15 NOVEMBER 1994
PART 2

AD-A286 752

76 10

Proceedings of the Sixth Joint Magnetism and Magnetic Materials - Intermag Conference

1186 ONE THOUSAND ONE HUNDRED EIGHTY SIX
95-01204

DTIC ELECTE APR 1 3 1994 F

DISTRIBUTION STATEMENT A
Approved for public release;
Distribution Unlimited

AMERICAN INSTITUTE OF PHYSICS

JOURNAL OF APPLIED PHYSICS

CODEN: JAPIAU
ISSN: 0021-8979

Editor

Steven J. Rothman
Argonne National Laboratory
Argonne, IL

Associate Editors at Argonne National Laboratory

Robert C. Birtcher
Gian P. Felcher
R. E. Holland
John N. Mundy
Simon R. Phillpot

Editorial Board

Term ending 31 December 1994
William R. Frensley (Univ. of Texas at Dallas)
Julia M. Phillips (AT&T Bell Labs, Murray Hill, NJ)
Paul M. Solomon (IBM, Yorktown Heights, NY)

Term ending 31 December 1995
Ulrich Gösele (Max Planck Inst., Halle, Germany)
William L. Johnson (Caltech, Pasadena, CA)
William F. Krupke (Lawrence Livermore Lab, CA)

Term ending 31 December 1996
Gene F. Dresselhaus (MIT, Cambridge, MA)
Allen M. Goldman (Univ. Minnesota, Minneapolis)
Klaus H. Ploog (Paul Drude Inst., Berlin, Germany)
Robert Sinclair (Stanford Univ., Stanford, CA)

Editorial Office

Diane M. Kurtz, *Editorial Supervisor*

Editorial Staff: Catherine M. Dial, *Assistant to the Editor;* Jennifer A. Smeets, *Secretary*

AIP Editorial Operations
John T. Scott, *Manager*

AIP Production
Deborah McHone, *Editorial Supervisor*
Elizabeth Belmont, *Journal Coordinator*
Julia Macklin, *Chief Production Editor*
Cindy Klingensmith, *Senior Production Editor*

The *Journal of Applied Physics* (ISSN: 0021-8979) is published semimonthly by the American Institute of Physics, 500 Sunnyside Blvd., Woodbury, NY 11797-2999. Second-class postage paid at Woodbury, NY, and additional mailing offices. POSTMASTER: Send address changes to *Journal of Applied Physics*, AIP, 500 Sunnyside Blvd., Woodbury, NY 11797-2999.

© 1994 by the American Institute of Physics.

The *Journal of Applied Physics* is the American Institute of Physics' (AIP) archival journal for significant new results in applied physics. The journal publishes articles that emphasize understanding of the physics underlying modern technology. There are two issues per month. The subject coverage includes, but is not limited to, experimental or theoretical physics applied to all aspects of materials: for example, charge and mass transport, superconductivity, magnetism; surfaces, interfaces, thin films, crystal lattice defects; electrical, optical, magnetic, and structural properties; processing; ion implantation. Materials covered include semiconductors, superconductors, metals and alloys, amorphous materials, and oxides. Other important topics are: electrical, optical, and magnetic devices; optics and lasers; nonlinear optics; electrical discharges; acoustics. The Proceedings of the Annual Conference on Magnetism and Magnetic Materials is a regular feature. *Applied Physics Reviews* is a series of occasional review articles on similar subjects.

Submit manuscripts (3 copies) to Editor, *Journal of Applied Physics,* Argonne National Laboratory, Bldg. 203, Room R-127, 9700 South Cass Avenue, P.O. Box 8296, Argonne, IL 60439-8296.

Subscription Prices* (1994)	U.S.A. & Poss.	Can., Mex., Central & S. Amer. & Caribbean	Foreign Surface Mail	Air Freight — Europe, Asia, Africa & Oceania	Optional Air Freight — Europe, Asia, Africa & Oceania
Members†	$190	$270	$270	-----	$380
Nonmembers	$1655	$1735	-----	$1945‡	-----

*The journal is available on microfiche at $190 per year to members and $1655 per year at the nonmember rate.
†AIP Member and Affiliated Societies. ‡Includes air freight service.

Back-Number Prices: 1994 single copies: $80. Prior to 1994 single copies: $24 for members; $80 for nonmembers. Prices for conference supplements available on request.

Subscription, renewals, and address changes should be addressed to *AIP Circulation and Fulfillment Division (CFD), 500 Sunnyside Blvd., Woodbury, NY 11797-2999.* Allow at least six weeks advance notice. For address changes please send both old and new addresses and, if possible, include a mailing label from a recent issue.

Claims, Single Copy Replacement and Back Volumes: Missing issue requests will be honored only if received within six months of publication date (nine months for Australia and Asia). Single copies of a journal may be ordered and back volumes are available in print or microform. Members—contact AIP Member Services at (516) 576-2288; (800) 344-6901. Nonmember subscribers—contact AIP Subscriber Services at (516) 576-2270; (800) 344-6902.

Page Charge and Reprint Billing: Contact: AIP Publication Page Charge and Reprints—CFD, 500 Sunnyside Blvd., Woodbury, NY 11797-2999; (516) 576-2234; (800) 576-6909.

Copying Fees: Copying of articles beyond that permitted by the Fair Use provisions (Sections 107 and 108) of the U.S. Copyright Law requires payment of fees. The code at the bottom of the first page of each article gives the fee for each copy of the article. Fees should be paid through the *Copyright Clearance Center (CCC), 222 Rosewood Drive, Danvers, MA 01923.* Persons desiring to photocopy materials for classroom use should contact CCC's Academic Permissions Service.

The item-fee code for this publication is 0021-8979/94 $6.00.

Permission For Other Use: Permission is granted to quote from the journal with the customary acknowledgment of the source. To reprint a figure, table, or other excerpt requires in addition the consent of one of the original authors and notification to AIP. Reproduction for advertising or promotional purposes, or republication in any form, is permitted only under license from AIP, which will normally require that the permission of one of the authors also be obtained. Direct inquiries to: Office of Rights and Permissions, American Institute of Physics, 500 Sunnyside Blvd., Woodbury, NY 11797-2999.

Document Delivery: For information on obtaining copies of individual articles, contact AIP Circulation and Fulfillment Division, 500 Sunnyside Blvd., Woodbury, NY 11797-2999; phone: (516) 576-2277; (800) 344-6908; fax: (516) 394-9704; E-mail: elecprod@pinet.aip.org.

Online Availability: Abstracts of journal articles published by the AIP and its Member Societies are available in bibliographic databases on major online hosts. The abstracts are also available in the SPIN database via the AIP online service, PINET (Physics Information Network). PINET also offers Advance Abstracts, a current awareness service with abstracts of research papers up to three months prior to their publication in AIP or Member Society Journals. Call (800) 874-6383 or (516) 576-2262 for further information.

PROCEEDINGS OF THE SIXTH JOINT MAGNETISM AND MAGNETIC MATERIALS–INTERMAG CONFERENCE

DTIC
ELECTE
MAR 01 1995
S D
G

20–23 June 1994
Albuquerque, New Mexico

Accesion For
NTIS CRA&I
DTIC TAB
Unannounced
Justification
By
Distribution /
Availability Codes
Dist | Avail and / or Special
A-1

Edited by
W. Yelon, W-Y. Ching,
Y. Idzerda, and F. E. Pinkerton

Journal of Applied Physics
Volume 76, Number 10, Part II, 1994

19950222 049

DISTRIBUTION STATEMENT A
Approved for public release;
Distribution Unlimited

Library of Congress Catalog Card Number: 94-79021
International Standard Book Number: 1-56396-403-1
CONF-940629—Vol. 1
Copyright © 1994 by the American Institute of Physics
Published by the American Institute of Physics
500 Sunnyside Blvd., Woodbury, New York 11797-2999
Printed in the United States of America

All papers in this volume, and in previous Proceedings of the Conference on Magnetism and Magnetic Materials published in this series, have been reviewed for technical content. The selection of referees, review guidelines, and all other editorial procedures are in accordance with standards prescribed by the American Institute of Physics.

6M^{3}I
6th JOINT MAGNETISM AND MAGNETIC MATERIALS–INTERMAG CONFERENCE
20–23 JUNE 1994
Albuquerque, New Mexico

Accesion For	
NTIS CRA&I	☒
DTIC TAB	☐
Unannounced	☐
Justification	
By	
Distribution /	
Availability Codes	
Dist	Avail and / or Special
A-1	

Sponsored by

The American Institute of Physics
The Magnetics Society
of the
Institute of Electrical and Electronics Engineers

In cooperation with

The Minerals, Metals, and Materials Society
The American Society for Testing and Materials
The Office of Naval Research
The American Ceramic Society

The Conference is especially grateful to

THE OFFICE OF NAVAL RESEARCH
for its support of the expenses of foreign and interdisciplinary speakers

CONTRIBUTORS TO THE 6TH JOINT MAGNETISM
AND MAGNETIC MATERIALS–INTERMAG CONFERENCE

The Conference expresses its appreciation to the following organizations for their generous support.

Applied Magnetics
BASF Magnetics GmbH
Crucible Magnetics
Eastman Kodak Company
F. G. Jones Associates, Ltd.
Fujitsu Ltd.
General Electric Company
Hewlett-Packard Company
Hitachi, Ltd.
IBM Corporation
Innovative Instruments Incorporated
Intervac, Inc.
KJS Associates, Inc.-Magnetic Engineering
Lakeshore Cryotronics, Inc.
Magnequench
Magnetic Materials Producers Association
Magnetics
NEC Corporation
Nortronics
O. S. Walker Company
Quantum Corporation
Seagate Technology
Soohoo Associates, Inc.
TDK Corporation
3M
Toda Kogyo Corporation
UGIMAG, Inc.

DTIC QUALITY INSPECTED 4

Conference Organization

Sixth Joint Magnetism and Magnetic Materials–Intermag Conference

General Conference Chairman

S. H. Charap

Program Committee

J. A. Borchers
A. Chaiken
C-L. Chien
W-Y. Ching
E. D. Dahlberg
R. E. Fontana, Jr.
P. George
H. Gill
M. Gyorgy
G. Hadjipanayis
Y. Idzerda
R. Indeck
R. Katti
D. Lambeth
D. Lavers
H. Leupold
S. McKay
J. Monson
J. L. Nix
F. E. Pinkerton
R. Robinson
M. Russak
D. Ryan
I. K. Schuller
N. Smith
G. Spratt
H. Suhl
T. Suzuki
P. Trouilloud
B. Van Dover
R. Victora
W. Yelon

Publications Chairman

A. Chaiken
W-Y. Ching
R. E. Fontana, Jr.
Y. Idzerda
D. Lavers
J. Monson
J. L. Nix
F. E. Pinkerton
W. Yelon

Treasurer

C. Perlov

Program Chairmen

F. Hellman
M. E. Re

Publicity

W. C. Cain

Industrial Support

R. S. Indeck

Local Chairman

M. Yapuncich

Chairman Elect

K. Hathaway

MMM Advisory Committee

D. L. Huber, *Chairman*
F. E. Pinkerton, *Secretary*

Term Expires 1994	Term Expires 1995	Term Expires 1996
I. A. Beardsley	R. J. Celotta	K. B. Hathaway
J. E. Crow	W. D. Doyle	W. Yelon
E. D. Dahlberg	G. E. Fish	G. P. Felcher
E. Della Torre	R. R. Katti	P. M. Levy
A. J. Freeman	D. R. Krahn	D. J. Sellmyer
F. B. Hagedorn	J. W. Lynn	
I. S. Jacobs	G. A. Prinz	
J. E. Opfer	B. J. Shula	
F. E. Pinkerton		
D. D. Stancil		

IEEE Magnetics Society

D. A. Thompson, *President*
J. E. Opfer, *Vice President*
D. D. Stancil, *Secretary-Treasurer*
S. H. Charap, *Past President*

Administrative Committee

Term Expires 1994	Term Expires 1995	Term Expires 1996
J. A. Christner	P. P. Biringer	G. E. Fish
E. Della Torre	R. F. Hoyt	H. S. Gill
W. D. Doyle	R. M. Josephs	R. B. Goldfarb
F. Friedlaender	J. H. Judy	R. S. Indeck
C. M. Perlov	D. N. Lambeth	R. A. Johnson
D. J Shula	M. Parvadi-Hovarth	F. E. Luborsky
D. D. Stancil	S. Uchiyama	J. A. Nyenhuis
T. Suzuki	P. E. Wigen	Y. Sugita

Sponsoring Society Representatives

American Institute of Physics

J. T. Scott

IEEE Magnetics Society

C. D. Graham

Cooperating Society Representatives

The Minerals, Metals, and Materials Society

M. Hong

ASTM Comm. A-6

K. H. Moyer

Office of Naval Research

K. B. Hathaway

American Ceramic Society

B. B. Ghate

PREFACE

The 6th Joint MMM-INTERMAG Conference was held in the Albuquerque Convention Center, June 20–23, 1994. Continuing a practice inaugurated at the 1993 MMM Conference in Minneapolis, the conference was preceded by a Sunday afternoon tutorial session sponsored by the Education Committee of the IEEE Magnetics Society. This accommodates particularly those attendees staying over the Saturday night before the conference. This year's topic was "Magnetic Multilayers: Fundamental Issues to Applications." The tutorial was particularly timely and played to a standing-room-only audience.

In addition to the usual invited papers, there were eight invited symposia; there were three on topics relating to magnetic and magneto-optic recording, and one each on magnetic microscopy, magnetic aftereffect, giant magnetoresistance, magneto-impedance, and neutron scattering studies of vortex structures in superconductors. There was also an evening panel discussion on units in magnetism. The session was lively, but failed to reach closure.

The conference was a marked success. It was larger than any previous Joint Conference. It was also generally agreed that the program, facilities, and environment were excellent. It was attended by 1227 participants. A total of 1444 abstracts were submitted from 36 countries. Of these, 497 originated in the U.S., 178 were from Japan, 155 from Russia, and 119 were from China (PRC and ROC), accounting for 66% of submissions. The program committee accepted 1048 abstracts (73%) for presentation.

Once again we are publishing, in this volume of the Journal of Applied Physics and in the associated volume of the IEEE Transactions on Magnetics, fully refereed papers based upon the conference presentations. The Transactions volume includes 368 contributed papers and 11 invited papers and constitutes the INTERMAG Proceedings for 1994; the Journal volume includes 280 contributed papers and 47 Invited papers and constitutes the MMM Proceedings for 1994. As usual, all fully paid registrants at the conference receive both volumes. Subscribers to either periodical will receive only the corresponding volume with their subscription. Both volumes contain the complete Table of Contents.

The conference reception at the "Los Amigos Round-Up Ranch" was sold out. Despite heavy rain that kept all activities indoors, this reception was a great success, with perhaps more thorough mingling of attendees than would have occurred in good weather.

Finally, I would like to thank the dedicated and talented volunteers on the Steering Committee and the very professional team of Courtesy Associates personnel for an exceptional job.

Stanley H. Charap
General Chairman
6th Joint MMM-INTERMAG Conference
Carnegie Mellon University
Pittsburgh, Pennsylvania, U.S.A.

JOURNAL OF APPLIED PHYSICS Vol. 76, No. 10, Pt. 2, 15 November 1994
CODEN: JAPIAU ISSN: 0021-8979

 Table of Contents for the Papers Appearing in the *IEEE Transactions on Magnetics*

Hard Magnets: Nitrides, Films, and Ferrites

6035	High field magnetization measurements of Sm_2Fe_{17}, $Sm_2Fe_{17}C_x$, and $Sm_2Fe_{17}C_xH_{5-x}$	O. Isnard, S. Miraglia, M. Guillot, D. Fruchart, K. H. J. Buschow
6038	X-ray structural studies of nitrogen diffusion in Dy_2Fe_{17}	Er. Girt, Z. Altounian, X. Chen, Ming Mao, D. H. Ryan, M. Sutton, J. M. Cadogan
6041	Atomic diffusion mechanism and diffusivity of nitrogen into Sm_2Fe_{17}	Chris N. Christodoulou, Norikazu Komada
6044	Effect of nitrogen on the properties of hard magnets	M. Melamud, L. H. Bennett, R. E. Watson
6047	Theoretical analysis of the spin-density distributions in $Y_2Fe_{17}N_3$ and $Y_2Fe_{17}C_3$	W. Y. Ching, Ming-Zhu Huang, Xue-Fu Zhong
6050	Study on the effect of the previous hydrogenation of the nitride formation of a Sm_2Fe_{17}(4 at. % Nb) alloy	H. W. Kwon, I. R. Harris
6053	The effects of hydrogen disproportionation, desorption, and recombination on the structure and magnetic properties of $Sm_2Fe_{17}N_x$ and $NdFe_{10}Mo_2N_x$ compounds	Jun Yang, Shengzhi Dong, Weihua Mao, Ping Xuan, Yingchang Yang
6056	Phase formation in melt-spun Nd-Fe-Mo-Ti alloys	F. E. Pinkerton, C. D. Fuerst, J. F. Herbst
6059	In-plane magnetized YIG substrates self-biased by SmCo based sputtered film coatings	F. J. Cadieu, H. Hegde, E. Schloemann, H. J. Van Hook
6062	Transverse susceptibility and magnetic anisotropy of CoTi-doped barium hexaferrite single crystals	G. Zimmermann, K. A. Hempel
6065	Preparation of high-coercivity fine barium ferrite powder	W. A. Kaczmarek, B. W. Ninham
6068	Nitriding studies of aligned high anisotropy $ThMn_{12}$-type $NdFe_{11}Co_{1-y}Mo_yN$ film samples (abstract)	A. Navarathna, P. Samarasekara, H. Hegde, R. Rani, F. J. Cadieu

Magnetic Anisotropy in Thin Films and Multilayers

6069	Theoretical predictions of interface anisotropy in the presence of interdiffusion (invited)	J. M. MacLaren, R. H. Victora
6075	Magnetic anisotropy of metal/Co/metal and metal/Co/insulator sandwiches	Michael H. Wiedmann Brad N. Engel, Charles M. Falco
6078	Effect of submonolayer coverage on magnetic anisotropy of ultrathin cobalt films M/Co/Au(111) with M=Au, Cu Pd	P. Beauvillain, A. Bounouh, C. Chappert, R. Mégy, S. Ould-Mahfoud, J. P. Renard, P. Veillet, D. Weller, J. Corno
6081	Effects of Ar-ion implantation and annealing on structural and magnetic properties of Co/Pd multilayers	John Q. Xiao, K. Liu, C. L. Chien, L. F. Schelp, J. E. Schmidt
6084	Sputtering pressure effects and temperature-dependent magnetism of Co/Pd multilayers	S. Y. Jeong, Z. S. Shan, P. He, J. X. Shen, Y. B. Zhang, J. A. Woollam, D. J. Sellmyer
6087	Magnetoelastic effect in Co/Pd multilayer films	Young-Suk Kim, Sung-Chul Shin
6090	Interface processing in multilayer films	R. J. Pollard, M. J. Wilson, P. J. Grundy
6093	Anomalous interface magnetism in ultrathin Co films with in-plane anisotropy	F. O. Schumann, M. E. Buckley, J. A. C. Bland

(Continued)

6096 FMR studies of magnetic properties of Co and Fe thin films on Al_2O_3 and MgO substrates — Yu. V. Goryunov, G. G. Khaliullin, I. A. Garifullin, L. R. Tagirov, F. Schreiber, P. Bödeker, K. Z. Bröhl, Ch. Morawe, Th. Mühge, H. Zabel

6099 The relationship between the microstructure and magnetic properties of sputtered Co/Pt multilayer films (abstract) — Y. H. Kim, Amanda K. Petford-Long, J. P. Jakubovics

6100 Identification of magnetoelastic and magnetocrystalline anisotropy contributions in ultrathin epitaxial Co(110) films (abstract) — J. Fassbender, Ch. Mathieu, B. Hillebrands, G. Güntherodt, R. Jungblut, M. T. Johnson

Coupling and Transport in Unusual Systems

6101 Nature of half-metallic ferromagnets: Transport studies — J. S. Moodera, D. M. Mootoo

6104 Magnetoresistance and magnetic properties of NiFe/oxide/Co junctions prepared by magnetron sputtering — T. S. Plaskett, P. P. Freitas, N. P. Barradas, M. F. da Silva, J. C. Soares

6107 Changes in resistivity behavior of metallic glass $Fe_{70}Ni_{12}B_{16}Si_2$ due to molybdenum substitution for nickel — A. K. Bhatnagar, B. Seshu, K. D. D. Rathnayaka, D. G. Naugle

6110 Anisotropic magnetism and resistivity of an $Al_{70}Ni_{15}Co_{15}$ decagonal quasicrystal — J. T. Markert, J. L. Cobb, W. D. Bruton, A. K. Bhatnagar, D. G. Naugle, A. R. Kortan

6113 Mössbauer effect investigation of the pentagonal approximant phase in the Fe-Nb system — R. A. Dunlap, J. Kyriakidis, M. Yewondwossen

6116 Short period oscillations in the Kerr effect of 4*d*- and 5*d*-transition metal wedges on Co films (invited) (abstract) — A. Carl, D. Weller

6117 Magnetoresistance of CuNiCo ternary alloys (abstract) — R. S. Beach, D. Rao, A. E. Berkowitz

Kondo, Mixed Valence, and Heavy Fermions I

6118 Enhancement of the localized behavior in $CeNi_{0.8}Pt_{0.2}$ Kondo compound replacing Ce by magnetic ions (Pr,Nd) — J. C. Gómez Sal, J. A. Blanco, J. I. Espeso, J. Rodríguez Fernández, D. Gignoux

6121 Low-temperature phase diagram of YbBiPt — R. Movshovich, A. Lacerda, P. C. Canfield, J. D. Thompson, Z. Fisk

6124 Quadrupolar effects in $PrCu_2Si_2$ — R. Osborn, E. A. Goremychkin

6127 Mixed valence in a generalized Hubbard model — A. N. Kocharian, G. R. Reich

6130 Consequences of competing hybridization for magnetic ordering in correlated-electron lattices — Carlos Sanchez-Castro, Bernard R. Cooper, Kevin S. Bedell

6133 Antiferromagnetic order in superconducting UPt_3: An x-ray magnetic scattering study (invited) — E. D. Isaacs, P. Zschack, A. P. Ramirez, C. S. Oglesby, E. Bucher

6137 Non-Fermi liquid ground states in strongly correlated *f*-electron materials (invited) (abstract) — M. B. Maple

6137 Magneto-oscillatory phenomena in highly correlated metals (invited) (abstract) — S. R. Julian, G. J. McMullan, C. Pfleiderer, F. S. Tautz, G. G. Lonzarich

Novel Hard Magnets

6138 New rare-earth intermetallic phases $R_3(Fe,M)_{29}X_n$: (R=Ce, Pr, Nd, Sm, Gd; M=Ti, V, Cr, Mn: and X=H, N, C) (invited) — J. M. Cadogan, Hong-Shuo Li, A. Margarian, J. B. Dunlop, D. H. Ryan, S. J. Collocott, R. L. Davis

6144 Structural and magnetic properties of $R_3(Fe,T)_{29}$ compounds — C. D. Fuerst, F. E. Pinkerton, J. F. Herbst

6147 Magnetic and crystal structure of the novel compound $Nd_3Fe_{29-x}Ti_x$ — Z. Hu, W. B. Yelon

6150 Magnetic properties of interstitially modified $Nd_3(Fe,Ti)_{29}X_y$ compounds (X=H, C, and N) — D. H. Ryan, J. M. Cadogan, A. Margarian, J. B. Dunlop

(Continued)

6153 Phase equilibria in the Fe-rich corner of the Nd-Fe-Ti ternary alloy system at 1100 °C — A. Margarian, J. B. Dunlop, R. K. Day, W. Kalceff

6156 Magnetic properties of $Sm_2Fe_{14-x}Co_xSi_2$-based quasiternary compounds — F.-M. Yang, W. Gong, G. C. Hadjipanayis

6159 Mössbauer study of permanent-magnet :naterials: $Sm_2Fe_{17-x}Al_x$ compounds — I. A. Al-Omari, S. S. Jaswal, A. S. Fernando, D. J. Sellmyer

6162 Neutron diffraction and magnetic studies of $Nd_2Fe_{17-x-z}Al_xSi_z$ — Z. Hu, W. B. Yelon

6165 New magnetic material based on $SmCo_4B$ — Hideaki Ido, Osamu Nashima, Takehiro Takahashi, Kiwamu Oda, Kiyohiro Sugiyama

Macroscopic Quantum Tunneling/Spin Glasses

6168 Dissipation in macroscopic quantum tunneling and coherence in magnetic particles (invited) — Anupam Garg

6174 Evidence for quantum mesoscopic tunneling in rare-earth layers — M. J. O'Shea, P. Perera

6177 Bloch states of a Bloch wall — Hans-Benjamin Braun, Daniel Loss

6180 Magnetic properties of cubic $R_xY_{1-x}Al_2$ (R=Dy, Tb) intermetallic random anisotropy magnets (invited) — A. del Moral, J. I. Arnaudas, C. de la Fuente, M. Ciria, E. Joven, P. M. Gehring

6186 Correlation decay in low-dimensional spin glasses — A. N. Kocharian, A. S. Sogomonian

6189 Relaxation and spin correlations in ^{119}Sn-doped a-$Fe_{90}Sc_{10}$ — D. Wiarda, D. H. Ryan

6192 Field-dependent susceptibility aging in CuMn spin glasses — P. W. Fenimore, M. B. Weissman

6195 Quantum tunneling in magnetic particles (invited) (abstract) — D. P. DiVincenzo

6196 Remanent magnetization of AgMn spin glasses (abstract) — Emily Engle, E. Dan Dahlberg

6197 Calculated field cooled and zero field cooled magnetizations of the three-dimensional Ising spin glass using Monte Carlo hard-spin mean-field theory (abstract) — Edwin A. Ames, Susan R. McKay

Symposium on Magneto-Impedance

6198 Giant magneto-imoedance and magneto-inductive effects in amorphous alloys (invited) — L. V. Panina, K. Mohri, K. Bushida, M. Noda

6204 Very large magneto-impedance in amorphous soft ferromagnetic wires (invited) — K. V. Rao, F. B. Humphrev, J. L. Costa-Krämer

6209 Sensitive field- and frequency-dependent impedance spectra of amorphous FeCoSiB wire and ribbon (invited) — R. S. Beach, A. E. Berkowitz

Kondo, Mixed Valence, and Heavy Fermions II

6214 Heavy fermion behavior of U_2T_2X compounds — L. Havela, V. Sechovský, P. Svoboda, M. Diviš, H. Nakotte, K. Prokeš, F. R. de Boer, A. Purwanto, R. A. Robinson, A. Seret, J. M. Winand, J. Rebizant. J. C. Spirlet, M. Richter, H. Eschrig

6217 Incommensurate antiferromagnetic phase in UNiGe — V. Sechovský, L. Havela, P. Svoboda, A. Purwanto, Allen C. Larson, R. A. Robinson, K. Prokeš, H. Nakotte, F. R. de Boer, H. Maletta

6220 Magnetic susceptibility and electronic specific heat of Anderson lattice with finite f-band width — Sunil Panwar, Ishwar Singh

6223 Electrical resistivity and thermoelectric power of heavy fermions and mixed-valence systems — Sunil Panwar, Ishwar Singh

(Continued)

6226 Understanding the great range of magnetic ordering behavior in correlated *f*-electron systems — Q. G. Sheng, B. R. Cooper

6229 Discovery of τ=2/9 iock-in in holmium — D. A. Tindall, C. P. Adams, M. O. Steinitz, T. M. Holden

$R_2FE_{14}B$ Hard Magnets and Applications

6232 Die-upset Nd-Fe-Co-B magnets from blends of dissimilar ribbons — C. D. Fuerst, E. G. Brewer

6235 Evidence for reversal by nucleation in RE-Fe-B die-upset magnets — L. Henderson Lewis, Y. Zhu, D. O. Welch

6238 Microstructure and magnetic properties of mechanically alloyed anisotropic Nd-Fe-B — J. Wecker, H. Cerva, C. Kuhrt, K. Schnitzke, L. Schultz

6241 Preparation and transmission electron microscope investigation of sintered $Nd_{15.4}Fe_{75.7}B_{6.7}Cu_{1.3}Nb_{0.9}$ magnets — Johannes Bernardi, Josef Fidler

6244 Fe-Nd-C-based ingot permanent magnets by solid-state transformation — M. Leonowicz, H. A. Davies, S. Wojciechowski

6247 Generation of highly uniform fields with permanent magnets (invited) — M. G. Abele

6253 Fabrication of multipolar magnetic field sources — H. A. Leupold, G. F. McLane

6256 Kinetic studies on solid-HDDR processes in Nd-Fe-B-type alloys — O. Gutfleisch, M. Verdier, I. R. Harris

6259 Study of desorbed hydrogen-decrepitated anisotropic Nd-Fe-B powder using x-ray diffraction — G. P. Meisner, V. Panchanathan

6262 The electrochemical hydrogenation of NdFeB sintered alloys — Kuo En Chang, Garry W. Warren

6265 Relation of remanence and coercivity of Nd,(Dy)-Fe,(Co)-B sintered permanent magnets to crystallite orientation — A. S. Kim, F. E. Camp, H. H. Stadelmaier

6268 Comparison of magnetic methods for the determination of texture of permanent magnets — G. Asti, R. Cabassi, F. Bolzoni, S. Wirth, D. Eckert, P. A. P. Wendhausen, K.-H. Müller

6271 Magnetic-field orientation and coercivity — Brandon Edwards, D. I. Paul

Magnetic Multilayer Coupling

6274 Magnetic structures and interactions in Ho/Y, Ho/Lu, and Ho/Er superlattices (invited) — R. A. Cowley, D. F. McMorrow, A. Simpson, D. Jehan, P. Swaddling, R. C. C. Ward, M. R. Wells

6278 Epitaxial ferromagnetic MnAs thin films grown by molecular-beam epitaxy on GaAs: Structure and magnetic properties — M. Tanaka, J. P. Harbison, M. C. Park, Y. S. Park, T. Shin, G. M. Rothberg

6281 Co/CoAl magnetic superlattices on GaAs — J. De Boeck, C. Bruynseraede, H. Bender, A. Van Esch, W. Van Roy, G. Borghs

6284 Investigations of the interplay between crystalline and magnetic ordering in Fe_3O_4/NiO superlattices — D. M. Lind, J. A. Borchers, R. W. Erwin, J. F. Ankner, E. Lochner, K. A. Shaw, R. C. DiBari, W. Portwine, P. Stoyonov, S. D. Berry

6287 Magnetic characterization of epitaxial $Y_5Fe_6O_{12}/Bi_3Fe_5O_{12}$ and $Y_5Fe_3O_{12}/Eu_1Bi_2Fe_5\ O_{12}$ heterostructures grown by pulsed laser deposition — B. M. Simion, R. Ramesh, V. G. Keramidas, G. Thomas, E. Marinero, R. L. Pfeffer

6290 Interlayer correlations and helical spin ordering in MnTe/CdTe multilayers (abstract) — V. Nunez, T. M. Giebultowicz, W. Faschinger, G. Bauer, H. Sitter, J. K. Furdyna

6291 Interlayer coupling in antiferromagnetic EuTe/PbTe superlattices (abstract) — T. M. Giebultowicz, V. Nunez, G. Springholz, G. Bauer, J. Chen, M. C. Dresselhaus, J. K. Furdyna

6292 Heat capacity measurements of antiferromagnetic CoO/NiCoO superlattices (abstract) — E. N. Abarra, K. Takano, F. Hellman, A. E. Berkowitz

(Continued)

6293 Exchange coupling, interface structure, and perpendicular magnetic anisotropy in Tb/Fe multilayers (abstract) — J. Tappert, J. Jungermann, B. Scholz, R. A. Brand, W. Keune

6294 Interfacial contributions to magnetic anisotropy in metal/semiconductor systems (abstract) — B. T. Jonker, H. Abad, J. J. Krebs

Fine Particles

6295 The magnetization density profile of a grain boundary in nickel (invited) — M. R. Fitzsimmons, A. Röll, E. Burkel, K. E. Sikafus, M. A. Nastasi, G. S. Smith, R. Pynn

6301 Magnetic and magnetocaloric properties of melt-spun Gd_xAg_{100-x} alloys — C. D. Fuerst, J. F. Herbst, R. K. Mishra, R. D. McMichael

6304 Thickness dependence of the magnetic and electrical properties of $Fe:SiO_2$ nanocomposite films — S. S. Malhotra, Y. Liu, J. X. Shen, S. H. Liou, D. J. Sellmyer

6307 Calculation of magnetic moments in Ho_2C_3 nanocrystals — S. A. Majetich, J. O. Artman, C. Tanaka, M. E. McHenry

6310 Kramers's rate theory, broken symmetries, and magnetization reversal (invited) — Hans-Benjamin Braun

6316 Magnetic properties of nanophase cobalt particles synthesized in inversed micelles — J. P. Chen, C. M. Sorensen, K. J. Klabunde, G. C. Hadjipanayis

6319 Magnetic and structural properties of vapor-deposited Fe-Co alloy particles — S. Gangopadhyay, Y. Yang, G. C. Hadjipanayis, V. Papaefthymiou, C. M. Sorensen, K. J. Klabunde

6322 Extended x-ray-absorption fine-structure studies of heat-treated fcc-$Fe_{50}Cu_{50}$ powders processed via high-energy ball milling — P. Crespo, A. Hernando, A. Garcia Escorial, K. M. Kemner, V. G. Harris

6325 Structure analysis of coprecipitated $ZnFe_2O_4$ by extended x-ray-absorption fine structure — B. Jeyadevan, K. Tohji, K. Nakatsuka

6328 Magnetic anisotropy of small clusters and very thin transition-metal films — H. Dreyssé, J. Dorantes-Dávila, Š. Pick, G. M. Pastor

6331 Structure and magnetic properties of $Nd_2Fe_{14}B$ fine particles produced by spark erosion (abstract) — H. Wan, A. E. Berkowitz

Macroscopic Quantum Tunneling

6332 Thermal equilibrium noise with $1/f$ spectrum in a ferromagnetic alloy: Anomalous temperature dependence — S. Vitale, A. Cavalleri, M. Cerdonio, A. Maraner, G. A. Prodi

6335 Experimental observation of magnetostochastic resonance — A. N. Grigorenko, P. I. Nikitin, A. N. Slavin, P. Y. Zhou

Critical Phenomena, Spin Glasses, and Frustrated Magnets

6338 Critical magnetic susceptibility of gadolinium — R. A. Dunlap, N. M. Fujiki, P. Hargraves, D. J. W. Geldart

6341 Monte Carlo simulation of Ising models with dipole interaction — U. Nowak, A. Hucht

6344 Magnetic phase diagrams of $NdRu_2Si_2$ and $TbRu_2Si_2$ compounds — M. Salgueiro da Silva, J. B. Sousa, B. Chevalier, J. Etourneau

6347 Study of critical properties of the Potts model by the modified variational cumulant expansion method — N. G. Fazleev, Hao Che, J. L. Fry, D. L. Lin

6350 Phase transition in a system of interacting triads — H. T. Diep, D. Loison

6353 Critical behavior of the random Potts model — B. M. Khasanov, S. I. Belov, D. A. Tayurskii

6356 Influence of exchange bond disorder on the magnetic properties of $(Pd_{1-x}Fe_x)_{95}Mn_5$ near T_c — Z. Wang, X. Qi, H. P. Kunkel, Gwyn Williams

6359 Magnetic transitions at high fields in $(Fe,Mn)_3Si$ alloys — H. J. Al-Kanani, J. G. Booth, J. W. Cable, J. A. Fernandez-Baca

6362 Critical behavior of the two-dimensional easy-plane ferromagnet — Alessandro Cuccoli, Valerio Tognetti, Paola Verrucchi, Ruggero Vaia

(Continued)

6365 Magnetic anomaly in insulator-conductor composite materials near the percolation threshold — L. V. Panina, A. S. Antonov, A. K. Sarychev, V. P. Paramonov, E. V. Timasheva, A. N. Lagarikov

6368 Time dependence effects in disordered systems — K. O'Grady, M. El-Hilo, R. W. Chantrell

6371 Magnetization of amorphous $Fe_{0.82}B_{0.18}$ and $Fe_{0.90}Zr_{0.10}$ compounds with additions of Tb — S. J. Clegg, J. H. Purdy, R. D. Greenough, F. Jerems

6374 Magnetic ordering in the three-dimensional site frustrated Heisenberg model — Morten Nielsen, D. H. Ryan, Hong Guo, Martin Zuckermann

6377 Mössbauer measurements of spin correlations in a-$(Fe,Ni)_{90}Zr_9Sn$ — D. Wiarda, D. H. Ryan

6380 Study of the spin glass transition of amorphous FeZr alloys using small angle neutron scattering — K. Mergia, S. Messoloras, G. Nicolaides, D. Niarchos, R. J. Stewart

6383 Study of magnetohistory effects in $YFe_{12-x}Mo_x$ (x=1.5–3.0) — Yi-Zhong Wang, Bo-Ping Hu, Gui-Chuan Liu, Lin Song, Kai-Ying Wang, Ji-Fan Hu, Wu-Yan Lai

Symposium on Slow Relaxation/Magnetic Aftereffect

6386 Magnetic viscosity, fluctuation fields, and activation energies (invited) — R. Street, S. D. Brown

6391 Analysis and interpretation of time dependent magnetic phenomena (invited) — L. Folks, R. Street

6396 Ubiquitous nonexponential decay: The effect of long-range couplings? (invited) — E. Dan Dahlberg, D. K. Lottis, R. M. White, M. Matson, E. Engle

6401 Mesoscopic model for the primary response of magnetic materials (invited) — R. V. Chamberlin

6407 Models of slow relaxation in particulate and thin film materials (invited) — R. W. Chantrell, A. Lyberatos, M. El-Hilo, K. O'Grady

6413 Time dependence of switching fields in magnetic recording media (invited) — M. P. Sharrock

Ultrathin Films and Overlayers

6419 Magnetic and structural instabilities of ultrathin Fe(100) wedges (invited) — S. D. Bader, Dongqi Li, Z. Q. Qiu

6425 Magnetic and structural instabilities of ferromagnetic and antiferromagnetic Fe/Cu(100) — Dongqi Li, M. Freitag, J. Pearson, Z. Q. Qiu, S. D. Bader

6428 Impurity hyperfine fields in metastable body centered cubic Co — J. Dekoster, B. Swinnen, M. Rots, G. Langouche, E. Jedryka

6431 Ferromagnetism and growth of Ru monolayers on C(0001) substrates — G. Steierl, R. Pfandzelter, C. Rau

6434 Spin reorientation transition in Ni films on Cu(100) — S. Z. Wu, G. J. Mankey, F. Huang, R. F. Willis

6437 Magnetization-related transport anomalies in metal/ferromagnetic insulator heterostructures — G. M. Roesler, Jr., M. E. Filipkowski, P. R. Broussard, M. S. Osofsky, Y. U. Idzerda

6440 Lorentz electron microscopy studies of magnetization reversal processes in epitaxial Fe(001) films — E. Gu, J. A. C. Bland, C. Daboo, M. Gester, L. M. Brown, R. Ploessl, J. N. Chapman

6443 Magnetic response of ultrathin Fe on MgO: A polarized neutron reflectometry study — S. Adenwalla, Yongsup Park, G. P. Felcher, M. Teitelman

6446 Roughness dependent magnetic hysteresis of a few monolayer thick Fe films on Au(001) — Y.-L. He, G.-C. Wang

6449 Fluctuation effects in ultrathin films — S. T. Chui

6452 Magnetic studies of fcc Co films grown on diamond (abstract) — J. A. Wolf, J. J. Krebs, Y. U. Idzerda, G. A. Prinz

(Continued)

6452 A Monte Carlo study of the temperature dependence of magnetic order on ferromagnetic and antiferromagnetic surfaces: Implications for spin-polarized photoelectron diffraction (abstract) — F. Zhang, S. Thevuthasan, R. T. Scalettar, R. R. P. Singh, C. S. Fadley

X-ray Magneto-optics

6453 X-ray magnetic circular dichroism in the near and extended absorption edge structure (invited) — G. Schütz, P. Fischer, K. Attenkofer, M. Knülle, D. Ahlers, S. Stähler, C. Detlefs, H. Ebert, F. M. F. de Groot

6459 Discussion of the magnetic dichroism in the x-ray resonance scattering — Peter Rennert

6462 Experimental investigation of dichroism sum rules for V, Cr, Mn, Fe, Co, and Ni: Influence of diffuse magnetism — W. L. O'Brien, B. P. Tonner, G. R. Harp, S. S. P. Parkin

6465 Spin-specific photoelectron diffraction using magnetic x-ray circular dichroism — J. G. Tobin, G. D. Waddill, X. Guo, S. Y. Tong

6468 Enhanced magnetic moment and magnetic ordering in MnNi and MnCu surface alloys — W. L. O'Brien, B. P. Tonner

6471 Observation of x-ray magnetic circular dichroism at the Rh $M_{2,3}$ edge in Co-Rh alloys — G. R. Harp, S. S. P. Parkin, W. L. O'Brien, B. P. Tonner

6474 Circular magnetic x-ray dichroism for rare earths — H. König, Xindong Wang, B. N. Harmon, P. Carra

6477 Circular dichroism in core-level photoemission from nonmagnetic and magnetic systems: A photoelectron diffraction viewpoint (abstract) — A. P. Kaduwela, H. Xiao, S. Thevuthasan, C. Westphal, M. A. Van Hove, C. S. Fadley

6477 Elemental determination of the magnetic moment vector (abstract) — H.-J. Lin, G. Meigs, C. T. Chen, Y. U. Idzerda, G. A. Prinz, G. H. Ho

Coupled Multilayers, Thin Films, and GMR

6478 Hybrid NiFeCo-Ag/Cu multilayers: Giant magnetoresistance, structure, and magnetic studies — J. D. Jarratt, J. A. Barnard

6481 Giant magnetoresistance in NiFe-Ag granular alloys — F. Badía, A. Labarta, X. Batlle, M. L. Watson

6484 Anisotropic giant magnetoresistance induced by magnetoannealing in Fe-Ag granular films — J. G. Na, C. T. Yu, X. G. Zhao, W. Y. Lai, H. L. Luo, J. G. Zhao

6487 Influence of microstructure on magnetoresistance of FeAg granular films — Chengtao Yu, Ye Yang, Yuqing Zhou, Shuxiang Li, Wuyan Lai, Zhenxi Wang

6490 Magnetic properties of FeSi-SiO_2 granular films — Z. S. Jiang, X. Ge, J. T. Ji, H. Sang, G. Guo, Y. W. Du, S. Y. Zhang

6493 Hysteresis of binary clusters — Ivo Klik, Jyh-Shinn Yang, Ching-Ray Chang

6496 Some specific features of fine Fe and Fe-Ni particles — Yu. V. Baldokhin, P. Ya. Kolotyrkin, Yu. I. Petrov, E. A. Shafranovsky

6499 Magnetoresistance of the magnetically ordered icosahedral quasicrystals Al-Pd-Mn-B — M. H. Yewondwossen, S. P. Ritcey, Z. J. Yang, R. A. Dunlap

6501 Electrical transport in amorphous Fe-Mn-Zr alloys — V. Srinivas, A. K. Nigam, G. Chandra, D. W. Lawther, M. Yewondwossen, R. A. Dunlap

6504 Field dependence of nuclear magnetic resonance in molecular beam epitaxy grown Co(111)/Cu multilayers — T. Thomson, H. Kubo, J. S. Lord, P. C. Riedi, M. J. Walker

6507 Dependence of giant magnetoresistance in Co/Cu multilayers on the thickness of the Co layers — A. M. Shukh, D. H. Shin, H. Hoffmann

6510 Vertical inhomogeneity of the magnetization reversal in antiferromagnetically coupled Co/Cu multilayers at the first maximum — R. Mattheis, W. Andrä, L. Fritzsch, J. Langer, S. Schmidt

6513 Magnetic and structural studies of sputtered Co/Cu multilayer films — J. D. Kim, Amanda K. Petford-Long, J. P. Jakubovics, J. E. Evetts, R. Somekh

(Continued)

6516 Influence of crystal structure on the magnetoresistance of Co/Cr multilayers — Y. Liou, J. C. A. Huang, Y. D. Yao, C. H. Lee, K. T. Wu, C. L. Lu, S. Y. Liao, Y. Y. Chen, N. T. Liang, W. T. Yang, C. Y. Chen, B. C. Hu

6519 Giant magnetoresistance peaks in CoNiCu/Cu multilayers grown by electrodeposition — S. Z. Hua, D. S. Lashmore, L. Salamanca-Riba, W. Schwarzacher, L. J. Swartzenruber, R. D. McMichael, L. H. Bennett, R. Hart

6522 High sensitivity GMR in NiFeCo/Cu multilayers — S. Gangopadhyay, S. Hossain, J. Yang, J. A. Barnard, M. T. Kief, H. Fujiwara, M. R. Parker

6525 Multidomain and incomplete alignment effects in giant magnetoresistance trilayers — Y. U. Idzerda, C.-T. Chen, S. F. Cheng, W. Vavra, G. A. Prinz, G. Meigs, H.-J. Lin, G. H. Ho

6528 Interface alloying and magnetic properties of Fe/Rh multilayers — K. Hanisch, W. Keune, R. A. Brand, C. Binek, W. Kleemann

6531 Heat treatment to control the coercivity of Pt/Co multilayers — J. Miller, P. G. Pitcher, D. P. A. Pearson

6534 Magnetostriction and magnetic properties of iron-cobalt alloys multilayered with silver — Tamzin A. Lafford, M. R. J. Gibbs, R. Zuberek, C. Shearwood

6537 Stabilization of the hexagonal close-packed phase of cobalt at high temperature — N. P. Barradas, H. Wolters, A. A. Melo, J. C. Soares, M. F. da Silva, M. Rots, J. L. Leal, L. V. Melo, P. P. Freitas

6540 Observation and computer simulation of static magnetization process in soft magnetic thin film — Zhigang Wang, Ikuya Tagawa, Yoshihisa Nakamura

6543 Magnetic and structural properties of Fe-FeO bilayers — X. Lin, A. S. Murthy, G. C. Hadjipanayis, C. Swann, S. I. Shah

6546 Ferromagnetic-ferromagnetic tunneling and the spin filter effect — P. LeClair, J. S. Moodera, R. Meservey

6549 Theory of Brillouin light scattering from spin waves in multilayers with interlayer exchange and dipole coupling — A. N. Slavin, I. V. Rojdestvenski, M. G. Cottam

6552 Spin wave spectra in semi-infinite magnetic superlattices with nonuniaxial single-ion anisotropy — E. L. Albuquerque

6555 Ground state of antiferromagnetic systems in a magnetic field and in the presence of surfaces — L. Trallori, P. Politi, A. Rettori, M. G. Pini, J. Villain

6558 Magnetoresistance of ultrathin Co films grown in UHV on Au(111): Crossover from granular to continuous film behavior versus Co thickness (abstract) — C. Dupas, E. Kolb, J. P. Renard, E. Vélu, M. Galtier, M. Mulloy, D. Renard

6559 The micromagnetics of periodic arrays of defects in trilayers with interlayer exchange coupling (abstract) — H. A. M. van den Berg

6560 FMR doublet in two-layer iron garnet films (abstract) — A. M. Grishin, V. S. Dellalov, E. I. Nikolayev, V. F. Shkar, S. V. Yampolskii

6560 Influence of the dipole interaction on the direction of the magnetization in thin ferromagnetic films (abstract) — A. Moschel, K. D. Usadel

Fine Particles

6561 Coercivity and switching field of single domain γ-Fe_2O_3 particles under consideration of the demagnetizing field — Paul L. Fulmek, Hans Hauser

6564 Structural and magnetic characterization of Co particles coated with Ag — J. Rivas, R. D. Sánchez, A. Fondado, C. Izco, A. J. García-Bastida, J. García-Otero, J. Mira, D. Baldomir, A. González, I. Lado, M. A. López Quintela, S. B. Oseroff

6567 Magnetic properties of Fe clusters in NaY zeolite — J. A. Cowen, K. L. Tsai, J. L. Dye

(Continued)

6570	Preparation and microwave characterization of spherical and monodisperse $Co_{20}Ni_{80}$ particles	G. Viau, F. Ravel, O. Acher, F. Fiévet-Vincent, F. Fiévet
6573	Coercivity of Fe-SiO_2 nanocomposite materials prepared by ball milling	Anit K. Giri, C. de Julián, J. M. González
6576	Nuclear magnetic resonance study of the magnetic behavior of ultrafine Co clusters in zeolite NaY	Y. D. Zhang, W. A. Hines, J. I. Budnick, Z. Zhang, W. M. H. Sachtler
6579	Perfluorocyclobutane containing aromatic ether polymers as planarization materials for alternative magnetic media substrates	Donald J. Perettie, Jack Judy, Qixu Chen, Rick Keirstead
6582	Anomalous perpendicular magnetoanisotropy in Mn_4N films on Si(100)	K. M. Ching, W. D. Chang, T. S. Chin, J. G. Duh, H. C. Ku
6585	Formation kinetics of polycrystalline $Eu_{2-x}Ce_xCuO_{4-y}$ obtained from a sol-gel precursor	P. A. Suzuki, R. F. Jardim, S. Gama
6588	Thermal decay of *N* coupled particles	Ivo Klik, Ching-Ray Chang, Jyh-Shinn Yang
6591	Influence of size and magnetocrystalline anisotropy on spin canting anomaly in fine ferrimagnetic particles	D. H. Han, J. P. Wang, Y. B. Feng, H. L. Luo
6594	Magnetic properties of nanometer-sized Fe_4N compound (abstract)	Y. B. Feng

Giant Magnetoresistance

6595	Theory of the negative magnetoresistance of ferromagnetic-normal metallic multilayers (invited)	L. M. Falicov, Randolph Q. Hood
6601	Giant magnetoresistance in Co/Cu multilayers after annealing	T. R. McGuire, J. M. Harper, C. Cabral, Jr., T. S. Plaskett
6604	Magnetoresistance and magnetization oscillations in Fe/Cr/Fe trilayers	R. Schad, C. D. Potter, P. Beliën, G. Verbanck, V. V. Moshchalkov, Y. Bruynseraede, M. Schäfer, R. Schäfer, P. Grünberg
6607	Structural and magnetic properties of Co/Ag multilayers	E. A. M. van Alphen, P. A. A. van Heijden, W. J. M. de Jonge
6610	Magnetic states of magnetic multilayers at different fields	P. A. Schroeder, S.-F. Lee, P. Holody, R. Loloee, Q. Yang, W. P. Pratt, Jr., J. Bass
6613	Investigation of the magnetic structures in giant magnetoresistive multilayer films by electron microscopy	L. J. Heyderman, J. N. Chapman, S. S. P. Parkin
6616	Distribution of current in spin valves (abstract)	Bruce A. Gurney, Virgil S. Speriosu, Harry Lefakis, Dennis R. Wilhoit
6616	A comparison of the giant magnetoresistance and anisotropic magnetoresistance in Co/Cu sandwich films (abstract)	B. H. Miller, E. Youjun Chen, Mark Tondra, E. Dan Dahlberg
6617	Enhanced magnetoresistance in chromium doped Fe/Cr multilayers (abstract)	Noa M. Rensing, Bruce M. Clemens
6617	Low field giant magnetoresistance and oscillatory interlayer exchange coupling in polycrystalline and (111)-oriented permalloy/Au multilayers (abstract)	S. S. P. Parkin, T. A. Rabedeau, R. F. C. Farrow, R. Marks
6618	Giant magnetoresistance at low fields in $[(Ni_xFe_{1-x})_yAg_{1-y}]$/Ag multilayers prepared by molecular beam epitaxy (abstract)	R. F. C. Farrow, R. F. Marks, A. Cebollada, M. F. Toney, D. Dobbertin, R. Beyers, S. S. P. Parkin, T. A. Rabedeau
6619	Effects of domains on magnetoresistance (abstract)	Shufeng Zhang, Peter M. Levy

$Fe_{16}N_2$: Giant Moment or Not (Panel Discussion)

6620	The synthesis, structure, and characterization of α''-$Fe_{16}N_2$ (invited)	K. H. Jack
6626	Magnetism of α''-$Fe_{16}N_2$ (invited)	Robert M. Metzger, Xiaohua Bao, Massimo Carbucicchio
6632	The magnetization of bulk $\alpha''Fe_{16}N_2$ (invited)	J. M. D. Coey

(Continued)

6637	Magnetic and Mössbauer studies of single-crystal $Fe_{16}N_2$ and Fe-N martensite films epitaxially grown by molecular beam epitaxy (invited)	Yutaka Sugita, Hiromasa Takahashi, Matahiro Komuro, Katsuya Mitsuoka, Akimasa Sakuma
6642	Magnetic moment of α''-$Fe_{16}N_2$ films (invited)	Migaku Takahashi, H. Shoji, H. Takahashi, H. Nashi, T. Wakiyama, M. Doi, M. Matsui
6648	Enhanced Fe moment in nitrogen martensite and $Fe_{16}N_2$ (invited)	W. E. Wallace, M. Q. Huang
6653	Enhancement of the formation of $Fe_{16}N_2$ on Fe films by Co additions (invited)	Yoshiharu Inoue, Shigeto Takebayashi, Toshio Mukai

Preparation and Physics of Artificially Structured Magnets

6656	Properties and measurement of scanning tunneling microscope fabricated ferromagnetic particle arrays (invited)	A. D. Kent, S. von Molnár, S. Gider, D. D. Awschalom
6661	Magnetic properties of amorphous nanocolumns created by heavy ion irradiation of paramagnetic YCo_2 thin films (invited)	D. Givord, J. P. Nozières, M. Ghidini, B. Gervais, Y. Otani
6667	Magnetic wire and box arrays (invited)	Atsushi Maeda, Minoru Kume, Takashi Ogura, Kazuhiko Kuroki, Takashi Yamada, Madoka Nishikawa, Yasoo Harada
6671	Ferromagnetic filaments fabrication in porous Si matrix (invited)	Sergey A. Gusev, Natalia A. Korotkova, Dmitry B. Rozenstein, Andrey A. Fraerman
6673	Single-domain magnetic pillar array of 35 nm diameter and 65 Gbits/in.^{2} density for ultrahigh density quantum magnetic storage	Stephen Y. Chou, Mark S. Wei, Peter R. Krauss, Paul B. Fischer
6676	Magnetic properties of nanostructured thin films of transition metal obtained by low energy cluster beam deposition	V. Dupuis, J. P. Perez, J. Tuaillon, V. Paillard, P. Mélinon, A. Perez, B. Barbara, L. Thomas, S. Fayeulle, J. M. Gay
6679	Size effects on switching field of isolated and interactive arrays of nanoscale single-domain Ni bars fabricated using electron-beam nanolithography	Mark S. Wei, Stephen Y. Chou

Itinerant Magnetism and Electronic Structure I

6682	Itinerant electron metamagnetism and related phenomena in Co-based intermetallic compounds (invited)	T. Goto, H. Aruga Katori, T. Sakakibara, H. Mitamura, K. Fukamichi, K. Murata
6688	Local and nonlocal density functional studies of FeCr	David J. Singh
6691	Temperature-dependent electronic structure and ferromagnetism of bcc iron	W. Nolting, A. Vega
6694	Theory for itinerant electrons in noncollinear and incommensurate structured magnets (invited)	J. Kübler, L. M. Sandratskii, M. Uhl
6700	Verwey transition in magnetite: Mean-field solution of the three-band model	S. K. Mishra, Z. Zhang, S. Satpathy
6703	Wannier states in magnetite	Trao Her, Carel Boekema
6705	Orbital ordering and magneto-optical effects in CeSb	V. P. Antropov, B. N. Harmon, A. I. Liechtenstein

Hard Magnets I

6708	Magnetic properties of $Sm_2(Fe,V)_{17}N_y$ coarse powder	Shunji Suzuki, Shinya Suzuki, Masahito Kawasaki
6711	Mössbauer study of $R_2Fe_{17}C_x$ (R=Tb,Dy) as-quenched intermetallics compounds	Hua-Yang Gong, Bao-Gen Shen, Lin-Shu Kong, Lei Cao, Wen-Shan Zhan, Zhao-Hua Cheng, Fang-Wei Wang

(Continued)

6714	Magnetic properties of $Tm_2Fe_{17}C_x$ ($0 \leq x \leq 2.8$) compounds prepared by melt spinning	Bao-Gen Shen, Lin-Shu Kong, Lei Cao, Hua-Yang Gong, Fang-Wei Wang, Zhao-Hua Cheng, Jian-Gao Zhao
6717	Kerr microscopy observation of carbon diffusion profiles in $Sm_2Fe_{17}C_x$	J. Zawadzki, P. A. P. Wendhausen, B. Gebel, A. Handstein, D. Eckert, K.-H. Müller
6720	Neutron-diffraction study on the structure of $Nd(TiFe)_{12}N_x$ and $Nd(TiFeCo)_{12}N_x$ alloys	Shu-Ming Pan, Hong Chen, Zu-Xiong Xu, Ru-Zhang Ma, Ji-Lian Yang, Bai-Sheng Zhang, De-Yan Xue, Qiang Ni
6722	Synthesis and magnetic properties of $PrFe_{12-x}Mo_x$ and $PrFe_{12-x}Mo_xN_y$ ($0.5 \leq x \leq 1.0$; $y \approx 1$)	O. Kalogirou, V. Psycharis, L. Saettas, D. Niarchos
6725	Study of permanent magnetic properties of the 1-12 nitrides with Nd and Pr	Ying-Chang Yang, Qi Pan, Ben-Pai Cheng, Xiao-Dong Zhang, Zun-Xiao Liu, Yun-Xi Sun, Sen-Ling Ge
6728	Structural and magnetic properties of $Ce(Fe,M)_{12}N_x$ interstitial compounds, M=Ti, V, Cr, and Mo	Qi Pan, Zun-Xiao Liu, Ying-Chang Yang
6731	Neutron-diffraction and Mössbauer effect study of the $Tb_2Fe_{17-x}Al_x$ solid solutions	G. K. Marasinghe, S. Mishra, O. A. Pringle, Gary J. Long, Z. Hu, W. B. Yelon, F. Grandjean, D. P. Middleton, K. H. J. Buschow
6734	Structure and magnetic anisotropy of $Sm_2Fe_{17-x}Al_xC$ ($x=2$–8) compounds prepared by arc melting	Zhao-Hua Cheng, Bao-Gen Shen, Jun-Xian Zhang, Fang-Wei Wang, Hua-Yang Gong, Wen-Shan Zhan, Jian-Gao Zhao
6737	Uniaxial magnetic anisotropy in Fe-rich 2:17 compounds with *sp* substitutions	R. A. Dunlap, Z. Wang, M. Foldeaki
6740	Magnetic properties of $R_2Fe_{17-x}Ga_x$ compounds (R=Y, Ho)	J. L. Wang, R. W. Zhao, N. Tang, W. Z. Li, Y. H. Gao, F. M. Yang, F. R. de Boer
6743	Magnetic properties of $Sm_2(Fe_{1-x}Ga_x)_{17}$ ($x=0-0.5$) compounds and their nitrides	W.-Z. Li, N. Tang, J.-L. Wang, Fuming Yang, Y. W. Zeng, J. J. Zhu, F. R. de Boer
6746	Structure and magnetic properties of arc-melted $Sm_2(Fe_{1-x}Co_x)_{14}Ga_3C_2$ compounds	Bao-gen Shen, Lin-shu Kong, Fang-wei Wang, Lei Cao, Bing Liang, Zhao-hua Cheng, Hua-yang Gong, Hui-qun Guo, Wen-shan Zhan
6749	Neutron diffraction and Mössbauer effect study of the structure of $DySi_xFe_{11-x}CoN$ alloys	Shu-ming Pan, Hong Chen, Den-ke Liu, Zu-xiong Xu, Ru-zhang Ma, Ji-lian Yang, Bai-sheng Zhang, De-yan Xue, Qiang Ni
6751	A full electron LMTO-ASA study of electronic band structure and magnetic properties for $RFe_{11}TiN_x$ (R=Y, Nd, Sm; $x=0,1$)	W. Y. Hu, J. Z. Zhang, Q. Q. Zheng, C. Y. Pan
6754	Magnetic properties and molecular field theory analysis of $RFe_{10}Mo_2$ alloys	Xie Xu, S. A. Shaheen
6757	Magnetic alignment in powder magnet processing	S. Liu
6760	Sputter synthesis of $TbCu_7$ type Sm(CoFeCuZr) films with controlled easy axis orientation	H. Hegde, P. Samarasekara, R. Rani, A. Navarathna, K. Tracy, F. J. Cadieu
6763	Metastable $Nd_2(Fe_{1-x}Co_x)_{23}B_3$ ($0 \leq x \leq 1.0$) compounds with the 2:23:3-type structure	Bao-gen Shen, Bo Zhang, Fang-wei Wang, Jun-xian Zhang, Bing Liang, Wen-shan Zhan, Hui-qun Guo, Jian-gao Zhao
6766	Magnetic properties of $(Nd_{0.9}R_{0.1})_5Fe_{17}$ with R=Sm, Gd, and Y	Cong-Xiao Liu, Yun-Xi Sun, Zun-Xiao Liu, Chin Lin

(Continued)

6769	New permanent magnetic MnBiDy alloy films	Fang Ruiyi, Fang Qingqing, Zhang Sheng, Peng Chubing, Dai Daosheng

Symposium on Neutron Scattering Studies of Vortex Structures in Superconductors

6772	Neutron scattering studies of the vortex lattice in niobium and 123 superconductors (invited)	N. Rosov, J. W. Lynn, T. E. Grigereit
6778	Vortex structures in $YBa_2Cu_3O_7$ (invited)	B. Keimer, J. W. Lynn, R. W. Erwin, F. Dogan, W. Y. Shih, I. A. Aksay
6784	Small-angle neutron scattering study of the flux-line lattice in a single crystal of $Bi_{2.15}Sr_{1.9}CaCu_2O_{8+x}$ (invited)	M. Yethiraj, H. A. Mook, E. M. Forgan, R. Cubitt, M. T. Wylie, D. M. Paul, S. L. Lee, J. Ricketts, P. H. Kes, K. Mortensen
6788	Neutron diffraction from the vortex lattice in the heavy fermion superconductor UPt_3 (invited) (abstract)	R. N. Kleiman, G. Aeppli, D. J. Bishop, C. Broholm, E. Bucher, N. Stüchelli, U. Yaron, K. N. Clausen, B. Howard, K. Mortensen, J. S. Pedersen
6789	Small angle neutron scattering from the vortex lattice in $2H$-$NbSe_2$ (invited) (abstract)	P. L. Gammel, U. Yaron, D. A. Huse, R. N. Kleiman, R. Batlogg, C. S. Oglesby, E. Bucher, D. J. Bishop, T. E. Mason, K. Mortensen

Giant Magnetoresistance in Granular Magnetic Systems

6790	Giant magnetoresistance in sputtered Cr-Fe heterogeneous alloy films	K. Takanashi, T. Sugawara, K. Hono, H. Fujimori
6793	Origin of giant magnetoresistance effect in granular thin films	Atsushi Maeda, Minoru Kume, Satoru Oikawa, Kazuhiko Kuroki
6796	Evolution of structure and magnetoresistance in granular Ni(Fe,Co)/Ag multilayers: Dependence on magnetic layer thickness	X. Bian, X. Meng, J. O. Ström-Olsen, Z. Altounian, W. B. Muir, M. Sutton, R. W. Cochrane
6799	Magnetoresistance in (Fe–Co)/Ag films	A. Tsoukatos, D. V. Dimitrov, A. S. Murthy, G. C. Hadjipanayis
6802	Interaction effects and magnetic ordering in GMR alloys	S. J. Greaves, M. El-Hilo, K. O'Grady, M. Watson
6805	Magnetic structure of the spin valve interface	D. M. C. Nicholson, W. H. Butler, X.-G. Zhang, J. M. MacLaren, B. A. Gurney, V. S. Speriosu
6808	Theory of transport in inhomogeneous systems and application to magnetic multilayer systems	W. H. Butler, X.-G. Zhang, D. M. C. Nicholson, J. M. MacLaren
6811	The effect of interactions on GMR in granular solids	M. El-Hilo, K. O'Grady, R. W. Chantrell
6814	Giant magnetoresistance in spinodally decomposed Cu–Ni–Fe films	L. H. Chen, S. Jin, T. H. Tiefel, T. C. Wu
6817	Relaxation of magnetoresistance and magnetization in granular $Cu_{90}Co_{10}$ obtained from rapidly quenched ribbons	P. Allia, C. Beatrice, M. Knobel, P. Tiberto, F. Vinai
6820	Magnetic and magnetotransport properties of granular $Cu_{85}Fe_{15}$ prepared by mechanical alloying	Siddharth S. Saxena, Jinke Tang, Young-Sook Lee, Charles J. O'Connor
6823	Granular giant magnetoresistive materials and their ferromagnetic resonances (abstract)	M. Rubinstein, B. N. Das, N. C. Koon, D. B. Chrisey, J. Horwitz
6824	Magnetoresistance of granular Cu-(Co,Fe) and Cu-Co-B (abstract)	R. v. Helmolt, J. Wecker, K. Samwer

Hard Magnets II

6825	Evolution of recombination in a solid HDDR processed $Nd_{14}Fe_{79}B_7$ alloy	N. Martinez, D. G. R. Jones, O. Gutfleisch, D. Lavielle, D. Peré, I. R. Harris

(Continued)

6828	Effects of HDDR treatment conditions on magnetic properties of Nd-Fe-B anisotropic powders	H. Nakamura, R. Suefuji, S. Sugimoto, M. Okada, M. Homma
6831	The use of polytetrafluoroethylene in the production of high-density bonded Nd-Fe-B magnets	C. Tattam, A. J. Williams, J. N. Hay, I. R. Harris, S. F. Tedstone, M. M. Ashraf
6834	Evidence of domain-wall pinning in W-doped (NdDy)(FeCo)B sintered magnets	T. Y. Chu, T. S. Chin, C. H. Lin, J. M. Yao
6837	Magnetic properties of rare-earth compounds of the $RCo_{10}Mo_2$ type	D. C. Zeng, N. Tang, T. Zhao, Z. G. Zhao, K. H. J. Buschow, F. R. de Boer
6840	Magnetic hardening by crystallization of amorphous precursors using very high heating rates	C. de Julián, J. M. González, C. Morón
6843	Magnetic phase diagrams of YCo_4B-based components	Z. G. Zhao, R. de Boer, K. H. J. Buschow, Y. P. Ge, J. Y. Wang
6846	A systematic study on stability of flux in Nd-Fe-B magnets consolidated by direct joule heating	H. Fukunaga, H. Tomita, M. Wada, F. Yamashita, T. Toshimura
6849	Studies of Mössbauer spectrum on $Sm_2(Fe,Ga)_{17}C_{1.5}$ alloy	Hong Chen, Zu-xiong Xu, Ru-zhang Ma, Shu-ming Pan, Bao-gen Shen, De-yan Xue, Qiang Ni
6851	Low-temperature behavior of thermopower in rare-earth iron borides $R_2Fe_{14}B$ (R=Nd, Sm, Gd, Tb, Dy, Ho, Er)	R. P. Pinto, M. E. Braga, M. M. Amado, J. B. Sousa, K. H. J. Buschow
6853	Effects of field orientation on field uniformity in permanent magnet structures	J. H. Jensen, M. G. Abele
6856	Lightweight, distortion-free access to interiors of strong magnetic field sources	H. A. Leupold, E. Potenziani, II, A. S. Tilak
6859	Laminar construction of spheroidal field sources with distortion-free access	H. A. Leupold, A. S. Tilak, E. Potenziani, II
6862	Effect of magnetization profiles on the torque of magnetic coupling	Der-Ray Huang, Gwo-Ji Chiou, Yeong-Der Yao, Shyh-Jier Wang
6865	A magnetic coupling without parasitic force for measuring devices	Jean-Paul Yonnet, Jérôme Delamare
6868	Accurate determination of permanent magnet motor parameters by digital torque angle measurement	M. A. Rahman, Ping Zhou
6871	A three-material passive *dI/dt* limiter	S. J. Young, F. P. Dawson, A. Konrad
6874	An extended magnet in a passive *dI/dt* limiter	S. J. Young, F. P. Dawson, A. Konrad
6877	Effects of additives on magnetic properties of sheet Sr-Ba ferrite magnets	Young Jei Oh, In Bo Shim, Hyung Jin Jung, Jae Yun Park, Seung Iel Park, Young Rang Um, Young Jong Lee, Seung Wha Lee, Chul Sung Kim

Spin Waves and Other Excitations

6880	Critical scattering of electromagnetic waves on spin fluctuations in nonsaturated magnetic films under acoustic pump	I. E. Dikshtein, R. G. Kryshtal, A. V. Medved
6883	Light scattering from spin waves in MnF_2	M. G. Cottam, V. P. Gnezdilov, H. J. Labbé, D. J. Lockwood
6886	Controlling high frequency chaos in circular YIG films	D. W. Peterman, M. Ye, P. E. Wigen
6889	Study of spin wave resonance in a superconductor with paramagnetic impurities	I. A. Garifullin, Yu. V. Goryunov, G. G. Khaliullin
6892	Two-magnon absorption in Nd_2CuO_4	V. L. Sobolev, Yu. G. Pashkevich, H. L. Huang, I. M. Vitebskii, V. A. Blinkin

(Continued)

6895 Surface precession solitons (surface "Magnetic drops") in uniaxial magnetics (abstract) — Yurij Bespyatykh, Igor Dikshtein, Sergey Nikitov

6895 Nonlinear self-localized surface spin waves in ferromagnets (abstract) — Alan Boardman, Yurij Bespyatykh, Igor Dikshtein, Sergey Nikitov

6896 Spin wave dispersion in ferromagnetic nickel (abstract) — J. M. Rejcek, J. L. Fry, N. G. Fazleev

6897 Ferromagnetic resonance and Brillouin light scattering from epitaxial Fe_xSi_{1-x} films on Si(111) (abstract) — M. Mendik, Z. Frait, H. von Känel, N. Onda

Hyperfine Field, Mössbauer Effect, and NMR

6898 Nuclear secondary echo in ferromagnets caused by quadrupole and Suhl–Nakamura interactions — V. I. Tsifrinovich

6900 A Mössbauer effect study on the acicular cobalt ferrite particles — J. G. Na, D. H. Han, J. G. Zhao, H. L. Luo

6903 X-ray photoelectron spectroscopy and Mössbauer study of $Ho(Fe_{1-x}Mn_x)_2$ compounds — Y. J. Tang, Y. B. Feng, H. L. Luo, S. M. Pan

6906 Hyperfine fields of mercury in single-crystalline cobalt — J. G. Marques, J. G. Correia, A. A. Melo, J. C. Soares, E. Alves, M. F. da Silva

6909 Simulation of nuclear magnetic resonance spin echoes using the Bloch equation: Influence of magnetic field inhomogeneities — J. A. Nyenhuis, O. P. Yee

6912 Correlation of magneto-volume effects and local properties of the Fe_2Ti-laves phase (abstract) — J. Pelloth, R. A. Brand, W. Keune

Symposium on Giant Magnetoresistance in Compounds

6913 Giant magnetoresistance effects in intermetallic compounds (invited) — V. Sechovský, L. Havela, K. Prokeš, H. Nakotte, F. R. de Boer, E. Brück

6919 Giant magnetoresistance related transport properties in multilayers and bulk materials (invited) — H. Sato, H. Henmi, Y. Kobayashi, Y. Aoki, H. Yamamoto, T. Shinjo, V. Sechovsky

6925 Intrinsic giant magnetoresistance of mixed valence La-A-Mn oxide (A=Ca,Sr,Ba) (invited) — R. von Helmolt, J. Wecker, K. Samwer, L. Haupt, K. Bärner

6929 Colossal magnetoresistance in La-Ca-Mn-O ferromagnetic thin films (invited) — S. Jin, M. McCormack, T. H. Tiefel, R. Ramesh

6934 Giant magnetoresistance in *f*-electron systems (invited) (abstract) — Tadao Kasuya, Takashi Suzuki

Superconductivity I

6935 Theory of spin dynamics in the metallic cuprates (invited) — Qimiao Si, Yuyao Zha, K. Levin

6941 Hydrostatic pressure on $HgBa_2CaCu_2O_{6+\delta}$ and $HgBa_2Ca_2Cu_3O_{8+\delta}$ — F. Chen, L. Gao, R. L. Meng, Y. Y. Xue, C. W. Chu

6944 Magnetoconductivity of $Bi_2Sr_2Ca_{1-x}Y_xCu_2O_{8+\delta}$ in fluctuation regime — C. P. Dhard, S. N. Bhatia, P. V. P. S. S. Sastry, J. V. Yakhmi, A. K. Nigam

6947 Straightened voltage effect in high-T_c superconductors — A. Grishin, J. Niska, B. Loberg, H. Weber

6950 Long-time magnetic relaxation measurements on a quench melt growth YBCO superconductor — L. H. Bennett, L. J. Swartzendruber, M. J. Turchinskaya, J. E. Blendell, J. M. Habib, H. M. Seyoum

6953 Surface barriers and two-dimensional-collective pinning in single crystal $Nd_{1.85}Ce_{0.15}CuO_{4-\delta}$ superconductors — F. Zuo, S. Khizroev, Xiuguang Jiang, J. L. Peng, R. L. Greene

6956 On vector generalization of the critical state model for superconducting hysteresis — I. D. Mayergoyz

6959 Proximity effect in MBE-grown superconducting/spin-glass multilayers — Carlos W. Wilks, Brad N. Engel, Charles M. Falco

(Continued)

6962 Heterodyne microwave mixing in a superconducting $YBa_2Cu_3O_{7-x}$ coplanar waveguide circuit containing a single engineered grain boundary junction — R. G. Seed, C. Vittoria, A. Widom

6965 Superconducting $YBa_2Cu_3O_{7-x}/Y_4Ba_3O_9$ multilayers: Field independent critical current and dimensional crossover (abstract) — Jun-Hao Xu, A. M. Grishin, K. V. Rao

6965 Schematic frictional model for interacting vortices in an isotropic superconducting plate (abstract) — J. S. Kouvel, S. J. Park

Magnetic Multilayer Coupling II

6966 Spin-polarized photoemission from quantum well and interface states (invited) — C. Carbone, E. Vescovo, R. Klăsges, W. Eberhardt, O. Rader, W. Gudat

6972 Recent progress in the theory of interlayer exchange coupling (invited) — P. Bruno

6977 Exchange anisotropy in films, and the problem of inverted hysteresis loops — Amikam Aharoni

6980 Ruderman–Kittel–Kasuya–Yosida polarizations in inhomogeneous media — W. Baltensperger, J. S. Helman

6983 Spin reversal in Co/Au(111)/Co trilayers — V. Grolier, J. Ferré, M. Galtier, M. Mulloy

6986 Effect of coupling on magnetic properties of uniaxial anisotropy NiFeCo/TaN/NiFeCo sandwich thin films — T. Yeh, L. Berg, B. Witcraft, J. Falenschek, J. Yue

6989 Antiferromagnetic versus ferromagnetic coupling in Fe/Cr(107) and Cr/Fe(107) — A. Vega, H. Dreyssé, C. Demangeat, A. Chouairi, L. C. Balbás

6992 Influence of Cr growth on exchange coupling in Fe/Cr/Fe(100) (invited) (abstract) — Joseph A. Stroscio, D. T. Pierce, J. Unguris, R. J. Celotta

6993 Exchange magnetic coupling through nonmagnetic insulator spacers (abstract) — Shufeng Zhang

Magnetostriction I

6994 Fabrication of magnetostrictive actuators using rare-earth (Tb,Sm)-Fe thin films (invited) — T. Honda, K. I. Arai, M. Yamaguchi

7000 Preparation and applications of magnetostrictive thin films — E. Quandt, B. Gerlach, K. Seemann

7003 Magnetostriction in TbDyFe thin films — P. J. Grundy, D. G. Lord, P. I. Williams

7006 Application of the ratio d/χ to the investigation of magnetization processes in giant-magnetostrictive materials — A. R. Piercy, S. C. Busbridge, D. Kendall

7009 Magnetization, Young's moduli, and magnetostriction of rare-earth–iron eutectic alloys with $R=Tb_{0.6}Dy_{0.4}$ — A. E. Clark, M. Wun-Fogle, J. P. Teter, J. B. Restorff, S. F. Cheng

7012 Theory of magnetostriction with application to Terfenol-D — R. D. James, D. Kinderlehrer

7015 Recent developments in modeling of the stress derivative of magnetization in ferromagnetic materials — D. C. Jiles, M. K. Devine

7018 Magnetization and magnetostriction curves from micromagnetics — Antonio DeSimone

7021 Magnetostriction of melt-spun Dy-Fe-B alloys — S. H. Lim, T. H. Noh, I. K. Kang, S. R. Kim, S. R. Lee

7024 Magnetic properties and magnetostriction in grain-oriented $(Tb_xDy_{1-x})(Fe_{1-y}Mn_y)_{1.95}$ compounds — .. Kobayashi, I. Sasaki, T. Funayama, M. Sahashi

7027 Stress effect on the magnetization of Dy in the $Dy/DyFe_2$ eutectic — J. P. Teter, S. F. Cheng, J. R. Cullen

7030 Direct measurements of magnetostrictive process in amorphous wires using a scanning tunneling microscope (abstract) — J. L. Costa, J. Nogués, K. V. Rao

7031 Tunable bistability from magnetostriction (abstract) — A. S. Arrott, J.-G. Lee

(Continued)

Itinerant Magnetism and Electronic Structure II

7032	Influence of Stoner-type excitations on the formation of magnetization and magnetic order in disordered metal-metalloid alloys	A. K. Arzhnikov, L. V. Dobysheva, E. P. Yelsukov
7034	Magnetic susceptibility studies in Gd_2CuO_4 below 300 K	J. Mira, J. Castro, J. Rivas, D. Baldomir, C. Vázquez-Vázquez, J. Mahía, A. López-Quintela, D. Fiorani, R. Caciuffo, D. Rinaldi, T. Jones, S. B. Oseroff
7037	Cluster model studies on the electronic and magnetic properties of $LaCo_{13}$ and $La(Fe_xAl_{1-x})_{13}$ alloys	G. W. Zhang, X. G. Gong, Q. Q. Zheng, J. G. Zhao
7040	Structure, transport and thermal properties of UCoGa	A. Purwanto, R. A. Robinson, K. Prokeš, H. Nakotte, F. R. de Boer, L. Havela, V. Sechovský, N. C. Tuan, Y. Kergadallan, J. C. Spirlet, J. Rebizant
7043	The effect of Mn on the magnetic properties of YFe_2	Jian-Wang Cai, Yuan-Bing Feng, He-Lie Luo, Zhi Zeng, Qing-Qi Zheng
7046	Effects of Al substitution in Nd_2Fe_{17} studied by first-principles calculations	Ming-Zhu Huang, W. Y. Ching
7049	Magnetic and crystallographic order in α-manganese	A. C. Lawson, Allen C. Larson, M. C. Aronson, S. Johnson, Z. Fisk, P. C. Canfield, J. D. Thompson, R. B. Von Dreele
7052	Magnetic field dependence of T_c of EuB_6 (abstract)	A. Lacerda, T. Graf, J. L. Sarrao, M. F. Hundley, D. Mandrus, J. D. Thompson, Z. Fisk

Nanocomposite Magnets

7053	Two- and three-dimensional calculation of remanence enhancement of rare-earth based composite magnets (invited)	T. Schrefl, R. Fischer, J. Fidler, H. Kronmüller
7059	Aligned two-phase magnets: Permanent magnetism of the future? (invited)	R. Skomski
7065	Nanocomposite $R_2Fe_{14}B$/Fe exchange coupled magnets	L. Withanawasam, A. S. Murphy, G. C. Hadjipanayis, R. F. Krause
7068	Influence of nitrogen content on coercivity in remanence-enhanced mechanically alloyed Sm-Fe-N	K. O'Donnell, C. Kuhrt, J. M. D. Coey
7071	Coercivity of Ti-modified (α-Fe)-$Nd_2Fe_{14}B$ nanocrystalline alloys	J. M. Yao, T. S. Chin, S. K. Chen
7074	Magnetization processes in remanence enhanced materials (invited) (abstract)	R. Street, P. Allen, J. Ding, E. Feutrill, L. Folks, P. A. I. Smith, R. C. Woodward

Magnetic Multilayer Coupling III

7075	Magnetic order and spin-flop transition in Co-Re multilayers	Z. Tun, W. J. L. Buyers, I. P. Swainson, M. Sutton, R. W. Cochrane
7078	Interlayer exchange coupling versus ferromagnetic layer thickness in asymmetric Co/Ru/Co trilayer films	L. Zhou, Z. Zhang, P. E. Wigen, K. Ounadjela
7081	Magnetic layer thickness dependence of the interlayer exchange coupling in (001) Co/Cu/Co	P. J. H. Bloemen, M. T. H. van de Vorst, M. T Johnson, R. Coehoorn, W. J. M. de Jonge
7084	Cumulative interface roughness and magnetization in antiferromagnetically coupled NiCo/Cu multilayers	X. Meng, X. Bian, R. Abdouche, W. B. Muir, J. O. Ström-Olsen, Z. Altounian, M. Sutton
7087	Coercivity and magnetization process versus dipolar coupling in $Ni_{80}Fe_{20}$/Cu/Co/Cu spin valves	R. Kergoat, J. Miltat, T. Valet, R. Jerome

(Continued)

7090	Observation of large biquadratic coupling of FeCo through Mn (invited) (abstract)	M. E. Filipkowski, C. J. Gutierrez, J. J. Krebs, G. A. Prinz
7091	Magnetic dipole mechanism for biquadratic interlayer coupling (abstract)	S. Demokritov, E. Tsymbal, P. Grünberg, W. Zinn, Ivan K. Schuller
7092	Polarized neutron reflectivity studies of biquadratic coupling in [Fe/Cr] (100) and [Fe/Al] (100) superlattices and films (invited) (abstract)	J. F. Ankner, A. Schreyer H. Zabel, J. A. Borchers, C. F. Majkrzak, M. Schäfer, J. A. Wolf, P. Grünberg, M. E. Filipkowski, C. J. Gutierrez, J. J. Krebs, G. A. Prinz

Critical Phenomena

7093	Monte Carlo histogram calculation of the critical exponents of an $Fe_xMg_{1-x}Cl_2$ Ising model (invited)	Laura Hernández, H. T. Diep
7099	Simultaneous surface and bulk magnetic properties investigations by using simultaneous gamma, x-rays and conversion electron Mössbauer spectroscopy: Method and experimental results	A. S. Kamzin, L. A. Grigor'ev, A. F. Ioffe
7102	Magnetic properties of Fe_xCu_{1-x} granular alloy films	Peng Chubing, Chen Haiying, Li Guozhong, Dai Daosheng
7105	New possibilities offered by high resolution Fourier transform spectroscopy in studying magnetic phase transitions	M. N. Popova
7108	How does mean-field theory work in magnetic multilayer systems?	Xiao Hu, Yoshiyuki Kawazoe
7111	Magnetic properties of the one-dimensional Heisenberg compounds (3-X-anilinium)$_8$[CuCl$_6$]Cl$_4$; X=Br, I	Gayatri Vyas, Leonard W. ter Haar
7114	Comparison of two-dimensional Heisenberg and two-dimensional *XY* model behaviors in Pd(1.2 at. % Fe) films	J. D. McKinley
7117	The effects of frustrated biquadratic interactions on the phase diagrams and criticality of the Blume–Emery–Griffiths model (abstract)	Daniel P. Snowman, Susan P. McKay
7117	Magnetic phase transitions in CsEr(MoO$_4$)$_2$ and KDy(MoO$_4$)$_2$-chain-layered Ising compounds (abstract)	E. N. Khats'ko, A. S. Cherny

Superconductivity II

7118	Na-doping effect on the magnetic properties of the YBCO ceramics	T. Nurgaliev, S. Miteva, I. Nedkov, A. Veneva, M. Taslakov
7121	Properties of polycrystalline samples of $Nd_{2-x}Ce_xCuO_{4-y}$ obtained from a sol-gel precursor	V. B. Barbeta, R. F. Jardim, L. Ben-Dor, M. B. Maple
7124	Magnetic ordering of Pr in $Pb_2Sr_2PrCu_3O_8$	W. T. Hsieh, W-H. Li, K. C. Lee, J. W. Lynn, J. H. Shieh, H. C. Ku
7127	Annealing temperature and O_2 partial pressure dependence of T_c in $HgBa_2CuO_{4+\delta}$	Q. Xiong, Y. Cao, F. Chen, Y. Y. Xue, C. W. Chu
7130	Penetration of electromagnetic fields into superconductors with gradual resistive transition	I. D. Mayergoyz
7133	Study of the frequency and low-field dependence of ac susceptibility in YBaCuO	M. Zazo, L. Torres, J. Iñiguez, C. de Francisco, J. M. Muñoz
7136	Effects of Ga doping on the magnetic ordering of Pr in $PrBa_2Cu_3O_7$	W-H. Li, C. J. Jou, S. T. Shyr, K. C. Lee, J. W. Lynn, H. L. Tsay, H. D. Yang
7139	Galvanomagnetic properties of quasi-one-dimensional superconductors	K. Yu. Arutyunov, N. P. Danilova, A. A. Nikolaeva
7142	Remanent magnetization of layered and isotropic superconductors (abstract)	Yu. V. Bugoslavsky, A. A. Minakov, S. I. Vasyurin
7143	Two types of additional maxima in magnetization curves of layered superconductors (abstract)	Yu. V. Bugoslavsky, A. A. Minakov
7143	"Effective radius" of the 4*f* electrons in $REBa_2Cu_3O_7$, RE=Dy, Ho, Er (abstract)	Yu. A. Koksharov, P. K. Silaev
7144	Helicoidal, magnetic vortex in a current-carrying superconductor in a longitudinal magnetic field: New exact solution (abstract)	Yuri A. Genenko

(Continued)

Magnetostriction II

7145 Ga substitution effect on magnetic and magnetostrictive properties of $TbFe_2$ compounds — Y. J. Tang, Y. B. Feng, H. L. Luo, S. M. Pan

7148 Comparison of the dynamic magnetomechanical properties of $Tb_{0.27}Dy_{0.73}Fe_2$ and $Tb_{0.30}Dy_{0.70}Fe_2$ — D. Kendall, A. R. Piercy

7151 Anisotropy in twinned terfenol-D crystals — D. G. Lord, D. Harvey

7154 Device oriented magnetoelastic properties of $Tb_xDy_{1-x}Fe_{1.95}$ (x=0.27, 0.3) at elevated temperatures — K. Prajapati, R. D. Greenough, A. G. Jenner

7157 Influence of hydrogen on the magnetic properties of Terfenol-D — L. Ruiz de Angulo, J. S. Abell, I. R. Harris

7160 Control of Terfenol-D under load — A. G. Jenner, R. D. Greenough, D. Allwood, A. J. Wilkinson

7163 Pressure dependencies of magnetostrictive strain and d coefficient in Terfenol-D after thermal or magnetic annealing — N. Galloway, R. D. Greenough, A. G. I. Jenner, M. P. Schulze

7166 Effect of bias magnetic field on the magnetostrictive vibration of amorphous ribbons — Naoshi Asuke, Tatsuru Namikawa, Yohtaro Yamazaki

7169 AUTHOR INDEX

IEEE TRANSACTIONS ON

MAGNETICS

NOVEMBER 1994 VOLUME 30 NUMBER 6 IEMGAQ (ISSN 0018-9464)

A PUBLICATION OF THE IEEE MAGNETICS SOCIETY

PART I OF TWO PARTS

Sixth Joint Magnetism and Magnetic Materials—International Magnetics Conference Albuquerque, New Mexico, June 20-23, 1994

Journal of Applied Physics Table of Contents 3774
IEEE Magnetics Society 1994 3791
Conference Organization 3793
Contributors 3794
Preface 3795
Introduction 3796

Symposium on Advanced Magnetic Recording

Outlook for Maintaining Areal Density Growth Rate in Magnetic Recording—*E. Grochowski and D. Thompson* 3797
Design, Fabrication and Testing of Spin-Valve Read Heads for High Density Recording—*C. Tsang, R. Fontana, T. Lin, D. Heim, V. Speriosu, B. Gurney and M. Williams* 3801
Advanced Read Channels for Magnetic Disk Drives—*T. Howell, W. Abbott and K. Fisher* 3807

GMR and Spin Valve Sensors for Magnetic Recording

Application of Giant Magnetoresistive Elements in Thin Film Tape Heads—*W. Folkerts, J. Kools, T. Rijks, R. Coehoorn, M. De Nooijer, G. Somers, J. Ruigrok, and L. Postma* 3813
High Sensitivity, GMR, 1 Micron Wide, End-on, Ganged, Read Head Sensors—*E. Chen, A. Pohm, J. Daughton, J. Brown and W. Black* 3816
Magnetoresistance of Symmetric Spin Valve Structures—*T. Anthony, J. Brug, and S. Zhang* 3819
Micromagnetics of GMR Multilayer Sensors at High Current Densities—*N. Smith* 3822
Size and Self-Field Effects in Giant Magnetoresistive Thin Film Devices—*R. Cross, S. Russek, and S. Sanders, M. Parker, J. Barnard, and S. Hossain* 3825
High Frequency Permeability Measurements On $Ni_{76}Fe_{10}Co_{14}$/Cu Giant Magnetoresistive Multilayers—*W. Doyle, H. Fujiwara, S. Hossain, A. Matsuzono, and M. Parker* 3828
Unshielded Spin-Valve Sensors Exchange-Biased by Thin TbCo Layers—*J. Leal, N. Oliveira, L. Rodrigues, A. Sousa, and P. Freitas* 3831
Magnetoresistance Studies of NiCoO Exchange Biased Spin-valve Structures—*C-L. Lin, J. Sivertsen, and J. Judy* 3834
Highly Sensitive Giant Magnetoresistance in NiFe/(Ni/Fe/Cu)n/NiFe Thin Films—*A. Kouchiyama, T. Miyauchi, and K. Watanabe* 3837

Magnetoresistive Thin Film Recording Heads

Flux-Guided MR Head for Very Low Flying Height—*T. Koshikawa, Y. Ohtsuka, Y. Ikegawa, H. Tanaka, J. Toda, and Y. Mizoshita* 3840
Performance Characteristics of a 4-Terminal Vertical Magnetoresistive/Inductive Head—*T. Shibata, N. Saito, H. Narisawa, Y. Soda, and T. Sekiya* 3843
Electrical Characteristics of a 500 Mb/in^2 Slanted Contact MR Head—*J. Fernandez-de-Castro, P. George and R. Machelski* 3846
Exchange Biasing Schemes for MR Disk Heads—*S. Yuan* 3849
Comparative Experimental Study of Exchange Biased Symmetric and Antisymmetric Dual Magnetoresistive Heads—*I. Trindade and M. Kryder* 3852

Stability and Biasing Characteristics of a Permanent Magnet Biased SAL/MR Device—*S. Liao, T. Torng, and T. Kobayashi* 3855
Numerical Analysis of Sensitivity Distribution for MR Strips Stabilized by Permanent Magnet Films—*K. Kikuchi, T. Kobayashi, T. Kawai, and A. Sakuma* 3858
Study of SAL-Biased MR Heads with Patterned Permanent Magnet Bias—*Y. Guo, J-G. Zhu, and S. Liao* 3861
Design and Fabrication of Unshielded Dual-Element Horizontal MR Heads—*J. Guzman, K. Mountfield, M. Kryder, R. Bojko, and R.E. Jones, Jr.* 3864
Simulation of Micromagnetic and Magnetoresistive Response in a Shielded Permalloy Strip—*T. Koehler* 3867

Inductive Thin Film Recording Heads

Writing Performance of Narrow Gap Heads Made with Sputtered Laminated FeN Materials on 3800 Oe Coercivity Media—*H. Hu, L. Vo, T. Nguyen, N. Robertson, M. Re, and C. Jahnes* 3870
Modeling of Narrow Track Thin Film Write Head Fields—*M. Kryder and W-Y. Lai* 3873
Performance Evaluation of Different Pole Geometries in Thin Film Heads—*S. Batra, A. Torabi, M. Mallary, S. Ramaswamy, and S. Marshall* 3876
The Effect of Rise Time and Field Gradient on Nonlinear Bit Shift in Thin Film Heads—*A. Torabi, M. Mallary, and S. Marshall* 3879
Write Induced Track Misregistration Due to Magnetic Center Shifts in Thin Film Inductive Heads—*M. Salo, Y. Tang, and T. Gallagher* 3882
Inductance Fluctuation, Domain Instability and Popcorn Noise in Thin Film Heads—*F. Liu and M. Kryder* 3885
Stress Effects of Water Sorption in Cure Baked Photoresist Underlayers on the Magnetic Easy Axis of Permalloy Film Overlayers—*P. Kasiraj, C. Moylan, and R. Fontana* 3888
Off-Track Capability of a Pole Trimmed Thin Film Head—*K. Fukuda, M. Sakai, N. Yamanaka, A. Iijima, and M. Matsuzaki* 3891
An Improvement of Thin Film Inductive Heads—*Y. Sakurai, T. Ishiguro, K. Katagiri, T. Kuriyama, and Y. Ichinose* 3894
Perpendicular Contact Recording Head with High Moment Laminated FeAlN/NiFe Pole Tips—*S. Wang, E. Louis, J. Wolfson, R. Anderson and M. Kryder* 3897
Multi-Track Submicron-Width Recording with a Novel Integrated Single Pole Head in Perpendicular Magnetic Recording—*H. Muraoka and Y. Nakamura* 3900

Magnetic Recording Heads

A Thin Film Head for HD-VCRs—*H. Ohmori, T. Yamamoto, M. Shoji, Y. Sugiyama, K. Hayashi, and M. Hayakawa* 3903
Low Inductance Double-Sided Metal-in-Gap Nano Composite Slider Using Fe-Ta-N Magnetic Film System for 250 Mb/in^2 Recording—*R. Goto, T. Kawai, M. Yamazaki, F. Tsuneda, S. Suwabe, I. Sakaguchi, and A. Iwama* 3909
Effects of Nitrogen Content on the Microstructure and Magnetic Properties of FeTaN Films—*J-C. Lin, L-J. Chen, and C-J. Chen* 3912
Microstructure and Magnetic Properties of FeTaN Films—*E. Haftek and J. Barnard* 3915
Electrochemical Corrosion Study of High Moment Thin Film Head Materials—*S. Gangopadhyay, V. Inturi, J. Barnard, M. Parker, H. Saffarian, and G. Warren* 3918
Stress, Microstructure and Materials Reliability of Sputter-Deposited Fe-N Films—*P. Narayan and Y. Kim* 3921
FeSiN Films for a Narrow Track Head—*M. Kadono, T. Yamamoto, M. Michijima, M. Kyoho, T. Matsuda, and T. Muramatsu* 3924
X-ray Diffraction and Magnetic Properties of Rapid Thermal Annealed Sendust Films—*M. Ullah, K. Coffey, M. Parker, and J. Howard* 3927
Thick and Stress-Free Sendust Films on Silicon for Recording Heads Cores—*J. Daval, B. Bechevet, J. Arroyo, B. Valon, M-F. Armand, and H. Joisten* 3930
Correlation between Noise-After-Write and Magnetic Domain Structure Conversions in Thin-Film Heads by Electron Microscopy—*K. Kobayashi* 3933
The Thin Film Head for VCR—*T. Suzuki, I. Abe, T. Mizuguchi, O. Morita, and H. Takino* 3936
Off-Track Characteristics of Laminated Heads in Azimuth Recording—*M. Ura, H. Kobayashi, S. Horibata, K. Sato, and H. Shibata* 3939

Thin Film Magnetic Recording Media

Effect of Cobalt Oxide Addition on Co-Pt Media—*R. Ranjan, M. Lu, T. Yamashita, and T. Chen* 3942
Exchange Anisotropy in Metal-Evaporated Tapes—*G. Bottoni, D. Candolfo, and A. Checchetti* 3945
Interdiffusion and Grain Isolation in Co/Cr Thin Films—*Y. Feng and D. Faughlin, and D. Lambeth* 3948
NiAl Underlayers for CoCrTa Magnetic Thin Films—*L-L. Lee, D. Laughlin, and D. Lambeth* 3951
Effect of Very Thin Cr-Underlayer on the Magnetic and Recording Properties of CoCrTa Thin-Film Media—*B. Lal, M. Tobise, and T. Shinohara* 3954
Advanced Multilayer Thin Films for Ultra-High Density Magnetic Recording Media—*P. Glijer, J. Sivertsen, and J. Judy* 3957
Magnetic Properties and Crystallography of Double-Layer CoCrTa Thin Films with Various Interlayers—*Y. Feng, D. Laughlin, and D. Lambeth* 3960
High Coercivity and Low Noise Media Using Glass Substrate—*X. Tang, B. Reed, R. Zubeck, D. Hollars, and K. Goodson* 3963
A Study of Magnetic Recording Media on Glass Substrates—*S. Duan, B. Zhang, C. Gao, G. Rauch, J. Pressesky, and A. Schwartz* 3966
Relation between Microstructure of Grain Boundary and the Intergranular Exchange in CoCrTa Thin Film for Longitudinal Recording Media—*J. Nakai, E. Kusumoto, M. Kuwabara, T. Miyamoto, M. Visokay, K. Yoshikawa, and K. Itayama* 3969
The Dependence of Compositional Separation on Film Thickness for Co-Cr and Co-Cr-Ta Magnetic Recording Media—*D. Rogers, Y. Maeda, and K. Takei* 3972
Magnetic and Recording Characteristics of Bicrystalline Longitudinal Recording Medium Formed on an MgO Single Crystal Disk Substrate—*M. Futamoto, M. Suzuki, N. Inaba, A. Nakamura, and Y. Honda* 3975
Microstructure and Recording Properties of Bicrystal Disks with GaAs Substrates—*J. Ding and J-G. Zhu* 3978
Coercivity-Gradient Bi-Layered Thin-Film Media for Longitudinal Recording—*B. Lal and T. Shinohara* 3981
Effects of Highly Permeable Keeper Layer on Transition Shifts for Thin Film Media—*G. Mian, P-K. Wang, W. Reed, R. Zubeck, and D. Hollars* 3984
Transition Noise Spectral Measurements in Thin Film Media—*G. Lin and H. Bertram* 3987
The Relationship of Medium Noise to System Error Rate in a PRML Channel—*J. Fitzpatrick, H. Bertram, X. Che, L. Barbosa, and G. Lin* 3990
Texture-Induced Modulation Noise and Its Impact on Magnetic Performance—*E. Wu, J. Peske, and D. Palmer* 3996
Experimental and Micromagnetic Study of Track Edge Noise Reduction Effect in Mutilayer Thin Film Media—*X-G. Ye, T. Lam, and J-G. Zhu* 3999
Interaction Fields and Media Noise in CoPtCr Thin Films—*P. Huang, J. Harrell, M. Parker, and K. Johnson* 4002
Soft Error Rate Dependence on MrT for Thin Film Media—*O. Allegranza and M. Yang* 4005
Effect of Ta on the Structure, Magnetic Properties, and Recording Performance of CoCrTaPt/Cr Thin Film Media—*K. Sin, J. Sivertsen, and J. Judy* 4008
Magnetic Properties and Recording Performance of Multilayer Films of CoCrTa, Co CrPtTa, and CoCrPtTa with CoCrPtB—*L. Song, R. Gardner, S. McLaurin, and M. Sedighi* 4011
Pd/Co Multilayers for Perpendicular Magnetic Recording—*B. Liarson, J. Perez and C. Baldwin* 4014
Polarization-Dependent EXAFS Studies of Chemical and Structural Anisotropy in Sputter-Deposited $Co_{78}Cr_{22}$ Films—*K. Kemner, V. Harris, W. Elam, and J. Lodder* 4017
Soft Magnetic and Crystallographic Properties of $Ni_{81}Fe_{19}/Co_{67}Cr_{33}$ Multilayers as Backlayers in Perpendicular Recording Media—*S. Nakagawa, T. Ichihara, and M. Naoe* 4020
High Coercivity in Co-Cr Films for Perpendicular Recording Perpared by Low Temperature Sputter-Deposition—*N. Honda, J. Ariake, K. Ouchi, and S. Iwasaki* 4023
Oxygen Effect on the Microstructure and Magnetic Properties of Binary CoPt Thin Films for Perpendicular Recording—*T. Hikosaka, T. Komai, and Y. Tanaka* 4026
Micromagnetic Domain Observations of Co-Cr Films by Neutron Scattering—*K. Takei, J. Suzuki, Y. Maeda, and Y. Morii* 4029
High Coercivity FeSmN Thin Films for Longitudinal Magnetic Recording Media—*D. Wang and W. Doyle* 4032
Nanostructures of Sm-Co on Cr Thin Films—*Y. Liu, B. Robertson, Z. Shan, S. Malhotra, M. Yu, S. Renukunta, S. Liou, and D. Sellmyer* 4035

Magnetic Properties and Microstructure of Sputtered CoSm/X(X = Ti,V,Cu and Cr) Thin Films—*Y. Okumura, H. Fujimori, O. Suzuki, N. Hosoya, X. Yang, and H. Morita* 4038
Magnetic Properties of $(Co_{93}Cr_7)$-P-Pt/Cr Thin Films for Longitudinal Magnetic Recording Media—*H. Sohn, S. Seol, T. Kang, K. Shin, T. Lee, and P. Jang* 4041
Effects of CoTi-Doping on Longitudinal Barium Ferrite Thin Film Media—*X. Sui and M. Kryder* 4044
Longitudinal Recording Performance of Sputtered Barium Ferrite Media on a Carbon Rigid Disk Substrate—*S. Rosenblum, H. Hayashi, J. Li, and R. Sinclair* 4047
Temperature and Orientation Effects on the Magnetic Properties of Doped Barium Ferrite Thin Films—*J. Li, R. Sinclair, S. Rosenblum, and H. Hayashi* 4050
Ba Ferrite Thin Films with Large Statuation Magnetization Deposited by Sputtering in Mixture of Xe, Ar, and O_2—*N. Matsushita, K. Noma, and M. Naoe* 4053
Fabrication and Magnetic Studies of (Co,Zn)-Doped γ-Fe_2O_3 Thin Films—*P. Kuo, Y. Yao, J. Chen, C. Lin, Y. Lo, and J. Huang* 4056

Particulate Magnetic Recording Media

An Investigation of the Archivability of Metal Particle Tape—*P. Sides, G. Spratt, and P. Kampf* 4059
Degradation of Passivated Iron Particles in Humid Atmospheres—*C-S. Jung, G. Bond, S. Raghavan, and R. Emrick* 4065
Protection of Fe Pigments with Amine-Quinone Polymers—*D. Nikles, J. Cain, A. Chacko, and R. Webb* 4068
Dispersion Quality of Magnetic Tapes Prepared from a Waterborne Formulation—*S. Cheng, H. Fan, J. Harrell Jr., A. Lane, and D. Nikles* 4071
Thermal Effects in Small Metallic Particles—*R. Veitch, H. Richter, P. Poganiuch, H. Jakusch, and E. Schwab* 4074
Influence of the Doping on the Time-Dependent Magnetic Behaviour of Fine Particles—*G. Bottoni, D. Candolfo, and A. Cecchetti* 4077
Switching Field Characteristics of Individual Iron Particles by MFM—*Y. Luo and J-G. Zhu* 4080
FMR Spectra of Oriented γ-Fe_2O_3, Co-γ-Fe_2O_3, CrO_2 and MP Tapes—*Y. Yu and J. Harrell* 4083
High Speed Coherent Switching Below the Stoner-Wohlfarth Limit—*L. He, W. Doyle and H. Fujiwara* 4086
Magnetization Reversal in Magnetic Tapes with Sequential Field Pulses—*P. Flanders, W. Doyle, and L. Varga* 4089
Hexaferrite Particles Prepared by Sol-Gel Technique—*C. Surig, K. Hempel, and D. Bonnenberg* 4092
Mean Field Interaction and Transverse Susceptibility—*C-R. Chang and J-S. Yang* 4095
Magnetic Thermal Stability of Mn and Co Volume-Doped Acicular Iron Oxide Particles—*D. Han, J. Wang, Y. Feng, H. Luo, and J. Na* 4098
Transverse Susceptibility and Remanence Characteristics of Barium Ferrite Hand Spread Coatings as a Function of Milling Time—*P. Sollis, P. Bissell, and R. Chantrell* 4101
Preparation and Magnetic Properties of (Co,Zn)-Doped γ-Fe_2O_3 Particles—*C. Lin, P. Kuo, J. Chen, and Y. Yao* 4104
Magnetic Properties of Composite Ba-Ferrite Particles Containing α-Fe—*S. Kitahata and M. Kishimoto* 4107
(Ni,Ti), (Ni,Sn) and (Zn,Ti) Substituted Barium Ferrite Particles Prepared by a Flux Method with δ-FeOOH as a Precursor—*T. Chin, M. Deng, S. Hsu, and C. Lin* 4110

Head/Disk Interface for Magnetic Recording

Tribological Behavior of Thin Film Rigid Disks with Regular Dot Array Texture on Carbon Overcoats—*H. Tanaka, F. Ishikawa, K. Gomi, N. Yamaguchi, and Y. Miyake* 4113
Isotropic Thin Film Texture for Alternative Substrates—*T. Kogure, Y. Matsuno, T. Itoh, and C. Shima* 4116
Sputter-Induced Random Micro Texturing on NiP Plated Aluminum and Alternate Substrates—*E. Teng, P. Nguyen, and A. Eltoukhy* 4119
Numerical Simulation of the Steady State Flying Characteristics of a 50% Slider with Surface Texture—*M. Wahl and F. Talke* 4122
Tribological and Recording Performance of Carbon-Coated Thin Film Head Sliders on Unlubricated and Lubricated Thin Film Media—*G. Wang, T-A. Yeh, J. Sivertsen, J. Judy and G-L. Chen* 4125
Slider/Disk Separation at Rest—*H-L. Leon and S. Chapman* 4128

The Development and Implementation of a Flying Height Tester Calibration Standard—*Y. Li, A. Menon, and P. Goglia* 4131
Performance of Hard DLC Protective Film Prepared by PECVD Method for Thin Film Magnetic Disk—*K. Iechika, Y. Kokaku, M. Ootake, K. Abe, K. Tani, and H. Inaba* 4134
The Role of Disk Carbon and Slider on Water Adsorption—*M. Smallen, J. Lee, A. Chao, and J. Enguero* 4137
Lubricant Bonding Via Hydrogen Bond Network—*K. Sano, H. Murayama, and F. Yokoyama* 4140
Environmental Effects on Phosphazene Lubricated Computer Hard Disks—*M. Yang, F. Talke, D. Pereitie, T. Morgan, and K. Kar* 4143
Vapor Lubrication of Thin Film Disks—*K. Coffey, V. Raman, N. Staud, and D. Pocker* 4146
Single-Pass Flaw Detector for Magnetic Media—*W. Huber* 4149
Mechanically-Induced Readback Errors in Contact Recording—*J. Spong, M. Dovek, and G. Vurens* 4152
A Study of the Head Disk Interface Shock Failure Mechanism—*S. Kumar, V. Khanna, and M. Sri-Jayantha* 4155
Design and Performance of Novel Air Bearing Slider—*M. Matsumoto, Y. Takeuchi, H. Agari, and H. Takahashi* 4158
Vibro-Loading of Magnetic Head Assembly for Hard Disk Drives—*K. Aruga, S. Yoneoka, and T. Ohwe* 4161
Non-Invasive Take-Off/Touch-Down Velocity Measurements—*K. Klaassen, J. Van Peppen, and R. Eaton* 4164
Measurement of Flying Height on Carbon Overcoated Sliders—*K. Lue, C. Lacey, and F. Talke* 4167
Slider Vibrations Induced by Ramp-Suspension Interaction During the Ramp Loading Process—*T-C. Fu and D. Bogy* 4170
Ultra Low Flying Height Measurements Using Monochromatic and Phase Demodulated Laser Interferometry—*T. McMillan and F. Talke* 4173
Friction and Wear of Particulate and ME Magnetic Tapes Sliding Against a Mn-Zn Ferrite Head in a Linear Mode—*B. Bhushan and J. Lowry* 4176
Measurement of Head Wear Rates Using Custom High Sensitivity Electrical Elements—*R. Dee, K. Franzel, J. Cates, and R. Crowell* 4179
Running Characteristics of MIG Heads Against MP, Barium Ferrite and ME Tapes—*T. Tsuchiya and B. Bhushan* 4182
Deformation of Laminated Tapes—*R. Sundaram* 4185
Biquadratic Surface Fits for Two-Dimensional Interferometric Head/Tape Spacing—*E. Baugh and F. Talke* 4188
Drive-Level Flying Height Meaurements and Altitude Effects—*Y. Deng, H-C. Tsai, and B. Nixon* 4191

Magnetic Recording Systems and Coding

Space Data Storage Systems and Technologies—*R. Katti* 4194
The Effects of MR Induced Non-Linearities on Channel Performance—*K. Chopra, L. Nix, and K. Taberski* 4200
Effects of MR Head Track Profile Characteristics on Servo Performance—*D. Cahalan and K. Chopra* 4203
A New MR Head Track Following Method for Submicron Track Servo on Rigid Disks—*B. Tan, G. Pan, D. Mapps* 4206
Characterization of Magnetizing Process for Pre-Embossed Servo Pattern of Plastic Hard Disks—*S. Tanaka, Y. Imai, O. Morita, D. Dericotte, K. Kurokawa, T. Kashiwagi, and H. Takino* 4209
Two-Dimensional Coding for a Multi-Track, Maximum-Likehood Digital Magnetic Storage System—*P. Davey, T. Donnelly, and D. Mapps* 4212
Spectral Properties of (d,k) Codes with Multiple Spacing—*C. Menyennett and H. Ferreira* 4215
A System Architecture for Multi-Level Decision Feedback Equalization—*J. Kenney* 4218
Improved Equalization for Digital Recording Using Nonlinear Filtering and Error Confinement—*S. Nair and J. Moon* 4221
Adaptive Time Optimal Control of a Disk Drive Actuator—*S. Weerasooriya, T. Low, and Y. Huang* 4224
A High-Performance and Low-Profile Moving-Magnet Actuator for Disk Drives—*T. Yamada, S. Koganezawa, K. Aruga, and Y. Mizoshita* 4227

Magnetic Recording Modeling and Phenomena

Thermal Instability at 10 Gbit/in^2 Magnetic Recording—*P-L. Lu and S. Charap* 4230
A Practical Nonlinear Model for Magnetic Recording Channels—*W. Zeng and J. Moon* 4233

A Generalized Frequency Domain Nonlinearity Measurement Method—*X. Che, M. Peek and J. Fitzpatrick* 4236
A Time-Correlation Method of Calculating Nonlinearities Utilizing Pseudorandom Sequences—*X. Che and P. Ziperovich* 4239
Magnetic Force Microscopy Study of Edge Overwrite Characteristics in Thin Film Media—*J-G. Zhu, Y. Luo, and J. Ding* 4242
Experimental Study of Track Edge Noise Distribution in Narrow Track Recording—*T. Lam, J-G. Zhu, and T. Arnoldussen* 4245
Comparison of Magnetic Fields on Thin-Film Heads and Their Corresponding Bit Patterns Using Magnetic Force Microscopy—*P. Rice, B. Hallet, and J. Moreland* 4248
Determination for the Narrow Read Width of Thin Film Magnetic Recording Head Using Error Rate Model—*M. Huang, R. Chu, Y. Hsia, and T. Tran* 4251
Edge Effects in Narrow Track Recording Using Symmetric and Asymmetric Write Pole Geometries—*E. Wu and J. Peske* 4254
Modeling and Measurement of Hard-Magnet Biasing Strengths of MR-SAL Structures—*S. Yuan, S. Liao, and T. Kobayashi* 4257
Moving Vector Preisach Hysteresis Model and δ_M Curves—*F. Ossart, R. Davidson, and S. Charap* 4260
Angular Dependence of Magnetization in Recording Media—*T. Templeton, A. Arrott, and Y. Yoshida* 4263
Physically Based Information Science of Magnetic Recording II. Physical Sources of Medium Noise—*D. Porter, J. O'Sullivan, R. Indeck, and M. Muller* 4266
A Model for Threshold and Timing Error Rate Versus Off-Track Position—*J. Alexander* 4269
Relationship between Overwrite and Transition Shift in Perpendicular Magnetic Recording—*H. Muraoka, S. Ohki, and Y. Nakamura* 4272
Modeling Study of Isolated Read-Back Pulses from Keepered Longitudinal Thin Film Media Using the Boundary Element Method—*J. Loven, Y. Guo, K. Sin, J. Judy, and J-G. Zhu* 4275
Calculation of Head Sensitivity Function from 3-D Magnetic Fields—*E. Burke, R. Gomez, R. Madabhushi, and D. Mayergoyz* 4278
Gauge Testing of Transition Jitter Measurements for Longitudinal Thin Film Magnetic Recording—*M. Huang, R. Chu, Y-T. Hsia, and T. Tran* 4281

Computational Magnetics

Fast Actuator Modeling by Finite Element Method—*K. Takeuchi, M. Shimizu, K. Okazaki, T. Nakata, N. Takahashi, and K. Fujiwara* 4284
Design Techniques for Reduction of Reluctance Torque in Brushless Permanent Magnet Motors—*S. Hwang and D. Lieu* 4287
Modeling of the Influence of Coil Winding Pattern on Tooth Forces in Brushless DC Motors—*G. Jang and D. Lieu* 4290
Modelling and Computation of Nonlinear Magnetic Fields in Linear Step Motors by Finite Element Method—*S. Khan and A. Ivanov* 4293
Utilizing Genetic Algorithms for the Optimal Design of Electromagnetic Devices—*G. Uler, O. Mohammed, and C-S. Koh* 4296
Eddy Current Losses in Saturable Magnetic Materials—*V. Machado* 4299
Perturbed H-Method Without the Lagrange Multiplier for Three-Dimensional Nonlinear Magnetostatic Problems—*I. Saitoh* 4302
Bifurcation Diagram and Large Energy Dissipation Caused by Chaotic Domain-Wall Motion—*H. Okuno, Y. Sugitani and T. Homma* 4305
Hysteresis Modeling of Recording Media with an Interacting Stoner-Wohlfarth Particles System—*A. Stancu and C. Papusoi* 4308
Optimizing Strategy for MR Imaging Gradient Coils—*K. Adamiak, A. Czaja, and B. Rutt* 4311
Electromagnetic Field Analysis in Rotational Electric Machines Using Finite Element-Analytical Hybrid Method—*B. Chao, S. Chen, Z. Liu, and T. Low* 4314
Modeling and Torque Analysis of Permanent Magnet Spindle Motors for Disk Drive Systems—*Z. Liu, C. Bi, C. Tan and T-S. Low* 4317
Genetic Algorithms for Nondestructive Testing in Crack Identification—*A. Arkadan, T. Sareen, and S. Subramaniam* 4320
Analysis of Axial-Field Actuators—*E. Furlani and M. O'Brien* 4323
Modelling the Effects of Eddy Current Losses on Frequency Dependent Hysteresis in Electrically Conducting Media—*D. Jiles* 4326

The Finite Element Solutions of Moving Conductor Eddy Current Problems Based on Triangular Elements—*Z. Wang, G. Dawson, T. Eastham, and Z. Liu* 4329
An Improved Technique for Nonlinear Magnetic Problems—*M. Chiampi, M. Repetto, and D. Chiarabaglio* 4332
Asymptotic Boundary Conditions for Axisymmetric Finite Element Electrostatic Analysis—*Q. Chen, A. Konrad, and S. Baronijan* 4335
Enclosure Losses in High Power Systems—*P. Ryff, T. Fawzi, and A. Hussein* 4338
Two Dimensional Magnetization Model for Anisotropic Soft Magnetic Sheets—*T. Waeckerle and M. Mekhiche* 4341
Domain Walls Interactions with Attractive and Repulsive Defects in the Garnet Films—*V. Karpasyuk and M. Bulatov* 4344
Experimental Analysis of Reversible Processes in Soft Magnetic Materials—*V. Basso, M. Bue, and G. Bertotti* 4347
An Adaptive Mesh Numerical Algorithm for the Solution of 2D Néel Type Walls—*J. Miltat and M. Labrune* 4350
Simulation of Vertical Bloch Lines Non-Reciprocal Dynamics—*V. Dobrovitski, A. Logginov, and A. Nikolaev* 4353
Analytical Expressions for Barkhausen Jump Size Distributions—*F. Hunt and R. McMichael* 4356
Magnetization Reversal Processes Reuled by Grain Interactions: Analysis of Their Dependence on the Direction of the Demagnetizing Field—*J. Gonzalez, R. Ramirez, R. Rueda, L. Dominguez, and J. Gonzalez* 4359
A Model for Lorentz Microscopy and Magnetic Behaviour of Longitudinal Thin Film with an Irregular Lattice—*N. Walmsley, C. Dean, A. Hart, D. Parker and R. Chantrell* 4362
A Fast, Smooth Vector Hysteresis Model with Adjustable Interactions—*T. Hoffend Jr. and M. Vos* 4365
The Input Dependent Preisach Model with Stochastic Input as a Model for Aftereffect—*C. Korman and I. Mayergoyz* 4368
Identification of Parameters in an Accommodation Model—*F. Vajda and E. Della Torre* 4371
Parameter Identification of the Complete-Moving-Hysteresis Model for HTS Steel—*G. Kahler, E. Della Torre, and F. Vajda* 4374
Magneto-Dynamic Field Computation Using a Rate-Dependent Preisach Model—*D. Philips, L. Dupre, and J. Melkebeek* 4377
Computational Hysteresis in Modeling Magnetic Systems—*D. Kinderlehrer and L. Ma* 4380
Numerical Implementation and Testing of New Vector Isotropic Preisach-Type Models—*A. Adly* 4383
Algorithm for Fast Implementation of Vector-Type Preisach Hysteresis Models—*G. Friedman and D. Ahya* 4386
Effect of Damping on Dynamic Distortion in Magnetic Garnet Material—*A. Bagneres, M. Redijal, and F. Humphrey* 4389

Magneto Optic Recording, Media, and Materials

Thermomagnetic Recording Behavior in the NdTbDyFeCo/DyFeCo-Ultrathin Bilayer—*T. Kawase, M. Ishida, S. Hoshina, A. Takakuwa, S. Nebashi, and T. Shimoda* 4392
Ar-Sputtered Pt/Co Multilayers with Large Anisotropy Energy and Coercivity—*P. Carcia, M. Reilly, Z. Li, and H. Van Kesteren* 4395
Nanostructure and Chemical Inhomogeneity in TbFe Magneto-Optical Films—*M. Kim, J. Bow, R. Carpenter, J. Liu, S. Kim, S. Lee, W. Kim, and J. Yoon* 4398
Domain Wall Mobility Meaurements in Magneto-Optic Media—*M. Du and M. Kryder* 4401
Effect of Grooves on Magnetization Reversal in Amorphous TbFeCo Thin Films—*S. Gadetsky, T. Suzuki, J. Erwin, and M. Mansuripur* 4404
Magnetic and Magneto-Optical Properties of Tb-Fe-Co/Ta Multilayers—*K-B. Song, H. Ito, and M. Naoe* 4407
Magneto-Optic Read Channel Modeling in Presence of Bloom—*I. Ozgunes and B. Kumar* 4410
Optimum Design of Optical Storage Media for Drive Compatibility—*T. McDaniel, K. Rubin, and B. Finkelstein* 4413
Deposition of Garnet Thin Films by Metallo-Organic Decomposition (MOD)—*A. Azevedo, S. Barthulwar, W. Eppler and M. Kryder* 4416
Faraday Rotation of Bismuth Substituted Terbium Iron Garnets—*M. Guillot, H. Gall, J. Desvignes, and M. Artinian* 4419

Composition Dependence of the Magnetooptical Properties of HoIG:Al Single Crystals—*J. Ostorero and M. Guillot* 4422
Microstructure of Re-Tm Films and Anisotropy of Domain Wall Motion—*T. Pokhil and E. Nikolaev* 4425
Thermal Stability of Sputtered GdDYFeCo Films with Trilayer Structure—*Y. Uchihara, K. Tanase, Y. Suzuki and K. Torazawa* 4428
Low Temperature Crystal Growth of MnBi Films—*M. Nakada and M. Okada* 4431
Exchange Stiffness Constant and Effective Gyromagnetic Factor of Gd, Tb and Nd Containing, Amorphous Rare Earth-Transition Metal Films—*C. Mathieu, B. Hillebrands, and D. Raasch* 4434
Optical Property Influence on Magneto-Optics of CoNi and TbCo Multilayers on Noble Metal Alloy Substrates—*J. Hilfiker, Y. Zhang, and J. Woollam* 4437
Anisotropy and Magneto-Optical Properties of Sputtered Co/Ni Multilayer Thin Films—*Y. Zhang, J. Woollam, S. Shan, J. Shen, and D. Sellmyer* 4440
Coexistence of Antiferromagnetic and Ferromagnetic Clusters in Ccmpositionally Modulated Amorphous Fe_xZr_{100-x}($66 < x \leq 85$) Thin Films—*B-I. Cho, W. Win, A. Manthiram, and R. Walser* 4443
Preparation of Bi-YIG Particles for Display Device—*N. Kawai, E. Komuro, T. Namikawa, Y. Yamazaki, and T. Hirano* 4446
Giant Magnetic Kerr Rotation for MnSbPt Films with NiAs Structure—*M. Takahashi, H. Shoji, Y. Hozumi, T. Wakiyama, Y. Takeda and Y. Itakura* 4449
Magnetic and Magneto-Optical Properties of (Co-Bi)/Pt and Co/(Pt-Bi) Multilayers—*T. Suzuki, S. Iwata, H. Brandle and D. Weller* 4455
First Principles Study of Magneto-Optical Properties of Half-Metallic Heusler Alloys: NiMnSb and PtMnSb—*X. Wang, V. Antropov, and B. Harmon* 4458
Magneto-Optic Properties of Macroscopic Ferrimagnets—*R. Gambino and P. Fumagalli* 4461
Novel Bulk Iron Garnets for Magneto-Optic Magnetic Field Sensing—*M. Deeter, S. Bon, G. Day, G. Diercks, and S. Samuelson* 4464

Symposium on Magnetic Microscopy

High Resolution Magnetic Force Microscopy of Domain Wall Fine Structures—*R. Proksch, S. Foss, and E. Dahlberg* 4467
A Magnetic Force Microscopy Analysis of Soft Thin Film Elements—*W. Rave, L. Belliard, M. Labrune, A. Thiaville, and J. Milat* 4473
Coherent Magnetic Imaging by TEM—*J. Chapman, A. Johnston, L. Heyderman, S. McVitite, and W. Nicholson* 4479

Magnetic Microscopy and Imaging

An Ultra-High Resolution Single-Domain Magnetic Force Microscope Tip Fabricated Using Nanolithography—*S. Chou, M. Wei, and P. Fischer* 4485
Analysis of 3-D Magnetic Fields Measured Using a Magnetic Force Scanning Tunneling Microscope—*E. Burke, R. Gomez, and I. Mayergoyz* 4488
Magneto-Optical Faraday Effect Probed in a Scanning Tunneling Microscope—*M. Prins, M. Van Der Wielen, D. Abraham, H. Van Kempen, and H. Van Kesteren* 4491
Methods for Wide-Field Kerr Imaging of Small Magnetic Devices—*P. Trouilloud, B. Petek, and B. Argyle* 4494
Absolute Magnetometry of Thin Cobalt Films and Co/Cu Multilayer Structures at Nanometer Spatial Resolution—*M. Mankos, Z. Yang, M. Scheinfein, and J. Cowley* 4497
A New Surface Microscope for Magnetic Imaging—*K. Grzelakowski, T. Duben, E. Bauer, H. Poppa, and S. Chiang* 4500
Optimization of Thin Film Tips for Magnetic Force Microscopy—*K. Babcock, V. Elings, M. Dugas, and S. Loper* 4503
Surface Structure of Fe_3O_4 (110) Studied by Scanning Tunneling Microscopy—*R. Jansen, B. Nelissen, D. Abraham, H. Van Kempen, and V. Brabers* 4506
Imaging Surface Conditions of Ferromagnetic Steel Using Barkhausen Technique—*M. Negley and D. Jiles* 4509

Microwave and Millimeter Devices

Oriented Barium Hexaferrite Thick Films Grown on C-Plane and M-Plane Sapphire Substrates—*P. Dorsey, D. Chrisey, J. Horwitz, P. Lubitz and R. Auyeung* 4512

Ferrite-Superconductor Microwave Phase Shifters—*G. Dionne, D. Oates, and D. Temme* 4518
Characteristics of the Quasi-Optical Reflection Circulator—*N. Harris, G. Dionne, J. Weiss and B. Lax* 4521
Novel Design of Tunable MMW Magnetic Filter—*H. How, T-M. Fang and C. Vittoria* 4524
Polycrystalline $Y_3Fe_5O_{12}$ Garnet Films Grown by a Pulsed Laser Ablation Technique—*C. Yang, S. Kim and Y. Kim* 4527
Low Energy Ion Bombardment and Surface Spin Pinning in Yttrium Iron Garnet Films—*A. Chernakova and D. Stancil* 4530
High Impedance Anisotropic Composite Manufactured from Ferromagnetic Thin Films for Microwave Applications—*O. Archer, P. Jacquart, J. Fontaine, P. Baclet, and G. Perrin* 4533
Comparison of the Auxiliary Vector Function and Adjoint Methods in Solving Anisotropic Media Electromagnetic Problems—*C. Krowne* 4536
Effects of Annealing on the Microwave Properties of Spin-Spray Ni-Zn Ferrites—*P. Lubitz, S. Lawrence, F. Rachford, and B. Rappoli* 4539
Investigation of High Frequency Permeability of Thin Amorphous Wires—*O. Acher, P. Jacquart, and C. Boscher* 4542
Microwave Polymer-Ferroxide Film Absorbers—*I. Nedkov, L. Milenova, and N. Dishovsky* 4545
Drop-On Circulator Design at X and Ka Bands—*H. How, T-M. Fang, and C. Vittoria* 4548
Magnetic Steerable Ferrite Patch Antenna Array—*H. How, T-M. Fang, D-X. Guan and C. Vittoria* 4551
Microwave Absorbing Properties of Sintered Ni-Zn Ferrite—*S-S. Kim, D-H. Han, and S-B. Cho* 4554

Instrumentation and Measurement Techniques

Current Distribution in Spin-Valve Structures—*R. Beech, J. Daughton and W. Kude* 4557
Improved Eddy-Current Decay Method for Resistivity Characterization—*A. Kos and F. Fickett* 4560
Magnetostriction Measurements with a Laser Doppler Velocimeter—*T. Nakata, N. Takahashi, M. Nakano, K. Muramatsu and M. Miyake* 4563
DC Biased Capacitance Method for Measuring Thin Film Magnetostriction and ΔE-Effect—*Y. Lee, Y. Shin, P. Herr, K. Lee, H. Kim, S. Han, I. Kang and J. Rhee* 4566
Design of a Digitally Based ΔE Measurement System—*S. Hogsdon, P. Squire, and D. Atkinson* 4569
Measurement of Magnetostriction in Self-Biased Shielded Magnetoresistive Heads—*J. Cates, R. Crowell, and R. Dee* 4572
Flexible Test System for Measurement of Magnetoresistance in Ferrromagnetic Films—*K. Franzel and R. Dee* 4575
Magneto-Optical High Resolution Measurement of Small Displacements between Light Beams of Different Color—*J. Hochreiter, F. Haberl, H. Hauser, and M. Gaugitsch* 4578
Magnetic Inclination Meaurement and Signal Transmission System for Trench Wall Constructions—*K. Vorlicek, H. Hauser, and M. Franz* 4581
Calculations of the Sensitivity Function of a Mis-Aligned Thin Film in a Mallinson Coil Set—*S-W. Hsu* 4584
Pitfalls in the Determination of Magnetic Permeability—*J. Bernards, A. Kuiper, H. De Wit and E. Van De Reit* 4587
Influence of DC Bias Field, Excitation and Detection Frequencies on Magnetic Barkhausen Noise Analysis—*L. Sipahi* 4590
Variation of Coercivity of Ferromagnetic Material During Cyclic Stressing—*Z. Gao, Z. Chen, D. Jiles, and S. Biner* 4593
Assessment of Creep Damage of Ferromagnetic Material Using Magnetic Inspection—*Z. Chen, M. Govindaraju, D. Jiles, S. Biner, and M. Sablik* 4596
Induction Motor Iron Losses Meaurement with Static Converter Supply Using a Slotless Rotor Test Bench—*A. Boglietti, P. Ferraris and M. Lazzari* 4599
Permanent Magnet Variable Flux Sources—*O. Cugat, P. Hansson, and J. Coey* 4602
10 GHz Cylindrical Cavity Resonator for Characterization of Surface Resistance of High T_c Superconducting Bulk and Thin Films—*M. Kumar, G. Srivastava, and N. Kataria* 4605

Magnetic Sensors

Magnetic Field Sensors Using GMR Multilayer—*J. Daughton, J. Brown, E. Chen, R. Beech, A. Pohm, and W. Kude* 4608
Thin-Film Magnetic Sensor Using High Frequency Magneto-Impedance (HFMI) Effect—*M. Senda, O. Ishii, Y. Koshimoto, and T. Toshima* 4611

New Method for Extracting Signals Generated by Magnetoresistive Sensors—*B-Z. Kaplan and E. Paperno* 4614
Integrated MR Sensors for Automobile—*O. Akiyama, H. Konna, D. Inami, and Y. Kuraishi* 4617
Thin-Film and Micro-Fiber Permalloy Magnetoresistors. A Comparison—*P. Ciureanu, P. Rudkowski, J. Ström-Olsen, and A. Yelon* 4620
Quick Response Large Current Sensor Using Amorphous MI Element Resonant Multivibrator—*K. Inada, K. Mohri, and K. Inuzuka* 4623
Sensitive Magneto-Inductive Effect in Amorphous Wires Using High Pass Filter and Micro Field Sensor—*K. Bushida and K. Mohri* 4626
A Torque Transducer Utilizing Two Oppositely Polarized Rings—*I. Garshelis and C. Conto* 4629
In-Process Detection of Torque on a Drill Using Magnetostrictive Effect—*I. Sasada, N. Suzuki, T. Sasaoka, and K. Toda* 4632
Construction of Electromagnetic Rotation Sensor Using Compound Magnetic Wire and Measurement at Extremely Low Frequency Rotations—*S. Abe and A. Matsushita* 4635
Modulation Effect in the Magnetic Shield with Magnetic Shaking—*I. Sasada* 4638
A New Microstrip Pickup Coil for Thin-Film Permeance Meters—*I. Kawazu, M. Yamaguchi, and K. Arai* 4641
Study of the New Eddy Current Non-Destructive Testing Sensor on Ferrromagnetic Materials—*S. Nath, B. Wincheski, J. Fulton, and M. Namkung* 4644
Silicon Micromachined Two-Dimensional Galvano Optical Scanner—*N. Asada, H. Matsuki, K. Minami and M. Esashi* 4647

Alternative Memories, Magnetic Separation and Fluids

Analysis of 0.1 to 0.3 Micron Wide, Ultra Dense GMR Memory Elements—*A. Polm, R. Beech, P. Bade, E. Chen, and J. Daughton* 4650
Magnetic Cage Filters—*R. Gerber and P. Lawson* 4653
The Small Particle Limit for Electromagnetic Separation—*D. Fletcher and R. Gerber* 4656
The Electromagnetic Separation of Metals from Insulators—*D. Fletcher, R. Gerber, and T. Moore* 4659
Vortex Magnetic Separation(VMS)—*Z. Li and J. Watson* 4662
The Development of a Magnetic Hydrocyclone for Processing Finely Ground Magnetite—*R. Freeman, N. Rowson, T. Veasey, and I. Harris* 4665
Selective Collection of Non-Magnetic Rutile and Quartz by Means of a Magnetic Reagent by HGMS—*Q. Liu and F. Friedlaender* 4668
Initial Susceptibilities of Magnetic Fluids Dispersing Mn-Zn Ferrite and Cobalt Ferrite Particles—*K. Nakatsuka and B. Jeyadevan* 4671
Experimental Observations of the Magnetic Flux Control Characteristics of Magnetic Fluid by Means of an Orthogonal Magnetic Field—*H. Oka* 4674
Use of Magnetic Fluid in a Current to Pressure Transducer—*R. Potter* 4677
Finite Element Calculation of Forces on a DC Magnet Moving Over an Iron Rail—*D. Rodger, N. Allen, P. Coles, S. Street, P. Leonard, and J. Eastham* 4680
Magnetic Design of a Cathodic Arc and Sputtering Polyvalent Source for Vapour Deposition—*N. Heras, A. Torrado, J. Barandiaran and J. Goikoetxea* 4683
Modification of the Nozzle Flow Using Electromagnetic Induction—*L. Kadar, P. Biringer and J. Lavers* 4686

Biomagnetism and Magnetochemistry

Conduction System Ablation Using Ferrite Rod for Cardiac Arrythmia—*T. Hoshino, T. Sato, A. Masai, K. Sato, H. Matsuki, K. Seki, H. Sato, K. Kishiro, S. Urabe and K. Kido* 4689
Ferrite Plating on Porous Silica Microspheres for Ultrasonic Contrast Agents—*M. Zhang, Q. Zhang, T. Itoh, and M. Abe* 4692
Diamagnetic Properties of Fibrin and Fibrinogen—*M. Iwasaka, S. Ueno, and H. Tsuda* 4695
Parting of Water by Magnetic Fields—*S. Ueno and M. Iwasaka* 4698
Enzymatic Activity of Plasmin in Strong Magnetic Fields—*M. Iwasaka, S. Ueno, and H. Tsuda* 4701
Hybrid MCG and ECG Approach to Medical Diagnosis in Human Heart—*T. Doi, S. Hayano, and Y. Saito* 4704
Metal Uptake and Separation Using Magnetotactic Bacteria—*A. Bahaj, P. James and I. Croudace* 4707

Measurement of Auditory Evoked Brain Responses Elicited by Ipsilateral and Contralateral Ear Stimulation with a High-Sensitivity SQUID System—*T. Yoshiura, S. Ueno, K. Iramina, and K. Masuda* 4710
Magnetic Orientation of Red Blood Cell Membranes—*T. Suda and S. Ueno* 4713
Source Localization of Auditory Evoked Magnetic Fields During Waking and Sleep Stages—*K. Iramina and S. Ueno* 4716
Long Latency Motor Evoked Responses to Magnetic Stimulation of the Spinal Roots in the Human Neck—*A. Kyura, A. Hyodo, S. Ueno, M. Fujiki and T. Matsuda* 4719
Magneto-Chemical Characteristics of Copper-Cobalt Catalysts—*A. Murty, U. Donatto, J. Washington, T. Hoard, M. Akundi, and C. Harris* 4722
Structural and Magnetic Characteristic of a Novel Method of $Fe_2O_3 \Rightarrow Fe_3O_4$ Reduction by Magneto-mechanical Activation—*W. Kaczmarek, I. Onyszkiewicz, and B. Ninham* 4725
Ferromagnetic Interactions Through End-On Azido Bridges in a Nickel (II) Dimer: $[Ni_2(C_{15}H_{11}N_3)_2(H_2O)\ (N_3)_3]ClO_4.H_20$—*R. Cortes, L. Lezama, T. Rojo, M. Urtiaga, and M. Arriortua* 4728

Levitation, Propulsion, and Power and Control Magnetics

Optimal Design of the Electromagnetic Levitation with Permanent and Electro Magnets—*Y-K. Tzeng and T. Wang* 4731
A New Electromagnetic Levitation System for Rapid Transit and High Speed Transportation—*T. Wang and Y-K. Tzeng* 4734
Experimental Investigation and 3-D Modelling of Linear Variable-Reluctance Machine with Magnetic-Flux Decoupled Windings—*C-T. Liu and J-L. Kuo* 4737
Levitational Melting of Several Kilograms of Metal with a Cold Crucible—*H. Tadano, M. Fujita, T. Take, K. Nagamatsu, and A. Fukuzawa* 4740
Study of Permanent Magnet Arrangements for Superconducting Passive Bearings—*M-C. Marion-Pera and J-P. Yonnet* 4743
A Compact Magnetic Suspension with Only One Axis Control—*J. Delamare, J-P. Yonnet, and E. Rulliere* 4746
A Passive Damper for Magnetic Suspension—*V. Nguyen, J. Delamare, and J-P. Yonnet* 4749
Three Dimensional Force Prediction in a Model Linear Brushless DC Motor—*J. Moghani, J. Eastham, R. Akmese, and R. Hill-Cottingham* 4752
A Novel High Power Converter for Non-Contact Charging with Magnetic Coupling—*H. Sakamoto and K. Harada* 4755
Development of Film Transformer—*S. Hayano, Y. Midorikawa, and Y. Saito* 4758
A New Inductor Having a Noise Filtering Capability—*Y. Midorikawa, S. Hayano, and Y., Saito* 4761
Fundamental Characteristics of Molten Metal Flow Control by Linear Induction Motor—*K. Fujisaki, J. Nakagawa, and H. Misumi* 4764
Trial Construction of New Magnetic Skew Gear Using Permanent Magnet—*S. Kikuchi and K. Tsurumoto* 4767

Soft Materials, Amorphous Materials and Crystalline Alloys

The Field Induced Magnetic Anisotropy in Amorphous Co-RE Alloys Films—*G. Suran, K. Roky, J. Sztern, F. Machizaud and J. Mackowski* 4770
Influence of Boron on the Magnetic and Transport Properties of FeZr Amorphous and Nanocrystalline Alloys—*J. Barandiaran, P. Gorria, J. Sal, L. Barquin, and S. Kaul* 4776
High Electrical Resistivity and Permeability of Soft Magnetic Granular Alloys—*H. Fujimori, S. Mitani, T. Ikeda, S. Ohnuma* 4779
Engineering Magnetostriction Measurements of Annealed FeSiB Amorphous Wires—*D. Atkinson and P. Squire* 4782
Induced Anisotropy in Nanocrystalline FeCuNbSiB—*M. Emura, A. Severino, A. Santos, and F. Missell* 4785
High-Field Magnetization Meaurements on a Ferromagnetic Amorphous Alloy from 295 to 5 K—*P. Szymczak, C. Graham, Jr., and M. Gibbs* 4788
Effects of Chemical Etching on the Asymmetric Magnetization Reversal in Amorphous Magnetic Alloy—*K. Shin, C. Graham, Jr. and P. Zhou* 4791
Influence of the As-Cast State on the Crystallization Process and Magnetic Properties for FeSiBCuNb Wires—*P. Marin, A. Olofinjana, M. Vazauez and H. Davies* 4794

Nanostructured Materials for Soft Magnetic Applications Produced by Fast dc Joule Heating—*P. Allia, P. Tiberto, M. Baricoo, M. Knobel, and F. Vinai* 4797
Creep Induced Magnetic Anisotropy in Nanocrystaline Fe-Cu-Nb-Si-B Alloys—*G. Herzer* 4800
Domain Structure Studies by Means of High Resolution ΔE Measurements—*S. Hogsdon, P. Squire, and D. Atkinson* 4803
Magnetic and Magnetoelastic Properties of Amorphous Fe-Si-B-C Films—*A. Mattingley, C. Shearwood and M. Gibbs* 4806
In-Plane Moment Canting in Amorphous $Fe_{78}B_{13}Si_9$ in Applied Fields Measured Using Polarized Mössbauer Spectroscopy—*Q. Pankhurst, S. Betteridge, J. Jiang and M. Gibbs* 4809
Effects of Nanocrystallization on the Magnetostriction of Co-Based Amorphous Alloys—*J. Gonzalez, N. Murillo, J. Blanco, P. Quintana, E. Amano and R. Valenzuela* 4812
Effect of Crystallization on Magnetic Domain Structure of Thinned Amorphous FeSiBCuNb Ribbons—*S. Zhou, Y. Wang, J. Ulvensoen and R. Hoier* 4815
The Effect of Surface Layers on Powder Loss in Amorphous Ribbon Materials—*T. Meydan and N. Derebasi* 4818
Influence of Scratching on Domain Structure and Power Loss in Amorphous Ribbons—*N. Derebasi, T. Meydan and G. Derebasi* 4821
A Comparative Study of Processes for the Production of Structured Barium Ferrite Films—*P. Gago-Sandoval, R. Carey, D. Newman, B. Thomas, S. Palmer, T. Jackson and R. Welch* 4824
Limiting Velocity of the Steady State Domain Wall Motion in the Presence of the Field Normal to the Anisotropy Axis—*V. Sobolev, H. Huang, and S. Chen* 4827
Effects of Creep Damage, Shot Peening, and Case Hardening on Magnetic Barkhausen Noise Analysis—*L. Sipahi* 4830
Computation of Intrinsic Permeability from Measured Permeability: Soft Ferromagnetic Thin Films—*J. Rusat and F. Durbin* 4833
Epitaxial Growth and Magnetic Properties of Fe Films on Si Substrates—*S. Yaegashi, T. Kurihara, K. Sato, and H. Segawa* 4836
Electrical and Physical Characterization of SiFe Sheets Insulation—*M. Marion-Pera and T. Waecherle* 4839
Obtention of a Strong (100)[001] Texture Component Based on a Hot-Rolling Process in 3% Al-Fe—*C. Talowski, T. Waeckerle, and B. Cornut* 4842
Soft Magnetic Properties of Fe-M-B-Cu (M = Hf, Zr, Nb) Alloys with Nanocrystalline and Amorphous Hybrid Structure—*J. Lee, K. Kim, T. Noh, I. Kang, and Y. Yoo* 4845
Microstructure and Magnetic Properties of Nanocrystalline bcc Fe-Nb-B Soft Magnetic Alloys—*A. Makino, S. Yoshida, A. Inoue, and T. Masumoto* 4848
Effects of the Interlayers on the Magnetic Properties in Fe-Hf-C/Ceramics Multilayer Films—*J. Choi, J. Lee, S. Han, H. Kim and I. Kang* 4851
Magnetic Viscosity and Activation Volume in Domain Wall Pinning—*D. Ng, C. Lo, and P. Gaunt* 4854
The Dependence of Magnetoacoustic Emission on Magnetic Induction and Specimen Thickness—*D. Ng, C. Lo, S. Cheng and J. Jakubovics* 4857
Performance and Noise Attenuation Mechanism of Noise Reduction Transformer—*T. Yanada, T. Matsuda, O. Ichinokura, and T. Jinzenji* 4860
Variation of the Localised Flux Densities in the Amorphous Toroidal Tansducer Core—*M. Goktepe and T. Meydan* 4863
Finite Element Analysis on Characteristics of Rotary Transformers—*Y-T. Huang, C-J. Chen, and W-B. Shu* 4866
Magnetic Properties of (Fe,Co)-B-Al-Nb Alloys with Ultrafine Grain Structure—*Y. Cho, Y. Kim, C. Kim, K. Lee, and T. Kim* 4869

Ferrites and Domain Walls

Effect of Heat Treatment on the Microstructure and Magnetic Properties of Polycrystalline MnZn Ferrites—*M. Ramesh, R. Crowell, and S. Dey* 4872
Low Temperature Fired NiCuZn Ferrite—*J-Y. Hsu, W-S. Ko, H-D. Shen and C-J. Chen* 4875
Correlation between Magnetic and Structural Properties of $Ni_{80}Fe_{20}$ Sputtered Thin Films Deposited on Cr and Ta Buffer Layers—*R. Jerome, T. Valet, and P. Galtier* 4878
FeGdN: a New Soft Magnetic Metallic Thin Film Material—*E. Van De Riet* 4881
Magnetic Properties of Nanostructure Controlled FeAlSi/FeAlSiO Multilayers—*M. Hiramoto, O. Inoue, and K. Kugimiya* 4884
Supersaturated A2 Solid Solution Induced by Ball Milling in the Fe-Si System: Structural and Magnetic Characterization and Thermal Stability—*M. Abdellaoui, E. Gaffet, T. Barradi, and F. Faudot* 4887

Forsterite Film and Grain Growth in 3% Si Steel—*M. Cunha and M. Cesar* 4890
Dynamic Preisach Model Interpretation of Power Losses in Rapidly Quenched 6.5% SiFe—*V. Basso, G. Bertotti, F. Fiorillo, and M. Pasquale* 4893
The Magnetic and Structural Properties of Ferrite Plated NiZn-Ferrite Films—*C. Williams, M. Abe, T. Itoh, and P. Lubitz* 4896
Ferrite Plating of Fe_3O_4 Films Using Alternate Electric Current—*Q. Zhang, T. Itoh and M. Abe* 4900
Dependence of the Magnetic Disaccommodation Spectrum of YIG with Sintering Temperature—*L. Torres, M. Zazo, J. Iniguez, C. De Francisco, and J. Munoz* 4903
Fine Powder Ferrite for Multilayer Chip Inductors—*H-M. Sung, C-J. Chen, W-S. Ko and H-C. Lin* 4906
Theoretical Analysis and Experimental Research on the Approach-Staturation Curve of Polycrystalline Hexagonal Planar Ferrites—*S. Zhu, H. Chen, F. Wen, and Y. Zhang* 4909
Studies of the Stoichiometrical Variation of Epitaxial $Fe_{3-(1-\delta)}O_4$ Thin Films—*E. Lochner, K. Shaw, R. DiBari, W. Portwine, P. Stoyonov, S. Berry, and D. Lind* 4912
Magnetic Domain Behavior of Cu-Co Spinel Ferrite Systems—*S. Patil and R. Dabhade* 4915
Structure and Magnetic Properties of $Gd_{1-x}Sr_xFeO_{3-\delta}$ Compounds—*C. Kim, Y. Um, S. Park, S. Ji, Y. Oh, J. Park, J. Lee, and C. Yo* 4918
Experimental Study of Local Dynamic Potential Well of Isolated Domain Wall—*V. Synogach and V. Gornakov* 4921
Effects of Surface Stress on Barkhausen Effect Emissions: Model Predictions and Comparison and X-ray Diffraction Studies—*D. Jiles and L. Suominen* 4924
The Effect of Curvature on Domain Wall Energy and Thickness—*J. Jatau and E. Della Torre* 4927

Magnetic Semiconductors and New Materials

Synthesis and Properties of $Cd_{1-x}Mn_xS$ Diluted Magnetic Semiconductor Nanoparticles—*R. Bandaranayake, M. Smith, J. Lin, H. Jiang, and C. Sorensen* 4930
Magnetic and Structural Properties of Laser Deposited Lithium Ferrite Films—*S. Oliver, C. Vittoria, G. Balestrino, S. Martellucci, G. Petrocelli, A. Tebano and P. Paroli* 4933
Magneto-Optical Properties of CdMnTe Films on Quartz Glass and Sapphire Substrates in the Transparent, Visible Region—*M. Imamura, K. Ogata, M. Tokubuchi, and M. Nakahara* 4936
Studies of Structural, Magnetic and Transport Properties of a New Series $R_3Cu_3Sb_4$ (R = La,Ce,Pr,Gd)—*Z. Hossain, S. Patil, R. Nagarajan, L. Gupta, R. Vijayaraghavan, and C. Godart* 4939
Magnetic Ordering in $(U_{0.5}Tb_{0.5})Co_2Ge_2$ Studied by AC-Susceptibility and Neutron-Diffraction Measurements—*M. Kuznietz, H. Pinto, H. Ettedgui, and M. Melamud* 4942
Soft Magnetic Properties of Nano-Structure-Controlled Magnetic Materials—*Y. Sugaya, O. Inoue, and K. Kugimiya* 4945
Microstructure and Magnetic Properties of Semi-Hard Fe-Co-B-Cu Alloys Formed by Rapid Solidification—*A. Zaluska, G. Rudkowska, P. Rudkowski and J. Strom-Olsen* 4948
Structural and Magnetic Properties of RFe_6Ge_6 (R=Y, Gd, Tb, Er) Compounds—*Y. Wang, D. Wiarda, D. Ryan, and J. Cadogan* 4951
Superparamagnetism of Ferrite Particles Dispersed in Spherical Polymeric Materials—*C. O'Connor, Y-S. Lee, J. Tang, V. John, N. Kommareddi, M. Tata, G. McPherson, J. Akkara, and D. Kaplan* 4954
Magnetic Properties of $Sm_3(Fe, Ti)_{29}N_5$ Compounds—*F. Yang, B. Nasunjilegal, W. Gong, and G. Hadijipanayis* 4957
Magnetic Properties of Two New Compounds: $Pr_2Ni_3Si_5$ and $Ho_2Ni_3Si_5$—*C. Mazumdar, R. Nagarajan, L. Gupta, R. Vijayaraghavan, C. Godart, and B. Padalia* 4960
Spin Reorientation Transitions in $RFe_{11.35}Nb_{0.65}$ (R = Dy, Er)—*K-Y. Wang, Y-Z. Wang, B-P. Hu, and W-Y. Lai* 4963
Magnetic Properties of RNi_4B (R=rare Earth Metal)—*N. Hong, T. Holubar, G. Hilscher, M. Vybornov, and P. Rogl* 4966
High Field Magnetization Study of the $Gd_2Fe_{17}H_x$ System—*O. Isnard, S. S. Miraglia, D. Fruchart, and M. Guillot* 4969
The Effects of Arsenic Doping on the Magnetic Properties of $CuCr_2Se_4$—*J. Tang, L. Li, S. Saxena, A. Puri, A. Falster, and W. Simmons, Jr.* 4972
Magnetic Properties of the Solid Solution $NdGa_{1-x}Ge_x$—*Y. Grin, O. Sichevich, and K. Hiebl* 4975

CONFERENCE AUTHOR INDEX 4978

High field magnetization measurements of Sm_2Fe_{17}, $Sm_2Fe_{17}C_x$, and $Sm_2Fe_{17}C_xH_{5-x}$

O. Isnard and S. Miraglia
Laboratoire de Cristallographie, CNRS 166X, 38042 Grenoble Cedex, France

M. Guillot
Service National des Champs Intenses, CNRS 166X, 38042 Grenoble Cedex, France

D. Fruchart
Laboratoire de Cristallographie, CNRS 166X, 38042 Grenoble Cedex, France

K. H. J. Buschow
Philips Research Laboratories, P.O. Box 80000, 5600 JA Eindhoven, The Netherlands

The magnetic properties of ferromagnetic compounds of Sm_2Fe_{17}, $Sm_2Fe_{17}C_{0.6}$, and $Sm_2Fe_{17}C_{0.6}H_{4.4}$ were investigated. Sm_2Fe_{17} nitrides, carbides, and carbohydrides are suitable for making high performance permanent magnets. The high field magnetization measurements performed up to 200 kOe in continuous fields are reported. In this article, the isothermal magnetization curves measured between 2 and 300 K on powder samples embedded in a resin and then aligned under a magnetic field of about 10 kOe in order to get oriented samples are presented. The magnetic anisotropy constants K_1 and K_2 are determined taking into account the angular distribution of the grains axis. The results are discussed in light of previously reported data and then the effects of C or H on the Sm contribution to the anisotropy is compared to that of N. It is shown that carbon and hydrogen have opposite influence on the Sm anisotropy and it is suggested that a wide range of magnetic anisotropy can be obtained depending on the H and C content. The influence of both interstitial elements H and C on magnetic features such as the Curie temperature and the saturation magnetization is analyzed.

The search for new hard permanent magnet materials has recently concentrated on the ternary carbides and nitrides $R_2Fe_{17}C_x$ and $R_2Fe_{17}N_x$. The crystallographic and magnetic properties of the R_2Fe_{17} compounds have been known for many years[1–3] and in a recent article we have reported in detail on the magnetic properties[4] of $Sm_2Fe_{17}N_3$, $Sm_2Fe_{17}D_5$, and $Pr_2Fe_{17}N_3$. Following our previous high field magnetization, we will concentrate in this article on the properties of $Sm_2Fe_{17}C_x$ and $Sm_2Fe_{17}C_xH_{5-x}$ compounds.

Samples of Sm_2Fe_{17} were prepared by induction melting in cold crucible under argon atmosphere, whereas $Sm_2Fe_{17}C_{0.6}$ has been obtained by arc furnace. The samples were found to be mainly single phase with small traces of iron in the case of $Sm_2Fe_{17}C_x$. The x-ray patterns of the rhombohedral compounds were indexed using the hexagonal multiple cell. Hydrogenation was performed in a stainless steel autoclave under hydrogen gas pressure of about 5 MPa leading to a stable hydride. The hydrogen uptake was determined by gravimetric methods and confirmed by volumetric estimation. The accuracy of the hydrogen concentration can be evaluated to about 0.1 hydrogen atom per formula unit; The Curie temperature was determined using Faraday-type torque balance.

Magnetic measurements were performed using an automatic system provided with a cryostat associated to a calorimeter which has been described in detail elsewhere.[5] The magnetization experiments were carried out in a continuous field up to 200 kOe produced by a water-cooled Bitter magnet. No single crystals were available due to the decrepitation process which is known to occur when hydrogen is inserted in R_2Fe_{17} compounds.[6,7] All the samples were sieved down to a particle size smaller than 25 μm. Then the powder was mixed with epoxy resin and subsequently aligned at room temperature using an orientation field of typically 10 kOe.

The crystal structure of the Sm_2Fe_{17} alloys is well established; its crystal symmetry is R-3m whose lattice parameters are reported in Table I. De Mooij and Buschow[8] as well as Gueramian and co-workers[9,10] have shown that $R_2Fe_{17}C_x$ phases can be obtained from a $R_2Fe_{14}C$ series depending upon the heat treatment. R_2Fe_{17} carbides correspond to the high temperature phase and $R_2Fe_{14}C$ correspond to the low temperature phases. Helmholdt *et al.*[11] have shown using

TABLE I. Structural data and Curie temperature of $Sm_2Fe_{17}X_y$ compounds (X=H, C, N).

	T_c (K)	a (Å)	c (Å)	V (Å^3)	c/a
Sm_2Fe_{17}	385	8.554	12.443	788	1.4426
$Sm_2Fe_{17}H_5$	565	8.682	12.550	819	1.4455
$Sm_2Fe_{17}N_3$	755	8.744	12.658	838	1.4476
$Sm_2Fe_{17}C_{0.6}$	485	8.608	12.463	780	1.4478
$Sm_2Fe_{17}C_{0.6}H_{4.4}$	583	8.699	12.565	832	1.4444

 0021-8979/94/76(10)/6035/3/$6.00 © 1994 American Institute of Physics

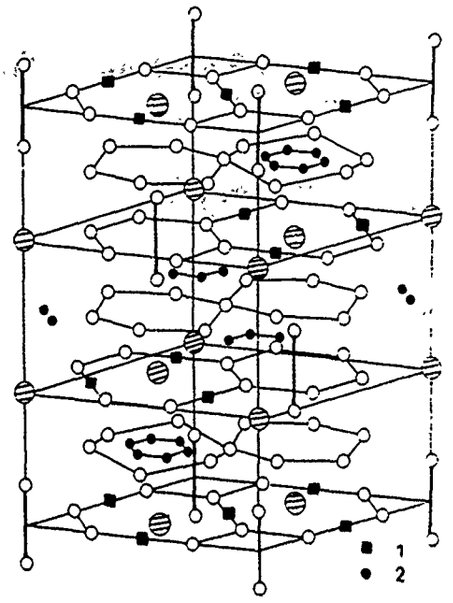

FIG. 1. R_2Fe_{17} crystal structure; large and small circles refer to rare earth and iron, respectively. Octahedral and tetrahedral sites are labeled 1 and 2, respectively.

neutron diffraction experiments that carbon atoms are accommodated within the crystal lattice on an interstitial site called 6*c*. This site can be seen as a pseudooctahedral site with two rare-earth and four iron atoms at the corners. The exclusive occupancy of this 6*c* site has been confirmed by a more recent work.[8]

The large difference in radii between iron and rare-earth atoms leads to large interstitial sites which are often used in rare-earth iron intermetallic compounds to insert hydrogen. Since hydrogen is significantly smaller than C or N, it does not only go to the octahedral site but also into some tetrahedral sites represented in Fig. 1. The location of hydrogen or deuterium in the R_2Fe_{17} lattice has been shown by neutron diffraction[12,13] and is discussed in detail elsewhere. All these atoms are located in the neighborhood of the rare-earth atoms, their influence on the crystal electric field by acting on the rare-earth site is expected to be important. This has been confirmed frequently for N (Refs. 4,14–17) and sometimes for C.[19] The influence of hydrogen on the magnetic features of the R_2Fe_{17} compounds has attracted less attention till now[19,20] but a recent study[4] has shown that the influence of hydrogen on the rare-earth anisotropy is opposite to that of nitrogen. Here we study $Sm_2Fe_{17}C_x$ and $Sm_2Fe_{17}C_xH_{5-x}$ in order to compare the influence of C to that of N and H. Insertion of H in a R_2Fe_{17} carbide is expected to occur in the two interstitial sites: (i) the remaining octahedral site not occupied by C atoms, (ii) the tetrahedral site.[21] These assumptions have been recently confirmed for $Th_2Fe_{17}C_xH_y$ [21] and $R_2Fe_{17}C_xH_y$ (R=Ce,Nd,Ho,...).[22] No neutron diffraction determination is possible on such phases due to the high absorption cross section of Sm for thermal neutrons,[23] nevertheless Sm compounds are expected to behave as others R_2Fe_{17} compounds do.

Insertion of light elements (H, C, or N) in Sm_2Fe_{17} alloys induces a significant lattice expansion. It is worth noting that even for the largest interstitial element, C or N, the symmetry of the host alloy is retained in the interstitial containing compound, no change of structure is observed in Sm compounds. It is not always the case since R_2Fe_{17} (R=Er, Tb, Ho, or even Y) alloys which are known to crystallize in $P6_3/mmc$ symmetry are observed to retain their rhombohedral structure for high carbon content.[24,25] As expressed by Table I, the lattice parameters of the nitrided compounds are larger than that of other interstitial compounds. Whatever the interstitial element used, the increase of the lattice occurs mainly in the basal plain (a,b) of the hexagonal cell, the expansion along the c axis being less pronounced. The volume expansion per interstitial atom deduced from Table I is in close agreement with previous results[21] obtained on Th_2Fe_{17} compounds. Insertion of hydrogen induces an expansion of about 2.3 Å^3/atom which is about one-third of that induced by carbon or nitrogen.

Results reported in Table II show that whatever the interstitial element used the saturation magnetization of the ternaries are significantly higher than that of the Sm_2Fe_{17} compound. In spite of a higher content in interstitial atoms, the hydride or carbohydride compounds exhibit a lower magnetization than $Sm_2Fe_{17}N_3$.

Studying several $Sm_2Fe_{17}C_x$ compounds with different carbon contents Grössinger *et al.*[18] have shown that for concentrations higher than $x=0.5$ the magnetic anisotropy is uniaxial. The magnetization curves measured for $Sm_2Fe_{17}C_{0.6}$ (Fig. 2) reveal a positive value of K_1 at 4.2 K thus confirming the measurements of Grössinger *et al.*[18] and Ding *et al.*[26] It is known that the iron sublattice anisotropy in $R_2Fe_{17}C_x$ compounds remains planar whatever the iron content;[27] the uniaxial character of the $Sm_2Fe_{17}C_{0.6}$ com-

TABLE II. Saturation magnetization and anisotropy constants measured for the $Sm_2Fe_{17}X_y$ compounds (X=H, C, N) at both 4.2 and 300 K.

	4.2 K			300 K		
	M_s (μ_B/*fu*)	K_1 (MJ/m^3)	K_2 (MJ/m^3)	M_s (μ_B/*fu*)	K_1 (MJ/m^3)	K_2 (MJ/m^3)
Sm_2Fe_{17}	29.9	−3.0±0.4	$\|K_2\|$<0.1	26.3	−1.75±0.3	$\|K_2\|$<0.05
$Sm_2Fe_{17}H_5$	34.9	−3.8±0.25	0.55±0.3	31.5	−2.80±0.2	0.55±0.2
$Sm_2Fe_{17}N_3$	40.5	10.8±0.4	−4.1±0.4	37.8	10.4±0.4	−5±1
$Sm_2Fe_{17}C_{0.6}$	33.7	2.0±0.25	−0.2±0.2	29.4	1.25±0.20	−0.4±0.2
$Sm_2Fe_{17}C_{0.6}H_{4.4}$	35.1	−2.0±0.3	−0.1±0.02	32.2	−2.0±0.25	0.07±0.0

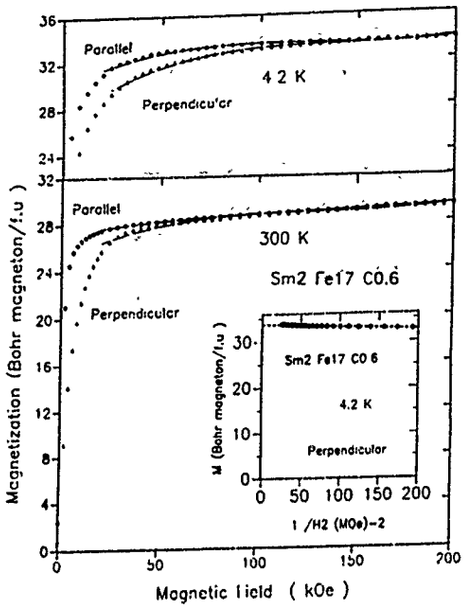

FIG. 2. Magnetization curves of $Sm_2Fe_{17}C_{0.6}$ at 4.2 and 300 K. Inset: $1/H^2$ extrapolation.

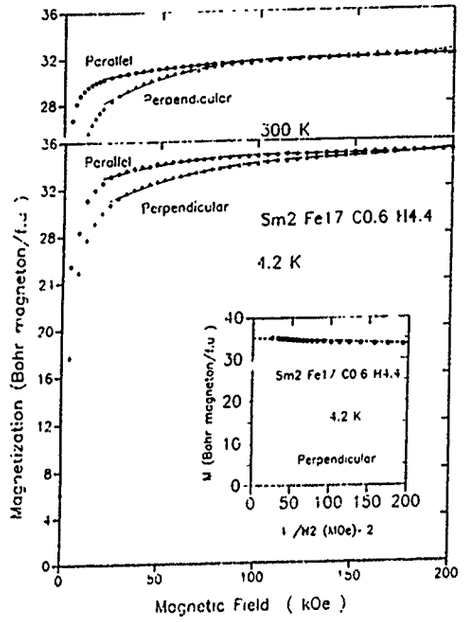

FIG. 3. Magnetization curves of $Sm_2Fe_{17}C_{0.6}H_{4.4}$ at 4.2 and 300 K. Inset: $1/H^2$ extrapolation.

pound is thus due to the contribution of Sm which overcomes that of the Fe sublattice. The insertion of only 0.6 carbon per formula unit is enough to change the sign of the Sm anisotropy from easy plane in Sm_2Fe_{17} to easy axis in $Sm_2Fe_{17}C_{0.6}$. The anisotropy of the rare-earth sublattice is in this structure very sensitive to the interstitial concentration. The measurements performed on $Sm_2Fe_{17}C_{0.6}H_{4.4}$ show that addition of hydrogen within the crystal structure leads to a huge effect on the magnetocrystalline anisotropy since our measurements reveal a change of the sign of the low order parameter K_1 which became negative in $Sm_2Fe_{17}C_{0.6}H_{4.4}$ (Fig. 3). This result is in good agreement with previous experiments on $Sm_2Fe_{17}H_5$ compounds. Nitrogen or carbon insertion have opposite effects. ^{155}Gd Mössbauer[28,29,19] studies have shown that the major effect of the interstitial elements is to modify the quadrupolar interaction on the rare-earth site. The modification of the R contribution to the magnetic anisotropy is thus due to the change of the CEF acting on the rare-earth site. It is worth noting that $Sm_2Fe_{17}C_{0.6}H_{4.4}$ exhibits higher K_1 values than $Sm_2Fe_{17}H_5$ confirming that the role played by carbon on the Sm magnetic anisotropy is opposite to that of hydrogen. It is thus interesting to notice that depending on the H and C concentration, a large range of the anisotropy field should be accessible in the $Sm_2Fe_{17}C_xH_y$ system.

[1] D. Givord, Ph.D. thesis, Université de Grenoble, 1973.
[2] K. H. J. Buschow, J. Less-Comm. Met. **11**, 20 (1966).
[3] P. C. M. Gubbens, Thesis, University of Delft, 1977.
[4] O. Isnard, S. Miraglia, M. Guillot, and D. Fruchart, J. Appl. Phys. **76**, 5988 (1994).
[5] J. C. Picoche, M. Guillot, and A. Marchand, Physica B **155**, 407 (1989).
[6] O. Isnard, Ecole Nationale Supérieure de Physique de Grenoble (I.N.P.G.), Stage de D.E.A., 1989.
[7] O. Isnard, Ph.D. thesis, University of Grenoble, 1993.
[8] O. Isnard, J. L. Soubeyroux, D. Fruchart, T. H. Jacobs, and K. H. J. Buschow, J. All. Comput. **186**, 135 (1992).
[9] M. Gueramian, Ph.D. thesis, University of Geneva, Switzerland, 1991.
[10] M. Gueramian, A. Bezinge, K. Yvon, and J. Muller, Solid State Commun. **64**, 639 (1987).
[11] R. B. Helmholdt and K. H. J. Buschow, J. Less-Comm. Met. **155**, 15 (1989).
[12] O. Isnard, S. Miraglia, J. L. Soubeyroux, D. Fruchart, and A. Stergiou, J. Less-Comm. Met. **162**, 273 (1990).
[13] O. Isnard, S. Miraglia, D. Fruchart, and J. Desportes, J. Magn. Magn. Mater. **103**, 157 (1991).
[14] M. Katter, J. Wecker, L. Schultz, and R. Grossinger, J. Magn. Magn. Mater. **83**, L14 (1990).
[15] S. Miraglia, J. L. Soubeyroux, C. Kolbeck, O. Isnard, D. Fruchart, and M. Guillot, J. Less-Comm. Met. **171**, 51 (1991).
[16] T. S. Zhao, X. C. Kou, R. Grossinger, and H. R. Kirchmayr, Phys. Rev. B **44**, 2846 (1991).
[17] H.-S. Li and J. M. Cadogan, Solid State Commun. **80**, 905 (1991).
[18] R. Grössinger, X. C. Kou, T. H. Jacobs, and K. H. J. Buschow, J. Appl. Phys. **69**, 5596 (1991).
[19] O. Isnard, P. Vuillet, A. Blaise, J. P. Sanchez, S. Miraglia, and D. Fruchart, J. Magn. Magn. Mater. **131**, 83 (1993).
[20] O. Isnard, S. Miraglia, D. Fruchart, and J. Desportes, J. Magn. Magn. Mater. **103**, 157 (1991).
[21] O. Isnard, S. Miraglia, J. L. Soubeyroux, D. Fruchart, J. Deportes, and K. H. J. Buschow, J. Phys. Condens. Mater. **5**, 5481 (1993).
[22] Isnard *et al.* (to be published).
[23] Bacon, *Neutron Diffraction* (Oxford University Press, New York, 1962).
[24] X. C. Kou, R. Grossinger, T. H. Jacobs, and K. H. J. Buschow, Physica B **168**, 181 (1991).
[25] H. Sun, B.-P. Hu, H.-S. Li, and J. M. D. Coey, Solid State Commun. **74**, 727 (1990).
[26] J. Ding and M. Rosenberg, J. Less-Common Met. **168**, 335 (1991).
[27] H. Sun, Ph.D. thesis, Trinity College, Dublin, 1992.
[28] M. W. Dirken, R. C. Thiel, R. Coehoorn, T. H. Jacobs, and K. H. J. Buschow, J. Magn. Magn. Mater. **94**, L15 (1991).
[29] M. W. Dirken, R. C. Thiel, T. H. Jacobs, and K. H. J. Buschow, J. Less-Comm. Met. **168**, 269 (1991).

X-ray structural studies of nitrogen diffusion in Dy_2Fe_{17}

Er. Girt, Z. Altounian, X. Chen, Ming Mao, D. H. Ryan, M. Sutton, and J. M. Cadogan[a)]
Centre for the Physics of Materials, Department of Physics, McGill University, 3600 University Street, Montréal, Québec, Canada H3A 2T8

The reaction between N_2 and Dy_2Fe_{17} has been studied by thermopiezic analysis on 20–25 μm sized powders in the temperature range 400–500 °C. Partially nitrided powders were analyzed using CuK_α x-ray diffraction and thermomagnetic techniques. Both high angle x-ray and thermomagnetic data show only the presence of Dy_2Fe_{17} and $Dy_2Fe_{17}N_{3-\delta}$ ($\delta<0.3$) with no evidence of intermediate compositions. The results of the x-ray diffraction experiments at several Bragg peaks were simulated using a two phase model structure: a Dy_2Fe_{17} core with a $Dy_2Fe_{17}N_3$ surface layer. The results show that at low temperatures the nitride layer is too thin to account for all of the nitrogen absorbed by the sample, indicating that a significant amount of the nitrogen diffused into the core of the particles, presumably along grain boundaries.

During a gas–solid reaction, nitrogen diffuses into R_2Fe_{17} (R=rare earth), occupying interstitial sites and expanding the lattice without changing the crystal structure. The enhancement of the magnetic properties was observed[1] as a result of interstitial nitrogen diffusion in R_2Fe_{17}. Neutron powder diffraction[2] showed that the R_2Fe_{17} and $R_2Fe_{17}N_3$ phases are in equilibrium during the reaction. However, it was observed[3,4] that a continuous solid solution $R_2Fe_{17}N_x$ ($0<x<3$) is formed on annealing partially nitrided powders. In this study we use x-ray diffraction and thermomagnetic techniques to characterize nitrogen diffusion in the 2-17 structure. Nitrogen diffusion in the 2-17 structure typically occurs above 350 °C, and significant diffusion through extended defects such as grain boundaries at 400 °C has been observed using metallography.[5]

The polycrystalline Dy_2Fe_{17} alloy was prepared by induction melting of appropriate amounts of Dy and Fe, followed by vacuum annealing at 1173 K for two weeks. Induction melting ensures homogeneity of alloys and mass loss was below 0.03% during preparation. The homogenized ingot was ground and sieved to select powder sizes between 20 and 25 μm. The powder size was confirmed by scanning electron microscopy. Nitrogen diffusion was performed in a thermopiezic analyzer (TPA) at a starting pressure of 1 bar and temperatures ranging from 400 °C (590 min) to 500 °C (25 min) to obtain $Dy_2Fe_{17}N_{0.85}$. The amount of nitrogen diffused into the sample was obtained directly from the gas pressure change in the TPA. Structural analyses on Dy_2Fe_{17}, before and after the gas–solid reaction, were carried out using CuK_α radiation on an automated Nicolet–Stöe powder diffractometer with a graphite monochromator in the diffracted beam. Thermomagnetic analyses were done using a Perkin–Elmer thermogravimetric analyzer (TGA) in a small field gradient.

The x-ray diffraction pattern of $Dy_2Fe_{17}N_{0.85}$ is shown in Fig. 1. As a consequence of nitriding, a new phase was formed with the same structure as Dy_2Fe_{17} but with the Bragg peaks shifted towards lower angles indicating an expansion of the unit cell. This shift is shown more clearly in Fig. 2, where the (300) peaks of $Dy_2Fe_{17}N_{0.85}$ (top) are compared with those (bottom) of pure Dy_2Fe_{17} (N_0) and $Dy_2Fe_{17}N_3$ (N_3). $Dy_2Fe_{17}N_{0.85}$ clearly contains both $Dy_2Fe_{17}N_3$ and unreacted Dy_2Fe_{17}. The position of the Dy_2Fe_{17} peak is shifted towards lower angles, due to the expansion of the unreacted core, while that of $Dy_2Fe_{17}N_3$ is shifted slightly towards higher angles. Careful examination of the (332) Dy_2Fe_{17} and $Dy_2Fe_{17}N_3$ diffraction peaks (inset of Fig. 1), which are well separated, shows no evidence of the existence of an intermediate composition phase. Using TGA two distinct Curie temperatures, $T_{c1}=128$ °C and $T_{c2}=445$ °C are detected as shown in Fig. 3. T_{c1} is 28 °C higher than the Curie temperature of Dy_2Fe_{17} and T_{c2} is 5 °C lower than the Curie temperature of $Dy_2Fe_{17}N_3$. The x-ray and the TGA data are thus in agreement, as T_c changes with the lattice expansion of Dy_2Fe_{17}. Even if the observed experimental data only show the existence of Dy_2Fe_{17} and $Dy_2Fe_{17}N_3$, they are not at equilibrium at 500 °C. After subsequent annealing for 60 h at 480 °C, a uniform $Dy_2Fe_{17}N_{0.85}$ solid solution was obtained. Further work is in progress to study this equilibrium phase. Because $Dy_2Fe_{17}N_3$ and Dy_2Fe_{17} are not in equilibrium, we tried to estimate the amount of the undetected intermediate phase (in the interface between $Dy_2Fe_{17}N_3$ and Dy_2Fe_{17}) by comparing the x-ray patterns of crushed $Dy_2Fe_{17}N_{0.85}$, shown in Fig. 2(b), with

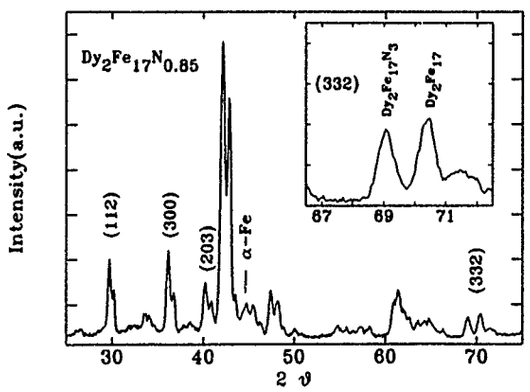

FIG. 1. The x-ray diffraction pattern of $Dy_2Fe_{17}N_{0.85}$ for nitrogen diffused at 500 °C for approximately 25 min. Inset: (332) peak of $Dy_2Fe_{17}N_{0.85}$.

[a)]On leave from School of Physics, The University of New South Wales, Sydney, NSW 2052, Australia.

 0021-8979/94/76(10)/6038/3/$6.00 © 1994 American Institute of Physics

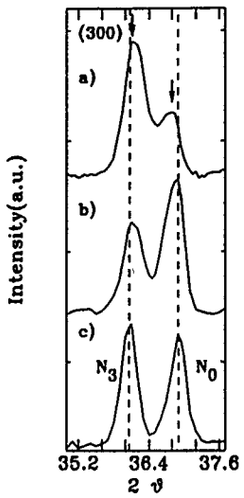

FIG. 2. (a) The (300) diffraction peak of $Dy_2Fe_{17}N_{0.85}$ (powder sizes between 20 and 25 μm). (b) The diffraction peak of the subsequently crushed $Dy_2Fe_{17}N_{0.85}$. (c) The (300) peak of a mixture of pure Dy_2Fe_{17} and $Dy_2Fe_{17}N_3$ powders in the ratio 1:1.

those (bottom of Fig. 2) of pure Dy_2Fe_{17} (N_0) and $Dy_2Fe_{17}N_3$ (N_3). Note that for the crushed $Dy_2Fe_{17}N_{0.85}$ powder the x-ray peaks are mostly relaxed to the unshifted positions. Fitting shows that the possible amount of the intermediate phase is much lower than the amount of the $Dy_2Fe_{17}N_3$ phase.

Nitrogen distribution can be estimated from the ratio of the intensities of the diffraction peaks by using a simple model where the core is nitrogen-free and the surface layer is fully nitrided as shown schematically in Fig. 4. Estimating the volume fractions is complicated because the $Dy_2Fe_{17}N_3$ phase coats the Dy_2Fe_{17} phase and so attenuates the x-ray scattering. In a multilayered system the intensity of the reflected beam from the ith layer can be expressed as

$$I_i = I_0 e^{-\Sigma_{j=1}^{i-1}(2d_j\mu_j/\sin\theta)} \int_0^{d_i} e^{-2x\mu_i/\sin\theta}\, dx \int dS, \quad (1)$$

where I_0 and θ are the intensity and angle of the incident beam, d_i and μ_i are the thickness and absorption coefficient of the ith layer, respectively, and S is the surface area illuminated by the beam. The term $e^{-\Sigma_{j=1}^{i-1}(2d_j\mu_j/\sin\theta)}$ comes from the attenuation of the x-ray beam from the top $(i-1)$ layers. For the two layer model, the intensity ratio becomes

$$I_1/I_2 = (\mu_2/\mu_1)(e^{2d_1\mu_1/\sin\theta} - 1), \quad (2)$$

where we have neglected the term $e^{-2d_2\mu_2/\sin\theta}$ as $d_2 \approx 20$ μm and $\mu_2 = 1.577$ μm^{-1}.

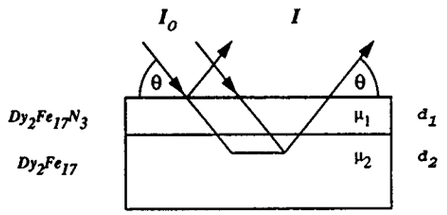

FIG. 4. Two layer model structure used to calculate x-ray diffraction patterns.

The relative intensities (I_1, I_2) were estimated by a simultaneous fitting of the measured (112), (300), and (203) Bragg peaks to Eq. (1) where each Bragg peak is a combination of two Gaussians with position p_i and width w_i ($i = 1,2$), representing the contributions from $Dy_2Fe_{17}N_3$ and Dy_2Fe_{17}. The widths, w_1 and w_2, are adjusted during the fitting. We note that this model assumes that the nitrogen diffuses uniformly through the bulk of the material. Figure 5 shows the CuK_α x-ray diffraction patterns of $Dy_2Fe_{17}N_{0.85}$ samples nitrided at 500 °C. The solid lines in Fig. 5 are the fits to the experimental data and the dotted lines are the contributions of Dy_2Fe_{17} and $Dy_2Fe_{17}N_3$ calculated from the model. Assuming that the average particle has a rectangular shape with the dimensions $20\times15\times10$ μm^3 (this particle shape is an approximate representation deduced from scanning electron microscope photographs) we obtain, using the calculated thicknesses of the layers, that for nitrogen diffusion at 500 °C approximately 90% of the nitrogen can be accounted for by the intensity of the fully nitrided peak. This shows that almost the entire amount of nitrogen is in the surface layer (the penetration of the CuK_α in Dy_2Fe_{17} is restricted to approximately 1–2 μm). To observe the nitrogen

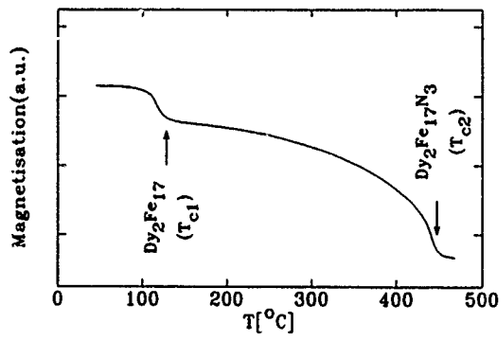

FIG. 3. Thermogravitometric analyses of $Dy_2Fe_{17}N_{0.85}$. T_{c1} correspond to the Curie temperature of the Dy_2Fe_{17} and T_{c2} to Curie temperature of the $Dy_2Fe_{17}N_3$ phase.

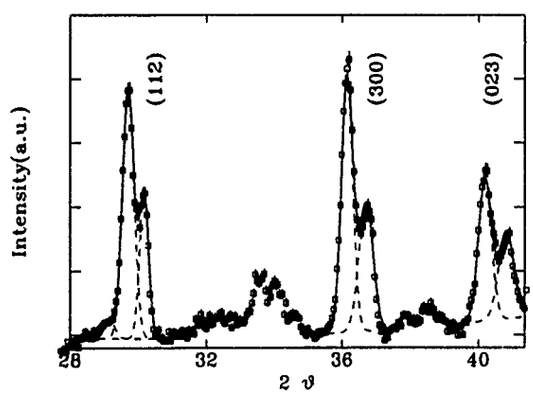

FIG. 5. Simultaneous fitting of (112), (300), and (023) peaks using a two layer model structure. The solid lines are contributions of Dy_2Fe_{17} and $Dy_2Fe_{17}N_3$ calculated from the model.

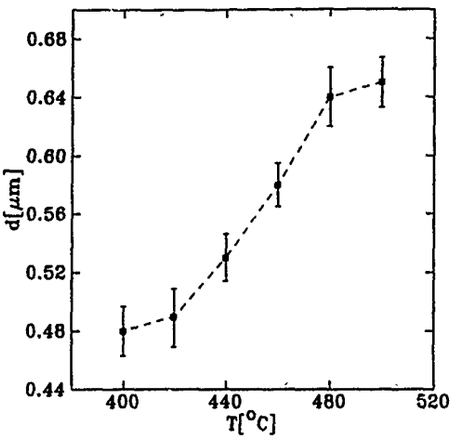

FIG. 6. Effect of reaction temperature on the apparent $Dy_2Fe_{17}N_3$ layer thickness derived from fits to the x-ray diffraction patterns. All samples have the same nominal nitrogen content.

distribution at different temperatures we introduced the same amount of nitrogen (a bulk average of 0.85 atoms per unit formula) to 20–25 μm sized powders at temperatures between 400 and 500 °C.

The values for the thicknesses of the nitrided layer versus the nitriding temperature is shown in Fig. 6. Despite the fact that all of the nitrided samples have the same nominal composition, the $Dy_2Fe_{17}N_3$ surface layer is clearly thinner in the samples prepared at lower temperatures. In the absence of any evidence for the formation of an intermediate composition nitride phase, we attribute the apparent nitrogen deficit to the formation of the nitride phase at depths within the particles beyond the penetration range of the CuK_α radiation ($\approx$1 μm). For this to happen, the nitrogen must find more rapid diffusion paths than bulk diffusion allows, presumably along extended defects such as grain boundaries. Above 480 °C, the two layer model accounts for over 90% of the absorbed nitrogen, and we conclude that for these temperatures nitrogen transport is dominated by bulk diffusion.

In conclusion, using x-ray diffraction and a thermomagnetic technique only Dy_2Fe_{17} and $Dy_2Fe_{17}N_3$ phases were observed. The thickness of the nitrogen layer was obtained by fitting x-ray diffraction peaks with a two phase model structure: a $Dy_2Fe_{17}N_3$ surface layer and a Dy_2Fe_{17} core. Significant nitrogen diffusion through extended defects such as grain boundaries was observed at temperatures below 480 °C.

The research was supported by grants from the Natural Sciences and Engineering Research Council of Canada, and Fonds pour la Formation de Chercheurs et l'Aide à la Recherche, Québec. J. M. C. was partially supported by an International Scientific Exchange grant from NSERC.

[1] J. M. D. Coey and H. Sun, J. Magn. Magn. Mater. **87**, L251 (1990).
[2] O. Isnard, J. L. Soubeyroux, S. Miraglia, D. Fruchart, L. M. Garcia, and J. Bartolomé, Physica B **183**, 624 (1992).
[3] M. Katter, J. Wecker, C. Kuhrt, L. Schultz, and R Grössinger, J. Magn. Magn. Mater. **117**, 419 (1992).
[4] T. Mukai and T. Fujimoto, J. Magn. Magn. Mater. **103**, 165 (1992).
[5] C. C. Colucci, J. Magn. Magn. Mater. **125**, 161 (1993).

Atomic diffusion mechanism and diffusivity of nitrogen into Sm_2Fe_{17}

Chris N. Christodoulou and Norikazu Komada
Central Research Institute, Mitsubishi Materials Corporation, 1-297 Kitabukuro-cho, Omiya, Saitama 330, Japan

An atomic diffusion mechanism (voidal diffusion) is proposed where nitrogen atoms migrate inside the Sm_2Fe_{17} lattice by jumping from a $9(e)$ site into a thermodynamically unstable tetrahedral $18(g)$ site and subsequently into a new $9(e)$ site. For the first time, the anisotropic nature of diffusion and growth kinetics together with direct observation of the diffusion fields by Bitter domain patterns have been taken into account and employed for nitrogen diffusivity measurements. The planar and axial preexponential factors were found to be $D_{OX}=0.72\times10^{-6}$ $m^2 s^{-1}$ and $D_{OZ}=2.26\times10^{-6}$ $m^2 s^{-1}$, respectively. The activation enthalpy, ΔH, for diffusion was found to be 143 kJ/mol.

I. INTRODUCTION

The metastable $Sm_2Fe_{17}N_3$ compound is an attractive material for permanent magnets.[1] It can be prepared by direct reaction of Sm_2Fe_{17} particles with N_2 gas. The reaction involves a slow diffusion of N atoms from the surface to the center of the particles. In order to improve the observed low diffusivity it is important to understand the atomic diffusion mechanism operating in this particular case. Such a mechanism has been proposed recently by Christodoulou and Takeshita[2] and Christodoulou and Komada.[3] The present article represents a study of the anisotropic diffusion and experimental results supporting the proposed atomic diffusion mechanism presented. The planar (D_{OX}) and axial (D_{OZ}) preexponential factors and activation enthalpy (ΔH) of the nitrogen diffusivity into Sm_2Fe_{17} are also reported.

II. EXPERIMENT

Clean Sm_2Fe_{17} particles were prepared by applying the interstitial hydrogen absorption desorption process on large pieces of a Sm_2Fe_{17} homogenized alloy.[1] Most of the particles were single grains and only those with particle size of larger than 100 μm were used for the diffusion experiments. The diffusion experiments were performed at temperatures of 400 and 425 °C for 20, 50, and 100 h and at 450 and 475 °C for 5, 10, 20, and 50 h. The pressure was monitored to be constant at 1 atm. Each experiment (temperature-time combination) was conducted twice. The $Sm_2Fe_{17}N_x$ phase was identified by Bitter domain patterns (colloidal solution of magnetite) formed on polished particles which were prealigned in a magnetic field. The thickness of the domain patterns were measured and averaged for at least 20 particles obtained in each run. Phase analysis was also performed by x-ray diffraction (CuK_α) and by thermomagnetic analysis (TMA).

III. THE ATOMIC DIFFUSION MECHANISM

A detailed description of the mechanism can be found in Refs. 2 and 3. Nitrogen atoms can migrate by jumping from a $9(e)$ site into a thermodynamically unstable tetrahedral $18(g)$ site and subsequently into a new $9(e)$ site (Fig. 1). In such a migration path, nitrogen atoms have to encounter an enormous energy barrier accounting for the energy needed to overcome the strong bonding from its nearest neighbors (Fe and especially the Sm atoms) and more importantly for the strain energy needed to break through of the octahedral face [Fe(f)-Sm(c)-Fe(h)] and in through the tetrahedral face [Fe(h)-Sm(c)-Fe(h)]. Although the $18(g)$ sites cannot accommodate any nitrogen atom in an equilibrium fashion,[4] their presence plays a key role for the diffusion of the nitrogen atoms. The temperature dependence of the diffusivity can be written[3] as $D_{XX}=D_{OX}\exp(-\Delta H/RT)$ along the planar α axes and $D_{ZZ}=D_{OZ}\exp(-\Delta H/RT)$ along the c axis, where T is the absolute temperature and R is the gas constant (8.314 J mol^{-1} K^{-1}). Also, it can be shown[3] that the anisotropic ratio of D_{XX}/D_{ZZ} is equal to $\frac{5}{8}(\alpha/c)^2$, where α and c are the lattice parameters of Sm_2Fe_{17}. By substituting $\alpha=8.549$ Å and $c=12.441$ Å, D_{XX}/D_{ZZ} takes the value of 0.3. In the case where the diffusing atoms (like hydrogen) are allowed to move inside the $18(g)$ "circular tunnel" (Fig. 1), the anisotropic ratio of D_{XX}/D_{ZZ} can be as large as $\frac{9}{4}(\alpha/c)^2$ or 1.07 (essentially isotropic).

IV. THE KINETICS OF $Sm_2Fe_{17}N_3$ GROWTH

The solution of the diffusion equation for the nitrogen concentration, $C(x)$, inside the diffusion layer in the case of large particles (almost flat surface) and short times (no overlapping of diffusion fields) can be approximated with that in a semi-infinite medium (Fig. 2) and is given by

$$C(x)=C_s\,\mathrm{erfc}[(x-L)/2\sqrt{(Dt)}], \tag{1}$$

where C_s is the constant surface and growing phase ($Sm_2Fe_{17}N_3$) concentration (Ref. 5), L is the thickness this phase ($Sm_2Fe_{17}N_3$), D is nitrogen diffusivity assumed to be constant, t is the time, and x measures from the surface of the particle.

For diffusion controlled growth

$$C_sL=\int_0^t -D\left[\frac{\partial C(x)}{\partial x}\right]_L dt. \tag{2}$$

From Eq. (1)

$$\left[\frac{\partial C(x)}{\partial x}\right]_L=-\frac{C_s}{\sqrt{\pi Dt}}. \tag{3}$$

By combining Eqs. (2) and (3) and integrating we get

 0021-8979/94/76(10)/6041/3/$6.00 © 1994 American Institute of Physics

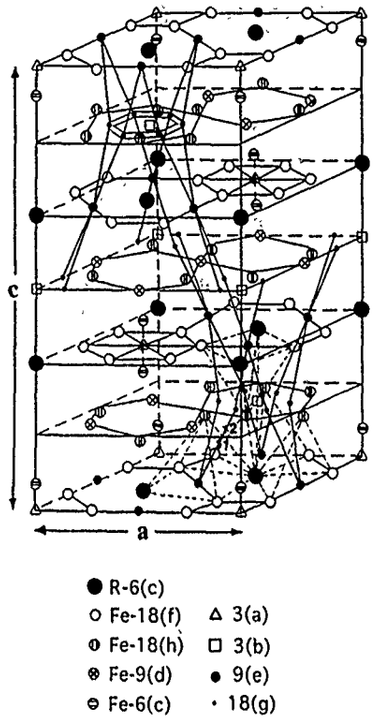

FIG. 1. Schematic representation of the hexagonal cell of the Sm_2Fe_{17} ($R\bar{3}m$) structure and the atomic jump network [single solid lines connecting the 9(e) with the 18(g) sites] of the nitrogen atoms during voidal diffusion. Double solid lines connecting the 18(g) sites represent the "circular tunnel" through where hydrogen atoms can be tunneled. The saddle point configurations, SPC1 and SPC2, are marked by "$\times$."

$$L=(2/\sqrt{\pi})\sqrt{Dt}. \tag{4}$$

The tangent of the concentration profile at the beginning of the diffusion layer (Fig. 2) defines a diffusion length, $D_\lambda = \sqrt{\pi Dt}$, which represents the effective penetration of nitrogen atoms where the magnetocrystalline anisotropy of the nitrogen containing Sm_2Fe_{17} is assumed to become axial and exhibits a domain structure as observed in the Bitter domain patterns. It is to be noted that the nitrogen-free Sm_2Fe_{17} phase does not form any observable domain patterns. The observable thickness of the Bitter domain pattern will be

$$d=L+D_\lambda=[(2/\sqrt{\pi})+\sqrt{\pi}]\sqrt{Dt}. \tag{5}$$

The diffusivity at a particular temperature and direction (planar or axial) will be:

$$D=\pi d^2/(2+\pi)^2 t=D_0\exp(-\Delta H/RT), \tag{6}$$

where, d is measured along that particular direction.

V. RESULTS—DISCUSSION

Typical Bitter domain patterns of nitrogenated Sm_2Fe_{17} particles are shown in Fig. 3. Particles with their c axis perpendicular to the observation plane exhibit a uniform "maze-type" domain pattern around the particle reflecting the uniaxial magnetocrystalline anisotropy and the isotropic nature of diffusivity in the c plane. Particles with their c axis on the observation plane exhibit a "parallel lines-type" domain pattern with deeper penetration reflecting both the uniaxial

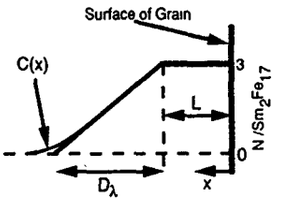

FIG. 2. Growth of $Sm_2Fe_{17}N_3$ from the surface to the center of a Sm_2Fe_{17} grain.

magnetocrystalline and diffusion anisotropy. A typical x-ray diffraction (XRD) pattern and a thermomagnetic analysis (TMA) trace for particles nitrogenated at 475 °C for 20 h are shown in Fig. 4.

By fitting the data in Table I for planar diffusivity according to Eq. (6), the preexponential factor, D_{OX}, and the activation enthalpy, ΔH, were found to be $(0.72\pm0.05)\times10^{-6}$ m^2 s^{-1}, and (143 ± 10) kJ mol^{-1}, respectively (Fig. 5). Applying the same for the axial diffusivity, the preexponential factor, D_{OZ}, and the activation enthalpy, ΔH, were found to be 1.21×10^{-6} m^2 s^{-1} and 139 kJ mol^{-1}, respectively. According to the proposed model, ΔH should be the same along xy and z axes. The experimentally determined values of 143 and 139 kJ mol^{-1} are essentially the same as expected from the proposed model. The degree of confidence for the data obtained for the planar diffusivity is greater than that for the axial diffusivity because the orientation of the particles could be unambiguously confirmed by the uniformity of the thickness of the domains formed around the particles. In the case of the axial diffusivity small misorientations of the particles are very difficult to be detected still revealing "parallel lines-type" of domain patterns. Therefore, the value of ΔH equal to (143 ± 10)

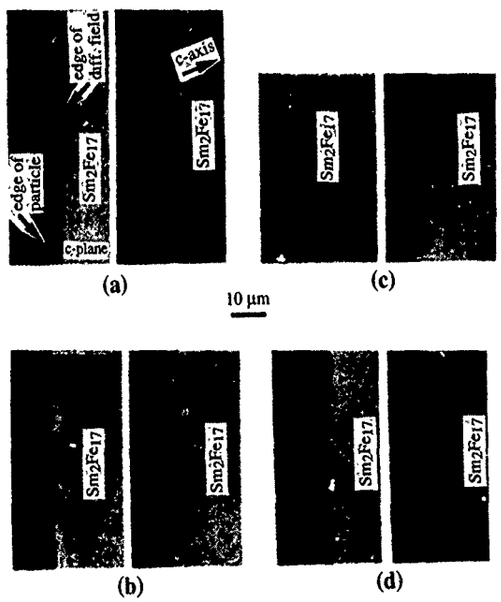

FIG. 3. Bitter domain patterns for Sm_2Fe_{17} particles nitrogenated at (a) 425 °C (50 h), (b) 425 °C (100 h), (c) 475 °C (5 h), and (d) 475 °C (10 h).

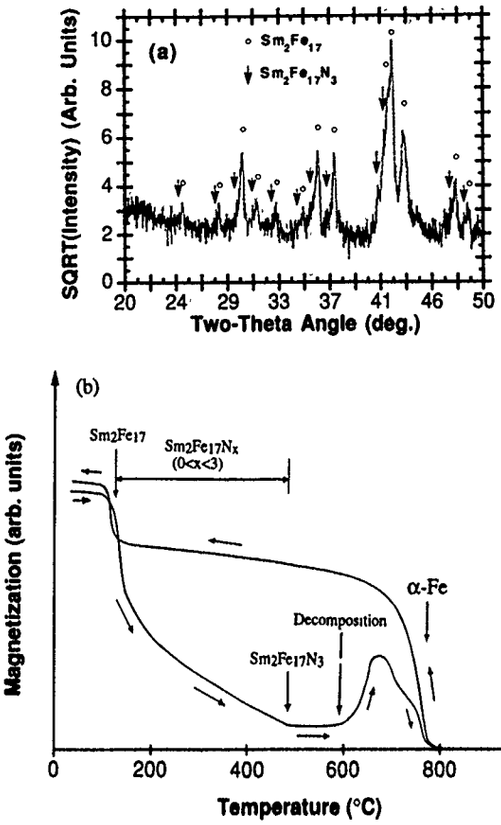

FIG. 4. X-ray diffraction pattern (a) and thermomagnetic analysis (b) of Sm_2Fe_{17} particles nitrogenated at 475 °C for 20 h. They confirm the presence of Sm_2Fe_{17} and $Sm_2Fe_{17}N_3$ phases together with the diffusion layer of $Sm_2Fe_{17}N_x$ ($0<x<3$).

kJ mol^{-1} is considered to be the correct one. Since ΔH was confirmed to be the same along xy and z axes, this restriction can be applied in order to obtain a refined value of D_{OZ} which is very sensitive to ΔH. Hence, $D_{XX}/D_{ZZ}=D_{OX}/D_{OZ}=(d_x/d_z)^2$, where d_x and d_z are the observed thicknesses of the domain patterns along x and z, respectively, at the same temperature and time. From this, the preexponential factor, D_{OZ}, was found to be $(2.26 \pm 0.15)\times 10^{-6}$ m^2 s^{-1}. The D_{OX}/D_{OZ} ratio is 0.32 ± 0.04, a value which is very close to 0.30 predicted by the atomic

TABLE I. The planar (d_x) and axial (d_z) average thicknesses of the Bitter domain patterns for Sm_2Fe_{17} particles nitrogenated at different temperatures and times.

Time (h)	d (μm)	400 °C	425 °C	450 °C	475 °C
5	d_x=	···	···	2.33	3.47
	d_z=	···	···	4.33	6.13
10	d_x=	···	···	3.30	4.90
	d_z=	···	···	6.02	8.66
20	d_x=	1.93	3.05	4.67	6.91
	d_z=	3.65	5.76	8.13	11.85
50	d_x=	3.06	4.82	7.38	10.96
	d_z=	5.41	8.39	12.66	18.80
100	d_x=	4.32	6.82	···	···
	d_z=	7.64	11.57	···	···

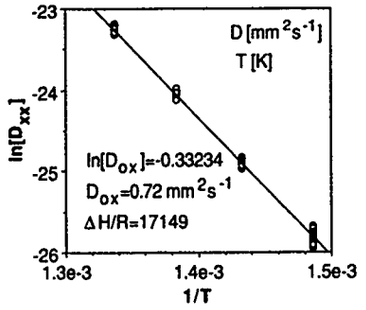

FIG. 5. Arrhenius plot of the planar diffusivity (D_{XX}) vs $1/T$.

diffusion mechanism. This value also suggests that during diffusion, nitrogen atoms are not permitted to move inside the $18(g)$ "circular tunnel,"[3] something expected to be occurring in hydrogen diffusion.

The activation entropy for diffusion,[3] ΔS, can be estimated to be $-0.343R$ through $D_{OX}=\gamma\tilde{\nu}\exp(\Delta S/R)$, where $\gamma=1.015\times10^{-6}$ m^2 s^{-1}, and $\tilde{\nu}=10^{13}$ s^{-1}. Such a negative activation entropy is attributed to the large increase in the vibrational frequencies of the atoms influenced by diffusion. The ratio of the vibrational frequency during diffusion to the initial one, ν_i'/ν_{io}, can be estimated[3] to be 1.4. Such a value is physically reasonable based on the fact that a nitrogen atom has to squeeze through and come in close contact with the atoms at the two saddle point configurations, SPC1 and SPC2 (Fig. 1).

The high value of the activation enthalpy for diffusion (143 kJ mol^{-1}) is indicative of the large energy barrier which a nitrogen atom encounters during its migration from one $9(e)$ site to another. This value falls within the limits predicted by Christodoulou and Komada[3] and it mostly accounts for the huge strain energy needed for a nitrogen atom to break through the two saddle point configurations, SPC1 and SPC2.

It is difficult to compare the values of D_0 and ΔH obtained in the present study with others published in the literature[6–8] because this is the first time that the anisotropic nature of the diffusivity and growth kinetics have been taken into account together with direct observation of the diffusion fields. Nevertheless, the present values compare favorably to the values obtained by Skomski and Coey[8] but are much higher than the ones reported in Refs. 6 and 7.

[1] C. N. Christodoulou and T. Takeshita, IEEE Trans. Magn. **MAG-92-245**, 53 (1992).

[2] C. N. Christodoulou and T. Takeshita, *Proceedings of the 1st International Conference on Processing Materials for Properties*, Honolulu, Hawaii, Nov. 7–10 1993, edited by H. Henein and T. Oki (TMS, Warrendale, PA, 1993), pp. 293–296.

[3] C. N. Christodoulou and N. Komada, J. Alloys Comp. **206**, 1 (1994).

[4] C. N. Christodoulou and T. Takeshita, J. Alloys Comp. **198**, 1 (1993).

[5] C. N. Christodoulou and T. Takeshita, J. Alloys Comp. **202**, 173 (1993).

[6] J. M. D. Coey, J. F. Lawler, Hong Sun, and J. E. M. Allen, J. Appl. Phys. **69**, 3007 (1991).

[7] H. Kaneko, T. Kurino, and H. Uchida, *Proceedings of the 7th International Symposium on Magnetic Anisotropy and Coercivity in Rare Earth Transition Metal Alloys* (University of Western Australia, Canberra, Australia, 1992), pp. 320–330.

[8] R. Skomski and J. M. D. Coey, J. Appl. Phys. **73**, 7602 (1993).

Effect of nitrogen on the properties of hard magnets

M. Melamud[a] and L. H. Bennett
National Institute of Standards and Technology, Gaithersburg, Maryland 20899

R. E. Watson
Brookhaven National Laboratory, Upton, New York 11973

The enhancement of magnetic properties of RE-TM hard magnet materials, such as RE_2Fe_{17}, upon nitriding is studied using the Wigner–Seitz (Voronoi) construct. In analogy with other RE-TM nitrides, it is concluded that nitrogen has a strong preference to occupy the octahedral $9e$ site in the 2:17 compounds, to the exclusion of the other proposed sites. Additional materials are suggested as candidates for nitriding on the basis of the availability of such an octahedral site. The site preference and its effect on the magnetism in RE_2Fe_{17} is discussed in relation to the Wigner–Seitz cell of the atoms. The magnetic moments on the iron are shown to be correlated with the WS cell volumes, and this dependence differs from that associated with αFe.

Renewed interest in the RE-Fe 2:17 hard magnets[1] has arisen because of the enhanced magnetic properties achieved by alloying them with nitrogen (or carbon). The addition of nitrogen causes an increase in lattice parameters, Curie temperature, sublattice magnetic moment, and anisotropy field. It has been observed theoretically[2,3] and experimentally[4,5] that iron atoms exhibit different moments on different sites in RE_2Fe_{17} and its nitride.

While there is no argument in the literature about these changes, and it has been agreed by all authors that nitrogen is interstitial (not substitutional), different sites have been suggested by different authors. Pr_2Fe_{17} and the other RE_2Fe_{17} compounds discussed in this work are those having the Th_2Zn_{17} structure—space group $R\bar{3}m$ (Table I). The sites suggested for N (or C) in the same space group are $3a$,[6] $9e$,[5,7] $18h$,[8] and $18g$.[9] One of the principal purposes of this paper is to address the problem of where in fact the nitrogen resides in the nitrided compounds. The choice is quite clear if one notes the behavior[10] of ordered TM nitride compounds.

The Wigner–Seitz (WS) cell construct has previously been suggested[11] as a method for studying the relationship of crystal structure and properties, especially with regard to magnetic properties of hard magnets. WS (or Voronoi) polyhedra furnish a useful measure of the local environment of an atom, including a description of the site symmetry of the atom, and a catalog of what atoms constitute its nearest neighbors. A modified WS construction[11,12] also accounts for the relative sizes (i.e., atomic radii) of the various atoms. It has been also observed[11] using the WS construct that "disclination nets" pass through those metal sites which have the largest magnetic moments. (Disclinations are chemically important bond lines.) The nets defined by these disclinations have been shown to be correlated with the anisotropy axes of hard magnets.[11] Structural factors, in addition to Invar-type volume effects, are expected to be important to local $3d$ magnetism in the hard magnets.

Wigner–Seitz cell construction has been employed to derive a measure of the local site volumes, and explore their correlations with the magnetic moments.[11] In αMn, for example, if we assume that all the Mn atoms have the same radius, then the WS cells have different volumes. Relating these volumes to the magnetic moments at the four Mn sites in αMn, a nearly linear relation is found. A similar result is obtained for the four Fe sites in the hard magnet, Pr_2Fe_{17} Ref. 12 (Table I). The relationship of the WS atomic volume and the disclinations to the enhancement of the magnetic properties are discussed in this paper, and suggestions for possible new hard magnet nitrides are given.

Based on calculations of the WS polyhedra for a wide array of TM metalloids[10] (with up to 50% metalloid content) it has been shown that each metalloid prefers a certain local environment defined by a special WS cell. One specific example is nitrogen which is always found in the (0 6) octahedral environment. [This environment competes with the higher coordinated (0 3 6) ninefold Bernal environment in the $3d$ metal carbides. In the $4d$-$5d$ carbide group (except for Nb_2C) the carbides have joined the nitrides in displaying only an (0 6) metalloid environment.[10] Boron is normally encountered in an (0 3 6) or (0 2 8) Bernal environment.] In analogy with these TM nitrides, we conclude that it would be extraordinary (i.e., indicative of a most unusual TM—N bonding) if nitrogen occupied anything other than the octahedral $9e$ site in the 2:17 compounds.

We have calculated the WS polyhedra for the Pr_2Fe_{17} and $Pr_2Fe_{17}N_3$ (assuming full occupancy) with nitrogen occupying any one of the suggested sites. The method of calculation is described elsewhere.[12] The results are presented[13] in Table I. Only in the $9e$ site is the WS polyhedron for nitrogen (0 6), namely, an octahedral array of six nearest neighbors. The other sites result in different, nonstable, polyhedra which have very small facets or edges and in some cases (e.g., $3a$ site) the resulting distances to neighboring atoms are too small.

Table II lists hard magnet materials, in addition to the Pr_2Fe_{17}, which were found to have enhanced magnetism upon nitriding. In all of these, the nitrogen is found to be in an octahedral (0 6) environment. These include $NdFe_{10}V_2$ and $NdFe_{10}Mo_2$, both having the $ThMn_{12}$ structure,[14] the hexagonal 2:17 (Tm_2Ni_{17}),[15] and the Fe_nN (n=3,4,8). In the lower part of Table II(a), we propose some other hard magnet

[a]Permanent address: Nuclear Research Center, Negev, P.O. Box 9001, Beer-Sheva 84190, Israel.

 0021-8979/94/76(10)/6044/3/$6.00 © 1994 American Institute of Physics

TABLE I. Wigner–Seitz polyhedra (Ref. 13) of the atoms in Pr_2Fe_{17} and its nitride, with nitrogen in the 9*e* site of space group $R3m$. The measured magnetic moments in μ_B are given where known (Refs. 4 and 5). The WS cells of other sites suggested by some authors for nitrogen are shown in the lower part of the table.

		Pr_2Fe_{17}			$Pr_2Fe_{17}N_3$		
Atom	Site	Moment	Poly	Volume	Moment	Poly	Volume
Pr	6*c*	···	(0 0 12 8)	31.95	3.4	(0 3 6 14)	32.12
Fe1	6*c*	2.46	(0 0 12 2)	12.14	2.9	(0 0 12 2)	12.82
Fe2	9*d*	2.03	(0 0 12)	11.23	2.3	(0 0 12)	11.84
Fe3	18*f*	2.03	(0 1 10 2)	11.71	2.1	(0 1 10 2)	11.83
Fe4	18*h*	2.03	(0 0 12)	12.17	2.5	(0 1 10 2)	12.48
N	9*e*	···	···	···	···	(0 6)	3.35
N	3*a*		as proposed			(0 6 0 2)	1.68
N	18*h*		by some authors			(0 5 2)	1.62
N	18*g*					(2 2 2 2)	3.01

TABLE II. (a) WS polyhedra of the atoms in a number of hard magnet materials, before and after nitriding, assuming full N occupancy. The definitions of the polyhedra designations are given in (b). In the lower part of (a) we list the WS cells for the proposed sites (listed in the text) for nitrogen in materials not yet known to be nitrided. Due to partial RE and TM occupancy in $PrFe_7$, two possibilities are shown for TM3. (b) Shorthand designation defining various polyhedra types (Ref. 13) computed in some RE-TM-metalloid hard magnet materials, encountered in Table II(a). The designations are sorted according to total number of facets on the polyhedra. Different designations are defined for the three different types of atoms. For the metalloids, the *O* designates the octahedral environment, the *T* and *U* are the nine-fold and ten-fold Bernal environments, respectively.

(a)

	RE1	RE2	TM1	TM2	TM3	TM4	TM5	TM6	B	N
Pr_2Fe_{17}	*A*		*M*	*K*	*L*	*K*				
$Pr_2Fe_{17}N_3$	*D*		*M*	*K*	*L*	*L*				*O*
Tm_2Ni_{17}	*A*	*A*	*M*	*K*	*L*	*K*				
$Tm_2Ni_{17}N_3$	*D*	*D*	*M*	*K*	*L*	*L*				*O*
$NdFe_{10}V_2$	*A*1		*K*	*M*	*K*					
$NdFe_{10}V_2N$	*C*		*K*	*M*	*L*					*O*
$NdFe_{10}Mo_2$	*A*1		*K*	*M*	*K*					
$NdFe_{10}Mo_2N$	*C*		*K*	*M*	*L*					*O*
αFe			*M*4							
Fe_3N			*M*3							*O*
Fe_4N			*K*3	*M*3						*O*
Fe_8N			*M*4	*M*4	*N*					*O*
$NdNi_5$	*A*		*K*1	*K*						
$NdNi_5N_3$	*E*		*K*1	*M*1						*O*
$CeCo_4B$	*A*	*A*4	*K*1	*L*					*T*	
$CeCo_4BN_{1.5}$	*E*	*A*4	*K*1	*M*1					*T*	*O*
$PrFe_7$	*A*	*A*	*M*	*K*	*K*1/*L*	*K*				
$PrFe_7N_{1.5}$	*A*	*D*	*M*	*K*	*K*1/*L*	*K*				*O*
$Nd_2Fe_{14}B$	*A*2	*A*3	*L*	*K*	*K*	*M*	*L*	*K*	*T*	
$Nd_2Fe_{14}BN_{0.5}$	*B*	*A*3	*L*	*K*	*K*	*M*	*L*	*K*	*U*	*O*

(b)

	Rare earth	Facets		Transition metal	Facets		Metalloid	Facets
A	(0 0 12 8)	20	*K*	(0 0 12)	12	*O*	(0 6)	6
*A*1	(0 0 16 4)	20	*K*1	(0 3 6 3)	12			
*A*2	(0 2 8 10)	20	*K*2	(0 2 8 2)	12			
*A*3	(0 1 10 9)	20	*K*3	(0 12)	12			
*A*4	(0 6 0 14)	20						
B	(0 1 10 10)	21	*L*	(0 1 10 2)	13	*T*	(0 3 6)	9
C	(0 2 8 12)	22	*M*	(0 0 12 2)	14	*U*	(0 2 8)	10
			*M*1	(0 2 8 4)	14			
			*M*3	(0 6 8)	14			
			*M*4	(0 6 0 8)	14			
D	(0 3 6 14)	23	*N*	(0 5 2 8)	15			
E	(0 6 0 20)	26						

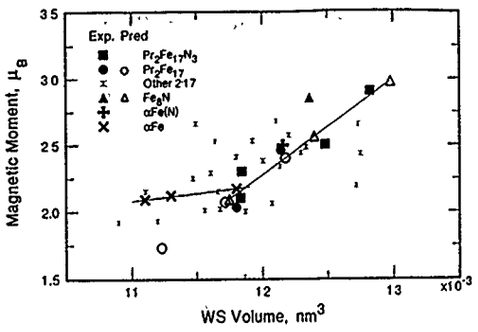

FIG. 1. Relation between the WS cell volume and magnetic moment per Fe atom in Pr_2Fe_{17} and its nitride. Also shown are results for iron nitride (Fe_8N), for αFe under pressure, and for αFe containing 1% N. Experimental and predicted values are represented by different symbols. The lines are the results of linear regression for (1) iron and (2) Pr_2Fe_{17} and its nitride. Also shown are values for Y, Nd, and Gd 2:17 compounds (Ref. 18).

materials which we have found have optional sites for nitrogen, with the same octahedral (0 6) WS cell as above. It is possible that these will also exhibit enhanced magnetic properties. The list includes RE-TM materials of the 1:5 ($CaCu_5$ and the related $CeCo_4B$), the 1:7 ($PrFe_7$) and the 2:14:1 ($Nd_2Fe_{14}B$) structures. The suggested sites for the nitrogen are $3f$ in space group $P6/mmm$, $9e$ in $R\bar{3}m$, and $2b$ in $P4_2/mnm$, respectively.

Iron volumes calculated from WS cell constructions are correlated with the known iron magnetic moments,[4,5] as can be seen in Fig. 1. $Pr_2Fe_{17}N_3$ is used as an example because of the availability of high-resolution neutron diffraction measurements,[5] which provide accurate moments for the four iron sites. The moments on the iron atoms for Pr_2Fe_{17} were derived[4] from Mössbauer experiments. Only the moment for the $6c$ site was resolved, and an average moment was assigned to the other three iron sites. We therefore have six experimental points, to which a linear regression has been applied, and predicted moments for the different sites were computed using their WS volumes. The average of the resulting moments for the three sites ($9d$, $18f$, and $18h$) is $2.18\mu_B$, as compared to the experimental value of $2.03\mu_B$.[4]

Another technologically relevant magnet is represented on Fig. 1, namely, Fe_8N, which is under study for use in reading heads.[16] The known experimental average moment for this material is $2.8\mu_B$ (at room temperature), shown in Fig. 1 using the average volume of the WS cells of these three sites. The iron atoms are in the three sites $4e$, $4d$, and $8h$ of space group $I4/mmm$. Predicted moments for the three sites are also shown on Fig. 1, as calculated from the WS site volumes using the same linear regression used for Pr_2Fe_{17}. The average value of these predicted moments is $2.7\mu_B$, in good agreement with the experimental value of $2.8\mu_B$. (The calculated band theoretical values[3] give an average of $2.4\mu_B$.)

Figure 1 includes also results[17] for αFe (as a function of pressure, at 0, 80, and 122 kbar). There seems to be a well-defined slope for these results, which is different from that in the 2:17 materials. This means that there are other factors which play an important role, such as coordination number, types of neighbors and the different exchange resulting from RE-TM in addition to Fe-Fe exchange. This result is supported by the observation[16] that an increase of ~0.5%–1% in the lattice parameter of αFe is accompanied by an increase of ~15% in its moment, resulting from the addition of a small amount of nitrogen. This result is shown in Fig. 1 to lie on the steeper line, off the αFe line. Other experimental and calculated critically collected[18] RE-TM data have been included in Fig. 1. A substantial scatter is seen resulting from inconsistencies even for the same material, and because not all values are saturation moments. There is no space to discuss this here.

The addition of the nitrogen into the structure in Pr_2Fe_{17} causes some changes in the topology of the WS cells of the neighboring atoms, which are probably correlated with the change in electron density caused by the nitrogen, and likely contribute to the break in slope. The main result is that the three fivefold facets connecting the RE to the Fe4 neighbors change into sixfold facets, thus incorporating the Fe4 into the sixfold disclination net and enhancing this net upon nitriding.

This work was supported by the Division of Materials Sciences, U.S. Department of Energy, under Contract No. DE-AC02-76CH00016.

[1] R. Grössinger and X. C. Kou, presented at Magnetism, Magnetic Materials and their Applications, Section II, La Habana, Cuba, 1991; H. Sun, J. M. D. Coey, Y. Otani, and D. P. F. Hurley, J. Phys. Condens. Matter **2**, 6465 (1990); K. H. J. Buschow, R. Coehoorn, D. B. deMooij, K. de Waard, and T. H. Jacobs, J. Magn. Magn. Mater. **97**, L35 (1990); J. M. D. Coey, H. Sun, J. Magn. Magn. Mater. **87**, L251 (1990).
[2] B. Szpunar, W. E. Wallace, and J. Szpunar, Phys. Rev. B **36**, 3782 (1987).
[3] A. Sakuma, J. Magn. Magn. Mater. **102**, 127 (1991).
[4] P. C. M. Gubbens, J. J. Van Loef, and K. H. J. Buschow, J. Phys. (Paris) Colloq. 6, Suppl. 12, **35**, C6-617 (1974); P. C. M. Gubbens, J. H. F. van Apeldoorn, A. M. van der Kraan, and K. H. J. Buschow, J. Phys. F **4**, 921 (1974).
[5] J. K. Stalick, J. A. Gotaas, S. F. Cheng, J. Cullen, and A. E. Clark, Mater. Lett. **12**, 93 (1991).
[6] S. Luo, Zh. Liu, G. Zhang, X. Pei, W. Jiang, and Wenwang Ho, IEEE Trans. Magn. **MAG-23**, 3095 (1987); S. Luo, G. Zhang, Zh. Liu, X. Pei, W. Jiang, and Wenwang Ho, *ibid.* **70**, 311 (1987).
[7] J. M. D. Coey, J. R. Lawler, H. Sun, and J. E. M. Allan, J. Appl. Phys. **69**, 3007 (1991); R. b. Helmholdt and K. H. J. Buschow, J. Less-Common Metals **155**, 15 (1989).
[8] H. H. Stadelmaier, E.-Th. Henig, G. Schneider, and B. Grieb, Mater. Lett. **7**, 155 (1988).
[9] Q. W. Yan, P. L. Zhang, Y. N. Wei, K. Sun, B. P. Hu, Y. Z. Wang, G. C. Liu, C. Gao, and Y. F. Cheng, Phys. Rev. B **48**, 2878 (1993).
[10] R. E. Watson and L. H. Bennett, Phys. Rev. B **43**, 11642 (1991).
[11] M. Melamud, L. H. Bennett, and R. E. Watson, Scr. Metall. **21**, 573 (1987); R. E. Watson, L. H. Bennett, and M. Melamud, J. Appl. Phys. **63**, 3136 (1988); L. H. Bennett, R. E. Watson, and M. Melamud, J. Phys. (Paris) **49**, C8-537 (1988).
[12] R. E. Watson and L. H. Bennett, J. Alloys Comp. **197**, 271 (1993).
[13] The notation for a WS cell is $(a,b,c,d,...)$ for a polyhedron having "a" triangular facets, "b" four-sided facets, "c" five-sided facets, etc.
[14] X. Chen, L. X. Liao, Z. Altounian, D. H. Ryan, and J. O. StromOlsen, J. Magn. Magn. Mater. **111**, 130 (1992).
[15] Y. Otani, D. P. F. Hurley, Hong Sun, and J. M. D. Coey, J. Appl. Phys. **69**, 5584 (1991).
[16] X. Bao, R. M. Metzger, and W. D. Doyle, J. Appl. Phys. **73**, 6734 (1993); C. Gao, W. D. Doyle, and M. Samsuzzoha, J. Appl. Phys. **73**, 6579 (1993).
[17] D. Guenzburger and D. E. Ellis, Phys. Rev. B **31**, 93 (1985).
[18] G. J. Long, O. A. Pringle, F. Grandjean, and K. H. Buschow, J. Appl. Phys. **72**, 4845 (1992), and references therein.

Theoretical analysis of the spin-density distributions in $Y_2Fe_{17}N_3$ and $Y_2Fe_{17}C_3$

W. Y. Ching, Ming-Zhu Huang, and Xue-Fu Zhong
Department of Physics, University of Missouri-Kansas City, Kansas City, Missouri 64110

The electronic structures and spin-density distributions in $Y_2Fe_{17}N_3$ and $Y_2Fe_{17}C_3$ are calculated using the self-consistent spin-polarized orthogonalized-linear-combination-of-atomic-orbitals method. The N or C atoms are assumed to occupy the $(9e)$ sites in the rhombohedral structure. The Fe $(18f)$ and N or C at the $(9e)$ site form covalent bonds which result in a very nonspherically symmetric spin-density distribution. The calculation shows a reduced moment for the Fe $(18f)$ sites due to doping. However, the moments at other sites are increased due to lattice expansion. There are some differences in the spin-density distribution between N and C at the $(9e)$ site. By comparing with the results of calculation on the pure Y_2Fe_{17} at different volumes, changes in moment enhancement and density of states at the Fermi level due to lattice expansion alone and that due to the chemical effect of introducing N or C are separated.

It has been well established that nitrogen (N) or carbon (C) doping in the rare-earth-Fe permanent magnets R_2Fe_{17} can raise the Curie temperature (T_c) substantially.[1,2] This is generally attributed to lattice expansion in the doped samples which increases the Fe-Fe interatomic distances and the exchange interactions. A large number of calculations exist which show the increase in the spin-magnetic moments on different Fe sites and significant changes in the density of states (DOS) at the Fermi level E_F upon N doping.[3–7] However, it is difficult to provide a direct explanation of the increase in T_c based on the electronic structure results since the electronic structure is a zero temperature entity. Mohn and Wohlfarth developed a theory based on a spin fluctuation mechanism which links with electronic structure to the T_c of a magnetic material.[8]

In spite of recent calculations on the electronic structure of the R_2Fe_{17} phases[3,9] and their nitroginated samples,[3–7] several questions remain unresolved. (1) The calculated spin moment on each Fe site is in general agreement with experiment, but discrepancies exist for specific sites such as Fe $(18f)$ and $(18h)$ in Y_2Fe_{17}.[10] The manner in which the spin moments have been obtained by different computational methods has not been fully scrutinized. (2) Separation of a chemical effect and volume expansion with introduction of N is important in understanding the mechanism for T_c enhancement. (3) It is generally assumed that the effects of the N doping or C doping on different R_2Fe_{17} crystals are similar. Realistic calculations may show subtle differences. (4) There is a fundamental question as to whether the local spin density approximation (LSDA) of the density functional theory on which almost all of the theoretical calculations are based, is good enough to answer the question of T_c enhancement. It is well known that the LSDA can give the wrong ground state in the case of elemental Fe crystals.[13]

In order to further understand some of these problems, we have carried out self-consistent, spin-polarized calculations on $Y_2Fe_{17}N_3$ and $Y_2Fe_{17}C_3$. Together with our previous calculations on pure Y_2Fe_{17} with different volume expansions,[10] we are able to separate the effects due to volume expansion and chemical doping. We focus on the details of the spin-density distribution in the vicinity of the doping sites as well as on the differences between systems with different dopings, i.e., N versus C.

We use the orthogonalized-linear-combination-of-atomic-orbitals (OLCAO) method in the LSDA. The procedures of the calculation have been described in the literature[14,15] and will not be repeated. A minimal atomiclike basis set consisting of orbitals of Y, Fe, N (C) which are expanded in terms of Gaussians in real space is employed. The crystal parameters used are listed in Table I. Three special **k** points are used in the self-consistent iterations, while in the final calculation, secular equations are solved at 11 special **k** points in the irreducible wedge of the Brillouin zone of the trigonal cell. The final charge and spin densities are calculated from the resulting eigenfunctions at these 11 **k** points with proper corrections for the core orthogonalization applied. The spin-magnetic moments at each site are ob-

TABLE I. Calculated properties for Y_2Fe_{17}, $Y_2Fe_{17}N_3$, and $Y_2Fe_{17}C_3$ crystals.

Crystal	Y_2Fe_{17}	Y_2Fe_{17}	$Y_2Fe_{17}N_3$	$Y_2Fe_{17}C_3$
Lattice constants:				
a (Å)	8.46	8.654	8.653	8.72
c (Å)	12.41	12.693	12.677	12.677
Volume (V/V_0):	1.00	1.07	1.069	1.072
Site moments (μ_B):				
Y $(6c)$	−0.63	−0.72	−0.46	−0.47
Fe $(6c)$	2.52(2.17)	2.70	2.55(2.71)	2.59(2.43)
Fe $(9d)$	2.05(2.01)	2.41	2.50(2.39)	2.56(2.01)
Fe $(18f)$	2.37(1.81)	2.50	2.02(2.36)	1.77(1.92)
Fe $(18h)$	2.10(1.77)	2.42	2.31(2.12)	2.19(1.75)
N or C $(9e)$			−0.07	−0.22
Total Fe moment (μ_B):	37.97	42.13	38.58	36.60
T_c (K) exp.:	325		697 694	698
DOS at E_F, $N(E_F)$ in unit of states per eV cell:				
$N(E_F)(\uparrow)$	11.2	6.0	7.6	10.0
$N(E_F)(\downarrow)$	16.4	12.6	8.0	9.5

 0021-8979/94/76(10)/6047/3/$6.00 © 1994 American Institute of Physics

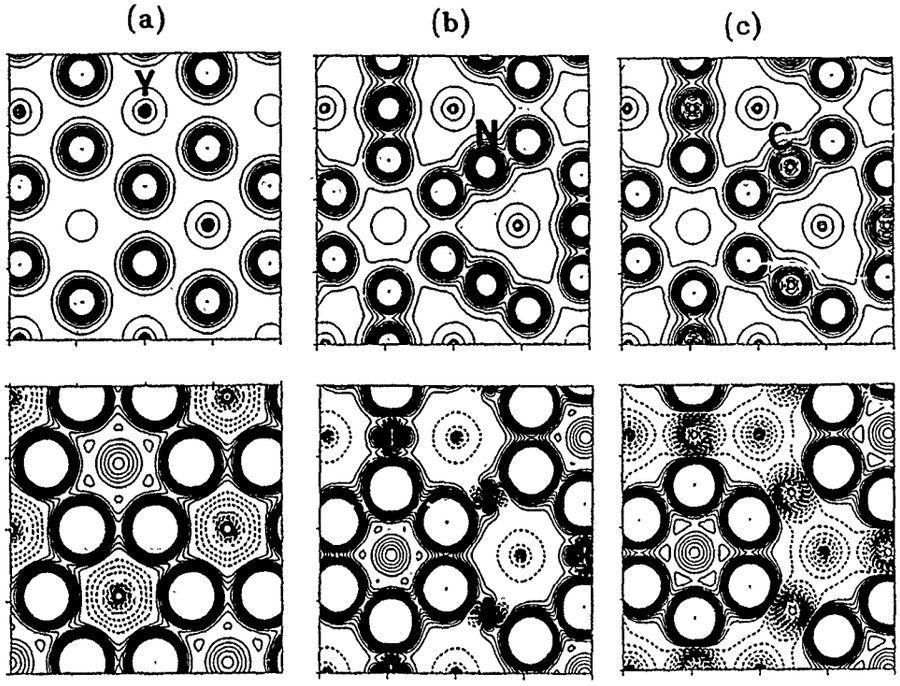

FIG. 1. Calculated charge density (left panel) and spin density (right panel) for (a) Y_2Fe_{17} (top), (b) $Y_2F_{17}N_3$ (middle), and (c) $Y_2Fe_{17}C_3$ (bottom) at approximately the same volume. The contour lines are 0.01, 0.02, 0.04, 0.06, 0.08, 0.10, 0.15, 0.20, 0.25, 0.30, 0.40, 0.50 for charge density and plus or minus of 0.001, 0.002, 0.003, 0.004, 0.006, 0.008, 0.01, 0.015, 0.020, 0.030, 0.040, 0.050. Negative numbers are indicated by dashed contours.

tained by using the Mulliken scheme[17] based on the eigenfunctions and the overlap matrix elements.

The calculated charge-density and spin-density maps on a plane perpendicular to the c axis and containing the Fe ($18f$) sites, the Y atom, and the doping elements are shown in Fig. 1 for Y_2Fe_{17}, $Y_2Fe_{17}N_3$, and $Y_2Fe_{17}C_3$. All three crystals have the same cell volumes. In the calculation for $Y_2Fe_{17}N_3$ and $Y_2Fe_{17}C_3$, we used the internal parameters which determine the atomic positions for $Nd_2Fe_{17}N_x$ as measured by Kajitani *et al.*[16] The results of Fig. 1 can be summarized as follows: (1) In the absence of the doping elements, Fe ($18f$) and Y have rather spherical charge- and spin-density distributions. The Y atom is negatively polarized. (2) When N atoms are introduced at the $9e$ site, expansion of the lattice and changes in the internal parameters make the $9e$ site of sufficient size to accommodate N. There is a significant covalent bonding character between Fe-$3d$ and N-$2p$ electrons in forming a tight Fe-N-Fe unit. The spin density at these sites shows significant distortion from spherical symmetry. The highly nonsymmetric charge- and spin-density distributions have some implications on the proper magnitude of spin-magnetic moments at these sites. (3) Although the moments at the N site are small and negatively polarized, the spin-density map shows that they form pairs of positive and negative lobes. (4) There are some differences in the spin-density distributions due to N and C dopings. For C, there is no lobe structure and the negative polarization at the C site is actually larger.

In Table I, we list the calculated spin moments at each site based on the Mulliken scheme. Also included are the results for Y_2Fe_{17} at zero expansion and some measured data for comparison. Based on these results, we can see that (1) Although the effect of volume expansion increases the negative polarization on the Y atom, the doping actually reduces it. (2) There is a significant reduction of moments on Fe ($18f$) next to N (C) when they are covalently bonded. (3) At other Fe sites, the increase in the moments can be accounted for mainly by the effect of volume expansion, but the chemical effect of doping is important and appears to be site specific. (4) C is slightly more negatively polarized than N and has a bigger influence on the Fe ($18f$) site and less influence on the Fe ($18h$) site.

The calculated numbers in Table I can be compared with the recent experimental Mössbauer data from Chen *et al.*[12] for Y_2Fe_{17}, $Y_2Fe_{17}N_{2.3}$, and $Y_2Fe_{17}C_2$ by dividing the reported hyperfine field data by a rather arbitrary factor of 14.8 T/μ_B. These numbers are listed in parenthesis in Table I. The comparison is only approximate because the samples are not stoichiometric in composition while the calculation assumes the ideal structure. Still, the relative magnitudes of the Fe moments should be meaningful. In the case of undoped Y_2Fe_{17} at equilibrium volume, it has been pointed out that the agreement between calculation and experiment on the relative magnitudes of Fe moments at various sites is marginal at best.[10] On the other hand, the results of different theoretical calculations using different methods are quite close.[10] This reflects either a fundamental inadequacy in the LSDA theory for the magnetic properties of the system of rare-earth-iron magnets, or that the theoretically calculated values may not correspond to quantities that the experiments actually measure. In the doped samples, the experimental data measure an increase of moments on all Fe sites. Our

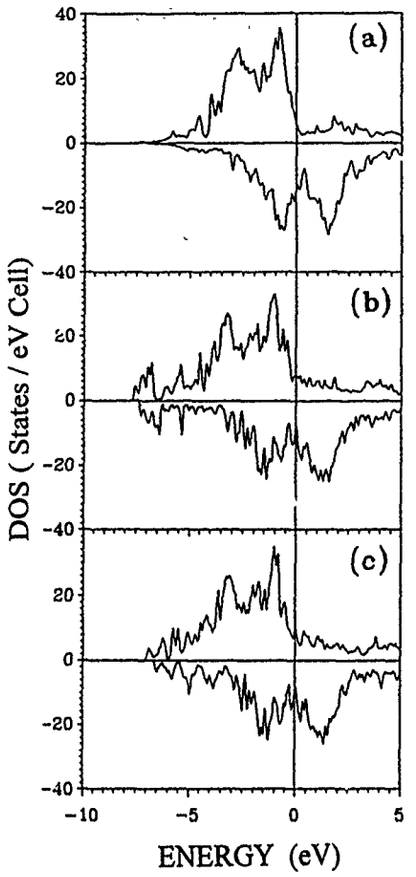

FIG. 2. Calculated total DOS for (a) Y_2Fe_{17}, (b) $Y_2Fe_{17}N_3$, and (c) $Y_2Fe_{17}C_3$ at approximately the same volume. Positive values are for the majority spin band and negative values for the minority spin band.

calculation shows this to be the case, except for the Fe ($18f$) site where there is a large decrease. Jaswal *et al.*[4] obtained the same moment as ours for this site. In the present calculation, the Mulliken scheme was used which gives the effective charges on each atom for the majority and minority spin cases. The difference is taken as the spin moment for that site. The Mulliken scheme for charge partitioning is approximate since it assumes an equal overlap for different atomic pairs. This simple scheme works best when the wave functions are not too extended, and the atoms in the system are more or less of the same size and have similar ranges of interatomic distances.

In the doped sample, the N or C are introduced to interstitial sites. Lattice expansion and local symmetry variation result in quite different interatomic separations. The Mulliken scheme may not work well in these cases. A better approach is to perform a three dimensional real space integration of the charge densities as was done by us in the case of some insulating crystals.[18] With a highly nonsystematic distribution as shown in Fig. 1, this is obviously not an easy job. In addition, the criterion for partitioning the charge or the spin density in real space is always subject to a certain degree of arbitrariness. It may be pointed out that in the linear muffin-tin orbital (LMTO)- or atomic sphere approximation (ASA)-type of calculations,[3,4,9] spin moments are not based on the Mulliken scheme, but on the difference of majority and minority spin charges inside the atomic spheres. The charges outside the atomic spheres are zero. The calculated spin moments depend somewhat on the choice of atomic sphere radii. In compact systems in which the charge distribution is more or less spherical, this approach gives quite accurate moments. However, in doped systems where the spin-density distribution is nonspherical, such an approach may not be reliable.

Figure 2 shows the calculated total DOS for the majority and minority spin bands in Y_2Fe_{17}, $Y_2Fe_{17}N_3$, and $Y_2Fe_{17}C_3$. As can be seen, doping does modify the DOS profiles. Projected partial DOS (not shown) for N and C show that the N states are in the range of -5.3 and -7.5 eV, while those of C are between -2.5 and -7.0 eV. The calculated DOS at E_F are listed in Table I. For the majority band, the reduction in the DOS at E_F in $Y_2Fe_{17}N_3$ by almost a factor of 2/3 is mainly due to lattice expansion. In $Y_2Fe_{17}C_3$, the effect of C doping increases $N(E_F)$ and is largely compensated for by the volume effect. For the minority band, lattice expansion alone reduces $N(E_F)$, and upon doping, it decreases further to about half of the value for undoped Y_2Fe_{17} at equilibrium volume. Thus chemical effect of doping is most pronounced in the $N(E_F)$ for the spin down band and in the moment of the Fe ($18f$) site.

ACKNOWLEDGMENTS

This work was supported by the DOE Grant No. DE-FG02-84ER45170. M.-Z. Huang was partially supported by a grant from the National Natural Science Foundation of China under Grant No. 188074.

[1] J. M. D. Coey and H. Sun, J. Magn. Magn. Mater. **87**, L251 (1990).
[2] H. Sun, J. M. D. Coey, Y. Otani, and D. P. F. Hurley, J. Phys. Condens. Matt. **2**, 6465 (1990).
[3] T. Beuerle, P. Braun, and M. Fahule, J. Magn. Magn. Mater. **94**, L1' (1991).
[4] S. S. Jaswal *et al.*, Phys. Rev. Lett. **67**, 644 (1991); S. S. Jaswal, IEEE Trans. Magn. **28**, 2322 (1992).
[5] Z. Q. Gu and W. Lai, J. Appl. Phys. **71**, 3911 (1992).
[6] Z. Gu, W. Lai, X.-F. Zhong, and W. Y. Ching, Phys. Rev. B **46**, 13874 (1992).
[7] Z. Zeng, Q. Q. Zheng, W. Y. Lai, and C. Y. Pan, J. Appl. Phys. **73**, 6916 (1993).
[8] P. Mohn and E. P. Wohlfarth, J. Phys. F **17**, 2421 (1987).
[9] R. Coehoorn, Phys. Rev. B **39**, 13072 (1989).
[10] M.-Z. Huang and W. Y. Ching (unpublished).
[11] Z. Altonian, X. Chen, L. X. Liao, D. H. Ryan, and J. O. Ström-Olsen, J. Appl. Phys. **73**, 6017 (1993).
[12] X. Chen, D. H. Ryan, Z. Altounian, and L. X. Liao, J. Appl. Phys. **73**, 6038 (1993).
[13] See, for example, P. Fulde, Y. Kakehashi, and G. Stollhoff, in *Metallic Magnetism*, edited by H. Capellmann (Springer, Berlin, 1987), p. 159.
[14] W. Y. Ching, Y.-N. Xu, B.-N. Harmon, J. Ye, and T. C. Leung, Phys. Rev. B **42**, 4460 (1990).
[15] W. Y. Ching, J. Am. Ceram. Soc. **73**, 3135 (1990).
[16] T. Kajitani, Y. Morii, S. Funahashi, T. Iriyama, K. Kobayashi, H. Kato, Y. Nakagawa, and K. Hiraya, J. Appl. Phys. **73** (10), 6032 (1993).
[17] R. S. Mulliken, J. Am. Chem. Soc. **23**, 1833 (1955).
[18] Y.-N. Xu and W. Y. Ching, Phys. Rev. Lett. **65**, 895 (1990); Phys. Rev. B **48**, 4335 (1993).
[19] M. Z. Huang, X.-F. Zhong, and W. Y. Ching (to be published).

Study on the effect of the previous hydrogenation of the nitride formation of a Sm_2Fe_{17}(4 at. % Nb) alloy

H. W. Kwon
Department of Material Science and Engineering, The National Fisheries University of Pusan, Pusan, South Korea

I. R. Harris
School of Metallurgy and Materials, The University of Birmingham, Birmingham, B15 2TT, England

In order to find an effective means of production of the interstitial $Sm_2Fe_{17}N_x$-type nitride, an alloy modification by the addition of small amount of alloying element (4 at.% Nb) and a hydrogenation treatment prior to the nitriding process have been employed. The effect of previous hydrogenation on the nitride formation of the Sm_2Fe_{17}(4 at. % Nb) alloy has been investigated systematically by means of thermopiezic analysis, thermomagnetic analysis, and vibrating sample magnetometer. It has been found that the previous hydrogen treatment facilitates significantly the formation of the nitride, and this may be due to the clean surface and the finer size of the particles caused by the hydrogen decrepitation. It has also been found that the combination of the alloy modification with the addition of Nb and the previous hydrogen treatment can be utilized effectively for the production of a $Sm_2Fe_{17}N_x$-type nitride.

INTRODUCTION

The $Sm_2Fe_{17}N_x$-type nitride material has been considered to be a potential candidate for the permanent magnetic application.[1–5] It is apparent, however, that there are some practical difficulties in the preparation of the Sm_2Fe_{17} N_x-type nitride material. The cast Sm_2Fe_{17}-type alloys, from which the interstitial $Sm_2Fe_{17}N_x$-type nitride is produced, have a severe structural inhomogeneity. The Sm_2Fe_{17} compound is formed through the peritectic reaction between the previously crystallized solid Fe and the liquid Sm-rich phase,[6] thus leading to the common presence of a considerable amount of free iron(α-Fe) in the cast ingot. In order to overcome this practical difficulty, a modification of the microstructure of the cast Sm_2Fe_{17} alloy by a substitution of M (M=Nb, Ta) for Fe in the alloy has been attempted, and it has been revealed that[7,8] the addition of certain transition elements, such as Nb and Ta to the Sm_2Fe_{17}-type alloy, modifies the crystallizing behavior, thus suppressing the presence of the free iron. The poor kinetics of the nitride formation reaction of the Sm_2Fe_{17}-type alloy is also a limiting factor for the preparation of the nitride material. Because the kinetics of the reaction is so slow, the Sm_2Fe_{17}-type alloy is processed commonly into a fine powder form (typical particle size less than 10 μm) in order to improve the kinetics. Many practical difficulties associated with the powder preparation or handling are, therefore, inevitable. In the present study, in an attempt to find an effective means of production of the interstitial $Sm_2Fe_{17}N_x$-type nitride, a combination of an alloy modification by the small addition of alloying element (4 at. % Nb) and a hydrogenation treatment prior to the nitrogenation process has been employed. The effect of the previous hydrogenation on the formation of the nitride has been investigated in more detail.

EXPERIMENTAL WORK

A Sm_2Fe_{17} alloy containing 4 at. % Nb was prepared using an induction furnace at 1400 °C and supplied by Rare Earth Products (Widnes, UK). The microstructure of the alloy was examined using an optical microscope or a scanning electron microscope (SEM), and the phase analysis of the alloy was performed by a SEM equipped with electron probe microanalysis (EPMA) facility. The supplied as-cast alloy was subjected to a hydrogenation treatment prior to the nitriding process. The hydrogenation was carried out at 300 °C, and it was followed by a degassing treatment at 450 °C under vacuum better than 0.05 mbar. The hydrogenation and the degassing were repeated four times in order to achieve a full decrepitation (it has been found that the Sm_2Fe_{17}-type alloy shows a poor decrepitation behavior with a simple hydrogenation treatment[9]). The cycle hydrogen treated alloy (hereafter the cycle hydrogenated alloy is in a hydrogenated state after the cycle treatment unless stated otherwise) was pulverized for 1 h using an automatic agate pulverizer in a glove box filled with high purity nitrogen gas (oxygen content in the glove box is less than 150 ppm). The as-cast alloy was also pulverized under the same conditions as the one for the cycle hydrogen treated alloy for comparison. The obtained powder materials were then nitrogenated at the temperature range of 450–500 °C for various periods under nitrogen gas (nitrogen pressure: ~1 bar). The nitrided material was then milled for 24 h under cyclohexane using a ball mill (mass ratio of material to steel ball=1:20). A TPA (thermopiezic analysis[10]) was employed in order to study the nitrogenation behavior of the as-cast or the cycle hydrogenated alloy powders. The magnetic properties of the nitrided material were characterized by means of VSM (vibrating sample magnetometer) or TMA (thermomagnetic analysis). For the VSM measurement, the nitride powder was aligned and bonded with wax under the magnetic field of 20 kOe, and the measurement was performed along the aligning direction.

RESULTS AND DISCUSSION

The microstructure of the as-cast alloy examined by a SEM is shown in Fig. 1. It is apparent that the microstructure

 0021-8979/94/76(10)/6050/3/$6.00 © 1994 American Institute of Physics

FIG. 1. SEM (backscattered electron image) photograph showing the microstructure of the as-cast Sm_2Fe_{17} (4 at. % Nb) alloy.

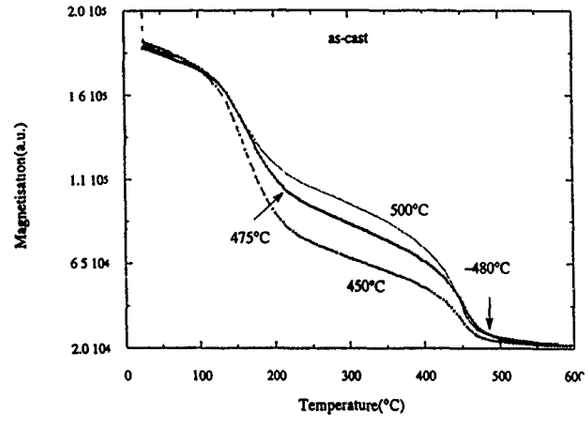

FIG. 3. TMA results for the nitride materials nitrogenated for 4 h at various temperatures using the as-cast alloy powder.

consists of a mixture of the matrix phase and eutectic phase. A minor island phase is also observed in the alloy. The x-ray microanalysis (EPMA) result shows that the matrix phase has a chemical composition of Sm_2Fe_{17} stoichiometry and the eutectic is a mixture of Sm_2Fe_{17} and $NbFe_2$ Laves phase. The island phase has a composition of $NbFe_2$ Laves phase. There is no evidence for the presence of the free iron in the alloy, which is a common feature of the conventional Sm_2Fe_{17} alloy. The as-cast alloy can, therefore, be used straightaway for the production of the Sm_2Fe_{17} nitride without any homogenizing treatment.

Figure 2 shows the TPA traces for the as-cast or the cycle hydrogenated alloy powders carried out under nitrogen gas (nitrogen pressure: ~1 bar). It appears that for the as-cast alloy powder, the nitrogen pressure in the reaction chamber begins to decrease from around 290 °C and a rapid drop is observed above 480 °C, indicating that the as-cast alloy absorbs the nitrogen from around 290 °C and most rapidly at around 480 °C. Meanwhile, for the cycle hydrogenated alloy the pressure drop occurs from around 170 °C, and a rapid increase in the pressure is observed from around 250 °C up to around 450 °C. This pressure increase is due to the desorption of hydrogen from the hydrogenated alloy. The pressure increase is stopped at around 450 °C and then followed by a rapid decrease, indicating that the hydrogen desorption is almost completed at 450 °C and the nitrogen absorption takes place rapidly above this temperature. It can be seen from these results that the cycle hydrogenated alloy powder can pick up the nitrogen at significantly lower temperature with respect to the as-cast alloy powder. This suggests that the hydrogen addition to the Sm_2Fe_{17}-type alloy prior to the nitrogenation may facilitate the formation of a $Sm_2Fe_{17}N_x$-type nitride.

Figures 3 and 4 show the TMA results for the materials nitrided for 4 h at various temperatures using an as-cast or a cycle hydrogenated alloy powder. For both materials, the TMA curves exhibit two deflections at around 150 °C and 480 °C. Those reflections correspond to the Curie temperatures of the unreacted Sm_2Fe_{17} phase and the formed $Sm_2Fe_{17}N_x$-type nitride, respectively. It appears that the deflections at 480 °C are much greater for the cycle hydrogenated alloy than for the as-cast alloy at any nitriding temperature used in the present study, indicating that the nitride can be formed more easily from the hydrogenated material with respect to the as-cast material at the same condition. The nitrided material nitrogenated at 500 °C using the as-cast alloy powder exhibits a large deflection at around 150 °C,

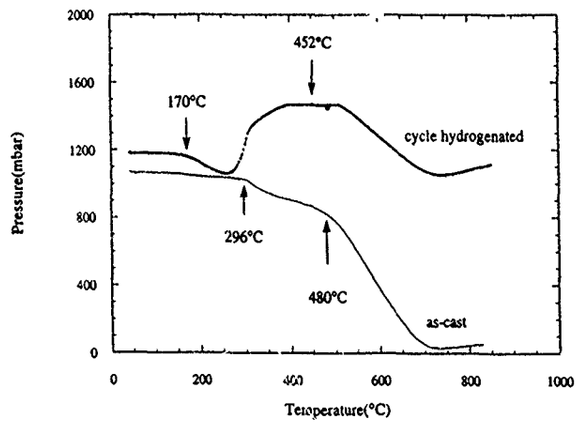

FIG. 2. TPA traces for the as-cast or the hydrogen treated alloy powders under nitrogen.

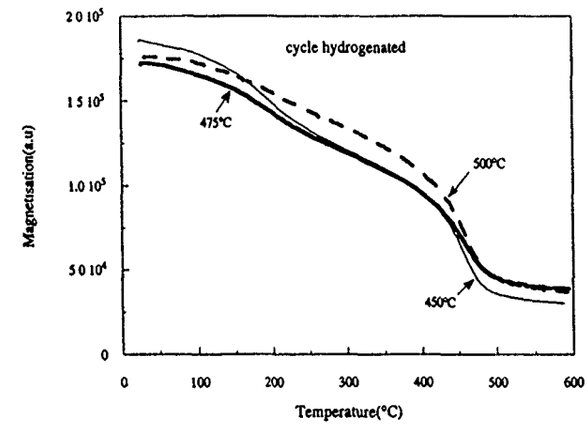

FIG. 4. TMA results for the nitride materials nitrogenated for 4 h at various temperatures using the cycle hydrogen treated alloy powder.

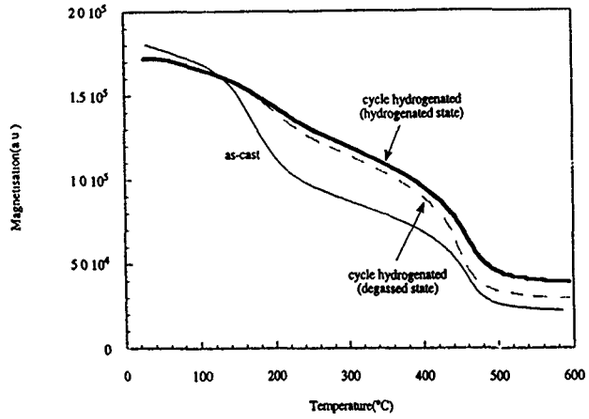

FIG. 5. TMA results for the nitride materials nitrogenated at 475 °C for 4 h using the alloy powders under various conditions.

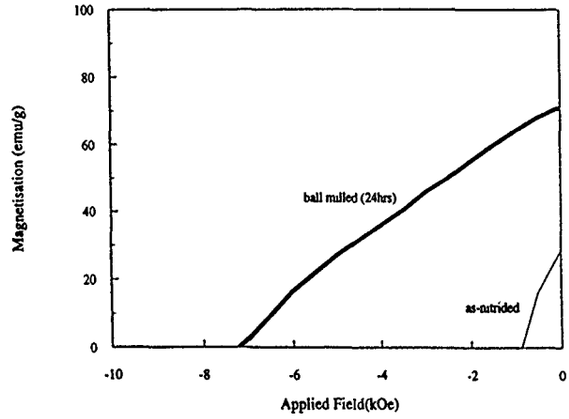

FIG. 6. VSM measurements on the nitride material nitrogenated at 475 °C for 15 h using the cycle hydrogen treated alloy powder.

indicating that there is still a significant amount of the unreacted Sm_2Fe_{17} phase after the nitrogenation. There is, however, little evidence for the presence of the unreacted Sm_2Fe_{17} phase for the cycle hydrogenated alloy powder. These results, together with the results of TPA (Fig. 2), indicate clearly that the previous hydrogenation treatment on the as-cast alloy may facilitate the formation of the nitride. Figure 5 shows the TMA result for the nitrided material which is previously cycle hydrogenated and then degassed prior to being subjected to the nitrogenation at 475 °C. The degassing was carried out *in situ* in the nitriding rig at 475 °C until a vacuum better than 5×10^{-6} Torr was achieved. The nitrogenation was carried out immediately after the degassing. The TMA results for the nitride materials obtained from the nitrogenation at 475 °C using the as-cast or the cycle hydrogenated alloy powders (the cycle hydrogenated alloy powder was in the hydrogenated state prior to the nitrogenation) duplicated from Figs. 3 and 4 are also included in Fig. 5 for comparison. The comparison between the TMA results for the nitrided materials nitrogenated using the as-cast or the cycle hydrogenated alloy powders may reveal the effect of previous hydrogen addition to the Sm_2Fe_{17}-type parent alloy on the nitride formation. It is worth noting that the TMA curves for the nitride materials nitrogenated using the cycle hydrogenated alloy powders which are in the hydrogenated or degassed state appear not to be significantly different. This result indicates that the addition of hydrogen to the Sm_2Fe_{17}-type parent alloy may not influence significantly the nitrogenation reaction of the alloy. It can be concluded, therefore, that the easier formation of nitride caused by the previous hydrogenation may be due to the decrepitation which results in a clean surface and a finer particle size.

The magnetic characterizations performed using a VSM for the nitride material obtained from the nitrogenation of the cycle hydrogenated material at 475 °C for 15 h are shown in Fig. 6. The material immediately after the nitrogenation exhibits poor permanent magnetic properties. The properties are however, improved markedly by the post-nitriding milling for 24 h. The poor properties of the as-nitrided materials may be due to the coarse particle size, and the marked improvement of the properties of the milled material may be attributed to the fine particle size of the nitride. The milled material has a significantly high coercivity (over 7 kOe).

CONCLUSION

The effect of previous hydrogen treatment on the nitride formation of the Sm_2Fe_{17}-type alloy modified with the addition of small amount of Nb has been investigated. It has been found that previous hydrogen treatment facilitates significantly the formation of the nitride, and this may be due to the clean surface and the finer size of the particles caused by the hydrogen decrepitation. The present study also shows that the combination of an alloy modification with the addition of Nb and a previous hydrogenation can be utilized as an effective means of production of a $Sm_2Fe_{17}N_x$-type nitride.

[1] J. M. D. Coey and H. Sun, J. Magn. Magn. Mater. **87**, L251 (1990).
[2] H. Sun, J. M. D. Coey, Y. Otani, and D. P. F. Hurley, J. Phys. Condens. Matter **2**, 6465 (1990).
[3] M. Katter, J. Wecker, L. Schultz, and R. Grossinger, J. Magn. Magn. Mater. **92**, L14 (1990).
[4] K. H. Buschow, Rep. Prog. Phys. **54**, 1123 (1991).
[5] B. P. Hu, and J. M. D. Coey, J. Less-Common Metals **171**, 33 (1991).
[6] W. G. Moffatt, *The Handbook of Binary Phase Diagrams* (General Electric Company, New York, 1978).
[7] A. E. Platts, I. R. Harris, and J. M. D. Coey, J. Alloys and Compounds, **185**, 251 (1992).
[8] B. Saje, A. E. Platts, S. Kobe Besenicar, I. R. Harris, and D. Kolar (to be published).
[9] H. W. Kwon and I. R. Harris, Proceedings of the 13th International Workshop on RE Magnets and Their Applications (1994), p. 805.
[10] D. H. Ryan, and J. M. D. Coey, J. Phys. E **19**, 693 (1986).

The effects of hydrogen disproportionation, desorption, and recombination on the structure and magnetic properties of $Sm_2Fe_{17}N_x$ and $NdFe_{10}Mo_2N_x$ compounds

Jun Yang, Shengzhi Dong, Weihua Mao, Ping Xuan, and Yingchang Yang
Department of Physics, Peking University, Beijing 100871, People's Republic of China

Hydrogen disproportionation, desorption, and recombination (HDDR) has been used as a pretreatment to prepare high performance $Sm_2Fe_{17}N_x$ and $NdFe_{10}Mo_2N_x$ compounds. Isotropic $Sm_2Fe_{17}N_x$ and $NdFe_{10}Mo_2N_x$ compounds with intrinsic coercivity larger than 12 and 4 kOe have been obtained by nitriding the HDDR-treated powders, respectively. It is found that the magnetic properties are sensitively dependent on the time and temperature of the HDDR process, which determine the grain size, nitrogen content, and the amount of α-Fe in the nitrides.

I. INTRODUCTION

$Sm_2Fe_{17}N_x$ and $Nd(Fe,M)_{12}N_x$ compounds have been discovered as potential new permanent magnetic candidates since 1990.[1,2]

HDDR, as a pretreatment, has been successfully used in the preparation of isotropic $Sm_2Fe_{17}N_x$ and $NdFe_{10}Mo_2N_x$ compounds. The relationship between preparation, structure, and magnetic properties of HDDR treated $Sm_2Fe_{17}N_x$ and $NdFe_{10}Mo_2N_x$ compounds will be presented in this article.

II. EXPERIMENTAL METHODS

Alloys of stoichiometric composition were prepared by arc melting 99.5 wt % pure materials in a purified argon atmosphere. The ingots were heat treated at 1050 °C for 2 days and a week for Sm_2Fe_{17} and $NdFe_{10}Mo_2$ compounds, respectively. The compounds were pulverized into powders with size ranging from 1 to 70 μm, then they were hydrided at 250–1100 °C for 1–5 h. Subsequently, the hydrided compounds were degassed at the above mentioned temperature for 1–4 h. Nitrogenation was carried out in the temperature range from 480 to 510 °C for 2–4 h, then rapidly cooled to room temperature. X-ray diffraction was used to determine the structure.

Powder samples of cylindrical shape were prepared by embedding the powders in epoxy resin, and some were aligned in a 10 kOe field. Hysteresis loops were measured in an applied field of $H=1.4$ T on a vibrating sample magnetometer and $H=7$ T on a superconducting quantum interference device (SQUID) magnetometer. The Curie temperatures were determined from M-T curves obtained with a vibrating sample magnetometer operating in a temperature range from 300 to 1000 K in a field of $H=0.1$ T.

The microstructural changes are observed by powder x-ray diffraction and scanning electron microscopy (SEM). The grain size of the HDDR treated nitrides was determined from observations by transmission electron microscopy (TEM).

III. RESULTS AND DISCUSSIONS

A. Phase formation, structure, and intrinsic magnetic properties

From x-ray diffraction, thermomagnetic measurements, and SEM observations, the alloys are identified as single phase except for a small amount of $SmFe_3$ in the Sm_2Fe_{17} alloy. When hydriding and nitriding the compounds at 250 and 500 °C, respectively, the rhombohedral and tetragonal structure of the Sm_2Fe_{17} and $NdFe_{10}Mo_2$ compounds were retained but with an increase in lattice parameters. Table I lists the lattice parameters a, c, unit cell volume V, Curie temperature T_c, and saturation magnetization M_S as well as the anisotropy field H_A of the compounds and their hydrides and nitrides. It can be seen that hydrogenation and nitrogenation can both increase the Curie temperature and saturation magnetization of the compounds and nitrogenation can change the easy magnetization direction from easy basal plane to easy c axis for the Sm_2Fe_{17} compound and from easy cone to easy c axis for the $NdFe_{10}Mo_2$ compound due to the change of second order crystal field coefficient A_{20} in the phases upon nitrogenation.

TABLE I. The lattice parameters a,c, unit cell volume V, and its relative change $\Delta V/V$, Curie temperature T_c, saturation magnetization M_S, and anisotropy field H_A of Sm_2Fe_{17} and $NdFe_{10}Mo_2$ compounds and their hydrides and nitrides at room temperature.

Compound	Structure	a (A)	c (A)	V (A^3)	$\Delta V/V$ (%)	T_c (K)	M_S (emu/g)	H_A (T)
Sm_2Fe_{17}	Rhomb.	8.561	12.45	790.4		438	105.5	
$Sm_2Fe_{17}H_y$	Rhomb.	8.673	12.54	817.0	3.37	563	120.6	
$Sm_2Fe_{17}N_x$	Rhomb.	8.736	12.67	837.0	6.0	748	137.8	15.6
$NdFe_{10}Mo_2$	Tetra.	8.593	4.784	353.3		374	65.59	
$NdFe_{10}Mo_2H_y$	Tetra.	8.614	4.796	355.9	0.72	427	74.86	
$NdFe_{10}Mo_2N_x$	Tetra.	8.662	4.818	361.5	2.32	538	86.04	8.4

 0021-8979/94/76(10)/6053/3/$6.00 © 1994 American Institute of Physics

B. Determination of HDDR parameters

HDDR includes two main processes: hydrogenation and hydrogen desorption. In both of them, time and temperature are vital to the obtained permanent magnetic properties of $Sm_2Fe_{17}N_x$ and $NdFe_{10}Mo_2N_x$ compounds. However, the correct powder size is a prerequisite for the proper HDDR treatment. For comparison, we chose the nitrogenation treatment of 500 °C for 3 h as determined in our previous studies.[3]

Figure 1 shows the demagnetization hysteresis loops of $Sm_2Fe_{17}N_x$ powder samples with an average particle size of 1, 10, and 70 μm with hydrogenation at 500 °C for 3 h and dehydrogenation treatment at 750 °C for 2 h and subsequently nitrogenation treated at 500 °C for 3 h. The results show that the optimized particle size is between 4 and 10 μm in both $Sm_2Fe_{17}N_x$ and $NdFe_{10}Mo_2N_x$ compounds. Powder particles smaller or larger than these size are deleterious to magnetic properties.

X-ray diffraction study of Sm_2Fe_{17} and $NdFe_{10}Mo_2$ compounds after hydrogenation treatment at temperatures from 250 to 1100 °C for 4 h shows that when the hydrogenation temperature is lower than 300 °C, for example, at 250 °C, the $Sm_2Fe_{17}H_y$ and $NdFe_{10}Mo_2H_y$ compounds are formed. At temperatures higher than 500 °C, Sm_2Fe_{17} and $NdFe_{10}Mo_2$ compounds decompose into a mixture of RH_{2-3} and α-Fe(Mo). When temperatures are higher than 1050 °C, Sm_2Fe_{17} and $NdFe_{10}Mo_2$ are partially recombined in the hydrogen atmosphere at 1 bar pressure. However, only when dehydrogenation was carried out at 700–800 °C, can the mixture of RH_{2-3} and α-Fe(Mo) recombine fully into Sm_2Fe_{17} and $NdFe_{10}Mo_2$ compounds. As an example, the x-ray diffraction patterns of the recombined Sm_2Fe_{17} compounds is shown in Fig. 2 in contrast with the decomposed mixture of SmH_{2-3} and α-Fe. The permanent magnetic properties also reveal that the best values were obtained by hydrogen absorption and desorption treatment at 700–800 °C.

Figures 3 and 4 show the effects of hydrogenation and hydrogen desorption time on the permanent magnetic properties of $Sm_2Fe_{17}N_x$ compounds. It can be seen that the best

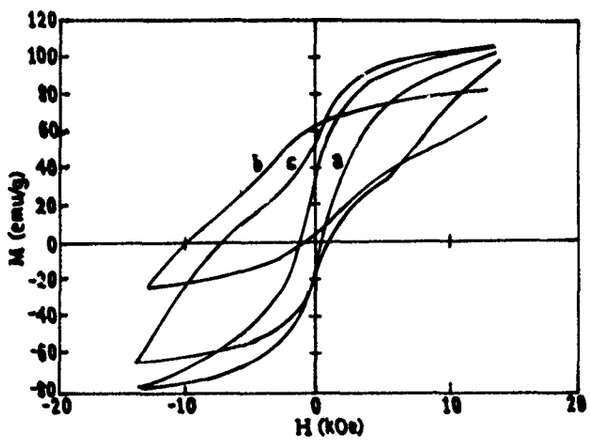

FIG. 1. The hysteresis loops of $Sm_2Fe_{17}N_x$ compounds of average powder particle size $d=1$ μm (a), 10 μm (b), 70 μm (c) by HDDR and nitrogenation treatment as described in the text.

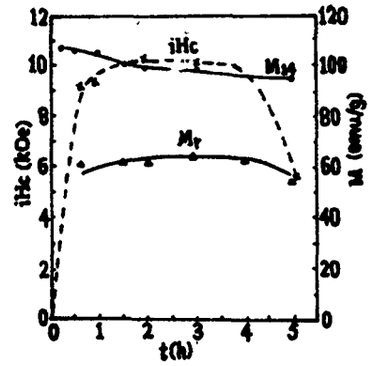

FIG. 2. The permanent magnetic properties of $Sm_2Fe_{17}N_x$ compound powders with the variation of hydrogenation time t (h) at 750 °C.

permanent magnetic properties are obtained at hydrogenation times between 2 and 4 h and a dehydrogenation time of 2 h. Furthermore, we can see from Fig. 4 that the permanent magnetic properties are sensitively dependent on the hydrogen desorption time. Figure 5 shows the hysteresis loops of thus treated $Sm_2Fe_{17}N_x$ and $NdFe_{10}Mo_2N_x$ compounds. From these data, coercivities of 12 and 4 kOe have been obtained for $Sm_2Fe_{17}N_x$ and $NdFe_{10}Mo_2N_x$, respectively.

C. Phase transformation in the HDDR process

As observed in Sec. II, the permanent magnetic properties are sensitive to the hydrogenation temperature, time, and especially to the hydrogen desorption time. X-ray diffraction studies have shown that the HDDR process is a reaction of diffusional phase transformation, which consists of the following two processes:

$$Sm_2Fe_{17}+H_2=SmH_{2-3}+\alpha\text{-Fe}, \tag{1a}$$

$$NdFe_{10}Mo_2+H_2=NdH_{2-3}+\alpha\text{-Fe(Mo)} \tag{1b}$$

and

$$SmH_{2-3}+\alpha\text{-Fe}=Sm_2Fe_{17}, \tag{2a}$$

$$NdH_{2-3}+\alpha\text{-Fe(Mo)}=NdFe_{10}Mo_2. \tag{2b}$$

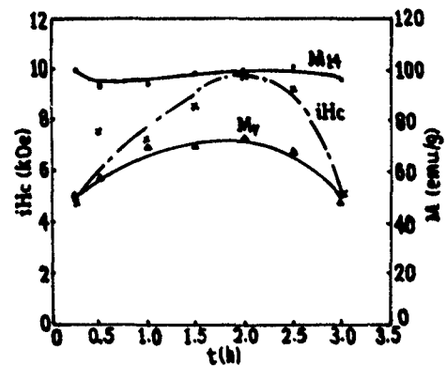

FIG. 3. The permanent magnetic properties of $Sm_2Fe_{17}N_x$ compound powders with the variation of dehydrogenation time t (h) at 750 °C.

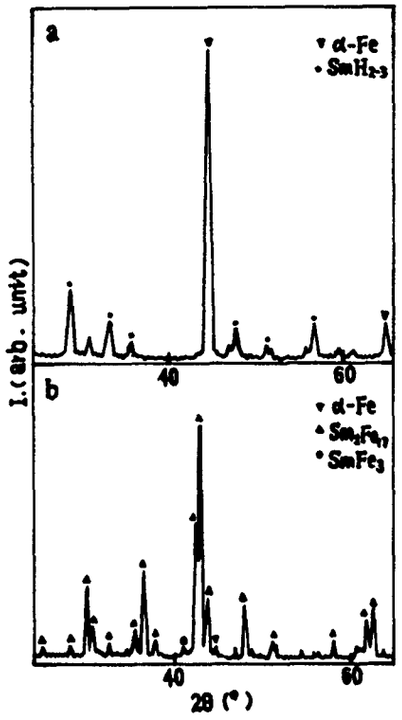

FIG. 4. The x-ray diffraction patterns of Sm_2Fe_{17} compound hydrogenated at 750 °C for 3 h (a) and dehydrogenated at 750 °C for 2 h (b).

In process (1), the reaction begins from the adsorption of H_2 on the particle surface and its decomposition into H atoms, then the H atoms diffuse along grain boundaries, and crystal defects such as twin grain boundaries jump through interstitial sites into the lattice. This results in its decomposition into a mixture of $Nd(Sm)H_{2-3}$ and α-Fe(Mo), which also requires the diffusion of Nd(Sm) and Fe(Mo) atoms to form clusters of $Nd(Sm)H_{2-3}$ and α-Fe(Mo). Therefore, when we hydrogenated bulk $NdFe_{10}Mo_2$ or Sm_2Fe_{17} compounds at 750 °C, the disproportionation process occurs preferentially in the grain boundary region, as shown in Fig. 6. It can be seen that the $Sm(Nd)H_{2-3}$ phase surrounds the α-Fe(Mo) phase and constitutes a maze pattern. From SEM observations, we also see that the size of α-Fe(Mo) and $Sm(Nd)H_{2-3}$ phases increases with hydrogenation temperature and time, because the diffusion rate of H, Nd(Sm), and Fe(Mo) atoms increases with increasing temperature, and the diffusion distance of these atoms increases with time.

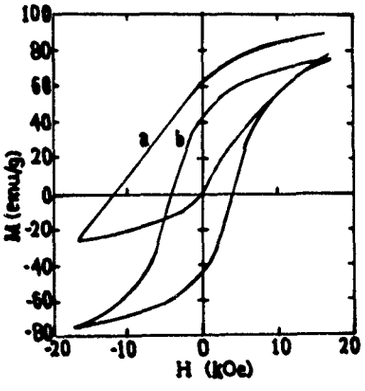

FIG. 5. The hysteresis loops of $Sm_2Fe_{17}N_x$ (a) and $NdFe_{10}Mo_2N_x$ (b) compounds magnetized at a field $H=1.4$ T after optimized HDDR and nitrogenation treatment.

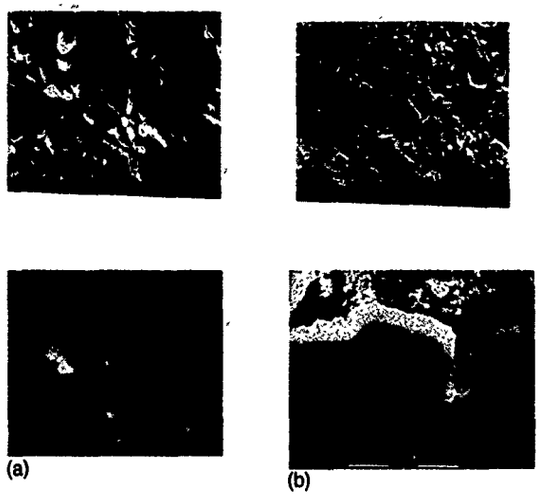

FIG. 6. The SEM backscattered electron graphs of Sm_2Fe_{17} and $NdFe_{10}Mo_2$ compounds after hydrogenation at 750 °C for 3 h (a) and dehydrogenation at 750 °C for 2 h (b).

In processes (2), the reaction starts with the detachment of H atoms from $Sm(Nd)H_{2-3}$, simultaneously, the Fe and R atoms will rapidly diffuse into each other to recombine into the original compounds but with much smaller grain size as shown also in Fig. 6. The size of the recombined grains is vital to permanent magnetic properties of the nitrogenated samples because it determines the nitrogen content, x, and the amount of the α-Fe phase as well as the amount of reverse domain nucleation sites. The grain size is determined mainly by the desorption temperature and time. Certainly, the size of the cluster of the mixture, which is controlled by the hydrogenation time and temperature, will influence the recombined grain size. The grain size in the optimized permanent magnets is around 0.3 to 0.5 μm for $Sm_2Fe_{17}N_x$ and $NdFe_{10}Mo_2N_x$ compounds as determined from transmission electron microscopy (TEM) observations.[3]

[1] J. M. D. Coey and H. Sun, J. Magn. Magn. Mater. **87**, L251 (1990).
[2] Y. C. Yang, X. D. Zhang, S. L. Ge, L. S. Kong, Q. Pan, S. Huang, and L. Yang, *Proceedings of the 6th International Symposium on Magnetism Anisotropy and Coercivity in RE-TM Alloys*, edited by S. G. Sanker (Carnegie Mellon University, Pittsburgh, PA, 1990), p. 190.
[3] Proceedings of the 12th International Works on RE Magnets and their Application, Canberra, July, 1992, p. 44.
[4] S. Z. Zhou, J. Yang, M. C. Zhang, F. B. Li, and R. Wang, as in Ref. 8, p. 44.

Phase formation in melt-spun Nd-Fe-Mo-Ti alloys

F. E. Pinkerton, C. D. Fuerst, and J. F. Herbst
Physics Department, General Motors Research and Development Center, 30500 Mound Road, Warren, Michigan 48090-9055

We report for the first time the range of $ThMn_{12}$-type crystal structure formation in melt-spun Nd-Fe-Mo-Ti ribbons. These materials, which combine the melt-spun microstructure with the favorable intrinsic magnetic properties of the $NdFe_{12-x}(Mo,Ti)_x$ phase, are important as precursors to the formation of hard magnetic materials by nitrogen absorption. Alloys with compositions $Nd_{1.15}Fe_{10+x}Mo_{2-2x}Ti_x$ ($0 \leq x \leq 1$), which grade the composition smoothly between the two end point alloys $Nd_{1.15}Fe_{10}Mo_2$ and $Nd_{1.15}Fe_{11}Ti$, were melt spun at quench wheel velocities 5 m/s$\leq v_s \leq$30 m/s. From x-ray diffraction patterns we construct a phase formation diagram as a function of Ti content x and wheel speed v_s. We find that the desired $ThMn_{12}$ structure is obtained only in ribbons quenched at low v_s. At higher speeds, the ribbons quench instead into the disordered $TbCu_7$-type crystal structure. Further, the $ThMn_{12}$ structure is considerably less stable at the Ti-rich end of the composition range than at the Mo-rich end: for $Nd_{1.15}Fe_{10}Mo_2$, the $ThMn_{12}$ structure is obtained for $v_s \leq 17.5$ m/s, whereas in $Nd_{1.15}Fe_{11}Ti$ only ribbons quenched at $v_s = 5$ m/s are of the $ThMn_{12}$ type. Heat treatments of $Nd_{1.15}Fe_{11}Ti$ ribbons melt spun at 30 m/s confirm the relatively difficult formation of the $ThMn_{12}$ structure type; annealing temperatures in excess of 1000 °C are required to form the $ThMn_{12}$ crystal structure.

I. INTRODUCTION

Compounds of the type $R(Fe,T)_{12}N_y$ (where R=rare earth and T includes Ti, Mo, and V) having the tetragonal $ThMn_{12}$ crystal structure have received increasing scrutiny as potential permanent magnet materials since the discovery by Yang *et al.*[1] that the Curie temperature T_C, saturation magnetization M_s, and magnetocrystalline anisotropy field H_A of $RFe_{11}Ti$ can be enhanced by nitrogen absorption. In the nitrided form, the most promising candidate materials are those with R=Nd, for which large saturation magnetizations and uniaxial anisotropies are obtained. In the case of T=Mo, for example, the anisotropy changes from basal plane in $NdFe_{10}Mo_2$ to uniaxial in $NdFe_{10}Mo_2N_y$ ($y \approx 1$).[2-4] Of T=Ti, Mo, and V, the nitrides of the Ti representative have been reported to have the most favorable intrinsic magnetic properties,[5] with $4\pi M_s = 13.7$ kG and $H_A = 80$ kOe at room temperature, and $T_C = 470$ °C (740 K). Magnetic hardening of the Ti materials to obtain substantial intrinsic coercivity, however, has proven to be difficult: coercivities of only 1.4–2.5 kOe have been reported in mechanically alloyed powders.[6,7] This appears to be due to the formation of a phase having the disordered, hexagonal $TbCu_7$ structure[8] which impedes formation of $NdFe_{11}Ti$ characterized by the $ThMn_{12}$ structure. Greater success has been obtained in nitrides of $NdFe_{10}Mo_2$, where coercivities of 6–9 kOe have been reported by nitriding rapidly quenched ribbons either directly quenched to a microcrystalline state,[9] or else melt spun at high wheel speeds and then annealed.[10] The generation of high coercivity by both of these techniques relies on the formation of $ThMn_{12}$-type material in the ribbons prior to nitriding.

In this article we examine phase formation in melt-spun $Nd_{1.15}Fe_{10+x}Mo_{2-2x}Ti_x$ ribbons ($0 \leq x \leq 1$) as the quench rate is varied by changing the quench wheel surface velocity v_s. The above alloy formulation transforms the composition smoothly between the end point compositions $NdFe_{10}Mo_2$ and $NdFe_{11}Ti$. We will show that slow quench wheel velocities favor the formation of the $ThMn_{12}$-type crystal structure, whereas higher wheel speeds quench the alloy into the disordered $TbCu_7$-type structure. We have previously reported that the $ThMn_{12}$ structure is obtained in ribbons quenched at wheel speeds up to about $v_s = 17.5$ m/s in $NdFe_{10}Mo_2$, but that ribbons spun at $v_s = 20$ m/s and above quench into the $TbCu_7$ structure.[9] Here we find that compositions at the Ti-rich end are much more readily quenched into the $TbCu_7$ structure at wheel speeds at and above $v_s = 10$ m/s. High quench rate Nd-Fe-Ti ribbons can be converted into the $ThMn_{12}$ structure by annealing at temperatures above 1000 °C.

II. EXPERIMENTAL DETAILS

Starting ingots of the form $Nd_{1.15}Fe_{10+x}Mo_{2-2x}Ti_x$ ($x = 0$, 0.25, 0.5, 0.75, and 1) were made by induction melting the pure elemental constituents in an argon atmosphere. $ThMn_{12}$-type Nd-Fe-Mo compounds form over a range of Mo contents from $NdFe_{11}Mo$ to $NdFe_{9.5}Mo_{2.5}$; we selected $NdFe_{10}Mo_2$ as the $x = 0$ end point for this alloy series because it is stable, the melt-spun cognate has been well characterized in our previous study,[9] and it forms high coercivity ribbon powder upon nitriding.[9,10] Excess Nd was included in the alloys because our prior work on nitriding of Nd-Fe-Mo precursor ribbons demonstrated that extra Nd was beneficial for obtaining large coercivities.[9] The ingots were rapidly quenched by melt spinning the molten alloy through a 0.60–0.65 mm orifice onto the surface of a Cr-plated copper quench wheel. The quench rate was adjusted by varying the surface velocity v_s of the wheel. The ribbons were ground to −325 mesh (<45 μm particle size), and x-ray diffraction patterns using Cu-K_α radiation were obtained. Powders made from $NdFe_{11}Ti$ ribbons melt spun at $v_s = 30$ m/s were annealed in vacuum for 10 min at temperatures ranging from

 0021-8979/94/76(10)/6056/3/$6.00 © 1994 American Institute of Physics

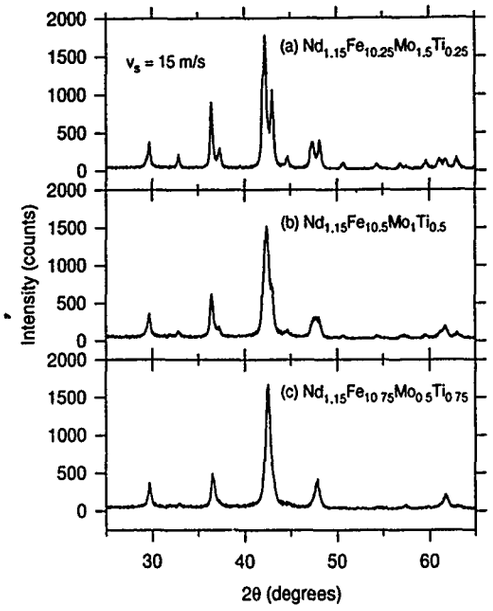

FIG. 1. X-ray diffraction patterns for $Nd_{1.15}Fe_{10+x}Mo_{2-2x}Ti_x$ ribbons melt spun at 15 m/s: (a) $x=0.25$, (b) $x=0.5$, and (c) $x=0.75$.

600 to 1100 °C in order to establish the stability of the $TbCu_7$-type material produced at high wheel speeds.

III. RESULTS AND DISCUSSION

The $ThMn_{12}$ structure is readily formed in $Nd_{1.15}Fe_{10}Mo_2$ ribbons when the wheel speed is less than or equal to 17.5 m/s.[9] At high wheel speeds, above 20 m/s, the ribbons quench instead into the disordered $TbCu_7$ structure type. The x-ray diffraction patterns in Fig. 1 illustrate the effect on phase composition of moving toward Ti-rich alloys. With the wheel speed fixed at 15 m/s, patterns are shown for (a) $Nd_{1.15}Fe_{10.25}Mo_{1.5}Ti_{0.25}$ ribbons, (b) $Nd_{1.15}Fe_{10.5}Mo_1Ti_{0.5}$ ribbons, and (c) $Nd_{1.15}Fe_{10.75}Mo_{0.5}Ti_{0.75}$ ribbons. Like its pure Mo cognate, the $x=0.25$ sample has a clean $ThMn_{12}$ diffraction pattern. At $x=0.5$, however, the diffraction pattern has begun to transform into that characteristic of the $TbCu_7$ structure, and hence it represents a partially disordered material. Line broadening due to decreased grain size alone cannot account for the observed changes in the diffraction pattern. At $x=0.75$, the transformation into the disordered $TbCu_7$ structure is complete.

From x-ray diffraction patterns like those of Fig. 1 we construct in Fig. 2 the phase formation diagram as a function of composition x (abscissa) and wheel speed v_s (ordinate). The filled circles represent samples which fall clearly within the $ThMn_{12}$ structure type, whereas the open circles represent samples having the $TbCu_7$-type structure. Partially filled circles denote samples which do not cleanly fall into either one of the two structure types, and signify in most cases a partially transformed material. The demarcation between the two structure types moves to significantly lower wheel speeds with increasing Ti content, indicating that the formation of the disordered $TbCu_7$ structure is much more favorable at high Ti content.

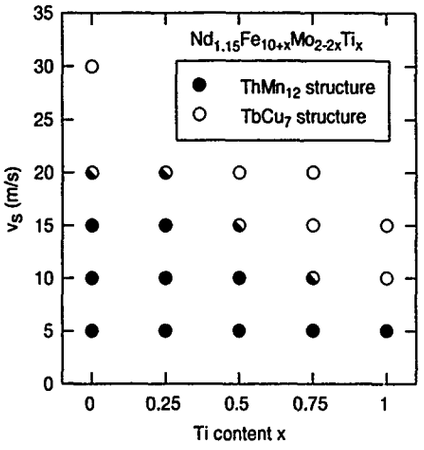

FIG. 2. Phase formation in melt-spun Nd-Fe-Mo-Ti ribbons: (●) $ThMn_{12}$, (○) $TbCu_7$ structure. Half-filled symbols represent partially transformed material.

Lattice parameters as a function of Ti content are shown in Fig. 3 for the $ThMn_{12}$-type ribbons quenched at a wheel speed of 5 m/s. The lattice constants were obtained from the d spacings of the well defined and isolated 301 and 002 diffraction peaks, and checked against the positions of several additional peaks. Contraction of the lattice with increasing Ti content x occurs predominantly in the basal plane, while the change in the c-axis lattice spacing is small. Although the $ThMn_{12}$ structure is maintained throughout the composition range, the lattice constants do not obey Vegard's law: a minimum in each of the lattice constants is observed at about $x=0.75$.

Figure 4 shows x-ray diffraction patterns of $NdFe_{11}Ti$ ribbons melt spun at a wheel speed of 30 m/s and subsequently annealed for 10 min at temperatures between 700 and 1100 °C. The as-spun ribbons, shown in Fig. 4(a), have a few weak diffraction peaks, at line positions consistent with

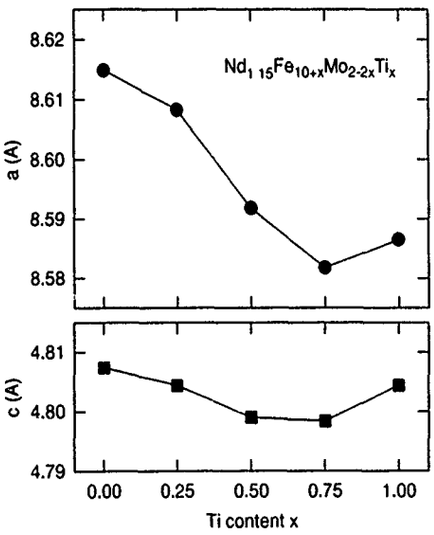

FIG. 3. Lattice parameters a and c for $Nd_{1.15}Fe_{10+x}Mo_{2-2x}Ti_x$ ribbons melt spun at $v_s=5$ m/s as a function of Ti content x.

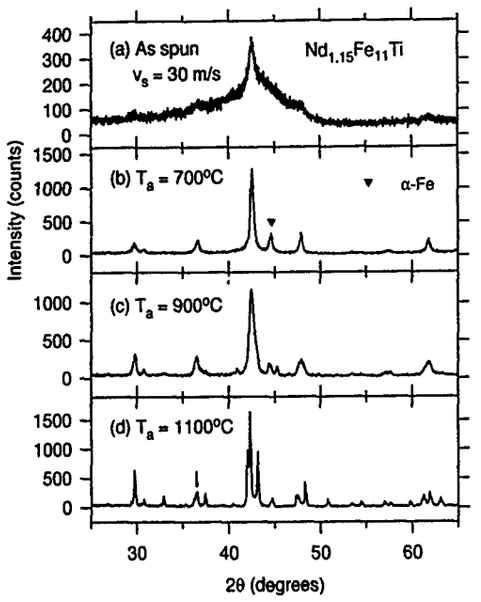

FIG. 4. X-ray diffraction patterns of $Nd_{1.15}Fe_{11}Ti$ ribbons for several annealing temperatures: (a) as spun, (b) 700 °C, (c) 900 °C, and (d) 1100 °C.

the $TbCu_7$ structure, on top of a broad amorphous background. When annealed at 700 °C [Fig. 4(b)], a well-defined $TbCu_7$ line pattern emerges, in agreement with the work of Itsukaichi *et al.*[11] A small amount of α-Fe is also present in this sample. The $TbCu_7$ structure is maintained for annealing temperatures up to 900 °C [Fig. 4(c)], where a close examination shows additional structure in the diffraction peaks indicating that the material has begun to transform into the $ThMn_{12}$ structure. The transformation is complete at 1100 °C, where the diffraction pattern is almost entirely $ThMn_{12}$-like (small impurity peaks are observed at 2θ =26.8°, 30.8°, 40.5°, and 53.5°). The relatively high annealing temperature required to transform the ribbons corroborates the phase formation diagram of Fig. 2, emphasizing the relative difficulty in forming the $ThMn_{12}$-type structure in Ti-rich ribbons.

In conclusion, we have established the phase formation diagram of melt-spun $Nd_{1.15}Fe_{10+x}Mo_{2-2x}Ti_x$ as the composition is changed smoothly between $Nd_{1.15}Fe_{10}Mo_2$ and $Nd_{1.15}Fe_{11}Ti$ and the quench wheel speed is varied from 5 to 30 m/s. The $ThMn_{12}$ crystal structure, which is favorable for the formation of hard magnetic material by nitriding, is obtained only a low wheel speeds. At higher speeds, the ribbons quench into the disordered $TbCu_7$ structure. The $TbCu_7$ structure is particularly stable at the Ti-rich end of the composition range, and in $NdFe_{11}Ti$ the $ThMn_{12}$ structure is obtained only by quenching at very low speeds (v_s=5 m/s) or by annealing the ribbons at temperatures above 1000 °C. This poses a serious challenge to the generation of useful coercivity in $ThMn_{12}$-type Nd-Fe-Ti-nitride.

ACKNOWLEDGMENTS

We wish to thank C. B. Murphy for his assistance in preparing the melt-spun ribbons, as well as A. Wims and M. Balogh of the Analytical Chemistry Department for the x-ray diffraction scans.

[1] Y.-C. Yang, X.-D. Zhang, L.-S. Kong, Q. Pan, and S.-L. Ge, Solid State Commun. **78**, 317 (1991).
[2] M. Anagnostou, C. Christides, M. Pissas, and D. Niarchos, J. Appl. Phys. **70**, 6012 (1991).
[3] X. Chen, L. X. Liao, Z. Altounian, D. H. Ryan, and J. O. Ström-Olsen, J. Magn. Magn. Mater. **111**, 130 (1992).
[4] Y. Z. Wang, G. C. Hadjipanayis, Z. X. Tang, W. B. Yelon, V. Papaefthymiou, A. Moukarika, and D. J. Sellmyer, J. Magn. Magn. Mater. **119**, 41 (1993).
[5] Y.-C. Yang, X.-D. Zhang, S.-L. Ge, Q. Pan, L.-S. Kong, H. Li, J.-L. Yang, B.-S. Zhang, Y.-F. Ding, and C.-T. Ye, J. Appl. Phys. **70**, 6001 (1991).
[6] M. Endoh, K. Nakamura, and H. Mikami, IEEE Trans. Magn. **MAG-28**, 2560 (1992).
[7] W. Gong and G. C. Hadjipanayis, IEEE Trans. Magn. **MAG-28**, 2563 (1992).
[8] Y. Khan, Acta Crystallogr. Sec. B **29**, 2502 (1973).
[9] F. E. Pinkerton, C. D. Fuerst, and J. F. Herbst, J. Appl. Phys. **75**, 6015 (1994).
[10] Z. X. Tang, E. W. Singleton, and G. C. Hadjipanayis, J. Appl. Phys. **73**, 6254 (1993); Z. X. Tang, G. C. Hadjipanayis, and V. Papaefthymiou, J. Alloys Compounds **194**, 87 (1993).
[11] T. Itsukaichi, M. Umemoto, I. Okane, and S. Hirosawa, J. Alloys Compounds **193**, 262 (1993).

In-plane magnetized YIG substrates self-biased by SmCo based sputtered film coatings

F. J. Cadieu and H. Hegde
Physics Department, Queens College of CUNY, Flushing, New York 11367

E. Schloemann and H. J. Van Hook
Raytheon Research Division, 131 Spring Street, Lexington, Massachusetts 02173

Highly anisotropic SmCo based films with the $TbCu_7$-type structure have been sputter deposited directly onto YIG substrates. The SmCo crystallites have the *c* axes approximately randomly splayed about the substrate plane such that the easy direction of magnetization of the SmCo film is in the film plane. The in-plane static energy product of the SmCo film layers was about 16 MG Oe. In-plane vibrating sample magnetometer hysteresis loops of the SmCo film and YIG substrate exhibit a composite form with the YIG field reversal shifted into the first quadrant by the looping field from the SmCo film layer. Approximately 4×4 mm^2 pieces of YIG substrate have been measured to determine the YIG bias field and field required for reverse saturation of the YIG as a function of the SmCo based film layer thickness to YIG substrate thickness. It is observed that for SmCo to YIG thickness ratios greater than 0.22, the looping field from the SmCo film layer is sufficient to saturate the YIG magnetization in the reverse direction. SmCo film thicknesses in the range from 80 to 120 μm have been used in these studies. Special boundary layers have been used to promote thick film adhesion to the YIG substrates.

INTRODUCTION

Magnetic ceramics are often used in microwave circuits to provide an active element for microwave circulators and isolators. In use the magnetization of the magnetic ceramic is generally saturated through the use of bulk pieces of magnet surrounding the device.[1,2] Such an arrangement is not amenable to direct film integration of such devices. To provide an alternative arrangement in which the magnetic ceramic can be biased we have deposited SmCo based permanent magnet film layers directly onto YIG substrates. The SmCo based films were directly crystallized onto the YIG substrates such that the permanent magnet film layer has the easy axis of magnetization strongly aligned onto the substrate plane. The looping field of the SmCo film layer then acts to bias the YIG substrate in the reverse direction. The YIG bias field level and the field required for complete reverse field saturation of the YIG has been studied as a function of the SmCo film layer thickness to YIG substrate layer thickness. Permanent magnet film layer thicknesses from 80 to 120 μm have been studied. To promote adhesion of such films onto the YIG substrates special boundary layers have been used.

EXPERIMENT

Highly anisotropic SmCo based films containing traces of Cu and Zr as in SmCo based 2-17 magnets have been RF sputter deposited onto polished YIG substrates. The substrates were heated so that the deposit crystallized upon deposition into a single phase $TbCu_7$-type structure.[3] The nominal film Sm concentration was 14 at. %. The sputtering conditions were adjusted so that the *c* axes of the $TbCu_7$ structure were in the film plane and nearly randomly splayed about the film plane.[4] To promote thick film adhesion a boundary layer of dense Al was deposited onto the polished YIG substrates before the SmCo based deposition.[5] The magnetic properties were measured at room temperature to ±18 kOe using a vibrating sample magnetometer (VSM). In addition, a bipolar power supply was used to sweep the low field region for certain samples. Sample pieces of SmCo based film and YIG substrate were cut for VSM measurements using a diamond wire saw.

RESULTS AND DISCUSSION

Figure 1 shows the cross section of a 118 μm thick SmCo based film that was directly crystallized onto a 635 μm thick YIG substrate. A 1.5 μm boundary layer of dense aluminum was first sputter deposited onto the YIG substrate to promote film adhesion. The resulting film and YIG substrate can be patterned by photolithography methods or cut

FIG. 1. The cross section of a 118 μm thick SmCo based film with in-plane anisotropy directly crystallized onto a boundary layer coated YIG substrate is shown. The YIG substrate is along the left edge of the figure.

 0021-8979/94/76(10)/6059/3/$6.00 © 1994 American Institute of Physics

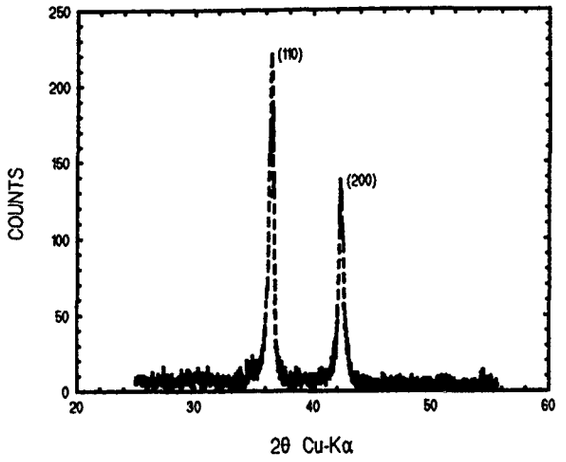

FIG. 2. An x-ray diffractometer trace, CuKα radiation, of the SmCo film of Fig. 1 is shown. Note that the crystallites have the c axes aligned onto the film plane.

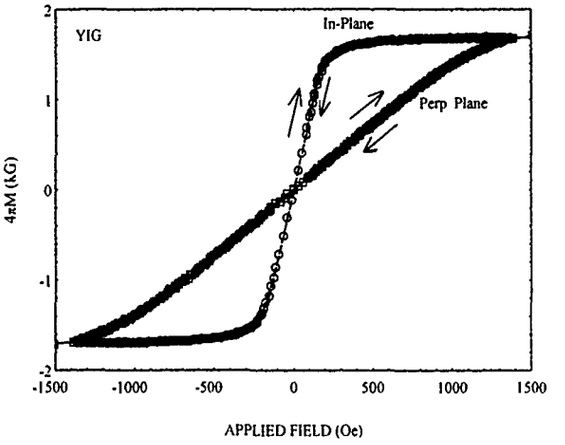

FIG. 4. Hysteresis loops measured in-plane and perpendicular to the plane of a 635 μm thick YIG piece are shown. The YIG area was 4.3×4.5 mm^2. Arrows are shown to indicate that each loop retraces itself.

as desired without the film and substrate delaminating. The SmCo based film was crystallized into the $TbCu_7$ disordered 1-5 type structure. An x-ray diffractometer trace of such a film is shown in Fig. 2. The only lines above background correspond to the (110) at 2Θ=36.43° and the (200) reflection at 42.25°. It should be noted that all crystallites have the c axes aligned onto the plane of the substrate, but that there is a nearly random splaying of the c axes about the film plane. In some cases the SmCo based film was sputter deposited with a mask used to form a pattern in the film deposited onto the YIG substrate. The hysteresis loops measured in the film plane and perpendicular to the plane for a piece removed from the mask are shown in Fig. 3. In this way the magnetic properties of the SmCo based film can be measured from the same sputter deposition as used for the SmCo film layer deposited onto the YIG substrate. The magnetic properties show that the easy direction of magnetization of the SmCo film layer is in the film plane. The typical remanent flux density is approximately 8 kG which is consistent with a random splaying of the crystallites in two dimensions. The expected remanent to saturation flux density in this case is $2/\pi$=0.64.[6] The room temperature static energy product of the SmCo based film is ≈16 MG Oe. In this particular case the room temperature $_iH_c$ = 6.0 kOe so that the energy product is not coercivity limited.

Figure 4 shows in-plane and perpendicular to the plane hysteresis loops for a bare YIG substrate piece measuring 4.3×4.5×0.635 mm^3. Arrows are shown to indicate that each loop retraces itself with no apparent hysteresis to the scale shown. The YIG flux density passes through zero for zero applied field so that the YIG bias value is zero. For this size piece a reverse in-plane applied field of 200 Oe is required to saturate the bare YIG substrate. The perpendicular applied field required for saturation is about 1200 Oe. The field values required for saturation are set by the demagnetization field due to the shape of the YIG piece.

Figure 5 shows the composite in-plane hysteresis loop of

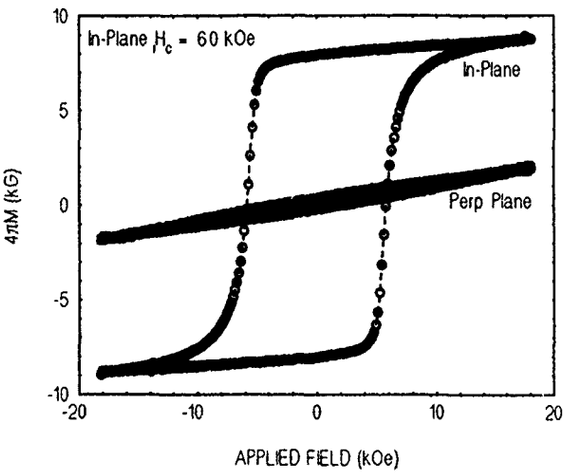

FIG. 3. Hysteresis loops are shown measured in-plane and perpendicular to the plane for a 118 μm thick $TbCu_7$-type SmCo based film.

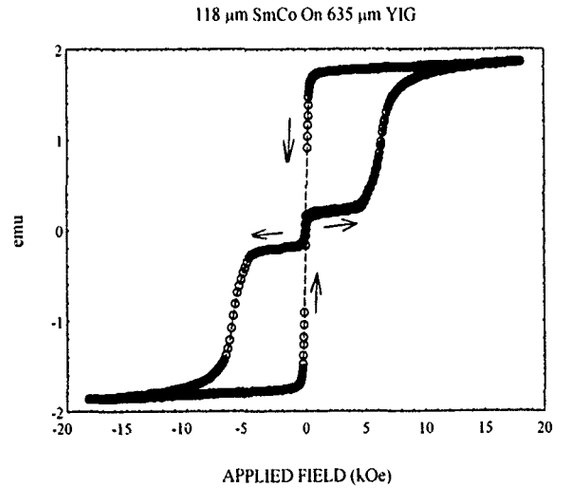

FIG. 5. An in-plane hysteresis loop for 118 μm thick SmCo based film deposited onto a 635 μm thick polished YIG substrate are shown. Arrows indicate the magnetization progression.

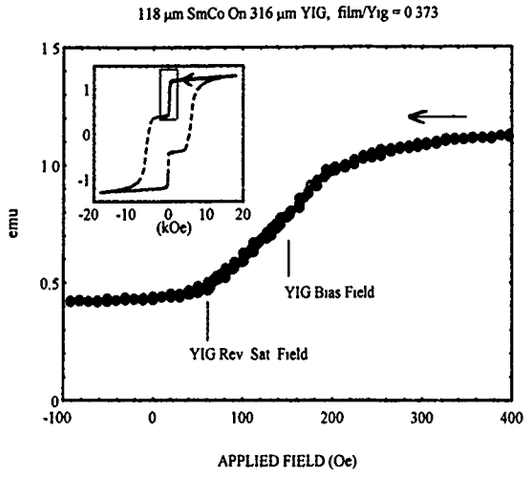

FIG. 6. An in-plane hysteresis loop for a 118 μm thick SmCo film on a 316 μm thick YIG substrate is shown in the inset. The main figure shows an expanded field view of the region indicated by the rectangle. The YIG bias level due to the presence of the SmCo film is indicated as well as the field at which the YIG becomes saturated in the reverse direction. Note that the YIG is saturated in the reverse direction when the applied field is still +60 Oe in the opposite direction. The arrow indicates that the applied field was decreased.

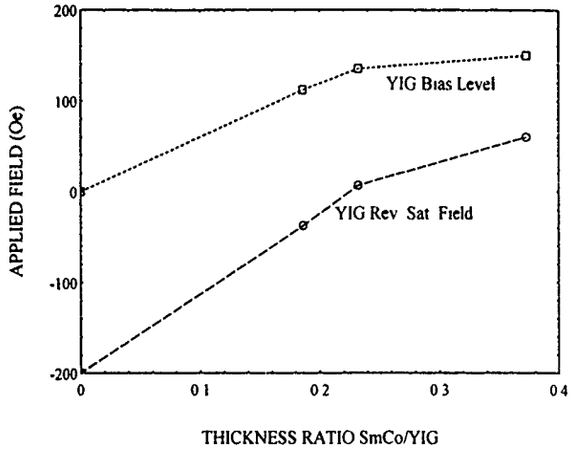

FIG. 7. The YIG bias level and the applied field level following magnetization at which the YIG becomes saturated in the reverse direction as a function of the SmCo to YIG thickness ratio are shown.

a 118 μm thick SmCo based film as deposited onto a 635 μm thick YIG substrate. The applied field range shown is from $\pm$20 kOe. Arrows on the curve indicate the magnetization and demagnetization progression. For the upper branch the sharp drop near $H=0$ is when the YIG emu value reverses. In this case the SmCo and YIG substrate size measured was 3.5×3.3 mm^2. The relative SmCo to YIG emu value jumps are in the ratio of the remanent flux density of the SmCo layer times the thickness of the SmCo layer to the saturation flux density of the YIG layer times the YIG thickness. The remanent SmCo flux density is 8.0 kG while that of the YIG is 1.7 kG. A SmCo to YIG film thickness ratio of 1.7/8.0 $=0.21$ would show the YIG reverse saturation step level at the zero net emu level. For Fig. 5 the SmCo to YIG thickness ratio is 0.186 and thus the YIG emu contribution exceeds the SmCo contribution.

Hysteresis loops were measured to saturation in the film plane for a 118 μm thick SmCo based film on a YIG substrate for successive steps as the YIG substrate was mechanically thinned. Figure 6 shows the SmCo-YIG magnetization progression as the field was swept from $\pm$18 kOe. The decrease in the total SmCo-YIG emu value due to the YIG magnetization reversal is shown with an expanded scale as the applied field was lowered from +400 to -100 Oe, as indicated by the arrow direction. This expanded scale region corresponds to the rectangular region indicated in the inset figure. The expanded scale date was collected with a field step size of a few Oe. The expanded scale part of the figure shows that the YIG reversal occurred before the applied field had been reduced to zero. For the substrate thinning step shown in Fig. 6 the YIG substrate thickness was 316 μm for a film to YIG thickness ratio of 0.373. In this case it should be noted that the YIG bias field value due to the presence of the SmCo film is 150 Oe. The internal field of the YIG is thus zero when the applied field has only been lowered to +150 Oe. In this case the YIG reverse emu value has saturated when the applied field has been reduced to +60 Oe. The looping field from the SmCo based layer is thus sufficient to completely saturate the YIG in a reverse direction when the external applied field is $\leq$60 Oe. The looping field from such a SmCo based film has been used similarly to bias permalloy strips[7] and in the construction of a magneto-optic waveguide isolator.[8]

Figure 7 shows the YIG bias level, and the field required for reverse saturation of the YIG, as a function of the SmCo to YIG thickness ratio. For SmCo to thickness ratios of $>$0.22 the magnetization of the YIG is reverse saturated by the presence of the SmCo layer. The YIG bias level and the field required for reverse YIG saturation become closer together as the YIG thickness is decreased because the demagnetization values decrease.

ACKNOWLEDGMENTS

This work was supported by a subcontract from the Raytheon Company (F. J. C.) as a part of the ARPA sponsored Ferrite Development Consortium. Work at QC supported in part by AFOSR.

[1] J. D. Adam, M. R. Daniel, P. R. Emtage, and S. H. Talisa, *Magnetostatic Waves*, Physics of Thin Films Vol. 15, editors M. H. Francombe and J. L. Vossen (Academic, San Diego, 1991).
[2] E. Schloemann and R. E. Blight, IEEE Trans. Microwave Theory Tech. MTT-**34**, 1394 (1986).
[3] F. J. Cadieu, H. Hegde, and K. Chen, J. Appl. Phys. **67**, 4969 (1990).
[4] F. J. Cadieu, J. Appl. Phys. **61**, 4105 (1987).
[5] F. J. Cadieu, H. Hegde, and K. Chen, IEEE Trans. Magn. MAG-**25**, 3788 (1989).
[6] F. J. Cadieu. *Permanent Magnet Thin Films*, Physics of Thin Films Vol. 16 (Academic, San Diego, 1992).
[7] H. Hegde, S. U. Jen, K. Chen, and F. J. Cadieu, J. Appl. Phys. **73**, 5926 (1993).
[8] M. Levy, R. Scarmozzino, R. M. Osgood, F. J. Cadieu, and H. Hegde, J. Appl. Phys. **75**, 6286 (1994).

Transverse susceptibility and magnetic anisotropy of CoTi-doped barium hexaferrite single crystals

G. Zimmermann and K. A. Hempel
Institut für Werkstoffe der Elektrotechnik, Aachen University of Technology, Templergraben 55, 52056 Aachen, Germany

Measurements of the reversible transverse susceptibility (RTS) were performed on $BaFe_{12-x-y}Co_xTi_yO_{19}$ single crystals with doping concentrations $x \approx y \leq 0.77$ under different angles ϑ_0 between the easy axis and applied field. For intermediate doping concentrations the occurrence of a peak in the RTS curve for $\vartheta_0=90°$ indicates that the domain walls are not free to move. This assumption is confirmed further by the large component of the RTS being out of phase with respect to the excitation field H_E. The phase angle of the initial susceptibility measured parallel to the easy axis becomes maximum at a characteristic excitation field value $H_{E,C}$ and a relaxation of the susceptibility is observed if H_E steps from zero to a value larger than $H_{E,C}$. Using the RTS curve for $\vartheta_0=0$ and assuming that the peak of the RTS is located at the same field strength as if the particle were single domain, the first-order anisotropy field $H_A=2K_1/(\mu_0 M_s)$ and the second-order anisotropy constant K_2 can be determined. The values found this way are compared to results from magnetization-curve analysis and from other authors.

I. INTRODUCTION

Due to their wide applicability, *M*-type barium hexaferrites with substitutions of Co^{2+} and Ti^{4+} were the subject of many theoretical and experimental investigations.[1] Most of the experimental work was done on isotropic polycrystalline powder samples and aimed at the dependence of saturation magnetization and magnetic anisotropy on the doping concentration.[2,3]

There was an attempt recently to clarify the resulting and partially conflicting theories of magnetization and anisotropy by analyzing magnetization curves of single crystals over a wide range of fields and temperatures.[4] One focal point of this investigation was the independent determination of the first- and second-order anisotropy constants K_1 and K_2. The aim of this paper is to present new data for these constants obtained by measurements of the reversible transverse susceptibility (RTS) on $BaFe_{12-x-y}Co_xTi_yO_{19}$ single crystals at room temperature. Results from analysis of the magnetization curve in the magnetically hard direction are given for comparison, and the observed time dependence of the initial susceptibility is described in order to give more insight into the magnetization process.

II. TRANSVERSE SUSCEPTIBILITY

The reversible transverse susceptibility (RTS), which measures the change of magnetization in the direction of a small excitation field applied perpendicular to a bias field **H**, was investigated theoretically for uniaxial single-domain particles by Aharoni *et al.*[5] In the case of perpendicular orientation of bias field **H** and easy axis ($\vartheta_0=90°$), the theory predicts an infinite RTS in the (**H**, easy axis), plane at field strengths sufficient for saturation. Assuming a single crystal with an ellipsoidal shape, coinciding crystalline and rotational axes, and demagnetizing factors $N_\parallel$ and $N_\perp$ parallel and perpendicular to these axes, the saturating field is given by

$$H_s = H_A\left(1+\frac{2K_2}{K_1}\right)+(N_\perp - N_\parallel)M_s = H_A' + \frac{2K_2}{K_1}H_A,$$

where $H_A=(2K_1)/(\mu_0 M_s)$ is the first-order anisotropy field, $K_{1,2}$ are the first- and second-order anisotropy constants, M_s the saturation magnetization, and $\mu_0=4\pi\times10^{-7}$ (V s)/(A/m).

If the direction of **H** coincides with the easy axis of the particle ($\vartheta_0=0$), the transverse susceptibility measurement yields H_A', which is not influenced by K_2.[6,7] Thus, the comparison between H_s and H_A' in principle gives the opportunity to determine both the anisotropy constants of a single-domain particle. If, on the other hand, a multidomain single crystal is considered, the theory predicts a jump of the RTS at the transition into the single-domain state. Since in practice there is no sharp kink, as expected theoretically, it is generally impossible to get information about K_2 from RTS measurements of multidomain particles.[8]

III. DETERMINATION OF ANISOTROPY CONSTANTS

We investigated five irregularly shaped $BaFe_{12-x-y}Co_xTi_yO_{19}$ single crystals, which were prepared by slow cooling[9] of $BaO\text{-}BaF_2\text{-}B_2O_3$ melts (Table I). The samples were oriented in a field of 1600 kA/m and fixed using liquid adhesive. Subsequently, we measured the magnetization curves parallel and perpendicular to the easy axis in a vibrating sample magnetometer and the RTS under dif-

TABLE I. Dopant concentrations, weight, and saturation magnetization of the investigated single crystals.

	$BaFe_{12-x-y}Co_xTi_yO_{19}$			
Sample	x	y	m (10^{-3} g)	M_s (kA/m)
1	0	0	17.9	380
2	0.09	0.1	14.3	372
3	0.40	0.45	19.9	365
4	0.58	0.58	43.0	333
5	0.77	0.77	46.4	310

 0021-8979/94/76(10)/6062/3/$6.00 © 1994 American Institute of Physics

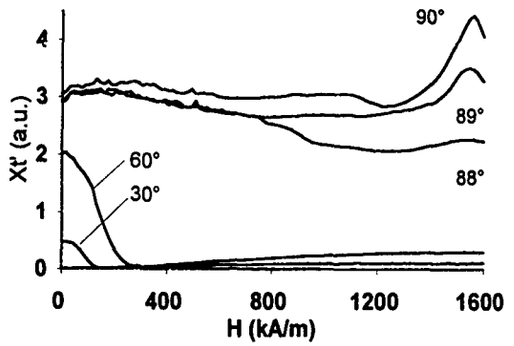

FIG. 1. In-phase component of the RTS of sample 2 for different angles ϑ_0. The measuring frequency was 5 kHz and the excitation field strength 15 A/m.

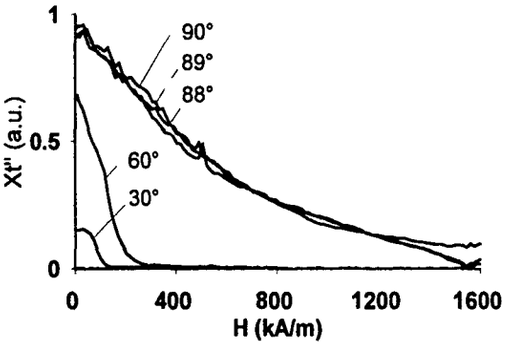

FIG. 2. Out-of-phase component of the RTS of sample 2 under the same conditions as in Fig. 1.

ferent angles ϑ_0 with an experimental setup similar to that described in Ref. 7, each time starting with a field of 1600 kA/m.

Whereas the undoped single crystal exhibits a qualitatively good agreement with the theoretical RTS curves for the multidomain case, a peak of the RTS occurs for $\vartheta_0=90°$ even for the small doping concentration $x\approx 0.1$ (Fig. 1). If x and y increase, the RTS curves become more and more similar to the curves predicted by single-domain theory, indicating that the domain walls do not move without energy consumption (as presumed for the theoretical investigation).[8] The location of the peak, as well as its shape, do not depend on the measuring frequency in the range between 1 and 150 kHz and on the strength of the excitation field which was increased to 90 A/m.

Identifying the field of the RTS peak with H_s and using the RTS curve and the magnetization curve for $\vartheta_0=0$ for the determination of H_A', $N_\parallel$, and $N_\perp$, the values of H_A and K_2 given in Table II are yielded. In addition, we evaluated H_A and K_2 using a Sucksmith–Thompson (ST) plot of the magnetization curve in the magnetically hard direction.[10] The room temperature values of H_A obtained in Ref. 4 by the same method are given for comparison.

IV. OUT-OF-PHASE COMPONENT AND TIME DEPENDENCE

The assumption of a damped domain wall motion is confirmed further by the appearance of a large out-of-phase component of the RTS for samples 2, 3, and 4 (Fig. 2). In order to get more insight into this effect, we measured the initial susceptibility parallel to the easy axis. Figure 3 shows the dependence of the phase angle of the initial susceptibility on the strength of the excitation field H_E, where we use $\underline{\chi}=\chi'-i\chi''$ ($i=\sqrt{-1}$). The most striking result is the existence of a maximum for the three samples with low and medium degree of doping at a characteristic excitation field $H_{E,C}$ of about 45 Å/m. The χ''/χ' ratio depends weakly on the measuring frequency in the 1–150 kHz range (Fig. 4). As a corresponding effect in the time domain, a relaxation of the susceptibility with a time constant τ of about 20 s at room temperature can be observed on samples 2, 3, and 4 (Fig. 5), provided that H_E steps from zero to a value larger than a threshold value $H_{E,T}\approx H_{E,C}$. If the temperature is increased up to 50 °C, τ decreases to one-tenth of its room-temperature value and becomes undetectable with our measuring equipment at a temperature of 100 °C. If we thus assume a thermally activated process with $\tau=\tau_0\exp(\Delta W/kT)$, we yield $\tau_0\approx 2\times10^{-11}$ s and $\Delta W\approx 0.7$ eV at a rough estimate. A similar activation energy, as well as the existence of a threshold field, was found by Enz *et al.*[11] on Si-doped YIG and ascribed to a diffusion aftereffect[12] involving electron transitions between Fe^{2+} and Fe^{3+} ions. It is remarkable, in this context, that Šimša *et al.* deduced from their measurements a preferred occupation of $12k$ instead of $4f_2$, sites by the Co and Ti ions in the hexagonal fundamental cell in case of

TABLE II. First-order anisotropy field H_A and second-order anisotropy constant K_2 determined by RTS measurement and Sucksmith–Thompson plot (ST), respectively. The $H_A^{(4)}$ values are given in Ref. 4 and were obtained by the ST method.

x	$H_{A,RTS}$ (kA/m)	$K_{2,RTS}$ (MJ/m³)	$H_{A,ST}$ (kA/m)	$K_{2,ST}$ (MJ/m³)	$H_{A,ST}^{(4)}$ (kA/m)
0	1381	···	1289	≤0.001	1305
0.09	1370	0.006	1270	0.002	1241
0.40	1069	0.007	914	0.005	···
0.58	531	0.019	429	0.012	454
0.77	135	0.03	175	0.029	40

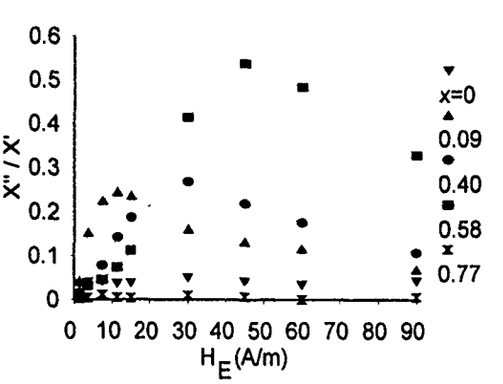

FIG. 3. Phase angle of the initial susceptibility as a function of the excitation field strength H_E. The measuring frequency was 1 kHz

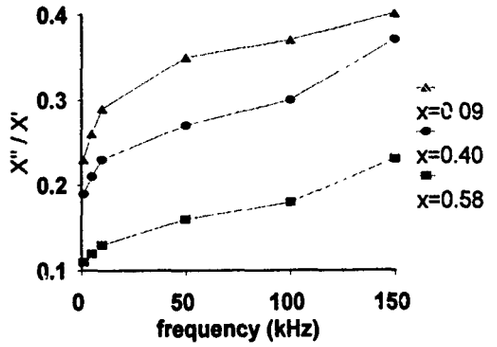

FIG. 4. Phase angle of the initial susceptibility as a function of the measuring frequency. The excitation field strength was 15 A/m.

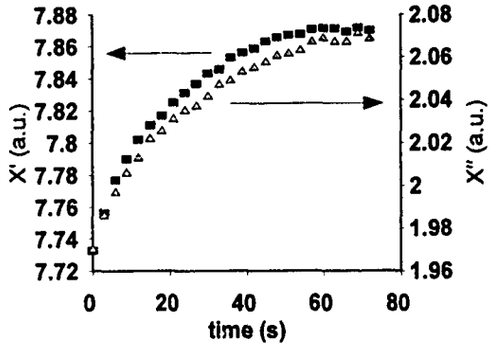

FIG. 5. Relaxation of the initial susceptibility of sample 3 at room temperature. The excitation field is applied parallel to the easy axis and steps from 0 to 30 A/m.

increasing dopant concentrations.[4,13] The present results are not sufficient to enlighten the conceivable connection between these observations.

V. CONCLUSION

The first-order anisotropy field values determined by measurement of the reversible transverse susceptibility parallel to the easy axis of the single crystals and by analysis of the magnetization curve in the perpendicular direction are in a good agreement with the results of other authors.[2,3,4]

By contrast, the values obtained for the second-order anisotropy constant differ both for the two methods used here and in comparison with results published elsewhere. On one hand, this reflects the general difficulty in the experimental determination of K_2; on the other hand, it might indicate that the observed curvature of the magnetization curves is not due to the influence of the second-order anisotropy constant. Despite a possibly large error in the absolute value of K_2, both methods however do not indicate a decrease for higher dopant concentrations, as was found by other authors.[4]

The existence of a peak in the reversible transverse susceptibility as well as the appearance of a large out-of-phase component indicates a heavily impeded wall motion for intermediate doping concentrations. This assumption is confirmed by time domain measurements, which show a relaxation of the initial susceptibility with a thermally activated relaxation time. Further investigations are necessary to clarify the suggestive interpretation of these results in terms of a diffusion damped domain wall motion, possibly due to distribution of the Co and Ti ions on energetically different lattice sites depending on the direction of magnetization.

ACKNOWLEDGMENT

The authors would like to thank Dr. K. Fischer from IPHT Jena for the growth of the crystals.

[1] Landolt-Börnstein, *Numerical Data, New Series III* (Springer, Berlin, 1982), Vol. 4b.
[2] D. J. De Bitetto, J. Appl. Phys. **35**, 3482 (1964).
[3] C. Surig, K. A. Hempel, and F. Schumacher, J. Magn. Magn. Mater. **117**, 441 (1992).
[4] Z. Šimša, R. Gerber, R. Atkinson, and P. Papakonstantinou, Ferrites: Proc. ICF 6, Tokyo and Kyoto, Japan, 1992 (unpublished).
[5] A. Aharoni, E. M. Frei, S. Shtrikman, and D. Treves, Bull. Res. Counc. Isr. A **6**, 215 (1957).
[6] H. J. Richter, J. Appl. Phys. **67**, 3081 (1990).
[7] G. Zimmermann, J. Appl. Phys. **73**, 8436 (1993).
[8] G. Zimmermann and K. A. Hempel, IEEE Trans. Magn. **28**, 3126 (1992).
[9] Z. Šimša, P. Görnert, A. J. Pointon, and R. Gerber, IEEE Trans. Magn. **26**, 2789 (1990).
[10] W. Sucksmith and F. E. Thompson, Proc. R. Soc. London Ser. A **225**, 362 (1954).
[11] U. Enz and H. van der Heide, J. Appl. Phys. **39**, 435 (1968).
[12] J. F. Janak, J. Appl. Phys. **34**, 3356 (1963).
[13] E. W. Gorter, Proc. IEE **104B**, 255S (1957).

Preparation of high-coercivity fine barium ferrite powder

W. A. Kaczmarek and B. W. Ninham
Research School of Physical Sciences and Engineering, Australian National University, Canberra, A.C.T. 0200, Australia

The structural and magnetic properties of the thermally activated transformation from nanostructural material, mechanically disordered and decomposed $BaFe_{12}O_{19}$ ferrite powder to pure crystalline phase, have been studied by x-ray diffraction, scanning electron microscopy, and vibrating sample magnetometry analysis techniques. All experiments were performed on as-milled (1000 h) in air, and in vacuum and annealed Ba-ferrite samples (4 h at 773 and 1273 K). In parallel with the structure and particle morphology changes, we investigate the influence of heat treatment on the powder M-H hysteresis parameters in relation to the preparation routes, i.e., powder obtained by ball milling in air and vacuum, and annealed in air or vacuum.

I. INTRODUCTION

The first experiments dealing with the effect of milling on the magnetic properties of barium ferrite were conducted more than twenty years ago.[1,2] However, particles obtained were well above the single-domain critical size (~1 μm at room temperature); and the results of magnetic measurements were ambiguous because they reflect the influence of structural deformation and lattice defects. Likewise, simple milling techniques used in those studies suffered from lack of control and precision in prescribing required milling conditions. Only in a recently introduced new type of ball mills can the milling process be controlled with required precision.[3,4] The present report is part of a wider project in which the influence of effects induced during mechanical processing on the gas-solid state surface interface on complex oxide systems is investigated. The influence of ball milling of $BaFe_{12}O_{19}$ ferrite powder on its structure and particle morphology was described in a previous paper.[5] In this study, along with the structure changes we investigate the influence of heat treatment on the powder particle morphology and magnetic properties in relation to preparation routes, i.e., powder obtained by ball milling in air and vacuum.

II. EXPERIMENT

High-purity (99.99 wt %) barium ferrite powder ($BaFe_{12}O_{19}$) with particle size distribution in the 0.5–50-μm range from Alfa Products/Johnson-Matthey was used as a starting material. Starting sample characterization and mechanical ball milling preparation details were described extensively in the previous paper.[5] An additional two samples were obtained by milling in air and in low-pressure "technical" vacuum (~10^2 Pa) for 1000 h. All three samples will be denoted in this paper as Ba-ferrite, A1000, and V1000, respectively. Heat treatment was performed on A1000 and V1000 powders at temperatures of 773 and 1273 K in air atmosphere, and in vacuum (sealed quartz tube) for 4 h. The experiments then yielded samples designated: for air milled material AA773, AA1273 (annealed in air) and AV773, AV1273 (annealed in vacuum) samples and for vacuum milled powder VA773, VA1273 (annealed in air) and VV773, VV1273 (annealed in vacuum) respectively. Particle morphology was examined by direct observation of gold-coated samples on a JEOL SEM 6400 scanning electron microscope. Structural characterization was performed using a Philips x-ray powder diffractometer employing Co $K\alpha$ (λ =1.789 nm) radiation. Supplementary thermo-gravimetric experiments were performed in a Shimadzu TGA-50H system. The dc magnetic field behavior of the material was investigated from the initially magnetized sample using a vibrating sample magnetometer PAR 155. All magnetic measurements were performed at room temperature on disk-shaped (4 mm) samples.

III. RESULTS AND DISCUSSION

A. X-ray diffraction

X-ray diffraction (XRD) patterns of as-milled powders are presented in Figs. 1(a) and 2(a). For sample A1000 two main crystalline phases were distinguished: dominant lines characteristic for α-Fe_2O_3 structure indexed and marked by F(hkl), and the remaining, most intense, reflections from barium ferrite marked as (B) and indexed below for sample AA1273. In the early study,[1] directly after milling no second phase was detected by XRD analysis (only subsequently, after annealing at 1273 K). Comparing the above with the XRD pattern for sample V1000, a strong tendency to form disordered phase was found. Peaks observed belong to the hematite phase, but additional broad features were assumed to be from nanocrystalline Ba-ferrite phase. Annealing at 773 K shows a complex mixture of two phases, and the influence of air pressure during heat treatment was observed. Characteristic XRD lines for both structures are clearly visible, and the broad feature (2θ=36° and $\Delta 2\theta$=10.5°) of V1000 has a tendency to disappear. XRD patterns from AV773 and VV773 are more similar than those seen for air-annealed powders. We assume that unlike the air-milled sample, the vacuum-milled sample has oxygen deficiency. Annealing in air allows restoration of stoichiometric proportions. Heat treatment at 1273 K for 4 h produces complete hexagonal structure restoration for either vacuum- or air-annealed samples and, contrary to results presented above for lower annealing temperature, present XRD patterns are the same. In Figs. 1(d) and 2(d) powder samples annealed in air are presented. We note that particle crystallographic structure is uninfluenced by different annealing atmosphere and the time required for "recrystallization," or to annihilate any defect induced by ball milling is relatively short when compared to

 0021-8979/94/76(10)/6065/3/$6.00 © 1994 American Institute of Physics

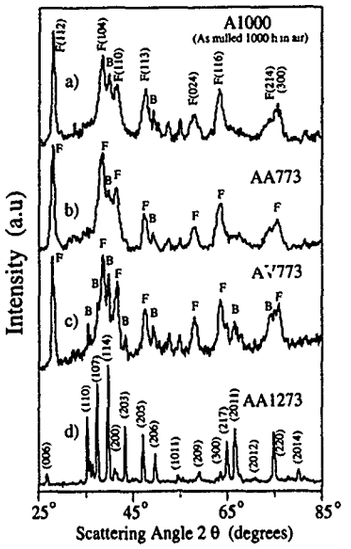

FIG. 1. XRD patterns evolution of the air-milled $BaFe_{12}O_{19}$ powder for different annealing temperatures. Peaks are indexed by: F: α-Fe_2O_3 and B: $BaFe_{12}O_{19}$.

that usually expected for "ordinary powder process." Partial decomposition during prolonged milling cannot produce completely separated hematite and barium oxide particles. Rather, it takes place as a microscale phase separation, and produces multigrain nanostructural particles of the three phases. Then, the subsequent reaction requires only a short-distance diffusion between the grains within a particle.

B. Scanning electron microscopy

In Fig. 3, SEM micrographs of A1000 and V1000 as-milled powders as compared with samples annealed at 1273 K are presented. Different behavior was observed for each. As a result of milling, instead of clusters of fine particles

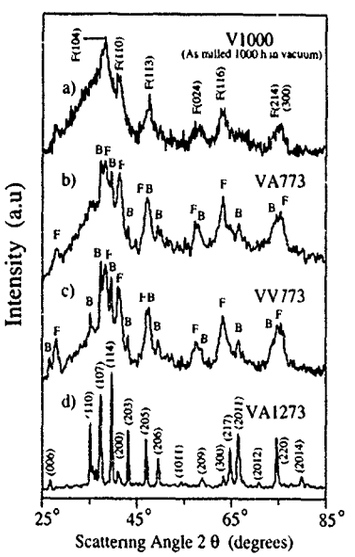

FIG. 2. XRD patterns evolution of the vacuum-milled $BaFe_{12}O_{19}$ powder for different annealing temperatures.

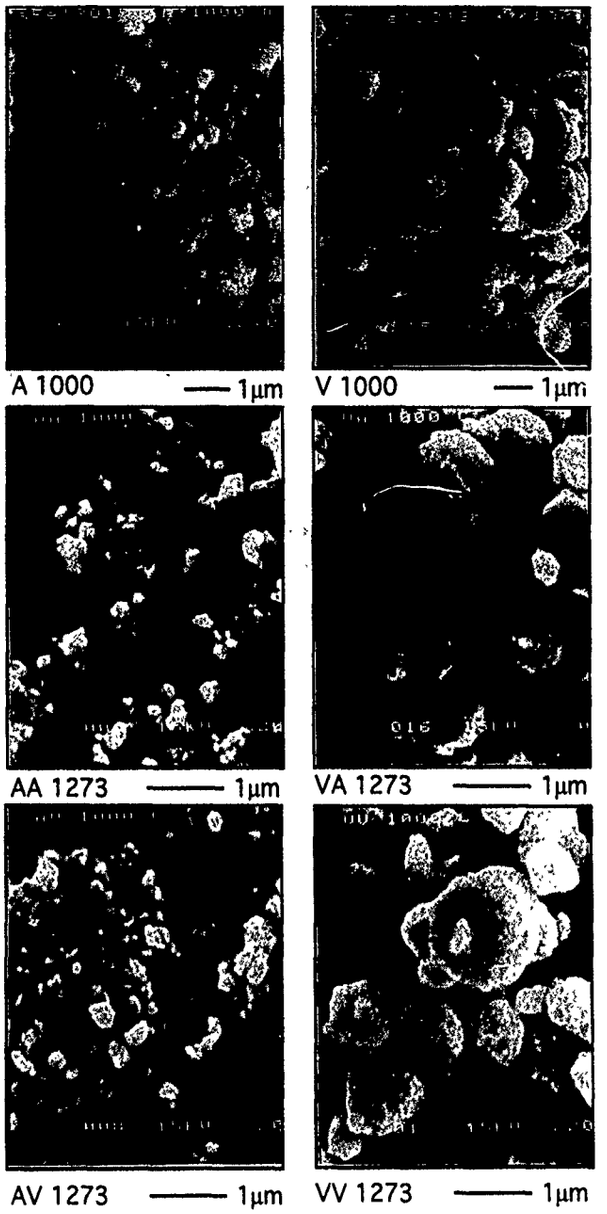

FIG. 3. SEM analysis of as-milled (A1000) and (V1000), and annealed at 1273 K in air (AA and VA) and vacuum (AV and VV) powders.

seen for the first powder, a tendency to form larger and more spherical particles can be noticed for the vacuum milled powder. Annealing at both 773 and 1273 K (air or vacuum) of A1000 and V1000 powders results in the same particle characteristics, as compared with material before annealing. Due to the short time of heat treatment, individual particle shape was found to be insensitive to process temperature and atmosphere. After annealing the particle size remains in the range 0.1–0.4 μm and 1–3 μm, respectively, for air- and vacuum-milled powders.

C. Magnetic properties

From early reports on magnetic properties of milled barium ferrite it has been well established that overall mag-

TABLE I. Values of magnetic hysteresis parameters: volume saturation, remanence, and coercivity. All parameters measured at room temperature. Maximum magnetic field applied 1 T.

Sample	M_s (kA/m)	M_r (kA/m)	H_c (kA/m)
$BaFe_{12}O_{19}$	380.0	254.7	74.4
A1000	13.0	2.7	44.6
AA773	28.4	5.3	99.5
AV773	52.1	25.2	187.8
AA1273	347.8	222.8	445.6
AV1273	344.1	203.5	393.9
V1000	13.8	3.2	35.0
VA773	13.9	3.6	58.5
VV773	22.9	5.6	60.9
VA1273	335.4	197.6	434.5
VV1273	343.0	199.2	429.7

netic properties are greatly affected by milling and annealing processes.[1,2] Our findings confirm these conclusions. From the results of hysteresis measurements performed at room temperature presented in Table I, it is clear that for as-milled samples A1000 and V1000 all parameters are extremely low by comparison with the premilled powder. After subsequent annealing at 773 K, only minimal changes of hysteresis parameters are observed. The most significant improvement of overall magnetic properties was recorded for powders annealed at 1273 K. Magnetic hysteresis curves for some of these powders are presented in Fig. 4 and all parameters are listed in Table I.

We note that after annealing at 1273 K hysteresis parameters are weakly dependent on the milling air pressure. However, slightly higher M_s values were observed for air-milled powders AA1273 and AV1273. On the other hand, annealing in air promotes minimally higher H_c values. We assume that different particle morphology as seen in Fig. 3 is directly responsible for magnetic parameter value fluctuations. It is obvious that independently of particle size, for either air- or vacuum-milled powders, the observed M_s values are close to values measured for a starting powder (~90%), but of importance is the fact that the coercivity increases over six times and reaches a value 445.6 kA/m. This value is typical of chemically coprecipitated fine Ba-ferrite powders where perfect crystal structure assures a defect and stress-free spin arrangement with high magnetocrystalline anisotropy energy.[6] According to the Stoner and Wohlfarth theory of coherent rotation,[7] the theoretical coercivity for a random assembly of Ba-ferrite particles would be $H_c = 0.96\ K_1/M_s = 664$ kA/m (substituting $K = +33$ MJ/m^3 and $M_s = 390$ kA/m). The last value is higher than any experimental value ever obtained on mechanically processed powders. Mössbauer spectroscopy results in the same powders will be presented subsequently.[8]

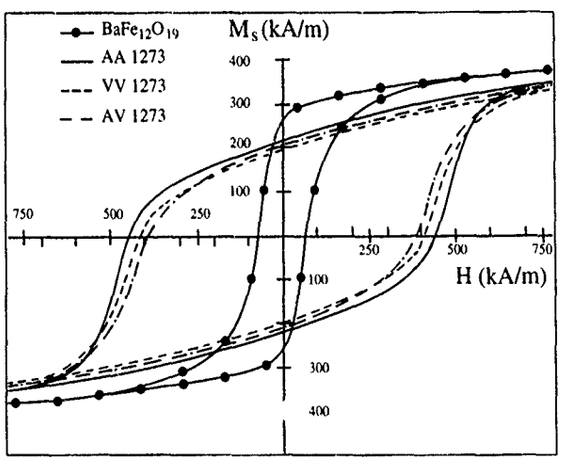

FIG. 4. Magnetization in a function of external magnetic field showing the effect of annealing at 1273 K on milled Ba-ferrite powders.

IV. CONCLUSIONS

We found that, depending on milling atmosphere (air or vacuum), the final average particle sizes are different ~0.3 and ~1 μm, respectively, with multiphase nanostructure. Low values of magnetization and coercivity, characteristic for decomposed Ba-ferrite, were found for as-prepared samples. With heat treatment, structural and magnetic properties were altered, but the particle morphology is retained. Annealing at 773 K produces more obvious changes in magnetic properties; however, with powders annealed at higher temperature, significant values $M_s = 335.4-347.2$ kA/m and $H_c = 393.9-445.6$ kA/m were obtained. The M_s value is near the typical value for Ba-ferrite powder (<10%), but the H_c value was improved quite remarkably, by a factor of six, as a result of fine crystal grain size produced by short annealing time.

[1] K. Haneda and H. Kojama, J. Am. Ceram. Soc. **57**, 68 (1973).
[2] M. H. Hodge, W. R. Bitler, and R. C. Bradt, J. Am. Ceram. Soc. **56**, 497 (1973).
[3] A. Calka and A. P. Radlinski, Mater. Sci. Eng. A **134**, 1350 (1991).
[4] W. A. Kaczmarek and B. W. Ninham, IEEE Trans. Magn. **MAG-30**, 732 (1994).
[5] W. A. Kaczmarek, J. Mater. Sci. (in press).
[6] O. Kubo, T. Ido, and H. Yokoyama, IEEE Trans. Magn. **MAG-18**, 1122 (1982).
[7] E. C. Stoner and E. P. Wohlfarth, Philos. Trans. R. Soc. London A **240**, 599 (1948).
[8] S. J. Campbell, W. A. Kaczmarek, and G. M. Wang, ICM Warsaw (1994).

Nitriding studies of aligned high anisotropy $ThMn_{12}$-type $NdFe_{11}Co_{1-y}Mo_yN$ film samples (abstract)

A. Navarathna, P. Samarasekara, H. Hegde, R. Rani, and F. J. Cadieu[a)]
Physics Department, Queens College of CUNY, Flushing, New York 11367

Highly aligned film samples of $ThMn_{12}$-type $NdFe_{12-y-z}Co_yMo_z$, $y+z\approx1$, have been directly crystallized onto heated substrates by rf sputtering. The deposited films have then been nitrided at different nitriding pressures and temperatures to determine the optimum conditions to maximize the coercivity. The films have generally been (002) textured so that the easy axis of magnetization of the nitrided films is perpendicular to the film surface. For low Co concentrations it has been possible to enhance the saturation flux densities, the coercivity, and the anisotropy field of the nitrided samples. Maximum room temperature coercivities and anisotropies of 11.3 and 145 kOe were obtained for a $ThMn_{12}$-type $Nd_{8.9}Fe_{80.3}Co_{6.0}Mo_{4.8}N$ (002) textured film sample. At lower temperatures the coercivity and anisotropy rose smoothly to 29.5 and ≈200 kOe respectively by 10 K. Based on nitriding studies on similar films, all nitride sites should be occupied at ≈1 N per $ThMn_{12}$ formula unit for the high coercivity films. Previously $NdFe_{11}Co_{0.5}Mo_{0.5}N$ films were reported with a room temperature BH_{max}=46.3 MGOe at 293 K and 59.6 MGOe at 10 K.[1] In general, films that have been made to exhibit a gradient in any one component have exhibited lower energy products due to either a reduced coercivity or to shouldered hysteresis loops.

[a)]Supported by Army Research Office.

[1] A. Navarathna, H. Hegde, R. Rani, K. Chen, and F. J. Cadieu, IEEE Trans. Magn. **29**, 2812 (1993).

 0021-8979/94/76(10)/6068/1/$6.00 © 1994 American Institute of Physics

Theoretical predictions of interface anisotropy in the presence of interdiffusion (invited)

J. M. MacLaren
Department of Physics, Tulane University, New Orleans, Louisiana 70118

R. H. Victora
Imaging Research and Advanced Development, Eastman Kodak Company, Rochester, New York 14650-2017

The first *ab initio* electronic structure calculations of the magnetocrystalline anisotropy of superlattices with imperfect interfaces are presented. Specifically the possibility of an interdiffusion between the layers at the interface in Co/Pd and Co/Pt superlattices is considered. The electronic structure calculations use the local spin-density formalism as implemented with the layer Korringa–Kohn–Rostoker method. Interdiffusion at the interface is modeled in two distinct ways. In the first approach a diffuse interface is represented by ordered arrangement of substitutions, while in the second approach interdiffusion is assumed to produce a substitutionally disordered random alloy on the layers at the interface, which is solved using the coherent potential approximation. The calculated interface anisotropies for superlattices with perfect and imperfect interfaces are, on average, modeled accurately by a simple Néel-type model. This model always predicts a reduction in magnetic anisotropy resulting from the presence of defects.

I. INTRODUCTION

Recently there has been considerable effort aimed at developing high-density magneto-optic storage devices. One proposed method for reading the stored data is to use the polar Kerr effect. A prerequisite for using this technique is a medium with perpendicular magnetic anisotropy, since this leads to optimal coupling between the incident light and the magnetic media. Transition-metal superlattices have a number of desirable properties which make them potential magneto-optic media, including large Kerr rotations, which are still significant at short wavelengths, and perpendicular anisotropy for certain multilayer geometries.

Perpendicular magnetic recording also offers the potential of higher aerial storage densities than longitudinal recording because of the properties of the demagnetization fields. Many short-period magnetic multilayers exhibit a perpendicular anisotropy resulting from the influence of the interfaces, despite the tendency for in-plane anisotropy caused by demagnetization energies. Beyond a critical multilayer period, the volume anisotropy will dominate the influence of the interfaces and in-plane anisotropy results. While the volume term always favors in-plane magnetization in a thin-film geometry, the interface term can in principle produce either a longitudinal or a perpendicular contribution to the magnetic anisotropy. In most of the magnetic multilayers it appears that the interface contributions favor perpendicular anisotropy. The range of superlattice periods which have the desired perpendicular anisotropy clearly depends on the relative strengths of the interface and volume terms. The value of the interface anisotropy depends upon the quality of the interface, thus, the strength of the magnetic anisotropy and the range of superlattice periods which exhibit useful perpendicular anisotropy will depend on sample preparation. Thus, it is of great interest to understand and predict the influence of defects on the magnetic anisotropy energy.

The magnetocrystalline anisotropy energy in transition metals is electronic in origin and results from the spin-orbit interaction. The magnetic anisotropy can be obtained theoretically from an electronic structure calculation by computing the electronic energy as a function of the spin direction. These types of calculations are, however, challenging owing to the small changes of energy (as compared to the total electronic energy) accompanying changes in the magnetization direction. Calculations for the elemental magnets Fe, Ni, and Co[1,2] predicted incorrect easy axes of magnetization for Co and Ni and while finding the correct easy axis for Fe the value of the anisotropy energy was too small. Systems with lower symmetry such as artificial free-standing monolayers,[3] embedded monolayers, surface overlayers,[3–5] and superlattices[6,7] typically have anisotropies which are an order of magnitude bigger and are large enough that the anisotropy energy can be reliably calculated using electronic structure theory.

In this article first-principles electronic structure calculations and a simple symmetry model are used to study the influence of defects produced by interdiffusion on the magnetic anisotropy. In particular, superlattices with three ordered arrangements of defects are considered. For the specific case of Co/Pd these are: (1) $1(Co_3Pd_1)/1(Pd_4)$ and $1(Co_3Pd_1)/2(Pd_4)$—a Pd substitution in the Co layer of 1Co/1Pd or 1Co/2Pd; (2) $1(Co_4)/1(Co_1Pd_3)/1(Pd_4)$—a Co substitution in one of the Pd layers of 1Co/2Pd; and (3)

 0021-8979/94/76(10)/6069/6/$6.00 © 1994 American Institute of Physics

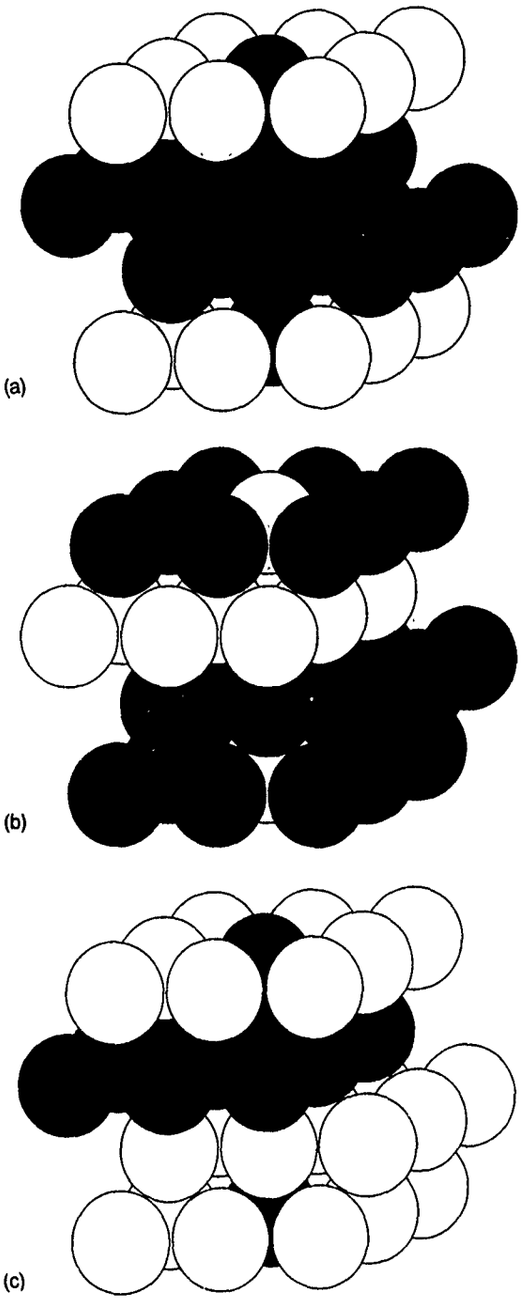

FIG. 1. Crystal structures of ordered arrangement of superlattice defects. Light and dark spheres correspond to Co and Pd/Pt atoms, respectively. (a) Monolayer substitution; (b) monolayer adatom; and (c) bilayer substitution.

$1(Co_4)/1(Co_3Pd_1)/1(Pd_4)$—a Pd substitution in one of the Co layers of 2Co/1Pd. These three defect structures are denoted as a monolayer substitution, monolayer adatom and bilayer substitution, respectively, and are shown in Fig. 1. The notation adopted is that all atoms between parentheses belong to the same layer, thus $1(Co_4)$ is a single layer with four Co atoms in the two-dimensional layer unit cell. For each of these structures, the defects are only connected at third nearest neighbors, a separation at which the defects are assumed to be essentially isolated.

In addition to these ordered defect structures, we have also studied the magnetic anisotropy of 1Co/3Pd and 1Co/3Pt superlattices where the interdiffusion between Co and Pd or between Co and Pt at the interface produces a substitutionally disordered random alloy. The profile of Co interdiffusion has been chosen to follow a trapezoidal distribution, i.e., $1(Co_{1-2x}Pd_{2x})/1(Co_xPd_{1-x})/1Pd/1(Co_xPd_{1-x})$ and $1(Co_{1-2x}Pt_{2x})/1(Co_xPt_{1-x})/1Pt/1(Co_xPt_{1-x})$ for various values of x. This composition profile is one which is consistent with experimental x-ray studies[8] where interdiffusion is often seen to occur. In all cases the atoms were assumed to lie on a perfect fcc lattice whose lattice constant was taken to be a weighted average of the constituent atoms. This choice was consistent with all the experimental x-ray determinations of the superlattice crystal structure.[9]

II. THEORY

A. Electronic structure theory

The electronic structure of both ordered and disordered superlattices is found self-consistently using the layer Korringa–Kohn–Rostoker (LKKR) method within the local-spin-density approximation.[10] The Janak, Moruzzi, and Williams[11] parameterization of the exchange correlation energy and potentials has been used. Unlike other studies where the spin-orbit interaction has been included in a second variational step using self-consistent potentials obtained in the absence of the spin-orbit interaction,[1,3,6] the calculations reported in this article solve the Kohn–Sham equations self-consistently with the spin-orbit interaction when the magnetization is normal to the superlattice. The longitudinal magnetization calculation is treated as a perturbation on the self-consistent solution for the perpendicular orientation of the magnetization. The energy difference is obtained using the force theorem[12] which we have found to give essentially identical answers to within numerical accuracy to full self-consistent results with a longitudinal magnetization. Calculations with an in-plane magnetization are significantly more time consuming because of the lower symmetry.

The LKKR method has been described in detail in Ref. 10. In this section, therefore, we present a brief outline of the method, paying attention mainly to those aspects that are unique to this work.

The potentials are assumed to be spherically symmetric within contiguous muffin-tin spheres and a constant in the interstitial region (the muffin-tin approximation). This approximation is known to be accurate for close-packed metallic structures, and since the anisotropy energy is predominantly determined by the d states which are primarily located within the muffin-tin spheres, it is an excellent approximation for the anisotropy energies of the metallic superlattices discussed in this article.

Inside the muffin-tin spheres the Hamiltonian can be conveniently partitioned into the usual scalar relativistic H_{SR} and spin-orbit H_{SO} terms. In Rydberg atomic units, which are assumed throughout this work, H_{SR} is given by

$$H_{SR} = -\frac{1}{2M}\begin{pmatrix}\nabla^2 & 0\\ 0 & \nabla^2\end{pmatrix} + \begin{pmatrix}V_\uparrow & 0\\ 0 & V_\downarrow\end{pmatrix}$$

$$-\frac{1}{4M^2c^2}\begin{pmatrix}\frac{\partial V_\uparrow}{\partial r}\frac{\partial}{\partial r} & 0\\ 0 & \frac{\partial V_\downarrow}{\partial r}\frac{\partial}{\partial r}\end{pmatrix}. \quad (1)$$

This term is spin dependent but diagonal in spin space. The spin-orbit interaction in Rydberg atomic units is given by

$$H_{SO}=\frac{1}{2M^2c^2}\frac{\partial V}{\partial r}LS=\frac{1}{4M^2c^2}\frac{\partial V}{\partial r}\begin{pmatrix} l_z & l_- \\ l_+ & -l_z\end{pmatrix}. \quad (2)$$

The forms of H_{SR} and H_{SO} are taken from Koelling and Harmon.[13]

In the above equations, $V_\uparrow$ and $V_\downarrow$ are the spin-up and spin-down one-electron potentials, V is the average of spin-up and spin-down potentials, c is the speed of light, $M=1/2+(E-V)/2c^2$ is the effective electron mass, $l_+=l_x+il_y$ and $l_-=l_x-il_y$ are the raising and lowering orbital angular momentum operators, and l_x,l_y,l_z are the Cartesian components of the orbital angular momentum operator. In the spin-orbit term H_{SO}, V is chosen to be the average of the spin-up and spin-down potentials to ensure that this term is Hermitian for real energies. H_{SO} couples spin-up and spin-down wave functions and this mixing depends upon the direction of the magnetization. The matrix elements of H_{SO} can be readily obtained by using spinors appropriate for a magnetization direction specified by the polar angles θ and ϕ,[4]

$$|\uparrow\rangle=\begin{pmatrix}\cos(\theta/2)e^{-i\phi/2}\\ \sin(\theta/2)e^{i\phi/2}\end{pmatrix}, \quad |\downarrow\rangle=\begin{pmatrix}\sin(\theta/2)e^{-i\phi/2}\\ -\cos(\theta/2)e^{i\phi/2}\end{pmatrix}. \quad (3)$$

Writing the solution to this effective Schrödinger equation as a product of radial solutions, spherical harmonics, and spinors, defined by Eq. (3), results in a set of coupled differential equations which are solved by standard techniques.

In contrast to most electronic techniques which calculate single-particle wave functions and eigenvalues, the LKKR method uses multiple scattering theory to obtain the one-electron Green's function at a given energy and wave vector in the Brillouin zone. The valence charge density is obtained from the imaginary part of the Green's function from integrations over the two-dimensional Brillouin zone and over energy from the bottom of the valence band to the Fermi energy, rather than from the sum of squares of occupied orbitals. This energy integral is performed numerically as a contour integral in the complex plane which ensures rapid convergence of both energy and Brillouin zone integrations.

Multiple scattering theory provides a convenient framework for calculating the Green's function by combining the atoms together to form the solid in a recursive manner. In a LKKR calculation the solid is partitioned into planes of atoms within which only two-dimensional translational symmetry is assumed. The multiple scattering is then factored into intra- and interlayer terms. First the scattering properties of the unique layers are found from those individual atoms. Multiple scattering within each layer is solved in the angular-momentum basis whose size scales with the number of atoms in the layer. Multiple scattering between the layers is solved using the layer coupling algorithms, derived for low-energy electron-diffraction theory,[14] in a plane-wave basis whose size is independent of the number of layers. Computing times scale roughly cubically in the number of atoms per layer and linearly in the number of layers rather than as the cube of the total number of atoms in the unit cell as is typical for most conventional electronic structure methods. This makes the LKKR method a very efficient technique for studying superlattice electronic structure since typically each layer has a simple structure and all the complexity in the superlattice lies in the stacking together of the layers.

The coherent potential approximation (CPA) provides a technique for describing the electronic structure of the random substitutionally disordered alloy by appropriately averaging different configurations,[15] and when combined with multiple scattering theory provides a first-principles density functional theory of alloys.[16] The physical picture behind the CPA is as follows: A mean field treatment of the alloy allows the construction of an effective medium which has translational invariance. Each atomic component in the alloy has the electronic structure of that particular atom embedded in this effective medium. The concentrations of atoms can be made site dependent, thus, realistic interdiffusion profiles can be modeled. The details of the implementation of the CPA within the LKKR method are given in Ref. 17.

The basis set included s, p, and d partial waves to describe the scattering in the layers from the individual muffin-tin potentials. In order to converge the anisotropy energy to 4 μRy, 13 plane waves to describe the interlayer scattering, 135 k points per irreducible Brillouin zone wedge, and 48 energy points were needed. The spin-orbit interaction lowers the symmetry of the crystal, thus care must be taken to include all inequivalent wedges of the Brillouin zone.

B. Simple theory

Results of our previous electronic structure calculations[7] showed that the magnetic anisotropy had significant contributions from all points in the Brillouin zone and that Pd atoms distant from the interface contributed negligible amounts to the anisotropy. This suggested that the magnetic anisotropy could be interpreted in terms of a real space model with near-neighbor interactions and that only Co-Co and Co-Pd or Co-Pt interactions were important.

Symmetry dictates that the lowest-order contribution to the magnetic anisotropy is $L(\hat{R}\cdot\hat{\mathrm{M}})^2$ where L is the interaction strength, $\hat{R}$ is an interatomic unit vector, and $\hat{M}$ is a unit vector pointing along the magnetization direction. The total anisotropy of the superlattice can be found by summing the basic interaction over all nearest-neighbor pairs of atoms. In the Co/Pd multilayers the simple model is parameterized by the geometrical arrangement of the atoms, and by two constants L_f describing Co-Co interactions, and L_m describing Co-Pd interactions. A similar pair of constants are needed to describe the Co/Pt system. The philosophy of this model is the same as that suggested by Néel in 1954 in his study of surface anisotropy;[18] differences include the use of two parameters to characterize the two different interactions, and the correction of some algebraic errors in Néel's original work.

In contrast to our previous work[7] where explicit numerical values for the different atomic interactions were required

TABLE I. Energies of superlattices with ordered arrangements of defects.

Defect		Perfect		Difference	
System	Energy (μRy)	System	Energy (μRy)	LKKR	Simple theory
$1(Co_3Pt)/1(Pt_4)$	186	$1(Co_4)/1(Pt_4)$	389	$-4.2K_p$	$-4.0K_p$
$1(Co_3Pd)/1(Pd_4)$	46	$1(Co_4)/1(Pd_4)$	72	$-2.9K_p$	$-4.0K_p$
$1(Co_3Pt)/2(Pt_4)$	98	$1(Co_4)/2(Pt_4)$	322	$-5.6K_p$	$-4.0K_p$
$1(Co_3Pd)/2(Pd_4)$	165	$1(Co_4)/2(Pd_4)$	242	$-2.5K_p$	$-4.0K_p$
$1(Co_4)/1(CoPt_3)/1(Pt_4)$	393	$1(Co_4)/2(Pt_4)$	322	$+1.8K_p$	$-2.0K_p$
$1(Co_4)/1(CoPd_3)/1(Pd_4)$	173	$1(Co_4)/2(Pd_4)$	242	$-2.3K_p$	$-2.0K_p$
$1(Co_4)/1(Co_3Pt)/1(Pt_4)$	211	$2(Co_4)/1(Pt_4)$	240	$-1.0K_p$	$-2.0K_p$
$1(Co_4)/1(Co_3Pd)/1(Pd_4)$	-29	$2(Co_4)/1(Pd_4)$	30	$-16K_p$	$-2.0K_p$

to quantify the simple theory, in the case of superlattices with interfacial defects the changes in anisotropy can always be expressed as a fraction of that found in the perfect structure. This obviously makes the results more useful in interpreting experimental results.

First we will derive an expression for the anisotropy of an unstrained (111) superlattice which is composed of n layers per cell where the probability of finding a Co atom on layer j is given by P_j. All nearest-neighbor atoms are contained either within the plane or in the adjacent planes for this superlattice orientation, thus it is more convenient to consider the effective interactions between atoms in the same plane W_0, and the effective interactions between atoms in adjacent planes W_1. These effective interactions take into account the geometric arrangement of the atoms in the [111] planes. A superscript m or f is added to differentiate between ferromagnetic-paramagnetic and ferromagnetic-ferromagnetic atom interactions. Specifically W_0^f sums the interaction between a Co atom and six Co first nearest neighbors in a [111] plane, while W_0^m sums the interaction between a Co atom and six Pd or Pt first nearest neighbors in a [111] plane. Similar definitions apply to W_1^f and W_1^m. All four of these effective interactions can be expressed in terms of the basic interatomic interactions L_f and L_m. Using these effective interactions gives the following for the magnetic anisotropy of the disordered superlattice:

$$2K_i=\sum_{j=1}^{n} P_j^2W_0^f+2(1-P_j)P_jW_0^m+P_jP_{j+1}W_1^f$$
$$+P_j(1-P_{j+1})W_1^m+(1-P_j)P_{j+1}W_1^m. \quad (4)$$

Two identities can be derived immediately since the anisotropy of the pure material and the 50:50 alloy are zero because of the cubic symmetry. This yields

$$W_0^f+W_1^f=W_0^m+W_1^m=0. \quad (5)$$

Using these relations and noting that the n-layer superlattice has two interfaces per unit cell it follows that the interface anisotropy for the imperfect interface K_i can be simply obtained from that of the perfect interface K_p by

$$K_i=\tfrac{1}{2}K_p\sum_{j=1}^{n}(P_j-P_{j+1})^2, \quad (6)$$

where the interface anisotropy of the ordered superlattice is

$$K_p=W_1^m-\tfrac{1}{2}W_1^f. \quad (7)$$

In a similar way one can derive expressions for the reduction in anisotropy energy of the three ordered defects; They are $4K_p$, for the monolayer substitution, and $2K_p$ for the monolayer adatom and bilayer substitution. A simple geometric picture would suggest that a Pd substitution in the Co monolayer would modify two interfaces and thus might be expected to reduce the anisotropy by $2K_p$, while the Co adatom and the bilayer substitution only modify one interface and thus might be expected to reduce the anisotropy by K_p. The simple Néel theory predicts that the influence of the defects is twice as large as naively expected, demonstrating the dramatic effect of defects on the magnetic interface anisotropy.

1Co/5Pd superlattices fabricated under a variety of different experimental conditions show a wide variation in the measured magnetic anisotropy. A 1Co/5Pd superlattice grown by molecular-beam epitaxy has the largest anisotropy of 5.9×10^7 erg/cm^2 (Ref. 19), and a 1Co/5Pd superlattice grown epitaxially in UHV had an anisotropy of 4.9×10^7 erg/cm^2 (Ref. 20). Sputtered 1Co/5Pd superlattices made by different groups have anisotropies of 2.6×10^7 erg/cm^2 (Ref. 21) and 2.4×10^7 erg/cm^2 (Ref. 22), respectively. These can be compared to the theoretical values for a perfect 1Co/5Pd superlattice of 6.6×10^7 erg/cm^2 (Ref. 7) and 8.7×10^7 erg/cm^2 (Ref. 6). All of the experimental superlattices will contain defects, with the sputtered samples having the largest concentration. The range of values observed is clearly consistent with the theoretical expectations for superlattices with defects.

III. RESULTS AND DISCUSSION

Table I shows the calculated anisotropies for all of the ordered defects in Co/Pd and Co/Pt. As was stated in the previous section, the simple theory predicts a reduction of $4K_p$ for Pd and Pt substitutions in a Co monolayer. The results of the electronic structure theory for substitutions in the Co monolayer also show a reduction in the anisotropy. In previous work on perfect Co/Pd superlattices[7] we have noticed that the simple model reproduces average trends in the magnetic anisotropy while the results of electronic structure

TABLE II. Energies of superlattices with random arrangements of defects.

Defect		Perfect		Difference	
System	Energy (μRy)	System	Energy (μRy)	LKKR	Simple theory
$1(Co_{0.8}Pt_{0.2})/1(Co_{0.1}Pt_{0.9})/1Pt/1(Co_{0.1}Pt_{0.9})$	16.8	1Co/3Pt	64.6	$-1.5K_p$	$-1.0K_p$
$1(Co_{0.8}Pd_{0.2})/1(Co_{0.1}Pd_{0.9})/1Pd/1(Co_{0.1}Pd_{0.9})$	28.8	1Co/3Pd	56.6	$-1.0K_p$	$-1.0K_p$
$1(Co_{0.6}Pt_{0.4})/1(Co_{0.2}Pt_{0.8})/1Pt/1(Co_{0.2}Pt_{0.8})$	8.0	1Co/3Pt	64.6	$-1.8K_p$	$-1.6K_p$
$1(Co_{0.6}Pd_{0.4})/1(Co_{0.2}Pd_{0.8})/1Pd/1(Co_{0.2}Pd_{0.8})$	14.6	1Co/3Pd	56.6	$-1.5K_p$	$-1.6K_p$

calculations for individual systems can show significant deviations from the predictions of the simple theory. The standard deviation of the fit in this case was $1.2K_p$. These variations can probably be explained by noting that while each point in the Brillouin zone contributes to the anisotropy, certain points are more important than others and that these points are superlattice dependent.

For the four monolayer substitutions studied, the average reduction is $3.8K_p \pm 1.4K_p$ which is statistically the same as the simple theory prediction of $4K_p$. In the case of the ordered defects structures with substitutions in the Co bilayer and Co substitutions in the Pd or Pt layer (last four lines of Table I) the simple theory predicts a reduction of $2K_p$ in the anisotropy. The agreement between the electronic structure results and the simple theory is clearly not as good. Excluding the 2Co/1Pd superlattice, leads to an average reduction of $0.5K_p \pm 1.7K_p$ which is still consistent with the simple theory though the standard deviation is larger. Defect-free 2Co/1Pd has a much smaller anisotropy than simple theory would predict and thus it is not too surprising that the introduction of defects produces an anomalous result.

Since the simple theory works best in an average sense one might expect better agreement between the predictions of the simple model and the results of the electronic structure calculations for superlattices where the defects are placed in a random manner. To model a realistic interdiffusion profile we have assumed a trapezoidal distribution; this distribution is consistent with the x-ray-diffraction data which we have examined. The superlattices which we have examined are $1(Co_{1-2x}Pd_{2x})/1(Co_{1-x}Pd_x)/1Pd/1(Co_{1-x}Pd_x)$ and $1(Co_{1-2x}Pt_{2x})/1(Co_{1-x}Pt_x)/1Pt/1(Co_{1-x}Pt_x)$ for $x=0.1$ and 0.2. The results of the LKKR CPA and the predictions of the simple theory are shown in Table II. The Néel-type model predicts a reduction of $1.0K_p$ and $1.6K_p$ for $x=0.1$ and $x=0.2$, respectively. Electronic structure theory gives $1.2K_p \pm 0.4K_p$ for the former and $1.6K_p \pm 0.2K_p$ for the latter, in excellent quantitative agreement with the simple theory. Simple theory also reproduces the results of the individual first-principles calculations as well as the average trend, and deviations are significantly smaller than those seen in the ordered calculations. The better agreement is attributed to the fact that the LKKR CPA calculations represent ensemble averages of many possible superlattices with the same layer compositions. Thus, the assumption of uniform contributions to the anisotropy from points in the Brillouin zone, implicit in the Néel-like theory, is likely to be a better approximation.

IV. CONCLUSIONS

Using the LKKR electronic structure method we have performed first-principles calculations of the magnetocrystalline anisotropy energy of a superlattice with imperfect interfaces. Both ordered arrangements of defects and a random substitutional alloy have been studied. Using a simple Néel-type theory, expressions for the expected changes in anisotropy associated with each type of defect have been derived. Detailed comparisons show the value of the simple symmetry-based model as a quantitative predictor of the expected trends. The imperfect superlattices where the interdiffusion causes a random arrangement of defects are expected to be a more realistic model of the experimental interface, and in this situation the simple theory is both found and expected to be more useful. We have shown that the influence of imperfections is generally larger than geometric arguments would suggest, and that defects act to reduce the magnetic anisotropy.

ACKNOWLEDGMENTS

J.M.M. acknowledges partial support from the Louisiana Quality Education Support Fund under Grant No. LEQSF (1991-1994)-RD-A-30, and thanks Dr. D. D. Johnson for useful discussions about the construction of self-consistent electronic potentials within the coherent potential approximation.

[1] G. H. O. Daalderop, P. J. Kelly, and M. F. H. Schuurmans, Phys Rev. B **41**, 11 919 (1990).
[2] G. Y. Guo. W. M. Temmerman, and H. Ebert, Physica B **172**, 61 (1991).
[3] J. G. Gay and R. Richter, J. Appl. Phys. **61**, 3362 (1987); R. Wu, C. Li, and A. J. Freeman, J. Magn. Magn. Matter. **99**, 71 (1991).
[4] C. Li, A. J. Freeman, H. J. F. Jansen, and C. L. Fu, Phys. Rev. B **42**, 5433 (1990).
[5] G. Y. Guo, W. M. Temmerman, and H. Ebert, J. Phys. Condens. Matter **3**, 8205 (1991).
[6] G. H. O. Daalderop, P. J. Kelly, and M. F. H. Schuurmans, in *Science and Technology of Nanostructured Magnetic Materials*, edited by G. C. Hadjipanayis and G. A. Prinz (Plenum, New York, 1991), p. 185; Phys. Rev. B **42**, 7270 (1990).
[7] R. H. Victora and J. M. MacLaren, Phys. Rev. B **47**, 11 919 (1990); J. M. MacLaren and R. H. Victora, IEEE Trans. Magn. **MAG-29**, 3034 (1993).
[8] X. Yan, T. Egami, E. E. Marinero, R. C. Farrow, and C. H. Lee, J. Mater. Res. Soc. **7**, 1309 (1992); N.-H. Cho, K. M. Krishnan, C. A. Lucas, and R. C. Farrow, J. Appl. Phys. **72**, 5799 (1992), J. A. Bain, B. M. Clemens, H. Notarys, E. E. Marinero, and S. Brennan, J. Appl. Phys. **74**, 996 (1993).
[9] B. N. Engel, M. H. Wiedmann, R. A. Van Leeuwen, C. M. Falco, L. Wu, N. Nakayama, and T. Shinjo, Appl. Surf. Sci. **60-61**, 776 (1992); B. N.

Engel, C. D. England, R. A. Van Leeuwen, M. H. Wiedmann, and C. M. Falco, J. Appl. Phys. **70**, 5873 (1991).
[10] J. M. MacLaren, S. Crampin, D. D. Vvedensky, and J. B. Pendry, Phys. Rev. B **40**, 12 164 (1989); J. M. MacLaren, S. Crampin, D. D. Vvedensky, R. C. Albers, and J. B. Pendry, Comput. Phys. Commun. **60**, 365 (1990).
[11] J. F. Janak, V. L. Moruzzi, and A. R. Williams, Phys. Rev. B **12**, 1257 (1975).
[12] A. R. MacKintosh and O. K. Anderson, in *Electrons at the Fermi Surface*, edited by M. Springford (Cambridge University Press, Cambridge, 1980).
[13] D. D. Koelling and B. N. Harmon, J. Phys. C **10**, 3107 (1977).
[14] J. B. Pendry, *Low Energy Electron Diffraction* (Academic, London, 1974).
[15] P. Soven, Phys. Rev. **156**, 809 (1967).
[16] B. L. Györffy, Phys. Rev. B **5**, 2382 (1972); J. S. Faulkener and G. M. Stocks, Phys. Rev. B **21**, 3222 (1980).
[17] J. M. MacLaren, A. Gonis, and G. Schädler, Phys. Rev. B **45**, 4392 (1992).
[18] L. Néel, J. Phys. Radium **15**, 225 (1954).
[19] B. N. Engel, C. D. England. R. A. Van Leeuwen, M. H. Wiedmann, and C. M. Falco, Phys. Rev. Lett. **67**, 1910 (1991).
[20] F. J. A. den Broeder, W. Hoving, and P. J. H. Bloemen, J. Magn. Magn. Mater. **93**, 562 (1991).
[21] H. J. G. Draaisma, W. J. M. de Jonge, and F. J. A. den Broeder, J. Magn. Magn. Mater. **66**, 351 (1987).
[22] Value interpolated from measured anisotropies of Co/Pd_4 and Co/Pd_6 taken from D. G. Stinson and S.-C. Shin, J. Appl. Phys. **67**, 4459 (1990).

Magnetic anisotropy of metal/Co/metal and metal/Co/insulator sandwiches

Michael H. Wiedmann, Brad N. Engel, and Charles M. Falco
Physics Department and Optical Sciences Center, University of Arizona, Tucson, Arizona 85721

In situ polar Kerr-effect measurements have been used to study the magnetic anisotropy of MBE-grown Au(111)/Co/X and Pd(111)/Co/X sandwiches, where X is the nonmagnetic metal Ag, Au, Cu, and Pd or the insulator MgO. For the metals it was recently found that the magnitude of the Co/X perpendicular interface anisotropy is strongly peaked at ~1 atomic layer (1.5–2.5 Å) coverage. To investigate structural influences on the anisotropy, reflection high-energy electron diffraction (RHEED) and low-energy electron diffraction (LEED) have been used to measure changes resulting from overlayer coverage. Analysis of digitized RHEED images captured every ~1 Å during metal overlayer coverage shows no abrupt change of the in-plane lattice constant. The out-of-plane lattice spacing has also been investigated as a function of nonmagnetic metal coverage by measuring LEED I-V curves along the (0,0) rod. In the case of Cu, where the LEED behavior is nearly kinematic, no evidence was seen of any abrupt structural changes at ~1 atomic layer coverage. These results suggest the observed peak in magnetic anisotropy is not structural in origin. To further study this phenomenon, the influence of an insulating overlayer, MgO, on the perpendicular magnetic properties has been measured.

I. INTRODUCTION

A fundamental understanding of the magnetic anisotropy arising from the interface between magnetic and nonmagnetic metal films is an important current problem in magnetism. Of particular interest for optical data storage applications are material systems that display perpendicular anisotropy, such as Au/Co and Pd/Co. Possible explanations advanced for this strong anisotropy include the reduced coordination symmetry,[1] altered electronic structure,[2] and localized epitaxial strain at the interface between two different materials.[3] Previously, we have investigated influences on the interface anisotropy by varying overlayer coverage and material species.[4,5] For Ag, Au, and Cu we have found that the magnitude of the Co/metal perpendicular interface anisotropy is strongly peaked at ~1 atomic layer coverage.

In this article we report on detailed structural characterization of the metal overlayers by reflection high-energy electron diffraction (RHEED) and low-energy electron diffraction (LEED). We also investigated the effects of an insulating overlayer (MgO) on the magnetic properties of single crystal Co films grown on Au(111) surfaces.

II. EXPERIMENT

The results reported here are for Co films in the thickness range 2 Å$\leq t_{Co} \leq$30 Å deposited on 500-Å-thick buffer layers of either Pd(111) and Au(111). The buffer layers were grown on annealed, Co-seeded GaAs(110) substrates. We used an effusion cell for Pd deposition at 0.15 Å/s, and optical-feedback-controlled electron-beam evaporators to deposit the Au (0.1 Å/s), Co (0.25 Å/s), Cu (0.1 Å/s), and MgO (~2 Å/s). All deposition rates were determined from Rutherford backscattering spectrometry (RBS) analysis of thick calibration films. The background pressure for the metals was $\leq 5\times10^{-10}$ Torr during deposition and $\leq 1\times10^{-8}$ Torr for the insulator. The crystalline quality of the films was monitored during growth with RHEED. The RHEED images were captured with a charge-coupled-device (CCD) camera system capable of resolving changes in in-plane lattice spacings of ~1%. A reverse-view LEED system with an identical CCD camera was used to measure changes in perpendicular lattice spacings upon coverage by measuring intensity versus voltage (I-V) curves of the specular beam. The growth must be interrupted after each coverage step in order to rotate the sample stage to perform LEED. I-V curves can be completed in less than 20 min with minimal surface contamination between depositions.

Magnetic and magneto-optic characterization of the samples was carried out by *in situ* polar Kerr-effect measurements. The sample can be transferred between the deposition chamber of our molecular-beam-epitaxy (MBE) system and another connected ultrahigh-vacuum chamber ($P<2\times10^{-10}$ Torr) where it is aligned between the poles of an external electromagnet. The magnetic field is applied along the sample normal with a maximum field of ±2.2 kOe. We use a 50 kHz photoelastic modulator and lock-in–amplifier–based detection scheme with a HeNe laser to measure the polar Kerr ellipticity of the sample as a function of applied field.

III. STRUCTURAL CHARACTERIZATION OF METAL OVERLAYERS

The role of crystal structure in our observed coverage-dependent anisotropy is an important question that is difficult to address. Because magnetic anisotropy is very sensitive to the local environment, subtle changes in atomic spacings could cause significant effects. We have used RHEED and LEED to investigate coverage-dependent changes in the surface lattice spacing. Using RHEED, we have measured intensity profiles across a streak pattern of a Co surface as it is progressively covered with Au.[6] Starting with a 30 Å Co film deposited on a 500 Å Au(111) buffer layer, RHEED images were captured every 4 s during uninterrupted Au deposition at a rate of 0.1 Å/s, giving a coverage interval of ~0.4 Å. At the coverage equivalent of 1 atomic layer (2.4 Å), the diffraction peak is composed of contributions from both bulk Au and bulk Co spacings. After 2 atomic layers of coverage, the peak is dominated by diffraction from the bulk Au spac-

 0021-8979/94/76(10)/6075/3/$6.00 © 1994 American Institute of Physics

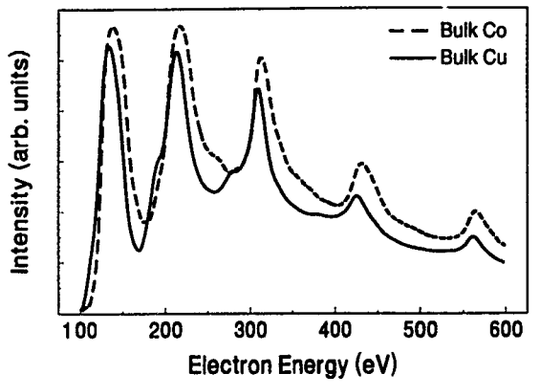

FIG. 1. LEED I-V curves of (0,0) specular beam for Co(111) surface and a thick Cu film (200 Å) deposited on top of it.

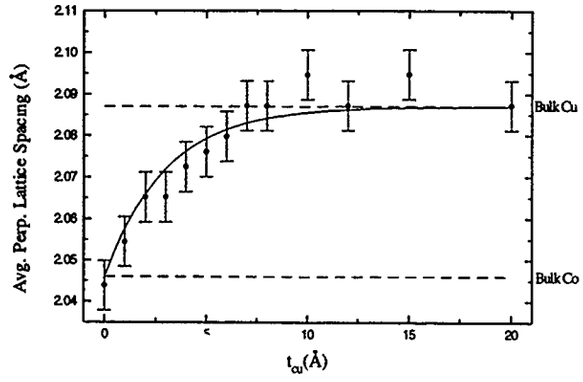

FIG. 2. Change in average perpendicular lattice spacings determined from shifts in lowest-energy peak locations in Fig. 1. The continuous curve is calculated assuming bulk Co and Cu lattice constants and a mean sampling depth of 3 Å. There is no evidence of any abrupt change at 1 atomic layer coverage.

ing. Because the Au immediately grows incoherently and strain free, these measurements suggest that the Co in-plane lattice spacing is unaffected by the Au overlayer. A similar experiment was carried out for a Cu overlayer on Co, where the two materials have a roughly 2% lattice mismatch. In this case we also see no abrupt changes in the surface lattice spacing.

Because the RHEED geometry is only sensitive to the in-plane lattice spacings, we can obtain information about the out-of-plane spacings from LEED versus I-V measurements. Although not as rigorous as a full dynamical analysis, one can determine the average out-of-plane lattice spacing of the top few monolayers from measured I-V curve of the specular or (0,0) beam. This simple analysis is only valid for materials which show weak or no multiple scattering. The average lattice spacing is deduced by comparison of the resulting intensity peak locations to calculated Bragg peaks. In this article we report results from I-V curves of the (0,0) beam of Cu deposited on Co(111). In this case, the overlayer is a different material from the substrate and therefore this analysis provides a combined weighted average lattice spacing of both materials. As an example of the sensitivity of this technique, Fig. 1 shows an I-V curve of a clean Co(111) surface and that from a bulklike thick Cu film deposited on top of the Co surface. The two representative curves show well-defined Bragg peaks which are slightly shifted from each other. To measure the effect of the overlayer as it is grown, I-V curves were taken after each of many Cu depositions of ~1 Å each (the equivalent of 0.5 atomic layers of Cu). As the bare Co is increasingly covered with Cu we observe a continuous shift from the Co peak positions to the Cu peak positions. Further deposition of Cu beyond 8 Å coverage does not change the location of the peaks. These peaks can be associated with Bragg diffraction by taking into account an inner potential correction, indicating that both the materials Co and Cu behave nearly kinematically. The peak location of the specularly reflected beam can be calculated from the following relation.[7]

$$2(E^B+V_0)\cos^2\theta=(n\pi/d)^2, \tag{1}$$

where E^B are the Bragg energies, V_0 is the inner potential, θ is the angle of incidence, n the order of the peak, and d the out-of-plane lattice constant. The energies and distances are given in hartrees, 1 hartree=27.18 eV, and bohrs, 1 bohr =0.529 Å, respectively. The angle of incidence of the electron beam was ~7° in the ⟨11-2⟩ azimuth. The measured spectra of the Cu(111) surface are very similar to those measured by Reid.[8] We have measured the inner potential shift for bulk Co and bulk Cu to be 7.7 and 8.5 eV, respectively. It should be noted that we do not know how the inner potential V_0 varies as Cu is deposited; however, because the two bulk values are nearly the same, we used their average (8.1 eV) in all of our calculations. This causes only a small uncertainty in our determined lattice spacings and is included in the error estimates.

From the shifts in the Bragg peaks upon coverage we can calculate changes in the average out-of-plane lattice spacing according to Eq. (1), and which are shown as the circles in Fig. 2. Here we have used the lowest-energy peak at 137 eV which is the most surface sensitive with a mean sampling depth of only ~3 Å. The mean free path of LEED electrons at 137 eV is roughly 6 Å;[7] however, in a reflection-diffraction experiment in which a monoenergetic beam must enter and exit the crystal, the mean sampling depth is half the value of the mean free path. We have also calculated the coverage dependence of the average lattice constant that would be expected if both the Co and Cu remain at their bulk spacings. This average spacing is calculated using depth-dependent weighting factors derived assuming an exponential decay of the LEED electrons with a probing depth of 3 Å. The calculated solid curve in Fig. 2 is in good agreement with the measured data indicating that, to within our uncertainty, Cu grows at its bulk perpendicular lattice constant on the Co surface. We see no evidence of any abrupt structural changes of greater than ~0.6% at ~1 atomic layer coverage that would correlate with our observed peak in the anisotropy at this coverage.

We have also taken LEED I-V spectra of the specular beam for Au and Pd overlayers on Co. Both materials show strong multiple scattering where the peaks do not correspond

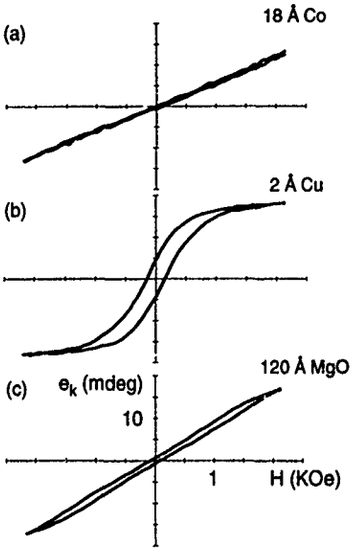

FIG. 3. *In situ* polar Kerr ellipticity loop from: (a) uncovered 18 Å Co on Au(111); (b) 2 Å Cu deposited on 18 Å Co; (c) 120 Å MgO deposited on 2 Å Cu.

to Bragg peaks and therefore the above simple analysis cannot be applied.

IV. MAGNETIC CHARACTERIZATION OF MgO OVERLAYERS

In order to further study this phenomenon we have measured the influence of an insulating overlayer, MgO, on the perpendicular magnetic properties. For the noble metals Ag, Au, and Cu, for which we observe the anomalous anisotropy behavior near 1 atomic layer coverage, there is also a hybridization between the ferromagnetic metal and the overlayer electronic states.[9] In the case of an insulating MgO overlayer this electronic interaction between the ferromagnetic material and overlayer is extremely weak.[10] Therefore, one would not expect significant changes in anisotropy upon insulator coverage.

The deposition of the MgO was carried out by *e*-beam evaporation. RBS analysis of the MgO film showed a 1:1 stoichiometric ratio of Mg to O, in agreement with previously reported results from *e*-beam-evaporated MgO.[11] We have also carried out Auger electron spectroscopy on the samples immediately after deposition. The Auger spectra of the deposited MgO film agree with those in the literature.[12] Thus, we do not expect any oxidation of the metal surface due to dissociation of MgO.

Figure 3 shows polar Kerr ellipticity loops of 18 Å Co deposited on a thick Au(111) buffer layer, 2 Å Cu deposited on the bare Co, and ~120 Å MgO deposited on top of the Cu. The initial magnetic moment of the bare Co is in plane. As we previously reported, upon coverage with just 2 Å of Cu we see a large increase in the perpendicular anisotropy. Interestingly, after depositing a MgO cap of ~120 Å thickness we observe a decrease in the perpendicular anisotropy. The MgO shows polycrystalline growth as evidenced by the disappearance of the Cu RHEED streak pattern. In a different experiment we started with a perpendicularly magnetized 4 Å Co film with a coercive field of $H_c \approx 470$ Oe; subsequent deposition of ~30 Å polycrystalline MgO reduces the coercive field to $H_c \approx 70$ Oe with no change in the magnitude of the measured ellipticity.

It is surprising to find such a large change in anisotropy since the electronic interaction between the metals and MgO should be very weak. It is possible that the MgO overlayer induces strain in the Co. Unfortunately, because MgO grows polycrystalline in this case we are unable to use *in situ* structural characterization techniques to investigate changes due to MgO coverage. Work is in progress to investigate other insulating materials.

V. SUMMARY

We have used RHEED and LEED to investigate structural influences on the perpendicular anisotropy of Co(111) ultrathin films upon coverage with the noble metals Ag, Au, and Cu. Neither RHEED nor LEED show evidence for abrupt changes in surface and out-of-plane lattice spacings for Au and Cu, respectively. We have also investigated the effect of an insulating overlayer (MgO) on the magnetic anisotropy with *in situ* polar Kerr-effect measurements and observe a reduction in the perpendicular anisotropy.

ACKNOWLEDGMENTS

This work was supported by the U.S. Department of Energy Grant No. DE-FG03-93ER45488 and the Optical Data Storage Center at the University of Arizona. The authors gratefully acknowledge J. Leavitt for RBS measurements.

[1] L. Néel, J. Phys. Radium **15**, 376 (1954).
[2] A. J. Freeman and R. Wu, J. Magn. Magn. Mater. **100**, 497 (1991).
[3] C. Chappert and P. Bruno, J. Appl. Phys. **64**, 5736 (1988).
[4] B. N. Engel, M. H. Wiedmann, R. A. Van Leeuwen, and C. M. Falco, J. Appl. Phys. **73**, 6192 (1993).
[5] B. N. Engel, M. H. Wiedmann, R. A. Van Leeuwen, and C. M. Falco, Phys. Rev. B **48**, 9894 (1993).
[6] B. N. Engel, M. H. Wiedmann, and C. M. Falco, J. Appl. Phys. **75**, 6401 (1994).
[7] M. A. Van Hove, W. H. Weinberg, C.-M. Chan, *Low Energy Electron Diffraction*, Springer Series in Surface Sciences Vol. 6 (Springer, Berlin, 1986).
[8] R. J. Reid, Surf. Sci. **29**, 603 (1972).
[9] A. J. Freeman and C. L. Fu, J. Appl. Phys. **61**, 3356 (1987).
[10] C. Li and A. J. Freeman, Phys. Rev. B **43**, 780 (1991).
[11] L. S. Hung, L. R. Zheng, and T. N. Blanton, Appl. Phys Lett. **60**, 3129 (1992).
[12] C. D. Wagner and P. Biloen, Surf. Sci. **35**, 82 (1973).

Effect of submonolayer coverage on magnetic anisotropy of ultrathin cobalt films M/Co/Au(111) with M=Au, Cu, Pd

P. Beauvillain, A. Bounouh, C. Chappert, R. Mégy, S. Ould-Mahfoud, J. P. Renard, and P. Veillet
Institut d'Electronique Fondamentale URA CNRS022, Université Paris-Sud, 91405 Orsay, France

D. Weller
IBM Almaden Research Center, 650 Harry Road, San Jose, California 95120-6099

J. Corno
Institut d'Optique Théorique et Appliquée, URA CNRS014, Université Paris-Sud, 91405 Orsay

Using *in situ* polar magneto-optical Kerr-effect measurements, the variation of the Kerr rotation and magnetic anisotropy of a (0001)Co ultrathin film on a (111)Au substrate has been precisely recorded, during the first stages of the growth of an overlayer of metal M=Au, Cu, and Pd. As reported earlier, a drastic increase of the magnetic anisotropy was observed, with a peak around 1 monolayer of overlayer thickness. From a careful study of the variation of the remanent Kerr rotation, it could be shown that only the interface contribution to the anisotropy changes with the overlayer thickness, while the bulk contribution remains mostly constant. The overall behavior can be interpreted in terms of electronic effects in the metal overlayer, acting on the interface anisotropy via band hybridization at the interface.

Considerable work has been devoted in the last few years to the study of the magnetic anisotropy in ferromagnetic ultrathin films.[1] Besides the magnetocrystalline interface anisotropy introduced by Néel,[2] strain-induced magnetoelastic anisotropy[3] or spin polarization of the interface layer in the nonmagnetic substrate[4] have been proposed to explain the observed behaviors of anisotropy versus the ferromagnetic film thickness, or for different nonmagnetic metal substrates. A new powerful way to investigate the origin of the magnetic anisotropy in ultrathin films is to measure its development *in situ*, during the first stages of the growth of an interface between the film and a metallic overlayer. It has been reported recently[5–7] that the coercivity and the perpendicular anisotropy of Co ultrathin films on Pd(111) and Au(111) substrates exhibit drastic increase with only submonolayer coverage by Cu, Ag, Au, and Pd, while a clear peak is observed around one atomic layer (AL) of overlayer thickness; however, owing to the complexity of *in situ* experiments, only total anisotropy for one Co thickness could be measured.[7,8] We have proposed[6] an original method, based on the analysis of the evolution versus the Co film thickness t_{Co} of the polar magneto-optical Kerr (PMOKE) rotation at remanence. We report here a detailed application of this method to the case of a (0001)Co film on a (111)Au substrate, upon coverage by a metal M=Au, Cu, or Pd.

Details of our sample preparation method have been published previously.[6,9] To achieve maximum precision and reliability in our study of the magnetic properties versus films thicknesses, we grow stepped-wedge samples using a moving shutter between sample and evaporation sources. For each sample, ten 1-mm-wide steps are made, with increasing Co thicknesses. Then the M overlayer is grown in successive thin (0.5–1 AL) layers, and after completion of each new layer, comprehensive PMOKE and reflection high energy electron diffraction (RHEED) scans are performed by moving the sample in front of a fixed e^- or laser beam.

As we reported earlier, a smoothing of the free surface with 1–2 ML of Au coverage is observed by RHEED.[6] This is a major phenomenon, which involves an important reorganization of the Co layer to rub out at least short-range roughness. It may be attributed to a surfactant effect of Au: Indeed, the surface energy of (111)Au is lower than the (0001)Co one. This behavior is not observed for Cu and Pd coverage.

Our PMOKE configuration, in which both magnetic field and laser beam are perpendicular to the sample, allows direct determination of the anisotropy coefficients only for films magnetized in plane, and provided that sufficiently high fields can be applied to saturate the magnetization of the sample. In the present study, this would restrict the determination to only a few selected values of t_{Co}.[7,8] To get an evaluation of the variation of the anisotropy coefficients for any t_{Co} and t_M combination we have proposed[6] an original method that uses the fact that, for hcp Co thin films, the two first anisotropy coefficients K_1 and K_2 have comparable magnitude (with $K_2>0$), and the change in easy axis from perpendicular to in plane with t_{Co} occurs via an intermediate state where the easy direction lies on a cone of half-angle γ. Provided the sample remains in a single-domain state, which is likely at least for low to intermediate values of γ, the ratio of the remanent to saturated Kerr rotations θ_R/θ_S, in this intermediate state, should be equal to $\cos(\gamma)$, given by

$$\cos(\gamma)=[(-2\pi M_S^2+K_1+2K_2)/2K_2]^{1/2}. \quad (1)$$

Here, M_S is the saturation magnetization, which in the following we shall assume constant and equal to the bulk value.

Assuming that K_2 does not change much with t_{Co} (this assumption is confirmed *a posteriori* at the end of this article), a good characterization of the dependence of K_1 vs t_{Co} is given by the crossover thickness t^* at which $\theta=45°$. By introducing for K_1 the usual expressions with interface anisotropies K_{S1} and K_{S2}, respectively, for the first (Co/Au) and second (vacuum/Co or M/Co) interfaces, and a volume contribution K_v, one obtains the expression

 0021-8979/94/76(10)/6078/3/$6.00 © 1994 American Institute of Physics

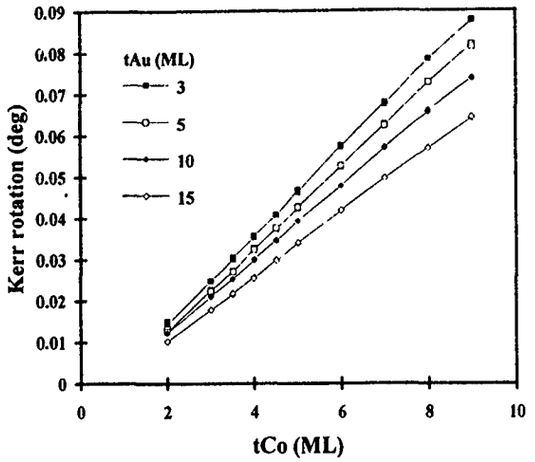

FIG. 1. Saturation polar Kerr rotations measured on a Au/Co/Au(111) sandwich vs the Co thickness t_{Co} for different values of the overlayer thickness t_{Au}.

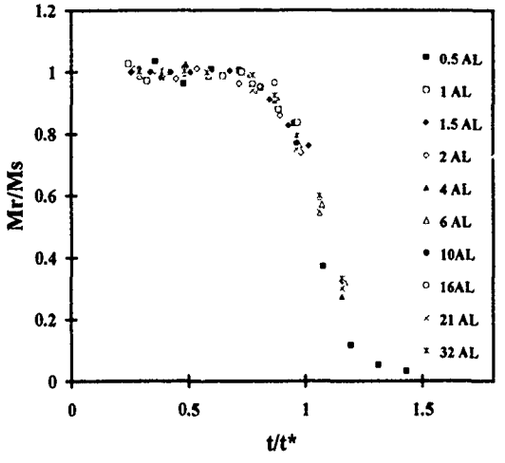

FIG. 2. Normalized remanent Kerr rotation vs normalized Co thickness, measured on a Au/Co/Au(111) sandwich for different values of the Au overlayer thickness (see legend inside the figure).

$$K_{S1}+K_{S2}=t^*(2\pi M_s^2-K_v-K_2). \quad (2)$$

Furthermore, if both volume contributions K_v and K_2 do not depend on the overlayer thickness t_M, one can easily see by combining Eqs. (1) and (2) that, for a given metal M, the θ_R/θ_S vs t_{Co} dependencies for any t_M values should superimpose on the same θ_R/θ_S vs (t/t^*) scaling curve.

Examples of hysteresis loops measured *in situ* at different stages of the interface growth have been given earlier.[6] For t_{Co} values above 7 AL (4 AL for Cu coverage), where the loops are not perfectly square, the maximum magnetic field in our setup is too low to allow direct determination of θ_S. For lower t_{Co} values the measured θ_S values vary linearly with t_{Co}, as can be seen for Au coverage in Fig. 1. To evaluate θ_S for any Co thickness, we thus extrapolate this linear variation to higher t_{Co} values. By high-field (20 kOe) measurements in air on samples with a thick coverage, we checked that this extrapolation is valid at least up to 15 AL of Co. An important effect seen in Fig. 1 is the occurrence of a nonzero intersect with the t_{Co} axis, in agreement with Ref. 10. This can be attributed to an interface effect. A more detailed study will be published elsewhere.[11]

Figures 2 and 3 display the variation of θ_R/θ_S vs t/t^*, respectively, for Au and Pd coverages. In both cases, within experimental precision all points appear well on the same scaling curve. This good agreement with scaling hypothesis confirms that K_2 is rather constant and does not change much with t_{Co}. A similar behavior is obtained for Cu coverage. Those curves appear actually more rounded than the ones calculated for perfect films.[12] This can be easily accounted for by introducing a narrow distribution of anisotropy coefficients, which could originate from nonuniform Au substrate roughness, or from inhomogeneous densities of stacking faults or strains.

As stated above, this scaling behavior allows us to assume confidently that measurement of t^* versus overlayer thickness characterizes precisely the variation of the interface anisotropy $K_{S1}+K_{S2}$ vs t_M. The variation of t^* vs t_M for M=Cu, Au, and Pd is given in Fig. 4. We observe a very fast increase in t^* at the very beginning of the overlayer growth. For Cu and Au, a narrow peak appears around $t_{Cu}=1.0$ AL (respectively, $t_{Au}=1.5$ AL), followed by a subsequent decrease of t^* toward saturation. A smoother increase of t^* is observed with M=Pd, as in Ref. 8. In agreement with previous reports,[5–8] the coercivity of perpendicularly magnetized Co films ($t_{Co}<t^*$) displays a dependence versus t_M very similar to that of t^*. Note also that the value of t^* that we measure on uncovered Co film ($t^*=4.3$ ML) is in very good agreement with that reported previously.[12]

Not much can be said at this point on the evaluation of absolute values of $K_{S1}+K_{S2}$, which would require knowledge of K_v and K_2 for each overlayer metal M. One can, however, observe that the scaling curves of Figs. 2 and 3 are very similar, which leads one to expect similar values for K_v and K_2 for M=Au and Pd. It is difficult to conclude for M=Cu, as a much smaller perpendicular anisotropy results

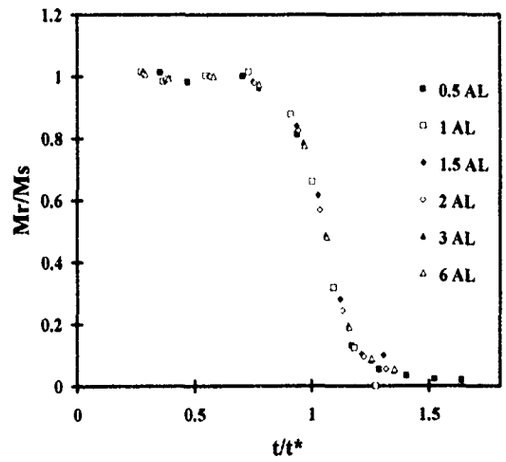

FIG. 3. Normalized remanent Kerr rotation vs normalized Co thickness measured on a Pd/Co/Au(111) sandwich for different values of the Pd overlayer thickness (see legend inside the figure).

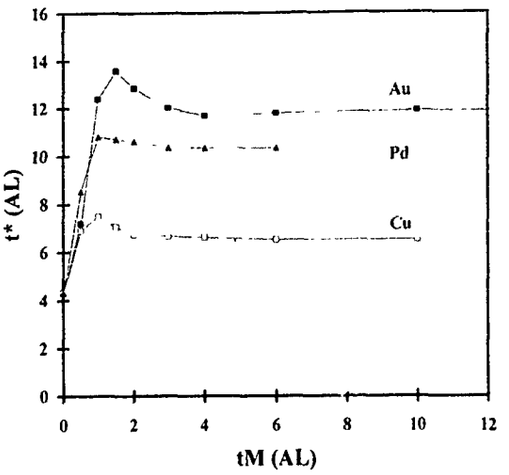

FIG. 4. Variation vs M overlayer thickness t_M of the Co thickness t^* where the remanent Kerr rotation is equal to $1/\sqrt{2}$ times the saturation Kerr rotation, for M=Au, Cu, and Pd.

in a narrow observation range, and thus in less precise evaluations. Nevertheless to get comparative values of interface anisotropies for all coverages, we have assumed one set of volume coefficients K_v and K_2, measured on similar Au/Co/Au samples,[13] and made the assumptions that: (i) in the Au/Co/Au sandwich both interfaces have the same K_S; (ii) the first (Co/Au) interface keeps the same K_S for any coverage. This last assumption in particular corresponds to the intuitive feeling that, after deposition of several atomic layers of Co, deposition of a thin overlayer should not change much the first interface. The obtained values of K_S are given in Table I. Note that the interface anisotropies for thick coverages are in good agreement with previously reported ones.[1] One interesting result is the negative (in-plane) interface anisotropy of the vacuum/Co interface, in agreement with theoretical predictions.[14]

The most interesting behavior remains the peaked dependence of the anisotropy versus t_M. We have shown here, for the first time, that the changes occur in the "interface" contribution. In principle, strain-induced anisotropy (MEA) can give a pseudo-volume term,[3] which, as observed here, should be higher for Au and Pd coverage, those metals having a large lattice mismatch with Co. This MEA is unlikely to be the dominant contribution here, as it could explain neither the negative sign of K_S for the vacuum/Co interface, nor the peak, nor even the amplitude of the change in K_S for Au and Pd coverage. Also, a t_M-dependent relaxation of the distance between subinterface and interface atomic planes in Co could contribute. However, the most likely origin of the behavior reported here is an evolution with t_M of the electronic band structure of the metallic overlayer, acting on the interface anisotropy through band hybridization with the Co. Indeed, very important changes have been observed by photoemission on electronic structures of ultrathin layers of Cu on Co(0001),[15,16] or Au. Moreover, in both cases the t_M dependence of the band structure bears striking similarities with the behavior displayed in Fig. 4 here, with, for instance, the existence of specific two-dimensional (2D) electronic structures for 1–1.5 AL coverage that relax very rapidly toward the bulk structure with further deposition of less than 1 AL. The existence of such 2D structures requires abrupt and flat interfaces. In this scheme, the more rounded behavior observed here for Pd coverage could be attributed to some alloying at the interface, as we have evidenced earlier on similar samples.

Finally, we cannot rule out the occurrence of a small spin polarization in the Au or Cu monolayer on Co, as observed recently at the Co/Cu interface.[17]

This research has been sponsored by a HCM-EEC program.

TABLE I. Interface anisotropy coefficients evaluated from the measured t^* displayed in Fig. 4. We assumed one set of volume anisotropy constants for all overlayer metals, measured on similar Au/Co/Au sandwiches (Ref. 13): $K_v=5.8\times10^6$ erg/cm^3 and $K_2=1\times10^6$ erg/cm^3. The peak values have been estimated for respective thicknesses 1.5, 1, and 1 AL of Au, Cu, and Pd overlayers.

	K_S	
Interface	Peak value (erg/cm^2)	Thick overlayer (erg/cm^2)
Vacuum/Co		−0.17
Au/Co	0.83	0.58
Cu/Co	0.17	0.06
Pd/Co	0.53	0.48

[1] W. J. M. de Jonge, P. J. H. Bloemen, and F. J. A. den Broeder in *Experimental Investigations of Magnetic Anisotropy*, Ultrathin Magnetic Structures, Vol. 1.3, edited by B. Heinrich and J. A. C. Bland (Springer, Berlin, 1994).
[2] L. Néel, J. Phys. Radium **15**, 225 (1954).
[3] C. Chappert and P. Bruno, J. Appl. Phys. **64**, 5736 (1988).
[4] D. Weller, H. Brändle, R. F. C. Farrow, R. F. Marks and G. H. Harp, NATO Advanced Science Institute Series 309, 1993, p. 201.
[5] B. N. Engel, M. H. Wiedmann, R. A. Van Leeuwen, and C. M. Falco, J. Magn. Magn. Mater. **126**, 532 (1993).
[6] S. Ould-Mahfoud, R. Mégy, N. Bardou, B. Bartenlian, P. Beauvillain, C. Chappert, J. Corno, B. Lecuyer, G. Sczigel, P. Veillet, and D. Weller, Mater. Res. Soc. Symp. Proc. **313**, 251 (1993).
[7] M. H. Wiedmann, B N. Engel, R. A. Van Leeuwen, K. Mibu, T. Shinjo, and C. M. Falco, Mater. Res. Soc. Symp. Proc. **313**, 531 (1993).
[8] B. N. Engel, M. H. Wiedmann, R. A. Van Leeuwen, and C. M. Falco, Phys Rev. B Rapid Commun. **48**, 9894 (1993).
[9] D. Renard and G. Nihoul, Philos Mag. B **55**, 75 (1987).
[10] S. Visnovsky, M. Nyvlt, V. Prosser, J. Ferré, G. Pénissard, D. Renard, and G. Sczigel, J. Magn. Magn. Mater. **128**, 179 (1993).
[11] P. Beauvillain, A. Bounouh, C. Chappert, R. Megy, and P. Veillet, in 1994 International Colloquium on Magnetic Films and Surfaces.
[12] R. Allenspach, M. Stampanoni, and A Bischof, Phys. Rev. Lett. **65**, 3344 (1990)
[13] V. Grolier, J. Ferré, A. Maziewski, E. Stefanowicz, and D. Renard, J. Appl. Phys. **73**, 5939 (1993).
[14] P. Bruno, Phys. Rev. B **39**, 865 (1989).
[15] J. E. Ortega, F. J. Himpsel, G. J. Mankey, and R. F. Willis, Phys. Rev. B **47**, 1540 (1993).
[16] D. Hartmann, W. Weber, A. Rampe, S. Popovic, and G. Güntherodt, Phys. Rev. B **48**, 16837 (1993).
[17] S. Pizzini, C. Giorgetti, A. Fontaine, E. Dartyge, G. Krill, J. F. Bobo, and M. Piecuch, Mater. Res. Soc. Symp Proc **313**, 625 (1993).

Effects of Ar-ion implantation and annealing on structural and magnetic properties of Co/Pd multilayers

John Q. Xiao, K. Liu, and C. L. Chien
Department of Physics and Astronomy, The Johns Hopkins University, Baltimore, Maryland 21218

L. F. Schelp and J. E. Schmidt
Institute de Física, Universida de Federal do Rio Grande do Sul, Porto Alegre, Brazil

The contrasting effects of ion implantation and thermal annealing on structural and magnetic properties of Co/Pd multilayers have been studied. Ion implantation causes local damage to the multilayers, resulting in enhanced magnetization due to the polarization of the neighboring Pd. Thermal annealing generates massive interdiffusion across the interfaces into the formation of Co-Pd alloys with a lower magnetization. Effects on coercivity and remanence have also been studied.

Magnetic multilayers have been the subject of numerous studies[1,2] owing to their unusual properties and potential applications. Novel properties such as enhanced magnetization, large (sometimes perpendicular) magnetic anisotropy, tailored spin structures, and giant magnetotransport properties, have been uncovered. Among the multilayers, Co/Pd has been extensively studied in recent years,[3,4] stimulated by both fundamental interests and technological applications. For constituent layers with very small thicknesses, the perpendicular anisotropy together with substantial Kerr effect have led to the application of Co/Pd multilayers in magneto-optical recording media.[5]

While the novel properties of multilayers are intimately related to the high degree of structural coherency of the layered structure, a complete understanding of the relationship between interfacial characteristics and physical properties remains lacking. In this work we have systematically altered the interfacial characteristics of Co/Pd multilayers using ion implantation and thermal annealing, and studied the resultant structural and magnetic properties. Our studies show that these two methods give rise to very different effects on the multilayer structure.

The Co/Pd multilayer samples have been deposited onto glass substrates using two electron-beam-deposition sources in a vacuum of 1×10^{-8} mbar. The samples are denoted as $[\text{Co}(x\ \text{Å})/\text{Pd}(y\ \text{Å})]_n$, where x and y are the Co and Pd layer thicknesses, respectively, and n is the number of repeats of the Co/Pd bilayers. One set of samples with $[\text{Co}(10\ \text{Å})/\text{Pd}(59\ \text{Å})]_{18}$ has been subjected to 230 keV of Ar^+ implantation at room temperature at a low current density of 50 nA/cm^2 to avoid sample heating. Low fluences of 1×10^{13}–5×10^{14} ions/cm^2, which are small compared with 1 monolayer of ions (1×10^{15} ions/cm^2), have been used. Another set of samples of $[\text{Co}(14\ \text{Å})/\text{Pd}(44\ \text{Å})]_{18}$ have been thermally annealed for 30 min in a helium atmosphere at various temperatures up to 700 K. Structural characteristics of all the samples have been made by a θ-2θ x-ray diffractometer with Cu$K\alpha$ radiation. Magnetic properties have been measured using a vibrating sample magnetometer (VSM) with the magnetic field parallel to the film plane.

Figure 1 shows the x-ray-diffraction data of the as-prepared and the ion-implanted $[\text{Co}(10\ \text{Å})/\text{Pd}(59\ \text{Å})]_{18}$ samples. The as-prepared sample [Fig. 1(a)] shows several satellite peaks near the Pd(111) peak. Because Co layers are thin and have a much lower scattering factor, no substantial diffraction peaks near the Co(111) peak are revealed nor expected. It is well known that the intensity of the satellite peaks is dictated by the layer profile and the repeatability of the bilayers. The structural coherence of the multilayers is manifested by the width of the diffraction peaks. From the width of the main diffraction peak, beyond the instrumental width, the structural coherence length L has been determined to be about 270 Å, which is about four bilayers. These results show that the as-prepared sample has a well-defined layer structure with [111] crystalline orientation.

Figures 1(b)–1(e) show the diffraction data for ion-implanted samples of $[\text{Co}(10\ \text{Å})/\text{Pd}(59\ \text{Å})]_{18}$ with Ar fluence varying from 5×10^{13} to 7.5×10^{14} ions/cm^2. Several features are noted for samples within this fluence range. For increasing fluence, the satellite peaks decrease progressively in intensity but remain observable in all cases. More important, the width of the main diffraction stays essentially the same as that of the as-prepared sample. These results indicate that layer structure and the structural coherence length L remain intact, but the layer profile becomes more diffuse as a result of ion implantation.

A contrasting situation occurs when the Co/Pd multilay-

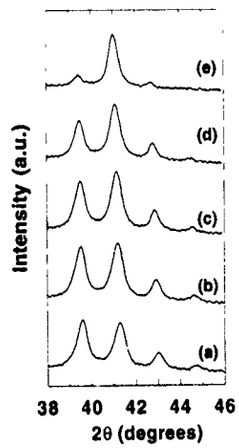

FIG. 1. X-ray spectra of (a) as-prepared sample and the implanted samples. (b) 5×10^{13}, (c) 1×10^{14}, (d) 5×10^{14}, and (e) 7.5×10^{14} ions/cm^2.

 0021-8979/94/76(10)/6081/3/$6.00 © 1994 American Institute of Physics

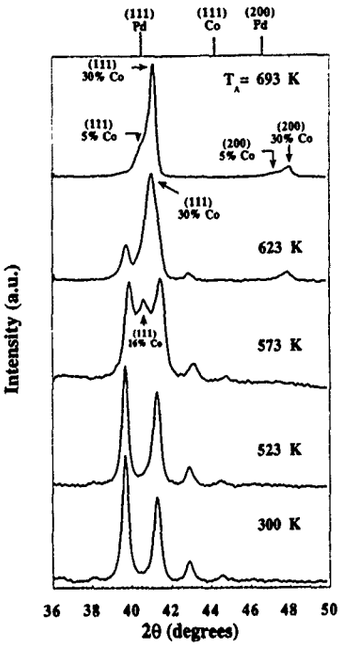

FIG. 2. X-ray spectra of samples annealed at different temperatures T_A. The peak positions corresponding to bulk Co and Pd are shown at the top. Alloys with different compositions have also been indexed.

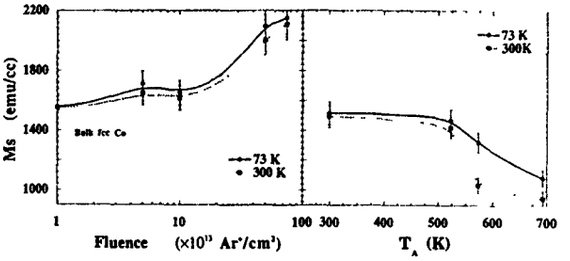

FIG. 3. Saturation magnetization in unit of emu/cm^3 of Co at 300 K (dotted curves) and 73 K (solid curves) as functions of fluences (left-hand side) and annealing temperatures (right-hand side).

ers have been thermally annealed at various annealing temperatures T_A. The x-ray-diffraction data of the as-prepared (T_A=300 K) and representative data of the annealed samples (T_A up to 693 K) of [Co(14 Å)/Pd(44 Å)]$_{18}$ are shown in Fig. 2. Discernible change of the diffraction are observed for $T_A \geq 523$ K; most notably a diminution of the satellite peak intensity and the appearance of additional diffraction peaks. It is useful to recall that Co and Pd form fcc Co-Pd alloys over the entire composition range. The lattice parameter of the alloy decreases monotonically from that of pure Co to that of pure Pd. At the top of Fig. 2 the locations of the diffraction peaks of Co(111) and Pd(111) are shown, and the (111) peak of a Co-Pd alloy falls between those of Co(111) and Pd(111) according to the composition. At T_A=573 K, in addition to the satellite peaks, a new peak, corresponding to $Co_{16}Pd_{84}$, appears. At T_A=623 K both the (111) and (200) peaks of $Co_{30}Pd_{70}$, in addition to the remanence of the satellite peaks, are observed. Finally, at T_A=693 K, only (111) and (200) peaks corresponding to predominantly $Co_{30}Pd_{70}$ and a small portion of Co_5Pd_{95} are observed. There are no satellite peaks remaining, and the layer structure has been completely destroyed. It may be noted that, if the Co and Pd atoms in [Co(14 Å)/Pd(44 Å)]$_{18}$ were mixed completely and uniformly, one would have obtained an alloy of $Co_{30}Pd_{70}$, which is very similar to the alloy composition found.

From the above results, it is clear that both ion implantation and thermal annealing can cause deterioration of the multilayers; however, the processes with which the layer structure and the interfaces are compromised are very different in the two cases. At low fluence, ion implantation causes local damages of the layer structure, while most of the layer structure and the structural coherence of the multilayer remain intact. On the other hand, thermal annealing is far more disruptive. It promotes interdiffusion of all the constituent atoms at the interfaces, very efficiently destroying the multilayers even at moderate annealing temperatures. Furthermore, due to the interdiffusion, the multilayer rapidly converges to the terminal and homogeneous alloy composition.

These conclusions made from structural studies are corroborated by the magnetic properties. It is useful first to recall the magnetic properties of Co_xPd_{100-x} alloys of which the magnetic ordering temperature T_C increases rapidly and monotonically with Co content. The values of T_C are less than 300 K for the alloys with low Co content ($x<10$).[6] The magnetic moment per atom of Co-Pd alloys also rises monotonically with Co content. However, because of the strong polarization effect on the Pd atoms by the nearby Co atoms (also known as the giant moments), these polarized Pd atoms contribute significantly to the magnetization.

The saturation magnetization M_s of the Co/Pd multilayers after ion implantation and thermal annealing are shown in Fig. 3. First of all, the as-prepared samples have a higher M_s than that of bulk fcc Co, owing to the well-known polarization effect of Pd. The enhanced magnetization has also been observed in other Co/Pd and Fe/Pd (Ref. 7) multilayers. Most remarkably, after ion implantation, there is further enhancement of M_s, and M_s has a weak temperature dependence; the values at 77 and 300 K are similar. This indicates that, as the interfaces are systematically disrupted by ion implantation, more Pd atoms are exposed and polarized by the displaced Co, hence a larger M_s. Furthermore, most of the magnetic species remain strongly coupled to share a high value of T_C. Quite the contrary, the thermally annealed samples show a decrease in M_s and a stronger temperature dependence in M_s. Both of these observations, which are consistent with another group's results,[8] are the results of the formation of Co-Pd alloys with relatively low Co contents, hence lower values of T_C.

In Fig. 4, the magnetic coercivity H_c for the implanted [Fig. 4(a)] and the annealed [Fig. 4(b)] samples are shown. We discuss the annealed samples first. Changes in H_c occur when the formation of the Co-Pd alloy appears at $T_A \geq 523$ K. Higher values of T_A result in large values of H_c, and H_c shows similar behaviors at the three temperatures (77, 150, and 300 K) measured. For the ion-implanted samples, H_c for the ion-implanted samples with higher fluences ($\geq 5\times10^{14}$

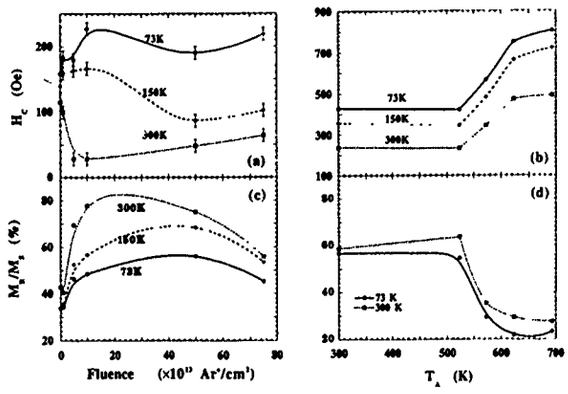

FIG. 4. In-plane coercivity H_c and squareness M_r/M_s at different temperatures as functions of fluences (left-hand side) and annealing temperatures (right-hand side).

ions/cm^2) has similar temperature dependencies as the annealed samples. The results for the low fluences are, however, more complex. In particular, the results of the implanted samples with fluences less than 1×10^{14} ions/cm^2 suggest the possibility of a phase(s) with low ordering temperature (<300 K). The precise nature of these possible phases, albeit of low sample content, has not been ascertained.

Finally, we turn to remanent magnetization M_r expressed as the squareness M_r/M_s shown in Figs. 4(c) and 4(d). After ion implantation with low fluence, the squareness becomes larger, suggesting an increase in the in-plane anisotropy. At high fluence, the squareness decreases due to the presence of Co-Pd alloy phases. In the annealed samples, the predominant evolution of the multilayer is toward the formation of Co-Pd alloys, which generally give rise to lower squareness.

In conclusion, we have observed via structural and magnetic properties the very different effects on the Co-Pd multilayer due to ion implantation and thermal annealing. Ion implantation causes local damage to the interfaces while maintaining the layer structure, whereas thermal annealing promotes massive interdiffusion toward the formation of Co-Pd alloys. Consequently, contrasting behaviors in saturation magnetization and other magnetic properties have been observed.

Work at JHU has been supported by NSF Grant No. DMR92-00280. Work at UFRGS has been supported by CNPq, FAPERGS, and FINEP in Brazil.

[1] See, for example, *Physics, Fabrication and Applications of Multilayered structures*, edited by P. Dhez and C. Weisbuch (Plenum, New York, 1988).
[2] L. M. Faclicov *et al.*, J. Mater. Res. **5**, 1299 (1990).
[3] P. F. Carcia, A. D. Meinhaldt, and A. Suna, Appl. Phys. Lett. **47**, 178 (1985).
[4] B. N. Engel, C. D. England, R. A. Van Leeuwen, M. H. Wiedmann, and C. M. Falco, J. Appl. Phys. **70**, 5873 (1991).
[5] M. J. A. M. Greidanus and W. B. Zeper, MRS Bull. **15**, 31 (1990).
[6] R. M. Bozorth, P. A. Wolfe, D. D. Davis, V. B. Compton, and J. H. Wernick, Phys. Rev. **122**, 1157 (1961).
[7] F. J. A. den Broeder, H. C. Donkersloot, H. J. G. Draaisma, and W. J. M. de Jonge, J. Appl. Phys. **61**, 4317 (1987); J. R. Childress, A. Schuhl, J.-M. George, O. Durand, P. Galtier, V. Cros, K. Ounadjela, R. Kergoat, and A. Fert, in *Magnetism and Structure in Systems of Reduced Dimension* (Plenum, New York, 1993).
[8] F. J. A. den Broeder *et al.*, J. Phys. (Paris) Colloq. **8**, C-1663 (1988).

Sputtering pressure effects and temperature-dependent magnetism of Co/Pd multilayers

S. Y. Jeong,[a] Z. S. Shan, P. He, J. X. Shen, Y. B. Zhang, J. A. Woollam, and D. J. Sellmyer

Behlen Laboratory of Physics and Center for Materials Research and Analysis, University of Nebraska, Lincoln, Nebraska 68588-0113

The temperature dependence of the sputtering Ar pressure effects on magnetic properties and the coercivity mechanism of Co(2 Å)/Pd(13 Å) multilayers were studied as the sputtering Ar pressure varied from 3–15 mTorr and the temperature from 300 to 35 K. It is found that the roughness of the interfaces or film surface increases with increasing sputtering pressure, the anisotropy increases with decreasing temperature and increasing Ar pressure and shows a maximum at $P_{Ar}\approx 12$ mTorr, and the coercivity increases with Ar pressure and shows stronger temperature dependence at higher Ar pressure. The coercivity mechanism was analyzed in terms of the coercivity predicted by Kronmüller's theory [Phys. Status Solidi B **144**, 385 (1987)]. Wall pinning is found to be the main mechanism and the size of the pinning site increases slightly as the Ar pressure increases.

I. INTRODUCTION

Co/Pd multilayers have been studied intensively in the last decade for pure and applied reasons.[1–3] For the Co/Pd multilayers with nanoscale Co layer, the interfacial magnetism, which is strongly influenced by the preparation conditions, plays a crucial role in determining the magnetic behavior. Hashimoto *et al.*,[4] de Haan *et al.*,[5] Shin *et al.*,[6] and He *et al.*[7] have reported the Ar pressure effects on magnetic properties at room temperature. It is found that the coercivity increases with increasing Ar pressure P_{Ar} during deposition and the anisotropy increases monotonically with increasing P_{Ar} (up to $P_{Ar}\approx 56$ mTorr),[5] or shows a maximum at $P_{Ar}=10$ mTorr.[4,6]

In this article the temperature dependence of the sputtering pressure effects on magnetism was studied as the temperature varied from 300 to 35 K. The coercivity mechanism was investigated in terms of the initial magnetization curves and minor loops at different temperatures, and comparisons were made to Kronmüller's model.[8]

II. EXPERIMENT

[Co(2 Å)/Pd(13 Å)]×35 (35 is the number of bilayers) multilayers were deposited onto glass substrates by dc magnetron sputtering under pressure $P_{Ar}=3$, 6, 9, 12, and 15 mTorr. All five samples were fabricated in one vacuum run to insure identical preparation conditions except for the Ar pressure.

The structure properties were characterized with the x-ray diffraction and atomic force microscopy (AFM) and the magnetic properties were measured by an alternating gradient force magnetometer (AGFM) with the temperature changed from 300 to 35 K. The coercivity $H_c(T)$ and magnetization $M(T)$ data were obtained from the perpendicular hysteresis loops and the measured anisotropy $K_u'(T)$ data were determined from the area between the parallel and perpendicular magnetization curves.

[a]Permanent address: Department of Physics, Gyeongsang National University, Chinju 660-701, Korea.

III. RESULTS AND DISCUSSIONS

A. Structure properties

Figure 1 shows the small-angle x-ray-diffraction patterns. It is seen clearly that the amplitude of the diffraction peaks decreases with increasing sputtering Ar pressure and when the sputtering pressure is greater than 9 mTorr, the diffraction peaks become obscure. This is attributed to the roughness of the interfaces which increases as the sputtering pressure increases since the sputtered Co and Pd atoms experienced more collisions with Ar atoms and form larger clusters at the growing film surface.

Figure 2 shows the AFM pictures of samples sputtered at (a) $P_{Ar}=3$ mTorr and (b) 15 mTorr and it is found that the surface roughness in Fig. 2(b) is much larger than that in Fig. 2(a). If the surface roughness may be regarded as the accumulation of the roughness of all individual layers or interfaces, Fig. 2 indicates clearly that the interfaces have larger roughness when sputtered in the higher Ar pressure, which is consistent with the result in Fig. 1.

B. Temperature character of pressure effects on magnetic properties

The Ar pressure dependence of the anisotropy K_u ($K_u = K_u' + 2\pi M_s^2$) as the temperature varied from 300 to 35 K is demonstrated in Fig. 3. It is seen that K_u increases as the temperature decreases. As the pressure increases K_u first increases, then decreases and shows a small peak at $P_{Ar}=12$ mT for all temperatures. This behavior is qualitatively consistent with earlier work[4,6] except that our peaks are rather small; K_u shows larger Ar pressure dependence at lower temperature. The origin of such K_u behavior is attributed to the interfacial magnetism which strongly depends on the polarization of Pd atoms at the interfaces[9,10] and the morphology of interfaces. As the temperature decreases the induced Pd moment increases which enhances the K_u. Hashimoto and co-workers[4] have explained qualitatively the behavior of Ar pressure dependence of K_u in terms of the stress-induced anisotropy because the stress in the film changes from compressive to tensile as the Ar pressure increases. Recently Vic-

 0021-8979/94/76(10)/6084/3/$6.00 © 1994 American Institute of Physics

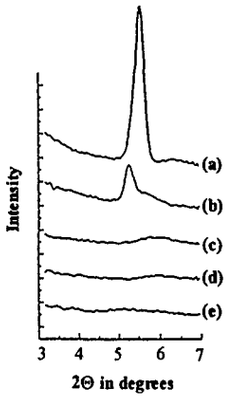

FIG. 1. Small-angle x-ray diffraction for Co(2 Å)/Pd(13 Å) deposited at different Ar sputtering pressures: (a) 3 mTorr; (b) 6 mTorr; (c) 9 mTorr; (d) 12 mTorr; and (e) 15 mTorr.

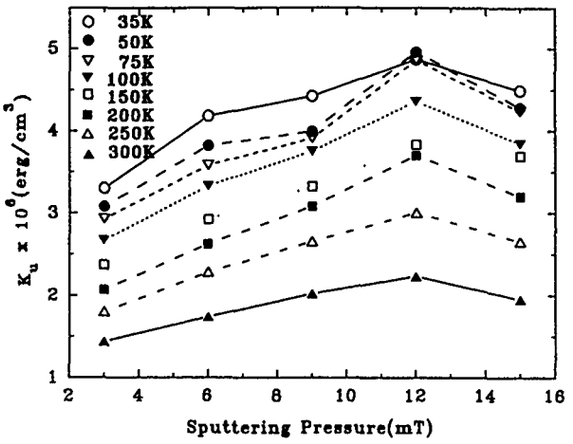

FIG. 3. Sputtering Ar pressure dependence of measured anisotropy K_u' at different temperatures.

tora and MacLaren[11] employed the symmetry-derived model based on summing $L(\mathbf{M}\cdot\mathbf{R})^2$ pair interactions (where $\mathbf{M}$ is the magnetization direction, $\mathbf{R}$ is the vector connecting the two atoms, and L is an interaction parameter) to calculate anisotropy for Co/Pd and Co/Pt multilayers. We intend to use this approach to calculate the K_u behavior quantitatively.

The sputtering pressure dependence of coercivity H_c as the temperature varied from 300 to 35 K is shown in Fig. 4(a). The coercivity increases monotonically with increasing P_{Ar} and shows stronger P_{Ar} dependence at the lower temperature. This behavior cannot be attributed fully to the change of K_u as shown in Fig. 3. In order to understand such behavior properly, we also need to consider the pinning effect of the domain-wall motion which is discussed in more detail in the following section.

The temperature dependence of H_c is shown in Fig. 4(b): H_c increases as the temperature decreases and shows stronger temperature dependence at higher P_{Ar}. The physical origins of this feature are discussed below.

C. Coercivity mechanism

In order to study the coercivity mechanism the initial curves and minor loops were measured at room and low temperature. All these curves show the typical domain-wall pinning feature: The magnetization is small at low applied field H_a and increases rapidly while H_a reaches a threshold value H_{th} which corresponds to the field required to exceed the pinning barrier. As the temperature decreases the thresh-

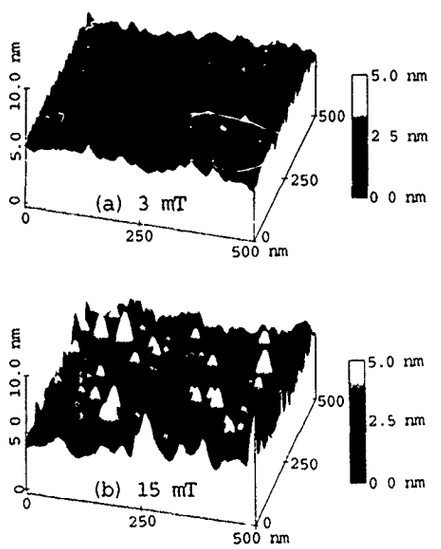

FIG. 2. AFM micrographs of Co(2 Å)/Pd(13 Å) deposited at Ar sputtering pressure of: (a) 3 mTorr and (b) 15 mTorr.

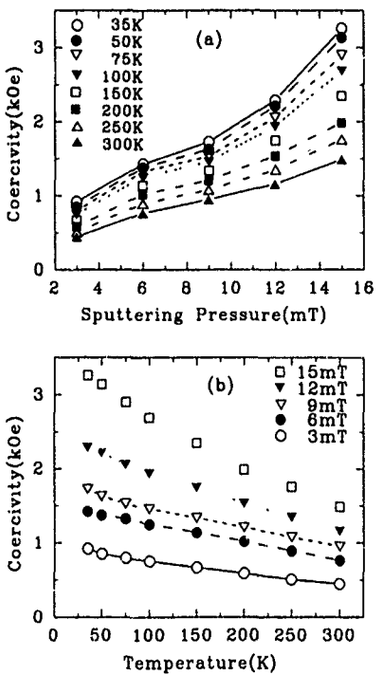

FIG. 4. (a) Sputtering Ar pressure dependence of coercivity at different temperature and (b) temperature dependence of coercivity at different sputtering Ar pressure

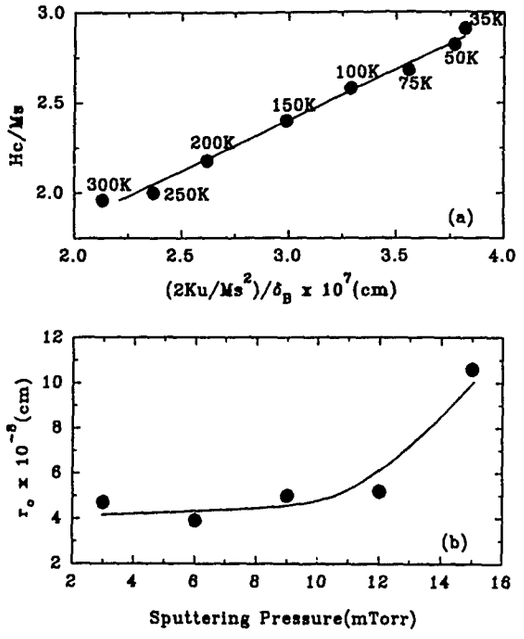

FIG. 5. (a) A linear fitting to the experimental data after Eq. (1) and the r_0 obtained is 4.7 Å. (b) The sputtering Ar pressure dependence of the estimated size of the pinning site.

old field H_{th} increases because of the decreasing thermal activation energy as predicted by Kirby *et al.*[12]

Kronmüller's formulas[8] were used to analyze the coercivity mechanism in more detail. If wall pinning is the dominant mechanism, the coercivity $H_c(T)$ is given by

$$H_c(T)=\kappa(r_0/\delta_B)(2K_u/M_s)-N_{\text{eff}}M_s \quad \text{for} \quad r_0 \ll \delta_B \qquad (1)$$

and

$$H_c(T)=\kappa'(\delta_B/r_0)(2K_u/M_s)-N_{\text{eff}}M_s \quad \text{for} \quad r_0 \gg \delta_B, \qquad (2)$$

where κ and κ' are both related to the exchange coupling constants and the anisotropy constants, r_0 is the size of the pinning site, and N_{eff} is a demagnetization factor. The wall width δ_B is given by $\pi(A/K)^{1/2}$, where A and K are exchange constant and anisotropy,[13] respectively.

Figure 5 is an example of the fitting curve based on Eq. (1) for the sample prepared at 3 mTorr Ar pressure. Similar fittings for all samples (P_{Ar}=6, 9, 12, and 15 mTorr) have been performed. The fact that the $[H_c/M_s, (2K_u/M_s^2)/\delta_B]$ experimental points measured at different temperatures are on a straight line implies that the domain-wall pinning is the dominant mechanism.

From the fits we could estimate the size of the pinning sites for each sample. The estimated sizes are 4.7, 3.9, 5.0, 5.2, and 10.6 Å for the samples prepared at P_{Ar}=3, 6, 9, 12, and 15 mTorr, respectively [see Fig. 5(b)]. The estimated values show that the size of the pinning site increases with increasing sputtering pressure. Equation (1) also tells us that $H_c(T)$ depends on the r_0K_u product. Although K_u decreases with increasing P_{Ar} for P_{Ar}>12 mTorr (as shown in Fig. 3), H_c still increases with increasing P_{Ar} for P_{Ar}>12 mTorr [as shown in Fig. 4(a)] because r_0 increases, and we have pointed out this feature earlier.

IV. CONCLUSIONS

The variation of the anisotropy and coercivity as a function of temperatures is closely related to the polarization of the Pd atoms at the interfaces and the film morphology which was controlled by the sputtering Ar pressure. The dominant mechanism for the coercivity is the wall pinning and the size of the pinning sites increase with increasing the sputtering pressure.

ACKNOWLEDGMENTS

We gratefully acknowledge financial support from NSF under Grant No. DMR-9222976. We thank A. Runge for assistance and helpful discussions.

[1] P. F. Carcia, A. D. Meinhaldt, and A. Suna, Appl. Phys. Lett. **47**, 78 (1985).
[2] N. Engel, C. P. England, R. A. Van Leeuwen, M. H. Wiedman, and C. M. Falco, Phys. Rev. Lett. **67**, 1910 (1991).
[3] F. J. A. den Broeder, H. C. Donkersloot, H. J. G. Draaisma, and J. M. de Jonge, J. Appl. Phys. **61**, 437 (1987).
[4] S. Hashimoto, Y. Ochiai, and K. Aso, J. Appl. Phys. **66**, 4909 (1989).
[5] P. de Haan, Q. Meng, T. Katayama, and J. C. Lodder, J. Magn. Magn. Mater. **113**, 29 (1992).
[6] S. C. Shin, J. H. Kim, and D. H. Ahn, J. Appl. Phys. **69**, 5664 (1991).
[7] P. He, Z. S. Shan, J. A. Woollam, and D. J. Sellmyer, J. Appl. Phys. **73**, 5954 (1993).
[8] H. Kronmüller, Phys. Status Solidi B **144**, 385 (1987); H. Kronmuller, K. D. Durst, and M. Sagawa, J. Magn. Magn. Mater. **74**, 291 (1988).
[9] R. M. Bozorth, P. A. Wolff, D. D. Davis, V. B. Compton, and J. H. Wernick, Phys. Rev. **122**, 1157 (1961).
[10] Z. S. Shan, P. He, C. Moore, J. Woollam, and D. J. Sellmyer, J. Appl. Phys. **73**, 6057 (1993).
[11] R. H. Victora and J. M. MacLaren, Phys. Rev. B **47**, 11 583 (1993).
[12] R. D. Kirby, J. X. Shen, R. J. Hardy, and D. J. Sellmyer, Phys. Rev. B **49**, 10 810 (1994).
[13] T. Suzuki, H. Notarys, D. C. Dobbertin, C. J. Lin, D. Weller, D. C. Miller, and G. Gorman, IEEE Trans. Magn. **MAG-28**, 2754 (1992).

Magnetoelastic effect in Co/Pd multilayer films

Young-Suk Kim and Sung-Chul Shin
Department of Physics, Korea Advanced Institute of Science and Technology, Kusung-Dong, Yusung-Gu, Taejon 305-701, Korea

In situ measurements of the stress are reported, and the magnetoelastic contribution to the magnetic anisotropy is clarified, in Co/Pd multilayer films prepared by dc magnetron sputtering. The stress was varied between 2.36×10^{10} and 4.22×10^{10} dyn/cm^2 in the Co sublayer of the film with an abrupt drop of the stress in the Co sublayer thicker than about 5 Å. This abrupt change seems to be related with a structural transition of a coherent-to-incoherent matching at the interface with thickening the sublayer. The stress-induced anisotropy of the samples having perpendicular magnetic anisotropy is found to be 40%–80%, compared to Néel's surface anisotropy.

I. INTRODUCTION

Co-based multilayer films are of great interest today because of their novel properties and potential technical applications.[1,2] In particular, the perpendicular magnetic anisotropy observed in those materials has been attracting wide attention for the application of the materials to magnetic and magneto-optical recording. Co/Pd multilayer films have been reported to show the perpendicular magnetic anisotropy for the samples having a Co sublayer thinner than about 8 Å and Pd sublayer thicker than about 5 Å.[3–6] The perpendicular magnetic anisotropy in this system is generally believed to be related to the change in the magnetic anisotropy of the interfacial atoms as a consequence of the reduced symmetry in their surroundings, as Néel first suggested.[7] However, recent studies have indicated that the stress-induced magnetic anisotropy also plays a role, especially for the samples prepared by sputtering.[5] In this article, we report *in situ* measurements of the stress and clarify the magnetoelastic contribution to the magnetic anisotropy in Co/Pd multilayer films.

II. EXPERIMENT

Co/Pd multilayer films were prepared by dc magnetron sputtering from 2-in.-diam Co and Pd targets on 4-cm-long, 1.1-cm-wide, and 130-μm-thick glass substrates at the Ar sputtering pressure of 10 mTorr. The distance between the substrate and the sputtering source was 12.7 cm. An edge of the substrate was fixed by a cantilever holder. The multilayer structure was achieved by alternately exposing the substrate to two sputtering sources via a reciprocating shutter. Typical deposition rates of Co and Pd were 0.53 and 0.81 Å/s, respectively.

The stress of a multilayer film was measured *in situ* during the deposition using a homemade optical displacement detection system as depicted in Fig. 1. A displacement sensor, composed of 38 optical fibers of 50 μm core diameter, was installed behind the free end of the substrate. The back side of the substrate was coated by 1000-Å-thick Al to enhance the reflectivity. A change in the gap distance between the sensor and the substrate, caused by the stress of a deposited film, was detected by measuring a corresponding change in the reflectivity from the back side of the substrate. The sensitivity of the displacement sensor used in this study was 0.059 V/μm and it turned out to be good enough to detect the stress caused by a deposition of a monatomic layer of Co or Pd. The multilayer structure was examined by low- and high-angle x-ray diffractometry. The magnetization was measured by a vibrating sample magnetometer (VSM) and the magnetic anisotropy was measured using a torque magnetometer at an applied field of 10 kOe.

III. RESULTS AND DISCUSSION

All samples in this study developed low-angle x-ray-diffraction peaks irrespective of the sublayer thickness, which suggests the existence of the multilayer structure in those samples. High-angle x-ray diffraction studies revealed that the samples were polycrystalline grown along the [111] cubic orientation.

Figure 2 shows a typical results of *in situ* measurement of the gap distance between the substrate and the optical probe with the deposition time for the sample having 8-Å-thick Co sublayers and 9-Å-thick Pd sublayers. The positive slope for the Co sublayer implies the existence of a tensile stress in the layer, while, the negative slope for the Pd sublayer implies a compressive stress in the layer. This result is as expected, since the d spacing of the (111) matching plane of Co is 9.9% smaller than that of Pd; however, it is inter-

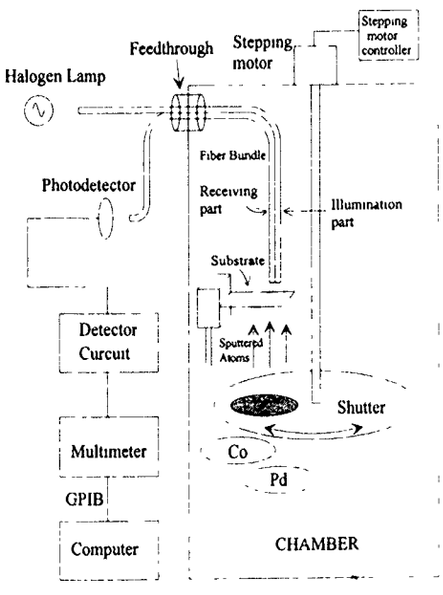

FIG. 1. Schematic configuration of an *in situ* stress measurement system.

 0021-8979/94/76(10)/6087/3/$6.00 © 1994 American Institute of Physics

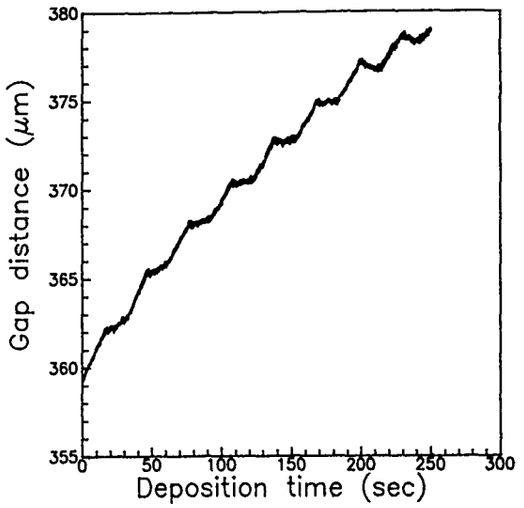

FIG. 2. A plot of the gap distance vs deposition time for the sample having 8-Å-thick Co and 9-Å-thick Pd layers.

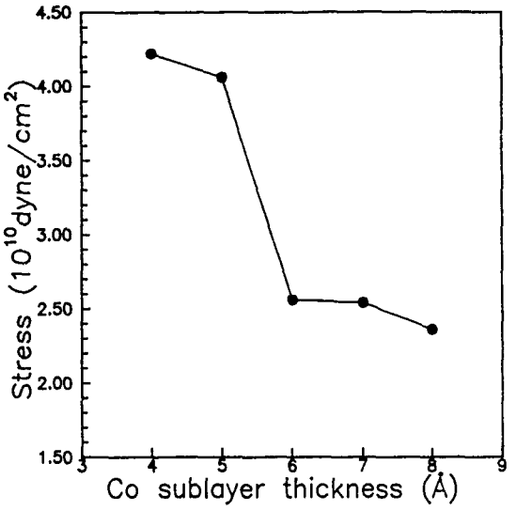

FIG. 4. A plot of the stress vs the Co sublayer thickness for a series of the samples having a constant Pd sublayer thickness of 9 Å.

esting to note that the slopes of the Co and Pd sublayers are changed with increasing sublayer thickness. To see the variation of the stress with the sublayer thickness, we calculate the stress existed in each sublayer using the well-known Stoney formula[8] as follows:

$$\sigma = \frac{E_s t_s}{3l^2(1-\nu_s)} \frac{\Delta d}{\Delta t_f}, \tag{1}$$

where E_s, ν_s, l, and t_s are Young's modulus, Poissons's ratio, and the length and thickness of a substrate, respectively, Δd is the change of the gap distance and Δt_f is the change of the film thickness. $E_s = 1.51\times10^{12}$ dyn/cm^2, $\nu_s = 0.3$, $l = 3$ cm, and $t_s = 130$ μm are used in the calculation.

Using Eq. (1) we plot the stress as a function of the sublayer of Co and Pd in Fig. 3. Since the Co sublayer was deposited first, the Co sublayers are expressed by the odd numbers and the Pd sublayers by the even numbers. The

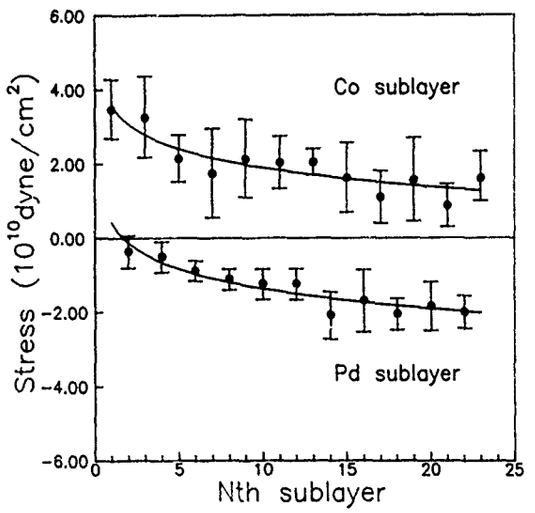

FIG. 3. A plot of the stress as a function of the Nth sublayer of Co and Pd.

error bar corresponds to the root-mean-square deviation of the mean stress of the Nth sublayer, which was obtained by taking the derivative at 100 points in each sublayer in Fig. 2. The stress in a multilayer film is mainly caused by two origins: an adhesion of the film to the substrate and the lattice mismatch between two dissimilar adjacent sublayers. The behavior of the stress with the sublayer thickness in Fig. 3 implies that an influence of the substrate yields a tensile stress with a maximum of 2.00×10^{10} dyn/cm^2 in the sublayer, possibly due to a smaller thermal-expansion coefficient of the glass substrate than the Co/Pd multilayer. This effect is monotonically decreased and seems to be negligible when the film is thicker than about 100 Å. Therefore, that a very small compressive stress observed in the first several Pd sublayers is not surprising; in this thickness range the tensile stress due to the substrate is appended to a compressive stress caused by the lattice mismatch. From Fig. 3 we note that the lattice mismatch between Co and Pd layers yields a 2.36×10^{10} dyn/cm^2 tensile stress for the Co sublayer and a 1.81×10^{10} dyn/cm^2 compressive stress for the Pd sublayer in this particular sample, which is larger than the stress of e-beam-evaporated samples.[9]

Interestingly enough, we have observed that the stress of the Co/Pd multilayer film was suddenly dropped with increasing the Co sublayer thickness. Figure 4 shows a plot of the stress versus the Co sublayer thickness for a series of the samples having a constant Pd sublayer thickness of 9 Å. A distinct drop in the stress can be seen when the Co sublayer thickness is larger than about 5 Å. Since the samples were prepared on the same glass substrates at the same sputtering conditions, the contribution other than the lattice mismatch to the stress of the film should be the same. Therefore, a sudden drop in the stress is believed to be related with a structural change from a coherent to incoherent interfacial matching between Co and Pd sublayers with increasing the Co sublayer thickness. The critical thickness for a coherency-incoherency transition observed in our sample agrees with a theoretical value of ~5 Å estimated by den

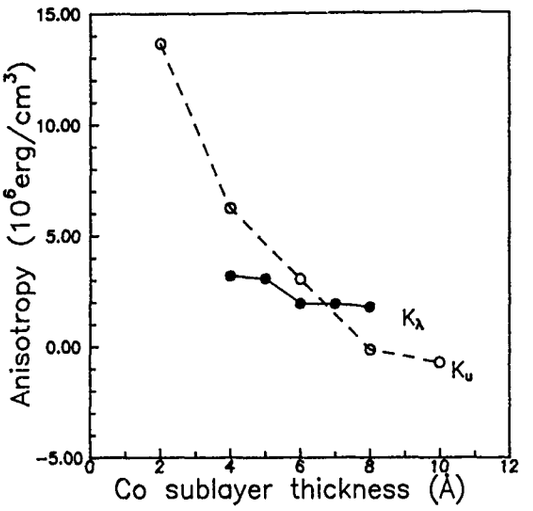

FIG. 5. A plot of the anisotropy energy K_u and the stress-induced anisotropy K_λ as a function of the Co sublayer thickness.

Broeder and co-workers.[1] The structural transition is under investigation by transmission x-ray diffractometry and will be published elsewhere.

In our system the perpendicular magnetic anisotropy exists for the samples having a Co sublayer thinner than about 8 Å as seen in Fig. 5. The anisotropy energy K_u associated with a multilayer can be described phenomenologically[4] as $K_u = 2K_s/t_{Co} + K_v$, where K_s is the interface anisotropy and K_v is the volume anisotropy. For a coherent multilayer K_s is only due to Néel's surface anisotropy and the strain-induced anisotropy is contained in K_v; however, for an incoherent case the misfit strain anisotropy may contribute to K_s.[1]

When the lattice mismatch is much larger than the magnetostriction coefficient as in Co/Pd multilayers the stress-induced magnetic anisotropy energy K_λ is given by[10]

$$K_\lambda = -\tfrac{3}{2}\lambda\sigma_{Co}, \tag{2}$$

where λ is the magnetostriction coefficient and σ_{Co} is the stress of the Co sublayer. Because of a negative λ for Co/Pd multilayers[11] the strained Co sublayer yields a positive perpendicular anisotropy energy. In Fig. 5 the stress-induced anisotropy K_λ is plotted, together with the magnetic anisotropy energy K_u. As seen in the figure, K_λ of $\sim 3.11\times10^6$ and $\sim 1.87\times10^6$ erg/cm^3 are obtained for the coherent and incoherent samples, respectively. The Néel surface anisotropy K_N in our samples, obtained from a plot of $K_u t_{Co}$ vs t_{Co} is estimated 0.16 erg/cm^2. The contribution of K_N to K_u for the samples showing perpendicular magnetic anisotropy is estimated to be between 2.7×10^6 and 8×10^6 erg/cm^3. Hence, the magnetoelastic contribution to the perpendicular magnetic anisotropy is 40%–80% in comparison with the contribution by Néel's surface anisotropy.

IV. CONCLUSIONS

We have investigated the effect of the stress on the magnetic anisotropy in Co/Pd multilayer films prepared by dc sputtering. *In situ* measurements of the stress have revealed that multilayers had a tensile stress of 2.36×10^{10}–4.22×10^{10} dyn/cm^2 in the Co sublayers. An abrupt reduction of the stress was observed when the Co sublayer thickness was larger than 5 Å, which is believed to be caused by a coherent-to-incoherent transition. It was found that for the perpendicular magnetic anisotropy of our samples, the magnetoelastic contribution due to the lattice mismatch is much comparable to the contribution by Néel's surface anisotropy.

ACKNOWLEDGMENT

This work was supported by Korea Research Foundation and Center for Interface Science and Engineering of Materials.

[1] F. J. A. den Broeder, W. Hoving, and P. J. H. Bloemen, J. Magn. Magn. Mater. **93**, 562 (1991), and references therein.
[2] S.-C. Shin, Appl. Surf. Sci. **65/66**, 110 (1993).
[3] P. F. Carcia, A. D. Meinhaldt, and A. Suna, Appl. Phys. Lett. **47**, 178 (1988).
[4] H. J. G. Draaisma, W. J. M. de Jonge, and F. J. A. den Broeder, J. Magn. Magn. Mater. **66**, 351 (1987).
[5] S. Hashimoto, Y. Ochiai, and K. Aso, J. Appl. Phys. **66**, 4909 (1989).
[6] D. G. Stinson and S.-C. Shin, J. Appl. Phys. **67**, 4459 (1990).
[7] L. Néel, J. Phys. Radium **15**, 225 (1954).
[8] G. G. Stoney, Proc. R. Soc. London Sect. A **82**, 172 (1909).
[9] H. Awano, Y. Suzuki, T. Yamazaki, T. Katayama, and A. Itoh, J. Appl. Phys. **68**, 4569 (1990).
[10] H. Awano, Y. Suzuki, T. Yamazaki, T. Katayama, and A. Itoh, IEEE Trans. Magn. **MAG-26**, 2742 (1990).
[11] A. Yamaguchi, S. Ogu, W. H. Soe, and R. Yamamoto, Appl. Phys. Lett. **62**, 1020 (1993).

Interface processing in multilayer films

R. J. Pollard, M. J. Wilson, and P. J. Grundy
Joule Physics Laboratory and Science Research Institute, University of Salford, Greater Manchester M5 4WT, United Kingdom

We have investigated the effect of ion modification of multilayer growth and ion etching of multilayer interfaces on perpendicular anisotropy and giant magnetoresistance in sputter deposited Co/Pt and Co/Cu multilayers. These two properties are thought to be particularly sensitive to the form of the interface profile in multilayers. We find that the ion-assisted deposition conditions used degrade both perpendicular anisotropy and GMR through interface smoothing and mixing. In contrast, thermal annealing and first experiments in ion etching show that GMR can be increased by smoothing of the Co/Cu interfaces.

INTRODUCTION

Co/Pt and Co/Cu MLs are believed to exhibit structure sensitive magnetic anisotropy[1–3] and giant magnetoresistance.[4] We have used such systems as models in preliminary investigations of the effect of ion beam-assisted sputter deposition, ion beam etching, and thermal annealing on these properties.

EXPERIMENT

The MLs were deposited in a UHV-compatible magnetron sputtering system equipped with dc magnetrons and a 3 cm Kaufman ion source. The Co, Pt, and Cu layers were deposited onto glass substrates by ion-assisted deposition, i.e., the ion beam (0–400 eV, 2 mA) on and irradiating the ML during growth, or by ion etching, i.e., with the deposition interrupted and the top surface of each Co layer irradiated with the ion beam for 10 s. The deposition rate was about 0.1 nm s^{-1}.

The magnetic hysteresis loops were measured in a VSM (Co/Cu MLs) or in a Kerr M/O loop plotter (Co/Pt MLs). Anisotropy (Co/Pt MLs) was investigated by torque magnetometry, and magnetoresistance (Co/Cu MLs) was measured by the standard four probe dc method. Some basic structural changes were inferred from x-ray diffraction measurements. All measurements were carried out at room temperature.

RESULTS AND DISCUSSION

Figure 1(a) shows the polar Kerr hysteresis loops for a series of three $15x$(0.4 nm Co/1.2 nm Pt) MLs deposited by ion-assisted growth. It can be seen that as the ion energy is increased the loops depart more and more from squareness and the coercivity of the MLs decreases. The shearing of the loops is reflected in the torque curves of Fig. 1(b), which show a gradual decrease in the torque amplitude with increasing ion energy. The negative slope at $\theta=0$ confirms the normal to the ML as the easy direction (θ is the angle between the normal to the ML and the field direction) for the 0 eV (no ion flux) and 100 eV MLs. However, for 200 eV the torque curve is clearly modified with the appearance of a change of slope near zero torque and $\theta=0$. These changes indicate that the effective perpendicular anisotropy decreases with increasing ion energy from a value of $\approx 6\times10^5$ J m^{-3} for the "unassisted" ML and that the easy direction of magnetization rotates from the normal to the ML towards the plane. A similar result has been obtained for ion beam etching of a series of $7x$(0.4 nm Co/1.2 nm Pt) MLs. Again, a decrease in torque and perpendicular anisotropy with increasing ion energy was observed.

Sputter deposited Co/Pt MLs with thicker ($\geq$0.8 nm) Co layers do not show such strong perpendicular anisotropy.[5,6] Figure 2(a) gives polar Kerr loops for a series of four 15

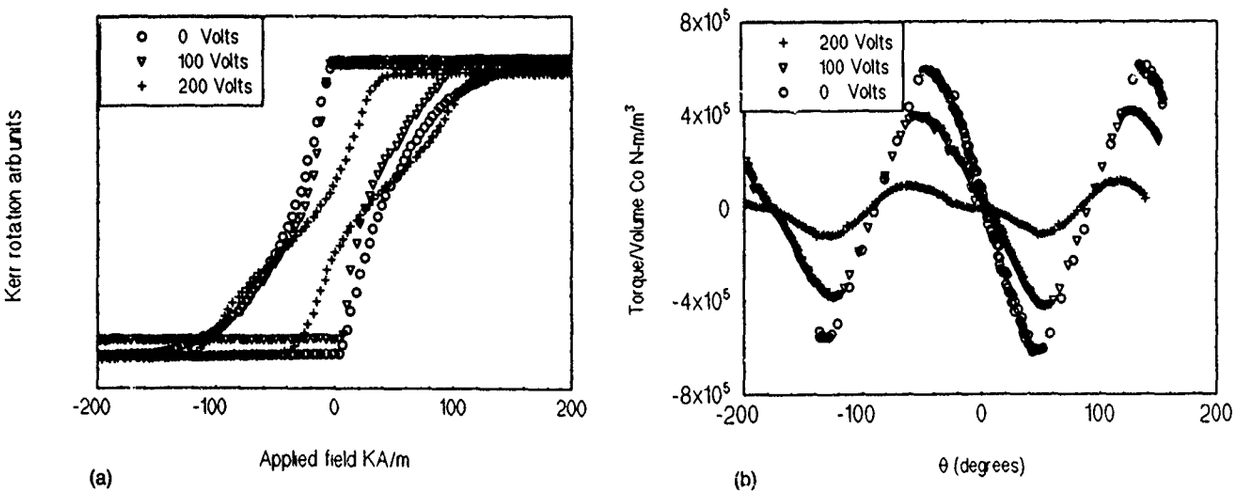

FIG. 1. Polar Kerr loops (a) and torque curves (b) for $15x$(0.4 nm Co/1.2 nm Pt) MLs for different beam energies/voltages in ion-assisted deposition.

 0021-8979/94/76(10)/6090/3/$6.00 © 1994 American Institute of Physics

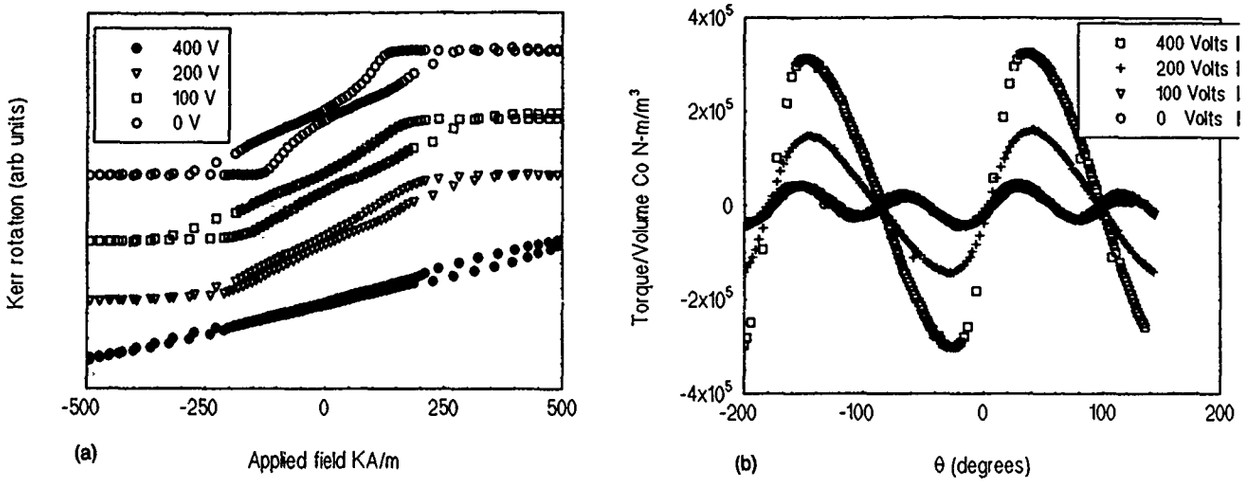

FIG. 2. As in Fig. 1 but for $15x$(1.2 nm Co/1.2 nm Pt) MLs.

×(1.2 nm Co/1.2 nm Pt) MLs deposited with ion assistance at 0, 100, 200, and 400 eV. These perpendicular loops change gradually with increasing shear and decreasing coercivity until at 400 eV the loop has the shape typical of a hard axis loop. The torque curves for these MLs, given in Fig. 2(b), change from two similar curves of small amplitude for 0 and 100 eV, which can be analyzed in terms of an easy cone of magnetization about the normal to the ML, which is isotropic in its plane, to curves for 200 and 400 eV for which the easy direction is clearly in the plane of the ML as signified by the positive slope of the torque curve at $\theta=0$.

X-ray diffraction confirmed the layered and textured structure of the low energy ion-assisted and etched MLs. Increasing the beam energy in ion-assisted deposition eventually destroys the layered structure as indicated by the ratio of the ⟨111⟩ maximum to the first satellite maximum, I_{111}/I_{sat}. For the 0, 100, 200, and 400 eV MLs described in Fig. 2, I_{111}/I_{sat} was measured as 1.7, 1.6, 2.3, and ∞, respectively.

Turning to the Co/Cu systems, Figs. 3(a) and 3(b) show the VSM hysteresis loops and magnetoresistance loops for four ion-assisted $20x$(1 nm Co/2 nm Cu) MLs. These MLs are structured for the second maximum in the GMR oscillation.[4,7] It can be seen in Fig. 3(a) that the ML deposited without ion assistance (0 eV) gave a sheared magnetic hysteresis loop having a lower remanence than MLs deposited with ion assistance suggesting some definite antiferromagnetic coupling between the Co layers in the 0 eV ML. Figure 3(b) shows a GMR of 15% for this ML. The figures also show that ion assistance in the deposition gradually destroys the properties of the ML; it reduces the amount of antiferromagnetic coupling in the ML and it eventually produces a much less sheared hysteresis loop at 200 eV, Fig. 3(a). There is a concomitant decrease in the GMR ratio to almost zero, Fig. 3(b).

Thermal annealing and x-ray measurements[8] show that the GMR in Co/Cu MLs is destroyed along with the layered structure at temperatures above about 300 °C. However, an

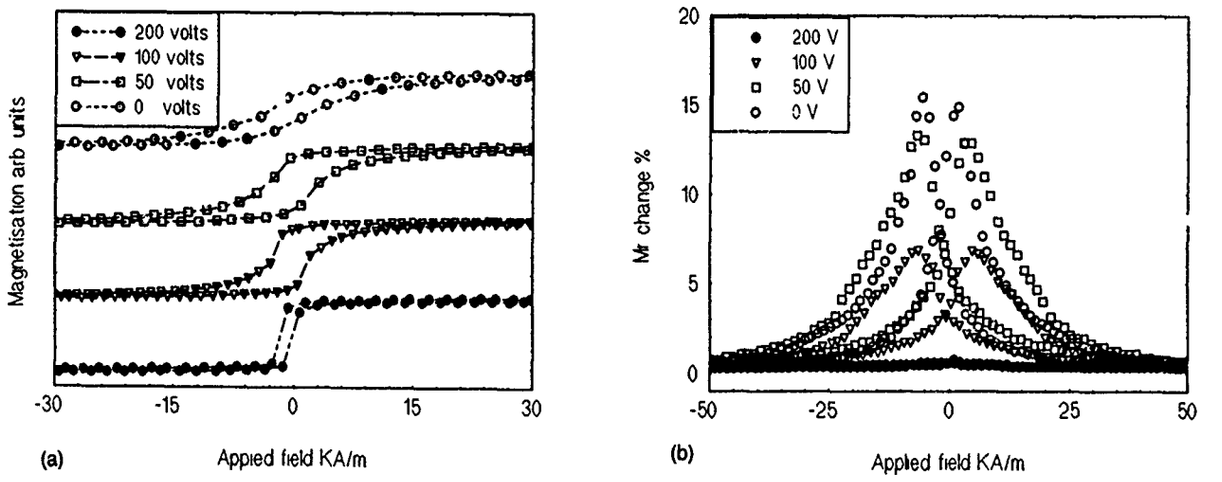

FIG. 3. VSM hysteresis (a) and GMR (b) loops for $20x$(1 nm Co/2 nm Cu) ion-assisted MLs.

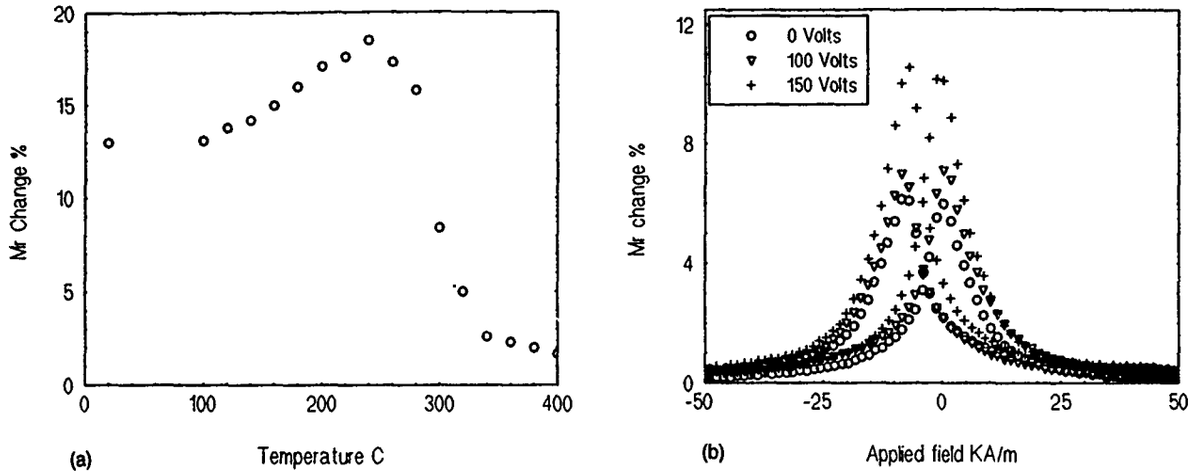

FIG. 4. GMR loops for (a) thermally annealed and (b) ion etched 16x(1 nm Co/2 nm Cu) MLs.

increase in GMR can be observed in annealing at lower temperatures. This is illustrated in Fig. 4(a) for a 16×(1 nm Co/2 nm Cu) ML where the GMR increases by about 50% up to 250 °C. Significantly, we have found that ion etching can also produce an improvement in GMR. Figure 4(b) shows GMR loops for a series of MLs having the structure 10×(1 nm Co/2 nm Cu) in which the Co surfaces have been ion etched at different energies. There is a clear improvement in GMR at energies up to 150 eV. We have some evidence that this effect is followed by a decrease at energies greater than 200 eV.

In the ion-assisted depositions the ratio of the ion to atom fluxes can be calculated as $j_i/j_a \approx 2$ and there is sufficient energy transferred in collisions of the ions with the condensing and condensed atoms to cause surface displacements and densification of the microstructure of the growing layers.[9] However, certainly at the higher energies, there is a possibility of atom mixing by the ion bombardment at any interface as the deposition progresses and this will encourage a less sharp compositional profile in the ML. No material loss from the MLs was detected up to ion energies of 200 eV and measurable sputtering of the growing ML is only expected at energies greater than 300 or 400 eV.

In ion etching, modification of the surface and near-surface regions of the interrupted structure can be expected. As the individual layers in the MLs discussed here are less than ten atomic layers thick, and some are of the order of two to three atomic layers, there is a possibility of modification and mixing at the interface below the treated surface. Monte Carlo simulations show that for the Co/Cu MLs, with 10 nm Co and 20 nm Cu layers, this effect is not significant for 100 eV ions, but at 200 eV mixing of Co into Cu occurs over a region ≈0.4 nm in width across the interface below the etched surface. In the Co/Pt MLs, considerable displacement of atoms from the 0.4-nm-thick Co layer into the underlying Pt layer is predicted at 100 eV, but in the case of the 1.2 nm Co layers, this is only significant at energies above 300 eV.

The effects in the ion treated Co/Pt MLs discussed here can be compared to those reported for Co/Pt MLs sputter-deposited in "thermalizing" conditions,[1] which result in rougher interfaces and coarser microstructures and stronger perpendicular anisotropy and larger coercivities. We can therefore reasonably interpret our results for the loss of perpendicular anisotropy in Co/Pt MLs in terms of surface smoothing at the lower ion energies and microstructural modification involving mixing and roughening of the interface at higher energies.

The progressive loss of GMR and antiferromagnetic coupling in the ion-assisted Co/Cu MLs may have been due to modification of the microstructure and texture of the layers and/or interface regions. The initial increase in GMR in the low energy ion etched MLs, and in the thermally annealed structures, followed by a loss at higher energies, suggests strongly that increased electron scattering was caused by interface/surface smoothing. We plan to investigate these suggested microstructural and interface changes by high resolution electron microscopy and x-ray reflectometry.

[1] P. F. Carcia, Z. G. Li, and W. B. Zeper, J. Magn. Magn. Mater. **121**, 452 (1993).
[2] B. Rodmacq, M. Vaezzadeh, B. George, and Ph. Mangin, J. Magn. Magn. Mater. **121**, 213 (1993).
[3] W. B. Zeper, H. W. van Kesteren, B. A. J. Jacobs, P. F. Carcia, and J. M. Spruit, J. Appl. Phys. **70**, 2264 (1991).
[4] M. E. Tomlinson, R. J. Pollard, D. G. Lord and P. J. Grundy, J. Magn. Magn. Mater. **111**, 79 (1992).
[5] S. J. Greaves, P. J. Grundy, and R. J. Pollard, J. Magn. Magn. Mater. **121**, 532 (1993).
[6] W. B. Zeper, F. J. A. M. Greidanus, P. F. Carcia, and C. R. Fincher, J. Appl. Phys. **65**, 4971 (1989).
[7] S. S. P. Parkin, R. Bhadra, and K. P. Roche, Phys. Rev. Lett. **66**, 2152 (1991).
[8] M. E. Tomlinson, R. J. Pollard, D. G. Lord, P. J. Grundy, and Z. Chun, IEEE Trans. Magn. **MAG-28**, 2662 (1992).
[9] K-H. Muller, in *Materials Modification and Growth Using Ion Beams*, Vol. 93, edited by U. J. Gibbon, A. E. White, and P. P. Pronko (MRS, Pittsburgh, PA, 1987), p. 275.

Anomalous interface magnetism in ultrathin Co films with in-plane anisotropy

F. O. Schumann, M. E. Buckley, and J. A. C. Bland
Cavendish Laboratory, Madingley Road, Cambridge CB3 OHE, United Kingdom

Using the magneto-optical Kerr effect, we have observed a striking sensitivity of the magnetic properties of ultrathin Co/Cu(001) films to submonolayer coverages of Cu. In particular large nonmonotonic changes of the coercive field H_c, the height of the *M-H* loop (magneto-optical signal), and the ratio S of remanent and saturation magnetizations are observed. With increasing Cu thickness the coercivity first sharply decreases, reaching a minimum at around 0.2 monolayer (ML) followed by a gradual increase. In contrast, the magneto-optical signal is found to peak strongly at the same Cu overlayer thickness of 0.2 ML, decaying in magnitude with further Cu coverage.

I. INTRODUCTION

It is now well established experimentally that nonmagnetic overlayers can drastically affect the magnetic properties of ultrathin magnetic films as reported by Przybylski *et al.*[1] and Weber *et al.*[2] More recently, Engel *et al.*[3] have shown the influence of ultrathin Cu, Ag, and Pd overlayers on the perpendicular magnetism of Co/Pd(111) films, where the coercive field exhibits a nonmonotonic dependence on the nonmagnetic overlayer thickness. It is therefore of interest to test the effect of a nonmagnetic overlayer in the ultrathin regime for a film with in-plane anisotropy. The Co/Cu(001) system displays in-plane anisotropy,[4–7] and upon coating with several monolayers (ML) of Cu, a reduction of the Curie temperature,[8] and of the out-of-plane anisotropy[9] and coercive field[10] are known to occur.

II. EXPERIMENT

The experiments were carried out in an ultrahigh vacuum chamber with a base pressure of 1.0×10^{-10} mbar, and a pressure of less than 5.0×10^{-10} mbar during Co and Cu deposition. Ar^+ sputtering (1 kV) and annealing up to 700 K resulted in a clean and well-ordered Cu(001) surface. Magneto-optical Kerr effect in the transverse geometry[4] has been employed for recording hysteresis loops, with the magnetic field aligned along the ⟨110⟩ easy axis.[4,6] Co and Cu films were grown with the sample at 300 K with typical deposition rates of 0.1 ML/min for Co and 0.05 ML/min for Cu (judged using the Auger peak heights and, for the Co, the sharp onset of ferromagnetic order as a guide).[10] All magnetic measurements were performed at 300 K.

III. RESULTS AND DISCUSSION

The thickness d_{Co} of the Co layers has been varied between 1 and 2 d_c, where d_c is the critical thickness at which long-range order occurs at 300 K. The absolute value of d_c is between 1 and 1.7 ML.[7–9,11,12]

In Fig. 1 we display several *M-H* loops of a $1.6d_c$ Co/Cu(001) film obtained during growth of the Cu overlayer. Clearly minute coverages reduce H_c drastically and change S, the ratio of remanent magnetization to saturation magnetization. Surprisingly, the squarest loop is obtained for a small Cu overlayer thickness of approximately 0.2 ML. A careful analysis of all *M-H* loops during this growth sequence reveals a nonmonotonic dependence M_{sat} (the loop amplitude) and H_c on Cu thickness d_{Cu} as shown in Fig. 2, and of S (not shown). In particular the coercivity exhibits a sharp minimum at the thickness at which S and M_{sat} peak.

For all Co thicknesses studied, qualitatively similar variations in each of these quantities are observed, except that the nonmonotonic behavior of S is less pronounced for thinner films, for which S is closer to unity than for the

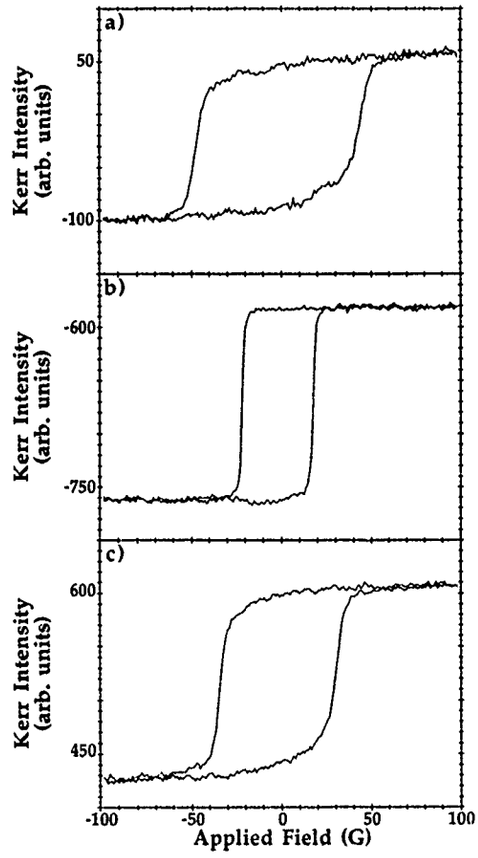

FIG. 1. Various *M-H* loops of a $1.6d_c$ thick Co/Cu(001) film during a Cu overlayer growth sequence, with Cu overlayer thickness d_{Cu} of 0.04, 0.16, and 0.36 ML for (a)–(c), respectively.

 0021-8979/94/76(10)/6093/3/$6.00 © 1994 American Institute of Physics

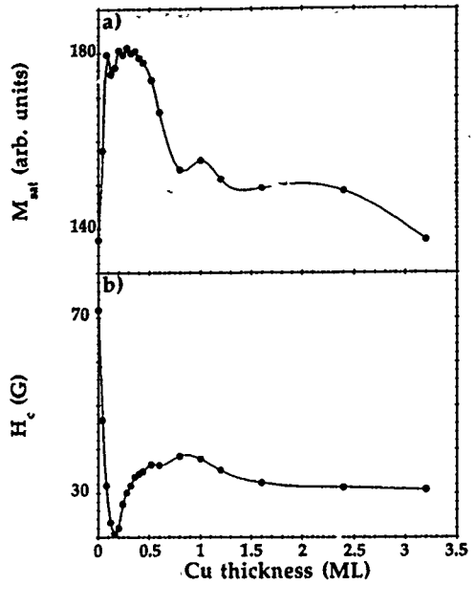

FIG. 2. The results of a careful analysis of the Cu overlayer growth sequence of a $1.6d_c$ thick Co/Cu(001) film are shown, revealing the nonmonotonic behavior of the saturation magneto-optical signal M_{sat} in (a), and the coercive field H_c in (b).

thicker Co films. We define the peak enhancement as follows:

$$\Delta = \frac{M_{sat}(d_{Cu}) - M_{sat}(0)}{M_{sat}(0)} \quad \text{with } d_{Cu} = 0.2 \text{ ML.} \qquad (1)$$

We can now summarize the main experimental findings for all the structures studied as follows: H_c always rapidly drops by roughly a factor of ~3, and Δ is always of the order of 20% upon the deposition of only 0.2 ML of Cu.

In Fig. 3 we show the thickness dependence of M_{sat} of a $1.5d_c$ thick Co/Cu(001) film. We notice again a nonlinear behavior in the submonolayer range as in Fig. 2. At higher coverages we see a noticeable drop of M_{sat} below the value for the uncovered Co/Cu(001) film, which is more pronounced than that which would be caused by optical attenuation through the Cu layer. A low-energy electron diffraction study of the energy dependence of the Bragg peak intensity

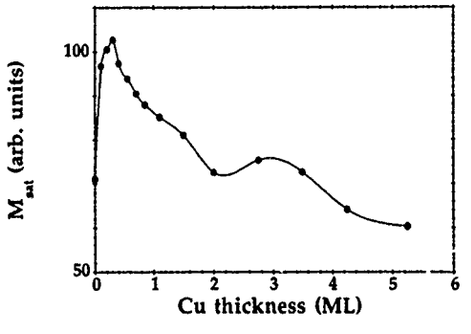

FIG. 3. The behavior of M_{sat} for a $1.5d_c$ thick Co/Cu(001) film. Note M_{sat} drops below the value for the uncovered film at high Cu coverages.

maxima for the (00) beam did not indicate strong changes in the perpendicular lattice parameter occurring upon Cu deposition.

The drop in H_c may indicate a drastic change in the magnetic anisotropy. A correlation between the change in perpendicular anisotropy and coercivity induced by an overlayer is reported by Engel *et al.*[3,13] for Cu-coated Co/Pd films. We would like to point out that Schneider *et al.*[8] report that the coercive field of films grown at 300 K is much higher than for those of identical thickness grown at 450 K. This observation is consistent with our data if we assume that the films grown at high temperatures correspond to the coated structures we have studied, as suggested by the observation by Kief *et al.*[14] that surface Cu segregation occurs at elevated temperatures.

The increase in magneto-optical signal with Cu deposition is surprising. We find that the degree of enhancement due to the 0.2 ML Cu overlayer is comparable with the increase in magnetic signal that would occur for an equivalent increase in the Co thickness. Schneider *et al.*[8] report a reduction of the Curie temperature T_C upon Cu deposition: therefore one might expect a reduction of M_{sat} upon Cu deposition. Since H_C and M_{sat} change with Cu overlayer thickness d_{Cu}, it is feasible that T_C could also be a general function of d_{Cu}, with the reported reduction[8] being the limiting behavior at higher Cu coverages. However, because T_C increases rapidly with Co thickness,[8,15] any effects due to a change in T_C should be more pronounced for films with a thickness of $1.1d_c$ than for those of $1.7d_c$; our findings show a similar behavior for all Co thicknesses. We can therefore rule out changes in the Curie temperature as a possible mechanism for the enhancement in loop amplitude we observe.

At present we cannot rule out the possibility that the deposition of small amounts of Cu acts like a "surfactant," improving the structural quality of the film. This is suggested by the almost perfectly square loop shown in Fig. 1(b) for 0.2 ML Cu coverage. However, further Cu deposition causes the loop to become less square, which contradicts this explanation at higher thicknesses. Also the peak enhancement is difficult to explain via surfactant effect. It is also possible that the Cu overlayer affects magnetic domain pinning or domain wall energies.

In our opinion, the most likely mechanism for the behavior we observe is that the evolving interface electronic structure influences the magnetic properties (anisotropy in particular). Recent calculations by Freeman[16] show that the presence of a Cu overlayer considerably influences the magnetism of fcc Co/Cu(001). The anomalous anisotropy behavior observed by Engel *et al.*[3,13] is believed to arise from the interface electronic structure, although we note that in this case the maximum effect is obtained for a nonmagnetic overlayer thickness of around 0.8 ML. In our view, the significance of the present work is that it implies that "anomalous" interface-induced changes in the magnetic properties may also occur for films with planar anisotropy, suggesting that a common mechanism may apply in both cases.

IV. SUMMARY

In summary, we have observed a nonmonotonic dependence of magnetic properties of ultrathin Co/Cu(001) films upon coating with submonolayers of Cu that may originate in the electronic structure of the interface. Most important, we report an enhancement of the magneto-optical signal upon deposition of 0.2 ML Cu. Surprisingly, these observations suggest that features analogous to the anomalous anisotropy in perpendicular Co/Pd(111) films[3,17] also occur in the in-plane Co/Cu(001) system. These results emphasize the importance of the interaction between the substrate and the magnetic layer, which can give rise to striking and largely unexplored effects in the submonolayer range.

ACKNOWLEDGMENTS

We thank the Royal Society, SERC, and the EEC for financial support.

[1] M. Przybylski and U. Gradmann, Phys. Rev. Lett. **59**, 1152 (1987).
[2] W. Weber, D. Kerkmann, D. Pescia, D. A. Wesner, and G. Guntherodt, Phys. Rev. Lett. **65**, 2058 (1990).
[3] B. N. Engel, M. H. Wiedmann, R. A. Van Leuwen, and C. M. Falco, Phys. Rev. B **48**, 9894 (1993).
[4] D. Kerkmann, Appl. Phys. A **49**, 523 (1989).
[5] H. P. Oepen, M. Benning, H. Ibach, C. M. Schneider, and J. Kirschner, J. Magn. Magn. Mater. **86**, L137 (1990).
[6] H. P. Oepen, J. Magn. Magn. Mater. **93**, 116 (1991).
[7] B. Heinrich, J. F. Cochran, M. Kowalewski, J. Kirschner, Z. Celinski, A. S. Arrott, and K. Myrtle, Phys. Rev. B **44**, 9348 (1991).
[8] C. M. Schneider, P. Bressler, P. Schuster, K. Kirschner, J. J. de Miguel, and R. Miranda, Phys. Rev. Lett. **64**, 1059 (1990).
[9] P. Krams, F. Lauks, R. L. Stamps, B. Hillebrands, and G. Güntherodt, Phys. Rev. Lett. **69**, 3674 (1992).
[10] F. O. Schumann and J. A. C. Bland, J. Appl. Phys. **73**, 5945 (1993).
[11] L. Smardz, U. Koebler, D. Kerkmann, F. Schumann, D. Pescia, and W. Zinn, Z. Phys. B **80**, 1 (1990).
[12] M. T. Kief, G. J. Mankey, and R. F. Willis, J. Appl. Phys. **69**, 5000 (1992).
[13] B. N. Engel, M. H. Wiedmann, R.A. Van Leeuwen, and C. M. Falco, J. Appl. Phys. **73**, 6192 (1993).
[14] M. T. Kief and W. F. Egelhoff, Jr., Phys. Rev. B **48**, 10 785 (1993).
[15] F. Huang, M. T. Kief, G. J. Mankey, and R. F. Willis, Phys. Rev. B **49**, 3962 (1994).
[16] D. Wang, R. Wu, and A. J. Freeman, J. Magn. Magn. Mater. **129**, 237 (1994).
[17] P. Beauvillain, A. Bounouh, C. Chappert, R. Mégy, S. Ould-Mahfond, J. P. Renard, P. Veillet, and D. Weller (these proceedings).

FMR studies of magnetic properties of Co and Fe thin films on Al_2O_3 and MgO substrates

Yu. V. Goryunov, G. G. Khaliullin, and I. A. Garifullin
Kazan Physicotechnical Institute, 420029 Kazan, Russian Federation

L. R. Tagirov
Kazan State University, 420008 Kazan, Russian Federation

F. Schreiber, P. Bödeker, K. Bröhl, Ch. Morawe, Th. Mühge, and H. Zabel
Institut für Experimentalphysik, Ruhr-Universität Bochum, 44780 Bochum, Germany

The effect of substrates on the magnetic properties has been studied for Co and Fe films both on Al_2O_3 $(11\bar{2}0)$ and MgO (001) substrates by using ferromagnetic resonance techniques. For Fe(C01)/MgO(001) samples the thickness dependence of the magnetocrystalline constant and of the effective magnetization values have been determined from the in-plane angular variation of the resonance field H_0. Different reasons for the thickness dependencies of these parameters are discussed. For $Co(111)/Al_2O_3(11\bar{2}0)$ the angular variation of H_0 exhibits an uniaxial anisotropy, for which several causes are discussed. For $Co(11\bar{2}0)/MgO(100)$ a four-fold in-plane anisotropy was observed which is due to the twinned structure of these samples.

I. INTRODUCTION

Magnetic properties of thin films are affected to a large degree by interfacial effects arising from the interaction of the film with the substrate. Understanding these interface anisotropies in thin ferromagnetic layers is also very important for dealing with the more complex problem of magnetic multilayers and in particular with the analysis of exchange coupling. Recently, anisotropy measurements using the longitudinal Kerr effect were carried out on cobalt films grown by molecular beam epitaxy (MBE)[1] and on iron films prepared by rf sputtering techniques.[2] For the observed anisotropies possible sources for the film/substrate interaction were suggested. However, final conclusions can only be drawn after detailed investigations of the thickness and temperature dependences of the anisotropy have been carried out. It is well known that the ferromagnetic resonance (FMR) technique is a powerful tool for the study of magnetic anisotropies. Here we report the results of a FMR study of the in-plane anisotropy of Co and Fe films on Al_2O_3 $(11\bar{2}0)$ and MgO(001) substrates over wide temperature and thickness ranges.

II. EXPERIMENT

Cobalt films were grown by MBE techniques on $Al_2O_3(11\bar{2}0)$ and MgO(001) substrates. During film growth the substrate temperature was held constant at T_s=620 K for the sapphire substrate and at T_s=300 K for the magnesium oxide substrates. The sample preparation and the growth conditions are described in more detail in Ref. 3. Some films were exposed later to high temperatures (470 K) at a hydrogen atmosphere of about 100 mm Hg. For one sample the effect of the substrate temperature on the anisotropy was also examined.

The Fe films were grown by rf sputtering on MgC(001) substrates at 300 K in a 5×10^{-1} Pa pure Ar (99.999%) plasma with a growth rate of 0.1 Å/s. Further details are provided in Ref. 4. In order to prevent oxidation, the iron films were covered by a protective gold layer of 40 Å thickness.

The structural properties of films were studied by out-of-plane and in-plane x-ray scattering experiments. It should be noted that the structural quality of our rf sputtered films come close to the quality of the MBE grown epitaxial films.[4] The epitaxial relation of bcc Fe(100) on fcc MgO(100) follows the 45° epitaxy expected from the bulk lattice constants, i.e., the Fe[100] in-plane axis is parallel to the MgO[110] axis. Thin Co films on Al_2O_3 $(11\bar{2}0)$ substrates grow in a fcc or hcp structure depending on the film thickness with either the (111)-axis or (0001) pointing perpendicular to the film plane. Co films on MgO(100) substrates grow in the hcp structure with the $(11\bar{2}0)$ plane parallel to the film plane.

FMR experiments were carried out at 9.4 GHz in the temperature range from 20 to 400 K. The angular dependencies of the spectra were observed with both the dc magnetic field and the high frequency field in the film plane.

III. RESULTS

A. Fe/MgO

The results of the FMR measurements were analyzed using the standard formalism (see, e.g., Ref. 5). Magnetic free energy was taken consisting of a Zeeman $F_Z=-MH\sin\theta\cos(\phi-\phi_H)$, a demagnetization $F_D=2\pi M^2\cos^2\theta$, and a magnetocrystalline anisotropy term

$$F_C=\tfrac{1}{4}K_1(\sin^2 2\theta+\sin^4\theta\sin^2 2\phi), \quad (1)$$

where $\theta(\theta_H)$ and $\phi(\phi_H)$ are the angles of the magnetization M (magnetic field H) with respect to the film normal and to the x axis in the film plane (xy plane), respectively. In our geometry $\theta_H=\pi/2$.

By fitting the four-fold angular dependence of the resonance field position H_0, the $4\pi M$ value and the cubic anisotropy constant K_1 were determined. In Fig. 1 K_1 is plotted as a function of the reciprocal film thickness L^{-1} and in Fig.

 0021-3979/94/76(10)/6096/3/$6.00 © 1994 American Institute of Physics

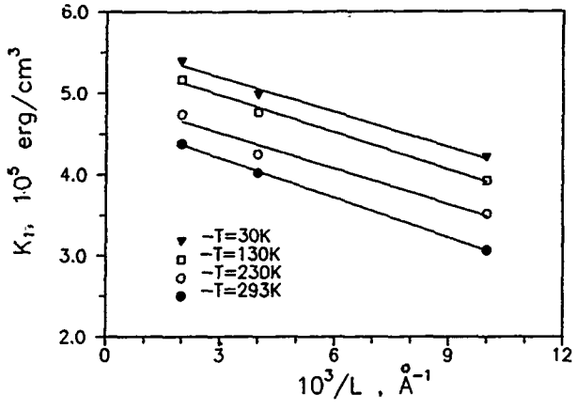

FIG. 1. The anisotropy constant K_1 for Fe(001) on MgO(001) plotted as a function of reciprocal Fe film thickness and for different temperatures.

2 $4\pi M$ is plotted as a function of temperature and for the different film thicknesses. These data clearly show a thickness dependence of K_1 and of $4\pi M$.

The thickness dependence of K_1 may be caused by the epitaxial misfit between film and substrate. If the epitaxial stress is located within a few atomic layers near the interface, we expect K_1 to vary inversely proportional with the film thickness because K_1 represents the volume density of the anisotropy energy. X-ray scans from these films revealed structural features which are consistent with this interpretation.[4]

The thickness dependence of $4\pi M$ comes as a surprise, at least for the thickness range studied here. However, it should be stressed that our FMR experiments cannot distinguish between an apparent decrease and a real reduction of the saturation moment due to interface effects. These possibilities shall be discussed in the following.

An apparent renormalization of the saturation moment could be caused by epitaxial misfit stresses. In this case a term accounting for the magnetostriction effects should be included in the expression for the free energy. The angular dependence of this contribution is similar to that for the demagnetization term. Therefore, in the expression for the free energy the effective value $4\pi M_{\text{eff}}$ should be used. Evaluating the contribution from the magnetostriction effect to $4\pi M_{\text{eff}}$, the correct sign is recovered, but the magnitude is far from being able to explain the reduction.

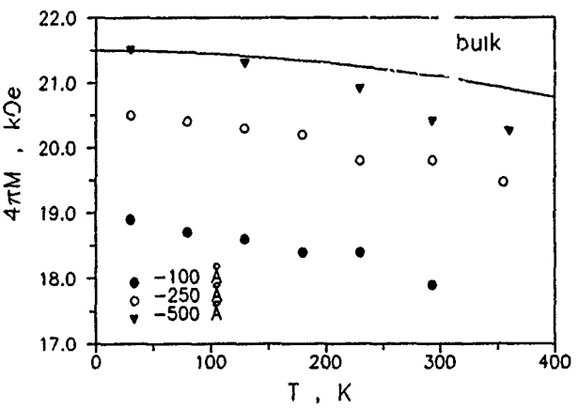

FIG. 2. The temperature dependence of the $4\pi M$ value plotted for all studied samples.

A more important contribution to the apparent reduction of $4\pi M_{\text{eff}}$ may come from the axial crystal field generated by interfaces. This uniaxial anisotropy field leads to perpendicular anisotropy of thin films.[7] Estimates show that this reason is partly responsible for the apparent reduction of $4\pi M_{\text{eff}}$ as observed by FMR.

At this point we would like to discuss the possibilities for a real reduction of the net magnetic moment. Early observations of moment reductions in rather thick films[8] could be discarded because of oxide formations on film surfaces resulting in "dead layers" (see. e.g., Ref. 9). However, this seems not to be the case here because of the use of a protective gold layer. From a theoretical point of view, band structure calculations lead, in general, to moment enhancements at (inter)surfaces due to band narrowing effects (see, e.g., Refs. 10 and 11). However, in these calculations, possible quantum fluctuation effects of the local moments cannot be incorporated. They are important at real interfaces resulting from random anisotropy fields and changes of the sign of the exchange coupling. In our case, for instance, antiferromagnetic (super)exchange interaction between Fe spins via oxygen ions at the Fe/MgO interface can be expected. Then the ground state would not correspond to a fully saturated ferromagnetic moment of the film. Strong frustrations of the exchange coupling may even lead to some canting of the spins near the surface or interface ("surface magnetic reconstruction"[12,13]).

B. Co/ Al_2O_3

FMR measurements on the angular variation of the resonance field H_0 showed a uniaxial in-plane anisotropy, which can be described by the free energy:

$$F_C = K_1 \sin^2\theta + K_2 - \sin^4\theta (K_u/2)\sin^2\theta \cos 2\phi. \quad (2)$$

Figure 3 shows the temperature dependence of the in-plane uniaxial anisotropy field $H_u = K_u/M$ for two samples with t_{Co}=120 Å and t_{Co}=350 Å. For the t_{Co}=120 Å thick sample the H_u value increases with decreasing temperature, whereas for the sample with t_{Co}=350 Å, H_u is reduced as compared to the thinner sample and is nearly temperature independent. After annealing the thin sample in a hydrogen atmosphere, the H_u value drops and approaches the H_u value for the thick sample. Moreover, we noticed that lowering the substrate temperature during film growth has the effect of decreasing the H_u and its temperature dependence seems to disappear.

From these observations at least two contributions to the uniaxial anisotropy can be inferred. The temperature dependent part may be caused by strains arising from the difference in thermal expansion coefficients of the substrate and the film. This part depends on the growth temperature and decreases after annealing at temperatures lower than the growth temperature. The temperature independent part may be due to internal oxidation of Co atoms along the oxygen

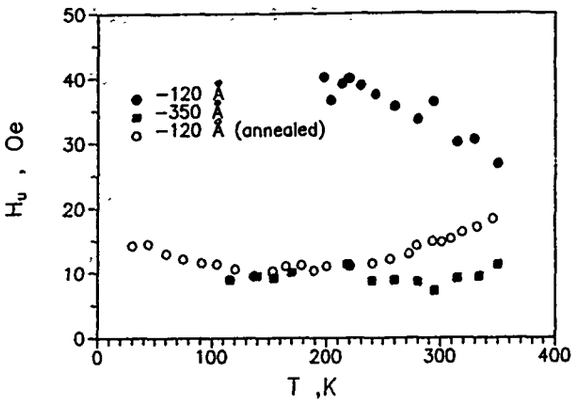

FIG. 3. The temperature dependence of the in-plane uniaxial anisotropy field $H_u=K_u/M$ shown for two samples of Co(111)/ $Al_2O_3(11\bar{2}0)$ with film thicknesses $t_{Co}=120$ Å and $t_{Co}=350$ Å. In addition, the data for the thinner sample are shown before and after annealing.

chains on the Al_2O_3 $(11\bar{2}0)$ surface as was suggested in Ref. 2, or due to the existence of an array of steps on the surface of the substrate which creates uniaxial in-plane anisotropy, as observed by Heinrich *et al.*[14]

C. Co/MgO

The in-plane angular variation of the FMR resonance field clearly exhibits a four-fold anisotropy for Co on MgO(001) similar to anisotropies usually observed for cubic crystals in the (100) plane. In contrast to Fe, the Co films have hcp $(11\bar{2}0)$ orientation with the c axis in the film plane. By surface x-ray scattering methods it was established that the Co films on MgO exhibit a twinned structure with the c-axis oriented parallel to the MgO[100] and MgO[010] directions. This twin structure, in turn, causes an apparent four-fold structural and hence a four-fold magnetic in-plane anisotropy. It can be supposed that the strong exchange interaction provides the coupled uniform motion of moments of different crystal domains, thus generating a single FMR-resonance line. For the anisotropy contributions of the two crystallographic domains the averaged magnetocrystalline term can be written as:

$$F_C=-\tfrac{1}{2}(K_1+2K_2)\sin^2\theta+\tfrac{3}{8}K_2\sin^4\theta + \tfrac{1}{8}K_2\sin^4\theta\cos 4\phi. \quad (3)$$

Here K_1 and K_2 are the first- and second-order uniaxial magnetocrystalline anisotropy constants. In this case the values measured in FMR are $H_i=4\pi M+H_{A1}+H_{A2}/2$ and H_{A2} ($H_{A1}=K_1/M$ and $H_{A2}=K_2/M$). If for $4\pi M$ the bulk value is assumed, a negative value for H_{A1} is obtained, indicating that $4\pi M$ is reduced. This reduction is most likely due to the reasons already discussed above for the case of Fe/MgO.

IV. CONCLUSIONS

FMR measurements of MBE grown Co films and of rf sputtered Fe films on the Al_2O_3 $(11\bar{2}0)$ and MgO (001) substrates have been performed over a wide temperature range and for several film thicknesses. For all studied systems, film/substrate interactions were detected. The particular anisotropy observed depends on the specific substrate material chosen and on the preparation conditions such as substrate temperature during growth. Thus, for iron films on the MgO(001) substrates, a reduction of the $4\pi M_{\text{eff}}$ value in comparison to the bulk saturation moment was observed with decreasing thickness. It was argued that this effect may possibly be caused by surface contributions to the out-of-plane axial anisotropy. An additional contribution may come form an interface reduction of the saturation moment. In the case of Co/Al_2O_3 samples with the Co fcc [111] axis perpendicular to the film plane a strong and unexpected uniaxial in-plane anisotropy was observed. This anisotropy probably arises in part from the difference of the thermal expansion coefficients of the film and the substrate and in part from the oxidation of Co along oxygen chains on the $Al_2O_3(11\bar{2}0)$ surface or from step arrangement on the surface of the substrate. Finally, for Co films on MgO(001) substrates a four-fold in-plane anisotropy was observed due to the twinned hcp structure of the film and a decrease of the $4\pi M_{\text{eff}}$ value was obtained resembling the Fe/MgO system.

ACKNOWLEDGMENTS

The work in Germany was funded by the Deutsche Forschungsgemeinschaft (SFB 166) and by the DFG supported German-Russian exchange program "Physics of Novel Materials," which are both gratefully acknowledged.

[1] N. Metoki, Th. Zeidler, A. Stierle, K. Bröhl, and H. Zabel, J. Magn. Magn. Mater. **118**, 57 (1991).
[2] N. Metoki, M. Hofelich, Th. Zeidler, Th. Mühge, Ch. Morawe, and H. Zabel, J. Magn. Magn. Mater. **121**. 137 (1993).
[3] K. Bröhl, P. Bödeker, N. Metoki, A. Stierle, and H. Zabel, J. Cryst. Growth **127**, 682 (1993).
[4] Th. Mühge, A. Stierle, N. Metoki, U. Pietsch, and H. Zabel, Appl. Phys. A (in press).
[5] C. Chappert, K. Le Dang, P. Beauvillian, H. Hurdequint, and D. Renard, Phys. Rev. B **34**, 3192 (1986).
[6] J. R. MacDonald, Phys. Rev. **106** 890 (1957).
[7] L. Néel, Compt. Rend. **237**, 1623 (1953).
[8] A. Drigo, Nuovo Cimento, **8**. 498 (1951).
[9] H. Hoffmann, Z. Angew. Phys. **13**, 149 (1961).
[10] C. Li and A. J. Freeman, Phys. Rev. B **43**, 780 (1991).
[11] A. J. Freeman and R. Wu, Progr. Theor. Phys. (Suppl.) **106**, 397 (1991).
[12] S. E. Trullinger and D. L. Mills, Solid State Commun. **12**, 819 (1973).
[13] A. Blandin, Solid State Commun. **13**, 1537 (1973).
[14] B. Heinrich, A. S. Arrott, J. F. Cohran, H. B. Urquhart, K. Myrtle, Z. Celinski, and Q. M. Zhong, Mater. Res. Symp. Proc. **151**, 177 (1989).

The relationship between the microstructure and magnetic properties of sputtered Co/Pt multilayer films (abstract)

Y. H. Kim, Amanda K. Petford-Long, and J. P. Jakubovics
Department of Materials, University of Oxford, Parks Road, Oxford OX1 3PH, United Kingdom

Co/Pd multilayer films (MLFs) are of interest because of their potential application as high-density magneto-optical recording media. Co/Pd MLFs with varying Co and Pd layer thicknesses were grown by sputter-deposition onto (100) Si wafers. X-ray diffraction and high resolution electron microscopy were used to study the microstructure of the films, and Lorentz microscopy was used to analyze their magnetic domain structure. The films show an fcc crystal structure with a compromised lattice parameter and a strong (111) crystallographic texture in the growth direction. The compromised interplanar spacing parallel to the surface increased with decreasing thickness ratio (t_{Co}/t_{Pd}), and the columnar grain size decreased with increasing Pd layer thickness. Films with t_{Co}=0.35 nm and t_{Pd}=2.8 nm (columnar grain diameter 20 nm) showed promising magnetic properties, namely a high perpendicular magnetic anisotropy (1.85×10^5 J m^{-3}), with a perpendicular coercivity of 98.7 kA m^{-1}, a perpendicular remanence ratio of 99%, and a perpendicular coercivity ratio of 88%. The magnetic domains were uniform and of a narrow stripe type, confirming the perpendicular easy axis of magnetization. The Curie temperature was found to be about 430 °C. Films of pure Co and Pd, grown for comparison, also showed columnar grain structure with grain-sizes of the same order as those seen in the MLFs. In addition the Pd films showed a (111) textured fcc structure.

 0021-8979/94/76(10)/6099/1/$6.00 © 1994 American Institute of Physics

Identification of magnetoelastic and magnetocrystalline anisotropy contributions in ultrathin epitaxial Co(110) films (abstract)

J. Fassbender, Ch. Mathieu, B. Hillebrands, and G. Güntherodt
2. Physikalisches Institut, RWTH Aachen, 52056 Aachen, Germany

R. Jungblut and M. T. Johnson
Philips Research Laboratories, Prof. Holstlaan 4, 5656 AA Eindhoven, The Netherlands

Magnetic anisotropies of ultrathin transition-metal films are inherently related to their structural properties. In ultrathin films the large fraction of atoms located at the film interface generates strong interface anisotropies, whereas elastic strain fields caused by the forced registry of atoms at the substrate/film interface induce magnetoelastic anisotropy contributions.[1–3] So far the experimental confirmation of the transition from these thin-film properties to bulk anisotropy properties, characterized by a dominating magnetocrystalline anisotropy, has not yet been presented. Magnetic anisotropies reflect, depending on their origin, both the crystallographic symmetry and the symmetry of the film geometry. For a clear separation between magnetoelastic, magnetocrystalline and Néel-type interface anisotropy contributions, the film symmetry and thickness must be chosen such that the respective different anisotropy contributions appear with different symmetries and film thickness dependencies. This is the case for (110)-oriented fcc Co films. In the present study we use the Brillouin light-scattering technique for the determination of the anisotropy contributions. An analysis of the spin-wave frequency measured as a function of the in-plane direction of the external field and the film thickness yields information about all relevant anisotropies. The samples used were molecular-beam-epitaxy grown in ultrahigh vacuum. Onto a Cu (110) single-crystal substrate a wedge-type sample and two staircase-shaped samples with distinct thicknesses in the range of 8–110 Å were grown. To obtain symmetric Co/Cu interfaces the Co layers were covered with a 12 Å Cu layer. Finally, a 25-Å-thick Au protective layer was deposited. Low-energy electron-diffraction studies were used to obtain the structural data of the films. All relevant anisotropy contributions—the magnetocrystalline anisotropy, and the uniaxial in-plane and out-of-plane anisotropy contributions—were determined. Three different anisotropy regimes are observed as a function of the Co layer thickness d_{Co}. This thickness regime up to 13 Å is dominated by the magnetoelastic anisotropy contributions as a result of the pseudomorphic film growth of the Co layer. For Co layer thicknesses larger than 13 Å we find a reduction of the magnetoelastic anisotropy contributions. This is structurally correlated to an anisotropic relaxation of the in-plane Co lattice constant. In the regime of $d_{Co}>50$ Å we observe a thickness-independent value for the magnetocrystalline anisotropy contribution $K_1=-8.5\times10^5$ erg/cm^3. This anisotropy contribution is largely suppressed for $d_{Co}<50$ Å. This finding might either indicate a breakdown of the usually postulated linear superposition principle of magnetic anisotropy contributions to the free anisotropy energy, or it might point to a subtle modification of the electronic band structure. At the onset of the magnetocrystalline anisotropy we find a change in the easy magnetization direction from ⟨001⟩ for thin Co films to ⟨111⟩ for thicker ones. For a more detailed discussion see Ref. 4.

This work is supported by Deutsche Forschungsgemeinschaft through SFB 341.

[1] P. Krams, F. Lauks, R. L. Stamps, B. Hillebrands, and G. Güntherodt, Phys. Rev. Lett. **69**, 3677 (1992).
[2] P. Krams, B. Hillebrands, G. Güntherodt, and H. P. Oepen, Phys. Rev. B **49**, 3633 (1994).
[3] R. Jungblut, M. T. Johnson, J. aan de Stegge, A. Reionders, and F. J. A. den Broeder, J. Appl. Phys. **75**, 6424 (1994).
[4] J. Fassbender, Ch. Mathieu, B. Hillebrands, G. Güntherodt, R. Jungblut, and M. T. Johnson (unpublished).

 0021-8979/94/76(10)/6100/1/$6.00 © 1994 American Institute of Physics

Nature of half-metallic ferromagnets: Transport studies

J. S. Moodera and D. M. Mootoo
Francis Bitter National Magnet Laboratory, Massachusetts Institute of Technology, Cambridge, Massachusetts 02139-4307

The half-metallic ferromagnetic compounds due to the absence of states at E_F for minority spin electrons, as predicted by band theory, should exhibit unique features in their transport properties. Transport measurements conducted as a function of T and H for NiMnSb and PtMnSb thin films show interesting behavior. In $H=0$, the resistivity versus T shows the absence of the T^2 dependence at low temperature found in ferromagnets such as Fe, Ni, etc. The Hall constant increases significantly below about 100 K for both compounds; NiMnSb shows a factor of seven increase. Transverse magnetoresistance changes sign between 295 and 4.2 K. Transport data seem to imply a drop in the carrier density and a large increase in their mobility at low temperatures, which is consistent with zero density of states for minority spins at E_F, but additional measurements are needed to clarify theoretical understanding.

I. INTRODUCTION

The prediction of an energy gap for the minority spin carriers at the Fermi level (E_F) in certain Heusler alloys has not yet been verified.[1] Such materials have been called as half-metallic ferromagnets, in that only majority spin carriers occupy the Fermi level, leading to 100% polarized conduction electrons. Among several compounds which may be classified as HMF, NiMnSb, and PtMnSb are the two compounds that have been studied the most.[2–4] However, very limited transport measurements have been carried out. The study on polycrystal and single-crystal bulk samples of NiMnSb and PtMnSb by Otto *et al.*[3] covers the resistivity and Hall-effect measurements in the whole temperature range, from the ferromagnetic Curie temperature to the liquid-helium range. However, detailed temperature variation of ρ at low T is lacking. For normal ferromagnets such as Fe, Ni, and Co near liquid-helium temperatures, ρ varies as T^2 due to spin flip scattering of charge carriers by magnons.[5,6] In the case of an HMF material the absence of spin-down states at E_F is expected to change the character of spin scattering, leading to the absence of spin flip scattering for the majority spin carriers, with ρ vs T not showing T^2 dependence at low temperatures. The ultimate test of the theoretical prediction is the direct measurement of spin polarization of conduction electrons which can be performed by spin-polarized tunneling technique. In order to carry out tunneling, thin films are orders of magnitude better than single crystals for preparing planar tunnel junctions. In addition, careful transport measurements can be performed with relative ease and sensitivity. In this paper we concentrate on the magnetotransport properties of thin films of NiMnSb and PtMnSb compounds.

II. EXPERIMENTAL

Thin films of NiMnSb and PtMnSb were prepared by three-source coevaporation on glass substrates held at 450–500 °C. After annealing these films at the deposition temperatures for 20 min, they were cooled to room temperature by turning off the heater. Films were analyzed by x-ray diffraction, EDX, and Auger depth profiling to confirm the formation of correct phase and chemical composition. Film surfaces showed nonstoichiometry down to several tens of Å and beyond that, 1:1:1 ratio of the three elements were observed within the accuracy of the Auger analysis. In order to prepare tunnel junctions over these films the surface was cleaned by Ar ions at shallow incident angle and immediately covered with Al_2O_3 by sputtering onto these films using a sapphire target. Aluminum thin films, 40 Å thick, served as the top electrode. Tunnel junction preparation was carried out in a modified ion milling system. Optimum conditions for obtaining useful junctions are yet to be found.

Magnetotransport measurements of these films were carried out in the temperature range of 300–1.1 K and applied magnetic field up to 20 T, using a water-cooled Bitter magnet. Results of these measurements are presented below.

III. RESULTS AND DISCUSSION

For both NiMnSb and PtMnSb the resistivity decreased with temperature as shown in Fig. 1. For these films ρ at 300 K is higher than that reported by Otto *et al.*[3] for single crystals of NiMnSb and PtMnSb. In the case of NiMnSb, ρ decreases more rapidly below about 100 K, whereas PtMnSb shows a nearly uniform drop in ρ. Detailed low-temperature variation of resistance for both compounds is shown in Fig. 2. Below ~15 K the resistance decreased *linearly* with temperature. This is different from the T^2 dependence of ρ observed for normal ferromagnets such as Fe, Ni, and Co in this temperature range,[5] and also observed by us for a pure Fe film prepared under similar conditions as used for NiMnSb and PtMnSb films.

Transverse magnetoresistance of both PtMnSb and NiMnSb films was negative at 295 K, all the way to 20 T. At liquid-helium temperatures it changed to a positive value for

 0021-8979/94/76(10)/6101/3/$6.00 © 1994 American Institute of Physics

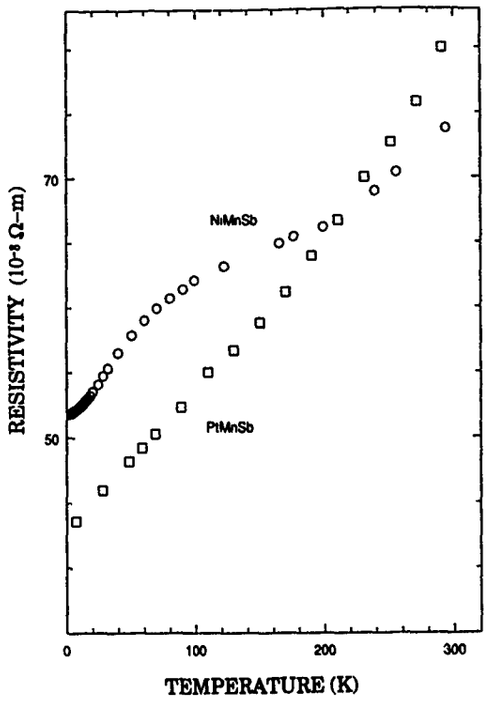

FIG. 1. Temperature variation of resistivity for NiMnSb and PtMnSb compound thin films. Note the rapid drop in resistivity below ~100 K for NiMnSb.

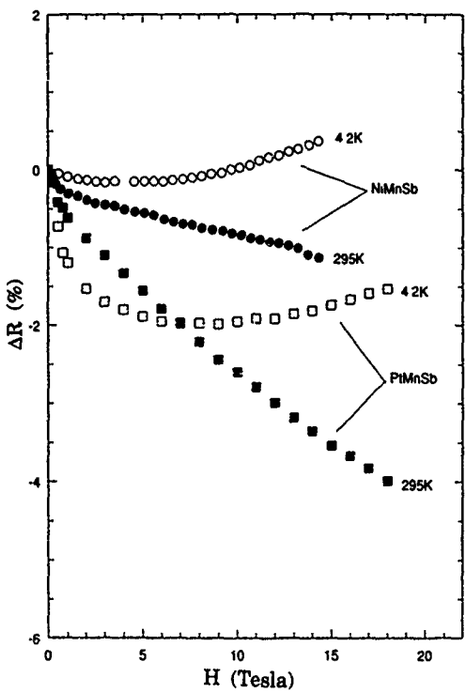

FIG. 3. Transverse magnetoresistance of NiMnSb and PtMnSb in high applied magnetic fields.

NiMnSb, the change occurring below ~50 K. However, in the case of PtMnSb, at low temperatures, magnetoresistance started out negative and then increased with increasing H beyond ~7–8 T. These results are shown in Fig. 3. Both films showed a decrease in resistance from 0 to ~1 tesla at all temperatures, expected for a ferromagnetic films in a field due to the buildup of magnetization. PtMnSb has higher values of ΔR compared to NiMnSb.

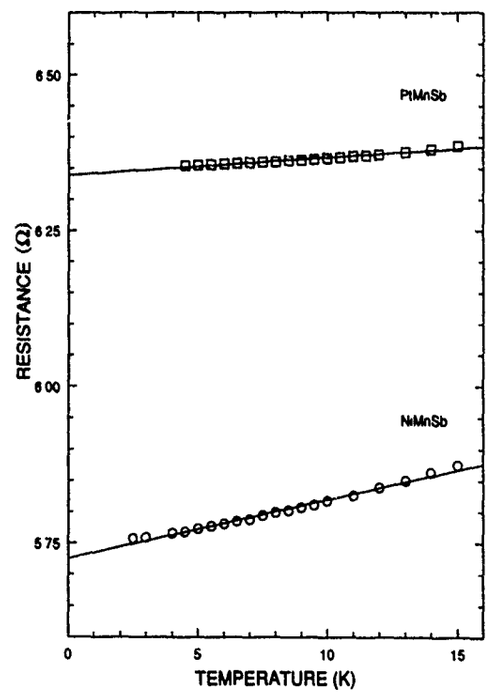

FIG. 2. Detailed temperature dependence of resistance for NiMnSb and PtMnSb compound thin films at low temperatures, showing linear dependence. Lines through the data points are linear fits.

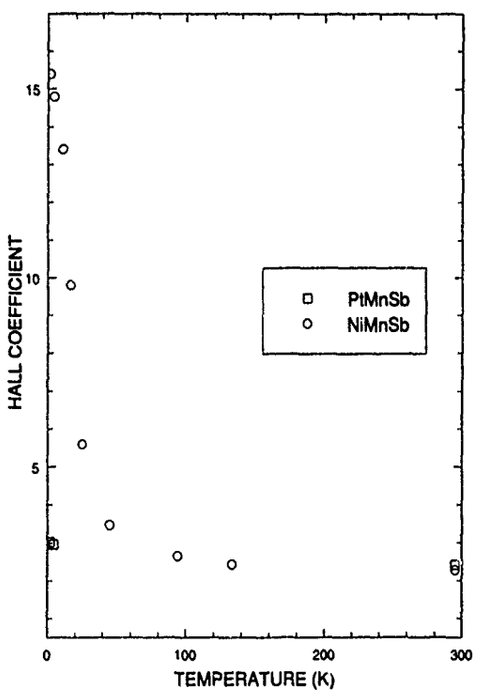

FIG. 4. Hall coefficient (in units of 10^{-10} m^3 A^{-1} S^{-1}) variation as a function of temperature for NiMnSb and PtMnSb films.

The Hall effect, as expected for a ferromagnetic material, showed two components as a function of applied magnetic field. In fields up to ~1 T, a large anomalous Hall voltage was observed and beyond which the ordinary Hall voltage (positive) increased linearly with H. The anomalous part decreased as T decreased, consistent with an increase in the film magnetization. Ordinary Hall constant (R_0) plotted in Fig. 4 as a function of T shows a small increase down to ~100 K, below which it increases significantly by about 20% for PtMnSb and by a factor of 7 in the case of NiMnSb. Similar behavior was observed earlier by Otto *et al.*[3] in polycrystalline bulk samples.

The transport properties of the above HMF compounds thus show unique features. There are no theoretical models to explain this behavior. The temperature variation of ρ is interesting, particularly the linear dependence of ρ vs T. According to theoretical prediction, if there are no spin-down states at E_F, then spin flip scattering for spin-up charge carriers due to magnons is forbidden. This will lead to the absence of T^2 dependence of ρ and to an increase in the mobility of the charge carriers. Since the Curie temperature of PtMnSb and NiMnSb are 582 and 730 K, respectively,[2] one may not expect many magnons at near-helium temperatures. This means absence of T^2 dependence of ρ does not provide conclusive proof for the absence of spin-down states at E_F. In addition, scattering processes such as electron-phonon, electron-electron, etc., can give rise to nontrivial ρ-T dependence. However, ordinary Hall coefficient increase by a large amount as T decreases shows significant changes in the carrier concentration and mobility. Caution should be exercised in the above interpretation since in NiMnSb, for example, the Fermi surface consists of three hole sheets and parts of it are electron-like.[1] In any case, a factor of seven increase in R_0 for NiMnSb indicates a decrease in the carrier density at low temperature. The mobility also has to increase considerably in order to explain the drop in the resistivity in the same temperature region. Between 4.2 and 295 K the saturation magnetization does not change more than 5%–6% for NMS. Within limits, the above *ad hoc* interpretation of the Hall and resistivity data appears to be consistent with the prediction of a gap for minority spin carriers at E_F. Although HMF is not quite like a semiconductor, transport behavior of our films is somewhat similar to that seen in doped or narrow-gap semiconductors. If the minority spin gap is much smaller than the predicted 0.5 eV in NiMnSb, then its effects can be realized only at lower temperatures where thermal activation across the gap becomes negligible. Presence of small quantities of other phases, below the detection limit of powder x-ray diffraction, can also dilute the HMF effect in these materials. Negative magnetoresistance at higher temperatures for NiMnSb may be interpreted as due to inelastic s-d scattering, which reduces to negligible values at low temperatures, which in turn is due to reduced thermal fluctuations and to the absence of spin-down states at E_F. This tentative explanation again depends on the presence of an energy gap for minority spin carriers. In PtMnSb the corresponding energy gap is even smaller[1] and hence the effects are smaller. The effect seen in the transport measurements can also result from a structural phase transition below room temperature. The above conjectures need more support from further studies on these compounds. For instance, thermal conductivity, specific heat, and MOKE measurements as a function of temperature and magnetic field will certainly shed more light onto the nature of these compounds. In addition, structural studies below room temperature are necessary.

IV. CONCLUSIONS

In summary, NiMnSb and PtMnSb compound thin films show interesting temperature changes of resistivity and Hall coefficient. This behavior appears to be consistent with the band structure calculation for these half-metallic compounds. However, study of other properties is needed to confirm the above observation.

ACKNOWLEDGMENTS

We gratefully acknowledge the Office of Naval Research for financial support for this research under ONR Grant No. N00014-92-J-1847. We greatly appreciate the keen interest shown in this work by R. Meservey and P. Tedrow. We thank L. Berger and K. Hathaway for their valuable comments. Our sincere thanks to S. Sears and C. Baik for their technical assistance.

[1] R. A. deGroot, F. M. Mueller, P. G. van Engen, and K. H. J. Buschow, Phys. Rev. Lett. **50**, 2024 (1983); K. E. H. M. Hanssen and P. E. Mijnarends, Phys. Rev. B **34**, 5009 (1986).
[2] P. G. van Engen, K. H. J. Buschow, R. Jongebreur, and M. Erman, J. Appl. Phys. Lett. **42**, 202 (1983); K. Watanabe, Trans. Jpn. Inst. Met. **17**, 220 (1976).
[3] M. J. Otto, R. A. M. van Woerden, P. J. van der Valk, J. Wijngaard, C. F. van Bruggen, and C. Haas, J. Phys.: Condens. Matter **1**, 2351 (1989).
[4] R. Kabani, Ph.D. thesis, Tufts University, 1992 (unpublished).
[5] G. K. White and S. B. Woods, Philos. Trans. R. Soc. London A **251**, 273 (1958).
[6] T. Kasuya, Prog. Theor. Phys. **16**, 58 (1956); I. Mannari, *ibid.* **22**, 335 (1959).

Magnetoresistance and magnetic properties of NiFe/oxide/Co junctions prepared by magnetron sputtering

T. S. Pläskett and P. P. Freitas[a)]
INESC, R. Alves Redol 9-1, 1000 Lisbon, Portugal

N. P. Barradas, M. F. da Silva, and J. C. Soares
INETI, EN10, 2685 Sacavem, Portugal

NiFe/oxide/Co junctions were fabricated by magnetron sputtering for studies of polarized electron transport across the insulating barrier. Al_2O_3, Al-Al_2O_3, and MgO insulating barriers were prepared with junction resistances from 0.5 to 116 Ω. The *I-V* characteristics at room temperature are linear. For low barrier resistance, the magnetoresistance of the structure is dominated by the anisotropic magnetoresistance of the ferromagnetic electrodes. For the higher barrier resistances, a different magnetoresistance effect is observed, which is tentatively related to tunneling or spin-valve effects across the insulating junction.

I. INTRODUCTION

Ferromagnetic/insulator/ferromagnetic junctions have been studied in the past[1-3] in order to clarify the effect of spin polarization on the tunneling current across the insulating barrier. These experiments were carried out at low temperatures in the tunneling regime of the *I-V* curve. A change in the junction zero-bias conductance was observed, which depended on the relative magnetic state of the bottom and top electrodes. Due to the relative size of electrode and junction resistances, the magnetoresistance (MR) of the ferromagnetic electrode was neglected.

Recently,[4] work has been reported on NiFe/Al-Al_2O_3/Co junctions. These authors claim spin-tunneling effects at room temperature, although it is not clear how the MR of the ferromagnetic electrodes was avoided.

In this paper we describe a study of NiFe/oxide/Co structures, where three types of oxide barriers were prepared, reactively sputtered Al_2O_3 and MgO, and thermally oxidized Al-Al_2O_3. A systematic study of junction resistance, *I-V* characteristics, oxide structure, and magnetoresistance behavior is reported. We find that when junction resistance is of the order of the electrode resistance, electrode MR dominates. For junction resistance much larger than electrode resistance, the observed magnetoresistance is ascribed to tunneling across the oxide.

II. EXPERIMENTAL METHOD

The samples were prepared by magnetron sputtering in a system with a base pressure of 1×10^{-7} Torr. The ferromagnetic and insulating layers were deposited through metallic masks to produce the cross pattern shown in Fig. 1(a). The junction has an active area of 1 mm^2, and the oxide layer is deposited through a circular mask with a diameter of 5 mm in order to prevent shorts between the top and bottom electrodes. The ferromagnetic electrodes were deposited at a rate of 1 Å/s in a magnetic field of 100 Oe to induce an easy-axis direction along the $Ni_{81}Fe_{19}$ and Co bars.

The insulating oxide layers were prepared by thermal oxidation of a metallic Al layer, and by reactive rf sputtering of Al_2O_3 or MgO in a mixed Ar/O_2 atmosphere, containing 2%–10% O_2 by volume, from metallic Al and Mg targets. The reactive sputtering of the oxide layers was done at power densities of 1 W/cm^2, rates of 0.1–0.2 Å/s, at an Ar pressure of 1.5 mTorr. In the thermal oxidation method, a thin layer of Al was deposited on top of the NiFe electrode. The sample was brought to atmosphere and oxidized in air for 36–100 h to produce an Al-Al_2O_3 layer. The Co layer was then deposited. The oxide thickness was varied from 25 to 300 Å, and electrode thickness was either 400 or 1500 Å.

The oxidation process was studied by Rutherford backscattering (RBS). For this purpose a thin Si⟨100⟩/NiFe(50 Å)/$Al_2O_3(t)$/Co(50 Å) structure was prepared without breaking vacuum. Figure 2 shows the oxygen content, obtained by RBS, for a series of samples with various Al_2O_3 thicknesses.

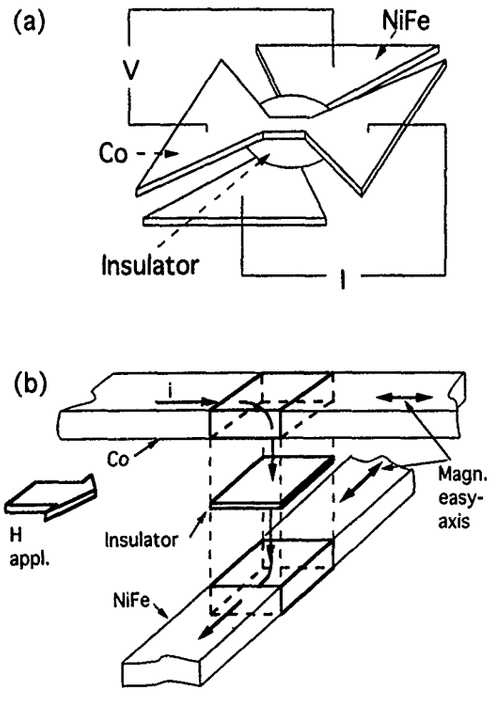

FIG. 1. (a) Schematic diagram of the ferromagnet/insulator/ferromagnet cross structure; (b) enlarged view of the junction area.

[a)]Also at IST, Av.Rovisco Pais, 1600, Lisbon, Portugal.

 0021-8979/94/76(10)/6104/3/$6.00 © 1994 American Institute of Physics

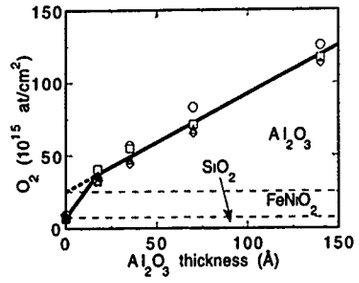

FIG. 2. Oxygen content determined by RBS analysis, for the reactively rf-sputtered Al_2O_3 junctions. The symbols represent different angles of incidence of the beam from 0° to 75°.

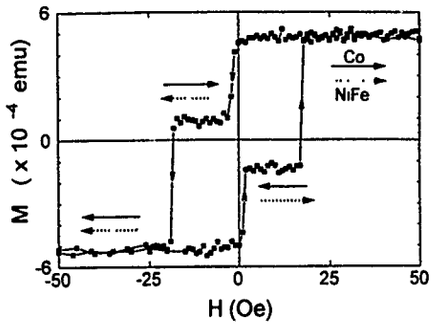

FIG. 3. Magnetization hysteresis loop for a NiFe/Al-Al_2O_3/Co structure with the field applied parallel to the Co easy axis (long axis of the bar). The arrows show the relative orientation of the NiFe and Co magnetizations.

The oxygen content is proportional to the oxide thickness, and the slope indicates an Al_2O_3 stoichiometry. The extrapolation to the origin corresponds to a NiFe oxide layer of 20 Å. The measured O_2 content at the origin is due to the SiO_2 native layer on the substrate. The main conclusion is that during the initial growth of the Al_2O_3 layer, the NiFe is being oxidized.

The main problem with these thin oxide layers is the existence of pinholes, leading to a low junction resistance of a few ohms. Also, the junction resistance sometimes decreases significantly at current densities as low as 0.1 A/cm^2. This occurs through irreversible dielectric breakdown taking place for fields of the order of 2×10^5 V/cm.

III. RESULTS AND DISCUSSION

Table I summarizes the oxide type and thicknesses studied, and the measured junction and electrode resistances. The junction resistance includes both insulator and electrode resistances. The electrode resistance in the junction area was measured using the same geometry as shown in Fig. 1, but without the oxide layer. A simple calculation of this resistance shows that most of the current in the junction area is in-plane. Notice that high junction resistances were observed only for MgO barriers. In this case, junction resistance is about 800 times higher than electrode resistance. For the Al oxides, most junction resistances are of the order of the electrode resistance.

TABLE I. Oxide types, thicknesses, junction resistance, and electrode resistance in the junction area.

	Junction		Electrodes	
Insulator	t (Å)	R (Ω)	t(each) (Å)	R(total) (Ω)
Al_2O_3	100	0.4	1000	
	400	20	400	0.75
Al-Al_2O_3	40	1.0	400	0.75
	60	1.4	400	0.75
	100	0.9	400	0.75
	200	0.4	400	0.75
MgO	150	116	1500	0.15
	100	0.4	1500	0.15

One signature used to indicate tunneling is a nonlinear behavior of the I-V curve. This has been shown at low temperatures for Fe/Ge/Co,[1] and Ni/NiO/(Ni,Fe,Co) junctions. Our I-V characteristics at room temperature are linear over four orders of magnitude, and therefore give no evidence for tunneling across the oxides.

Another signature for tunneling across an insulating barrier comes from the magnetoresistance measurement. Slonzceski's theory for spin tunneling across an insulating barrier[5] predicts that the magnetoresistance is a function of the cosine of the angle between the magnetizations in both electrode layers. In Fig. 1(b) we show the junction structure under study. The easy axis on both electrodes are at 90° to each other, such that we will always have one of the layers in a hard direction when the field is applied along one of the electrode bars. With this structure, one of the magnetizations reverses by rotation, therefore producing a configuration where the angle between the two magnetizations varies from 0° to 180°.

Figure 3 shows the hysteresis loop for a NiFe/Al-Al_2O_3/Co structure where the electrode thickness is 400 Å, oxide thickness is 40 Å, and the junction resistance is 1.0 Ω. The applied field is parallel to the Co easy axis. The NiFe is in a hard-axis direction and should start reversing at a 4 or 5 Oe positive field. This is not observed. The curve is shifted giving rise to 100% remanence at $H=0$. This may indicate a ferromagnetic 2–3 Oe pinhole coupling. Between −5 and −20 Oe the magnetizations of the Co and NiFe layers are antiparallel.

Figures 4(a)–4(d) show the magnetoresistance behavior for the same sample, for different orientations of the applied field, either parallel to the Co easy axis (a), parallel to the NiFe easy axis (b), or at ±45° to the Co easy axis (c) and (d). The main conclusion of these results is that the observed MR comes from the anisotropic magnetoresistance produced by the in-plane current component in each electrode [see Fig. 1(b)]. In Fig. 4(a) the Co reverses by domain-wall motion leading to no AMR. On the other hand, the NiFe is perpendicular to the in-plane current component at saturation, and becomes parallel at near-zero field, leading to the observed positive AMR. In Fig. 4(b) the NiFe now reverses by domain-wall motion (no AMR), and the Co rotates from perpendicular to the in-plane current at saturation to parallel to

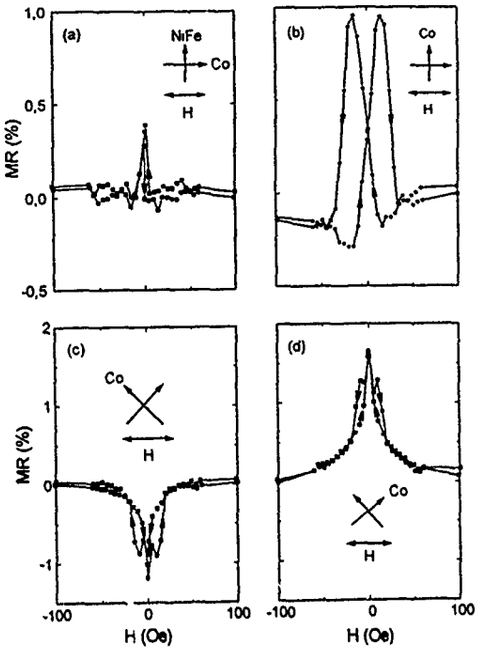

FIG. 4. Magnetoresistance for the same structure shown in Fig. 3, but with the magnetic field applied along different orientations. The angular dependence of the MR comes from the anisotropic magnetoresistance of the ferromagnetic electrodes. Junction resistance is of same order as electrode resistance.

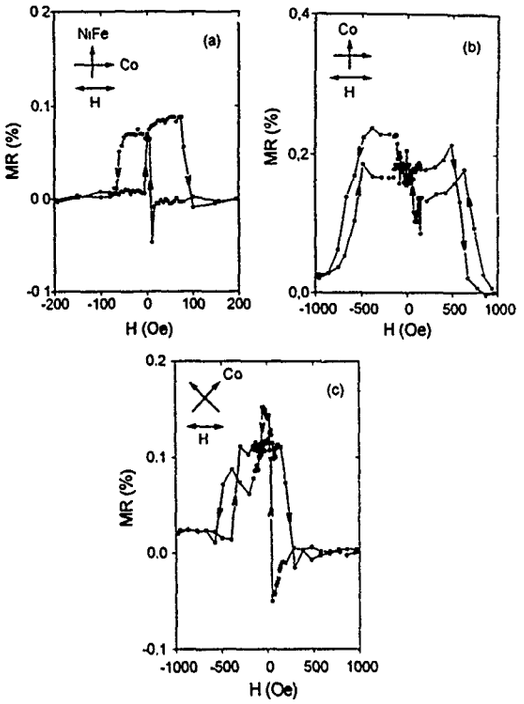

FIG. 5. Magnetoresistance for a NiFe/MgO/Co structure, where the junction resistance is much larger than electrode resistance. No AMR is observed.

the in-plane current at zero field. The definite proof of AMR is the negative magnetoresistance found in Fig. 4(c), where both the NiFe and Co at zero field have magnetization components perpendicular to the current. This result is not unexpected since in this sample the junction resistance is 1.0 Ω, which is of the order of the electrode resistance in the junction area.

On the other hand, on one of the NiFe/MgO/Co samples, the junction resistance is about 800 times larger than the electrode resistance, and it is now possible to probe the junction MR. In this case, the voltage across the electrode arms comes mainly from the junction. Figure 5 shows the measured MR signal, for an electrode thickness of 1500 Å and oxide thickness of 150 Å. Contrary to the sharp positive and negative MR peaks shown in Fig. 4, which are characteristic from electrode AMR, Fig. 5 shows essentially positive MR for all orientations. In Fig. 5(a) plateaus occur in the MR at low fields, when the magnetizations of the electrodes are antiparallel. This geometry, and the measured hysteresis loop is similar to that described in Fig. 3. These MR results are characteristic of tunneling or spin-valve effects.[3,4]

The details of Figs. 5(b) and 5(c) are not yet fully understood, and are being investigated with respect to the possible exchange coupling between MgO and the NiFe or Co layers, and the formation of magnetic oxide compounds at the interfaces. When dielectric breakdown occurred in this same sample, and junction resistance dropped to 3.5 Ω, the electrode AMR became comparable to the junction signal. Again, we emphasize that the MgO junctions show linear I-V curves at room temperature. This may indicate that the observed MR has a different origin than tunneling.

The main conclusion of this study is that further work is needed in order to produce stable, high-resistive junctions, with high dielectric breakdown. Only in this case can the junction contribution to the perpendicular MR be measured. Whether tunneling effects across insulating layers can be observed at room temperature, remains an open question.

ACKNOWLEDGMENTS

This work was partially supported by STRDA/C/CEN/461/92 program. One author (N.P.B.) was supported by a CIENCIA/JNICT stipend.

[1] M. Julliere, Phys. Lett. **54A**, 225 (1975).
[2] P. M. Tedrow and R. Meservey, Phys. Rev. B **7**, 318 (1973).
[3] S. Maekawa and U. Gäfvert, IEEE Trans. Magn. **MAG-18**, 707 (1982).
[4] T. Yaoi, S. Ishio, and T. Miyazaki, J. Magn. Soc. Jpn. **16**, 303 (1992).
[5] J. Slonczewski, Phys. Rev. B **39**, 6995 (1989).

Changes in resistivity behavior of metallic glass $Fe_{70}Ni_{12}B_{16}Si_2$ due to molybdenum substitution for nickel

A. K. Bhatnagar[a] and B. Seshu
School of Physics, University of Hyderabad, Hyderabad 500134, India

K. D. D. Rathnayaka and D. G. Naugle
Department of Physics, Texas A & M University, College Station, Texas 77843

The changes in the resistivity behavior of metallic glass $Fe_{70}Ni_{12-x}Mo_xB_{16}Si_2$ are reported as a function of Mo substitution (x=0, 2, 4, and 6) for Ni at temperatures between 300 and 1.5 K.

The temperature dependence of the resistivity of many magnetic and nonmagnetic metallic glasses below room temperature results from a number of scattering mechanisms, and localization and Coulomb interaction effects in the highly disordered structures. Metallic glasses with Fe-rich composition based on $Fe_{80}B_{20}$ and $Fe_{80}B_{20-x}Si_x$, which are ferromagnetic, normally show a positive temperature coefficient of resistivity (TCR) at room temperature, and their resistivity exhibits a minimum in its value usually at a temperature (T_{min}) below 20 K. Addition of Ni or Co for Fe in such systems does not shift T_{min} very much but addition of Cr or Mn does change the resistivity substantially as far as T_{min} is concerned. It is known that a substitution of Mo, a nonmagnetic metal, reduces the Curie temperature (T_C) of $Fe_{80}B_{20}$ (Ref. 1) and $(Fe_{1-x}Mo_x)_{75}P_{16}B_6Al_3$ (Ref. 2) appreciably, the effect of Mo being more drastic in the latter glass. On the other hand, substitution of Mo in a metallic glass like $Fe_{70}Ni_{12}B_{16}Si_2$ does not change T_C and magnetic properties as much as in the above two mentioned metallic glasses.[3] The similarity of magnetic properties of Cr and Mo substituted Fe-B-Si glasses has motivated us to investigate whether a similarity in the resistivity behavior also exists in these two types of glasses. We present measurements of the resistivity of the metallic glass system $Fe_{70}Ni_{12-x}Mo_xB_{16}Si_2$. These glasses remain ferromagnetic at room temperature (RT) and below even for x=6. We compare the results with those reported for Cr substitution in ferromagnetic glasses and discuss them qualitatively.

$Fe_{70}Ni_{12-x}Mo_xB_{16}Si_2$ samples (S0, S2, S4, and S6, corresponding to x=0, 2, 4, and 6, respectively) were prepared at Allied Signal. The ribbons were 0.5 cm wide and 20 μm thick. Glassy structure was confirmed by x-ray diffraction and differential scanning calorimetry. The resistance was measured between 300 and 1.5 K using the four-probe dc method. The temperature was changed quasicontinuously with a 5–10 K/h drift in temperature. The samples were enclosed in a double can, one in high vacuum with an inner can for the samples having 0.1 Torr of He gas for good thermal contact. Changes in the resistance with an accuracy of better than two parts in 10^5 were detected. The accuracy in the room-temperature resistivity is determined by geometrical factors. Curie temperature (T_C) determined by a vibrating sample magnetometer as well as by differential scanning calorimetry are in good agreement with each other.

The normalized resistivity $r(T)=\rho(T)/\rho_0$, where ρ_0 is the resistivity at the ice point, is plotted in Figs. 1 and 2 as a function of temperature. Table I lists room-temperature resistivities ρ(RT), temperature coefficient of resistivity (TCR) defined as $[\rho^{-1}(d\rho/dT)]$, assuming linear T dependence of ρ near RT, and Curie temperatures (T_C) for the samples. The resistivity increases with the addition of Mo, the initial increase being about 30% for x=2 after which the change is about 5 $\mu\Omega$ cm/Mo at. %. The TCR, the magnitude of which is typical of most metallic glasses, decreases with increasing room-temperature resistivity, hence with Mo concentration. This is expected from Mooij's correlation.[4] Although samples S4 and S6 have ρ(RT) higher than 150 $\mu\Omega$ cm, the TCRs for these samples are still positive at 300 K.

The temperature dependence of normalized resistivity $r(T)$ (Figs. 1 and 2) exhibits substantial changes as the Mo concentration increases. Sample S0 behaves typically as other iron-rich metallic glasses like $Fe_{80}B_{20}$, with almost linear behavior near 300 K. A minimum in resistivity is observed at 15 K, and below this temperature the resistivity ratio shows a negative TCR. For S2 the temperature dependence becomes less pronounced, and exhibits a resistivity minimum at about 45 K. However, the resistivity minimum is much broader than that for S0. Higher Mo concentration changes the resistivity behavior significantly. The minimum shifts to much higher temperatures. T_{min} values for S4 and S6 are 195 and 232 K, respectively. Because T_{min} for S6 is close to room temperature, its negative TCR range is much

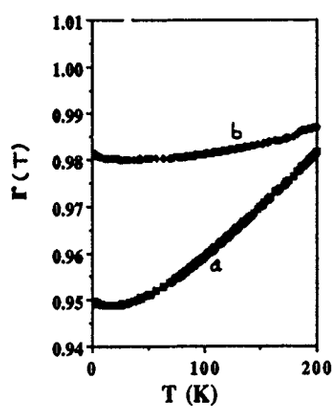

FIG. 1. Normalized resistivity $r(T)$ vs temperature T: (a) $Fe_{70}Ni_{12}B_{16}Si_2$ (sample S0) and (b) $Fe_{70}Ni_{10}Mo_2B_{16}Si_2$ (sample S2).

[a]Present address: Department of Physics, Texas A & M University, College Station, TX 77843.

 0021-8979/94/76(10)/6107/3/$6.00 © 1994 American Institute of Physics

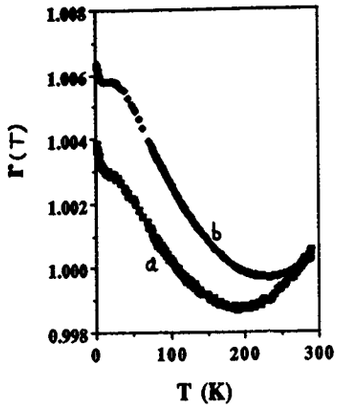

FIG. 2. Normalized resistivity $r(T)$ vs temperature T: (a) $Fe_{70}Ni_8Mo_4B_{16}Si_2$ (sample S4) and (b) $Fe_{70}Ni_6Mo_6B_{16}Si_2$ (sample S6).

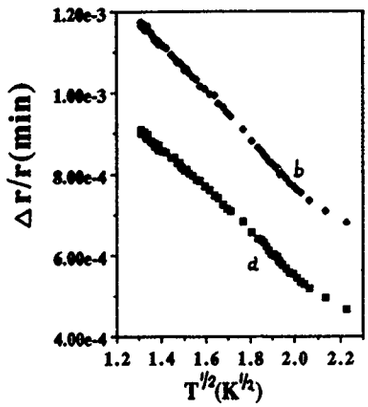

FIG. 3. $\Delta r/r(\min)$ vs $T^{1/2}$ for samples (a) $Fe_{70}Ni_{12}B_{16}Si_2$, and (b) $Fe_{70}Ni_{10}Mo_2B_{16}Si_2$ for $T<T_{\min}$.

larger than for the other samples. The total change in resistivity from RT to $T=T_{\min}$ for S0 is about 5% while this change is less than 1% for other samples. These figures also show that $r(T)$ of both samples S4 and S6 exhibits a weak maximum followed by another weak minimum at lower temperature. The broad resistivity minimum for S2 may be considered as the precursor to the development of a second minimum. Similar results have been reported for glassy $Fe_{80-x}Cr_xB_{20}$ (Ref. 5) and $Fe_{80-x}Mo_xB_{20}$ (Ref. 1) although it has been reported that $T_{\min}$ for glassy $Fe_{80-x}Mo_xB_{20}$ (Ref. 6) increases with x up to $x=4$ but then reduces for $x=6$ while we find that, for our sample S6, $T_{\min}$ is larger than that for S4. We speculate that this difference may be due to the presence of Ni in this glass. A reasonable linear correlation between $T_{\min}$ and ρ(RT), and $T_{\min}$ and T_C within experimental uncertainty is observed. These correlations indicate the possible importance of roles played by the structural disorder and the magnetic property of the samples in addition to other physical mechanisms in determining the behavior of their minimum in resistivity. The temperature at which a local maximum in resistivity is observed for S4 and S6 is practically the same for both samples, while the temperature $T_{\min 2}$, at which the second resistivity minimum is observed, decreases slightly with increasing Mo concentration. Values of $T_{\min}$ and $T_{\min 2}$ are listed in Table I. Errors in these values are determined by the flatness of the resistivity variation near these temperatures.

For discussion purposes we shall divide temperature intervals as follows: (1) $T>T_{\min}$, (2) $T<T_{\min 2}$, and (3) $T_{\max}<T<T_{\min}$. For $T>T_{\min}$, the resistivity ratio $r(T)$ can be fitted to a second-order polynomial in T with a linear coefficient of the order of 10^{-4} K^{-1}, and a quadratic coefficient of the order of 10^{-7} K^{-2} between 200 and 300 K indicating the possibility of a contribution from magnetic scattering to the total resistivity.[7] For lower temperatures but above $T_{\min}$, a quadratic fit in T adequately describes $r(T)$ which may include the T^2 magnetic scattering term[7] in addition to the T^2 contribution as predicted by Ziman's theory.[8] Data for S4 and S6 samples were also fitted to the second-order polynomial in T for $T>T_{\min}$ which resulted in a linear term with a negative coefficient of about 5×10^{-5} (K^{-1}) and a positive quadratic term of the order of 10^{-7} (K^{-2}). The T^2 term, we believe, is due to the magnetic scattering[7] since the Ziman theory predicts a linear T dependence near RT. The negative linear term is most probably the contribution due to the incipient localization effect as expected from Mooij's correlation with ρ(RT). In the negative TCR region, it is controversial as to whether the increase in $\rho(T)$ of ferromagnetic glasses is due to a "Kondo-type effect," structural disorder induced two level states, or weak localization and Coulomb interaction effects. Numerous reports indicate that the temperature dependence of resistivity of many magnetic and nonmagnetic metallic glasses can be fitted to $T^{1/2}$ reasonably well below T, at which minimum in resistivity is observed, with negative slope as predicted by Coulomb interaction theories.[9] To check whether our samples show the similar trend, we have plotted, in Figs. 3 and 4, $\Delta r/r(\min)=[\rho(T)-\rho(\min)]/\rho(\min)$ vs $T^{1/2}$ for $T<T_{\min}$ for S0 and S2, and $T<T_{\min 2}$ for S4 and S6. It is seen that it exhibits a linear behavior, and that the slopes for all of these samples are approximately constant (-5×10^{-4} $K^{1/2}$). A similar observation was reported for $Fe_{80-x}Cr_xB_{20}$ samples for $x<20$.[5] According to the Coulomb interaction theory,[9] the major contribution to the resistivity arises from the diffusion channel which predicts an additional term to the conductivity, which in absence of spin-orbit interaction is given by[5]

$$\sigma_D(H,T)=\frac{1.3}{\sqrt{2}}\frac{e^2}{4\pi^2\hbar}\left(\frac{k_BT}{\hbar D}\right)^{1/2}\times\left\{\frac{4}{3}+\lambda^{j=1}(F)\left[\frac{3}{2}+\frac{g_3(h)^2}{1.3}\right]\right\},$$

where

TABLE I. Various measured parameters for $Fe_{70}Ni_{12-x}Mo_xB_{16}Si_2$ metallic glasses. For explanation of symbols see the text.

x (at. %)	ρ(RT) (±5%) ($\mu\Omega$ cm)	TCR (RT) (K^{-1})	$T_{\min}$ (K)	$T_{\max}$ (K)	$T_{\min 2}$ (K)	T_C (K)
0	109	2.64×10^{-4}	15±2	···	···	700
2	139	8.94×10^{-5}	45±5	···	···	635
4	152	3.04×10^{-5}	195±2	22±2	13±2	558
6	161	1.38×10^{-5}	232±2	20±2	10±2	476

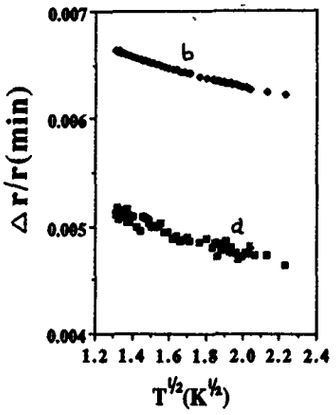

FIG. 4. $\Delta r/r(\min)$ vs $T^{1/2}$ for samples (a) $Fe_{70}Ni_8Mo_4B_{15}Si_2$, and (b) $Fe_{70}Ni_6Mo_6B_{16}Si_2$ for $T<T_{min2}$.

$$\lambda^{j=1}(F)=\frac{32}{3F}\left[1+\frac{3F}{4}-\left(1+\frac{F}{2}\right)^{3/2}\right]$$

is a measure of the electron-phonon interaction. The function $g_3(h)$, where $h=g\mu_B H/k_B T$, has the asymptotic form $0.056h^2$ for $h\ll 1$ and $(h^{1/2}-1.3)$ for $h\gg 1$. Various constants have the usual meaning. We have calculated an upper limit for D, the diffusion constant, from this expression by taking the limit $\lambda^{j=1}=0$ and find it to be $\sim 3.5\times10^{-5}$ and 7.8×10^{-5} m^2/s for S0 and S6 samples. These are typical values (within a factor of 2) reported for other metallic glasses. Hence, the assumption that the temperature dependence of the resistivity of $Fe_{70}Ni_{12-x}Mo_xB_{16}Si_2$ at temperatures below 10 K is dominated by the Coulomb interaction effects seems to be a reasonable one.

We have also plotted $\Delta r/r(\min)$ vs $T^{1/2}$ for S4 and S6 in the region $T_{max}<T<T_{min}$ in Fig. 5 since these samples show two minima in $\rho(T)$. It is clearly seen that $\Delta r/r(\min)$ shows

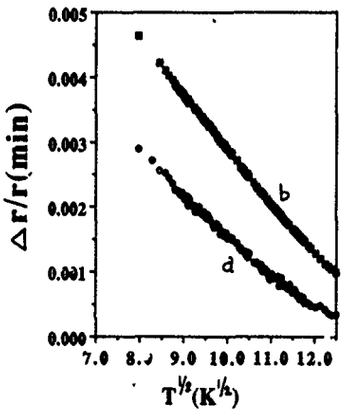

FIG. 5. $\Delta r/r(\min)$ vs $T^{1/2}$ for samples (a) $Fe_{70}Ni_8Mo_4B_{16}Si_2$, and (b) $Fe_{70}Ni_6Mo_6B_{16}Si_2$ for $T_{max}<T<T_{min}$.

a linear dependence on $-T^{1/2}$ in this temperature interval also. We also find that $\Delta r/r(\min)$ for these samples can be fitted to an expression $(a-b\ln T)$ equally well in this temperature interval which is predicted by either two-level tunneling or Kondo-type magnetic scattering,[10] however, the coefficient b is about one order of magnitude greater than that found for $Fe_{80}B_{20-x}C_x$ and similar metallic glasses.[7] The slope of $\Delta r/r(\min)$ vs $T^{1/2}$ in this temperature range is only about one and a half times larger than that found below T_{min2}. Whether this $T^{1/2}$ temperature dependence is due to Coulomb interaction effects or not is difficult to conclude at this time although one would expect these effects not to be appreciable at such large temperatures. Most probably, the higher-temperature region has resistivity contributions from other mechanisms, e.g., magnetic scattering, localization effects, etc., as well, and one needs to do additional measurements like the magnetic field dependence of $r(T)$ to get a better understanding.

Thus, the resistivity behavior of $Fe_{70}Ni_{12-x}Mo_xB_{16}Si_2$ is similar to that of Fe-Cr-B metallic glasses,[3] i.e., the temperature dependence of resistivity shows two minima as Mo concentration is increased. Since it is very difficult to make high concentration Mo amorphous samples, it is difficult to determine whether T_{min} (observed at larger temperatures) would start decreasing for large Mo concentration samples or not. Similarity of Mössbauer spectra of Mo and Cr substituted Fe-B-Si/Fe-Ni-B-Si and Fe-B-Cr samples, the fast decrease in Curie temperature with concentration, and the similar behavior of resistivity indicates that Mo in these glasses induces an "interaction" similar to that of Cr. It has been suggested[2] that this interaction is an "antiferromagnetic" type based on the observations of the fast decrease of Curie temperature of $(Fe_{1-x}Mo_x)_{75}P_{16}B_6Al_3$ with increasing Mo concentration, and the similarity of Mössbauer spectra of $Fe_{80-x}M_xB_{20}$ (M=Cr, Mo). A more detailed analysis and measurements of the magnetic field dependence of the resistivity minima and maximum need to be done in order to fully elucidate the role of Mo in this metallic glass system. Such measurements are in progress.

We thank Dr. V. R. V. Ramanan for providing samples. This work was supported at the University of Hyderabad by the Department of Atomic Energy (India), and at Texas A & M by the Robert A. Welch Foundation (A-0514).

[1] H. J. V. Nielsen, Solid State Commun. **30**, 239 (1979).
[2] C. L. Chien and H. S. Chen, J. Appl. Phys. **50**, 1574 (1979).
[3] N. R. M. Rathnam, Ph.D. thesis, University of Hyderabad, India.
[4] J. H. Mooij, Phys. Status Solidi A **17**, 521 (1983).
[5] M. Olivier, J. O. Ström-Olsen, and Z. Altounian, Phys. Rev. B **35**, 333 (1987).
[6] D. F. Jones, G. Stroink, Z. M. Stadnik, and R. A. Dunlap, Mater. Sci. Eng. **99**, 208 (1988).
[7] S. N. Kaul, W. Kettler, and M. Rosenberg, Phys. Rev. B **33**, 4987 (1986).
[8] See, for example, D. G. Naugle, J. Phys. Chem. Solids **45**, 367 (1984).
[9] P. A. Lee and T. V. Ramakrishnan, Rev. Mod. Phys. **57**, 287 (1985).
[10] R. Harris and J. O. Ström-Olsen, in *Glassy Metals II*, edited by H. Beck and H.-J. Guntherodt (Springer, Berlin, 1984), p. 325.

Anisotropic magnetism and resistivity of an $Al_{70}Ni_{15}Co_{15}$ decagonal quasicrystal

J. T. Markert and J. L. Cobb
Department of Physics, University of Texas, Austin, Texas 78712

W. D. Bruton, A. K. Bhatnagar, and D. G. Naugle
Department of Physics, Texas A&M University, College Station, Texas 77843

A. R. Kortan
AT&T Bell Laboratories, Murray Hill, New Jersey 07974

We report the results of dc magnetization and electrical resistivity studies of a single-domain $Al_{70}Ni_{15}Co_{15}$ decagonal quasicrystal. The temperature dependence and anisotropy of the electrical resistivity are in excellent agreement with previous results for a similar sample. The magnetic properties were determined by superconducting quantum interference device magnetometry over the temperature range 1.8–300 K for magnetic fields between 10 Oe and 10 kOe. The magnetic behavior can be characterized by a weak ferromagnetic component $M_0(H)$ which saturates in moderate fields ($H \approx 1$ kOe) and a differential susceptibility, $\chi_0 = \Delta M/\Delta H$, obtainable from the high-field data. The observed magnetization $M = \chi_0 H + M_0$ is slightly anisotropic and essentially temperature independent below room temperature. For H parallel to the quasicrystal axis, we observe $\chi_{0\parallel} = 7.1 \times 10^{-7}$ emu/g and $M_{0\parallel} = 2.0 \times 10^{-3}$ emu/g. For H perpendicular to the quasicrystal axes, we obtain $\chi_{0\perp} = 8.2 \times 10^{-7}$ emu/g and $M_{0\perp} = 1.7 \times 10^{-3}$ emu/g. An anisotropic and weak superconducting transition was observed at $T = 3.2$ K, corresponding to a superconducting volume fraction of only $\sim 10^{-3}$.

Although a great deal of experimental effort has been directed at understanding the unusual nature of quasicrystalline materials,[1] only recently, with the discovery of the two-dimensional decagonal quasicrystals,[2,3] has it been possible to make a direct comparison between properties in the quasicrystalline and periodic directions of the same material. The decagonal quasicrystalline material $Al_{70}Ni_{15}Co_{15}$ was recently[4] shown to exhibit appreciable transport anisotropy. In this work, we verify the transport properties observed in Ref. 4 and present the results of dc magnetic measurements; the magnetic data indicate a weak anisotropy in the conduction electron susceptibility and the presence of small quantities of both ferromagnetic and superconducting inclusions in the single-domain $Al_{70}Ni_{15}Co_{15}$ quasicrystal studied.

The single-grain crystal used in this study ($\sim 0.6 \times 0.6 \times 3$ mm^3) was prepared and characterized in a similar manner to that used for specimens previously described.[5] The temperature dependence of the anisotropic resistivity was determined from conventional four-terminal measurements with careful placement of voltage and current leads. The magnetic data were obtained at temperatures in the range 1.8–300 K using a Quantum Design model MPMS superconducting quantum interference device (SQUID) magnetometer. Because of the small signal from the ~7 mg quasicrystal, a custom sample holder was employed which utilized a cancellation of Pauli paramagnetic and Langevin core diamagnetic contributions, resulting in an extremely low background signal. For example, at $T = 50$ K with $H = 10$ kOe, a background moment of only $\sim 1 \times 10^{-6}$ emu was obtained, compared to the quasicrystal moment of $\sim 6 \times 10^{-5}$ emu (i.e., only a 1–2% typical correction). A point-by-point subtraction of the sample holder background was used for all data to avoid possible nonlinearities in the background response. For the observed susceptibilities, demagnetization effects were negligible.

Figures 1 and 2 both define the geometries used in this study and show the results of the electrical resistivity measurements. The resistivity in the periodic direction (perpendicular to the quasicrystal axes) of Fig. 1 exhibits the positive temperature coefficient expected for delocalized electronic states in a metal. However, in the quasiperiodic

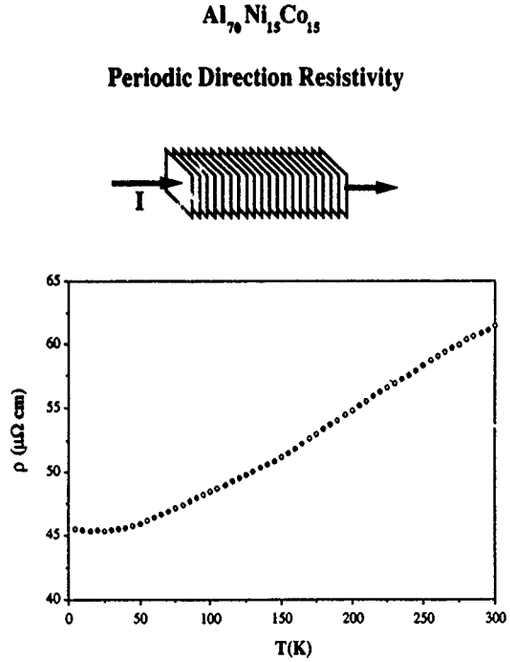

FIG. 1. The resistivity in the periodic direction as a function of temperature for a single-domain specimen of the decagonal quasicrystal $Al_{70}Ni_{15}Co_{15}$.

 0021-8979/94/76(10)/6110/3/$6.00 © 1994 American Institute of Physics

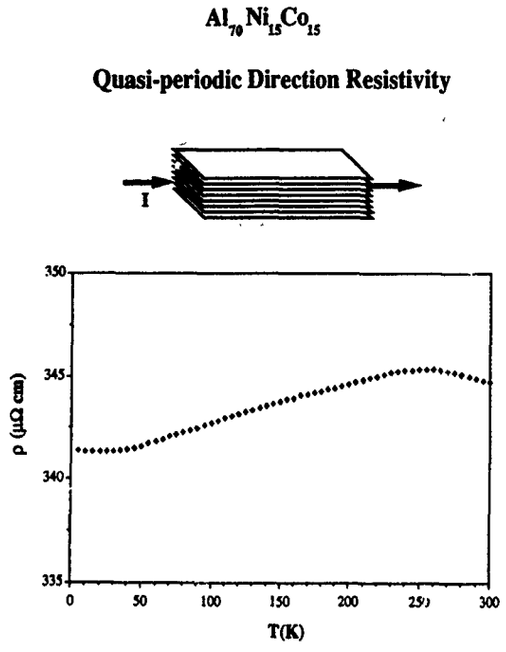

FIG. 2. The resistivity in the quasicrystalline direction as a function of temperature for a single-domain specimen of the decagonal quasicrystal $Al_{70}Ni_{15}Co_{15}$.

direction, Fig. 2, we observe the resistivity to increase with decreasing temperature between ~250 and 300 K, and then decrease before levelling off at low temperatures. As mentioned above, this result is in good agreement with a previous study[4] using the Montgomery method, where such nonmetallic behavior was argued to be consistent with phonon-assisted tunneling of carriers in extended states.

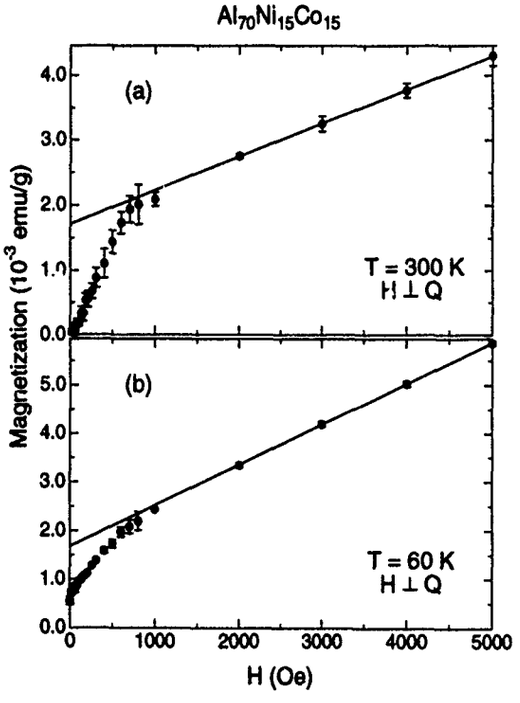

FIG. 3. Isothermal magnetization at (a)$T=300$ K and (b)$T=60$ K as a function of magnetic field applied parallel to the periodic direction of $Al_{70}Ni_{15}Co_{15}$.

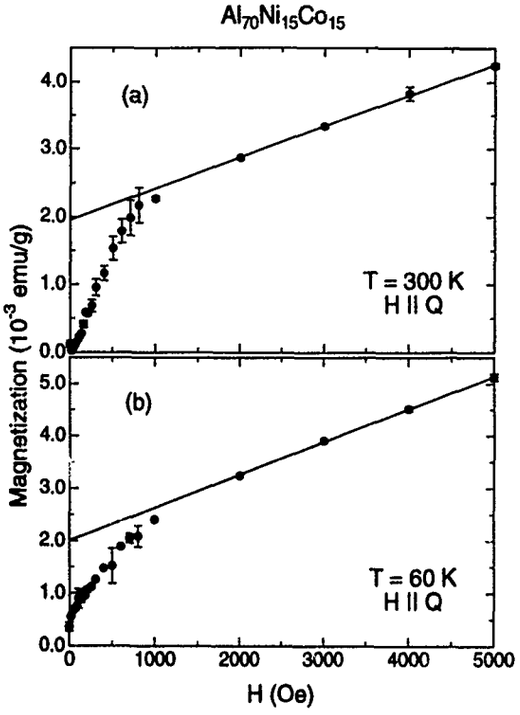

FIG. 4. Isothermal magnetization at (a) $T=300$ K and (b) $T=60$ K as a function of magnetic field applied parallel to the quasicrystalline direction of $Al_{70}Ni_{15}Co_{15}$.

In Figs. 3(a) and 3(b) are shown isothermal magnetization data as a function of the external magnetic field, taken with the field perpendicular to the quasicrystalline axes, for $T=300$ and 60 K, respectively. Similar data are shown in Fig. 4 for the magnetic field applied parallel to a quasicrystalline axis. The nonlinear behavior may be characterized by a ferromagnetic component which saturates in moderate fields ($H\approx 1$ kOe) followed by the more usual linear increase in magnetization with field at higher fields. Several observations are in order. First, the overall behavior is nearly isotropic and essentially temperature independent. Such temperature-independent behavior implies that whatever is responsible for the ferromagnetic component (whether it be clusters, inclusions, or paramagnons) cannot be attributed to extremely small nanoclusters, which would be expected to exhibit superparamagnetic behavior above some blocking temperature. Second, the ferromagnetic component exhibits remanence at 60 K [note the y intercept of the data in Figs. 3(b) and 4(b)], which disappears at room temperature. The lines in Figs. 3 and 4 are linear fits to the high-field region where the ferromagnetic component has presumably saturated. The intercepts of these lines with the magnetization axes provide the saturated moment of the ferromagnetic component, with temperature-independent values of $M_{0\perp}=(1.7\pm0.1)\times10^{-3}$ emu/g for H perpendicular to the quasicrystal axes and $M_{0\parallel}=(2.0\pm0.1)\times10^{-3}$ emu/g for H parallel to the quasicrystal axis. If the anisotropy in M_0 is attributed to shape anisotropy of the possible inclusions or

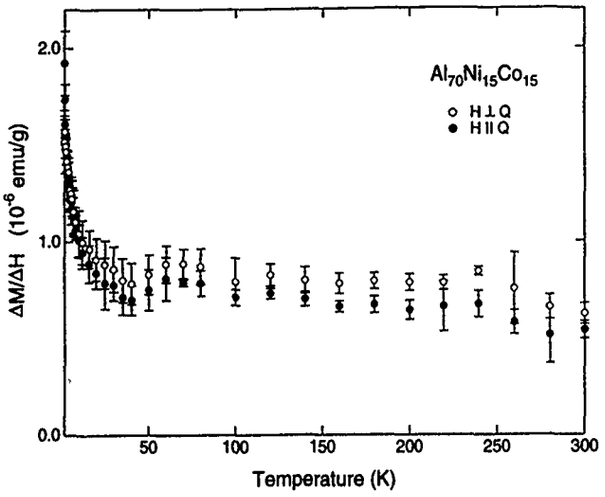

FIG. 5. High-field differential susceptibility, $\chi_0 \equiv \Delta M/\Delta H$, as a function of temperature for magnetic fields applied both perpendicular (open circles, $H \perp Q$) and parallel (filled circles, $H \| Q$) to the quasicrystalline direction of $Al_{70}Ni_{15}Co_{15}$.

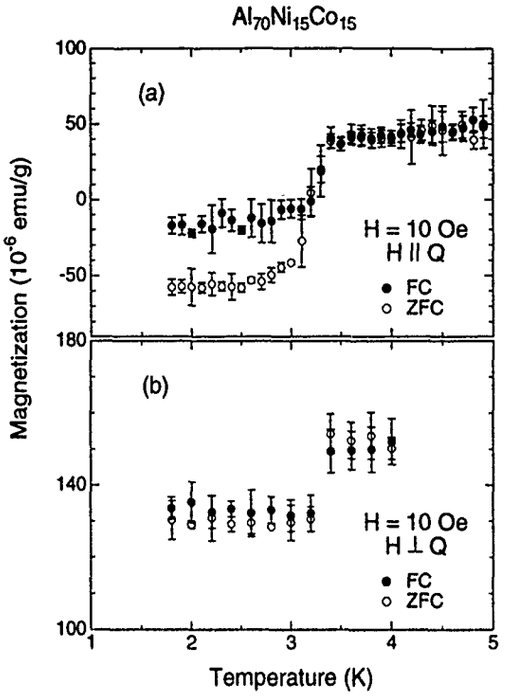

FIG. 6. Magnetization as a function of temperature in a field $H = 10$ Oe applied (a) parallel to the quasicrystalline direction and (b) perpendicular to the quasicrystalline direction for $Al_{70}Ni_{15}Co_{15}$. Both zero-field cooled (ZFC) and field-cooled (FC) data are shown.

clusters, this would imply (for ferromagnetism) that their shape is prolate with the shorter axis perpendicular to the quasicrystal direction, a reasonable result. We point out, however, that the observed values of M_0 correspond to only about $1\times10^{-3}\mu_B$ per formula unit of $Al_{70}Ni_{15}Co_{15}$, a rather small ferromagnetic component.

To obtain the underlying field-independent susceptibility (the slope of the lines in the high-field regions of Figs. 3 and 4), magnetization data were taken as a function of temperature between 1.8 and 300 K for applied fields $H = 5$ and 10 kOe. The intrinsic susceptibility was then defined by $\chi_0 \equiv \Delta M/\Delta H$. The results are shown in Fig. 5. The data are essentially temperature independent between about 30 and 250 K, with a Curie-like impurity tail at low temperatures. The Curie-like term corresponds, for example, to only $\sim 2\times10^{-3}$ free Co^{2+} moments per formula unit of $Al_{70}Ni_{15}Co_{15}$. A small but persistent anisotropy in the value of χ_0 is observable in Fig. 5. The average values of the data for temperatures between 30 and 250 K are $\chi_{0\perp} = 8.2\times10^{-7}$ emu/g and $\chi_{0\|} = 7.1\times10^{-7}$ emu/g. Such values are appreciably higher than that reported[4] for $Al_{65}Cu_{15}Co_{20}$, where $\chi_0 \approx -1\times10^{-7}$ emu/g; that small value was attributed to a nearly *sp*-like band at the Fermi energy. The larger value for $Al_{70}Ni_{15}Co_{15}$ is somewhat unexpected, given the similar transport properties of the two materials. If one estimates a contribution to χ_0 due to core diamagnetism of $\chi_{\text{core}} \approx -1.5\times10^{-7}$,[6] the bare density of states from the resulting χ_0 value is $N(E_F) \approx 160$ states eV^{-1} per formula unit of $Al_{70}Ni_{15}Co_{15}$, or $N(E_F) \approx 1.6$ states eV^{-1} $atom^{-1}$. However, this may be an overestimate, since we have neglected any possible Van Vleck paramagnetism (e.g., due to Co^{3+}), which is difficult to determine.

Finally, in Fig. 6, we show magnetization data as a function of temperature taken under both zero-field-cooled (ZFC) and field-cooled (FC) conditions in a field of $H = 10$ Oe. A weak superconducting transition is observable at $T = 3.2$ K; the strength of the signal corresponds to a superconducting volume fraction of only $-4\pi\chi_v \approx 10^{-3}$. One candidate for superconductivity in this temperature regime would be inclusions of amorphous aluminum. The signal for $H \| Q$ (Q is the quasicrystalline direction) is about five times larger than for $H \perp Q$. Such behavior is opposite of that expected for demagnetization effects due to prolate inclusions parallel to the quasicrystalline planes; however, for small inclusions, penetration depth effects may dominate shape anisotropy.

In summary, we have reported electrical resistivity and dc magnetization measurements on a single-domain decagonal quasicrystal of $Al_{70}Ni_{15}Co_{15}$. The anisotropic resistivity was in good agreement with earlier measurements. Weak superconducting, Curie-like, and ferromagnetic contributions were observed, presumably due to defects. A dominant temperature-independent susceptibility of $\sim 7\times10^{-7}$ emu/g, with $\sim 10\%$ anisotropy, was observed.

This work was supported by the National Science Foundation under Grant No. DMR-9158089 and the Robert A. Welch Foundation under Grants Nos. F-1191 and A-0514.

[1] See, e.g., *Physics of Quasicrystals*, edited by P. J. Steinhart and S. Ostlund (World Scientific, Singapore, 1987).
[2] L. X. He, Y. K. Wu, and K. H. Kuo, J. Mater. Sci. Lett. **7**, 1284 (1987).
[3] A. P. Tsai, A. Inoue, and T. Masumoto, Mater. Trans. **30**, 300 (1989).
[4] S. Martin, A. F. Hebard, A. R. Kortan, and A. F. Theil, Phys. Rev. Lett. **67**, 719 (1991).
[5] A. R. Kortan *et al.*, Phys. Rev. B **40**, 9397 (1989).
[6] L. N. Mulay and E. A. Boudreaux, *Theory and Applications of Molecular Diamagnetism* (Wiley, New York, 1976).

Mössbauer effect investigation of the pentagonal approximant phase in the Fe-Nb system

R. A. Dunlap, J. Kyriakidis, and M. Yewondwossen
Department of Physics, Dalhousie University, Halifax, Nova Scotia B3H 3J5, Canada

The formation of the pentagonal Frank–Kasper phase (μ phase) in the $Fe_{50+x}Nb_{50-x}$ system near $x=0$ has been investigated. The effects of composition and heat treatment on the phase diagram of this system have been studied. Only the as-cast $x=0$ alloy was found to consist of a pure μ phase. X-ray diffraction patterns indicate the existence of a phase with a high degree of structural order but considerable chemical disorder. A Mössbauer spectrum of the μ-phase material exhibits a room-temperature quadrupole split doublet with $\Delta=0.209$ mm/s and an isomer shift $\delta=-0.289$ mm/s relative to α-Fe. A shell model analysis of the spectrum indicates a structure with a high degree of order. Results are discussed in terms of measurements on related icosahedral and decagonal phase materials.

I. INTRODUCTION

Mössbauer effect studies of quasicrystals have been important for an understanding of the microstructure of these novel materials. A recent review of these studies has been presented by Dunlap and Lawther.[1] A number of methods for the interpretation of Mössbauer spectra of quasicrystalline materials have been presented in the literature and the information which can be obtained from these measurements depends crucially on the techniques applied to their analysis. The comparison of results from quasicrystalline materials and those of related crystalline phases has been important in understanding the relationship of Mössbauer spectral parameters and microstructural details. In the present work we have considered Mössbauer measurements of the pentagonal approximant phase in the Fe-Nb system. These results will be interpreted in the context of results for related quasicrystalline materials.

II. EXPERIMENTAL METHODS

Samples of $Fe_{50+x}Nb_{50-x}$ were prepared by melting high-purity elemental components in an argon arc furnace for compositions with $x=0,2$. Materials were studied as-cast and after annealing for four days at 1000 °C and water quenching. Room-temperature Cu K_α x-ray diffraction patterns were made of all samples using a Siemens D500 scanning diffractometer. Room-temperature ^{57}Fe Mössbauer effect studies were performed using a constant acceleration Wissell System II spectrometer and a $Pd^{57}Co$ source. The intrinsic linewidth of the spectrometer for ^{57}Fe is 0.23 mm/s (FWHM).

III. RESULTS

All alloys studied here showed the presence of the pentagonal μ phase. However, only the as-cast $x=0$ sample was free from the presence of impurity phases. This analysis is consistent with the phase formation studies of the Fe-Nb system reported by Raman.[2] Further investigations presented in the present manuscript are confined to the single-phase sample.

X-ray diffraction peaks for the μ phase were well defined with a typical linewidth of $\Delta(2\theta)\leq 0.2°$ (FWHM), indicating a high degree of structural order. The peak locations and relative intensities obtained in this work along with those calculated for the μ phase (W_6Fe_7 structure) with $a=4.928$ Å and $c=26.83$ Å are given in Table I. The peak locations are in excellent agreement with the calculated values[3] for the lattice parameters as indicated above. The anomalies in the measured intensities for some of the diffraction peaks are an indication of the presence of substantial chemical disorder on the lattice sites.

The room-temperature ^{57}Fe Mössbauer effect spectrum of the pentagonal phase of Fe-Nb is illustrated in Fig. 1. This spectrum shows the existence of a symmetric quadrupole split doublet. Although the individual lines cannot be resolved, the shape and width of the absorption peak indicate that it is not a singlet. A fit to this spectrum using a Lorentzian doublet yields the mean quadrupole parameters as indicated in Table II. The linewidth of the component lines, 0.29 mm/s, is slightly greater than the intrinsic linewidth of the spectrometer but is substantially less than that found for similar fits to spectra of quasicrystalline materials; typically

TABLE I. X-ray diffraction scattering length and relative peak intensities for pentagonal $Fe_{50}Nb_{50}$ measured in the present work and calculated for the pentagonal Frank–Kasper phase.

	Measured		Calculated	
Index	d (Å)	I	d (Å)	I
1 1 0	2.470	86	2.471	72
0 1 10	2.273	67	2.278	46
0 0 12	2.238	18	2.242	18
1 1 6	2.163	100	2.165	75
2 0 1	2.131	45	2.133	35
1 0 11	2.120	53	2.124	43
2 0 4	2.037	17	2.039	16
0 2 5	1.987	31	1.985	29
1 1 9	1.903	15	1.905	15
0 1 13/2 0 7	1.867	11	1.866	15
3 0 0	1.426	16	1.426	20
2 1 10	1.385	15	1.386	33
3 0 6	1.359	22	1.359	32
0 1 19/1 2 13	1.348	22	1.348	48
0 0 21/1 1 18	1.278	20	1.279	60
0 2 17	1.270	9	1.273	21
2 2 0	1.236	20	1.236	100

 0021-8979/94/76(10)/6113/3/$6.00 © 1994 American Institute of Physics

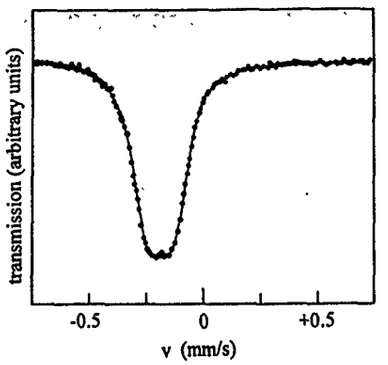

FIG. 1. Room-temperature ^{57}Fe Mössbauer effect spectrum of the pentagonal phase of $Fe_{50}Nb_{50}$. The solid line is a least-squares fit to the shell model.

about 0.36 mm/s.[1] This excess linewidth is, presumably, the result of local disorder in the structure as evidenced by the anomalous x-ray peak intensities and which produces a corresponding distribution of local Fe environments. This behavior can be accounted for in the analysis of the Mössbauer effect spectrum by fitting the data to a shell model distribution of quadrupole splittings of the form[1,4]

$$P(\Delta)=\left(\frac{\Delta}{\sigma}\right)^{n}\exp\left(-\frac{\Delta^2}{2\sigma}\right), \qquad (1)$$

where n and σ are fitted parameters. The symmetric nature of the spectrum indicates the lack of correlation between isomer shift and quadrupole splitting distributions. A detailed computer analysis confirms this assumption. The results of the shell model analysis for this spectrum are given in Table III and the calculated $P(\Delta)$ is illustrated in Fig. 2.

IV. DISCUSSION AND CONCLUSIONS

The existence of a decagonal[9] and icosahedral[10] phase in the Fe-Nb system has been demonstrated by electron diffraction studies of rapidly quenched samples; although single-phase materials have not yet been prepared. Table I compares the mean quadrupole parameters of the pentagonal Fe-Nb phase with several other icosahedral and decagonal materials. The mean quadrupole splitting of Fe-Nb is somewhat less than in Al-based icosahedral[5] and decagonal[7] alloys where Fe atoms are believed to exist in a highly anisotropic environment analogous to the transition metal site environments in the outer shell of the MacKay icosahedra of a cubic approximant phase (e.g., α-AlMnSi) or in the sites of a two-dimensional Penrose tiling, respectively. On the other hand, the quadrupole splitting of Fe-Nb is much greater than that in typical Ti-based icosahedral alloys.[11,12] where the Fe atoms are believed to reside in highly symmetric sites at the center of an icosahedral cluster.

TABLE II. Results of room-temperature Mössbauer effect studies of some quasicrystalline and related materials; i=icosahedral, d=decagonal, p=pentagonal, *=this work.

Alloy	Structure	Δ (mm/s)	δ (mm/s)	Reference
$Al_{62.5}Cu_{25}Fe_{12.5}$	i	0.369	+0.234	5
$Ti_{56}Ni_{23}Fe_5Si_{16}$	i	0.06	−0.170	6
$Al_{75}Pd_{15}Fe_{10}$	d	0.372	+0.185	7
$Fe_{50}Nb_{50}$	p	0.209	−0.289	*

TABLE III. Comparison of shell model parameters for pentagonal Fe-Nb (p) and some icosahedral (i) alloys. *=this work.

Alloy	Phase	n	σ (mm/s)	Reference
$Al_{70}Ta_{10}Fe_{20}$	i	1.14	0.363	8
$Al_{62.5}Cu_{25}Fe_{12.5}$	i	1.44	0.283	5
$Al_{80}Fe_{11}Mo_9$	i	1.48	0.351	8
$Al_{86}Fe_{0.28}Mn_{13.72}$	i	1.70	0.144	1
$Fe_{50}Nb_{50}$	p	5.2	0.088	*

The negative isomer shift observed in this alloy is indicative of an anomalously high electron density at the Fe probe sites. This is expected on the basis of the presence of a large concentration of early transition metal (M) atoms in the alloy. The value of δ observed here is consistent with measurements of dilute MFe alloys and near neighbor effects of dilute M impurities in Fe (see Ref. 13 and references therein).

The parameters obtained from shell model fits to several quasicrystalline alloys are compared with the data for pentagonal Fe-Nb in Table III. The present results are anomalous in two respects; an unusually large value of the parameter n and an unusually low value of the parameter σ, when compared with all results for quasicrystalline alloys reported to date.[1] The relationship of these parameters to the detail of the microstructure has been discussed by Dunlap *et al.*[8] Specifically, n near unity and a large value of σ are characteristic of a highly disordered (e.g., amorphous) structure, while increasing values of n (and correspondingly smaller values of σ) are characteristic of an increase in the degree of microstructural order. This inverse correlation between the values of n and σ is characteristic of the relationship between the shell model and the distribution of local Fe environments in the material and is illustrated for typical data for quasicrystalline and related materials in Fig. 3. Typically quasicrystalline materials have values of n in the range of 1–2, with more highly ordered materials (as evidenced from other ex-

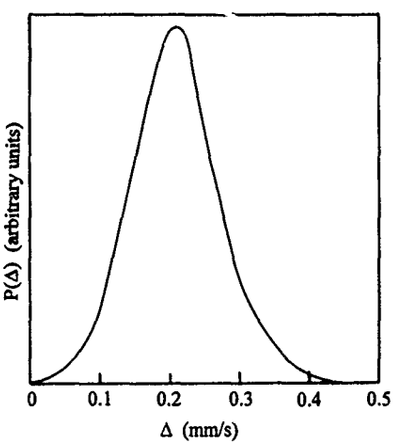

FIG. 2. Quadrupole splitting distribution, $P(\Delta)$, for the spectrum of Fig. 1 as obtained from the shell model.

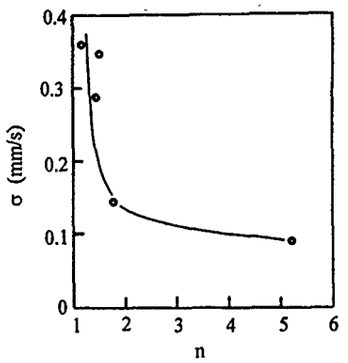

FIG. 3. Relationship between the shell model fitting parameters n and σ for several quasicrystalline and related materials.

perimental techniques) giving $n \approx 2$. The value of $n=5.2$ obtained in the present work for pentagonal Fe-Nb indicates a much greater degree of order in this crystalline approximant phase than in similar quasicrystalline phases. This, presumably, is indicative of the existence of translational symmetry in the approximant phase which is lacking in the quasicrystalline phase. In more specific terms, n is related to the number of independent distortion vectors d, which are necessary to describe the structure as $n=d-1$. The present studies clearly point to the differences which exist between the microstructure of quasicrystals and their crystalline approximants.

ACKNOWLEDGMENTS

This work was supported by the Natural Sciences and Engineering Research Council of Canada and the Faculty of Graduate Studies, Dalhousie University.

[1] R. A. Dunlap and D. W. Lawther, Mater. Sci. Eng. Rep. R **10**, 141 (1993).
[2] A. Raman, Proc. Ind. Acad. Sci. A **65**, 256 (1967).
[3] P. I. Kripyakevich, E. I. Gladyshevskii, and R. V. Skolozdra, Sov. Phys. Crystall. XPhys. Crystall. **12**, 525 (1968).
[4] G. Czjzek, Phys. Rev. B **25**, 4908 (1982).
[5] D. W. Lawther and R. A. Dunlap, J. Non-Cryst. Solids **153/154**, 45 (1993).
[6] D. Bahadur, V. Srinivas, R. A. Dunlap, R. C. O'Handley, and M. E. McHenry, Philos. Mag. B **60**, 871 (1989).
[7] D. W. Lawther and R. A. Dunlap, J. Non-Cryst. Solids **153/154**, 49 (1993).
[8] R. A. Dunlap, R. C. O'Handley, M. E. McHenry, and V. Srinivas, Struct. Chem. **2**, 501 (1991).
[9] A. Q. He, Q. B. Yang, and H. Q. Ye, Philos. Mag. Lett. **51**, 69 (1990).
[10] A. Q. He, H. Q. Ye, and K. H. Kuo, Scr. Metall. **23**, 533 (1989).
[11] R. A. Dunlap, M. E. McHenry, R. C. O'Handley, V. Srinivas, and D. Bahadur, Phys. Rev. B **39**, 1942 (1989).
[12] R. A. Dunlap, R. C. O'Handley, M. E. McHenry, and R. Chatterjee, Phys. Rev. B **37**, 8484 (1988).
[13] R. Ingalls, *Mössbauer Isomer Shifts* (North-Holland, Amsterdam, 1978), p. 361.

Short period oscillations in the Kerr effect of 4*d*- and 5*d*-transition metal wedges on Co films (invited) (abstract)

A. Carl and D. Weller
IBM Almaden Research Center, San Jose, California 95120-6099

We report a novel type of short period oscillations in electron-beam evaporated Co films covered with wedge-shaped films of Pt, Au, and Pd. Oscillatory behavior, with periods in the range 2–3 Å, is observed both in the saturation polar Kerr angle and in the high field susceptibility, as a function of the wedge position (see Fig. 1). The structures of the type buffer/Co/X wedge/Y cap were made by high vacuum evaporation using fused silica as substrates. They consist of a 200 Å Pt buffer layer, a thin Co layer revealing a perpendicular easy magnetization axis, a transition metal wedge (X) with thickness in the range 0–25 Å, and a thin Cu or Au cap (Y) layer. The presence of oscillations depends critically on the choice of the cap-layer Y. They are distinctly different from long and short range period oscillations observed in magnetic sandwich or multilayer structures, since there is only one magnetic film involved. The present results will be discussed in the framework of spin polarized quantum well states.

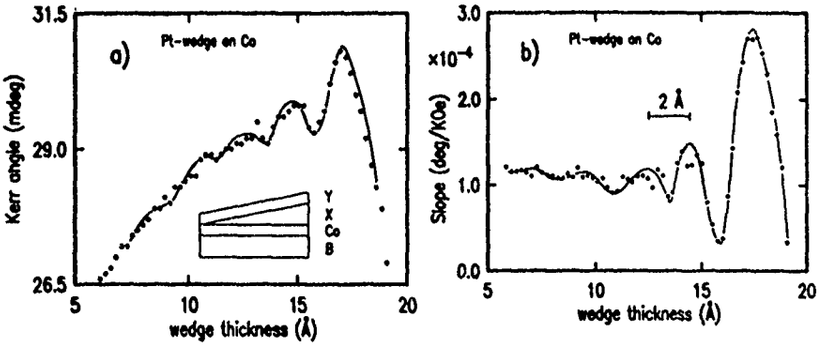

FIG. 1. Oscillatory behavior as a function of the wedge position.

 0021-8979/94/76(10)/6116/1/$6.00 © 1994 American Institute of Physics

Magnetoresistance of CuNiCo ternary alloys (abstract)

R. S. Beach, D. Rao, and A. E. Berkowitz
Center for Magnetic Recording Research, University of California, San Diego, La Jolla, California 92093

Magnetoresistance (MR) measurements on four film samples of the ternary alloy CuNiCo were performed at room temperature in fields $H \leq 20$ kOe. Following growth by sputtering onto thermally oxidized Si substrates, the films (100–200 nm thick) were annealed between 1 and 6 h at temperatures $T_A = 200$, 350, 500, and 700 °C. The samples display anisotropic magnetoresistances (AMR) for $H < 100$ Oe of up to 3% at room temperature for $Cu_{20}Ni_{53}Co_{27}$ ($T_A = 350$ °C). Despite the fact that in the bulk these alloys tend to phase separate into Co rich and Co poor regions, we find evidence for giant magnetoresistance (i.e., an isotopic negative component to the MR) in only one sample, $Cu_{51}Ni_{17}Co_{31}$, after a 6 h, 700 °C anneal. In the as-deposited condition, samples $Cu_{20}Ni_{53}Co_{27}$ and $Cu_{13}N_{41}Co_{46}$ display a pronounced asymmetry between the resistance decrease for H applied perpendicular to the current I and the corresponding increase for H parallel to I which substantially exceeds the 1:2 ratio in bulk materials or the 1:1 ratio expected for a thin film. The large observed values of AMR (more evident in samples with low Cu concentrations) are likely linked to AMR in binary CuCo alloys, which are known to exhibit large AMR.[1] The disparity between the MR for H parallel and perpendicular to the current we attribute to magnetic anisotropy induced during fabrication.

[1] O. Jaoul *et al.*, J. Magn. Magn. Mater. **5**, 23 (1977).

 0021-8979/94/76(10)/6117/1/$6.00 © 1994 American Institute of Physics

Enhancement of the localized behavior in $CeNi_{0.8}Pt_{0.2}$ Kondo compound replacing Ce by magnetic ions (Pr,Nd)

J. C. Gómez Sal
Facultad de Ciencias, Universidad de Cantabria, 39005 Santander, Spain

J. A. Blanco
Departamento de Física, Universidad de Oviedo, 33007 Oviedo, Spain

J. I. Espeso and J. Rodríguez Fernández
Facultad de Ciencias, Universidad de Cantabria, 39005 Santander, Spain

D. Gignoux
Laboratoire Louis Néel, CNRS, 166X, 38042 Grenoble Cedex, France

The substitution of Ce by magnetic ions such as Pr or Nd in the $CeNi_{0.8}Pt_{0.2}$ Kondo ferromagnetic compound not only favors the magnetic interactions increasing the Curie temperatures, but also disturbs the coherence of the Kondo lattice state leading to a decrease of the Kondo temperatures and an increase of the Ce intrinsic magnetic moment. These effects have been studied by resistivity, magnetization, and neutron diffraction.

$CeNi_xPt_{1-x}$ is among the cerium-based compounds one of the systems which presents a clear relationship between the cerium state and the cell volume.[1] The orthorhombic CrB-type structure is kept through the whole series from CePt to CeNi. The variation of the cell volume gives rise to changes in the magnetic properties according to the rule "the $4f$-sd conduction-band hybridization increases with decreasing cell volume." The substitution of Ce ions by nonmagnetic Y or La strongly supports this fact.[2] A mostly localized Ce^{3+} behavior is observed for the larger volume compounds (CePt or $Ce_{1-y}La_yNi_xPt_{1-x}$) while CeNi or $Ce_{1-y}Y_yNi_{0.8}Pt_{0.2}$, with smaller volumes, show an enhanced Pauli paramagnetism or Kondo impurity behavior. From CePt, the compounds are Kondo ferromagnets with T_K (Kondo temperature) increasing with the decreasing volume. $CeNi_{0.8}Pt_{0.2}$ is the compound with the largest T_c (Curie temperature) but close to the crossover between the localized and delocalized regime, according to the Doniach diagram.[3]

Recent specific-heat measurements[4] give electronic coefficients γ with a maximum ($\gamma \approx 200$ mJ/K^2 mol) for $CeNi_{0.8}Pt_{0.2}$. The description of C_{mag} and the relative variation of T_K and γ along the series could be interpreted in the framework of an $S=1/2$ resonant level model extended to Kondo lattices using a mean field approach as developed by Bredl, Steglich, and Schotte.[5] Neutron-diffraction studies[6] allowed us a direct estimation of the Ce intrinsic magnetic moment. As can be seen in Fig. 1, the magnetic moment is much smaller than that of the free Ce^{3+} ion ($2.14\mu_B$) and it progressively reduces with the Ni concentration as a consequence of the enhancement of the hybridization, showing the increasing importance of Kondo interactions with the volume decrease. It is worth to mention that the diluted (La or Y) compounds have magnetic moments according to the corresponding volume effects (see Fig. 1).

The substitution of Ce by magnetic atoms such as Pr or Nd must not only produce a decrease of the volume but also have a direct influence on the magnetic interactions. We present here the resistivity, magnetization, and neutron-diffraction studies performed in two diluted compounds: $Ce_{0.9}Pr_{0.1}Ni_{0.8}Pt_{0.2}$ and $Ce_{0.9}Nd_{0.1}Ni_{0.8}Pt_{0.2}$, referred to as (Pr) and (Nd) henceforth. These experiments are compared with the results from the "nondiluted compound" $CeNi_{0.8}Pt_{0.2}$, referred to as (Ce). Resistivity, magnetization, and neutron-diffraction experiments were performed at the Universidad de Cantabria, at the Laboratoire Louis Néel (Grenoble), and on the D1B diffractometer of the ILL (Grenoble), respectively.

We have not observed drastic changes in the general shape of resistivity due to the Pr or Nd substitution (Fig. 2).

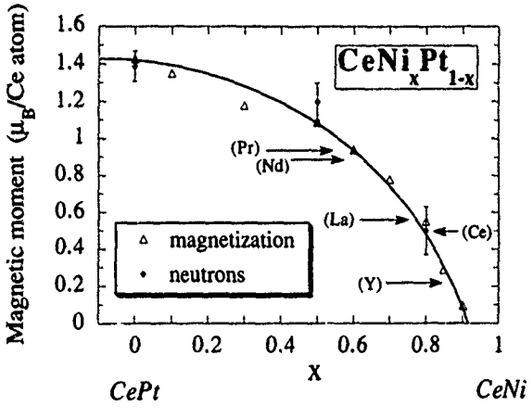

FIG. 1. Magnetic moment of the Ce atoms as a function of the Ni content in the $CeNi_xPt_{1-x}$ series. The moments of the diluted compounds have been situated with arrows pointing to the solid line used as a visual guide.

 0021-8979/94/76(10)/6118/3/$6.00 © 1994 American Institute of Physics

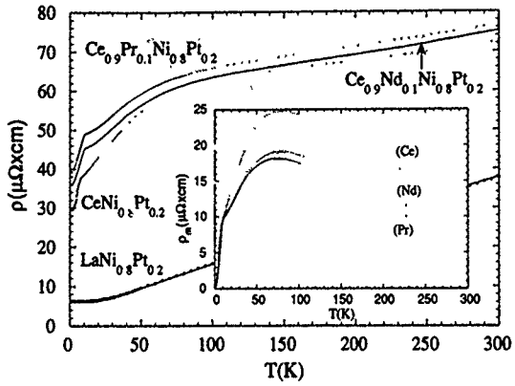

FIG. 2. Thermal variation of the electrical resistivity. Insert: magnetic contribution to the resistivity ρ_m.

The magnetic contributions, obtained by subtraction of the isomorphous $LaNi_{0.8}Pt_{0.2}$ resistivity and a constant residual resistivity term, present a broad maximum attributed to the crystal-field effects which are quite strong in these low-symmetry compounds. The position of the maximum, which is related to the crystal-field-level scheme, does not seem to be very sensitive to the introduction of these small concentrations of Pr and Nd. The negative slope of ρ_{mag} at high temperatures is related to Kondo interactions, being slightly reduced by Nd or Pr substitutions. The Curie temperatures 10.2 and 9.8 K, deduced from the kinks in (Pr) and (Nd) respectively, are slightly higher than that of $CeNi_{0.8}Pt_{0.2}$ (8.6 K) and they coincide with those obtained from the Arrot plots of the magnetization measurements.

The magnetization curves at 1.5 K for the three compounds are presented in Fig. 3. They are characteristic of a ferromagnetic behavior but the (Pr) and (Nd) curves present a notably larger magnetization. At 80 kOe they are far from saturation. The extrapolated values of M ($H=0$, $T=1.5$ K) are 0.28, 0.35, and $0.34\mu_B$/formula for (Ce), (Pr), and (Nd), respectively, thus showing the enhancement of the effective magnetic moment on the rare-earth site. The reciprocal susceptibilities follow a Curie–Weiss law with averaged effec-

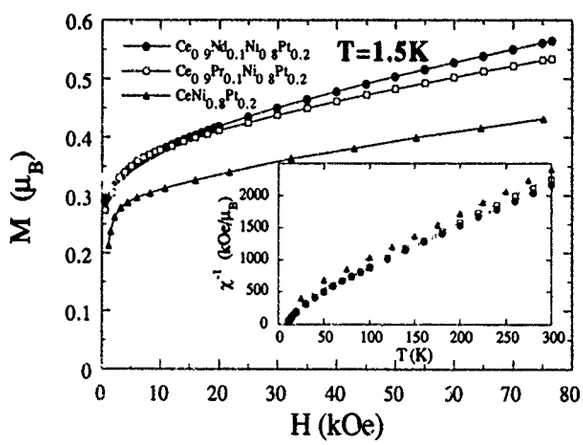

FIG. 3. Magnetization curves at 1.5 K. Insert: thermal dependence of the reciprocal susceptibility.

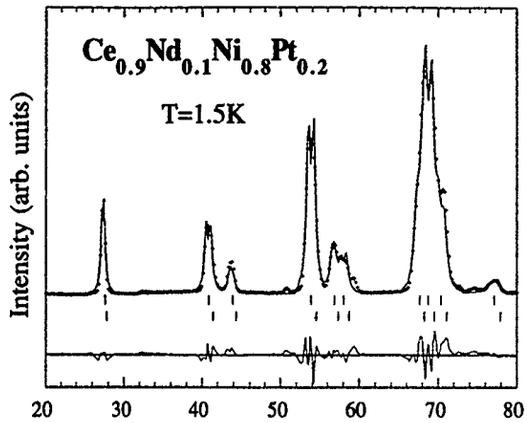

FIG. 4. Rietveld refinements of the neutron-diffraction patterns for $Ce_{0.9}Nd_{0.1}Ni_{0.8}Pt_{0.2}$ at 1.5 K. Vertical marks correspond to the reflexion of the two crystalline observed phases. $Ce_{0.9}Pr_{0.1}Ni_{0.8}Pt_{0.2}$ presents a similar pattern.

tive magnetic moments very close to the Ce^{3+} free-ion value and leading to paramagnetic Curie temperatures. $\theta_p=-49$, -40 K, and -43 K, for (Ce), (Pr), and (Nd), respectively.

The neutron-diffraction patterns (Fig. 4), present the same characteristics of the rest of the series and previous diluted compounds.[6] All of these compounds, prepared in a cold crucible induction furnace and annealed for a few days, present a splitting on the peaks corresponding to the CrB structure. The only way to interpret such diagrams is to consider a kind of spinodal segregation of phases of the same structure with slight differences in the cell parameters. With these hypotheses the Rietveld refinements give quite accurate fits, assuming that Pr or Nd atoms are randomly distributed in the same ($4c$) site occupied by Ce atoms. The obtained crystallographic data are presented in Table I. As expected, we find a slightly smaller volume for (Pr) or (Nd).

The diagrams obtained at 1.5 K (in the ordered range) do not present supplementary new peaks, but only an increase of the intensity of some of them. The magnetic peaks are the same as those detected in other magnetic compounds of this system,[6] corresponding to the same collinear ferromagnetic structure, with the magnetic moments in the c direction. Due to the weak magnetic contributions, the determination of the magnetic structure has been performed from the difference diagrams (1.5–15 K) using the Rietveld method.[7]

The magnetic intensities are noticeably higher for (Pr) or (Nd) than for $CeNi_{0.8}Pt_{0.2}$. In order to estimate the Ce magnetic moment value, we have considered an average magnetic moment $\langle\mu\rangle=0.9\mu_{Ce}+0.1\mu_{(Pr\text{ or }Nd)}$ in each rare-earth ($4c$) site, taking $\mu_{Pr}=3.20\mu_B$ and $\mu_{Nd}=3.27\mu_B$ which correspond to the free-ion values $\mu=g_J J\mu_B$. Then, the only parameter to be fitted is the μ_{Ce} value. The magnetic rare-earth form factors were taken from Ref. 8. The obtained values must be considered just as an estimate which gives a minimum limit for the cerium intrinsic moment, because we have not considered the crystal-field effects on Nd and Pr. For example, in the isomorphous NdNi compound, the crystal field reduces the Nd magnetic moment to $2.7\mu_B$.[9] We obtain $0.92\pm0.05\mu_B$ for (Pr) and $0.89\pm0.05\mu_B$ for (Nd). These val-

TABLE I. Crystallographic and magnetic data.

	V (Å^3)	Phase %	Average V (Å^3)	R_{Bragg} (%)	T_c (K)	μ (μ_B/Ce atom)	R_{mag} (%)
	178.7	52.0		4.8			
(Ce)	----------		175.2	----------	8.6	0.50(5)	18.2
	171.3	48.0		6.6			
	178.1	42.7		4.8			
(Pr)	----------		174.7	----------	10.2	0.92(5)	12.2
	172.2	57.3		4.9			
	178.7	44.1		4.9			
(Nd)	----------		174.4	----------	9.8	0.89(5)	19.6
	171.3	55.9		5.6			

ues are much larger than that found for $CeNi_{0.8}Pt_{0.2}$ ($0.5\pm0.05\mu_B$). These moments are indicated by arrows over the general trend presented in Fig. 1.

From all of these data we can deduce that the introduction of 10% of Pr and Nd atoms in the $CeNi_{0.8}Pt_{0.2}$ Kondo ferromagnet enhances the exchange Ruderman–Kittel–Kasuya–Yoshida interactions leading to a noticeably increase of the Curie temperatures and very slight modifications of the crystal-field scheme.

If we only take into account the very small volume decrease caused by the Pr or Nd introduction, it should be expected an enhancement of the hybridization; however, it is clear from our results that the Kondo interactions are reduced. The experimental results that support this assertion are: (i) the decrease of the absolute value the paramagnetic Curie temperatures, which are related to T_K; (ii) the higher values of the magnetization, at 80 kOe for (Pr) and (Nd) (see Fig. 3); (iii) above all, the noticeable increase of the Ce intrinsic magnetic moments found in (Pr) and (Nd) by neutron diffraction (see Table I).

Figure 1 has been used to illustrate the effects of the different dilutions. On one hand, the substitution of Ce by nonmagnetic ions, $Ce_{0.8}La_{0.2}Ni_{0.8}Pt_{0.2}$ and $Ce_{0.8}Y_{0.1}Ni_{0.8}Pt_{0.2}$, leads to magnetic moments higher and lower than that of $CeNi_{0.8}Pt_{0.2}$, according to the volume effects. And, on the other hand, the Ce magnetic moment changes appearing with the introduction of Pr and Nd magnetic ions are opposite to those expected by pure volume effects.

The present results show that the dilution of Ce by magnetic atoms disturbs the coherence of the Kondo lattice state increasing the magnetic interactions and favoring the tendency to a localized behavior of the Ce ions. This is not the case of Y nonmagnetic dilutions for which a clear tendency to the delocalized behavior was observed. This means that the Kondo lattice behavior needs to be understood not only as a consequence of the large $4f$-sd conduction-band hybridization but also as a cooperative phenomenon of coherence between the Ce magnetic ions.

This work was supported by Spanish CICYT (MAT93-0691).

[1] D. Gignoux and J. C. Gómez Sal, J. Appl. Phys. **57**, 3125 (1985).
[2] J. M. Barandiarán, J. A. Blanco, D. Gignoux, J. C. Gómez Sal, J. Rodríguez Fernández, and J. Voiron, J. Magn. Magn. Mater. **90 & 91**, 145 (1990).
[3] S. Doniach, in *Valence Instabilities and Related Narrow Band Phenomena*, edited by R. D. Parks (Plenum, New York, 1976), p. 169.
[4] J. A. Blanco, M. de Podesta, J. I. Espeso, J. C. Gómez Sal, C. Lester, M. A. McEwen, M. Patrikios, and J. Rodríguez Fernández, Phys. Rev. B **49**, 15126 (1994).
[5] C. D. Bredl, F. Steglich, and K. D. Schotte, Z. Phys. B **29**, 327 (1978).
[6] J. C. Gómez Sal, J. I. Espeso, J. Rodríguez Fernández, J. A. Blanco, and J. Rodríguez Carvajal, Solid State Commun. **87**, 863 (1993).
[7] J. Rodríguez Carvajal, FULLPROF: A program for Rietveld Refinement and Pattern Matching Analysis (Abstracts of the Satellite Mett. 15th Congress of the International Union of Crystallography, Tolouse, 1991), p. 127.
[8] C. Stassis, H. W. Deckman, B. N. Harman, J. P. Desclaux, and A. J. Freeman, Phys. Rev. B **15**, 369 (1977).
[9] R. Lemaire and D. Paccard, in Les Elements des Terres Rares, (edited by CNRS, Paris, 1970), Vol. 2, p. 231.

Low-temperature phase diagram of YbBiPt

R. Movshovich, A. Lacerda, P. C. Canfield,[a] J. D. Thompson, and Z. Fisk[b]
Los Alamos National Laboratory, Los Alamos, New Mexico 87545

Resistivity measurements are reported on the cubic heavy-fermion compound YbBiPt at ambient and hydrostatic pressures to ≈19 kbar and in magnetic fields to 1 T. The phase transition at T_c=0.4 K is identified by a sharp rise in resistivity. That feature is used to build low-temperature H-T and P-T phase diagrams. The phase boundary in the H-T plane follows the weak-coupling BCS expression remarkably well from T_c to $T_c/4$, while small hydrostatic pressure of ≈1 kbar suppresses the low-temperature phase entirely. These effects of hydrostatic pressure and magnetic field on the phase transition are consistent with an spin-density-wave (SDW) formation in a very heavy electron band at T=0.4 K. Outside of the SDW phase at low temperature, hydrostatic pressure increases the T^2 coefficient of resistivity, signaling an increase in heavy-fermion correlations with hydrostatic pressure. The residual resistivity decreases with pressure, contrary to trends in other Yb heavy-fermion compounds.

Interest in the compound YbBiPt has been sparked by the very large coefficient of the linear-in-temperature contribution to the heat capacity, γ=8 J/mol K^2, that develops at low temperatures.[1] If a substantial part of that heat capacity is due to the heavy-fermion nature of the ground state, that value of γ makes YbBiPt the "heaviest" fermion compound known to date. Inelastic neutron scattering[2] suggests that some fraction of this large γ may be due to the existence of low-lying crystal-field excitations; however, separation of these and intrinsic heavy-fermion contributions has not been possible. The heat capacity data also revealed a phase transition at 0.4 K as a small, but rather sharp, peak in the C vs T curve. It is the nature of that transition that is the subject of this article, together with the clues it may provide to the properties of the ground state of the system. To address these questions we have studied the electrical resistivity as a function of pressure and applied magnetic fields and we argue that these results are consistent with the development of a spin-density wave (SDW) below 0.4 K in a heavy-mass band of conduction electrons.

Single-crystal samples of YbBiPt were grown from an excess Bi flux.[3] X-ray diffraction confirms the samples to be face-centered cubic with the half-Heusler structure at room temperature. Neutron diffraction shows no evidence for a structural transition to 27 K.[2] Resistance measurements were made in standard four-probe and Montgomery[4] configurations. Pressure was generated in a self-clamping Be-Cu cell with Fluorinert FC-75 as the hydrostatic pressure medium. The pressure at low temperatures was established from the shift in the superconducting transition of a piece of high-purity lead mounted near the sample.

Results of four-probe ac resistivity measurements under hydrostatic pressure below ≈4 kbar are displayed in Fig. 1 for the rod-shaped sample in which the current flow was close to being parallel to the (100) crystallographic direction. Data for P=0 kbar curve show a sharp kink at T=0.4 K. The rise in resistivity below T_c suggests a decrease in the number of conduction electrons that could arise from partial gapping of the Fermi surface. Combination of this effect and the magnetic nature of the transition[1] suggests SDW as a candidate for the nature of T=0.4 K transition. The curve at P=0.78 kbar displays similar behavior, with the transition temperature shifted very slightly downward; however, application of 1.20 kbar suppresses any resistive signature for the low-temperature phase transition. The inset in Fig. 1 shows the P-T phase diagram, with data points identified from the kinks in the resistivity curves, as in Fig. 1, as function of pressure. The point at P=0.84 kbar is obtained from a curve not shown in the Fig. 1. The dashed line represents the approximate pressure above which there is no resistive signature for a phase transition. The dotted line through the data points corresponds to the pressure dependence of the transition temperature of $(dT_c/dP)_{P\to 0}$=−14 mK/kbar. The behavior of the transition temperature is highly nonlinear, and

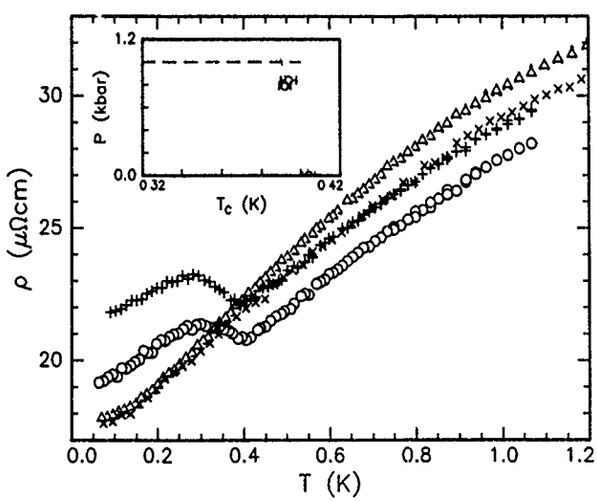

FIG. 1. Resistivity of a single-crystal rod-shaped sample of YbBiPt under hydrostatic pressure: (○) 0 kbar; (+) 0.78 kbar; (×) 1.20 kbar; (△) 3.92 kbar. Inset: transition temperature T_c vs applied hydrostatic pressure, obtained from the kinks in curves shown in the main body of the figure. Dashed line: approximate pressure that suppresses the low-temperature phase. Dotted line passes through the data points, with a slope $(dT_c/dP)_{P\to 0}$=−14 mK/kbar. The low-temperature phase is suppressed by pressure between 0.84 and 1.20 kbar.

[a]Present address: Ames Laboratory/Iowa State University, Ames, IA 50011.
[b]Present address: Florida State University, Tallahassee, FL 32306.

 0021-8979/94/76(10)/6121/3/$6.00 © 1994 American Institute of Physics

very strong. Hydrostatic pressure has been an important tool for investigating the SDW transition in Cr. The transition temperature is suppressed rapidly by pressure, at the rate of $(dT_N/dP)_{P\to 0}=-5.1$ K/kbar.[5] Such a strong dependence on pressure is seen as a consequence of the delicate Fermi surface nesting that results in a SDW transition. The high sensitivity to relatively small pressure on the order of 1 kbar is consistent with the 0.4 K transition in YbBiPt being due to a Fermi surface instability. Extending the analogy with Cr,[6] analysis of data similar that of Fig. 1 for $P=0$ kbar (Ref. 7) results in a value for a weak-coupling SDW gap of $\Delta(T=0)/k_BT_c=1.65\pm0.15$. This is close to the minimum value of 1.764 for the two-band model of itinerant antiferromagnetism.[8] For comparison, in Cr it was found[6] that $\Delta(T=0)/k_BT_N=2.3$.

To further investigate this transition we performed a series of resistance measurements in a magnetic field. The two samples used were of a "Montgomery type," thin square platelets, each oriented to have one pair of long edges along the magnetic field. Both samples displayed anisotropic resistivity,[7] and the direction of the largest increase in V/I was longitudinal for one of the samples and transverse for the other. One reason for choosing such a geometry was the expectation that magnetic field might reorient the SDW domains with different order parameters, as was demonstrated for Cr,[9] and produce a single-domain sample. In one of the samples we indeed observed a small downward kink in V/I, in the direction which had a larger resistivity at zero field, while sweeping temperature at a fixed field of 2.5 kG. This would imply that reversal of the direction of the larger resistivity has taken place. However, temperature sweeps in fields greater than 2 kG are increasingly difficult since the phase boundary of the low-temperature phase becomes rather independent of temperature, as described below.

Figure 2(a) displays results of temperature sweeps for one of the samples described above in which the excitation current was transverse to magnetic field. The phase transition temperature is easily identified by sharp kink in V/I. Figure 2(b) shows V/I at 350 mK for the same sample but with the current flow parallel to the applied field. We identify the sharp kink at 2.1 ± 0.1 kG in the derivative with respect to H as the transition magnetic field for that temperature. This identification is consistent with the results of the temperature sweep at 2 kG, which gives a transition temperature of 350 ± 10 mK. Similar identifications were then made for magnetic field sweeps at 100 and 200 mK.

Figure 3 displays the resulting magnetic-field temperature phase diagram for the low-temperature phase of YbBiPt. The solid curve is the functional dependence of the BCS energy gap scaled to pass through the points $T_c=0.4K$, $H=0$ on the x axis and $T=0$, $H=3.1$ kG on the y axis. The curve fits the data very well, indicating the weak-coupling nature of the transition in the whole temperature range studied. In contrast to Cr, in which T_N is independent of magnetic fields up to $H=16$ T,[10] YbBiPt follows mean field behavior expected of an itinerant antiferromagnetism.

We now turn our attention to the resistive behavior of YbBiPt at pressures sufficiently high that evidence for a phase transition is not found. Figure 4 shows the

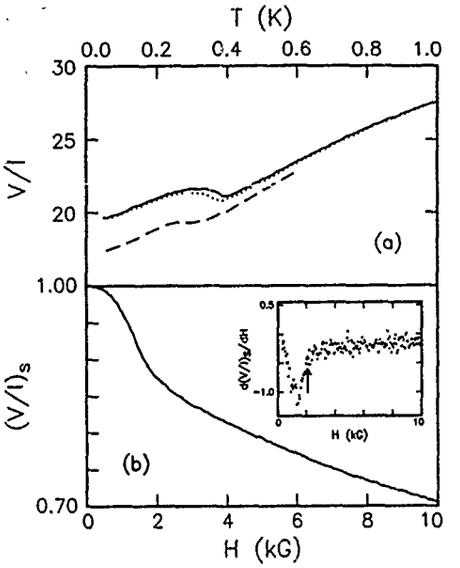

FIG. 2. (a) Temperature sweeps at constant magnetic field: (solid line) $H=0$ kG; (dotted line) $H=1$ kG; (dashed line) $H=2$ kG. Kinks in V/I curves are taken as signaling transition temperatures for given fields. (b) Magnetic-field sweep at a constant temperature of $T=350$ mK, $(V/I)_s=(V/I)/[V/I(H=0)]$. Inset: derivative of the curve shown in (b). The sharp kink indicated by the arrow at a field $H=2.1\pm0.01$ kG represents the phase transition at $T=350$ mK.

temperature-dependent resistivity at pressures between ≈4 and 19 kbar. Data for all curves can be fit very well by $\rho(T)=\rho_0+AT^2$ below $T=300$ mK, as expected for a Fermi liquid. In this Fermi liquid regime $\sqrt{A}$ was shown[11] to be proportional to γ for a large number of Ce and U heavy-fermion compounds. The inset in Fig. 4 shows A as a function of pressure and indicates an increase in the heavy-fermion correlations with pressure. Similar systematics with pressure are observed in other Yb heavy-fermion compounds.[12] The decrease of the residual resistivity ρ_0 with

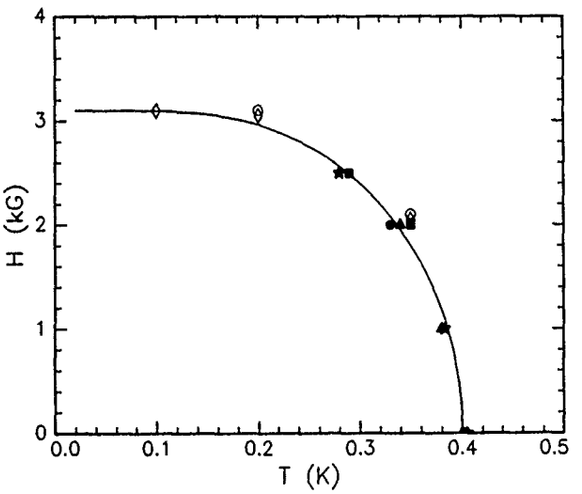

FIG. 3. Magnetic-field temperature phase diagram for the low-temperature phase of YbBiPt. The solid and open symbols are results of the temperature and magnetic field sweeps, respectively. The solid line is a BCS curve fixed by the points $H,T=0$ and $H=0$, T_c.

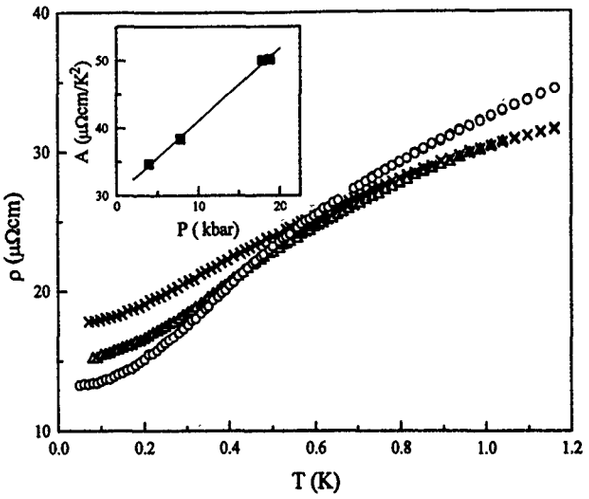

FIG. 4. Resistivity of YbBiPt in the high-pressure phase: (O) 18.79 kbar; (△) 7.83 kbar; (×) 3.92 kbar. Inset: T^2 coefficient of $\rho(T)$ vs pressure; straight line is a guide to the eye.

pressure, however, is rather anomalous. In other Yb compounds the residual resistivity increases with pressure, possibly reflecting its Kondo hole origin.[13] The decrease of ρ_0 with pressure in YbBiPt may be due to purely band-structure effects. The REBiPt series (RE is an element of the rare-earth series) exhibits a systematic progression from small gap semiconductor in Nd to metallic behavior in Yb,[14] as the RE series is traversed from the left- to right-hand side, i.e., as the size of the RE ion diminishes. Pressure would reduce the volume of the unit cell of YbBiPt even further, possibly increasing the carrier density and reducing resistivity.

In summary, the phase boundary in the H-T plane of the low-temperature state of YbBiPt follows the weak coupling BCS-like expression expected of an SDW transition. This identification is supported further by the extreme pressure dependence of the transition temperature, with the low-temperature phase being suppressed by pressures of ≈1 kbar. Above that pressure-induced transition, the heavy-fermion nature of YbBiPt appears to be enhanced further with increased pressure. We suggest that investigating YbBiPt at higher pressures yet may yield interesting information on a transition regime between heavy-fermion and antiferromagnetic behaviors.

We want to thank Dr. Günter Sparn for help with constructing apparatus and Dohn Arms for writing some of the software. We also acknowledge Dr. S. A. Trugman, Dr. Ward Beyerman, Dr. H. R. Ott, Dr. L. P. Gorkov, and Dr. A. J. Millis for stimulating discussions. Special thanks go to Dr. Alexander Balatsky for numerous discussions of data. Work at Los Alamos was performed under the auspices of the U.S. Department of Energy.

[1] Z. Fisk, P. C. Canfield, W. P. Beyerman, J. D. Thompson, M. F. Hundley, H. R. Ott, E. Felder, M. B. Maple, M. A. Lopez de la Torre, P. Visani, and C. L. Seaman, Phys. Rev. Lett. **23**, 3310 (1991).
[2] R. A. Robinson, M. Kohgi, T. Osakabe, P. C. Canfield, T. Kamiyama, T. Nakane, Z. Fisk, and J. D. Thompson, Physica B **186-188**, 550 (1993); R. A. Robinson (unpublished).
[3] P. C. Canfield and Z. Fisk, Philos. Mag. B **65**, 1117 (1992).
[4] H. C. Montgomery, J. Appl. Phys. **42**, 2971 (1971).
[5] T. Mitsui and C. T. Tomizuka, Phys. Rev. **137**, A564 (1965).
[6] D. B. McWhan and T. M. Rice, Phys. Rev. Lett. **19**, 846 (1967).
[7] R. Movshovich, A. Lacerda, P. C. Canfield, J. D. Thompson, and Z. Fisk (to be published).
[8] P. A. Fedders and P. C. Martin, Phys. Rev. **143**, 245 (1966).
[9] W. B. Muir and J. O. Ström-Olsen, Phys. Rev. B **4**, 988 (1971).
[10] Z. Barak, E. Fawcett, D. Feder, G. Lorincz, and M. B. Walker, J. Phys. F **11**, 915 (1981).
[11] K. Kadowaki and S. B. Woods, Solid State Commun. **58**, 307 (1986).
[12] J. D. Thompson, H. A. Borges, Z. Fisk, S. Horn, R. D. Parks, and G. L. Wells, in *Theoretical and Experimental Aspects of the Valence Fluctuations and Heavy Fermions*, edited by L. C. Gupta and S. K. Malik (Plenum, New York, 1987), p. 151.
[13] T. Graf, J. M. Lawrence, and J. D. Thompson (private communication).
[14] P. C. Canfield, J. D. Thompson, W. P. Beyerman, A. Lacerda, M. F. Hundley, E. Peterson, and Z. Fisk, J. Appl. Phys. **70**, 5800 (1991).

Quadrupolar effects in $PrCu_2Si_2$

R. Osborn
Materials Science Division, Argonne National Laboratory, Argonne, Illinois 60439-4845

E. A. Goremychkin[a)]
ISIS Science Division, Rutherford Appleton Laboratory, Chilton, Didcot, Oxon, OX11 0QX, United Kingdom

As part of a systematic study of the crystal-field (CF) potential in RCu_2Si_2 compounds (R=Ce, Pr, Nd, Tb, Ho, Er) using inelastic neutron scattering, the CF level scheme and potential in the antiferromagnet $PrCu_2Si_2$ both above and below T_N has been determined. There have been recent speculations that the quadrupole moment of $PrCu_2Si_2$ has been quenched by the quadrupolar Kondo effect. Using the CF potential derived from the results, the quadrupole moment Q_2 of $PrCu_2Si_2$ has been calculated and it has been compared to the other members of the RCu_2Si_2 series. The temperature dependence of the quadrupole moment of $PrCu_2Si_2$ is significantly weaker than all the other compounds, e.g., it is approximately five times smaller than in $HoCu_2Si_2$. Therefore, it is the CF potential which is responsible for quenching Q_2 at low temperature rather than a quadrupolar Kondo effect. Furthermore, the CF Schottky contribution to C/T vs T^2 is approximately linear above T_N and explains the anomalously high linear term in the specific heat. However, the evolution of the CF potential across the rare-earth series provides evidence of an enhanced hybridization contribution to the CF potential of $PrCu_2Si_2$, intermediate between the heavy fermion $CeCu_2Si_2$ and the other rare-earth compounds.

I. INTRODUCTION

There has been considerable interest in f-electron systems, particularly uranium alloys such as $U_{0.2}Y_{0.8}Pd_3$ (Refs. 1 and 2) and $UCu_{3.5}Pd_{1.5}$,[3] displaying non-Fermi liquid scaling of their thermodynamic properties at low temperatures. One possible microscopic mechanism to explain these observations is the $N=2$ multichannel Kondo effect produced by orbital scattering of the conduction electrons.[4] This quadrupolar Kondo effect is expected to quench the local quadrupole moment of the f electrons just as the single-channel Kondo effect screens the local magnetic moment and suppresses magnetic ordering. It has recently been proposed that anomalies in the thermodynamic and structural properties of $PrCu_2Si_2$ and related isostructural compounds might also be evidence of quadrupolar Kondo interactions.[5,6] The extrapolation of C/T vs T^2, measured in the paramagnetic phase of $PrCu_2Si_2$ (T_N=21 K), to T=0 appears to give evidence for a large electronic contribution to the specific heat with γ=225 mJ mol^{-1} K^{-2}.[6] Since there is no evidence of conventional Kondo-like behavior in the magnetic susceptibility or resistivity, there has been speculation that quadrupolar Kondo scattering is responsible for the high γ. This suggestion is given further weight by the absence of a c/a lattice anomaly at low temperatures, comparable to those seen in all the other RCu_2Si_2 (R denotes rare earth) compounds, implying that the Pr^{3+} quadrupole moment has been quenched.

When the anomalous properties of $PrCu_2Si_2$ were first reported, it was pointed out that a knowledge of the crystal-field (CF) potential is essential to assess the validity of these ideas.[6] Apart from making a substantial contribution to the thermodynamic properties, the CF also determines the f-electron wave functions, in the absence of strong hybridization, and consequently the quadrupole moment. We have been conducting a systematic investigation of the magnetic properties of RCu_2Si_2 compounds using neutron diffraction and inelastic neutron scattering.[7–10] Inelastic neutron scattering (INS) is the most reliable method of determining the CF potential in intermetallic compounds since it measures directly the energies and dipole matrix elements of transitions between CF levels. One aim of our work is to measure the CF potential across the rare-earth series in order to determine whether the CF in the heavy-fermion compound $CeCu_2Si_2$ is anomalous compared to the "normal" rare-earth compounds. We have now established the CF parameters for R=Ce, Pr, Nd, Tb, Ho, and Er and discuss some of the consequences of these results here with particular reference to the praseodymium compound. Full details of this work will be published in Ref. 9.

II. EXPERIMENTAL RESULTS

The samples were prepared by arc melting stoichiometric quantities of the constituent elements, with no measurable weight loss. After annealing at 700 °C, nearly all peaks observed in neutron-diffraction measurements could be indexed with the $ThCr_2Si_2$-type structure and only a few very weak reflections in the light rare earths indicated minor contamination by other phases. The INS measurements were performed at the pulsed spallation neutron source ISIS (Rutherford Appleton Laboratory, U.K.) on the time-of-flight chopper spectrometer HET, using incident energies between 10 and 60 meV, and on the high-resolution inverse geometry spectrometer IRIS to resolve low-energy transitions.

The rare-earth ions in RCu_2Si_2 occupy sites with tetragonal point group symmetry. In the paramagnetic phase, the appropriate CF Hamiltonian is

$$H_{CF}=B_2^0O_2^0+B_4^0O_4^0+B_4^4O_4^4+B_6^0O_6^0+B_6^4O_6^4 \quad (1)$$

[a)]On leave from: I. M. Frank Laboratory of Neutron Physics, Joint Institute for Nuclear Research, Dubna, Head Post Office, P.O. Box 79, Moscow, Russia, CIS.

 0021-8979/94/76(10)/6124/3/$6.00 © 1994 American Institute of Physics

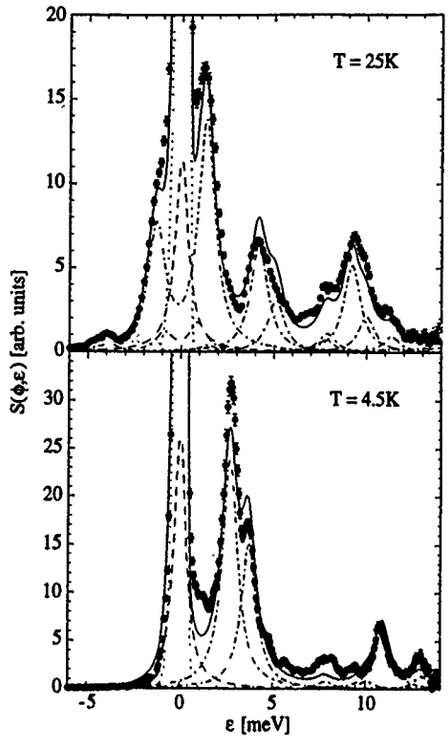

FIG. 1. Neutron inelastic scattering from $PrCu_2Si_2$ measured at 4.5 and 25 K on HET with an incident energy of 15 meV integrated over scattering angles of 9°–29°. The solid line is the profile of the crystal-field model described in the text including Lorentzian broadening and, at 4.5 K, a molecular field. The dashed line is the quasielastic scattering, the dashed-dotted lines are the inelastic transitions, and the dotted line is the elastic nuclear scattering.

where O_n^m are the Steven's operator equivalents and B_n^m are the phenomenological CF parameters. The influence of antiferromagnetic ordering on the excitation spectrum has been taken into account in the molecular-field approximation. An example of the HET spectra on $PrCu_2Si_2$, measured both above and below T_N, with an incident energy of 15 meV and summed over scattering angles from 9° to 29°, is shown in Fig. 1. The spectra taken at 136°, where the nuclear scattering is strongest, show that the phonon contribution in this energy range is negligible at low angles, so the observed peaks are all magnetic.

The solid lines in Fig. 1 are the results of a profile refinement of the CF model after establishing the approximate CF parameters using a comprehensive stepwise search. The resulting parameters are $B_2^0=-(6.28\pm0.15)\times10^{-2}$ meV, $B_4^0=(1.48\pm0.15)\times10^{-3}$ meV, $B_6^0=(5.27\pm0.07)\times10^{-5}$ meV, $B_4^4=(2.24\pm0.06)\times10^{-2}$ meV, and $B_6^4=-(3.80\pm0.03)\times10^{-4}$ meV, and the corresponding level scheme in the paramagnetic phase is shown in Fig. 2. The INS spectrum measured at 4.5 K shows that the molecular field H_{mf} changes the level splittings, energies, and transition probabilities significantly in the antiferromagnetic state. Nevertheless, it was fitted using the same CF parameters as in the paramagnetic phase with $H_{mf}=(10.4\pm0.6)$ T. Therefore, the CF model describes the measured profiles reasonably well both above and below T_N with some discrepancies due probably to the use of a common linewidth for all the transitions and to the neglect of

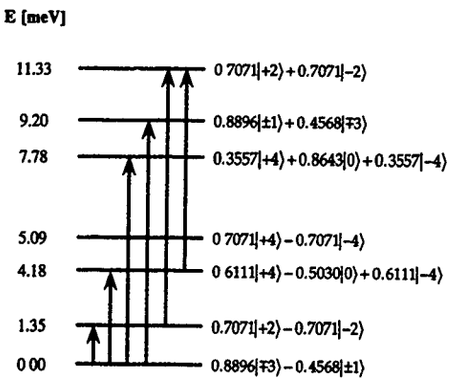

FIG. 2. Energy-level scheme for $PrCu_2Si_2$ in the paramagnetic phase with the crystal-field parameters given in the text. The arrows mark the dipole-allowed transitions.

dispersion in the antiferromagnetic state. We have performed similar analyses for the other rare-earth compounds. In each case, the CF potential was determined without ambiguity with the possible exception of $TbCu_2Si_2$ where the transitions are not well enough resolved to guarantee a unique solution.

III. DISCUSSION

As we stated in Sec. I it has been proposed that $PrCu_2Si_2$ shows unconventional (quadrupolar Kondo) heavy-fermion behavior.[5] One immediate result of our CF analysis is to explain the apparently high value of γ. The calculated CF contribution, consisting of a number of overlapping Schottky peaks, is approximately linear in C/T vs T^2 for about 20 K above T_N and extrapolates to the value 282 mJ mol^{-1} K^{-2} at $T=0$. Once this Schottky contribution has been subtracted, C/T is close to zero within the uncertainties of this analysis so there is no evidence of an enhanced electronic contribution to the specific heat. A second result is to explain the absence of the lattice anomaly at low temperatures. Figure 3 shows the calculated temperature dependence of the quadrupole moments $Q_2=\frac{1}{2}\alpha_J\langle O_2^0\rangle$ of RCu_2Si_2 using the measured CF parameters. Q_2 is proportional to the size of the lattice anomaly assuming the magnetoelastic coupling is linear in

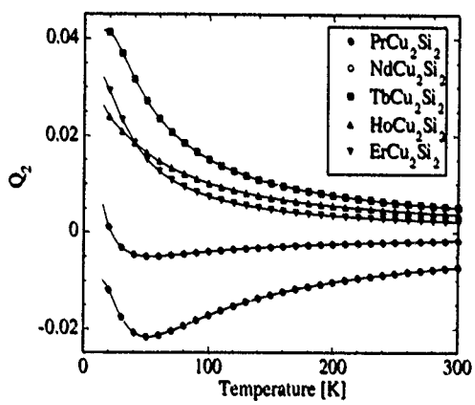

FIG. 3. Temperature dependence of the quadrupole moment Q_2 of RCu_2Si_2 compounds (R=Pr,Nd,Tb,Ho,Er).

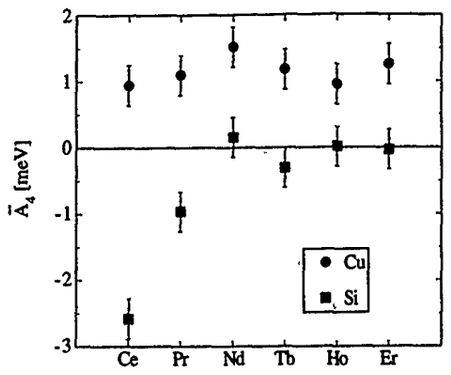

FIG. 4. Superposition model parameters $\tilde{A}_4$(Cu) and $\tilde{A}_4$(Si) for RCu_2Si_2 compounds (R=Pr,Nd,Tb,Ho,Er) assuming A_4^4 and A_6^4 are positive.

the tetragonal strain.[11] Although the absolute value of Q_2 in $PrCu_2Si_2$ at room temperature is slightly greater than the heavy rare earths, its temperature dependence is much weaker. For example, its variation between 300 and 20 K is five times weaker than in $HoCu_2Si_2$ making any attendant lattice anomaly difficult to see. Since the quadrupole moment of the CF ground state in $PrCu_2Si_2$ is relatively small, the increase in Q_2 is suppressed as the excited CF levels are depopulated. Therefore, it is the CF potential which reduces Q_2 at low temperature, not a quadrupolar Kondo effect. Nevertheless, the size of T_N indicates that orbital exchange contributions may be necessary to explain the scale of magnetic interactions in $PrCu_2Si_2$.[10,12]

Analyzing the CF potential in the framework of the superposition model (SM) allows a direct comparison of the different ligand contributions in the RCu_2Si_2 compounds. A detailed discussion of the use of this model is given in Refs. 7 and 8. Here we discuss briefly the systematics of this analysis across the rare-earth series. There is an ambiguity about the relative signs of B_4^4 and B_6^4 but both solutions show a systematic evolution of the two ligand contributions, $\tilde{A}_4$(Cu) and $\tilde{A}_4$(Si), to the CF potential with a substantial increase in the magnitude of the silicon term and a smaller decrease in the magnitude of the copper term. We discuss in Ref. 7 our reasons for favouring positive values of A_4^4 and A_6^4 and show these results in Fig. 4 ($B_n^m = \theta_n A_n^m \langle r^n \rangle$ where θ_n are the Steven's factors and $\langle r^n \rangle$ are the $4f$ radial integrals). In $NdCu_2Si_2$ and the heavy rare earths, the silicon contribution is small in comparison with the copper contribution which is nearly constant across the series. However, a large negative silicon contribution has developed in $CeCu_2Si_2$ indicating an enhanced hybridization between the rare-earth $4f$ electrons and the Si s-p orbitals. The SM analysis does therefore show evidence of the same hybridization in $PrCu_2Si_2$ but on a substantially reduced scale.

IV. CONCLUSION

Our solution of the CF potential of $PrCu_2Si_2$ shows that the anomalous thermodynamic and structural properties observed in earlier investigations can be understood in the framework of a conventional f-electron system split by the crystal field. Both the enhanced linear term in the specific heat and the apparent quenching of the Pr^{3+} quadrupole moment are reproduced by our CF model. However, the expanded radial wave functions of the f electrons, compared to the heavier rare earths, are reflected in an enhanced hybridization contribution to the CF potential by the silicon ligands as earlier observed in $CeCu_2Si_2$.

ACKNOWLEDGMENTS

This work is supported by the U.S. Department of Energy, Basic Energy Sciences—Materials Sciences, under Contract No. W-31-109-ENG-38. E.A.G. would like to acknowledge the financial support and hospitality of the Rutherford Appleton Laboratory.

[1] C. L. Seaman, M. B. Maple, B. W. Lee, S. Ghamaty, M. S. Torikachvili, J.-S. Kang, L. Z. Liu, J. W. Allen, and D. L. Cox, Phys. Rev. Lett. **67**, 2882 (1991).
[2] B. Andraka and A. M. Tsvelik, Phys. Rev. Lett. **67**, 2886 (1991).
[3] B. Andraka and G. R. Stewart, Phys. Rev. B **47**, 3208 (1993).
[4] D. L. Cox, Phys. Rev. Lett. **59**, 1240 (1987).
[5] E. V. Sampathkumaran and I. Das, Physica B **186-188**, 328 (1993).
[6] E. V. Sampathkumaran, I. Das, R. Vijayaraghavan, K. Hirota, and M. Ishikawa, Solid State Commun. **78**, 971 (1991).
[7] E. A. Goremychkin and R. Osborn, Phys. Rev. B **47**, 14 280 (1993).
[8] E. A. Goremychkin, A. Yu. Muzychka, and R. Osborn, Physica B **179**, 184 (1992).
[9] E. A. Goremychkin, A. Yu. Muzychka, R. Osborn, J. B. Forsyth, and E. Lidström (unpublished).
[10] E. A. Goremychkin, R. Osborn, and A. Yu. Muzychka (unpublished).
[11] N. Rüssmann, H. U. Häfner, and D. Wohlleben, in *International Conference on Crystalline Electric Field Effects in f-Electron Magnetism*, Wroclaw, Poland, 1981, edited by R. P. Guertin, W. Suski, and Z. Zolnierek (Plenum, New York, 1982), p. 333.
[12] M. Giraud, P. Morin, and D. Schmitt, J. Magn. Magn. Mater. **52**, 41 (1985).

Published without author corrections

Mixed valence in a generalized Hubbard model

A. N. Kocharian[a] and G. R. Reich
Physics Department, Union College, Schenectady, New York 12308

A generalized Hubbard model involving two kinds of spinless fermions with different masses is proposed to explain the properties of mixed-valence compounds. An equivalence between the proposed model and an effective anisotropic antiferromagnetic Heisenberg model with external field is established in the strong-interaction limit. The ground-state energy and partition function are obtained analytically using generalized mean field theory which, for bipartite lattices, allows the system to be reduced to an equivalent two-site problem. The analytic behavior of the valence and compressibility under variation of pressure and the phase diagram in the ground state and at finite temperature are investigated. The conditions for a first-order transition depending on the position of the f band are obtained, taking into account the effect of local hybridization between the s and f states. The known anomalies in the behavior of n_f and χ in mixed-valence systems are interpreted in analogy with the magnetization and susceptibility in the corresponding pseudospin model.

Many phenomena in heavy-fermion compounds, high-T_c superconductors, quantum crystals, etc. have been modeled either with a single-band Hubbard model[1] or a spinless Falicov–Kimball (FK) (or closely related) model.[2–4] These models are also often used to explain phase diagram anomalies and interesting valence behavior in mixed-valence compounds under change of temperature and pressure (see, e.g., Ref. 5). Aside from some details of electron structure these two models can be studied together as particular cases of a more general model (GM),

$$H_{\mathrm{GM}}=-t_1\sum_{\langle ij\rangle} c_{i\uparrow}^{+}c_{j\uparrow}-t_2\sum_{\langle ij\rangle} c_{i\downarrow}^{+}c_{j\downarrow}+U\sum_{i} c_{i\uparrow}^{+}c_{i\uparrow}c_{i\downarrow}^{+}c_{i\downarrow}$$

$$-\frac{H}{2}\sum_{i}(c_{i\uparrow}^{+}c_{i\uparrow}-c_{i\downarrow}^{+}c_{i\downarrow}), \tag{1}$$

which includes hopping terms and intrasite repulsion ($U>0$) for two different kinds of particles. For $t_1=t_2$ it is, of course, a Hubbard model with an applied magnetic field. Although Eq. (1) is written in the language of electron creation operators with spin indices, an equivalent Hamiltonian could be written using band or orbital indices, as in the FK model. In other words, the $c_{\uparrow}^{+}$, $c_{\downarrow}^{+}$ operators in Eq. (1) can be replaced with creation operators f^{+}, a^{+} representing spinless fermions in the f and s bands. The field strength H in this case represents the energy difference between the centers of the two bands, which in mixed-valence materials can be changed with pressure. For $t_1=0$, this is equivalent to the FK model. In the strong interaction limit $U\to\infty$ the GM reveals some interesting relations between the two models, and helps to explain the connections between such phenomena as superfluity and excitonic insulators, antiferromagnetism (or charge-density waves) and valence-density waves, ferromagnetism, and pure integer valency. In addition, viewed as a generalization of the FK model there are significant advantages to using Eq. (1) for describing mixed-valence compounds. In the pure FK model, for example, mixed-valence states can appear only as a spatially periodic lattice of ions,[4] with $n_f=0$ or 1, a kind of orbital antiferromagnetism. The generalized model, however, also permits a liquidlike state of uniform, noninteger valence, as has been seen experimentally,[5] and it correctly predicts the first-order transitions seen in those materials under change of temperature and pressure.

It is convenient to rewrite the GM Hamiltonian, replacing the creation operators by Hubbard operators[1] so that $c_{i\sigma}^{+}=X_i^{\sigma 0}+\sigma X_i^{2-\sigma}$ and the Hamiltonian takes the symmetrized form $H_{\mathrm{GM}}=\Sigma_{i,\Delta}H(i,i+\Delta)+H(i+\Delta,i)$, where Δ is summed over the lattice vectors, and $H(i,j)$ can be written in terms of two-site operators as follows:

$$\begin{aligned}H(i,j)=&-t_1(X_i^{\uparrow 0}X_j^{0\uparrow}+X_i^{2\downarrow}X_j^{\downarrow 2})-t_2(X_i^{\downarrow 0}X_j^{0\downarrow}+X_i^{2\uparrow}X_j^{\uparrow 2})\\&-t_1(X_i^{\uparrow 0}X_j^{\downarrow 2}+X_i^{2\downarrow}X_j^{0\uparrow})+t_2(X_i^{\downarrow 0}X_j^{\uparrow 2}+X_i^{2\uparrow}X_j^{0\downarrow})\\&+U/2(X_i^{22}+X_j^{22})-H/4(X_i^{\uparrow\uparrow}+X_j^{\uparrow\uparrow}-X_i^{\downarrow\downarrow}-X_j^{\downarrow\downarrow}).\end{aligned} \tag{2}$$

While the first two terms in Eq. (2) represent simple hopping, the second two are interconfiguration fluctuation terms and can be removed by a suitable unitary transformation as in Ref. 6. In the strong interaction limit the transformed Hamiltonian can be expanded to any order in powers of $t_{1,2}/U$. Projecting the transformed Hamiltonian onto the subspace of singly occupied states, exactly at half-filling ($n_{\uparrow}+n_{\downarrow}=1$) gives, to lowest order, an effective Hamiltonian

$$H_{\mathrm{eff}}=-\frac{t_1^2+t_2^2}{2U}\sum_{\langle ij\rangle}(X_i^{\uparrow\uparrow}X_j^{\downarrow\downarrow}+X_i^{\downarrow\downarrow}X_j^{\uparrow\uparrow})+\frac{t_1t_2}{U}\sum_{\langle ij\rangle}(X_i^{\uparrow\downarrow}X_j^{\uparrow\uparrow}+hc)-\frac{H}{2}\sum_{i}(X_i^{\uparrow\uparrow}-X_i^{\downarrow\downarrow}). \tag{3}$$

Since the Hubbard operators $X^{\alpha\beta}$ generate an $SU(2)$ algebra, and their commutation relations are isomorphic to those of the pseudospin operator L ($2L^z=X^{\uparrow\uparrow}-X^{\downarrow\downarrow}$ and $L^{+}=X^{\uparrow\downarrow}$), the effective Hamiltonian above can be written in the form

$$H_{\mathrm{eff}}=J_{\parallel}\sum_{\langle ij\rangle}(2L_i^zL_j^z-\tfrac{1}{2})+J_{\perp}\sum_{\langle ij\rangle}(L_i^{+}L_j^{-}+hc)-H\sum_{i}L_i^z, \tag{4}$$

with $J_{\parallel}=(t_1^2+t_2^2)/2U$ and $J_{\perp}=t_1t_2/U$. Thus, to lowest order, the GM is strictly equivalent to an anisotropic antiferromagnet with external field. Using analogies of this kind one may advantageously translate the substantial existing knowledge about spin systems to mixed-valence systems.

The transformed Hamiltonian is valid for all t_1, t_2, and in earlier work[7] the case $t_1\ll t_2$ was described. It is also easy

[a]Permanent address: Yerevan Physics Institute, Yerevan, Armenia 375036.

 0021-8979/94/76(10)/6127/3/$6.00 © 1994 American Institute of Physics

to show that taking $t_1=t_2$ (Hubbard model) gives a spin analog equivalent to Anderson superexchange,[8] H_{An}. Here we examine in greater detail the FK-like case $t_1\to 0$. Expanding the resulting effective Hamiltonian to fourth order gives

$$H_{Is}=\frac{t_2^2}{U}\sum_{nn} L_i^z L_j^z+\frac{t_2^4}{U^3}\sum_{nnn} L_i^z L_j^z-H\sum_i L_i^z+\text{const} \quad (5)$$

so that any exact results from the Ising model can be easily transferred to the FK model in the strong interaction limit. In particular, one expects the appearance of a spatially ordered phase in the GM in two dimensions, similar to results described earlier[4] about the appearance of a chessboard structure of f fermions in $D\geq 2$ in the symmetric case ($H=0$). We show below, however, that even with $H\neq 0$, there is a region where the chessboard structure is stabile. Higher-order corrections as in Eq. (5) are important for their implications regarding additional spatially ordered phases for $H\neq 0$.

Comparing the Anderson Hamiltonian H_{An} with H_{Is} above, we see that the difference between the Hubbard and FK models in the strong interaction limit is no more than that between a classical Ising system and a quantum antiferromagnet. Thus, exactly at half-filling the FK model can be considered to be a classical analog of the Hubbard model. Below we show that, in spite the fact that $J_\parallel \geq J_\perp$, the inclusion of a finite, small bandwidth for the f states changes the character of the phase transition from second to first order and stabilizes the quantum-liquid (QL) state with strong excitonic correlations.

All these effects can be derived analytically using a generalized mean field approximation (GMFA) for bipartite systems, i.e., those consisting of two sublattices A and B. Taking the most general decoupling scheme for Hubbard operators in Eq. (3) the Hamiltonian can be reduced to the two-site form,

$$H_{\text{eff}}^{MF}=(-J_\parallel z\tilde{n}_{2a}-H/2)X_1^{\uparrow\uparrow}+(-J_\parallel z\tilde{n}_{2f}-H/2)X_1^{\downarrow\downarrow}+(-J_\parallel z\tilde{n}_{1a}-H/2)X_2^{\uparrow\uparrow}+(-J_\parallel z\tilde{n}_{1f}-H/2)X_2^{\downarrow\downarrow}+J_\perp z\Delta_2(X_1^{\uparrow\downarrow}+X_1^{\downarrow\uparrow})$$
$$+J_\perp z\Delta_1(X_2^{\uparrow\downarrow}+X_2^{\downarrow\uparrow})+J_\parallel z(\tilde{n}_{1f}\tilde{n}_{2a}+\tilde{n}_{1a}\tilde{n}_{2f})-2J_\perp z\Delta_1\Delta_2, \quad (6)$$

where z is the coordination number of the lattice, and we have introduced the order parameters $\Delta_{1,2}=\langle X_{1,2}^{\sigma-\sigma}\rangle$ for the excitonic correlations (orbital mixing) in xy plane and $\eta=\langle X_1^{-\sigma-\sigma}-X_2^{-\sigma-\sigma}\rangle$ for the spatial orbital ordering in z plane. The number of particles n_1 and n_2 on the A and B sites is then $n_1=\tilde{n}_{1f}+\tilde{n}_{1a}$ and $n_2=\tilde{n}_{2f}+\tilde{n}_{2a}$ and the total number of particles on the two sublattices, exactly at half-filling, is $n_1+n_2=2$.

After diagonalization of Eq. (6) one can find eigenstates $E_{1,2}^{\pm}$ and the partition function Z depending on Δ, η, and $m=2\tilde{n}_f-1$. The analysis of self-consistent equations for these gives the dependence of the valence $\tilde{n}_f$ on the position of the f level H,

$$h=\frac{H}{2J_\parallel z}=mg+\sqrt{m^2+(g^2-1)\eta^2(m)}. \quad (7)$$

Analysis of Eq. (7) reveals many phases, which are shown in Fig. 1. In a strong magnetic field we have ferromagnetic ordering or integer valence (IV) states $\tilde{n}_f=0$ or 1. On decreasing the magnitude of h, the system undergoes a transition into an excitonic insulator at $h^*=1+1/g$. In this region $\tilde{n}_f$ changes linearly with h, $\tilde{n}_f=h/h^*$. This phase most closely resembles a uniform QL with strong hole-particle correlations, and with $(2m_0+1)/2<\tilde{n}_f<1$, where $m_0=\sqrt{[(g-1)/(g+1)]}$. For h between $\pm\sqrt{(g^2-1)}\,\tilde{n}_f$ is multivalued until some critical field $\pm h_0$ where the system undergoes a first-order transition from a mixed state with $\eta\neq 0$, $\Delta\neq 0$, in which valence-density waves (VDW) coexist with the QL, into a pure spatially ordered phase with VDW. When the mass of the f fermions goes to infinity we obtain at $T=0$ two consecutive jumps from IV states into VDWs with $\tilde{n}_f=\tilde{n}_s=1/2$, as shown in Fig. 1. It is also possible to obtain such a transition in systems with short-range electron-phonon interactions.[10] The transition, however, becomes continuous at any finite temperature. Thus, the stabilized excitonic phase is ruled out in the ground state whenever we exclude a finite bandwidth for f states, and there is no possibility to obtain a first-order transition in the FK model at finite temperatures. From Eq. (7) one can easily find the compressibility $\chi=-d\tilde{n}_f/dp$, which is small in IV configurations and in spatially ordered phases ($\tilde{n}_f=1/2$), but in the QL phase becomes constant $\chi=1/h^*$. The value increases with pressure, and reaches a maximum near the transition into the mixed state. Such behavior has been seen in experiments in SmS under pressure.[5,10]

The inclusion of local hybridization in the GM $V(c_\uparrow^+c_\downarrow+c_\downarrow^+c_\uparrow)$ would be the same as considering the GM in presence of a transverse magnetic field $V(L^++L^-)$. This factor is of an excitonic type and increases the tendency toward a first-order transition from a spatially ordered phase into QL state with strong excitonic correlations.

If we consider the Ising-type interaction ($t_1\to 0$) to all orders in t/U, which includes the antiferromagnetic long-range interactions with all neighbors (analogous to a classical gas with Coulomb repulsion,[11] then an infinite number of incommensurate modulated phases is found between the ferromagnetic and the VDW "antiferromagnetic" ordered phases in the one-dimensional case. This means that the FK model at $U\to\infty$ can be converted into an Ising model with long-range antiferromagnetic interactions. The crystallization of f particles into a periodic structure and dielectric splitting of the f band has been found in the 1D case.[12] The similarity between the ground-state energy and the partition functions of the FK model and the classical lattice gas has also been found recently for the 1D case.[13]

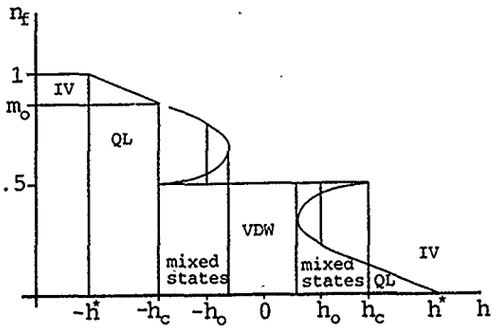

FIG. 1. The occupation number $\tilde{n}_f$ as a function of h in a generalized Hubbard model at $0<1/g<1$.

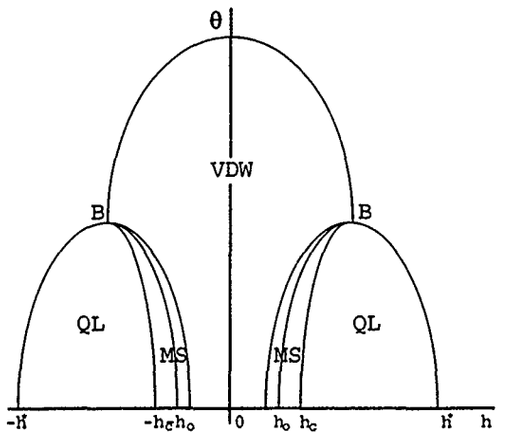

FIG. 2. The predicted h-T phase diagram for the generalized model for $D\geq 3$.

The thermodynamic behavior of our system can be analyzed easily. From analysis of these equations one can easily find the thermodynamic characteristics, and investigate the phase diagram at finite temperatures. The schematic phase diagram of critical temperatures versus magnetic field (or pressure) of the GM in the strong interaction limit is shown in Fig. 2. In some cases[14] the transition from the VDW to the QL state can be realized through an intermediate mixed state (MS), where the first-order transition line is split into two lines terminating in tetracritical point B. One first order phase transition from the QL into the VDW state is also possible by increasing the temperature at constant field (pressure) (see Fig. 2). Physically, this result is connected with the fact that excitonic effects, which are absent at high temperatures, become important at low temperatures. The phase boundary between the QL and VDW states indicates an increase of entropy for the spatially ordered phase with temperature. The bicritical point T_{bc} and spinodals, which are characteristic of the first-order transition, are also seen in Fig. 2. We expect that in the 3D case only a finite number of commensurate crystalline ordered phases exists at finite temperatures and can survive near the equilibrium line in the VDW region. At high pressures, near the IV phase the transition from QL into normal state is smooth, and its dependence on the magnetic field is logarithmic $T_c=-J_\perp/\ln(h-h^*)$. This result means that the excitonic effect by itself cannot give rise to a first-order transition and is possible only near the boundary of a spatially ordered phase. The high-temperature compressibility in the normal paramagnetic phase behaves as predicted in mean field theory, $\chi=d\tilde{n}_f/dP=C/(T-T_c^*)$, where T_c^* and C are the Curie–Weiss temperature and the Curie constant. Thus, all anomalies in the behavior of n_f and χ in mixed-valence systems can be interpreted in analogy with the temperature dependence of the magnetic moment and susceptibility of a Heisenberg–Ising system under variation of external field.

Using analogies between the FK model at $U\rightarrow\infty$ and the antiferromagnetic Ising or classical lattice-gas model, we can predict spatial ordering (VDW). In addition the long-range interactions for the Ising model (see Ref. 11) give rise to numerous other modulated long-range-ordered phases and, similarly, using an analogy with the classical lattice-gas model, one can predict an infinite number of phase transitions with charge-density wave states under change of pressure in the FK model. Thus, the thermodynamic behavior as well as the value of all critical exponents for FK model can be obtained using analogies with exactly solvable one- and two-dimensional Ising or lattice gas models. Even a small bandwidth causes a the appearance of a valence fluctuation term (or spin-flop terms in the effective Heisenberg Hamiltonian), and drastically changes the properties of the system. In spite of the fact that the exact solution of the 2D Heisenberg–Ising model is not known, it is possible to reach some conclusions about the ground-state properties and correlation function behavior even in this case.[15] For example, at low temperatures the bounds obtained in Ref. 16 rule out the possibility of excitonic condensation in 2D lattices, but allow power-law-like decay for excitonic correlations in the GM, which can be of the Kosterlitz–Thouless type, whenever t_1 or t_2 is different from zero.

The participation of ANK was made possible by the Union College Fund for Former Soviet/Eastern European Scholars established by an anonymous donor.

[1] J. Hubbard, Proc. R. Soc. London Sect. A **277**, 273 (1964).
[2] L. M. Falicov and J. C. Kimball, Phys. Rev. Lett. **22**, 997 (1969).
[3] V. L. Emery, Phys. Rev. B **14**, 2989 (1976); A. N. Kocharian and D. I. Khomskii, Sov. Phys. JETP **44**, 404 (1976); Solid State Commun. **18**, 985 (1976); N. Sh. Izmailian, A. N. Kocharian, P. S. Ovnanian, and D. I. Khomskii, Fiz. Tverd. Tela **23**, 2977 (1981).
[4] U. Brandt and R. Schmidt, Z. Phys. B **63**, 45 (1986); B **67**, 43 (1987); B **75**, 365 (1989); B **79**, 295 (1990); T. Kennedy and E. H. Lieb, Physica A **138**, 320 (1986); A **140**, 240 (1986); Q. Si, G. Kotliar, and A. Georges, Phys. Rev. B **2**, 1261 (1992); J. K. Freericks, *ibid.* P. **48**, 14 797 (1993).
[5] J. M. Lawrence, P. S. Riseborough, and R. D. Parks, Rep. Prog. Phys. **44**, 1 (1981); C. M. Varma, Rev. Mod. Phys. **48**, 219 (1976).
[6] A. N. Kocharian and P. S. Ovnanian, Z. Phys. B **83**, 161 (1991).
[7] A. N. Kocharian and A. S. Saakian, Physica B **199&200**, 582 (1994).
[8] P. W. Anderson, Phys. Rev. **115**, 2 (1959).
[9] H. Matsuda and T. Matsubara, Prog. Theor. Phys. **17**, 19 (1957).
[10] D. I. Khomskii, Sov. Phys. Usp. **22**, 879 (1979).
[11] V. L. Pokrovsky and G. V. Uimin, J. Phys. C **11**, 3535 (1978).
[12] R. Lyzwa, Phys. Lett. A **164**, 323 (1992).
[13] C. Gruber, J. L. Lebowitz, and N. Macris, Phys. Rev. B **48**, 4312 (1993).
[14] M. Fisher and D. Nelson, Phys. Rev. Lett. **32**, 1350 (1974).
[15] T. Kennedy, E. Lieb, and B. Siram Shastry, Phys. Rev. Lett. **61**, 2583 (1988).
[16] A. N. Kocharian and A. G. Sogomonian, Physica B **194–196**, 445 (1994)

Consequences of competing hybridization for magnetic ordering in correlated-electron lattices

Carlos Sanchez-Castro[a] and Bernard R. Cooper
Department of Physics, West Virginia University, Morgantown, West Virginia 26506-6315

Kevin S. Bedell
Los Alamos National Laboratory, Los Alamos, New Mexico 87545

A method is presented for calculating the f-f ion interaction in systems where a d-electron species also hybridizes with the same Fermi sea. For the physical systems of interest, typically the f species is a light rare earth (e.g., Ce or Pr) or a light actinide (U) involving a partially filled f shell and the d species is a transition-metal ion; and there may be experimental evidence of competition between magnetic ordering of the f and d electron systems (e.g., when f is U and d is Mn). The method treats first the strong hybridization between the d and the conduction electrons to obtain a new ground state with delocalized d electrons. Then it calculates the f-f ion interaction by perturbation theory. The mechanisms by which the d electrons modify the f-f ion interaction are identified.

In recent years there has been considerable interest in the behavior of partially delocalized light-rare-earth and actinide systems where cooperative hybridization between a lattice of somewhat delocalized f-electron ions and the non-f-band electrons gives rise to orbitally driven magnetic ordering phenomenology characterized by extremely high anisotropy in the equilibrium, excitation, and critical behavior, and often by anomalously strong damping of the excitations.[1] The theory of this magnetic ordering and associated behavior is by now well developed[1] when a lattice of only a single f-electron species, such as cerium or uranium, is present. Interest in generalizing this understanding to the situation where there is a d-electron species also present is strongly motivated by the competition between magnetic d and f electrons that occurs in compounds[2,3] of the $ThCr_2S_2$-type structure of the type UMn_2X_2 and RMn_2X_2 [where R is a rare earth (Ce, Pr, Nd) and X is Si,Ge]. If the Mn is replaced by another transition metal, there is no magnetic moment on the transition metal. For the light-rare-earth/Mn compounds[2] there is magnetic ordering of Mn moments, with ordering temperatures above 300 K, that either is ferromagnetic or is antiferromagnetic with Mn planes that are ferromagnetic in alternating directions; and the rare-earth sublattices show no ordering. Quite different magnetic ordering behavior occurs for the corresponding heavy-rare-earth compounds where the more localized f electrons presumably have negligible hybridization, and where typically there is evidence of magnetic ordering on the rare-earth site. For the UMn_2X_2 compounds[3] the magnetic moment of the uranium sublattice is strongly coupled with that of the Mn sublattices.

In this article we present a method for calculating the f-f ion interaction in a system where both magnetic f electrons and d electrons on a lattice (or different sublattices) hybridize with a common band sea. The method treats first the strong hybridization of the d electrons with the band sea to construct a new ground state and then proceeds to treat the f hybridization by perturbation theory. Although we explicitly assume that the d species has no moment, the method can be generalized to the case where it does by introducing spin-polarized bands.

We start by writing the Anderson lattice Hamiltonian for a system of d and f electrons hybridizing with a common conduction band as

$$H=H_c+H_f+H_d, \tag{1}$$

where $H_c = \Sigma_{\mathbf{k}\sigma}\epsilon_{\mathbf{k}}c^{\dagger}_{\mathbf{k}\sigma}c_{\mathbf{k}\sigma}$ is the conduction-band Hamiltonian and $c^{\dagger}_{\mathbf{k}\sigma}$ is a creation operator for a conduction electron with wave vector $\mathbf{k}$ located in the first Brillouin zone and spin σ. Here

$$H_\alpha=\sum_{ia m}\epsilon_\alpha l^{\dagger}_{iam}l_{iam}+\frac{1}{2}\sum_{\substack{iamm'\\ m\neq m'}}U_\alpha l^{\dagger}_{iam}l_{iam}l^{\dagger}_{iam'}l_{iam'}$$

$$+\frac{1}{\sqrt{N_s}}\sum_{\substack{iam\\ \mathbf{k}\sigma}}(V^{(\alpha)}_{\mathbf{k}\sigma m}e^{-i\mathbf{k}\cdot\mathbf{R}_i}c^{\dagger}_{\mathbf{k}\sigma}l_{iam}+\text{c.c.}), \tag{2}$$

where $\alpha=\{f,d\}$, $l^{\dagger}_{ifm}=f^{\dagger}_{im}$ is a creation operator for a localized f electron located in the ith unit cell with total angular momentum j_α and projection of the latter along the quantization axis m, $l^{\dagger}_{idm}=d^{\dagger}_{i\sigma}$ is a creation operator for a localized d electron located at the origin of the ith unit cell with spin σ, and we have neglected the orbital degeneracy for the d electron system. Here N_s is the number of unit cells in the crystal and the d hybridization matrix element for simplicity is taken to be a constant, V_d.

For a general f-d electron system, both species can interact strongly with each other by modifying the Fermi band sea. Here, we consider the case where the f species is in the Ruderman–Kittel–Kasuya–Yoshida (RKKY) interaction dominated regime with local magnetic moments in contrast to the heavy fermion regime with quenched moments due to the formation of conduction–f-electron singlets. For such a system, the most significant renormalization of the Fermi band sea is due to the hybridization with the d electrons. Thus, we propose a method where we first approximately diagonalize the terms in the Hamiltonian involving the con-

[a]Present address: Los Alamos National Laboratory, Los Alamos, NM 87545.

 0021-8979/94/76(10)/6130/3/$6.00 © 1994 American Institute of Physics

duction electrons and the d electrons to obtain renormalized bands and then, afterward, treat the hybridization of the f species as a perturbation. The d hybridization effect introduces the well-known mixed valence nature of the renormalized bands and determines the enhancement in the density of states (DOS). An enhanced DOS plus various residual interactions between the d electrons not considered here could lead to a spontaneous magnetic moment for the d electrons. We consider the case where this does not happen; however, we believe that by introducing spin polarized bands, a generalization of this method can be achieved.

The d hybridization effect, however, is different than for simple metals since electron correlation effects between the narrow d bands electrons are significant and the intraatomic Coulomb interaction must be explicitly taken into account. To take those correlations effects into account, we have assumed that $U_d \to \infty$ and introduced a slave boson formalism[4-6] to diagonalize $H_c + H_d$ in a mean field approximation. The resulting Hamiltonian H_{c-d}^{MF} is one of hybridizing bands and can be diagonalized by a canonical transformation to yield renormalized bands[5,6] given by

$$H_{c-d}^{\mathrm{MF}} = \sum_{\mathbf{k}n\sigma} \epsilon_{\mathbf{k}n} a_{\mathbf{k}n\sigma}^{\dagger} a_{\mathbf{k}n\sigma} + N_s \Lambda (r^2 - 1), \tag{3}$$

where $n=1,2$ is a band index, $\epsilon_{\mathbf{k}n} = \frac{1}{2}[\epsilon_{\mathbf{k}} + \tilde{\epsilon}_d + (-1)^n E_{\mathbf{k}}]$ are the hybridized band energies, $E_{\mathbf{k}} = [(\epsilon_{\mathbf{k}} - \tilde{\epsilon}_d)^2 + 4\tilde{V}_d^2]^{1/2}$, $\tilde{\epsilon}_d = \epsilon_d + \Lambda$ is the renormalized d energy level, and Λ is the corresponding energy shift. Here $\tilde{V}_d = V_d r$ is the renormalized d hybridization matrix element and r is the hybridization renormalization factor. Both Λ and r are expectation values of slave boson fields over the coherent equilibrium states and are determined by minimizing the mean field free energy[5,6] with respect to them. The hybridized band creation operators are given by[5,6]

$$a_{\mathbf{k}n\sigma}^{\dagger} = \gamma_{n,1}(k) \hat{d}_{\mathbf{k}\sigma}^{\dagger} + \gamma_{n,2}(k) c_{\mathbf{k}\sigma}^{\dagger}, \tag{4}$$

where $\gamma_{n,m}$ is an orthogonal matrix, $\hat{d}_{\mathbf{k}\sigma}^{\dagger} = \sum_i e^{i\mathbf{k}\cdot\mathbf{R}_i} \hat{d}_{i\sigma}^{\dagger}/N_s^{1/2}$, and $\hat{d}_{i\sigma}^{\dagger}$ is the slave fermion creation operator representing the $|d_{\sigma}^{(1)}\rangle_{\mathbf{R}_i}$ configuration. The limit of $U_d = 0$ can be formally obtained from the above equations by setting $r=1$ and $\Lambda=0$. The slave boson average r also gives the average electron occupation of a d site n_d by $n_d = 1 - r^2$, i.e., r^2 is a measure of the degree of delocalization or itineracy of the d electrons.[5,6] In other words, in the infinite U_d limit a conduction electron can jump to a d site only if it is empty and this results in a factor $V_d^2 r^2 = V_d^2(1 - n_d)$ in the transition probability.

Now, by replacing $H_c + H_d$ by H_{c-d}^{MF} in Eq. (1), and expressing the f hybridization term in terms of the renormalized band operators, we obtain an effective Hamiltonian in which the f electrons hybridize with two renormalized bands that already contain the effects of the d electron hybridization and is given by

$$H = H_{c-d}^{\mathrm{MF}} + \sum_{i,m} \epsilon_f f_{im}^{\dagger} f_{im} + \frac{1}{2} \sum_{\substack{imm' \\ m \neq m'}} U_f f_{im}^{\dagger} f_{im} f_{im'}^{\dagger} f_{im'}$$

$$+ \frac{1}{\sqrt{N_s}} \sum_{imk n\sigma} (\tilde{V}_{\mathbf{k}n\sigma m}^{(f)} e^{-i\mathbf{k}\cdot\mathbf{R}_i} f a_{\mathbf{k}n\sigma}^{\dagger} f_{im} + \mathrm{c.c.}), \tag{5}$$

where $\tilde{V}_{\mathbf{k}n\sigma m}^{(f)} = V_{\mathbf{k}\sigma m}^{(f)} \gamma_{n,2}(k)$ is a renormalized f hybridization matrix element. The renormalized f hybridization matrix element takes into account the mixed valence nature of the renormalized bands, i.e., an electron in a state $|\mathbf{k}n\sigma\rangle$ and energy $\epsilon_{\mathbf{k}n}$ has a probability $\gamma_{n,2}(k)^2$ of being in a conduction-band state and hopping into the localized f state. The calculation of an effective magnetic Hamiltonian for the f ions starting from Eq. (5) is accomplished by a combination of a Schrieffer–Wolff (SW) transformation and perturbation theory.[6] Two distinct physical processes contribute to the two-ion interaction: (1) an induced interaction mediated by the interchange of a particle-hole excitation in the conduction band; (2) a kinetic superexchange contribution due to an effective hopping or banding interaction between the localized electrons that results after applying the SW transformation to the Anderson Hamiltonian. The resulting ionic interaction between two localized f^1 electrons located at sites i and j is given by

$$h_{ij} = -\sum_{m,m'} E_{m'm;mm'}(\mathbf{R}_i - \mathbf{R}_j) f_{im'}^{\dagger} f_{im} f_{jm}^{\dagger} f_{jm'}. \tag{6}$$

For a matrix element of the form

$$\tilde{V}_{\mathbf{k}\sigma m}^{(f)} = \sqrt{4\pi} V_f \gamma_{n,2}(k) Y_{3,m-\sigma}(\hat{k}) \times \langle 3,1/2,m-\sigma,\sigma | 3,1/2.j,m \rangle,$$

where $Y_{l,m}(\hat{k})$ is a spherical harmonic, $\langle 3,1/2,m-\sigma,\sigma|3,1/2,j,m\rangle$ is a Clebsch–Gordon coefficient for a spin-orbit coupled f state, and a quantization axis along $\mathbf{R}_i - \mathbf{R}_j$, it can be shown that the asymptotic behavior of the range function is given by[1,6] $E_{m'm;mm'} = g(m,m')E(R)$. The factor

$$g(m,m') = \delta_{|m|,1/2} \delta_{|m'|,1/2}$$

remains unchanged from the case where there are no d electrons and implies a highly anisotropic interaction that favors having two ions point their charge along the bonding axis ($m = \pm 1/2$) thereby developing a small covalent bonding energy and causing the ionic orbital moments to align perpendicular to the bonding axis.[1] The radial factor $E(R)$ is a complicated function of the renormalized f hybridization and renormalized bands.[6]

To explore the physics that comes out of this approach, we have done a model calculation for a system of f ions with $j=5/2$ and d electrons with $s=1/2$. The conduction band was assumed to be parabolic with a bandwidth $W=5$ eV. We took ϵ_d and ϵ_f to be 0.3 and 1 eV below the conduction Fermi surface, respectively. Before hybridization, the d band holds 1 electron per site and the conduction band 0.6 electrons per site, and therefore after hybridization the lower hybridized band holds 1.6 electrons per site. The various parameters were chosen as follows: $V_d = 1$ eV, $V_f = 0.1414$ eV, $U_f = 3.0$

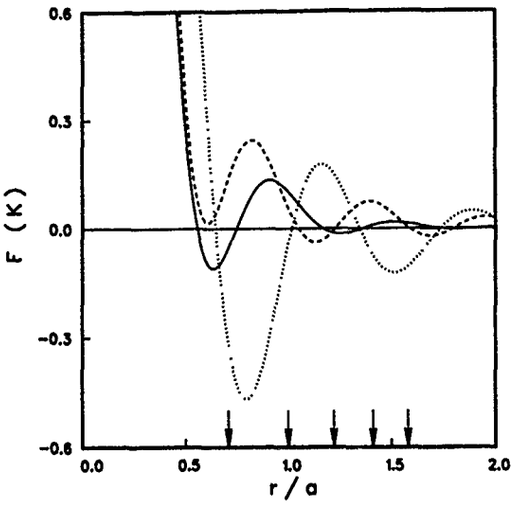

FIG. 1. The range function (intersite coupling strength) as a function of the ratio of the distance between the two f sites to the unit-cell fcc lattice constant a. Here the solid, dashed, and dotted curves correspond to $E_{V,U}$, E_V, and E_0, respectively. The arrows indicate the nearest-neighbor distances for a fcc lattice.

eV, and U_d infinite. In Fig. 1 we show the calculated f-f ion interaction range function under different circumstances: (1) by taking into account the hybridization and correlations between the d electrons as outlined here, $E_{V,U}$ (solid curve); (2) by treating the hybridization of the d electrons but neglecting their correlations, i.e., $U_d=0$, E_V (dashed curve); and (3) by neglecting both the hybridization and correlations between the d electrons, E_0 (dotted curve). We note that both $E_{V,U}$ and E_V oscillate more rapidly with distance than E_0 due to renormalizations in the partial densities of states with a net effect of electrons spilling from the d band into the conduction band.[7] The difference between $E_{V,U}$ and E_V is due to the correlations between the d electrons which are significant for the case considered here. A detailed analysis of these results is presented elsewhere.[6]

In conclusion, we have presented a method to compute the f-f ion interaction in systems where both d and magnetic f electrons hybridize with a conduction band. Our calculations elucidate some of the mechanisms by which two different transition shell species can interfere with each other through cooperative hybridization with a common Fermi band sea. We found that correlations between the d electrons in addition to hybridization must be taken into account in the calculation of the f-f interaction.

[1] B. R. Cooper, R. Siemann, D. Yang, P. Thayamballi, and A. Banerjea, in *Handbook on the Physics and Chemistry of the Actinides*, edited by A. J. Freeman and G. H. Lander (North-Holland, Amsterdam, 1985), Chap. 6, pp. 435–498; B. R. Cooper, Q. G. Sheng, S. P. Lim, C. Sanchez-Castro, N. Kioussis, and J. M. Wills, J. Magn. Magn. Mater. **108**, 10 (1992), and references therein.

[2] A. Szytula and I. Szott, Solid State Commun. **40**, 199 (1981); A. Szytula, in *Handbook of Magnetic Materials*, edited by K. H. J. Buschow (Elsevier, Amsterdam, 1991), Vol. 6, Chap. 2, pp. 139–148.

[3] V. Sechovsky and L. Havela, in *Handbook of Ferromagnetic Materials*, edited by E. P. Wohlfarth and K. H. J. Buschow (Elsevier, Amsterdam, 1988), Vol. 4, pp. 309 ff.

[4] A. J. Millis and P. A. Lee. Phys. Rev. B **35**, 3394 (1987).

[5] C. Sanchez-Castro, K. S. Bedell, and B. R. Cooper, Phys. Rev. B **47**, 6879 (1993).

[6] C. Sanchez-Castro, B. R. Cooper, and K. S. Bedell (unpublished).

[7] J. M. Ziman, *Electrons and Phonons* (Oxford University Press, London, 1960), p. 125.

Antiferromagnetic order in superconducting UPt_3: An x-ray magnetic scattering study (invited)

E. D. Isaacs
AT&T Bell Laboratories, 600 Mountain Avenue, Murray Hill, New Jersey 07974

P. Zschack
Oak Ridge Institute for Science and Education, Brookhaven National Laboratory, Upton, New York 11973

A. P. Ramirez, C. S. Oglesby, and E. Bucher[a)]
AT&T Bell Laboratories, 600 Mountain Avenue, Murray Hill, New Jersey 07974

The temperature dependence of the antiferromagnetic order in superconducting UPt_3 has been measured using x-ray resonance magnetic scattering. The magnetic Bragg intensity at $Q=(1/2,0,2)$ grows linearly from $T_N=5$ K to $T\cong 0.6$ K ($T_{C+}=0.53$ K), where it becomes suppressed with temperature to a reduction of $\sim 6\%$ at $T=180$ mK. These results demonstrate a coupling of the superconducting and antiferromagnetic order parameters and are consistent with a suppression in the magnitude of the ordered moments below T_c when compared with previously obtained neutron-scattering data.

UPt_3 has emerged as a model system in which to study unconventional superconductivity.[1] The unconventional nature can be seen, for example, in the anisotropic response of bulk measurements in the superconducting phase, such as the ultrasound attenuation,[2] magnetic penetration depth,[3] flux lattice,[4] and tunneling,[5] which shows indirect evidence that the superconducting gap is anisotropic and that the Cooper pairs carry orbital angular momentum, e.g., *d*-wave pairing. It has been suggested that the rich phase diagram of UPt_3 for example, the splitting of the superconducting transition observed by specific heat,[6] arises from a breaking of the orbital degeneracy by a coupling of the superconducting order parameter to another symmetry-breaking field in the system.[7] Scattering studies, which are a direct microscopic probe, have pointed to several possible symmetry-breaking fields. Neutron-scattering[8,9] measurements have shown a coupling of superconductivity to the weak antiferromagnetic order in UPt_3, while electron-scattering[10] studies have suggested the possibility of a coupling between superconductivity and an incommensurate structural modulation of the lattice. While these different results are tantalizing they point to the need for more microscopic measurements. Therefore, we have used x-ray magnetic diffraction to study the interplay of magnetism and superconductivity in UPt_3. X-ray scattering is the only microscopic probe, along with neutron scattering, that is sensitive to the very small ordered moment found in this heavy fermion system. We show that there is a large suppression of the antiferromagnetic scattering intensity below the superconducting transition temperature T_{C+}, demonstrating a direct coupling between the superconducting and antiferromagnetic order parameters in UPt_3. Applying the polarization selection rules unique to x-ray resonance scattering and comparing our results to the previous neutron-scattering measurements of Aeppli *et al.*,[8] we show that the suppression of the magnetic scattering in the superconducting phase is consistent with a suppression in the magnitude of the ordered moment below T_C.

Our x-ray scattering measurements have been performed at Beamline X14A at the National Synchrotron Light Source at Brookhaven National Laboratory.[11] Monochromatic x rays (3.728 keV) are horizontally focused at the sample by a sagittally bent, double-crystal Si(111) monochromator collecting up to 5 mrad, and vertically focused by an x-ray mirror to a spot size of approximately 1 mm^2. The mirror serves the additional function of low-pass filter, helping to suppress the higher-order components passed by the monochromator (e.g., $\lambda/4$ at $E=14.912$ keV). A neon or argon gas proportional counter is used as a detector with an energy resolution of approximately 750 eV which allows us to separate the remaining higher-order contamination from λ, and gives us a direct measure of the instrumental resolution function.

The UPt_3 sample is mounted in vacuum on the mixing chamber of an Oxford Instruments dilution refrigerator. The temperature of the sample is monitored with a Ge diode sensor mounted on the mixing chamber next to the sample. The refrigerator is fitted into a cryostat with three concentric cylindrical Be windows (two thermal shields, one at 4 K and a second at 77 K, and a vacuum shroud at 300 K). The cryostat is mounted on a two-circle diffractometer with a horizontal scattering plane, i.e., the plane of the synchrotron orbit. With this geometry we can access a larger volume in reciprocal space than the more conventional vertical scattering plane, while keeping the vertical axis of the cryostat within $\pm 10°$ of vertical. This is necessary in order to keep the ^{3}He dilute/rich interface inside the mixing chamber. Because of the larger beam divergence in the horizontal plane (the 5 mrad acceptance of the monochromator) the momentum resolution is defined by v slits just before the monochromator and scattering slits before the detector to be $\Delta q\cong 8\times 10^{-3}$ Å^{-1} (see Fig. 2). An additional advantage to the horizontal scattering plane is that for the magnetic reflection at $\mathbf{Q}=(1/2,0,2)$ there is significant suppression of the diffuse and higher-order ($\lambda/4$) scattering at $\mathbf{Q}=(2,0,8)$ that would otherwise saturate the detector. This suppression is due to the polarization factor, which for a Bragg angle of $\theta\cong 44.6°$ [$\mathbf{Q}=(1/2,0,2)$ with $E=3.728$ keV] is $\cos^2(2\theta)\cong 2\times 10^{-4}$.

The UPt_3 sample that we use is cut from the same boule

[a)]Also at University of Konstanz, Konstanz 7750, Germany.

 0021-8979/94/76(10)/6133/4/$6.00 © 1994 American Institute of Physics

that was used in muon spin relaxation measurements.[3] The boule was grown by the float-zone refining method and annealed at 1230 °C for 40 h in vacuum and slowly cooled to room temperature. The specific heat shows the now well-known splitting of the superconducting transition with $T_{C+} \cong 0.530$ K and $T_{C-} \cong 0.427$ K. The superconducting coherence length is about 120 Å as determined with muon spin relaxation by Broholm *et al.* in a sample cut from the same boule.[3] Our sample is a 5-mm-diam×1-mm-thick disk with a shiny, polished surface whose normal is within 1° of c^*. UPt_3 has the hexagonal closed-pack Ni_3Sn structure with the $P6_3/mmc$ space group. In this article Bragg reflections are expressed using Miller indices with reciprocal lattice vectors $a^*=b^*=4\pi/a\sqrt{3}=1.264$ Å^{-1} and $c^*=2\pi/c=1.285$ Å^{-1}. The antiferromagnetic transition at $T_N \cong 5$ K corresponds to a doubling of the unit cell along $[h,0,0]([0,k,0])$ with the moments aligned along $[h,0,0]$ $([0,k,0])$.[12] Thus, the magnetic Bragg peaks occur at half-order positions, e.g., $Q=(h+1/2,0,l)$ for integer values of h and l. The sample is fixed on the mixing chamber with the $(h,0,l)$ plane normal to the horizontal scattering plane such that the (1/2,0,2) magnetic Bragg reflection is specular $[\theta=1/2(2\theta)_{Bragg}]$. This configuration optimizes our sensitivity to a rotation of the ordered moments in the basal plane, given the polarization selection rules associated with resonant magnetic scattering (see below).[13]

In order to measure the very small ordered moment in UPt_3 of $(0.02\pm0.005)\mu_B$ we use the recently developed technique of x-ray resonance magnetic scattering.[14,15] In previous work it was demonstrated that the weak antiferromagnetic ordering could be measured in the heavy fermion superconductor URu_2Si_2 $(0.04\mu_B)$[16] by tuning the incident x-ray energy to the peak of the so-called "white line" feature at the uranium M_{IV} absorption edge at $E=3.728$ keV. The lower curve in Fig. 1 shows the integrated scattering intensity versus energy in UPt_3 of the magnetic Bragg reflection at $Q=(1/2,0,2)$ corrected for both background and absorption (upper curve) at $T=0.25$ K. This resonance corresponds to a dipole transition from the $3d_{3/2}$ core state to an unoccupied $5f_{5/2}$ orbital. The quantum-mechanical contact between the $5f_{5/2}$ states and the s,p, and d bands is what gives rise to the interesting low-temperature properties in this system, including the weak antiferromagnetism that we are probing. The measurements described in this article are carried out at the peak of the profile where the magnetic signal is a maximum. Since the penetration depth is a minimum at the same energy (~1/2 μm), and since the crystal quality could have an effect on both the superconducting and antiferromagnetic coherence lengths, we determine whether the crystal quality of the bulk is the same as near the surface by measuring the sample mosaic. This is shown in the inset in Fig. 1 where we plot mosaic scans (intensity versus sample angle θ) at $Q=(0,0,2)$ for $E=7.59$ keV with a penetration depth of ~1 μm and for $E=16.0$ keV with a penetration depth of ~10 μm. Similar scans are also seen for $E=3.728$ keV at the peak of the white line. These scans were taken with higher angular resolution than the magnetic scans, i.e., $\Delta\theta=0.2$ mrad. The mosaic widths differ by less than 5% leading us to believe that the crystal quality of the bulk and

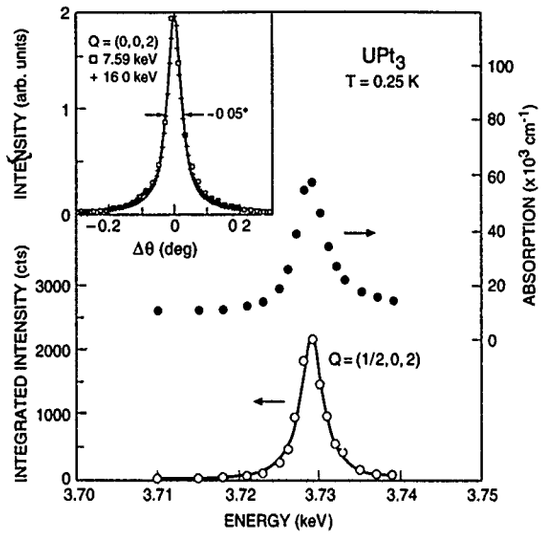

FIG. 1. X-ray magnetic scattering resonance profile at the M_{IV} edge in UPt_3 ($\mu \cong 0.04$ μ_B). The lower curve shows the magnetic scattering intensity at $Q=(1/2,0,2)$ as a function incident energy for $T=0.25$ K. The solid line is a Lorentzian fit to the data which has been corrected for background and absorption. The absorption profile is shown in the upper curve. Inset: The mosaic widths for incident x-ray energies 7.59 keV (○) and 16.00 keV (+) are shown to be nearly the same ($\Delta\theta_{FWHM} \sim 0.05°$) demonstrating that the crystal quality near the surface (<1 μm) is similar to the bulk (10 μm).

surface region are the same. It is interesting to note that an as-grown (unannealed) sample cut from the same boule has a considerably broader mosaic width of 0.33° and a superconducting transition which is suppressed to $T=0.4$ K with no evidence of a splitting in the specific heat.

Figure 2 shows a longitudinal (θ-2θ) scan through the magnetic Bragg reflection at $Q=(1/2,0,2)$ for $T=0.25$ K.

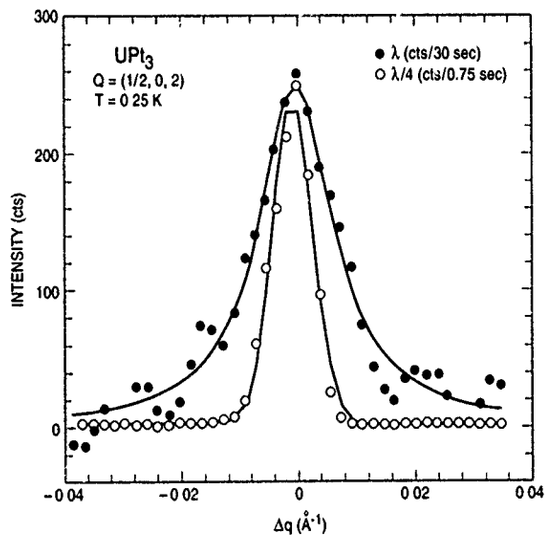

FIG. 2. Longitudinal scans (θ-2θ) through the magnetic (1/2,0,2) and charge (2,0,8) (collected at λ/4) Bragg reflections at $T=0.25$ K. The width of the (2,0,8) charge peak is a direct measure of the resolution function of our spectrometer. From a fit of a Lorentzian to the data we determine the magnetic correlation length to be $\xi \cong 185$ Å.

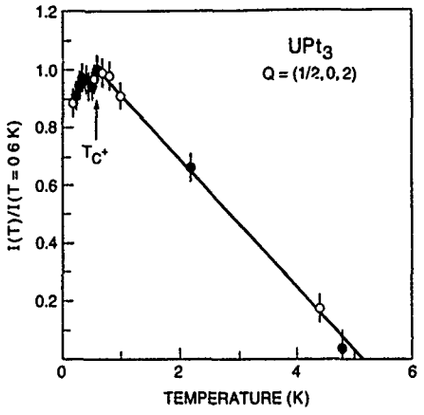

FIG. 3. Integrated scattering intensity of the magnetic reflection at $Q=(1/2,0,2)$ as a function of temperature corrected for background and normalized to fluorescence. The solid circles reflect temperatures for which intensities were measured repeated times for both cooling and warming. The arrow indicates the position of the upper superconducting transition at $T_{C+}=0.53$ K.

The peak intensity of the scan is a remarkable 10 counts/s. A temperature-independent ($0.2\ \text{K}<T<10\ \text{K}$) diffuse background, due primarily to unresolved fluorescence, of about 30 counts/s has been subtracted from the scan. The line shape of the longitudinal scan (solid line) is a Lorentzian convoluted with the nearly triangular resolution function. The resolution function, which we recall is determined by slits, is measured simultaneously by collecting the higher-order scattering ($\lambda/4$) at $Q=(2,0,8)$ shown by the open circles in Fig. 2. A fit to the data gives a full width at half maximum of $\xi^{-1}=0.013\ \text{Å}^{-1}$, corresponding to a magnetic correlation length of approximately 185 Å. This is not much larger than the superconducting coherence length as determined by muon spin rotation (see Ref. 3). There is no measurable change in the magnetic correlation length above T_{C+} at $T=2.3$ K. This lack of long-range order with a similar correlation length has been observed with neutron scattering.[8] This is additional evidence that the near-surface magnetization as measured by x-ray resonance magnetic scattering is similar to that of the bulk as measured by neutrons.

The principle result of our experiment is shown in Fig. 3. Here we plot the background corrected integrated intensity of the magnetic Bragg peak at $Q=(1/2,0,2)$ as a function of temperature, normalized to the value at $T=0.6$ K, near T_{C+}. The solid lines are least-squares linear fits to the data above and below T_{C+}, respectively, and cross at $T\cong 0.61$ K. The data have been normalized to the fluorescence to correct for scattering volume effects due to variations in x-ray beam position on the sample. The remaining systematic errors are shown by the error bars which are estimated from repeated scans at several temperatures (solid circles) taken for both warming and cooling. The scattering intensity shows a relatively abrupt onset at $T_N=5$ K and grows as (T_N-T) to $T=0.6$ K. While this linearity is consistent with mean field behavior, it extends over an unusually large temperature range to approximately $T_N/10$. Similar behavior is observed in the heavy fermion superconductor URu_2Si_2, where the magnetic scattering intensity increases linearly until it saturates near $T_N/10$ ($T_N=17$ K) with a small ordered moment ($\mu\cong 0.04\mu_B$).[15,17] The reason for this unusual behavior is not well understood. Below $T=0.6$ K there is a kink and a subsequent suppression with temperature to a reduction of approximately 6% at $T=180$ mK, the base temperature of this measurement. The dip in the order parameter just above T_C at $T=0.45$ K is about twice the size of the estimated error bars and, as such, will require further study.

The reduction of the magnetic Bragg intensity at $Q=(1/2,0,2)$ below T_{C+} can arise from one of the following possibilities: (i) a rotation of the ordered moment, or (ii) a suppression in the magnitude of the ordered moment. First we examine case (i). Our sensitivity to the orientation of the ordered moment arises from the resonant magnetic scattering polarization selection rules. With the incident x-ray energy tuned to the peak of the uranium M_{IV} edge (see Fig. 1) the polarization dependence of the resonance magnetic scattering cross section is given by $|-(\boldsymbol{\epsilon}_f^*\times\boldsymbol{\epsilon}_i)\cdot\mathbf{z}|^2$, where $\boldsymbol{\epsilon}_i$ and $\boldsymbol{\epsilon}_f$ are the polarization of the electric field of the incident and scattered photons, respectively, and $\mathbf{z}$ is a unit vector along the direction of the ordered moment $\boldsymbol{\mu}$.[13] For the geometry of our experiment $(\boldsymbol{\epsilon}_f^*\times\boldsymbol{\epsilon}_i)=-\mathbf{k}_i/|\mathbf{k}_i|$, where $\mathbf{k}_i$ is the wave vector of the incident photon, and we recall that $\boldsymbol{\mu}$ lies in the hexagonal basal plane. Because of our choice of scattering geometry we are particularly sensitive to a rotation of the moments, i.e., $\mathbf{k}_i\cdot\mathbf{z}$ is nearly linear in the orientation of $\boldsymbol{\mu}$. A 6% suppression would imply a spin rotation of only 2°, assuming that the rotation is purely in plane, which is justified because the in-plane magnetic susceptibility is larger than along $\mathbf{c}$.[18] We recall that the size of the suppression observed with magnetic neutron scattering was ~5%, which is very similar in magnitude to our results.[8] However, because the geometry and polarization selection rules for that measurement were different $[|\mathbf{Q}\times(\boldsymbol{\mu}\times\mathbf{Q})|^2$, where $\mathbf{Q}=(1,1/2,0)$ is the total neutron momentum transfer], a larger rotation would be required to produce the same suppression. Thus, we conclude that, within the error bars of our experiment, the reduction of the magnetic scattering intensity below T_{C+} is most likely due to a reduction in the magnitude of the ordered moment and not a rotation. This conclusion is reinforced when we consider that the observation of a reduction in the magnetic intensity due to rotation would require dominant chirality in the basal plane, which is not known to exist in the absence of a magnetic field. It would be more likely that an equal distribution of domains with clockwise and counterclockwise rotations should exist, which would average out and produce no net change in the scattering intensity.

In conclusion, we have measured the antiferromagnetic Bragg reflection at $\mathbf{Q}=(1/2,0,2)$ to $T=180$ mK using x-ray resonance magnetic scattering. The kink in the scattering intensity, which occurs very near the upper superconducting transition at $T_{C+}=0.53$ K, is evidence that superconductivity influences antiferromagnetism in UPt_3. The 6% reduction in scattering intensity that we observe is very similar in magnitude to what was previously observed with neutron scattering, but with quite different scattering geometry and polarization selection rules. This leads us to conclude that the reduction arises from a suppression of the ordered moment

rather than a rotation. Such a reduction points to a direct coupling of the two order parameters, which in turn points to the anisotropic nature of the superconductivity. While we cannot explicitly determine the nature of this anisotropy with this measurement, it is consistent with the general picture in which the formation of an anisotropic superconducting gap (e.g., which vanishes along lines on the Fermi surface) competes with the highly anisotropic antiferromagnetic state.[19] In this scenario antiferromagnetism could provide the symmetry breaking field that gives rise to the rich superconducting phase diagram in UPt_3.

We are indebted to Gabriel Aeppli and Rafael Kleiman for enlightening discussions. We also acknowledge Hugh Williams and Mitch Nelson. Oak Ridge National Laboratory Beamline X14A is supported by the Division of Materials Sciences and Division of Chemical Sciences, U.S. Department of Energy under Contract No. DE-AC05-840R21400 with Martin Marietta Energy Systems, Inc.

[1] M. Siegrist and K. Ueda, Rev. Mod. Phys. **63**, 239 (1991); Z. Fisk and G. Aeppli, Science **260**, 38 (1993).
[2] D. J. Bishop, C. M. Varma, B. Batlogg, and E. Bucher, Phys. Rev. Lett. **53**, 1009 (1984); B. S. Shivaram, Y. H. Jeong, T. F. Rosenbaum, and D. G. Hinks, Phys. Rev. Lett. **56**, 1078 (1986).
[3] C. Broholm, G. Aeppli, R. N. Kleiman, D. R. Harshman, D. J. Bishop, E. Bucher, D. Ll. Williams, E. J. Ansaldo, and R. H. Heffner, Phys. Rev. Lett. **65**, 2062 (1990).
[4] R. N. Kleiman, C. Broholm, G. Aeppli, E. Bucher, N. Stücheli, D. J. Bishop, K. N. Clausen, K. Mortensen, J. S. Pedersen, and B. Howard, Phys. Rev. Lett. **69**, 3120 (1992).
[5] G. Goll, H. von Löhneysen, I. K. Yanson, and L. Taillefer, Phys. Rev. Lett. **70**, 2008 (1993).
[6] R. A. Fisher *et al.* Phys. Rev. Lett. **62**, 1311 (1989).
[7] E. Bount, C. Varma, and G. Aeppli, Phys. Rev. Lett. **64**, 3074 (1990); R. Joynt, *ibid* **71**, 3015 (1993).
[8] G. Aeppli, D. J. Bishop, C. Broholm, E. Bucher, K. Siemensmeyer, M. Steiner, and N. Stüsser, Phys. Rev. Lett. **63**, 676 (1989).
[9] S. M. Hayden, L. Taillefer, C. Vettier, and J. Flouquet, Phys. Rev. B **46**, 8675 (1992).
[10] P. A. Midgley, S. M. Hayden, L.Taillefer, B. Bogenberger, and H. von Löhenysen, Phys. Rev. Lett. **70**, 678 (1993).
[11] A. Habenshuss, G. E. Ice, C. J. Sparks, and R. A. Neiser, Nucl. Instrum. Methods Phys. Res. **266**, 215 (1988).
[12] A. I. Goldman, G. Shirane, G. Aeppli, B. Batlogg, and E. Bucher, Phys. Rev. B **34**, 6564 (1986).
[13] J. Luo, G. T. Trammell, and J. P. Hannon, Phys. Rev. Lett. **71**, 287 (1993).
[14] D. Gibbs, D. R. Harshman, E. D. Isaacs, D. B. McWhan, D. Mills, and C. Vettier, Phys. Rev. Lett. **61**, 1241 (1988).
[15] E. D. Isaacs, D. B. McWhan, C. Peters, G. E. Ice, D. P. Siddons, J. B. Hastings, C. Vettier, and O. Vogt, Phys. Rev. Lett. **62**, 1671 (1989).
[16] E. D. Isaacs, D. B. McWhan, R. N. Kleiman, D. J. Bishop, G. E. Ice, P. Zschack, B. D. Gaulin, T. E. Mason, J. D. Garrett, and W. J. L. Buyers, Phys. Rev. Lett. **65**, 3185 (1990).
[17] T. E. Mason, B. D. Gaulin, J. D. Garrett, Z. Tun, W. J. L. Buyers, and E. D. Isaacs, Phys. Rev. Lett. **65**, 3189 (1990).
[18] P. H. Frings and J. Franse, Phys. Rev. B **31**, 4355 (1985).
[19] G. Aeppli, E. Bucher, C. Broholm, J. K. Kjems, J. Baumann, and J. Hufnagel, Phys. Rev. Lett. **60**, 615 (1988).

Non-Fermi liquid ground states in strongly correlated *f*-electron materials (invited) (abstract)

M. B. Maple
Department of Physics and Institute for Pure and Applied Physical Sciences, University of California, San Diego, La Jolla, California 92093-0319

Strongly correlated electron materials, especially the high transition temperature (T_c) cuprate superconductors and heavy fermion rare earth and actinide compounds, have been the focus of intense investigation in recent years. The unusual normal state properties of the high T_c cuprates have been ascribed by some researchers to a non-Fermi liquid (NFL) metallic state, while the anomalous properties of certain heavy fermion U-based superconductors such as UBe_{13} have been attributed to NFL behavior due to a two-channel quadrupolar Kondo effect.[1] Although NFL behavior has not been established in any of the U-based heavy fermion superconductors, evidence for its occurrence in an *f*-electron material has been found in the U alloy system $Y_{1-x}U_xPd_3$.[2] Subsequently, NFL behavior was observed in a number of other *f*-electron alloy systems, including $Sc_{1-x}U_xPd_3$, $UCu_{3.5}Pd_{1.5}$, $Th_{0.1}U_{0.9}Be_{13}$, $Th_{1-x}U_xRu_2Si_2$ ($x \leq 0.07$), $Th_{1-x}U_xPd_2Al_3$, $La_{0.9}Ce_{0.1}Cu_2Si_2$, and $CeCu_{5.9}Au_{0.1}$. Evidence for NFL behavior in $Y_{1-x}U_xPd_3$ and related systems is reviewed and discussed within the context of possible microscopic mechanisms. Some systematics of the NFL low temperature behavior observed in several *f*-electron materials include a linear temperature dependence of the electrical resistivity $\rho \sim 1 - aT$ with the coefficient a either >0 or <0, a logarithmically diverging specific heat $C/T \sim -\ln T$, and $T^{1/2}$ asymptotic behavior of the magnetic susceptibility $\chi \sim 1 - T^{1/2}$.

Supported by the U.S. NSF under Grant No. DMR-9107698 and the U.S. DOE under Grant No. DE-FG03-86ER45230.

[1] D. L. Cox, Phys. Rev. Lett. **59**, 1240 (1987).
[2] C. L. Seaman, M. B. Maple, B. W. Lee, S. Ghamaty, M. S. Torikachvili, J.-S. Kang, L. Z. Liu, J. W. Allen, and D. L. Cox, Phys. Rev. Lett. **67**, 2882 (1991).

Magneto-oscillatory phenomena in highly correlated metals (invited) (abstract)

S. R. Julian, G. J. McMullan, C. Pfleiderer, F. S. Tautz, and G. G. Lonzarich
Cavendish Laboratory, Cambridge CB3 0HE, United Kingdom

A central question in the physics of interacting electron systems is whether conditions exist under which the conventional Landau description fails to describe the low energy excitations of the "normal" metallic state. Measurements of the temperature and magnetic field dependences of the magnetization and resistivity—in particular of the de Haas–van Alphen and Shubnikov effects which provide sensitive probes of microscopic processes in metals—are currently being used to examine this question. Advances in material preparation and detection techniques have made it possible to conduct exhaustive studies in selected examples of systems of highly correlated *d* and *f* electrons. Most of our results will be shown to be consistent with the broad predictions of the Landau model. In some extreme circumstances, however, near low temperature transitions as a function of hydrostatic pressure or applied magnetic field, evidence has been collected which appears difficult to reconcile with the standard model of the metallic state.

 0021-8979/94/76(10)/6137/1/$6.00 © 1994 American Institute of Physics

New rare-earth intermetallic phases $R_3(Fe,M)_{29}X_n$: (R=Ce, Pr, Nd, Sm, Gd; M=Ti, V, Cr, Mn; and X=H, N, C) (invited)

J. M. Cadogan and Hong-Shuo Li
School of Physics, The University of New South Wales, Sydney NSW 2052, Australia

A. Margarian
Department of Applied Physics, University of Technology, Sydney NSW 2007 and CSIRO Division of Applied Physics, Lindfield NSW 2070, Australia

J. B. Dunlop
CSIRO Division of Applied Physics, Lindfield NSW 2070, Australia

D. H. Ryan
Department of Physics, McGill University, Montréal, Québec H3A 2T8, Canada

S. J. Collocott
CSIRO Division of Applied Physics, Lindfield NSW 2070, Australia

R. L. Davis
Australian Nuclear Science and Technology Organisation, Lucas Heights NSW 2234, Australia

New rare-earth (R), iron-rich ternary intermetallic compounds of the form $R_3(Fe,M)_{29}$ with the monoclinic $Nd_3(Fe,Ti)_{29}$ structure (space group $P2_1/c$, #14, Z=2) have recently been shown to form with R=Ce, Nd, Pr, Sm, and Gd, and M=Ti, V, Cr, and Mn. This novel structure is derived from the alternate stacking of Th_2Zn_{17} and $ThMn_{12}$-type segments and contains two R sites and fifteen Fe(M) sites. Reported Curie temperatures of the 3:29 compounds range from 296 K (R=Ce, M=Cr) to 524 K (R=Sm, M=V). The 3:29 compounds all show improved magnetic properties after interstitial modification with H or N; in particular, room-temperature coercivity has been reported in $Sm_3(Fe,Ti)_{29}N_5$, making this compound a candidate for possible permanent-magnet applications. In this article we will review the work carried out to date on the 3:29 compounds.

The past ten years have witnessed a renewed interest in the structural and magnetic properties of rare-earth (R), iron-rich intermetallic compounds. These intermetallics often show potential for application as permanent-magnet materials, as in the case of $Nd_2Fe_{14}B$, and much effort has been devoted to the search for intermetallic systems whose magnetic properties might surpass those of $Nd_2Fe_{14}B$, which is limited in application by its comparatively low Curie temperature.[1] Two families of intermetallics, the rhombohedral $R_2(Fe,M)_{17}$ and tetragonal $R(Fe,M)_{12}$ compounds, have received special attention since they are both able to absorb N and C as interstitial atoms, with remarkable improvements in their magnetic properties resulting. In fact, $Sm_2Fe_{17}N_{3-\delta}$ and $Nd(Fe,Ti)_{12}N_{1-\delta}$ both have uniaxial anisotropy and Curie temperatures over 700 K.

As early as 1990, Jang and Stadelmaier[2] demonstrated that the tetragonal $NdFe_{11}Ti$ phase is unstable at temperatures below about 1000 °C, decomposing into $Nd_2(Fe,Ti)_{17}$, Fe_2Ti, and α-Fe(Ti), a fact missed by many workers. In 1992, whilst studying the conditions of formation of $NdFe_{11}Ti$, with a view to preparing single-phase material for subsequent nitrogenation and ultimately $NdFe_{11}TiN_{1-\delta}$ based permanent magnets, Collocott *et al.*[3] reported the formation of a new high-temperature phase in the Fe-rich corner of the Nd-Fe-Ti ternary phase diagram (see also Margarian *et al.*[4]). The new structure was given as $Nd_2(Fe,Ti)_{19}$ by Collocott *et al.*[3] and its x-ray diffraction (XRD) pattern was indexed on the basis of a (2a,4c) superstructure of the hexagonal $TbCu_7$ structure. The $Nd_2(Fe,Ti)_{19}$ compound had a rather low Curie temperature of 411 K but absorption of nitrogen gave a roughly 50% increase in Curie temperature. However, the easy direction of magnetization is in the basal plane (referred to the underlying hexagonal $TbCu_7$ cell) for both the parent and nitride compounds, precluding its use as a permanent magnet.

There are a number of reports of Sm-Fe-Ti and Nd-Fe-Ti phases at around the same composition as the $Nd_2(Fe,Ti)_{19}$ compound of Collocott *et al.*[3] For example, Saito *et al.*[5] and Ohashi *et al.*[6] both observed a transformation from a tetragonal $ThMn_{12}$ structure to a disordered hexagonal $TbCu_7$ structure in rapidly quenched $SmFe_{11}Ti$ as the quenching rate increased. Similarly, Katter *et al.*[7] observed a transformation from the rhombohedral Th_2Zn_{17} structure to the $TbCu_7$ structure in Sm-Fe alloys around the 1:9 composition, and Neiva *et al.*[8] reported the formation of a 1:7 phase with composition $Sm(Fe,Ti)_9$. Jang and Stadelmaier[2] reported a Ti-stabilized $NdFe_7$ phase in as-cast alloys. At the same conference at which Collocott *et al.* reported the formation of the $Nd_2(Fe,Ti)_{19}$ phase,[3] Hirosawa *et al.*[9] reported the formation of a $Nd(Fe,Ti)_9$ phase with the $TbCu_7$ structure during a study of the formation of the $ThMn_{12}$-type $NdFe_{11}Ti$ phase. A common feature of many of these reports is the transformation from the 2:17 or 1:12 structures to the disordered 1:7

 0021-8979/94/76(10)/6138/6/$6.00 © 1994 American Institute of Physics

structure by rapid solidification with increasing quenching rate.

At the 38th Annual MMM Conference in Minneapolis in November 1993, Cadogan *et al.*[10] reported that the new $Nd_2(Fe,Ti)_{19}$ structure is monoclinic with a cell derived from that of $TbCu_7$. At the same conference, Li *et al.*[11] reported the observation of a $Pr_2(Fe,Ti)_{19}$ phase in a study of the $(Pr_{1-x}Ti_x)Fe_5$ compounds. During discussions at the MMM Conference we learned that the General Motors group (Fuerst *et al.*) had also observed the formation of a new structure in samples of the form $NdFe_{9.5-x}M_x$ ($x=0.5$ for M=Ti, 1.5 for M=Cr and $x>3.5$ for M=Mn) with virtually identical XRD patterns to that of our $Nd_2(Fe,Ti)_{19}$ sample.[3,10] Fuerst *et al.*[12] were the first to suggest that the new phase belongs to the $P2_1/c$ space group, which was later confirmed by x-ray[13] and neutron[14] powder diffraction work. The structural determinations[13,14] also showed that the stoichiometry previously referred to as $Nd_2(Fe,Ti)_{19}$ is in fact $Nd_3(Fe,Ti)_{29}$. The $R_3(Fe,Ti)_{29}$ phase is now known to form with R=Sm,[15] Pr,[11] Ce,[16] and Gd,[17] in addition to R=Nd.

In this article we shall review the structural and magnetic properties of the new $R_3(Fe,M)_{29}$ phases.

In the original paper by Collocott *et al.*[3] the new Nd-Fe-Ti phase was denoted $Nd_2(Fe,Ti)_{19}$ and found to form with high-temperature annealing (1100 °C). This structure only forms for a Ti content in the range 3.8–5.1 at. % and was indexed as a (2a,4c) superlattice of the hexagonal $TbCu_7$ structure. Earlier work by Ivanova, Shcherbakova, and co-workers[18,19] also showed evidence of a new structure in the $R_2(Fe_{0.91}V_{0.09})_{17}$ (R=Y, Nd, Sm, and Gd) compounds and these workers described the crystal cell as being a (5a,5c) superlattice of the hexagonal $CaCu_5$ structure for R=Y and a distorted orthorhombic variant of the hexagonal $CaCu_5$ structure for R=Nd, Sm, and Gd. The similarities between the XRD patterns of the $Sm_2(Fe_{0.91}V_{0.09})_{17}$ sample of Shcherbakova *et al.*[19] and the $Nd_2(Fe,Ti)_{19}$ sample of Collocott *et al.*[3] strongly suggest that these samples in fact have the same crystal structure.

The structure of $Nd_2(Fe,Ti)_{19}$ was reported as monoclinic by Cadogan *et al.*[10] and Fuerst *et al.*,[12] the latter group suggesting the $P2_1/c$ space group and also that the crystal cell contained six $NdFe_{9.5-x}M_x$ units, on the basis of density measurements.

The final structural refinement was obtained from x-ray powder diffraction work by Li *et al.*[13] who confirmed the monoclinic $P2_1/c$ space group and showed that the correct stoichiometry of the new phase is $Nd_3(Fe,Ti)_{29}$ with two formula units per cell. The 3:29 stoichiometry represents a difference of 1.7% from the original 2:19 stoichiometry. At the same time, Yelon and co-workers[14] refined the 3:29 structure by neutron powder diffraction, and there is excellent agreement between these two structural refinements. In Fig. 1 we show the powder XRD patterns (Cu$K\alpha$ radiation) of $Nd_3(Fe,Ti)_{29}$, together with those of $Nd_2(Fe,Ti)_{17}$ and $Nd(Fe,Ti)_{12}$ for comparison, and in Fig. 2 we show the crystal structure of $Nd_3(Fe,Ti)_{29}$ (courtesy of Hu and Yelon[14]).

The structure of $Nd_3(Fe,Ti)_{29}$ is intermediate between the well-known rhombohedral Th_2Zn_{17} and tetragonal $ThMn_{12}$ structures. The common feature of all these structures is that

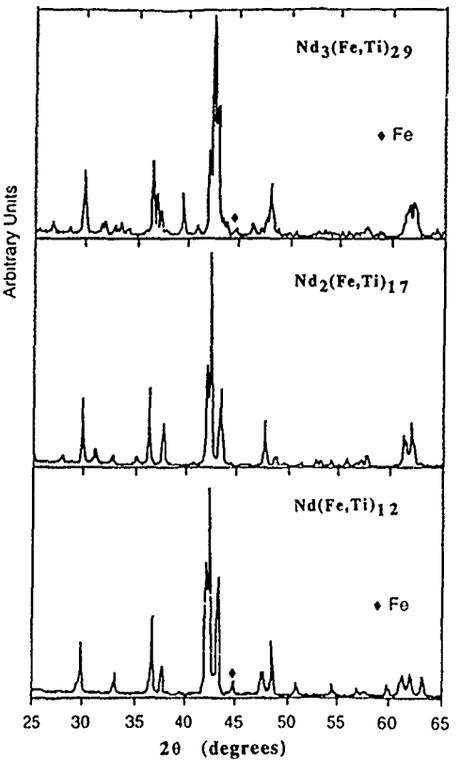

FIG. 1. X-ray powder diffraction patterns (Cu$K\alpha$) of monoclinic $Nd_3(Fe,Ti)_{29}$, rhombohedral $Nd_2(Fe,Ti)_{17}$ and tetragonal $Nd(Fe,Ti)_{12}$.

they are formed by the replacement of R atoms by T-T "dumb-bells" in the hexagonal RT_5 structure. This process may be described by the equation

$$R_{1-x}(2T)_xT_5 \rightarrow RT_y$$

with the 2:17 structure corresponding to a $\frac{1}{3}$ replacement and the 1:12 structure corresponding to a $\frac{1}{2}$ replacement. The new 3:29 structure corresponds to a $\frac{2}{5}$ replacement and is formed by the alternate stacking of 2:17 and 1:12 segments, in the

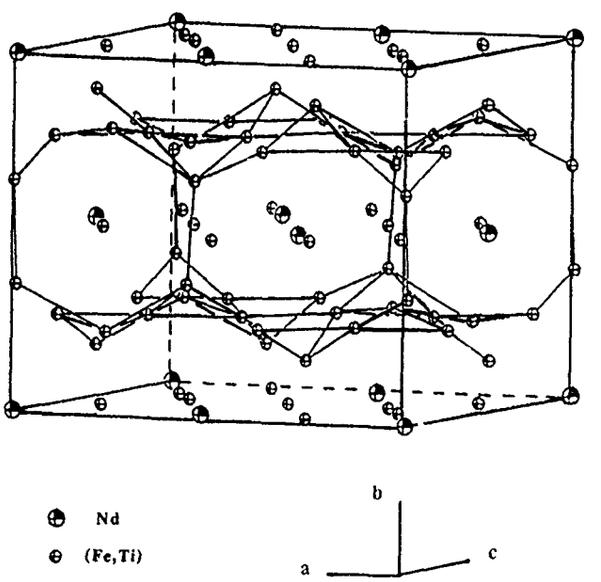

FIG. 2. Monoclinic unit cell of $Nd_3(Fe,Ti)_{29}$ (Ref. 14).

TABLE I. Lattice parameters and indexation cells used in the analysis of x-ray and neutron diffraction data on the $R_3(Fe,M)_{29}$ compounds. The atomic content of the M atom is at. %. [* The indexation of $Y_2(Fe,V)_{17}$ by Shcherbakova *et al.*[19] was given in both hexagonal and orthorhombic forms for comparison with their other $R_2(Fe,V)_{17}$ compounds. The lattice parameter a is therefore determined by $a=b\sqrt{3}$ since Shcherbakova *et al.* indexed $Y_2(Fe,V)_{17}$ as a true hexagonal structure.]

R	M	at. % M	a(Å)	b(Å)	c(Å)	β(°)	Cell	Ref.
Y	V	8.1	24.3	···	20.9	···	hexag.	18
Y	V	8.1	42.09	24.30	20.90	···	ortho-hex	*19
Nd	V	8.1	42.80	24.31	21.04	···	ortho.	19
Sm	V	8.1	42.60	24.27	20.99	···	ortho.	19
Gd	V	8.1	42.45	24.30	20.86	···	ortho.	19
Nd	Ti	4.1	9.88	···	16.96	···	hexag.	3
Nd	Ti	4.1	10.644	8.585	9.755	96.92	mono.	10
Nd	Ti	4.8	10.65	8.59	9.75	96.9	mono.	12,30
Nd	Ti	4.1	10.641	8.5913	9.748	96.928	mono.	13
Nd	Ti	3.9	10.6628	8.6056	9.7610	96.996	mono.	14
Nd	Ti	3.6	10.62	8.58	9.73	96.912	mono.	22
Sm	Ti	6.1	10.65	8.58	9.72	96.98	mono.	15
Sm	Ti	6.3	10.62	8.56	9.72	96.972	mono.	22
Sm	Ti	3.8	10.63	8.57	9.72	97.0	mono.	30
Ce	Ti	5.0	10.56	8.49	9.68	96.7	mono.	30
Pr	Ti	4.5	10.63	8.59	9.74	96.892	mono.	22
Pr	Ti	4.7	10.64	8.63	9.76	97.1	mono.	30
Ce	Cr	12.8	10.53	8.45	9.63	96.8	mono.	30
Nd	Cr	14.3	10.60	8.55	9.71	96.8	mono.	12
Nd	Cr	13.8	10.59	8.56	9.71	96.9	mono.	30
Sm	Cr	14.1	10.56	8.51	9.68	96.9	mono.	30
Nd	Mn	33.3	10.65	8.61	9.75	96.9	mono.	12

ratio 1:1. Such structural relationships were considered by Stadelmaier in 1984,[20] who indeed predicted the occurrence of a number of novel structures including the 3:29 structure. Stadelmaier showed that such new structures must have one edge length equal to $a_0\sqrt{3}$ where a_0 is the relevant lattice parameter of the 1:5 cell. Both structural refinements of $Nd_3(Fe,Ti)_{29}$ (Refs. 13,14) have $b\sim a_0\sqrt{3}$, in agreement with Stadelmaier's criterion. In Table I we give the lattice parameters and indexation cells of the various $R_3(Fe,M)_{29}$ compounds studied to date.

TABLE II. Atomic positions and lattice parameters of $Nd_3(Fe_{0.955}Ti_{0.045})_{29}$ obtained from the x-ray powder diffraction pattern refinement according to the space group $P2_1/c$.[13]

Atom	Site	x	y	z
Nd	$2a$	0	0	0
Nd	$4e$	0.5925(4)	0	0.1851(1)
Fe	$2d$	1/2	1/2	0
Fe	$4e_1$	0.8570(5)	1/2	0.2141(1)
Fe	$4e_2$	0.2570(5)	1/2	0.0141(1)
Fe	$4e_3$	4/5	0.785(1)	1/10
Fe	$4e_4$	4/5	0.215(1)	1/10
Fe	$4e_5$	0.628(1)	0.638(2)	0.1858(1)
Fe	$4e_6$	0.628(1)	0.362(2)	0.1858(1)
Fe	$4e_7$	0	0.853(2)	1/2
Fe	$4e_8$	0.892(1)	0	0.284(2)
Fe	$4e_9$	4/5	1/4	7/20
Fe	$4e_{10}$	4/5	3/4	7/20
Fe	$4e_{11}$	0.706(1)	1/2	0.411(2)
Fe	$4e_{12}$	0.410(2)	3/4	0.072(4)
Fe	$4e_{13}$	0.597(2)	3/4	0.444(4)
Fe	$4e_{14}$	0	3/4	1/4
	R_p=8.8%		a=10.641(1) Å	
	R_{wp}=11.9%		b=8.5913(8) Å	
	R_{expt}=5.9%		c=9.748(1) Å	
	R_{Bragg}=5.6%		β=96.928(6)°	
			Z=2	

The monoclinic $R_3(Fe,M)_{29}$ structure contains two R sites (2a and 4e) and fifteen Fe(M) sites (2d and fourteen 4e sites), and in Table II we give the atomic positions of these sites, deduced by Li *et al.*[13] from x-ray powder diffraction. The relationships between the lattice parameters of the 3:29 and 1:5 structures are

$$a=\sqrt{(2a_0)^2+(c_0)^2}$$

$$b=\sqrt{3}a_0$$

$$c=\sqrt{(a_0)^2+(2c_0)^2}$$

$$\beta=\arctan\left(\frac{2a_0}{c_0}\right)+\arctan\left(\frac{a_0}{2c_0}\right),$$

and in Fig. 3 we show the relationship between the 3:29 and 1:7 crystal cells.[10] In Fig. 4 we show a schematic representation of the dumb-bell substitution sequence, projected onto the (110) plane of the $CaCu_5$ structure, for the 2:17, 3:29, and 1:12 structures.[13]

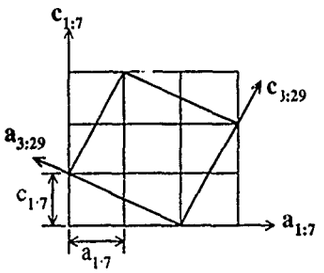

FIG. 3. Crystallographic relationship in the a-c plane between the monoclinic unit cell of $Nd_3(Fe,Ti)_{29}$ and the hexagonal $TbCu_7$ cell (Ref. 10).

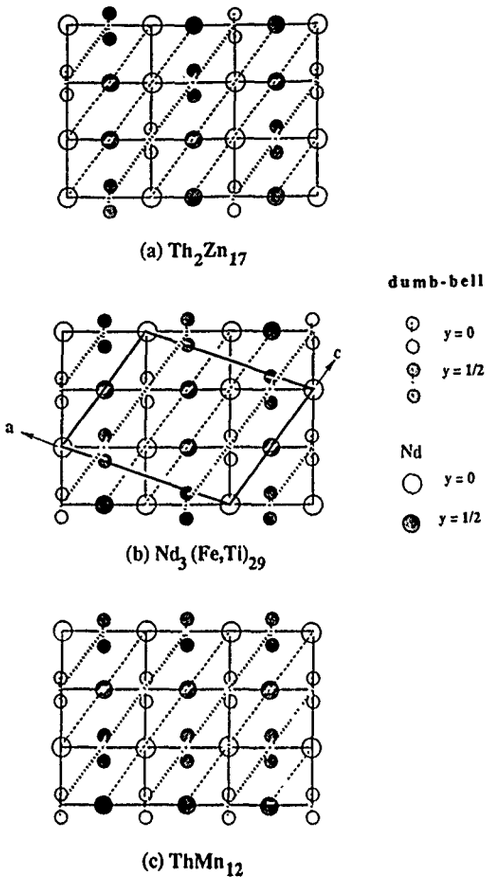

FIG. 4. Schematic representation of the geometrical relationship and the dumb-bell substitution sequence, in a projection onto the (110) plane of the hexagonal $CaCu_5$ structure for the 3:29, 2:17, and 1:12 structures (Ref. 13).

The rhombohedral 2:17 structure forms with light R atoms by a regular dumb-bell replacement in the 1:5 structure, and we therefore suggest that the new monoclinic 3:29 structure will also form only for light R (including Gd). It is quite likely that a different structure derived from the stacking of *hexagonal* 2:17 and tetragonal 1:12 segments will exist for 3:29 compounds with heavy R atoms. It is also likely that other intermediate phases based on the stacking of the rhombohedral 2:17 and tetragonal 1:12 segments will exist, besides 3:29. For example, a 2:1 stacking ($\frac{3}{8}$ dumb-bell replacement) would correspond to a 5:46 phase, whereas a 1:2 stacking ($\frac{3}{7}$ dumb-bell replacement) would correspond to a 4:41 phase.

Hu and Yelon[14] drew attention in their paper to the fact that the crystal structure of 3:29 shows a distinct stacking along the *b* direction which is reminiscent of the $Nd_2Fe_{14}B$ structure, in that there is an alternating stacking of R-containing and R-free layers. Furthermore, they pointed out that the distinction between the dumb-bell and non-dumb-bell Fe sites is not as clear-cut as in the 2:17 and 1:12 structures, since the 3:29 structure exhibits a number of rather short Fe-Fe bonds (<2.45 Å). Taking advantage of the fact that Ti has a negative neutron scattering length, Hu and Yelon demonstrated that the Ti atoms in $Nd_3(Fe,Ti)_{29}$ occupy sites with a low Nd coordination. In a subsequent paper, Hu and Yelon[21] presented a comprehensive summary of the bond lengths in $Nd_3(Fe,Ti)_{29}$ and showed that the distribution in bond length is virtually continuous over the range 2.36–3.01 Å, in contrast to the $Nd_2(Fe,Ti)_{17}$ and $Nd(Fe,Ti)_{12}$ compounds. In their paper, Hu and Yelon also reported the formation of $Nd_3(Fe,V)_{29}$ and $Nd_3(Fe,Al)_{29}$, but no structural details were presented.

The $R_3(Fe,M)_{29}$ compounds are ferromagnetic with Curie temperatures in the range 296 K [R=Ce, M=Cr (Ref. 30)] to 524 K [R=Gd, M=V (Ref. 19)]. XRD experiments on magnetically aligned powder samples of $Nd_3(Fe,Ti)_{29}$ (Ref. 22) and $Sm_3(Fe,Ti)_{29}$ (Ref. 15) indicate that the easy direction of magnetization is in the *a*-*b* basal plane (hexagonal description), along [201], whereas the powder neutron diffraction results of Hu and Yelon[14,21] were interpreted in

TABLE III. Intrinsic magnetic parameters (Curie temperature, saturation magnetization and anisotropy field) of the $R_3(Fe,M)_{29}$ compounds (*=12 K measurement and ×=77 K measurement).

R	M	at. % M	T_c (K)	M_{sat}(4 K) (μ_B/f.u.)	M_{sat}(RT) (μ_B/f.u.)	B_a(4 K) (T)	B_a(RT) (T)	Ref.
Y	V	8.1	439	41	···	3.8	···	18
Y	V	8.1	439	41	···	···	···	19
Nd	V	8.1	480	50	···	···	···	19
Sm	V	8.1	490	41	···	23.9	17.3	19
Gd	V	8.1	524	24	···	···	···	19
Ce	Ti	5.0	322	47.0	31.4	···	···	30
Pr	Ti	4.5	373	56.4*	46.2	6.3*	4.0	22
Pr	Ti	4.7	393	60.7	45.4	···	···	30
Nd	Ti	4.1	480	46.3	42.1	···	···	3
Nd	Ti	4.1	411	57.3	48.6	···	···	10
Nd	Ti	4.8	424	58.9	44.5	···	···	12
Nd	Ti	3.9	361	···	···	···	···	21
Nd	Ti	3.6	396	58.2*	47.6	9.8*	7.7	22
Nd	Ti	4.1	426	···	···	···	···	26
Nd	Ti	5.0	419	58.5	44.8	···	···	30
Sm	Ti	6.1	486	46.0×	43.8	···	···	15
Sm	Ti	6.3	452	50.8*	43.6	7.8*	5.8	22
Sm	Ti	3.8	469	51.6	45.2	···	···	30
Ce	Cr	12.8	296	35.4	···	···	···	30
Nd	Cr	14.3	417	45.0	33.4	···	···	12
Nd	Cr	13.8	410	45.3	34.5	···	···	30
Sm	Cr	14.1	423	38.6	31.1	···	···	30
Nd	Mn	33.3	<295	17.1	···	···	···	12

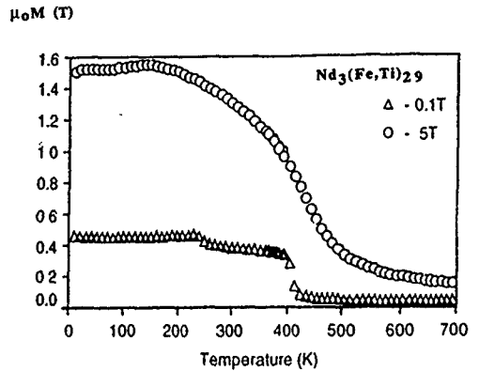

FIG. 5. Magnetization curves for $Nd_3(Fe,Ti)_{29}$ in applied fields of 0.1 and 5 T (Ref. 10).

terms of the magnetically easy direction being the crystal a-axis at 295 K. The saturation magnetization of $Nd_3(Fe,Ti)_{29}$ is 58 μ_B/f.u. at 4 K and 47 μ_B/f.u. at 295 K, and its anisotropy field B_a=7.7 T at 295 K and 9.8 T at 12 K.[10,22] In Table III we summarize the intrinsic magnetic properties of the various $R_3(Fe,M)_{29}$ compounds.

The temperature dependence of the magnetization of $Nd_3(Fe,Ti)_{29}$ presented by Cadogan *et al.*[10] (Fig. 5) shows clear evidence of a magnetization reorientation around 220 K (B_{appl}=0.1 T), and recent low-temperature neutron work by Hu and Yelon[21] confirms a shift in the easy direction of magnetization away from the crystal a axis (at 295 K) to the a-b plane (at 12.5 K). Our analysis of ^{57}Fe average hyperfine fields, deduced from Mössbauer measurements, also supports the occurrence of a spin reorientation at low temperatures.[23] Other evidence of magnetization reorientations in the form of FOMPs (first-order magnetization processes) has been reported by Fuerst *et al.*[12] who observed a FOMP in the magnetization of $NdFe_{9.0}Ti_{0.5}$ measured on fixed powders at 5 K; the observed FOMP field is 2.0 T. Yang *et al.*[15] also observed a FOMP in $Sm_3(Fe,Ti)_{29}$ by singular-point detection measurements; their FOMP fields are 2.2 T at 77 K and 3.0 T at 4 K. The exact nature of the magnetization reorientations in $Nd_3(Fe,Ti)_{29}$ are as yet unclear.

Finally, Fuerst *et al.*[12] reported that their $NdFe_{6.0}Mn_{3.5}$ sample had a coercive field of 3.8 kOe at 5 K, whereas their $NdFe_{9.0}Ti_{0.5}$ and $NdFe_{8.0}Cr_{1.5}$ samples had coercivities less than 1.2 kOe.

Shcherbakova *et al.*[19] demonstrated that their $R_2(Fe_{0.91}V_{0.09})_{17}$ (R=Y, Nd, Sm, and Gd) phases all absorb nitrogen with substantial increases in Curie temperature ensuing (see Table IV). Significantly, they also found an easy [001] direction of magnetization (hexagonal description) in $Sm_2(Fe_{0.91}V_{0.09})_{17}N_{2.5}$ and measured anisotropy fields B_a of 23.9 T at 4 K and 17.3 T at 260 K. The formation of a carbide $Y_2(Fe_{0.91}V_{0.09})_{17}C_{1.0}$, which had a modest 30 K increase in Curie temperature over the parent phase, was also reported by these authors.

Collocott *et al.*[3] showed that $Nd_3(Fe,Ti)_{29}$ absorbs nitrogen, with a 5.4% increase in volume and a 45% increase in Curie temperature resulting. However, their XRD patterns on magnetically aligned powder samples showed that both the parent and nitride compounds had a-b planar anisotropy.

Yang *et al.*[24] reported the formation of $Sm_3(Fe,Ti)_{29}N_5$ with a 7.1% volume increase relative to the parent phase. The Curie temperature of the nitride was 750 K compared to 486 K for the parent phase and, importantly, $Sm_3(Fe,Ti)_{29}N_5$ shows c-axis anisotropy. The anisotropy field of $Sm_3(Fe,Ti)_{29}N_5$ is 18.1 T at 4 K, and Yang *et al.*[24] were able to develop a coercivity of $\mu_0 H_{c_i}$ = 1.3 T at 4 K. Subsequent work by Hu *et al.*[25] on ball-milled $Sm_3(Fe,Ti)_{29}N_5$ produced a maximum energy product $(BH)_{max}$ of 105 kJ m^{-3} after ball milling for 4.5 h.

Ryan *et al.*[26] have studied the absorption of hydrogen and nitrogen by $Nd_3(Fe,Ti)_{29}$ using thermopiezic analysis, thermogravimetric analysis (TGA), and ^{57}Fe Mössbauer spectroscopy, and found that the addition of hydrogen leads to a significant increase in Curie temperature but very little change in Fe moment, whereas the addition of nitrogen increases both parameters. Attempts to form a $Nd_3(Fe,Ti)_{29}$ carbide were unsuccessful due to disproportionation of the material, although a "magnetic event" was observed by TGA at 660 K which was tentatively assigned to a $Nd_3(Fe,Ti)_{29}C_x$ phase.

As mentioned earlier, the 3:29 structure is formed by the 1:1 alternate stacking of 2:17 and 1:12 segments and Li[27] has identified the interstitial sites available to N or C atoms in the 3:29 structure by considering the interstitial sites in the 1:12 and 2:17 structures. There are two 4e interstitial sites with the special atomic positions $(\frac{1}{5}\frac{1}{2}\frac{2}{5})$ and $(\frac{1}{2}\frac{1}{4}\frac{1}{4})$, giving a maximum N content of $Nd_3(Fe,Ti)_{29}N_4$ according to the relation

TABLE IV. Intrinsic magnetic properties and volume expansions of the $R_3(Fe,M)_{29}N_x$ compounds [×=12 K measurement and * refers to $Nd_3(Fe,Ti)_{29}H_x$].

R	M	at. % M	×	ΔV(%)	T_c (K)	M_{sat}(4 K) (μ_B/f.u.)	M_{sat}(RT) (μ_B/f.u.)	B_a(4 K) (T)	B_a(RT) (T)	Ref.
Y	V	8.1	4	···	706	···	···	···	···	19
Nd	V	8.1	4	···	706	···	···	···	···	19
Sm	V	8.1	4	6	743	···	···	···	···	19
Gd	V	8.1	4	···	728	···	···	···	···	19
Nd	Ti	4.1	4	5.4	695	···	57.6	···	···	3
Nd	Ti	4.1	4.5	6.5	723	···	···	···	···	26
Sm	Ti	6.1	5	7.1	750	60.9	53.3	18.1	12.8	24
Nd	Ti	4.1	6.1*	2.2	>548	···	···	···	···	26
Pr	Ti	4.5	5.4	6.9	700	68.8×	63.6	13.9×	7.5	22
Nd	Ti	3.6	4.7	5.4	725	61.3×	61.7	19.4×	8.1	22
Sm	Ti	6.3	3.8	5.3	710	59.4×	52.3	14.3×	10.7	22

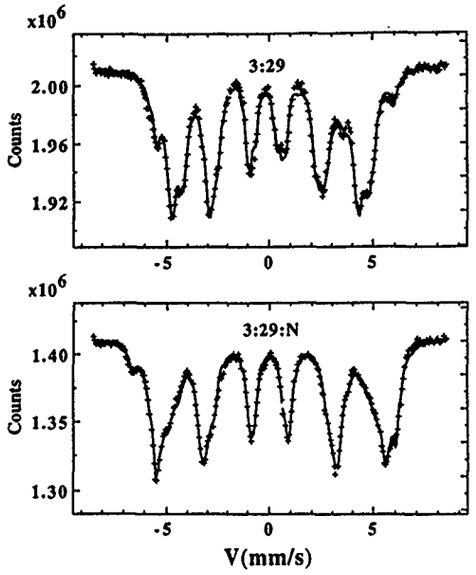

FIG. 6. ^{57}Fe Mössbauer spectra of $Nd_3(Fe,Ti)_{29}$ and $Nd_3(Fe,Ti)_{29}N_{4.5}$ obtained at 12 K with a ^{57}CoRh source (Ref. 26).

$$R_2M_{17}N_3+RM_{12}N_1\rightarrow R_3M_{29}N_4.$$

Ryan and Cadogan[26] calculated the sizes of the holes in the 3:29 structure and found that all holes capable of accommodating interstitial H, N, or C are 4*e* sites. The two largest holes have radii of 0.64 and 0.59 Å and are thus able to accommodate N or C, giving $R_3M_{29}X_4$ as the maximum interstitial X content. The next largest hole has a radius of 0.45 Å, which is too small for N or C but can accommodate H, giving a maximum H content of $R_3M_{29}H_6$, as observed.[26]

In Table IV we summarize the work on interstitially modified 3:29 compounds. The interstitial contents are approximate values, and we note that the results on the $Sm_3(Fe,Ti)_{29}$ nitride by Yang *et al.*[24] and Hu *et al.*[25] give a nitrogen content of N_5. Ryan *et al.*[26] calculated a nitrogen content of $N_{4.5}$ in $Nd_3(Fe,Ti)_{29}N_x$ but caution that such results with $N_{>4}$ may be due to partial decomposition of the samples.

The room-temperature ^{57}Fe Mössbauer spectra of $Nd_3(Fe,Ti)_{29}$ and its nitride were presented by Cadogan *et al.*,[28] along with spectra of $Nd_2(Fe,Ti)_{17}$ and $Nd(Fe,Ti)_{12}$ for comparison. The $Nd_3(Fe,Ti)_{29}$ phase has an average ^{57}Fe hyperfine field $\langle B_{hf}\rangle$ of 20.8 T at 295 K which corresponds to an average Fe moment of 1.33 μ_B, assuming a conversion factor of 15.6 T/μ_B.[29] The corresponding $\langle B_{hf}\rangle$ values of $Nd_2(Fe,Ti)_{17}$ and $Nd(Fe,Ti)_{12}$ are 15.4 and 24.8 T, respectively. The $\langle B_{hf}\rangle$ of $Nd_3(Fe,Ti)_{29}N_4$ is 29.6 T at 295 K, the 42% increase in field being attributed to the N-induced increase in Curie temperature of about 200 K. Subsequent low-temperature (12 K) ^{57}Fe Mössbauer studies by Ryan *et al.*[26] gave $\langle B_{hf}\rangle$ values of 29.0 and 33.4 T for $Nd_3(Fe,Ti)_{29}$ and $Nd_3(Fe,Ti)_{29}N_{4.5}$, respectively. The $\langle B_{hf}\rangle$ values of $Nd_3(Fe,Ti)_{29}H_{6.1}$ are 30.2 and 26.4 T at 12 and 295 K, respectively.[26] Given the large number of Fe sites in the $Nd_3(Fe,Ti)_{29}$ structure (15 sites) and the effects of site occupation by Ti in $Nd_3(Fe,Ti)_{29}$, one can only deduce the average hyperfine parameters from the Mössbauer spectra, with any certainty. In Fig. 6 we show the ^{57}Fe Mössbauer spectra of $Nd_3(Fe,Ti)_{29}$ and $Nd_3(Fe,Ti)_{29}N_{4.5}$ obtained at 12 K with a ^{57}CoRh source.

Interestingly, a comparison of $\langle B_{hf}\rangle$ of $Nd_3(Fe,Ti)_{29}$ at 12 and 295 K (Ref. 26) with saturation magnetization results[22] suggests that the low-temperature magnetic structure of $Nd_3(Fe,Ti)_{29}$ is noncollinear (Cadogan *et al.*[23]).

[1] J. F. Herbst, Rev. Mod. Phys. **63**, 819 (1991); K. H. J. Buschow, Rep. Prog. Phys. **54**, 1123 (1991).
[2] T. S. Jang and H. H. Stadelmaier, J. Appl. Phys. **67**, 4957 (1990).
[3] S. J. Collocott, R. K. Day, J. B. Dunlop, and R. L. Davis, in Proceedings of the Seventh International Symposium on Magnetic Anisotropy and Coercivity in R-T Alloys, Canberra, July 1992, p. 437.
[4] A. Margarian, J. B. Dunlop, R. K. Day, and W. Kalceff (these proceedings).
[5] H. Saito, M. Takahashi, and T. Wakiyama, J. Appl. Phys. **64**, 5965 (1988).
[6] K. Ohashi, R. Osugi, and Y. Tawara, in Proceedings of the Tenth International Workshop on RE Magnets and their Applications, Kyoto, 1989, pp. 13–22.
[7] M. Katter, J. Wecker, and L. Schultz, J. Appl. Phys. **70**, 3188 (1991).
[8] A. C. Neiva, F. P. Missell, B. Grieb, E.-T. Henig, and G. Petzow, J. Less Common Met. **170**, 293 (1991).
[9] S. Hirosawa, K. Makita, T. Ikegami, and M. Umemoto, Proceedings of the Seventh International Symposium on Magnetic Anisotropy and Coercivity in Rare-Earth Transition Metal Alloys, Canberra, July 1992, pp. 389–402.
[10] J. M. Cadogan, H.-S. Li, R. L. Davis, A. Margarian, J. B. Dunlop, and P. B. Gwan, J. Appl. Phys. **75**, 7114 (1994).
[11] H.-S. Li, Suharyana, J. M. Cadogan, G. J. Bowden, J.-M. Xu, S. X. Dou, and H. K. Liu, J. Appl. Phys. **75**, 7120 (1994).
[12] C. D. Fuerst, F. E. Pinkerton, and J. F. Herbst, J. Magn. Magn. Mater. **129**, L115 (1994).
[13] H.-S. Li, J. M. Cadogan, R. L. Davis, A. Margarian, and J. B. Dunlop, Solid State Commun. **90**, 487 (1994).
[14] Z. Hu and W. B. Yelon (unpublished).
[15] F.-M. Yang, B. Nasunjilegal, H.-Y. Pan, J.-L. Wang, R.-W. Zhao, B.-P. Hu, Y.-Z. Wang, H.-S. Li, and J. M. Cadogan (unpublished).
[16] A. Margarian, J. B. Dunlop, and S. J. Collocott (to be published).
[17] J.-M. Xu, H.-S. Li, J. M. Cadogan, S. X. Dou, and H. K. Liu (to be published).
[18] G. V. Ivanova, Y. V. Shcherbakova, Y. V. Belozerov, A. S. Yermolenko, and Y. I. Teytel, Phys. Met. Metallogr. **70**, 63 (1990).
[19] Y. V. Shcherbakova, G. V. Ivanova, A. S. Yermolenko, Y. V. Belozerov, and V. S. Gaviko, J. Alloys Compounds **182**, 199 (1992).
[20] H. H. Stadelmaier, Z. Metallkd. **75**, 227 (1984).
[21] Z. Hu and W. B. Yelon (these proceedings).
[22] A. Margarian, J. B. Dunlop, S. J. Collocott, H.-S. Li, J. M. Cadogan, and R. L. Davis, submitted to the Eighth International Symposium on Magnetic Anisotropy and Coercivity in R-T Alloys, Birmingham, September 1994.
[23] J. M. Cadogan, D. H. Ryan, A. Margarian, and J. B. Dunlop (to be published).
[24] F.-M. Yang, B. Nasunjilegal, J.-L. Wang, H.-Y. Pan, W.-D. Qing, R.-W. Zhao, B.-P. Hu, Y.-Z. Wang, G.-C. Liu, H.-S. Li, and J. M. Cadogan (unpublished).
[25] B.-P. Hu, G.-C. Liu, Y.-Z. Wang, B. Nasunjilegal, R.-W. Zhao, F.-M. Yang, H.-S. Li, and J. M. Cadogan, J. Phys. Condens. Matter **6**, L197 (1994).
[26] D. H. Ryan, J. M. Cadogan, A. Margarian, and J. B. Dunlop (these proceedings).
[27] H.-S. Li (private communication).
[28] J. M. Cadogan, R. K. Day, J. B. Dunlop, and A. Margarian, J. Alloys Compounds **201**, L1 (1993).
[29] B.-P. Hu, H.-S. Li, and J. M. D. Coey, Hyp. Int. **45**, 233 (1989).
[30] C. D. Fuerst, F. E. Pinkerton, and J. F. Herbst (these proceedings).

Structural and magnetic properties of $R_3(Fe,T)_{29}$ compounds

C. D. Fuerst, F. E. Pinkerton, and J. F. Herbst
Physics Department, General Motors NAO Research and Development Center, 30500 Mound Road, Warren, Michigan 48090-9055

We report the formation of several members of the recently discovered class of $R_3(Fe,T)_{29}$ compounds and some of their intrinsic properties. Focusing on materials with T=Ti and Cr, we have prepared $R_3(Fe,Ti)_{29}$ (R=Ce, Pr, Nd, Sm) and $R_3(Fe,Cr)_{29}$ (R=Ce, Nd, Sm) compounds which all feature the novel monoclinic crystal structure first established for $Nd_3(Fe,Ti)_{29}$. In each of the Ti- and Cr-containing groups the Ce member has the smallest magnetization, Curie temperature, and unit cell, suggesting that the Ce ion is tetravalent, or nearly so, in this family of materials. We observed no evidence of $R_3(Fe,Ti)_{29}$ phase formation for R=Y, Gd, Dy, and Er. Our magnetization measurements indicate that only $Nd_3(Fe,Ti)_{29}$ and $Nd_3(Fe,Cr)_{29}$ exhibit spin reorientations, at temperatures of 235 and 145 K, respectively.

I. INTRODUCTION

A new class of rare earth-iron (R-Fe) compounds stabilized by a third element (T) has recently been discovered to form. The class was recognized initially as having the $R_2(Fe,T)_{19}$ stoichiometry, with $Nd_2(Fe,Ti)_{19}$ (Refs. 1–3), and $Nd_2(Fe,Cr)_{19}$, $Nd_2(Fe,Mn)_{19}$ (Ref. 3) as representatives; alloys of nominal composition $R_2(Fe_{0.91}V_{0.09})_{17}$ are also likely members.[4] Its prototypical lattice symmetry was identified as monoclinic and was found to correspond to the $P2_1/c$ space group (No. 14 of Ref. 5).[3] Structural investigations of the Nd-Fe-Ti phase by neutron[6] as well as x-ray[7] powder diffraction have since established that the precise stoichiometry is $R_3(Fe,T)_{29}$. Here we report the preparation and characterization of several other members of this fascinating class of compounds, including two Ce-based representatives: $R_3(Fe,Ti)_{29}$ (R=Ce, Pr, Nd, Sm) and $R_3(Fe,Cr)_{29}$ (R=Ce, Nd, Sm).

II. SAMPLE PREPARATION AND PHASE FORMATION

Ingots for this inquiry were prepared by induction melting high-purity elemental constituents in boron nitride crucibles. Our starting compositions contained 2%–10% excess rare earth relative to the $R_3(Fe,T)_{29}$ stoichiometry. The ingots were heat treated in vacuum for periods between five days and three weeks at various temperatures T_A to maximize the amount of $R_3(Fe,T)_{29}$ component. For the T=Ti (Cr) materials an anneal temperature T_A=1100 °C (1000 °C) was most appropriate, with the exception of $Ce_3(Fe,Ti)_{29}$ and $Ce_3(Fe,Cr)_{29}$, both of which required a much lower T_A of 900 °C. Phase occurrences were monitored by x-ray diffraction and electron beam microprobe analyses. The latter indicated (i) a rare earth concentration of 9.4±0.1 at. % for the principal phase, in excellent agreement with the $R_3(Fe,T)_{29}$ stoichiometry, and (ii) the values of x given in Table I for the specific $R_3Fe_{29-x}T_x$ compositions.

The heat-treated (R=Ce, Pr, Nd; T=Ti) materials were essentially single-phase $R_3(Fe,Ti)_{29}$. To illustrate this point with a representative example, Fig. 1 compares the Cu-K_α x-ray powder diffraction pattern of $Pr_3Fe_{27.5}Ti_{1.5}$ with a pattern calculated for that compound using the sites and nuclear position parameters obtained by Hu and Yelon[6] for $Nd_3(Fe,Ti)_{29}$. In the other samples contaminant phases detected by the electron microprobe analyses included $R(Fe,T)_{12}$, $R_2(Fe,T)_{17}$, $R(Fe,T)_2$, and α-Fe admixed with the element T. Figure 2 compares the observed Cu-K_α x-ray spectra of the annealed Ce-Fe-Ti and Ce-Fe-Cr ingots. The former [Fig. 2(a)] is essentially single-phase $Ce_3Fe_{27.4}Ti_{1.6}$, while the analytical results indicate that the latter [Fig. 2(b)] contains, in addition to the principal $Ce_3Fe_{24.9}Cr_{4.1}$ phase, minor amounts of $CeFe_{9.9}Cr_{2.1}$, $Fe_{0.8}Cr_{0.2}$, and $CeFe_{1.9}Cr_{0.1}$.

In our opinion the $R_3(Fe,T)_{29}$ phases are "high temperature" materials in the sense that they are not thermodynamically stable at room temperature. Put another way, they crystallize only at temperatures above some minimum value. To test this conjecture we heat treated an as-cast $Sm_{3.3}Fe_{27.5}Ti_{1.5}$ ingot for five days at 900 °C [well below T_A=1100 °C found to yield material chiefly composed of monoclinic

TABLE I. Crystallographic and magnetic properties of $R_3Fe_{29-x}T_x$ compounds. The monoclinic lattice parameters are a, b, c, and β; the unit cell volume is $V=abc\sin\beta$; ρ is the density derived from the lattice constants; T_C is the Curie temperature; and $4\pi M_s$ is the saturation magnetization.

R	Ce	Pr	Nd	Sm
T	Ti	Ti	Ti	Ti
x	1.6	1.5	1.6	1.2
a (Å)	10.56	10.64	10.65	10.63
b (Å)	8.49	8.63	8.59	8.57
c (Å)	9.68	9.76	9.75	9.72
β	96.7°	97.1°	96.9°	97.0°
V (Å^3)	862	880	886	878
ρ (g/cm^3)	7.81	7.58	7.65	7.79
T_C (K)	322	393	419	469
$4\pi M_s$(5 K) (kG)	12.7	15.9	15.4	13.7
$4\pi M_s$(295 K) (kG)	8.5	11.9	11.8	12.0
R	Ce	Nd	Sm	
T	Cr	Cr	Cr	
x	4.1	4.4	4.5	
a (Å)	10.53	10.59	10.56	
b (Å)	8.45	8.56	8.51	
c (Å)	9.63	9.71	9.68	
β	96.8°	96.9°	96.9°	
V (Å^3)	851	873	864	
ρ (g/cm^3)	7.90	7.74	7.90	
T_C (K)	296	410	423	
$4\pi M_s$(5 K) (kG)	9.7	12.1	10.4	
$4\pi M_s$(295 K) (kG)	···	9.2	8.4	

 0021-8979/94/76(10)/6144/3/$6.00 © 1994 American Institute of Physics

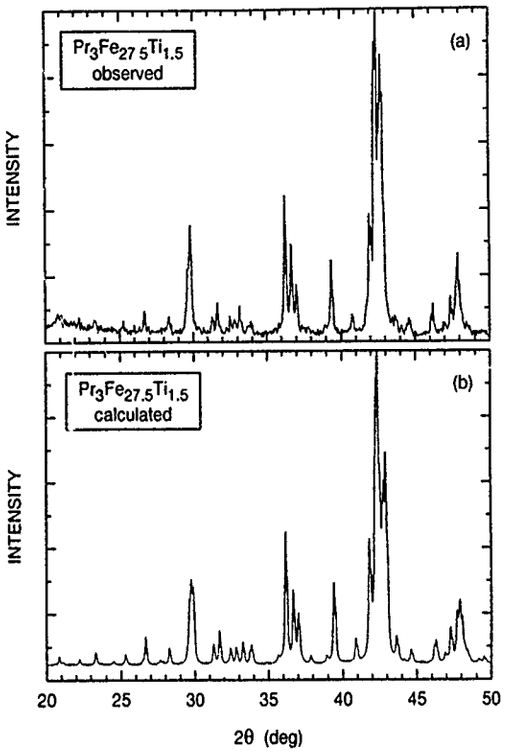

FIG. 1. (a) Cu-K_α x-ray powder diffraction pattern observed for $Pr_3Fe_{27.5}Ti_{1.5}$. (b) Pattern calculated for $Pr_3Fe_{27.5}Ti_{1.5}$ using crystallographic information from Ref. 6 and lattice constants (see Table I) inferred from (a).

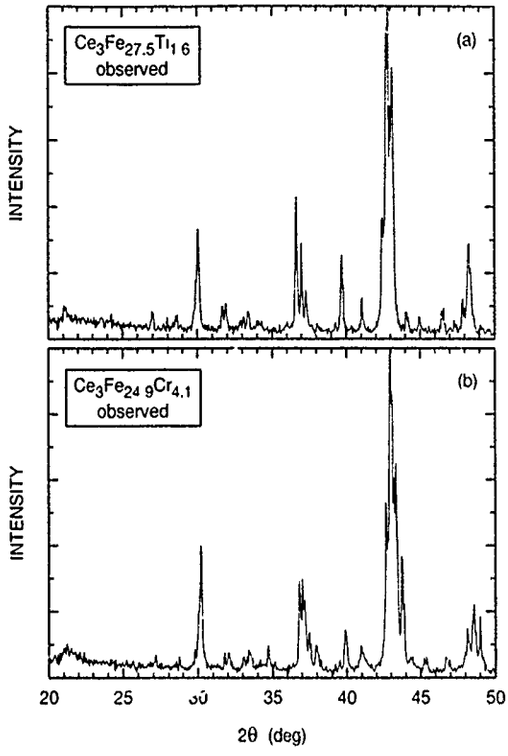

FIG. 2. Observed Cu-K_α x-ray powder diagrams for (a) $Ce_3Fe_{27.4}Ti_{1.6}$ and (b) $Ce_3Fe_{24.9}Cr_{4.1}$.

$Sm_3(Fe,Ti)_{29}$]. The x-ray pattern of the $T_A = 900$ °C sample closely resembles a pattern calculated for $SmFe_7$ having the rhombohedral $ThFe_4Co_4$-type defect structure,[8,9] which, judging from the similarity of their x-ray signatures, is related to the rhombohedral Th_2Zn_{17}-type structure characterizing Sm_2Fe_{17}.

Using compositions and anneal schedules similar to those employed for the materials of Table I we attempted to form $R_3(Fe,Ti)_{29}$ compounds with R=Y, Gd, Dy, and Er. All these samples, however, consisted primarily of material having the hexagonal Th_2Ni_{19}-type structure.[10,11] We surmise that monoclinic $R_3(Fe,Ti)_{29}$ does not form for Y and the heavy rare earths, for which a hexagonal Th_2Ni_{19} type [or hexagonal Th_2Ni_{17} type for slightly lower (Fe+Ti):R ratios] is the stable low temperature phase. Apparently monoclinic $R_3(Fe,Ti)_{29}$ can be formed only when the equilibrium room temperature phase has a rhombohedral structure of the $ThFe_4Co_4$ or Th_2Zn_{17} variety.

It is doubtful that $R_3(Co,Ti)_{29}$ compounds occur, at least for the light rare earths. A Nd-Co-Ti ingot annealed at 1000 °C principally contained Th_2Zn_{17}-type material.

III. RESULTS AND DISCUSSION

Crystallographic and magnetic information on the $R_3(Fe,T)_{29}$ compounds investigated here is summarized in Table I. The lattice parameters a, b, c, and β (corresponding to the second monoclinic setting, $\beta \neq 90°$) were inferred from the x-ray diagrams. The lanthanide contraction is evident from the decrease of a, b, and c as the atomic number of the rare earth constituent increases from Pr to Sm. The largest decline with R atomic number is shown by b, analogous to the larger decline of c in the tetragonal $R_2Fe_{14}B$ series (cf. Ref. 12). The common behavior likely reflects the fact that the R ions in $R_3(Fe,T)_{29}$ [$R_2Fe_{14}B$] reside in planes normal to the b direction[6,7] [c direction]. Through the $R_2Fe_{14}B$ series the basal plane cell constant a is confined to a narrow range by the particularly stable trigonal prisms of the $Nd_2Fe_{14}B$-type structure,[12] and we speculate that local atomic coordination effects restrict, in a similar way, the variation of a and c with R in the $R_3(Fe,T)_{29}$ series.

We determined Curie temperatures (T_C) by differential scanning calorimetry, and magnetization measurements were performed from 5 to 295 K with a vibrating sample magnetometer using a maximum applied field of 9 T. Values of T_C and the saturation magnetization ($4\pi M_s$) at 5 and 295 K are included in Table I.[13] For both the T=Ti and T=Cr groups T_C and $4\pi M_s$(5 K) are lowest for the Ce member, as is the (room temperature) unit cell volume V. Together these facts strongly suggest that the Ce ion is essentially tetravalent (i.e., has no $4f$-derived magnetic moment) in the $R_3(Fe,T)_{29}$ class of compounds.

If we assume that the Ce moment is zero, the $4\pi M_s$(5 K) values for $Ce_3Fe_{27.4}Ti_{1.6}$ and $Ce_3Fe_{24.9}Cr_{4.1}$ imply average Fe moments of ~1.7 and ~1.4 μ_B for the Ti and Cr materials, respectively. These average Fe moments together with the $4\pi M_s$(5 K) results for the other compounds indicate that the R moments are near their free ion values. Magnetization versus temperature measurements in a small applied field, 1 kOe, revealed spin reorientations of the easy magnetization

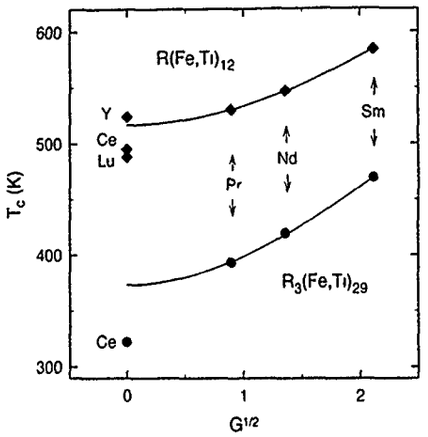

FIG. 3. Curie temperatures T_C of $R_3(Fe,Ti)_{29}$ (●) and $R(Fe,Ti)_{12}$ (♦) compounds vs $G^{1/2}$. The curves are specified by Eqs. (1)–(3) for the R=Pr, Nd, and Sm compounds of each series with the parameters given in the text.

direction at $T_s \cong 235$ K in $Nd_3Fe_{27.4}Ti_{1.6}$ and $T_s \cong 145$ K in $Nd_3Fe_{24.6}Cr_{4.4}$, but in none of the other compounds in Table I. Our $T_s(Nd_3Fe_{27.4}Ti_{1.6})$ agrees well with the measurements of Cadogan *et al.*[14] The slightly larger low-temperature magnetization of $Pr_3Fe_{27.5}Ti_{1.5}$ as compared with that of $Nd_3Fe_{27.4}Ti_{1.6}$ may reflect a noncollinear moment arrangement in the latter below T_s.

As is often the case for rare earth-transition metal series, T_C is an increasing function of the effective rare earth spin, gauged by $G^{1/2}$ where $G \equiv (g-1)^2 J(J+1)$ is the de Gennes factor for an R ion having gyromagnetic ratio g and total angular momentum quantum number J. This is shown for the T=Ti compounds by the filled circles of Fig. 3, which displays T_C vs. $G^{1/2}$. Ascribing the magnetism to Fe-Fe and R-Fe exchange interactions and neglecting R-R exchange, we can write $T_C(G)$ in the nearest-neighbor, mean-field approximation of the two-sublattice Heisenberg model, which is used widely in analyzing systematic T_C behavior in rare earth-transition metal compound series, as

$$T_C(G) = \tfrac{1}{2} T_C(0)(1+\sqrt{1+\gamma G}), \tag{1}$$

where

$$3k_B T_C(0) = Z_{FF} S_F (S_F+1) j_{FF} \tag{2}$$

and

$$\gamma = 4\left(\frac{Z_{FR} Z_{RF}}{Z_{FF}^2}\right) \frac{1}{S_F(S_F+1)} \left(\frac{j_{RF}}{j_{FF}}\right)^2. \tag{3}$$

Here Z_{AB} is the number of B neighbors of atom A (A,B≡R or Fe), S_F the Fe spin, and j_{AB} the exchange interaction energy of the A and B *spins*. A negative j_{RF} implies ferromagnetic coupling of light R and Fe *moments* and antiferromagnetic coupling of heavy R and Fe *moments*. From the work of Hu and Yelon[6] we estimate $Z_{FF}=10$, $Z_{FR}=2$, and $Z_{RF}=18$, and we take $S_F=1$ since the average Fe moment is $\sim 2\ \mu_B$ and the corresponding g factor can be expected to be near 2. A least-squares fit of Eqs. (1)–(3) to the Curie temperatures of the (R=Pr, Nd, Sm; T=Ti) compounds, in which the R ion is presumably trivalent, yields $j_{FF} \cong 2.4$ meV and $j_{RF} \cong -1.5$ meV. The fit generates the lower curve in Fig. 3 and provides excellent accommodation of the experimental results; the departure of $T_C(Ce_3Fe_{27.4}Ti_{1.6}) \cong 322$ K from the trend underscores the likelihood that Ce is tetravalent. For comparison purposes Fig. 3 also displays T_C values (diamonds) for the cognate $R(Fe,Ti)_{12}$ compounds.[15,16] A corresponding fit to them (the same estimates for Z_{AB} and S_F can be used)[15] yields $j_{FF} \cong 3.3$ meV and $j_{RF} \cong -1.4$ meV and is shown by the upper curve in Fig. 3. The stronger Fe-Fe exchange is responsible for the fact that the $R(Fe,Ti)_{12}$ Curie temperatures are 120–170 K higher than those of their $R_3(Fe,Ti)_{29}$ counterparts.

ACKNOWLEDGMENTS

It is a pleasure to thank M. P. Balogh, C. B. Murphy, G. W. Smith, R. A. Waldo, and A. M. Wims for their contributions to this work. We are also grateful to J. M. Cadogan and W. B. Yelon for useful discussions.

[1] S. J. Collocott, R. K. Day, J. B. Dunlop, and R. L. Davis, *Proceedings of the Seventh International Symposium on Magnetic Anisotropy and Coercivity in Rare-Earth Transition Metal Alloys*, Canberra, 1992 (Rare-earth Information Center, Ames, IA, 1992), p. 437.
[2] J. M. Cadogan, R. K. Day, J. B. Dunlop, and A. Margarian, J. Alloys Compounds **201**, L1 (1993).
[3] C. D. Fuerst, F. E. Pinkerton, and J. F. Herbst, J. Magn. Magn. Mater. **129**, L115 (1994).
[4] G. V. Ivanova, E. I. Teitel', and E. V. Shcherbakova, Phys. Met. Metallogr. **75**, 274 (1993).
[5] *International Tables for X-ray Crystallography*, edited by N. Henry and K. Lonsdale (Kynoch, Birmingham, 1952), Vol. 1, p. 99.
[6] Z. Hu and W. B. Yelon, Solid State Commun. **91**, 223 (1994).
[7] H-S. Li, J. M. Cadogan, R. L. Davis, A. Margarian, and J. B. Dunlop, Solid State Commun. **90**, 487 (1994).
[8] P. Villars and L. D. Calvert, *Pearson's Handbook of Crystallographic Data for Intermetallic Phases* (ASM International, Metals Park, OH, 1991), Vol. 3, p. 3392.
[9] A. E. Ray, Acta Crystallogr. **21**, 426 (1966).
[10] Reference 8, Vol. 4, p. 4713.
[11] D. Givord, F. Givord, R. Lemaire, W. J. James, and J. S. Shah, J. Less-Common Met. **29**, 389 (1972).
[12] J. F. Herbst, Rev. Mod. Phys. **63**, 819 (1991).
[13] We also find $T_C \cong 100$ K for the monoclinic Nd-Fe-Mn compound reported in Ref. 3.
[14] J. M. Cadogan, H-S. Li, R. L. Davis, A. Margarian, S. J. Collocott, J. B. Dunlop, and P. B. Gwan, J. Appl. Phys. **75**, 7114 (1994).
[15] H.-S. Li and J. M. D. Coey, in *Handbook of Magnetic Materials*, edited by K. H. J. Buschow (North-Holland, Amsterdam, 1991), Vol. 6, p. 1.
[16] S. F. Cheng, Y. Xu, S. G. Sankar, and W. E. Wallace, in *Proceedings of the Sixth International Symposium on Magnetic Anisotropy and Coercivity in Rare Earth-Transition Metal Alloys*, edited by S. G. Sankar (Carnegie–Mellon University, Pittsburgh, 1990), p. 400.

Magnetic and crystal structure of the novel compound $Nd_3Fe_{29-x}Ti_x$

Z. Hu and W. B. Yelon
University of Missouri Research Reactor, Columbia, Missouri 65211

The structure of the compound previously reported as $Nd_2Fe_{19-x}Ti_x$ has been solved by powder neutron diffraction, which reveals a monoclinic cell and a stoichiometry of $Nd_3Fe_{29-x}Ti_x$ ($x=1.24$) and two formula units per unit cell. This low symmetry, and the large number of crystallographically unique sites (17), lead to a wide range of Fe—Fe bond lengths (from 2.36 to 3.01 Å) in a nearly continuous band. The phase forms through the replacement of two-fifths of the rare earths in the RFe_5 phase by Fe-Fe dumbbells. The magnetic moments at room temperature lie along the monoclinic a axis with an average iron moment of 1.05 μ_B, while the magnetic moments at 12.5 K lie in the a-b plane with an average iron moment of about 1.36 μ_B.

I. INTRODUCTION

Binary rare-earth (R)-Iron (Fe) compounds are unsuitable for permanent magnet application due to their low Curie points. $Nd_2Fe_{14}B$, nitrides and carbides of R_2Fe_{17} and $RFe_{12-x}T_x$, where T is a transition element,[1–3] and pseudobinary compounds such as $R_2Fe_{17-x}T_x$, where T is Si, Al, or Ga, have significantly enhanced Curie points compared to the parent binary phases.[4–6] Studies of these materials have recently led to the discovery of a new pseudobinary phase, first identified as $R_2Fe_{17-x}T_x$ with a structure different from the well known Th_2Zn_{17} and Th_2Ni_{17} types,[7,8] then identified as $R_2Fe_{19-x}T_x$[9–11] and which has now been shown to have stoichiometry $R_3Fe_{29-x}T_x$.[12,13] This compound was originally formed with T=Ti at about 6% Fe/Ti replacement and has also been shown to form at higher replacement levels with Cr and Mn.[9] In attempting to form doubly-substituted $RFe_{12-x}T_x$, this phase was also formed with a V+Al replacement.[14] The monoclinic cell of this new phase is related to the $CaCu_5$ structure, and an approximate x-ray structure determination, based on the idealized positions of the $CaCu_5$ structure, was recently reported.[12] At the same time, powder neutron diffraction was used for an exact solution in which the magnetic moments at room temperature were also reported.[13] In this article the neutron diffraction results are extended to low temperature, further structural details are reported, and the results for $R_3Fe_{29-x}T_x$ are compared to those of Ti substituted Nd_2Fe_{17} and $NdFe_{12}$. These three different phases can be considered as modifications of the $CaCu_5$ structure with differing degrees of Fe-Fe dumbbell replacement of some of the rare earths.

II. RESULTS

The room-temperature and 12.5-K results of the neutron diffraction analysis of $Nd_3Fe_{27.76}Ti_{1.24}$ are given in Table I. The structure adapted from Ref. 13 is shown in Fig. 1. The layered structure is apparent from the figure in which only the shortest bonds (<2.4 Å) are shown. Although not constrained by symmetry, all of the Fe/Ti and Nd atoms in the first layer lie within 0.06 Å of the $y=0$ plane. In the second layer, which contains only Fe/Ti atoms, most are found very close to $y=\frac{1}{4}$. The atoms that deviate from this are clearly visible in the figure and are displaced due to the presence of Nd atoms nearly directly above or below them. The arrangement of the Fe/Ti atoms in this layer forms a nearly perfect hexagonal grid. As previously discussed, both the stacking of layers with and without rare earth, and the hexagonal arrangement, are also seen in $R_2Fe_{14}B$.[15] Other projections of the $R_3(Fe/Ti)_{29}$ structure show planes of atoms, although none so clearly as seen in this direction. This is a reflection of the relatively close-packed nature of the structure.

Table I also gives the coordinates used in the x-ray study.[12] Relatively few of these were refined, but the generally good agreement between these two sets of coordinates is an indication of the small deviation of this structure from the parent structure from which it is derived. It is easy to see that the R_2Fe_{17} structure is derived from the RT_5 structure ($CaCu_5$) by replacement of one-third of the rare earths by Fe-Fe pairs. It has been pointed out that the RFe_{12} structure can be formed from the same parent by replacement of one-half of the rare earths by the Fe-Fe dumbbells. The new compound, $R_3(Fe/T)_{29}$, is produced in the same fashion by replacement of two-fifths of the rare earths. This appears to be entirely regular and leads to the stoichiometric compound observed here. In Nd_2Fe_{17}, the dumbbell is clearly visible and the Fe—Fe bond length is unusually small—2.36 Å. In RFe_{12}, the dumbbells are less apparent, but it is important to note that this compound contains at least one T atom per unit cell and is thus expanded with respect to the idealized, but nonexistent pure Fe phase.

Because of the low symmetry and the large number of Fe sites, there are many more distinct bonding pathways in this compound than in either the R_2Fe_{17}- or RFe_{12}-type structures. The minimum bond length is 2.36 Å, as is seen in Nd_2Fe_{17}, but it is less separated from the other bonds, which form a continuous band up to at least 3 Å. The longest bonds are associated with the 14 coordinated Fe atoms shown in Table I, but similar 14-fold coordination is also seen in the R_2Fe_{17} and RFe_{12} structures. The Fe atoms have from one to three Nd neighbors, but the Ti atoms are found only at the three sites with a single Nd neighbor. Neutron diffraction data for $Nd_2Fe_{16.07}Ti_{0.93}$ and $NdFe_{10.9}Ti_{1.1}$ were also collected and analyzed, and the same Ti environment was observed in these compounds.

The range of bond lengths around each site and the average bond lengths are given in Table II for $Nd_3Fe_{27.76}Ti_{1.24}$, $Nd_2Fe_{16.07}Ti_{0.93}$, and $NdFe_{10.9}Ti_{1.1}$. This table excludes

 0021-8979/94/76(10)/6147/3/$6.00 © 1994 American Institute of Physics

TABLE I. Refinement results for $Nd_3Fe_{27.76}Ti_{1.24}$; space group: P21/C; cell volume=889.00 Å^3.

Atom, site	Neutron x	Neutron y	Neutron z	X ray[b] x	X ray[b] y	X ray[b] z	Neutron Ti%	Neutron coord.	Neutron 295 K (μm)	Neutron 12.5 K (μm)
Nd, 2*a*	0	0	0	0	0	0		20Fe	1.8(1)	2.2(2)
Nd, 4*e*	0.402(1)	0.007(2)	0.815(6)	0.408	0	0.81		19Fe	1.0(1)	1.4(1)
Fe, 2*d*	0.5	0	0.5	0.5	0	0.5		10Fe+2Nd	1.1(1)	1.2(2)
Fe, 4*e*1	0.110(1)	0.001(1)	0.722(1)	0.1063	0	0.7127		10Fe+2Nd	1.5(1)	1.5(2)
Fe, 4*e*2	0.291(1)	0.002(2)	0.094(1)	0.2937	0	0.0875		9Fe+3Nd	1.2(1)	1.4(2)
(Fe/Ti), 4*e*3	0.257(1)	−0.002(2)	0.526(1)	0.2552	0	0.5104	30.50	13Fe+1Nd	1.5(2)	1.8(2)
(Fe/Ti), 4*e*4	0.137(1)	0.001(3)	0.292(1)	0.1448	0	0.2896	21.40	13Fe+1Nd	1.3(1)	1.8(2)
Fe, 4*e*5	0.632(1)	0.143(1)	0.681(1)	0.6376	0.1401	0.6812		10Fe+2Nd	0.8[a]	1.2(2)
Fe, 4*e*6	0.806(1)	0.225(1)	0.088(1)	0.8	0.2147	0.1		10Fe+2Nd	1.2(1)	1.5(1)
Fe, 4*e*7	0.597(1)	0.243(1)	0.433(1)	0.6034	0.25	0.4535		9Fe+3Nd	0.6[a]	1.1(2)
Fe, 4*e*8	−0.004(1)	0.247(2)	0.257(1)	0	0.25	0.25		10Fe+2Nd	0.6(1)	1.1(3)
Fe, 4*e*9	0.406(1)	0.247(1)	0.062(1)	0.4195	0.25	0.0891		9Fe+3Nd	0.7[a]	1.2(3)
Fe, 4*e*10	0.802(1)	0.248(1)	0.847(1)	0.8	0.25	0.85		10Fe+2Nd	0.2(2)	0.8(3)
Fe, 4*e*11	0.197(1)	0.257(1)	0.161(1)	0.2	0.25	0.15		10Fe+2Nd	1.2(1)	1.6(2)
Fe, 4*e*12	0.204(1)	0.293(1)	0.410(1)	0.2	0.2853	0.4		10Fe+2Nd	0.9(1)	1.0(1)
Fe, 4*e*13	0.376(1)	0.355(1)	0.812(1)	0.3624	0.3599	0.8188		10Fe+2Nd	1.0(1)	1.4(2)
(Fe/Ti), 4*e*14	0.005(1)	0.356(1)	0.004(2)	0.0067	0.3542	−0.0034	10.30	13Fe+1Nd	1.1(1)	1.4(2)

Cell parameters and agreement factors of neutron and x-ray diffraction results

	a, Å	*b*, Å	*c*, Å	β	R_p	R_{wp}	R_{mag}	χ^2
Neutron 295 K	10.6628(2)	8.6056(2)	9.7610(2)	96.996(1)	3.61%	4.74%	5.95%	1.69
Neutron 12.5 K	10.6486(2)	8.6050(2)	9.7660(2)	96.833(1)	3.92%	5.23%	6.05%	2.04
X-ray[b]	10.6258	8.5814	9.7282	96.89	13.20%	16.10%		

[a]Moment unstable when refined—constrained to the average.
[b]X-ray data cited from Ref. 10 and transformed to the comparable coordinates.

Fe—Fe bonds over 2.8 Å that are assumed to contribute little or no magnetic energy. As already discussed, the Nd_2Fe_{17} parent has a short 2.36-Å bond. In the Ti-substituted compound, however, this bond has expanded to 2.47 Å due to the strong preference for the dumbbell Fe site by the larger Ti atom. The high symmetry of the RFe_{12} phase produces two groups of bonds, long and short, with a gap between. The other two compounds have a broader distribution. Table III gives the overall average bond lengths for these three samples (and Nd_2Fe_{17}) as well as their Curie points. For $Nd_3Fe_{27.76}Ti_{1.24}$, two values are given, including bond lengths to 2.8 and 2.99 Å. The dependence of the Curie point on bond length in other NdFe compounds[16] has previously been noted and a similar relationship is observed here if one does not include the very long Fe—Fe bonds, which obviously contribute little to the magnetic exchange energy.

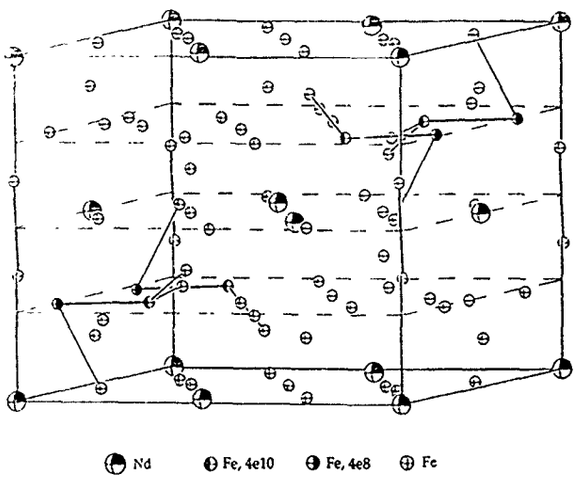

FIG. 1. Monoclinic unit cell of $Nd_3Fe_{29-x}Ti_x$ with the *B* axis up. The layers with $y=1/4$, 1/2, and 3/4 are drawn as well as the Fe—Fe bonds under 2.4 Å.

TABLE II. Site bond length range and average bond length.

$Nd_2Fe_{16.03}Ti_{0.97}$ Site	BLR	ABL	$Nd_3Fe_{27.76}Ti_{1.24}$ Site	BLR	ABL
Fe, 6*c*	2.4748–2.7998	2.7001	Fe, 2*d*	2.4443–2.6272	2.5040
Fe, 9*d*	2.4568–2.6278	2.4994	Fe, 4*e*1	2.4016–2.7278	2.5694
Fe, 18*f*	2.4569–2.7998	2.5991	Fe, 4*e*2	2.4567–2.7098	2.5567
Fe, 18*h*	2.4778–2.6628	2.5636	Fe, 4*e*3	2.4629–2.7687	2.6198
			Fe, 4*e*4	2.4629–2.7779	2.6624
			Fe, 4*e*5	2.3795–2.7705	2.5947
$NdFe_{10.9}Ti_{1.1}$			Fe, 4*e*6	2.3575–2.6845	2.5550
Site	BLR	ABL	Fe, 4*e*7	2.4059–2.7400	2.5527
Fe, 8*i*	2.4723–2.7464	2.6014	Fe, 4*e*8	2.3808–2.6526	2.5222
Fe, 8*j*	2.4935–2.6692	2.6247	Fe, 4*e*9	2.4654–2.7705	2.5790
Fe, 8*k*	2.4011–2.6242	2.5188	Fe, 4*e*10	2.3575–2.7779	2.5005
			Fe, 4*e*11	2.4045–2.6878	2.5256
BLR=bond length range			Fe, 4*e*12	2.4679–2.7850	2.5907
ABL=average bond length			Fe, 4*e*13	2.4586–2.6747	2.5464
			Fe, 4*e*14	2.3803–2.7957	2.6271

TABLE III. The overall average bond length (OABL) and Curie temperature.

Compound	OABL	T_c (K)	Comments
$Nd_2Fe_{16.03}Ti_{0.97}$	2.5811	383	
$NdFe_{10.9}Ti_{1.1}$	2.5814	530	
Nd_2Fe_{17}	2.5801	330	
$Nd_3Fe_{27.76}Ti_{1.24}$	2.5801	361	no bond>2.8 Å
	2.5929		no bond>2.99 Å

The magnetic moments are also given in Table I. For $Nd_3Fe_{27.76}Ti_{1.24}$ at room temperature, the Fe moment refinements were unstable on a few sites, oscillating about relatively small values. These were constrained to their average, while the others were allowed to refine freely. The overall average site moments of $Nd_3Fe_{27.76}Ti_{1.24}$, $Nd_2Fe_{16.07}Ti_{0.93}$, and $NdFe_{10.9}Ti_{1.1}$ at room temperature are 1.05, 1.95, and 2.36 μ_B, respectively. The moments of $Nd_3Fe_{27.76}Ti_{1.24}$ are found to lie along the a axis. The moments of $Nd_2Fe_{16.07}Ti_{0.93}$ are found to lie perfectly in the basal plane, while the moments of $NdFe_{10.9}Ti_{1.1}$ are found to lie perfectly along the c axis.[17] The Fe and Nd atoms couple ferromagnetically in all three compounds, suggesting that the reported enhancement in the Curie point through interstitial substitution could lead to highly desirable properties due to their high Nd:Fe ratio. For $Nd_3Fe_{27.76}Ti_{1.24}$ at 12.5 K, the easy direction is found to be changed from the a axis at room temperature to the a-b plane at 12.5 K. It was found that the component ratio, μ_x/μ_y, on all sites is close to 0.6 when every component was refined independently. Then a constraint was made to keep all site moments in the same direction and with a component ratio of 0.6. The amplitudes of the site moments at 12.5 K given in the last column of Table I, as expected, are larger than that at room temperature. The overall average iron site moment of $Nd_3Fe_{27.76}Ti_{1.24}$ at 12.5 K is $1.36\mu_B$. This low value may be due to the fact that nearly all sites have at least some very short (<2.45 Å), presumably antiferromagnetic, bonds. It is particularly interesting to note that one Fe site, $4e10$, has three short bonds and refines with the smallest moment at both temperatures. A second site, $4e8$, has two such bonds and has the second smallest moment at room temperature, which remains small at 12.5 K. In contrast, Fe4 and Fe5 have the largest 12.5-K moments, average bond lengths over 2.6 Å, and no short bonds.

III. CONCLUSIONS

The new pseudobinary rare earth-iron phase, $Nd_3Fe_{27.76}Ti_{1.24}$, was studied by neutron diffraction and compared with Ti-substituted Nd_2Fe_{17} and $NdFe_{12}$ compounds. The structures of all those three compounds are related to the structure of RT_5, with differing degrees of Fe-Fe dumbbell replacement of the rare earth. The Ti atoms were found to occupy those sites with a single Nd neighbor in all three compounds. A dependence of the Curie points on bond length similar to other NdFe compounds was observed. The Nd sublattice couples ferromagnetically to the Fe sublattice in all three compounds with different easy directions, that is, a axis for $Nd_3Fe_{27.76}Ti_{1.24}$, basal plane for $Nd_2Fe_{16.03}Ti_{0.97}$, and c axis for $NdFe_{10.9}Ti_{1.1}$, respectively. An easy direction change, from the a axis to a-b plane, for $Nd_3Fe_{27.76}Ti_{1.24}$ was observed when the temperature was lowered from 295 to 12.5 K.

ACKNOWLEDGMENTS

The authors would like to thank Dr. J. M. Cadogan and his collaborators for providing the sample $Nd_3Fe_{27.76}Ti_{1.24}$ used in this study, for the early report of the x-ray study, and for helpful discussions. We would also like to thank Dr. C. Fuerst and the General Motors group for providing samples $Nd_2Fe_{16.03}Ti_{0.97}$ and $NdFe_{10.9}Ti_{1.1}$ and a preprint of their work. Useful discussions with Dr. F. K. Ross are also greatly appreciated.

[1] J. J. Croat, J. F. Herbst, R. W. Lee, and F. E. Pinkerton, Appl. Phys. Lett. **44**, 148 (1984).
[2] J. M. D. Coey and H. Sun, J. Magn. Magn. Matter. **87**, L251 (1990).
[3] D. B. de Mooij and K. H. J. Buschow, J. Less Common Met. **142**, 349 (1988).
[4] G. J. Long, G. K. Marasinghe, S. Mishra, O. A. Pringle, F. Grandjean, K. H. J. Buschow, D. P. Middleton, W. B. Yelon, F. Pourarian, and O. Isnard, Solid State Comm. **88**, 761 (1993).
[5] W. B. Yelon, H. Xie, G. J. Long, O. A. Pringle, F. Grandjean, and K. H. J. Buschow, J. Appl. Phys. **73**, 6029 (1993).
[6] Z. Hu, W. B Yelon, S. Mishra, G. J. Long, O. A. Pringle, D. P. Middleton, K. H. J. Buschow, and F. Grandjean, J. Appl. Phys. **76**, 443 (1994).
[7] G. V. Ivanova, E. I. Teitel, and E. V. Shcherbakova, Phys. Met. Metallogr. **15**, 274 (1993).
[8] Y. V. Shcherbakova, G. V. Ivanova, A. S. Yermolenko, Y. V. Belozerov, and V. S. Gaviko, J. Alloys Compounds **182**, 199 (1992).
[9] S. J. Collocott, R. K. Day, J. B. Dunlop, and R. L. Davis, in Proceedings of the Seventh International Symposium on Magnetic Anisotropy and Coercivity in Rare-Earth Transition Metal Alloys, Canberra, 1992, p. 437.
[10] J. M. Cadogan, H.-S. Li, R. L. Davis, A. Margarian, S. J. Collocott, J. B. Dunlop, and P. B. Gwan, J. Appl. Phys. **75**, 7114 (1994).
[11] C. D. Fuerst, F. E. Pinkerton, and J. F. Herbst, J. Magn. Magn. Mater. **129**, L115 (1994).
[12] H.-S. Li, J. M. Cadogan, R. L. Davis, A. Margarian, and J. B. Dunlop, Solid State Commun. **90**, 487 (1994).
[13] Z. Hu and W. B. Yelon, Solid State Commun. **91**, 233 (1994).
[14] Z. Hu and W. B. Yelon (unpublished).
[15] J. F. Herbst, J. J. Croat, F. E. Pinkerton, and W. B. Yelon, Phys. Rev. B **29**, 4176 (1984).
[16] W. B. Yelon and G. C. Hadjipanayis, IEEE Trans. Magn. **28**, 2316 (1992).
[17] W. B. Yelon, Z. Hu and C. D. Fuerst (unpublished).

Magnetic properties of interstitially modified $Nd_3(Fe,Ti)_{29}X_y$ compounds (X=H, C, and N)

D. H. Ryan and J. M. Cadogan[a)]
Centre for the Physics of Materials and Department of Physics, McGill University, 3600 University Street, Montréal, Québec H3A 2T8, Canada

A. Margarian
Department of Applied Physics, University of Technology, Sydney NSW 2007 and CSIRO Division of Applied Physics, Lindfield NSW 2070, Australia

J. B. Dunlop
CSIRO Division of Applied Physics, Lindfield NSW 2070, Australia

The effects of light atom intercalation on the magnetic properties of the monoclinic compound $Nd_3(Fe,Ti)_{29}$ have been studied by Mössbauer spectroscopy and thermogravimetric analysis. Maximum contents of 4 nitrogen atoms and 6 hydrogen atoms per formula unit have been achieved, consistent with structural calculations. The associated lattice expansion ranges from 2% in the hydride to 6.5% in the nitride. Attempts to introduce carbon were unsuccessful as the material decomposed rapidly during the reaction. Both hydrogen and nitrogen additions lead to substantial increases in the magnetic ordering temperature, but only the nitrogen leads to an increase in the iron moment.

I. INTRODUCTION

The search for high-performance magnetic materials, which was revived by the discovery of the $R_2Fe_{14}B$ system, has been expanded greatly by the observation that significant improvements can be obtained through the intercalation of alloys by a variety of light atoms. Often this intercalation process can be used to transform otherwise useless materials into highly promising permanent magnet candidates. The most striking examples of this are the R_2Fe_{17} alloys, which have ordering temperatures only slightly above room temperature, but the addition of either carbon or nitrogen by gas-phase reaction leads to a greatly enhanced T_c and, in the case of the Sm alloy, substantial uniaxial anisotropy.[1]

In 1992, Collocott *et al.* reported the existence of a new, iron-rich, phase in the Nd-Fe-Ti phase diagram.[2] Subsequent x-ray[3] and neutron[4] diffraction measurements showed that the alloy structure belonged to the monoclinic $P2_1/c$ space group, and that the correct stoichiometry was $Nd_3(Fe,Ti)_{29}$. The composition lies between the tetragonal $Nd(Fe,Ti)_{12}$ and rhombohedral $Nd_2(Fe,Ti)_{17}$ phases, and the 3-29 structure can be viewed as an alternating stack of these 1-12 and 2-17 units.[3] The magnetic ordering temperatures of the 3-29 compounds are in the range 411–486 K.[5] Previous work has shown that this phase absorbs nitrogen readily, exhibiting large increases in both T_c and magnetization.[6]

In this paper we report a more extensive study of the effects of H, C, and N interstitial modification on the magnetic properties of $Nd_3(Fe,Ti)_{29}$.

II. EXPERIMENTAL METHODS

$Nd_3(Fe,Ti)_{29}$ samples were prepared by arc melting appropriate amounts of 99.9% purity Nd, Ti, and Fe under Ti-gettered argon. Single-phased alloys were obtained by annealing at 1373 K for 72 h under argon in sealed quartz tubes, followed by water quenching. Structural measurements were made using Cu-K_α radiation on an automated Nicolet–Stoe diffractometer. Ordering temperatures were determined on a Perkin–Elmer TGA-7 by recording the apparent mass as a function of temperature in a small field gradient. ^{57}Fe Mössbauer spectra were obtained on a conventional constant acceleration spectrometer using a 25-mCi ^{57}CoRh source. Low-temperature spectra were obtained using a vibration-isolated closed-cycle He fridge. Calibration and isomer shifts are referred to α-Fe at room temperature. The $Nd_3(Fe,Ti)_{29}$ unit cell contains 6 Nd atoms on two sites, and 58 Fe atoms distributed among 15 distinct sites, one being a $2d$ and the remaining 14 being $4e$ sites. It is clear from the spectra in Figs. 1 and 2 that few of the subspectra arising from the 15 Fe sites are resolved, especially at room temperature. We have therefore fitted the spectra using the minimum number of subspectra needed to reproduce the most obvious features of the spectra. The number used varied from 3 in the case of the as-annealed material at room temperature, to 6 in the cases of the nitride and hydride at 12 K.

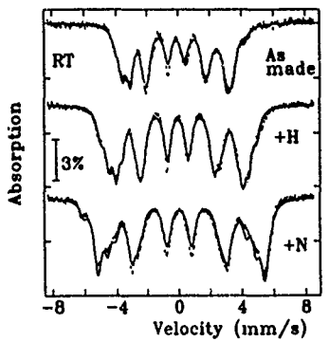

FIG. 1. Room-temperature Mossbauer spectra of $Nd_3(Fe,Ti)_{29}$ as-annealed, and with hydrogen and nitrogen added

[a)]On leave from School of Physics, University of New South Wales, Sydney NSW 2052, Australia.

 0021-8979/94/76(10)/6150/3/$6.00 © 1994 American Institute of Physics

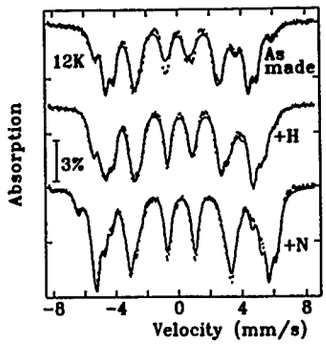

FIG. 2. Mössbauer spectra of $Nd_3(Fe,Ti)_{29}$ as-annealed, and with hydrogen and nitrogen added measured at 12 K.

The intercalation reactions were carried out at various temperatures in a thermopiezic analyzer (TPA) using hydrogen, nitrogen, and acetylene as sources of H, N, and C, respectively.

III. RESULTS AND DISCUSSION

Substantial amounts of hydrogen are absorbed readily by $Nd_3(Fe,Ti)_{29}$. Heating to 300 °C at 40 °C/min in ~1.6 bar of H_2 leads to a hydrogen uptake of over 6 H/formula unit (f.u.), with no evidence of decomposition. While the hydride appears stable at room temperature (no evolution of the material was apparent on the ~1-day timescale needed to record a Mössbauer spectrum), it decomposed rapidly on heating, making an accurate determination of T_c problematic. The value of 548 K given in Table I represents a lower limit, the value obtained on re-cooling was typically 100 K lower, reflecting a significant loss of hydrogen. The room temperature Mössbauer spectrum (Fig. 1) exhibits a substantially increased average hyperfine field; however, the measurement at 12 K (Fig. 2) shows this to be almost entirely due to the higher ordering temperature. The measured lattice expansion is ~2%, giving an effective volume change per hydrogen atom of ~2.0 Å^3, close to values typical of intermetallic hydrides.[7]

Nitrogen also reacts easily with this alloy. Annealing for 70 h in 1.6 bar of N_2 at 400 °C takes the reaction close to completion and yields nitrogen contents of ~4.5 N/f.u. Higher apparent concentrations (~5.8 N/f.u.) can be achieved by annealing at higher temperatures (e.g., 500 °C); however, the observed ordering temperature does not increase, and there is evidence of α-Fe precipitation. The 6.5%

TABLE I. Summary of magnetic and structural changes resulting from the addition of H, C, or N to $Nd_3(Fe,Ti)_{29}$.

Sample	T_c (K)	$\langle B_{hf} \rangle$ (T) 12 K	$\langle B_{hf} \rangle$ (T) RT	$\Delta V/V$ (%)
$Nd_3(FeTi)_{29}$	426	29.0	21.0	...
$Nd_3(FeTi)_{29}H_{6.1}$	>548	30.2	26.4	2.2±0.5
$Nd_3(FeTi)_{29}C_y$	~660	...	...	...
$Nd_3(FeTi)_{29}N_{4.5}$	723	33.4	31.0	6.5±0.7

TABLE II. The four largest voids in the $Nd_3(Fe,Ti)_{29}$ alloy system, derived from an analysis of the crystal structure. The $4e_3$ is assumed to be unoccupied as it is too small for nitrogen, and only coordinated by Fe atoms.

Site	Location x	y	z	Radius (Å)	Coordination	Occupied by
$4e_1$	0.49	0.75	0.23	0.64	2-Nd 4-Fe	HCN
$4e_2$	0.20	0.50	0.40	0.59	2-Nd 4-Fe	HCN
$4e_3$	0.10	0.51	0.95	0.45	4-Fe	empty(?)
$4e_4$	0.44	0.23	0.92	0.42	1-Nd 3-Fe	H

volume expansion corresponds to a volume change of ~7 Å^3/N atom, as found in the R_2Fe_{17} nitrides.[1] The Mössbauer spectra show a substantial increase in the hyperfine field both at room temperature and 12 K. Values listed in Table I are in close agreement with those reported earlier.[5] As in the 2-17 and 1-12 alloys, nitriding leads to an increase both in T_c and in the average Fe moment.

The carbide does not form easily. Conditions appropriate for 1-12 or 2-17 alloys tend to lead to a disproportionation reaction, with the principal magnetic phases being Fe_3C (possibly containing some of the Ti) and α-Fe. Even short duration (~30 min) anneals at temperatures between 350 and 500 °C led to partially decomposed samples. It therefore appears that in this phase, the competition from the disproportionation reaction is too strong, and the carbide tends not to form in significant amounts. A magnetic event at ~660 K is tentatively associated with a $Nd_3(Fe,Ti)_{29}C_y$ phase; however, the actual carbon content is unknown. Given the mixture of magnetic phases present, no attempt was made to extract Mössbauer parameters.

An analysis of the 3-29 structure yields only a very limited number of holes large enough to accommodate interstitial atoms (see Table II), and all of them are 4e sites (the 2a and 2d sites are occupied by Nd and Fe, respectively, and both the 2b and 2c sites lie inside other atoms). The two largest voids have radii of 0.64 and 0.59 Å, and could hold either carbon or nitrogen atoms. Full occupancy of these sites by nitrogen would yield a composition of $Nd_3(Fe,Ti)_{29}N_4$. This composition is also consistent with the 3-29 structure being derived from alternate stacking of 1-12 and 2-17 units, which can hold 1 and 3 nitrogen atoms, respectively. Our measured nitrogen content of 4.5 N/f.u. probably results from a partial decomposition of the material, with the excess nitrogen in the form of neodymium nitride. The next hole is only 0.45 Å in radius, far too small to accept either nitrogen or carbon. While this site is large enough to take a hydrogen atom,[7] the coordination solely by Fe atoms may make the environment energetically unattractive. The next largest site with one Nd neighbor has a radius of 0.42 Å and is more likely to be the hydrogen location. Occupation of the three largest rare-earth coordinated holes by hydrogen gives the composition $Nd_3(Fe,Ti)_{29}H_6$, as observed.

In conclusion, adding hydrogen leads to a significant increase in T_c, but essentially no change in the iron moment, whereas nitrogen leads to an increase in both parameters. These results are similar to those found in the 1-12 and 2-17 rare-earth iron alloys. Attempts to make the carbide were unsuccessful due to a rapid disproportionation of the mate-

rial. An examination of the crystal structure shows that the hydrogen and nitrogen concentrations achieved are the maximum values allowed.

ACKNOWLEDGMENTS

This work was supported by grants from the Natural Sciences and Engineering Research Council of Canada (NSERC) and le Fonds pour la Formation de Chercheurs et l'Aide à la Recherche de la Province du Québec. J. M. C. was partially supported by an NSERC International Scientific Exchange grant.

[1] Z. Altounian, X. Chen, L. X. Liao, D. H. Ryan, and J. O. Ström-Olsen, J. Appl. Phys. **73**, 6017 (1993).
[2] S. J. Collocott, R. K. Day, J. B. Dunlop, and R. L. Davis, Proceedings of the Seventh International Symposium on Magnetic Anisotropy and Coercivity in R-T Alloys, Canberra, 1992, p. 437.
[3] J. M. Cadogan, H. S. Li, R. L. Davis, A. Margarian, S. J. Collocott, J. B. Dunlop, and P. B. Gwan, J. Appl. Phys. **75**, 7114 (1994).
[4] Z. Hu and W. B. Yelon, Solid State Commun. **91**, 223 (1994).
[5] J. M. Cadogan, R. K. Day, J. B. Dunlop, and A. Margarian, J. Alloys and Comp. **201**, L1 (1993).
[6] J. M. Cadogan, H. S. Li, A. Margarian, J. B. Dunlop, D. H. Ryan, S. J. Collocott, and R. L. Davis (these proceedings).
[7] D. G. Westlake, J. Less Common Met. **90**, 251 (1983).

Phase equilibria in the Fe-rich corner of the Nd-Fe-Ti ternary alloy system at 1100 °C

A. Margarian
Department of Applied Physics, University of Technology, Sydney, Broadway 2007 and CSIRO Division of Applied Physics, Lindfield 2070, Australia

J. B. Dunlop and R. K. Day
CSIRO Division of Applied Physics, Lindfield 2070, Australia

W. Kalceff
Department of Applied Physics, University of Technology, Sydney, Broadway 2007, Australia

High-temperature phase relations in the Fe-rich corner of the Nd-Fe-Ti ternary alloy system have been investigated and an equilibrium phase diagram has been constructed at 1100 °C. Arc-melted and annealed alloys of systematically varying compositions were characterized utilizing scanning electron microscopy, an energy dispersive x-ray microanalysis system (EDS), x-ray diffraction, and optical metallography. Three major phases have been identified, the well known $Nd(Fe,Ti)_{12}$ "1:12" ($ThMn_{12}$-type structure) and $Nd_2(Fe,Ti)_{17}$ "2:17" (Th_2Zn_{17}-type structure) compounds, and a phase with approximate composition $Nd_2(Fe,Ti)_{19}$ "2:19." The crystal structure of the latter phase has very recently been solved, and the "ideal" composition shown to be $Nd_3(Fe,Ti)_{29}$ "3:29." Quantitative EDS data has been used to identify the compositional limits for the three major phases. Annealing the "1:12" and "3:29" ternary phases at 900 °C results in a slow decomposition into $Nd_2(Fe,Ti)_{17}$, Fe_2Ti, and α-Fe(Ti).

I. INTRODUCTION

Intensive research during the past 25 years has seen the emergence of many rare-earth iron transition metal intermetallic compounds with technologically interesting magnetic properties. $Nd_2Fe_{14}B$ has many of the properties of an ideal permanent magnet, such as a high-remanence, large uniaxial magnetocrystalline anisotropy and low cost, yet its low Curie temperature (310 °C) restricts its applications to temperatures below 150 °C.

Nd-Fe-Ti alloys with the tetragonal $ThMn_{12}$-type structure, and especially their nitrides, have magnetic properties comparable to those of $Nd_2Fe_{14}B$ and are therefore possible candidates for permanent magnets. In attempting to prepare single-phase samples of $Nd(Fe,Ti)_{12}$, Collocott *et al.*[1] found a second ternary compound, with nominal composition $Nd_2(Fe,Ti)_{19}$. The structure of the "2:19" phase has been solved from powder x-ray diffraction[2] and neutron diffraction[3] data, and the ideal composition shown to be $Nd_3(Fe,Ti)_{29}$. To further understand the formation and interrelationships of phases in the Fe-rich section of the Nd-Fe-Ti ternary alloy system, we have carried out a systematic investigation of a range of alloy compositions and constructed an equilibrium-phase diagram at a temperature of 1100 °C.

II. EXPERIMENTAL PROCEDURE

Alloys weighing 2 g were prepared from Nd, Fe, and Ti of ≥99.9% purity by argon-arc melting on a water-cooled copper hearth. The samples were then wrapped in tantalum foil, encapsulated in sealed quartz tubes under an atmosphere of argon gas, and annealed for 3 days at 1100 °C, followed by a water quench. Selected samples were also given a second annealing treatment at 900 °C for periods of 7 and 21 days. Samples were characterized by powder x-ray diffraction using Cu $K\alpha$ radiation, optical metallography, and scanning electron microscopy (SEM) using a JEOL 35CF equipped with a Robinson backscatter electron detector and a LINK energy dispersive x-ray microanalysis system (EDS).

III. RESULTS AND DISCUSSION

Microstructural investigation of the alloys was carried out utilizing backscatter electron (BSE) imaging and x-ray microanalysis. Generally, backscattered electrons provide excellent contrast between phases of different mean atomic number in a polished section of sample. In our samples, where there are two or more phases with similar compositions, BSE imaging alone does not provide sufficient contrast and etching with a 2% solution of nitric acid in alcohol (Nital) was necessary to generate topological contrast.

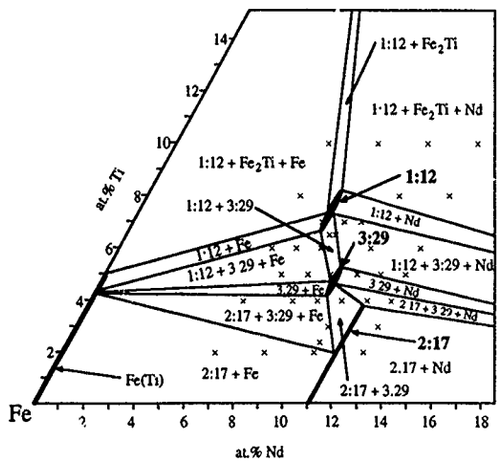

FIG. 1. Fe-rich corner of the Nd-Fe-Ti phase diagram at 1100 °C. ("×" represents annealed compositions analyzed).

 0021-8979/94/76(10)/6153/3/$6.00 © 1994 American Institute of Physics

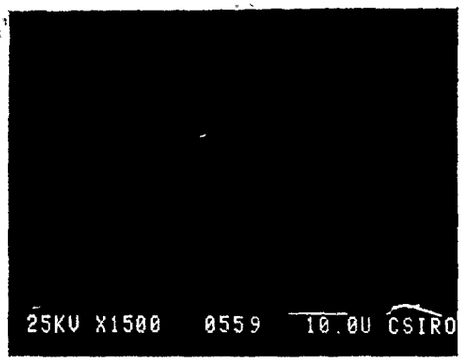

FIG. 2. Backscattered electron image of an etched $Nd_6Fe_{88}Ti_6$ alloy (major phase—1:12, depression—3:29 and dark region—Fe).

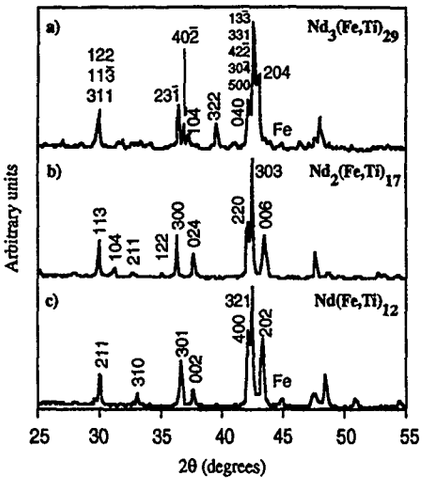

FIG. 3. X-ray diffraction spectra for the Fe-rich Nd-Fe-Ti phases: (a) $Nd_3(Fe,Ti)_{29}$, (b) $Nd_2(Fe,Ti)_{17}$, and (c) $Nd(Fe,Ti)_{12}$ (CuK_α radiation).

Detailed examination of alloys in the Fe-rich corner of the Nd-Fe-Ti ternary alloy system at 1100 °C revealed the existence of two ternary phases, $Nd(Fe,Ti)_{12}$, $Nd_3(Fe,Ti)_{29}$ [previously reported as $Nd_2(Fe,Ti)_{19}$], and the pseudobinary $Nd_2(Fe,Ti)_{17}$ phase, and allowed us to construct the ternary phase diagram shown in Fig. 1. Figure 2 shows a backscattered electron image of a $Nd_6Fe_{88}Ti_6$ composition (in the 1:12+3:29+Fe phase field) annealed at 1100 °C and etched with Nital. The 3:29 phase (depression) could not be observed prior to etching. The compositional limits for all the major phases were determined by quantitative x-ray microanalysis, although this was complicated by the strong overlap which exists between the Nd L and Fe K series lines. The Nd compositions were normalized by reference to a single phase sample of Nd_2Fe_{17} prepared with minimal weight loss (<0.1%) during arc melting and annealing. It was observed that the Nd content remained constant (to ±0.2%) within each of the three major phases, with only the Fe:Ti ratio changing. The compositional limits for the three major phases are presented in Table I.

Jang and Stadelmaier reported[4] the existence of two ternary phases in Nd-Fe-Ti alloys: the "1:12," and a $TbCu_7$-type (1:7) phase with a higher Nd content (≈12 at. %) than in the substituted binary $Nd_2(Fe,Ti)_{17}$, whereas the "3:29" reported here has a Nd content of 9.4 at. %, significantly lower than in the 2:17. Neiva *et al.*[5] have reported the formation of a $Sm(Fe,Ti)_9$ phase with a hexagonal $TbCu_7$-type structure at 1000 °C.

X-ray diffraction spectra of the major phases are shown in Fig. 3. The "1:12" [Fig. 3(c)] has the tetragonal $ThMn_{12}$-type structure, which is relatively common in R-Fe-T systems (R=a rare-earth and T=a transition element), but does not exist as a binary RFe_{12} phase except for the case of $SmFe_{12}$ thin films prepared by sputtering.[6,7] $Nd_2(Fe,Ti)_{17}$ [Fig. 3(b)] has the rhombohedral Th_2Zn_{17}-type structure and exists with up to 3.8 at. % of the Fe substituted by Ti.

$Nd_3(Fe,Ti)_{29}$ [Fig. 3(a)] has a complex structure that was originally indexed on a $2\times a$ and $4\times c$ superlattice of hexagonal $TbCu_7$.[1] The x-ray diffraction data has subsequently been reindexed on the basis of a monoclinic lattice[2,8] and very recently the structure was solved independently from powder x-ray diffraction[2] and neutron diffraction[3] data. The crystal structure is monoclinic ($P2_1/c$) with lattice parameters $a=1.064$ nm, $b=0.859$ nm, $c=0.975$ nm, and $\beta=96.928°$, and the "ideal" composition is $Nd_3(Fe,Ti)_{29}$. Figure 4 illustrates the crystallographic relationship in the a-c plane between the monoclinic unit cell of $Nd_3(Fe,Ti)_{29}$ and the hexagonal $TbCu_7$ lattice. Crystallographic data for the three major phases can be found in Table II. The "3:29" phase is not restricted to the Nd-Fe-Ti system, but also exists in R-Fe-Ti (R=Sm,[9,10] Ce,[9] Pr,[11] and Gd[12]) and in Nd-Fe-T (T=Cr, and Mn[8]).

Investigations into the thermal stability of $Nd(Fe,Ti)_{12}$ and $Nd_3(Fe,Ti)_{29}$ have shown that they are only stable at elevated temperatures. Annealing the compounds at a temperature of 900 °C results in a slow decomposition to

TABLE I. Compositional ranges of the three major phases.

Phase	Composition (at. %)		
	Nd	Fe	Ti
$Nd_2(Fe,Ti)_{17}$	11.0	balance	0–3.8
$Nd_3(Fe,Ti)_{29}$	9.4	balance	4.0–5.1
$Nd(Fe,Ti)_{12}$	7.9	balance	6.5–8.1

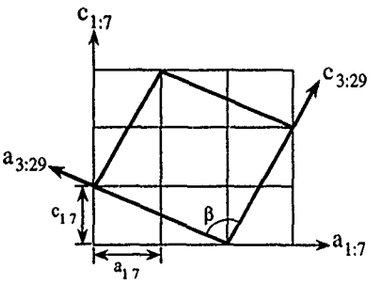

FIG. 4. Crystallographic relationship in the a-c plane between the unit cell of monoclinic $Nd_3(Fe,Ti)_{29}$ and the $3\times a$ and $3\times c$ superlattice of $TbCu_7$.

TABLE II. Crystallographic data for the three major phases.

Phase	Structure	Crystal type	Lattice parameters			
			a (nm)	b (nm)	c (nm)	β (°)
2:17	rhombohedral	Th_2Zn_{17}	0.860	···	1.251	···
3:29	monoclinic	$Nd_3(Fe,Ti)_{29}$	1.064	0.859	0.975	96.92
1:12	tetragonal	$ThMn_{12}$	0.859	···	0.479	···

$Nd_2(Fe,Ti)_{17}$, Fe_2Ti, and α-Fe(Ti), and this observation is in agreement with the findings of Jang and Stadelmaier,[4] that $Nd(Fe,Ti)_{12}$ is unstable at low temperatures. Itsukaichi *et al.*[13] also showed that mechanically alloyed Nd-Fe-Ti powder with the 1:12 composition does not crystallize in the $ThMn_{12}$ structure after a heat treatment at 800 °C.

IV. CONCLUSION

We have constructed an equilibrium-phase diagram for the Fe-rich corner of the Nd-Fe-Ti alloy system at 1100 °C, and determined the composition ranges for the major phases: tetragonal $Nd(Fe,Ti)_{12}$, monoclinic $Nd_3(Fe,Ti)_{29}$, and rhombohedral $Nd_2(Fe,Ti)_{17}$. $Nd(Fe,Ti)_{12}$ and $Nd_3(Fe,Ti)_{29}$ become thermodynamically unstable on cooling below some temperature between 900 and 1000 °C. $Nd(Fe,Ti)_{12}$, and especially its nitride $Nd(Fe,Ti)_{12}N_x$, are being examined as candidates for new permanent magnets, and this low-temperature instability will have profound implications on material processing.

ACKNOWLEDGMENTS

A. Margarian and J. B. Dunlop wish to thank D. Dunne and G. Delamore (Department of Materials Engineering, University of Wollongong) for helpful discussions.

[1] S. J. Collocott, R. K. Day, J. B. Dunlop, and R. L. Davis, in Proceedings of the Seventh International Symposium on Magnetic Anisotropy and Coercivity in Rare-Earth Transition Metal Alloys, Canberra, 1992, p. 437.
[2] H.-S. Li, J. M. Cadogan, R. L. Davis, A. Margarian, and J. B. Dunlop, Solid State Commun. **90**, 487 (1994).
[3] Z. Hu and W. B. Yelon Solid State Commun. **91**, 223 (1994).
[4] T. S. Jang and H. H. Stadelmaier, J. Appl. Phys. **67**, 4957 (1990).
[5] A. C. Neiva, F. P. Missel, B. Grieb, E.-T. Henig, and G. Petzow, J. Less Common Met. **170**, 293 (1991).
[6] F. J. Cadieu, H. Hedge, A. Navarathna, R. Rani, and K. Chen, Appl. Phys. Lett. **59**, 875 (1991).
[7] D. Wang, S. H. Liu, P. He, D. J. Sellmyer, G. C. Hadjipanayis, and Y. Zhang, J. Magn. Magn. Mater. **124**, 62 (1991).
[8] C. D. Fuerst, F. E. Pinkerton, and J. F. Herbst, J. Magn. Magn. Mater. **129**, L115 (1994).
[9] A. Margarian, J. B. Dunlop, and S. J. Collocott (unpublished results).
[10] F.-M. Yang, B. Nasunjilegal, H.-Y. Pan, J.-L. Wang, R.-W. Zhao, B.-P. Hu, Y.-Z. Wang, H.-S. Li, and J. M. Cadogan (unpublished).
[11] H.-S. Li, Suharyana, J. M. Cadogan, G. J. Bowden, J.-M. Xu, S. X. Dou, and H. K. Liu, J. Appl. Phys. **75**, 7120 (1994).
[12] H.-S. Li and J. M. Cadogan (unpublished results).
[13] T. Itsukaichi, M. Umemoto, I. Okane, and S. Hirosawa, J. Alloys Compounds **193**, 262 (1993).

Magnetic properties of $Sm_2Fe_{14-x}Co_xSi_2$-based quasiternary compounds

F.-M. Yang
Institute of Physics, Chinese Academy of Sciences, P.O. Box 603, Beijing 10080, China

W. Gong and G. C. Hadjipanayis
Department of Physics and Astronomy, University of Delaware, Newark, Delaware 19716-2570

The structural and magnetic properties of the off-stoichiometric R_2Fe_{17}-type $Sm_2Fe_{14-x}Co_xSi_2$ compounds with $0 \leqslant x \leqslant 7$ have been investigated by x-ray diffraction, thermomagnetic analysis, and magnetic measurements. Substitution of Co for Fe leads to an increase in Curie temperature, $\Delta T_c = 303$ K for samples with x from 0 to 7. The saturation magnetization M_s increased with increasing Co content at first and then decreased. A maximum saturation magnetization $M_s = 124$ emu/g was obtained at x about 4. The anisotropy changes from planar $x < 4$ to uniaxial $x \geqslant 4$ with $H_a = 23$ kOe for $x = 7$. Introduction of N leads to an increase in lattice constants causing a further enhancement in the Curie temperature and anisotropy field. The best properties were obtained for the $Sm_2Fe_{10}Co_4Si_2N_{2.3}$ compound with $T_c = 742$ K, H_a (300 K) = 175 kOe.

I. INTRODUCTION

Research in the field of permanent magnets intensified after the discovery of the R-Fe-B compounds[1,2] whose superior magnetic properties led to the high performance Nd-Fe-B type permanent magnets[3] which are being used in a wide variety of applications, most notably in the computer industry. However, the low Curie temperature and large temperature coefficients of B_r and H_c limit the temperature range of applications of Nd-Fe-B magnets. Recently the $R(FeT)_{12}$ compounds (T=Al, Cr, Mo, Si, Ti, V, and W) with the $ThMn_{12}$-type structure have been investigated extensively.[4,5] Recently, it has been found that 2:17-type rare-earth iron carbides and nitrides[4] show excellent intrinsic magnetic properties for permanent magnet applications.[6] A new type of ternary compounds with nominal composition $R_2Fe_{14-x}Co_xSi_2$ which crystallize in the off-stoichiometric 2:17-type structure has been studied[7,8] with R=Y or a heavy rare-earth element.

In this work, a detailed study of the structural and magnetic properties of the $Sm_2Fe_{14-x}Co_xSi_2$ nitrides was performed and some of the results are presented and discussed.

II. EXPERIMENT

$Sm_2Fe_{14-x}Co_xSi_2$ compounds with $x = 0-7$ were prepared by arc-melting the constituent elements which had at least 99.9% purity. The ingots were melted several times to ensure homogeneity. The as-cast ingots, without any annealing, were then pulverized to an average particle size of 20–30 μm and the powder samples obtained were heated in purified N_2 under a pressure of about 1.7 atm at 520 °C for 4–16 h to form the $Sm_2Fe_{14-x}Co_xSi_2N_y$ nitrides. The value of y was determined to be $2 < y < 3$ by weighing the samples before and after nitrogenation.

X-ray diffraction was employed to determine the structure and the lattice parameters. The x-ray diffraction patterns of the magnetically aligned powder samples obtained at room temperature were used to determine the easy magnetization direction (EMD) of the compounds. Thermomagnetic curves were measured by means of a vibrating sample magnetometer (VSM) with an applied field of 500 Oe, and the Curie temperature T_c was derived from M^2 vs T plots. The magnetization curves were measured by means of a superconducting quantum interference device magnetometer with applied fields up to 65 kOe at temperatures between 4.2 K and room temperature. The saturation magnetization M_s was derived by means of M vs $1/H^2$ plots, using the high field part of the magnetization curves.

The anisotropy fields H_a were derived from the extrapolated intersection of the two magnetization curves, measured with the field parallel and perpendicular to the alignment direction.

III. RESULTS AND DISCUSSION

A. $Sm_2Fe_{14-x}Co_xSi_2$ compounds

X-ray diffraction and thermomagnetic analysis show that all the investigated as-cast $Sm_2Fe_{14-x}Co_xSi_2$ alloys are of

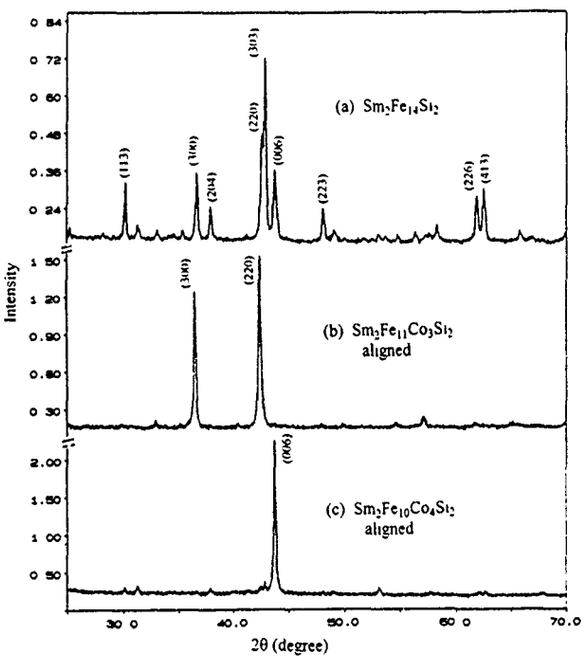

FIG. 1. X-ray diffraction patterns of $Sm_2Fe_{14}Si_2$, $Sm_2Fe_{11}Co_3Si_2$, and $Sm_2Fe_{10}Co_4Si_2$ compounds ($\lambda = 1.5418$ Å).

 0021-8979/94/76(10)/6156/3/$6.00 © 1994 American Institute of Physics

TABLE I. The lattice parameters a and c, unit cell volume V, room temperature saturation magnetization M_s, anisotrop field H_a, and easy magnetization direction EMD in $Sm_2Fe_{14-x}Co_xSi_2$ compounds.

x	a (Å)	c (Å)	V (Å^3)	M_s (emu/g)	H_a (kOe)	EMD
0	8.484	12.340	772.78	118		plane
1	8.477	12.388	770.87	120		plane
2	8.487	12.613	774.33	123		plane
3	8.456	12.338	764.00	124		plane
4	8.459	12.379	764.62	124	8	c axis
5	8.439	12.338	760.88	122	13	c axis
6	8.414	12.301	753.96	120	21	c axis
7	8.404	12.293	751.28	112	23	c axis

single phase. The x-ray diffraction patterns have been indexed on the basis of the Th_2Zn_{17}-type structure. Figure 1, curve (a) shows an example for the $Sm_2Fe_{14}Si_2$ compound. Substitution of Co for Fe does not lead to any change in the crystal structure even for $x=14$. The lattice constants a and c exhibit a small decrease with increasing Co concentration. Experimental data in Table I show the lattice constants a and c as functions of Co concentration. The average decrease upon Co substitution is only 0.1% per Co atom. The average lattice constants are $a=8.252$ Å and $c=12.356$ Å, which are 1.3% and 1.5% smaller than those of the Sm_2Fe_{17} compound, respectively.

Figure 2, curve (A) shows the Curie temperature T_c as a function of Co concentration. It can be seen that T_c increases nearly linearly with Co content, from 514 K for $x=0$ to 817 K for $x=7$. The average increase upon Co substitution was determined to be 55 K per Co atom. It is worth noting that the Curie temperature of the $Sm_2Fe_{14}Si_2$ is about 100 K higher than that of the Sm_2Fe_{17} compound.

The saturation magnetization at room temperature as a function of Co content is summarized in Table I. It can be seen that the saturation magnetization M_s increases with increasing Co content, at first going through a maximum of 124 emu/g at $x\sim3$ and then it decreases with increasing Co content. The increase of the saturation magnetization at room temperature for smalier Co contents results from the enhancement in Curie temperature.

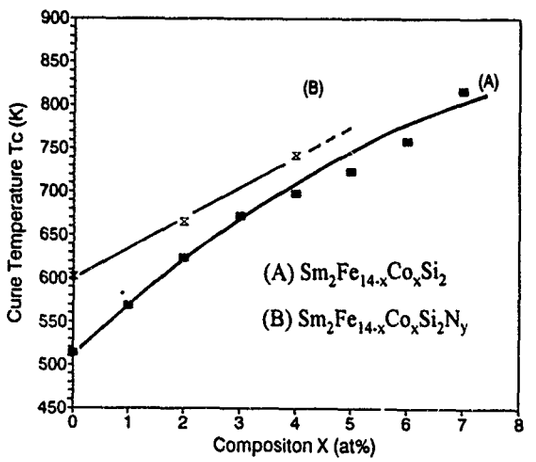

FIG. 2. Curie temperature T_c as a function of x in $Sm_2Fe_{14-x}Co_xSi_2$ compounds and their nitrides. (A) is $Sm_2Fe_{14-x}Co_xSi_2$ samples and (B) is $Sm_2Fe_{14-x}Co_xSi_2N_y$ when $x=0$, $y=2.6$, and $x=4$, $y=2.3$.

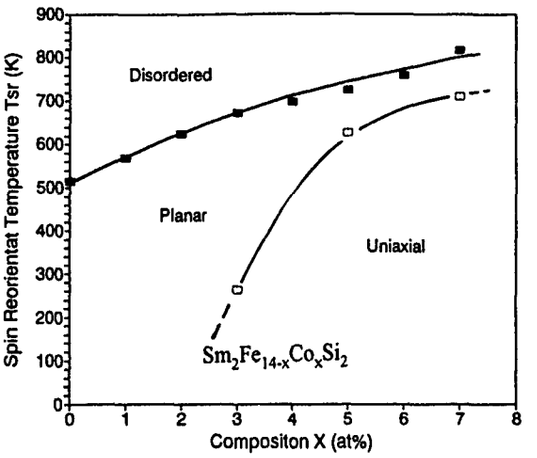

FIG. 3. A spin phase diagram for $Sm_2Fe_{14-x}Co_xSi_2$ compounds.

$Sm_2Fe_{14}Si_2$ exhibits a planar anisotropy. With increasing Co content, the magnetocrystalline anisotropy changes from planar to uniaxial at an x value between 3 and 4 (Table I).

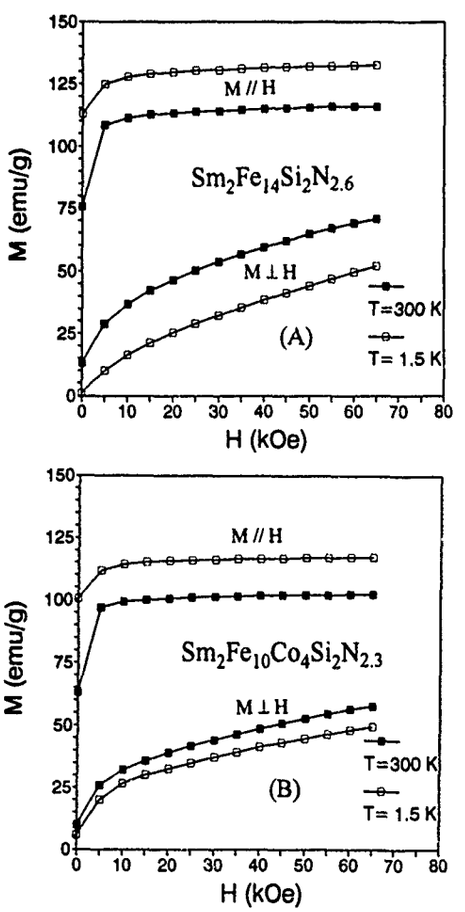

FIG. 4. Magnetization curves of the aligned powder samples, measured parallel (∥) and perpendicular (⊥) to the external magnetic fields.

TABLE II. The lattice parameters a, c, unit cell volume expansion, $\Delta V/V$, Curie temperature T_c, saturation magnetization M_s, anisotropy field and easy magnetization direction for $Sm_2Fe_{14-x}Co_xSi_2N_y$, and the parent compounds.

Compound	a (Å)	c (Å)	$\Delta V/V$ (%)	T_c (K)	M_s (emu/g) 1.5 K	M_s (emu/g) 300 K	H_a (kOe) 1.5 K	H_a (kOe) 300 K	EDM
$Sm_2Fe_{14}Si_2$	8.484	12.340		514	134	118			plane
$Sm_2Fe_{14}Si_2N_{2.6}$	8.633	12.478	4.2	602	133	117	227	157	c axis
$Sm_2Fe_{10}Co_4Si_2$	8.459	12.379		698	136	124		8	c axis
$Sm_2Fe_{10}Co_2Si_2N_{2.3}$	8.633	12.460	5.0	742	128	113	276	175	c axis

Figures 1(b) and 1(c) shows the x-ray diffraction patterns on the magnetically aligned powder samples of the $x=3$ and 4 compounds, respectively. For compounds with $x\leqslant 3$, a substantial increase in the $(h,k,0)$ reflection intensities and disappearance of $(0,0,l)$ lines show that the samples have easy plane magnetocrystalline anisotropy, in contrast with the compounds with $x\geqslant 4$; in the latter only the $(0,0,l)$ reflection intensity substantially increased, which shows a uniaxial magnetocrystalline anisotropy at room temperature. It can be seen that for the compounds with $x\leqslant 3$, H_a is very small due to the planar anisotropy, whereas for the compounds with $x\geqslant 4$, H_a increases with increasing Co content, changing from $H_a=8$ kOe for $x=4$ to $H_a=23$ kOe for $x=7$.

A spin phase diagram is shown in Fig. 3. It is clear that the spin reorientation temperature T_{sr} increases monotonously with increasing Co content. This suggests that substitution of Co for Fe leads to an increase in the contribution to the uniaxial anisotropy resulting from the Sm and Co sublattices.

B. $Sm_2Fe_{14-x}Co_xSi_2$ nitrides

$Sm_2Fe_{14-x}Co_xSi_2$ nitrides with $x=0$ and 4 have been prepared with the values of y determined to be $2<y<3$. The nitrides maintain the Th_2Zn_{17}-type structure, but with remarkable unit-cell volume expansions compared with the hosts. The x-ray diffraction patterns of $Sm_2Fe_{10}Co_4Si_2N_y$ (a), compared with that of the parent compound (B). The unit-cell volume expansion is 4.2% for $x=0$ ($y=2.6$) and 5% for $x=4$ ($y=2.3$). The introduction of nitrogen leads to an increase in Curie temperature from 514 to 602 K for $x=0$ and from 698 to 742 K for $x=4$, respectively. The increase in T_c may be partly associated with the unit cell volume expansion. The values of T_c for $Sm_2Fe_{14-x}Co_xSi_2N_y$ compounds are also shown in Fig. 2 [curve (B)]. Introduction of nitrogen also changed the anisotropy in $Sm_2Fe_{14}Si_2$ from planar to uniaxial at room temperature with an anisotropy field $H_a=157$ kOe and led to an increase in the room-temperature anisotropy field of $Sm_2Fe_{10}Co_4Si_2$ from 8 kOe for the parent compound to 175 kOe for the nitride. A very large anisotropy field was observed at low temperature, $T=1.5$ K, $H_a=227$ kOe for $Sm_2Fe_{14}Si_2N_{2.6}$ and $H_a=276$ kOe for $Sm_2Fe_{10}Co_4Si_2N_{2.3}$, respectively. The detailed experimental data are summarized in Table II and Fig. 4[(A) and (B)].

IV. CONCLUSIONS

The off-stoichiometric R_2Fe_{17}-type $Sm_2Fe_{14-x}Co_xSi_2$ compounds with $x=0$ to 7 crystallize in the Th_2Zn_{17}-type structure. Substitution of Co for Fe leads to an increase in Curie temperature T_c from 514 K for $x=0$ to 817 K for $x=7$. The room-temperature saturation magnetization increases from 118 emu/g for $x=0$ to 124 emu/g for $x=4$ and then it decreases slightly with increasing Co content. Co substitution enhances the uniaxial anisotropy and the spin reorientation temperature T_{sr}. The anisotropy changes from planar in $Sm_2Fe_{14-x}Co_xSi_2$ to uniaxial for $x\geqslant 4$. The anisotropy field is 23 kOe for $x=7$.

Introduction of N leads to an increase in lattice constant and unit cell volume, causing a further enhancement in Curie temperature. Furthermore, introduction of N results in a further increase in the contribution to uniaxial anisotropy from the Sm sublattice. It has been found that for the $Sm_2Fe_{10}Co_4Si_2N_{2.3}$ compound, $T_c=742$ K, M_s (300 K) $=113$ emu/g and H_a (300 K)$=175$ kOe.

[1] G. C. Hadjipanayis, R. C. Hazelton, and K. R. Lawless, Appl. Phys. Lett. **43**, 797 (1983).
[2] J. J. Croat, J. G. Herbst, R. W. Lee, and F. E. Pinkerton, J. Appl. Phys. **55**, 2078 (1984).
[3] M. Sagawa, S. Fujimura, N. Togawa, H. Yamamoto, and Y. Matsuura, J. Appl. Phys. **55**, 2083 (1984).
[4] Y. Z. Wang and G. C. Hadjipanayis, J. Magn. Magn. Mater. **87**, 375 (1990).
[5] W. Gong and G. C. Hadjipanayis, IEEE Trans. Magn. **MAG-28**, 2563 (1992).
[6] J. M. D. Coey and H. Sun, J. Magn. Magn. Mater. **87**, L251 (1990).
[7] F. Pourarian, R. T. Obermyer, and S. G. Sankar, J. Appl. Phys. **75**, 6262 (1994).
[8] F. Pourarian, R. Obermyer, Y. Zheng, S. G. Sankar, and W. E. Wallace, J. Appl. Phys. **73**, 6272 (1993).

Mössbauer study of permanent-magnet materials: $Sm_2Fe_{17-x}Al_x$ compounds

I. A. Al-Omari, S. S. Jaswal, A. S. Fernando, and D. J. Sellmyer
Behlen Laboratory of Physics and Center for Materials Research and Analysis, University of Nebraska, Lincoln, Nebraska 68588-0111

The Fe^{57} Mössbauer spectra of $Sm_2Fe_{17-x}Al_x$, where $x=0$, 1.0, 2.0, 3.0, and 4.0, have been measured at room temperature and analyzed. The ternary compounds $Sm_2Fe_{17-x}Al_x$ have the rhombohedral Th_2Zn_{17} structure. Mössbauer measurements showed that all the compounds studied were ferromagnetic. The average hyperfine field was found to decrease with the increasing aluminum concentration, which is in qualitative agreement with magnetic measurements. The decrease in the average hyperfine field was from 224 kOe at $x=0$ to 174 kOe at $x=4$. By fitting the spectra we found that the hyperfine fields for the iron sites decrease in the order $6c$, $9d$, $18f$, and $18h$. The measured average isomer shift relative to α-iron was found to increase linearly with x. Analysis of the spectra showed that Al atoms occupy the $6c$, $18h$, and $18f$, but not $9d$, Fe sites and the fraction of occupancy of Al was found to depend on x.

I. INTRODUCTION

It has been discovered recently that the hard-magnet properties of Fe-rich intermetallic compounds improve considerably upon nitrogenation.[1-3] Efforts are underway to see if substitutional impurities can accomplish the same goal. Compounds of the type $R_2Fe_{17-x}M_x$, (R=Ho, Y, Sm, Ce, Pr, and Nd; M=Al, Ga, V, Co, and Ni) have been studied[3-6] and their magnetic ordering temperatures were found to increase by substituting other elements for iron. Weitzer *et al.*[7] found that the Curie temperature (T_c) changed from 265 K for Ce_2Fe_{17} to 385 K for $Ce_2Fe_{15}Al_2$, and from 335 K for Nd_2Fe_{17} to 440 K for $Nd_2Fe_{15}Al_2$ and to 520 K for $Nd_2Fe_{15}Ga_2$. Effects of Al substitution on the magnetic anisotropy and Curie temperature of $Sm_2Fe_{17-x}Al_x$ compounds have been studied by Wang and Dunlap.[8] They found that T_c for these compounds depends on the Al concentration (x) and it reaches a maximum of 471 K for $Sm_2Fe_{14}Al_3$, compared to 391 K for the parent compound Sm_2Fe_{17}. They found also that the anisotropy changed from planar for $x\leq 1$ to uniaxial for $x\geq 3$. These changes in T_c and the anisotropy are promising improvements to the permanent-magnet properties of the parent compounds. Low-temperature measurements for $Sm_2Fe_{17-x}Al_x$ by McNeely and Oesterreicher[9] showed that the magnetization of these compounds decreases by 83% as x increases from 0 to 9.5. The coercive force (H_c) increases by increasing x and it reaches a value of 15 kOe with $x=9.5$ at $T=4.2$ K. In this article we report on Mössbauer studies for $Sm_2Fe_{17-x}Al_x$ to understand the effect of Al on their magnetic properties and the site occupation of the different Fe sites. Also we use Mössbauer spectroscopy to look for small amounts of α-Fe in these compounds.

II. EXPERIMENTAL PROCEDURE

Bulk samples of $Sm_2Fe_{17-x}Al_x$ with $x=0$, 1, 2, 3, and 4 were prepared by arc melting the elemental constituents in a water-cooled copper boat in a flowing-argon gas atmosphere. All the starting elements used were at least of 99.99% purity. The alloys were melted several times to insure homogeneity. The samples were wrapped separately in tantalum foils and heat-treated below 3×10^{-6} Torr vacuum at 1000 °C for about 72 h, and subsequently quenched in water.

Room-temperature x-ray diffraction measurements on powder samples using Cu $K\alpha$ radiation showed only the rhombohedral Th_2Zn_{17} structure with a small amount of α-Fe. The magnetization of the compounds was measured at 5 and 300 K with a superconducting quantum interference device (SQUID) and alternating force gradient magnetometer (AFGM), respectively.

The samples for Mössbauer spectroscopy were prepared by sprinkling a thin layer of the powder of $Sm_2Fe_{17-x}Al_x$ on a piece of tape. The samples were studied by using a Ranger Mössbauer spectrometer, model MS1200. The velocity drive of this spectrometer operates in the constant acceleration mode. Co^{57} in Pd was used as the γ-ray source in this experiment. All the isomer shifts were measured relative to α-iron at room temperature and α-iron was also used for calibration.

III. RESULTS AND DISCUSSION

Figure 1 shows the room-temperature Mössbauer spectra and the fitting (the solid curves) for $Sm_2Fe_{17-x}Al_x$ with $x=0$, 1, 2, 3, and 4. The spectra show that all the samples are magnetically ordered for all values of x and all of them have different subspectra with different magnetic hyperfine fields. A standard program was used to fit the spectra, where each spectrum was fitted with a set of seven subspectra, which is similar to the previous models used by Ping *et al.*,[10] Long *et al.*,[11] and Yelon *et al.*[12] for 2:17 compounds. The weak features indicated by arrows in Fig. 1 are the first and sixth lines due to α-Fe in samples with $x=1$ and 2. From the relative intensity of the subspectrum the atomic percentage of α-Fe was estimated to be less than 2%. For the rhombohedral Th_2Zn_{17} structure there are four different iron sites, $6c$, $9d$, $18f$, and $18h$, with different environments. Previous Mössbauer measurements by Long *et al.*[11,13] for Nd_2Fe_{17} and

 0021-8979/94/76(10)/6159/3/$6.00 © 1994 American Institute of Physics

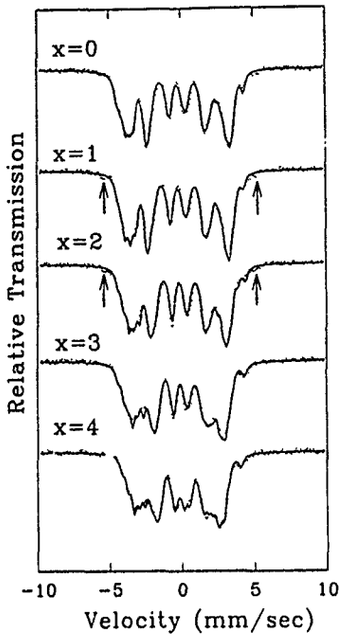

FIG. 1. Room-temperature Mössbauer spectra of $Sm_2Fe_{17-x}Al_x$ compounds. The solid curves represent the fitting. Arrows indicate the first and sixth lines due to α-Fe.

$Nd_2Fe_{17}N_{2.6}$, Mössbauer and neutron diffraction by Yelon *et al.*[12] for $Nd_2Fe_{17-x}Al_x$, and Mössbauer measurements by Hu *et al.*[10] for $R_2Fe_{17}N_{3-\delta}$ showed that the hyperfine fields decrease in the order $6c$, $9d$, $18f$, and $18h$. The $6c$ site has the largest hyperfine field since it has the largest number of iron nearest neighbors. In our fitting and analysis of the data we kept the same order. The seven subspectra used in fitting correspond to one spectrum for $6c$ and two subspectra for each of the other three sites with the relative intensity 2:1. The parent compound Sm_2Fe_{17} was studied for comparison with other compounds and other data. The average hyperfine field for different sites and for different Al concentrations was found to decrease with increasing concentration of the nonmagnetic element, Al, as seen in Fig. 2. This decrease is in qualitative agreement with the magnetization measurements by McNeely and Oesterreicher.[9] The average hyperfine field for the parent compound was 224 kOe which is in good agreement with other values of 221 kOe by Hu *et al.*[10]

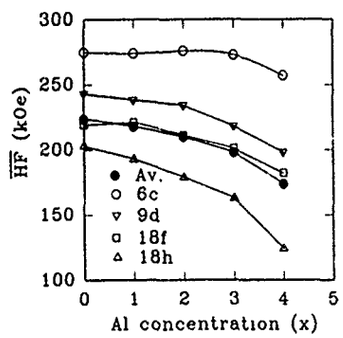

FIG. 2. Dependence of the average hyperfine field for the different Fe sites of $Sm_2Fe_{17-x}Al_x$ on the Al concentration x, at $T=295$ K.

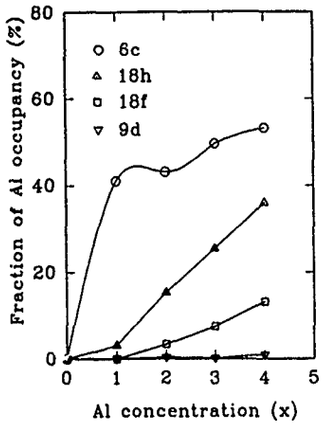

FIG. 3. Dependence of the percentage fraction of aluminum occupancy for different sites on the Al concentration x.

and 216 kOe by Long *et al.*[11] for related compounds. The Curie temperature for these compounds increases with x and reaches a maximum at $x=3$: T_c changes from 391 K for Sm_2Fe_{17} to 471 K for $Sm_2Fe_{14}Al_3$.[8] This increase of 20% in T_c in spite of the decrease in the average hyperfine field by 12% must be due to the increase in the interatomic exchange interactions upon volume expansion.

The intensity of each subspectrum is proportional to the Fe-site occupation. Using the fitted intensities we calculated the percentage of iron and aluminum at each site. Figure 3 shows the percentage fraction of Al occupancy of each site for the different sites and for different concentrations. From this figure we see that Al prefers to go to the different sites in the order $6c$, $18h$, and $18f$, but not $9d$, which has the smallest Wigner–Seitz cell volume. This is in agreement with previous observations on $Nd_2Fe_{17-x}Al_x$ by Yelon *et al.*[12]

The average isomer shift $\overline{(IS)}$ relative to α-iron was found to increase linearly by increasing the Al concentration as shown in Fig. 4, where the circles are the experimental $\overline{IS}$ and the solid line is the linear fit. The parameters for the linear fitting are given by the equation

$$\overline{IS}(\text{mm/s}) = -0.12 + 0.03x.$$

Figure 4 shows that $\overline{IS}$ is negative and the magnitude of $\overline{IS}$ decreases with increasing Al concentration. This decrease

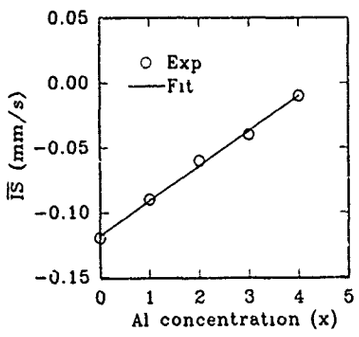

FIG. 4. Dependence of the average isomer shift $\overline{(IS)}$ relative to α-iron for $Sm_2Fe_{17-x}Al_x$ compounds on the Al concentration x.

means a decrease in the probability of finding the s electrons at the nucleus that can be attributed to the expansion of the cell volume. $\delta\overline{IS}/\delta \ln V$ for these compounds was 3.0 mm/s compared to 1.13 mm/s for α-Fe given by Shenon and Wagner[14] and 1.5–2.3 mm/s for R_2Fe_{17} and $R_2Fe_{17}N_{3-\delta}$ at 15 K given by Hu *et al.*[10] The present value is higher than the other values due to the smaller change in the cell volume compared to the others.

IV. CONCLUSIONS

Samples of $Sm_2Fe_{17-x}Al_x$ magnetic compounds have been fabricated and studied by Mössbauer spectroscopy. These compounds have rhombohedral Th_2Zn_{17} single phase with less than 2% α-Fe impurity. All the samples studied are ferromagnetic and the average hyperfine fields, and hence the magnetic moments, are found to decrease as x increases from 0 to 4. Therefore the increase in T_c with x up to $x=3$ must be due to the increase in interatomic exchange interactions between Fe atoms with volume expansion. Adding more Al lowers the exchange interaction due to the decrease in the number of Fe-Fe nearest neighbors, thereby lowering the T_c for $x>3$. Aluminum is found to occupy the three iron sites $6c$, $18h$, and $18f$ with varying degrees of occupancy, but not the $9d$ site. The change in isomer shift with increasing Al concentration corresponds to the decreasing s-electron density at the nucleus caused by the volume expansion.

ACKNOWLEDGMENT

The authors would like to thank the United States Department of Energy (DOE) for the support under Grant No. DE-FG2-86ER45262.

[1] X. P. Zhong, R. J. Radwanski, F. R. De Boer, T. H. Jacobs, and K. H. J. Buschow, J. Magn. Magn. Mater. **86**, 333 (1990).
[2] J. M. D. Coey and H. Sun, J. Magn. Magn. Mater. **87**, L251 (1990).
[3] B. P. Hu and J. M. D. Coey, J. Less-common Metals **142**, 295 (1988).
[4] M. Valeaun, N. Plagaru, and E. Burzo, Solid State Commun. **89**, 519 (1994).
[5] B.-G. Shen, F. Wang, L. Kong, and L. Cao, J. Phys.: Condens Matter **5**, L685-1688 (1993).
[6] T. H. Jacobs, K. H. J. Buschow, G. F. Zhou, X. Li, and F. R. de Boer, J. Magn. Magn. Mater. **116**, 220 (1992).
[7] F. Wertzer, K. Hiebl, and P. Rogl, J. Appl. Phys. **65**, 1989.
[8] Z. Wang and R. A. Dunlap, J. Phys.: Condens. Matter **5**, 2407–2414 (1993).
[9] D. McNeely and H. Oesterreicher, J. Less-common Metals **44**, 183 (1976).
[10] B.-P. Hu, H.-S. Li, H. Sun, and J. M. D. Coey, J. Phys.: Condens. M **3**, 3983 (1991).
[11] Gary J. Long, S. Mishra, O. A. Pringle, F. Grandjean, and K. H. J. Buschow, J. Appl. Phys. (to be published).
[12] W. B. Yelon, H. Xie, Gary J. Long, O. A. Pringle, F. Grandjean, and K. H. J. Buschow, J. Appl. Phys. **73**, 6029 (1993).
[13] Gary J. Long, O. A. Pringle, F. Grandjean, and K. H. J. Buschow, J. Appl. Phys. **72**, 4845 (1992).
[14] D. L. Williamson, in *Mössbauer Isomer Shifts*, edited by G. K. Shenoy and F. E. Wagner (North-Holland, Amsterdam 1978), p. 317.

Published without author corrections

Neutron diffraction and magnetic studies of $Nd_2Fe_{17-x-z}Al_xSi_z$

Z. Hu and W. B. Yelon
University of Missouri Research Reactor, Columbia, Missouri 65211

The Al and Si double-substituted 2:17 phase, $Nd_2Fe_{17-x-z}Al_xSi_z$, was prepared and analyzed using neutron powder diffraction and SQUID magnetization measurements. Rietveld analysis of the neutron diffraction data indicates that the lattice parameters are close to a linear combination of the corresponding single-substitution compounds. The unit cell could be expanded or contracted, depending on the Al/Si ratio. The aluminum and silicon fractional occupancy on the different crystallographic sites in the double-substitution compounds are related to those of single-substitution compounds. The SQUID measurements show that all samples in this study have Curie points higher than that of the unsubstituted compound. For a Si/Al ratio of 2:1, the Curie point, 492 K, was found at a total substituent content less than in the singly substituted Si compound with the same T_c.

I. INTRODUCTION

The substitution of aluminum for iron in Nd_2Fe_{17} raises the Curie temperature and leads to an expansion in the unit cell volume.[1] In this kind of compound, it is believed that the lattice expansion is sufficient to decrease antiferromagnetic exchange and enhance the ferromagnetic exchange.[2] When silicon is used as the substituent for iron in Nd_2Fe_{17}, the lattice contracts upon substitution, which would normally be expected to lower the Curie temperature. However, the Curie temperatures of the compounds are strongly increased.[3,4] The enhancement of magnetic properties with Si substitution is apparently related to the expansion of the lattice in the $9d$-$18h$ plane.[3] It may be expected that a combined substitution of Fe by Si and Al at the appropriate level could lead to further enhancement of the magnetic properties. In this paper, neutron diffraction and magnetic studies of the Al and Si double-substituted 2:17 phase, $Nd_2Fe_{17-x-y}Al_xSi_y$, are presented.

II. EXPERIMENT

Samples of $Nd_2Fe_{17-x-y}Al_xSi_y$ used in this study were prepared by rf induction melting of the constituent elements of purity 99.9–99.995% in a water-cooled copper boat under flowing argon at the Graduate Center for Materials Research, University of Missouri-Rolla. The ingots were annealed at 980 °C for one week. The ingots were then crushed and ground in an acetone bath for neutron diffraction studies or SQUID measurements. Neutron diffraction data were collected at the University of Missouri Research Reactor using the linear position-sensitive detector diffractometer at room temperature on approximately 2 g samples in 24 h. The neutron wavelength was 1.4783 Å. The data were measured from 5°–105° in 2θ. The Curie temperatures, T_c, were measured by SQUID using a Quantum Design MPMS System.

The neutron diffraction powder patterns were analyzed by the Rietveld method using the FULLPROF program[5] for multiphase refinement including magnetic structure refinement. α-Fe (5.62–8.57% in volume) was observed in all samples.

III. RESULTS AND DISCUSSIONS

The refinement results are given in Table I. Since each sample has some α-Fe (5–8% in volume) as the second phase, the stoichiometry of the compounds differs from the nominal composition. However, by using the site-effective scattering length and assuming the nominal Si/Al ratio, the stoichiometry of the compounds can be determined (see Appendix). The results are given in Table I. In a previous study,[2] the unit cell volume increased in the Al-only substituted compound, $Nd_2Fe_{17-x}Al_x$, at a rate of 9 $Å^3$/Al, while the unit cell volume decreased in the Si-only substituted compound, $Nd_2Fe_{17-y}Si_y$, at a rate of 3.4 $Å^3$/Si.[4] It is found that the unit cell volume, as well as the cell parameters, a and c, are close to a linear combination of that of the corresponding single-substitution compounds. The deviations are in the range of ±0.11%. The unit cell could, thus, be expanded or contracted, depending on the Al/Si ratio. All double-substitution compounds were found to have a higher c/a ratio than the pure Nd_2Fe_{17} phase. The site occupancies of the substituents in double-substitution compounds are not a simple addition of the Al occupancies and the Si occupancies of corresponding single-substitution compounds. Unfortunately, the substituent occupancies cannot be determined directly from the neutron refinements. However, they can be determined using a few reasonable assumptions. Previous studies show that no Al occupies the $9d$ site in the $Nd_2Fe_{17-x}Al_x$ compounds up to $x=8$, since the $9d$ is the smallest site,[1,2] and no Si occupies the $6c$ sites in $Nd_2Fe_{17-y}Si_y$ compounds up to at least $y=4.2$, since the $6c$ is the largest site.[4] In $Nd_2Fe_{17-x-y}Al_xSi_y$, it is assumed that (a) no Al atoms occupy the $9d$ sites, (b) no Si atoms occupy the $6c$ sites, and (c) the average bond length of the $18h$ sites depends only on the occupancies of Al and Si on this site. The dependence functions of the $18h$ site average bond length of single-substitution compounds are applied to double-substitution compounds. The results for the separate Al and Si site occupancies (see Appendix) are given in Table II. These appear reasonable in comparison to the singly substituted results, but an anomalous x-ray scattering study, combined with the neutron data, would be useful to uniquely fix the occupancies. Figure 1 shows the dependence of site occupancies upon the substituent contents for those samples

 0021-8979/94/76(10)/6162/3/$6.00 © 1994 American Institute of Physics

TABLE I. Refinement results of $Nd_2Fe_{17-x-y}Al_xSi_y$ solid solution.

x,y parameter	$x=0$ $y=0$	$x=0.92$ $y=0.93$	$x=1.82$ $y=0.87$	$x=0.91$ $y=1.79$	$x=1.57$ $y=1.58$	$x=2.83$ $y=1.02$	$x=2.14$ $y=2.09$	$x=2.68$ $y=2.69$
a	8.6002(1)	8.5925(3)	8.6288(3)	8.5785(3)	8.6043(2)	8.6413(2)	8 6060(4)	8.6274(3)
c	12.4835(2)	12.5156(5)	12.5572(6)	12.5194(5)	12.5446(4)	12.5878(3)	12.5473(7)	12.5509(5)
c/a	1.4515	1.4566	1.4552	1.4594	1.4579	1.4567	1.458	1.4548
V	799.631	800.233	810.414	797.879	804.352	814.101	804.976	809.074
μ, Nd, 6c	2.1(2)	2.2(3)	2.8(3)	2.8(2)	2.2(3)	2.1(2)	2.1(3)	1.7(3)
μ, Fe, 6c	2.5(2)	2.8(5)	2.5(4)	2.7(2)	2.4(4)	1.9(3)	2.2(4)	1.6(3)
μ, Fe, 9d	1.7(2)	1.8(1)	1.8(1)	1.8(1)	1.8(1)	1.2(1)	1.8(1)	2.1(4)
μ, Fe, 18f	2.4(2)	1.7(2)	2.6(3)	2.4(2)	2.3(2)	2.2(2)	2.5(3)	2.0(4)
μ, Fe, 18h	1.7(2)	1.8(3)	2.3(3)	2.2(3)	1.9(3)	1.9(2)	2.1(4)	1.6(4)
$\mu(z)/\mu(x)$	0	0	0	0	0.33	0 5	1 2	1.7
R	5.48	4.68	5.60	5.20	5.06	4.68	6.04	6.72
R_{wp}	7.09	6.39	7.71	7.12	6.63	6.30	8.60	9.31
R_{mg}	6.22	10.20	14.10	10.60	10.60	10.70	11.90	8.97
χ^2	3.11	1.93	3.47	2.99	2.54	2.33	4.41	5.01
T_c, K	330	455	470	492	480	462	470	390
α-Fe	6.95	5.62	8.57	7.74	7.43	5.98	7.16	6.46
6c, ASBL[a]	2.675	2.676	2.686	2.680	2.684	2.685	2.681	2.689
9d, ASBL	2.494	2.494	2.503	2.495	2.499	2.505	2.497	2.504
18f, ASBL	2.579	2.582	2.592	2.586	2.590	2.595	2.590	2.591
18h, ASBL	2.566	2.564	2.576	2.560	2.568	2.580	2.568	2.576

[a]ASBL=average site bond length.

with an approximate Al/Si ratio of one. In the singly substituted compounds, either the 9d or 6c sites remain full of Fe and, therefore, the remaining sites must, on average, have a higher than random substituent occupancy. In the present case, both sites are occupied and therefore there is a lower total occupancy of the remaining 18f and 18h sites. It is found that the 18f site takes up less substituent, while the 18h site fills at roughly the same rate as in the singly substituted compounds. Table I also gives the bond lengths and the average bond length of each site. It was found that the average bond length increases in 6c, 9d, and 18f sites in all samples in this study. On the 18h site, the average bond length increases in some samples and decreases in other samples, depending on the Al/Si ratio and the total substituent content.

The site magnetic moment of these compounds are also given in Table I. It was found that the Nd sublattice couples ferromagnetically to the Fe sublattice in all compounds. For those samples of low total substituent content, the magnetic moments lie in the basal plane. For those samples of high total substituent content, canted magnetic structures were observed. However, the refinement was not stable for the sample of highest content and the minimum was found by iteration of the $\mu(z)/\mu(x)$ ratio. An easy direction change was found in $Nd_2Fe_{17-y}Si_y$ only with $y>3$ (Ref. 4) but not found in $Nd_2Fe_{17-x}Al_x$ up to $x=9$.[2] It is possible that an easy axis system could be produced at a lower substituent content than is found in any singly substituted compound. The Curie temperatures, measured by SQUID, are also given in Table I. All compounds have a Curie point higher than that of the pure Nd_2Fe_{17} phase, which is 330 K. The Curie temperature was found to depend on both the total substituent content and the Al/Si ratio, and those compounds with a higher Si/Al ratio have higher Curie points, indicating that Si has a stronger effect on the ferromagnetic exchange than Al. In the $Nd_2Fe_{17-x}Al_x$, the maximum Curie temperature, about 460 K, is found for x of approximately three. In $Nd_2Fe_{17-y}Si_y$, the maximum Curie temperature, about 495 K, is at y of about 3.7. The maximum Curie point of the double-substitution compounds (with the limited Al and Si contents and their ratio in this study) was found to be 492 K, similar to that of Si-only substitution compounds. The total substituent content is significantly lower than in the singly substituted compound (2.7 compared to 3.7, about 27% less),

TABLE II. Site occupancies of Al and Si in $Nd_2Fe_{17-x-y}Al_xSi_y$.

x,y parameter	$x=0$ $y=0$	$x=0.92$ $y=0.93$	$x=1.82$ $y=0.87$	$x=0.91$ $y=1.79$	$x=1.57$ $y=1.58$	$x=2.83$ $y=1.02$	$x=2.14$ $y=2.09$	$x=2.68$ $y=2.69$
Al%, 6c	0.00	4.35	5.87	5.66	7.87	7.01	14.21	24.44
Si%, 6c	0.00	0.00	0.00	0.00	0.00	0.00	0.00	0.00
Al%, 9d	0.00	0.00	0.00	0.00	0.00	0.00	0.00	0.00
Si%, 9d	0.00	5.84	6.95	7.42	10.36	7.88	14.87	16.32
Al%, 18f	0.00	3.78	5 78	3.16	5.49	15.25	10.88	11.94
Si%, 18f	0.00	0.00	0.00	4.30	2.30	0.00	6.33	17.83
Al%, 18h	0.00	10.13	22.24	10.16	18.02	29.57	19.96	24.86
Si%, 18h	0.00	12.47	11.13	21.79	18.89	13.18	21.11	18.97

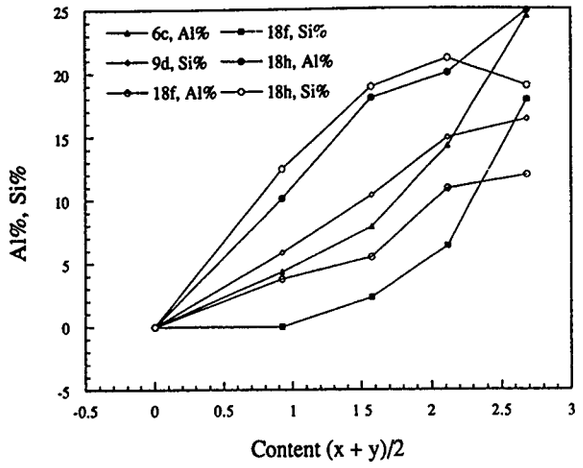

FIG. 1. The percentage substituents found on the four iron sites as a function of $(x+y)/2$ for samples with an approximate Al/Si ratio of one.

which is important because the lower substituent content means less reduction in the magnetization of the compound. It is possible that the higher Fe content on the $18f$ site plays a role in the observed enhancement in the magnetic properties. Note that the magnetic moment on this site is relatively large in most of the specimens.

ACKNOWLEDGMENTS

The authors would like to thank Dr. W. J. James, University of Missouri-Rolla, for help in preparing samples, the Division of Materials Research of the U.S. National Science Foundation for Grant No. DMR 9305782, and M. Seewoster for helping in preparing tables and figures.

APPENDIX

For a double-substitution 2:17 phase, $Nd_2Fe_{17-x-y}Al_xSi_y$, the effective scattering lengths of the four iron sites are

$$cb_{fe}=x_1b_{al}+y_1b_{si}+(0.167-x_1-y_1)b_{fe}, \quad \text{(A1)}$$

$$db_{fe}=x_2b_{al}+y_2b_{si}+(0.167-x_2-y_2)b_{fe}, \quad \text{(A2)}$$

$$fb_{fe}=x_3b_{al}+y_3b_{si}+(0.167-x_3-y_3)b_{fe}, \quad \text{(A3)}$$

$$hb_{fe}=x_4b_{al}+y_4b_{si}+(0.167-x_4-y_4)b_{fe}, \quad \text{(A4)}$$

where c, d, f, and h are refined Fe site occupancies. b_{al}, b_{si}, and b_{fe} are the scattering lengths of Al, Si, and Fe, respectively. x_i ($i=1$, 2, 3, and 4) are Al site occupancies and y_i ($i=1$, 2, 3, and 4) are Si site occupancies.

To solve for the eight unknowns, x_i and y_i, four more independent equations are needed:

(a) No Al or Si out of the 2:17 phase, then

$$\Sigma x_i/\Sigma y_i=(W_{al}/M_{al})/(W_{si}/M_{si}), \quad \text{(A5)}$$

where W_{al} and W_{si} are the starting weights of Al and Si, and M_{al} and M_{si} are the atomic weights of Al and Si, respectively.

(b) No Al atoms occupy the $9d$ sites,

$$x_2=0. \quad \text{(A6)}$$

(c) No Si atoms occupy the $6c$ sites,

$$y_1=0. \quad \text{(A7)}$$

(d) The average bond length of the $18h$ sites depends only on the occupancies of Al and Si on this site. The dependence functions of the $18h$ site average bond length of single-substitution compounds can be applied to double-substitution compounds. The site average bond length for the $18h$ sites depends only on the substituent occupancies.

$$ABL_h=f_h(x_4)+f'_h(y_4)-ABL_0, \quad \text{(A8)}$$

where ABL_h is the refined h site average bond length of $Nd_2Fe_{17-x-y}Al_xSi_y$, ABL_0 is the refined h-site average bond length of Nd_2Fe_{17}, $f_h(x)$ is the dependence function of the h site average bond length on Al occupancy in $Nd_2Fe_{17-x}Al_x$, which was extracted from the Al-only substituted compounds in a previous study.[2] $f'_h(y)$ is the dependence function of the h-site average bond length on Si occupancy in $Nd_2Fe_{17-y}Si_y$, which was extracted from the Si-only substituted compounds in a previous study.[4]

By solving the independent equations (A1)–(A8), x_i ($i=1$, 2, 3, and 4) and y_i ($i=1$, 2, 3, and 4) are determined.

[1] W. B. Yelon, H. Xie, G. J. Long, O. A. Pringle, F. Grandjean, and K. H. J. Buschow, J. Appl. Phys. **73**, 6029 (1993).
[2] G. J. Long, G. K. Marasinghe, S. Mishra, O. A. Pringle, Z. Hu, W. B. Yelon, D. P. Middleton, K. H. J. Buschow, and F. Grandjean, J. Appl. Phys. (in press).
[3] G. J. Long, G. K. Marasinghe, S. Mishra, O. A. Pringle, F. Grandjean, K. H. J. Buschow, D. P. Middleton, W. B. Yelon, F. Pourarian, and O. Isnard, Solid State Commun. **88**, 761 (1993).
[4] Z. Hu *et al.* (unpublished).
[5] FULLPROF Rietveld refinement code by J. Rodriquez-Carjaval, Institute Laue-Langevin, Grenoble, France.

New magnetic material based on $SmCo_4B$

Hideaki Ido, Osamu Nashima, and Takehiro Takahashi
Department of Applied Physics, Tohoku Gakuin University, Tagajo 985, Japan

Kiwamu Oda and Kiyohiro Sugiyama
The Research Center for Extreme Materials, Osaka University, Toyonaka, Osaka 560, Japan

The compound $SmCo_4B$ is a hard magnetic material; however, the saturation moment and the Curie temperature need to be increased for the compound to be a candidate for a permanent magnetic material. For this purpose, Fe substitution for the Co and Pr substitution for the Sm of $SmCo_4B$ have been attempted. In addition, the nitrogenation of $SmCo_2Fe_2$ is also attempted. The magnetic characteristics of $SmCo_2Fe_2B$ have been investigated in a pulsed high magnetic field up to 350 kOe. and the data are compared with those of other related compounds investigated in this work. The compound with more Fe content, $SmCo_{1.7}Fe_{2.3}B$, has been successfully made, and $T_C=794$ K and saturation moment $M_s=81.4$ emu/g at 300 K have been obtained. It is found that the Fe substitution does not decrease the uniaxial magnetic anisotropy. Heat treatments in nitrogen gas at 500 °C of $SmCo_2Fe_2B$ have brought about significant increases of magnetization; however, the increase of T_C is only about 20 K and the crystal volume is unchanged to within experimental uncertainty.

It has been known[1,2] that boron substitution for the Co of RCo_5 (R=rare earth) leads to a formation of compound systems with discrete B content expressed by the general formula $R_{n+1}Co_{3n+5}B_{2n}$ $(n=0,1,2,\ldots,)$. In our previous papers,[3,4] we focused on the Sm system of hard magnetic materials. The compound $SmCo_4B$ is especially interesting because it has a huge uniaxial magnetic anisotropy at $T=4.2$ K. However, both the saturation moment and the Curie temperature are about half of those of $SmCo_5$. It is also known[4] that Fe and Pr substitutions increase the magnetization as well as the Curie temperature of $SmCo_4B$. In order to improve the magnetic characteristics of $SmCo_4B$ for a hard magnetic material, three kinds of trials have been made in this work: the first is to re-examine the magnetic characteristics of $SmCo_{4-x}Fe_xB$ in a high magnetic field; the second is to make samples with greater Fe content than $x=2$ in $SmCo_{4-x}Fe_xB$ and also to create Pr substitution for the Sm; the last is to make nitrogen-absorbed samples of $SmCo_2Fe_2B$. Magnetic and crystallographic measurements have been performed and discussed for the samples mentioned above.

Samples in the present study were prepared by an arc furnace. The melting was repeated generally more than six times to homogenize the composition of the melts. Especially in the case of $SmCo_{1.7}Fe_{2.3}B$, ingots of Co, Fe, and B with desired ratio of mass were first melted ten times, and then the ingot thus prepared was melted together with a suitable mass of Sm at least six times. This method seems to be effective to obtain a single phase of the compound with a large content of Fe. Several days of heat treatment at about 1000 °C was generally made to homogenize the ingots obtained by the arc melting. By this method, we obtained a single phase of $SmCo_{1.7}Fe_{2.3}B$, which implies that there is hope that higher Fe contents are attainable, but not certainty. In the case of the $Sm_{0.7}Pr_{0.3}Co_2Fe_2B$ compound, the sample prepared included a small amount of the 2:17 phase and a very small amount of the 1:5 phase. If composition loss of the Sm and B occurs during the melting process, we will have the three phase samples mentioned above.[2] Excess nominal composition of Sm and B will be needed to obtain a single phase of $Sm_{0.7}Pr_{0.3}Co_2Fe_2B$. The crystal structures of $CaCu_5$ type for $SmCo_5$ and $CeCo_4B$ type for $SmCo_4B$, etc., are illustrated in Fig. 1. The lattice parameters of $SmCo_{1.7}Fe_{2.3}B$ have been determined by x-ray diffraction to be $a=5.138$ A and $c=6.948$ A, which are larger than $a=5.087$ A and $c=6.89$ A for $SmCo_4B$, respectively. About 3% volume expansion occurs by the Fe substitution.

Magnetization curves have been measured in a pulsed high magnetic field up to 35 T(=350 kOe) for field-oriented samples of $SmCo_5$, $SmCo_4B$, and $SmCo_2Fe_2B$. Particle size of powdered samples is generally less than 32 μm in diameter. The magnetization curves of $SmCo_5$ and $SmCo_4B$ are similar to our previous data.[3] The anomalous behavior of the magnetization curve with $H\|c$ at around $H=0$ for $SmCo_4B$ is considered to be caused by the experimental method: the magnetization in the process of decreasing external field is first measured in the region from $H=35$ T to $H=0$ and then the cylindrical field-oriented sample direction was reversed to measure the magnetization in the region from $H=0$ to

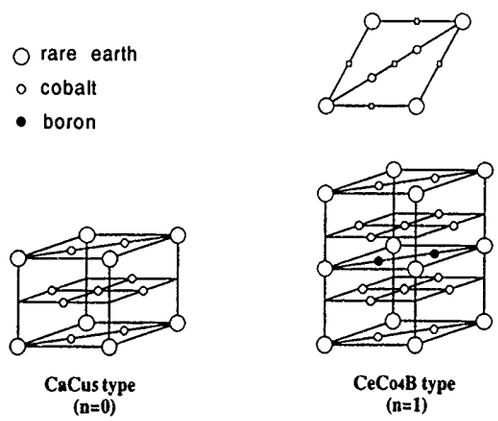

FIG. 1. Crystal structure of $CaCu_5$ and $CeCo_4B$ type. The square symbols in the basal plane indicate the sites that nitrogen atoms may occupy if the nitride is formed.

 0021-8979/94/76(10)/6165/3/$6.00 © 1994 American Institute of Physics

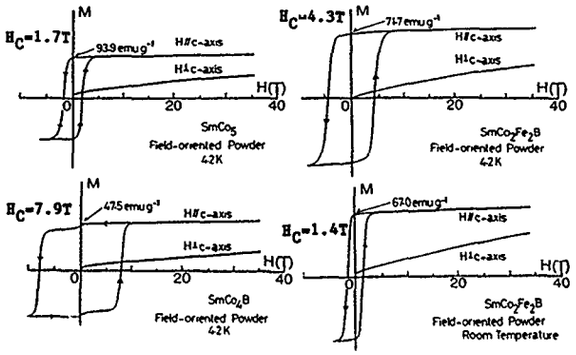

FIG. 2. Magnetization curves measured in pulsed magnetic field for field-oriented samples of $SmCo_5$ and $SmCo_{4-x}Fe_xB$ with $x=0$ and 2. C indicates the direction of field orientation.

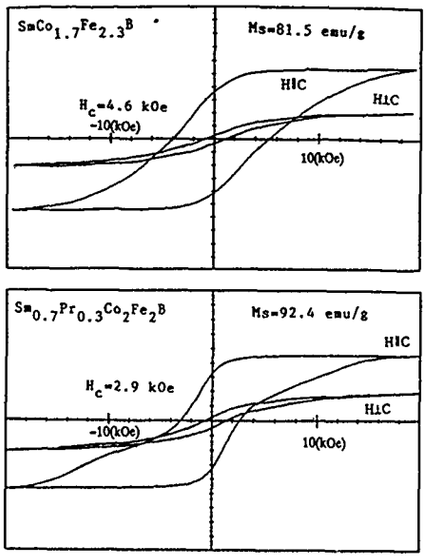

FIG. 3. Magnetization curves for field-oriented samples of $SmCo_{1.7}Fe_{2.3}B$ and $Sm_{0.7}Pr_{0.3}Co_2Fe_2B$. C indicates the direction of field orientation. The coercivity H_c is defined as an average of H_c in the processes of decreasing and increasing fields.

$H=-10$ T. The magnetization curve in the process of increasing field was measured by a similar method. The data for $SmCo_2Fe_2B$ at $T=4.2$ and 300 K are obtained for the first time in this work. Coercivity H_c, which depends on the various factors, is also shown for the respective samples in Fig. 2. As seen in Fig. 2, the magnetization curves with $H\perp c$ have a small amount of residual magnetization at $H=0$, which means a slight lack of alignment of the field-oriented samples. To avoid the error in the estimation of anisotropy field H_A due to the lack of alignment, the linear part of the initial magnetization curve with $H\perp c$ is moved in parallel so as to start from the origin, and then the anisotropy field is determined as the magnetic field at which the straight line corresponding to the linear part mentioned above reaches the spontaneous magnetization. The anisotropy field has been determined by this method for the respective sample in Fig. 2. The saturation magnetization values have been calibrated by making use of the data for the loose powder of each sample. Anisotropy constant K_1 has been calculated by the equation of $K_1=(1/2)M_sH_A$, where M_s is the spontaneous magnetization per unit volume.

The magnetization curves for the field-oriented samples of $SmCo_{1.7}Fe_{2.3}B$ and $Sm_{0.7}Pr_{0.3}Co_2Fe_2B$ have been measured in a magnetic field up to 20 kOe. The data are shown in Fig. 3. In this case, the particle size is larger than that of the samples in Fig. 2, but less than 32 μm. Since there is considerable lack of alignment and also the maximum field used is only 20 kOe in Fig. 3, it is hard to obtain a reliable value of anisotropy field. Rough values of H_A in both cases in Fig. 3 have been estimated to be about 120 kOe by a method similar to that used in Fig. 2. The magnetic data mentioned above are summarized in Table I together with Curie temperatures determined by a magnetic balance in this work. Some data in Table I are taken from references cited therein. We can see some important points in Table I. The magnetization of $SmCo_4B$ is considerably increased; however, the anisotropy constant remains almost unchanged by the Fe substitution. The magnetization of $YCo_{4-x}Fe_xB$ is known to increase with x.[9,10] It has also been clarified by Onodera *et al.*[10] that both Fe and Co moments increase with x. A similar mechanism, which occurs also in the Fe-Co alloy, must occur in $SmCo_{4-x}Fe_xB$. A fundamental concern is also in the magnetic state of the Sm sublattice; however, we do not discuss it here. According to Dung *et al.*,[9] the anisotropy constant K_1 at $T=4.2$ K of YCo_4B and $YCo_{2.5}Fe_{1.5}B$ take about -4×10^6 erg/cm^3 and -1×10^7 erg/cm^3, respectively. These values are negligibly small compared with those of $SmCo_4B$ and $SmCo_2Fe_2B$ at $T=4.2$ K, which means that the K_1 value in the Sm system mentioned above is supplied mainly by the Sm sublattice. The data of K_1 in Table I suggest that the Sm-sublattice anisotropy is enhanced by the Fe substitution. Therefore, to make $SmCo_4B$ a candidate for permanent magnet materials, we only need to increase the magnetization and the Curie temperature of $SmCo_4B$ by Fe substitution as much as possible. As seen in Table I, the Curie temperature of $SmCo_{1.7}Fe_{2.3}B$ is about 1.6 times higher than that of $SmCo_4B$. The Pr substitution is also effective to increase the magnetization. In the case of $YCo_{4-x}Fe_xB$, the maximum Fe content seems to be $x=1.5$,[9] which means the

TABLE I. Magnetic data of $SmCo_4B$ and related compounds. T_C, Curie temperature; M_s, saturation magnetization; H_A, anisotropy field in the unit of Tesla; K_1, anisotropy constant. Saturation induction equals $4\pi M_s\rho$ (Gauss), where specific mass ρ is 8.58 for $SmCo_5$ and 8.54 for other compounds.

	T_C (K)	M_s (emu/g)	H_A (T)	K_1 (10^7 erg/cm^3)
$SmCo_5$	959[5]–1020[6]	93.7(4.2 K)	71(4.2 K)	28.6
		90(300 K)		15[7]–18[8]
$SmCo_4B$	500[4]	47.5(4.2 K)	110(4.2 K)	22.3
			120(4.2 K)[3]	24.3[3]
$SmCo_2Fe_2B$	782[4]	71.7(4.2 K)	74	22.6
	732	70.2(77 K)	81	24.2
		67.1(300 K)	51	14.6
$SmCo_{1.7}Fe_{2.3}B$	794	81.4(300 K)		
$Sm_{0.7}Pr_{0.3}Co_2Fe_2B$	749	92.4(300 K)		

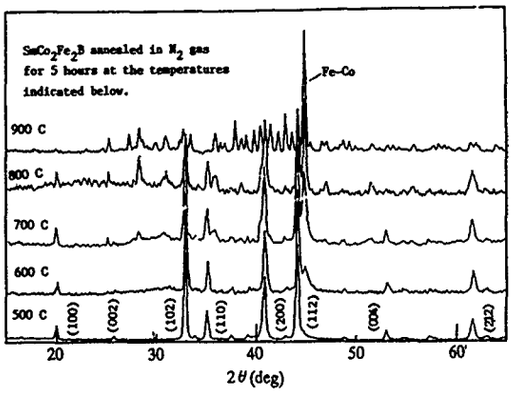

FIG. 4. X-ray diffraction patterns for $SmCo_2Fe_2B$ powder annealed in N_2 gas for 5 h at the indicated temperatures.

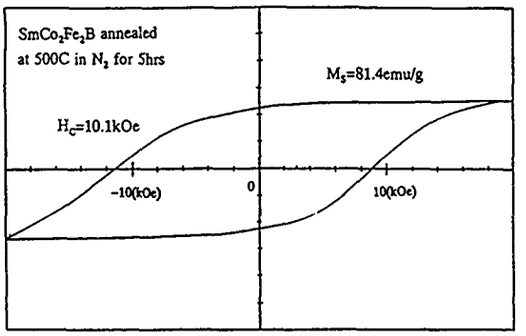

FIG. 6. Hysteresis loop of field-oriented $SmCo_2Fe_2B$ powder annealed at 500 °C in N_2 gas for 5 h. Definition of H_c is the same as those in Fig. 3.

maximum Fe content in $RCo_{4-x}Fe_xB$ seems to depend on the kind of rare earth R.

As mentioned in the preceding section, the three phases of $Sm_{0.7}Pr_{0.3}Co_2Fe_2B$ could be attributed to the composition shift during the melting process, so if appropriate initial nominal composition is found, it will be possible to obtain the single phase sample of $Sm_{0.7}Pr_{03}Co_2Fe_2B$.

To improve the magnetic characteristics of the materials mentioned in Sec. III, the nitrogenation will be another effective method. In this work, heat treatments of $SmCo_2Fe_2B$ powder in atmospheric N_2 gas have been carried out at various temperatures. X-ray diffraction patterns of the sample after the heat treatments are shown in Fig. 4. The heat treatments at temperatures above 600 °C seem to promote the precipitation of Fe-Co alloy. Therefore, nitrogenation of $SmCo_2Fe_2B$ was tried at 500 °C in N_2 gas for 5, 10, and 24 h. Magnetization curves measured for loose powders at 300 K are shown in Fig. 5. These data clearly show an effect of heat treatments in N_2 gas. The saturation magnetization increases more than 10%; however, x-ray diffraction patterns before and after the heat treatment do not bring about significant volume expansion. The Curie temperatures that are shown in the inset of Fig. 5 also do not show a clear difference, although an N_2 gas effect is seen in the magnetizations. It is not clear at present whether the sample absorbed nitrogen into the inner part of the crystal. A hysteresis loop of the heat treated N_2 gas for 5 h is shown in Fig. 6. The coercivity takes a very similar value to that of the sample without heat treatment in N_2 gas. The crystallographic site that the nitrogen atom may occupy is shown by the open square symbols, which is the site similar to the $9e$ site in Sm_2Fe_{17}[11] in Fig. 1. Since the four near neighboring sites around the square site are occupied by Co or Fe atoms in equal probability in the present case, the probability that all the four sites are occupied by Fe atoms will be $(\frac{1}{2})^4$. Therefore, if the nitrogen atom is supposed to occupy the square site with four Fe surroundings, the possible formula of nitride of $SmCo_2Fe_2B$ will be $SmCo_2Fe_2BN_{0.1875}$, which means that the quantity of nitrogen that may be absorbed by the sample is small, unlike the case of Sm_2Fe_{17}. This may be one of the reasons why nitrogen is not easily absorbed by $SmCo_2Fe_2B$.

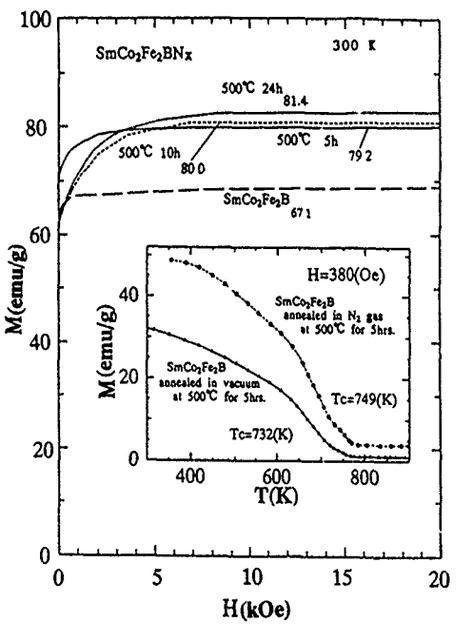

FIG. 5. Magnetization curves for $SmCo_2Fe_2B$ loose powders. 500 °C, 24 h indicates that the sample was annealed in N_2 gas at 500 °C for 24 h. The inset shows the temperature dependence of the magnetization of $SmCo_2Fe_2B$ annealed in two different conditions.

[1] Yu. B. Kuzuma, N. S. Bilonizhko, S. I. Mykhalenko, G. F. Stepanova, and N. F. Chaban, J. Less-Common Met. **67**, 51 (1979).
[2] P. Rogl, in *Handbook on the Physics and Chemistry of Rare Earths*, edited by K. A. Gschneidner and L. Eyring (North-Holland, Amsterdam, 1984), Vol. 6, p. 335.
[3] H. Ido, K. Sugiyama, H. Hachino, M. Date, S. F. Cheng, and K. Maki, Physica B **177**, 265 (1992).
[4] H. Ido, H. Ogata, and K. Maki, J. Appl. Phys. **73**, 6269 (1993).
[5] A. S. Ermolenko and Ye. V. Shcherbakova, Fiz. Met. Matalloved **48**, 275 (1979).
[6] R. Lemaire, Cobalt **32**, 132 (1966).
[7] H. P. Klein and A. Menth, AIP Conf. Proc. **18**, 1177 (1974).
[8] A. S. Ermolenko, *Proceedings of the International Conference on Magnetism 1973* (Nauka, Moscow, 1974), Vol. I (1), p. 231.
[9] T. T. Dung, N. P. Thuy, N. M. Hong, and T. D. Hien, J. Appl. Phys. **69**, 4633 (1991).
[10] H. Onodera, S. G. Kang, H. Yamauchi, and Y. Yamaguchi, J. Magn. Magn. Mater. **127**, 296 (1993).
[11] J. M. D. Coey and S. Hong, J. Magn. Magn. Mater. **87**, L251 (1980).

Dissipation in macroscopic quantum tunneling and coherence in magnetic particles (invited)

Anupam Garg
Department of Physics and Astronomy, Northwestern University, Evanston, Illinois 60208

For quantum phenomena involving a macrovariable such as the total moment of a ferromagnetic particle, or the Néel vector of an antiferromagnetic one, environmental couplings play a crucial role. The effect of such couplings, or dissipation, is studied, with emphasis on the nuclear spin environment. It is shown that magnetic macroscopic quantum tunneling (MQT) and coherence (MQC) both become harder to see. Quantitative calculations are presented for the tunneling rate in MQT, and the tunnel splitting and ac susceptibility for MQC. A recent claim to have seen MQC in a resonance experiment on ferritin is critically discussed and the absorption is found to be at least 1500 times larger than predicted by MQC.

I. INTRODUCTION

Even the best quantum mechanics texts[1] sometimes state that for billiard balls and cannon shells, the de Broglie wavelength is so absurdly small that any quantum mechanical effect such as two-slit diffraction would be washed out by the limited resolution of any measurement apparatus. This is usually taken as sufficient reason for the inadvisability of applying quantum mechanics to such objects. Yet, if one were to press the issue, and ask what the practical difficulties would be in experimentally verifying quantum effects in such cases, one would soon conclude that the small de Broglie wavelength was completely overshadowed by another phenomenon, namely, interaction with the environment. Different particle trajectories would be correlated with very different states of the rest of the universe, so that even if the trajectories ended with the particle in the same position, the environment would not, and the interference terms in the square of the total amplitude would vanish by virtue of the zero overlap between the states of the environment. To put it another way, the environment would "measure" the trajectory taken by the particle, and one would never obtain the case of indistinguishable alternatives.[2]

This view of the quantum mechanics of macroscopic objects has been developed considerably further by Leggett and his co-workers over the last decade.[3] Interaction with the environment, or dissipation, as it has come to be called, is *the* feature which distinguishes macroscopic objects from microscopic ones. It is usually present in myriads of ways, and one would have to go to impossible lengths to eliminate it for the vast majority of macroscopic systems. As Leggett has pointed out, the two phenomena likely to yield the most unambiguous evidence of quantum behaviour are macroscopic quantum tunneling (MQT), or the decay of a metastable state, and macroscopic quantum coherence (MQC), or the resonance between degenerate states (see Fig. 1). Most of the early work was done with a view of seeing MQT and MQC of the order parameter in Josephson junction based systems,[4–9] but in the last few years, small magnetic particles have emerged as potential candidates too.[10,11] The macrovariable is the total magnetic moment of the particle if it is ferromagnetic, or the Neél vector if it is antiferromagnetic, and the different states correspond to different directions of these vectors. Other magnetic systems such as domain walls have also been proposed.[12]

It is essential to realize at the outset that MQT and MQC are very different phenomena, especially when environmental couplings are considered. In general, both become harder to see, but the effect on MQC is more severe. The essential requirement for MQC is degeneracy. If the bottoms of the wells of the MQC potential in Fig. 1 are nondegenerate by much more than the tunnel splitting, the mixing between the states localized near the well bottoms will be negligible, and one will not see any MQC. The environment can be viewed as giving rise to a dynamically fluctuating potential for the system. If this potential is asymmetric for most of the time, or if the degeneracy persists for times much less than the tunneling time, MQC will be reduced. Another way of saying this is that phase coherence must be maintained for much longer durations in MQC than MQT (inverse of the tunnel splitting versus the small oscillation period in the metastable well), and is therefore more easily destroyed by an environment. In fact, for ohmic and subohmic dissipation, as defined in Ref. 7(b), the environment can suppress MQC completely, localizing the particle in the initial well![8]

The purpose of this paper is to discuss dissipation in magnetic particle systems. The dissipation mechanisms which have been studied to date include phonons,[13,14] nuclear spins,[15] and Stoner excitations and eddy currents in metallic magnets.[16] Except for nuclear spins and Stoner excitations, the other mechanisms are generally weak. We will focus only on nuclear spins, and refer the reader to the literature for the rest. The work, for the most part, elaborates on Refs. 15(a) and 15(b), which deal, respectively, with MQT and MQC. We will consider MQT in Sec. II. We rebut

 0021-8979/94/76(10)/6168/6/$6.00 © 1994 American Institute of Physics

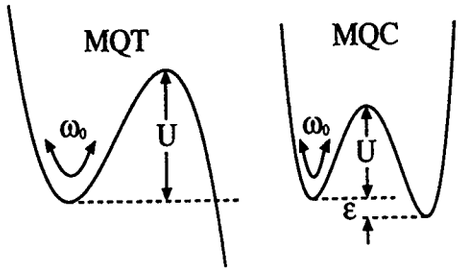

FIG. 1. Potentials for MQT and MQC. For MQC, the bias ϵ must be small.

Chudnovsky's recent statement that nuclear spins are unimportant,[17] and explicitly obtain the WKB exponent in the presence of dissipation. We find that unless the number of magnetic nuclei is less than a few percent of the atomic magnetic moments, the exponent is multiplied by a factor of order unity. If the exponent is as large as 20 or 30 in the absence of dissipation, this can substantially reduce the escape rate. We consider MQC in Sec. III, and show that even for systems where magnetic nuclei are rare, the suppression of MQC can be large. As a technical point, we note that unlike the case of MQT, for the MQC problem, nuclear spins cannot be reduced to an equivalent bath of harmonic oscillators. Because $\omega_n \ll \omega_e$, where ω_n and ω_e are the nuclear and electronic Larmor frequencies, the nuclei act almost as a c-number bias field, and sizeable resonance occurs only when the net nuclear spin polarization in a given particle is zero. Since the polarization decreases with increasing temperature T, we predict that MQC may be enhanced with increasing T in some range. We also suggest double resonance experiments—driving the nuclear polarization to zero by a strong rf pulse at ω_n should enhance the MQC signal while the nuclear polarization relaxes. We apply our results to Awschalom *et al.*'s claim to have seen MQC in antiferromagnetic ferritin particles.[18] When nuclear spin dissipation is included in a previous calculation of the expected power absorption,[19] the experimental signal is found to be too large by a factor exceeding 1500. Taken with previously discussed difficulties,[20] this renders the possibility of MQC occurring in ferritin rather implausible.

II. NUCLEAR SPINS AND MQT

Consider an isolated, nonmetallic, ~50 Å radius, single domain, ferromagnetic particle, at a temperature well below the anisotropy gap. Let us suppose that it has $N \sim 10^4$–10^5 atomic moments, each of spin s, and magnetogyric ratio γ. The total magnetic moment $\mathbf{M}$ then has essentially fixed magnitude $M_0 = Ns\hbar\gamma$, and its direction $\hat{\mathbf{M}}$ is the only dynamical variable left. In the presence of an external field $\mathbf{H}$, the Hamiltonian is given by

$$\mathscr{H}(\hat{M}) = E_{an}(\hat{M}) + \frac{1}{2v_0} N_{ij} M_i M_j - \mathbf{M}\cdot\mathbf{H}. \tag{2.1}$$

The three terms are due to crystal anisotropy, shape anisotropy, and the dipole coupling; v_0 is the particle volume, and N_{ij} is a shape dependent tensor with trace 4π. The first two terms will combine to create easy and hard directions for $\mathbf{M}$, which will in general not be along the crystal axes. This point must be kept in mind if one ever reaches the stage of doing single particle experiments, as it raises the issue of how the magnetic axes are to be found. We will denote the easy axis by $\hat{z}$, the hard axis by $\hat{y}$, and assume that $\mathbf{H} \| -\hat{z}$. [For results for small misalignments of $\mathbf{H}$, see Ref. 13(b).] The state $\mathbf{M} \| \hat{z}$ is then metastable with respect to $\mathbf{M} \| -\hat{z}$. As the field strength is increased, the barrier from $\mathbf{M} \| \hat{z}$ to $\mathbf{M} \| -\hat{z}$ will be lowered, and eventually vanish at some "coercive field" H_c. Since the tunneling rate is low for large barriers, we anticipate that we will need $H \approx H_c$ to see appreciable tunneling, and parametrize H as $H = (1-\epsilon)H_c$, where $\epsilon \ll 1$. Writing $\hat{\mathbf{M}}$ in terms of polar angles θ and ϕ, and subtracting a constant term, we arrive at the general Hamiltonian (model III in Ref. 10)

$$\mathscr{H}(\theta,\phi) = K_1\theta^2(\epsilon - \theta^2/4) + K_2\theta^2 \sin^2\phi. \tag{2.2}$$

Here, K_1 and K_2 are shape plus crystal anisotropy coefficients ($K_1 > K_2 > 0$). For hard magnets, we expect these to be close to the crystal anisotropy coefficients. In any case, we expect that per unit volume, $K_1 \sim K_2 \sim 10^6$–10^7 ergs/cm^3.

The quantum mechanical dynamics of $\mathbf{M}$ can be specified by giving the action and using path integrals to calculate any desired amplitude. For tunneling rates, it is better to use the "imaginary time" or Euclidean action, and this is given by

$$S_0[\hat{\mathbf{M}}] = \int [\mathscr{H}(\theta,\phi) - i\gamma M_0 \cos\theta\dot{\phi}(\tau)]d\tau. \tag{2.3}$$

The escape rate from an MQT potential such as in Fig. 1 can generally be written as $\Gamma_0 = c\omega_0 \exp(-S_0^{\rm cl}/\hbar)$, where ω_0 is the small oscillation frequency in the metastable well, c is a constant of order unity, and $S_0^{\rm cl}$ is the least or "classical" action for trajectories crossing the barrier. For our problem, ω_0 is the frequency for small amplitude precession of $\mathbf{M}$ around the stable direction $\theta = 0$—essentially the ferromagnetic resonance frequency—which from Eqs. (2.2) and (2.3) is $\omega_p = (2\gamma/M_0)(K_1K_2\epsilon)^{1/2}$. (Note that K_1, K_2, and M_0 are all proportional to the particle volume, so that ω_p is an intensive quantity.) As for the exponent $S_0^{\rm cl}/\hbar$, it can be obtained by standard WKB or instanton techniques,[10,13(b),(c),21] and it is useful to write it in three equivalent ways:

$$\frac{S_0^{\rm cl}}{\hbar} = \frac{8M_0}{3\hbar\gamma}\sqrt{\epsilon^3 r} = \frac{8Ns}{3}\sqrt{\epsilon^3 r} = \frac{16U}{3\hbar\omega_p}. \tag{2.4}$$

Here, $r = K_1/K_2$, $U = K_1\epsilon^2$ is the barrier height, and N is the total number of atomic moments in the particle. The second form follows from the first on recalling that $M_0 = Ns\hbar\gamma$, and the last form reveals a general feature for all smooth potentials, namely, that the WKB exponent is of order $U/\hbar\omega_p$. The second form shows explicitly that tunneling becomes harder as the number of moments increases, and makes the need for keeping ϵ small absolutely clear. Since $\omega_p \sim 10^{10}$ s^{-1}, one must have $S_0 < 30$, say, to have any hope of getting a reasonable value for Γ_0. Since $r > 1$, and $s > 1/2$, it follows that we must have $\epsilon < 0.037$ for $N = 10^4$ and $\epsilon < 0.008$ for $N = 10^5$. Surprisingly, these values correspond to fairly big exit angles (the classical turning points) of 22° and 10°, so

that the tunneling can justifiably be called macroscopic, although it does require rather fine tuning of ϵ, i.e., the applied field **H**.

Let us now include the nuclear spins.[15(a)] We consider only the nuclei of the magnetic atoms, as this is enough to illustrate our central point that nuclear spin dissipation suppresses tunneling. Hyperfine fields at magnetic atoms' nuclei are often ~100 T.[22] Transferred hyperfine fields at the nuclei of nonmagnetic atoms and dipolar fields at nuclei outside the particle are smaller, and their effect is weaker, although it could be included with minor modification of the treatment to follow. Suppose there are N_n magnetic nuclei, each with spin **I**, and magnetogyric ratio γ_n. It suffices to take an isotropic hyperfine tensor, and to neglect the applied and demagnetization fields. The total interaction Hamiltonian for all nuclear spins is then

$$\mathscr{H}_n = -A\sum_k \mathbf{I}_k\cdot\mathbf{s}_k, \tag{2.5}$$

where $\mathbf{s}_k$ is the atomic spin on the kth atom, and A is the hyperfine coupling. The hyperfine field is given by $H_n = As$, and the nuclear Larmor frequency is $\omega_n = AIs/\hbar$. We will only consider the case of zero temperature ($T=0$). The issue of how to correctly calculate $T\neq 0$ escape rates is not completely clear to the author, but if the common procedure of finding the imaginary part of the free energy is used, one can show that the canonically averaged escape rate is always less than the rate in the absence of dissipation.[23] The $T=0$ case thus gives the maximum dissipative suppression of the escape rate, and a comparison of the exponent in this rate with U/k_BT also provides an estimate of the crossover temperature between thermal activation and quantum tunneling.

To calculate the rate Γ with dissipation, we consider an initial state $|\hat{z},\{-I\}\rangle$, where $\hat{\mathbf{z}}$ is the orientation of $\hat{\mathbf{M}}$, and $\{-I\}$ indicates that $I_z=-I$ for all nuclear spins. We then calculate the quantity

$$Q(T) = \langle \hat{\mathbf{z}},\{-I\}|e^{-(\mathscr{H}+\mathscr{H}_n)T/\hbar}|\hat{\mathbf{z}},\{-I\}\rangle \tag{2.6}$$

as $T\to\infty$, and compare the result with $\exp(-E_0+i\Gamma/2)T/\hbar$. (Note that T is now a time, and not the temperature.) The amplitude for the nuclear spins not to flip for any given **M** trajectory is found to very good approximation by perturbation theory, and the final result is[15(a)] that $Q(T)$ can be written entirely in terms of an effective action $S_{\rm eff}=S_0+S_1$ for **M**, where S_0 is given by Eq. (2.3), and

$$S_1[\theta] = N_n\frac{Is^2}{8\hbar}A_x^2\int_0^T\int_0^T[\theta(\tau_1)-\theta(\tau_2)]^2 \times e^{-\omega_n|\tau_{12}|}d\tau_1 d\tau_2. \tag{2.7}$$

Note that this effective action would also be given by a bath of harmonic oscillators, with a spectral density $J(\omega)\sim\delta(\omega-\omega_n)$. This illustrates the Caldeira–Leggett argument[4] that as long as any one bath degree of freedom is weakly perturbed, the bath can be regarded as a collection of harmonic oscillators for understanding the dynamics of the system. We shall see that this description of the nuclear breaks down completely for the case of MQC.

The new rate $\Gamma\propto\omega_p\exp(-S_{\rm eff}^{\rm cl})$, where $S_{\rm eff}^{\rm cl}$ is the least value of $S_{\rm eff}$. (The change in the prefactor in Γ is much less important and will be ignored.) Following Refs. 4(b) and 24, we define $u=\omega_p\tau$, $\theta(\tau)=2\epsilon^{1/2}z(u)$, and

$$\sigma[z] = (\hbar\omega_p/4U)S_{\rm eff}[\theta(\tau)]. \tag{2.8}$$

The problem is characterized by two dimensionless parameters, given by

$$\mu = N_nI\epsilon(\hbar\omega_p/U), \quad \eta=\omega_n/\omega_p, \tag{2.9}$$

in terms of which, we can write

$$\sigma[z] = \int du(\dot{z}^2+z^2-z^4) + \frac{\mu\eta^2}{8}\int\int[z(u)-z(u')]^2 \times e^{-\eta|u-u'|}du\,du'. \tag{2.10}$$

We shall denote the minimum value of $\sigma[z]$ by $b(\mu,\eta)$. Thus, without dissipation, $b=4/3$, and the bounce, or best trajectory, is $z=\operatorname{sech} u$. Taking $H_n\sim$1–100 T, and $\omega_p\sim10^{10}$ s^{-1}, we get $\eta\sim$0.01–1. To estimate μ, let us take $\epsilon\sim10^{-3}$, and $\hbar\omega_p/U\sim1/5$ (any smaller value would lead to a very small bare tunneling rate). If the magnetic nucleus has a high abundance, so that $N_n\simeq N\sim10^5$, we get $\mu\gtrsim10$. If, on the other hand, $N_n/N\sim10^{-2}$, as is the case for natural isotopic mixtures of Fe and Ni, $\mu\simeq0.1$

[Before minimizing Eq. (2.10), we address a recent opinion by Chudnovsky[17(a)] stating that nuclear spin dissipation can largely be ignored. For weak or moderate dissipation, the relevant combination of μ and η turns out to be $\mu\eta/2$, which as we can see from above can be of order unity in many cases. Chudnovsky rewrites $\mu\eta/2=h_{hf}/H_c\epsilon$, where h_{hf} is the field at the atomic moments due to the nuclei. As $h_{hf}/H_c\sim10^{-2}$ for systems with high abundance of magnetic nuclei, a value of order unity for $\mu\eta/2$ can arise only if $\epsilon\lesssim0.01$, a condition which is thought to be not realistic by Chudnovsky. We have shown earlier, however, that small values of ϵ are compelled upon us by the need to have $S_0<30$. Since the second term in Eq. (2.10) is positive, we see that the WKB exponent is always increased by dissipation—in fact, $b(\mu,\eta)$ is a monotonically increasing function of μ—the restrictions on ϵ apply with even greater force. Far from being unrealistic, small values of ϵ are a necessary precondition for observing MQT.]

The Euler–Lagrange equation for the least action trajectory is

$$\frac{d^2z}{du^2} = z-2z^3+\frac{\mu\eta^2}{4}\int_{-\infty}^{\infty}[z(u)-z(u')]e^{-\eta|u-u'|}du', \tag{2.11}$$

and the boundary conditions are $z(u)\to0$ as $u\to\pm\infty$. Denoting Fourier transforms by tildes, Eq. (2.11) can be rewritten in the frequency domain as

$$\tilde{z}(\omega) = 2\widetilde{z^3}(\omega)G(\omega), \tag{2.12}$$

$$G^{-1}(\omega) = 1+\omega^2+\frac{\mu\eta}{2}\frac{\omega^2}{\omega^2+\eta^2}. \tag{2.13}$$

Note that $\widetilde{z^3}(\omega)\neq\tilde{z}^3$. The inverse Fourier transform of Eq. (2.12) gives

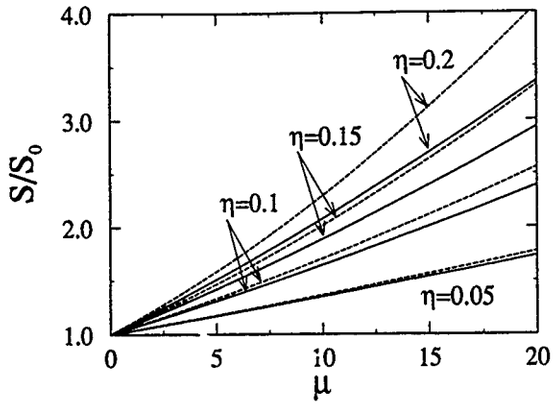

FIG. 2. Multiplicative dissipative correction to the WKB exponent (solid lines), and upper bound from Ref. 17(b) (dashed lines).

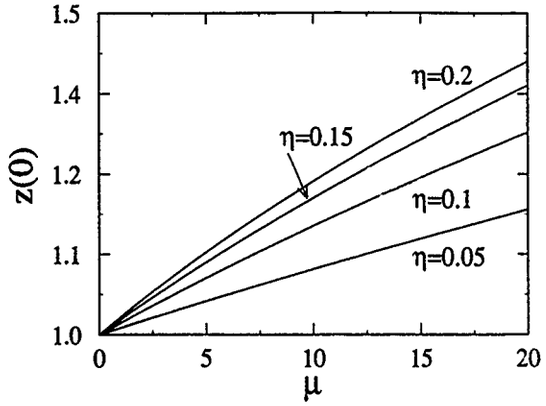

FIG. 3. Maximum excursion of the bounce with dissipation.

$$z(u)=\sum_{j=\pm}\int_{-\infty}^{\infty}z^3(u')R_j e^{-\beta_j|u-u'|}du', \tag{2.14}$$

where

$$\beta_\pm^2=\tfrac{1}{2}(1+\tfrac{1}{2}\mu\eta+\eta^2)\mp\tfrac{1}{2}[(1+\tfrac{1}{2}\mu\eta+\eta^2)^2-4\eta^2]^{1/2},$$
$$R_\pm=(\eta^2-\beta_\pm^2)/\beta_\pm(\beta_-^2-\beta_+^2). \tag{2.15}$$

In a large interesting part of parameter space, we have $\eta\ll 1$, but $\mu\eta$ is arbitrary. In this limit, to leading order in η we have

$$\beta_+=\eta u_b,\quad \beta_-=u_b^{-1},$$
$$R_+=\tfrac{1}{2}\mu\eta^2u_b^2,\quad R_-=u_b, \tag{2.16}$$

where $u_b=(1+\mu\eta/2)^{-1/2}$. From Eqs. (2.14)–(2.16) we see that $z(u)$ varies on two quite different time scales. The short time scale β_-^{-1} and associated amplitude (which is governed by R_-) are both of order unity. The long time scale diverges as $\eta\to 0$, but the amplitude, which is governed by R_+ is $O(\eta)$. In fact we can show that asymptotically, as $u\to\infty$,

$$z(u)\approx z_\infty e^{-\beta_+u};$$
$$z_\infty=2R_+\int_0^\infty z^3(u)\cosh(\beta_+u)du. \tag{2.17}$$

The integral is clearly convergent and of order unity. The approximation B of Ref. 15(a) is obtained by simply neglecting the R_+ term in Eq. (2.14), and using Eq. (2.16) for R_- and β_-.

To solve for $z(u)$ numerically, we iterate Eq. (2.14). [This is better than iterating Eq. (2.12), as $\tilde{z^3}(\omega)$ entails a double integral.] As noted by Chang and Chakravarty,[24] however, one must beware of a dangerous relevant direction in this iteration, but this can be efficiently eliminated following their procedure. At the nth iteration, we insert the solution $z_n(u)$ on the right-hand side of Eq. (2.14) and multiply it by a parameter λ_n to get $z_{n+1}(u)$. The only difference with Ref. 24 is that we must choose $\lambda_{n+1}=\lambda_n\xi^{-3}$, where $\xi=z_{n+1}(0)/z_n(0)$. Once the pair $[\lambda_j,z_j(u)]$ has converged, we scale to $\lambda=1$ via the equation $z(u)=\lambda_j^{1/2}z_j(u)$.

In Fig. 2 we show the calculated multiplicative correction to the nondissipative action $[S/S_0=3b(\mu,\eta)/4]$. The dashed lines are the upper bounds from the method of Ref. 17(b). In Fig. 3, we plot the maximum value $z(0)$, which, multiplied by $2\epsilon^{1/2}$ gives the typical exit angle with dissipation. By choosing different meshes for integrating Eq. (2.14) and different points beyond which the asymptotic form (2.17) is employed, we estimate that our numerics are accurate to about 1%.

As an illustration, for $\mu=10$ and $\eta=0.1$, $S/S_0=1.65$, and so if $S_0/\hbar$ were 25, the escape rate would be reduced by the rather large factor of $10^{-7.0}$. In the author's opinion, the best hope for seeing MQT lies in using materials—natural or isotopically enriched—with few nuclear moments, for which $\mu\approx 0.1$. If $\mu\eta\ll 1$, a useful formula is $S/S_0\approx 1+3\mu\eta/4$.

III. NUCLEAR SPINS AND MQC

The setup for MQC[15(b)] is the same as that for MQT, except that now there is no external field. In other words, we consider an isolated, insulating, ferro- or antiferromagnetic (FM or AFM) particle at nearly zero temperature, with $N_e\lesssim 10^4$ atomic moments. Suppose anisotropy (crystal and/or shape) creates an easy direction for $\mathbf{M}$ or the Néel vector $\hat{l}$. If there are no external fields, time reversal invariance ensures that the opposite direction is also easy, and resonance between these directions then becomes a possibility. We look at this phenomenon in this section.

The tunnel splitting Δ for a potential such as that labeled MQC in Fig. 1 is generically given in terms of the barrier height U and the small oscillation frequency ω_0 by a WKB formula like that for the escape rate: $\Delta\sim\hbar\omega_0\exp(-cU/\hbar\omega_0)$. Since ω_0 for AFM resonance is generally higher than that for FM resonance, we will get bigger Δ's with AFM particles.[11] We will therefore couch our discussion in terms of AFM particles, although it can be trivially altered to fit the FM case. A significant point, as noted by Barbara and Chudnovsky,[11(a)] is that in the AFM case, due to finiteness of the particle, the number of spins on the two sublattices (in the simplest case) will not be equal, and the particle will have a net moment $\mathbf{M}$. We expect $\mathbf{M}$ to follow $\hat{l}$ adiabati-

cally, and MQC could be detected by measuring the ac susceptibility χ'', which is related by standard formulas to the correlation function

$$C(t)=\langle \mathbf{M}(t)\cdot\mathbf{M}(0)\rangle = M_0^2\langle \hat{l}(t)\cdot\hat{l}(0)\rangle. \tag{3.1}$$

As noted in Sec. I, Awschalom *et al.*[18] claim to have seen just such MQC in particles of ferritin, an iron storage protein[25] in the form of a hollow shell of 75 Å inner diameter, that can be filled with an inorganic compound close in composition and structure to ferrihydrite or hydrated α-Fe_2O_3. This core is believed to be antiferromagnetic, and Awschalom *et al.* ascribe the peak in their χ'' to resonance of the Néel vector. Some relevant parameters as given by them are as follows: The sample has $N_g=38\,000$ ferritin particles, each containing $N_e=4500$ Fe^{3+} ions, of which 43 are uncompensated, giving $M_0=|\mathbf{M}|=217\ \mu_B$. At $T=29.5$ mK, the resonance frequency is $\nu_r=\Delta/h=940$ Hz, the peak susceptibility $\chi''(\nu_r)=3.8\times10^{-11}$ emu/G, the full width at half maximum intensity (FWHM) is $\simeq$50 kHz, and the ac field used to see the resonance is $H_{ac}=10^{-5}$ G.

We consider a two-sublattice uniaxially anisotropic antiferromagnetic particle with N_e atomic moments or spins, each of magnitude s. Denoting the spin directions on the sublattices by unit vectors $\hat{\mathbf{n}}_1$ and $\hat{\mathbf{n}}_2$, we have the obvious hamiltonian[11(b),26,27]

$$\mathscr{H}_e=J\hat{\mathbf{n}}_1\cdot\hat{\mathbf{n}}_2-K(\hat{\mathbf{n}}_{1z}^2+\hat{\mathbf{n}}_{2z}^2), \tag{3.2}$$

where $J\gg K>0$. (We will use the subscripts e and n to denote electronic and nuclear spin quantities.) By integrating out[11(b)] $\mathbf{M}\propto(\hat{\mathbf{n}}_1+\hat{\mathbf{n}}_2)$ we get the following Euclidean action for $\hat{l}$:

$$S_0[\hat{l}(\tau)]=\frac{N_e^2s^2}{8J}\int(\dot{\theta}^2+\sin^2\theta\,\dot{\phi}^2)+2K\int\sin^2\theta, \tag{3.3}$$

where θ and ϕ are the polar angles of $\hat{l}$. Standard instanton or WKB methods[11,26] give the tunnel splitting as $\Delta_0=(\hbar\omega_e/\pi)e^{-B}$, where $\omega_e=4(JK)^{1/2}/N_es$ is the AFM resonance frequency, and $B=2N_es(K/J)^{1/2}$ is the action for one instanton. Note that ω_e^{-1} is the instanton width or the "time spent under the barrier." For typical values of J and K, $\omega_e/2\pi\sim10^{11}$–10^{13} Hz. Even for a weak ferromagnet such as α-Fe_2O_3, $\omega_e/2\pi\sim10$ GHz. Because the WKB exponent $B\propto N_e$, Δ will be unlikely to exceed a few MHz if $N_e\gtrsim5000$.

Next, as in Sec. II, let N_n of the magnetic ions have magnetic nuclei. The total interaction Hamiltonian is the same as Eq. (2.5):

$$\mathscr{H}_{en}=-A\sum_{i=1}^{N_n}\mathbf{I}_i\cdot\mathbf{s}_i. \tag{3.4}$$

For simplicity we consider only $I=1/2$. For ferritin, the relevant nucleus is ^{57}Fe, I *is* 1/2, and Mössbauer data[25] give a hyperfine field of 50 T, a typical value for magnetic ions.[22] This yields $\omega_n=As/\hbar=(2\pi)68.5$ MHz. We thus have three well separated frequency scales in the problem: $\omega_e\gg\omega_n\gg\Delta_0/\hbar$.

Because $\omega_e\gg\omega_n$, the nuclear spins are essentially static during the time it takes for $\hat{l}$ to tunnel, and they act almost like a c-number external field. If we map our system onto an equivalent pseudospin 1/2, with the states $|\hat{l}\|\pm\hat{z}\rangle\rightarrow|\pm\rangle$, Eq. (3.2) becomes the tunneling term $\Delta_0\sigma_x$. Equation (3.4) is equivalent to a magnetic field along the z axis proportional to the nuclear polarization $p=2\Sigma_k\zeta_kI_k^z$, where $\zeta_k=\pm1$ depending on the sublattice, and the total Hamiltonian becomes

$$\mathscr{H}_0=\Delta_0\sigma_x/2-\hbar\omega_np\sigma_z/2. \tag{3.5}$$

Since $\omega_n\gg\Delta_0$ and since p changes in steps of unity, it follows that there is negligible mixing between $|+\rangle$ and $|-\rangle$ unless $p=0$. To put it another way, suppose $p\neq0$ and $\hat{l}\|\hat{\mathbf{z}}$ initially. If $\hat{l}$ were to now switch to $-\hat{\mathbf{z}}$, Eq. (3.4) implies that the energy of the nuclei (and hence the total system) would change by $Asp=p\hbar\omega_n\gg\Delta_0$. Since resonance occurs only between nearly degenerate states, we must have $p=0$.

Thus, unlike an ohmic bath, the main effect of nuclear spins is not to renormalize Δ_0. Instead, the amplitude of $C(t)$ is reduced from its non dissipative value (which we shall calculate below) by f_0, the probability for having $p=0$:

$$f_0=(2\pi N_n)^{-1/2}[\cosh(\beta\hbar\omega_n/2)]^{-N_n}, \tag{3.6}$$

where $\beta=1/k_BT$. Since f_0 decreases rapidly with increasing N_n, it pays to work with an element with almost no nuclear magnetism. For ferritin, although the abundance of ^{57}Fe is 2.25%, giving $N_n=101$, we get $f_0=0.034$ at 29.5 mK and $\omega_n/\gamma_n=50$ T.

To include relaxation we argue that coherence will persist from time 0 to time t only if there are no nuclear T_1 processes in this interval. If the T_1 time for one nuclear spin is T_{1n}, $C(t)$ will decay as the probability for no T_1 processes, i.e., as $\exp(-t/N_nT_{1n})$. With $N_n\simeq100$, T_{1n} must be of order a few seconds for the resonance to be observable.

[What about a state with $p\neq0$? Such a state can resonate only if at least p nuclear spins flip along with $\hat{l}$. The frequency for this can be shown[15(b)] to be of order $\Delta_0N_n^{p/2}(\omega_n/\omega_e)^p\ll\Delta_0$. This resonance also decays as $\exp(-t/N_nT_{1n})$, so most of the spectral weight in χ'' is shifted into a broad background near $\omega=0$.]

We now find χ'' and the resonant power absorption. As the ac field $|\mathbf{H}_{ac}(t)|\ll H_a$, the anisotropy field, it cannot cause direct $|+\rangle\leftrightarrow|-\rangle$ transitions. Instead it shifts the $|\pm\rangle$ energies by $\mp M_0H_{ac}^z(t)$. Adding a perturbation term $-M_0H_{ac}^z(t)\sigma_z$ to Eq. (3.5) we obtain a standard NMR Hamiltonian. Introducing T_1 and T_2 for the MQC resonance itself (note that $T_1\neq T_{1n}$), and including the nuclear polarization reduction factor, we get

$$\chi''(\omega)=f_0N_g\frac{\beta\Delta}{\hbar}\frac{M_0^2T_2}{1+(\delta T_2)^2}, \tag{3.7}$$

where δ is the detuning.

From Ref. 18 (see especially the erratum), we have the actual power absorption as $\pi\nu_r\chi''(\nu_r)H_{ac}^2=1.1\times10^{-21}$ W. On the other hand, Eq. (3.7) predicts a peak power of 7.1×10^{-25} W, 1500 times too small. In fact, we have overestimated the expected signal size. First, there is randomness in the angle between $\mathbf{H}_{ac}$ and $\mathbf{M}$'s of different ferritin grains. Then, there are $N_p\simeq8000$ protons per ferritin. If we take the local field at the protons to be about 100 G, which is not unreasonable, the Zeeman splitting is 0.43 MHz, not so different from ν_r. Hence, the net proton spin polarization must

also be quite small for MQC to occur, which reduces χ'' further. [The reduction factor is $11(2\pi N_p)^{-1/2}=0.05$, if we assume that states differing in energy by less than 2Δ can mix, which implies that the proton polarization must be less than 5.] There are simply not enough two-level systems in the MQC interpretation of the data in Ref. 18 to give the large absorption seen. A microscopic interpretation would not suffer from this problem, and seems less remote to the author.[19]

ACKNOWLEDGMENTS

It is a pleasure to thank W. P. Halperin for his sustained interest in this work, and for many useful discussions. This work was supported by the National Science Foundation through Grant Nos. DMR-9102707 and DMR-9306947.

[1] R. P. Feynman, R. B. Leighton, and M. Sands, *The Feynman Lectures on Physics*, Vol. III (Addison–Wesley, New York, 1965). See the final paragraph of Sec. 1-6.

[2] Indeed, the description we have given is precisely von Neumann's view of measurement in quantum mechanics. See, e.g., K. Gottfried, *Quantum Mechanics* (Benjamin, New York, 1966), Chap. IV.

[3] See A. J. Leggett, in *Chance and Matter*, edited by J. Souletie, J. Vannimenus, and R. Stora (North-Holland, Amsterdam, 1987) for a review of MQT and MQC.

[4] A. O. Caldeira and A. J. Leggett, (a) Phys. Rev. Lett. **46**, 211 (1981); (b) Ann. Phys. (N.Y.) **149**, 374 (1984); **153**, 445(E) (1984).

[5] R. F. Voss and R. A. Webb, Phys. Rev. Lett. **47**, 265 (1981); L. D. Jackel *et al.*, *ibid.* **47**, 697 (1981); S. Washburn, R. A. Webb, R. F. Voss, and S. M. Faris, *ibid.* **54**, 2417 (1984); D. B. Schwartz, B. Sen, C. N. Archie, and J. Lukens, *ibid.* **55**, 1547 (1985); **57**, 266 (1986).

[6] J. M. Martinis, M. H. Devoret, and J. Clarke, Phys. Rev. Lett. **55**, 1543 (1985); M. H. Devoret, J. M. Martinis, and J. Clarke, *ibid.* **55**, 1908 (1985). See J. Clarke *et al.*, Science **239**, 992 (1988) for a review, and references to [illegible] experimental work.

[7] (a) S. Chakrav[illegible], and A. J. Leggett, Phys. Rev. Lett. **52**, 5 (1984); (b) A. J. Leggett, S. Chakravarty, A. T. Dorsey, M. P. A. Fisher, A. Garg, and W. Zwerger, Rev. Mod. Phys. **59**, 1 (1987).

[8] S. Chakravarty, Phys. Rev. Lett. **49**, 681 (1982); A. J. Bray and M. A. Moore, *ibid.* **49**, 1546 (1982).

[9] S. Han, J. Lapointe, and J. Lukens, Phys. Rev. Lett. **66**, 810 (1991). These workers do not attain low enough dissipation to see MQC, but they nevertheless see novel features in the incoherent relaxation of the trapped flux that were predicted in Ref. 7.

[10] E. M. Chudnovsky and L. Gunther, Phys. Rev. Lett. **60**, 661 (1988).

[11] (a) B. Barbara and E. M. Chudnovsky, Phys. Lett. A **145**, 205 (1990); (b) I. V. Krive and O. B. Zaslavskii, J. Phys. Condens. Matter **2**, 9457 (1990).

[12] P. C. E. Stamp, Phys. Rev. Lett. **66**, 2802 (1991); E. M. Chudnovsky, O. Iglesias, and P. C. E. Stamp, Phys. Rev. B **46**, 5392 (1992).

[13] (a) A. Garg and G.-H. Kim, Phys. Rev. Lett. **63**, 2512 (1989); (b) J. Appl. Phys. **67**, 5669 (1990); (c) Phys. Rev. B **43**, 712 (1991).

[14] H. Simanjuntak, J. Low Temp. Phys. **90**, 405 (1992).

[15] A. Garg, (a) Phys. Rev. Lett. **70**, 1541 (1993), and (b) submitted to Phys. Rev. Lett.; N. V. Prokofev and P. C. E. Stamp, J. Phys: Cond. Matter **5**, L663 (1993).

[16] G. Tatara and H. Fukuyama, Phys. Rev. Lett. **72**, 772 (1994); and submitted to J. Phys. Soc. Jpn.

[17] (a) E. M. Chudnovsky, Phys. Rev. Lett. **72**, 1134 (1994); (b) see also the reply, A. Garg, *ibid.* **72**, 1135 (1994). Note that the figure herein is wrong. The correct bounds are shown in Fig. 2.

[18] D. D. Awschalom, J. F. Smyth, G. Grinstein, D. P. DiVincenzo, and D. Loss, Phys. Rev. Lett. **68**, 3092 (1992), **71**, 4279(E) (1993).

[19] A. Garg, Phys. Rev. Lett. **71**, 4249 (1993); see also D. D. Awschalom *et al.*, *ibid.* **71**, 4276 (1993).

[20] A. Garg, Phys. Rev. Lett. **70**, 2198 (1993); D. D. Awschalom *et al.*, *ibid.* **70**, 2199 (1993).

[21] M. Enz and R. Schilling, J. Phys. C **19**, 1765 (1986); *ibid.* **19**, L711 (1986); J. L. van Hemmen and A. Sütö, Europhys. Lett. **1**, 481 (1986); Physica **141B**, 37 (1986).

[22] E. A. Turov and M. P. Petrov, *Nuclear Magnetic Resonance in Ferro- and Antiferromagnets* (Wiley, New York, 1972).

[23] A. I. Larkin and Yu. Ovchinnikov, Sov. Phys. JETP **85**, 1510 (1984); H. Grabert and U. Weiss, Z. Phys. B **56**, 71 (1984); W. Hontscha, P. Hanggi, and E. Pollak, Phys. Rev. B **41**, 2210 (1990).

[24] L. D. Chang and S. Chakravarty, Phys. Rev. B **29**, 130 (1984).

[25] See P. M. Harrison and T. H. Lilley, in *Iron Carriers and Iron Proteins*, edited by T. M. Loehr (VCH, 1989) for a review on ferritin, and a comprehensive bibliography.

[26] J.-M. Duan and A. Garg, Physica B **194-196**, 323 (1994).

[27] J.-M. Duan and A. Garg (unpublished) have noted that under Eq. (3.2), $\mathbf{M}\cdot\hat{z}$ is rigorously conserved, and to describe its tunneling, one must include transverse anisotropy. Although Eq. (3.2) is seriously limited in its describing experiments, we will still use it here, as the detailed form of the instanton is unimportant; only that $\omega_e \gg \omega_n$ matters.

Evidence for quantum mesoscopic tunneling in rare-earth layers

M. J. O'Shea and P. Perera
Department of Physics, Cardwell Hall, Kansas State University, Manhattan, Kansas 66506-2601

We report on finite size effects and evidence for quantum mesoscopic tunneling (QMT) in thin isolated rare-earth layers prepared in the form of R/Mo multilayers where R represents Tb, Dy, or $Dy_{50}Co_{50}$. The magnetic transition temperature T_c decreases with decreasing magnetic layer thickness and is discussed within a finite size scaling theory. Evidence for QMT is found in magnetic relaxation measurements in these systems with a sharp crossover to a temperature-independent magnetic relaxation regime at low temperatures. The Tb system has a crossover temperature T_0 of 20 K, the largest value reported so far for this crossover.

When magnetic materials are prepared with one or more dimensions close to atomic dimensions, their properties are significantly modified by finite size effects and effects associated with their interface. New phenomena, not seen in the bulk, may also appear. In this work we discuss the properties of ultrathin rare-earth based layers and will show (i) that the transition temperature T_c is depressed in thin layers due to finite size effects[1,2] and (ii) that there is evidence for quantum mesoscopic tunneling[3] via magnetic relaxation measurements. This latter phenomenon is the subject of much current research[3,4] and we find a crossover temperature T_0, below which the magnetic viscosity is temperature independent, of 20 K for the Tb system. This is the highest crossover temperature reported so far.

The systems we report on here are of the form $R(d$ nm)/Mo (18 nm) with at least five bilayers and are prepared by sputtering. R represents Dy, $Dy_{50}Co_{50}$, or Tb. Both Tb and Dy are ferromagnetically ordered at low temperatures,[5] while $Dy_{50}Co_{50}$ is ferrimagnetically ordered.[6] The Mo layer is thick enough that no interactions can occur between neighboring rare-earth layers so that they are magnetically isolated. We have previously reported on the magnetic anisotropy associated with the interface in some of these systems.[7] Examples of x-ray diffractometers using Cu $K\alpha$ radiation at small angles and large angles are shown in Fig. 1 for selected Dy/Mo multilayers. A thinner Mo layer is used for the small-angle diffraction measurement so that the small-angle maxima associated with the bilayer spacing may be seen. The Dy layers are polycrystalline as can be seen from the presence of all the significant large angle peaks associated with the Dy hexagonal structure (peaks in the range 28°–36°). The peak at 41° is associated with the Mo body centered cubic structure. For Dy layer thickness below about 30 nm the crystalline peaks associated with hexagonal Dy become broad indicating structural disorder within the layer. The x-ray diffractograms for the Tb and $Dy_{50}Co_{50}$ systems confirm that they are also layered. While the intralayer structure in Tb is polycrystalline like Dy, the intralayer structure for the $Dy_{50}Co_{50}$ system is amorphous for all layer thicknesses with only a broad maximum in the x ray diffractogram at large angles.

Figure 2 shows field-cooled (FC) and zero-field-cooled (ZFC) magnetizations for selected samples from the Dy series measured with increasing temperature. The applied field is in the plane of the multilayer so that demagnetization effects are negligible. The value of T_c, the magnetic transition temperature, is estimated from the initial rise in magnetization. A Curie–Weiss plot is shown as an inset in Fig. 2 and the Curie–Weiss temperature T_{cw} is determined by extrapolating the high-temperature linear portion of the plot to the temperature axis. Both T_c and T_{cw} agree within experimental error with the bulk values for Dy. Figure 3 shows a plot of T_c versus Dy layer thickness. T_c shows a gradual decrease with decreasing layer thickness and at about 10 nm decreases more rapidly. For systems with no anisotropy, T_c should go to zero in the 2-d limit since it has been shown that no magnetic ordering exists for a 2-d Heisenberg system of spins.[8] Inclusion of anisotropy modifies this result and allows magnetic ordering to occur in 2-d.[9] It is expected from finite size scaling arguments that as the thickness of a magnetic layer is reduced, its transition temperature T_c should show a reduction.[1] Such effects have been seen in some transition metal thin-film systems.[2] The dependence of T_c on film

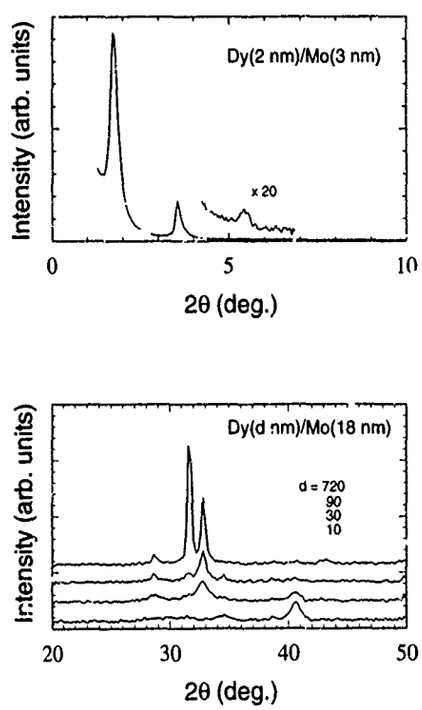

FIG. 1. X-ray diffractograms at small and large angles for selected Dy/Mo multilayers using Cu-$K\alpha$ radiation.

 0021-8979/94/76(10)/6174/3/$6.00 © 1994 American Institute of Physics

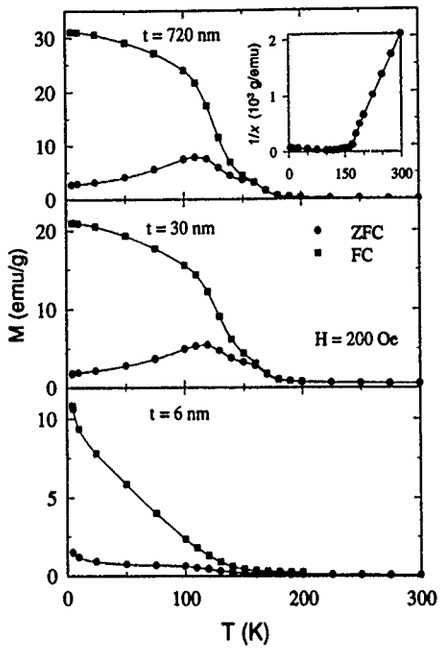

FIG. 2. Field-cooled (FC) and zero-field-cooled (ZFC) magnetizations in an applied field of 200 Oe for selected samples from the Dy (d nm)/Mo (18 nm) multilayer series. The inset shows a Curie–Weiss plot. The solid lines are guides to the eye.

thickness for thin films is expected to follow the finite size scaling relation[2]:

$$[T_c(\infty)-T_c(n)]/T_c(n)=[(n-n')/n_0]^{-\lambda}, \qquad (1)$$

where $T_c(\infty)$ is the bulk value of T_c and $T_c(n)$ is the value of T_c for a film of thickness n monolayers. n_0 and n' are microscopic lengths of order the size of a unit cell, and λ is an exponent to be determined. This exponent can also be calculated and is ~ 1.5 for a thin film assuming Ising spins.[10] The measurement of λ serves as a test of the finite size model used to calculate it. The solid line of Fig. 3 represents a fit to Eq. (1) using data with $d>5$ nm ($n>17$). The values of λ, n_0, and n' are 1.5, 1.2, and 0.3 nm, respectively (assuming a monolayer is 0.3 nm) with error bars of 20%. The λ is in agreement with the approximate theoretical prediction. The data deviate from the fitted curve at small t most likely because the structure of the layer changes from crystalline to highly disordered as seen in x-ray diffractograms. These fitted values are close to those found for transition metal based thin layers.[2]

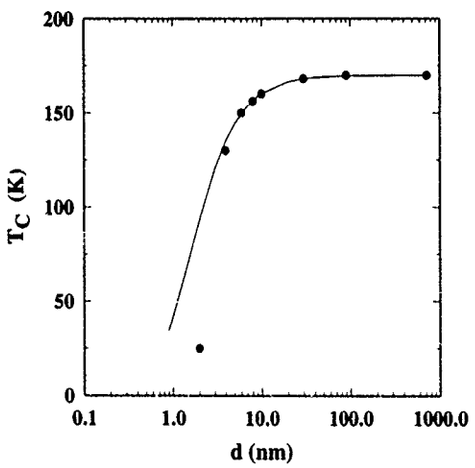

FIG. 3. Magnetic ordering temperature T_c vs magnetic layer thickness for the Dy (d nm)/Mo (18 nm) multilayer series. The solid line represents a curve fit using Eq. (1).

At low enough temperatures quantum tunneling rather than thermal excitation processes are predicted to dominate magnetic reversal. This tunneling process is often referred to as quantum mesoscopic tunneling (QMT) because the number of atomic moments coherently tunneling is inferred to be of order 10^3 in systems studied so far.[4] Magnetic reversal processes involving QMT include magnetic reversal within a single domain and tunneling of a domain wall through a pinning site.[11] These processes are of fundamental interest and are also of practical interest since they may be important in devices of nanometer dimensions.

In our thin films we expect that magnetic reversal is dominated by domain wall movement. Under these circumstances the measured rate of magnetic relaxation when the

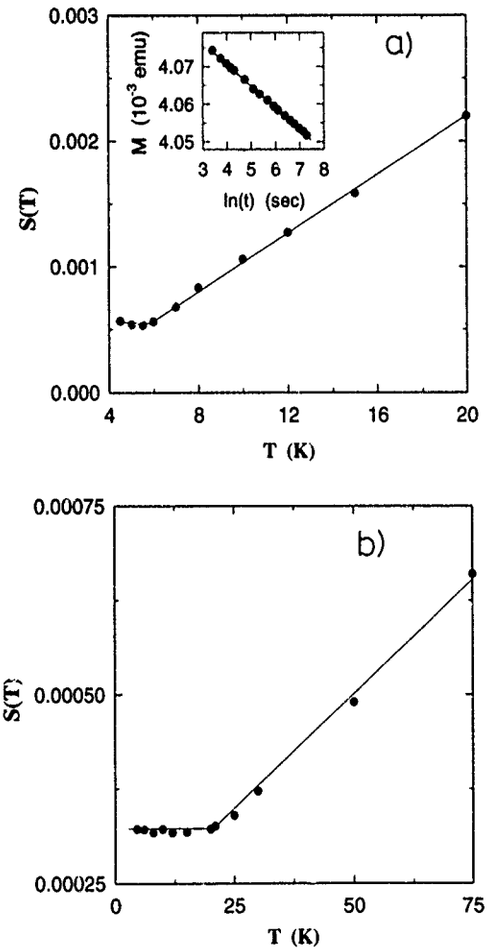

FIG. 4. $S(T)$, the magnetic viscosity, as a function of temperature for (a) Dy (90 nm)/Mo (18 nm) and (b) Tb (77 nm)/Mo (18 nm) multilayers for a measuring field of -100 Oe. The solid lines are guides to the eye. The inset in (a) shows an example of a logarithmic time (t) dependence of magnetization (M) at 8 K. The solid line represents a least-squares fit to the data.

applied field is switched from one value to another should be independent of temperature if domain wall motion occurs by quantum tunneling. We find that the time dependence of magnetization can be parameterized accurately by a logarithmic decay at short times ($<2\times10^3$ s) thus

$$M(t)=M_0[1-S(T)\ \ln(t)]. \tag{2}$$

$S(T)$, the magnetic viscosity, is a measure of the rate of change of magnetization. Both thermal relaxation and tunneling will contribute to $S(T)$. In this experiment the sample is field cooled to a temperature T in an applied field of 1000 Oe. The applied field is then switched to a new value, in our case -100 Oe, and the magnetic relaxation $M(t)$ is measured.

The inset of Fig. 4(a) shows the time dependence of $M(T)$ for the Dy (90 nm)/Mo (18 nm) multilayer at $T=8$ K and as can be seen it conforms to a logarithmic dependence on time. $S(T)=(1/M_0)dM/d\ \ln(t)$ is determined from the slope and the solid line in the insert of Fig. 4(a) is a least-squares fit. Figure 4 shows the calculated $S(T)$ from the relaxation measurements as a function of temperature for a Dy and a Tb multilayer. For the Dy multilayer there is a crossover at 6 K to a regime where $S(T)$ is independent of temperature within our experimental error. In the case of the Tb multilayer where we have data over a wide range of temperatures in the temperature-independent regime, it can be seen that the crossover from the temperature dependent to temperature-independent region is sharp within the accuracy of our experiment. This sharpness, expected from QMT if dissipation is not important, together with the temperature-independent $S(T)$ is strong evidence in favor of a QMT interpretation of these results in these systems.

There is a large difference in the crossover temperatures T_0 for the Tb and the Dy system with Tb, at 20 K, being considerably larger than Dy at 6 K. We note that while we have considered a QMT interpretation of these results, theoretical estimates in the limit of large anisotropy predict T_0 should be proportional to the atomic moment and the square root of the product of the planar and c-axis anisotropy.[11] For Dy and Tb the c-axis anisotropies are 5×10^8 and 5.5×10^8 ergs/cc, respectively, and the planar anisotropies are 7.5×10^6 and 2.4×10^6 ergs/cc, respectively.[12] Since the magnetic moments of Tb and Dy are within 8% of each other this simple model suggests that Dy should have a higher T_0 and Tb and so is unable to explain the large value of T_0 for Tb compared to Dy. We are currently preparing other anisotropic elemental rare earths in layer form to determine if any correlation exists between the microscopic magnetic anisotropy and the measured T_0.

This work was supported by NSF OSR92-55223 and NSF DMR91-23831.

[1] M. E. Fisher and A. E. Ferdinand, Phys. Rev. Lett. **19**, 169 (1967); A. E. Ferdinand and M. E. Fisher, Phys. Rev. **185**, 832 (1970).
[2] F. Huang, G. J. Mankey, M. T. Kief, and R. F. Willis, Appl. Phys. **73**, 6760 (1993), and references therein.
[3] E. M. Chudnovsky and L. Gunther, Phys. Rev. Lett. **60**, 661 (1988); Phys. Rev. B **37**, 9455 (1988).
[4] J. Tejada, X. X. Zhang, and E. M. Chudnovsky, Phys. Rev. B **47**, 14977 (1993); B. Barbara and E. M. Chudnovsky, Phys. Lett. A **145**, 205 (1990); D. D. Awschalom, M. A. McCord, and G. Grinstein, Phys. Rev. Lett. **65**, 783 (1990).
[5] S. Legvold, in *Ferromagnetic Materials*, edited by E. P. Wohlfarth (North-Holland, Amsterdam, 1980), Vol. 1, p. 183.
[6] K. Moorjani and J. M. D. Coey, *Magnetic Glasses* (Elsevier, Amsterdam, 1984), Chap. VI.
[7] P. Perera and M. J. O'Shea, J. Appl. Phys. **70**, 6212 (1991).
[8] N. D. Mermin and H. Wagner, Phys. Rev. Lett **17**, 1133 (1966).
[9] D. L. Mills, J. Magn. Magn. Mater. **100**, 515 (1991).
[10] K. Binder and P. C. Hohenberg, Phys. Rev. B **9**, 2194 (1974).
[11] See Section VII of E. M. Chudnovsky, O. Iglessias, and P. C. E. Stamp, Phys. Rev. B **46**, 5392 (1992).
[12] J. J. Rhyne and A. E. Clarke, J. Appl. Phys. **38**, 1379 (1967).

Bloch states of a Bloch wall

Hans-Benjamin Braun and Daniel Loss
Department of Physics, Simon Fraser University, Burnaby, British Columbia V5A 1S6, Canada

Bloch walls in mesoscopic ferromagnets can tunnel between periodically arranged pinning sites leading to a Bloch band. The quantum spin phase gives rise to a spin parity dependent shift in the dispersion. Static external magnetic fields induce magnetization oscillations and provide a magnetic analogue of the Josephson effect.

The possibility of macroscopic quantum tunneling in small magnetic particle has attracted much interest both theoretically[1,2] and experimentally.[3,4] Susceptibility measurements[4] on small antiferromagnetic grains of diameter $\simeq 70$ Å have shown coherent quantum tunneling of the sublattice magnetization through an anisotropy barrier. On the other hand, ferromagnetic domain walls exhibit a high mobility and low coercivities, facts that renders them suitable candidates for displaying macroscopic quantum phenomena (MQP). It has been proposed[5] that domain walls can collectively tunnel out of a single pinning potential by applying an external magnetic field.

In this paper we focus on another possible manifestation of MQP: the coherent tunneling of a Bloch wall between periodically arranged pinning centers in an insulating ferromagnet. Such pinning centers can be caused by the discreteness of the lattice itself or by a magnetic superlattice created, e.g., by ion substitution. We show that there is a finite tunneling probability of the Bloch wall between pinning sites and that, as a result, the low-energy states will form a Bloch band. The topological term gives rise to a shift in the band structure depending on spin quantum number and pinning separation. We determine the bandwidth and show that the decohering effect of the spin waves is negligible below 100 mK for typical material parameters. In addition we demonstrate that a constant magnetic field induces magnetization oscillations in analogy to Bloch oscillations of a Bloch electron in a uniform electric field. This "magnetic Josephson effect" does not have a classical counterpart and thus provides a unique signature of macroscopic quantum coherence. To observe domain wall tunneling, the wall area has to be small. Thus we consider elongated particles (or ferromagnetic "wires") of length L with a cross-sectional area of about 100 nm^2. For these lateral dimensions and at temperatures of interest, transverse spin waves are completely frozen out and the system behaves effectively one-dimensional.

Consider a Heisenberg Hamiltonian with anisotropies on a simple cubic lattice with lattice constant a

$$\mathcal{H}=-\tilde{J}\sum_{\langle i,j\rangle}\mathbf{S}_i\cdot\mathbf{S}_j-\tilde{K}_y\sum_i (S_i^y)^2+\tilde{K}_z\sum_i (S_i^z)^2, \tag{1}$$

where $\mathbf{S}_i$ is the spin operator at the ith lattice site. The first term describes nearest-neighbor interaction with exchange constant $\tilde{J}$; the next terms represents easy- and hard-axis anisotropies with constants $\tilde{K}_z>\tilde{K}_y>0$. For thin long slabs of materials like YIG, $\tilde{K}_z$ originates from shape anisotropy. For the 1D approximation to hold, the sample should have lateral dimensions smaller than the minimal length scale $a[\tilde{J}/\tilde{K}_z]^{1/2}$. Next, we introduce coherent spin states defined by $\mathbf{\Omega}_i\cdot\mathbf{S}_i|\mathbf{\Omega}_i\rangle=S|\mathbf{\Omega}_i\rangle$, where S is the spin quantum number (units such that $\hbar=1$) and $\mathbf{\Omega}=(\sin\theta\cos\phi,\ \sin\theta\sin\phi,\ \cos\theta)$ is a vector on the unit sphere.

To find the tunneling rate it is appropriate to consider the imaginary time transition amplitude between two coherent state configurations expressed as a path integral,

$$\langle\{\Omega_b\}|e^{-\beta H}|\{\Omega_a\}\rangle=\int\mathcal{D}\phi\mathcal{D}(\cos\theta)e^{-S_E[\phi,\theta]}. \tag{2}$$

The Euclidean action is given by

$$S_E[\phi,\theta]=\int_0^\beta d\tau\int_{-L/2}^{L/2}dx\left[iN_A\frac{S}{a}\partial_\tau\phi(1-\cos\theta)+\mathcal{H}\right], \tag{3}$$

and contains the energy density

$$\mathcal{H}=N_A\{J[\sin^2\theta(\partial_x\phi)^2+(\partial_x\theta)^2]-K_y[\sin^2\theta\sin^2\phi-1]+K_z\cos^2\theta\}, \tag{4}$$

where $J=\tilde{J}S^2a$, $K_{y,z}=\tilde{K}_{y,z}S^2/a$. The first term in the integrand of Eq. (3) arises from the overlap of the coherent spin states at adjacent imaginary time steps. For a single spin and for closed trajectories it has the form of a Berry phase. The term $\propto\cos\theta\partial_\tau\phi$ together with the energy density $\mathcal{H}$ reproduces in saddle point approximation $\delta S_E=0$ the micromagnetic Landau–Lifshitz equations. According to our microscopic derivation, there is an additional term $\propto\partial_\tau\phi$ which, as a total derivative, does not affect the classical equations of motion. However, in quantum mechanics all paths contribute to the transition amplitude Eq. (2) and therefore this term can lead to interference effects.[6]

The Bloch wall

$$\phi_0(x)=-\pi/2+2\tan^{-1}(e^{x/\delta}), \tag{5}$$

is confined to the easy-plane $\theta=\pi/2$ and is a solution of $\delta S_E=0$ which connects two different easy-axis anisotropy minima within the wall width $\delta=\sqrt{J/K_y}$. It is degenerate with all Bloch walls $\phi_0(x-X)$ that arise by a rigid translation by X which have the energy $E_0=4N_A\sqrt{JK_y}$.

We now focus on the decohering influence of the spin waves on the motion of the domain wall. A moving Bloch wall induces scattering between the spin wave states and thus affects the quantum coherence of the system. To investigate this effect quantitatively, we can introduce small fluctuations around the moving Bloch wall and construct an effective action for the Bloch wall position X. For simplicity and since the hard-axis anisotropy is large in high-purity materials such as YIG, we first eliminate the out of easy-plane degree of

 0021-8979/94/76(10)/6177/3/$6.00 © 1994 American Institute of Physics

freedom. Expanding Eq. (3) to second order in $p \equiv \cos\theta - \pi/2$ and performing the resulting Gaussian integrals, the transition amplitude Eq. (2) takes the form $\int \mathscr{D}\phi \exp\{-S_{SG}\}$ with the sine-Gordon (SG) action

$$S_{SG}[\phi] = N_A \int d\tau dx \left[i \frac{S}{a} \partial_\tau \phi + \kappa (\partial_\tau \phi)^2 + J(\partial_x \phi)^2 + K_y \cos^2 \phi \right], \tag{6}$$

including a topological term $\propto \partial \phi$. The elimination of the out of easy-plane fluctuations gives rise to the kinetic term $\kappa(\partial_\tau \phi)^2$ with $\kappa = S^2/(4K_z a^2)$. The action of Eq. (6) correctly reproduces the long-wavelength excitations of Eq. (3) to order $\mathscr{O}(K_y/K_z)$. The "velocity of light" $c \equiv \sqrt{J/\kappa}$ in the SG model is the asymptotic spin wave velocity.

Spin wave fluctuations around the Bloch wall Eq. (5) (which also satisfies $\delta S_{SG}=0$) are described by

$$\phi(x,\tau) = \phi_0(x-X) + \varphi(x-X,\tau). \tag{7}$$

Here $X(\tau)$ represents the instantaneous position of the Bloch wall. Since a rigid translation of the Bloch wall is already described by the coordinate X in the first term on the rhs of Eq. (7), the spin waves φ do not contain the zero energy "Goldstone mode" $d\phi_0/dx$. Maintaining this constraint, Eq. (7) can be inserted into S_{SG} and the transition amplitude $\int \mathscr{D}\phi \exp\{-S_{SG}\}$ can be brought to a form with X and φ as independent variables. Note that this constraint gives rise to a nontrivial Faddeev–Popov determinant, which, however, leads to a correction of order $O(1/N_A S)$.[8] In contrast to the standard Caldeira–Leggett model which contains a coupling which is linear in both the system and environment variables, the coupling occurs here to second order in the spin wave amplitudes. Nevertheless, we can eliminate the spin waves[8] and obtain the following effective action for the Bloch wall coordinate

$$S_X = \int_0^\beta d\tau \left\{ -i\pi S \frac{N_A}{a} \dot{X} + \frac{M}{2} \dot{X}^2 \right\} + \frac{1}{2} \int_0^\beta d\tau \int_0^\tau d\sigma K(\tau-\sigma)[X(\tau)-X(\sigma)]^2. \tag{8}$$

The first term is the topological term while the second term is the kinetic energy of the Bloch wall where $M = 4N_A\kappa/\delta$ is the Döring mass. The third term is the damping term due to the scattering of spin waves. For low temperatures, the damping kernel takes the Caldeira–Leggett form $K(\tau) = (1/\pi)\int_0^\infty d\omega J(\omega) D_\omega(\tau)$ with $D_\omega(\tau) = e^{-\omega|\tau|}$. The spectral function is given by $J(\omega) = (\omega/2\delta c)\Theta(\omega - 2c/\delta)\sqrt{\omega^2 - (2c/\delta)^2}$ and reflects the anisotropy gap of the spin wave excitations. Thus the damping effect of the spin waves can indeed be treated within a Caldeira–Leggett model although the underlying microscopic coupling involves term which is second order in the magnons (see also Appendix C of Ref. 7).

As we shall see below, the characteristic time scale of X is much larger than the decay time $\tau_c = \delta/(2c)$ of the damping kernel. In this case damping leads to a small renormalization of the Döring mass of the order $O(1/N_A S)$ and shall therefore be neglected henceforth.

We now turn to the tunneling of a Bloch wall in a periodic array of pinning sites with distance d that is assumed to be an integral multiple of a. Such pinning sites can be incorporated into the action (6) by substituting K_y with the term $K_y - K_v \Sigma_n \delta(x-nd)$. If the domain wall center (at which the easy-axis anisotropy is maximally frustrated) coincides with one of these pinning sites, the energy will be lowered and the domain wall becomes pinned. Then inserting Eq. (7) with Eq. (5) into this new action and assuming that $d \ll \delta$, we recognize that pinning can be described by adding the potential $2V_0 \int d\tau \sin^2(\pi X/d)$ to Eq. (8). The resulting action is now equivalent to the action of a single particle in a periodic potential, e.g., like an electron in a crystal potential. The topological term then plays the role of the electromagnetic gauge potential. Performing an instanton calculation[9] we can then extract the dispersion relation for Bloch wall states

$$\epsilon(k) = -\Delta/2 \cos(kd + \pi S N_A d/a), \tag{9}$$

where the bandwidth is given by $\Delta = 4\omega_I \sqrt{S_0/2\pi} \times \exp(-S_0)$ with instanton action $S_0 = (4/\pi) d\sqrt{V_0 M}$ and frequency $\omega_I = (2\pi/d)\sqrt{V_0/M}$. The topological phase thus induces a shift in the dispersion by $\pi S N_A d/a$.

To give some quantitative estimates of this effect we consider material parameters (at $T=0$) of YIG: $J = 1.65\times10^{-21}$ erg cm, $K_y = 9.61\times10^{-11}$ erg/cm, where a cell with lattice constant $a = 6.2$ Å contains one $S=5/2$ spin implying a saturation magnetization of $M_0 = 194$ Oe (i.e., $K_z = 2\pi M_0^2 a^2 = 9.1\times10^{-10}$ erg/cm), wall width $\delta = 414$ Å, and spin wave velocity $c = 6\times10^4$ cm/s.

An external field in the direction of the easy axis induces a Zeeman coupling term $-2\mathscr{M} M_0 H_{ext} X$ which has to be added to the action Eq. (8). The potential strength is related to the coercivity H_c, at which the barrier vanishes, via $V_0/\mathscr{M} = M_0 H_c d/\pi$. If we choose $d = 3a$ and $H_c = 2$ Oe, we have $\omega_I = 1.45\times10^{10}$ s^{-1}, and $|\dot{X}/c| \leq 2\omega_I \tau_c d/\pi\delta \simeq 2\times10^{-2}$. For $N_A \simeq 260$, the domain wall contains $N_A \delta/a \simeq 1.7\times10^4$ tunneling spins, and the bandwidth is $\Delta/\hbar = 5\times10^5$ s^{-1}. For $d = a$, the bandwidth becomes $\Delta/\hbar = 6\times10^9$ s^{-1}.

Next, we address some striking experimental consequences resulting from this Bloch band structure: Bloch oscillations and the magnetic equivalent of the Josephson effect where a constant external magnetic field H along the easy axis induces an oscillatory magnetization.

Let us recall that the effective behavior of the domain wall in the presence of a periodic pinning array corresponds to the behavior of a single Bloch particle in the presence of a periodic potential and can be described by an effective Hamiltonian, $P^2/2M + 2V_0 \sin^2(\pi X/d)$, where P is the momentum operator conjugate to the wall position X, and V_0 is given above. We choose $d = 3a$ and for simplicity we assume $SN_A d/a$ to be an even integer and thus drop the topological term. The corresponding kinetic energy of the unperturbed ($V_0 = 0$) Bloch particle at the zone boundaries, $k = \pm \pi/d$, is given by $\epsilon_0 = (\hbar^2/2M)(\pi/d)^2 = 10$ mK k_B, for the particular parameter values chosen above for YIG. Thus we find that $\epsilon_0/V_0 = 0.06$, and hence we are in the tight binding limit (as

opposed to the nearly free limit) where the Bloch particle is strongly localized around the potential minima, and with band structure Eq. (9). The lowest band gap E_G is of the order of $\sqrt{2\epsilon_0 V_0} = 0.35V_0$, and thus much larger than the band width Δ, since $\Delta/V_0 = 2.5\times10^{-5}$. Next we consider a dynamic situation and apply to the sample an external magnetic field with H the component along the easy axis. This field drives the domain wall via the Zeeman term, $FX = 2\mathcal{A}M_0HX$. From the standard semiclassical equation of motions for a Bloch particle,[8,10] given by

$$v = \frac{1}{\hbar}\frac{\partial \epsilon}{\partial k} = v_0 \sin[k(t)d],$$

where $v_0 = \Delta d/(2\hbar)$, and $\hbar\dot{k} = F$, we then find that for constant H the domain wall position $X(t)$ performs Bloch oscillations of amplitude $\delta X = \Delta/F$ and Bloch frequency $\omega_B = Fd/\hbar$. These Bloch oscillations result then in oscillations of the magnetization along the easy axis, with amplitude $\delta M = 2N_A g\mu_B(S/a)\delta X$, and with the same Bloch frequency ω_B. Let us now give some illustrative numbers for the set of values $(H, \omega_B, \delta X, \delta M)$: $A = (2\times10^{-5}$ Oe, 5×10^6 s^{-1}, $a = 6.2$ Å, 2600 μ_B), $B = (10^{-5}$ Oe, 5×10^5 s^{-1}, $d = 3a = 18.6$ Å, 7800 μ_B), $C = (7\times10^{-7}$ Oe, 2×10^4 s^{-1}, $\delta = 414$ Å, 2×10^5 μ_B), and $D = (10^{-10}$ Oe, 8 s^{-1}, 0.2 mm, 10^9 μ_B). Thus we see that the smaller the applied field, the larger is the oscillatory response, clearly a striking and unique quantum signature without classical counterpart. Note that these Bloch oscillations are the magnetic analogue of the Josephson effect: a driving constant field (H) results in an oscillatory response (magnetization). Moreover, if the external field is oscillatory in time we expect to see resonance effects in the magnetization.

Very similar to recent experiments on magnetic grains,[4] observations could be performed on ensembles consisting of many identical particles (say 10–100 for case B), by using superconducting quantum interference device (SQUID) magnetometers. If the particles are well separated, the Bloch oscillations are independent and in phase. Thus the magnetization oscillations add up coherently irrespective of the individual easy-axis orientations. To minimize a broadening of the Bloch period the spread of the particle size distribution should be small.

We emphasize that for the above field values Zener interband transitions can be safely ignored even for astronomically long observation times. Indeed, the Zener tunneling probability is given by $P = e^{-A}$, with WKB exponent $A = \pi^2 E_G^2/(4\epsilon_0 Fd) > 8\times10^4$, if $H < 4\times10^{-5}$ Oe, and thus $\omega_B P$ is virtually zero for the above values. Zener transitions occur when P becomes of order one, i.e., $H \approx H_c = 2$ Oe; in this case the Bloch oscillations vanish and the domain wall runs down the pinning "washboard potential."

Finally, preliminary theoretical results[8] suggest that the presence of dissipative effects due to magnons and phonons is negligible also for the dynamics of Bloch oscillations. The fact that damping can be expected to be weak is also supported by the recent observation of macroscopic quantum coherence in small magnetic grains over very long times.[4]

This work has been supported by the Swiss National Science Foundation (H.B.B.) and by the NSERC of Canada (S.L. and H.B.B.).

[1] J. L. van Hemmen and S. Süto, Europhys. Lett. **1**, 481 (1986); M. Enz and R. Schilling, J. Phys. C **19**, 1765 (1986).
[2] E. M. Chudnovsky and L. Gunther, Phys. Rev. Lett. **60**, 661 (1988); B. Barbara and E. M. Chudnovsky, Phys. Lett. A **145**, 205 (1990).
[3] C. Paulsen *et al.*, Phys. Lett. A **161**, 319 (1991).
[4] D. D. Awschalom, J. F. Smyth, G. Grinstein, D. P. DiVincenzo, and D. Loss, Phys. Rev. Lett. **68**, 3092 (1992).
[5] W. Riehemann and E. Nembach, J. Appl. Phys. **55**, 1081 (1984); P. C. E. Stamp, Phys. Rev. Lett. **66**, 2802 (1991).
[6] D. Loss, D. P. DiVincenzo, and G. Grinstein, Phys. Rev. Lett. **69**, 3233 (1992); J. van Delft and C. Henley, *ibid.* **69**, 3237 (1992).
[7] A. O. Caldeira and A. J. Leggett, Ann. Phys. **149**, 347 (1983).
[8] H. B. Braun and D. Loss (unpublished).
[9] R. Rajaraman, *Solitons and Instantons* (North-Holland, Amsterdam, 1982).
[10] C. Kittel, *Quantum Theory of Solids* (Wiley, New York, 1963); J. B. Krieger and G. J. Iafrate, Phys. Rev. B **33**, 5494 (1986); **38**, 6324 (1988).

Magnetic properties of cubic $R_xY_{1-x}Al_2$ (R=Dy, Tb) intermetallic random anisotropy magnets (invited)

A. del Moral, J. I. Arnaudas, C. de la Fuente, M. Ciria, and E. Joven
Unidad de Magnetismo, Departamento de Física de la Materia Condensada and ICMA, Universidad de Zaragoza and CSIC, 50009 Zaragoza, Spain

P. M. Gehring
Department of Physics, Brookhaven National Laboratory, Upton, New York 11793

A short review is made of the key magnetic properties of dilute cubic $R_xY_{1-x}Al_2$ (R=Tb, Dy) intermetallics, in order to show their main magnetic features. Dilution by Y introduces a weak random magnetic anisotropy (RMA). The rich magnetic phase diagram is described, including paramagnetic (P), spin glass (SG), correlated spin glass (CSG), random ferromagnetic (RFM), and ferromagnetic (F) phases, with a triple point and two multicritical ones. The paper deals with the induced macroscopic magnetic anisotropy cooling in a magnetic field below T_{SG} or T_{CSG} transition temperatures, which can be either unidirectional or uniaxial or both. High-field (3 T) magnetostriction in Tb series shows, for x=0.48, 0.59, 0.87, a decrease of the Callen α exponent ($\lambda_t \sim m^{\alpha}$, m=reduced magnetization) below 3. The Sompolinsky irreversibility parameter Δ has been determined for the Tb series in the SG regime, and a replica model is presented to explain the $\Delta(T)$ dependence. The character of the P→SG or P→CSG transitions is addressed, through the scaling of nonlinear susceptibility (SG regime) or a ferromagnetic-like scaling of magnetization, respectively. From quasielastic neutron scattering around $\mathbf{Q}$=[1,1,1] we determine the temperature dependence of the magnetic correlation length in $Dy_{0.8}Y_{0.2}Al_2$, which peaks, but does not diverge at T_c. A magnon excitation at 3.5 meV is reported for x=0.8.

I. INTRODUCTION

$R_xY_{1-x}Al_2$ (R=Dy, Tb) are *crystalline* cubic Laves phase compounds. We have extensively studied their magnetic properties using as probes: low- and high-field magnetization, ac magnetic susceptibility, ferromagnetic-like scalings, law of approach to saturation,[1] Arrott plots, observation of transition lines, existence of Edwards–Anderson (EA) parameter,[2] hysteresis,[3] magnetic anisotropy measurements,[4] Bragg and small-angle neutron scattering (SANS),[5] and magnetostriction.[6] These measurements have revealed the compounds as *weak* random magnetic anisotropy (RMA) systems, exhibiting a very rich variety of magnetic phases and transitions,[7] likely never observed together in a RMA system. Of the possible origins for the RMA, the most likely is the strong magnetoelastic coupling, because of the local strains introduced by the Y^{3+} substitutions.[1] In Fig. 1 we show the magnetic phase diagrams (MPD) for the Dy and Tb series. The Dy system exhibits paramagnetic (P), spin glass (SG), and correlated spin glass (CSG) phases, with a triple point (TP) at x_{tr}=0.30.[1] At 0 K a first-order transition from CSG to ferromagnet (FM), driven by coherent cubic anisotropy, is observed at x_t=0.62, remaining up to x_t' = 0.87, where the FM phase extends up to the line boundary FM-P, with a tricritical point at T_t' = 45.4 K.[7] At x_t=0.62, a boundary between CSG and a quasiferromagnetic or random ferromagnetic phase (RFM) appears, with an ending tricritical point at T_t=29.5 K. For $x>x_t$ the line of transitions RFM-P shows a crossover exponent ϕ_Δ=0.80±0.08.[7] Law of approach to saturation allows an estimation of D/J_0, e.g., ≈0.04 for x=0.83, between the strength of the random crystal field (CEF) D, and the *positive* exchange interaction J_0 according to positive paramagnetic Curie temperature θ. An increase of such ratio with decreasing x is likely.[1,7] The MPD of $Tb_xY_{1-x}Al_2$ has not been yet explored in such detail, only up to x=0.50, showing P, SG, CSG phases (see Fig. 1), with a TP at x_{tr}=0.27, T_{tr}=8.6 K.[8]

The aim of this paper is to present the magnetic properties of the RMA system $R_xY_{1-x}Al_2$ (Dy, Tb), showing some previous work and adding new results recently obtained. In particular: the field-induced macroscopic anisotropy in $Dy_xY_{1-x}Al_2$, together with rotational hysteresis found (Sec. II); CEF origin magnetostriction, showing that in Callen's[9] mp law in $Tb_xY_{1-x}Al_2$, $p<3$ (Sec. III); the Sompolinsky[10] irreversibility order parameter Δ in Tb series (Sec. IV); aspects of the critical behavior at the P-SG and P-CSG transitions in Tb series, from magnetization measurements, together with neutron scattering around T_C (P→CSG or RFM)

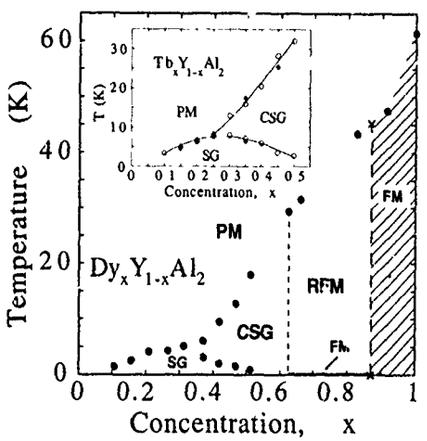

FIG. 1. Magnetic phase diagram for $Dy_xY_{1-x}Al_2$ compounds. Inset: the $Tb_xY_{1-x}Al_2$ one [(○) from ac susceptibility; (♦) from the "branching points" of Fig. 4(b)].

 0021-8979/94/76(10)/6180/6/$6.00 © 1994 American Institute of Physics

in the Dy series, and the magnetic correlation length temperature dependence. The amount of work reported is large, and the presentation is succinct.

II. FIELD-INDUCED MACROSCOPIC ANISOTROPY AND ROTATIONAL HYSTERESIS

We will address three points: the symmetry of the field-induced macroscopic anisotropy (FIMA), the rotational hysteresis of anisotropy torque, and the differences in the torque curve symmetries, when cooling above or below the coercive field. The samples were single crystals of $Dy_xY_{1-x}Al_2$ (x =0.3, 0.4, 0.6), i.e., at the CSG phase. The anisotropy torque L_k was measured from the magnetization perpendicular to the rotating magnetic field **B** on plane (110), because $L_k=M_\perp B$. A complication is the coherent cubic anisotropy (CA), which was averaged out by measuring in fields so weak as to have the crystals divided in six ⟨100⟩ domains, so that $\langle \mathbf{M}_s\rangle=0$, for the sample average spontaneous magnetization. We developed[4] a model, based on Henley *et al.* and Saslow[11] ones, which predicts the appearance of FIMA anisotropy both unidirectional (UD) and uniaxial (UA). Starting with the Hamiltonian,

$$H=J_0\sum_{\substack{\alpha,\beta\\ i<j}} S_i^\alpha S_j^\beta+D\sum_{i,\alpha}(\hat{a}_i^\alpha S_i^\alpha)^2, \tag{2.1}$$

where $\hat{a}_i$ are the local RMA easy axes (EA), i stands for sites, and α for spin components. It is possible to show[4] from Eq. (2.1) that the FIMA energy becomes,

$$E_k^{\mathrm{RMA}}=-K_{\mathrm{RMA}}\cos\theta-2K_{\mathrm{RMA}}\cos^2\theta, \tag{2.2}$$

with $K_{\mathrm{RMA}}=(4/15)\mathrm{N}(\mathrm{D}^2/J_0)$ (N, ion number per unit volume). To this energy me must add the CA, so the total anisotropy torque becomes

$$\Gamma(\theta)=-K_{\mathrm{RMA}}(\sin\theta+2\sin 2\theta)-(K_1/4+K_2/64)$$
$$\times\sin 2\theta-(3K_1/8+K_2/16)\sin 4\theta+\cdots, \tag{2.3}$$

where K_1, K_2 are CA constants, about 10^3 higher than K_{RMA}.

We did two experiments: cooling in the low measuring field, H_m and cooling in a larger field $H_{\mathrm{FC}}>1$ kOe and measuring in the lower one ($\mathbf{H}_{\mathrm{FC}}\|\langle 100\rangle$, easy axis). In addition H_{FC} can be larger or smaller than the coercive field H_c,[1,2] which makes two different situations. The magnetization will be $\mathbf{M}=\chi\mathbf{H}+\mathbf{M}_r$, where χ is the isotropic cubic susceptibility and $\mathbf{M}_r$, the remanent magnetization after FC, which can be a complicated object. (i) We first address the case when both UD and UA FIMA's have been produced. In Fig. 2(a) we show the torque curves for x=0.30, 0.40 below T_C for FC and H_m=0.25 kOe, above H_c. At this field, K_1 and K_2 are very small. Fourier analysis of Γ shows $\sin\theta$ and $\sin 2\theta$ components, indicating the presence of both anisotropies, although for x=0.4 the the UD character is stronger. Extrapolation to H_m=0 of $K_{\mathrm{RMA}}(H_m)$ obtained from the $\Gamma(\theta)\sin\theta$ component amounts to 127 and 225 J/m^3, respectively, at 3.8 K. We notice that the Γ_2 coefficient (of $\sin 2\theta$) is not $2\Gamma_1$ (of $\sin\theta$), because of the CA contamination, which practically disappears below ≅0.70 kOe. In fact a combined plot of $\Gamma_2-2\Gamma_1$ and $(K_1/4+K_2/64)$ gives a linear relation, extrapolating to zero. Model Eq. (2.2) has thus been established. Notice the existence of a constant torque Γ_0 whose origin should be a $\mathbf{M}_r$ component, rotating in phase with **H**, limited by the shortest spin relaxation times. (ii) A second point is that there is a crossover from $H_m<H_c$ to $H_m>H_c$, i.e., from unidirectional plus uniaxial FIMA's to unidirectional alone [π and 2π periods in $\Gamma(\varphi)$ curves, respectively, where φ in the rotating field angle]. These experiments were done with $H_{\mathrm{FC}}\gg H_c$. This is shown in Fig. 2(b) for x=0.6, where H_c=0.39 kOe at T=3.8 K and H_{FC}=3 kOe, in going from H_m=0.23 to 1.0 kOe. The same behavior is observed for the other concentrations. In the first situation ($H_m<H_c$), $\mathbf{M}_r$ remains fixed along ⟨100⟩ cooling direction, whereas in the

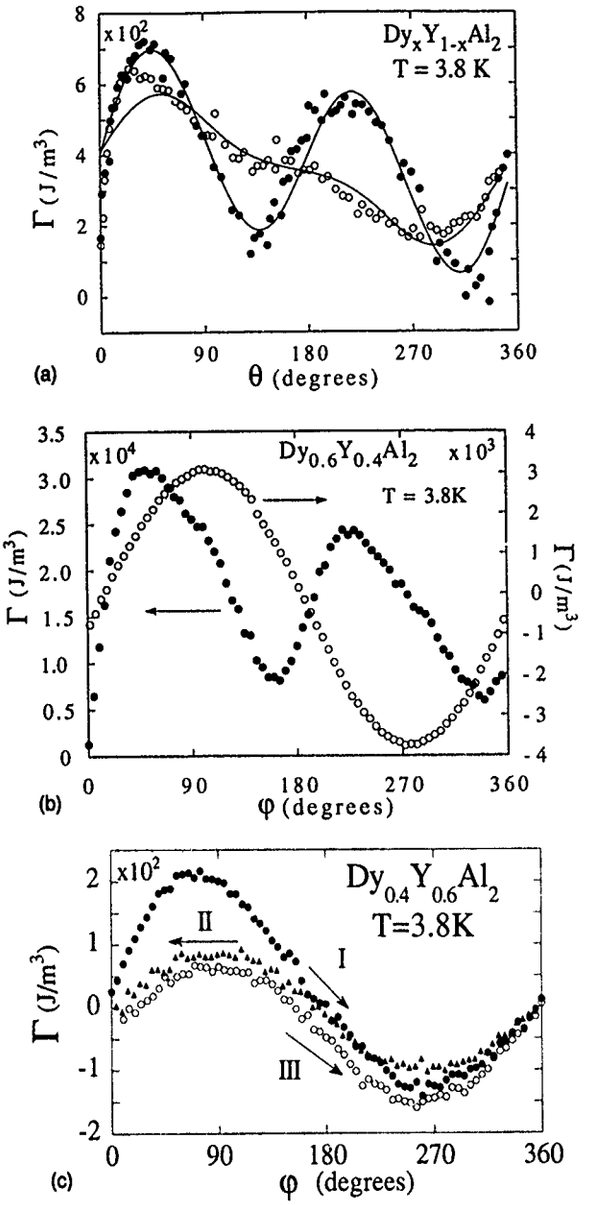

FIG. 2. (a) Magnetic anisotropy torque vs θ angle curves for $Dy_xY_{1-x}Al_2$: x=0.30, (●); x=0.40 (○). The full lines are the theoretical fits, according to Eq. (2.3). (b) Torque curves vs φ angle for $Dy_{0.60}Y_{0.40}Al_2$, for applied fields: (○) 0.23 kOe, (●) 1.0 kOe. The cooling field was 3 kOe (see meaning of φ in text). (c) Torque curves vs φ angle for $Dy_{0.40}Y_{0.60}Al_2$ for applied field 80 Oe. The arrows show the sense of successive rotations. The cooling field was 1 kOe.

second one $\mathbf{M}_r$ splits in three components: one fixed to $\langle 100\rangle$ (Γ_1 torque), a rotating one out of phase with $\mathbf{H}$ (Γ_2 torque), and one at a constant angle with $\mathbf{H}$ (Γ_0 torque), due to the mechanism suggested.

From K_{RMA} one obtains D^2/J_0 (=0.007 and 0.01 K for x=0.3 and 0.4, respectively), which allows a *separate* estimation of D and J_0. Since we found above that $D/J_0 \cong 0.04$, we now have $D \cong 0.2$ K and $J_0 \cong 5$ K. (iii) We now consider the rotational hysteresis, which suggests metastable states in these RMA systems. In Fig. 2(c) we notice, for x=0.4, H_{FC}=1 kOe and H_m=0.080 kOe, at 3.8 K, a strong hysteresis (φ=0 to π) between the first clockwise rotation and the second counterclockwise rotation, the hysteresis disappearing afterwards. An explanation for the transient in the initial $L_k(\varphi)$ curve is that the spins with the shortest relaxation times easily follow the field, the slowest ones following it later on (curves II and III). The hysteresis increases strongly when $H_m > H_c$, as expected. Similar behavior is found for the other concentrations.

III. MAGNETOSTRICTION: VIOLATION OF m^3 LAW

It has been predicted[12] that when the local RMA field satisfies $H_{\mathrm{RMA}} > H$, but $H \ll H_{\mathrm{ex}}$ (H and H_{ex} are the applied and exchange fields, respectively), so one is in the ferromagnet with wandering axis regime (FWA),[13] that noticeable deviations from the Callen and Callen[9] law for CEF-origin shape magnetostriction λ_t are expected: $\lambda_t \sim m^p$, with $p<3$, $m=M(T)/M(0)$ being the reduced magnetization. It can be shown that[12]

$$\frac{\lambda_t(T)}{\lambda_t(0)} = \frac{\langle\langle O_2^0(\mathbf{J})\rangle\rangle_c}{\langle O_2^0(\mathbf{J})\rangle_c}, \quad \frac{M(T)}{M(0)} = \frac{\langle\langle O_1^0\rangle\rangle_c}{\langle O_1^0\rangle_c}, \tag{3.1}$$

where O_2^0 and O_1^0 are Stevens operators, functions of the angular momentum $\mathbf{J}$, $\langle\cdots\rangle$ is the thermal average and $\langle\cdots\rangle_c$ is the average over the local easy axis disorder. For large J, we express O_n^0 in terms of site spin wave (sw) deviation operators, a, a^+, but introducing c and c^+ numbers representing the static spin deviations, writing $a=(1+u)\alpha+v\alpha^++c$, where the (u,v) numbers account for sw scattering by the RMA disorder, and α are Bose operators. Then it can be shown that in the FWA regime, where sw are proper:

$$\frac{M(T)}{M(0)} = \frac{1-J^{-1}\langle\langle a^+a\rangle\rangle_c}{1-J^{-1}\{\langle cc^+\rangle_c+\langle v^2\rangle_c\}},$$

and

$$\langle\langle O_{20}(T)\rangle\rangle_c = 3J^2-J(J+1)-3(2J-1)\langle\langle a^+a\rangle\rangle_c + 6J^2[1-m(T)]^2,$$

with $m(T)=\langle\langle J_z\rangle\rangle_c/J$. Combining the above four equations gives[12]

$$\frac{\lambda_t(T)}{\lambda_t(0)} = \left[\frac{M(T)}{M(0)}\right]^p, \tag{3.2}$$

where

$$p = \frac{3[J(2J-1)-6\delta J+\delta(1+4\delta)]}{[J(2J-1)-6\delta J+3\delta(1+2\delta)]},$$

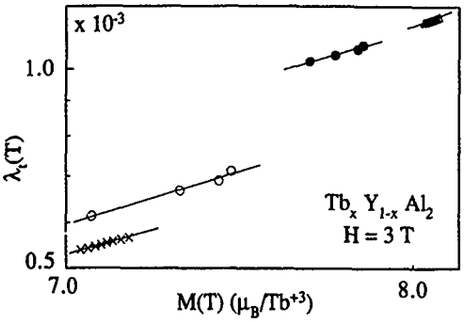

FIG. 3. Double logarithmic plots of magnetostriction $\lambda_t(T)$ vs $M(T)$, at H=3 T, and for $T<20$ K, for $Tb_xY_{1-x}Al_2$, for x=0.49 (x), 0.60 (○), 0.87 (●), and 1(Δ) compounds. The slopes give the exponent p [see Eq. (3.2)].

with $\delta=J[1-m(0)]$, proportional to the RMA disorder 0 K magnetization quantum defect $\Delta(0)=1-m(0)$. The important result is that $p<3$.

We have searched for this m^3 violation in $Tb_xY_{1-x}Al_2$ (x=0.49, 0.60, and 0.87) compounds, measuring $\lambda_t(T)$ and $M(T)$ up to 12 T, from 1.5 K. In Fig. 3(a) we show low-temperature ($T<20$ K) plots of λ_t vs M at H=3 T, where we can assume $H > H_{\mathrm{RMA}}$. From them we obtain the p values: 2.3 (x=0.49); 2.7 (x=0.60); 2.65 (0.87), smaller than for the good ferromagnet $TbAl_2$, $p=3.0\pm0.1$. As expected, p increases with H, becoming quite close to 3 for H=12 T. Also, from p expression we can evaluate $\Delta(0)$:0.24 (x=0.49); 0.16 (x=0.60); 0.18 (x=0.87). These values are slightly higher than those obtained from the ratio $M(0,H)/Ng J\mu_B$:0.19, 0.16, and 0.12 respectively, this reduction likely being due to the magnetization induced by the strong cubic anisotropy. Notice that the extrapolated 0 K Tb^{3+} magnetic moment in $Tb_xY_{1-x}Al_2$ is unquenched,[14] (9.0±0.3) μ_B, allowing us to take $M(0)=NgJ\mu_B$, i.e., excluding RMA effects.

IV. FC AND ZFC MAGNETIZATION IRREVERSIBILITY: ASSOCIATED ORDER PARAMETER Δ

Our best studied system demonstrating the irreversibility between FC and ZFC magnetizations is Tb, for $0.15 \leqslant x \leqslant 0.50$. The behavior is quite different in the SG and CSG regimes. At CSG regime one observes [Fig. 4(a)] a branching point between FC and ZFC magnetizations at T_C, followed by a broad maximum for the ZFC isofield, both magnetizations rapidly decreasing when approaching T_{SG}. For SG regime, only a branching point is observed coincident with the cusp [Fig. 4(b)]. The $M_{\mathrm{ZFC}}-M_{\mathrm{FC}}$ difference decreases with increasing field, finally merging. Strong relaxation was found for $H \cong H_c$, at the ZFC branch, for both SG and CSG regimes.

The usual order parameter considered for SG systems is that of Edwards–Anderson (EA), q, conveniently redefined[15] for RMA systems. Although useful, there are difficulties with q: it has nonzero value for $T > T_{\mathrm{SG}}$ even at zero applied field, and there are subtle theoretical difficulties with the replica method. Therefore it seems worthwhile to use the FC-ZFC irreversibility to define an additional order parameter, in the way proposed by Sompolinsky[10] using a dynamical model

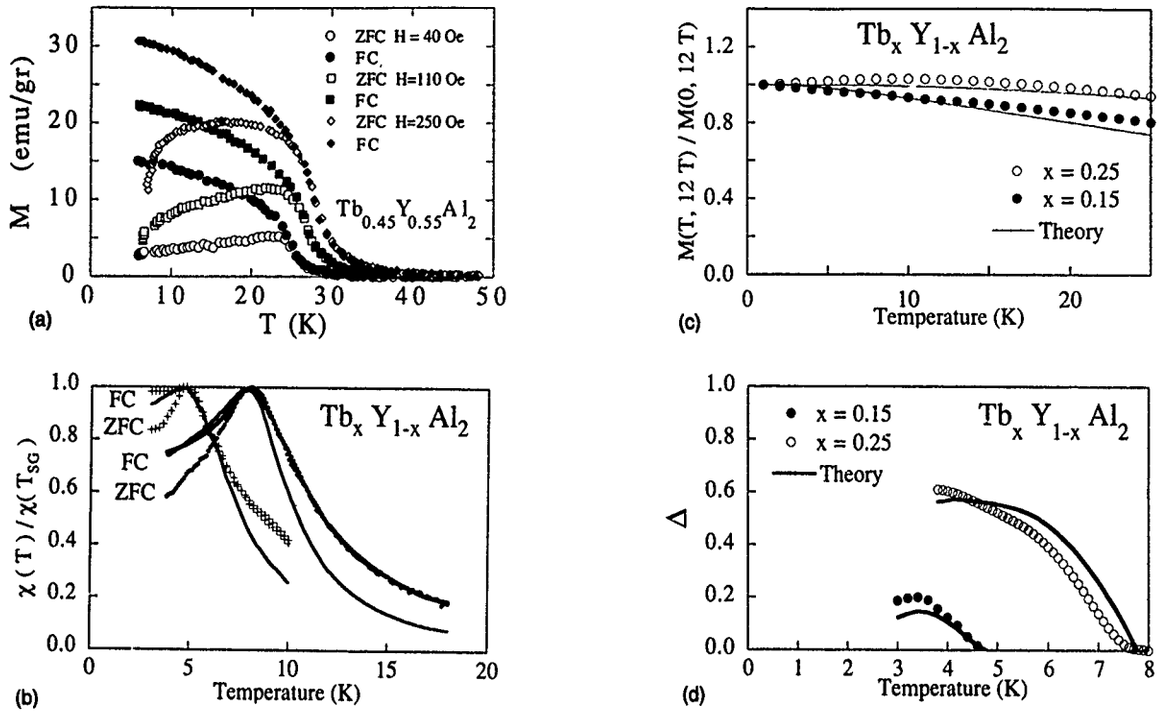

FIG. 4. (a) Field-cool (FC) and zero-field-cool (ZFC) isofield curves for $Tb_{0.45}Y_{0.55}Al_2$ compounds at increasing fields. (b) The same as (a) for $Tb_xY_{1-x}Al_2$: (●), $x=0.25$ at $H=26$ Oe; (+), $x=0.15$ at $H=3.6$ Oe. The full lines are the theoretical calculations for the χ_{FC} susceptibility. (c) Reduced magnetization $M(T,12\text{ T})/M(0,12\text{ T})$ for $Tb_xY_{1-x}Al_2$: (●), $x=0.15$; (○), $x=0.25$. The full lines are the theoretical fits (see text for details). (d) Irreversibility order parameter Δ vs temperature for $Tb_xY_{1-x}Al_2$: $x=0.15$ (●), $H=3.6$ Oe; $x=0.25$ (○), $H=26$ Oe (see text for details). The full line is the theoretical calculation.

where time-variable spin noise and time-persistent noise due to RMA are combined with TAP[16] theory. The resulting irreversibility parameter Δ becomes

$$\Delta=\frac{T}{C}(\chi_{FC}-\chi_{ZFC}), \tag{4.1}$$

where χ_{FC} and χ_{ZFC} are low field susceptibilities and C is the Curie constant. The equilibrium χ_{FC} susceptibility is amenable to calculation as (M/H) for very small H(few Oe). We developed a replica-MF model for RMA systems[15] where $M(T,H)=Ng\mu_B\langle\langle J_z\rangle\rangle_c$ has the form

$$\langle\langle J_z\rangle\rangle_c=\int_{-\infty}^{\infty}\frac{dx}{\sqrt{2\pi}}e^{-x^2/2}\frac{\mathrm{Tr}(J_z\exp\{\alpha J_z^2+[\gamma x+\beta\theta(g-1)^2\,m/g+\beta g\mu_B H]J_z\})}{\mathrm{Tr}\exp[\cdots]} \tag{4.2}$$

with $\beta\equiv 1/K_BT$ and $m=M(N\mu_B)^{-1}$. The parameters α and γ depend[15] on the CEF parameter D, on the quadrupolar moment $p=\langle\langle J_z^2\rangle\rangle_c$, and on $q=\langle\langle J_z\rangle^2\rangle_c$. $\theta=zJ_0$ is the paramagnetic Curie temperature, and z is the R^{3+} NN number. Then, to evaluate M, p, and q, we need a knowledge of the parameters J_0 and D. We obtain D from the condition $q(T_{SG},0)=0$ by extrapolation, and we obtain J_0, together with a refinement of D, from a self-consistent calculation of M, q, and p, and fitting $M(T,H)$ to the experiment. In Fig. 4(c) we show the high-field (12 T) measurements of $M(T)$ for $x=0.15$ and 0.25, together with the best theoretical fits. The resulting values were for $x=0.15$, $D=0.5$ K, and $J_0=16$ K ($z=0.6$), and for $x=0.25$, $D=0.7$ K, and $J_0=18$ K ($z=1$). In Fig. 4(d) we present $\Delta(T)$ for both x, at $H=3.6$ and 26 Oe, respectively: note that $\Delta(T_{SG},H)=0$. Figure 4(b) shows $\chi_{FC}(T)$, calculated from Eq. (4.2) for those fields. From Eq. (4.1) we have calculated $\Delta(T)$ for both compounds, the agreement with experiment is reasonably good [Fig. 4(d)].

V. CRITICAL BEHAVIOR, PHASE TRANSITIONS, AND NEUTRON SCATTERING

A still open question is if a RMA spin glass undergoes at T_{SG} a phase transition. The answer can be obtained by a scaling analysis of the nonlinear susceptibility χ_{NL}, which is proportional to the singular component of q.[2,17] Similarly for the CSG or RFM phases one is tempted to see if the magneti-

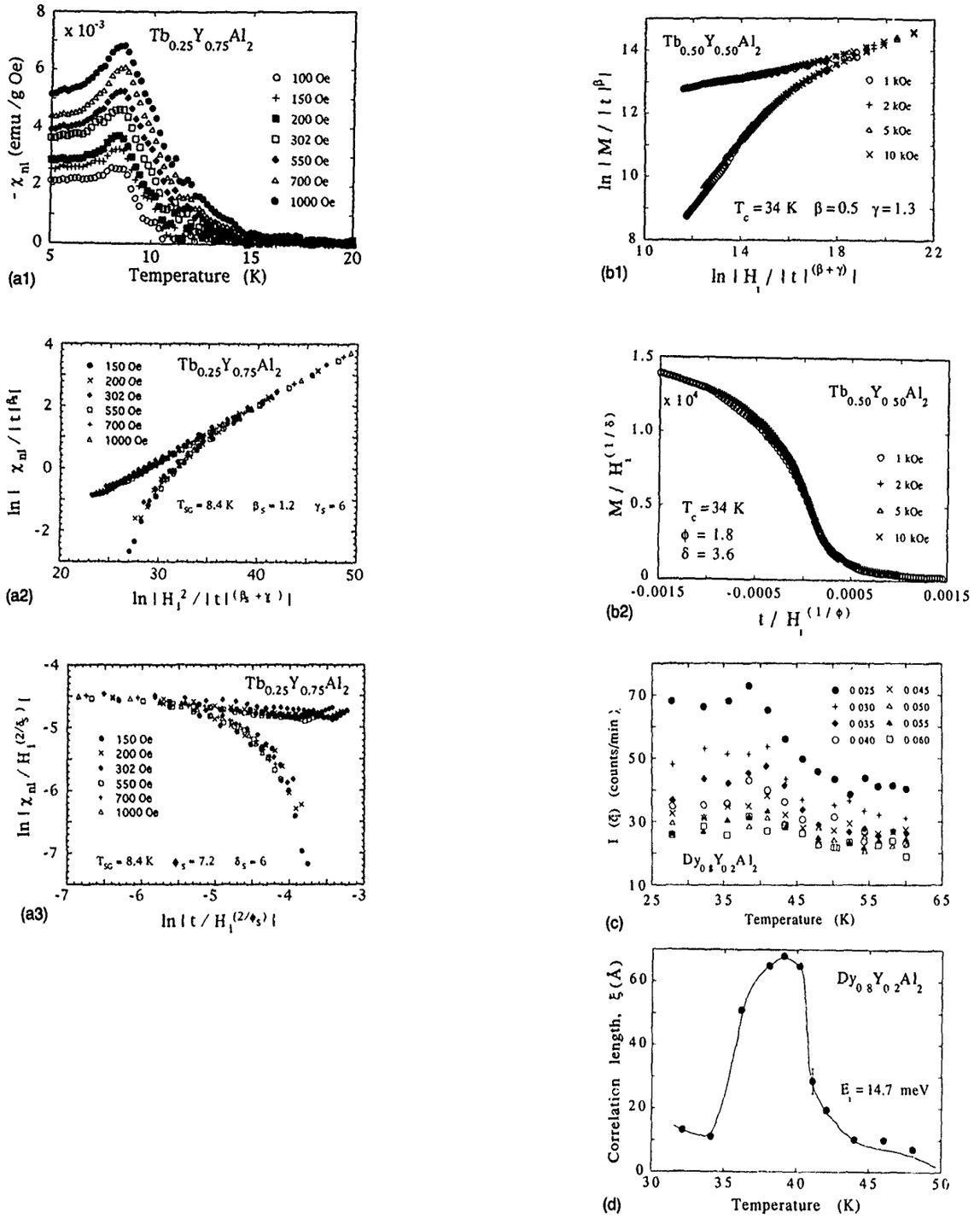

FIG. 5. (a1) Nonlinear susceptibility χ_{NL} vs temperature for $Tb_{0.25}Y_{0.75}Al_2$ at increasing magnetic fields; (a2) double logarithmic (β_s, γ_s) scaling for $x=0.25$; (a3) the same as (a2), (δ_s, ϕ_s) plot. H_i is the internal field. (b1) Double logarithmic ferromagnetic-like (β,γ) scaling plot for $Tb_{0.50}Y_{0.50}Al_2$. The upper branch is for $T<T_c$. H_i is the internal field. (b2) The same as (b1) scaling plot (δ,ϕ) for $Tb_{0.50}Y_{0.50}Al_2$. (c) Scattered neutron intensity, $I(\mathbf{q})$, vs temperature for different momentum transfer $\mathbf{q}=(2\pi/a)$ $[\xi,\xi,\xi]$ (ξa^* values are shown within the graph), around $\mathbf{Q}=(2\pi/a)$ [1,1,1], for $Dy_{0.80}Y_{0.20}Al_2$ (a, the lattice constant). (d) Magnetic correlation length temperature dependence for $Dy_{0.80}Y_{0.20}Al_2$ (see text for details). The line is an eye guide.

zation satisfies a critical scaling similar to ferromagnets and a ferromagnetic-like neutron scattering around T_c. We will address these points in $Tb_xY_{1-x}Al_2$ compounds, together with neutron scattering around T_c for $Dy_{0.8}Y_{0.2}Al_2$.

(i) Critical scaling of χ_{NL} of $Dy_xY_{1-x}Al_2$ has been extensively studied elsewhere[2] and we will focus here on the Tb series at SG regime. The nonlinear susceptibility was obtained as $\chi_{NL}=\chi(H)-\chi_0$, where the linear one χ_0 was

TABLE I. Nonlinear susceptibility χ_{nl} scaling exponents for the series $Tb_xY_{1-x}Al_2$ at the SG regime (s label). Ferromagnetic-like exponents at the CSG regime (no label). The transition temperatures and fractal dimensionality $d_f=d\phi_s/(\phi_s+\beta_s)$ are included. For χ_{nl} exponents: (*) are from (β_s,γ_s) scaling, (+) from (δ_s,ϕ_s), ($) from scaling at T_{SG}, and (#) from scaling laws. Error bars are ±0.1 in β_s and ±0.5 in γ_s, δ_s, and ϕ_s.

Compound	T_{SG} (K)	β_S	γ_S	δ_S	ϕ_S	d_f
0.15	4.7			5.0($)		
0.20	6.8	1.2(*)	6.0(*)	6.0(#)	7.2(#)	
				5.0($)		2.5
0.25	8.5	1.2(*)	6.0(*)	6.0(#)	7.2(#)	
		1.2(#)	6.0(#)	6.0(+)	7.2(+)	2.5
Compound	T_c (K)	β	γ	δ		ϕ
$TbAl_2$	97	0.40±0.05	1.25±0.05	4.1±0.01		1.65±0.01
0.50	34	0.5±0.5	1.3 ±0.1	3.6±0.1		1.80±0.1

accurately measured at a few Oe. In Fig. 5(a1) we show $\chi_{NL}(T)$ for $x=0.25$, the variation being similar for $x=0.15$, 0.20. No shift with H is found, signaling T_{SG} as a fixed point. Two kinds of scalings:[17] $-\chi_{NL}/H^{2/\delta_s}=f(|t|/H^{2/\phi_s})$ and $-\chi_{NL}/|t|^{\beta_s}=f(H^2/|t|^{\beta_s+\gamma_s})$ were performed [see Figs. 5(a2) and 5(a3), with the best data "collapses"], in order to determine the pairs of exponents (δ_s,ϕ_s) and (β_s,γ_s), and to verify the scaling laws; also the first scaling was performed at T_{SG}, where $\chi_{nl}\approx H^{2/\delta_s}$ [$t=(T-T_{SG})/T_{SG}$ is the reduced temperature]. All exponents are in Table I, scaling laws being reasonably well obeyed, as well as universality, although exponents markedly differ from MF theory.[17] We conclude that the $P\rightarrow$SG transition is a true phase transition for RMA $Tb_xY_{1-x}Al_2$ compounds, as was shown for the Dy ones.[2]

In the CSG regime we performed a ferromagnetic-like scaling for $x\geq 0.40$, akin to such a character according to Arrott plots, where the demagnetizing limit is almost reached at $x=0.35$. The relations were $M/|t|^{\beta}=f(H/|t|^{\beta+\gamma})$ and $M/H^{1/\delta}=f(t/H^{1/\phi})$, in order to check for the scaling laws. For $TbAl_2$, a good $3d$-Heisenberg ferromagnet,[14] we obtain the exponents in Table I. In Figs. 5(b1) and 5(b2) we show the (γ,β) and (δ,ϕ) best data "collapses," with the exponents quoted in Table I, for $x=0.5$. It is clearly not a ferromagnet, because of the nonleveling-off of the $T<T_c$ branch. Those exponents are related to those for a $3d$-Heisenberg ferromagnet (f), using the Arrott–Noakes[1] equation of state: $\delta=(\epsilon+2)\beta_f/(1+2\gamma_f)$, $\beta=[(\epsilon+2)/2]\beta_f$, with $\epsilon=4-d$. These relations are well followed in the Dy series but not in the Tb one, likely due to the stronger cubic anisotropy and weaker RMA of the Tb compounds.

(ii) Zero energy transfer neutron scattering at $E_i=14.7$ meV was performed at the triple-axis $H4M$ spectrometer at BNL for $x=0.8$ compound, around $Q=a^*[111]$ for $q=a^*[\zeta,\zeta,\zeta]$ momentum transfer with $\zeta a^*=0.03$–0.058 $Å^{-1}$, in the range 8.7–66 K. In Fig. 5(c) we see that the scattered intensity peaks around $T_c=38$ K, in agreement with magnetization and χ_{ac} measurements. We tried a Lorentzian (L)[18] fit to the magnetic intensity I_m (after subtracting I at 60 K), i.e., $I_m(q,T)=A/(q^2+\xi^{-2})$, in order to measure the magnetic correlation length ξ. Below 36 K it was necessary to fit by $L+L^2$.[18] This indicates that above and just below T_c, the "critical" fluctuations are spin waves (sw), and that below 36 K static RMA disorder becomes important. In Fig. 5(d) we show $\xi(T)$, not diverging at T_c, an indication of the absence of long-range ferromagnetic order. This develops, for the longitudinal magnetization,[18] at finite T only above $x=0.87$.[1] We should mention that we have very recently observed a sw excitation at $\mathbf{Q}=a^*[2,2,-0.4]$ of 3.5 meV for $x=0.8$ at 10 K, a confirmation of the predicted existence of spin waves in weak RMA quasiferromagnets.[18]

ACKNOWLEDGMENTS

We acknowledge the Spanish DGICYT for support with Grant No. PB-90-1014. Useful discussions with J. Cullen, C. Ritter, M. B. Salamon, G. Shirane, and J. Schweizer including work not presented here are fully appreciated.

[1] A. del Moral and J. I. Arnaudas, J. Magn. Magn. Mater. **62**, 71 (1986); A. del Moral, P. M. Gehring, J. I. Arnaudas, and M. B. Salamon, J. Phys. C **8**, 1233 (1988); P. M. Gehring, M. B. Salamon, A. del Moral, and J. I. Arnaudas, Phys. Rev. B **41**. 9134 (1990).
[2] A. del Moral, J. I. Arnaudas, and P. M. Gehring, J. Phys. Condens. Matter **6**, 4779 (1994).
[3] J. I. Arnaudas, A. del Moral, and J. S. Abell, J. Magn. Magn. Mater. **61**, 370 (1986).
[4] A. del Moral, M. Ciria, J. I. Arnaudas, J. S. Abell and Y. J. Bi, J. Appl. Phys. **75**, 5850 (1994).
[5] A. del Moral, J. I. Arnaudas, M. R. Ibarra, P. A. Algarabel, and J. Schweizer, J. Magn. Magn. Mater. **83**, 160 (1990); A. del Moral, J. I. Arnaudas, P. A. Algarabel, and M. R. Ibarra, Spanish Sci. Res. using neutron scatt. tech., Pub. Univ. Cantabria, 1991, p. 156; A. del Moral, J. Shweizer, J. I. Arnaudas, M. B. Salamon, C. Ritter, E. Joven, P. M. Gehring, P. A. Algarabel, and J. Cullen, J. Magn. Magn. Mater. **104-107**, 243 (1992).
[6] C. de la Fuente, A. del Moral, and J. I. Arnaudas (unpublished).
[7] A. del Moral, J. I. Arnaudas, P. M. Gehring, M. B. Salamon, C. Ritter, E. Joven, and J. Cullen, Phys. Rev. B **47**, 7892 (1993).
[8] E. Joven, A. del Moral, and J. I. Arnaudas, J. Appl. Phys. **69**, 5069 (1991).
[9] E. R. Callen and H. B. Callen, Phys. Rev. **129**, 578 (1963).
[10] H. Sompolinsky, Phys. Rev. Lett. **47**, 935 (1981); Phys. Rev. B **23**, 1371 (1981).
[11] C. L. Henley, H. Sompolinsky, and B. I. Halperin, Phys. Rev. B **25**, 5849 (1982); W. Saslow, *ibid.* **35**, 3454 (1987).
[12] J. Cullen and A. del Moral, J. Magn. Magn. Mater. **83**, 157 (1990).
[13] E. M. Chudnowsky, W. M. Saslow, and R. A. Serota, Phys. Rev. B **33**, 251 (1986).
[14] A. del Moral, J. I. Arnaudas, M. R. Ibarra, J. S. Abell, and E W. Lee, J. Phys. C **19**, 579 (1986).
[15] A. del Moral and J. I. Arnaudas, Phys. Rev. B **40**, 7192 (1989).
[16] D. J. Thouless, P. W. Anderson, and R. G. Palmer, Philos. Mag. **35**, 593 (1977).
[17] M. Suzuki, Prog. Theor. Phys. **74**, 1175 (1985).
[18] A. del Moral and J. Cullen, J. Magn. Magn. Mater. (to be published).

Correlation decay in low-dimensional spin glasses

A. N. Kocharian[a)]
Physics Department, Union College, Schenectady, New York 12308

A. S. Sogomonian
Yerevan Physics Institute, Yerevan 375036, Armenia

A new method to investigate the two-point correlation function decay in a finite size random spin system and at finite temperatures is proposed. It is applicable to systems with cyclic boundary conditions and in any local or uniform magnetic field. The efficiency of this method is presented in the case of an isotropic XY spin glass model with Gaussian bond distribution in external field. Using unitary $U(1)$ gauge transformation and operator inequalities we have obtained explicit upper bounds for generalized spin-glass susceptibility $\kappa(T,R)$ that describes off-diagonal transverse magnetization in two dimensional random XY spin lattices at finite temperatures. It is found that the slowest possible decay for susceptibility in random XY spin glass is of the Kosterlitz–Thouless-type with power-law decay in 2D, and the exponential type in 1D, at low temperatures. These upper bounds rule out the possibility of the corresponding magnetic ordering in 1D and 2D isotropic XY spin glasses at finite temperatures.

INTRODUCTION

During the last two decades, the problem of random spin systems have attracted the interest of many physicists. This is because among the systems considered there are simplest examples of the random models such as Ising spin glasses or random XY model with nearest neighbor or long-range interactions.[1,2] These systems are characterized by a competition between ferromagnetic and antiferromagnetic interactions and a huge number of their experimental examples have been studied. As a result, conventional magnetic long-range order is impossible. In the mean field approach we can obtain numerous thermodynamic states and suggest the existence of the line of phase transitions at finite temperatures in the presence of a magnetic field.[3] On the other side, there is evidence that the nature of the random spin system (planar XY model with spin dimensionality n equals 2) at finite temperatures and in low dimensions may be close to the classical XY model in the 2D case and correspondingly quite different from the simple mean field picture. The essential difference is in the properties of the low temperature phase.

There are many doubts about the possibilities of obtaining real phase transitions in such systems at sufficiently low temperatures. For all these models, one believes, an upper critical dimension exists, and the critical properties associated with the transition are modified due to fluctuations below this critical dimension. In other words, the main problem is whether or not phase transitions are possible in real three dimensional space at finite temperatures for random spin systems. This circumstance depends on lowest critical dimensionality d_c; and if $d_c>3$, then phase transitions are ruled out, and if $d_c\leqslant 3$, then there is a possibility of obtaining a real finite temperature transition. Unfortunately, there are no exact results corresponding to the value of parameter d_c in spin glasses. The same question can be stated also in two dimensional spin glasses, where it would be possible to obtain the finite temperature transition, in the case when spins are frozen randomly and we have neither ferromagnetic nor antiferromagnetic states, but more of the spin liquid type.

In this paper, we propose a new method for investigation of the upper bound behavior of two-point correlation functions of such random systems as the isotropic XY spin glass model with long-range interactions with the Gaussian bond distribution at sufficiently low temperatures and in an arbitrary magnetic field in one and two dimensional lattices. Below, we show that the upper bound for generalized spin susceptibility at low temperatures in 2D lattices is power-law like. These results rigorously rule out any possibility of the corresponding long-range ordering in 1D and 2D random XY models at nonzero temperatures. The suggested approach has been used before to obtain upper bounds for correlation function decay in low dimensional Hubbard model as well as for correlation functions in anisotropic Heisenberg–Ising like models with arbitrary spin.[4,5]

SPIN-GLASS MODEL

As is known, the Hamiltonian of the random XY model with long-range interactions in the presence of local longitudinal magnetic field is represented in the form

$$H_{S.G.}=\sum_{i,j} J_{ij}(S_i^xS_j^x+S_i^yS_j^y)-\sum_i H_i,S_i^zV. \tag{1}$$

The main distinction from the usual XY model is that the value of the exchange integral J_{uv} in (1) is random and given by a Gaussian bond distribution function $\phi(J_{uv})$, where each J_{uv} is statistically independent of all others,

$$\phi(J_{uv})=\frac{1}{\sqrt{2\pi\sigma_{uv}}}\exp\left(-\frac{J_{uv}^2}{2\sigma_{uv}}\right), \tag{2}$$

where $\sigma_{uv}=\langle J_{uv}^2\rangle-\langle J_{uv}\rangle^2$ is the dispersion of the system.

For the random spin lattices all physical and thermodynamical expectation values for correlation functions $\langle....\rangle_T$ must be averaged also by parameter J_{uv} with distribution function:

[a)]Permanent address: Yerevan Physics Institute, Yerevan 37503, Armenia

 0021-8979/94/76(10)/6186/3/$6.00 © 1994 American Institute of Physics

$$(\langle \ldots \rangle_T)_J = \int \langle \ldots \rangle_T \phi(J_{uv}) dJ_{uv}. \quad (3)$$

The thermal expectation in (3) is defined by $\langle \ldots \rangle_T = \lim 1/N \, \mathrm{Tr}(\ldots \exp[-\beta H])/\mathrm{Tr}(\exp[-\beta H])$, where we replace the infinite lattice with a finite one of linear dimension N with periodic boundary conditions and take the limit $N \to \infty$.

To prove the restrictions on the correlation functions we use unitary $U(1)$ gauge transformation $T(\theta) = \Pi \exp[\theta_i(S_{iz})]$, where θ is an arbitrary function on the hypercubic lattice, and the identity $\mathrm{Tr}[A \exp(-\beta H)] = \mathrm{Tr}[T(\theta) A T^{-1}(\theta)] \exp[-\beta T(\theta) H T^{-1}(\theta)]$ with $\beta = 1/T$. In the following[4] we also let $\theta = i\varphi$ be pure imaginary, and in this case the transformation is no longer unitary. To get upper bound for different correlation functions we also use some operator inequalities.[4-6]

The transverse susceptibility in the regular XY model, which is defined from the two-point correlation function, can be represented in the form

$$A_{ij} = \lim_{N \to \infty} 1/N \langle S_i^x S_j^x + S_i^y S_j^y \rangle_T \leq B_{ij}, \quad (4)$$

where upper bound $B(R)$ for two-point correlation function $A(R)$ at sufficiently large distances $R = i - j$ in regular lattices is defined by

$$B = \exp\left[-2 \ln R + 2T^{-1} \left(\sum_{uv} \left| J_{uv} [\cosh(\varphi_u - \varphi_v) - 1] \right| \right) \right]. \quad (5)$$

This expression depends on the exchange parameter J_{uv} and variables φ_u and φ_v, which are unique solution of Poisson equation $-\Delta \varphi_u = q(\delta_{x,v} - \delta_{y,u})$ on the hypercubic lattices and they satisfy the same conditions as in Ref. 4. The positive charge q is defined later from optimization condition and constants δ and L exist depending on parameters of the system and lattice dimensionality, so when for arbitrary u and v with $|u - v| \leq L$, $|\varphi_u - \varphi_v| \leq q\delta$.[6]

Correspondingly, for the XY spin glass model, the generalized susceptibility is defined by

$$\chi = \lim \frac{1}{2N} \sum_{ij} [\langle S_i^+ S_j^- + S_i^- S_j^+ \rangle_T^2]_J, \quad \text{when } N \to \infty, \quad (6)$$

and interesting two-point correlation function must be averaged by parameter J_{uv}. Then, using integral inequalities after a Gaussian integration with (2), we obtain the upper bound for correlation function for 2D random spin glass system:

$$[\langle S^+(R) S^-(0) + h.c. \rangle_T^2]_J \leq D \exp\left(-4 \ln R + 4T^{-2} \sum_{uv} \sigma_{uv} [\cosh(\varphi_u - \varphi_v) - 1]^2 \right). \quad (7)$$

Using the properties of the parameters φ_u and φ_v, we get a restriction on the expression $\alpha = \cosh(\varphi_u - \varphi_v) - 1$ and obtain the final upper bound relation for 2D spin glass correlation function, when $N \to \infty$ and $\varphi_R \geq q \ln R / 2\pi J$:

$$[\langle S^+(R) S^-(0) + h.c. \rangle_T^2]_J \leq D \exp[-f(T,Q) \ln R], \quad (8)$$

where

$$f(T,Q) = \frac{1}{2\pi} \left(Q - \frac{J^2}{4T^2} (\cosh Q - 1) \right).$$

The parameter D in (7) and (8) weakly depends on the temperature, which appears to be due to a Gaussian integration:

$$D = (2\pi\sigma)^{-1/2} \int dJ_{uv} \exp[-(J_{uv} - 2\sigma_{uv}\beta\alpha)^2 / 2\sigma_{uv}].$$

The expression $f(T,Q)$ depends on the effective dimensionless parameter $Q = 4q/J$. The optimization of the bound relation (7) by the parameter Q gives the condition

$$1 - \frac{J^2}{2T^2} \sinh Q \cdot (\cosh Q - 1) = 0. \quad (9)$$

The same type of calculations gives the upper bound for the 1D case, where $\varphi_r \geq qr/J$:

$$[\langle S^+(r) S^-(0) + h.c. \rangle_T^2]_J \leq D \exp[-f_1(T,Q) r], \quad (10)$$

where

$$f_1(T,Q) = 4Q - \frac{4J^2}{T^2} (\cosh Q - 1)^2.$$

The main result contained in Eqs. (8) and (9) does not depend on magnetic field and shows that when the parameter R goes to infinity the two-point correlation function for off-diagonal transverse magnetization goes to zero. This means that it is impossible to obtain a phase transition in 2D random lattices at any finite temperature and for an arbitrary value of magnetic field (local or uniform). On the other hand, the investigation of the upper bound in Eqs. (8) and (9) shows that the slowest possible decay at low temperatures is power-law like, which in principle does not exclude the possibility of a Kosterlitz–Thouless-like phase transition in 2D spin glass.[7] But in contrast to Ref. 7, the critical exponent $f(T)$ in (8) at low temperatures is proportional to T.[2/3] This means that in random lattices transverse magnetization of the correlation function decays faster than in regular spin lattices.[4,5] The indication about Kosterlitz–Thouless-like behavior can also be obtained from the comparison of changing characters for correlation functions under the temperature for upper bound correlation length of our system with those known for the classical XY model. Indeed, in both cases we have similar logarithmic behavior for correlation lengths at high temperatures. The correlation length, which is a power function at low temperatures and becomes logarithmic at high temperatures, apparently reflects a nonmonotonic variation of the thermodynamic state with the temperature.

On the other hand, from Eq. (8) one can obtain that in the zero field the upper bound for susceptibility diverges at low temperatures, when the corresponding critical exponent becomes less then 2. Such a behavior indicates the possibility of a certain phase transition similar to the Kosterlitz–Thouless-type, even in the random two-dimensional spin system at nonzero temperature.

Corresponding investigations in the 1D case from Eq. (10) show that the upper bound decays exponentially with

the distance, in spite of the fact that the high temperature behavior remains as in the 2D case with large spin. The obtained upper bounds do not exclude the possibility of some kind of long range ordering for a two dimensional random spin system at zero temperature. Corresponding lower bound relations until now have been obtained only for the regular Heiseberg–Ising-like 2D systems in the ground state.[8] It is believed that vector Heisenberg spin glasses with $n=3$ do not have an equilibrium phase transition in the 3D case, but that the observed experimental transitions result from small anisotropicity, which causes a crossover to an Ising-like transition. The approach suggested here is applicable for both randomness and long-range interaction simultaneously and can be used for investigations of critical behavior in the presence of the magnetic field for a large class of random spin quantum systems, which are invariant under the global rotation around the z axis.

Thus, the method developed for finding upper bounds gives results sharpening the Mermin–Wagner theorem for regular lattices as well as for a random system with long-range interactions.

One of us (A.N.K.) acknowledges support of the Union College Fund for Former Soviet/Eastern European Scholars established by an anonymous doctor.

[1] S. F. Edwards and P. W. Anderson, J. Phys. F **5**, 965 (1975).
[2] D. Sherrington and S. Kirpatrick, Phys. Rev. Lett. **35**, 1972 (1975).
[3] J. R. L. de Almeida and D. J. Thouless, J. Phys. A **11**, 983 (1978).
[4] T Koma and H. Tasaki, Phys Rev. Lett. **68**, 3247 (1992).
[5] A Kocharian and A. Sogomonian, Physica C **194–196**, 445 (1994)
[6] A. McBryan and T. Spencer, Commun. Math. Phys **53**, 299 (1977).
[7] J. M. Kosterlitz and D. J. Thouless, J. Phys. C **6**, 1181 (1973)
[8] T Kennedy, E. H Lieb, and B. Sriram Shastry, Phys. Rev Lett **61**, 2583 (1988).

Relaxation and spin correlations in ^{119}Sn-doped a-$Fe_{90}Sc_{10}$

D. Wiarda and D. H. Ryan
Centre for the Physics of Materials and the Department of Physics, McGill University, Rutherford Building, 3600 University Street, Montréal, Québec, Canada H3A 2T8

Combined ^{119}Sn and ^{57}Fe Mössbauer measurements have been made on a Sn-doped sample of a-Fe-Sc both around T_{sg} (117±2 K) to examine the onset of order, and at 12 K to investigate spin correlations. The different time scales probed by the Sn and Fe Mössbauer transitions allow us to confirm that cluster relaxation effects do not contribute to the ordering at T_{sg}, while the large transferred hyperfine field (B_{hf}) at the Sn sites, in an alloy known to exhibit isotropic spin freezing, is inconsistent with the simple view of the transferred field arising as a vector sum over the nearest-neighbor moments.

I. INTRODUCTION

Amorphous iron-rich Fe-Sc alloys are unique among the iron-rich early transition metal-iron glasses, in that they do not exhibit a strong dependence of the magnetic ordering temperature on composition.[1] In contrast to a-Fe_xZr_{100-x} where the ordering temperature drops from 260 K at $x=88$ to 160 K at $x=93$,[2] the ordering temperature in a-Fe_xSc_{100-x} is essentially constant at 105 K in the range $89 \leqslant x \leqslant 91$ accessible by melt spinning.[3] Examination of the scaling behavior of the susceptibility around T_{sg} indicates that the material is a borderline spin glass, just sufficiently frustrated to destroy the ferromagnetic order,[4] a result that is confirmed by in-field Mössbauer measurements[5] which show that the system directly enters a noncollinear state at T_{sg}, and does not pass through the intermediate ferromagnetic phase seen in less frustrated materials.[1] More recent magnetization measurements have demonstrated that the system does not exhibit a spontaneous moment at any temperature.[6] An alternative view of the ordering proposes the existence of superparamagnetic clusters, which block in random orientations at T_{sg}.[7] This seems extremely unlikely in view of the close agreement between χ_{ac}[4,8] and Mössbauer[3] determinations of the ordering temperature, measurements with vastly different characteristic time scales.[5]

We present here a combined ^{57}Fe and ^{119}Sn Mössbauer study of a ^{119}Sn-doped a-Fe-Sc alloy. The two Mössbauer measurements are made in the same way, and on the same equipment, thus eliminating instrumental and calibration differences; however, the lifetime of the ^{119}Sn excited state is a factor of 5.5 times shorter than that of ^{57}Fe, so that the two measurements probe very different time scales, allowing us to examine the possible role that cluster freezing may play in the ordering at T_{sg}. Furthermore, as Sn has no local moment, the transferred hyperfine field at the ^{119}Sn nuclei contains information about the magnetic correlations among the neighboring Fe moments.

II. EXPERIMENTAL METHODS

Ingots for melt spinning were prepared in an arc furnace under titanium-gettered argon. The Sc (99.9%) was first premelted and then alloyed with the ^{119}Sn. Enriched ^{119}Sn (isotopic purity 82.9%) was used in order to get ~8 mg ^{119}Sn per 1 g sample weight and ensure a convenient absorption in the ^{119}Sn spectra. The Sc-Sn alloy was then added to an appropriate quantity of Fe (99.98%), and melted several times to ensure homogeneity. Melt spinning was done under a helium atmosphere onto a copper wheel, and yielded ribbons ~1 mm wide and ~10 μm thick. The amorphous structure of the sample was verified by x-ray diffraction and room-temperature Mössbauer spectroscopy. Differential scanning calorimetry showed that the crystallization temperature for this material was 810 K, close to the value of 822 K reported for a-$Fe_{90}Sc_{10}$,[3] confirming that the addition of 1% Sn does not significantly affect the glass. The amorphous ribbons were mounted on tape in order to make a Mössbauer absorber. A single thickness was used for the ^{57}Fe spectra while six layers were used for the ^{119}Sn measurements. The Mössbauer spectra were taken using a conventional constant acceleration spectrometer with a ^{57}CoRh source for the ^{57}Fe spectra and a $Ca^{119}SnO_3$ source for the ^{119}Sn spectra. The temperature was varied by means of a vibration-isolated closed-cycle He cryostat.

The ^{57}Fe spectra were fitted using two Gaussian distributions to describe the hyperfine field distribution. For the ^{119}Sn spectra a single Gaussian distribution with different widths on the low- and high-field side of the peak field was used. As the sample is an amorphous ribbon, the relative intensity of lines 2 and 5 cannot be fixed *a priori* to its powder average value. Therefore it was fitted in the ^{57}Fe spectra and then set to 2 (the value found in the fits to the ^{57}Fe spectra) for the ^{119}Sn spectra. A linear correlation between the isomer shift and the hyperfine field was assumed in order to fit the slight asymmetry in the spectra.

III. RESULTS AND DISCUSSION

A conventional method for determining magnetic ordering temperatures is to record the transmitted intensity of Mössbauer radiation at zero velocity as a function of temperature. As the spectrum broadens at T_{sg}, the peak absorption falls, and the zero-velocity count rate increases. The data for the ^{57}Fe thermal scan are shown in Fig. 1. T_{sg} is identified with the marked change in slope at 119±1 K. The procedure has to be modified for ^{119}Sn as the isomer shift displaces the peak absorption above T_{sg} to +1.8 mm/s relative to the source at rest. The spectrometer is therefore run at a constant velocity chosen to maximize the absorption at room temperature, and the observed drift in count rate on cooling above

 0021-8979/94/76(10)/6189/3/$6.00 © 1994 American Institute of Physics

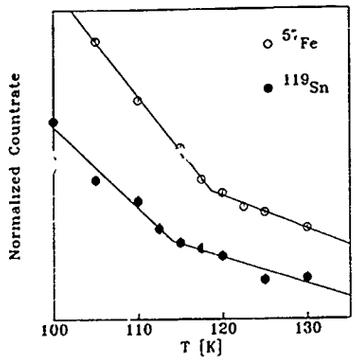

FIG. 1. Mossbauer thermal scans for a-$Fe_{90}Sc_9Sn_1$ at zero velocity for ^{57}Fe (○) and at ~1.8 mm/s for ^{119}Sn (●), showing the discontinuity at T_{sg}.

T_{sg} seen in Fig. 1, is due to the spectrum center moving as a result of the second-order Doppler shift. A clear break in slope is observed at 114±2 K.

Given that ^{119}Sn samples on a shorter time scale than ^{57}Fe, we would expect the Sn data to give a significantly higher ordering temperature if blocking of superparamagnetic clusters were the origin of the magnetic order. Such clusters would appear frozen at higher temperatures when observed at higher frequencies. However, the two Mössbauer measurements yield the same ordering temperature within error (it is interesting to note that the Sn value is actually slightly lower, rather than significantly higher). Assuming that T_{sg} does reflect a blocking of superparamagnetic clusters, we can calculate the energy barrier for magnetization reversal[9] and thus the change in blocking temperature on going from ^{57}Fe to ^{119}Sn. This calculation indicates that the ^{119}Sn transition would be at ~150 K if such a model were appropriate, rather than 114 K as observed. We can therefore rule out relaxation effects or cluster blocking as contributing to the ordering of a-Fe-Sc.

Unlike earlier work on Sn-doped a-Fe-Zr which showed no effect of the Sn additions on the magnetic ordering temperature,[10] the Sn-doped sample does exhibit a slightly higher ordering temperature than that of earlier materials; however, we do not believe that the ~14 K increase reflects a significant modification of the magnetic structure. The most convenient way to modify the magnetic properties of a-Fe-Sc is to add hydrogen. This leads to profound changes in both T_c (rises to ~310 K) and the iron moment (increases to $\sim 2.2\mu_B$, the average hyperfine field rises to 31.3 T),[3] but the material still lacks the critical behavior characteristic of a ferromagnet.[4] Therefore it seems reasonable to conclude that if a 200 K increase in T_c leaves the system still in a strongly spin-glass like state, a 14 K increase will have negligible effects on the magnetic structure.

The Mössbauer spectra obtained at 12 K for the two transitions are shown in Fig. 2. Both are clearly magnetically split, reflecting the ordering of the iron moments. The fit to the ^{57}Fe spectrum yields an average hyperfine field of 22.8 T, indistinguishable from previous values obtained on Sn-free materials,[3,5] and further reinforcing the view that the addition of Sn has not significantly affected the magnetic ordering. Curiously, the ^{119}Sn spectrum also yields a large average

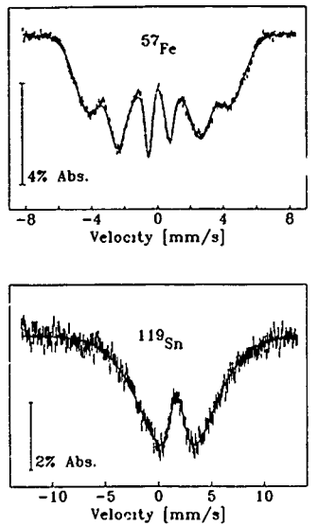

FIG. 2 Mossbauer spectra measured at 12 K a-$Fe_{90}Sc_9Sn_1$ for ^{57}Fe (top) and ^{119}Sn (bottom).

field: 5.1±0.2 T. If the local magnetic order were essentially isotropic, as would be expected in a spin glass, the contributions from the neighboring Fe moments would be random and therefore largely cancel at a Sn site. Such a situation would then yield a small ratio between the observed transferred Sn field and the Fe field (assumed proportional to the Fe moments). The value obtained here is 0.22±0.01, essentially the same as that found in the less frustrated a-$Fe_{92}Zr_7Sr_1$ (Ref. 10) and the almost ferromagnetic a-$Fe_{90-x}Ni_xZr_9Sn_1$.[11] Assuming that the transferred field at the ^{119}Sn results from a vector sum over the moments on the Fe nearest neighbors, and that the coordination number in the glass is ~12, then going from fully collinear to isotropic order should lead to a factor of 4 drop in the Sn/Fe hyperfine field ratio, a prediction that is completely inconsistent with our observations. Similar measurements on Mn-containing spin glasses[12,13] have also reported large transferred fields, leading to the rather unlikely speculation that the spin glass is dominated by significant ferromagnetic short-ranged correlations.[13] Since it is highly unlikely that the addition of 1 at % Sn makes the a-Fe-Sc alloy essentially ferromagnetic, without increasing either T_c or the iron moment, we are forced to conclude that even in an isotropically ordered material (i.e., a spin glass), the ^{119}Sn nuclei measure the magnitude of the average iron moment, rather than the vector sum of the randomly oriented neighboring moments.

[1] D H Ryan, in *Recent Progress in Random Magnets*, edited by D. H. Ryan (World Scientific, Singapore, 1992).
[2] D H Ryan, J. M. D. Coey, E Batalla, Z. Altounian, and J. O. Strom-Olsen, Phys Rev. B **35**, 8630 (1987)
[3] D. H. Ryan, J. O. Strom-Olsen, W. B. Muir, J. M Cadogan, and J. M. D. Coey, Phys. Rev. B **40**, 11208 (1989).
[4] H. Ma, Z. Wang, H P. Kunkel, G. Williams, D. H. Ryan, and J O Strom-Olsen, J. Magn. Magn. Mater. **104-7**, 89 (1992).
[5] Hong Ren and D H. Ryan, J. Appl. Phys. **73**, 5494 (1993)
[6] Hong Ren and D H. Ryan (unpublished).
[7] M. Ghafari, R K Day, J. B. Dunlop, and A. C McGrath, J Magn. Magn. Mater **104-7**, 1668 (1992).

[8]R. K. Day, J. B. Dunlop, C. P. Foley, M. Ghafari, and H. Pask, Solid State Commun **56**, 843 (1935).
[9]D. H. Jones, Hyp. Int. **47**, 289 (1989).
[10]Hong Ren and D. H. Ryan, Phys. Rev. B **47**, 7919 (1993).
[11]D. Wiarda and D. H. Ryan (these proceedings).
[12]B. Window, J. Phys C **2**, 2380 (1969).
[13]V. Drago, E. Baggio-Saitovitch, and M. M. Abd-Elmeguid, Hyp. Int. **51**, 1061 (1989).

Field-dependent susceptibility aging in CuMn spin glasses

P. W. Fenimore and M. B. Weissman
Department of Physics, University of Illinois at Urbana–Champaign, 1110 West Green Street, Urbana, Illinois 61801-3080

A "hole" is found to develop in the dc field-dependent ac susceptibility of CuMn spin glasses when the material is cooled or aged in a field. Comparisons are made with analogous experiments on structural glasses at low temperature. The hole is not compatible with independent two-level systems. The significance of the width (in H) of this hole is discussed.

Recent work on aging of the ac dielectric susceptibility $\epsilon(f)$ in several dissimilar insulating glasses found that a "hole" can form in $\epsilon(f)$ versus applied dc electric field **E** when the dielectric is aged in an electric field at low temperatures for times in the range 10^3–10^5 s.[1] The detailed time and frequency dependence of this hole has been shown to be inconsistent with a model consisting of a simple superposition of quantum two-level systems (TLS).[2] The most plausible source of such aging effects lies in multistate relaxations, such as those responsible for the well-known (but not well understood) large aging effects in spin glasses.[3] In this paper we describe experiments, analogous to the dielectric experiments, on the time and magnetic field dependence of the magnetic susceptibility, $\chi(f)\equiv\chi'(f)+i\chi''(f)$, in metallic spin glasses.

Spin glasses are good candidates for these experiments for several reasons. (i) Previous work has clearly established that there are large aging effects below the spin-glass temperature.[3] (ii) In metallic spin glasses there is almost certainly a continuous phase transition at the spin-glass freezing temperature T_G,[4] which provides a well-defined energy scale for interactions in spin glasses. Since the low-temperature excitations of the structural glasses do not have a known phase transition, an appropriate energy scale for interactions in glasses is unclear. (iii) Spin-glass experiments may be conducted in the classical (high-temperature) regime. Dielectric aging has been studied in the tunneling regime and comparison with spin glasses should shed light on the importance of quantum mechanical effects.

We have examined CuMn with 4 at. % Mn and 12 at. % Mn and CuMnAu with 4 at. % Mn and 1 at. % Au. We have also measured a CuSiMn (4.2 at. % Si, 0.3 at. % Mn) sample as a control. The spin-glass temperature of the control sample is lower than the temperature range in which we took data (T_G<5 K). The 4% samples are cylindrical and have two overlapping cuts along their length to reduce the contribution to χ'' from eddy currents.[5] The 12% sample is a small segment of an annulus about 2 cm in radius. The overall dimensions of this sample are comparable to the 4% samples. The control sample is a ~1-cm-long section of the body of a silicon-bronze screw. All the samples have masses near 1 g. The measurements were made in a 1 T commercial (Quantum Design) ac susceptometer. The measurements were made at 3 Hz, about the highest frequency (allowing fastest data collection) for which the eddy current background could be accurately subtracted.

The spin glass is initially field cooled (usually at 300 Oe) from $\sim 2T_G$ to a working temperature below T_G. A non-zero cooling field is used to make sure that the effects of equilibrating at a particular field are not confused with any special properties of $H=0$. The fields used were always small enough to stay the strongly irreversible spin-glass regime at the measurement temperature.[5] The sample is then aged at that field for about 5000 s. The field is then changed to a new (second) field for a few minutes, during which time the initial values of χ' (3 Hz) and χ'' (3 Hz) are measured. The applied field is then changed back to its initial value and the sample is allowed to age before the next measurement is performed. By repeating this **H**-cycling procedure, all at fixed T, we make a map of initial χ vs **H**. Since, empirically, this map does not depend substantially on the order in which we cycle to the measurement fields, long-term distortion of the curve caused by the field history at the measuring temperature does not seem to be a problem.

All three of these spin glasses show a substantial hole in $\chi(f,H)$ versus magnetic field (H) (see Fig. 1). To a first approximation, the center of the hole is simply shifted by cooling in different fields. The hole in $\chi(f,H)$ for these SGs is short lived, compared with the lifetime of the hole in $\epsilon(f,E)$ of structural glasses (except SiO_2).[1] (Because of this effect slow scans of the applied field are not feasible.)

The hole depth for χ'' is ~30% of the initial value of χ'' and for χ' it is ~3% of the initial value. These numbers contrast with the structural glasses where the hole depth in ϵ' is only ~0.1%. Monitoring χ'' allows us to separate slow, relaxational spin dynamics from fast spin dynamics (e.g., spin dynamics near the attempt rate) that contribute to χ'. This is important because there is no guarantee that the

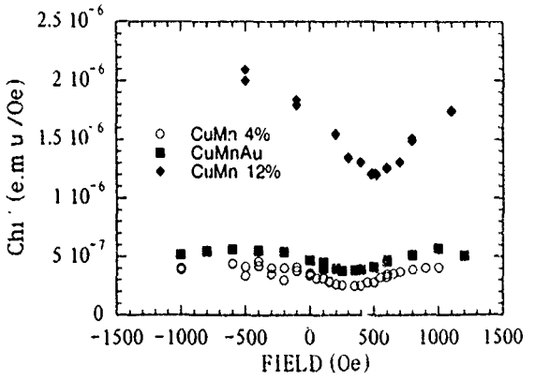

FIG. 1 The hole in χ'' vs field for three different spin glasses at $0.5T_G$. The measurements were made at 3 Hz

 0021-8979/94/76(10)/6192/3/$6.00 © 1994 American Institute of Physics

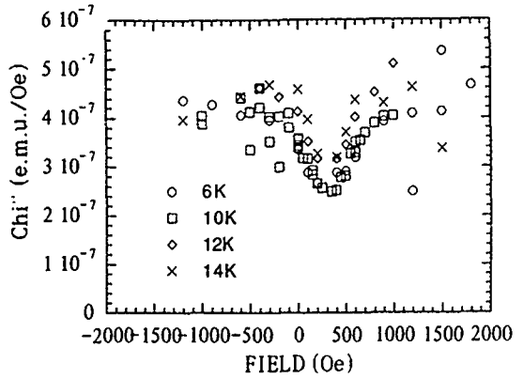

FIG. 2. The hole in χ'' vs field for four temperatures in CuMn 4 at. % Mn. The data were taken at 3 Hz.

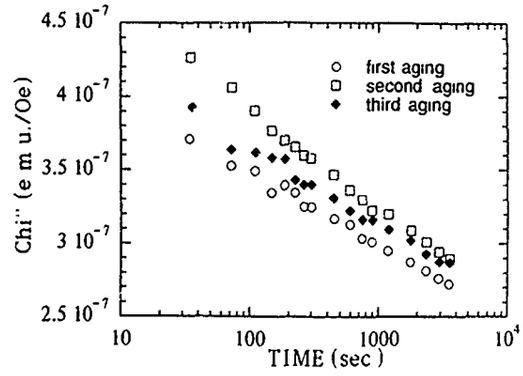

FIG. 3. Time dependence of the relaxation of χ'' in CuMn 4 at. % Mn at 10 K. The data were taken at 3 Hz.

"fast" spin dynamics have the same aging properties as those near 1 Hz.

The width of the hole in χ'' is ~300 Oe at 10 K and is slightly narrower at higher temperatures (see Fig. 2). The weak T dependence of this width, from 0.3 to $0.7T_G$, contrasts with the strong temperature dependence of the $\epsilon(f,\mathbf{E})$ hole between 50 and 500 mK.[1]

For sufficiently large ΔH (~300 Oe), the increase in χ saturates, indicating that nearly all the spin configurations whose fluctuations give χ'' (3 Hz) are sufficiently changed by fields of ~300 Oe to cease to contribute to χ'' (3 Hz). That is, by changing H by 300 Oe, one sees a different set of fluctuators, ones which have not had a chance to relax to the smaller values of χ'' (3 Hz). Further change of H simply gives a different set of new fluctuators, which are still not aged.

One expects that H has little effect on the dynamics of active spin clusters until $\mu\Delta H$ becomes greater than k_BT, where μ is the net magnetic moment of the rearranging spin cluster. (When, however, $\mu\Delta H > k_BT$, a new set of fluctuating objects will be responsible for χ''.) Since the net moment of a spin cluster in a spin-glass scales as the square root of the number of spins, and since a Mn ion in Cu has a moment about $2\mu_B$, the characteristic number of spins involved in the clusters as $\mathbf{H}$ is changed is about 10^5 at 10 K. This number of spins is fairly constant in the samples we have examined. However, the relations among this number, the number of spins involved in individual coherent thermal flips at fixed H,[6] and the number of spins which are within a volume throughout which such coherent groups interact[6] are not yet clear to us.

If instead of briefly visiting other fields and building up a map of initial, unaged χ vs $\mathbf{H}$, we field cool in $+\mathbf{H}_1$, age the sample, change to $-\mathbf{H}_1$ and allow the sample to age further, we can see the long time behavior of the hole. The relaxations are roughly logarithmic in time (Fig. 3). Observing this second relaxation (and also a third relaxation, this time back at $+\mathbf{H}_1$) allows us to compare the field-cooled behavior with field-jump behavior.

For equal aging times the second aging does not reach as low a χ'' value as the first. Even a brief excursion from the field cooled $+\mathbf{H}_1$ to $-\mathbf{H}_1$ mostly resets the (third) aging of χ'' on return to $+\mathbf{H}_1$. Nonetheless, at long times the third aging (at $+\mathbf{H}_1$) is intermediate to the first and second, indicating that some small part of the $+\mathbf{H}_1$ hole survives to long times at $-\mathbf{H}_1$.

In contrast, the aging of χ' at $+\mathbf{H}_1$ is not mostly restarted by brief excursions to $-\mathbf{H}_1$ (see Fig. 4). For times shorter than about 1000 s at $-\mathbf{H}_1$, the initial χ' on return to $+\mathbf{H}_1$ is still lower than any value of χ' recorded at $-\mathbf{H}_1$. We assume that this behavior indicates that the very fast relaxations which contribute substantially to χ' age in a very different way than the clusters responsible for χ''.

In conclusion, conventional spin glasses in a classical temperature regime show field-dependent aging effects similar to those of structural glasses in the quantum regime. The spin-glass susceptibility holes, however, are deeper than those of the structural glasses, and generally show more rapid relaxation. Our results strongly reinforce the theoretical conclusion[2] that the main explanation of dielectric aging will be found in multisite cooperative effects, such as are known to be present in spin glasses, rather than in the simple TLS picture.

Several prior pieces of evidence strongly support this view. The decay in $\epsilon'(f)$ is very strongly dependent on f.[1] Thus the frequency dependence of ϵ' strongly ages. Since,

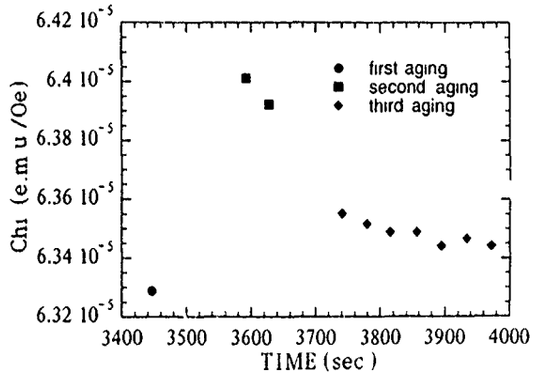

FIG. 4. χ' vs time for CuMn 4 at % Mn at 10 K. The data point at early times is in the first part of the aging. Note that χ' drops between the second and third aging fields. The data were taken at 3 Hz.

by Kramers–Kronig, the frequency dependence of ϵ' is essentially ϵ'', ϵ'' must also show very strong aging effects (as does χ'' in spin glasses). At frequencies much less than the attempt rate, it is very unlikely that χ'' or ϵ'' comes from anything other than relaxational effects (i.e., tunneling processes at low temperature and activated processes at higher temperatures). Since a simple noninteracting two-state system with a characteristic rate comparable to the measurement frequency does not have some other longer time associated with it, it cannot produce a slowly aging χ'' or ϵ''.

It is known from fluctuation experiments in mesoscopic samples of metallic glasses that their low-temperature structural fluctuations (in both the tunneling and activated regimes) are not strictly two-state systems.[7] Interactions lead to slow fluctuations in the characteristic rate and duty cycle of the individual (configurational) fluctuations. These fluctuations are probably the equilibrium analog of the dielectric aging. Since the detailed properties of the fluctuators vary over long times, one expects long time relaxations into configurations with minimal free energy. Unless some unexpected symmetry precludes average differences in susceptibility between the high free-energy configurations and the minimum, the susceptibilities will slowly relax. The sign of the relaxation (toward lower susceptibilities) is consistent with a simple correlation: the barrier heights seen from a low free-energy configuration tend to be higher than those seen from a high free-energy configuration, as would be expected if energies of the transition states did not differ from each other. It is probably no coincidence that similar mesoscopic experiments on CuMn show extremely strong interactions, to the point that nothing like two-state systems exists,[6] and that CuMn shows much stronger aging effects.[3]

In the mesoscopic noise experiments on amorphous metals, a whole new set of fluctuating objects could be obtained by thermal cycling to ~50 K and back,[7] just as a whole new fluctuation pattern can be obtained by cycling a mesoscopic spin glass to T_G.[6] If the analogy between interacting TLS in amorphous materials and interacting spins in spin glasses turns out to be meaningful, then the ~100 mK temperature scale of the dielectric hole measurements probably corresponds to a similar low temperature in the spin-glass experiments. It will be interesting to investigate whether the quantitative differences between the aging in the two types of systems are primarily the result of this different experimental temperature scale or of some more fundamental factor, such as the strength of the interactions versus the local energy asymmetries. At any rate, the quantum mechanical nature of the TLS does not seem to be an essential aspect of the aging.

This work was supported by NSF DMR-93-05763, using facilities of the MRL (NSF DMR-89-20538). We thank M. B. Salamon and L. J. P. Ketelson for two of the samples.

[1] S. Rogge, D. J. Salvino, B. Tigner, and D. D. Osheroff, Physica B **194-196**, 407 (1994).
[2] H. M. Carruzzo, E. R. Grannan, and C. C. Yu (unpublished).
[3] M. Lederman, R. Orbach, J. Hammann, M Ocio, and E. Vincent, Phys. Rev. B **44**, 7403 (1991).
[4] K. H. Fischer and J. A. Hertz, *Spin Glasses* (Cambridge University Press, Cambridge, 1991).
[5] L. J. P. Ketelsen and M. B. Salamon, Phys. Rev. B **33**, 3610 (1986).
[6] M. B. Weissman, Rev. Mod. Phys. **65**, 829 (1993); N. E. Israeloff, G. B. Alers, and M. B. Weissman, Phys Rev. B **44**, 12613 (1991); M. B. Weissman, N. E. Israeloff, and G. B. Alers, J Magn. Magn Mater **114**, 87 (1992).
[7] G. A. Garfunkel, G. B. Alers, and M. B Weissman, Phys. Rev. B **41**, 4901 (1990).

Quantum tunneling in magnetic particles (invited) (abstract)

D. P. DiVincenzo
IBM Research Division, T. J. Watson Research Center, P.O. Box 218, Yorktown Heights, New York 10598

Recent advances both in materials preparation techniques for ultrafine magnetic particles, and in low-temperature magnetometry, have made possible the observation of a new kind of collective quantum-mechanical phenomenon. In our studies[1] of horse-spleen ferritin particles (naturally occurring 75 Å iron-oxide crystallites), a resonance in the magnetic susceptibility is observed at low temperature (<200 mK) and exceedingly low ambient magnetic fields (of order 10^{-3} Gauss and below). I will discuss the accumulation of evidence which indicates that this resonance arises from the quantum tunneling of the magnetization between the ferritin particles's two easy-axis states. This involves a unique collective effect: the orientation of the thousands of spins in the particle flip over as a unit, passing through an energy barrier. I will discuss various new theoretical results which have been stimulated by these recent experiments. For example, quantum mechanics predicts that the tunneling behavior is radically different for particles with even and odd number of iron atoms,[2]—in particular, tunneling is predicted to be forbidden in the odd case. Finally, I will discuss the possibilities for quantum effects in a new class of nanoscopic Fe particles, produced by a novel STM deposition technique by A. Kent. It is clear that new materials preparation techniques will continue to provide novel testing grounds for quantum theory.

Work done in collaboration with D. D Awschalom, J. F. Smyth, G. Grinstein, D. Loss, and E. Chudnovsky.

[1] D. D. Awschalom, J. F. Smyth, G. Grinstein, D. P. DiVincenzo, and D. Loss, Phys. Rev. Lett. **68**, 3092 (1992); **71**, 4276(E) (1993)
[2] D Loss, D. P DiVincenzo, and G. Grinstein, Phys. Rev. Lett. **69**, 3232 (1992).

 0021-8979/94/76(10)/6195/1/$6.00 © 1994 American Institute of Physics

Remanent magnetization of AgMn spin glasses (abstract)

Emily Engle and E. Dan Dahlberg
School of Physics and Astronomy, University of Minnesota, Minneapolis, Minnesota 55455

Plots of the dc demagnetization remanence, I_d, versus the isothermal remanent magnetization, I_r, have been used to determine the presence of interactions in concentrated magnetic systems.[1] In terms of interacting entities within the system, the standard interpretation of these plots is that positive (negative) curvature indicates the presence of demagnetizing (magnetizing) interactions between the magnetic entities.[2,3] We will report the first such analysis made on a spin glass (the archetypal spin glass system AgMn, with three Mn concentrations). As prescribed, I_d and I_r were normalized and plotted against each other. All of the plots of zero-field quenched specimens have positive curvature, indicating the presence of demagnetizing interactions. In these measurements the sample shape dependent demagnetizing field was not a factor because the magnetizing field was applied parallel to the long axis of the foils (0.50 in. × 0.15 in. ×~0.005 in.). These results are consistent with a recent model for slow relaxation[4] wherein interactions, not disorder, determine the quasilogarithmic time dependence of relaxation processes in these systems.

This work is supported by the Air Force Office of Scientific Research, Grant No. AF/FA9620-92-J-0185

[1] O Henkel, Phys. Status Solidi **7**, 919 (1964).
[2] E. P Wohlfarth, J. Appl. Phys. **29**, 595 (1958).
[3] M. Fearon, R. W. Chantrell, and E. P. Wohlfarth, J Magn. Mater. **86**, 197 (1990).
[4] D. K. Lottis, R. M. White, and E. D. Dahlberg, Phys Rev. Lett. **67**, 362 (1991).

 0021-8979/94/76(10)/6196/1/$6.00 © 1994 American Institute of Physics

Calculated field cooled and zero field cooled magnetizations of the three-dimensional Ising spin glass using Monte Carlo hard-spin mean-field theory (abstract)

Edwin A. Ames and Susan R. McKay
Department of Physics and Astronomy, University of Maine, Orono, Maine 04469-5709

We have studied the ±J Ising spin glass in a uniform magnetic field by using Monte Carlo hard-spin mean-field theory,[1] implemented on a 24×24×24 lattice with periodic boundary conditions. This method modifies the conventional mean-field approach to retain frustration by placing a spin of unit magnitude at each nearest neighbor. Each spin's direction is chosen using the hard spin condition, which preserves the site's average magnetization. The method yields an average magnetization at each site and permits the exploration of stable and metastable states within the spin-glass phase and their overlaps. By direct calculation of the free energy of each final state, stability and metastability can be distinguished. The resulting average magnetizations display realistic history dependence. For example, the calculated field cooled magnetization remains roughly constant below the freezing temperature, T_g, whereas the zero field cooled magnetization rises to a cusp as temperature is increased below T_g, as is observed experimentally. Aging phenomena are also reproduced within this method, since varying the number of Monte Carlo steps at each temperature and field corresponds to altering the waiting time.

[1] R. R. Netz and A. N. Berker, Phys. Rev. Lett. **66**, 377 (1991); J. Appl. Phys. **70**, 6074 (1991).

 0021-8979/94/76(10)/6197/1/$6.00 © 1994 American Institute of Physics

Giant magneto-impedance and magneto-inductive effects in amorphous alloys (invited)

L. V. Panina, K. Mohri, K. Bushida,[a] and M. Noda
Department of Electrical Engineering, Nagoya University, Nagoya 464, Japan

Recent experiments have discovered giant and sensitive magneto-impedance and magneto-inductive effects in FeCoSiB amorphous wires. These effects include a sensitive change in an ac wire voltage with the application of a small dc longitudinal magnetic field. At low frequencies (1–10 kHz) the inductive voltage drops by 50% for a field of 2 Oe (25%/Oe) reflecting a strong field dependence of the circumferential permeability. At higher frequencies (0.1–10 MHz) when the skin effect is essential, the amplitude of the total wire voltage decreases by 40%–60% for fields of 3–10 Oe (about 10%/Oe). These effects exhibit no hysteresis for the variation of an applied field and can be obtained even in wires of 1 mm length and a few micrometer diameter. These characteristics are very useful to constitute a highly sensitive microsensor head to detect local fields of the order of 10^{-5} Oe. In this paper, we review recently obtained experimental results on magneto-inductive and magneto-impedance effects and present a detailed discussion for their mechanism, developing a general approach in terms of ac complex impedance in a magnetic conductor. In the case of a strong skin effect the total wire impedance depends on the circumferential permeability through the penetration depth, resulting in the giant magneto-impedance effect.

I. INTRODUCTION

Recently, much work has been done on giant magnetoresistance because of its importance for applications in various magnetic sensors and especially in magnetic heads for recording. The problem, however, is not well understood, and experimental results are far from practical applications, as the effect is observed at rather high magnetic fields and suffers strong hysteresis. On the other hand, giant and sensitive magneto-inductive (MI) and magneto-impedance (**MI**) effects have been found in soft magnetic FeCoSiB amorphous wires[1–6] and ribbons.[7,8] These effects include a sensitive change in an ac voltage in these materials with the application of a small dc magnetic field, and are thus an ac analog of giant magnetoresistance. The effects have been reported to be the strongest for an amorphous wire of a composition $Fe_{4.3}Co_{68.2}Si_{12.5}B_{15}$. In a low frequency range of 1–10 kHz, which is typical of the MI effect, the inductive component of an ac wire voltage decreases by 50% for a longitudinal field of 2–5 Oe. At higher frequencies (0.1–10 MHz) where the skin effect is essential the giant **MI** effect occurs: the amplitude of the total wire voltage decreases by 40%–60% under the influence of a longitudinal field of 3–10 Oe. No hysteresis has been observed. The giant MI and **MI** effects can be observed in wires with a few micrometer diameter and 1 mm length. These results suggest establishing a new microsized sensitive magnetic head and a sensor head for information storage devices.

In this work we present a comprehensive study of the MI and **MI** effects in FeCoSiB amorphous wires including both a brief review of the recently obtained experimental results and their analysis on the basis of the ac complex impedance of a magnetic wire with a domain structure. Some new results for FeCoMoSiB amorphous ribbons are presented as well. We demonstrate that both effects have a classical electromagnetic origin and, hence, are not connected with the conventional magnetoresistance. All the experimental data can be explained in terms of a field dependence of impedance as a result of the transverse magnetization (with respect to current direction) and the skin effect.[6,9–11] In general, large and giant magneto-impedance effects are possible in many other soft magnetic materials of various geometries.

Because of the skin effect, an ac current, $I=I_0\exp(-j\omega t)$, tends to be concentrated near the surface of a conductor, changing its impedance $\hat{Z}$. The current distribution depends not only on the shape of the conductor and frequency but also on the transverse permeability μ. If μ is a sensitive function of an external field H_{ex} in a high frequency region this dependence reveals itself in the impedance behavior through the penetration depth, resulting in a sensitive voltage response: $V(\omega,H_{ex})=\hat{Z}[\omega,\mu(\omega,H_{ex})]I$. At low frequencies, when the skin effect is negligible, the first order term in an expansion of $\hat{Z}(\omega)$ in powers of frequency is responsible for the voltage field dependence. This term is represented by the internal inductance, which is proportional to the static transverse permeability. The general approach of impedance is thus helpful to explain both the low and high frequency field effects on ac voltage.

An FeCoSiB amorphous wire can be considered as one of the most suitable material to observe the magneto-impedance effects. It has fine soft magnetic properties because of its nearly zero magnetostriction constant $\lambda\cong-10^{-7}$. The negative magnetostriction results in a circumferential anisotropy and, consequently, a domain structure with circu

[a]Unitika Ltd. R & D, Uji 611, Japan.

 0021-8979/94/76(10)/6198/6/$6.00 © 1994 American Institute of Physics

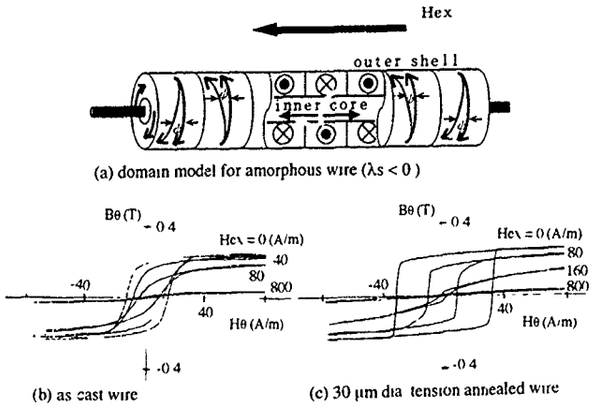

FIG. 1 Magnetic structure (a) and circular hysteresis loops (b), (c) of FeCoSiB amorphous wires in the presence of a longitudinal field.

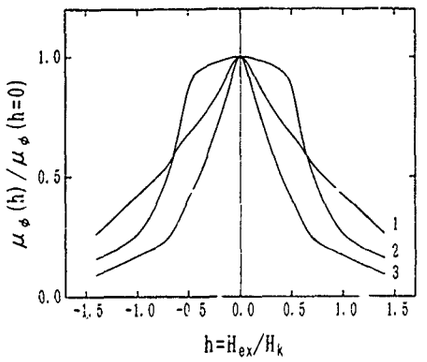

FIG. 2. Theoretical dependencies (obtained on the basis of hysteresis loop calculations, Ref. 9) of the maximal circumferential permeability on a reduced longitudinal field $h=H_{ex}/H_K$. The anisotropy axis deviations $2\Delta\alpha$ are: 1—45°, 2—10°, 3—20°.

lar domains situated along the wire. The current flowing through the wire generates an easy axis driving field which causes a circular magnetization by the domain wall movement. The external longitudinal field H_{ex}, being a hard axis field with respect to the circular magnetization, suppresses the circular flux change. As a result, the circumferential permeability having a high value of the order of 10^4 for $H_{ex}=0$, decreases rapidly with the application of the field. This sensitive field dependence of the circumferential permeability, which maintains till high frequencies at which the skin effect is essential (but the domain wall motion is not completely damped by eddy currents), is responsible for the magneto-impedance effects in wires.

This paper is organized as follows: In Sec. II we review the existing experimental and theoretical results on the static magnetic properties of negative magnetostrictive amorphous wires since they eventually determine the field dependence of the impedance. In Sec. III the experimental magneto-inductive and magneto-impedance characteristics recently obtained by the present authors are summarized. For comparison, new data for FeCoMoSiB amorphous ribbons are presented. In Sec. IV the concept of the magneto-impedance effect is put forward. In Sec. V the calculated magneto-impedance characteristics for wires are presented, and the analysis of the experimental results is given, showing a reasonable agreement.

II. STATIC MAGNETIC PROPERTIES OF FeCoSiB AMORPHOUS WIRES

The magnetic structure of amorphous wires made by rapid quenching process is dominated by stress induced anisotropy.[12–14] In the case of negative magnetostrictive wires ($\lambda<0$), the stress distribution results in a core and sheath magnetic structure with magnetization parallel to the wire axis in the inner core and circular in the outer shell. The corresponding magnetic structure with ring domains spaced along the wire is shown in Fig. 1(a). This structure is retained even for slightly negative ($\lambda=-10^{-7}$) magnetostrictive wires of a composition $Fe_{4\,3}Co_{68\,2}Si_{12\,5}B_{15}$ which are used in the present investigation without loss of generality.

An as-cast wire has a diameter of 120 μm. Smaller diameter wires (down to 30 μm) can be obtained by cold drawing an as-cast one and then tension annealing. During tension annealing a higher circumferential anisotropy is induced. For a relatively high annealing tension (>2 kg/mm^2) the circumferential magnetization is considered to exist in the entire wire However, the effective anisotropy field H_K is still very small (~1 Oe). If the wire is shortened down to 1–3 mm, H_K increases due to the demagnetizing effect and is about several Oe. The length effect on the anisotropy is much stronger for as-cast wires.

The circumferential anisotropy allows the wire to be magnetized by flowing through it a current which creates a circular easy axis driving field H_φ. The circular magnetization proceeds mainly by the movement of circular (or ring) domains along the wire, resulting in a sharp hysteresis with the maximum of the differential permeability of the order of 10^4 for a 1 kHz current (see Fig. 1). Then a sensitive circumferential magnetic flux change can be made to occur due to a small ac wire current. The magnetic field H_{ex} applied along the wire axis suppresses the circular magnetization by wall movement, since H_{ex} is a hard axis field with respect to the circumferential anisotropy. As H_{ex} is increased and the rotational portion of the remagnetization grows, there is a gradual transition from almost a square loop to a linear one[1–3] as can be seen in Fig. 1. This process is accompanied by rapid reduction in the circumferential permeability μ_φ. In Ref. 9 the change in hysteresis loops under the influence of H_{ex} was considered for a practical case of a nonuniform circumferential anisotropy. The result for the maximal differential permeability as a function of H_{ex} for different averaged anisotropy axis inclinations, $\Delta\alpha$, relative to the circular direction, is presented in Fig. 2. For some optimum values of $\Delta\alpha$, the permeability sensitively decreases with increasing h for $h=H_{ex}/H_K<1$. For higher fields ($h>1$) corresponding to the longitudinal saturation, the permeability slowly decreases, being consistent with the pure rotational magnetization. The proper anisotropy can be established by corresponding tension annealing.[3]

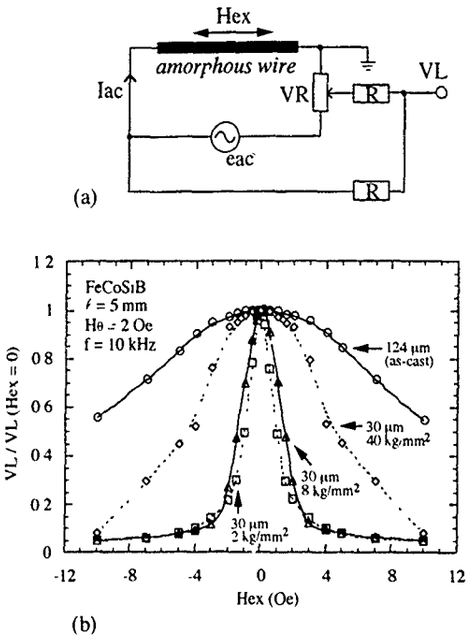

FIG. 3. Experimental circuit for measurement of V_L (a), and reduced amplitude of that voltage plotted as a function of H_{ex} for as-cast and tension annealed amorphous wires (b)

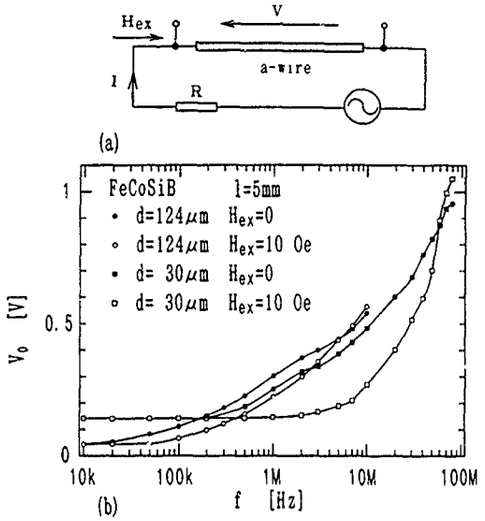

FIG. 4. Experimental circuit (a) and measured frequency dependencies of the voltage amplitude with H_{ex} as a parameter for a 124 μm diameter as-cast wire and a 30 μm diameter tension annealed wire (b).

III. EXPERIMENTAL RESULTS

The unique circumferential magnetic properties of FeCoSiB amorphous wires are attractive for the application of those wires as a sensitive flux detection element, since the change in the circular magnetization due to an ac wire current affects the voltage across the wire ends. In the case of a relatively low frequency current, when the skin effect is negligible, the change in the circular magnetic flux is considered to generate an additional inductive voltage,[15] V_L, which is determined by the internal part of the self inductance of a wire, $L_i = l\mu_\varphi/2$, where μ_φ corresponds to the averaged differential permeability and l is the wire length. The magnetoinductive effect can be measured by utilizing a resistor bridge circuit as shown in Fig. 3(a). A series of narrow peaks periodically spaced on the time axis then can be observed.[1–3] The peak height V_{L0} sharply decreases with the application of a longitudinal magnetic field H_{ex} by 50% at relatively low fields of 2–10 Oe as can be seen in Fig. 3(b). The sharp form of V_L is consistent with the nearly rectangular hysteresis loop for $H_{ex}=0$. There is also a consistency between the experimental dependencies $V_{L0}(H_{ex})$ and calculated dependencies for the maximum permeability $\mu_\varphi(H_{ex})$ shown in Fig. 2. Theoretical curves 2,3 characterized by a smaller anisotropy axis distribution $\Delta\alpha$ correspond to those seen in the case of tension annealed wires with a stronger circumferential anisotropy. Curve 1 is typical for as-cast wires with much broader anisotropy axis distribution.

It was proposed in Refs. 5 and 6 to utilize a high frequency current for which the total wire voltage is sensitive to the magnetic field. As the frequency is increased above some characteristic value ω^*, the amplitude V_0 of the total wire voltage increases as seen in Fig. 4. The value of ω^* increases with the application of the field as well as for a smaller diameter wire ($\omega^*/2\pi$ is about 20 and 200 kHz for 120 and 30 μm diameters, respectively, at $H_{ex}=0$). Such behavior shows that the skin effect is of predominant importance. At frequencies above $\omega^*(H_{ex}=0)$ there is a big difference between the behaviors of $V_0(\omega)$ for $H_{ex}=0$ and in the presence of the field. As a result, for a given frequency above this critical value the voltage amplitude decreases sensitively with the application of the field. For example, a drop in voltage by 50% can be reached by applying a field of about 10 Oe for a 30 μm diameter amorphous wire as seen in Fig. 5. The cut-off frequency of H_{ex} is 1/10 that of the ac wire current.

Figure 6(a) compares the wave forms for a magnetizing current at 1 MHz and the voltage at zero external field and a field of 10 Oe. The wave form of the voltage at zero field clearly exhibits a nonlinear behavior, supporting the idea that at high frequencies the magnetization processes such as domain wall displacement affect the total wire voltage. The voltage form, however, is not so far from the sinusoidal one (especially at higher frequencies), probably because the domain walls are already quite damped by eddy currents. Therefore the concept of a complex impedance $\hat{Z}=Z'+jZ''$, as the ratio between the harmonic complex voltage and cur-

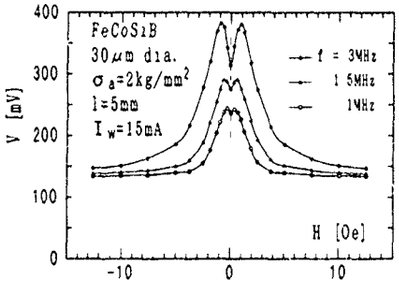

FIG 5. Voltage amplitude as a function of H_{ex} at various current frequencies for 30 μm diameter tension annealed wires.

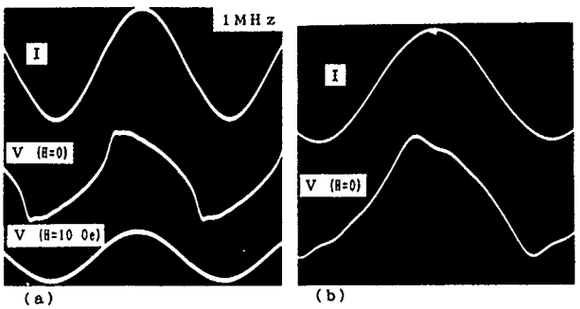

FIG. 6. Wave forms of current and voltage at different fields in (a) and frequencies in (b).

rent, can be employed to describe the observed effects at higher frequencies. Thus, the decrease in the wire voltage by applying the longitudinal field means the corresponding change in $\hat{Z}$. In this sense the effect was named as a magneto-impedance effect.

A giant **MI** effect can be found in various soft magnetic materials. However, in the case of a longitudinal (along the current and field direction) magnetic structure the **MI** effect is less sensitive and observed for higher fields, as in the case of FeCoSiB amorphous ribbons.[8] We measured the **MI** effect in ribbons of a composition $Fe_4Co_{67}Mo_2Si_{15}B_{10}$ as shown in Fig. 7. The voltage drop by 15%–20% is observed for fields of 20–30 Oe.

IV. IMPEDANCE OF A MAGNETIC WIRE

In this section we consider the field dependence of the complex impedance of a magnetic conductor. All the results are given for a wire with a circular domain structure since at present the main experimental data have been obtained in such materials. We employ Gaussian units.

A. Low frequency case

Let us consider a wire in which an ac current $I=I_0\exp(-j\omega t)$ is flowing. The current generates a circular magnetic field $H\varphi$ which magnetizes the wire in the circular direction. This circular magnetization affects the voltage across the wire ends. At low frequencies, when the skin effect is negligible, it is simply written as

$$V=RI+\langle E_z\rangle l. \tag{1}$$

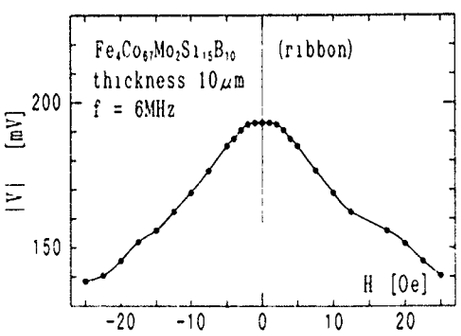

FIG 7 Magneto-impedance effect in $Fe_4Co_{67}Mo_2Si_{15}B_{10}$ amorphous ribbons of 10 μm thickness.

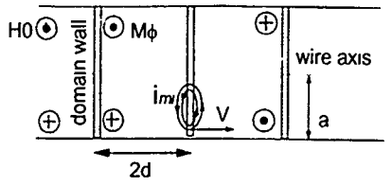

FIG. 8. Circular domain model for eddy current distribution calculations.

Here R is the ordinary resistance, and $\langle E_z\rangle$ is the averaged electric field due to change in the circular magnetization caused by $H_\varphi=2Ir/ca^2$:

$$E_z(r)=-\frac{j\omega}{c^2}I\int_0^r\frac{2r'\,dr'}{a^2}\mu_\varphi(r'),\quad r\leqslant a, \tag{2}$$

where a is the wire radius, μ_φ has to be defined as a differential permeability $\mu_\varphi=dB_\varphi/dH_\varphi$. Averaging Eq. (2) over the wire cross section allows us to represent Eq. (1) in a standard form $V=\hat{Z}(\omega)I$ using the wire impedance

$$\hat{Z}=R-j(\omega/c^2)L_i,\quad L_i=2l\left\langle\int_0^r\mu_\varphi r'\,dr'/a^2\right\rangle. \tag{3}$$

It follows from Eq. (3) that at a low frequency the field dependence of the impedance is attributed to its inductive term which is proportional to the differential circumferential permeability.

B. High frequency case

We can expect that with increasing frequency the dependence of $\hat{Z}$ on the field becomes more essential. In the case of thin wires with homogeneous magnetization changing linearly with an ac magnetizing field, the impedance can be calculated exactly for any frequency, i.e., without neglecting the skin effect:[16]

$$\hat{Z}=-(j\omega/c^2)L_e+RkaJ_0(ka)/2J_1(ka),$$
$$k=(1+j)/\delta_m,\quad \delta_m=c/\sqrt{2\pi\omega\sigma\mu_\varphi}, \tag{4}$$

where $L_e=2l\ln(l/a)$ is the external part of the self inductance of the wire, δ_m is the penetration depth in a magnetic media with the linear permeability μ_φ, σ is the conductivity, and J_0, J_1 are Bessel functions. In the case of a strong skin effect $a/\delta_m\gg 1$, the high frequency expansion of Eq. (4) gives

$$\hat{Z}=R(a/2\delta_m)-j\omega[L_e+L_i(2\delta_m/a)]/c^2. \tag{5}$$

It follows from Eq. (5) that at high frequencies (but L_e can be still neglected) $\hat{Z}\propto(\omega\mu_\varphi)^{1/2}$ since the penetration depth in magnetic materials depends on permeability as $\delta_m=\delta/\mu_\varphi^{1/2}$ [$\delta=c/(2\pi\omega\sigma)^{1/2}$ is a nonmagnetic penetration depth] and the internal inductance is proportional to μ_φ. Thus, in the high frequency region, when the skin effect can not be ignored, the total impedance of a magnetic wire is proportional to the root of the circumferential permeability.

This simple consideration already gives the idea of the **MI** effect and is helpful for the understanding of the experimental data described in Sec. III. However, for a quantitative comparison we have to consider the dynamic character of the

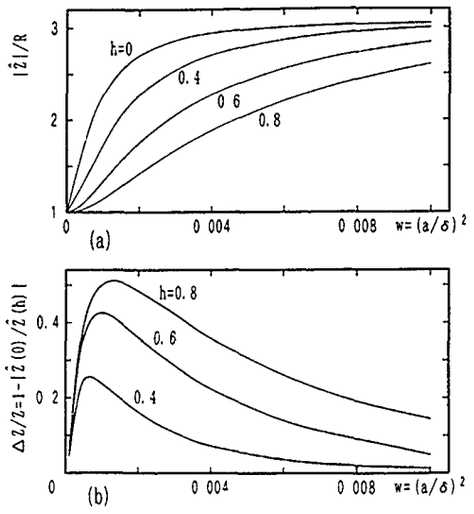

FIG. 9. Frequency dependence of the impedance $[|\hat{Z}|/R$ in (a), and $\Delta Z/Z = 1-|\hat{Z}(h)/\hat{Z}(0)|$ in (b)] with $h=H_{ex}/H_K$ as a parameter. The calculation was done with the theoretical dependence $\mu_\varphi(H_{ex})$ shown in Fig. 2 by curve 3, $\mu_\varphi(H_{ex}=0)=10^4$, $d/a=1/3$, $1/\sigma=130\ \mu\Omega$ cm

magnetization process. In the case of a wire with circular domains, while $H_{ex}<H_K$, the main contribution to the circular magnetization arises from the domain wall motion which generates local eddy currents. In Eq. (4) we ignored these microscopic currents. However, they are known to result in the excess losses[17] and damped domain wall movement. The exact calculation of the total current distribution inside the wire (due to the outer shape and domain wall displacements) cannot be done analytically. This problem can be considered in the effective medium approximation[18,19] in which the microscopic eddy currents i_{mi} are averaged on the domain wall scale. Then classical expression (4) for the impedance can be still used but with the effective permeability $\tilde{\mu}_\varphi$ incorporating i_{mi} and substituting for μ_φ.

The effective magnetic permeability depends on a concrete type of the domain structure. The calculation of $\tilde{\mu}_\varphi$ can be done by considering that the wall motion generating the eddy current field H_{mi} occurs under the influence of the averaged field $\langle H\rangle$ which includes some external field H^0 and the field H_{mi}. Then, if the eddy current field is known, we have the self-consistent condition to calculate $\tilde{\mu}_\varphi: \tilde{\mu}_\varphi H^0=\langle\mu_\varphi(H^0+H_{mi})\rangle$. The analytical solution for the eddy current field distribution is known for some simple domain structures as in the case of a sheath with periodical bar domains.[20] Recently an analytical result has been obtained for a wire with circular domains around it with a periodic spacing $2d$, as shown in Fig. 8. In this case, which is a prime interest here, the effective permeability can be written in the form[10]

$$\tilde{\mu}_\varphi=\mu_\varphi/(1-j\omega/\omega_{rel}), \tag{6}$$

$$\omega_{rel}=c^2/16\pi\mu_\varphi\sigma ad\sum_n g_n, \tag{7}$$

$$g_n=\left(\int_0^{\lambda_n} xJ_1(x)dx\right)^2 \coth(\lambda_n d/a)/\lambda_n^5 J_2^2(\lambda_n),$$

where ω_{rel} is a characteristic relaxation frequency, λ_n are such that $J_1(\lambda_n)=0$. The series in Eq. (7) is rapidly converging and is equal to 0.053 for $d\geqslant a/3.8$. From Eqs. (6) and (7) it follows that if the initial permeability μ_φ is a function of the magnetic field, the parameter $\tilde{\mu}_\varphi$ will also sensitively depend on the field while $\omega<\omega_{rel}$. In the limit $\omega\gg\omega_{rel}$ the effective permeability tends to be $\tilde{\mu}_\varphi\cong jc^2/(0.9\pi ad\omega)$ and is independent of μ_φ and, hence, of the field.

It should be noted that the eddy current losses in the case under consideration prove to be about 3 times lower than that for a bar domain structure.[20] Due to this the permeability maintains its low frequency value till higher frequencies and the condition $\omega^*=c^2/2\pi a^2\sigma\mu_\varphi<\omega<\omega_{rel}$ is easier satisfied, in the case of a wire with circular domains.

V. MAGNETO-IMPEDANCE CHARACTERISTICS

To describe quantitatively the magneto-impedance effect in negative magnetostrictive amorphous wires we will use expression (4) which is valid for any frequency together with the frequency dependent magnetic permeability defined by Eqs. (6) and (7). For the initial permeability entering Eq. (6) we will use the result of Ref. 9 shown in Fig. 2. We can assume that those field dependencies are valid for the linearized permeability as well.

First, let us investigate a high frequency $(a/\delta_m\gg 1)$ expansions of the impedance, substituting the complex permeability in Eq. (5),

$$\hat{Z}=R(a/2\delta)(\sqrt{\mu_R}-j\sqrt{\mu_L})-j\omega L_e/c^2,$$
$$\mu_R=|\tilde{\mu}_\varphi|+\tilde{\mu}''_\varphi,\quad \mu_L=|\tilde{\mu}_\varphi|-\tilde{\mu}''_\varphi. \tag{8}$$

It follows from Eq. (8) that at high frequencies such that $\omega^*<\omega<\omega_{rel}$ both the resistive and inductive components of $\hat{Z}$ depend on the permeability and contribute to the dependence of $\hat{Z}(H_{ex})$. At $\omega/\omega_{rel}\gg 1$ the ratio $\mu_L/\mu_R\approx(\omega_{rel}/2\omega)^2$ and tends to be zero, so the wire behaves as a resistive element (see experimental wave forms in Fig. 6). However, under this condition the dependence of $\hat{Z}$ on H_{ex} disappears since the permeability becomes independent of the field.

The frequency dependence of the impedance in the presence of the external field is shown in Fig. 9. We use the reduced frequency $w=(a/\delta)^2$. The reduced external field $h=H_{ex}/H_K$ is chosen to be $h<1$ since we are concerned with the permeability associated with domain wall displacement. Figure 9(a) shows the module of the impedance $|\hat{Z}|$ as a function of w. The considerable field dependence occurs in some frequency range $1<w\mu_\varphi<\omega_{rel}/\omega^*$ where the skin effect is suitable but the magnetic permeability μ_φ still has relatively high values. As a result, the relative change in the impedance $\Delta Z/Z=1-|\hat{Z}(H_{ex})/\hat{Z}(0)|$ by the external field has a maximum which achieves 50% at $h=0.8$ as shown in Fig. 9(b). Such impedance behavior is consistent with the experimental results. In Fig. 10 the **MI** ratio $\Delta Z/Z$ is compared with the experimental data obtained on amorphous wires of different diameters, showing a satisfactory agreement. In accordance with the skin effect, the maximum of $\Delta Z/Z$ shifts to lower frequencies for a larger diameter wire.

In Fig. 11 the field dependence of $\Delta Z/Z$ is shown for some frequencies. The plot is shown symmetrically since the

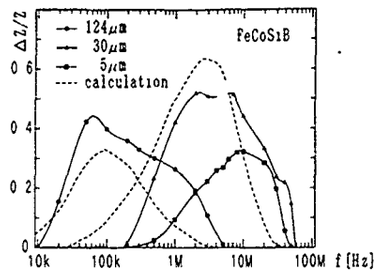

FIG. 10. Experimental and calculated frequency dependencies of $\Delta Z/Z$ at H_{ex}=10 Oe for a 124 μm diameter as-cast wire [$\mu_\varphi(H_{ex}=0)$=9800] and a 30 μm diameter tension annealed wire [$\mu_\varphi(H_{ex}=0)$=13 000]. The data for a 5 μm diameter wire obtained by etching are shown for a comparison.

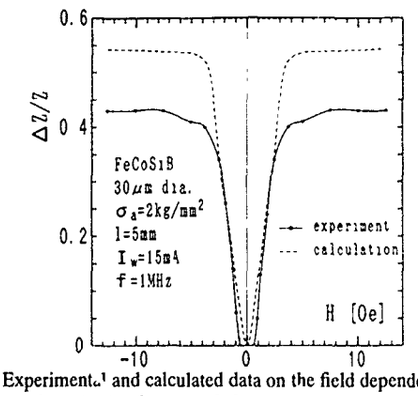

FIG. 12. Experimental and calculated data on the field dependence of $\Delta Z/Z$ for a 30 μm diameter tension annealed wire.

static permeability does not exhibit hysteresis with respect to h. Here the case of $h>1$ is considered as well. At such fields, a wire is longitudinally magnetized and the circumferential permeability is associated with only the magnetization rotation. In the frequency range under consideration it can be assumed to be frequency independent. The **MI** ratio rapidly increases at fields lower than the anisotropy field H_K ($h<1$), and it increases little at fields higher than H_K ($h>1$). Such behavior reflects the field dependence of the static permeability that was used for the impedance calculation (curve 3 in Fig. 2). In Fig. 12 the experimental and calculated curves are shown for a 30 μm diameter tension annealed wire, showing a reasonable agreement.

It should be noted, that with increasing frequency the rotational permeability becomes important even at $h<1$, since the wall motion becomes more and more damped. The longitudinal field stimulates the rotational process while $h<1$, and the corresponding permeability has a maximum at $h=1$. This tendency can be seen in Fig. 5 for higher frequencies.

VI. CONCLUSION

We can conclude that the magneto-impedance effect has a classical electromagnetic origin and is a general phenomenon in soft magnetic conductors. At high frequencies when the skin effect is strong, the impedance is subject to the current distribution which sensitively depends on the transverse magnetic properties. The most sensitive magneto-impedance effect can be expected in soft magnetic materials with domain walls perpendicular to the current and external field direction. In this case the change in $\hat{Z}$ of the order of 50% can be reached with fields of the order of the anisotropy field. This configuration is realized in negative magnetostrictive amorphous wires having a circular domain structure.

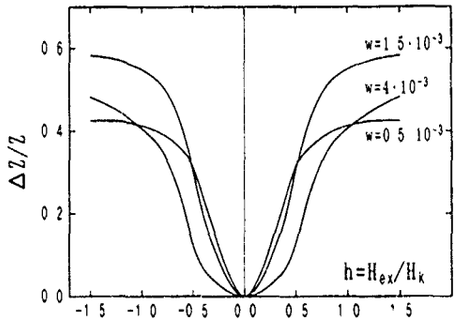

FIG. 11. Field dependencies of the **MI** ratio $\Delta Z/Z$ for various frequency w.

[1] K. Mohri, K. Kawashima, T. Kohzawa, Y. Yoshida, and L. V. Panina, IEEE Trans. Magn. **28**, 3150 (1992).
[2] K. Mohri, K. Kawashima, T. Kohzawa, and H. Yoshida, IEEE Trans. Magn. **29**, 1245 (1993).
[3] K. Kawashima, T Kohzawa, H Yoshida, and K. Mohri, IEEE Trans Magn **29**, 3168 (1993).
[4] K. Bushida and K. Mohri, in Abstract Book of the 6th Joint MMM-INTERMAG Conference (AR-09), New Mexico, June 1994.
[5] K. Bushida, M. Noda, L. V. Panina, H. Yoshida, T. Uchiyama, and K. Mohri, J. Magn. Soc. Jpn. **18**, 493 (1994).
[6] K. Mohri, K. Bushida, M. Noda, H. Yoshida, L. V Panina, and T. Uchiyama, IEEE Trans. Magn. (to be published).
[7] V. E. Makhotkin, B. P. Shurukhin, and V. A. Lopatin, Sensors Actuators A **25–27**, 759 (1991)
[8] F. L. A. Machado, B. L. da Silva, S M. Rezende, and C. Martins, J. Appl Phys. **75**, 6563 (1993).
[9] L V Panina, H. Katoh, K. Mohri, and K. Kawashima, IEEE Trans. Magn. **29**, 2524 (1993).
[10] L V. Panina and K. Mohri, J. Magn. Soc. Jpn. **18**, 245 (1994).
[11] L. V. Panina and K Mohri, Appl. Phys. Lett. **65**, 1189 (1994)
[12] K. Mohri, F. B. Humphrey, J. Yamasaki, and F. Kinoshita, IEEE Trans. Magn. **21**, 2017 (1985).
[13] F. B. Humphrey, K. Mohri, J. Yamasaki, H. Kawamura, and R. Malmhall, *Proceedings of the Symposium on Magnetic Properties of Amorphous Metals* (Elsevier Science, Amsterdam, 1987), p. 110
[14] J. Liu, R. Malmhal, L. Arnberg, and S. J. Savage, J. Appl. Phys. **67**, 4238 (1990).
[15] A. Hernando and J. M. Barandiaran, J. Phys. D **11**, 1539 (1978)
[16] L. D. Landau and E. M. Lifshitz, *Electrodynamics of Continuous Media* (Pergamon, Oxford, 1975), p. 195.
[17] H. J. Williams, W. Shockley, and C. Kittel, Phys. Rev. **80**, 1090 (1950)
[18] G. A. Niklasson and C. G. Granquist, J. Appl. Phys **55**, 3382 (1983).
[19] A. P. Vinogradov, L V. Panina, and A. K. Sarychev, Sov. Phys. Dokl **34**, 530 (1989).
[20] R H Pry and C P. Bean, J. Appl. Phys **29**, 532 (1958).

Very large magneto-impedance in amorphous soft ferromagnetic wires (invited)

K. V. Rao, F. B. Humphrey,[a] and J. L. Costa-Krämer
Department of Condensed Matter Physics, Royal Institute of Technology, Stockholm, Sweden

Changes in the impedance, ≈600%/Oe, at axial fields less than 1 Oe nave been observed in the presence of a 90 kHz, few mA current through a soft, nearly zero magnetostrictive wire. In this 125 μm diameter CoFeSiB amorphous wire we observe a total change of 160% at the maxima of the impedance in dc fields less than 2 Oe. A systematic study of the role of induced anisotropy in the axial, circumferential, and helical directions on the magneto-impedance shows that the largest effect is seen in the wire annealed to obtain circumferential easy axis using a 15 mA ac current passing through it. Both the axial hysteresis loops and the observed *I-V* characteristics reflect the induced anisotropies. The observed dependence of the inductance change on the type of the anisotropy induced in these wires can be modeled in terms of an interplay between the induced anisotropy, reversing ac field, and the axial dc field.

I. INTRODUCTION

Recently, there has been considerable interest in the giant-magneto-resistive (GMR), phenomena observed in a wide variety of magnetic materials such as multilayers, granular, and other heterogeneous structures. For device applications a large change in GMR per Oe at room temperature and low external fields is of interest.

In this paper we elucidate the role of induced anisotropies to explain the large changes in the magneto-impedance observed[1] in a nearly zero magnetostrictive wire at external fields as low as 1 Oe. Amorphous wires, produced by injecting a melt through a continuously moving fluid,[2]develop a unique microstructure because of the axial direction in which it is cast and the homogeneous radial rapid cooling process during solidification.[3] Such transition metal based amorphous wires are found to possess unique soft magnetic properties which are already used in applications as sensors.[4] In a Co-Fe-Si-B amorphous wire with the absence of crystalline anisotropy it is now possible to tailor[5] a nearly zero magnetostrictive ($\lambda_s < 10^{-9}$) wire in which we can induce axial, circumferential, or helical anisotropies with practically no dispersion and study the response of such a system to external fields. The magne o-inductive properties found in such tailored wires are promising for developing novel low field sensors.

II. EXPERIMENT

In order to study in depth the role of the type of induced anisotropy we have specially prepared the amorphous wires in a well defined magnetic state with axial, circumferential, and helical anisotropies using the following procedure: four 45 cm long, 125 μm diameter wires of nominal composition $(Co_{94}Fe_6)_{72.5}Si_{12.5}B_{15}$, were used. Three of these were annealed in air using a current of 350 mA for 30 min. During this anneal, the field direction on each wire was carefully controlled so that a well defined induced magnetic anisotropy would develop. One wire was annealed in the presence of an axial dc field to obtain an axial anisotropy. Another was annealed with only the ac current to induce a circumferential anisotropy. The third, was annealed using a dc current in the presence of an axial dc field of such a value as to create a 45° helix at the wire surface.

The axial hysteresis loops of the wires were measured with a conventional induction technique hysteresis loop tracer. It uses a primary coil 27 cm long, 3 cm diameter, with a field to current constant of 22.9 Oe/A. A 31 Hz sinusoidal current is fed to the primary, the voltage across a resistor connected in series with the primary coil fed to the *X* channel of an oscilloscope. The voltage induced in a 1000 turn 0.8 cm long secondary, properly compensated for the applied field, is integrated and displayed in the *Y* channel of the oscilloscope where the longitudinal hysteresis loops are monitored.

The *I-V* characteristics of the wires were studied passing an ac current through the wire and a resistor connected in series. We use an oscilloscope to visualize the voltage across 35 cm of the amorphous wire against the voltage across the resistor. The current through the wire creates a circumferential field of about 0.031 Oe per mA at the surface. An FFT spectrum analyzer, model SR760 from Stanford Research Systems, was used to measure the different spectral components of the magneto-impedance. In this work we present the amplitude of the first harmonic of the voltage as a function of the axial field for the above mentioned wires.

III. RESULTS AND DISCUSSION

In Fig. 1 the longitudinal hysteresis loops for the amorphous wires as-quenched, and annealed under different conditions are displayed. The saturation magnetization value for the wire is found to be about 5700 G. The as-quenched wire [Fig. 1(A)] reaches magnetic saturation at a field of about 0.5 Oe with $M_r/M_s \approx 0.61$. The axial anisotropy wire [Fig. 1(B)] clearly displays an axial easy direction of the magnetization ($M_r/M_s \approx 1$) with H_c of about 0.035 Oe. The wire with circumferential anisotropy [Fig. 1(C)] exhibits a hysteretic loop typical when a magnetic field is applied along a hard axis direction ($M_r/M_s \approx 0$) with H_k of about 1.3 Oe. The wire with induced helical anisotropy [Fig. 1(D)] displays a loop with an intermediate behavior for which

[a]Visiting from Boston University

 0021-8979/94/76(10)/6204/5/$6.00 © 1994 American Institute of Physics

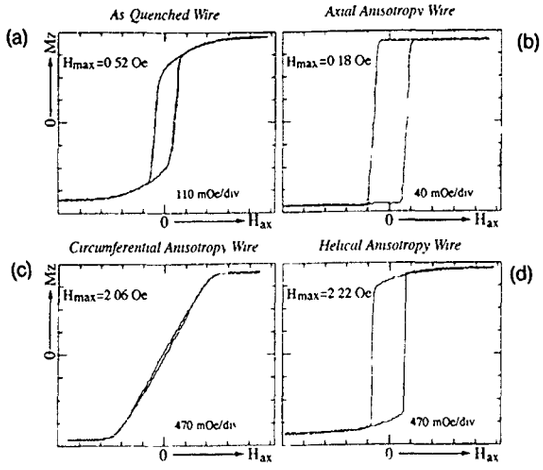

FIG. 1. Longitudinal hysteresis loops for $(Co_{94}Fe_6)_{72.5}Si_{12.5}B_{15}$ wire in the (A) as-quenched, and current annealed under different conditions for induced (B) axial anisotropy, (C) circumferential anisotropy, and (D) helical anisotropy.

$M_r/M_s=0.85$ which corresponds to an average orientation of the magnetization of 32° with respect to the axis. If we assume a 45° orientation of the magnetization at the surface, which decreases monotonically as we proceed radially inwards, to an axial orientation at the center of the wire, we estimate a theoretical average angle to be 30.7°, which is quite close to the measured value of 32°. This wire axially saturates at an external field of about 1.5 Oe.

The frequency dependence of the *I-V* characteristics at zero applied axial magnetic field for the same wire is shown in Fig. 2. On the vertical axis we display the voltage across 35 cm of wire and, on the horizontal axis, the voltage across a resistor in series with the wire which is proportional to the current amplitude value. As observed, at low frequencies in all cases the resistive (linear and reversible) component of the impedance dominates. The slope of this linear part is related to the dc resistance of the wire (about 35 Ω). As the frequency of the ac current is increased, the inductive component of the impedance develops. Notice that the *I-V* loop closes at the current amplitude which saturates the sample along the circumferential direction, proportional to the circumferential anisotropy field. Accordingly, the area under the inductive peak should be proportional to the frequency of the excitation and the amount of circumferential flux which is being switched. The position of the maximum of the peak in the inductive component provides us with the circumferential coercive field at which the maximum flux change takes place.

As seen in Fig. 2(A), the as-quenched wire has a small inductive component of the impedance even for 100 Hz fre-

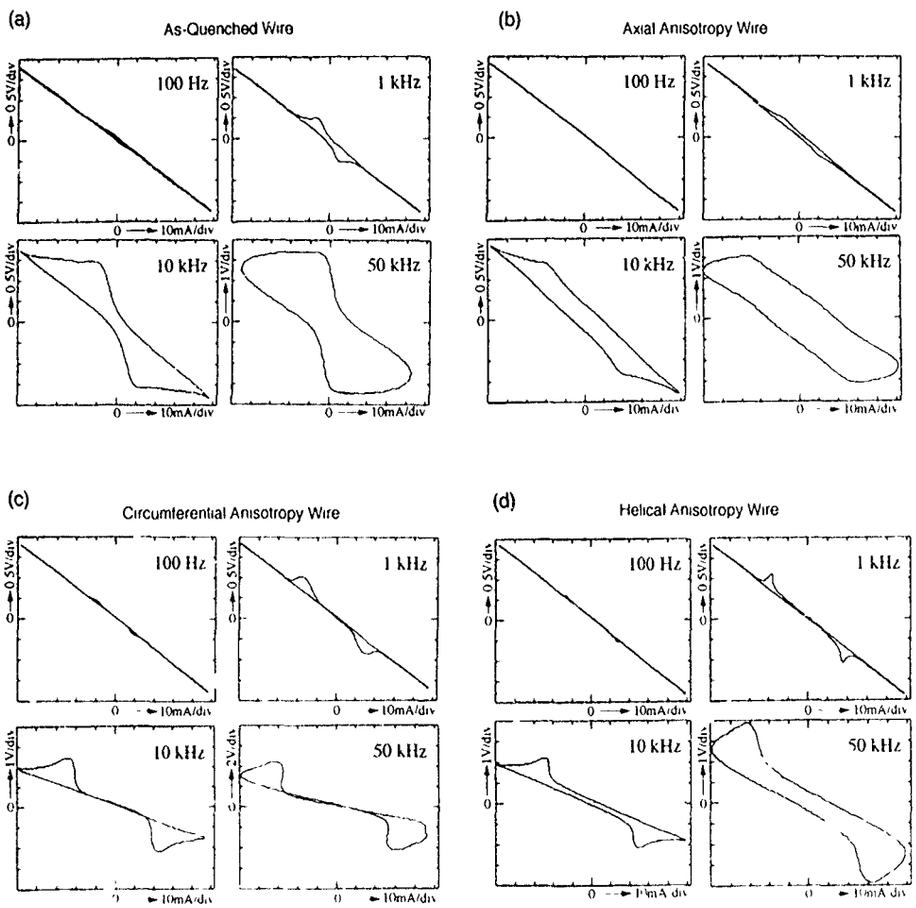

FIG. 2. Frequency dependence of the *I-V* characteristics for $(Co_{94}Fe_6)_{72.5}Si_{12.5}B_{15}$ wire in the (A) as-quenched, and current annealed under different conditions for induced (B) axial anisotropy, (C) circumferential anisotropy, and (D) helical anisotropy.

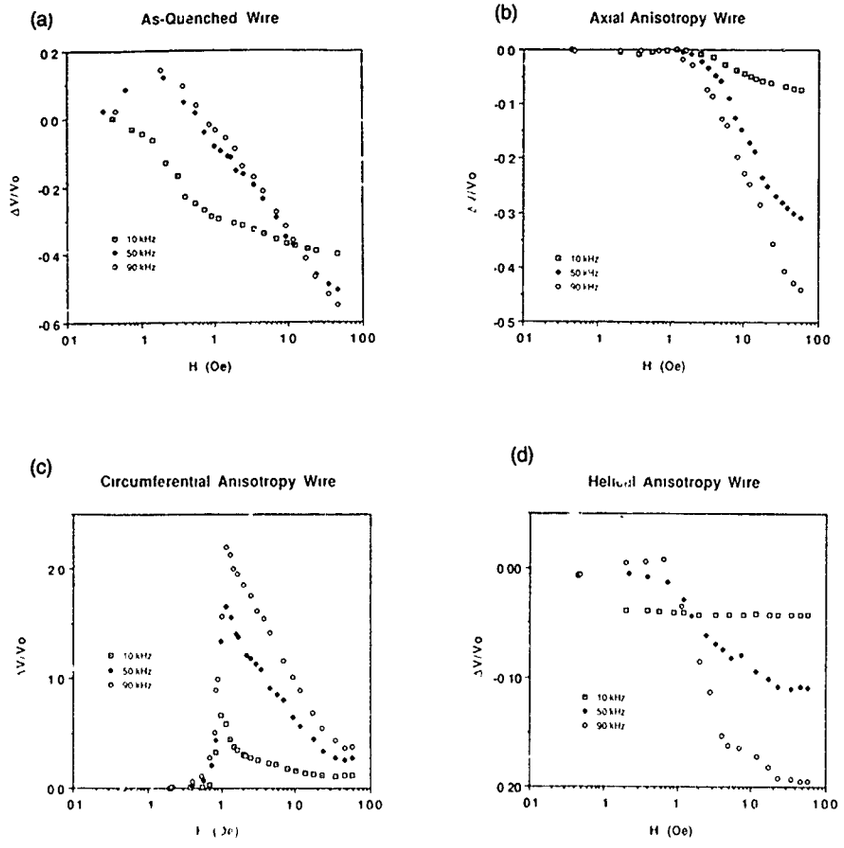

FIG. 3. Magneto-impedance measured with 3 mA at 10, 50, and 90 kHz for $(Co_{94}Fe_6)_{72.5}Si_{12.5}B_{15}$ wire in the (A) as-quenched, and current annealed under different conditions for induced (B) axial anisotropy, (C) circumferential anisotropy, and (D) helical anisotropy.

quency. On increasing the frequency of the current, the inductive component grows and is displaced toward higher current values, indicating the displacement of the circumferential coercive field as we increase the frequency of the excitation. This is concomitant with a decrease of the circular susceptibility. For the induced axial anisotropy wire [Fig. 2(B)] we do not observe a significant inductive component of the impedance at 100 Hz. In a similar fashion to the as-quenched wire, the inductive component increases as the current frequency is increased. The wire with circumferential anisotropy [Fig. 2(C)] displays the inductive bumps separated by a central linear and reversible part up to 50 kHz current frequency. This suggests the existence of a critical circumferential switching field below which there is no significant circumferential flux change and accordingly no axial inductive voltage. At a threshold the circumferential magnetization switches, as noticed by the appearance of the inductive component of the voltage. Notice also that, as before, the inductive component of the impedance displaces to higher current amplitude values on increasing the current frequency. For the wire with induced helical anisotropy [Fig. 2(D)] we observe a mixture of the previous two behaviors, i.e., a displacement of the inductive peaks plus a broadening of the *I-V* loop. The observed behavior could be viewed as a mixture of the axial and circumferential *I-V* characteristics.

The inductive component shown in the various wires of Fig. 2 can be identified by using an axial field. In all the wires, when a 100 Oe axial field is applied, each of the curves collapse to a diagonal resistive line. The inductive component disappears, leaving pure resistive behavior. Consequently, the deviation from the resistive behavior at a given frequency and amplitude of the current, provides a measure of the magnitude of the impedance change from zero to saturation.

We now discuss the evolution of the magneto-impedance in the wire with a well tailored anisotropy. The actual field evolution of the voltage between the ends of the wire depends both on the amplitude of the ac current and on the magnetic anisotropy. In. Fig. 3 the amplitude of the fundamental of the impedance as a function of the axial dc field is presented at three different frequencies (10, 50, and 90 kHz) when a 3 mA ac current is flowing through the wires with different induced anisotropies. A 3 mA current flowing through the wires creates a maximum circumferential field at the surface of about 0.1 Oe. This field will try to oscillate the magnetization circumferentially. The amount of flux change (and accordingly the axial inductive voltage) will depend on the magnitude and relative orientation of the anisotropy and the applied ac field. It will also depend on the magnetic softness of the material which in amorphous materials is primarily determined by the magnitude and sign of the magnetostriction. On applying an axial field, we modify the zero field domain structure tilting the average magnetization toward the axis, and, consequently, change the relative orien-

tation of the average magnetization to the applied circumferential field, resulting in the magneto-inductive voltage changes. This voltage change will thus reflect the change of circular susceptibility at the frequency of the excitation as we proceed towards axial saturation, in the external field.

For the as-quenched wire [Fig. 3(A)] at 10 kHz we observe a continuous decrease of the inductive voltage as a function of the axial field, demonstrating partly a decrease of the circular susceptibility as we align the magnetization axially. On increasing the current frequency the inductive voltage first increases and then decreases. This may be caused by an increase in the average circular susceptibility at that frequency values as we align the magnetization axially. At high enough axial field values a pure resistive behavior is expected, the magneto-impedance is then saturated.

The axial anisotropy wire [Fig. 3(B)] displays the magneto-impedance at the three selected frequencies. Below 1 Oe there is no significant change of the magneto-impedance. As the field increases further, the magneto-impedance starts to decrease, demonstrating the reduction of the amplitude of the circumferential flux oscillations created by the current's self-field.

In the case of the circumferential anisotropy wire, the magnetization is oriented circumferentially in the demagnetized state. Below the circumferential critical switching field there is no circumferential flux change [central part of the *I-V* characteristic, Fig. 2(C)]. However, the situation changes on applying an axial field. When the applied axial field overcomes the effect of the circumferential anisotropy, the magnetization will rotate toward the axial direction. The circumferential susceptibility is expected to increase. The magneto-impedance data for this wire [Fig. 3(C)] is consistent with this picture. A sharp rise in the inductive component of the impedance at about 0.8 Oe, reaching a maximum value at about 1 Oe is observed. On increasing the axial field further, the circular susceptibility decreases, eventually to zero resulting in no inductive voltage. Notably, the maximum change in the impedance is 220% at 90 kHz, with a maximum slope at field values between 0.8 and 1.1 Oe of about 300%/Oe!

The magneto-impedance for the helical anisotropy wire [Fig. 3(D)] displays a behavior qualitatively similar to the as-quenched wire with a lower axial saturation field. At 10 kHz current frequency a continuous decrease of the voltage is observed as the axial dc field is raised, while at higher frequencies the initial slope tends to be positive. The low axial saturation field of the magneto-impedence might be explained in terms of a smaller circumferential susceptibility, as compared with the as-quenched wire case at the same current value. The axial field required to stop the magnetization oscillations in the circumferential direction is accordingly smaller.

The remarkable magneto-impedance behavior for the wire with circumferential anisotropy, can be seen in more detail in Fig. 4. The relative change in voltage is seen as a function of the axial field for different ac currents through the wire at a constant frequency of 90 kHz as a parameter.

As the amplitude of the ac current is increased [see Fig. 4(A)], the impedance threshold is displaced to lower axial

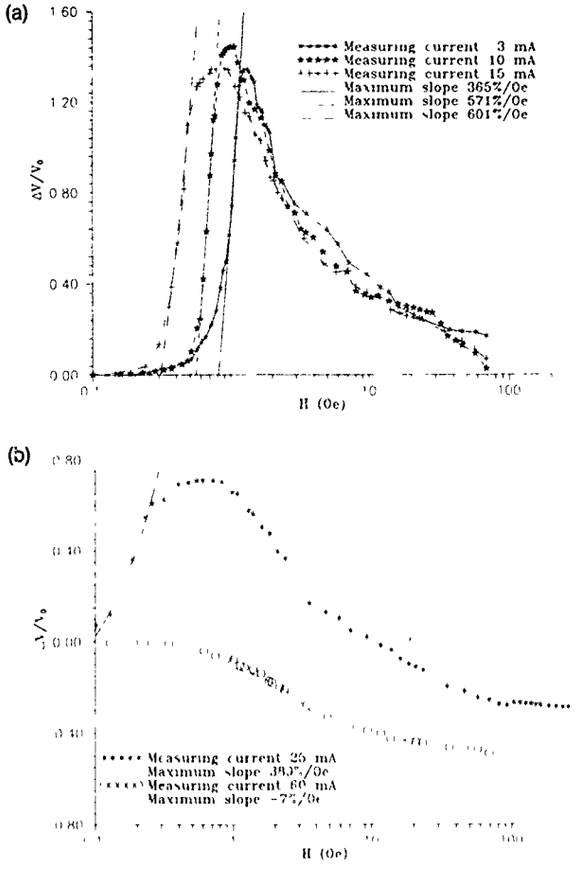

FIG. 4. Dependence of the magneto-impedance on the current amplitude at 90 kHz for a $(Co_{94}Fe_6)_{72.5}Si_{12.5}B_{15}$ wire with induced circumferential anisotropy at (A) 3, 10, and 15 mA and (B) 25 and 60 mA.

fields. This can be understood in terms of the balance between the circumferential anisotropy, the applied axial dc and circumferential ac fields. As the amplitude of the ac circumferential field is increased, the dc field required to tilt the magnetization such that the ac circumferential field manages to set the magnetization to oscillate in the circumferential direction is decreased. On increasing the current amplitude further [as seen in Fig. 4(B)], a value is reached for which all the circumferential flux is oscillating at zero axial field. When this value is reached, the behavior of the magneto-impedance changes to a continuous decrease in amplitude as the axial field is increased as shown by the open circles (60 mA).

IV. CONCLUSIONS

Current annealing proves to be a powerful method to tailor magnetic responses, particularly the magneto-impedance, of amorphous soft ferromagnetic wires.

The magneto-impedance effect has been studied in low magnetostrictive amorphous wires with different easy magnetization axes. The observed current, frequency, and axial field dependencies of the magneto-impedance support the view of an effect related to the soft magnetic properties of

the wire, i.e., voltage changes caused by large circular magnetic flux variations driven by the field generated by the current.

The nature of the magnetic anisotropy is an essential ingredient in the description of the effect. The field and current dependencies of the magneto-impedance are markedly different for axial and circumferential anisotropies, i.e., domain orientations parallel and perpendicular to the applied dc field. As expected, the characteristics of the changes in the impedance are found to be maximum in the wire with induced circumferential magnetic anisotropy. A maximum change of +220% in the impedance value at an external field of about 1 Oe, and a slope of 600%/Oe at axial field values below 1 Oe in the presence of a 15 mA, 90 kHz current are found in this wire. A quantitative analysis of the magneto-impedance and its dependence on the applied external dc fields in the presence of ac currents through the wires will be presented elsewhere.

ACKNOWLEDGMENTS

It is a pleasure to acknowledge technical help from Jan-Erik Schuch and Göran Alterland. This work has been supported by the Swedish funding agencies TFR and NUTEK.

[1] K. Mohri, T. Kohzawa, K Kawashima, H. Yoshida, and L. V. Panina, IEEE Trans. Magn. **28**, 3150 (1992).

[2] T. Masumoto, I. Ohnaka, A. Inoue, and M. Hagiwara, Scr. Metall. **15**, 293 (1981).

[3] J. L. Costa and K. V. Rao, *Physics of Magnetic Materials* (World Scientific, Singapore, 1990), pp. 279–293.

[4] F. B Humphrey, RQ8, Sendai, Japan, paper 27011-1, August 22–27, 1993.

[5] J. L. Costa-Kramer, Ph.D. thesis, Royal Institute of Technology, Stockholm, Sweden, February 1994.

Sensitive field- and frequency-dependent impedance spectra of amorphous FeCoSiB wire and ribbon (invited)

R. S. Beach and A. E. Berkowitz[a)]
Center for Magnetic Recording Research, University of California, San Diego, La Jolla, California 92093

Conflicting reports of large magnetoresistive and magnetoinductive effects in amorphous FeCoSiB wires and ribbons prompted the impedance measurements reported here. The spectra ($0 \leq f \leq 3.2$ MHz) were obtained at room temperature using a commercial impedance analyzer both as functions of axial magnetic field ($-140 < H_A < 140$ Oe) and sense current ($1 \leq I_{rms} \leq 60$ mA). The phase shift due to the test leads was carefully measured and subtracted from the raw data to resolve the spectra into resistive $R(f)$ and reactive $X(f)$ components. We find for the $Fe_{4.3}Co_{68.2}Si_{12.5}B_{15}$ wire (120 μm diameter) and ribbon (20 μm thick) that both $R(f)$ and $X(f)$ depend strongly on frequency and magnetic field. For $H_A=0$, each component increases monotonically with frequency, with $R(f=0) \approx 1$ Ω/cm and $X(f=0)=0$. In high fields ($H_A=140$ Oe), $R(f)$ and $X(f)$ are nearly frequency independent. The field-dependent response is sharply peaked about $H_A=0$; the full width at half maximum is FWHM$\leq$20 Oe, typically. The change in $R(f)$ and $X(f)$ between these two extremes is extraordinarily large; 4.5 Ω/cm at $f=1$ MHz is a typical value for the wire. The sensitivity of the magnetoresistive response is 44% of the dc resistance per Oe for $f=1$ MHz. Qualitatively similar phenomena were observed for the $Fe_{7.5}Co_{67.5}Si_{15}B_{10}$ ribbon, although the field and frequency dependences of the spectra are less pronounced than for the wire. We discuss a model which describes the spectra quantitatively, using classical electrodynamics.

I. INTRODUCTION

In spite of the fact that amorphous ferromagnetic materials have zero magnetocrystalline anisotropy, magnetic isotropy has not been attained in the laboratory. The small, yet finite coercivities, permeabilities less than simple theoretical predictions, and the unusual domain structures characteristic of these materials demonstrate the presence of anisotropy despite their amorphous microstructure. It is generally believed that the anisotropy observed in amorphous ferromagnets is predominantly due to magnetostriction. Magnetostriction anisotropy is governed by the alloy composition, which determines the value of the magnetostriction coefficient λ, and stress fields which result from the fabrication process. Amorphous ferromagnetic wires are produced by quenching a molten stream in water. This process results in wires with a radially directed stress field and, consequently, anisotropy fields that are either radial or circumferential, depending on the sign of λ.

Due to their potential uses in transformers and transducers, the magnetic properties of amorphous ferromagnets in the frequency domain have been studied extensively. These materials typically exhibit high permeabilities and low losses, characteristics desirable for many high-frequency applications. The permeability, in particular, is dependent upon the anisotropy field, the domain structure, and the magnitude and topology of the magnetic field acting on the material.

Recent work by the authors,[1] by Mohri and co-workers,[2] and several others[3–5] has focused on ac electrical transport phenomena in amorphous FeCoSiB alloys. These researchers have demonstrated firstly that the impedance $Z(f)=R(f)+iX(f)$ of certain amorphous wire and ribbon samples is a very strong function of the frequency f of the drive current, and secondly, that this strong frequency response can be virtually eliminated by the application of a magnetic field H_A of the order of 10 Oe. Such amorphous materials have the potential to be used as simple, extremely sensitive magnetic field detectors.

In our research, we have found that a sensitive magnetoresistance $R(f,H_A)$ accompanies the previously observed[2] field-dependent reactance $X(f)$ of amorphous FeCoSiB wires. At room temperature and for $f \geq 3$ MHz, the net magnetoresistance exceeds 600% of the dc wire resistance. This large response enables us to detect changes in the applied field of less than 0.001 Oe. The impedance spectra of as-cast FeCoSiB ribbon have also been measured, and we observe field-dependent effects that are of the same order of magnitude, but somewhat smaller than those for wires. For the case of wires, we are able to fit the spectra to a straightforward model that is based on classical electrodynamics.

II. EXPERIMENTAL

All of the data presented herein were obtained using a Schlumberger 1260 impedance analyzer running in constant current amplitude mode. The FeCoSiB ribbon and wire samples were first cut to lengths of 3 cm and cleaned in a solution of HCl and ZnCl. Two current leads were attached to the ends of the samples, and two voltage leads, 1.4 cm apart, were attached between these. All the connections were made with Ag paint. The contact resistances were less than 1 Ω. The samples were mounted inside a grounded chassis box which was connected to the analyzer with four coaxial cables. The cables were roughly 40 cm long and permitted the samples to sit within a Helmholtz coil (diameter 30 cm), which produced a dc magnetic field -140 Oe$<H_A<140$ Oe

[a)]Also at Department of Physics, University of California, San Diego, La Jolla, CA 92093.

 0021-8979/94/76(10)/6209/5/$6.00 © 1994 American Institute of Physics

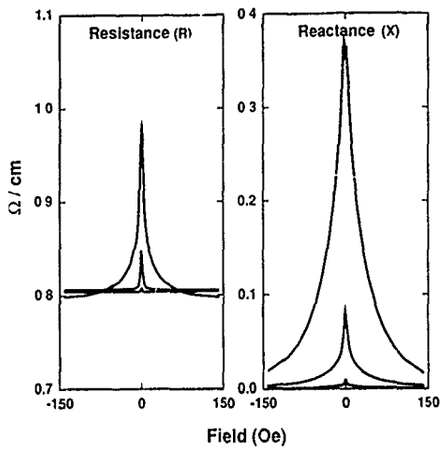

FIG. 1. The impedance of an amorphous $Fe_{75}Co_{67.5}Si_{15}B_{10}$ ribbon $Z=R+iX$ vs magnetic field $(-140<H_A<140$ Oe) for three sense current frequencies, $f=10$ kHz, 100 kHz, and 1 MHz. The peak at $H_A=0$ grows dramatically with increasing f. Note also the frequency dependence of the peak widths.

along the lengths of the samples. The samples were aligned with their long axes (parallel to the current) normal to the earth's magnetic field. All the data were collected at room temperature.

The measured impedance spectra $Z(f,H_A)$ were resolved into resistive R and reactive X components by subtracting the previously determined impedances of the instrumentation and test leads from the raw data. This null correction amounted to approximately 10% of the measured wire signal for $f=1$ MHz. Frequency sweeps (100 Hz$<f<$3 MHz) and current amplitude sweeps (0.5 mA$<I_{rms}<$60 mA) were controlled by computer. Field sweeps were performed manually. The applied field had no direct observable effect on the experimental apparatus.

III. IMPEDANCE $Z(f,H_A)$ OF AMORPHOUS FeCoSiB RIBBON AND WIRE

A. Ribbon

In this paper we discuss the impedance spectra $Z(f,H_A)$ obtained from FeCoSiB ribbon and wire samples under the influence of an axially applied magnetic field H_A. We expect that these materials are very soft ferromagnets, with dc coercivities considerably less than 1 Oe, although this was confirmed only for the ribbon sample.

The 0.9-mm-wide by 20±3-μm-thick $Fe_{75}Co_{675}Si_{15}B_{10}$ ribbon was prepared by melt spinning by J. L. Walter of the General Electric Research and Development Center. The amorphous structure of the ribbon was verified by x-ray diffraction. The as-cast ribbon has a resistivity $\rho=145$ $\mu\Omega$ cm. It exhibits only a small anisotropic magnetoresistance of $\sim$0.1% at room temperature, and a small linear decrease of $R(H_A)$ for fields $H_A>5$ kOe. This behavior is typical of ferromagnetic $3d$ metals and alloys. In Fig. 1 we show the response of the ribbon impedance (in units of Ω/cm ribbon) to a magnetic field applied along the ribbon's length, at drive current frequencies of 10 kHz, 100 kHz, and 1 MHz. The drive current amplitude used in collecting these data was $I_{rms}=10$ mA. The dc impedance (not shown) is flat on this scale, and is purely real. For frequencies f other than zero, peaks in both the resistance R and reactance X appear, centered about $H_A=0$. Both the magnitudes *and* widths of the peaks in R and X grow monotonically with frequency. For $f=1$ MHz, the magnetoresistance ratio is $(R_{max}-R_{sat})/R_{sat}=23\%$. The dc resistance $R_{dc}=0.8$ Ω/cm is apparently equal to R_{sat}, the ac resistance in the limit of high H_A. The relative change in reactance for $f=1$ MHz is $\Delta X/R_{sat}=X_{max}/R_{sat}=46\%$. We note that the widths of the resistive and reactive responses are different. The full widths at half maximum of the resistance curves FWHM$=2\Delta H_R$ are less than those for the reactance $2\Delta H_X$ for each value of f shown. The magnitudes of these peaks ΔR and ΔX, and their widths ΔH_R and ΔH_X are given in Table I. Parameters which serve to quantify the sensitivities of the resistive and reactive responses are $(1/\Delta H_R)(\Delta R/R)$ and $(1/\Delta H_X)(\Delta X/R)$. For $f=1$ MHz, these are, respectively, 4.3%/Oe and 1.8%/Oe. We observe relatively little response in either R or X when H_A is perpendicular to the current.

TABLE I. The relative magnitudes and widths of the peaks in R and X for a $Fe_{75}Co_{67.5}Si_{15}B_{10}$ ribbon, taken from Fig. 1. The resistance for $f=0$ is $R_{dc}=0.8$ Ω/cm.

Frequency	10 kHz	100 kHz	1 MHz
$\Delta R/R$	0.4%	5.5%	23%
$\Delta X/R$	1.1%	10.1%	46%
ΔH_R	1.0 Oe	1.8 Oe	5.3 Oe
ΔH_X	3.5 Oe	7.2 Oe	25 Oe

Impedance spectra $(0<f<3$ MHz) in zero field and for $H_A=140$ Oe are displayed in Fig. 2. The zero-field reactance exhibits negative curvature for the entire frequency range, and linearly approaches a value $X=0$ at $f=0$. On the contrary, the resistance displays positive curvature up to $f=1.5$ MHz; for $f>1.5$ MHz, the curvature of $R(f)$ is negative. Similar zero-field behavior, very much smaller in magnitude, was previously observed[6] for FeCoSiMoB ribbons.

The spectra are rendered nearly completely flat by a 140 Oe magnetic field, as shown in the Fig. 2. The resistance

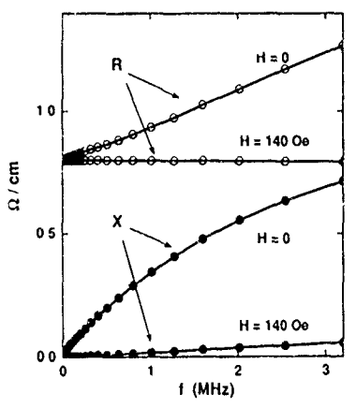

FIG 2. Impedance spectra for the amorphous $Fe_{75}Co_{675}Si_{15}B_{10}$ ribbon for zero applied field, and for an axially applied field of 140 Oe Close inspection of the figure reveals an inflection point at $f=1.5$ MHz The 140 Oe field suppresses the frequency responses almost completely

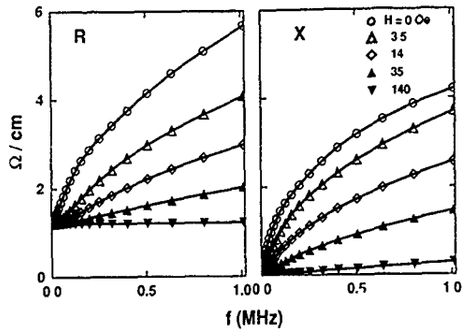

FIG. 3. Impedance spectra of a $Fe_{43}Co_{68.2}Si_{12.5}B_{15}$ wire for axially applied magnetic fields H_A=0, 3.5, 14, 35, and 140 Oe. Solid lines connect points at fixed H_A.

$R(f)$ has no visible slope for this field. One will note a small positive slope in $X(f,H_A=140\ \text{Oe})$, which is consistent with the different widths of $R(H_A)$ and $X(H_A)$ found in the field scans of Fig. 1. Note that ΔR is less than ΔX for all frequencies $f<3$ MHz. At a frequency of $f=3.2$ MHz, $\Delta R/R=59\%$ and $\Delta X/R=89\%$.

B. Wire

The nominally amorphous $Fe_{43}Co_{68.2}Si_{12.5}B_{15}$ wire sample was fabricated by the technique of quenching in rotating water[7] by the Unitika Corp. of Japan. We are grateful to R. Hasegawa for making it available to us. The wire has a 120 μm diameter, and a resistivity $\rho=135\ \mu\Omega$ cm. Impedance spectra obtained from this sample in various axially applied magnetic fields are displayed in Fig. 3. These share many characteristics with the ribbon spectra, shown in Fig. 2. Both $R(f)$ and $X(f)$ increase monotonically with frequency, and are driven to lower values by the axial field, but the magnitudes of the responses are $\Delta R/R=370\%$ and $\Delta X/R=350\%$ for a frequency $f=1$ MHz, an order of magnitude larger than for the ribbon. Like the ribbon, $X(f)$ also exhibits negative curvature and vanishes for $f=0$, but the curvature in $R(f)$ is predominantly negative for $0<f<1$ MHz (where that for the ribbon is positive). However, as f approaches zero, the second derivative of $R(f)$ becomes positive. This behavior is clearly evident in Fig. 4, where we show $Z(f)$ for $H_A=1.4$ Oe. At higher frequency, both $R(f)$ and $X(f)$ increase as $f^{1/2}$. For $H_A=0$, the inflection point which separates the two regimes occurs for $f=60$ kHz. A $H_A=140$ Oe applied field virtually flattens the resistive frequency response ($R(f,H_A=140\ \text{Oe})\cong R_{sat}$), and like the ribbon, only a small positive slope remains in $X(f)$ for $H_A=140$ Oe. This particularly simple form of $Z(f)$ at high field, for which $R(f)\cong R_{sat}$ and $X(f)\cong 0$, is easily explained: when the sample is saturated, the anomalous magnetic effects disappear, and we observe flat spectra (for $0<f<1$ MHz) typical of nonmagnetic materials.

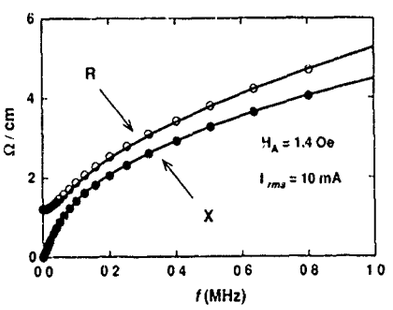

FIG. 4. The impedance spectrum $R(f)$ and $X(f)$ for the $Fe_{43}Co_{68.2}Si_{12.5}B_{15}$ wire subjected to an axial magnetic field $H_A=1.4$ Oe (the amplitude of the sense current is 10 mA rms). Note the inflection point in $R(f)$ for $f\approx 60$ kHz. The solid lines shown are a fit to Eq. (2) using two parameters.

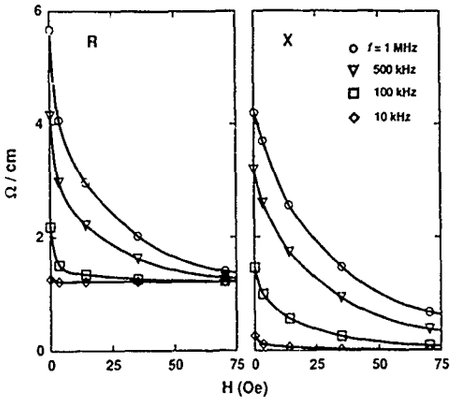

FIG. 5. Data from Fig. 3 plotted vs the applied field ($0<H_A<140$ Oe). (Data for $H_A=75$ Oe were not included in Fig. 3 for clarity.) We observe little difference between these data and those obtained by scanning H_A with f fixed.

Figure 5 shows data taken from Fig. 3 in the H_A-Z plane (we also show additional points for $H_A=75$ Oe). The lines join data obtained at a fixed frequency. The data display a pronounced increase in R and X as H_A is reduced to zero. For all values of H_A, both R and X increase with increasing frequency, and at high field tend to their respective dc limits. The widths of the curves also increase monotonically with frequency, as for the ribbon. We observe no hysteretic effects associated with sweeping frequency at fixed magnetic field, rather than sweeping field at fixed frequency. Table II displays $\Delta R/R$, $\Delta X/R$, and the widths ΔH_R and ΔH_X obtained from the wire. For $f=3.2$ MHz, $\Delta X/R=470\%$ and $\Delta R/R=620\%$. For the wire, as well as the ribbon, $\Delta H_R<\Delta H_X$. The sensitivities of the resistive and reactive responses for $f=1$ MHz are extraordinarily high: $(1/\Delta H_R)(\Delta R/R)=44\%/\text{Oe}$ and $(1/\Delta H_X)(\Delta X/R)=16\%/\text{Oe}$.

TABLE II. Relative magnitudes and widths for the $Fe_{43}Co_{68.2}Si_{12.5}B_{15}$ wire sample taken from Fig. 5. The resistance at $f=0$ is $R_{dc}=1.2\ \Omega$/cm.

Frequency	10 kHz	100 kHz	1 MHz
$\Delta R/R$	4%	80%	370%
$\Delta X/R$	21%	120%	350%
ΔH_R	1.5 Oe	1.9 Oe	8.5 Oe
ΔH_X	2.7 Oe	8.3 Oe	21.5 Oe

IV. MODEL FOR SPECTRA

Two characteristics common to the spectra of both wire and ribbon are the negative curvatures of the reactances $X(f)$ and the inflection points in the resistances $R(f)$; the latter separates the low frequency behavior, dominated by positive curvature, from that at high f, where the curves are concave down. For the case of the wire, both R and X increase with $f^{1/2}$ in the high f limit. Such features are characteristic of the impedance of nonmagnetic wires.[8] However, for a wire of the same diameter and resistivity (120 μm and 135 $\mu\Omega$ cm), these features should appear for $f\cong 10$ MHz, not at the onset frequency $f\cong 15$ kHz observed.

The magnetic response to the field produced by the drive current is evidently the mechanism which gives rise to the tremendous frequency dependences of the ribbon and wire impedances. (The effect of Joule heating on the spectra was previously found to be unimportant.[1]) The domain structure[9] of amorphous FeCoSiB wire is determined by its negative magnetostriction coefficient $\lambda\cong -10^{-7}$ in combination with quenched-in radial tensile stress. The resulting magnetic easy direction is circumferential (at least near the wire's surface). The domain structure is broken along the wire's length into alternate left- and right-handed circumferential domains. Evidently, this magnetic structure is highly susceptible to the field of a current flowing in the wire.

We model the impedance spectra of the wire using Maxwell's equations. The response to the field generated by the drive current is governed by the circumferential permeability, denoted μ_ϕ. We assume that μ_ϕ does not depend on position. This is a crude approximation; the core of the wire, very probably, is longitudinally magnetized.[9] Nevertheless, it is correct to first order. From Maxwell's equations we deduce that the skin depth for a wire with circumferential anisotropy is

$$\delta=\frac{c}{2\pi}\sqrt{\rho/\mu_\phi f}, \tag{1}$$

from which follows[8]

$$Z=R+iX=\frac{1}{2}R_{dc}ka\,\frac{J_0(ka)}{J_1(ka)}, \tag{2}$$

where the J_i are Bessel functions of the first kind, R_{dc} is the $f=0$ resistance of the wire (per cm), a the wire radius, and

$$k=(1+i)\,\frac{a}{\delta}.$$

The data may be fit to Eq. (2), with μ_ϕ a real constant.[1] Here we include the possibility that μ_ϕ is frequency dependent. We assume that this arises from a damped magnetic response, characterized phenomenologically by a relaxation time τ. The permeability $\mu_\phi=\mu'_\phi+\mu''_\phi$ is then given by[10]

$$\mu'_\phi=1+\frac{4\pi\chi_0}{1+\omega^2\tau^2},\quad \mu''_\phi=\frac{4\pi\chi_0\omega\tau}{1+\omega^2\tau^2},$$

where χ_0 is the susceptibility for $f=0$ and $\omega=2\pi f$. The solid lines in Fig. 4 are a fit with two parameters, $1+4\pi\chi_0=\mu_\phi(f=0)=6074$ and $1/\tau=10.45$ MHz. A rigorous model of the impedance would include nonlinear terms in the magnetic response to the drive current (saturation of the circumferential magnetization being the most obvious nonlinear phenomenon not contained in the above), as well as a frequency dependent relaxation time. In its present form, the model describes the data extremely well, especially considering the approximations we have made.

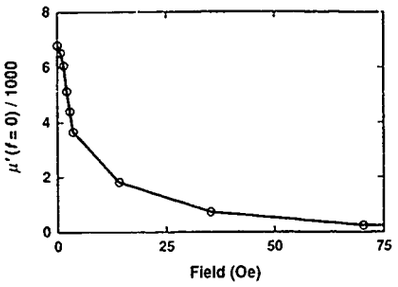

FIG. 6 Field dependence of the fitting parameter $\mu'(f=0,H_A)=1+4\pi\chi_0(H_A)$ of Eq. (3). The points were obtained by fitting data from Fig. 3 to Eq. (2) using Eqs. (1) and (3).

The permeability was so determined from the $Z(f)$ shown in Fig. 3 for a variety of H_A. Its value at zero frequency $\mu_\phi(f=0)$ (purely real) vs H_A is shown in Fig. 6. The sharp decrease in $\mu_\phi(f=0,H_A)$ for a relatively small increase in H_A parallels that in $Z(f,H_A)$. For $H_A=140$ Oe, $\mu_\phi(f=0,H_A)$ is reduced from its value of 6805 at $H_A=0$ by a factor of 75. When the magnetization is forced to lie parallel to the wire axis, the circumferential permeability approaches $\mu_\phi=1$ (Ref. 11 suggests a plausible mechanism for the field dependence of μ_ϕ). We infer that, for a fixed frequency, the skin depth δ grows roughly by a factor of 10 as H_A increases to 140 Oe from zero, and that the wire resistance is subsequently diminished. The relaxation frequency $1/\tau$ appreciably affects the quality of the fit only for $H_A<3$ Oe. In this range, $1/\tau$ increases sharply from $1/\tau=3.3$ MHz for $H_A=0$ and rises to $1/\tau>40$ MHz, beyond which frequency the addition of a damping term has a negligible effect for the frequency range fit ($0<f<1$ MHz). This behavior may possibly be due to the increased importance of rotational processes for higher H_A, and more rapid relaxation.

We believe that the same mechanism is responsible for the impedance of the ribbon sample. Because the domain structure is not known for this sample, we decline to make a quantitative comparison of the ribbon and wire spectra. We may, however, compare the two frequencies for which $R(f, H_A=0)$ exhibits an inflection point; their ratio is 25. Assuming that this is the frequency for which the skin depth is equal to the thickness of the sample, we arrive at a ratio of effective permeabilities which is of the order of one.

V. DRIVE CURRENT DEPENDENCE

The frequency-dependent part of the resistance $R-R_{sat}$ for $H_A=0$ is shown in Fig. 7 versus drive current amplitude 0.5 mA$<I_{rms}<$60 mA (data taken from Ref. 1). Note that the ordinate is set on a logarithmic scale. The current amplitude dependence of X is qualitatively similar.[1] The current scans (I_{rms} increasing) were performed for fixed frequencies $f=1$ kHz, 10 kHz, 100 kHz, and 1 MHz. For $f=1$, 10, and 100

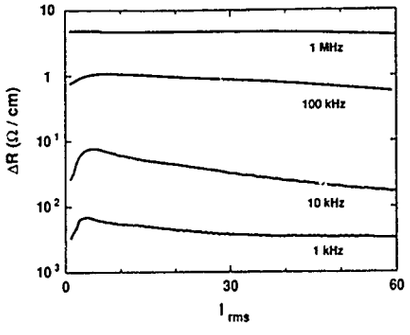

FIG. 7. Dependence of the magnetoresistance $\Delta R(f,I_{rms})$ on the amplitude of the drive current I_{rms}. Note the peak in $\Delta R(f,I_{rms})$ for $I_{rms}<1$ MHz, and the decrease in $\Delta R(f,I_{rms})$ for $I_{rms}>10$ mA at all f. The applied field is $H_A=0$.

kHz, there are peaks evident in the data at $I_{rms}=4.0$, 5.5, and 8.0 mA, respectively. This maximum vanishes for $f\geq 1$ MHz. Each data set also exhibits a gradual decrease for $I_{rms}>10$ mA. The fields at the surface of the wire are $H_\phi=2.5$, 3.0, and 4.5 Oe at the peak positions. Since it is reasonable to expect that the wire magnetizes by domain wall motion at low f, we suggest that the peak in $R(f,I_{rms})$ corresponds to the onset of domain wall motion, i.e., the circumferential coercive force. The absence of a peak in $R(f,I_{rms})$ for $f>1$ MHz is possibly due to the dominance of rotational processes at these relatively high frequencies. The decrease in R for $I_{rms}>10$ mA may result from saturation of the circumferential magnetization for a current-dependent fraction of the cycle. Experiments are in progress that will test these speculations by imaging the magnetization dynamics.

VI. CONCLUSION

A complete picture of the magnetic-field-dependent impedance spectra of amorphous ferromagnetic materials has only begun to take shape. Over the last few years a handful of groups have reported fragments of the whole. The reactance of amorphous wires possessing negative magnetostriction was found to depend sensitively on applied field;[2] a large magnetoresistance for such wires was reported for $f=82$ Hz (Ref. 4) (we observe no magnetoresistance at this low frequency); and an ac magnetoresistance, which scales linearly with f, was reported for FeCoSiB ribbons.[3] In our work we have determined that the impedance spectra of amorphous FeCoSiB wire and ribbon consist both of resistive and reactive components, each of which displays a precipitous decrease in a moderate magnetic field parallel to the sense current. We have been able to describe the effect in wires quantitatively, using a phenomenological model based on classical electrodynamics. The existence of qualitatively similar spectra for amorphous FeCoSiB ribbon demonstrates that the phenomenon is somewhat robust, and that it is not dependent on a particular domain structure.

At high frequency, the resistance is sensitive to smaller fields than the reactance. Why the widths ΔH_R and ΔH_X are different, and why they increase with frequency are unanswered questions at present (we note that the sensitivity increases with f). A possible explanation for the latter is that the circumferential anisotropy K_ϕ (and the resistivity) is dependent on position. Due to the quenching process, one expects this quantity to be greater near the wire surface. The current runs closer to the surface at higher frequencies, and the effective anisotropy field thus increases with frequency

Currently, the most sensitive giant magnetoresistive (GMR) materials have $(1/\Delta H_R)(\Delta R/R_{sat})<1\%$/Oe at room temperature. The sensitivity of the amorphous wire discussed in this paper to an applied field is more than an order of magnitude larger than this for $f=1$ MHz. It is expected that further developments in this nascent field will increase the sensitivity substantially. There is vast technological potential in the phenomenon of magneto-impedance, and many scientific questions still unanswered.

ACKNOWLEDGMENTS

The authors would like to express their appreciation to R. Hasegawa, F. E. Spada, and F. T. Parker for valuable conversations and assistance with the experiment. This research was performed under an ATP grant administered by the National Storage Industries Consortium (NSIC) and NSF Grant No. DMR-90-10908.

[1] R. S. Beach and A. E. Berkowitz, Appl. Phys Lett. **64**, 3652 (1994).
[2] K. Mohri, T Kohzawa, K. Kawashima, H. Yoshida, and L. V. Panina, IEEE Trans. Magn. **MAG-28**, 3150 (1992).
[3] F. L. A. Machado, B. L. da Silva, S. M. Rezende, and C. S. Martins, J. Appl. Phys. **75**, 6563 (1994).
[4] K. Mandal and S. K. Ghatak, Phys. Rev. B **47**, 14233 (1993)
[5] K. V. Rao, F. B. Humphrey, and J. L. Costa-Kramer (these proceedings)
[6] A. K. Agarwala and L Berger, J Appl Phys. **57**, 3505 (1985).
[7] I. Ohnaka *et al*, Proceedings of the 4th International Conference on Rapidly Quenched Metals, Sendai, 1981.
[8] L. D. Landau and E. M. Lifschitz, *Electrodynamics of Continuous Media*, 2nd ed. (Pergamon, New York, 1984).
[9] J. Yamasaki, K. Mohri, H. Kawamura, H. Takamure, F. B. Humphrey, and R. Malmhall, IEEE Trans. J. Magn. Jpn. **4**, 360 (1989).
[10] D. J Craik, *Structure and Properties of Magnetic Materials* (Pion, London, 1971)
[11] L. V. Panina, H Katoh, and K Mohri, IEEE Trans Magn. **29**, 2524 (1993).

Heavy fermion behavior of U_2T_2X compounds

L. Havela, V. Sechovský, P. Svoboda, and M. Diviš
Department of Metal Physics, Charles University, Ke Karlovu 5, 121 16 Prague 2, The Czech Republic

H. Nakotte, K. Prokeš, and F. R. de Boer
Van der Waals-Zeeman Laboratory, University of Amsterdam, Valckenierstraat 65, 1018XE Amsterdam, The Netherlands

A. Purwanto and R. A. Robinson
LANSCE, Los Alamos National Laboratory, Los Alamos, New Mexico 87545

A. Seret, J. M. Winand, J. Rebizant, and J. C. Spirlet
Institute for Transuranium Elements, European Commission, Joint Research Centre, D-76125 Karlsruhe, Germany

M. Richter and H. Eschrig
MGP Research Group "Electron Systems," Technical University Dresden, D-01062 Dresden, Germany

Magnetic and specific-heat studies of U_2T_2X compounds show a frequent occurrence of the γ enhancement in conjunction with the onset of antiferromagnetic ordering. The largest value of 830 mJ/mol K^2 was observed in U_2Pt_2In, which is nonmagnetic down to 1.2 K. Variations of electronic structure are documented by optimized relativistic LCAO calculation.

I. INTRODUCTION

Magnetic and other electronic properties of light actinides in intermetallic compounds are strongly affected by the hybridization of the $5f$ states with electronic states of ligands. In compounds with transition metals, the most significant delocalizing effect comes from the $5f$-d hybridization, which is reduced with filling the d band. The reason follows from electronic structure calculations, which show how the gradual filling of the d states leads to a reduced overlap of the $5f$ states, forming a band pinned at E_F, with the d transition metal states, which are pushed down to higher binding energies. Thus irrespective of stoichiometry or crystal structure we can observe variations of the $5f$ electron magnetism, with a crossover from nonmagnetic to magnetic ground state by the end of transition metal series. There is a common belief that heavy fermion phenomena occur only with very narrow $5f$ bands, which do not order magnetically (or which show very small ordered moments). However, it remains an open question as to why the onset of magnetism is *not* accompanied by a significant γ enhancement in many cases. In other words, the heavy fermion compounds remain rather unique and it is unclear where to place them in the systematics of other uranium intermetallics.

Here we describe results of investigations of the recently discovered compounds of the U_2T_2X type,[1] which can contribute to heavy fermion research due to a systematic occurrence of γ enhancement. The U and Np compounds of the 2:2:1 stoichiometry exist with nearly all transition metals of the Fe, Co, and Ni column. X represents Sn or In. They all crystallize in the tetragonal U_3Si_2 structure type with U-U distances in the range 3.45–3.8 Å.[1]

II. EXPERIMENTAL RESULTS

We studied polycrystalline samples prepared by arc melting stoichiometric amounts of the constituent elements. Most of them were single phase. A several percent contamination was found in U_2Pt_2In (UPt) and in U_2Ir_2Sn and U_2Ir_2In (UIr).

Most of the compounds with Ni, Pd, and Pt display antiferromagnetic (AF) order at low temperatures. The only exception is **U_2Pt_2In**, which exhibits a strongly enhanced susceptibility χ at low temperatures (23×10^{-8} m^3/mol at 4.2 K—note that 1 mol f.u. contains 2 U atoms). No phase transition was indicated in the specific heat down to 1.2 K. The $\chi(T)$ dependence (Fig. 1) can, at high temperatures, be approximated by a modified Curie–Weiss (MCW) law similar to the majority of compounds described here:

$$\chi = C/(T-\Theta_p)+\chi_0, \tag{1}$$

yielding for U_2Pt_2In the parameters $\mu_{\rm eff}=2.4$ μ_B/U, $\Theta_p=-106$ K, and $\chi_0=9.7\times10^{-8}$ m^3/mol. Below 100 K, $\chi(T)$ deviates from the MCW fit towards larger χ values. The low-temperature data are contaminated by the UPt impurity[2] (which has spontaneous magnetization of 0.4 μ_B/U below $T=25$ K[3]), but the large susceptibility at 4.2 K was confirmed by high-field magnetization measurements. The specific heat displays a pronounced upturn of C/T vs T (Fig. 2), which is insensitive to applied magnetic field of 5 T. Although the fit involving a $T^2 \ln T$ term accounts well for the data only in a very limited temperature range (up to 5 K), it can be used to estimate the γ value in the zero K limit, $\gamma\cong830$ mJ/mol K^2.

The highest ordering temperatures were observed in the two Pd compounds, **U_2Pd_2Sn** ($T_N=41$ K) and **U_2Pd_2In** ($T_N=38$ K). The susceptibility analysis in terms of Eq. (1) yields smaller negative Θ_p values (−30 and −32 K for Sn and In, respectively) than in other compounds from this series. The relatively strong $5f$ localization is indicated by sizeable U magnetic moments (1.89 and 1.40 μ_B, respec-

 0021-8979/94/76(10)/6214/3/$6.00 © 1994 American Institute of Physics

tively) determined from neutron-diffraction experiments. They show in both cases a noncollinear AF structure with moments within the basal plane and oriented along directions of the [110] type.[4] Despite magnetic ordering, a pronounced upturn in the C/T vs T dependence was found also for U_2Pd_2In, leading to γ=393 mJ/mol K^2 (65 mJ/mol K^2 is obtained by extrapolation from paramagnetic range). No such upturn was found in U_2Pd_2Sn, but the linear coefficient of the specific heat was still high: γ=203 mJ/mol K^2. The $5f$ local-moment magnetism in the Pd compounds is corroborated by the magnetic entropy estimate ($1-2\times R$ ln ?).

Unlike U_2Pt_2In, **U_2Pt_2Sn** is magnetically ordered (T_N=15.5 K). A much smaller magnetic entropy (about 0.2 $\times R$ ln 2) is suggestive of itinerant magnetism. γ=334 mJ/mol K^2 was extracted from the low-temperature range, whereas 390 mJ/mol K^2 can be obtained above T_N.

U_2Ni_2In exhibits a similar behavior (T_N=15 K). Magnetic susceptibility analysis in terms of Eq. (1) yields $\Theta_p=-80$ K and μ_{eff}=2.0 μ_B/U. The low-temperature γ=200 mJ/mol K^2 is substantially smaller than the high-temperature value of 350 mJ/mol K^2. The magnetic entropy is about 0.4$\times R$ ln 2.

U_2Ni_2Sn orders below T_N=25 K. In the paramagnetic range, μ_{eff} can be described by Eq. (1) yielding μ_{eff}=2.3 μ_B/U, $\Theta_p=-110$ K, and $\chi_0=1.8\times10^{-8}$ m^3/mol. We are aware that the presence of the χ_0 term can be an artifact due to the averaging the anisotropic χ values in polycrystal.

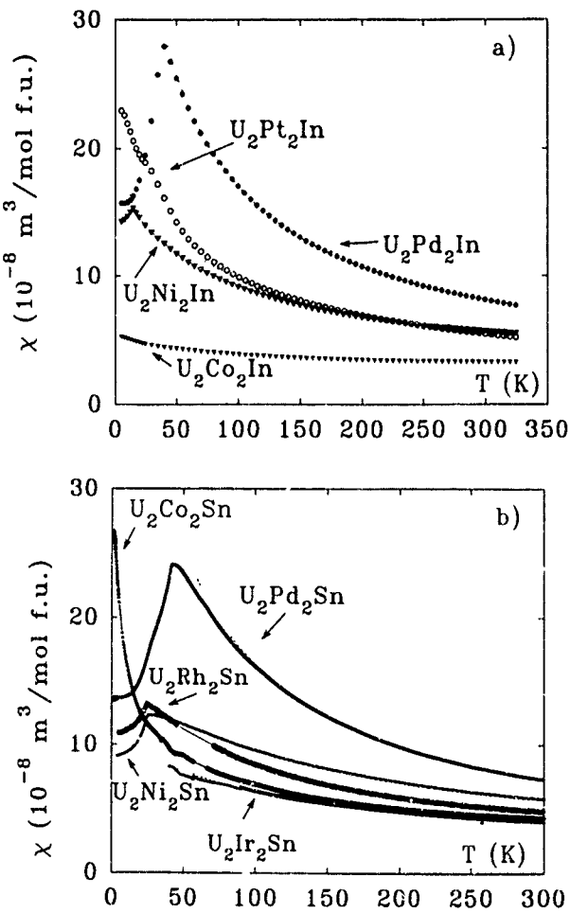

FIG 1 Temperature dependence of magnetic susceptibility of (a) U_2T_2In and (b) U_2T_2Sn The dotted lines shown in some cases are the MCW fits

Regarding other compounds, we have found magnetic ordering in **U_2Rh_2Sn** with T_N=24 K. A weak magnetic entropy of 0.4×R ln 2 is again indicative of a strongly itinerant $5f$ magnetism, but the γ value is rather low (131 mJ/mol K^2).

Besides U_2Pt_2In, some other nonmagnetic compounds exhibit spin-fluctuation features: **U_2Co_2Sn**, **U_2Ni_2In**, and **U_2Ir_2Sn**. They display γ values ranging from 130 (U_2Ir_2Sn) to 280 mJ/mol K^2 (U_2Rh_2In) (a strong upturn in C/T is found in U_2Co_2Sn and a weaker one in U_2Rh_2In). Finally, the presumably most itinerant $5f$ states cause a weak itinerant paramagnetism in **U_2Co_2In** (γ=32 mJ/mol K^2) and **U_2Ru_2Sn** (20 mJ/mol K^2).

Assessing variations of properties in the group of U_2T_2X compounds, we can deduce the following trends: (i) The $5f$ localization increases within each transition metal series towards the right end of the periodic table. This is similar to findings in other groups of light actinide compounds. (ii) The U_2T_2In compounds have a weaker tendency to magnetic ordering than their U_2T_2Sn counterparts.

III. ELECTRONIC STRUCTURE CALCULATIONS

To follow electronic structure variations in the system of U_2T_2In compounds, we performed calculations using the optimized HLCAO[5] method in a fully relativistic version.[6]

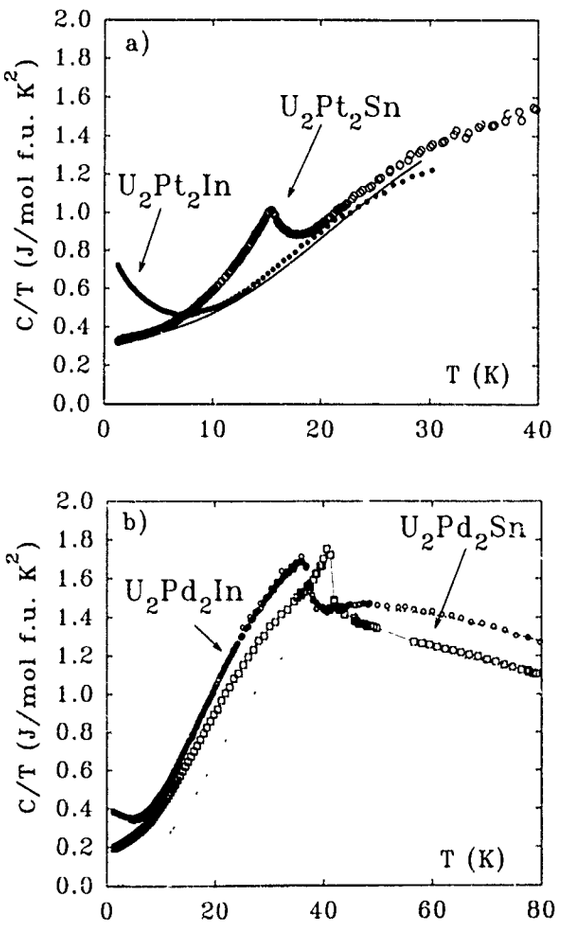

FIG. 2. C/T vs T plots of (a) U_2Pt_2X and (b) U_2Pd_2X The dotted lines show the Debye background approximating the high-temperature specific heat. For U_2Pt_2Sn (full line) it is shifted down to fit to the low-temperature γ.

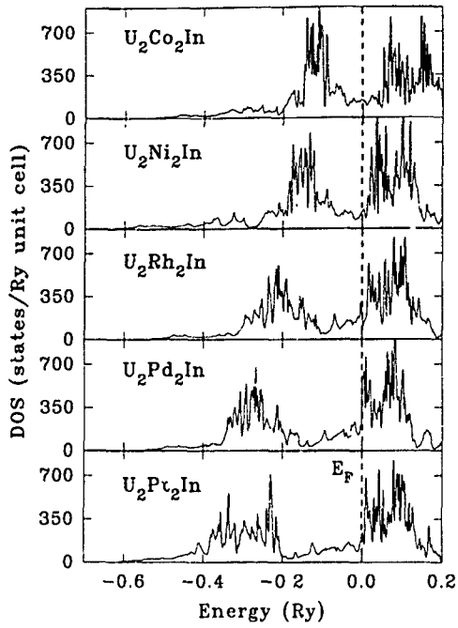

FIG. 3. Calculated total density of states of U_2T_2In.

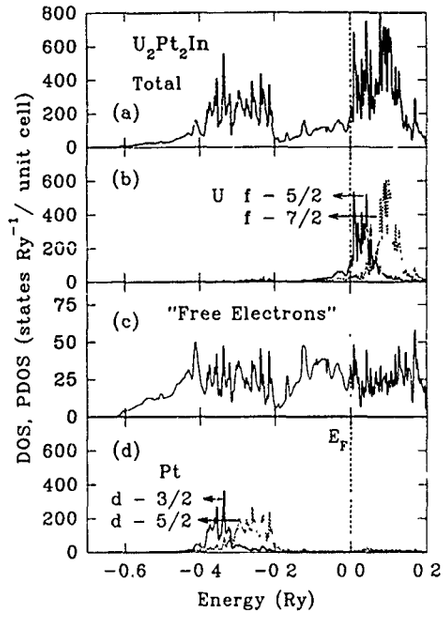

FIG. 4. Calculated total and orbital-projected density of states for U_2Pt_2In.

Self-consistency is treated by the Kohn–Sham density-functional theory in the local-density approximation (LDA).

The total densities of states (DOS) for U_2T_2In (T=Co, Ni, Rh, Pd, Pt) calculated fully relativistically are displayed in Fig. 3. The obtained spectra are characterized by a nearly free-electron background of s-, p-, and uranium $6d$ electrons, which extends to about 0.6 Ry below E_F. In all cases bonding and antibonding band groups are well separated by a broad and deep minimum around E_F. The orbital-projected DOS for the $5f$ and T-d orbitals (see, e.g., U_2Pt_2In shown in Fig. 4) indicate that the bonding (antibonding) states are predominantly T-$d(5f)$. There is, however, an appreciable amount of covalency—the $5f(T$-$d)$ contribution to the bonding and the antibonding states, respectively. The estimate of the contribution of a direct $5f$-$5f$ overlap to the width of the f-projected DOS proved that the $5f$-d hybridization appreciably enhances the $5f$ bandwidth.[6]

Practically no electron transfer from U to T was found in U_2Pd_2In. But it does increase with decreasing population of the d states. As expected, the spin-orbit splitting of Co- and Ni-$3d$ states is small, with moderate spin-orbit splitting in Rh- and Pd-$4d$ states (0.02 Ry), and the largest splitting in Pt-$5d$ and U-$5f$ states (0.1 Ry).

The Fermi level gradually shifts from the top of the bonding band in U_2Co_2In to the bottom of the antibonding band in U_2Ni_2In, U_2Rh_2In, and U_2Pt_2In, and finally into the antibonding band in U_2Pd_2In, which displays much weaker transfer of $5f$ (and $4d$) electrons into free-electron states. This reduced transfer may be understood as the result of shifting down of the Pd-$4d$ states compared to the Ni-$3d$ states or Pt-$5d$ states. The experimentally observed development in the γ values is qualitatively consistent with the trends in the calculated DOS at the Fermi level $N(E_F)$. We have also partitioned the total DOS into different contributions and the change of total DOS at E_F can be mainly ascribed to the variations of $N(E_F)^{U}_{f5/2}$.

Since the width of the covalence gap (>1 eV) exceeds the exchange splitting of elemental Co and Ni, any possible magnetism should arise from $5f$ electrons only. Applying the LDA Stoner theory, we have obtained the Stoner product $I \times N(E_F)$=0.6, 1.3, 2.0, 11.5, and 3.1 for U_2Co_2In, U_2Ni_2In, U_2Rh_2In, U_2Pd_2In, and U_2Pt_2In, respectively. Therefore the observed nonmagnetic ground state of U_2Co_2In and magnetic ground state of U_2Ni_2In and U_2Pd_2In are qualitatively consistent with our calculations. The nonmagnetic heavy fermion behavior of U_2Rh_2In and U_2Pt_2In cannot be described by our LDA calculations, which lead to a Stoner instability.

ACKNOWLEDGMENTS

This work is a part of the research program of the "Stichting voor Fundamenteel Onderzoek der Materie (FOM)." It was also supported by the U.S.–Czechoslovak Science and Technology Joint Fund under Project No. 93039 and by the Grant Agency of Czech Republic (Grant No. 202/93/0184). Support to A.S. and J.M.W. given in the frame of the EC funded training program Human Capital and Mobility is acknowledged.

[1] M. N. Peron, Y. Kergadallan, J. Rebizant, D. Meyer, J. M. Winand, S Zwirner, L Havela, H. Nakotte, J. C. Spirlet, G. M Kalvius, E Collineau, J. L. Oddou, C. Jeandey, and J. P. Sanchez, J Alloys Comp **201**, 203 (1993)

[2] The standard procedure for elimination of ferromagnetic impurity was applied on measurements in B=2 and 4 T But several percent of ferromagnetic impurity in a paramagnetic matrix means normally a very severe contamination, and the resulting "impurity-free" data are much less reliable, also partly due to a field dependence of the impurity magnetization

[3] P. H Frings and J. J M. Franse, J. Magn. Magn Mater **51**, 141 (1985)

[4] A. Purwanto, R. A. Robinson, L. Havela, V. Sechovský, P Svoboda, H. Nakotte, K. Prokeš, F R. de Boer, A. Seret, J. M Winand, J Rebizant, and J. C Spirlet, Phys. Rev. B (in press).

[5] H. Eschrig, *Optimized LCAO Method and the Electronic Structure of Extended Systems* (Springer, Berlin, 1989), M. Richter and H Eschrig, Solid State Commun. **72**, 263 (1989)

[6] M. Diviš, M. Richter, and H Eschrig, Solid State Commun **90**, 99 (1994).

Incommensurate antiferromagnetic phase in UNiGe

V. Sechovský, L. Havela, and P. Svoboda
Department of Metal Physics, Charles University, CZ 121 16 Praha 2, Czech Republic

A. Purwanto, Allen C. Larson, and R. A. Robinson
LANSCE, Los Alamos, National Laboratory, Los Alamos, New Mexico 87545

K. Prokeš, H. Nakotte, and F. R. de Boer
Van der Waals–Zeeman Laboratory, University of Amsterdam, NL 1018XE Amsterdam, The Netherlands

H. Maletta
BENSC, Hahn-Meitner-Institut, D 14 109 Berlin, Germany

By specific-heat, magnetization, electrical resistivity, and neutron-diffraction measurements on a single crystal we have confirmed that UNiGe orders antiferromagnetically below 50.5 K into an incommensurate phase with $\mathbf{q}=(0,1/2,-1/2)\pm(0,\delta,\delta)$, $\delta\sim0.15$. δ decreases continuously with decreasing temperature to ~0.123 at 41.5 K, where the incommensurate phase vanishes in a first-order phase transition and a commensurate antiferromagnetic structure with $\mathbf{q}=(0,1/2,1/2)$ sets in and remains stable down to the lowest temperatures. If a magnetic field sufficient to induce a metalmagnetic transition (1–5 T) is applied along the c axis, both antiferromagnetic phases are transformed to an uncompensated AF phase with $q=(0,1/3,1/3)$ yielding a nonzero magnetization $M\approx1/3\times M_S$. The latter structure is destroyed and a complete alignment of U moments is achieved in fields above 10 T. The strikingly different B-T diagrams observed for a magnetic field applied along different crystallographic directions reflect strongly anisotropic exchange interactions.

I. INTRODUCTION

UNiGe belongs to the isostructural group of the UTX compounds (T=transition metal, $X=p$ metal), which crystallize in the orthorhombic TiNiSi-type structure. The nearest-neighbor uranium atoms in this structure form zigzag chains along the a axis. The coordination of U atoms is intimately connected with the anisotropy of bonding of $5f$ orbitals, which has serious consequences for the symmetry of the $5f$-electron magnetism.[1] Specifically, in UNiGe and other isostructural UTX compounds, the easy-plane magnetocrystalline anisotropy with the hard-magnetization direction along the a axis is observed as a rule.[1,2] This is manifest in the low-temperature magnetization, which is small and linearly dependent on the magnetic field up to 35 T applied along the a axis. For the other two field directions (along b and c) almost saturated magnetization M_S due to aligned U moments of 1.45 μ_B is attained above metalmagnetic transitions.[2] Note that the magnetization curves at 4.2 K display two metalmagnetic transitions at 17 and 25 T in the field applied along b (and at 3 and 10 T in $B\|c$). In both field geometries, the magnetization observed above the first transition amounts to approximately $1/3\times M_s^2$.

For some time, UNiGe was believed to order magnetically around 42 K,[2–7] although some indications of another transition around 50 K could be seen in the specific-heat data of Kawamata *et al.*.[7] Moreover, controversial conclusions about the magnetic structure at low temperatures could be found in the literature.[6,8] This unsatisfactory situation motivated us to perform an extensive study of a well-defined single crystal of UNiGe, which was governed by a Czochralski technique in a tri-arc furnace at the University of Amsterdam. Besides measurements of bulk properties (magnetization, electrical resistivity, and specific heat) over wide temperature and external magnetic-field intervals, we have performed extensive neutron-diffraction experiments. Results and experimental details of bulk measurements were published elsewhere,[2,9] along with preliminary neutron data indicating the existence of the incommensurate antiferromagnetic phase (IAFP) below 50 K[11]. In this paper we concentrate on both the temperature and magnetic-field stability of the IAFP in the complex magnetic phase diagram of UNiGe.

II. RESULTS AND DISCUSSION

The specific heat of UNiGe exhibits a sharp peak at 41.5 K and a weaker maximum around 50 K (see Fig. 1). The first-order magnetic phase transition at 41.5 K is also clearly reflected in the magnetization and resistivity.[2,9] Closer inspection of magnetization and electrical resistivity results, however, also reveals around 50 K slight (but well noticeable

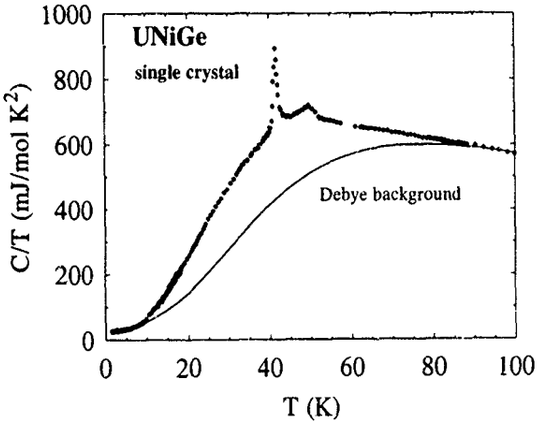

FIG. 1. Temperature dependence of the specific heat of UNiGe

 0021-8979/94/76(10)/6217/3/$6.00 © 1994 American Institute of Physics

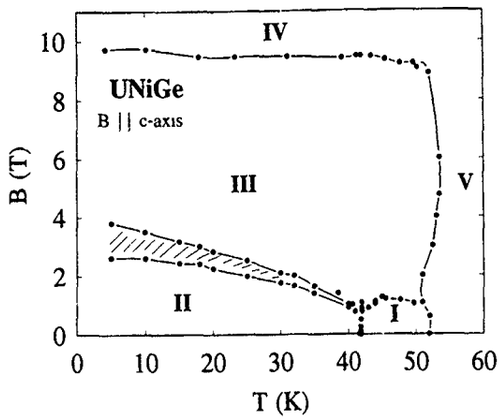

FIG. 2 Magnetic phase diagram of UNiGe in B parallel to the c axis, as determined from magnetization and neutron-diffraction measurements. (I) incommensurate antiferromagnetic phase, $\mathbf{q}=(0,1/2,-1/2)\pm(0,\delta,\delta)$, (II) commensurate antiferromagnetic phase, $\mathbf{q}=(0,1/2,1/2)$, (III) uncompensated antiferromagnetic phase, $\mathbf{q}=\pm(0,1/3,1/3)$, (IV) phase with "ferromagnetically" aligned U moments, and (V) paramagnetic phase.

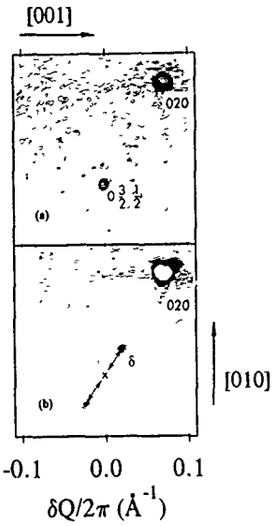

FIG. 3. Magnetic reflections in the vicinity of the 0, 3/2, −1.2 at (a) 20 K and (b) 46 K

in $\partial M/\partial T$ and $\partial\rho/\partial T$) anomalies, which corroborate the conclusion about the magnetic origin of this phase transition.

In order to obtain better knowledge of magnetic phases and transitions in UNiGe we performed neutron-diffraction experiments on the same single crystal at BENSC (on E2 and E4) and LANSCE (on SCD). The obtained magnetic phase diagram shown in Fig. 2 contains essential information from studies in magnetic fields applied along the c axis.

A. Zero magnetic field, $T\leqslant 41.5$ K

All observed magnetic reflections can be indexed as $h,k/2,1/2$ (with $k,1$ odd), suggesting the AF structure with $\mathbf{q}=(0,1/2,1/2)$ in agreement with Ref. 6. The U moments are locked in the b-c plane. The temperature dependence of the intensities of the magnetic reflections indicates that the U moment decreases slowly with increasing temperature.[11] At 40 K, the ordered U moments retain about 90% of the low-temperature value. The magnetic intensities then decrease abruptly at the 41.5 K first-order phase transition, where the low-temperature phase vanishes.

B. Zero magnetic field, $T\geqslant 41.5$ K

A crucial point of our research has been to indicate an IAFP, which propagates within the b-c plane. For this purpose experiments on the flat cone diffractometer E2 in Berlin and the single-crystal diffractometer SCD with an area detector at Los Alamos were indispensable. Both types of experiments provided compatible results confirming the existence of an IAFP with $\mathbf{q}=(0,1/2,-1/2)\pm(0,\delta,\delta)$. For illustration, we display in Fig. 3 typical patterns recorded on SCD in Los Alamos at 20 and 46 K, in which the difference between the respective magnetic states is manifest. Whereas at 20 K the 0, 3/2, −1/2 is characteristic for the commensurate AF phase stable below 41.5 K, this reflection is absent at 46 K and instead two satellites shifted by $\pm(0,0.141,0.141)$ indicate the presence of the IAFP. After identifying this phase, its stability and temperature evolution of δ were studied on E4 in Berlin. The results are displayed in Fig. 4 The IAFP emerges just above 41.5 K. The characteristic reflections 0, $k/2\pm\delta$, $-1/2\pm\delta$ reach a maximum intensity already around 43 K and then diminish continuously with increasing temperature. The reflections are at the limit of detectability at 50 K, but some residual intensity can be seen in the background up to approximately 53 K. The parameter δ varies from ~0.123 at 41.5 to 0.15 at 50 K. The transition at 41.5 K is apparently of the first-order type in contrast to the second-order transition around 50.5 K.

C. $B\leqslant 6$ T, $E\|c$, $T\leqslant 41.5$ K

The first metalmagnetic transition exhibits a large hysteresis.[11] The critical fields and the hysteresis (marked by the hatched region in Fig. 2) decrease with increasing temperature. When sweeping the field upwards, the $0,k/2,1/2$ reflections disappear rapidly around the transition. On the

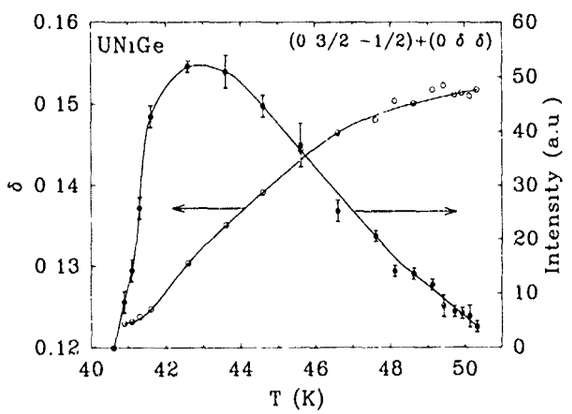

FIG 4 Temperature dependence the integral intensity and the parameter δ of the $(0,1/2,-3/2)\pm(0,\delta,\delta)$ reflection

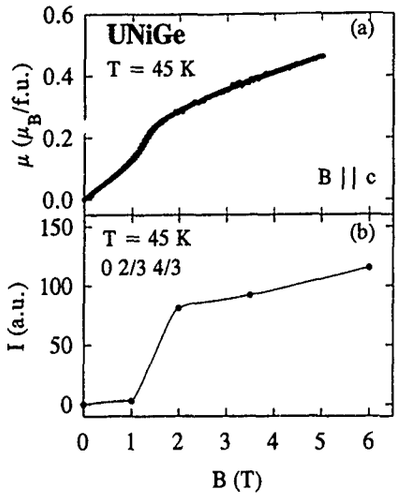

FIG. 5. Field scans of (a) magnetization and (b) the 0 2/3 4/3 reflection at 45 K.

other hand, $h,k/3,1/3$-type reflections and magnetic contribution to nuclear reflections emerge (following the magnetization dependence closely).[11] The metalmagnetic state connected with the uncompensated AF structure therefore has $\mathbf{q}=(0,1/3,1/3)$. This leads to the collinear arrangement of the U magnetic moments oriented along the c axis with the $++-$ stacking simultaneously along the b and c axis, which gives rise to the magnetization $M=1/3\times M_s$ in agreement with the above-mentioned result from magnetization measurements.

D. $B\leq 6$ T, $B\|c$, $T\geq 41.5$ K

The IAFP is stable in magnetic fields up to about 1 T, where it starts to transform gradually to phase III. This field correlates well with that of the metalmagnetic transition shown in Fig. 5(a). The $0,k/3,1/3$ reflections representing the phase III persist up to ~51 K, where a first-order transition (in contrast to the second-order transition in zero field) to the high-temperature paramagnetic phase takes place as shown in Fig. 5(b).

When the magnetic field is applied along the b axis a two-step metalmagnetic process appears. However, the critical fields of the metalmagnetic transitions are considerably higher, indicating pronounced anisotropy of the exchange interactions.

To analyze magnetic phases in U intermetallics, models considering the relation of U coordination and the type of anisotropy can be employed. The experimental findings in UNiGe corroborate the empirical rules[1] relating the symmetry of the bonding of the $5f$ orbitals in a particular structure to the type of magnetocrystalline anisotropy. The strong bonding axis (a axis in UNiGe and structure-related UTX compounds) determines the hard-magnetization direction whereas the magnetic moments are locked perpendicular to the hard direction (in the b-c plane in UNiGe). The exchange interaction along the strong bonding axis (plane) is usually strong and ferromagnetic, whereas the considerably weaker interaction(s) in the perpendicular direction(s) mediate the coupling between the ferromagnetic chains (planes). These interactions are frequently frustrated and a sequence of incommensurate and commensurate phases can be observed[12] when temperature is decreased.

ACKNOWLEDGMENTS

The work was sponsored by the U. S.–Czechoslovak Science and Technology Joint Fund (Project No. 93039), by the Czech Grant Agency (Project No. 93/202/0184) and the "Stichting voor Fundamenteel Onderzoek der Materie" (FOM). The experiments at HMI were supported by the CEC HCM programs "Go West" (V.S.) and Large Facilities (K.P.). Work at Los Alamos was funded in part by the division of Basic Energy Sciences of the U. S. Department of Energy.

[1] V. Sechovský, L. Havela, H Nakotte, F.R. de Boer, and E Brück, J. Alloys Comp. (in press)
[2] L. Havela, V. Sechovský, F. R. de Boer, E. Bruck, and H. Nakotte, Physica B **177**, 159 (1992).
[3] R. Troc and V. H. Tran, J. Magn. Magn. Mater. **73**, 38 (1988).
[4] K. H. J. Buschow, E. Bruck, R. G. van Wierst, F. R. de Boer, L Havela, V. Sechovský, P. Nozar, E. Sugiura, M. Ono, M. Date, and A. Yamagishi, J Appl. Phys **67**, 5215 (1990).
[5] S. Kawamata, K. Ishimoto, H. Iwasaki, N. Kobayashi, Y. Yamaguchi, T. Komatsubara, G. Kido, T Mitsugashira, and Y Muto, J. Magn. Magn. Mater. **90–91**, 513 (1990).
[6] A. Murasik, P. Fischer, R.Troc, and V. H. Tran, J. Phys. Condens. Matter **3**, 1841 (1991).
[7] S. Kawamata, H. Iwasaki, and N. Kobyashi, J. Magn. Magn. Mater. **104–107**, 55 (1990)
[8] S. Kawamata, K. Ishimoto, Y. Yamaguchi, and T. Komatsubara J. Magn. Magn. Mater. **104–107**, 51 (1990).
[9] K. Prokeš, H Nakotte, E. Bruck, F R. de Boer, L. Havela, V. Sechovský, P. Svoboda, and H. Maletta, IEEE Trans. Magn. (in press).
[10] F. R. de Boer, K. Prokeš, H. Nakotte, E. Bruck, P Svoboda, V Sechovský, L. Havela, and H. Maletta, Physica B (in press)
[11] V. Sechovský, L Havela, A. Purwanto, A. C. Larson, R. A. Robinson, K Prokeš, E. Bruck, F R. de Boer, P Svoboda, H Maletta, and M Winkelmann, J Alloys Comp. (in press).
[12] D Gignoux and D. Schmitt, Phys. Rev. B **48**, 12682 (1994).

Magnetic susceptibility and electronic specific heat of Anderson lattice with finite *f*-band width

Sunil Panwar and Ishwar Singh
Department of Physics, University of Roorkee, Roorkee 247667, India

We study an extension of the periodic Anderson model by considering finite f-band width. A variational method recently developed, has been used to study the temperature dependence of the average valence of magnetic susceptibility χ_s and electronic specific heat C_v for different values of the f-band width. As f-band width increases, the low-temperature peak in χ_s and C_v becomes more broad and shifts towards the high-temperature region.

I. INTRODUCTION

A class of certain lanthanide and actinide intermetallic compounds, now known as heavy fermions, show a variety of anomalous electronic and magnetic properties.[1-4] At high temperatures, there is a Curie–Weiss-like magnetic susceptibility χ_s. χ_s can be fitted to $(T-\theta)^{-1}$ where $\theta<0$ and there are large effective moments ($>\mu_B$). However, at low temperatures, χ_s shows T^2 dependence and tends to a constant value which for heavy-fermion systems is greatly enhanced over the value expected for a normal metal. The data on the electronic specific heat C_v also show interesting features. In general C_v varies linearly with temperature at very low temperature, $C_v=\gamma T$, which is the behavior expected for a Fermi liquid. In the recent past, the periodic Anderson model (PAM)[5] has been widely accepted as a model for understanding the basic electronic and magnetic properties of mixed valence and heavy fermion materials. Since there is an overlap of 5-f orbitals (thereby giving rise to a finite f-band width) in actinide materials,[6] we consider an extension of the PAM by considering finite f-band width. Recently, an extension to the Anderson model in which direct f-f hopping is included has been studied by several authors.[7-9] This model has been studied by several authors using the variational method.[10-14] Recently, we developed a variational method[15-20] to study the ground state and thermodynamic properties of PAM. We use this variational method here to study the PAM including finite f-band width. In Sec. II we give the basic formulation for the magnetic susceptibility and electronic specific heat. In Sec. III we discuss our results.

II. BASIC FORMULATION

The orbitally nondegenerate periodic Anderson model including finite band width of f electrons is described by the Hamiltonian

$$H=\sum_{k\sigma}\epsilon_k c^{+}_{k\sigma}c_{k\sigma}+\sum_{ij\sigma}T_{ij}b^{+}_{i\sigma}b_{j\sigma}-\sum_{ik\sigma}V_{ik}(c^{+}_{k\sigma}b_{i\sigma}+\text{h.c.})+\frac{U}{2}\sum_{j\sigma}n^{f}_{j\sigma}n^{f}_{j-\sigma}, \tag{1}$$

where

$$T_{ij}=\frac{1}{N}\sum_{k}E_k e^{ik(R_i-R_j)}. \tag{2}$$

Here, E_k is the f-band energy and other symbols have their usual meanings.

For simplicity, we assume that the form of the f band is the same as that of the conduction band. The f band is represented by the expression

$$E_k=\epsilon_f+A\left(\epsilon_k-\frac{W}{2}\right), \tag{3}$$

where A is a positive constant less than unity. Here W and AW are the band widths of conduction band and f band, respectively. For $A=0$, $E=\epsilon_f$ is the position of the f level.

In the k space, the Anderson–Hamiltonian may be written as

$$H=\sum_{k\sigma}\epsilon_k c^{+}_{k\sigma}c_{k\sigma}+\sum_{k\sigma}\left[\epsilon_f+A\left(\epsilon_k-\frac{W}{2}\right)\right]b^{+}_{k\sigma}b_{k\sigma}-\sum_{k\sigma}v_k(c^{+}_{k\sigma}b_{k\sigma}+\text{h.c.})+\frac{U}{2}\sum_{j\sigma}n^{f}_{j\sigma}n^{f}_{j-\sigma}. \tag{4}$$

Here we are considering strongly interacting (i.e., $U\to\infty$) case. In this case the probability of f^2 configuration is very small. The variational wave function which projects the f^2 configuration out, may be written as (Panwar and Singh[15])

$$|\psi\rangle=\prod_{k\sigma}[1+A_{k\sigma}(1-n^{f}_{-\sigma})b^{+}_{k\sigma}c_{k\sigma}]|F\rangle \tag{5}$$

when $|F\rangle=\Pi_{k\le k_{F,\sigma}}c^{+}_{k\sigma}|0\rangle$ is the Fermi sea of conduction electrons and $A_{k\sigma}$ the variational parameters. It can be seen that the resultant states are in the form of two quasiparticle bands; the lower (−) and upper (+) of quasiparticle spectra are given by

$$E^{\pm}_{k\sigma}=\frac{1}{2}\left\{\left[(1+AP_f)\epsilon_k+\epsilon_f P_f-\frac{AWP_f}{2}\right]\pm\sqrt{\left((1-AP_f)\epsilon_k-\epsilon_f P_f+\frac{AWP_f}{2}\right)^2+4V_k^2P_f^2}\right\}. \tag{6}$$

The A_k's are given by

 0021-8979/94/76(10)/6220/3/$6.00 © 1994 American Institute of Physics

$$A_k^{\pm}=\frac{1}{2V_kP_f^2}\left\{\left[\epsilon_k(1-AP_f)-\epsilon_fP_f+\frac{AWP_f}{2}\right]\right.$$
$$\left.\pm\sqrt{\left[\epsilon_k(1-AP_f)-\epsilon_fP_f+\frac{AWP_f}{2}\right]^2+4V_k^2P_f^2}\right\}, \tag{7}$$

where

$$P_f=(1-n^f_{-\sigma}).$$

At finite temperature, the number of conduction electrons and f electrons are given by (taking the total number of electrons such that the Fermi level lies in the lower band)

$$n^c_{k\sigma}=\left[\frac{f^-_{k\sigma}}{1+(A^-_{k\sigma})^2P_f^2}+\frac{f^+_{k\sigma}}{1+(A^+_{k\sigma})^2P_f^2}\right]$$
$$n^f_{k\sigma}=\left[\frac{(A^-_{k\sigma})^2P_f^3f^-_{kr}}{1+(A^-_{k\sigma})^2P_f^2}+\frac{(A^+_{k\sigma})^2P_f^3f^+_{kr}}{1+(A^+_{k\sigma})^2P_f^2}\right]. \tag{8}$$

Here Fermi functions $f^-_{k\sigma}$ and $f^+_{k\sigma}$ are given by

$$f^{\pm}_{k\sigma}=\frac{1}{\exp[\beta(E^{\pm}_{k\sigma}-\mu)]+1} \tag{9}$$

where μ is the chemical potential and $\beta=1/k_BT$.

A. Magnetic susceptibility

In the presence of a static magnetic field B, the f level is $E_f-g\sigma u_BB$; $E_f=\epsilon_f+A(\epsilon_k-W/2)$. The static magnetic susceptibility for the lower branch of quasiparticle spectra is given by

$$\chi_s=gu_B\sigma\frac{\partial}{\partial B}[n^f_\sigma-n^f_{-\sigma}]\Big|_{B\to0}. \tag{10}$$

Putting n^f_σ's from Eq. (8) one gets, after some algebra, the expression of susceptibility [in units of $(g\mu_B)^2$] at finite temperature[16] in the paramagnetic region.

B. Electronic specific heat

At finite temperature, the ground state energy is given by

$$\langle E\rangle=\sum_{k\sigma}[(E^-_{k\sigma}-\mu)f^-_{k\sigma}+(E^+_{k\sigma}-\mu)f^+_{k\sigma}]. \tag{11}$$

The electronic specific heat C_v is obtained by differentiating energy $\langle E\rangle$ with respect to temperature T. The total electronic specific heat gets the contribution from both the lower as well as the upper quasiparticle bands. It is given by

$$C_v=\frac{\partial\langle E\rangle}{\partial T}=\frac{\partial}{\partial T}\sum_{k\sigma}[(E^-_{k\sigma}-\mu)f^-_{k\sigma}+(E^+_{k\sigma}-\mu)f^+_{k\sigma}]. \tag{12}$$

III. RESULTS AND DISCUSSIONS

In these calculations, we have considered a tight-binding conduction band which is centered around zero energy with conduction band width $W=2.0$ eV. The total number of electrons per site (n^C+n^f) has been taken to be 1.5. The f-band width is $AW=2$ A. V is fixed on 0.25 eV. Figures 1(a) and 1(b) show the variation of average valence n^f and magnetic susceptibility χ_s^0 with parameter A, respectively, at $T=0$ K. In Fig. 1(a) curve I shows variation for the f-level position $\epsilon_f=-0.4$ and curve II for $\epsilon_f=0.0$. Here we find a smooth variation of n^f with A. We have also seen that for a constant value of A, n_f increases slowly with increasing temperature.

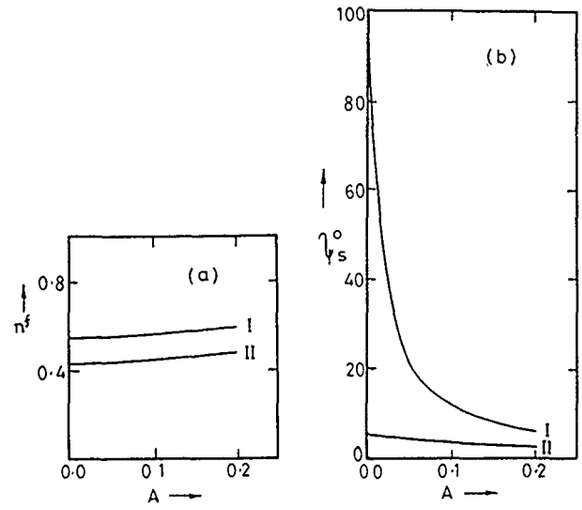

FIG. 1. (a) Variation of average valence n^f with A at $T=0$ K with tight-binding conduction band for different effective positions of f level. Curve I for $\epsilon_f=-0.4$, curve II for $\epsilon_f=0.0$ V is fixed on 0.25. (b) Variation of magnetic susceptibility χ_s^0 [in units of $(g\mu_B)^2$] with A at $T=0$ K with tight-binding conduction band for different effective positions of f level Curve I for $\epsilon_f=0.0$, curve II for $\epsilon_f=0.2$. V are fixed on 0 25.

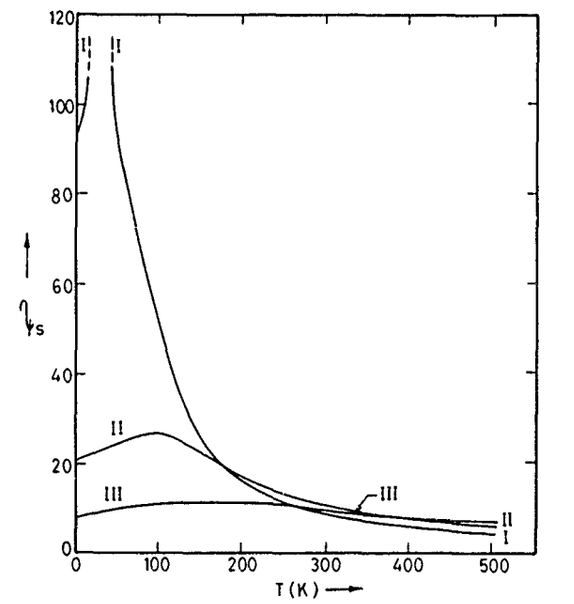

FIG. 2. Magnetic susceptibility χ_s [in units of $(g\mu_B)^2$] as a function of temperature for different A with tight-binding conduction band $V=0$ 25 and $\epsilon_f=0.0$ Curve I for $A=0$ 0, curve II for $A=0$ 05, and curve III for $A=0$ 15 Dashed part of curve I shows the divergence of χ_s in the temperature range 10–50 K

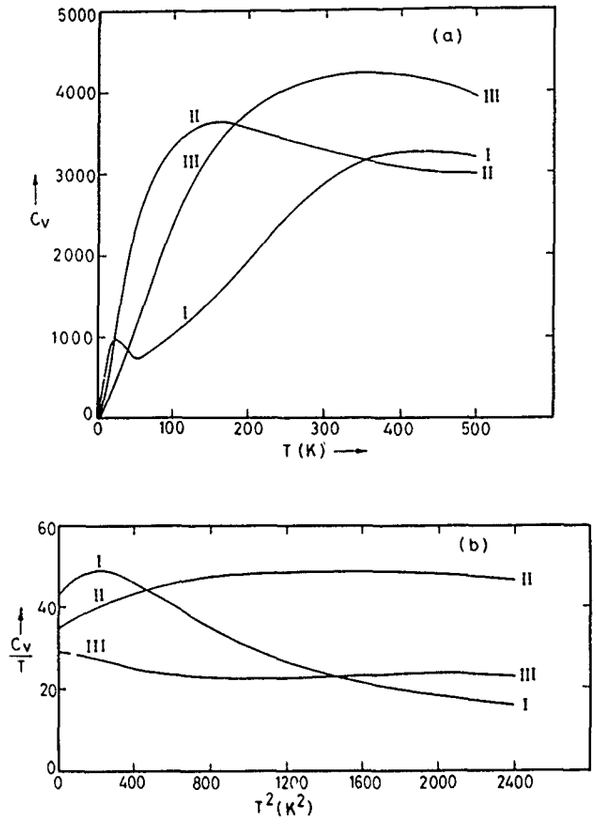

FIG. 3. (a) Variation of specific heat C_v with temperature with tight-binding conduction band for different values of A. Curve I is for $A=0.0$, curve II for $A=0.05$, and curve III for $A=0.15$. ϵ_f are fixed on -0.4. (b) Variation of specific heat coefficient C_v/T with temperature with tight-binding conduction band for different values of A. Curve I is for $A=0.0$, curve II for $A=0.05$, and curve III for $A=0.15$. ϵ_f are fixed on -0.4.

While in Fig. 1(b), curve I shows variation for $\epsilon_f=0.0$ and curve II for $\epsilon_f=0.2$. χ_s^0 increases rapidly as A is lowered.

We have shown results of magnetic susceptibility $\chi_s(T)$ in Fig. 2 for different A. ϵ_f is fixed on 0.0. Curve I stands for $A=0.0$, curve II for $A=0.05$, and curve III for $A=0.15$. The behavior of $\chi_s(T)$ is interesting. At low temperature $\chi_s(T)$ rises up to a maximum. This low-T peak in χ_s gets sharpened as A reduces from 0.15 to 0.10 and finally diverges at $A=0.0$. Also as the f level goes down, χ_s increases and we have a sharper peak at low temperature. This susceptibility behavior is characteristic of many mixed-valence compounds like $CeSn_3$, $CePd_3$, and of many Ce and U-heavy fermion systems like $CeAl_3$ and UPt_3.[21,22] As A increases, the f-band width increases and as a result the density of f states reduces and thereby reduces the Pauli susceptibility term.

Figures 3(a) and 3(b) show the variation of specific heat C_v and specific heat coefficient C_v/T, respectively, with temperature for different values of parameter A. ϵ_f is fixed on -0.4. Curve I shows variation for $A=0.0$, curve II for $A=0.05$, and curve III for $A=0.15$. Here $C_v(T)$ increases linearly at low temperature, and has a maxima near $T_{max}=25$ K at $A=0.0$. As A increases, the maximum is less pronounced and much broader and shifts towards higher temperature region. Also as A increases, the maxima in C_v/T at low temperature becomes wider and is less pronounced and in some cases disappears. We have a more sharp peak in C_v or C_v/T at low temperature as the f level goes down for a constant value of A. This behavior of specific heat curves has been the main characteristic of many mixed valence and heavy fermion materials like $NpSn_3$.[23]

From the above results of $\chi_s(T)$ and $C_v(T)$, one can conclude that by increasing the f-band width, we are making the "Fermi-liquid" nature of f electrons to be more pronounced.

ACKNOWLEDGMENTS

One of the authors (S.P.) is thankful to the Council of Scientific and Industrial Research (India) for financial support. I.S. is thankful to the Department of Science and Technology (India) for financial support.

[1] G. R. Stewart, Rev. Mod. Phys. **56**, 755 (1984).
[2] *Theory of Heavy Fermions and Valence Fluctuations*, edited by T. Kasuya and T. Saso (Springer, New York, 1985).
[3] P. Flude, J. Keller, and G. Zwichnage, *Solid State Physics*, edited by H. Ehrenreich and D Turnbull (Academic, New York, 1988), Vol 41
[4] U. Rauchschwalbe, Physica, **147B**, 1 (1987).
[5] S. Doniach, Physica (Utrecht) B **91**, 231 (1977), H. J. Leder and B. Muhlschlegel, Z. Phys. B **29**, 341 (1978); K. Yamada and K. Yosida, Prog. Theor. Physics (Kyoto) **76**, 621 (1986); K Yamada, K. Okada, and K. Yoshida, Prog Theor. Phys. (Kyoto) **77**, 1097, 1297 (1987)
[6] *The Actinides: Electronic Structure and Related Properties*, edited by J. B. Darby, Jr. and A. J Freeman (Academic, New York, 1974), Vol. I, p. 51.
[7] A. P. Harrington, D K Roy, and G. A. Gehring, J. Phys. C: Solid State Phys. **21**, 5007 (1988)
[8] S. M. M. Evans, T. Chung, and G A. Gehring, J. Phys. Condens. Matter **1**, 10473 (1989).
[9] S. Panwar and I Singh (unpublished).
[10] B. H. Brandow, Phys. Rev. B **33**, 215 (1986); J. Magn. Magn Mater. **63–64**, 264 (1987); Solid State Commun. **69**, 915 (1989)
[11] T. M. Rice and K. Ueda, Phys. Rev. Lett. **55**, 995 (1985); Phys Rev. B **34**, 6420 (1986)
[12] C M Varma, W. Weber, and L. J. Randall, Phys. Rev B **33**, 1015 (1986).
[13] A. Oguchi, Prog. Theor. Phys. (Kyoto) **77**, 278 (1987); P Fazekas, Solid State Commun **60**, 431 (1986).
[14] T Yanagisawa, Phys. Rev B **37**, 2050 (1988).
[15] S. Panwar and I. Singh, Solid State Commun. **72**, 711 (1989).
[16] S. Panwar and I Singh, Phys. Status Solidi B **168**, 583 (1991)
[17] S. Panwar and I Singh, Solid State Commun **85**, 239 (1993).
[18] S. Panwar and I. Singh, Phys. Status Solidi B **175**, 487 (1993).
[19] S. Panwar and I. Singh, Phys. Rev. B **50** (1994)
[20] S. Panwar, Ph.D. thesis, 1992 (unpublished).
[21] B. H. Brandow, Phys Rev. B **37**, 250 (1988), T Yanagisawa, *ibid* **38**, 9099 (1988).
[22] P H. Frings, J. J M. Franse, F. R de Boer, and A. Monovsky, J Magn. Magn **31–34**, 240 (1983).
[23] R. J Trainor, M B. Brodsky, B D. Dunlap and G. K. Shenoy, Phys. Rev Lett. **37**, 1511 (1976).

Electrical resistivity and thermoelectric power of heavy fermions and mixed-valence systems

Sunil Panwar and Ishwar Singh
Department of Physics, University of Roorkee, Roorkee 247667, India

Representing the heavy fermions and mixed-valence systems by the periodic Anderson model, we have used the variational method to study the temperature dependence of electronic transport properties of these systems. The electrical resistivity $\rho(T)$ and thermoelectric power $Q(T)$ calculated show the features experimentally observed in these materials. In the low-temperature region $\rho(T)$ and $Q(T)$ increase rapidly. Toward high-temperature region, $Q(T)$ changes sign.

I. INTRODUCTION

The experimental results of electrical resistivity $\rho(T)$ of many heavy fermion systems (e.g., $CeAl_3$, $CeCu_2Si_2$, $CeCu_6$, UBe_{13}) at low temperatures show anomalous behavior.[1-5] $\rho(T)$ increases with increasing temperature in the very low-temperature region (known as the Fermi-liquid region or coherence region), reaching a maximum and then decreasing slowly like $\ln T$ (known as the Kondo region or independent-impurity region). The negative temperature coefficient (NTC) of the resistivity in the high-temperature regime is usually interpreted as a manifestation of the Kondo effect in a concentrated system.[1,2] The thermoelectric power $Q(T)$ also exhibits characteristic anomalies when compared to the thermoelectric power of usual metals. $Q(T)$ is very large in the case of these materials. It shows a maximum at a relatively low temperature T^*. In some heavy fermion systems like UPt_3,[6] $Q(T)$ changes sign at temperatures $T>T^*$. In the recent past it has been suggested that the low-temperature coherent Fermi-liquid phase may very well be represented by the periodic Anderson model (PAM) where one considers the coherent hybridization between conduction states and the f states on all N sites.[7-11]

Recently we developed a variational method to study the ground-state and thermodynamic properties of PAM.[11-15] We use this variational method here to study electrical resistivity and thermoelectric power of heavy fermion (HF) and mixed-valence (MV) systems within PAM. The details of the variational method may be found in Ref. 11. In the recent past, the characteristic anomalies in $\rho(T)$ and $Q(T)$ have been described by the frequency dependent relaxation time resulting from quasiparticle-quasiparticle scattering. In Ref. 16, the frequency dependence of the self-energy contains this information. We have not taken into account such lifetime effects in our variational approach. In this work, we suggest that the scattering mechanism is impurity scattering with a frequency independent mean free path and we have taken into account only the energy dependence of different factors like density of states appearing in the expression of $\rho(T)$ and $Q(T)$. We have used the Mott's formula for the electrical conductivity which takes the explicit energy dependence of the mean free path. Below we give the basic formulation for electrical resistivity and thermoelectric power. In Sec. III we discuss our results.

II. BASIC FORMULATION

The orbitally nondegenerate periodic Anderson model is described by the Hamiltonian

$$H=\sum_{k\sigma}\epsilon_k c^+_{k\sigma}c_{k\sigma}+\epsilon_f\sum_{\iota\sigma}b^+_{\iota\sigma}b_{\iota\sigma}-\sum_{k\sigma}V_k(c^+_{k\sigma}b_{k\sigma}+\text{h.c.})+\frac{U}{2}\sum_{j\sigma}n^f_{j\sigma}n^f_{j-\sigma}, \tag{1}$$

where symbols have their usual meanings.

A. Weak interaction case

In the weak-interaction case, where Coulomb interaction U is small and all the three configurations f^0, f^1, and f^2 are energetically possible, the variational wave function has been taken as in k space

$$|\Psi_0\rangle=\prod_{k\sigma}(1+A_{k\sigma}b^+_{k\sigma}c_{k\sigma})|F\rangle, \tag{2}$$

with $|F\rangle$ as the conduction-electron state and A_k the variational parameters. It can be easily seen that the resultant states are in the form of two quasiparticle bands; the lower branch of quasiparticle spectra is given by

$$E^-_k=1/2\left[\left(\epsilon_k+\epsilon_f+\frac{Un^f}{2}\right)-\sqrt{\left(\epsilon_k-\epsilon_f-\frac{Un^f}{2}\right)^2+4V_k^2}\right]. \tag{3}$$

B. Strong interaction case

In the high interaction case, where U is very large and the probability of f^2 configuration is very small, the variational wave function which projects the f^2 configuration out may be written as

$$|\Psi\rangle=\prod_{k\sigma}[1+A_{k\sigma}(1-n^f_{-\sigma})b^+_{k\sigma}c_{k\sigma}]|F\rangle. \tag{4}$$

For this case, the corresponding expression of E^-_k is

$$E^-_k=\tfrac{1}{2}[(\epsilon_k+\epsilon_f P_f)-\sqrt{(\epsilon_k-\epsilon_f P_f)^2+4V_k^2P_f^2}]. \tag{5}$$

C. Electrical resistivity

We are not interested here in the absolute value of resistivity and thermoelectric power but only in the variation of resistivity and thermoelectric power with temperature. In the

 0021-8979/94/76(10)/6223/3/$6.00 © 1994 American Institute of Physics

low-temperature regime, we assume the resistivity is produced by the impurities in the system. Then we use the electrical conductivity formula given by Mott[17]

$$\sigma(T)=\int\left(-\frac{\partial f_k^-}{\partial E_k^-}\right)\tilde{\sigma}(E_k^-)dE_k^-, \tag{6}$$

where $\tilde{\sigma}(E_k^-)$ can be written as

$$\tilde{\sigma}(E_k^-)=\sigma_0[N^c(E_k^-)]^2, \tag{7}$$

$$\sigma_0=\frac{2\pi e^2\hbar^3}{m^2}|D_E|^2_{\text{av}}. \tag{8}$$

The symbols in σ_0 are given in Ref. 17. σ_0 has been taken as a constant in our calculations. f_k^- is the Fermi function for the lower branch of the quasiparticle spectrum and $N^c(E_k^-)$ is the density of (lower part of) perturbed conduction states.

D. Thermoelectric power

The thermoelectric power $Q(T)$ may be written in terms of $\tilde{\sigma}(E_k^-)$ [17] in the following way

$$Q(T)=Q_0\frac{\int dE_k^-(-\partial f/\partial E_k^-)(E_k^--\mu)\tilde{\sigma}(E_k^-)}{\int dE_k^-(-\partial f/\partial E_k^-)\tilde{\sigma}(E_k^-)}, \tag{9}$$

where

$$Q_0=\frac{1}{e}. \tag{10}$$

III. RESULTS AND DISCUSSIONS

In these calculations we have considered a tight-binding conduction band which is centered around zero energy with a conduction-band width $W=2.0$ eV. The total number of elec-

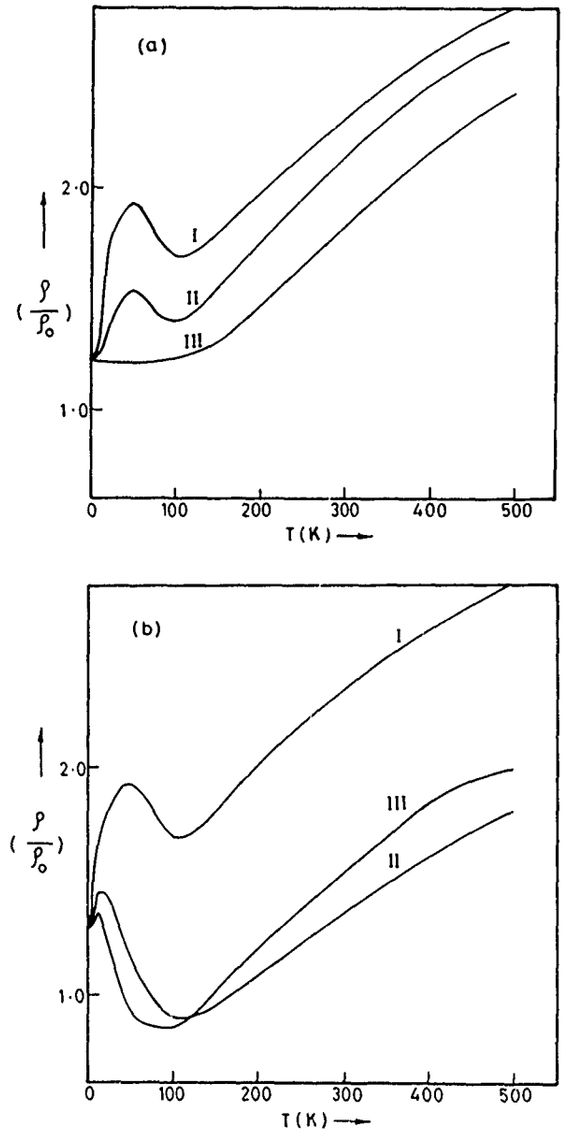

FIG. 1. Electrical resistivity ρ as a function of temperature for the tight-binding conduction-band case (a) $V=0.25$, $U=\infty$, curve I for $\epsilon_f=-0.6$, curve II for $\epsilon_f=-0.4$, and curve III for $\epsilon_f=-0.2$. (b) $V=0.25$, $\epsilon_f=-0.6$, curve I for $U=\infty$, curve II for $U=1.0$, and curve III for $U=0.5$

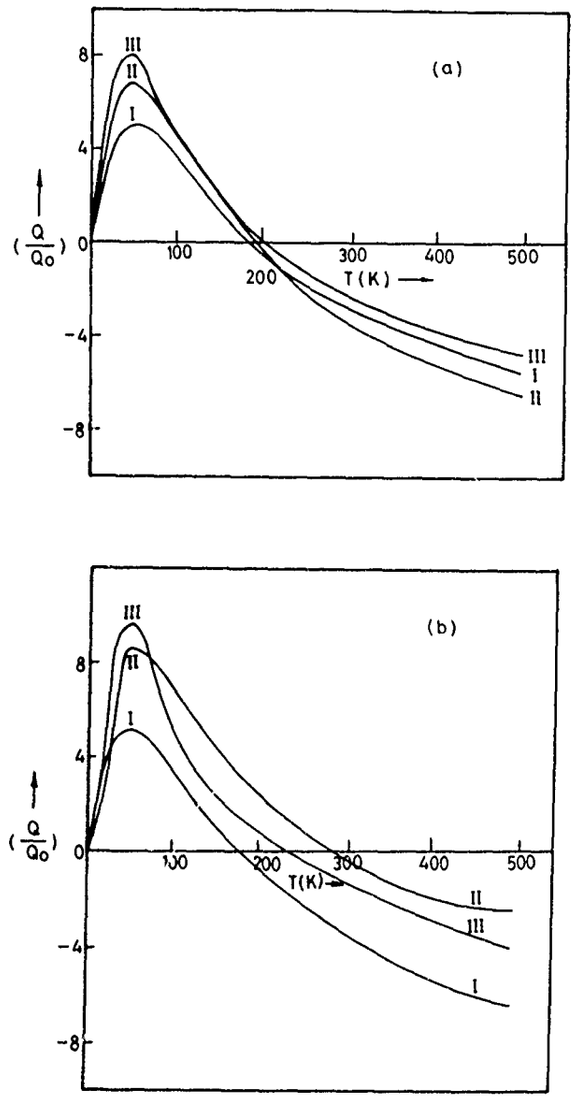

FIG. 2. Variation of thermoelectric power Q with temperature for tight-binding conduction-band case (a) $V=0.25$, $U=\infty$, curve I for $\epsilon_f=-0.6$, curve II for $\epsilon_f=-0.4$, and curve III for $\epsilon_f=-0.2$. (b) $V=0.25$, $\epsilon_f=-0.6$, curve I for $U=\infty$, curve II for $U=1.0$, and curve III for $U=0.5$

trons per site (n^c+n^f) has been taken to be 1.5. We have calculated here the temperature dependence of $\rho(T)$ for different effective positions of f level ϵ_f and with finite as well as infinite U. The results are shown in Fig. 1. Fig. 1(a) shows $\rho(T)$ for $\epsilon_f=-0.6$, -0.4, and -0.2 eV. We obtain the typical behavior in $\rho(T)$ with a rapid increase $\sim T^2$ at low temperatures, a maximum near $T_{max}=50$ K, and a NTC for higher temperatures. As f level ϵ_f shifts downward with respect to Fermi energy ϵ_F, $\rho(T)$ increases more sharply in the low-T regime; as a result, the peak in $\rho(T)$ becomes even sharper with a larger NTC. Figure 1(b) shows $\rho(T)$ for different interactions: $U=0.5$, 1.0, and ∞. Here when U is increased the resistivity increases and the peak at low temperature gets sharpened. These resistivity results are in qualitative agreement with experimental results for $YbAgCu_4$ (HF compound) and $CePd_3$ (MV compound).[16] It may be noted here that we have not considered the phonon contribution to resistivity, which is appreciable toward the high temperatures.

Corresponding results for the temperature dependence of the thermoelectric power $Q(T)$ are shown in Fig. 2. We observe the extremum in $Q(T)$ approximately at the same temperature T_{max}, where the resistivity has its maximum and this extremum in $Q(T)$ is also present when $\rho(T)$ does not have the maxima as in $\epsilon_f=-0.2$, in complete agreement with the experimental findings. We obtain a change of the sign of $Q(T)$ for relatively high temperatures. Our $Q(T)$ results match qualitatively with the experimental result of Visser *et al.*[6] for the HF compound UPt_3.

Our main conclusions are (1) Both types of resistivity behaviors (viz., with or without maxima at low T) can be obtained within the same treatment by changing slightly only one parameter like ϵ_f. (2) The relevant mechanism responsible for the temperature dependence of $\rho(T)$ and $Q(T)$ is the special type of dispersion curve of these systems, because of which they have a very high quasiparticle density of states. We have considered here the orbitally nondegenerate Anderson Hamiltonian. It explains much valence fluctuation and heavy fermion physics, at least qualitatively.

[1] G. R. Stewart, Rev. Mod. Phys. **56**, 755 (1984).
[2] N. Grewe and F. Steglich, in *Handbook on the Physics and Chemistry of Rare Earths*, edited by K. A. Gschneidner (North-Holland, Amsterdam, 1991), Vol. 14.
[3] P. Fulde, J. Keller, and G. Zwichnage, Solid State Phys. **41**, 1 (1988).
[4] U. Rauchschwalbe, Physica **147B**, 1 (1987).
[5] *Theory of Heavy Fermions and Valence Fluctuations*, edited by T. Kasuya and T. Saso (Springer, New York, 1985).
[6] A. D. E. Visser, A. Menovsky, and J. J. M. Franse, Physica **147B**, 81 (1987).
[7] S. Doniach, Physica **91B**, 231 (1977).
[8] H J. Leder and Muhlschlegel, Z. Phys. **B29**, 341 (1978).
[9] K. Yamada and K. Yosida, Prog Theor. Phys **76**, 621 (1986)
[10] K. Yamada, K Okada, and K. Yosida, Prog. Theor. Phys. **77**, 1097 (1987).
[11] S Panwar and I. Singh, Solid State Commun. **72**, 711 (1989).
[12] S. Panwar and I. Singh, Phys. Status Solidi B **168**, 583 (1991)
[13] S. Panwar and I. Singh, Solid State Commun. **85**, 239 (1993).
[14] S Panwar and I. Singh, Phys. Status Solidi B **175**, 487 (1993)
[15] S. Panwar, Ph.D. thesis, 1992
[16] H. Schweitzer and G. Czycholl, Phys. Rev. Lett **67**, 3724 (1991).
[17] N. F. Mott, *Metal-Insulator Transitions* (Taylor and Francis, London, 1974), p. 26.

Understanding the great range of magnetic ordering behavior in correlated *f*-electron systems

Q. G. Sheng and B. R. Cooper
Department of Physics, West Virginia University, Morgantown, West Virginia 26506-6315

The magnetic ordering behavior of correlated f-electron systems varies widely. With regard to the value of the ordered moments, there are systems of saturated moment (e.g., CeSb), of moment somewhat reduced from the saturated value (e.g., UTe), of very small moment (e.g., UPt_3) and of no moment at all (e.g., $CeCu_2Si_2$). We show that such wide diversity in magnetic ordering is a manifestation of the competition between (1) hybridization and exchange interaction and (2) localization and itinerancy. By analyzing these effects, we develop a theory which organizes the diverse magnetic behavior into a unified picture describable through one model Hamiltonian. An important feature of this analysis is that we recognize and treat the effect of band-f Coulomb exchange simultaneously with that of band-f hybridization. Rather than adopting the standard analysis using the "Kondo resonance"–"Kondo compensation" concept, the development of this theory offers a new approach to treat the correlated f-electron state. The present theory naturally leads to a nonmagnetic singlet "Kondo state" which is one of the possible states, along with other magnetic states which the system could be in, when the conditions determining the state of the system favor that choice. The f orbital motions and spin-orbital coupling are given full consideration in the theory.

I. INTRODUCTION

For correlated f-electron systems, one interesting and not yet fully understood fact is that their magnetic ordering behavior has wide diversity. On one hand, there are "Kondo lattice" materials, in which the localized ordered moments are very small or vanishing; on the other hand, there are materials having strong magnetic ordering with almost saturated moments. Between the two extremes, there are a variety of materials with ordered magnetic moments ranging from very small to very large, while their magnetic structures also have rich complexities.[1] Can such diverse f magnetism be understood on the basis of one unified picture?

There are a variety of approaches to treat the correlated f-electron systems. For most of these approaches, the foundation of the theoretical framework is the concept of "Kondo resonance"–"Kondo compensation," and there are a large number of publications based on this line of thought.[2] In this work, we propose an alternative approach to treat the correlated f-electron systems, which has nothing to do with the concept of Kondo resonance–Kondo compensation. This theory covers the diverse f magnetism, and it naturally leads to the nonmagnetic singlet "Kondo state" as one of the possible states, along with other magnetic states, which the system could be in, depending on what the conditions favor. It shows how the diversity in f magnetism rests on the fundamental aspects of the f-electron systems, including the roles of hybridization versus exchange interaction, localization versus itinerancy, and the f orbital motion.

We describe the theory in three steps: (1) for a single atom, considering only the spins of electrons; (2) also for a single atom, including the f orbital motion; (3) forming a crystal using atoms described by (1) and (2).

II. STEP 1

Consider a single isolated atom which has two orbitals: an f orbital $|f\rangle$ and a ligand orbital $|l\rangle$. Assume the following Hamiltonian for this atom:

$$H_{\text{atom}}=\epsilon_l\sum_\sigma l_\sigma^\dagger l_\sigma+\epsilon_f\sum_\sigma f_\sigma^\dagger f_\sigma+U f_\uparrow^\dagger f_\uparrow f_\downarrow^\dagger f_\downarrow$$

$$+V\sum_\sigma (l_\sigma^\dagger f_\sigma+\text{h.c.})-J\sum_{\sigma\sigma'} f_\sigma^\dagger f_{\sigma'} l_{\sigma'}^\dagger l_\sigma, \quad (1)$$

where ϵ_f and ϵ_l are the energies of $|f\rangle$ and $|l\rangle$, respectively; $f_\sigma^\dagger$ and $l_\sigma^\dagger$ create an electron with spin σ in $|f\rangle$ and $|l\rangle$, respectively; U is the f-f Coulomb repulsion; V is the hybridization between the two orbitals; and J is the exchange Coulomb interaction between f and ligand electrons. Suppose $\epsilon_l>\epsilon_f$. Hamiltonian (1) is the Anderson Hamiltonian plus a J interaction. The inclusion of J leads to significant magnetic consequences, which have been shown by first-principle calculations for several materials,[3] and will be further analyzed later.

Consider the case that the atom has two electrons. Neglect double occupancy of $|f\rangle$ by assuming $U\to\infty$. When $V=0$ and $J=0$, the system has a fourfold degenerate ground state, which, having one electron in $|f\rangle$ and the other in $|l\rangle$, has an energy $E_0=\epsilon_l+\epsilon_f$. The fourfold degenerate states can be grouped into a spin singlet $|\Phi_{S=0}\rangle$ and a spin triplet $|\Phi_{S=1}\rangle$:

$$|\Phi_{S=0}\rangle=\frac{1}{\sqrt{2}}(f_\uparrow^\dagger l_\downarrow^\dagger-f_\downarrow^\dagger l_\uparrow^\dagger)|0\rangle, \quad (2a)$$

$$|\Phi_{S=1}^{M=+1}\rangle=f_\uparrow^\dagger l_\uparrow^\dagger|0\rangle;$$

$$|\Phi_{S=1}^{M=0}\rangle=\frac{1}{\sqrt{2}}(f_\uparrow^\dagger l_\downarrow^\dagger+f_\downarrow^\dagger l_\uparrow^\dagger)|0\rangle; \quad (2b)$$

 0021-8979/94/76(10)/6226/3/$6.00 © 1994 American Institute of Physics

$$|\Phi_{S=1}^{M=-1}\rangle = f_{\uparrow}^{\dagger} l_{\downarrow}^{\dagger} |0\rangle.$$

The system has a singlet excited state, which, having two electrons in $|l\rangle$, has an energy $E_{ex}=2\epsilon_l$:

$$|\Phi_{ex}\rangle = l_{\uparrow}^{\dagger} l_{\downarrow}^{\dagger} |0\rangle. \tag{3}$$

When V is turned on but J is kept to zero, the system has the following changes: (i) The singlet $|\Phi_{S=0}\rangle$ mixes slightly with $|\Phi_{ex}\rangle$, lowers its energy by $\Delta E \simeq 2V^2/(\epsilon_l - \epsilon_f)$, and becomes the actual ground state. (ii) The triplet $|\Phi_{S=1}^{M=0,\pm 1}\rangle$ does not mix with $|\Phi_{S=0}\rangle$ or $|\Phi_{ex}\rangle$; its energy remains unchanged and becomes a low-lying excited state. (iii) $|\Phi_{ex}\rangle$ mixes slightly with $|\Phi_{S=0}\rangle$, and raises its energy by $\Delta E \simeq 2V^2/(\epsilon_l - \epsilon_f)$.

The above picture contains the key elements of the Kondo problem: at low temperatures ($T \ll \Delta E$), the system is bound in the nonmagnetic singlet state; as the temperature rises, the triplet state becomes populated and the system develops magnetic moments; at high temperatures ($T \gg \Delta E$), the singlet and triplet states are equally populated, and the f and ligand electrons can be seen as effectively decoupled. The foregoing treatments and discussions involving V were given by Fulde[4] and readers can find the details therein.

On the other hand, when J is turned on but V is kept to zero, the splitting of the ground state is reversed. The exchange energy is $+J$ for the singlet $|\Phi_{S=0}\rangle$ and $-J$ for the triplet $|\Phi_{S=1}\rangle$. Thus the ground state splits by $\Delta E = 2J$, and since $J>0$, the triplet instead of the singlet is the ground state. Therefore J tends to destroy the Kondo state driven by V and maintains magnetic moments for the system.

Ultimately, whether the system is in the nonmagnetic Kondo state or a magnetic state depends on whether V or J prevails. This opens the door for understanding the "Kondo-like" f phenomena and the non-Kondo magnetic f phenomena by a single model Hamiltonian.

III. STEP 2

We now do the same kind of analysis as in step 1, but with the f orbital motion included. We show that the features in step 1 are not fortuitous because of the neglect of the f orbital motion; instead, they are intrinsic to the f-electron systems. The atomic Hamiltonian is

$$H_{atom} = \epsilon_l \sum_{\sigma} l_{\sigma}^{\dagger} l_{\sigma} + \epsilon_f \sum_{m\sigma} f_{m\sigma}^{\dagger} f_{m\sigma} + \sum_{m\sigma} (V_m l_{\sigma}^{\dagger} f_{m\sigma} + \text{h.c.})$$

$$- J \sum_{m\sigma\sigma'} f_{m\sigma}^{\dagger} f_{m\sigma'} l_{\sigma'}^{\dagger} l_{\sigma}, \tag{4}$$

where m indicates the orbital state of $|f\rangle$. We have dropped U from Eq. (4) by excluding double occupancy of $|f\rangle$ from our discussion. Considering that in a lattice the orbital motion of the ligand states are largely quenched by the crystal field, we assume $|l\rangle$ is an s wave. Then J is m independent but V_m is not. We also include spin-orbit coupling in the following discussion by restricting the f electron to the $j=5/2$ states $|f_\mu\rangle$.

When $J=0$ and $V=0$, the ground state $|j,\nu\rangle$ ($E_0 = \epsilon_l + \epsilon_f$) is 12-fold degenerate, in which the total angular momentum j of the system can be $j=5/2 \pm 1/2$; and the excited state $|\Phi_{ex}\rangle$ ($E_{ex}=2\epsilon_l$) is the same as in Eq. (3).

When V is turned on but J kept zero, the resulting 13×13 Hamiltonian matrix has the following form:

$$\begin{pmatrix} E_{ex} & \tilde{V}_1 & \tilde{V}_2 & \tilde{V}_3 & \cdots & \tilde{V}_{12} \\ \tilde{V}_1^* & E_0 & 0 & 0 & \cdots & 0 \\ \tilde{V}_2^* & 0 & E_0 & 0 & \cdots & 0 \\ \tilde{V}_3^* & 0 & 0 & E_0 & \cdots & 0 \\ \vdots & \vdots & \vdots & \vdots & \ddots & \vdots \\ \tilde{V}_{12}^* & 0 & 0 & 0 & \cdots & E_0 \end{pmatrix}, \tag{5}$$

where $\tilde{V}_m$ is V_m multiplied by some coefficient. The elements of matrix (5) are all zero except those on the first row, first column, and the diagonal. This leads to the following eigenequation:

$$[(E_0-\lambda)(E_{ex}-\lambda) - 6\tilde{V}^2](E_0-\lambda)^{11} = 0, \tag{6}$$

where

$$\tilde{V}^2 \equiv \frac{1}{7} \sum_{m=-3}^{3} |V_m|^2. \tag{7}$$

As a result, the system has: (i) an 11-fold state $|\Phi_1\rangle$, which is purely $|j\nu\rangle$, and has an energy E_0; (ii) a singlet $|\Phi_0\rangle$, which is $|j\nu\rangle$ dominant but mixes slightly with $|\Phi_{ex}\rangle$, and has an energy $E_0 - \Delta E$; (iii) a singlet which is $|\Phi_{ex}\rangle$ dominant but mixes slightly with $|j\nu\rangle$, and has an energy $E_{ex} + \Delta E$, which we simply denote as $|\Phi_{ex}\rangle$. These are similar to the spin-only case: the 12-fold degenerate ground state splits into an actual ground-state singlet $|\Phi_0\rangle$ and a low-lying excited state multiplet $|\Phi_1\rangle$, and $|\Phi_0\rangle$ is the only one of these states which mixes with $|\Phi_{ex}\rangle$ through V, while $|\Phi_1\rangle$ is not affected by V. $\Delta E \simeq 6\tilde{V}^2/(\epsilon_l - \epsilon_f)$ and the singlet $|\Phi_0\rangle$ is

$$|\Phi_0\rangle \simeq \left[1 + \frac{6\tilde{V}^2}{(\epsilon_l - \epsilon_f)^2}\right]^{-1/2} \times \left(\sum_{\nu=-3}^{3} \frac{V_\nu^*}{\sqrt{7}\tilde{V}} |3,\nu\rangle + \frac{\sqrt{6}\tilde{V}}{\epsilon_l - \epsilon_f} l_{\uparrow}^{\dagger} l_{\downarrow}^{\dagger} |0\rangle \right). \tag{8}$$

By applying the condition that $V_{-m} = (-1)^{3+m} V_m^*$, one can verify that $\langle \Phi_0 | \mathbf{j} | \Phi_0 \rangle = 0$. Thus in $|\Phi_0\rangle$, an f $j=5/2$ moment and a ligand $s=1/2$ spin result in a nonmagnetic singlet, the Kondo state. $|\Phi_1\rangle$ is magnetic since $\langle \Phi_1 | \mathbf{j} | \Phi_1 \rangle \neq 0$. We conclude that the forming of the Kondo state can be regarded as a consequence of the local correlations. In contrast, in the theory of Kondo compensation it is not clear how an f $j=5/2$ moment can be fully "compensated" by conduction electrons without the hardly reasonable consequence of consuming five conduction $s=1/2$ spins.

We now turn on J. One can verify that the J interaction does not change the $|\Phi_0\rangle$ and $|\Phi_1\rangle$ states resulting from the V interaction, but simply shifts these states by different amounts. As a result, the 11-fold degenerate $|\Phi_1\rangle$ splits: Some levels move toward $|\Phi_0\rangle$, and some do not. If J is large enough, the lowest level from $|\Phi_1\rangle$ can cross over the V-induced gap ΔE and become the actual ground state, oth-

erwise, $|\Phi_0\rangle$ remains the actual ground state. Also similar to the spin-only case, whether the nonmagnetic singlet or the magnetic multiplet is the ground state depends on whether V or J prevails.

So far, we have seen that the key elements of step 1 remain when f orbital motion is included. A new aspect also emerges with the inclusion of f orbital motion. Unlike the spin-only case, $|\Phi_0\rangle$ and $|\Phi_1\rangle$ are not eigenstates of the total moment $\hat{j}_z$. This causes the system to respond to a magnetic field (external or internal) with complicated magnetic configurations. Thus a crystal formed by such atoms, if being magnetic, can have complicated magnetic structures. In contrast, the spin-only model can only have simple magnetic structures.

IV. STEP 3

We now construct a crystal using atoms described by steps 1 and 2. We call the interactions within an atom, which are represented by atomic Hamiltonians (1) and (4) and lead to atomic states $|\Phi_0\rangle$, $|\Phi_1\rangle$, and $|\Phi_{ex}\rangle$, local correlations. We call the overlaps between electronic wave functions from different atoms, together with the interactions between electrons from different atoms, nonlocal correlations. The nonlocal correlations, by driving the system toward itinerancy, tend to suppress the local effects, while the local correlations tend to preserve the local effects, and to suppress the itinerancy.

We maintain that, for a large number of materials, the suppression of the local effects by the nonlocal correlations is small. In other words, the atomic states $|\Phi_0\rangle$, $|\Phi_1\rangle$, and $|\Phi_{ex}\rangle$ resulting from the local correlations will be sustained to a large extent, while being dressed by the onset of nonlocal correlations. Based on this premise, we take $|\Phi_0\rangle$, $|\Phi_1\rangle$, and $|\Phi_{ex}\rangle$ as the starting states, and adiabatically turn on the nonlocal correlations. The result is the self-banding of these atomic states, which leads to density spectra $|\Psi_0(\mathbf{k})\rangle$, $|\Psi_1(\mathbf{k})\rangle$, and $|\Psi_{ex}(\mathbf{k})\rangle$, which are associated with $|\Phi_0\rangle$, $|\Phi_1\rangle$, and $|\Phi_{ex}\rangle$, respectively.

Such spectra are of two-electron representation, since $|\Phi_0\rangle$, $|\Phi_1\rangle$, and $|\Phi_{ex}\rangle$ are two-electron states. The effects of local correlations are completely built into the two-electron wave function, thus completely represented by the two-electron spectra. If we choose single-electron states as bases to form a spectrum, the local correlation effects cannot be represented in the spectrum so directly and completely.

$|\Psi_{ex}(\mathbf{k})\rangle$ forms a wide band, since $|\Phi_{ex}\rangle$ is a product of two $|l\rangle$s, which are spatially extended. $|\Psi_0(\mathbf{k})\rangle$ forms a narrow band, since $|\Phi_0\rangle$ is a product of one $|f\rangle$ and one $|l\rangle$, and $|f\rangle$ is spatially very small. $|\Psi_1(\mathbf{k})\rangle$ also forms a narrow band. We neglect the mixing between $|\Psi_0(\mathbf{k})\rangle$, $|\Psi_1(\mathbf{k})\rangle$, and $|\Psi_{ex}(\mathbf{k})\rangle$, since it will not change our discussion. We can also see that the Fermi level is always in the vicinity of narrow peaks from $|\Psi_0(\mathbf{k})\rangle$ and $|\Psi_1(\mathbf{k})\rangle$ by simple counting of the electron occupation.

We now have a two-component spectrum near the Fermi level: a nonmagnetic $|\Psi_0(\mathbf{k})\rangle$ component and a magnetic $|\Psi_1(\mathbf{k})\rangle$ component. The local V and J interactions determine which component is lower, and how much it is lower; the nonlocal correlations determine how wide they are, and the local and nonlocal correlations together determine how much they overlap. This opens a wide range of possibilities depending on by what proportion the two components are occupied, and such wide possibilities lead to a wide range of magnetic behaviors. Three such possibilities are: (a) $|\Psi_0(\mathbf{k})\rangle$ is occupied but $|\Psi_1(\mathbf{k})\rangle$ is empty, which leads to a nonmagnetic Kondo state; (b) $|\Psi_0(\mathbf{k})\rangle$ and $|\Psi_1(\mathbf{k})\rangle$ both are partially occupied, which leads to reduced moments; (c) $|\Psi_1(\mathbf{k})\rangle$ is occupied but $|\Psi_0(\mathbf{k})\rangle$ is empty, which leads to strong magnetism.

The above possibilities correspond to the case when the f population is close to 1. If we include the wide band $|\Psi_{ex}(\mathbf{k})\rangle$ into our discussion, it also opens the possibilities of reduced f population: the more $|\Psi_{ex}(\mathbf{k})\rangle$ is populated, the less the f population the system has.

From the description above, we see that this theory opens the door to understanding diverse f magnetism by addressing the fundamental aspects of the correlated f-electron systems, such as hybridization versus exchange interaction, localization versus itinerancy, and Kondo state versus magnetized state. As for the Kondo state, it comes from a new approach which is completely different, fundamentally, than the Kondo resonance–Kondo compensation theory. In this theory, the alternative possibility of the Kondo state and the magnetic states appears naturally as a consequence of local correlations.

More work is needed to see if the approach proposed here can be developed into a comprehensive theory of correlated f-electron systems. (We also point out that the part of the theory described in step 3 is only a preliminary illustration, and a more elaborate analysis will be published elsewhere.) To reach this goal, more aspects need to be addressed, such as: the spatial and time distribution of electrons in $|\Psi_0(\mathbf{k})\rangle$ and $|\Psi_1(\mathbf{k})\rangle$, magnetic excitations due to electronic scattering between $|\Psi_0(\mathbf{k})\rangle$ and $|\Psi_1(\mathbf{k})\rangle$, and effective mass and susceptibility of electrons in $|\Psi_0(\mathbf{k})\rangle$ or $|\Psi_1(\mathbf{k})\rangle$.

ACKNOWLEDGMENT

This research is supported through the National Science Foundation under Grant No. DMR91-20333.

[1] B. R. Cooper, R. Siemann, D. Yang, P. Thayamballi, and A. Banerjea, in *Handbook on the Physics and Chemistry of Actinides*, edited by A. J. Freeman and G. H. Lander (North-Holland, Amsterdam, 1985), Vol. 2, Chap. 6, pp. 435–500.

[2] The number of publications in this area is huge. We refer to two publications which gave an overview of this area: J. M. Lawrence and D. L. Mills, Comments Cond. Mat. Phys. **15**, 163 (1991); A. C. Hewson *The Kondo Problem to Heavy Fermions* (Cambridge University, Cambridge, 1993).

[3] Q. G. Sheng and B. R. Cooper, J. Appl. Phys. **69**, 5472 (1990); J. Appl. Phys. **70**, 6083 (1991); Phys. Rev. B **50**, 1965 (1994).

[4] P. Fulde, *Electron Correlation in Molecules and Solids* (Springer, Berlin, 1991), p. 268.

Discovery of τ=2/9 lock-in in holmium

D. A. Tindall and C. P. Adams
Department of Physics, Dalhousie University, Halifax, Nova Scotia, Canada B3H 3J5

M. O. Steinitz
Department of Physics, St. Francis Xavier University, Antigonish, Nova Scotia, Canada B2G 1C0

T. M. Holden
Neutron and Condensed Matter Science, AECL-Research, Chalk River, Ontario, Canada K0J 1J0

The complex magnetic behavior of holmium is a well-established experimental fact and has been studied by a variety of experimental techniques, including magnetization, x-ray diffraction, thermal expansion, and heat capacity. Our recent studies have focused on using neutron diffraction to study the temperature and field dependence of the helimagnetic structure. The pitch of the helix is described by τ, the spiral wave vector. τ usually varies smoothly with temperature but tends to lock in at various values that are commensurate with the lattice when a field is applied. These lock-ins provide clues to the nature of the different magnetic phases and, up to now, all the lock-ins have corresponded to features of the magnetic phase diagram obtained from magnetization measurements. However, recent experiments have revealed a previously unobserved lock-in at τ=2/9 rlu in a 1.4 T b-axis field. It shares the same general features of other lock-ins except that it does not correspond to any feature of the magnetic phase diagram.

Neutron diffraction has been particularly useful in determination of the magnetic structure and the nature of the ordering of magnetic substances. Holmium is one of the materials that has been frequently studied in this way.[1-4] For our part, we have used neutron diffraction to study holmium and its intricate magnetic phase diagram,[5-9] and used the results to supplement the information yielded by the various other experimental techniques.[10-19] One phenomenon which has been extensively investigated,[6-9] using neutron diffraction, is the lock-in behavior of the spiral wave vector τ.

We have found lock-ins in holmium for magnetic fields applied in different directions: specifically at τ=1/4 and 1/5 rlu (reciprocal lattice units) in a 3 T c-axis field.[5-7] τ=1/6 rlu is the "original" lock-in which occurs in zero field below the Curie temperature (T_c=20 K).[1] More recently, we have observed lock-ins at τ=1/4 and 5/18 for b-axis fields of 1.4 and 3 T.[8,9] In this paper we report our most recent studies, which have revealed a previously unobserved lock-in at τ=2/9 rlu which occurs at 75 K (in a 1.4 T b-axis magnetic field). The discovery of this lock-in is of particular interest for two reasons. First of all, τ=2/9 is part of a series of commensurate values arising from a simple spin-slip model.[2,20,21] Second, while all of the previously observed lock-ins correspond to features of the magnetic phase diagram seen in magnetization measurements,[13] this is not the case for the τ=2/9 lock-in. Given the previous correspondence between lock-ins and phase transitions, this raises the question of why this lock-in was not observed in magnetization measurements.

Measurements were made on the N5 triple-axis spectrometer at the Chalk River Laboratories of AECL-Research in Chalk River, Ontario. The scattering experiments were done elastically at an incident neutron energy of 8.23 THz, corresponding to a wavelength of 0.155 nm. The holmium sample was a high-purity single crystal roughly 2×1×1 cm, provided by Pechan and Stassis[3] and used in our previous neutron studies. The sample was mounted in the M2 cryostat,[22] which provided a horizontal field with less than a 2% variation in the field over the sample volume. The cryostat allows a range of temperatures from 4.2 K to room temperature, fields up to 3 T, and 350° access for the neutron beam. The sample was mounted so that we could observe the (h01) reflections. A platinum resistance thermometer was used to control the temperature of the sample and a carbon glass thermometer used to read the temperature. The thermometers were mounted in the copper base to which the sample mount was also connected. The temperatures were high enough, and the field was low enough, that magnetoresistance effects on the thermometers were negligible.

Holmium in its antiferromagnetic state (between 20 and 132 K in zero applied magnetic field) has a helimagnetic structure with the moments in the basal planes ferromagnetically aligned, but with the direction of alignment in the plane changing in angle as one moves from plane to plane along the c axis. The pitch of the helix is given by the spiral wave vector τ, which represents the periodicity in reciprocal space (for example, if the helix has a period of four lattice constants, then τ=1/4 rlu). The effect of the magnetic structure on the neutron-diffraction pattern is to produce magnetic satellite peaks offset by τ from the nuclear peaks in reciprocal space, for instance at (10$\pm\tau$). Since the magnetic cross section and the nuclear cross section are comparable under our experimental conditions, the primary peak and its satellites are roughly of the same, relatively large, intensity. We measured τ by scanning in the c^* direction, through both the satellite and the corresponding nuclear peak, carefully measuring their positions (determined using a Gaussian fit), and then obtaining the difference. In zero field τ decreases smoothly, from a value of 5/18 (0.2778) rlu at the Néel temperature (T_N=132 K), to 1/6 rlu at the Curie temperature. However, in the presence of an applied magnetic field, we have found that τ becomes locked in, causing the τ versus temperature curve to flatten out at certain values of τ that are commensurate with the lattice. As a locked-in region is entered in a temperature sweep, there is also a distinct anomaly

 0021-8979/94/76(10)/6229/3/$6.00 © 1994 American Institute of Physics

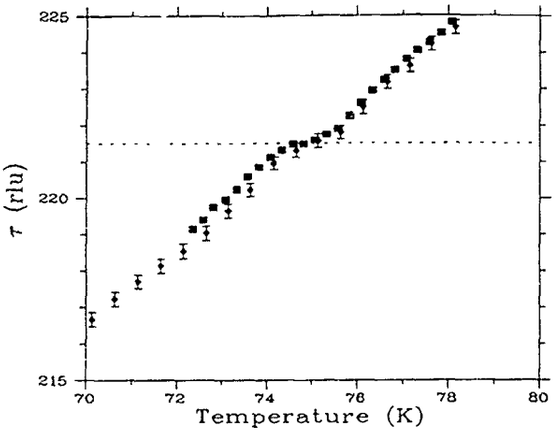

FIG 1. τ vs temperature in a 1.4 T b-axis field showing the 2/9 lock-in highlighted by the dashed line. Initial coarse runs are shown by ◆, and the finer temperature runs shown by ■

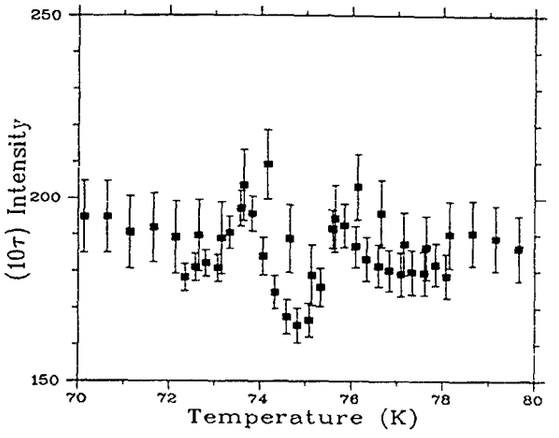

FIG. 2. (10τ) intensity vs temperature for the same runs as in Fig. 1 Notice the sharp anomaly in the lock-in region which has been present for all lock-ins observed so far.

in the intensity of the magnetic satellite. The occurrence of this anomaly is not understood, but it is very useful for identifying the lock-ins. The absolute error in τ is estimated to be ± 0.0010 rlu and relative error between the scans better than ± 0.0001 rlu. The absolute error in τ arises from uncertainty in the lattice parameters which are needed to measure distances in reciprocal space. Unfortunately, data for the thermal expansion of holmium in the presence of a 1.4 T field are not available and, given the large magnetostriction of holmium, it is unlikely that the use of zero-field thermal-expansion data in this region would give the lattice parameters to sufficient accuracy. The relative error arises from the counting statistics and least-squares-fitting procedure.

In Fig. 1 we show a plot of τ versus temperature for a 1.4 T b-axis field. This plot clearly shows the lock-in at which τ is 0.2215 ± 0.0010 rlu, corresponding to $\tau = 2/9$ rlu, at a temperature of 75 K. Despite the fairly modest field value, the lock-in is prominent and has a width of roughly 1.5 K for the flattened region, very similar to the widths of the lock-ins at much higher field values. Figure 1 also shows the reproducibility from run to run. There are two runs shown: one at a coarse temperature step of 0.5 K and another finer run at 0.25 K between the scans. The two plots are almost identical. A lock-in at 2/9 rlu is not altogether unexpected since it is one of the commensurate values that arises out of a simple spin-slip analysis. Although the spin-slip model was devised as a description of low-temperature phenomena (below 70 K), and is based on the detection of low-temperature phenomena (below 70 K), and is based on the detection of 5τ and 7τ peaks,[2,20] there may be some basis for its use in high-field situations where extra stabilizing effects may be present. The associated intensity anomaly is shown in Fig. 2. It is often useful to use the peaks in intensity to characterize the width of the lock-in, since they are sharply defined compared to the edges of the lock-in region on the τ vs T plot. If we examine this region of the magnetic phase diagram, obtained from magnetization measurements,[13] we find that this point falls below the closest coexistence curve by 0.4 T. In addition, if one follows this coexistence curve to zero field, one finds that this curve is associated with $\tau = 1/5$ and not 2/9 rlu. It thus appears that a branch of the phase diagram has been missed in the magnetization measurements. On looking at the magnetization measurements of Willis *et al.*,[13] it is seen that some of the magnetization anomalies are quite subtle and it is, perhaps, not too surprising that one might have been missed.

As well as the previously undiscovered 2/9 lock-in, we have also observed lock-ins at 1/4 and 5/18 rlu for the 1.4 T b-axis field. We have previously reported the 5/18 lock-in and compared it to the 5/18 lock-in for a 3 T b-axis field.[23] In that paper we mentioned that the width of the 5/18 lock-in appeared to vary as the square of the field, but this is not the case for the 1/4 lock-in. In Fig. 3 we show the 1/4 lock-in for a 1.4 T b-axis field, drawn to the same scale as Fig. 1 of our previous work.[9] Using the intensity anomaly to characterize the widths, we obtain a ratio of widths, (2.2 K/0.8 K)=2.8 compared with (3 T/1.4 T)^2=4.6, so our simple generalization does not apply here. This may have to do with the twisting of the phase diagram that occurs in this region compared

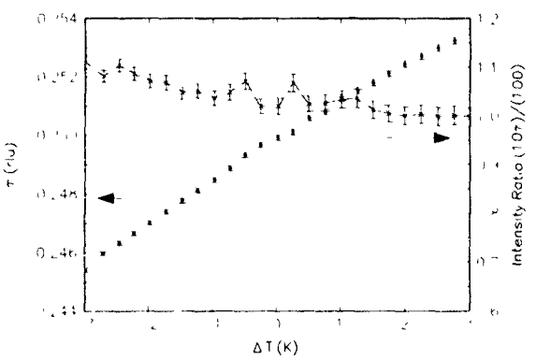

FIG. 3. τ vs the difference in temperature (ΔT) away from 99.6 K, in a 1.4 T b-axis field is shown by ● The 1/4 lock-in is much less prominent than in a 3 T field, and probably would have been overlooked if not for the intensity anomaly The ratio of the (10τ) intensity to that of the (100) nuclear peak is shown by ×.

to the higher temperature region and also the c-axis phase diagram. We also note that in the 1.4 T b-axis field the width of the 1/4 lock-in is less than half that of the 2/9 lock-in and is much less prominent.

There is also some question of how the 2/9 lock-in would manifest itself at higher fields. Due to the high magnetization under such conditions, and the size of our sample, we have experienced difficulties in the past with bending of the sample mount by the forces and/or torques on the sample. These problems occurred in the region from 80 to 95 K in which there were two distinct phases present.[9] Assuming that there is another 2/9 coexistence curve on the phase diagram, we would hope to be able to observe some sort of anomalous behavior in this region for $\tau=2/9$ rlu. This is not the case, and it appears as though some other interaction is dominating in this region. Clearly this region is deserving of further study at higher field values.

We gratefully acknowledge the financial support of the Natural Sciences and Engineering Research Council of Canada and the Canadian Institute for Neutron Scattering. We also thank AECL-Research, Chalk River, for the use of their excellent facilities and it is a pleasure to thank the staff of the Neutron and Condensed Matter Science Branch, especially Larry MacEwan, Peter Moss, Mel Potter, and Don Tennant. We are indebted to M. J. Pechan and C. Stassis for the loan of the sample.

[1] W. C. Koehler, J. W. Cable, M K Wilkinson, and E. O. Wollan, Phys. Rev. **151**, 414 (1966).
[2] W C. Koehler, J W Cable, H. R. Child, M. K. Wilkinson, and E. O. Wollan, Phys. Rev. **158**, 450 (1967).
[3] M. J. Pechan and C Stassis, J. Appl. Phys. **55**, 1900 (1984).
[4] J. A. Tarvin and J. Eckert, Solid State Commun. **30**, 375 (1979).
[5] D. R. Noakes, D. A. Tindall, M. O. Steinitz, and N Ali, J Appl Phys. **67**, 5274 (1990).
[6] D. A. Tindall, M. O. Steinitz, M. Kahrizi, D. R. Noakes, and N. Ali, J. Appl. Phys **69**, 5691 (1991).
[7] D. A. Tindall, M. O. Steinitz, and T. M. Holden, Phys Rev B **47**, 5463 (1993).
[8] D. A. Tindall, M. O. Steinitz, and T. M. Holden, J. Phys. Condens. Matter **4**, 9927 (1992).
[9] D. A. Tindall, M. O. Steinitz, and T M. Holden, J Appl. Phys. **73**, 6543 (1993).
[10] M. C. Lee, R. A. Treder, and M. Levy, J. Phys. Chem. Solids **36**, 1281 (1975).
[11] A. M. Simpson, M. H. Jericho, and M C. Jain, Can J. Phys. **54**, 1172 (1976).
[12] S. B. Palmer and E. W. Lee, Proc. R. Soc. London, Ser. A **327**, 519 (1972).
[13] F. Willis, N. Ali, M. O. Steinitz, M. Kahrizi, and D. A. Tindall, J. Appl. Phys. **67**, 5277 (1990).
[14] K. D. Jayasuriya, S. J. Campbell, and A. M. Stewart, J. Phys. F **15**, 225 (1985)
[15] D. Gibbs, D. E. Moncton, K L D'Amico, J Bohr, and B. H. Grier, Phys. Rev. Lett. **55**, 234 (1985).
[16] J. Bohr, D. Gibbs, D. E. Moncton, and K. L. D'Amico, Physica **140A**, 349 (1986).
[17] J. J Rhyne, S. Legvold, and E. T. Rodine, Phys Rev **154**, 266 (1967).
[18] D. A. Tindall, M. O. Steinitz, and M L. Plumer, J. Phys. F **7**, L263 (1977)
[19] M. O. Steinitz, M. Kahrizi, and D. A. Tindall, Phys. Rev. B **36**, 783 (1987).
[20] D. Gibbs, J. Less-Common Met **148**, 109 (1989).
[21] A. M. Venter, P de V. du Plessis, and E. Fawcett, Physica B **180&181**, 290 (1992).
[22] D. C. Tennant, N. Kerley, and N. Killoran, Rev Sci. Instrum. **60**, 136 (1989).
[23] D. A. Tindall, C. P. Adams, M. O Steinitz, and T. M. Holden, J Appl Phys. **75**, 6318 (1994).

Die-upset Nd-Fe-Co-B magnets from blends of dissimilar ribbons

C. D. Fuerst and E. G. Brewer
Physics Department, GM Research and Development Center, 30500 Mound Road, Warren, Michigan 48090-9055

We prepared die-upset Nd-Fe-Co-B magnets from melt-spun ribbon powders which were a series of blends of two ribbon alloys. One alloy was always ternary Nd-Fe-B (no cobalt), and in the other cobalt replaced up to half of the iron. Differential scanning calorimeter measurements revealed that during hot working, the cobalt diffused across ribbon boundaries, effectively redistributing the transition metal concentration throughout the magnet. Instead of anomalies indicating the Curie temperatures of the two original ribbon compositions, we found a single transition consistent with the average cobalt concentration in the magnet. However, the transition was broader than expected, suggesting that the homogenization was incomplete. These results are new evidence of massive diffusion occurring between ribbons, changing the microstructure and facilitating the deformation of the otherwise rigid 2-14-1 magnet.

I. INTRODUCTION

Hot deformation, or die upsetting, was first presented as a viable process for greatly enhancing (>60%) the remanence of magnets produced from melt-spun Nd-Fe-B ribbons, by Lee *et al.* in the early 1980s.[1,2] Mishra and Lee[3] have described the microstructure of die-upset magnets as platelet-shaped grains (50–100 nm thick and 200–600 nm in diameter) where the short dimension corresponds to the c axis of the tetragonal $Nd_2Fe_{14}B$ crystalline[4] phase. The deformation process not only encourages anisotropic grain growth, but also causes the alignment of the grains with the c axis along the press direction (perpendicular to the flow of material). Optimizing alignment while maintaining sufficient coercivity has resulted in extremely high-energy products, nearly 50 MGOe, in melt-spun 2-14-1 magnets.[5,6]

The success of die upsetting depends on a fine-grained microstructure in the starting material. Suitable grain sizes can be easily obtained by melt spinning at moderate quench conditions.[5,7] It has also been demonstrated that mechanically alloyed[8] and hydrogen, decomposition, desorption, and recombination (HDDR)[9,10] materials can be used as precursors for die-upset magnets. During die upsetting there is a burst of grain growth at high temperatures (1000–1100 K), creating a coarser-grained structure within a relatively short period of time (~1 min). Material is diffusing between regions as smaller grains vanish and are replaced by the new larger platelet-shaped grains. The diffusion momentarily softens the matrix, permitting the deformation which in turn leads to the crystallographic alignment of the microstructure. Once the new microstructure stabilizes, the matrix becomes essentially rigid and further die upsetting is impossible.

In this paper, we have used differential scanning calorimeter (DSC) measurements of the Curie temperature (T_C) to characterize the extent of iron and cobalt diffusion within the die-upset magnet. These measurements are sensitive to the specific heat of the material which experiences an abrupt change in slope at T_C. This effect is very similar to that observed in thermal expansion measurements near T_C.[11–16]

II. EXPERIMENTAL DETAILS

We used our standard sample preparation techniques which have been extensively described elsewhere.[5,17] The melt-spun ribbons were crushed to less than 60 mesh and sieved to remove fine particles (less than 270 mesh). The composition of the ribbons was ~14 at. % neodymium, 6 at. % boron, and the remainder transition metal $TM=(Fe_{1-x}Co_x)$, where $0 \leq x \leq 0.5$.

Ribbon blends were prepared by mixing cobalt-free ($x_0=0$) ribbons with cobalt-containing ribbons ($x_1>0$). The average cobalt concentration (x_{avg}) depended on the weight ratios ($1-w$ and w) of the ribbons and can be approximated as $x_{avg} \cong (1-w)x_0 + wx_1$ or $x_{avg} \cong wx_1$ since $x_0=0$. At the extremes, $w=0$ and $w=1$, the powders consisted of a single composition with a cobalt concentration of x_0 and x_1, respectively.

The blends of ribbon powders were hot pressed to produce fully dense precursors (about 16 g). Subsequent die upsetting reduced sample heights by just over 50%. Magnetic properties were measured with a hysteresis graph after premagnetizing in a pulsed magnetic field (100 KOe). The remanences (B_r) for magnets with moderate cobalt levels ($x_{avg} \leq 0.2$) were in the range 12–12.5 kG; the coercivities (H_{ci}) were slightly more variable, 7–10 kOe. At higher cobalt concentrations ($0.2 < x_{avg} \leq 0.25$) the remanences tended to be lower, $B_r \sim 11$ kG with no commensurate change in coercivity. In general, the reduced energy products, $(BH)_{max}/(B_r/2)^2$, were in the range 0.9–0.95. Above $x_{avg} \sim 0.3$, the coercivities dropped off considerably.

A high-speed diamond saw was used to cut small (2 $\times 3 \times 3$ mm^3) samples weighing about 135 mg for the differential scanning calorimeter (DSC) measurements. We used a Perkin–Elmer model System-7 DSC with a temperature scan rate of 25 K per minute and a 25 ml per minute flow of argon

 0021-8979/94/76(10)/6232/3/$6.00 © 1994 American Institute of Physics

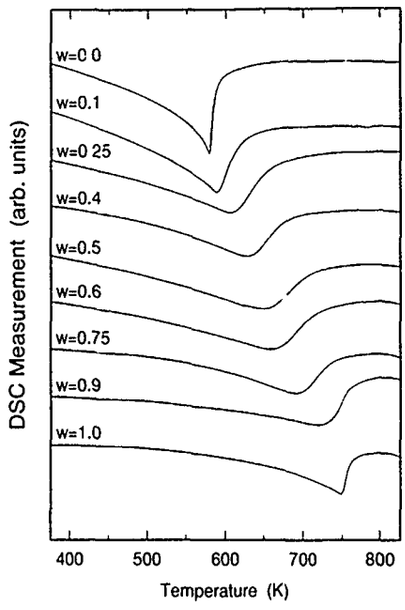

FIG. 1. DSC measurements of nine die-upset magnets produced by combining different weight fractions, $1-w$ and w, of two ribbon alloys, $x_0=0$ and $x_1=0.2$. For clarity, the measurements have been displaced vertically with the single-alloy magnets at the top ($w=0$) and bottom ($w=1$). The exothermic heat flow is upward.

gas. The DSC data have been adjusted to level the overall slope and were plotted in the figures with the exothermic direction of heat flow upward.

III. RESULTS AND DISCUSSION

The DSC measurements labeled $w=0$ and $w=1$ in Fig. 1 are characteristic of magnets from single-ribbon alloys. There is a relatively sharp minimum in each curve corresponding to T_c. Both transitions occurred at temperatures appropriate for their respective cobalt content, $T_c=588$ K for the $x_0=0$ cobalt-free alloy ($w=0$) and $T_c=757$ K for the $x_1=0.2$ cobalt-containing alloy ($w=1$).[18,19] However, when die-upset magnets were made from mixtures of these two ribbon alloys ($0<w<1$), there was no evidence of either of these transitions in the DSC measurements. Instead, the measurements revealed a single minimum or transition centered on the T_c expected for an alloy with a cobalt level equal to x_{avg}. Clearly the diffusion of iron and cobalt within the matrix is sufficient to create a material with nearly uniform cobalt distribution. This requires more than intergranular diffusion; rather, material transport is necessary over distances encompassing two or more ribbon particles.

It is also clear from Fig. 1 that the homogenization of the composition was incomplete, because rather than sharp transitions similar to the end points ($w=0$ and $w=1$), the blends produced broadened transitions, suggesting that small variations in cobalt concentrations between regions persisted. The greatest broadening occurred in the range $0.4\leq w\leq 0.8$, just where one would expect the greatest statistical variation in the average composition. The variation can be reduced by grinding the ribbon powders, which increases the number of

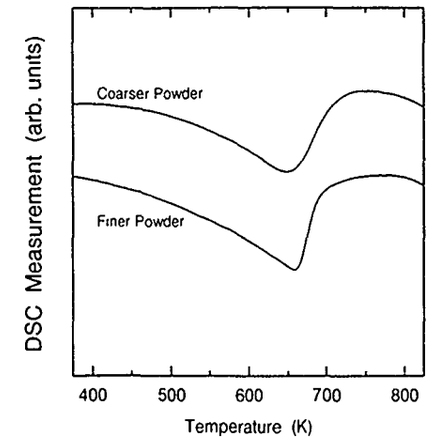

FIG. 2. DSC measurements on two die-upset magnets, both produced from a blend of equal weight fractions ($w=0.5$) of two ribbon alloys, one cobalt-free ($x_0=0$) and the other cobalt containing ($x_1=0.2$). The upper curve was typical for magnets made from as-crushed coarse powder, less than 60 mesh (<250 μm) and greater than 270 mesh (>53 μm). The lower curve was obtained from a magnet made from powder ground to finer than 325 mesh (<45 μm). The exothermic heat flow is upward.

particles within a given volume. The result can be seen in Fig. 2, which shows DSC measurements from two magnets with identical overall compositions, one produced from our standard (coarse) powder and the other with powder ground to less than 270 mesh (fine powder). The fine powder produced a sharper transition, consistent with less statistical variation and more uniform cobalt distribution.

Figure 3 shows DSC measurements for a series of magnets containing half cobalt-free ribbons and half cobalt-

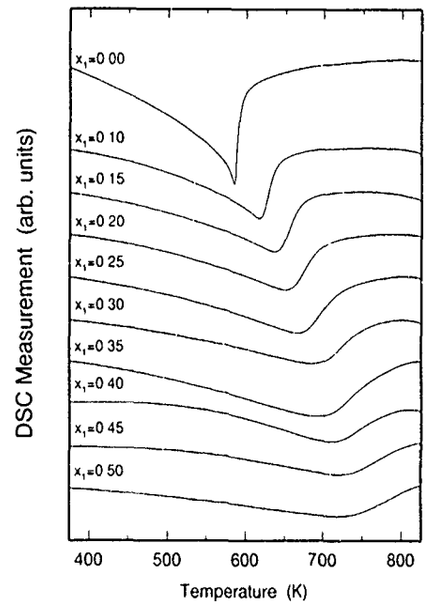

FIG. 3. DSC measurements of ten die-upset magnets, nine of which were produced by combining equal weight fractions ($w=0.5$) of cobalt-free ribbon alloys ($x_0=0$) and cobalt-containing ribbon alloys ($x_1>0$). The tenth magnet (top) contained no cobalt ($x_0=x_1=0$). The exothermic heat flow is upward.

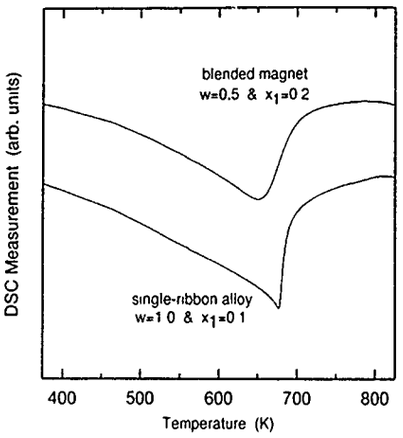

FIG 4. DSC measurements of two die-upset magnets, each with the same average cobalt content, $x_{avg}=0.1$. The first magnet (bottom) was prepared from a single ribbon alloy ($w=1$) containing cobalt, $x_1=0.1$. The second magnet (top) was prepared from a blend ($w=0.5$) of cobalt-free ribbons ($x_0=0$) and cobalt-containing ribbons ($x_1=0.2$). The exothermic heat flow is upward.

containing ribbons ($x_1>0$). The curve labeled $x_1=0$, corresponding to the single-ribbon alloy with no cobalt, is provided for comparison. In each case, the minimum corresponds to the anticipated T_c for a 2-14-1 alloy with a cobalt concentration of x_{avg}. The broadening increases monotonically with increasing x_1 until the transition is almost unrecognizable for the highest x_1 values. Even broader transitions might be possible at higher cobalt levels (up to $x_{avg}=0.5$), but the coercivities of die-upset magnets become very poor for $x_{avg}>0.3$.

We have also compared the DSC measurements of similarly prepared magnets with the same average cobalt concentration (see Fig. 4). Here both magnets have $x_{avg}=0.1$, but one was prepared from powders of a single-ribbon alloy ($w=1$ and $x_1=0.1$) and the other from blended ribbons ($w=0.5$ and $x_1=0.2$). The apparent Curie temperatures were both near 675 K, but the minimum was broader for the blended r agnet.

IV. SUMMARY

We have shown that DSC measurements can be used to characterize the relative distribution of iron and cobalt within die-upset 2-14-1 magnets. When compared to single-ribbon alloy magnets, the anomaly associated with T_c was considerably broader for magnets produced from blends of cobalt-free ribbons and cobalt-containing ribbons. When blending two ribbon powders, the broadest transitions were seen with nearly equal weight fractions. Since the broadening is controlled by regional variations in composition, the effect can be maximized by using coarse powers and selecting powders with large compositional differences, $x_1 \gg x_0$. Despite the broadening, the transition temperatures indicate that massive diffusion across ribbon boundaries has significantly homogenized the composition of the magnet. A more controlled study of particle size could reveal more precisely the diffusion distances involved.

ACKNOWLEDGMENTS

The authors have benefited greatly from discussing with J. F. Herbst, J. W. Herchenroeder, and R. K. Mishra. We are very grateful to C. B. Murphy for preparing the melt-spun ribbons and to P. Johnson for his assistance with our magnetic measurements.

[1] R. W. Lee, Appl. Phys. Lett **46**, 790 (1985).
[2] R. W. Lee, E. G. Brewer, and N. A. Schaffel, IEEE Trans. Magn. **MAG-21**, 1958, (1985).
[3] R. K. Mishra and R. W. Lee, J. Magn. Magn. Mater. **54-57**, 450 (1986).
[4] J. F. Herbst, J. J. Croat, F. E. Pinkerton, and W. B. Yelon, Phys. Rev. B **29**, 4176 (1984).
[5] C. D. Fuerst and E. G. Brewer, J. Appl. Phys. **73**, 5751 (1993)
[6] R. K. Mishra and V. Panchanathan, J. Appl. Phys. **73**, 6470 (1993).
[7] M. Leonowicz, H. A. Davies, and R. A Buckley, IEEE Trans. Magn. **MAG-29**, 2794 (1993).
[8] L Schultz, K. Schnitzke, and J. Wecker, J. Magn Magn Mater. **80**, 115 (1989).
[9] P. J. Mcguiness, X J Zhang, K. G. Knoch, X. J. Yin, M. J Wyborn, and I. R. Harris, J. Magn Magn. Mater. **104**, 1169 (1992).
[10] P. J. Mcguiness, C. Short, A. F Wilson, and I. R. Harris, J. Magn. Magn. Mater. **184**, 243 (1992).
[11] A. V. Andreev, A. V. Deryagin, S M. Zadvorkin, and S. V. Terent'ev, Sov. Phys. Solid State **27**, 987 (1985).
[12] K H. J. Bushow, J. Less-Common Metals **118**, 349 (1986).
[13] K. H. J. Bushow and R. Grossinger, J. Less-Common Metals **135**, 39 (1987).
[14] Ben-pei Cheng, Ying-chang Yang, Shou-can Fu, and W. J. James, J. Appl. Phys. **61**, 3586 (1987).
[15] H. Fujii, H. Nagata, Y. Uwatoko, T. Okamoto, H. Yamamoto, and M. Sagawa, J. Magn. Magn. Mater. **70**, 331 (1987).
[16] M. R. N. Pouryazdi, G. W. Johnson, and A. J. Moulson, J. Mater. Sci. **28**, 249 (1993).
[17] C. D. Fuerst, E G. Brewer, R. K. Mishra, Yem :. Zhu, and D. O. Welch, J Appl. Phys. **75**, 4208 (1994).
[18] C. D. Fuerst, J. F Herbst, and E. A. Alson, J Magn. Magn. Mater. **54-57**, 567 (1986).
[19] C. D. Fuerst and J. F. Herbst, J Appl. Phys. **66**, 1782 (1989).

Evidence for reversal by nucleation in RE-Fe-B die-upset magnets

L. Henderson Lewis, Y. Zhu, and D. O. Welch
Department of Applied Science, Brookhaven National Laboratory, Upton, New York 11973

Electron microscopy and initial magnetization studies at elevated temperatures were performed on two die-upset rare-earth magnets with bulk compositions $Nd_{13.75}Fe_{80.25}B_6$ and $Pr_{13.75}Fe_{80.25}B_6$. In both compositions the intergranular phase is amorphous and occurs primarily on those surfaces parallel to the tetragonal 2-14-1 phase c axis. The intergranular phase is enriched in iron relative to the bulk grain, with an average width of 8–12 Å in the Nd-based magnet and 15–20 Å in the Pr-based magnet. The initial magnetization curves and the dependence of the coercivity upon maximum magnetizing field both increase linearly with a common slope and then saturate, consistent with nucleation-dominated behavior. These results suggest that the dominant reversal mechanism in these magnets is nucleation of reversed domains in the iron-rich intergranular region of reduced anisotropy.

I. INTRODUCTION

Not only are magnets based on the $RE_2Fe_{14}B$ tetragonal intermetallic compounds more economical to manufacture than other rare-earth-based magnetic compounds, but they possess impressive energy products which significantly exceed those of prior-existing magnets.[1] However, a major drawback of this class of magnets is their high-temperature coefficient of coercivity, which causes the coercivity to fall steadily to unacceptably low values for temperatures much above 400 K. One method to compensate for this behavior is to increase the coercivity of the magnet[2] so that it more closely approaches its theoretical maximum value, the anisotropy field ($2K_1/M_S$), which is around 90 kOe for $Nd_2Fe_{14}B$ at room temperature.[3] Such directed engineering would be greatly facilitated by the identification of the dominant mechanism of magnetization reversal in these magnets. It is generally agreed upon in the literature that sintered 2-14-1 magnets attain their coercivity by the nucleation of reversed domains.[4] In constrast, the limiting mechanism which controls magnetic reversal in the $RE_2Fe_{14}B$ die-upset magnets produced by melt-quench methods remains an open question. Some researchers believe that strong pinning of domain walls by a nonmagnetic intergranular phase determines the coercivity in these magnets.[5,6] However, other studies comparing sintered and melt-spun magnets have concluded that the nucleation mechanism is dominant in both die-upset and sintered magnets, and recent data obtained from magnetic viscosity measurements[10] performed on melt-quenched magnets support this claim.

In order to identify definitively and understand the reversal mechanism operative in the 2-14-1-based die-upset magnets, it is necessary to investigate simultaneously the microstructural and the magnetic properties.[11] We present here some microstructural, microcompositional, and initial magnetization evidence which suggests that the dominant reversal mechanism in these magnets is the nucleation of reversed domains.

II. EXPERIMENTAL PROCEDURES

Both high-resolution analytical transmission electron microscopy (TEM) and magnetic measurements were performed on two (2-14-1)-based die-upset rare-earth magnets, with bulk compositions $Nd_{13.75}Fe_{80.25}B_6$ and $Pr_{13.75}Fe_{80.25}B_6$, obtained from the General Motors Research and Development Center. The magnets were manufactured by standard hot-deformation processing:[12] overquenched melt-spun ribbons were hot pressed at 750 °C and then further deformed at 800 °C to produce oriented die-upset magnets. Additional processing details are contained in Refs. 13 and 14.

The analytical electron microscopy was performed on the intergranular phases and the boundaries of deformed grains using both a VG Instruments HB-501 and a JEOL 2000FX transmission electron microscope. The samples were thinned with mechanical dimpling followed by argon-ion milling at room temperature. Over 30 unique grain-boundary regions were examined in the Pr-based sample while 10 were examined in the Nd-based sample.

The initial magnetization curves and the dependence of the coercivity upon maximum magnetizing field at elevated temperatures were investigated in the range 350 K$\leqslant T\leqslant$425 K in applied fields up to 20 kG using a superconducting quantum interference device (SQUID) magnetometer manufactured by Quantum Design. Each sample was machined down to the approximate dimensions 1.3 mm×1.3 mm×2.0 mm and was subsequently sealed in a quartz capillary tube of 2 mm (i.d.)×3 mm (o.d.) to avoid the possibility of oxidation during measurement. Prior to each minor loop measurement the magnets were thermally demagnetized by heating to 30° above their nominal 2-14-1 Curie temperatures and then cooled in zero field to the measuring temperature. The resultant hysteresis loops were corrected for demagnetization using the equation[15]

$$H_{\text{demag}}=4\pi M_s\times(2/\pi)\times\arcsin(1/1+q), \tag{1}$$

where q is the dimensional ratio. H_{demag} was corrected further a constant multiplicative factor of 0.815, obtained from a measurement of low coercivity nickel.

III. RESULTS

The microstructures of both the Nd-based and the Pr-based die-upset magnets are very similar. As described in previous publications[16–18] the materials are highly anisotropic, consisting mostly of platelet-shaped grains of the 2-14-1 phase stacked parallel to their c axes and separated

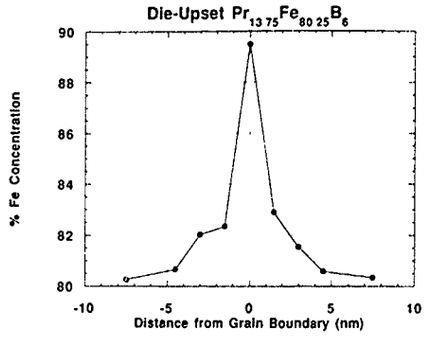

FIG. 1. Iron concentration for $Pr_{13.75}Fe_{80.25}B_6$ as a function of distance from grain boundary.

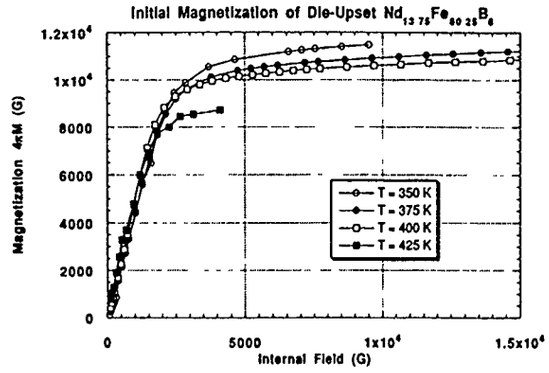

FIG. 3. Initial magnetization curves for die-upset $Pr_{13.75}Fe_{80.25}B_6$ at various temperatures.

from one another by a thin intergranular phase. The average dimensions of the deformed grains are 600 nm±150 nm in length by 150 nm±75 nm in width. A certain fraction of the grains are larger and equiaxed; these contain a speckling of precipitates in the grain interior which was not found in the more deformed grains. Mishra[18] estimated this fraction of larger grains to be around 15%. During our studies it was found that the intergranular phase is amorphous and its presence is dependent upon the nature of the grain boundary in question: there appears to be no intergranular phase in (001) twist boundaries parallel to the tetragonal basal plane. The average width of the intergranular phase is 8–12 Å in the Nd-based magnet and 15–20 Å in the Pr-based magnet. The high-resolution analytical electron microscope studies reported here show that, for both the Nd-based and the Pr-based compositions, the intergranular phase is enriched in iron relative to the bulk grain composition. Figure 1 illustrates the iron concentration profile in Pr-Fe-B upon traveling from one grain to another across the intergranular phase; it is to be noted that the iron concentration in the bulk grain is near 80%. Figure 2 gives a histogram of the relative ratio of iron to praseodymium in the grain-boundary region versus that in the grain interior for a sampling of 30 grain boundaries. The trends for iron in the Nd-based sample were found to be very similar to those shown here for the Pr-based sample.

The magnetic data are illustrated in Figs. 3 and 4 for Pr-Fe-B. The results for Nd-Fe-B look very similar. Figure 3 shows the initial magnetization curves at various temperatures. The initial curves of both samples show a steep temperature-independent rise in the magnetization, followed by an approach to saturation that is temperature dependent. Figure 4 illustrates the development of the coercivity in Pr-Fe-B with maximum applied field. As was the case with the initial magnetization curves, the coercivities initially develop rapidly and level out to a constant, temperature-dependent value.

IV. DISCUSSION

Structurally, nucleation may be controlled by small numbers of relatively large defects whereas pinning requires a regular distribution of defects, such as fine precipitates, to be present in the material.[19,20] For efficient pinning it is desired that the magnetic properties of the two phases constituting the material be very different.[11] The microstructure of these magnets more closely matches that of a material characterized by nucleation reversal because the deformed grains, which comprise ~85% of the sample, are largely free of precipitates.

The high-resolution microcompositional analyses reported here clearly show an enrichment of iron in the grain-boundary region relative to the grain itself, for a sampling of

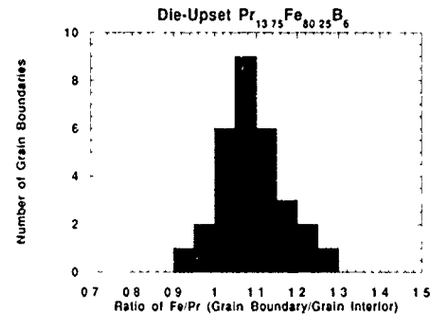

FIG 2. Histogram depicting Fe/Pr ratio for the grain-boundary phase vs the grain interior.

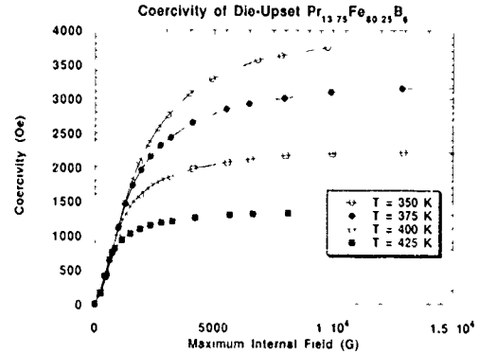

FIG. 4. Coercivity vs maximum applied field for die-upset $Pr_{13.75}Fe_{80.25}B_6$

30 grain boundaries. Additionally, this grain-boundary phase is not found to evenly wet all surfaces of the 2-14-1 main phase particles, but rather is found mainly on those boundaries parallel to the c axis. These results differ considerably from those of Mishra,[18] obtained by lower-resolution methods, who reported a grain-boundary phase with a composition close to the eutectic phase $Nd_{70}Fe_{30}$ (or $Pr_{70}Fe_{30}$) and which coats each grain uniformly. We do not doubt that a phase with a composition close to $Nd_{70}Fe_{30}$ does exist in these materials, especially since the excess rare-earth present in these magnets must be present somewhere in the microstructure. However, the exact distribution within the microstructure of rare-earth-rich and iron-rich grain boundaries, as well as intragranular phases, remains to be determined.

The presence of excess iron in the grain-boundary phase has several important consequences with regards to intergrain interactions. One result is that the grains are most probably exchange coupled as well as magnetostatically coupled. The micromagnetic origins of the coercivity in fine-grained material strongly depend upon the type of coupling between the grains. Recent numeric micromagnetic calculations[21] of nucleation fields of 2D magnetic structures demonstrate that if grains have direct exchange interactions, the entire sample can easily demagnetize after reversal of one grain.

The presence of a ferrous intergranular phase, which may well be magnetic, also allows for the existence of lower-anisotropy sites for reverse magnetization nucleation while at the same time it may reduce the probability of domain wall pinning at the intergranular phase. As is stated by Livingston,[19] pinning is a necessary requirement, even in nucleation-controlled magnets, to avoid catastrophic reversal originating at low-coercivity regions. In these magnets a likely place for pinning to occur is at the larger RE-rich nonmagnetic pockets found along some of the grain boundaries and at grain-boundary triple points.

Our magnetic data strongly suggest that the coercivity of these magnets develops by the nucleation of reverse domains. A distinguishing characteristic between nucleation-dominated and pinning-dominated materials is the behavior of the initial susceptibility. A low initial susceptibility of a thermally demagnetized magnet implies that no free domain wall displacement occurs, because the walls are pinned within the crystallites. This results in only very small changes of magnetization for fields less than a critical unpinning field. Magnets that exhibit a high initial susceptibility have domain walls that move easily, implying that no domain-wall pinning occurs within the crystallites.[9,22] The initial magnetizations of the Pr-based magnets, Fig. 3, show a high initial susceptibility which is independent of temperature.

Another distinguishing characteristic between nucleation-controlled and pinning-controlled magnets is the development of the coercivity with applied field. Hadjipanayis and Kim[22] state that for nucleation-dominated magnets the coercivity H_c increases linearly with magnetizing field and then saturates, whereas in those magnets characterized by pinning the coercivity is almost negligible up to a critical field and then it suddenly increases to saturation. Figure 4 clearly shows that these 2-14-1 die-upset magnets behave in the former manner at elevated temperatures. The common slope of the H_c vs H_a curve implies that these nucleation sites are structural features, but are thermally sensitive.

V. CONCLUSIONS

Evidence is presented which strongly suggests that the development of coercivity at elevated temperatures in die-upset $RE_2Fe_{14}B$ magnets is probably dominated by the nucleation of reversed domains. It is likely that these reversed domains nucleate at reduced-anisotropy sites residing within the iron-rich grain-boundary phase, observed using high-resolution analytical TEM. However, the origin of the temperature dependence of the coercivity, which was attributed by Pinkerton and Fuerst[5,6] to strong pinning, still remains to be clarified.

The above conclusions suggest methods to improve the temperature coefficient of coercivity in die-upset $RE_2Fe_{14}B$ magnets. An ideal microstructure for a nucleation-type magnet consists of grains of a magnetically hard phase that are exchange isolated from one another.[11] Therefore, segregation of nonmagnetic atoms to the grain-boundary phase via metallurgical manipulation would produce higher-coercivity magnets. In fact, preliminary work along those lines has been done by Fuerst and Brewer[23] in which an increase of coercivity was observed in die-upset Nd-Fe-B magnets upon introduction of noble-metal elements to the melt-spun ribbons.

ACKNOWLEDGMENTS

We are grateful to C. D. Fuerst for providing us with samples and for helpful discussions. This research was sponsored by U.S. DOE Laboratory Directed Research and Development Program, Contract No. DE-AC02-76CH00016.

[1] J. F. Herbst, Rev. Mod Phys. **63**, 819 (1991).
[2] G. C. Hadjipanayis, K. R. Lawless, and R. C. Dickerson, J. Appl. Phys. **57**, 4097 (1985).
[3] K. H. J Buschow, Mater. Sci. Rep. **1**, 1 (1986)
[4] J. F. Herbst and J. J. Croat, J. Magn. Magn. Mater. **100**, 57 (1991).
[5] F. E Pinkerton and C. D. Fuerst, J. Appl. Phys. **69**, 5817 (1991)
[6] F. E. Pinkerton and C. D. Fuerst, J. Magn. Magn. Mater **89**, 139 (1990).
[7] M. Grönefeld and H. Kronmuller, J. Magn Magn. Mater. **88**, L267 (1990).
[8] K -D. Durst and H. Kronmuller, J. Magn. Magn. Mater. **68**, 63 (1987).
[9] D. Givord, Q. Lu, M. F. Rossignol, P Tenaud, and T. Viadieu, J Magn. Magn. Mater. **83**, 183 (1990).
[10] L. Folks, R. Street, and R. Woodward, J. Appl. Phys. **75**, 6271 (1994).
[11] R. Ramesh and G. Thomas, Mater. Sci. Eng B **3**, 435 (1989).
[12] R. W. Lee, Appl. Phys. Lett. **46**, 790 (1985).
[13] C. D Fuerst and E. G. Brewer, J. Appl. Phys. **73**, 5751 (1993).
[14] C. D. Fuerst, E. G. Brewer, R K. Mishra, Y. Zhu, and D. O. Welch, J. Appl. Phys. **75**, 4208 (1994).
[15] D. J. Craik, *Structure and Properties of Magnetic Materials* (Pion, London, 1971), p. 23
[16] T.-Y. Chu, L Rabenberg, and R. K Mishra, J. Appl. Phys. **69**, 6046 (1991).
[17] R. K. Mishra, T.-Y. Chu, and L. Rabenberg, J. Magn. Magn. Mater. **84**, 88 (1990).
[18] R. K. Mishra, J. Appl Phys **62**, 967 (1991)
[19] J. D Livingston, IEEE Trans Magn **MAG-23**, 2109 (1987).
[20] J. J Becker, IEEE Trans. Magn. **MAG-12**, 965 (1976)
[21] T Schrefl, H. F. Schmidts, J. Fidler, and H. Kronmuller, IEEE Trans. Magn. **MAG-29**, 2878 (1993).
[22] G C Hadjipanayis and A. Kim, J Appl Phys **63**, 3310 (1988)
[23] C. D. Fuerst and E. G Brewer, J Appl Phys. **69**, 5826 (1991).

Microstructure and magnetic properties of mechanically alloyed anisotropic Nd-Fe-B

J. Wecker, H. Cerva, C. Kuhrt, K. Schnitzke, and L. Schultz[a)]
Siemens AG, Research Laboratories, Erlangen and Munich, Germany

Mechanically alloyed Nd-Fe-B powders with additions of Dy, Co, and Ga were hot compacted to magnetically isotropic materials and then deformed by die upsetting to obtain anisotropic magnets. Magnets can be processed either with a medium coercivity H_{ci} of 7.8 kA/cm but with a high-energy product $(BH)_{max}$ of 330 kJ/m^3 or with a coercivity of 21.2 kA/cm and a lower $(BH)_{max}$ of 192 kJ/m^3. Plane-view transmission electron microscopy (TEM) pictures show nearly equiaxed $Nd_2Fe_{14}B$ grains. In cross section, the grains display the typical platelet form known from MQ 3-type magnets with a length of about 300 nm and a height of 100 nm. Characteristic for mechanically alloyed materials are up to 500 nm large globular NdO_x particles distributed regularly throughout the microstructure which inhibit the anisotropic grain growth. In addition 5–20 nm small NdO_x precipitates are found within some $Nd_2Fe_{14}B$ grains. X-ray diffraction studies also indicate that the degree of texturing after die upsetting is smaller for mechanically alloyed than for melt-spun materials. High-resolution TEM experiments did not show any grain boundary phase usually found in melt-spun materials; however, this needs to be confirmed.

I. INTRODUCTION

The small grain sizes of rapidly quenched or mechanically alloyed Nd-Fe-B prohibit the preparation of anisotropic magnets by an alignment of the respective powders in an external magnetic field. Anisotropy can be induced by hot compaction of the ribbons or powders to fully dense isotropic magnets followed by hot deformation.[1,2] From transmission electron microscopy (TEM) analysis of melt-spun Magnequench (MQ)-type magnets it was concluded that the alignment proceeds by a combination of grain boundary sliding and grain boundary migration.[3] For mechanically alloyed materials a detailed investigation of the microstructure and its correlation to the magnetic properties remained to be done. First preliminary experiments already showed the presence of Nd oxides in both the isotropic and the die-upset samples.[4]

II. EXPERIMENTAL

Mechanically alloyed Nd-Fe-B powders were prepared by high-energy ball milling in a planetary ball mill or in an attritor with typical batch sizes of 30 or 300 g (milling time 48 h). For comparison we also prepared rapidly quenched ribbons by conventional melt spinning. The compositions of the different samples are given below. The as-milled powders or the as-quenched ribbons were hot compacted to cylindrical magnets (diameter $d=10$ mm, height $h=10$ mm) followed by a die-upset process. For both processes the temperatures were between 720 and 750 °C for mechanically alloyed powders and at 690 °C for the melt-spun ribbons with a deformation ratio h_0/h of 4 (h_0 and h being the heights of the magnets before and after deformation). Magnetic measurements were done in a vibrating sample magnetometer after magnetizing the samples in a field of 50 kA/cm. For TEM analysis, the cylinders were sliced parallel and perpendicular to the press direction. The samples were ground and ion milled and were examined in a transmission electron microscope (JEOL 2000 FX). Chemical microanalysis was done by energy dispersive x-ray analysis (EDX).

III. RESULTS

A. Magnetic properties

As for sintered or melt-spun Nd-Fe-B, the properties of mechanically alloyed magnets can be tailored to the desired needs by a proper choice of alloying additions. Figure 1 shows the demagnetization curve of a magnet with a remanence J_r of 1.32 T and thus with a high-energy product $(BH)_{max}$ of 333 kJ/m^3. Because of the low rare-earth content, the coercivity H_{ci} is rather low. H_{ci} can be increased by nearly a factor of 3 by the partial substitution of Nd by Dy via an increase of the anisotropy field. However, because of

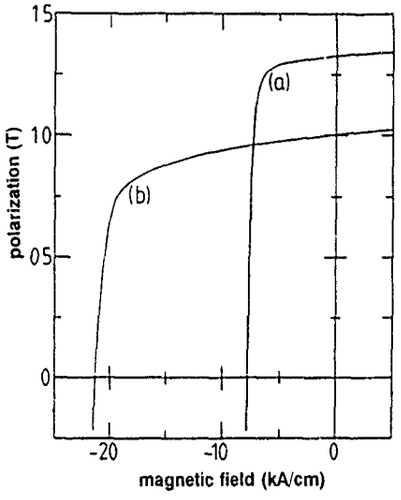

FIG. 1. Demagnetization curves of two anisotropic mechanically alloyed magnets with compositions of $Nd_{15.5}Fe_{72}Co_6Ga_{0.5}B_6$ (curve a) and of $Nd_{14}Dy_3Fe_{68}Co_{7.5}Ga_{0.75}B_{6.75}$ (curve b).

[a)]Institute for Solid State and Materials Research, Dresden, Germany

 0021-8979/94/76(10)/6238/3/$6.00 © 1994 American Institute of Physics

TABLE I. Coercivity, H_{ci}, remanence, J_r, remanence ratio, $R=J^{\parallel}/J^{\perp}$, and energy product, $(BH)_{max}$, of die-upset magnets with different Nd concentrations

	H_{ci} (kA/cm)	J_r (T)	R	$(BH)_{max}$ (kJ/m^3)
$Nd_{13.5}Fe_{73}Co_6Ga_{0.5}B_7$	3.6	0.87	1.3	97
$Nd_{14.5}Fe_{72}Co_6Ga_{0.5}B_7$	7.7	1.30	4.8	313
$Nd_{15.5}Fe_{71}Co_6Ga_{0.5}B_7$	8.8	1.27	4.0	311
$Nd_{16.5}Fe_{70}Co_6Ga_{0.5}B_7$	9.8	1.19	2.8	265
$Nd_{14}Fe_{71.4}Co_8Ga_{0.6}B_6$[a]	7.1	1.36	4.3	350

[a]Melt-spun material.

the antiferromagnetic coupling of the Dy to the transition metal sublattice the remanence decreases (Fig. 1). The simultaneous addition of Co improves the temperature dependence of the magnetic properties and guarantees a coercivity of 9.0 kA/cm even at 150 °C necessary, e.g., for the substitution of Sm-Co magnets in electromotors.

For mechanically alloyed Nd-Fe-B, the texturing of fully dense magnets by die upsetting is only possible above a rare-earth concentration of 14 at %. Below this critical value hardly any anisotropy develops and J_r remains low (Table I). Above, one obtains energy products greater than 300 kJ/m^3 and H_{ci} increases with the Nd content in the same way as for MQ magnets.[5] The ratio, $R=J^{\parallel}/J^{\perp}$, of the remanences measured parallel and perpendicular to the press direction is a measure of the degree of texturing and shows values above 4. For higher Nd concentrations $(BH)_{max}$ decreases probably because of nonmagnetic impurity phases. The magnet prepared for comparison from melt-spun ribbons with a Nd concentration of 14 at % but with a slightly different concentration of the remaining elements had a $(BH)_{max}$ of 350 kJ/m^3 (Table I).

B. Microstructure

Cross-sectional TEM images which were taken parallel to the press direction show the typical platelet form of the $Nd_2Fe_{14}B$ (Φ) grains known from MQ-type magnets[3] with a length and a height of about 300 and 100 nm, respectively (Fig. 2). The flat surfaces of the grains are normal to the press direction and to the c axis of the tetragonal unit cell. In plane view, the grains are nearly equiaxed. Characteristic for mechanically alloyed magnets are up to 500 nm large Nd-oxide particles distributed regularly throughout the microstructure which were already observed previously.[4] EDX analysis proves that the main metallic constituents of these oxides are Nd and Dy. The particles show a sponge-like contrast and their diffraction patterns can be assigned to cubic NdO and Nd_2O_3. A characteristic feature is the fact that in their vicinity the growth of the Φ grains to flat platelets is inhibited as can be seen in Fig. 3 where the oxide particle in the center is marked by an arrow. Besides these intergrain oxides we also frequently observe 5–20 nm small precipitates within $Nd_2Fe_{14}B$ (see arrows in Fig. 2) which by EDX analysis are identified as oxides. Such intragrain oxides were also observed in sintered magnets and are probably hexagonal Nd_2O_3.[6] We have not observed the metallic intergranular phase found in MQ-3 magnets[3] (Fig. 4). Instead the grain boundary appears to be free of a minority phase and the lattice planes of neighboring Φ grains directly meet at the grain boundary.

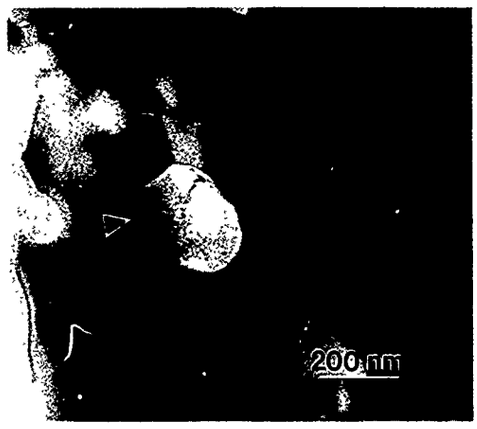

FIG. 3 Cross-section bright-field TEM image of die-upset $Nd_{14}Dy_3Fe_{62}Co_{14}Ga_{0.75}B_{6.25}$. The large oxide grain marked by the arrow inhibits the growth of $Nd_2Fe_{14}B$ to the typical platelet shape seen in Fig. 1.

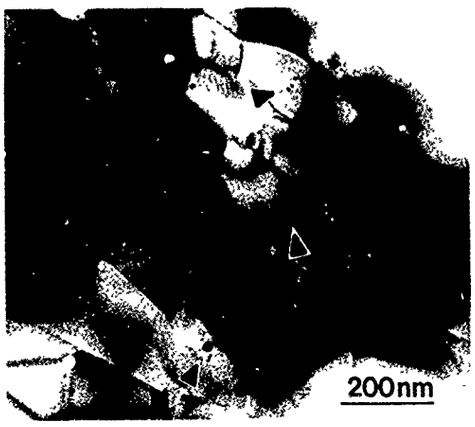

FIG 2 Cross-section bright-field TEM image of die-upset $Nd_{15.5}Dy_{2.5}Fe_{65}Co_{10}Ga_{0.75}B_{6.25}$ The arrows mark oxide inclusions in $Nd_2Fe_{14}B$ grains

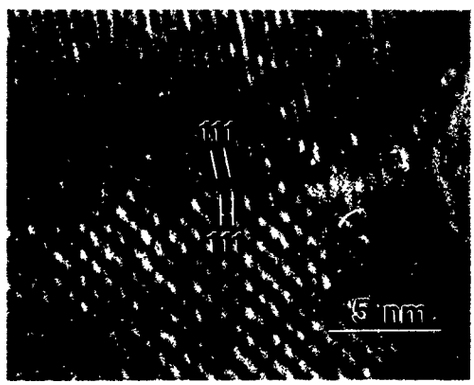

FIG 4. High-resolution image showing the grain boundary between $Nd_2Fe_{14}B$ grains in die-upset $Nd_{15.5}Dy_{2.5}Fe_{65}Co_{10}Ga_{0.75}B_{6.25}$

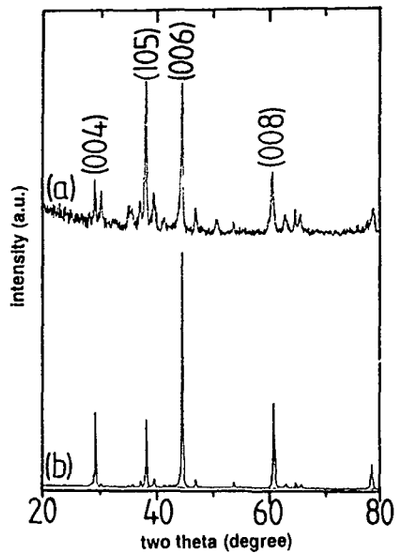

FIG. 5. X-ray diffraction pattern of die-upset mechanically alloyed Nd-Fe-B (curve a) compared to melt-spun materials (curve b).

The texturing during die upsetting becomes also evident in x-ray diffraction patterns taken in $\Theta/2\Theta$ geometry which show prominent (001) peaks (Fig. 5) indicative of an alignment of the c direction normal to the surface of the magnet. Compared to the MQ-type magnet, however, the intensity of the (105) line is higher [Fig. 5(b)], hinting to a smaller degree of orientation in the mechanically alloyed material.

IV. DISCUSSION

Mechanical alloying like conventional sintering is a powder metallurgical technique to prepare high performance permanent magnets. Therefore, the presence of oxides in the microstructure is not unexpected. Indeed, by chemical analysis we detect an oxygen content of up to 0.5 wt % in the final magnet which is comparable to sintered magnets. The oxygen contamination is introduced to about 0.2 wt % with the starting powders and the rest coming from the uptake during processing. Since the oxygen forms rare-earth oxides, the amount of the Nd-rich intergranular phase which is supposed to be necessary for texturing via the anisotropic grain growth[3] should be reduced. This explains why we do not observe a crystallographic alignment for too low Nd concentrations (<14 at %), i.e., when the Nd surplus is almost completely reacted to Nd oxides in contrast to the samples prepared from melt-spun ribbons which have an oxygen content below 0.1 wt %. $Nd_2Fe_{14}B$ has no plasticity at the temperatures used for die upsetting but shows brittle fracture[7] and therefore, the grain boundary phase indeed also should be present in our materials but obviously to a smaller amount. The observation of no grain boundary phase in the TEM experiments does not unambiguously prove that there is no Nd-rich phase at all because of only too few analyses we did. Also, the micrograph may have been taken from a part of the grain boundary which is not decorated by the Nd-rich phase. However, grain boundary phases were previously detected in the isotropic compacted magnets.[4]

The bimodal size distribution of oxide particles, i.e., large intergrain oxides and small particles within the $Nd_2Fe_{14}B$ were also observed in high-strength NiAl-based alloys and seem to be characteristic of mechanically alloyed materials.[8] So far, it is not clear to what extent the lack of texturing in the vicinity of large oxide particles (cf. Fig 3) is a direct consequence of their presence which prevents grain growth. Or if it results from the local absence of the Nd-rich phase which accelerates diffusional mass transport because it is liquid at the deformation temperatures. But both factors do reduce the remanence and thus the energy product as can be seen by comparing the mechanically alloyed and the melt-spun samples (Table I). Since the occurrence of oxides at least under practical conditions can never be prevented in powder metallurgy the energy product of mechanically alloyed magnets will always be somewhat lower than for respective MQ-type materials whereas the coercivities do not show any significant difference. For the latter magnets a $(BH)_{max}$ of 335 kJ/m^3 was obtained with an even lower Nd concentration of 13.7 at % and a comparable deformation ratio.[5] Some improvement of the texturing of mechanically alloyed magnets may be possible by trying to introduce a low melting grain boundary phase artificially. For example, small amounts of diffusion alloyed Zn additives were shown to increase not only the coercivity of die-upset MQ magnets but also the remanence.[9]

ACKNOWLEDGMENTS

The authors gratefully acknowledge valuable discussions with W. Rodewald and technical assistance by F. Körner and K. Rostek. This work was supported by the BRITE/Euram program of the European Union.

[1] R. W Lee, E. G Brewer, and N. A Schaffel, IEEE Trans. Magn. **MAG-21**, 1958 (1985)
[2] L. Schultz, K Schnitzke, and J Wecker, J Magn Magn Mater **80**, 115 (1989).
[3] R K. Mishra, J. Mater Eng. **11**, 87 (1989).
[4] C. Koestler, M. Chandramouli, G. Thomas, and L. Schultz, J Magn. Magn Mater. **110**, 264 (1992).
[5] C. D. Fuerst and E. G. Brewer, J. Appl. Phys. **73**, 5751 (1993).
[6] J. Fidler, IEEE Trans. Magn. **MAG-23**, 2106 (1987).
[7] C. Kuhrt, L. Schultz, K. Schnitzke, S. Hock, and R Behrensmeier, Appl Phys. Lett. **59**, 1418 (1991).
[8] S. Dymek, M. Dollar, S J. Hwang, and P. Nash, Mater. Res. Soc. Symp Proc. **238**, 1117 (1993).
[9] C D. Fuerst and E. G. Brewer, Appl. Phys. Lett **56**, 2252 (1990)

Preparation and transmission electron microscope investigation of sintered $Nd_{15.4}Fe_{75.7}B_{6.7}Cu_{1.3}Nb_{0.9}$ magnets

Johannes Bernardi and Josef Fidler
Institute of Applied and Technical Physics, T. U. Vienna, Wiedner Hauptstrasse 8-10, A-1040 Vienna, Austria

Sintered magnets were prepared from jet-milled and hydrogen-decrepitated jet-milled Nd-Fe-B:(Cu,Nb) powder. The HD process started after heating the cast material up to 200 °C. A single-step annealing treatment at 525 °C improved the magnetic properties of all samples. Magnets prepared from the jet-milled powder required a short time sintering (<60 min) to obtain optimum coercivity but had poor density. Magnets prepared from the HD powder showed a higher remanence and energy density product but a slightly smaller coercivity than the magnets prepared from the jet-milled powder. The sintered and annealed magnets contain a multiphase microstructure. Nb was found as small precipitates within the hard magnetic grains and as intergranular boride phase. The addition of Cu lowers the melting point of the liquid phase during sintering and leads to the formation of an orthorhombic NdCu phase that is partly replacing the Nd-rich intergranular phases. The intergranular δ-phase $Nd_6Fe_{13}Cu$ was found regularly in the annealed samples. Nd_2Fe_{17} was not detected in the investigated samples.

I. INTRODUCTION

The magnetic properties of $Nd_2Fe_{14}B$ magnets can be improved by the substitution of expensive Dy and Co and/or by the addition of two types of dopant elements that influence the microstructure in a similar way.[1] Type I dopants ($M1$=Al, Cu, Zn, Ga, Ge, Sn) form binary $M1$-Nd or ternary $M1$-Fe-Nd compounds, while type II dopants ($M2$=Ti, V, Nb, Mo, W) form $M2$-B or $M2$-Fe-B borides. In a previous investigation we showed that the addition of Ga and Nb leads to good magnetic properties.[2] Small amounts of Cu improved the workability of hot worked magnets[3] and led to the formation of new intergranular phases like NdCu.[4] The purpose of this work was to study the microstructure and the magnetic properties of a Dy and Co-free magnet containing a type I (Cu) and a type II (Nb) dopant.

II. EXPERIMENT

The alloy with the nominal composition $Nd_{15.4}Fe_{75.7}B_{6.7}Cu_{1.3}Nb_{0.9}$ was supplied by Treibacher Chemische Werke. Magnets were prepared by the powder-metallurgical sintering process from jet-milled powder (A) and from hydrogen decrepitated (HD) and jet-milled powder (B). The average diameter of powder A was 2.9 and 1.75 μm of powder B, respectively (determined by FSSS). An initial temperature of 200 °C was necessary to start the HD process at +1 bar H_2 pressure. Green compacts were pressed at 200 MPa transverse to the direction of the aligning field of 1.25 T. Sintering was done at temperatures from 1040 to 1120 °C for different times followed by a single-step annealing treatment. The magnetic properties were determined with a hysteresigraph at room temperature. The microstructure of the magnets was investigated by means of analytical transmission electron microscopy in a JEOL 200CX microscope fitted with two energy dispersive x-ray detectors, a high take-off angle Si detector and a low take-off angle Ge detector for light element analysis. Electron transparent samples were produced by grinding and following ion-beam thinning.

III. RESULTS

A. Magnetic properties

The magnets produced from powder A were sintered between 1080 and 1120 °C. The density of the samples and the remanence increased with increasing sintering temperature while the coercivity increased for the samples sintered for short times (40–60 min) at lower temperatures. A single-step annealing treatment at 525 °C improved the magnetic properties. The magnet with the highest coercive field was sintered at 1080 °C for 40 min and annealed at 525 °C. That sample showed a coercive field of 910 kA/m and a remanence of 1.14 T, but had a poor density (<7 g/cm^3).

The magnets produced from the HD powder B were sintered between 1040 and 1090 °C. Good magnetic properties were achieved after a single-step annealing treatment at 525 °C (Fig. 1). At comparable sintering temperatures the HD magnets showed a higher remanence and energy product but a slightly reduced coercivity than the magnets produced from powder A.

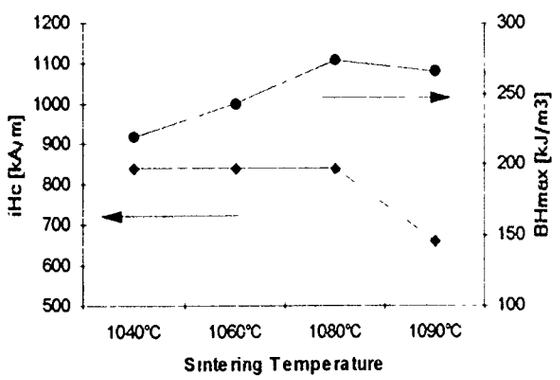

FIG. 1. Magnetic properties of the sintered and annealed $Nd_{15.4}Fe_{75.7}B_{6.7}Cu_{1.3}Nb_{0.9}$ magnets produced from the HD powder. All samples were sintered for 1 h and annealed at 525 °C.

 0021-8979/94/76(10)/6241/3/$6.00 © 1994 American Institute of Physics

TABLE I. Phases found in the sintered and annealed $Nd_{15.4}Fe_{75.7}B_{6.7}Cu_{1.3}Nb_{0.9}$ magnet.

Phase	Composition	Structure
ϕ	$Nd_2Fe_{14}B$ with Cu substitutions	Tetragonal
$p\phi$	Nb containing precipitates within ϕ	Hexagonal NbFeB
η	Intergranular $Nd_{1+\epsilon}Fe_4B_4$	Tetragonal
ιB	Intergranular NbFeB	Hexagonal NbFeB
$n1$	Intergranular Nd rich (+Fe)	fcc
$n2$	Intergranular Nd rich	hcp
cu	Intergranular NdCu	Orthorhombic
δ	$Nd_6Fe_{13}Cu$	Tetragonal
no	Nd_2O_3 impurities	Rhombohedral

B. Microstructure of the magnets

A magnet from set A, sintered at 1080 °C for 40 min and annealed at 525 °C, was chosen for the transmission electron microscope (TEM) investigation. The phases detected in that magnet are summarized in Table I. The magnet contained a multiphase microstructure consisting of the hard magnetic phase (ϕ), two types of boride phases (η and ιB), several Nd-rich intergranular phases, and the δ-phase $Nd_6Fe_{13}Cu$.

Like in the case of the Ga- and Nb-doped magnets,[2] the hard magnetic $Nd_2Fe_{14}B$ phase (ϕ) was found with a high amount of spherical NbFeB precipitates $p\phi$ with a diameter up to 50 nm as shown in Fig. 2. But some ϕ grains did not show any precipitates. Intergranular boride phases occurred as grains with a diameter up to several microns as hexagonal NbFeB (ιB) and as tetragonal $Nd_{1+\epsilon}Fe_4B_4(\eta)$. Both intergranular boride phases usually contained a high density of crystal defects (Fig. 3). Nd-rich intergranular phases were found with fcc ($n1$) or hcp ($n2$) crystal structure. The fcc phase ($n1$) usually contained some Fe or oxygen as in Ref. 5. In addition an intergranular orthorhombic NdCu phase (cu) was partly replacing the Nd-rich phases (n1) and (n2). Figure 4 shows the NdCu phase besides a Nd-rich phase and a hard magnetic grain with the corresponding x-ray spectra. Nd_2O_3 was found as an impurity phase. The tetragonal

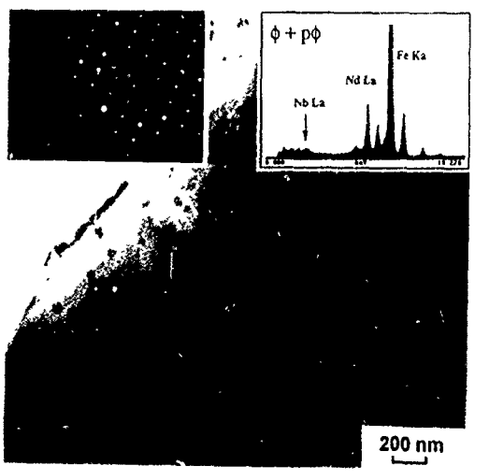

FIG 2. Micrograph of the hard magnetic phase ϕ containing a high amount of spherical NbFeB precipitates $p\varphi$

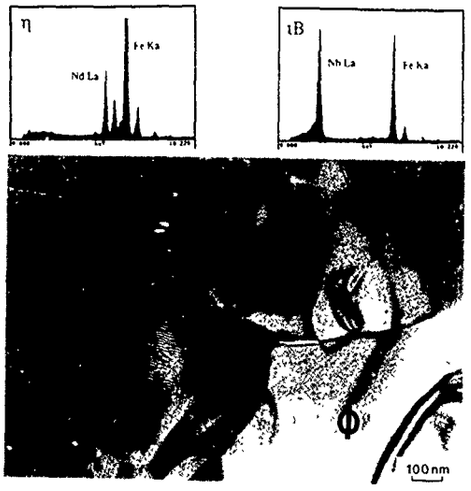

FIG. 3. Micrograph of the intergranular boride phases $Nd_{1+\epsilon}Fe_4B_4$ (η) and NbFeB (ιB) with the corresponding x-ray spectra besides a hard magnetic grain ϕ.

δ-phase $Nd_6Fe_{13}Cu$ that is in equilibrium with Nd and NdCu in the ternary Nd-Fe-Cu phase diagram[6] was found quite regularly as a separate grain with a size up to several microns in the $Nd_{15.4}Fe_{75.7}B_{6.7}Cu_{1.3}Nb_{0.9}$ magnet (Fig. 5). Nd_2Fe_{17} was not detected in the investigated sample.

IV. DISCUSSION

Ternary Nd-Fe-B magnets have a poor temperature stability and bad corrosion resistance. To overcome these problems, Dy and Co are widely added to magnets. The addition of dopants helps to produce magnets with good magnetic properties without the expensive heavy rare-earth element Dy and without Co. From the ternary Nd-Fe-M1 phase diagrams it is clear that type I dopants like Cu, Al, or Ga lower the melting temperature of the liquid phase during sintering. On the other hand, the wettability of the liquid phase is different for Cu, Al, and Ga, respectively. Improved wettability of the liquid phase leads to a better decoupling of the hard

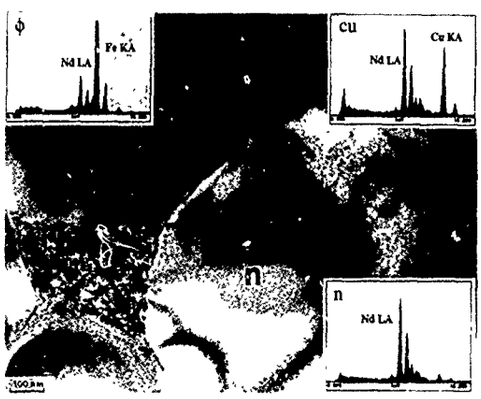

FIG 4. NdCu phase (cu) and a Nd-rich phase (n) besides a hard magnetic grain (ϕ) The NdCu phase is partly replacing the Nd-rich intergranular phases.

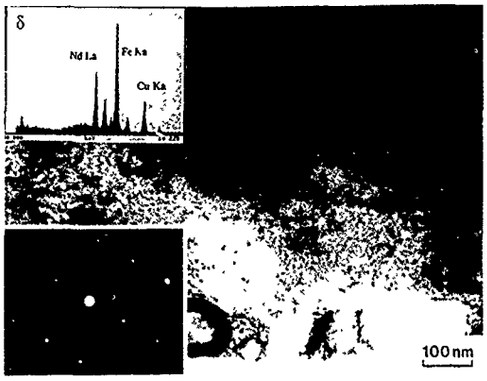

FIG. 5. Micrograph of a $Nd_6Fe_{13}Cu$ grain (δ phase) with the corresponding x-ray spectrum. This phase is found quite regularly in the $Nd_{15.4}Fe_{75.7}B_{6.7}Cu_{1.3}Nb_{0.9}$ magnet

magnetic grains[1] and therefore to an improved coercivity. In the case of Cu poor wettability leads to a lower density and lower coercivity of the magnets compared with Al- and Ga-doped magnets. In addition binary $M1$-Nd and ternary $M1$-Fe-Nd ($M1$=Cu, Al, Ga) occur, partly replacing the fcc and hcp Nd-rich intergranular phases that are mainly responsible for the bad corrosion resistance of Nd-Fe-B magnets. In the investigated $Nd_{15.4}Fe_{75.7}B_{6.7}Cu_{1.3}Nb_{0.9}$ magnet, the orthorhombic NdCu phase and the tetragonal δ-phase $Nd_6Fe_{13}Cu$ were found regularly, and the corrosion resistance was improved, compared with Nd-Fe-B sintered magnets. According to the ternary Nd-Fe-Cu phase diagram,[6] at the Nd-rich side Nd is in equilibrium with NdCu and with the δ phase. The Nd_2Fe_{17} phase, which is also in equilibrium with Nd and the δ phase, was not observed in this magnet. This could be due to a sufficiently high Cu concentration in the liquid phase during annealing which prefers the formation of the δ phase instead of the soft magnetic Nd_2Fe_{17} phase. Nb shows a low solubility at sintering temperature within the hard magnetic phase[7] and forms NbFeB precipitates within the $Nd_2Fe_{14}B$ phase as well as intergranular NbFeB grains that also help to decouple the hard magnetic grains.

Compared to ternary Nd-Fe-B magnets, where the HD process allows a lowering of the sintering temperature,[8] the sintering temperature of the HD-processed Cu- and Nb-doped powder could not be reduced to obtain high coercive fields. This explains why wettability is not improved by Cu addition. For a given sintering temperature the remanence and the energy density product of the HD magnets was larger than that of the magnets prepared by the standard jet-milling process. The main advantage of Nd-Fe-B:Cu magnets is the improved corrosion resistance compared with Nd-Fe-B magnets. Nb-addition suppresses the formation of α-Fe.

ACKNOWLEDGMENTS

This work was part of the CEAM stimulation EC programme and was partly supported by the Austrian Ministry for Science and Research (BRITE/EURAM Project BREU-0150-M).

[1] J Fidler, in *Proceedings of the 7th International Symposium on Magnetic Anisotropy and Coercivity in RE-TM Alloys*, edited by B. Street (The University of Western Australia, 1992), pp 11–22
[2] J. Bernardi, J Fidler, M. Seeger, and H. Kronmuller, IEEE Trans Magn. **MAG-29**, 2773 (1993).
[3] T. Shimoda, K Akioka, O Kobayashi, T. Yamagami, and A. Arai, in *Proceedings of the 11th Workshop on RE Magnets and their Applications*, edited by S. G. Sankar (Cargnegie Mellon University Press, Pittsburgh, 1990), pp. 17–28.
[4] J. Fidler and J Bernardi, J. Appl Phys. **70**, 6456 (1991)
[5] J. Fidler, K. G. Knoch, H. Kronmuller, and G. Schneider, J Mater. Res. **4**, 806 (1989).
[6] C Muller, B. Reinsch, and G Petzow, Z. Metal **83**, 845 (1992).
[7] W. Rodewald, B Wall, and J. P. Jacquet, CEAM II Final Report, Group M 34, 1991.
[8] I. R. Harris and P. J. McGuiness, in *Proceedings of the 11th Workshop on RE Magnets and their Applications*, edited by S. G. Sankar (Cargnegie Mellon University Press, Pittsburgh, 1990), pp 29–48

Fe-Nd-C-based ingot permanent magnets by solid-state transformation

M. Leonowicz, H. A. Davies,[a] and S. Wojciechowski
Department of Materials Science and Engineering, Warsaw University of Technology, Narbutta 85, 02-524 Warszawa, Poland

The effects of composition, annealing temperature, and annealing time on the magnetic properties and microstructure of $Fe_{66}M_2Nd_{20}C_{9.5}B_{0.5}$ (M=Ga,Nb,Cu,Al) ingot magnets are presented. It has been found that the magnitude of the hard magnetic properties, which evolve during the solid-state transformation $Fe_{17}Nd_2C_x$ to $Fe_{14}Nd_2C$, depends on the additive elements. These additions which decrease the melting temperature of the intergranular phase accelerate the transformation process and those which increase this temperature retard the transformation. Coercivities up to 880 kA/m combined with a remanence 0.58 T were produced in alloy ingots with Cu. The initial grain size was found to be crucial in producing good magnetic properties and coercivities as high as 980 kA/m were achieved for Fe-Nd-C-B alloy magnets hot pressed from microcrystalline melt spun ribbon. A modest increase of remanence (~0.7 T) was achieved by die-upset forging of ingot alloys.

I. INTRODUCTION

The principal routes for the production of RE-Fe-B permanent magnets are those based on liquid phase sintering,[1] or on melt spinning,[2] followed by resin bonding or hot working the crushed ribbon.[2] Both technologies are based on powder processing. However, there are two systems for which useful coercivities can be obtained in the cast state. Fe-Pr-B ingot magnets exhibit coercivities up to 1000 kA/m and partly columnar alloys show remanences of ~0.7 T.[3,4] The second system is based on the $Fe_{14}Nd_2C$ compound.[5–8] Its structure and intrinsic magnetic properties are broadly comparable with those of $Fe_{14}Nd_2B$.[5] The possibility of producing cast magnets is attractive due to the simplicity of the processing, low cost, and the ability to manufacture net shape products without the need for handling powders or ribbon. The Fe-Nd-C system is interesting also because the $Fe_{14}Nd_2C$ compound forms by a solid-state peritectoid reaction, which occurs below 900 °C.[6] Small addition (0.05%) of boron accelerates the nucleation rate of the $Fe_{14}Nd_2C$ phase, increases the transformation temperature (~1050 °C), and reduces the annealing time.[7]

In this study the possibility of achieving useful coercivities in the Fe-M-Nd-C-B (M=Cu,Ga,Nb,Al) ingot magnets, within a relatively short annealing time of a few hours was investigated and the temperature-microstructure relations were analyzed.

II. EXPERIMENTAL PROCEDURE

The $Fe_{66}M_2Nd_{20}C_{9.5}B_{0.5}$ (M=Ga,Nb,Cu,Al) alloys were made by induction melting the pure elements under an argon atmosphere. The ingot magnets were prepared by annealing the ingots in evacuated silica tubes. The $Fe_{68}Nd_{20}C_{9.5}B_{0.5}$ alloy was also prepared in ribbon form by melt spinning in an argon atmosphere and the crushed ribbon was subsequently hot pressed at 700 °C in argon. The magnetic properties were measured using an Oxford VSM with maximum applied field of 5 T. Phase identification was performed by x-ray diffraction. Microstructural observations were made using scanning electron and optical microscopy. The Curie temperature and the melting point of the grain boundary phase were evaluated in a Perkin–Elmer DSC-2 scanning calorimeter.

III. RESULTS AND DISCUSSION

The effects of annealing temperature on the magnetic properties of the $Fe_{68}Nd_{20}C_{9.5}B_{0.5}$ alloy are shown in Fig. 1. The alloy was annealed for a constant time of 5 h. The $Fe_{14}Nd_2C$ compound first appeared at 800 °C but due to only partial transformation at this temperature, the remanence (J_r) was relatively low. Both J_r and coercivity ($_JH_c$) achieved

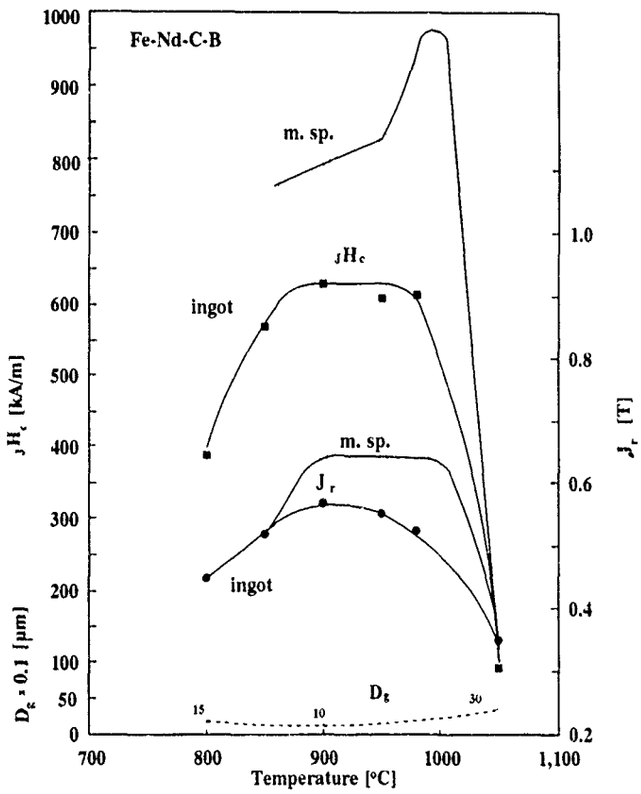

FIG. 1 Magnetic properties for $Fe_{68}Nd_{20}C_{9.5}B_{0.5}$ ingot and melt spun (m sp.) ribbon alloys annealed at different temperatures for 5 h. Mean grain size for the ingot alloy is also shown.

[a] Department of Engineering Materials, University of Sheffield, Sheffield S1 4DU, United Kingdom

 0021-8979/94/76(10)/6244/3/$6.00 © 1994 American Institute of Physics

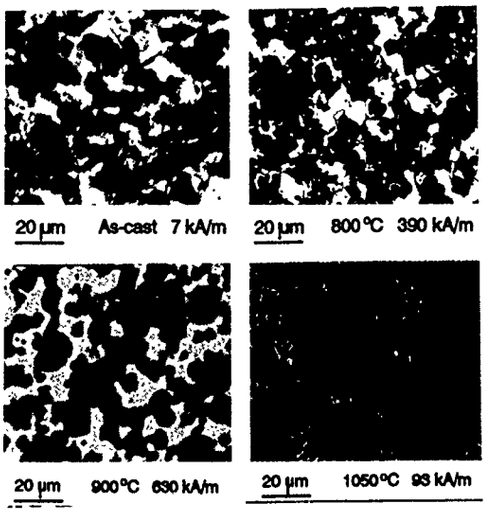

FIG 2. SEM micrographs for $Fe_{68}Nd_{20}C_{9.5}B_{0.5}$ ingots: as-cast ($_JH_c$=7 kA/m), and annealed for 5 h at 800 °C ($_JH_c$=380 kA/m), 900 °C ($_JH_c$=630 kA/m), and 1050 °C ($_JH_c$=93 kA/m). Backscattered electrons images

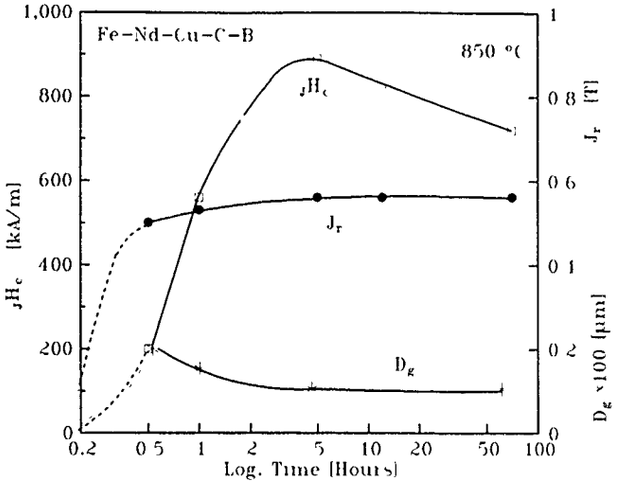

FIG 3. Magnetic properties and mean grain size for $Fe_{66}Cu_2Nd_{20}C_{9.5}B_{0.5}$ ingot magnets after annealing at 850 °C for different times.

maxima at 900 °C and the shape of the demagnetization curve for this sample indicated that the material consisted largely of the $Fe_{14}Nd_2C$ phase. Samples annealed at 1050 °C appeared to contain much soft magnetic phase and this temperature seemed to be close to the point of equilibrium coexistence of the $Fe_{14}Nd_2C$ and $Fe_{17}Nd_2C_x$ phases. The mean grain size (D_g) for the cast ingot alloy was inversely proportional to the amount of $Fe_{14}Nd_2C$ phase and showed a minimum of ~10 μm for the sample annealed at 900 °C. The coercivity of the magnets correlated closely with the grain size. Samples having a much smaller grain size (~50 μm) produced by hot pressing of rapidly solidified ribbon exhibited $_JH_c$ up to 300 kA/m higher than the ingot magnets of the same composition.

Fe-Nd-C-B alloys crystallized from the melt formed a fine dendritic microstructure. These elongated grains became equiaxed during annealing, firstly as $Fe_{17}Nd_2C_x$ (~15 μm), then reducing their size to ~10 μm, on decomposition to $Fe_{14}Nd_2C$. Long time annealing (70 h) at 850 °C did not result in coarsening of the microstructure. In contrast, the alloys annealed at 1050 °C were transformed by a small proportion only so that the final structure consisted of large grains (~30 μm) of mostly $Fe_{17}Nd_2C_x$ phase (Fig. 2).

The effect of annealing time on the magnetic properties was investigated for the $Fe_{66}Cu_2Nd_{20}C_{9.5}B_{0.5}$ alloy. The as-cast alloy was magnetically very soft but $_JH_c$ of 880 kA/m was developed after annealing for 5 h at 850 °C (Fig. 3). Significant coercivity appeared after a relatively short annealing time of 0.5 h. The reaction was completed after about 4 h annealing. For the longer annealing times at 850 °C a decrease of coercivity was observed though J_r was almost unchanged at a level of 0.58 T. X-ray diffraction analysis for this alloy showed patterns typical of the $Fe_{17}Nd_2C_x$ and $Fe_{14}Nd_2C$ structures for the as-cast and annealed (70 h at 850 °C) samples, respectively. The microstructure observations showed a decreasing grain size from ~20 μm for the specimen annealed for 0.5 h to ~10 μm for the fully transformed material.

Partial substitution for iron was made in a series of alloys $Fe_{66}M_2Nd_{20}C_{9.5}B_{0.5}$ with M=Ga,Nb,Cu,Al. These elements M were known to increase the coercivity of the Fe-Nd-B type magnets, mostly by changing the properties of the boundary phases.[9] The magnetic properties of substituted alloys are shown in Table I. The ternary and Cu-containing alloys exhibited high $_JH_c$ after very short annealing times, starting from 1 h, within the temperature range 850–1000 °C. Somewhat longer times were required for the Ga-containing alloy whereas the alloys with Nb and Al additions, even after long time annealing (five days), were only partially transformed and showed considerable proportions

TABLE I Magnetic properties for $Fe_{66}M_2Nd_{20}C_{9.5}B_{0.5}$ (M=Ga,Nb,Cu,Al) ingot alloys annealed at 900 °C.

Composition	$_JH_c$ (kA/m)	J_r (T)	$(BH)_{max}$ (kJ/m^3)	Annealing time
$Fe_{68}Nd_{20}C_{9.5}B_{0.5}$	630	0.58	50	5 h
$Fe_{68}Nd_{20}C_{9.5}B_{0.5}$ melt spun	980	0.65	66	5 h
$Fe_{66}Cu_2Nd_{20}C_{9.5}B_{0.5}$	880	0.58	51	5 h
$Fe_{66}Ga_2Nd_{20}C_{9.5}B_{0.5}$	620	0.56	48	5 h
$Fe_{66}Nb_2Nd_{20}C_{9.5}B_{0.5}$	550	0.55	40	5 days
$Fe_{66}Al_2Nd_{20}C_{9.5}B_{0.5}$	420	0.55	37	5 days

TABLE II. Curie temperatures T_c and melting temperatures of the boundary phases T_e for as-cast and annealed $Fe_{66}M_2Nd_{20}C_{9.5}B_{0.5}$ (M=Ga,Nb,Cu,Al) alloys.

Composition	Treatment	T_c (°C)	T_e (°C)
$Fe_{68}Nd_{20}C_{9.5}B_{0.5}$	as-cast	···	707
	annealed	311	707
$Fe_{66}Cu_2Nd_{20}C_{9.5}B_{0.5}$	as-cast	···	587, 639
	annealed	312	523, 575
$Fe_{66}Ga_2Nd_{20}C_{9.5}B_{0.5}$	as-cast	···	702
	annealed	312	637
$Fe_{66}Nb_2Nd_{20}C_{9.5}B_{0.5}$	as-cast	···	717
	annealed	312	717
$Fe_{66}Al_2Nd_{20}C_{9.5}B_{0.5}$	as-cast	···	>727
	annealed	312	>727

of a soft magnetic phase. Results of the DSC analysis, presented in Table II, showed no change of the Curie temperature which suggested that no substantial amounts of the additives entered the $Fe_{14}Nd_2C$ phase. However, quite large differences in the melting points of the boundary phase were found. The multiphase grain boundaries melt in several stages which, due to the equipment limitations, we were able to measure only up to 727 °C. The lowest melting point was exhibited by the Cu-containing alloy which, on the DSC trace, showed a small primary melting peak at 523 °C and a large melting effect starting at 575 °C. This alloy had the best magnetic properties in the ingot state which moreover were developed within a short annealing time.

It has not been possible in the present study to establish whether the other alloys exhibit multistage melting because their incipient melting temperatures. The Al-containing alloy did not show a melting effect up to 727 °C. The two alloys having the highest melting temperatures of the intergranular phases, i.e., containing Nb and Al, did not transform completely to the $Fe_{14}Nd_2C$ phase even after a very long annealing time within the whole temperature range 800–1000 °C. Thus, it seems plausible that the properties of the intergranular liquid phase affects the kinetics of the peritectoid transformation, either acting as an aid to the process by increasing diffusivity across the phase boundary or retarding the diffusion and stabilizing the $Fe_{17}Nd_2C_x$ phase.

To increase J_r of the magnets attempts were made to produce anisotropic microstructures by hot deformation. Die-upset forging of cast alloys resulted in a modest increase of the remanence with a substantial decrease of the coercivity, as is shown in Fig. 4 for $Fe_{66}Ga_2Nd_{20}C_{9.5}B_{0.5}$ alloy. The reduced coercivity exhibited by the die-upset forged magnets we relate to squeezing out of the specimen the Nd-rich boundary phase which separates the hard magnetic grains. This appears to be more pronounced for the magnets containing additional elements which lower melting point of the boundary phase.[10]

IV. CONCLUSIONS

A coercive ingot material, with $_JH_c$ up to 880 kA/m, was fabricated by solid-state transformation during heat treatment

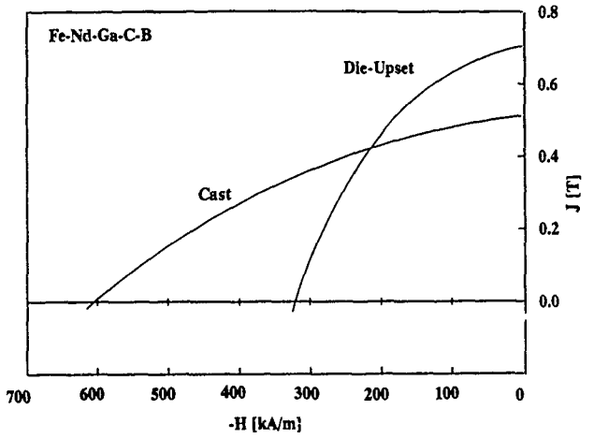

FIG. 4. Cast and die-upset forged $Fe_{66}Ga_2Nd_{20}C_{9.5}B_{0.5}$ alloys.

of Fe-Nd-C-B type ingot alloys. The useful annealing temperatures were in the range 800–1000 °C. Annealing times of a few hours was found to be sufficient to achieve complete transformation for $Fe_{68}Nd_{20}C_{9.5}B_{0.5}$ and for Cu, and Ga-added alloys. However, only small volume fractions of $Fe_{14}Nd_2C$ were obtained for Nb- and Al-containing alloys. The kinetics of the peritectoid transformation were found to be affected by the melting temperature of the intergranular phases. The elements which lower this temperature are considered to act as an aid to the process by increasing diffusivity across the phase boundary and the elements that increase melting point can inhibit the process and effectively stabilize the $Fe_{17}Nd_2C_x$ phase. The optimally annealed alloys had mean grain sizes of ~10 μm and their coercivity showed strong dependence on the initial microstructure before the heat treatment. Some increase of the remanence (~0.7 T) was achieved after die-upset forging of cast alloys.

ACKNOWLEDGMENTS

Financial support from the Polish National Committee for Scientific Research and from the British Council is gratefully acknowledged.

[1] M. Sagawa, S Fujimura, N. Togawa, H. Yamamoto, and Y. Matsuura, J. Appl. Phys. **55**, 2083 (1984).
[2] J. J Croat, J. F. Herbst, R. W Lee, and F. E Pinkerton, J Appl. Phys **50**, 2078 (1984).
[3] T Shimoda, K. Akioka, O Kobayashi, and T Yamagami, IEEE Trans. Magn **MAG-25**, 4099 (1989).
[4] G. J. Mycock, R N J. Faria, and I. R Harris, J. Appl Phys. **73**, 6497 (1993).
[5] K. H. J. Buschow, Rep. Prog Phys. **54**, 1123 (1991)
[6] D B de Mooij and K H J. Buschow, J. Less-Common Metals **142**, 349 (1988)
[7] J. Eisses, D B. de Mooij, K H J. Buschow, and G. Martinek, J Less-Common Metals **171**, 17 (1991).
[8] B Grieb, K Fritz, and E.-Th Henig, J Appl Phys **70**, 6447 (1991)
[9] M. Leonowicz, J Magn. Magn. Mater **83**, 211 (1989).
[10] M Leonowicz, H. A. Davies, M A Al-khafaji, T A. Keates, and M W Crabbe, J Appl Phys (to be published).

Generation of highly uniform fields with permanent magnets (invited)

M. G. Abele
New York University School of Medicine, New York, New York 10016

A review of a design methodology of permanent magnets composed of magnetic materials with quasilinear demagnetization characteristics is presented. The paper focuses on the design of efficient permanent magnets for applications that require strong and highly uniform fields. The compensation of the field distortion caused by design constraints and fabrication tolerances is one of the aspects of magnet design discussed in this paper. A design procedure based on active filter structures that restore a required degree of field uniformity is reviewed.

I. INTRODUCTION

The evolution of the design of permanent magnets in recent years has been prompted by the development of high-energy product rare-earth magnetic materials. The characteristics of these alloys, and, in particular, their high intrinsic coercive force, have extended the use of permanent magnets to a number of applications. Compared to electromagnets, permanent magnets have the obvious advantage of requiring no external power supply and no maintenance cost. Their basic disadvantages are the high cost of the magnetic material, the technological problems of achieving any desired distribution of magnetization, and the difficult operations of preparing and assembling the magnetic blocks.

The most striking property of modern rare-earth materials is their quasilinear demagnetization characteristics. This property has led to the introduction of new design approaches that depart drastically from the traditional magnet designs where only approximate numerical solutions are possible due to the highly nonlinear characteristics of older magnetic alloys.[1] Exact mathematic solutions of the field generated by the new material have resulted in novel magnetic structures that differ from traditional magnetic circuits both in terms of geometry and field properties as well.[2–4]

At present, the most significant application of large permanent magnets is found in nuclear magnetic resonance imaging in medicine, where the size of a magnet is dictated by the dimensions of the human body and the field strength is selected on the basis of imaging requirements. Superconductive magnets still have the lion's share of the medical field and their technology is constantly improving in terms of size, self-shielding property, and reduction of maintenance of the cryogenic equipment. On the other hand, the advantages of permanent magnets justify the current efforts to reduce their cost, weight, and size. At present, the main application of permanent magnets is found in the low to medium field strength.[5] Two major challenges face the designer: generation of high fields of the order of the remanence within acceptable limits of size and weight, and reduction of the complexity of the problem of compensation of field distortions due to practical design constraints and magnetization tolerances.[6]

II. BASIC MAGNETIC STRUCTURES

The quasilinear demagnetization characteristics of modern magnetic materials is the basis of the development of a linear theory of the design of permanent magnets that relegates the nonlinear effects to a perturbation of basic linear solutions.[7–9]

The design of a magnet is the classical inverse problem where once the field is assigned within a region of interest, the designer must find the configuration of the magnetic structure capable of generating such a field. On one hand, the designer faces the problem of the indeterminacy of the solution of the inverse problem. On the other hand, the indeterminacy makes it possible to satisfy specific requirements by choosing the solution among several categories of magnetic structures, in order to satisfy specific design requirements.

Once a field distribution is specified within a given region, it is always possible to generate such a field with a magnetic structure that encloses the assigned region. As an example, consider the problem of generating a two-dimensional periodic field with a period $4z_0$ along the z coordinate of a prismatic cavity of rectangular cross section of dimensions $2x_1$, $2y_1$. The field is independent of the x coordinate and on the plane $y=0$ is oriented in a direction perpendicular to the plane, as indicated in the schematic of Fig. 1.

The scalar potential within the prismatic cavity is

$$\Phi = \frac{H_0}{k} \sinh ky \cos kz, \tag{1}$$

where $k=\pi/2z_0$ and H_0 is the amplitude of the field intensity on the $y=0$ plane. Equation (1) describes the field of an undulator.[10] A structure that generates the periodic field with-

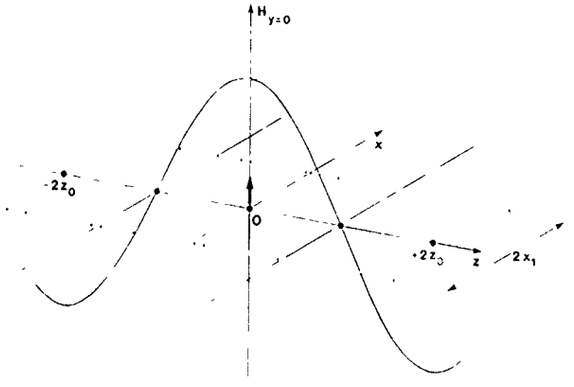

FIG. 1. Periodic two-dimensional field.

 0021-8979/94/76(10)/6247/6/$6 00 © 1994 American Institute of Physics

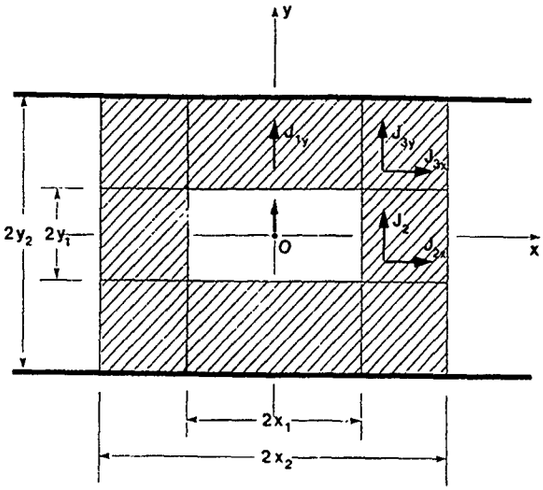

FIG. 2. Cross section of undulator.

out introducing harmonics is shown in Fig. 2, where the magnetic material is distributed between the cavity and an external rectangular boundary of dimensions $2x_2$, $2y_2$.

The two sides of the external boundary perpendicular to the y axis interface with a high magnetic permeability material that closes the flux of the magnetic induction. The flux does not cross the sides perpendicular to the x axis. These two sides are also equipotential and, as a consequence, they interface with external nonmagnetic media. In the first quadrant the components of the remanence of the magnetic material are

$$
\begin{aligned}
&J_{1x}=0, \quad J_{1y}=-\mu_0 H_0 \frac{\sinh ky_2}{\sinh k(y_2-y_1)}\cos kz, \\
&J_{2x}=-\frac{\mu_0 H_0}{k(x_2-x_1)}\sinh ky \cos kz, \quad J_{2y}=0, \\
&J_{3x}=-\frac{\mu_0 H_0}{k(x_2-x_1)}\frac{\sinh ky_1}{\sinh k(y_2-y_1)}\sinh k(y_2-y)\cos kz, \\
&J_{3y}=-\mu_0 H_0 \frac{\sinh ky_2}{\sinh k(y_2-y_1)}\frac{x_2-x}{x_2-x_1}\cos kz.
\end{aligned}
\tag{2}
$$

Equation (2) shows that both magnitude and orientation of the remanence are a function of position. In general, a nonuniform field requires a nonuniform distribution of magnetization in the magnetic structure; this could be very difficult, if not impossible, to implement in practice. Thus even if an exact solution is found, the design and fabrication of a magnetic structure would have to be an approximation of the theoretical model. An exception is found in the generation of a uniform field in which case the exact solution of the design problem yields structures of uniformly magnetized polyhedrons that can be fabricated from standard blocks of magnetic material.

The existence of a design solution with uniformly magnetized polyhedrons is based on a condition that relates the geometry of the polyhedrons that compose the magnetic structure and the uniform remanence $\mathbf{J}$ of each polyhedron.[7] A uniform field is found in each polyhedron if and only if at each point common to n interfaces between polyhedrons the remanences and the orientations of the interfaces satisfy the condition

$$
\sum_{h=1}^{n} \boldsymbol{\tau}_h \cdot \boldsymbol{\eta}_h \times (\mathbf{J}_{h-1}-\mathbf{J}_h)=0, \tag{3}
$$

where $\boldsymbol{\eta}_h$ is a unit vector perpendicular to the hth interface between polyhedrons of remanences $\mathbf{J}_{h-1}$, $\mathbf{J}_h$, oriented from the medium of remanence $\mathbf{J}_{h-1}$ to the medium of remanence $\mathbf{J}_h$, and $\boldsymbol{\tau}_h$ is a unit vector in the plane of the hth interface, perpendicular to the line common to the n interfaces and pointing away from the hth interface.

The magnetic structures that satisfy condition (3) can be classified in several categories characterized by different properties: yoked magnets where the flux of the induction generated by the magnet closes through an external yoke of high permeability material, yokeless magnets where the flux is confined within the same structure of the magnetic material without the need of an external yoke, and hybrid magnets combining both yoked and yokeless structures that optimize the magnet efficiency for a particular geometry and field intensity within the magnet cavity.

A fourth category includes magnets that take full advantage of linear demagnetization characteristics with small values of the magnetic susceptibility. In the ideal limit of zero susceptibility, the magnetic material is perfectly transparent to the field generated by other sources. Thus the field within the region of interest can be increased by superimposing the field generated by independent magnets. In the particular case of yokeless magnets, this is achieved by a multiplicity of magnets inserted one inside each other around the region of interest.

An example of yoked magnet is presented in Fig. 3(a), which shows a section of a two-dimensional magnet designed to generate a uniform field inside a prismatic cavity of rectangular cross section. The heavy line in the schematic of Fig. 3(a) represents the external yoke. A characteristic feature of such a magnet is the presence of the nonmagnetic regions between the blocks of magnetized material. The flux of the induction in these regions does not circulate within the cavity and is the equivalent of the fringe field in a traditional magnet.

Figure 3(b) shows an example of yokeless magnet that is characterized by a combination of an internal structure that interfaces with the cavity and an external structure designed to confine the field. The magnet of Fig. 3(b) is also designed around a prismatic cavity of rectangular cross section. In general the basic difference between yoked and yokeless structures is that a yokeless magnet requires a larger amount of magnetic material to perform the double function of generating and confining the field. An important property of a two-dimensional yokeless magnet is that its geometry is independent of the orientation of the field within the cavity.[7]

An example of hybrid magnet designed around the same cavity of Figs. 3(a) and 3(b) is shown in Fig. 3(c); it combines a yoked component of magnetic material with yokeless structures of triangular cross section where the magnetic induction is zero. As a consequence, the total flux of the mag-

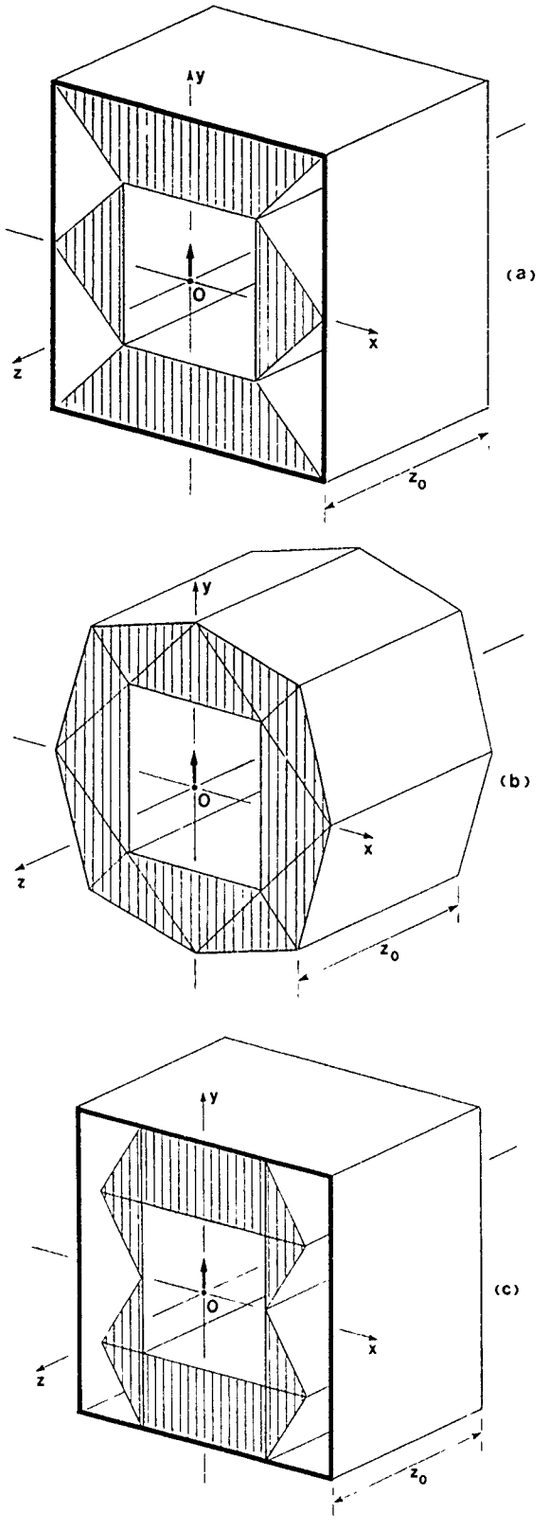

FIG. 3. Examples of two-dimensional magnets with the same internal prismatic cavity: (a) yoked, (b) yokeless, (c) hybrid.

netic induction flows through the cavity and closes through the yoke. In Fig. 3(c) the heavy line that represents the yoke can be closed without interfacing with the components of triangular cross section and no field is found in the region between these components and the yoke. One observes that Fig. 2 is another example of hybrid structure.

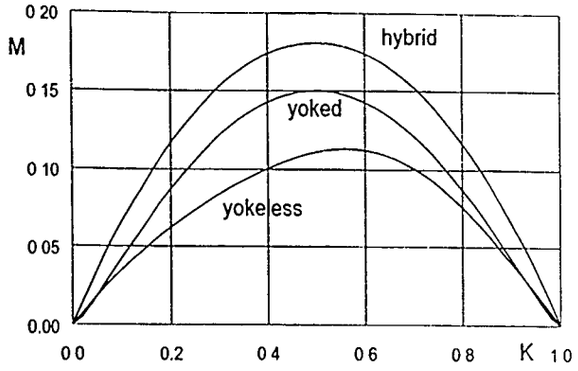

FIG. 4. Figure of merit of three magnets with the same cavity geometry.

If the same magnetic material is used in all the components of a magnetic structure designed to generate a uniform field intensity H_0 within the cavity, one can define the parameters

$$K=\mu_0\frac{H_0}{J_0},\quad M=K^2\frac{V_c}{V_m}, \tag{4}$$

where J_0 is the remanence and μ_0 is the magnetic permeability of a vacuum. M is the figure of merit of the magnet and V_c, V_m are the volumes of the cavity and of the magnetic material, respectively. Figure 4 shows the plotting of the figure of merit of the three magnetic structures of Fig. 3 versus K for the dimensions of the cavity cross section $2x_0=4y_0$. The hybrid structure exhibits the highest value of M, and the yokeless the lowest. M attains its maximum in the range $0.5<K<0.6$ for the three magnets, and it decreases to zero as the field within the cavity approaches the value of the remanence. This is due to the fact that as the field increases, the outside layer of magnetic material becomes less and less efficient in contributing to the field within the cavity.

By virtue of Eqs. (4) and Fig. 4, the volume of the magnetic material diverges at $K=1$, and, as a consequence, the structures of Fig. 3 cannot generate a field equal or larger than the remanence. The upper limit $K=1$ is removed by multilayer structures, like the schematic of Fig. 5 which shows a number m of concentric yokeless magnets around a regular polygonal cavity of n sides. If m is the number of layers, the values of K and M of the structure of Fig. 5 are

$$K=m\left(1-\cos\frac{\pi}{n}\right),\quad M=\frac{K^2}{\cos^{-2m}(\pi/n)-1}. \tag{5}$$

Even if a structure like Fig. 5 makes it possible to generate values $K>1$, the optimum design condition is achieved for large values of n and a large number of layers at $K\approx0.8$ and $M\approx0.16$. An example of multilayer structure is the two layer, two-dimensional magnet with a square cross-section cavity shown in Fig. 6 where the internal layer generates a field corresponding to $K=0.51$. The total value of K of this magnet is $K\approx0.79$ and its figure of merit is $M\approx0.13$.

The optimum design of a multilayered magnet is a structure of hybrid layers that combines materials with different remanences. Specifically, the figure of merit attains its maximum in multilayered structures where the highest value of

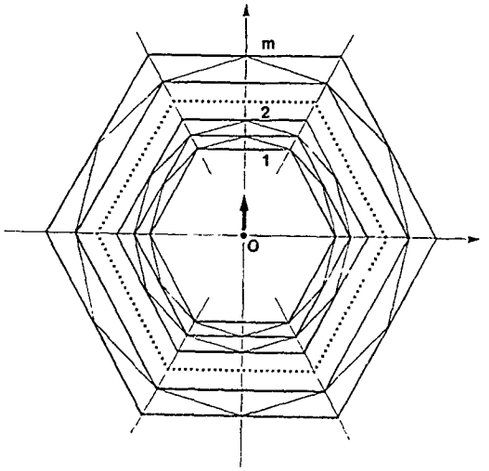

FIG. 5. Multilayer structures.

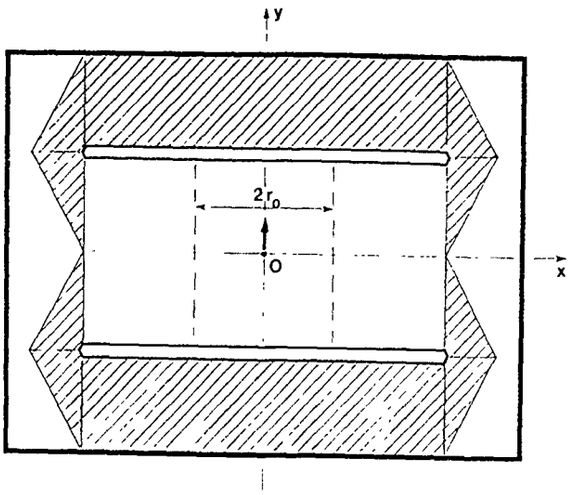

FIG 7. Insertion of high magnetic permeability plates

the remanence is used for the internal layer and the remanence of the other layers decrease with the distance of each layer from the cavity. The absolute maximum value of the figure of merit is 0.25 regardless of geometry and distribution of magnetization.[11]

III. OPEN MAGNETS

A magnet cavity has to be closed to achieve a perfectly uniform field. In practice a magnet must be open to access the region of interest. For instance, a magnet may be a section of length $2z_0$ of one of the structures illustrated in Fig. 3 open at both ends. The distortion of the field due to the opening reduces the region of the cavity where an acceptable degree of uniformity is found. In applications requiring a moderate field uniformity a simple solution is the choice of a sufficiently large dimension $2z_0$, of the order of several times the dimension of the region of interest. However, in applications like NMR imaging in medicine, where the uniformity has to be of the order or better than 10^{-5}, this approach would lead to extremely large values of $2z_0$. In this case, the compensation of the field distortion becomes the most critical problem that faces the designer in order to keep magnet dimensions and cost within practical limits.

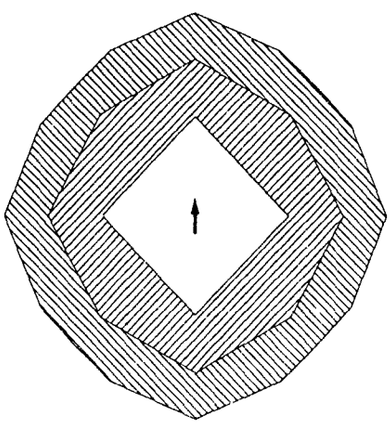

FIG. 6 Two-layer yokeless magnet

The field distortion results not only from the opening of the magnet cavity but also from the fabrication tolerances, and in particular from the magnetization tolerance of the magnetic materials. The magnitude of the remanence may vary by a few percent and the orientation of the remanence may vary by a few degrees. While the effects of the magnet opening may be corrected in the design phase, the compensation of fabrication and magnetization tolerances must be accomplished in the shimming of the assembled magnet. However, the same logic followed in the design phase can be applied to derive the shimming procedure from the field measurements in the assembled magnet.

Because of the quasilinearity of the magnetized material, the compensation of the field distortion in the design phase can be accomplished by designing a compensating structure to be added to the main structure of the magnet. A number of solutions can be adopted involving magnetic materials as well as ferromagnetic components.[7] The quantitative derivation of these solutions can be obtained by expressing the field distortion in terms of the spectrum of its spatial harmonics. Consider the type of magnets where the interface between cavity and magnetic material includes two parallel planes perpendicular to the magnetic field in the cavity. The region of the expansion in the spatial harmonics can be a cylinder of radius r_0 containing the region of interest, with its axis parallel to the field, and closed by two thin plates of high magnetic permeability material inserted at the two interfaces perpendicular to the field as indicated in the schematic of Fig. 7. The plates must be sufficiently thin in order not to affect the figure of merit of the magnet.

The two plates in Fig. 7 act as magnetic mirrors of the field inside the cavity and at the same time they are an effective filter of the high spatial frequency components of the field distortion generated by the magnetization tolerances.[12]

Within the region of the cylinder between the plates, the scalar potential of the field is

$$\Phi=\Phi_0\frac{y}{y_0}+\sum_{m,n} I_m\left(n\pi\frac{r}{y_0}\right)$$

$$\times(a_{m,n}\cos m\psi+b_{m,n}\sin m\psi)\sin\left(n\pi\frac{y}{y_0}\right), \tag{6}$$

where Φ_0 is a constant; r, ψ, y are the cylindrical coordinates, $a_{m,n}$, $b_{m,n}$ are the amplitudes of the harmonics, and I_m is the modified Bessel function

$$I_m\left(n\pi\frac{r}{y_0}\right)=i^{-m}J_m\left(in\pi\frac{r}{y_0}\right). \tag{7}$$

If H_0 is the uniform field intensity within the magnet cavity, the quantity

$$\frac{1}{y_0}\Phi_0+H_0 \tag{8}$$

represents the loss of the field intensity within the region of interest. Usually this loss can be tolerated and the compensation procedure can be confined to the correction of the nonuniformity expressed by the summation on the right-hand side of Eq. (6). As a consequence the amount of magnetic material necessary to perform the compensation reduces to only a fraction of the total material of the magnet.

IV. COMPENSATION OF FIELD DISTORTION

Once the distortion of the field is defined by its spectrum, the compensation can be performed by means of a filter structure located outside the cylindrical surface; this is designed to eliminate the dominant harmonics $a_{m,n}$, $b_{m,n}$ up to the point where the residue of the harmonics expansion is within an acceptable value. An essential part of the filter is a structure that allows the control of the potential of the surface of the two high permeability plates in Fig. 7 outside the cylindrical region selected for the expansion. This is accomplished in each plate by means of elements of magnetized material sandwiched between the main body of the plate and a number of magnetically insulated high permeability plates that interface with the cavity.[13] If the dimensions of the insulated plates are large compared to the thickness of the sandwiches, the scalar potential of each insulated plate relative to the main plate is a linear function of the amount of magnetic material magnetized in the direction perpendicular to the plate and is independent of the position of the material in the space between the insulated plate and the main plate. Consequently, the effect of each sandwich on the field within the cavity is controlled by the mechanical precision of fabrication of the plates and by the amount of material of each sandwich. This structure leads itself to a mechanical tuning of the filter both in the construction of the magnet as well as in its final shimming.

A schematic of filter structures inserted in each plate is shown in Fig. 8 where individual elements of the filter structure are arranged on a circular pattern. The distribution of potential of the elements of the filter is computed to generate harmonics equal in amplitude and opposite sign of the harmonics of order m of the spectrum of the field of the magnet. Thus the maximum value of m of the harmonics to be compensated determines the minimum number of the elements of the filter. The potential of each element determines the amount and magnetization of the material to be inserted in the element. Because of the linearity of the relationship between potential of each element of the filter and its filling, the compensation of the distortion is achieved by the addition of the amount of material required by each harmonic.

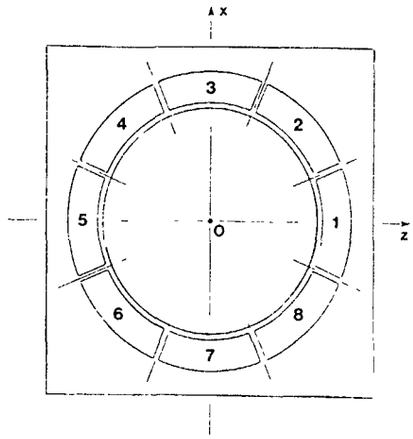

FIG. 8. Schematic of filter composed of eight elements inserted in each high permeability plate.

The elements of the filter on the plate of Fig. 8 alone are one part of the entire filter designed to compensate any harmonic of indices m,n. To generate a spectrum containing a specified number of n harmonics, the filter structure must contain also elements distributed in a number of additional rings on the main plates as well as in the region between the plates. Obviously the complete filter structure cannot interfere with the access to the region of interest. Therefore the filter elements distributed between the plates must occupy only a part of the full circle, as indicated in the schematic of Fig. 9, which shows filter elements located on the $y=0$ plane.

A typical spectrum of the harmonics of the field distortion is shown in Table I which corresponds to a rectangular

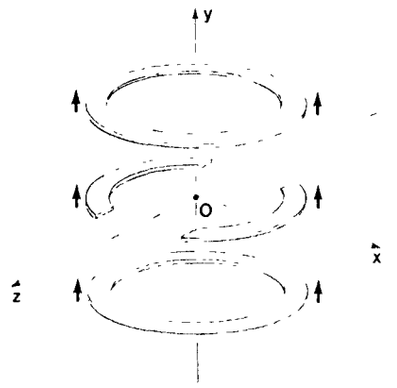

FIG. 9. Filter structure with elements distributed on the $y=0$ plane.

TABLE I. Typical spectrum of harmonics in a yoked magnet.

m	n	$a_{m,n}$	$n\pi a_{m,n} I_m(n\pi r/y_0)$
0	1	1.5×10^{-4}	1.3×10^{-3}
0	2	$\sim 10^{-6}$	$\sim 10^{-4}$
2	1	6.5×10^{-4}	1.8×10^{-3}
2	2	$\sim 10^{-7}$	$\sim 10^{-6}$
4	1	4.2×10^{-4}	1.0×10^{-4}
4	2	$\sim 10^{-6}$	$\sim 10^{-5}$

prismatic cavity open on opposite sides, with cavity dimensions $2z_0=2x_0=4y_0$. The values of the amplitude of the harmonics listed in Table I correspond to a yoked structure designed for $K=0.5$ with the two main plates inserted in the cavity. Because of symmetry, all amplitudes $b_{m,n}$ are zero and the spectrum reduces to the harmonics of even order m. If the required degree of uniformity is such that harmonics with values $a_{m,n}<10^{-6}$ can be disregarded, only harmonics of order $n=1$, with the exception of the harmonics ($m=0$, $n=2$), ($m=4$, $n=2$), constitute the spectrum that must be compensated. Thus in this particular case, the filter structure can be implemented following the schematic of Fig. 9. Table II lists the values of the three elements numbered in the schematic of the filter structure shown in Fig. 8 that cancel the harmonics ($m=0$, $n=1$), ($m=2$, $n=1$), ($m=4$, $n=1$). By symmetry, the potential of the other elements are

$$\delta\Phi_8=\delta\Phi_6=\delta\Phi_4=\delta\Phi_2,$$
$$\delta\Phi_5=\delta\Phi_1, \quad \delta\Phi_7=\delta\Phi_3. \tag{9}$$

The filter structure based on the control of the potential of the filter elements by means of magnetic material is the active equivalent of the passive pole pieces of traditional magnets whose geometry is designed to achieve the desired field configuration. The ability to control the amount of material inside each element of the filter structure extends the use of the filter to the correction of the effects of magnetic and fabrication tolerances. The final shimming of a magnet can be performed by extracting the harmonics from the measurement of the field in the fully assembled magnet and by correcting the potential of each element of the filter either by inserting additional magnetic material or by changing the orientation of the material inside each element.

TABLE II. Potential of the filter elements relative to the main plate.

$\delta\Phi_1/\Phi_0$	$\delta\Phi_2/\Phi_0$	$\delta\Phi_3/\Phi_0$
0.17	0.0016	−0.064

V. CONCLUDING REMARKS

The new design approaches are already being adopted for the commercial development of permanent magnets and the application of permanent magnet technology to the field of medical imaging is expanding. In the low-field range, a remarkably compact 0.2 T ferrite magnet has been successfully development by Esaote Biomedica of Italy. In the medium field range, Sumitomo Special Metals of Japan, which has pioneered the use of permanent magnets in medical imaging, has recently developed a powerful 0.45 T Nd.Fe.B magnet designed for whole body imaging.

As new higher-energy product materials are being developed,[14] smaller and more efficient magnetic structures can be designed. With an expanding range of applications, the cost of these new materials is bound to decline steadily, and as the cost per unit energy decreases, more powerful magnets are becoming a viable solution in large scale applications requiring field energies of the order of 10^5 J/m^3 or larger.

[1] R. J. Parker, *Advances in Permanent Magnetism* (Wiley, New York, 1990).
[2] K. Halbach, Nucl. Instrum. Methods **169**, 1 (1980).
[3] H. Zijlstra, Philips J. Res **40**, 259 (1985)
[4] H. A. Leupold and E. Potenziani, An Overview of Modern Permanent Magnet Design US Army SLCET, TR-90-6, August 1990
[5] T. Miyamoto, H. Sakurai, and M. Aoki, Tenth International Workshop on Rare-Earth Metals and their Applications, Kyoto, May 1989, pp 113–120
[6] M. G. Abele, Tenth International Workshop on Rare-Earth Magnets and their Applications, Kyoto, May 1989, pp. 121–130.
[7] M. G Abele, *Structures of Permanent Magnets* (Wiley, New York, 1993).
[8] M G Abele, J. Magn. Magn Mater. **83**, 276 (1990).
[9] M. G Abele and H. A. Leupold, J. Appl Phys. **67**, 4644 (1990).
[10] H. A. Leupold, E Potenziani II, and M G Abele, J Appl. Phys **67**, 4653 (1990).
[11] M. G. Abele and H. Rusinek, J Appl. Phys. **67**, 4644 (1990)
[12] M. G. Abele and H. Rusinek, IEEE Trans. Magn **MAG-29**, 2908 (1993).
[13] M. G. Abele, H. Rusinek, F. Bertora, and A Trequattrini, J Appl. Phys. April (1994).
[14] K. J. Strnat, Proc. IEEE **78**, 923 (1990)

Fabrication of multipolar magnetic field sources

H. A. Leupold and G. F. McLane
U. S. Army Research Laboratory, Fort Monmouth, New Jersey 07703

The emergence of high-energy-product permanent magnets has made possible the generation of extraordinarily high magnetic fields in the internal working spaces of relatively small structures. The widespread use of such structures has been hampered by the variety and complexity of their magnetic components and the concomitant difficulty and expense of manufacture. This paper describes approaches to fabrication and assembly that should significantly ease both fabricational and economic problems. Examples of these approaches are given for the production of cylindrical multipolar sources (magic rings, quadrupolar electron beam guides) and spherical dipolar sources (magic spheres).

I. INTRODUCTION

The high-energy-product permanent magnet materials afford shell-like structures that produce in their internal chambers fields that are much higher than those obtainable from the conventional structures that can be made of the older materials such as the alnicos. Unfortunately for many such structures the required distributions of the magnetization are complex and require components with many different magnetic orientations. This augments the difficulty and expense of the manufacture.

Two particularly useful configurations are the so-called magic rings (really cylindrical shells) and magic spheres.[1,2] In the cylinder, the magnetization is uniform in magnitude, has no z component, and varies in direction γ with the azimuthal angle as $\gamma=2\phi$ [see Fig. 1(a)]. If a circular section of such a cylinder is rotated about its polar axis, its locus forms a spherical shell or magic sphere like that shown in Fig. 1(b).

The cylinders and spheres produce in their internal chambers uniform fields of $H_c=B_r \ln(r_o/r_i)$ and $H_s=(4/3)B_r \ln(r_o/r_i)$, respectively. Here B_r, r_o, r_i are the magnetic remanence and outer and inner radius, respectively. These formulas show that fields of any magnitude are possible for either structure if the ratio r_o/r_i is made large enough. However, the field's logarithmic dependence on outer radius results in prohibitive bulks for fields much in excess of 20 kOe in the cylinder and about 27 kOe for the sphere. Within these limits, however, performance is quite impressive. A sphere of 8 cm diameter produces 20 kOe in a cavity of 2.5 cm diameter with a material of B_r equal to 12 kG.

II. ASSEMBLY OF A MAGIC RING

In practice the continuous magnetic structure of rings and spheres is approximated by an array of segments each of uniform magnetization within its boundaries which changes abruptly upon passage to a neighboring segment (Fig. 1). Therefore many different orientations are needed in the magic ring and, it would seem, many different operations to produce them. These operations can be reduced to one by the following considerations.

If a cylindrical tube is aligned and uniformly magnetized perpendicularly to its principal axis one notes that every possible orientation of the magnetization relative to the local radius is represented. Therefore, only a simple rearrangement of cylindrical segments is needed to form the desired magic ring [Fig. 2(a)].[3] Alternatively each segment can be rotated 180° about its local radius to obtain the same results [Fig. 2(b)]. Either procedure obviates the necessity of multiple magnetizations on many different cylindrical segments.

III. MULTIPOLAR RINGS

A similar procedure may be used to form rings and cylinders of higher order polarity. Of these probably the most useful is the quadrupole, which is extensively employed in the focusing of charged particle beams.[1] A typical arrangement is that of Fig. 3 which shows that the magnetic orientation goes as $\gamma=4\phi$. Because the orientation changes twice as fast with ϕ as in the dipolar structure, it follows that the orientation increment between adjacent segments of given size is twice as great while twice as many segments of a given orientation are needed. For example, the initial uniform magnetization of a cylinder yields only one radially oriented segment that points inward while for a quadrupole, two such are needed. This problem can be solved by the magnetization of two cylinders and then the procedure of Fig. 4 to form two slightly different segmented approximations to ideal quadrupolar cylinders.

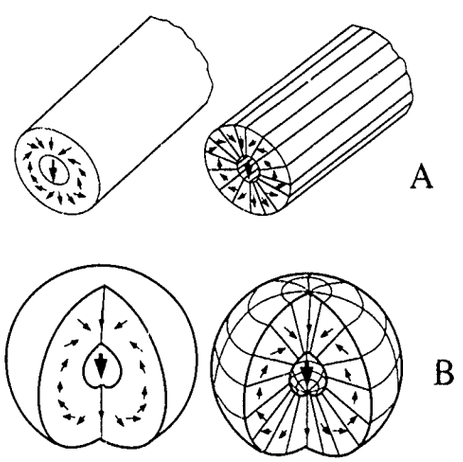

FIG 1 Permanent magnet structures with segmented approximations (A) magic ring, (B) magic sphere

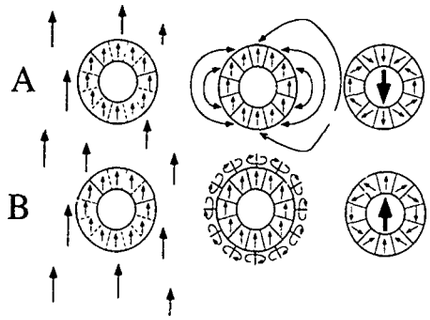

FIG. 2. Assembly of a magic ring by (A) rearrangement of segments after uniform magnetization, (B) rotation of segments about local axes after magnetization.

Alternatively a ring could be segmented before magnetization with every other piece elevated above the original stack, revolved $2\pi/n$ about the original axis and stacked as shown in Fig. 5. The stack would then be uniformly magnetized with the correct number of each type of required segment. After a π rotation of each segment about its local radius and an angular contraction of the gapped stack into a half cylinder with two identical semidisc layers, the said layers are appropriately joined at their equatorial planes as illustrated in Fig. 5.

Similar procedures are used to form multipolar rings of higher order. In general $n/2$ stack layers of m/n segments each are used, where n is the desired multipolar order and m is the total number of segments needed to attain the required structural fineness.

IV. MAGIC SPHERES

A magic sphere is made from magic ring slices that have been beveled to form the melon-slice shapes of Fig. 6. These are then assembled, tangerine-like, into the required magic sphere. Unfortunately this involves the possible, but inconvenient, step of machining a magnetized ring. Unfortunately the uniform magnetization of a spherical segment and its subsequent rotation about the local radius does not work with

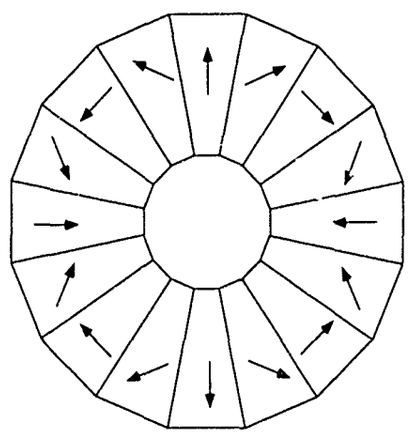

FIG 3 Cylindrical quadrupolar cross section

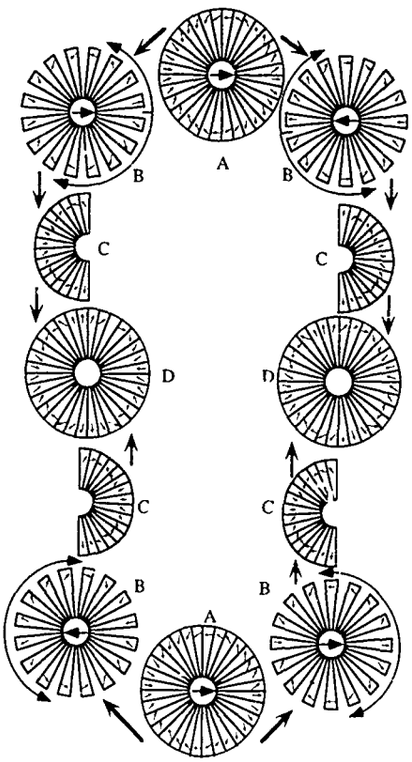

FIG 4 formation of two quadrupole sources from two dipole sources (A) Start with two dipolar structures. (B) Separate every other segment from adjacent segments to form two new structures for each original structure (C) Compress structures B in direction of circular arrows to form structures C. (D) Assemble structures C to form structures D

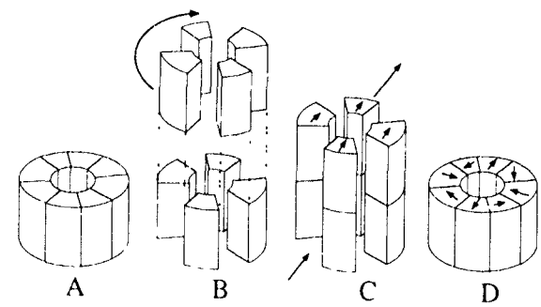

FIG 5 Conversion of an unmagnetized ring into a quadrupolar ring.

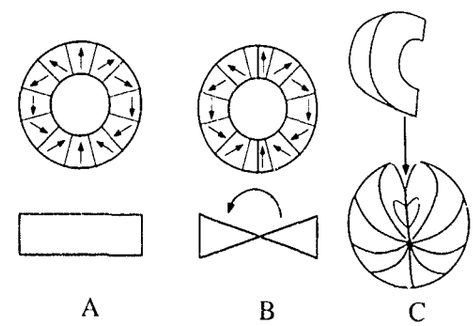

FIG 6 Fabrication of a magic sphere by a beveling of magic rings

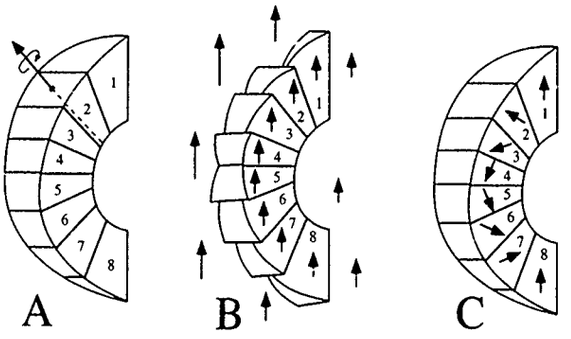

FIG 7. Manufacture of a magic sphere without the machining of magnetized segments (A) rotation of segments, (B) magnetic field applied, (C) rotation of segments back to initial positions.

the sphere as with the ring. The lengths of the areas that subtend the width of a segment on the spherical surface depend on the polar angle. This results in a mismatch when the required rotation about the local radius leaves the shorter arc where the larger should be and vice versa. This difficulty can be avoided by a rotation of the segment prior to magnetization as in Fig. 7. After magnetization the segments are rotated back into their initial positions with the correct magnetic orientations.

V. SUMMARY

Multipolar cylinders and dipolar spheres can all be magnetically oriented in a single uniform magnetization. In the case of the sphere this can be done either before or after the necessary machining. The machining for the sphere can be minimized to a single bevelling operation on magic ring segments instead of the cutting of many compound angles on a multiplicity of different spherical segments.

[1] K. Halbach, Proceedings of the 8th International Workshop on Rare-Earth Cobalt Magnets, University of Dayton, Dayton, OH, 1985, p. 123
[2] H. A. Leupold and E. Potenziani, IEEE Trans. Magn. **MAG-23**, 3628 (1987).
[3] H A Leupold, Mater Res Soc Symp Proc. **96**, 279 (1987).

Kinetic studies on solid-HDDR processes in Nd-Fe-B-type alloys

O. Gutfleisch, M. Verdier, and I. R. Harris
School of Metallurgy and Materials Science, University of Birmingham, Birmingham B15 2TT, United Kingdom

The kinetics of solid-HDDR (hydrogenation, disproportionation, desorption, recombination) processing of Nd-Fe-B-type alloys have been characterized by means of *in situ* electrical resistivity measurements and hydrogen absorption and desorption studies on nondecrepitated samples. The fundamental differences in reaction rate and mechanism between a $Nd_{16}Fe_{76}B_8$ as-cast and a homogenized stoichiometric $Nd_2Fe_{14}B$ alloy at $T=800$ °C and $p(H_2)=0.7$ bar are reported. The disproportionation and recombination rates were found to be significantly lower in the stoichiometric alloy, particularly in the case of the latter. The onset of the disproportionation and recombination reaction in $Nd_{16}Fe_{76}B_8$ in a temperature range of $T=780-880$ °C under hydrogen atmosphere was investigated and these reactions were found to depend critically on the pressure. Low-temperature recombination at $T=620$ °C was studied by the development of the Curie-point resistance anomaly of the $Nd_2Fe_{14}B$ matrix phase. It has been shown that the amount of reformed $Nd_2Fe_{14}B$ matrix phase during recombination can be monitored by this method.

I. INTRODUCTION

The hydrogenation, disproportionation, desorption, recombination (HDDR) process has been reported as a method of producing highly coercive Nd-Fe-B-based powder via a hydrogen-induced structural change; this powder can be used for the production of Nd-Fe-B-type hot pressed and bonded magnets (see, for example, Refs. 1 and 2). Heating under a hydrogen atmosphere results in the decrepitation of the ingot which is described as the HD process.[3] The disproportionation reaction occurs at elevated temperatures and results in the formation of an intimate mixture of α-Fe, Nd-hydride, and Fe_2B. On desorbing the hydrogen, the different constituents recombine to form the thermodynamically stable $Nd_2Fe_{14}B$ phase. The main microstructural feature of the HDDR process is the conversion of the coarse grained $Nd_2Fe_{14}B$ phase into a material with submicron grain size.

The kinetics of the disproportionation and recombination reactions, which depend on alloy composition, initial microstructure, temperature, and hydrogen pressure, can be monitored by means of *in situ* electrical resistivity measurements of the nondecrepitated material by introducing the hydrogen at elevated temperatures ($T\sim800$ °C).[4,5] This type of reaction can be referred to as solid-HDDR.[6] In this article it is reported how *in situ* electrical resistivity measurements during solid-HDDR processing can be employed to study the differences in kinetics and reaction mechanisms in Nd-Fe-B-type alloys with and without the presence of Nd-rich grain boundary material. Other factors such as hydrogen pressure and the absence of grain boundary melting are also examined.

II. EXPERIMENT

The *in situ* electrical resistivity measurement employed is based on the standard four-probe method and can be used up to 1000 °C under vacuum or hydrogen atmosphere. Detailed procedures have been given elsewhere.[5] Materials under investigation were as-cast $Nd_{16}Fe_{76}B_8$ and stoichiometric $Nd_2Fe_{14}B$ alloy which was homogenized at 1060 °C for 264 h under vacuum.[7] After homogenization, a small area fraction of ~2% free Fe dendrites was found to be present in the material. The microstructure of the $Nd_{16}Fe_{76}B_8$ alloy is typical of "Neomax"-type alloys with this composition,[8] whereas the stoichiometric alloy is virtually free of Nd-rich phase.

The overall HDDR kinetics of the two alloys were investigated at $T=800$ °C and $p(H_2)=0.7$ bar. The electrical resistivity and hydrogen absorption and desorption pressures were recorded in order to monitor the disproportionation and recombination reactions. In addition, a fully disproportionated $Nd_{16}Fe_{76}B_8$ alloy was heated from 700 to 1000 °C under various hydrogen pressures to provide further information about the contributions of the different constituents in the disproportionated mixture to the overall electrical resistivity. In order to investigate the onset of the disproportionation and recombination reactions of a $Nd_{16}Fe_{76}B_8$ alloy under hydrogen, the pressure was varied at different isotherms between $T=780$ and 880 °C. The resistivity of $Nd_2Fe_{14}BH_x$ or NdH~2, α-Fe, and Fe_2B as a function of hydrogen content was recorded. Rapid changes in resistivity were interpreted as the onset of the disproportionation or recombination reactions.[4,5] Controlled recombination at $T=620$ °C was achieved by monitoring the hydrogen desorption behavior and the development of the Curie-point resistance anomaly of the reformed $Nd_2Fe_{14}B$ matrix phase. At this temperature, the desorption of the hydrided Nd-rich grain boundary phase is avoided and hence melting of the grain boundary material is also avoided. The observed changes in resistivity will be derived entirely from transformations within the matrix phase. The disproportionated material was then cooled under hydrogen to room temperature and reheated to $T=620$ °C under vacuum to desorb for 2 h and cooled again, this cycle was repeated until the material was fully recombined.

III. RESULTS AND DISCUSSIONS

A. Comparison of HDDR kinetics between a Nd-rich and a stoichiometric alloy

A schematic diagram for a complete HDDR experiment monitored by measuring the electrical resistivity has been reported previously.[5] Resistivity, hydrogen absorption and

 0021-8979/94/76(10)/6256/3/$6.00 © 1994 American Institute of Physics

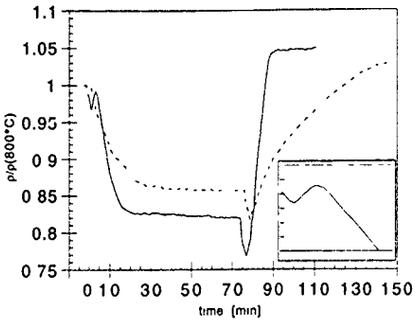

FIG. 1. Isothermal part of the electrical resistivity vs time monitoring the S-HDDR process at $T=800$ °C and $p(H_2)=0.7$ bar for an as-cast $Nd_{16}Fe_{76}B_8$ (solid line) and a stoichiometric $Nd_2Fe_{14}B$ alloy (dashed line); hydrogen introduction at $t=0$ min and vacuum at $t=75$ min. Inset shows the initial variations in more detail.

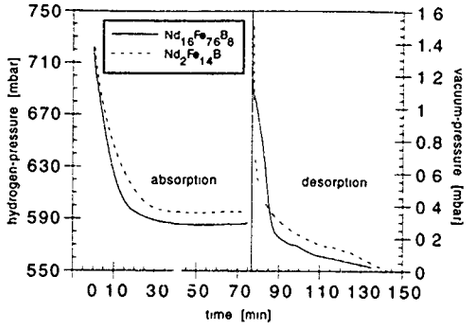

FIG. 2. Hydrogen absorption and desorption behavior during disproportionation and recombination of a $Nd_{16}Fe_{76}B_8$ as-cast (solid line) and a stoichiometric $Nd_2Fe_{14}B$ alloy (dashed line) at $T=800$ °C and $p(H_2)=0.7$ bar.

desorption pressures, and temperature are recorded. During heating and cooling the magnetic and phase transitions are delineated. The rapid decrease in resistivity after the introduction of hydrogen at elevated temperatures corresponds to the disproportionation process and can be attributed mainly to the formation of free iron. Another contribution arises from the formation of the Nd-hydride. On evacuating the system, the $NdH_{2\pm x}$ phase desorbs and the sudden decrease in resistivity can be attributed to the dissociation of Nd-hydride into Nd which subsequently recombines with the other constituents resulting in an increase in resistivity.

Figure 1 shows the isothermal part of the electrical resistivity versus time, which delineates the S-HDDR process at $T=800$ °C and $p(H_2)=0.7$ bar for the $Nd_{16}Fe_{76}B_8$ as-cast and the stoicl iometric $Nd_2Fe_{14}B$ alloy. It can be seen that the disproportionation and recombination reaction rates are higher for the $Nd_{16}Fe_{76}B_8$ alloy. Shortly after the introduction of hydrogen a small maximum (see inset in Fig. 1) in the resistivity curve of the $Nd_{16}Fe_{76}B_8$ alloy can be observed, and this can be related to the rapid hydrogenation of the Nd-rich grain boundary resulting in the formation of $NdH_{2\pm x}$. Further studies, which will be published elsewhere, have shown that the hydrogenation of the grain boundary phase results in the solidification of this phase, which has its melting point at $T=650$ °C.[8] For the stoichiometric alloy no such maximum is observed, consistent with the absence of the Nd-rich grain boundary phase in this alloy. Microstructural characterization[6] has shown that the material is fully disproportionated when a constant, equilibrium resistivity is attained and the same applies for the recombination reaction. The resistivity data indicate that the $Nd_{16}Fe_{76}B_8$ alloy is fully disproportionated after 19 ± 2 min of exposure to hydrogen at $p(H_2)=0.7$ bar and fully recombined after 20 ± 2 min of desorption at $T=800$ °C. The corresponding times for the stoichiometric $Nd_2Fe_{14}B$ alloy are 29 ± 2 and 71 ± 2 min, respectively (for identical sample thicknesses of $t=0.8$ mm). Thus, both reactions are much slower for the stoichiometric alloy. These changes in resistivity correspond to the hydrogen absorption and desorption pressure behaviors shown in Fig. 2. The slightly smaller quantity of hydrogen absorbed in the stoichiometric $Nd_2Fe_{14}B$ alloy can be attributed to the absence of Nd-rich phase in this material.[10]

These studies could indicate that the N ...n grain boundary phase has a significant influence on the kinetics of the HDDR reactions. It was reported earlier[6] that the hydrogen diffuses either in the hydrided Nd-rich phase or at the interface between this phase and the matrix phase. It was shown[6] that the disproportionation reaction begins at the Nd-rich/$Nd_2Fe_{14}B$ boundaries and proceeds towards the center of the original grains. For the stoichiometric $Nd_2Fe_{14}B$ alloy no such fast transport paths exist, which could explain the lower reaction rates in this material. A reverse mechanism can be assumed for the desorption of hydrogen during the recombination reaction. However, it is interesting to note that, in particular, the latter process is much slower in the $Nd_2Fe_{14}B$ alloy, which could indicate that the Nd-rich grain boundary phase plays an additional role in the recombination process.

B. Onset of disproportionation and recombination in as-cast $Nd_{16}Fe_{76}B_8$

Figure 3 shows the electrical resistivity and the hydrogen desorption behavior of a disproportionated $NdH_{\sim2}$, α-Fe, Fe_2B mixture between $T=750$ and 1000 °C under an initial pressure of $p(H_2)=35$ mbar. The measurements revealed the Curie-point resistance anomaly of α-Fe at $T=770\pm5$ °C and

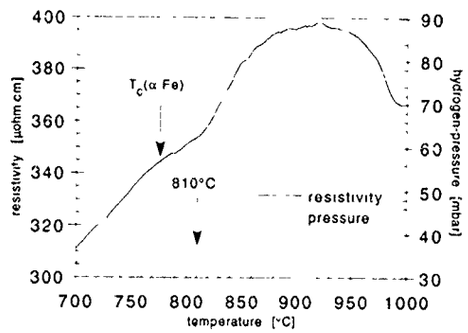

FIG. 3 Electrical resistivity and hydrogen desorption behavior between $T=750$ and 1000 °C under an initial pressure of $p(H_2)=35$ mbar of a disproportionated $NdH_{\sim2}$, α-Fe, Fe_2B mixture

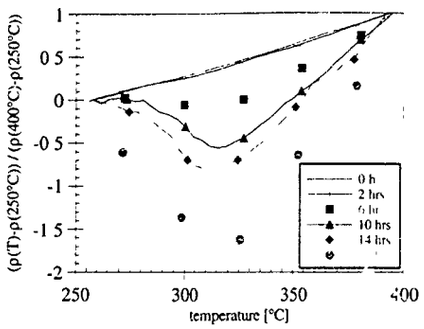

FIG. 4. Ratio of $[\rho(T)-\rho(250\,^{\circ}\mathrm{C})]/[\rho(400\,^{\circ}\mathrm{C})-\rho(250\,^{\circ}\mathrm{C})]$ vs temperature monitoring the development of the Curie point of an as-cast $Nd_{16}Fe_{76}B_8$ alloy for different stages of recombination at $T=620\,^{\circ}\mathrm{C}$.

a major desorption at $T=810\pm5\,^{\circ}\mathrm{C}$ causing another change in slope in the resistivity curve. This event can be interpreted as recombination under a hydrogen atmosphere. It was observed that, the higher the pressure, the higher the temperature for the desorption event. The pressure changes at higher temperatures can be attributed to the desorption of the Nd-rich grain boundary phase (to be published) and this corresponds with a fall in the resistivity.

Starting from a recombined material, the hydrogen pressure was increased step by step and the "equilibrium" resistivity was measured at different isotherms. It was found that, at $T=880\,^{\circ}\mathrm{C}$, for example, the 2-14-1-hydride shows a Sieverts'-type behavior before the sharp onset of the disproportionation reaction at $p(H_2)=0.46$ bar. These studies indicate that the start of the disproportionation and recombination reactions depend critically on the stability of NdH_2, which is determined by hydrogen pressure and processing temperature. A hysteresis effect[11] for the NdH_2 was found as the data for the onset of disproportionation and recombination were derived from absorption and desorption isotherms, respectively. These results are in agreement with work by Takeshita and Nakayama,[12] who reported, on the basis of x-ray diffraction measurements, that the disproportionated mixture will recombine above 1000 °C under a hydrogen pressure of 1 bar.

C. Low-temperature recombination in as-cast $Nd_{16}Fe_{76}B_8$

At conventional HDDR-processing temperatures (750–850 °C) it can be assumed that the Nd-rich grain boundary phase will remelt after the hydrogen is fully desorbed, whereas at $T=620\,^{\circ}\mathrm{C}$ the microstructural changes will occur in a solid-solid reaction as the Nd-rich grain boundary phase remains in the solid, hydrided state. Figure 4 shows the development of the Curie-point anomaly by evaluating the resistivity data during the heating stage of the cycling procedure described in part II. The ratio $[\rho(T)-\rho(250\,^{\circ}\mathrm{C})]/[\rho(400\,^{\circ}\mathrm{C})-\rho(250\,^{\circ}\mathrm{C})]$ is plotted over the temperature range of $T=250$–$400\,^{\circ}\mathrm{C}$. At $T=620\,^{\circ}\mathrm{C}$, the different stages during recombination can be monitored and the amount of reformed $Nd_2Fe_{14}B$ matrix phase can be estimated, because the observed changes are due entirely to transformations in the matrix phase. After 18 h at $T=620\,^{\circ}\mathrm{C}$, no further changes occur and therefore it can be assumed that the material is fully recombined. The pattern in the overall resistivity behavior is similar to that of a stoichiometric alloy at $T=800\,^{\circ}\mathrm{C}$. The development of the magnetic properties and the microstructural changes during the different stages of recombination will be reported elsewhere.[13]

IV. CONCLUSIONS

The fundamental differences in HDDR-reaction kinetics and mechanisms between a $Nd_{16}Fe_{76}B_8$ as-cast and a homogenized stoichiometric $Nd_2Fe_{14}B$ alloy at $T=800\,^{\circ}\mathrm{C}$ and $p(H_2)=0.7$ bar have been characterized by means of *in situ* electrical resistivity measurements and hydrogen sorption studies on nondecrepitated samples. The absence of the Nd-rich grain boundary phase in the stoichiometric alloy causes the disproportionation and recombination rates to be significantly lower. The Nd-rich phase not only acts as a transport path for the hydrogen, but effects in particular the desorption/recombination reaction. The onset of the disproportionation and recombination reactions under hydrogen atmosphere in a temperature range of $T=780$–$880\,^{\circ}\mathrm{C}$ depend critically on the hydrogen pressure. Desorption at $T=620\,^{\circ}\mathrm{C}$ revealed the different stages during re-formation of the $Nd_2Fe_{14}B$ matrix phase. At this temperature the recombination process is a solid-solid reaction.

ACKNOWLEDGMENTS

Thanks are due to the SERC and the European Commission for support of the general research program of which the work forms part and for the provision of an EC-fellowship (OG).

[1] I R Harris, Proceedings of the 12th International Workshop on Rare Earth Magnets and their Applications, Canberra, Australia, 1992, p 347
[2] T. Takeshita and R. Nakayama, Proceedings of the 12th International Workshop on Rare-Earth Magnets and their Applications, Canberra, Australia, 1992, p 670
[3] P. J. McGuiness, E J. Devlin, I R. Harris, E Rozendaal, and J Ormerod, J Mater. Sci **24**, 2541 (1989).
[4] O. Gutfleisch, M Verdier, and I R Harris, J Alloys Comp **196**, L19 (1993).
[5] O. Gutfleisch, M Verdier, I. R. Harris, and A. E Ray, IEEE Trans Magn **MAG-29**, 2872 (1993).
[6] O Gutfleisch, N Martinez, M. Verdier, and I. R. Harris, J. Alloys Comp. **204**, L21 (1994).
[7] X. ' Zhang, Ph.D thesis, University of Birmingham, UK, 1991
[8] P. J McGuiness, X J Zhang, and I R Harris, J. Less-Common Metals **158**, 359 (1990).
[9] G Schneider, E T Henig, G Petzow, and H H Stadelmaier, Z Metallkd. **77**, 755 (1986).
[10] P J. McGuiness, I R Harris, U D Scholz, and H Nagel, Z. Phys Chem Neue Folge **163**, 687 (1989)
[11] K H. J Buschow, P C. P. Bouten, and A R Miedema, Rep. Prog Phys **45**, 937 (1982)
[12] T Takeshita and R Nakayama, Proceedings of the 11th International Workshop on Rare-Earth Magnets and their Applications, Pittsburgh, 1990, p 49
[13] N Martinez, D G. R Jones, O. Gutfleisch, D Lavielle, D. Pere, and I R Harris, to be presented at INTERMAG-MMM 1994.

Study of desorbed hydrogen-decrepitated anisotropic Nd-Fe-B powder using x-ray diffraction

G. P. Meisner
Physics Department, GM NAO Research and Development Center, Warren, Michigan 48090-9055

V. Panchanathan
GM Magnequench, Anderson, Indiana 46013

The intrinsic magnetic coercivity (H_{ci}) of Nd-Fe-B-based permanent magnet material is profoundly affected by hydrogen absorbed during the hydrogen decrepitation (HD) process for producing anisotropic powders from bulk anisotropic hot-deformed MAGNEQUENCH (MQ) magnets. Hydrogen (H) content and x-ray diffraction measurements clarify the effects of H and desorption temperature (T_d) on the intrinsic magnetic anisotropy (IMA) of the $Nd_2Fe_{14}B$-type phase and the nature of the intergranular phases, both of which are crucial for high H_{ci}. The Nd-rich intergranular phase disproportionates during HD, initially forming a microcrystalline Nd-hydride phase, possibly Nd_2H_5. For $T_d \leq 220$ °C, H remains in the $Nd_2Fe_{14}B$-type phase, severely degrading the IMA, which causes a low H_{ci}. For 220 °C$\leq T_d \leq$250 °C, enough H desorbs from the $Nd_2Fe_{14}B$-type phase and the IMA recovers its large prehydrided value, and the microstructure supports a high $H_{ci} \leq 10$ kOe in spite of the H disproportionated intergranular phase. Only for $T_d > 250$ °C is H_{ci} degraded by the microstructure, corresponding to further H desorption and the microcrystalline Nd-hydride phase becoming well-crystallized NdH_2. The NdH_2 phase decomposes with continued H desorption and at $T_d > 580$ °C recombines to re-form the Nd-rich intergranular phase of prehydrided MQ material. H is completely desorbed above 580 °C and $H_{ci} > 11$ kOe, nearly that of the prehydrided MQ magnets.

Anisotropic permanent magnet powder is of considerable importance in high performance bonded magnet production. The $Nd_2Fe_{14}B$-type phase[1,2] of Nd-Fe-B-based magnets has a very large intrinsic magnetic anisotropy[3] (IMA) that orients the magnetic moments uniaxially in the tetragonal lattice, and such magnets potentially have a very large bulk magnetic anisotropy. Melt-spun Nd-Fe-B ribbons are easily crushed into powder and used in bonded magnets directly but are nearly isotropic, consisting of randomly oriented crystallites.[4,5] Hot-pressing ribbons followed by hot-deformation results in substantial crystallite alignment[6,7] without degrading the high intrinsic magnetic coercivity (H_{ci}), yielding highly anisotropic permanent magnets. Fabrication of hot-deformed magnets with specific shapes and alignment directions while achieving grain alignment throughout, however, is difficult. Powders produced from hot-deformed Nd-Fe-B-based magnets remain anisotropic, and bonded magnets using such powder can be made highly anisotropic by aligning the powder grains in an applied magnetic field during the bonding process.[8–15]

Powders of Nd-Fe-B-based material can be mechanically ground,[8–11] a difficult process[15] that degrades H_{ci} of the smallest powder grains,[12] and the magnetic properties of the powder are not consistent from lot to lot.[16] An alternate method is hydrogen decrepitation (HD)[13–15] where hydrogen (H) absorbing interstitially in the $Nd_2Fe_{14}B$-type phase causes spontaneous pulverization. Incorporation of H into the $Nd_2Fe_{14}B$-type lattice, however, dramatically reduces the IMA[17] which in turn greatly degrades H_{ci}. Desorption of H after HD is therefore necessary to recover high performance magnetic properties. In previous work,[18] we studied H desorption and magnetic properties of HD hot-deformed Nd-Fe-B-based (MQ3) magnets. In this paper we present chemical analysis and x-ray diffraction measurements on HD MQ3 anisotropic powders as a function of desorption temperature (T_d).

The Nd-Fe-B-based material for this study was H-containing powder of HD[19] MQ3-E alloy.[20] Direct chemical analysis[21] yielded the H content in HD MQ3 powder as a function of T_d. These results along with the curve for H_{ci},[18] are shown in Fig. 1 where four T_d regions are quite apparent. X-ray diffraction spectra,[22] Fig. 2, correspond to the $Nd_2Fe_{14}B$-type major phase plus a few diffraction peaks from minor phases. For $T_d \leq 240$ °C, Figs. 2(a)–2(c), the peaks for the $Nd_2Fe_{14}B$-type phase are slightly broadened and shifted to lower angles. The shift is considerably less than for the fully hydrided state, Fig. 3(a), but quite evident from the position of the (301) peak. A small amount of H evidently remains in the $Nd_2Fe_{14}B$-type phase until $T_d \cong 240$ °C.

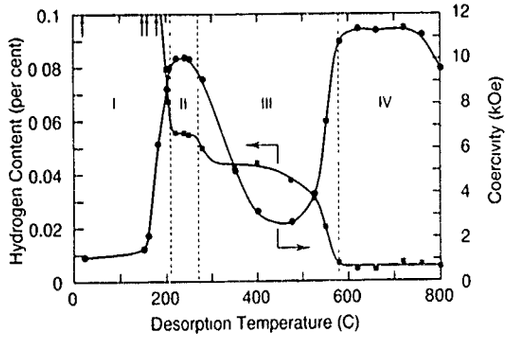

FIG. 1 Hydrogen content and magnetic coercivity H_{ci} vs desorption temperature T_d for HD MQ3 powder Vertical dashed lines delineate four regions of desorption temperature, vertical arrows indicate H contents greater than 0 1 wt %, and solid lines are guides for the eye

 0021-8979/94/76(10)/6259/3/$6.00 © 1994 American Institute of Physics

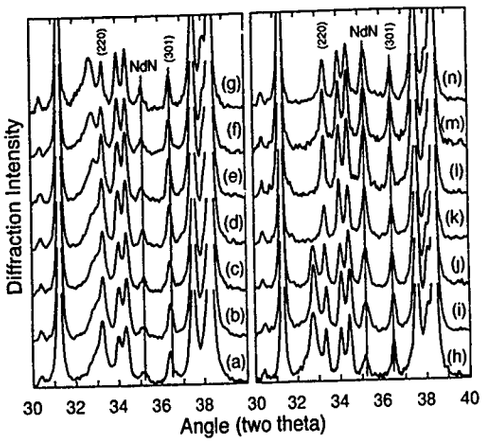

FIG. 2. X-ray diffraction spectra for HD MQ3 powders desorbed at (a) 200 °C, (b) 220 °C, (c) 240 °C, (d) 250 °C, (e) 280 °C, (f) 350 °C, (g) 400 °C, (h) 475 °C, (i) 520 °C, (j) 550 °C, (k) 580 °C, (l) 620 °C, (m) 660 °C, and (n) 720 °C. The vertical line at 36.55° indicates the (301) peak of the $Nd_2Fe_{14}B$-type phase and at 35.2° indicates the (111) peak of NdN.

The minor phase peaks are obvious from a comparison of the observed spectra, Fig. 2, with a calculation for unhydrided $Nd_2Fe_{14}B$, Fig. 3(b). The peak near 35.2°, which increases in intensity monotonically with T_d, is the (111) peak of NdN due to a small amount of nitrogen contamination, and this has been observed previously in heat-treated Nd-Fe-B-based materials.[23] Another minor phase peak occurs near 32.8°. In the fully hydrided material, Fig. 3(a), the (220) peak of the $Nd_2Fe_{14}B$-type phase shifts from ~33.3° to ~33.0° and obscures this minor phase peak. In the desorbed samples, the 32.8° peak is a broad shoulder and has low intensity at low T_d values, Figs. 2(a)–2(d). It becomes a true peak at 280 °C, Fig. 2(e), grows in intensity and sharpens, Figs. 2(f)–2(j), until 580 °C where it disappears, Figs. 2(k)–2(n). This dependence on T_d of the intensity and shape of this mino. phase peak at 32.8° correlates very well with H content and H_{ci}, Fig. 1. This minor phase peak corresponds to a binary Nd-hydride phase and is evidence that H disproportionation during HD occurs for some part of the sample.

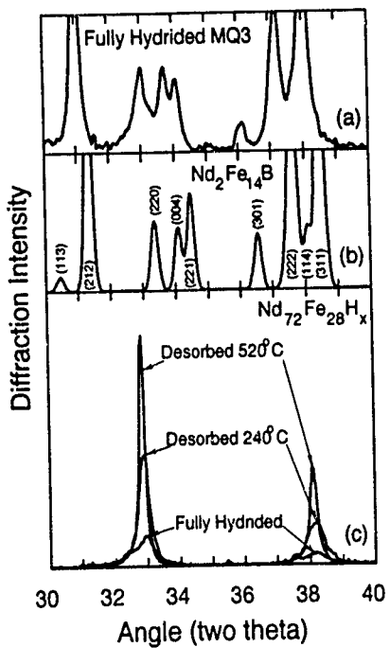

FIG 3. X-ray diffraction spectra for (a) fully hydrided HD MQ3 powder (not desorbed), (b) the $Nd_2Fe_{14}B$-type phase (calculation) where (hkl)'s are the Miller indices of the diffraction peaks, and (c) H disproportionated $Nd_{72}Fe_{28}$ fully hydrided, desorbed at 240 °C, and desorbed at 520 °C

A Nd-rich alloy approximating the intergranular phase in MQ materials, $Nd_{72}Fe_{28}$, was induction melted and then hydrided.[24] The spectra for this alloy after hydriding and after desorbing at 240 and 520 °C consist of Nd-hydride and iron peaks, confirming H disproportionation of this alloy. The Nd-hydride peaks for the fully hydrided $Nd_{72}Fe_{28}$ phase are broad and have low intensity, but as H is removed at higher T_d, the peaks increase in intensity and move slightly to lower diffraction angles, Fig. 3(c). Although the Nd-hydride peaks increase their intensity by a factor of ~7.5 compared to the fully hydrided state, the iron peak (not shown) remains at a very low intensity, approximately that of the peak at ~38.1° for fully hydrided $Nd_{72}Fe_{28}H_x$. H disproportionation of the $Nd_2Fe_{14}B$-type phase, however, results in a very high intensity iron peak.[23] Because iron peaks are not observed in the spectra for any of the desorbed samples, we conclude the Nd-hydride phase in HD MQ3 desorbed powder is a disproportionation product of the Nd-rich intergranular phase and not of the $Nd_2Fe_{14}B$-type phase.

The coercivity of H_{ci} of MQ3 materials arises from both the large IMA of the $Nd_2Fe_{14}B$-type phase that provides rigidity to the underlying magnetism, and a suitable microstructure involving grain boundaries and intergranular phases that provide effective pinning sites for magnetic domain walls.[25] The independent effects of H on these two conditions for large H_{ci} cause the dramatic H_{ci} behavior of HD MQ3 powder as a function of T_d shown in Fig. 1. In the HD process[19] the $Nd_2Fe_{14}B$-type phase and the Nd-rich intergranular phase absorb a considerable amount of H. The H content can be estimated from the total rare-earth (RE) content[20] to be 0.43 wt % for a molar concentration RE:H =1:2 (i.e., corresponding to $RE_2Fe_{14}BH_x$ with $x=4$). Conversely, with no H in the $Nd_2Fe_{14}B$-type phase and assuming that the intergranular phase disproportionates into REH_2, the H content estimated from the amount of RE exceeding $RE_2Fe_{14}B$ stoichiometry in the MQ3 alloy is 0.074 wt %. Thus, the measured H content of 0.055 wt %, region II of Fig. 1, is consistent with all the H desorbed from the $Nd_2Fe_{14}B$-type phase and the residual H only in the intergranular phase. The profound degrading effect of H on H_{ci} via the IMA of the $Nd_2Fe_{14}B$-type phase is therefore limited to low T_c, region I, and this result agrees with our previous conclusions based on first quadrant magnetization data for these materials.[26]

The nature of the hydrided intergranular phase also has a profound effect on H_{ci}. The intergranular phase H disproportionates during HD and only degrades H_{ci} slightly for $T_d<280$ °C, regions I and II. The low H_{ci} in region I is due only to the low IMA of the hydrided $Nd_2Fe_{14}B$-type phase.

The microstructural contribution to H_{ci}, i.e., strong domain wall pinning, remains suitable for high H_{ci} although different from that of prehydrided MQ3 magnets. Once the IMA of the $Nd_2Fe_{14}B$-type phase has recovered its large value, region II, H_{ci} regains a high value of $\geq$10 kOe. The value of $H_{ci}\geq$14 kOe of the prehydrided MQ3 magnet is not quite achieved, however, implying that H disproportionated intergranular phase microstructure is less effective in domain wall pinning than the original MQ3 microstructure.

Because of the broad Nd-hydride peak at 32.8° in Figs. 2 and 3(c), it is possible that a H-induced amorphous-like phase exists in the intergranular areas below 280 °C, regions I and II, or a microcrystalline Nd_2H_5-type phase, which is a tetragonal superstructure of the face-centered-cubic NdH_2-type phase. Crystallization of the disproportionated intergranular phases occurs above 280 °C, region III, and corresponds to H_{ci} decreasing strongly, some of the residual H desorbing, and the shoulder in x-ray diffraction spectra at 32.8° in Fig. 2 shifting and sharpening into a well-defined peak. This behavior is also evident in the diffraction spectra of hydrided $Nd_{72}Fe_{28}$, Fig. 3(c), as H is desorbed. This result suggests a microcrystalline Nd_2H_5-type phase decomposes to a well-crystallized NdH_2-type phase, where the lattice constants of Nd_2H_5, $a=0.54322$ nm and $c/2=0.5454$ nm,[27] are slightly smaller than that of NdH_2, $a=0.54678$ nm.[28] Eventually, sufficient H desorbs at higher temperatures causing the NdH_2-type phase itself to decompose and react with the other disproportionated intergranular phases to recombine and form the a Nd-rich intergranular phase similar to that of the prehydrided MQ3 alloy. This accounts for the gradual recovery of H_{ci} above 475 °C, Fig. 1, and the correspondingly gradual decrease in H content. Some of the degradation of H_{ci} in region III occurs because of annealing effects on the microstructure. This has been observed for MQ3 materials annealed without H,[29–31] but H seems to cause a much greater degradation of H_{ci}.

Above 580 °C, region IV, NdH_2 diffraction peaks are absent, Fig. 2, H is completely desorbed, and H_{ci} is high, Fig. 1. Although H_{ci} is higher in region IV than region I, it does not return to the prehydrided value of $\geq$14 kOe. We conclude that H disproportionation desorption and recombination of the intergranular phase cause a nonrecoverable decrease in domain wall pinning strength of the intergranular phase relative to prehydrided MQ3 magnets. Also, the NdN contamination indicates a nonrecoverable decomposition of the Nd-rich intergranular phase has occurred and is presumably detrimental to H_{ci}. Finally, the drop in H_{ci} at 800 °C in region IV of Fig. 1 is undoubtedly due to the detrimental effects of annealing and grain growth on the microstructure of MQ3 material generally.

We thank Dr. Raja K. Mishra and Earl G. Brewer for useful discussions, Charles B. Murphy and Daniel J. Van Wingerden for technical assistance, and Dr. Jan F. Herbst and Dr. John J. Croat for much encouragement and support.

[1] J. F Herbst, J J. Croat, F. E Pinkerton, and Y. B Yelon, Phys. Rev B **29**, 4176 (1984).
[2] For a review, see J F Herbst, Rev. Mod. Phys. **63**, 819 (1991).
[3] R. Grossinger, X K Sun, R. Eibler, K. H. J. Bushchow, and H. R Kirchmayr, J Magn. Magn. Mater. **58**, 55 (1986)
[4] R. K. Mishra, J. Magn. Magn. Mater. **54-57**, 450 (1986).
[5] R. K. Mishra, in *High Performance Permanent Magnet Materials*, Mater. Res Soc. Symp. Proc Vol 96, edited by S. G. Sankar, J F Herbst, and N. C. Koon (Materials Research Society, Pittsburgh, 1987), p. 83.
[6] R. K. Mishra and R. W. Lee, Appl. Phys. Lett. **49**, 733 (1986)
[7] R. K. Mishra, J. Appl. Phys. **62**, 967 (1987).
[8] Y. Nozawa, K Iwasaki, S Tanigawa, M Tokunaga, and H. Harada, J Appl. Phys. **64**, 5285 (1988).
[9] L. J. Eshelman, K. A. Young, V. Panchanathan, and J J Croat, J Appl Phys **64**, 5293 (1988).
[10] J. J. Croat, IEEE Trans Magn. **25**, 3550 (1989).
[11] M. Tokunaga, Y. Nozawa, K Iwasaki, S. Tanigawa, and H. Harada, J Magn. Magn. Mater. **80**, 80 (1989).
[12] G. P. Meisner and E. G. Brewer, Report PH-1577, General Motors NAO Research and Development Center (1989), p. 25 (unpublished)
[13] I. R. Harris, C Noble, and T. Bailey, J. Less-Common Metals **106**, L1 (1985).
[14] V. Panchanathan, A. T. McMullen, J. J. Croat, M. Doser, and R. W Ribitch, J. Appl Phys **70**, 6465 (1991).
[15] M. Doser, V. Panchanathan, and R K Mishra, J Appl Phys. **70**, 6603 (1991).
[16] V Panchanathan, J Mater Eng **13**, 129 (1991).
[17] K. Oesterreicher and H. Oesterreicher, Phys. Status Solidi A **81**, K61 (1984), see also Ref. 1, pp. 863–4, and references therein.
[18] G. P. Meisner and V. Panchanathan, J. Appl Phys. **73**, 6482 (1993).
[19] HD was performed by Hoeganaes Corp., Riverton, NJ, at 150 psi H_2. The sample self-heated to 130 °C during H absorption
[20] E-alloy nominal composition in weight per cent 30 5% tot ' rare earth, 2.5% Co, 1% B, 76% Fe. The billets were obtained from MAGNEQUENCH.
[21] Chemical analysis for hydrogen was performed by Sherry Laboratories, Inc., 2203 S. Madison St , Muncie, IN 47307
[22] We performed x-ray diffraction measurements and analysis using a Philips APD1700 Automated Powder Diffraction System (Co K_α radiation), see G P. Meisner and E G. Brewer, J Appl. Phys. **72**, 1 (1992).
[23] G. P. Meisner and V. Panchanathan, J. Appl. Phys. **74**, 3514 (1993)
[24] Hydrogen reacts with $Nd_{72}Fe_{28}$ exothermically, causing self-heating to well above 100 °C. Our sample was prepared by further heating in ~1 atm H_2 to 500 °C and cooling in H_2 to room temperature in ~10 min
[25] The microstructure of hot-deformed rapidly solidified Nd-Fe-B is such that the grain boundary and intergranular phase regions do not promote nucleation of reverse magnetic domains. A strong-pinning model of H_{ci} agrees well with observed magnetic properties See F E Pinkerton and C D Fuerst, J. Appl. Phys. **67**, 4753 (1990); F E Pinkerton and C. D. Fuerst, J Magn. Magn. Mater. **89**, 139 (1990); and F. E. Pinkerton and C. D. Fuerst, J. Appl. Phys. **69**, 5817 (1991).
[26] Absorbed H in the $Nd_2Fe_{14}B$-type phase allows a higher degree of magnetic saturation for randomly oriented powders in moderate applied magnetic fields compared to prehydrided material and samples desorbed above ~220 °C See Ref 17
[27] P Knappe, H Muller, and H. W. Mayer, J Less-Common Metals **95**, 323 (1983)
[28] J E Bonnet and J. N. Daou, J Appl Phys **48**, 964 (1977).
[29] R. K Mishra, E G. Brewer, and R W. Lee, J. Appl. Phys **63**, 3528 (1988).
[30] V. Panchanathan, U. S Patent No 4 900 374 (13 February 1990).
[31] E. G. Brewer, U S Patent No 4 966 633 (30 October 1990)

The electrochemical hydrogenation of NdFeB sintered alloys

Kuo En Chang and Garry W. Warren
Department of Metallurgical and Materials Engineering, The University of Alabama, P.O. Box 870202, Tuscaloosa, Alabama 35487

The absorption of hydrogen by NdFeB alloys in aqueous solution has been investigated using dc electrochemical methods and x-ray diffraction. Immersion of the NdFeB alloy in 0.1 M H_2SO_4 results in the formation of the $Nd_2Fe_{14}BH_{2.7}$ hydride phase as indicated by x-ray diffraction analysis. The hydrogen entering the NdFeB lattice is believed to result from the preferential acid dissolution or etching of the Nd-rich phase. The hydrogen absorption and desorption behavior of sintered NdFeB alloys, $(NdDy)_{15}Fe_{78.3}Al_{0.7}B_6$ and $(NdDy)_{15}Fe_{67}Co_5V_4Al_2B_7$, have been compared with that of a $LaNi_5$ alloy utilizing an electrochemical technique. $LaNi_5$ is capable of absorbing extremely high quantities of hydrogen as a metal hydride. The level of hydrogen absorbed by the three alloys was compared by "charging" electrodes of each alloy in 6 M KOH at a constant cathodic current, followed by a constant anodic "discharge" current. An arrest in the resulting potential versus time curve during discharge indicates the oxidation of the hydride, i.e., of absorbed hydrogen, formed during the cathodic charging process. Results indicate that both NdFeB alloys absorb hydrogen in aqueous solution. Similar experiments performed on a set of samples with varying total rare-earth (TRE) content showed that the amount of hydrogen absorbed is proportional to TRE content. Anodic potentiodynamic polarization after charging shows that the corrosion rate increases as the level of absorbed hydrogen increases.

I. INTRODUCTION

The magnetic properties of NdFeB and similar alloys are significantly affected by the hydrogen absorption of the $Nd_2Fe_{14}B$ phase.[1–3] Therefore an understanding of the hydrogen absorption behavior of NdFeB materials is important. Cast NdFeB alloy can absorb significant amounts of hydrogen relatively easily at room temperature even at hydrogen pressures as low as 1 bar.[4] The reactive nature of the NdFeB alloy with respect to hydrogen has also been attributed to the presence of the neodymium-rich phase at the grain boundaries, and the amount of hydrogen absorbed by the NdFeB alloys increases with rare-earth content.[5] It has also been suggested that the poor corrosion resistance of the sintered NdFeB alloys is due, at least in part, to the presence of the Nd-rich phase.[6,7] However, until now a correlation between hydrogen absorption and corrosion behavior of the sintered NdFeB alloys has not been demonstrated.

The preferential dissolution of the Nd-rich phase in the grain boundaries in acidic solutions, due to its lower electrochemical potential with respect to the $Nd_2Fe_{14}B$ phase,[7] results in the simultaneous evolution of hydrogen. Results presented in this work suggest that part of this hydrogen is absorbed by the $Nd_2Fe_{14}B$ matrix, producing a lattice expansion of the $Nd_2Fe_{14}B$ unit cell which can be measured by x-ray diffraction analysis.[8]

Hydrogen absorption of similar rare-earth materials, e.g., $LaNi_5$,[9,10] have been widely examined using an electrochemical charge/discharge technique. The method involves the application of a constant (galvanostatic) cathodic current resulting in hydrogen evolution, a portion of which forms a metal hydride. Stored hydrogen can then be removed by reversing the current flow. This reaction can be represented by the redox equation

$$M + xH_2O + xe^- = MH_x + xOH^-,$$

where x represents the number of hydrogen atoms absorbed by the alloy and MH_x is the hydride phase of the alloy. A plot of the potential versus time during discharge shows an arrest (a region of constant potential) characteristic of materials which absorb hydrogen and which represents the oxidation of the hydride. The charge passed during this arrest is a measure of the hydrogen absorbed.[9–12]

This technique has been used to examine the tendency of NdFeB alloys to absorb hydrogen from aqueous solution, to compare NdFeB with the known behavior of $LaNi_5$, and to examine its potential effect on the corrosion behavior of NdFeB. Results presented here show that the corrosion mechanism of NdFeB must involve hydrogen and that absorbed hydrogen has a detrimental effect on corrosion resistance.

II. EXPERIMENTAL MATERIALS AND TECHNIQUES

Four types of materials were utilized in this investigation, as follows: (1) $(NdDy)_{15}Fe_{78.3}Al_{0.7}B_6$, in both powder and sintered form, subsequently referred to as NdFeB alloy, (2) $(NdDy)_{15}Fe_{67}Co_5V_4Al_2B_7$ in both powder and sintered form, subsequently referred to as NdFeB-Co-V alloy, (3) cast $LaNi_5$, containing about 0.14 wt % of a catalyst, and (4) a set of four sintered NdFeB alloys, similar to those in (1), but with varying total rare-earth (TRE) content (29, 31, 33, and 37 wt %). All samples were supplied by Rhone Poulenc Basic Chemicals Co. A Rigaku D/Max-2BX x-ray diffractometer with Cu K_α radiation was used for structure determinations of NdFeB powders before and after etching in 0.1 M H_2SO_4. A Nikon optical microscope with image analysis system was used for microstructural observations. dc electrochemical techniques were performed using an EG&G model 273A potentiostat, and a three electrode glass cell. Working electrodes were prepared using samples of the sintered or cast materials described above. The reference electrode was

 0021-8979/94/76(10)/6262/3/$6.00 © 1994 American Institute of Physics

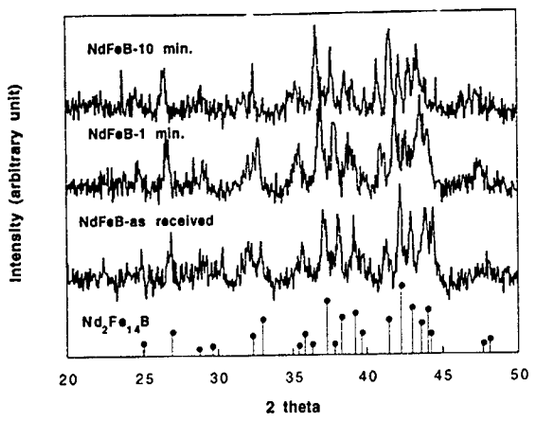

FIG 1. X-ray diffraction patterns for $(NdDy)_{15}Fe_{78.3}Al_{0.7}B_6$ powders before and after etching in 0.1 M H_2SO_4

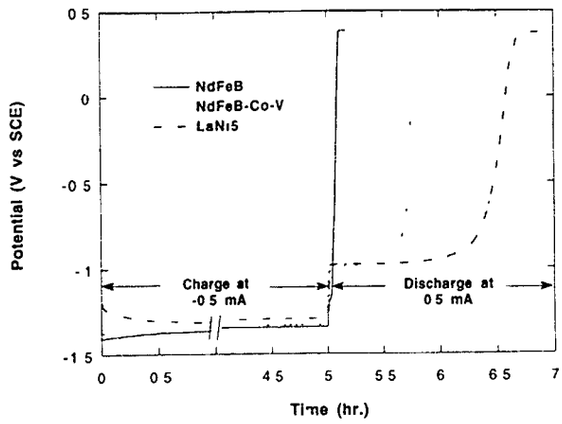

FIG. 2 Galvanostatic charge/discharge data for NdFeB, NdFeB-Co-V, and $LaNi_5$ alloys in 6 M KOH.

saturated calomel, and the counterelectrode was Pt. The 6 M KOH electrolyte was purged with nitrogen for at least 1 h prior to each experiment. The working electrode was polished to 600 grit, rinsed, dried, immersed in the electrolyte, and the open circuit or rest potential allowed to equilibrate for at least 1 h. Current densities were obtained by dividing measured current by the geometric cross-sectional area.

III. RESULTS

A. Hydrogen absorption from aqueous solution

Upon immersion of the NdFeB alloy powder (38–53 μm diameter) in 0.1 M sulfuric acid solution, gas evolution was observed to occur. After filtering, the powders were thoroughly rinsed with distilled water, and dried in a dessicator for 24 h. Dry powders were then pressed into pellets for x-ray diffraction analysis. Figure 1 shows x-ray diffraction data of NdFeB alloy powders after immersion in H_2SO_4 for 1 and 10 min. For comparison, patterns are also included for as-received powder and $Nd_2Fe_{14}B$. As can be seen, the patterns are similar but show a distinct shift toward smaller diffraction angles as etching time increases This shift reveals that the overall tetragonal structure of the NdFeB is retained but with measurably larger lattice parameters. Lattice constants were calculated from the x-ray data and are presented in Table I. Results indicate that the amount of hydrogen absorbed by the NdFeB powder increases in the first minute, rapidly achieving "saturation" and relatively constant a- and c-axis lattice parameters. The changes in total volume during the etching process for as-received and hydrided NdFeB alloys are in good agreement with those reported by Oesterreicher.[13] Based on these results the hydride phase formed after etching in 0.1 M H_2SO_4 is close to $Nd_2Fe_{14}BH_{2.7}$.

TABLE I Crystallographic data for NdFeB alloys and their hydrides.

Compounds	a (Å)	c (Å)	V (Å^3)	$\Delta V/V$ (%)
$(NdDy)_{15}Fe_{78.3}Al_{0.7}B_6$	8.80	12 29	951	··
$(NdDy)_{15}Fe_{78.3}Al_{0.7}B_6H_x$	8 94	12.39	990	4.1
$Nd_2Fe_{14}B$ (Ref 13)	8.79	12 17	940	···
$Nd_2Fe_{14}BH_{2.7}$ (Ref 13)	8.93	12 36	985	4.8

B. Electrochemical absorption/desorption of hydrogen

The relationship between the charge/discharge process for the sintered NdFeB and $LaNi_5$ alloys was compared using the galvanostatic charge/discharge technique. Samples were charged for 5 h at a constant cathodic current of −0.5 mA, immediately followed within 30 s by the application of a 0.5 mA constant anodic current until the sample was fully discharged as indicated by an increase in potential to about 0.45 V. Additional cycles were obtained by repeating the process. Experimental results for the first cycle of the NdFeB, NdFeB-Co-V, and $LaNi_5$ alloys are shown in Fig. 2. The lengthy arrest in potential of the $LaNi_5$ alloy at −1.0 V is characteristic of the discharge of stored hydrogen and is the basis for the proposed use of this material in metal hydride batteries.[14] By comparison, the NdFeB and NdFeB-Co-V alloys also show evidence of hydrogen absorption, though to a lesser degree than $LaNi_5$ in this measurement.

C. Effect of total rare-earth content

Since previous researchers have shown that hydrogen absorption increases with TRE[5] and have suggested a connection between TRE and corrosion resistance,[6] this effect has also been investigated. Results of the microstructural examination and image analysis of a set of samples with vary-

TABLE II. The volume fraction and the average grain size of the $Nd_2Fe_{14}B$ phase for sintered NdFeB alloys with varying TRE.

TRE (wt %)	TRE (at. %)	Vol. fraction of the $Nd_2Fe_{14}B$ phase	Avg of grain size of the $Nd_2Fe_{14}B$ phase
29 0	12 9	0.83	25 0±9.5 μm
31 0	14 0	0 79	19.5±5 8 μm
33.0	15 2	0.77	18 5±5 8 μm
37.0	17 5	0.73	15 8±4 8 μm

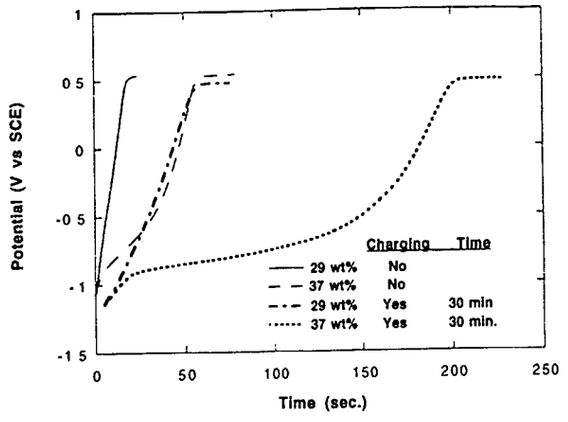

FIG. 3. Potential vs time for sintered NdFeB (29 and 37 wt % TRE) during anodic discharge (1 mA) in 6 M KOH with and without prior cathodic charging

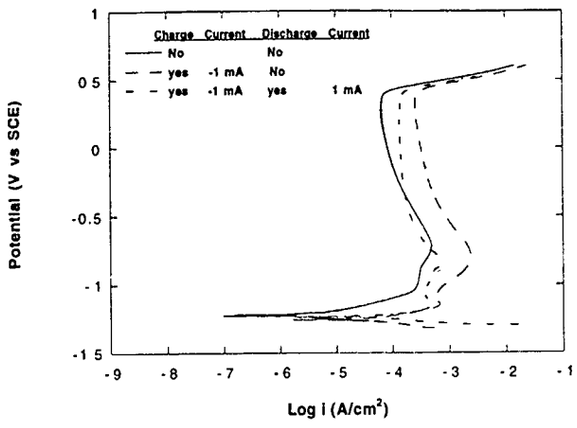

FIG. 4. Anodic polarization curves for sintered NdFeB (37 wt % TRE) in 6 M KOH; scan rate=2 mV/s.

ing TRE (29, 31, 33, and 37 wt %) after polishing to 0.05 μm and a 10 s etch in 10% nital are given in Table II. As expected, the volume fraction of the $Nd_2Fe_{14}B$ phase decreases with TRE, corresponding to an increase in the Nd-rich grain-boundary phase.[5] A slight decrease in grain size of the $Nd_2Fe_{14}B$ matrix with increasing TRE was also observed.

These samples were also subjected to a charge/discharge process. Charging was accomplished with a cathodic current of -1.0 mA for 30 min, followed by discharging with an anodic current of 1.0 mA. The potential during discharge was measured and results are shown in Fig. 3 for sintered NdFeB alloys with 29 and 37 wt % TRE, respectively. For comparison data are also shown for the same samples but without prior cathodic charging. Interestingly, the samples without cathodic charging show some evidence of a discharge process, which likely indicates the presence of a small amount of absorbed hydrogen even in the as-received state. Figure 3 also shows a clear increase in hydrogen absorption with increasing TRE. Over the range of TRE contents examined, the increase in hydrogen absorbed is roughly linear with TRE.

D. Effect of hydride formation on anodic polarization

Anodic potentiodynamic polarization curves were also measured for the four alloys with varying TRE before and immediately after the charge/discharge process. Results for the 37 wt % TRE alloy are shown in Fig. 4; behavior of the other samples was generally the same. Three curves are shown in Fig. 4: (1) as-received, without charging or discharging, (2) with charging only but without anodic discharging, and (3) with charging and discharging. As can be seen, after a complete charge/discharge cycle the observed current at low applied potentials is significantly higher than that of the as-received sample. This suggests that the corrosion resistance of the sintered NdFeB alloys is degraded upon absorbing and desorbing hydrogen.

IV. CONCLUSIONS

(1) The $(NdDy)_{15}Fe_{78.3}Al_{0.7}B_6$ powder has been shown to absorb hydrogen upon exposure to 0.1 M H_2SO_4. Based on the change in lattice constants the level of hydrogen absorbed corresponds fairly closely to an overall composition of $Nd_2Fe_{14}BH_{2.7}$.

(2) This study clearly shows that the sintered NdFeB and NdFeB-Co-V alloys both absorb hydrogen during the application of a cathodic current. Furthermore, these results suggest that the amount of hydrogen absorbed increases with increasing TRE as has been suggested by Scholz.[5]

(3) A comparison of anodic potentiodynamic polarization on samples before charging, after charging, and after complete discharging shows that the corrosion resistance of the sintered NdFeB alloys is degraded upon absorbing and desorbing hydrogen.

[1] K. H. J. Buschow, in *Ferromagnetic Materials*, edited by E. P. Wohlfarth and K. H. J. Buschow (Elsevier Science, North Holland, Amsterdam, 1984), Vol 4, p. 109.
[2] F. Pourarian, M. Q Huang, and W. E Wallace, J Less-Common Met. **120**, 63 (1986).
[3] J M. D Coey, A. Yaouanc, D. Fruchart, R Fruchart, and P L'Héritier, J Less-Common Met. **131**, 419 (1987).
[4] I. R. Harris and P. J. McGuiness, in *Proceedings of the Eleventh International Workshop on Rare Earth Magnets and their Applications* (Carnegie Mellon University Press, Pittsburgh, PA, 1990), p. 29.
[5] U. D. Scholz and H. Nagel, in *Concerted European Action on Magnets*, edited by I V. Mitchell (Elsevier Science, London, 1989), p 521
[6] A. S. Kim and F. E Camp, J. Mater Eng. **13**, 175 (1991).
[7] H Nakamura, A. Fukuno, and T. Yoneyama, in *Proceedings of the Tenth International Workshop on Rare Earth Magnets and their Applications* (Society of Non-Traditional Technology, Tokyo, 1989), p 315
[8] B. Rupp, A. R. Resnik, D Shaltiel, and P Rogl, J Mater Sci **23**, 2133 (1988).
[9] J J G. Willems, Philips J. Res. Suppl. **39**, 1 (1984).
[10] C Iwakura, T. Asaoka, H. Yoneyama, T Sakai, H. Ishikawa, and K Oguro, Nippon Kagaku Kaishi **1988**, 1482 (1988).
[11] J. H. N. van Vucht, F. A. Kuijpers, and H C A. M. Bruning, Philips Res Rep **25**, 133 (1970)
[12] H. F Bittner and C. C. Badcock, J. Electrochem. Soc. **130**, 193C (1983).
[13] K. Oesterreicher and H Oesterreicher, Phys Status Solidi A **85**, K61 (1984)
[14] C Iwakura, Y. Kajiya, H. Yoneyama, T. Sakai, K. Oguro, and H Ishikawa, J. Electrochem. Soc **136**, 1351 (1989).

Relation of remanence and coercivity of Nd,(Dy)-Fe,(Co)-B sintered permanent magnets to crystallite orientation

A. S. Kim and F. E. Camp
Crucible Research Center, Pittsburgh, Pennsylvania 15205-1022

H. H. Stadelmaier
Department of Materials Science and Engineering, North Carolina State University, Raleigh, North Carolina 27695-7907

For sintered permanent magnets based on $Nd_2Fe_{14}B$ having magnetically oriented crystallites, a simple method of measuring the degree of alignment by x-ray diffraction is described, using the inverse pole figure technique. The results are related to a distribution function for the easy axis which is a direct measure of remanence. The fraction of the ideal [001] texture component in both Nd-Fe-B and Nd,Dy-Fe,Co-B magnets is enhanced by doping with oxygen, resulting in a measurable increase in remanence and improved loop squareness. The observed increase of the intrinsic coercivity $_iH_c$ with better crystallite orientation is also discussed.

I. INTRODUCTION

The remanence in sintered permanent magnets based on the phase $Nd_2Fe_{14}B$ is maximized by aligning the powdered particles of the magnet alloy in a magnetic field before pressing. While this results in a large fraction of crystallites with the easy axis in or near the field direction, the orientation is never perfect. The purpose of this study is twofold: (i) to describe a simple method of measuring the degree of alignment and relate it to the remanence and (ii) to report a method of enhancing the fraction of the ideal [001] texture component by doping with oxygen. In particular, it will be shown what improvement in the remanence can be expected when the easy axis lies within a cone described by an orientation distribution of a given angular width. The effect of orientation on the intrinsic coercivity $_iH_c$ will also be discussed.

II. TEXTURE

The methods of quantitatively assessing the crystal orientation in a sintered magnet are essentially twofold: (i) The intensity of an x-ray reflection corresponding to the easy axis, i.e., $(00l)$ for Nd-Fe-B magnets, is measured directly as the magnet axis is tilted out of the reference orientation, the normal to the magnet surface. The angle at which the intensity drops to 1/2 is a measure of the textural quality. A way of doing this by using a pole figure device for full orientation has been described by Chang *et al.*[1] A simpler modification of this technique utilizes the decoupled θ scan for an $(00l)$ reflection and describes a line through a pole figure which is assumed to be that of a fiber texture.[2] Again, the width of tilt at half maximum is a measure of texture. (ii) A specimen with the reflecting surface normal to the magnet axis is subjected to a standard Bragg 2θ scan. In an anisotropic magnet only reflections with low (h,k) and high (l), including $(00l)$, are observed. Then the orientation is derived from the known angles between the observed (hkl) and $(00l)$, or their poles, and the orientation distribution is derived by comparing their intensities to the corresponding intensities in a specimen with random orientation of the crystallites. Meisner and Brewer[3] have performed a more sophisticated analysis in which two reference directions are used. They have also shown that calculated powder intensities are in good agreement with those measured on a random powder sample of Nd-Fe-B, and our analysis will use the former. This method has been described by Tenaud *et al.*[4] and used by Kawai *et al.*[5] in connection with axial to conical spin reorientation in Nd-Fe-B. The technique has been known to metallurgists for some time as the "inverse pole figure" method.[6,7] It uses a single reference direction (the axis of the anisotropic magnet), which is assumed to be the direction of the scattering vector. In the present study, the fraction of $(00l)$ in a direction tilted by a given angle from the scattering vector is determined from the set of available (hkl) and is used to determine the cause of remanence enhancement resulting from the addition of oxygen under otherwise equal experimental conditions. It should be pointed out that the texture difference between specimens observed here can be seen by visual inspection of a pair of diffraction patterns. The goal is to make this observation more quantitative and, specifically, to determine whether the improvement in remanence can be accounted for by the sharpening of the texture. As for the distribution function used in Sec. IV, it has not been suggested previously but has the advantage of mathematical simplicity.

III. EXPERIMENT

Sintered magnets were prepared with two compositions, in wt %, 30.5Nd, 2.5Dy, 63.4Fe, 2.5Co, 1.1B (in at. % 14.0Nd, 1.0Dy, 75.4Fe, 2.8Co, 6.8B) referred to as A and B and 32.5Nd, 66.4Fe, 1.1B (14.9Nd, 78.4Nd, 6.7B), specimens C and D. Of each composition one batch (A and C) was prepared by conventional methods, employing rigid tool compaction of the powder, and another batch (B and D) was subjected to additional oxygen pickup during powder processing prior to pressing. The final oxygen analyses of the magnets (in wt %) were: A (0.22), B (0.50), C (0.24), D (0.41). The method of adding oxygen was apparently not critical to its effect on grain orientation and it could be introduced during jet milling or following milling. The hysteresis loops were measured on a hysteresisgraph, independently at both laboratories. The x-ray diffraction patterns

 0021-8979/94/76(10)/6265/3/$6 00 © 1994 American Institute of Physics

TABLE I. Ratio J_r/J_s of remanence to saturation polarization for orientation distributions $f(\theta)=\cos^m\theta$ having cone angle width $\theta^*_{1/2}$ at $f(\theta)=1/2$.

$\theta_{1/2}$	m	$J_r/J_s=(m+1)/(m+2)$
90	0	0.500
45	2	0.750
27.0	6	0.875
22.2	9	0 909
17 9	14	0.938
13.7	24	0.962
9 5	50	0 981
0	∞	1.000

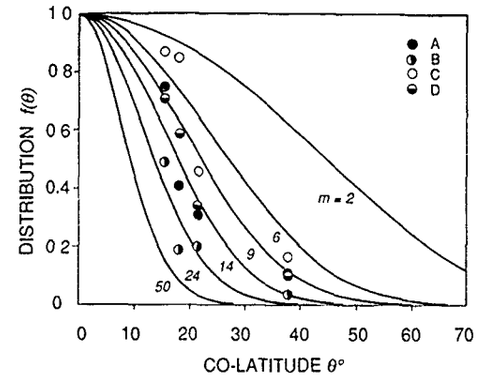

FIG. 1. Hypothetical and experimental distribution of tetragonal (001) poles.

were taken on a standard diffractometer (Cu $K\alpha$ radiation). The specimen surface that was perpendicular to the magnet axis was placed in the Bragg reflecting orientation to provide a measure of the deviation from the ideal grain orientation. No useful intensities are obtained unless the samples are metallographically polished to remove the surface layer disturbed by grinding (it is known that the 2-14-1 phase can undergo plastic deformation[8]). The intensities of the six prominent reflections were normalized to calculated intensities for a random orientation of the crystallites following the procedure for obtaining inverse pole figures.[6,7]

IV. ORIENTATION AND REMANENCE

If the magnet were a single crystal, or had an ideal grain orientation with the easy axis normal to the surface, the diffraction pattern would show only reflections $(00l)$ with even values of l, namely (004) and (006) in the range investigated (Bragg $2\theta\leqslant 50°$). Because of the imperfect orientation, additional reflections having low (h,k) and high l are observed and permit the assessment of the preferred orientation. In a cylindrical magnet the crystal orientation represents a fiber texture with the magnet axis as the fiber axis. For a given (hkl) the corresponding tetragonal c axis (001) lies on a cone with half-angle θ, where θ is now the colatitude in spherical polar coordinates. Therefore the observation of reflections having high l that are aligned with the magnet axis contain information on the distribution of the (001) poles. This is necessarily so because in the tetragonal system there exists one and only one off-axis (001) pole for every pole (hkl) that is in line with the magnet axis.

The distribution of (001) poles can be modeled to describe the impact of misorientation on the remanence. In the range $0\leqslant\theta\leqslant\pi/2$, let this distribution be $f(\theta)$. Then the number of poles in a ring of width $d\theta$ on the surface of a unit sphere is $2\pi f(\theta)\sin\theta d\theta$. The contribution of these poles to the magnetization in the direction of the magnet axis is obtained by multiplying with $\cos\theta$. It follows directly that the ratio of remanence to saturation polarization for an assumed square hysteresis loop must be

$$\frac{\int_0^{\pi/2} f(\theta)\sin\theta\cos\theta d\theta}{\int_0^{\pi/2} f(\theta)\sin\theta d\theta},$$

where the denominator serves to normalize the expression to a constant total number of poles in the hemisphere. A useful distribution function is $\cos^m\theta$ because for it the integrals have simple solutions so that the ratio J_r/J_s takes on the form $(m+1)/(m+2)$. It is immediately obvious that for $m=0$, $J_r/J_s=1/2$ (familiar result for random orientation) and for $m\to\infty$, $J_r/J_s=1$ (delta function, perfect orientation). Table I gives some examples of J_r/J_s for various orientation distributions $f(\theta)$ characterized by the cone angle at half maximum $(f=1/2)$. It shows the improvement in remanence that can be expected from sharpening the orientation. For example, when the cone angle is decreased from 18° to 9.5°, J_r/J_s increases by 4.6%. A corresponding set of plots of $f(\theta)=\cos^m\theta$ is shown in Fig. 1; the significance of the data points is discussed in the next section.

TABLE II Observed reflections with low (h,k) and high l showing (i) calculated intensities for a random orientation, normalized to $I/I_0=100$ for the strongest reflection (140), (ii) angles between (hkl) and (001) poles, and (iii) experimental intensities treated as inverse pole figure data

	Intensity	Cone angle	Intensities normalized to random orientation			
hkl	(random)	$°\theta$	A	B	C	D
004	9	0	1 00	1.00	1.00	1.00
124	89	37.8	0.11	0.04	0.17	0 10
015	50	15 5	0 75	0.49	0 87	0.71
115	25	21 4	0 31	0.20	0.46	0.34
006	25	0	1 00	1 00	1 00	1.00
116	8	18 1	0.41	0 19	0.85	0 59

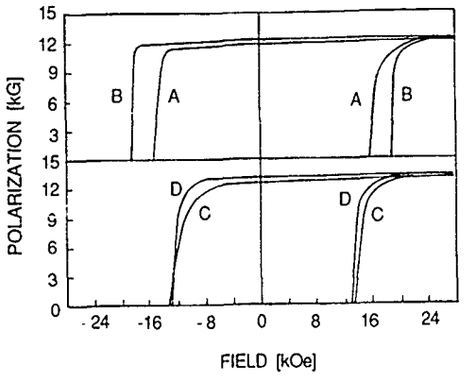

FIG. 2 Hysteresis loops of undoped (A and C) and oxygen-doped (B and D) sintered magnets.

V. EXPERIMENTAL RESULTS

The intensities as processed for an inverse pole figure are proportional to the volume fraction of grains with (hkl) poles in the direction of the magnet axis and, conversely, to the volume fraction of (001) poles in a direction tilted away from the axis by θ. Therefore they can be plotted directly over the distributions of Fig. 1. Table II shows the angle θ by which the easy axis [001] is tilted against the magnet axis for a given (hkl). It is derived from $tg^2\theta=(c/a)^2(h^2+k^2)/l^2$, and obviously the higher the (h,k) and the lower the l, the larger θ will be. Table II also contains information on the four test specimens A, B, C, D: calculated intensities for a powder pattern[9] with a random orientation of the crystallites and inverse pole figure intensities normalized by setting a weighted average intensity of (004) and (006) equal to 1. The reduction in the non-$(00l)$ reflections by going from A to B and from C to D is evident. It is also seen that the particle alignment in the Co-, Dy-containing magnets A and B is superior to that in the simpler ternaries. The reduced intensities in Table II represent a distribution for which the data points are plotted in Fig. 1. It is obvious from Fig. 1 that the experimental data show considerable scatter and do not follow the $\cos^m\theta$ distribution closely (nor do they fit a Gaussian distribution function) but tend to have steeper flanks. Nevertheless, the trend is clear: untreated specimens A and C have a broader orientation distribution than the corresponding oxygen-treated specimens B and D. Fitting the data to the curves allows a rough estimate of the expected improvement in remanence A→B and C→D, namely, 3.6% and 3.9%, respectively. The corresponding experimental increments are 4.2% and 4.7%. Supporting magnetization curves are shown in Fig. 2. The improvement in loop squareness in the oxygen-doped magnets B and D is evident.

VI. COERCIVITY

The coercivity is also affected by the oxygen treatment that causes the sharpening of the orientation. In the Co-, Dy-containing specimens A and B, one sees a concomitant increase in ${}_iH_c$ that is intuitively plausible from the orientation effect in the Stoner–Wohlfarth theory for a single-domain particle. The detailed model of Schrefl *et al.*[10] describing the reduction of the nucleation field for reversed domains at the grain boundaries of $Nd_2Fe_{14}B$ also predicts this orientation effect for coercivity. The crossing of the magnetization curves C and D in Fig. 2 is contrary to this behavior so that the curve with the higher remanence and the better alignment now has the lower intrinsic coercivity. Unlike the pair A and B, magnets C and D apparently have an orientation dependence of the critical field for magnetization reversal that does not decrease with the loss of alignment. It has to be conceded that the influence of oxygen on coercivity may well be a more complex one and simply results from changes in the "grain boundary phase," which is known to be fcc rather than hexagonal in many magnets, an effect that has long been attributed to the oxygen impurity, see e.g., Yang *et al.*[11]

VII. CONCLUSIONS

It has been shown that by using a simple powder diffractometer technique, information on grain alignment in sintered magnets can be obtained without resorting to a full pole figure determination. The trend of permanent magnet properties found in the Co-, Dy-containing magnets is already present in Stoner–Wohlfarth theory for single-domain particles. For it the remanence goes with $J_s\cos\theta$, and both remanence and coercivity decrease together when the orientation deviates from $\theta=0$. Therefore it is plausible that the remanence enhancement resulting from the oxygen treatment is an orientation effect, and the x-ray diffraction data support this interpretation. To what should the observed ability of the oxygen-treated magnets to show improved orientation be attributed? This can only be speculated, but it appears to be based on the ability of the powder particles to better maintain their magnetic orientation in the pressing operation. This might be loosely described as a reduction in friction between the particles that results from the oxygen treatment of the powder. It is remarkable that the ability of the powders to retain their orientation during pressing is so sensitive to alloy chemistry, as seen not only in the effect of oxygen doping but also in the difference between the alloys containing Co and Dy and the simpler ternary alloys.

[1] W C. Chang, T B. Wu, and K S Liu, J Appl Phys. **63**, 3531 (1988)
[2] S Z Zhou, Y. X Zhou, and C D. Graham, Jr., J Appl. Phys. **63**, 3534 (1988).
[3] G. P Meisner and E. G. Brewer, J. Appl Phys **72**, 2659 (1992).
[4] P Tenaud, A Chamberbord, and F Vanoni, Solid State Commun. **63**, 303 (1987)
[5] T Kawai, B. M. Ma, S G Sankar, and W E Wallace, J Appl Phys. **67**, 4610 (1990)
[6] L. K. Jetter, C J McHargue, and R O. Williams, J Appl. Phys **27**, 368 (1956).
[7] B. D. Cullity, *Elements of X-ray Diffraction* (Addison–Wesley, Reading, MA, 1978), p 319
[8] H H. Stadelmaier and N C Liu, Mater Lett. **4**, 304 (1986)
[9] W. Wong-Ng, H. McMurdie, B Paretzkin, C Hubbard, and A Dragoo, JCPDS Card No 39-473, Int Center for Diffraction Data, Swarthmore, PA, 1989
[10] T Schrefl, H F Schmidts, J Fidler, and H Kronmuller, J Appl Phys **73**, 6510 (1973)
[11] J -P Yang, S H. Pi, Y P. Kim, and Y G Kim, J Magn Magn. Mater **110**, L261 (1992)

Comparison of magnetic methods for the determination of texture of permanent magnets

G. Asti and R. Cabassi
Dipartimento di Fisica, Universita'di Parma, Italy

F. Bolzoni
Istituto MASPEC del CNR, Parma, Italy

S. Wirth, D. Eckert, P. A. P. Wendhausen, and K.-H. Müller
Institut fur Festkörper- und Werkstofforschung Dresden, P.O. Box, 01171 Dresden, Germany

The singular point detection (SPD) technique as well as a least-mean-square procedure of fitting trial texture functions to demagnetization curves (DMC) were applied in order to determine the orientation density of the tetragonal axes of the $Nd_2Fe_{14}B$ crystallites in sintered Nd-Fe-B magnets with different degrees of grain alignment. Both methods are less complicated than calculating the texture function from x-ray-diffraction data. The orientation densities obtained by both methods agree fairly. Analytically, they can be described as a Gaussian or a sum of cosine-power functions of the angle between the local tetragonal axis and the texture axis. This agreement is a test for the DMC method which can also be used for materials showing much larger anisotropy fields than the maximum available measuring field. The SPD and DMC methods can also be applied to measure the temperature dependence of the anisotropy field H_A of the magnetic main phase in noncompletely textured polycrystalline materials. By means of the DMC method additionally the spontaneous polarization J_s as well as the anisotropy constants K_1 and K_2 can be determined. As expected, the values of H_A of our sintered Nd-Fe-B samples, measured up to 140 °C, are nearly independent of the degree of texture and are in agreement with those reported in literature. This confirms that SPD as well as DMC can be used to measure intrinsic magnetic properties for materials which can hardly be prepared as single crystals, such as interstitial compounds made by gas–solid reactions.

I. INTRODUCTION

In typical modern permanent magnet materials such as sintered Nd-Fe-B the magnetic main phase is crystallographically uniaxial and the crystal c axis is a magnetically easy one. The orientation density of the easy axis is rotationally symmetric in a good approximation and can be described by a texture function $f(\alpha)$, normalized by

$$\int_0^{\pi/2} d\alpha \sin\alpha\, f(\alpha) = 1, \tag{1}$$

where α is the angle between the local easy axis and the texture axis.[1] The classical procedure to calculate $f(\alpha)$ from an adequate set of x-ray-diffraction data[2] is expensive. Alternative methods, based on magnetic measurements, have been reported.[1,3,4] The angular dependence of remanence induction B_r can be used, as described in Ref. 1, if B_r is controlled by rotational demagnetization processes only. Unfortunately, the remanence of nucleation controlled materials such as sintered Nd-Fe-B or Zn-bonded $Sm_2Fe_{17}N_3$ is affected by the presence of domains in the grains of the sample surface. This difficulty is avoided by the singular point detection (SPD) technique[5] which was applied to texture analysis in Ref. 3. In fact, by this method one detects a sharp peak in the second derivative d^2J/dH^2 of the polarization J versus the applied magnetic field H, exactly located at the anisotropy field H_A. The amplitude of the peak is proportional to the volume fraction of crystallites oriented with their easy axes perpendicular to H. In Ref. 4 the width σ_g of a Gaussian density,

$$f(\alpha) \sim \exp(-\alpha^2/2\sigma_g^2), \quad 0 \leq \sigma_g < \infty \tag{2}$$

was fitted to major demagnetization curves in the first quadrant of the J-H plane, where H is the applied field corrected for demagnetization effects. Additionally, this fitting procedure yields the anisotropy constants K_1, K_2 and the spontaneous polarization J_s (if the volume fraction of the main phase is known) and works even for measuring fields H considerably smaller than $H_A = (2K_1 + 4K_2)/J_s$. It was successfully applied to bonded $Sm_2Fe_{17}N_x$[4,6] and sintered Nd-Fe-B.[7]

Fitting parameters such as σ_g from Eq. (2) are texture parameters summarizing the information included in $f(\alpha)$.

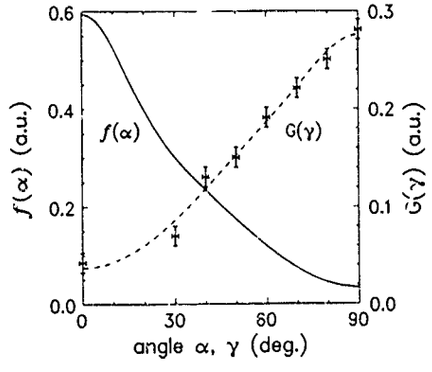

FIG. 1. SPD peak amplitude $G(\gamma)$ of the sintered $Nd_{16}Fe_{78}B_6$ sample A2 and its fitted texture function $f(\alpha) = 0.034 + 0.34\cos^2\alpha + 0.22\cos^{20}\alpha$

 0021-8979/94/76(10)/6268/3/$6.00 © 1994 American Institute of Physics

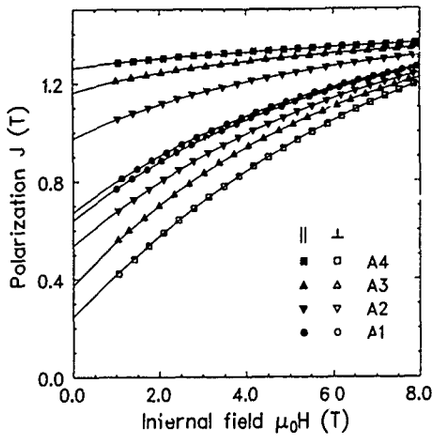

FIG. 2. Demagnetization curves of the sintered $Nd_{16}Fe_{78}B_6$ samples A1–A4 with different degrees of texture, measured at $T=20$ °C, parallel (∥) and perpendicular (⊥) to the texture axis. The solid lines are fitted demagnetization curves based on the trial texture function from Eq. (2)

The definition of a texture parameter may also be independent of the special type of $f(\alpha)$, as in the case of the standard deviation σ, which is given by

$$\sigma^2 \equiv \overline{\alpha^2} = \int_0^{\pi/2} d\alpha \sin\alpha\, f(\alpha)\alpha^2. \tag{3}$$

II. EXPERIMENTAL AND THEORETICAL METHODS

Sintered $Nd_{16}Fe_{78}B_6$ magnets were prepared in the usual powder metallurgical way.[7] To obtain four samples A1–A4 with different degrees of texture, various values of the magnetic field were used during the compacting process. Magnetic properties from room temperature up to 140 °C were measured by a vibrating-sample magnetometer with applied fields up to 8 T.

The SPD measurements were performed as described in Ref. 3. A computer program has been developed for the automatic measurement of the amplitude of the SPD peak. The adopted criterion is to measure the difference in the slope of d^2J/dH^2 at the two inflection points located at both sides of the peak. The applied field H forms an angle γ with the texture axis z and is in the x-z plane. The SPD peak amplitude $G(\gamma)$ is proportional to the volume fraction of crystallites having their c axes in a plane perpendicular to H. If ϕ denotes the azimuth of the c axis with respect to x-z plane, we have $\cos\alpha = \cos\phi \sin\gamma$ and

$$G(\gamma) = 2/\pi \int_0^{\pi/2} d\phi\, F(\cos\phi \sin\gamma), \tag{4}$$

where $F(\cos\alpha) = f(\alpha)$ is the texture function from Eq. (1).

The integral equation (4) was numerically solved by fitting the power series

$$F(\cos\alpha) = \sum_i b_i \cos^{2n_i}\alpha \tag{5}$$

to measured values of $G(\gamma)$, where a small number of terms turns out to be sufficient.

Trial demagnetization curves were computed taking into consideration only coherent rotational processes based on anisotropy constants up to K_2, neglecting the internal magnetic

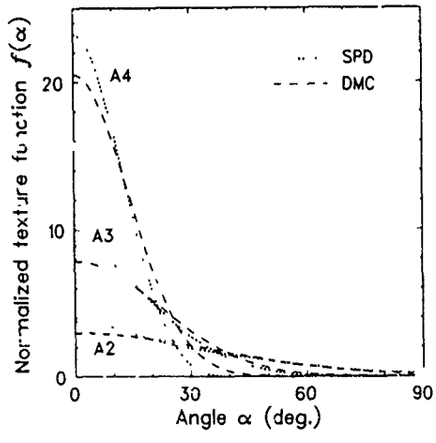

FIG 3 Texture functions for samples A2, A3, and A4 SPD $f(\alpha) = b_0 + b_1 \cos^{n_1}\alpha + b_2 \cos^{n_2}\alpha$ fitted to SPD data DMC $f(\alpha) \sim \exp(-\alpha^2/2\sigma_g^2)$ fitted to the curves of Fig 2

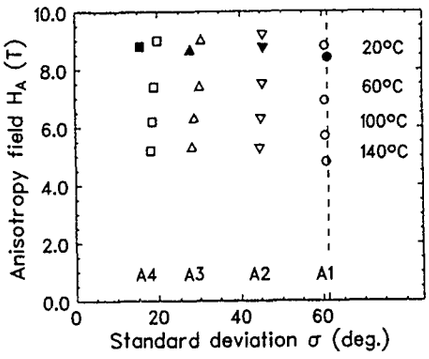

FIG 4 Anisotropy field H_A and texture parameter σ from Eq. (3). Open symbols: values from a fit to the demagnetization curves of the samples A1–A4 for different temperatures; closed symbols: the corresponding room-temperature values obtained from SPD data

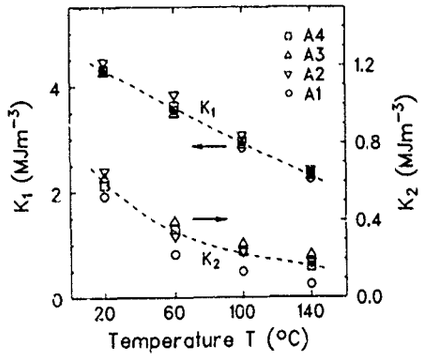

FIG 5 Temperature dependence of the anisotropy constants K_1 and K_2 of samples A1–A4, calculated from fitted demagnetization curves

stray fields, using the trial texture function of Eq. (2). Then the calculated J vs H curves, depending on trial values of σ_g, J_s, K_1, and K_2, were fitted by a least-mean-square fit to the experimental curves, measured above $\mu_0 H = 1.5$ T in order to avoid domain-wall processes. Three criteria were used to test the applicability of the trial function: (i) the remaining variance of the numerical fit should be sufficiently small, (ii) the texture parameter must not depend on temperature, and (iii) the fitted values of K_1, K_2, J_s must not depend on the degree of easy-axis alignment. Finally, the fitted texture function as well as the obtained anisotropy field H_A were compared with those determined by the SPD method.

TABLE I. Texture parameter σ [from Eq. (3)] fitted to SPD and DMC measurements In the case of SPD data Eq (4) was approximately solved using the series expansion (5) as well as the Gaussian (2).

Sample	SPD $\Sigma b_i \cos^{2n_i} \alpha$ (deg)	SPD Gaussian (deg)	DMC Gaussian (deg)
Ideally isotropic		61 2	
A1	≈61	≈61	60.7
A2	45 8	47 5	45 4
A3	27.8	28 6	29 2
A4	15 7	15.8	18.6
Ideally textured		0.0	

III. RESULTS AND DISCUSSION

In Fig. 1 the angular dependence of the measured peak amplitude $G(\gamma)$ of the little textured sample A2 and the corresponding fitted texture function $f(\alpha)$ are shown as a typical example for the SPD analysis.

The Gaussian texture function (2) yields a very good fit for the demagnetization curves (DMCs) of our samples A1–A4, measured perpendicularly and parallel to the texture axis (see Fig. 2). A typical value of the residual variance of the numerical calculation is 10^{-7} T^2.

The texture functions obtained from demagnetization curves are fairly similar to those calculated from SPD data, as shown in Fig. 3. This is an encouraging result because very different experimental procedures are used. Due to the normalization factor $\sin \alpha$ in Eqs. (1) and (3), the deviations of $f(\alpha)$ at $\alpha \approx 0$ in Fig. 3 have only a small weight for physical quantities.

As a consequence of this result, the values of standard deviation σ summarized in Table I do not much depend on the type of the applied measuring procedure.

Figure 4 presents the temperature dependence of the anisotropy field H_A and the standard deviation σ, both obtained from demagnetization curves, as well as the corresponding room-temperature values calculated from SPD data. For all the samples, σ shows a small temperature dependence as expected for a correct texture parameter. The small difference in the values of H_A obtained from SPD and DMC measurements, respectively, may be due to the magnetostatic interaction between the $Nd_2Fe_{14}B$ particles, which was neglected in this study. The effect of this interaction on SPD measurements was considered in Ref. 8. In the case of DMC analysis the influence of internal magnetostatic fields has not yet been systematically investigated.

The DMC results of the anisotropy constants K_1 and K_2 determined from differently textured samples yield sufficiently small variations for all investigated temperatures (Fig. 5). The temperature dependence of K_1 and K_2 is in good agreement with the data from Ref. 9. The room-temperature value of H_A is comparable to that presented in Ref. 10 for a single crystal, but $K_2 = 0$ at $T = 293$ K was obtained there.

In summary, DMC as well as SPD analysis yield fairly correct data on texture and intrinsic magnetic properties because both techniques are based on reversible rotation of the local magnetic polarization. Contrary to other elementary magnetization processes, reversible rotation is not very sensitive to chemical and topological details in the nanometer range of microstructure.

[1] S. Shtrikman and D Treves, J Appl. Phys. **31**, 58S (1960).
[2] D. Givord, A. Lienard, R Perrier de la Bathie, P. Tenaud, and T. Viadieu, J Phys Paris Colloq **46**, C6-313 (1985).
[3] G. Asti, F Bolzoni, and L. Pareti, J. Magn Magn. Mater. **83**, 270 (1990).
[4] M. Katter, J Wecker, C. Kuhrt, L. Schultz, and R. Grossinger, J Magn. Magn Mater **117**, 419 (1992).
[5] G Asti and S. Rinaldi, J Appl Phys **45**, 3600 (1974)
[6] K.-H. Muller, D. Eckert, P. A P Wendhausen, A. Handstein, S. Wirth, and M. Wolf, IEEE Trans Magn. **MAG-30**, 586 (1994)
[7] D Eckert, A. Handstein, K -H Muller, R Grossinger, and M Katter, Proceedings of the 12th International Workshop on RE Magnets and their Applications, Canberra, 1992, p 180
[8] G Asti, F Bolzoni, and R Cabassi, J. Appl. Phys **73**, 323 (1993).
[9] K -D. Durst and H. Kronmuller, J Magn Magn Mater. **59**, 86 (1986)
[10] F Bolzoni, O Moze, and L Pareti, J. Appl Phys. **62**, 615 (1987).

Magnetic-field orientation and coercivity

Brandon Edwards
Mathematics Department, Portland State University, Portland, Oregon 97207

D. I. Paul
Materials Science and Engineering Department, Massachusetts Institute of Technology, Cambridge, Massachusetts 02139

The relationship between the coercive force and the angle of the applied field of an infinite magnetic medium containing a planar defect have been analyzed. A domain-wall pinning dominated coercivity was assumed and the spatial dependence of the magnetization in the direction normal to the plane of the defect was taken into account. The results show that the coercivity must be about two orders of magnitude smaller than the anisotropy field for the inverse cosine curve to be a good approximation. Some of the results with experimental work on $Fe_{77}Nd_{15}B_s$ are compared. In addition, the existence of a decrease in the domain-wall pinning coercivity as a function of the angle between the applied magnetic field and the anisotropy for certain ranges of parameters—a behavior previously thought to have only occurred in the angular dependence of a nucleation dominated coercivity—is shown.

A central issue in the study of permanent magnets such as NdFeB and SmCo has been the understanding of the magnetic reversal mechanism at the coercive field H_c.[1,2]

An important aspect of this problem is the angular dependence of the coercive field. The angular dependence in sintered RFeB magnets has been measured by the group at CNRS in Grenoble.[3] They find that for $H_c=10$ kOe at room temperature the increase of H_c with θ_H, the angle of the applied field with respect to the easy direction of magnetization, corresponds approximately to a $1/\cos(\theta_H)$ relationship, a theoretical derivation of which had been carried out in a previous paper.[4] For $H_c \sim 17$ kOe, there is a reduced increase in H_c with θ_H. Finally, a decrease in H_c as θ_H increases occurs at small θ_H values in PrFeB magnets. The authors of Ref. 3 state that they are unable to understand the last result on the basis of either coherent rotation or domain-wall propagation.

Results by both Sakuma *et al.*[5] and Kronmuller *et al.*[6] indicate that there exists ranges of magnetic parameter values wherein coercivity limited by the nucleation of domain walls shows deviations from the $1/\cos(\theta_H)$ or inverse cosine angular dependence, but it is generally accepted that coercivity limited by domain-wall pinning follows the inverse cosine relation, thus yielding insight into the mechanism of magnetic reversal through analyzing the angular dependence of the coercivity of different materials. We shall show that this is not so, that there also exist strong deviations from the inverse cosine relation when domain-wall pinning is the mechanism limiting magnetization reversal.

In 1990, Sakuma *et al.*[15] presented theoretical derivations of the coercivity as a function of the angle of the applied field for the case of a domain-wall nucleation dominated coercivity in a material containing a defect. Their methods, first introduced by Friedberg and Paul,[7] took into account the spatial dependence of the magnetization.

In this paper, we derive the angular dependence of the coercive force for domain-wall pinning. We also take into account the spatial dependence of the magnetization.

Let us consider an array of magnetic dipoles representing the host magnetic material containing a defect lying within the region $x=-D/2$ to $x=D/2$. The host matrix has uniform magnetization M_1, first-order anisotropy constant K_1, and first-order exchange energy constant A_1. The impediment has entirely independent magnetic properties K_2, M_2, and A_2. The easy axis of magnetization is in the direction of the z axis and an external magnetic field H is being applied at an angle θ_H as measured from the z axis in the y-z plane. The orientation of a given dipole in the array is taken as the angle θ measured from the z axis in the y-z plane. We assume a one dimensional spatial dependence for the angle θ. The orientations of the end dipoles are fixed with $\theta=0°$ at $x=-\infty$ and $\theta=180°$ at $x=\infty$, signifying the presence of a Bloch wall along the array. We wish to find the value, H_c, of the external magnetic field for which the wall can no longer be held by the impediment and thus magnetic reversal of the entire medium occurs. This model has already been discussed for the case in which the external magnetic field is applied in the same direction as the easy axis of magnetization ($\theta_H=0°$).[7,8]

The total energy for the ith region ($i=1,2,3$) is given by

$$E_i=\int_{x_1}^{x_2}\left[K_i \sin^2(\theta)-HM_i \cos(\theta-\theta_H)+A_i\left(\frac{d\theta}{dx}\right)^2\right]dx. \tag{1}$$

Minimizing the energy in the three regions using the boundary conditions that $\theta=0°$ and $180°$ at $x=-\infty$ and ∞, respectively, and that $A_i(d\theta/dx)$ is continuous at $x=-D/2$ and $D/2$, we get Eq. (2) where η is given by Eq. (3):

$$W=\int_{\cos(\theta_2)}^{\cos(\theta_1)}(\sin\theta)^{-1}[\sin^2(\theta)-hFE^{-1}\cos(\theta-\theta_H)+\eta]^{-1/2}d\cos(\theta), \tag{2}$$

$$\eta=(E^{-1}-1)\sin^2(\theta_1)-hE^{-1}(1-F)\cos(\theta_1-\theta_H)+hE^{-1}\cos(\theta_H). \tag{3}$$

 0021-8979/94/76(10)/6271/3/$6.00 © 1994 American Institute of Physics

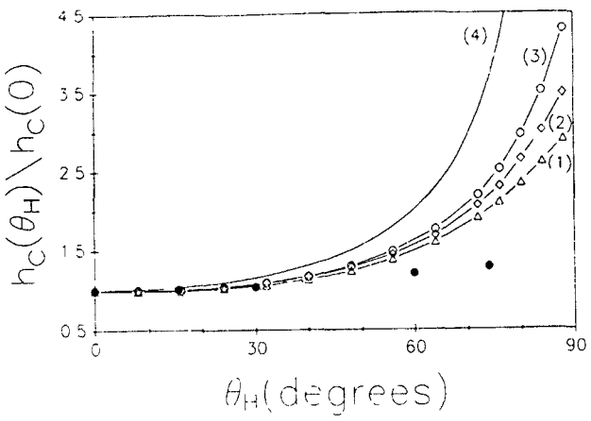

FIG 1. Ratio of the normalized coercive forces $h_c(\theta_H)/h_c(0)$ as a function of the angle of the external field with respect to the anisotropy axes θ_H, for a constant normalized defect width $W=2$ and constant ratio $F=0.8$ Curve (1) is for $E=0.4$, curve (2) is for $E=0.5$, and curve (3) is for $E=0.6$ Curve (4) shows the $1/\cos(\theta_H)$ angular dependence generally accepted to be characteristic of a domain-wall pinning dominated coercivity The solid circles are measurements on the angular dependence of $Fe_{77}Nd_{15}B_8$ (see Ref. 6)

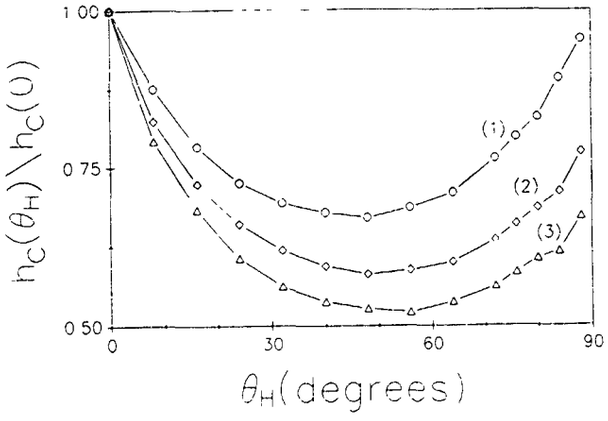

FIG 2 Same as Fig 1 with the normalized defect width $W=2$. Curve (1) is for $E=F=0.1$, curve (2) is for $E=F=0.05$, and curve (3) is for $E=F=0.025$.

The relationship between the quantities θ_1 and θ_2 (the orientation of the dipoles at $x=-$ and $D/2$, respectively), are given by

$$(1-E^{-1})\sin^2(\theta_2)+hE^{-1}(1-F)\cos(\theta_2-\theta_H)+hE^{-1}\cos(\theta_H)+\eta=0, \quad (4)$$

along with the condition $\cos(\theta_1)>\cos(\theta_2)$.

Here we have also introduced the dimensionless parameters E, F, h, and W:

$$E=\frac{A_2K_2}{A_1K_1}, \quad F=\frac{A_2M_2}{A_1M_1}, \quad h=\frac{HM_1}{K_1}, \quad W=\frac{D}{\delta},$$

used in Ref. 8, where D is the actual width of the defect and $\delta=(A_2/K_2)^{1/2}$ is the domain-wall half-width within the defect region.

Given a value for the normalized external field h and θ_H, there is a set of θ_1's for which a θ_2 in $(\theta_1,180°)$ satisfying Eq. (4) will exist and $W(\theta_1,\theta_2)<\infty$, where $W(\theta_1,\theta_2)$ is determined by Eq. (2). This gives rise to a set $\{W_{\theta 1}\}$ of normalized defect widths. These are values of W for which there exists a static domain-wall solution that satisfies the given boundary condition. In particular, $\theta(-\infty)=0°$ and $\theta(\infty)=180°$ are satisfied and thus a domain wall is still present. Thus, for all widths W in $\{W_{\theta 1}\}$, the field h is insufficient to drive the wall over the defect.

The minimum W_c of the set $\{W_{\theta 1}\}$ corresponds to the critical width at which h is sufficient to drive the wall over the defect region and magnetic reversal begins. As one would suspect, it was found that W_c increases as a function of h. Thus any field smaller than h would be insufficient to drive the wall across a defect of width $W_c(h)$ as contrasted to a field greater than h. Therefore $h_c=h$ is the coercive force corresponding to the given defect width $W_c(h)$.

Figure 1 shows the ratio of the normalized coercive forces $h_c(\theta_H)$ and $h_c(0)$ versus the angle of deviation θ_H of the external field with respect to the anisotropy axes. The normalized defect width W and ratio F are held constant at values 2 and 0.8, respectively. The ratio E ranges from 0.4 to 0.6, corresponding to a large change in the magnetic parameters A_t and/or K_t across the boundaries $x=-D/2$ and $x=D/2$. We have included for comparison the normalized angular dependence $h_c(\theta_H)/h_c(0)=1/\cos(\theta_H)$, generally accepted as the angular dependence curve characteristic of a domain-wall pinning dominated coercivity. We notice that our curves deviate significantly from the inverse cosine curve for this range of E and value of F and W with the deviation decreasing as E approaches unity. Also included in this figure are measurements of the normalized angular dependence of the coercive force for $Fe_{77}Nd_{15}B_8$ done by Kronmuller *et al.*[6]

In Fig. 2, the ratios E and F take on very small values ranging from 0.025 to 0.1 and the normalized defect width W is again held constant at the value of 2. This range for E and F corresponds to differences within the material parameters A_t, K_t, and M_t between the host matrix and the defect region of up to two orders of magnitude. For these small values of E and F, we see a very pronounced decrease in $h_c(\theta_H)/h_c(0)$ as θ_H increases from zero. Physically, the external field required to drive the domain wall across the defect is decreased when applied in directions deviating from the anisotropy axes, with the minimum required field occurring at $\theta_H\approx 50°$. Note that for $E=F=0.025$, applying the external magnetic field at 55° with respect to the anisotropy axes will reduce the coercive force by approximately one half that required to demagnetize the material with a field parallel to the anisotropy axes.

The last figure, Fig. 3, plots h_c vs W rather than $h_c(\theta_H)/h_c(0)$ vs θ_H. We do this for the values of θ_H ranging from 5° to 80°. The ratios E and F are held constant at 0.5 and 0.75, respectively. Notice that for a given value of θ_H, when W is greater than approximately 1.5, there are essentially no further changes in h_c.

In Fig. 1 as well as in subsequent work we see that as E and F approach 1, the angular dependence approaches the inverse cosine relation. Physically, the parameters E and F

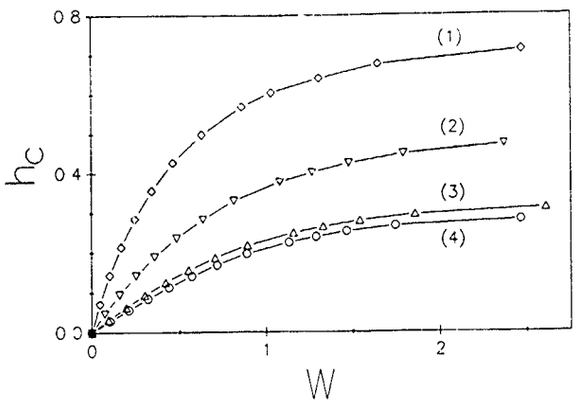

FIG. 3 Normalized coercive force h_c as a function of the normalized defect width W for the values $E=0.5$ and $F=0.75$. Curve (1) is for $\theta_H=80°$, curve (2) is for $\theta_H=65°$, curve (3) is for $\theta_H=35°$, and curve (4) is for $\theta_H=5°$.

approach 1 when the changes in the magnetic parameters A_t, M_t, and K_t between the host material and defect become negligible. This is the basic criterion for the $1/\cos(\theta_H)$ angular dependence to take over. In the analysis of the normalized coercive force for $\theta_H=0°$ done by Friedberg and Paul,[7] it was shown that as E and F converge to 1, $H_c(0)/H_A$ goes to zero. Therefore the criterion mentioned above is similar to the arguments made in previous works for the occurrence of a $1/\cos(\theta_H)$ curve for values $H_c \ll H_A$.[4,6,9]

We find that a change in A_t between the host and defect material, causing a decrease in both E and F, produces the greatest deviation from the inverse cosine curve while a change in K_t, causing a decrease in E alone, produces a slightly smaller deviation, and finally, the smallest deviation is produced by a change in M_t between the host and defect material, causing a decrease in F alone. Therefore the exchange energy seems to be the most influential in determining the appearance of the inverse cosine angular dependence.

As seen in Fig. 3, at any given θ_H, $h_c(\theta_H)$ as a function of W becomes essentially constant for $W>1.5$. This asymptotic behavior in $h_c(\theta_H)$ as a function of W was shown for $\theta_H=0°$ by Paul.[8] We see now that it is exhibited at values of θ_H other than 0° and from this conclude that the behavior of an angular dependence curve, $h_c(\theta_H)/h_c(0)$, is only a function of W for W less than approximately 1.5.

Figure 2 shows a "dip" in the normalized coercive force as θ_H increases. Indeed, not only is the increase with θ_H shown in our model not as great as that predicted by the inverse cosine curve, but for small E and F (<0.5 if $W\sim2$), h_c actually decreases as θ_H increases from 0°. Physically, this means that for these values of the parameters E, F, and W it is easier in general to demagnetize the material by applying the external field in directions other than along the anisotropy axes. The maximum decrease in h_c for small E and F occurs at $\theta_H\sim50°$.

We have found that little or no dip is seen in the angular dependence when either E or F has value close to unity. It appears that both E and F must be small together in order for a significant dip to be present. This suggests that the exchange energy, present in both of the parameters E and F, takes on a dominant role in the cause of this dip.

It has been shown by Friedberg and Paul[7] that as W approaches zero, the value of $H_c(0)/H_A$ approaches zero. Therefore we would expect that for small values of W, the angular dependence curve will be close to $1/\cos(\theta_H)$. However, the "critical width" above which the angular dependence significantly deviates from $1/\cos(\theta_H)$ will depend on the values of A_2/A_1, H_2/H_1, and M_2/M_1. In particular, we have found that if A_2/A_1 decreases from 0.75 to 0.03 (a factor of 25), this critical width is reduced by one order of magnitude. Calculations along these lines suggest that it is necessary for H_c to be approximately two orders of magnitude smaller than H_A for $1/\cos(\theta_H)$ to be a good approximation for the angular dependence.

The normalized angular dependence of the coercivity measured as a function of the applied field angle for $Fe_{77}Nd_{15}B_8$[6] has been included in Fig. 2 for comparison with our theoretical curves. As will be noticed, the fit of this data to our curves leaves something to be desired, as was the case when this data was compared to other theoretical work.[5,6] There needs to be more experimental work.

The nucleation dominated angular dependence curves derived in Ref. 5 as well as the pinning dominated curves in this paper show a decrease in h_c as a function of θ_H for certain parameter values. Although for given values of E, F, and W, the model in Ref. 5 and our model may give entirely different looking curves; as a whole one cannot look at an angular dependence curve to determine the coercive force mechanism without explicit knowledge of the parameters E, F, and W. These qualitative similarities are seen to be true when comparing our curves to nucleation dominated angular dependence curves derived from other models as well.[6,9] This indicates that caution must be used if one is trying to determine whether a certain material's coercivity is pinning or nucleation dominated by comparing its angular dependence curve with theory.

[1] M Sugana, S. Fuyimoia, N. Tagaua, H Yamomoto, and Y Matsura, J. Appl Phys **55**, 2083 (1984)
[2] J. J Croat, J F Herbst, R W Lee, and F. E Pinkerton, J. Appl. Phys **55**, 2078 (1984).
[3] D. Elbaz, D. Givord, S. Hirosawa, F. P. Missell, M F Rossignol, and V Villas-Boas, J Appl Phys **69**, 5492 (1991).
[4] D. Givord, P. Tenaud, and T. Viadieu, J Magn Magn Mater **72**, 247 (1988).
[5] A. Sakuma, S. Tamigawa, and M Tokunaga, J Magn. Magn Mater **84**, 52 (1990).
[6] H Kronmuller, K D Durst, and G. Martinek, J Magn Magn Mater. **69**, 149 (1987)
[7] R. Friedberg and D I. Paul, Phys Rev. Lett **34**, 1234 (1975)
[8] D. I. Paul, J Appl. Phys. **53**, 1649 (1982)
[9] D Givord, Q Lu, M F Rossignol, P Tenaud, and T Viadieu, J. Magn. Magn. Mater. **83**, 183 (1990)

Magnetic structures and interactions in Ho/Y, Ho/Lu, and Ho/Er superlattices (invited)

R. A. Cowley, D. F. McMorrow,[a] A. Simpson, D. Jehan, P. Swaddling, R. C. C. Ward, and M. R. Wells
Oxford Physics, Clarendon Laboratory, University of Oxford, Parks Rd., Oxford 0X1 3PU, United Kingdom

Ho/Y and Ho/Er superlattices have been grown by molecular-beam epitaxy using a Balzers UMS 630 instrument. The superlattices were grown on a sapphire substrate with an Nb buffer and Y seed layer. X-ray-diffraction techniques were used to characterize the crystallographic structure and neutron-diffraction techniques to determine the magnetic structures. The results for the Ho/Y systems were consistent with long-range order being formed coherently through the whole superlattice. The moments in the Ho layers were aligned in the basal plane and most of the structures could be described by helical structures with a turn angle between holmium planes of Ψ_H and between nonmagnetic Y planes Ψ_Y. Ψ_Y is found to be largely independent of temperature or superlattice, while Ψ_H decreases with decreasing temperatures and at low temperatures takes a commensurate value, so as to take advantage of the basal plane anisotropy. The results for the Ho/Er superlattices differ because the Er has a magnetic moment and the anisotropy favors alignment along the c axis. Between the ordering temperature of bulk Ho and bulk Er, the results are similar to those of the Ho/Y superlattices. The ordering propagates through the Er layers but the Er moments are not ordered. At lower temperatures the Er moments order in a cycloidal (a/c) structure with the basal plane components having fairly long-range coherence with the Ho moments, but the c-axis components having no coherence from one Er layer to the next.

I. INTRODUCTION

Rare-earth superlattices show a number of novel and interesting properties as has been reviewed by Majkrzak *et al.*[1] We have extended this work particularly to the superlattices containing Ho, and have studied superlattices of Ho with the nonmagnetic elements Y[2] and Lu,[3] and also Ho and the magnetic element Er. Bulk Ho orders magnetically below 132 K into a helical magnetic phase in which the moments align ferromagnetically in each basal plane but rotate from one plane to the next by an angle Ψ_H which decreases on decreasing temperature from 52° at the T_N to an average of 30° below 18 K, when the moments also tip out of the basal plane to form a cone phase. One of the interesting aspects of Ho is the existence of a series of long period commensurate spin-slip structures,[4] due to the basal plane anisotropy. Our choice of Ho superlattices was therefore made to see if Ho/Y superlattices behaved similarly to the Dy/Y superlattices previously studied, to determine the effect of the basal plane anisotropy on the magnetic structures, and to determine the structures of the Ho/Er superlattices in which the Ho and Er have competing anisotropies.

The superlattices were grown by molecular-beam epitaxy in Oxford using a Balzers UMS 630 facility. The technique followed was developed by Kwo *et al.*[5] and has been described in detail.[2] The superlattices are grown on a sapphire substrate with a 500 Å Nb buffer layer and a 1000 Å Y seed layer before the superlattice and capped by a 300 Å Y layer to prevent oxidation of the magnetic material. The chemical and crystallographic quality of the superlattice is then determined using x-ray diffraction. Typically the superlattices have a mosaic spread of 0.16°, a chemical coherence length of about 2200 Å, and an interface width of about 5 atomic planes.

The magnetic structures were determined by neutron-scattering techniques using triple axis spectrometers at the DR3 reactor of the Risø National Laboratory. Typically, 5 meV incident neutrons were selected with a pyrolytic graphite monochrometer, and second-order contaminant neutrons were suppressed with a cooled Be filter. A pyrolytic graphite analyzer was used to ensure that only elastically scattered neutrons were detected. The collimation was typically from reactor to detector $60'-30'-30'-120'$ and gave a resolution in the scattering plane of 0.01 $Å^{-1}$. The samples, whose growth direction is always perpendicular to the c axis, were aligned with the (hol) plane in the scattering plane and mounted in a variable-temperature cryostat so that the temperature could be controlled to 0.1 K. The scattered intensity was determined as the wave-vector transfer was scanned along the $(00l)$ and $(10l)$ directions. The former provides information about the basal plane ordering of the magnetic moments, while the latter gives intensities dependent on both the basal plane and c-axis moments.

II. RESULTS FOR HO/Y SUPERLATTICES

The results for the Ho/Y superlattices have been published[2] and so the results will only be briefly summarized

[a]Permanent address. Physics Dept., Danish AEK, Risø, Roskilde, DK 4000 Denmark

 0021-8979/94/76(10)/6274/4/$6 00 © 1994 American Institute of Physics

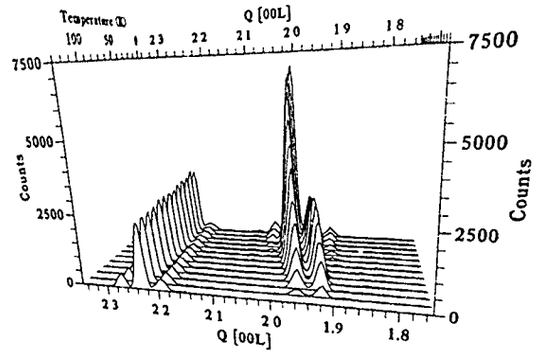

FIG 1. The neutron-scattering intensity (Ref. 2) observed from a $(Ho_{40}Y_{15})_{50}$ superlattice along $(00l)$ at a series of temperatures at intervals of 10 K from 130 to 10 K. The nuclear (002) scattering is temperature independent and the magnetic scattering grows with decreasing temperature. Note that even at 120 K, the magnetic scattering is two peaks showing long-range coherence.

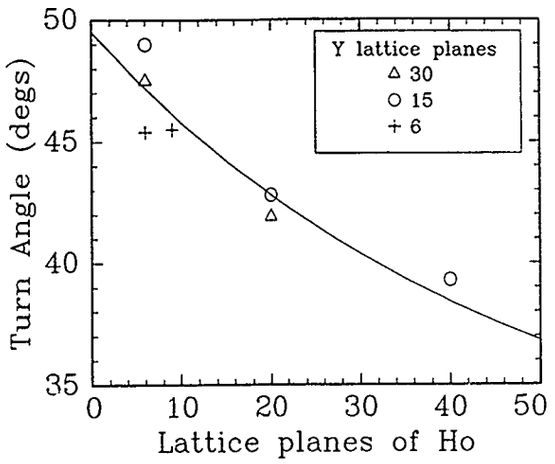

FIG. 3 The turn angle (Ref 2) Ψ_H for Ho in various superlattices showing that at least for thick superlattices, Ψ_H is largely independent of the Y thickness and that Ψ_H is close to a commensurate spin-slip value The solid line is a guide to the eye, and the errors are about the symbol size

here. The neutron scattering as a function of temperature from the $Ho_{40}Y_{15}$ superlattice is shown in Fig. 1 and shows the growth of the magnetic scattering with decreasing temperature. The magnetic scattering at every temperature shows several separate peaks showing that the ordering is always coherent through the nonmagnetic Y blocks. In this respect the result is similar to that found for the Dy/Y system.[1]

A more detailed description requires a model. We have used a model in which there is a turn angle between the magnetic moment direction on successive Ho planes Ψ_H, and one between successive Y planes Ψ_Y, and moments on both the Ho and Y planes. The fits showed that the data were consistent with no moment on the Y planes, and the same Ho block lengths and interface widths as the crystallographic fits to the x-ray data. Consequently, in the final fits, only Ψ_H, Ψ_Y, and the moment on the Ho planes were allowed to vary while the block lengths and interface thicknesses were taken from the x-ray results.

The model gave a good description of the results and the parameters for the $Ho_{40}Y_{15}$ sample are shown in Fig. 2. The Y turn angle Ψ_Y is independent of temperature and was indeed found to be the same and constant for all the Ho/Y superlattices. The Ho turn angle Ψ_H was found to decrease with decreasing temperature but less markedly than for a pure Ho film or bulk Ho. Presumably the decrease with decreasing temperature arises largely from the effect of the ordering on the turn angle[6] as in bulk Ho, while the difference between the behavior of bulk Ho and the Ho superlattices is due at least in part to the clamped lattice parameters and consequent strain of the Ho in the superlattice, as found in Dy/Y superlattices.[1]

The low-temperature Ho turn angles for several Ho/Y superlattices are shown in Fig. 3, and are largely independent of the Y block thickness and increase steadily with decreasing Ho block thickness. The samples with more than eight Ho planes, for which interdiffusion is not too severe, all have Ψ_H close to the turn angle for a commensurate spin-slip structure, 40°, 42 9°, 45°, and 48°. These spin-slip structures also show higher harmonics of the magnetic satellites, but interestingly these did not show the separate peaks of the main magnetic satellites, only a single broad peak, whose width was consistent with the scattering from an isolated Ho block. The conclusion is that, while the primary magnetic satellites show coherence in phase and chirality through the nonmagnetic Y blocks, the extra spin-slip features of the structures are not coherent from one magnetic block to the next.

Similar measurements[3] have been made for the Ho/Lu system. The basic results are very similar to those obtained for the Ho/Y system except for:

(1) The Lu turn angle Ψ_L is 40° and possibly varies more from system to system than that of Ψ_Y.
(2) The turn angles for Ψ_H are less than those of bulk Ho at the same temperature.

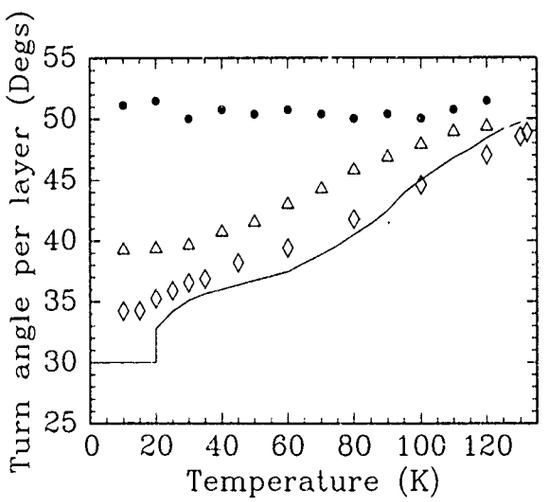

FIG 2. The temperature dependence (Ref. 2) of the turn angles Ψ_H (△), Ψ_Y (○) for the $Ho_{40}Y_{15}$ superlattice. Also shown is Ψ_H (◇) for an epitaxially grown Ho film and for bulk Ho (solid line) The errors of the fitting are shown by the point size

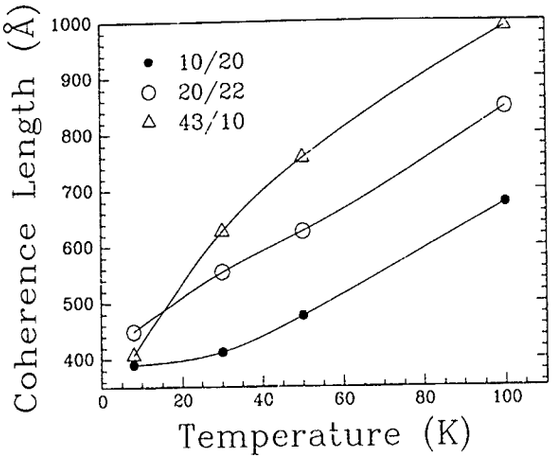

FIG. 4. The temperature dependence of the coherence length for the basal plane ordering of Ho/Er superlattices. The data were obtained from the scattering along (00l) and have been corrected for the resolution effects (Ref 10).

(3) A basal plane ferromagnetic phase with $\Psi_H=0$ was obtained at low temperatures below 30 K in samples such as $Ho_{20}Lu_{15}$, and successive Ho blocks then ordered parallel or antiparallel, dependent on the number of Ho layers. This structure does not occur in bulk Ho and probably results from the strain of the Ho in Ho/Lu superlattices as shown for Dy/Lu superlattices.[7]

III. RESULTS OF Ho/Er SUPERLATTICES

The Ho/Er superlattices are of interest because the crystal field anisotropy for Er favors alignment of the magnetic moments along the c axis. Bulk Er has a longitudinally modulated structure below $T_N=84$ K, which on cooling below 52 K becomes a cycloidal phase[8] with the moments largely confined to the a/c plane above 18 K and a cone phase below 18 K. Thus, between 84 and 20 K, the crystal fields in Er and Ho favor alignment in different directions.

We have studied several different Ho/Er superlattices. At high temperatures, above the ordering temperature of bulk Er, the results are qualitatively similar to those of the Ho/Y systems. There is a long-range coherent basal plane helical structure, and fits suggest that there is a negligible moment associated with the Er atoms and that the turn angle in the Er is 51±1°. The turn angle associated with the Ho is similar to that of bulk Ho. This result shows that the long-range basal plane order propagates through the Er layers even without simultaneously ordering the Er moments. The magnetic coherence length of the structure is many superlattice periods ~600 Å. Similar results[9] have been found in Dy/Er superlattices above 85 K.

On cooling below the erbium transition temperature the scattering changes. First, the width of the peaks along (00l) increased, showing that the correlation length associated with the basal plane structure decreases; see Fig. 4. Second, the scattering along (10l) consisted of sharp peaks, presumably associated with the basal plane structure and, in addition, a broad peak, as shown for the Ho_{20}/Er_{22} sample at 8 K

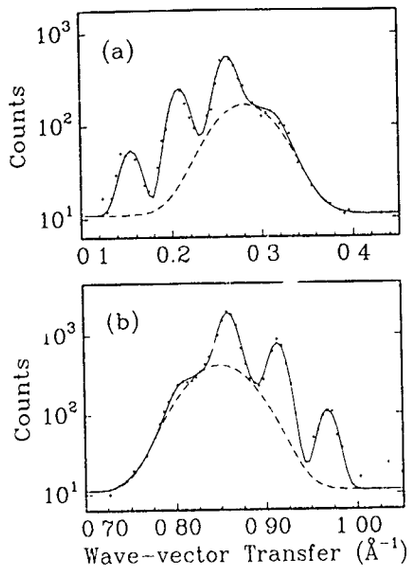

FIG. 5. The scattering (Ref. 10) observed for a scan along (10l) for the $Ho_{20}Er_{22}$ system at 8 K. The fit is to a series of Gaussian peaks, the narrow peaks arise from the basal plane ordering and the broad peak from the longitudinal ordering. The latter peak gives a correlation length of about the thickness of a single Er layer.

in Fig. 5. Fits to Gaussian peaks show that the widths of the sharp components increase in the same way with decreasing temperatures as the peaks observed along (00l), while the broad peak has a width corresponding to scattering from a single Er block and a position to a turn angle similar to that of bulk Er at the same temperature, see Fig. 6.

A model which accounts for this behavior assumes that the Ho moments align in a basal plane helix, while the Er moments align in an a/c cycloid with the basal plane components of the cycloid coherent with the Ho moments, but the sense of rotation of the cycloid is randomly clockwise or anticlockwise, destroying any coherence of the c-axis mo-

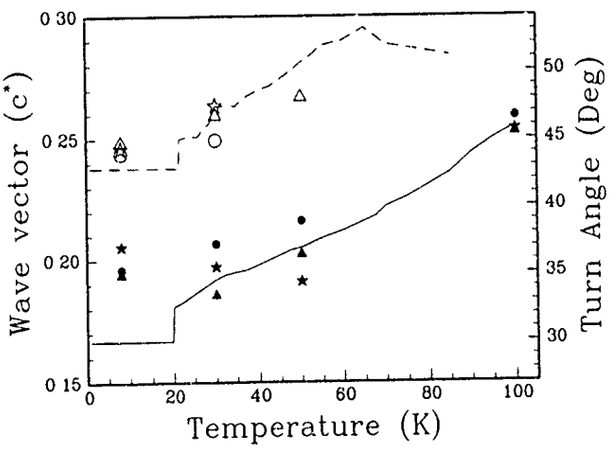

FIG 6 The turn angles Ψ_H and Ψ_E for the holmium and erbium moments (from the broad longitudinal peak) The Ho values are the filled symbols and solid line for the bulk while the Er values are the dashed line and open symbols The symbols correspond to $Ho_{20}Er_{22}$ (△), $Ho_{10}Er_{20}$ (*), and $Ho_{43}Er_{10}$ (○)

ments between the different Er layers. This model is clearly consistent only if the Ho and Er turn angles have values such that the different structures match up at the boundaries of the layers. Full details of the models will be published elsewhere.[10]

The lack of the long-range coherence, particularly for the c-axis, was surprising because long-range coherence has been observed in the Er/Y system.[11]

IV. SUMMARY AND DISCUSSION

The magnetic structures of Ho/Y, Ho/Lu, and Ho/Er superlattices have been determined using neutron-scattering techniques. The results for Ho/Y and Ho/Lu superlattices are qualitatively similar to those of Dy/Y and other superlattices, in that long-range coherent magnetic structures are produced in which the order propagates through the nonmagnetic layers. As for Dy/Y and Dy/Lu superlattices,[1,7] the strain in the Ho/Y layers means that the Ho turn angle is larger than in bulk Ho, while in the Ho/Lu layers it is smaller. The basal plane anisotropy leads, at low temperatures, to spin-slip commensurate structures within each Ho layer, but there is no coherence of the spin-slip aspects of the structure from one layer to the next. In the case of the Ho/Lu superlattices, there is a new phase in which the Ho forms basal plane ferromagnetic layers which are oriented either ferromagnetically or antiferromagnetically with neighboring layers.

The Ho/Er structures are more complicated because the Er moments are aligned by the crystal field along the c axis. Above the ordering temperature of Er, the structure is a long-range helical ordering, similar to that of the Ho/Y superlattices but with zero net moment on the Er atoms. On cooling Er below the ordering temperature, the correlation length decreases for the basal plane ordering and the results are consistent with the holmium ordering as a basal plane helix and the erbium in a cycloidal, a/c-plane structure. The basal plane moments of both the Ho and Er are coherent over several superlattice repeats, but the c-axis Er moments are coherently ordered only over single Er layers. Different parts of the cycloidal ordering are randomly clockwise or anticlockwise in sense.

Part of the importance of these results lies in the information they provide about the nature of the magnetic interactions in the superlattices. Conventionally the magnetic interactions are taken to be of the RKKY form, which suggests an interaction of the form $\mathbf{S}_1.\mathbf{S}_2$, of a magnitude which oscillates in sign with a period determined by the Fermi surface. This interaction is of long range and has usually been taken to explain the propagation of the magnetic ordering through quite large nonmagnetic Ho blocks. In the absence of more detailed calculations, however, we do not find this wholly convincing. The long-range order propagates through Y and Lu layers containing as many as 30 planes of Y in each layer. This is much longer range than the exchange constants deduced from spin-wave measurements of the bulk rare earths[8] which we believe give a better estimate of the RKKY interaction than the calculations.[1] Furthermore, the transition temperatures of the Ho/Y superlattices decrease only slightly as the Ho layer thickness decreases, and are largely independent of the Y layer thickness.[2] They are consistently higher than those of the Ho/Y alloys with the same average composition. Finally, when the Ho/Lu superlattices[3] or the Gd/Y or Dy/Y superlattices[1] order into basal plane ferromagnetic layers, the ordering through the Lu layers changes from propagation of a helical ordering to an ordering which is either ferromagnetic or antiferromagnetic. This change in the effect of the Y layers is inconsistent with the simple RKKY interaction, and not convincingly explained by existing calculations.[12]

The results for the Ho/Er system are also not readily understood. How does the order propagate through the Er layers above T_N for Er without producing ordering in the Er layers? Once the Er moments begin to order, it is difficult to understand why the coherence length of the basal plane ordering decreases, or why there is no propagation of the longitudinal ordering through the Ho layers, as would be expected if the interaction had the simple $\mathbf{S}_1.\mathbf{S}_2$ form.

One possible explanation of the results is to consider the band structure of the magnetically ordered structure, when the electrons at the new superzone gaps must have conduction-band spin-wave functions associated with the nature of the magnetic ordering.[6] This then leads to a long-range interaction only if the metals have similar band structures and for only the spin ordering which forms the initial spin-density wave. We intend exploring this model elsewhere.

ACKNOWLEDGMENTS

We are grateful to K. N. Clausen who helped with the measurements. Financial support was provided by the Science and Engineering Research Council in the U.K. and by the E.U. under the Large Scale Facility Programme.

[1] C. F. Majkrzak, J. Kwo, M. Hong, Y. Yafet, D. Gibbs, C. L. Chien, and J. Bohr, Adv. Phys. **40**, 99 (1991).
[2] D. A. Jehan, D. F. McMorrow, R. A. Cowley, R. C. C. Ward, M. R. Wells, N. Hagmann, and K. N. Clausen, Phys. Rev. B **48**, 5594 (1993). D. F. McMorrow, D. A. Jehan, R. A. Cowley, P. P. Swaddling, R. C. C. Ward, M. R. Wells, N. Hagman, and K. N. Clausen, Europhys. Lett. **23**, 523 (1993).
[3] D. F. McMorrow, D. A. Jehan, P. P. Swaddling, R. A. Cowley, R. C. C. Ward, M. R. Wells, and K. N. Clausen, Physica B **192**, 150 (1993). P. P. Swaddling, D. F. McMorrow, J. A. Simpson, M. R. Wells, R. C. C. Ward, and K. N. Clausen, J. Phys. Condens. Matter **5**, L481 (1993).
[4] D. Gibbs, D. E. Moncton, K. L. D'Amico, J. Bohr, and B. H. Grier, Phys. Rev. Lett. **55**, 234 (1985); R. A. Cowley and S. E. Bates, J. Phys. C **21**, 4113 (1988).
[5] J. Kwo, E. M. Gyorgy, D. B. McWhan, F. J. DiSalvo, C. Vettier, and J. E. Bower, Phys. Rev. Lett. **55**, 1402 (1985).
[6] R. J. Elliott and F. A. Wedgewood, Proc. Phys. Soc. London **81**, 846 (1963); **84**, 63 (1964).
[7] R. S. Beach, J. A. Borchers, A. Matheny, R. W. Erwin, M. B. Salamon, B. Everitt, K. Pettit, J. J. Rhyne, and C. P. Flynn, Phys. Rev. Lett. **70**, 3502 (1993).
[8] E. A. Cowley and J. Jensen, J. Phys. Condens. Matter **4**, 9673 (1992).
[9] W. T. Lee, H. Kaiser, J. J. Rhyne, K. Dumesnil, C. Dufour, Ph. Mangin, G. Marchal, R. W. Erwin, and J. A. Borchers, J. Appl. Phys. **75**, 6477 (1994).
[10] J. A. Simpson, D. F. McMorrow, R. A. Cowley, D. A. Jehan, R. C. C. Ward, and M. R. Wells, Phys. Rev. Lett. **73**, 1162 (1994).
[11] J. J. Rhyne, M. B. Salamon, C. P. Flynn, R. W. Erwin, and J. A. Borchers, J. Magn. Magn. Mat. **129**, 39 (1994).
[12] Y. Yafet, J. Kwo, M. Hong, C. F. Majkrzak, and T. O'Brien, J. Appl. Phys. **63**, 3453 (1988).

Epitaxial ferromagnetic MnAs thin films grown by molecular-beam epitaxy on GaAs: Structure and magnetic properties

M. Tanaka[a] and J. P. Harbison
Bellcore, 331 Newman Springs Road, Red Bank, New Jersey 07701

M. C. Park, Y. S. Park, T. Shin, and G. M. Rothberg
Department of Materials Sciences and Engineering, Stevens Institute of Technology, Hoboken, New Jersey 07030

We have studied structural and magnetic properties of epitaxial MnAs thin films with various thicknesses (L=1.0–200 nm) on GaAs substrates. The MnAs thin films were grown at 200–250 °C on an As-rich disordered $c(4\times4)$ (001) GaAs surface by molecular-beam epitaxy (MBE). The growth direction of the MnAs was found to be along the $[\bar{1}100]$ axis of the hexagonal unit cell. X-ray spectra of the MnAs at room temperature have two peaks, indicating that the present MBE-grown MnAs films consist of the hexagonal ferromagnetic phase and orthorhombic paramagnetic phase. Magnetization measurements revealed that the MnAs thin films have perfectly square hysteresis characteristics with relatively high remnant magnetization M_r=300–567 emu/cm^3 and low coercive field H_c=65–926 Oe, compared with those of epitaxial MnGa and MnAl thin films reported previously.

Epitaxial ferromagnetic thin films grown directly on semiconductors have generated much interest, since (1) high structural quality and submicrometer uniformity is expected in epitaxial monocrystalline thin films, leading to high reliability in small scale devices and (2) such heteroepitaxy of dissimilar materials can lead to a new class of device applications having properties both of ferromagnetic materials and of semiconductors.[1] Among a number of material choices, using III-V compound semiconductors like GaAs as a substrate allows the coupling of magnetism with high-speed semiconductor electronics/photonics, offering a wide range of possibilities for the fabrication of new hybrid magnetic-semiconductor devices. However, none of the elemental metals can meet the following stringent requirements: the ferromagnetic metals must grow epitaxially on GaAs, must be thermodynamically stable with no reaction with GaAs, and must be morphologically stable on GaAs.[2]

We have found that some metallic compounds can satisfy these requirements.[3–6] Ferromagnetic tetragonal MnAl[3,4] and MnGa,[5,6] Mn-based metallic compounds having common III-column atoms with AlAs and GaAs, have been grown by molecular-beam epitaxy (MBE) on GaAs substrates. Furthermore, very recently, we have successfully grown another ferromagnetic metallic compound, MnAs, by MBE on GaAs substrates.[7] This magnetic binary compound based on arsenic is more compatible with conventional III-V MBE. Though we have reported the initial results on the MBE growth on MnAs thin films on GaAs,[7] no detailed and systematic studies have been done on the MnAs/GaAs system. In this paper, we present structural and magnetic properties of the epitaxial MnAs with various thicknesses (L =1.0–200 nm) grown on (001) GaAs substrates.

In the bulk Mn-As system, MnAs at the stoichiometric composition ($Mn_{50}As_{50}$) has a thermodynamically stable ferromagnetic phase (α phase) at room temperature.[8] The Curie temperature of the ferromagnetic αMnAs is 40 °C, slightly above room temperature. The crystal structure of the αMnAs is hexagonal of NiAs type, with lattice constants of a=0.3725 nm and c=0.5713 nm, as shown in Fig. 1. At the stoichiometric composition, this ferromagnetic MnAs phase extends up to 40 °C, and paramagnetic βMnAs of a MnP-type orthorhombic structure (with lattice constants of a=0.366 nm, b=0.636 nm, and c=0.572 nm) and paramagnetic γMnAs of a NiAs-type hexagonal structure exist at 40–125 °C and above 125 °C, respectively.

The MBE growth was performed in a conventional III-V MBE machine (Riber 2300) with a Mn effusion cell. After growing a 100 nm thick undoped GaAs buffer layer on a (001) GaAs substrate at 5°0 °C, the substrate temperature T_s was cooled to ~200 °C, watching the reflection high-energy electron-diffraction (RHEED) patterns. During the cooling process, the surface reconstruction of the GaAs changed from (2×4) to $c(4\times4)$ in the RHEED. When the As_2 flux

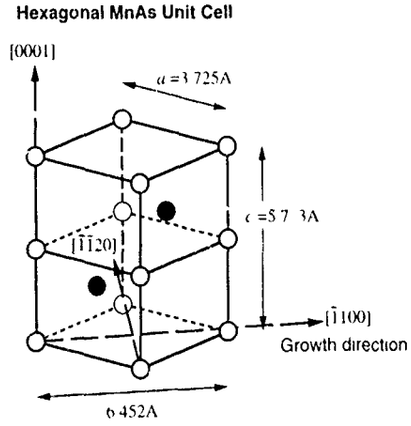

FIG 1 The crystal structure of the ferromagnetic MnAs is hexagonal of NiAs type, with lattice constants of a=0 3725 nm and c=0 5713 nm The growth direction is also shown in the figure

[a]Present address Department of Electrical Engineering, University of Tokyo, 7-3-1 Hongo, Bunkyo-ku, Tokyo 113, Japan

 0021-8979/94/76(10)/6278/3/$6 00 © 1994 American Institute of Physics

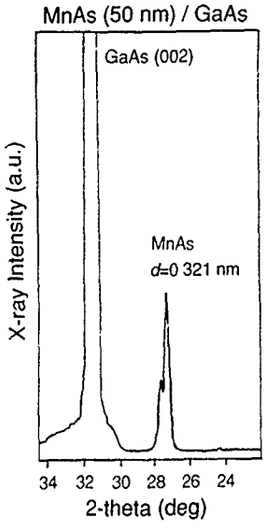

FIG 2. X-ray spectrum of a MBE-grown 50 nm thick MnAs film along the direction perpendicular to the substrate, measured at room temperature (20 °C).

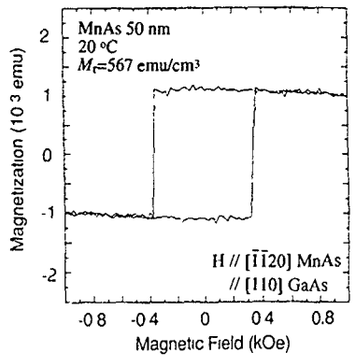

FIG 3. M-H characteristics of a 50 nm-thick MnAs at room temperature (20 °C), when the magnetic field was applied along the [1̄1̄20] axis of MnAs (//[110] GaAs). Almost perfectly square hysteresis characteristics are seen.

was supplied to the $c(4\times4)$ GaAs surface for a few minutes at 200 °C, the surface reconstruction changed from $c(4\times4)$ to *disordered* $c(4\times4)$ surface [$d(4\times4)$], where the half order streaks in the RHEED are weakened, indicating disorder caused by the accumulation of extra As atoms.[9] Then the Mn shutter was opened to grow MnAs thin films with various thicknesses ($L=1.0$–200 nm) on the $d(4\times4)$ GaAs surface at 200–250 °C with a growth rate of ~50 nm/h. The As/Mn ratio was set at 2.0–5.0. Under these growth conditions, the growth rate of MnAs is determined only by the Mn flux as in the growth of GaAs and related III-V semiconductors.

Figure 2 shows an x-ray spectrum of a 50 nm thick MnAs along the direction perpendicular to the substrate, measured at room temperature (20 °C). Similar x-ray results were obtained for all the other MnAs thin films grown under the same growth procedure and conditions. A huge peak at 31.6° is the (002) reflection of the GaAs substrate. The other two peaks around 28° are from the MnAs thin film. The stronger peak shows a lattice spacing of $d=0.321$ nm, corresponding to the (1100) reflection of hexagonal αMnAs. This indicates that the growth direction of the ferromagnetic MnAs is along the [1̄100] (see Fig. 1). A minor peak is also seen at the shoulder of the major peak, showing a lattice spacing of 0.317 nm, which corresponds to the (020) reflection of the orthorhombic βMnAs. In bulk MnAs, the hexagonal-orthorhombic transition is known to occur at the Curie temperature ($T_c=40$ °C) through very slight lattice distortions, since the two structures are very similar. In the present MBE-grown MnAs films, the paramagnetic βMnAs coexists with ferromagnetic αMnAs at room temperature (20 °C), though the major part of the film is the α phase. The reason for the existence of the β phase below T_c is unclear, but its formation might be the way MnAs relaxes the strains caused by the misfit to the GaAs substrate.

To investigate the epitaxial relationship in the present MnAs/GaAs system, RHEED patterns were observed along various azimuths during the growth. The RHEED measurements showed that the in-plane lattice constants are very close to those of hexagonal αMnAs, and the epitaxial relationship was found to be [1̄1̄20] [0001] MnAs//[110][1̄10] GaAs.

We have performed magnetization measurements on the MnAs thin films, with the thicknesses ranging from 1 to 200 nm, at room temperature using vibrating sample magnetometry. All the MnAs films have strong magnetic anisotropy, and the easy magnetization axis was found to be in plane, along the [1̄1̄20] axis of the hexagonal lattice of MnAs, which is parallel to the [110] axis of GaAs. Almost perfectly square hysteresis characteristics were seen as shown in Fig. 3, which is taken from the 50 nm thick MnAs, when the magnetic field was applied along the [1̄1̄20] axis of MnAs (//[110]GaAs), whereas almost no hysteresis was observed when the field is applied along the [0001] (c axis) of MnAs (//[1̄10]GaAs) or perpendicular to the film plane. This indicates that the MBE-grown MnAs thin films have strong magnetic anisotropy. We find this to be true for all thicknesses studied (1.0–200 nm). The values of remnant magnetization M_r and coercive field H_c of the 50 nm MnAs are 567 emu/cm^3 and 396 Oe, respectively, as shown in Fig. 3. This M_r value is slightly lower than that of bulk MnAs (600–700 emu/cm^3), but much higher than the best values (225–270 emu/cm^3) we have obtained for MBE-grown MnGa[5] and MnAl[10] thin films. The H_c value of the MnAs is much lower than that (1.1–5.0 kOe) of the MnGa and MnAl. The high M_r and low H_c with perfect squareness in the hysteresis characteristics are very attractive for future device applications including magnetic digital memory.

Figure 4 shows the thickness dependence of the room-temperature (20 °C) magnetic properties, saturation magnetization M_s and coercive field H_c of the epitaxial MnAs thin films on GaAs. The thickness dependence of the M_s is peculiar, having its maximum value at a thickness of 50 nm. The decrease of M_s when the thickness is greater than 50 nm could be related to the increase of surface roughness and deterioration of the epitaxial quality, as observed in the RHEED. The value of H_c increases from 65 Oe at 1 nm to 926 Oe at 10 nm, taking the maximum value, and then decreases again to 108 Oe at 200 nm. Some very thin films of

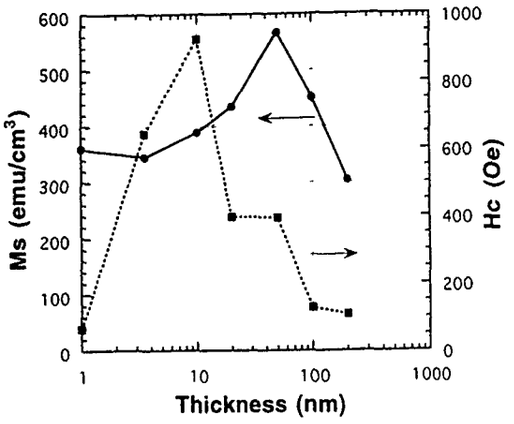

FIG. 4. Thickness dependence of the room-temperature (20 °C) magnetic properties, saturation magnetization M_s and coercive field H_c of the epitaxial MnAs thin films on GaAs

Fe and Co have been reported to show low coercive fields that increase with thickness.[11,12] On the other hand, the decrease of H_c may result from structurally related phenomena that affect the nucleation and movement of magnetic domains. These behaviors of M_s and coercive field H_c are not fully understood at this stage, but it is important for some applications to achieve high M_s(>300 emu/cm^3) and tailorable H_c (50–1000 Oe) in the low-field range (<1 kOe).

In summary, we have obtained epitaxial ferromagnetic MnAs thin films on (001) GaAs substrates by MBE. The growth direction of the ferromagnetic αMnAs was found to be along the $[\bar{1}100]$ axis. X-ray measurements showed that the MBE-grown MnAs films consist of ferromagnetic αMnAs and paramagnetic βMnAs. Magnetization measurements revealed that the MnAs thin films have perfectly square hysteresis characteristics with relatively high remnant magnetization M_r=301–567 emu/cm^3 and low coercive field H_c=65–926 Oe.

The authors wish to thank T. Sands, T. L. Cheeks, and V. G. Keramidas of Bellcore for their collaborations and support. One of the authors (M. T.) acknowledges the constant encouragement of Professor T. Nishinaga of the University of Tokyo. M. T. also thanks the Japan Society for the Promotion of Science (JSPS) for partial financial support.

[1] G. A. Prinz, Science **250**, 1092 (1990)
[2] T. Sands, C. J. Palmstrom, J. P. Harbison, V. G Keramidas, N Tabatabaie, T. L. Cheeks, R. Ramesh, and Y. Silberberg, Mater. Sci. Rep. **5**, 99 (1990); J. P. Harbison, T. Sands, C. J Palmstrom, J DeBoeck, L T. Florez, and V. G. Keramidas, 11th Record of Alloy Semiconductor Physics and Electronics, Kyoto, 1992 July (unpublished), p. 7.
[3] T. Sands, J. P. Harbison, M. L. Leadbeater, S J. Allen, Jr., G. W. Huli, R. Ramesh, and V. G. Keramidas, Appl. Phys. Lett **57**, 2609 (1990).
[4] J. P. Harbison, T. Sands, R. Ramesh, L. T. Florez, B. J. Wilkens, and V. G. Keramidas, J. Cryst Growth **111**, 978 (1991).
[5] M Tanaka, J. P. Harbison, J. DeBoeck, T. Sands, B Phillips, T. L. Cheeks, and V. G. Keramidas, Appl. Phys. Lett **62**, 1565 (1993).
[6] M. Tanaka, J. P. Harbison, T Sands, B. A. Phillips, J. DeBoeck, T L. Cheeks, L. T. Florez, and V. G. Keramidas, Mater. Res Soc. Symp. Proc. **313**, 507 (1993).
[7] M. Tanaka, J. P. Harbison, T. Sands, T. L. Cheeks, V. G. Keramidas, and G. M. Rothberg, J. Vac Sci. Technol. B **12**, 1091 (1994).
[8] G. E Bacon and R. Street, Nature **175**, 518 (1955); *Binary Alloy Phase Diagram*, 2nd ed., edited by T. B. Massalski, H. Okamoto, P. R. Subramanian, and L. Kacprzak, (American Society of Metals, Metals Park, OH, 1990), Vol. 1, p 295, and references therein.
[9] I. Kamiya, H. Tanaka, D. E. Aspnes, L. T. Florez, E Colas, J P Harbison, and R. Bhat, Appl Phys. Lett. **60**, 1238 (1992)
[10] T. L. Cheeks, M. J. S. P. Brasil, J. De Boeck, J. P Harbison, T. Sands, M. Tanaka, A. Scherer, and V G. Keramidas, J Appl Phys. **73**, 6121 (1993).
[11] M. Senda and Y Yagai, J. Appl. Phys. **65**, 3157 (1989).
[12] M. T Kief, G J. Mankey, and R. F Willis, J Appl. Phys **69**, 5000 1991)

Co/CoAl magnetic superlattices on GaAs

J. De Boeck, C. Bruynseraede, H. Bender, A. Van Esch,[a] W. Van Roy, and G. Borghs
IMEC, 75 Kapeldreef, B3001 Leuven, Belgium

Co/CoAl multilayers are grown by molecular beam epitaxy on AlAs/GaAs (001). CoAl is used as a template for the epitaxy of Co. From RHEED and lattice matching considerations bcc Co is expected, but thicker Co layers are probably fcc with stacking faults. The crystallographic structure of the Co layers is unclear at present. Room-temperature magnetization and magnetoresistance data are presented. Co/CoAl multilayers with various CoAl thickness all show in-plane magnetic anisotropies along ⟨110⟩. Uniaxial anisotropy along ⟨110⟩ is found to increase with increasing thickness of the CoAl layers in the multilayers. The magnetoresistive effect as a function of the orientation of the current path and the applied field is ascribed to domain-wall effects and internal Lorentz magnetoresistance.

I. INTRODUCTION

Metal epitaxy on semiconductors has received great interest over the past years, motivated by the need for stable ohmic contacts and Schottky barriers for submicrometer device structures and buried metal layers for novel devices.[1] Recently, progress has been made in epitaxy of ferromagnetic metal thin films on III-V's such as elemental Fe[2] and Co[3,4] and Mn-III compounds such as MnAl,[5] MnGa[6] on GaAs. The combination of ferromagnetic thin films and semiconductor heterostructures is expected to lead to novel device concepts. Epitaxy of elemental metals on III-V is a problem because single-variant epitaxy, morphological smoothness, and thermodynamical stability are never simultaneously achieved. Fe and Co are known to react with the semiconductor at relatively low temperatures and buried thin films coalesce upon regrowth. Intermetallic phases, however, are more suitable as candidates for stable metal epitaxy on semiconductors and a lot of effort has been invested in the study of transition-metal aluminides (TMAl) such as NiAl and CoAl.[7,8] The lattice parameter of, e.g., CoAl (a_0=0.2861 nm) is close to half the lattice parameter of GaAs and to that of bcc Co (a_0=0.2819 nm), while the large fraction of group-III elements reduces the reactivity at the metal/III-V interface. Furthermore, the use of TM aluminides as templates and interlayers in magnetic superlattices has shown to be successful in ferromagnetic/metallic thin-film heterostructures such as MnAl/NiAl on AlAs/GaAs.[9] In this work we study the use of CoAl as a template for Co epitaxy on GaAs and as interlayer in a magnetic Co/CoAl multilayer and present data on the magnetic properties of multilayers with varying CoAl thicknesses.

II. EXPERIMENT

The samples were grown using a Riber 2300 molecular-beam epitaxy system equipped with a 10 keV electron gun for reflection high-energy electron-diffraction (RHEED) observations during growth. For the evaporation of Co an EPI high-temperature cell is used with either a BeO or Al_2O_3 crucible. For the III-V growth, standard *K* cells and an EPI valved As-cracker source are employed.

The structure of the samples is characterized using transmission electron microscopy (TEM) and the magnetic properties are studied using an alternating gradient field magnetometer (AGFM 2900, Princeton Meas. Corp.) in addition to magnetoresistance measurements.

III. RESULTS AND DISCUSSION

Prior to the metal epitaxy, a GaAs buffer is grown on the GaAs (001) undoped substrates. On top of the GaAs buffer an AlAs layer of 10 nm is grown, the thickness of which is controlled using RHEED oscillations. The substrate is subsequently cooled to about 150 °C while the As background pressure is reduced by shutting the As valve and reducing the temperature in the cracking zone to about 300 °C. At that time the Co cell temperature is increased to the operating point. Co and Al beam equivalent pressures are equalized for CoAl growth using a Bayard–Alpert gauge. The background pressure was reduced below 3×10^{-10} Torr.

For the CoAl template, we have adopted the growth sequence as described[8] by Tanaka *et al.* Upon the AlAs (001) $c(4\times4)$ reconstructed surface, a ML of Co is deposited, followed by CoAl codeposition. Although CoAl can be grown at 350 °C on AlAs, the lower substrate temperature (150 °C) is chosen in an attempt to stabilize Co "bcc."[4] In this paper we report on a set of samples with a heterostructure of $10\times$(6 Å Co/t Å CoAl) with 2.5 Å$<t<$15 Å. The Co thicknesses are estimated from CoAl RHEED oscillations and assuming a_0(Co)=0.2819 nm. All samples are terminated by a CoAl layer.

The growth of the heterostructure is monitored using RHEED. The intensity of the RHEED specular spot decreases during cobalt deposition at 150 °C on the AlAs buffer. Upon deposition of the CoAl layer, the intensity recovers and clear oscillations are visible. CoAl adopts the structure of the ordered variant of the bcc CsCl (a_0=0.2861 nm). Initially, the RHEED streaks are relatively broad, suggesting that initial roughness is present, probably due to interaction of the Co with the As present on the AlAs $c(4\times4)$ surface. The RHEED patterns demonstrate the desirable ep-

[a]LTHV–Catholic University Leuven, Celestijnenlaan 200D, B3001 Leuven, Belgium

 0021-8979/94/76(10)/6281/3/$6.00 © 1994 American Institute of Physics

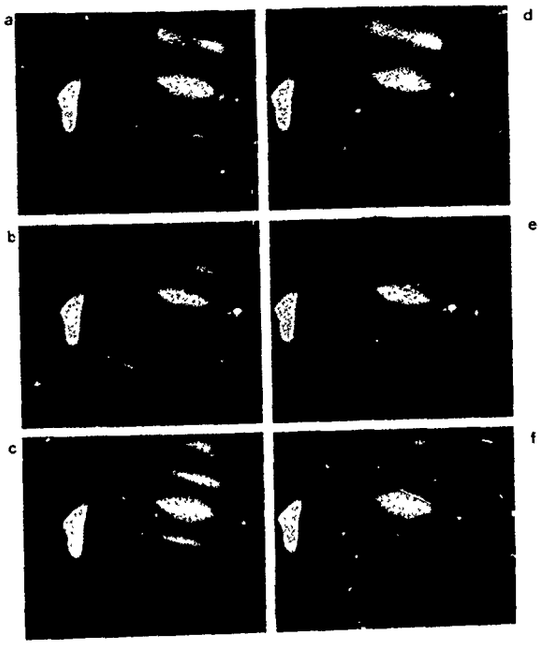

FIG. 1. RHEED images of (a)–(c) Co and (d)–(f) CoAl layers, forming the last period of a (6 Å Co/5 Å CoAl)×10 multilayer on AlAs/GaAs. The images are taken along different azimuths: (a) and (d) ⟨100⟩, (b) and (e) ⟨110⟩, and (c) and (f) ⟨1$\bar{1}$0⟩.

itaxial relation (001)[110] CoAl‖(001)[110]AlAs. Both the interface roughness and the epitaxial relation are confirmed by TEM.

A first Co layer was subsequently deposited on the CoAl template while rotating the sample holder for optimum uniformity until completion of the heterostructure. The rest of the structure is fabricated by keeping the Co cell open and shutting the Al periodically. The deposition times for each layer are in the range of 30–90 s. The RHEED images during growth of all multilayer samples are indicative of epitaxy in a cubic phase for both the Co and CoAl layers. Figure 1 shows a set of RHEED pictures taken from Co [Figs. 1(a)–1(c)] and CoAl [Figs. 1(d)–1(f)], forming the last period of a 10×(6 Å Co/5 Å CoAl) multilayer.

The crystallographic structure of the Co layers is presently still unclear. Given the close lattice match to CoAl and the RHEED data suggesting cube-on-cube epitaxy, one would expect the bcc Co phase to appear. Preliminary NMR[10] data on multilayer samples with thicker Co (≈9 Å) layers where RHEED showed additional spots around the central streak for Co suggest that the Co structure is fcc with stacking faults, which is surprising given the lattice constant of fcc Co (a_0=0.3545 nm) which does not correspond closely to CoAl (misfit≈24%). A more detailed structural investigation is under way.

Figures 2(a)–2(f) show the results of the room-temperature in-plane magnetization measurements (M/Ms) as a function of crystallographic direction, for samples with different CoAl spacer thicknesses. For all the samples we find an anisotropy in the plane. The saturation magnetization (Ms) typically ranges between 650 and 700 emu/cc.

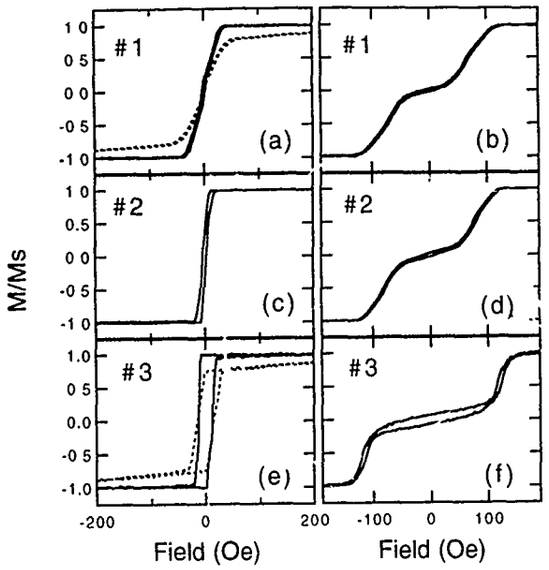

FIG. 2. AGFM magnetization measurements (300 K) for 10×[Co (6 Å)/CoAl (t Å)] along the different crystallographic directions. (a), (c), and (e) [1$\bar{1}$0] (full line) (b), (d), and (f), [110], and (d) and (e) ⟨100⟩ (dotted line). The CoAl thickness t is varied: 5 (No 1), 10 (No. 2), and 15 Å (No 3).

The samples with 5 Å CoAl spacers [Figs. 2(a) and 2(b), No. 1] exhibit a steplike M-H behavior with very little remanence in all directions. A difference between the two orthogonal ⟨110⟩ directions is visible. One of these directions has a saturation field which is a factor of 3 larger (Hs[110] =120 Oe, 9.55 kA/m) compared to the orthogonal [1$\bar{1}$0]. With increasing thickness of the CoAl spacers {No. 2: 10 Å [(c),(d)] and No. 3: 15 Å [(e),(f)]}, the uniaxial anisotropy becomes more pronounced. The remanence of the [110] direction increases to nearly 100% ($Mr=Ms$) for CoAl≈15 Å, while a steplike hysteresis with small remanence is observed in the orthogonal direction. The ⟨100⟩ directions represent a hard magnetic axis of the thin film as illustrated by

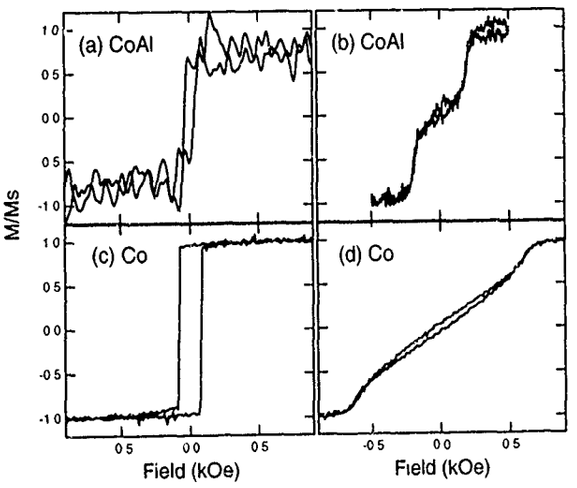

FIG 3 AGFM magnetization measurements (300 K) and for (a) and (b) 60 Å CoAl and (c) and (d) 36 Å Co along (a) and (c) [1$\bar{1}$0] and (b) and (d) [110]

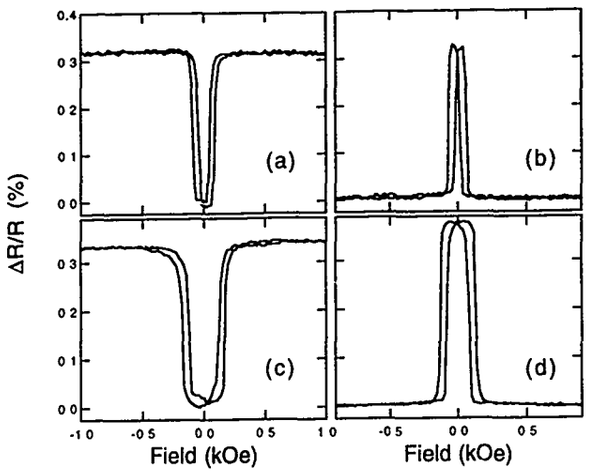

FIG. 4. Room-temperature magnetoresistance data from two Co/CoAl multilayers [(a) and (b), No. 1 and (c) and (d), No. 2; see text and Fig. 2] with different CoAl thicknesses. In all cases the applied magnetic field (H) is orthogonal to the easy axis ([1$\bar{1}$0]), and either (a) and (c) orthogonal or (b) and (d) parallel to the current direction.

the dotted curves in Fig. 2 [(a) and (e)]. Similar uniaxial anisotropic behavior has been observed for single layers of Fe[11] on GaAs (110) and Co[4] on GaAs (001).

Besides the thickness of the CoAl spacer layer, its magnetic properties will influence the magnetic and transport behavior of the heterostructure. It is known[12] that Co-rich CoAl behaves ferromagnetically. AGFM measurements (300 K) on a 60 Å thick CoAl layer on AlAs/GaAs show a very weak ferromagnetic behavior of about 17 emu/cc [Figs. 3(a) and 3(b)]. We also tested a 36 Å thick Co layer on a CoAl template. RHEED showed a complex pattern of additional spots indicating structural changes in the cobalt layer. AGFM measurements of this sample are shown in Figs. 3(c) and 3(d). These thicker, single layers of Co and CoAl display the same in-plane anisotropic behavior as the Co/CoAl multilayers discussed above.

Figure 4 shows the in-plane magnetoresistance curves (300 K) for samples No. 1 and No. 3 (see Fig. 2). The magnetic field is applied perpendicular to the easy direction. When the current is along the easy axis (and orthogonal to the applied field), the resistance increases from its zero-field value to its saturation value (+0.3%) [Figs. 4(a) and 4(c)]. When the current and the applied field are parallel, the resistance at saturation is about 0.3% lower than the zero-field resistance [Figs. 4(b) and 4(d)]. In each case, when the magnetic field is applied in the direction of the easy axis, the resistance of the film does not change appreciably around $H=0$. For the measurements repeated at 77 K identical results were observed. This resistance behavior is attributed to a combined effect of domain wall and carrier interaction and Lorentz magnetoresistance.[13] In the case of resistance decrease, the internal Lorentz magnetoresistance is removed at saturation. In the case of resistance increase, a larger Lorentz action is present at saturation. The influence of the domain (wall) structure on the resistance can be important, but the actual domain configuration is unknown at present.

IV. SUMMARY

The epitaxial growth of Co/CoAl multilayers on AlAs/GaAs is described, using CoAl as a template for cobalt epitaxy. The crystallographic structure of the Co layers is unclear at present. From RHEED and lattice matching considerations bcc Co is expected but thicker Co layers are probably fcc. Co/CoAl multilayers with various CoAl thickness all show in-plane magnetic anisotropies along ⟨110⟩. Magnetoresistive effects at low fields are ascribed to domain-wall effects and internal Lorentz magnetoresistance.

ACKNOWLEDGMENTS

The authors would like to thank Professor Ewa Jedryka (Magnetic NMR Laboratory, Polish Academy of Sciences, Warsawa, Poland) for the NMR measurements. C. Bruynseraede acknowledges financial support from the IWONL (Belgium). W. Van Roy acknowledges financial support as a Research Assistant of the National Fund for Scientific Research (Belgium).

[1] T. Sands, C. J. Palmström, J. P. Harbison, V. G. Keramidas, N. Tabatabaie, T. L. Cheeks, R. Ramesh, and Y. Silberberg, Mater. Sci. Rep. **5**, 99 (1990).
[2] J. J. Krebs, B. T. Jonker, and G. A. Prinz, J. Appl. Phys. **61**, 2596 (1987); G. A. Prinz, Science **250**, 1092 (1990).
[3] G. A. Prinz, Phys. Rev. Lett. **54**, 1051 (1985).
[4] S. J. Blundell, M. Gester, J. A. C. Bland, C. Daboo, E. Gu, M. J. Baird, and A. J. Ives, J. Appl. Phys. **73**, 5948 (1993).
[5] T. Sands, J. P. Harbison, M. L. Leadbeater, S. J. Allen, Jr., G. W. Hull, R. Ramesh, and V. G. Keramidas, Appl. Phys. Lett. **57**, 2609 (1990).
[6] M. Tanaka, J. P. Harbison, J. De Boeck, T. Sands, B. Philips, T. L. Cheeks, and V. G. Keramidas, Appl. Phys. Lett. **62**, 1565 (1993).
[7] T. Sands, J. P. Harbison, R. Ramesh, C. J. Palmström, L. T. Florez, and V. G. Keramidas, Mater. Sci. Eng. B **6**, 147 (1990).
[8] M. Tanaka, N. Ikarashi, H. Sakakibara, K. Ishida, and T. Nishinaga, Appl. Phys. Lett. **60**, 835 (1992).
[9] M. Tanaka, J. P. Harbison, T. Sands, B. Philips, T. L. Cheeks, J. De Boeck, L. T. Florez, and V. G. Keramidas, Appl. Phys. Lett. **63**, 839 (1993).
[10] E. Jedryka (private communication).
[11] G. A. Prinz, G. T. Rado, and J. J. Krebs, J. Appl. Phys. **53**, 1087 (1982).
[12] S. R. Butler, J. E. Hanlon, and R. J. Wasilewski, J. Phys. Chem. Solids **30**, 1929 (1969).
[13] S. S. P. Parkin, Appl. Phys. Lett. **63**, 1989 (1993).

Investigations of the interplay between crystalline and magnetic ordering in Fe_3O_4/NiO superlattices

D. M. Lind, J. A. Borchers,[a] R. W. Erwin,[a] J. F. Ankner,[b] E. Lochner, K. A. Shaw, R. C. DiBari, W. Portwine, P. Stoyonov, and S. D. Berry

Department of Physics, Center for Materials Research and Technology (MARTECH) and the National High Magnetic Field Laboratory, Florida State University, Tallahassee, Florida 32306-3016

Using SQUID magnetometry and both x-ray- and neutron-diffraction techniques, we have studied the structural and magnetic ordering of a series of Fe_3O_4/NiO superlattices grown by MBE. X-ray diffraction reveals that the superlattices are coherent, single phase crystals with narrow interfaces. Symmetry differences between the Fe_3O_4 spinel and NiO rocksalt structures lead to interfacial stacking faults, manifested in some diffraction intensities. Analysis of the neutron-diffraction spectra show that the NiO antiferromagnetic ordering is coherent through several superlattice bilayers, while the Fe_3O_4 magnetic ordering is confined to individual interlayers by stacking faults in all superlattices but those with thinnest ($\leq$10 Å) NiO interlayers. Neutron diffraction and SQUID magnetometry have been used to study the Fe_3O_4 Verwey phase transition in thin-layered superlattices. The charge ordering in superlattices such as $[Fe_3O_4$ (75 Å)$|$NiO (9 Å)$]_{500}$, below the Verwey transition, directly observable in (4, 0, 1/2) neutron intensities, indicates a shift to higher temperature of the charge ordering transition from the bulk Fe_3O_4 T_{Verwey} at 123 K. We also describe ongoing efforts to extract the moment distribution in these superlattices from field dependent high-angle neutron diffraction.

I. INTRODUCTION

We report recent studies of the magnetic ordering in multilayers composed of iron oxide and nickel oxide. The iron oxide is prepared in the magnetite spinel (Fe_3O_4) phase which orders ferromagnetically, and the nickel oxide in its rocksalt-structured cubic phase which orders antiferromagnetically. Both of these materials order magnetically with short-range coupling, allowing us to study effects due to the local interfacial magnetic coupling and interfacial-driven strain. Studies of the structural and magnetic ordering of these layered materials have been performed by combining SQUID magnetometry with neutron- and x-ray-diffraction techniques.

II. CRYSTAL GROWTH AND CHARACTERIZATION

For this work oriented single-crystalline thin films of NiO and Fe_3O_4, and superlattice structures composed of these two materials, have been grown on polished (100)-oriented MgO substrates using oxygen plasma-assisted molecular-beam epitaxy.[1] NiO, MgO, and Fe_3O_4, each cubic crystalline structures, exhibit good pseudomorphic growth on each other due to the small lattice mismatch (0.3%–0.9%) among the cubic rocksalt structure of NiO and MgO and the half spacing of the cubic spinel Fe_3O_4 structure. These single-crystal structures have excellent repeat regularity and high crystalline coherence. The high degree of superlattice coherence is observable in data taken for x-ray (400) and neutron (222) peaks, in Fig. 1, for scans along the crystal growth direction for a $[Fe_3O_4$(75 Å)$|$NiO(9 Å)$]_{500}$ superlattice. The sharpness of the interfacial structures formed is indicated by the large number of superlattice sidebands, and the fact that the peaks do not broaden with increasing Q is a function of the high repeat regularity of the superlattices. The growth mode and structure of these films has been studied using x-ray, neutron, and *in situ* electron diffraction, with supportive work done using electron microscopy.[1–3] We report briefly the characterization of our films with these methods, and then address the present work.

X-ray and neutron diffraction indicate that individual layers down to 8.5 Å thick grow single crystalline, with the in-plane lattice spacing expanded to align in registry with the MgO substrate lattice. This is accompanied by a small layer-thickness-dependent tetragonal lattice distortion due to the

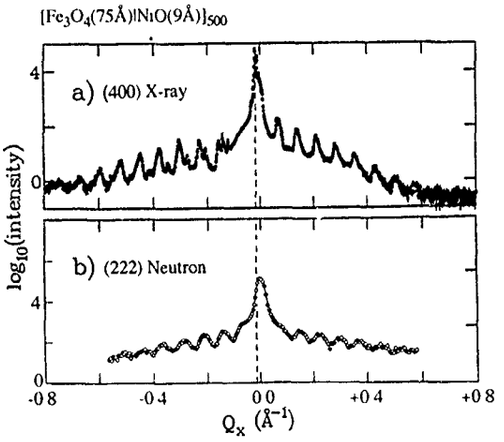

FIG. 1 (a) Room-temperature x-ray-diffraction scan through the (400) reflection for the $[Fe_3O_4$(75 Å)$|$NiO(9 Å)$]_{500}$ superlattice as a function of the the wave vector Q_x along the crystal growth direction, with the Q vector indexed relative to the position of the central Bragg peak. (b) Neutron-diffraction scan at 80 K through the (222) peak of the same sample. The central Bragg reflection is partially obscured by scattering from the MgO substrate, which is indicated by a dashed line

[a]Reactor Radiation Division, NIST, Gaithersburg, MD 20899
[b]MURR, University of Missouri, Columbia, MO 65211.

 0021-8979/94/76(10)/6284/3/$6.00 © 1994 American Institute of Physics

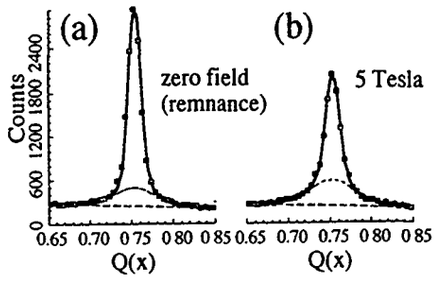

FIG. 2. Intensity profiles for (111) neutron reflection along [100] from a $[Fe_3O_4(33\ Å)|NiO(67\ Å)]_{300}$ superlattice at 30 K (a) at zero field (in remnance) and (b) at 5 T applied field. The dashed line is the Gaussian fit to the intensity of the broad (Fe_3O_4) component, and the solid line is the sum of the two (NiO and Fe_3O_4) Gaussian fits. Note the trends in the broad (Fe_3O_4), and narrow (NiO) components with field.

epitaxial and interfacial lattice mismatches.[2] The crystalline coherence of the layered structures are long range (>1500 Å),[1,2] although coherence of the Fe_3O_4 layers across intervening NiO interlayers (of thickness ≥15 Å) is limited by interfacial stacking faults. Although the underlying oxygen sublattice in the NiO and Fe_3O_4 structures is continuous across the interfaces, alignment of Fe tetrahedral sites in Fe_3O_4 is not uniquely defined with respect to that oxygen sublattice, and thus there is not a unique alignment of Fe_3O_4 unit cells across the intervening NiO spacer layers. The accompanying reduction in Fe_3O_4 coherence has been modeled[3] using a Hendricks–Teller description of the stacking faults.[4]

III. NEUTRON DIFFRACTION

Neutron diffraction indicates that the NiO orders antiferromagnetically in alternating (111) planes with a magnetic coherence that extends over several superlattice bilayers, and that coupling to adjacent Fe_3O_4 layers with a higher (T_c=858 K) ordering temperature causes an enhancement in the NiO Néel temperature above bulk T_N (520 K) in thin-layered superlattices.[2,3] The Fe_3O_4 magnetic coherence is limited to individual layers in all superlattices but those with the thinnest NiO interlayers by the structural stacking faults. The nature of this extended coherence in thinnest NiO-layered superlattices is not entirely understood. Although the highest temperature accessible with those studies (675 K) is far below the Fe_3O_4 Curie Temperature in the films, the results indicated that the NiO ordering enhancement is consistent with a mean field-type model that includes strong magnetic coupling across the interfaces.[3]

In the present work, one of our studies focused on the magnetic ordering of layered Fe_3O_4 and NiO structures as a function of applied field between 0 and 5 T. The studies were performed on BT-9, a triple-axis spectrometer at the National Institute of Standards and Technology reactor. During the experiments, the superlattices and thin films were aligned with the surface normal [400] and one of the [022] in-plane axes in the scattering plane to allow access to the (222), (111), and (022) reflections. The normal to the scattering plane (the [0$\bar{2}$2] direction) is chosen to be the externally applied field direction. We find changes with increasing field in the (111) and (022) neutron reflections, comprised in part from the magnetic scattering from the individual Fe_3O_4 and NiO layers. These changes suggest that the spins reorient with respect to the applied field direction in a manner consistent with bulk results. Figure 2 shows intensity profiles along [100] for the (111) reflection from a $[Fe_3O_4$ (33 Å)|NiO (67 Å)$]_{300}$ superlattice (a) at zero applied field (in remnance) and (b) at 5 T.

Because of the short-range magnetic ordering of the Fe_3O_4 layers and the long-range ordering of the NiO layers within the superlattices, the (111) neutron reflection intensity can be separated into two overlapping profiles, one short and broad, and the other tall and narrow.[3] The former has a large contribution from the Fe_3O_4 ferrimagnetic ordering, and the latter is due entirely to NiO antiferromagnetic ordering. In the superlattices, the NiO peak intensity decreases, and the Fe_3O_4 intensity increases, with increasing applied field. These changes in intensity may indicate an in-field low-energy state for the NiO layers with moments aligned perpendicular to the applied field (and probe direction), while in the Fe_3O_4 layer moments align parallel to the applied field. Neutron scattering also indicates that the saturation fields for these samples are larger than in bulk. In addition, in the superlattice spectra, Fe_3O_4 neutron linewidths show no change with field, but the NiO peak shows a small but consistent broadening trend with increasing field. This broadening indicates a reduction of NiO coherence length and domain size with increasing field. An equivalent broadening of neutron reflections with increasing field is not seen in either bulk or single-thin-film NiO samples.

Another sequence of studies we performed dealt with the influence of superlattice layering on the Verwey transition manifested in the iron oxide layers. The interlayer coupling and strain of the superlattice structure affects temperature and form of the Fe_3O_4 Verwey transition, a magnetic, conductivity, and structural transformation that accompanies a charge ordering of the Fe^{+3} and Fe^{+2} ions in magnetite. The Fe_3O_4 Verwey transition in the bulk (~123 K) is highly sensitive both to the exact stoichiometry of the iron oxide and to the presence of strain, and is accompanied by a lattice distortion to an orthorhombic structure, a large step downward in electron conductivity, and a shift in magnetic anisotropy, as the sample is lowered below the ordering temperature in the iron spinel materials.

Recently, Aragon *et al.*[5] have used neutron-diffraction techniques to investigate the Verwey transition in bulk Fe_3O_4, on single-crystalline samples of about 1 cm^3 volume. One sample in their study was prepared with exact Fe_3O_4 stoichiometry, while another was deficient in iron ($Fe_{3-\delta}O_4$ with δ=0.006). The charge ordering was manifested by the presence of reflections which appear below the Verwey transition (T~123 K) at the ($4n$, 0, 1/2) positions. The line shapes and temperature dependence of these peaks were used to study the nature of the charge ordering of the below-Verwey state. The charge ordering present below the transition temperature loses its long-range coherence due to lack of available charge in the nonstoichiometric sample, as evidenced by a broadening of the peak line shape, and a smear-

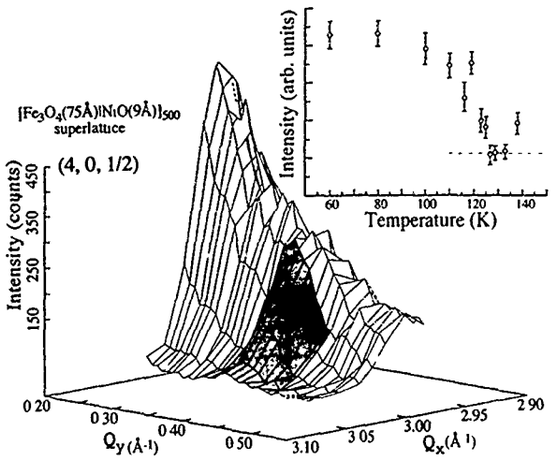

FIG. 3. Two-dimensional plot of the intensity for neutron reflection around the (4, 0, 1/2) peak at 80 K for scattering from a $[Fe_3O_4(75\ Å)|NiO(9\ Å)]_{500}$ superlattice. The reflection is partially obscured by a ridge of intensity due to the (400) reflection from the MgO substrate, and appears as a shoulder on the edge of the ridge (shaded area). Inset: Temperature dependence of the (4, 0, 1/2) reflection. The total intensity decays to the ridge background intensity (dashed line), indicating the extinction of the reflection peak intensity by 127 K

ing and lowering of the transition temperature, when compared to the pure Fe_3O_4 sample.

We have performed comparable measurements to probe the Verwey transition in a small subset of our grown films and superlattices,[6] which have a sample volume a factor of 1000 times less than those used by Aragon *et al.* The charge ordering, manifested by the appearance of the (4, 0, 1/2) peak, is seen both for a thick (3 μm) Fe_3O_4 film and for one of our superlattices, a sample containing very thin NiO layers—$[Fe_3O_4\ (75\ Å)|NiO\ (9\ Å)]_{500}$. Figure 3 shows the (4, 0, 1/2) peak for this latter sample superimposed on an intensity ridge associated with the MgO substrate (400) peak. The data in the figure were taken at 80 K, well below the Verwey ordering temperature. The inset in Fig. 3, also for the $[Fe_3O_4\ (75\ Å)|NiO\ (9\ Å)]_{500}$ superlattice, shows the integrated intensity of the (4, 0, 1/2) peak as a function of temperature near the Verwey transition. We can track this intensity to obtain an order parameter for the Verwey charge ordering, and obtain a transition temperature of about 128 K, several degrees above the bulk stoichiometric T_{Verwey}. Resolution limits do not allow for a full determination of whether the Verwey charge ordering is truly long range.

The amplitude of the temperature-dependent (4, 0, 1/2) peak follows another signal of the Verwey transition quite well: SQUID measurements at low applied fields (~1000 Oe) of the moment in the film, a technique for probing the Verwey transition first employed by Weiss and Forrer.[7] This method also gives a transition temperature for the superlattice *increased* to about 128 K. Since only a depression of the transition temperature due to nonstoichiometric samples has been previously observed, either by Aragon *et al.*[5] or in earlier work by Honig and co-workers,[8] we feel it is likely that the increase seen here is due to the strain in the superlattice, an effect which is being studied further.[6] For other superlattice samples, the ordering due to the Verwey transition with increasing NiO layer thickness is found to be entirely suppressed by the superlattice structure, and may be further evidence of increasing strain in the Fe_3O_4 layers.

We conclude that neutron diffraction, when supported by other complementary techniques, shows strong evidence for the influence of interfacial coupling and strain on the magnetic and structural ordering of layered iron oxide and nickel oxide heterostructures. The magnetic-field response of the ordering shows modifications from bulklike behavior influenced by interfacial coupling. Also, the Verwey transition, clearly associated with both structural and magnetic ordering effects, is *shifted to higher temperature* in the thin NiO-layered superlattice, and entirely suppressed in thicker NiO-layered samples.

ACKNOWLEDGMENTS

We gratefully acknowledge the research support of the National Science Foundation under Grant No. DMR-9206870 and the Office of Naval Research under Grant No. N000014-92-J-1356. Aspects of this work have been carried out at NIST research reactor facilities of the Department of Commerce, and that support is also generously acknowledged.

[1] D. M. Lind, S. D Berry, G. Chern, H. Mathias, and L. R. Testardi, Phys. Rev. B **45**, 1838 (1992).
[2] D. M. Lind, S.-P. Tay, S. D. Berry, J. A. Borchers, and R. W. Erwin, J Appl. Phys. **73**, 6886 (1993); D. M. Lind, *Proceedings of the Sixth International Conference on Ferrites (ICF 6), Tokyo and Kyoto, 1992*, edited by T. Yamaguchi and M. Abe (Japanese Society of Powder and Powder Metallurgy, Tokyo, 1992), p. 866.
[3] J. A. Borchers, R. W. Erwin, S. D. Berry, D. M. Lind, E. Lochner, and K. A. Shaw, Appl. Phys. Lett **64**, 381 (1994), J. A. Borchers, R. W. Erwin, S D. Berry, D. M. Lind, J. Ankner, E. Lochner, K. A. Shaw, and D Hilton (unpublished).
[4] S. Hendricks and E. Teller, J. Chem Phys. **10**, 147 (1942).
[5] R. Aragón, P. M. Gehring, and S. M. Shapiro, Phys. Rev. Lett. **70**, 1635 (1993).
[6] S. D. Berry, J. A. Borchers, R. W. Erwin, D. M. Lind, E. Lochner, K. A. Shaw, and P. Stoyonov (unpublished).
[7] D. Weiss and R. Forrer, Ann. Phys. **12**, 279 (1929).
[8] Z. Kalol and J. M. Honig, Phys. Rev B **40**, 9090 (1989); R Aragón, R. J. Rasmussen, J. P. Shepherd, J. W. Koenitzer, and J. M. Honig, J. Magn. Magn. Mater. **54–57**, 1335 (1986).

Magnetic characterization of epitaxial $Y_5Fe_eO_{12}/Bi_3Fe_5O_{12}$ and $Y_5Fe_3O_{12}/Eu_1Bi_2Fe_5O_{12}$ heterostructures grown by pulsed laser deposition

B. M. Simion
Department of Materials Science and Mineral Engineering, University of California at Berkeley, Berkeley, California 94720

R. Ramesh and V. G. Keramidas
Bell Communications Research, Red Bank. New Jersey 07701

G. Thomas
Department of Materials Science and Mineral Engineering, University of California at Berkeley, Berkeley, California 94720

E. Marinero
IBM Almaden Research Facility, San Jose, California 95120

R. L. Pfeffer
U. S. Army Research Laboratory, Fort Monmouth, New Jersey 07703

Epitaxial $Y_3Fe_5O_{12}$(YIG)/$Bi_3Fe_5O_{12}$(BIG) and YIG/$Eu_1Bi_2Fe_5O_{12}$(EBIG) heterostructures have been grown on [111] oriented single-crystalline gadolinium-gallium-garnet substrates by pulsed laser deposition. The effects of the layer thickness ratios on the composition, microstructure, and magnetic properties of the films have been studied employing x-ray diffraction, Rutherford backscattering spectroscopy, vibration sample magnetometry, and Kerr magnetometry. All films under investigation are single crystalline, in the [111] orientation. The multilayered heterostructures displayed superior magnetic properties in comparison to their single crystalline monolayer counterparts, deposited at the same conditions. The YIG/BIG heterostructures indicate increased in-plane saturation magnetic moments, approaching the maximum saturation value in bulk YIG. The YIG/EBIG heterostructures show a definite reorientation of the magnetic moment in the out-of-plane direction, a new set of increased saturation magnetization values that go even above that recorded for the bulk YIG, as well as an increase in coercivity.

The magneto-optical rewritable media embody the combination between the relatively infinite writing capability of a magnetic material with the mechanical system stability of an optical reading device and the high recording density of an optical medium. However, this imposes new constraints on the properties of these novel materials, as well as raising new challenges from a materials science point of view. Such requirements as perpendicular magnetic anisotropy, large magnetic coercivity, stable material structure, good corrosion resistance, low medium noise, fairly low Curie temperatures, and high magneto-optical effects are just a few in a large list. The launch of the first generation of commercially viable rewritable magneto-optical devices has already increased the storage capacity of the 3.5 in. disk format by an order of magnitude, compared to magnetic floppies. Yet this first generation of magne o-optical media is operating in the long-wavelength (infrared) range of the spectrum, intrinsically implementing a density limit on the read information (since the physical size of the data unit is diffraction limited by the wavelength of the reading radiation). The operation of the present media in a lower wavelength regime (such as green or even blue radiation) is made impractical by the low magneto-optical effect response of the material. Hence new materials are being considered for the next generation of magneto-optical storage media.

Three material systems are considered the front runners on the list of new potential candidates for magneto-optical applications: the rare-earth transitional metal alloys, the Co/Pt multilayers, and the ferrimagnetic iron garnets. Each of these systems offer attractive features, while displaying a series of disadvantages.

The rare-earth iron garnets have the highest magneto-optical response in the green blue range, display an unsurpassed corrosion resistance, and the rather loose structure, while extremely complicated, is capable of accommodating a large variety of ionic species. Furthermore, the position of the ions in the structure, being solely determined by the ionic radius, is completely unambiguous (such as in the spinel structure). Among the disadvantages, one can cite the high deposition temperature of the garnet phase and the relatively low signal-to-noise of the polycrystalline garnet films.

A large variety of chemical species may be substituted in the garnet lattice, resulting in different magnetic and magneto-optical properties. Because the garnet structure contains four sublattices, of which the oxygen sublattice is common to all garnets, an epitaxial deposition of layers of garnets with different compositions can easily be achieved.

We have grown by pulsed laser deposition (PLD) a series of thin-film superlattice heterostructures of rare-earth iron garnets, on [111] oriented single crystalline paramagnetic gadolinium-gallium-garnet (GGG) substrates. Layers with the following stoichiometries were grown: $Y_3Fe_5O_{12}$(YIG), $Bi_3Fe_5O_{12}$(BIG), and $Eu_1Bi_2Fe_5O_{12}$(EBIG). A 248 nm KrF excimer laser, with an energy density of 3.3 J/cm^2 and a frequency of 10 Hz, was used for film depositions. The depositions were carried out in O_2 ambient at pressures between 100 and 700 mTorr, and temperatures were between 500 and 800 °C for all single layer structures. The multilayer films were all grown at 600 °C for reasons out-

 0021-8979/94/76(10)/6287/3/$6.00 © 1994 American Institute of Physics

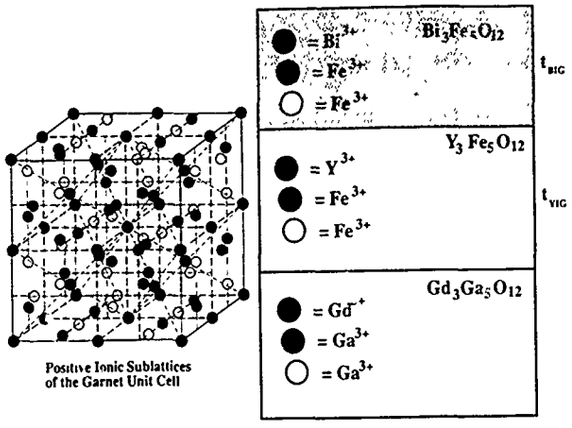

FIG. 1. Typical two layer YIG/BIG heterostructure with the corresponding unit cell.

lined elsewhere.[1] All films were cooled at an average 10 °C/min, in an O_2 ambient with a pressure of 1 atm.

Figure 1 shows a typical two layer YIG/BIG heterostructure with the corresponding unit cell. For simplicity, only the positive ions positions are shown. Note that in going from the YIG layer to the BIG layer, the composition changes solely by substituting Bi^{3+} ions in all Y^{3+} positions, without changing the unit-cell symmetry from one film to another.

Before growing thin-film heterostructures, we had to calibrate the laser system and optimize the different garnet structures' deposition conditions. As part of the initial calibration experiments we tried to replicate the results of a similar study on epitaxial growth of YIG on single crystalline GGG by PLD announced previously in the literature.[2] In their report, Dorsey *et al.* indicated that the variation of deposition ambient oxygen pressure affected the anisotropy direction, such that a low oxygen pressure growth generated an in-plane magnetic anisotropy while a high-pressure deposition led to an out-of-plane anisotropy. We have deposited single crystalline single layers of YIG on GGG, at 800 °C, and at ambient pressures of 100, 200, and 700 mTorr, respectively. Figure 2 shows the three hysteresis loops for in-plane (VSM) measurements (made by applying a magnetic field parallel to the surface of the film). A close study of the figure reveals that while the saturation magnetization of the low-pressure specimen (100 mTorr) is the lowest of the three, its hysteresis loop displays the most squareness. The saturation magnetization values of the three films do not show a systematic variation with pressure. Dorsey *et al.* hinted that the reduction of the in-plane magnetization loop squareness could be associated with a change in anisotropy direction as a function of deposition ambient pressure.

Figure 3 shows the results of the out-of-plane VSM measurement of the three variable deposition pressure samples. The comparison of these hysteresis loops with the ones in Fig. 2 indicate that for all three specimens the anisotropy is in plane. Although the 700 mTorr film displays a relative squareness of the loop, the low saturation values and the high applied field required to achieve an out-of-plane saturation suggest that the increased O_2 pressure during deposition is negatively affecting the magnetic behavior of the single crys-

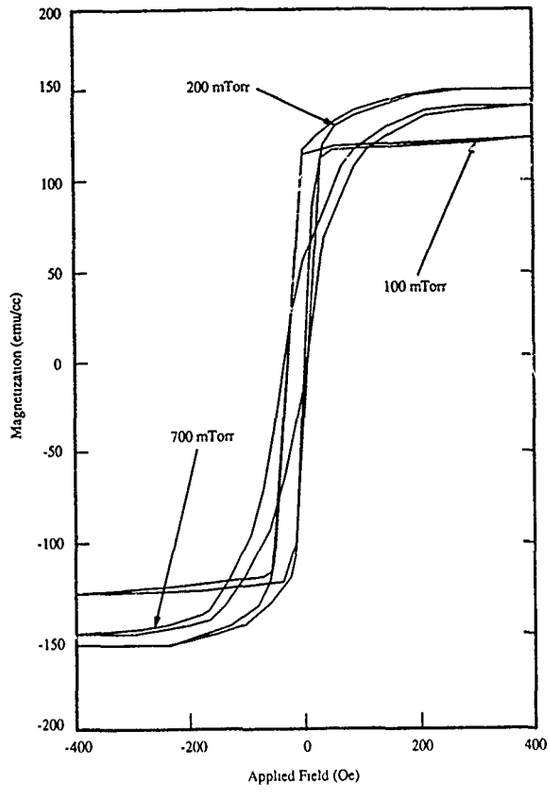

FIG. 2. The three hysteresis loops for in-plane (VSM) measurements.

talline YIG films grown at 800 °C on GGG substrates. Hence we carried all our depositions at 100 mTorr ambient pressure.

The x-ray θ-2θ measurements were made normal to the film surface. As indicated elsewhere,[3] the x-ray spectra consistently contained only two peaks: the [444] peak of the garnet film phase and the [444] peak of the garnet substrate phase. The conclusion of these experiments is that, even if the films are polycrystalline, all the grains are oriented such that the [111] direction is normal to the film surface.

It was noted that the saturation magnetizations of the multilayer heterostructures do not follow the rule of mixtures using as limits the bulk values (of the single layers grown at the same temperature), but rather using as the upper limit the bulk value for YIG grown at 800 °C. A close study of the x-ray-diffraction pattern also shows that the out-of-plane lattice parameter of the YIG layers varies with the YIG content of the 600 °C heterostructures, approaching the lattice parameter of the YIG monolayer deposited at 800 °C, not of the one grown at 600 °C.[1]

The YIG/BIG series, while generating some very encouraging results, could not be considered as potential materials for magneto-optical applications, since the anisotropies of all of the samples were in plane.

The role played by partial substitution of the ions occupying the dodecahedral sublattice of the garnet structure with rare-earth atoms has been widely investigated.[4,5] Of the rare earths, Sm, Eu, and Tb are known to give high positive K_u values in substituted garnets $R_{3-x}Bi_xFe_5O_{12}$, while Y, Gd, and Dy generate small K_u values. We have attempted to sub-

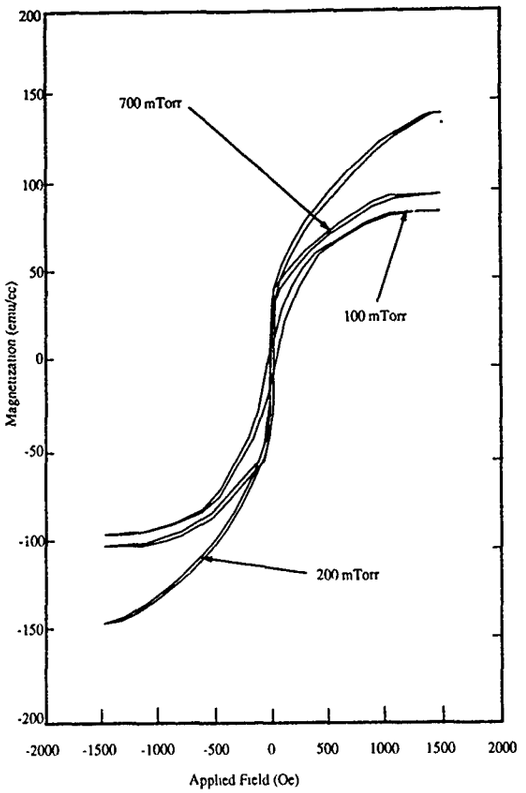

FIG. 3. The results of the out-of-plane VSM measurement of the three variable deposition pressure samples.

stitute one Eu^{3+} ion/formula unit, and deposited a new heterostructure series by growing alternating YIG and EBIG single crystalline layers.

The immediate effect of replacing one third of the Bi ions in the BIG structure by Eu ions is the change in anisotropy direction of the EBIG films, of similar thickness, from in plane to out of plane. The addition of Eu also seems to increase the coercive field.

Figure 4 shows a comparison of out-of-plane hysteresis loops of four multilayer EBIG/YIG films. Similar to the YIG/BIG series, the overlaying of YIG and EBIG monolayers produces increased saturation values. The increments appear to linearly follow the content of YIG. The highest saturation value is achieved for a ratio of 5:1 between the YIG layers and the EBIG layers thicknesses, while the lowest saturation magnetization is achieved for the film containing excess EBIG in a ratio of 3:1 to YIG. Note that while the value of the saturation goes up with the YIG content, the squareness of the hysteresis loops is also reduced, indicating an apparent change in the magnetic anisotropy direction from out of plane to in plane. This is consistent with the total composition of the film, which approaches the YIG single layer condition. In contrast, the films containing excess EBIG show decreasing saturation magnetization with the increased EBIG content, as they approach the EBIG single layer condition. At the same time, the films containing excess EBIG have displayed increased coercivity values in comparison to the specimens with large YIG content.

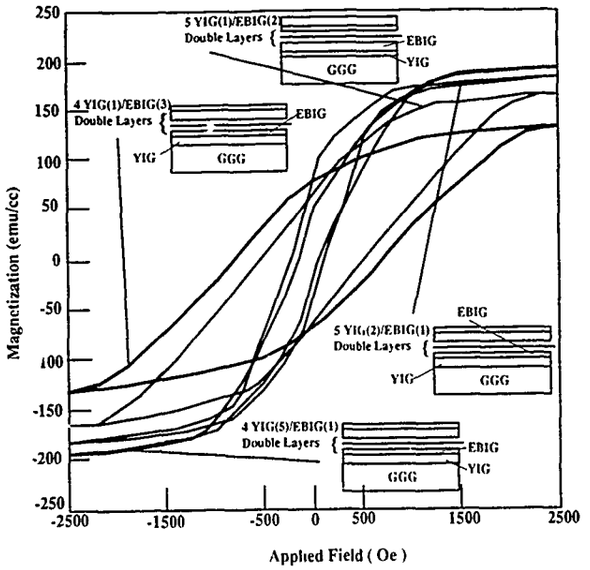

FIG. 4. A comparison of out-of-plane hysteresis loops of four multilayer EBIG/YIG films.

A magneto-optical hysteresis loop of a thin-film superlattice which has a ratio of EBIG to YIG layer thicknesses of 3:1 showed the best Kerr effect response in the series. The maximum rotation angle measured is 13 250 deg/cm, while the coercivity is 1.10 kOe. The values measured for coercivity during the Kerr rotation analysis are usually larger than those measured by VSM. This can be explained by the highly localized interaction with the specimen of the Kerr measurement and by the averaging character of the VSM analysis.

The exact effect of Eu addition on the magnetic and magneto-optical properties of the YIG/EBIG series are not completely understood at the present time. In contrast to the YIG/BIG series, the x ray of the YIG/EBIG series did not show any kind of structural fluctuation as a result of thickness modifications in the constituent layers. The tendency of the EBIG rich heterostructures to have high coercivities and a distinct out-of-plane anisotropy can be linked to the Eu substitution. However, further detailed measurements of new films must be carried out before we can conclusively decide if the observed effects are due solely to the Eu addition, to an increased stress in the film structure, or to a combination of factors.

Part of this work was supported by the Director, Office of Energy Research, Office of Basic Energy Sciences, Materials Science Division of the United States Department of Energy under Contract No. DE AC03-76SF000098.

[1] B. M. Simion, R Ramesh, V. G. Keramidas, R. L. Pfeffer, and G Thomas (unpublished)
[2] P. C. Dorsey, S. E. Bushell, R. G. Seed, and C. Vittoria, J. Appl. Phys. **74**, 1242 (1993).
[3] B. M. Simion, R. Ramesh, V. G. Keramidas, R L Pfeffer, G Thomas, and E. Marinero, in *Epitaxial Oxide Thin Films*, edited by D. K. Fork, J. M. Phillips, R. Ramesh, and R. H. Wolf (Materials Research Society, Pittsburgh, 1994), pp. 67–72.
[4] S. Geller, Z. Kristallogr **125**, 1 (1967).
[5] P Hansen, C. P. Klages, and K. Witter, J. Appl. Phys **63**, 2058 (1988).

Interlayer correlations and helical spin ordering in MnTe/CdTe multilayers (abstract)

V. Nunez
University of Maryland, College Park, Maryland 20742 and National Institute of Standards and Technology, Gaithersburg, Maryland 20899

T. M. Giebultowicz
George Mason University, Fairfax, Virginia 22030

W. Faschinger, G. Bauer, and H. Sitter
J. Keppler Universität Linz, Austria

J. K. Furdyna
University of Notre Dame, Notre Dame, Indiana 46556

Mn-VI/II-VI superlattices belong to the family of artificial multilayered structures composed from zinc-blende II-VI semiconducting compounds and Mn chalcogenides using MBE and ALE. While all naturally existing crystals of MnTe have the NiAs (hexagonal) structure, the zinc-blende form is a fcc Heisenberg antiferromagnet with dominant nearest neighbor interactions. The magnetic properties of such frustrated systems are strongly influenced by lattice mismatch strain. For example, *tensile* strain produces an incommensurate helical antiferromagnetic phase with an *in-plane* axis.[1] The strain and therefore helical period increases with thickness of CdTe, but in the presently studied samples is weak enough to allow investigation of the onset of incommensurate helical effects. In previously studied MBE-grown Mn-VI/Zn-VI systems,[1,2] the nonmagnetic spacers were too thick to allow interlayer coupling. We report neutron diffraction studies of new MnTe/CdTe superlattices prepared by ALE with extremely thin CdTe spacers (from 2 to 6 monolayers). The results indicate the formation of spin helices, consistent with the tensile nature of strain in the MnTe layers. In addition, the widths of the AF diffraction peaks and the presence of satellite peaks clearly indicate that the magnetic interactions propagate through the CdTe spacers, introducing coherence between the helices in different MnTe layers. The nature of the interaction responsible for this transfer is not yet clearly understood. Some possible mechanisms are discussed.

Supported in part by NSF Grant. No. DMR 9121353.

[1]T. M. Giebultowicz *et al.*, Phys. Rev. B **46**, 12076 (1992).
[2]T M. Giebultowicz *et al.*, Phys. Rev. B **48**, 12817 (1993).

 0021-8979/94/76(10)/6290/1/$6.00 © 1994 American Institute of Physics

Interlayer coupling in antiferromagnetic EuTe/PbTe superlattices (abstract)

T. M. Giebultowicz
George Mason University, Fairfax, Virginia 22030

V. Nunez
University of Maryland, College Park, Maryland 20742 and National Institute of Standards and Technology, Gaithersburg, Maryland 20899

G. Springholz and G. Bauer
J. Keppler University at Linz, Linz, Austria

J. Chen and M. S. Dresselhaus
Massachusetts Institute of Technology, Cambridge, Massachusetts 02139

J. K. Furdyna
University of Notre Dame, Notre Dame, Indiana 46556

We report neutron diffraction studies of magnetic correlations in MBE-grown (111) EuTe/PbTe multilayers. Bulk EuTe is a type-iI fcc antiferromagnet. This structure consists of ferromagnetic (FM) sheets of spins on (111)-type planes which are coupled antiferromagnetically to one another. In EuTe/PbTe the lattice mismatch strain selects an arrangement of the FM sheets parallel to the multilayer plane. Thus, in the case of an odd number of EuTe monlayers, there should be a nonzero magnetic moment—in other words, such superlattices are expected to behave as ferrimagnets, not anitferromagnets. This has been confirmed by recent SQUID studies.[1] As suggested by the above model, the dipolar fields arising from the lack of total moment compensation may introduce interlayer magnetic coupling, even though in this system there are no carriers that can transfer magnetic interactions across the nonmagnetic spacers through the RKKY mechanism, which is usually the case in coupled magnetic multilayered systems. Our experiments have indeed revealed clear magnetic superlattice peak patterns in several samples. The results of measurements in high external fields (up to 6 T) bring further support for the dipolar nature of the observed interlayer coupling. However, in some contrast to the expected scenario, the most pronounced coupling effects were seen in the case of an even number of monolayers. Possible explanations of this fact (e.g., higher-order terms in dipolar fields, or structural imperfections) are discussed.

Supported in part by NSF Grant No. DMR 9121353.

[1] J. Chen, Z. Wang, M. Dresselhaus, G. Dresselhaus, G. Springholz, and G. Bauer (in press).

 0021-8979/94/76(10)/6291/1/$6.00 © 1994 American Institute of Physics

Heat capacity measurements of antiferromagnetic CoO/NiCoO superlattices (abstract)

E. N. Abarra
Physics Department 0319, University of California, San Diego, La Jolla, California 92093-0319

K. Takano
Physics Department 0319, University of California, San Diego, La Jolla, California 92093-0319 and Center for Magnetic Recording Research, CMRR-0401, University of California, San Diego, La Jolla, California 92093-0401

F. Hellman
Physics Department 0319, University of California, San Diego, La Jolla, California 92093-0319

A. E. Berkowitz
Physics Department 0319, University of California, San Diego, La Jolla, California 92093-0319 and Center for Magnetic Recording Research, CMRR-0401, University of California, San Diego, La Jolla, California 92093-0401

We present heat capacity and magnetic measurements of antiferromagnetic (AFM) CoO/$Ni_{0.5}Co_{0.5}O$ superlattices grown by reactive sputtering. X-ray data verify the structure and the high quality of the superlattice. Neutron-diffraction studies of similar superlattices have shown AFM ordering through several bilayers despite the short-range nature of the spin interaction in the constituent materials.[1] We have recently developed a unique thin film microcalorimeter capable of measuring thin films from 1.5 K to well above room temperature,[2] permitting specific heat measurements on these superlattices for the first time. Magnetic measurements were made by coupling the superlattices to a 30 nm $Ni_{81}Fe_{19}$ overlayer and measuring the temperature dependence of the exchange anisotropy field. We examine the effect of exchange coupling at the interfaces by varying the thickness of the bilayers and their constituents. When the layers of the CoO/$Ni_{0.5}Co_{0.5}O$ superlattice are thin, we observe a single broad heat capacity peak at a temperature between the Néel temperatures of bulk CoO and $Ni_{0.5}Co_{0.5}O$. This peak is at a temperature that corresponds to the superlattice magnetic blocking temperature, the temperature at which the exchange field goes to zero. For thicker layers, we observe the disappearance of the superlattice peak, and the emergence of two broad peaks close to the individual Néel temperatures of CoO and $Ni_{0.5}Co_{0.5}O$. We compare the temperature dependence of the specific heat of the superlattices to various models.

Work was supported by NSF Grant Nos. 88-10374 and DMR-90-10908.

[1] J. A. Borchers, M J. Carey, R. W. Erwin, C. F Majkrzak, and A. E. Berkowitz, Phys. Rev Lett. **70**, 1878 (1993).
[2] D. W. Delinger, E. N. Abarra, K. Allen, P. W. Rooney, M. T. Messer, S. K. Watson, and F. Hellman, Rev. Sci. Instrum. **65**, 946 (1994).

 0021-8979/94/76(10)/6292/1/$6.00 © 1994 American Institute of Physics

Exchange coupling, interface structure, and perpendicular magnetic anisotropy in Tb/Fe multilayers (abstract)

J. Tappert, J. Jungermann, B. Scholz, R. A. Brand,
and W. Keune
Laboratorium für Angewandte Physik, Universität Duisburg, D 47048 Duisburg, Germany

Tb/Fe multilayer films are known to show perpendicular magnetic anisotropy (PMA), which is interesting for potential applications in magneto-optical data storage. We demonstrate by using ^{57}Fe Mössbauer probe layers and x-ray diffraction that part of the Tb-deposited-on-Fe (Tb/Fe) interface remains chemically sharp and crystalline bcc Fe. This part is associated with an unexpectedly strong antiferromagnetic exchange coupling of the Fe to the Tb layers. We find by using both conventional and circularly polarized radiation that part of the interface and core bcc Fe but none of the amorphous Fe is strongly coupled to Tb. This behavior is qualitatively explained by a structural model including regions with a sharp Tb/bcc-Fe interface, where PMA originates from Tb ions that experience the broken symmetry of the crystal electric field at the interface. The extrapolated isomer shift at $T=0$ K of the amorphous phase located at the Fe-deposited-on-Tb (Fe/Tb) interface was found to be different from that of the amorphous phase located at the Tb/Fe interface, suggesting a different amorphous structure at both interfaces.

 0021-8979/94/76(10)/6293/1/$6.00 © 1994 American Institute of Physics

Interfacial contributions to magnetic anisotropy in metal/semiconductor systems (abstract)

B. T. Jonker, H. Abad, and J. J. Krebs
Naval Research Laboratory, Washington, D.C. 20375-5343

It has been empirically established that the net anisotropy exhibited by even a simple metal epitaxial film is strongly effected by the interactions at the metal/semiconductor interface, although the mechanisms have not been systematically addressed and remain an open issue. An Fe(001) film, for example, is expected to exhibit a four fold symmetry in the in-plane magnetic anisotropy, consistent with the crystalline surface symmetry. Such films grown on a bulk GaAs(001) surface, however, exhibit a significant uniaxial anisotropy (twofold symmetry). It has been speculated that this uniaxial anisotropy arises from the strongly directional bonds of the substrate surface, based on a model that assumes a bulk-terminated, unreconstructed zinc-blende (001) surface.[1] This model fails to explain, however, the nearly ideal fourfold symmetry observed for similar Fe(001) films on the ZnSe(001) surface,[2] which has an identical crystalline structure as GaAs and differs in lattice constant by only 0.25%. We propose here a conceptual model to account for these pronounced differences, which describes how contributions to the net magnetic anisotropy arise from the formation of the interface and early stages of the metal film growth. We suggest that these contributions originate in the initial metal adsorption sites and subsequent bond or site filling, and are strongly dependent on the semiconductor surface reconstruction. We compare this model with results for Fe growth on several surface reconstructions.

This work was supported by the Office of Naval Research.

[1] J. J. Krebs, B. T. Jonker, and G. A. Prinz, J. Appl. Phys. **61**, 2596 (1987).
[2] B. T. Jonker, J. J. Krebs, G. A. Prinz, and S. B. Qadri, J. Cryst. Growth **81**, 524 (1987); J. Appl. Phys. **61**, 3744 (1987).

 0021-8979/94/76(10)/6294/1/$6.00 © 1994 American Institute of Physics

The magnetization density profile of a grain boundary in nickel (invited)

M. R. Fitzsimmons
Manuel Lujan Jr., Neutron Scattering Center, Los Alamos National Laboratory, Los Alamos, New Mexico 87545

A. Röll
Sektion Physik der Universität Munchen, München, Germany

E. Burkel
Friedrich-Alexander Universität, Erlangen-Nürnberg, Germany

K. E. Sikafus and M. A. Nastasi
Los Alamos National Laboratory, Los Alamos, New Mexico 87545

G. S. Smith and R. Pynn
Manuel Lujan Jr., Neutron Scattering Center, Los Alamos National Laboratory, Los Alamos, New Mexico 87545

We report the measured atomic and magnetization densities of a nickel twist grain boundary averaged over its lateral dimensions as a function of distance from the interface plane. The presence of a reconstructed interface region (the grain boundary) sandwiched between two single-crystal nickel films that were hot-pressed together was confirmed with grazing incidence x-ray diffraction. From reflection data taken using unpolarized neutrons, the atomic density profile of the grain boundary was determined to be (85±5)% of the bulk density when averaged over twice the grain-boundary width of (8±1) nm. Using this information in conjunction with the reflectivity data taken from the nickel sample with polarized neutrons reflection, the magnetic moment of a nickel atom was found to be between 18% and 52% larger in the twist grain boundary than in the bulk. The enhancement of the magnetic moment at the grain boundary is believed to result from the reduced atomic density of the interface region. Owing to this reduction in density, the magnetization density of the nickel interface is only somewhat enhanced, about 10%, compared to that of bulk nickel.

I. INTRODUCTION

Interesting magnetic behavior with great technological potential has been observed in a number of materials, particularly those containing a large fraction of internal interfaces. For example, interfaces play an important role in the giant magnetoresistance[1] and magnetic anisotropy[2] of some nanocrystalline and multilayered systems that may be used in future recording media or in magnetic reading and writing heads. The magnetocrystalline anisotropy of grain boundaries may determine whether a material is magnetically hard[3]—making a good permanent magnet, or soft[4]—making a good transformer core.

Considerable emphasis has been placed on studies of interfacial magnetism using calculational methods. In one calculation, Tersoff and Falicov[5] report a 34% enhancement in the magnetization of the (001) nickel surface compared to the bulk. The enhancement is a consequence of a narrowing of the *d*-orbital density of states and a dehybridization of the *sp-d* bands of nickel. These effects are attributed to the reduced coordination of a nickel atom at a (001) surface. Recently, Chrzan *et al.*[6] have calculated a reduction in the magnetization of a {111} stacking fault in nickel of about 2% compared to the bulk. They attribute the reduction to a broadening of band states caused by the close proximity of atoms in the [111] direction in the region of the stacking fault. Schaefer[7] has deduced from magnetometry measurements of consolidated ultrafined-grained nickel that the magnetic moment of nickel in the interfacial regions is reduced compared to bulk nickel. In the present work, we report an enhancement in the magnetic moment of nickel atoms in a planar grain boundary that we believe to be related to its *reduced* atomic density.

II. FABRICATION OF THE NICKEL TWIST GRAIN BOUNDARY

A. Bicrystal sample preparation

The grain boundary was manufactured by hot-pressing two thin single-crystal films of nickel to form a nickel bicrystal. An electron-beam evaporator was used to deposit nickel [Ni(1) in Fig. 1] onto the polished surface of a (001)MgO substrate heated to 825 K in a vacuum chamber with a base pressure of 10^{-5} Pa.[8] A second deposition of a mixture of naturally occurring nickel and ^{62}Ni was made onto a cleaved (001)NaCl single-crystal substrate.[9] The mass fractions of the natural nickel and ^{62}Ni used in the second deposition were chosen so that the average scattering length density of the nickel mixture was close to zero. By making the second film [Ni(2) in Fig. 1] nearly transparent to neutrons, the neutron reflectivity of the grain boundary was enhanced. During the second deposition, the NaCl crystal was

 0021-8979/94/76(10)/6295/6/$6.00 © 1994 American Institute of Physics

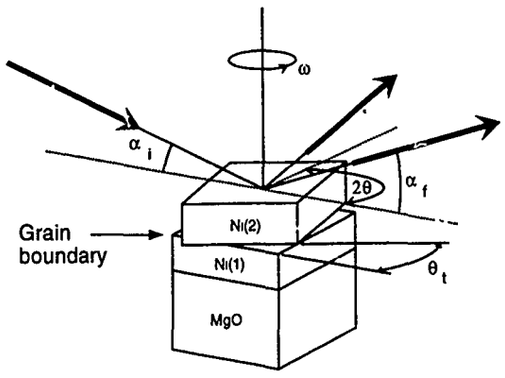

FIG. 1. Schematic diagram showing radiation incident on the nickel bicrystal at an angle of α_i, and reflected from the sample by α_f. The rotation of the sample about its surface normal is ω, and the rotation of the detector about the surface normal is 2θ. The crystal labeled as Ni(1) was grown on a MgO single-crystal substrate. The [001] edge of this crystal is misoriented by $\theta_t = 19.7°$ relative to that of the lower nickel crystal Ni(2), which was grown on a NaCl substrate.

heated to 600 K, and a potential of +1 kV was applied to the substrate relative to the vacuum chamber. After deposition, the two nickel films, with lateral dimensions of 3 cm by 3 cm, were placed face to face in a pressure cage such that the [100] edges of the films formed a twist angle of $\theta_t = 19.7°$ in the (001) plane. The twist angle for a $\Sigma = 37$ twist grain boundary, in which the positions of 1 in every 37 atoms coincide when projected onto the interface plane, is 18.9°. The small difference between the twist angles of the sample and that of a $\Sigma = 37$ boundary suggests that the boundary studied here is likely to have a special geometry with a high degree of symmetry, i.e., one with a relatively small unit cell.

After heating the substrates to 333 K, carbon monoxide was introduced into the oven at a pressure of 1 atm for 20 min. During this time, the native oxide on the nickel films was reduced into nickel carbonyl (the Mond process).[10] Next, the carbon-monoxide and nickel-carbonyl gases were evacuated, restoring the base pressure of the oven (10^{-5} Pa), and the bicrystal sintered at 773 K for 3 h. After cooling to room temperature in vacuum, the sample was removed from the pressure cage, and placed in water to dissolve the NaCl substrate. The resulting sample consisted of a grain boundary sandwiched between the two nickel crystals on the MgO substrate (see Fig. 1).

B. X-ray-diffraction measurements of the bicrystal and grain boundary

X-ray-diffraction measurements were made under conditions of grazing incidence, using the HASYLAB synchrotron in Hamburg, Germany, in order to characterize the quality of the bicrystal and grain boundary.[11] The mosaic spread of the nickel film on its MgO substrate was 1.3°, while that of the upper film, which was grown on NaCl, was 0.3°. Transmission electron microscopy of the latter film showed it to be relatively free of microtwins. The diffuse scattering of x rays reflected from the bicrystal was observed in order to determine whether the interface between the two nickel films contained voids. No modulation of the diffuse scattering with departure angle (α_f in Fig. 1) was observed, suggesting that the bicrystal interface was free of voids.[11]

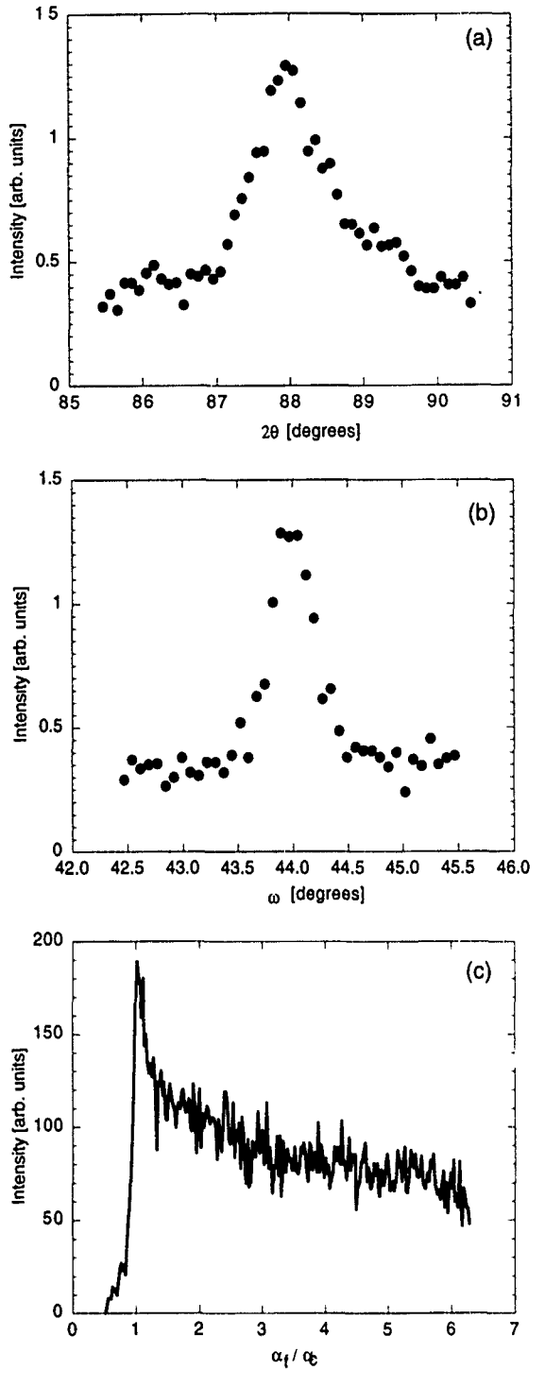

FIG. 2. The x-ray intensity measured under conditions of grazing incidence and integrated over departure angle α_f is shown as a function of (a) scattering angle 2θ, when the sample was optimized to excite a Bragg reflection from the grain boundary, and (b) sample orientation ω, when the detector was positioned at the intensity maximum in 2θ. (c) The x-ray intensity measured as a function of α_f normalized to the critical angle α_c for nickel and the radiation used, when 2θ and ω were optimized to produce a maximum of diffracted radiation. The smoothly varying profile beyond $\alpha_f/\alpha_c = 1$ is characteristic of a thin interfacial region.

A plot of the x-ray intensity integrated over the length of the position sensitive detector, i.e., α_f, as a function of scat-

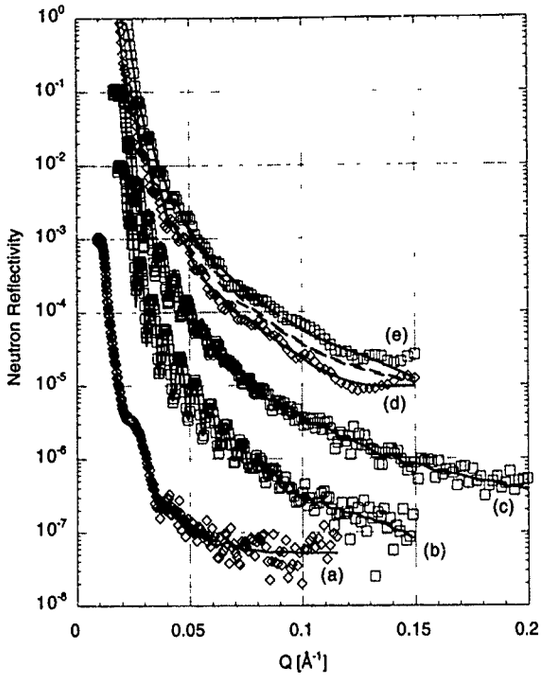

FIG. 3. The unpolarized-neutron reflectivities of the nickel films on (a) NaCl (◇) and (b) MgO (□) substrates, and (c) the nickel bicrystal (□). The solid lines for (a) and (b) were calculated from the scattering length density profiles shown in Fig. 4. The solid line for (c) was calculated using the atomic density profile of the grain boundary shown in Fig. 5(a). The polarized-neutron reflectivities for the R_- (◇) and R_+ (□) cross sections are shown in (d) and (e). The dashed lines were calculated using a magnetic moment for nickel that was constant throughout the bicrystal. The solid lines were calculated using an enhanced magnetic moment [Fig. 5(b)] at the grain boundary.

tering angle 2θ (see Fig. 1), when the sample was oriented to excite a grain-boundary reflection (one corresponding to the 12,12,0 reflection indexed in the coordinate system of a $\Sigma=37$ grain boundary) is shown in Fig. 2(a). A plot of the intensity measured as a function rotation angle about the normal to the sample surface, ω (see Fig. 1), when the detector is positioned at the intensity maximum in Fig. 2(a) is shown in Fig. 2(b). These measurements demonstrate that Bragg reflection is well localized within the reciprocal-lattice plane corresponding to the projection of atom positions onto the interface plane of the bicrystal. When the detector position and sample orientation were optimized to produce a maximum of intensity at the position corresponding to the 12,12,0 grain-boundary reflection, the rodlike intensity profile shown in Fig. 2(c) was measured as a function of departure angle α_f from the sample surface. The rodlike form is characteristic of scattering from spatially limited or thin reconstructed interfaces. The presence of the rodlike distribution of intensity at the position of a grain-boundary reflection, and its absence in single-crystal films containing no grain boundary, is evidence that the bicrystal interface had reconstructed during the sintering process to form a grain boundary.[11–13]

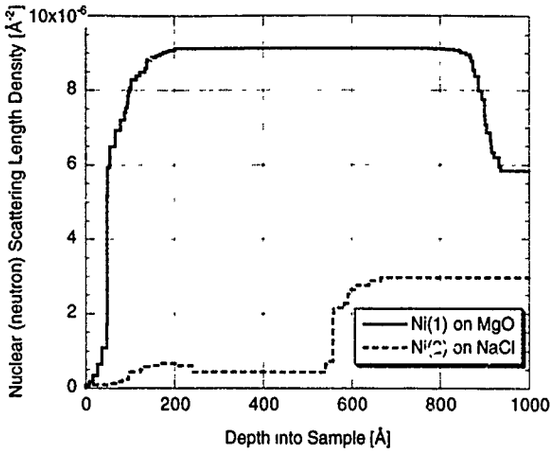

FIG. 4. The nuclear (neutron) scattering length density profiles deduced for the nickel on MgO sample (solid line) and the nickel on NaCl sample (dashed line) from fits to the reflectivity data in Figs. 3(a) and 3(b).

III. EXPERIMENTAL RESULTS AND DISCUSSION

A. The atomic density profile of the nickel grain boundary

The reflectivities of two nickel films, which were grown under conditio. s identical to those used to make the bicrystal but on different NaCl and MgO substrates, were obtained with unpolarized neutrons at the Manuel Lujan Jr. Neutron Scattering Center (LANSCE).[14] These reflectivity curves are shown in Figs. 3(a) and 3(b) (open symbols) as a function of scattering vector magnitude, $Q=4\pi\sin(\alpha_i)/\lambda$, where λ is the wavelength of the radiation (determined using the time-of-flight technique), and α_i is the angle of incidence of the radiation onto the sample surface. The scattering length density profiles $\beta(z)$, deduced as a function of depth into the nickel films from the reflectivity data, are shown in Fig. 4. The solid curves in Figs. 3(a) and 3(b) were calculated from the density profiles using the Parratt formalism.[15] From the fit to the nickel-MgO data, and using the published scattering length for natural nickel (10.3×10^{-5} Å[16]), the average atomic (number) density of the nickel film, $n_0=0.0895\pm0.0005$ Å^{-3}, was deduced. This density is somewhat less than the density of bulk nickel, 0.0913 Å^{-3}. Similar reductions in the densities of thin films compared to their bulk counterparts have been observed in other metal systems.[11,17] Using the value of n_0, the neutron-scattering length of the null scattering ^{62}Ni-nickel mixture was deduced to be $(4.8\pm0.5)\times10^{-6}$ Å (more than 20× smaller than that of natural nickel) from the fit to the nickel-NaCl data. This information is used later.

The reflectivity of unpolarized neutrons from the nickel bicrystal is shown in Fig. 3(c). In determining the scattering length density profile of the nickel bicrystal, the air-nickel and nickel-MgO interfaces of this sample were assumed to be identical to those previously determined. This assumption is reasonable, since no significant differences between the air-nickel and nickel-MgO interfaces of other similarly prepared samples have been observed. The portions of the scattering length density profile for the bicrystal that were per-

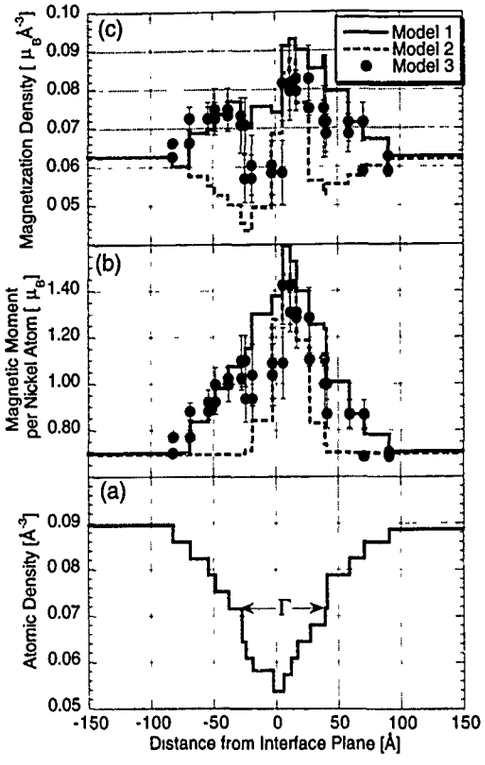

FIG. 5. (a) The atomic density of the grain boundary deduced as a function of distance away from the interface plane from a fit of the bicrystal model (described in the text) to the reflectivity data in Fig. 3(c). (b) The magnetic moment of nickel deduced as a function of distance from the interface plane for model 1 (solid curve), model 2 (dashed curve), and model 3 (●) described in the text. (c) The magnetization density of the grain boundary calculated for the three models.

turbed to fit the data were those belonging to the overall thicknesses of the two nickel films and the atomic density of the grain-boundary region. The atomic density profile deduced for the grain boundary is shown in Fig. 5(a). The reflectivity curve calculated for this model is shown as the solid curve in Fig. 3(c). The minimum density of the grain boundary, occurring at the interface plane, is (60±6)% of the film density. The full width Γ, where the density is halfway between the minimum and bulk densities, is (8±1) nm. The mean grain-boundary density, when averaged over twice its width, is (85±5)% of n_0.

The mean density is similar to those calculated from atomic structures of gold grain boundaries, which have been deduced from quantitative x-ray-diffraction measurements;[12,13] however, the nickel boundary is considerably broader than the gold boundaries. The boundary widths deduced for the two gold grain boundaries are believed to be about 1 nm.[12,13] Since the twist angles of the two gold grain boundaries (θ_t=36.9° and 22.6°) were larger than that of the nickel grain boundary (θ_t=19.7°), the nickel boundary is expected to be broader than the gold grain boundaries, although perhaps not as broad as observed. Interestingly, grain-boundary widths in nanocrystalline nickel also appear to be quite large. Recently, Aus *et al.*[18] have reported boundary widths of 5 nm deduced from magnetometry measurements, while Valiev[19] has measured widths of 10 nm using high-resolution transmission electron microscopy. The large boundary widths, which seem to be typical of nickel, may be due to the ferromagnetic nature of the material. For example, the magnetic anisotropy of a grain boundary may influence and in turn be influenced by the atomic structure of the boundary. To date, the magnetic effects have been largely ignored in theoretical calculations of grain-boundary structures, so theoretical calculations may be underestimating the structural widths of grain boundaries in magnetic materials.

B. The magnetization profile of the nickel grain boundary

The reflectivities of a nickel-MgO sample and the bicrystal were remeasured at LANSCE using neutrons with polarization states antiparallel and parallel to the 0.1 T magnetic field applied along the sample surface.[20] The field strength is considerably larger than that needed to saturate thin iron films along their hard axes,[21] so both nickel samples, whose saturation magnetizations are much less than iron, should have been fully saturated during the reflectivity measurements. Two reflection cross sections, R_- and R_+,[22] corresponding to the two neutron polarization states (antiparallel and parallel), were measured for each sample. In the case of the nickel-MgO sample, the difference in Q between the critical edges for the R_- and R_+ reflectivity curves was used to calculate the average magnetic moment of μ_{Ni}=(0.7±0.1) μ_B for the sample. This value is in good agreement with the literature value of 0.6 μ_B for bulk nickel.[23]

Since the polarization state of the reflected radiation was not determined in this study, the reflectivity cross sections R_- and R_+ may be contaminated by scattering processes occurring within the sample that actively change the polarization state of the neutron radiation. These processes may occur in samples that are not fully saturated, or have a large degree of magnetocrystalline anisotropy.[22] In the latter case, the magnetic moment deduced from R_+ and R_- would represent the component of the total moment in the direction of the applied magnetic field. Measurements of the polarization state of the reflected radiation, i.e., all four scattering cross sections of the sample, are in progress at LANSCE.

The R_- and R_+ cross sections for the nickel bicrystal are shown as the open symbols in Figs. 3(d) and 3(e). The dashed curves in this figure were calculated from a model that used the atomic density profile previously determined for the bicrystal, the nuclear scattering lengths for each nickel film, and the value of μ_{Ni}, to calculate the nuclear and magnetic contributions to the scattering length density profile of the bicrystal. For $Q>0.07$ Å^{-1}, no splitting is discernible between the calculated profiles (dashed curves), when a clear splitting is seen in the data. Since the large-Q region is most sensitive to spatially limited features like the grain boundary, poor agreement here suggests that the magnetic moments of atoms in the grain boundary may be different from the bulk.

The agreement between the calculated profiles and the data could be significantly improved when the magnetic moment of nickel atoms in the grain boundary were made to be larger than μ_{Ni}. By varying only the decay of the magnetic moment from a maximum at the interface plane (correspond-

ing to an abscissa value of zero in Fig. 5) to μ_{Ni} at a position where the grain-boundary density equals n_0 much better agreement was obtained. This variation in magnetic moment is shown by the solid line in Fig. 5(b) and is called model 1. The optimum value of (1.6±0.3) μ_B at the interface plane produced the solid curves in Figs. 3(d) and 3(e). When averaged over twice the grain-boundary width, 2Γ, the magnetic moments of nickel atoms in the interfacial region are about (52±12)% larger than the magnetic moment measured for the film.

A second model (model 2), which represented the variation of the magnetic moment of nickel by a Gaussian function centered at the interface plane, was also explored. In this model the height and width of the Gaussian function were optimized to produce the dashed curves in Fig. 5. A peak moment of (1.5±0.2) μ_B was obtained. The full width at half maximum in the profile of the magnetic moment was (3±1) nm. In this model the magnetic width of the grain boundary is considerably smaller than its structural width of (8±1) nm. Theoretical calculations suggest that changes in symmetry, coordination number, and density can alter the magnetic moments of atoms. If these predictions are correct, then the magnetic moments of the atoms closest to the interface plane would be most affected by the change of atomic structure that occurs at grain boundaries. In particular, the coordination number of an atom would be expected to remain unchanged unless it were located quite closely to the interface plane. If the magnetic moment of an atom is most affected by its coordination number, rather than changes in atomic density, then the magnetic width of a grain boundary might be smaller than its structural width.

In a third model (model 3), the magnetic moment [(●) in Fig. 5(b)] for each step in the atomic density profile [Fig. 5(a)] was perturbed independently to yield a good fit to the data. Even though the magnetic moments of nickel atoms away from the grain boundary were no longer constrained to be μ_{Ni}, as in the earlier model, the magnetic moments of these atoms, nevertheless, tended toward this value. The optimum magnetic moment at the grain-boundary plane was still enhanced [a value of (1.4±0.2) μ_B was obtained] compared to the bulk, although the increase was not as large as that deduced from the previous models.

All the models predict an enhancement of the magnetic moment of nickel at the grain-boundary interface. When averaged over twice the grain-boundary width, we find enhancements in the magnetic moment of nickel ranging from a low of 18% for model 2 to a high of 52% for model 1. The enhancement deduced from the best-fitting model, model 3, is (38±3)%. Since the magnetization density is the product of magnetic moment and atomic density, which is reduced at the nickel grain boundary, the magnetization density of the interface is only sightly enhanced compared to the bulk. The magnetization densities of the interfaces [Fig. 5(c)] calculated using models 1 and 3 are 20% and 10% greater than the bulk, respectively, when integrated over the grain-boundary region, while a small decrease of 6% is predicted from model 2. In other words, the large enhancements in the *magnetic moments* of nickel at the grain boundary are mostly negated by the reduction of its atomic density to yield a *magnetization density* that is only about 10% greater than the bulk.

IV. CONCLUDING REMARKS

We believe that reduction of atomic density and change in symmetry at a grain boundary will alter its density of states (of *d* orbitals in nickel), leading to the observed enhancement in the magnetic moments of nickel atoms in the grain boundary. In support of this hypothesis, we point out that Chrzan *et al.*[6] have attributed a calculated *reduction* in the magnetic moments of nickel atoms at a {111} stacking fault to the close proximity of atoms near this interface. Another calculation has shown that the reduced coordination of an ideal (100) nickel surface alters its density of states, which produces a 32% enhancement in the magnetic moments of nickel atoms at the surface compared to the bulk.[5] The trend in the two theoretical calculations is in agreement with our observations of an enhanced magnetic moment and reduced atomic density of one particular nickel grain boundary. Nickel grain boundaries with different twist angles and crystallographic orientations will have different crystal structures, and so might have different magnetic structures. Comparisons between these structures, measured with techniques developed for this study, with calculations of theoreticians for a variety of grain boundaries will lead to a better understanding of interfacial magnetism, and its effects on the macroscopic magnetic properties of materials like multilayered and nanophase systems which contain many interfaces.

Interestingly, Schaefer[7] has reported a *reduction* in the magnetic moment of nickel at grain boundaries in samples composed of consolidated nickel crystallites with grain sizes of 10 nm. This conclusion was made based upon magnetization measurements using a SQUID and vibration magnetometer. The difference between the conclusion reached by Schaefer and that in the present study, where evidence for an increase in the magnetic moment of nickel at a grain boundary was seen, may be due to several factors.

First, the magnetometry technique measures the magnetization of the entire sample, and so does not specifically measure the magnetization of interfaces. If, for example, a portion of the nanocrystalline sample were not magnetic when the entire sample was thought to be magnetic, then a reduced magnetic moment would be calculated for the sample, since its measured magnetization would not have been as large as would have been the case had the entire sample been magnetic. We note that antiferromagnetic order is suppressed in 11 nm grains of chromium (to at least 20 K).[24] If magnetic order can also be suppressed in ultrafine-grained nickel, then a portion of the sample studied by Schaefer may not have been ferromagnetic, possibly resulting in a diminished sample magnetization. Depending upon the amount of material which was not ferromagnetic, a diminished magnetization might be measured for the entire sample even if the magnetic moment of nickel is generally increased in the grain boundaries.

Second, microstrain introduced into the nanocrystalline sample during high-pressure compaction, which was not likely to have been relieved at ambient temperature used during the compaction process, may affect the magnetic proper-

ties of the material in a manner that may not have occurred in the bicrystal sample. For example, strain is known to affect the magnetic anisotropy and magnetoelastic energies of ferromagnets[25] and the magnetic structure of coarse-grained chromium.[26] Considerable microstrain is usually found in nanocrystalline metals[24,27] and is likely to be present in nanocrystalline nickel.[28] Since the bicrystal was annealed at high temperature, the grain boundary in this sample should be relatively strain-free compared to those in nanocrystalline nickel. The different conclusions reached by Schaefer and this study might be attributed to differences in the strain contents of two sample, if microstrain can change the magnetic moments of atoms in grain boundaries.

Third, the grain boundary studied in the bicrystal experiment may not be representative of grain boundaries found in nanocrystalline materials. For example, the grain boundary in the bicrystal sample was known from the x-ray-diffraction observations to be reconstructed, i.e., to have formed a relaxed structure. On the other hand, the nanocrystalline sample, at least on the onset of the magnetometry measurements, was likely to contain grain boundaries in unrelaxed configurations owing to the relatively low diffusivity of nickel at ambient temperature compared to the annealing temperature used to make the bicrystal (773 K). The magnetic moment of nickel may be increased in a relaxed grain boundary compared to an unrelaxed one. Furthermore, the grain boundary studied here is special in that its unit cell is reasonably small—containing only 37 atoms per atomic plane. Randomly oriented grain boundaries, which are characterized by large unit cells, should occur more frequently in as-compacted nanocrystalline nickel that the special grain boundary studied in this work. Efforts are in progress to determine whether the magnetic moments of nickel atoms in grain boundaries with other orientations differ from the moment reported for the $\Sigma=37$ twist grain boundary.

Finally, as the grain size of a nickel crystallite becomes comparable to the structural width of a grain boundary, which may be relatively large for nickel,[18,19] interactions across crystallites between different interfaces may perturb their structures from those of interfaces found in coarser-grained materials. If the magnetic structure of an interface is coupled to its atomic structure, then interactions between neighboring grain boundaries that produce alterations in their atomic structures may also lead to changes in their magnetizations, particularly in an ultrafine-grained materials such as that studied by Schaefer. These interactions would not be present in the bicrystal sample, since the surface and nickel-MgO interface of the sample are a few tens to hundreds of nanometers away from the grain-boundary interface.

While bicrystal experiments such as this one may not provide information relevant to as-compacted nanocrystalline materials, these experiments do provide valuable information about the magnetizations of planar interfaces, such as those present in multilayered materials. In particular, model bicrystal experiments can be designed to study specific problems that might be encountered in the development of magnetic multilayer devices. For example, bicrystals containing controlled amounts of impurity solutes can be fabricated and studied to determine how the magnetic properties of interfaces change as impurity atoms segregate to the bicrystal interfaces.

ACKNOWLEDGMENTS

This study was supported by the U. S. Department of Energy under Contract No. W-7405-ENG-36 with the University of California, and the German Federal Ministry for Research and Technology (BMFT) under the Contract No. 03PE1LMU/2. The Manuel Lujan Jr., Neutron Scattering Center is a national user facility funded by the U. S. Department of Energy Office of Basic Energy Science. We acknowledge valuable discussions with Dr. A. C. Lawson and Dr. R. A. Robinson. The use of the D4 and W1 beam lines at HASYLAB, Germany, and the equipment of Risø National Laboratories, Denmark for the x-ray measurements are acknowledged. The support of Professor J. Peisl is gratefully acknowledged.

[1] P. M. Levy, Science **256**, 972 (1992).
[2] J. C. Slonczewski, J. Appl. Phys. **73**, 5957 (1993).
[3] S. Mørup and G. Christiansen, J. Appl. Phys. **73**, 6955 (1993).
[4] G. Herzer, IEEE Trans. Magn. **26**, 1397 (1990).
[5] J. Tersoff and L. M. Falicov, Phys. Rev. B **26**, 6186 (1982).
[6] D. C. Chrzan, L. M. Falicov, J. M. MacLaren, X.-G. Zhang, and A. Gonis, Phys. Rev. B **43**, 9442 (1991).
[7] H.-E. Schaefer, in *Mechanical Properties and Deformation Behavior of Materials Having Ultra-Fine Microstructures*, edited by M. A. Nastasi, D. M. Parkin, and H. Gleiter, NATO ASI Series 233 (Kluwer, Dordrecht, 1993), p. 81.
[8] S. Chikazumi, J. Appl. Phys. **32**, 81S (1961).
[9] A. Chambers and M. Prutton, Thin Solid Films **1**, 235 (1967).
[10] L. Mond, C. Langer, and F. Quincke, J. Chem. Soc. **57**, 749 (1890).
[11] M. R. Fitzsimmons and E. Burkel, Phys. Rev. B **47**, 8436 (1993).
[12] M. R. Fitzsimmons and S. L. Sass, Acta Metall. **36**, 3103 (1988).
[13] M. R. Fitzsimmons and S. L. Sass, Acta Metall. **37**, 1009 (1989).
[14] G. S. Smith and W. A. Hamilton, in *Condensed Matter Research at LANSCE*, edited by D. K. Hyer, Report No. LALP 90-7 (1990) (unpublished).
[15] L. G. Parratt, Phys. Rev. **95**, 359 (1954).
[16] L. Koester, H. Rauch, and E. Seymann, At. Data Nucl. Data Tables **49**, 66 (1991).
[17] E. Kay and S. M. Rossnagel, in *Handbook of Ion Beam Processing Technology*, edited by J. J. Cumo, S. M. Rossnagel, and H. R. Kaufman (Noyes, Park Ridge, NJ, 1989), p. 170.
[18] M. J. Aus, B. Szpunar, A. M. El-Sherik, U. Erb, G. Palumbo, and K. T. Aust, Scr. Metall. **27**, 1639 (1992).
[19] R. Z. Valiev, in *Nanophase Materials*, edited by G. C. Hadjipanayis and R. W. Siegel, NATO ASI Series 260 (Kluwer Academic, Dordrecht, The Netherlands, 1994), pp. 275–282.
[20] M. R. Fitzsimmons, G. S. Smith, R. Pynn, M. A. Nastasi, and E. Burkel, Physica B **198**, 169 (1994).
[21] Th. Zeidler (private communication).
[22] A. Schreyer, Th. Zeidler, Ch. Morawe, N. Metoki, H. Zabel, J. F. Ankner, and C. F. Majkrzak, J. Appl. Phys. **73**, 7616 (1993).
[23] *Handbook of Chemistry and Physics*, 57th ed., edited by R. C Weast (CRC, Cleveland, 1976), p. E-120.
[24] M. R. Fitzsimmons, J. A. Eastman, R. A. Robinson, A. C. Lawson, J. D. Thompson, R. Mavshovich, and J. Satti, Phys. Rev. B **48**, 8245 (1993).
[25] E. Fawcett, Rev. Mod. Phys. **60**, 209 (1988).
[26] G. E. Bacon and N. Cowlam, J. Phys. C **2**, 238 (1969).
[27] M. R. Fitzsimmons, J. A. Eastman, M. Muller-Stach, and G. Wallner, Phys. Rev. B **44**, 2452 (1991).
[28] J. A. Eastman (private communication).

Magnetic and magnetocaloric properties of melt-spun Gd_xAg_{100-x} alloys

C. D. Fuerst, J. F. Herbst, and R. K. Mishra
Physics Department, General Motors NAO Research and Development Center, 30500 Mound Road, Warren, Michigan 48090-9055

R. D. McMichael
National Institute of Standards and Technology, Gaithersburg, Maryland 20899

With the object of assessing their magnetocaloric properties, we have prepared Gd_xAg_{100-x} alloys (x=50, 70, 75, 77.5, 80, 100) by melt spinning. The microstructures of the melt-spun ribbons were investigated by x-ray diffraction and transmission electron microscopy. Data from field- and temperature-dependent magnetization measurements were used to calculate the field-induced entropy change ΔS. The Gd-only ribbons are characterized by a single ΔS peak near 280 K. For the Gd_xAg_{100-x} ($70 \leq x \leq 80$) materials ΔS contains another peak in the 100–120 K range which we ascribe to an amorphous, ferromagnetic Gd-Ag component. We find melt-spun $Gd_{50}Ag_{50}$ ribbons to consist primarily of crystalline GdAg (cubic CsCl structure), which is antiferromagnetic.

It is well known that the field-induced entropy change ΔS of a magnetic material can be exploited as a basis for solid-state refrigeration, with potential for application in the room-temperature range as well as at cryogenic temperatures.[1–3] Recent calculations[4,5] and experiments[6,7] have shown that materials containing nanometer-sized magnetic regions can produce larger values of ΔS than conventional ferromagnets or paramagnets over certain intervals of temperature (T) and applied field (H). To maximize this effect, it is important that the magnetic phase have a large intrinsic magnetization and, to minimize heating due to hysteresis, low magnetocrystalline anisotropy. Both of these demands are satisfied by gadolinium. Furthermore, it is desirable for the magnetic particles to be at least partially separated by nonmagnetic material to reduce magnetic interactions between them.

With these considerations in mind we have investigated, and here report, measurements of $\Delta S(T)$ for Gd_xAg_{100-x} alloys which were prepared by the rapid solidification technique of melt spinning. We chose a rapid quenching method with the objective of forming small magnetic particles or clusters, and the Gd-Ag system was selected since its equilibrium phase diagram indicates that ferromagnetic Gd (Curie temperature $T_c \cong 293$ K) and antiferromagnetic GdAg (Neel temperature $T_n \sim 140$ K) are essentially immiscible.

Ingots of Gd_xAg_{100-x} (x=50, 70, 75, 77.5, 80) were prepared by induction melting high-purity elemental constituents. Each ingot was melt spun, again under argon, by ejecting molten alloy through an orifice (0.6 mm diameter) in a quartz crucible onto the surface of a chrome-plated copper disk (25 cm diameter). The quench rate was varied by changing the surface velocity v_S of the disk. A quench rate corresponding to v_S=20 m/s was used for all the silver-containing alloys, and v_S=30 m/s was used to produce the Gd-only material.

Ribbon microstructures were examined by both x-ray powder diffraction and transmission electron microscopy (TEM). Figures 1 and 2 display Cu K_α x-ray diffractograms for the x=100, 80, 77.5 and x=75, 70, 50 materials, respectively. It is clear from Fig. 1(a) that the Gd-only ribbons are comprised of hexagonal Gd grains with some preferential orientation along the [001] direction since the (002) and (004) reflections are of greater intensity than those calculated for an isotropic distribution [vertical bars in Fig. 1(a)]. Selected area diffraction in the TEM confirms this interpretation. Figure 3(a) shows that the Gd ribbons consist of irregular grains approximately 0.5 μm in size and have some alignment along the [001] direction, which was normal to the surface of the quench wheel. In addition to [100]-oriented hexagonal Gd crystallites, the x-ray diagram of the $Gd_{80}Ag_{20}$

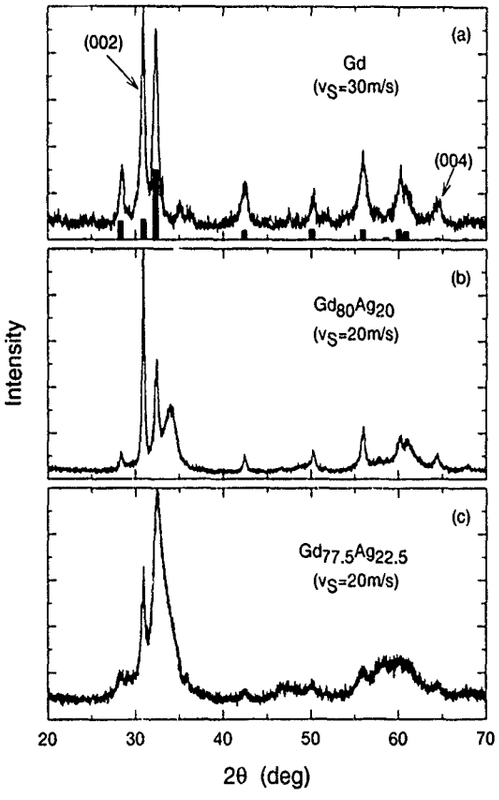

FIG. 1. Cu K_α x-ray powder-diffraction patterns of melt-spun Gd_xAg_{100-x} ribbons. (a) Gd, the vertical bars denote line positions and intensities for isotropic, hexagonal Gd metal. (b) $Gd_{80}Ag_{20}$ (c) $Gd_{77.5}Ag_{22.5}$.

 0021-8979/94/76(10)/6301/3/$6.00 © 1994 American Institute of Physics

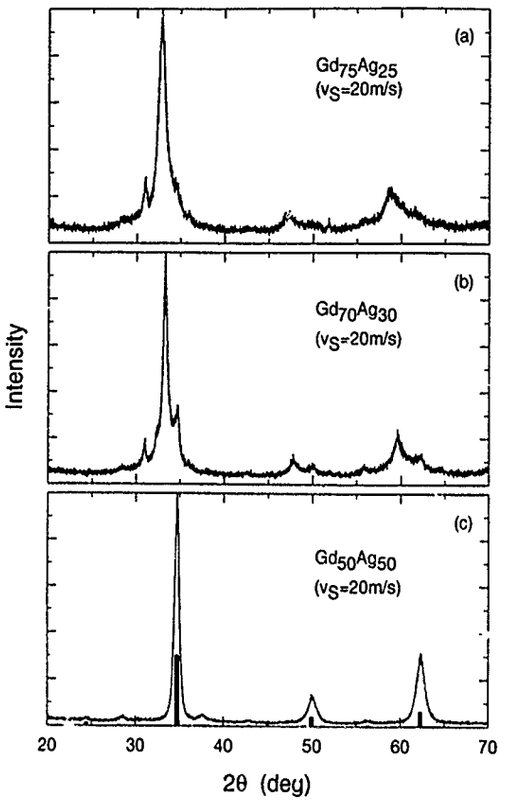

FIG 2. Cu K_α x-ray powder-diffraction patterns of melt-spun Gd_xAg_{100-x} ribbons. (a) $Gd_{75}Ag_{25}$. (b) $Gd_{70}Ag_{30}$. (c) $Gd_{50}Ag_{50}$; the vertical bars denote line positions and intensities for isotropic, cubic GdAg.

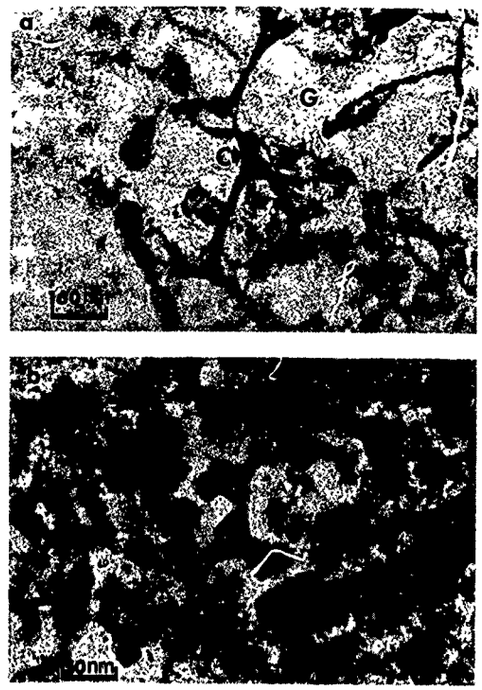

FIG. 3. TEM micrographs of melt-spun (a) Gd (G denotes a hexagonal Gd grain and C indicates a cubic form of Gd situated at the grain boundaries) and (b) $Gd_{77.5}Ag_{22.5}$ (regions labeled A are amorphous $Gd_{50}Ag_{50}$; hexagonal Gd particles are signified by G).

ribbons [Fig. 1(b)] also suggests an amorphous Gd-Ag component. Ribbons melt spun from the eutectic composition $Gd_{77.5}Ag_{22.5}$ contain a substantial amorphous fraction, as shown by Fig. 1(c); the corresponding TEM micrograph of Fig. 3(b) reveals small (<100 Å) Gd grains embedded in an amorphous matrix having an overall composition near $Gd_{50}Ag_{50}$ estimated by microchemical analysis.

From the x-ray pattern for the $Gd_{75}Ag_{25}$ ribbons, Fig. 2(a), we infer that the amorphous fraction is even larger than that of the $Gd_{77.5}Ag_{22.5}$ sample since the features are more diffuse than those of Fig. 1(c). Some hexagonal Gd is still present and persists in the $Gd_{70}Ag_{30}$ ribbons as well [Fig. 2(b)]; comparison of Figs. 2(a) and 2(b) indicates less amorphous Gd-Ag phase in the $Gd_{70}Ag_{30}$ ribbons. Similar to Fig. 3(b), TEM analysis of the $Gd_{70}Ag_{30}$ ribbons again reveals Gd grains interspersed in an amorphous matrix having a composition near $Gd_{50}Ag_{50}$, in addition to a small amount of crystalline GdAg. No gadolinium component is apparent in the x-ray diagram of melt-spun $Gd_{50}Ag_{50}$, Fig. 2(c); the ribbons are principally composed of fine-grained crystalline GdAg, whose reflections are illustrated by the vertical bars in Fig. 2(c). TEM of this material shows GdAg grains with an average diameter of ~100 Å.

Magnetic moment versus temperature curves for the melt-spun ribbons investigated here, as well as for a bulk Gd ingot sample, are displayed in Fig. 4; the measurements were performed in a maximum applied field of 9 kOe, which was

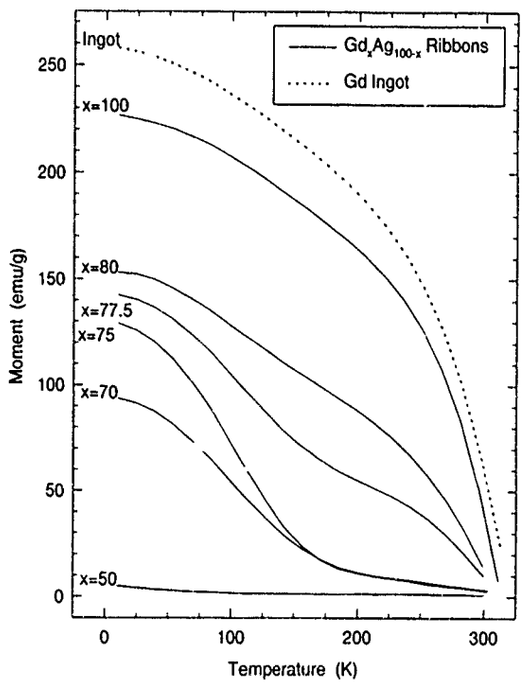

FIG. 4. Magnetic moment vs temperature for melt-spun Gd_xAg_{100-x} ribbons (x=50, 70, 75, 77.5, 80, 100) and for a Gd ingot sample measured in an applied magnetic field of 9 kOe.

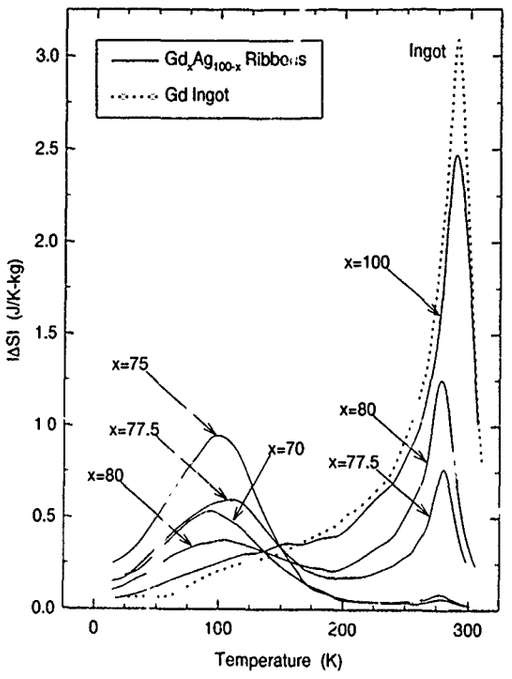

FIG. 5. Entropy change ΔS of melt-spun Gd_xAg_{100-x} ribbons (x=70, 75, 77.5, 80, 100) and of a Gd ingot sample in a 9 kOe applied magnetic field.

sufficient to saturate the magnetization in each case. The observed low-temperature moment for the Gd-only (x=100) ribbons, ~215 emu/g (~6.1 μ_B/Gd), is 20% lower than the 268 emu/g (7.55 μ_B/Gd) value for elemental gadolinium metal, as comparison with the bulk Gd curve in Fig. 4 shows. The disparity is puzzling. Some of it can be attributed to nonmagnetic contaminants such as oxides, but our TEM work indicates that secondary phases comprise no more than 5 vol % of the ribbons. We speculate, therefore, that particle size effects may also contribute to the moment reduction. Gadolinium moments in the 5–7 μ_B range have been reported in several amorphous binary alloys,[8] and a moment of only 3 μ_B/Gd has been observed in clusters containing fewer than 100 Gd atoms.[9]

For the Gd_xAg_{100-x} ribbons with $70 \leq x \leq 80$, the data of Fig. 4 strongly suggest the presence of two ferromagnetic components, one with a Curie temperature in the vicinity of 100 K and a second near the $T_c \cong 293$ K value for bulk Gd metal. Hauser[10] prepared amorphous Gd_xAg_{100-x} alloys in the $20 \leq x \leq 100$ interval by sputtering and found them to be ferromagnetic, with T_c essentially linear in x with $T_c \sim 100$ K at x=50. We conclude, therefore, that the amorphous component detected by x-ray diffraction and TEM in our $70 \leq x \leq 80$ melt-spun ribbons is ferromagnetic Gd_xAg_{100-x} with $x \sim 50$.

In contrast, the magnetization curve for the $Gd_{50}Ag_{50}$ (20 m/s) ribbons in Fig. 4 mirrors the susceptibility versus temperature curve reported by Walline and Wallace[11] for crystalline, antiferromagnetic GdAg, consistent with our microstructural analyses of that material. It is quite surprising that the $x \sim 50$ component of the Gd-richer $70 \leq x \leq 80$ ribbons is amorphous, while $Gd_{50}Ag_{50}$ melt spun at the same quench rate (v_S=20 m/s) is crystalline. To satisfy one of our original objectives it would have been preferable for the former materials to contain crystalline GdAg [which would be paramagnetic at T_c(Gd)] to magnetically isolate the Gd particles.

We calculated the field-induced entropy change ΔS from the magnetization data (measured as a function of both applied magnetic field H and temperature T) by making use of the Maxwell relation $(\partial S/\partial H)_T = (\partial M/\partial T)_H$, which implies

$$\Delta S = \int_0^H \left[\frac{\partial M(H',T)}{\partial T} \right]_{H'} dH'. \quad (1)$$

Figure 5 displays ΔS vs T for the melt-spun $70 \leq x \leq 100$ ribbons and for the Gd ingot sample. The Gd-only ribbon material features a single peak near 290 K which corresponds well with T_c of bulk Gd, as comparison with the Gd ingot curve in Fig. 5 demonstrates. The four other ribbon curves in Fig. 5 exhibit two peaks. One is centered in the 100–120 K interval and is generated by the ferromagnetic, amorphous $Gd_{50}Ag_{50}$ component; the variation of the maximum with x is relatively small and is undoubtedly associated with compositional variation in the amorphous fraction. Most pronounced in the x=77.5 and x=80 ribbons, the second peak occurs at $T \sim 280$ K and arises from the Gd constituent; the ~100 Å particle size reduces T_c somewhat from the bulk value of 293 K.

Both ΔS structures for the $70 \leq x \leq 80$ ribbons in Fig. 5 are quite broad; the height of each is considerably smaller than that of the Gd-only ribbons, which is in turn somewhat reduced from that of the Gd ingot. These results reinforce earlier findings[4–7] that a fine-particle morphology can markedly modify the temperature distribution of ΔS. Figure 5 suggests that the x=70 and x=75 materials may be of interest for magnetic refrigeration in the 100 K regime. While the x=77.5 and x=80 ribbons do contain small Gd particles, further effort is required, at least in the Gd-Ag system, to separate them in a nonferromagnetic matrix. We intend to explore heat treatment as a possible means for converting the amorphous $Gd_{50}Ag_{50}$ component into antiferromagnetic GdAg while minimizing growth of the Gd grains.

[1] C. V. Brown, J. Appl. Phys. **47**, 3673 (1976).
[2] H. Oesterreicher and F. T. Parker, J. Appl. Phys. **55**, 4334 (1984).
[3] J. A. Barclay, Adv. Cryogen. Mater. **33**, 719 (1988).
[4] R. D. McMichael, R. D. Shull, L. J. Swartzendruber, L. H. Bennett, and R. E. Watson, J. Magn. Magn. Mater. **111**, 29 (1992).
[5] L. H. Bennett, R. D. McMichael, L. J. Swartzendruber, R. D. Shull, and R. E. Watson, J. Magn. Magn. Mater. **104–107**, 1094 (1992).
[6] R. D. McMichael, J. J. Ritter, and R. D. Shull, J. Appl. Phys. **73**, 6946 (1993).
[7] R. D. McMichael, R. D. Shull, L. H. Bennett, C D. Fuerst, and J. F. Herbst, NanoStructured Mater. **2**, 277 (1993).
[8] K. H. J. Buschow and N. M. Beekmans, in *Rapidly Quenched Metals III*, Proceedings of the Third International Conference on Rapidly Quenched Metals (The Metals Society, London, 1978), Vol. 2, p. 133; K H. J. Buschow, Solid State Commun. **27**, 275 (1978).
[9] D. C. Douglass, J. P. Bucher, and L. A. Bloomfield, Phys. Rev. Lett. **68**, 1774 (1992).
[10] J. J. Hauser, Phys. Rev. B **12**, 5160 (1975).
[11] R. E. Walline and W. E. Wallace, J. Chem. Phys. **41**, 3285 (1964). These authors emphasize that the susceptibility behavior of GdAg below 200 K is anomalous.

Thickness dependence of the magnetic and electrical properties of Fe:SiO_2 nanocomposite films

S. S. Malhotra
Behlen Laboratory of Physics and Center for Materials Research and Analysis, University of Nebraska, Lincoln, Nebraska 68588-0111

Y. Liu
Center for Materials Research and Analysis, University of Nebraska, Lincoln, Nebraska 68588-0111 and Department of Mechanical Engineering, University of Nebraska, Lincoln, Nebraska 68588-0656

J. X. Shen, S. H. Liou, and D. J. Sellmyer
Behlen Laboratory of Physics and Center for Materials Research and Analysis, University of Nebraska, Lincoln, Nebraska 68588-0111

Nanocomposite $Fe_{80}(SiO_2)_{20}$ films with thickness from 150 to 5000 Å have been prepared by rf magnetron sputtering from a composite target. The crystallites in the $Fe_{80}(SiO_2)_{20}$ films have a bcc structure with the average size of 46–66 Å which was determined by transmission electron microscopy. As indicated by the thickness dependence of resistivity, the stacking and connectivity of the crystallites depend on the thickness of the films. The magnetic properties also depend on the microstructure which changes with the thickness of the films. The magnetic coercivity of the films increases with the thickness of the film, reaches a maximum, and then decreases. The maximum coercivity of 400 Oe at 300 K and 1200 Oe at 5 K was observed for a film with a thickness of about 700 Å.

I. INTRODUCTION

Nanocomposite materials have the form of small crystallites dispersed in a matrix which may be insulating or metallic. The magnetic properties of nanocomposite materials depend on the microstructure of the films which can be controlled by either changing the size of crystallites and/or the separation distance between the crystallites. It has been shown that the crystallites size and the intercrystallite distance of the nanocomposite Fe:SiO_2 system can be systematically changed by varying the Fe volume fraction.[1–6] The average crystallite size in the films for a fixed volume fraction can also be varied by changing the substrate temperature.[7] For the films with lower metal volume fraction the crystallites are isolated whereas for the films with higher metal volume fraction the crystallites are well connected.[8] For the Fe:SiO_2 films with a Fe volume fraction near 50% the crystallites begin to form a percolating network. As the thickness of the film is decreased, the number of crystallites connecting together in the film-normal direction decreases and a change in the electrical and magnetic properties is expected. In this work we investigated the thickness dependence of magnetic and electrical properties of the Fe:SiO_2 films.

II. EXPERIMENTAL PROCEDURE

The nanocomposite Fe:SiO_2 films were prepared by rf magnetron sputtering from a composite target. The sputtering targets were prepared by sintering a mixture of pressed Fe and SiO_2 powders. The sputtering gas was 5 mTorr of Ar, and the films were deposited on glass substrates at room temperature. The films used in this study have a target composition of $Fe_{80}(SiO_2)_{20}$ (55 vol. % of Fe). The film thickness ranged from 150 to 5000 Å. The microstructure of the films was studied by using a JEOL 2010 high-resolution transmission electron microscope (HRTEM) and electron diffraction. The magnetization and the coercive force were measured using a commercial alternating-gradient force magnetometer and a SQUID magnetometer. The resistivity was measured in a standard four-point probe configuration.

III. RESULTS AND DISCUSSION

The electron-diffraction pattern of the $Fe_{80}(SiO_2)_{20}$ films with a thickness of 700 Å is shown in Fig. 1. The electron-

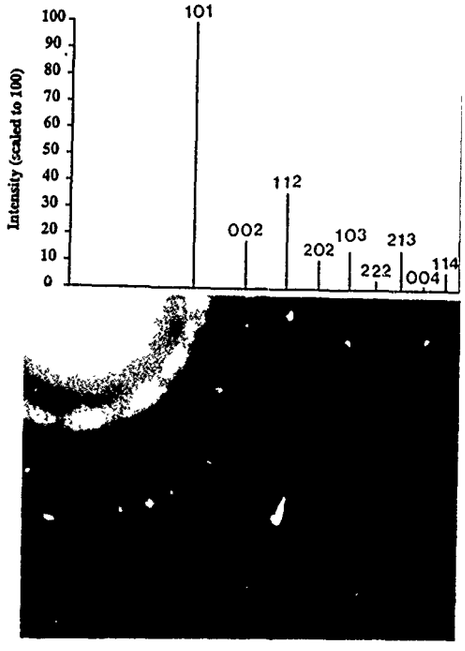

FIG. 1. Electron-diffraction pattern of $Fe_{80}(SiO_2)_{20}$ film with a thickness of 700 Å.

 0021-8979/94/76(10)/6304/3/$6.00 © 1994 American Institute of Physics

FIG. 2. HRTEM image for the $Fe_{80}(SiO_2)_{20}$ film with a thickness of 700 Å.

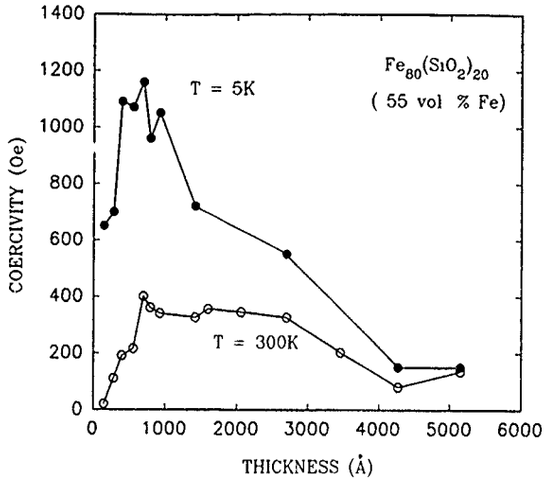

FIG. 4. Magnetic coercivities measured at 300 and 5 K vs thickness for the $Fe_{80}(SiO_2)_{20}$ films.

diffraction pattern of the films show a α-Fe structure with the (110), (200), (211), etc. rings present. The d spacing of the (110) peak as deduced from x-ray diffraction is 2.03 Å, which is close to the lattice parameter of α-Fe. The electron-diffraction pattern of the film can be indexed to α-Fe and there is no evidence of contribution from any Fe oxide phases; this is also confirmed by Mössbauer spectroscopy. The hyperfine field as calculated from the Mössbauer spectra is 330 kOe, which is close to the value for α-Fe. The morphology of the crystallites as revealed by the HRTEM image for the $Fe_{80}(SiO_2)_{20}$ films with a thickness of 700 Å is shown in Fig. 2. The average particle size of the Fe crystallites is 46–66 Å and the Fe crystallites are mostly isolated in an amorphous SiO_2 matrix. The Fe crystallites have a clear boundary with the SiO_2 matrix. The fringes on the crystallites represent the lattice spacing of Fe.

The thickness dependence of the resistivity for the $Fe_{80}(SiO_2)_{20}$ films is shown in Fig. 3. It is seen that the resistivity decreases as the film thickness increases and above 700 Å the resistivity decreases drastically, indicating that the films form a better connecting network of Fe crystallites. The plane view HRTEM image shows that the Fe crystallites are isolated in the SiO_2 matrix, so the drastic change in resistivity for the films with thickness above 700 Å may be likely due to the change in stacking and connection of the Fe crystallites. The inset of Fig. 3 shows the resistivity versus film thickness for 700–4273 Å thick films. As the film thickness increases from 700 to 4273 Å, the resistivity changes from 5.6×10^{-2} to 1.8×10^{-4} Ω cm.

The magnetic coercivity measured at 300 and 5 K of the $Fe_{80}(SiO_2)_{20}$ films versus thickness is shown in Fig. 4. The magnetic properties depend on the thickness of the film. It is observed that as the film thickness increases the magnetic coercivity increases, goes through a maximum, and then decreases The maximum coercivity of about 400 Oe at 300 K and 1200 Oe at 5 K was obtained for a film with a thickness of about 700 Å. As the film thickness increases, the change in magnetic coercivity measured at 5 K is more pronounced compared to the magnetic coercivity measured at 300 K for the films with thicknesses less than 1200 Å.

Figure 5 shows the dependence of magnetic coercivity with temperature for $Fe_{80}(SiO_2)_{20}$ films with different thicknesses. The magnetic coercivity decreases as the temperature

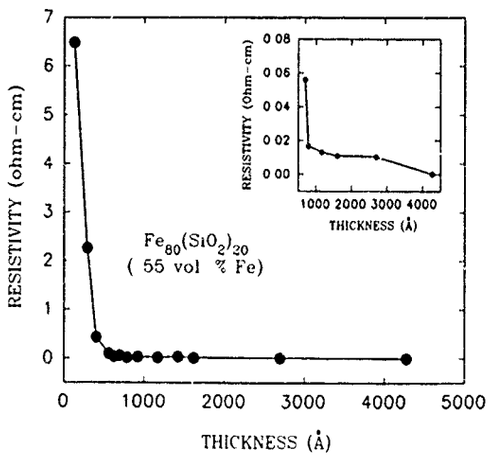

FIG 3. Resistivity vs thickness for the $Fe_{80}(SiO_2)_{20}$ films.

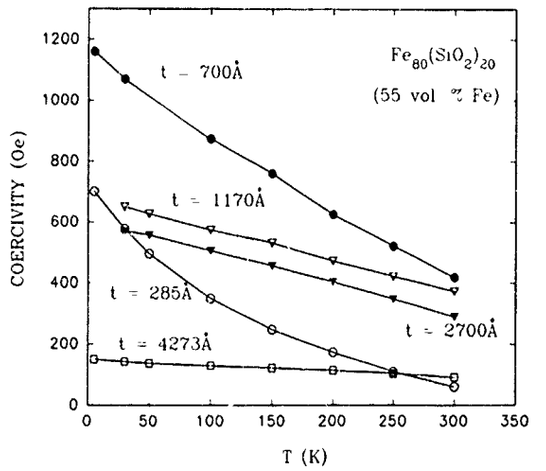

FIG. 5. Magnetic coercivities vs temperature of the $Fe_{80}(SiO_2)_{20}$ films with different thicknesses

increases. The temperature dependence of coercivity with a film thickness more than 1000 Å is almost linear, whereas the film with a thickness of 285 Å has a $T^{1/2}$ dependence. The $T^{1/2}$ dependence of coercivity for a thin film is characteristic of a system of superparamagnetic particles below the blocking temperature.[9] As the film thickness increases the number of connected crystallites also increases, i.e., the interaction between the crystallites increases and one observes a change in the magnetic properties of the films.

IV. SUMMARY

We have prepared Fe:SiO_2 nanocomposite films with different thicknesses. The size of the α-Fe crystallites for the $Fe_{80}(SiO_2)_{20}$ films ranges from 46 to 66 Å. The resistivity of the $Fe_{80}(SiO_2)_{20}$ films decreases with increasing film thickness. Above 700 Å the resistivity drops drastically, indicating that the crystallites form a better connecting network in the thick films. The magnetic coercivity for the $Fe_{80}(SiO_2)_{20}$ films depends on the microstructure which changes with the thickness of the films.

ACKNOWLEDGMENT

We are grateful for support from the National Science Foundation under Grant No. OSR 9255225.

[1] J. L. Dormann, P. Gibart, G. Suran, and C. Sella, Physica **86–88B**, 1431 (1977).
[2] G. Xiao and C. L Chien, Appl. Phys. Lett. **51**, 1280 (1987).
[3] S. H. Liou and C. L. Chien, Appl. Phys. Lett. **52**, 512 (1988).
[4] M. J. Carey, F. T. Parker, and A. E. Berkowitz, Mater Res. Soc. Symp Proc. **195**, 445 (1990).
[5] Y. Kanai and S. H. Charap, J. Appl. Phys. **69**, 4478 (1991).
[6] A. Tsoukatos, H. Wan, G. C. Hadjipaniyas, V. Papaefthymoiu, A. Kostikos, and A. Simonpolous, J. Appl. Phys. **73**, 6967 (1993).
[7] S. H. Liou and C. L. Chien, J. Appl. Phys. **63**, 4240 (1988).
[8] B. Abeles, in *Applied Solid State Science, Advances in Material and Device Research*, edited by R. Wolf (Academic, New York, 1976).
[9] B. D. Cullity, *Introduction to Magnetic Materials* (Addison Wesley, Menlo Park, CA, 1972).

Calculation of magnetic moments in Ho_2C_3 nanocrystals

S. A. Majetich,[a] J. O. Artman, and C. Tanaka
Department of Physics, Carnegie Mellon University, Pittsburgh, Pennsylvania 15213-3890

M. E. McHenry
Department of Materials Science and Engineering, Carnegie Mellon University, Pittsburgh, Pennsylvania 15213-3890

A general approach to the computation of effective magnetic moments in rare-earth carbides is described, and details of this calculation for Ho^{3+} ions in Ho_2C_3 are presented. This calculation is designed to explain the reduced magnetic moments, relative to free ion values, measured by dc SQUID magnetometry for Ho_2C_3 nanocrystals. Crystal-field splittings of the rare-earth ion in a particular symmetry site are determined by the operator equivalent method. Using the eigenvalues and eigenfunctions of the crystal-field Hamiltonian, the effective magnetic moment is then determined. For Ho^{3+} ions in Ho_2C_3, this method predicts a reduced magnetic moment, but the degree of reduction depends on the energy-level splittings and, therefore, the temperature. This magnetic moment is compared with previous experimental results, and the implications of the formal carbon charge, screening, and temperature are discussed.

I. INTRODUCTION

Carbon-coated gadolinium and holmium sesquicarbide nanocrystals have been prepared in a carbon arc, and the details of their synthesis, structure, and measured magnetic behavior have been reported previously.[1,2] The gadolinium ions in Gd_2C_3 have an $^8S_{7/2}$ electronic ground state which is unaffected by the crystal field. However, the Ho^{3+} ions found in Ho_2C_3 do not show the free ion behavior. For a $^5I_8$ electronic ground state, the predicted effective moment, $g[J(J+1)]^{1/2}$, is 10.61 μ_B, but $\mu_{\text{eff}}\sim 7.5$ μ_B was found experimentally.[2] Here we present the details of a crystal-field calculation for Ho^{3+} ions in Ho_2C_3, aimed at understanding the reduced magnetic moment, and in laying the groundwork for similar calculations for other rare-earth sesquicarbides, dicarbides, and rare-earth-containing fullerenes.

II. CRYSTAL-FIELD CALCULATIONS

The free ion energy levels are perturbed by a crystal field. The Hamiltonian for this perturbation, H_{CF}, can be written in terms of operator equivalents, O_n^m,

$$H_{\text{CH}}=\sum_{n,m} B_n^m O_n^m, \quad m\leq n. \tag{1}$$

The crystal-field intensity parameters, B_n^m, are given by the expression

$$B_n^m=[-|e|/4\pi\epsilon_0]\langle r^n\rangle\Theta_n\gamma_{nm}N_{nm}. \tag{2}$$

Here $\langle r^n\rangle$ is the expectation value for the nth power of the f-electron radius and Θ_n is the Stevens' factor, both of which are tabulated for various rare earth ions.[3,4] N_{nm} is the coefficient for the Tesseral harmonic Z_n^m, and γ_{nm} is the lattice sum over the neighboring ions, which have fixed positions and charges for a particular structure. The operator equivalents O_n^m are functions of J_+, J_-, J_z, and J. The eigenstates for the ion perturbed by the crystal field are generated from superpositions of free ion $|JM\rangle$ states. This method, reviewed by Hutchings,[3] has recently been used to calculate the energy levels of the rare-earth ions inside C_{60} molecules.[5] Here we use this information to calculate the effective magnetic moment per ion μ_{eff} for Ho_2C_3.

III. ENERGY LEVELS AND EIGENSTATES OF Ho^{3+} IN Ho_2C_3

Ho_2C_3 has a body-centered-cubic structure ($I\bar{4}3d$) with the Ho^{3+} ions in positions of C_3 site symmetry. To model the crystal field experienced by a Ho^{3+} ion in this solid, we included 11 neighboring carbon atoms and the 12 closest Ho^{3+} neighbors (Fig. 1). The atomic positions were taken from published x-ray and neutron data for bulklike Ho_2C_3 powder,[6] and the only free parameter was the charge on the carbon atoms. In many carbide molecules[6] and solids,[7] bonding occurs between the metal atom and C_2^{n-} dimer units, and the formal charge varies with the material.[7] Previous results for Ho_2C_3 suggest that the holmium ions carry a 3+ charge, and the carbon dimers have a reduced charge because they donate electrons to a conduction band.[6] In our calculations the formal dimer charge was varied between 2− and 4−. The calculated lattice sums γ_{nm} over the near-neighbor Ho^{3+} ions shown in Fig. 1 contributed only about 10% of the total, showing that the carbon dimers dominate the crystal field of a holmium ion in Ho_2C_3.

Since the holmium ions have C_3 site symmetry, only some of the operator equivalents contribute to the crystal-field Hamiltonian:

$$H_{\text{CF}}(C_3)=B_2^0O_2^0+B_4^0O_4^0+B_6^0O_6^0+B_4^3O_4^3+B_6^3O_6^3+B_6^6O_6^6 +B_{4t}^3O_{4t}^3+B_{6t}^3O_{6t}^3+B_{6t}^6O_{6t}^6. \tag{3}$$

Here B_{nt}^m refers to the imaginary part of B_n^m, and the crystal axes were chosen to minimize the contributions from the B_{6t}^3 and B_{6t}^6 terms.

Using the free ion basis set, $|JM\rangle$, with $J=8$, the 17×17 matrix was diagonalized to determine the energy eigenvalues E_i and the eigenfunctions $|\Psi_i\rangle$:

$$|\Psi_i\rangle=\sum a_{iM}|JM\rangle. \tag{4}$$

[a]Author to whom correspondence should be addressed.

 0021-8979/94/76(10)/6307/3/$6.00 © 1994 American Institute of Physics

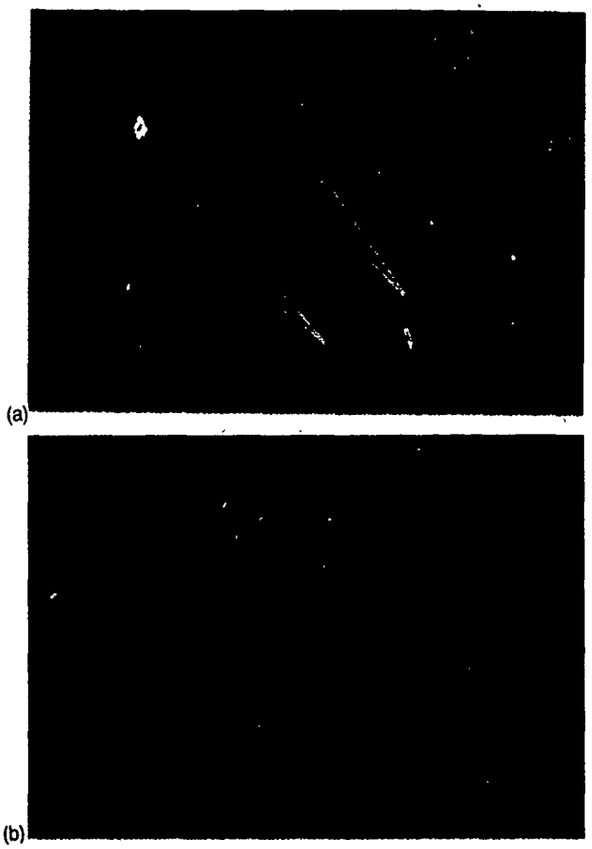

FIG. 1. (a) Ho^{3+} ion with 11 nearest-neighbor Ho^{3+} ions. (b) Ho^{3+} ion with 12 nearest-neighbor carbide ions.

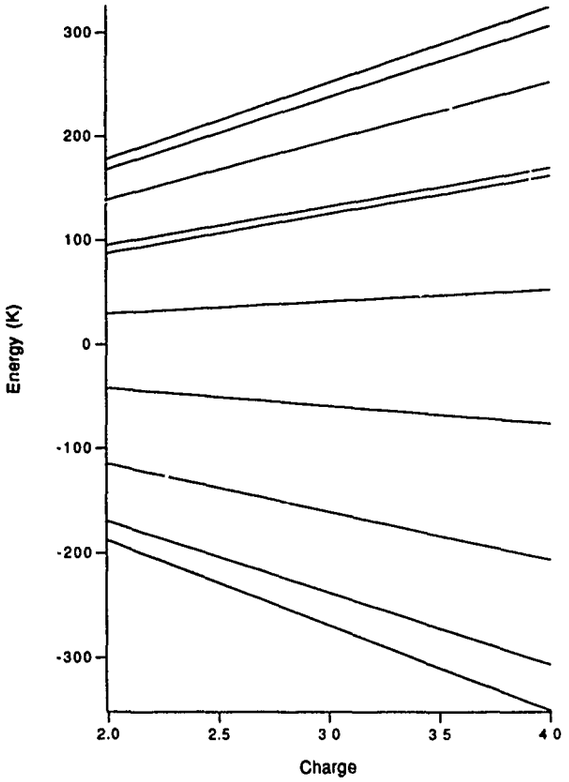

FIG. 2. Energy levels of Ho^{3+} as a function of carbon dimer charge magnitude. Energies are relative to that of a free Ho^{3+} ion. A more detailed description of the energy eigenstates for the dimer charge of -2.0 is found in Table I.

From group theory, the $J=8$ electronic ground state for a free Ho^{3+} ion should split into five $^1\Gamma_1$ states and six $^2\Gamma_2$ states when perturbed by a C_3 crystal field. As shown in Table I, the formal calculation did indeed result in six doublets and five singlet states. While the energy-level splittings varied with the formal charge on the carbon dimer, the relative ordering was the same (Fig. 2), and the makeup of the energy eigenstates was not significantly affected. The lowest doublet consisted predominantly of $M=+8$ and -8 states, and the next lowest doublet was mainly $M=+7$ and -7 states. For all formal charge values there is significant population of excited states at 300 K.

IV. MAGNETIC MOMENT OF Ho^{3+} IN Ho_2C_3

In the limit of small H/T, the paramagnetic susceptibility is given by

TABLE I. Ho_2C_3 eigenvectors for C_2^2.

Eigenvector (energy)
$\|\Psi_{1,2}\rangle=0.988\|\pm8\rangle+(\pm0.142-0.056i\|\pm5\rangle$, $[E_{1,2}/k=0.00$ K]
$\|\Psi_{3,4}\rangle=0.986\|7\pm\rangle+(\pm0.149-0.063i)\|\pm4\rangle$, $[E_{3,4}/k=18.39$ K]
$\|\Psi_5\rangle=(-0.505-0.479i)\|6\rangle+(-0.117-0.040i)\|3\rangle+0.002i\|0\rangle+(-0.112-0.051i)\|-3\rangle+0.696\|-6\rangle$, $[E_5/k=72.87$ K]
$\|\Psi_6\rangle=0.697\|6\rangle+(0.109-0.049i)\|3\rangle+(0.024-0.010i)\|0\rangle+(-0\ 113+0.040i)\|-3\rangle+0.506-0.479i)\|-6\rangle$, $[E_6/k=72.96$ K]
$\|\Psi_{7,8}\rangle=\mp0.003\|\pm4\rangle+(0.022\pm0\ 04i)\|\pm1\rangle+(\mp0.164-0.079i)\|\mp2\rangle+0.971\|\mp5\rangle+(0.142-0.056i)\|\mp8\rangle$, $[E_{7,8}/k=145.56$ K]
$\|\Psi_9\rangle=(-0.136-0.057i)\|7\rangle+(0.002-0\ 002i)\|5\rangle+0.880\|4\rangle+(-0.010)+0.011i)\|2\rangle+(0.154\cdots0.081i)\|1\rangle+(0.078-0.011i)\|-1\rangle+(0.032+0.007i)\|2\rangle$ $+(-0\ 326+0\ 234i)\|-4\rangle+(0.006+0.001i)\|-5\rangle+(-0.035+0.057i)\|-7\rangle$, $[E_9/k=217.00$ K]
$\|\Psi_{10}\rangle=(-0.001+0.001i)\|5\rangle+(0.035-0.008i)\|2\rangle+(-0\ 169-0.089i)\|\cdots1\rangle+0.967\|-4\rangle+(0.149-0.063i)\|-7\rangle$, $[E_{10}/k=217.00$ K]
$\|\Psi_{11}\rangle=(-0.112-0.048i)\|6\rangle+0.681\|3\rangle+(0.076-0.194i)\|0\rangle+(0.501+0\ 461i)\|-3\rangle+(0.115+0.041i)\|-6\rangle$, $[E_{11}/k=275.36$ K]
$\|\Psi_{12}\rangle=(0.112-0.047i)\|6\rangle+(-0\ 464+0.503i)\|3\rangle+(-0.169+0.073i)\|0\rangle+0.684\|-3\rangle+(0.110-0.050i)\|-6\rangle$, $[E_{12}/k=283.13$ K]
$\|\Psi_{13}\rangle=(0.006-0.009i)\|8\rangle+(-0.165-0.076i)\|5\rangle+(0.962\|2\rangle+(0.181-0.082i)\|-1\rangle+(-0.011-0.038i)\|-4\rangle+(-0.004-0.003i)\|-7\rangle$, $[E_{13}/k=326\ 61$ K]
$\|\Psi_{14}\rangle=(0.003-0.003i)\|7\rangle+(-0.011+0.038i)\|4\rangle+(0.001+0.001i)\|2\rangle+(-0.181-0.082i)\|1\rangle+0.962\|-2\rangle+(0.165-0.076i)\|-5\rangle$ $+(-0.004-0.003i)\|-8\rangle$, $[E_{14}/k=326.61$ K]
$\|\Psi_{15}\rangle=(0.001-0.001i)\|8\rangle+(0.001+0.002i)\|5\rangle+(-0.179-0.085i)\|2\rangle+0.961\|-1\rangle+(0.172-0.082i)\|-4\rangle+(0.006-0.014i)\|-7\rangle$, $[E_{15}/k=355.84$ K]
$\|\Psi_{16}\rangle=(0.006+0.014i)\|7\rangle+(0.001+0.001i)\|5\rangle+(-0\ 172-0.081i)\|4\rangle+(-0.014+0.002i)\|2\rangle+0.959\|1\rangle+(0.055-0.038i)\|-1\rangle+(0.179-0.085i)\|-2\rangle$ $+(0.007-0.011i)\|-4\rangle+(0.001-0.025i)\|-5\rangle+(-0.001i)\|-7\rangle+(-0.001-0.001i)\|-8\rangle$, $[E_{15,16}/k=355.84$ K]
$\|\Psi_{17}\rangle=(0.005+0.019i\|6\rangle+(-0.177-0.085i)\|3\rangle+0.960\|0\rangle+(0.177-0.085i)\|-3\rangle+(0.005-0.019i)\|-6\rangle$, $[E_{17}/k=365.73$ K]

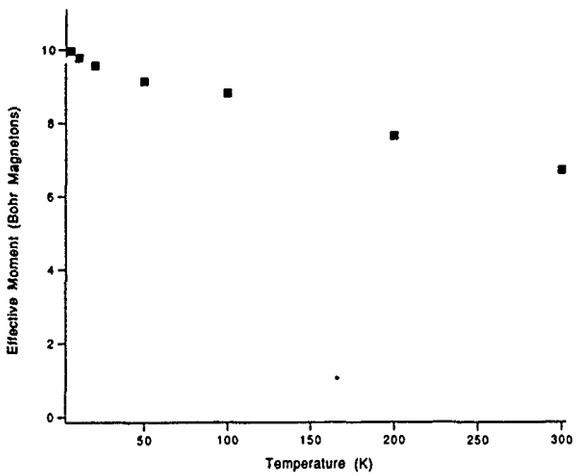

FIG. 3. Effective magnetic moment for Ho^{3+} with a carbon dimer charge of -2.0 as a function of temperature, with assumptions concerning off-diagonal elements as noted in the text.

$$\chi_{pm}=N\mu_B^2 g^2 J(J+1)/3kT=N\mu^2/3kT, \tag{5}$$

for a free rare-earth ion with ground-state angular momentum J. Here μ is the magnetic moment of the free ion. In the full quantum-mechanical treatment,[8] χ depends on the statistical averaging over the energy eigenstates. While there are several contributions,[9] the effective magnetic moment determined from the magnetization curve measured with a SQUID magnetometer is related to the low-frequency term

$$\chi=\left(\frac{N\mu_B^2 g^2}{3kT}\right) \times \frac{\sum_J \sum_M \langle JM|M^2 \exp(-E_J/kT)|JM\rangle}{\sum_J \sum_M \langle JM| \exp(-E_J/kT)|JM\rangle}. \tag{6}$$

For Ho^{3+} ions in the Ho_2C_3 crystal field, we treated only the ground electronic state multiplet, which has $J=8$. The next lowest electronic state in the free ion, $^5I_7$, lies over 5000 cm^{-1} higher in energy and is not appreciably populated in the experimental measurements.[10] With the crystal-field eigenfunctions and eigenvalues, the expression for χ is

$$\chi=\left(\frac{N\mu_B^2 g^2}{3kT}\right) \frac{\sum_i \sum_M \langle JM|a_{iM}^* a_{iM} M^2 \exp(-E_i/kT)|JM\rangle}{\sum_i \sum_M \langle JM|a_{iM}^* a_{iM} \exp(-E_i/kT)|JM\rangle},$$

$$=N\mu_{\text{eff}}^2/3kT. \tag{7}$$

The effective moment per Ho^{3+} ion, μ_{eff}, differs from the free ion moment because of the removal of the free ion degeneracy, and because the crystal-field splittings lead to a temperature-dependent moment. Figure 3 shows the temperature dependence of the moment for the case where the carbon dimer charge equals -2.0. For larger carbon dimer charge values, the temperature-dependent drop-off is less pronounced.

Earlier SQUID magnetometry measurements[2] yielded a temperature-averaged value of $\mu_{\text{eff}}=7.5\ \mu_B$. There the data were scaled as a function of H/T, and results from all temperatures were fit simultaneously.[11] Experiments are underway to study the degree of temperature dependence in order to place limits on the carbon dimer charge. Refinements in the crystal-field calculations to incorporate screening of the conduction electrons will also have an impact on the energy-level splittings, and therefore on the temperature dependence of the magnetic moment.

V. CONCLUSIONS

Crystal-field calculations were performed to determine the ground-state energy-level splittings for Ho^{3+} ions in Ho_2C_3. The energy eigenstates were used to calculate the low-frequency paramagnetic susceptibility and the effective magnetic moment. In comparison with SQUID magnetometry measurements, this calculation underestimates the reduction of the magnetic moment. However, information concerning important fitting parameters may be obtained by detailed temperature-dependent measurements of μ_{eff}.

Note added in proof: A marked increase in the magnetic moment with increasing temperature has been observed experimentally, thought the error bars for fits of the high-temperature data are quite large. When the data taken at different temperatures are scaled and fit as a group, the low-temperature contributions dominated in the determination that $\mu_{\text{eff}}=7.5\ \mu_B$.

ACKNOWLEDGMENTS

M.E.M. and S.A.M. would like to thank the National Science Foundation for support through NYI Awards No. DMR-9258450 and No. DMR-9258308, respectively. Support from the Carnegie Mellon University SURG program and the assistance of E. M. Brunsman, C.-S. Niu, P. Sivaramakrishnan, and the CMU Buckyball Project members have also been valuable.

[1] S. A. Majetich, J. O. Artman, M. E. McHenry, N. T. Nuhfer, and S. W. Staley, Phys. Rev. B 48, 16845 (1993).
[2] E. M. Brunsman, M. E. McHenry, S. A. Majetich, J. O. Artman, M. De Graef, S. W. Staley, R. Sutton, E. Bortz, S. Kirkpatrick, K. Midelfort, J. Williams, and B. Brunett, J. Appl. Phys. **75**, 5879 (1994).
[3] M. T. Hutchings, in *Solid State Physics*, edited by F. Seitz and D Turnbull (Academic, New York, 1964), pp. 227–276.
[4] W. E Wallace, S. G. Sankar, and V. U S. Rao, Structure and Bonding **33**, 1 (1977).
[5] M. E. McHenry and S. G. Sankar (unpublished).
[6] M. Atoji and Y. Tsunoda, J. Chem Phys. **54**, 3510 (1971).
[7] G. J. Miller, J. K. Burdett, C. Schwartz, and A. Simon, Inorganic Chemistry **25**, 4437 (1986).
[8] J. H Van Vleck, Phys. Rev. **29**, 727 (1927); **30**, 31 (1927), **31**, 587 (1928).
[9] S. V. Vonsovskii, *Magnetism* (Wiley, New York, 1974), Vol 1, pp 120–126..
[10] G. H. Dieke, *Spectra and Energy Levels of Rare Earth Ions in Crystals* (Wiley, New York, 1968).
[11] In this sample, electron diffraction has shown the presence of cubic α-Ho_2C_3. No evidence of Ho_5C_{19} has been observed. In comparing the experimental and calculated values, a factor of 1/3 should be introduced in the susceptibility formula to account for random orientations of the individual crystals.

Kramers's rate theory, broken symmetries, and magnetization reversal (invited)

Hans-Benjamin Braun
Department of Physics, Simon Fraser University, Burnaby, British Columbia V5A 1S6, Canada

The theory of thermally induced magnetization reversal in small particles is reviewed. The conventional Néel–Brown theory for uniform magnetization reversal and its derivation from Kramers's rate theory are first discussed. For sufficiently elongated particles, however, a nonuniform energy barrier ("nucleus") has lower energy than the uniform barrier and thus yields a lower coercivity. This coercivity reduction is shown to occur also for vanishing hard-axis anisotropy when the nucleus breaks the rotational symmetry around the easy axis. The prefactor of the Arrhenius factor is calculated for uniform and nonuniform barriers.

I. INTRODUCTION

Recent years have witnessed tremendous progress in the preparation of magnetic particles on the scale of a few nanometers. Such particles typically exhibit two degenerate equilibrium directions of the magnetic moment which are separated by an anisotropy barrier.

As the thermal energy k_BT approaches the barrier energy, thermal fluctuations drive the magnetization from the metastable state over the lowest-energy barrier into the adjacent anisotropy minimum. Recent experiments on a single particle[1] or lithographically produced arrays[2] of even smaller particles reveal a coercivity that is substantially smaller than that predicted by standard theories of magnetization reversal.

The most widely used theory is that by Néel[3] and Brown.[4] It is based on the picture that all spins within the grain are aligned and behave like a single large magnetic moment. The switching rate out of the metastable state is then given by the Arrhenius factor $\exp[-E_s/k_BT]$ where the barrier energy E_s is proportional to the total anisotropy energy and thus to the particle volume.

With increasing aspect ratio of the particle, this assumption of a uniform magnetization becomes questionable. A recent study[5] which includes the exchange interaction of magnetic moments along an idealized long particle with constant cross section has indeed shown that the energy exhibits a saddle point corresponding to a localized deviation ("nucleus") from the initial metastable state. This nucleus can also be viewed as a soliton-antisoliton pair.[6]

These exact results showed that several previous concepts have to be thoroughly revised: For sufficiently elongated particles, the barrier energy is proportional to the cross-sectional area of the particle rather than the particle volume. Second, the concept of an "activation volume" is misleading: Even if the nucleus represents an already reversed domain delimited by two domain walls [see Fig. 1(ii)], the barrier energy is not proportional to the volume of the reversed domain but rather equals the total energy of the delimiting domain walls. Third, it can be shown that the energy decreases monotonically from the saddle point until the magnetization is reversed. This is in contrast to a saddle point of assumed curling symmetry (where the radial component of the magnetization vanishes). Such a constraint requires the magnetization at the "backbone" in the cylinder center to remain in the initial state even if the magnetization outside this central region is reversed. This obstructs the way down from the putative saddle point of curling symmetry by an additional energy barrier of topological origin which in the case of a continuous magnetization distribution is even infinitely high. This can only be avoided by breaking the rotational symmetry of the magnetization distribution at the cylinder center. For small particle diameters, we are then led to an effectively one-dimensional model[5] that will be described below.

The purpose of this article is twofold. We start with a review of the theory of uniform magnetization reversal with particular emphasis on the difference between the rotationally symmetric case of a single easy-axis anisotropy[3,4] and the case of an additional hard-axis anisotropy.[7,8] These results have been derived by a variety of methods and unfortunately no recent review exists in the literature. Therefore, Kramers's rate theory is presented in the Appendix in a form which can be readily extended to nonuniform situations or systems of interacting particles.

In Sec. IV it is shown that in elongated particles a spatially localized deviation ("nucleus") from the metastable state provides the lowest barrier. The same nucleus also exists for vanishing hard-axis anisotropy where it breaks the rotational symmetry. This symmetry breaking gives rise to a Goldstone mode of zero energy which corresponds to an infinitesimal rotation of the saddle-point structure around the easy axis. By taking advantage of this symmetry, the statistical part of the prefactor is evaluated exactly for all values of the external field.

II. MODEL

Let us first consider an elongated particle of constant cross section $\mathcal{A}$. The energy of a one-dimensional (1D) magnetization configuration $\mathbf{M}(x,t)$ of constant magnitude $|\mathbf{M}|=M_0$ is given by

$$E=\mathcal{A}\int_{-L/2}^{L/2}dx\left\{\frac{A}{M_0^2}\left[\left(\frac{\partial M_x}{\partial x}\right)^2+\left(\frac{\partial M_y}{\partial x}\right)^2+\left(\frac{\partial M_z}{\partial x}\right)^2\right]+\frac{K_h}{M_0^2}M_z^2-\frac{K_e}{M_0^2}M_x^2-H_{\mathrm{ext}}M_x\right\}. \tag{2.1}$$

The particle length L is assumed to be considerably larger[9] than the domain-wall width $\sqrt{A/K_e}$. For particle diameters of the order of $\sqrt{A/K_e}$ or smaller, transverse fluctuations are

 0021-8979/94/76(10)/6310/6/$6.00 © 1994 American Institute of Physics

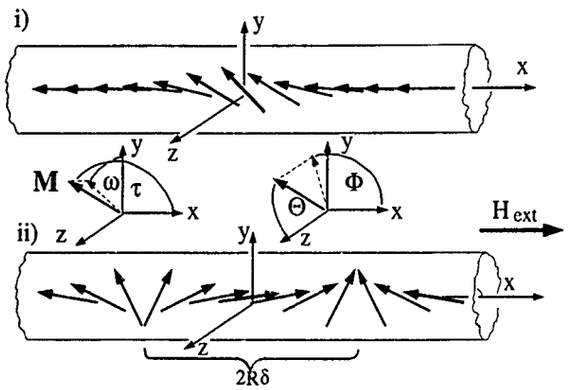

FIG. 1. The nucleus (3.2) for nonuniform magnetization reversal at (i) large external fields ($h\to 1$) and (ii) small external fields. For vanishing hard-axis anisotropy, this configuration is degenerate with all configurations that arise by a rotation around the easy axis.

suppressed and a 1D treatment is justified. The first term in the integrand of Eq. (2.1) is the exchange interaction between adjacent magnetic moments along the particle. The next two terms are effective easy and hard-axis anisotropies of strengths $K_e, K_h > 0$, respectively. They incorporate both crystalline and demagnetizing contributions.[10] For example, for an infinitely long sample of circular cross section, we have $K_e = K_{e,\mathrm{cryst}} + \pi M_0^2$, $K_h = K_{h,\mathrm{cryst}}$, where $k_{e,\mathrm{cryst}}$, $k_{h,\mathrm{cryst}}$ are crystalline anisotropy constants. The last term in Eq. (2.1) describes the interaction with an external field H_{ext} along the easy axis, which is conveniently expressed as

$$h = H_{\mathrm{ext}} M_0 / 2K_e . \tag{2.2}$$

It is appropriate to use spherical coordinates,

$$\mathbf{M}/M_0 = (\sin\theta\cos\phi, \sin\theta\sin\phi, \cos\theta),$$

where $\phi = \phi(x,t)$ and $\theta = \theta(x,t)$. The energy (2.1) then takes the form

$$E = \mathscr{A}\int_{L/2}^{L/2} dx \left\{ A\left[\left(\frac{\partial\theta}{\partial x}\right)^2 + \sin^2\theta\left(\frac{\partial\phi}{\partial x}\right)^2\right] + K_h\cos^2\theta - K_e(\sin^2\theta\cos^2\phi - 1) - H_{\mathrm{ext}}M_0(\sin\theta\cos\phi + 1)\right\}, \tag{2.3}$$

which is measured relative to the metastable state antiparallel to the external field. The magnetization is assumed to obey the Landau–Lifshitz–Gilbert equations

$$\frac{\partial \mathbf{M}}{\partial t} = -\gamma \mathbf{M}\times\mathbf{H}_{\mathrm{eff}} + \left(\frac{\alpha}{M_0}\right)\mathbf{M}\times\frac{\partial\mathbf{M}}{\partial t},$$

with $\mathbf{H}_{\mathrm{eff}} = -\delta\mathscr{E}/\delta\mathbf{M}$, which can be expressed as

$$\begin{aligned}(1+\alpha^2)\frac{M_0}{\gamma}\sin\theta\frac{\partial\phi}{\partial t} &= \frac{\delta\mathscr{E}}{\delta\theta} - \frac{\alpha}{\sin\theta}\frac{\delta\mathscr{E}}{\delta\phi},\\ (1+\alpha^2)\frac{M_0}{\gamma}\frac{\partial\theta}{\partial t} &= -\frac{1}{\sin\theta}\frac{\delta\mathscr{E}}{\delta\phi} - \alpha\frac{\delta\mathscr{E}}{\delta\theta},\end{aligned} \tag{2.4}$$

where $\mathscr{E} = E/\mathscr{A}$ is the energy per area and $\delta/\delta\phi$ denotes a functional derivative. The terms containing $\alpha > 0$ describe damping. For small values of the damping constant, the α dependence of the left-hand side (lhs) can be neglected.

The uniform configuration ($\phi_m = \pi$, $\theta_m = \pi/2$) antiparallel to the external field represents a metastable state while the state ($\phi_0 = 0$, $\theta_0 = \pi/2$) parallel to the external field is the minimum of the energy (2.1). In the following we investigate the energy barriers that separate these two states.

III. UNIFORM MAGNETIZATION REVERSAL

If the dimensions of a magnetic grain are smaller than a domain-wall width, the exchange energy dominates over demagnetizing contributions. The individual atomic magnetic moments are aligned and the system can be described by a uniform magnetization $\mathbf{M}$=const. The energy of an arbitrarily shaped particle of volume V is then given by

$$E = V[-K_e(\sin^2\theta\cos^2\phi - 1) + K_h\cos^2\theta - H_{\mathrm{ext}}M_0(\sin\theta\cos\phi + 1)]. \tag{3.1}$$

For $0 < h < 1$, the metastable state (ϕ_m, θ_m) is then separated from the stable state (ϕ_0, θ_0) by two equivalent barriers defined by

$$\cos\phi_s^{(0)} = -h, \quad \theta_s^{(0)} = \pi/2, \tag{3.2}$$

which have the energy

$$E_s^{(0)} = VK_e(1-h)^2. \tag{3.3}$$

In the vicinity of the saddle point, the energy (3.1) can be expanded to second order in the fluctuations $\varphi = \phi - \phi_s^{(0)}$, $p = \pi/2 - \theta$,

$$E \simeq E_s^{(0)} + V[-K_e(1-h^2)\varphi^2 + K_h p^2]. \tag{3.4}$$

The φ fluctuations are thus unstable while the out of easy-plane fluctuations are stable. In the vicinity of the metastable state the energy becomes

$$E \simeq V\{K_e(1-h)\varphi_m^2 + [K_e(1-h) + K_h]p_m^2\}, \tag{3.5}$$

where φ_m, θ_m are now the stable fluctuations away from the metastable point, i.e., $\varphi_m = \phi - \pi$, $p_m = \pi/2 - \theta$.

The uniform magnetization $\mathbf{M}$ obeys the equations of motion (2.4) with $\mathscr{E}$ replaced by the energy density E/V and with the functional derivatives replaced by partial derivatives. The dynamics near the saddle point is obtained by inserting Eq. (3.4) into Eq. (2.4). In particular we are interested in the motion away from the saddle point, i.e.,

$$[\varphi_+(t), p_+(t)] = e^{\lambda_+ t}(\varphi_+, p_+) \quad (\lambda_+ > 0),$$

which obeys

$$\begin{aligned}(1+\alpha^2)\frac{M_0}{2\gamma}\lambda_+\varphi_+ &= -K_h p_+ + \alpha K_e(1-h^2)\varphi_+,\\ (1+\alpha^2)\frac{M_0}{2\gamma}\lambda_+ p_+ &= -K_e(1-h^2)\varphi_+ - \alpha K_h p_+ .\end{aligned} \tag{3.6}$$

Note that the Landau–Lifshitz equation (2.4) is not consistent with the fluctuation-dissipation theorem since it lacks random forces which result from the coupling to the heat bath. Without such random forces, the magnetization would never be driven out of a metastable state. Such a term could

be added as a random field[4] to the right-hand side (rhs) of Eq. (2.4) to form a Langevin equation. However, it is only necessary to consider the stochastic dynamics near the saddle point, and we give a derivation of the corresponding Fokker–Planck equation in the Appendix.

Using the result Eq. (A11) of the Appendix, we obtain for the switching rate[7,8] out of the metastable state

$$\Gamma=\frac{\lambda_+}{\pi}\left(\frac{(K_e/K_h)(1-h)+1}{1+h}\right)^{1/2}e^{-\beta E_s^{(0)}}, \tag{3.7}$$

where we have included a factor of 2 due to the existence of the two equivalent saddle points (3.2). The escape frequency[7,8] follows from Eq. (3.6),

$$\lambda_+=\frac{\gamma/M_0}{1+\alpha^2}\{-\alpha[K_h+K_e(h^2-1)] + \sqrt{\alpha^2[K_h+K_e(1-h^2)]^2+4K_hK_e(1-h^2)}\}. \tag{3.8}$$

For weak hard-axis anisotropy, i.e., $\beta V K_h<1$ and $K_e>K_h$, the out of easy-plane fluctuations become large and the system behaves as if $K_h=0$. In this case, there is a degenerate class of energy barriers which arise from the configuration (3.2) by rotation around the easy axis. Equation (A12) then yields the switching rate[3,4]

$$\Gamma=\frac{\alpha}{1+\alpha^2}\frac{2\gamma(K_e)^{3/2}}{M_0}\left(\frac{\beta V}{\pi}\right)^{1/2}(1+h)(1-h)^2e^{-\beta E_s^{(0)}}. \tag{3.9}$$

Although Eq. (3.9) has been derived in the moderately damped regime, it is proportional to the damping constant α which is a characteristic of underdamped theories.

IV. NONUNIFORM MAGNETIZATION REVERSAL

Let us now return to the case of an elongated particle as described in Sec. II. The metastable state (ϕ_m,θ_m) along the sample and antiparallel to the external field is now separated from the stable state (ϕ_s,θ_s) by the nonuniform energy barrier (see Fig. 1),

$$\tan\frac{\phi_s}{2}=\frac{\cosh[(x-x_0)/\delta]}{\sinh R},\quad \theta_s=\frac{\pi}{2}, \tag{4.1}$$

where $\operatorname{sech}^2 R=h$ and $\delta=\sqrt{A/K_e}\coth R$. $2\delta R$ is the distance between the soliton and antisoliton constituting the nucleus (see Fig. 1). We have restricted ourselves to one of the two equivalent saddle points $\pm\phi_s$. The arbitrary position x_0 of the nucleus along the sample gives rise to a Goldstone mode of zero energy in the spin-wave spectrum. ϕ_s solves the Euler–Lagrange equations,

$$-(A/K_e)d^2\phi/dx^2+\sin\phi\cos\phi+h\sin\phi=0,$$

with the boundary condition that ϕ merges asymptotically into the metastable state. The corresponding barrier energy is

$$E_s=8\sqrt{AK_e}\mathscr{B}(\tanh R-R\operatorname{sech}^2 R), \tag{4.2}$$

where the first term is the deformation energy and the second term is the Zeeman energy of the nucleus. Equation (4.2) has three important features as follows.

(i) E_s is proportional to the sample cross-sectional area and the energy $8\sqrt{AK_e}\mathscr{B}$ of two π Bloch walls. This is in contrast to the uniform barrier energy (3.3) which is proportional to the volume. For sufficiently elongated particles, this leads to a lower coercivity than theories discussed in the previous section.

(ii) For small external fields ($R\to\infty$), where the nucleus consists of a reversed domain delimited by two domain walls, the barrier energy is twice the domain-wall energy. This shows the invalidity of the "activation volume" concept which assumes that the barrier energy equals the total anisotropy energy of the reversed domain.

(iii) The saddle point is connected to the stable state via a path of decreasing energy. Consider the sequence of configurations that arise from Eq. (4.1) if we fix δ at the value $\sqrt{A/K_e}\coth R_0$ but vary R between 0 and ∞. The energy of such configurations is

$$E=8\sqrt{AK_e}\mathscr{B}(\tanh R-R\operatorname{sech}^2 R_0),$$

which increases from 0 (for $R=0$) to E_s at $R=R_0$ and then decreases monotonically until the domain walls leave the sample and the magnetization is reversed. The way down from the saddle point is thus not obstructed by intermediate saddle points. As mentioned in Sec. I, this latter problem can arise for saddle points of curling symmetry.

We are now going to investigate the energy near the saddle point ϕ_s. Expanding Eq. (2.3) to second order in the fluctuations $\varphi(x)=\phi(x)-\phi_s(x)$ and $p(x)=\pi/2-\theta(x)$ around the saddle point, we obtain

$$E\simeq E_s+\mathscr{B}\int dx\ \varphi\mathscr{H}^{s\varphi}\varphi+\mathscr{B}\int dx\ p\mathscr{H}^{sp}p, \tag{4.3}$$

with the operators

$$\mathscr{H}^{s\varphi}=A\left[-\frac{d^2}{dx^2}+\delta^{-2}V_-\left(\frac{x}{\delta},R\right)\right], \tag{4.4}$$

$$\mathscr{H}^{sp}=A\left[-\frac{d^2}{dx^2}+\delta^{-2}V_+\left(\frac{x}{\delta},R\right)\right]+K_h. \tag{4.5}$$

The potentials are defined by

$$V_\pm(\xi,R)=1-2\operatorname{sech}^2(\xi+R)-2\operatorname{sech}^2(\xi-R) \pm 2\operatorname{sech}(\xi+R)\operatorname{sech}(\xi-R). \tag{4.6}$$

Two eigenfunctions of the eigenvalue problems $\mathscr{H}^{s\varphi,p}\chi_n^{s\varphi,p}=E_n\chi_n^{s\varphi,p}$ are exactly known: the Goldstone mode

$$\chi_1^{s\varphi}\propto\operatorname{sech}(x/\delta-R)-\operatorname{sech}(x/\delta+R)$$

of zero energy which corresponds to a translation of the nucleus, and the ground state

$$\chi_0^{sp}\propto\operatorname{sech}(x/\delta-R)+\operatorname{sech}(x/\delta+R)$$

of energy $E_0^{sp}=K_h$. Since the former eigenfunction has one node and the latter eigenfunction represents the ground state of $\mathscr{H}^{sp}$, there is exactly one eigenfunction with negative energy. This proves the instability of the nucleus. Inserting Eq. (4.3) into the Landau–Lifshitz equations (2.4), we recognize that the decay mode of the nucleus

$$[\varphi_+(x,t),p_+(x,t)]=e^{\lambda_+ t}[\varphi_+(x),p_+(x)],$$

with $\lambda_+>0$ obeys the following eigenvalue problem:

$$\begin{aligned}(1+\alpha^2)\frac{M_0}{2\gamma}\lambda_+\varphi_+&=-\mathscr{H}^{sp}p_+-\alpha\mathscr{H}^{s\varphi}\varphi_+,\\(1+\alpha^2)\frac{M_0}{2\gamma}\lambda_+p_+&=\mathscr{H}^{s\varphi}\varphi_+-\alpha\mathscr{H}^{sp}p_+.\end{aligned}\tag{4.7}$$

For the derivation of the switching rate we refer to the Appendix. For $h\to 1$, Eq. (A11) can be evaluated exactly[11] and we obtain the switching rate

$$\Gamma=\left(\frac{6}{\pi^3}\right)^{1/2}\frac{8\gamma K_e}{M_0}\frac{L}{\sqrt{A/K_h}}\sqrt{\beta\mathscr{A}\sqrt{AK_e}}(1-h)^{7/4}e^{-\beta E_s}.\tag{4.8}$$

This result is plotted in Fig. 2 which clearly illustrates the coercivity reduction compared to uniform reversal. For small K_h, i.e., $\beta\mathscr{A}\sqrt{A/K_e}K_h<1$, this result is not valid and we have to investigate an energy density with vanishing hard-axis anisotropy $K_h=0$. The energy (2.1) then exhibits rotational symmetry around the easy x axis. To account for this symmetry, it is more convenient to measure the polar angle from the external field, i.e.,

$$\mathbf{M}/M_0=(\cos\tau,\ \sin\tau\cos\omega,\ \sin\tau\sin\omega)$$

(see Fig. 1). $\tau_s(x)=\phi_s(x)$ solves the Euler–Lagrange equations in these new parameters, but it is completely degenerate with configurations that arise from Eq. (4.1) by a rotation around the easy axis by an angle $0\leq\omega_s<2\pi$ (see Fig. 1): A given saddle-point structure (τ_s,ω_s) thus breaks the rotational symmetry and there must be a corresponding (Goldstone) mode of zero energy in the spin-wave spectrum which corresponds to an infinitesimal rotation of the nucleus around the easy axis. As is shown in the Appendix, this rotation is equivalent to the ground state χ_0^{sp} of $\mathscr{H}^{sp}$ which acquires zero energy for $K_h=0$. The explicit knowledge of the rotational and the translational Goldstone mode allows the evaluation of the statistical prefactor for all values of h,[11] and we obtain from the Appendix

$$\Gamma=\frac{\tilde{\lambda}_+}{1+\alpha^2}\frac{64\gamma K_e}{\pi M_0}\beta\mathscr{A}L\frac{(1-h)^2}{h}e^{-\beta E_s},\tag{4.9}$$

where for $\alpha\gtrsim 1$, $\tilde{\lambda}_+=\alpha|E_0^{s\psi}|$ Inserted into Eq. (4.9), this vlaue for $\tilde{\lambda}_+$ also provides a good approximation of the switching rate for $\alpha\lesssim 1$. The prefactor in Eq. (4.9) remains finite since for small h,[11] we have $E_0^{s\varphi}=-2hK_e$ and for $h\to 1$, $E_0^{s\varphi}=-3(1-h)K_e$.

V. DISCUSSION

We have presented magnetization reversal rates for uniform and nonuniform magnetization reversal. It has been shown that for elongated particles, a spatially localized nucleus gives rise to a lower coercivity than a uniform barrier. This is also valid for the case of a vanishing hard-axis anisotropy as is illustrated in Fig. 2, where the switching rate is plotted as a function of the external field. The following material parameters have been used: $A=5\times10^{-7}$ erg/cm, $K_e=\pi M_0^2=7\times10^5$ erg/cm^3, $M_0=480$ Oe, $\gamma=1.5\times10^7$ Oe^{-1} s^{-1}, $T=300$ K, $K_h=K_e/5$, and $\alpha=0.05$. Note that the value of the prefactor considerably affects the value of the rate as is illustrated by the three curves for nonuniform reversal which all have the same Arrhenius factor.

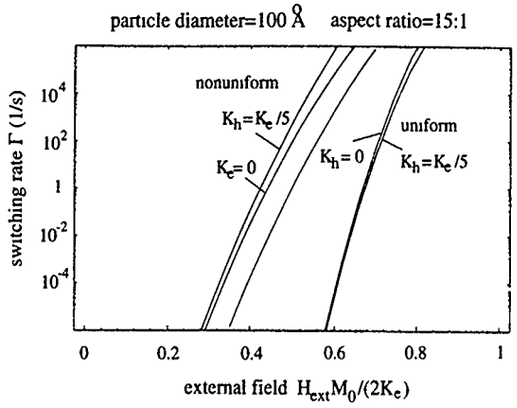

FIG. 2. Magnetization reversal rate for uniform and nonuniform reversal The dashed line is the approximation of "constant attempt frequency" $\Gamma\approx(2\gamma K_e/M_0)\exp(-\beta E_s)$.

In view of recent experiments, one should keep in mind that the coercivity changes drastically[12] with the angle between the external field and the particle axis. A precise alignment of the particle with respect to the field is therefore extremely important.

Note that we have assumed a constant cross section of the particle. If the particle cross section is not constant, nonuniform barriers at different x_0 are no longer degenerate but they form a distribution of energy barriers. A single particle can therefore behave like an ensemble of many particles.

So far we have neglected effects that occur at the particle ends. The present treatment, however, also allows a first estimate for nucleation occurring at the particle ends. Assuming that the anisotropy persists to the very end of the particle and that the magnetization obeys open boundary conditions $d\mathbf{M}/dx(\pm L/2)=0$, the nucleus (4.1) with $x_0=-L/2$ restricted to $x>0$ describes the nucleation of a domain wall at the sample end at $x=-L/2$. The corresponding barrier energy is then half that of the nucleus $E_s/2$. In a real sample, however, the demagnetizing energy will lead to a decrease of the easy-axis anisotropy from $K_e=K_{e,\mathrm{cryst}}+\pi M_0^2$ to $K_e=K_{e,\mathrm{cryst}}$ at the sample end and thus lead to a modification of this picture. Finally, it should be noted that this behavior could be investigated experimentally by artificially pinning the sample ends by, e.g., a high-coercivity material.

ACKNOWLEDGMENTS

The author kindly acknowledges discussions with A. Arrott, H. N. Bertram, A. Kent, M. Lederman, and H. Suhl. This work has been supported by the Swiss National Science Foundation and by NSERC of Canada.

APPENDIX

In this appendix we construct a Fokker–Planck equation for the magnetization dynamics and derive the corresponding switching rate. We focus on the moderately damped regime and barriers which are high compared to the thermal energy k_BT. Since the prefactor is of the order 10^{10} s^{-1}, this condition is satisfied even for large switching rates.

The present formalism which is based on work by Kramers and Langer[13] allows us to rederive the results of Zürcher[7] and Klik and Gunther[8] in a simple way. In addition, this method can be readily extended to interacting particles and nonuniform magnetization configurations.[5,11]

To simplify notation, it is convenient to use dimensionless units defined by $[x] = \sqrt{A/K_e}$, $[E/V] = 2K_e$, $[t]=(1+\alpha^2)M_0/(2\gamma K_e)$. Introducing the vectors $\psi=(\varphi,p)$, $h=(h_{s\varphi},h_{sp})$ with $h_{s\varphi}=h^2-1$, $h_{sp}=k_h/k_e$, the energy (3.4) near the saddle point reads $E\simeq E_s^{(0)}+\frac{V}{2}\Sigma_i h_i\psi_i^2$. The equations of motion linearized around the saddle point take the following form:

$$\frac{\partial\psi_i}{\partial t}=-\sum_j M_{ij}h_j\psi_j(t), \tag{A1}$$

where M is a matrix with $M_{11}=M_{22}=\alpha$, $M_{12}=-M_{21}=1$. The unstable mode $\psi_i(t) = e^{\lambda_+ t}\psi_i^+$ with $\lambda_+>0$ [Eq. (3.6)] thus obeys the equation

$$\lambda_+\psi_i^+=-\sum_j M_{ij}h_j\psi_j^+ . \tag{A2}$$

Rather than investigating the stochastic trajectories $\psi_i(t)$ that arise by adding noise terms to Eq. (A1) we now focus on the probability $\rho(\psi_i)\Pi_i\, d\psi_i$ of finding the system in a phase-space volume element $\Pi_i\, d\psi_i$ around the state ψ_i. The dynamics of this probability distribution is then governed by the Fokker–Planck equation

$$\frac{\partial\rho}{\partial t}+\sum_i \frac{\partial J_i}{\partial\psi_i}=0, \tag{A3}$$

with the probability current

$$J_i=-\sum_j M_{ij}\left(h_j\psi_j+\frac{1}{\tilde\beta}\frac{\partial}{\partial\psi_j}\right)\rho. \tag{A4}$$

Note that due to the structure of M only the diagonal part contributes to the second term in Eq. (A4). Equation (A3) can be formally derived from a Langevin equation with Gaussian white noise, but it is more instructive to consider the following heuristic motivation: (i) The coefficient of ψ_i in Eq. (A4) is constructed such that $\partial\langle\psi_i\rangle/\partial t=\langle\partial\psi_i/\partial t\rangle$. (The expectation value is defined as $\langle f\rangle=\int\Pi_i d\psi_i f\rho$); (ii) the coefficient of the derivative is determined such that the equilibrium distribution near the saddle point,

$$\rho_{eq}=Z^{-1}\exp\left[-\tilde\beta\left(e_s^{(0)}+\tfrac{1}{2}\sum_i h_i\psi_i^2\right)\right], \tag{A5}$$

is a static solution of Eq. (A3) with vanishing current, where $\tilde\beta=\beta V$ and $e_s^{(0)}=E_s^{(0)}/V$. Z is the normalization with respect to the vicinity of the metastable state.

Equation (A3) represents a continuity equation in phase space. The "leakage" of the system out of a certain region of phase space, e.g., the vicinity of the metastable state, is thus given by the flux through the boundary of this region. Due to the Boltzmann factor $\exp(-\beta E)$, this flux will be maximal around the saddle point which represents the connection of lowest energy between the metastable and the stable state. The goal of calculating the switching rate out of the metastable state thus amounts to the evaluation of the total probability current of a stationary nonequilibrium distribution through a surface near the saddle point.

Since we consider high barriers, the desired nonequilibrium probability distribution ρ will thus approach an equilibrium distribution in the vicinity of the metastable state while it has to vanish beyond the saddle point. Following Kramers, the stationary nonequilibrium distribution is assumed to factorize as follows near the saddle point:

$$\rho=\rho_{eq}F(u), \tag{A6}$$

where F depends on the single coordinate $u=\Sigma_i U_i\psi_i$ (even in the case of arbitrarily many degrees of freedom), with coefficients U_i to be determined. Inserting Eq. (A6) with Eq. (A5) into Eq. (A3) and using $\partial\rho/\partial t=0$ we obtain

$$-\sum_{ij} M_{ij}h_i\psi_i U_j\frac{dF}{du}+\frac{1}{\tilde\beta}\sum_{ij} M_{ij}U_iU_j\frac{d^2F}{du^2}=0, \tag{A7}$$

where the above boundary conditions imply $F(-\infty)=1$, $F(\infty)=0$. The consistency of the ansatz requires this to be a differential equation in u alone, and thus

$$\sum_{ij} M_{ij}h_i\psi_iU_j=\kappa u,\quad \frac{1}{\tilde\beta}\sum_{ij} M_{ij}U_iU_j=\gamma\kappa. \tag{A8}$$

First we note that $\Sigma_{ij}M_{ij}U_iU_j = \alpha\Sigma_i U_i^2$ and thus $\gamma\kappa>0$. To elucidate the meaning of κ we remark that the first equation in Eq. (A8) is solved by $U_j=h_j\psi_j^+$ and therefore $\kappa=-\lambda_+<0$. The constant γ will cancel in the final result. Equation (A7) then takes the form $-u\,dF/du+\gamma\,d^2F/du^2=0$ and the boundary conditions on F are satisfied by the solution

$$F(u)=\frac{1}{\sqrt{2\pi|\gamma|}}\int_u^\infty du\,\exp\left(-\frac{u^2}{2|\gamma|}\right). \tag{A9}$$

Inserting Eqs. (A9) and (A6) into Eq. (A4) we obtain

$$J_i=-\frac{1}{\tilde\beta}\sum_j M_{ij}U_j\rho_{eq}\frac{dF}{du}.$$

The switching rate is then given by the total probability flux through a surface near the saddle point which we choose for convenience to be $u=0$,

$$\Gamma=\int_{u=0} dS\sum_i U_iJ_i=\lambda_+\left(\frac{|\gamma|}{2\pi}\right)^{1/2}\int_{-\infty}^{\infty}\prod_i d\psi_i\,\delta(u)\rho_{eq}. \tag{A10}$$

The equilibrium probability density thus has to be evaluated near the saddle point where it is given by Eq. (A5). Using $\delta(u)=\int(dq/2\pi)\exp(iqu)$ we perform first the integration over the stable directions and then over q. The coefficient of the resulting final Gaussian integration over the unstable mode is negative although the energy decreases along this unstable direction. This follows from Eq. (A8) which implies that $\Sigma_i U_i^2/h_i=\tilde\beta\gamma<0$. Since ρ_{eq} is strongly peaked around the metastable state, we can use a Gaussian approximation and obtain $Z = \Pi_i\sqrt{2\pi/\tilde\beta h_{mi}}$ where $h_{m\varphi}=1-h$ and

$h_{mp}=1-h+K_h/K_e$ are the coefficients in a quadratic expansion of the energy (3.5). We thus finally obtain for the switching rate

$$\Gamma=\frac{\lambda_+}{2\pi}\left(\frac{\Pi_i h_{mi}}{\Pi_i|h_i|}\right)^{1/2} e^{-\tilde{\beta}e_s^{(0)}}, \tag{A11}$$

where λ_+ is the decay frequency of the nucleus and the remaining term is the ratio of the partition functions evaluated in Gaussian approximation at the saddle point and the metastable state respectively. In the derivation of Eq. (A11) it has been assumed that there is only one single saddle point. Since Eq. (3.2) defines two equivalent saddle points, Eq. (A11) has to be multiplied by a factor of 2 to yield the result (3.7).

Note that the result (A11) is completely general and can be extended to other situations with artibrarily many degrees of freedom such as interacting particles and spatially nonuniform situations.

We now focus on the situation of a vanishing hard-axis anisotropy $K_h=0$. In this case, $h_{sp}=K_h/K_e$ becomes zero and the formerly stable direction at the saddle point becomes flat. There is now a completely degenerate class of saddle points which is conveniently expressed in terms of τ and ω as in Sec. IV. The saddle point is then given as in Eq. (3.2), $\cos\tau_s^{(0)}=-h$, but as a consequence of the rotational symmetry around the easy axis the azimuthal angle $0\leqslant\omega_s^{(0)}\leqslant 2\pi$ is arbitrary.

Since the previous treatment required the existence of a stable direction at the saddle point, the derivation of the switching rate now proceeds along somewhat different lines. The difficulty arises when we try to perform the integration in Eq. (A10) over the variable $\psi_2\equiv p$ which diverges since $h_{sp}=0$. The infinite integration domain in Eq. (A10) is, however, only sensible if the Gaussian approximation of the partition function provides a sufficiently fast decay. Since this integration is related to the rotational degeneracy, it is inadequate to use an infinite integration domain. It rather has to be replaced by a finite integration over the angle $\omega_s^{(0)}$. Since a rotation around the easy axis by an angle $d\omega$ corresponds to a fluctuation $dp/\sin\tau_s^{(0)}$, the correct value for the integral is

$$\int dp_2=\sin\tau_s^{(0)}\int_0^{2\pi}d\omega_s^{(0)}=2\pi\sin\tau_s^{(0)},$$

which replaces the former term $\sqrt{2\pi/\beta h_{sp}}$ in Eq. (A11). In dimensionless units the rate becomes

$$\Gamma=\lambda_+\left(\frac{h_{m\varphi}h_{mp}}{|h_{s\varphi}|}\right)^{1/2}\left(\frac{\tilde{\beta}}{2\pi}\right)^{1/2}\sin\phi_s^{(0)}e^{-\beta E_s^{(0)}}, \tag{A12}$$

where $\phi_s^{(0)}$ is given by Eq. (3.2) and the dimensionless escape frequency $\lambda_+=\alpha(1-h^2)$ follows from Eq. (3.6).

For *nonuniform* configurations, we obtain by an adaptation of the previous method[11] the following expression of the switching rate:

$$\Gamma=\lambda_+\mathscr{L}\left(\frac{\beta\mathscr{A}}{2\pi^3}\right)^{1/2}\left(\frac{\det\mathscr{H}^{m\varphi}}{\det'|\mathscr{H}^{s\varphi}|}\right)^{1/2}\left(\frac{\det\mathscr{H}^{mp}}{\det\mathscr{H}^{sp}}\right)^{1/2}e^{-\beta E_s}, \tag{A13}$$

which is expressed in dimensionless units. Since there are two degenerate saddle points $\pm\phi_s$, a factor of 2 has been included in Eq. (A13). "det" denotes now the infinite product [see Eq. (A11)] of the eigenvalues of the fluctuation operators and the prime denotes omission of the eigenvalue $E_1^{s\varphi}=0$. $\mathscr{H}^{m\varphi}=-d^2/dx^2+1-h$, $\mathscr{H}^{mp}=\mathscr{H}^{m\varphi}+K_h/K_e$ describe fluctuations around the metastable state (ϕ_m,θ_m) and $\mathscr{L}=L\sqrt{E_s/2\mathscr{A}}\sqrt{AK_e}$ arises from the integration over the translational Goldstone mode $\chi_1^{s\varphi}$. In the limit $h\to 1$, Eq. (A13) can be evaluated analytically[11] with the result (4.8).

For vanishing hard-axis anisotropy $K_h=0$, the result (A13) fails since the ground state of $\mathscr{H}^{sp}$ acquires zero energy and needs a special treatment in the derivation of the rate formula: A rigid rotation around the easy axis by an angle $d\omega$ corresponds to the fluctuation $d\varphi(x)=0$, $dp(x)=\sin\phi_s(x)d\omega$. Since $\sin\phi_s\propto\chi_0^{sp}$, we also have $dp(x)=\chi_0^{sp}dp_o$, and the integration over the mode amplitude p_0 in the Gaussian integral in Eq. (A10) can be expressed as

$$\int dp_0=\left(\int_{-\infty}^{+\infty}dx\,\sin^2\phi_s\right)^{1/2}\int_0^{2\pi}d\omega$$

$$=4\pi(\tanh R+R\,\mathrm{sech}^2 R,$$

which replaces the factor $\sqrt{2\pi/\beta\mathscr{A}E_0^{sp}}$ that arises for $K_h\neq 0$. This fact allows an analytic evaluation of the statistical prefactor for all values of h. Using the exact results[11] for the fluctuation determinants, we obtain Eq. (4.9) after reinstating units.

[1] M. Lederman, D. R. Fredkin, R. O'Barr, S. Schultz, and M. Ozaki, J. Appl. Phys. **75**, 6217 (1994).
[2] A. Kent, S. von Molnár, S. Gider, and D D. Awschalom (these proceedings).
[3] L. Néel, Ann. Géophys. **5**, 99 (1949).
[4] W. F. Brown, Phys. Rev. **130**, 1677 (1963).
[5] H. B. Braun, Phys. Rev. Lett. **71**, 3557 (1993).
[6] H. B. Braun and O. Brodbeck, Phys. Rev Lett. **70**, 3335 (1993).
[7] U. Zurcher, Diploma thesis, University of Basel, 1985.
[8] I. Klik and L. Gunther, J. Stat. Phys. **60**, 473 (1990).
[9] In Ref. 12 it has been shown that below a particle length $L_{crit}=2\pi\sqrt{A/K_e}/\sqrt{1-h^2}$ only uniform saddle points exist, provided that the magnetization obeys open boundary conditions $d\mathbf{M}/dx(x=\pm L/2)=0$.
[10] In his criticism of Ref. 5, A. Aharoni (unpublished) overlooks that demagnetizing effects are already absorbed in the definition of K_e.
[11] H. B. Braun, Phys. Rev. B (in press).
[12] H. B. Braun and H. N. Bertram, J. Appl. Phys. **75**, 4609 (1994).
[13] H. A Kramers, Physica **7**, 284 (1940); J. S. Langer, Ann. Phys. **54**, 258 (1969).

Magnetic properties of nanophase cobalt particles synthesized in inversed micelles

J. P. Chen and C. M. Sorensen
Department of Physics, Kansas State University, Manhattan, Kansas 66506

K. J. Klabunde
Department of Chemistry, Kansas State University, Manhattan, Kansas 66506

G. C. Hadjipanayis
Department of Physics and Astronomy, University of Delaware, Newark, Delaware 19716

Cobalt particles were prepared with the microemulsion method in the binary system of DDAB (didodecyldimethylammonium bromide)/toluene by reduction of $CoCl_2$ with $NaBH_4$. The average particle size of the as-prepared samples could be varied from 1.8 to 4.4 nm by controlling the concentration of $CoCl_2$ in the solution of DDAB in toluene. TEM studies showed that the particles were quite uniform and well isolated. The particle sizes determined from magnetic data were consistent with those measured by TEM. The coercivity of the particles at 10 K increased from 640 to 1250 Oe as particle size increased from 1.8 to 4.4 nm. The blocking temperature of the particles increased from 19 to 50 K for the same size range. The saturation magnetization σ_s at 2 K increased with decreasing particle size. The value of σ_s of the particles with average size of 1.8 nm was about 200 emu/g, which is 20% higher than the bulk value. This implies that the magnetic moment per atom is enhanced in the nanoparticle system.

I. INTRODUCTION

Nanoscale materials show novel properties that are often significantly different from the bulk due to fundamental changes in coordination, symmetry, and confinement. In magnetic materials advantage has been taken, for a considerable time, of the variation of magnetic properties of fine particles due to effects such as single domains, superparamagnetism, and surface interaction. Only recently, however, have magnetic studies proceeded into the ultrasmall regions where more fundamental changes will occur as the bulk transforms to the atomic. In this work we describe the synthesis of nanoscale metallic cobalt particles using an inversed micelle synthesis method. A consistent set of size dependent magnetic data are obtained, the most surprising of which show an enhanced, relative to the bulk, magnetic moment per Co atom.

II. EXPERIMENTAL METHODS

Cobalt particles were prepared by the microemulsion method in the binary system of DDAB/toluene.[1,2] $NaBH_4$ was used to reduce $CoCl_2$ to produce Co particles. First $CoCl_2 \cdot 6H_2O$ was dissolved in a deoxygenated 11 wt % DDAB solution in toluene at concentrations of 0.005–0.02 M. The reagent was trapped in the empty micelles and formed a blue transparent solution. Then a 10 M $NaBH_4$ aqueous solution was added on the condition of $[BH_4]:[Co^{2+}]=3:1$ and stirred. It eventually turned from blue to black and formed a stable colloid. The colloid was dried in a glove bag with all the toluene evaporated and formed a paste sample. The cobalt particles were uniformly distributed in the DDAB matrix.

The x-ray spectrum of a paste sample showed only the (111) peak of fcc cobalt. Since the concentration of cobalt in the sample is about 0.6 wt %, the other weaker peaks were in the noise.

When we studied the dependence of the spontaneous magnetization on temperature at low field for zero-field cooled samples, we found that the particles were not pure metallic cobalt when the mole ratio of water to DDAB was much larger than one. Figure 1 shows the data for two samples with the same preparation except the water content. In sample A 60 μl of 5 M $NaBH_4$, whereas in sample B 30 μl of 10 M $NaBH_4$, was added to 10 ml of 0.01 M $CoCl_2$ solution in DDAB/toluene. Sample A shows two peaks in Fig. 1, while its saturation magnetization was just 50% of that of sample B, which had only one peak in σ vs T plot. The two peaks imply two magnetic phases in sample A. In nonmicroemulsion systems we have shown[3] how water causes the borohydrate reduction to create Co_2B whereas Co is created in the absence of water. Thus we interpret the results for sample A to imply that both Co and Co_2B particles

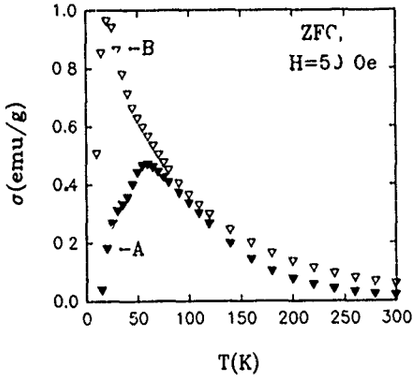

FIG. 1. Temperature dependence of the spontaneous magnetization at $H=50$ Oe for zero-field cooled samples A and B. In sample A 60 μl of 5 M $NaBH_4$, whereas in sample B 30 μl of 10 M $NaBH_4$, was added to 0.01 M $CoCl_2$ solution in DDAB/toluene The peak at 20 K in both A and B is due to Co; the peak at 60 K in A is due to Co_2B.

 0021-8979/94/76(10)/6316/3/$6 00 © 1994 American Institute of Physics

FIG. 2. TEM photograph of the cobalt particles with an average particle size of 3.3 nm.

were produced. On the other hand, in sample B only Co is produced. There was, of course, water present in sample B. But at low concentration (one H_2O molecule per DDAB molecule in sample B) the water must be fixed by the hydrophilic part of the DDAB and unable to participate in the Co reduction. We remark that Pileni *et al.*[4] found the oxidation states of copper metallic clusters changed with the change of water content in the micelles.

With the above results in mind, we controlled the ratio of $[H_2O]$:[DDAB] below 1.5 to make pure metallic cobalt. The particle size was varied by changing the $CoCl_2$ concentration in the DDAB/toluene system from 0.005 to 0.02 M. We have also tried to increase the particle size by increasing the reaction temperature to 50 °C, but no obvious change was observed.

III. RESULTS AND DISCUSSION

A TEM study was carried out to size the particles and study their morphology. The particle diameter changed from 1.8 to 4.4 nm as the $CoCl_2$ concentration increased from 0.005 to 0.02 M. Figure 2 is a TEM picture of one sample with an average diameter of 3.3 nm. The particles are well separated and their sizes are narrowly distributed.

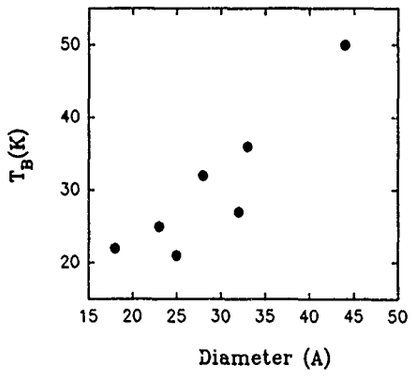

FIG. 3. The blocking temperature as a function of size for Co particles

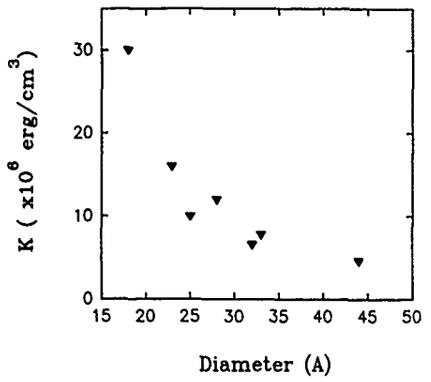

FIG. 4. Relation between the anisotropy constant and size of Co particles.

The magnetic properties were measured by a SQUID magnetometer. All the particles were in the superparamagnetic state at room temperature. The sample was cooled in zero field to 2 K, and then magnetization was measured as a function of temperature in a 50 Oe field to determine the blocking temperature. The relation between the blocking temperature and the particle size is shown in Fig. 3. The blocking temperature increased as particle size increased, which is consistent with the behavior of fine particles.

The blocking temperature should roughly satisfy the relationship

$$T_B = \frac{KV}{30k_B}, \tag{1}$$

where K is the anisotropy constant, k_B Boltzmann's constant, and V the average volume of the particle. With the knowledge of the blocking temperature and the particle size, we calculated the anisotropy constant for the Co particles as shown in Fig. 4. The calculated anisotropy is larger than the bulk value of fcc cobalt (2.7×10^6 erg/cm^3)[5,6] and increases with the decrease of particle size.

At 10 K, all the samples were in the ferromagnetic state. The coercivities of different samples are shown in Fig. 5. As particle size increased, the coercivity increased, which is the behavior of single-domain particles caused by thermal effects.

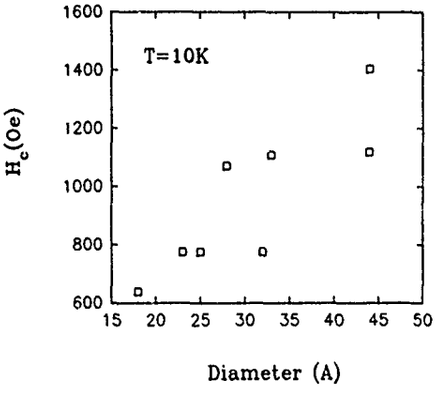

FIG. 5. Size dependence of coercivity of Co particles at 10 K

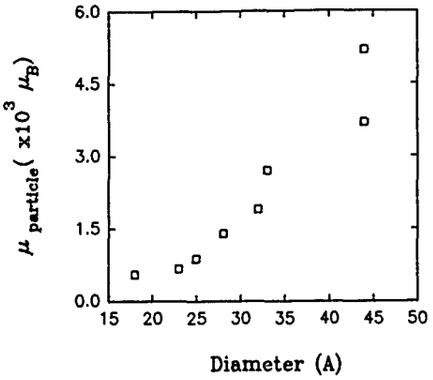

FIG. 6. Magnetic moment per particle determined from σ_s and susceptibility and for different samples at temperatures higher than T_B.

Above the blocking temperature, the magnetic anisotropy energy barrier of the single-domain particles is overcome by thermal energy and superparamagnetism occurs. The magnetic moment per particle was calculated from the susceptibility and saturation magnetization. The results are shown in Fig. 6 as a function of the TEM determined size.

All the above results are consistent with the properties of ultrafine particles. The saturation magnetization (σ_s) of the cobalt particles at 2 K (Fig. 7) showed surprising behavior. The particles were not saturated even at 5.5 T despite their large moments. To obtain σ_s we plotted σ vs $1/H$ and extrapolated to $1/H \rightarrow 0$. Figure 8 shows the relation between the saturation magnetization and the particle size. The magnetizations are larger than the bulk value of cobalt and increase with decreasing particle size. For the smallest particles, the saturation magnetization was about 200 emu/g, about 20% larger than the bulk value of fcc cobalt, which is

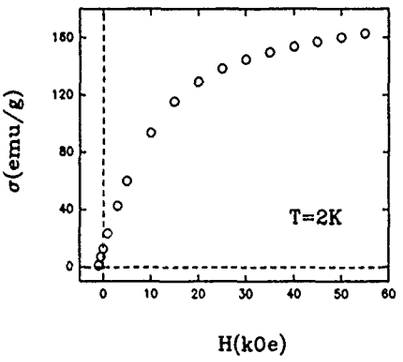

FIG. 7. Magnetization as a function of field at 2 K for a sample with the average particle size of 3.3 nm.

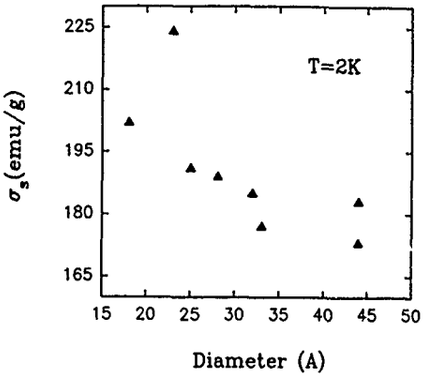

FIG. 8. Saturation magnetization of Co particles at $T=2$ K (bulk $\sigma_s=166$ emu/g).

166 emu/g.[7] An enhancement of the magnetic moment per atom in cobalt has been observed in free cobalt clusters[8] and ultrathin Co/Ag(001) films,[9] and has been predicted by theoretical calculations[10,11] this is the first time that the enhancement has been observed in supported cobalt particles.

IV. CONCLUSIONS

We have successfully made cobalt fine particles with the size varying from 1.8 to 4.4 nm. The Co particles are single-domain particles and in superparamagnetic state at room temperature. The anisotropy constants in our Co particles are larger than that of bulk material. An enhanced magnetic moment per Co atom compared to the bulk was observed. This enhancement increases with decreasing size to be ~20% greater than bulk for 1.8 nm particles. This result is consistent with theoretical calculations and experimental results in free cobalt clusters.

ACKNOWLEDGMENT

This work was supported by NSF Grant No. 9013930.

[1] J. P. Wilcoxon, US Patent No. 5147841 (1992).
[2] J. P. Chen, C. M. Sorensen, K. J. Klabunde and G. C. Hadjipanayis, J. Appl. Phys. **75**, 5846 (1994).
[3] G. N. Glavee, K. J. Klabunde, C. M. Sorensen, and G. C. Hadjipanayis, Langmuir **8**, 771 (1992); Inorg. Chem. **32**, 474 (1993).
[4] M. P. Pileni, J. Phys. Chem. **97**, 6961 (1993).
[5] W. D. Doyle and P. J. Flanders, in *International Conference of Magnetism*, Nottingham, 1964 (The Institute of Physics and the Physical Society, Bristol, 1965), p. 751.
[6] W. A. Sucksmith and J. E. Thompson, Proc. R. Soc. London Ser. A **225**, 362 (1954).
[7] M. Nishikawa, E. Kita, T. Erata, and A. Tasaki, J. Magn. Magn. Mater **126**, 303 (1993).
[8] J. P. Bucher, D. C. Douglass, and L. A. Bloomfield, Phys. Rev. Lett. **66**, 3052 (1991).
[9] J. A. C. Bland, A. D. Johnson, R. D. Bateson, and H. J. Lauter, J. Magn. Magn. Mater. **104**, 1798 (1992).
[10] C. Y. Yang, K. H. Johnson, D. R. Salahub, J Kaspar, and R. P. Messmer, Phys. Rev. B **24**, 5673 (1981).
[11] Z. Li and B. Gu, Phys. Rev. B **47**, 13611 (1993).

Magnetic and structural properties of vapor-deposited Fe-Co alloy particles

S. Gangopadhyay,[a] Y. Yang, and G. C. Hadjipanayis
Department of Physics, University of Delaware, Newark, Delaware 19716

V. Papaefthymiou
University of Ioannina, 453 32 Ioannina, Greece

C. M. Sorensen
Department of Physics, Kansas State University, Manhattan, Kansas 66506

K. J. Klabunde
Department of Chemistry, Kansas State University, Manhattan, Kansas 66506

The structural and magnetic properties of two Fe-Co alloy particles with composition $Fe_{100-x}Co_x(x=45,65)$ were studied using x-ray diffraction, x-ray photoelectron spectroscopy, transmission electron microscopy, superconducting quantum interference device magnetometry, and Mössbauer spectroscopy. The particles were nearly spherical in shape with an average particle size around 350 Å. Particles formed long chains and showed a core/shell particle morphology. X-ray diffraction and Mössbauer studies showed the presence of bcc α-Fe-Co and $CoFe_2O_4$ phases with the former as the majority phase in $Fe_{55}Co_{45}$ and the latter the majority phase in $Fe_{35}Co_{65}$. The room-temperature coercivities of both of these samples were much higher than those in Fe particles with values exceeding 2.2 kOe. The $Fe_{35}Co_{65}$ sample showed a drastic temperature dependence of coercivity from 1.5 kOe at 300 K to 15 kOe at 10 K. The structural and magnetic data suggest a core/shell morphology with the surface oxide layer having a very important impact on both the magnitude and temperature dependence of the coercivity of the whole particle.

Previous studies on Fe, Co, and Ni particles prepared by gas evaporation have shown large coercive forces with values of 1050, 1200, and 100 Oe, respectively.[1] Transmission electron microscopy (TEM) and Mössbauer studies indicated a core-shell particle structure with a metallic core surrounded by the corresponding oxide shell. Micromagnetic calculations[2] and experimental studies[3] on passivated and unpassivated γ-Fe_2O_3 particles have shown that the thickness and magnetic state of the oxide layer affects the switching fields and hence the coercivity of the particle. In passivated Fe and Co particles the hysteresis behavior was found to be strongly dependent on the amount of surface oxidation and the magnetic interaction at the core-shell interface was claimed to be responsible for the high coercivity.[4] Previous work[5] on Fe-Co alloy particles has shown coercivities exceeding 2.5 kOe which are much higher than those of either Fe or Co particles. A similar behavior has been observed on elongated Fe-Co particles prepared by electrodeposition[6] and the high coercivity was attributed to the presence of a cobalt ferrite oxide layer on the surface of the particle.

In the present paper we try to understand the origin of the high coercivity of Fe-Co alloy particle samples by comparing their structural, microstructural, and magnetic properties.

Two Fe-Co alloy particle samples prepared by the gas evaporation method were obtained from Vacuum Metallurgical Co., Japan.

The structure of the particles was determined by x-ray diffraction (XRD) and selected area diffraction (SAD) patterns. The particle size was determined by transmission electron microscopy (TEM) and their composition was deter-

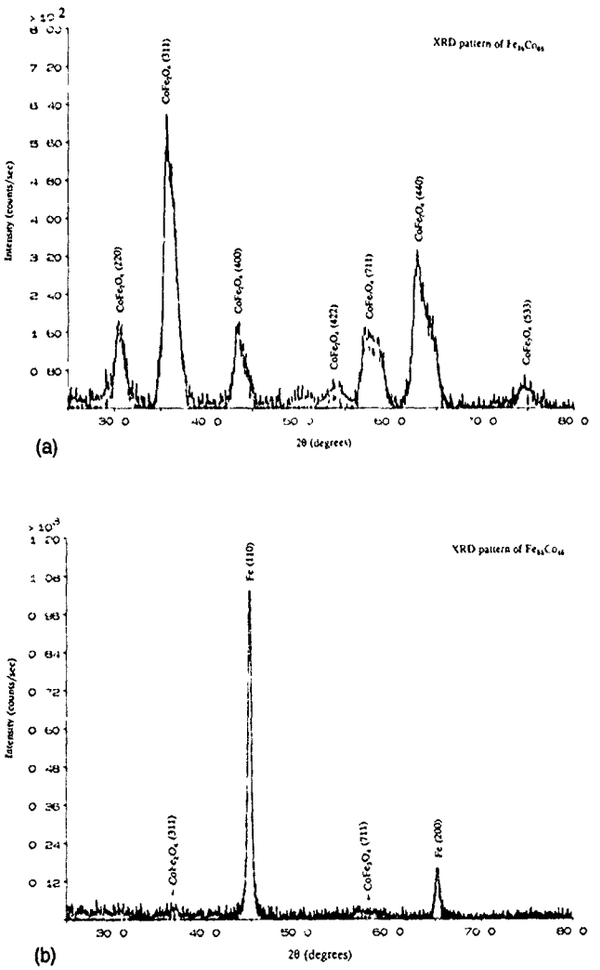

FIG. 1. XRD patterns of the Fe-Co samples. (a) $Fe_{35}Co_{65}$, (b) $Fe_{55}Co_{45}$

[a]Current address. Center for MINT, University of Alabama,Tuscaloosa, AL 35847.

 0021-8979/94/76(10)/6319/3/$6.00 © 1994 American Institute of Physics

FIG. 2. Bright-field TEM micrographs of (a) $Fe_{55}Co_{45}$ and (b) $Fe_{35}Co_{65}$.

mined by energy dispersive x-ray analysis (EDAX). X-ray photoelectron spectroscopy (XPS) was used to probe and characterize the surface of the particles. The magnetic properties were measured by both a vibrating sample magnetometer (VSM) and a superconducting quantum interference device (SQUID) magnetometer. Mössbauer spectroscopy was also carried out to determine the type of the oxides present.

The two samples studied had a nominal composition $Fe_{100-x}Co_x$ with $x=45$ and 65. EDAX measurements gave the x values of 43 and 64, respectively.

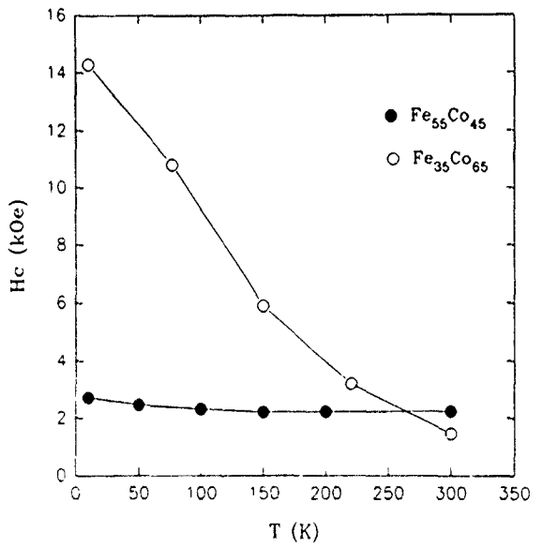

FIG 3. Temperature dependence of coercivity in the two Fe-Co samples.

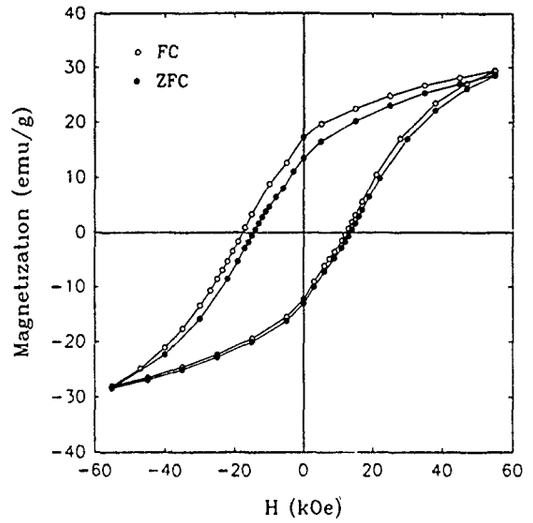

FIG. 4. Zero-field-cooled (ZFC) and field-cooled (FC) hysteresis loop in an $Fe_{35}Co_{65}$ sample.

The x-ray diffraction pattern of $Fe_{55}Co_{45}$ was dominated by bcc Fe-Co, with few extremely weak and broadened peaks corresponding to $CoFe_2O_4$ [Fig. 1(a)], while the pattern of $Fe_{35}Co_{65}$ showed strong and relatively broadened peaks corresponding to $CoFe_2O_4$ [Fig. 1(b)]. The asymmetric broadening of the $CoFe_2O_4$ peaks may be due to the small grain size and the off-stoichiometric composition of $CoFe_2O_4$. The presence of an Fe/FeCo phase could not be detected unambiguously due to the overlap of its d spacing with that of the asymmetric broadened peaks of the $CoFe_2O_4$ phase. Selected area diffraction (SAD) patterns agreed with the XRD results.

Bright-field micrographs obtained for the two samples revealed that the particles were about spherical in shape and formed a long chain-like structure. The average grain size of the two samples was about the same and ~350 Å (Fig. 2). The particles in the $Fe_{35}Co_{65}$ sample showed a very distinct contrast between the inside core area and surface shell region as shown in Fig. 2(b).

The magnetic properties of these samples were measured in the temperature range from 10 to 300 K. $Fe_{35}Co_{65}$ showed an M_s around 30 emu/g while in $Fe_{55}Co_{45}$ M_s was much

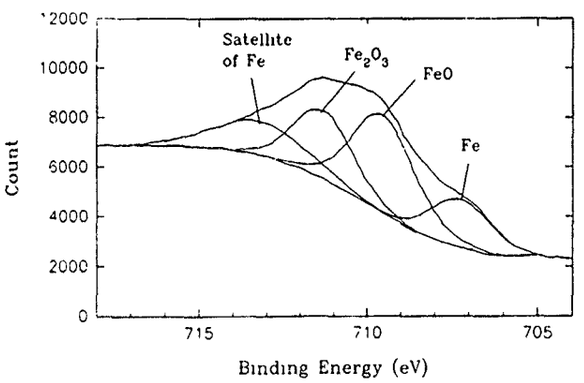

FIG. 5. XPS spectra of $Fe_{55}Co_{45}$.

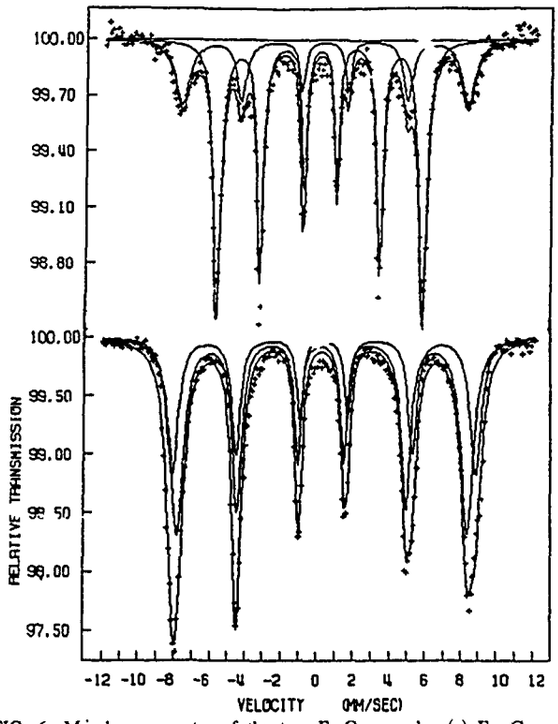

FIG. 6. Mössbauer spectra of the two Fe-Co samples (a) $Fe_{55}Co_{45}$, (b) $Fe_{35}Co_{65}$.

higher, over 170 emu/g. Such a difference in the magnetization of the two samples could be due to the presence of a large amount of $CoFe_2O_4$ in $Fe_{35}Co_{65}$ as compared to $Fe_{55}Co_{45}$, and to possible surface spin pinning in the former because of a thicker cobalt ferrite shell. The decrease in M with increasing T (10–300 K) was only about 5%. The remanence was about 0.5 in both the samples. The temperature dependence of coercivity for the two samples was quite different, as shown in Fig. 3. The coercivity of the $Fe_{35}Co_{65}$ sample was ~1.5 kOe at 300 K and increased to 15 kOe at 10 K (about 900% increase) while the coercivity of the $Fe_{55}Co_{45}$ sample was 2.2 kOe at 300 K and increased slightly to 2.7 kOe at 10 K (only 25% increase).

Field-cooled hysteresis loops on both samples showed a shift to the left (Fig. 4) with the value of the shift much larger in the $Fe_{35}Co_{65}$ sample (about 3 kOe in $Fe_{35}Co_{65}$ and 0.5 kOe in $Fe_{55}Co_{45}$ at 10 K). The shift in the field-cooled (FC) loops (H_{cool}=20 kOe) is believed to be the result of exchange interaction at the interface of a core-shell particle morphology. The larger amount of shift in $Fe_{35}Co_{65}$ is consistent with the presence of a thicker cobalt ferrite shell.

XPS is a sensitive technique to detect the type of oxides on the surface of the particles. The presence of the Fe-Co oxides was determined by deconvoluting the asymmetric broadening of the higher-energy edge of the metallic Fe and Co peaks. Figure 5 shows the spectrum of $Fe_{55}Co_{45}$ around the binding energy of Fe. These data show clearly the presence of surface oxides in both samples. Because XPS probes the surface layer, a thin Fe-O layer on the surface can result in a corresponding peak in the spectrum.

TABLE I. Mössbauer parameters δ is the isomer shift. ΔE_Q is the quadrupole splitting. H is the hyperfine field.

Sample	δ(mm/s)	ΔE_Q(mm/s)	H(kOe)	ΔH(kOe)	%	Phase
$Fe_{55}Co_{45}$	0.40	0.02	504	20	28	$(Fe,Co)_3O_4$
	0.14	−0.004	362	80	72	Fe-Co
$Fe_{35}Co_{65}$	0.37	0.018	506	15	*A*	$(Fe,Co)_3O_4$
	0.51	−0.02	529	12	*B*	

Mössbauer spectra for $Fe_{55}Co_{45}$ showed a mixture of Fe-Co alloy and cobalt ferrite while the spectrum of $Fe_{35}Co_{65}$ showed only $CoFe_2O_4$ (Fig. 6). The ratio of Fe^{3+} at the A and B site was 1.6:1 instead of 1:1, indicating an off-stoichiometric $CoFe_2O_4$. The Mössbauer parameters are listed in Table I. The fact that no FeO has been observed with Mössbauer indicates a small percentage of this oxide (<5%). This is different in XPS, where a thin FeO layer on the surface can result in a corresponding peak in the spectrum.

The XRD and Mössbauer results on the Fe-Co alloy particles indicated a core-shell particle morphology. In $Fe_{55}Co_{45}$ the core is a bcc Fe-Co alloy while the shell consists of Fe-Co oxides with $CoFe_2O_4$ as the majority oxide. In $Fe_{35}Co_{65}$ the core/shell morphology is composed of stoichiometric and off-stoichiometric $CoFe_2O_4$, respectively.

Based on the present and our previous experiments with passivated Fe particles,[4] we believe that the $CoFe_2O_4$ oxide layer plays an important role in the magnetic properties of the particles. It results in a large surface-pinning force, which impedes the rotation of magnetization near the interface layer toward the direction of the external field, and thus it leads to the high coercivity and nonsaturation effects even at 55 kOe. The anisotropy constant K_1 of $CoFe_2O_4$ is much higher than that of Fe_3O_4 (the values are 2×10^6 and -1.1×10^5 erg/cm^3 at room temperature, respectively[7]) and has a strong temperature dependence: K_1 (0 K) is almost an order of magnitude higher than K_1 (300 K).[8] This large temperature dependence of K_1 explains the drastic temperature dependence of the coercivity in $Fe_{35}Co_{65}$.

This work has been supported by NSF-CHE-9013930. The Fe-Co alloy particle samples were supplied by Dr. M. Oda of Vacuum Metallurgical Co., Japan.

[1] S. Gangopadhyay, G. C. Hadjipanayis, B Dale, C M. Sorensen, and K. J. Klabunde, Nanostruct. Mater. **1**, 77 (1992).
[2] M. E. Schabes, J. Appl. Phys. **67**, 5149 (1990)
[3] T. Miyahara and K. Kawakami, IEEE Trans. Magn. **MAG-23**, 2877 (1987).
[4] S. Gangopadhyay, G. C. Hadjipanayis, S. I. Shah, C. M. Sorensen, K J. Klabunde, V. Papaefthymiou, and A. Kostikas, J. Appl. Phys. **70**, 5888 (1991).
[5] A. Tasaki, M. Oda, S. Kashu, and C. Hayashi, IEEE Trans. Magn. **MAG-15**, 1540 (1979).
[6] R. B. Falk and G. D. Hooper, J. Appl. Phys. Suppl. **32**, 190S (1961).
[7] B. D. Cullity, *Introduction to Magnetic Materials* (Addison–Wesley, Reading, 1972), p. 234.
[8] J. Kanamori, in *Anisotropy and Magnetostriction of Ferromagnetic and Antiferromagnetic Materials, Magnetism*, edited by G. T. Rado and H Suhl (Academic, New York, 1963), p. 174.

Published without author corrections

Extended x-ray-absorption fine-structure studies of heat-treated fcc-$Fe_{50}Cu_{50}$ powders processed via high-energy ball milling

P. Crespo and A. Hernando
Instituto de Magnetismo Aplicado, P.O. Box 155, Las Rozas, 28230 Madrid, Spain

A. Garcia Escorial
CENIM-CSIC, Avenida, Gregoria del Amo 8, 28040 Madrid, Spain

K. M. Kemner and V. G. Harris
U.S. Naval Research Laboratory, Washington, DC 20375

The local structure and chemistry of a ferromagnetic fcc-$Fe_{50}Cu_{50}$ solid solution obtained through high-energy ball milling were measured before and after heat-treatment-induced decomposition using extended x-ray-absorption fine-structure measurements. The decomposition is first evident with the phase separation of α-Fe after a heat treatment at 523 K. Analysis of the residual fcc component revealed that the Fe atoms were predominantly surrounded by other Fe atoms, suggesting that the Fe has coalesced within the fcc structure. The Fe atoms within the fcc phase likely exist in low-spin clusters which provide an explanation for the reduced values of low-temperature magnetization previously measured in annealed samples [P. Crespo *et al.*, Phys. Rev. B **48**, 7134 (1993)].

Much research has been focused on the Fe_xCu_{1-x} system since it was shown that the miscibility of Fe in fcc-Cu can be greatly enhanced, $0 \leq x \leq 0.6$, through high-energy ball milling.[1–4] In recent work,[3,4] some of the authors have reported on the magnetic and structural properties of a ferromagnetic fcc-$Fe_{50}Cu_{50}$ solid solution processed using high-energy ball milling. Their findings indicate anomalous magnetic behavior for heat-treated samples in the intermediate stages of decomposition. Specifically, a significant decrease of the low-temperature magnetization relative to the value measured for the as-milled sample was observed in annealed samples where multiple phases are present. This behavior cannot be accounted for by a nucleation and growth decomposition where the alloy separates into pure fcc-Cu and bcc-Fe components. Alternatively, these authors have suggested a spinodal mechanism to describe the decomposition process. In an attempt to elucidate the decomposition mechanism in this material we have measured the average local structure and chemistry around the Fe and Cu sites before and after heat treatments using extended x-ray-absorption fine-structure (EXAFS) measurements.

Powder samples, having a nominal composition of $Fe_{50}Cu_{50}$, were fabricated by high-energy ball milling Fe powder with Cu foil for a period of 400 h in a Fritsch vibrating mill. X-ray-diffraction measurements of the milled powder revealed only Bragg peaks corresponding with a single fcc phase having a lattice parameter of 3.641 Å. Samples of the as-milled FeCu powders were annealed under flowing argon gas to temperatures ranging from 523 to 923 K at a rate of 20 K/min and were then allowed to cool. Details of sample processing and characterization, including results of x-ray-diffraction, Mössbauer effect, and magnetization measurements, have been reported in Ref. 4.

A portion of the as-milled and annealed powders were examined using the NRL materials analysis beamline, X23B, at the National Synchrotron Light Source (Brookhaven National Laboratory, Upton, NY). The x-ray-absorption spectra near the Fe and Cu K absorption edges were collected in conversion electron mode after attempts to employ the transmission mode failed due to our inability to grind the powder to the scale required for EXAFS measurements. In using the conversion electron technique we applied a generous amount of the powder over a still-wet coating of colloidal graphite on a substrate of commercial grade Al foil. As per this technique, the absorption spectra was measured as normalized sample current (see Ref. 5 for details of the operation and performance of the conversion electron cell used here).

Following established EXAFS analysis procedures[6] the fine structure extending from 20 to 600 eV above the absorption edges were first normalized to the edge step height and energy, then fitted with a cubic spline curve to remove a low-frequency background oscillation, and converted to photoelectron wave-vector (k) space. These data were then Fourier transformed to radial coordinates in order to obtain direct information of the structure and atomic symmetry around the Fe and Cu sites. Quantitative information of the local structure and chemistry around the Fe sites were obtained by further fitting the near-neighbor peak of the Fourier-transformed EXAFS data with empirical and theoretical standards. EXAFS data for the as-milled sample were fit using theoretical EXAFS spectra generated by the FEFF codes (ver. 3.11) developed by Rehr and co-workers.[7] Alternatively, the fitting of data collected from annealed samples, where multiple phases were present, was performed using empirical standards of bcc-Fe and fcc-FeCu (simulated using the Fe EXAFS collected from the as-milled sample). These empirical standards were chosen because the x-ray-diffraction measurements indicate that bcc-Fe precipitates from the solid solution upon heat treatment. We assume that the remaining fcc phase consists of both Fe and Cu atoms still in solution. All fits were performed in k-space using a least-squares-fitting algorithm.

Information of the local structure and chemistry around the Fe and Cu sites is contained in the Fourier transform of their respective EXAFS data. These data for the as-milled sample are presented in Fig. 1 with similar data collected

 0021-8979/94/76(10)/6322/3/$6.00 © 1994 American Institute of Physics

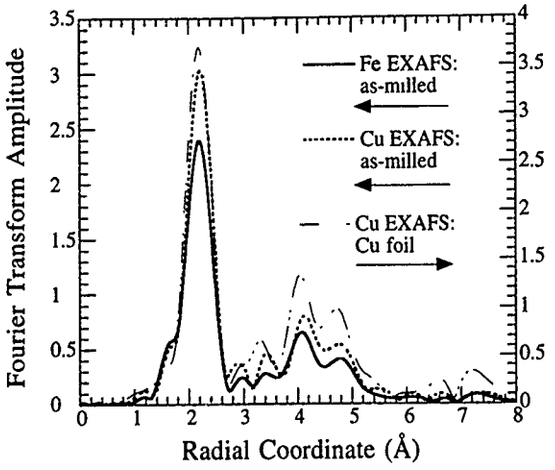

FIG. 1. Fourier-transformed Fe and Cu EXAFS from the as-milled $Fe_{50}Cu_{50}$ sample. Similar data collected from a fcc-Cu standard are shown for comparison. All data were transformed using k^2-weighting and k-ranges of 2.5–12.5 $Å^{-1}$. Electron phase-shift corrections have not been included, therefore radial distances do not correspond directly with bond lengths.

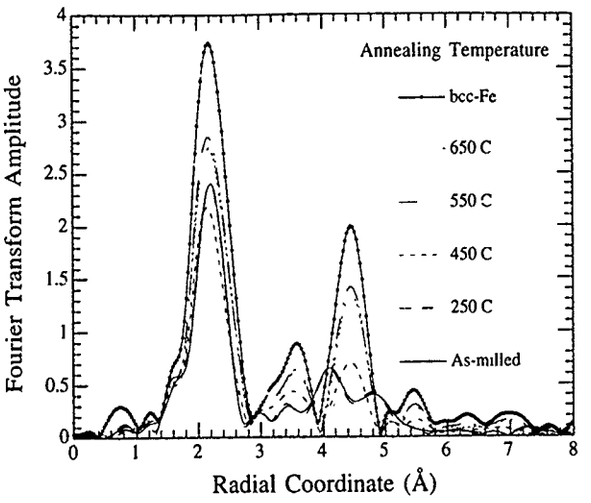

FIG. 2. Fourier-transformed Fe EXAFS data for the as-milled sample and those samples annealed at T=523, 723, 823, and 923 K. All data were transformed using k^2-weighting and k-ranges of 2.5–12.5 $Å^{-1}$. Electron phase-shift corrections have not been included, therefore radial distances do not correspond directly with bond lengths.

from a Cu foil used here to represent the fcc structure. Data corresponding with the as-milled sample are shown to resemble closely the fcc structure of the Cu standard in both the relative amplitude and radial distance of Fourier peaks appearing over the range of 1–5 Å. Slight changes in relative amplitude and distance of these Fourier peaks between the milled sample data and the fcc Cu standard can be attributed to the increased structural disorder of the milled powder and the smaller diameter of the Fe atom, respectively.

Fitting of the near-neighbor peak of the EXAFS data presented in Fig. 1 using FEFF generated EXAFS spectra indicates that the first coordination shell around both the Fe and Cu atoms consists of a mixture of Fe and Cu atoms which reflect a stoichiometry of $Fe_{48}Cu_{52}$, a result consistent within the uncertainty of the EXAFS fitting analysis with the nominal composition of the starting powder mixture. This analysis establishes that atomic level mixing has occurred around Fe and Cu sites due to the ball milling operation and indeed an fcc solid solution exists. Attempts to include a bcc component to the fit resulted in a significant deterioration of the least-squares-fitting parameter, as did attempts to simulate coherent fcc-Fe clusters within the Cu matrix. Further details of this analysis will be presented elsewhere.

Fitting of both the Fe and Cu EXAFS data found a Cu—Fe(Fe—Cu) bond of 2.60±0.02 Å, significantly larger than the sum of the Goldsmidt radii (assuming a coordination of 12), 2.55 Å. However, this result is consistent with x-ray-diffraction measurements of the as-milled powder[2] which indicate a larger lattice parameter for the solid solution, a_0=3.641 Å, than that of fcc Cu, a_0=3.615 Å. The Fe—Fe and Cu—Cu bonds are measured to be 2.53±0.01 Å. Taken together, the resulting EXAFS lattice parameter, 3.627±0.02 Å, matches within the EXAFS fitting uncertainty to the value obtained by XRD. The distorted bond distance of the Cu—Fe correlation is apparently responsible for the distorted lattice measured by XRD. However, at this time we can only speculate that the repulsion between the Fe and Cu atoms arises from an electronic interaction brought about by the filled d-band of Cu interacting with the unfilled d-band of Fe.

Figure 2 depicts the Fourier-transformed Fe EXAFS data for the as-milled and annealed samples illustrating the evolution of local structure around the Fe site as a function of heat-treatment temperature. All the data presented in Fig. 2 are shown on the same x and y axes without offset or normalization to allow for the direct comparison between samples annealed at different temperatures. The as-milled sample and the sample annealed at 523 K have nearly identical transform profiles, indicating that the local structure around the Fe atoms remains largely unchanged after this low-temperature anneal. However, the data corresponding with the sample annealed at 723 K displays significant changes in the Fourier features appearing over the r range of 3–5 Å (uncorrected for electron phase shifts). This transform illustrates features common to both bcc and fcc structures, indicating that the Fe atoms exists in both phases after this heat treatment. Evidence for the bcc phase is seen in the large peak appearing near 3.5 Å which corresponds with the cube-diagonal unit-cell site and the body-centered site of the adjacent cell. Anneals at still higher temperatures are seen to further advance the chemical and phase separation: The Fourier-transformed data for samples annealed at 823 and 923 K closely match the bcc Fe transform presented in Fig. 2 in both relative amplitude and radial distance of Fourier peaks.

Information of the local chemical environment at different stages of decomposition would be very useful in providing insight to the nature of the decomposition mechanism and in turn assist in our understanding of the magnetic properties. However, because the photoelectron backscattering amplitudes of the Cu and Fe atoms are similar, it is difficult to extract information of the local chemistry from a qualitative inspection of the data presented in Fig. 2. To this end, we have performed a quantitative fitting analysis of the near-

neighbor Fourier peak for all samples whose data appear in Fig. 2. Because the Fe atom may occupy more than one inequivalent site in these partially decomposed samples, depending upon the nature of the decomposition and the annealing temperature, it is difficult to fit the EXAFS data using only FEFF generated EXAFS spectra. This difficulty arises from the increasing number of independent variables (used in fitting) corresponding with each inequivalent site. Hence, we chose to fit these data using empirical standards of bcc-Fe and fcc-FeCu. Through this approach multiple inequivalent Fe sites in the annealed samples are simplified to two, those existing in bcc and fcc symmetries. This modeling does not take into account the variation in local chemistry around the absorbing atom. It does, however, provide a means of measuring the relative fraction of atom which occupies those sites differentiated by symmetry made possible by the differences in local atomic symmetry between the bcc and fcc structures.

The results of the fitting analysis of the annealed samples are presented graphically in Fig. 3. The inset plot illustrates the experimental Fourier-filtered Fe EXAFS data of the near-neighbor region and the best-fit calculation for the sample annealed at 723 K. The as-milled sample and the sample annealed at 523 K are measured to contain only an fcc component to the near-neighbor environment of Fe. After an anneal at 723 K, however, 30% of the sample exists in a bcc phase with 70% remaining in the fcc phase. Anneals at 823 and 923 K further advance the decomposition with a bcc atom fraction growing to 68% and 72%, respectively. The error bars presented in Fig. 3 represent a 100% increase in the goodness of fit parameter, indicating a significant deterioration relative to the best fit. The increase in error bar for samples annealed at 823 and 923 K is attributed to the gradual change in chemistry of the residual fcc phase with increasing annealing temperature. In these samples the empirical fcc-FeCu standard becomes a poor simulation of the fcc component.

The observed magnetic behavior reported in Refs. 3 and 4 cannot be explained by a simple nucleation of fcc-Cu and bcc-Fe from the as-milled fcc solid solution. The decrease of low-temperature magnetization (relative the value of the as-milled powder) with the appearance of the bcc phase suggests that a significant amount of Fe must exist in a low-spin state, either as small clusters of fcc-Fe or dilute Fe in fcc-Cu. To investigate this hypothesis, we have isolated the fcc component of a partially decomposed sample, namely the sample annealed at 723 K which was found previously to have a 30% bcc component. EXAFS modeling of the fcc component of this sample using FEFF generated theoretical EXAFS spectra indicates that the average environment of the Fe sites in this phase is dominated by Fe neighbors at a ratio of 10:1. In theory, with 30% of the Fe in the bcc phase, the fcc phase should have a composition near $Fe_{20}Cu_{80}$, if it were to remain a solid solution. If this was the case the local environment of Fe would be dominated by Cu neighbors at a ratio of 4:1. This result provides evidence that the Fe atoms in the residual fcc phase have coalesced within the Cu matrix during the heat-treatment-induced decomposition. Furthermore, it is likely that these fcc clusters of Fe are sufficiently small so as to exist in a low-spin state, thus providing an explanation for the reduced magnetization at low temperatures reported in Refs. 3 and 4.

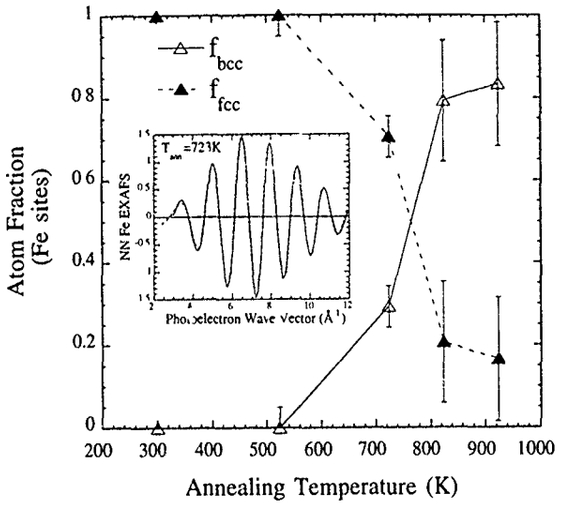

FIG. 3. Atomic fraction of Fe atoms occupying bcc and fcc sites in heat-treated samples as a function of annealing temperature. Results were derived from EXAFS fitting of the near-neighbor (NN) region of the Fourier-transformed data presented in Fig. 2 using empirical standards. The inset plot illustrates the experimental Fourier-filtered NN Fe EXAFS data for the sample annealed at 723 K and the best-fit calculation. Error bars reflect a 100% increase in the least-squares-fitting parameter. The lines connecting the data points are presented to illustrate the qualitative trend with annealing temperature.

This work, in part, has been supported by the Spanish CICYT through Projects No. Mat. 92-0491 and No. Mat. 92-0404. A. Hernando acknowledges support of the BBV Foundation. The EXAFS measurements were carried out at the National Synchrotron Light Source (Brookhaven National Laboratory, Upton, NY), which is sponsored by the U.S. Department of Energy (Division of Material Science and Division of Chemical Sciences of the Office of Basic Energy Sciences). KMK acknowledges support from the National Research Council-Naval Research Laboratory research associate program.

[1] K. Uenishi, K F. Kobayashi, S. Nasu, H. Hatano, K. N. Ishihara, and P H Shingu, Z. Metallkd. **82-3**, 132 (1992).
[2] A. R. Yavari, P. J. Desre, and T. Benameur, Phys. Rev. Lett. **68**, 2235 (1992).
[3] A. Hernando, P. Crespo, A. Garcia Escorial, and J M. Barandiaran, Phys. Rev. Lett. **70**, 3521 (1993).
[4] P. Crespo, A. Hernando, R. Yavari, O. Drbohlav, A Garcia Escorial, J. M. Barandiaran, and I. Orue, Phys. Rev. B **48**, 7134 (1993).
[5] D. E. Sayers and B. A Bunker, in *X-ray Absorption. Basic Principles of EXAFS, SEXAFS, and XANES*, edited by D. C. Koningsberger and R. Prins (Wiley, New York, 1988).
[6] W T. Elam, J P. Kirkland, R A. Neiser, and P. D. Wolf, Phys. Rev. B **38**, 26 (1988).
[7] J. J. Rehr, J. Mustre de Leon, S. I Zabinsky, and R. C. Albers, J. Am. Chem. Soc. **113**, 5135 (1991).

Structure analysis of coprecipitated $ZnFe_2O_4$ by extended x-ray-absorption fine structure

B. Jeyadevan, K. Tohji, and K. Nakatsuka
Department of Resources Engineering, Tohoku University, Aramaki, Aoba, Aoba-ku, Sendai 980, Japan

Though the anomalous antiferromagnetism of zinc ferrite was a subject of intensive studies in the past, the unusually high magnetization of coprecipitated zinc ferrite at low temperatures has drawn renewed interest among researchers. The local structures of zinc ferrites around Fe and Zn atoms are measured using extended x-ray-absorption fine structure and the results are discussed in correlation with their magnetic properties. The structure around the Zn atom was found to differ between zinc ferrite produced by ceramic and coprecipitation techniques. The position of the second-nearest neighbor of the Zn atom for coprecipitated zinc ferrite was shorter than the one produced by the ceramic method. This suggests the possible occupation of the Zn atoms in the octahedral sites and the cause for the unusually high magnetization in coprecipitated zinc ferrite. Furthermore, the intensity of the peak is weak compared to the one produced by the ceramic method. This is thought to be due to the deformation induced by the occupation of zinc ions in the octahedral sites, causing a decrease in the structural periodicity.

I. INTRODUCTION

Zinc ferrite ($ZnFe_2O_4$) is usually assumed to be a completely normal spinel with zinc ions exclusively occupied in the tetrahedral sites. This is described as an anomalous antiferromagnetic substance with a Néel temperature around 10 K. The magnetic behavior of $ZnFe_2O_4$ has drawn much interest and has been a subject of intensive studies.[1,2] To explain the anomalous behaviors, it has been suggested that small amount of Fe ions occupy tetrahedral (A) sites and the Fe(A) ions and their 12 nearest neighbors at octahedral (B) sites form a cluster. Each of the Fe (B) spins is coupled with the Fe (A) spins by AB interaction which is much stronger than the BB interaction.[3] These experiments have been carried out on polycrystalline samples prepared by the ceramic method. However, very recent research on ultrafine $ZnFe_2O_4$ prepared by the coprecipitation technique,[4] with a defect-free crystal structure,[5] has showed unusually higher magnetization.[6] Furthermore, the magnetization was found to vary with particle size and takes a maximum around 8 nm diameter.[7,8] In this paper, we report the results of structure analysis of coprecipitated $ZnFe_2O_4$ using extended x-ray-absorption fine structure (EXAFS), in search of an answer to the high magnetization observed in coprecipitated $ZnFe_2O_4$. This may solve the unresolved problem of scientific interest and provide clues to produce particles with high magnetization.

II. EXPERIMENT

A. Sample preparation and characterization

The $ZnFe_2O_4$ samples were prepared by the following procedure:

(a) Ceramic method—The powders of ZnO and Fe_2O_3 of chemical grade were mixed at a mole ratio of 1:1 in a mechanical mixer. The mixture was calcined at 1373 K for 3 h in oxidizing atmosphere and cooled slowly. Then the product was ground in a mechanical grinder for 1 h. After, it was calcined again at 1373 K for 3 h in the oxidizing atmosphere, slowly cooled to room temperature, and ground to powder again.

(b) Coprecipitation technique—The coprecipitated $ZnFe_2O_4$ was prepared by the method described in Ref. 4.

(c) Coprecipitation followed by annealing—The coprecipitated $ZnFe_2O_4$ is calcined at 1373 K for 3 h, cooled slowly, and ground to powder in a grinder.

The ferrites prepared by the above methods were examined by x-ray diffraction. The local structure was analyzed using EXAFS by measuring the absorption spectra at Fe and Zn K-edges. The sample was mixed with polythelene and pellets were made. The magnetization of these products were also measured in a vibration sample magnetometer (VSM) in the 5 K to room temperature range.

III. RESULTS AND DISCUSSION

A. Magnetization of $ZnFe_2O_4$

The magnetization temperature curves of $ZnFe_2O_4$ prepared by the methods described in the previous section was measured using VSM in the temperature range 5–293 K at 6 kOe are given in Fig. 1. As can be seen, the magnetization shows an increase with decreasing temperature and attains maximum around 20 K, in the case of $ZnFe_2O_4$ produced by the ceramic method and coprecipitation followed by annealing. But, in the case of coprecipitated $ZnFe_2O_4$, the magnetization continues to increase with decreasing temperature and the increase at 6 K is about 16× that of the value at room temperature. The x-ray-diffraction analysis confirmed that $ZnFe_2O_4$ produced by all three methods crystallized in the spinel structure and the cation distribution in the structure is believed to be the main cause for the differences in magnetic behavior among zinc ferrites prepared by different methods. The reason for higher magnetization has been suggested to be due to high concentration of magnetic clusters in coprecipitated zinc ferrite. Neutron-diffraction studies have revealed a high concentration of Fe ions in the A sites that form clusters with the Fe atoms in the B sites. It also has been reported that the $ZnO:Fe_2O_3$ ratio of coprecipitated

 0021-8979/94/76(10)/6325/3/$6.00 © 1994 American Institute of Physics

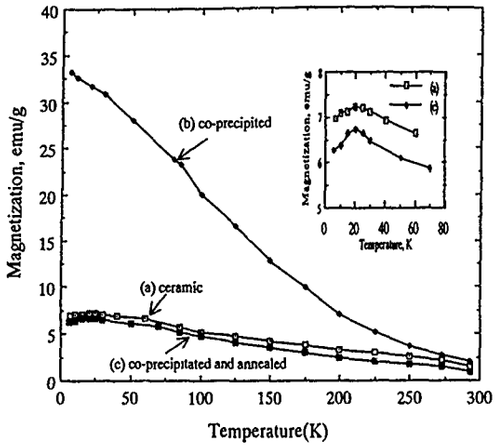

FIG. 1. Magnetization temperature curves of $ZnFe_2O_4$ produced by different methods.

$ZnFe_2O_4$ is the same as that of the one produced by the ceramic method, meaning that there is no density difference among the ferrite produced by different methods. Therefore the concentration increase of Fe ions in *A* sites would lead to the occupation of zinc ions in the *B* sites. To find an explanation for the above differences, structure information of zinc ferrites is necessary.

B. EXAFS of $ZnFe_2O_4$

EXAFS is an ideal tool to investigate the local structure of matter. The local structure information, such as interatomic distances (in the case of spinel structure, this would lead to the determination of the sites occupied by the atoms), coordination number, and the kind of surrounding atoms around a selected x-ray absorbing atom could be studied.

The EXAFS spectra of $ZnFe_2O_4$ prepared by the methods described in Sec. II at the Fe *K*-edge are measured and the Fourier transform of the above spectra are given in Fig. 2. The two intensive peaks in the Fourier transform are centered around distances of 1.45 and 2.6 Å. In the case of $ZnFe_2O_4$, if we assume the Fe atoms to occupy exclusively

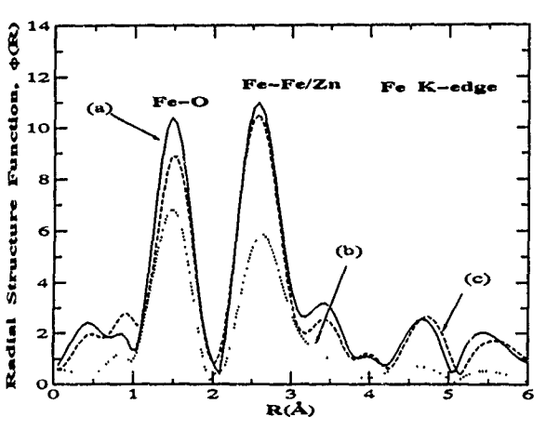

FIG. 2. Fourier transforms of $ZnFe_2O_4$ prepared by (a) the ceramic method, (b) coprecipitation, and (c) coprecipitated and annealed, at the Fe *K*-edge.

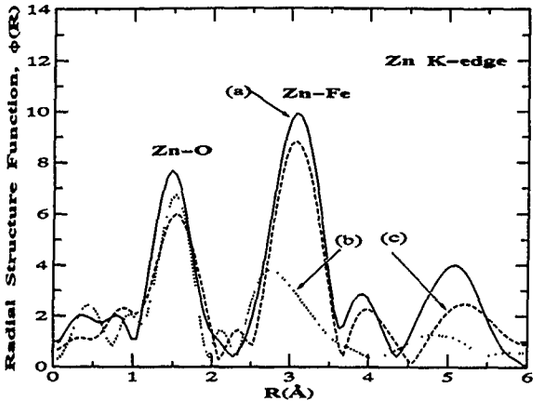

FIG. 3. Fourier transforms of $ZnFe_2O_4$ prepared by (a) the ceramic method, (b) coprecipitation, and (c) coprecipitated and annealed, at the Zn *K*-edge.

in the octahedral sites, the second-nearest peak is a result of the scattering from Fe-Fe atoms and Fe-Zn atoms, where Zn atoms are occupied exclusively in the *A* sites.

Considering the peak intensities between $ZnFe_2O_4$ samples, it could be seen that the peak intensity of coprecipitated $ZnFe_2O_4$ is weak compared to the samples produced by other methods. As far as the peak positions are concerned, the distance between the central atom and the second-nearest peak is marginally greater in the case of coprecipitated $ZnFe_2O_4$.

EXAFS spectra of $ZnFe_2O_4$ at the Zn *K*-edge were measured. Fourier transforms of the same are given in Fig. 3. The two intensive peaks in the Fourier transform are centered around 1.5 and 3.1 Å in the case of $ZnFe_2O_4$ produced by the ceramic method and coprecipitation followed by annealing, whereas, in the case of coprecipitated $ZnFe_2O_4$, the peaks centered around 1.6 and 2.8 Å and the intensity of the peak at 2.8 Å was very weak compared the ones produced by other methods.

The Fourier transform of the spectra at Fe and Zn *K*-edges for $ZnFe_2O_4$ produced by ceramic and coprecipitation methods showed considerable difference in amplitude of radial structure function. A similar observation was made by Maeyama *et al.*[9] for $ZnFe_2O_4$ of 56 and 5 nm diameters. The reduction in radial structure function, which is directly related to the coordination number, was considered due to the increase in the surface atomic layer for finer particles. The broadening of the metal-metal peak in the Zn *K*-edge has been considered due to the amorphous state of the sample.

In our study, if we consider the second-nearest peak in the Fourier transform of the spectrum at the Zn *K*-edge in all three samples, it is clear that the peak of coprecipitated $ZnFe_2O_4$ has become broader and the peak maximum lies at a distance shorter than in the other two cases. The peak broadening can be caused as a result of (a) the disordered state of the sample and (b) scattering from atoms two different distances; i.e., the peak is a result from the contribution of two different peaks. If it is true that the zinc atoms occupy only the *A* sites, it is not possible to get a response at shorter atomic distance than that of $ZnFe_2O_4$ produced by the ceramic method.

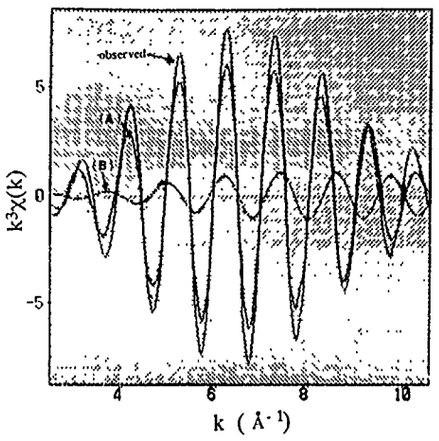

FIG. 4. The inverse Fourier transform of the second peak (Zn-Fe) in Fig. 3(a) and the contributions from shells (a) Zn(A)-Fe(B) and (b) Zn(B)-Fe(B).

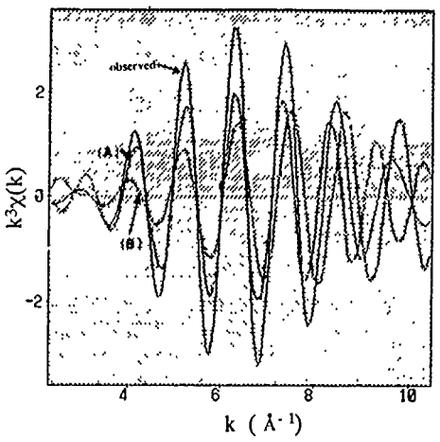

FIG. 5. The inverse Fourier transform of the second peak (Zn-Fe) in Fig. 3(b) and the contributions from shells (a) Zn(A)-Fe(B) and (b) Zn(B)-Fe(B).

Assuming that Zn atoms are occupied in both tetrahedral and octahedral sites and the main contribution of the scattering to be only from shells Zn(B)-Fe(B) at 2.98 Å and Zn(A)-Fe(B) at 3.48 Å [even though the scattering from Zn(B)-Fe(B), Zn(B)-Zn(B) at 2.98 Å and Zn(A)-Fe(B), Zn(B)-Fe(A) at 3.48 Å shells are possible], curve fitting as well as individual contributions of these scatterings were evaluated. The values of the Debye–Waller factor and mean free path were determined from the analysis of zinc ferrite prepared by the ceramic method and were used in the analysis of coprecipitated and coprecipitated and annealed zinc ferrite. The best fit obtained for the second-nearest peak in Fig. 3(a) gave a value of $R=2.7\%$. The individual contribution of the scattering from shells Zn(A)-Fe(B) and Zn(B)-Fe(B), are given in Fig. 4 and it can be seen that the scattering is contributed to almost only by shell Zn(A)-Fe(B). But, in the case of coprecipitated zinc ferrite (fit $R=2\%$), in addition to the contribution of Zn(A)-Fe(B) scattering, a considerable contribution from Zn(B)-Fe(B) is also observed and is shown in Fig. 5. Also, when the coprecipitation followed by annealing sample was analyzed, it resembled very much that produced by the ceramic method.

This suggests that the shift as well as the broadening of the peak at a shorter distance is a result of the zinc atoms occupying the octahedral sites, too. In coprecipitated zinc ferrite, this may be possible, as the cation distributions are in a metastable state as they are produced at low temperature within a short period of time. If they are brought to higher temperature, stability is achieved and the Zn ions take the most stable position in A sites. This is demonstrated in the results on coprecipitated and annealed samples. The occupation of the zinc atoms in the octahedral sites may have caused some deformation which has reduced the periodicity of the structure and may have caused the reduction in the amplitude radial structure function.

Furthermore, the occupation of zinc ions in both tetrahedral and octahedral sites may have led to a magnetization mechanism which is different to the one observed in antiferromagnetic substances, or on the other hand, the concentration increase in Fe ions in tetrahedral sites due to the occupation of zinc ions in octahedral sites may have caused an increase in the concentration of magnetic clusters formed through AB interaction and leading to magnetization increase. However, it could be said that the cation distribution in coprecipitated zinc ferrite is the cause for the higher magnetization.

IV. CONCLUSION

The results of EXAFS analysis on coprecipitated zinc ferrite have suggested that the zinc ions are occupied both in A and B sites. The resulted cation distribution is believed to have caused the increase in magnetization, and the occupation of Zn ions in the B sites is believed to have led to the deformation in the structure that reduces the periodicity of the structure, causing a decrease in radial structure function amplitude.

[1] V. Konig, E. F. Bertaut, V. Gros, M. Mitrikov, and G. Chol, Solid State Commun. **8**, 759 (1970).
[2] F. K. Lotgering, J. Phys. Chem. Solids **27**, 139 (1966).
[3] S. Ligenza, Phys. Status Solidi B, **75**, 315 (1976).
[4] T. Sato, IEEE Trans. Magn. **MAG-6**, 295 (1970).
[5] T. Sato, K. Haneda, M. Seki, and T. Iijima, Appl. Phys. A **50**, 13 (1990).
[6] T. Sato, K. Haneda, M. Seki, and T. Iijima, *Proceedings of the International Symposium on the Physics of Magnetic Materials* (World Scientific, Singapore, 1987), p. 210.
[7] T. Sato, K. Haneda, T. Iijima, and M Seki, Proceedings of the Sixth International Conference on Ferrites, (unpublished), p. 984.
[8] T. Kamiyama, K. Haneda, T. Sato, S Ikeda, and H. Asano, Solid State Commun. **51**, 563 (1992)
[9] S. Maeyama, T. Kawamura, H. Ishii, and T. Sato, Applied Physics Meeting, Japan, 1985 (unpublished), p. 368

Magnetic anisotropy of small clusters and very thin transition-metal films

H. Dreyssé
IPCMS-GEMME, UMR CNRS 46, 23 rue du Loess, BP 20 CR, 67037 Strasbourg, France

J. Dorantes-Dávila
Instituto de Física, UASLP, Alvaro Obregón 64, 78000 San Luis Potosí, México

Š. Pick
J. Heyrovský Institute of Physical Chemistry, Academy of Sciences of the Czech Republic, Dolejskova 3, CZ-182 23 Prague 8, Czech Republic

G. M. Pastor
Deparamento de Física de la Materia Condensada, Facultad de Ciencias, C-III, Universidad Autónoma de Madrid, 28049 Madrid, Spain

The magnetic anisotropy of $3d$-TM clusters is studied in the framework of a d-electron tight-binding Hamiltonian including hopping, Coulomb, and spin-orbit interactions on the same electronic level. Results for the magnetic anisotropy energy and spin-polarized DOS are given as a function of the bond length for the Fe_6 cluster. In particular it is shown that the MAE may be qualitatively related to the projections of the orbital moment along the magnetization directions, and that the "in-plane" anisotropy can be of the same order of magnitude as the "perpendicular" anisotropy. Using the same Hamiltonian, the problem of the convergence of the magnetic anisotropy energy of very thin films is revisited. By the choice of a basis which mixes spherical harmonics. it is shown that the irregular oscillations of the MAE versus the band filling disappear. For Co(111) excellent stability of the in-plane anisotropy as observed experimentally was found. Finally, the crystal-field effects are also discussed.

I. INTRODUCTION

Considerable attention has been devoted during the last years to the study of the magnetic anisotropy of low-dimensional systems. The number of papers presented during this meeting attests to the vitality of the research on thin metallic overlayers. For clusters experimental results show that the magnetic anisotropy plays an important role in the observed relaxation of the cluster magnetic moments in an external field.[1,2] However, from a theoretical point of view, very little on the magnetic anisotropy of clusters is known, contrary to the case of thin films. The purpose of this paper is to propose an unified theoretical framework able to describe the magnetic anisotropy of clusters, i.e., of systems having a finite number of inequivalent sites; the case of very thin film can be seen as a particular simple situation.

The calculations are performed in the real space by using a tight-binding Hubbard-type Hamiltonian. The magnetic anisotropy energy (MAE) is the total-energy difference for two different magnetization directions which can be chosen without restrictions. For clusters we consider directions which do not necessarily correspond to the symmetry axis of the cluster, which may result in Jahn–Teller instabilities. In analogy to magnetic thin films, we assume a *perpendicular* magnetization direction as well as one or two *in-plane* directions. In this way we can discuss not only the perpendicular but also the in-plane anisotropy. This is of considerable interest since so far very few quantitative results based on an electronic theory are known about the importance of the latter.

II. MAGNETIC ANISOTROPY OF SMALL CLUSTERS

In this work we extend a theoretical framework originally developed to describe, without spin-orbit coupling, clusters[3] and it is used with success to study low-dimensional systems[4] to include the spin-orbit interactions. This Hamiltonian includes hopping, Coulomb, and spin-orbit interactions on the same footing and can be written as

$$H=\sum_{\substack{\alpha,\beta,\sigma\\ i\neq j}} t_{ij}^{\alpha\beta}\hat{c}_{i\alpha\sigma}^{+}\hat{c}_{j\beta\sigma}+H_C+H_{\mathrm{SO}}. \tag{1}$$

Here $\hat{c}_{i\alpha\sigma}^{+}$ ($\hat{c}_{i\alpha\sigma}$) refers to the creation (annihilation) an operator of an electron with spin σ at atomic site i in the orbital α ($\alpha\equiv xy,yz,zx,x^2-y^2,3z^2-r^2$), and $t_{ij}^{\alpha\beta}$ to the hopping integrals between the orbitals α and β at sites i and j.

The Coulomb interaction H_C in the unrestricted Hartree–Fock approximation is given by

$$H_C=\sum_{i\alpha\sigma}\Delta\epsilon_{i\sigma}\hat{n}_{i\alpha\sigma}-E_{\mathrm{dc}}, \tag{2}$$

where $\Delta\epsilon_{i\sigma}=\Sigma_{\sigma'}U_{\sigma\sigma'}(\nu_{i\sigma'}-\nu_0)$ are the site and spin dependent d-level shift due to the redistribution of the spin-polarized electron density ($\hat{n}_{i\alpha\sigma}=\hat{c}_{i\alpha\sigma}^{+}\hat{c}_{i\alpha\sigma}$). $\nu_{i\sigma}=\Sigma_{\alpha}\langle\hat{n}_{i\alpha\sigma}\rangle$ refers to the average d-electron occupation at site i and spin σ and ν_0 the corresponding average d occupation in the paramagnetic solution of the bulk. The correction due to double counting is given by $E_{\mathrm{dc}}=(1/2)\,\Sigma_{i\sigma,j\sigma'}U_{\sigma\sigma'}\nu_{i\sigma}\nu_{j\sigma'}$.[3] Notice that the spin-quantization direction is taken to be parallel to the magnetization direction $\langle\mathbf{S}\rangle$. For the spin-orbit interaction H_{SO} the following single-particle, intraatomic approximation is used:

$$H_{\mathrm{SO}}=-\xi\sum_{i,\alpha\sigma,\beta\sigma'}(\mathbf{L}_i\cdot\mathbf{S}_i)_{\alpha\sigma,\beta\sigma'}\hat{c}_{i\alpha\sigma}^{+}\hat{c}_{i\beta\sigma'}. \tag{3}$$

Here $(\mathbf{L}_i\cdot\mathbf{S}_i)_{\alpha\sigma,\beta\sigma'}$ refers to the intraatomic matrix elements of $\mathbf{L}\cdot\mathbf{S}$, which couple the up- and down-spin manifolds and which depend on the relative orientation between $\langle\mathbf{S}\rangle$ and the

 0021-8979/94/76(10)/6328/3/$6.00 © 1994 American Institute of Physics

cluster structure. The spin-polarized charge distribution, and in particular the spin moments, are determined *self-consistently* by imposing the global charge-neutrality condition $\Sigma_{i\sigma}\nu_{i\sigma}=Nn_d$.

The electronic energy E_δ, from which the MAE is derived, is calculated from

$$E_\delta=\Sigma_{i\alpha\sigma}\int_{-\infty}^{\epsilon_F}\epsilon\rho_{i\alpha\sigma}(\epsilon)d\epsilon-E_{\rm dc}, \tag{4}$$

where δ refers to the magnetization direction (e.g., $\delta\equiv x,y,z$) and $\rho_{i\alpha\sigma}$ to the local density of states (DOS). The MAE is obtained from the change in the electronic energy E_δ associated with a change in the orientation of the magnetization $\langle\mathbf{S}\rangle$ with fixed position of the ions. The DOS $\rho_{i\alpha\sigma}(\epsilon)$ are computed by using the recursion method.[5] A special care must be taken in the self-consistent treatment of the Hamiltonian, in order to avoid any numerical incertitude.[6] In the case of a free-standing pure transition-metal mono- or bilayer, all sites are equivalent. For clusters it is no more the case and charge transfers occurring.

In these calculations we use parameters corresponding to Fe as given in Ref. 3 with a spin-orbit coupling constant ξ=0.05 eV.[7] Since in the clusters the value of the bond length d is somewhat uncertain, we have performed a systematical study in terms of d/d_B, where d_B is the bulk bond length.

In Fig. 1 the results obtained for the Fe_6 cluster are reported. Other clusters have been studied.[6] General trends emerge. For all studied clusters the spin moment along the magnetization direction depends very weakly on the direction of magnetization. Therefore only the results for perpendicular magnetization are reported. Clearly it is found that the variations of the MAE versus d/d_B are related to variations of the spin moment and the resulting changes in the densities of states. However, no simple rule can be given to explain these spin-flips. For very large values of d/d_B, the magnetization is saturated as expected. Before the spin-flip, the variation of the MAE and $\langle S_Z\rangle$ are continuous functions of d/d_B. This is no longer the case when a spin-flip occurs. As seen in Fig. 1 this charge redistribution can even change the sign of the MAE. For other Fe_N clusters,[6] many spin-flips can be present.

The *in-plane* anisotropy can be defined here as the difference between E_x and E_y. For Fe_6, this *in-plane* anisotropy is of the same order of magnitude as the *perpendicular* one. Similar results have been found for other Fe_N clusters.[6] The value of the MAE for this Fe cluster (around 1 meV per atom) is of the same order of magnitude as the corresponding values for very thin films. For a small value of d/d_B the perpendicular orientation is more favorable, whereas for d/d_B larger than 0.95, it is more favorable to align the magnetization along the x direction.

Assuming that interactions between unlike spins can be omitted, Bruno found within a second-order perturbation theory that the MAE is proportional to the difference of the projection of the orbital moment along the two considered magnetization directions.[7] Surprisingly, the MAE is found to follow qualitatively this simple law, especially for large values of d/d_B, where the spin moment is saturated. As already mentioned, the *in-plane* anisotropy is found to be important (more than 0.5 meV for d/d_B larger than 0.95). This result, which could seem surprising in comparison with perfect 2D film, is consistent with the large difference observed for the projection of the orbital moment along the x and y directions. The origin of these values is related to the very small size of the cluster (six atoms here). Similar behaviors have been observed for other Fe_N clusters.

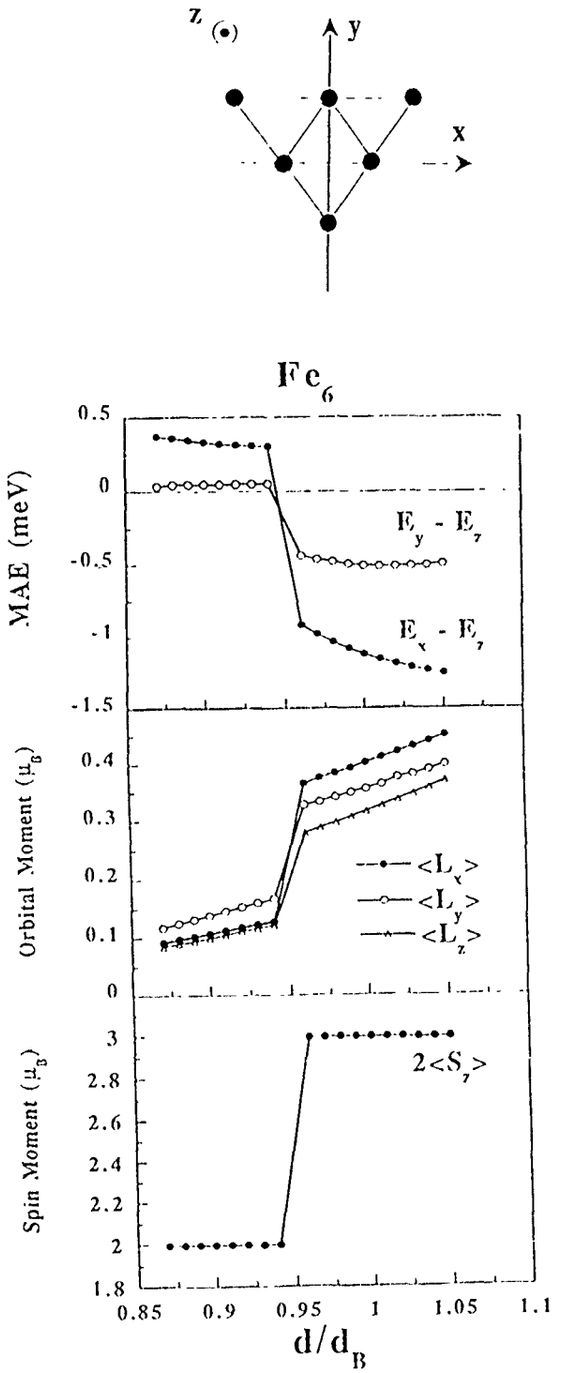

FIG. 1 The magnetic anisotropy energy per atom (meV), orbital moment, and spin moment of a Fe_6 cluster as a function of the bond length d/d_B (d_B=bulk bond length). The assumed cluster structure and the considered directions of magnetization are illustrated.

III. CONVERGENCE OF THE VERY THIN FILMS' MAGNETIC ANISOTROPY ENERGY

Some calculations for thin films or multilayers indicate that the MAE is very sensitive to band-structure details near the Fermi level and the MAE versus the band filling presents many oscillations.[8] According to other works, these oscillations are numerical artifacts.[9] In any case it is clear that the problems can be traced back to the energy-band crossing in the Brillouin zone. Recently, we have studied the MAE for transition-metal free-standing mono- and bilayers[10] by using the tight-binding Hamiltonian used in this work. A formal analysis, based on the moments theory, indicates that the MAE versus the band filling can be described by a "canonical" curve which crosses zero four times when the *d*-band occupation varies from 0 to 10.[10] In fact, the MAE curves were plagued by irregular oscillations which have been related to band crossings. Later, however, various tests on systems having little symmetry have suggested that this explanation is not valid. So we have reconsidered the problem.

In previous calculations we used, here as in the previous section, a basis of spherical harmonics (the spatial parts are eigenfunctions of the orbital moment operator without a spin-orbit interaction). We shall denote this basis as nonmixed (NM). Without spin-orbit coupling for strong ferromagnetism, the partial density of states corresponding to the minority-spin is identically zero in a large part of the majority-spin band energy region. However, when any spin-orbit interaction is considered, this partial density of states acquires a nonzero component in this region. In such a case, the method used in our previous work to get the Green's functions matrix elements is not well suitable. In order to avoid this problem, we build a mixed (M) basis where each vector contains a mix of all representations present in the original NM basis. Numerical calculations have shown that 25 levels of the continued fractions within the M basis are, at least, as precise as 150 levels within the NM basis for films. In this case the irregular oscillations disappear and one to two orders of magnitude for the computer time are gained.[11] For clusters, the NM basis is satisfactory since the finite size of the cluster allows consideration of a number of levels for the continuous fractions which is large enough to get perfect convergence.

Experimental results indicate that a free-standing Co (111) monolayer presents strong *in-plane* anisotropy.[12] Using the empirical relation between magnetic moment and exchange splitting values,[13] a value of exchange splitting of 1.9 eV is appropriate. Strong in-plane anisotropy is found. However, as it can be inferred from Fig. 2, this result is quite insensitive to the value of the exchange splitting. Moreover, introducing a crystal-field shifting does not modify significantly the magnetic anisotropy energy for the Co(111) monolayer. This stability should be related to the fact that the Co spin moment is almost satured.

In summary, a unified theoretical framework has been proposed to determine the magnetic properties of transition-metal small clusters and thin films by considering the spin-orbit coupling. The MAE has been derived. We found that in most cases the MAE can be related to the projections of the orbital moment along the considered magnetization directions. However, complete self-consistent calculations must be performed. Since a real-space method is used, this approach should provide a way to determine from the electronic structure the preferred magnetization direction of adsorbed clusters. Work is under progress.

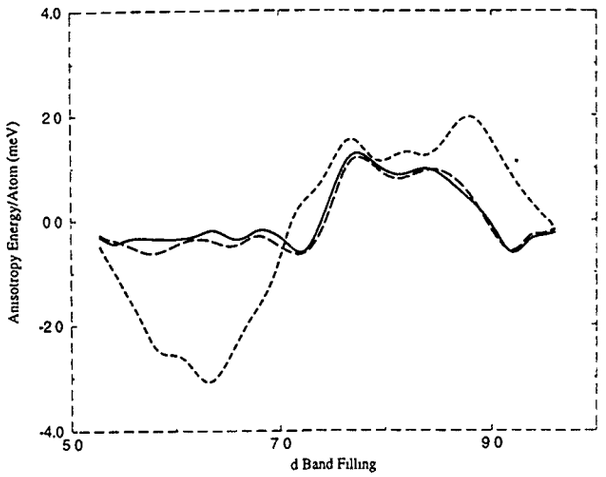

FIG. 2. Magnetic anisotropy energy per atom (meV) vs the *d*-band filling for a (111) monolayer calculated in the M basis with 25 continued fraction levels. In the full (long dashed) line, the result for the exchange splitting of 2.9 (1.9) eV is given. The dashed line corresponds to the exchange splitting of 1.9 eV and nonzero crystal-field splitting of 0.4 eV. Negative values correspond to the favorable perpendicular direction of the magnetization.

ACKNOWLEDGMENTS

The authors would like to thank the Laboratoire de Physique du Solide in Nancy, where this work has been initiated, for kind hospitality. We would like to thank also P. Kocinski for nice discussions. This work has been supported partially by a CONACYT-CNRS research grant.

[1] I. M. L. Billas, J. A. Becker, A. Châtelain, and W. A. de Heer, Phys. Rev. Lett. **71**, 4067 (1993); W. A. de Heer, P. Milani, and A. Châtelain, Phys. Rev. Lett. **65**, 488 (1990).

[2] J. P. Bucher, D. G. Douglas, and L. A. Bloomfield, Phys. Rev. Lett. **66**, 3052 (1991); J. P. Bucher, in *From Clusters to Crystals*, edited by P. Jena, S. N. Khanna, and B. K. Rao (Kluwer Academic, Boston, 1992).

[3] G. M. Pastor, J. Dorantes-Dávila, and K. H. Bennemann, Physica B **149**, 22 (1988); Phys. Rev. B **40**, 7642 (1989).

[4] A. Chouairi, H. Dreyssé, H. Nait-Laziz, and C. Demangeat, Phys. Rev. B **48**, 7735 (1993), and references therein.

[5] R. Haydock, in *Solid State Physics* (Academic, New York, 1980), Vol. 35, p. 216.

[6] J. Dorantes-Davila, Š. Pick, G. M. Pastor, and H. Dreyssé (in press).

[7] P. Bruno, Phys. Rev. B **39**, 865 (1989); Ph. D. thesis, Université de Paris Sud, 1989.

[8] G. H. O. Daalderop, P. J. Kelly, and M F H. Schuurmans, Phys. Rev. B **41**, 11919 (1990); Phys. Rev. Lett. **71**, 2165 (1993).

[9] D.-S. Wang, R. Wu, and A. J. Freeman, Phys. Rev. Lett. **70**, 869 (1993); Phys. Rev. B **47**, 14932 (1993); Phys. Rev. Lett. **71**, 2166 (1993).

[10] Š. Pick and H. Dreyssé, Phys. Rev. B **46**, 5802 (1992); **48**, 13588 (1993); Solid State Commun. **84**, 627 (1992).

[11] Š. Pick, J. Dorantes-Dávila, G. M. Pastor, and H. Dreyssé, Phys. Rev. B (in press).

[12] S. Ould-Mahfoud, R. Megy, N. Bardou, B. Bartenlian, P. Beauvillain, C. Chappert, J. Corno, B. Lecuyer, G. Sczigel, P. Veillet, and D. Weller, Mater. Res. Soc. Symp. Proc. **313**, 251 (1993); M. H. Wiedmann, B. N. Engel, R. A. Van Leeuwen, Ko Mibu, T. Shinjo, and C. M. Falco, Mater. Res. Soc. Symp. Proc. **313**, 531 (1993).

[13] F. J. Himpsel, J. Magn. Magn Mat. **102**, 261 (1991).

Structure and magnetic properties of $Nd_2Fe_{14}B$ fine particles produced by spark erosion (abstract)

H. Wan and A. E. Berkowitz
Center for Magnetic Recording Research, M/S 0401, University of California, San Diego, La Jolla, California 92093-0401

At present $Nd_2Fe_{14}B$ is the best permanent magnet because of its extremely high coercivity and energy product. Optimum properties of $Nd_2Fe_{14}B$ magnets can be attained by producing single domain particles, and then aligning and compacting them. Due to the high reactivity of the Nd constituent, it is challenging to produce and handle a large amount of fine particles of this material. We have prepared fine particles of $Nd_2Fe_{14}B$ by spark erosion with various dielectric media. Yield, size, size distribution, structure, and magnetic properties are discussed. The $Nd_2Fe_{14}B$ particles were made by the shaker pot spark erosion method.[1] Relaxation oscillators or a pulse generator were used to power the spark erosion. Commercial Neomax 35 was employed as the primary material. The dielectric media were liquid Ar, Ar gas, and hydrocarbons, which provided an oxygen free environment. Structure and size were studied by TEM, SEM, and x-ray diffraction. Magnetic properties were measured by VSM with temperatures in the range of 4.2–1200 K. The particles produced in these three different dielectric media had different microstructures and crystal structures. The particles made in Ar gas were pure $Nd_2Fe_{14}B$ phase. The particles made in liquid Ar were a mixture of amorphous and crystalline $Nd_2Fe_{14}B$, because the liquid Ar provided a much higher quench rate than Ar gas, which produced some amorphous $Nd_2Fe_{14}B$. Upon annealing, the amorphous particles became crystalline. The fine particles produced in hydrocarbons, such as pentane and dodecane, had more complex mixed phases, since the rare earth reacted with the hydrocarbons during the sparking process. The phases were NdC_2, α-Fe, and amorphous and crystalline $Nd_2Fe_{14}B$. The effects of power parameters, such as voltage and capacitance, on particle size were investigated. Particle sizes from 20 nm to 50 μm were obtained. We concentrated on $Nd_2Fe_{14}B$ fine particles made in liquid Ar and Ar gas. Particles were classified by centrifuging and sizes were confirmed by TEM and x-ray diffraction. The size dependence of coercivity, anisotropy, and magnetization of these $Nd_2Fe_{14}B$ particles will be discussed.

[1] A. E. Berkowitz and J. L. Walter, J. Mater. Res. **2**, 277 (1987).

 0021-8979/94/76(10)/6331/1/$6.00 © 1994 American Institute of Physics

Thermal equilibrium noise with $1/f$ spectrum in a ferromagnetic alloy: Anomalous temperature dependence

S. Vitale, A. Cavalleri, M. Cerdonio, A. Maraner, and G. A. Prodi
Department of Physics, University of Trento and Centro di Fisica degli Stati Aggregati ITC-CNR, I-38050 Povo, Trento, Italy

We report on the magnetization noise in a soft ferromagnetic alloy for frequencies $f<10$ Hz, temperatures $T<4.2$ K, and excitation field amplitudes <150 μA/m. The spectra agree, without any adjustable parameter, with the fluctuation dissipation formula and the measured complex susceptibility of the material. The spectra show a $1/f$ shape coming from a frequency-independent imaginary susceptibility χ_0''. χ_0'' is found to be proportional to T above $\approx$2.5 K but tends to be independent of T below this value. After annealing the sample to relieve the internal stresses, χ_0'' is found nearly temperature independent above $\approx$2.5 K and to sharply increase by decreasing the temperature below that value. We discuss these findings in terms of the hopping of the magnetization by activation or tunneling.

I. INTRODUCTION

Thermal magnetic noise with $1/f$ power spectrum has been reported now in a variety of systems at low temperature including soft ferromagnetic alloys,[1] spin glasses,[2] and high T_c superconductors.[3] The noise originates from a frequency-independent quasiequilibrium imaginary susceptibility χ_0'' that produces, via the standard fluctuation dissipation formula, to a magnetization noise with spectrum $S_M(\omega)=(2k_BT/\mu_0)(V\chi_0''\omega)$, with T,V, and ω the temperature, the sample volume, and the angular frequency, respectively.

A frequency-independent imaginary susceptibility translates,[1] in the time domain, to a logarithmic relaxation of the magnetization after a stepwise field excitation. This is a close analogue of the phenomenon detected in relaxation experiments, and often referred to as magnetic viscosity, where instead the sample is driven far from equilibrium by large field steps. Magnetic viscosity is attributed to the existence of a collection of simple exponential relaxations with distributed time constants[4] each one due to the escape of the magnetization outside some local free energy minimum. If the escape occurs by thermal activation, the logarithmic relaxation rate is predicted[4] to be proportional to T while any nonthermal relaxation mechanism, like for instance quantum tunneling, would lead to a temperature-independent rate.

At equilibrium this picture should be rephrased[5] in terms of the hopping of the system between nearby free energy minima with distributed lifetimes. The dependence of χ_0'' on the temperature is then related both the mechanism underlying the hopping, whether thermal activation or not, and to the energy differences Δ between the minima. If the lifetime of each minimum is regulated by thermal activation and if Δ is in turn distributed from zero to a value much higher than k_BT, then (see Sec. IV) $\chi_0''\propto T$, again in analogy with relaxation experiments.

This last prediction has recently been contradicted[5] for some amorphous ferromagnetic alloys where χ_0'' has been found to be temperature independent from 4.2 K down to $T\approx100$ mK. It is tempting to think that a temperature-independent χ_0'' could occur if the hopping takes place by some dissipative tunneling mechanism.[6] This interpretation would be favored if one could observe a crossover from the observed temperature-independent regime to the temperature-dependent one due to thermal activation.

In search of a material where such a crossover is displayed within the temperature range accessible by our method, we have studied the temperature dependence of χ_0'' for a soft crystalline alloy that has already been reported[7] to show magnetic viscosity and the related thermal $1/f$ noise at 4.2 K.

II. EXPERIMENTAL METHODS

The sample studied is a strip wound toroid made of 68 turns of a $\approx$3-μm-thick ribbon of Ultraperm alloy. Ultraperm is a soft alloy of nominal composition $Fe_{12}Ni_{77}Cu_5Mo_4$. Measurements have been performed both before and after annealing the sample for 3 h at 950 °C in saturated atmosphere of hydrogen to relief stresses. The linear reversible relative permeability has been measured to be $|\mu|=180\pm10$ before the annealing and $|\mu|=210\pm10$ at 4.2 K after it.

Complex susceptibility measurements have been performed as described in detail elsewhere.[1,5,8] Here we only remind that they are based on the measurement of the complex self-inductance $L=L'i-L''$ of a superconducting transformer coupled to the sample on one side and to a commercial rf superconducting quantum interference device (SQUID) on the other hand.

The ac field amplitudes used to measure the complex susceptibility are always less than 150 μA/m and the sample behaves for such small signals as a linear device.[1,7]

The data for the phase Φ_L of the transformer inductance result from the subtraction of a proper blank measurement obtained substituting the pick-up coil coupled to the sample with a test coil with the same value of self-inductance. In the

 0021-8979/94/76(10)/6332/3/$6.00 © 1994 American Institute of Physics

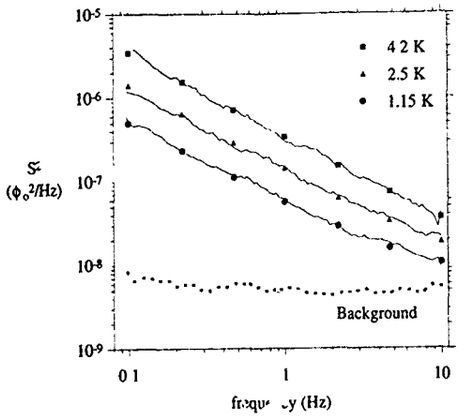

FIG. 1. Spectral noise density at the SQUID output for some different temperatures. The continuous noisy lines are the experimental spectral densities. The broken line is the SQUID background noise. The symbols represent the noise calculated from Eq. (1) using the measured values of the complex susceptibility.

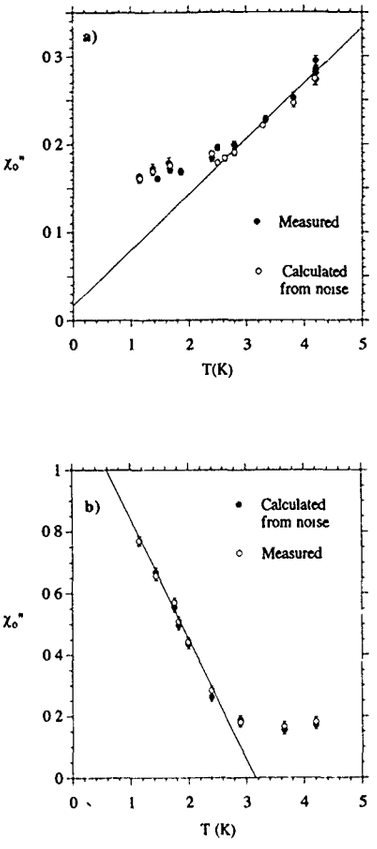

FIG. 2. The average imaginary susceptibility between 0.1 and 10 Hz χ_0'' as a function of the temperature. Closed symbols represent the values as directly measured. Open symbols are the values calculated from noise using fluctuation dissipation formula. (a) Data for the sample before the annealing. The solid line is a linear least-square fit to data above 2.5 K. (b) Data after the annealing. The solid line is a linear least-square fit to data below 2.5 K.

0.1 Hz/10 Hz frequency range the method achieves an accuracy for Φ_L of $\approx 10^{-3}$ deg, while the modulus $|L|$ is measured with a $\approx 0.5\%$ relative accuracy. These figures translate, for the sample discussed here, to an accuracy of about 0.005 for χ'', apart from the uncertainty in the geometrical conversion factor from inductance to susceptibility (see below).

The data for L are converted to a complex susceptibility $\chi = \chi' - i\chi''$, using standard formulas for coils and transformer cores. This conversion has a relative accuracy not better than 10% but we stress that any inaccuracy in the conversion is of no consequence when calculating the thermal noise. In fact the flux noise at the SQUID output S depends on L as[8]

$$S = 2k_B T(M^2/|L|^2)(L''/\omega) + S_0, \tag{1}$$

where S_0 is the SQUID background noise and M is the mutual inductance between the SQUID and the transformer.

The spectral densities S and S_0 are measured by standard fast Fourier transform methods.[1,5]

The sample temperature was regulated by lowering the pressure above the liquid helium bath and was measured by a calibrated germanium resistor.

III. RESULTS

In Fig. 1 the spectral noise density S^2 in the presence of the sample is reported as a function of the frequency for three different temperatures. Also, in Fig. 1 the measured background noise S_0 is shown. The noisy continuous lines are the measured spectral densities while the symbols represent the noise predicted by using Eq. (1) and the measured values of L and S_0. A fit to the experimental noise spectra with a constant plus a power law gives always exponents in the range 1.00 ± 0.03.

The imaginary susceptibility χ'' of the sample between 0.1 and 10 Hz is found to be frequency independent.

The mean imaginary susceptibility between 0.1 and 10 Hz χ_0'' is reported as a function of the temperature in Fig. 2 both for the sample before the annealing [Fig. 2(a)] and for the annealed one [Fig. 2(b)]. The values of χ_0'' as calculated from the noise by inverting Eq. (1) are also reported in Fig. 2.

Neither the data in Fig. 2(a) nor those in Fig. 2(b) can be fit to a single straight line in the whole temperature range explored, a chi square test of the linear best fit giving a probability of random occurrence not larger than 10^{-6}.

Above 2.5 K the data in Fig. 2(a) are well fitted to a simple proportionality law with a slope of 0.063 ± 0.004 K^{-1}. Below that temperature the data show a much reduced temperature dependence.

In Fig. 2(b) the data above 2.5 K are nearly temperature independent while those below 2.5 K can be fit to a straight line with a marked negative slope of -0.38 ± 0.02 K^{-1}.

The loss factor $\tan\delta = \chi''/\chi'$ in the frequency range 0.1/10 Hz, is easily calculated from the above figures to be in the range $\tan\delta \approx 5/10 \times 10^{-4}$ for both samples.

IV. DISCUSSION

The good agreement between the noise calculated from Eq. (1) and the measured one shows[1,5,8] that the sample is

acting as a linear device at thermal equilibrium. This is of no surprise as the applied field variation is less than a part in 10^5 of the coercive field of ≈ 10 A/m≈ 0.10 Oe.

If the susceptibility of the sample results from many contributions,[9] each one coming from an ordinary exponential relaxation with time constant τ, $\chi=\hat{\chi}[1+i\omega\tau]^{-1}$, a frequency-independent imaginary susceptibility is obtained by assuming that $\ln(\tau)$ is uniformly distributed between two values $\ln(\tau_1)$ and $\ln(\tau_2)$ such that the angular frequency of the measurement ω is $1/\tau_1 \ll \omega \ll 1/\tau_2$. In this case $\chi \approx \hat{\chi} \ln^{-1}(\tau_1/\tau_2)$ $[-\ln(\omega\tau_1)-i(\pi/2)]$ and $\chi_0''=i(\pi/2)$ $[\hat{\chi}/\ln(\tau_1/\tau_2)]$. Notice that the loss factor is then $\tan\delta=-\pi[2\ln(\omega\tau_1)]$. Even assuming that $\tau_1 \approx 10^{-12}$ s, a lower limit to any magnetic relaxation process, one gets $\tan\delta \approx 0.06$ at 0.1 Hz, a value much larger than the experimental one. However the above one is still a reasonable model, provided that only a fraction of the total susceptibility is contributed by the mentioned distributed relaxation mechanism.

Let us now discuss the observed dependence of χ_0'' on T within the model that assumes a collection of independent two levels systems, with distributed lifetimes and level splitting. The complex susceptibility of each system is

$$\chi=\frac{\mu_0 V m^2}{8k_BT}\cosh(\Delta/2k_BT)^{-2}\frac{1}{1+i\omega\tau}, \tag{2}$$

where m is the difference in magnetization between the two levels.

In Eq. (2) τ is given by $\tau=\tau_+/(1+e^{-\Delta/k_BT})$, where τ_+ is the mean lifetime of the upper energy level. This is given, for thermal activation, by $\tau_+=\tau_0 e^{E/k_BT}$ with E the height of the free energy barrier that prevents the escape, while it is expected to be a much slower function of the temperature for a nonthermal hopping mechanism like, for instance, quantum tunneling. As a consequence, for broadly distributed time constants, the prefactor $1/\ln(\tau_1/\tau_2)$ in χ_0'' is proportional to T for thermal activation[9] and it is expected to be instead almost temperature independent if the hopping occurs by tunneling.

A second important feature of Eq. (1) is the prefactor $\cosh(\Delta/2k_BT)^{-2}(8k_BT)^{-1}$ in the susceptibility. By introducing the two simplest hypotheses on the distributions of Δ one can calculate the two following limits: If Δ is uniformly distributed between 0 and $\Delta_{\max} \gg k_BT$ the prefactor becomes temperature independent while in the opposite limit of $\Delta_{\max} \ll k_BT$, i.e., with almost degenerate levels, it becomes proportional to $1/T$ as in a pure Curie law.

One can then predict the four following limiting temperature dependencies for χ_0'': (1) nondegenerate levels and thermal activation: $\chi_0'' \propto T$; (2) degenerate levels and thermal activation: temperature-independent χ_0''; (3) nondegenerate levels and fully nonthermal hopping: temperature-independent χ_0''; (4) degenerate levels and fully nonthermal hopping: $\chi_0'' \propto 1/T$.

Thus, if the levels are nondegenerate, a crossover from a nonthermal hopping regime to a thermal activation one would show up as a transition from a temperature-independent χ_0'' to a $\chi_0'' \propto T$ above the crossover temperature T_c. On the contrary, in the case of degenerate levels, the same crossover would appear as a transition from a $\chi_0'' \propto 1/T$ low temperature branch to a temperature-independent χ_0'' above T_c.

The data of Fig. 2 can be at least qualitatively explained if one assumes then that at $T_c \approx 2.5$ K a crossover occurs from a nonthermal to a thermal hopping regime of, e.g., a domain wall portion between two pinning sites; in addition one has also to assume that the annealing procedure, by removing the internal stresses of the material, makes the difference of the pinning energies of the two sites much less than k_BT.

It is tempting to compare the observed $T_c \approx 2.5$ K to the one predicted by theoretical models for tunneling of domain walls[6,10,11] in the bulk. These models predict that $T_c \approx (\hbar g/k_B)B_e \approx 1.3$ K(B_e/1 T) with g the gyromagnetic factor. B_e is an effective magnetic field that can be, for instance, the internal saturation field B_s for high anisotropy materials or $B_e \approx \sqrt{K\mu_0}$, with K the anisotropy energy density, for low anisotropy ones like that considered here. The observed crossover corresponds then to $B_e \approx 2$ T, a field much larger than the value $\sqrt{K\mu_0} \approx 0.02$ T typical of permalloys but still of the order of the internal saturation field of the sample. To ascribe the observed crossover to the model above one would then require the additive hypothesis that some local or surface anisotropy field could exceed by a large factor the average anisotropy of the material. We believe that a definitive explanation of the observations goes beyond the purport of the present data.

ACKNOWLEDGMENTS

This work was supported by the European Economic Community within the project "Effets Quantistiques en Nano-magnetisme." It is a real pleasure to acknowledge many enlightening discussions with B. Barbara, A. E. Berkowitz, G. Bertotti, G. Durin, E. Chudnovsky, and J. Tejada.

[1] G. A Prodi, S Vitale, M. Cerdonio, and P. Falferi, J. Appl. Phys. **66**, 5984 (1989).
[2] M. Ocio, H. Bouchiat, and P. Monod, J. Phys. Lett. **46**, L647 (1985).
[3] F C. Wellstood *et al.*, Phys. Rev. Lett. **70**, 89 (1993)
[4] R. Street and J. C. Woolley, Proc. Phys. Soc. A **62**, 562 (1956).
[5] S. Vitale *et al.*, J. Appl. Phys. **72**, 4820 (1992)
[6] P. C. E. Stamp, E M. Chudnovsky, and B. Barbara, Int. J Mod. Phys. B **6**, 1355 (1992)
[7] M. Cerdonio, P. Falferi, R. Macchietto, G. A. Prodi, and S. Vitale, J. Magn. Magn. Mater. **101**, 92 (1991).
[8] S. Vitale, G. A. Prodi, and M. Cerdonio, J. Appl. Phys. **65**, 2130 (1989).
[9] See for instance: G. Durin, M. Cerdonio, P Falferi, G. A. Prodi, and S. Vitale, J. Appl Phys. **73**, 5363 (1993), and references therein.
[10] D. D Awshalom, D. P. DiVincenzo, and J. F. Smyth, Science **258**, 414 (1992); D. D Awshalom, M A. McCord, and G. Grinstein, Phys. Rev. Lett. **65**, 783 (1992), J. Tejada, X X. Zhang, Ll Balcells, J. Appl. Phys. **73**, 6709 (1993).
[11] E. M. Chudnovsky, O. Iglesias, and P. C. E Stamp, Phys. Rev. **46**, 5392 (1992).

Published without author corrections

Experimental observation of magnetostochastic resonance

A. N. Grigorenko and P. I. Nikitin
General Physics Institute, 38 Vavilov str., Moscow, Russia 117942

A. N. Slavin
Physics Department, Oakland University, Rochester, Michigan 48309

P. Y. Zhou
Knogo Corporation, 350 Wireless Boulevard, Hauppauge, New York 11788

We report an observation of magnetostochastic resonance (MSR) in bistable magnetic systems. MSR manifests itself as a peak of a response of such a system to a periodic field as a function of the noise strength. Bi-substituted ferrite-garnet films with uniaxial anisotropy were used as simple examples of bistable systems. Noise was produced by (i) thermal fluctuations of an effective magnetic field and (ii) externally applied "noiselike" magnetic fields. The position of the peak depended dramatically on the magnitude of applied dc fields, so that dc fields of about 1 mOe in the spatial scale of 10 μm were measured. MSR applications to various tunneling phenomena such as tunneling of magnetization in small magnetic particles are discussed.

Recently, peculiarities of the response of a bistable magnetic system to a periodic magnetic field in the presence of noise have been predicted.[1] It was shown that the signal-to-noise ratio has a peak at some noise strength. This phenomenon was called magnetostochastic resonance (MSR) and turned out to be an excellent tool for investigation of various tunneling phenomena. It enables us to evaluate basic tunneling characteristics in case, e.g., of quantum magnetization tunneling and electron tunneling that depends upon magnetization. Besides, MSR provides a new method for magnetic field detection in the nanometer scale.

To model the theory in a simple system we detect MSR in a bistable ferrite-garnet film. In this article detailed description of experimental procedures is given and applications of the phenomenon to magnetic field measurements are discussed.

Let us recall main features of the magnetostochastic theory. Uniform magnetization dynamics of a bistable system is considered. An angle θ between magnetization and the easy axis is taken as the generalized coordinate of the system. The system is located in one of the minima in the absence of noise. An application of a periodic magnetic field H_{ac} (the ac field) along the easy axis changes the potential energy of the system each half of a period as shown in Figs. 1(b) and 1(c). The change of the magnetization angle θ will be referred to as a magnetization signal. In the absence of noise this change is determined by the stiffness of the potential minimum in which the system is located. The presence of noiselike magnetic fields of some origin results in magnetization changes even in the absence of the ac field. These changes are usually called noise.

In the presence of noiselike magnetic fields and the ac field the transitions between minima are possible. It means that for one-half of a period the system will move over the barrier from the higher minimum to the deeper one and for the other half of the period the system will move back, if the noise strength is sufficient enough. In this case the magnetization signal is determined by an "average" potential stiffness and is much greater than that in the absence of noise. This leads to a peak in the signal-to-noise ratio at some noise strength.[1]

The experimental setup is shown in Fig. 1. To model the phenomenon a thin easy-axis ferrite-garnet film, with high g factor, was chosen as a bistable magnetic system. An additional in-plane magnetic field H_{in} was used to lower the potential barrier between minima and to remove domains out of the sample. A periodic field H_{ac} was applied along the film's easy-axis z. The angle θ between the net magnetization of the illuminated part of the film and the easy-axis z was chosen to be the generalized coordinate of the system. The changes of the angle θ were detected by means of the Faraday effect. The magneto-optical signal (MO signal) S is given by $S = KF_0 \cos^2[\varphi + \alpha(M_z/M_0)]$, where K is a constant that describes photodiode efficiency, F_0 is the total light flux, φ is an angle between the polarizer and the analyzer, $M_z = M_0 \cos\theta$ is the z component of total magnetization M_0, and α is a Faraday rotation angle of the film. In the performed experiments the condition $\alpha M_z/M_0 \ll \varphi$ was satisfied. It means that the MO signal was simply proportional to the studied magnetization signal, which was defined in the introduction as a change of the angle θ.

It follows from the equation that the MO signal does not depend upon the size of the light spot on the film in the absence of noise. However, thermally induced noiselike magnetic fields depend upon the sample volume: the smaller the volume, the bigger the strength of the effective fields H_{eff}, which influence the uniform magnetization dynamics. It allowed us to register the film response to the ac field for

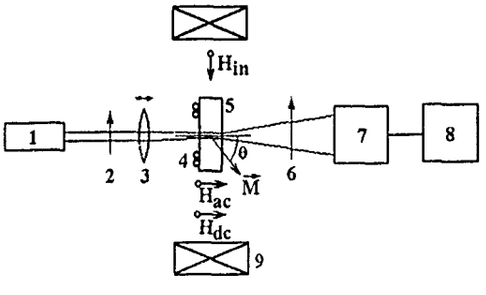

FIG. 1. The experimental installations: (1)—a laser, (2)—a polarizer, (3)—a lens, (4)—coils for magnetic fields production, (5)—a ferrite-garnet film, (6)—an analyzer, (7)—a photodetector, (8)—a narrow bandwidth nanovoltmeter, (9)—magnets.

 0021-8979/94/76(10)/6335/3/$6.00 © 1994 American Institute of Physics

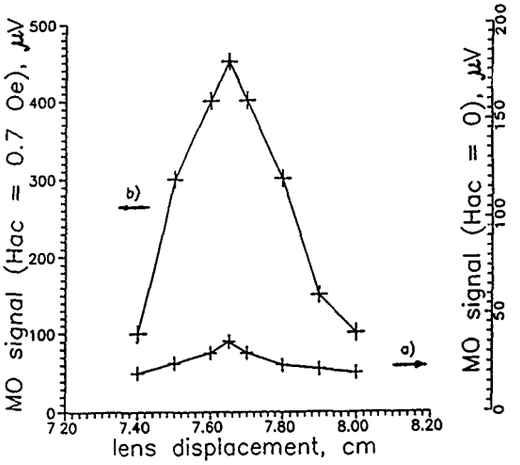

FIG. 2. (a) MO signal in the absence of the ac field, (b) MO signal in the presence of the ac field of 0.7 Oe and frequency 3 kHz, both vs the distance between the lens and the sample.

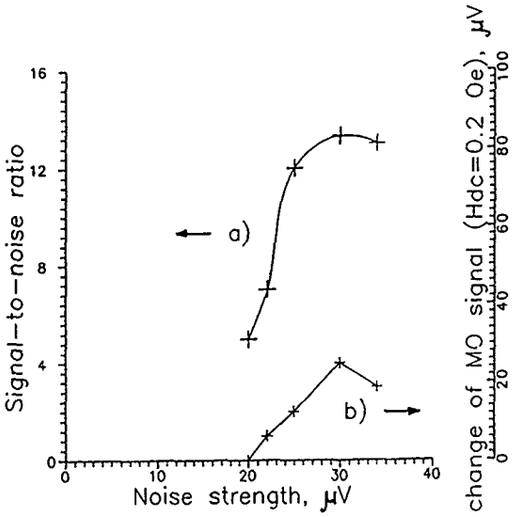

FIG. 3. (a) The MSR curve and (b) the change in the MO signal in the presence of the ac field due to application of the dc field of 0.2 Oe. The sample is the same as in Fig. 2.

various noise strengths by changing the size of the light spot where magnetization changes were detected. For this a special lens was used. Also, an external coil powered by amplified currents from a closed diode was used as a generator of white noiselike magnetic fields H_{ext}.

The measurements were carried out in the following way. First, the amplitude of the ac field was set to zero, $H_{ac}=0$, and MO signals were measured by the photodetector and the narrow bandwidth nanovoltmeter for various sizes of the light spot on the sample. Then, the ac field was applied perpendicular to the film, see Fig. 1, and MO signals were measured in relation to the distance between the lens and the sample. The signal-to-noise ratio is the quotient of the MO signal in the presence of the ac field over the MO signal in the absence of the ac field. Using measured signals, we calculated signals-to-noise ratios for different samples and found MSR curves. Analogous procedures were used in case of externally applied noiselike magnetic fields. In this case the noise strength was varied by a change of the amplification gain of the noise generator.

In Fig. 2(a) typical MO signals in the absence of the ac field are plotted as a function of the distance between the lens and the sample. The distance of 7.7 cm corresponds to the minimal light spot size of 5 μm. As an example, the curves are presented for the sample with composition $(LuBi)_3(FeGa)_5O_{12}$ and parameters: the thickness—7 μm, the anisotropy field—1200 Oe, the domain period—22 μm, magnetization—70 G, the dimensionless Gilbert damping constant—0.16. Figure 2(a) shows MO signals in the presence of the ac field having an amplitude 0.7 Oe and a frequency 3 kHz. Using points from Figs. 2(a) and 2(b), the signal-to-noise ratio can be calculated for various noise strengths, which gave us the typical MSR curve shown in Fig. 3(a). Other films also demonstrated such dependence.

MSR curves for the case of externally applied noiselike magnetic fields were also detected. They have the same form as shown in Fig. 3.

The position of the stochastic resonance peak depends upon the frequency of the ac field. It was found that the peak position moved into the higher fluctuation strength region for a higher frequency of the ac field.

The most interesting result was obtained when an additional dc magnetic field H_{dc} was applied perpendicular to the film, see Fig. 1. Such a field removes the degeneracy of the minima of the magnetic potential and reduces the MO signals, which are measured in the presence of the ac field. The greatest MO signal in the presence of the ac field is observed when the total external field has only the in-plane component and the potential minima are degenerate. This fact was used to adjust the sample position between magnets, which were exploited to produce the in-plane field H_{in}.

The changes of MO signals due to application of the dc field were studied for various noise strengths and for various amplitudes of the dc field. In these experiments the amplitude of the ac field was chosen to be 0.2–1.0 Oe. Figure 3(b) demonstrates this change for the dc field with an amplitude of 0.2 Oe as a function of the noise strength. The change of MO signal in the presence of the ac field due to the dc magnetic field as a function of the amplitude of the dc field is shown in Fig. 4. The curves shown in Fig. 3(b) and in Fig. 4 are the same for both directions of the dc field. This fact was also used to position the sample in the external magnetic field.

It is interesting to note two important features of the change of the MO signal in the presence of ac field due to the dc fields. This change has linear dependence upon the amplitude of the dc field, see Fig. 4. In addition, the MO signals are very sensitive to the applied constant fields. For example, dc magnetic fields as small as 1 mOe were detected in our experiments. It means that MSR can be successfully used for sensor development.

Let us consider results obtained in terms of the stochastic theory[2,3] and its particular application to magnetization dynamics.[1] There are two important parameters which describe resonance: the energy barrier and the Kramers time. The energy barrier between the minima of the magnetic po-

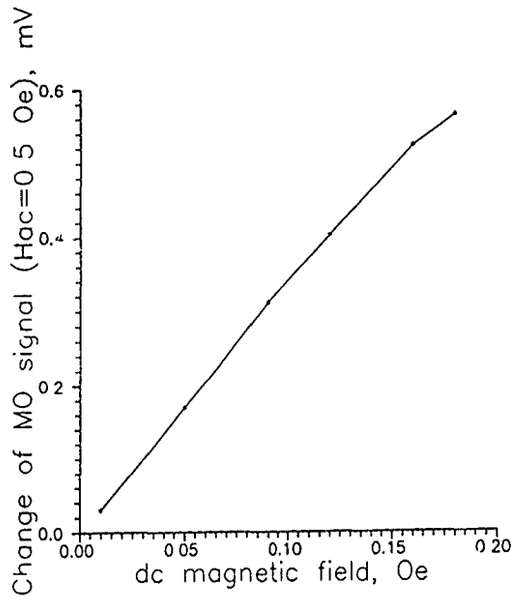

FIG. 4. The change of the MO signal in the presence of the ac filed due to application of the dc field as a function of the amplitude of the dc field. The lens position corresponds to the resonance peak. The sample is the same as in Fig. 2.

tential of an easy-axis ferromagnetic film in the presence of an in-plane field H_{in} is given by $\Delta U = (H_a M_0 v \epsilon^2/2)$, where H_a is the anisotropy field, v is the sample volume, and $\epsilon = 1 - H_{in}/H_a$. The Kramers transition rate for the z component of magnetization in the effective potential[1] can be found as $\nu_{Kr} = (\alpha\gamma\epsilon H_a/\sqrt{2}\pi)\exp[-(H_a M_0 v \epsilon^2/2k_B T)]$, where α is the dimensionless Gilbert damping constant, γ is the gyromagnetic ratio, k_B is the Boltzmann constant, T is the temperature, and ϵ is assumed to be small. (The definition of the anisotropy field differs in factor 2 in comparison with that of Ref. 1.)

It is necessary to know the value of the in-plane field in order to calculate ΔU and ν_{Kr}. The in-plane field was produced by two magnets (ϕ 5 cm, 1800 G) mounted on movable holders, whereas the sample was placed in the region of the maximum homogeneity of the field. To evaluate the in-plane field, the response to the periodic field has been used. This response has the peculiarity at the magnitude of the in-plane field which is equal to the magnitude of the anisotropy field. It was found that the difference between the in-plane field applied in resonance experiments and the anisotropy field of the sample was smaller than 0.2–0.4 Oe for thermal "noise" magnetic fields, which was determined by the accuracy of measurements of magnets positions and the magnitude of the in-plane field. Since the anisotropy fields of studied films were of the order of 1000 Oe, it means that $\epsilon = 1 - H_{in}/H_a < 4\times10^{-4}$ in our experiments. In case of external noiselike magnetic fields $\epsilon < 3\times10^{-2}$.

It allows us to put bounds on the energy barriers and the Kramers transition rates. Taking $H_a = 1200$ Oe, $\epsilon = 3\times10^{-4}$, $M_0 = 70$ Oe, $v = 1.4\times10^{-10}$ cm^3, $\alpha = 0.16$, $\gamma = 10^8$ (Oe s)$^{-1}$, $T = 293$ K for the peak of resonance curve shown in Fig. 3(a), we find that $\Delta U < 5.2\times10^{-13}$ ergs and $\nu_{Kr} > 21$ Hz. The energy barrier and the Kramers transition rate in case of external noiselike magnetic fields were $\Delta U < 5.2\times10^{-11}$ ergs and $\nu_{Kr} > 10^{-4}$ Hz. The effective magnetic field that corresponds to the energy barrier $H_{eff} = (H_a\epsilon^2)/2$ was $H_{eff} < 10^{-4}$ Oe for thermally induced magnetic fields and $H_{ext} < 1$ Oe for the external noise. Since amplitudes of the periodic test fields were 0.03–0.7 Oe, the resonance curves were detected in the nonlinear regime, which means that the ac field made one minimum of the bistable potential disappear for each half of the period. The small value of H_{eff} required to maintain the in-plane field of the order of 1000 Oe with the accuracy better than 0.2 Oe. For this, experimental installations were mounted on a stabilized optical platform. To loosen the constraint on the stability of the in-plane field, it is necessary to detect the magnetization response in smaller volumes than those of our experiments. The promising way to solve the problem is to detect magnetization by means of the Kerr effect instead of the Faraday effect. In this case the effective depth in which magnetization is detected can be as small as wavelength of the light. It allows one to reduce the detection volume by a factor of 10. The best MSR application will be the detection of magnetization tunneling in small magnetic particles, since they inherently have small volumes.

It should be noted that samples vibrations in the external magnetic field and random magnetic fields, which contributed to the change of the in-plane field, lead to the change in basic resonance parameters (2), (3) and, hence, to the reduction of the resonance peak. Mechanical vibrations and random fields, which result in the magnetic field perpendicular to the film, contributed to the independent upon volume magnetization noise.

Finally, we would like to emphasize the important influence of the dc magnetic fields applied perpendicular to the film on the magnetization response to the ac field in the presence of noise. Such a field removes the degeneracy of the energy minima, changes the system distribution in the absence of the periodic test field, and changes the hopping rates between the energy minima. Thus, the magnetization response to the ac field depends upon the presence of small dc magnetic fields and noise. The theoretical treatment of the bistable system susceptibility to the dc field in the presence of the ac field and noise is beyond the scope of the article.

The authors are indebted to Professor Chudnovsky for sending copies of his papers and for helpful discussions. One author (A.N.G.) acknowledges the financial support of the Soros International Science Foundation, by Grant No. M8L000.

[1] A. N. Grigorenko, V. I. Konov, and P. I. Nikitin, JETP Lett. **52**, 593 (1990).
[2] B McNamara and K. Wiesenfeld, Phys. Rev. A **39**, 4854 (1989).
[3] R. F. Fox, Phys. Rev. A **39**, 4148 (1989).

Critical magnetic susceptibility of gadolinium

R. A. Dunlap
Department of Physics, Dalhousie University, Halifax, Nova Scotia B3H 3J5, Canada

N. M. Fujiki
Department of Telecommunications, Sendai National College of Technology, Kami-Ayashi, Aoba-Ku, Sendai 989-31, Japan

P. Hargraves and D. J. W. Geldart
Department of Physics, Dalhousie University, Halifax, Nova Scotia B3H 3J5, Canada

An extensive analysis of ac magnetic susceptibility measurements of single-crystal gadolinium is presented. The demagnetization-corrected c-axis data are analyzed on the basis of a power law of the form $\chi_c = At^{-\gamma}$ where t is the reduced temperature above T_c. Our results yield effective values of $T_c = 293.57$ K and $\gamma = 1.327$. The basal plane susceptibility is expressed as a parametric equation in terms of the c-axis susceptibility $\chi_{ab}^{-1} = B' + C'\chi_c^{-y/\gamma}$. The exponent y, which is related to the critical exponent associated with the specific heat α as $y = 1 - \alpha$, is determined by our analysis to be $y = 1.01(2)$. This gives a temperature scale associated with the anisotropy as $t_{\text{anis}} = 2.0 \times 10^{-3}$. These results are interpreted in the context of the effects of dipolar interactions in the critical region.

I. INTRODUCTION

The critical magnetic properties of gadolinium have recently been reported by several authors.[1–8] Although early measurements on Gd[9–12] led to certain ambiguities concerning the proper universality class for this ferromagnet, recent studies using a variety of experimental techniques have provided a consistent picture of the critical behavior which has a firm foundation on modern theoretical predictions. This behavior has been shown to be complex and to be dominated in the critical region by the presence of magnetic dipole–dipole interactions. The recent analysis of basal plane ac susceptibility by Stetter *et al.*[8] is contrary to this interpretation and these authors have suggested the Gd exhibits three-dimensional Ising behavior and that sample imperfections limit the asymptotic critical behavior. It is the purpose of the present investigation to consider the reasons for these apparent inconsistencies, to provide a new analysis of experimental results and to interpret these data in the context of recent theoretical predictions in order to provide a consistent and comprehensive understanding of the static critical magnetic behavior of gadolinium.

II. EXPERIMENTAL METHODS AND DATA ANALYSIS

A single crystal of high purity gadolinium with a resistivity ratio of $\rho(295\text{ K})/\rho(4.2\text{ K}) = 156$ was cut into the form of a cube with an edge length 0.249 ± 0.005 cm and the c-axis oriented along one of the cube edges. Further details of the sample preparation have been reported in Ref. 6. Measurements of the ac susceptibility have been performed[6,7] for two crystallographic orientations; with the c axis along the applied ac field direction and with one of the basal plane axes along the field direction.

The c-axis susceptibility in the critical region is defined for $t \to 0^+$ by the power law of the form

$$\chi_c = At^{-\gamma}, \tag{1}$$

where the reduced temperature t is defined in terms if the Curie temperature T_c as

$$t = \left| \frac{T_c - T}{T_c} \right|. \tag{2}$$

In contrast to the c-axis susceptibility which diverges as T_c is approached from above, the basal plane susceptibility remains finite and is described by

$$\chi_{ab}^{-1} = B + Ct^y, \tag{3}$$

where the exponent y is related to the critical exponent for the specific heat α by[7]

$$y = 1 - \alpha. \tag{4}$$

The susceptibilities given in the above expressions are intrinsic quantities and are independent of sample geometry. The actual measured susceptibilities are the demagnetization limited external quantities and are related to the intrinsic quantities by the demagnetization factor N as, e.g.,

$$\frac{1}{\chi_{c,\text{ext}}} = \frac{1}{\chi_{c,\text{int}}} + N \tag{5}$$

and similarly for the basal plane susceptibility. Since. in our experimental measurements the sample geometry was chosen to be cubic, the demagnetization factors for the c-axis and the basal plane susceptibility were identical. Equation (5) may be used in conjunction with Eqs. (1) and (3) to express the extrinsic quantities as

 0021-8979/94/76(10)/6338/3/$6.00 © 1994 American Institute of Physics

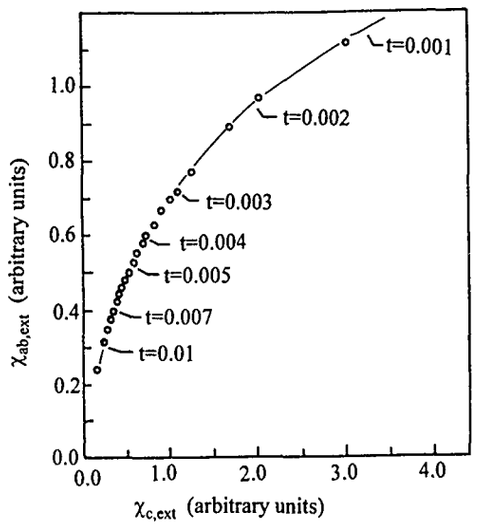

FIG. 1. Measured basal plane susceptibility as a function of measured c-axis susceptibility. Each point represents measurements of the susceptibility along the two directions at the same temperature. The reduced temperature scale as obtained from a fit to T_c for the c-axis data is indicated in the figure.

$$\chi_{c,\mathrm{ext}}^{-1}=A^{-1}t^{y}+N, \tag{6}$$

and

$$\chi_{ab,\mathrm{ext}}^{-1}=B+Ct^{y}+N. \tag{7}$$

In these expressions the coefficients A, B, and C and the exponents γ and y are fitted parameters. While the Curie temperature may be obtained by independent methods and the demagnetization factor may be estimated on the basis of geometric considerations, it is essential to determine the values of the parameters in Eqs. (6) and (7) in a consistent manner. It is clear from the form of Eq. (7) that the values of B and N cannot be determined independently from the basal plane data. It should also be noted that since $|\alpha|\ll 1$, then $y\approx 1$ and the value of C is highly correlated to the value of $B+N$. Because N is the same in Eqs. (6) and (7) it is possible to combine these two expressions and to fit the c axis and basal plane data simultaneously. Solving both expressions for t gives

$$\chi_{ab,\mathrm{ext}}^{-1}=B'+C'\left[\frac{\chi_{c,\mathrm{ext}}^{-1}-N}{N}\right]^{y/\gamma}, \tag{8}$$

where B' is given by $B+N$ and C' may be expressed in terms of C and A. This expression is valid for a given value of t and requires that experimental measurements for the c axis and basal plane orientations be made for the same values of temperature (as is the case for our measurements). This expression allows B', γ, and y to be determined in a consistent manner for both the c axis and basal plane data without the need to know T_c. Fitted values of these parameters may then be used to obtain T_c from a fit to Eq. (1) for the c-axis data.

TABLE I. Fitted parameter values for the critical susceptibility of gadolinium.

Parameter	Value	Uncertainty
A	1728	1.0
B	0.524	0.005
N	3.84	0.02
γ	1.327	0.002
y	1.01	0 01
T_c	293.57	0.02

III. RESULTS AND DISCUSSION

Measured basal plane susceptibility as a function of c-axis susceptibility measured at the same temperature is illustrated in Fig. 1. Parameters obtained from least-square fits to Eqs. (1) and (8) are given in Table I along with uncertainties based on a statistical analysis of the fits.

Although the use of a cubic sample in our studies results in a large demagnetization correction, it is precisely the use of this geometry which allows for a direct comparison of the c-axis and basal plane behavior in the critical region without the need to apply these corrections. Perhaps the ideal sample geometry in this respect would be a sphere. However, the likelihood of introducing additional defects during the machining is an important consideration in the choice of a cubic sample. The anisotropic nature of the critical behavior is readily apparent from our measurements for reduced temperatures less than about 10^{-2} and this, in itself, provides evidence to support our choice of the model based on dipolar interactions as described above for the analysis of these data. A direct measurement of the importance of the dipolar interactions may be obtained on the basis of the above treatment. A reduced temperature scale for the dipolar interactions is expressed in terms of the coefficients in Eqs. (2) and (3) as[7]

$$t_{\mathrm{anis}}=(B/A)^{1/\gamma}. \tag{9}$$

Using the values of these parameters as given in Table I, t_{anis} is found to be 2.2×10^{-3}. This corresponds to an actual temperature difference between T_{anis} and T_c of 0.65 ± 0.10 K. This is in good agreement with theoretical predictions[7,13,14] for the crossover temperature to anisotropic dipolar behavior in this system; $\Delta T=T_{\mathrm{anis}}-T_c=0.45$ K, and previous investigations involving an independent analysis of c-axis and basal plane susceptibility data.

In a comparison of recent experimental studies of Gd it is essential to consider differences in sample quality and geometry and their effects on measured magnetic properties. Of particular relevance in this respect is the relationship of the sample used in the recent study by Stetter *et al.*[8] and that used for our own investigation. Stetter *et al.*[8] have used a 300 Å film grown with the Gd basal plane parallel to the (110) surface of a tungsten substrate. It is clear from the annealing studies reported by these authors that their as-deposited films show magnetic behavior which is severely influenced by the presence of defects. Even after annealing at 870 K these authors base their data analysis on a model involving the existence of imperfections which cause a spread in Curie temperatures of 1 K. No further improvement in the sharpness of the transition was observed for

higher temperature anneals. Stetter *et al.*[8] have suggested that the behavior which we attribute to dipolar effects may actually be the result of sample imperfections as they occur on a temperature scale comparable to the T_c smearing observed in the thin-film experiment. The following evidence would seem to be against this interpretation for the following reasons:

(1) The samples used in our studies and in those of Stetter *et al.*[8] have been prepared by different methods and it would be highly coincidental if the level and type of imperfections in the two samples yielded precisely the same influence on the magnetic properties.

(2) There is no evidence on the basis of our resistivity studies of single-crystal Gd of any smearing of T_c on a reduced temperature scale of about 10^{-4} (see Ref. 5), or in the c-axis ac susceptibility data reported previously.[6,7] This is also the case for other studies of the magnetic properties of bulk Gd samples reported in the literature.[1–4]

Our own studies,[6,7] as well as those of others, e.g., Hohenemser and co-workers,[1–4] indicate that the critical temperature region of Gd exhibits complex crossover behavior over an experimentally observable range of reduced temperatures and it is not likely that measured critical properties will be asymptotic. Instead, critical exponents derived from studies of Gd should be treated as effective exponents for the particular range of reduced temperatures studied and that the values of these exponents will inevitably be dominated by anisotropic effects which result from the presence of dipolar interactions. This behavior of critical properties has been shown to result from a crossover pattern from exchange dominated Heisenberg behavior far above T_c to isotropic dipolar to anisotropic dipolar close to T_c.

The present analysis provides additional evidence for the behavior described above and indicates that, by the proper choice of sample geometry and measurement of data at proper temperature intervals, meaningful results which demonstrate the anisotropic dipolar character of gadolinium can be obtained without the need for an independent knowledge of the Curie temperature or the sample demagnetization factor.

ACKNOWLEDGMENT

This work was supported by grants from the Natural Sciences and Engineering Research Council of Canada.

[1] A. R. Chowdhury, G. S. Collins, and C. Hohenemser, Phys. Rev. B **30**, 6277 (1984).
[2] A. R. Chowdhury, C. S. Collins, and C. Hohenemser, Phys Rev. B **33**, 6231 (1986).
[3] G. S. Collins, A. R. Chowdhury, and C. Hohenemser, Phys. Rev. B **33**, 4747 (1986).
[4] A. R. Chowdhury, G. S. Collins, and C. Hohenemser, Phys. Rev. B **33**, 5070 (1986).
[5] D. J. W. Geldart, K. De'Bell, J. Cook, and M. J. Laubitz, Phys. Rev. B **35**, 8876 (1987).
[6] P. Hargraves, R. A. Dunlap, D J. W. Geldart, and S. P Ritcey, Phys. Rev. B **38**, 2862 (1988).
[7] D. J. W. Geldart, P. Hargraves, N. M. Fujiki, and R A. Dunlap, Phys. Rev Lett. **62**, 2728 (1989).
[8] U. Stetter, M. Farle, K. Baberschke, and W. G. Clark, Phys. Rev B **45**, 503 (1992).
[9] E. A. S. Lewis, Phys. Rev. B **1**, 4368 (1970).
[10] D. S Simons and M. B. Salamon, Phys Rev. B **10**, 4680 (1974)
[11] G. H. J. Wantenaar, S. J. Campbell, D H. Chaplin, T. J. McKenna, and G. V. H. Wilson, J. Phys. C **13**, L863 (1980).
[12] C. D. Graham, J. Appl. Phys. **36**, 1135 (1965)
[13] M. E. Fisher and A. Aharony, Phys. Rev. Lett. **30**, 559 (1973).
[14] N. Fujiki, K. De'Bell, and D. J. W. Geldart, Phys. Rev. B **36**, 8512 (1987)

Monte Carlo simulation of Ising models with dipole interaction

U. Nowak and A. Hucht
Theoretische Tieftemperaturphysik, Universität Duisburg, 47048 Duisburg, Germany

Recently, a new memory effect was found in the metamagnetic domain structure of the diluted Ising antiferromagnet $Fe_xMg_{1-x}Cl_2$ by domain imaging with Faraday contrast. Essential for this effect is the dipole interaction. We use a Monte Carlo method to simulate the low-temperature behavior of diluted Ising antiferromagnets in an external magnetic field. The metamagnetic domain structure occurring due to the dipole interaction is investigated by graphical representation. In the model considered, the antiferromagnetic state is stable for an external magnetic field smaller than a lower boundary B_{c1} while for fields larger than an upper boundary B_{c2} the system is in the saturated paramagnetic phase, where the spins are ferromagnetically polarized. For magnetic fields in between these two boundaries a mixed phase occurs consisting of ferromagnetic domains in an antiferromagnetic background. The position of these ferromagnetic domains is stored in the system: after a cycle in which the field is first removed and afterwards applied again the domains reappear at their original positions. The reason for this effect can be found in the frozen antiferromagnetic domain state which occurs after removing the field at those areas which have been ferromagnetic in the mixed phase.

The three-dimensional Ising model with an antiferromagnetic exchange interaction undergoes a first-order phase transition from an antiferromagnetic to a paramagnetic saturated phase for low temperatures during an increase of the homogeneous external magnetic field. Because of demagnetizing field effects in experimental systems like $FeCl_2$ there occurs a mixed phase for external fields $B_{c1} \leq B \leq B_{c2}$.[1] In theoretical considerations the existence of a mixed phase is often neglected since dipole interactions have to be considered in order to investigate the mixed phase. Especially in Monte Carlo simulations, the dipole interaction can hardly be taken into account for lattices large enough to investigate domain structures due to its long-range nature: for each spin flip the number of operations to calculate the change in energy scales with the number of spins in the system. However, we used a specially adjusted algorithm to do these calculations efficiently. The details of our method will be published elsewhere.

In this paper, we perform simulations in order to get a deeper understanding of a new memory effect that was found recently in the mixed-phase domain structure of the diluted Ising antiferromagnet $Fe_xMg_{1-x}Cl_2$ by domain imaging with Faraday contrast.[2] The position and shape of paramagnetic saturated domains which grow within the antiferromagnetic state while the field is increasing, is stored in the sense that the domains reappear even after a cycle in which the field is first removed and afterwards again applied. Essential for an investigation of this effect is obviously the dipole interaction, since it is this long-range interaction which is responsible for the occurrence of a mixed phase.

The diluted Ising antiferromagnet in an external magnetic field (DAFF) is an ideal system to study random field behavior theoretically as well as experimentally since it is believed to be in the same universality class as the random field Ising model (RFIM).[3] A well-known feature of the DAFF is the formation of a domain state with extremely long relaxation times (for an overview see Ref. 4). This domain state is frozen even for zero field and it is obtained by either cooling the system in an external field from the paramagnetic high-temperature phase or by decreasing the field correspondingly. The mechanisms which are responsible for the hysteretic properties of the DAFF have been investigated experimentally,[5,6] theoretically,[7] and in computer simulations.[8–11] In the following, we will show that the understanding of the hysteretic behavior of the DAFF is essential for an understanding of the memory effect.

The Hamiltonian of an Ising model with dipole interaction in units of the coupling constant reads

$$H = \sum_{\langle i,j \rangle} \epsilon_i \epsilon_j \sigma_i \sigma_j - B \sum_i \epsilon_i \sigma_i + d \sum_{i,j} \frac{\epsilon_i \epsilon_j \sigma_i \sigma_j}{r_{i,j}^3} (1 - 3 \cos^2 \theta_{i,j})$$

where $\sigma_i = \pm 1$ are the spins and the $\epsilon_i = 0,1$ represent the dilution $p = 5\%$. In the first sum $\langle i,j \rangle$ means all combinations of spins which are nearest neighbors. The exchange interaction favoring antiferromagnetic alignment of spins is set equal to one. The second sum represents the interaction with the external magnetic field B. The third sum is over all combinations of spins and d represents the strength of the dipole interaction ($d = 0.5$ in this case). $r_{i,j}$ is the distance between two spins on sites i and j and θ is the angle between the z axis (the direction of the external field) and the distance vector $\mathbf{r}$. In order to simplify the model we restrict ourselves to a two-dimensional system with open boundary conditions representing one plane of the experimental system. As we will see the qualitative behavior of the experimental system is well described by our model as far as the domain structure is concerned, which is responsible for the memory effect.

We use an antiferromagnetic long-range ordered system as the initial spin configuration. The simulation is done at very low temperature, $T = 0.1$. The system builds up a saturated-domain state for a field of $B = 2.65$ which is within the mixed phase, then we investigate the development of this domain state during a field cycle to zero field, $B = 0$, and

 0021-8979/94/76(10)/6341/3/$6.00 © 1994 American Institute of Physics

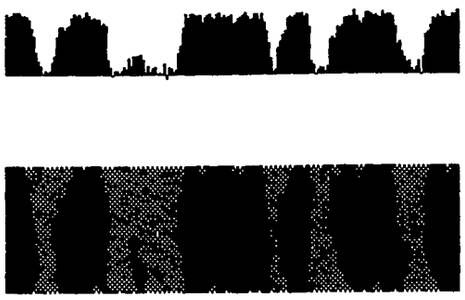

FIG. 1. Spin configuration and column magnetization of the simulated system as explained in the text: a metamagnetic domain configuration in the mixed phase.

then back to the mixed phase, $B=2.65$. The time that is needed to equilibrate the system is a few hundreds of Monte Carlo steps per spin.

The system has a size of 190×50 ($x\times z$), i.e., 190 columns and 50 rows. The figures show spin configurations of the simulated system as well as the mean magnetization of the columns of the system. The external magnetic field is aligned with the easy axis of the spins, the z direction. Each site of the two-dimensional square lattice is represented by a square, the vacancies of the system are shown as black, upspins as grey and downspins as white squares. The mixed phase (Fig. 1) consists of antiferromagnetic domains (checkerboardlike) and paramagnetic saturated (ferromagnetic) domains (grey, "spinup"). In the latter domains the spins are aligned with the field. The domains have the form of stripes. This follows directly from the nature of the dipole interaction which favors those spins to order ferromagnetically which are on lattice sites placed along the direction of the easy axis leading to the development of ferromagnetically ordered columns. Also shown in the upper part of Fig. 1 is the column magnetization, i.e., the mean magnetization of each column of the system. This quantity corresponds to the Faraday contrast that is observed in experiments. Since the domains are striped there is a sharp contrast between antiferromagnetic domains (magnetization$\approx$0) and paramagnetic saturated domains (magnetization$\approx$1/per spin).

Lowering the field to zero the saturated domains vanish (Fig. 2) and the magnetization decreases to nearly zero. However, an accurate analysis of this zero-field spin configuration shows that it is not completely antiferromagnetically long-range ordered. Instead, those regions of the system

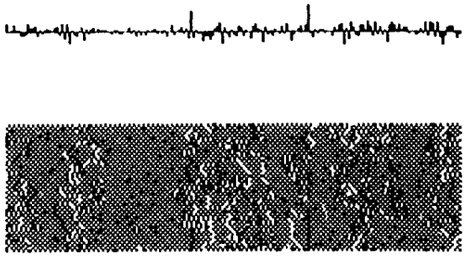

FIG. 2 Spin configuration and column magnetization of the simulated system an antiferromagnetic domain configuration after removing the field.

FIG. 3. Spin configuration and column magnetization of the simulated system: the metamagnetic domain configuration after applying the field again.

which have been paramagnetic saturated in the field now consist of an antiferromagnetic domain structure corresponding to the domain state of a DAFF after field decreasing. Why does this happen?

In a field-decreasing procedure the antiferromagnetic–paramagnetic phase boundary is crossed in a direction from the paramagnetic to the antiferromagnetic phase. In this case, due to the unconventional dynamics of the DAFF which follows from random-field pinning, the system cannot develop a long-range ordered state. Instead, it freezes in an antiferromagnetic domain state. This effect is the reason for the unconventional structure of the system after removing the external field. In regions of the system which have been paramagnetic saturated in the mixed phase, a frozen antiferromagnetic domain state develops while in the regions of the system which have been antiferromagnetic nothing changes, the long-range order persists. The nonexponential dynamics of antiferromagnetic domains in a DAFF after removing the external field has been investigated earlier (see Ref. 12; and references therein). The domains are frozen and remain practically constant on time scales accessible for observation. Note that due to the existence of antiferromagnetic domains and domain walls, respectively, there is a finite column magnetization. This magnetization is small compared to the magnetization of a saturated domain but it is larger than the magnetization of an antiferromagnetic column which is also not exactly zero due to fluctuations of the vacancy distribution in our finite system.

After applying the magnetic field again, once more a configuration of striped antiferromagnetic domains arises (Fig. 3). Comparing this configuration with the original domain configuration (Fig. 1) one finds that the original domain configuration is nearly reproduced, at least in that sense that paramagnetic saturated domains grow first at those places which have been paramagnetic saturated before. This is the memory effect. Its origin is the antiferromagnetic domain configuration of the system after removing the field (Fig. 2). The regions which consist of an antiferromagnetic domain state are less stable than the long-range ordered regions since the first contain domain walls. These regions are the first in which saturated domains during an increase of the external field occur, restoring the original metamagnetic domain configuration.

This work was supported by the Deutsche Forschungsgemeinschaft through Sonderforschungsbereich 166.

[1] J. F. Dillon, Jr., E. Yi. Chen, and H. J. Guggenheim, Phys. Rev. B **18**, 377 (1978).
[2] J. Mattsson, J. Kushauer, D. Bertrand, J. Ferré, and W. Kleemann, J. Mag Mag. Mater. **130**, 216 (1994).
[3] S. Fishman and A. Aharony, J. Phys. C **12**, L729 (1979).
[4] D. P. Belanger and A. P. Young, J. Mag. Mag. Mater. **100**, 272 (1991).
[5] R. J. Birgeneau, R. A. Cowley, G. Shirane, and H. Yoshizawa, J. Stat. Phys. **34**, 817 (1984); D. P. Belanger, S. M. Rezende, A. R. King, and V. Jaccarino, J. Appl. Phys. **57**, 3294 (1985).
[6] U. A. Leitão, W. Kleemann, and I. B. Ferreira, Phys. Rev. B **38**, 4765 (1988); P. Pollak, W. Kleemann, and D. P. Belanger, Phys. Rev. B **38**, 4773 (1988).
[7] J. Villain, Phys. Rev. Lett. **52**, 1543 (1984).
[8] G. S. Grest, C. M. Soukoulis, and K. Levin, Phys Rev B **33**, 7659 (1986).
[9] U. Nowak and K. D. Usadel, Phys. Rev. B **39**, 2516 (1989).
[10] U. Nowak and K. D. Usadel, Phys. Rev B **44**, 7426 (1991).
[11] U. Nowak and K. D. Usadel, Phys. Rev B **46**, 8329 (1992).
[12] S-J. Han, D. P. Belanger, W. Kleemann, and U. Nowak, Phys. Rev. B **45**, 9728 (1992).

Magnetic phase diagrams of $NdRu_2Si_2$ and $TbRu_2Si_2$ compounds

M. Salgueiro da Silva and J. B. Sousa
Centro de Física Universidade Porto and IFIMUP (IMAT), Portugal

B. Chevalier and J. Étourneau
Laboratoire Chimie du Solide-CNRS, Université Bordeaux I, France

Here we report a detailed study providing complete H-T phase diagrams for both $NdRu_2Si_2$ and $TbRu_2Si_2$ intermetallic compounds, based on high resolution SQUID magnetization measurements, in the temperature range 2–300 K and in applied magnetic fields up to 5 T, using c-axis magnetically oriented powders. For $NdRu_2Si_2$, our results are in good agreement with recent neutron diffraction work under applied magnetic fields, confirming the appearance of an intermediate (temperature and field) ferrimagnetic phase responsible for the two-step metamagnetic process observed in the temperature range 16–22.5 K. Our isofield magnetization curves provide unambiguous evidence on the decomposition of this ferrimagnetic phase into ferromagnetic and antiferromagnetic components. Furthermore, at low temperatures and low fields, we observe, in this compound, the presence of thermal irreversibility effects. For $TbRu_2Si_2$, we present an experimental account, on its H-T phase diagram, which shows striking differences with respect to that of $NdRu_2Si_2$. In particular, the ferrimagnetic phase, which sets in at 50 K, persists down to the lowest temperature. In addition, we observe reentrant ferrimagnetism in this compound (ferri-ferro-ferri) under applied fields in the range 28–31 kOe.

I. INTRODUCTION

The ternary intermetallic compounds $NdRu_2Si_2$ and $TbRu_2Si_2$ crystallize in the tetragonal $ThCr_2Si_2$-type crystal structure, with magnetic moments only at the rare-earth sites. Due to their strong crystal field magnetic anisotropy, they behave as uniaxial materials, with the moments always directed along the tetragonal c axis.

The first neutron diffraction measurements on these compounds, at zero magnetic field, have shown interesting sequences of magnetic phases at low temperatures, specially in the case of $NdRu_2Si_2$.[1]

At the Néel point, T_N=23.5 K, $NdRu_2Si_2$ undergoes a second-order phase transition from the paramagnetic state into a pure sinusoidal amplitude modulated phase, with modulation vector [0.13, 0.13, 0]. As temperature decreases below approximately 16 K, the growth of higher-order harmonics takes place and the structure squares up, reducing its entropy. This process is completed at $T_C \approx 8$ K, at which the system becomes partially ferromagnetic (FE), through a second-order phase transition. Below this temperature, the coexistence of both the FE and square-wave modulated phases was observed.

At zero field, $TbRu_2Si_2$ orders below T_N=55 K, through a first-order phase transition, in a [0.23, 0, 0] modulated phase which squares up at low temperatures.

The application of a magnetic field along the tetragonal c axis induces the appearance of new phases through the inversion of moments at those sites where the internal field is small. At intermediate fields, similar ferrimagnetic (FI) phases stabilize in both compounds. In $NdRu_2Si_2$, a FI phase consisting of a FE component and antiferromagnetic (AF) modulations [0.13, 0.13, 0] and [0.26, 0, 0] in the temperature range 16 K$<T<$23 K, for magnetic fields from 5.5 to 8 kOe, has been reported.[2] In $TbRu_2Si_2$, a FI structure with a FE component and [0.23, 0, 0], [0.23, 0.23, 0] AF modulations has been observed at 4.2 K.[3]

The aim of our present work was to determine the complete magnetic phase diagram of both compounds through SQUID magnetization measurements. These measurements were performed in powder samples whose grains were magnetically oriented. The original samples were prepared as described in Ref. 1.

A. $NdRu_2Si_2$

Typical isothermal magnetization curves of $NdRu_2Si_2$, are presented in Fig. 1. We see that for magnetic fields in the range 5 kOe $<H<$8.5 kOe a FI phase stabilizes from 22.5 K down to 16 K, the temperature at which the zero-field AF phase starts squaring-up.[1] Below 16 K, a single-step AF–FE magnetization process is observed. This suggests that the metamagnetic transition to the FI phase is only possible when the nearly pure sinusoidal amplitude modulated structure is the starting phase at zero field.

According to Ref. 2, this FI phase has a complex structure consisting of a FE and two AF components, [0.13, 0.13, 0] and [0.26, 0, 0]. Such decomposition of the FI phase is consistent with our isofield magnetization curves (see Fig. 2). Indeed, the usual AF cusplike behavior of the magnetization near T_N persists for fields up to ~8.5 kOe. Starting at ~5 kOe and up to ~8.5 kOe, the shape of the isofield magnetization curves can be viewed as a superposition of an AF (cusplike) contribution which is partially masked by an increasingly important FE one. Above ~8.5 kOe, no AF behavior is seen to exist and the system behaves as a typical ferromagnet.

At low fields ($H<$1 kOe), as temperature decreases below 10 K, the magnetization increases in a FE-like way, reaching a maximum around 5 K. Besides, it shows thermal

 0021-8979/94/76(10)/6344/3/$6.00 © 1994 American Institute of Physics

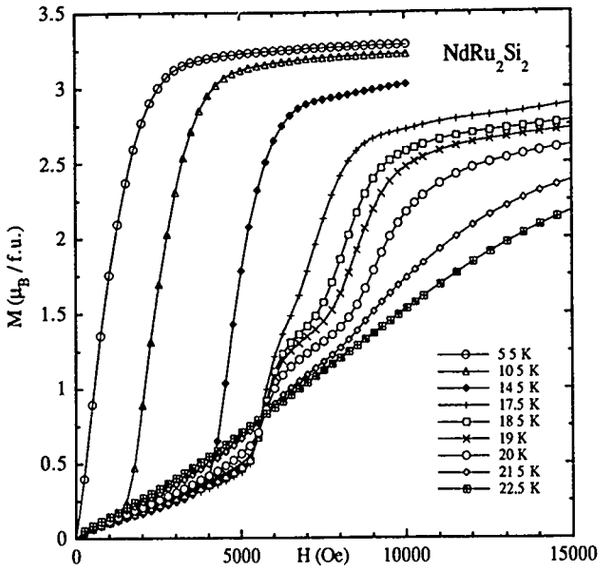

FIG 1. Isothermal magnetization curves of $NdRu_2Si_2$ at several temperatures.

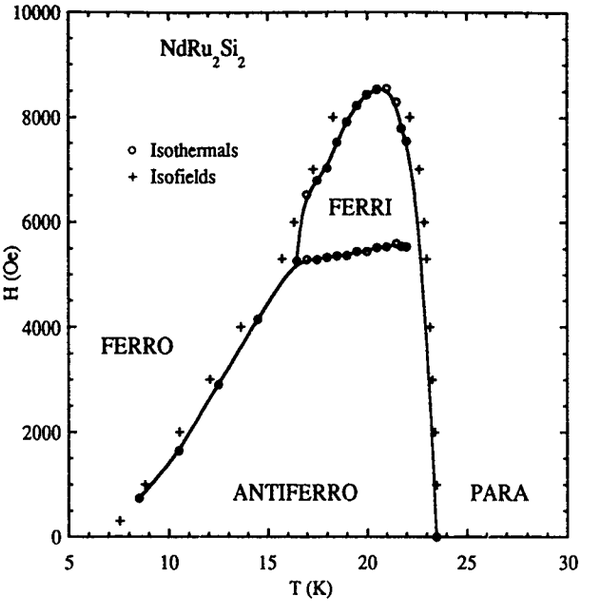

FIG. 3. H-T magnetic phase diagram of $NdRu_2Si_2$.

irreversibility effects, such as the difference between the zero field cooled (ZFC) and field cooled (FC) measurements. Such magnetic behavior may be the result of the competition between FE and AF phases which were reported to coexist in this region.[1]

The magnetic phase diagram (Fig. 3) was completed with both isothermal and isofield results. We notice that the phase line separating the AF and FI regions is not horizontal, as in Ref. 2. All other features of our phase diagram are in good agreement with Ref. 2.

B. $TbRu_2Si_2$

A clear two-step metamagnetic process is observed, characterized by two critical fields, H_{c1} and H_{c2}, which persists from the lowest temperature up to about 50 K, i.e., in almost all the ordered temperature range (see Fig. 4). We also observed the existence of magnetic hysteresis above H_{c1}. At this field, the magnetization jumps to an intermediate FI plateau with approximately half the saturation moment, jumping again at H_{c2} towards saturation. The intermediate phase in the range $H_{c1}<H<H_{c2}$ has been identified at 4.2 K

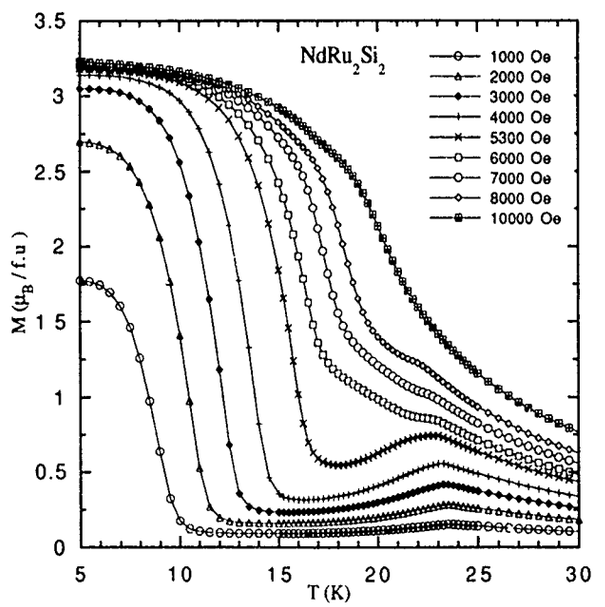

FIG 2 Isofield magnetization curves of $NdRu_2Si_2$ at several applied magnetic fields.

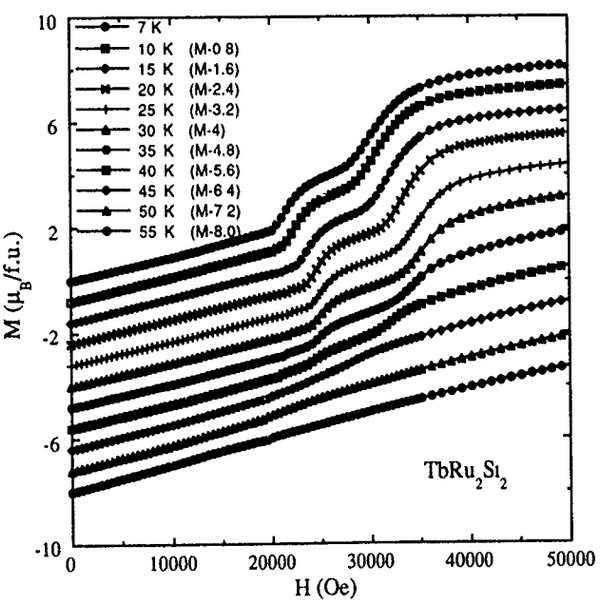

FIG. 4. Isothermal magnetization curves of $TbRu_2Si_2$ at several temperatures.

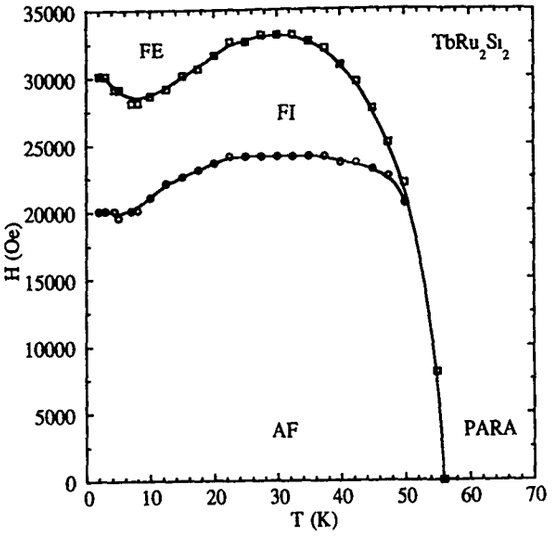

FIG. 5. H-T magnetic phase diagram of $TbRu_2Si_2$.

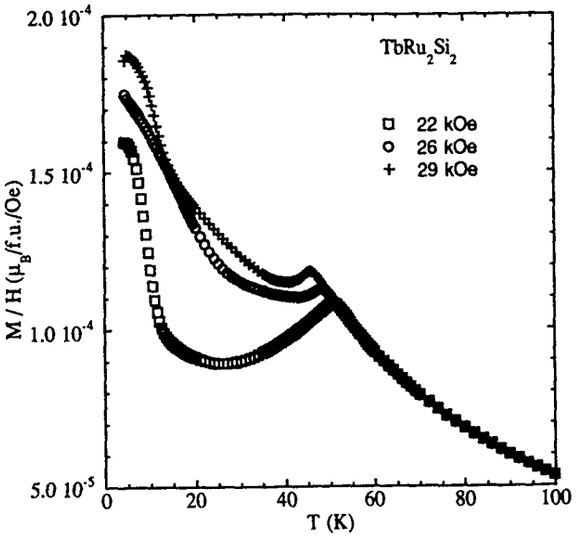

FIG. 6. Isofield M/H curves of $TbRu_2Si_2$ at several applied magnetic fields.

by neutron diffraction[3] as a complex two-dimensional modulated structure with a FE component and AF modulations [0.23, 0, 0], [0.23, 0.23, 0].

The observed regular increase of the magnetization below H_{c1}, characteristic of the development of a FE component, is attributed to the growing of higher-order harmonics in the AF [0.23, 0, 0] structure as H approaches H_{c1}.[3] The sudden enhancement of this FE component is made possible only at H_{c1} where an additional [0.23, 0.23, 0] modulation sets in.

The obtained H-T phase diagram (see Fig. 5) is divided into three main ordered regions: AF for $H<H_{c1}$ and $T<T_N$; FI resulting from the superposition of two-dimensional AF modulations and a FE component, for $H_{c1}<H<H_{c2}$ and $T<50$ K; FE for $H>H_{c2}$. As shown in Fig. 5, this compound exhibits reentrant ferrimagnetism (FI–FE–FI) under applied fields in the range 28–31 kOe and the FI phase is seen to persist down to the lowest temperature. The isofield curves near this field range also illustrate this phenomenon (see Fig. 6). For a field well within the FI region, e.g., $H=26$ kOe, and after the initial cusplike AF behavior just below T_N, the magnetization increases regularly with decreasing temperature. However, for a field intercepting both FE and FI regions, e.g., $H=29$ kOe, a noticeable change in slope takes place as temperature crosses the transition from the FI to the FE phases, at about 15 K. The magnetization reaches a maximum at a lower temperature which coincides with the transition from the FE back to the FI region. At $H=22$ kOe, the AF region is seen to extend over a wider temperature range.

II. CONCLUSION

The H-T phase diagrams of $NdRu_2Si_2$ and $TbRu_2Si_2$ were obtained from SQUID magnetization measurements on powder samples.

While in $NdRu_2Si_2$, the high field FI phase exists only for intermediate temperatures, in the case of $TbRu_2Si_2$ the FI phase persists down to the lowest temperature and behaves as a reentrant phase for 28 kOe$<H<$31 kOe.

A common feature of both diagrams lies in the fact that the respective intermediate FI phases set in through the appearance of an additional AF modulation. In the resulting FI structure, a larger number of magnetic moments is expected to detect a reduced exchange field and thus flip in a smaller applied field.[4]

ACKNOWLEDGMENTS

We acknowledge Dr. T. Shigeoka for kindly sending us a copy of his manuscript on the H-T phase diagram of $NdRu_2Si_2$, before publication. This work was partially supported by the JNICT-CNRS and STRDA/C/CEN/522/92 Project.

[1] B Chevalier, J. Etourneau, S. Quezel, and J. Rossat-Mignod, J Less Common Metals **111**, 161 (1985)
[2] T Shigeoka, N Iwata, T. Kishino, M. Nishi, Y. Oohara, and H. Yoshizawa (private communication).
[3] T. Shigeoka, S Kawano, N. Iwata, and H. Fujii, Physica B **180-181**, 82 (1992)
[4] D. Gignoux and D. Schmitt, Phys Rev. B **48**, 12682 (1993).

Study of critical properties of the Potts model by the modified variational cumulant expansion method

N. G. Fazleev,[a] Hao Che, and J. L. Fry
Department of Physics, University of Texas at Arlington, Arlington, Texas 76019-0059

D. L. Lin
Department of Physics and Astronomy, State University of New York at Buffalo, Buffalo, New York 14260

The modified variational cumulant expansion (VCE) method valid for the whole temperature range and for arbitrary fields is developed to study the critical properties of the general q-state Potts model used to stimulate various magnetic systems. The series expansion is generated directly in terms of the Potts Hamiltonian. The free energy and the internal energy are calculated up to the third-order cumulant terms for the d-dimensional hypercubic q-state Potts model. The expression for the critical temperature T_c is derived in a closed form which allows to determine T_c up to arbitrary order cumulant terms. The modified VCE method eliminates the unphysical first-order phase transition at the mean-field critical point in the internal energy of the Potts model which plagues the conventional VCE method.

As a generalization of the Ising model to more than two components, the Potts model has become a subject of intense theoretical studies. In the absence of an exact solution for the general q-state Potts model, series expansions remain one of the most powerful tools in the theoretical studies of this model.[1] However, the critical behavior of the Potts model has been studied by generating series expansions only in the limiting cases of low and high temperatures.[1] In this paper, a modified variational cumulant expansion (VCE) method is developed to study the critical properties of the general q-state Potts model in the whole temperature range. This modified VCE expansion is generated directly in terms of the Potts Hamiltonian. The expressions for the free energy and the internal energy for the d-dimensional hypercubic q-state Potts model are obtained up to the third-order cumulant terms valid for the whole temperature range. A procedure is developed to eliminate the unphysical first-order phase transition at the mean-field critical temperature for the corrections higher than the first order, which plagues the VCE method.[2] This procedure is tested for the Potts model with second- ($q=2$, $d=2$) and first- ($q=4$, $d=3$) order phase transitions.

The Hamiltonian of the general Potts model can be expressed as[1]

$$H=-J\sum_{\langle i,j\rangle}\delta(\sigma_i,\sigma_j)-H\sum_i\delta(\sigma_i,0), \tag{1}$$

where $\sigma_i=0,1,2,...,q-1$ specifies the spin states at the site i, J stands for the coupling constant, and H is the external field. In applying the VCE method[2] one first introduces a trial Hamiltonian $H_0(\xi_i)$ with variational parameters ξ_i and expands the free energy of the Hamiltonian H of a real system as a series of cumulants averaged over $\exp(-H_0/kT)$. The first-order expression for the free energy is minimized to determine the variational parameters, which are then substituted back into the free energy expansion or higher-order cumulants. The action for the system is defined as $S=-H/kT$. Our trial action $S_0=-H_0/kT$ is chosen as follows

$$S_0=\sum_i\sum_{k=0}^{q-1}\xi_k\delta(\sigma_i,k) \tag{2}$$

where $\xi_k=1+(q-1)\cdot s$ for $k=0$ and $\xi_k=1-s$ for $k=1,2,...,q-1$. Here s is the variational parameter which serves as the order parameter of the system. The asymmetric state ξ_i ($i=0$) is chosen to account for the symmetry breaking below the critical temperature $T_c(H)$ ($s=0$). When $T>T_c(H)$, symmetry should be retained, i.e., $\xi_k=$const, ($k=0,1,2,...,q$), which implies that $s=0$. The VCE of the free energy up to the order m can be expressed as[2]

$$W_m=W_0-\sum_{n=1}^{m}\frac{1}{n!}\langle(S-S_0)^n\rangle_c \tag{3}$$

where W_0 is the free energy of the corresponding trial system, the symbol $\langle...\rangle_c$ denotes the cumulant average of the considered quantity over the Boltzmann weight $\exp(S_0)$. The order parameter s is determined as a function of J/kT by minimizing the first-order free energy with respect to s.

The free energy and the internal energy are calculated up to the third order in the cumulant terms. The results of calculations within the VCE method of the internal energy of the Potts model with a second-order phase transition ($q=2$, $d=2$) are plotted in Fig. 1. It follows from Fig. 1 that the first-order internal energy is continuous as it should be, while the second- and third-order internal energies have discontinuities which occur at the mean-field critical point $[kT_c(1)/J=2]$. As it follows from the comparison with the exact results, this is the unphysical phase transition which plagues the VCE method.[2]

The central issue for the VCE method is how to determine the variational parameters (s for the present case). Within the VCE method the value of the order parameter is calculated only to the first order.[2] This is actually the pure variational result which gives the mean-field results when the trial action is chosen in the mean-field form.[3] Thus, the ex-

[a]Permanent address Kazan State University, Kazan 420008, Russia.

 0021-8979/94/76(10)/6347/3/$6.00 © 1994 American Institute of Physics

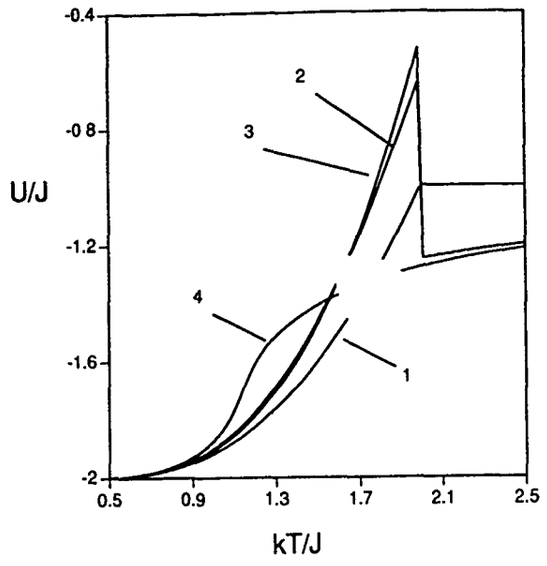

FIG. 1. VCE results for internal energy vs temperature for the $q=2$ and $d=2$ Potts model. The curves 1, 2, and 3 are the internal energy calculated up to first-, second-, and third-order cumulant terms, respectively. Curve 4 is the exact result.

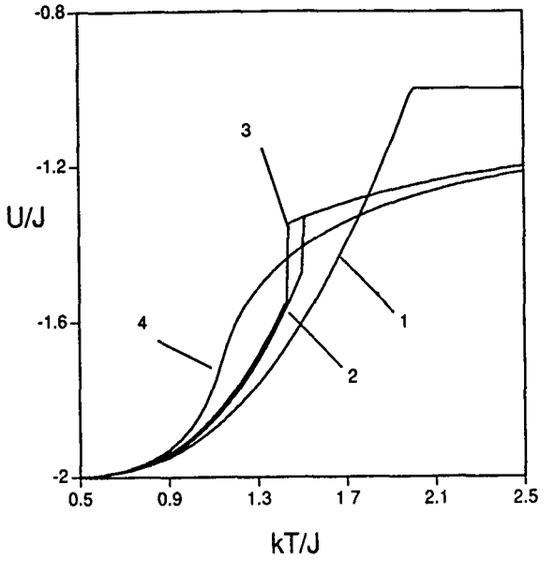

FIG. 2. Modified VCE results for internal energy vs temperature for the $q=2$ and $d=2$ Potts model. Curves 1, 2, and 3 are the internal energy calculated up to first-, second-, and third-order cumulant terms, respectively. The exact result is curve 4.

pansions with the order higher than one would carry the features of the first-order expansion. This leads to the appearance of the unphysical phase transition at the mean-field critical point.

To eliminate the unphysical phase transition we use a procedure based on some conjectures for the location of the true critical temperature $T_c(m)$ for the mth order VCE. From the general symmetry consideration, the order parameter s should take value zero when $T>T_c(m)$ for the mth order expansion. It is therefore reasonable to expect that the values $s=0$ corresponds to the global extremum (not necessarily the global minimum) of $W_m(T,s)$ for $T>T_c(m)$ and that $s=0$ remains to be the solution as temperature decreases until it reaches the critical temperature when this solution becomes "unstable," and then s changes to another solution which becomes "stable." These considerations lead to the following two equations which determine the critical temperature $T_c(m)$ and critical order parameter s_c

$$\begin{aligned} &W_m(T_c,0)=W_m(T_c,s_c) \\ &\frac{\delta}{\delta s}[W_m(T,s)]|_{s=s_c}=0, \end{aligned} \tag{4}$$

with

$$\left.\frac{\delta^2 W_m(T,s)}{\delta s^2}\right|_{s=0} \times \left.\frac{\delta^2 W_m(T,s)}{\delta s^2}\right|_{s=s_c} \geq 0. \tag{5}$$

For systems with the second-order phase transition $s_c=0$ and the equality (5) holds. The order parameter $s(T,m)$ within this approach is determined by

$$s(T,m)=\begin{cases} 0 & \text{for } T>T_c(m) \\ s(T,1) & \text{for } T<T_c(m) \end{cases}. \tag{6}$$

The internal energy of the Potts model with the second-order ($q=2$, $d=2$) phase transitions is recalculated by means of the modified VCE method up to the third order in the cumulant terms and the results are plotted in Fig. 2. As it follows from Fig. 2, the unphysical phase transition at the mean-field critical point has been eliminated and the overall features have been much improved although the higher-order internal energies still have discontinuities, which are shifted to $T_c(s,m)$ and are strongly reduced. The results of calculations of the internal energy of the Potts model with the first-order ($q=4$,

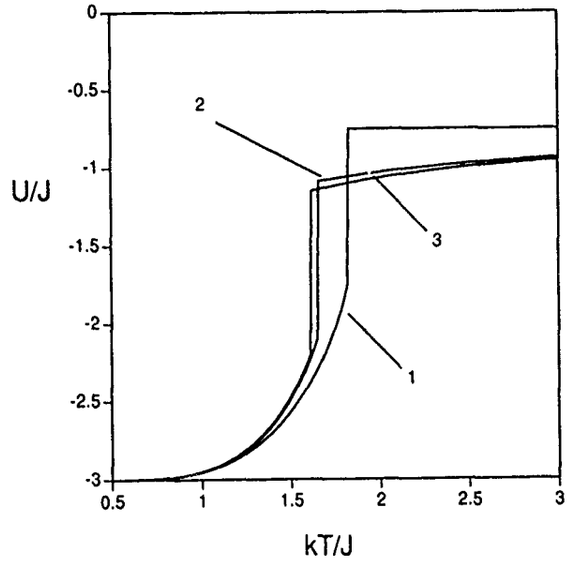

FIG. 3. Modified VCE result for internal energy vs temperature for the $q=4$ and $d=3$ Potts model. Curves 1, 2, and 3 are the internal energy calculated up to first-, second-, and third-order cumulant terms, respectively.

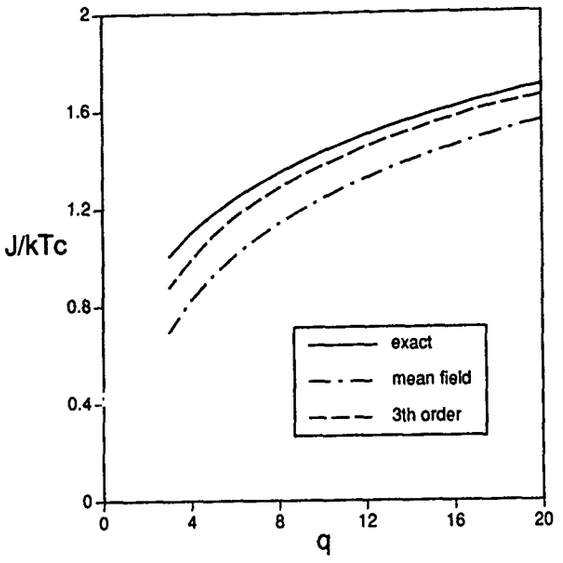

FIG. 4. Inverse of the critical temperature vs q for the $d=2$ Potts model.

$d=3$) phase transition are presented in Fig. 3. It follows from Fig. 3, that the discontinuity in the internal energy, which is a characteristic feature of the first-order phase transition, is present to all orders. As a test of our conjecture on the definition of the critical temperature, which is crucial for the modified VCE method, we calculated the first- and third-order critical temperatures for the two-dimensional Potts model with q varying from 3 to 20. The results of the calculation together with the exact ones are presented in Fig. 4. As it follows from Fig. 4 the results of calculations converge to the exact one, thus supporting our conjecture.

In summary, we have developed the modified VCE method valid for the whole temperature range to study critical behavior of the general q-state Potts model. The free energy and the internal energy for the d-dimensional hypercubic q-state Potts model are calculated up to the third-order cumulant terms. It is shown that by analyzing the cumulant expansions the expression for the critical temperature T_c is derived in a closed form which allows to determine T_c up to arbitrary orders. It is found that the first-order cumulant term gives results which coincide with the mean-field results as expected. The modified VCE method eliminates the unphysical first-order phase transition at the mean-field critical temperature in the internal energy of the Potts model which plagues the conventional VCE method. Calculation of T_c for q varying from 3 to 20 shows that the results obtained up to the first- and third-order cumulant terms converge toward the exact results.

This work was supported by The National Research Council (The Cooperation in Applied Science and Technology Grant), the Texas Advanced Research Program, The Robert A. Welch Foundation, and the Texas Advanced Technology Program.

[1] F. Y. Wu, Rev. Mod. Phys. **54**, 235 (1982)
[2] X. Zheng, Z. G. Tan, and D. C. Xian, Nucl. Phys. B **287**, 171 (1987).
[3] L. Mittag and M. J. Stephen, J. Phys. A **7**, L109 (1974).

Phase transition in a system of interacting triads

H. T. Diep and D. Loison
Groupe de Physique Statistique, Université de Cergy-Pontoise 49, Avenue des Genottes, B.P. 8428, 95806 Cergy-Pontoise Cedex, France

The present work is motivated by the controversy on the nature of the phase transition on the Heisenberg stacked triangular antiferromagnet (STA). In particular, the renormalization group with $4-\epsilon$ expansion suggests a new universality class, while the renormalization group with $2+\epsilon$ expansion using a nonlinear σ (NLS) model shows that the transition, if not mean-field tricritical or first order, is of the known $O(4)$ universality class. In order to verify this conjecture, we study here an equivalent system obtained from the STA by imposing the local rigidity as has been used in the NLS model. The results show that none of the scenarios predicted by the NLS model is found. The critical exponent $\nu=0.48\pm0.05$ is quite different from the original STA without local rigidity, indicating that the local rigidity changes the nature of the transition. It is also different from that of $O(4)$. It means that successive transformations used to buildup the NLS model from the original STA may lead to the $O(4)$ universality class.

I. INTRODUCTION

Phase transitions in frustrated spin systems have been extensively investigated during the last decade.[1] In particular, the nature of the phase transition in the stacked triangular antiferromagnets (STA) with Heisenberg spins interacting via nearest-neighbor (nn) bonds has been widely studied. This system belongs to a general family of periodically canted spin systems known as helimagnets. Recent extensive Monte Carlo (MC) simulations which are more precise than early MC works[2] have shown that the transition in STA is of second order with the critical exponents quite different from those of known universality classes.[3–5] The body-centered tetragonal helimagnet has also shown almost the same critical exponents.[6] Using a renormalization group (RG) technique in a $4-\epsilon$ perturbative expansion, Kawamura[7] has suggested a new universality class for that transition. However, by using a RG technique for a nonlinear σ (NLS) model with a $2+\epsilon$ expansion, Azaria *et al.*[8–10] showed that the transition, if not of first order or mean-field tricritical, is of second order with the known $O(4)$ universality class. This situation is embarrassing since the RG technique with $2+\epsilon$ and $4-\epsilon$ expansions usually yields the same result in three dimensions for nonfrustrated systems. Furthermore, it is clear that none of the scenarios predicted by Azaria *et al.* was verified by the above-mentioned independent MC simulations of the Heisenberg STA.[3–5]

The purpose of this paper is to find out the reason of the disagreement between the $2+\epsilon$ and the MC results. To this end, we study by the histogram MC simulation technique,[11,12] the approximated system used in the NLS model[8–10] and to compare the MC results with those performed on the original STA.[3–5] The approximated system, as seen in Sec. II, is in fact, obtained from the STA by neglecting local fluctuations while keeping the symmetry of the original Hamiltonian.

Section II is devoted to the description of our model and method. Results are shown and discussed in Sec. III. Concluding remarks are given in Sec. IV.

II. MODEL AND METHOD

Let us consider the STA with nn interaction. The ground state (GS) is characterized by a planar spin configuration where the three spins on each triangle form a 120° structure with either left or right chirality. Thus, the GS degeneracy is twofold in addition to the global rotation. The Hamiltonian is given by

$$H=J\sum_{ij}\mathbf{S}_i.\mathbf{S}_j \tag{1}$$

where S_i denotes the classical Heisenberg spin of unit length at the ith site, $J(>0)$ is the interaction between two nn spins, and the sum runs over all nn pairs. The Hamiltonian (1) has been used in previous MC simulations[3–5] which all give the same critical exponents within statistical errors: $\nu=0.59\pm0.01$, $\beta=0.28\pm0.02$, $\gamma=1.25\pm0.03$, and $\alpha=0.40\pm0.01$.

Following Azaria *et al.*[10] we take the continuum limit at each triangle by putting the three spins at its center. In doing so for all triangles, we generate a new superlattice [see Fig. 1(a)]. In the NLS model, the local rigidity was assumed, i.e., the sum of the three spins on each triangle is set to zero.[8–10,13] The resulting model is a system of triads each of which is defined by the three orthogonal unit vectors $\mathbf{e}_i(x)(i=1,2,3)$ which replace the spins at the center of the xth triangle in Fig. 1(a). The original spins at the xth triangle are obtained by a linear combination of $\mathbf{e}_i(x)(i=1,2,3)$. The system of triads is shown in Fig. 1(b). Note that the third vectors $\mathbf{e}_3(x)$ which are perpendicular to the figure sheet are not shown for clarity. Since there is no more frustration by geometry, one can take indifferently ferromagnetic or antiferromagnetic interaction between nn triads with the following Hamiltonian

$$H_t=-\sum_{xy}\sum_{i=1,2,3}K_i(x,y)\mathbf{e}_i(x).\mathbf{e}_i(y), \tag{2}$$

where $K_i(x,y)$ is the interaction between the two ith unit vectors sitting at the nn, xth, and yth, triads. The original STA is now transformed into a triad system which is defined on a simple cubic lattice. Strictly speaking, the STA corre-

 0021-8979/94/76(10)/6350/3/$6 00 © 1994 American Institute of Physics

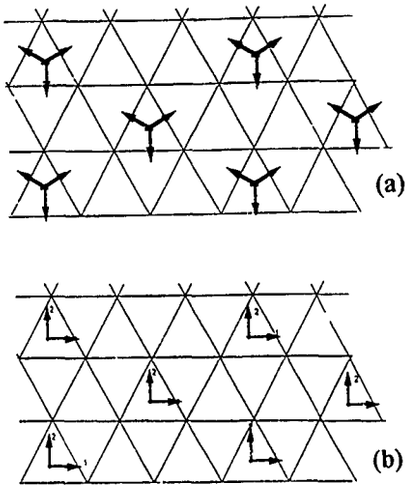

FIG. 1. (a) The continuum limit of the ground state of the STA is taken by putting the spins on each triangle at its center (b) system of triads which is equivalent to the Heisenberg STA with local rigidity. The third unit vectors perpendicular to the figure sheet are not shown.

sponds to the case where the interactions between one of the unit vectors, say $\mathbf{e}_3(x)$, are zero.[10] We will consider in this paper not only this case but also the symmetric case where all $K_t(x,y)$ are equal. Since the interactions in (1) are site independent, all interactions for the triad system are also site independent, i.e., $K_t(x,y)=K_t$.

Before showing our results, let us emphasize that the model considered in this paper is equivalent to the Heisenberg model on the STA *only within the so-called local rigidity condition.*

The method used here is the histogram MC technique which has been recently developed by Ferrenberg and Swendsen to study phase transitions.[11,12] The reader is referred to these papers for details. In our simulations, we use a simple cubic lattice of linear size $L=10,12,14,16,18,20$ sites with periodic boundary conditions. In general, we discarded 500 000 MC steps per triad for equilibrating and calculated the energy histogram as well as other physical quantities over 1–2 M MC steps. We first estimate roughly the transition temperature T_0 at each size and calculate at T_0 the energy histogram as well as the following quantities:

$$\langle C\rangle=\frac{(\langle E^2\rangle-\langle E\rangle^2)}{Nk_BT^2}, \tag{3}$$

$$\langle \chi\rangle=\frac{N(\langle O^2\rangle-\langle O\rangle^2)}{k_BT}, \tag{4}$$

$$\langle (O)'\rangle=\langle OE\rangle-\langle O\rangle\langle E\rangle, \tag{5}$$

$$\langle (O^2)'\rangle=\langle O^2E\rangle-\langle O\rangle^2\langle E\rangle, \tag{6}$$

$$\langle (\ln O)'\rangle=\frac{\langle OE\rangle}{\langle O\rangle}-\langle E\rangle, \tag{7}$$

$$\langle (\ln O^2)'\rangle=\frac{\langle O^2E\rangle}{\langle O^2\rangle}-\langle E\rangle, \tag{8}$$

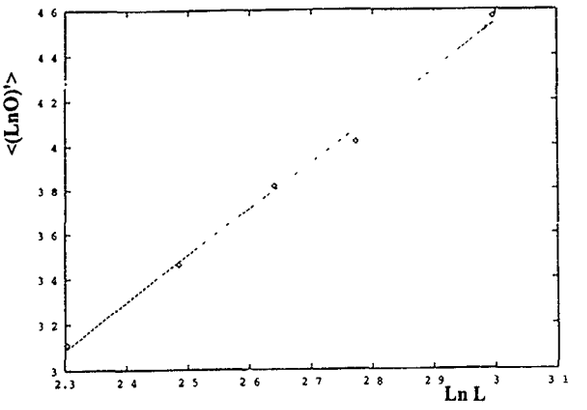

FIG. 2. $\langle(\ln O)'\rangle$ vs $\ln L$. The slope is $1/\nu=2.08$.

$$\langle V\rangle=1-\frac{\langle E^4\rangle}{3\langle E^2\rangle^2}, \tag{9}$$

$$\langle U\rangle=1-\frac{\langle O^4\rangle}{3\langle O^2\rangle^2}, \tag{10}$$

$$\langle (U)'\rangle=\langle UE\rangle-\langle U\rangle\langle E\rangle, \tag{11}$$

where E is the internal energy of the system, T the temperature, O the order parameter, C the specific heat per site, χ the magnetic susceptibility per site, U the fourth-order cumulant, V the fourth-order energy cumulant, $\langle ...\rangle$ means the thermal average, and the prime denotes the derivative with respect to $\beta=1/(k_BT)$. Using the energy histogram at T_0, one can calculate physical quantities at neighboring temperatures, and thus the transition temperature at each size is known with precision.[11,12]

III. RESULT

Let us show the results for the two following cases.

A. $K_1=K_2=K$, $K_3=0$

The system in this case is equivalent to the STA with local rigidity. The transition is found of second order. Using the finite size scaling for the maxima of $\langle C\rangle$, $\langle\chi\rangle$, $\langle(\ln O)'\rangle$, etc.[11,12] we obtained the critical temperature for the infinite system which is $T_c(\infty)=1.5325\pm0.0020$. The exponent ν can be obtained from the inverse of the slope of $\langle(\ln O)'\rangle$ [and $\langle(\ln O^2)'\rangle$] versus $\ln L$. This is shown in Fig. 2 where $\nu=0.48\pm0.05$. The critical exponents γ and β are obtained by plotting $\ln\langle O\rangle$ and $(\ln\langle\chi\rangle)$ vs $\ln L$, respectively (not shown here). They are $\beta=0.22\pm0.04$ and $\gamma=1.15\pm0.07$. These exponents are completely different from those of the original STA (without local rigidity) (see values of exponents given in the preceding section). They are also different from those of the $O(4)$ universality class which are $\nu=0.74$, $\beta=0.39$, $\gamma=1.47$.

There are two things we learn from these results: (i) the local rigidity changes the nature of the phase transition; (ii) when one starts with the local rigidity, one does not find the scenarios predicted by the NLS model in $2+\epsilon$ expansion.[10] It means that the subsequent approximations used in the theoretical calculation,[10] for instance, the continuum limit performed at some steps, may alter the nature of the transition

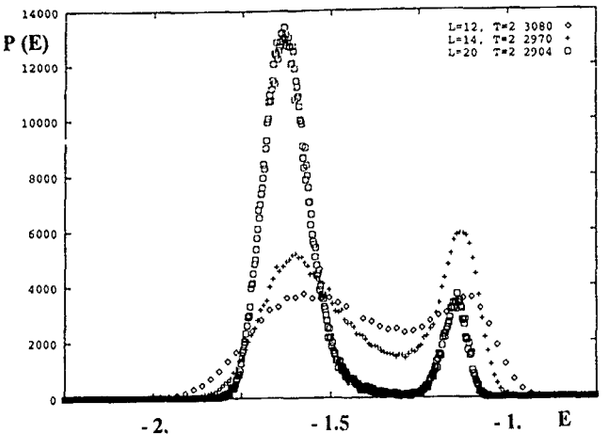

FIG. 3. Energy histogram $P(E)$ for $L=12$ at $T=2.3080$ (diamonds), for $L=14$ at $T=2.2970$ (crosses), and for $L=20$ at $T=2.2904$ (squares). Bimodal distribution characteristic of first-order transition is seen. E is internal energy per unit vector $\mathbf{e}_i(x)(i=1,2,3)$

found by MC simulation for the discrete lattice system. We believe that the continuum limit used in the NLS model excludes possible topological defects which can change the transition nature.

B. $K_1=K_2=K_3=K$

In this case, we find a strong first-order transition. This is unexpected since the symmetry of the Hamiltonian is invariant with respect to the previous case. We show in Fig. 3 the energy histogram $P(E)$ performed for several lattice sizes at the transition temperature of each size. The bimodal distribution characteristic of a first-order transition is seen. The two maxima, which are separated by a continuum for small sizes, show a real discontinuity between them for $L=20$. Note that for $L=20$ the two maxima do not have the same height because the temperature at which the simulation was performed is not precisely the transition temperature. Another signature of the first order is the fact that the energy cumulant $\langle V\rangle$ does not tend to 2/3 at the transition for increasing size as it should be in a second-order transition. Instead, it decreases with increasing size to reach the value of 0.628 for $L=20$. The maxima of $\langle C\rangle$ and $\langle\chi\rangle$ vary as L^3, providing another evidence of the first-order character. Details will be shown elsewhere.

At this stage, it is interesting to note that there should be a critical value of K_3 between 0 and 1 where the transition undergoes a crossover from second to first order. The determination of this tricritical point is left for a future study.

IV. CONCLUSION

Here we have studied a system of interacting triads which is equivalent to the STA if one neglects local fluctuations by imposing a local rigidity on all triangles. In the case which is equivalent to the Heisenberg STA ($K_1=K_2=K$, $K_3=0$), we do not find the same critical exponents as those found for the STA. It means that the local rigidity changes the nature of the transition. The obtained critical exponents are, in addition, different from those of $O(4)$ found in the NLS calculation. We think that during the successive transformations of the initial STA to build the NLS model,[10] some ingredients may have been lost, though the system symmetry is preserved. In the case where $K_1=K_2=K_3=K$, we find that the transition is unexpectedly of first order, though the symmetry of the system does not change with respect to the case where $K_1=K_2=K$, $K_3=0$. We hope that this work will stimulate further theoretical investigations on the nature of phase transition in helimagnets.

ACKNOWLEDGMENTS

The authors wish to thank P. Azaria and B. Delamotte for suggesting this problem and for helpful discussion.

[1] *Magnetic Systems with Competing Interactions*, edited by H. T. Diep (World Scientific, Singapore, in press).
[2] H. Kawamura, J Appl. Phys. **63**, 3086 (1988), J. Phys. Soc Jpn. **58**, 584 (1989)
[3] H. Kawamura, J. Phys. Soc. Jpn. **61**, 1299 (1992); and in *Recent Advances in Magnetism of Transition Metal Compounds*, edited by A. Kotani and Suzuki (World Scientific, Singapore, 1992).
[4] D. Loison and H. T Diep, Phys. Rev. B (in press).
[5] T. Bhattacharya, A. Billoire, R. Lacaze, and Th. Jolicoeur, J. Phys. I France **4**, 181 (1994)
[6] H. T. Diep, Phys. Rev. B **39**, 397 (1989).
[7] H. Kawamura, Phys. Rev. B **38**, 4916 (1988).
[8] P. Azaria, B. Delamotte, and Th. Jolicoeur, Phys. Rev. Lett. **64**, 3175 (1990).
[9] P. Azaria, B. Delamotte, and Th. Jolicoeur, J. Appl. Phys. **69**, 6170 (1990).
[10] P. Azaria, B. Delamotte, F. Delduc, and Th. Jolicoeur, Nucl. Phys. B **408**, 485 (1993).
[11] A. M. Ferrenberg and R. H. Swendsen, Phys. Rev. Lett. **61**, 2635 (1988).
[12] A. M. Ferrenberg and R. H. Swendsen, Phys. Rev. Lett. **63**, 1195 (1989).
[13] T Dombre and N. Read, Phys. Rev. B **39**, 6797 (1989).

Critical behavior of the random Potts model

B. M. Khasanov, S. I. Belov, and D. A. Tayurskii
Physics Department, Kazan State University, Kazan 420 008, Russia

The phase transition in the continual random n-component Potts model is studied by the renormalization group method. It is shown that for the three-dimensional model and $n=3$ the phase transition is to be of the first order. In the case $n=2$ which corresponds to the random Ising model the stable fixed point exists as early as in the one-loop approximation of renormalization group equations.

In the Potts model each lattice site can be in one of n possible states. The energy of interaction between neighboring sites is equal to ϵ_0 for the sites being in the same states and to $\epsilon_1 > \epsilon_0$ in the opposite case. The Landay theory predicts the first-order phase transition due to the third-order vertex in the Hamiltonian of continual Potts model with tensor order parameter. On the other hand, it was shown in Refs. 1 and 2 that the strong fluctuations can lead to continuous transition in pure Potts model.

The static point defects which do not cause the matrix ordering in their localization lead to the local change of the effective Hamiltonian constants. One of the most simple defects is the defectlike "random temperature," but there are a number of situations where coupling constants may vary in a random way. In general, the third- and the fourth-order random potentials should be included in the reduced Hamiltonian. In this paper, we shall consider the critical behavior of continuous analogy of the random lattice Potts model and take into account local changes of all effective parameters in Hamiltonian.

Earlier it was shown that for the random P-model (the system with symmetric nonsingular and traceless tensor order parameter) its critical behavior was experimentally undistinguishable from pure model. The reason for it is that the stable fixed points of renormalization group equations in random and pure systems are located very closely to each other.[3]

For the model we consider the Hamiltonian has the form:[4]

$$\mathbf{H}=\frac{1}{2!}\int_{\mathbf{q}_1\mathbf{q}_2}\nu_2(\mathbf{q}_1\mathbf{q}_2)Q_{\alpha\beta}(\mathbf{q}_1)Q_{\alpha\beta}(\mathbf{q}_2)+\frac{1}{3!}\int_{\mathbf{q}_1\mathbf{q}_2\mathbf{q}_3}\nu_3(\mathbf{q}_1\mathbf{q}_2\mathbf{q}_3)Q_{\alpha\beta}(\mathbf{q}_1)Q_{\beta\gamma}(\mathbf{q}_2)Q_{\alpha\gamma}(\mathbf{q}_3)$$
$$+\frac{1}{4!}\int_{\mathbf{q}_1\mathbf{q}_2\mathbf{q}_3\mathbf{q}_4}\nu_4(\mathbf{q}_1\mathbf{q}_2\mathbf{q}_3\mathbf{q}_4)Q_{\alpha\beta}(\mathbf{q}_1)Q_{\alpha\beta}(\mathbf{q}_2)Q_{\gamma\delta}(\mathbf{q}_3)Q_{\gamma\delta}(\mathbf{q}_4)+\frac{1}{4!}\int_{\mathbf{q}_1\mathbf{q}_2\mathbf{q}_3\mathbf{q}_4}\nu_4'(\mathbf{q}_1\mathbf{q}_2\mathbf{q}_3\mathbf{q}_4)$$
$$\times Q_{\alpha\beta}(\mathbf{q}_1)Q_{\beta\gamma}(\mathbf{q}_2)Q_{\gamma\delta}(\mathbf{q}_3)Q_{\delta\alpha}(\mathbf{q}_4). \tag{1}$$

Here $Q_{\alpha\beta}(\mathbf{q})$ is the Fourier transform of symmetric, diagonal, and traceless tensor of rank n, $\int_q=\int d^d\mathbf{q}/(2\pi)^d$. ν_2,ν_3,ν_4 are the random fields for which we suppose the translational invariance of all averages and the absence of the long-range correlations. The average value of ν is transformed according to the full space group of the system without impurities and can be obtained by the averaging over a probability distribution of fields ν in the Hamiltonian

$$\langle\nu_2(\mathbf{q}_1\mathbf{q}_2)\rangle=(r+q_1^2)\,\delta(\mathbf{q}_1+\mathbf{q}_2),$$
$$\langle\nu_2(\mathbf{q}_1\mathbf{q}_2\mathbf{q}_3)\rangle=B\,\delta(\mathbf{q}_1+\mathbf{q}_2+\mathbf{q}_3),$$
$$\langle\nu_4(\mathbf{q}_1\mathbf{q}_2\mathbf{q}_3\mathbf{q}_4)\rangle=C\,\delta(\mathbf{q}_1+\mathbf{q}_2+\mathbf{q}_3+\mathbf{q}_4),$$
$$\langle\nu_4'(\mathbf{q}_1\mathbf{q}_2\mathbf{q}_3\mathbf{q}_4)\rangle=U\,\delta(\mathbf{q}_1+\mathbf{q}_2+\mathbf{q}_3+\mathbf{q}_4). \tag{2}$$

The renormalization group transformation change also averages $\langle\delta\nu\delta\nu\rangle$ as well as parameters B, C, and U. Here $\delta\nu$ denotes the deviation from the translation invariance $\nu=\nu+\delta\nu$. In the three-dimensional space it is necessary to consider the following cumulants:

$$\langle\delta\nu_i(\mathbf{q}_1\mathbf{q}_2)\,\delta\nu_j(\mathbf{q}_3\mathbf{q}_4)\rangle=\Delta_{ij}(\mathbf{q}_1+\mathbf{q}_2+\mathbf{q}_3+\mathbf{q}_4),$$
$$\Delta_{ij}\in(\Delta_{rr},\Delta_{BB},\Delta_{rB},\Delta_{rC},\Delta_{rU}). \tag{3}$$

The functions $B(T)\equiv\Gamma_3$ and $C(T)=\Gamma_4^i$ (i is a number of the fourth-order invariant) are the irreducible vertices at zero momentum for the Hamiltonian (1). Besides those vertices there are a number of effective impurity vertices: the vertex Δ_{rr} has the same dimension as Γ_4, the vertex Δ_{rB} is equivalent to the fifth-order invariant in the Hamiltonian, and vertices $\Delta_{BB},\Delta_{rC},\Delta_{rU}$ are equivalent to the sixth-order invariant. For the continuous transition all vertices depend on correlation radius κ by means of the power law

$$\Gamma_k\propto g_k\kappa^{2k-d(k-2)-k\eta/2}, \tag{4}$$

where η is the Fisher critical exponent. One can obtain the Gell-Mann-Low-like equations for dimensionless invariant charges $g_k\in(B,C,U,\Delta_{ij})$

$$\frac{\partial g_k}{\partial t}=\Psi_k(g). \tag{5}$$

 0021-8979/94/76(10)/6353/3/$6.00 © 1994 American Institute of Physics

TABLE I. The fixed points of renormalization group Eq. (5) for $n=3$.

	$O(2)$	A_+	A_-	$O'(2)$	A'_+	A'_-	A'_1	A'_2	U
B^2	0	2	$\frac{18}{43}$	0	2.27	0.54	0.19	5.64	0
C	$\frac{3}{20}$	$\frac{1}{4}$	$\frac{15}{43}$	$\frac{3}{8}$	0.3	0.44	0.33	1.47	0
Δ_{rr}	0	0	0	$\frac{1}{16}$	0.03	−0.12	0.04	0.1	$-\frac{1}{16}$
Δ_{rB}	0	0	0	0	0.004	−0.05	0.01	−0.45	0
Δ_{BB}	0	0	0	0	0.04	−0.03	0.02	1.43	0
Δ_{rC}	0	0	0	0	−0.008	−0.03	0.0007	−0.31	0

where $t=\ln \kappa^2$. For arbitrary n there are eight such equations. For $n=3$ the two fourth-order invariants in (1) are connected by means of equality $TrQ^4=(TrQ^2)^2/2$. In this case the number of equations is reduced to six, but they are still rather complicated. The numerical solution gives the fixed points with positive B^2 and C that is summarized in Table I.

The first three fixed points with $\Delta=0$ earlier obtained in Ref. 1, describe the critical behavior of the Potts model without impurities. The fixed point A_+ is the saddle point while the stable point A_- is the stable focus. The Hamiltonian flow of renormalization group equations that is going through the fixed point A_+ divides the phase diagram into two parts. Flows from the one part are going to the line 01 of the Fig. 1 on which the first-order phase transition occurs, and flows from another—to the fixed point A_-, where the second-order phase transition takes place. For the random Potts model the only one stable fixed point is the A'_-. In the real physical system the cumulants Δ_{rr} and Δ_{BB} are by definition a positive definite quantities. The flow lines make it impossible for a point that starts in the region with $\Delta_{ii}>0$ to flow after renormalization into the region with $\Delta_{ii}<0$ (Fig. 2). Thus, the fixed point A'_- is inaccessible to physical systems. Hence, the phase transition in the random three component Potts model described by the Hamiltonian (1) is the phase transition of the first order. It is important to note that the fixed point A_- of the pure system is unstable with respect only to Δ_{BB} and Δ_{rC}. All given fixed points in Table I are in the region of values B^2 and C that is stable about condensate separation. Presently, results for the continual model are correlated with the lattice model mentioned at the beginning are discussed. By means of functional integration, the lattice model may be presented as a field theory with a nonpolinomial interaction potential in which all bare constants are connected. It is not obvious that the expansion up to the fourth-order invariants in (1) is sufficient to describe the phase transition in a lattice model. However, if that is the case then Hamiltonian (1) will correspond to the lattice model only with the definite correlations between the bare parameters in (1). After that the critical behavior of a lattice model will described only by the same phase flow of renormalization group equations. Probably, this flow line will go near the fixed point A_- or A'_1. In this case, one can obtain the critical exponent of susceptibility γ from equation

$$1-\gamma^{-1}=\frac{n+1}{3}C-\frac{3(n-2)}{2n}B^2-2\Delta_{rr}, \tag{6}$$

Therefore $\gamma=1.3$. If the flow line passes near A_+ or A'_+, then $\gamma=0.6$. In order to investigate the critical properties for $n>3$ one has to solve eight equations like (5). This problem is rather complicated in comparison with the three-component system. Therefore, we will discuss only impurities of "random temperature" type, i.e., $\Delta_{rr}\neq 0$. In this regime the unstable fixed point for $n=4$ and the stable fixed point for $n\geq 5$ with B^2, $U>0$, and $C,\Delta_{rr}<0$ could be obtained. There are not stable fixed points in the physical region with $B^2,\Delta_{rr}>0$.

If we take $B=0$ in the Hamiltonian (1) and consider the limit $n\to\infty$ (in this case, the condition $TrQ=0$ becomes irrelevant), then the stable unphysical fixed point with $U=1/12$, $C=1/(4n)$, $\Delta_{rr}=-1/48$, and the stable fixed point $U=1/6$, $C=1/(2n)$, $\Delta_{rr}=0$ appear. The latest point describes the critical properties of the spherical model with cubic anisotropy. Calculating the exponent γ for it

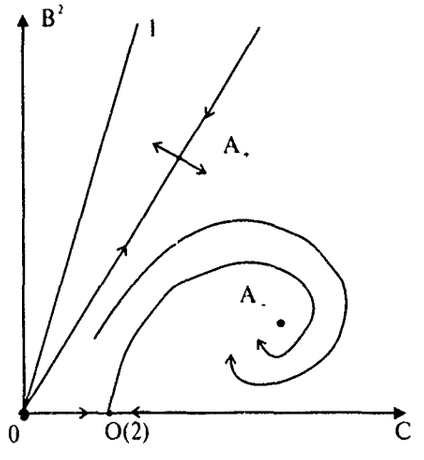

FIG. 1 Flow diagram for pure model, $n=3$.

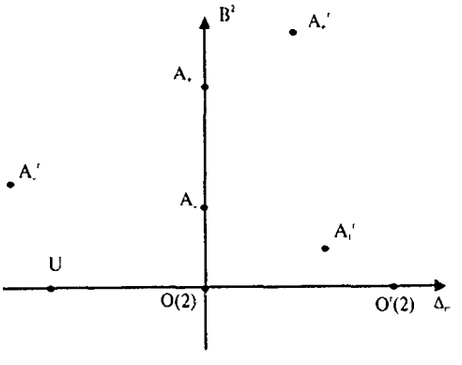

FIG 2. The fixed points on the (B^2,Δ_{rr}) plane for $n=3$.

$$1-\gamma^{-1}=\frac{n}{3}C+U,$$

we have $\gamma=3/2$. In the three-loop approximation the stable fixed point is equal to $nC=0.480$, $U=0.176$, $\Delta_{rr}=0$, and $\gamma=1.43$. It happens that in the zero order to $1/n$ the renormalization group equation for vertex U and the critical exponent η depend only on U, so the value of η for the spherical model with cubic anisotropy is equal to η of the Ising model. The same results were obtained in Ref. 5 where the perturbation theory on vertex C was used. Note that if one can take only $C\neq 0$ in the Hamiltonian (1) (spherical model) then the well-known result in three-dimensional space $\gamma=2$ follows. The limit of large n considered here is of consequence with the statement that for $n\to\infty$ and $d>2$ the interaction of fluctuations C disappears while the value nC remains finite and the expansion over $1/n$ can be effective.

The case $n=2$ that corresponds to the Ising model is the subject of special interest. Here, the third-order vertex B does not influence the critical behavior, and corresponding to it, charge g_3 drops out of Eqs. (5). This circumstance follows from the symmetry of the Potts model for $n=2$. Besides, here as well as for $n=3$, there is only one fourth-order invariant in (1), so the total number of variables is reduced to three: C and two cumulants Δ_{rr} and Δ_{rC}. If $\Delta_{rC}=0$, Eqs. (5) are degenerated in the one-loop approximation and do not have nontrivial solutions. There is no degeneracy in the two-loop approximation, but at the same time the fixed point describing the critical behavior in the pure Ising model is absent. The pure and random fixed points appear only in the three-loop approximation.[6] Assuming that $\Delta_{rC}\neq 0$, one can get nontrivial random stable fixed point even in the one-loop approximation: $C=0.390$, $\Delta_{rr}=0.051$, $\Delta_{rC}=-0.002$. Using (6) it is easy to find susceptibility exponent γ. Other critical exponents are expressed through γ and η with the help of the scaling relation laws. One can use two approaches in order to find the value of γ in the three-dimensional renormalization perturbation theory: (i) to substitute into (6) the fixed point coordinates and to reverse the obtained value; (ii) on the first inverse Eq. (6) and to expand γ as a series of C and Δ_{rr}, then the fixed point coordinates into obtained expressions are substituted. As a result, we find for γ and the heat capacity exponent α the following values, calculated in the following ways, respectively: $\gamma=1.4$, $\alpha=-0.1$, and $\gamma=1.29$, $\alpha=0.07$. Higher-order terms of perturbation theory (it is necessary to consider the three-loop approximation) lead to the small increase of γ and can essentially change the value of α. Even in the one-loop approximation, two ways of calculations give the opposite signs of α. Hence, the obtained results do not allow to estimate reliably estimate the value of the random exponent α. It is a very reasonable possibility that this cannot also be made in the three-loop approximation as it was shown in Ref. 6 for the "random temperature" impurities. Using Harris' arguments[7] it is possible to show that two different kinds of the disorder variables Δ_{rr} and Δ_{rC} do not change the statement[6] that critical exponent α must be negative.

The work of B.Kh. was supported, in part, by a Sloan Foundation Grant awarded by the American Physical Society and the work of D.T. was supported, in part, by a Soros Grant awarded by the International Science Foundation.

[1] A. L. Korzhenevskii Zh. Eksp. i Teor. Fiz. **75**, 1474 (1978) (in Russian).
[2] A. L. Korzhenevskii, Fiz. Tverd. Tela. **20**, 359 (1978) (in Russian).
[3] B. M. Khasanov and S. I. Belov, Fiz. Tverd. Tela. **36** (1994) (in Russian).
[4] R. G. Priest and T. C. Lubensky, Phys. Rev. B **13**, 4159 (1976).
[5] A. Aharony, Phys. Rev. Lett. **31**, 1494 (1973).
[6] A. I. Sokolov and B. N. Shalaev, Fiz. Tverd. Tela **23**, 2058 (1981) (in Russian); I. O. Mayer, A. I. Sokolov, and B. N. Shalaev, Ferroelectrics **95**, 93 (1989); I. O. Mayer, J. Phys. A **22**, 2815 (1989).
[7] A. B. Harris, J. Phys. C **7**, 1671 (1974).

Published without author corrections

Influence of exchange bond disorder on the magnetic properties of $(Pd_{1-x}Fe_x)_{95}Mn_5$ near T_c

Z. Wang, X. Qi, H. P. Kunkel, and Gwyn Williams
Department of Physics, University of Manitoba, Winnipeg, Manitoba R3T 2N2, Canada

A summary of a detailed study of the field and temperature dependent ac susceptibility of a series of ternary $(Pd_{1-x}Fe_x)_{95}Mn_5$ alloys near the ferromagnetic ordering temperature T_c is presented. By following the behavior of the crossover line (a line of maxima in the field dependent susceptibility *above* T_c, the maxima moving upwards in temperature but decreasing in amplitude with increasing field) it is possible to catalog the influence of exchange bond disorder on aspects of the critical behavior. These ternary systems are not soft ferromagnets and thus asymptotic critical exponents are difficult to estimate using this technique. Nevertheless, effective exponents (i.e., obtained away from the critical point) clearly reflect the presence of significant variance in the distribution of exchange bonds.

I. INTRODUCTION

$(Pd_{1-x}Fe_x)$ $(0.01 \leqslant x < 0.25)$ is a well-known ferromagnet[1] and $Pd_{95}Mn_5$ is a spin glass.[2] In the frequently referenced approach[3] in which the exchange bond distribution that exists in such metallic systems is approximated by a Gaussian, the mean value of this distribution thus exceeds its variance in the former system, while in the latter this inequality is reversed.

Binary $Pd_{1-x}Fe_x$ ($x \simeq 0.014$–0.016) is a nearly ideal example of a soft ferromagnet.[1] Internal fields as low as $H_i \simeq 1$ Oe are capable of revealing structures normally associated with critical fluctuations at a second-order phase transition, and a detailed analysis of this structure yields critical exponents[1] ($\gamma = 1.36 \pm 0.03$, $\beta = 0.39(5) \pm 0.015$, $\delta = 4.5 \pm 0.15$) close to the values predicted by the isotropic, three-dimensional Heisenberg model[4] using renormalization group techniques ($\gamma = 1.386$, $\beta = 0.365$, $\delta = 4.8$). Binary $Pd_{1-x}Mn_x$ ($x \geqslant 0.05$) is a spin glass, characterized by a divergence in the nonlinear susceptibility[5,6] (the associated exponents having been most recently reported[6] as $\gamma = 2.0 \pm 0.2$, $\beta = 0.9 \pm 0.15$, $\delta \simeq 3$). Ternary $(Pd_{1-x}Fe_x)_{95}Mn_5$ ($x = 0.0035$) remains[7,8] as one possible example of a system exhibiting sequential phase transitions following detailed studies,[8] viz. near $T_c \simeq 9$ K the field- and temperature-dependent susceptibility exhibits features associated with critical fluctuations near a second order paramagnetic to ferromagnetic transition (but with some indication of the influence of variance in the exchange bond distribution), while at lower temperature, $T_{SG} \simeq 4.1$ K, the nonlinear response displays a marked (but *not* divergent) anomaly.

Here we present a summary of comparable measurements on ternary $(Pd_{1-x}Fe_x)_{95}Mn_5$. At rather higher Fe concentrations ($x \simeq 0.016$–0.022), these samples have correspondingly higher ferromagnetic ordering temperatures, and the "reentrant" transition is also suppressed. For this reason we have focused attention on the detailed behavior of the field- and temperature-dependent response near T_c, and on the influence exerted on this response by the exchange disorder expected in such systems.

II. EXPERIMENTAL DETAILS

Samples were prepared individually in an argon arc furnace from high purity starting materials using a well-established sequence of inverting, remelting, cold rolling, and annealing steps,[1,9] to ensure homogeneity. Field- and temperature-dependent ac susceptibility data were collected continuously using a previously described[1] phase-locked susceptometer on samples of typical dimensions (17×2×0.1) mm;[3] both the ac excitation field (50 m Oe rms at 2.4 kHz) and static biasing fields up to 1 k Oe were applied along the largest specimen dimension. The data were corrected for background and demagnetizing effects, as described previously.[1]

III. RESULTS AND DISCUSSION

Figure 1 reproduces the zero-field susceptibility in binary Pd-1.6 at. % Fe [Fig. 1(a)], and in ternary $(Pd_{1-x}Fe_x)_{95}Mn_5$ ($x = 0.0035$ [Fig. 1(c)] and 0.016 [Fig.

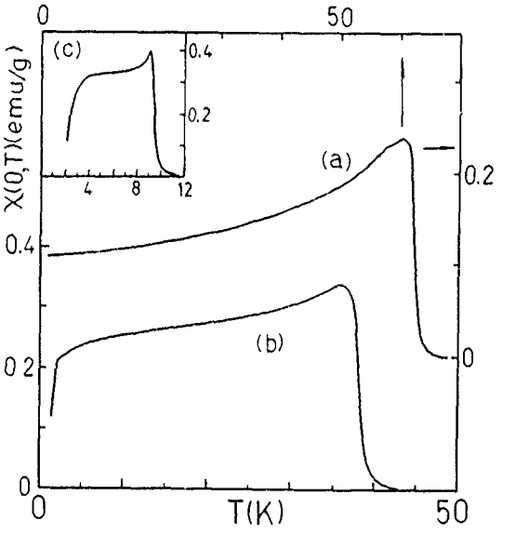

FIG 1. The zero-field susceptibility $\chi(0,T)$ (in emu/g) plotted against temperature (in K) for (a) Pd + 1.6 at. % Fe, (b) (Pd + 1.6 at. % Fe)$_{95}$Mn$_5$, and (c) (Pd + 0 35 at. % Fe)$_{95}$Mn$_5$.

 0021-8979/94/76(10)/6356/3/$6.00 © 1994 American Institute of Physics

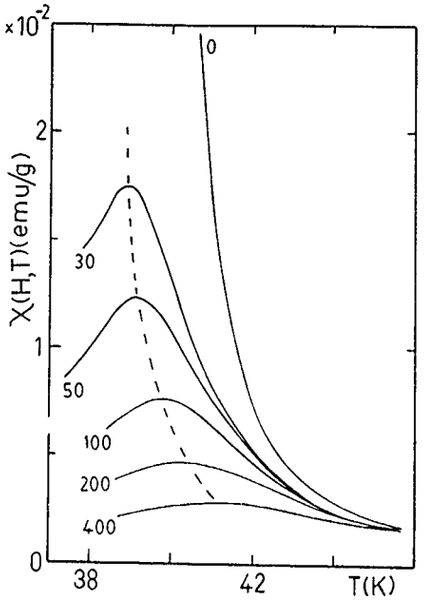

FIG. 2. The susceptibility $\chi(H,T)$ (in emu/g) plotted against temperature T (in K) for (Pd+1.6 at. % Fe)$_{95}$Mn$_5$; the numbers marked against each curve are the estimated, superimposed (internal) fields H_i (in Oe). The dashed line represents the crossover line.

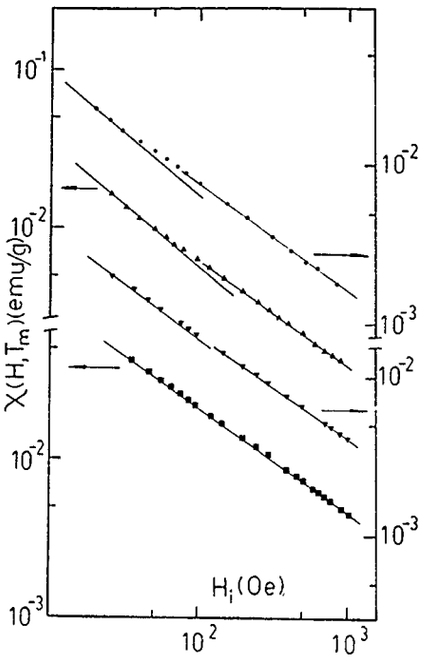

FIG. 3. The *peak* susceptibility $\chi(H,T_m)$ (in emu/g), taken from data similar to that shown in Fig 2, plotted against the internal field H_i (in Oe) on a double logarithmic scale for $(Pd_{1-x}Fe_x)_{95}Mn_5$, with $x=1.6$ at. % Fe (●), 1.8 at. % Fe (▲), 2.0 at. % Fe (▼) and 2.2 at % Fe (■). The lines drawn yield the $\delta^*(H)$ values listed in Table I.

1(b)]), so that the general features of the behavior of these systems can be compared and contrasted. While the characteristic structure usually associated with reentrant behavior is evident in Fig. 1(c), the lower (reentrant) transition is suppressed in both binary and ternary samples with higher Fe concentration. Nevertheless, as is clear from a comparison of Figs. 1(a) and 1(b), the ferromagnetic ordering temperature T_c is lowered by the addition of Mn. Figure 2 details the influence of superimposed static biasing fields on Fig. 1(b) near 40 K; such fields suppress the principal (Hopkinson) maximum enabling a secondary peak structure to be observed. These latter peaks decrease in amplitude and move upwards in temperature as the applied field increases; they are a characteristic signature[1,10] of critical fluctuations at a second-order paramagnetic to ferromagnetic transition, and their locus defines the crossover line.[10,11] In terms of the usual[12] scaling law expression for the field (h) and temperature (t) dependent susceptibility $\chi(h,t)$

$$\chi(h,t)=t^{-\gamma}F\left(\frac{h}{t^{\gamma+\beta}}\right)=h^{(1/\delta)-1}G\left(\frac{h}{t^{\gamma+\beta}}\right), \tag{1}$$

[with $h\sim H_i/T_c$ and $t=(T-T_c)/T_c$ in the usual notation], the temperature T_m of these critical (secondary) peaks varies with fields as [1,10]

$$t_m=(T_m-T_c)/T_c\propto\left(\frac{H_i}{T_c}\right)^{1/(\gamma+\beta)}, \tag{2}$$

while the critical peak amplitude $\chi(h,t_m)$ behaves as

$$\chi(h,t_m)\propto h^{1/\delta-1}. \tag{3}$$

Equations (2) and (3) along with the more conventional dependence of the zero-field susceptibility on (reduced) temperature above T_c, viz:

$$\chi(0,t)\propto t^{-\gamma}, \tag{4}$$

have provided the basis for a detailed analysis of the critical behavior in a variety of systems.[1,10]

Here, however, two factors conspire to preclude such a detailed analysis; (a) fields in excess of $H_i\simeq 15$ Oe are required initially to resolve critical peak structure, and (b), even when these peaks are resolved they are considerably broader than those in the corresponding binary $Pd_{1-x}Fe_x$ samples. The influence of point (a) can be seen in Fig. 3 which tests Eq. (3) via a double logarithmic plot of the peak susceptibility $\chi(H,T_m)$ (evident in Fig. 2) against internal field (H_i); in the case of the 1.6 and 1.8 at. % Fe samples the line drawn at *low* field corresponds to the 3D-Heisenberg model value of $\delta=4.8$ while the higher field slope yields an *effective* exponent $\delta^*(H)\sim 3$ (the mean-field value). This fall in the effective exponent $\delta^*(H)$ with increasing field is well cataloged[1,10] in systems with exchange bond disorder. The field dependence of the effective exponent $\delta^*(H)$ is not so evident in the 2.0 and 2.2 at. % Fe specimens as even larger fields H_0 (listed in Table I) are required to resolve critical peak structure in them.

Figure 4 tests the predictions of Eq. (2) and also illustrates the difficulties introduced as a result of point (b) above. Briefly, in the most favorable cases,[1,10] t_m can be plotted against H_i on a double logarithmic scale, the slope of which yields the crossover exponent $(\gamma+\beta)$. Here the diffuse nature of the critical peaks renders this procedure inappropriate since T_m (and hence t_m) cannot be established with sufficient accuracy. The best that can be done is a linear plot of the peak temperature T_m against $(H_i)^{0.57}$ ($[\gamma+\beta]^{-1}=0.57$

TABLE I. A compilation of parameters deduced from ac susceptibility data on $(Pd_{1-x}Fe_x)_{95}Mn_5$.

				$\delta^*(H)$	
x (at. % Fe)	T_c (K)	T_c[a] (K)	H_0 (Oe)	Low field	High field
0.35	9.3±0.02	7.5±0.03	3	4.1±0.1	4.1±0.1
1.6	38.0±0.2	61.5±0.2	15	4.8±0.2	3.0±0.2
1.8	41.6±0.3	69.1±0.2	25	4.8±0.4	3.0±0.2
2.0	44.9±0.5	75.4±0.3	28	3.7±0.4	3.0±0.2
2.2	47.9±0.5	80.6±0.5	35	3.0±0.2	3.0±0.2

[a]For the corresponding binary (Mn free) PdFe sample (Ref. 1).

for Heisenberg model exponents), which indicates that these data are generally consistent with such model exponents within the rather appreciable scatter evident here. The intercept from such plots yields the T_c estimates listed in Table I.

Further effects of exchange bond disorder are provided in Fig. 5 where, rather than to test Eq. (4) directly, the effective Kouvel–Fisher susceptibility exponent[13]

$$\gamma^*(t) = d\ \ln[\chi(0,t)]/d\ \ln(t) \tag{5}$$

is plotted against t for the 2.0 at. % Fe sample. The nonmonotonic variation of this effective exponent with temperature—specifically the peak in $\gamma^*(t)$ *above* T_c near

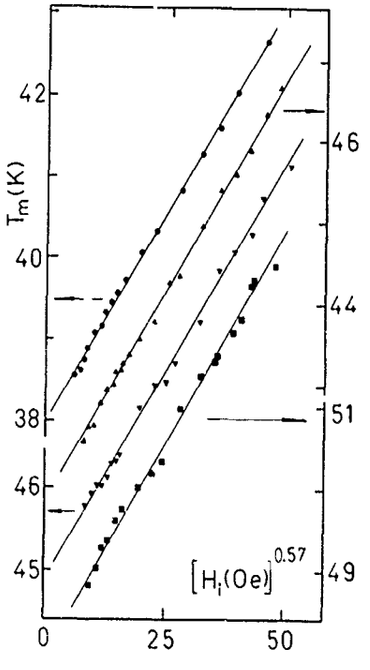

FIG. 4. The susceptibility peak temperature T_m (in K) plotted against internal field H_i (in Oe) raised to the power $(\gamma+\beta)^{-1}=0.57$. Symbols are the same as those used in Fig. 3.

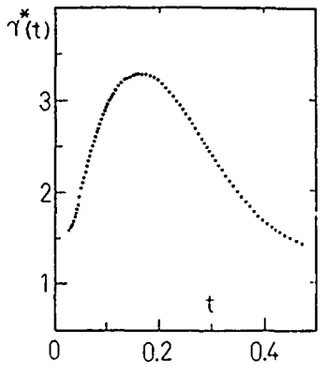

FIG. 5. The Kouvel–Fisher effective susceptibility exponent $\gamma^*(t)$ plotted against reduced temperature t for the (Pd+2.0 at. % Fe)$_{95}$Mn$_5$ specimen.

$t\simeq 0.16$—is well documented in systems with bond disorder,[1,10,14] confirming the conclusions drawn from the data shown in Fig. 3.

IV. SUMMARY

A detailed study of the field- and temperature-dependent ac susceptibility near the ferromagnetic ordering temperature T_c in $(Pd_{1-x}Fe_x)_{95}Mn_5$ indicates a significant suppression in the value for T_c following the addition of Mn. Within the framework of an S–K like model,[3] this represents a marked reduction of the mean value/second moment ratio for the exchange bond distribution. The field and temperature dependence of the effective exponents $\delta^*(H)$ and $\gamma^*(t)$ indicate that this distribution retains a substantial width/second moment although the width cannot exceed the mean value as the reentrant transition is suppressed.

ACKNOWLEDGMENT

Support for this work from the Natural Sciences and Engineering Research Council (NSERC) of Canada is gratefully acknowledged.

[1] C. Büscher, T. Auerswald, E. Scheer, A. Schroder, H. V. Löhneysen, and H. Claus, Phys. Rev. B **46**, 983 (1992); Z. Wang, H. P. Kunkel, and G. Williams, J. Phys.: Condens. Matter **4**, 10385 (1992).
[2] B. R. Coles, H. Jamieson, R. H. Taylor, and A. Tari, J. Phys. F: Metal Phys. **5**, 565 (1975).
[3] D. Sherrington and S. Kirkpatrick, Phys. Rev. Lett. **32**, 1792 (1975); K. Binder and A. P. Young, Rev. Mod. Phys. **58**, 801 (1986).
[4] L. C. LeGuillou and J. Zinn-Justin, Phys. Rev. B **21**, 3976 (1980).
[5] E. C. Zastre, R. M. Roshko, and G. Williams, Phys. Rev. B **32**, 7597 (1985).
[6] B. R. Coles and G. Williams, J. Phys. F: Metal Phys. **18**, 1279 (1988).
[7] B. H. Verbeek, G. J. Nieuwenhuys, H. Stocker, and J. A. Mydosh, Phys. Rev. Lett. **40**, 586 (1978).
[8] H.P. Kunkel and G. Williams, J. Magn. Magn. Mater. **75**, 98 (1988).
[9] Z. Wang, thesis, University of Manitoba, 1990.
[10] G. Williams, in *Magnetic Susceptibility of Superconductors and Other Spin Systems*, edited by R. A. Hein, T. L. Francavilla, and D. H. Liebenberg (Plenum, New York, 1991)
[11] H. P Kunkel, R. M. Roshko, and G. Williams, Phys. Rev. B **37**, 5880 (1988).
[12] H. E. Stanley, in *Introduction to Phase Transitions and Critical Phenomena* (Clarendon, Oxford, 1971).
[13] J. S. Kouvel and M. E. Fisher, Phys. Rev. A **136**, 1626 (1964).
[14] S. N. Kaul, J Magn. Magn. Mater. **53**, 5 (1985); Phys. Rev. B **38**, 9178 (1988).

Magnetic transitions at high fields in $(Fe,Mn)_3Si$ alloys

H. J. Al-Kanani and J. G. Booth
Joule Physics Laboratory, Salford University, Salford M5 4WT, United Kingdom

J. W. Cable and J. A. Fernandez-Baca
Solid State Division, Oak Ridge National Laboratory, Oak Ridge, Tennessee 37831-6393

In the series of ordered DO_3 solid solutions $Fe_{3-x}Mn_xSi$, field-induced transitions have previously been found to occur for antiferromagnetic alloys with values of x near 1.70. The present work has determined a region of composition in which antiferromagnetism is the low-field, low-temperature state and gives the variation of the critical field as a function of temperature and composition. The critical field decreases approximately quadratically with temperature and rises to beyond 6 T in the range of composition from $1.6 \leqslant x \leqslant 1.8$. Neutron diffraction indicates that the antiferromagnetic axis is shifted from the [111] direction and that in a 5 T field the antiferromagnetic component of the scattering is reduced considerably from that in zero field. However, no corresponding increase in ferromagnetic component is observed within experimental error and Arrott plots suggest the high-field state is still largely antiferromagnetic.

I. INTRODUCTION

Fe_3Si and Mn_3Si are known to form solid solutions with the DO_3 ordered structure. The substitution of Mn for Fe in forming the series $Fe_{3-x}Mn_xSi$ results in a selective site occupation which has been fully described in earlier papers.[1,2] The present paper is concerned with the magnetic properties of the compounds in the compositional range $1.6 \leqslant x \leqslant 1.8$. These properties derive from the occupation of the A and C sites by Mn atoms, the B site being already fully occupied.[1] Magnetization studies show that the zero field magnetization $\sigma_{0,T}$ for these compounds decreases below a "reorientation temperature" T_R (~65 K) to give a smaller saturation magnetization $\sigma_{0,0}$. The previous work has shown that $\sigma_{0,0}$ is zero at $x = 1.70$ beyond which antiferromagnetism is the low temperature, low-field state. The present work stems from the observation[2] that for the alloys with $x = 1.70$ and 1.75 a field-induced transition from antiferromagnetism to another magnetic state occurs at temperatures below T_R. We have extended this work considerably to determine the alloy compositions for which this transition occurs (i.e., for which antiferromagnetism is the low-temperature, low-field state) and the variation of the critical fields as a function of temperature and composition. We have also attempted to determine the high field magnetic state of the compounds by comparing the neutron diffraction patterns in zero field and in a field of 5 T as a function of temperature, as well as examining the Arrott plots.

II. EXPERIMENTAL DETAILS

The material used for this investigation was prepared in an identical manner to that employed in the earlier examinations.[1,2] The new material consisted of alloys with x having values of 1.60, 1.625, 1.65, and 1.80. X-ray examination of the alloys indicated all to be single phase alloys. The quenched samples in powder form were examined in field up to 12 T using the Manchester and Salford Vibrating Sample Magnetometer facility over the temperature range 2–300 K. Data acquisition is by microprocessor control in which at a given temperature the field is swept automatically from 0 to 12 T and back to 0 within about 20 min. The critical field was taken to be that at which the differential susceptibility $d\sigma/dH$ was a maximum. Neutron diffraction measurements as a function of field and temperature were obtained at the HFIR Reactor, Oak Ridge National Laboratory using a wavelength of 1.42 Å. 24 h isothermal scans were normally employed with the field applied vertically, perpendicular to the scattering vector. Rietveld plots were obtained above the magnetic ordering temperatures allowing the site occupations and compositions to be refined.

III. RESULTS

The determination of the composition at which $\sigma_{0,0}$ becomes zero was made more difficult by the observation that for $x = 1.60$ and 1.625 the low-temperature properties of the alloys (in common with those of alloys having smaller values of x (Ref. 1) are dependent on previous magnetic field history. Since a demagnetizing facility was not available magnetization measurements at each temperature were obtained only after cooling in zero field from the paramagnetic state. Following this procedure it was established that $\sigma_{0,0}$ is zero for $x = 1.60$ and 1.625, although as indicated in the inset to Fig. 1, a magnetic measurement produces a large remanent moment in these cases which is associated with the transition fields being very small. Such effects are not observed for $x > 1.65$. A typical field transition is shown in Fig. 1 for the alloy with $x = 1.80$. The transition occurs over a wide range of field and is accompanied by considerable hysteresis at the lowest temperatures suggesting a first-order phase transition and possibly a large magnetostrictive effect. It is possible therefore to define two critical fields. At the lowest temperatures the difference between these two fields is often large, of the order of 1 T. At low fields the magnetization increases linearly with field as expected for an antiferromagnetic material but above the transition the observed curvature suggests an unsaturated state. The variation of the mean critical fields with temperature and composition is illustrated in Fig. 2 where a quadratic decrease with increasing temperature is seen (the results for $x = 1.75$ are included for comparative purposes). The solid lines are a fit to $H^* = (1 - T^{*2})$ where

 0021-8979/94/76(10)/6359/3/$6.00 © 1994 American Institute of Physics

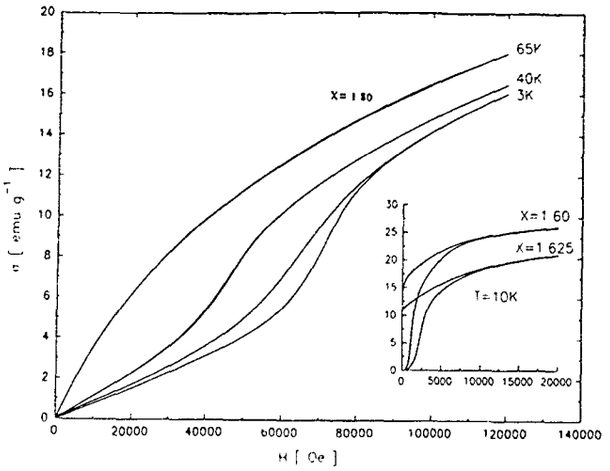

FIG. 1. Typical variation of magnetization with applied field at several temperatures below T_R for $Fe_{1.20}Mn_{1.80}Si$ Inset: low field data at low temperatures for $x=1.60$ and $x=1.625$.

the asterisks indicate reduced critical fields and temperatures, i.e., $H^*=H_c(T)/H_c(0)$ and $T^* =T/T_R$. Arrott plots were obtained both above and below T_R. Figure 3(a) shows that for $x=1.8$ above T_R the intercept on the H/σ axis approaches the origin as the temperature falls towards the ordering temperature. Information on the high-field state below T_R is provided by the Arrott plots shown in Fig. 3(b) for which the intercept on the H/σ axis retreats away from the origin as the temperature continues to fall. This behavior has recently been shown to be characteristic of an antiferromagnetic state[3] and will be discussed below. The situation for the other alloys is complicated by the appearance of a ferromagnetic region in a narrow temperature range above T_R. This is also reflected in the Arrott plots of those materials. Table I gives the approximate values of T_R and T_C versus x.

Neutron diffraction was carried out on the alloy with $x=1.65$ at the following temperatures and fields: 130 K and zero field in the paramagnetic regime; 80 K and zero field in

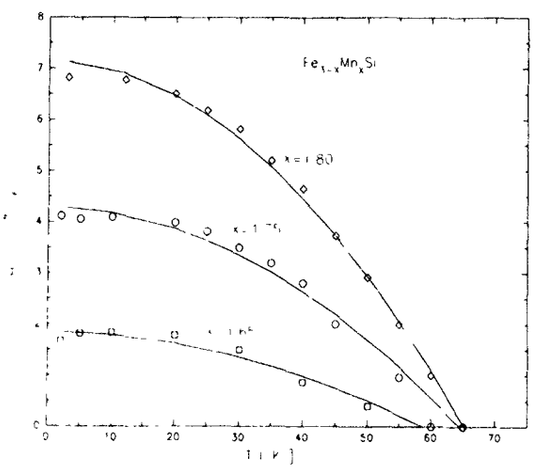

FIG. 2. Mean transition field vs temperature for the alloys discussed in this paper. Data for $x=1.75$ is included from Ref. 2 for comparative purposes. The solid lines are fits to the data using $H_C(T)/H_C(0)=[1-(T/T_R)^2]$.

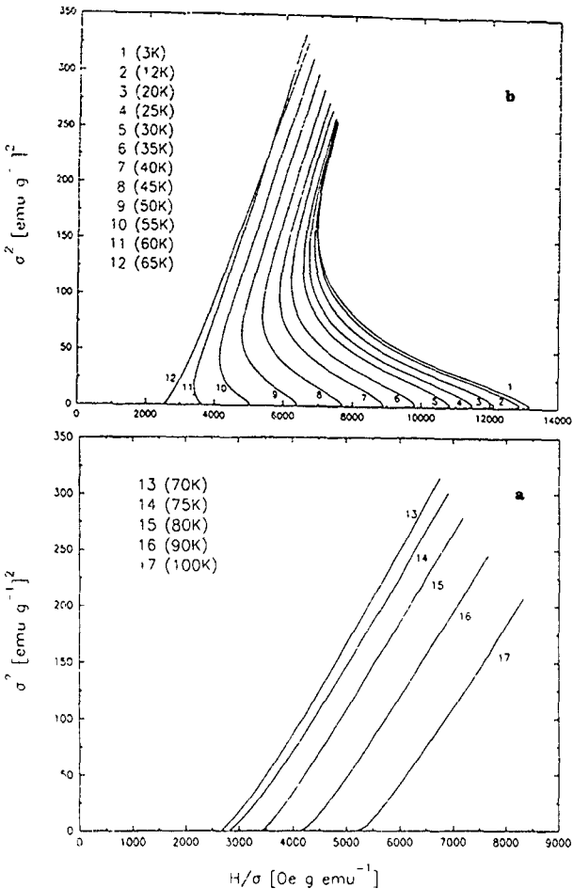

FIG. 3. Arrott plots for $Fe_{1.20}Mn_{1.80}Si$ (a) above T_R and (b) below T_R.

a regime where the alloy is weakly ferromagnetic; 4.2 K and zero field where the alloy is antiferromagnetic; 4.2 K and 5 T at which field the transition to another magnetic phase has occurred. For the results from the paramagnetic regime (130 K) the composition and site occupations were refined by a Rietveld plot which included parameters taking into account a small preferred orientation. The refined composition corresponded to $x=1.64$ and the following site occupation: (A) (0.32 Mn+0.68 Fe), (B) Mn, (C) as (A), and (D) Si. Figure 4(a) shows the results in zero field at 4.2 K and this is compared with the equivalent results in a field of 5 T in Fig. 4(b). The very small peaks in Fig. 4 were not observed at 130 K and indicate the antiferromagnetic order.

TABLE I. Approximate values of T_R and T_C vs x for the series $Fe_{3-x}Mn_xSi$.

x	T_R (K)	T_C (K)
1.60	60	125
1.625	60	118
1.65	60	80
1.70	60	75
1.75	65	...
1.80	65	...

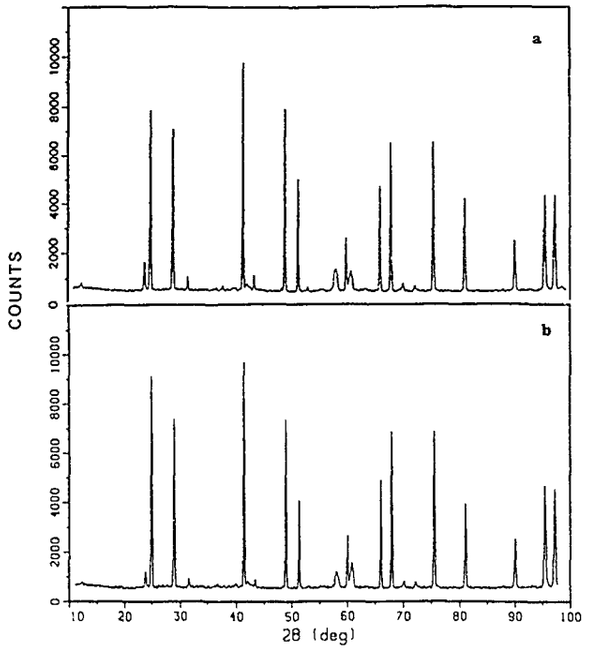

FIG. 4. $Fe_{1.35}Mn_{1.65}Si$ neutron diffraction patterns at 4.2 K with (a) $H=0$ and (b) $H=5$ T.

IV. DISCUSSION

The remarkable feature of Fig. 3 is the observation that below T_R the Arrott plot intercepts on the H/σ axis retract from the origin. It has recently been shown using the Landau theory of phase transitions[3] that such behavior is characteristic of systems with coupled antiferromagnetic and ferromagnetic components with $T_N<T_C$ and theoretical curves similar to those in Fig. 3 have been obtained. It is possible that the high-field state remains predominantly antiferro- (or ferri-) magnetic and that further transitions at even higher fields might be expected. The magnetization and neutron diffraction data have previously been shown to be consistent with a model in which in the zero field the Mn moments on alternate B sites ($\sim 2\ \mu_B$ independent of x in this range of x) are canted at opposing angles to the magnetic axis and it is assumed that at T_R these moments "flip" to become parallel to the moments on A and C sites. In the composition range considered here the previous neutron diffraction data has indicated that the moments on A and C sites are practically zero so that the BB antiferromagnetic interactions dominate and indeed become stronger as x increases beyond 1.5. The

TABLE II. Comparison of the observed structure factors of the superlattice lines in 0 and 5 T fields for $Fe_{1.35}Mn_{1.65}Si$.

1/2 (hkl)	Field ON q^2F^2/F^2_{220}	Field OFF q^2F^2/F^2_{220}	F^2_{ON}/F^2_{OFF}
111	0.007	0.010	0.70
311	0.055	0.091	0.60
331	0.050	0.076	0.66
511+333	0.028	0.041	0.68
531	0.041	0.073	0.56
533	0.016	0.042	0.39
551	0 029	0.060	0.48

neutron diffraction results in Fig. 4 show that the intensities of the superlattice peaks in zero field are much reduced by the application of a 5 T field. Since the applied field is perpendicular to the scattering vector one might expect that any reduction in the antiferromagnetic alignment would correspond to the appearance of a ferromagnetic component and that this would be reflected in an increase in the scattering at the nuclear peaks. The structure factors for the latter are such that one would expect the (111) line, which contains only the contribution from the B site, to be most sensitive to an increase in ferromagnetic alignment but within experimental error the intensity remains the same. Table II gives the effect of field on the intensities of the superlattice lines showing, in general, a reduction to some 57% of the zero-field value. The application of a magnetic field alters the basic antiferromagnetic arrangement but it seems likely that the resultant state is another unsaturated one. To explain the observations this state must be such as to contribute only very small ferromagnetic components to the scattering.

Clearly further work on this most interesting region of concentration is required and further neutron diffraction and μSR investigations are planned.

ACKNOWLEDGMENTS

The assistance of SERC/Neutron Beam Research Committee and Martin Marietta Inc. in enabling the neutron diffraction aspects of this work to be carried out is gratefully acknowledged.

[1] S. Yoon and J. G Booth, J. Phys. F: Metal Phys. 7, 1079 (1977)
[2] H. Al-Kanani, J. G. Booth, and S. Yoon, J. Appl. Phys. 73, 5671.
[3] K.-U. Neumann, J. Crangle, N. K Zayer, and K. R. A. Ziebeck, *Proceedings of Summer School, Bialowieza, Poland, 1993* (Warsaw University Press, Warsaw, Poland, 1994).

Critical behavior of the two-dimensional easy-plane ferromagnet

Alessandro Cuccoli, Valerio Tognetti, and Paola Verrucchi
Dipartimento di Fisica dell'Università di Firenze, Largo E. Fermi 2, I-50125 Firenze, Italy

Ruggero Vaia
Istituto di Elettronica Quantistica del Consiglio Nazionale delle Ricerche, Via Panciatichi 56/30, I-50127 Firenze, Italy

The critical behavior of 2D magnetic easy-plane systems has mainly been studied by the classical XY model. However, the z components of the spins have to be considered in order to describe real systems, and their fluctuations cannot positively be neglected when quantum effects are to be included, quantum spins being intrinsically three-component objects. Therefore, Monte Carlo simulations are performed for the Heisenberg ferromagnet with easy-plane anisotropy (XXZ model) on a two-dimensional square lattice with a twofold aim: first, to obtain accurate quantitative results about the critical behavior of the classical model, showing the relevant role played by the out-of-plane fluctuations; second, to open the way for approaching the quantum thermodynamics by means of the effective Hamiltonian method that reduces the quantum thermodynamics of the XXZ ferromagnet to the investigation of an effective classical model with temperature-dependent renormalized interaction parameters. Specific heat, magnetic susceptibility, and correlation length are calculated in the critical region for lattice sizes up to 128×128. These quantities preserve the Kosterlitz–Thouless behavior of the XY model. For the transition temperature of the classical $XX0$ model we obtain the estimate $k_B T_c/(J\tilde{S}^2)=0.69\pm0.01$.

The two-dimensional XXZ model is described by the Hamiltonian

$$\hat{\mathcal{H}}=-\frac{1}{2}J\sum_{i,d}[(\hat{S}_i^x\hat{S}_{i+d}^x+\hat{S}_i^y\hat{S}_{i+d}^y)+\lambda\hat{S}_i^z\hat{S}_{i+d}^z]. \tag{1}$$

The index $i\equiv(i_1,i_2)$ labels the sites of a two-dimensional Bravais lattice, and $d\equiv(d_1,d_2)$ represents the displacements of the z nearest-neighbors of each site. The easy-plane anisotropy is represented by the dimensionless parameter $\lambda(|\lambda|<1)$. For $\lambda=0$ the above Hamiltonian describes the $XX0$ model (also called "quantum XY model").

In this paper, we are mainly concerned with the classical counterpart of Eq. (1). For our purposes it is sufficient to take the spins in Eq. (1) as classical vectors of length $\tilde{S}$, i.e., $\hat{S}_i\to\tilde{S}\mathbf{s}_i$ with the classical vectors $\mathbf{s}_i$ varying onto the unit sphere $|\mathbf{s}_i|=1$. The natural energy scale is then $\epsilon=J\tilde{S}^2$, so we define a dimensionless reduced temperature $t=k_BT/\epsilon$. The classical XXZ Hamiltonian reads

$$\mathcal{H}=-\frac{\epsilon}{2}\sum_{i,d}[(s_i^x s_{i+d}^x+s_i^y s_{i+d}^y)+\lambda s_i^z s_{i+d}^z]. \tag{2}$$

This system belongs[1] to the universality class of the planar (or XY) model (i.e., $s_i^z\equiv0$), that is characterized by the Berezinskii-Kosterlitz-Thouless[2] (BKT) phase transition at $t_c\simeq0.89$.[3,4] The transition is driven by the unbinding of vortex pairs,[5] and its peculiar characteristics are that for $t<t_c$ the correlation function $\langle\mathbf{s}_i\cdot\mathbf{s}_j\rangle$ displays a power law decay, $\sim|\mathbf{i}-\mathbf{j}|^{-\eta(t)}$, whereas for $t>t_c$ its behavior is exponential. Moreover, the susceptibility and the correlation length have an exponential divergence for $t\to t_c^+$, although long-range order is also absent in the low-temperature phase, i.e., $\langle\mathbf{s}_i\rangle=0$ at any T.

In the case of the XXZ model the out-of-plane components s_i^z of the spins can fluctuate and give a $t_c(\lambda)$ lower than the value for the XY model. In the isotropic limit $\lambda\to1$ the transition disappears logarithmically,[1] $t_c\sim[-\ln(1-\lambda)]^{-1}$.

Kawabata and Bishop[6,7] performed pioneering Monte Carlo (MC) simulations of the classical XXZ model, and obtained estimates of the transition temperature confirming the theoretical asymptotic dependence of $t_c(\lambda)$. Their result in the $XX0$ limit is $t_c(\lambda=0)=0.78\pm0.03$.

As the first step to approach the quantum model by means of the effective Hamiltonian,[8] we have reconsidered the classical $XX0$ model producing accurate thermodynamic data and giving a quantitative description of the relevant quantities in the transition region. We present here MC results for the $XX0$ model, i.e., for $\lambda=0$. The MC sample consists of a square lattice of $L\times L$ classical spins, with periodic boundary conditions, and we considered lattices with $L=32$, 64, 128. The simulations were based on single spin moves, using a combination of the Metropolis and the overrelaxed algorithm.[4] The former consists in rotating a single spin at random, and accepting the resulting configuration after the Metropolis test; the maximum amplitude of the move is such that 45%–55% of the trial moves are accepted. The overrelaxed algorithm[4] is a reflection of the in-plane component of one single spin with respect to the in-plane component of the resultant of its nearest neighbors; this move leaves the energy unchanged and is always accepted. The advantage is in the reduction of the MC critical slowing down, in spite of the fact that this algorithm is local. One MC step is defined as N_O overrelaxed sequential sweeps through the two sublattices whose sites $\mathbf{i}\equiv(i_1,i_2)$ have even and odd i_1+i_2, plus N_M Metropolis random sweeps (i.e., L^2 randomly chosen spins are moved). For each run the system has been equilibrated for 1000 steps with $N_O=0$ and $N_M=2$, i.e., 2000 Metropolis steps have been employed in order to take the system in a typical equilibrium configuration before accumulating data. After a preliminary series of test runs we

 0021-8979/94/76(10)/6362/3/$6.00 © 1994 American Institute of Physics

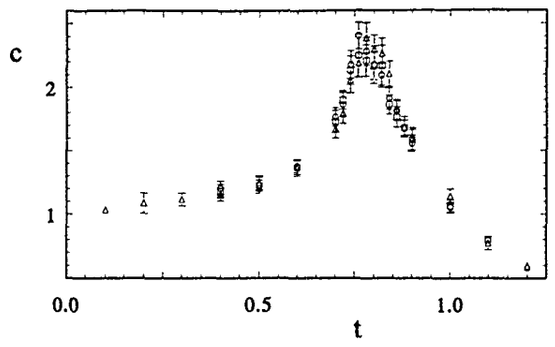

FIG. 1. Specific heat per site c vs reduced temperature $t=k_BT/\epsilon$. MC data for $L=32$ (triangles), 64 (squares), and 128 (circles).

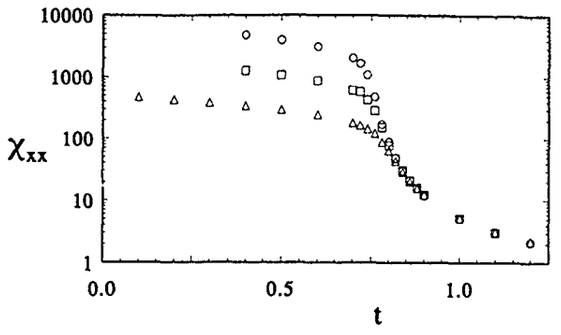

FIG. 2. The in-plane magnetic susceptibility χ_{xx} vs temperature. MC data for $L=32$ (triangles), 64 (squares), and 128 (circles).

observed that the initial configuration chosen (spins aligned along one axis, or random) does not affect the subsequently accumulated averages, within the statistical uncertainty, at all the temperatures we used. The averages were accumulated for 10 000 steps with $N_O=4$ and $N_M=2$. For each quantity with measured values Q_i at the ith MC step, the average is calculated as $Q=\langle Q_i\rangle$ and in order to account for MC correlation effects its variance σ_Q is multiplied by 2τ, where the *decorrelation* MC time τ is defined by the fit $\langle Q_{i+n}Q_i\rangle-\langle Q_i^2\rangle\sim e^{-n/\tau}$. For all quantities τ turns out to be less than 10 for $t>t_c$, and increases by one order of magnitude for $t\ll t_c$.

We have calculated the internal energy per spin $u=L^{-2}\langle\mathscr{H}\rangle$, the specific heat per spin

$$c=L^{-2}(k_BT)^{-2}\langle(\mathscr{H}-\langle\mathscr{H}\rangle)^2\rangle, \tag{3}$$

the magnetization $m^\mu=\langle s_i^\mu\rangle$ ($\mu=x,y,z$), the spin-row correlation function

$$C^{\mu\mu}(r)=\langle S_i^\mu S_{i+r}^\mu\rangle, \tag{4}$$

where $S_{i_2}^\mu\equiv\Sigma_{i_1}s_{i_1i_2}^\mu$, and the in-plane **k**-dependent susceptibility

$$\chi_k^{\mu\mu}=L^{-2}\left\langle\left|\sum_i s_i^\mu e^{ik\cdot i}\right|^2\right\rangle, \tag{5}$$

which for $k=0$ gives the magnetic susceptibility $\chi_{\mu\mu}$. The correlation length ξ_μ has been obtained in two ways: by means of an exponential fit of the spin-row correlation function (accounting for periodicity, the fitting function is $\cosh[(L/2-r)/\xi_\mu]$) and by an Ornstein–Zernicke fit of $\chi_k^{\mu\mu}\sim(k^2+\xi_\mu^{-2})^{-1}$, using the lowest six irreducible values of k. The two determinations coincide within the MC uncertainty.

The results for the specific heat $c(t)$ depend weakly on the lattice size L, as it appears from Fig. 1, and do not give rise to divergencies. The temperature dependence of the specific heat shows a peak around $t=0.78$, similar to the one observed in the planar model[3,4] at a temperature $t\simeq 1.15t_c$; then, if the similarity would be quantitatively correct, the BKT transition temperature of the $XX0$ model should be expected to be around $t_c\simeq 0.7$.

The finite-size saturation at low temperatures is apparent in the data we obtained for the in-plane susceptibility $\chi_{xx}(t)$, and the in-plane correlation length $\xi_x(t)$ (Figs. 2 and 3). Indeed, when ξ_x is comparable with L, L becomes the dominant length scale of the system, and the first consequence is that the measured ξ_x is linear in L, i.e., ξ_x/L is independent of L (see Fig. 3). At the same time, these figures show that the data at temperatures where $\xi_x(t)$ are smaller than $\sim L/3$ are unaffected by finite-size effects, and can be taken as reliable estimates of the infinite lattice values. For the 128 $\times$128 lattice this happens for temperatures larger than $\sim$0.75.

As for the direct estimate of the critical temperature, we have made use of BKT fits with the trial function

$$f(t;a,b,t_c)=ae^{b(t-t_c)^{-\nu}},\quad(\nu\equiv 1/2). \tag{6}$$

Also, the power-law fit, typical of second-order phase transitions,

$$g(t;a,\nu,t_c)=a(t-t_c)^\nu \tag{7}$$

has been considered for comparison. In Table I we report the results for t_c obtained from weighted fits to the data points for $t\geq 0.76$ and those for $t\geq 0.78$, respectively. The second case is reported in Fig. 4. The BKT form (6) appears to be superior, both because it displays a more favorable $\chi^2/_{\mathrm{DOF}}$ with respect to the power law, and because there is agree-

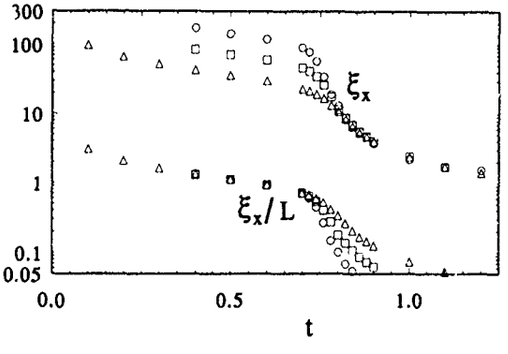

FIG. 3. The in-plane correlation length ξ_x vs temperature. The data points for ξ_x/L show the onset of finite-size scaling when $\xi_x\sim L$ MC data for $L=32$ (triangles), 64 (squares), and 128 (circles)

TABLE I. Results for the critical temperature t_c from weighted fits to the in-plane susceptibility $\chi_{xx}(t)$ and correlation length $\xi_x(t)$. MC data for the 128×128 lattice. Data sets for $t \geq 0.76$ and for $t \geq 0.78$, with power law and BKT fitting functions following Eqs. (7) and (6) in the text. $\chi^2/_{DOF}$ represents the sum of the squared deviations from the fit divided by the number of degrees of freedom (DOF).

Data	Fit	t_c	$\chi^2/_{DOF}$
χ_{xx}	power	0.742±0.003	3.86
$t \geq 0.76$	BKT	0.694±0.002	0 45
χ_{xx}	power	0.752±0.003	2.10
$t \geq 0.78$	BKT	0.697±0.003	0.43
ξ_x	power	0.721±0.004	3.10
$t \geq 0.76$	BKT	0.681±0.005	2.02
ξ_x	power	0.727±0.008	3.24
$t \geq 0.78$	BKT	0.679±0.011	2.29

ment among the values obtained for t_c, whereas those for the power law are not in agreement. At present, we are computing more accurate data for giving a final answer about the BKT character of the transition, and determining the critical exponent ν, that here is kept fixed to the BKT value $\nu=0.5$. The results for t_c obtained through $\chi_{xx}(t)$ are more accurate since $\chi_{xx}(t)$ is a direct product of the MC simulations. Therefore, at present there is good evidence that the classical $XX0$ model undergoes a BKT transition at $t_c=0.69\pm0.01$. This value turns out to be much lower than the one (0.78) estimated by Kawabata and Bishop.[7] In our opinion their

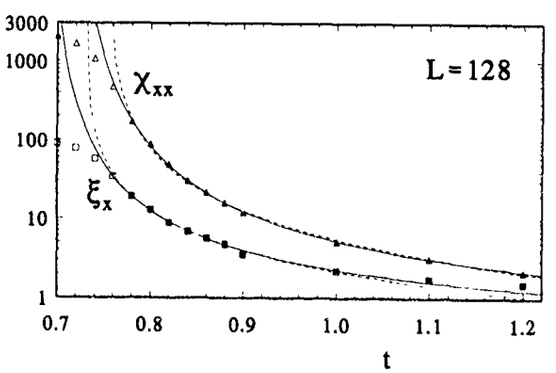

FIG. 4. MC data at $L=128$ for the magnetic susceptibility χ_{xx} and the correlation length ξ_x vs temperature. The solid and dashed curves report the best fits obtained using Eqs. (6) and (7), respectively (see also Table I), with the data at $t \geq 0.78$ (data with open symbols are excluded from the fit).

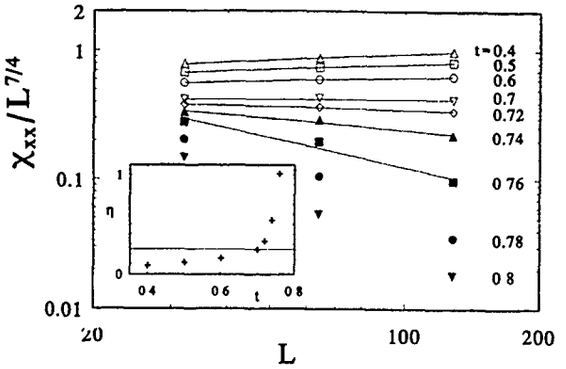

FIG. 5. MC data for $\chi_{xx}/L^{7/4}$ vs L, at different temperatures. Below t_c a linear behavior with positive slope $1/4-\eta(t)$ is displayed as expected for a BKT system. The inset shows the corresponding values of $\eta(t)$.

determination suffered from the poorer statistics ($N_O=0$, $N_M=1$, 6000 steps) and the smaller lattice size ($L=40$). In addition, they have extrapolated t_c by looking for the crossover where the correlation function ceases to be exponential. Since the crossover is strongly dominated by finite-size effects, they got an overestimated t_c.

For $t \leq t_c$ the susceptibility satisfies the finite-size scaling relation $\chi_{xx} \sim L^{2-\eta(t)}$, where the exponent $\eta(t)$ increases with t and should reach the BKT critical value $\eta(t_c)=1/4$. Therefore, in Fig. 5 we report a log–log plot of the dependence of $\chi_{xx}/L^{7/4}$ on L in such a way that the dependence at $t \leq t_c$ is linear with a slope that at the critical temperature decreases to $1/4-\eta(t_c)=0$. Even though at each t there are only three data points, it is possible to roughly estimate $\eta(t)$ by taking the linear fits shown in Fig. 5. As reported in the inset, $\eta(t)$ behaves in the expected way; the critical value, $\eta=0.25$, is indeed reached at about $t \simeq 0.7$, consistent with the above estimate of t_c.

[1] S. B. Khokhlachev, Zh Exp. Teor Fiz **70**, 265 (1976); S. Hikami and T. Tsuneto, Progr. Theor. Phys. **63**, 387 (1980)
[2] V. L. Berezinskii, Zh Eksp. Teor. Fiz. **59**, 907 (1970); J. M. Kosterlitz and D. J. Thouless, J. Phys. C **6**, 1181 (1973)
[3] J. Tobochnik and G. V. Chester, Phys. Rev. B **20**, 3761 (1979).
[4] R. Gupta, J. DeLapp, G. G. Batrouni, G. C. Fox, C. F. Baillie, and J. Apostolakis, Phys. Rev. Lett. **61**, 1996 (1988); R. Gupta and C F Baillie, Phys. Rev. B **45**, 2883 (1992).
[5] J. Villain, J. Phys. (Paris) **36**, 581 (1975).
[6] C. Kawabata and A. R Bishop, Solid State Commun **42**, 595 (1982).
[7] C. Kawabata and A. R. Bishop, Solid State Commun **60**, 169 (1986)
[8] A. Cuccoli, V Tognetti, P. Verrucchi, and R. Vaia, Phys Rev. A **45**, 8418 (1992); Phys. Rev. B **46**, 11601 (1992); J. Appl. Phys **75**, 5814 (1994)

Magnetic anomaly in insulator-conductor composite materials near the percolation threshold

L. V. Panina
Department of Electrical Engineering, Nagoya University, Nagoya 464, Japan

A. S. Antonov, A. K. Sarychev, V. P. Paramonov, E. V. Timasheva, and A. N. Lagarikov
Scientific Association IVTAN, Russian Academy of Science, Moscow 127412, Russia

The effective magnetic permeability of composite materials containing fine iron particles of 1–2 μm size is investigated theoretically and experimentally. This permeability is considered due to both the ferromagnetic properties of iron and the generation of eddy currents by an alternating magnetic field. An analytical result shows that as the percolation threshold is approached, the skin effect in large conducting clusters dominates, suppressing the ferromagnetic behavior for any value of frequency. As a result of this, the effective permeability tends to become zero near the percolation threshold, having a "ν" form anomaly. The experimental data for frequencies of 6–10 GHz where the skin depth is of the order of a particle size, clearly exhibit a sharp decrease near the percolation threshold in the real part of the effective magnetic permeability. We believe this is the first observation of a possible magnetic anomaly in a percolating system.

I. INTRODUCTION

The study of composite materials has been the subject of considerable interest in recent years because of their possible technological applications. The mixture of metal and insulator particles with the concentration of metal particles p close to the percolation threshold p_c at which the system first exhibits a nonzero conductivity has a number of anomalies in electrophysical properties. For example, the dielectric constant and the inductance of percolating materials become infinite on approaching p_c.[1–3] In Refs. 4–6 it has been reported on a divergence in the limit $p \to p_c$ ($p < p_c$) for the imaginary part of the magnetic permeability associated with eddy currents induced in the system by an alternating magnetic field. These investigations have ignored the effects of the inductive interactions of currents, however, these effects are of predominant importance near p_c and allowance for them removes the divergence of the magnetic permeability[7] which tends to become zero at $p \to p_c$.

In the present paper, we investigate both theoretically and experimentally the effective magnetic permeability $\mu_{\text{eff}} = \mu'_{\text{eff}} + i\mu''_{\text{eff}}$ of a percolating system composed of fine iron particles. The eddy current contribution to μ_{eff} becomes dominant near p_c even if the skin effect in a single particle is weak. The reason for this is related to the appearance of large conducting clusters in the vicinity of the percolation threshold. The induced magnetic moments of those clusters substantially suppress the ferromagnetic properties, resulting in a sharp drop in μ_{eff} at $p \to p_c$. We observed this behavior in a mixture with iron inclusions of 1–2 μm size in the frequency region of 6–10 GHz.

II. EFFECTIVE MAGNETIC PERMEABILITY OF COMPOSITE MATERIAL

The proximity of a composite system to the percolation threshold is characterized by the value of the correlation length ξ which defines the typical magnitude of fluctuations. Near the percolation threshold ξ varies with concentration as $|(p_c - p)/p_c|^{-\nu}$, with $\nu = 0.88$,[8] tending towards infinity at $p \to p_c$. The composite material placed in an electromagnetic field can be described by the effective magnetic permeability, μ_{eff}, and the dielectric constant, ϵ_{eff}, if the wavelength of this field λ is smaller than the correlation length ξ. The most general analytical approach for calculating μ_{eff} and ϵ_{eff} is to use the effective medium approximation,[9–11] in which the influence of all the other particles on a selected one reduces to the replacement of the environment by some effective medium with μ_{eff} and ϵ_{eff}. The effective magnetic permeability μ_{eff} of an n-component percolating system can be found from the following equation[11]

$$\sum_j^n p_j \alpha_j(\mu_{\text{eff}}) = 0, \tag{1}$$

where p_j, $\alpha_j(\mu_{\text{eff}})$ are the concentration and the magnetic polarizability of the j-th component. For a magnetic particle of a spherical shape the polarizability is of the form

$$\alpha_m(\mu_{\text{eff}}) = 3(\mu_m - \mu_{\text{eff}})/4\pi(2\mu_{\text{eff}} + \mu_m) \tag{2}$$

$$\mu_m = \mu[2\, f(ka)]/[1 - f(ka)], \quad k = (1+i)/\delta$$

$$f(x) = 1/x^2 - \cot(x)/x, \quad \delta = c(2\pi\sigma\omega\mu)^{-1/2}, \tag{3}$$

where μ_m substitutes for the magnetic permeability μ in the case of a conducting particle if the skin effect is essential ($\delta < a$), a is the particle size and σ is its conductivity.

To extend Eq. (1) for the case of a cluster structure which exists near p_c, the averaged magnetic polarizability of clusters α_{cl} due to eddy currents has to be included in Eq. (1). Each cluster represents a set of doubly connected regions having a scale-invariant drop structure. It is assumed that, relative to the alternating magnetic field, a doubly connected cluster is equivalent to a contour of size identical to the characteristic size l of this cluster,[7] then the averaged polarizability can be written in the form

 0021-8979/94/76(10)/6365/3/$6.00 © 1994 American Institute of Physics

$$\langle \alpha_{cl} \rangle = \int_a^{\xi} \tilde{\alpha}_{cl}(l, \mu_{\text{eff}}) F(l) dl, \tag{4}$$

$$F = B_1 l^{-3} \begin{cases} 1/l, & p < p_c \\ 1/l + B_2 \delta(l-\xi), & p > p_c \end{cases}$$

where $F(l)$ is the size distribution of doubly connected clusters and $\tilde{\alpha}_{cl}$ is the total polarizability of doubly connected clusters. B_1 and B_2 are certain normalization constants independent of ξ. The additional term $\propto \delta(l-\xi) l^{-3}$ appearing in $F(l)$ above the percolation threshold is attributed to a regular conducting structure. By analogy to a contour placed in a medium with the magnetic permeability μ_{eff}, the parameter $\tilde{\alpha}_{cl}(l)$ can be written in the form

$$\tilde{\alpha}_{cl} = -A \mu_{\text{eff}} l^3 / Z, \quad Z = \mu_{\text{eff}} \ln l/a + Z_{cl};$$

$$Z_{cl} = \mu_m/4 + i(\delta_m/a)^2, \quad \delta_m \gg a,$$

where A is a correction factor independent of both μ_{eff} and l.

For a binary mixture with a nonmagnetic dielectric matrix, effective medium Eq. (1) which accounts for all kinds of polarizabilities (2) and (4) reduces to the form

$$\mu_{\text{eff}} = 1 + 3p\mu_{\text{eff}}(\mu_m - 1)/(2\mu_{\text{eff}} + \mu_m) - \mu_{\text{eff}} B_1 \int_a^{\xi} \frac{(l^{-1} + B_2 \theta(p) \delta(l-\zeta)) dl}{\mu_{\text{eff}} \ln (l/a) + Z_{cl}}, \tag{5}$$

where $\theta(p) = 0$ for $p \leqslant p_c$ and $\theta(p) = 1$ for $p > p_c$. Far from p_c ($\xi \to a$) the last term can be neglected and Eq. (5) reduces to the standard form for noncontacting inclusions.[11] In the opposite limit of $p \to p_c$ ($\xi \to \infty$), Eq. (5) ensures the dominance of the induced magnetic moments of large clusters even in the case of a weak skin effect ($\delta \gg a$). It can be clear from the asymptote of μ_{eff} for $\xi/Z_{cl} \to \infty$

$$\mu_{\text{eff}}(\xi/Z_{cl} \to \infty) = [1 - \exp(1/B_1)] Z_{cl} / \ln(\xi/a). \tag{6}$$

It follows from Eq. (6) that at any fixed frequency the effective permeability tends to become zero on approach to the percolation threshold. This conclusion is valid for p approaching p_c from both $p < p_c$ and $p > p_c$. For $\mu' > 1$, near p_c a "ν"-form anomaly appears on the plot of $\mu'_{\text{eff}}(p)$, as can be seen in Fig. 1(a). The corresponding anomaly in the imaginary part μ''_{eff} arises in the immediate vicinity of p_c. For lower frequency this behavior is seen closer to p_c.

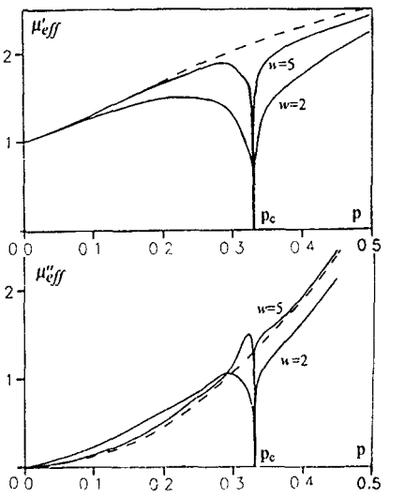

FIG. 1. Concentration dependencies of the effective magnetic permeability $\mu_{\text{eff}} = \mu'_{\text{eff}} + i\mu''_{\text{eff}}$ calculated from Eq. (5) for different values of $w = \delta/a$. The dashed lines correspond to the case of noncontacting inclusions [Eq (5) at $\xi \to a$] The other parameters were chosen as follows: $B_1 = B_2 = 1$, $\mu' = 4$, $\mu'' = 9$.

III. EXPERIMENT

As a ferromagnetic composite material we used a polymer matrix—butadiene-nitrile rubber—with fine iron particles of an elongated form with a maximal size of 1–2 μm and an axis ratio of 3/5. A composite material was formed by a tape casting method. Flexible composite film obtained with thickness of 0.1 mm were packed and rolled to have a required thickness and concentration.

The measurement technique was based on the method of a standing wave in a rectangular or a coaxial waveguide.[12] The experimental setup is shown in Fig. 2. The measurements were made for frequencies from 1 to 10 GHz (below 4 GHz a coaxial waveguide was used). A sample in the form of a slab or a ring disc of thickness $d = 0.5$–1 mm occupied the whole cross section of the waveguide. The magnetic permeability and the dielectric constant can be obtained from a pair of measurements of the complex reflection factor ζ for two different positions of the specimen in the waveguide, defined by the distances h_1 and h_2 from the shorting plate as seen in Fig. 2. The result for μ_{eff} and ϵ_{eff} can then be averaged over various pairs of h_1 and h_2. In the case of a composite material near p_c there is a question if the sample can be considered macroscopically homogeneous so that μ_{eff} and ϵ_{eff} can be applicable. As long as the effective parameters can be used, the values of μ_{eff} and ϵ_{eff} have to be independent of the chosen sample positions. The dependence of μ_{eff} and ϵ_{eff} on h_1 and h_2 would give an indication that samples are not homogeneous and the effective parameters cannot be used. Thus, the method of arbitrary sample positions allows us to test whether the composite material has μ_{eff} and ϵ_{eff} at a given frequency and concentration.

Solving a standard problem of electromagnetic wave propagation in a waveguide,[13] one can relate the parameters $\check{\mu}_{\text{eff}}$ and $\check{\epsilon}_{\text{eff}}$ to the reflection factor ζ, or the input impedance $Z_{\text{in}} = (1+\zeta) Z_0/(1-\zeta)$ through the following expressions

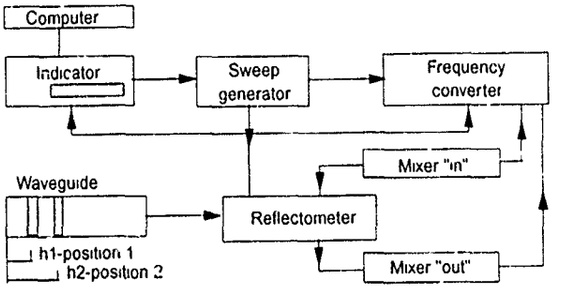

FIG. 2 Experimental scheme

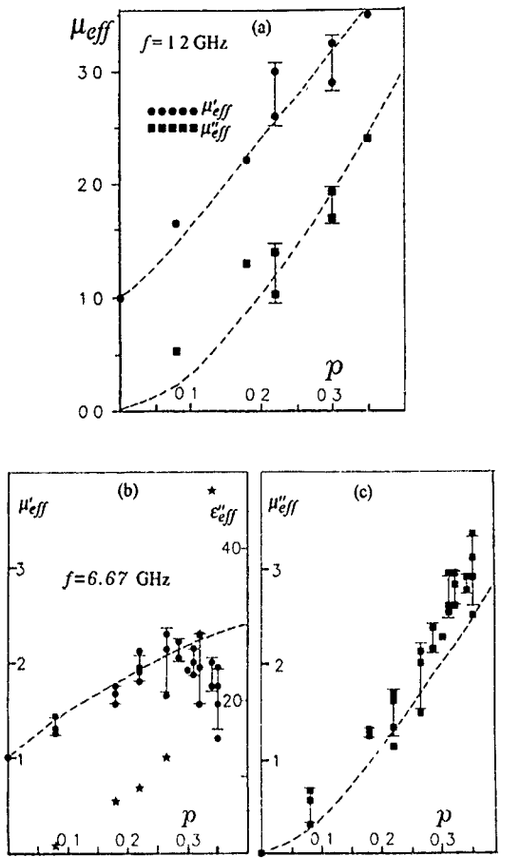

FIG. 3. Experimental concentration dependencies of the effective magnetic permeability for frequencies 1.2 GHz in (a) and 6.67 GHz in (b) and (c). In (b) the concentration dependence of the imaginary part of the dielectric constant is given to determine the percolation threshold. The dashed lines were obtained by using a simplex method to fit the effective medium equation for noncontacting particles, which is valid far from p_c. We used this equation in the form $\mu_{\text{eff}}=1+p\mu_{\text{eff}}(\mu_m-1)/[(1-n)\mu_{\text{eff}}+n\mu_m]$, where n is a correction factor for a particle shape (for $n=1/3$ it coincides with (5) far from p_c). The fitting parameters were $n=0.15$, $\mu'=8$, $\mu''=11$ for 1.2 GHz, $\mu'=4$, $\mu''=9$ for 6.67 GHz.

$$\mu_{\text{eff}}/\sqrt{\epsilon_{\text{eff}}\mu_{\text{eff}}-(\lambda_0/\lambda_c)^2}=Z_{\text{eff}}/Z_0,$$

$$\sqrt{\epsilon_{\text{eff}}\mu_{\text{eff}}-(\lambda_0/\lambda_c)^2}=k\lambda_0/2\pi;$$

$$-i(Z_{\text{eff}}/Z_0)\tan(kd)=(Z-Z_{\text{in}})/(ZZ_{\text{in}}-1);$$

$$Z=-iZ_0\tan[2\pi h\sqrt{1-(\lambda_0/\lambda_c)^2}/\lambda_0], \tag{7}$$

where Z_0 is the characteristic impedance of a waveguide, λ_c is the cutoff wave length. Equations (7) are valid for both rectangular and coaxial waveguides. By applying (7) to two sample positions: $h=h_1$ and $h=h_2$, both complex parameters $\check{\mu}_{\text{eff}}$ and $\check{\epsilon}_{\text{eff}}$ can be found.

IV. EXPERIMENTAL RESULTS AND DISCUSSION

Figure 3 shows the concentration dependencies of the complex magnetic permeability for different frequencies. The value of the percolation threshold $p_c=0.35$ corresponds to a sharp increase in the imaginary part of the effective dielectric constant. At a relatively low frequency (<2 GHz) the parameter $\mu_{\text{eff}}(p)$ increases with concentration up to the percolation limit. On the other hand, as the frequency is increased above 6 GHz, the real part of the magnetic permeability considerably decreases near p_c. The magnetic permeability of iron particles is estimated to be $\mu'=4$, $\mu''=9$ at a frequency of 6.7 GHz, then the effective permeability of a composite with noncontacting inclusions has to monotonically increase. Therefore, we can relate the drop in $\mu'_{\text{eff}}(p)$ to the formation of large percolation clusters.

According to our analysis (see Fig. 1), an anomaly in μ_{eff} at $p\to p_c$ appears at any frequency, however, it shifts closer to p_c at lower frequency. In the limit of ($\delta\gg a$) it exists just in the immediate vicinity of p_c and can hardly be found experimentally. This is probably the case with Fig. 3(a), since at a frequency of 1 GHz the skin depth δ in an iron particle is estimated to be about 2 μm and $\delta/a>3$ (where a is a minimal size of a particle), then the percolation effect is not seen in a sufficiently large concentration region, and the behavior of $\mu_{\text{eff}}(p)$ can be well described by a standard effective medium equation which follows from (5) at $\xi\to a$ (far from p_c), as shown in Fig. 3(a) in dashed lines. However, the sharp drop in $\mu'_{\text{eff}}(p)$ which is seen near p_c for frequencies above 6 GHz ($\delta/a\sim1$) is not consistent with the noncontacting particle equation. The values of $\mu''_{\text{eff}}(p)$ are also higher. Comparing such behavior with that shown in Fig. 1, we can conclude that at certain frequencies ($\delta/a<1$) the effective magnetic permeability of a composite material near p_c can be greatly affected by the magnetic moments induced by eddy currents in large conducting clusters. This effect can strongly suppress the ferromagnetic properties of a composite, resulting in an anomaly in $\mu_{\text{eff}}(p)$ on approaching the percolation threshold.

[1] D. M. Grannan, J. C. Garland, and D. B. Tanner, Phys. Rev. Lett. **46**, 375 (1981).
[2] G. A. Nicklasson and C. G. Granqvist, J. Appl. Phys. **55**, 3382 (1984).
[3] A. P. Vinogradov, A. N. Lagar'kov, and A. K. Sarychev, Pis'ma Zh. Eksp Teor. Fiz. **40**, 296 (1984) [JETP Lett. **40**, 1083 (1984)].
[4] P. G. De Gennes, C. R. Acad. Sci. **292**, 701 (1981).
[5] M. J. Stephen, Phys Lett. A **87**, 67 (1981)
[6] R. Rammal, T C. Lubensky, and G. Toulouse, J. Phys. Lett. **44**, L65 (1983).
[7] A. N. Lagar'kov, L. V. Panina, and A. K. Sarychev, Zh Eksp. Teor. Fiz. **93**, 215 (1987) [JETP **66**, 123 (1987)].
[8] D. Stuffer, *Introduction to Percolation Theory* (Taylor and Francis, London, 1985).
[9] S. Kirkpatrick, Rev. Mod. Phys. **45**, 574 (1973).
[10] A. K. Sarychev and A. P. Vinogradov, Phys. Status Solidi B **117**, K113 (1983).
[11] A. P. Vinogradov, L. V. Panina, and A K Sarychev, Sov. Phys Dokl. **34**, 530 (1989).
[12] G. Franceshetti, Alta Fregneza **36**, 757 (1967).
[13] R. Plonsey and R. E. Collin, *Principles and Applications of Electromagnetic Fields* (McGraw-Hill, Tokyo, 1961), p 370

Time dependence effects in disordered systems

K. O'Grady and M. El-Hilo
Magnetic Materials Research Group, University of Wales, Bangor, Gwynedd LL57 1UT, United Kingdom

R. W. Chantrell
Department of Physics, Keele University, Keele, Staffordshire ST5 5BG, United Kingdom

In this paper the time variation of the thermoremanent magnetization (TRM) is examined. From a simple theory based on the relaxation of magnetic moments over the associated energy barrier we explain the various forms for the time variation of thermoremanent magnetization. For a narrow distribution of energy barriers the variation of TRM with $\ln(t)$ is predicted to be concave downwards when the relaxation takes place over barriers less than the average barrier. For barriers greater than the average barrier the variation of TRM vs $\ln(t)$ is predicted to be concave upwards. In the region where the relaxation takes place over barriers close to the average barrier the variation is initially concave downward and then concave upward.

I. INTRODUCTION

Thermoremanent magnetization is usually measured in the following way: the system is cooled in the presence of a dc magnetic field from a temperature where all moments can fluctuate rapidly between energy minima to a temperature where some of these fluctuations become slower and take place over the measured time scale. Finally the magnetic field is switched off and the remanence obtained is called the TRM.

Time dependence of magnetization is a well-known phenomenon and arises due to the fact that there is a finite time for transitions over the energy barrier. According to this phenomenology the time dependence of the remanent magnetization is given by Néel[1]

$$M_r(t)=M_r(0)e^{-t/\tau}, \tag{1}$$

where τ is the relaxation time and in zero field τ^{-1} is given by

$$\tau^{-1}=f_0 e^{-\Delta E/kT}, \tag{2}$$

where ΔE is the height of the barrier for reversal. For the case where ΔE is distributed and the distribution function of the barriers over which fluctuations are taking place remains approximately constant during the time of observation, following Street *et al.*,[2] the formalism of Eqs. (1) and (2) gives

$$M_r(t)\propto \ln(t). \tag{3}$$

The time variation of TRM is often measured and used as one of the characteristics of the disordered system since this variation is usually observed not to follow a $\ln(t)$ law. Hence the time variation of TRM in spin glass and other disordered systems is often analyzed using empirical expressions like the stretched exponential function, $M_r(t)=M_r(0)\exp(-t/\tau_p)^{1-n}$,[3-5] where τ_p is the characteristic relaxation time and n is the time-stretched exponent. In other studies the time variation of TRM has been described in terms of a power law $M_r(t)\propto t^{-a}$,[6] and on other occasions a product of power law and stretched exponential functions was used.[7]

Recently, further attempts have been made in order to explain the nonlinear $\ln(t)$ behavior of $M_r(t)$ in a reentrant ferromagnet.[8] In Ref. 8 the $M_r(t)$ data were analyzed in terms of a percolation model of relaxation which was proposed earlier by Chamberlin *et al.*[9] In this new model similar expressions to that of Eqs. (1) and (2) were used and in addition a distribution of cluster sizes was introduced

$$M_r(t)=M_r(0)\int_0^\infty x^{10/9}\exp(-x^{2/3})e^{-t/\tau_p}dx, \tag{4}$$

where $\tau_p=f_\pm e^{\pm C/x}$ is the relaxation time, the $(-)$ and $(+)$ signs are associated with slow and fast relaxations, respectively, and $C=C'\Delta/kT$ where C' is an adjustable parameter. The new formalism of Eq. (4) contains the physics of the problem unlike the empirical powers n and a as used in previous models. However, in Eq. (4) the distribution function and energy barrier have been calculated using an assumed model. The analysis of the $M_r(t)$ data according to Eq. (4) suggested that the change of the curvature in $M_r(t)$ vs $\ln(t)$ curves as the temperature increases is due to different relaxation regimes, i.e., slow and fast. Due to the treatment of the $M_r(t)$ problem via Eq. (4), the origin of the curvature in the $M_r(t)$ and its variation with temperature was used to infer different types of dynamic behavior.

In this paper we show that the experimentally observed behavior can be reproduced using a simple model in which the energy barrier and its distribution are independent of temperature.

II. THEORY

For a system with a distribution of energy barriers $f(\Delta E)$ Eq. (1) becomes

$$M_r(T,t)=M_r(H,T,t_w)\int_0^\infty e^{-t/\tau(\Delta E)}f(\Delta E)d\Delta E, \tag{5}$$

where ΔE can have various origins like cluster sizes, anisotropy, and orientation effects. $M_r(H,T,t_w)$ is the initial remanent magnetization, a quantity which at a given cooling field and temperature, depends on the aging time t_w, i.e., the waiting time that elapses after the system has reached the required measuring temperature while the field is still on. Also in Eq. (5) we assume that the field is switched to zero in an extremely short time, otherwise the time dependence during switching should be taken into account.[10,11]

 0021-8979/94/76(10)/6368/3/$6.00 © 1994 American Institute of Physics

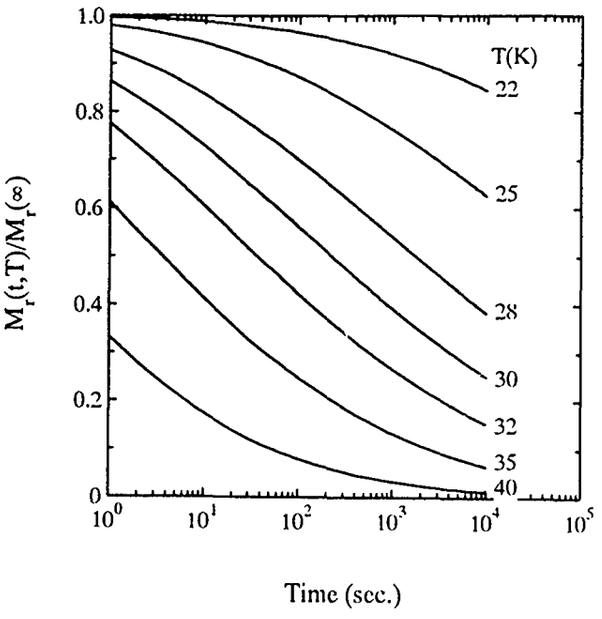

FIG. 1. The time dependence of thermoremanent magnetization at different temperatures for a system with a narrow distribution of energy barriers.

Equation (5) can be rewritten in terms of a distribution of reduced energy barriers $f(y)$ where $y=\Delta E/\Delta E_m$, then

$$M_r(T,t)=M_r(H,T,t_w)\int_0^\infty e^{-t/\tau(y)}f(y)dy, \tag{6}$$

where $\tau^{-1}(y) = f_0 e^{-a_m(T)y}$, $a_m(T)=\Delta E_m/kT$, and ΔE_m is the average barrier in the system. Assuming a distribution function of energy barriers with a certain value of ΔE_m and standard deviation σ, an exact numerical calculation for Eq. (6) can be made and the data of $M_r(T,t)$ at different temperatures can be fitted using only two parameters ΔE_m and σ. For a system with a narrow distribution of energy barriers, the calculated $M_r(T,t)/M_r(\infty)$ curves at different temperatures are shown in Fig. 1 where $M_r(\infty)\equiv M_r(H_{sat})$ which is the TRM obtained in a saturating cooling field. In these calculations a log-normal distribution function of reduced energy barriers were used, $f(y) = \exp\{ - [\ln(y)]^2/2\sigma^2\}/\sqrt{2\pi}\sigma y$ with $\Delta E_m=1.2\times10^{-13}$ erg, and $\sigma=0.18$. The form of $f(y)$ can be easily determined by measuring the temperature variation of the maximum TRM, i.e., cooling in a saturating field, then $f(y)\propto dM_r(H_{sat})/dT$.[12] Thus the form of the distribution is not an adjustable parameter and can be determined by experiment. The data shown in Fig. 1 exhibit similar behavior as those always observed for disordered systems.[4,5,8] Thus, from first-principles Eq. (6) can describe the shape of $M_r(T,t)$ vs $\ln(t)$ curves at all temperatures without the need to imply a phase transition or using different forms of the relaxation rate at different temperatures. In order to describe the origin of the curvature in the $M_r(t)$ vs $\ln(t)$ curves Eq. (6) can be simplified and an analytical expression can be derived following our previous work.[13,14]

The function $e^{-t/\tau(y)}$ varies strongly with y about the critical energy barrier y_c which can be defined when $t=\tau(y_c)$. Hence, for $y<y_c$ the fluctuations between minima happen very quickly and the system exhibits no remanence, while for $y>y_c$ the moments show remanence and time-dependent behavior. Using this criterion Eq. (6) can be simplified to

$$M_r(T,t)=M_r(H,T,t_w)-M_r(H,T,t_w)\int_0^{y_c}f(y)dy, \tag{7}$$

where y_c is given by

$$y_c=\frac{kT}{\Delta E_m}\ln(tf_0). \tag{8}$$

Equation (7) is a good approximation to Eq. (6) and gives the same behavior for $M_r(t)$ vs $\ln(t)$ curves as those shown in Fig. 1. In addition, an analytical solution for Eq. (7) can be obtained by expanding $f(\Delta E)$ about y_c due to the fact that time-dependence effects are mainly due to fluctuations over barriers close to y_c.[14] Then, Eq. (7) can be rewritten as

$$M_r(t,T)=M_r(t_0,T)-M(H,T,t_w)\int_{y_c(t_0)}^{y_c(t_0)+\delta y_c}f(y)dy, \tag{9}$$

where $\delta y_c=y_c(t)-y_c(t_0)=\ln(t/t_0)/a_m(T)$ and t_0 is the initial time of measurement. $M_r(t_0,T)$ is the initial TRM at $t=t_0$ and it is given by: $M_r(t_0,T) = M_r(H,T,t_w) - M_r(H,T,t_w)\int_0^{y_c(t_0)}f(y)dy$. Now by expanding $f(y)$ about $y_c(t_0)$ the change in the remanent magnetization with time is given by

$$\Delta\bar{M}_r(t,T)=-\sum_{n=0} f^n[y_c(t_0)][\Delta\ln(t)/a_m(T)]^{n+1}, \tag{10}$$

where $\Delta\bar{M}_r=\bar{M}_r(t)-\bar{M}_r(t_0)$ is the change in remanence normalized to $M_r(H,T,t_w)$, $f^n=d^nf(y)/dy^n$, and $\Delta\ln(t)=\Delta\ln(t/t_0)$. For constant $f(y)$, Eq. (10) gives a logarithmic time dependence of $\Delta M_r(t)$ which is consistent with Eq. (3). However, in general, $f(y)$ is not a constant function and higher orders of $\Delta\ln(t)$ should be considered when $f(y)$ varies with y around the critical barrier. The higher order terms in the series expansion are found to become increasingly important as the distribution becomes narrower.[14] Thus, in general, the $\Delta M_r(t)$ vs $\Delta\ln(t)$ curve can be represented by a series expansion in $\Delta\ln(t)$ and the number of terms required to describe the data depends on the behavior of the function $f(y)$ about y_c. In order to show explicitly the origin of the curvature changes in $\Delta M_r(t)$ vs $\Delta\ln(t)$ curves, at any instant t, the slope of this variation is given by

$$\frac{d\bar{M}_r(t,T)}{d\ln(t)}=-\frac{kT}{\Delta E_m}f(y_c). \tag{11}$$

Thus, according to Eq. (11) the slope of $\Delta\bar{M}_r(t)$ vs $\Delta\ln(t)$ at any instant is directly proportional to $f(y_c)$. Thus, at very low temperatures where fluctuations are due to the small energy barriers $\Delta E<\Delta E_m$, i.e., y_c is at the left-hand side of the distribution, thus in this region $f(y)$ is increasing with y and the slope is increasing which causes the variation of $\Delta\bar{M}_r(t)$ vs $\Delta\ln(t)$ to be concave downward. Since $y_c\propto T$, at higher temperatures the fluctuations of moments will taking place over barriers $\Delta E>\Delta E_m$, where $f(y)$ is decreasing with y

and accordingly the slope $\Delta \tilde{M}_r(t)/\Delta \ln(t)$ at any instant will be decreasing with y_c and cause the variation to curve upward. Thus, in the case where fluctuations are taking place over barriers around ΔE_{m_2}, i.e., about the peak in the distribution, the variation of $\Delta \tilde{M}_r(t)$ vs $\Delta \ln(t)$ will initially curve downwards and finally curve upwards and in the intermediate range it will exhibit some degree of linearity due to those fluctuations associated with the most probable energy barrier within the system, i.e., at the peak where $f(y_c)$ remains constant.

Thus from this simple theory the shape of the $\Delta M_r(t)$ vs $\Delta \ln(t)$ curve and the degree of nonlinearity is directly related to the distribution of energy barriers within the system and not necessarily to the type of the relaxation regime. The relaxation mechanism at all temperatures is governed by the same dynamic equation [Eq. (2)]; however the contribution of these fluctuations to the remanence is determined by the distribution of energy barriers.

A. The effects of aging on TRM

In the work of Li *et al.*[8] effects of aging were measured and showed that the initial value of TRM $[M_r(t_w)]$ depends on the waiting time t_w at the required measuring temperature while the cooling field (H) is still applied. The effects of t_w can also be derived from first principles using the rate equation which can be solved to give[11]

$$M_r(H,T,t_w) = [M_r(H,T,0) - M_e] \int_0^\infty e^{-t/\tau(y,H)} f(y)\,dy + M_e, \qquad (12)$$

where $M_e = [\tau_-^{-1}(H) - \tau_+^{-1}(H)]/[\tau_-^{-1}(H) + \tau_+^{-1}(H)]$ is the equilibrium magnetization and τ_-^{-1} and τ_+^{-1} are the relaxation rates into the field direction and out of the field direction, respectively. Thus the value of $M_r(t_w)$ obtained before switching the field depends on the arrangement of moment axes with respect to the cooling field. Hence the aging observations in Ref. 8 suggest that t_w must depends on the detailed distribution of spins and is currently the subject of further work.

B. Previous treatment of the problem

The time dependence of remanent magnetization in spin glasses has been discussed by Aharoni.[15] Similar formalism to that of Eq. (5) was considered, but a distribution of relaxation times rather than a distribution of energy barriers was used. In addition a gamma distribution function of $f(\tau)$ was assumed in order to obtain an analytical solution for Eq. (5). In this formalism, the data for $M_r(t)$ at a given temperature can be fitted using two parameters, the mean and width of the gamma distribution of relaxation. Hence, according to the formalism of Aharoni the analysis of the $M_r(t,T)$ curves gives an average relaxation time and width for every temperature whereas our formalism in terms of the energy barrier distribution gives an average energy barrier (ΔE_m) and width (σ) for the whole system. In addition, the form of $f(\Delta E)$ can be determined directly from experiment and is not assumed. Furthermore, by linking the problem to the energy barrier distribution, the origin and shape of the curvature in the $\Delta M_r(t)$ vs $\Delta \ln(t)$ can be explained.

III. CONCLUSIONS

In this paper, a simple first principle theory for the time dependence of TRM in disordered magnetic systems is described. The theory shows that the origin and shape of the curvature in the $M_r(t)$ vs $\ln(t)$ data at different temperatures are mainly due to the form of the distribution of energy barriers. For a system with a narrow distribution of energy barriers a similar variation of $M_r(t,T)$ to those observed in a disordered system can be predicted without the need to assume different relaxation regimes at different temperatures.

[1] L Néel, J. Phys Radiat. **12**, 339 (1951).
[2] R. Street and J. C. Woolley, Proc. Phys. Soc. A **62**, 562 (1949)
[3] R. V. Chamberlin, G. Mozurkewich, and R. Orbach, Phys. Rev Lett. **52**, 867 (1984).
[4] I. Yeung, W. Ruan, and R M. Roshko, J. Magn. Magn. Mater. **74**, 59 (1988).
[5] R. M. Roshko and W. Ruan, J. Magn. Magn. Mater. **104-107**, 1613 (1992).
[6] J. Ferré, J Rajchenbach, and H. Maletta, J. Appl Phys. **52**, 1697 (1981).
[7] S. H. Kim and P. D Battle, J. Magn. Magn Mater. **123**, 273 (1993).
[8] D. Li, R. M. Roshko, and G. Yang, J. Appl. Phys. **75**, 5844 (1994).
[9] R. V. Chamberlain, and D. H. Haines, Phys. Rev. Lett. **65**, 2197 (1990).
[10] A. Aharoni and E. P. Wohlfarth, J. Appl. Phys. **55**, 1664 (1984).
[11] M. El-Hilo, K O'Grady, H. Pfeifferand, and R. W. Chantrell, J. Magn. Magn. Mater. **104-107**, 1580 (1992).
[12] M. El-Hilo and K. O'Grady, IEEE Trans. Magn **26**, 1807 (1990)
[13] M. El-Hilo, K. O'Grady, and R. W. Chantrell, J. Magn. Magn. Mater. **109**, L164 (1992).
[14] M. El-Hilo, K. O'Grady, and R. W. Chantrell, J. Magn. Magn. Mater. **123**, 30 (1993).
[15] A. Aharoni, J. Appl. Phys. **57**, 4702 (1985).

Magnetization of amorphous $Fe_{0.82}B_{0.18}$ and $Fe_{0.90}Zr_{0.10}$ compounds with additions of Tb

S. J. Clegg, J. H. Purdy, R. D. Greenough, and F. Jerems
Department of Applied Physics, The University of Hull, Hull HU6 7RX, United Kingdom

The addition of Tb to melt spun iron-boron or iron-zirconium compounds raises the magnetostriction to practically useful levels (≥450 ppm) at room temperature. The present work examines the corresponding compositional and temperature dependencies of the magnetization in $Tb_x(Fe_{0.82}B_{0.18})_{1-x}$ for $0 \leq x \leq 0.5$ and $Tb_y(Fe_{0.90}Zr_{0.10})_{1-y}$ for $0 \leq y \leq 0.1$. Increasing the Tb content in Fe-B compounds decreases the room-temperature magnetization towards a compensation point and lowers the Curie temperature T_c. In Fe-Zr compounds, Tb increases the room-temperature magnetization and raises T_c. Magnetic phase diagrams are presented for each group of compounds and exchange frustration effects identified by comparing the observed temperature dependencies of the reduced magnetization with predictions from the Handrich mean field model. Only 3 at. % Tb in Fe-Zr is sufficient to annul exchange fluctuations, but in Fe-B compounds exchange frustration persists throughout the compositional range.

I. INTRODUCTION

Magnetostriction in amorphous compounds is of theoretical interest to understand how macroscopic anisotropic strains are developed from randomly oriented moments and of practical importance as an alternative to crystalline highly magnetostrictive pseudobinary rare-earth (RE)-iron compounds for applications.[1,2] Amorphous compounds with RE =Sm, Dy, or Tb prepared by melt spinning[3] or sputtering[4] develop useful levels of magnetostriction (~500 ppm). Iron-boron and iron-zirconium amorphous compounds can be melt spun with relative ease and hence the present choice of two groups of compounds, $RE_x(Fe_{0.82}B_{0.18})_{1-x}$ with $0 \leq x \leq 0.50$ and $RE_y(Fe_{0.90}Zr_{0.10})_{1-y}$ with $0 \leq y \leq 0.10$; terbium is selected for the RE ion because of its outstanding magnetostrictive properties. However, as terbium is added to each of the chosen groups of compounds, changes in their room-temperature magnetostrictions are markedly different.[5] Hence, the present study of magnetic properties was undertaken in order to obtain a better understanding of their behavior to assist in theoretical calculations of magnetoelastic coupling and, in the longer term, enhance the room-temperature magnetomechanical properties for practical applications.

II. EXPERIMENTAL TECHNIQUES

Polycrystalline compounds in the ranges $Tb_x(Fe_{0.82}B_{0.18})_{1-x}$ for $0 \leq x \leq 0.5$ and $Tb_y(Fe_{0.90}Zr_{0.10})_{1-y}$ for $0 \leq y \leq 0.1$ were produced using start material of at least $3N$ purity. Melt spinning was conducted in an argon atmosphere, producing samples 30–50-μm thick, 1–2-mm wide and of varying lengths. X-ray diffraction (XRD) has been employed to ensure that all samples were amorphous. Using CuK_α radiation, angles corresponding to the position of the intensity maxima have been used to estimate the average interatomic spacings. A vibrating sample magnetometer (VSM) was employed to measure magnetization from ~4 K to the Curie temperatures with dc fields up to 1000 kA m^{-1}. Curie temperatures were obtained from differential scanning calorimetry (DSC) for Tb-Fe-B alloys and from magnetization measurements for Tb-Fe-Zr alloys.

The random anisotropy (RA)–ferromagnetic (F) phase boundaries were detected with ac susceptibility measurements for the iron-boron compounds[6] and in the iron-zirconium compounds by comparing field annealed and zero field annealed temperature dependent magnetization data.[7]

III. RESULTS

RE-Fe-B: Room temperature data for the variation of saturation magnetization with Tb content (Fig. 1), are in agreement with previous measurements[5] which showed that the materials are magnetically soft. A compensation point at $x=0.22$ is due to antiferromagnetic (AF) coupling between the iron and terbium subnetworks. The magnetization at 1000 kA m^{-1} has been measured as a function of temperature from 4.2 K to T_c, for each Tb composition. Competing effects of local anisotropy and exchange interactions are evident, viz: at high temperatures ($T < T_c$) the system appears to

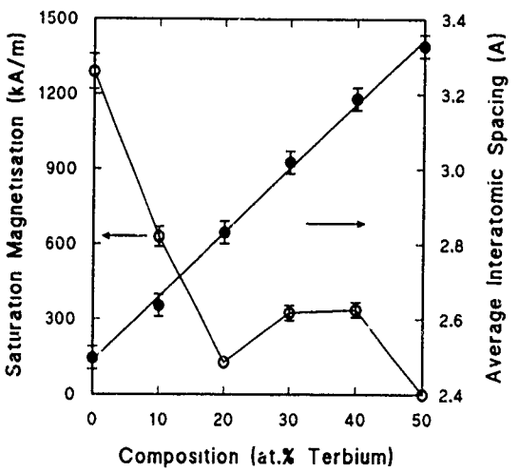

FIG. 1 Saturation magnetization (○) and average interatomic spacing (●) as a function of Tb content in $Tb_x(Fe_{0.82}B_{0.18})_{1-x}$.

 0021-8979/94/76(10)/6371/3/$6.00 © 1994 American Institute of Physics

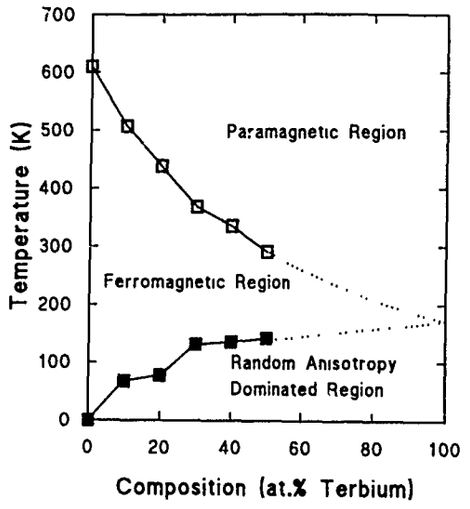

FIG. 2. Magnetic phase diagram for Tb-Fe-B showing T_c(□) and T_f (■).

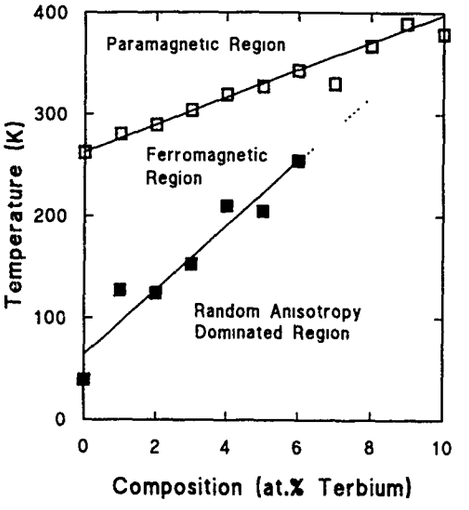

FIG. 4. Magnetic phase diagram for Tb-Fe-Zr showing T_c (□) and T_f (■).

be magnetically ordered, but with sufficiently high Tb content at low temperatures, random local anisotropy begins to dominate, which causes a "freezing" of the magnetic moments. The fields employed are then insufficient to align all the moments leading to an apparent decrease in magnetization at low temperatures below the "spin freezing" temperature T_f. These features of magnetic behavior are summarized in a magnetic phase diagram (Fig. 2).

RE-Fe-Zr: The variation of saturation magnetization with terbium content at room temperature (Fig. 3) demonstrates a different behavior to the RE-Fe-B system. The magnetization is seen to increase with the addition of Tb up to 9 at. %, before dropping sharply as further Tb is added. From magnetization measurements as a function of temperature,[7] a magnetic phase diagram has been constructed (Fig. 4). The addition of terbium again has the effect of "freezing" the magnetic moments at low temperatures although values for T_f are much higher than for the Tb-Fe-B system. A little extrapolation of the RA-F phase boundary indicates that at room temperature (~295 K) each of the three magnetic phases can be obtained in the range 2–8 at. % Tb.

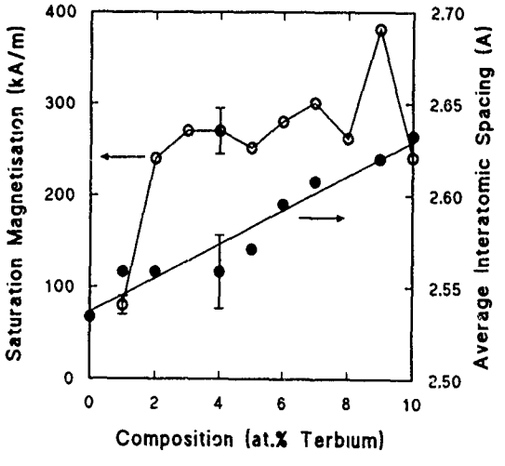

FIG. 3. Saturation magnetization (○) and average interatomic spacing (●) as a function of Tb content in $Tb_x(Fe_{0.90}Zr_{0.10})_{1-x}$.

IV. DISCUSSION AND CONCLUSIONS

In both the magnetic phase diagrams (Figs. 2 and 4) a region has been labeled "ferromagnetic" based on the observed magnetization versus applied field curves. However, previous work on similar metallic glasses without rare earths, by Buchholtz *et al.*,[5] (Metglas 2605 S2), Cowley *et al.*[9] ($Fe_{83}B_{17}$) and Thomas *et al.*[10] (VAC 0040), indicates that in the absence of any well-defined anisotropy, exchange fluctuations disturb the collinear structure. Present data for the reduced magnetization as a function of temperature have therefore been compared with Handrich's mean field model[11] in which the reduced magnetization is expressed as

$$\sigma = \tfrac{1}{2}[B_s(x)(1+\Delta)+B_s(x)(1-\Delta)] \qquad (1)$$

where $B_s(x)=\tanh(x)$, $x=(3S/S+1)(\sigma/\tau)$, S is the spin quantum number, τ is the ratio T/T_c, and Δ is the level of exchange fluctuation. Even with the limitations of a mean field model, it is presently observed that in *iron-boron* compounds (Fig. 5), for either 10 or 50 at. % Tb, $\Delta=0.5$, indicating exchange fluctuations persist regardless of the amount of Tb, consistent with the previous observation of noncollinear moments in metallic Fe-B glasses. For $Fe_{0.90}Zr_{0.10}$ (Fig. 6) the best fit to the experimental reduced magnetization data is achieved with $\Delta=0.6$, but with the addition of Tb, Δ quickly decreases to zero, implying that frustration effects are lifted with only 3 at. % Tb.

The lowering of the room-temperature magnetization and T_c with the addition of Tb to Fe-B can be explained by the antiferromagnetic coupling of terbium-iron moments which lowers the overall exchange. Reduction in the exchange frustration in Fe-Zr accounts for the increase in both the room-temperature magnetization and T_c.

With the addition of only 3 at. % Tb to Fe-Zr, the total lifting of frustration effects cannot be attributed directly to

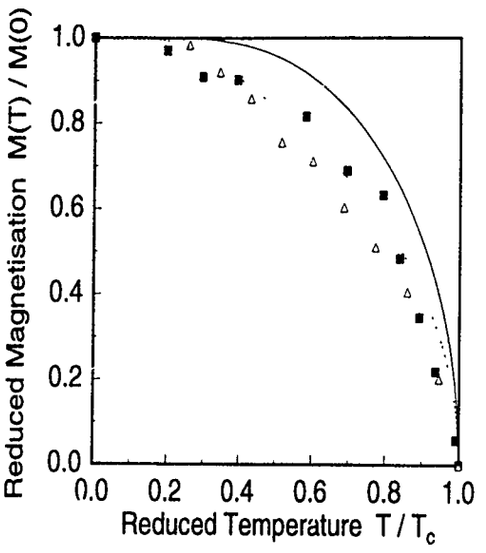

FIG. 5. Reduced magnetization as a function of reduced temperature for $Tb_x(Fe_{0.82}B_{0.18})_{1-x}$ where $x=10\%$ (■) and $x=50\%$ (△) with theoretical predictions from the Handrich model for $\Delta=0.5$ (·····) and $\Delta=0$ (——).

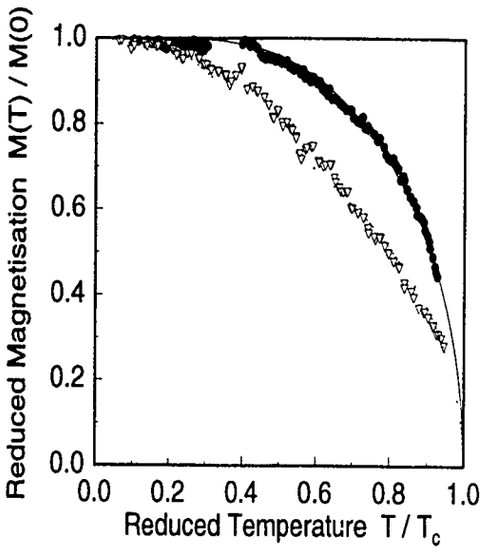

FIG. 6. Reduced magnetization as a function of reduced temperature for $Tb_y(Fe_{0.90}Zr_{0.10})_{1-y}$ where $y=0$ at. % (▽) with Handrich fit for $\Delta=0.6$ (.....) and $y=3$ at. % (●) with Handrich fit for $\Delta=0$ (——)

Fe-Tb bond effects and in the light of previous work by Ryan,[12] changes in mean interatomic separation is likely to be a significant factor. According to Ryan, exchange in the Fe-Zr system is very sensitive to nearest-neighbor distances and changes the sign from positive to negative below 2.4 Å. From the present data (Fig. 3) the mean interatomic spacing for $Fe_{0.90}Zr_{0.10}$ is ~2.5 Å, so that a small but significant number of Fe-Fe pairs will be antiferromagnetically coupled. With the addition of 3 at. % Tb, the mean interatomic spacing increases slightly but is sufficient for the majority of Fe-Fe pairs to be coupled ferromagnetically.

Finally, there are the, as yet, unexplained increases in the room-temperature magnetostriction as Tb is added to either the Fe-B or Fe-Zr compounds. Present observations show that these increases are not simply due to increases in T_c. What is common to both groups of compounds is the change in average interatomic spacing which increases by ~7% for the addition of ~10 at. % Tb. While this alone cannot explain the observed magnetostrictive effects, it is significant when the local field gradients at the Tb ion sites are considered. Work is in progress to quantify their effects on the magnetostriction.

ACKNOWLEDGMENT

The authors thank SERC, DRA (Holton Heath) and the staff of the Department of Applied Physics for their assistance.

[1] A. E. Clark, in *Ferromagnetic Materials*, edited by E. P. Wohlfarth (North-Holland, Amsterdam, 1980), Chap. 7.

[2] R. D. Greenough and M. P. Schulze, in *Intermetallic Compounds*, edited by J. H. Westbrook and R. L. Fleischer (Wiley, New York, 1994), Vol. 2, Chap. 17, pp. 389–406.

[3] S. J. Clegg and R. D. Greenough (unpublished).

[4] H. Fujimori, J. Y. Kim, S. Suzuki, H. Morita, and N. Kataoka, J. Magn. Magn. Mater. **124**, 115 (1993).

[5] R. D. Greenough, T. J. Gregory, S. J. Clegg and J. H. Purdy, J. Appl. Phys. **70**, 6534 (1991).

[6] S. J. Clegg, Ph. D. thesis, University of Hull, UK, 1992.

[7] J. H. Purdy, Ph. D. thesis, University of Hull, UK, 1992.

[8] F. Bucholtz, K. P. Koo, A. Dandridge, and G. H. Sigel, J. Magn. Magn. Mater. **54**, 1607 (1985).

[9] R. A. Cowley, N. Cowlam, and L. D. Cussens, J. de Phys Colloque **C8**, 1285 (1988).

[10] A. P. Thomas, M. R. J. Gibbs, and P. T. Squire, IEEE Trans. Mag. **MAG-26**, 1406 (1990).

[11] K. Handrich, Phys. Status Solidi **32**, K55 (1969).

[12] D. H. Ryan and J. M. Coey, Phys Rev. B **35**, 8630 (1987).

Magnetic ordering in the three-dimensional site frustrated Heisenberg model

Morten Nielsen, D. H. Ryan, Hong Guo, and Martin Zuckermann
Centre for the Physics of Materials, Department of Physics, McGill University, 3600 University Street, Montreal, Quebec H3A 2T8, Canada

We study transverse spin freezing in the site frustrated three-dimensional classical Heisenberg model using Monte Carlo simulations. For small values of the site randomness, there is no transverse spin freezing in the ferromagnetic state. As the fraction of the antiferromagnetic sites is increased beyond 16%, we observed that the transverse component of the spins freeze in random directions at temperatures below some value T_{xy}. Similar behavior is observed in the antiferromagnetic state. We compare results of this model to those of the bond frustrated model. Finally an approximate phase diagram of this model is presented.

I. INTRODUCTION

Recent experimental studies[1-3] of partially frustrated magnetic systems have demonstrated the existence of a transverse spin freezing phenomenon below the ferromagnetic transition. Such a freezing is characterized by the sudden increase of the local spin length, as measured by Mössbauer spectroscopy, when the temperature is lowered below some value T_{xy}. This behavior is found for a range of frustrations in systems such as a-Fe_xZr_{1-x} and $Au_{1-x}Fe_x$.[1] In a recent paper,[4] we examined theoretically the spin freezing phenomenon and the critical behavior of a bond frustrated three-dimensional Heisenberg model. Our Monte Carlo calculations gave results in qualitative agreement with the experimental findings. In particular, we found that at a low temperature T_{xy} below the Curie temperature T_c, the transverse spin component freezes out, leading to an increase in the total spin length.[4]

The bond-frustrated model seems to describe the transverse spin freezing in systems such as a-Fe_xZr_{1-x}, where there is only one magnetic compound, and the magnetic interaction are determined from nearest-neighbor distances. However, there are other magnetic systems for which this model is not appropriate. An example is $Eu_{1-x}Gd_xS$ in which the spin glass phase is induced by site frustration.[5] Theoretically, site randomness can be introduced by replacing a fraction f of ferromagnetic sites by antiferromagnetic sites. If f is small then no frustration is expected. However, at larger values of f when the antiferromagnetic sites start to form a percolating network, the randomness will lead to frustration and change the magnetic behavior of the system. Thus, we expect that site frustration will give rise to a somewhat different phase diagram compared with the bond frustration model, especially for transverse spin freezing which crucially depends on the degree of frustration. It is the purpose of this work to investigate the behavior of the site frustrated Heisenberg model using Monte Carlo simulations.

II. MODEL

We consider a system of classical Heisenberg spins $\mathbf{S}_i$ on a simple cubic lattice in zero magnetic field. The Hamiltonian is given by $H=-\Sigma_{n\,n} J_{ij}\mathbf{S}_i\mathbf{S}_j$. Here, J_{ij} is the exchange interaction between nearest-neighbor spins on lattice sites i and j, respectively. We introduce site randomness into the system by replacing a fraction f of ferromagnetic sites by antiferromagnetic sites. The values for the Curie temperature of the ferromagnetic Heisenberg model ($f=0$) and the Néel temperature of the antiferromagnetic Heisenberg model ($f=1$) are identical, $T_H=1.44J$.

The model with site frustration was investigated using the standard Metropolis Monte Carlo method. A three-dimensional system of 8^3 spins on a simple cubic lattice was initiated with high-temperature configurations.[6] The system was then annealed via 25 temperature intervals to a low temperature of $0.0005T_H$. At each temperature, statistical averages of relevant physical quantities were taken. A calculation of the relaxation time for temperatures away from T_H revealed that about 2000 Monte Carlo steps per spin (MCSs) were needed to reach equilibrium at such temperatures, and a larger number of MCSs were needed close to T_H where critical slowing down becomes important. After the system reached equilibrium, statistical averages of physical quantities were collected over 4000 MCSs. We found that fluctuations in the energy were indeed Gaussian distributed for 4000 MCSs thus our choice of the number of steps was reasonable. Finally, results for ten different realizations of the site randomness for a given f were averaged. The values of f used in the simulations ranged from 0 to 1 and we were thus able to calculate the entire magnetic phase diagram for the system.

We compute a time average of the spin components and of the square of the transverse spin components at each site, i.e.,

$$\mathbf{m}_i=\frac{1}{\tau}\sum_{\tau'=1}^{\tau}\mathbf{S}_i(\tau')$$

and

$$m_{\perp i}^2=\frac{1}{\tau}\sum_{\tau'=1}^{\tau}[S_{ix}(\tau')^2+S_{iy}(\tau')^2]$$

where, as mentioned above, $\tau=4000$ MC steps. From these local quantities we calculate the following spatially averaged quantities: (1) the root-mean-square spin length $S_{\rm rms}=1/N\Sigma_{i=1}^{N}(\mathbf{m}_i\cdot\mathbf{m}_i)^{1/2}$, (2) the bulk magnetization $M_f=1/N|\Sigma_{i=1}^{N}\mathbf{m}_i|$, (3) the staggered magnetization

 0021-8979/94/76(10)/6374/3/$6.00 © 1994 American Institute of Physics

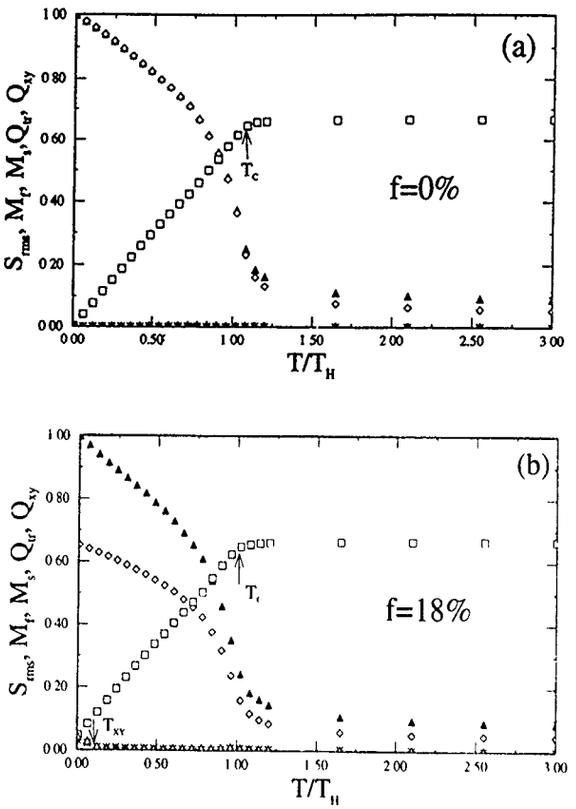

FIG. 1. Temperature dependence of the different spin averages. (▲) $S_{\rm rms}$, (◇) M_f, (*) M_s, (□) $Q_\perp$, and (△) Q_{xy} T_c is the temperature where $Q_\perp$ starts to decrease from 2/3. (a) $f=0$; (b) $f=18\%$. T_{xy} in (b) is the temperature where Q_{xy} becomes nonzero.

$M_s=1/N|\Sigma_{i=1}^{N}\mathcal{S}\mathbf{m}_i|$, where $\mathcal{S}$ is a matrix with the symmetry of the antiferromagnetic structure of the lattice, (4) the mean square of the spin projection on the x-y plane $Q_\perp=1/N\Sigma_{i=1}^{N}m_{\perp i}^2$; (5) the x-y projection of the time-averaged spin components $Q_{xy}=1/N\Sigma_{i=1}^{N}(m_{ix}^2+m_{iy}^2)$. The last two quantities take into account ordering in the x-y plane and may therefore exhibit the onset of anisotropy and spin freezing in the system.

III. RESULTS

Figures 1(a) and 1(b) show data for quantities M_f, $S_{\rm rms}$, M_s, $Q_\perp$, and Q_{xy} as functions of temperature, for several values of site frustration f. In Fig. 1(a) the pure ferromagnetic case ($f=0$) is shown. This shows, as expected, that the order parameter M_f and the local spin length $S_{\rm rms}$ are identical below the critical temperature T_c (which is equal to T_H in this case), as the system orders to a collinear configuration. Above T_c, $Q_\perp$ takes the value 2/3 since the spins are randomly rotating in three dimensions thus spending 2/3 of the time in the transverse plane where $Q_\perp$ is computed. Below T_c, $Q_\perp$ decreases to zero at $T=0$ as expected for $f=0$. Naturally the quantity Q_{xy} is zero for all T when $f=0$ since there is no spin freezing.

Up to $f\approx0.16$, the behavior is similar to the $f=0$ case. As we further increase the site randomness f, interesting features start to show. Figure 1(b) are the data for $f=0.18$. Here, we can see that Q_{xy} becomes nonzero at a low temperature T_{xy}. Since Q_{xy} measures the time-averaged length of the spin components in the transverse plane, a nonzero value of Q_{xy} signals the freezing out of that component. In this situation $Q_\perp$, the mean square of the spin projection on the x-y plane, remains nonzero as T approaches 0. For a simple cubic lattice there are six neighboring spins per site, thus we expect that, on average, all the spins will be affected when the site randomness reaches 16%–17%. Indeed, spin freezing is observed around this value of frustration. This is very different from the behavior of the bond-frustrated system. There, any finite f gives rise to the transverse freezing.[4] In the bond frustrated system, frustration is induced by just replacing one ferromagnetic bond by an antiferromagnetic bond. In the site frustrated model, however, the replacement of a single ferromagnetic site by an antiferromagnetic site only decreases the bulk magnetization and has no other effect. Frustration for the site frustrated model can only occur when there are at least two neighboring antiferromagnetic sites. This occurs on average at a value given by $f=q^{-1}$ where q is the coordination number of the lattice. For our case, $q=6$ at $f=0.167$. Finally we notice the different values of M_f and $S_{\rm rms}$ below T_c: part of the difference is now contributed by the transverse spin freezing as $S_{\rm rms}$ is the vector sum of the z as well as the transverse components of the spins. For higher values of f, all features are similar to those of Fig. 1(b). Due to more frustration in the system with higher f, it is easier to freeze out the transverse spin components, thus T_{xy} has increased to higher values.

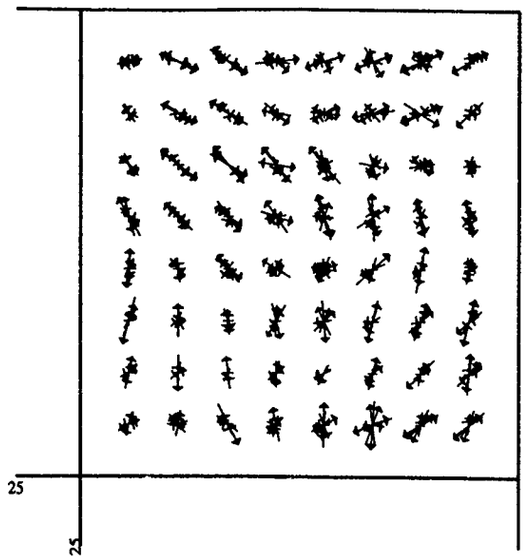

FIG. 2. Time averaged spin configuration for $f=36\%$ and $T=0.12T_H$ of a 8^3 system projected onto the x-y plane. Each point therefore is a stack containing eight spins.

An interesting result is the behavior of the staggered magnetization as f is increased from zero. We found that M_{st} starts to have nonzero values at the same temperature as T_{xy}. This seems to indicate that in the x-y plane the spin components freezes antiferromagnetically. To see this, we plot a typical configuration of the spin components in the x-y plane in Fig. 2 for $f=0.36$ at $T=0.12T_H$. Indeed, we see that the

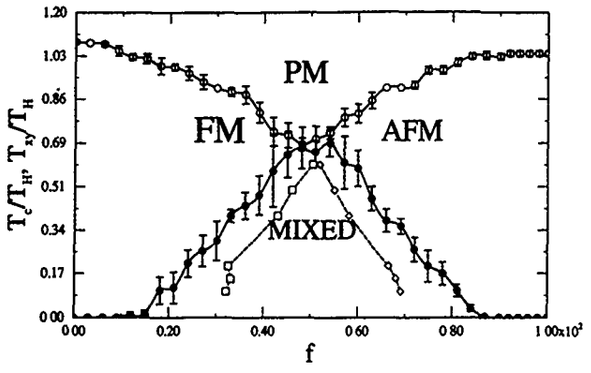

FIG. 3. An approximate phase diagram of the model. Open circles are temperatures T_c. Solid circles are temperatures T_{xy}. The dashed line with open boxes and diamonds roughly separates the mixed phase from the FM and AFM regions. The line is determined from the peak position in the susceptibility as we sweep f at fixed temperature. The error bars are determined as standard deviation from ten realizations of site randomness for each value of f.

transverse components try to order antiferromagnetically.

In Fig. 3 we present an estimate of the phase diagram for this model. The phase transition lines from the paramagnetic state (PM) to the ferromagnetic (FM) and antiferromagnetic (AFM) states were determined by calculating the susceptibility of the system. We took the peak position of the susceptibility as the transition point.[7] The T_{xy} line was determined as the temperature where $Q_\perp$ just became nonzero. We note that there is no phase transition across the line of T_{xy} and it represents the short-range behavior of the transverse spin freezing. The onset of the freezing occurs at frustration $f\sim16\%$ in the ferromagnetic state, and $f\sim84\%$ in the antiferromagnetic state. At these values of f, the phase transition temperature T_c starts to decrease. In the region between $f=45\%$ and $f=55\%$, T_c and T_{xy} merge together.

Apart from the usual states, at the middle region of the phase diagram there is a state we termed "mixed phase." We found that in the mixed phase $Q_\perp$ remains nonzero down to zero temperature and, in fact, it has rather substantial values at low temperatures. For instance with $f=51\%$, $Q_\perp\approx0.45$ at $T=0$. We have checked from the spin configurations that this large value of $Q_\perp$ was due to the fact that many spins lie almost completely in the transverse plane in the mixed phase, and that they actually form antiferromagnetic configurations (Fig. 2). Thus this part of the phase diagram is characterized by ferromagnetic domains pointing in the z direction mixed with antiferromagnetic domains pointing in the transverse plane. We have performed simulations to compute the susceptibility at fixed temperatures by sweeping f. A peak occurred in the susceptibility at the broken line in the phase diagram which separates the FM and AFM from the mixed phase. Unfortunately, we were not able to determine the nature of the region near this line as extremely large simulations are needed to determine whether there is a true phase transition from the FM or AFM states to the mixed phase as f or T is varied. We hope to report such a study in the future.

IV. CONCLUSIONS

Our Monte Carlo simulations on the site frustrated Heisenberg model give qualitatively similar results to those of the bond frustrated model. In particular the transverse spin freezing phenomena are observed which lead to an increase of the local spin length. However, the frustration does not set in until the site randomness reaches ~16%. Thus, the transverse spin freezing temperature T_{xy} remains zero until f reaches that value. We have observed a mixed phase for large values of the site randomness at low temperatures. Such a disordered phase is characterized by the configurations of mixed ferromagnetic and antiferromagnetic domains. Finally we have estimated the phase diagram of this model and it is in qualitative agreement with experimental findings.[5]

ACKNOWLEDGMENTS

This work was supported by the Natural Sciences and Engineering Research Council of Canada and le Fonds pour la Formation de Chercheurs et l'Aide à la Recherche de la Province du Québec.

[1] D. H. Ryan, J. O. Ström-Olsen, R. Provencher, and M. Townd, J. Appl. Phys. **64**, 5787 (1988).
[2] R A. Brand, V. Manns, and W. Keune, in *Heidelberg Colloquium on Spin Glasses, Lecture Notes in Physics*, (Springer, New York, 1983), Vol. 192, p. 79.
[3] B. Huck and J Hesse, J. Magn. Magn. Mater. **78**, 247 (1989).
[4] J. R. Thomson, H Guo, D. H. Ryan, M. J. Zuckermann, and M. Grant, J. Appl. Phys. **69**, 5231 (1991), Phys. Rev. B **45**, 3219 (1992).
[5] A. Berton, J Chaussy, J. Odin, R. Rammal, J. Souletie, J. L. Tholence, R. Tournier, F. Holtzberg, and S. Von Molnar, J. Appl. Phys. **52**, 1763 (1981).
[6] To check finite size effects some simulations were performed using 20^3 spins and qualitatively the same results were obtained.
[7] To accurately determine the transition points a proper finite size scaling analysis should be performed, as was done in Ref. 4 However, here we are only interested in the general phase behavior, thus we simply took the peak position of the susceptibility as the transition temperature.

Mössbauer measurements of spin correlations in a-$(Fe,Ni)_{90}Zr_9Sn$

D. Wiarda and D. H. Ryan
Centre for the Physics of Materials and the Department of Physics, McGill University, Rutherford Building, 3600 University Street, Montréal, Québec H3A 2T8, Canada

The local spin structure of the partially frustrated amorphous $Fe_{90-x}Ni_xZr_9Sn$ system was investigated by Mössbauer spectroscopy for $x=1,3$. The magnetic probe atom ^{57}Fe and the nonmagnetic ^{119}Sn were used to monitor the local correlation of the spins. The additional Ni renders the system less frustrated. We measured the temperature dependence of the hyperfine fields of the two probe atoms. The ratio $\langle B_{hf}(^{119}Sn)\rangle/\langle B_{hf}(^{57}Fe)\rangle$ rises with increasing temperature. This is in contrast to the temperature independence found for this ratio in $Fe_{92}Zr_7Sn$. A similar rise was found in the crystalline spin-glass AuFe where the slope was much larger and was related to a loss of longitudinal correlations.

INTRODUCTION

In amorphous and crystalline materials with competing antiferromagnetic (AF) and ferromagnetic (FM) exchange couplings two magnetic transitions have been observed in the low to medium frustration range.[1] The first transition marks the onset of ferromagnetic ordering at T_c. At the second transition temperature, T_{xy}, the transverse degrees of freedom freeze.[1,2] Overlaying the gross ordering behavior, are a series of phenomena associated with magnetic correlations and excitations. Neutron depolarization[3] and Lorentz microscopy[4] clearly show the existence of long-range ($\sim$10 μm) magnetic correlations which appear at T_c and persist through T_{xy}, consistent with the formation of a ferromagnetic state. By contrast, small angle neutron scattering reveals significant contributions from short-range ($\sim$10 nm) correlations,[5] which are sensitive to both magnetic transitions, and exist well above T_c.

One way to probe short-range magnetic correlations is to use Mössbauer spectroscopy. For a magnetic probe atom like ^{57}Fe the main contribution to the measured hyperfine field stems from the local moment of the atom itself. For a nonmagnetic probe atom like ^{119}Sn only the transferred fields from the neighboring magnetic moments contribute to the measured hyperfine field. If the spin structure is collinear, then the fields from the neighboring moments should add coherently, and a large transferred field should be observed at the nonmagnetic site, while a noncollinear or random spin structure should lead to a partial cancellation of the contributions and thus a smaller transferred field. The ratio of the (transferred) ^{119}Sn field to the (generating) ^{57}Fe field contains information about the degree of collinearity, and the temperature dependence of the ratio can be used to scale out the large changes due to thermal fluctuations, and reveal smaller effects due to changes in spin structure. This technique has been used to study spin correlations in several frustrated magnetic systems. In amorphous $Fe_{92}Zr_7Sn_1$, where the frustration arises through the distance dependence of the Fe-Fe direct exchange interaction, the transverse spin components were found to be correlated[6] as no change in the field ratio was observed on cooling through T_{xy}. Similarly, in AuFe, where the frustration is due to competition between long-ranged Ruderman–Kittel–Kasuya–Yosida (RKKY) and nearest-neighbor direct exchange interactions, both ^{196}Au and ^{119}Sn Mössbauer resonances have been employed, and clear evidence for strongly correlated transverse spin components was obtained.[7,8] However, more detailed examination of the temperature dependence of the $^{119}Sn/^{57}Fe$ field ratio, revealed evidence for a decay in the longitudinal spin correlations on cooling,[6] a result that is consistent with observations on similar compositions by neutron depolarization.[3]

In order to further understand the behavior of the field ratio it is necessary to study a range of frustrated magnetic systems. We have previously reported work on the a-$(Fe_{1-x}Mn_x)_{78}G_{22}$ system (G is a mixture of glass forming elements like Si, B, Al, P), which is frustrated through the addition of manganese,[9] however interpretation is complicated by the large magnetic moment of the Mn atoms. Here we report work on a simpler system, a-$(Fe_{90-x}Ni_x)_{90}Zr_{10}$, in which the addition of Ni reduces the frustration in the alloy, raising T_c and suppressing the transverse spin freezing transition.[10] In addition to the reduction of noncollinearity with increasing nickel content, the excitations become better behaved.[11] No spin waves were observed by inelastic neutron scattering for $x=0$, and while spin waves are seen below T_c for $x=1$, they soften on cooling, and were not resolved below $0.1T_c$. Well-defined spin waves are present for $x\geqslant 5$. Nickel carries a relatively small moment in this system ($\sim 0.6\mu_B$[12]) and as it is only present in low concentrations, its direct effects on the ^{119}Sn hyperfine field should be small. Therefore, the dominant contributions to the ^{119}Sn field should come from changes in the magnetic structure. The two samples considered here contain 1 and 3 at. % nickel; insufficient nickel to render the materials ferromagnetic.

EXPERIMENTAL METHODS

Ingots for melt spinning were prepared by first melting appropriate quantities of Zr (99.8%) and Ni (99.99%) in an arc furnace under titanium-gettered argon, then the Fe (99.98%) was added and the constituents were alloyed by rf melting under an Ar atmosphere. Enriched ^{119}Sn was used in order to get approximately 8 mg ^{119}Sn per 1 g sample weight to ensure a usable absorption in the ^{119}Sn spectra. Melt spinning was done under a helium atmosphere on to a copper wheel. The amorphous structure of the sample was verified by x-ray diffraction, DSC measurements, and room-temperature Mössbauer spectroscopy. The resultant amor-

 0021-8979/94/76(10)/6377/3/$6.00 © 1994 American Institute of Physics

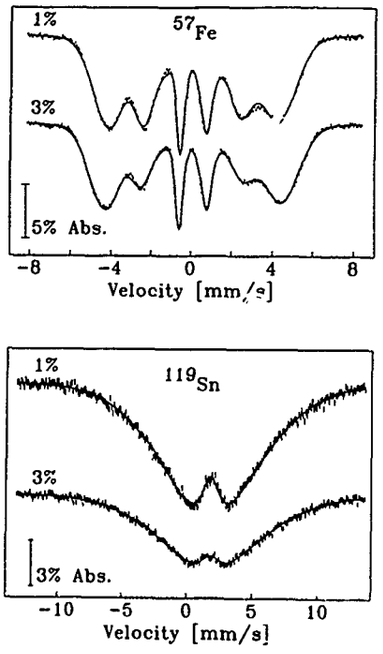

FIG. 1. ^{57}Fe and ^{119}Sn Mossbauer spectra for $Fe_{90-x}Ni_xZr_9Sn$ taken at 12 K.

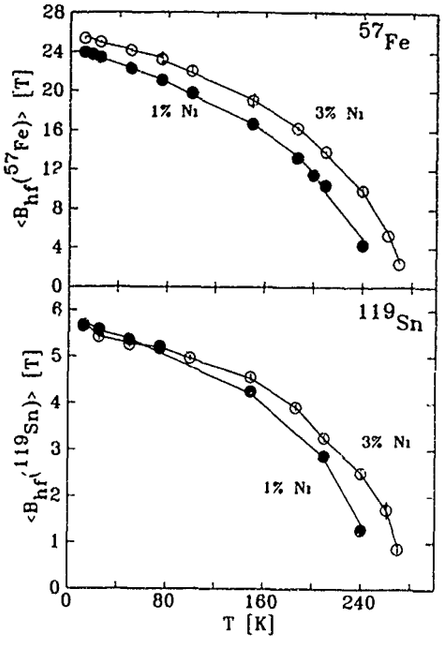

FIG. 2. Temperature dependence of the average ^{57}Fe and ^{119}Sn hyperfine fields for the two compositions of $Fe_{90-x}Ni_xZr_9Sn$.

phous ribbons were mounted on tape in order to make a Mössbauer absorber. The MS spectra were taken with a conventional constant acceleration spectrometer with a ^{57}Co/Rh source for the ^{57}Fe spectra and a $Ca^{119}SnO_3$ source for the ^{119}Sn spectra. The temperature was varied by means of a vibration-isolated, closed cycle He cryostat or a continuous flow cryostat.

The ^{57}Fe spectra were fitted using two Gaussian distributions to describe the hyperfine field distribution. For the ^{119}Sn spectra a single Gaussian distribution with different widths on the low and high field side was used. As the sample is an amorphous ribbon the intensity of the 2nd and 5th lines could not be fixed to its powder average value. Therefore the intensity was fitted in the ^{57}Fe spectra, and then set to the value found in those fits (~1) in order to fit the ^{119}Sn spectra. A linear correlation between the isomer shift and the hyperfine field was assumed in order to fit the slight asymmetry in the spectra. Spectra taken at 12 K for the different compositions and the two probe atoms along with the fits are shown in Fig. 1.

RESULTS

As expected, T_c increases on adding Ni, being 247±5 K for $x=1$ and 270±5 K for $x=3$, compared with 230±5 K for $x=0$. The temperature dependence of the average ^{57}Fe and ^{119}Sn hyperfine fields is given in Fig. 2. The curves show Brillouin-like behavior in all cases, and the derived T_c for each alloy is the same for both the Fe and Sn measurements, confirming that the Sn probes the same magnetic behavior as Fe.

The ^{57}Fe hyperfine field at 12 K rises on adding nickel, increasing 4% on going from $x=0$ to $x=1$, and a further 6% on going to $x=3$. The width of the hyperfine field distribution also narrows slightly. These results are in accordance with more collinear ordering, and the increased magnetization observed in this system on adding Ni.[10]

The behavior of the ^{119}Sn transferred hyperfine field however, is less straightforward. The shapes of the ^{119}Sn spectra shown in Fig. 1 are different, reflecting a 4% increase in the width of the hyperfine field distribution on going from $x=1$ to $x=3$, however, this broadening does not translate into an increased average. It is immediately apparent from Fig. 2, that the average Sn field at 12 K does not match the increase in the iron moment derived both from magnetization measurements and the ^{57}Fe Mössbauer spectra. In clear contrast to the ^{57}Fe data, the average ^{119}Sn hyperfine field does not change with composition, and the slight difference in temperature dependence, apparent in Fig. 2, simply reflects the higher T_c of the $x=3$ sample.

Plotting the ratio: $\langle B_{hf}(^{119}\mathrm{Sn})\rangle/\langle B_{hf}(^{57}\mathrm{Fe})\rangle$ (Fig. 3) reveals another puzzle. Since the Sn field does not increase with the Ni content, the Sn/Fe field ratio decreases on moving to the less frustrated, and thus more collinear, sample. Furthermore, a clear temperature dependence is apparent, with a slope of $\sim 1.5\times10^{-4}$ K^{-1}, at least an order of magnitude greater than the largest slope consistent with the data from $Fe_{92}Zr_7Sn_1$.[6] This slope should also be compared with the much stronger temperature dependence of $\sim 9\times10^{-4}$ K^{-1} observed in AuFe by ^{119}Sn Mössbauer spectroscopy. In the case of AuFe, the decline in the field ratio on cooling was interpreted as evidence for a loss of longitudinal order, a conclusion consistent with neutron depolarization measurements. However in the case of a-$Fe_{90-x}Ni_xZr_{10}$ no temperature dependence was seen for $x=0$, and adding nickel reduces frustration, making the system more ferromagnetic.

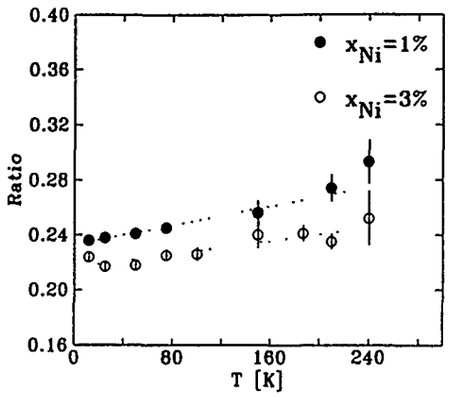

FIG. 3. Temperature dependence of the ratio $\langle B_{hf}(^{119}\mathrm{Sn})\rangle/\langle B_{hf}(^{57}\mathrm{Fe})\rangle$ for the two compositions of $Fe_{90-x}Ni_xZr_9Sn$.

Two possible conclusions can be reached. (i) There is, in fact, a loss of collinear order on cooling in a-$Fe_{90-x}Ni_xZr_{10}$. Independent confirmation of this behavior will be difficult to obtain, as the effect is quite small. The reduction of thermal fluctuations on cooling from 100 to 0 K, leads to a factor of two increase in the magnetization, while the change in the field ratio, and hence in the degree of collinearity, over the same temperature range is only about 1%. Unambiguously separating these two contributions would be extremely difficult. The existence of a collinearity loss in this system is unexpected since magnetization and neutron scattering measurements both show that the material becomes more ferromagnetic with increasing Ni content. Moreover, a more frustrated, binary a-Fe-Zr alloy showed no evidence of a collinearity decay. (ii) The Sn hyperfine field does not probe correlations between the neighboring Fe moments in the simple manner proposed, perhaps as a result of a greater tendency to form covalent bonds. The failure of the Sn field to rise with the increase in the Fe moment certainly provides support for this view. However, both ^{196}Au and ^{119}Sn Mössbauer measurements in AuFe yielded the same result, and confirmed neutron depolarization measurements. This agreement suggests that Sn does not sample its environment any more selectively than Au, and also shows that a loss of collinear order does yield the correct signature in the hyperfine field ratio. It is possible that the additional Ni leads to changes in the Fe moments which are not probed by the Sn. For example, even small changes in the orbital contribution to the iron moment can have significant effects on the ^{57}Fe hyperfine field,[13] but would not be seen by neighboring Sn atoms. It is not clear why the temperature dependence of such effects should differ from that of the average moment so as to yield a temperature dependent field ratio.

[1] D. H. Ryan, in *Recent Progress in Random Magnets*, edited by D. H. Ryan (World Scientific, Singapore, 1992).
[2] I. Mirebeau, M. Hennion, S. Mitsuda, and Y. Endoh, in *Recent Progress in Random Magnets*, edited by D. H. Ryan (World Scientific, Singapore, 1992).
[3] S. Mitsuda, S. Senoussi, and I. Mirebeau, J. Phys. Soc. Jpn. **60**, 136 (1991); B. V. B. Sarkissian, J. Phys.: Condens. Matter **3**, 961 (1991).
[4] S. Senoussi, S. Hadjoudj, P. Jouret, J. Bilotte, and R. Fourmeaux, J. Appl. Phys. **63**, 4086 (1988).
[5] J. Rhyne, R. W. Erwin, J. A. Fernandez-Baca, and G. E. Fish, J. Appl. Phys. **63**, 4080 (1988).
[6] H. Ren and D. H. Ryan, Phys. Rev. B **47**, 7919 (1993).
[7] M. M. Abd-Elmeguid, H. Micklitz, R. A. Brand, and W. Keune, Phys. Rev. B **33**, 7833 (1986).
[8] A. Ait-Bahammou, C. Meyer, F. Hartmann-Boutron, Y. Gros, and I. A. Campbell, J. Phys. C **8**, 1157 (1988).
[9] D. Wiarda, H. Ren, and D. H. Ryan, *Proceedings of The International Conference on the Applications of the Mössbauer Effect Vancouver, August 1993*, Hyperfine Interaction (to be published).
[10] S. Bao-gen, X. Rufeng, Z. Jiang-gao, and Z. Wen-shan, Phys. Rev. B **43**, 11005 (1991).
[11] J. A. Fernandez-Baca, J. J. Rhyne, G. E. Fish, M. Hennion, and B. Hennion, J. Appl. Phys **67**, 5223 (1990).
[12] Z. M. Stadnik, P. Griesbach, G. Dehe, P. Gütlich, and T. Miyazaki, Phys. Rev. B **35**, 430 (1987).
[13] F. van der Woude and G. A. Sawatzky, Phys. Rep. **12**, 335 (1974).

Study of the spin glass transition of amorphous FeZr alloys using small angle neutron scattering

K. Mergia and S. Messoloras
Solid State Physics Section, University of Athens, Panepistimioupolis, 157 84 Zografos, Greece

G. Nicolaides and D. Niarchos
NCSR "Demokritos," Institute of Material Science, 15310 Aghia, Paraskevi, Greece

R. J. Stewart
J. J. Thomson Physical Laboratory, University of Reading, Reading RG6 2AF, United Kingdom

SANS experiments of an amorphous $Fe_{90}Zr_{10}$ alloy were carried out in the temperature region 20–300 K with and without the application of a magnetic field. The scattering versus temperature for different Q values (zero field cooled magnetization) shows two transitions at T_c=240 K and T_f=40 K. However, both transitions are not observed in magnetic field (2.6 kG) cooling down curves. By switching off the magnetic field and warming up the sample only the transition at T_f=40 K is observed. Application of a magnetic field at different temperatures in a zero field cooled sample reduces the scattering; the scattering returns to its initial value after switching off the field.

INTRODUCTION

Amorphous $Fe_{1-x}Zr$ alloys, where $x \approx 0.1$, exhibit an unusual complex magnetic behavior. At T_c=240 K they exhibit a transition from the paramagnetic state to the long-range ferromagnetic (FM) ordering, whereas at the lower temperature $T_f(H=0)=40$ K another transition to a "spin-glass-like" (SG) (reentrant) state occurs.[1] Most of the experimental evidence referred to the T_f transition could be explained by the coexistence and competition of ferromagnetic and antiferromagnetic interactions.[2] Recent magnetization and Mössbauer measurements[3] of the $Fe_{90}Zr_{10}$ alloy have been interpreted as being consistent with finite ferromagnetic clusters in a ferromagnetic matrix.[4] However, questions have been raised as to whether the T_f transition is indeed a FM to true SG state transition. The ac susceptibility could be explained by either a SG transition or domain pinning effects. TEM and Lorentz microscopy studies[5] have revealed the existence of magnetic domains down to 6 K. However, SANS experiments[6,7] on $Fe_{91}Zr_9$ revealed the existence of two different spin–spin correlation lengths, the longest persisting up to temperatures even higher than T_c, whereas the shortest appears below T_c.

In this paper, we report small angle neutron scattering (SANS) measurements of an amorphous $Fe_{90}Zr_{10}$ alloy. The two transitions in zero field cooled (ZFC) magnetization, reported previously, are observed around the same temperatures. However, in a FC sample only the lower temperature transition (T_f) is observed. Interesting results are obtained when a field is applied after cooling the sample at different temperatures.

EXPERIMENT

Amorphous $Fe_{90}Zr_{10}$ alloy was prepared in an argon atmosphere by the melt spinning method. The amorphicity of the alloy was verified by x-ray diffraction. ac susceptibility measurements showed two transitions at 40 and 240 K. Ribbons of about 1 g were stuck together and their low angle scattering was measured using the LOQ instrument at the spallation source ISIS, Rutherford-Appleton Laboratory, England. In this instrument a neutron wavelength band from 0.22 to 1 nm is utilized. The averaged counts from the different wavelength bands are pulled together giving a Q-range ($Q=4\pi \sin\theta/\lambda$) from 0.07 to 2.0 nm^{-1}. The scattering of this alloy was measured in the temperature range 300–15 K with or without the application of a magnetic field.

RESULTS AND DISCUSSION

The change in the scattering versus temperature in zero magnetic field is shown in Fig. 1. These measurements were obtained during the cooling of the sample; a few spectra were repeated during the warming up and showed that the scattering was reversible. From Fig. 1 we clearly observe two transitions: the first at 240 K and the second at around 40 K. From 300 to 250 K the scattering remains almost constant. Below 250 K a gradual increase in the scattering is observed which peaks at 230 K. As the temperature de-

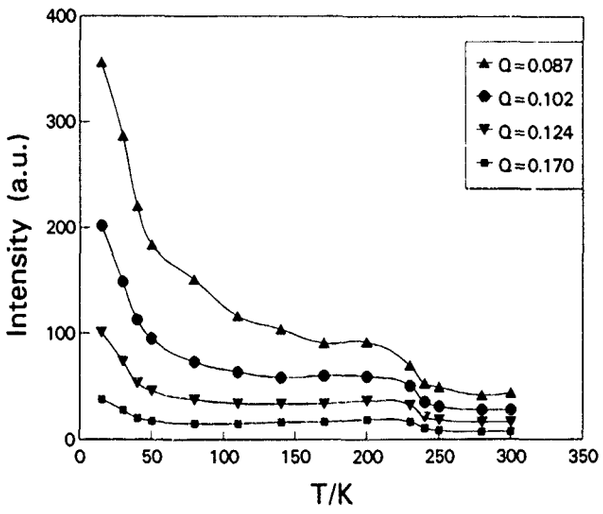

FIG. 1. Scattering vs temperature at different Q values. The sample has been cooled in zero field (the solid lines are a guide to the eye).

 0021-8979/94/76(10)/6380/3/$6.00 © 1994 American Institute of Physics

creases from 230 K the scattering for $Q>0.12$ nm^{-1} remains almost constant, whereas for lower Q values a continuous increase in the scattering is observed. At around 40 K a sharp increase in the scattering for all Q values is observed. These two transition temperatures coincide with those observed from ac susceptibility measurements carried out on the same sample.

The transition at 240 K has been attributed to a transition from a paramagnetic state to a long-range ferromagnetic ordering. In a ferromagnetic system the neutron scattering within the static approximation is given by a Lorentzian form (L)

$$I(Q)=\frac{A}{Q^2+\kappa^2}, \tag{1}$$

where κ is the inverse spin correlation length which approaches zero at the phase transition. In order to examine whether the scattering follows a Lorentzian line shape the data were plotted as $1/I(Q)$ vs Q^2. The data do not show a linear behavior when the whole experimental Q range is used. However, if we restrict our attention to the low Q region (0.07 to 0.6 nm^{-1}), we observe two linear regions, and in the temperature range 300–110 K. The Q value of the inflection decreases with temperature (at 250 K around $Q=0.5$ nm^{-1}) and is not observed within the experimental window below 110 K. These results are very similar to those discussed by Rhyne *et al.*[7]

As discussed above, the data in a plot of $1/I(Q)$ vs Q^2 [Eq. (1)] are curved and the departure from the Lorentzian-type shape increases as the temperature decreases. At these temperatures irreversibility effects have been observed in ac susceptibility measurements and if we assume a random anisotropy system the scattering can be expressed in Lorentzian plus Lorentzian-squared ($L-L2$) form[8]

$$I(Q)=\frac{A}{Q^2+\kappa^2}+\frac{B}{(Q^2+\kappa^2)^2}. \tag{2}$$

A least-squares fit of the experimental intensities to Eq. (2) using the full Q range gives physically meaningful values ($\kappa^2>0$) only in the temperature range 240–110 K. This is the temperature region in which the intensity varies slowly with temperature (Fig. 1). The value of the coefficient A decreases with temperature (around 30% from 240 to 110 K), whereas the correlation length as determined from κ^2 increases with temperature from 7.5 nm at 240 to 19 nm at 110 K. The decrease of A with temperature is in accordance with the behavior expected from a normal ferromagnet. It should be noted that the experimental intensity and that calculated from the fitted A, B, and κ values agree very well apart from a small deviation at the very low Q values. It has been proposed that the spin clusters can be presented by a Maxwellian distribution.[7] However, by using such a model it is difficult to fit the whole Q range and the values of A increase with decreasing temperature. Thus, we can only say that the L-$L2$ Eq. (2) describes the experimental data in the temperature regions defined from the first transition at $T_c=240$ K to the onset of the second one. In order to understand the origin of the low-Q scattering experiments in an even lower Q range are required. The interpretation of the scattering at temperatures around the two transitions probably requires a more sophisticated model.

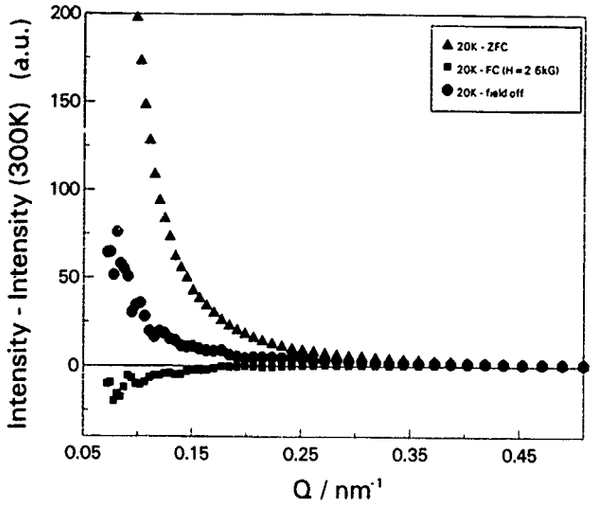

FIG. 2. The effects of the magnetic field at 20 K. The scattering at room temperature has been subtracted from all spectra. Triangles: ZFC, squares: FC from 300 K, circles: scattering after switching off the magnetic field.

The application of a magnetic field at 300 K reduces the scattering. This reduction is initially proportional to the field and at 5 kG saturation has been reached. The field-dependent scattering cannot be described by the simple Lorentzian form of Eq. (1). However, a plot of the $\ln[I(Q)]$ vs $\ln Q$ exhibits a linear behavior for the whole Q range and the slope obtained is around 2. This shows that the scattering after the application of the magnetic field can be described with a function of the form A/Q^2. This behavior is expected from an ordered ferromagnetic system.

Cooling the sample from 300 K in a 2.6 kG field, we observe no change in the scattering with temperature. Neither of the two transitions is observed. By switching off the magnetic field at 20 K the scattering increases, but it does not reach the value of the scattering observed during the cooling of the sample with zero magnetic field (Fig. 2). The increase of the scattering observed after switching off the field at 20 K occurs within 5 min, the time required to obtain the first measurement. No change in the scattering is observed in subsequent measurements, while remaining at 20 K. Warming up, we observe the lower transition at 40 K. However, the higher transition at $T_c=240$ K is not observed (Fig. 3), the scattering slowly increases to its original 300 K value in zero field.

In order to examine the spin reorientation at different temperatures, a magnetic field was applied after cooling the sample to a specific temperature (230, 110, 80, and 40 K). The change in the scattering induced by the field occurs within less than 2 min (time of the measurement) and the scattering returns to its previous value by switching off the magnetic field within the same time interval. In Fig. 4 the effect of the magnetic field ($H=2.6$ kG) applied after the sample was cooled at 230 K is presented. For comparison, the scattering obtained when the same field is applied at 300

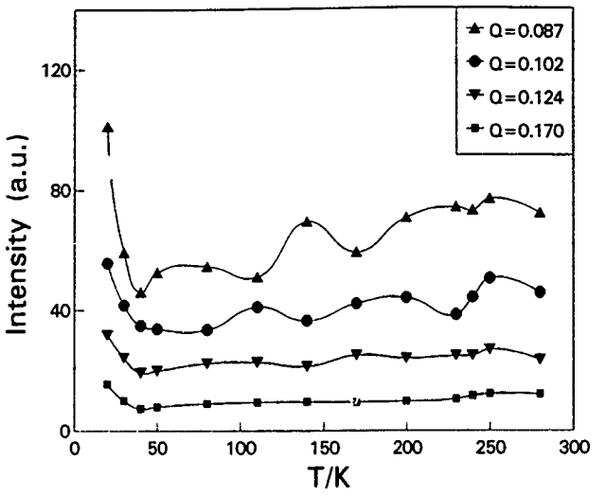

FIG. 3. Scattering vs temperature at different Q values during the heating of the sample in zero field from 20 to 300 K. The sample was previously cooled in a magnetic field of 2.6 kG.

K is also presented. In order to show the effect of the magnetic field, the scattering at room temperature has been subtracted from all the spectra. The field-induced scattering for the low Q values is lower than the 300 K scattering in zero field. As Q increases it reaches the 300 K scattering, further increases to peak at 0.44 nm^{-1}, then decreases to the 300 K scattering at Q around 1.2 nm^{-1} (see inset of Fig. 4) and remains unchanged for $Q>1.2$ nm^{-1}. As the temperature of cooling is reduced these effects become less pronounced and the field-induced scattering at 40 and 300 K almost coincide.

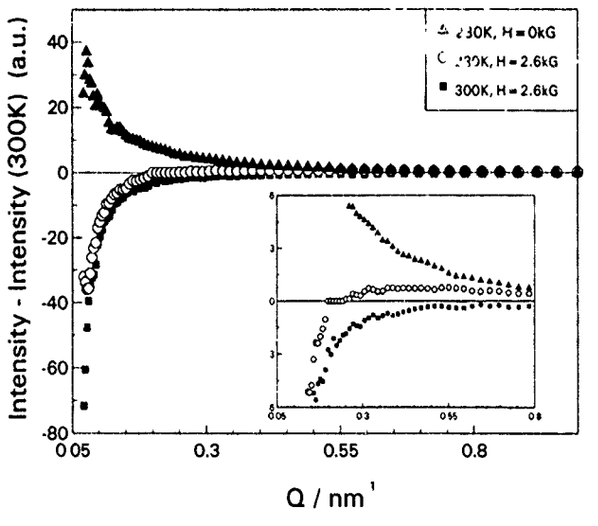

FIG. 4. The effect of a 2.6 kG magnetic field after the sample was cooled at 230 K. The scattering at room temperature has been subtracted from all spectra. Triangles: ZFC to 230 K, circles: cooling from 300 to 230 K in zero field and application of a magnetic field of 2.6 kG, squares: application of 2.6 kG at 300 K.

CONCLUSIONS

The ZFC SANS from an amorphous $Fe_{90}Zr_{10}$ alloy shows two transitions at 240 and 40 K which coincide with those observed from ac susceptibility measurements carried out on the same sample. The scattering in the temperature range 300–110 K and in the low Q region shows a behavior which departs from either L or L-$L2$ form [Eqs. (1) and (2)]. This scattering cannot be attributed to chemical effects or clustering since it is temperature dependent. If we ignore the low Q scattering we can fit a L-$L2$ equation to the data only in the range 240–110 K. The correlation length obtained from such a fit increases with temperature from 7.5 to 19 nm and the coefficient A which contain contributions from both finite range spin waves and from the static spin glass order decreases with temperature as expected. The 300 K scattering is reduced with the application of a magnetic field and saturation is observed at 5 kG. No change in the scattering is observed during the cooling of the sample from 300 to 20 K. The temperature independence of the scattering during cooling and its form (A/Q^2) indicate an ordered ferromagnetic system. By warming up the sample after switching off the field at 20 K only the lower transition at T_f=40 K is observed. The switching off of the field unlocks the spin cluster units which undergo their transition at 40 K. The unlocking of the spin clusters is not complete since the scattering at 20 K, after switching off the field, is not restored to its ZFC value. The FM matrix remains frozen at low temperatures and the scattering slowly recovers to its previous value at 300 K without showing the T_c=240 K transition. The application of a magnetic field after cooling the sample to a specific temperature results in a reduction of the scattering. The effect is more pronounced at 40 K where the field has almost the same effect as when applied at room temperature. No hysteresis is observed in the restoration of the scattering to its previous value after switching off the field. We may assume that the field mainly modifies the spin cluster units. At 40 K a larger part of the sample is occupied by the spin clusters so the effect is greater. This is in agreement with the unlocking of the spin clusters when the magnetic field is switched off at 20 K after a field cooling of the sample.

ACKNOWLEDGMENTS

We would like to thank the British Council and the Greek General Secretariat of Science and Technology for financial support and the SERC for the use of ISIS facilities. The contribution of Dr. R. Heenan and Dr. S. King during the experiments is appreciated.

[1] G. K. Nicolaides, W. Gong, G. C. Hadjipanayis, and K. V. Rao, J. Mater. Sci. Eng. **99**, 69 (1988).
[2] M. Gabay and G. Toulouse, Phys. Rev. Lett. **47**, 201 (1981).
[3] S. N. Kaul, V. Siruguri, and G. Chandra, Phys. Rev. **45**, 12343 (1992).
[4] S. N. Kaul and V. Siruguri, J. Phys.: Condens. Matter **4**, 505 (1992); S. N. Kaul, J. Phys.: Condens. Matter **3**, 4027 (1991).
[5] S. Senousi, S. Hadjouj, P. Pouret, J. Bilotte, and R. Fourmeaux, J. Appl. Phys. **63**, 4086 (1988); Z. Wronski, A. J. Janicki, and H. Matyja, J. Mater. Sci. Lett. **2**, 5 (1983).
[6] J. J. Rhyne and G. E. Fish, J. Appl. Phys. **57**, 3407 (1985).
[7] J. J. Rhyne, J. A. Fernadez-Baca, and G. E. Fish, J. Appl. Phys. **61**, 4080 (1988).
[8] A. Aharony and E. Pytte, Phys. Rev. B **27**, 5872 (1983).

Study of magnetohistory effects in $YFe_{12-x}Mo_x$ (x=1.5–3.0)

Yi-Zhong Wang
San Huan Research Laboratory, Chinese Academy of Sciences, P. O. Box 603, Beijing 100080, People's Republic of China and Department of Physics, Utah State University, Logan, Utah 84322

Bo-Ping Hu and Gui-Chuan Liu
San Huan Research Laboratory, Chinese Academy of Sciences, P. O. Box 603, Beijing 100080, People's Republic of China

Lin Song, Kai-Ying Wang, and Ji-Fan Hu
San Huan Research Laboratory, and Institute of Physics, Chinese Academy of Sciences, P. O. Box 603, Beijing 100080, People's Republic of China

Wu-Yan Lai
Institute of Physics, Chinese Academy of Sciences, P. O. Box 603, Beijing 100080, People's Republic of China and Department of Physics, Utah State University, Logan, Utah 84322

Magnetohistory effects in $YFe_{12-x}Mo_x$ (x=1.5–3.0) have been investigated. The freezing temperature T_f increases with increasing Mo concentration. Irreversible behavior still appears in an applied field up to 6 T for $YFe_{9.5}Mo_{2.5}$. These magnetohistory behaviors may be understood by domain-wall pinning.

I. INTRODUCTION

Since 1990, when $Sm_2Fe_{17}N_3$ and $NdFe_{11}TiN$ compounds were discovered,[1,2] interstitial compounds have been intensively investigated due to their excellent magnetic properties for permanent magnet applications. Anagnoston *et al.*[3] and Wang *et al.*[4] first studied the series of $RFe_{10}Mo_2$ nitrides and the series of $NdFe_{12-x}Mo_x$ nitrides, respectively. The studies showed that the $RFe_{12-x}T_x$ series with T=Mo has different magnetic behavior from the other series with T=Ti, V, Cr, W, and Si.[5,6] Recently, $YFe_{12-x}Mo_x$ and their nitrides were also investigated by Sun *et al.* in order to get information on the magnetic properties of the Fe sublattice.[7,8] Some magnetohistory effects were observed in both $YFe_{10}Mo_2$ and $LuFe_{10}Mo_2$ by Christides *et al.*[9] These magnetohistory phenomena are very close to the behavior which exists in spin glasses and amorphous alloys.[10] The authors in Ref. 9 believed that such phenomena result from the variation of Fe–Fe distances for $YFe_{10}Mo_2$ and $LuFe_{10}Mo_2$ on different Fe sites and the distribution of Mo atoms leads to a randomness of the exchange interaction and an establishment of noncollinear-type of magnetic order (helimagnetic structure). However, such a mechanism is still a matter of debate. In fact, magnetohistory phenomena are often exhibited by some rare-earth transition-metal alloys, for example, in YCo_2Ni_3 observed in 1976[11] and recently in $Ho_2Fe_{17-x}Al_x$[12] and $R_2Fe_{14-x}Mn_xC$.[13] The narrow-Bloch-wall pinning mechanism developed by Barbara *et al.* in the early 1970's[14] for understanding the huge coercive force in the crystalline rare-earth-transition metal alloys has been used to explain the magnetohistory effects.[13]

In this work, we investigate the magnetohistory effects of the series alloys of $YFe_{12-x}Mo_x$ (x=1.5–3.0) and discuss the origin of these effects.

II. EXPERIMENT

Alloys of $YFe_{12-x}Mo_x$ with x=1.5, 2.0, 2.5, and 3 were prepared by arc melting from 99.9% starting materials under an argon gas atmosphere and then vacuum annealed at 1100 °C for 24 h. By x-ray diffraction and thermomagnetic analysis, all samples were found to be single phase with $ThMn_{12}$-type structure. Experimental data of structural and intrinsic magnetic properties have been reported separately.[15] Samples of cylindrical shape with a diameter of 3 mm and a length of 6 mm were made at room temperature by aligning the alloy powders along the cylinder axis in a magnetic field of 1 T and fixing their direction with epoxy resin. The low-temperature thermomagnetic data were obtained using an extraction sample magnetometer in the temperature range from 1.5 to 300 K in an applied field up to 6 T.

III. RESULTS AND DISCUSSION

Figure 1 shows the temperature dependence of the magnetization of $YFe_{12-x}Mo_x$ series ($1.5<x<3.0$) in an applied field of 0.045 T after zero-field cooling (ZFC) and field cooling (FC) processes. Here the ZFC curve is obtained by cooling the sample from room temperature to 1.5 K in zero applied field, and then measuring the magnetization with the increase of temperature in a certain applied field, while the FC curve is produced by cooling the sample in the same applied field. The thermomagnetic cycle of ZFC and FC processes exhibits an irreversible behavior. Values of the magnetization after ZFC are obviously lower than those after FC. The ZFC and FC magnetization curves are coincident at high temperatures and are separate at low temperatures. The irreversible phenomena observed here in the $YFe_{12-x}Mo_x$ series are similar to that in $YFe_{10}Mo_2$.[9] Moreover, the freezing temperature T_f, which is marked by the arrows at the cusps of the ZFC curves in the figure, decreases with decreasing Mo concentration.

Figure 2 shows the temperature dependence of the ZFC and FC magnetization curves in different applied fields for the $YFe_{9.5}Mo_{2.5}$ compound. It can be seen that T_f decreases with increasing applied field. Even if the applied field goes up to 6 T, the irreversible behavior does not vanish. This is

 0021-8979/94/76(10)/6383/3/$6.00 © 1994 American Institute of Physics

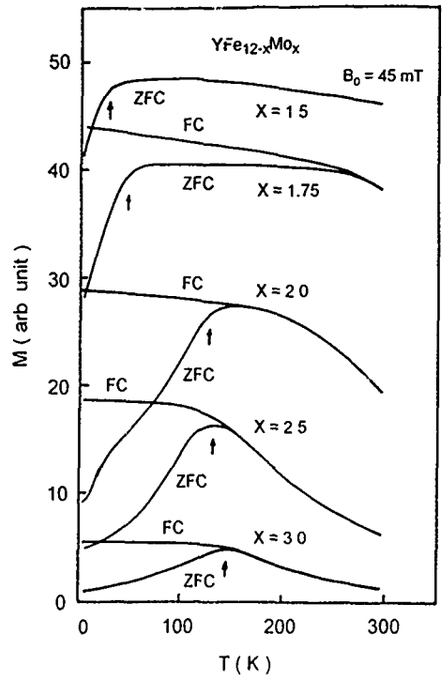

FIG. 1. Temperature dependence of the magnetization of $YFe_{12-x}Mo_x$ by zero-field cooling and field cooling. The arrows mark the freezing temperature T_f.

different from the case of $YFe_{10}Mo_2$, observed by Christides *et al.*,[9] where the irreversible phenomenon disappeared when the applied field went up to 0.7 T.

Understanding the magnetohistory effects observed in rare-earth transition-metal intermetallic compounds has been

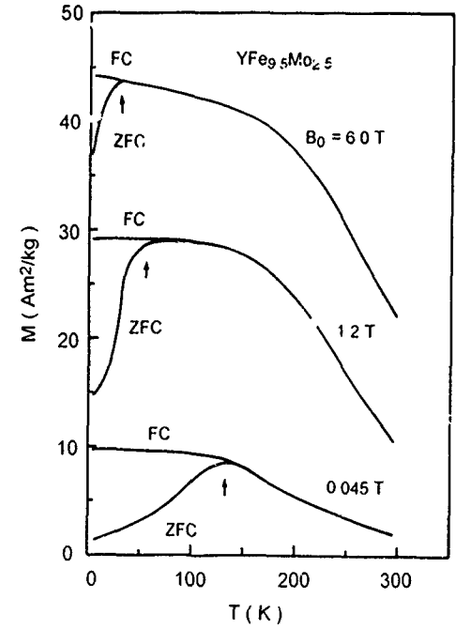

FIG. 2. Temperature dependence of magnetization of $YFe_{9.5}Mo_{2.5}$ by zero field cooling and field cooling in different applied fields. The arrows mark the freezing temperature T_f.

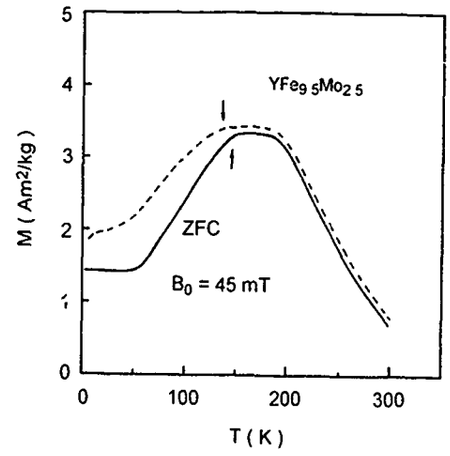

FIG. 3. Temperature dependence of magnetization of $YFe_{9.5}Mo_{2.5}$ by zero-field cooling for thermal demagnetized ingot (solid line) and magnetized ingot (dashed line). The arrows mark the freezing temperature T_f.

an interesting subject for scientists working on magnetism. The magnetohistory effects may be described in terms of cluster glasses[10] or in terms of the narrow-Bloch-wall.[12,13] For the magnetohistory, effects observed in $RFe_{10}Mo_2$ (R=Y and Lu) were explained in terms of cluster glasses by the authors in Ref. 9, which were established by a competition between the positive and negative exchange interactions due to the variation of Fe–Fe distances in different lattice sites, since the Fe–Fe interactions with short interatomic distance (~0.24 nm) may cause the antiferromagnetic coupling, but the authors did not explain why there is no magnetohistory effect in $GdFe_{10}Mo_2$ which has similar lattice parameters to $YFe_{10}Mo_2$.[3] A recent neutron-powder-diffraction study on $YFe_{12-x}Mo_x$[8] at a temperature of 10 K showed that all the Fe atomic magnetic moments are parallel over the three crystallographic sites. This does not support the proposal made by the authors in Ref. 9. For the cluster glass model, the magnetohistory effect is independent from the magnetic domain structure. Figure 3 shows two types of ZFC curves for $YFe_{9.5}Mo_{2.5}$. It can be seen that at 1.5 K the thermal demagnetized ingot has a lower magnetization value than the ingot magnetized in a field of 6 T at 200 K. This indicates that the magnetohistory effect observed here is associated with the distribution of the domain wall. Therefore the narrow-Bloch-wall model may be suitable for explaining the magnetohistory effects in $YFe_{12-x}Mo_x$.

The neutron-powder-diffraction study on $YFe_{12-x}Mo_x$[8] at a temperature of 10 K also showed that the Mo has an atomic magnetic moment of 1.0 μ_B which is antiparallel to the Fe-sublattice magnetization and the Mo atoms are mainly distributed on 8*i* sites. The distribution of Mo substitution in the iron sites in $YFe_{12-x}Mo_x$ may cause the necessary fluctuation of the exchange interaction and anisotropy to form the pinning of domain walls, so that irreversible magnetic behavior occurs at low temperatures. This is similar to that observed in YCo_2Ni_3.[11] If the nonmagnetic Y is replaced by magnetic R, which enhances the relative value of magnetocrystalline anisotropy to exchange interaction, the magneto-

history effects in $RFe_{12-x}Mo_x$ can be expected. We have found that the magnetohistory effects do exist in $RFe_{12-x}Mo_x$ with light rare-earth R=Pr, Nd, and Sm.[16] The reason for the absence of magnetohistory effects in $GdFe_{10}Mo_2$[9] may be attributed to the magnetic Gd^{3+} which couples antiparallel to Fe and parallel to Mo. The magnetic Gd sublattice smoothes the magnetic fluctuation caused by Mo atoms.

In conclusion, magnetohistory effects in $YFe_{12-x}Mo_x$ (x =1.5–3.0) have been investigated and may be understood by domain-wall pinning. The experimental data give a strong evidence that magnetohistory effects are related to the domain structures rather than the cluster glasses.

[1] J. M. D. Coey and H. Sun, J. Magn. Magn. Mater. **87**, L251 (1990).
[2] Y. C. Yang, X. D. Zhang, L. S. Kong, Q. Pan, and S. L. Ge, Appl. Phys. Lett. **58**, 2042 (1991).
[3] M. Anagnostou, C. Christides, and D. Niarchos, Solid State Commun. **788**, 681 (1991).
[4] Y. Z. Wang, B. P. Hu, X. L. Rao, G. C. Liu, L. Yin, W. Y. Lai, W. Gong, and G. C. Hadjipanayis, J. Appl. Phys. **73**, 6251 (1993).
[5] X. C. Kou, C. Christides, R. Grossinger, H. R. Kirchmayr, and A. Kostikas, J. Magn. Magn. Mater. **105-107**, 1341 (1992).
[6] Y. Z. Wang, B. P. Hu, X. L. Rao, G. C. Liu, L. Song, L. Yin, and W. Y. Lai, J. Appl. Phys. **75**, 6226 (1994).
[7] H. Sun, M. Akayama, K. Tatami, and H. Fujii, Physica B **183**, 33 (1993).
[8] H. Sun, Y. Morii, H. Fujii, M. Akayama, and S. Funahashi, Phys. Rev. B **48**, 13333 (1993).
[9] C. Christides, A. Kostikas, G. Zouganelis, and V. Psyharis, Phys. Rev. B **47**, 1220 (1993).
[10] K. Moorjani and J. M. D. Coey, *Magnetic Glasses* (Elsevier, Amsterdam, 1984).
[11] H. Oesterreicher, F. T. Parker, and M. Misroch, Solid State Commun. **19**, 539 (1976).
[12] T. H. Jacobs, K. H. J. Buschow, G. F. Zhou, X. Li, and F. R. de Boer, J. Magn. Magn. Mater. **116**, 220 (1992).
[13] T. H. Jacobs, K. H. J. Buschow, R. Verhoef, and F. R. de Boer, J. Less-Common Metals **157**, L11 (1990).
[14] B. Barbara, C. Becle, R. Lemaire, and D. Paccard, J. Phys. (Paris), **32**, C1-299 (1971).
[15] Y. Z. Wang, B. P. Hu, L. Song, K. Y. Wang, and G. C. Liu, J. Phys.: Condens. Matter (to be published).
[16] Y. Z. Wang, B. P. Hu, J. F. Hu, G. C. Liu, K. Y. Wang, and W. Y. Lai, (unpublished).

Magnetic viscosity, fluctuation fields, and activation energies (invited)

R. Street
Research Centre for Advanced Mineral and Materials Processing, Nedlands 6009 Australia

S. D. Brown
Department of Physics, Keele University, Keele, Staffordshire ST5 5B9, United Kingdom

Time dependence of magnetization in ferromagnetic materials was first described towards the end of the 19th century. Subsequently, two types of mechanisms responsible for time dependent behavior were identified and became known as "diffusion" and "fluctuation" after-effect or viscosity. The former depends on thermally induced motion of impurity atoms. The latter is a consequence of thermal activation of irreversible domain processes such as domain-wall motion and the nucleation of domains of reverse magnetization. Fluctuation viscosity affects, to a greater or smaller extent, all magnetic materials subject to hysteresis. In the late 1940s descriptions of magnetic viscosity in terms of fluctuation fields (Néel) and activation energy distributions (Street and Woolley) were developed. The two approaches will be described. An analysis of the time dependent phenomena exhibited by magneto-optical films will be presented as a simple example of the application of activation energy modeling.

I. INTRODUCTION

Two different types of magnetic viscosity or after-effect have been recognized. The first observations of the time dependence of magnetization in a constant field were made by Ewing[1] and Rayleigh[2] in their measurements of the magnetic properties of soft magnetic materials. Later Preisach[3] and others observed a different kind of time dependence in the magnetization of harder magnetic materials. Different processes are involved in the two effects. In the first, magnetic processes are affected by the diffusion of impurity atoms and the temperature dependence of the magnetic effects are typical of diffusion processes. The phenomenon underlying Preisach's observations affect all magnetic materials which exhibit hysteresis. The magnetization processes of these materials exist in metastable states which transform to stable states by a combination of field induced transitions and thermal activation. Under constant field conditions the evolution of magnetization is the result of thermal activation of irreversible magnetization processes. Observations of magnetic viscosity are made by measuring the magnetization $M(t)$ as a function of time elapsed after a discontinuous increment of magnetic field. In many cases, over restricted ranges of elapsed time,

$$M(t)=S \ln t+\text{const}, \tag{1}$$

where the parameter S depends on the point of measurement on the magnetization curve. S also depends on the demagnetization factor of the sample on which measurements are made.

Two independent descriptions of the effects of thermal activation on magnetization were given by Street and Woolley[4,5] and Néel.[6,7] The latter considered the effects associated with thermally induced random fluctuations of spontaneous magnetization vectors in terms of a fluctuation field:

$$H(t)=H_f(Q+\ln t), \tag{2}$$

where Q is a constant and H_f is known as the fluctuation field. The time dependence of irreversible magnetization is obtained in terms of the irreversible susceptibility χ_{irr} as

$$M_{\text{irr}}(t)=\chi_{\text{irr}} H(t)=S \ln t+\text{const}, \tag{3}$$

where $S=\chi_{\text{irr}} H_f$.

In the approach adopted by Street and Woolley to magnetic viscosity, thermally activated rate processes involving metastable states with a distribution of activation energies are considered. Thus $N(E)\,dE$ is the number per unit volume of metastable states having, at a given field H, activation energies lying between E and $E+dE$.

II. MODELS

A domain model exhibiting field dependent metastability is based on the work of Stoner and Wohlfarth[8] in which they examined the magnetic behavior of anisotropic single domain particles. The results of many studies of magnetic viscosity have been discussed in terms of this model. A simple case of an aligned uniaxial domain subjected to a demagnetizing field H is shown in Fig. 1. It is assumed that the magnetization proceeds by coherent rotation.

In the case of an assembly of noninteracting aligned particles with a distribution of volume $f(V)\,dV$, the distribution of activation energy at a fixed field will be given by $Kf(V)\,dV\,(1-H/H_k)^2$. The variation of the activation energy E as a function of H is shown in Fig. 2. The activation energy distribution functions at two different values of field

 0021-8979/94/76(10)/6386/5/$6.00 © 1994 American Institute of Physics

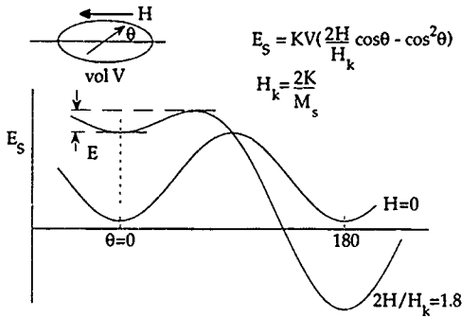

FIG. 1. Energy of an aligned uniaxial domain as a function of the angle between the field and the magnetization vector at two different fields. The activation energy for reversal is indicated.

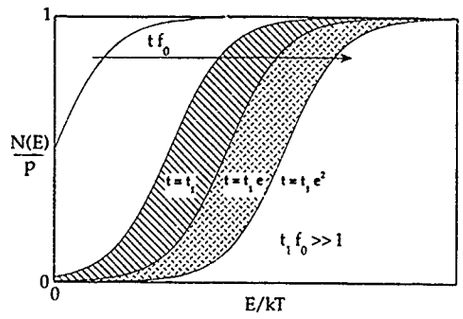

FIG. 3. The distribution of energy barriers $N(E)/p$ as a function of E/kT for various values of time after a discontinuous step change in field. The model assumes that at $t=0$, $N(E)=p$ for all E. For values of $tf_0 \gg 1$ the curve sweeps out equal areas in equal logarithmic increases in time (the shaded regions).

are also indicated. It is clear that determination of the field variation of activation energy requires measurements to be made at constant values of magnetization.

Other examples of magnetization processes which involve metastable states include domain-wall motion subject to weak and strong pinning[9,10] and the nucleation of domains of reverse magnetization.[11]

As noted by Street and Woolley[4,5] the rate of transformation of metastable to stable states is given by

$$\frac{d}{dt}N(E)dE = -f_0 N(E)dE\ \exp\left(-\frac{E}{kT}\right), \tag{4}$$

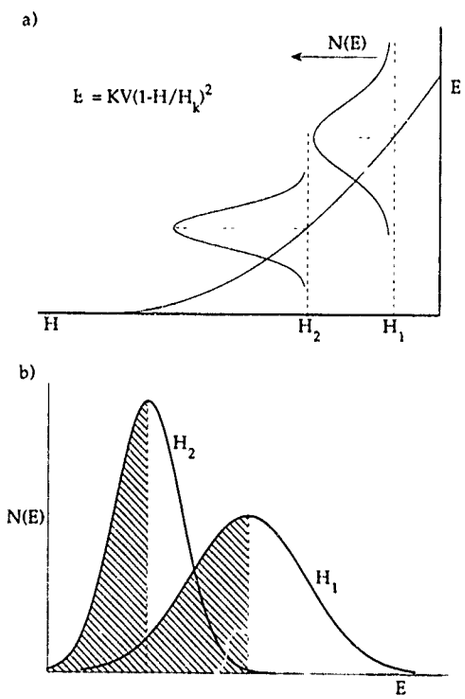

FIG. 2. (a) Activation energy as a function of demagnetizing field for an aligned uniaxial domain. The distribution of activation energies due to a distribution of volumes is indicated at two values of field. (b) The distribution of activation energies at two values of field. To determine $\partial E/\partial H$, measurements must be made at constant magnetization, represented by the shaded area.

where f_0 is the attempt frequency, assumed to be constant.

The solution to Eq. (4) is

$$N(E) = N_0(E)\exp[-tf_0\ \exp(-E/kT)], \tag{5}$$

where $N_0(E)$ is the initial number of metastable states per unit volume with activation energies lying between E and $E+dE$ at $t=0$.

For the case that the initial value of the distribution function $N_0(E)$ is independent of E and equals a constant p, Eq. (5) becomes

$$N(E)/p = \exp[-tf_0\ \exp(-E/kT)]. \tag{6}$$

The variations of the ratio $N(E)/p$ as a function of E/kT with the dimensionless product tf_0 as parameter are shown in Fig. 3. Assuming that each successful activation makes the same contribution to the magnetization, the total change in magnetization of the assembly from time $t=0$ to t_1 is proportional to the area between the curve at $t=t_1$ and the $N(E)/p$ axis. For values of the parameter $tf_0 \gg 1$ the curve sweeps out equal areas in equal logarithmic increases in time. That is, the magnetization increases logarithmically with time in accordance with the experimentally observed variation, Eq. (1). Making the simplifying assumption that each successful activation involves a change in magnetic moment μ, the viscosity parameter S is given by

$$S = \mu p kT. \tag{7}$$

Changes in magnetization may also be achieved by stepwise changes in the applied field ΔH. It may be shown that the irreversible susceptibility χ_{irr} is given by[12]

$$\chi_{irr} = \mu p\ \frac{\partial E}{\partial H}. \tag{8}$$

Hence

$$\frac{S}{\chi_{irr}} = H_f = \frac{kT}{\partial E/\partial H}; \tag{9}$$

cf. Eq. (3).

Conventionally, the quantity H_f has been derived from measurements of S and χ_{irr}. The operational definition of χ_{irr} to be substituted in Eq. (9) is a matter of some uncertainty in

materials, such as high coercivity permanent magnets, which exhibit pronounced time dependence of magnetization. It has been shown that in this context,[13]

$$\chi_{\rm irr}=\left.\frac{\partial M_{\rm irr}}{\partial H}\right|_{\dot{M}}. \tag{10}$$

An alternative method of deriving values of H_f from experimental observations of time dependence is discussed by Folks and Street.[14]

At a given point on a magnetization curve, H_f is a measure of $\partial E/\partial H$, the variation with field of the activation energy of the irreversible metastable processes which are active at that point. For example, the $\partial E/\partial H$ vs H curve for an assembly of aligned Stoner–Wohlfarth domains is given by the slope of the $E_{\rm ac}$ vs H curve of Fig. 2, i.e., a linear decrease as the magnitude of the reverse field is increased. In the case of the activation of aligned nuclei of reverse magnetization,

$$\frac{\partial E}{\partial H}=vM_{\rm sp}, \tag{11}$$

where v and $M_{\rm sp}$ are the volume and spontaneous magnetization of the nucleus.

Some interesting features arise from the study using an activation energy model of the time dependence of a system in which the metastable states all have the same value of activation energy $E(H)$. Specifically, we consider a thin film in which there exist identical uniaxial grains each of volume V. The magnetic moment of a grain VM_s may be aligned only either in a positive or negative direction with respect to the normal of the plane of the film.

Let N_t be the total number of grains per unit volume of the film and N_+ and N_- be the number of grains per unit volume aligned in the positive and negative directions, respectively. Then $N_t=N_++N_-=1/V$ and the intensity of magnetization of the film when $N=N_+$ is given by

$$M=N_tVM_s(2N/N_0-1)$$

or

$$m=2n-1, \tag{12}$$

where

$$m=M/M_s$$

and

$$n=N/N_0.$$

The rate equation is

$$\frac{dn}{dt}=-f_0n\,\exp\left[-\frac{E(H)}{kT}\right]. \tag{13}$$

Solving Eq. (13) and substituting for n from Eq. (12) gives

$$m=2\,\exp(-t/\tau)-1, \tag{14}$$

where

$$\tau=\frac{1}{f_0}\exp\left[\frac{E(H)}{kT}\right].$$

The variations of m as a function of $\ln t$ with $E(H)/kT$ as parameter are shown in Fig. 4.

E as a function of H may be derived from Eq. (14) by considering constant $m=m_c$ conditions which implies

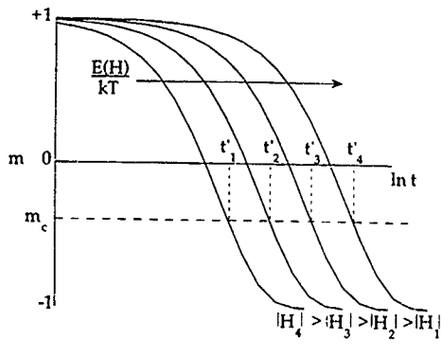

FIG. 4. The decay of magnetization with $\ln t$ for a uniaxial perpendicular thin film at various fixed values of field. The coercivity is clearly time dependent.

$$2\,\exp(-t'/\tau)=m_c+1, \tag{14a}$$

where t' = time at which $m=m_c$ for a given value of τ. Thus,

$$-\frac{t'}{\tau}=\ln\left(\frac{m_c+1}{2}\right). \tag{14b}$$

Substituting for τ from Eq. (14) gives

$$t'\,\exp\left[-\frac{E(H)}{kT}\right]=-\frac{1}{f_0}\ln\left(\frac{m_c+1}{2}\right)=\text{const.} \tag{14c}$$

Hence

$$\ln t'-E(H)/kT=\text{const.} \tag{15}$$

The derivative of both sides of Eq. (15) with respect to H may be cast in the form

$$\Delta\,\ln t'=\frac{1}{kT}\left.\frac{\partial E}{\partial H}\right|_M\Delta H. \tag{16}$$

The associated values of ΔH and $\Delta \ln t'$ in Eq. (16) are derived from the constant values of H associated with successive m vs $\ln t$ curves and the $\ln t$ coordinates of the points of intersection of the line $m=m_c$ with those curves.

The value of H_f may be derived from the gradient of the curve ΔH vs $\ln t$ since

$$\Delta H=\frac{kT}{\left.\partial E/\partial H\right|_M}\ln t'=H_f\ln t'. \tag{17}$$

III. EXPERIMENTAL APPLICATION TO THIN FILMS

The above analysis has been applied to study the time dependence and mechanisms of magnetization reversal in Tb-Fe-Co films by Brown *et al.*[15] Magneto-optic magnetometer measurements were made of the time dependence of the magnetization of thin films of Tb-Fe-Co when subjected to various fixed values of reversing field. The experimental results obtained using a 48.5 nm thick film of $Tb_{0.22}(Fe_{0.9}Co_{0.1})_{0.78}$ are shown in Fig. 5. Associated values of H_a and $\ln t'$, obtained from the intersections of the experimental curves with lines $m=m_c$ within the range $-0.9\leq m_c\leq 0.9$, are plotted in Fig. 6. The average of the five values of H_f is 87.3 ± 1 Oe. It follows that the activation energy of the process responsible for magnetization reversal

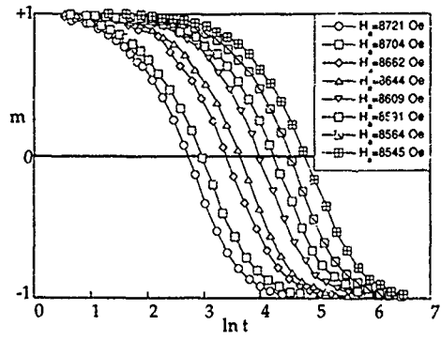

FIG. 5. Experimental results for the decay of magnetization with $\ln t$ at fixed values of reversing field for a 48.5 nm thick film of $Tb_{0.22}(Fe_{0.9}Co_{0.1})_{0.78}$. Note the similarity with Fig. 4.

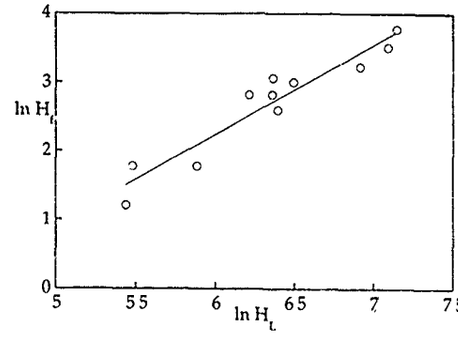

FIG. 7. The Barbier plot of $\ln H_f$ vs $\ln H_L$ for the data of Labrune *et al* (see Ref. 16). The slope of the line is 1.22.

in this film is a linear function of field, at least over the measured range of 8.55–8.76 kOe, and within the range $-0.9 \leq m_c \leq 0.9$. This observation is consistent with the view that magnetization reversal proceeds by activation of reversal of magnetization in regions of constant volume v. Using a value of 86 G for the spontaneous magnetization of the material of the film, v was found to be 5.5×10^{-18} cm^3, the volume of a sphere of diameter 22 nm.

Labrune *et al.*[16] have also measured the time dependence of magnetization processes in rare-earth-transition-metal alloys including alloys of Gd-Fe and of GdTbFe. Application of the above analysis to their results, which are given in detail for a GdTbFe film, show that at $m=0$ a linear relation exists between ΔH and $\ln t'$ [Eq. (16)], leading to a value of $H_f=18.9$ Oe. It appears in this case that H_f is not independent of m, decreasing by approximately 10% as m decreases from 1 to -1.

The apparent coercivity H_c of magneto-optic films, i.e., that field at which the holomagnetization is zero, depends on the time at which the measurement of m is made after the reversing field is switched on. The shorter the time, the higher the apparent coercivity will be. There exists a limiting field H_L for which the activation energy is zero. In this circumstance, reversal of magnetization will occur in a time $t=1/f_0$.

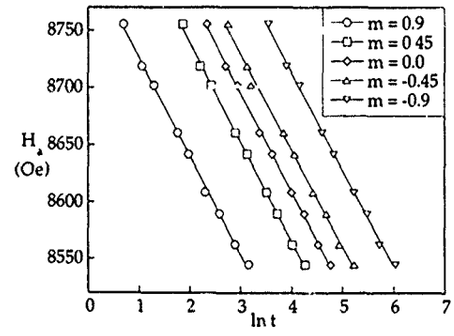

FIG. 6. Associated values of H_a and $\ln t$ from the intersections of lines of constant m with the experimental curves in Fig. 5. The average slope of the five lines is 87.3±1 Oe, which is equivalent to the fluctuation field H_f.

The value of H_L may be calculated using Eq. (17) assuming that the value of H_c', say at time $t=1$ s, is known and that the value of H_f remains constant over the field range H_c' to H_L:

$$H_L = H_c' + H_f \ln f_0 \cong H_c' + 21 H_f,$$

taking $f_0 \approx 10^9$ Hz.

In the case of the TbFeCo film considered above, $|H_L| = 11.01$ kOe.

Labrune *et al.*[16] have provided data for 11 different samples of GdFe and GdTbFe alloys having values of H_c ranging from about 200 to 1300 Oe. These data have been used to construct the Barbier plot of $\ln H_L$ vs $\ln H_f$ shown in Fig. 7. The slope of the line is 1.22. Wohlfarth[17] found in an analysis of a Barbier plot of data for different materials with coercivities ranging from 1 to 1000 Oe that the slope was 1.37.

Extension of the activation energy analysis of the magnetic properties of thin films leads to information on the mechanisms responsible for the growth of regions of reverse magnetization.[15,16] Details of the fractal or other nature of the magnetization of thin films may also be obtained from observations of time dependent behavior.

IV. CONCLUSIONS

The important information derived from magnetic viscosity measurements concerns the variation of the fluctuation field H_f as a function of magnetic state parameters. Reliable values of H_f, derived from the slope of M vs $\ln t$ curves and irreversible susceptibility χ_{irr} as $H_f = S/\chi_{irr}$, can only be obtained when χ_{irr} is carefully defined as $\partial M_{irr}/\partial H|_{M_{irr}}$.

The value of measurements of H_f lies in the fact that its definition involves $\partial E/\partial H|_M$, the variation with field of the activation energy of the metastable states responsible for irreversible magnetization at the point of measurement. It then becomes possible to check numerical values of $\partial E/\partial H|_M$ against the predictions of postulated models of magnetic behavior.

The application of activation energy modeling of magnetic behavior of some magneto-optic films is particularly simple. It produces information on the growth of magnetized regions and the micromagnetic structure of the films.

[1]J. A. Ewing, Philos. Trans. R. Soc. London **176**, 569 (1885).
[2]Rayleigh, Proc. R. Soc. London **46**, 249 (1889).
[3]F. Preisach, Z. Phys. **94**, 277 (1935).
[4]R. Street and J. C. Woolley, Proc. Phys. Soc. London, Sect. B **62**, 141 (1949).
[5]R. Street and J. C. Woolley, Proc. Phys. Soc. London, Sect. B **63**, 509 (1950).
[6]L. Néel, J. Phys. Radiat. **11**, 49 (1950).
[7]L. Néel, J. Phys. Radiat. **12**, 339 (1951).
[8]E. C. Stoner and E. P. Wohlfarth, Philos. Trans. R. Soc. London, Ser. A **52**, 562 (1949).
[9]P. Gaunt, Philos. Mag. B **48**, 261 (1983).
[10]P. Gaunt, IEEE Trans. Magn. **19**, 2030 (1983).
[11]S. Chikazumi, J. Magn. Magn. Mater. **54–57**, 1551 (1986).
[12]R. Street, J. C. Woolley, and P. B. Smith, Proc. Phys. Soc. London, Sect. B **65**, 679 (1952).
[13]Y. Estrin, P. G. McCormick, and R. Street, J. Phys: Condens. Matter **1**, 4845 (1989).
[14]L. Folks and R. Street (these proceedings).
[15]S. D. Brown, R. Street, R. W. Chantrell, and P. W. Haycock (unpublished).
[16]M. Labrune, S. Andrieu, F. Rio, and P. Bernstein, J. Magn. Magn. Mater. **80**, 211 (1989).
[17]E. P. Wohlfarth, J. Phys. F **14**, L155 (1984).

Analysis and interpretation of time dependent magnetic phenomena (invited)

L. Folks and R. Street
Research Centre for Advanced Mineral and Materials Processing, The University of Western Australia, Nedlands 6009, Australia

Time dependence of intensity of magnetization is the result of thermal activation of metastable domain processes. The simple (M,H) representation of magnetic behavior may be extended to include time dependent effects using a constitutive equation. Magnetic processes may be described by the movement of a point over a three-dimensional surface with coordinates M, H, and $\dot{M}$. The parameters required to define the surface, Λ (or fluctuation field H_f) and χ, may be derived from measurements of the time dependence of magnetization. A review of the utilization of the constitutive equation is given and simple methods for obtaining the material parameters from conventional magnetic viscosity measurements (under constant applied field conditions) are described. Measurements of Λ in particular provide additional quantitative information on magnetization processes which may be compared with predictions of proposed models of magnetization. The results of measurements of Λ and susceptibility χ for CrO_2 powders and sintered and melt-quenched rare earth-transition metal borides are presented. Conclusions about the magnetization mechanisms of these materials are discussed.

I. INTRODUCTION

Hysteresis in ferromagnets arises from domain processes which progress through states of metastable equilibrium. Examples are

(1) coherent or incoherent rotation of magnetization in single domain particles (Stoner and Wohlfarth[1]),
(2) pinning and unpinning of domain boundary walls (Gaunt[2,3]), and
(3) nucleation of domains of reverse magnetization (Chikazumi[4]).

Transitions from metastable to stable states may be achieved by the supply of activation energy, for example, by changing the applied field or by thermal agitation. At constant field, thermal activation alone may lead to significant variations in magnetization, amounting in some cases[5] to greater than 20% of the saturation magnetization in 10^2 s. Time dependence of magnetization under constant field conditions is referred to as magnetic viscosity or magnetic aftereffect. All ferromagnets subject to hysteresis exhibit time dependence of magnetization to a greater or lesser extent. As a general rule time dependent behavior is more pronounced in higher coercivity materials (Barbier[6]). It follows that the representation of the magnetic behavior by (M vs H) data is incomplete in that time dependence is neglected. Investigations of magnetic viscosity were described by Street and Woolley[7] in 1948 and Néel[8] in 1949 and led to phenomenological descriptions of time dependent behavior in terms of distributions of activation energies and fluctuation fields, respectively.

Estrin *et al.*[9] developed an alternative approach by analogy with the phenomenological description of plastic deformation of crystals. The magnet analog of plastic strain and stress were taken as the irreversible component of intensity of magnetization M_{irr} and the internal magnetic field H_i acting on the sample, respectively. The time dimension was introduced through $\dot{M}_{irr}$, the choice of which was determined by the Arrhenius relation

$$\dot{M}_{irr}(E)=\dot{M}_{irr}(E_0)\exp\left(-\frac{E(H)}{kT}\right), \tag{1}$$

from which

$$\ln \dot{M}_{irr}(E)=\ln \dot{M}_{irr}(E_0)-\frac{E(H)}{kT}, \tag{2}$$

where $\dot{M}_{irr}(E_0)$ is the rate of change of M_{irr} for activation energy $E(H)=0$.

Then, the constitutive equation of state is written in differential form:

$$dH_i=\frac{1}{\chi^i_{irr}}\,dM_{irr}+\Lambda\; d\,\ln(\dot{M}_{irr}), \tag{3}$$

where

$$\chi^i_{irr}=\left.\frac{\partial M_{irr}}{\partial H_i}\right|_{M_{irr}} \quad \text{and} \quad \Lambda=\left.\frac{\partial H_i}{\partial \ln \dot{M}_{irr}}\right|_{M_{irr}}. \tag{4}$$

Hence *isothermal* magnetization behavior may be represented by the movement of a point on a three-dimensional surface in $(M,H,\dot{M})$ space defined by Eq. (3), for which the intrinsic irreversible susceptibility χ^i_{irr} and Λ are required as functions of M. The functional dependence of both the intrinsic irreversible susceptibility χ^i_{irr} and Λ can be determined from magnetic viscosity measurements. In this paper the use of the constitutive equation to describe the field and time dependence of magnetization is discussed.

II. MAGNETIC VISCOSITY MEASUREMENTS

The constitutive equation may be applied to predict the behavior of magnetic systems subject to specified time constraints and initial conditions, e.g., predictions of the M vs H curves as the field is varied at uniform rates (conventional hysteresis curves).[10] Conventionally, measurements of magnetic viscosity are carried out at constant applied field, i.e., during the measurements, $\dot{H}_a=0$. The solution of Eq. (3) for M as a function of t requires the specification of the initial values of M_{irr} and $\dot{M}_{irr}$ at the origin of time for the measure-

 0021-8979/94/76(10)/6391/5/$6.00 © 1994 American Institute of Physics

ment. For simplicity, consider a specimen which has zero demagnetization factor. Then $\dot{H}_i=\dot{H}_a=0$ and the differentiation of Eq. (3) leads to

$$\dot{H}_i=\frac{1}{\chi'_{irr}}\dot{M}_{irr}+\Lambda\frac{\ddot{M}_{irr}}{\dot{M}_{irr}}=0. \tag{5}$$

The solution of Eq. (5), assuming that Λ and χ'_{irr} are independent of M during a magnetic viscosity experiment, is

$$M_{irr}=M_{irr}(0)+\Lambda\chi'_{irr}\ln(t+t_0), \tag{6}$$

where $M_{irr}(0)$ is the value of M_{irr} at $t=0$ and $t_0=\Lambda\chi'_{irr}/\dot{M}_{irr}(0)$. $\dot{M}_{irr}(0)$ is the rate of change of irreversible magnetization at $t=0$.

Equation (6) may be written as

$$M_{irr}=\text{const}+S(0)\ln(t+t_0), \tag{7}$$

where

$$S(0)=\Lambda\chi'_{irr}. \tag{8}$$

It is customary to present magnetic viscosity data in the form of $M(t)$ vs $\ln(t)$ graphs. It follows from Eq. (7) that $M(t)$ will be a linear function of $\ln(t)$ only for times of observation $t\gg t_0[=S/\dot{M}_{irr}(0)]$ and when S is constant over the range of values of M_{irr} observed during a magnetic viscosity measurement. Nonlinear $M(t)$ vs $\ln(t)$ curves arising from both these causes have been observed.[5,11]

An expression for the parameter Λ, which has dimensions in Oersteds, introduced in the constitutive equation (3) may be obtained by differentiation of Eq. (2) with respect to H_i by

$$\left.\frac{\partial\ln\dot{M}_{irr}}{\partial H_i}\right|_{M_{irr}}=-\frac{1}{kT}\left.\frac{\partial E(H_i)}{\partial H_i}\right|_{M_{irr}}=\frac{1}{\Lambda}, \tag{9}$$

i.e.,

$$\left.\frac{\partial E}{\partial H_i}\right|_{M_{irr}}=-\frac{kT}{\Lambda}. \tag{10}$$

The slope of the M_{irr} vs $\ln(t+t_0)$ is written $S(0)$ to denote that it applies to measurements on specimens with demagnetizing factor $D=0$.

The parameter Λ is directly related to the field dependence of the activation energy required to activate the irreversible domain processes responsible for magnetic viscosity effects. The value of $(\partial E/\partial H_i)|_{M_{irr}}$ is determined by the physical nature of the domain processes involved. Expressions for $\partial E/\partial H$ for different models of magnetization behavior may be calculated and compared with measured values of Λ. In Néel's model of viscosity[8] the effects of thermal energy on magnetization were represented by a fictitious fluctuation field H_f which is identical with the parameter Λ.

For example, consider a material consisting of aligned uniaxial ferromagnetic grains with spontaneous magnetization M_{spont} initially magnetized in the positive direction. If demagnetization proceeds by reversal of magnetization from nuclei of negative magnetization of fixed volume v then,

$$\frac{\partial E}{\partial H}=-vM_{spont}. \tag{11}$$

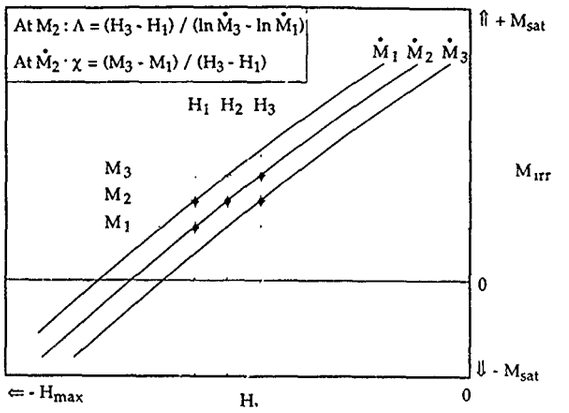

FIG. 1. Illustration of determination of Λ from experimental data.

From Eq. (10) for this idealized model,

$$v=\frac{kT}{\Lambda M_{spont}}. \tag{12}$$

Thus, in principle, additional quantitative information about the mechanisms of magnetization may be obtained from measurements of Λ.

Cammarano[12] has pointed out the interrelation of Λ and χ which arises from consideration of Eq. (3) as a perfect differential, i.e.,

$$\frac{\partial}{\partial\ln\dot{M}_{irr}}\left(\frac{1}{\chi'_{irr}}\right)=\frac{\partial}{\partial M_{irr}}(\Lambda). \tag{13}$$

It follows that if Λ is constant independent of M then χ'_{irr} is independent of $\dot{M}_{irr}$. A characteristic feature of many permanent magnet materials is that Λ is constant over large ranges of values of M. Also, within these ranges of M it has been shown that experimental values of χ'_{irr} are independent of $\dot{M}_{irr}$ as predicted by Eq. (13).[13]

III. FINDING Λ AND χ

Using the definitions given in Eq. (4), Λ and χ'_{irr} may be evaluated from data obtained from magnetic viscosity experiments as illustrated in Fig. 1. In order to construct these graphs, which are almost invariably derived from results of measurements on specimens with nonzero demagnetization factors D, it is necessary to account for the demagnetizing fields, i.e., $H_i=H_a-DM_{tot}$ where M_{tot} is the measured intensity of magnetization, and it is also required to derive values of M_{irr} as $(M_{tot}-M_{rev})$, where M_{rev} is the reversible component of intensity of magnetization.

The variation of magnetization for a specimen with demagnetization factor D may be derived from the constitutive equation as

$$M_{tot}=M_{tot}(0)+t'_0\dot{M}(0)\ln\left(1+\frac{t}{t'_0}\right), \tag{14}$$

where

$$t_0' = \frac{\Lambda \chi_{\rm irr}^i}{\dot{M}(0)} \frac{1}{(1+D\chi_{\rm tot}^i)}.$$

The values of the susceptibilities are obtained from slopes of the M vs H curves taken at constant $\dot{M}_{\rm irr}$.

The variation of $M_{\rm tot}$ is predicted to be a linear function of $\ln(t + t_0')$ but the slope

$$S(D) = \frac{\Lambda \chi_{\rm irr}^i}{1+D\chi_{\rm tot}^i} = \frac{S(0)}{1+D\chi_{\rm tot}^i} = \frac{\Lambda(\chi_{\rm tot}^a - \chi_{\rm rev}^a)}{1-D\chi_{\rm rev}^a}. \quad (15)$$

If $D\chi_{\rm rev}^a \ll 1$, then

$$\Lambda \doteq \frac{S(D)}{(\chi_{\rm tot}^a - \chi_{\rm rev}^a)}. \quad (16)$$

Equation (16) has been widely used to determine Λ. However, it follows from the above that unequivocal values of Λ will be obtained from Eq. (16) only if $\chi_{\rm tot}^a$ is evaluated as $(\partial M_{\rm tot}/\partial H_a)|_{\dot{M}_{\rm irr}}$.

The magnetic viscosity data required to construct graphs of the form shown in Fig. 1 may be obtained by measuring the time dependence of magnetization at different constant values of applied field on both the initial magnetization (first quadrant) curve and the demagnetization (second and third quadrant) curve. Measurements are made using a vibrating sample magnetometer under computer control. If a demagnetizing curve is to be measured, the sample is first exposed to a saturating field in the positive direction. Then the field is ramped to some negative value and held constant while the magnetic viscosity is recorded. A small recoil curve is then performed by ramping the field first in a positive direction by an amount which is small compared to Λ, then in a negative direction back to the measurement field. The field is then either ramped in a negative direction to the next measurement field and the process repeated (called a "multiple step per loop" experiment) or cycled through negative saturation and back to positive saturation before continuing to the next measurement field (called a "single step per loop" experiment). The small curves are used to estimate $\chi_{\rm rev}^a$ at the measurement field. The experimental technique is illustrated in Fig. 2.

Some care should be taken with sample preparation in the case of bulk materials as the condition of the surface and nonuniform magnetization may have a significant impact on the magnetic behavior.[14] It is best that measurements of bulk materials be performed on well polished spheres[15] so that the impact of the surface is minimized and the demagnetizing factor is known. Then Eq. (16) may be used to find Λ.

IV. RESULTS AND DISCUSSION

The mechanisms of magnetization in permanent magnets and in particulate recording media are of continuing interest in the search for improved materials. Comparisons may be made of the measured values of the parameters Λ and χ with those predicted by models of magnetic processes.

For example, measurements performed on a sample of acicular CrO_2 particles, commonly used as a recording medium, are shown in Fig. 3. The specimen, of volume 0.134 cm^3, was prepared by embedding 0.120 g of CrO_2 powder in

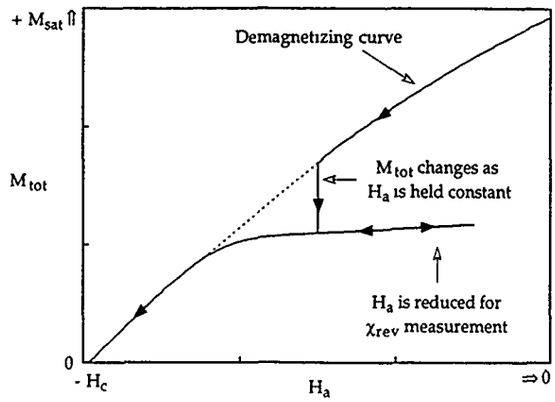

FIG. 2. Schematic of experimental technique. The magnetic viscosity is measured at a constant value of H_a for a period of time. Then the applied field is ramped towards zero by a small amount and the apparent reversible susceptibility determined from the slope of $M_{\rm tot}$ vs H_a. The field is then ramped in a negative direction to the next measurement field.

paraffin wax, hence the average density of CrO_2 in the specimen was 0.895 g cm^{-3}. The magnetization curve and the hysteresis curve for this sample are shown in Fig. 3(a). Figure 3(b) shows the values of Λ, calculated as described above, as a function of the specific magnetization σ during

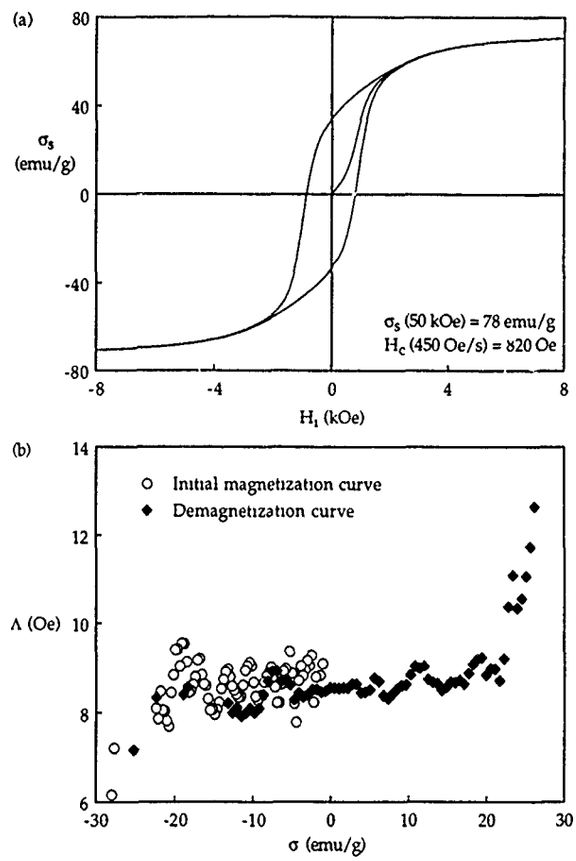

FIG. 3. (a) Magnetization curve and hysteresis curve for CrO_2 particles measured at room temperature with a maximum field of 50 kOe and a ramp of 450 Oe/s. (b) Λ vs specific magnetization for CrO_2 particles at room temperature with a maximum field of 50 kOe.

the magnetizing of the sample (from a thermally demagnetized state) and the demagnetization curve. Over the range of specific magnetization from +20 to −20 emu g^{-1} for the demagnetizing curve, the results reported here may be represented by a line $\Lambda=8.52+0.02\,\sigma$. Within experimental error, for initial magnetization Λ is independent of σ within the range 0 to −25 emu g^{-1} and its value is 8.7±0.4 Oe.

The CrO_2 particle volumes V, estimated from SEM images, are about 4×10^{-16} cm^3 compared with the value of 6.2×10^{-16} cm^3 reported by de Witte *et al.*[16] The activation volume v calculated from Eq. (12) using $\Lambda=8.6$ Oe and $M_{spont}=330$ G is 1.5×10^{-17} cm^3 which is about 4% of the particle volume. A similar ratio was obtained by de Witte *et al.*[16]

As another example, the hysteresis curve and the variation of Λ with M_{irr} for a polished 5 mm diameter sphere of sintered $Pr_2Fe_{14}B$ material are shown in Fig. 4. Over the range +400 to −400 G, $\Lambda=99.5-0.02\,M_{irr}$. Over this range the activation volume, calculated from Eq. (12) using $M_{spont}=1100$ G, $v=3.79\times10^{-19}+6.26\times10^{-23}\,M_{irr}$, has linear dimensions corresponding to about six crystalline unit cells.[17] Givord *et al.*[18] have related v to δ^3, where δ is the average domain-wall width in the material. For sintered permanent magnet materials of the Nd-Fe-B type initial magnetization involves the movement of domain boundary walls through individual grains. The discontinuous nature of this motion has been observed in the form of Barkhausen pulses.[19] Attempts to observe time dependent behavior here have been unsuccessful, presumably because of the small values of activation energy required to release the domain walls from pinning centers within the grains. Values of $\chi^i_{irr}|_{\dot{M}_{irr}}$ as functions of M_{irr} are shown in Fig. 4(c). The different symbols represent measurements made at different values of $\dot{M}_{irr}$. All the values lie on the same curve which, since Λ is almost independent of M_{irr}, is a consequence of Eq. (13).

Towards the ends of the ranges of magnetization it is not possible to make accurate measurements of Λ or χ^i_{irr} since the curves of constant $\dot{M}_{irr}$ converge and Eq. (4) becomes difficult to evaluate with certainty. It follows that for a given material there is a limited range of magnetization over which reliable measurements of Λ and χ^i_{irr} may be made.

The observations on both CrO_2 and $Pr_2Fe_{14}B$ show that Λ is approximately constant over a substantial part of the total change of intensity of magnetization. These results are consistent with the assumption that the major part of magnetization reversal in both materials results from activation of nuclei of reverse magnetization having volumes which are substantially independent of M. There is additional evidence to support this supposition in the case of $Pr_2Fe_{14}B$, specifically the ease with which the material may be magnetized and the dependence of coercivity on the maximum magnetizing field.[20]

The case of magnetization reversal of acicular particles has been considered by Sharrock.[21] He notes that theoretical studies by Schabes and Bertram[22] have concluded that a strong field applied to one end of an acicular particle tends to switch the magnetization of the entire particle by means of a propagating magnetic reversal—a microscopic analog of the classic Sixtus and Tonks experiment.[23] A mechanism of this kind would be consistent with the proposition that magnetization reversal may be initiated by thermal activation in a small volume of the particle.

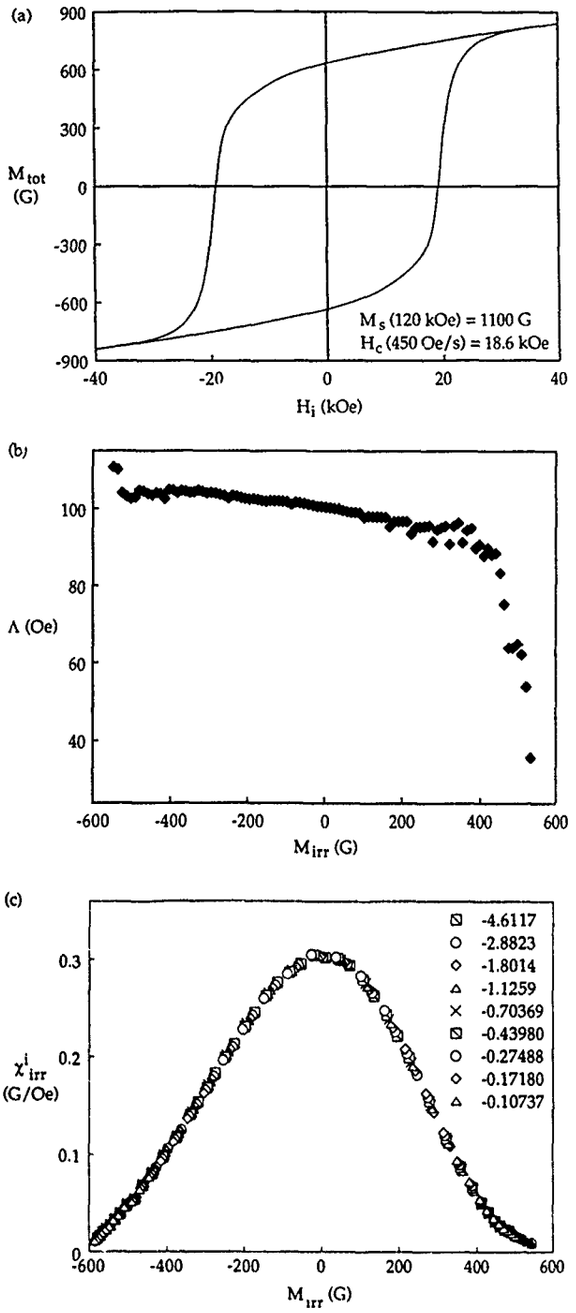

FIG. 4. Measurements of a sample of sintered $Pr_2Fe_{14}B$ at room temperature with a maximum field of 50 kOe and $H_a=450$ Oe/s. (a) A hysteresis curve. (b) Λ vs M_{irr}. (c) χ^i_{irr} vs M_{irr} at many values of $\dot{M}_{irr}$ as indicated in the legend.

V. SUMMARY

Time dependent magnetization may be analyzed in terms of a constitutive equation involving variables H_i, M_{irr} and two parameters $\Lambda(M_{irr})$ and $\chi^i_{irr}(M_{irr})$. The functions $\Lambda(M_{irr})$ and $\chi^i_{irr}(M_{irr})$ may be determined experimentally from mag-

netic viscosity experiments. For representative magnetic recording media (CrO_2) and high-energy permanent magnet materials (PrFeB) the $\Lambda(M_{irr})$s are found to be slowly varying functions of M_{irr} and the $\chi^i_{irr}(M_{irr})s$ are peaked around $M_{irr}=0$.

The constitutive equation with values of $\Lambda(M_{irr})$ and $\chi^i_{irr}(M_{irr})$ for a particular material may be used to analyze its time dependent magnetization with given external constraints, e.g., with an applied field ramped at a uniform rate or under impulsive field conditions.

[1] E. C. Stoner and E. P. Wohlfarth, Philos. Trans. R. Soc. London **240**, 599 (1948).
[2] P. Gaunt, Philos. Mag. B **48**, 261 (1983).
[3] P. Gaunt, IEEE Trans. Magn. **19**, 2030 (1983).
[4] S. Chikazumi, J. Magn. Magn. Mater. **54–57**, 1551 (1986).
[5] R. Street, L. Folks, and S. Hirosawa, Proceedings of the Sixth International Symposium on Magnetic Anisotropy and Coercivity in Rare-Earth Transition Metal Alloys, Pittburgh, 1990, edited by S. G. Sankar (Carneigie Mellon University Press, Pittsburgh, 1990), pp. 1–11.
[6] J.-C. Barbier, Ann. Phys. (Paris) **12**, 84 (1954).
[7] R. Street and J. C. Woolley, Proc. Phys. Soc. London, Sect. A **62**, 562 (1949).
[8] L. Néel, Ann. Géophys. **5**, 99 (1949).
[9] Y. Estrin, P. G. McCormick, and R. Street, J. Phys.: Condens. Matter **1**, 4845 (1989).
[10] R. Street, P. G. McCormick, L. Folks, and R. Newman, J. Magn. Magn. Mater. **104–107**, 371 (1992).
[11] M. El-Hilo, K. O'Grady, and R. W. Chantrell, J. Magn. Magn. Mater. **109**, L164 (1992).
[12] R. Cammarano, Ph.D. thesis, The University of Western Australia, 1993.
[13] R. Street, P. G. McCormick, and L. Folks, J. Magn. Magn. Mater. **104–107**, 368 (1992).
[14] H. Nishio, H. Yamamoto, M. Nagakura, and M. Uehara, IEEE Trans. Magn. **26**, 257 (1990).
[15] L. Folks, R. Street, G. Warburton, and R. C. Woodward, Meas. Sci. Technol. **5**, 1 (1994).
[16] A. M. de Witte, K. O'Grady, G. N. Coverdale, and R. W. Chantrell, J. Magn. Magn. Mater. **88**, 183 (1990).
[17] J. F. Herbst, Rev. Mod. Phys. **63**, 819 (1991).
[18] D. Givord, A. Lienard, P. Tenaud, and T. Viadieu, J. Magn. Magn. Mater. **67**, L281 (1987).
[19] P. J. Thompson (private communication).
[20] S. Chikazumi, J. Magn. Magn. Mater. **54–57**, 1551 (1986).
[21] M. P. Sharrock, IEEE Trans. Magn. **26**, 193 (1990).
[22] M. E. Schabes and H. N. Bertram, IEEE Trans. Magn. **25**, 3662 (1989).
[23] K. J. Sixtus and L. Tonks, Phys. Rev. **37**, 93 (1931).

Ubiquitous nonexponential decay: The effect of long-range couplings? (invited)

E. Dan Dahlberg and D. K. Lottis
School of Physics and Astronomy, University of Minnesota, Minneapolis, Minnesota 55455

R. M. White
Department of Electrical and Computer Engineering, Carnegie Mellon University, Pittsburgh, Pennsylvania 15213

M. Matson and E. Engle
School of Physics and Astronomy, University of Minnesota, Minneapolis, Minnesota 55455

Many physical systems exhibit a dynamic response referred to either as slow relaxation, a quasilogarithmic time dependence, or a stretched exponential response. Historically this time dependence has been attributed to the presence of disorder which creates a distribution of relaxation times. In two papers [D. K. Lottis, E. Dan Dahlberg, J. Christner, J. I. Lee, R. Peterson, and R. White, J. Appl. Phys. **63**, 2920 (1988); D. K. Lottis, R. M. White, and E. Dan Dahlberg, Phys. Rev. Lett. **67**, 362 (1991)], we have shown that this time dependence can alternatively be explained to be a consequence of interactions or couplings. In the model, the interactions between relaxing spins, the dipole–dipole couplings, drive the system from an initial state towards equilibrium. As the system relaxes, the dipolar energy is reduced and the driving force diminishes. This process gives rise to the observed slow relaxation-time dependence in a very natural manner. To guarantee the absence of disorder, the model considers the dipolar coupling or interaction between relaxing spins with a mean-field approximation, the demagnetization field. Another feature observed in physical systems which the model explains is the nonmonotonic temperature dependence of the logarithmic decay slope. In addition to a description of the model, measurements to determine the presence of interactions in some of the systems will be discussed.

I. INTRODUCTION

A remarkable number of diverse physical systems exhibit the phenomenon which is referred to as slow relaxation.[1] The manifestation of this phenomenon is best explained graphically, as in Fig. 1, where the temporal decay of the remanent magnetization of an archetypal spin glass, AgMn, is shown. The system was prepared by cooling from high temperature to low temperatures with a magnetic field applied. This process results in a magnetization in the system known as the remanent magnetization. As can be seen, the field cooled magnetic state of the system relaxes after the removal of the cooling field with the remanent magnetization decaying quasilogarithmically with time. Other systems which exhibit this strange time dependence in response to an external stimulus include the trapped flux in superconductors,[2] the decay of the charge carriers in amorphous semiconductors,[3] and the strain fields or structure in glasses and polymers,[1] to name a few. That these systems are so diverse yet exhibit the same relaxation dynamics has confounded researchers in their quest for a simple explanation of this phenomenon.

We recently developed an explanation in which interactions or couplings between the relaxing entities are responsible for this seemingly ubiquitous time dependence.[4,5] In what follows, we will develop this view of slow relaxation starting with the simple Debye relaxation model. This will be followed by an extensive discussion of how it explains various observed features in physical systems. How to more fully test the applicability of the model is discussed at the end of the discussion session.

II. INTERACTION MODEL SYSTEM

As a starting point for understanding this phenomenon, it is useful to recall the expected response of a relaxing system, Debye relaxation. Debye relaxation can be understood by considering the relaxation of a collection of two level systems with an energy barrier (E_b) separating the levels as shown in Fig. 2. Each entity (one may call them either particles, spins, or moments) in the collection acts independently of all others. If the system of N particles is prepared

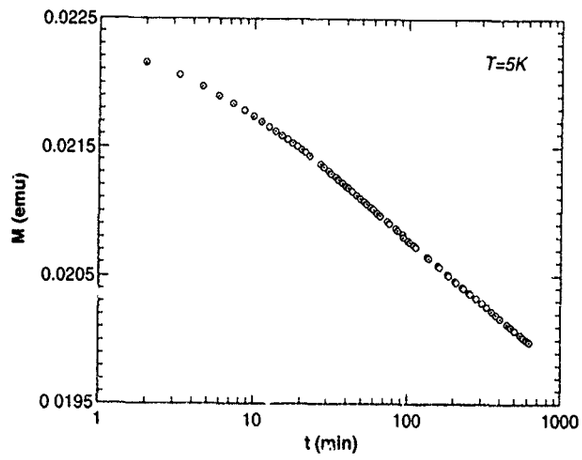

FIG. 1. An example of slow relaxation. The system is an alloy of 7.8% Mn in Ag The sample was cooled in a field of 3 kG which resulted in a remanent magnetization. The resulting decay was observed after removal of the cooling field.

 0021-8979/94/76(10)/6396/5/$6.00 © 1994 American Institute of Physics

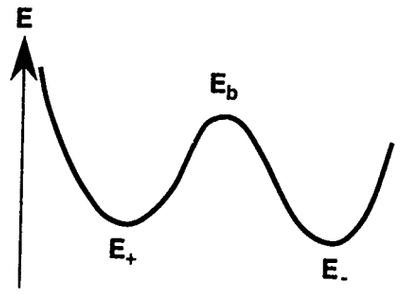

FIG. 2. A two level system with the energy minima separated by an energy barrier. This system provides a useful description for a number of physical systems and, in the absence of interactions, a collection of these systems with identical parameters exhibits an exponential time dependence.

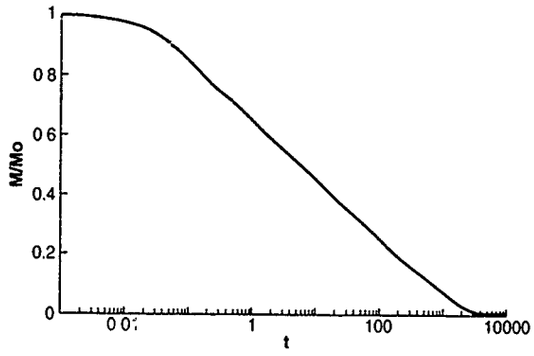

FIG. 3. The effects of disorder on exponential decay. This artificial relaxation curve is the result of averaging the relaxation curves for five exponential decays. The decay times are 0.1, 1, 10, 100, and 1000 s. Note that the quasilogarithmic time dependence is roughly a decade less than the number of decades in the average.

with all the particles in the higher energy state, it will relax to a distribution of particles in the higher energy state (or up state, E_+) and lower energy state (or down state, E_-) where the ratio of the number of particles in the up state to the down state will be given by the Boltzmann factor, $\exp(-\beta\Delta E)$, where β is k_BT and ΔE is (E_+-E_-). The dynamics of this relaxation process depend upon the attempt frequencies for the particles in the up and down states to try to get over the barrier, ω_+ and ω_-, respectively, in addition to the three energies defined above and in Fig. 2. By recognizing that the number of particles hopping over the barrier at any given instant from the up state to the down state depends upon the number of particles in that state at that instant, N_+, one is led to the differential equation for dN_+/dt,

$$\frac{dN_+}{dt} = -\omega_+ N_+ \exp[-\beta(E_b-E_+)] + \omega_- N_- \exp[-\beta(E_b-E_-)]. \quad (1)$$

This differential equation includes the possibility for particles in the down state to return to the up state. By assuming that the attempt frequencies ω_+ and ω_- are equal, and recognizing that the total number of particles $N=N_++N_-$, this equation can be rewritten as

$$\frac{dN_+}{dt} = -\omega N_+ \exp[-\beta(E_b-E_+)] + \omega(N-N_+)\exp[-\beta(E_b-E_-)]. \quad (2)$$

A solution to this differential equation leads to a decaying N_+ which is exponential in time, described by a single relaxation time τ; the τ is of the form $\tau=\omega^{-1}\exp(E_{\text{barrier}}/kT)$. This exponential decay is generally referred to as Debye relaxation. Although this derivation is very straightforward, as stated earlier, many systems do not obey this relationship.

Rather than abandon this simple model, it has long been the usual practice to assume distributions of energies E_+, E_-, and E_b which gives rise to a distribution of relaxation times, i.e., a distribution of τ's. As an example, a system containing five discreet τ's, each separated by a decade, provides a quasilogarithmic relaxation over four decades in time. To illustrate this, Fig. 3 is the relaxation of a system of particles with equal numbers of particles having relaxation times of 0.1, 1, 10, 100, and 1000 s. This may seem to be a rather large amount of disorder to be present in a physical system, but because the τ's are exponential functions of energy, this distribution corresponds to a spread in energy barriers of only one decade, approximately. Clearly, with this approach, most investigations of the relaxation processes of the various physical systems argue that the energy distribution is the measured entity. For one example of this approach, the temperature dependence of the relaxation rate has been used by the Grenoble spin-glass group to determine the energy distribution using $T\ln(t)$ scaling.[6]

An alternative view of slow relaxation was presented by some of us in a series of publications starting in 1988.[4,5] The fundamental premise for the model is that interactions, without any disorder, can result in the quasilogarithmic relaxation observed in so many physical systems.

The model system we developed consists of a plane of spins or magnetic moments with an anisotropy energy such that the energy minima are with the moments aligned perpendicular to the plane, i.e., the energy minima states are up and down states which are perpendicular to the plane. These spins interact through dipole–dipole interactions which are treated in a mean-field approximation. In the ground state this system contains no net magnetization, with one spin up for every spin down. When the system is saturated along the positive z axis, the demagnetizing field of the system will be along the negative z axis, driving the system back to equilibrium. Because the remanent field decreases as equilibrium is approached, the thermal energy needed to overcome the anisotropy energy barrier increases. This slows the relaxation process over time, leading to quasilogarithmic relaxation. As will be shown later, if there were no interactions the system would still relax but since the barriers remain at their maximum height, the decay, with an exponential time dependence, would take a much longer time.

In this model each moment has a uniaxial magnetic anisotropy energy of the form $-K_u v\cos^2(\phi)$, where v is the volume of the spin grain, ϕ the angle between the spin vector and the positive z axis, and K_u a positive constant. This system of particles fits the two level model presented earlier; E_+ and E_- occur at values of $\phi=0$ and π and are degenerate

at an energy $-K_u v$. Assuming coherent rotation of the individual magnetic moments, the energy barrier maximum E_b occurs at $\pi/2$ and has a value of 0.

In the presence of an external magnetic field applied along the $\phi=\pi$ direction (taken to be the negative z-axis direction), the magnetic energy $M_s H v \cos(\phi)$, where M_s is the saturation magnetization of the spin grain, must be considered in addition to the anisotropy energy. This gives a total energy per particle of

$$E=-K_u v \cos^2(\phi)+M_s H v \cos(\phi). \tag{3}$$

There are two important changes when a magnetic field is applied. First, the energy minima are no longer degenerate although they still occur for $\phi=0$ and π. Second, the energy barrier is no longer at $\phi=\pi/2$. The value of ϕ corresponding to E_b is obtained by the usual process of differentiating and setting the result to zero. Using the E_b determined above and the E_+ and E_- determined from $\phi=0$ and π, respectively, the differential equation which describes the dynamics of the moments is then given by

$$\frac{dN_+}{dt}=-\omega_+ N_+ e^{-\beta\left[\frac{v}{4K_u}(M_s H-2K_u)^2\right]}+\omega_- N_- e^{-\beta\left[\frac{v}{4K_u}(M_s H+2K_u)^2\right]}, \tag{4}$$

where N_+ is the number of spins pointing up, N_- the number of spins pointing down, ω_+ and ω_- the attempt frequencies, and $\beta=1/K_b T$. This expression is an explicit development of Eq. (2) and would therefore describe the usual Debye relaxation with an exponential time dependence as in Eq. (3). In general, the attempt frequencies for the + and − spins are functions of the applied magnetic field and are not equivalent. However, setting the ω_+ and ω_- to be equal and independent of the applied field introduces little error as the relaxation is dominated by the argument of the exponential, not the prefactor. Therefore in the remaining discussion they will be given by ω.

This expression, of course, neglects any coupling between the particles. In particular, the dipole–dipole coupling between the magnetic moments of the particles is lacking. As the particles are arranged in a plane and restricted by the anisotropy energy to orient perpendicular to the plane, the dipolar interaction energy would be a minimum for the case where the alternating spins are antiparallel to each other, i.e., a dipolar antiferromagnet. In order to guarantee the absence of disorder, the dipolar couplings between the spins can be treated with an average or mean-field approximation, the demagnetization field. For the limiting case of planar symmetry with the magnetization perpendicular to the plane, as is appropriate for the present situation, this gives a field of $-4\pi M$ where $M=M_s(N_+-N_-)/N$, where N is the total number of moments. Defining ΔN such that $N_{+(-)}=N/2+(-)\Delta N/2$ (so $\Delta N=N_+-N_-$), one obtains

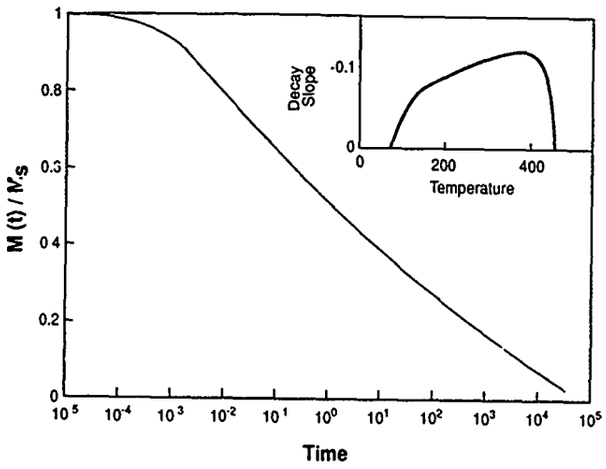

FIG. 4. An example of a slow decay of the model system given by Eq. (5). For this decay the relevant parameters are $K=5\times10$ ergs/cm, $M=200$ emu/cm, $T=300$ K, $v=2\times10^{-18}$ cm^3, and $\omega=\omega=2\times10^4$ s^{-1}. Note that the decay is measured over nine decades in time. The inset in the figure is the temperature dependence of the logarithmic slope of the decay taken at a time of 100 s. The nonmonotonic behavior of the slope is observed in magnetic and superconducting systems (see Refs. 12 and 2).

$$\frac{d\Delta N}{dt}=-\omega\left(\frac{N}{2}+\frac{\Delta N}{2}\right)\exp\left[-\frac{\beta v}{K_u}(2\pi M_s^2\Delta N/N-K_u)^2\right]+\omega\left(\frac{N}{2}-\frac{\Delta N}{2}\right)\exp\left[-\frac{\beta v}{Ku}(2\pi M_s^2\Delta N/N+K_u]^2\right]. \tag{5}$$

This nonlinear differential equation now describes the situation where the magnetic field of the spins are driving the system to a state with equal numbers of up and down spins. As the relaxation progresses, the field which drives the system decreases and thus the relaxation slows down. The result of this decreasing drive field is shown in Fig. 4. This figure is a numerical solution to the differential equation with the parameters listed in the figure caption. As shown, the relaxation rate slows down as the system relaxes. This quasilogarithmic time dependence occurs over six decades in time.

Several comments are necessary concerning this relaxation. The first is that although the data exhibit a quasilogarithmic time dependence, there is absolutely no disorder in the system. The couplings are treated in a mean-field approximation such that it is only the average field, $2\pi M_s\Delta N/N$, which enters the expression. The second is that various functional forms of slow dynamics must be considered, and while the data here is plotted against the log of time, it can also be fitted to a stretched exponential over several decades. Maybe without much surprise, it would appear that fitting to various functional forms of slow dynamics must be considered carefully before completely ascribing the behavior to a single one. Finally, for times longer than about 4×10^4 s, the slowly decaying function becomes exponential.[7] This long time regime can be understood by considering the limit in Eq. (4) where ΔN becomes small enough that the exponential is dominated by the K_u. In this limit, the differential equation becomes linear and the decay is expo-

nential. In the other time extreme, at short times, the initial time dependence is a result of the attempt frequency ω chosen for the generation of this data (about 10^9 s^{-1} for this figure).

The long time observation makes another point clear, that the relaxation is not slow; it is actually fast. If there were no interactions, the full energy barrier height would be present at all times; with interactions present, the barrier height is a function of the state of the system, but it is always less than it would be without the interactions. To further explain, if two otherwise identical systems, one with and one without couplings, were prepared in a state with all the spins parallel, they would both relax to a state with equal numbers of up and down spins. The main difference is that in the system without interactions there would be little decay until the time decade which is equivalent to the relaxation time over the full barrier height.[8]

III. DISCUSSION

To summarize the constraints of the model, we must note that it is for particles with constant magnetization, uniaxial anisotropy, and considers only coherent rotation for the magnetization reversal process in a single particle. Although the model system certainly exhibits a reasonable time dependence, it is necessary to show that the model does have a basis in fact with physical systems. We have previously shown that the decay of the remanent magnetization in thin films of CoCr can be fitted to the model over a limited magnetization decay range.[5] However, the volume of the magnetic entities, the only adjustable parameter in the fit, was several orders of magnitude smaller than that measured by electron microscopy. Although seemingly problematic, simple calculations show that this is a reasonable volume for a domain wall in one of the cobalt rich particles in the CoCr. This would indicate, at the very least, that the coherent rotation assumption is incorrect, a fact consistent with observed domain reversal in small particles.

Another feature which appears in many systems which exhibit this slow relaxation is a nonmonotonic decay slope. This feature is usually considered anomalous since one would expect any thermally activated process to accelerate at higher temperatures. However, the magnetization decay in superconductors,[2,9] ferrofluids,[10] and the CoCr alloys[11] exhibits a maximum as a function of temperature. This characteristic has been used as evidence that there is a collective transition of the decaying system. In the present model, this anomalous feature occurs in a very natural fashion for the following reason.

All experiments are constrained to measure the decay in a fixed time window. For example, in a SQUID magnetometer measurement, it may be that the measurements start approximately 1 min after a change in the external field. The measurements may then proceed for times up to hours or days. In any event, the time range of 1 min–1 day sets the measurement time window, and the decay slopes at all temperatures and initial states are defined in this window. At low temperatures, even though the interactions may be large, there is not enough thermal energy for the system to decay in the time window. At sufficiently high temperatures, the decay process is so rapid that, by the time the measurements start, the system has already relaxed, and again in the time window of the measurements, there is no measurable decay. Between these two extremes the decay rate measured in the time window goes through a maximum. If one could measure the initial decay rate, which occurs at zero time, it would continue to increase. The inset in Fig. 4 shows the temperature dependence of the decay slope from the model at the fixed time of 100 s (or a factor of $10^6\times$ the attempt frequency).

Another test of the applicability of the model is to confirm the presence of interactions. In the case of the magnetic aftereffect in ferromagnets, there was work which showed how the demagnetization factor altered the measured dynamics.[12] In this work, the larger the demagnetization factor, the more resistant the system was to being magnetized. This fact is consistent with Eq. (5) where the interaction or coupling term, $2\pi M_s \Delta N/N$, has a different numerical constant from 2π. In the case of superconductors, the frozen flux is associated with trapped vortices. Each vortex acts as a single magnetic dipole which can interact with the others via the dipole–dipole coupling. With only a very general argument, Tinkham used a similar rationale to get the logarithmic time dependence of the flux decay.[13]

For general applicability, one needs to determine the presence of interactions in these systems and their relevance to the magnetization process. We have previously used an approach developed by Wohlfarth[14] and Henkel[15] plotting the remanent magnetizations in what are referred to as Henkel plots. In that work[16] we were successful in showing how known interactions in a system, the perpendicular-to-the-plane demagnetization field, explained the observed remanances. It is important to note that Henkel plots may suffer from a nonrandom demagnetized state. Thus it would be best to work with a system which can be annealed prior to measurement. For this reason, and because it is an archetypal slow relaxation system, we have recently been studying the Henkel plots of spin glasses. Although in a preliminary stage, we note that all Henkel plots on the spin glass Ag:Mn indicate interactions are in fact present.[17]

A final comment to make is that the interactions in the model are treated to assure that disorder is not present and so the interactions must be responsible for any slow relaxation. In real systems, the interaction range is finite; therefore disorder is present. For example, starting from a saturated sample, after the very first spin or moment flips, its neighbors see a different dipolar field than the spins farther away. As the system evolves, this situation is exacerbated. So in the interaction driven model presented here, with the mean-field approximation, the slow relaxation occurs as a result of the couplings and disorder does not play a role. In real systems, with finite ranged interactions, some disorder is always present. The relevant question is then how important this disorder is compared to the interactions. To test this question, disorder must be included in the calculations, a process we have recently begun.[8]

It is important to point out that in addition to the work presented here, the model has been used by others with the inclusion of a domain-wall energy term, to model the magnetization process in magneto-optic media.[18]

As a final note, although the model developed here has focused on condensed-matter systems, there are other physical systems which are manifestly affected by interactions. A very simple way to understand how interactions can dominate the relaxation process is to consider radioactive decay. Most sophomore level modern physics textbooks derive the Debye relaxation law for β decay. This relaxation derivation is also applicable to other decays, such as U^{235} provided the decaying nuclei are well separated so that there are no interactions, i.e., independent decay. In the case of U^{235}, when the radioactive nuclei are close enough so that there are interactions, the decay process is changed considerably!

ACKNOWLEDGMENTS

This work was supported under AFOSR Grant No. AF/FA 9620-92-J-0185/P00003. One of the authors, E.D.D., would like to thank Dr. R. Kirby, Dr. J. Souletie, Dr. C. Dasgupta, Dr. M. Sharrock, Dr. J. Kakalios, Dr. R. Chantrell, Dr. K. O'Grady, Dr. O. Valls, and Dr. G. Mazenko for a number of interesting and relevant discussions over the course of these investigations.

[1] K. L. Ngai, Comments Solid State Phys. **9**, 127 (1979); **9**, 141 (1979).
[2] M. Tuomenen, A. M. Goldman, and M. L. Mecartney, Phys. Rev. B **37**, 548 (1988).
[3] J. Kakalios, R. Street, and C. Jackson, Phys. Rev. Lett. **59**, 1037 (1987).
[4] D. K. Lottis, R. M. White, and E D. Dahlberg, Phys. Rev. Lett. **67**, 362 (1991).
[5] D. K. Lottis, E. D. Dahlberg, J. Christner, J. I. Lee, R. Peterson, and R. White, J. Appl. Phys. **63**, 2920 (1988).
[6] J. J. Prejean and J. Souletie, J. Phys. (Paris) **41**, 1335 (1980).
[7] J. Shore (private communication).
[8] M. E. Matson, D. K. Lottis, and E. D. Dahlberg, J. Appl. Phys. **75**, 5475 (1994).
[9] C. W. Hagen and R. Griessen, Phys. Rev. Lett. **62**, 2857 (1989).
[10] W. Luo, S. R. Nagel, T. F. Rosenbaum, and R. E. Rosensweig, Phys. Rev. Lett. **67**, 2721 (1991).
[11] D. K. Lottis, E. D. Dahlberg, J. A. Christner, J. I. Lee, R. L. Peterson, and R. M. White, J. Phys. (Paris) C **8**, 407 (1988).
[12] R. Street, J. C. Woolley, and P. B. Smith, Proc. R. Soc. London, Ser. B **65**, 679 (1952).
[13] M. Tinkham, *Introduction to Superconductivity* (McGraw-Hill, New York, 1975), p. 178.
[14] E. P. Wohlfarth, J. Appl. Phys. **29**, 595 (1958).
[15] O. Henkel, Phys. Status Solidi **7**, 919 (1964).
[16] J. Skorjanec, J. Close, N. Kirchner, P. Iverson, and E. D. Dahlberg, J. Appl. Phys. **73**, 6671 (1993).
[17] E. Engle and E. D. Dahlberg (unpublished).
[18] R. D. Kirby, J. X. Shen, R. J. Hardy, and D. J. Sellmyer, **49**, 10 810 (1994) and D. J. Sellmyer, R. D. Kirby, and S. S. Jaswal, *Magnetism of Amorphous Metals and Alloys*, edited by J. A. Fernandez-Baca and W. Y. Ching (World Scientific, Hong Kong, 1994), Chap. 8.

Mesoscopic model for the primary response of magnetic materials (invited)

R. V. Chamberlin
Department of Physics and Astronomy, Arizona State University, Tempe, Arizona 85287-1504

A model for the relaxation of thermal fluctuations is applied to the dynamical response of magnetic materials. Systems investigated include paramagnets, spin glasses, and ferromagnets. The key feature which distinguishes the model is that it describes the behavior of localized normal modes (e.g., magnons), *not* barrier hopping or domain-wall motion. Mathematical approximations to the model reproduce several previously used empirical formulas, such as the stretched exponential, power-law, and logarithmic time dependences, but the unapproximated model gives generally better agreement with observed response. Data of sufficient quality and range allow quantitative confirmation of all assumptions of the model. The model provides a common physical basis for observed magnetic after-effects, the magnitude and distribution of Landau–Lifshitz damping parameters, and $1/f$ noise.

I. INTRODUCTION

Despite the fact that all classical systems must ultimately relax exponentially, single relaxation rate (Debye-like) behavior is rarely observed in condensed matter. Nevertheless, some remarkably "universal" empirical expressions have been used to characterize the observed response from many different materials. Since 1854,[1] the most popular empirical expression for characterizing amorphous materials has been the Kohlrausch–Williams–Watts stretched exponential $M(t) \propto e^{-(t/\tau)^{\beta}}$. For crystals, the Curie–von Schweidler power law[2] $M(t) \propto t^{-\beta}$ is often preferred. For magnetic after-effects, the Néel[3,4] logarithmic time dependence $M(t) \propto \log(t/\tau)$ is also popular. These empirical expressions are simple mathematical formulas that give generally good agreement with a wide variety of measurements. Unfortunately, they are also common mathematical approximations to a wide variety of models; hence demonstrating agreement with these formulas tells you nothing about the physical mechanism of response. Furthermore, all of these formulas have infinite slope at $t=0$; hence they must only be approximations valid over a limited time range. Indeed, measurements over sufficient range invariably demonstrate deviations from such simple mathematical formulas.

Here we review a physical model for the observed response of condensed matter. The model is based on two assumptions: that nonexponential relaxation is due to a heterogeneous distribution of exponentially relaxing regions, and that these regions obey elementary thermodynamics. Various mathematical approximations to the model reproduce all of the previously used empirical formulas, but the unapproximated model gives generally better agreement with observed behavior. The model provides a physical description for the dynamical behavior of dozens of different systems including dielectric, structural, and thermal response in liquids, glasses, polymers, and crystals.[5–8] Here we focus on application to magnetic systems,[6,7,9–11] including resonance spectra, magnetic after-effects, and $1/f$ noise in paramagnets, spin glasses, and ferromagnets.

II. MESOSCOPIC MODEL

We assume that nonexponential response is due to a heterogeneous distribution of independently relaxing regions, that we call "dynamically correlated domains" (DCDs). Perhaps the earliest picture of dynamical heterogeneity was the 1907 Einstein model for the specific heat of solids, in which it was assumed that each atom was an independent harmonic oscillator.[12] In 1912, Debye recognized that, due to interactions between local sites, a solid can lower its energy by dynamical correlation into normal modes.[13] Examples of normal modes include phonons, polaritons, and magnons. In a perfect harmonic crystal, all normal modes are infinite plane waves; in real systems, however, some normal modes may become localized. Even in simulated perfect crystals, some normal modes are localized by assuming realistic (anharmonic) interactions, but direct observation often requires suppression of the plane-wave excitations.[8] In real systems, intrinsic inhomogeneities may augment the localization of normal modes.

Considerable evidence indicates that dynamical heterogeneity is common in condensed matter. In glass-forming liquids, four-dimensional (4D) NMR measurements[14] unambiguously establish that nonexponential relaxation is due to a heterogeneous distribution of independently relaxing regions (DCDs) that become homogeneous only after essentially all of the primary response is complete; typical diameters are found to be ~35 Å.[15] In spin glasses, neutron-scattering measurements,[16] and the 2D to 3D crossover,[17] indicate dynamical heterogeneity on a scale of 40–1000 Å. In EuS crystals, the thermal hysteresis of the remanent magnetization can only be explained by regions with distinct dynamical behavior, while the relaxation of this remanence quantitatively confirms a specific distribution of DCDs. It is important to emphasize that DCDs are related to a dynamical correlation length, *not* a region of static order. For example, in pure Fe at low temperatures, statically aligned regions are macroscopic, while the magnetic exchange length[18] $l_{ex} = \sqrt{A/M_s^2}$ (A is the anisotropy energy and M_s the saturation magnetization) gives $l_{ex} \sim 80$ Å, suggesting that each statically aligned region contains a myriad of independently relaxing DCDs, as is quantitatively confirmed from the observed magnetic response.

Generally, the relaxation rate of a DCD (w_s) will depend on its size s, where s is the number of responding particles (proportional to volume) in the domain. For a distribution of

 0021-8979/94/76(10)/6401/6/$6.00 © 1994 American Institute of Physics

sizes (n_s), and size-dependent initial response (M_s), the net relaxation is the weighted sum over all sizes: $M(t)=\Sigma_{s=0}^{\infty} n_s M_s e^{-tw_s}$. A change of variable ($w_s=1/\tau$) may be used to convert this sum to include the customary distribution of relaxation times, but we prefer to parameterize relaxation in terms of DCD size; since s is a thermodynamic variable, the expressions for n_s and M_s will be simpler.

The size dependences of n_s, M_s, and w_s are obtained by assuming simple thermodynamics. Thermodynamic extensivity suggests that the net response of a DCD should be proportional to its size, $M_s \propto s$. The central-limit theorem suggests that near thermodynamic equilibrium, DCDs should have a Gaussian size distribution $n_s \propto e^{-[(s-\bar{s})/\sigma]^2}$, where σ is the variance about an average size $\bar{s}$. Detailed balance suggests that, if the system is to approach thermodynamic equilibrium, relaxation rates between energy levels separated by an amount δE_s must vary as $w_s \propto e^{-\delta E_s/2k_BT}$. The key feature which distinguishes our approach is that we consider the relaxation of localized normal modes (e.g., magnons, phonons, polaritons, etc.), for which energy-level spacings are *inversely* proportional to size: $\delta E_s \propto 1/s$.

The fact that normal-mode energy-level spacings generally vary inversely proportional to size may be pictured in many ways. In a simple magnon picture,[19] the bandwidth (Δ) depends only on the local spin and exchange integral, independent of domain size, whereas the number of excitations that fill this bandwidth is proportional to the number of spins in the domain; hence $\delta E_s \sim \Delta/s$. In fact, this is the thermodynamic requirement that densities of states are extensive quantities, $\delta N/\delta E_s \propto s$, so that the energy spacing between adjacent ($\delta N=1$) levels is $\delta E_s \propto 1/s$. Of course, we are not the first to consider finite-size effects in condensed matter. In 1937, Fröhlich[20] calculated the energy spacing for quantized excitations in perfect spheres, and obtained the textbook expression $\delta E_s \propto 1/D^2 \propto 1/s^{2/3}$. In 1962, Kubo[21] recognized that imperfections in real systems break the degeneracies inherent in perfect spheres, yielding $\delta E_s \propto 1/s$. Thus $\delta E_s \propto 1/s$ for mesoscopic systems governed by either quantum mechanics, or thermodynamics. We implement this requirement to obtain relaxation rates that vary exponentially with *inverse* size.

Combining the ingredients of finite-size thermodynamics, using $x=s/\sigma$ and converting the sum over all sizes to an integral, the net relaxation of an ergodic system (e.g., rapidly relaxing crystal or liquid) becomes

$$M(t)=M_0\int_0^{\infty} dx\, x e^{-(x-\tilde{x})^2} e^{-tw_\infty e^{-C/x}}. \tag{1}$$

Equation (1) has four adjustable parameters: the prefactor (M_0) accommodates the magnitude of response, the asymptotic relaxation rate (w_∞) governs the time scale of relaxation, the correlation coefficient (C) controls the spectral width, whereas the scaled average size ($\tilde{x}=\bar{s}/\sigma$) influences the magnitude, time scale, and width of response. Note[7] for simple relaxation between adjacent energy levels, detailed balance yields $C<0$, and Eq. (1) may be approximated by the stretched exponential with w_∞ the slowest relaxation rate, whereas if relaxation requires activation over an intermediate energy barrier, $C>0$ (see Sec. IV) and Eq. (1) may be approximated by a power law with w_∞ the fastest relaxation rate.

In principal, both $\tilde{x}$ and C could adjust the spectral shape of Eq. (1). Experimentally, however, for all ergodic systems that we have examined, the ratio ($\tilde{x}/C$) is constant, independent of temperature. For example, from the dielectric susceptibility of glass-forming salol over 24 K we find[7] $\tilde{x}/C=-0.182\pm0.003$. Furthermore, we find a similar ratio from dozens of measurements on many different glass-forming liquids, and even $\tilde{x}/C=0.197\pm0.02$ from magnetic relaxation in single-crystal Fe.[11] We now speculate as to a possible reason for this "universality."

A specific expression for the correlation coefficient (C) in the relaxation rate ($w_s=w_\infty e^{-C\sigma/s}$) may be obtained by combining detailed balance with Fermi's golden rule. The transition rate from energy E_i to E_f is $w_{i\to f} \propto |V_{i\to f}|^2 \times \sqrt{(n_f/n_i)}$, where $V_{i\to f}$ ($=V_{f\to i}$) is a matrix element that connects the initial and final states, and $n_f/n_i = e^{-(E_f-E_i)/k_BT}$ is the factor that ensures detailed balance. At normal temperatures ($k_BT \gg \delta E_s \sim \Delta/\bar{s}$), thermal fluctuations strongly influence transitions between levels, so that the matrix element is dominated by the probability that a fluctuation will cause the initial and final energies to overlap, $V_{i\to f} \propto P_{i=f}$. Near thermal equilibrium[22] $P_{i=f} \propto \exp[-(E_f-E_i)^2 F''(E_e)/2k_BT]$, where $F''(E_e)=sf''(E_e)$ and $f''(E_e)$ is the Helmholtz free-energy curvature *per particle* about the equilibrium energy. The net relaxation rate into equilibrium is obtained by integrating over all possible initial states

$$W_s \sim \int_{-\infty}^{\infty} dE_i |P_{i=e}|^2 \sqrt{(n_e/n_i)} \propto e^{1/[16sf''(E_e)k_BT]},$$

yielding[7] $C=-1/[16\sigma f''(E_e)k_BT]$, so $\tilde{x}/C=-16\bar{s}f''(E_e)k_BT$. As expected for response that is governed by thermal fluctuations, the relaxation rate is independent of Δ, consistent with a ratio of shape parameters in Eq. (1) that does not depend on the details of interactions in a substance.

Some thermodynamic identities can be used to simplify $\tilde{x}/C$. The free-energy curvature of an average-sized DCD may be written[23]

$$\bar{s}f''(E) \equiv (\partial^2/\partial E^2)(E-TS) = -T(\partial^2 S/\partial E^2) = 1/(TC_V)$$

(where $C_V=\partial E/\partial T$ is the "heat capacity" of an average-sized DCD due to excitations that contribute to observed response), so that $\tilde{x}/C=-16k_B/C_V$. For a system of N classical particles, the law of Dulong and Petit gives $\tilde{x}/C=-16/3N$, leaving no explicit temperature dependence. Of course, with decreasing temperature, the heat capacity per particle diminishes, $C_V<3k_B$, while the number of particles in an average-sized DCD increases, $\bar{s}>N$. Evidently, since $\tilde{x}/C$ is found to be constant, the effective number of classical degrees of freedom must not change, $\bar{s}c_V=3Nk_B$. Finally, we speculate that N corresponds to the minimum number of classical particles necessary to support nontrivial excitations in three dimensions, $N\sim 3^3$, which gives $\tilde{x}/C \approx -0.198$. Empirically, regardless of interpretation, Eq. (1) with $\tilde{x}/|C| = 0.19\pm0.02$ provides excellent agreement with observed re-

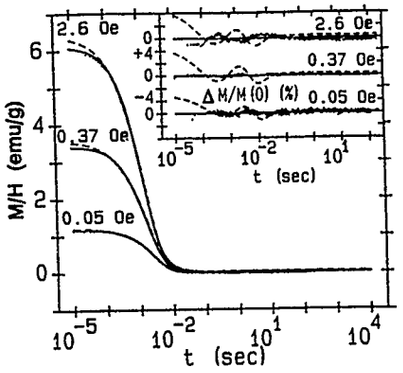

FIG. 1. Relaxation of the remanent magnetization in a single-crystal whisker of Fe at 4.2 K after removing three different fields. Dashed curves are best fits to the data using the stretched exponential function. Solid curves are best fits to the data using Eq. (1) with $\tilde{x}/C=0.20$. Inset: deviation between the data, model function (solid line at each origin), and stretched exponential.

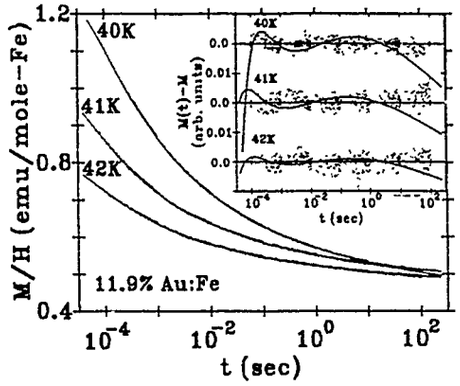

FIG. 2. Relaxation of the remanent magnetization in an 11.9%Au:Fe sample at three temperatures above the spin-glass transition $T_g=39$ K. Solid curves are the best fits to the data using Eq. (2). Inset: deviation between the data, model function (solid line at each origin), and simple power law.

sponse from a wide variety of ergodic systems with only one parameter governing the width and entire shape of the response.

Nonergodic systems (e.g., slowly relaxing crystals or glasses) have quenched (local) randomness that may be characterized by the Poisson-like distribution from percolation theory: $sn_s \propto s^{1-\theta}e^{-(C's)^{\zeta}}$. For isotropic excitations in highly correlated ($p>p_c$) systems, the size-scaling exponents are $1-\theta=10/9$ and $\zeta=2/3$, with $C' \propto |p-p_c|^{2.2}$. Using $x=C's$, the net relaxation of a nonergodic system becomes

$$M(t)=M_0\int_0^{\infty} dx\, x^{10/9}e^{-x^{2/3}}e^{-tw_{\infty}e^{-C/x}}. \tag{2}$$

Equation (2) has only three adjustable parameters: again M_0 accommodates the magnitude of response and w_{∞} governs the time scale of relaxation, while the width and entire shape of the response is controlled by the single parameter C. For example, if $C=0$ the relaxation is size independent, yielding single relaxation rate (Debye-like) behavior, whereas if $|C|\gg 1$, the spectral width is extremely broad. Here, for response that is governed by thermal fluctuations, the correlation coefficient is given by $C=-C'/[16f''(E_e)k_BT]$.

III. EXPERIMENTAL EVIDENCE FOR THE MODEL

Measurements of magnetic response were made using a SQUID magnetometer. Features of the magnetometer include a nonconducting sample region (to minimize eddy-current effects), and a critically damped low-impedance solenoid for fields (H) of 0.05–70 Oe that can be removed within 5 μs. With a standard dc SQUID sensor coupled to a high-speed voltmeter, the magnetometer is capable of measurements from 10^{-5} to 10^4 s after removing H.

Figure 1 shows the relaxation of the primary magnetic response in a single-crystal whisker of Fe at 4.2 K after removing three different fields.[11] Best fits using the stretched exponential show significant deviations from the observed behavior, while Eq. (1) with $\tilde{x}/|C|=0.20$ gives excellent agreement. Figure 2 shows the magnetic relaxation in an 11.9% Au:Fe sample at three temperatures above the spin-glass transition $T_g=39$ K.[9] The inset shows that a simple power law gives good agreement over four or five orders of magnitude in time, but when the entire range of data are considered, Eq. (2) gives significantly better agreement. Figure 3 shows magnetic relaxation in a single crystal of EuS at three temperatures below the Curie transition $T_c=16.57$ K.[10] Linear fits to the data show that the relaxation is approximately logarithmic, but again, best fits using Eq. (2) are significantly better.

We have documented statistical, qualitative, and quantitative evidence for the validity of the mesoscopic model. Statistically, compared to previously proposed response functions, in addition to giving superior agreement with observed magnetic response from paramagnets, spin glasses, and ferromagnets, the model also provides better agreement with the observed dielectric, structural, and thermal response from dozens of liquids, glasses, polymers, and crystals.[5] Furthermore, no other previously proposed response function can fully account for the qualitative behavior of the high-frequency dielectric absorption in glass-forming liquids.[7]

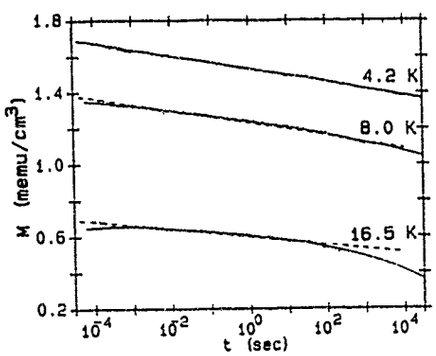

FIG. 3 Relaxation of the remanent magnetization in single-crystal EuS at three temperatures below the Curie transition $T_c=16.57$ K. Dashed lines are best logarithmic fits to the data. Solid curves are best fits to the data using Eq. (2).

Most convincing, however, is the quantitative confirmation of the size-scaling exponents.

The size distribution used in Eq. (1) [$xn_x \propto x^{1-\theta}e^{-(x^\zeta-\bar{x})^2}$] assumes thermodynamic extensivity ($1-\theta=1$) and that DCD size obeys the central-limit theorem ($\zeta=1$). For data of sufficient quality and range, it is possible to release these exponents as additional adjustable parameters, so that the only place where size scaling is fixed is in the exponent of the relaxation rate, $w_x=w_\infty e^{-Cx^\beta}$ with $\beta=-1$. For example, if response was a surface effect or if domain radius was the appropriate parameter of randomness, one would expect $1-\theta=2/3$ or $\zeta=1/3$, respectively. From magnetic relaxation in single-crystal whiskers of Fe, we find $1-\theta=0.92\pm0.12$ and $\zeta=0.99\pm0.08$, quantitatively confirming all assumptions of the model: volume response $1-\theta=1$, random DCD sizes $\zeta=1$, *and* relaxation rates vary exponentially with inverse size $\beta=-1$; otherwise $1-\theta$ and ζ would adjust to compensate. Similarly, the size distribution used in Eq. (2) ($xn_x \propto x^{1-\theta}e^{-x^\zeta}$) assumes the Poisson-like size distribution from percolation theory ($\zeta=2/3$) and thermodynamic extensivity ($1-\theta=10/9$). From magnetic relaxation in single-crystal EuS we find $1-\theta=1.10\pm0.02$ and $\zeta=0.669\pm0.004$, again quantitatively confirming all assumptions of the model. Alternatively, within experimental uncertainty, Eqs. (1) and (2) are the correct response functions for these data.

IV. APPLICATIONS OF THE MODEL

Since the model provides a physical mechanism for the primary response of condensed matter, it may be used to interpret a variety of observed behavior. For example, the model has been used to identify ergodicity in amorphous systems, and provide an explanation for observed non-Arrhenius temperature dependences of relaxation rates.[8] Here we will focus on application to magnetic materials, specifically the observed magnitude and distribution of Landau–Lifshitz damping parameters, and $1/f$ magnetic noise.

When $C>0$, the size-dependent relaxation rate ($w_x=w_\infty e^{-C/x}$) implies that larger DCDs have faster relaxation rates. $C>0$ (as is observed for the primary magnetic response of Fe) can only occur if relaxation requires activation over an intermediate barrier, where $f''(E)<0$ gives $C\propto 1/f''(E)>0$. Qualitatively, large DCDs have many degrees of freedom that facilitate traversal of a potential barrier, whereas small domains are relatively rigid, and hence require many attempts before relaxing. In the Landau–Lifshitz formalism, a fundamental attempt frequency is the Larmor precession rate $\omega=|\gamma|B$, where $|\gamma|=17.6\times10^6$ (rad/s)/G for pure electron spins.[24] If this precession is related to the asymptotic relaxation rate $w_\infty\sim|\gamma|B$, then $w_{\bar{x}}=w_\infty e^{-C/\bar{x}}$ gives a connection between the gyromagnetic precession and average relaxation rates, providing a physical explanation for the Landau–Lifshitz damping parameter $\alpha\approx w_{\bar{x}}/w_\infty=e^{-C/\bar{x}}$. Indeed, from SQUID measurements of magnetic relaxation in Fe we find $\alpha\approx e^{-1/(0.197\pm0.02)}\approx0.006$, consistent with the damping parameter found from ferromagnetic-resonance linewidths at much higher frequencies: $\delta B=32$ Oe at $f_0=9.2$ GHz and $\delta B=158$ Oe at 36.2 GHz[25] give $\alpha=(\delta B)|\gamma|/(4\pi f_0)\approx0.005$. Thus the mesoscopic model provides an explanation for both the magnitude, and distribution, of Landau–Lifshitz damping parameters in Fe. Furthermore, approximately half of the commercially available ferrite materials[26] have damping parameters consistent with $\alpha\approx e^{-1/(0.19\pm0.02)}$. However, other materials have quite different damping parameters, suggestive of alternative relaxation mechanisms. Most notably, highly polished YIG crystals have the lowest microwave loss of any material, with $\alpha\sim10^{-4}$. Such extraordinarily low loss is attributable[27] to an absence of orbital contributions, and nearly spherical charge distribution, for the ferric ions in YIG; thus the spins are decoupled from the "universal" lattice vibrations which govern the relaxation in many other materials.

Another common property that may be attributed to mesoscopic thermal fluctuations is $1/f$ noise. Electrical $1/f$ noise has been known for many years,[28] but magnetic measurements of sample noise have only been possible with recent advancements in SQUID magnetometry.[29] Within the fluctuation dissipation theorem, noise is proportional to $1/f$ times the out-of-phase (absorption) component of response, $\overline{M^2}(f)=k_BT\chi''(f)/\pi^2 f$. Thus only systems with infinitely broad absorption peaks (corresponding to logarithmic time relaxation) will exhibit purely $1/f$ noise. Of course, no physical system can have an infinitely broad absorption peak, as evidenced by deviations from logarithmic relaxation when measured over sufficient time range; similar deviations must also occur in $1/f$ noise. Indeed, magnetic noise spectra[29] from spin glasses exhibit very broad, *asymmetrical* deviations from $1/f$ behavior, consistent with relaxation rates that vary exponentially with *inverse* size, which is the key feature of our model. Furthermore, deviations from $1/f$ behavior become more conspicuous near T_g, similar to the increased deviations from logarithmic relaxation observed in EuS near T_c. Using Eq. (2), $1/f$ times the out-of-phase component of the Fourier transform of $-dM(t)/dt$ yields a specific expression for the equivalent noise spectrum:

$$\overline{M^2}(f)=\frac{2k_BT}{\pi}M_0\int_0^\infty dx\, x^{10/9}e^{-x^{2/3}}\frac{1/w_x}{1+(2\pi f/w_x)^2}, \tag{3}$$

where $w_x=w_\infty e^{-C/x}$. Although electrical measurements on small samples have shown that $1/f$ noise is often caused by a distribution of independently relaxing regions,[30] available magnetic measurements have not allowed quantitative confirmation of Eq. (3). Nevertheless, magnetic relaxation that is characterized by Eq. (1) or (2) may yield apparent $1/f$ noise. For example, Fig. 4 shows equivalent noise spectra of ferromagnetic EuS, demonstrating qualitative agreement with measured noise spectra,[29] and the difficulty in distinguishing from hypothetical $1/f$ behavior.

V. CONTRAST WITH PREVIOUS PICTURES

Domain-wall motion is an established mechanism of magnetic response. Usually, wall motion occurs on short time scales ($<10^{-5}$ s), outside the time window of our SQUID magnetometer, but by extrapolating the observed response to $t=0$, an estimate of the relative contribution of

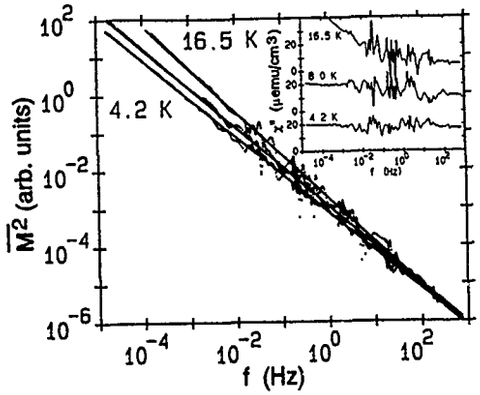

FIG. 4. Equivalent noise spectra in ferromagnetic EuS, from the imaginary part of the susceptibility (inset), as determined from the data of Fig. 3. Solid lines are the best power-law fits to the data [$\overline{M^2}(f) \propto 1/f^{\beta}$], yielding β of 1.007, 1.046, and 1.14 at temperatures of 4.2, 8.0, and 16.5 K, respectively.

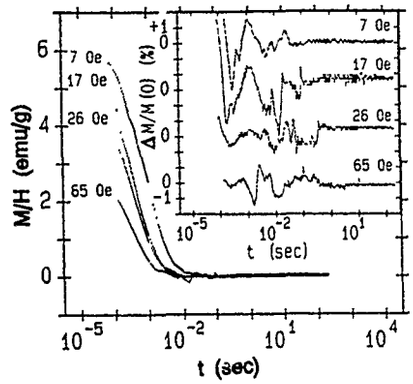

FIG. 6. Relaxation of the remanent magnetization in Fe at 4.2 K after removing four relatively large fields. Inset: deviation of the data from Eq. (1), showing small jumps and spikes (Barkhausen noise) due to domain-wall adjustments during the primary magnon relaxation.

such fast response mechanisms can be obtained. As shown in Fig. 5 for the magnetic relaxation of Fe, after removing small fields ($H<0.1$ Oe), the response accounted for by our mesoscopic model is only about 20% of the initial (infield) response; 80% of the initial response occurs before 10^{-5} s, presumably due to domain-wall motion. However, with increasing field the fraction of slow response increases, until $H>1$ Oe where essentially 100% of the initial response can be accounted for by magnon relaxation over the available time window. At still higher fields ($H>3$ Oe, Fig. 6), relatively small jumps and spikes appear, indicative of minor domain-wall adjustments (Barkhausen noise) during the otherwise smooth magnon response. Evidently, the magnetic relaxation is so slow that domain walls (which traverse the sample in $<10^{-5}$ s) cannot carry any magnetization reversal. Instead, these "proto-walls" merely break the degeneracy between regions where magnons will eventually relax the spins into distinct static alignments; magnetization evolves smoothly from saturation without any significant contribution from wall motion.

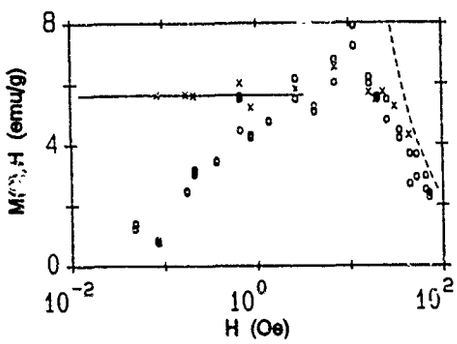

FIG. 5. Field dependence of initial (in field) susceptibility M/H (×) from before H was removed, and extrapolated initial response $M(0)/H$ (□) from Eq. (1), of an Fe whisker at 4.2 K. For $H<0.1$ Oe, only 20% of the in-field response is accounted for by Eq. (1). For $H>1$ Oe, essentially 100% of the in field response can be accounted for by magnon relaxation over the available time window.

Many investigators have considered slow relaxation due to coherent domain rotation via barrier hopping. Such coherent domains are assumed to be rigidly aligned in a common direction, with only a few degrees of freedom, similar to a rigid rod governed by classical mechanics. Generally, barrier heights are assumed to increase with increasing domain size, $\delta E_s \propto s^{\beta}$ with $\beta>0$. In contrast, we consider relaxation of low-energy internal degrees of freedom (e.g., magnons) governed by thermodynamics, for which $\beta=-1$. Our approach has some favorable features. First, even at low temperatures in highly ordered ferromagnets, where rigidly aligned spin behavior might be expected to occur, magnons are found to govern the static magnetization, hence they should also contribute to the dynamical properties. Second, it is generally assumed that slow relaxation of a rigidly aligned domain requires activation over an intermediate energy barrier. In contrast, for $C<0$, normal-mode relaxation involves simple transitions between adjacent energy levels, thus requiring only detailed balance. (Although some systems do have $C>0$, indicating relaxation over an intermediate barrier, since $\delta E_s \propto s^{\beta}$ with $\beta=-1$, large DCDs relax faster than small DCDs, as expected for systems with internal degrees of freedom.) Third, since $w_x \propto e^{-C/x}$, there is considerable asymmetry in the relation between domain size and relaxation rate, so that relatively symmetrical, and hence more physically reasonable, size distributions (e.g., Gaussian or percolation) provide good agreement with most frequently observed asymmetrical responses. Finally, within experimental uncertainty for a variety of systems, $\beta=-1$ has been confirmed quantitatively.

VI. CONCLUSIONS

A model is presented that provides a physical description for the primary response of condensed matter. The model is based on the assumption that nonexponential response is due to a heterogeneous distribution of independently relaxing regions, and that these regions obey simple thermodynamics. The model gives superior agreement with the observed response from dozens of different materials, including magnetic after-effects in paramagnets, spin glasses, and ferro-

magnets. Data of sufficient quality and range, including SQUID measurements of single-crystal EuS and whiskers of Fe over nine orders of magnitude in time, allow quantitative confirmation of all aspects of the model. The model provides a common physical basis for several previously used empirical expressions, such as the stretched exponential, power-law, and logarithmic time dependences. Furthermore, the model provides a physical explanation for other properties commonly found in the dynamical response of magnetic materials, including the magnitude and distribution of Landau–Lifshitz damping parameters, and $1/f$ noise.

ACKNOWLEDGMENTS

I thank R. Böhmer, M. R. Scheinfein, and K. E. Schmidt for helpful discussions.

[1] R. Kohrausch, Pogg. Ann. Phys. **91**, 56 (1854).
[2] J. Curie, Ann. Chim. Phys. **6**, 244 (1889).
[3] R. Street and J. C. Woolley, Proc. Phys. Soc. London Sec. A **62**, 562 (1949).
[4] L. Néel, J. Phys. (Paris) **11**, 49 (1950).
[5] R. V. Chamberlin and M. R. Scheinfein, Ultramicroscopy **47**, 408 (1992).
[6] R. V. Chamberlin, in *On Clusters and Clustering*, edited by P. J. Reynolds (Elsevier, New York, 1993), p. 393.
[7] R. V. Chamberlin, Phys. Rev. B **48**, 15638 (1993).
[8] R. V. Chamberlin and D. W. Kingsbury, J. Non-Cryst. Solids (in press).
[9] R. V. Chamberlin and D. N. Haines, Phys. Rev. Lett. **65**, 2197 (1990).
[10] R. V. Chamberlin and F. Holtzberg, Phys. Rev. Lett. **67**, 1606 (1991).
[11] R. V. Chamberlin and M. R. Scheinfein, Science **260**, 1098 (1993).
[12] A. Einstein, Ann. Phys. **22**, 180 (1907).
[13] P. Debye, Ann. Phys. **39**, 789 (1912).
[14] K. Schmidt-Rohr and H. W. Spiess, Phys. Rev. Lett. **66**, 3020 (1991).
[15] K. Schmidt-Rohr, J. Clauss, and H. W. Spiess, Macromolecules **25**, 3273 (1992).
[16] S. A. Werner, Comments Cond. Mat. Phys. **15**, 55 (1990); S. A. Werner (private communication).
[17] P. Granberg, J. Mattsson, P. Nordblad, L. Lundgren, R. Stubi, J. Bass, D. L. Leslie-Pelecky, and J. A. Cowen, Phys. Rev. B **44**, 4410 (1991), and references therein.
[18] M. E. Schabes and H. N. Bertram, J. Appl. Phys. **64**, 1347 (1988).
[19] C. Kittel, *Introduction to Solid State Physics*, 5th ed. (Wiley, New York, 1976), p. 468.
[20] H. Fröhlich, Physica **4**, 406 (1937).
[21] R. Kubo, J. Phys. Soc. Jpn. **17**, 975 (1962).
[22] R. Kubo, K. Matsuo, and K. Kitahara, J. Stat. Phys. **9**, 51 (1973).
[23] H. B. Callen, *Thermodynamics and an Introduction to Thermostatistics*, 2nd ed. (Wiley, New York, 1985); J. Dyre (private communication).
[24] T. H. O'Dell, *Ferromagnetodynamics* (Wiley, New York, 1981).
[25] Z. Frait and B. Heinrich, J. Appl. Phys. **35**, 904 (1964).
[26] W. H. von Aulock, *Handbook of Microwave Ferrite Materials* (Academic, New York, 1965).
[27] C. W. Chen, *Magnetism and Metallurgy of Soft Magnetic Materials* (North-Holland, New York, 1977).
[28] M. B. Weissman, Rev. Mod. Phys. **60**, 537 (1988).
[29] H. Bouchiat and M. Ocio, Comments Cond. Mat. Phys. **14**, 163 (1988).
[30] C. T. Rogers and R. A. Buhrman, Phys. Rev. Lett. **53**, 1272 (1984).

Models of slow relaxation in particulate and thin film materials (invited)

R. W. Chantrell and A. Lyberatos
Physics Department, Keele University, Keele, Staffordshire ST5 5BG, United Kingdom

M. El-Hilo and K. O'Grady
Magnetic Materials Research Group, SEECS, University of Wales, Bangor, Gwynedd LL57 1UT, United Kingdom

The development of a number of models of slow relaxation in magnetic materials is reviewed. A phenomenological theory based on the intrinsic energy barrier is shown to explain the form of time dependence of the magnetization, including the logarithmic time dependence observed for systems with a relatively wide distribution of energy barriers. This formulation gives rise to useful analytical results which give generally good qualitative agreement with experiment. The slow relaxation is related to the irreversible magnetic behavior via a fictitious fluctuation field H_f which itself determines a quantity called the activation volume V_{act}. Both H_f and V_{act} are related to the magnetization reversal process. For granular materials V_{act} is generally smaller than the grain size. Computer simulations based on the Monte Carlo method are applied to the investigation of the behavior of thin films with perpendicular anisotropy. Detailed comparisons of the simulation with experimental data demonstrate the relationship between V_{act} and the micromagnetic magnetization reversal mode. Some recent models introducing thermal agitation into the micromagnetic formalism are discussed.

I. INTRODUCTION

In general, models of magnetization reversal proceed by determining the minimum energy state and following its evolution until at some field the minimum disappears and an irreversible transition to a new state occurs. This approach is valid for magnetization reversal at absolute zero temperature. However, at a finite temperature a different phenomenology, involving determination of the energy barriers, must be adopted. A considerable amount of work has been carried out using a simple formalism based on a distribution of energy barriers. This approach has proved extremely useful in producing analytical results which give generally good qualitative agreement with experiment, thereby illuminating the physical processes involved. Here we start by outlining the energy barrier distribution formalism and introducing the concepts of the fluctuation field and activation volume. These highlight the major deficiencies of the phenomenology, which are principally the neglect of the detailed nature of the magnetization reversal mechanisms and interaction effects. The remainder of the article is devoted to consideration of computational studies of slow relaxation.

II. ANALYTICAL MODELS FOR TIME DEPENDENCE

In magnetic materials the time-dependence effects arise due to the fact that there is a finite relaxation time τ required for the magnetization vector to rotate from one minimum to another. The origin of the energy barrier is a material property and since its magnitude depends on experimental conditions such as magnetic field, these factors govern the probability of thermally activated transitions. Almost any phenomenology shows that the probability of a transition is given by[1]

$$\tau^{-1}=f_0 \exp(-\Delta E/kT), \tag{1}$$

where f_0 is the attempt frequency which depends on the properties of the material and ΔE is the height of the energy barrier for reversal.

In general the time variation of the magnetization of any system can be characterized by a simple differential equation:

$$\frac{dM(t)}{dt}=-\frac{M(t)-M_e}{\tau}, \tag{2}$$

where $M_e=M(t=\infty)$ is the equilibrium magnetization. In principle the time variation of magnetization can be described by solving Eq. (2).

For the case of a noninteracting system which contains a distribution of energy barriers the solution of Eq. (2) gives

$$M(t)=B+A\int_0^\infty e^{-t/\tau(y)}f(y)dy, \tag{3}$$

where $B=M(\infty)$ and $A=M(t=0)-M(\infty)$ are time-independent constants. $f(y)$ is the distribution of energy barriers and $y=\Delta E/\Delta E_m$ is the reduced energy barrier relative to the average barrier ΔE_m of the system. $\tau^{-1}(y)=f_0\exp(-\alpha y)$ is the inverse of the relaxation time and $\alpha=\Delta E_m/kT$. According to Eq. (3) the time-dependent behavior is most sensitive to two parameters which characterize the relevant distribution of energy barriers for the system, i.e., the average energy barrier of the system ΔE_m and the width of the distribution.

Figure 1 shows the exact calculations of the integral in Eq. (3) at different values of α for a narrow ($\sigma=0.18$) and distribution of energy barriers. In these calculations a log normal distribution of energy barriers was used. The change in the values of α can arise from temperature changes or magnetic field changes. These calculations show that for a narrow distribution of energy barriers the decays exhibit non-

 0021-8979/94/76(10)/6407/6/$6.00 © 1994 American Institute of Physics

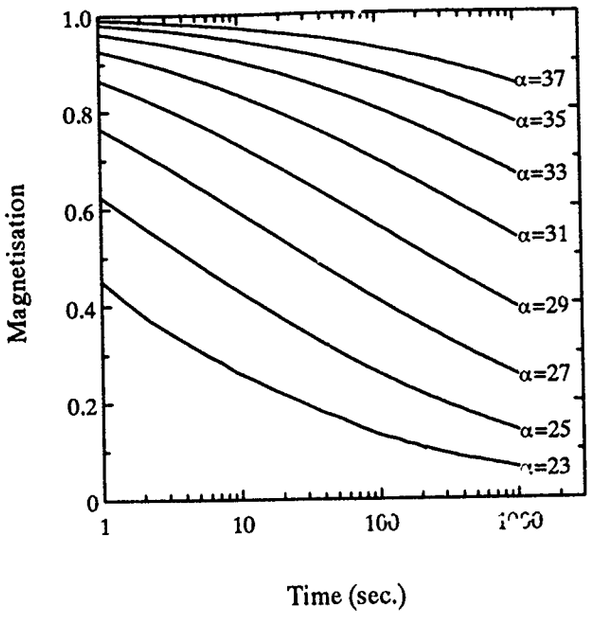

FIG. 1. The time variation of magnetization at different values of α for a narrow distribution of energy barriers (σ=0.18).

linear logarithmic time-dependent behavior. For a wide distribution of energy barriers a $\ln(t)$ law is a good approximation over the range of time examined.

In order to understand the physical interpretation of these results and examine the role of the energy barrier distribution, it is possible to simplify the integral in Eq. (3) using the critical energy barrier of activation (ΔE_c). This critical barrier can be defined in such a way that activation over barriers lower than ΔE_c happens so quickly that $e^{-t/\tau(y<y_c)} \simeq 0$. With $e^{-t/\tau} \simeq 1$ for $y > y_c$ Eq. (3) becomes

$$M(t) = B + A - A \int_0^{y_c(t)} f(y)dy, \tag{4}$$

where $y_c = \Delta E_c / \Delta E_m$ is the reduced critical barrier for reversal and is given using Eq. (1) by

$$y_c = \frac{1}{\alpha} \ln(t f_0). \tag{5}$$

According to Eq. (4) the rate of change of $M(t)$ with $\ln(t)$ is given by

$$\frac{dM(t)}{d\ln(t)} = -\frac{A}{\alpha} f(y_c). \tag{6}$$

This result explains the shapes of any $M(t)$ vs $\ln(t)$ curve where the slope of the $M(t)$ vs $\ln(t)$ curve at any instant is directly linked to the behavior of the distribution function about the critical barrier above which thermal activation is taking place.[2] Thus the data shown in Fig. 1 can be explained as being due to significant variation of $f(y_c)$ during the time-dependent process. In the case of a wide distribution of energy barriers, the variation of $M(t)$ vs $\ln(t)$ is almost linear due to the fact that $f(y_c)$ does not change appreciably about the critical barrier as in the case of a narrow distribution. An analytical expression of Eq. (4) can be derived by representing the behavior of $f(y)$ about y_c using a series expansion[3,4]

$$M(t) = M(t_0) - A \sum_{n=0} f^n(y_c) \left[\frac{\Delta \ln(t)}{\alpha} \right]^{n+1}, \tag{7}$$

where

$$M(t_0) = B + A - A \int_0^{y_c(t_0)} f(y)dy$$

and $\Delta \ln(t) = \ln(t/t_0)$ and t_0 is the initial time of measurement. $f^n(y_c)$ is the nth differential of the distribution function evaluated at y_c. Equation (7) shows that for a constant probability of activation

$$M(t) = M(t_0) - \frac{A}{\alpha} \Delta \ln(t), \tag{8}$$

which is the well-known logarithmic time dependence of magnetization.[5] However in general $f(y)$ is not constant and higher order terms become important as the variation of the distribution function about y_c becomes steeper. In Ref. 3 the higher order coefficients are found to be proportional to $(1/\sigma^2)^n$ and hence as the width of the distribution increases the higher order terms in the expansion will vanish.

III. THE FLUCTUATION FIELD AND ACTIVATION VOLUME

The concept of the fluctuation field was introduced by Néel[1,6] who assumed that thermal agitation could be represented by a fictitious field $H_f(t)$ which he showed to be a linear function of $\ln(t)$. As a result the magnetization can be written as

$$M = M_0 \pm \chi_{irr} H_f(t). \tag{9}$$

Equation (9) directly relates the time-dependent changes to the irreversible susceptibility χ_{irr} defined as $\Delta M_{irr}/\Delta H$ where ΔM_{irr} is the small change in the irreversible component of magnetization resulting from a small increment of field ΔH, χ_{irr} is often measured as the slope of the dc-demagnetization remanence curve. Thus, as is intuitively reasonable, the time-dependent changes are related to the irreversible magnetic behavior of the system. The meaning of the fluctuation field is however, unclear from Eq. (9) and is still the matter of some debate. It would seem that the fluctuation field is intimately linked with the micromagnetics of magnetization reversal, as will be demonstrated here in the case of materials with perpendicular anisotropy. A rather different definition of the fluctuation field in terms of the time-dependence coefficient was given by Wohlfarth[7] as

$$S = \chi_{irr} H_f. \tag{10}$$

Thus, in principle independent measurements of S and χ_{irr} can be use to determine H_f. A considerable amount of experimental work has been carried out using this approach. This shows H_f to be a parameter dependent on a number of factors such as the volume and anisotropy field distributions[8,9] and interparticle interactions.[10]

It is also found that H_f is dependent on the magnetization reversal mechanism of the material. This is often dis-

cussed in terms of an "activation volume" V_{act} which can be defined following Wohlfarth[7] on dimensional grounds as

$$V_{act}=\frac{kT}{M_s H_f}, \tag{11}$$

where M_s is the bulk saturation magnetization of the material. V_{act} is perhaps most useful in studying the behavior of granular materials, which have a well-defined volume V for comparison with V_{act}. Generally speaking it is found that V_{act} is significantly smaller than V for elongated particles.[11,12] Flanders and Sharrock[13] have also measured particle sizes via time-dependence measurements. Although the measured volumes are in principle different from V_{act}, they are also generally found to be smaller than V for elongated particles. A similar situation is found for alumite thin films,[14] a case to be discussed in more detail later. Although the activation volume is a useful quantity in the study of granular materials it is perhaps less so in relation to domain wall processes since the equivalent physical volume is more difficult to define. In general it is perhaps more useful to concentrate on H_f, which is directly related to the material properties. Recent work[15] has shown that the form of H_f depends upon the distribution of energy barriers $f(\Delta E)$. For a single energy barrier it can be shown that

$$H_f=-kT/[\partial \Delta E/\partial H] \tag{12a}$$

while for a relatively wide distribution

$$H_f=-kT/[\partial \Delta E/\partial H]_{\Delta E=\Delta E_c}, \tag{12b}$$

where the differential is evaluated at the critical energy barrier defined earlier. Equation (12b) is the definition of H_f originally given by Gaunt,[16] and has been the starting point of a number of attempts (e.g., Ref. 17) to explain the relation between H_f and the coercive force, the so-called Barbier plot.[18] It is relatively easy to study H_f using analytical theories for simple model systems. The problem of determining H_f via micromagnetic calculations for more realistic systems is at a very early stage. Essentially the problem is that via Eq. (12) H_f is related to the energy barrier, which is not determined in the standard micromagnetic approach. This problem will be considered in detail in the final section of the article.

Finally we briefly indicate here the approach to magnetic viscosity based on a constitutive equation.[19] This phenomenological approach has proved very useful in the study of magnetic viscosity, especially via the definition of new methods of determining H_f. These methods avoid the determination of χ_{irr} [necessary for the direct determination of H_f using Eq. (10)] which itself is a quantity dependent on the measurement time. Details of this approach are given in the current issue.[20]

IV. MODELS OF TIME DEPENDENCE IN THIN FILMS WITH PERPENDICULAR ANISOTROPY

The first simulation of time-dependent magnetic behavior for an interacting many-particle system was made in 1936[21] using a Monte Carlo technique. We shall describe the model in some detail here, since it essentially forms the basis of most subsequent treatments. The first study[21] considered a three-dimensional lattice of particles interacting via a magnetostatic field. An important result of this study, which also features strongly in recent work is the fact that logarithmic time dependence can result in a system with a single intrinsic energy barrier due to a spread of interaction energies. Thus the disorder which appears necessary for logarithmic time dependence has an intrinsic contribution from the probabilistic nature of the reversal process itself.

Simulations of films with perpendicular anisotropy were prompted by the experimental work of Dahlberg *et al.*[22] on CoCr films, who observed a strong time dependence of the magnetization (driven by the demagnetizing field) which resulted in a time decay of a recorded signal. In the recording context we also note the work of Charap[23] who has used a Monte Carlo model to study the thermal stability of written information in longitudinal granular media. Because of the strong demagnetizing fields in the transition region the thermal stability is much reduced, leading to the conclusion that the ultimate lower limit of grain size in conventional recording is significantly larger than the superparamagnetic limit which is often assumed.

A. A Monte Carlo model

Central to the calculations is the determination of the energy barrier, which essentially governs the transition rate via the Arrhenius–Néel law. The film is considered to consist of a collection of grains with anisotropy easy axes oriented perpendicular to the film plane. In practice there will be a distribution of easy axis directions about the normal to the plane. However, the time dependence is most strongly dependent on the large demagnetizing fields and the spread of interaction energies and consequently the disorder due to the easy axis distribution is neglected. The grains are assumed to interact via the magnetostatic field, which can be calculated using standard techniques such as the fast Fourier transform or the Bethe–Peierls–Weiss approximation used in Ref. 21. In addition it is possible to introduce an exchange interaction which is necessary for the simulation of magneto-optical films. Assuming coherent rotation within individual grains the energy barrier is given by

$$\Delta E=KV(1-H_{tot}/H_K)^2, \tag{13}$$

where $H_{tot}=H+H_{int}$ is the sum of the applied and magnetostatic interaction field, respectively. Each individual grain has a characteristic relaxation time determined by the energy barrier and the Arrhenius–Néel law, Eq. (1). The numerical simulation is most efficiently carried out using an algorithm described by Binder.[24] The algorithm is as follows:

(1) The time is set to $t=0$.
(2) t' is sampled at random from a distribution $Nr\exp(-Nrt')$ where N is the number of particles and $r=\max\{r_\nu\}$ where r_ν is the relaxation rate of the νth particle: $r_\nu = f_0 \exp(-\Delta E_\nu/kT)$.
(3) A moment ν is selected at random, $1\leq\nu\leq N$.
(4) With probability r_ν/r we accept the reversal.
(5) Steps (2) to (4) are repeated until an equilibrium state is reached.

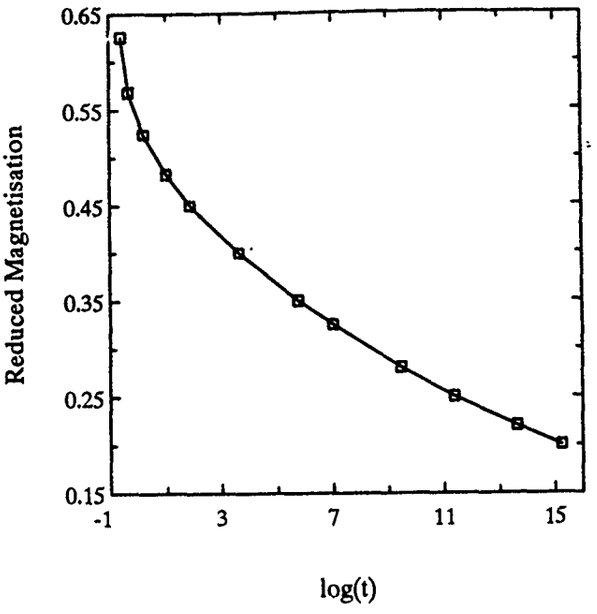

FIG. 2. Time variation of magnetization in a perpendicular thin film.

This approach has the advantage of scaling the steps along the time axis according to the transition rate at a given point in the process. Consequently it is possible to simulate the magnetic relaxation efficiently over extremely large time scales.

Simulations were first carried out in zero applied field[25] on an ensemble of particles of identical size, consisting of prolate ellipsoids with a 7:1 aspect ratio. As shown in Fig. 2 over many orders of magnitude the decay is nonlogarithmic. However, over the typical experimental time scale an approximately logarithmic slow relaxation is predicted, in agreement with experiment. Within this region it is possible to define a coefficient of magnetic viscosity S. The temperature dependence of S shows slow monotonic increase to a broad maximum followed by a rapid decrease to zero. This is broadly in agreement with experiment, indicating that the essential features of the model, in terms of interaction effects, are correct. There is however, a major discrepancy in the grain size predicted from a fit between theory and experiment which is very small in comparison with the physical size of the CoCr columns. This can be interpreted in terms of a micromagnetic model of magnetization reversal. Generally, magnetization reversal in elongated particles takes place by incoherent rotation, which can be viewed as the nucleation of a volume of reverse magnetization followed by propagation of the reversed area throughout the particle. The energy involved with the nucleation is clearly less than required to reverse the whole particle by rotation. Consequently a reduced effective volume for the model simulations is not unreasonable. The micromagnetic implications of this observation will be described in the final sections of the article.

B. Analytical models of slow relaxation in perpendicular media

In the Monte Carlo simulations there is a strong contribution to the logarithmic time dependence arising from the disorder produced by the interaction field distribution. However, materials with perpendicular magnetization have a unique feature in that logarithmic time dependence can occur as a result of the macroscopic demagnetizing field. A simple mean-field model can give very useful results in comparison with experiment. Mean-field models have been proposed by Lottis *et al.*[26] and Lyberatos *et al.*[27] Consider a material with perpendicular anisotropy and particle size V with a distribution function $f(V)$. The interactions are represented by a mean-field formalism, the total field being the sum of the applied field and demagnetizing field, i.e., $H=H-N_dM$. The variation of magnetization with time is the interval t_0 to t given by

$$M(V,t)=M(V,t_0)+[M_e(V)-M(V,t_0)] \times[1-e^{-(t-t_0)\tau^{-1}}], \tag{14}$$

where $M(t_0)$ and M_e are the reduced initial and equilibrium values of the magnetization, respectively. If the relaxation time is given by the Arrhenius–Néel law it can be shown that M_e and τ are given by

$$M_e(V)=\tanh(M_sHV/kT), \tag{15}$$

and

$$\tau^{-1}(V)=2\,f_0\exp\left[-\frac{KV}{kT}(1+h^2)\right] \times\cosh\left(\frac{M_sVH}{kT}\right) \quad \text{for } |h|<1$$

and

$$\tau^{-1}(V)=f_0 \quad \text{for } |h|\geq 1, \tag{16}$$

where $h=H/H_K$. In order to calculate the time evolution of the magnetization we approximate the decay by a series of discrete time intervals that can be made arbitrarily small thereby approximating a continuous process. Thus, taking into account the particle size distribution we have that

$$M(t_{n+1})=M(t_n)+\int [M_e(V,M)-M(V,M)] \times\{1-\exp[-(t_{n+1}-t_n)\tau^{-1}(V,M)]\}f(V)dV \tag{17}$$

the transcendental nature of Eq. (17) is stressed here by writing M_e and τ as explicit functions of M. In Ref. 27 a numerical solution of Eq. (17) was made using a log normal volume distribution. The results do not depend strongly on the form of $f(V)$ as long as this is narrow.

The analytical results agree qualitatively with the computational studies. An initial rapid demagnetization is followed by a quasilogarithmic region. The initial demagnetization arises because in the strong demagnetizing field the relaxation times are short and also $M_e=-1$. Ultimately of course as the time-dependent process proceeds the demagnetization field decreases and the system tends to a state of zero magnetization. An approximate analytical approach to the problem of relaxation in perpendicular media has been carried out by Chantrell *et al.*[28] which clarifies certain features of the experimental data and reinforces the intimate relation-

ship between slow relaxation and micromagnetics. Starting from the Eq. (2) and assuming coherent rotation, it can be shown that for large demagnetizing fields the magnetization is a solution of the equation

$$\int dM \exp[\beta(1-h^2)]/(1+M) = -tf_0, \tag{18}$$

where $\beta = KV/kT$, and in zero field $h = N_d M/H_k$. Using a steepest descent approach it can be shown that the magnetization at remanence decreases logarithmically with a normalized time-dependence coefficient $S_r = d(M/M_r)/d\ln(t)$ given by

$$S_r = \tfrac{1}{5}\beta^{-1/2}. \tag{19}$$

This approximate equation is valid for relatively short time scales. A more detailed treatment shows S_r to be a slowly decreasing function of $\ln(t)$ (in agreement with experiment) with the magnetization decay tending to an exponential as $t \to \infty$. It should be stressed that the volume in Eq. (19) is in principle the physical volume rather than the activation volume defined earlier. In Ref. 28 a comparison is made with the experimental behavior of alumite media, which consist of elongated metal particles oriented perpendicular to the plane and which are prepared by the deposition of iron into oxidized aluminum. It has been experimentally demonstrated that alumite samples reverse incoherently by a mechanism close to curling.[29] Essentially it is found that Eq. (19) is obeyed well for alumite, however the best fit to the data is obtained using an effective activation volume equal to 0.05 times the physical column volume. Given that alumite exhibits incoherent reversal of a type which might be thought of as nucleation of a reversal followed by propagation, this small activation volume seems intuitively reasonable. However, a complete understanding of this phenomenon requires a very detailed micromagnetic study, which is the subject of the final section of this article.

V. THERMAL ACTIVATION: THE MICROMAGNETIC APPROACH

Thus far all the theoretical developments have been based on the assumption of magnetization reversal by coherent rotation in single domain particles. However, the comparison with experiment leads inevitably to the conclusion that magnetization reversal involves thermally activated nucleation followed by propagation of the reverse domain. The latter process may be hindered by pinning, in which case the movement of a domain wall from a pinning site is itself a thermally activated process. It should perhaps be stressed that this presents a problem fundamentally outside the classical micromagnetic formalism. Micromagnetism is based on the determination of stationary states and their evolution with respect to changes in external parameters such as the applied magnetic field. Magnetization reversal occurs when the local energy minimum in which the system is situated disappears resulting in a transition to a new stationary state. Modern investigation using numerical techniques generally determines stationary states using the Landau–Lifschitz dynamic equation. This approach more reliably determines the stationary state after magnetization reversal. However, this approach is not valid at a finite temperature. Here we outline two rather different theories of micromagnetism at a finite temperature, the first valid for short time scales and the second applicable to slow dynamic behavior.

A. Langevin dynamics formalism

This approach takes account of collective magnetic excitations in the system, recognizing that ultimately thermal agitation occurs via spin waves. The theory is essentially an extension of Brown's model[30] of thermal activation to systems with large numbers of degrees of freedom. The dynamic behavior of a spin is governed by the Landau–Lifschitz equation

$$\frac{d\mathbf{M}}{dt} = \gamma_0 \mathbf{M}\times\mathbf{H} + \frac{\lambda}{M}\mathbf{M}\times(\mathbf{M}\times\mathbf{H}), \tag{20}$$

where γ is the gyromagnetic ratio and λ is the damping parameter. At a finite temperature the stochastic dynamics of the spin can be described by adding a fluctuating "random field" term to the deterministic field arising from interaction effects in addition to the applied field. Thus Eq. (20) becomes the Langevin equation of the problem. Using this formalism Brown[30] derived an analytical expression for the relaxation time associated with thermally activated reversal of a single particle. A model of thermal activation in a micromagnetic system of coupled spins has been proposed by Lyberatos *et al.*[31] Briefly, the technique involves linearization of the equation of motion followed by a transformation into the normal coordinates which essentially decouples the equations. The statistics of the random field can then be determined using the fluctuation dissipation theorem. This model was first used to study magnetization reversal in the simplest micromagnetic system of a pair of magnetostatically coupled particles.[32] Essentially, the set of integrated Langevin equations is solved numerically, leading to a switching behavior resembling a random walk over the energy barrier. Among the results given in Ref. 32 are detailed calculations of the pre-exponential factor f_0 in the Arrhenius–Néel law. In particular, a dependence of f_0 on the applied field and strength of coupling between the particles was demonstrated. In addition thermal agitation was shown to have a profound effect on the reversal process itself. Significant deviations from the deterministic (symmetric fanning) mode are found at a finite temperature, the magnitude of which depends on the temperature and the interparticle coupling. This has two important effects from the micromagnetic viewpoint. First, a reversal to an antiparallel state after switching becomes possible in addition to the parallel state expected at zero temperature. Second, it is found that there appears a temperature dependence of the effective energy barrier. Physically this is because of the departure from the ideal reversal mode induced by thermal perturbations as a result of which many unsuccessful reversal attempts are made in directions other than those leading to the saddle point of the transition. We note that these effects are important for reversal over low energy barriers, i.e., reversals involving very short time scales. The model described here cannot realistically be applied to rever-

sals in slow dynamic time scales. In order to study slow dynamics it is necessary to calculate energy barriers directly. This is a problem which is being given increasing attention. In the following, we outline some recent energy barrier approaches.

B. Energy barrier models

Slow relaxation in multivariate systems such as a particle in the micromagnetic formalism is best approached by direct determination of the energy barrier and the determination of the relaxation time using the Arrhenius–Néel law [Eq. (1)]. However, the determination of the minimum energy barrier on a complex energy surface is a difficult problem and one not amenable to the usual micromagnetic approach. An early model was given by Lyberatos and Chantrell.[33] This model uses a minimization approach to determine the energy barrier. The algorithm was found to give physically reasonable results for the variation of energy barrier with particle size, leading ultimately to the prediction of a peak in the variation of H_c with particle diameter, in agreement with the early experimental work of Kneller and Luborsky.[34] An interesting result, which highlights the importance of the thermal effects is the prediction of a thermally induced flower to vortex state transition in zero field. This assists nucleation via a mechanism close to curling and leads to a lower coercivity than predicted by the previous computations.[35] However, this approach, although providing useful physical results, significantly overestimates the energy barrier, and a number of other approaches have been adopted.

The study of energy barriers in the micromagnetic problem is thus of considerable importance. For the simplest case of two interacting particles analytical approaches[36,37] have given useful results and in particular[37] it was shown that the activation volume is related to the change of magnetization required to reach the saddle point of the transition, which is consistent with the definition proposed by Gaunt.[16] The superparamagnetic transition has also been studied via numerical approaches in a chain of spheres.[38] However, both these approaches rely on constrained optimization, which is known to lead to potential numerical problems in complex systems. A more recent development is a novel random search ridge method for saddle point detention on hypersurfaces. Essentially a ridge method is used, employing the linear fluctuation theory outlined earlier[31] to choose the initial direction of search for the ridge. This enhances the simulation by the introduction of the lowest eigenmodes into the thermal activation problem. A detailed study of the topology of the energy surface for three interacting particles using this technique will be published elsewhere.[39]

ACKNOWLEDGMENTS

The financial support of SERC and the EC CAMST project is gratefully acknowledged.

[1] L. Néel, J. Phys. Rad. **12**, 339 (1951).
[2] M. El-Hilo, K. O'Grady, and R. W. Chantrell, J. Magn. Magn. Mater. **109**, L164 (1992).
[3] M. El-Hilo, K. O'Grady, and R. W. Chantrell, J. Magn. Magn. Mater. **123**, 30 (1993).
[4] K. O'Grady, M. El-Hilo, and R. W. Chantrell (these proceedings).
[5] R. Street and J. C Woolley, Proc. Phys. Soc. A **62**, 562 (1949).
[6] L. Néel, Ann. Geophys. **5**, 99 (1949).
[7] E. P. Wohlfarth, J. Phys. F **14**, 1155 (1984).
[8] M. El Hilo, S. H. Uren, K. O'Grady, J. Popplewell, and R. W. Chantrell, IEEE Trans. Magn. **MAG-26**, 244 (1990).
[9] M. El Hilo, K. O'Grady, H. Pfeiffer, R. W. Chantrell, and R. J. Veitch, IEEE Trans. Magn. **MAG-28**, 2689 (1992).
[10] M. El Hilo, K. O'Grady, and R. W. Chantrell, IEEE Trans. Magn. **MAG-27**, 4666 (1991).
[11] A. M. de Witte, K. O'Grady, and R. W. Chantrell, J. Magn. Magn. Mater. **120**, 187 (1993).
[12] A. M. de Witte, K. O'Grady, G. N. Coverdale, and R. W. Chantrell, J. Magn. Magn. Mater. **88**, 183 (1990).
[13] P. J. Flanders and M. P. Sharrock, J. Appl. Phys. **62**, 2918 (1987).
[14] A. Lyberatos, R. W. Chantrell, E. R. Sterringha, and J. C. Lodder, J. Appl. Phys. **70**, 4431 (1991).
[15] M. El Hilo, L. Folks, R. W. Chantrell, K. O'Grady, and R. Street (to be published).
[16] P. Gaunt, J. Appl. Phys. **59**, 4129 (1986).
[17] J. F. Liu and H. L. Luo, J. Magn. Magn. Mater. **86**, 153 (1990).
[18] J. C. Barbier. Ann. Phys. Paris **9**, 84 (1954).
[19] R. Street, P. G. McCormick, and L. Folks, J. Magn. Magn. Mater. **104–107**, 368 (1992).
[20] L. Folks and R. Street (these proceedings).
[21] R. W. Chantrell, A. Lyberatos, and E. P. Wohlfarth, J. Phys. F **16**, L145 (1986).
[22] D. K. Lottis, E. H. Dahlberg, J. A. Christner, J. I. Lee, R. L. Peterson, and R. M. White, J. Appl. Phys. **63**, 2920 (1988).
[23] Y Kanai and S. H. Charap, IEEE Trans. Magn. **MAG-27**, 4972 (1991).
[24] K. Binder, *Monte Carlo Methods in Statistical Physics* (Springer, Berlin, 1979), p. 33.
[25] A. Lyberatos, R. W. Chantrell, and A. Hoare, IEEE Trans. Magn. **MAG-26**, 222 (1990).
[26] D. Lottis, R. M. White, and E. D. Dahlberg, J. Appl. Phys. **67**, 5187 (1990).
[27] A. Lyberatos, R. W. Chantrell, E. R. Sterringha, and J. C. Lodder, J. Appl. Phys. **70**, 4431 (1991).
[28] R. W. Chantrell, A. Lyberatos, H. Pfeiffer, E. R. Sterigha, and J. C. Lodder (to be published).
[29] G. T. Huysmans, J. C. Lodder, and Y. Wakui, J. Appl. Phys. **64**, 2016 (1988).
[30] W. F. Brown, Jr., Phys. Rev. **130**, 1677 (1963).
[31] A. Lyberatos, D. V. Berkov, and R. W. Chantrell, J. Phys: Condens. Matter **5**, 8911 (1993).
[32] A Lyberatos and R. W. Chantrell, J. Appl. Phys. **73**, 6501 (1993).
[33] A. Lyberatos and R. W. Chantrell, IEEE Trans. Magn. **MAG-26**, 2119 (1990).
[34] E. Kneller and F. E. Lubrovsky, J. Appl. Phys. **34**, 656 (1963).
[35] M. E. Schabes and H. N. Bertram, J. Appl. Phys. **64**, 1349 (1988).
[36] W. Chen, S. Zhang, and H. N. Bertram, J. Appl. Phys. **71**, 5579 (1988).
[37] A. Lyberatos, J. Appl. Phys. (in press).
[38] P. V. Headriksen, G. Christansen. C. Morup, and S. Morup, J. Magn. Magn. Mater. **132**, 207 (1994).
[39] A. Lyberatos and R. W. Chantrell (to be published).

Time dependence of switching fields in magnetic recording media (invited)

M. P. Sharrock
Digital Media Laboratory, 3M, 236-3C-02, 3M Center, St. Paul, Minnesota 55144-1000

Coercivity and other experimental measures of switching field depend upon the time scale of interest. This time-scale dependence has practical importance in magnetic recording, because the effective time scales of writing and storage are very different. A simple model accounts for the time-scale dependence of coercivity in terms of the thermally assisted crossing of an energy barrier whose height is reduced by the applied field. Fitting this barrier-crossing model to data provides an estimate of the volume that must switch magnetization direction in overcoming the barrier. The assumption of Stoner–Wohlfarth reversal is used to obtain an initial estimate of the dependence of the barrier height on the field. With some adjustment of the resulting energy expression, the model gives good agreement between calculated switching volume and actual particle volume for advanced recording particles of three types: acicular oxide, acicular metal, and barium ferrite platelets. The model can be used to estimate minimum practical particle volumes for use in magnetic recording. Switching due to fields nearly perpendicular to the particle's preferred axis, sometimes used as a measure of the anisotropy field, also shows the effect of thermal assistance. The switching volume determined from such measurements, like that from coercivity, approximates the particle volume.

I. INTRODUCTION

Current magnetic recording media encode information, whether digital or analog, as magnetized zones in the surface of a tape or disk. The minimum dimension of these features is on the order of a micrometer (typically 0.5 μm in advanced applications). This paper will focus on media of the particulate construction,[1] as opposed to those made by thin-film deposition. A particulate medium consists of a support material upon which is coated a dispersion of magnetic particles in organic polymers, along with solvents, lubricants, and other necessary components. Usually the coating is exposed to a magnetic field before drying in order to impart a magnetic orientation to the particles. The particles have maximum dimensions, length for acicular particles and diameter for platelets, on the order of a tenth micrometer (0.05–0.2 μm, for advanced materials). They are generally assumed because of their size to be single-domain particles. The particle size is extremely important to the recording resolution, signal-to-noise properties, and magnetic stability of the medium.[2] Recent years have seen significant reduction in particle sizes of all compositions used in recording.

One of the most important magnetic properties of the particles used in a recording medium is the *remanent coercivity*, which is essentially the median switching field. For convenience, the *intrinsic coercivity* (applied field that reduces magnetization to zero after saturation in the opposite direction) is more commonly specified; it is often (and here) referred to simply as the *coercivity*. The coercivity value determines the field needed to record, and also to erase or overwrite, information on the medium. Thus it must not be excessively large. The coercivity must, however, be adequately large to prevent long-term demagnetization during the desired life of the information (typically years); this implies adequate resistance to fields from both internal and external sources.

Time-dependent magnetic phenomena have been well known for over 40 years,[3,4] and were in fact described over a century ago.[5] In particular, the coercivity value depends upon the time scale of the process used to induce magnetic reversal. That is, the value of the fixed field required to reduce magnetization to zero from saturation decreases as one increases the time that it is allowed to act. Similarly, the coercivity measured in a swept-field hysteresis loop increases with the sweep rate.[2,6,7]

These time-dependence considerations are highly relevant to magnetic recording technology, in which the time scale of the writing process may be on the order of 10^{-8} s and that of the desired storage stability on the order of 10^{+8} s. The usual laboratory methods cannot investigate behavior over this huge range, covering 16 orders of magnitude, although recent pulsed-field experiments[8] have begun to probe behavior at and below its lower end. A vibrating-sample magnetometer (VSM) typically has a time scale on the order of 1 s, and a 60-Hz magnetometer has an effective time scale of 10^{-5}–10^{-6} s.[7] The model described here and previously[2,6,7] allows the interpretation of such laboratory experiments in terms of physical quantities and also the extrapolation to the much longer and shorter time scales of interest in recording. Reducing the switching volume has the effect of increasing the amount by which the "writing coercivity" exceeds the "storage coercivity." Thus the trend toward smaller particles for benefits in signal-to-noise ratio, resolution, and surface smoothness will at some point be limited by time-dependence considerations. This potential limitation has been discussed in the past[2] and will be reevaluated in Sec. IV.

II. MEASUREMENTS AND MODEL

The essential origin of time-dependent magnetic behavior in small particles is the thermally assisted process of crossing an energy barrier that occurs in magnetic switching.[3,4,9–11] The conventional Arrhenius formulation for the rate constant r, the probability per unit time of successful crossing, is

 0021-8979/94/76(10)/6413/6/$6.00 © 1994 American Institute of Physics

$$r = A \exp(-\Delta E/kT). \quad (1)$$

The factor A is assumed to have a negligible dependence on field and temperature; k is Boltzmann's constant and T is the absolute temperature. The role of an externally applied magnetic field is to decrease the energy barrier ΔE until switching occurs on the time scale of interest. Equation (1) would suggest that in the presence of a constant opposing field, the magnetic moment $m(t)$ of a collection of particles decays exponentially with time t from an initial saturated value m_0 as

$$m(t) = m_0[2 \exp(-rt) - 1]. \quad (2)$$

This exponential behavior would in fact be observed for an ensemble of noninteracting particles having identical magnetic properties. Particles in actual recording media, however, exhibit distributions of particle size and shape (and possibly composition). This distribution of physical properties leads to a distribution of magnetic properties, which may be further complicated by the variety of interparticle magnetic interactions that can occur. The result is that observed behavior is nonexponential.[12] The decay of $m(t)$ in the presence of a constant field is often found to approximate a linear dependence on some power of the logarithm of time.[13] Such a function can be viewed as the superposition of many exponential decays, representing a distribution of magnetic properties such as switching field. Another way of measuring time dependence is the recording of hysteresis loops of differing sweep rates;[6,7,14] by combining an ac instrument (e.g., 60 Hz) with a VSM, this technique can allow a greater range of time scales than is convenient in constant-field decays. In both types of experiments, one must take the distribution of properties into account. A straightforward way of doing this is to focus attention on the center, or peak, of the switching-field distribution (SFD) and to consider the coercivity as representing the material at this peak. It will be assumed that in some approximation the peak of the SFD is associated with the peak of the distribution of other relevant parameters, such as switching volume. In other words, the coercivity characterizes the switching of the most typical, or significant, particles in the sample. (One needs to assume also that substantially the same material is represented by the peak of the SFD at all time scales of interest.) Obtaining constant-field decay curves that represent the same part of the SFD [that is, the same value of the measured moment $m(t)$] over a significant range of time values can be difficult. Over a limited time range, curves for significantly different field values may occur at very different $m(t)$ values and thus represent different parts of the SFD. The slopes of the curves will in fact reflect the height of the SFD for these fields.[15,16] The switching volumes associated with these points of the SFD may well be different. In order to concentrate on one part (the peak) of the SFD, a large range of experimental time scales may be more easily attained by using hysteresis loops, and the resulting coercivity values, for different sweep rates. The loops present their own difficulties, however. One must assign an effective time scale, t in Eq. (1), to the experimental sweep rate. This assignment can be done;[7,13,17] as expected, the t value is approximately inversely proportional to the sweep rate but also depends upon the strength of the time-dependent effects shown by the sample.

Equation (1) will be used with the above assumptions and interpretations. The factor A in Eq. (1) is an "attempt frequency" for barrier crossing. It can be estimated in a number of ways,[10] including simple precession, and appears to be on the order of 10^9 s^{-1}. A range of values around this estimate will be considered.

The energy barrier ΔE depends upon the value of a volume that is called below the "switching volume" and designated by V. This parameter is defined here as *the volume of material that must rotate magnetically in the process of overcoming the rate-limiting energy barrier*. In switching by coherent rotation, this would be expected to be the entire particle volume (assumed single-domain at the sizes of interest). In more complex reversal modes, the switching volume might be a fraction of the particle volume,[18] the portion that must rotate in order to initiate the reversal process of the whole particle. If reversal is incoherent but simultaneous, however (as in fanning[19]), V might conceivably be the entire particle volume.

The model assumes single-domain particles having uniaxial magnetic anisotropy, with anisotropy energy of the form $K \sin^2 \theta$ (angle θ between the preferred axis and the moment vector). For the case of the applied field being exactly aligned with the preferred axis and opposing the initial magnetization,[6,9]

$$\Delta E = KV(1 - H/H_o)^2, \quad (3)$$

with

$$H_o = 2K/M. \quad (4)$$

The first-order anisotropy constant is designated by K, the magnetization intensity of the particle by M, and the external field strength by H. (Note: $\Delta E = 0$ for $H = H_o$.) The switching volume V used here cannot be identified with the "activation volume" V_{act} discussed by others.[15,16,20] V_{act}, as usually defined, is explicitly field dependent. For the special case of perfect alignment of H with the preferred axis, V_{act} can be interpreted in terms of the change in magnetic moment, projected onto the preferred axis, that occurs in overcoming the barrier [Ref. 20, Eq. (26), and Ref. 16, Eq. (12)]. The V used here can best be identified with the value of the "critical volume"[16] *that applies when the field is equal to the coercivity*.

The case of perfect alignment of field and preferred axis is an improbable one in a collection of particles having even a modest distribution of orientations. Actual recording media have substantial distributions, despite efforts to orient them. [Typical ratios of remanent to saturated moment near 0.8 indicate mean deviations of roughly $\cos^{-1}(0.8)$, or 35°, from the intended direction.] Victora[21] has presented a theoretical argument that with the field not aligned with the preferred axis, the exponent in Eq. (3) is expected to be 3/2, for very general anisotropy, even including interactions. The Stoner–Wohlfarth (SW) model of reversal[22] also indicates an exponent that can differ from 2. Using the approximation of Pfeiffer,[23] one can use the SW model to write

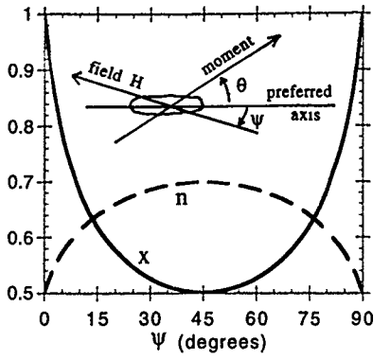

FIG. 1. Dependence of Stoner–Wohlfarth parameters, used in Eqs. (6)–(9), on the (minimum) angle ψ between the applied field and the preferred axis of a particle.

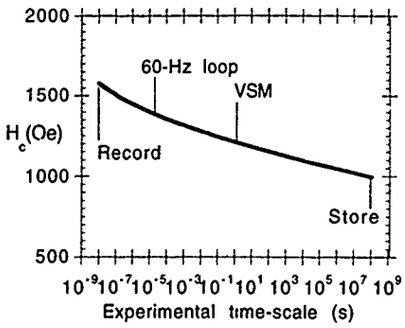

FIG. 2. Plot of Eq. (10), which models the dependence of measured coercivity on time scale t, for $H_0=1800$ Oe, $n=1/2$, $A=2\times10^9$ s^{-1}, $V=3.0\times10^{-17}$ cm^3, and $M=300$ emu/cm^3. Relevant time scales for magnetic recording and experimental measurements are shown.

$$\Delta E=KV(1-H/H_o)^m, \tag{5}$$

with

$$H_o=2xK/M, \tag{6}$$

and

$$m\approx 0.86+1.14x. \tag{7}$$

For later convenience, subsequent expressions will use the definition

$$n\equiv 1/m. \tag{8}$$

As in the case of perfect alignment, $\Delta E=0$ for $H=H_0$. The dependence of H_0 (that is, of x) on the angle ψ between the field direction and the preferred axis is the familiar SW one:

$$x=[\cos^{2/3}(\psi)+\sin^{2/3}(\psi)]^{-3/2}. \tag{9}$$

Figure 1 shows this behavior ($x=1.0$ for $\psi=0°$ or 90°; $x=0.5$ for $\psi=45°$). Using Eqs. (5)–(8) and defining coercivity $H_c(t)$ as the field that produces reversal of half of the sample in time t,

$$H_c(t)=H_o\{1-[(kT/KV)\ln(At)]^n\}. \tag{10}$$

(A relatively insignificant factor of 0.693, shown in earlier work,[2,6] has been absorbed into A for convenience.) Figure 1 shows the behavior of the exponent n in the SW model, using the Pfeiffer approximation. Figure 2 shows a plot of Eq. (10) for typical parameters, where the experimental time scale t is the duration of a constant or pulsed field and/or the equivalent values for swept-field experiments.[7] As was stated above, the coercivity is interpreted as representing the switching of material at the peak of the SFD and also the peaks of other relevant distributions. Thus Eq. (10) is taken to represent the most "typical" particles in the medium.

III. RESULTS

Equation (10) has four unknowns: H_o, A, n, and the product KV. If one is willing to assume plausible values for A and n, the other two can be determined from two measured coercivity values of sufficiently differing time scales. This has been done in the past, using a VSM and a 60-Hz instrument.[2,6] Further, if the magnetization intensity M is known, K and V can be determined separately, using Eqs. (6) and (7). These calculations allow the interpretation of the time dependence of coercivity in terms of physical parameters, and also the extrapolation to coercivity values for the experimentally difficult recording and storage time scales.[2,6] If more than two experimental time scales are available, determination of more than two parameters is possible. Figure 3 shows data and a typical fit for a tape containing cobalt-modified acicular iron oxide particles. As in all coercivity measurements reported here, the applied field direction coincides with the direction of intended magnetic orientation in the sample; the preferred axes of individual particles are distributed around this direction. The oxide particles are relatively small examples of this type of material, about 0.2 μm long, and are commonly used in advanced video and data tapes. The data are from a VSM, run at various sweep rates, and a 60-Hz instrument. Four parameters are still too many to fit meaningfully. Therefore a value of A was chosen and fitting was done on H_0, KV, and n. Equivalently good fits were achieved over a range of A values. Figure 4 shows the relationship between fitted n and assumed A. The switching volume V was computed, using Eqs. (6) and (7), with a magnetization M of 340 emu/cm^3. The value of V depends upon the assumed value of A, but not very sensitively. However, it is very interesting that the best agreement between V and the

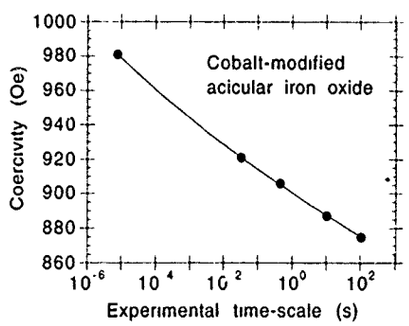

FIG. 3. Experimental data showing measure coercivity vs experimental time scale t, for tape containing acicular cobalt-modified iron oxide particles. Line is a fit of Eq. (10), for $A=3\times10^9$ s^{-1}, and is the basis for one of the points in Fig. 4. The fitting parameters are H_0, n, and the product KV.

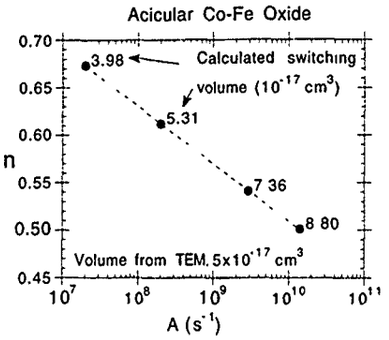

FIG. 4. Plot of values of n vs chosen values of A, obtained by fitting Eq. (10) to the data in Fig. 3. Magnetization M is 340 emu/cm^3; this is used to calculate the value of the switching volume V from the fitted values of H_0, n, and the product KV that result for each value of A. The dotted line shows a least-squares fit, yielding $n=1.115-0.0606[\log(A/s^{-1})]$.

particle volume estimated from transmission electron microscopy (TEM) occurs for n approximately 0.63, close to the 2/3 predicted by Victora[21] and for A about 10^8 s^{-1}, in reasonable agreement with results of Doyle *et al.*[8] The value of 0.63 for n is somewhat lower than would be expected in SW reversal for the sample's degree of orientation. The remanence-to-saturation ratio is 0.88, which indicates average angular deviations of nearly 30°. The SW model [Eqs. (7)–(9); Fig. 1] predicts an n value of 0.68 for this angle.

Another sample studied was a tape containing barium ferrite platelets, of a type currently of interest for advanced applications. This experimental tape had a relatively low degree of magnetic orientation (remanence-to-saturation ratio of 0.63), which tends to minimize the interaction effects. These can be very strong in barium ferrite,[24,25] especially when highly oriented.[26] Because of the low degree of orientation, n will be initially estimated as 0.7. This is the maximum allowed in SW reversal; see Fig. 1. The measured coercivities were 1460 Oe for the 60-Hz loop and 1290 Oe for the VSM run at 13 Oe/s sweep rate. The effective t values for these measurements can be estimated[7] as 1.5×10^{-5} s and 0.8 s, respectively. The hysteresis loops were recorded to limits of ±3240 Oe (the maximum possible) with the 60-Hz instrument, and ±2940 Oe with the VSM. These limits provide that the ratio of maximum applied field to measured coercivity is approximately the same in the two instruments, in order to avoid the possibility that one produces more complete saturation of the sample than the other. (This precaution is necessary only because of the relatively low 60-Hz field capability relative to this sample.) The results of fitting, using 0.7 for n, 10^9 s^{-1} for A, and 300 emu/cm^3 for M, are given in Table I.

In addition, remanence coercivities were measured in the following way: A fixed reverse field, opposite the direction of initial magnetization by a field of 11 kOe, was applied. Periodically, the reverse field was shut off and the remanence measured. The total accumulated field exposure time required to reduce remanence to zero was taken to be the t value for remanence coercivity H_r equal to this reverse field. The results were t values of 10 and 290 s for H_r values of 1350 and 1300 Oe, respectively. The results of fitting these values, using the same values for n, A, and M, are also shown in Table I.

The agreement between the two coercivity methods with regard to V is good. The average is given in Table I, with a measure of the uncertainty resulting from their spread. The 9% increase in H_0 from the first to the second line is typical of a remanence coercivity relative to the coercivity from a scanned loop. These results are not very sensitive to the value chosen for A; variation over the range 2×10^8–3×10^9 s^{-1} produces an insignificant difference (3%–5%) in H_0 and V.

TEM pictures indicate that most of the particles have volumes of 2–3×10^{-17} cm^3. The factor-of-2 discrepancy between the model calculation of V and the apparent particle size may not be significant, in view of various assumptions made in the model and the difficulty of estimating representative TEM volumes. (Particle size is quite nonuniform.) The discrepancy is largely removed (calculated $V\approx2\times10^{-17}$ cm^3) if $n\approx0.6$, close to the value found for the acicular oxide. This n value would in SW reversal [Eqs. (7) and (9); Fig. 1] be appropriate for a very well oriented sample, which is not the case.

It seems worthwhile to investigate the possibility that the switching volume V is less than the total particle volume because of an incoherent mode of switching. This would be plausible in view of recent theoretical work.[27] The method of Flanders and Shtrikman,[28] applied previously to barium ferrite anisotropy studies,[25,29] allows measurement of switching by only those particles whose preferred axes lie nearly perpendicular to the applied field, as in Fig. 5. Even if switching at lower ψ values in the usual coercivity measurement is incoherent, the nearly perpendicular field very likely produces parallel rotation of the moment throughout the particle, and thus coherent switching. In SW reversal, by Eqs. (7)–(9) (Fig. 1), the value of n is expected to be close to 0.5 and that of x to 1.0. In this study, switching was measured for particles having ψ in the range 85°–90°. The field needed to produce this switching was measured as a function of the duration of application. The results, shown in Fig. 6, have a large amount of scatter, possibly as a result of deviations from isolated-particle behavior due to interactions. The fit of Eq. (10), using 0.5 for n, yields the values shown in the last line of Table I, for $M\approx300$ emu/cm^3.

Both the "remanence coercivity" and the "perpendicular switching" methods use the measurement of remanent moment after the application and removal of a field. Therefore their H_0 values can be directly compared (Table I). The ratio of these two values, 4800/1850=2.6, exceeds the maximum ratio, 2.00, that the SW model (Fig. 1) can explain between switching fields for different angles. (Recall that because of the low degree of orientation the coercivity measurement represents particles near the center of the curves in Fig. 1.) Therefore it is likely that some form of incoherent switching occurs in the coercivity measurement. The agreement of the values for V shown in the last two lines of Table I is perhaps remarkable in view of the fact that different reversal modes may be involved.

A third material chosen for this study was a tape con-

TABLE I. Ba ferrite.

Method	Initial magnetizing field (kOe)	H_0 (Oe)	V (10^{-17} cm^3)
Coercivity	3	1700	1.28
Remanence coercivity	11	1850	1.10
Average of above two	...	...	1.2±0.1
Perpendicular switching	11	4800±300	1.3±0.4

taining metal particles (MP). As with the barium ferrite, the coercivity values were measured from loops where the ratio of maximum field to coercivity was the same for the 60-Hz magnetometer and the VSM. These instruments gave, respectively, 1735 Oe from a loop of ±3170 Oe and 1650 Oe for ± 3000 Oe. The resulting fit to Eq. (10) yields (with values of 2/3 for n, 10^9 s^{-1} for A, and 1800 emu/cm^3 for M)

$$H_0=1860 \text{ Oe}, \quad \text{and}, \quad V=0.73\times10^{-17} \text{ cm}^3.$$

This value of V represents only the metallic core of the particle; this core is surrounded by the oxide shell produced by the passivation process. Chemical analysis, magnetic moment, and particle mass density, together with TEM pictures, indicate that the core is only about 35% of the particle volume and that the shell is only weakly magnetic. The TEM pictures also show that particle volume is about $3–4\times10^{-17}$ cm^3. Thus the actual particle core volume appears to be about 1.2×10^{-17} cm^3, nearly twice the calculated value of V. As in the case of the barium ferrite particles in this study, the discrepancy is removed if n is set to approximately 0.6. Again, for SW reversal, this is not consistent with the degree of orientation in actual media. Equations (7)–(9) require a value of less than 10° for ψ to give an n value of 0.6; this would imply a remanence-to-saturation ratio of 0.99. The MP tape studied had a ratio of 0.85.

IV. DISCUSSION AND CONCLUSIONS

The results presented here represent magnetic switching behavior for particulate recording media representing the current state of the art in three materials: acicular oxide, barium ferrite, and metallic particles. All show significant

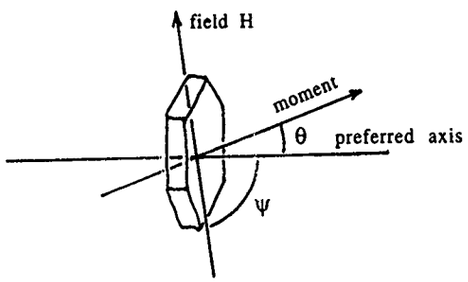

FIG. 5. Diagram of particle in the presence of field nearly perpendicular to preferred axis; ψ is less than, but close to, 90°. Remanence will switch from right to left if moment rotates past the energy barrier.

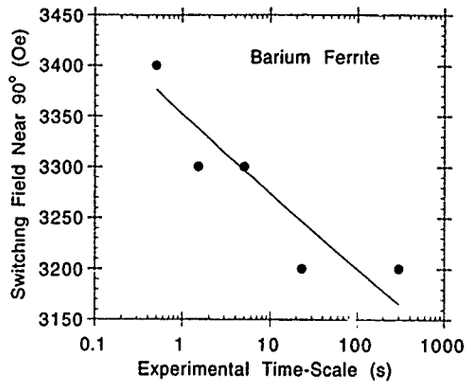

FIG. 6. Plot of measured value of near-perpendicular switching field vs field application time t. Angle ψ was in the range 85°–90° in the experiment. The fit was done for $A=10^9$ s^{-1} and $n=1/2$. The fitting parameters are H_0, n, and the product KV.

time-scale dependence in typical laboratory experiments. The thermally assisted barrier-crossing model discussed here is successful in analyzing this time-scale dependence. Using SW reversal,[22,23] the model determines switching volumes that are within a factor of 2 of particle volumes estimated from TEM pictures. With the assignment of the exponent n to a value of 0.6, rather than 0.7 as determined from SW reversal for typical particulate orientation, the agreement is essentially perfect (within the precision of determining TEM volumes). The good agreement between calculated V and particle volume for n values of 0.6, rather than 0.7, may indicate that the dependence of ΔE on applied field is not accurately given by SW reversal. Regardless of the reversal model used, however, the barrier-crossing model described here can be expected to be useful in extrapolating from coercivities measured in the laboratory to the much shorter and longer times relevant to magnetic recording and storage of information.

By using Eq. (10) to estimate coercivities that would be relevant to writing and storage time scales, one can obtain an estimate of the smallest particle volumes practical for magnetic recording. If the highly arbitrary criterion is adopted that the coercivity relevant to 3-year storage (10^{+8} s) be no less than one half of the value relevant to 10-MHz writing (10^{-8} s),[2] then for $A=10^9$ s^{-1} and $n=0.6$,

$$(KV)_{\text{minimum}}=4.3\times10^{-12} \text{ ergs}. \tag{11}$$

This is 106× the room-temperature value of kT; Lu and Charap found significant decay of simulated high-density recorded transitions for a KV value of $60kT$.[30]

Using Eqs. (6) and (7), Eq. (11) can be rewritten as

$$V_{\text{minimum}}=6.1\times10^{-12} \text{ ergs}/H_0M, \tag{12}$$

where V_{minimum} will be expressed in cm^3 if H_0 is in Oe and M in emu/cm^3. The difference between Eq. (12) and similar expressions discussed earlier[2] is the use of Eqs. (5)–(7) in place of Eqs. (3) and (4). Equation (12), however, does not take account of the differing need for long-term coercivity in materials of very different magnetization intensity. A simple way of estimating this need is through the familiar expres-

sion of Williams and Comstock[31] for the magnetic transition length that results from self-demagnetization:

$$a = B_r d / 2\pi H_c . \tag{13}$$

In Eq. (13), B_r is the remanent induction for the medium (in G), d the recording depth, and H_c the coercivity (in Oe). This expression essentially says that a medium having a higher B_r value needs a higher H_c value in order to resist transition broadening. If the transitions occur at spacing b, then a reasonable degree of transition sharpness requires

$$a \leqslant b/4 \approx d/2. \tag{14}$$

Equations (13) and (14) together give

$$H_c \geqslant B_r/\pi. \tag{15}$$

With Eq. (15) as a lower limit for H_c (10^8 s), and 2200 Oe as an assumed practical upper limit for the writing coercivity H_c (10^{-8} s), Eq. (10) can again be used to estimate the minimum practical particle volume. With $A=10^9\ s^{-1}$ and $n=0.6$, $V_{\text{minimum}}=4\times10^{-18}$ cm^3 for barium ferrite and 1.1×10^{-18} cm^3 for the metallic core of MP. Assuming a passivation shell thickness comparable to that of current MP, the latter value implies a volume of $3\text{–}4\times10^{-18}$ cm^3 for the entire MP particle (M=300 and 1800 emu/cm^3, B_r=1400 and 3000 G for barium ferrite and MP, respectively).

The estimated minimum practical particle volumes given above for MP and barium ferrite are nearly identical; the lower self-demagnetization and absence of a passivation shell in barium ferrite media compensate for the higher value of M that would otherwise appear to give an advantage to MP [Eq. (12)]. These calculated values of V_{minimum} are substantially smaller than the volumes of the smallest currently available particles ($2\text{–}4\times10^{-17}$ cm^3). Thus the model discussed here argues that particulate media technology can advance significantly further toward smaller particles and the resulting higher signal-to-noise ratios.

The barrier-crossing model discussed here will become invalid at time scales on the order of $1/A$ or less. The values of A used here would imply that this limitation occurs at a time scale of about 1 ns (10^{-9} s), at least for barium ferrite and MP. In fact, the observations of Doyle *et al.*[8] made with extremely short field pulses have shown a pronounced increase of the required switching field with decreasing pulse duration at just this order of magnitude. The point at which this increase is considered to be significant is somewhat arbitrary. Equation (10), with parameters typical of advanced media, gives a 1%–2% increase of switching field with each halving of the field exposure time t, for times approaching the $At \approx 1$ condition. If one defines the onset of the regime where the model is no longer adequate as the pulse width where the switching field rises about 10% (an order of magnitude more rapidly) per octave, then this appears to occur at about 0.6 ns for MP and about 1.5 ns for barium ferrite [Figs. 3(a) and 4(a) of Ref. 8]. In data-recording terms, the required switching field begins to deviate significantly from that predicted by Eq. (10) somewhere around 1 Gbit/s for both materials. Since the data rates in anticipated recording systems are generally on the order of 10–100 Mbit/s per channel, recording processes will probably stay within the regime of the model discussed here during the foreseeable future, for both MP and barium ferrite.

ACKNOWLEDGMENTS

The author is grateful to R. L. Brott, W. D. Doyle, T. R. Hoffend, S. F. Kistler, and D. P. Stubbs for constructive critical reading of the manuscript, to J. T. McKinney for valuable discussion and suggestions, to J. W. Mackay and J. S. Roden for providing sample media, and to W. M. Scantlin and H. Nozu for support and encouragement.

[1] M. P. Sharrock, IEEE Trans. Magn. **25**, 4374 (1989).
[2] M. P. Sharrock, IEEE Trans. Magn. **26**, 193 (1990).
[3] L. Néel, Ann. Geophys. **5**, 99 (1949).
[4] R. Street and J. C. Wooley, Proc. Phys. Soc. London, Sect. A **62**, 562 (1949).
[5] J. A. Ewing, Philos. Trans. R. Soc. London **176**, 523 (1885).
[6] M. P. Sharrock and J. T. McKinney, IEEE Trans. Magn. **MAG-17**, 3020 (1981).
[7] P. J. Flanders and M. P. Sharrock, J. Appl. Phys. **62**, 2981 (1987).
[8] W. D. Doyle, L. He, and P. J. Flanders, IEEE Trans. Magn. **29**, 3634 (1993).
[9] C. P. Bean and J. D. Livingston, J. Appl. Phys. **30**, 120S (1959).
[10] W. F. Brown, Jr., J. Appl. Phys. **30**, 130S (1959).
[11] E. P. Wohlfarth, J. Electron. Control **10**, 33 (1961).
[12] R. M. Kloepper, B. Finkelstein, and D. P. Brunstein, IEEE Trans. Magn. **MAG-20**, 757 (1984).
[13] S. B. Oseroff, D. Franks, V. M. Tobin, and S. Schultz, IEEE Trans. Magn. **MAG-23**, 2871 (1987).
[14] A. M. de Witte, M. El-Hilo, K. O'Grady, and R. W. Chantrell, J. Magn. Magn. Mater. **120**, 184 (1993).
[15] K. Song, M. R. Parker, and J. W. Harrell, J. Magn. Magn. Mater. **120**, 180 (1993).
[16] A. Lyberatos, R. W. Chantrell, and K. O'Grady, *Nanophase Materials: Synthesis, Properties, and Applications,* edited by G. C. Hadjipanayis and R. W. Siegel (Kluwer Academic, NATO ASI Series E, Applied Sciences, 1994), Vol. 260, pp. 653–662.
[17] R. W. Chantrell, G. N. Coverdale, and K. O'Grady, J. Phys. D **21**, 1469 (1988).
[18] M. E. Schabes and H. N. Bertram, IEEE Trans. Magn. **25**, 3662 (1989).
[19] I. S. Jacobs and C. P. Bean, Phys. Rev. **100**, 1060 (1955).
[20] P. Gaunt, J. Appl. Phys. **59**, 4129 (1986).
[21] R. H. Victora, Phys. Rev. Lett. **63**, 457 (1989).
[22] E. C. Stoner and E. P. Wohlfarth, Philos. Trans. R. Soc. London, Ser. A **240**, 599 (1948).
[23] H. Pfeiffer, Phys. Status Solidi A **118**, 295 (1990)
[24] P. I. Mayo, R. M. Erkkila, A. Bradbury, and R. W. Chantrell, IEEE Trans. Magn. **26**, 1894 (1990).
[25] M. P. Sharrock, IEEE Trans. Magn. **26**, 225 (1990).
[26] D. E. Speliotis and W. Lynch, J. Appl. Phys. **69**, 4496 (1991).
[27] T. Chang and J.-G. Zhu, IEEE Trans. Magn. **29**, 3619 (1993).
[28] P. J. Flanders and S. Shtrikman, J. Appl. Phys. **33**, 216 (1961).
[29] D. E. Speliotis, IEEE Trans. Magn. **26**, 1891 (1990).
[30] P.-L. Lu and S. H. Charap, J. Appl. Phys. **75**, 5768 (1994).
[31] M. L. Williams and R. L. Comstock, AIP Conf. Proc. **5**, 738 (1972).

Magnetic and structural instabilities of ultrathin Fe(100) wedges (invited)

S. D. Bader, Dongqi Li, and Z. Q. Qiu[a)]
Materials Science Division, Argonne National Laboratory, Argonne, Illinois 60439

An overview is provided of recent efforts to explore magnetic and related structural issues for ultrathin Fe films grown epitaxially as wedge structures onto Ag(100) and Cu(100). Experiments were carried out utilizing the surface magneto-optic Kerr effect. Ordinary bcc Fe is lattice matched to the primitive unit cell of the Ag(100) surface. Fe wedges on Ag(100) can be fabricated whose thick end has in-plane magnetic easy axes due to the shape anisotropy, and whose thin end has perpendicular easy axes due to the surface magnetic anisotropy. A spin-reorientation transition can thus be studied in the center of the wedge where the competing anisotropies cancel. The goal is to test the Mermin–Wagner theorem which states that long-range order is lost at finite temperatures in an isotropic two-dimensional Heisenberg system. Fe wedges on Cu(100) can be studied in like manner, but the lattice matching permits fcc and tetragonally distorted fcc phases to provide structural complexity in addition to the interplay of competing magnetic anisotropies. The results of these studies are new phase identifications that help both to put previous work into perspective and to define issues to pursue in the future.

I. INTRODUCTION

It is of interest to explore magnetic instabilities associated with competing anisotropies in ultrathin epitaxial films. A simple approximation is to equate the two dominant contributions to the anisotropy energy density

$$\frac{2K_s}{t}=2\pi M^2.$$

This provides the condition for which the "shape" anisotropy ($-2\pi M^2$) balances out the surface anisotropy ($2K_s/t$), where K_s is the surface anisotropy constant, t is the thickness of the magnetic film, and M is the magnetization. The underlying assumptions are that any other anisotropy terms can be ignored, *and* that the magnetization orientation within the film is uniform (i.e., all spins point in the same direction). The critical thickness for spin reorientation is

$$t_R=\frac{K_s}{\pi M^2}.$$

For $t<t_R$ the easy axis of magnetization is perpendicular to the film plane (i.e., vertical), while for $t>t_R$ the easy axis is in plane. The question is what happens in the vicinity of $t=t_R$?

Recent theoretical treatments and ideas can be summarized. First, in an isotropic two-dimensional (2D) Heisenberg system there is no long-range order at finite temperature. This is known as the Mermin–Wagner theorem.[1] Hence, spin melting might be expected to occur in the vicinity of t_R. Pescia and Pocrovsky[2] used a renormalization group approach to consider thermal fluctuations, and concluded that the spin reorientation occurs as a phase transition at a temperature T_R which can be less than the Curie temperature T_C. They used the idea of Jensen and Bennemann[3] of a transition driven by the entropy of disorder on going from a uniaxial to a planar spin configuration as temperature increases. Morr, Jensen, and Bennemann[4] recently used a Greens function approach within the random phase approximation to phenomenologically describe the loss of long-range order in the vicinity of the spin-reorientation phase transition. However, it is known that even arbitrarily small anisotropies can restore long-range order.[5] Therefore, it also may be necessary to explore the additional anisotropies, such as arise from the bulk or from finite-size effects, or from higher-order terms in the expansions of the anisotropies than the dominant terms that vary as the square of the magnetization. The higher-order terms can manifest themselves in the vicinity of t_R where the dominant anisotropy terms vanish. Experimentally, ultrathin magnetic films are always grown on a substrate for which lattice constants and thermal expansion coefficients tend to be mismatched to some degree. Thus, epitaxial strain also can influence the magnetic surface or interface anisotropy. This has been treated recently for a test case, for example, by Victora and MacLaren[6] who used electronic structure calculations.

Alternatively, it also becomes important to explore nonuniform magnetization configurations. For example, Yafet and Gyorgy[7] considered the conditions necessary to stabilize ferromagnetic stripe domains in an atomic monolayer that possesses strong surface magnetic anisotropy. They found that while the short-range part of the dipolar interaction gives rise to the familiar $-2\pi M^2$ shape anisotropy term, the long-range part, which can be represented as a domain wall-wall interaction, can result in a lower energetic state than the uniformly magnetized case. The wall-wall interaction, however, has to be evaluated explicitly for the domain configuration under consideration. The domain size will reach an experimentally observable magnitude in the vicinity of the spin-

[a)]Permanent address: Physics Dept., University of California, Berkeley.

 0021-8979/94/76(10)/6419/6/$6.00 © 1994 American Institute of Physics

reorientation transition. Thieville and Fert[8] treated twisted spin configurations using a micromagnetic approach. Alternatively, Erickson and Mills[9] reached similar conclusions for canted spin structures by considering spin wave excitations in 2D films. They found that the excitation energy becomes imaginary in a gap region near the spin-reorientation transition, implying that there exists a static spin-density wave in real space in this region (i.e., the stripe domain structure). A striped domain structure in a 2D film can be viewed as a one-dimensional (1D) ordered system. It is well known that 1D ordered states are unstable against thermal fluctuations. Indeed, Kashuba and Pokrovsky[10] examined 2D striped domains by means of renormalization group methods and found that while thermal fluctuations destroy the regular *spatial* distribution of the stripe domains predicted by Yafet and Gyorgy[7] for the $T=0$ case, the *orientation* of the domain walls remains stable in the presence of thermal fluctuations. Therefore, they reached the conclusion that the 2D stripe domains can be mapped onto the smectic liquid-crystal case.

It is of interest to discuss in more detail the issue of a film of fixed thickness that undergoes a temperature-dependent spin-reorientation transition from perpendicular at low $T(T<T_R)$ to in plane at high $T(T>T_R)$. The question arises as to the existence of a temperature gap ΔT for which either long-range order disappears or for which a uniform magnetization configuration is unstable with respect to canting, twisting, or domain formation. Erickson and Mills roughly estimate a value of $\Delta T/T_R \sim 0.5\%$ for an ultrathin Fe film. A gap due to domain formation can be appreciably larger in magnitude than this estimate. This is because the gap would signal the T range over which the scale of the domain structure shrinks to dimensions that are less than the sample size or probing length.

Much has been said about 2D spin-reorientation phenomena so far, but perhaps the most fascinating aspect to appreciate is that it is predicated on the existence of perpendicular surface anisotropy that is strong enough to compete with the shape anisotropy of the film. For Fe the shape anisotropy gives rise to an ~20 kG demagnetizing field. Thus, the surface anisotropy must be quite substantial in magnitude. Néel[11] was the first to recognize that unusually strong surface anisotropies relative to bulk anisotropies can exist. The bulk magnetocrystalline anisotropy was first attributed to the spin-orbit interaction by Van Vleck.[12] Néel recognized that strong spin-orbit interactions could arise from the broken symmetry at the surface. Much more recently Gay and Richter[13] performed the first computational study to confirm that strong surface anisotropies can be anticipated in particular systems. Wang, Wu, and Freeman[14] have contributed the most recent state-of-the-art advances to this demanding approach.

Gradmann[15] was the first to experimentally identify perpendicular easy axes attributed to strong surface anisotropy He recently reviewed his work that dates back to the 1960s on a variety of films, in an outstanding book chapter. Jonker *et al.*[16] reawakened interest in the surface anisotropy issue in 1986. They attributed the nonobservation of spin polarization in photoemission experiments on Fe/Ag(100) films as being due to the existence of vertical easy axes, and to the technical constraint that the spin detectors employed in their experiments were only sensitive to *in-plane* magnetization components. Recent work on surface magnetic anisotropy in ultrathin films have been reviewed in a variety of publications.[17]

Another experimental manifestation of strong surface anisotropies can be observed in enhanced coercivity (H_c) values displayed in the ultrathin regime. The earliest studies of this type are due to Hirsch[18] who observed a factor of ~5 enhancement in H_c for ultrathin Fe interleaved with Cu. Bader[19] documented a number of systems for which H_c peaks in the monolayer region. Engel *et al.*[20] have observed H_c peaks in monolayer-range films that occur as a function of the thickness of a nonmagnetic overcoating layer. This can be due to electronic effects or morphological (i.e., wetting) changes in the magnetic layer. Gradmann has documented similar examples of coercivity and anisotropy changes due to nonmagnetic overcoats.[15]

The first experimental identifications of temperature-dependent 2D spin-reorientation transitions in transition-metal films are due to Pappas, Kämper, and Hopster.[21] They studied both Fe/Ag(100) and Fe/Cu(100). A ΔT range of ~20–30 K was identified that had vanishingly small remanence. Allenspach and Bischof[22] subsequently imaged the magnetic domains of Fe/Cu(100) and observed striped domains with smectic liquid-crystal-like orientational order, as described by Kashuba and Pokrovsky.[10] However, the question is still not answered as to whether the spontaneous magnetization, as opposed to the average magnetization, is at all reduced or not in the immediate vicinity of the spin-reorientation transition.

In the present work we describe recent surface magneto-optic Kerr effect (SMOKE) contributions to this fundamental problem in 2D magnetism. We first examine Fe/Ag(100) for which magnetic instabilities can be studied without concern for structural instabilities, since Fe is well lattice matched to the Ag(100) square net. Then we progress to the more complex case of Fe/Cu(100) which can exhibit similar spin-reorientation behavior to Fe/Ag(100), but also possesses structural instabilities.

fcc Fe(100) is lattice matched to Cu(100). In the ultrathin limit a tetragonally distorted fcc structure is stable. This fct structure relaxes to an undistorted fcc structure upon increasing the Fe thickness.[23] The fct phase is itself unusual for an element. Only elemental Sn has a naturally occurring fct phase. In the case of Fe/Cu(100) the fct structure is stabilized epitaxially. (This is one of the attributes of modern thin-film-magnetism research—the ability to artificially stabilize new phases.) Eventually, thicker Fe films grown on Cu(100) transform to the equilibrium bcc structure. bcc(110) epitaxial relationships to fcc(100) have been described elsewhere.[24] Metastable phases, therefore, abound in Fe/Cu(100) as a function of growth temperature and Fe thickness. The fct spin-reorientation transition, for example, is only found for low-T growth ($T \leq 200$ K). At higher temperatures the fct structure relaxes to fcc and the magnetic properties change dramatically, as studied recently by Thomasen *et al.*[25] and Li *et al.*[28] Thus, Fe/Cu(100) provides a system rich in magnetic and structural instabilities. The interplay of these instabilities has intrigued, challenged, and stymied a whole generation of

modern researchers. An enormous collective effort has been devoted to this system. It is the prototype chosen by many who seek a rite of passage into the realm of surface magnetism.

II. EXPERIMENTAL DETAILS

Background information on the sample preparation, characterization, and magneto-optic-measurement techniques appear elsewhere.[26–28] For the sake of completeness we briefly mention that the Fe samples were prepared by ultrahigh vacuum evaporation, also known as molecular beam epitaxy. The Fe wedges are formed by linear translation of the substrate behind a mask during growth. Evaporation rates are in the range of 1 monolayer (ML) every ~2–3 min. The wedges have a slope of ~0.2 ML/mm for Fe/Ag and ~1.5 ML/mm for Fe/Cu. The slopes are substantially larger for the Fe/Cu wedges in order to scan the broader region of interest that includes a range of the fct, fcc, and bcc phases. The crystals were ~1 cm in length, and the laser beam for the SMOKE studies was focused to ~0.2 mm. Thus ~50 discrete positions could be sampled along a wedge. The substrates were prepared utilizing standard surface-science techniques involving sputter-anneal cycles. Low- and high-energy electron diffraction (LEED and RHEED) were used to characterize the substrates and films. RHEED oscillations during Fe growth are published in Refs. 27 and 28.

Magneto-optic Kerr-effect measurements were made at the He-Ne laser line using p-polarized light. The films were magnetized using a split-coil superconducting solenoid that provides a homogeneous field with low trapped flux at zero current (<10 Oe). Hysteresis loops were generated with no attempt to convert to ellipticity units. Ellipticities are reported elsewhere for related film structures.[29] The important point for the present studies is that the signal is proportional to the magnetization. The remanent magnetization M_R was used to track the phase transitions in order to avoid possible field-induced transitions. The hysteresis loops are used to identify the easy axis of magnetization. Square polar loops identify vertical easy axes, while square longitudinal loops identify in-plane easy axes. To obtain polar or longitudinal signals the sample was positioned appropriately within the solenoid to face one of two orthogonal laser stations used to generate the data. Thus, it was necessary to rotate the sample by 90° between full scans of a wedge to obtain data for both configurations. This introduced an absolute uncertainty in the positioning of the beam along the wedge, but it presented no obvious problem for our purposes. The hysteresis loops permitted the H_c values to be obtained. They were used to identify the structural transitions for Fe/Cu and to augment the spin-reorientation studies for both systems.

III. RESULTS

A. Fe/Ag(100)

The spin-reorientation transition for Fe/Ag(100) is shown in Figs. 1(a) and 2. Figure 1(a) displays the transition as a function of temperature for a fixed Fe thickness. This is the manner in which the transition was studied originally by Pappas *et al.*[21] who used polarized electron scattering to

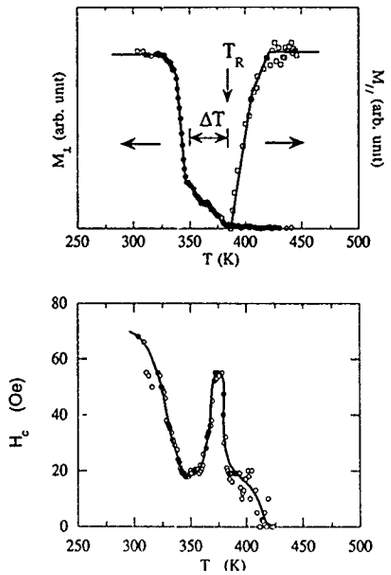

FIG. 1. The perpendicular and parallel components of the remanent magnetization for a 6.0 ML Fe film grown on Ag(100) vs temperature are shown in (a) and the corresponding coercivities from polar SMOKE measurements are shown in (b). The noise in the longitudinal Kerr data (parallel magnetization component) is greater than that in the polar data because of the inherent weakness on the longitudinal signal, as mentioned in the text

identify a region ΔT with vanishing magnetization. The high signal-to-noise ratio and data density in Fig. 1(a) enables one to discern an asymmetric ramp structure within the pseudogap encompassed by ΔT. Thus, if the remanence vanishes, it does so over a very limited T range (a few kelvin at most), as estimated by Erickson and Mills. Note that M_R in Figs. 1(a) and 2 are normalized to the film thickness, and the longitudinal and polar M_R values at saturation are normalized to each other for clarity. (The polar signal is ~25 times as intense as the longitudinal signal, as expected.) The question that Fig. 1(a) raises is what is the root cause of the remanence decrease within ΔT? Is long-range ferromagnetic order lost anywhere within this region, as might be anticipated from the Mermin–Wagner theorem? How do domains or other nonuniform spin configurations manifest themselves within ΔT? If long-range order does not vanish, do enhanced thermal fluctuations in 2D suppress the magnetization even

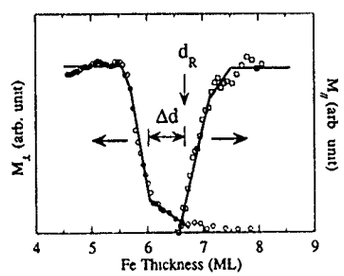

FIG. 2. Perpendicular and parallel components of the remanent magnetization at room temperature along an Fe/Ag(100) wedge.

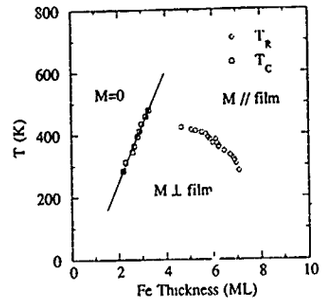

FIG. 3. Magnetic phase diagram of Fe/Ag(100).

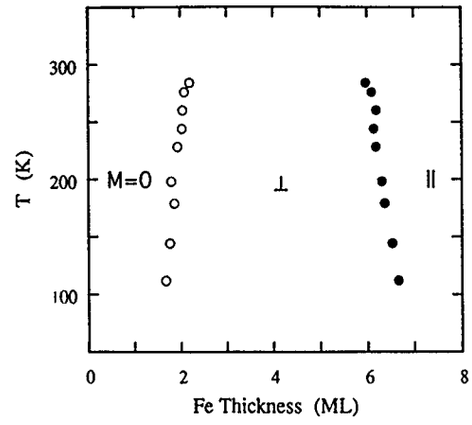

FIG. 4. Boundaries of the uniform ferromagnetic phase with vertical easy axis for an fct Fe/Cu(100) wedge as a function of measurement temperature and Fe thickness. The left-hand boundary delineates the onset of detection of a ferromagnetic signal, while the right-hand boundary terminates in a transition to the spin-in-plane fct phase.

partially due to the system becoming more isotropic in the vicinity of T_R? These questions should motivate future progress in the field.

Figure 2 provides similar data to Fig. 1(a) but as a function of Fe thickness along a wedge. The region Δd and the point d_R are defined operationally in an analogous manner to ΔT and T_R in Fig. 1(a). The asymmetric ramp structure within Δd is very similar in appearance to that observed in Fig. 1(a) within ΔT. The same questions apply as outlined above. It is interesting to note that Kashuba and Pokrovsky[10] have found that their calculations linearize to first-order expansion in both T and d in the vicinity of T_R and d_R, as observed experimentally in Figs. 1(a) and 2.

To augment Fig. 1(a) further, we show the corresponding H_c data in Fig. 1(b). The transition at T_R is defined by a peak in H_c which is almost 3 times as large as its value at $(T_R-\Delta T)$. For $T>T_R$ the value of H_c drops precipitously because the vertical axis becomes a hard direction for the magnetization. For $T<(T_R-\Delta T)$, H_c decreases substantially as T increases. Thus, the hysteresis loops are shrinking in area in this interval as T increases. This can be due to enhanced thermal fluctuations as T_R is approached, or to the fluidity of the domain structure. The peak in H_c at T_R, in any case, represents a striking observation and a challenge to interpret.

Figure 3 summarizes results for the spin-reorientation phase-boundary determinations for Fe/Ag(100). The data represent measurements taken along wedges at different temperatures. The pseudogap regions are not indicated in Fig. 3, but Curie temperatures T_C are shown for some initial Fe thicknesses. The Curie transitions are found to be 2D-Ising-like, as described in Ref. 27. The Curie transitions can be examined to provide an estimate of the intrinsic width that might apply also to the spin-reorientation transitions. The 3%–5% tails reported at T_C imply that the correlation length is limited by finite-size effects to ~100 Å, which corresponds to a typical terrace width in a metallic single crystal.[27] Thus, with inclusion of the Curie transitions, Fig. 3 delineates the $M=0$, $M_{\parallel}$, and $M_{\perp}$ phase regions.

B. Fe/Cu(100)

The region of stability of vertical easy axes for Fe/Cu(100) was first explored systematically by Liu *et al.*[30] They constructed a phase diagram to represent the metastability of the system by plotting growth temperature versus Fe thickness for a large number of films. Vertical easy axes were observed in a region bounded by a thickness of ~6 ML Fe and growth temperatures that do not extend very much above room temperature. The onset of ferromagnetic signals for the thinnest films occurred between ~1 and 3 ML. Figure 4 shows a somewhat different mapping than that of Liu *et al.*[31] for one of our wedged samples grown at low temperature. Figure 4 is analogous to the plot of the Fe/Ag(100) data in Fig. 3. The left-hand boundary in Fig. 4 represents the onset of detection of ferromagnetic signals with vertical easy axis (i.e., T_C), while the right-hand boundary represents the termination of the vertical ferromagnetic phase (i.e., T_R). The left-hand boundary is believed to be influenced by the non-ideal morphology of the films (i.e., intermixing) as well as by decreased T_C values for decreasing film thickness.

Subsequent to the work of Liu *et al.*[31] interest focused on the region beyond the right-hand boundary of Fig. 4. It became clear that two phases exist in this region depending on growth temperature. For low temperature (~100 K) growth the spin-reorientation transition ensues, as for Fe/Ag(100). This occurs even if the samples are annealed to the

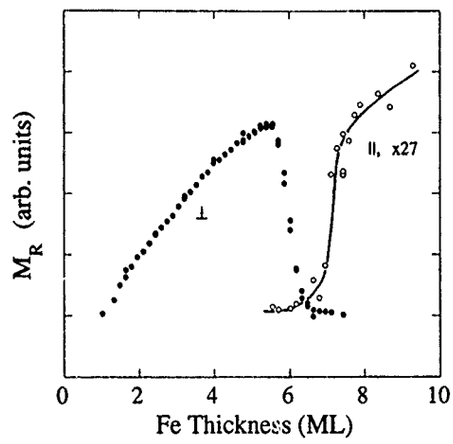

FIG. 5. Spin-reorientation transition for Fe/Cu(100).

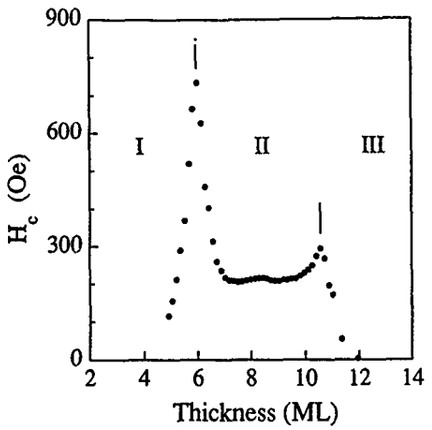

FIG. 6. Coercivities along a wedge of Fe/Cu(100) illustrating peaks at the phase transitions. The left-hand transition is from the fct (I) to the fcc phase (II), while the right-hand transition is to the bcc structure (III).

vicinity of room temperature after growth, as in the work of Ref. 21. For example, the spin reorientation is shown in Fig. 5 for a wedge grown at 190 K, annealed at room temperature, and measured at 110 K. However, different results are obtained for room-temperature growth. Xhonneux and Courtens[31] found evidence for a nonmagnetic phase beyond the 6–7 ML Fe phase boundary. Thomasen *et al.*[25] further clarified the new phase identification as having a surface ferromagnetic "live" layer with vertical easy axis. Li *et al.*[28] more recently confirmed the work of Thomasen *et al.*[25] and, further, found evidence that the ferromagnetic surface is the termination of an antiferromagnetic (AFM) phase. Antiferromagnetism does not manifest itself directly in SMOKE measurements, so further explanation is necessary. While Ref. 25 observed a constant magnetization in the region of interest, Li *et al.*[28] found that upon cooling the constant signal developed peaks of monolayer-type amplitude. For an AFM structure built up of alternating ferromagnetic (100) sheets, a peak would arise due to an uncompensated ferromagnetic sheet whenever there is an odd number of total layers in the structure.

Structural studies indicate that the AFM phase corresponds to the relatively undistorted fcc structure. The $M_\perp$ ferromagnetic phase that precedes it in Fe thickness corresponds to the unrelaxed fct structure. The spin-reorientation transition takes place within the fct structure, and the transition to fcc is suppressed at low-temperature growth. The fct structure is probably strain stabilized under these conditions due to the morphology of the interface and/or to magnetostriction effects. In this latter regard, Hembree *et al.*[32] recently documented for Fe/Cu(100) striking field-induced metastable states attributed to magnetoelastic effects. It is also of interest to speculate on the relationship of the AFM fcc phase identified by Li *et al.*[28] to that observed in γ-Fe coherent precipitates in Cu host alloys. For the bulk alloys the Néel temperature T_N is low as is the magnetic moment ($<1\mu_B$).[33] For the films the magnetic ordering temperature is much higher (200–250 K) suggestive that the moments may also be larger. However, it remains to be determined to what extent the surface ferromagnetic layer boosts the properties (T_N and μ) of the underlying AFM film.

Finally, with increasing Fe thickness the bcc phase is reached at ~10–12 ML Fe. The bcc films are ferromagnetic with in-plane easy axis dictated by the shape anisotropy. The coercivity exhibits striking peaks at the phase transitions, as shown in Fig. 6 for a wedge than spans the fct-fcc transition as well as the bcc transition. The coercivity provides a convenient way to track phase boundaries between fct-fcc, fcc-bcc, and fct-bcc, as well as for the spin-reorientation transition. The most recent magnetic phase diagram for the growth of Fe/Cu(100) is presented in Ref. 28.

IV. SUMMARY

Recent SMOKE studies for Fe/Ag(100) and Fe/Cu(100) were highlighted. The documentation of the spin-reorientation transition for Fe/Ag(100) provides detailed corollary measurements to those of Refs. 21 and 22. A suppressed but nonvanishing remanent magnetization was found within most of the pseudogap region in temperature and Fe thickness that characterizes the phase transition. The coercivity also exhibits a pronounced peak. The role of thermal fluctuations in a nearly isotropic 2D Heisenberg system is quite dramatic and can suppress long-range order and/or give rise to domain structures with unusual characteristics.

For fct Fe/Cu(100) the spin-reorientation transition occurs for low-temperature ($\lesssim$200 K) growth. However, for room-temperature growth the ferromagnetic fct phase with vertical easy axis transforms to an AFM fcc phase with a surface ferromagnetic live layer. Fe films of ~10–12 ML transform to the equilibrium bcc ferromagnetic structure with in-plane easy axis of magnetization. The Fe/Cu(100) system offers complexity associated with the interplay of magnetic and structural transitions. However, coercivity peaks can be used to track a variety of its phase transitions. The underlying mechanisms for achieving phase stability and that control coercive behavior remain a challenge to pursue in the future.

ACKNOWLEDGMENT

This work was supported by the U.S. DOE Basic Energy Sciences-Materials Sciences under Contract No. W-31-109-ENG-38.

[1] M. D. Mermin and H. Wagner, Phys. Rev. Lett. **17**, 1133 (1966).
[2] D. Pescia and V. L. Pokrovsky, Phys. Rev. Lett. **65**, 2599 (1990); **70**, 1183 (1993); P. Politi, A. Rettori, and M. G. Pini, *ibid.* **70**, 1182 (1993).
[3] P. J. Jensen and K. H. Bennemann, Phys. Rev. B **42**, 849 (1990).
[4] D. K. Morr, P. J. Jensen, and K. H. Bennemann (unpublished).
[5] M. Bander and D. L. Mills, Phys. Rev. B **38**, 12 015 (1988).
[6] R. H. Victora and J. M. MacLaren, Phys. Rev. B **47**, 11 583 (1993).
[7] Y. Yafet and E. M. Gyorgy, Phys. Rev. B **38**, 9145 (1988).
[8] A. Thiaville and A. Fert, J. Magn. Magn. Mater. **113**, 161 (1992).
[9] R. P. Erickson and D. L. Mills, Phys. Rev. B **43**, 10715 (1991); **46**, 861 (1992).
[10] A. Kashuba and V. L. Pokrovsky, Phys. Rev. Lett. **70**, 3155 (1993); Phys. Rev. B **48**, 10 335 (1993).
[11] L. Néel, J. Phys. Radium **15**, 225 (1954).
[12] J. H. Van Vleck, Phys. Rev. **52**, 1178 (1937).
[13] J. G. Gay and R. Richter, Phys. Rev. Lett. **56**, 2728 (1986).
[14] D.-s Wang, R. Wu, and A. J. Freeman, Phys. Rev. B **47**, 14 932 (1993).
[15] U. Gradmann, in *Handbook of Magnetic Materials*, edited by K. H. J. Buschow (North-Holland, Amsterdam, 1993), Vol. 7, p. 1.

[16] B. T. Jonker, K.-H. Walker, E. Kisker, G. A. Prinz, and C. Carbone, Phys. Rev. Lett. **57**, 142 (1986).
[17] T. Shinjo, Surf. Sci. Rep. **12**, 49 (1991); see articles in J. Magn. Magn. Mater. **100** (1991); J. Ferré, in *Magnetism, Magnetic Materials, and Their Applications*, edited by F. Leconbue and J. L. Sanchez Llamazares (IOP, Bristol, 1992), p. 167: H. C. Siegmann, J. Phys.: Condens. Matter **4**, 8395 (1992); B. Heinrich and J. F. Cochran, Adv. Phys. **42**, 523 (1993); see chapters in *Ultrathin Magnetic Structures*, edited by J. A. C. Bland and B. Heinrich (Springer, Berlin, 1994), Vols. I and II; R. Allenspach, J. Magn. Magn. Mater. **129**, 160 (1994).
[18] A. A. Hirsch, in *Basic Problems in Thin Film Physics*, edited by R. Niedermayer and H. Mayer (Vandenhoeck and Ruprecht, Göttingen, 1966), p. 477.
[19] S. D. Bader, Ultramicroscopy **47**, 355 (1992); Proc. IEEE **78**, 909 (1990).
[20] B. N. Engel, M. H. Wiedmann, R. A. VanLeeuwen, and C. M. Falco, Phys. Rev. B **48**, 9894 (1993).
[21] D. P. Pappas, K.-P. Kämper, and H. Hopster, Phys. Rev. Lett. **64**, 3179 (1990) [Fe/Cu(100)]; D. P. Pappas, K.-P. Kämper, B. P. Miller, H. Popster, D. E. Fowler, A. C. Luntz, C. R. Brundle, and Z.-X. Shen, J. Appl. Phys. **69**, 5209 (1991) [Fe/Cu(100)]; D. P. Pappas, C. R. Brundle, and H. Hopster, Phys. Rev. B **45**, 8169 (1992) [Fe/Cu(100) and Fe/Ag(100)].
[22] R. Allenspach and A. Bischof, Phys. Rev. Lett. **69**, 3385 (1992).
[23] H. Mangnan, D. Chandesris, B. Villette, O. Heckmann, and J. Lecante Phys. Rev. Lett. **67**, 859 (1991).
[24] F. Scheurer, R. Allenspach, P. Xhonneux, and E. Courtens, Phys. Rev. B **48**, 9890 (1993); K. Kalki, D. D. Chambliss, K. E. Johnson, R. J. Wilson, and S. Chiang, Phys. Rev. B **48**, 18 334 (1993).
[25] J. Thomasen, F. May, B. Feldmann, M. Wuttig, and H. Ibach, Phys. Rev. Lett. **69**, 3831 (1992).
[26] Z. Q. Qiu, J. Pearson, and S. D. Bader, Phys. Rev. Lett. **70**, 1006 (1993).
[27] Z. Q. Qiu, J. Pearson, and S. D. Bader, Phys. Rev. B **49**, 8797 (1994).
[28] D. Li, M. Freitag, J. Pearson, Z. Q. Qiu, and S. D. Bader, Phys. Rev. Lett. **72**, 3112 (1994); and these proceedings.
[29] Z. Q. Qiu, J. Pearson, and S. D Bader, Phys. Rev. B **45**, 7211 (1992); **46**, 8195 (1992).
[30] C. Liu, E. R. Moog, and S D. Bader, Phys. Rev. Lett. **60**, 2422 (1988).
[31] P. Xhonneux and E. Courtens, Phys. Rev. B **46**, 556 (1992).
[32] G. G. Hembree, J. Drucker, S. D. Healy, K. R. Hein, Z. J. Yang, and M. R. Scheinfein, Appl. Phys. Lett. **64**, 1036 (1994).
[33] Y. Tsunoda, N. Kunitomi, and R. M. Nicklow, J. Phys. F **77**, 2447 (1987).

Magnetic and structural instabilities of ferromagnetic and antiferromagnetic Fe/Cu(100)

Dongqi Li, M. Freitag,[a] J. Pearson, Z. Q. Qiu,[b] and S. D. Bader
Materials Science Division, Argonne National Laboratory, Argonne, Illinois 60439

Fe wedges epitaxially grown on Cu(100) have been employed to investigate the interplay between magnetic and structural instabilities. 2–4 monolayer (ML) clean Fe films grown at room temperature are ferromagnetic with perpendicular easy axes. bcc Fe films>11 ML thick are ferromagnetic with in-plane easy axes. Most importantly, 6–11 ML fcc Fe films are antiferromagnetic and have a ferromagnetic surface. Films grown below 200 K and annealed to room temperature do not exhibit the antiferromagnetic phase, but remain ferromagnetic and undergo a spin-reorientation transition from perpendicular to in plane at ~6 ML. A new phase diagram for Fe/Cu(100) is proposed as a function of thickness and growth temperature. In addition, an impurity-stabilized layer-by-layer growth that persists to 30–40 ML Fe is also reported.

Iron, especially fcc Fe, is intrinsically unstable magnetically in the sense that its nearest-neighbor exchange interaction can be either positive (ferromagnetic) or negative (antiferromagnetic), depending on structural details.[1,2] Fe films grown onto Cu(100), in particular, form various structural and magnetic phases to illustrate the tendency toward instability.[3–9] In the current work, we focus on these instabilities and their interplay to achieve a better understanding of the relation between structure and magnetism. Most important, we observe an antiferromagnetic phase with a ferromagnetic surface for 6-11 monolayer (ML) films of Fe grown on Cu(100) at ambient temperature. The different magnetic phases are displayed in a new magnetic phase diagram. In addition, an impurity-induced layer-by-layer growth of Fe on Cu(100) is observed that persists into the 30–40 ML regime.

Sample preparation proceeded first via mechanical and electrochemical polishing of the Cu(100) substrate, and then via sputtering and annealing (600 °C) cycles in the ultrahigh vacuum chamber. Fe was evaporated from an alumina crucible with a typical evaporation rate of 0.7 Å/min. The base pressure of the chamber was 1×10^{-10} Torr, and the pressure during deposition was $2\text{–}5\times10^{-10}$ Torr. The ordering and cleanness of the crystal and the films were confirmed with reflection high-energy electron diffraction (RHEED), low-energy electron diffraction (LEED), and Auger spectroscopy. The Fe wedges were grown while moving the substrate behind a mask during evaporation to define a slope of ~1.5 ML/mm. The substrate temperature during growth is denoted as T_s. The magnetic properties were studied *in situ* by means of the surface magneto-optic Kerr effect (SMOKE). A He-Ne laser beam focused to 0.2 mm was used to scan along the wedge to obtain hysteresis loops for different Fe thicknesses. The height of the Kerr loop in remanence is denoted as M_R, due to its relation to the remanent magnetization. First the results of "dirty" growth will be presented. The remainder of the article will then be devoted to the properties of clean films.

Quite striking behavior is observed for dirty growth. In that case persistent layer-by-layer growth can be obtained (see Fig. 1) as judged by relatively undamped RHEED oscillations up to 32 ML Fe. The oscillations resume after restarting the stopped deposition (not shown in Fig. 1) and persist to 40 ML, where the experiment was terminated. This is surprisingly thick for a metastable phase. The LEED patterns before and after deposition were both $c(2\times2)$, which is a common pattern for contaminated fcc(100) surfaces. Auger measurements indicate an oxygen level of 10–20 at. % for both the substrate and the film. The chamber pressure during this dirty deposition was 2×10^{-9} Torr, which is significantly higher than that for the clean films to be reported herein. It is apparent that the layer-by-layer growth of the metastable fcc Fe shown in Fig. 1 is extrinsically stabilized by impurities, as can be qualitatively understood. There are two factors that mitigate against persistent layer-by-layer epitaxial growth. One involves the thermodynamic argument that opposes the wetting of a high-surface-free-energy species (Fe) on a low-surface-free-energy substrate (Cu). Three-dimensional growth would be anticipated in such a case. The other factor is that the slight lattice mismatch between fcc Fe (3.59 Å) and Cu (3.61 Å) should cause strain in the film and lead to a critical thickness for epitaxial growth. The impurities appear to act as surfactants to lower the surface free energy of Fe so

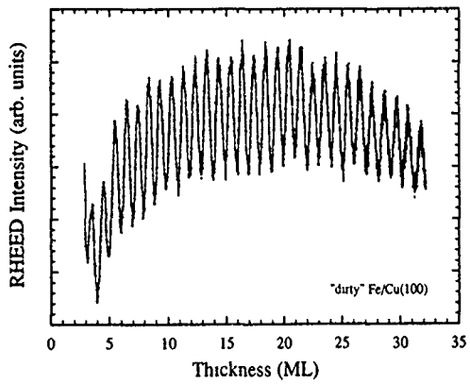

FIG. 1. RHEED intensity oscillations for a dirty deposition of Fe on Cu(100). The persistent oscillation, indicative of layer-by-layer growth, are impurity induced, as discussed in the text. The deposition rate was 0.64 Å/min T_s=315 K.

[a]Present address: IGV der KFA, Jülich, Germany.
[b]Permanent address: Physics Dept., Univ. of California, Berkeley.

 0021-8979/94/76(10)/6425/3/$6.00 © 1994 American Institute of Physics

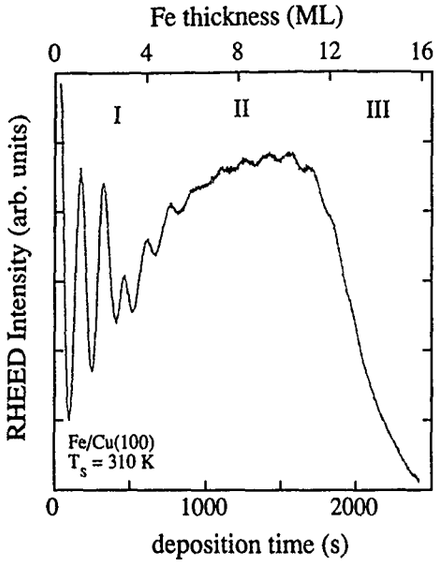

FIG. 2. RHEED intensity oscillations for Fe grown on Cu(100) at 310 K. Regions I–III are labeled as in Ref. 3.

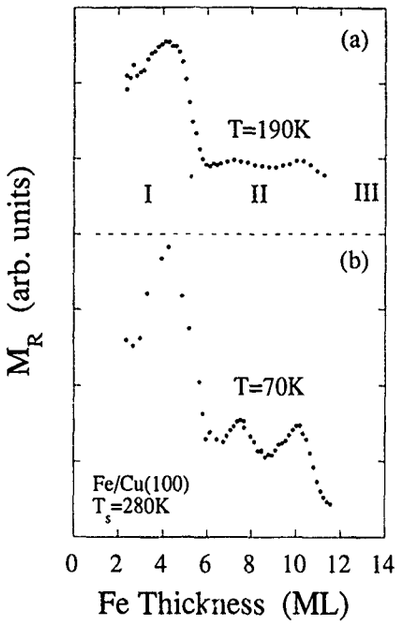

FIG. 3. Perpendicular remanent magnetization from polar SMOKE vs thickness across an Fe wedge grown at T_s=280 K and measured at 190 K (a) and 70 K (b). Region II has a enhanced surface ferromagnetic layer and antiferromagnetic underlayers as discussed in the text.

that it can wet the Cu(100) surface. Such an effect was discussed by Egelhoff *et al.*,[10] who point out that various atoms can serve as surfactants for 1 ML Fe/Cu(100) and related systems, and that some impurity atoms can float to the surface during growth to continue to activate layer-by-layer growth. The impurities may also serve as defect centers to help release film strain and to thwart the transition into the equilibrium bcc phase. Thus, impurity surfactant agents can provide a promising way to extend the study of epitaxial growth of metastable phases.

The growth characteristics of clean Fe films on Cu(100), as documented in Fig. 2, are more complex than the behavior shown in Fig. 1. Three growth regions are delineated in Fig. 2 for films grown above 250 K on the (1×1) Cu(100) substrate with no detectable C or O Auger signals, in agreement with previous studies.[3] No in-plane lattice-constant differences are observed by RHEED or LEED between the first two thickness regions as Fe grows into pseudomorphic face-centered structures. Region I has been attributed to a face-centered tetragonal (fct) phase and region II to the fcc phase.[11] Region II exhibits regular oscillations characteristic of a tendency toward layer-by-layer growth. The sharp decay of the RHEED intensity on going from region II to III at ~11 ML has been attributed to the onset of three-dimensional growth of bcc Fe.[3,7,8]

Different magnetic properties accompany the structural phases of regions I–III. For films grown above 250 K, the magnetic easy axis changes from perpendicular to in plane at ~11 ML. The magnetic anisotropy is dominated by the shape anisotropy in region III. In region I the surface anisotropy yields a perpendicular easy axis. Most strikingly, there is a dramatic change in the magnetic properties between regions I and II from the ferromagnetic phase to an antiferromagnetic phase with a ferromagnetic surface. This is shown in Fig. 3. The remanent magnetization obtained from our magneto-optic measurements increases initially in region I with Fe thickness as expected for a ferromagnetic film. At ~5 ML Fe, however, the magnetic signal drops to ~30%–40% of its maximum value. In addition, in region II the remanent magnetization forms a two-peaked structure between 6 and 11 ML which is most apparent at low temperature. These observations suggest that the bulk of the Fe film is antiferromagnetic with alternating layers of spins pointing out of or into the surface. There is a relatively constant magnetic signal in region II at relatively high temperature (right below T_C). And the signals at the valleys do not go to zero in the temperature range we performed our experiments. These facts suggest that the surface layer is ferromagnetic, as reported in Ref. 9, and has an enhanced magnetic order. The antiferromagnetic order is more significantly reduced by thermal fluctuations than is the ferromagnetic surface order. This unique magnetic phase was observed only when the substrate was clean and the pressure during deposition was $<5\times10^{-10}$ Torr. A recent theoretical calculation[12] suggests that the for 4–11 ML of fcc Fe on Cu(100), the surface and one subsurface layer are ferromagnetically aligned while the underlayers are antiferromagnetically aligned, in general agreement with our experimental observations. It is noted that the peak separation in our experiments is ~2.6 ML instead of 2 ML. Such an incommensurate magnetic structure is not indicated by the calculation of Kraft *et al.* It could relate to the quantization of the electronic states and the corresponding spin density wave in a finite thickness film.

The richness of magnetic phases of Fe/Cu(100) is demonstrated in the new magnetic phase diagram shown in Fig. 4. Region I contains the ferromagnetic phase with perpendicular magnetic anisotropy. A nonmagnetic region <2 ML, not delineated in Fig. 4, is presumably due to a reduced

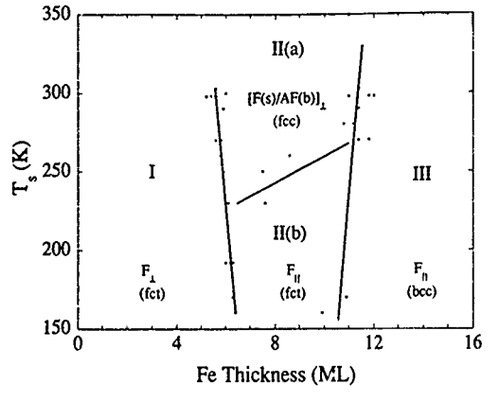

FIG. 4. Magnetic phase diagram with respect to growth temperature and Fe thickness. In region I, the films are ferromagnetic with perpendicular easy axes (fct). In region II(a) the films are AF and the surface is ferromagnetic (fcc). In region II(b), the films are ferromagnetic with in-plane easy axes (fct). In region III, the films are ferromagnetic with in-plane easy axes (bcc). (Measurements were performed in the range of 110–190 K.)

Curie temperature. Thick films (>10–11 ML) are bcc and possess in-plane ferromagnetic magnetization. At the intermediate thicknesses of region II different phases can be formed depending on the substrate temperature. For low-temperature deposition, where the fct-to-fcc phase transition is suppressed, a spin-reorientation transition occurs into region II(b) wherein the easy axis changes from perpendicular to in plane.[9] For growth temperatures higher than ~250 K, the newly identified antiferromagnetic phase with the live ferromagnetic surface layer appears in region II(a), as discussed above.

The difference in structure between regions I and II for ambient-temperature-grown films is believed to be the difference in interlayer spacing.[11] The initial phase is a fct structure with interlayer spacing different from the in-plane lattice constant. Such a distortion appears to stabilize ferromagnetic ordering. The second phase is the more isotropic fcc phase[11] which is antiferromagnetic and has a ferromagnetic surface. Because of the magnetic instability of fcc Fe, a small lattice distortion can drive the system into either antiferromagnetic or ferromagnetic states with different anisotropies. Recent work reported that fcc Fe grown on diamond (capped with Cu) is also ferromagnetic, but with in-plane anisotropy.[13] This might be consistent with the expected in-plane compression of Fe on diamond (lattice constant of 3.51 Å) as opposed to the expected in-plane expansion of Fe on Cu(100).

In conclusion, we investigated the ferromagnetic and antiferromagnetic phases of Fe/Cu(100) which correlate with its structural phases. We observe a new antiferromagnetic phase with a live ferromagnetic surface. We propose a new magnetic phase diagram for the growth of Fe on Cu(100). We also observe impurity-induced layer-by-layer growth of Fe on Cu(100) that persists to at least ~40 ML.

This work was supported by US DOE BES-MS under Contract No. W-31-109-ENG-38.

[1] J. S. Kouvel and R. H. Wilson, J. Appl. Phys. **32**, 435 (1961).
[2] C. S. Wang, B. M. Klein, and H. Krakauer, Phys. Rev. Lett. **54**, 1852 (1985); V. L. Moruzzi, P. M. Marcus, K. Schwarz, and P. Mohn, Phys. Rev. B **34**, 1784, (1986); F. J. Pinski, J. Staunton, B. L. Gyorffy, D. D. Johnson, and G. M. Stocks, Phys. Rev. Lett. **56**, 2096 (1986).
[3] J. Thomassen, F. May, B. Feldmann, M. Wettig, and H. Ibach, Phys. Rev. Lett. **69**, 3831 (1992).
[4] C. Liu, E. R. Moog, and S. D. Bader, Phys. Rev. Lett. **60**, 2422 (1988).
[5] D. P. Pappas, K.-P. Kamper, and H. Hopster, Phys Rev. Lett **64**, 3179 (1990); D. P. Pappas, C. R. Brundle, and H. Hopster, Phys. Rev. B **45**, 8169 (1992).
[6] R. Allenspach and A. Bischof, Phys. Rev. Lett. **69**, 3385 (1992).
[7] P. Xhonneux and E. Courtens, Phys. Rev. B **46**, 556 (1992); F. Scheurer, R. Allenspach, P. Xhonneux, and E. Courtens, *ibid.* **48**, 9890 (1993).
[8] K. Kalki, D. D. Chambliss, K. E. Johnson, R. J. Wilson, and S. Chiang, Phys. Rev. B **48**, 18 344 (1993); K. E. Johnson, D. D. Chambliss, R. J. Wilson, and S. Chiang, J. Vac. Sci. Technol A **11**, 1654 (1993).
[9] D. Li, M. Freitag, J. Pearson, Z. Q. Qiu, and S. D. Bader, Phys. Rev. Lett. **72**, 3112 (1994), and references therein.
[10] W. F. Egelhoff, Jr. and D. A. Steigerwald, J. Vac. Sci. Technol. A **7**, 2167 (1989); D. A. Steigerwald, I Jacob, and W. F. Egelhoff, Jr., Surf. Sci. **202**, 472 (1988).
[11] H. Magnan, D. Chandesris, B. Villette, O. Heckmann, and J. Lecante, Phys. Rev. Lett. **67**, 859 (1991).
[12] T. Kraft, P. M. Marcus, and M. Scheffler, Phys. Rev. B **49**, 11511 (1994).
[13] D. P. Pappas *et al.*, Mater. Res. Soc. Symp. Proc. **313**, 369 (1993).

Impurity hyperfine fields in metastable body centered cubic Co

J. Dekoster, B. Swinnen, M. Rots, and G. Langouche
Instituut voor Kern-en Stralingsfysica, K. U. Leuven, Celestijnenlaan 200D, B-3001 Leuven, Belgium

E. Jedryka
Institute of Physics, Polish Academy of Sciences, Al. Lotnikow 32/46, PL-02 668 Warsaw, Poland

A new spectrum component is observed in Mössbauer spectra of thin body centered cubic Co layers doped with ^{57}Co which have previously been shown to be in this metastable state with nuclear magnetic resonance. It is characterized with a large magnetic hyperfine field (31.2 T) and an isomer shift nearly equal to that of α-Fe. The decrease of the isomer shift in bcc Co with respect to hcp Co is consistent with a smaller $s-d$ charge transfer in bcc Co as compared to hcp Co. The influence of structure on the hyperfine field in a Co crystal is reflected in the decrease of the magnetic hyperfine field of Fe in bcc Co as compared to hcp Co and is similar to the volume dependence of the magnetic hyperfine fields in a Co crystal.

Over the last years magnetic films and superlattices grown with molecular beam epitaxy have attracted considerable attention in the search for new materials with unusual magnetic and structural properties. Recently it has been shown that a metastable body centered cubic Co phase can be grown on GaAs, Fe, and in Co/Fe superlattices.[1–4] One of the properties which is expected to be strongly dependent on the structure of a Co crystal is the magnetic hyperfine field. The characterization of the bcc phase was therefore established with NMR spectroscopy which showed a NMR frequency at 199 MHz for bcc Co, a value which is about 10% lower than the known NMR frequencies in fcc and hcp Co. The purpose of the present study is to use radioactive ^{57}Co as a probe material for the magnetic hyperfine fields in these layers. A ^{57}Fe source experiment in which the Mössbauer isotope is the daughter isotope of ^{57}Co is one of the few methods to measure the hyperfine interaction at Fe in a thin metastable bcc Co crystal. ^{57}Fe-NMR measurements or absorber Mössbauer measurements would require a much larger concentration of Fe into Co. The introduction of ^{57}Co as a radioactive probe in the Co phase under investigation offers at least five orders of magnitude of sensitivity as compared to absorber experiments.[5] There are two more distinct advantages in the use of Mössbauer spectroscopy to study ^{57}Co in bcc Co: first, one can be completely confident that the Fe atoms will occupy Co sites, as ^{57}Co is expected to take a regular substitutional lattice site in bcc Co and second, ^{57}Fe is the best Mössbauer probe with a high recoil-less fraction and a good sensitivity of the isomer shift (δ) to pressure.[6] In such source experiments it is generally believed that the atomic configuration surrounding the probe atom is not modified during the extremely short lifetime of the excited Mössbauer state, i.e., the ^{57}Fe directly probes the bcc Co atomic configuration.

It is intriguing to notice that the hyperfine field at ^{59}Co in a Co crystal determined with NMR is quasilinearly decreasing with the atomic volume of the specific Co phase studied (hcp, fcc, or bcc Co). A similar behavior is observed in the pressure dependence of the magnetic hyperfine field in a Co crystal, i.e., the magnitude of the hyperfine field is decreasing with the volume.[7] The pressure effect on the hyperfine field is however an order of magnitude smaller than the observed decrease of the hyperfine field of bcc Co with respect to hcp Co. In recent years several studies, both theoretical and experimental, have been performed to explain systematic trends and the pressure dependence of the magnetic hyperfine fields of impurity atoms into ferromagnetic host metals such as Co, Fe, and Ni.[7,8] The experimental determination of the magnetic hyperfine field in a metastable magnetic phase such as bcc Co might shed some light on the dependence of the magnetic hyperfine field of impurity atoms on the structure of the crystal phase under investigation. Co is, just like Fe, a unique material which can take the form of three crystallographically different magnetic phases. In the present study the hyperfine field of Fe in bcc Co is determined with Mössbauer spectroscopy and compared with the known hyperfine field of Fe and its volume dependence in hcp Co. In addition Mössbauer spectroscopy is sensitive to the atomic volume via the isomer shift. We will demonstrate that the decrease of the hyperfine field of Fe in bcc Co with respect to hcp Co is certainly not a volume effect but more likely is due to a coordination effect.

Samples were prepared by implanting 80 keV radioactive ^{57}Co with a dose of 10^{14} atoms/cm^2 into Co/Fe superlattices grown with molecular beam epitaxy. The metastable bcc Co epitaxy on Fe (001) is possible because of the small lattice mismatch of 1.6% between the predicted bcc Co phase ($a=2.82$ Å) and an (1×1) construction on Fe ($a=2.87$ Å). $[Fe_xCo_y]_{20}$ superlattices with various Co layer thickness ($x=25$ Å, 6 Å$<y<$24 Å) were prepared on MgO (001) substrates. Details of the preparation conditions can be found elsewhere.[9] The Mössbauer spectra were recorded at 300 K using a sodiumferrocyanide absorber (SFC). The δ values are expressed as absorber isomer shift with respect to SFC.

NMR measurements on these samples revealed a metastable state for Co characterized with a frequency of 199 MHz, a value which is lower than the Co frequency in fcc (217 MHz) and hcp Co (220–228 MHz). The metastable state is attributed to Co in a bcc phase and relaxes for this growth direction to the regular hcp phase only for Co layer thickness above 24 Å.[10] Co/Fe superlattices with Co thickness smaller than 24 Å are expected to contain the following atomic configurations for the implanted ^{57}Co probe atoms: α-Fe, bcc Co, Co/Fe interface region, and a possible surface

 0021-8979/94/76(10)/6428/3/$6.00 © 1994 American Institute of Physics

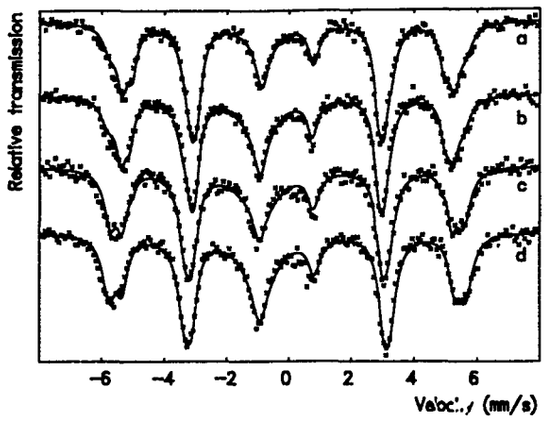

FIG. 1. Mössbauer spectra of bcc Co/Fe superlattices with various Co layer thickness [24 Å (a), 18 Å (b), 12 Å (c), and 6 Å (d)] implanted with 10^{14} ^{57}Co measured at 300 K with respect to a sodiumferrocyanide absorber.

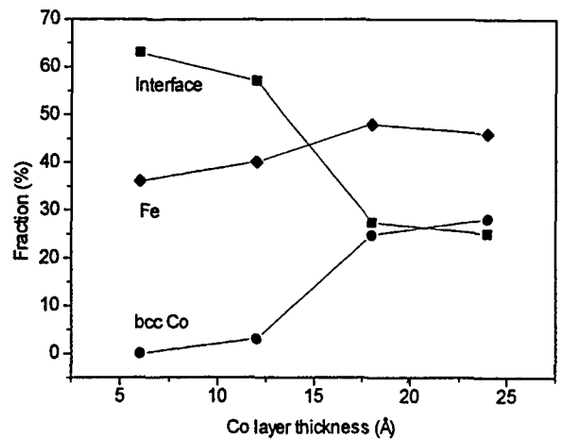

FIG. 2. Relative contribution of the magnetic spectrum components of Mössbauer spectra of bcc Co/Fe superlattices for various Co layer thickness [(♦) α-Fe, (●) bcc Co, (■) CoFe interface].

oxide layer. Figure 1 shows the ^{57}Fe Mössbauer spectra of Co/Fe superlattices with different Co-layer thickness. For the layer with 6 Å Co only two magnetic spectrum components are present. The hyperfine field of the first spectrum component and its isomer shift are within error limits equal to that of α-Fe [B=33.1 T]. The second component has a hyperfine field of 35.4 T and an isomer shift δ=0.10 mm/s. It is reasonable to attribute this component to Fe in the Co/Fe interface region since it is almost equal to the hyperfine field of Fe in an equiatomic Co/Fe alloy. With increasing Co layer thickness in addition to the above-mentioned magnetically split components a third spectrum component is observed with a slightly lower hyperfine field [B=31.0 T (12 Å Co), B=31.4 T (18 Å Co), and B=31.2 T (24 Å Co)]. The assumption that this new component is due to Fe in bcc Co is justified by two observations: first, the increase of the relative contribution of this component with Co layer thickness is accompanied by a decrease of the interface component (see Fig. 2) and is similar to the increase of the NMR component at 199 MHz, and second, this hyperfine field component is clearly lower than the known hyperfine fields of Fe in hcp Co and in Co/Fe alloys. Therefore we attribute it to Fe in bcc Co and estimate the hyperfine field of Fe in bcc Co to be 31.2(2) T. Finally, a nonmagnetic single line component with δ=0.90 mm/s is observed in all the Mössbauer spectra and is probably due to the presence of an oxide layer. The contribution of this spectrum component is decreasing with increasing Co layer thickness which reflects the higher resistance of Co to oxidation as compared to Fe.

The bcc Co spectrum component is characterized by an isomer shift which is only slightly smaller than the isomer shift of the α-Fe component and consequently is also smaller than the isomer shift in hcp Co. The isomer shift is well know to be proportional to the electron density at the nucleus and thus depends on the atomic volume. The behavior in bcc Co is opposite to what can be expected from the volume dependence of the Fe isomer shift in hcp Co. The isomer shift of Fe in hcp Co decreases with pressure[6] and one might expect an increase of the isomer shift for bcc Co since it has a larger volume then hcp Co. The decrease of the isomer shift in bcc Co can however be explained by a smaller $s-d$ charge transfer in bcc Co with respect to hcp Co. It is therefore supporting without really proving such a charge transfer effect which has been proposed a long time ago to explain the stronger volume dependence of the isomer shift in the bcc metals then in the close packed fcc and hcp metals.[6]

Recently the hyperfine interaction of Cd in bcc Co/Fe superlattices was studied with the angular correlation technique.[11] Also in these measurements a new value for the hyperfine field of Cd is observed which is substantially lower than the known hyperfine fields of Cd in fcc and hcp Co. It is remarkable that the hyperfine fields for Co, Fe, and Cd in the three Co phases are increasing almost linearly with the atomic density of the specific Co phase (see Fig. 3) and that the slope of this behavior reflects the difference of the experimental volume dependence of the hyperfine field of Co, Fe, and Cd in hcp Co. In pressure measurements one observed $d\ln B/dp=0.3\times10^{-3}$ kbar^{-1} for Fe,[12] $d\ln B/dp=0.615\times10^{-3}$ kbar^{-1} for Co,[7] and $d\ln B/dp=1.04\times10^{-3}$ kbar^{-1} for Cd[7] in hcp Co. The mag-

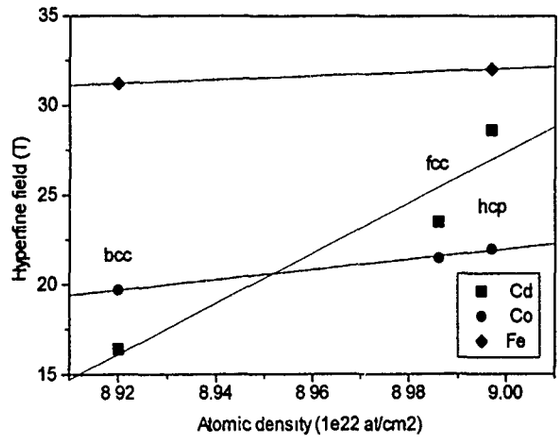

FIG. 3. Hyperfine fields of Co (●), Fe (♦), and Cd (■) in hcp, fcc, and bcc Co vs the atomic density of the specific Co phase.

nitude of the hyperfine field of Cd is decreasing much more rapidly with the atomic volume than that of Co and Fe, respectively. It is therefore tempting to associate the decrease of the hyperfine field in bcc Co with respect to hcp Co to a volume effect. However if one estimates the hyperfine field changes for bcc Co from the experimental volume dependence one gets a value which is much lower than the experimentally observed changes of the hyperfine fields of bcc Co. The corresponding microscopic change when going from a fcc to a bcc crystal is however predominantly governed by a change in the specific coordination. In the analysis of the transferred hyperfine field it is common to use a formalism proposed a long time ago by Stearns.[8] This model proposes that the transferred hyperfine field due to $4s$ neighbor conduction electron polarization (B_Σ) can be obtained by a summation over the neighboring atoms with a specific contribution ΔBi for each neighbor shell.: $B_\Sigma = \Sigma_1 n_i \Delta B_i$. Experimentally the different contributions have been determined up to the fifth-neighbor shell in fcc Co.[13] If one scales the fcc values to a bcc structure under the assumption that ΔBi has a Ruderman–Kittel–Kasuya–Yosida behavior and that the contributions in a specific shell for fcc Co have the same sign as in bcc Co one obtains a transferred hyperfine field for bcc Co which is a few tesla smaller than in fcc Co. This result is merely supporting the fact that the decrease of the hyperfine field in bcc Co is due to a structure effect. Finally it is noteworthy that recent theoretical calculations[14] based on a spin-polarized Korringa–Kohn–Rostoker (SP-KKR) formalism performed for bcc Co/Fe alloys show that the hyperfine field for pure bcc Co is about 20 T a value which is almost in perfect agreement with the NMR value we obtain for bcc Co in Co/Fe superlattices.

[1] G. A. Prinz, Phys. Rev. Lett. **54**, 1051 (1985).
[2] H. Li and B. P. Tonner, Phys. Rev. B **40**, 10 241 (1989).
[3] Ph. Houdy, P. Boher, F. Giron, F. Pierre, C. Chappert, P. Beauvillain, K. Le Dang, P. Veillet, and E. Velu, J. Appl. Phys. **69**, 5667 (1991).
[4] J. Dekoster, E. Jedryka, C. Mény, and G. Langouche, Europhys. Lett. **22**, 433 (1993).
[5] *Hyperfine Interactions of Defects in Semiconductors*, edited by G. Langouche (Elsevier, Amsterdam, 1992).
[6] D. L. Williamson, *Mossbauer Isomer Shifts*, edited by G. K. Shenoy and F. E. Wagner (North-Holland, Amsterdam, 1978), p. 317 and references therein.
[7] B. Lindgren and Y. K. Vijay, Hyp. Int. **9**, 379 (1981), and references therein.
[8] M. B. Stearns, Phys. Rev. B **8**, 4383 (1973).
[9] J. Dekoster, E. Jedryka, C. Mény, and G. Langouche, J. Magn. Magn. Mater. **121**, 69 (1993).
[10] E. Jedryka *et al.* (to be published).
[11] B. Swinnen, J. Dekoster, G. Langouche, and M. Rots (unpublished).
[12] I. N. Nikolaev and I. Yu. Bezotosnyi, Sov. Phys.-Solid State **21**, 1679 (1979).
[13] T. M. Shavishvilli and I. G. Kiliptari, Phys. Status Solidi **92**, 39 (1979).
[14] H. Ebert, H. Winter, D. D. Johnson, and F. J. Pinski, J. Phys. Cond. Matter **2**, 443 (1990).

Ferromagnetism and growth of Ru monolayers on C(0001) substrates

G. Steierl, R. Pfandzelter, and C. Rau
Department of Physics and Rice Quantum Institute, Rice University, Houston, Texas 77251

The magnetic and growth properties of Ru monolayers on C(0001) are studied using spin-polarized secondary electron emission and Auger electron spectroscopy (AES). Using AES, we find that the initial growth of Ru on C(0001) occurs *laterally* until the first monolayer is completed. One monolayer-thin Ru film shows ferromagnetic order below a surface Curie temperature of approximately 250 K. The in-plane magnetization saturates in small applied fields of a few tenths of an Oe. This is the first observation of spontaneous, long-ranged, two-dimensional ferromagnetic order in an ultrathin film composed of a 4*d* transition metal.

Recent advances, both experimentally and theoretically, enable us to explore the possibility of inducing spontaneous, two-dimensional, long-ranged ferromagnetic order in elements that are paramagnetic in their bulk form. Interesting candidates are the paramagnetic 3*d*, 4*d*, and 5*d* transition metals.[1–6]

One way to address this interesting issue is to grow such a metal epitaxially on an adequate nonmagnetic substrate. Ferromagnetic order in such ultrathin films may be induced by the reduced coordination number and hence reduced interatomic hybridization, band structure effects due to the restriction to two dimensions and, compared to the bulk paramagnetic solid, an increased lattice constant imposed by pseudomorphic film growth.

As to ultrathin films of the 4*d*-transition metals, recent studies[2–10] have focused on Ru and Rh monolayers (ML) deposited on Ag(100) and Au(100) substrates. Theoretical works indicate that these systems should possess a ferromagnetic ground state.[2–6] Recent experiments for Rh on Ag(100) and on Au(100), however, failed to find any evidence for spontaneous, long-ranged ferromagnetic order,[13,14] or were inconclusive.[15] There is experimental evidence that an explanation for the discrepancies between theory and experiment can be found in the structural properties of the films deposited on these substrates: Schmitz *et al.*[16] propose that the equilibrium structure of Rh on Ag(001) is actually that of a sandwich with an Ag monolayer atop. Mulhollan *et al.*[14] find evidence for diffusion of Rh into the Ag matrix. Other authors do not rule out islanding.[13,14] These effects are indeed likely to prevent spontaneous, long-ranged ferromagnetic order.

Therefore we decided upon a different substrate and selected graphite C(0001) for the following reasons: similar to the noble metals, there is hardly a band overlap with the 4*d*-transition metals due to the low density of states near the Fermi level, which should prevent strong hybridization with the 4*d* bands. Moreover, the graphite (0001)-surface is known to be very flat, possessing only few steps and nearly no defects. This should considerably suppress interdiffusion. As film material we selected Ru, which has a hexagonal bulk lattice structure with an in-plane nearest neighbor distance which is almost twice that of graphite. Despite the difference in the surface free energy, epitaxial or pseudomorphic growth of metastable Ru with a lattice slightly stretched (5%) compared to the bulk should be favored.[11,12]

To study the growth and magnetic properties, we used Auger electron spectroscopy (AES) and spin polarized secondary electron emission (SPSEE). For many metal-on-metal systems, it was already shown, that AES is a very suitable technique to distinguish between various types of initial growth modes (lateral growth, islanding, intermixing).[19] We recorded the Auger intensity of the substrate and that of the adsorbate line as function of coverage or deposition time. The lateral growth and the completion of a ML is evident from the *linear* increase in the signal and the abrupt change in slope in both plots.

In SPSEE, an unpolarized electron beam of energy of a few keV is used to induce the emission of secondary electrons from the sample. The electron spin polarization (ESP) of the emitted secondary electrons is a direct measure of the surface magnetization. For SPSEE, we use an einzellens system with a 90° cylindrical energy analyzer connected to a 20 keV Mott polarimeter.

As substrate, we use highly oriented, pyrolytic graphite (HOPG) ($8\times15\times1$ mm^3) with a standard distribution of the *c* axes $\sigma=0.2°$ and randomly oriented *a* axes. The HOPG sample is cleaved in air. No further *in situ* treatment is necessary, because the extremely low gas adsorption efficiency guarantees a clean surface for ample time. The sample is mounted on a manipulator between the pole caps of an electromagnet and can be cooled to liquid nitrogen temperatures. The temperature is monitored using a copper-constantan thermocouple. Ru (purity 99.95%) is evaporated using electron beam evaporation (evaporation rate: 0.03 ML/min). The film thickness is monitored by using a quartz microbalance. AES is performed using a cylindrical mirror analyzer (CMA). During the magnetic measurements, the residual gas pressure amounted to $\approx3\times10^{-10}$ mbar; during the evaporation, it increased to $\approx8\times10^{-10}$ mbar.

The growth of Ru on C(0001) was studied by measuring peak-to-peak heights of differentiated Auger lines versus deposition time. In Fig. 1, dN/dE vs E Auger spectra of the clean and the Ru covered graphite surface are given. The graphite spectrum shows one peak at 272 eV. The Ru spectrum is more complicated with nearly symmetric peaks at

 0021-8979/94/76(10)/6431/3/$6.00 © 1994 American Institute of Physics

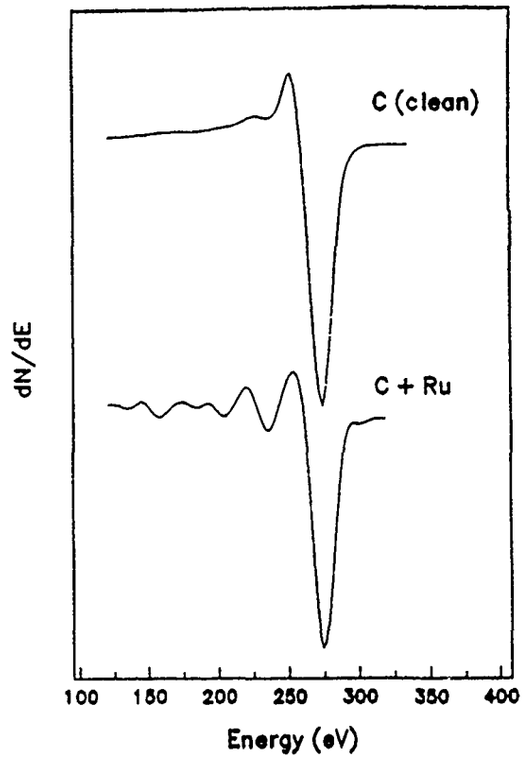

FIG. 1. Differentiated Auger spectra for the clean and Ru covered C(0001) surface.

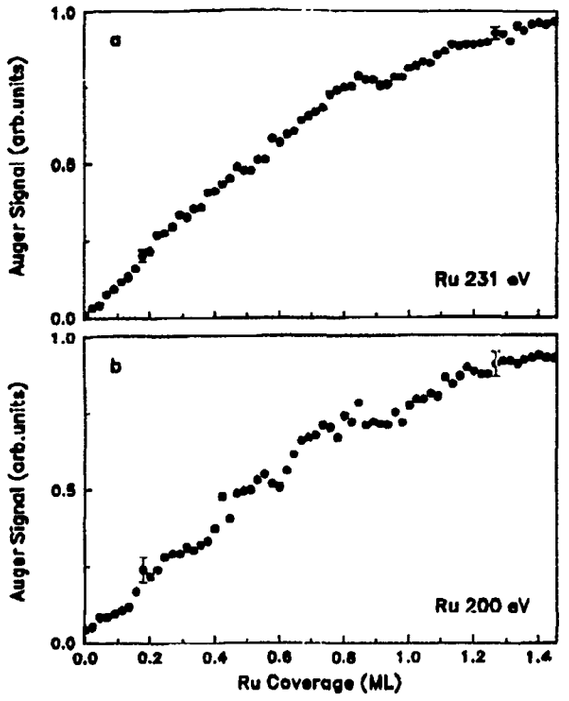

FIG. 2. Auger peak-to-peak height vs Ru coverage on C(0001) of the (a) Ru 231 eV and (b) Ru 200 eV line. The coverage is referred to the atomic density of the bulk Ru(0001) plane.

273, 231, 200, and 160 eV.[20] The most prominent Ru peak at 273 eV overlaps with the graphite peak, therefore, we used the smaller Ru peaks as adsorbate Auger signal. A quantitative analysis of the substrate Auger signal was already the subject of several studies.[21]

In Fig. 2(a), the peak-to-peak heights of the Ru 231 eV Auger line is shown. The x-axis scale is converted from deposition time to coverage, using the quartz reading, calibrated by a geometrical factor. We refer the coverage to the atomic density of the (0001) plane in bulk Ru and assume the sticking coefficient to be one. The Auger signal increases linearly up to a coverage of nearly 1 ML, where a breakpoint occurs. For higher coverages, the Auger signal increases further and reveals a smaller slope. These results are confirmed by the Ru 200 eV Auger signal [Fig. 2(b)], although the data points show a little more scattering due to the smaller signal.

The linear increase of the Auger signal shows that Ru grows laterally until the graphite surface is homogeneously covered, and the first Ru ML completed. From our data, it is unlikely that Ru continues to grow in a layer-by-layer mode (Frank–van der Merwe). Our findings point to a Stranski–Krastanov growth mode (three-dimensional islands on top of a ML) for the following reasons: The (average) slope ratio between the data beyond and below the breakpoint is 0.42, which is smaller than the value 0.70 calculated for layer-by-layer growth using an inelastic mean free path $\lambda=0.82$ nm for 231 eV electrons and a thickness $d=0.214$ nm for one Ru layer.

In Fig. 3(a), we show the peak-to-peak heights of the composite C 272 eV+Ru 273 eV Auger signal. The signal decreases linearly until a sharp breakpoint occurs at nearly 1 ML. These findings are even clearer, when we take only the graphite contribution of the composite Auger line [Fig. 3(b)]. The substrate signal then shows the qualitative behavior as expected for lateral growth and confirms the findings from the adsorbate signal.

To summarize, we find that Ru grows laterally on the graphite surface until the first ML is completed. Beyond the first ML, the data indicate that Ru begins to form three-dimensional islands, i.e . Ru seems to grow on C(0001) in a Stranski–Krastanov mode. These findings are corroborated by our scanning tunneling microscopy measurements, showing in the range of submonolayer coverage lateral growth of Ru.[17]

Next, we report on the magnetic properties of Ru ML films. Initially, we measured the ESP as function of small applied fields up two 2 Oe which were reversed in order to calibrate for instrumental asymmetries. From the magnetization curves, we find that saturation is reached at field strengths of a few tenths of an Oe.

For more refined checks on the effect of instrumental asymmetries on the measured ESP, we used the nonmagnetic surface of the graphite crystal and performed the same procedure as for the Ru films. We find that the small applied fields have no effect on the measured ESP.

The results of the SPSEE experiment are shown in Fig.

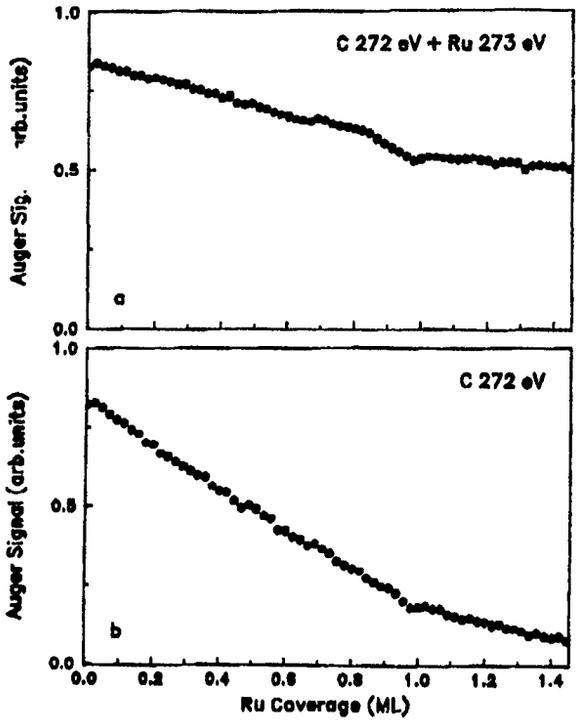

FIG. 3. Auger peak-to-peak height vs Ru coverage on C(0001) of (a) the composite C 272 eV+Ru 273 eV line, and (b) the C 272 eV line only. (b) is obtained from the composite signal in (a) by subtracting the Ru 231 eV Auger intensity multiplied by a factor of 2.35.[13] The coverage is referred to the atomic density of the bulk Ru(0001) plane. Statistical errors are contained withint the symbol size.

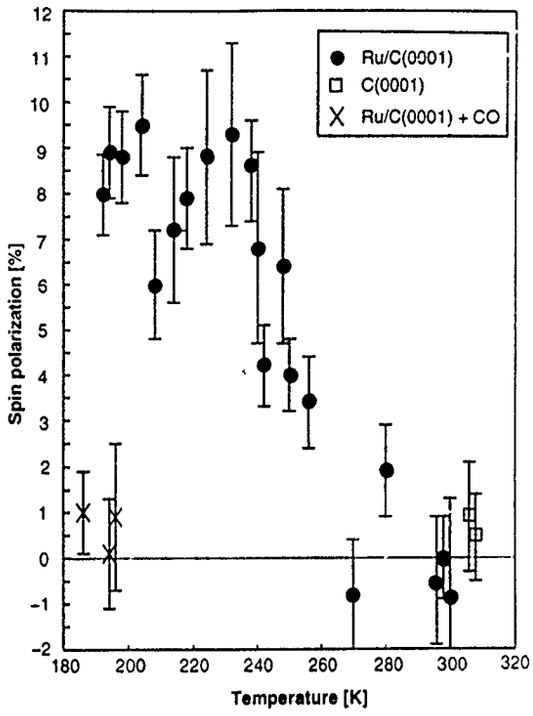

FIG. 4. ESP of 3 eV electrons as function of temperature for a ML-thin Ru film on C(0001) (solid circles), for the clean C(0001) surface (open squares), and for the CO covered Ru ML film on C(0001) (crosses).

4. Solid circles represent the ESP of a Ru ML film as function of temperature T. The low temperature value of the ESP is between +8% and +9%, i.e., the film is indeed ferromagnetic. The positive sign indicates a predominance of electrons with magnetic moment oriented parallel to the applied magnetizing field. With increasing temperature, the ESP drops to zero within a narrow temperature range. This behavior of the ESP is completely reversible. It is not the intent of the present publication to evaluate the critical exponent of the two-dimensional (2D) phase transition near the surface Curie temperature T_{Cs}, which is located at around 250 K.

We performed additional SPSEE measurements on adsorbate covered Ru ML films. At 300 K, we exposed the clean Ru film to 10 L of CO, which is the saturation coverage of CO at the clean Ru/C(0001) surface. From Fig. 4 (crosses), it can be directly seen that chemisorption of CO results in zero ESP within the experimental errors which is identical to the result we obtain for the clean graphite surface (see Fig. 4, open squares).

In conclusion, we have demonstrated that Ru can be grown laterally on a HOPG C(0001) surface until the first ML is completed. We find that the deposited Ru ML film is ferromagnetic below a surface Curie temperature $T_{Cs} \approx 250$ K. This is the first observation of 2D ferromagnetism of a 4*d* element.

We thank N. J. Zheng for experimental assistance. One of us (R.P.) is grateful to the Max Kade Foundation for granting a fellowship. This work was supported by the National Science Foundation, the Robert A. Welch Foundation, and the Texas Higher Education Coordinating Board.

[1] C. Rau, Appl. Phys. A **49**, 579 (1989).
[2] C. L. Fu, A. J. Freeman, and T. Oguchi, Phys. Rev. Lett. **54**, 2700 (1985).
[3] R. Wu and A. J. Freeman, Phys. Rev. B **45**, 7222 (1992).
[4] O. Eriksson, R. C. Albers, and A. M. Boring, Phys. Rev. Lett. **66**, 1350 (1991).
[5] M. J. Zhu, D. M. Bylander, and L. Kleinman, Phys. Rev. B **43**, 4007 (1991).
[6] S. Blugel, Phys. Rev. Lett. **68**, 851 (1992).
[7] C. Liu and S. D. Bader, Phys. Rev. B **44**, 12 062 (1991).
[8] G. A. Mulhollan, R. L. Fink, and J. L. Erskine, Phys. Rev. B **44**, 2393 (1991).
[9] H. Li, S. C. Wu, D. Tian, Y. S. Li, J. Quinn, and F. Jona, Phys. Rev. B **44**, 1438 (1991).
[10] P. J. Schmitz, W.-Y. Leung, G. W. Graham, and P. A. Thiel, Phys. Rev. B **40**, 11 477 (1989); and references therein.
[11] Z. Q. Qiu, J. Pearson, and S. D. Bader, Phys. Rev. Lett. **67**, 1646 (1991).
[12] E. Ganz, K. Sattler, and J. Clarke, Surf. Sci. **219**, 33 (1989).
[13] C. Argile and R. H. Rhead, Surf. Sci. Rep. **10**, 277 (1989).
[14] P. W. Palmberg, G. E. Riach, R. E Weber, and N. C. MacDonald, in *Handbook of Auger Electron Spectroscopy* (Physical Electronics Industries, Edina, 1972).
[15] M. J. VanStaden and J. P. Roux, Appl. Surf. Sci. **44**, 259 (1990), and references therein.
[16] M. P. Seah and W. A. Dench, Surf. Interface Anal. **1**, 2 (1979).
[17] N. L. Nunes, M. S. thesis, Rice University, 1994 (to be published).

Spin reorientation transition in Ni films on Cu(100)

S. Z. Wu, G. J. Mankey, F. Huang, and R. F. Willis
Department of Physics, The Pennsylvania State University, University Park, Pennsylvania 16802

The magnetic anisotropy of Ni films grown on single-crystal Cu(100) was studied *in situ* using the surface magneto-optic Kerr effect. The easy axis of magnetization lies in the plane of the film for ultrathin films and it is perpendicular to the film above a switching thickness. This behavior is attributed to a specific contribution to the magnetocrystalline anisotropy energy induced by a change in the film microstructure above a critical thickness. In the Ni/Cu(100) system, the magnetoelastic interface anisotropy favors perpendicular magnetization which becomes comparable to the shape anisotropy at the switching thickness. We compare the switching thickness and magnetization of films grown using different processing conditions.

For ultrathin ferromagnetic films, there is a magnetization reorientation phase transition where the easy axis of magnetization is perpendicular to the film surface and switches to in plane as film thickness is increased.[1,2] Within the framework of the magnetic Hamiltonian, this transition can be interpreted as the increasing dominance of the thickness-dependent shape anisotropy which favors in-plane magnetization overcoming the spin-orbit magnetocrystalline anisotropy term which favors perpendicular magnetization. In addition to a thickness-dependent transition, a reorientation transition can also occur as a result of varying temperature of a film with fixed thickness. The temperature dependence can be modeled with an empirical temperature-dependent coefficient for the spin-orbit term in the Hamiltonian.[3] This transition has been observed for Fe/Ag(100),[4] Fe/Cu(100),[5] and Co/Au(111).[6] For the Ni films studied in this work, there is a different behavior.

Bulk Ni is the canonical Heisenberg ferromagnet. It has a spin moment of 0.6 bohr magnetons,[7] a Curie temperature T_C of 627 K,[8] a critical exponent $\beta \sim 0.4$, and a weak magnetocrystalline anisotropy with the easy axis of magnetization in the [111] direction and the hard axis in the [100] direction.[9] Ni monolayers have been studied theoretically with the self-consistent local orbital method[10,11] and a perturbative tight-binding approach.[12] These calculations predict that a (100) oriented Ni monolayer has a preferred direction of magnetization in the plane of the film. More recent state-tracking first principals calculations demonstrate the magnetocrystalline anisotropy energy for monolayers is dependent on band filling and strain.[13,14] To what extent the results for truly two-dimensional monolayers can be used for describing the magnetic properties of films of finite thickness has yet to be determined. The critical behavior of Ni films on Cu(100) has been studied[15] and it was shown that the magnetic phase transition power law exponent crosses over from a two-dimensional *XY* model behavior to a three-dimensional Heisenberg model behavior at a film thickness of 7 monolayers (ML). These measurements show films thicker than a single monolayer exhibit two-dimensional magnetic properties.

Both Ni and Cu are fcc crystals with lattice constants of 3.52 and 3.61 Å, respectively, so Ni has a lattice constant 2.5% smaller than Cu. Ni films maintain an in-plane lattice constant identical to Cu up to a critical thickness of 10 ML.[16,17] The surface free energies for Ni and Cu are 2.45 and 1.85 J/m^2, respectively.[18,19] Since Cu has a surface free energy 0.6 J/m^2 lower than Ni, it tends to segregate to the surface at elevated temperatures.[20] In addition, Ni and Cu form a continuous series of solid solutions. In order to produce atomically smooth pseudomorphic layers of Ni on Cu, the films must be grown at a temperature high enough for the incoming Ni to form smooth layers yet low enough to suppress bulk diffusion which favors both alloy formation and surface segregation. The formation of a surface alloy can be detected by a reduced magnetization since Ni_xCu_{1-x} alloys are nonmagnetic when x is below 0.4.[21]

Our sample preparation procedures and film thickness calibration techniques have been reported before.[22] The magnetic behavior of films produced with three different processing conditions were studied in this work: Ni films grown at 300 K on a substrate roughened by 500 eV Ar^+ bombardment, Ni films grown at 300 K on a smooth substrate, and Ni films grown at 400 K on a smooth substrate. The composition of the samples was determined by Auger electron spectroscopy, with all of the films showing a small (<10%) but measurable amount of carbon and oxygen contamination. The magnetic properties were measured *in situ* by the surface magneto-optic Kerr effect (SMOKE) with the substrate cooled to 200 K.

To perform the SMOKE measurements, a linearly polarized He-Ne laser was incident on the sample surface at 70° from the surface normal with the polarization vector in the incident plane. The reflected light is analyzed by a Wollaston prism in combination with two photodiodes which allows simultaneous detection of the two orthogonal light components. The laser was rotated to ~0.08° from extinction in the null channel. By measuring ΔI, the difference between the Kerr intensity at remanence, the Kerr ellipticity can be derived: $\phi'' = \delta/4\Delta I/I$, where I is the Kerr intensity at zero net magnetization and δ is the angle the laser is rotated from extinction. A four-pole electromagnet applies the external magnetic field either parallel or perpendicular to the film plane with a maximum magnetic field of 150 Oe.[23] This arrangement allows the measurement of both the longitudinal and polar Kerr Effects.[24] A typical hysteresis loop is shown in Fig. 1, the height of the loop at zero external field is proportional to the remanent magnetization M_r and the external magnetic field at zero net magnetization is called the coercive field or coercivity H_c.

To study the magnetization of the films, we measured the

 0021-8979/94/76(10)/6434/3/$6.00 © 1994 American Institute of Physics

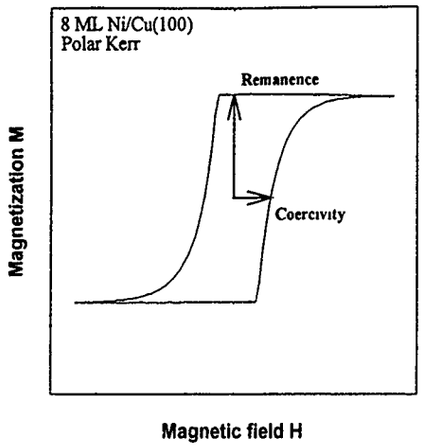

FIG. 1. A hysteresis loop for the out-of-plane magnetization of 8 ML Ni on smooth Cu(100) substrate grown at T_g=400 K. The magnetization at zero external field is the remanence. The external field at zero net magnetization is called the coercive field or coercivity.

remanence and coercivity as functions of Ni film thickness from 4 to 20 ML with the three different processing conditions. The results are shown in Figs. 2 and 3.

First we will examine the data for Ni films grown on a smooth Cu surface at the optimum growth temperature of 400 K. For film thicknesses below 8 ML, there are relatively weak Kerr ellipticities in both the parallel and perpendicular directions (Fig. 2). The magnitudes of the ellipticities cannot be directly compared because the polar and longitudinal Kerr effects have different sensitivities. The sensitivity for the polar Kerr effect is roughly ten times that of the longitudinal Kerr effect for our experimental setup, so the magnetization in the parallel direction is about ten times larger than the magnetization in the perpendicular direction. This is consistent with ferromagnetic resonance studies of Ni films on Cu(100) which showed the anisotropy energy favors in-plane magnetization below 7 ML.[25] The magnitudes of both components are comparable to those of films grown at 300 K indicating there is not a significant amount of alloying with the Cu substrate since this would result in a lower Kerr ellipticity for the 400 K growth temperature films.

The most striking difference between the films grown at 300 and 400 K on a smooth substrate is the behavior of the coercive field at low thickness (Fig. 3). The coercive field stays nearly constant for 400 K growth temperature films where it increases monotonically for the 300 K growth temperature films. This shows the films have different domain structure with the 400 K films exhibiting a behavior characteristic of single domain films and the monotonically increasing coercivity for the 300 K growth temperature films characteristic or multidomain structure with an increasing domain size as the film thickness is increased.

At 8 ML film thickness, there is an abrupt increase in both magnetizations. This abrupt increase in magnetizations is accompanied by a sudden change in the coercive fields as well. The coercive field in the perpendicular direction drops to half its initial value indicating that the easy axis of magnetization is now in the perpendicular direction. The coercive

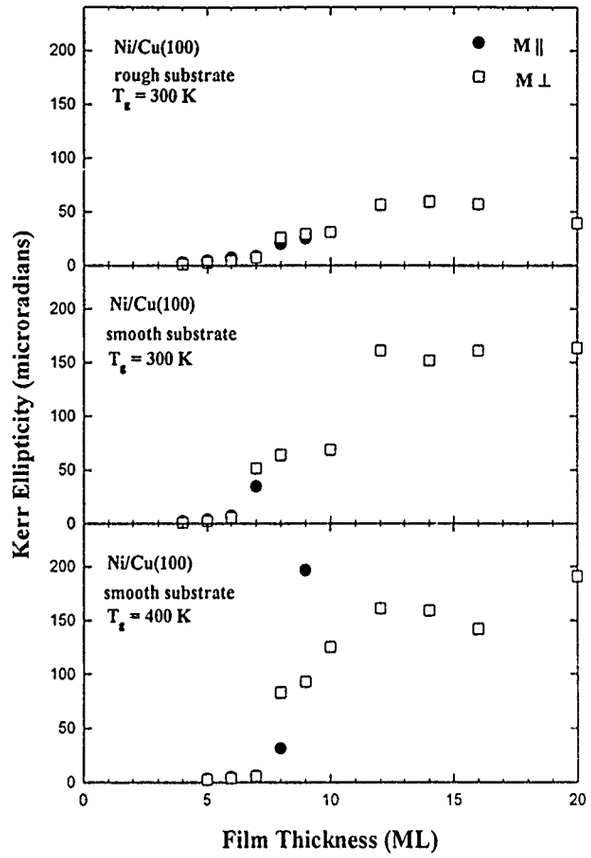

FIG. 2. Remanence vs Ni film thickness for three different film/substrate systems measured at temperature T=200 K. For each of the plots there is an abrupt increase in both parallel and perpendicular magnetizations at approximately 8 ML. Because of the limitation of our maximum applied magnetic field, the magnetization of the films could not be saturated in the parallel direction above 10 ML. This implies that the parallel component could also be increasing above this thickness.

field in the parallel direction increases sharply above the switching thickness, ultimately going above the maximum field attainable with our experimental apparatus. The slope of the perpendicular coercive field versus film thickness above the switching thickness is 1.2 Oe/ML. The abrupt change in the easy axis of magnetization is characteristic of a magnetic reorientation phase transition where the easy axis of magnetization changes from in plane to perpendicular at the switching thickness of 8 ML. This effect has been observed with x-ray magnetic circular dichroism measurements at a film thickness of 10 ML.[26]

We do not attribute the magnetization reorientation phase transition to any gross structural change since the LEED spots are similar both below and above the switching thickness for films grown at 400 K. However a subtle structural change occurs at thicknesses greater than 10 ML where the Ni(100) film transforms from a strained face centered tetragonal structure at low thickness with an in-plane lattice constant of the Cu substrate to a relaxed face centered cubic structure with an in-plane lattice constant identical to bulk Ni.[16] Small differences in the thickness where the structural strain relaxation change occurs may be due to different film preparation procedures or different levels of carbon and oxy-

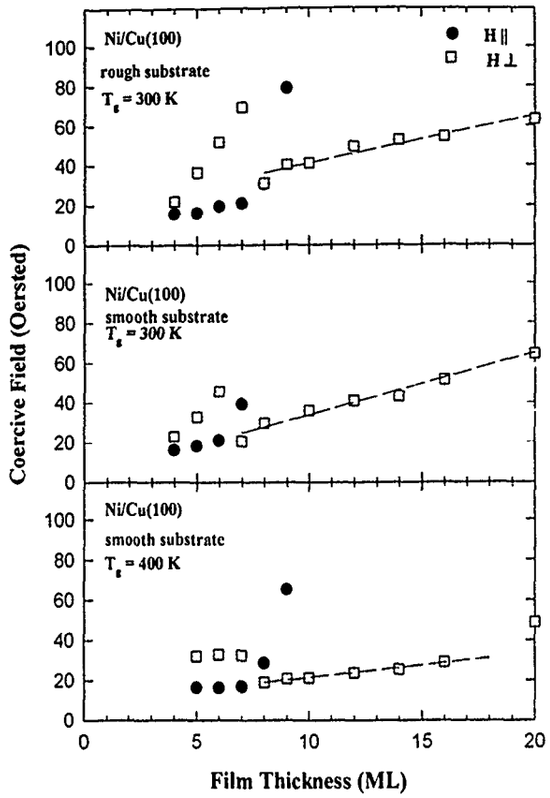

FIG. 3. Coercivity vs Ni film thickness for three different film/substrate systems measured at temperature T=200 K. For each of the systems, the coercivity in the perpendicular direction drops at the switching thickness indicating that the easy axis of magnetization is now in the perpendicular direction. The coercive field in the parallel direction increases sharply above the switching thickness, ultimately going above the maximum field attainable with our experimental apparatus.

gen contamination. This slight structural relaxation change nevertheless affects the anisotropy through the spin-orbit interaction It is sensitive to small changes in interatomic nearest-neighbor distances and by the different symmetry properties of the overlapping wave functions for the two structures. A recent calculation of the magnetocrystalline anisotropy energy showed that as a general trend, decreasing the atomic spacing will increase the energy term which prefers a perpendicular magnetization.[13,14]

In order to study the effect of interfacial strain on the switching thickness, we performed similar measurements for films deposited on a rough substrate. Interfacial roughness increases the amount of vertical strain and decreases the uniaxial anisotropy in films with perpendicular spontaneous magnetization.[27,28] The Kerr intensity for the films deposited on the rough substrate is significantly lower than that of the films deposited on a smooth substrate which shows that the magnetization of the rough films is reduced. Surprisingly, the switching thickness remains the same at 8 ML film thickness where there is a rapid decrease in the polar coercive field. However the polar Kerr ellipticity is three times weaker and the coercive field is twice as large as the films grown at 400 K. This reflects the different domain structure of the rough films and suggests that the structural change still occurs at 8 ML film thickness.

All these measurements show that the Ni films grown on Cu(100) have a predominantly in-plane magnetization for films below 8 ML thickness. Above a switching thickness the magnetization develops a strong out-of-plane component. We attribute this anomalous behavior to both structural and magnetic micromorphology of the Ni thin films. Ultrathin films of Ni have a multidomain magnetic microstructure which is a combination of perpendicular and in-plane domains, with the in-plane domains dominating below 8 ML. At a critical film thickness there is a structural transition and a perpendicular magnetization develops. The surface roughness can affect the magnetic strain anisotropy in a complicated fashion because the Ni layers can expand in both the in-plane and perpendicular direction. In the thinnest films, an in-plane interfacial strain anisotropy component is dominant. However, with increasing thickness, an out-of-plane component develops. The measurements indicate a mix of in-plane and out-of-plane magnetization domains, the latter shows a sudden increase at an onset thickness of 8 ML. At much greater film thickness, Ni/Cu(100) films show a transition back to in-plane magnetization.[29]

Funding for this research was provided by Grant No. NSF-DMR 9121736.

[1] D. Pescia and V. L. Pokrovsky, Phys. Rev. Lett. **65**, 2599 (1990).
[2] A. Kashuba and V. L. Pokrovsky, Phys. Rev. Lett. **70**, 3155 (1993).
[3] D. K. Morr, P. J. Jensen, and K. -H. Bennemann, Surf. Sci. **307–309**, 1109 (1994).
[4] Z. Q. Qiu, J. Pearson, and S. D. Bader, Phys. Rev. Lett. **70**, 1006 (1993).
[5] D. P. Pappas, C. R. Brundle, and H. Hopster, Phys. Rev. B **45**, 8169 (1992).
[6] C. Chappert, D. Renard, P. Beauvillain, J. P. Renard, and J. Seiden, J. Magn. Magn. Mater. **54–57**, 795 (1986).
[7] O. Eriksson, B. Johansson, R. C. Albers, A. M. Boring, and M. S. S. Brooks, Phys. Rev. B **42**, 2707 (1990).
[8] J. M. Leger, C. Loriers-Susse, and B. Vodar, Phys. Rev. B **6**, 4250 (1972).
[9] F. Brailsford, *Physical Principles of Magnetism,* edited by F. Brailsford (Van Nostrand, London, 1966).
[10] J. G. Gay and R. Richter, J. Appl. Phys. **61**, 3362 (1987).
[11] J. G. Gay and R. Richter, Phys. Rev. Lett. **56**, 2728 (1986).
[12] P. Bruno, Phys. Rev. B **39**, 865 (1989).
[13] D.-S. Wang, R. Wu, and A. J. Freeman, Phys. Rev. Lett. **70**, 869 (1993).
[14] D.-S. Wang, R. Wu, and A. J. Freeman, Phys. Rev. B **47**, 14932 (1993).
[15] F. Huang, M. T. Kief, G. J. Mankey, and R. F. Willis, Phys. Rev. B **49**, 3962 (1994).
[16] J. Zhang, Z. L. Han, S. Varma, and B. P. Tonner, Surf. Sci. **298**, 351 (1993).
[17] J. W. Matthews and J. L. Crawford, Thin Solid Films **5**, 187 (1970).
[18] A. R. Miedema and J. W. F. Dorleijn, Surf. Sci. **95**, 447 (1980).
[19] F. R. de Boer, R. Boom, W. C. M. Mattens, A. R. Miedema, and A. K. Niessen, *Cohesion in Metals,* edited by F. R. de Boer and D. G. Perrifor (North-Holland, Amsterdam, 1988), Vol. 1, p. 676.
[20] P. M. Ossi, Surf. Sci. **201**, L519 (1988).
[21] M. Hansen and K. Anderko, *Constitution of Binary Alloys* (McGraw-Hill, New York, 1985).
[22] F. Huang, G. J. Mankey, and R. F. Willis, Surf. Sci. Lett. **297**, L79 (1993).
[23] M. T. Kief, Ph.D. thesis, Pennsylvania State University, 1991.
[24] S. D. Bader, J. Magn. Magn. Mater. **100**, 440 (1991).
[25] B. Schulz, R. Schwarzald, and K. Baberschke, Surf. Sci. **307–309**, 1102 (1994).
[26] W. L. O'Brien and B. P. Tonner, Phys. Rev. B **49**, 15370 (1994).
[27] P. Bruno and J.-P. Renard, Appl. Phys. A **49**, 499 (1989).
[28] A. Yamaguchi, S. Ogu, and R. Yamamoto, J. Magn. Magn. Mater. **126**, 272 (1993).
[29] G. Bochi, C. A. Ballentine, H. E. Inglefield, S. S. Bogomolov, C. V. Thompson, and R. C. O'Handley, J. Appl. Phys. **75**, 6430 (1994).

Magnetization-related transport anomalies in metal/ferromagnetic insulator heterostructures

G. M. Roesler, Jr., M. E. Filipkowski, P. R. Broussard, M. S. Osofsky, and Y. U. Idzerda
Naval Research Laboratory, Code 6340, Washington, DC 20375-5343

Magnetoresistance measurements have been performed on epitaxial metal/ferromagnetic insulator bilayers. They are more sensitive to magnetic behavior at the interface of such structures than magnetization measurements. It is clear from the magnetoresistance data that previously reported slope discontinuities in the resistance versus temperature of such heterostructures are magnetic in origin. These studies demonstrate that the conduction electrons of the metal are coupled to the spins in the magnetic insulator, and act as probes of the magnetic state at the interface between the two materials. An example of the usefulness of this probe is shown by magnetoresistance measurements on a Ag/EuO bilayer.

Thin film heterostructures of nonmagnetic metals and magnetic insulators represent a new class of systems in which the interaction of conduction electrons and magnetism may be investigated. They are in some respects analogous to all-metallic magnetic heterostructures, which have demonstrated remarkable behaviors such as giant magnetoresistance[1] and antiferromagnetic coupling through interlayers.[2] The primary qualitative difference between an all-metallic heterostructure and one involving insulators is that the conduction electrons in the latter are confined to the metal layer (except for tunneling processes), and interaction with localized moments is essentially restricted to those at the interface. Measurements of the in-plane resistance versus temperature in such systems[3] contain a strong feature near the Curie temperature of the insulator, for sufficiently thin metallic layers. In this paper, we describe magnetization and magnetoresistance measurements on such structures. Not only do these measurements confirm that the resistivity anomaly previously seen is magnetic in origin, but they reveal the utility of resistivity measurements in probing the magnetic state at the metal/insulator interface.

The metal/ferromagnetic insulator structures were prepared under conditions of heteroepitaxy, in a VG system with a base pressure of 10^{-10} mbar, on the [100] plane of yttria-stabilized zirconia (YSZ) substrates. The ferromagnetic insulator used, EuO, was chosen for its relatively low Curie temperature of 70 K and ease of thin film preparation. Pressure during EuO deposition is typically 10^{-6} to 10^{-7} mbar due to outgassing of the boron nitride crucible containing the EuO. The lattice constants of EuO and YSZ are identical, 5.184 Å, although the oxygen lattices of the two are of different symmetry. At a deposition rate of about 0.2 Å/s, EuO was found to grow epitaxially and two dimensionally on YSZ, with some three dimensionality of the surface occurring after about three unit cells have been deposited. For consistency, all of the samples reported in this work involve 100 Å EuO layers grown at a substrate temperature of 300 °C. Our EuO films have shown 70 K Curie temperatures by magnetization and Kerr rotation measurements. We are unaware of other work in which EuO films have been prepared epitaxially, but EuS films have been epitaxially grown.[4] It is probably essential that ultrahigh vacuum conditions be used in the preparation of these metal/magnetic insulator structures, to ensure intimate contact, and to ensure that the thin metal layers needed to demonstrate coupling are of high quality. If thick metal layers are used, as in one study of a thick Pb/EuS bilayer,[4] coupling may be difficult to detect. In our samples, resistivity anomalies are not seen for metal layers thicker than 200 Å.

Metal layers are evaporated *in situ* after EuO growth is completed, at typical pressures of 10^{-8} to 10^{-9} mbar. Because resistance measurements, x-ray diffraction, etc. must be done *ex situ*, a 200 Å Si passivation layer is applied to all samples. This is important to prevent degradation of the EuO due to moisture, and to minimize oxidation of V films, since the magnetic oxides of V could influence the scattering in the films. Resistance measurements are four-terminal ac or dc measurements with contacts in a van der Pauw configuration.

Figure 1 contains a comparison of the resistance of two metal/ferromagnetic insulator bilayers, one composed of a 36 Å Ag layer on EuO, the other 45 Å of V on EuO. Slope discontinuities, such as those reported in Ref. 3, are evident in both sets of $R(T)$ data, at 50 K for the Ag/EuO bilayer and at 90 K for the V/EuO bilayer. *Whenever* a dR/dT discontinuity is observed in our V/EuO structures, it occurs at 90 K; and at 50 K in Ag/EuO structures (sometimes with an additional feature at 13 K). Thus, a common trait of these structures is a *characteristic temperature* T^* determined by the

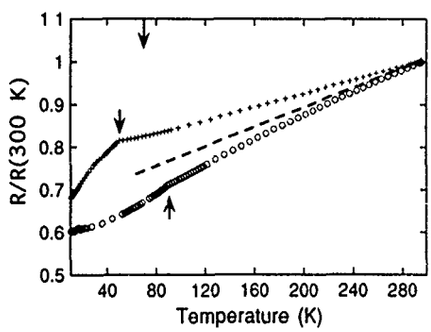

FIG. 1. The resistance of bilayers of 36 Å V on 100 Å EuO (circles) and 45 Å Ag on 100 Å EuO (crosses), normalized to room temperature. Arrows on the data show the location of T^* (dR/dT discontinuities) for the two samples. The top arrow is at the EuO Curie temperature (70 K). The dashed straight line is to make the curvature of the two data sets above T^* more apparent.

 0021-8979/94/76(10)/6437/3/$6.00 © 1994 American Institute of Physics

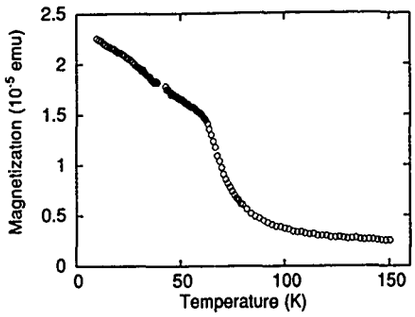

FIG. 2. Perpendicular magnetization of a 20 Å Ag film grown on 150 Å EuO on yttria-stabilized zirconia. The magnetization of the bare substrate has been subtracted from the data. Departure from Curie–Weiss behavior is apparent below about 70 K.

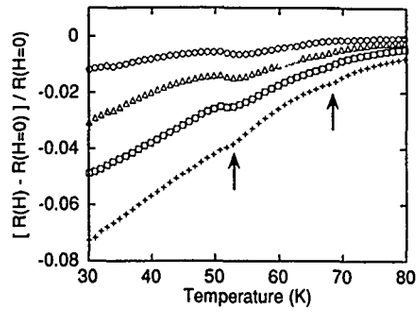

FIG. 3. Magnetoresistance of a 45 Å Ag film on 100 Å EuO in fields of (top to bottom) 1, 2, 3, and 4 T. The arrows indicate cusps in the 4 T data, which nearly correspond to Curie temperature of EuO (upper cusp), and to the slope discontinuity of the zero-field resistance that defines T^*_{Ag}.

metal element, and perhaps by other conditions such as strain or epitaxial arrangement. Figure 1 also illustrates some qualitative differences between the Ag/EuO and V/EuO samples we have grown. In the V-containing samples, the slope of the resistance always remains positive and has negative curvature down to T^*_V, whereas in Ag-containing samples, the resistance develops a positive curvature above T^*_{Ag}. For very thin (20 Å) Ag layers (not shown), *R(T)* exhibits a local maximum at T^*_{Ag}. This implies that the physics governing the scattering behavior in these two systems is qualitatively different. A further difference between V/EuO and Ag/EuO interfacial magnetism is apparent in the different values of T^* in the two systems. Compared to the bulk EuO Curie temperature of 70 K, T^*_V is shifted upward in temperature, whereas T^*_{Ag} is shifted downward.

The proximity of the *dR/dT* discontinuities to the EuO Curie temperature suggests that those features are magnetic in origin. Two experiments to confirm this, soft x-ray magnetic circular dichroism (SXMCD) and Hall effect, were reported in Ref. 3. No dichroism was observed in the SXMCD measurement, giving no confirmation of *d*-band splitting, and no anomalous Hall voltage was noted. A change in magnetic scattering due to magnetic ordering still seemed the most likely cause of the resistance anomalies. To verify this, magnetization and magnetoresistance measurements were performed on Ag/EuO heterostructures. Figure 2 shows the magnetization of a Ag/EuO bilayer measured on a SQUID magnetometer with the magnetic field perpendicular to the film plane. The magnetization of the bare substrate (weakly paramagnetic) has been subtracted from the data. Curie–Weiss behavior is evident at high temperatures. Departure from Curie–Weiss behavior begins in the 60–70 K range, but there is no distinct feature corresponding to T^*_{Ag}. This is not surprising if the anomaly at T^*_{Ag} represents an interfacial phenomenon, since any transition there involves only a fraction of the magnetic ions in the sample.

Magnetoresistance measurements proved more successful in resolving the bulk and interface behavior, and in associating the anomaly at T^*_{Ag} with magnetism. The magnetoresistance of a 45 Å Ag layer on EuO is shown in Fig. 3 for various magnetic fields applied perpendicular to the film plane. For fields of 1, 2, and 3 T, the magnetoresistance is nonmonotonic with temperature, having a maximum magnitude a few degrees above T^*_{Ag}, and a minimum magnitude at about T^*_{Ag}. At 4 T, the magnetoresistance is no longer nonmonotonic with temperature, but slope changes are visible both at the EuO Curie temperature and at T^*_{Ag}. Whatever the microscopic mechanism, a magnetic field strongly influences the scattering behavior at T^*_{Ag}. The magnetoresistance is negative even far above the Curie temperature, as is typical of systems containing disordered magnetic ions. One interpretation of the phenomenon at T^* is a reduction in scattering due to ordering of spins caused by local (exchange) fields. An ordering of perhaps one-quarter to one-half of the scattering centers would be consistent with the observed magnetoresistance.

Similar behavior has been observed in V/EuO heterostructures near T^*_V. The magnetoresistance of a V/EuO bilayer in a field of 1 T is shown in Fig. 4. The curve $\Delta R = \Delta R_0 (T_0/T)^2$, which is the magnetoresistance scaling expected for spin-flip scattering from disordered ions, is superimposed on the data. The close fit to the data at high temperatures and the abrupt departure just above T^*_V suggest that the maximum magnitude of magnetoresistance is due to an *extra scattering mechanism*, in addition to spin-flip scattering, which is significant within a few degrees of T^*.

These magnetization and magnetoresistance measurements demonstrate an association between magnetism and

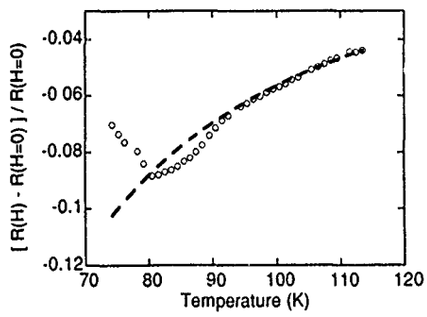

FIG. 4. Magnetoresistance of a 20 Å V film on 100 Å EuO in a field of 1 T. The dashed curve is $\Delta R = \Delta R_0 (T_0/T)^2$, where ΔR_0 is the magnetoresistance at $T_0 = 113$ K.

resistance anomalies in these metal/magnetic insulator heterostructures. The microscopic behavior responsible for this association could be as simple as alignment of the localized Eu^{++} spins by the molecular field of the EuO. Or a more complex phenomenon, such as a many-body polarization of the conduction electrons due to the overlap of their wavefunctions with the Eu^{++} f orbitals, could be responsible. Regardless of the mechanism, the conduction electrons respond to changes in scattering which are associated with magnetism, and therefore *act as probes of the magnetic state at the interface.*

We show as an example of the utility of this interaction the magnetic behavior of a Ag/EuO multilayer which exhibited a T^* of 13.5 K rather than the usual 50 K. Because the total thickness of this multilayer was over 500 Å, some surface roughness may have allowed contact between Ag and EuO planes not ordinarily in contact in thin bilayer samples. The resistance of the multilayer is shown in Fig. 5 for the magnetic field both in-plane and out-of-plane. With the field in-plane, the magnetoresistance is small and negative above T^*, and nearly zero below T^*. When the field is out-of-plane, magnetoresistance is strongly positive at low temperatures, and the downward shift of T^* is stronger than with the field in-plane. These measurements suggest that an in-plane anisotropy exists in this sample.

The coupling of conduction electrons to localized spins at a metal/magnetic insulator interface may in future prove to be useful both for probing the magnetic state of such interfaces and for understanding fundamental processes involved in electron-spin interactions. It will be important to develop an understanding of the microscopic processes which determine the magnetic and scattering behavior illuminated by these measurements. For example, two fundamental questions are why T^*_V and T^*_{Ag} are different, and why they are displaced in opposite directions from the Curie temperature of bulk EuO. Determining the role of epitaxy and interface arrangement in the behavior of these structures will be the subject of future studies. Also of interest is the nature of the 13 K anomaly in Ag/EuO films, which is only occasionally observed in these structures.

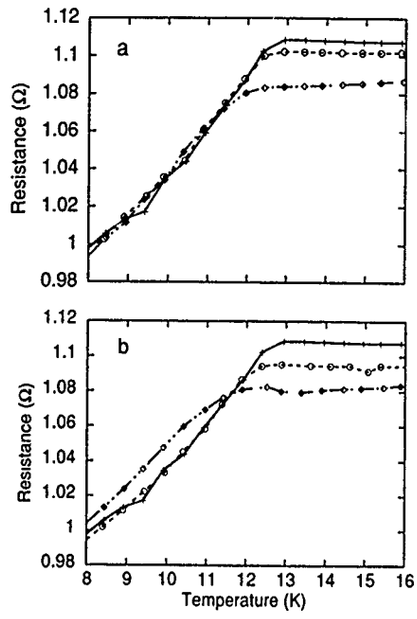

FIG. 5. Resistance in a magnetic field of an Ag/EuO multilayer of composition (20 Å Ag/30 Å EuO)$_{10}$, with magnetic field (a) in plane, and (b) out of plane. Magnetic field strengths: $H=0$ (crosses, solid curves), 2 T (circles, dashed curves), and 4 T (diamonds, dot-dashed curves).

We are grateful to A. Ehrlich, J. Krebs, J. S. Moodera, G. A. Prinz, and P. M. Tedrow for useful discussions. One of us (GMR) acknowledges the support of the National Research Council Postdoctoral Associateship program.

[1] M. N. Baibich, J. M. Broto, A. Fert, F. Nguyen Van Dau, F. Petroff, P. Eitenne, G. Creuzet, A. Friederich, and J. Chazelas, Phys. Rev. Lett. **61**, 2472 (1988).
[2] P. Grünberg, R. Schrieber, Y. Pang, M. B. Brodsky, and H. Sowers, Phys. Rev. Lett. **57**, 2442 (1986).
[3] G. M. Roesler, Jr., Y. U. Idzerda, P. R. Broussard, and M. S. Osofsky, J. Appl. Phys. **75**, 6679 (1994).
[4] W. Zinn, B. Saftic, N. Rasula, M. Mirabal, and J. Kohne, J. Magn. Magn. Mater. **35**, 329 (1983).

Lorentz electron microscopy studies of magnetization reversal processes in epitaxial Fe(C01) films

E. Gu, J. A. C. Bland, C. Daboo, M. Gester, and L. M. Brown
Cavendish Laboratory, University of Cambridge, Madingley Road, Cambridge CB3 OHE, United Kingdom

R. Ploessl and J. N. Chapman
Department of Physics and Astronomy, University of Glasgow, Glasgow G12 8QQ, United Kingdom

The magnetic domain structure and microscopic magnetization reversal processes in epitaxial Fe/GaAs(001) films with cubic anisotropy and in-plane easy axes have been investigated by a Lorentz microscope equipped with a magnetizing stage. For the films of a few hundred angstroms thickness we observe the single domain remanent state predicted for a two-dimensional film but find that domains play a crucial role in the magnetic reversal process. For reversal along the in-plane ⟨110⟩ directions (hard axes), magnetization reversal proceeds via a combination of coherent rotation and displacements of weakly pinned 90° domain walls at critical fields. For magnetization reversal along the in-plane ⟨100⟩ directions (easy axes), an irregular checkerboard domain structure develops at the critical field and both 180° and 90° domain walls coexist. The reversal of the domains with magnetization vector opposite to the applied field direction takes place by a combination of two 90° reorientations. We discuss how these processes are related to the magnetic anisotropies present in the film and the macroscopic M-H hysteresis curves.

I. INTRODUCTION

The magnetic properties of thin epitaxial Fe films and various types of Fe multilayer films grown on semiconductor substrates are of particular interest since they open up possibilities for a broad range of applications[1] and also permit fundamental studies in magnetism.[2–4] The structural and magnetic properties of these epitaxial Fe films are the focus of current experimental investigations.[3–5] Recently, the magnetization reversal processes in epitaxial Fe/GaAs(001) thin films have been studied by the longitudinal and transverse magneto-optical Kerr effects (MOKE).[4–6] From these studies, it is now clear that the simple coherent rotation model cannot explain all the details of the magnetization process in these Fe/GaAs(001) films and that magnetic domain processes play an important role in the magnetization reversal around the transition fields. However, to our knowledge, the detailed domain evolution during magnetization reversal in such epitaxial Fe films has not been reported.

II. EXPERIMENT

The Fe films were grown on As-desorbed GaAs(001) substrates in an ultra high vacuum chamber.[7] During growth, the pressure was less than 5×10^{-10} mbar. The optimum substrate temperature of 150 °C and a deposition rate of 1 Å min^{-1} were used for the Fe growth. To prevent oxidation, completed Fe films were covered by a Cr cap layer. In this work, a new selective chemical etching technique was employed to prepare Lorentz microscope specimens.[7] By using this method, an electron transparent uniform "window" (up to 300×300 μm in size) appropriate for magnetic domain studies can be fabricated. The macroscopic magnetization reversal behavior of the Fe films was studied using a MOKE magnetometer.[5,8] The magnetic domain structure in the Fe films was revealed using a Lorentz electron microscope equipped with a magnetizing stage.[9]

III. RESULTS

A. Microstructure

The epitaxial growth of bcc Fe films was confirmed by transmission electron diffraction. The surface topography of the Fe films was investigated by scanning tunneling microscopy (STM). STM images reveal that the films have a surface roughness amplitude of about 10 Å over lateral distance of several hundred angstroms. Detailed structural results are reported elsewhere.[10]

B. Microscopic magnetization reversal processes

1. ⟨110⟩ hard directions

For the applied field aligned parallel to the ⟨110⟩ in-plane hard direction, the MOKE hysteresis loop of an Fe(150 Å)/GaAs(001) film with cubic anisotropy (K_1/M=259 Oe, $K_u\sim0$) is inset in Fig. 1. It can be seen that initially there is a gradual decrease of the component of the magnetization parallel to the applied field direction from saturation as the field strength is reduced from the saturation value. An abrupt jump occurs at a small negative field followed by a further gradual decrease until negative saturation is reached. At this transition field, Barkhausen discontinuities are observed in the detailed MOKE loops indicative of the irreversible movement of domain walls.

To gain insight into the mechanisms by which the magnetic switching behavior described above took place, the Fe(150 Å)/GaAs(001) film was subjected to field cycles in the Lorentz microscope. First, a single domain state was induced by applying a magnetic field (H_i) along one of the ⟨110⟩ directions, say the [1$\bar{1}$0] direction. Then the field was reduced to zero. In the remanent state, the Fe film was found to be still in a single domain configuration. This single domain state persisted up to a critical reverse field strength $H_r = H^h_{crit}$ applied along the [$\bar{1}$10] direction at which domain walls were first observed (H^h_{crit} = 5.6 Oe for a field amplitude

 0021-8979/94/76(10)/6440/3/$6.00 © 1994 American Institute of Physics

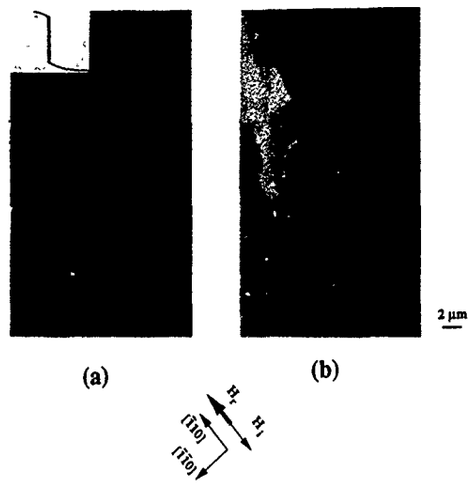

FIG. 1. Foucault images of an Fe(150 Å)/GaAs(001) film for the field applied along the hard axis. The component of induction mapped was parallel to the applied field direction for reverse field strengths ($H_r \| [1\bar{1}0]$) of (a) H^h_{crit}, (b) 1.10 H^h_{crit}. The MOKE hysteresis loop along this direction is inset.

of 120 Oe). Only a few domain walls appeared, extending several hundreds of microns across the whole area of the window. A Foucault image, sensitive to the component of induction parallel to the field direction and recorded at the critical field strength is shown in Fig. 1(a). In this image, a single wall running almost parallel to the $[1\bar{1}0]$ direction can be seen. Figure 1(b) shows what happened when the field strength was increased to a value of 1.10 H^h_{crit}. In this case the domain wall seen in Fig. 1(a) remained pinned at the original position but another domain wall moved into the field of view from the top right-hand corner. A further small increase of field led to the disappearance of domain walls from the whole of the visible area of the sample. Repetition of the field cycle described above showed that the fields at which walls appeared and disappeared were highly reproducible. Further, it was noted that Foucault images sensitive to magnetic induction perpendicular to the field direction were never found to show contrast variations, indicative of a constant (or zero) magnetization component in that direction. These images are consistent with the magnetization orientations indicated by the arrows shown in Fig. 1.

The overall magnetization reversal process for fields along the ⟨110⟩ direction can now be explained with reference to Fig. 2. As the field strength is reduced from a high value in the $[1\bar{1}0]$ direction, there is a tendency for the magnetization to rotate towards the nearest easy axis. While $[1\bar{1}0]$ lies midway between the easy [100] and $[0\bar{1}0]$ directions, in practice, the applied field will never be exactly along the intended direction with the result that the magnetization vector rotates towards whichever easy direction is closer to that of the field ([100] in Fig. 2). Hence, in the remanent state, the sample is uniformly magnetized as a single domain along this "preferred" easy direction. Application of a field of the opposite polarity (namely one parallel to $[\bar{1}10]$) leaves the film in its single domain state until, at the critical field, 90° walls are nucleated and these sweep across

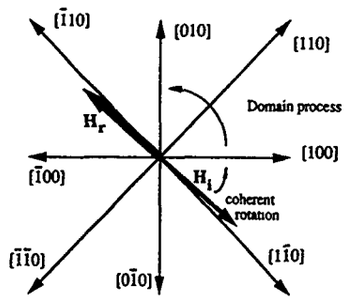

FIG. 2. Magnetization reversal process for applied fields near the ⟨110⟩.

the specimen introducing domains in which the magnetization is oriented along [010], the easy direction near to that of the applied field. Increasing the field strength by only a fraction of 1 Oe allows [010] oriented domains to grow through Barkhausen-like jumps, the jump distance observed being of the order of a few tens of microns. This part of the reversal process corresponds to the steep part of the MOKE loop. When it is complete the whole of the film is once again uniformly magnetized but the direction of magnetization has changed from the [100] direction to the [010] direction. Increasing the field strength further leads to the magnetization moving away from the $[01\bar{0}]$ direction towards that of the applied field. Very similar magnetization reversal behavior has also been observed for a 450 Å Fe film along the ⟨110⟩ hard axes.

2. ⟨100⟩ easy directions

Along the ⟨100⟩ easy directions, the Fe films exhibit a square hysteresis loop (the hysteresis loop is inset in Fig. 3). However, Barkhausen discontinuities are also observed at the transition field in the detailed minor hysteresis loop.

In the microscope, following a similar procedure to that used for the ⟨110⟩ direction, a single domain state was first induced, in this case by applying a field along $[0\bar{1}0]$. After removal of the field, no walls were observed in the sample, as is consistent with the square loop observed by MOKE. Magnetization reversal was then studied by applying successively greater fields parallel to [010]. No change was observed up to a field of H^e_{crit} = 7.8 Oe at which point domain walls suddenly appeared. A Foucault image, sensitive to the component of induction perpendicular to the field direction and recorded at the critical field strength is shown in Fig. 3(a). The evolution of the domain structure shown in Fig. 3(a) is shown for a field of 1.09 H^e_{crit} in Fig. 3(b). In both cases the domain structure is of the checkerboard type observed also in demagnetized Fe/MgO(001) films.[11,12] The magnetization distributions deduced from the images (the Foucault images, sensitive to the component of induction parallel to the field direction are not included in Fig. 3) are also shown in Fig. 3. Increasing the field above 1.13 H^e_{crit} led to a complete loss of domain walls with the sample returning to a single domain state, albeit with a reversed magnetization vector. A similar checkerboard domain pattern is also formed for reversal along the other easy axis.

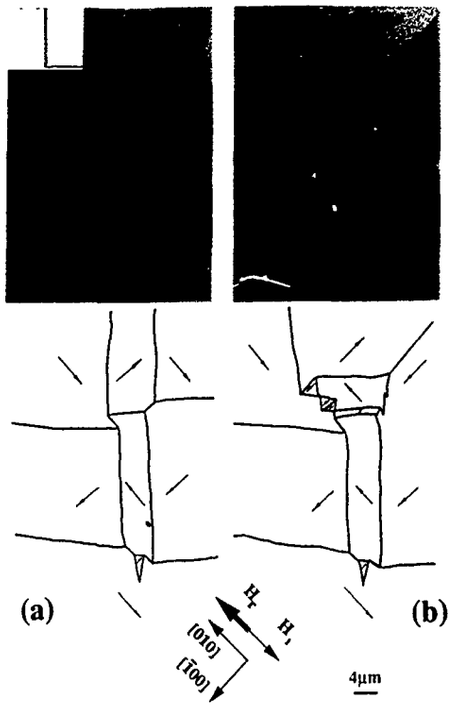

FIG. 3. Foucault images and magnetization distributions of the 150 Å Fe film for the field applied along the easy axis. The component of induction mapped in the images was perpendicular to the applied field direction for reverse field strengths ($H_r \| [010]$) of (a) H_{crit}^c, (b) 1.09 H_{crit}^c. The MOKE hysteresis loop along this direction is inset.

While a pure checkerboard domain structure comprises only 90° domain walls, some (generally short) 180° walls are observed in our structures. It can be seen that the 90° and 180° domain walls are aligned almost along the ⟨110⟩ and ⟨100⟩ directions, respectively. The 180° domain walls are assumed to arise from the combined action of the applied field and pinning centers.

In Figs. 3, domain wall displacements and the nucleation of new domains are observed. A detailed study of Figs. 3 shows that the reversal of the magnetization which is initially antiparallel to the applied field tends to take place not by a single reversal, but by a combination of two 90° reorientations. This two-step reversal process appears to involve both domain nucleation and wall displacements.

It is immediately clear that magnetic domains again play a crucial role in the reversal mechanism when the field is applied along a ⟨100⟩ direction. The main steps in the reversal process are summarized as follows. Since ⟨100⟩ directions are the easy axes for an Fe film with cubic anisotropy it is entirely reasonable that the magnetization should remain oriented along is initial direction (say $[0\bar{1}0]$) when the field is reduced to zero. Even if the applied field is not exactly parallel to the $[0\bar{1}0]$ direction, as mentioned in the previous section, during reduction of the field strength to zero, the magnetization will simply rotate to this $[0\bar{1}0]$ direction leaving a single domain remanent state. Since the $[0\bar{1}0]$ direction is the bisector of another two easy directions, [100] and $[\bar{1}00]$, there should be comparable probabilities for the magnetization to jump into either of these two easy directions as the strength of the field in the [010] direction is increased. Thereafter, further 90° transitions take place to introduce domains in which the magnetization is parallel to the applied field and, over a small field range, all four easy magnetization directions are present in the sample simultaneously. This structure is the checkerboard pattern but it exists only within a narrow field range. It is destroyed by a combination of further domain nucleation and wall motion of the kinds discussed above. For the 450 Å Fe/GaAs(001) film an irregular checkerboard pattern also develops for reversal along the easy directions.

IV. DISCUSSION AND CONCLUSIONS

Since all the magnetic domains observed have sizes (>1 μm) much larger than the lateral length of surface features revealed by STM, one may conclude that the domain size is not affected by the topography of these Fe/GaAs(001) films. For demagnetized ultrathin fcc Co/Cu(100) films, the magnetizations of the domains lie along each of the four easy in-plane axes but the walls are extremely irregular, suggesting a vanishing magnetostatic energy. [13,14] In our films, the domain walls are fairly straight and have a defined orientation with respect to the crystal axes. Therefore, these results show that the 150 Å thickness is sufficient for the magnetostatic energy contribution to the wall energy to be important.[10] Nonetheless, the films are still thin enough to be considered as almost two dimensional from the viewpoint of domain formation. A simple estimate of the energy associated with the checkerboard domain structure shows that the checkerboard domain is driven by the Zeeman energy at the coercive field.[10]

ACKNOWLEDGMENTS

We gratefully acknowledge the financial support for this work from the SERC and the Toshiba Corporation.

[1] G. A. Prinz, Sciecne **250**, 1092 (1990).
[2] G. A. Prinz and J. J. Krebs, Appl. Phys. Lett. **39**, 397 (1981).
[3] J. J. Krebs, B. T. Jonker, and G. A. Prinz, J. Appl. Phys. **61**, 2596 (1987).
[4] J. M. Florczak and E. Dan Dahlberg, Phys. Rev. B **44**, 9338 (1991).
[5] C. Daboo, R. J. Hicken, D E. P. Eley, M. Gester, S. J. Gray, A. J. R. Ives, and J A. C. Bland, J. Appl. Phys. **75**, 5586 (1994).
[6] J. M. Florczak and E. Dan Dahlberg, J. Magn. Magn. Meter. **104**, 399 (1992).
[7] E. Gu, C. Daboo, J. A. C. Bland, M. Gester, A. J. R Ives, L. M. Brown, N. A. Stelmashenko, and J. N Chapman, J. Magn. Magn. Mater. **126**, 180 (1993).
[8] C. Daboo, J. A C. Bland, R. J. Hicken, A. J. R. Ives, and M. J. Baird, Phys. Rev. B **47**, 11852 (1993).
[9] J. N. Chapman, S. McVitie, and S. J. Hefferman, J. Appl. Phys. **69**, 6078 (1991).
[10] E. Gu *et al.* (to be published).
[11] H. Sato and R. W. Astrue, J. Appl. Phys. **33**, 2956 (1962).
[12] H. Sato, R. S. Toth, and R. W. Astrue, J. Appl. Phys. **34**, 1062 (1963).
[13] H. P. Oepen, M. Benning, H. Ibach, C. M. Schneider, and J. Kirschener, J. Magn. Magn. Mater. **86** L 137 (1990).
[14] H. P. Oepen, J. Magn. Magn. Mater. **93**, 116 (1991).

Magnetic response of ultrathin Fe on MgO: A polarized neutron reflectometry study

S. Adenwalla, Yongsup Park, and G. P. Felcher
Argonne National Laboratory, Argonne, Illinois 60439

M. Teitelman
Russian Academy of Science, Nizhny Novgorod, Russia

The magnetization of ultrathin bcc Fe films (two and three monolayers) on MgO was measured and compared with the behavior predicted for a two-dimensional ferromagnet. The experiment indicated that no hysteresis was present in the magnetization. Instead, the magnetization at low temperature was affected by a marked field cooling effect. These observations lead to the conclusion that films of Fe on MgO of such thickness exhibit superparamagnetic behavior as if they were not entirely continuous. In contrast, films thicker than five monolayers exhibit a magnetic response close to that of bulk iron.

I. INTRODUCTION

A polarized neutron reflection (PNR) study of thin films of bcc iron on MgO recently published[1] showed some surprising features. Even the thinnest films (two monolayer thick) were found to be ferromagnetic. At low temperature a sizeable magnetic field (of the order of 1 kOe) was necessary to saturate the in-plane magnetization, while fields of a few oersted were sufficient to saturate thicker samples. The amplitude of the ferromagnetic moment was found to be 2.2 ± 0.2 μ_B/Fe atom regardless of the sample thickness, in contrast with a predicted enhancement[2] for the surface atoms close to 3 μ_B/Fe atom. In view of the unusual magnetization curve at low temperature the question was raised if these thin films of iron showed the elusive magnetic behavior expected for a two-dimensional ferromagnet.

A magnet in two dimensions differs in significant ways from its three-dimensional counterpart. The Mermin–Wagner theorem shows that in the absence of anisotropy there is no magnetic ordering at zero field.[3] At finite fields the field and temperature behavior of the magnetization is governed by the equation[4]

$$\frac{M}{M_0} = 1 + \frac{k_B T}{2\pi J} \ln[1 - \exp(-2\mu H/k_b T)]. \tag{1}$$

For $\mu H < kT$ the magnetization follows a loglike behavior. Over a large temperature range the magnetization induced at a given field decreases almost linearly with increasing temperature.

The technique used was PNR, the working of which has already been discussed in detail in the literature.[5] Here it was used to measure the magnetic moment, functioning as a sensitive magnetometer. The physical quantities observed by PNR, however, differ somewhat from those observed by regular magnetometry. In PNR it is assumed that the films are formed of uniform and flat layers. If the films are not entirely uniform, the mean amplitude has to be taken for each height in the film; the *roughness* also causes some of the neutrons to be scattered out of the specular beam. Second, only the component of the magnetization in the plane of the sample is measured. This component, however, can be obtained as an *absolute* value.

II. EXPERIMENT

The samples studied consisted of the equivalent of two, three, or eight monolayers of Fe evaporated onto the substrate at room temperature. The Fe was covered by a wedge-shaped coating of gold, with a mean thickness of 200 A. These samples had been used in a previous PNR experiment,[1] and they were similar to others used in extensive magneto-optical Kerr effect measurements.[6] However fresh samples, sputtered on MgO and covered with MgO as well, showed similar magnetic behavior. The measurements were taken at temperatures ranging from 25 to 300 K and magnetic fields from 20 to 7000 Oe at the reflectometer "POSY-I" at the Intense Pulsed Neutron Source at Argonne National Laboratory. Each data point presented here has been extracted from a measurement which took approximately 12 h.

Fitting the neutron reflectivity data, we obtain a saturated moment of $2.0 \pm 0.2 \mu_B$/Fe atom, showing no enhancement over the bulk value. Demagnetizing effects do not play a role since at this field the moment lies along the applied field direction.

Figure 1 shows the temperature variation of the magnetization of the three monolayers sample at 7 kOe. The magnetization decreases linearly with increasing temperature with a slope far greater than that of bulk iron. Is this the signature of a two-dimensional magnet? The low temperature magnetization curve (Fig. 2) shows saturation at about 1000 Oe and could not be fit to a log function. On the other hand, the magnetization had features not expected for a conventional ferromagnet. No evidence for hysteresis was found, as it was checked by reversing the field and then measuring the remnant magnetization. In addition, a very marked field cooling effect was present. On cooling from 275 K in a field of 7 kOe (FC), the remanent magnetization was about half the saturation value. The remanent magnetization dropped dramatically by cooling from room temperature in zero field. The two monolayers sample displayed essentially the same features as the three monolayer sample, but with worse statistics. The eight monolayer sample showed a clear hysteresis loop, with a H_c of 50 Oe at 35 K

 0021-8979/94/76(10)/6443/3/$6.00 © 1994 American Institute of Physics

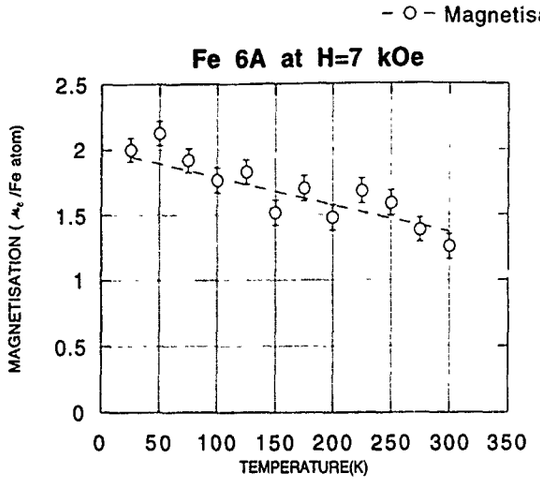

FIG. 1. Temperature dependence of the magnetization for the three monolayer sample. Data were taken at a field of 7 kOe. The dashed line is the Langevin function for particles of 1000 atoms.

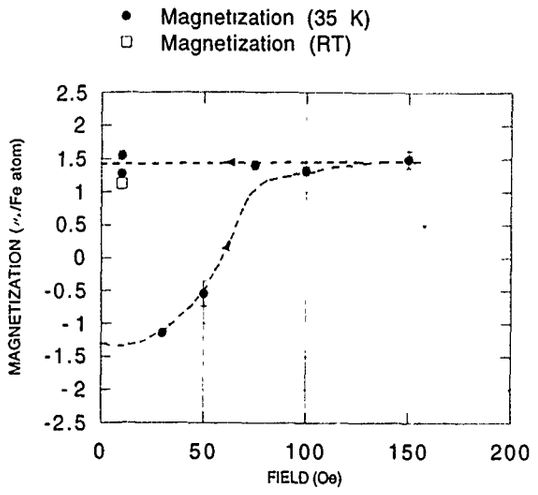

FIG. 3. Hysteresis loop at 35 K for the eight monolayer sample.

(see Fig. 3) and no appreciable variation with temperature of the magnetization at saturation.

III. DISCUSSION

The absence of hysteresis is indicative of superparamagnetism. Instead of a continuous thin film of Fe, the Fe forms islands on the surface of MgO. In a superparamagnetic material, in the absence of anisotropy, the component of magnetization in the field direction follows the Langevin function[4]

$$\frac{M}{M_0}=\coth\left(\frac{\mu H}{k_B T}\right)-\left(\frac{k_B T}{\mu H}\right), \tag{2}$$

where μ refers to the magnetization of the superparamagnetic particle, comprising a large number of atoms. Using the absolute value of the magnetization per Fe atom (obtained from fitting the neutron reflectivity data), we obtain the best fit to a Langevin function for islands of 1000 atoms in size. The calculated magnetization is presented in the form of dashed curves in Figs. 1 and 2; in Fig. 1 it is apparent that, even for superparamagnetic particles, the temperature variation of the magnetization is almost linear in a region not too close to the Curie temperature.

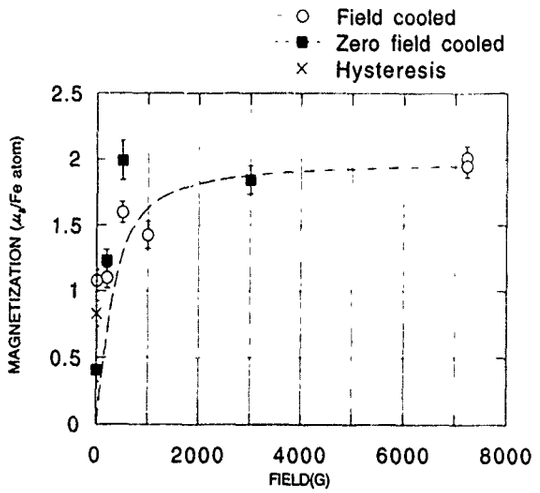

FIG. 2. Field dependence of the magnetization at 25 K of the three monolayer sample. The dashed line is the Langevin function for particles 1000 atoms in size.

According to the Langevin function the magnetization is null at zero field. However it is well known[4] that below a blocking temperature field cooling effects are present, which are interpreted as due to anisotropy. The anisotropy energy provides an energy barrier against rotation of the magnetization. If the sample is cooled in a magnetic field, and the the magnetic field is turned off, the magnetization relaxes exponentially with a time constant that is large well below the blocking temperature. A naïve calculation starting from the crystalline anisotropy of Fe gives a relaxation rate at 25 K of $\sim 10^{-9}$ s—a value which is far too small. Published measurements by Xiao *et al.*[7] on granular films confirm that the crystalline anisotropy is only a small contribution to the anisotropy energy barrier in superparamagnetic systems. We know that other anisotropies are present in our system, for instance shape anisotropy. The iron clusters are in reality thin flat islands; if they were not so, their magnetic moment would not have contributed appreciably to the magnetic reflectivity. As corroborating evidence, the magnetization of the eight monolayer Fe coverage seems to be that expected of a *continuous* film. What is not known is the detailed nature of these islands, and for that reason it is not possible at present to do further modeling: the notion itself of superparamagnetism is qualitative (because no interaction is assumed between the islands) and based on a a limited amount of observations. However, transmission electron microscopy characterization may allow us to make a more quantitative analysis.

The present study shows that films of Fe on MgO below a certain thickness do not have long range ferromagnetic ordering, such as has been observed for ultrathin Fe films on Cu,[8] Ag,[9] and Au.[10] The magnetic response can be explained in terms of superparamagnetism, which leads to the conclusion that, below a certain thickness, Fe on MgO aggregates in islands. This conclusion had been tentatively reached already by Liu *et al.*[6] on the basis of some magneto-optic measurements: below a thickness of four monolayers Fe films on MgO showed no Kerr effect signal. The lattice mismatch between MgO and Fe is only 4%; however, the difference in the surface energies (4010 nJ/mm^2 for Fe vs 1200 nJ/mm^2 for MgO) is large, which may account for the fact that at small thicknesses the Fe does not wet the MgO surface. Finally, the present measurements indicate that the magnetic moment of iron in these samples is not enhanced compared to the bulk value which is consistent with our conclusion that we have aggregates of particles in these samples.

ACKNOWLEDGMENTS

Work at Argonne was supported by the Department of Energy, Basic Energy Sciences, under Contract No. W31-109-ENG-38.

[1] Y. Y. Huang, C. Liu, and G. P. Felcher, Phys. Rev. B **47**, 183 (1993).
[2] C. Li and A. J. Freeman, Phys. Rev. B **43**, 780 (1991).
[3] N. D. Mermin and H. Wagner, Phys. Rev. Lett. **17**, 1133 (1966).
[4] I. S. Jacobs and C. P. Bean, in *Magnetism*, edited by G. T. Rado and H. Shul (Academic, New York, 1963), Vol. III, Chap. 6.
[5] G. P. Felcher, R. O. Hilleke, R. K. Crawford, J. Haumann, R. Kleb, and G. Ostrowski, Rev. Sci. Instrum. **58**, 609 (1987).
[6] C. Liu, Y. Park, and S. D. Bader, J. Magn. Magn. Mater. **111**, 225 (1992).
[7] Gang Xiao, S. H. Liou, A. Levy, J. N. Taylor, and C. L. Chien, Phys. Rev. B **34**, 7573 (1986).
[8] C. Liu, E. R. Moog, and S. D. Bader, J. Appl. Phys. **64**, 5325 (1988).
[9] A. Vaterlaus, M. Stampanoni, M. Aeschlimann, and F. Meier, J. Appl. Phys. **64**, 5331 (1988).
[10] W. Durr, M. Taborelli, O. Paul, R. Germar, W. Gudat, D. Pescia, and M. Landolt, Phys. Rev. Lett. **62**, 206 (1989).

Roughness dependent magnetic hysteresis of a few monolayer thick Fe films on Au(001)

Y.-L. He[a] and G.-C. Wang
Department of Physics, Rensselaer Polytechnic Institute, Troy, New York 12180-3590

We have studied quantitatively the surface and interface roughness of Fe films in a few monolayer regime on an Au(001) surface using the high-resolution low-energy electron diffraction technique. The hysteresis loops of those films were also measured *in situ* by the surface magneto-optical kerr effect technique. A correlation between the shape of hysteresis loops and the roughness of films was observed. The hysteresis loops are consistently squarelike for films with a two-dimensional (2D) smooth structure. For films with isolated three-dimensional (3D) islands structure, the hysteresis loops are typically stripelike. For films with a combination of 2D/3D structure, the loop shape is squarelike for longitudinal loops and stripelike for polar loops.

I. INTRODUCTION

The study of the relationship between ultrathin film morphology and magnetic properties on the atomic scale is a challenging subject. The magnetism is an electronically driven phenomenon. It depends not only on the arrangements of electrons in an atom but also on the structural arrangement of atoms in an ultrathin film. Advances in sample preparation techniques and availability of atomic scale characterization techniques have made it possible to prepare ultrathin films in a variety of structures.[1] If the magnetic property of films with known structure is measured, then the possibility of obtaining magnetic ultrathin films with desired characteristics increases.

Previous experimental studies on magnetic properties of ultrathin Fe films grown on an Au(001) surface under various growth conditions have been reported. For example, Liu and Bader[2] have observed perpendicular magnetic anisotropy in the Fe/Au(001) films grown at 100 K with thickness less than 2.8 monolayer (ML). In contrast, Fe/Au(001) films grown at room temperature have been shown to exhibit in-plane easy axes in the monolayer regime.[3,4] However, quantitative information on the roughness and structure of the as-grown films and their effects on magnetic properties are still lacking. In this article, we show there exists a strong dependence of magnetic hysteresis loops on the roughness of ultrathin Fe/Au(001) films in a few ML regime. There are three kinds of film roughness, two-dimensional (2D) smooth and continuous, three-dimensional (3D) isolated islands, and a mixture of 2D/3D, that can be prepared at room temperature by changing the deposition rate.

II. EXPERIMENT

All the experiments were performed in an ultrahigh vacuum chamber with a base pressure of 1×10^{-10} Torr. The chamber was equipped with surface magneto-optic kerr effect (SMOKE), high-resolution low-energy electron diffraction[5] (HRLEED), and Auger electron spectroscopy (AES) techniques. The details of our SMOKE setup have been presented elsewhere.[6] The magnetic field can be aligned either perpendicular or parallel to the sample surface by rotating the electromagnet 90° *in situ*. This allows the measurement of longitudinal and polar Kerr loops using the same electromagnet.

The perfection of the Au(001) substrate was characterized by angular profile measurements of diffraction beams from the surface. On a well-annealed surface, the size of ordered regions ranges from ~400 to ~600 Å. Ultrathin Fe films were prepared by thermal evaporation of Fe atoms from an Fe foil heated to ~1200 °C by electron bombardment. The growth rate and roughness of films were determined by analyzing the changes of angular profiles of the (00) diffraction beam measured from the Fe films/Au(001).

III. RESULTS AND DISCUSSION

A. Film growth and morphology

To monitor the growth morphology using HRLEED, we measure the change of angular profiles near an out-of-phase diffraction condition of film-substrate system during deposition. This is because the destructive interference of electrons is most sensitive to a surface or a film containing steps.[7] For example, if electrons scattered from adjacent terraces separated by a step of height d are out of phase, i.e., the electron path length is a half-integer number of the electron wavelength λ, then the diffraction intensity at the Bragg position decreases. The angular profile will broaden. This destructive interference condition is $d\cos\theta=\lambda/2$, where the θ is the angle of incidence and angle of diffraction for the specular diffraction beam and $\lambda=[150.4/E(\text{eV})]^{1/2}$. Reference 8 lists calculated and measured energies for the out-of-phase condition for the clean Au and Fe-Au systems.

The Fe films of a few ML thickness are prepared by the experience gained from the submonolayer growth.[8] Basically, the line shape of angular profiles broadens from that of the clean surface profile and then narrows with accumulated deposition time. At 110 s, the angular profile becomes nearly the same as that of the initial time. From the diffraction point of view, the Fe/Au(001) surface is virtually identical to the clean Au surface. We thus assign the Fe coverage as ~1 ML at 110 s, implying the growth rate is ~0.55 ML/min. The growth rate can be doubled by increasing the source temperature by 20 K. In this range of deposition rate, the growth mode is essentially layer-by-layer as evidenced by the full-

[a]Present address. Physics Department, University of Nebraska-Lincoln

 0021-8979/94/76(10)/6446/3/$6.00 © 1994 American Institute of Physics

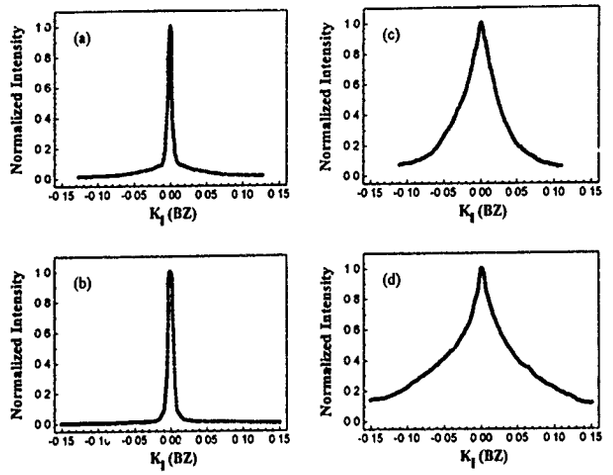

FIG. 1. Angular profiles of the (00) beam measured from Fe/Au(001) films: (a) and (b) 2D with ~2.0 ML coverage; (c) and (d) 3D film with ~2.1 MLE coverage. The energies of 27.5 eV (a) [28 eV for (c)] and 44 eV (b) [same for (d)] are near the out-of-phase conditions for Au-Fe and Fe-Fe steps, respectively. The $K_{\parallel}$ is the momentum transfer parallel to the surface and is in units of Brillouin zone [BZ=2π/(2.88 Å)].

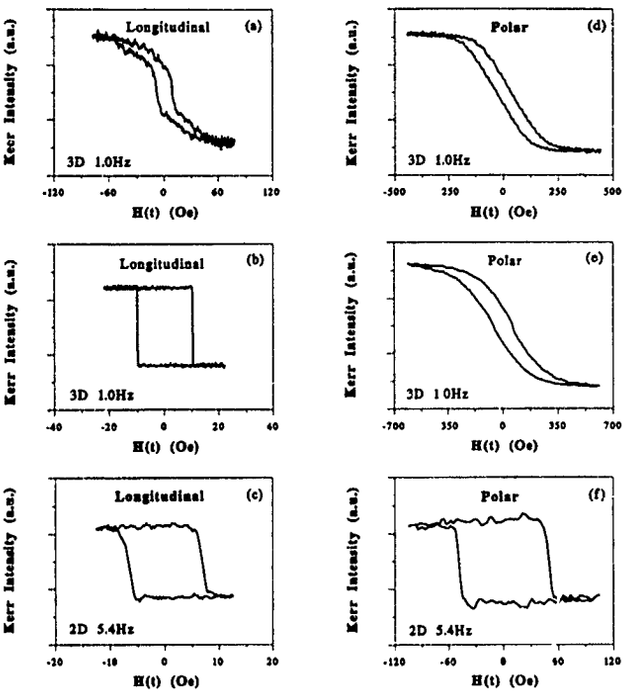

FIG. 3. Longitudinal and polar hysteresis loops measured from Fe films with various roughness as sketched in Fig. 2: (a) and (d) for 3D isolated islands, ~2.1 MLE; (b) and (e) for 3D islands on 2D smooth film, ~3.7 MLE; and (c) and (f) for 2D smooth film, ~2.0 ML. Note the arbitrary units in the Kerr intensity.

width-at-half-maximum (FWHM) oscillation and a smooth continuous film, denoted as 2D film, persists up to ~3 ML. It then crosses over to a 3D island growth mode. The angular profiles (raw data) near the out-of-phase conditions of Fe-Au (27.5 eV) and Fe-Fe (44 eV) from a 2D film of ~2 ML are shown in Figs. 1(a) and 1(b). Both profiles do not broaden significantly compared to that of the clean Au surface and indicate a relatively smooth and continuous film with low density of steps as sketched in Fig. 2(c).

If the growth rate was reduced below ~0.2 ML/min, 3D island growth occurs. There was no oscillatory behavior observed in the line shape of angular profiles with accumulated time as that observed in 2D layer-by-layer growth. Instead, the FWHM at the out-of-phase condition monotonically increases with time (not shown here). This is a characteristic of 3D growth. The rate dependence of growth mode is due to the growth kinetics and has been discussed elsewhere.[9] Figures 1(c) and 1(d) show the profiles measured near the out-of-phase conditions of Fe-Au (28 eV) and Fe-Fe (44 eV) from a film with ~2.1 ML equivalent (MLE) coverage. Comparing the profiles of Figs. 1(c) and 1(d) with that of Figs. 1(a) and 1(b), the profiles of Figs. 1(c) and 1(d) are considerably broader. A complete energy-dependent FWHM measurement shows maximum broadening peaks at ~28 and ~43 eV.[9,10] This result is consistent with the calculated destructive interference energy.[8] The coexistence of two types of steps (Fe-Au and Fe-Fe) supports that the film was grown in a 3D mode. The amount of broadening is inversely proportional to the average terrace width.[7] From the FWHM shown in Figs. 1(c) and 1(d), we estimate that the average terrace of isolated islands is ~60 Å. Also, the profile shape measured at the Fe-Fe out-of-phase is consistent with that from a multilayer thick film. A film with ~2.1 MLE coverage consisting of 3D islands isolated by nonmagnetic Au substrate is sketched in Fig. 2(a). The lateral size of the islands near the interface is smaller than the terrace of Au substrate (shaded area of ~400–600 Å). With sufficient amount of Fe deposits, e.g., ~3.7 MLE, the substrate is entirely covered by the film as sketched in Fig. 2(b).

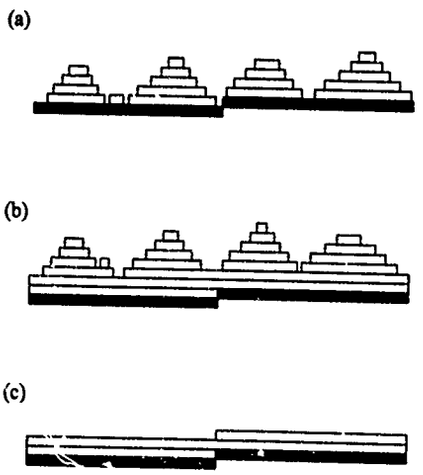

FIG. 2. Schematics of three ultrathin Fe/Au(001) films: (a) ~2.1 MLE, 3D isolated islands; (b) ~3.7 MLE, 3D continuous islands; and (c) ~2.0 ML, 2D continuous and smooth. The shaded area denotes the substrate (with a step), and the unshaded area denotes the films.

B. Magnetic hysteresis loops

Figure 3 shows hysteresis loops measured from two kinds of 3D films (~2.1 and ~3.7 MLE) and a 2D smooth film of ~2 ML. The polar loops measured from both 3D films are typically stripelike as shown in Figs. 3(d) and 3(e). However, the shape of longitudinal loops for the 3D films

depends on the film coverage. The longitudinal loop measured from ~2.1 MLE film is stripelike as shown in Fig. 3(a) but is square like for ~3.7 MLE film. In contrast there is no coverage-dependent loop shape for 2D films. The loops are squarelike in both directions as shown in Figs. 3(c) and 3(f).

Various shapes of hysteresis loops can be related to various film morphologies as follows. For a continuous and smooth film, the squarelike hysteresis loop shown in Fig. 3(c) is consistent with that of the dominant magnetization reversal process in the wall displacement and the easy axis is oriented in the surface plane. Due to the cubic symmetry observed in Fe film, the easy axis can also be oriented along the surface normal. Therefore, the polar hysteresis loop is also squarelike. See Fig. 3(f).

The stripelike shape of the hysteresis loops shown in Figs. 3(a) and 3(d) is consistent with the loop shape measured from single domains with various shapes and sizes. Note that from the 1×1 LEED pattern we learn that each Fe island has an epitaxial relation with respect to the Au(001) substrate, i.e., bulk bcc Fe lattice rotates 45° with respect to the fcc Au lattice. This rotation minimizes the lattice mismatch to less than 0.5%. The magnetization process involves rotation of spins in each single domain which requires larger applied field to reverse the spins and saturate the domains as compared with just domain wall movement. Each isolated ferromagnetic Fe island on the Au substrate may have its own demagnetization factor. The demagnetization factor depends on the structural shape and size of the Fe island. From the profile measurement we know the 3D film has a distribution of island size and height, therefore the demagnetizing field which is opposite to the applied field has various magnitude. When an external magnetic field is applied on the positive direction in either longitudinal or polar configuration, the domains magnetized in the opposite direction will be eliminated first. A further increase of the external field would rotate all domains into a saturation state at various external field strength.

The distinct shapes of hysteresis loops shown in Figs. 3(b) and 3(e) obtained in longitudinal and polar configurations result from a nearly in-plane magnetic anisotropy. The magnetic remanence is nearly the same as the saturation magnetization in the longitudinal direction which indicates that the easy axis is in the surface plane. In a polar configuration, the external field is perpendicular to the in-plane easy axis, which often leads to nearly linear hysteresis loop. However, for the 3D/2D film [Fig. 2(b)], there exist some isolated Fe islands which behave like the case of 3D islands sketched in Fig. 2(a) and contribute to the stripelike, or less linear loop shape. The conclusion of in-plane easy axis from our data is consistent with results from other experimental studies,[3,4] although the details of film morphologies were not presented.

Our result of anisotropy is not inconsistent with the prediction of perpendicular magnetic anisotropy for a free standing Fe ML.[11] At 1 ML, the easy axis is perpendicular to the surface. With increasing coverage (e.g., 2 ML), however, the demagnetization field tends to bring the easy axis to the surface plane. As a result, the hysteresis behavior in both polar and longitudinal configurations is similar to that observed in 2D flat films. That the easy axis is along the surface plane is also consistent with the smaller value of coercive field measured in the longitudinal direction compared with that in the polar direction. For 3D island films, the local variation of the demagnetization complicates the hysteresis behavior.

IV. CONCLUSIONS

Our study of both film morphology and hysteresis loop indicates that the shape of a loop is closely related to the roughness of a film. For a smooth film, one is most likely to observe squarelike loops [Figs. 3(c) and 3(f)]. For an isolated 3D islands film, one is likely to observe stripelike loops [Figs. 3(a) and 3(d)]. For films with continuous islands, the loops in the longitudinal configuration are squarelike. However, the loops in the polar configuration remain stripelike.

ACKNOWLEDGMENTS

We thank Professor S.-H. Liou and Professor J.-P. Woods for valuable discussions. This work was supported by the ONR under Grant No. N00014-91-J-1099.

[1] For a review, see L. M. Falicov, D. T. Pierce, S. D. Bader, R. Gronsky, K. B. Hathaway, H. J. Hopster, D. N. Lambeth, S. S. P. Parkin, G. Prinz, M. Salamon, I. K. Schuller, and R. H. Victora, J. Mater. Res. **5**, 1299 (1990).
[2] C. Liu and S. D. Bader, J. Vac. Sci. Technol. A **8**, 2727 (1990).
[3] S. D. Bader, E. R. Moog, and P. Grunberg, J. Magn. Magn. Mater. **53**, L295 (1986).
[4] W. Dürr, M. Taborelli, O. Paul, R. Germar, W. Gudat, D. Pescia, and M. Landolt, Phys. Rev. Lett. **62**, 206 (1989).
[5] U. Scheithauer, G. Meyer, and M. Henzler, Surf. Sci. **178**, 441 (1985).
[6] J.-P. Qian and G.-C. Wang, J. Vac. Sci. Technol. A **8**, 4117 (1990).
[7] M. Henzler, in *Electron Spectroscopy for Surface Analysis*, edited by H. Ebach (Springer, Berlin, 1977).
[8] Y.-L. He and G.-C. Wang, Phys. Rev. Lett. **71**, 3834 (1993).
[9] Y.-L. He, Ph.D thesis, Rensselaer Polytechnic Institute, Troy, NY, 1993.
[10] F.-Y. Liew, Y.-L. He, A. Chan, and G.-C. Wang, Surf. Sci. **273**, L461 (1992).
[11] J. G. Gay and R. Richter, Phys. Rev. Lett. **56**, 2728 (1986); C. L. Fu, A. J. Freeman, and T. Oguchi, *ibid.* **54**, 2700 (1985); D. S. Wang, Bull. Am. Phys. Soc. **38**, 370 (1993).

Fluctuation effects in ultrathin films

S. T. Chui
Bartol Research Institute, University of Delaware, Newark, Delaware 19716

We discuss finite temperature fluctuation of the domain walls and the magnetization **M** in ultrathin magnetic films where spins interact with short range exchange (J), anisotropy (K), and long range dipolar (g) couplings. Phase boundaries for a triangular lattice are obtained from Monte Carlo simulations as a function of J, g, and K. The transition temperature for the disappearance of the z magnetization as a function of the effective anisotropy field $K-g/0.1208$ is essentially unchanged as g becomes zero. This suggests a new physical picture that the change in the direction of **M** is closely connected with the Ising transition for $g=0$. Mean field calculation suggests *three* transitions where only M_z is finite at low temperature. As the temperature is increased (1) M_x becomes nonzero, (2) M_z becomes zero and eventually, (3) M_x becomes zero. To investigate fluctuation of domain walls their elastic energy are calculated. For Bloch walls perpendicular to the x axis separating spins along the z axis this energy is *negative* for a small enough wave vector. The competition of the stabilizing long range dipolar interaction and low dimensional fluctuation suggests the possibility of a finite temperature roughening of an array of one-dimensional Néel walls in the film.

I. MAGNETIZATION

In the ultrathin magnetic films, new physics occurs because of the competition between the stabilizing *long range* dipolar interaction and the *low dimensionality* fluctuation effects.[1] An example of this competition is provided for by the question of the existence of long range order. For two-dimensional (2D) systems, the fluctuation of the magnetization is of the order of $\int d^2qkT/\omega_q$. When the spins interact only with nearest neighbor exchange, $\omega_q \propto q^2$; the fluctuation is infinite and there is no long range order.[1] When the long range dipolar interaction is included, $\omega_q \propto q$ for some spin arrangements. The fluctuation becomes finite and long range order is restored.[2,3]

The interaction energy between the spins is $H=0.5\ \Sigma_{ij=xyz,RR'} V_{ij}(R-R')S_i(R)S_j(R')$ where $V=V_d+V_e+V_a$ is the sum of the dipolar energy $V_{dij}(R)=g(\delta_{ij}/R^3-3R_iR_j/R^5)$; the exchange energy $V_e=-J\delta(R=R'+d)\delta_{ij}$; and the anisotropy energy $V_a=-2K\delta(R=R')\delta_{iz}\delta_{jz}$. Here d denotes the nearest neighbors. For the experimental systems, J is much larger than g and K. However, without g and K there is no long-range order at any finite temperatures. We have studied the phase diagram (Fig. 1) as a function of the parameters J, K, and g for a triangular lattice with Monte Carlo simulations on a 60×60 lattice for 1.6×10^9 MC steps. The transition temperature is determined from the peak position of the magnetic susceptibility with a histogram technique.[4] We found that for small $K-g$, the transition temperature for the vanishing of M_z can be well approximated by $J/T_c=A+B\ \ln(\Delta/J)$ for constants A and B. Here Δ is the effective spin-wave gap energy given by $\Delta=K-g/0.12$. In the absence of the dipolar interaction ($g=0$), the magnetization disappears in the high temperature phase above T_c. $T_c=0$ for $K=0$ because of two-dimensional fluctuations. For $g\neq0$, there is an intermediate phase where the magnetization changes from perpendicular to in-plane above T_c, as is first observed experimentally.[5-8] *The constants A and B are unchanged to within the accuracy of the present calculation* (≈2%) *as g becomes nonzero.* This suggests a new physical picture, different from that of previous considerations,[9-11] that the driving force behind the change in the direction of the magnetization is the same as that causing the Ising transition for $g=0$ when the z magnetization disappears at a high enough temperature. After the z magnetization vanishes, the in-plane magnetization can still be stable in two-dimensional (2D) over a temperature range if the dipolar coupling is finite because of its long range nature. The temperature at which the x magnetization disappears depends mostly on only g and very little on K.

Allenspach and Bishof[8] observed that there are regions in temperature so that the in plane and the z-axis magnetization are both nonzero. We think that there are actually *two*

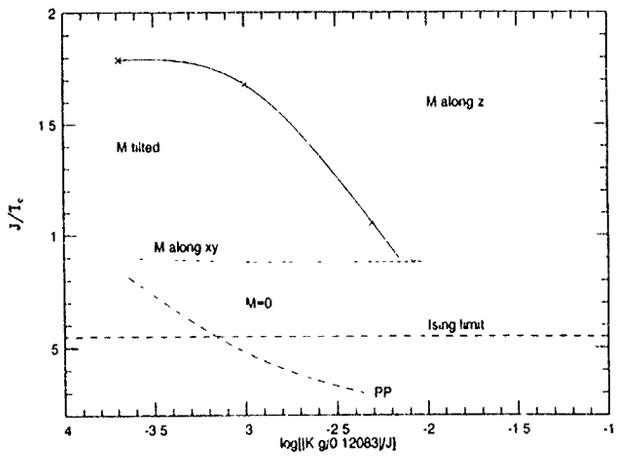

FIG. 1. Inverse transition temperatures for $g=0.12$ and different values of K. The different phases are as labelled. Lines are drawn connecting the points to guide the eye. The dotted line on the lower left corner is the theoretical results of Pescia and Prokrovsky; the horizontal line at the bottom is the asymptotic limit corresponding to the transition of the 2D triangular lattice.

 0021-8979/94/76(10)/6449/3/$6.00 © 1994 American Institute of Physics

transitions around T_c; one associated with the onset of the in-plane magnetization and the other one associated with the disappearance of the z-axis magnetization. The occurrence of a finite in plane magnetization depends on two issues. That the magnetization is not *completely* aligned along the z axis and that the fluctuation in the azimuthal direction is not infinite. These two transitions can be understood in more detail from a mean-field argument. Specifically, we assume the presence of two order parameters M_x and M_z and ask if these magnetizations can be self-consistently sustained. We get

$$M_x=\int_{-1}^{1} d\mu(1-\mu^2)^{0.5}\exp(-\beta E_z)I_1(\beta E_x)/Z';$$

$$M_z=\int_{-1}^{1} d\mu\ \mu\exp(-\beta E_z)I_0(\beta E_x)/Z';$$

$$Z'=\int_{-1}^{1} d\mu\exp(-\beta E_z)I_0(\beta E_x),$$

$$E_z=-K\mu^2-6J\mu M_z-g\mu M_z/0.75g_1,$$

$$E_x=(1-\mu^2)^{0\,5}(6J+0.5gc)M_x,$$

$\beta=1/kT$. When M_z is large, the spins are favored to align along the z axis with μ close to 1. A solution for M_x does not exist. When M_z is small *but not zero*, a solution for M_x is possible. The requirement that M_z be small restricts this onset of in-plane magnetization to close to T_c. In the limit of small M_x, the equation for M_z is similar to that in the 2D Ising model. Linearizing the equation for M_x we obtain the transition temperature T_2 for its onset as

$$T_2=(6J+0.5gc)\int d\mu\exp(-\beta E_z)(1-\mu^2)/2Z'',$$

where $Z''=\int d\mu\exp(-\beta E_z)$. A solution is possible even when M_z is nonzero. This implies that the onset of in-plane magnetization is distinct from the disappearance of the z axis magnetization. Detail numerical solutions of the mean field equations confirm the above argument.

Pescia and Pokrovsky[9] (PP) proposed that the spin-rotation transition temperature is given by $T_c=K^{-1}(K-g/g_1)12\pi J/\ln(3J/K)$. Their magnitude and functional dependence are very different from the Monte Carlo results. While no details of their calculation is available, we think the difference between their calculation and the present picture come from different assumptions of the fixed point Hamiltonian. More precisely, one can write the Hamiltonian in increasing power of q as

$$H=\Sigma_q-\Delta|S_z(q)|^2+\Sigma_{i,j=x,y}J_1q^2|S_q|^2+J_2q|S_z(q)|^2$$
$$+J_3\Sigma_{i,j=x,y}q_iq_jS_i(q)S_j(-q)/q$$

(Refs. 12 and 13) and follow the standard procedure[14,15] to derive renormalization group equations for the couplings Δ, J_i to first order in Δ/J_1, $J_{2,3}/J_1$. The bare dipolar coupling contributes to the initial values of Δ, J_1, and J_2, which possess different scaling trajectories ($n=3$):

$$d\Delta/dl=[2-(n-1)(T/2\pi J_1)]\Delta,$$

$$dJ_1/dl=-(n-2)T/2\pi-TJ_2/(32\pi J_1),$$

$$dJ_2/dl=[1-(n-1)T/J_12\pi]J_2/T,$$

$$dJ_3/dl=[1-(n-1)T/J_12\pi]J_3/T.$$

Thus it is not possible to have a single scaling equation for the dipolar coupling constant, as PP has assumed. Also, the functional form for the scaling equation for Δ does not depend on its initial value and thus, to first order in the small parameters g/J and K/J, remain the same whether the dipolar interaction is present or not; different from the conclusions of PP.

II. DOMAIN WALLS

Low-dimensional finite temperature fluctuation also affects domain walls. These effects are important in understanding domain formation, hysteresis and relaxation phenomena in the films. Whereas in three dimensional situations, domain walls are flat, recent experimental results[16–18] indicate that walls in ultra-thin films are not flat.

A magnetic domain wall is an interface between a spin-up region and a spin-down region. The statistical mechanics of interfaces have been actively studied over the last ten years. The movement of an interface usually proceeds not with the whole interface marching forward in unison but with part of the interface moving forward once at a time. This involves distorting the interface and thus the elastic energy and the roughness of the interface is an important consideration. The mobility of the interface in the presence of external pinning potentials is often discussed in terms of a roughening transition where the interfaces become rough and mobile if the temperature is higher than the roughening temperature. 2D interface in 3D systems roughens at a finite temperature.[19] 1D interfaces in 2D systems are always rough at any finite temperature. After the interface roughens, the free energy of steps becomes zero; the interface becomes mobile and the nature of the growth of domains becomes different. These studies assume that the interaction potential is short ranged.

The finite temperature statistical mechanics and dynamics of domain walls are often discussed in terms of a phenomenological model consisting of the elastic energy E_e to deform the wall and a pinning potential E_p that is due to the intrinsic periodic structure of the crystal lattice. For a deformation of wave vector q described by the displacement δr_q, the elastic energy is often assumed to be proportional to the strain squared, i.e., $E_e=A\Sigma_q q^2|\delta r_q|^2$. For magnetic domain walls in bulk materials, the physics is different. A Néel wall of width w located at position c is characterized by specifying the spin orientations at position $\mathbf{r}$ by the angles $\theta=\pi/2$, $\phi=\pi\tanh[(x-c)/w]/2$. The elastic energy is given by the domain wall energy change as c is changed by $\delta c=c_0[\cos(k.r)]$. In calculating this change, one ends up with the derivative of ϕ, which behaves like a δ function in the limit that the wave vector is less than the inverse domain wall width. We get $E_e=0.5\Sigma'_{RR'}V_{yy}(R-R')S_0^2(\delta c-\delta c')^2$. The prime on the summation indicates that we sum over those R,R' only at the $d-1$ dimensional undistorted wall position. V is proportional to the 2nd derivative of the $1/r$ Coulomb potential and is identical in form to the dynami-

cal matrix of the Wigner crystal in two dimensions, the Fourier transform of which can be summed with the Ewald sum technique.[20]

In the long wavelength limit the elastic energy is not proportional to q^2 but, because of the long range nature of the dipolar forces, is instead proportional to $|q|$ in 3D. In 2D, for magnetization in the plane, it is proportional to $q \ln(q)$ for a single 1D wall and to q/d for arrays of 1D domain walls separated by distances d. *Bloch walls perpendicular to the x axis separating domains with spins along the z axis are unstable against distortion in the long wavelength limit.*

Because of the different elastic behavior a 2D magnetic domain wall in 3D bulk systems is never rough at any temperature. On the other hand, in 2D films, a single wall in an n-layer system roughens at any finite temperature even when the dipolar interaction is included. For spins oriented along the y-axis separated by an *array* of Néels walls running perpendicular to the x axis a distance d apart, the problem can be related to the Knodo problem[21,22] via a Coulomb gas mapping.[19] The walls are flat for length scales less than d. There exist a temperature T_R above which the walls become rough. $T_R \approx 8\pi^2 g^2 \mu_B^2 n^2 a/d$ as the pinning strength approaches zero.

In conclusion, we presented in this article Monte Carlo results for the phase boundaries for ultrathin films as a function of the dipolar, z-axis anisotropy and exchange interactions. Our result suggests a new way of looking at the transition when the spins rotate into the plane. Renormalization group and mean field scenarios are discussed. We propose that there are three transitions associated with the disappearance of M_z and the onset and disappearance of M_x. We investigated finite temperature fluctuation of magnetic domain walls. For Bloch walls perpendicular to the x axis separating spins along the z axis this energy is *negative* for a small enough wave vector. The competition of the stabilizing long range dipolar interaction and low dimensional fluctuation suggests the possibility of a finite temperature roughening of an array of one dimensional Néel walls in the film.

This work is supported by the Office of Naval Research under Contract No. N00014-94-1-0213.

[1] N. D. Mermin and H. Wagner, Phys. Rev. Lett. **17**, 1133 (1966).
[2] Y. Yafet, J. Kwo, and E. M. Gyorgy, Phys. Rev. B **33**, 6519 (1986).
[3] R. P. Erickson, Phys. Rev. B **46**, 14 194 (1992).
[4] See, for example, K. Chen, A. M. Ferrenberg, and D. P. Landau, Phys. Rev. B **48**, 3249 (1993); A. M. Ferrenberg, in *Computer Simulation Studies in Condensed Matter Physics III*, edited by D. P. Landau, K. K. Mo, and H. B. Schuttler (Springer, Heidelberg, 1991).
[5] D. P. Pappas, K. P. Kamper, and H. Hopster, Phys. Rev. Lett. **64**, 3179 (1990).
[6] J. J. Krebs, B. J. Jonker, and G. A. Prinz, J. Appl. Phys. **63**, 3467 (1988).
[7] M. Stampanoni *et al.*, Phys. Rev. Lett. **59**, 2483 (1987).
[8] R Allenspach and A. Bischof, Phys. Rev. Lett. **69**, 3385 (1992).
[9] D. Pescia and V. L. Prokrovsky, Phys. Rev. Lett. **65**, 2599 (1990).
[10] P. J. Jensen and K. H. Bennemann, Phys. Rev. B **42**, 849 (1990).
[11] R. P. Erickson and D. L. Mills, Phys. Rev. B **46**, 861 (1992).
[12] For a discussion of the effect of the anisotropy and dipolar interaction in 3D systems, see A. Aharony, in *Critical Phenomena and Phase Transitions*, edited by C. Domb, M. Green, and J. Leibowitz (Academic, New York, 1980), Vol. 5.
[13] For a discussion of long range interactions in 2D Heisenberg systems, see J. Sak, Phys. Rev. B **15**, 4344 (1975).
[14] A. M. Polyakov, Phys. Lett. **59B**, 2483 (1987).
[15] R. Pelcovits and D. Nelson, Phys. Lett. **57A**, 23 (1976); D. Nelson and R. Pelcovits, Phys. Rev. B **16**, 2191 (1975).
[16] A. Berger, U. Linke, and H. P. Oepen, Phys. Rev. Lett. **68**, 839 (1992).
[17] J. Pommier, P. Meyer, G. Penissard, J. Ferre, P. Bruno, and D. Renard, Phys. Rev. Lett. **65**, 2054 (1990).
[18] P. Bruno *et al.*, J. Appl. Phys. **68**, 5759 (1990).
[19] S. T. Chui and J. D. Weeks, Phys. Rev. B **14**, 4978 (1976); Phys. Rev. Lett. **40**, 733 (1978).
[20] L. Bonsall and A. Maraduddin, Phys. Rev. B **15**, 1959 (1977).
[21] S. T. Chui, Phys. Rev. B **28**, 178 (1983), Appendix D.
[22] K. D. Schotte, Z. Phys. **230**, 99 (1970); see also, P. W. Anderson, *Basic Notions of Condensed Matter Physics* (Benjamin, New York, 1984).

Magnetic studies of fcc Co films grown on diamond (abstract)

J. A. Wolf,[a] J. J. Krebs, Y. U. Idzerda, and G. A. Prinz
Naval Research Laboratory, Code 6345, Washington, DC 20375

We report the first growth and characterization of fcc Co epitaxial films (t=10–130 nm) on diamond. Growth was carried out under UHV conditions in a commercial MBE machine and monitored during growth using RHEED which showed single crystal growth oriented with $\langle 100\rangle_{Co}\|\langle 100\rangle_{C}$. X-ray diffraction studies of the 130 nm sample demonstrated the single crystal fcc growth throughout the entire sample. Separate studies to determine growth mode and structure were carried out using angle-resolved Auger forward scattering. Vibrating sample and SQUID magnetometry yields a magnetic moment of $(1.05\pm0.1)\ 10^3$ emu/cm^3. Ferromagnetic resonance measurements carried out at 35 GHz yield a large cubic anisotropy K_1/M_S=(480±30)Oe and linewidth of only ΔH=100 Oe. Spin waves were observed in the thicker samples and the exchange constant determined to be $A_{Co}=1.09\times10^{-6}$ erg/cm. This work has been supported by the Office of Naval Research.

[a]NRC-NRL Research Associate.

A Monte Carlo study of the temperature dependence of magnetic order on ferromagnetic and antiferromagnetic surfaces: Implications for spin-polarized photoelectron diffraction (abstract)

F. Zhang, S. Thevuthasan,[a] R. T. Scalettar, R. R. P. Singh, and C. S. Fadley[b]
Department of Physics, University of California, Davis, California 95616

We have used Ising-model Monte Carlo calculations to study the magnetic order near cubic ferromagnetic and antiferromagnetic surfaces. The antiferromagnets were studied with and without frustrated next-nearest-neighbor interactions. Intralayer and interlayer spin-spin correlation functions have been calculated as a function of the relative coupling strength in the surface layer. If this coupling strength is more than a few times the bulk value, a distinct surface phase transition is observed at temperatures $T_{C,surf}$ or $T_{N,surf}$ that can be significantly above the corresponding bulk values, $T_{C,bulk}$ or $T_{N,bulk}$. These calculations suggest that previous spin-polarized photoelectron diffraction measurements on antiferromagnetic $KMnF_3(110)$[1] and $MnO(001)$[2] could in fact have been observing such surface transitions at $T_{N,surf}$ values of 2.7 and 4.5 times $T_{N,bulk}$, respectively.

Research sponsored by DOE, BES, Mat. Sci. Div. (Contract No. DOE-AC03-76SF00098) and ONR (Contract No. N00014-90-5-1457).

[a]Present address: Battelle Pacific Northwest Laboratory, Richland, WA 99352.

[b]Also at Materials Sciences Division, Lawrence Berkeley Laboratory, Berkeley, CA 94720.

[1]B. Sinkovic, B. D. Hermsmeier, and C. S. Fadley, Phys. Rev. Lett **55**, 1227 (1985).
[2]B. Hermsmeier, J. Osterwalder, D. J. Friedman, and C. S. Fadley, Phys. Rev. Lett. **62**, 478 (1989).

 0021-8979/94/76(10)/6452/1/$6.00 © 1994 American Institute of Physics

X-ray magnetic circular dichroism in the near and extended absorption edge structure (invited)

G. Schütz, P. Fischer, and K. Attenkofer
Institute für Experimental Physics II, University Augsburg, D 86135 Augsburg, Germany

M. Knülle, D. Ahlers, S. Stähler, and C. Detlefs
Physics Department E12, Technical University Munich, D 85747 Garching, Germany

H. Ebert
Institute für Physical Chemistry, University of Munich LMU, D 80333 Munich, Germany

F. M. F. de Groot
L.U.R.E, Bât. 209D, F 91405 Orsay, France

Magnetic circular dichroism (MCD) studies at K and L edges using hard and soft x rays are presented. The relation of this universal phenomenon in the x-ray absorption near-edge structure (XANES) and extended x-ray absorption fine structure (EXAFS) regions to local magnetic structures in the case of $3d$ and $4f$ elements is illustrated. The validity of atomic and band-structure pictures to describe the MCD in the XANES range are outlined and the applicability of sum rules and two-step vector coupling models to deduce spin and orbital moments of the absorbing atom as well as spin-density profiles from the experimental data are critically discussed. The correlation of the dichroic contribution in the EXAFS to the magnetic moments and spin densities of the neighboring atoms are addressed by systematic studies which provide new insights into the exchange phenomena of the interaction of spin-polarized electrons with ferromagnetic media. The potential but also the limitations of this new spectroscopy is demonstrated.

I. INTRODUCTION

X-ray circular magnetic dichroism (X-MCD) in core-to-valence transitions is a new powerful method to study in an element- and symmetry-selective manner the magnetic aspects of local electronic structures in magnetic media. The possibility of extracting local spin and orbital moments using "sum rules" deduced on the basis of an atomic approach[1,2] or in the local spin-density (LSD) formalism[3,4] by a comparison of the magnetic L_2- and L_3-dichroic spectra is one of the dominant subjects of interest. To date a correct interpretation of experimental spectra seems to be restricted to cases with either a localized character of the involved final states as, e.g., $3d$-$4f$ transitions in rare earth (RE) systems,[5,6] where an atomic picture[7] is adequate or to those with a delocalized behavior as, e.g., $1s$-$4p$ transitions in $3d$ elements and $2s$-$6p$ transitions in $4f/5d$ systems[8,9] and $2p$-$5d$ transitions in $5d$ elements,[3] where the band-structure approach has been adopted successfully.[10] For intermediate cases, however, as the $L_{2,3}$ edges in transition elements[5,11] and in REs,[9,12] a closed theoretical description is still a problem.

Although the occurrence of a dichroic contribution to the extended (EXAFS) [spin-polarized EXAFS (SPEXAFS)] has been proven to be a universal phenomenon,[4,13] theoretical calculations of the experimental spectra are not available but are on the way.[14] However, as demonstrated in the second part of this article, the systematics observed in several systems show that on the basis of simple two-step models interesting correlations of the SPEXAFS to the local magnetic short-range order can be found, which demonstrate the potential of this method to study magnetic structures on an atomic scale.

II. NEAR-EDGE MCD

A. Theoretical models

Large MCD effects (in some cases more than 20%) are found in the near-edge region within 20 eV above an absorption threshold. In this energy range the absorption cross section can be described by Fermi's golden rule.[15] In the case of bandlike final states, the single-particle density-of-states model describes the experimental spectra successfully. The energy dependence of the absorption cross section is given by the density profile of the final states with selected symmetry determined by dipole-selection rules times a nearly energy-independent matrix element. If the final states are well localized, two-particle interactions have to be included. These can be calculated explicitly using atomic multiplet[16] approaches. Here it is also possible to include solid state effects by adding crystal field terms to the Hamiltonian and hybridization of ligand character by an admixture of extra-atomic configurations such as in charge-transfer states.

In both cases, polarization effects and exchange splittings can be taken into account. Using fully relativistic spin-polarized Korringa–Kohn–Rostoker (KKR)–GF and linear muffin-tin orbital[10] band-structure approaches or spin-polarized versions of the linear augmented plane wave (LAPW) method,[7] the MCD L spectra of various heavier

 0021-8979/94/76(10)/6453/6/$6.00 © 1994 American Institute of Physics

transition metals such as magnetic $5d$ elements and Gd-metal have been successfully described in the single-particle picture, while on the other hand the experimental $M_{4,5}$-MCD spectra in RE systems are excellently reproduced by atomic calculations.[6]

On the basis of the atomic description sum rules have been developed recently,[1,2] which relate the difference and the sum of the dichroic signals ($\mu^{\pm}$) for reversed photon polarization $\mu_c := (\mu^+ - \mu^-)/2$ for the two spin-orbit initial states directly to the local spin and orbital moments of the partially filled final valence shell.

Based on a simple vector-coupling version of the band-structure approach, a similar relation between the normalized MCD spectra μ_c/μ_0 at the L_2 and L_3 edges times the unoccupied final state density and the local magnetic moments can be deduced.[4,9] Based on the Fano effect[8] the sensitivity of the dichroic signal to the spin and orbital moment originates from finite spin $\langle \sigma_z \rangle$ and orbital polarization $\langle l_z \rangle$ of the outgoing photoelectron in the propagation direction z of the circularly polarized photon. The photoelectron emitted from an unpolarized core state is thus considered as a polarized probe for the spin and orbital moment of the final states. The polarization values for a free electron wave are $\langle l_z \rangle = +3/4$ in an initial p state and $\langle \sigma_z \rangle = -1/2$ and $+1/4$ for the corresponding $p_{1/2}$ and $p_{3/2}$ spin-orbit partners.

In a simple spin-polarized version of Fermi's golden rule for pure spin-ferromagnetic systems,[8,9] the MCD signal is directly correlated to the spin density $\Delta\rho = \rho^+ - \rho^-$ of the final state by $[\mu_c/\mu_0](E) = \langle \sigma_z \rangle [\Delta\rho/\rho](E)$, which corresponds to $\mu_c(E) \sim -\Delta\rho(E)$ at the L_2 and $\mu_c(E) \sim +\Delta\rho(E)$ at the L_3 edges for $\mu_0(L_3) = 2\mu_0(L_2)$.[9]

Within the vector-coupling model the relation between the normalized MCD spectra μ_c/μ_0 and the spin and orbital moments is deduced to

$$\mu_S/\mu_B \sim -\tfrac{4}{3} \int \{[\mu_c/\mu_0]_{L_3}(E) - [\mu_c/\mu_0]_{L_2}(E)\} \rho(E) dE, \tag{1}$$

$$\mu_L/\mu_B \sim -\tfrac{4}{9} \int \{[\mu_c/\mu_0]_{L_3}(E) + 2[\mu_c/\mu_0]_{L_2}(E)\} \rho(E) dE. \tag{2}$$

Under the condition $\mu_0(L_3) = 2\ \mu_0(L_2)$ Eqs. (1) and (2) are equivalent to the sum rules, which are more appropriate in case of (nearly) isolated absorption profiles (white lines =WL) as, e.g., the $M_{4,5}$ edges in RE, while Eqs. (1) and (2) can be more easily applied in the case of more steplike absorption edges, e.g., the $L_{2,3}$ edges in heavier elements, without or with weakly indicated WL structure as in some RE and Pt and Au systems.

For K edges $\langle l_z \rangle$ amounts -1 and $\langle \sigma_z \rangle$ has the very small value of $\sim 10^{-2}$. Thus only weak MCD effects of less than 1% are expected for outer, bandlike final states with nearly quenched orbital moments, as, e.g., the $(4)p$ states in $3d$ elements or $(6)p$ in $4f/5d$ systems and no simple relation of the MCD profile and the local p moment exists.

B. Fe-metal layers

To demonstrate the reliability of the sum rules Eqs. (1) and (2), they are applied to $L_{2,3}$ MCD spectra of Fe-metal layers (cf. Fig. 1). The exact thicknesses of the 9.25 Å (A) and 24 Å (B) Fe layers (deposited on 300 Å Au on a glass substrate and protected by a 30 Å Al coverlayer) and the magnetic moments per atom of 2.07(3) μ_B for the thin (A) and 2.14(3) μ_B for the thicker sample (B) were determined via XFA and super conducting quantum interference device (SQUID) measurements, respectively.[20] The μ_c profiles are shown in Fig. 1(a) in addition to the spin-averaged μ_0 profile for the 9.25 Å (dashed line) and the 24 Å Fe layers (solid line). Corresponding theoretical spectra from fully relativistic spin polarized KKR calculation for iron metal are presented in Fig. 1(b).[10] The experimental data measured by total-yield detection in an applied external field of 0.2 T were taken at the DRAGON beamline (NSLS).

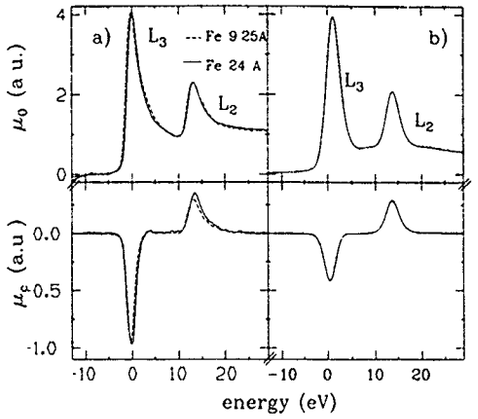

FIG. 1. Experimental absorption and dichroic profiles (a) at the Fe $L_{2,3}$ edges of Fe metal layers with thicknesses of 9.25 Å (dashed) and 24 Å (solid) in comparison with theoretical profiles from band-structure calculations (b). The experimental spectra correspond to raw and unsmoothed data with subtracted linear background.

Figure 1(a) shows, that the dichroic L_2 signal is significantly reduced relative to the L_3 signal causing a strong deviation from the ratio $\mu_c(L_2)/\mu_c(L_3) = -1$ expected for pure spin moments. This indicates the existence of an orbital moment coupled parallel to the spin moment [Eq. (4)]. Applying the sum rules one deduces a spin and orbital moment of $m_S \sim 2.19\mu_B$ $(2.29\mu_B)$ and $m_L \sim 0.25\mu_B$ $(0.21\mu_B)$ for samples A (B) taking into account $n = 4$ holes in the $3d$ level. The errors of these numbers due to the uncertainties of estimating the white line areas amounts to 20%. Very similar, somewhat smaller values of $m_S \sim 2.02\mu_B$ $(2.08\mu_B)$ and $m_L \sim 0.20\mu_B$ $(0.15\mu_B)$ (uncertainty about 5%) are found by applying Eqs. (3) and (4) using theoretical density of states profiles with an integrated value of $\int \rho(E) = 3.1$. These results are in excellent agreement with the results of the macroscopic measurements and confirm the expected increase of m_L with decreasing layer thickness.

Only the absolute values of m_L are larger than expected from theory and other measurements.[21] The spin polarized KKR calculation of the μ_0 and μ_c spectra seems to underestimate the values of μ_c and μ_0 at the L_2 edges, which could be an indication for the breakdown of the single-particle approach, as has been found for the $L_{2,3}$ MCD in the lighter $3d$ transition metals.

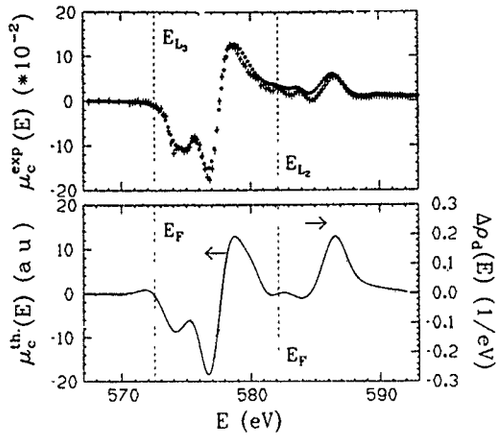

FIG. 2. Top: experimental dichroic absorption of CrO_2 at the L_3 and L_2 edges of chromium, measured at the SX700/3 (BESSY) (O) and DRAGON beamlines (NSLS) (+) with energy resolutions of about 900 and 500 meV, respectively. From the raw data only a constant offset has been subtracted. Bottom: theoretical dichroic absorption at the L_3 and L_2 edge of CrO_2, given by LMTO calculation (—) and the spin density of the $3d$ band above the Fermi level, given by LAPW band-structure calculations. The L_2 edge is rescaled by (-1) due to the negative photoelectron polarization. The vertical lines (···) mark the energy of the L_2 and L_3 edges, which are identical to the Fermi levels of the plotted spin densities.

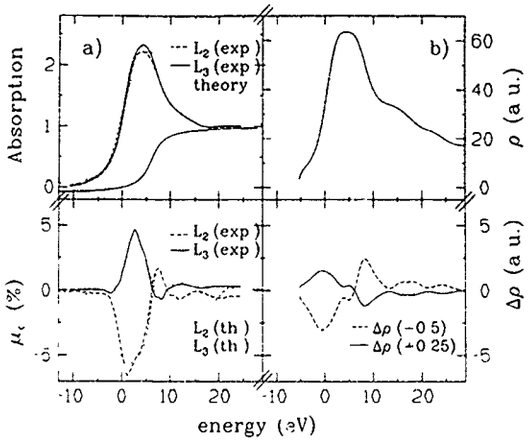

FIG. 3. (a) Experimental L_2 (dashed) and L_3 (solid) absorption (μ_0) (top) and corresponding dichroic profiles (μ_c) (bottom) of Gd-metal in comparison with theoretical unpolarized (dash-dotted) (top) and L_2 (dash-dotted), L_3 (dots) polarized profiles (bottom). The first inflection point of the absorption onset is chosen as the origin of the energy scale. The experimental absorption step is fitted by an arctan function (width 4 eV). (b) Theoretical total d spin-density profiles ($\rho=\rho^+ + \rho^-$) (top) and corresponding difference (b) ($\Delta\rho=\rho^+ - \rho^-$) broadened by core hole lifetime and experimental resolution and rescaled by -0.5 and $+.25$ at the $L_{2,3}$ edges, respectively. The dash-dotted line represents the theoretical MCD profile.

C. Cr $L_{2,3}$ MCD spectra

Going to lower Z within the $3d$ series due to the decrease of the $2p$ spin-orbit splitting below 10 eV it is difficult to separate the corresponding L_2 and L_3 parts in the spectra as seen in case of the Cr MCD in the half-metallic ferromagnet CrO_2 presented in Fig. 2. The dichroic profile is much more complex than in the heavier transition metals and even changes sign within the L_3 contribution. A comparison with the calculation of the dichroic effects for transition metal ions in the atomic approach[22] suggests that these models are more appropriate to reproduce the experimental findings and thus we have used a ligand field multiplet model (LFM), which includes the influence of the cubic crystal field on the local wave functions.[23] Setting the spin-orbit splitting to zero gives a reasonably good agreement between theory indicating the validity of the theoretical concept for the description of the MCD effects. The vanishing influence of an orbital momentum and correlated spin-orbit effects can also be verified by the application of the sum rules, which gives an upper limit of m_L of less than $10^{-2}\mu_B$. It can also be seen from the MCD spectra that it is difficult to deduce the corresponding spin moment in case of too close, i.e., not well resolved, $L_{2,3}$ absorption edges. That the LSD approach and the model Eqs. (1) and (2) are based on fails can be demonstrated by a comparison of the local unoccupied spin density of states $\Delta\rho$ shifted to the absorption edge with the μ_c profile, which show only rather poor similarities.

D. $L_{2,3}$ MCD in Gd-metal and $Eu_3Fe_5O_{12}$

Dichroic $L_{2,3}$ effects of several percent in REs have been found in all systems investigated up to now. Theoretical descriptions, however, have concentrated on Gd, as the fully relativistic band-structure approach by Ebert[10] and the calculations carried out by Carra *et al.*[17] which were also extrapolated to heavier RE metals.

However the description of the REs with nonzero $4f$ angular momentum is still an open problem. In particular the structures at the L_3 edges at negative energies, characteristic for all systems except Gd, have been proven to exhibit an atomic character.[24]

Although the ratios of the normalized Gd $L_{2,3}$ MCD profiles (both peak values and integrated areas) as seen in Fig. 3 are close to -2, i.e., the ratio of the spin-polarization factors, applying the sum rules Eqs. (1) and (2) leads to a spin moment of $-0.24\mu_B$ having the opposite sign compared to the theoretical calculations, which predict $\mu_S=+0.47\mu_B$ for the spin and $\mu_L=-0.04\mu_B$ for the orbital d moment.[25] The sum rules yield for the orbital moment a value of $-0.004\mu_B$ which is a factor of 10 too small compared with the theoretical prediction. Similar results are obtained even in the naive vector-coupling model ($\mu_S=-0.19\mu_B$ and $\mu_L=-0.002\mu_B$).

A direct comparison of the unbroadened theoretical Gd MCD profiles with unbroadened spin densities (Fig. 4) explains the breakdown of the validity of the basic assumptions Eqs. (1)–(2) are based on. Though the fine structures of the profiles coincide roughly, indicating a direct correlation between μ_c/μ_0 and $\Delta\rho/\rho$, the value of $\langle\sigma_z\rangle$ obviously becomes strongly energy dependent, amounting, e.g., to a value twice as high at the Fermi energy. Hence the small positive spin density leads to a strong line in the $L_{2,3}$ MCD spectrum at E_F and a negative spin moment.

The physical origin is a strong energy and spin dependence of the matrix element, since close to E_F the overlap of initial and final spin-up wave functions is much larger for the

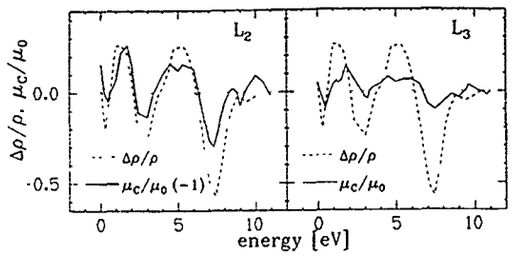

FIG. 4. Unbroadened theoretical $\Delta\rho/\rho$ profiles (dashed) and unbroadened theoretical μ_c/μ_0 profiles (solid) at the L_2 (left) and L_3 (right) edges in Gd-metal. The ratio $(\Delta\rho/\rho)/(\mu_c/\mu_0)$ is not constant with energy.

corresponding states of minority character, a fact, which has to be neglected in the models. But the MCD calculations (shown in Fig. 3) using the single particle band-structure approach reproduces this behavior exactly.

Applying the sum rules in the case of Eu $L_{2,3}$ MCD spectra (Fig. 5) in $Eu_3Fe_5O_{12}$ yields a spin moment of $-0.03\mu_B$ and an orbital moment of $+0.005\mu_B$. The moments obtained in the naive vector-coupling model amount to $-0.03\mu_B$ for the spin and $+0.007\mu_B$ for the orbital contribution. However, similar to Gd, these values lead to the wrong sign for the spin, which can again be drawn back to matrix-element effects. On the other hand, the expected opposite signs of μ_L and μ_S, induced in the $5d$ state by the intra-atomic $4f$-$5d$ coupling in lighter REs, seems to be directly manifested in the collapse of the L_3 MCD to the credit of a strong L_2 dichroic signal.

III. MAGNETIC EXAFS

A. Theoretical aspects

A phenomenological description of the measured effects is presented based on the simple vector-coupling "two-step" model, which has successfully been used to describe the near-edge MCD in the "spin-only" limit. In the first step, we assume that a free electron wave is going out with a spin

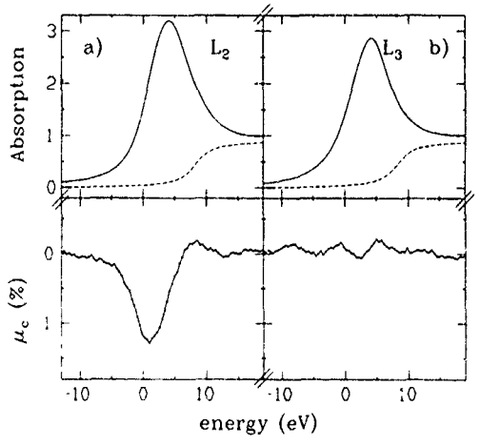

FIG. 5. (a) Experimental L_2 (a), L_3 (b) absorption (μ_0) (top) and dichroic profiles (μ_c) (bottom) of Eu in $Eu_3Fe_5O_{12}$. The absorption step is fitted by an arctan function (width 4 eV).

projection $\langle\sigma_z\rangle$ in photon-beam direction. If the magnetic moment of the neighboring atom, i.e., the spin of its majoritylike electrons, is also polarized in z direction, an exchange contribution to the Coulomb scattering potential is present in the scattering processes of the outgoing photoelectron. This should result in a magnetic contribution to the backscattering amplitude, which changes its sign with reversing the relative orientation of the photoelectron spins and the spins of the magnetic neighbors in the absorption process. In the conventional EXAFS formula the effect of exchange interaction in the scattering process is described by an additive exchange contribution (with index c) to the Coulomb-interaction parameters, i.e., the backscattering amplitude $F=F_0\pm F_c$, the phase shift $\phi=\phi_0\pm\phi_c$ and the mean free path $\lambda=\lambda_0\pm\lambda_c$. The strengths of the exchange contribution are within this simple model expected to scale directly with the spin-polarization parameter, i.e., $\langle\sigma_z\rangle\sim F_c, \phi_c, \lambda_c$.

Thus the conventional EXAFS (χ_0)[41] as function of the photoelectron de-Broglie wave-number k, which are described by a summation over the coordination shells located at distances r_j with N_j neighboring atoms and including the Debye–Waller factor D_j and "shake-off/on" processes at the central atom i (S_i), is transferred into a spin-polarized expression $\chi_c=\chi^+-\chi^-$ by

$$\chi_c(k)=\sum_j N_j S_i(k) D_j(k)\frac{e^{-2r_j/\lambda_{jo}}}{kr_j}\left(F_{jc}\sin(2kr_j+\varphi_{ijo})+\varphi_{ijc}F_{jo}\cos(2kr_j+\varphi_{ijo})+\frac{2r_j\lambda_{jc}}{\lambda_{jo}^2}F_{jo}\sin(2kr_j+\varphi_{ijo})\right). \quad (5)$$

B. Experimental results

1. $L_{2,3}$ SPEXAFS

SPEXAFS studies in the hard x-ray range have been performed in the transmission mode at HASYLAB (Hamburg) in various magnetic systems at the L edges in REs and $5d$ elements and at the K edges of $3d$ systems.[4]

For an analysis of the EXAFS and accordingly of the SPEXAFS to deduce structural information as, e.g., the distances r_j of next atoms and the coordination numbers N_j a sufficiently extended range of the $\chi_{0/c}$ spectra is Fourier transformed. Thus, this method is often not well practicable for energetically close following $L_{2,3}$ edges in $3d$ elements. This holds especially for the SPEXAFS analysis, since according to the simple picture the magnetic oscillation at the L_2 and L_3 edges should show identical structures but with opposite sign, which is found in all systems studied up to now as demonstrated in Fig. 6 at the Eu $L_{2,3}$ edges in the ferromagnetic Eu iron garnet ($Eu_3Fe_5O_{12}$).

If one takes into account a ratio of the amplitudes of -2, the χ_c profiles at the L_2 and L_3 edges are identical. The corresponding near-edges MCD signals (Fig. 5), behave completely different due to their dependence on the orbital moment. This proves that similar effects of the orbital polarizations can be neglected in the SPEXAFS interpretation. Only an additional contribution due to the small near-edge MCD at the iron K edge causes some deviation at the L_3

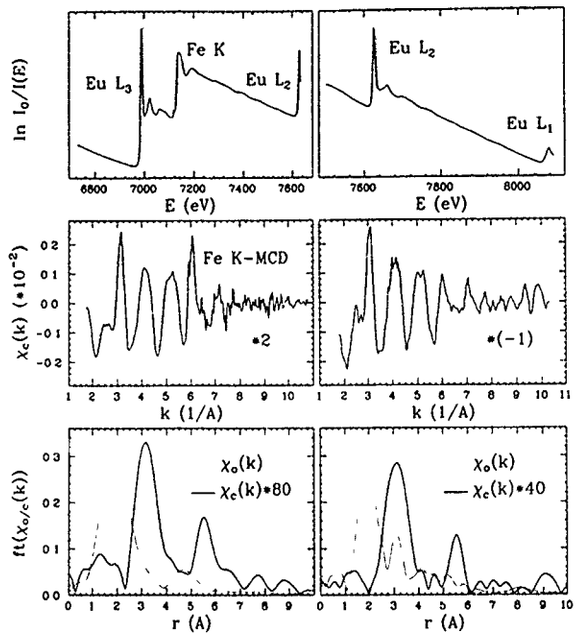

FIG. 6. Top: the absorption of $Eu_3Fe_5O_{12}$ between 6700 and 7680 eV (left) and between 7480 and 8120 eV (right), displaying the Fe K and the Eu L_3, L_2, and L_1 edges. Center: the SPEXAFS at the Eu L_3 (left) and L_2 edge (right) follow the same profile with a ratio of (-2). Bottom: the Fourier transform of the spin-averaged EXAFS (···) and SPEXAFS (—) of the Eu L_3 (left) and L_2 edge (right).

edge ($k=6$ Å^{-1}). Since in the simple picture the corresponding K-edge SPEXAFS are more than one order of magnitude smaller, they are nearly invisible in the L_3 SPEXAFS.

The Fourier transform (FT) of the polarization averaged EXAFS spectrum $f(\chi_0)$ (dashed line) and the corresponding SPEXAFS FT (solid line) $f(\chi_c)$ are significantly different. The FT of the L_3 EXAFS show very broad features due to the small transformation range limited by the Fe K edge. The prominent maximum in $f(\chi_o)$ resulting from the strong backscattering at the next oxygen neighbors has vanished in the SPEXAFS to the credit of an increase of the peaks at higher r values, which mark the positions of the next and over next iron Fe neighbors. They are small or almost invisible in the EXAFS FT. The $f(\chi_c)$ at the L_2 and L_3 edges are very similar demonstrating that the occurrence of the Fe K edge does not limit the k range in the magnetic spectra.

These studies show, that (nearly) nonmagnetic neighbors as the oxygen components on magnetic oxides do not contribute to the SPEXAFS and a clear distinction between magnetic and nonmagnetic neighborhood is possible. From the systematics observed by studies in various systems,[4,13] we have observed that the relative strength of the SPEXAFS rescaled by the photoelectron spin polarization

$$[\chi_c/\chi_0]/\langle\sigma_z\rangle=[f(\chi_c)/f(\chi_o)]\langle\sigma_z\rangle=2.4(3)\%\mu_S(\mu_B) \tag{6}$$

is directly proportional to the magnetic spin moment of the neighboring atoms. Thus, we expect, that the SPEXAFS spectroscopy gives even quantitatively new element-specific insights into the magnetic short-range order.

2. K-edge SPEXAFS

The highly precise measurements, which are possible in the transmission mode, allow us also to address $3d$ elements by K-edge SPEXAFS studies as demonstrated in case of Co-(fcc) and Ni-metal. As shown in Fig. 7, the χ_c oscillation at the K edges follow roughly the χ_0 structure except an additional contribution at a k region of 4–5 Å^{-1}. In this range multielectron contributions ($3p\rightarrow 3d$ transition) result in an additional line in the dichroic K spectra, which decreases strongly by going from Fe to Ni.[13] Following Eq. (6), we deduce a value of $\langle\sigma_z\rangle=+3.5(5)\%$ for the K SPEXAFS, which is somewhat larger than expected from the near-edge MCD effects.

Due to the small value of $\langle\sigma_z\rangle$ the statistics of the K SPEXAFS can be poor. But a more detailed analysis by an extraction of the exchange parameter from the experimental data allows also in this case a sufficiently quantitative analysis. Hereby the values F_{jo}, ϕ_{ijo}, and λ_{jo} are calculated by the FEFF code of Rehr[17] and the D_j and S_i values can be deduced by fitting the χ_o profiles. The F_c profile for Co and Ni indicate a significant different k dependence of the magnetic and Coulomb backscattering amplitude F_o, which seems to be correlated to the differences of the distribution of spin and charge density in the neighboring atom. The ratio of the Co and Ni F_c amplitudes scale directly with the ratio of the magnetic moments per atom. Thus the described analysis allows the determination of the average magnetic moment carried by a coordination shell with good accuracy even for noisy SPEXAFS data.

The amplitudes of F_c correspond to relatively large exchange contributions of the *elastic* scattering cross section of more than 20% per magnetic electron. On the other hand the

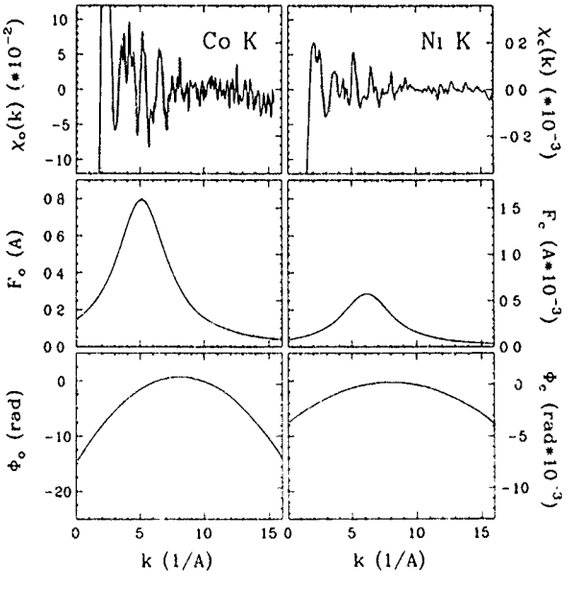

FIG. 7. Top: the EXAFS (···) and SPEXAFS (—), measured at the Co K (left) and Ni K edge (right) of Co fcc and Ni fcc metal. Center: the calculated spin-independent (···) and fitted spin-dependent part (—) of the backscattering amplitude of the first neighbor of Co fcc (left) and Ni fcc (right). Bottom: the corresponding calculated spin-independent (···) and fitted spin-dependent (—) phase shift.

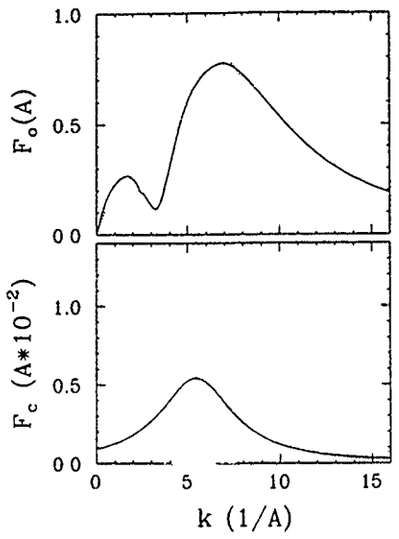

FIG. 8. The calculated spin-independent part F_0 (top) and fitted spin-dependent part F_c (bottom) of the backscattering amplitude for Co (···) and Cu (—) of a Co(5) Cu(4) multilayer.

exchange contributions to the phase shift, as seen from Fig. 7, are much smaller and the spin-dependent mean-free path of the order of less than 10^{-3} is found to be negligible. This demonstrates that the SPEXAFS analysis can also provide useful new information on the exchange phenomena in the interaction of spin-polarized electrons directly inside a solid and especially in comparison with corresponding results from surface-sensitive electron spectroscopies.

SPEXAFS studies can be applied even for multilayered systems (ML) to get information on the interface structures, as shown for Co/Cu systems. Our calculated distribution of the magnetic moments of 5Co/4Cu ML (Fig. 9) indicates a small Cu polarization corresponding to an average spin and orbital moment of $m_S(\mathrm{Cu})=0.0137\mu_B$ and $m_L=0.001\mu_B$, which agree well to our near-edge MCD studies at the NSLS, where we observed for the first time an induced Cu moment in this ML of $m_S(\mathrm{Cu})=0.014\mu_B$ and $m_L<0.002\mu_B$.[4]

In MLs with strongly different magnetic moments of both components as the Co/Cu systems the average magnetic moments of the *neighboring* Co and Cu atoms depend very sensitively on the sharpness of the interface. The ratio between the Co and Cu SPEXAFS amplitudes resulting from the exchange scattering at the first coordination shell should be about 7.3 for a sharp interface and reduced to ~1.9 for a complete intermixing of two adjacent atomic layers. Thus a comparison of the strengths of F_c deduced from the Co and Cu SPEXAFS in the ML (see Fig. 8) gives quantitative information on the quality of the interface. Their ratio of the amplitudes of ~2.0 are significantly smaller than the value of 7.3 estimated for an ideal structure and can be explained by an intermixing of close to 50% in the first Co and Cu at the interface.

ACKNOWLEDGMENTS

We would like to thank all colleagues involved in this work, G. Bayreuther, S. Parkin, J. Stöhr, A. Fontaine, C. T. Chen, H. Petersen , K. Schwarz, and P. Blaha. The help of the staffs at TU Munich, the University of Augsburg, at HASYLAB, BESSY, and NSLS is appreciated. This work is supported by the German Federal Minister of Research and Technology (BMFT) under Contract No. 05 5WO EAI.

[1] B. T. Thole, P. Carra, F. Sette, and G. van der Laan, Phys. Rev. Lett. **68**, 1943 (1992).
[2] P. Carra, B. T. Thole, M. Altarelli, and X. Wang, Phys. Rev. Lett. **70**, 694 (1993).
[3] R. Wienke, G. Schütz, and H. Ebert, J. Appl. Phys. **69**, 6147 (1991).
[4] G. Schütz, M. Knülle, and H. Ebert, Phys. Scr. **T49**, 302 (1993).
[5] F. Sette, C. T. Chen, Y. Ma, S. Modesti, and N. V. Smith, *Proceedings of 6th International Conference on X-ray Absorption Fine Structure*, edited by S. Samar Hasnain (Horwood, Chichester, UK, 1991), p. 96.
[6] J. Ph. Schillé, J. P. Kappler, Ph. Sainctavit, Ch. Cartier dit Moulin, C. Brouder, and G. Krill, Phys. Rev. B **48**, 9491 (1993).
[7] B. T. Thole, G. van der Laan, and G. A. Sawatzky, Phys. Rev. Lett. **55**, 2086 (1985).
[8] G. Schütz, W. Wagner, W. Wilhelm, P. Kienle, R. Zeller, R. Frahm, and G. Materlik, Phys. Rev. Lett. **58**, 73 (1987).
[9] G. Schütz, M. Knülle, R. Wienke, W. Wilhelm, W. Wagner, P. Kienle, and R. Frahm, Z. Phys. B **73**, 67 (1988).
[10] H. Ebert, P. Strange, and B. L. Gyorffy, J. Phys. Condens. Matter B **73**, 77 (1988); H. Ebert, B. Drittler, R. Zeller, and G. Schütz, Solid State Commun. **69**, 485 (1989); H. Ebert, G. Schütz, and W. M. Temmerman, Solid State Commun. **76**, 475 (1990).
[11] C. T. Chen, F. Sette, Y. Ma, and S. Modesti, Phys. Rev. B **42**, 7262 (1990); Y. U. Idzerda, L. H. Tjeng, H. J. Lin, G. Meigs, C. T. Chen, and J. Gutierrez, J. Appl. Phys. **73**, 6204 (1993).
[12] P. Fischer, G. Schütz, and G. Wiesinger, Solid State Commun. **76**, 777 (1990); P. Fischer, G. Schütz, S. Stähler, and G. Wiesinger, J. Appl. Phys. **69**, 6144 (1991).
[13] G. Schütz, R. Frahm, P. Mautner, R. Wienke, W. Wagner, W. Wilhelm, and P. Kienle Phys. Rev. Lett. **62**, 2620 (1989); M. Knülle, D. Ahlers and G. Schutz, Solid State Commun. (to be published).
[14] J. J. Rehr (private communication, 1994).
[15] J. C. Fuggle and J. E. Inglesfield, *Unoccupied Electronic States*, edited by J. C. Fuggle (Springer, Berlin, 1992).
[16] B. T. Thole, G. van der Laan, and P. H. Butler, Chem. Phys. Lett. **149**, 295 (1988).
[17] P. Carra, B. N. Harmon, B. T. Thole, M. Altarelli, and G. A. Sawatzky, Phys. Rev. Lett. **66**, 2495 (1991).
[18] U. Fano, Phys. Rev. **178**, 131 (1969).
[19] J. L. Erskine and E. A. Stern, Phys. Rev. B **12**, 5016 (1975).
[20] M. Knülle, G. Schütz, G. Bayreuther, and C. T. Chen, Solid State Commun. (to be published).
[21] P. Soderlind, O. Eriksson, B. Johansson, R. C. Albers, and A. M. Boring, Phys. Rev. B **45**, 12 911 (1992).
[22] G. van der Laan and B. T. Thole, Phys. Rev. B **43**, 13 401 (1991).
[23] F. M. F. de Groot, J. C. Fuggle, B. T. Thole, and G. A. Sawatzky, Phys. Rev. B **42**, 5459 (1990).
[24] P. Fischer, G. Schutz, S. Scherle, M. Knulle, S. Stahler, and G. Wiesinger, Solid State Commun. **82**, 857 (1992).
[25] J. Sticht and J. Kübler, Solid State Commun. **53**, 529 (1985).
[26] B. K. Teo, in *EXAFS Spectroscopy*, edited by D. C. Joy (Plenum, New York, 1981).
[27] J. J. Rehr, S. I. Zabinski, and R. C. Albers, Phys. Rev. Lett. **69**, 3397 (1992)

Discussion of the magnetic dichroism in the x-ray resonance scattering

Peter Rennert
Physics Department, Martin-Luther-University, Halle-Wittenberg, D-06099 Halle, Germany

The cross section for the x-ray resonance scattering is evaluated at the K edge for a transition metal like Ni. The Green function is calculated analytically from a model system. The differences in the spectra measured with different polarization can be explained from these results. The examples show that the shape of magnetic dichroism is very sensitive to the spin polarized p part of the Green function.

I. INTRODUCTION

The x-ray-resonance scattering or the anomalous scattering involves the variation of the intensity of a Bragg peak if the photon energy crosses an edge. Magnetic dichroism can be observed considering magnetic systems and using polarized x-ray sources. Recently magnetic dichroism at the K and L edge was analyzed theoretically for ferromagnetic $3d$ transition metals where the main source of dichroism is the spin polarization of the valence electrons.[1] The cross section

$$d\sigma/d\Omega' = r_0^2 |S(\mathbf{K})|^2 |M(\mathbf{q}'\boldsymbol{\epsilon}';\mathbf{q}\boldsymbol{\epsilon})|^2 \tag{1}$$

can be calculated by second order perturbation theory.[1–4] The order of magnitude is given by the square of the classical electron radius r_0.

The matrix element M [Eq. (30) of Ref. 1 with terms I to VII] depends on the photon wave vectors $\mathbf{q}$, $\mathbf{q}'$ and on the polarizations $\boldsymbol{\epsilon}$, $\boldsymbol{\epsilon}'$ of the incoming and outgoing photon, respectively. It contains terms which describe the Thomson scattering (I), the magnetic scattering (II), and the resonance scattering (III–VII). The terms VI and VII are neglected in the following discussion. The resonance terms depend on the structure of the unoccupied electron energy bands. It can be expressed by the Green function.

Experimental results for nickel were presented by Namikawa *et al.*[5] and Schütz *et al.*[6] Namikawa *et al.* observed magnetic dichroism for the (220) reflex with linear polarized light. The polarization was chosen in the scattering plane and the magnetization perpendicular to the scattering plane. Schütz *et al.* observed magnetic dichroism for the (222) reflex with circular polarized light. The magnetization was in the scattering plane. The results of both experiments differ from each other, and it is one aim of the paper to discuss the magnetic dichroism for different experimental conditions.

II. MODEL OF THE BAND STRUCTURE

In Eq. (30) of Ref. 1 the electron states of the unoccupied part of the electron energy bands are included in the Green function. The Green function is expanded into lattice harmonics, angular momentum parts in our example. The total Green function $G = G_\uparrow + G_\downarrow$ and the spin polarized part $G_s = G_\uparrow - G_\downarrow$ appear separately. Different parts of the Green function appear in the expressions III–VII. They are multiplied with factors containing the photon wave vectors and the polarizations. To discuss the influence of the different factors we use a simplified picture of the band structure with degenerate parabolic energy bands characterized by the position of the bottom $E_{l\sigma}^0$ and the width $W_{l\sigma}$ of the bands for the different angular momentum parts ($l = s,p,d$) and spin ($\sigma = \uparrow,\downarrow$). These values are taken from the band structure of nickel in the numerical discussion of the following chapters. In this model the Green function of the unoccupied states can be calculated analytically

$$G(E) = -\frac{3}{W}\left[1 - x_F + \frac{\alpha}{2}\ln\left(\frac{(1-\alpha)(x_F+\alpha)}{(x_F-\alpha)(1+\alpha)}\right)\right] \tag{2}$$

with

$$x_{Fl\sigma}^2 = (E_F - E_{l\sigma}^0)/W_{l\sigma} = n_{l\sigma}^{2/3}/(2l+1),$$
$$\alpha_{l\sigma}^2 = (E - E_{l\sigma}^0)/W_{l\sigma}. \tag{3}$$

$n_{l\sigma}$ is the number of l electrons with spin σ. The behavior of this function is shown in Figs. 1 and 2 for the p and d part, respectively. In our example the unoccupied part of the $p_\uparrow$ band lies in the range from the Fermi energy ($E_F = 0$) up to 17.4 eV. Thus, in Fig. 1 $D_\uparrow(E)$ is restricted to this range. The real part of the Green function $G_\uparrow$ has long tails below the Fermi energy. It changes the sign within the unoccupied region. Figure 2 shows the d part of the Green function. In our example the top of the majority band lies at 0.11 eV and the top of the minority band at 0.43, respectively. The spin density $\mathrm{Im}(-G_s/\pi)$ is positive in the range from the Fermi energy up to the top of the majority d band and then it

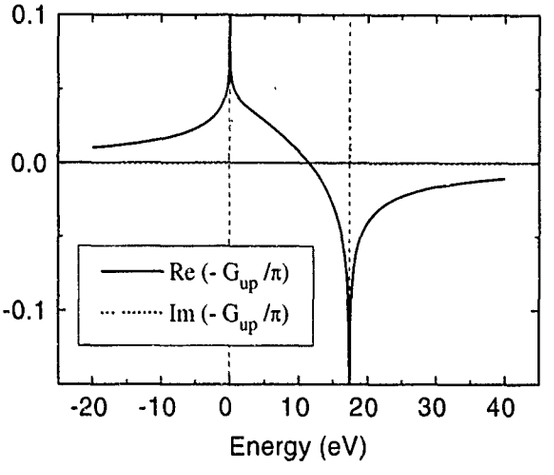

FIG. 1. The p part of the Green function $G_\uparrow$ multiplied with $-1/\pi$. $\mathrm{Im}(-G/\pi)$ is the density of states $D(E)$. The dashed lines indicate the Fermi energy ($E_F = 0$) and the top of the p band, respectively

 0021-8979/94/76(10)/6459/3/$6.00 © 1994 American Institute of Physics

becomes negative up to the top of the minority d band. Again the real part of the Green function has a long tail below the Fermi energy.

III. LINEAR POLARIZED LIGHT

The polarization is given by

$$\epsilon=\mathbf{u}_1 \sin\psi+\mathbf{u}_2 \cos\psi\, e^{i\xi}, \tag{4}$$

where $\mathbf{u}_1$ is chosen to be in the scattering plane (say yz plane) and $\mathbf{u}_2$ perpendicular to it. $\xi=0$ describes linear polarized light, $\xi=\pm\pi/2$ and $\psi=\pi/4$ circular polarized light. At first we choose $\xi=0$ and $\psi=\pi/2$ which corresponds to the experimental conditions of Namikawa *et al.*[5] We consider the two opposite ($\pm x$) directions of the magnetization and we get

$$\begin{aligned}|M^+|^2-|M^-|^2=&-2\sin(2\Theta)\Big[\cos(2\Theta)n(\mathbf{K})-\cos(2\Theta)\frac{2\pi}{3}\frac{\hbar\omega}{W_{p\uparrow}}N_p^2\,\mathrm{Re}\Big(-\frac{1}{\pi}W_{p\uparrow}G_p(E)\Big)\\&-\cos(4\Theta)\frac{2\pi}{15}\Big(\frac{\hbar\omega}{mc^2}\Big)^2\frac{\hbar\omega}{W_{d\uparrow}}(Z\alpha)^{-2}R_d^2\,\mathrm{Re}\Big(-\frac{1}{\pi}W_{d\uparrow}G_d(E)\Big)\Big]\Big(\frac{\pi}{3}\frac{\hbar\omega}{mc^2}\frac{\hbar\omega}{W_{p\uparrow}}R_pN_p[W_{p\uparrow}D_{ps}(E)]\Big)\\&-2\sin(2\Theta)\Big[\frac{\hbar\omega}{2mc^2}n_s(\mathbf{K})+\frac{\pi}{3}\frac{\hbar\omega}{mc^2}\frac{\hbar\omega}{W_{p\uparrow}}R_pN_p\,\mathrm{Re}\Big(-\frac{1}{\pi}W_{p\uparrow}G_{ps}(E)\Big)\Big]\\&\times\Big[\cos(2\Theta)\frac{2\pi}{3}\frac{\hbar\omega}{W_{p\uparrow}}N_p^2[W_{p\uparrow}D_p(E)]+\cos(4\Theta)\frac{2\pi}{15}\Big(\frac{\hbar\omega}{mc^2}\Big)^2\frac{\hbar\omega}{W_{d\uparrow}}(Z\alpha)^{-2}R_d^2[W_{d\uparrow}D_d(E)]\Big]\end{aligned} \tag{5}$$

for the difference of the intensities. R and N are radial integrals as listed in Table III of Ref. 1. The leading terms correspond to Eqs. (2) and (4) of Ref. 5. The notation follows Ref. 1.

Values for the charge formfactor $n(\mathbf{K})$ and for the magnetic formfactor $n_s(\mathbf{K})$ can be taken from Zukowski *et al.*[7] They are measured for the Bragg angle $2\Theta=90°$ which corresponds to $\hbar\omega=8.62$ keV for the (222) reflex. The K edge energy is 8333 eV. We have $2\Theta=94°$ for the (222) reflex and $2\Theta=73°$ for the (220) reflex. This is an important point, too. For the (222) reflex the charge form factor contributes with a small weight $\cos 2\Theta=-0.07$ whereas for the (220) reflex this weight is larger (0.28) and of opposite sign.

It should be noticed that the terms in Eq. (5) contain the factor $D(E)$. Therefore the spectrum of Namikawa *et al.* is restricted to the energy region of the unoccupied states. Furthermore there is no contribution to the dichroism from pure magnetic scattering. Figure 3 shows the results. The dichroism in the x-ray resonance spectrum is determined by the behavior of the p part of the Green function. We find negative values near the edge and positive values up to the top of the band. The shape of the curve is determined by the shape of density of states of the model. The spin polarization of the p band determines for the negative values near the edge. As known from Compton profiles[8,9] there is a negative spin po-

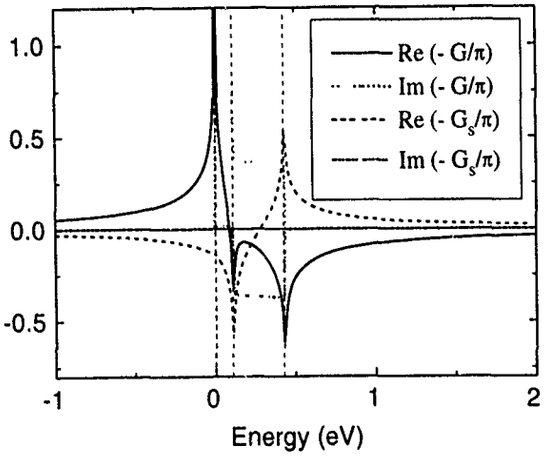

FIG. 2. The d part of the total Green function G and of the spin-polarized Green function G_s multiplied with $-1/\pi$. The dashed lines indicate the Fermi energy ($E_F=0$), the top of the majority d band, and the top of the minority d band, respectively.

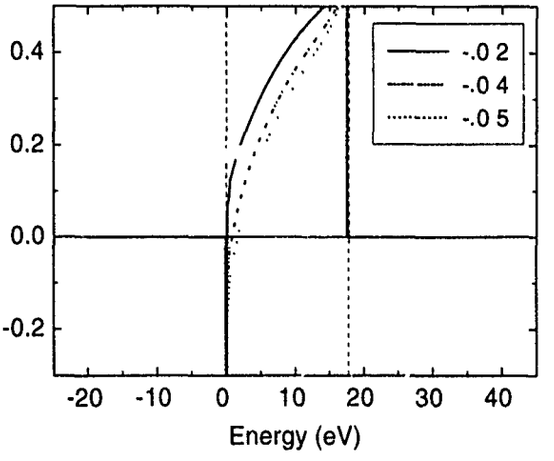

FIG. 3. Dichroism $\Delta I/(I_+ + I_-)$ for the scattering of linear polarized x rays near to the K edge. The spectrum is restricted to the energy range of the unoccupied part of p band. The numbers indicate the assumed value for the contribution of the p electrons to the magnetic moment per atom. The values are scaled by a factor 10^4.

larization of the p band in Ni with a contribution of $\approx -0.2\mu_B$. Figure 3 shows results for different values of the spin polarization. If we neglect this spin polarization at all then we do not get negative values near the edge. Thus, to discuss measured spectra it is important to calculate the spin polarization of the p band in detail.

The calculated values are smaller than the experimental one for Ni.[5,6] This is due to the simple model of the band structure. In the real band structure of Ni the spin polarization of the p band is larger near the Fermi energy whereas in the model it is uniform over the whole band.

IV. CIRCULAR POLARIZED LIGHT

Now we consider the polarization (4) which corresponds to the experiment of Schütz *et al.*[6] instead of Eq. (5) we get

$$
\begin{aligned}
|M^+|^2-|M^-|^2=\cos\Theta\Bigg\{&[\cos(2\Theta)+1]n(\mathbf{K})-[\cos(2\Theta)+1]\frac{2\pi}{3}\frac{\hbar\omega}{W_{p\uparrow}}N_p^2\,\mathrm{Re}\left(-\frac{1}{\pi}W_{p\uparrow}G_p(E)\right)\\
&-[\cos(4\Theta)+\cos(2\Theta)]\frac{2\pi}{15}\left(\frac{\hbar\omega}{mc^2}\right)^2\frac{\hbar\omega}{W_{d\uparrow}}(Z\alpha)^{-2}R_d^2\,\mathrm{Re}\left(-\frac{1}{\pi}W_{d\uparrow}G_d(E)\right)\Bigg]\\
\times\Bigg[&\frac{\hbar\omega}{2mc^2}n_s(\mathbf{K})+\sin^2\Theta\,\frac{\pi}{3}\frac{\hbar\omega}{mc^2}\frac{\hbar\omega}{W_{p\uparrow}}R_pN_p\,\mathrm{Re}\left(-\frac{1}{\pi}W_{p\uparrow}G_{ps}(E)\right)\Bigg]\\
-2\cos\Theta\Bigg(&\sin^2\Theta\,\frac{\pi}{3}\frac{\hbar\omega}{mc^2}\frac{\hbar\omega}{W_{p\uparrow}}R_pN_p[W_{p\uparrow}D_{ps}(E)]\Bigg)\Bigg[[\cos(2\Theta)+1]\frac{\pi}{3}\frac{\hbar\omega}{W_{p\uparrow}}N_p^2[W_{p\uparrow}D_p(E)]\\
+[\cos(4\Theta)+\cos(2\Theta)]&\frac{\pi}{15}\left(\frac{\hbar\omega}{mc^2}\right)^2\frac{\hbar\omega}{W_{d\uparrow}}(Z\alpha)^{-2}R_d^2[W_{d\uparrow}D_d(E)]\Bigg],
\end{aligned}
\tag{6}
$$

which has a quite different structure than Eq. (5). At first we find an essential contribution from the magnetic scattering—a term proportional to $n(\mathbf{K})\cdot n_s(\mathbf{K})$. Furthermore the contributions from the resonance scattering contain the real part of the Green function. As shown in Fig. 1 it has a long tail below the edge. This behavior explains the observation of Schütz *et al.* who found essential contributions below the edge in contrast to Namikawa *et al.*

Figure 3 shows the dichroism for our example. The constant contribution from the pure magnetic scattering was subtracted and only the resonance contribution is shown. In contrast to Fig. 4 we find a finite intensity below the Fermi energy, thus below the edge. Furthermore the range of negative values is much broader and the shape is similar to the behavior of the real part of the Green function in Fig. 1.

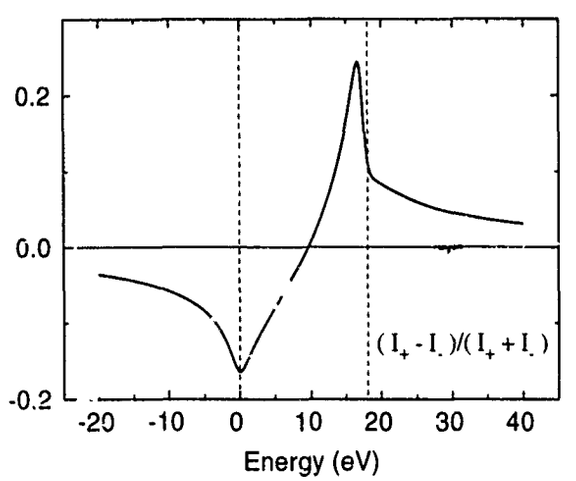

FIG. 4. Dichroism $\Delta I/(I_+ + I_-)$ for the scattering of circular polarized x rays near the K edge. The contribution of the pure magnetic scattering was subtracted. The dashed lines indicate the Fermi energy ($E_F=0$) and the top of the p band, respectively. The values are scaled by a factor 10^4.

V. CONCLUSIONS

We have calculated the magnetic dichroism in the x-ray resonance scattering in a model for the band structure, which can be evaluated analytically. The formulas and the numerical evaluation show what features of the band structure determine the characteristic peaks found in the experimental spectra. Clearly, the Green function has to be determined by a full band structure calculation to get consistence in respect to peak position and the order of magnitude with the experimental spectra in detail. Especially measurements with linear polarized light seems to more suitable, because the influence of the pure magnetic scattering is suppressed. In this case the spectrum sensitively depends on the spin-polarized part of the Green function.

[1] P. Rennert, Phys. Rev. B **48**, 13559 (1993).
[2] P. M. Platzman and N. Tzoar, Phys. Rev. B **2**, 3556 (1970).
[3] F. de Bergevin and M. Brunel, Acta Crystallogr. A **37**, 314 (1980).
[4] M. Blume, J. Appl. Phys. **57**, 3615 (1985).
[5] K. Namikawa, M. Ando, T. Nakajima, and H. Kawata, J. Phys. Soc. Jpn. **54**, 4099 (1985)
[6] G. Schutz (unpublished).
[7] E. Zukowski, J. M. Cooper, R. Armstrong, M. Ito, S. P. Collins, D. Laundy, and A. Andreejczuk, J. X-Ray Sci. Technol. **3**, 300 (1992).
[8] P. Rennert, G. Carl, and W. Hergert, Phys. Status Solidi B **120**, 273 (1983).
[9] Y. Kubo and S. Asano, Phys. Rev. B **42**, 4431 (1990).

Experimental investigation of dichroism sum rules for V, Cr, Mn, Fe, Co, and Ni: Influence of diffuse magnetism

W. L. O'Brien
Synchrotron Radiation Center, University of Wisconsin–Madison, Stoughton, Wisconsin 53589

B. P. Tonner
Synchroton Radiation Center, University of Wisconsin–Madison, Stoughton, Wisconsin 53589
and Department of Physics, University of Wisconsin–Milwaukee, Milwaukee, Wisconsin 53211

G. R. Harp and S. S. P. Parkin
IBM Almaden Research Center, San Jose, California 95120

Uncertainties in the application of the $\langle L_z\rangle/\langle S_z\rangle$ sum rule to experimental spectra of V, Cr, Mn, Fe, Co, and Ni are discussed. An important contribution to these uncertainties is the possible presence of dichroism due to diffuse magnetic moments, which are known to exist in Fe, Co, and Ni.

X-ray magnetic circular dichroism (XMCD) is the difference in the absorption cross section for photons with spin parallel and antiparallel to the sample magnetization. The $L_{2,3}$ absorption edges of the magnetically interesting $3d$ transition metals have readily measurable dichroism signals, making XMCD an excellent technique for the study of magnetism in ultrathin films and multilayers. Theoretical understanding of XMCD can be traced to work by Erskine and Stern[1] who predicted that the XMCD L_3/L_2 intensity ratio is equal to -1 for a simple atomiclike model. Early measurements on Ni by Chen *et al.*[2] found values substantially different than -1. Later, Smith *et al.*[3] showed that agreement with experiment could be improved by including the d-band spin-orbit interaction in the calculation. More recently, Thole *et al.*[4] and Carra *et al.*[5] have derived sum rules which relate the ground state expectation values $\langle L_z\rangle$ and $\langle S_z\rangle$ to the dichroism spectra of atoms. The derivation of these sum rules assumes excitations into d levels only and their application to solids is still controversial.[6] In this article we examine the details of the V, Cr, Mn, Fe, Co, and Ni $L_{2,3}$ XMCD spectra. We point out a number of trends in the spectra, some of which affect the application of the sum rules We also discuss dichroism due to diffuse magnetic moments and its effect on the application of the dichroism sum rules.

The experiments were performed on the 10M toroidal grating monochromator at the Synchrotron Radiation Center of the University of Wisconsin.[7] The samples were magnetized *in situ* by a 2 kG electromagnet. Absorption spectra, $\sigma(\hbar\omega)$, were obtained by measuring the total electron yield, $Y(\hbar\omega)$, by monitoring the sample drain current. All XMCD measurements were made on the remanent magnetization by reversing the sample magnetization and using a fixed incident polarization. We have completed several extensive tests of this technique[8] and have identified experimental conditions where the approximation $Y(\hbar\omega)\propto\hbar\omega\sigma(\hbar\omega)$ is valid.

In Fig. 1 we show the XMCD spectra of V, Cr, Mn, Fe, Co, and Ni. Samples were a V-Fe multilayer, a submonolayer film of Cr on Fe, a submonolayer film of Mn on Co, and Fe, Co, and Ni thin films grown on Cu(001), respectively. The energy of the maximum L_3 peak intensity in the linear absorption spectra is defined as the zero of the energy scale. We make the following observations of the results in Fig. 1. The separation between the L_3 and L_2 peaks decreases in going from Ni to V. For V and Cr the L_3 and L_2 features are not clearly separated. The L_3 peaks are predominantly of negative intensity and the L_2 peaks of positive intensity. The vanadium L_2 peak is the only exception to this. Ni and Co have negative shoulders, B, on the high energy side of the L_3 peak. For Ni, the main peak and shoulder are due to d^9 and d^8 initial state configurations, respectively.[9] We propose a similar identification for the shoulder in the Co spectra. There is also a nearly constant negative intensity feature between the shoulders B and the L_2 peaks in the Ni and Co spectra, gray arrows. The Fe L_3 peak is nearly symmetrical, having a small positive intensity shoulder. The Mn,

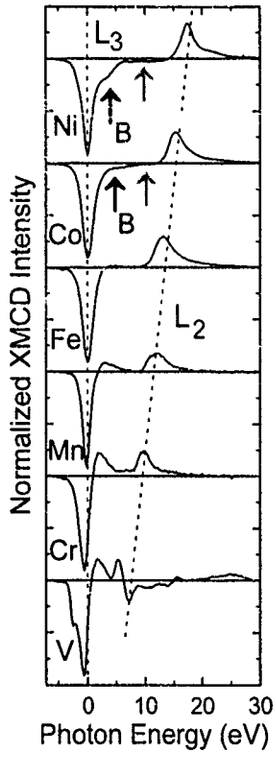

FIG. 1. V, Cr, Mn, Fe, Co, and Ni XMCD spectra shown normalized to constant L_3 peak height The shoulders labeled B are due to multiple initial state configurations. We identify the constant negative intensity features between B and L_2 in the Ni and Co spectra, gray arrows, as due to diffuse-magnetic moments

 0021-8979/94/76(10)/6462/3/$6 00 © 1994 American Institute of Physics

TABLE I. Diffuse moment, μ_{diff}, and ratio of diffuse moment to total moment, μ_{diff} (%), for Ni, Co, and Fe determined by calculation, Ref. 13, and by neutron diffraction (ND), Ref. 12. Values are given in μ_B/atom.

	Ni		Co		Fe	
	Theory	ND	Theory	ND	Theory	ND
μ_{diff}	−0.04	−0.105	−0.07	−0.28	−0.04	−0.21
μ_{diff}(%)	−7%	−17%	−4%	−16%	−2%	−10%

Cr, and V L_3 peaks have more pronounced positive intensity shoulders. These shoulders are present in atomic calculations for Mn, d^5, Cr d^4, and V d^2.[10] The asymmetry introduced by these shoulders shifts the peak maximum in the L_3 XMCD signal to −0.2, −0.6, and −0.8 eV relative to the maximum in the linear absorption spectra for Mn, Cr, and V, respectively.

We now discuss the application of the $\langle L_z\rangle/\langle S_z\rangle$, sum rule to our experimental results. From Carra *et al.*,[5]

$$\frac{\langle L_z\rangle}{\langle S_z\rangle}=\frac{4}{3}\frac{R_M+1}{R_M-2},$$

where $R_M=I(L_3)/I(L_2)$, the ratio of the integrated dichroism intensities. The only uncertainties involved in applying this sum rule are in the experimental separation of $I(L_3)$ and $I(L_2)$ and in the identification of dichroism intensities due to non-3d orbitals. We immediately see difficulties in applying this sum rule to the Cr and V data, since the L_3 and L_2 peaks are not clearly separated. In the Ni and Co spectra the constant negative intensity feature between the shoulder B and the L_2 peak must be identified. These features are present in other published spectra but have not been previously interpreted.[2,11] It is important to know whether or not this intensity is due to excitations into 3d orbitals. If it is not, then its intensity should not be included in the value for R_M. If this is the case, accurate models must be used to distinguish the non-3d contributions to the XMCD spectra.

A possible source of these constant negative intensity features is from diffuse magnetic moments. Polarized neutron diffraction studies have shown that diffuse magnetic moments are present in Fe, Co, and Ni.[12] This background magnetism is assumed to be caused by 4s electrons, whose spin is oppositely polarized to the 3d electrons. Recent band structure calculations on Fe, Co, and Ni[13] also predict a negative diffuse magnetic moment due to the sp-projected and interstitial moments. The results from these calculations and the neutron scattering experiments are summarized in Table I. Since $L_{2,3}$ absorption spectra are sensitive to both s- and d-electron levels, it is expected that diffuse magnetic moments will affect the XMCD spectra.

To show that the dichroism signal due to diffuse magnetic moments is consistent with the experiment we use a model similar to that developed by Erskine and Stern.[1] We assume that the empty d levels have minority spin character (↓) and that the diffuse magnetic moment is described by empty s levels which have majority spin character (↑). This simple model predicts an R_M of −1 for excitation into both the 3d(↓) and s(↑) levels. Note that the sign of the dichroism signal is the same for excitations into these oppositely polarized states. The sign at the L_3 edge for both 3d(↓) and s(↑) excitations is negative and the sign at the L_2 edge is positive for both excitations. Since there is no spin-orbit coupling in the s levels we expect $R_M=-1$ for transitions into s orbitals. Based on a comparison of radial matrix elements the diffuse XMCD should be small compared to the 3d XMCD.

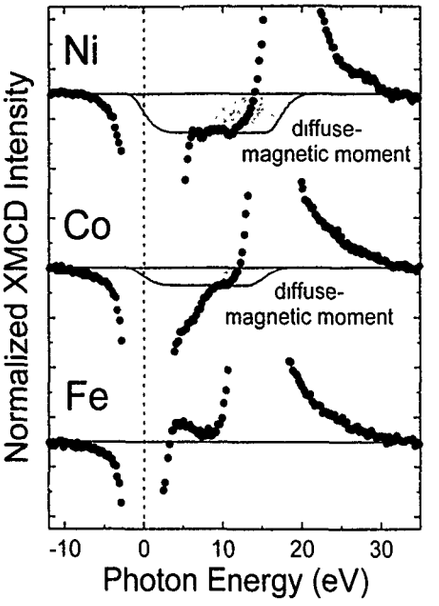

FIG. 2. Fe, Co, and Ni XMCD spectra from Fig. 1 shown on an expanded scale. XMCD signal due to diffuse-magnetic moments in Ni and Co, shaded area.

In Fig. 2 we show the same Ni, Co, and Fe spectra from Fig. 1 on an expanded scale together with the predicted XMCD signal due to diffuse magnetism for both Ni and Co. We observe no effects of diffuse magnetic moments in the Fe XMCD spectra. The positive going shoulder on the Fe L_3 may obscure such a feature, or the separation between the Fe L_2 and L_3 peaks may be too small. We also note that for Fe, Co, and Ni, the relative diffuse moment is smallest for Fe (Table I). The model we have used predicts a step-function line shape, which reflects a broad s band with nearly constant density of state. We have assumed that $R_M=-1$ so that the diffuse XMCD signal goes to zero above the L_2 edge. While the XMCD line shape due to diffuse magnetic moments is undoubtedly more complicated, this simple model serves to illustrate the importance of considering diffuse magnetism in XMCD.

We have determined $\langle L_z\rangle/\langle S_z\rangle$ for V, Cr, Mn, Fe, Co, and Ni, from our XMCD spectra both before and after subtracting contributions from diffuse moments. These values are given in Table II along with values determined by neutron diffraction[12] and band structure calculations[14] for Fe, Co, and Ni. Values of $\langle L_z\rangle/\langle S_z\rangle$ determined from XMCD are larger than values determined by neutron scattering and band structure calculations, but including diffuse moments improves the comparison for Co and Ni. The results in Table II show how different interpretations of weak features in the XMCD spectra greatly affect the application of the $\langle L_z\rangle/\langle S_z\rangle$

TABLE II. $\langle L_z\rangle/\langle S_z\rangle$ values obtained from results in Fig.1 and dichroism sum rules, compared to theoretical values, Ref. 14, and neutron diffraction (ND), Ref. 12. Values for Co and Ni were obtained both before and after subtracting the diffuse-XMCD signal. The calculated value for Co is for the fcc phase which is present in this experiment. Errors given for Cr are due to overlap of L_3 and L_2 dichroism signal.

	Ni	Co	Fe	Mn	Cr
XMCD	0.39	0.33	0.17	0.25	0.065±0.02
XMCD-DMM	0.28	0.25	···	···	···
Theory	0.22	0.15	0.08	···	···
ND	0.17	0.14	0.12	···	···

sum rule. Uncertainties of this nature may limit the usefulness of the $\langle L_z\rangle/\langle S_z\rangle$ sum rule to qualitative applications.

ACKNOWLEDGMENTS

This work was supported by the National Science Foundation Division of Materials Research under Grant No. DMR-94-13475. The Synchrotron Radiation Center is a national facility supported by the NSF Division of Materials Research.

[1] J. L. Erskine and E. A. Stern, Phys. Rev. B **12**, 5016 (1975).
[2] C. T. Chen, N. V. Smith, and F. Sette, Phys. Rev. B **43**, 6785 (1991).
[3] N. V. Smith, C. T. Chen, F. Sette, and L. F. Mattheiss, Phys. Rev. B **46**, 1023 (1992).
[4] B. T. Thole, P. Carra, F. Sette, and G. van der Laan, Phys. Rev. Lett. **68**, 1943 (1992).
[5] P. Carra, B. T. Thole, M. Altarelli, and X. Wang, Phys. Rev. Lett. **70**, 694 (1993).
[6] R. Wu, D. Wang, and A. J. Freeman, Phys. Rev. Lett. **71**, 3581 (1993).
[7] R. W. C. Hansen, W. L. O'Brien, and B. P. Tonner, Nucl. Instrum. Methods (in press).
[8] W. L. O'Brien and B. P. Tonner, Phys. Rev. B **50**, 2963 (1994).
[9] L. H. Tjeng, C. T. Chen, P. Rudolf, G. Meigs, G. van der Laan, and B. T. Thole, Phys. Rev. B **48**, 13 378 (1993).
[10] G. van der Laan and B. T. Thole, Phys. Rev. B **43**, 13401 (1991).
[11] Y. Wu, J. Stöhr, B. D. Hermsmeirer, M. G. Samant, and D. Weller, Phys. Rev. Lett. **69**, 2307 (1992).
[12] M. B. Stearns, in *Landolt-Bornstein Numerical Data and Functional Relationships in Science and Technology*, edited by H. P. J. Wijn (Springer, Berlin, 1986), Group 3 Vol. 19, Pt. A.
[13] O. Eriksson, A. M. Boring, R. C. Albers, G. W. Fernando, and B. R. Cooper, Phys. Rev. B **45**, 2868 (1992).
[14] P. Soderlind, O. Eriksson, B Johansson, R. C. Albers, and A. M. Boring, Phys. Rev. B **45**, 12 911 (1992).

Spin-specific photoelectron diffraction using magnetic x-ray circular dichroism

J. G. Tobin and G. D. Waddill[a)]
Department of Chemistry and Materials Science, Lawrence Livermore National Laboratory, Livermore, California 94550

X. Guo and S. Y. Tong
Laboratory for Surface Studies and Department of Physics, University of Wisconsin-Milwaukee, Milwaukee, Wisconsin 53201

The first observation of spin-dependent photoelectron diffraction using circularly polarized x rays is reported for monolayer ferromagnetic fcc Fe films on Cu(001). Circularly polarized x rays are used to produce spin-polarized photoelectrons from the Fe2p spin-orbit split doublet, and intensity asymmetries in the $2p3/2$ level of $\approx 3\%$ are observed. The asymmetry is dependent on the relative orientation of the x-ray polarization vector and the Fe magnetic moment. This spin-dependent technique promises the direct, element-specific determination not only of local atomic structure, but magnetic structure as well.

The last several years have witnessed a massive growth in the research and development of nanoscale magnetic materials. Perhaps the best review is provided by the Falicov report[1] on "Surface, Interface, and Thin-Film Magnetism." Three general lessons can be derived from this report. (1) Magnetism is one of those special cases where fundamental research can directly lead to technological applications; (2) the key to understanding and manipulation of magnetic properties is the subtle yet overwhelming interplay of atomic geometric structure and local magnetic properties. For example, the giant magnetoresistance effect (GMR), which is already being explored for technological exploitation,[2–4] appears to be intimately coupled to interfacial and thin film effects and probably will require elementally specific probes for an explicit determination of the underlying causes.[5–7] This also appears to be the case for spin valves,[8–10] another source of device miniaturization in read heads and magnetic sensors. [While it may eventually be found that these two effects are fundamentally connected, for now it appears that the GMR effect (up to 60%) is dependent upon an antiferromagnetic coupling through a nonferromagnetic layer while the spin valve effect ($\leqslant 10\%$) is associated with a loosely coupled ferromagnetic layer,[9] which can be controlled externally.] (3) The importance of probes with a direct spin dependence. A very recent illustration of this is the development of the magnetic x-ray circular dichroism using x-ray absorption[11–15] and photoemission[16,17] as a probe of surface, monolayer, and multilayer magnetism. It is this advantage that we propose to utilize, as will be described. However, before beginning that discussion, it is useful to summarize the state of of core-level photoelectron spectroscopy and diffraction at this point.

In the case of photoelectron spectroscopy and diffraction, there have been some significant strides recently. High resolution core-level spectroscopy has been demonstrated by Himpsel,[18] to be a sensitive measure of oxidation state of surface silicon. Photoelectron diffraction[19–21] has been shown to be a powerful probe of metal overlayer structure. Using the internal spin polarization of the 3s state of Mn, Fadley *et al.* have reported observation of spin-specific photoelectron diffraction in bulk systems,[22] and used it to study short range magnetic order. In attempting to extend such measurements to metal overlayer systems,[23] limitations to this method became apparent. The small 3s cross section, the overlap of the split peaks, the large background on which the peaks rode, and the generally unknown spin composition of the peaks all militate for a better defined approach. This approach must possess some sort of independent spin sensitivity or selectivity, such as that shown in Fig. 1, and a more rigorous analysis based upon multiple scattering theory. One avenue to better spin sensitivity is the utilization of spin detectors, which unfortunately carry with them a concomitant loss. (Efficiencies of 10^{-2}–10^{-4} are common, relative to unpolarized detection.) Despite this handicap to spin-polarized, core-level, photoelectron spectroscopy, the first results were reported by Kisker *et al.* and Carbone *et al.* looking at the shallow 3p (Ref. 24) and 3s (Refs. 25 and 26) levels of bulk Fe. Subsequently, the measurements have been extended to include magnetic overlayers, demonstrating effects such as antiferromagnetic coupling between substrate and overlayer.[27] (In parallel with this, spin-polarized photoemission studies of valence band structure have also been pursued. Recent examples include the investigations of quantum well state, by Johnson *et al.*[28] and Carbone *et al.*,[29] which suggest that these states are connected to oscillatory interlayer coupling. Johnson has also led the effort at NSLS to extend their spin-resolved measurements to include shallow core levels.)[30] Finally, Roth *et al.*[31] reported the observation of strong dichroism effects in the Fe 3p spectra using linear polarization, with and without spin detection, by using specific high symmetry geometries. These first studies were invariably done using *linearly* polarized soft x rays, and the spin sensitivity was provided by electron spin polarizers coupled to energy-analyzers. An alternative means to extract spin-specific information from core levels is to use circularly polarized x rays and the strong dipole selection rules that govern these transitions. The observation of photoemission circular dichroism was first demonstrated using the Fe 2p

a)Present address: University of Missouri-Rolla, Dept. of Physics, Rolla, MO 65401-0249

 0021-8979/94/76(10)/6465/3/$6.00 © 1994 American Institute of Physics

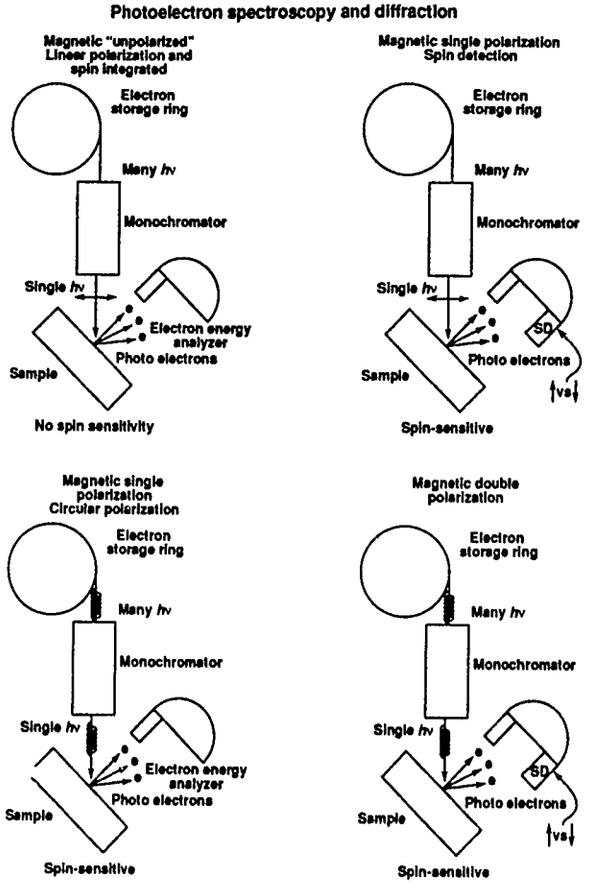

FIG. 1. This figure shows schematically the experimental setup. A single energy ($h\nu$) of electromagnetic radiation is selected from the broad continuum of synchrotron radiation using a monochromator. The photons cause the ejection of photoelectron, which are then collected by the angle ($\pm 3°$) and energy resolving detector. The photons can be linearly or circularly polarized. The electron energy analyzer can be coupled to a spin detector (SD).

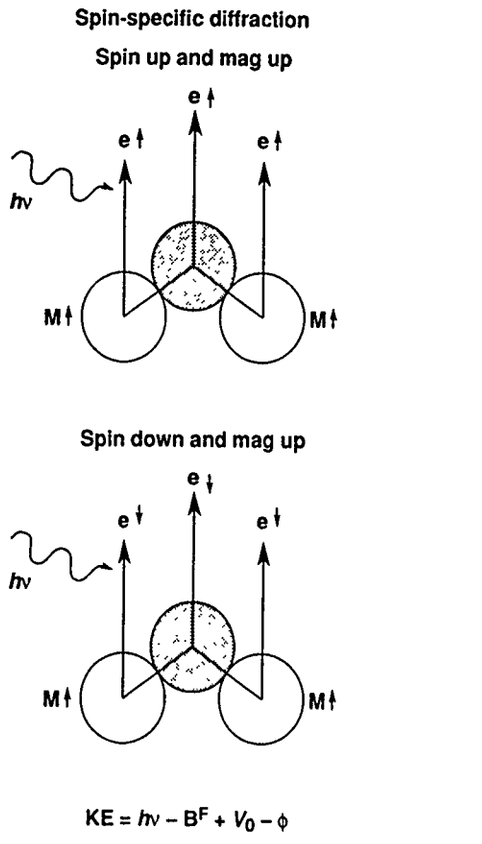

FIG. 2. This schematic illustrates the underlying cause of photoelectron diffraction: interference between the direct and scattered waves. The interference is dependent upon the details of the local geometry and the emission angles, the kinetic energy (KE), and the spin of the outgoing electron, as well as the sample magnetization. The kinetic energy is varied by scanning the photon energy, $h\nu$. The binding energy (B^F), the work function ($\varnothing$), and inner potential (V_0) are constant for a given state and material system.

states of bulk Fe by Baumgarten *et al.*[16] and then ultrathin films of Fe/Cu(001) by Waddill *et al.*[17] Subsequently, Kaindl *et al.* extended this work to rare-earth systems, with the observation of very strong effects.[32] More recently, a large circular dichroism in the Fe $3p$ emission from Fe/Cu(001) has been observed and quantitatively simulated,[33] using a spin-specific, fully relativistic, multiple scattering theory that can also explain the large linear dichroism that was previously observed.[31] It is this spin selectivity, based upon circular polarization of soft x rays, that we have used to perform spin-specific photoelectron diffraction.

In photoelectron diffraction, an electron is ejected from a core level and can scatter or diffract off of its nearest neighbors. In the usual experiments a small solid angle of electrons is collected and linearly polarized x rays are used as the excitation. From the energy or angular variations of the partial cross section, the local geometrical structure can be obtained. To gain sensitivity to local magnetic structure, the spin of the electron must come into play (Fig. 2). One way to do this is to use circularly polarized x rays as the excitation: In this case the $2p$ peaks will be intrinsically spin polarized. A naive atomic picture would predict that the $2p_{3/2}$ would be

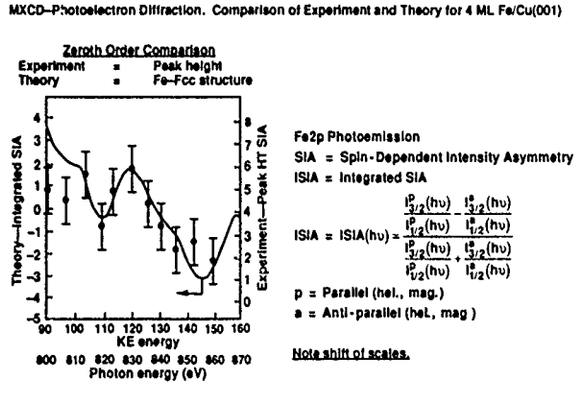

FIG 3. Spin-specific photoelectron diffraction using magnetic circular dichroism, for emission along the Cu[111] direction. Because the sample was perpendicularly magnetized, the x rays were incident normal to the surface. Experimental results are shown as data points with error bars. The theoretical results are from a spin-specific, multiple scattering calculation using an unrelaxed fcc model (a=3.6 Å) for the Fe

$\pm 25\%$ polarized and the $2p_{1/2}$ would be $\mp 50\%$ polarized. These spin-polarized electrons can then be used to determine local atomic magnetic structure, for example, to distinguish local antiferromagnetic ordering versus local ferromagnetic ordering.

In fact, we have already done the first such experiment. In Fig. 3 is an example of our data collected using ferromagnetic Fe/Cu(001) and circularly polarized x rays without spin detection. It should be noted that our measurements were done in mirror planes and with variation of both the magnetization and helicity, to remove other extraneous effects and as a cross-check upon our analysis. It is obvious from our spectra that there is a fundamental intensity asymmetry that is independent of exchange-induced peak shifting. A more thorough discussion is provided elsewhere.[34] Thus, spin-dependent photoelectron diffraction can provide a sensitivity to local magnetic order, similar to that demonstrated for spin-polarized extended x-ray-absorption fine structure.[35]

Work was performed under the auspices of the U.S. Department of Energy by the Lawrence Livermore National Laboratory under Contract No. W-7405-ENG-48. Work at Wisconsin was supported by the U.S. Department of Energy. The authors wish to thank Karen Clark for her clerical support. Discussions with James Brug were enlightening and enjoyable.

[1] L. M. Falicov, D. T. Pierce, S. D. Bader, R. Gronsky, K. B. Hathaway, H. J. Hopster, D. N. Lambeth, S. S. P. Parkin, G. Prinz, M. Salamon, I. K. Schuller, and R. H. Victora, J. Mater. Res. **5**, 1299 (1990).
[2] G. Avalos, San Ramon Valley Times, 20 August 1993.
[3] R. Pool, Science **261**, 984 (1993).
[4] T. L. Hylton, K. R. Coffey, M. A. Parker, and J. K. Howard, Science **261**, 1021 (1993).
[5] S. S. P. Parkin, Phys. Rev. Lett. **71**, 1641 (1993).
[6] A. C. Ehrlich, Phys. Rev. Lett. **71**, 2300 (1993).
[7] V. Grolier, D. Renard, D. Bartenlian, P. Beauvillian, C. Chappert, C. Dupas, J. Ferre, M. Galtier, E. Kolb, M. Mulloy, J. P. Renard, and P. Veillet, Phys. Rev. Lett. **71**, 3023 (1993).
[8] B. A. Gurney, V. S. Speriosu, J. P. Nozieres, H. F. Lefakis, D. R. Wilhoit, and D. U. Need, Phys. Rev. Lett. **71**, 4023 (1993).
[9] B. Dieny, V. S. Speriosu, S. Metin, S. S. P. Parkin, B. A. Gurney, P. Baumgart, and D. R. Wilhoit, J. Appl. Phys. **69**, 4774 (1991).
[10] B. Dieny, V. S. Speriosu, S. S. P. Parkin, B. A. Gurney, D. R. Wilhoit, and D. Mauri, Phys. Rev. B **43**, 1297 (1991).
[11] G. Schutz, W. Wagner, W. Wilhelm, P. Keinle, R. Zeller, R. Frahm, and G. Materlik, Phys. Rev. Lett. **58**, 737 (1987); G. Schutz, M. Knulle, R. Wienke, W. Wilhelm, W. Wagner, P. Kienle, and R. Frahn, Z. Phys. B **73**, 67 (1988); G. Schutz, R. Frahm, P. Mautner, R. Wienke, W. Wagner, W. Wilhelm, and P. Kienle, Phys. Rev. Lett. **62**, 2620 (1989).
[12] C. T. Chen, F. Sette, Y. Ma, and S. Modesti, Phys. Rev. B **42**, 7262 (1990); C. T. Chen, Y. U. Idzerda, H. J. Lin, G. Meigs, A. Chaiken, G. A. Prinz, and G. H. Ho, *ibid.* **48**, 642 (1993).
[13] J. G. Tobin, G. D. Waddill, and D. P. Pappas, Phys. Rev. Lett. **68**, 3642 (1992).
[14] Y. Wu, J. Stohr, B. D. Hermsmeier, M. G. Samant, and D. Weller, Phys. Rev. Lett. **69**, 2307 (1992).
[15] J. Stohr, Y. Wu, B. D. Hermsmeier, M. G. Samant, G. R. Harp, S. Koranda, D. Dunham and B. P. Tonner, Science **259**, 658 (1993).
[16] L. Baumgarten, C. M. Schneider, M. Petersen, F. Schafers, and J. Kirschner, Phys. Rev. Lett. **65**, 492 (1990).
[17] G. D. Waddill, J. G. Tobin, and D. P. Pappas, Phys. Rev. B **46**, 552 (1992).
[18] F. J. Himpsel, Appl. Phys. A **38**, 205 (1985).
[19] S. A. Chambers, T. J. Wagener, and J. H. Weaver, Phys. Rev. B **36**, 8992 (1987).
[20] W. F. Egelhoff, Jr., G. G. Tibbetts, M. H. Hecht, and I. Lindau, Phys. Rev. B **30**, 1052 (1984).
[21] J. G. Tobin, G. D. Waddill, H. Li, and S. Y. Tong, Phys. Rev. Lett. **70**, 4150 (1993).
[22] B. Sinkovic, B. Hermsmeier, and C. S. Fadley, Phys. Rev. Lett. **55**, 1227 (1985); B. Hermsmeier, J. Osterwalder, D. J. Friedman, and C. S. Fadley, *ibid.* **62**, 478 (1989); F. Zhang *et al.*, Bull. APS **39**, 904 (1994).
[23] J. G. Tobin, M. K. Wagner, X. Q. Gui, and S. Y. Tong, Mater. Res Soc. Symp. Proc. **208**, 283 (1991).
[24] C. Carbone and E. Kisker, Solid State Commun. **65**, 1107 (1988).
[25] F. U. Hillebrecht, R. Jungblut, and E. Kisker, Phys. Rev. Lett. **65**, 2450 (1990).
[26] C. Carbone, T. Kachel, R. Rochow, and W. Gudat, Z. Phys. B **79**, 325 (1990).
[27] F. U. Hillebrecht, C. H. Roth, R. Jungblut, E. Kisker, and A. Bringer, Europhys. Lett. **19**, 711 (1992).
[28] K. Garrison, Y. Chang, and P. D. Johnson, Phys. Rev. Lett. **71**, 2801 (1993).
[29] C. Carbone, E. Vescovo, D. Rader, W. Gudat, and W. Eberhardt, Phys. Rev. Lett. **71**, 2805 (1993).
[30] P. D. Johnson, Meeting of the Materials Research Society, San Francisco, CA, Spring 1993 (unpublished).
[31] C. Roth, F. U. Hillebrecht, H. B. Rose, and E. Kisker, Phys. Rev. Lett. **70**, 3479 (1993).
[32] K. Stark, E. Navas, L. Baumgarted, and G. Kaindl, Phys. Rev. B **48**, 1329 (1993); G. Kaindl, 1993 Meeting of the User Group of the Advanced Light Source, Berkeley, CA, October 1993 (unpublished).
[33] E. Tamura, G. D. Waddill, J. G. Tobin, and P. A. Sterne, Phys. Rev. Lett. **73**, 1533 (1994).
[34] G. D. Waddill, J. G. Tobin, Y. Guo, and S. Y. Tong, Phys. Rev. B 1 **50**, 6774 (1994).
[35] G. Schutz *et al.*, Phys. Rev. Lett. **62**, 2620 (1989).

Enhanced magnetic moment and magnetic ordering in MnNi and MnCu surface alloys

W. L. O'Brien
Synchrotron Radiation Center, University of Wisconsin-Madison, 3731 Schneider Drive, Stoughton, Wisconsin 53589

B. P. Tonner
Synchrotron Radiation Center, University of Wisconsin-Madison, 3731 Schneider Drive, Stoughton, Wisconsin 53589 and Department of Physics, University of Wisconsin-Mikwaukee, 1900 East Kenwood Blvd., Milwaukee, Wisconsin 53211

Two-dimensional, ordered surface alloys of MnCu and MnNi were grown on Cu(001) and Ni(001) substrates. These surface alloys, which have structures that are not present in the bulk phase diagram, are highly corrugated with a $c(2\times2)$ periodicity. The stability of these surfaces has been predicted theoretically to be due to a gain in magnetic energy of the Mn atoms. Using a combination of soft x-ray absorption spectroscopy and x-ray magnetic circular dichroism we find that Mn is in a high-spin state and is ferromagnetically ordered in the MnNi surface alloy. MnNi surface alloys have been grown with an easy axis of magnetization perpendicular to the surface.

Ultrathin films of Mn on Cu(001) and Ni(001) have received much attention recently due to the existence of stable surface alloys which form at 1/2 monolayer (ML) coverage.[1–4] These surface alloys form at room temperature and are characterized by $c(2\times2)$ low energy electron diffraction (LEED) patterns. LEED $I-V$ analysis,[1,2] shows that these surface alloys are highly corrugated with the Mn relaxing outwards by 0.3 Å on the Cu surface and 0.25 Å on the Ni surface, Fig. 1. This large outward relaxation results in a reduction of screening at the Mn sites, observable as large binding energy shifts in the Mn $3s$, $3p$, and $2p$ photoemission.[4] The stability of these highly corrugated surfaces has been attributed to a gain in magnetic energy of the Mn atoms and ferromagnetic ordering of the Mn atoms has been predicted.[1] Calculated magnetic moments for Mn in the surface alloys are high $\sim 4\mu_B$.[1]

In this article we investigate the magnetic properties of the MnCu and MnNi $c(2\times2)$ surface alloys using soft x-ray absorption spectroscopy[5] and x-ray magnetic circular dichroism (XMCD).[6,7] Both these techniques give element specific magnetic information. The line shape of the Mn $L_{2,3}$ absorption spectra has been shown to be sensitive to the ground state spin moment of the Mn atoms.[5] The XMCD signal, $\sigma_M = (\sigma_+ - \sigma_-)$, is the difference between the absorption spectra with the photon spin parallel (σ_+) and antiparallel (σ_-) to the sample magnetization, **M**. The average of the two spectra, $\sigma_0 = 1/2(\sigma_+ + \sigma_-)$, is in most circumstances considered to be identical to the linearly polarized absorption spectra. The intensity and sign of σ_M depends on the relative orientation of **M** and the photon spin, Σ, that is $\sigma_M \sim \Sigma \cdot \mathbf{M}$. This is an important property of XMCD since it allows the direction of **M** to be determined, allowing antiferromagnetic coupling to be distinguished from ferromagnetic coupling.[6,7] We present our XMCD spectra normalized to σ_0 at the L_3 peak, $\sigma_M(\hbar\omega)/\sigma_0(L_3)$, in order to discuss relative degrees of magnetic ordering.

The experiments were performed on the 10M toroidal grating monochromator at the Synchrotron Radiation Center of the University of Wisconsin. The beamline is equipped with a water-cooled copper aperture which allows the selection of either linear, left-handed or right-handed elliptically polarized photons in the energy range 200–900 eV. The degree of circular polarization for this instrument has been calculated to be $85\pm5\%$.[8] The samples were magnetized *in situ* by a 2 kG magnet and all XMCD measurements were made on the remanent magnetization at room temperature. All absorption measurements were made using the total electron yield by monitoring the sample drain current.[6] For perpendicular magnetization the photons were incident normal to the surface. For in-plane magnetization measurements the photon angle of incidence was 65° off normal (25° grazing). This reduces the in-plane σ_M signal by a factor of 0.9 (cos 25°) when compared to σ_M signals for perpendicular magnetization. We have corrected our measurements for this geometrical factor by multiplying the normalized in-plane σ_M spectra by 1/cos (25°).

Samples were made and measured in an ultrahigh vacuum system equipped with cryo-shrouded evaporation sources. Manganese was evaporated from an Al_2O_3 crucible at a rate of 1 ML in 5 min. The MnCu $c(2\times2)$ surface alloy was prepared by evaporation onto a clean Cu(001) single crystal at room temperature. A sharp $c(2\times2)$ pattern, as viewed by LEED, was formed at 1/2 ML coverage. The

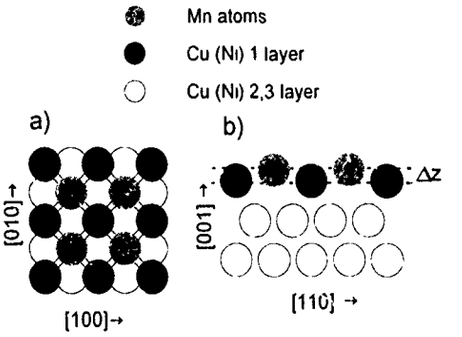

FIG. 1. Structural model of $c(2\times2)$ surface alloy (a) top view, (b) side view. Corrugation, Δz, is 0.3 Å for MnCu and 0.25 Å for MnNi.

 0021-8979/94/76(10)/6468/3/$6.00 © 1994 American Institute of Physics

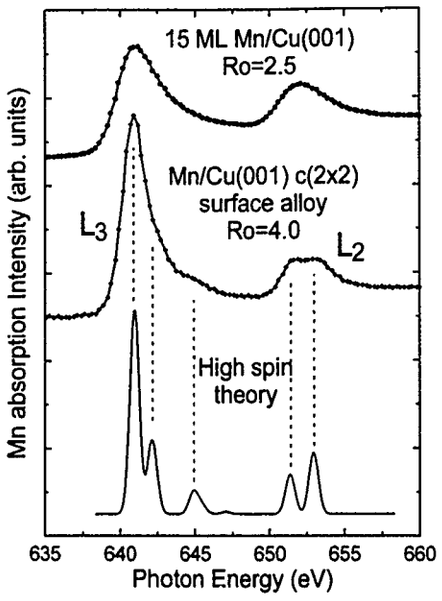

FIG. 2. (Top) Mn $L_{2,3}$ absorption spectrum, σ_0, for 15 ML of Mn on Cu(001), (middle) Mn $L_{2,3}\sigma_0$ for the Mn/Cu(001)$c(2\times2)$ surface alloy. (Bottom) Theoretical spectrum for high spin Hund's rule ground state, $S=5/2$, of d^5 Mn^{+2} from Ref. 11.

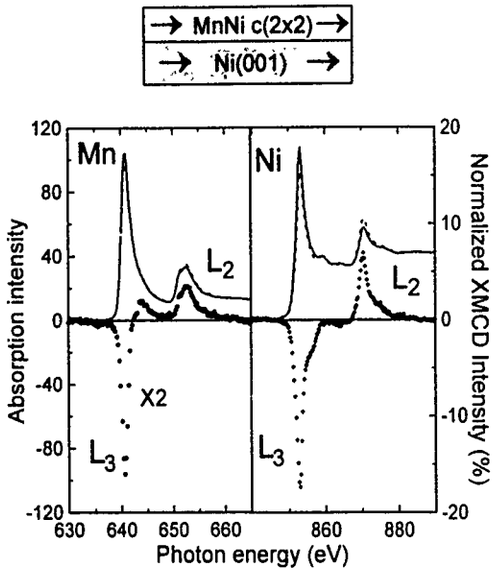

FIG. 3. (Top) Mn and Ni $L_{2,3}$ absorption spectra, σ_-, solid line, and σ_+, dashed line, for the MnNi $c(2\times2)$ surface alloy grown on Ni(001). (Bottom) Mn and Ni normalized XMCD spectrum, $\sigma_M(\hbar\omega)/\sigma_0(L_3)$, showing ferromagnetic ordering in both Mn and Ni and ferromagnetic alignment of Mn to Ni. The film was magnetized in plane along the [110] axis. The spectra have been multiplied by 1/cos(25)=1.1 to account for the photon angle of incidence.

MnNi surface alloy was grown on two types of fcc Ni(001) substrate: a Ni(001) single crystal and a 20 ML Ni(001) film grown on Cu(001). The ultrathin Ni films are known to have a perpendicular easy axis of magnetization, while the Ni(001) single crystal has an in-plane easy axis.[9] For both Ni(001) substrates a $c(2\times2)$ LEED pattern was formed after deposition of 1/2 ML of Mn. This pattern became much sharper after annealing to 400 K. The base pressure of the vacuum chamber was 5×10^{-11} Torr and the pressure during evaporation was 2×10^{-10} Torr.

In Fig. 2 we show the Mn $L_{2,3}$ absorption spectra, σ_0, for the MnCu surface alloy and a 15 ML film of Mn grown on Cu(001). The two spectra are shown normalized to the integrated L_2 intensity and are quite different. The spectrum for the surface alloy has two shoulders on the main L_3 peak and the L_2 feature appears as a doublet. The spectrum for the 15 ML film is comparatively featureless consisting of a single broad peak at both the L_3 and L_2 edges. Also the L_3/L_2 intensity ratio, R_0, is smaller than the 15 ML spectrum. The spectrum for the 15 ML film is very similar to the absorption spectra for bulk Mn.[10]

Also shown in Fig. 2 is the theoretical spectrum for high spin atomic Mn^{+2} d^5, $S=5/2$. This calculated spectrum is from Fig. 1(e) of Ref. 11 and includes spin-orbit coupling in the d levels. The only solid state effect included in the calculation is an 80% scaling of the electrostatic terms in the Hamiltonian to account for solid state screening. The calculated high spin spectrum is in good agreement with the experimental spectrum of the surface alloy. Each of the major features in the experimental spectrum are reproduced in the theoretical spectrum. The relative intensity ratios of the different features also agree well. A similar agreement is found for the Mn absorption spectrum in the MnNi surface alloy. These comparisons show that Mn in the MnNi and MnCu surface alloys are nearly atomiclike and have high spin moments.

It is informative to consider why the atomic calculation describes so well the Mn absorption spectra for these surface alloys. We first note that atomic calculations have been more successful than band structure calculations in explaining the nonstatistical behavior of the L_3/L_2 intensity ratio in the absorption spectra of first row transition metals.[10] This is due to the localization of the d orbitals involved in the transitions and the importance of many-body excitations. At the surface, d orbitals are further localized due to lower coordination. This leads to an enhanced surface moment in magnetic materials. The outward buckling of Mn in the surface alloys causes even more localization of the d orbitals resulting in an almost atomiclike Mn. The Hund's rule ground state for Mn d^5 is an $S=5/2$ state. Therefore, both the atomiclike σ_0 spectra and the high spin moment are due to the surface corrugation.

In Fig. 3 we show the Mn $L_{2,3}$ absorption spectra σ_+ and σ_- and their difference σ_M for the MnNi surface alloy grown on a Ni(001) single crystal. Mn is found to be ferromagnetically ordered with an in-plane easy axis of magnetization. Also shown in Fig. 3 is the Ni σ_+, σ_-, and σ_M spectra for the same sample. Both the Mn σ_M spectrum and the Ni σ_M spectrum are negative at the L_3 edge and positive at the L_2 edge. Mn is ferromagnetically aligned with the Ni substrate. This is unusual since bulk MnNi is antiferromagnetic at room temperature.[12] No remanent magnetization was found for either Mn or Ni for magnetization perpendicular to the surface. No remanent magnetization was found in any direction for the MnCu surface alloy.

The MnNi surface alloy was also grown on a 20 ML film

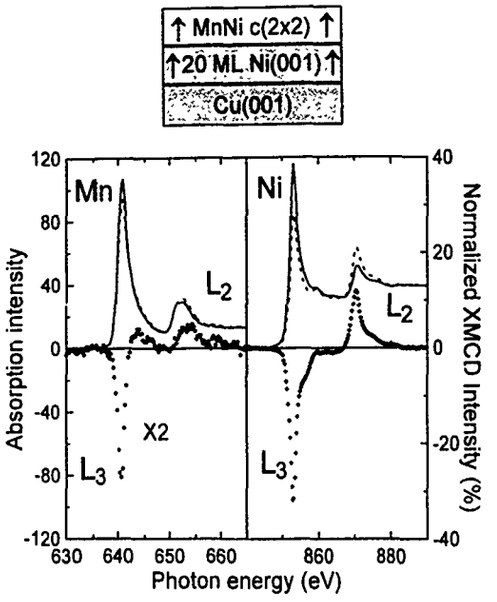

FIG. 4. (Top) Mn and Ni $L_{2,3}$ absorption spectra, σ_-, solid line, and σ_+, dashed line, for the MnNi $c(2\times2)$ surface alloy grown on a 20 ML film of Ni/Cu(001). (Bottom) Mn and Ni normalized XMCD spectrum, $\sigma_M(\hbar\omega)/\sigma_0(L_3)$ showing ferromagnetic ordering in both Mn and Ni and ferromagnetic alignment of Mn to Ni. The film was magnetized perpendicular to the surface. The intensities of the normalized XMCD spectrum are ~2 times greater than those for MnNi grown on Ni(001), Fig. 3.

of Ni deposited on Cu(001). These Ni films are known to have an easy axis of magnetization which is perpendicular to the surface.[9] XMCD studies of these films show they have a similar σ_M line shape as bulk Ni but that the normalized intensity is increased by almost a factor of 2.[9] This increase has been attributed to magnetic domains in the bulk sample, which are apparently absent in the thin films.[9] In Fig. 4 we show the Mn and Ni $L_{2,3}$ absorption spectra σ_+ and σ_- and their difference σ_M for the MnNi surface alloy grown on a 20 ML film and magnetized perpendicular to the surface. Once again the Mn is ferromagnetically ordered and aligned with the Ni substrate. No remanent magnetization was found for either Mn or Ni for magnetization parallel to the surface. The Mn σ_M line shape is similar for the surface alloy grown on the single crystal and the thin film. The normalized intensity of the Mn σ_M spectra is increased by a factor of ~2 for growth on the Ni thin film, consistent with the Ni σ_M results and the idea of magnetic domains in the bulk sample.

In conclusion, we have shown that Mn has a high spin moment in the MnCu and MnNi $c(2\times2)$ surface alloys. This high moment results from the corrugation of the surface which localizes the Mn d orbitals. We find Mn to be ferromagnetically ordered in the MnNi surface alloy but not in the MnCu surface alloy. Long range magnetic ordering does not affect the stability of these surface alloys. We believe that it is the formation of atomiclike Mn in the Hund's rule ground state which stabilizes the surface alloy. For the MnNi surface alloy we find that the Mn is ferromagnetically coupled to the Ni for substrates with in-plane and perpendicular easy axis of magnetization. This is unusual since bulk MnNi is antiferromagnetic at room temperature.

It is also possible to grow thicker compositionally ordered MnNi alloys with the $c(2\times2)$ surface structure.[3] We have measured the magnetism in these films using XMCD and have found ferromagnetic ordering for film thickness up to 4 ML. These results will be discussed in detail in a separate publication.[13]

This work was supported by the National Science Foundation, Division of Materials Research under Grant No. DMR-94-13475. The Synchrotron Radiation Center is a national facility supported by the NSF Division of Materials Research.

[1] M. Wuttig, Y. Gautier, and S. Blügel, Phys. Rev. Lett. **70**, 3619 (1993).
[2] M. Wuttig, C. C. Knight, T. Flores, and Y. Gauthier, Surf. Sci. **292**, 189 (1993).
[3] M. Wuttig, T. Flores, and C. C. Knight, Phys. Rev. B **48**, 12082 (1993).
[4] W. L. O'Brien, J. Zhang, and B. P. Tonner, J. Phys. Condens. Mat. **5**, L515 (1993).
[5] B. T. Tole, R. D. Cowan, G. A Sawatzky, J. Fink, and J. C. Fuggle, Phys. Rev. B **31**, 6856 (1985).
[6] W. L. O'Brien and B. P. Tonner, Phys. Rev. B **50**, 2963 (1994).
[7] Y. U. Idzerda, L. H. Tjeng, H.-J. Lin, C. J. Gutierrez, G. Meigs, and C. T. Chen, Surf. Sci. **287/288**, 741 (1993).
[8] R. W. C. Hansen, W. L. O'Brien, and B. P. Tonner, Nucl. Instrum. Methods (in press).
[9] W. L O'Brien and B. P. Tonner, Phys. Rev. B **49**, 15370 (1994).
[10] J. Fink, Th. Muller-Heinzerling, B. Scheerer, W. Speier, F. U. Hillebrecht, J. C. Fuggle, J. Zaanen, and G. A. Sawatzky, Phys. Rev. B **32**, 4899 (1985). J. Zaanen, G. A. Sawatzky, J. Fink, W. Speier, and J. C. Fuggle, *ibid.* **32**, 4905 (1985).
[11] G. van der Laan and B. T. Thole, Phys. Rev. B **43**, 13401 (1991).
[12] L. Pál, F. Krén, G. Kádár, P. Szabó, and T. Tarnóczi, J. Appl. Phys. **39**, 538 (1968).
[13] W. L. O'Brien and B. P Tonner, Phys. Rev. B (to be published).

Observation of x-ray magnetic circular dichroism at the Rh $M_{2,3}$ edge in Co-Rh alloys

G. R. Harp and S. S. P. Parkin
IBM Research Division, Almaden Research Center, 650 Harry Road, San Jose, California 95120-6099

W. L. O'Brien
Synchrotron Radiation Center, University of Wisconsin-Madison, 3731 Schneider Drive, Stoughton, Wisconsin 53589

B. P. Tonner
Synchrotron Radiation Center, University of Wisconsin-Madison, 3731 Schneider Drive, Stoughton, Wisconsin, 53589 and Department of Physics, University of Wisconsin-Milwaukee, 1900 East Kenwood Boulevard, Milwaukee, Wisconsin 53211

The $M_{2,3}$ edge of Rh in Co-Rh alloys shows measurable x-ray magnetic circular dichroism. Such dichroism is not present, however, for analogous alloys of Co-Ru. The induced Ru magnetic moment, if any, is thus demonstrated to be significantly smaller than the induced Rh moment in otherwise similar Co alloys.

X-ray magnetic circular dichroism (XMCD) is a useful technique for the study of magnetic systems. In XMCD, the absorption coefficient of circularly polarized x rays is measured as a function of photon energy. Near a core level absorption edge, the absorption coefficient is seen to vary depending on the cosine of the angle between the x-ray polarization and the sample magnetization. XMCD can be used to determine the net magnetization, projected onto the x-ray polarization axis, of the individual elemental species in a complex sample.

Published studies using XMCD have considered diverse systems, including the K_1 edge[1] and $L_{2,3}$ edge[2] of the $3d$ transition metals, the $L_{2,3}$ edge of the $5d$ transition metals,[3] and the $L_{2,3}$ earth of the rare-earth transition metals.[4]

Absent from this list are the $4d$ transition metals. The reason for this omission is that for the transition metals, the $L_{2,3}$ edge is preferred for XMCD because (a) it allows the study of the d-like valence electrons, and (b) because it has a high signal to background ratio for x-ray absorption.[5] However, the angle of incidence required in the energy range of the $4d$ $L_{2,3}$ absorption edges (2–3 kV), is typically close to Brewster's angle for most crystal monochromators (≈45°).[6] That is, the monochromators produce only linearly polarized x rays, independent of the polarization of the incident radiation. For example, with 100% circularly polarized incident radiation at the Rh L_2 edge (3146 eV), a Si(111) monochromator crystal would be held at 39° incident angle, and would reflect only 8% circularly polarized x rays. Given that the XMCD signal from Rh is only 4% using 85% polarized x rays (see below), systematic errors in, e.g., spectrum normalization make measurements at the Rh L edge unfeasible. Another approach toward the measurement of Rh XMCD is therefore indicated.

In this study, we evaluate the feasibility of XMCD measurements of $4d$ transition metal elements at the $M_{2,3}$ absorption edge. Although the estimated signal/background ratios are low, such experiments may be possible with currently available grating monochromators which produce x rays approaching 90% circular polarization in the energy range of interest for the M edges (300–600 eV). We present measurements made on intermetallic alloys close to the $Co_{75}Ru_{25}$, $Co_{75}Rh_{25}$, and $Co_{50}Rh_{50}$ compositions. The particular alloys were chosen based on their miscibility, remanent moment, and energy position of their respective absorption edges (e.g., Pd was omitted due to a conflict with the O $1s$ grating absorption edge).

The measurements were made at the Synchrotron Radiation Center in Stoughton, WI, on a 10 m toroidal grating monochromator. The alloys samples were prepared as 500–1000 Å thin films on fused quartz wafers by codeposition using magnetron sputtering at 500 °C. Alloy compositions were measured by electron microprobe analysis and absolute magnetizations were measured by superconducting quantum interference device magnetometry. The samples were transported to the synchrotron in air. To remove the resulting surface impurity layer, the films were sputtered in vacuum and annealed to ~300 °C prior to measurement. Residual oxygen impurity levels were small (less than 1 equivalent monolayer) as determined from the oxygen $1s$ core absorption peak. The samples were magnetized in-plane prior to the XMCD measurements, and were measured in remanence (zero applied field). We estimate the x rays had about 85%±5% circular polarization[7] and they were incident at ±65° from the surface normal upon the sample, with consecutive spectra taken at alternating angles. Absorption spectra were measured using a total electron yield technique. For more information on the measurement technique, see Ref. 7.

Figure 1 displays the XMCD data from the Co $L_{2,3}$ and Ru $M_{2,3}$ edges of a $Co_{75}Ru_{25}$ alloy. Here the solid and dashed curves are the absorption coefficients, $\alpha_{\pm 65°}$, taken in the two sample positions (magnetization 25° or 155° with respect to polarization, respectively), and the dotted curve their difference. Regarding this data, we wish to make several points: in the Co spectrum the signal to background ratio at the L_3 absorption edge is 4, while at the Ru M_3 edge it is 0.15, or about 25 times smaller. As a result, the Ru spectrum took much longer to collect (about 8 h) than the Co spectrum (about 40 min). The peak XMCD signal, χ_p, defined as $\chi_p = \max\,[(\alpha_{+65}-\alpha_{-65})/(\alpha_{+65}+\alpha_{-65})]$, is 0.032 at the Co edge, compared with 0.21 for a saturated epitaxial Co film.

 0021-8979/94/76(10)/6471/3/$6.00 © 1994 American Institute of Physics

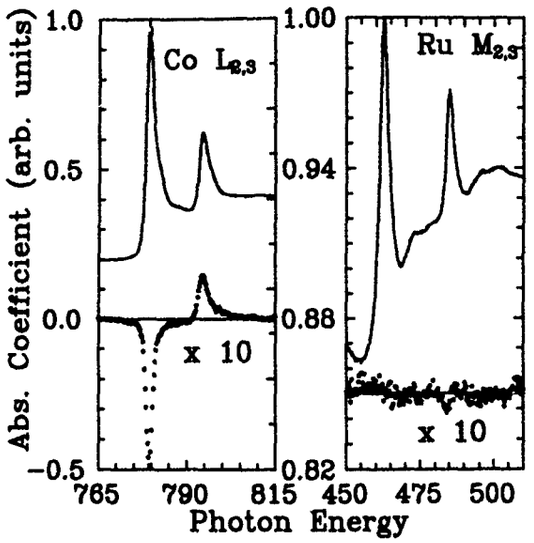

FIG. 1. Circularly polarized x-ray absorption spectra (solid and dashed curves) and their difference or dichroism (dotted curve) from a $Co_{75}Ru_{25}$ alloy. The Co $L_{2,3}$ edge shows significant dichroism but the Ru $M_{2,3}$ edge does not.

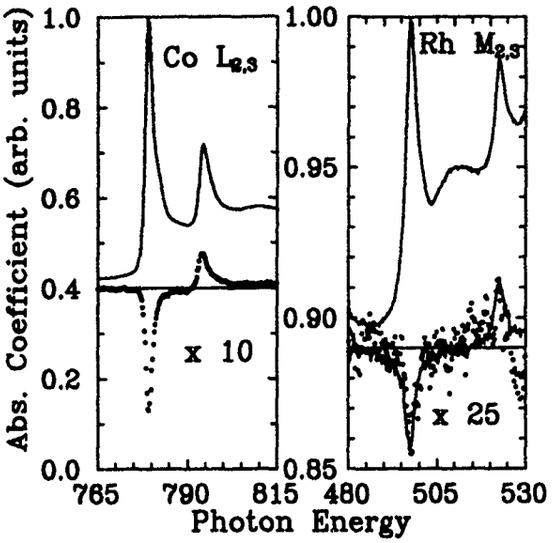

FIG. 3. Spectra analogous to Figs. 1 and 2, except for a $Co_{49}Rh_{51}$ alloy. The Rh atoms develop measurable magnetic moments in this alloy.

The low XMCD signal is caused by the low saturation magnetization in this alloy and by its low remanence (52%). At the Ru edge, however, no XMCD signal is seen. We conservatively place an upper bound on χ_p to be ≤ 0.005 at the Ru L_3 edge.

The data from the $Co_{75}Ru_{25}$ alloy can be compared with Fig. 2 showing spectra from a $Co_{77}Rh_{23}$ alloy. Here $\chi_p=0.12$ at the Co edge. At the Rh $M_{2,3}$ edge definite XMCD is seen, with $\chi_p=0.04$. The induced Rh moment is parallel to the Co moment. This alloy had 66% remanence, and we can extrapolate the XMCD measurement to determine that the saturation Rh χ_p for this alloy is 0.06. Mössbauer measurements of the Rh moment in $Fe_{75}Rh_{25}$ alloys indicate an induced Rh moment of $\sim 1\ \mu_B$.[8] If we assume that Rh develops a similar moment in Co alloys, we may deduce an approximate proportionality constant between χ_p for Rh and its moment, i.e., $\chi_p=0.06/\mu_B$.

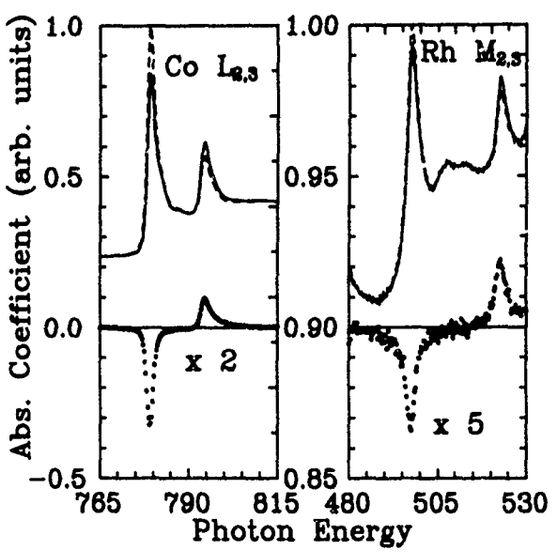

FIG. 2. Spectra analogous to Fig. 1, except for a $Co_{77}Rh_{23}$ alloy. Here significant dichroism is seen at the Rh $M_{2,3}$ edge, indicating that the Rh develops a significant magnetic moment.

Figure 3 shows spectra from a $Co_{49}Rh_{51}$ alloy. The Co edge has $\chi_p=0.025$. The Rh dichroism signal is only about 3 times the noise level, yet still measurable with $\chi_p=0.006$. This sample had 40% remanence, and based on the results from the previous paragraph, we find the saturation Rh moment in this alloy to be 0.25 μ_B. As a guide to the eye, we have superimposed a scaled version of the $Co_{77}Rh_{23}$ XMCD spectrum as a dashed curve.

This last result has particular significance to our understanding of the $Co_{75}Ru_{25}$ alloy (Fig. 1). Although the Ru alloy possessed remanent Co moments 1.3 times higher than in the $Co_{49}Rh_{51}$ alloy, no detectable Ru moment was found. If we assume the same proportionality constant between magnetic moment and χ_p for Ru as for Rh, we can place an upper bound on the saturation Ru moment in the $Co_{75}Ru_{25}$ alloy of approximately 0.16 μ_B. Thus we find that Ru and Rh behave qualitatively quite differently when alloyed with Co.

In summary, we have demonstrated the feasibility of XMCD measurements in the $4d$ transition metals using photon energies below 1000 eV. We find that the signal/background ratio at the $4d$ $M_{2,3}$ edge is about 25 times smaller than at the $3d$ $L_{2,3}$ edge, but that this edge can be effectively used to study XMCD in the $4d$ transition metals.

[1] See, e.g., G. Schütz, W. Wagner, W. Wilhelm, P. Keinle, R. Zeller, R. Frahm, and G. Materlik, Phys Rev. Lett. **58**, 737 (1987), H. Maruyama, T. Iwazumi, H. Kawata, A. Koizumi, M. Fujita, H Sakurai, F. Itoh, K. Namikawa, H. Yamazaki, and M. Ando, J. Phys. Soc. Jpn. **60**, 1456 (1991).

[2] See, e.g., C. T. Chen, F. Sette, Y. Ma, and S. Modesti, Phys. Rev. Lett. **42**, 7262 (1990); C. T Chen, N. V. Smith, and F. Sette, Phys. Rev. B **43**, 6785 (1991); J. G Tobin, G. D. Wadill, and D. P Pappas, Phys. Rev. Lett. **68**,

3642 (1992); Y. Wu, J. Stöhr, B. D. Hermsmeier, M. G. Samant, and D. Weller, *ibid.* **69**, 2307 (1992); W. L. O'Brien, J. Zhang, B. P. Tonner, J. Phys. Condens. Matter **5**, L515 (1993).
[3]G. Schütz, R. Weinke, W. Wilhelm, W. Wagner, P. Kienle, R. Zeller, and R. Frahm, Z. Phys. B **75**, 495 (1989).
[4]See, e.g., G. Schütz, M. Knülle, R. Weinke, W. Wilhelm, W. Wagner, P. Keinle, and R. Frahm, Z. Phys. B **73**, 67 (1988); H. Maruyama, T. Iwazumi, H. Kawata, A. Koizumi, M. Fujita, H. Sakurai, F. Itoh, K. Namikawa, H. Yamazaki, and M. Ando, J. Phys. Soc. Jpn. **60**, 1456 (1991).
[5]J. Stöhr and Y. Wu, in *New Directions in Research with Third Generation Soft X-ray Synchrotron Radiation Sources*, Proceedings of the NATO Advanced Study Institute (Kluwer Academic, The Netherlands, to be published).
[6]B. D. Cullity, *Elements of X-ray Diffraction* (Addison–Wesley, Reading, MA, 1956), p. 106.
[7]R. W. C. Hansen, W. L. O'Brien, and B. P. Tonner, Nucl. Instrum. Methods (to be published).
[8]G. Shirane, R. Nathans, and C. W. Chen, Phys. Rev. **134**, A1547 (1964).

Circular magnetic x-ray dichroism for rare earths

H. König,[a] Xindong Wang, and B. N. Harmon
Ames Laboratory, Iowa State University, Ames, Iowa 50011

P. Carra
E.S.R.F., B.P. 220, F-38043, Grenoble, France

Circular magnetic x-ray dichroism is a promising new tool for the study of spin and orbital moments in ferromagnetically ordered materials. For rare-earth systems the L_2 and L_3 edge dichroic spectra give information about the magnetic properties of the $5d$ conduction electrons. This article addresses a few of the key issues concerning the interpretation of the spectra. In particular, the quadrupole nature of the dichroic spectra below the L absorption edges and its angular dependence is discussed. The important role of the $4f$-$5d$ exchange in causing a large and important spin dependence in the $2p-5d$ matrix elements is likewise examined.

Because of the strong electronic correlations associated with the ground state of magnetic materials, there is an old but continuing problem on how to best formulate a model capable of quantitative analysis. With the advent of dedicated synchrotron sources a new tool, circular magnetic x-ray dichroism (CMXD), has become available and may eventually prove as valuable as magnetic neutron scattering in helping to sort out the microscopic details of the magnetic ground state. An attractive feature of CMXD is its ability to yield element and shell specific information about the separate spin *and* orbital magnetic moments, even in complicated magnetic materials. In this article we concentrate on several issues which arise when trying to interpret features of the observed spectra for the L edges in rare-earth materials. Although the first CMXD measurements on rare-earth materials (Gd and Th) were reported in 1988,[1] there already exists a fairly large literature on the subject, which we cannot adequately review in this short paper.

In the analysis of the L edge x-ray dichroism experiments on Gd a simple model was used to compare the experimental spectra with a theoretical spin difference d density of states.[1] The obvious disagreement was noted. The question arose whether when dealing with high energy photons and the creation of a core hole the single particle picture is valid. Certainly an atomic picture with full multiplet considerations is required for the M_4 and M_5 spectra of the rare earths (involving dipole transitions from the $3d$ core states to the highly local $4f$ states).[2] However a self-consistent, relativistic, spin-polarized band structure calculation was extremely successful in reproducing the dichroic spectra of Gd for the L_2 and L_3 edges,[3] thus indicating the single particle picture may be adequate for the very itinerant $5d$ states. The experimental data also exhibit some structure below the L_2 and L_3 absorption edges, and these features were quantitatively accounted for by using an atomic model to evaluate the $2p-4f$ quadrupole transitions.[3] Similar atomic calculations were carried out to explain the variation of these below edge features in the dichroic spectra across the entire heavy rare-earth series.[4] There is good agreement with experiment.[5] The reason these quadrupole features appear below the L edges is that the core hole is more attractive for the localized $4f$ states than for the itinerant $5d$ states.

These first calculations also included a quantitative prediction for confirming the quadrupolar character of the below edge structure. There is an expected difference in the angular dependence of the dipole and quadrupole spectra as one varies the direction of the magnetization relative to the wave vector of the incoming light.[3] For some rare earths (e.g., Ho and Er) the angular difference is expected to be large and was looked for experimentally, with no success.[6–8] We have speculated on possible explanations for the negative results of these experiments.[9] We believe the simplest explanation which should be checked first involves the lack of complete magnetic alignment that has been obtained so far in the experiments. There are two causes for the lack of alignment: (1) experiments done on powders that have the easy axis of grains misaligned (not the case for samples with grain alignment or with very small anisotropy), and (2) the misalignment caused by thermal fluctuations (not a problem at temperatures that are very low compared with the magnetic ordering temperature). To demonstrate the rather large sensitivity of the difference between dipole and quadrupole angular dependence to temperature, we consider an isolated ion of holmium. We neglect crystal field effects (which can also reduce the expected difference). The integrated spectra for the $2p-4f$ quadrupole transitions can be decomposed into two terms, one with a $P_1(\theta)=\cos(\theta)$ dependence, and the other with a $P_3(\theta)=[5\cos^2(\theta)-3]\cos(\theta)/2$ dependence.[10,11] The first term has an angular dependence identical to the $2p-5d$ dipolar transitions, so it is only the second term that gives the quadrupolar transitions at different angular dependence. If we take the $|JM\rangle$ $4f$ states as equally spaced in energy (no crystal field effects) and evaluate the magnitude of the factor multiplying the P_3 term for Ho, we get the dependence shown in Fig. 1. This figure indicates under ideal conditions, that if the experimental $4f$ moment is at 70% of its zero temperature saturated value, then the P_3 term is already reduced by a factor of 6! We are not aware of any experiments that have been done in such a way that the magnetic alignment was sufficient to make a definitive statement about the quadrupolar angular dependence, although several groups are planning such measurements in the near future.

Another interesting aspect of the L dichroic spectra for rare earths is the sign. It was a surprise when the first spectra for Gd were analyzed and interpreted as indicating more spin up than spin down unoccupied $5d$ states. This is inconsistent

[a]Also at E S R.F., B.P 220, F-38043 Grenoble, France

 0021-8979/94/76(10)/6474/3/$6 00 © 1994 American Institute of Physics

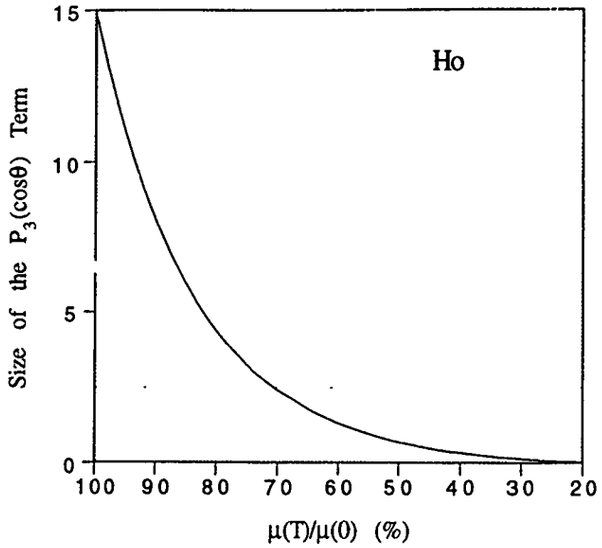

FIG. 1. The P_3 term for the quadrupolar part of the dichroic spectra of Ho as a function of the magnetic moment (relative to the zero temperature saturated moment).

with there being a net spin up conduction electron moment of 0.63 μ_B/atom moment. Figure 11 of Ref. 1 compares the difference in the $5d$ spin density of states (DOS) from a band structure calculation with that derived from the measured dichroic spectra. Based on a simple model the experimental spectra indicate a dominant positive spin DOS above E_F, while the theory has a dominant negative spin DOS. These authors comment "This obvious disagreement may indicate a modification of the $5d$ spin density spectrum by the polarized core hole created by absorption of a circularly polarized photon." This same sign problem has also recently been discussed for rare-earth intermetallic compounds by Giorgetti *et al.*[12] who suppose that it is due to an open $4f$ shell. As mentioned earlier, the full band structure calculations *with dipole matrix elements* are able to accurately reproduce the dipolar part of the experimental dichroic spectra above the L_2 and L_3 edges; so that it is not necessary to invoke core hole or many body interactions to explain the sign. In a previous publication we briefly discussed the resolution.[4] The $5d$ radial functions in rare earths with open $4f$ shells have a strong spin dependence. This is illustrated in Fig. 2 for the Gd atom. The $5d$ orbitals by themselves are too spread out and the $5d$ band too broad to support a magnetic ground state, and it is the $5d$ exchange interaction with the localized $4f$ orbitals (which have a peak in probability well within 1.0 au) that is responsible for inducing the magnetism in the conduction electron bands. The observed conduction electron moment scales with the total spin of the $4f$ states across the rare-earth series. The $2p$ radial function has its peak in probability just inside 0.1 au and the dipole matrix elements between the $2p$ and $5d$ orbitals are very spin dependent, with the matrix elements for the majority spin up $5d$ states being 20%–30% larger than the corresponding $5d$ spin down states at the same energy. The effect of the matrix elements is demonstrated in Figs. 3 and 4. In the first we plot the (up–down) difference in the DOS for Gd calculated with the linear aug-

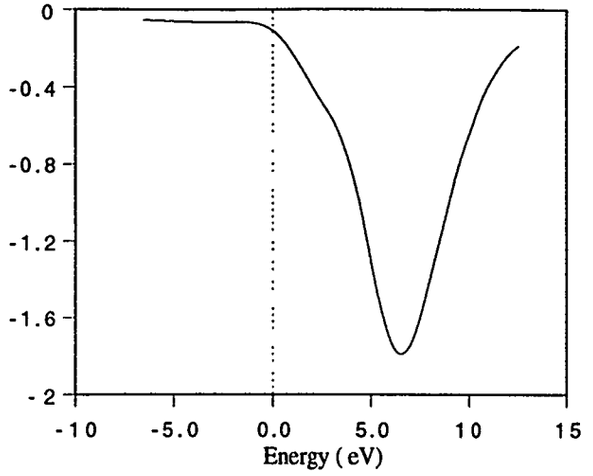

FIG. 3. The unoccupied spin up minus the spin down $5d$ DOS of Gd. The theoretical curve has been Lorentzian broadened by 6 eV.

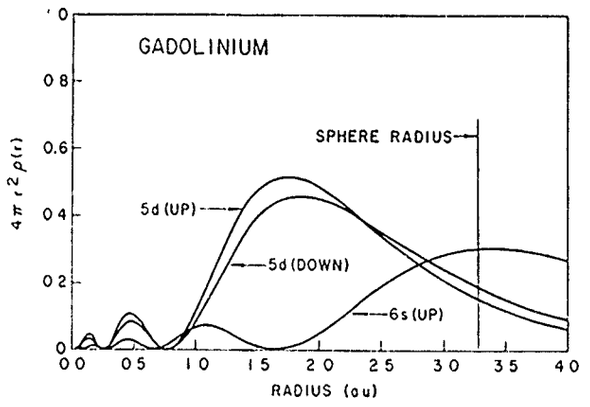

FIG 2 The spin up and spin down $5d$ radial functions for a neutral gadolinium atom.

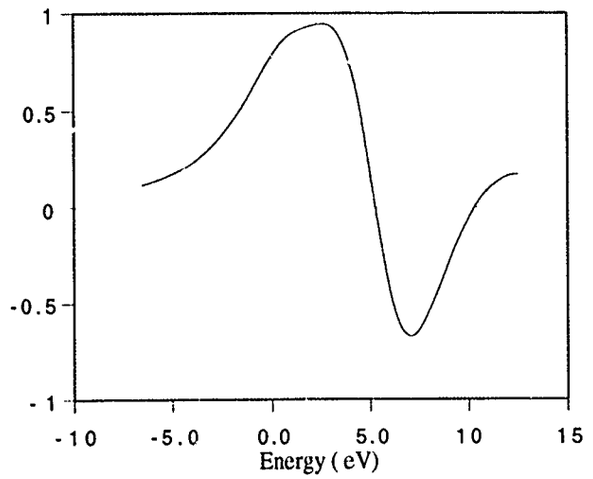

FIG. 4. The same as Fig 3 except the spin up density of states has been multiplied by 1.25 to approximate the spin-dependent matrix element effect for the dichroic spectra

mented plane waves (LAPW) method, using several energy panels above E_F. The DOS has been set to zero below E_F and broadened with a 6 eV Lorentzian. The broadening represents the large (~3.5 eV) core hole and final state lifetime and the experimental resolution. It can be seen that the spin down DOS dominates. Now we take the same data set and multiply the spin up DOS by 1.25 before making the subtraction. The results shown in Fig. 4 show that it is now the spin up spectrum that "wins." There is sufficient spin up d character to the bands extending to high energies that the integrated spectrum never switches sign to indicate a net spin down moment. This means that a recently derived sum rule[13] involving the net spin is invalid for the case of L edge spectra involving rare-earth $5d$ bands. It is interesting however that a related sum rule for the net orbital moment[14] yielded reasonable estimates when applied to the amorphous and crystalline $GdFe_2$ dichroic spectra.[15] It is still unclear if the orbital moment sum rule will retain its usefulness in all cases, and why.

We have benefited from conversations with Dr. V. P. Antropov and Dr. B. T. Thole, and with Professor A. I. Goldman and Professor G. Schütz. This work was supported by the U.S. Department of Energy, Office of Basic Energy Sciences, Materials Sciences Division. Ames Laboratory is operated for the U.S. Department of Energy by Iowa State University under Contract No. W7405-ENG.

[1] G. Schütz, M. Knülle, R. Wienke, W. Wilhelm, W.Wagner, P. Kienle, and R. Frahm, Z. Phys. B **73**, 67 (1988).
[2] B. T. Thole, G. van der Laan, J. C. Fuggle, G. A. Sawatsky, R. C. Karnatak, and J.-M. Esteva, Phys. Rev. B **32**, 5107 (1985).
[3] P. Carra, B. N. Harmon, B. T. Thole, M. Altarelli, and G. A. Sawatsky, Phys. Rev. Lett. **66**, 2495 (1991).
[4] X. Wang, T. C. Leung, B. N. Harmon, and P. Carra, Phys. Rev. B **47**, 9087 (1993).
[5] P. Fischer, G. Schütz, and G. Wiesinger, Solid State Commun. **76**, 777 (1990).
[6] P. Fisher, G. Schütz, S. Stähler, and G. Wiesinger, J. Appl. Phys. **69**, 6144 (1991).
[7] J. C. Lang, S. W. Kycia, X. Wang, B. N. Harmon, A. I. Goldman, D. J. Branagan, R. W. McCallum, and K. D. Finkelstein, Phys. Rev. B **46**, 5298 (1992).
[8] K. Shimomi, H. Maruyama, K. Kobayashi, A. Koizumi, H. Yamazaki, and T. Iawazumi, Jpn. J. Appl. Phys. **32-2**, 314 (1992).
[9] X. Wang, V. P. Antropov, B. N. Harmon, J. C. Lang, and A. I. Goldman, these proceedings.
[10] P. Carra and M. Altarelli, Phys. Rev. Lett. **64**, 1286 (1990).
[11] C. Brouder (unpublished).
[12] C. Giorgetti, S. Pizzini, E. Dartyge, A. Fontaine, F. Baudelet, C. Brouder, Ph. Bauer, G. Krill, S. Miraglia, D. Fruchart, and J. P. Kappler, Phys. Rev. B **48**, 12732 (1993).
[13] P. Carra, B. T. Thole, M. Altarelli, and X. Wang, Phys. Rev. Lett. **70**, 694 (1993).
[14] B. T. Thole, P. Carra, F. Sette, and G. van der Laan, Phys. Rev. Lett. **68**, 1943 (1992)
[15] J. C. Lang, X. Wang, V. P. Antropov, B. N. Harmon, A. I. Goldman, H. Wan, G. C Iadjipanayis, and K. D. Finkelstein, Phys. Rev. B **49**, 5993 (1994).

Circular dichroism in core-level photoemission from nonmagnetic and magnetic systems: A photoelectron diffraction viewpoint (abstract)

A. P. Kaduwela
Materials Sciences Division, Lawrence Berkeley Laboratory, Berkeley, California 94720

H. Xiao
Physics Department, University of California, Davis, California 95616

S. Thevuthasan
MSIN K2-12, Battelle Pacific Northwest Laboratory, Richland, Washington 99532

C. Westphal and M. A. Van Hove
Materials Sciences Division, Lawrence Berkeley Laboratory, Berkeley, California 94720

C. S. Fadley
Physics Department, University of California, Davis, California 95616 and Materials Sciences Division, Lawrence Berkeley Laboratory, Berkeley, California 94720

Magnetic circular dichroism (MCD) in x-ray absorption represents an exciting new technique for studying and imaging magnetic systems. However, there are to date relatively few studies of dichroism in the inherent process involved: photoelectron emission. We will here illustrate that photoelectron diffraction (PD) theory provides a fruitful way of analyzing dichroism data for both nonmagnetic and magnetic systems. Circular dichroism (CD) has been observed in core-level photoemission from nonmagnetic systems: C 1s from CO/Pd(111)[1] and Si $2p$ from Si(100)[2]. For CO/PD(111), chirality in the experimental geometry is readily discernible, but for Si(100), it is more difficult to define the chirality with simple vector relationships. PD effects implicitly contain all information on such core-level dichroism, and we will present multiple-scattering simulations of the observations to date. We will also discuss the role of such CD effects in core-level MCD measurements, using Fe $2p$ emission from magnetically aligned Fe(110)[3] as an example. The analysis of such MCD data has so far been qualitative.[3] We will present a more quantitative analysis including final-state effects such as the interference of $l\pm1$ photoelectron channels and spin-dependent scattering and diffraction.

[1] J. Bansmann *et al.*, Phys. Rev. B **46**, 13 496 (1992).
[2] H. Daimon *et al.*, Jpn. J. Appl. Phys. **32**, L000 (1993).
[3] L. Baumgarten *et al.*, Phys. Rev. Lett. **65**, 492 (1990).

Elemental determination of the magnetic moment vector (abstract)

H.-J. Lin, G. Meigs, and C. T. Chen
AT&T Bell Laboratories, 600 Mountain Avenue, Murray Hill, New Jersey 07974

Y. U. Idzerda and G. A. Prinz
Naval Research Laboratory, Washington, DC 20375

G. H. Ho,
University of Pennsylvania, Philadelphia, Pennsylvania 19104

Recently, we have shown that magnetic circular dichroism (MCD) can be used to obtain element specific magnetic hysteresis (ESMH) loops of heteromagnetic systems.[1] By using magnetic circular dichroism (MCD) we map the three orthogonal components of the magnetic moment vector of each element of a strongly (90°) coupled $Fe_{30}Co_{70}$/Mn/$Fe_{30}Co_{70}$ single crystal trilayer heterostructure as a function of applied magnetic field. The intensity of the MCD of the Mn $L_{2,3}$ absorption edges clearly shows that the Mn possesses a ferromagnetically aligned net magnetic moment. Furthermore, the individual element specific hystersis curves, when followed through the magnetic reversal process, reveals a detailed description of the magnetization reversal in the presence of both cubic anisotropy and strong exchange. This vividly demonstrates the capability of this technique to analyze the magnetic moment reversal process in the presence of strongly competing interactions.

[1] C. T. Chen, Y. U. Idzerda, H.-J. Lin, G. Meigs, A. Chaiken, G. A. Prinz, and G. H. Ho, Phys. Rev. B **48**, 642 (1993).

 0021-8979/94/76(10)/6477/1/$6.00 © 1994 American Institute of Physics

Hybrid NiFeCo-Ag/Cu multilayers: Giant magnetoresistance, structure, and magnetic studies

J. D. Jarratt and J. A. Barnard
Department of Metallurgical and Materials Engineering, The University of Alabama, Tuscaloosa, Alabama 35487-0202

Giant magnetoresistance (GMR), crystal structure, and magnetic properties have been investigated in sputtered $Ni_{66}Fe_{16}Co_{18}$-Ag/Cu hybrid granular multilayer thin films. High angle x-ray diffraction (HXRD) was used to reveal the overall film structure and growth texture and low angle XRD was used to investigate the periodicity and flatness of the multilayer structures. Hysteresis loops for the as-deposited Ag-rich films show superparamagnetic behavior (and conventional granular GMR) which does not saturate in 14 kOe. Very NiFeCo-rich films are magnetically soft and exhibit induced in-plane uniaxial anisotropy.

I. INTRODUCTION

Giant magnetoresistance (GMR) in magnetic/nonmagnetic multilayer thin films,[1] discontinuous multilayer films,[2,3] and in granular phase separated alloys[4–6] has been the subject of much recent study. We have recently investigated the composition dependence of GMR and structure in "thick" (>1000 Å) $Ni_{66}Fe_{16}Co_{18}$-Ag single layer phase separating films.[7] In this article we analyze the effect of layering and reduced dimensions on the same alloy in a multilayer geometry using Cu spacers.

II. EXPERIMENTAL METHODS

These films were computer-controlled dc magnetron sputter deposited at 100 W and two different sputtering pressures (2 and 15 mTorr) with ultrahigh purity argon in a Vac-Tec model 250 side sputtering system with a base pressure of 3×10^{-7} Torr onto Corning 7059 glass substrates. A permanent magnet was positioned behind each substrate providing a 90 Oe field parallel to the substrate. The granular layer was cosputtered from a $Ni_{66}Fe_{16}Co_{18}$ target partially covered with Ag foil. This resulted in a composition gradient that was perpendicular to the induced easy axis in the films. The composition of the granular layers ranged from $Ag_{20}FM_{80}$ to $Ag_{48}FM_{52}$ (at. %) for films deposited at 2 mTorr and from $Ag_{28}FM_{72}$ to $Ag_{72}FM_{28}$ for films deposited at 15 mTorr, where FM stands for the NiFeCo ferromagnetic portion of the film. The granular layer thickness was varied from 25 to 55 Å and the Cu spacer layer thicknesses investigated were 20 and 24 Å. The granular layers have a thickness gradient (the Ag-rich end is ~25% thicker than the Ag-poor end due to the faster sputtering rate of the Ag foil). The granular film thicknesses reported are the average thicknesses. Slightly better MR magnitudes were observed throughout in samples with a Cu spacer thickness of 20 Å rather than 24 Å. The sputtering rates were determined from reference film steps measured on a Dek-Tak IIA surface profilometer.

Composition was determined with a JEOL 8600 Electron Probe Microanalyzer. Magnetic properties were measured on a Digital Measurement Systems vibrating sample magnetometer model 880. X-ray diffraction (XRD) was performed on a Rigaku D/Max-2BX XRD System with thin film attachment. The MR measurements were made at room temperature using a four-point probe assembly with the applied current and easy axis of the film both perpendicular to the applied magnetic field except where designated on anisotropic magnetoresistance (AMR) results. The annealing (300 °C for 30 and 60 min) was done in a quartz tube wrapped in heating tape with an overpressure of flowing purified argon. A magnetic field of 50 Oe was maintained in the films' easy axis direction during the anneal using magnetic coils outside the tube.

III. EXPERIMENTAL RESULTS

Broadly speaking, two different as-deposited MR (dR/R_{max} with a maximum applied field of 12.5 kOe) behaviors were seen, where dR is the change in resistivity of the film from zero applied magnetic field to the maximum field and R_{max} is the resistivity of the film in the maximum applied field. In the Ag-rich compositions a very rounded MR profile was observed. As the NiFeCo component is increased the MR profile sharpens. A small low field AMR component (~0.2%) was observed in the most NiFeCo-rich samples. We were unable to saturate the GMR in the available field. The granular composition giving the largest GMR magnitudes for the samples prepared at 2 mTorr was $\sim Ag_{44}FM_{56}$ and for the 15 mTorr samples it was $Ag_{50}FM_{50}$, both being ~4%. The evolution of the GMR profile versus FM fraction for (NiFeCo-Ag 35 and 55 Å/Cu 24 Å)×10 appears in Fig. 1 (the profiles are offset for clarity). We note two important differences between the GMR observed in these hybrid structures and single layer films of the same granular alloy: the GMR magnitude is reduced by ~50% and the composition at

 0021-8979/94/76(10)/6478/3/$6.00 © 1994 American Institute of Physics

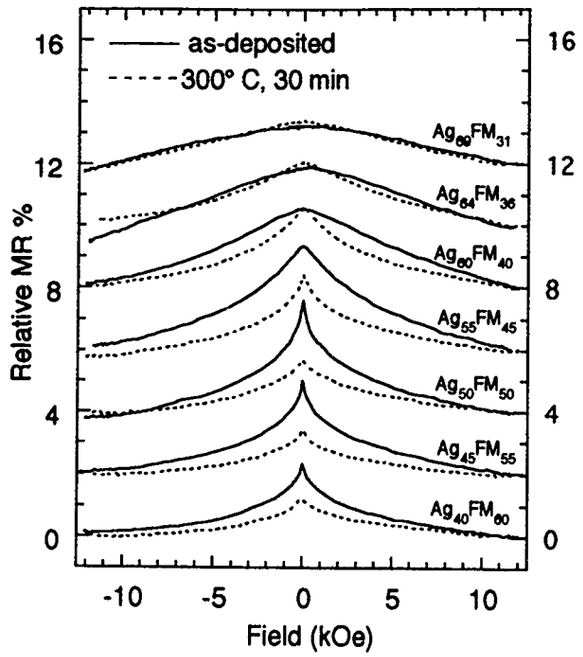

FIG. 1. MR loops for a series of granular layer compositions for as-deposited and annealed (300 °C, 30 min) hybrid granular multilayer films (NiFeCo-Ag 35 Å/Cu 24 Å)×10.

the maximum GMR is much more FM rich (~50% vs 30%) in the layered structures.[7] A significant reduction in MR ratio with film thickness has recently been reported in Co-Ag alloy films.[8] The same study also reported a slight increase in the Co composition corresponding to the maximum MR ratio in 200- vs 2000-Å-thick films. The composition shift we report is much larger, but our individual granular layers are also much thinner than 200 Å. This phenomenon may be associated with a transition from three-dimensional to quasi-two-dimensional behavior. The percolation threshold is much higher in a two-dimensional lattice than the corresponding three-dimensional lattice.[9]

Annealing caused a decrease in MR magnitude for the FM-rich samples while the overall profile was maintained.

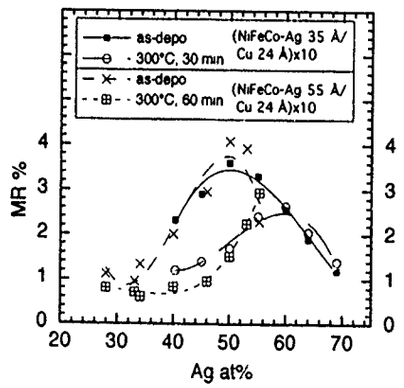

FIG 2. MR magnitude vs granular layer composition for as-deposited and annealed hybrid granular multilayer films (NiFeCo-Ag 35 Å/Cu 24 Å)×10 and (NiFeCo-Ag 55 Å/Cu 24 Å)×10. (The curves are guides for the eye.)

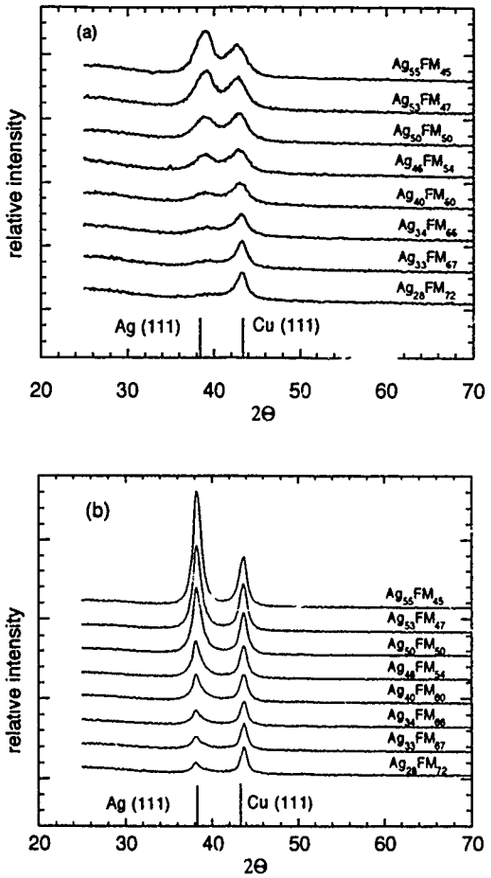

FIG. 3. High angle θ-2θ XRD scans for (a) as-deposited and (b) annealed (300 °C, 60 min) hybrid granular multilayer films (NiFeCo-Ag 55 Å/Cu 24 Å)×10.

Ag-rich films displaying an as-deposited broad profile experienced an increase in MR magnitude upon annealing along with a distinct sharpening of the MR peak. Beyond a critical Ag concentration, (~$Ag_{55}FM_{45}$ for 15 mTorr) the GMR magnitude increases with annealing (Fig. 2). A similar trend with a critical composition of $Ag_{50}FM_{50}$ was seen for samples prepared at 2 mTorr. This transition was previously

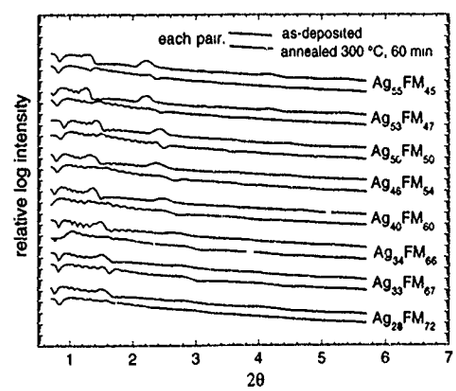

FIG. 4. Low angle θ-2θ XRD scans for an as-deposited and annealed (300 °C, 60 min) hybrid granular multilayer film [$Ag_{50}(NiFeCo)_{50}$ 55 Å/Cu 24 Å]×10.

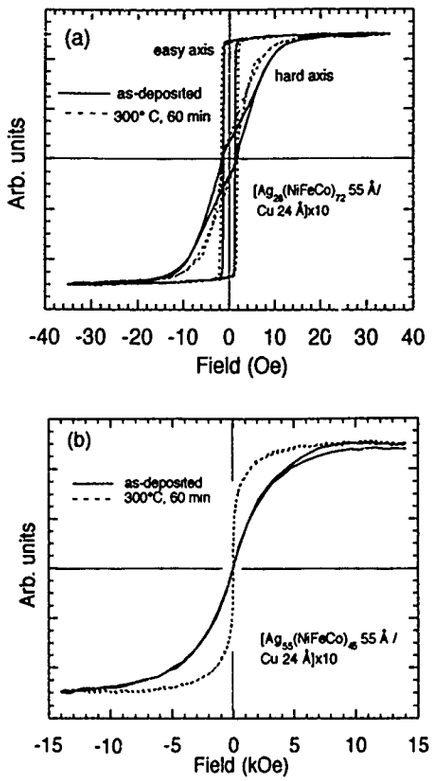

FIG. 5. *M-H* hysteresis loops for as-deposited and annealed (300 °C, 60 min) hybrid granular multilayer films with (a) both easy and hard axes shown for $[Ag_{28}(NiFeCo)_{72}$ 55 Å/Cu 24 Å$]\times 10$ and (b) easy-axis (this sample was nearly isotropic) loops for $[Ag_{55}(NiFeCo)_{45}$ 55 Å/Cu 24 Å$]\times 10$.

reported for single layer NiFeCo-Ag granular films grown at 15 mTorr with a more Ag-rich critical composition of $\sim Ag_{68}FM_{32}$.[7] Because the average FM particle size is expected to increase with the FM fraction, the critical concentration is naturally also associated with a critical FM particle size. Annealing shifts the maximum GMR composition to the more Ag-rich films (this is also found in single layer films).[7]

As-deposited high-angle XRD data revealed Cu(111) peaks consistently and increasing Ag(111) peak intensities with increasing percentage of Ag; the films are strongly (111) textured [Fig. 3(a)]. A systematic shift in the Cu(111) peak to lower angles with increasing Ag content is noted in the as-deposited films. The Cu(111) peaks are observed at angles lower than bulk values. Explicit NiFeCo peaks are not observed. Upon annealing, both the Cu and Ag(111) peaks sharpened and intensified with the Ag peak increase more pronounced [Fig. 3(b)]. Interestingly, following the anneal, the Cu(111) peak position is now independent of Ag content and its position is now at a slightly higher angle than bulk. The asymmetry of the Ag(111) peaks for annealed FM-rich samples may be associated with the growth of NiFeCo particles. The *d* spacing derived from Ag(111) peaks from the as-deposited films is smaller than the bulk Ag(111) value. Annealing causes an increase in the *d* spacing up to nearly the bulk value, in agreement with the single layer results.[7] The low-angle XRD (LXRD) peaks (Fig. 4) indicate reasonably good periodicity in the multilayer structure in the as-deposited state which allows for a calculation of the bilayer thickness, Λ, that agrees well with the calibrated sputtering rate data. Annealing has a small, nonsystematic effect on the LXRD spectra.

M-H hysteresis loops from very FM-rich (e.g., $Ag_{28}FM_{72}$) samples display induced uniaxial anisotropy that decreases slightly with annealing while the coercivity slightly increases [Fig. 5(a)]. These surprisingly soft loops, which display no further increase in *M* at higher fields, indicate that very FM-rich granular layers are behaving much like simple NiFeCo alloy layers. The NiFeCo alloy in the NiFeCo-Ag layer most likely forms a physically continuous matrix with the Ag existing as particles (an "inverted" granular layer). As the Ag concentration in the granular layer increased (ferromagnetic concentration decrease) the *M-H* loops tend toward superparamagnetism associated with a small FM component particle size [Fig. 5(b)]. Annealing of this Ag-rich sample results in a more easily saturated *M-H* loop probably resulting from an increase in FM component particle size.

IV. CONCLUSIONS

Layering of NiFeCo-Ag granular alloys with Cu spacers does not improve either the GMR magnitude or field sensitivity when compared with thick single layers of the same alloy. However, the composition dependence of GMR is strongly affected by the multilayer geometry with thin layers of NiFeCo-Ag separated by Cu behaving similar to thick single layers of much higher Ag content. We also find that very soft uniaxial multilayers can be grown with Ag compositions as high as 22% in the FM layer.

ACKNOWLEDGMENTS

The authors would like to thank Dr. Mike Bersch for his electron microprobe analysis. This work was supported by NSF-DMR-9301648. The use of the facilities at the Center for Materials for Information Technology at The University of Alabama, Tuscaloosa, AL is gratefully acknowledged.

[1] M. N. Baibich, J. M. Broto, A. Fert, F. Nguyen Van Dau, F. Petroff, P. Eitenne, G. Creuzet, A. Friederich, and J. Chazelas, Phys. Rev. Lett. **61**, 2472 (1988).
[2] T. L. Hylton, K. R. Coffey, M. A. Parker, and J. K. Howard, Science **261**, 1021 (1993).
[3] J. D. Jarratt and J. A. Barnard, Mater. Res. Soc. Symp. Proc. (in press).
[4] J. C. Xiao, J. S. Jiang, and C. L. Chien, Phys. Rev. Lett **68**, 3749 (1992).
[5] A. E. Berkowitz, J. R. Mitchell, M. J. Carey, A. P. Young, S. Zhang, F. E. Spada, F. T. Parker, A. Hutten, and G. Thomas, Phys. Rev. Lett. **68**, 3745 (1992).
[6] J. A. Barnard, A. Waknis, M. Tan, E. Haftek, M. R. Parker, and M. L. Watson, J. Magn. Magn. Mater. **114**, L230 (1992).
[7] A. Waknis, J. A. Barnard, and M. R. Parker, J. Appl. Phys. **75**, 6930 (1994).
[8] J. R. Mitchell and A. E. Berkowitz, J. Appl. Phys. **75**, 6912 (1994).
[9] D. Stauffer, *Introduction to Percolation Theory* (Taylor and Francis, London, 1985), p. 17.

Published without author corrections

Giant magnetoresistance in NiFe-Ag granular alloys

F. Badía, A. Labarta, and X. Batlle
Departament Física Fonamental, Universitat de Barcelona, Diagonal 647, 08028 Barcelona, Spain

M. L. Watson
Centre for Data Storage Materials, Coventry University, Priory Street, Coventry CVI 5FB, United Kingdom

Some FeNi-Ag granular films of composition $Fe_{11.43}Ni_{6.35}Ag_{82.22}$ (sample A) and $Fe_{7.62}Ni_{16.4}Ag_{75.98}$ (B) were prepared by using rf magnetron sputtering, and once deposited were rapidly annealed at 600, 650, and 750 °C. All samples displayed giant magnetoresistance. The zero-field-cooled and field-cooled processes evidence the segregation of ferromagnetic particles with a broad size distribution. The temperature and magnetic field dependence of the resistance is analyzed. The magnetoresistance follows a H^n law at high fields and it decays from its maximum value with a T^m behavior, with m approaching 1 at high fields.

I. INTRODUCTION

The discovery of giant magnetoresistance (GMR) effects in a variety of antiferromagnetically coupled transition-metal multilayers[1] has opened a new amazing research field not only from the fundamental point of view but also from the technological one. Recently, this extraordinary effect has also been found in granular alloys[2] consisting of a distribution of nonaligned nanocrystalline ferromagnetic particles embedded in a nonmagnetic metallic matrix. In both kinds of systems, the resistivity strongly drops as the magnetic field orients the magnetic moments. Concerning theoretical explanations, both the existence of a spin-dependent potential scattering either at the interfaces or in the bulk of ferromagnetic layers (or particles) and the role of the unfilled d bands of the transition metal constituent (through an asymmetric density of states for majority- and minority-spin d bands)[3,4] have been taken into account in order to correlate GMR with the microscopic parameters. The magnitude of GMR has been found to be a sensitive function of both the size of the ferromagnetic particles and the concentration of the ferromagnetic material in the alloy. The former effect is postulated to be due to the existence of an optimum particle size, determined by the conduction electron mean free path or spin diffusion length. Larger particles result in a reduction of GMR as a result of the decrease in particle surface-to-volume ratio.[3] The latter effect is believed to be due to the onset of percolation, which acts to couple the particles ferromagnetically.[1-3] We present in this article the temperature and magnetic field dependence of the resistance of NiFe-Ag granular alloys presenting GMR.[5]

II. EXPERIMENT

Ag-Ni-Fe films of thickness 200–300 nm were rf sputtered onto glass microscope slides using a Nordico 2000 sputtering system. The base pressure was less than 2×10^{-7} Torr, the sputtering pressure was 8 mTorr of argon and the sputtering power was 300 W. The target used consisted of a 4 in. Ag (99.999%) disc onto which were placed $Ni_{80}Fe_{20}$ and Fe 0.25 cm^2 squares arranged in a mosaic pattern. In order to promote post-deposition phase segregation and magnetic particle growth, strips of about 7 mm wide were rapidly thermally annealed in a custom built vacuum system. Three annealing temperatures were investigated: 600, 650, and 750 °C, and these were reached in 20 s, 2 min, and 3 min, respectively. Resistance and magnetoresistance (MR) of all samples were measured by an ac four-point probe technique in the temperature range 20–300 K and in magnetic fields up to 12 kOe. The relative geometry among the film plane, the electrical current, and the magnetic field was set by three ways: (a) the electrical current and the magnetic field are parallel to the film plane (parallel geometry); (b) the in-plane magnetic field is perpendicular to the electrical current (transversal geometry); and (c) the magnetic field is perpendicular to both the electrical current and the film plane (perpendicular geometry). The zero-field-cooled (ZFC) and field-cooled (FC) processes at low fields and the magnetization curves at 5 K up to 55 kOe were carried out by applying the magnetic field along the film plane using a superconducting quantum interference device magnetometer.

III. RESULTS AND DISCUSSION

The structure of some of the thin films ($d\approx50$ nm) were investigated by transmission electron microscopy (TEM) in a modified JEOL 2000 electron microscope. Films were deposited onto Si substrates into which a SiN covered window had been etched and were found to have a strong ⟨111⟩ texture. A number of films were also investigated by using a Philips x-ray diffraction (XRD) system. This confirmed the strong ⟨111⟩ texturing but in neither the TEM nor the XRD was any clear evidence of phase segregation of the Ni or Fe from the Ag matrix. Magnetic and transport properties were measured on films which had composition $Fe_{11.43}Ni_{6.35}Ag_{82.22}$ (sample A) and $Fe_{7.62}Ni_{16.4}Ag_{75.98}$ (sample B). As both samples were rapidly annealed at 600, 650, and 750 °C, we will refer to them as A(as cast), A(600), A(650), A(750), B(as cast), B(600), B(650), and B(750), respectively.

Figure 1 shows the ZFC-FC processes for sample A(650) measured at 100 Oe. The ZFC displays a broad maximum at $T_M\approx22$ K, suggesting the existence of a broad size distribution of ferromagnetic particles. As magnetic irreversibility persists up to high temperature, we expect very large particles to be present in the sample. We plot in Fig. 2 the magnetization curve of the same sample at 5 K. A detail of

 0021-8979/94/76(10)/6481/3/$6.00 © 1994 American Institute of Physics

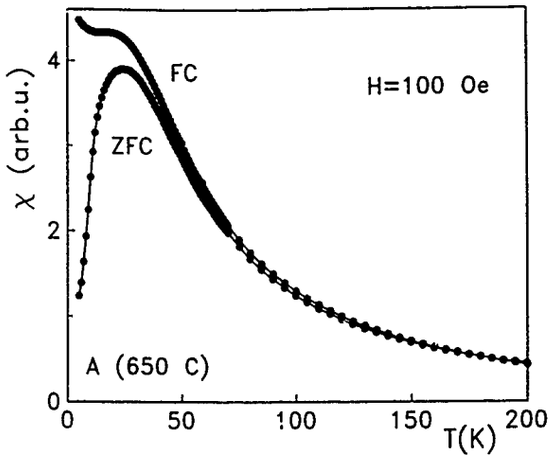

FIG. 1. ZFC and FC processes measured at 100 Oe for sample A(650).

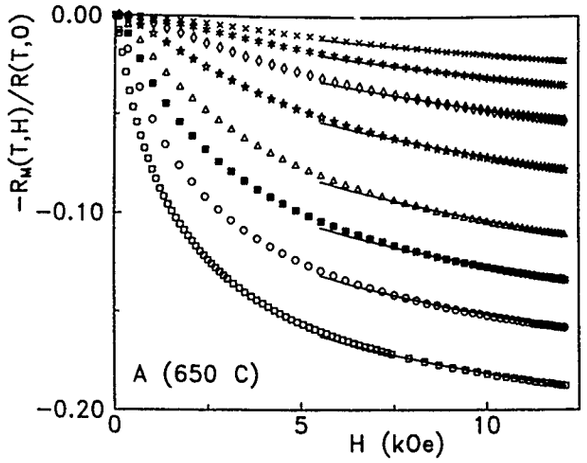

FIG. 3. $-R_M(T/H)/R(T,H=0)$ as a function of H at different temperatures for sample A(650) in the parallel geometry. Solids lines indicate the best fit of the data to the H^n law. Temperatures: (□) 21.6 K; (○) 46.1 K; (●) 73.6 K; (△) 102 K; (☆) 149.2 K; (◇) 196.4 K; (*) 245 K; (×) 290 K.

the hysteresis circle is displayed in the inset, showing that the coercive field is small (about 150 Oe).

The temperature dependence of the ratio $-R_M(T,H)/R(T,H=0)$ [with $R_M(T,H)=R(T,H=0)-R(T,H)$] in the parallel geometry for samples A(650) and B(650) are plotted in Figs. 3 and 4, respectively. All the rest of the samples display very similar experimental features. The maximum MR values are obtained for samples B(650) and A(650), suggesting that the optimum annealing temperature is about 650 °C in this Ag compositional range. MR is larger for sample B(650) than for sample A(650) because of the larger amount of ferromagnetic entities. As-cast samples display smaller MR than annealed samples due to the segregation of ferromagnetic particles in the latter. Results concerning the rest of annealing temperatures and other Ag compositions will be published elsewhere. Figures 3 and 4 evidence that MR is largely susceptible at low fields. We have also detected that MR is more susceptible in the in-plane geometries than in the perpendicular geometry, which is only due to the demagnetizing field (and it is not associated with an intrinsic in-plane magnetocrystalline anisotropy) because there is no difference between the MR in the parallel and transversal geometry. All measurements have been recorded with increasing and decreasing field, and we observe a slight irreversibility at low temperatures below the coercive field.

We have analyzed the temperature dependence of the MR as Mattson *et al.*[6] by defining the MR as $R_M(T,H)=R(T,H=0)-R(T,H)$, where $R(T,H)$ is the resistance measured at a temperature T and in an applied field H. The total resistance at T and H is assumed to be given by $R(T,H)=R_0+R_{sd}(T)+R_M(T,H)$, where R_0 is the resistance due to defects, $R_{sd}(T)$ is the temperature dependent resistance due to phonons and magnons. We show in Fig. 5 the temperature dependence of $R_M(T,H)$ at different fields for sample A(650). $R_M(T,H)$ displays a monotonic increase

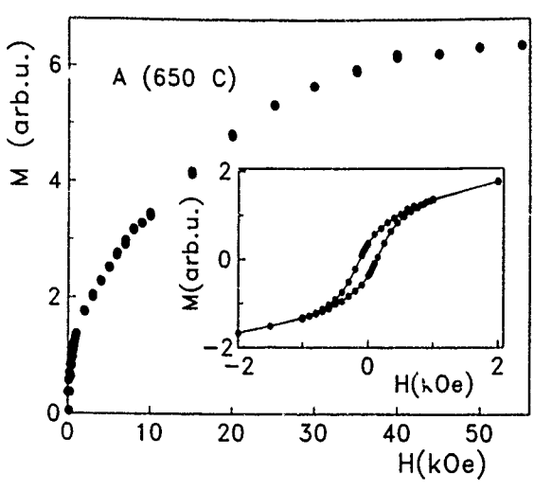

FIG. 2 Isothermal magnetization curve at 5 K for sample A(650). Inset: detail of the hysteresis cycle at 5 K for the same sample.

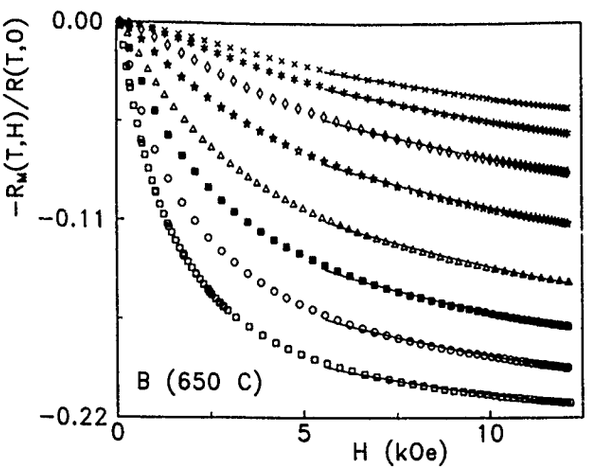

FIG. 4. $-R_M(T/H)/R(T,H=0)$ as a function of H at different temperatures for sample B(650) in the parallel geometry. Solids lines indicate the best fit of the data to the H^n law. Temperatures: (□) 21.5 K; (○) 45.9 K; (●) 73.7 K; (△) 102.4 K; (☆) 149.6 K; (◇) 197.8 K; (*) 245.9 K; (×) 282.1 K.

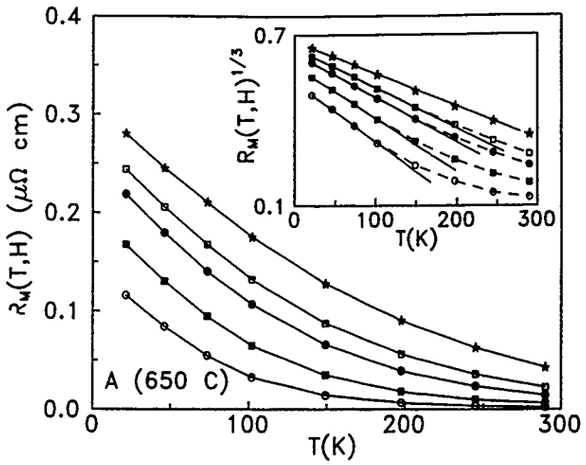

FIG. 5. $R_M(T,H)$ vs T at various fields for sample A(650). Magnetic fields: (○) 1 kOe; (■) 2 kOe; (●) 4 kOe; (□) 6 kOe; (☆) 12.1 kOe. Inset: $R_M(T,H)^{1/3}$ vs T at the same fields for the same sample.

as temperature goes down, which is in agreement with the progressive blocking of the ferromagnetic particles (Fig. 1). We plot in the inset of Fig. 5 the temperature dependence of $R_M(T,H)^{1/3}$ at various fields for the same sample. We notice that $R_M(T,H)^{1/3}$ is perfectly linear with T in the whole temperature range 20–290 K when the magnetic field is the maximum available in our experimental setup (H_{max}=12 kOe), and that the linear law $R_M(T,H)^{1/3}$ versus T is followed in a smaller temperature range as we reduce the magnetic field. The same 1/3 exponent and temperature dependence of $R_M(T,H)$ is found for sample B(650). If we extrapolate the data at T=0, we obtain the $R_M(T=0,H)$ and we may define $\Delta R_M = R_M(T=0,H) - R_M(T,H)$. The log-log plot of ΔR_M versus T is displayed in Fig. 6 for sample A(650) at 2 and 12.1 kOe. The slope of the plot yields the exponent m in the relationship $\Delta R_M \approx T^m$, and this power law gives us an idea of the underlying scattering mechanism. It is evidenced that the temperature range in which the power law is accomplished increases with magnetic field (as expected, since the MR saturates at large fields). The exponent m slightly increases with H and seems to tend to about 1, which is smaller than the $T^{3/2}$ and T^2 laws found by Mattson *et al.*[6] in Fe/Cr multilayers. These behaviors are attributed to the thermal excitation of magnons. The temperature dependence of the MR of granular materials is complicated by there being a distribution of particle sizes and therefore blocking processes. We might tentatively attribute the temperature dependence of ΔR_M at high fields to the thermal excitation of magnons with a smaller exponent in the T^m law due to the reduction of the magnetic system dimensionality.

Concerning the field dependence of the MR, we have observed that $R_M(T,H)/R(T,0)$ follows a H^n behavior at high fields (above about 6000 Oe), as was found by Nigam *et al.*[7] in $Au_{87}Fe_{13}$ cluster glass. Solids lines in Figs. 3 and 4 indicate the best fit of the data to the H^n law. The n-exponent monotonically increases with temperature, ranging from 0.18 at 21.6 K to 0.86 at 290 K for samples A(650), and from 0.13 at 21.5 K to 0.76 at 282.1 K for sample B(650). The error in n is about 0.02. This monotonic temperature behavior evidences the progressive blocking of the ferromagnetic particles, without being a freezing state corresponding to a spin glass behavior. Also, n is always smaller than the n=2 value expected for a pure paramagnetic state,[7] signaling that magnetic correlations persist even at room temperature and/or larger particles are still blocked at this temperature, since the size distribution of ferromagnetic particles seems to be very broad (see Fig. 1).

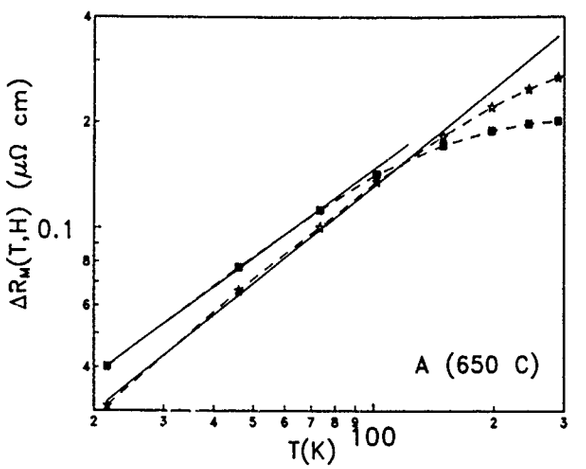

FIG. 6. Log-log plot of the temperature dependence of $\Delta R_M = R_M(T=0,H) - R_M(T,H)$, at (■) 2 kOe and at (☆) 12.1 kOe for the sample A(650). Solid lines correspond to the best fit of the data to a T^m law.

ACKNOWLEDGMENTS

We gratefully acknowledge the assistance of Professor J. Chapman and Dr. A. Johnston of the University of Glasgow who conducted the TEM investigations.

[1] M. N. Baibich *et al.*, Phys. Rev. Lett. **61**, 2472 (1988); G. Binach, P. Grunberg, F. Saurenbach, and W. Zinn, Phys. Rev. B **39**, 4828 (1989); W. P. Pratt, S. F. Lee, J. M. Slaughter, R. Loloee, P. A. Schroeder, and J. Bass, Phys. Rev. Lett. **66**, 3060 (1991).

[2] A. E. Berkowitz, J. R. Mitchell, M. J. Carey, A. P. Young, S. Zhang, F. E. Spada, F. T. Parker, H. Hutten, and G. Thomas, Phys. Rev. Lett. **68**, 3745 (1992); J. Q. Xiao, J. S. Jiang, and C. L. Chien, *ibid.* **68**, 3749 (1992); J. A. Barnard, A. Waknis, M. Tan, E. Haftek, M. R. Parker, and M. L. Watson, J. Magn. Magn. Mater. **114**, L230 (1992).

[3] S. Zhang, Appl. Phys. Lett. **61**, 1855 (1992); S. Zhang and P. M. Levy, J. Appl. Phys. **73**, 5316 (1993).

[4] L. Xing and Y. C. Chang, Phys. Rev. B **48**, 4156 (1993); L. Xing, Y. C. Chang, M. B. Salomon, D. M. Frankel, J. Shi, and J. P. Lu, *ibid.* **48**, 6728 (1993).

[5] J. S. Jiang, J. Q. Xiao, and C. L. Chien, Appl. Phys. Lett. **61**, 2362 (1992); M. L. Watson, J. A. Barnard, S. Hossain, and M. R. Parker, J. Appl. Phys. **73**, 5506 (1993).

[6] I. A. Campbell, A. Fert, and O. Jaoul, J. Phys. C **3**, S95 (1970); F. P. Freitas and L. Berger, J. Magn. Magn. Mater. **54–57** (1986); M. A. M. Gijs and M. Okada, *ibid.* **113**, 105 (1992); J. E. Mattson, M. E. Brubaker, C. H. Sowers, M. Conover, Z. Qiu, and S. D. Bader, Phys. Rev. B **44**, 9378 (1991).

[7] A. K. Nigam, S. Radha, and G. Chandra, J. Phys.: Condens. Matt. **5**, 9197 (1993).

Anisotropic giant magnetoresistance induced by magnetoannealing in Fe-Ag granular films

J. G. Na
Korea Institute of Science and Technology, Sungbuk, Seoul 136-791, Korea

C. T. Yu, X. G. Zhao, W. Y. Lai, H. L. Luo, and J. G. Zhao
State Key Laboratory of Magnetism, Institute of Physics, CAS, Beijing 100080, China

The effects of magnetoannealing on the giant magnetoresistance (GMR) in Fe_xAg_{100-x} granular films (X= 15, 26, 29, 33, 37, and 60) were investigated. The thin films were annealed in a presence of magnetic field of 3 kOe at different temperatures of 300, 400, and 500 °C using various annealing times. It is found that the anisotropic GMR characteristics were developed when Fe-Ag granular thin films were annealed in the presence of a magnetic field. The anisotropic GMR characteristics of the thin films were closely related to the magnetic anisotropy developed along the field direction during magnetoannealing.

I. INTRODUCTION

A considerable number of studies have been conducted on the giant magnetoresistance (GMR) effect in magnetic multilayers with antiferromagnetic interlayer coupling[1,2] and magnetic granular films with nonconnecting ferromagnetic particles embedded in a paramagnetic matrix,[3,4] due to their high potential for application for various kinds of sensors, i.e., a magnetic head for high recording density. Among these materials, the magnetic granular thin films are investigated by many researchers because they can be easily fabricated over large areas using usual thin film processes. Most of the work, however, is confined to the isotropic GMR in a microscopic point of view.

Traditionally it has been well known that the anisotropic properties of magnetic materials are used to maximize the required magnetic properties and magnetoannealing is one of the most convenient methods to develop the magnetic anisotropy in magnetic materials.

In this article, Fe_xAg_{100-x} (X=15, 26, 29, 33, 37, and 60) granular thin films were deposited on slide glasses (Qing Huang Dao Medical Glasses Co., 1.2 mm×26 mm×76 mm) and annealed in a presence of magnetic field of 3 kOe at different temperatures of 300, 400, and 500 °C in a vacuum of 5×10^{-3} Pa or a high purity nitrogen atmosphere to develop an anisotropic GMR. The effects of magnetoannealing on the GMR and magnetic properties of Fe-Ag granular thin films were investigated.

II. EXPERIMENTAL PROCEDURES

Ag-Fe granular thin films were prepared by dc magnetron sputtering. The target was composed of 6-cm-diam Ag disk (99.9 at. % purity) and iron chips (99.9 at. % purity). The composition of the granular thin films was controlled by adjusting the number of iron chips attached on the Ag disk. Prior to deposition, the target was presputtered at 0.5 Pa for 30 min. The sputter conditions are summarized in Table I.

The magnetic annealing of thin films was carried out at different temperatures of 300, 400, and 500 °C in a vacuum of 5×10^{-3} Pa or a high purity nitrogen (99.99%) atmosphere. There was no difference in the electrical and magnetic properties between vacuum and N_2-atmosphere annealed samples in this annealing temperature range. A magnetic field of 3 kOe was applied in an in-plane direction of the films.

The magnetoresistance was measured by using a conventional four-point configuration on a specimen of 3 mm×8 mm with the magnetic field of 20 kOe perpendicular to current within the film plane at room temperature. Two directions, i.e., parallel and perpendicular to the magnetic field direction of annealing were measured to compare the magnetic annealing effect of the thin films.

An x-ray diffractometer and a vibrating sample magnetometer were used to analyze the microstructure and magnetic properties of the films, respectively. A scanning electron microscope was used to analyze the composition of the thin films.

III. RESULTS AND DISCUSSION

Figure 1 shows the change of GMR as a function of Fe content in the as-sputtered Ag-Fe granular films. The GMR reported here is referenced to the maximum resistivity at zero magnetic field and it is defined as $\Delta\rho/\rho_{H=0}=(\rho_H-\rho_{H=0})/\rho_{H=0}$, where $\rho_{H=0}$ and ρ_H denote the resistivity at zero magnetic field and field H, respectively. One can see that the GMR value is very sensitively dependent upon the chemical composition of thin films. There is a narrow optimum composition range around $Fe_{29}Ag_{71}$, and in both the Fe-poor and Ag-poor regime the GMR decreases rapidly, which is in agreement with the result of Xiao *et al.*[5]

As-sputtered Fe-Ag thin films were annealed in a presence of magnetic field of 3 kOe at different temperatures of 300, 400, and 500 °C for various times. The structural change of the samples was characterized by x-ray diffraction.

TABLE I. Sputtering conditions for Fe-Ag granular thin films.

Background pressure	4×10^{-3} Pa
Sputter pressure	0.5 Pa
Sputter gas	Ar
Substrate temperature	room temperature
Input power	0.1 A×400 V dc
Film thickness	0.2 μm

 0021-8979/94/76(10)/6484/3/$6.00 © 1994 American Institute of Physics

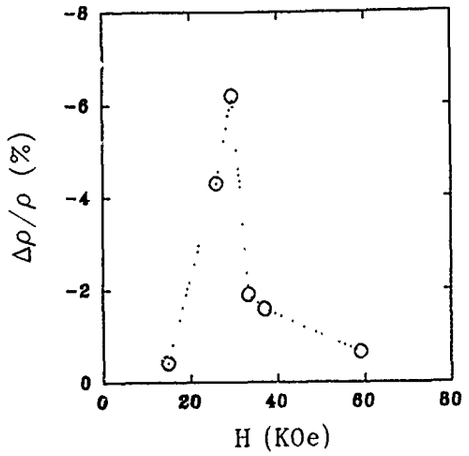

FIG. 1. The change of GMR as a function of Fe content in the as-sputtered Ag-Fe granular films.

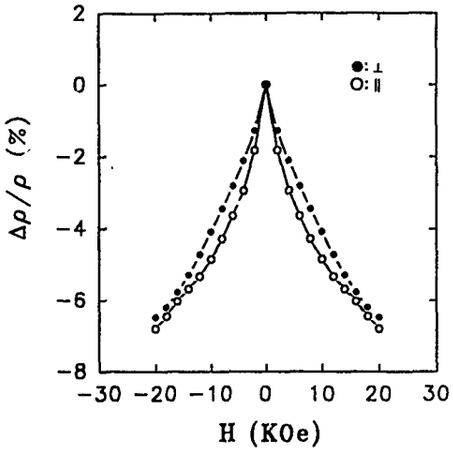

FIG. 3. GMR curves of easy and hard directions in $Fe_{29}Ag_{71}$ thin films annealed at 400 °C for 80 min in an N_2 atmosphere.

The diffraction patterns of $Fe_{29}Ag_{71}$ as sputtered and magnetoannealed at 400 °C for 30 min are shown in Fig. 2. For the as-sputtered film, a large peak attributable to (111) plane of Ag is detected, which indicates that a strong (111) preferred orientation was developed in the film. With magnetoannealing, the peak for (111) plane of Ag becomes sharp and a small broad peak around 44.3° is observed. The small peak may be attributed to (200) plane of Ag and (110) plane of Fe because d_{200} of Ag and d_{110} of Fe are similar. The intensity of the small peak was increased with increasing Fe content of thin films, which strongly suggested that the peak include the peak of (110) plane of Fe.

The anisotropic GMR characteristics are developed in annealed thin films with respect to the direction of magnetic field during annealing, i.e., parallel (easy) and perpendicular (hard). For the thin films annealed at 300 and 400 °C, the shape of the GMR curves was significantly different between the easy and hard direction of thin films. For $Fe_{15}Ag_{85}$ thin film annealed at 400 °C for 10 min, we observed that the GMR curve became almost linear in a hard direction. Figure 3 shows the GMR curves of $Fe_{29}Ag_{71}$ annealed at 400 °C for 80 min. As can be seen in Fig. 3, the GMR curve of the easy direction becomes sharper than that of the hard direction. The difference in GMR values between these two directions is not considerably large although GMR values in easy direction is always larger than those in the hard direction. However, there is the considerable difference in GMR values between easy and hard direction for the films annealed at 500 °C. Figure 4 shows the variation of GMR values of $Fe_{29}Ag_{71}$ with annealing time at different temperatures of 400 and 500 °C. It can be seen from Fig. 4 that the GMR values of these thin films increase with annealing time, reach the maximum at about 80 and 40 min, respectively, and decrease. The difference in GMR values between easy and hard direction is larger in the sample annealed at 500 °C than that at 400 °C. To understand the cause of this difference between easy and hard direction, the M-H loop of $Fe_{29}Ag_{71}$ annealed

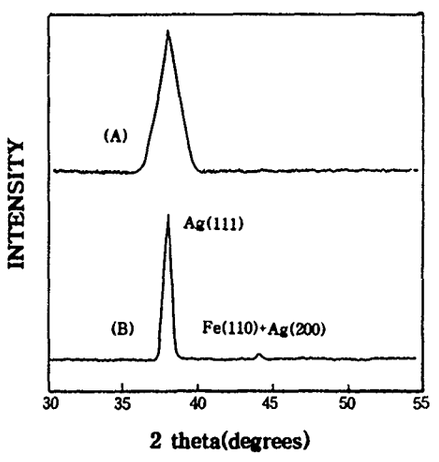

FIG. 2. X-ray diffraction patterns of $Fe_{29}Ag_{71}$ thin films as-sputtered(A) and magnetoannealed at 400 °C for 30 min in an N_2 atmosphere(B).

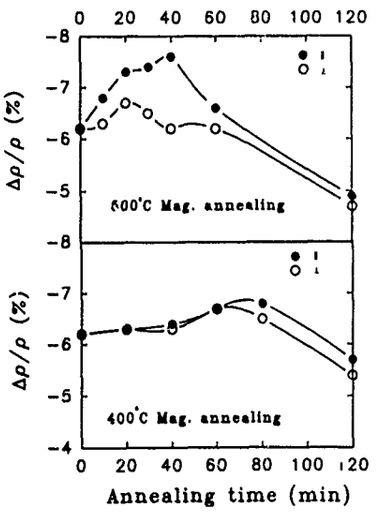

FIG. 4. The variation of GMR values of $Fe_{29}Ag_{71}$ with annealing time at different temperature of 400 (N_2 atmosphere) and 500 °C (vacuum atmosphere).

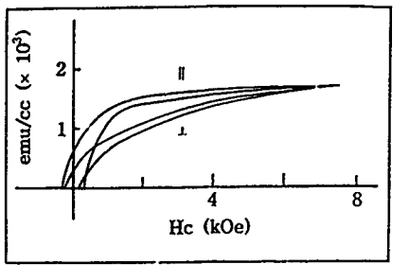

FIG. 5. The M-H loop of $Fe_{29}Ag_{71}$ thin film annealed at 500 °C for 40 min in a vacuum atmosphere.

at 500 °C for 40 min was measured and the result is shown in Fig. 5. The coercivities of easy and hard direction are 210 and 180 Oe, respectively, from Fig. 5. The difference in the M-H loop shape and coercivity indicates that the magnetic anisotropy is developed along the magnetic field direction during annealing. Therefore, the anisotropic GMR characteristics of Fe-Ag thin films annealed in the presence of magnetic field is closely related to the magnetic anisotropy because except for GMR measuring direction, the other conditions, e.g., sputtering condition, composition, annealing condition of thin films were the same. The small difference in GMR values between easy and hard direction in the sample annealed at 400 °C shown in Fig. 4 can be explained by small magnetic anisotropy due to low annealing temperature.

In this study, the origin of the magnetic anisotropy is not elucidated yet. Further study on this point is suggested.

IV. CONCLUSION

It is found that the anisotropic GMR characteristics were developed when Fe-Ag granular thin films were annealed in a presence of magnetic field. The shape of GMR curves was different between easy and hard direction when the thin films were annealed at 300 and 400 °C. But the difference of GMR values was small. For the thin films annealed at 500 °C, there was considerable difference in GMR values between easy and hard direction which was closely related with the magnetic anisotropy developed along the field direction during magnetoannealing.

[1] M. N. Baibich, J. M. Brote, A. Fert, F. Nguyen van Dau, F. Petoff, P. Etienne, G. Creuzet, A. Friederich, and J. Chazeles, Phys. Rev. Lett. **61**, 2472 (1988).
[2] R. E. Camley, and J. Barnas, Phys. Rev. **63**, 664 (1989).
[3] A. E. Berkowitz, J. R. Mitchell, M. J. Carey, A. P. Young, S. Zhang, F. E. Spada, F. T. Parker, A. Hutten, and G. Thomas, Phys. Rev. Lett. **68**, 3745 (1992).
[4] J. Q. Xiao, J. S. Jiang, and C. L. Chien, Phys. Rev. Lett. **68**, 3749 (1992).
[5] G. Xiao, J. Q. Wang, and P. Xiong, Appl. Phys. Lett. **62**, 420 (1993).

Influence of microstructure on magnetoresistance of FeAg granular films

Chengtao Yu, Ye Yang, Yuqing Zhou, Shuxiang Li, Wuyan Lai, and Zhenxi Wang
Institute of Physics, Chinese Academy of Sciences, P.O. Box 603, Beijing 100080, China

The magnetoresistance of FeAg granular films with optimum composition has been systematically studied as a function of film thickness. It was found that the giant magnetoresistance increases rapidly with increasing film thickness in the initial stage, and beyond about 500 Å the improvements become limited. The saturation field was also found to rise with increasing film thickness. Transmission electron microscope studies showed that with the increase of film thickness the microstructure becomes more homogeneous, with smaller grains and fewer structural defects such as twins. A discussion of the influence of microstructure on magnetoresistance and saturation field is presented.

I. INTRODUCTION

The discovery of giant magnetoresistance (GMR) in multilayer systems[1] and subsequently in granular films[2,3] has stimulated worldwide research activities, due to both its fundamental significance and its potential application to magnetic sensors. It has generally been agreed that in both multilayer systems and granular films the GMR arises from spin-dependent scattering occurring either at the surface of or within the magnetic entity. For granular films, however, there exists evidence[4] that interface scattering plays a dominant role in magnetoresistance (MR). The GMR is believed to be closely related to features of magnetic granules such as size, shape, and distribution. So far, much attention has paid to this problem both experimentally[5] and theoretically,[6,7] but it is still far from completely understood. Concerning the effect of the feature of magnetic particle, most of the experimental work has focused on post-deposition annealing, which is believed to promote grain growth or phase segregation. In several candidates suitable for fabricating granular films, Fe and Ag are virtually immiscible at equilibrium, and thus even for as-deposited FeAg film, large GMR has been observed[8] due to presence of iron precipitated during the material fabricating process. Therefore, the deposition process certainly plays an important role in structure evolution and thus affects the GMR.

In this article, we adopted the optimum composition of FeAg, focused on the influence of film thickness and attempted to reveal the influence of microstructure on MR.

II. EXPERIMENTS

FeAg granular films were prepared by magnetron sputtering from a composite target onto water cooled glass substrates at an Ar pressure of 0.5 Pa after a base pressure of better than 4×10^{-5} Pa was achieved. The composite target consisted of an Ag disk with small fan-shaped iron chips. Composition was adjusted by the number of iron chips placed on the Ag disk. Once the target was mounted, it was cleaned by extensive presputtering. In each batch, eight samples were produced, and the whole sputtering process was controlled by computer. A profilometer was employed to measure film thickness, and the steps for measurements were yielded by removing a strip of scotch tape placed on the substrate previously. The MR was measured by using a conventional four-terminal configuration on a specimen of 2×6 mm^2 with magnetic field perpendicular to current but within the film plane. The microstructure of the granular film was investigated by transmission electron microscope (TEM) and its composition was analyzed by energy dispersive analysis.

III. RESULTS AND DISCUSSION

For FeAg granular film the optimum nominal composition showing the largest MR was found to be about 17.5 vol % Fe, and in both the Fe-poor and Fe-rich regime the magnetoresistance decreased abruptly, which is consistent with the literature.[8] Energy dispersive analysis indicated that the nominal optimum composition actually contains 26 at. % iron, corresponding to a volume fraction of 20% Fe.

Figure 1 shows the MR curves for three as-deposited $Fe_{26}Ag_{74}$ samples with different thicknesses at a temperature of 1.5 K. The MR reported here is referenced to the maximum resistivity at zero field and is defined as $\Delta\rho/\rho_{H=0}=(\rho_H-\rho_{H=0})/\rho_{H=0}$, where $\rho_{H=0}$ and ρ_H denote the resistivity at zero field and field H, respectively, and $\Delta\rho$ represents the net change in resistivity. As can be seen in Fig. 1, the value of MR changes considerably in samples with different thicknesses. For a sample with a thickness of 120 Å, the MR at 60 kOe is −7.14%, while for sample with thickness of 1800 Å, it reaches −18%. From Fig. 1, it also should be noticed that with increasing thickness, not only the MR but also the saturation field increases. Even in the highest magnetic field available the MR curves are still far from

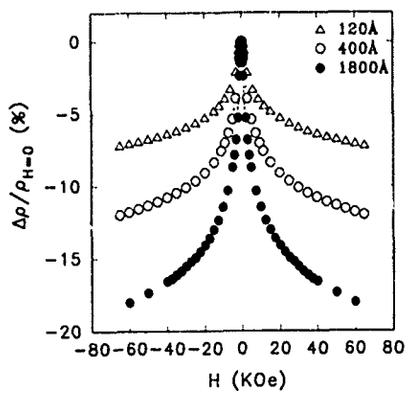

FIG. 1. Magnetic field dependence of MR for as-deposited $Fe_{26}Ag_{74}$ granular films with different thicknesses at temperature 1.5 K.

 0021-8979/94/76(10)/6487/3/$6.00 © 1994 American Institute of Physics

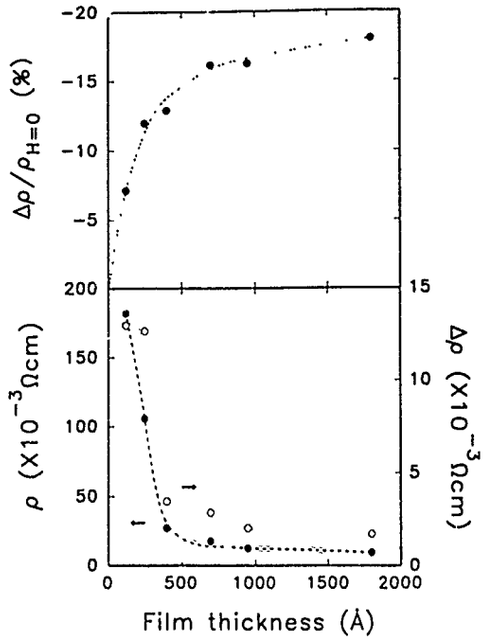

FIG. 2. MR $\Delta\rho/\rho_{H=0}$ (top), resistivity ρ, and the net change in resistivity $\Delta\rho$ (bottom) for $Fe_{26}Ag_{74}$ granular films as a function of film thickness at 1.5 K. Dashed lines are guides to the eye.

complete saturation, especially for thicker samples, and thus, to some extent, the MR values given here are underestimated.

Shown in Fig. 2 is the thickness dependence of the MR, from which it can be seen that with increase of film thickness the MR increases rapidly, and beyond about 500 Å, this change approaches saturation. What is also shown in Fig. 2 is the thickness dependence of both the zero-field resistivity ρ, and the net change in resistivity $\Delta\rho$ in a field of 60 kOe. It demonstrates that both ρ and $\Delta\rho$ drop abruptly with increasing thickness in the initial stage of deposition, but beyond about 500 Å both change moderately. However, it should be stressed that the drops in ρ are more significant than that in $\Delta\rho$, and this gives rise to the increasing trend of MR with film thickness. It is generally believed that for thinner films the role of surface scattering becomes significant relative to scattering occurring within the film, and consequently the resistivity rises. In addition, the existence of mismatch between film and substrate may result in high stress and structure defects such as twins, and these also enhance resistivity prominently. However, to some extent, the deposition process can be considered as an *in situ* annealing. Sputtering for a relatively long time may ease mismatch stress, alleviate disorder, and also promote precipitation, and as a result the resistivity decreases and MR rises. This structure evolution has been confirmed by TEM.

In Fig. 3 are shown bright-field (TEM) images for three $Fe_{26}Ag_{74}$ samples with different thicknesses, and in the upper-right-hand corners are the corresponding selected-area diffraction (SAD) patterns. Although energy dispersive analyses in nanomode indicated that the black areas contain considerably less concentration of iron than the white, the contrast does not necessarily imply an elemental difference.

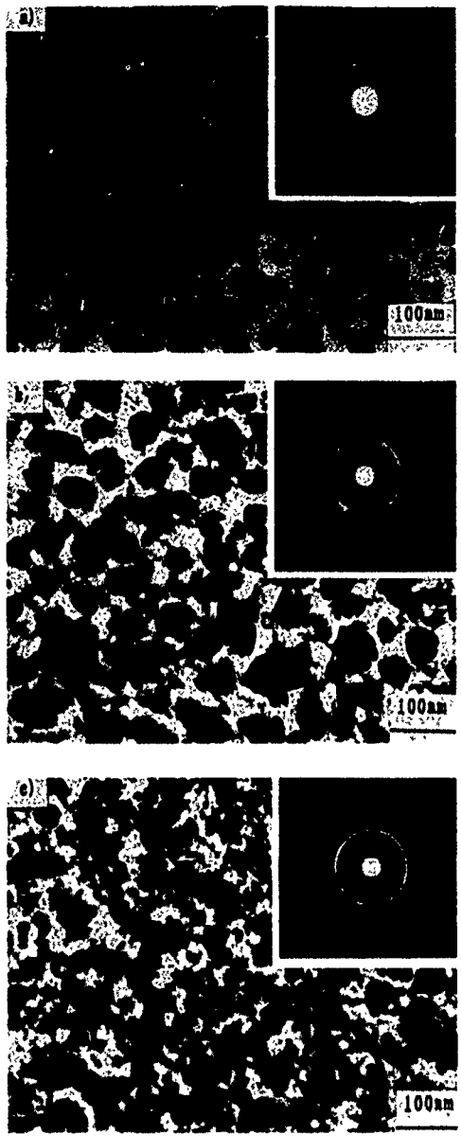

FIG. 3. Bright field (TEM) images and SAD patterns for $Fe_{26}Ag_{74}$ granular films with different thickness (a) 120 Å, (b) 400 Å, and (c) 1800 Å.

It also contains a contribution from crystal orientation. From Fig. 3, it can be seen that the thicker the film, the smaller the grains, and also the more homogeneous the microstructure. For the sample of 120 Å, the average grain size is on the order of 500 Å and the size distribution has a wide range, while for the sample of 1800 Å, the grain size decreases to the order of 200 Å or less and it also shows a tendency toward homogenization. This probably resulted from phase segregation rather than nucleation on structure defects. As a result, this process led to the existence of plenty of fine iron particles, which gave rise to difficulty in saturation as observed from the MR curves. Certainly, a great number of Fe precipitated particles would also contribute to improvements of the MR. Besides, it should be noted in the micrograph of the thinnest sample, which exhibited the maximum resistivity and the minimum MR, that a number of twins are visible. They would be expected to cause extra scattering and en-

hance resistivity. For thicker films, the possibility of increasing resistivity caused by small grain boundaries may be overwhelmed by eliminating giant twins and other defects as well as lowering the surface scattering fraction.

Although there exists evidence for the presence of fine Fe particles, it is difficult to determine the Fe and Ag phases separately by electron or x-ray diffraction because of the overlap between Fe and Ag spectral lines, and in particular the line broadening for especially fine grains or particles. All electron diffraction patterns shown in Fig. 3 can be indexed as those lines of fcc Ag, but they still show apparent differences. For the thinnest sample, the spectral rings are characterized by dispersive diffraction spots, which implies the existence of large grains or preferential crystal orientation. For thicker samples, those rings become complete and also broaden. It is an indication of the existence of fine grains with random orientation, promoted by phase segregation.

Further studies concerning the relation between microstructure and magnetic properties are presently being carried out.

IV. CONCLUSION

The MR of granular $Fe_{26}Ag_{74}$ films has been found to be sensitive to the film thickness, which, to some extent, determines the microstructure and reflects the film growth process. In the initial stage, the MR increases greatly with the increase of film thickness, and beyond about 500 Å the improvements approach saturation. The maximum value of MR observed in as-deposited $Fe_{26}Ag_{74}$ is -18%. Studies of the films with TEM and SAD demonstrated that the low values of MR for thinner samples are mainly attributable to the existence of a large number of defects, such as twins, as well as the increasing effects of surface scattering, while for thicker samples the increase of both MR and saturation field can be explained by relief of structural disorder and promotion of iron precipitation, caused by a relatively long time deposition, which may serve as an *in situ* annealing.

ACKNOWLEDGMENTS

This work was supported by Chinese National Laboratory of Magnetism and Sanhuan Corporation.

[1] M. N. Baibich, J. M. Broto, A. Fert, F. N. V. Dau, F. Petroff, P. Etienne, G. Creuzet, A. Friederich, and J. Chazelas, Phys. Rev. Lett. **61**, 2462 (1988).
[2] A. E. Berkowitz, J. R. Mitchell, M. J. Carey, A. P. Young, S. Zhang, F. E. Spada, F. T. Parker, A. Hutten, and G. Thomas. Phys. Rev. Lett. **68**, 3745 (1992).
[3] J. Q. Xiao, J. S. Jiang, and C. L. Chien, Phys. Rev. Lett. **68**, 3749 (1992).
[4] P. Xiong, G. Xiao, J. Q. Wang, J. Q. Xiao, J. S. Jiang, and C. L. Chien, Phys. Rev. Lett. **69**, 3220 (1992).
[5] C. L. Chien, J. Q. Xiao, and J. S. Jiang, J. Appl. Phys. **73**, 5309 (1993).
[6] M. R. Parker, J. A Barnard, D. Sealc, and A. Waknis, J. Appl. Phys. **73**, 5512 (1993).
[7] S. F. Zhang and P. M. Levy, J. Appl. Phys. **73**, 5315 (1993).
[8] G. Xiao, J. Q. Wang, and P. Xiong, Appl. Phys. Lett. **62**, 420 (1993).

Magnetic properties of FeSi-SiO_2 granular films

Z. S. Jiang, X. Ge, J. T. Ji, H. Sang, G. Guo, and Y. W. Du
National Laboratory of Solid State Microstructures, Nanjing University, Nanjing 210093, People's Republic of China

S. Y. Zhang
Department of Physics, Nanjing University, Nanjing 210093, People's Republic of China

The ferromagnetic resonance (FMR) spectra and coercivities of FeSi-SiO_2 granular films have been measured over a wide range of FeSi volume fractions (f_v). The films were prepared using the ion-beam sputtering technique and transmission electron microscopy showed that the FeSi alloy granules are embedded in a matrix of SiO_2. An enhanced coercivity (H_c), as high as 329 Oe at room temperature, is observed. For some samples, there are several resonance peaks in the FMR spectra, which include one major peak and several minor peaks. The major and minor peaks correspond to the usual uniform mode and spin-wave respectively. In our experiments, the field separations between the major and the minor peaks show a complex fashion. Our results are discussed in comparison with some theoretical models.

I. INTRODUCTION

Granular solids consist of nanometer size metal granules embedded in an immiscible matrix which may be insulating or metallic. Because of the unique microstructure of ultrafine particles, many interesting and potentially useful properties have been found in granular systems.[1,2] The magnetic behaviors of metal granules are very different from that of the bulk. In particular, intrinsic magnetic properties, such as saturation magnetization (M_s) and anisotropy constant (K), are changed dramatically and greatly enhanced coercivities are usually observed. Such properties, especially giant coercivity, show potential for applications, among them, as novel magnetic recording media.[3]

With the development of the technology of film fabrication and the advancement of structure analytic methods, the magnetic properties of granular metal films have been investigated intensively.[4–6] Recently, some studies have also been carried out in the granular alloy films.[7] However, many properties on these films are still unknown and need to be clarified. To further understand the magnetic properties in the important area of ultrafine alloy, we have successfully fabricated FeSi-SiO_2 granular alloy films using the ion-beam sputtering technique. In this paper, we will describe the preparation and characterization of the films. Using these samples, we have made detailed measurements on their coercivities and ferromagnetic resonance (FMR) spectra. Our experimental study shows that an enhanced coercivity, as high as 329 Oe at room temperature, has been achieved in the films. Furthermore, we found that in some of our samples, there are several resonance peaks in FMR spectra. In the following, we should first discuss the experimental setup, then we will present our results and compare them with some existing theories.

II. EXPERIMENTS

The granular FeSi-SiO_2 films were prepared by the ion-beam sputtering technique. The films were deposited onto glass substrates which were fixed at the temperature 300 °C. During deposition, an ambient pressure of 2×10^{-2} Pa of argon was maintained. The sputtering targets were mosaic targets of FeSi(97% Fe-3% Si) alloy and SiO_2. The fractional area of SiO_2 on the targets can be changed so that various samples in the range of FeSi volume fractions (f_v) between 0.25 and 1.0 are obtained. The composition of the samples was determined using electron microprobe analysis.

The microstructure of the samples was examined by transmission electron microscopy (TEM), electron diffraction, and x-ray diffraction. The magnetic properties of the films were measured by a vibration sample magnetometer (VSM) with magnetic fields up to 20 kOe, the external field was applied parallel to the plane of the films during the measurements. The FMR spectra of the samples were recorded using an electron paramagnetic resonance (EPR) spectrometer operating at 9.97 GHz, the angle between the applied dc field and film plane changed from 90° to 0°.

III. RESULTS AND DISCUSSION

We have prepared samples with various FeSi volume fractions f_v. The microstructure of the films is composition dependent, the typical TEM micrographs are shown in Fig. 1(a) for $f_v\approx0.45$ and Fig. 1(b) for $f_v\approx0.7$. For smaller value of f_v, one can see that fine and roughly spherical FeSi particles are separated by the host material. The particles are of the order of a few nm in diameter and have a rather narrow size distribution. While for larger f_v, the fine particles aggregate into large connected granules; this can be clearly seen in Fig. 1(b).

The coercivities (H_c) of the films were measured at room temperature by VSM with the external field parallel to the plane of the films. The dependence of H_c on f_v is shown in Fig. 2. One found that H_c first increases as f_v increases, after reaches a maximum $H_c\approx329$ Oe at $f_v\approx0.7$, H_c sharply drops as f_v further increases. We found that the increase in the region of H_c at smaller f_v corresponds to the situation where the size of fine particles increases, while the rapid drop of H_c corresponds to the case when these fine particles form granular networks. This is similar to the observations of Xiao *et al.*[3] The maximum coercivity of our granular samples is about 85 times that of sputtered pure FeSi films.

 0021-8979/94/76(10)/6490/3/$6.00 © 1994 American Institute of Physics

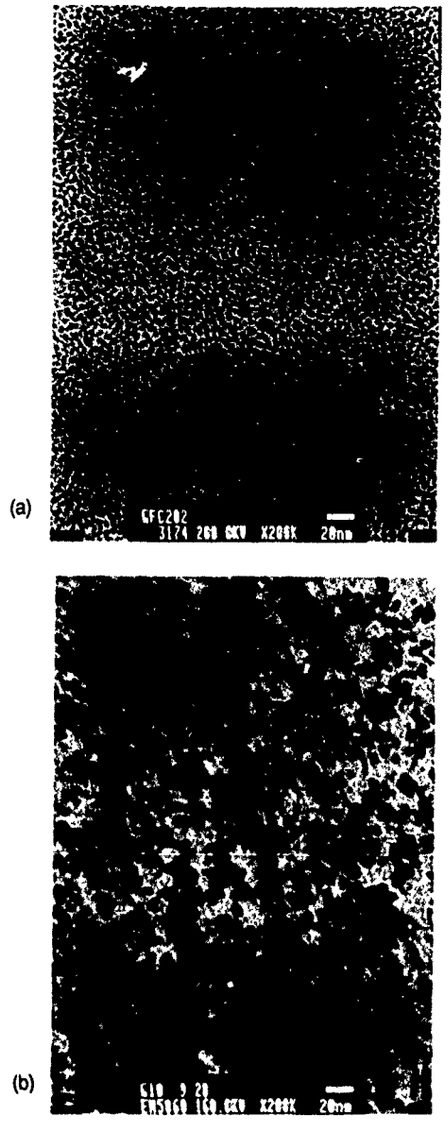

FIG. 1. TEM micrographs of FeSi-SiO_2 granular films (a) $f_v \approx 0.45$ and (b) $f_v \approx 0.7$.

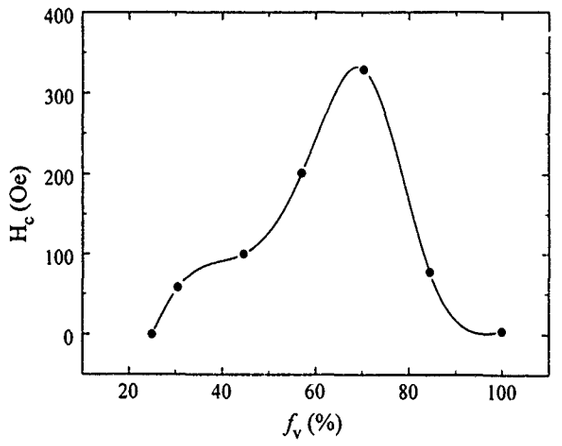

FIG. 2. Magnetic coercivities measured at 300 K of FeSi-SiO_2 granular films vs FeSi volume fraction f_v with the external field parallel to the film plane.

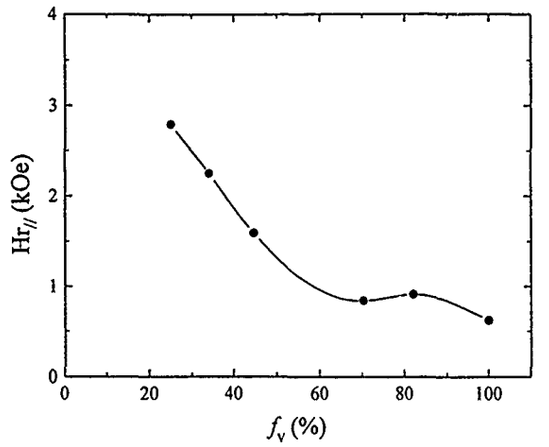

FIG. 3. The magnetic resonance field as function of FeSi volume fractions f_v for the applied dc field parallel to the film plane.

In comparison with Fe-SiO_2 granular solids, our maximum H_c is smaller. This is due to the fact that the FeSi alloy has a lower anisotropy constant than pure iron.

The FMR spectra of the samples were measured over a wide range of f_v at room temperature. Presented in Fig. 3 is the resonance field ($H_{r\|}$) obtained for applied dc field H in the film plane. $H_{r\|}$ decreases monotonically as f_v increases up to 0.6, then changes very little as f_v increases to 1. Our result indicates that the structure of the samples changes as f_v increases. The demagnetizing factor of our samples is reduced continuously as the fine particles gradually form uniform FeSi layer.

Figure 4 shows the dependence of the resonance fields H_r on θ for $f_v \approx 0.45$, with the θ denoting the angle between the applied dc field and film plane. When θ is close to 90°, there are several resonance peaks in the FMR spectra, which includes a major peak and four minor peaks. As θ changes from 90° to 0°, the positions of both the major and minor

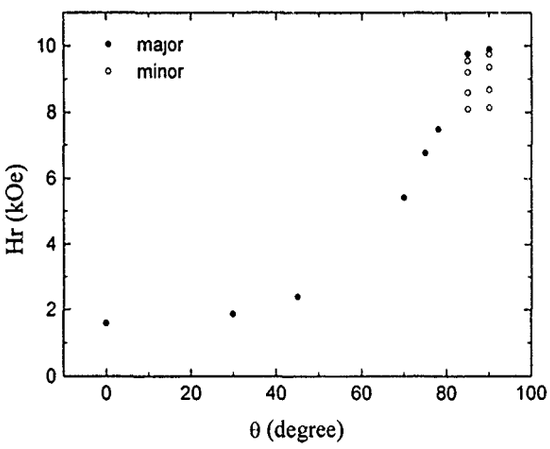

FIG. 4. The dependence of magnetic resonance field on the angle θ between the applied dc field and film plane for $f_v \approx 0.45$. The solid circles and the open circles correspond to the field positions of the major and minor peaks, respectively.

peaks shift towards low-field side. While the intensity of the major peak is almost unchanged, the intensities for the minor peaks become drastically reduced and disappear at the critical angle $\theta_c \approx 80°$. This behavior suggests that the major peak is the uniform mode and the minor peaks are spin-wave modes.[8] At $\theta=90°$, the separations between the first and the nth peak are about 150, 540, 1220, and 1760 Oe, respectively. The corresponding ratios are 1:3.6:8.1:11.7. The spin-wave resonance (SWR) theories[8–10] predict that this ratio should be proportional to n^2 or n depending on whether magnetic inhomogeneities are localized near the surface or distributed in the thickness of the films. Our result is within these two different cases and closer to the surface inhomogeneity model. This results from the fact that although a nanoscale volume inhomogeneity is characteristic of the granular films, there are abundant surfaces in our granular samples due to small size of particles, and magnetic inhomogeneities localized near metal-insulator interfaces may play an important role.

In conclusion, we have successfully prepared FeSi-SiO_2 granular films with different FeSi volume fractions using the ion-beam sputtering technique. Using these samples we have studied ferromagnetic resonance spectra and coercivities. We have observed a large H_c as high as 329 Oe. The FMR spectra for perpendicular configuration showed several peaks which can be attributed to the usual uniform mode and spin-wave modes. These materials open up a rich perspective for both fundamental investigations and technological applications.

ACKNOWLEDGMENTS

This work was supported by Grant 85-6 NMS, Grant NSFS and NAMCC, SKLM, and Grant JSNSF.

[1] J. A. A. J. Perenboom, P. Wyder, and F. Meier, Phys. Rep. **78**, 173 (1981).
[2] C. L. Chien, in *Science and Technology of Nanostructured Magnetic Materials: Granular Solids*, edited by G. C. Hadjipanayis and G. A. Prinz (Plenum, New York, 1991), p. 477.
[3] Gang Xiao and C. L. Chien, J. Appl. Phys. **63**, 4252 (1988).
[4] Y. Kanai and S. H. Charap, J. Appl. Phys. **69**, 4478 (1991).
[5] R. L. Holtz, P. Lubitz, and A. S. Edelstein, Appl. Phys. Lett. **56**, 943 (1990).
[6] A. Tsoukatos, H. Wan, and G. C. Hadjipanayis, J. Appl. Phys. **73**, 6967 (1993).
[7] A. Gavrin and C. L. Chien, J. Appl. Phys. **67**, 938 (1990).
[8] H. Puszkarski, Prog. Surf. Sci. **9**, 191 (1979).
[9] A. M. Portis, Appl. Phys. Lett. **2**, 69 (1963).
[10] F. Hoffmann, Solid State Commun. **9**, 295 (1971).

Hysteresis of binary clusters

Ivo Klik
Department of Physics, National Taiwan University, Taipei, Taiwan

Jyh-Shinn Yang
Division of General Education, National Taiwan Ocean University, Keelung, Taiwan

Ching-Ray Chang
Department of Physics, National Taiwan University, Taipei, Taiwan

A pair of parallel uniaxial particles with dipole-dipole coupling has, for bond angles $\beta=0$ and $\pi/2$, up to four locally stable configurations: $\uparrow\uparrow$, $\uparrow\downarrow$, $\downarrow\uparrow$, and $\downarrow\downarrow$. Assuming thermal relaxation via coherent rotation and a periodic driving field we solve a master equation for the occupation probabilities of these states and find the coercivity and switching field distribution of the ensemble of coupled particles. For either value of the bond angle we compare numerical solutions of the master equation with approximate expressions based on extremal analysis and find good agreement between the two.

There exists a vast body of literature dedicated to thermal relaxation effects in bistable systems while thermal relaxation in systems with more than two metastable minima has received, to date, but scant attention, a notable exception being the work of Pfeiffer.[1] We have recently[2] applied his master equation approach to an array of interacting, thermally relaxing bistable systems and we were able to demonstrate that the relaxation rates within such an array must be interpreted as rates of transitions between its metastable configurations. The simplest possible interacting array is formed by two identical, magnetostatically coupled uniaxial particles with individual energies $E^{(i)}=KV\sin^2\theta_i-M_sHV\cos\theta_i$ (K is anisotropy constant, V particle volume, M_s saturation magnetization, H is external field applied in the z direction, and θ_i is the angle spanned by the magnetization vector and applied field), and coupling $E_{\rm int}=r^{-3}\mathbf{M}_1\cdot\mathbf{M}_2-3r^{-5}(\mathbf{M}_1\cdot\mathbf{r})(\mathbf{M}_2\cdot\mathbf{r})$ where $\mathbf{r}=r(\sin\beta\mathbf{i}+\cos\beta\mathbf{k})$ is the radius vector joining the two particles and β the bond angle. The total energy is $E=E^{(1)}+E^{(2)}+E_{\rm int}$ and for brevity we write $\mathscr{E}=E/KV$ and $h=H/H_n$ ($H_n=2K/M_s$ is the nucleation field of an isolated particle). For bond angles $\beta=0$ and $\beta=\pi/2$ Chen *et al.*[3] found analytic expressions for the extremal energies and barrier heights of the system. We briefly summarize here their findings, write down our set of master equations,[2] and compute then the major hysteresis loop, coercivity, and switching field distribution as functions of the coupling strength $\rho=M_s^2V/(2Kr^3)$.

For either value of β there exist[3] up to four metastable states schematically represented as $\uparrow\uparrow$, $\downarrow\uparrow$, and $\uparrow\downarrow$ (these two are equivalent) and $\downarrow\downarrow$. Their energies are $\mathscr{E}_1=-\epsilon-4h$, $\mathscr{E}_2=\epsilon$, and $\mathscr{E}_3=-\epsilon+4h$, respectively; in these formulas $\epsilon=4\rho$ if $\beta=0$ and $\epsilon=-2\rho$ if $\beta=\pi/2$. For bond angle $\beta=0$ there exist three critical fields $h_{n_1}\geq h_p\geq h_{n_2}$,

$$h_{n_1}(\rho)=1+\rho, \tag{1}$$

$$h_p(\rho)=(1+\rho)(1-3\rho)^{1/2}(1-\rho)^{-1/2}, \tag{2}$$

$$h_{n_2}(\rho)=(1-3\rho)^{1/2}(1-\rho)^{1/2}. \tag{3}$$

The degree of metastability changes at the nucleation fields h_{n_i} while, as will be explained, at the critical field h_p only one of the relaxation channels changes and no change in the number of local minima takes place. There exist also three saddle points, labeled *a*, *b*, and *c*, with energies

$$\mathscr{E}^{(\alpha)}=1+3\rho^2+h^2\mp 2hh_{n_2}(\rho), \tag{4}$$

$$\mathscr{E}^{(c)}=2(1-\rho^2+h^2)/h_{n_1}(\rho), \tag{5}$$

where $\alpha=a$, b and the upper sign refers to the saddle *a*. The minimum and saddle point energies define [see Eq. (11) below] the barrier heights to be overcome by thermal relaxation). If $\beta=\pi/2$ then the system has again three critical fields $h_{n_1}\geq h_{n_2}\geq h_p$,

$$h_{n_1}(\rho)=(1-\rho)^{1/2}(1+3\rho)^{1/2}, \tag{6}$$

$$h_{n_2}(\rho)=1-3\rho, \tag{7}$$

$$h_p(\rho)=(1-3\rho)(1-\rho)^{1/2}(1+3\rho)^{-1/2}, \tag{8}$$

and three saddle points with energies

$$\mathscr{E}^{(\alpha)}=1-3\rho^2+h^2\mp 2hh_p(\rho), \tag{9}$$

$$\mathscr{E}^{(c)}=2[h^2+h_{n_2}(\rho)(1-2\rho)]/h_{n_2}(\rho). \tag{10}$$

As previously mentioned, there exist up to three physically distinct metastable configurations of the two-particle cluster. They correspond to local energy minima and we shall define

$$\kappa_{ij}^{(\alpha)}(h,\rho)=\kappa_{i\to j}^{(\alpha)}(h,\rho)=f_0\exp(-KV\mathscr{E}_{ij}^{(\alpha)}/T) \tag{11}$$

as the rate of thermally activated flux from the metastable state i to j passing through the saddle α. Here T is temperature ($k_B=1$), f_0 is the prefactor (we set[4] $f_0=e^{25}$ Hz) and the reduced barrier heights $\mathscr{E}_{ij}^{(\alpha)}=\mathscr{E}^{(\alpha)}-\mathscr{E}_i$.

For bond angle $\beta=0$ and applied field $|h|<h_{n_2}(\rho)$ the relaxation channels open in the two particle system may schematically be represented as $1\overset{a}{\leftrightarrow}2\overset{b}{\leftrightarrow}3$ where $1=\uparrow\uparrow$, $2=\downarrow\uparrow+\uparrow\downarrow$, and $3=\downarrow\downarrow$. The probabilities n_i (occupation numbers) that the system finds itself in the ith metastable state the satisfy[2] the equations

 0021-8979/94/76(10)/6493/3/$6.00 © 1994 American Institute of Physics

$$\dot{n}_1 = -2\kappa_{12}^{(a)} n_1 + \kappa_{21}^{(a)} n_2, \tag{12}$$

$$\dot{n}_2 = 2\kappa_{12}^{(a)} n_1 - (\kappa_{21}^{(a)} + \kappa_{23}^{(b)}) n_2 + 2\kappa_{32}^{(b)} n_3, \tag{13}$$

$$\dot{n}_3 = \kappa_{23}^{(b)} n_2 - 2\kappa_{32}^{(b)} n_3, \tag{14}$$

where $\dot{n}_i = dn_i/dt$. The factors 2 above have their origin in the degeneracy of the metastable state 2. The stationary state of Eqs. (12)–(14) is thermal equilibrium and it is easily shown[2] that in the decoupled limit one recovers the single particle result. In applied fields $h_{n_2} \leqslant |h| < h_p$ the local minima 2 do not exist so that

$$\dot{n}_1 = -\dot{n}_3 = -2\kappa_{13}^{(\alpha)} n_1 + 2\kappa_{31}^{(\alpha)} n_3 \tag{15}$$

and $n_2 \equiv 0$; $\alpha = b$ if $h > 0$ and $\alpha = a$ if $h < 0$, while $\alpha = c$ at fields $h_p \leqslant |h| < h_{n_1}$. The relaxation rates $\kappa_{ij}^{(\alpha)}$ are continuous across all critical fields $h_i(\rho)$ but equation sets (12)–(14) and (15) are discontinuous at the nucleation fields $\pm h_{n_2}(\rho)$ where the levels 2 vanish. In hysteresis calculations it is therefore necessary to verify that the vanishing intermediate states 2 are empty before the transition from the tristable to the bistable regime is made. The coercivity h_c is obviously bounded by the nucleation field h_{n_1}, $h_c \leqslant h_{n_1}$.

The case of bond angle $\beta = \pi/2$ and applied field $|h| < h_p$ is described by Eqs. (12)–(14). However, a direct relaxation channel opens between the states 1 and 3 if $h_p \leqslant |h| < h_{n_2}$ and we write[2] here

$$\dot{n}_1 = -2(\kappa_{12}^{(a)} + \kappa_{13}^{(c)}) n_1 + \kappa_{21}^{(a)} n_2 + 2\kappa_{31}^{(c)} n_3, \tag{16}$$

$$\dot{n}_2 = 2\kappa_{12}^{(a)} n_1 - (\kappa_{21}^{(a)} + \kappa_{23}^{(b)}) n_2 + 2\kappa_{32}^{(b)} n_3, \tag{17}$$

$$\dot{n}_3 = 2\kappa_{13}^{(c)} n_3 + \kappa_{23}^{(b)} n_2 - 2(\kappa_{31}^{(c)} + \kappa_{32}^{(b)}) n_3. \tag{18}$$

At $h_{n_1} > h \geqslant h_{n_2}$ the system has the two metastable states 1 and 2 and at $-h_{n_1} < h \leqslant -h_{n_2}$ the states 3 and 2. The evolution equations are

$$\dot{n}_2 = -\dot{n}_i = -\kappa_{2i}^{(\alpha)} n_2 + 2\kappa_{i2}^{(\alpha)} n_i, \tag{19}$$

where $i = 1$ and $\alpha = b$ for $h > 0$ while $i = 3$ and $\alpha = a$ for $h < 0$. In this case $h_c \leqslant h_{n_2}$. For either value of β the system is monostable in fields $|h| \geqslant h_{n_1}$.

Now let the applied field h vary with time as $h(t) = h_{n_1}(\rho)\cos 2\pi f t$ where f is the field sweep rate. At time $t = 0$, accordingly, $n_1 = 1$ and $n_2 = n_3 = 0$ in Eqs. (15) and (19). These are the initial conditions for the differential systems (12)–(15) describing the time evolution of the two particle cluster at bond angle $\beta = 0$ and for the systems (12)–(14), (16)–(19) corresponding to $\beta = \pi/2$. Their sample numerical[5] solutions are presented in Figs. 1 and 2 where we also introduce the reduced magnetization $m = 2(n_1 - n_3)$ and switching field distribution (SFD) $\chi = \partial m/\partial h$. In all cases we have chosen $q = KV/T = 42$ so that the half lifetime of an *isolated* particle is about one year.

At zero bond angle (Fig. 1) the antiparallel configurations 2 are energetically unfavorable and at the chosen temperature $n_2 \approx 0$ at all times for $\rho > 0.01$ (not shown in Fig. 1). The coercivity[6] $h_c(\rho, f)$ is shown in Fig. 3. Since $n_2 \approx 0$ the system may be treated as having only the two levels 1 and 3 approximately described by the evolution equation

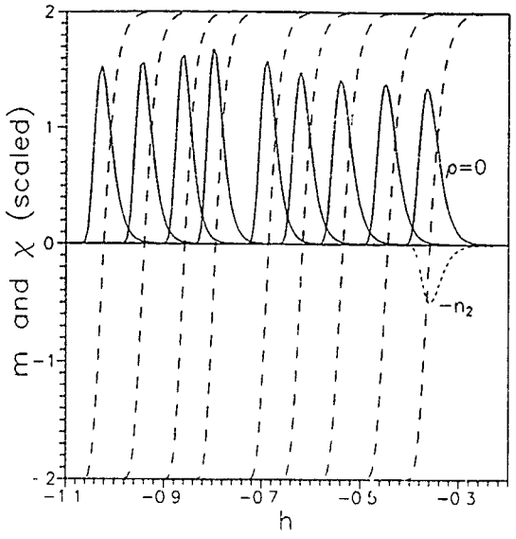

FIG. 1. Bond angle $\beta = 0$. Nonequilibrium magnetization $m[h(t)]$ (long dash) and switching field distribution $\chi[h(t)]$ (solid lines) vs applied field $h(t)$. Coupling strength $\rho = 0$ (rightmost curve, marked), 0.05, 0.10, 0.15, 0.20, 0.32 (the highest SFD peak shown here), 0.40, 0.50 and 0.60 (leftmost curve). For $\rho = 0$ we also show the probability $n_2[h(t)]$ (short dash), for all other values of ρ $n_2 \approx 0$ at all times. Sweep rate $f = 10^1$ Hz.

$\dot{n}_1 = -\Gamma n_1 = -\dot{n}_3$ where we retain only the dominant rate: $\Gamma = 2\kappa_{12}^{(a)}$ if $-h_p < h < 0$ and $\Gamma = 2\kappa_{13}^{(c)}$ if $-h_{n_1} < h < -h_p$; $\mathcal{A}_{12}^{(a)} = (h - h_{n_2})^2 + 4(2\rho + h)$ and $\mathcal{A}_{13}^{(c)} = 2(h + h_{n_1})^2/h_{n_1}$. At coercivity $n_1 = n_3 = 1/2$ and the SFD function has, approximately,[4] a maximum, $d\chi/dh|_{h=h_c} = 0$, so that

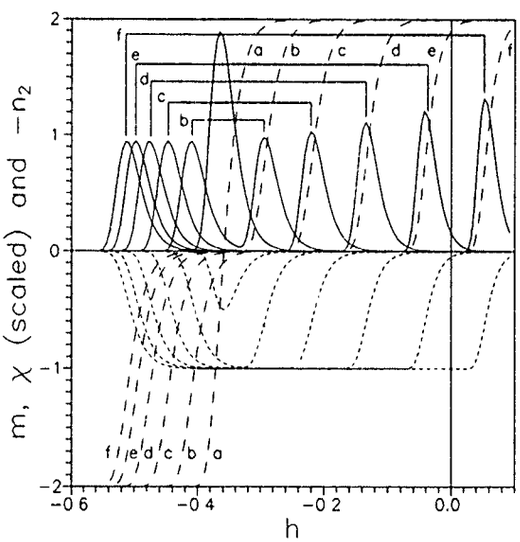

FIG. 2. Bond angle $\beta = \pi/2$. Nonequilibrium magnetization $m[h(t)]$ (long dash), switching field distribution $\chi[h(t)]$ (solid lines), and the probability $n_2[h(t)]$ (short dash, plotted as $-n_2$ for clarity) vs applied field $h(t)$. The magnetization curves labeled as a ($\rho = 0$), b ($\rho = 0.05$), c ($\rho = 0.10$), d ($\rho = 0.15$), e ($\rho = 0.20$), and f ($\rho = 0.25$). For $\rho > 0$ the SFD function has a minimum at coercivity and two flanking peaks which we connect by labeled braces. The curves $n_2(h)$ are unlabeled, the broadest curve corresponds to $\rho = 0.25$, the narrowest one (with max $n_2 = 1/2$) to $\rho = 0$. Note how stable the antiparallel states 2 become at large coupling strengths. Sweep rate $f = 10^1$ Hz.

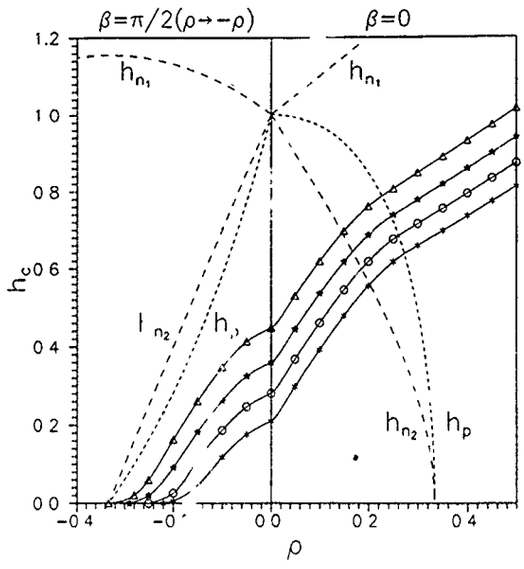

FIG. 3. The exact reduced coercivity (Ref. 6) $h_c(\rho,f)$ for bond angles $\beta=0$ and $\pi/2$. Sweep rates are $f=10^{-3}$ Hz (*), 10^{-1} Hz (○), 10^{1} Hz (☆), and 10^{3} Hz (△). Note in particular that at small interaction strengths $h_c \propto \rho$ for $\beta=0$ but $h_c \propto -\rho^2$ for $\beta=\pi/2$. Also shown are the nucleation fields h_{n_i} and the critical fields h_p.

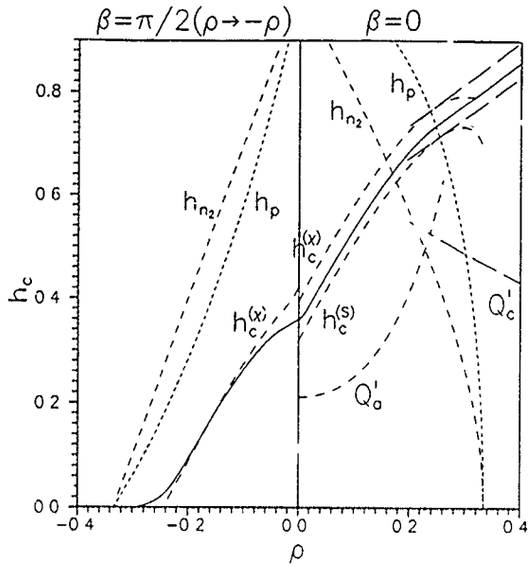

FIG. 4. The exact reduced coercivity (Ref. 6) $h_c(\rho,f)$ ($f=10^{1}$ Hz, solid line) compared with the approximate expressions $h_c^{(S)}$ [solution of Sharrock's formula (Ref. 7) $\beta=0$ only] and $h_c^{(x)}$ [solution of Eq. (21) for $\beta=0$ and Eq. (22) for $\beta=\pi/2$]. Approximate solutions based on $\mathcal{Q}_{12}^{(a)}$ (short dash) exist at $h_c<h_p$ and those based on $\mathcal{Q}_{13}^{(c)}$ (long dash) at $h_c>h_p$. To emphasize the matching at $h_c=h_p$ we extend both solutions a little into the unphysical region beyond h_p. Also shown are the (scaled) derivatives $Q_a'(h_c^{(x)})$ and $Q_c'(h_c^{(x)})$ (same markings as for coercivity).

$$2\pi f h_c \dot{m}(h_c) - \sigma(h_c)\ddot{m}(h_c) = 0, \tag{20}$$

$\sigma(h) = (h_{n_1}^2 - h^2)^{1/2}$. Substituting for $\dot{m}$ and $\ddot{m}$ we finally obtain

$$\ln(f_0/\pi f) - Q_\alpha(h_c) = \ln\{\sigma(h_c)[Q_\alpha'(h_c) - h_c/\sigma^2(h_c)]\}, \tag{21}$$

where $Q_\alpha(h_c) = q\mathcal{Q}_{ij}^{(\alpha)}(h_c)$ for brevity and $Q_\alpha' = dQ_\alpha/dh$. Without the right-hand side this is exactly Sharrock's formula[7] for coercivity and Fig. 4 shows that both the solution $h_c^{(x)}$ of Eq. (21) and the solution $h_c^{(S)}$ of Sharrock's formula provide a very good approximation to the exact solution $h_c(\rho)$. Regarding the SFD function $\chi(h)$ it was shown[4] that approximately $\chi_{\max}(h) \sim Q_\alpha'(h_c)$ so that according to Fig. 4 the SFD function $\chi(h)$ should attain the greatest height if $h_c(\rho)=h_p(\rho)$ and this trend is indeed observed in Fig. 1 and in its counterparts at other sweep rates.

At bond angle $\beta=\pi/2$ the evolution of the two particle cluster is dominated by the great stability[8] of the antiparallel configurations 2 (see Fig. 2), $n_2(h_c)\approx 1$ and the SFD function has a local *minimum* flanked by two local maxima. The two level approximation is obviously not applicable, yet an approximate expression for $h_c(\rho)$ follows from Eqs. (20) and (12)–(14) supplemented by the auxilliary extremal conditions $n_1(h_c)=n_3(h_c)$ and $\dot{n}_2(h_c)=0$:

$$2\kappa_{12}^{(a)}(h_c) - \kappa_{23}^{(b)}(h_c) = 2\pi f\sigma(h_c)[Q_a'(h_c) + Q_b'(h_c) - 2h_c/\sigma^2(h_c)], \tag{22}$$

where $Q_a/q = \mathcal{Q}_{12}^{(a)} = (h - h_{n_1})^2 + 4(h-\rho)$ and $Q_b/q = \mathcal{Q}_{23}^{(b)} = (h + h_{n_1})^2$. The solution $h_c^{(x)}$ of Eq. (22) is compared with the exact coercivity $h_c(\rho)$ in Fig. 4. An approximate expression for the SFD peak values $\chi_{\max}(h_c+\delta_1) > \chi_{\max}(h_c-\delta_2)$, $\delta_i>0$, is not known to us.

The evolution (master) equations of Sec. II are fairly complicated but we have shown here that at least the coercivity $h_c(\rho)$ may easily be found from the approximate Eqs. (21) and (22). It is remarkable that for $\beta=\pi/2$ and small ρ the exact coercivity is a nonlinear function of the coupling strength ($h_c \propto -\rho^2$) while this result cannot be obtained from the approximate Eq. (22) (compare Fig. 4) nor from a mean field theory.[9] Equations (21) and (22) fail if the hysteresis loop approaches the curve of equilibrium magnetization, i.e., at high temperatures or small sweep rates.

This research was sponsored by the National Science Council of ROC under Grant No. NSC 82-0208-M002-35.

[1] H. Pfeiffer, Phys. Status Solidi A **120**, 233 (1990); **122**, 377 (1990).
[2] I. Klik, C. R. Chang, and J. C. Yang (unpublished).
[3] W. Chen, S. Zhang, and H. N. Bertram, J. Appl. Phys. **71**, 5579 (1992).
[4] I. Klik, C. R. Chang, and H. L. Huang, Phys. Rev. B **47**, 8605 (1993). We recall that e^{25} Hz$\approx 10^{10}$ Hz. For experimental measurements of the prefactor see D. P. E. Dickson, N. M. K. Reid, C. Hunt, H. D. Williams, M. El-Hilo, and K. O'Grady, J. Magn. Magn. Mater. **125**, 345 (1993).
[5] W. H. Press, B. P. Flannery, S. A. Teukolsky, and W. T. Vetterling, *Numerical Recipes, FORTRAN Version* (Cambridge University Press, Cambridge, 1990), Sec. 15.6, p. 572.
[6] Our system is initially saturated in positive applied field so that it switches at negative coercive fields, but in the plots of Figs. 3 and 4 we apply the convention that $h_c(\rho)\geq 0$. Similarly, the solutions $h_c^{(x)}$ of Eqs. (21) and (22) are in fact negative.
[7] M. P. Sharrock, IEEE Trans. Magn. **MAG-26**, 193 (1990).
[8] We recall that the initial equilibrium susceptibility $\chi_{eq}(0)=8q(1+e^{-2q\rho})^{-1}$ for $\beta=0$ but $\chi_{eq}(0)=8q(1+e^{4q\rho})^{-1}$ for $\beta=\pi/2$.
[9] I. Klik and C. R. Chang (unpublished data based on Ref. 4); D. C. Jiles and D. L. Atherton, J. Magn. Magn. Mater. **61**, 48 (1986). Interactions are represented by the state dependent mean field $\bar{h}(t)=h(t)+\alpha m(t)$ where $m(t)$ is the instanteneous magnetization and α a small empirical constant; $h_c \propto \alpha$ if $|\alpha| \ll 1$.

Some specific features of fine Fe and Fe-Ni particles

Yu. V. Baldokhin, P. Ya. Kolotyrkin, Yu. I. Petrov, and E. A. Shafranovsky
Institute of Chemical Physics, Russian Academy of Sciences, Kosygin Ulitsa 4, 117977, GSP-1, Moscow V-334, Russia

By comparing results of Mössbauer spectroscopy and x-ray diffraction investigations of ultrafine Fe and Fe-Ni particles, a formerly stated supposition on the existence of two spin states of the fcc phase in pure iron and Fe-Ni alloys has been verified. Some structural peculiarities of particles under study have been observed also. For the pure bcc-Fe particles with an average diameter of 30 and 50 nm the existence of two hyperfine fields (H_1=330 kOe, H_2=360 kOe) at room temperature has been found. It is supposed that H_2 in the bcc phase could be considered as a remnant of a high spin state of the fcc-Fe phase at high temperature. Particles of Fe-Ni(30.3 wt %), Fe-Ni(35 wt %), and Fe-Ni(52 wt %) alloys with an average diameter ranging from 5 to 15 nm were studied also. Particles of Fe-Ni (30.3 wt %) and Fe-Ni(35 wt %) alloys with diameter of 5–8 nm had the bcc structure. A mixture of the bcc and fcc phases appeared with an increase of the particle size. At the same time only the fcc structure remained for the largest particles. The observed size structural dependences and the existence of the stable bcc phase in small particles can be explained by the martensite fcc-bcc transition.

I. INTRODUCTION

This work aims to study Fe and some binary system peculiarities under transition from bulk to fine particles in order to reveal some of their size-dependent properties and to understand the nature of these properties of the bulk itself more profoundly. Subjects of inquiry are chosen magnetic Fe and Fe-Ni fine particles. The change in the crystalline and hyperfine magnetic structure of small particles of Fe and Fe-Ni alloys enriched with Fe as compared with the bulk have been investigated. It is well known from experimental data and the theoretical point of view that some Fe-based alloys with fcc structure show many anomalies of physical properties. This variety of anomalies is named Invar anomalies and the most specific one is a behavior of the thermal expansion. The thermal expansion constant is practically equal to zero within a wide temperature range. The nature of the anomalies in fcc Invars is supposed to be due to (i) the peculiarities of the electron and magnetic structure, (ii) size-dependent properties of small particles, (iii) an influence of various composition, interatomic distances, a number of nearest neighbors, α-γ and antiferro-ferromagnetic transformations, and high and low spin states.

II. SAMPLE PREPARATION

The fine particles are produced with the so-called "gas evaporation" technique. The principle of the method lies in substance vapor condensation in an inert gas atmosphere which transfers the condensation heat from the arising aerosol particles to the reaction vessel walls (the solidification rate is about 10^4–10^5 deg/s). By varying the species and the pressure of the inert gas as well as the vessel size, it is possible to alter the average diameter of aerosol particles within a range from one to hundreds of nanometers. The particles obtained are deposited on the vessel walls and have a rather narrow size distribution (maximum deviation from the average value is usually no more than a double value).

III. EXPERIMENTAL RESULTS AND DISCUSSION

Analyzing thermodynamic functions as well as results of electric and magnetic measurements for pure iron and its alloys, Weiss[1] came to the conclusion that a high temperature fcc-Fe phase could exist in two spin electron states, one of which was antiferromagnetic (Néel temperature T_N=80 K, magnetic moment per atom μ=0.5 μ_B, lattice constant a=3.55±0.01 Å), and the other was ferromagnetic (Curie temperature T_C=1800 K, magnetic moment μ=2.8 μ_B, lattice constant a=3.64±0.01 Å). However, so far no direct proof has existed that the fcc phase in pure iron was possible in two spin states. In an attempt to clear up this question, we used the capability of small particles obtained by the condensation of a vapor substance in argon (gas evaporation technique), to retain their high temperature state.[2] A comparison of Mössbauer spectra with x-ray diffraction data on thermal expansion of such Fe particles gave a direct verification of Weiss's hypothesis[3] for the first time.

The Mössbauer spectra obtained at 300 K for particles with a diameter of about 50 nm are shown in Fig. 1.[3] Computer analysis of the initial powder revealed two spectra with the following hyperfine parameters: (1) an effective magnetic field on Fe nuclei H_1=330 kOe, a fraction of whole spectrum area S_1=37.8%, electric quadrupole interaction Δ_1=0, an isomer chemical shift δ_1=0 (δ is referred to metallic iron at room temperature), half a width of the first line $(\Gamma/2)_1$=0.55 mm/s (this spectrum corresponds to a slightly disordered bcc-Fe phase); (2) H_2=360 kOe, S_2=62.2%, δ_2=0.02 mm/s, Δ_2=0.1 mm/s, $(\Gamma/2)_2$=0.56 mm/s. The superposition of these two spectra demonstrated a complex magnetic structure of the sample. At the same time x-ray patterns showed the presence of only a bcc-Fe phase with a lattice constant a=2.866±0.002 Å. The Mössbauer spectrum of the powder was varied essentially by fast quenching to room temperature after heating in argon at T=800 °C for half an hour [Fig. 1(b)]. The area of such the spectrum with the H_2 component was extended to S_2=82% while the content of the bcc-Fe phase with the H_1 component was reduced

 0021-8979/94/76(10)/6496/3/$6.00 © 1994 American Institute of Physics

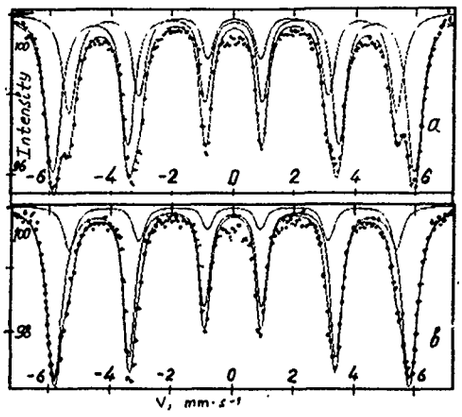

FIG. 1. Mössbauer spectra of Fe particles with a diameter of 50 nm: (a) the initial powder; (b) the same powder after heating at temperature $T=800$ °C for half an hour followed by quenching down to room temperature.

down to $S_1=18\%$. These results allowed us to suppose that the hyperfine magnetic field H_2 in the bcc phase could be considered as a remnant of a high spin state available in the fcc-Fe phase at high temperature.

It was interesting to ascertain to what degree the peculiarities of the Mössbauer spectra for Fe particles are retained in small particles of an Fe-Ni Invar alloy for which a stabilization of the high temperature fcc phase in iron is typical. Preliminary results of studies of Fe-Ni alloy particles have been published earlier.[4]

Particles of Fe-Ni(30.3 wt %), Fe-Ni(35 wt %), and Fe-Ni(52 wt %) alloys with an average diameter ranging from 5 to 15 nm were studied by x-ray diffraction and Mössbauer spectroscopy. Foil and wire alloys were used for preparing samples. They were evaporated within a vacuum chamber from W wire placed at the center of a beaker with a diameter of 10 cm. The vacuum chamber was filled with argon up to a given pressure ranging from 0.08 to 3.5 Torr and a swift sample evaporation was made. Metal vapor condensation in argon (the gas evaporation technique) resulted in ultrafine deposits on the beaker walls formed from spherical particles with a narrow size distribution. The following results were obtained from the x-ray diffraction measurements. (1) The lattice constants for even the smallest particles did not differ from those for a bulk solid. (2) The Fe-Ni(52 wt %) alloy retained the fcc structure whatever the particle size. (3) The Fe-Ni(30.3 wt %) and Fe-Ni(35 wt %) alloys in a bulk solid originally have a fcc structure with a small fraction of the bcc phase, while the particles with a diameter of 5–8 nm consist of only the bcc phase. As the particle size increases the content of the fcc phase rises while the fraction of the bcc phase is reduced. The bcc-fcc transition is completed entirely in Fe-Ni(35 wt %) particles with a diameter of about 12 nm though larger Fe-Ni(30.3 wt %) particles with a diameter of 15 nm have a conspicuous bcc phase fraction.

It should be noted that the observed structural size dependence and stable existence of the bcc phase in small particles of Fe-enhanced alloys run counter to the expected suppression of the martensite fcc-bcc transition in such particles.[5]

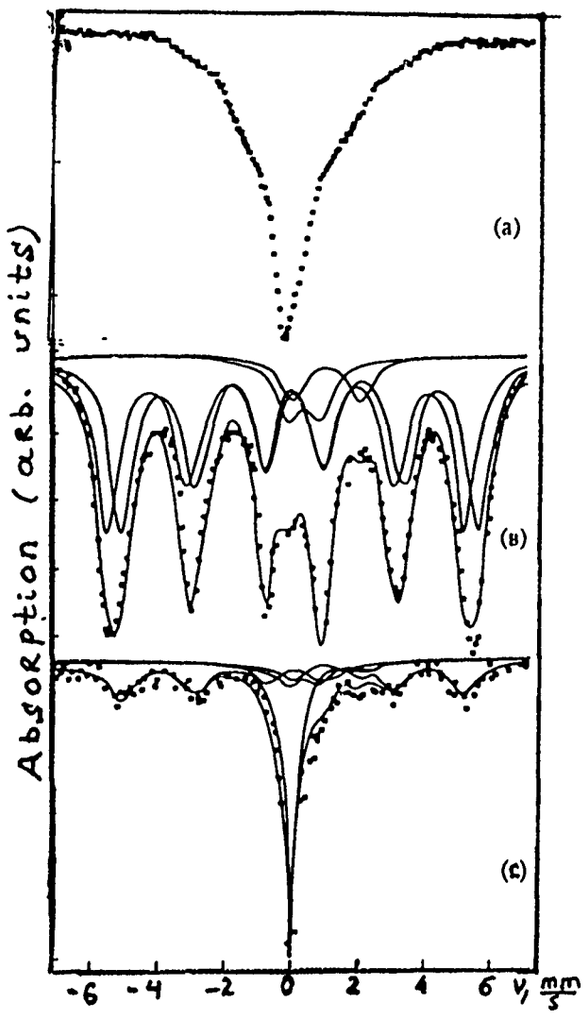

FIG. 2. Mössbauer spectra of Fe-Ni alloys: (a) Fe-Ni(30.3 wt %) foil; (b) Fe-Ni(35 wt %) powder with a mean particle size of 8 nm; (c) the same powder as a previous one heated at temperature $T=900$ °C for half an hour followed by quenching to room temperature.

Typical Mössbauer spectra for Fe-Ni alloys are shown in Fig. 2. The spectra of particles are quite different from spectra of foils. Parameters for the Mössbauer spectra of samples are listed in Table I. The spectrum for the Fe-Ni(30.3 wt %) foil displays a broad single line [Fig. 2(a)] while the spectra for Fe-Ni(35 wt %) foil and Fe-Ni(52 wt %) wire could be represented as two 6-line spectra: $H_1=278$ kOe ($S_1=44\%$), $H_2=238$ kOe ($S_2=56\%$), and $H_1=308$ kOe ($S_1=50\%$), $H_2=313$ kOe ($S_2=50\%$), respectively. In the case of the Fe-Ni(52 wt %) alloy its Mössbauer spectrum pattern and a crystalline structure keep under the transition from a bulk solid to particles with the diameter of 7 nm. The Fe-Ni(35 wt %) and Fe-Ni(30.3 wt %) alloys behave the other way around, that is the fcc structure of the bulk solid changes into bcc structure for the particles with a diameter of 5–8 nm. The form of the Mössbauer spectrum and the crystallographic features of the Fe-Ni(30.3% wt %) particles with about 15 nm diam, which contain both phases at the 1.3 fcc/bcc ratio, do not change after exposing samples at 77 K for 2 h.

TABLE I. Hyperfine size parameters for Fe-Ni samples at 298 K.[a]

d	H_{eff}	γ	ϵ	Cl	S
		30.3 Ni wt % sample			
15	330	−	−	−	43
	−	+	−	−	57
	345	−	−	−	44
8	318	−	−	−	44
	−	−	−	+	12
	345	−	−	−	33
	318	−	−	−	33
5	−	−	−	+	14
	−	−	+	−	20
	330	−	−	−	37
5.5	−	−	+	−	63
		35 Ni wt % sample			
	345	−	−	−	44
8	318	−	−	−	44
	−	−	−	+	12
	318	−	−	−	40
8[b]	−	+	−	−	43
	−	−	−	+	17

[a]d—particle size, nm; H_{eff}—hyperfine magnetic field, kOe; γ—single line with the isomer shift $\delta=-0.07$ mm/s corresponds to the fcc phase; ϵ—unresolved structure ("sagging wire"); Cl—clusters of Fe^{2+}, Fe^{3+} [see Fig. 2(b)]; S—relative area of subspectra, %.
[b]Sample after heating at $T=900$ °C for 2 h.

The spectrum for Fe-Ni(35 wt %) particles with a mean diameter of 8 nm, as shown in Fig. 2(b), could be represented by two 6-line spectra: $H_1=345$ kOe ($S_1=44\%$) and $H_2=318$ kOe ($S_2=44\%$) with a small fraction of Fe^{3+} and Fe^{2+} oxides. Practically the same value of H_1 and H_2 were observed for the Fe-Ni(30.3 wt %) particles with diameters in the range of 5–8 nm. When the Fe-Ni(30,3 wt %) and Fe-Ni(35 wt %) the smallest particles of 5–8 nm size were quenched from 900 °C to room temperature, the 6-line spectrum with $H_1=345$ kOe transformed into a central line ($S_1=43\%$, $\delta_1=-0.07$ mm/s) [Fig. 2(c)] with simultaneously about twice the increase of the particle size. This spectrum transformation is undoubtedly due to a bcc-fcc phase transition. This is also borne out with the appearance of the narrow central line ($S_1=57\%$, $\delta_1=-0.05$ mm/s) corresponding to the fcc phase side by side with the 6-line spectrum ($H_2=330$ kOe, $S_2=43\%$, $\delta_2=0.02$ mm/s, $\Delta_2=0.02$ mm/s) corresponding to the bcc phase for the Fe-Ni(30.3% wt %) particles with a mean diameter of 15 nm (see Table I).

IV. CONCLUSIONS

As in the case of the small particles of both pure iron and Fe-Ni alloy the Mössbauer spectra have a complex structure indicating, probably, the essential role of a high temperature Fe fcc modification which can be displayed in two different states depending on the size, the particle making conditions, and the heat treatment.

Though it has been recently shown theoretically that the ferromagnetic fcc Fe was unstable relative to tetragonal deformation, and hence it could not exist itself,[6] nevertheless in the case of pure iron the experimental results[3] evidence an availability of two spin states in the fcc Fe. As for the Fe-Ni Invar alloy in this case also the above given experimental results indicate the existence, at least, of two spin states in the fcc phase. So, in accordance with the theory[1] for the Fe-Ni(30.3 wt %) and Fe-Ni(35 wt %) particles the central paramagnetic peak in Fig. 2(c) apparently belongs to an antiferromagnetic low spin state of the fcc phase but one of the two Mössbauer spectrum components [Fig. 2(c)] with the higher hyperfine field ($H_1=345$ kOe) on Fe nuclei, probably, corresponds to the hereditary high spin magnetic structure of the fcc phase in a crystalline bcc structure of small particles. This last magnetic structure is formed during a particle making procedure. At the same time after the powder heat treatment at a temperature of 900 °C followed by a quenching to room temperature it transforms to the low spin state of the fcc phase simultaneously with the structural bcc-fcc transition.

ACKNOWLEDGMENT

Two of the authors (Y.I.P. and E.A.S.) would like to thank the International Science Foundation under Grant No. MJ8 000 for the partial financial support of this work.

[1] R. J. Weiss, Proc. Phys. Soc. London **82**, 281 (1963).
[2] Yu. I. Petrov, *Clusters and Small Particles* (Nauka, Moscow, 1986) (in Russian).
[3] Yu. V. Baldokhin and Yu. I. Petrov, Doklady RAN **327**, 87 (1992).
[4] Yu. V. Baldokhin, P. Ya. Kolotyrkin, I. I. Morozov, Yu. I. Petrov, and E. A. Shafranovsky, Doklady RAN **330**, 310 (1993).
[5] H. Asano, J. Phys. Soc. Jpn. **27**, 542 (1969).
[6] G. L. Krasko and G. R. Olson, J. Appl. Phys. **67**, 4570 (1990).

Magnetoresistance of the magnetically ordered icosahedral quasicrystals Al-Pd-Mn-B

M. H. Yewondwossen, S. P. Ritcey, Z. J. Yang, and R. A. Dunlap
Department of Physics, Dalhousie University, Halifax, Nova Scotia B3H 3J5, Canada

The transverse magnetoresistance has been measured for the newly discovered magnetically ordered icosahedral quasicrystals $Al_{70-x}Pd_{15}Mn_{15}B_x$ (x=0,2,4,6,8,10). Experiments were conducted at 4.2 K in magnetic fields up to 5.5 T. The results showed a systematic change as a function of boron concentration. The magnetoresistance for x=0,2,4,6 showed a negative field dependence which became weak with increasing x. The samples with x=8,10 showed a negative magnetoresistance at low fields, which became positive for higher applied fields. The minimum in the magnetoresistance shifted to lower field value with increasing boron content (to about 0.5 T for 10 at. %B). The analysis of the results has been based on the theory of three-dimensional weak localization, with a strong influence of spin-orbit scattering. The magnetoresistance is negative for low boron concentration due to weak spin-orbit scattering, and is positive for high boron concentration due to strong spin-orbit scattering.

I. INTRODUCTION

Since the first discovery of quasicrystals in Al-Mn alloys[1] the influence of the quasiperiodicity on the physical properties has been studied extensively. In particular, the effect of the local icosahedral symmetry on the magnetic and electronic properties has been of particular interest.[2,3] Quasicrystals show magnetic behavior that ranges from diamagnetic to ferromagnetic.[3] Most quasicrystalline materials have been reported to be either diamagnetic or paramagnetic, while a few have exhibited spin glasslike behavior.[3] Weak ferromagnetism has been found in Al-Ce-Fe,[4] Al-Mn-Ge,[5] and Al-Mn-Si.[6,7]

Recently a new class of Al-Pd-Mn-B quasicrystals with large magnetization ($\sim 5\times10^{-7}$ H m^2 kg^{-1}) and Curie temperatures around 500 K have been reported.[8] The room-temperature magnetization was found to increase with increasing B content in the series of alloys of the composition $Al_{70-x}Pd_{15}Mn_{15}B_x$. The magnetization is observed only in the metastable quasicrystalline phase and is not present in the equilibrium crystalline phase. In this work the magnetoresistance of $Al_{70-x}Pd_{15}Mn_{15}B_x$ has been investigated at 4.2 K. Weak localization theory is used to analyze the result and deduce the inelastic scattering time τ_i and spin-orbit scattering time τ_{so}.

II. EXPERIMENTAL METHODS

$Al_{70-x}Pd_{15}Mn_{15}B_x$ alloy ingots were prepared from high purity elements by arc melting followed by melt spinning onto a copper roller with a surface speed of 60 m s^{-1}. Resulting ribbons had cross sections of $\sim$25 μm thick by $\sim$1.5 mm wide. The single phase quasicrystalline nature of the ribbons was confirmed by room temperature x-ray diffraction using Cu-K_α radiation on a Siemens D500 scanning diffractometer. The magnetoresistance was measured at 4.2 K in a transverse field up to 5.5 T using a conventional four-point dc technique. The electrical leads were attached to the sample using silver loaded epoxy.

III. RESULTS AND DISCUSSION

Weak localization (WL) effects are manifested at low temperature as small quantum perturbations of the classical Boltzmann conductivity and can provide detailed information about the electron scattering processes. The theory of WL has had reasonable success in explaining the anomalous behavior of the transport properties of three-dimensional disordered systems.[9,10] The magnetoresistance is negative in the case of weak spin-orbit scattering systems, i.e., $\tau_i<\tau_{so}$. In the case of strong spin-orbit scattering systems the magnetoresistance is positive and $\tau_i>\tau_{so}$.

The magnetoresistance, $\Delta\rho/\rho^2$, due to WL effects is given as a function of the applied magnetic field, B, by the model of Altshuler *et al.*[11] as

$$\frac{\Delta\rho}{\rho^2}=\frac{\alpha e^2}{\pi h}\sqrt{\frac{2\pi eB}{h}}\left[\frac{1}{2}f_3\left(\frac{B}{B_i}\right)-\frac{3}{2}f_3\left(\frac{B}{B_{so}}\right)\right], \tag{1}$$

where

$$B_i=\frac{h}{8\pi eD\tau_i}, \tag{2}$$

$$B_{so}=B_i+\frac{h}{4\pi eD\tau_{so}} \tag{3}$$

and D is the diffusion coefficient and α accounts for uncertainties in sample geometry. The function $f_3(x)$ is the Kawabata function given by[12]

$$f_3(x)=\sum_{n=0}^{\infty}\left[2\left(n+1+\frac{1}{x}\right)^{1/2}-2\left(n+\frac{1}{x}\right)^{1/2}-\left(n+\frac{1}{2}+\frac{1}{x}\right)^{-1/2}\right]. \tag{4}$$

The transverse magnetoresistance measured at 4.2 K for the $Al_{70-x}Pd_{15}Mn_{15}B_x$ (x=0,2,4,6,8,10) alloys is shown in Fig. 1. The magnetoresistance is negative for $x\leqslant6$ and positive for x=8 and 10. Data have been fit to Eq. (1) using standard

 0021-8979/94/76(10)/6499/2/$6.00 © 1994 American Institute of Physics

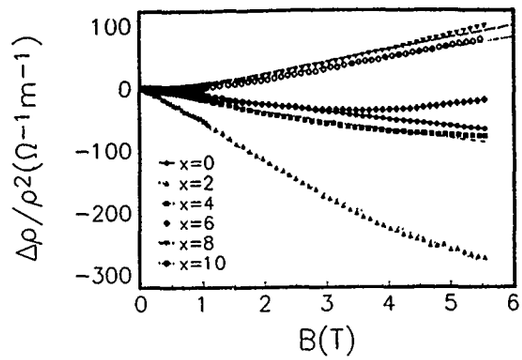

FIG. 1. The transverse magnetoresistance measured at 4.2 K for the $Al_{70-x}Pd_{15}Mn_{15}B_x$ (x=0,2,4,6,8,10) alloys. Least-squares fits to Eq. (1) are illustrated by the solid and broken lines.

nonlinear least-squares methods. The slowly converging function $f_3(x)$ used by Kawabata[12] was replaced by the more compact form proposed by Baxter *et al.*[13]

$$f_3(x)=2\left[\sqrt{2+\frac{1}{x}}-\sqrt{\frac{1}{x}}\right]-\left[\left(\frac{1}{2}+\frac{1}{x}\right)^{-1/2}+\left(\frac{3}{2}+\frac{1}{x}\right)^{-1/2}\right]+\frac{1}{48}\left(2.03+\frac{1}{x}\right)^{-3/2}. \quad (5)$$

The diffusion coefficient is taken to be 0.075 $cm^2\,s^{-1}$,[14] from literature values for similar Al-Mn-Pd based quasicrystals. The characteristic scattering times τ_i and τ_{so} are obtained as free parameters in the fits. The parameters obtained from these fits are summarized in Table I and fitted curves are illustrated in Fig. 1.

Equation (1) gives a good fit to the data for the two alloys with the strongest spin-orbit scattering and positive $\Delta\rho/\rho^2$, i.e., alloys with 8 and 10 at. % boron. The presence of strong spin-orbit scattering in these alloys is evidenced by the relative values obtained from the fits to the scattering times; $\tau_i > \tau_{so}$. The fit for alloys with weak spin-orbit scattering, i.e., alloys with 0, 2 and 4 at. % boron, indicates that the relative scattering times are $\tau_i < \tau_{so}$. The alloy with x=6 at. % boron exhibits complex behavior of $\Delta\rho/\rho^2$ as a function of applied field. Subsequently the function given in Eq. (1) does not provide a suitable fit to the experimental data for the alloy of this composition.

TABLE I. Scattering times and coefficient values obtained by fitting measured magnetoresistance data to Eq. (1).

x (at. %)	τ_i (10^{-10} s)	τ_{so} (10^{-10} s)
0	2.51	9.8
2	1.96	960
4	2.59	0.57
8	0.30	0.0015
10	0.22	0.0015

IV. CONCLUSIONS

The values of the parameters given in Table I as well as the qualitative behavior of the experimental data as illustrated in Fig. 1 demonstrate a crossover from weak spin-orbit scattering to strong spin-orbit scattering as a function of increasing boron content in the alloys. This crossover corresponds to a transition from $\tau_i < \tau_{so}$ to $\tau_i > \tau_{so}$ and a corresponding loss of phase coherence in the scattering. The present experimental results have demonstrated that the theory of WL gives at least a semiquantitative description of the magnetoresistance of magnetically ordered $Al_{70-x}Pd_{15}Mn_{15}B_x$ quasicrystals; in particular those which exhibit strong spin-orbit scattering. WL theory gives a poorer quantitative description of weak and intermediate spin-orbit scattering. The breakdown of the theory for similar cases in three-dimensional systems have been reported by other authors.[15] The increase in the spin-orbit component of the scattering which results from the increase in boron content of the alloys may be seen as an increase in the d-band density of states at the Fermi energy. This is consistent with the observed increase in the strength of the magnetic coupling in these alloys as indicated by an increase in the measured magnetization.[8]

ACKNOWLEDGMENTS

This research was funded by the Natural Science and Engineering Research Council of Canada, the Faculty of Graduate Studies, Dalhousie University, and the Killam Foundation.

[1] D. Shechtman, I. A. Blech, D. Gratias, and J. W. Cahn, Phys. Rev. Lett. **53**, 1951 (1984).
[2] S. J. Poon, Adv. Phys. **41**, 303 (1992).
[3] R. C. O'Handley, R. A. Dunlap, and M. E. McHenry, in *Handbook of Magnetic Materials*, edited by K. H. J. Buschow (North-Holland, Amsterdam, 1991), p. 453.
[4] J. G. Zhao, L. Y. Yang, Q. Fu, and H. Q. Guo, Suppl. Trans. JIM **29**, 497 (1988).
[5] A. P. Tsai, A. Inoue, T. Masumoto, and N. Kataoka, Jpn. J. Appl. Phys. **27**, L2252 (1988).
[6] R. A. Dunlap, M. E. McHenry, V. Srinivas, D. Bahadur, and R. C. O'Handley, Phys. Rev. B **39**, 1942 (1989).
[7] V. Srinivas and R. A. Dunlap, Mater. Sci. Eng. A **125**, 115 (1989).
[8] Y. Yokoyama, A. Inoue, and T. Masumoto, Mater. Trans. JIM **33**, 1012 (1992).
[9] G. Bergmann, Phys Rep. **107**, 1 (1984).
[10] P. A. Lee and T. V. Ramakrishnan, Rev. Mod. Phys. **57**, 287 (1985).
[11] B. L. Altshuler and A. G. Aronov, in *Electron-Electron Interaction in Disordered Systems*, edited by A. L. Efros and M. Pollak (North-Holland, Amsterdam, 1985), p. 1.
[12] A. Kawabata, Solid State Commun. **34**, 431 (1980).
[13] D. V. Baxter, R. Richter, M. L. Trudeau, R. W. Cochrane, and J. O. Strom-Olsen, J. Phys. (France) **50**, 1673 (1989).
[14] M. A. Chernikov, A. Bernasconi, C. Beel, and H. R. Ott, Europhys. Lett. **21**, 767 (1993).
[15] B. J. Hickey, D. Greig, and M. A. Howson, Phys. Rev. B **36**, 3074 (1987).

Electrical transport in amorphous Fe-Mn-Zr alloys

V. Srinivas
Department of Physics and Meteorology, Indian Institute of Technology, Kharagpur, India 721 302

A. K. Nigam and G. Chandra
Low Temperature Physics Division, Tata Institute of Fundamental Research, Bombay, India 400 005

D. W. Lawther
Department of Physics, University of Western Ontario, London, Ontario N6A 3K7, Canada

M. Yewondwossen and R. A. Dunlap
Department of Physics, Dalhousie University, Halifax, Nova Scotia B3H 3J5, Canada

The magnetic and electrical transport properties of amorphous Fe-Zr based alloys with compositions near 10 at. % Zr with various elements substituted for Fe are of particular interest. In the case of Mn substitutions the Curie temperature and the average magnetic moment decrease monotonically with increasing Mn content and the temperature dependence of the magnetization is significantly modified. The electrical transport properties of amorphous $Fe_{90-x}Mn_xZr_{10}$ (for $x=0$, 4, 8, and 12) over the temperature range of 4.2–300 K and the magnetoresistance for fields up to 4.0 T at 4.2 K are reported in the present work. A broad minimum in the resistivity is observed at around 255, 235, 200, and 180 K for the four compositions, respectively. In the case of the $x=8$ sample a second minimum occurs at around 50 K. The magnetoresistance of all samples shows a sharp increase for small fields and a linear field relationship for fields above about 0.1 T.

I. INTRODUCTION

The amorphous FeZr (a-FeZr) alloys with compositions near 10 at. % Zr form an interesting disordered magnetic phase. A variety of unusual properties, e.g., small Fe moment, low Curie temperature (T_C), a large high field susceptibility, etc., have been observed in these materials. The replacement of Fe with other $3d$-transition metals (TM) can introduce significant changes in the magnetic properties. In particular Mn substitutions[1] have the following effects on a-FeZr: (1) a monotonic decrease in T_c with increasing Mn content, (2) a large high field susceptibility for alloys with up to at least 10 at. % Mn, and (3) re-entrant behavior of the initial susceptibility for samples with Mn content up to at least 10 at. %.

As the Mn substituted alloys show re-entrant magnetic behavior over a wide range of compositions, i.e., 0–10 at. % Mn, these samples are a suitable means for investigating the details of the magnetic transitions in amorphous ferromagnets.[2,3] Few magnetic and electronic transport studies have been reported for Mn substituted a-FeZr alloys and these do not allow for well-defined conclusions concerning the inter-relationship of magnetism and electronic properties. In the present work we report the results of a detailed investigation of resistivity and magnetoresistance of a-$Fe_{90-x}Mn_xZr_{10}$ alloys over the temperature range of 4.2–300 K. Particular emphasis is placed on the regions near magnetic phase transitions with the idea of improving our understanding of the effects of magnetic interactions on electron scattering mechanisms.

II. EXPERIMENTAL METHODS

Amorphous alloys of the composition $Fe_{90-x}Mn_xZr_{10}$ with $x=0$, 4, 8, and 12 were prepared by arc melting high purity elemental components followed by quenching from the melt on to a single Cu roller in an argon atmosphere. X-ray diffraction patterns obtained using Cu $K\alpha$ radiation confirmed the amorphous nature of all as-prepared ribbons. The magnetic properties of the alloys were characterized by standard ac susceptibility measurements and will be presented in detail elsewhere.[4] Four-point resistivity and magnetoresistance measurements were carried out over the temperature range of 4.2–300 K in applied magnetic field from 0 to 4.5 T using standard dc techniques.

III. RESULTS AND DISCUSSION

The temperature dependence of the reduced electrical resistivity, $\rho(T)/\rho(300\text{ K})$ for the a-$Fe_{90-x}Mn_xZr_{10}$ samples is illustrated in Fig. 1. The magnetic data (observed T_C) and the resistivity data (T_{min}) of this series of alloys is shown in Fig. 2. It is clear from the figures that

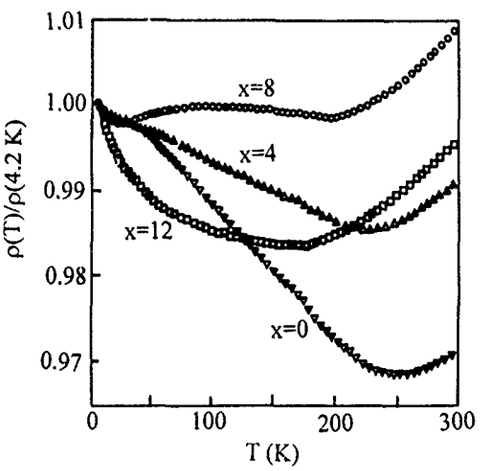

FIG. 1. $\rho(T)/[\rho(4.2\text{ K})]$ as a function of temperature for a-$Fe_{90-x}Mn_xZr_{10}$ with $x=0$, 4, 8, and 12.

 0021-8979/94/76(10)/6501/3/$6.00 © 1994 American Institute of Physics

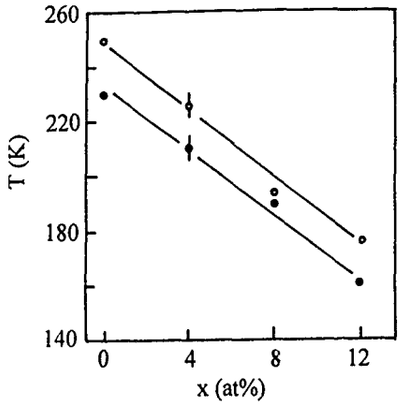

FIG. 2. T_{min} (○) and T_C (●) as a function of Mn concentration (x) for a-$Fe_{90-x}Mn_xZr_{10}$.

(1) all samples show a resistivity minimum at a temperature (T_{min}) near T_C,
(2) both T_C and T_{min} decrease by about 30% as x increases to 12 at. %,
(3) in the case of $x=0$ and $x=4$ a small anomaly in the resistivity at low temperatures (~20 K) is observed,
(4) a second minimum is observed at low temperatures for 8 at. % of Mn and a broad minimum is observed in the case of 12 at. % of Mn alloy.

These observations suggest that the resistivity minimum around T_C is closely correlated to the magnetic behavior. This is in agreement with the results of studies of pressure effects on T_C and T_{min} in similar alloys.[5]

Magnetoresistance data provide information about the microscopic magnetization and can aid in the understanding of the relationship between magnetic interactions and electron scattering mechanisms. Spin disorder scattering and the Kondo effect (in the case of dilute magnetic alloys) can account for the differences between the zero field and the in-field resistivity. This scattering is expected to be sensitive to magnetic ordering on a distance scale comparable to the electron mean free path in the alloys. On the other hand, the coherent-exchange scattering (CES) model, which is well suited to magnetic systems, takes into account the contribution to resistivity from coherent exchange scattering by neighboring ions and predicts that the change in resistivity due to magnetic ordering is either positive or negative depending on whether the interference between the scattered waves is constructive or destructive.

In order to determine the effects of an applied magnetic field on the resistivity minimum, we have carried out temperature dependent resistivity measurements in external fields of 0.7 and 4.0 T. Figure 3 illustrates that there is a shift in T_{min} as the applied field is increased. It is also evident that the external field suppresses the minimum. Transverse and longitudinal magnetoresistance measurements were carried out in a field of 4.5 T at 4.2 K and the results for samples with $x=0$, 4, 8, and 12 are shown in Fig. 4. The magnetoresistance increases monotonically with applied field and the slope is observed to be positive for both geometries. It is also

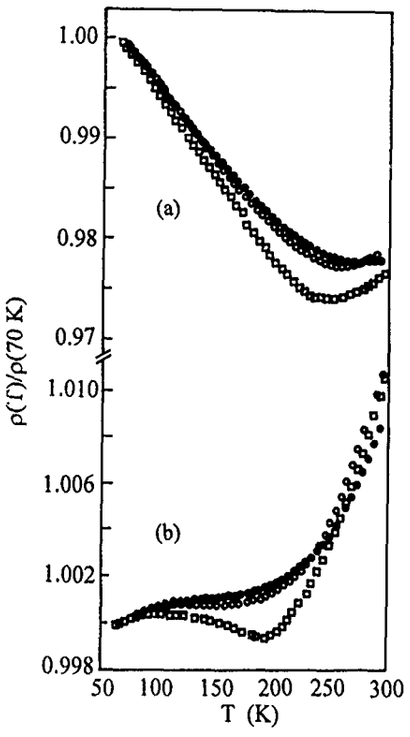

FIG. 3. Normalized resistivity, $\rho(T)/[\rho(70\text{ K})]$, as a function of temperature for a-$Fe_{90-x}Mn_xZr_{10}$ with (a) $x=0$ and (b) $x=8$ for different values of the applied magnetic field: 0 T (■); 0.7 T (○); and 4.0 T (●).

seen that the magnitude of the spontaneous resistive anisotropy decreases with increasing Mn concentration. The technical saturation is achieved at lower applied field values in the longitudinal mode than in the transverse case and this is an indication that the domain rotation process occurs at lower fields for the longitudinal geometry.

The present materials are concentrated magnetic alloys and variations in the exchange interaction between localized

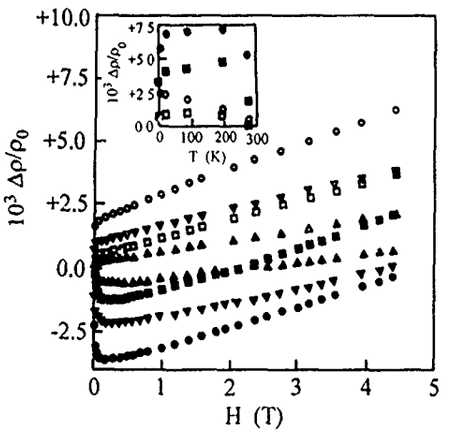

FIG. 4. $\Delta\rho/\rho_0=[\rho(H,T)-\rho(0,T)]/[\rho(0,T)]$ as a function of applied magnetic field for $x=0$ (●,○); $x=4$ (▼,▽); $x=8$ (■,□); and $x=12$ (▲,△). Closed symbols represent the transverse mode and open symbols represent the longitudinal mode. Inset: magnetoresistance as a function of temperature for $x=0$ (closed symbols) and $x=8$ (open symbols) in an applied field of 0.7 T (□,■) and 4.0 T (○,●).

moments at the first nearest-neighbor distance will result in the formation of regions of short range ferromagnetic and antiferromagnetic order. The large values of high field susceptibility which have been observed for the present series[1] have been interpreted in terms of weakly coupled antiferromagnetic spins and are a prerequisite for the existence of a Kondo anomaly. However, the longitudinal magnetoresistance as measured in the present work is positive at all temperatures (see insert in Fig. 4 for $x=0$ and 8) and this is inconsistent with the assumption that T_{min} is due to Kondo behavior. It is also seen that the magnetoresistance shows a maximum at a temperature near T_C. Similar behavior has also been observed in rare earth-transition metal alloys[6] and has been attributed to the effects of coherent exchange scattering. The present results are, therefore, consistent with the CES model and it is suggested that the magnetic and electronic transport behavior observed for the series of a-$Fe_{90-x}Mn_xZr_{10}$ alloys can be explained on the basis of this model.

[1] B. G. Shen, R. F. Xu, J. G. Zhao, and W. S. Zhan, Phys. Rev. B **43**, 11 005 (1991).
[2] S. N. Kaul, J. Appl. Phys. **61**, 451 (1987).
[3] G. E. Fish and J. J. Rhyne, J. Appl. Phys. **61**, 454 (1987).
[4] V. Srinivas, S. Ramakrishnan, G. Chandra and R. A. Dunlap (unpublished).
[5] K. Shirakawa, K. Fukamichi, T. Kaneko, and T. Masumoto, Sci. Rep. Res. Inst. Tohoku Univ. A **31**, 54 (1983).
[6] A. Fert and R. Asomoza, J. Appl. Phys. **50**, 1886 (1979).

Field dependence of nuclear magnetic resonance in molecular beam epitaxy grown Co(111)/Cu multilayers

T. Thomson, H. Kubo,[a] J. S. Lord, and P. C. Riedi
Department of Physics, University of St. Andrews, St. Andrews, Fife KY16 9SS, United Kingdom

M. J. Walker
Department of Physics, University of Leeds, Leeds LS2 9JT, United Kingdom

An initial study of the field dependence of ^{59}Co nuclear magnetic resonance (NMR) has been undertaken for two Co/Cu(111) multilayer films grown by molecular beam epitaxy. The multilayer structure of the films was nominally identical, $[Co(15\ Å)/Cu(7\ Å)]_{\times 20}$, however by growing the multilayers with similar structures on different buffer layers, Cu(200 Å) and Au(10 Å), saturation magnetoresistances $\Delta R/R$ of 4% and 22%, respectively, were obtained. The NMR signal in ferromagnetic materials arises due to the enhancement effect from the electronic magnetization. This enhancement effect is therefore a function of the domain structure and any external magnetic field. By applying a simple model of how the NMR enhancement factor varies with applied field, in the absence of a domain structure, the anisotropy fields at the interfaces and in the bulk were determined separately at $T=4.2$ K. These were then compared with the coercive field obtained from magnetization measurements. Our results show that at low temperature the anisotropy field at the interfaces is approximately equal to the coercivity obtained from magnetization measurements (260 Oe), while in the bulk the anisotropy field was found to be ~550 Oe for the low magnetoresistance sample with $\Delta R/R=4\%$, and ~1230 Oe for the high magnetoresistance sample with $\Delta R/R=22\%$.

I. INTRODUCTION

The technique of spin echo nuclear magnetic resonance (NMR) using the ^{59}Co nucleus has already provided significant structural information on Co/Cu(111) superlattices.[1–3] In particular it has been established that sharp interfaces in molecular beam epitaxy (MBE) grown Co/Cu(111) multilayers are not incompatible with giant magnetoresistance (GMR).[4] This article extends the NMR work on these materials by considering the field dependence of the NMR at a temperature of 4.2 K. Investigating the field dependence of the NMR in ferromagnetic materials allows the change in the enhancement factor of the signal intensity to be examined, which can then be related to the domain structure and anisotropy fields.

In MBE grown Co/Cu(111) multilayers the NMR frequency of the nuclei with parent atoms at a plane interface (nine nearest-neighbor Co atoms and three nearest-neighbor Cu atoms) is ~46 MHz below that of those nuclei in the bulk (12 nearest-neighbor Co atoms). This separation allows independent investigation of the magnetic environment associated with the interfaces and the bulk. If a magnetic field large enough to remove the domain structure is applied, the anisotropy field can be determined from the field dependence of the NMR signal. Hence the anisotropy field can be determined separately for the interfaces and the bulk.

II. THEORY

The utility of ^{59}Co NMR arises from the fact that the effective field (B_{eff}) experienced by a nucleus depends on the atomic environment of the parent atom. When applied to MBE grown Co/Cu(111) superlattices, B_{eff} is essentially determined by the parent atom and the surrounding nearest-neighbor atoms. Thus B_{eff} can be written as

$$B_{\text{eff}}=a\mu_{\text{self}}+b\Sigma\mu_i, \tag{1}$$

where the first term is due to the parent atom and the second term is due to the nearest neighbors. Work on Co/Cu alloys and multilayer materials[3,5,6] has shown that the second term contributes a discrete shift of about −16 MHz per atom when a nearest-neighbor Co atom is replaced by a Cu atom.

NMR is observable in ferromagnetic materials due to the enhancement effect.[7,8] The amplitude of the rf field experienced by a nucleus has two components: a regular component due to the applied rf field, and an enhanced component due to the oscillation of the electronic magnetization induced by the applied rf field. In a domain wall or in a domain within a low anisotropy material the enhancement factor is of the order of $\eta\approx 10^3$. Thus the response of the nuclei to an applied resonance rf field is largely determined by the electronic enhancement factor (η). In a spin echo experiment the magnitude of the received echo is also proportional to η.

The enhancement factor varies according to the situation of the electron spin moments responsible for the electronic magnetization. In the absence of domain walls the strength of the NMR signal for a particular environment can be related to the domain enhancement factor η_d where $\eta_d \gg 1$[8] by

$$\text{signal}\propto \eta_d \propto \frac{B_{\text{eff}}}{B_{\text{app}}+B_{\text{ani}}}, \tag{2}$$

where B_{eff} is the effective field at the nucleus, B_{app} is the applied field, B_{ani} is the anisotropy field experienced by the atoms under consideration.

[a]Permanent address: Dept. of Electronics, Fukuoka Institute of Technology, Wajira, Fukuoka, Japan.

 0021-8979/94/76(10)/6504/3/$6.00 © 1994 American Institute of Physics

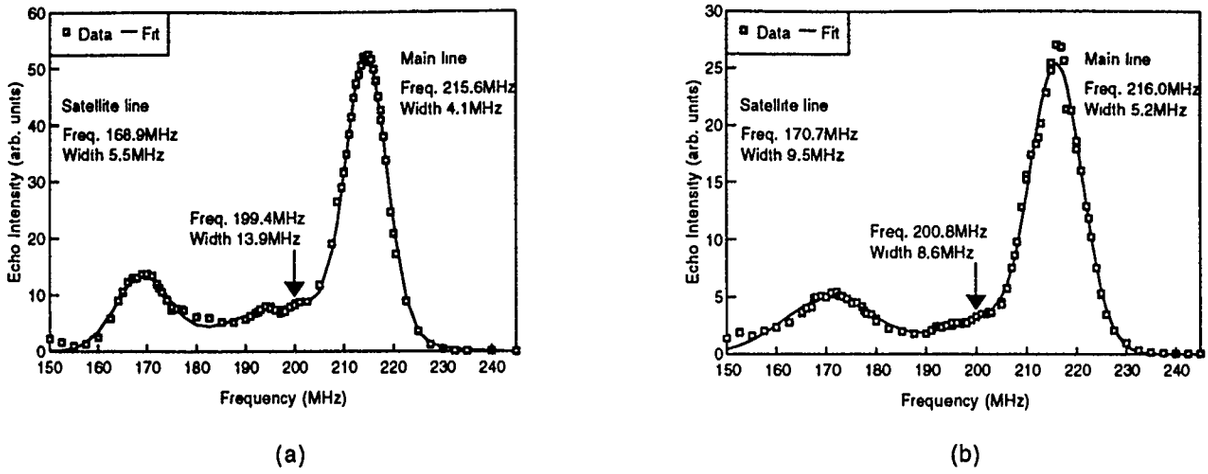

FIG. 1. ^{59}Co NMR spectrum for good quality Co/Cu(111) multilayer films (a) sample No. 66 $\Delta R/R=4\%$, (b) sample No. 56 $\Delta R/R=22\%$.

Thus by measuring the NMR intensity as a function of field, once a sufficiently large field has been applied to ensure that all the domain walls have been swept out, the anisotropy field can be determined.

III. EXPERIMENT

Two samples, Nos. 66 and 56, were produced under similar ultrahigh vacuum conditions by MBE[9] at the SERC facility located at the University of Leeds. The films were grown on GaAs(110) substrates with a Ge(500 Å)/Co(15 Å) buffer layer, a Cu(200 Å) seed layer was used for sample No. 66 and an Au(10 Å) seed layer for sample No. 56. The multilayer structure consisted of $[\text{Co}(15\text{ Å})\text{Cu}(7\text{ Å})]_{\times 20}$ with a thin Au cap to inhibit oxidation. The progress of the growth was monitored by *in situ* reflection high energy electron diffraction measurements and these confirmed that they were no

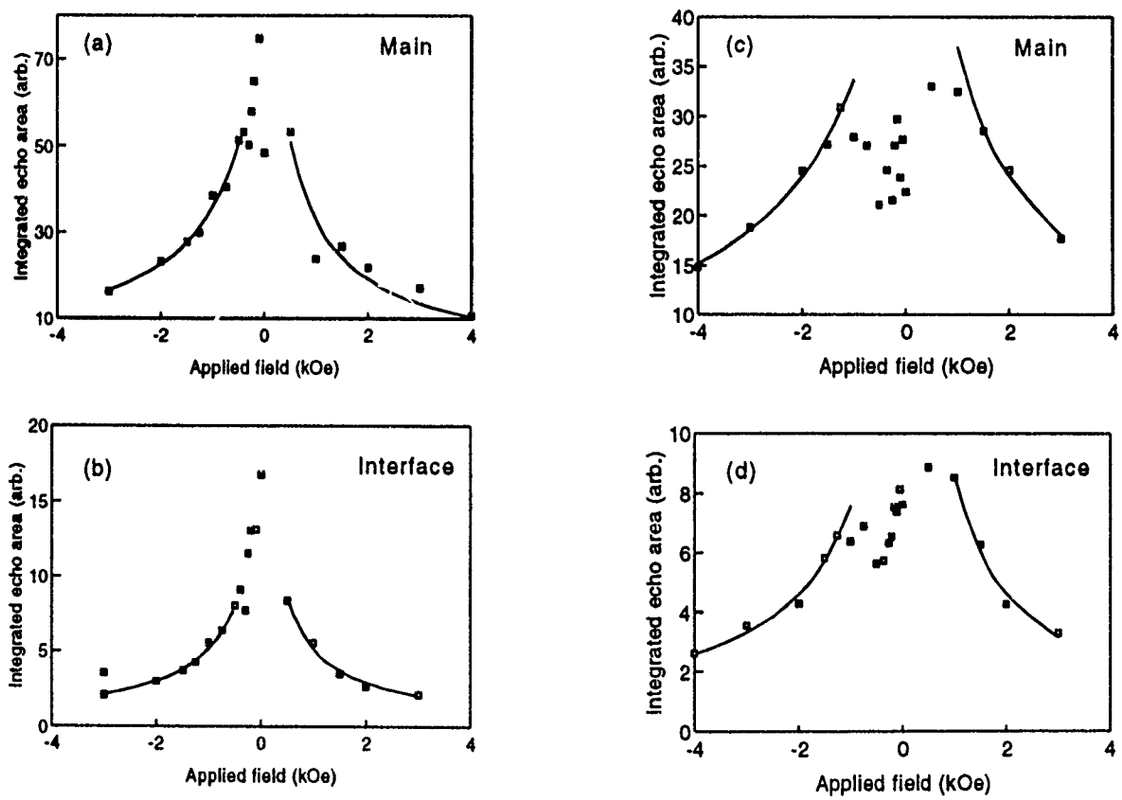

FIG. 2. Field dependence of ^{59}Co NMR integrated area for (a) sample No. 66 main peak (b) sample No. 66 interface peak (c) sample No 56 main peak, (d) sample No. 56 interface peak. A saturating field of 9 kOe was applied prior to each measurement.

TABLE I. Anisotropy fields determined from field dependence of NMR, coercivity measured on a VSM. NMR measured at 4.2 K and H_c at 8 K. Uncertainty in NMR measurements ~100 Oe.

Sample No.	$\Delta R/R$	Anisotropy field (Oe)		Coercive field (Oe)
		Bulk	Interface	
66	4%	550	340	260
56	22%	1230	360	260

gross structural differences between the films. However recent work[10] has confirmed that in these MBE grown materials an increase in the GMR is correlated with less interfacial roughness. The saturation magnetoresistance in a field of ~6 T and a temperature of $T=4.2$ K was $\Delta R/R=4\%$ for sample No. 66 while for No. 56, $\Delta R/R=22\%$.

The ^{59}Co NMR was measured using a swept frequency, coherently detected spin echo spectrometer.[11] The pulse power was adjusted to ensure the maximum response at each field and frequency. The data collected were corrected for ω^2 in the usual way. A further correction to allow for the variation in spin-spin relaxation time, T_2, as a function of frequency was also carried out. The final data therefore gave an accurate representation of the product of the enhancement effect and the number of nuclei in a particular atomic environment at all frequencies and fields.

The coercivity was measured at $T=8$ K in a PAR 4500 vibrating sample magnetometer (VSM) fitted with a CF1200 cryostat and a bipolar power supply.

IV. RESULTS AND DISCUSSION

The zero applied field spectrum, shown in Fig. 1 for both sample Nos. 66 and 56, demonstrates the typical features of a good quality Co/Cu(111) multilayer, with a peak at ~170 MHz associated with the 3×Cu, 9×Co nearest-neighbor configuration of a perfect interface, and a main peak at ~215 MHz due to Co atoms in a bulk fcc environment. The shift in the main peak frequency from the value of 217.4 MHz found in free fcc Co powder is due to strain caused by the lattice mismatch (2%) between Cu and Co which increases the atomic spacing of the Co in the plane of the film. The small echo intensity between these peaks is probably due to Co atoms surrounded by one or two Cu atoms.

Figure 2 shows the field dependence of the integrated echo intensity for both the main peak and interface peak of sample Nos. 66 and 56. The parameters obtained from fitting Eq. (2) are summarized in Table I. In order to ensure that the multilayer was in a single domain state the data was fitted over the range of applied field for which the gyromagnetic ratio (γ) had the value associated with free Co. The gyromagnetic ratio was determined from the shift in NMR peak frequency as a function of field. This shift was similar for both the interface and bulk peaks in a particular sample, and in the absence of domain structure was close to the free Co value of $\gamma=10.054$ MHz/T.

Table I shows that the interfacial anisotropy field determined from NMR measurements is, within error, the same for both samples and is similar to the coercivity. If these data are correlated, then it implies that magnetization reversal is nucleated at the interfaces. The anisotropy field measured for atoms in a bulk environment is larger than that measured at the interfaces, and shows significant differences between the two samples.

V. CONCLUSIONS

By examining the high field region of the field dependence of the NMR of Co/Cu multilayers, the NMR response can be fitted to a simple model that allows independent determination of the anisotropy field in the bulk and at the interfaces. Our results show that an anisotropy field, approximately equal to the coercivity, exists at the interfaces. The ratio of bulk to interface anisotropy was found to be approximately double for the sample exhibiting a stronger GMR effect.

ACKNOWLEDGMENTS

The authors wish to Dr. K. O'Grady of University College of North Wales for the magnetization measurements. The support of the U.K. Science and Engineering Research Council is also gratefully acknowledged.

[1] K. Le Dang, P. Veillet, Hui He, F. J. Lamelas, C. H. Lee, and R. Clarke, Phys. Rev. B **41**, 12 902 (1990).
[2] H. A. M. de Gronkel, K. Kopinga, W. J. M. de Jonge, P. Panissod, J. P. Schillé, and F. J. A. den Broeder, Phys. Rev. B **44**, 9100 (1992).
[3] C. Mény, P. Panissod, and R. Loloee, Phys. Rev. B **45**, 12 269 (1992).
[4] J. S. Lord, H. Kubo, P. C. Riedi, and M. J. Walker, J. Appl. Phys. **73**, 6381 (1993).
[5] S-I Kobayashi, K. Asayama, and J. Itoh, J. Phys. Soc. Jpn. **21**, 65 (1966).
[6] S. Nasu, H. Yasuoka, Y. Nakamura, and Y. Murakami, Acta Metall. **22**, 1057 (1974).
[7] M. A. H McCauseland and I. S. MacKenzie, Adv. Phys. **28**, 305 (1979).
[8] P. C. Riedi, Hyperfine Interact. **49**, 335 (1989).
[9] D. Grieg, M. J. Hall, C. Hammond, B. J. Hickey, H. P. Ho, M. A. Howson, M. J. Walker, N. Wiser, and D. G. Wright, J. Magn. Magn. Mater. **110**, L239 (1992).
[10] T. Thomson, P. C. Riedi, and D. Greig, Phys. Rev. B (in press).
[11] T. Dumelow and P. C. Riedi, Hyperfine Interact. **35**, 1061 (1987).

Dependence of giant magnetoresistance in Co/Cu multilayers on the thickness of the Co layers

A. M. Shukh,[a] D. H. Shin, and H. Hoffmann
Institut für Angewandte Physik III, Universitat Regensburg, 93053 Regensburg, Germany

The dependence of the giant magnetoresistance (GMR) on the thickness of the Co layers in Co/Cu multilayers was investigated experimentally. The thickness of the Cu layer was held constant at t_{Cu}=19 Å, which corresponds to the second maximum of the GMR ratio oscillating dependence on t_{Cu}. The Co layer thickness was varied from 4.8 to 79.0 Å. High resolution transmission electron microscopy showed the existence of the two-dimensional artificial superstructure with defined periodicity as well as sharp and flat interfaces. From wide angle x-ray diffraction it was concluded that at Co layer thickness below 40 Å the multilayers are polycrystalline with mainly fcc lattice structure and (111) texture. In the case of thicker Co layers indications of hcp Co could be found. The GMR ratio reaches a maximum at Co layer thickness about 11 Å. It was shown that the GMR in sputtered Co/Cu multilayers is due to spin scattering at the interfaces and resistance is strongly influenced by interface scattering.

I. INTRODUCTION

Considerable attention is paid in the literature to the giant magnetoresistance (GMR) effect observed in multilayers composed of alternating metal and ferromagnetic layers of special thicknesses. Since the discovery of GMR in Fe/Cr multilayers,[1] the effect has been observed in a variety of multilayer systems. At present the Co/Cu multilayers seem to be of the greatest interest because of the large GMR and of its weak temperature dependence.[2–4] Because of these properties this system could be a candidate for an application.

The dependence of the GMR in Co/Cu multilayers on the thickness of the Cu interlayers is well known from the previous publications.[2,3,5] However the influence of the Co layer thickness on the amount of the GMR has not been clarified yet. In this article we report about such experiments and their results.

II. EXPERIMENT

The multilayers Fe(100 Å)/[Co(t_{Co})/Cu(t_{Cu})]$_{20}$/Fe(50 Å) were deposited onto glass substrates (diameter 10 mm) at room temperature. The base pressure before the deposition was below 8×10^{-8} Torr and the Ar pressure during sputtering was kept 6.0 mTorr. The glass substrates were chemically cleaned and plasma etched just before the deposition.

An Fe buffer layer with the thickness t_{Fe}=100 Å and Fe protective layer at t_{Fe}=50 Å were dc magnetron sputtered, while the Co/Cu multilayers were deposited by rf sputtering. By experience, Co/Cu multilayers with the Fe buffer layer usually exhibit a much larger GMR ratio[4,6,7] than systems without an Fe buffer, especially in the case of Cu layer thickness below 10 Å. The deposition rates were between 1.8 and 3.0 Å/s, calibrated by x-ray fluorescence measurements. The thicknesses t_{Cu}, t_{Co}, and t_{Fe} were determined from the calibrated deposition rates and sputtering time as well as multilayer cross-sectional investigations by transmission electron microscopy (TEM). The multilayers showed the existence of a two-dimensional artificial superstructure with defined periodicity, as well as sharp and flat interfaces.

The magnetoresistance of the multilayers was investigated at room temperature by a four-point method. The electrical current was oriented in plane of the multilayers. The external magnetic field was applied in plane perpendicular to the current. The magnetoresistance ratio $\Delta R/R_s$ is defined by $\Delta R/R_s=(R_m-R_s)/R_s$, where R_m is a maximum value of the resistance, and R_s is resistance of multilayer at magnetic saturation in the applied magnetic field. The magnetization loops of the samples were taken by a vibrating sample magnetometer at room temperature. The structure of the multilayers was investigated using x-ray diffraction.

III. RESULTS AND DISCUSSION

For constant thickness of the Co layers (t_{Co}=10.8 Å) the oscillation of the GMR ratio $\Delta R/R_s$ with variation of the Cu interlayer thickness t_{Cu} coincides with the oscillation of the saturation field H_s. In the thickness interval 6.6 Å$\leq t_{Cu}\leq$30.4 Å we found three maxima for the GMR ratio $\Delta R/R_s$ and the saturation field H_s at t_{Cu} equal to 9, 19, and 30 Å, respectively. Our results are in good agreement with the results of other authors.[2,3,5] The maximum of the GMR ratio (ranging up to $\Delta R/R_s$=36% at room temperature) was always observed for the multilayers with the interlayer thickness $t_{Cu}\approx$9 Å. Regarding the thickness of the Cu layer the oscillation period is about 10 Å.

In this article the dependence of the GMR on the thickness of the Co layers t_{Co} at constant thickness of the Cu interlayers t_{Cu} should be investigated. A thickness t_{Cu}=19 Å (second maximum of the GMR ratio dependence on t_{Cu}) has been selected. By experience, at this thickness the experiments showed good reproducibility. Typical magnetoresistance loops for three samples with various thicknesses of the Co layers t_{Co} are given in Fig. 1 for t_{Co}=4.8, 18, and 79 Å, respectively.

Figure 2 shows the wide angle x-ray diffraction patterns of Co/Cu multilayers with various Co layer thicknesses. At $t_{Co}<$40 Å multilayers are fcc with predominantly (111) texture. The same was found in Co/Cu multilayers grown by molecular beam epitaxy.[8] With increasing t_{Co} all peaks shift

[a]Present address: Samsung Advanced Institute of Technology, P.O. Box 111, Suwon 440-600, Korea.

 0021-8979/94/76(10)/6507/3/$6.00 © 1994 American Institute of Physics

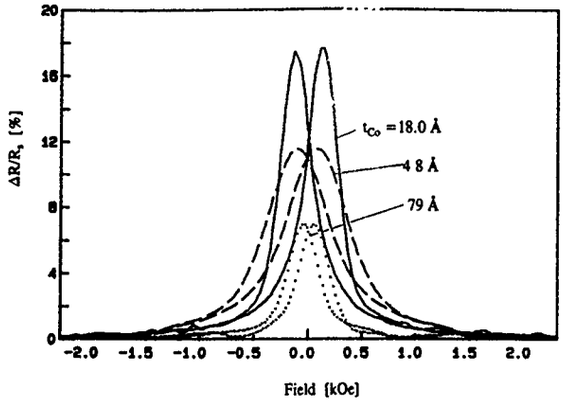

FIG. 1. Transverse magnetoresistance vs in-plane field for three multilayers of the form Fe(100 Å)/[Co(t_{Co})/Cu(19 Å)]$_{20}$/Fe(50 Å) for Co layer thicknesses 4.8, 18, and 79 Å at room temperature.

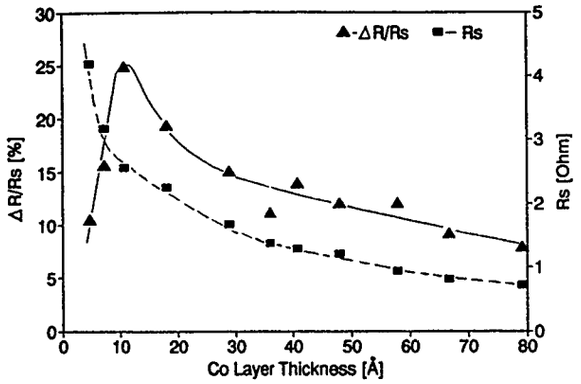

FIG. 3. GMR ratio $\Delta R/R_s$ and resistance R_s at magnetic saturation vs Co layer thickness for Fe(100 Å)/[Co(t_{Co})/Cu(19 Å)]$_{20}$/Fe(50 Å) multilayers.

toward the higher 2θ values (smaller value of the lattice, peculiar to the Co layers). The intensities of (111), (200), and other fcc peaks decrease but the intensity of a left-side satellite peak of (111) increases with t_{Co} increase. This peak approximately corresponds to (100) peak of hcp Co. The presence of the hcp phase in sputtered Co/Cu multilayers at t_{Co}=30 Å was observed by nuclear magnetic resonance spin-echo investigation.[9]

The dependences of the GMR ratio $\Delta R/R_s$ and the total resistance of the multilayers at magnetic saturation R_s on the thickness of the Co layers are given in Fig. 3. As can be seen from Fig. 3 the GMR ratio reaches a maximum ($\Delta R/R_s$=25%) at $t_{Co}\approx$11 Å and decreases with increasing thickness of the Co layers. The GMR ratio $\Delta R/R_s$ depends on ΔR as well as on R_s. Due to the film structure both values depend on different ways on the thickness t_{Co} of the Co layers. This needs to separate ΔR and R_s for the discussion.

The change of the resistance ΔR of the multilayers is given by the difference of the resistance of the multilayer system at antiparallel and parallel alignments of the magnetization of the adjacent ferromagnetic Co layers. This difference $\Delta R = R_m - R_s$ should be solely caused by the difference of the spin scattering due to the orientation of the magnetization. Figure 4 shows the dependence of ΔR on the reciprocal thickness $1/t_{Co}$ of the Co layers. From the straight line for all thicknesses above t_{Co}>10 Å it has to concluded that the observed GMR is due to interface spin scattering. This finding agrees with former results.[10] The decrease of ΔR at layer thickness t_{Co}<10 Å ($1/t_{Co}$>0.11/Å) will be discussed below.

The dependence of the resistance R_s of the multilayer at magnetic saturation on the thickness t_{Co} of the single Co layers is given in Fig. 3. Magnetic saturation means that the magnetic moment of all single layer Co films are parallel aligned, due to the applied external magnetic field. In this case we do not need to separate the spin-dependent part of scattering. The application of a model of parallel resistors allows us to obtain for the total conductance $1/R_s$

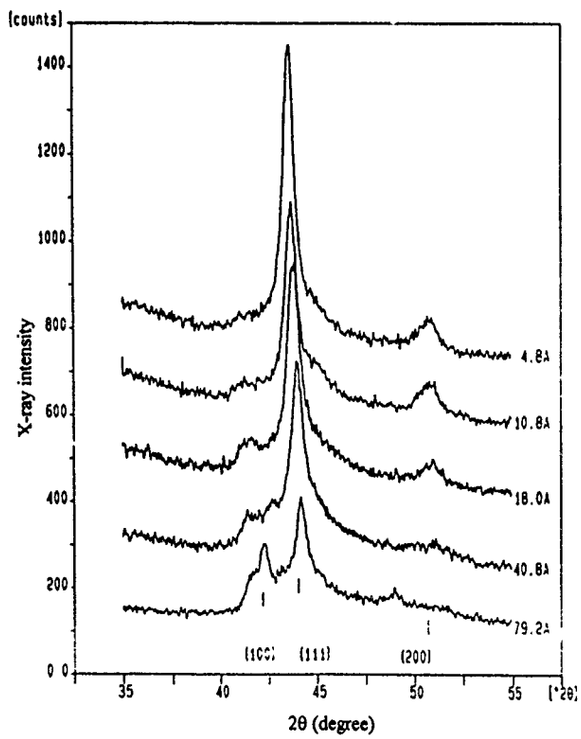

FIG. 2. Wide angle x-ray diffraction patterns of Co/Cu multilayers with various thickness of Co layers (Cu K_α radiation).

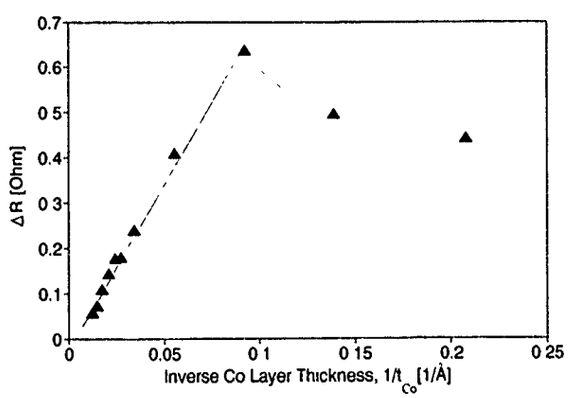

FIG. 4. Magnetoresistance change ΔR as a function of inverse Co layer thickness for the multilayers Fe(100 Å)/[Co(t_{Co})/Cu(19 Å)]$_{20}$/Fe(50 Å).

$$\frac{1}{R_s}=\frac{1}{R_{\text{Fe buffer}}}+\frac{1}{R_{\text{Fe prot}}}+N\left(\frac{1}{R_{\text{Cu}}}+\frac{1}{R_{\text{Co}}}\right), \tag{1}$$

where $R_{\text{Fe buffer}}$ and $R_{\text{Fe prot}}$ are resistances of the Fe buffer and Fe protection layers, respectively, N is the number of the Co/Cu periods of the multilayers, and R_{Cu} and R_{Co} are resistances of the single Cu and Co layers, respectively.

Since in the present experiments the thicknesses of the Fe buffer layer, of the Fe protection layer, of the Cu layers, and the number of periods were constant it is assumed in a first approximation

$$1/R_s=A+N/R_{\text{Co}} \tag{2}$$

with a constant value

$$A=(1/R_{\text{Fe buffer}})+(1/R_{\text{Fe prot}})+(N/R_{\text{Cu}}). \tag{3}$$

This constant value needs a special investigation, which has been shown in other publications.[10,11]

The dependence of the total resistance on the thickness t_{Co} of the Co layers has to be discussed on the thickness dependence of the resistivity of the films, including surface scattering and the fluctuation of the film thickness. These discussions have been given in the past.[11] For a very first approach it is assumed that the Co layers are continuous and of constant thickness. (The lower thicknesses will be discussed below.) In this case the resistance R_{Co} of a single Co layer depends on its thickness t_{Co} and is given by

$$R_{\text{Co}}=\rho_{\text{Co}}L_{\text{Co}}/W_{\text{Co}}t_{\text{Co}}, \tag{4}$$

where L_{Co} and W_{Co} are the length and width of the Co layers, respectively. Due to Sondheimer[12] approximation of Fuchs'[13] theory

$$\rho_{\text{Co}}=\rho^{\infty}_{\text{Co}}\left(1+\frac{3}{8}\frac{l^{\infty}_{\text{Co}}}{t_{\text{Co}}}\right), \tag{5}$$

where l^{∞}_{Co} and $\rho^{\infty}_{\text{Co}}$ are the mean free path of the electrons and the resistivity of infinite thick Co films, respectively. In the case $l^{\infty}_{\text{Co}}\gg t_{\text{Co}}$ which can be assumed in a very first approximation one obtains

$$\rho_{\text{Co}}=3l^{\infty}_{\text{Co}}\rho^{\infty}_{\text{Co}}/8t_{\text{Co}}, \tag{6}$$

and

$$R_{\text{Co}}=b/t^2_{\text{Co}}, \tag{7}$$

where

$$b=\frac{3}{8}\frac{L_{\text{Co}}}{W_{\text{Co}}}l^{\infty}_{\text{Co}}\rho^{\infty}_{\text{Co}}=\text{const.} \tag{8}$$

This leads to

$$1/R_s=A+(N/b)t^2_{\text{Co}}. \tag{9}$$

In Fig. 5 the inverse $1/R_s$ of the resistance R_s is plotted against the square t^2_{Co} of the thickness of the Co layers,

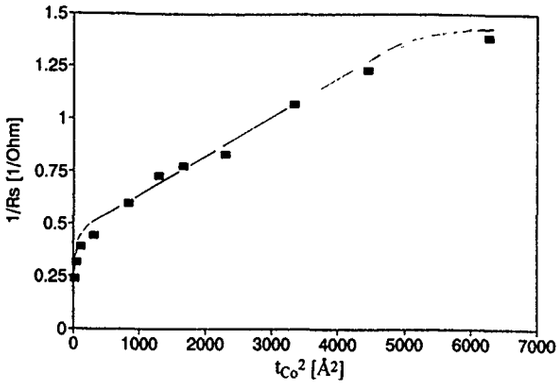

FIG. 5. Inverse resistance $1/R_s$ at magnetic saturation vs square thickness of Co layer for Fe(100 Å)/[Co(t_{Co})/Cu(19 Å)]$_{20}$/Fe(50 Å) multilayers.

which leads to a straight line. Deviation at large thickness are explained since there the approximation $l^{\infty}_{\text{Co}}\gg t_{\text{Co}}$ is not longer valid.

At small thickness $t_{\text{Co}}<25$ Å of the Co layer one has to take care of the layer roughness, which on mesoscopie scale leads to fluctuation of the layer thickness and increases the resistance. This effect is not included in the foregoing considerations. The system then is described by Co islands in a Cu matrix, which can be seen from Fig. 2.

ACKNOWLEDGMENTS

This work was supported by the EC Commission, Brussels, under Contract No. SC1*-CT88-0106. The authors are grateful to J. S. Lee and J. H. Choi at Samsung Advanced Institute of Technology for x-ray characterization and TEM investigation. We thank C. Dorner for technical support.

[1] M. N. Baibish, J. M. Broto, A. Fert, F. Nguyen Van Dau, F. Petroff, P. Eitenne, G. Creuzet, A. Friederich, and J. Chazelas, Phys. Rev. Lett. **61**, 2472 (1988).
[2] S. S. P. Parkin, R. Bhadra, and K. P. Roche, Phys. Rev. Lett. **66**, 2152 (1991).
[3] D. H. Mosca, F. Petroff, A. Fert, P. A. Schroeder, W. P. Pratt, Jr., and R. Laloee, J. Magn. Magn. Mater. **94**, L1 (1991).
[4] S. S. P. Parkin, Z G. Li, and D. J. Smith, Appl. Phys. Lett. **58**, 2710 (1991).
[5] M. E. Tomlinson, R. J. Pollard, G. D. Lord, and P. J. Grundy, J. Magn. Magn. Mater. **111**, 79 (1992).
[6] M. E. Tomlinson, R. J. Pollard, D. G. Lord, P. J. Grundy, and Z. Chun, IEEE Trans. Magn. **MAG-28**, 2662 (1992).
[7] C. Dorner, M. Haidl, and H. Hoffmann, J. Appl. Phys. **74**, 5886 (1993).
[8] F. J. Lamelas, C. H. Lee, Hui He, W. Vavra, and R. Clarke, Phys. Rev. B **40**, 5857 (1989).
[9] K. Le Dang, P. Veillet, E. Velu, S. S. Parkin, and C. Chappert, Appl. Phys. Lett. **63**, 108 (1993).
[10] T. Eckl, G. Reiss, H. Bruckl, and H. Hoffmann, J. Appl. Phys. **75**, 362 (1994).
[11] J. Vancea, Int. J. Mod. Phys. B **3**, 1455 (1989).
[12] E. H. Sondheimer, Adv. Phys. **1**, 1 (1952).
[13] K. Fuchs, Proc. Camb. Philos. Soc. **34**, 100 (1938).

Vertical inhomogeneity of the magnetization reversal in antiferromagnetically coupled Co/Cu multilayers at the first maximum

R. Mattheis, W. Andrä, L. Fritzsch, J. Langer, and S. Schmidt
Institut für Physikalische Hochtechnologie Jena, PF 100 239, D-07702 Jena, Germany

Magnetization behavior in antiferromagnetically (AFM) coupled multilayer systems was calculated by using an atomic layer model. Comparisons with the experimental results obtained on sputtered Co/Cu multilayers reveal remarkable differences in the magnetization reversal and in the field dependence of the magnetoresistance. Kerr loops measured from both sides of the stack display strong vertical differences. At the lower side near the Fe seed layer the magnetization reversal is in good agreement with that of our calculations whereas near the surface in large portions of the stack the AFM coupling is destroyed or varied. These effects are presumably caused by magnetic short circuits at defects in the multilayer structure. Cross-section transmission electron microscopy reveals growth defects which seem to be responsible for the deviations from the calculated ideal behavior.

I. INTRODUCTION

Due to their large magnetoresistance (MR) value up to 80% at room temperature,[1] Co/Cu multilayers are favored candidates for advanced magnetoresistive applications. A large scatter in the amplitude of the MR and also the saturation field, H_s has been found.[2–5] Defects in the multilayer stack causing magnetic short circuits (MSC) seem to be responsible. A linear correlation between the amplitude of the giant magnetoresistance (GMR) and the antiferromagnetically (AFM) coupled part of the stack was found.[4]

We prepared Co/Cu stacks on thermally oxidized Si wafers and glass plates. Details of the preparation are reported elsewhere.[5] Each Co/Cu stack consists of 24 pairs of 1.7 nm Co and x nm Cu with a 3.4 nm Co covering layer. In some samples a 5 nm Fe buffer layer was used. Magneto-optical investigations were performed using the longitudinal Kerr effect. For transmission electron microscopy a Philips CM 20 was used.

II. RESULTS AND DISCUSSION

A. Magnetization reversal and GMR calculated for ideal multilayers

Calculations of the magnetization reversal were performed using the atomic layer model (ALM).[6] Both systems, Co/Cu multilayers with and without Fe seed layer, were calculated assuming constant AFM coupling C_i between all Co layers and vanishing in-plane anisotropy. The field dependence of the MR was estimated by using the angle differences between nearest Co layers and their parallel connection to determine the total resistance.

A linear dependence of the magnetization and a parabolic dependence of the MR were obtained only for a stack with two Co layers ($n=2$) with no Fe buffer. In Fig. 1 the angle of magnetization of each individual Co layer for systems with even numbers of Co (4 and 24) layers is shown. The outermost Co layers, with only one neighboring Co layer, react most sensitively and strongly deviate from the cosine law throughout the whole magnetization process. The inner layers show strong differences only at low fields ($<0.25\ H/H_s$). Systems with an odd number of Co layers possess a nonvanishing residual magnetization at zero field, stable up to a threshold field H_{th} (Fig. 2). The value for H_{th} decreases with increasing number of Co layers. The resulting $M(H)$ curves are very similar to those with even number of bilayers for fields higher than H_{th}. Our MR curves are normalized with respect to the ordinate (at $H=0$) as well as to the abscissa (at $H=H_s$). The deviation from the parabolic curve is small for even n (Fig. 2). For odd n it decreases with increasing number n.

In the case of an Fe buffer the state at the remanence is determined by the Fe layer independent of the number n. Therefore, the angle dependence resembles that of one of the systems without an Fe buffer and odd n (Fig. 3). With increasing n the curves become more and more similar to those without an Fe buffer. In general, a nearly linear behavior of the AFM-coupled Co magnetization with increasing field is obtained with small deviations at low and high fields. A similar tendency was found for the magnetoresistivity.

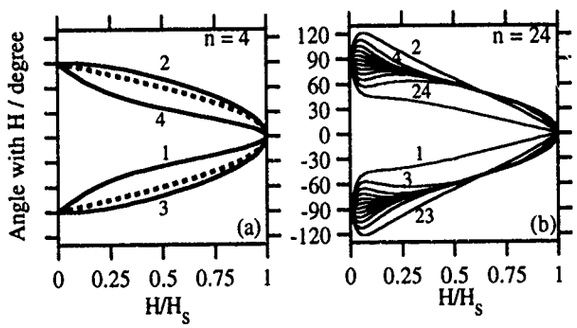

FIG. 1. Angle of the magnetization of each individual Co layer vs normalized field in a four bilayer (a) and a 24 bilayer (b) stack without an Fe buffer. The numbers indicated on the curves refer to the individual Co layer beginning from the substrate surface. In (a) the cosine law is shown as a dotted line. This is the exact solution obtained for $n=2$.

 0021-8979/94/76(10)/6510/3/$6.00 © 1994 American Institute of Physics

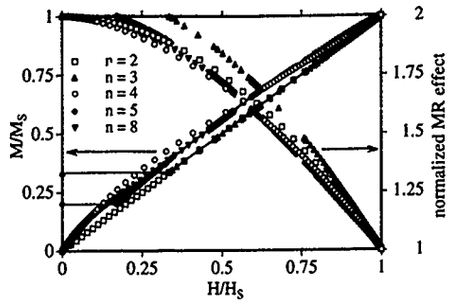

FIG. 2. Relative magnetization and normalized MR vs normalized field for different numbers of Co/Cu bilayers. The MR values were normalized to a value of 2 and 1 for zero field and saturation field H_s, respectively.

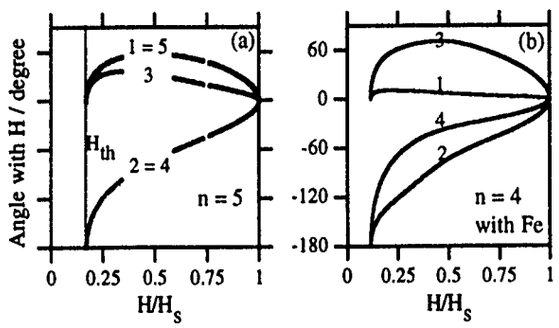

FIG. 3. Angle of the magnetization of each individual Co layer vs normalized field in a five bilayer stack without Fe buffer (a) and four bilayer stack with Fe buffer (b). In the stack without Fe buffer (a) the magnetization in the first and fifth layer as well as in the second and fourth layer is identical. Additionally in (a) the position of the threshold field is indicated.

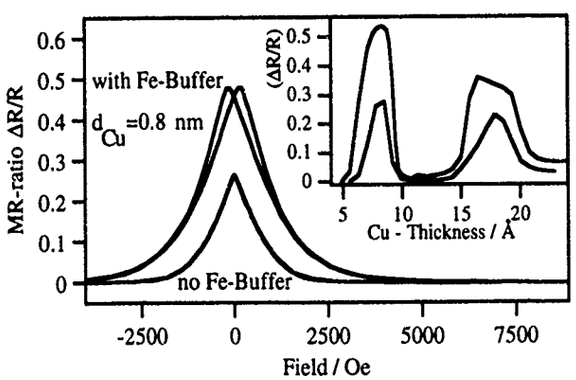

FIG. 4. Resistance vs applied field for our Co/Cu system with and without Fe buffer at the first maximum. The inset shows the amplitude of the GMR vs the thickness of the Cu spacer layer.

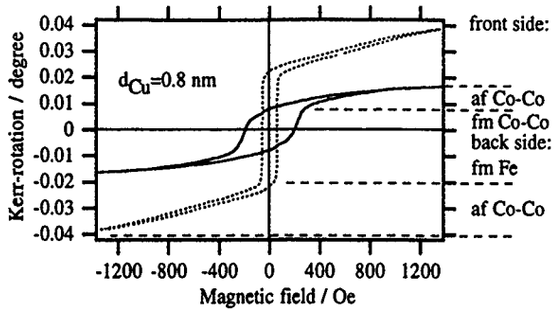

FIG. 5. Kerr loops from frontside (solid line) and backside (dotted line) of our Co/Cu system with Fe buffer. Backside means substrate side. The small Faraday rotation caused by the glass substrate was taken away. It is obvious that the AFM fraction measured from the backside is larger than that measured from the frontside. The ferromagnetic fraction detected from the backside is due to the Fe buffer.

B. Experimental results

An Fe buffer causes a strong increase in the amplitude of GMR and also of the saturation field H_s (Fig. 4). The measured dependence of $R(H)$ in both systems is different from the one calculated in A but nearly the same on glass and thermally oxidized silicon.

The magnetization reversal was studied by Kerr loops taken from both sides of the multilayers on glass substrates (information depth ≈25 nm).[7] For a multilayer with an Fe buffer (Fig. 5) the Kerr angle rotation resembles the calculated magnetization curve only at the lower part of the stack near the Fe buffer. Due to differences in H_c for Fe and Co (Fig. 5) we estimated that 100% of the lower and 60% of the upper part are AFM coupled: Bearing in mind the results of our structural investigations, layer defects concentrated in the upper part may be responsible for the observed behavior. The Kerr loops on Co/Cu multilayers without Fe buffers (Fig. 6) show a remarkable proportion of ferromagnetically coupled Co even near the substrate.

Cross-section transmission electron microscopy (XTEM) on stacks with Fe buffers (Fig. 7) reveals that the interfaces between Co and Cu get rougher with increasing distance from the substrate surface. At the arrow the metallic layers are interrupted and slightly shifted due to a grain boundary.

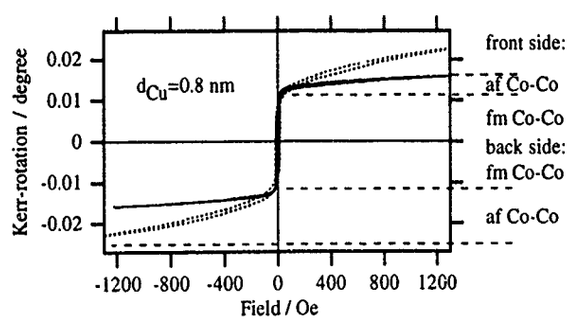

FIG. 6. Kerr loops from frontside (solid line) and backside (dotted line) of our Co/Cu system without Fe buffer. The small Faraday rotation caused by the glass substrate was taken away.

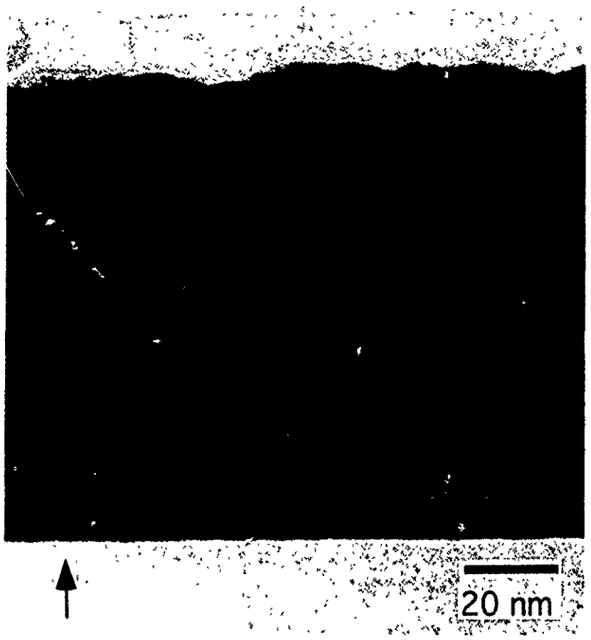

FIG. 7. Low magnification cross-sectional image of the system $Si/SiO_2/Fe(50\ Å)/[Co(17\ Å)/Cu(22\ Å)]_{24}/Co(34\ Å)$, underfocus. The arrow indicates a defect induced by a grain boundary. Co layers appear darker, Cu layers lighter.

In all other areas the metallic layers exhibit continuous straight lines without defects. The cross sections of multilayers without Fe buffers show smaller grains both in lateral and vertical dimension. Because of the greater number of grain boundaries it is reasonable that these systems contain more defects in their layer structure. Moreover, the interfaces between the layers are rougher compared to systems with Fe buffers.

C. Influence of structural defects

To check the influence of a lateral defect causing a MSC between neighboring Co layers a model similar to the ALM was used. The MSC was assumed to have the shape of a nearly straight line with a width of a few lattice constants. This may be caused by grain grooving at the grain boundary as is depicted in the marked region in Fig. 7. The two Co layers are magnetized in antiparallel directions for $H=0$ a great distance from the MSC. Due to the ferromagnetic exchange coupling at the MSC the magnetization directions are locally rotated towards the defect line. Taking into account the coupling between the two short circuited layers and including their nearest Co neighbors, the local magnetization distribution can be calculated. First estimations yielded a width of the magnetization distortion in the range of 10–100 nm depending on the coefficient of a AFM coupling.

III. CONCLUSIONS

Deviations from the simple cosine law for the calculated field dependence of the direction of magnetization were found in all systems with Fe buffer layer and in systems without Fe for $n>2$. These deviations are primarily limited to the outer layers on both sides. Comparisons between the calculated and measured magnetization and MR curves display remarkable differences. Depth selective Kerr loops show strong indications for vertical inhomogeneities. These are probably caused by defect regions responsible for the ferromagnetic part of the magnetic reversal of the upper layers. XTEM investigations reveal MSCs at grain boundaries which could be a possible source for the observed effects. The use of the Fe buffer layer seems to improve the perfection of the multilayer structure, at least for the first layers of the stack.

ACKNOWLEDGMENTS

We thank Dr. D. Hesse and Dr. S. Senz of the Max-Planck Institute in Halle for assistance with the TEM investigations and for many fruitful discussions.

[1] H. Kano, K. Kagawa, A. Suzuki, A. Okabe, K. Hayashi, and K. Aso, Appl. Phys. Lett. **63**, 2839 (1993).
[2] M. E. Tomlinson, R. J. Pollard, D. G. Lord, P. J. Grundy, and Z. Chun, IEEE Trans. Magn. **MAG-28**, 2662 (1992).
[3] S. S. P. Parkin, R. Bhadra, and K. P. Roche, Phys. Rev. Lett. **66**, 2152 (1991).
[4] G. Rupp and H. A. M. van den Berg, IEEE Trans. Magn. **MAG-29**, 3102 (1993).
[5] R. Mattheis, W. Andrä, Jr., L. Fritzsch, A. Hubert, M. Ruhrig, and F. Thrum, J. Magn. Magn. Mater. **121**, 424 (1993).
[6] W. Andrä, IEEE Trans. Magn. **MAG-2**, 560 (1966).
[7] G. Träger, L. Wenzel, and A. Hubert, Phys. Status Solidi A **131**, 201 (1992).

Magnetic and structural studies of sputtered Co/Cu multilayer films

J. D. Kim, Amanda K. Petford-Long, and J. P. Jakubovics
Department of Materials, University of Oxford, Parks Road, Oxford OX1 3PH, United Kingdom

J. E. Evetts and R. Somekh
Department of Metallurgy and Materials, University of Cambridge, Pembroke Street, Cambridge CB2 3QZ, United Kingdom

The structure and magnetic properties of sputtered Co/Cu multilayer films with various layer thicknesses have been studied. X-ray diffractometry and high resolution electron microscopy show the films to be polycrystalline with a fcc structure and strong [111] texture in the growth direction. The magnetoresistance (MR) of the films depends critically on Cu layer thickness (t_{Cu}), with maximum values for films with t_{Cu} around 1 nm. Large differences in saturating field are seen for films with t_{Cu} and t_{Co} differing by a nominal 0.1 nm. The magnetic domain structure, studied using Lorentz microscopy, shows strong dependence on t_{Cu}. High MR-value films showed evidence of antiphase magnetic domain boundaries. The high MR samples show antiferromagnetic coupling, with higher saturating fields than seen in the ferromagnetically coupled films.

I. INTRODUCTION

Multilayer films (MLFs) exhibiting giant magnetoresistance (GMR) are of interest both because of their fundamental properties and because of their potential development as magnetoresistive read heads and sensors. GMR was first discovered in Fe/Cr MLFs grown by molecular beam epitaxy,[1] and is attributed to the spin dependent scattering of conduction electrons, arising from the antiferromagnetic (AFM) alignment of the magnetization in adjacent Fe layers across the Cr layers. The interlayer exchange coupling associated with the AFM alignment is oscillatory with increasing nonmagnetic layer thickness.[2] Parkin *et al.* reported resistance changes up to 65% at room temperature, in an applied magnetic field of 10 kOe, for Co/Cu MLFs,[3] and in addition, the interlayer coupling constant of the Co/Cu MLFs has been reported to be about 8 times smaller than that of Fe(001)/Cr(001).[4] These properties make Co/Cu a promising system for magnetic sensors or magnetoresistive read heads to replace conventional inductive read heads.

In this article, we report the results of a study of the correlation of the microstructure and magnetic domain structure of sputtered polycrystalline Co/Cu MLFs with the MR and interlayer magnetic coupling.

II. EXPERIMENTAL TECHNIQUES

Co/Cu MLFs were deposited onto native oxide-coated Si (100) wafers in an UHV dc-magnetron sputtering system at the University of Cambridge. A series of 40 period MLFs, with Co layer thickness, t_{Co}, of 1.9 and 2.0 nm and t_{Cu} between 0.5 and 1.3 nm, were grown under 0.68 Pa of argon.

The crystallographic structure and periodicity of the MLFs were studied using a Philips x-ray diffractometer. The atomic-scale structure of the films, and the layer thicknesses, were determined from cross-sectional transmission electron microscopy (TEM) specimens using a JEOL 4000 EX HREM. Plan-view specimens were prepared for TEM and Lorentz microscopy by chemical or argon ion etching, or by floating the films off the substrates. Optical diffractogram (ODM) analysis of the high-resolution electron microscopy (HREM) negatives was used to determine the crystal structure of individual crystallites.

The magnetic domain structure was investigated by Lorentz microscopy, using the Foucault mode which reveals the magnetic domains as areas of different intensity. Use of a specially designed objective aperture mechanism[5] enabled high quality Foucault images to be obtained. Hysteresis curves were obtained at room temperature using an alternating gradient force magnetometer (AGFM) at Bangor University. An applied magnetic field of up to 3 kOe was used both parallel to and perpendicular to the film plane.

The MR of the Co/Cu MLFs was measured by the four-point probe method with magnetic fields parallel to both the film plane and the measuring current at room temperature. The MR ratio was calculated according to

$$r(H)=(R_H-R_{sat})/R_{sat},$$

where R_H is the resistance in an applied magnetic field H, and R_{sat} is the resistance under a saturating magnetic field.

III. RESULTS AND DISCUSSION

Figure 1 shows (a) small-angle and (b) high-angle x-ray diffraction (XRD) patterns from two Co/Cu MLFs with t_{Co}=2.0 nm, and t_{Cu}=0.5 and 1.0 nm. The strong low-angle peaks confirm the clear compositional modulation of the films, and the bilayer thicknesses calculated from the peaks using Bragg's law agree well with the nominal values. The high-angle patterns show a single strong peak between the bulk Cu and Co fcc 111 peak positions (calibrated against the Si 200 peak). With increasing Cu layer thickness the peak shifts toward lower angles. This shift, combined with the small peak width, suggests that large areas of the Co/Cu interfaces are coherent. The Co/Cu MLFs have a strong crystallographic texture, with a predominantly fcc structure and {111} parallel to the film plane. The difference in peak heights between curves A and B is due to differences in specimen area and is therefore not significant.

The [111] texture was confirmed by selected area electron diffraction of both plan-view and cross-sectional speci-

 0021-8979/94/76(10)/6513/3/$6.00 © 1994 American Institute of Physics

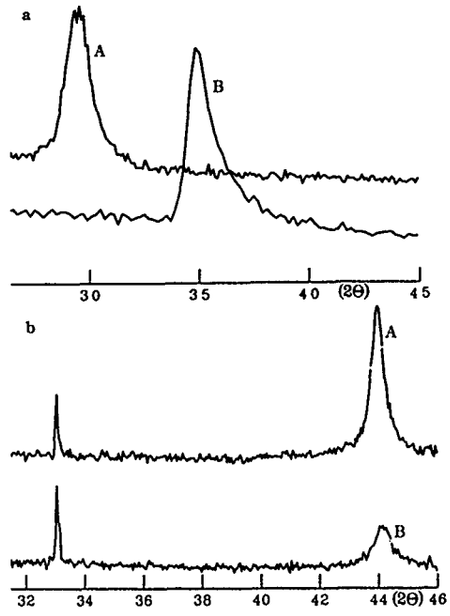

FIG. 1. (a) Low-angle and (b) high-angle XRD patterns from $(Co_{2.0\ nm}/Cu_{1.0\ nm})_{40}$ (curve A) and $(Co_{2.0\ nm}/Cu_{0.5\ nm})_{40}$ (curve B) MLFs. Vertical scale is the intensity in arbitrary units. A and B have been displaced vertically for clarity.

mens. ODM analysis of the HREM images show a dominant fcc structure with a lattice spacing in agreement with the high-angle XRD data. A typical HREM image of a cross-sectional specimen of a $(Co_{2.0\ nm}/Cu_{1.0\ nm})_{40}$ MLF is shown in Fig. 2(a). Textured columnar grains growing normal to the film plane are visible with a constant crystal structure across several layers and coherent Co/Cu interfaces. The columnar grain size, determined from both the XRD peak widths and the HREM images, has a value of about 11 nm for the film shown in Fig. 2. The film quality in all cases is very similar, as expected since the growth conditions were similar. Figure

FIG. 2. (a) HREM image of cross-sectional specimen of $(Co_{2.0\ nm}/Cu_{1.0\ nm})_{40}$ MLF. Columnar grain boundary is marked. (b) Part of same area shown in (a) taken out of focus to show position of layers. Light contrast Cu layers are arrowed.

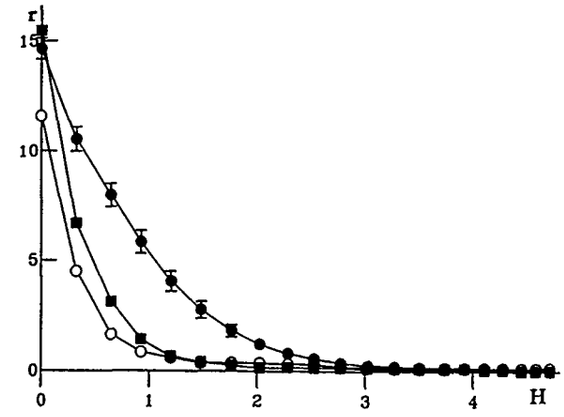

FIG. 3. Plots of r vs $\mathbf{H}$ (in kOe) for (a) $(Co_{2.0\ nm}/Cu_{1.0\ nm})_{40}$ (closed circles), (b) $(Co_{1.9\ nm}/Cu_{1.1\ nm})_{40}$ (closed squares), and (c) $(Co_{1.9\ nm}/Cu_{1.0\ nm})_{40}$ (open circles) MLFs. Note the decrease in saturating field for (b) and (c).

2(b) shows part of the same area of film, taken out of focus, to show the layers.

The MR ratio varies greatly for the films, depending on the thickness of the Cu layers, as has been observed by other authors.[6] The $(Co_{2.0\ nm}/Cu_{0.5\ nm})_{40}$ film shows zero MR, while films with t_{Cu} around 1 nm show saturation MR values around 15%, as can be seen in Fig. 3. Each curve is the average of three measurements on each of a number of samples with the same nominal layer thicknesses (circles—two samples, squares—three samples). The error bars are only shown for points for which they are larger than the symbols used. The most striking observation is the large decrease in saturating field for a change in nominal layer thickness of 0.1 nm, resulting in an increase in slope of the r vs $\mathbf{H}$

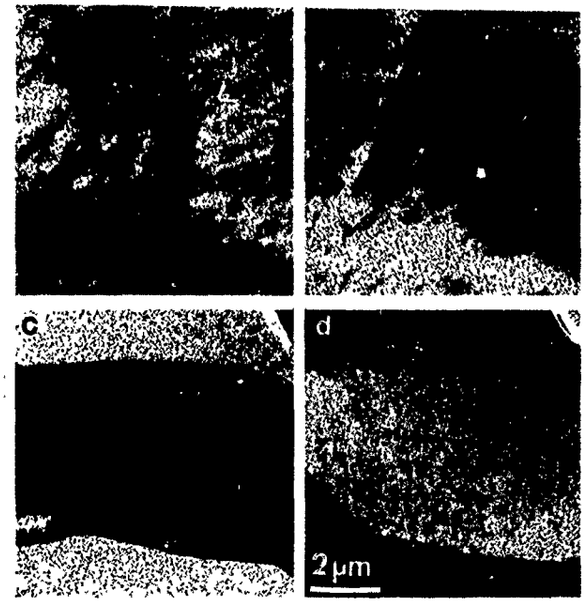

FIG. 4. Foucault images of magnetic domain structure in $(Co_{1.9\ nm}/Cu_{1.1\ nm})_{40}$ MLF showing AFM coupling, (a) and (b), and $(Co_{2.0\ nm}/Cu_{0.5\ nm})_{40}$ MLF showing FM coupling (c) and (d). Easy axis of magnetization in film plane for both films.

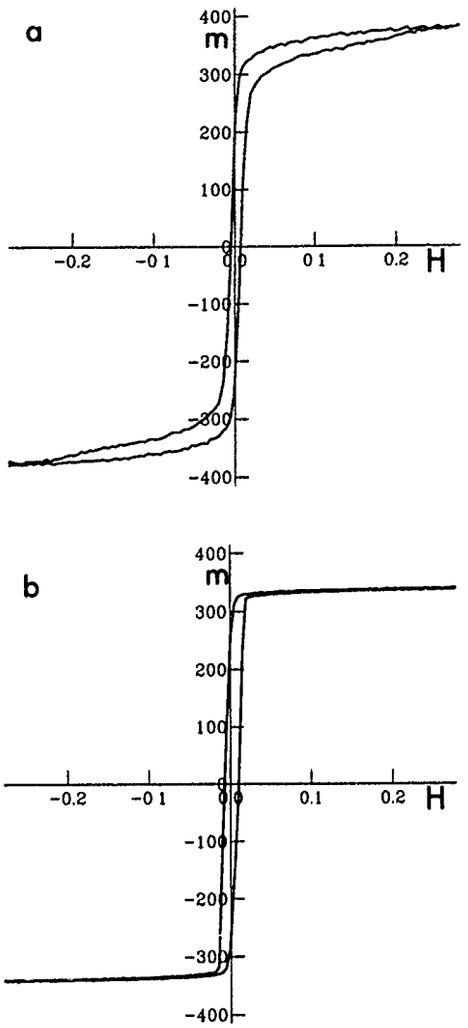

FIG. 5. Hysteresis loops (magnetic moment m in μemu against field H in kOe) obtained using an AGFM for (a) $(Co_{1.9\ nm}/Cu_{1.1\ nm})_{40}$ MLF showing AFM coupling, and (b) $(Co_{2.0\ nm}/Cu_{0.5\ nm})_{40}$ MLF showing FM coupling.

curve (a steep slope to this curve is required for films to be used as MR sensors and heads). The differences in r vs **H** may be related to differences in layer quality. TEM images of the $(Co_{2.0\ nm}/Cu_{1.0\ nm})_{40}$ films show the layers to be less flat than those in the t_{Co}=1.9 nm MLFs with more "faults" in the layers.

The value of MR ratio shown by the Co/Cu MLFs can be determined qualitatively from the type of magnetic domain structure observed. Figures 4(a) and 4(b) show the magnetic domain structure of a $(Co_{1.9\ nm}/Cu_{1.1\ nm})_{40}$ MLF (r=15%) imaged using the Foucault technique. The transition between areas showing bright and dark contrast occurs gradually rather than abruptly, with wavy rather than smooth boundaries. In addition, the overall change in contrast is relatively low. We attribute these features to the fact that the domain walls are in different positions in different layers, and to a relatively low degree of ferromagnetic (FM) coupling between the Co layers. The geometry of the domain pattern suggest that domains do not extend through the whole thickness of the MLF. This effect has also been observed in Fe/Cr MLFs.[7] The fact that domain contrast is visible is in agreement with the suggestion that antiphase domain boundaries parallel to the substrate are present,[8] and explains the fact that $r(0)$ is smaller than the ideal value for Co/Cu MLFs. In comparison, Figs. 4(c) and 4(d) show a pair of Foucault images illustrating the typical magnetic domain structure of a $(Co_{2.0\ nm}/Cu_{0.5\ nm})_{40}$ MLF, which shows a low MR. The strong magnetic domain contrast and regular domain shape show that the layer coupling is predominantly FM. Further evidence for the magnetic layer coupling is given by the shape of the hysteresis loops, as seen in Fig. 5 for films showing high $(Co_{1.9\ nm}/Cu_{1.1\ nm})$ and low MR $(Co_{2.0\ nm}/Cu_{0.5\ nm})$.

IV. CONCLUSIONS

The Co/Cu MLFs show a clear composition modulation and are polycrystalline, with columnar grains extending across several layers. The films have a strong (111) crystallographic texture with all layers showing a predominantly fcc structure. Coherent interfaces are observed between the Co and Cu layers over large areas. The magnetic domain contrast depends strongly on t_{Cu}, which determines the state of magnetic coupling. The samples with $t_{Co}\approx$2.0 nm and $t_{Cu}\approx$1.0 nm show the highest MR, and weak and irregular magnetic domain contrast. The magnetization measurements confirm that samples showing negligible MR exhibit FM coupling.

ACKNOWLEDGMENTS

We are grateful to the Magnetic Materials Research Group at UCNW Bangor for assistance with the magnetic measurements on the AGFM, and to the SERC, to CAMST and to the Royal Society (AKPL) for research support.

[1] M. N. Baibich, J. M. Broto, A. Fert, F. Nguyen van Dau, F. Petroff, P. Etienne, G. Creuzet, A. Friederich, and J. Chazeles, Phys. Rev. Lett. **61**, 2472 (1988).
[2] S. S. P. Parkin, N. More, and K. P. Roche, Phys. Rev. Lett. **64**, 2304 (1990).
[3] S. S. P. Parkin, Z. G. Li, and D. J. Smith, Appl. Phys. Lett. **58**, 2710 (1991).
[4] D. H. Mosca, F. Petroff, A. Fert, P. A. Schroeder, W. P. Pratt, Jr., and R. Laloee, J. Magn. Magn. Mater. **94**, L1 (1991).
[5] R. C. Doole, A. K. Petford-Long, and J. P. Jakubovics, Rev. Sci. Instrum. **64**, 1038 (1993).
[6] S. S. P. Parkin, R. Bhadra, and K. P. Roche, Phys. Rev. Lett. **66**, 2152 (1991).
[7] A. K. Petford-Long, R. C. Doole, A. Cerezo, J. S. Conyers, and J. P. Jakubovics, J. Magn. Mag. Mater. **126**, 117 (1993).
[8] R. J. Highmore, J. E. Evetts, and R. Somekh, J. Magn. Magn. Mater. **123**, L13 (1993).

Influence of crystal structure on the magnetoresistance of Co/Cr multilayers

Y. Liou
Institute of Physics, Academia Sinica, Taipei 115, Taiwan, Republic of China

J. C. A. Huang
Department of Physics, National Cheng Kung University, Tainan 701, Taiwan, Republic of China

Y. D. Yao
Institute of Physics, Academia Sinica, Taipei 115, Taiwan, Republic of China

C. H. Lee
Synchrotron Radiation Research Center, Hsinchu 300, Taiwan, Republic of China

K. T. Wu, C. L. Lu, and S. Y. Liao
Department of Physics, Fu Jen University, Taipei 242, Taiwan, Republic of China

Y. Y. Chen and N. T. Liang, W. T. Yang, C. Y. Chen, and B. C. Hu
Institute of Physics, Academia Sinica, Taipei 115, Taiwan, Republic of China

Epitaxial Co/Cr multilayers, and single-crystal Co thin films etc. have been grown on MgO and Al_2O_3 substrates with Cr and Mo as buffer layers by molecular beam epitaxy technique. From the structure and magnetoresistance studies, we have found that the ferromagnetic anisotropy of resistance (AMR) is strongly influenced by the buffer layer, but with negligible effect due to the variation of the structure of Co films. The AMR of Co film on Cr buffer layer is quite small (0.1%); however, the MR of Co/Cr multilayers is almost one order larger than the AMR of Co film on Cr buffer layer. An enhancement factor of 4 for the MR in Co/Cr multilayers by the interface roughness has been observed. This suggests that the effect due to the spin dependent scattering at the interfacial regions of the superlattice is larger than that due to the spin dependent scattering in the ferromagnetic layers for the MR in the Co/Cr multilayer system.

During the past several years, the magnetoresistance (MR) behaviors in many metallic multilayers have become the subject of considerable interest. Large (or giant) MR was first realized in Fe/Cr multilayer system,[1] and has been referred to as GMR. Relatively small MR occurs in the Co/Cr multilayers.[2] The MR in multilayers results from the spin dependent scattering of the conduction electrons which occurs both in the ferromagnetic layers and at the interfacial regions between the ferromagnetic and nonferromagnetic layers. It is quite different from the ferromagnetic anisotropy of resistance (AMR) in ferromagnetic systems, which depends on the direction of the magnetization.[3]

Epitaxial Co/Cr multilayers as well as single-crystal hcp-Co, fcc-Co, and polycrystal Co thin films have been grown on both MgO and Al_2O_3 substracts with Cr and Mo as buffer layers using an Eiko EL-10A molecular beam epitaxy (MBE) system with base pressure of $\sim 2\times10^{-10}$ Torr. Pure elements (≥99.99%) of Co, Cr, and Mo were evaporated from three independent e-beam evaporators. During deposition of the elements, the growth pressure was controlled at below 5×10^{-9} Torr, and the deposition rate at ~0.1 Å/s. To enable the growth of high-quality samples, polished and epitaxial grade MgO and Al_2O_3 substrates were chemically precleaned and rinsed in an ultrasonic cleaner. They were then outgassed at 900 to 1000 °C for at least 1/2 h under ultra high vacuum in the MBE system. For samples with a Mo (or Co) buffer layer, Mo (or Co) was deposited on the substrates at 900 (or 500) °C. The substrate temperature for all films during evaporating was kept between 300 and 350 °C. The crystallographic structure of the films were examined, throughout all the growth, by reflection high energy electron diffraction (RHEED). The interface roughness and the thickness of the superlattice structures were determined by the x-ray reflectivity analyses.

The magnetic properties of all the samples were studied by using a SQUID magnetometer. The AMR and MR measurements were carried out by the conventional four probe technique.

Before discussing the experimental data of AMR and MR in the CoCr system, we have to clarify their definition. The AMR in ferromagnetic films is defined by $(R_\parallel - R_\perp)/R_0$, where R_0 is the electrical resistance in zero internal magnetic field, and $R_\parallel$ and $R_\perp$ are the resistances when the saturated magnetization is parallel and perpendicular to the current, respectively.

The MR (or GMR) in multilayers is defined as $[R_{AF} - R_S]/R_S$, where R_S is the electrical resistance at saturated high magnetic field, and the spins in Co layers align in the field direction. R_{AF} is the electrical resistance when the field is removed, the Co layers adjacent to the Cr layer in-between exhibit antiferromagnetic coupling.

Crystal structures of thin films or multilayers may be considerably affected by the choice of buffer layers, substrates, and their orientations. In this study, we chose MgO(100), Al_2O_3 ($1\bar{1}02$), and Al_2O_3(0001) as substrates, and Cr and Mo as buffer layers to study the variation of AMR for Co films. In general, for Co grown on MgO(100) substrate without a buffer layer, an epitaxial fcc-Co film with (100) growth plane can be formed for Co thicknesses larger than about 60 Å, but for Co grown on an Al_2O_3(0001) substrate

 0021-8979/94/76(10)/6516/3/$6.00 © 1994 American Institute of Physics

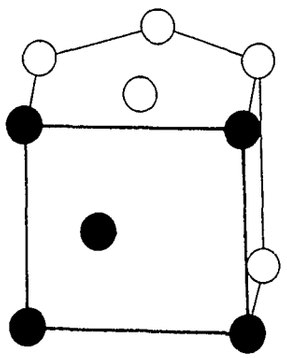

(a)

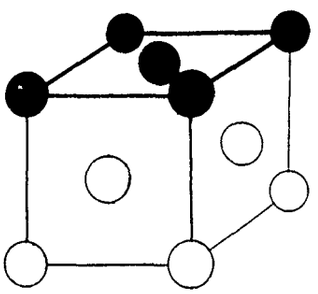

(b)

FIG. 1. Typical RHEED patterns of (a) hcp-Co(11$\bar{2}$0) plane viewed along [0001], and (b) fcc-Co(100) plane viewed along [011]. The surface with solid circles cutting with the unit cell of both hcp(11$\bar{2}$0) and fcc(100) Co are schematically illustrated below each RHEED pictures.

without a buffer layer, a polycrystal Co film was observed. In addition when we grow a thin buffer layer of Cr(100) about 20 Å on either MgO(100) or Al_2O_3(1$\bar{1}$02), then both RHEED and x-ray diffraction (XRD) studies show an hcp-Co structure with (11$\bar{2}$0) plane parallel to the (100) surface of Cr. For example, Fig. 1 shows the typical RHEED patterns of (a) hcp-Co(11$\bar{2}$0) plane viewed along [0001], and (b) fcc-Co(100) plane viewed along [011]. The surfaces with solid circles cutting with unit cell of hcp(11$\bar{2}$0) and fcc(100) are

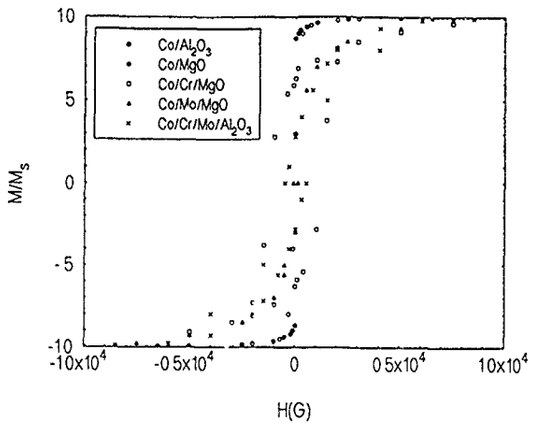

FIG. 2. The normalized magnetization as a function of magnetic field at room temperature for (a) Co/Al_2O_3, (b) Co/MgO, (c) Co/Cr/Mgo, (d) Co/Mo/MgO, and (e) $Co/Cr/Mo/Al_2O_3$.

schematically illustrated below each of the RHEED pictures.

Figure 2 shows the normalized magnetization as a function of the magnetic field at room temperature for 5 thin film samples (Co/Al_2O_3, Co/MgO, Co/Cr/MgO, Co/Mo/MgO, and $Co/Cr/Mo/Al_2O_3$). Generally speaking, the magnetization is saturated after roughly 6 kG for all the samples. Figure 3 presents the normalized difference of resistance as function of the magnetic field at room temperature for 5 thin film samples: (a) polycrystal Co on Al_2O_3 (0001), (b) fcc-Co(100) on MgO(100), (c) hcp-Co(11$\bar{2}$0) on Cr(100) which is on MgO(100), (d) hcp-Co(11$\bar{2}$0) on Mo(100) which is on MgO(100), and (e) hcp-Co(11$\bar{2}$0) on Cr(100) and Mo(100) which is on Al_2O_3(1$\bar{1}$02). One can see that the values of AMR for both polycrystal- and fcc-Co films without a buffer layer are roughly equal to 1.3%. However, the AMRs of all the Co films with either Cr or Mo as a buffer layer are roughly one order of magnitude smaller than that of Co films without a buffer layer. Therefore, we conclude that the effect to the AMR for Co films with different structure is negli-

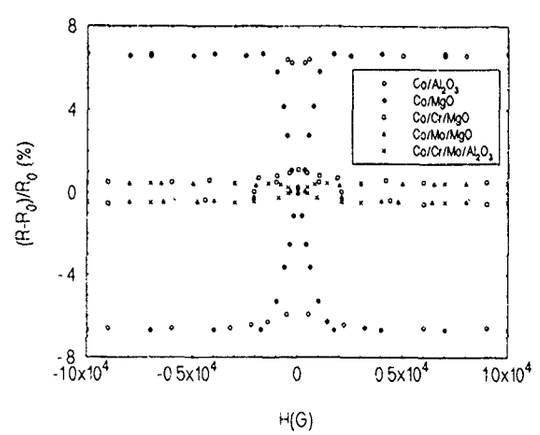

FIG. 3. The normalized difference of electrical resistance between magnetic field and zero field as a function of magnetic field at room temperature for (a) polycrystal Co/Al_2O_3, (b) fcc-Co/MgO, (c) hcp-Co/Cr/MgO, (d) hcp-Co/Mo/MgO, and (e) hcp-Co/Cr/Mo/Al_2O_3.

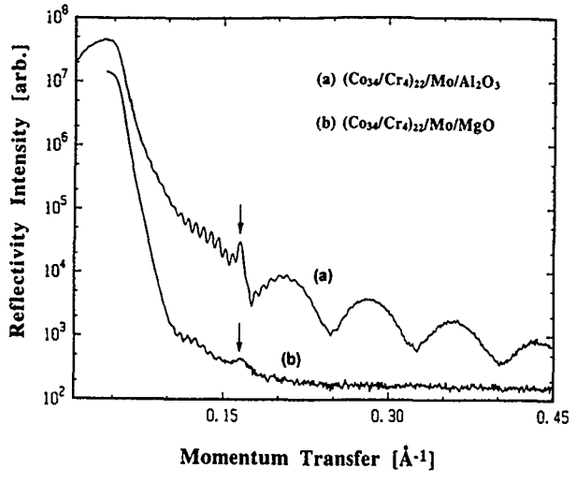

FIG. 4. X-ray reflectivity measurement of the samples (a) $(Co/Cr)_{22}/Mo/Al_2O_3$, and (b) $(Co/Cr)_{22}/Mo/MgO$. The arrow indicates the peak due to the period of the superlattice. The oscillation fringes pattern is due to the interference of the x-ray reflection between the two interfaces of Mo buffer layer and the interfaces of the total growth thickness.

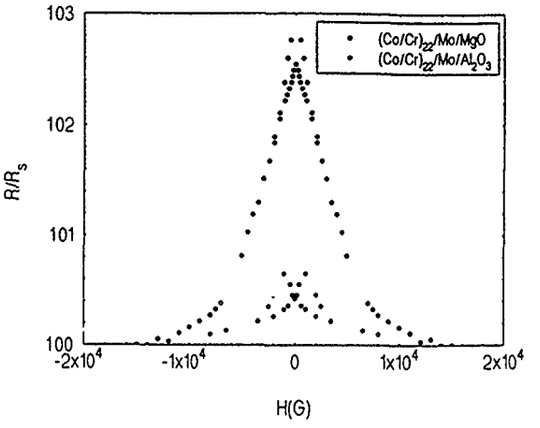

FIG. 5. The Normalized resistivity as a function of applied magnetic field at 10 K for (a) $(Co/Cr)_{22}/Mo/Al_2O_3$, and (b) $(Co/Cr)_{22}/Mo/MgO$ superlattices.

gible, if it is compared with the variation due to the addition of buffer layers of Cr and Mo. However, the exact mechanism of this reduction in AMR is not clear at present. It is noted that the buffer layers are not thick enough to shunt enough current to explain this reduction.

For Co/Cr multilayer samples, we have selected MgO(100), and $Al_2O_3(1\bar{1}02)$ as substrates. The thickness of each layer is varied from 4 to 30 Å for Cr, and from 20 to 40 Å for Co. We chose Cr as the first layer to form the multilayer structures. For samples without a Mo buffer layer, we found that the multilayers we made always had polycrystal structure if the thickness of the first Cr layer was less than 20 Å. This result tells us that it is difficult to grow epitaxial Co/Cr multilayers on either MgO or Al_2O_3 with Cr thickness less than 20 Å and Co thickness less than 60 Å. Therefore, we selected Mo as a buffer layer (about 100 Å) on both MgO and Al_2O_3 substrates to study the epitaxial behavior of the Co/Cr multilayer system. From the RHEED and XRD studies, both hcp-Co and bcc-Cr layers were identified for all the multilayer samples on either MgO or Al_2O_3 substrates. For the sake of comparison, Co/Cr multilayer samples with either MgO or Al_2O_3 as substrate were epitaxially grown side by side under the same batch of crystal growth process. Any difference between these two samples should be due to the different substrate only; e.g., the interface roughness of the multilayers is one of the important factors. For explanation, Fig. 4 shows result of the x-ray reflectivity measurement on two samples: (a) $(Co_{34\ Å}/Cr_{4\ Å})_{22}/Mo_{88\ Å}/Al_2O_3$, and (b) $(Co_{34\ Å}/Cr_{4\ Å})_{22}/Mo_{88\ Å}/MgO$. We can readily see that the reflectivity intensity drops more rapidly for the sample grown on MgO substrate. The reflectivity formula originally derived by Parratt[4] was used for the calculation of intensity reflected from a multiple-layer film on a substrate. Interfacial inhomogeneity due to roughness was included by adding effective Debye–Waller factors to each of the layers.[5,6] From this analysis the interface roughness of the sample grown on MgO is roughly 8 times larger than that on Al_2O_3.

The normalized electrical resistance as a function of applied field at 10 K for the above two superlattice samples are shown in Fig. 5. The MR, i.e., $(R-R_s)/R_s$, is roughly about 2.72%, and 0.65% for $(Co/Cr)_{22}/Mo/MgO$ and $(Co/Cr)_{22}/Mo/Al_2O_3$, respectively. This tells us that, roughly speaking, the MR is enhanced by a factor of 4 in the Co/Cr multilayers by the interface roughness. It is suggested that the effect by the spin dependent scattering at the interfacial regions of the superlattice is larger than that due to the spin dependent scattering in the ferromagnetic layers for the magnetoresistance in the Co/Cr multilayer system.

We are grateful for the financial support by the National Science Council of the ROC under Grant Nos. 82-0212-M006-002 (J.C.A.H.), 81-0204-M001-537 and 81-0212-M001-534 (Y.L.), and 83-0208-M001-082 (Y.D.Y.).

[1] M. N. Baibich, J. M. Broto, A. Fert, F. Nguyen Van Dau, F. Petroff, P. Etienne, G. Creuzet, A. Friederich, and J. Chazelas, Phys. Rev. Lett. **61**, 2472 (1988).
[2] S. S. P. Parkin, R. Bhadra, and K. P. Roche, Phys. Rev. Lett. **64**, 2304 (1990).
[3] J. Smit, Physica **16**, 612 (1951).
[4] L. G. Parratt, Phys. Rev. **95**, 359 (1954).
[5] P. Crove and L. Nevot, Rev. Phys. Appl. **15**, 761 (1980).
[6] L. Nevot, B. Pardo, and J. Corno, Rev. Phys. Appl. **23**, 1675 (1980).

Giant magnetoresistance peaks in CoNiCu/Cu multilayers grown by electrodeposition

S. Z. Hua
Department of Materials and Nuclear Engineering, University of Maryland, College Park, Maryland 20742

D. S. Lashmore
National Institute of Standards and Technology, Gaithersburg, Maryland 20899

L. Salamanca-Riba
Department of Materials and Nuclear Engineering, University of Maryland, College Park, Maryland 20742

W. Schwarzacher
Department of Physics, University of Bristol, Bristol, England

L. J. Swartzenruber, R. D. McMichael, and L. H. Bennett
National Institute of Standards and Technology, Gaithersburg, Maryland 20899

R. Hart
Department of Physics, University of Bristol, Bristol, England

Giant magnetoresistance (GMR) of CoNiCu/Cu multilayers grown by electrodeposition was measured as a function of the copper layer thickness and effects of the order of 14% were obtained. The copper layer thickness ranged from 0.7 to 3.5 nm. Two peaks in the magnetoresistance were observed. One was centered at a copper thickness of ~1.0 nm and the second was centered at ~2.3 nm. Comparison of the field dependence of the magnetoresistance with the field dependence of the magnetization, as determined by vibrating-sample magnetometer, suggests that the saturation field for GMR and the magnetization are similar for the larger copper thicknesses, but are strikingly different near 1.0 nm copper thickness. This observation suggests that the GMR is affected by different factors depending on the thickness of the copper layer.

I. INTRODUCTION

Since the discovery of giant magnetoresistance (GMR), a considerable amount of research has been focused on the origin of the GMR effect and on understanding oscillatory exchange coupling mechanisms.[1–3] In Fe/Cr multilayers, it is generally accepted that spin-dependent scattering causes the GMR effect and is related to interface roughness.[1,4] However, recent studies indicated that spin-independent scattering at interfaces reduces the GMR.[5] In the Co/Cu or CoNi/Cu systems, the GMR depends on substrate type, surface roughness and the nature of the underlayers and overlayers. There have been many reports[6,7] of observations of GMR in sputtered Co/Cu multilayers suggesting strong antiferromagnetic (AFM) coupling. Typically three oscillations of GMR were observed as the spacer thickness varied from 0.6 to 4.0 nm. In molecular beam epitaxy (MBE) grown Co/Cu multilayers,[8] the magnetization shows significant hysteresis. It also appears that incomplete AFM coupling exists although the GMR effect is still large. No oscillations are reported in some (111) oriented epitaxial Co/Cu multilayers,[9] while other textures of Co/Cu, apparently with nearly comparable structures and perfection, exhibit different AFM coupling strength with GMR values that are attributed to the nature of the buffer layers as well as to the texture.[10] These results suggest that the magnetic properties of Co/Cu are sensitive to: (1) interface roughness, (2) nature of buffer layer and (3) texture. In none of these early studies was strain explicitly considered.

We present GMR and vibrating-sample magnetometer (VSM) results of studies on CoNiCu/Cu multilayers grown electrochemically. The AFM and ferromagnetic (FM) coupling states were also studied by analysis of: (1) the field dependence of GMR and (2) the magnetization curves as a function of spacer layer thickness. Finally, our data suggest that the GMR behavior is affected by interfacial alloying at low copper thickness and by strain at large copper layer thickness.

II. EXPERIMENT

Multilayers were electrochemically deposited on a (100) textured electropolished thin copper foil (0.127 mm thick) at room temperature. Electrodeposition was performed from a sulfamate electrolyte containing Co^{2+}, Ni^{2+}, and Cu^{2+} ions in a single cell. The procedure has been described previously.[11–13] We used a cathode potential of −1.8 V vs saturated calomel electrode (SCE) for NiCo alloy deposition and a potential of −0.26 V vs SCE for copper deposition. Copper is codeposited with CoNi so that the real composition of magnetic layers is about $Co_{64}Ni_{31}Cu_5$. Finally, the copper substrate was dissolved by chemical etching, and the free standing multilayer was glued on glass to facilitate handling. In this study the CoNiCu layer thickness was held constant and the copper layer thickness was varied.

The composition of the films was measured using x-ray fluorescence which confirmed that the cobalt to nickel ratio in all the magnetic multilayers was about 2:1. Structure and

 0021-8979/94/76(10)/6519/3/$6.00 © 1994 American Institute of Physics

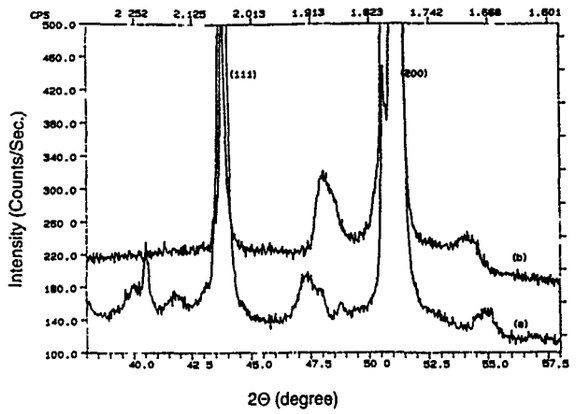

FIG. 1. A high angle x-ray diffraction pattern of [CoNiCu(2.2 nm/Cu(t_{Cu})]×400 multilayers with a t_{Cu} of 1.0 nm and (b) t_{Cu} of 2.3 nm. The vertical displacement is for clarity.

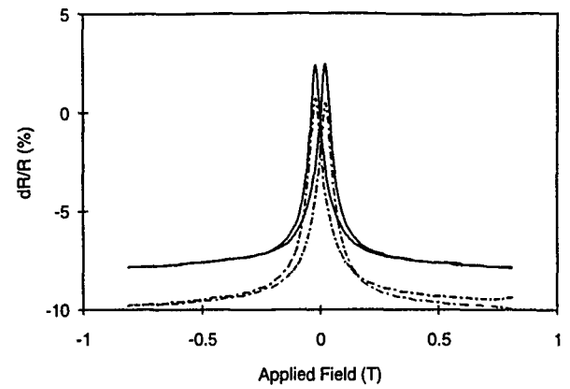

FIG. 2. Magnetoresistance of electrodeposited [CoNiCu(1.5 nm)/Cu(4.5 nm)]×250 multilayers measured at room temperature. The solid and dashed line show the data for longitudinal and transverse mode, respectively. Note that some drift was apparent at high fields for the transverse measurements.

periodicity of the multilayers were characterized by high angle x-ray diffraction and the MR measurement was performed by a four point probe technique at room temperature. Magnetic fields up to 0.8 T were applied in the film plane, both parallel and perpendicular to the current direction. Magnetization loops were obtained using a vibrating-sample magnetometer at room temperature.

III. RESULTS

High angle x-ray diffraction patterns from two of the CoNiCu/Cu multilayers are shown in Fig. 1. The high intensity (200) Bragg peak suggests a predominant (100) texture epitaxial to the substrate with some (111) contribution. The first order satellites indicate the presence of layers of well defined periodicity. In most samples the second order satellite was too weak to be observed. The superlattice period Λ is calculated from the satellite positions.[13] The observed increase in the Bragg peak width is believed due to an increase in coherence strain.[14]

A typical MR curve of a [CoNiCu(1.5 nm)/Cu(4.5 nm)] ×250 multilayer measured at room temperature is shown in Fig. 2. A 10% change resistivity was observed by changing the applied field from 0 to 0.1 T with a maximum sensitivity ~0.6%/mT in the linear slope region. Both longitudinal and transverse orientations were measured (Fig. 2). A symmetric change of almost the same amplitude was observed for both cases. The large isotropic magnetoresistance in both modes implies GMR behavior rather than isotropic normal magnetoresistance.

The variation of the maximum change in MR of [CoNiCu(2.2 nm)/Cu(t_{Cu})] multilayers as a function of copper thickness t_{Cu} is shown in Fig. 3. When the GMR saturation field exceeded the maximum 0.8 T available, the saturation value was determined by extrapolation. We observed a first GMR peak at a copper thickness of ~1.0 nm. Instead of a second oscillation of lower value, a large increase of GMR is observed at a copper layer thickness greater than 2.0 nm, giving rise to a broad peak centered at 2.3 nm. This result differs both from the results obtained from sputtered CoNi/Cu multilayers[15] and previous work for MBE grown Co/Cu (111) multilayers in which no oscillations were observed and in which the GMR decayed continuously with increasing copper thickness.

Further investigations of scattering mechanisms were carried out by a comparison of the GMR with the magnetization loops obtained by VSM. The magnetic field dependence of the GMR and of the corresponding magnetization are shown for the samples with copper layer thickness of 1.0 nm in Fig. 4(a) and 2.3 nm in Fig. 4(b). The shapes of the GMR curves observed with thin (~1.0 nm) and thick (~2.0 nm) copper layers [Figs. 4(a1) and 4(b1)] differ considerably. For the thinner copper layers, the GMR peak is broad with a small hysteresis suggesting stronger AFM coupling. As can be seen in Figs. 4(a2) and 4(b2), the coercivity increases with increasing copper thickness. Magnetization loops of these samples were measured at room temperature at fields up to 0.8 T [Figs. 4(a2) and 4(b2)]. As expected, incomplete AFM coupling is suggested in Figs. 4(a2) and 4(b2) by the gradu-

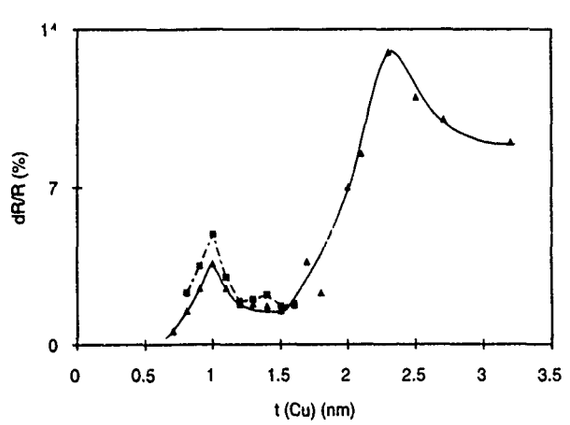

FIG. 3. Oscillation of GMR with variation of copper layer thickness. The thickness of the CoNiCu layer is 2.2 nm with 400 pairs of layers for all the samples. The squares indicate the measured maximum GMR data for applied field up to 0.8 T, and the triangle gives the extrapolated saturation GMR.

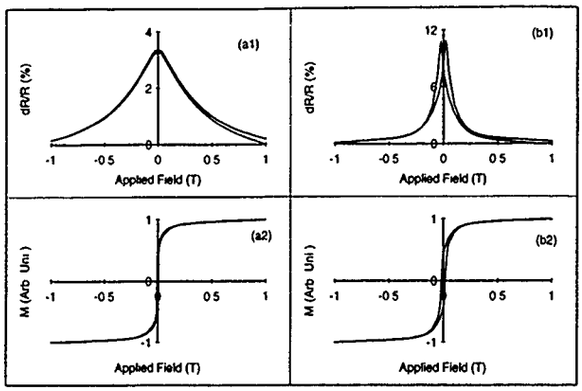

FIG. 4. The magnetic field dependence of GMR and magnetization of [CoNiCu(2.2 nm)/Cu(t_{Cu})]×400 multilayers for (a) t_{Cu}=1.0 nm, (b) t_{Cu}=2.3 nm. All the measurements have been carried out at room temperature and with the field parallel to the plane of the multilayer except when indicated.

ally increasing magnetization with increasing applied field as well as by the large remanent magnetization at low fields in all the samples. Remanent magnetization of around 70%–80% of saturation is consistent with the existence of some FM coupling between the magnetic layers. However, from previous work,[8,10] a small fraction of AFM coupling (~30% saturation magnetization) can still produce a reasonable GMR (~40%), which suggests that the AFM coupling may still be contributing to the GMR in our samples.

IV. DISCUSSION

We have observed a small increase in the GMR ratio (dR/R) at 1.0 nm copper thickness. We believe that this first peak is possibly due to AFM coupling and is analogous to that commonly observed in many Co/Cu and CoNi/Cu sputtered specimens.[6,7,15] The electrochemical process used in this study results in copper codepositing in the cobalt alloy layer. The copper content of the solution adjacent to the cathode is reduced during the deposition of copper and a gradient in this copper concentration will exist whose magnitude will be proportional to the thickness of the copper layer being deposited.[16] The subsequent cobalt layer will have a copper content inversely proportional to this gradient so that for thin copper layers the next cobalt alloy will be enriched in copper. The low GMR value of these thin (Cu) samples may be attributed to significant copper alloying while the thicker (Cu) specimens will have less copper contamination in the ferromagnetic layers and therefore larger GMR values.

The second GMR peak was found at ~2.3 nm, at a position consistent with predictions of Stiles[2] for a (200) textured copper spacer layer. The low frequency oscillation predicted by Stiles was not observed due, we believe, to surface roughness. However, unlike data presented for sputtered multilayers, our second peak is both higher and is significantly broader than reported in the published data for binary Co/Cu multilayers produced by sputtering.[6,7] The high angle x-ray diffraction patterns of the electrochemically produced specimens suggest that all the samples are epitaxial with low intensity symmetrical satellites around the [200] Bragg peak a small copper layer spacings, and well defined and high intensity but asymmetric satellites at larger copper layer spacings. The width of the Bragg peak increases with copper spacer thickness and may be due to increasing coherency strains as the copper layer thickness increases.[14] Both nickel and cobalt are magnetostrictive and so are sensitive to strains therefore, the broadening of the second peak is consistent with both a magnetorestrictive effect and to decreasing AFM/FM coupling strength as the copper thickness and resultant coherency strain increases.

The comparison of magnetization data with MR data for thin copper spacer layers (see Fig. 4) shows that a much higher field is required to saturate the MR suggesting strong AFM coupling. The small coercive field required to reverse the magnetization is consistent with this explanation. At higher copper layer thickness, good agreement between the saturation field of MR and the magnetization is obtained, possibly due to weaker AFM coupling. The large coercive field is consistent with decreased coupling for the thick copper spacer layers.

ACKNOWLEDGMENTS

The authors acknowledge the NSF for financial support S. H. under Contract No. DMR 9111516, W. Schwarzacher and R. Hart acknowledge support of NATO (North Atlantic Treaty Organization) under Grant No. CRG 910583.

[1] M. N. Baibich, J. M. Broto, A. Fert, F. Nguyen Van Dau, F. Petroff, P. Eitenne, G. Creuzet, A. Friederich, and J. Chazelas, Phys. Rev. Lett. **61**, 2472 (1988).
[2] M. D. Stiles, Phys. Rew. B **48**, 7238 (1993).
[3] P. M. Levy, S. Zhang, and A. Fert, Phys. Rev. Lett. **65**, 1643 (1990).
[4] B. A. Gurney, P. Baumgart, D. R. Wilhoit, B. Dieny, and V. S. Speriosu, J. Appl. Phys. **70**, 5867 (1991).
[5] V. S. Speriosu, J. P. Nozieres, B. A. Gurney, B. Dieny, T. C. Huang, and H. Lefakis, Phys. Rev. B **47**, 11579 (1993).
[6] A. Fert, A. Barthelemy, P. Etienne, S. Lequien, R. Loloee, D. K. Lottis, D. H. Mosca, F. Petroff, W. P. Pratt, and P. A. Schroeder, J. Magn. Magn. Mater. **104–107**, 1712 (1992).
[7] S. Honda, S. Ohmoto, R. Imada, and M. Nawate, J. Magn. Magn. Mater. **126**, 419 (1993).
[8] M. A. Howson, B. J. Hickey, J. Xu, and D. Greig, J. Magn. Magn. Mater. **126**, 416 (1993).
[9] E. Avdi, B. J. Hickey, D. Greig, M. A. Howson, M. J. Hall, J. Xu, M. J. Walker, N. Wiser, and P. de Groot, J. Appl. Phys. **73**, 5521 (1993).
[10] S. S. P. Parkin, R. F. Marks, R. F. C. Farrow, G. R. Harp, Q. H. Lam, and R. J. Savoy, Phys. Rev. B **46**, 9262 (1992).
[11] M. Alper, K. Attenborough, R. Hart, S. J. Lane, D. S. Lashmore, C. Younes, and W. Schwarzacher, Appl. Phys. Lett. **63**, 2144 (1993).
[12] D. S. Lashmore, Y. Zhang, S. Hua, M. P. Dariel, L. Swartzendruber, and L. Salamanca-Riba, Third International Symposium on Magnetic Materials, Procedures, and Devices, 1993 (in press).
[13] D. S. Lashmore, R. Oberle, M. P. Dariel, L. H. Bennett, and L. Swartzendruber, Mater. Res. Soc. Symp. Proc. **132**, 219 (1988).
[14] D. B. McWhan, *Synthetic Modulated Structures*, edited by L. L. Chang and B. C. Giesen (Academic, New York, 1985), p. 43.
[15] X. Bian, J. O. Strom-Olsen, Z. Altounian, Y. Huai, and R. W. Cochrane, Appl. Phys. Lett. **62**, 3525 (1993).
[16] A. R. Despic and V. D. Jovic, J. Electrochem. Soc. **134**, 3004 (1987).

High sensitivity GMR in NiFeCo/Cu multilayers

S. Gangopadhyay, S. Hossain, J. Yang, J. A. Barnard, M. T. Kief, H. Fujiwara, and M. R. Parker
Materials for Information Technology, Box 870209, University of Alabama, Tuscaloosa, Alabama 35487-0209

Magnetoresistance and magnetic hysteresis in NiFeCo/Cu soft magnetic multilayers with a fixed number of bilayers (six) and magnetic and spacer layer thickness but varying composition has been studied. The highest value of the transverse GMR obtained is 6.8% in a saturation field of ≈40 Oe at room temperature. Very high sensitivity, around 1%-2%/Oe and unconventional easy-axis hysteresis and GMR loop shapes have been observed. The analysis of the GMR effects and the associated hysteretic behavior by using a model that includes biquadratic exchange coupling suggests that the samples are composed of at least two distinctively different parts.

Much interest has focused, in recent months, on the development of giant magnetoresistive (GMR) thin film materials with high magnetic field sensitivity. High sensitivity here means a relatively large percentage change in electrical resistance per unit applied magnetic field. One recently described approach to high sensitivity[1,2] has been the fabrication of quasigranular NiFe/Ag multilayers with sensitivities approaching 1%/Oe. A major difficulty with this system is that these high sensitivities are only achieved after a high-temperature (~300 °C) anneal. High sensitivities have also been demonstrated in spin-valve structures,[3] but here again, some technical difficulties are apparent in the realization of effective antiferromagnetic exchange layers.

The thin film alloy system discussed in the present paper has been described elsewhere[4,5] in terms of its transverse (or hard-axis) GMR characteristics.[6] The system in question is NiFeCo/Cu in a six-bilayer configuration prepared by high rate dc magnetron sputtering. Its longitudinal (or easy-axis) GMR effect is characterized by an extremely sharp spin flop[7,8] transition of high field sensitivity in the range (typically, for these particular alloys) of 1% to 2%/Oe. A phenomenological model[9] of biquadratic coupling in GMR multilayers has been used to describe the data.

dc magnetron sputtering was used to prepare NiFeCo/Cu multilayers, using high purity argon (99.99%) gas at a base pressure $\leq 3\times10^{-7}$ Torr. Samples were sputtered at a power of 100 W and the argon pressure during sputtering was fixed at 2 mTorr. Corning 7059 glass at ambient temperature was used as the substrate and a permanent magnet (field ~60 Oe) was held behind the glass to induce uniaxial anisotropy. A split target consisting of a 4 in. $Ni_{80}Fe_{20}$ disk, partially covered with a Co foil, was used to sputter the magnetic layer, and an 8 in. Cu target was used for the spacer layer. The thickness of the magnetic and Cu layers was 16 and 23 Å, respectively. Sputtering rates were calculated from thickness measurements of reference films. Multilayer and crystal structure were studied using low and high angle x-ray diffraction (XRD). MR measurements were made using a linear four-point probe method with the current flowing in the film plane and along the induced easy-axis direction. The most widely used definition of GMR is as follows: $\Delta R/R \simeq [R(H)-R(H)_{sat})]/R(H_{sat})$. A vibrating sample magnetometer (VSM) was used for other magnetic characterization.

Eight samples with composition of the magnetic layer varying between $Ni_{67}Fe_{17}Co_{21}$ (sample No. 1) and $Ni_{44}Fe_{11}Co_{45}$ (sample No. 8) were obtained using the split target geometry, which was comprised of a $Ni_{80}Fe_{20}$ 4 in. disk covered partially with a Co foil.[10] Figure 1 shows a typical low and high angle (insert) XRD spectra for these multilayer structures. LXRD shows the first and second order Bragg reflections due the chemical modulation of the sample structure in addition to the intermediate reflections, which indicates good multilayer structure. The high angle XRD shows that the films have (111) texture. A single broad diffraction peak which is slightly shifted from the fcc-Cu (111) d spacing is observed (the film is 60% Cu by volume fraction). Small shifts in d spacing away from bulk values are common in as-deposited multilayers which are likely to be strained.

Figure 2 shows the easy (EA) and hard-axis (HA) hysteresis loops for four different compositions of the magnetic layer. As the Co concentration increases, a canted and/or antiparallel spin alignment starts to develop. This is shown by the arrows in Fig. 2(b). Also, notice the evolution of the "double" hysteresis loop and consequent vanishing of remanence as the composition approaches that of sample No. 6 and its reappearance with any further increase in the Co concentration (sample No. 8). Although the coercivity along the HA increases monotonically from sample No. 1 to No. 8, the EA coercivity and remanence have a minimum for sample No. 6. The length of the exchange coupled region "cd," marked in Fig. 2(c) also increases with Co concentration.

The change in the magnitude of HA and EA GMR and the length of region "cd" are plotted as a function of the sample position (or composition) in Fig. 3. A representative error bar resulting due to the gradient sample composition along the x axis and causing an associated error in the GMR value is marked on sample No. 1 (open circle). The length of the region "cd," which is related to the canted and/or antiparallel spin alignment in the sample is found to scale with the composition of the magnetic layer. Also, as the Co content increases (or from sample No. 1 to No. 8), GMR increases until sample No. 6, whereupon any further increase in Co causes a slight decrease in GMR. The sharp spin transitions [Fig. 2(b)] observed along the EA direction result in an extremely high sensitivity. This is shown in Fig. 4, where the EA GMR for sample No. 5 ($Ni_{58}Fe_{14}Co_{28}$/Cu) along with

 0021-8979/94/76(10)/6522/3/$6.00 © 1994 American Institute of Physics

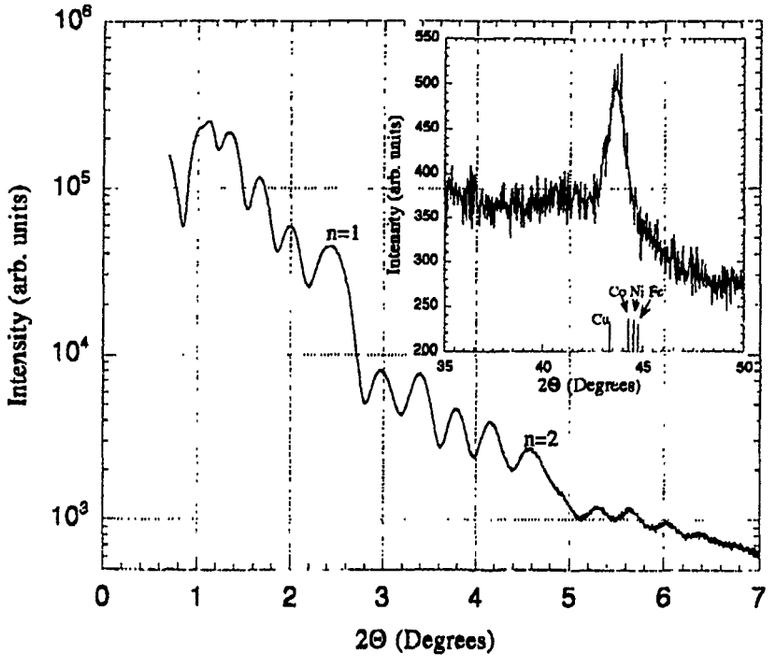

FIG. 1. A typical low- and high-angle XRD pattern of NiFeCo/Cu multilayer sample (No. 3). The relative position of the fcc-Ni (111), bcc-Fe(110), fcc-Co(111), and fcc-Cu(111) diffraction peaks are also marked.

its first derivative or $\Delta R/R$ per unit change in the field is plotted. To our knowledge, 2%/Oe is the highest sensitivity observed in magnetic multilayer or spin valve structures. But it should be pointed out that such a high sensitivity is only observed along the easy axis of the sample and it also features some hysteresis. Figure 5 compares the EA and HA GMR profiles. The HA GMR profile in this figure is typical of all the compositions studied, with a saturation field of 40–50 Oe and sensitivity of about 0.2%/Oe. The smooth variation in the MR along the HA indicates uniform magnetization rotation.

Figure 6 correlates the EA GMR and hysteresis curve profiles. The fields at which a change in the angle between the adjacent magnetic layers (marked with two arrows) takes place is marked by lower case letters *o* through *f* on the hysteresis loop. The corresponding transitions in the GMR loop are marked by the respective capital letters. The observed shape of the longitudinal GMR and hysteresis curve can be explained by considering a two phase magnetic sys-

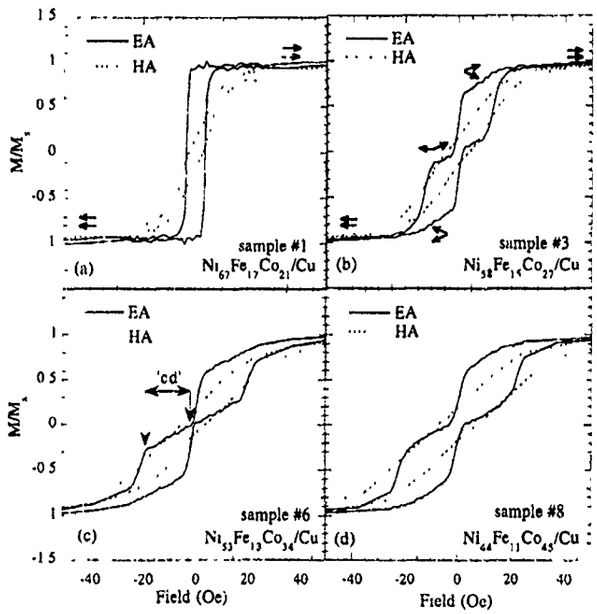

FIG. 2 Hysteresis loop profiles along the easy- and hard-axis directions for different compositions (marked on each figure) of the magnetic layer.

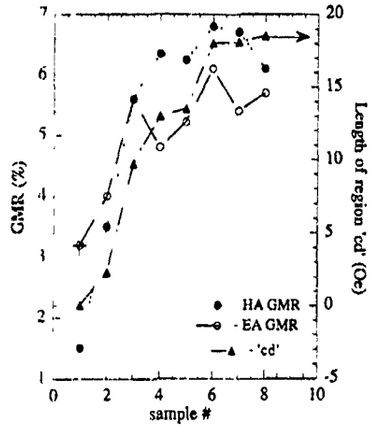

FIG. 3. Change in the magnitude of GMR along the easy and hard axis, and the length of region "*cd*" (defined in Fig. 2), as a function of the sample No. (or composition). The solid and dashed lines are drawn to guide the eye.

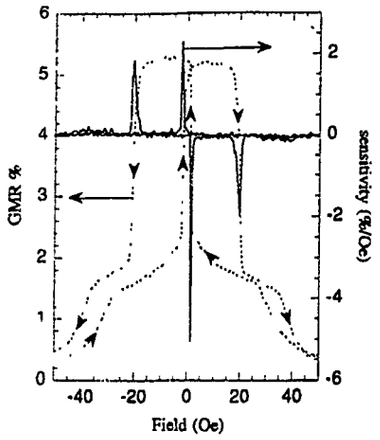

FIG. 4. EA GMR and sensitivity for sample No. 5, $Ni_{54}Fe_{15}Co_{31}$/Cu six bilayers.

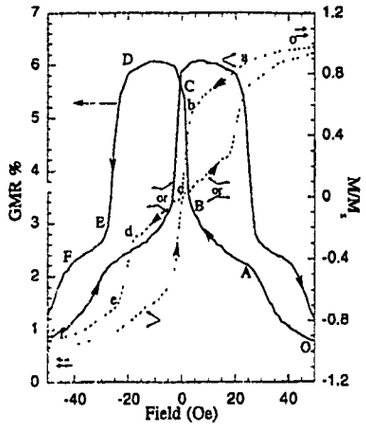

FIG. 6. GMR and hysteresis loop profiles for sample No. 6 ($Ni_{53}Fe_{13}Co_{34}$/Cu), measured along the EA.

tem. The total energy per unit volume of any one of the phases is approximately given[9] by

$$E(\theta_1,\theta_2)=\frac{H_k M}{4}(\sin^2\theta_1+\sin^2\theta_2)+\frac{M}{4}[H_1\cos(\theta_1-\theta_2)+H_2\cos^2(\theta_1-\theta_2)]-\frac{MH}{2}[\cos(\psi-\theta_1)+\cos(\psi-\theta_2)], \quad (1)$$

where θ_1 and θ_2 are the angles between the magnetizations and the easy-axes, depending on whether they are in the odd or even numbered layer, respectively. The angle between the magnetic field and the easy axis is ψ, and H_k, H_1, and H_2 are the effective uniaxial anisotropy, and first- and second-order (biquadratic) exchange fields, respectively. Minimization of the total energy [Eq. (1)] with respect to θ_1 and θ_2 results in a qualitative fit to the observed hysteresis and GMR loop shapes. For samples 2 to 8 this is achieved when the ratios H_k/H_1 and H_2/H_1 are ≥ 0.5. The scaling phenomenon of the length "cd" [in Fig. 2(c)] with the sample composition is ascribed to the increase of the ratio H_k/H_1. The sharp spin flops from b to c, which consequently causes a double hysteresis loop, are also predicted by this model.[9] However, only one magnetic phase described by Eq. (1) cannot explain certain features of the hysteresis and GMR loop shown in Fig. 6, such as the opening of the region o to a and e to f and the corresponding regions of the GMR loop labeled by the capital letters. One way of explaining this is to consider an independent magnetic phase described also by Eq. (1) with an independent set of variables H_k, H_1, and H_2. An overlap of two such phases can simulate the hysteresis and GMR loops observed in this study.

We have shown clearly in as-deposited sputtered NiFeCo/Cu multilayers a sharp, highly distinctive spin-flop transition of extremely high GMR sensitivity (>1%/Oe) along the easy axis. This study has also shown that this switching mechanism can be controlled by varying the Co concentration. A direct observation of the domains or magnetization direction at various fields may prove the presence of the biquadratic coupling and a two phase system as discussed in the text and predicted by theory.

This work has been supported by the National Storage Industry Consortium-Advanced Technology Project heads division program funded by the Department of Commerce.

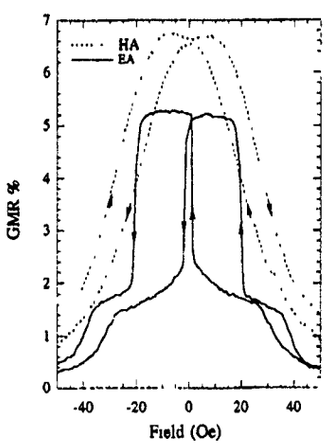

FIG. 5. Comparison of easy- and hard-axis GMR loop profiles for sample No. 5.

[1] G. P. Gerard and B. Rodmacq, IEEE Trans. Magn. **29**, 2732 (1993).
[2] T. L. Hylton, K. R. Coffey, M. A. Parker, and J. K. Howard, Science **261**, 1021 (1993).
[3] B. Dieny, V. S. Speriosu, S. S. P. Parkin, B. A. Gurney, D. R. Wilhoit, and D. Mauri, Phys. Rev. B **43**, 1297 (1991).
[4] M. R. Parker, S. Hossain D. Seale, J. A. Barnard, M. Tan, and H. Fujiwara, IEEE Trans. Magn. **30**, 358 (1994).
[5] S. Hossain, D. Seale, G. Qiu, J. Jarratt, J. A. Barnard, H. Fujiwara, and M. R. Parker, J. Appl. Phys. **75**, 7067 (1994).
[6] M. R. Parker, J. A. Barnard, S. Hossain, J. Yang, M. T. Kief, H. Fujiwara, R. W. Cross, A. B. Kos, S. E. Russek, and S. C. Sanders, Proc. CMPP'93, Dec. 1993, Leeds, UK.
[7] B. Dieny, J. P. Gavigan, and J. P. Rebouillat, J. Phys. **2**, 159 (1990).
[8] S. Hossain (unpublished).
[9] H. Fujiwara and M. R. Parker, J. Magn. Magn. Mater. **135**, L23 (1994).
[10] J. A. Barnard, A. Waknis, M. Tan, E. Haftek, M. R. Parker, and M. L. Watson, J. Magn. Magn. Mater. **114**, 203 (1992).

Multidomain and incomplete alignment effects in giant magnetoresistance trilayers

Y. U. Idzerda
Naval Research Laboratory, Washington, DC 20375

C.-T. Chen
AT&T Bell Laboratories, 600 Mountain Avenue, Murray Hill, New Jersey 07974

S. F. Cheng
Naval Surface Warfare Center, Silver Spring, Maryland 20903

W. Vavra and G. A. Prinz
Naval Research Laboratory, Washington, DC 20375

G. Meigs and H.-J. Lin
AT&T Bell Laboratories, 600 Mountain Avenue, Murray Hill, New Jersey 07974

G. H. Ho
Department of Physics, University of Pennsylvania, Philadelphia, Pennsylvania 19104

The element specific magnetic hysteresis curves of Fe/Cu/Co trilayer structures can be used in conjunction with the measured magnetoresistance curves to extract the coefficient of the giant magnetoresistance (GMR) independent of magnetic domain effects and incomplete alignment effects, allowing for a measure of the maximum attainable GMR for that trilayer. Information concerning the details of the trilayer switching can be extracted showing that sputtered polycrystalline films of Fe/Cu/Co deposited on Si switch their magnetization directions like multidomain Ising magnets.

I. INTRODUCTION

To understand and optimize trilayer and multilayer systems which exhibit giant magnetoresistance (GMR), an appreciable change of the resistance of the multilayer in response to an applied magnetic field, it is important to separate the intrinsic GMR, the maximum achievable change in the resistance, from extrinsic variations to the measured GMR. A clear example of an extrinsic modification to the magnetoresistance is the dependence of the resistance on micromagnetic details of the ferromagnetic film reversal.

The giant magnetoresistance as a function of the applied magnetic field, H, is typically defined as[1]

$$\mathrm{MR}(H)=\frac{R(H)-R(H_s)}{R(H_s)}, \tag{1}$$

where $R(H_s)$ is the film resistance at the saturation field H_s (the field where all ferromagnetic layers are fully aligned with each other). In the absence of anisotropic magnetoresistance, the maximum attainable magnetoresistance for a simple sandwich structure is understood to be the difference between the low resistance state of the sandwich, when the two films are fully aligned (at high field $>H_s$), and the high resistance state when the two films are fully anti-aligned (at low or zero field). For trilayer (sandwich) structures, an ideal switching behavior would result in square magnetic hysteresis loops and GMR curves with abrupt transitions separated by well defined plateau regions.[2] Unfortunately, the majority of reported systems display rounded hysteresis loops and peaks in the GMR curves.[1–3] Since the low resistance aligned film configuration can be achieved by application of a sufficiently large positive or negative magnetic field, the absence of plateaus in the GMR indicate that the fully anti-aligned magnetic film orientation is never achieved. Instead, during the moment reversal process, before the first ferromagnetic film has completely switched its magnetic orientation (establishing the anti-aligned state), the second magnetic film has already begun to reverse its moment direction.

There have been a large number of comparative studies which have attempted to determine variations of the intrinsic GMR on material and interface parameters (including magnetic layer and interlayer composition, layer thicknesses, and film and interface quality). Unfortunately, modifying these parameters may also dramatically affect the details of the film reversal process including the degree to which the two films are not completely anti-aligned. Any comparative studies of the GMR must first correct for, or eliminate these incomplete anti-alignment effects. To this end, we have developed a method to extract the coefficient of GMR, the maximum achievable GMR, from the nonideal magnetoresistance data, provided that the details of the magnetization reversal process of the two ferromagnetic films is known. For simplicity, we will consider only two models for the magnetization reversal process—the single domain xy model and the multidomain Ising model.

II. SINGLE DOMAIN *xy* MODEL

The single domain xy model treats each ferromagnetic film as a single magnetic domain with a constant total moment which can point in any direction in the film plane, but must remain in the film plane. The magnetization reversal is therefore accomplished by an in-plane rotation of the moment direction. Since magnetometry measures the projection of the magnetic moment along an analysis direction, typically coincident with the applied field direction, the mea-

 0021-8979/94/76(10)/6525/3/$6.00 © 1994 American Institute of Physics

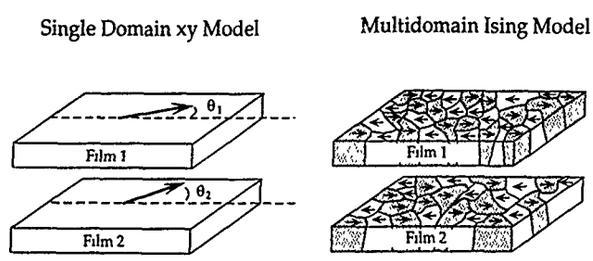

FIG. 1. Models for the magnetization reversal.

sured hysteresis loop can be used to determine the angle, θ, that the moment makes with the applied field direction

$$M_{xy}(H)=M_0\cos[\theta(H)], \tag{2}$$

where M_0 is the constant magnitude of the film magnetization vector.

If independent hysteresis loops of each of the magnetic films can be obtained, then a determination of the relative angles of both films as a function of applied field, and therefore the angle between the two magnetic films, can be made (a schematic of the two films is shown in the left-hand panel of Fig. 1). From the relative angles of each film, we can determine the magnetoresistance, given by[4,5]

$$\mathrm{MR}_{xy}(H)=G\sin^2\frac{\Delta\theta(H)}{2}=G\sin^2\left(\frac{\theta_1(H)-\theta_2(H)}{2}\right), \tag{3}$$

where G is the coefficient of the GMR and $\Delta\theta$ is the angle between the magnetic moments of the two single domain films. From the measured hysteresis curves of the two magnetic layers, we can then calculate the form of the magnetoresistance curve. By comparing this curve with the measured hysteresis curve, we can extract a value for G, the coefficient of magnetoresistance, which corresponds to the maximum achievable magnetoresistance.

III. MULTIDOMAIN ISING MODEL

The multidomain Ising model treats each magnetic film as if it were composed of many magnetic domains, each allowed to be oriented along with or opposed to the applied field direction. Now the magnetization reversal is accomplished through the abrupt magnetization reversal of the separate domains. The hysteresis loops, which reflect the net moment, are a measure of the fraction of the film pointing along the applied field

$$M_{\mathrm{Ising}}(H)=M_0[f^{\uparrow}(H)-f^{\downarrow}(H)], \tag{4}$$

where M_0 is the maximum moment and $f^{\uparrow}(f^{\downarrow})$ is the fraction of the film pointing along (opposed to) the field. For two magnetic layers, if the moment direction of domains in the two films are uncorrelated (i.e., the direction of the moment of a domain in one film is independent of the direction of the moment in a domain of the other film), then the measurements of the two independent hysteresis loops can be used to determine what fraction of the films are aligned and anti-aligned with each other. (A schematic of this model is shown in the right-hand panel of Fig. 1.)

In the simplest view, there are only two domain configurations which contribute to the overall resistivity, when the current flows between two domains of opposite orientation or between two domains of aligned orientation. Because these two configurations represent two well defined resistance states in parallel with each other, then if the domains are large compared to the mean spin scattering length[6] and if we ignore the additional resistivity associated with current flow between domains within the same magnetic layer (which would also depend on the distribution of domain sizes and domain configurations), then the total film resistance is just given by

$$R_T(H)=\frac{R_A}{f_A(H)}\|\frac{R_P}{f_P(H)}=\frac{R_AR_P}{R_Af_P-R_Pf_A}, \tag{5}$$

where $R_P(R_A)$ is the resistance of the film in the completely aligned (anti-aligned) configuration and $f_P(f_A)$ is the fraction of the film in the aligned (anti-aligned) state. The magnetoresistance can be expressed as (noting $f_P+f_A=1$)

$$\mathrm{MR}_{\mathrm{Ising}}(H)=\frac{R(H)-R_P}{R_P}=G\frac{f_A}{f_A+(R_A/R_P)f_P}, \tag{6}$$

where $G=(R_A-R_P)/R_P$. If $R_A\sim R_P$ (i.e., G is small) then

$$\mathrm{MR}_{\mathrm{Ising}}(H)\sim Gf_A=G[f_1^{\uparrow}(H)f_2^{\downarrow}(H)+f_1^{\downarrow}(H)f_2^{\uparrow}(H)], \tag{7}$$

where the term in the brackets is the fraction of the two films which are anti-aligned (in the absence of domain correlation).

IV. INDEPENDENT HYSTERESIS LOOPS

The major difficulty is of course in determining independently the hysteresis loops of the two magnetic films. Most magnetometry techniques determine the total hysteretic behavior of the system. Recently, we have developed a method to determine element-specific hysteresis loops of heteromagnetic materials.[7] By recording the absorption intensity of circularly polarized soft x-rays at each transition metal L_3 absorption edge as a function of applied field, the hysteretic behavior of each magnetic element in a compound or multilayer structure can be determined using magnetic circular dichroism (MCD).[8–12] In this way, the complicated conventional hysteresis curves can be resolved as a linear combination of simple elemental hysteresis curves. In the case of a multilayer system with different magnetic elements in each ferromagnetic layer, the separate element-specific magnetic hysteresis (ESMH) curves are now equivalent to the hysteretic behavior of the individual ferromagnetic layers.

To demonstrate this, an Fe/Cu/Co trilayer structure, known to exhibit a reasonable GMR effect,[13] was sputter deposited onto a Si(100) surface which was chemically degreased prior to the deposition. The multilayer film consists of 50 Å Fe film and a 50 Å Co film separated by 50 Å of Cu and capped with an additional 30 Å of Cu to prevent oxidation. The films were deposited in an argon gas of $\sim 3\times10^{-3}$ Torr at a rate of a few angstroms per second. X-ray absorption spectroscopy measurements showed that no oxidation of the buried Fe or Co layers has occurred. Details of the MCD setup have been described previously.[14,15]

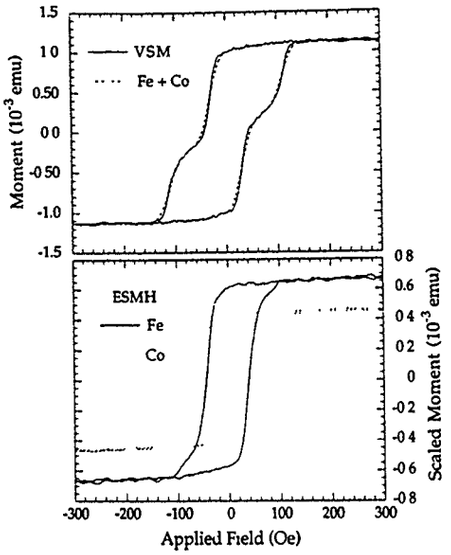

FIG. 2. Top panel: conventional total moment VSM hysteresis loop (solid line) and the summed element specific magnetic hysteresis loops for Fe and Co (dotted line). Bottom panel: ESMH loops for Fe and Co. The scaling values were determined by a best-fit of the summed data to the VSM data.

The conventional, total magnetic hysteresis behavior of this trilayer is shown in the top panel of Fig. 2. This hysteresis loop shows rounded transitions and is characteristic of non-ideal switching behavior. In the bottom panel are the scaled ESMH loops for Fe and Co. The weighting factors were determined by a least-squares-best fit of the summed data to the VSM data. These weighting factors, included in the ESMH loops of the lower panel of Fig. 2, give good agreement between the VSM spectra and the summed spectra, displayed as the dotted line in the top panel of Fig. 2. The differences in the spectra are attributed to film inhomogeneity and the different analyzed areas of the two magnetometry techniques.

From these elemental hysteresis loops, we can calculate the GMR curves for the single domain xy model and the multidomain Ising model. By comparing to the measured GMR curves (shown scaled to be aligned at the peaks in Fig. 3), not only are we able to extract a value for the coefficient of magnetoresistance, but we can differentiate which model is applicable to our multilayer. The two vertical axes are displayed in normalized MR values (MR/G) and vividly demonstrate the effects of the incomplete alignment. It is clear from these spectra that these films are best described by a multidomain Ising model (which is consistent with the polycrystalline nature of these films). From the value of the maximum measured GMR of 2.1% (corresponding to the peaks in the measured data in Fig. 3), we can extract a coefficient of GMR of 0.031 (3.1%), an increase of almost 50%. It is interesting to note that had the single domain xy model been the applicable description of the magnetization reversal, the extracted coefficient of GMR would be 0.068

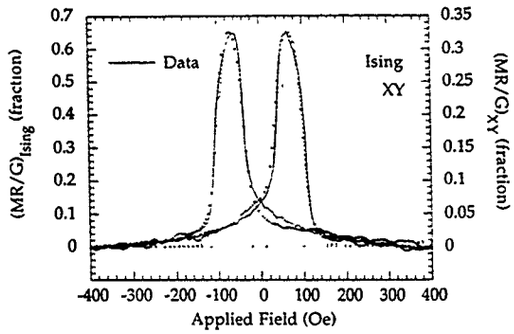

FIG. 3. Comparison of the measured magnetoresistance data (solid line) to the multidomain Ising model (dotted line) and the single domain xy model (dashed line). The coordinates are normalized values for the calculated spectra and the measured data is arbitrarily scaled to fit.

(6.8%) an increase of 200%! (The anisotropic magnetoresistance for this film is measured to be 0.4%.)

In summary, we have shown that in nonideal systems with peaked magnetoresistance curves and rounded hysteresis loops, the maximum measured GMR is reduced from the maximum attainable value by multidomain and incomplete alignment effects. We have also used ESMH measurements, in conjunction with the measured magnetoresistance curves, to extract the coefficient of GMR. In any comparative study of the GMR, it is this larger extracted coefficient which should be used.

ACKNOWLEDGMENTS

This research is supported by the Office of Naval Research. Work done at the National Synchrotron Light Source was supported by DOE, under Contract No. DE-AC02-76CH00016.

[1] W. P. Pratt, Jr., S.-F. Lee, J. M. Slaughter, R. Loloee, P. A. Schroeder, and J. Bass, Phys. Rev. Lett. **66**, 3060 (1991).
[2] A Chaiken, C. J. Gutierrez, J. J. Krebs, and G. A. Prinz, J. Magn. Magn. Mater. **125**, 228 (1993)
[3] For many examples, see, J. Appl. Phys. **73**, 5506 (1993).
[4] B. Dieny, P. Humbert, V. S. Speriosu, S. Metin, B. A. Gurney, P. Baumgart, and H. Lefakis, Phys. Rev. B **45**, 806 (1992).
[5] A. Chaiken, G. A. Prinz, and J. J. Krebs, J. Appl. Phys. **67**, 4892 (1990).
[6] The effect of small domains has been addressed by S. Zhang and P. Levy (private communication).
[7] C. T. Chen, Y. U. Idzerda, H.-J. Lin, G. Meigs, A. Chaiken, G. A. Prinz, and G. H. Ho, Phys. Rev. B **48**, 642 (1993).
[8] L. H. Tjeng, Y. U. Idzerda, P. Rudolf, F. Sette, and C. T. Chen, J. Magn. Magn. Mater. **109**, 288 (1992).
[9] J. G. Tobin, G. D. Waddill, and D. F. Pappas, Phys. Rev. Lett. **68**, 3642 (1992).
[10] Y. Wu, J. Stohr, B. D. Hermsmeier, M. G. Samant, and D. Weller, Phys. Rev. Lett. **69**, 2307 (1992).
[11] Y. U. Idzerda, L.-H. Tjeng, H.-J. Lin, C. J. Gutierrez, G. Meigs, and C. T. Chen, Phys. Rev. B. **48**, 4144 (1993).
[12] Y. U. Idzerda, C. J. Gutierrez, L.-H. Tjeng, H.-J. Lin, G. Meigs, and C. T. Chen, J. Magn. Magn. Mater. **127**. 109 (1993).
[13] A. Chaiken, P. Lubitz, J. J. Krebs, G. A. Prinz, and M. Z. Harford, Appl. Phys. Lett. **59**, 240 (1991).
[14] C. T. Chen, F. Sette, Y. Ma, and S. Modesti, Phys. Rev. B **42**, 7262 (1990): C. T. Chen, N. V. Smith, and F. Sette, *ibid.* **43**, 6785 (1991).
[15] C. T. Chen, Nucl. Instrum. Methods Phys. Rev. Sec. A **256**, 595 (1987); C. T. Chen, N. V. Smith, and F. Sette, Rev. Sci. Instrum. **60**, 1616 (1989); C. T. Chen, *ibid.* **63**, 1229 (1993).

Interface alloying and magnetic properties of Fe/Rh multilayers

K. Hanisch, W. Keune, R. A. Brand, C. Binek, and W. Kleemann
Laboratorium für Angewandte Physik, Universität Duisburg, D-47048 Duisburg, Germany

Rh(20 Å)/^{57}Fe(t_{Fe}) multilayers with Fe thicknesses t_{Fe} of 2, 5, 10, and 15 Å prepared by alternate evaporation in UHV have been investigated by x-ray diffraction (XRD), Mössbauer spectroscopy, and SQUID magnetometry. First- and second-order superstructure Bragg peaks (but no higher-order peaks) in small-angle XRD patterns suggest some compositional modulation. Mössbauer spectra taken at 4.2 K are characterized by a distribution $P(B_{hf})$ of hyperfine fields B_{hf}. Peaks observed in the $P(B_{hf})$ curves near 17 and 35 T are assigned to an fcc-RhFe interface alloy (~7–24 at. % Fe) with spin-glasslike properties and to a disordered ferromagnetic bcc-FeRh alloy (~96 at. % Fe), respectively. The magnetic transition temperature of the fcc alloy was found to be 23 and 45 K for t_{Fe}=2 and 5 Å, respectively, and B_{hf} follows a $T^{3/2}$ law. For t_{Fe}=2 Å, spin-glasslike behavior was observed by magnetometry.

Metallic multilayered films offer an exciting field for the exploration of magnetic properties in novel systems and at interfaces.[1] In a search for new multilayers with interesting magnetic behavior we have studied the Fe-Rh system. According to the thermodynamic Fe-Rh phase diagram[2] a wide solubility range exists at rather low temperatures on both the Fe-rich and Rh-rich side. Therefore, a tendency for interface-alloy formation may be expected in these multilayers. The properties of Fe/Rh interfaces are unknown so far.

We have prepared a series of Rh/Fe multilayers with constant Rh thickness (20 Å) by alternating evaporation of Rh and ^{57}Fe isotope (95% enriched) in an UHV system. The pressure during evaporation was $<5\times10^{-9}$ mbar. The substrates were polyimid foils for Mössbauer and magnetometric studies and Si wafers for small- and large-angle x-ray diffraction (XRD). To reduce intermixing, the substrate temperature was held at ~100 K during multilayer growth. Rh and ^{57}Fe were evaporated from a 2-kW electron-beam gun and a small resistively heated evaporation cell with alumina crucible, respectively. Four different types of multilayers have been prepared, namely [Rh(20 Å)/^{57}Fe(2 Å)]$_{100}$+Rh(20 Å), [Rh(20 Å)/^{57}Fe(5 Å)]$_{52}$+Rh(20 Å), [Rh(20 Å)/^{57}Fe(10 Å)]$_{30}$+Rh(20 Å), and [Rh(20 Å)/Fe(15 Å)]$_{20}$+Rh(20 Å). (All samples were coated by 20 Å Rh for protection.)

The small-angle XRD patterns (Fig. 1) exhibit a clear first-order superstructure Bragg peak for all samples, and an additional second-order peak for t_{Fe}=10 and 15 Å. This and the fact that no higher-order superstructure peaks have been detected (not shown in Fig. 1) demonstrates qualitatively that our samples are compositionally modulated structures with some degree of intermixing at the interfaces. The multilayer periodicity determined from Fig. 1 is 23.7, 24.9, 29.7, and 37.7 Å for t_{Fe}=2, 5, 10, and 15 Å, respectively, being in agreement with the nominal periodicity within 7% or better. The large-angle XRD patterns from our samples (not shown) exhibit a dominant fcc Rh(111)-Bragg peak and weaker peaks from higher-indexed Rh planes. However, the Rh peaks were found to be shifted slightly to higher Bragg angles upon increase of t_{Fe}, implying a fcc-lattice parameter (a_0) reduction with increasing Fe-film thickness from a_0=3.808 Å (pure Rh film) to 3.793, 3.780, 3.738, and 3.713 Å for t_{Fe}=2, 5, 10, and 15 Å, respectively. No pure bcc-Fe Bragg peaks could be detected. However, a shoulder (near $2\theta\approx40°$) on the low-angle side of the Rh(111) peak observed for the thicker Fe films (10 and 15 Å) may be assigned to a bcc (110) reflex with a corresponding bcc-lattice parameter which is enhanced (relative to that of pure bcc Fe) by 11.4% (for t_{Fe}=10 Å) and 10.0% (for t_{Fe}=15 Å). In view of the small-angle XRD and Mössbauer results (below) the observed reduction or increase in lattice parameter is interpreted by the main effect of interface-fcc-alloy formation or bcc-alloy formation, respectively. For fcc Fe-Rh alloys, our interpretation is qualitatively supported by the known decrease of a_0 with rising Fe content in the bulk.[3]

Mössbauer spectra measured at 4.2 K (Fig. 2) indicate magnetic hyperfine (hf) splitting at all Fe thicknesses. These spectra were least-squares fitted using a histogram distribution,[4] $P(B_{hf})$, of hyperfine fields B_{hf}. It was found necessary to include a small linear correlation between isomer shift δ and B_{hf}, given by about +0.004 mm s^{-1}/T.

For t_{Fe}=2 Å, the most-probable (peak) hf field, B_{hf}^{peak}, has a value of 16.8 T (Fig. 2) which is typical for that of a ~7 at. % Fe disordered fcc-Fe-Rh bulk alloy at 4.2 K.[5] This

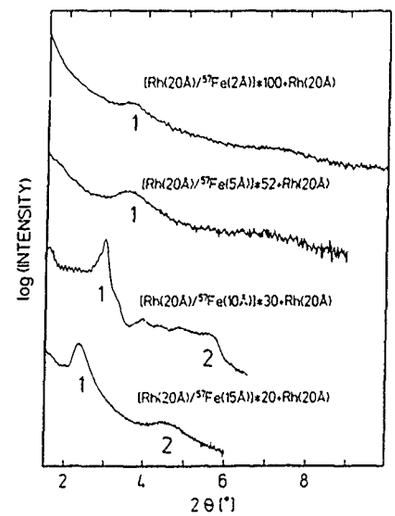

FIG. 1. Small-angle XRD patterns of Rh(20 Å)/^{57}Fe(t_{Fe}) multilayers with t_{Fe}=2, 5, 10, and 15 Å (from top) (Cu $K\alpha$ radiation).

 0021-8979/94/76(10)/6528/3/$6.00 © 1994 American Institute of Physics

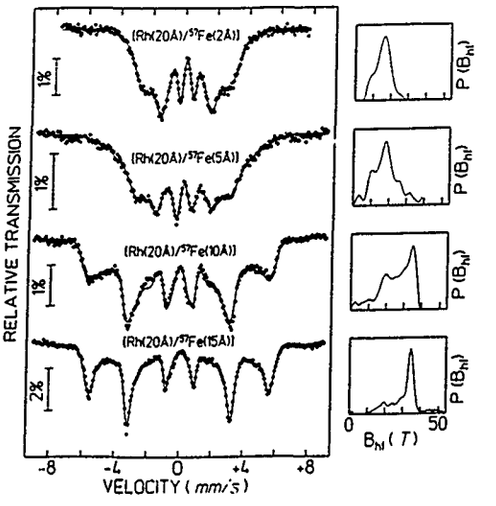

FIG. 2. Mössbauer spectra measured at 4.2 K and distributions $P(B_{hf})$ of Rh(20 Å)/^{57}Fe(t_{Fe}) multilayers for t_{Fe}=2, 5, 10, and 15 Å (from top).

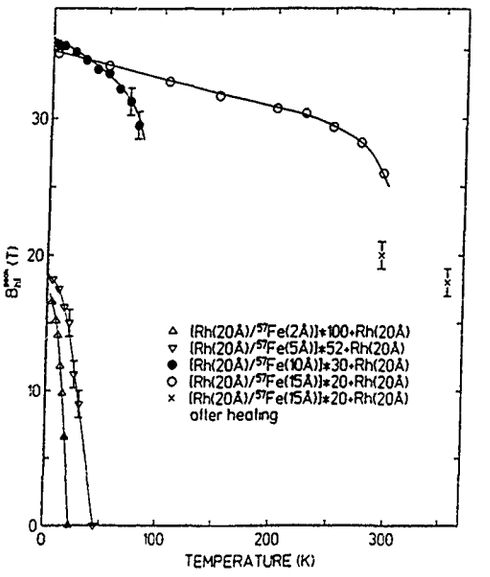

FIG. 3. Temperature dependence of B_{hf}^{peak} for t_{Fe}=2 Å (△), 5 Å (▽), 10 Å (●) and 15 Å (○). Crosses (×): for t_{Fe}=15 Å after annealing at 355 K.

suggests that the 2 Å ^{57}Fe film [~1 monolayer (ML) bcc Fe(110)] is completely alloyed with Rh resulting in an fcc-Fe-Rh alloy of average Fe concentration $c_{Fe}^{B_{hf}}$ of ~7 at. %. In the case of t_{Fe}=5 Å, $P(B_{hf})$ in Fig. 2 shows a pronounced peak at 18.2 T which demonstrates that this is also a pure fcc-RhFe multilayer. This hf field corresponds to $c_{Fe}^{B_{hf}}$ ~ 19 at. %, according to Ref. 5. We have also estimated the Fe concentration ($c_{Fe}^{a_0}$) in the fcc-alloy layer by comparing the measured lattice parameters (a_0) with those of bulk alloys.[3] Table I shows that $c_{Fe}^{a_0}$ values for 2 and 5 Å Fe are in rough agreement with corresponding $c_{Fe}^{B_{hf}}$ values. The calculated Rh thicknesses, $t_{Rh}^{fcc\ alloy}$, required for explaining the obtained $c_{Fe}^{B_{hf}}$ or $c_{Fe}^{a_0}$ values are given in Table I, too. (It was assumed that t_{Fe}=2 and 5 Å are completely alloyed). The $t_{Rh}^{fcc\ alloy}$ values obtained from $c_{Fe}^{B_{hf}}$ appear somewhat too large as compared to the deposited 20 Å-Rh layer, while those values deduced from $c_{Fe}^{a_0}$ appear to be reasonable. Table I indicates also the Fe concentration ($c_{Fe}^{T_f}$) obtained by comparing the measured (average) magnetic transition temperature T_f of our films (T_f=23±4 K for t_{Fe}=2 Å and T_f=45±7 K for t_{Fe}=5 Å, respectively, see Fig. 3) with the T_f vs c_{Fe} behavior of disordered fcc-RhFe alloys;[5] however, the corresponding (calculated) $t_{Rh}^{fcc\ alloy}$ values (Table I) are unreasonably high (e.g., 34 Å for t_{Fe}=5 Å). This very likely indicates that the T_f vs c_{Fe} behavior in ultrathin RhFe alloy layers deviates from that in bulk alloys as is the case for other spin glasses.[6] From the Mössbauer-line-intensity ratios the Fe-spin orientation in these samples was found to be nearly random which can be expected for spin-glass-type magnetism where a magnetic shape anisotropy is absent.

TABLE I. Estimated Fe concentrations $c_{Fe}^{T_f}$, $c_{Fe}^{B_{hf}}$ and $c_{Fe}^{a_0}$ of the fcc and bcc Rh–Fe alloy phase in Rh/Fe multilayers. $t_{Rh}^{fcc\ alloy}$ is the calculated Rh thickness consumed in fcc-alloy formation.

Rh(20 Å)/Fe(t_{Fe})	t_{Fe}=2 Å	t_{Fe}=5 Å	t_{Fe}=10 Å	t_{Fe}=15 Å
fcc phase				
$c_{Fe}^{T_f}$/at. %	7	12	24	...
($t_{Rh}^{fcc\ alloy}$)	(25 Å?)	(34 Å?)	(9.4 Å?)	...
$c_{Fe}^{B_{hf}}$/at. %	~7	~19	>25	>25
($t_{Rh}^{fcc\ alloy}$)	(25 Å?)	(20 Å?)	...	...
$c_{Fe}^{a_0}$/at. %	10	24	50	62
($t_{Rh}^{fcc\ alloy}$)	(17 Å)	(14.3 Å)	(3.0 Å)	(1.2 Å)
bcc phase				
$c_{Fe}^{B_{hf}}$/at. %	...	...	~96	~96

One can notice in Fig. 2 that the $P(B_{hf})$ curves (and the spectra) change drastically with increasing Fe thickness: the fcc-alloy distribution peak near ~17 T decreases gradually in relative intensity and shifts to slightly higher values, while simultaneously a new peak near 36 T (35 T) evolves and dominates at t_{Fe}=10 Å (or t_{Fe}=15 Å). This new peak is assigned to a disordered ferromagnetic bcc-Fe-Rh alloy. This follows from a comparison of our B_{hf}^{peak} values with those of Fe-rich disordered bcc-Fe-Rh bulk alloys.[7] We may estimate the average composition c_{Fe} of the bcc alloy in our multilayers by using the B_{hf} vs c_{Fe} curve in Ref. 7 (with B_{hf} in Ref. 7 corrected by a factor of 1.03 for the low temperature (4.2 K) used in our case). This leads to c_{Fe} ~96 at. % for t_{Fe}=10 and 15 Å in the bcc alloy (Table I).

The shape of the distribution $P(B_{hf})$ for t_{Fe}=10 Å (Fig. 2) demonstrates that fcc and bcc alloy phases coexist in this multilayer, (with the fcc-alloy distribution peak located at 19.8 T). Even for t_{Fe}=15 Å, the fcc-alloy distribution peak (at 20.0 T) is still present, together with a low-field distribution part (for B_{hf}<28 T). The relative area of the low-field or high-field (B_{hf}>28 T) distribution part provides values for the relative phase content (fcc or bcc) in the multilayer. In the case of t_{Fe}=10 Å we find that (36±15)% of the Fe atoms form the fcc-interface alloy (and 64% the bcc phase); for

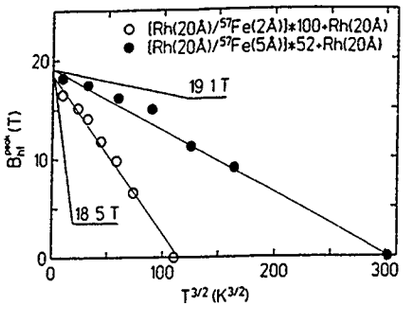

FIG. 4. B_{hf}^{peak} vs $T^{3/2}$ for t_{Fe}=2 Å (○) and 5 Å (●).

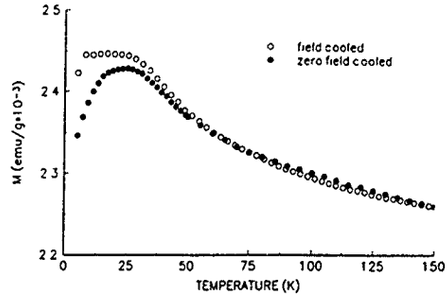

FIG. 5. Temperature dependence of magnetization in a Rh(20 Å)/^{57}Fe(2 Å) multilayer measured in B_{ext}=0.5 T, zero-field cooled (●) and field cooled (○).

t_{Fe}=15 Å, the corresponding values are (30±5)% (fcc) and 70% (bcc). This means that in the average a thickness of 3.6 Å Fe of the original 10 Å bcc-Fe layer is transformed to the fcc-interface alloy by interdiffusion; for the 15 Å Fe film, the corresponding value is 4.5 Å Fe. The Fe-spin direction of the bcc phase was observed to be preferentially oriented in the film plane indicating a shape anisotropy due to ferromagnetism.

It follows from the temperature dependence of B_{hf}^{peak} (Fig. 3) that the magnetic transition temperatures of the bcc phase (in multilayers with t_{Fe}=10 and 15 Å) are much higher than those of the fcc phase (with t_{Fe}=2 and 5 Å). For t_{Fe}=2 and 5 Å, $B_{hf}^{peak}(T)$ follows closely a $T^{3/2}$-spin wave law over the whole temperature range (Fig. 4). For t_{Fe}=15 Å, B_{hf}^{peak} shows a remarkable linear T dependence over a wide T range. It has been suggested that such a behavior is related to superparamagnetic relaxation of bcc-phase clusters.[8] However, as we have not observed a remarkable change at 150 K in the central component of the spectrum (not shown) even by applying fields up to 1 T, we may exclude superparamagnetism. Therefore, the linear T dependence observed can be explained by quasi-two-dimensional behavior of the bcc phase in the 15-Å sample, as predicted theoretically.[9] In contrast, the t_{Fe}=10 Å multilayer has been observed to be superparamagnetic by applying a magnetic field. After a measurement at 355 K and recooling to 295 K, an irreversible drop of B_{hf}^{peak} at 295 K occured. As we did not observe a change in $P(B_{hf})$ at 4.2 K after annealing, this drop in B_{hf}^{peak} could be due to a change in bcc Fe-film morphology (island formation) and a resulting change in the T dependence of B_{hf}^{peak} (possibly due to superparamagnetism).

The temperature dependence of the magnetization in the multilayer with t_{Fe}=2 Å (Fig. 5) indicates typical spin-glasslike behavior, i.e., different branches after zero-field cooling and during field cooling. It can be seen that the temperature of the maximum in the zero-field cooled magnetization (23±2 K) is in very good agreement with the magnetic transition temperature obtained from Mössbauer spectroscopy. This proves that interface fcc alloys with spin-glasslike properties can be obtained in Rh/Fe multilayers.

We are grateful to U. von Hörsten for technical assistance and sample preparation. This work was supported by the DFG (SFB166).

[1] For an overview of recent work, see Proceedings of the First International Symposium on Metallic Multilayers, Kyoto, Japan, 1993 [J. Magn. Magn. Mater **126** (1993)].
[2] O. Kubaschewski, *Iron Binary Phase Diagrams* (Springer, Berlin, 1992).
[3] C. C. Chao, P. Duwez, and C. C. Tsuei, J. Appl. Phys. **42**, 4282 (1971).
[4] J. Hesse and A. Rübartsch, J. Phys E **7**, 526 (1974).
[5] B. Window, G. Longworth, and C. E. Johnson, J. Phys. C **3**, 2156 (1970).
[6] H. Vloeberghs *et al.*, Europhys. Lett. **12**, 557 (1990).
[7] G. Shirane, C. W. Chen, P. A. Flinn, and R. Nathans, J. Appl. Phys. **34**, 1044 (1963).
[8] Z. Q. Qiu, S. H. Mayer, C. J. Gutierrez, H. Tang, and J. C. Walker, Phys. Rev. Lett. **63**, 1649 (1989).
[9] J. C. Levy and J. L. Motchane, J. Vac. Sci. Technol. **9**, 721 (1971), J. A. Davis, J. Appl. Phys. **36**, 3520 (1965).

Heat treatment to control the coercivity of Pt/Co multilayers

J. Miller, P. G. Pitcher, and D. P. A. Pearson
Johnson Matthey Tech. Center, Sonning Common, Reading RG4 9NH, United Kingdom

We report on controlled changes in the coercivity of sputter deposited Pt/Co multilayer films by thermal treatment under controlled atmospheres. The as-sputtered coercivities of typically 3.3 kOe can be increased to 10.5 kOe by annealing in air, however for coercivities greater than 6 kOe the rectangular ratio of the multilayer decreases with increasing coercivity. The loop shape can be regained and the coercivity decreased by annealing in a H_2/N_2 atmosphere.

I. INTRODUCTION

Pt/Co multilayers are a promising candidate for the next generation of magneto-optical recording material.[1,2] These multilayers have been found to have large polar Kerr rotations and coercivities in both evaporated and sputtered films.[3,4]

In this article we report on the effect on annealing in controlled atmospheres on the coercivity of sputtered Pt/Co multilayers.

II. EXPERIMENT

Pt/Co multilayers were magnetron sputtered using dual source deposition in an Ar atmosphere onto glass substrates. The multilayers all consisted of 9.5 periods of 8 Å Pt/3 Å Co (the Pt layer was deposited first and last). Pt/Co individual layer thicknesses were confirmed using x-ray diffraction and inductively coupled plasma emission spectrometry.

The magnetic and magneto-optical properties of the multilayers were examined using a polar Kerr loop plotter and a vibrating sample magnetometer (VSM), the maximum applied field was 8 kOe so VSM measurements could not be done on the higher coercivity samples. The multilayer microstructure was examined using x-ray diffraction (XRD) and transmission electron microscopy (TEM).

A post-deposition anneal was performed on the multilayers, the atmosphere was either air or 10% H_2 in N_2, the annealing temperature was varied between 100 and 400 °C. The air annealed multilayers were heated by placing on a heater block at the required temperature. The transition from room temperature to the anneal temperature was achieved in under 2 min. Samples were cooled to room temperature by placing them on a large aluminum block. Cooling took less than a minute. The multilayers annealed in H_2/N_2 atmospheres typically reached the anneal temperature in under 5 min and were force cooled reaching room temperature in under 5 min.

III. RESULTS AND DISCUSSION

The as-sputtered multilayers typically had coercivities of 3.3 kOe and hysteresis loops with a high rectangular ratio $r(=H_n/H_c)$, as shown in Fig. 1(a). The coercivity was found to increase on heating the multilayer in an atmosphere containing oxygen. Figures 1(b)–1(d) show the room temperature polar Kerr hysteresis loops obtained after the multilayers had been heated in air to 200 °C for 2, 8, and 240 min. Initially both the coercivity (H_c) and the nucleation field (H_n) increase with annealing time and the hysteresis loops maintain a high rectangular ratio (r), however the H_n reaches a maximum at 6.2 kOe while the H_c continues to increase to a maximum of 10.5 kOe (Fig. 2) resulting in a skewing of the hysteresis loop. The H_c increase could be reversed and the loop's original rectangular ratio regained by heating in a reducing atmosphere of 10% H_2/90% N_2. An as-sputtered multilayer had its coercivity increased from 3.3 to 8.2 kOe by heating in air to 160 and 185 °C for 20 and 27 min, respectively. The before and after polar Kerr loops being almost identical to those of Figs. 1(a) and 1(c). The coercivity was then reduced from 8.2 to 3.3 kOe and the original loop shape regained by heating for 30 min at 185 °C in a 10% H_2/90% N_2 gas mix.

The mechanism for the coercivity increase is thought to be related to oxygen incorporation into the film structure. Coercivity increases after annealing the sample in air[5,6] and also in vacuum have previously been reported.[7] Yamane *et al.*[8] obtained increases from 0.2 to 2 kOe in the coercivity of sputtered Pt/Co multilayers with a 500 Å Pt capping film. They concluded from similar work with thicker Pd/Co multilayer films that oxygen incorporation at the grain boundaries of the columnar microstructure caused domain wall binding resulting in the increase in the multilayer coercivity.[5] The reversible nature of the coercivity in a reducing atmosphere suggests a similar mechanism causes the coercivity increases observed in our films. The saturation

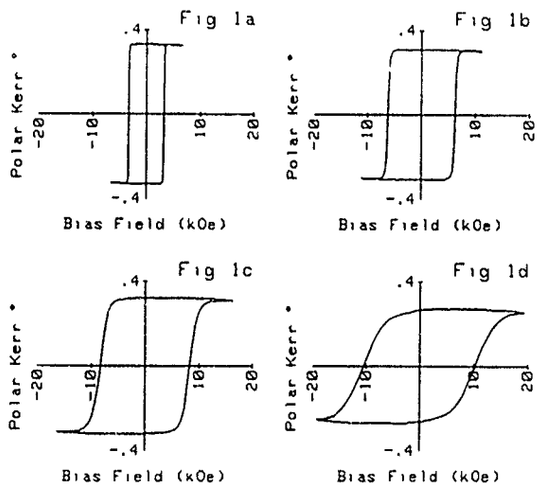

FIG. 1. Polar Kerr loops of Pt/Co multilayers after annealing at 200 °C, (a) as-sputtered, (b) 2 min, (c) 8 min, (d) 240 min.

 0021-8979/94/76(10)/6531/3/$6.00 © 1994 American Institute of Physics

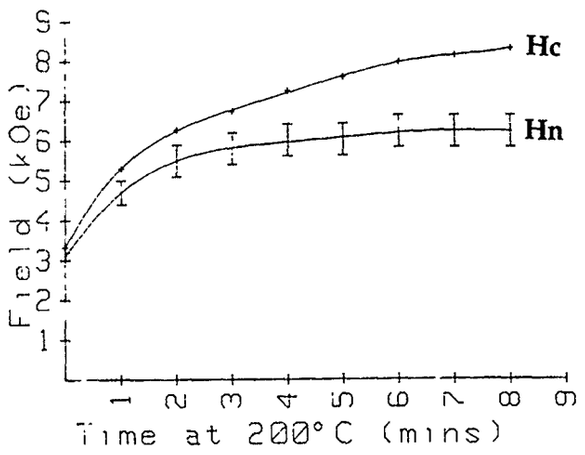

FIG. 2. Coercivity and nucleation variation with anneal time at 200 °C.

magnetization of our multilayers decreased as the multilayer coercivity increased from 3 to 6 kOe, this further suggests cobalt oxide formation as the cause of the increased coercivity.

A bright field TEM image of an as-sputtered multilayer is shown in Fig. 3. The multilayers are polycrystalline with a grain size of approximately 10 nm.

To examine the effect of the coercivity increase on the magnetization reversal mechanism initial magnetization curves were examined. A set of multilayers was demagnetized by heating to 400 °C for 15 s, the dwell time had to be short to avoid damaging the multilayer structure. Hashimoto *et al.*[1] have previously found that a 30 min anneal at 400 °C resulted in loss of perpendicular magnetic anisotropy and multilayer structure. However XRD measurements of our demagnetized multilayers showed that the satellite peaks of the multilayers were unchanged after thermal demagnetization. Figure 4 shows the initial magnetization curves for these multilayers. In Figs. 4(a)–4(c) the coercivity is a result of the difficulty in creating a reversed domain, since the magnetization initially increases from the demagnetized state at

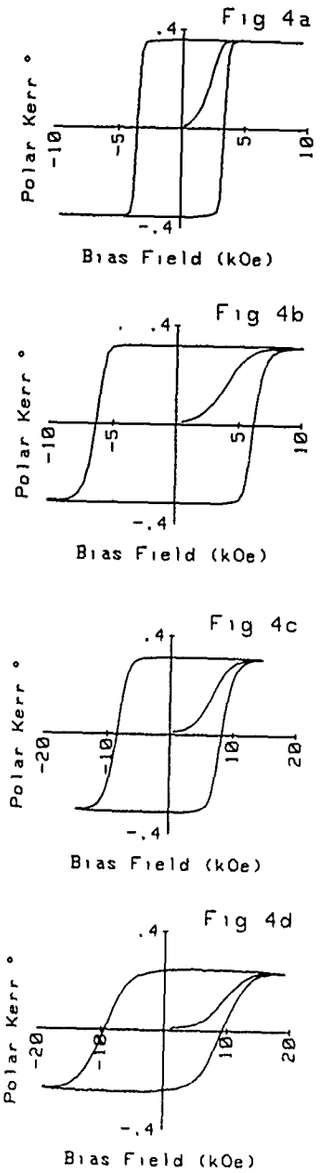

FIG. 4. Initial magnetization curves of thermally demagnetized Pt/Co multilayers.

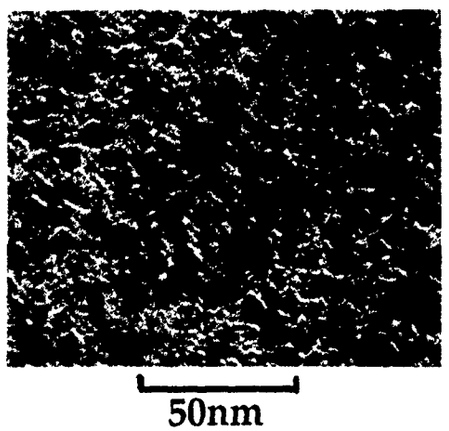

FIG. 3. TEM bright field image of an as-sputtered Pt/Co multilayer.

fields smaller than the nucleation field. In contrast the coercivity of the high coercivity multilayer in 4*d* is dominated by domain wall pinning. This is demonstrated by differentiating the polar Kerr signal with respect to the applied field, Figs. 5(a) and 5(b) are the differentials of Figs. 4(a) and 4(d) respectively. The rate of change of the initial magnetization as a function of applied field is different to that of the magnetization reversal in Fig. 5(a), where as in Fig. 5(b) both distributions are the same.

In summary the initial magnetization loops show that the coercivity increase is initially caused by an increase in the nucleation field. As the coercivity increases further, wall pinning becomes the dominant effect in determining the multilayer coercivity.

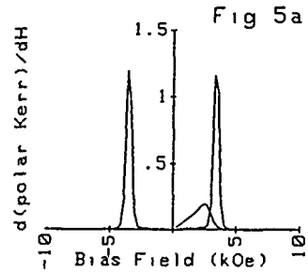

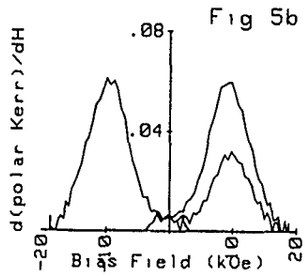

FIG. 5. Differential with respect to applied field of the initial magnetization curves.

IV. CONCLUSION

We have found that we can increase the coercivity of sputtered multilayers by annealing in air. The coercivity increase can be reversed by annealing in a 10% H_2 in N_2. The cause of the coercivity increase is thought to be oxygen incorporation in the multilayer, initially the effect is to increase the nucleation field of the multilayer however further coercivity increases are caused by domain wall pinning.

ACKNOWLEDGMENTS

We would like to thank the Centre for Data Storage Materials at Coventry University for use of the VSM and for informative discussions, Dr. L. Heyderman and Professor J. Chapman of Glasgow University for the TEM analysis and Dr. T. Hyde for the XRD analysis.

[1] S. Hashimoto, Y. Ochiai, and K. Aso, J. Appl. Phys. **67**, 2136 (1990).
[2] W. B. Zeper, F. J. A. M. Geridanus, P. F. Carcia, and C. R. Fincher, J. Appl. Phys. **65**, 4971 (1989).
[3] D. Weller, H. Brandle, and C. Chappert, J. Magn. Met. **121**, 461 (1993).
[4] P. G. Pitcher, J. Miller, D. P. A. Pearson, and P. D. Gurney, J. Magn. Soc. Jpn. **17**, S1 (1993).
[5] H. Yamane, N. Maeno, and M. Kobayashi, J. Appl. Phys. **73**, 334 (1993).
[6] J. Miller, D. P. A. Pearson, and P. G. Pitcher, European Patent No. 92311475.5.
[7] S. Sumi, Y. Kusumoto, Y. Teragaki, and K. Torazawa, J. Appl. Phys. **73**, 6835 (1993).
[8] H. Yamane, M. Kobayashi, N. Maeno, and K. Sato, Japanese Patent No 1-274039.

Magnetostriction and magnetic properties of iron-cobalt alloys multilayered with silver

Tamzin A. Lafford and M. R. J. Gibbs
Department of Physics, University of Sheffield, Sheffield, S3 7RH, United Kingdom

R. Zuberek
Institute of Physics, Polish Academy of Sciences, Al. Lotników 32/46, 02-668 Warsaw, Poland

C. Shearwood
Department of Physics, University of Sheffield, Sheffield, S3 7RH, United Kingdom

Commercially available Fe-Co alloys with Co contents of 50 and 24 wt. % have been rf sputtered to produce multilayers with noble metal (Ag or Cu) interlayers. Series with fixed Fe-Co or noble metal thicknesses have been produced, as have plain Fe-Co films. In all cases, the coercivities of the multilayers are significantly reduced from those exhibited by the plain alloy films. For example, a film of the alloy containing 50 wt. % Co had H_c=6.9 kA m^{-1}, whereas a multilayer with 12 nm Fe-Co layers and 2 nm Ag layers had H_c=480 A m^{-1}. The saturation magnetostriction is also enhanced, in some cases increasing by 60% over the expected bulk polycrystalline alloy value. For example, the literature λ_s value for a Fe-Co alloy containing 24% Co is about 28 ppm; in a multilayer with 12 nm alloy layers and 8 nm Ag layers, λ_s=45 ppm. The combination of high magnetostriction and low coercivity makes such materials as these attractive for their potential as stress sensor and actuation transducer elements.

I. INTRODUCTION

There is currently interest in many aspects of magnetic multilayers (e.g., giant magnetoresistance and magnetic and magneto-optic recording media). For sensor and transducer applications, high saturation magnetostriction, λ_s, in soft materials is desirable. Our investigations began with an iron-cobalt alloy of a composition known to have a value of λ_s(≈53 ppm) comparable with most conventional soft materials. Ag and Cu were chosen as the interlayers because they are noble metals, immiscible with Fe and Co, nonmagnetic, and are larger than Fe or Co atoms. We found that Ag interlayers in films sputtered from this alloy softened them considerably and, in some cases, caused enhancement of the magnetostriction.[1] Here, we report further investigations into the Fe-Co alloy/noble metal multilayer systems, including two types of alloy and various thicknesses. Results for Ag interlayers will be compared to those for multilayers containing Cu in order to give the first indication of an explanation for the observations.

II. EXPERIMENTAL METHODS

The multilayers were rf magnetron sputtered from alternate targets of commercially available alloys: HiSat50® (50% Fe, 50% Co with less than 0.2% Ta) or Permendur24® (24% Co, 75.4% Fe, 0.6% Cr) (Telcon Metals Ltd., U.K.); and Ag (99.99%) at 75 W. The background pressure was 2–5×10^{-7} Torr; during sputtering, the Ar pressure was 5 mTorr. The substrates were 26-μm-thick Kapton® polyimide (DuPont Ltd., U.K.); the substrate platen was water cooled. Typically 50 bilayers were deposited on each side of the substrate to equalize any film stresses. Two series types were made: (1) t_{Ag}=2 nm, $t_{HiSat50}$=2–12 nm or $t_{Permendur24}$=2–15 nm; (2) t_{Ag}=0.5–10 nm, $t_{HiSat50}$=12 nm, or $t_{Permendur24}$=10 nm. Results for the first HiSat50 series will be compared with those from multilayers with Cu in place of Ag interlayers (Cu target 99.99%). Plain alloy films were also deposited, 600 nm thick for HiSat50 on one side of the substrate and 2×600 nm thick for Permendur24, i.e., 600 nm on each side of the substrate. These thicknesses are comparable to the typical total thickness of Fe-Co alloy in the multilayers.

In-plane magnetic hysteresis loops were measured using a quasi-dc inductive magnetometer,[2] H_{max}=22 kA m^{-1}. Saturation magnetostriction was measured by small angle magnetization rotation (SAMR)[3] (see Ref. 1 for application to deposited samples) and strain-modulated ferromagnetic resonance (SMFMR).[4] The films were examined structurally using high-angle x-ray diffraction (XRD) in the θ-2θ mode with Cu-$K\alpha$ radiation.

III. RESULTS AND DISCUSSION

Electron probe microanalysis of sputtered HiSat50 films shows that they contain 45 wt % Fe, 55 wt. % Co, and approximately 0.2 wt. % Ta. A bulk polycrystalline alloy of this composition would have λ_s≈53 ppm; this is true for compositions ≈±5% of the nominal.[5]

XRD traces of the Fe-Co/Ag and Fe-Co/Cu multilayers show that the alloy layers are polycrystalline, with bcc structure and no significant crystallographic texture. Peaks due to fcc Ag generally coincide with alloy peaks, so it is not possible to say whether the Ag layers are textured. No XRD satellite peaks are seen, indicating that the alloy-noble metal interfaces are rough. This is supported by low-angle XRD and kinematic modeling. Ag layers are possibly not continuous for t_{Ag}<≈5 nm.[6]

The Scherrer equation[7] has been used with the bcc (110) peak widths to estimate the grain sizes in the films. (No account was taken of any possible inhomogeneous lattice strains, which also contribute to peak broadening.) Grain sizes in the HiSat50/2 nm Ag multilayers are 3–14 nm; in

 0021-8979/94/76(10)/6534/3/$6.00 © 1994 American Institute of Physics

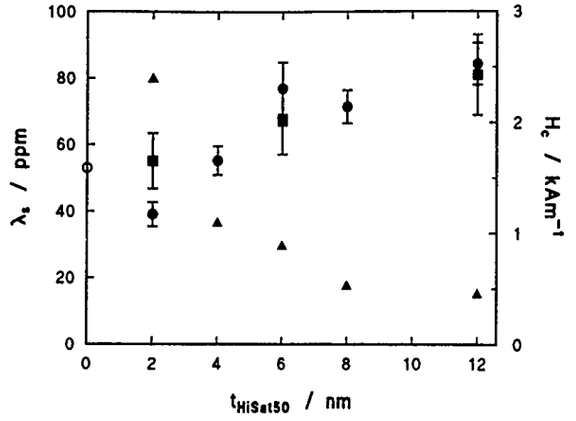

FIG. 1. Saturation magnetostriction of HiSat50/Ag multilayers. t_{Ag}=2 nm. ● λ_s, SAMR data; ■ λ_s, SMFMR data; ○ bulk polycrystalline λ_s (Ref. 5): Δ H_c. H_c plain alloy film=6 9 kA m^{-1}.

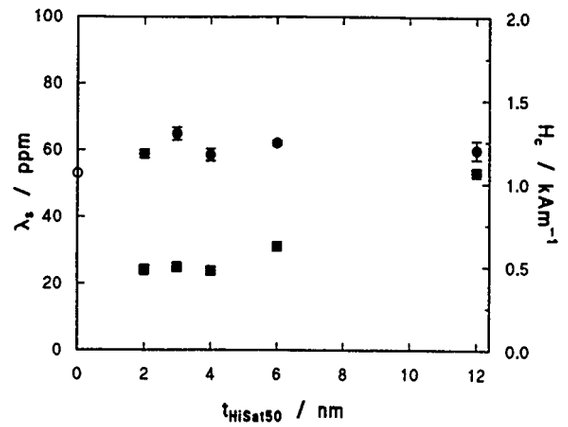

FIG. 2. Saturation magnetostriction and coercivity for HiSat50 (Ref. 5). H_c plain alloy film=6.9 kA m^{-1}.

HiSat50/2 nm Cu, 5–14 nm. Thicker alloy layers produce larger grains in both cases.

Average lattice strain was calculated from the XRD peak positions by comparison with bulk Ag d_{111} or the d_{110} spacing for the thick Fe-Co films. In the series with constant t_{Ag}=2 nm, for thinner alloy layers, the average Fe-Co d_{110} spacing perpendicular to the film plane is expanded (up to 1.0% for HiSat50, 1.6% for Permendur24). The spacing relaxes towards the plain film value for thicker alloy layers. The Ag(111) spacings show no trend with $t_{Fe\text{-}Co}$ but the lattice is contracted up to −1.0%. In multilayers with fixed $t_{Fe\text{-}Co}$ and varied t_{Ag}, there is contraction up to −1.0% in thinner Ag layers, tending weakly towards the bulk value as t_{Ag} increases. The Fe-Co d_{110} spacings follow the same pattern as Ag d_{111} as t_{Ag} varies. The HiSat50 d_{110} strain rises to +0.3% as t_{Ag} increases; similarly, the Permendur24 d_{110} strain rises to +1.1%. Please note that although these strains are perpendicular to the film plane, it does not follow that the in-plane strains are necessarily of opposite sign.[8]

We have already reported some results on HiSat50/2 nm Ag multilayers.[1] Here we add λ_s data obtained SMFMR measurements (Fig. 1), which confirm the validity of the SAMR technique for such samples. Enhancement of λ_s is observed for multilayers with thicker $t_{HiSat50}$ and t_{Ag}=2 nm; 83 ppm is the highest seen, compared with 53 ppm for bulk.[5] A significant reduction of H_c is seen for all the multilayers, compared to that of a plain 600 nm HiSat50 sputtered film.[1] H_c=450 A m^{-1} is observed for a multilayer containing 12 nm HiSat50 layers and 2 nm Ag layers (this is also the most magnetostrictive sample) compared to 6.9 kA m^{-1} for the plain HiSat50 film. H_c values for plain alloy films given here are underestimates, since these films were not saturated in the field available in the dc magnetometer. The values given are those for which M=0 on reducing the applied field from H_{max}=22 kA m^{-1}.

H_c and λ_s for HiSat50/2 nm Cu multilayers are presented in Fig. 2. The softening effect of interlayers is again seen with similarly low coercivities obtained, although the trend is opposite to that seen in the HiSat50/2 nm Ag multilayers (i.e., for Cu interlayers, *thinner* HiSat50 layers, with *smaller* grain sizes, give the softer films). λ_s is slightly enhanced over the bulk value[5] but the increase is not as large as that seen for thicker HiSat50 layers with Ag interlayers.

Figure 3 shows the effects of different thicknesses of Ag interlayers on the properties of multilayers with $t_{HiSat50}$=12 nm. It is thought that Ag layers become continuous only for $t_{Ag}>\approx$5 nm[6] and this may account for the dip in λ_s at around that value. The maximum H_c in this series occurs around t_{Ag}=8 nm.

These results are to be compared with those for multilayers containing Permendur24 (Figs. 4 and 5), which contains a greater proportion of Fe and has a lower bulk polycrystalline λ_s than HiSat50 (around 28 ppm).[5] Again, the alloy films are softened by the presence of Ag interlayers and λ_s is enhanced. H_c=560 A m^{-1} for a multilayer with 12 nm Permendur24 layers and 2 nm Ag layers, compared with 4.6 kA m^{-1} for a 2×600 nm plain film. The highest λ_s value observed is 45±3 ppm an increase of about 60% over the bulk value, for the multilayer 2×40 (10 nm Permendur24/10 nm Ag). A similar value is found for 2×50(10 nm Permendur24/2 nm Ag), which has low H_c. The differences in behavior between the Ag and Cu series may result from

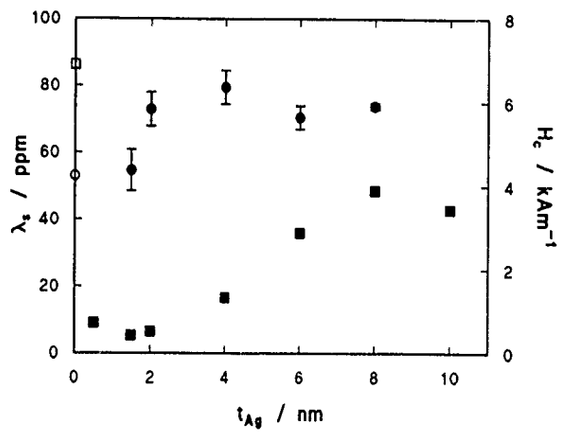

FIG. 3. Saturation magnetostriction and coercivity of HiSat50/Ag multilayers with fixed HiSat50 thickness ($t_{HiSat50}$=12 nm). ● λ_s, ■H_c. Open symbols: bulk alloy λ_s (Ref. 5) and H_c.

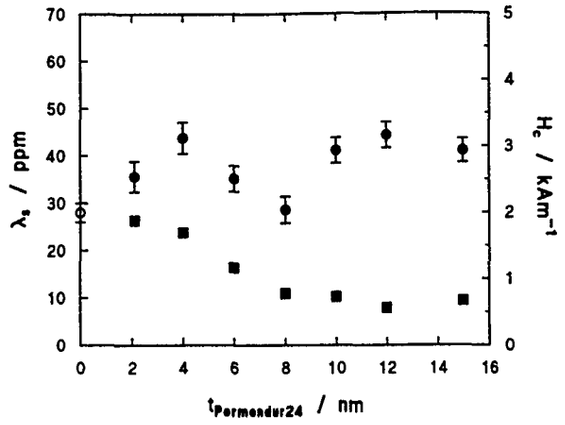

FIG. 4. Saturation magnetostriction and coercivity of Permendur24/Ag multilayers. t_{Ag}=2 nm. ● λ_s, ■ H_c, ○ bulk polycrystalline alloy λ_s (Ref. 5). Plain alloy film H_c=4.6 kA m^{-1}.

the different wetting characteristics of Cu and Ag on Fe and Co. The crystallographic strain perpendicular to the film plane in multilayers of HiSat50/2 nm Cu is slightly greater than in HiSat50/2 nm Ag multilayers. Although Ag is a larger

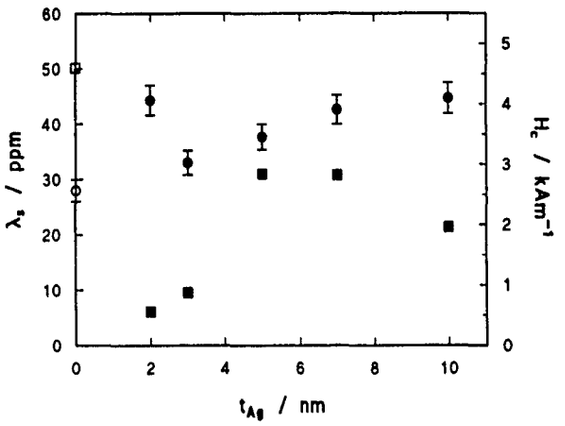

FIG. 5. Saturation magnetostriction and coercivity of Permendur24/Ag multilayers with fixed Permendur24 layer thickness ($t_{Permendur24}$=10 nm). ● λ_s, ■ H_c. Open symbols: bulk polycrystalline alloy λ_s (Ref. 5) and H_c.

atom than Cu (Ag a_0=0.41 nm, Cu a_0=0.36 nm) Cu has a larger Young's modulus (E_{Cu}=118 GPa, E_{Ag}=76 GPa)[9] so it strains less readily, forcing the alloy layer to strain more. The data we have do not permit a comparison of the roughness of the interfaces in the two systems, although we can state that neither is smooth. It appears that lattice strain is not the mechanism for enhancing λ_s; work is in progress regarding magnetization orientation effects.

IV. SUMMARY

Both Ag and Cu interlayers of various thicknesses reduce the coercivity of Fe-Co alloy sputtered films by up to an order of magnitude. In certain cases, λ_s is enhanced by nearly 60% over the value expected for bulk polycrystalline alloys of similar compositions. Some λ_s results taken by SAMR have been independently confirmed by SMFMR. Greater effects are seen in multilayers containing Ag interlayers than in those containing Cu interlayers; this difference is tentatively attributed to the difference in wetting of Ag and Cu on Fe and Co. It has been demonstrated that multilayers can be deposited which are simultaneously magnetically soft and highly magnetostrictive, a characteristic desirable in sensor and transducer applications.

ACKNOWLEDGMENTS

The UK Science and Engineering Research Council and British Technology Group fund this work; BTG retain intellectual property rights in this area. We gratefully acknowledge the help of B. Chapman with XRD.

[1] T. A. Lafford, M. R. J. Gibbs, and C. Shearwood, J. Magn. Magn. Mater. **132**, 89 (1994).
[2] P. T. Squire, S. M. Sheard, C. H. Carter, and M. R. J. Gibbs, J. Phys. E: Sci. Instrum. **21**, 1167 (1988).
[3] K. Narita, J. Yamasaki, and H. Fukunaga, IEEE Trans. Magn. **MAG-16**, 435 (1980).
[4] R. Zuberek, H. Szymczak, G. Suran, and K. Ounadjela, Thin Solid Films **188**, 1 (1990).
[5] R. M. Bozorth, *Ferromagnetism* (Van Nostrand, Reinhold, 1951).
[6] K. L. Chopra and M. R. Randlett, J. Appl. Phys. **39**, 1874 (1968).
[7] A. Guinier, *X-Ray Diffraction in Crystals, Imperfect Crystals and Amorphous Bodies* (Freeman, New York, 1963).
[8] A. F. Jankowski, J. Appl. Phys. **71**, 1782 (1992).
[9] C. R. Tottle, *An Encyclopedia of Metallurgy and Materials* (MacDonald and Evans, Plymourh, 1984).

Stabilization of the hexagonal close-packed phase of cobalt at high temperature

N. P. Barradas, H. Wolters, A. A. Melo, and J. C. Soares
CFNUL, Avenida Professor Gama Pinto, 2, P-1699 Lisboa Codex, Portugal

M. F. da Silva
INETI, EN No. 10, 2685 Sacavém, Portugal

M. Rots
IKS-KUL, Celestijnenlaan 200 D, B-3001 Leuven, Belgium

J. L. Leal, L. V. Melo, and P. P. Freitas
INESC, Rua Alves Redol, 9-1°, 1000 Lisboa, Portugal

The structure of thin cobalt films sputtered on a rhenium buffer was analyzed from room temperature to 963 K, using the perturbed angular correlation technique with the $^{111}In/^{111}Cd$ probe. The hyperfine field corresponding to the fcc phase, which is the stable one above 704 K, is never observed, and the measured hyperfine field follows closely a theoretical prediction for the hcp phase. This is a consequence of the good match between the cobalt and the Re hcp lattices that leads to the stabilization of the hcp phase up to 963 K.

I. INTRODUCTION

As the structure of magnetic thin films and superlattices (SLs) determines their magnetic properties, it becomes important to control it on a microscopic level, leading to the tailoring of materials with prespecified properties. Cobalt is one of the elements more frequently used in magnetic SLs. While its stable phase has a hcp structure below 704 K, above that temperature a phase transition to fcc is observed.[1] Total-energy band structure calculations at 0 K predict correctly the hcp phase as the stable one,[2] with the fcc and bcc phases slightly higher in energy. The small energy differences suggest however the possibility of occurrence of the fcc and bcc metastable phases, even at room temperature. The bcc phase was first obtained[3] by epitaxial growth of Co on (110) GaAs, and later[4] by epitaxial growth on (100) Fe. The fcc structure is generally presented in samples submitted to mechanical or thermal treatments.[1] Although the mechanism of the phase transition at 704 K is well known[5] and explained as corresponding to the slip of planes normal to the $\langle 0001 \rangle$ hcp and $\langle 111 \rangle$ fcc axes, its cause is still not yet understood. Temperature-dependent calculations of the total energy should be able to determine whether an energy crossover between the hcp and fcc phases exists.

In this work, the 704 K phase transition in Co thin films grown on a hcp rhenium buffer is investigated. Re was chosen due to the small mismatch $\Delta(c/a)=0.5\%$ relative to the Co hcp lattice. Measurements were carried out at temperatures up to 963 K, using the perturbed angular correlation (PAC) hyperfine interactions technique, based on the observation of the spin rotation of a ^{111}Cd probe implanted in the film. Since the magnetic hyperfine fields (HFFs) are well known for both Co phases, the method is very sensitive for following the phase transition in a microscopic way.

II. EXPERIMENTAL DETAILS

Co thin films on a Re buffer grown on glass and silicon substrates were produced with a modified argon sputtering apparatus (Alcatel SCM 540). The pressure in the target chamber before the introduction of argon was 5×10^{-8} Torr. Co was deposited by rf magnetron sputtering at 5 mTorr and Re was deposited by dc magnetron sputtering at 2.5 mTorr. The deposition rates were 0.04 and 0.1 nm/s, respectively. Film thickness was monitored *in situ* by the vibrating quartz crystal method, and checked with Rutherford backscattering (RBS) analysis.[6] The Co layers were 22, 34, and 40 nm thick for the films studied in this work. The Re buffer layer was 30 nm thick in all cases.

The Re buffer is highly structured with the c axis normal to the film surface, and the same orientation is observed by x-ray diffraction and cross-sectional high resolution transmission electron microscopy for the Co films.[7,8] This is a consequence of the good lattice match between the Co and Re hcp structures, where $\Delta(c/a)=0.5\%$.

The ^{111}Cd probe atom has been introduced in the films by implantation with 80 keV energy of the ^{111}In parent isotope to doses of about 10^{13} at./cm^2. The implantation range and width are 16 and 6 nm, respectively, so the probe is confined to the Co layers. The PAC technique measures the Larmor nuclear spin precession frequency induced by the magnetic HFF at the probe site. The Larmor frequency is observed in the oscillating anisotropy amplitude of the coincidence spectra of the 173–247 keV γ-γ cascade of ^{111}Cd. This is done by measuring the number of coincidences as a function of time, $N(\theta,t)$, using four detectors in the same plane at 90° angles, and calculating the usual anisotropy function $R(t)=2.[N(180^0,t)-N(90^0,t)]/[N(180^0,t)+2.N(90^0,t)]$. For a pure magnetic interaction, the $R(t)$ function is a sum of cosines with the Larmor frequency $\omega_L=-\mu B/I\hbar$ and its $2\omega_L$ harmonic, where B is the local field at the ^{111}Cd probe and μ the magnetic moment of the $I=5/2$ intermediate state of the cascade. The known weak electric field gradient of the hcp Co lattice leads to a small damping of the spectra,[9] and was taken into account in the calculations. In this way the experimental data have been fitted with a theoretical function using ω_L and the percentage

 0021-8979/94/76(10)/6537/3/$6.00 © 1994 American Institute of Physics

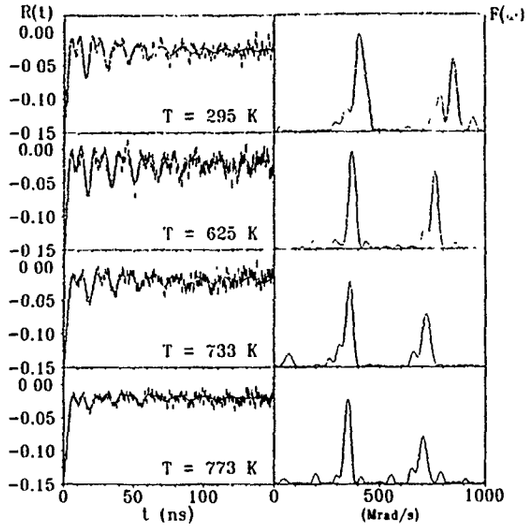

FIG. 1. PAC time spectra and corresponding Fourier transforms for one of the films.

of probe nuclei with a particular hyperfine interaction as adjustable parameters. The magnetic frequencies obtained following this analysis are also observed in the Fourier spectra, where the linewidth is broadened due to the quadrupole splitting.

Two setups were used, one with NaI(Tl), and the other with BaF_2 detectors. The time resolution of 2.3 ns for NaI(Tl) and 0.7 ns for BaF_2 allows the observation of the precession frequencies, with a 1% error mainly due to the error in the time calibration. The measurements have been performed as a function of temperature under 10^{-6} Torr pressure. The maximum temperatures reached for each of the films were, respectively, 963, 759, and 773 K. In each of the films several runs were done starting at room temperature. The frequencies obtained for the same temperature in different runs were the same within experimental errors, and the

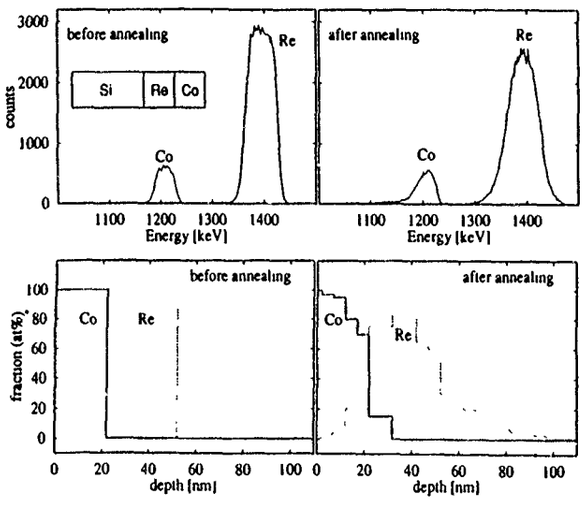

FIG. 2. RBS spectra and derived depth profiles of a Si/Re 30 nm/Co 22 nm film taken before and after 1 h annealing at 923 K.

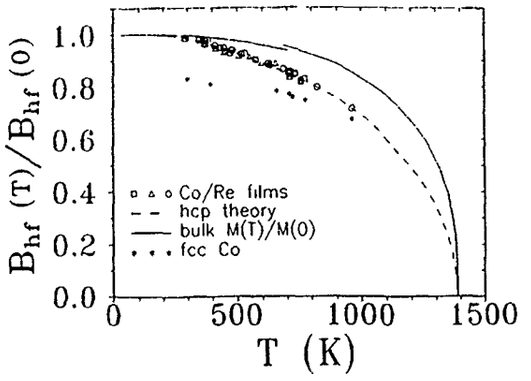

FIG. 3. Temperature dependence of the reduced hyperfine field at ^{111}Cd in Co, in Co/Re thin films. The full line represents the bulk magnetization. The dashed line is a theoretical prediction for the hcp field above the phase transition temperature (Ref. 13). The temperature dependence of the hyperfine field at ^{111}Cd in fcc Co (Refs. 13–15) is also shown.

temperature dependence of the frequency was also the same in the three films, so the results obtained will be treated as a single experiment.

RBS experiments were done using a 1.6 MeV He^+ beam detected by a 15 keV energy resolution detector located at 160° with the incidence direction in the Cornell geometry.

III. RESULTS

In Fig. 1 the spin rotation curves and their corresponding Fourier transforms are shown for one of the films, measured with the BaF_2 detectors setup at different temperatures. The normal to the plane of the film was in the detector plane, at 45° with two of the detectors. The field orientation is clearly reflected in the relative amplitudes of the ω_L and $2\omega_L$ frequencies. It is in the plane of the film, as already seen in Co/Re multilayers.[10] Separate experiments were done at room temperature with the film in different positions, leading to different ω_L and $2\omega_L$ amplitudes, confirming that orientation of the HFF. In Co single crystals the HFF is along the c axis at room temperature, and turns slowly to the basal plane between 500 and 600 K.[9] This reorientation of the magnetic moments does not occur in these thin films, due to the demagnetizing field.

The clearly separated satellites observed at the left of the ω_L and $2\omega_L$ peaks correspond to a well-known stacking fault defect.[11,12] This defect is due to the sputtering process and does not interfere with the determination of ω_L. Its fraction is maximum at room temperature, and decreases with annealing.

At temperatures higher then 800 K, new frequency components (not shown) are seen in the Fourier spectra. However, the ^{111}CdCo peaks are still clearly defined. RBS studies of the 22 nm Co film were done as function of annealing temperature. Below 823 K no change could be observed. The RBS spectra taken before and after 1 h annealing at 923 K are shown in Fig. 2, together with the derived depth profiles, showing clearly that diffusion occurred between the Co and Re layers. Therefore, the new frequency components are

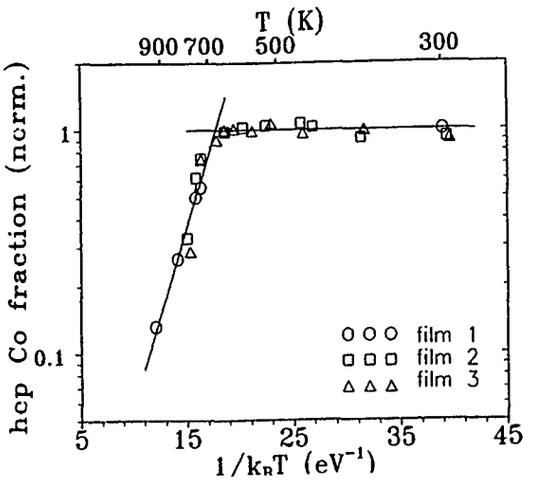

FIG. 4. Temperature dependence of the fraction of probes feeling a well-defined hyperfine field, normalized to the room temperature value.

likely to be related with a fraction of probes in the mixed region, while some remain in a pure Co environment, leading to the ^{111}CdCo field.

IV. DISCUSSION

The temperature dependence of the reduced HFF $B_{HF}(T)/B_{HF}(0\ K)$ is shown in Fig. 3 together with the bulk Co magnetization $M(T)/M(0\ K)$[1] and the HFF of ^{111}Cd in fcc Co.[13–15] It is clear that throughout the temperature range of this experiment, the temperature dependence of the measured field is smooth and in very good agreement with the one expected for hcp Co; indeed, the fcc field is never observed, and the known 10% discontinuity of the HFF that takes place at the phase transition is not present, which proves that no fcc phase is present. Also, the deviation from the bulk magnetization of the HFF of Cd and other 4 *sp* impurities in Co has been explained previously by Lindgren *et al.*[13] In this model a temperature dependent *sd* hybridization contributes a local field at the probe site adding up with the conduction electron contribution. Their calculation for the HFF of Cd in hcp Co is given as the dashed line in Fig. 3. The HFF obtained in the present study is in very good agreement with the predicted values above the phase transition temperature, confirming that the hcp structure was retained as a metastable phase throughout the temperature range attained.

The fraction of probes feeling the well-defined HFF of Cd in hcp Co is shown in Fig. 4 as function of temperature, normalized to its room temperature value. The solid line is a fit to the data above 625 K assuming an Arrhenius law. The extrapolation of the fit to a 1.0 normalized fraction of probe nuclei in substitutional positions in a pure Co environment yields $T(f=1.0)=$ 655 K. This is 150 K below the occurrence of mixing between the Co and Re layers, so the decrease observed must be related to diffusion of the probes out of the Co layer.

V. CONCLUSIONS

The hcp structure of Co was retained above the fcc phase transition temperature and up to 963 K, as a metastable phase, by growing thin Co films on Re substrates. No fcc phase was observed, and the temperature dependence of the hyperfine field at the Cd site in the Co films above the usual phase transition temperature of 704 K follows closely a theoretical prediction for the hcp field.

ACKNOWLEDGMENTS

N.P.B. and J.L.L. acknowledge grants from JNICT under Programa Ciência, and partial support by the ERASMUS program. H.W. acknowledges a grant from the Alexander von Humboldt Foundation under the Feodor von Lynen Programme.

[1] R. Tebble and D. Craik, *Magnetic Materials* (Wiley, New York, 1969), p. 69.
[2] B. Min, T. Oguchi, and A. Freeman, Phys. Rev. B **33**, 7852 (1986).
[3] G. A. Prinz, Phys. Rev. Lett. **54**, 1051 (1985).
[4] H. Li and B. Tonner, Phys. Rev. B **40**, 10241 (1989).
[5] Z. Nishiyama, Tohoku Sci. Rep. **25**, 79 (1936).
[6] L. Melo, I. Trindade, M. From, P. P. Freitas, N. Teixeira, M. F. da Silva, and J. C. Soares, J. Appl. Phys. **70**, 7370 (1991).
[7] J. L. Leal, N. P. Barradas, J. C. Soares, M. F. da Silva, M. Rots, and P. P. Freitas, *Proceedings of the Symposium on Magnetic Ultrathin Films, Multilayers, and Surfaces, San Francisco, April 1993* (Materials Research Society, Pittsburgh, 1993), p. 773.
[8] N. P. Barradas, J. L. Leal, J. C. Soares, M. F. da Silva, P. P. Freitas, M. Rots, S. I. Molina, and R. Garcia, Nucl. Instrum. Methods B **85**, 202 (1994).
[9] N. P. Barradas, M. Rots, A. A. Melo, and J. C. Soares, Phys. Rev. B **47**, 8763 (1993).
[10] N. P. Barradas, J. L. Leal, H. Wolters, M. F da Silva, A. A. Melo, J. C. Soares, L. V. Melo, P. P. Freitas, B. Swinnen, and M. Rots, J. Magn. Magn. Mater. **121**, 80 (1993).
[11] C. Allard, G. S. Collins, and C. Hohenemser, Phys. Rev. B **32**, 4839 (1985).
[12] F. Raether, D. Wiarda, K. P. Lieb, J. Chevallier, and G. Weyer, Z. Phys. B **73**, 467 (1989).
[13] B. Lindgren, S. Bedi, and R. Wappling, Phys. Scr. **18**, 26 (1978).
[14] B. Lindgren and Y. Vijay, Hyp. Int. **9**, 379 (1981).
[15] M. Senba, P. Raghavan, W. Semmler, and R. Raghavan, Hyp. Int. **9**, 449 (1981).

Observation and computer simulation of static magnetization process in soft magnetic thin film

Zhigang Wang, Ikuya Tagawa, and Yoshihisa Nakamura
Research Institute of Electrical Communication, Tohoku University, Sendai 980-77, Japan

We have developed a new numerical micromagnetic simulator based on the curling particle assembly model and the finite element method which describes the static magnetization process in soft magnetic films successfully, and which exhibits many details of that process. Compared to conventional numerical treatment of the magnetic structure in soft magnetic films, e.g., the Landau–Lifshits–Gilbert equation method, recently proposed Monte Carlo method, our approach has the following advantages: high calculation speed, arbitrary meshing size, and good agreement with experiment.

I. INTRODUCTION

Studying the static magnetization process in soft magnetic thin film is of interest for domain-control technology. As a conventional analytic method, the Landau–Lifshits–Gilbert (LLG) equation method has been well used.[1,2] Recently a Monte Carlo method was proposed[3] which uses random numbers to calculate an approximate result for eventual phenomena such as unknown magnetization distribution in soft magnetic films.

In this article a new numerical micromagnetic simulator based on the curling particle assembly model[4] and the finite element method (FEM) is developed. Compared to the other methods, our approach has the following advantages: high calculation speed, arbitrary meshing size, and good agreement with experiment.

Magnetic structures of rectangularly striped permalloy film, which can be typically used for magnetoresistive head, are modeled. The easy magnetic axis is aligned in the transverse direction. At the beginning, the spontaneous subdomain configuration for a stripe of a given length/width ratio is simulated by determining the minimum free energy. The static magnetization process due to a slowly changing external field is then simulated. The above simulation results are generally in agreement with Bitter pattern experiments.

II. OBSERVATION

The sample for the Bitter pattern experiment is a rectangular $Ni_{80}Fe_{20}$ film (thickness=100 nm, width=10 μm) formed by rf sputtering, photolithography, and ion-etching process. An anisotropic field H_k=4.2 Oe is induced along the width direction by applying a field of 15.5 Oe in the same direction while sputtering. The samples were coated by a thin magnetic colloidal solution and the domains were observed under an optic microscope.

The static magnetization process for a stripe with the length/width ratio of 2:1 is shown in Fig. 1. Based on the equilibrium ground state of the closure domain pattern, a uniform external field H is applied along the transverse and longitudinal directions. The common rule is that those domains with magnetizations parallel to H grow whereas those domains with magnetizations antiparallel to H shrink and therefore magnetic walls move. Eventually a single domain state is achieved at a field H_s. We find that H_s along the longitudinal direction is about 10 Oe, and is much smaller than the value of 50 Oe determined for H_S along the transverse direction.

III. DESCRIPTION OF SIMULATOR

The flow chart of our simulator is shown in Fig. 2. A soft magnetic film is divided into an array of $n \times m$ square cells, where each cell is assumed to be an assembly of a certain number of magnetic particles. The angle of the magnetization in each particle is chosen such that it minimizes the energy function which covers the exchange, anisotropy, demagnetizing, and external field terms according to the curling model. The magnitude and direction of the magnetization (magnetization vector) of each cell is determined by computing the arithmetic mean of those of all particles in that cell. The magnetic properties of each particle are determined by forcing the calculated hysteresis curve, with the aid of our hysteresis curve simulator,[4] to resemble the measured curve in shape. The parameters to be adjusted for the curling model are shown in Table I. The adjusted parameters are as follows:

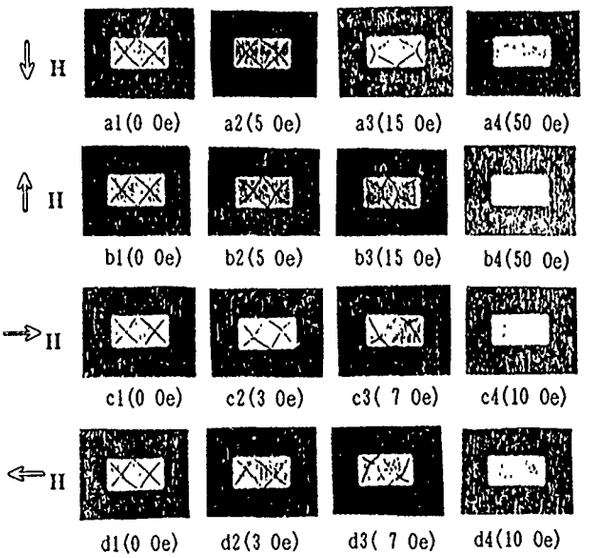

FIG 1. The Bitter pattern experiment

 0021-8979/94/76(10)/6540/3/$6.00 © 1994 American Institute of Physics

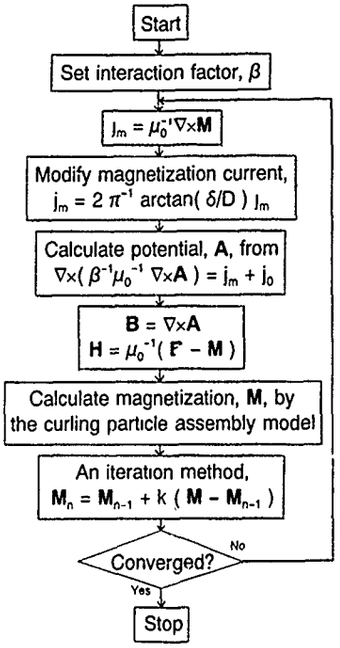

FIG. 2. Flow chart.

the curling model parameter $S=(1.08H_k/H_c)^{1/2}=3.37$, $M_s=700$ emu/cc, $H_c=0.4$ Oe, $\sigma_{H_c}/H_c=0.1$, $H_k=4.2$ Oe, $\sigma_{H_k}/H_k=0.1$, $\sigma_\theta=10$ deg.

In general two-dimension model the thickness of the film is assumed as large enough. To realize the quasi-three-dimension (FEM) simulation of very thin film, we have to correct the demagnetizing field by a factor $(2/\pi)\arctan(\delta/D)$, where δ and D are the thickness and width of the film, respectively. This is because the demagnetizing factor of a long stripe thin film with the thickness δ and the width D is appropriately $(2/\pi)\arctan(\delta/D)$ in the transverse direction. In FEM program, however, we cannot separate the demagnetizing field from the total field, so that we modified the magnetization current j_m instead of the demagnetizing field, as shown in Fig. 2.

TABLE I. The adjusted parameters for the curling model.

Magnetic property	Distribution function	Parameters to be adjusted
Curling model parameter		S
Saturation magnetization		M_s
Coercive field	Gauss distribution	Average H_c, standard deviation σ_{H_c}/H_c
Anisotropic field	Gauss distribution	Average H_k, standard deviation σ_{H_k}/H_k
Direction distribution of easy axis	Gauss distribution	Average θ, standard deviation σ_θ

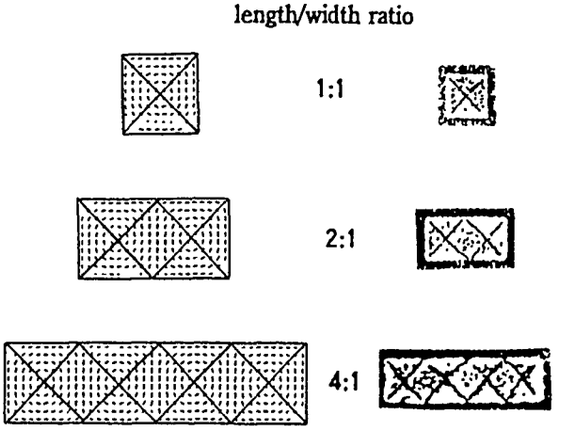

FIG. 3. The spontaneous subdomain configuration.

It is taken for granted to assume a mean field interaction[5] between particles for permalloy. The mean magnetic field is assumed to be proportional to the intensity of the mean magnetization in the surroundings of the particle. For simplicity, we take the mean field as $H_{\text{mean}}=\alpha B/\mu_0$, where B is the magnetic flux density and α is a constant. The effective field in a soft magnetic film is then expressed as

$$H_{\text{eff}}=H+H_{\text{mean}}=H+\alpha B/\mu_0=(1+\alpha)H+\alpha M/\mu_0. \tag{1}$$

Here H is the magnetostatic field which consists of the externally applied field and the demagnetizing field. The equation expressing the relationship between the flux density B and the field H then results in

$$B=\mu_0 H_{\text{eff}}+M=(1+\alpha)(\mu_0 H+M)=\beta(\mu_0 H+M), \tag{2}$$

where $\beta=1+\alpha$ which represents the interparticle mean field interaction. Applying Ampere's law $\nabla\times H=j$, the essential equation of FEM becomes

$$\nabla\times\left(\frac{1}{\beta\mu_0}\nabla\times A\right)=j_0+j_m, \tag{3}$$

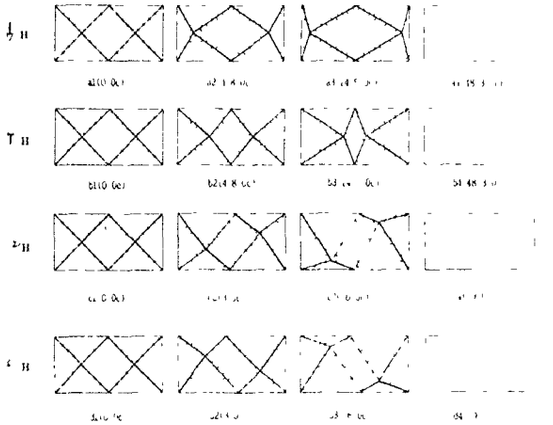

FIG. 4. The simulated static magnetization process.

where A ($B=\nabla\times A$) is the vector potential. The solved magnetization M in every cell is converted into an equivalent magnetization current by $j_m=\mu_0^{-1}(\nabla\times M)$ and the substituted into the magnetization current term j_m in Eq. (3). This procedure is repeated until the final equilibrium state is reached.

IV. SIMULATED RESULTS

By making use of the above micromagnetic model, the spontaneous states of the well-known closure domain pattern are given in Fig. 3 for various length/width ratios. For comparison, the corresponding Bitter patterns are also shown in the same figure.

Then the static magnetization process due to a slowly changing field is simulated. The uniform external field H is induced by a pair of Helmholtz coils. Figure 4 is a example for a 2:1 stripe which demonstrates good agreement with the Bitter pattern experiment in Fig. 1. Further, this simulation can explain the phenomenon that the walls of the main domain become less well defined in Fig. 1(c3) and Fig. 1(d3) and finally disappear completely in the Bitter pattern experiment. It is because of the large-angle rotation of the moments in the main domain, as shown in Fig. 4(c3) and Fig. 4(d3). In other words, from this simulation we can observe clearly the two major magnetization mechanisms: wall displacement and magnetization rotation.

V. CONCLUSION

Attempts to simulate the static magnetization process in soft magnetic film using the particle assembly model yield good agreement with experiment. In the future it may be interesting to find a direct microscopic evidence in physical structure.

[1] T. L. Gilbert, Phys. Rev. **100**, 1243 (1955).
[2] Z. Guo and E. D. Torre, Digests of INTERMAG'93, AC-06, Stockholm, Sweden, 1993.
[3] K. Tan, I. Tagawa, and Y. Nakamura, Proceeding of the 1994 IEICE Annual Conference, C-496, Keioh University, April 1994 (unpublished).
[4] Y. Nakamura and I. Tagawa, IEEE Trans. Mag. **MAG-25**, 4159 (1989).
[5] I. Tagawa and Y. Nakamura, IEEE Trans. Magn. **MAG-29**, 3981 (1993).

Magnetic and structural properties of Fe-FeO bilayers

X. Lin, A. S. Murthy, and G. C. Hadjipanayis
Department of Physics & Astronomy, University of Delaware, Newark, Delaware 19716

C. Swann
Bartol Research Institute, Newark, Delaware 19716

S. I. Shah
Dupont Experimental Station, Wilmington, Delaware 19808

The structural and magnetic properties of sputtered Fe/Fe-O films were studied by x-ray photoelectron spectroscopy (XPS), Rutherford backscattering spectroscopy, transmission electron microscopy, and superconducting quantum interference device. XPS studies showed the presence of FeO and Fe_2O_3 on the surface of as-made samples. Microstructure studies showed a uniform nanostructure with the grain size in the range of 50–150 Å with smaller grains corresponding to thinner films. The coercivity at 10 K was found to increase substantially with decreasing film thickness below 60 Å. A high H_c (2.7 kOe) was observed in samples with a thickness about 20 Å. Magnetization curves showed a planar anisotropy with a shifted hysteresis loop characteristic of an exchange anisotropy between the Fe and Fe-O coating. The coercivity was found to drop steeply with increasing temperature. This may be attributed to the superparamagnetic behavior of the Fe-O surface layer.

I. INTRODUCTION

During the last several years, iron oxide thin films have been extensively investigated because of their unusual magnetic properties and potential application in high density recording media.[1–5] In these studies, iron oxide thin films were prepared by a variety of methods, including reactive rf sputtering from iron targets in a mixed O_2 and Ar atmosphere. The structural and magnetic properties of the films were found to strongly depend on the oxygen flow rate, the substrate temperature and the thickness of the film. Different iron oxides (FeO, Fe_3O_4, α-Fe_2O_3, and γ-Fe_2O_3) were found in films with thickness in the range from several hundred to several thousand angstroms.

Very few studies have been conducted on iron-iron oxide systems.[6–8] Schneider *et al.*[7] found a high coercivity in Fe-Fe_2O_3 annealed at 200 °C. However, Ruf and Gambino[8] observed a strong exchange anisotropy in sputtered Fe-FeO layered films instead of a high coercivity. Recent studies on Fe-Fe oxide fine particles showed a high coercivity and exchange anisotropy at low temperatures consistent with a core-shell particle morphology.[9]

In this study we extended the studies on Fe-Fe oxide particles to bilayer films made by dc magnetron sputtering. Iron oxide was formed by direct oxidation of the surface of the as-made Fe film.

II. EXPERIMENTAL PROCEDURE

A dc planar magnetron sputtering system was used to prepare the Fe-Fe oxide bilayers. The sputtering target used was a 99.9% Fe disk 2 in. in diameter and 0.053 in. in thickness. The distance between the target and the water cooled substrate holder was 13.5 cm. The sputtering chamber was initially pumped down to 7×10^{-8} Torr by a crypopump and then the Fe film was deposited onto a kapton substrate by sputtering in a 5 mTorr Ar atmosphere. Aluminum and carbon-coated copper grids were also used as substrates to study the structural and microstructural properties of the film. The thickness of the films was between 20 and 200 Å. Soon after the film was made, a small amount of ambient air was introduced into the system to passivate the surface of Fe films under three different pressures (335, 735 and 1070 mTorr) for 2 h at the ambient room temperature (we use the same passivation conditions as in Fe particles[9]). The as-made samples were protected by depositing a 100 Å Ag coating layer on top of the bilayers.

The Fe-Fe oxide bilayer thickness was measured by Rutherford backscattering spectroscopy (RBS) and the surface composition and depth profile were studied by x-ray photoelectron spectroscopy (XPS). The crystal structure of bilayers was determined from selected area electron diffraction (SAD) data and the microstructure was studied using a JEOL JEM-2000 FX transmission electron microscope (TEM). The magnetic properties were studied using a superconducting quantum interference device (SQUID) magnetometer.

III. RESULTS AND DISCUSSION

Figure 1 shows two bright field micrographs and a selected area diffraction pattern of a 112 Å sample sputtered at 1.0 Å/s and oxidized at 1.07 Torr air. A uniform and continuous distribution of grains could be seen from the bright field pictures. The grain size determined by the line intercept method was observed to increase from 50 to 150 Å as the thickness of the samples increased from 20 to 200 Å. For films with the same thickness but with different sputtering rates and oxidation pressures, the grain size was found not to vary significantly. From selected area electron diffraction patterns, bcc α-Fe and fcc Ag were recognized. The apparent absence of reflections from the oxide layer in the diffraction pattern is probably due to the very small grain size and the small thickness of the oxide layer.

Figure 2 shows a typical XPS spectrum of an Fe-Fe oxide sample. The asymmetric broadening of the higher energy

 0021-8979/94/76(10)/6543/3/$6.00 © 1994 American Institute of Physics

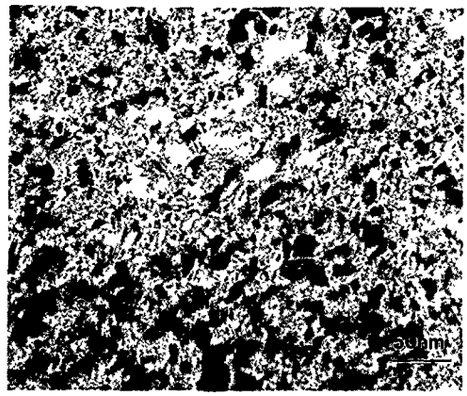

(a)

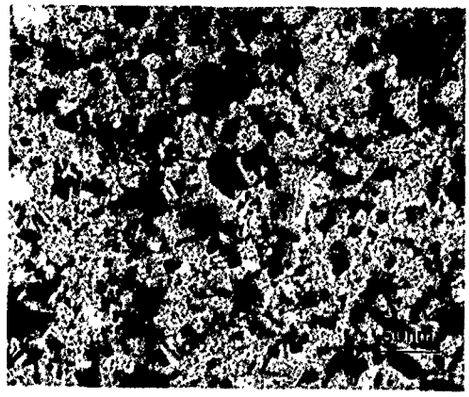

(b)

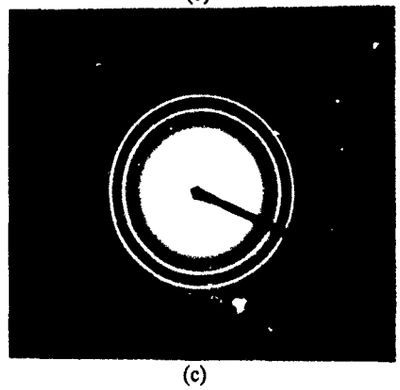

(c)

FIG. 1. Bright field micrographs of two samples sputtered at 1.0 Å/s and oxidized at 1.07 Torr. (a) 56 Å and (b) 112 Å thick, (c) SAD pattern of sample in (b).

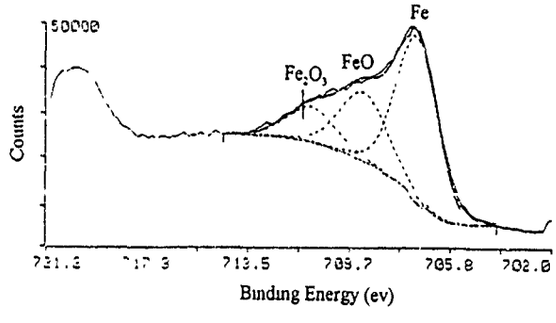

FIG. 2. XPS spectrum of an Fe-Fe oxide bilayer sample with thickness of 80 Å.

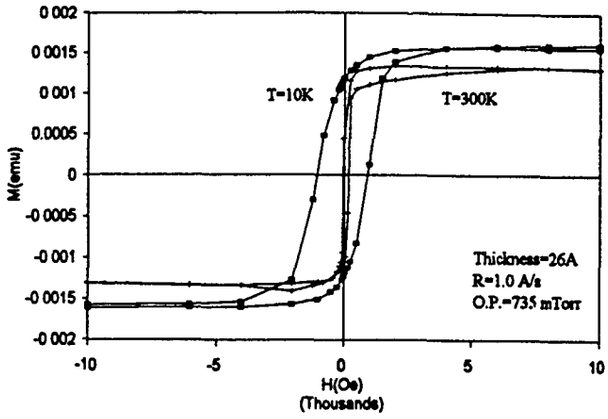

FIG. 3. Hysteresis loops of an Fe-Fe oxide sample at 10 and 300 K.

edge of the metallic Fe peak was deconvoluted to determine the type and amount of Fe oxides present. After argon etching for about 40 Å, the peak due to Fe became stronger, indicating that the oxides were on the surface of the Fe film. Figure 3 shows typical hysteresis loops for an Fe-Fe oxide sample at 10 and 300 K. The shifted loop (shift by about 120 Oe) indicates the presence of exchange anisotropy at the interface of α-Fe and Fe-O phases. The loop shift was found to be smaller in thicker films.

Magnetization studies perpendicular and parallel to the film plane showed an anisotrop · in the film plane in a sample of thickness of 112 Å, which had been sputtered at 1.0 Å/s and passivated at 1.07 Torr (Fig. 4). The lack of perpendicular anisotropy is consistent with previous studies[10] which showed that oxygen contamination reduces the uniaxial surface anisotropy in Fe films having a thickness of several monolayers. With the increasing thickness, the surface anisotropy energy is further reduced and the easy axis becomes planar.

The coercivity of Fe-Fe oxide bilayers was found to depend strongly on both the total film thickness and temperature. H_c showed a large increase in samples with thickness below 60 Å reaching a value about 2.7 kOe in a 20 Å thick film (Fig. 5). In samples with a larger thickness, the coercivity was almost a constant, ~250 Oe. The thickness depen-

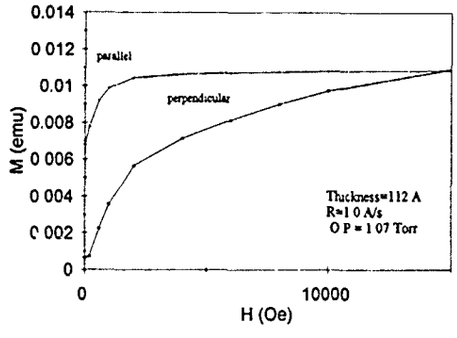

FIG. 4. Magnetization curves parallel and perpendicular to the film plane in an Fe-Fe oxide sample.

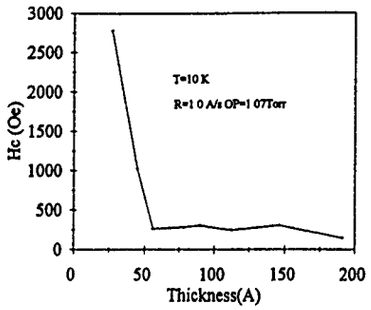

FIG. 5. Thickness dependence of H_c in Fe-Fe oxide bilayers.

dence of H_c may be influenced by both the grain size and the amount of iron oxide in the sample. The grain size is larger in thicker films and this may lead to a multidomain structure with a reduced coercivity. However, the grain size is well below the single domain size of iron particles (200 Å) even in the 200 Å thick sample, and therefore the size does not play a significant role here. On the other hand the relative amount of iron oxide present in the bilayers is much higher in thinner films leading to a stronger effective exchange coupling between the iron and iron-oxide layers and therefore a higher coercivity. The latter assumption is consistent with the fact that the coercivity of films with less oxidation is lower. The quantitative aspect of this interaction remains to be further investigated.

The coercivity decreases substantially with increasing temperature, as shown in Fig. 6. At room temperature, the coercivity is small but at lower temperature it increases substantially. This behavior may be caused by the magnetic behavior of the Fe-O coating which may become superparamagnetic at temperatures above 100 K. This is further supported by the thermomagnetic data (Fig. 7) which show a magnetic transition below room temperature possibly associated with the blocking temperature of Fe-O.

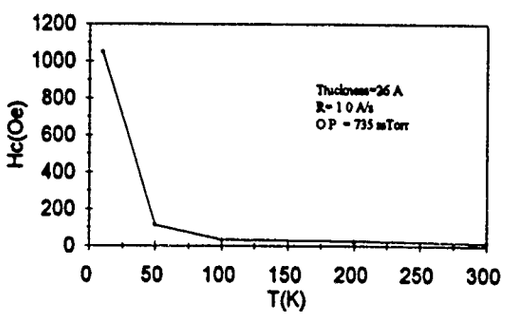

FIG. 6. Temperature dependence of H_c in an Fe-Fe oxide sample.

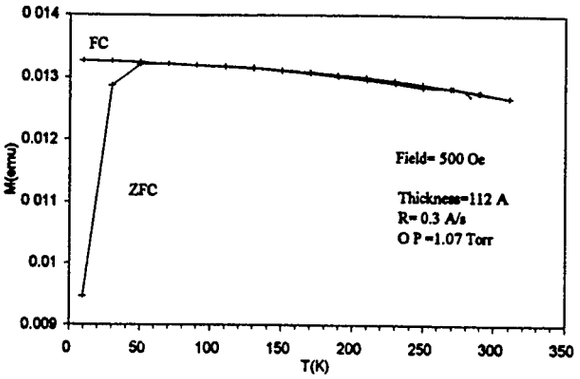

FIG. 7. Magnetization as a function of temperature of an Fe-Fe oxide sample at an applied field of 500 Oe. (ZFC: zero field cooled; FC: field cooled.)

IV. CONCLUSIONS

Fe-Fe oxide bilayers were made by dc magnetron sputtering method. The oxide layer was formed by passivating the surface of Fe film. The thin film was observed to have a uniform distribution of grains and the grain size increased with the increasing thickness from 20 to 200 Å. A high coercivity (2.7 kOe) was observed in a sample of 20 Å, deposited at 1.0 Å/s and passivated at 1.07 Torr air. A displaced hysteresis loop was observed in samples indicating a strong anisotropy at the iron-iron oxide interface. The coercivity was found to decrease substantially when the film thickness increased above 60 Å and the temperature increased above 100 K. The latter behavior was attributed to the superparamagnetic behavior of the Fe-O coating which might consist of very fine grains that had a blocking temperature around 100 K.

ACKNOWLEDGMENT

This work was supported by NSF DMR-9307676.

[1] Y. K. Kim and M. Oliveria, J. Appl. Phys. **75**, 431 (1994).
[2] J. K. Lin, J. M. Sivertsen, and J. H. Judy, J. Magn. Magn. Mater. **54**, 1659 (1986).
[3] C. Ortiz, T. Manoubi, and C. Colliex, J. Phys. **C8**, 2009 (1988).
[4] S. Urabe, T. Numata, S. Inokuchi, and Y. Sakurai, Jpn. J. Appl. Phys. **25**, 1134 (1986).
[5] S. Dhara, G. L. Malhotra, A. C. Rastogi, and B. K. Das, Thin Solid Films **209**, 116 (1992).
[6] W. H. Meiklejohn, J. Appl. Phys. **29**, 454 (1958).
[7] J. W. Schneider, A. M. Stoffel, and G. Trippel, IEEE Trans. Magn. **MAG-9**, 183 (1973).
[8] R. R. Ruf and R. J. Gambino, J. Appl. Phys. **55**, 2628 (1984).
[9] S. Gangopadhyay, G. C. Hadjipanayis, S. I. Shah, C. M. Sorensen, K. J. Klaubunde, V. Papaefthymiou, and A. Kostikas, J. Appl. Phys. **70**, 5888 (1991).
[10] J. F. Cochran, B. Heinrich, A. S. Arrott, K. B. Urquhart, J. R. Dutcher, and S. T. Purcell, J. Phys. **C8**, 1671 (1988).

Published without author corrections

Ferromagnetic-ferromagnetic tunneling and the spin filter effect

P. LeClair,[a] J. S. Moodera, and R. Meservey
Francis Bitter National Magnet Laboratory, Massachusetts Institute of Technology, Cambridge, Massachusetts 02139

Tunneling characteristics of a ferromagnetic-antiferromagnetic-ferromagnetic (FM-AFM-FM) thin film tunnel junction were studied in high magnetic fields with a view to investigate magnetic coupling by the tunneling process. Gd_2O_3, a stable oxide which undergoes antiferromagnetic ordering below about 3.9 K, was chosen as the tunnel barrier between the ferromagnetic electrodes Gd and permalloy. Tunnel characteristics showed as much as 32% decrease in junction resistance in an applied field of 20 T, below 4.2 K. The resistance behavior as a function of H can be explained by two different effects: firstly, the change in tunnel conductance due to change in the relative magnetization of the two FM electrodes in low H; secondly, the spin filter effect in high fields, due to the exchange splitting of the Gd_2O_3 conduction band.

I. INTRODUCTION

In the past few years, there have been many investigations with multilayer magnetic thin films. For example, if two magnetic films are separated by a thin nonmagnetic layer, then the current flowing in such a trilayer depends on the relative magnetization direction of the magnetic film.[1] This is the case whether the current flow is by the tunneling process or in plane through the entire length of the trilayer. Several trilayer systems in non-tunneling work (generally, with a metallic film interlayer) have shown the characteristics needed to fabricate field-activated devices.[1] When tunneling occurs between two ferromagnets, interesting effects can be expected if it is assumed that spin is conserved in the tunneling process.[2] Having two ferromagnetic electrodes with different coercive fields, one can expect the tunnel conductance to be dependent on the relative magnetization of the two electrodes.[3–7] When the two electrodes are aligned parallel, a maximum in conductance is expected; the opposite is true for an antiparallel arrangement. The effects of FM-I-FM tunneling and the change in the relative magnetization direction have been observed to bring up to 2%–3% change in junction resistance.[4,6] A simple model[4] gives the change in tunnel conductance due to the change in the relative magnetization directions equal to $2P_1P_2$, where P_1 and P_2 are the conduction band spin polarizations of the electrodes. For example, taking P_1=34% for Gd and P_2=30% for NiFe, one expects a change of 20% in the tunnel conductance. However, the observed change for various combinations of FM electrodes and barriers is far less than the expected value based on the simple model. Earlier, using a NiO_x barrier in FM-FM tunneling showed limited success.[4–6] This deviation can be partially accounted for by impurities in the tunnel barrier, magnetic domain walls, and insufficient field to align the electrodes fully.[6] Recent theoretical studies have also indicated a small effect.[7] The present work is about the study of an antiferromagnetic layer intervening two ferromagnetic layers, with a view to investigate magnetic coupling by the tunneling process. Gd_2O_3, a stable oxide which undergoes antiferromagnetic ordering below ~3.9 K,[8] was chosen for this study. In Gd/Gd_2O_3/NiFe tunnel junctions, a large effect on the junction resistance is observed upon the application of a magnetic field. The present experiments show that the latter effect is related to the spin filter effect, similar to that observed by Moodera *et al.*[9] Nowak and Rauluszkiewicz have recently reported excellent domain structure study in the tunnel junction area and about 2.5%–7.7% change in tunneling resistance for Gd/GdO_x/Fe junction in a field of ~80 Oe which they partially attribute to the spin filter effect.[10] However, the exchange splitting due to the applied field, $2\mu H$, in their case is only ~7 μeV and is too small compared to the reported barrier height of 0.276 eV to effectively show significant spin filter effect.

II. EXPERIMENT

Thin film junctions of Gd/Gd_2O_3/NiFe were prepared on LN_2 cooled glass substrates by vacuum evaporation. Metal masks were used to obtain the tunnel junction cross pattern. Initially, 40 nm cross strips of Gd were deposited. The Gd_2O_3 barrier was then created by oxygen glow discharge of the Gd film surface. NiFe long strips of 18 nm were then deposited. The preparation process was entirely *in situ*. Two out of the 72 junctions were selected to be mounted on a probe to measure the resistance as a function of magnetic field and temperature down to liquid helium temperatures. The magnetic field was applied parallel to the junction plane. Two kinds of measurements were done: R_J was measured as a function of applied field up to 20 T; second, I-V characteristics were plotted at H=0 and H=20 T up to 300 mV bias across the junction. The four terminal resistance measurement was used to avoid contact and lead resistance.

III. RESULTS AND DISCUSSION

Tunnel junction resistance was observed to increase as temperature decreased, showing the semiconducting nature of the Gd_2O_3 tunnel barrier. At temperatures 4.2 K and below, a significant drop in junction resistance was seen with applied magnetic field. Figure 1 shows the variation of tunnel junction resistance as a function of magnetic field, taken at 1.1 K for a representative sample. As seen in Fig. 1, junction resistance showed a sharp initial decrease of ~6%, in low fields, region A(A′), followed by a slight increase in region B(B′) where it nearly regains its original value. Some

[a]Present address: Phillips Academy, Andover, MA 01810.

 0021-8979/94/76(10)/6546/3/$6.00 © 1994 American Institute of Physics

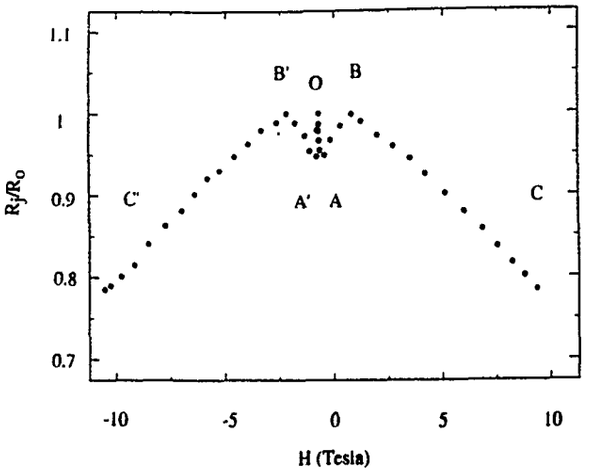

FIG. 1. Tunnel junction resistance variation with magnetic field. Data taken at $T=1.1$ K.

other junctions did not show this rise after the first decrease in resistance. In higher H, a more gradual and greater change in R_J is seen, and by $H=10$ T, the change is ~20% [region C(C′)]. As seen in Fig. 1, R_J variation is not simple and straightforward. However, invoking the phenomena of tunneling conductance dependence on the relative magnetization directions of the two electrodes and the spin filter model, one can try to explain the general trend of the data. Although not shown in Fig. 1, R_J vs H was measured up to 20 T, where R_J decreased by ~32%. The magnetoresistance of the electrodes alone was measured and found to have a negligible contribution to the junction resistance change.

The I-V characteristics of the junctions were measured in $H=0$ and $H=20$ T at various temperatures. Data reported here is for $T=1.1$ K; data at 4.2 K or less showed qualitatively similar behavior, while at higher temperatures R_J varied only a few percent. Shown in Fig. 2 is current density (J) versus voltage at 1.1 K, in $H=0$ and $H=20$ T. The J-V curves are typical of junctions with good barriers. The current-voltage characteristic of a tunnel junction has been theoretically derived by Simmons,[11] based on a trapezoidal tunnel barrier. The tunnel current density is given approximately by

$$J=J_0\left\{\left(\phi-\frac{V}{2}\right)\exp\left(-A\left(\phi-\frac{V}{2}\right)^{1/2}\right]-\left(\phi+\frac{V}{2}\right)\times\exp\left(-A\left(\phi+\frac{V}{2}\right)^{1/2}\right]\right\}, \quad (1)$$

where $J_0=(e^2/2\pi h)s^{-2}$ and $A=(4\pi s/h)(2m)^{1/2}$, with s being the barrier thickness, and ϕ is the barrier height. By fitting the J-V curves to Eq. (1), tunnel barrier height (ϕ) was obtained for $H=0$ and $H=20$ T separately. This fit is also shown in Fig. 2. The barrier thickness (s) was found to be 3.05 nm. In $H=0$, the mean barrier height was 0.4105 eV, while at $H=20$ T it was found to be 0.4006 eV. Thus the mean barrier height decreased by 9.9 meV in 20 T field.

R_J variation seen in Fig. 1 may now be explained as follows. At low H, the ~6% decrease in R_J(A,A′) can be due to ferromagnetic-ferromagnetic tunneling with the relative magnetization of the electrodes changing from antiparallel to parallel direction. Region O represents the antiparallel alignment. This change is still quite low when compared to the expected 20% change[4] as discussed above, but the values in this region are quite similar to those observed by others.[3–7] The effects due to the relative magnetization direction dominate at low H. The increase in region B(B′) is not fully understood at this time; for example, exchange anisotropy at the AFM-FM interface may be at least partially responsible.

In high fields, the change in junction resistance is more gradual and greater as well. Simmons' tunneling theory shows that a decrease in R_J is possible when ϕ or s is decreased. In the present case, the change cannot be due to a decreasing barrier thickness, since s is Gd_2O_3 thickness, which is fixed. Such behavior was observed recently by Moodera *et al.*[9] in tunnel junctions with antiferromagnetic EuSe barriers. There, the variation of the barrier height was

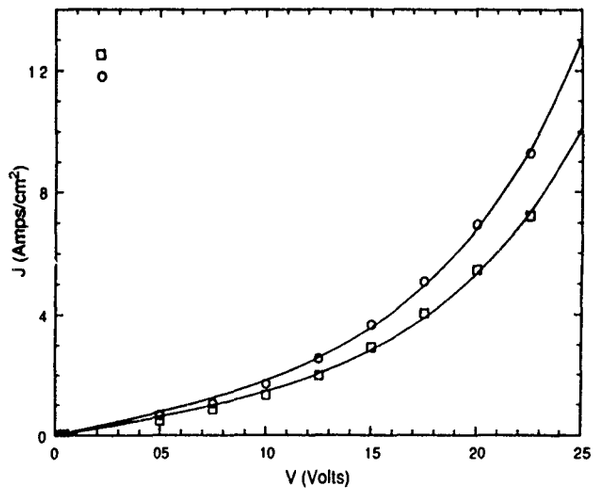

FIG 2 J-V characteristics taken at 1.1 K in $H=0$ and 20 T (□ and ○, respectively) applied field. Solid line is the fit to Simmons' theory [Eq. (1)].

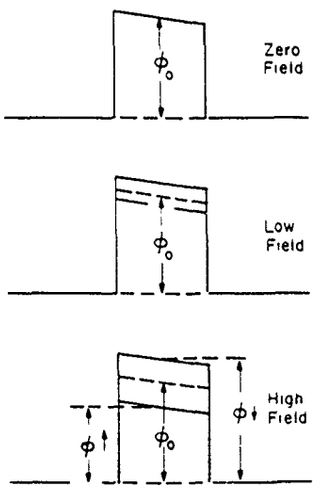

FIG. 3 Schematic of conduction band exchange splitting of the antiferromagnetic Gd_2O_3 tunnel barrier and the spin filter effect.

attributed to the AFM to FM phase change in EuSe in an applied H, leading to exchange splitting in EuSe and resulting in an energy separation of spin up and spin down bands (see Fig. 3). Since Gd_2O_3 is antiferromagnetic, applying a strong magnetic field can be expected to drive it towards a ferromagnetic phase. The magnetic moment of the Gd^{3+} ion, $7.8\mu_b$,[12] is conductive to such a phase change. The exchange splitting (2Δ) in a field is given by the Zeeman energy, $2\ \mu H$, where μ is the magnetic moment of Gd^{3+} ions in Gd_2O_3. The exchange splitting value is for the splitting of the bottom of the conduction band in Gd_2O_3, similar to europium chalcogenides.[13,14] The change in barrier height as expected from the exchange splitting, $2\ \mu H$, is 9.03 meV at 20 T, which is in close agreement with the observed change of 9.9 meV from $H=0$ to $H=20$ T. This clearly shows that the change in barrier height is closely associated with the conduction band splitting in Gd_2O_3. This energy separation causes the spin up band to be at a lower energy than the spin down band, resulting in preferential selection of spin up electrons in the tunneling process, and thus decrease in resistance as well as spin polarization of the tunneling electrons (Fig. 3), leading the tunnel barrier to serve as a "spin filter." Applied field effectively "tunes" the barrier height. The spin filter effect dominates at high H and temperatures close to and below the Neél temperature of Gd_2O_3, $T_n=3.9$ K.

Simmons' tunnel current equation [Eq. (1)] can be modified for the spin up and spin down current densities as follows:

$$J_{\downarrow,\uparrow}=\frac{J_0}{2}\left\{\left(\phi_{\downarrow,\uparrow}-\frac{V}{2}\right)\exp\left[-A\left(\phi_{\downarrow,\uparrow}-\frac{V}{2}\right)^{1/2}\right]-\left(\phi_{\downarrow,\uparrow}+\frac{V}{2}\right)\exp\left[-A\left(\phi_{\downarrow,\uparrow}+\frac{V}{2}\right)^{1/2}\right]\right\}, \quad (2)$$

where $\phi_{\downarrow,\uparrow}$ are the barrier heights, respectively, for the spin up and spin down tunneling electrons. The barrier heights for spin up and spin down tunneling electrons are $\phi-\mu H$ and $\phi+\mu H$ respectively. So, at 20 T, $\phi_\downarrow$ was taken to be 0.4096 eV, and $\phi_\uparrow$ was taken to be 0.3916 eV. Now that spin up and spin down barrier heights are known, spin polarization can be found by evaluating J for the spin up and spin down energy bands. Spin polarization was found by defining $P=(J_\uparrow-J_\downarrow)/(J_\uparrow+J_\downarrow)$,[9] which gave values of 17%–23%. This does not take into account spin scattering or other effects.

IV. SUMMARY

In conclusion, FM-FM tunneling has been studied. The present work shows that the junction resistance variation with H of the $Gd/Gd_2O_3/NiFe$ tunnel structure can be explained by two distinct effects; namely, FM-FM tunneling and the spin filter effect. Exchange splitting in H, given by the Zeeman energy, explain the J-V characteristics quite well. This latter effect also causes spin polarization of the tunneling electrons. The low H results are in agreement with previous studies,[3–7] and the high H results are similar to those seen in EuSe junctions by Moodera *et al.*[9]

ACKNOWLEDGMENTS

One of the authors (P.L.) would like to thank the Research Science Institute for making much of his stay at the Francis Bitter National Magnet Laboratory at MIT possible. Funding for this research is provided by the Office of Naval Research (ONR Grant No. N00014-92-J-1847) and the National Science Foundation NSF Grant No. DMR-9023400).

[1] G. A. Prinz, Science **250**, 1092 (1990); S. S. P. Parkin, Phys. Rev. Lett. **71** (1993), and references cited therein; M. Johnson, *ibid.* **70**, 2142 (1993).
[2] P. M. Tedrow and R. Meservey, Phys. Rev. Lett. **26**, 192 (1971); P. M. Tedrow and R. Meservey, Phys. Rev. B **7**, 318 (1973).
[3] M. Julliere, Phys. Lett. **54A**, 225 (1975).
[4] S. Maekawa and U. Gafvert, IEEE Trans. Magn. **MAG-18**, 707 (1982).
[5] Y. Suezawa and Y. Gondo, in *Proceedings of the International Symposium on Physics of Magnetic Materials*, edited by M. Takahashi, S. Maekawa, Y. Gondo, and H. Nose (World Scientific, Singapore, 1987), p. 303.
[6] R. Kabani, J. S. Moodera, P. M. Tedrow, and R. Meservey, Materials Research Society Extended Abstracts, 1990 (unpublished), pp. 177–179.
[7] J. C. Slonczewski, Phys. Rev. B **39**, 6995 (1989).
[8] A. E. Miller, R. J. Jeilinek, K. A. Gschneidner, Jr., and B. C. Gerstein, J. Chem. Phys. **55**, 2647 (1971).
[9] J. S. Moodera, X. Hao, G. A. Gibson, and R. Meservey, Phy. Rev. Lett. **61**, 637 (1988); J. S. Moodera, R. Meservey, and X. Hao, *ibid.* **70**, 853 (1993).
[10] J. Nowak and J. Rauluszkiewicz, J. Magn. Magn. Mater. **109**, 79 (1992).
[11] J. G. Simmons, J. Appl. Phys. **34**, 1793 (1963).
[12] S. Arajs and P. V. Colvin, J. Appl. Phys. **33**, 2517 (1962).
[13] A. Mauger and C. Godart, Phys. Rep. **141**, 51 (1986).
[14] P. Wachter, in *Handbook on the Physics and Chemistry of Rare Earths*, edited by K. A. Gschneidner, Jr. and L. Eyring (North-Holland, Amsterdam, 1979), Chap. 19.

Theory of Brillouin light scattering from spin waves in multilayers with interlayer exchange and dipole coupling

A. N. Slavin
Physics Department, Oakland University, Rochester, Michigan 48309

I. V. Rojdestvenski and M. G. Cottam
Physics Department, University of Western Ontario, London, Ontario N6A 3K7, Canada

An analytic Green-function theory is developed for the dipole-exchange spin waves and their Brillouin light-scattering spectra in perpendicularly magnetized magnetic multilayers and superlattices. We consider periodic structures consisting of a large number of similar ferromagnetic layers separated by nonmagnetic spacers. The dipole-dipole and exchange coupling are included between magnetic layers, as well as within the layers.

We extend our previously developed analytic theories of Brillouin light scattering from dipole-exchange spin waves in magnetic films[1] and double layers[2] to the cases of perpendicularly magnetized magnetic superlattices consisting of alternating layers of a ferromagnet and a nonmagnetic spacer. The effects of dipole-dipole and exchange interactions (both intralayer and interlayer) are included. We obtain explicit approximate expressions for the spectrum of the collective spin wave modes of a superlattice. Numerical examples for Fe/spacer superlattices are presented.

We assume a perpendicularly magnetized multilayer structure consisting of N identical magnetic layers separated by identical nonmagnetic spacers. The energy density W of the system can be written as

$$W=\frac{1}{4VN}\sum_{i,j}\int d\mathbf{r}\,d\mathbf{r}'\mathbf{M}^*_{\mathbf{r}i}(2\hat{G}_{\mathbf{r}\mathbf{r}'ii}\delta_{ij}+\hat{G}_{\mathbf{r}\mathbf{r}'ij})\mathbf{M}_{\mathbf{r}'j}$$
$$-\frac{1}{VN}\sum_{j}\int d\mathbf{r}H_{\mathbf{r}j}M^z_{\mathbf{r}j}, \tag{1}$$

where V is the volume of each magnetic layer (labeled by i and j) and $\mathbf{M}_{\mathbf{r}i}$ is the total magnetization at position $\mathbf{r}$ in layer i. The second term describes the Zeeman interaction with the static magnetic field, assumed to be $H\hat{\mathbf{z}}$ in all layers. The tensor $\hat{G}_{\mathbf{r}\mathbf{r}'ij}$ represents dipole and exchange interactions, with the diagonal term $\hat{G}_{\mathbf{r}\mathbf{r}'ii}$ corresponding to a single film case. We take the dipole and intralayer exchange interaction tensors in the same form as for a single film[1] and assume for the interlayer exchange

$$W_{ile}=-\frac{\pi\alpha}{\tilde{L}NV}\sum_{i,j}\beta\int d\mathbf{r}\,d\mathbf{r}'\mathbf{M}^*_{\mathbf{r}i}\mathbf{M}_{\mathbf{r}'j}\delta(\rho-\rho'), \tag{2}$$

where $\tilde{L}$ is the superlattice periodic length (i.e., the sum of a spacer thickness and a magnetic layer thickness), and α is a constant of intralayer exchange[3] related to exchange constant $\mathcal{A}$ by $\alpha=\mathcal{A}/(2\pi M_0^2)$, where M_0 is the saturation magnetization (assumed to be the same in all layers). Also $\beta=\mathcal{A}_{12}/\mathcal{A}$ is an effective interlayer exchange parameter defined as in Ref. 2. The sum is over the adjacent layers, and ρ and ρ' are the in-plane components of $\mathbf{r}$ and $\mathbf{r}'$.

Next we rewrite W, using the linearized Holstein–Primakoff representation[4] as before,[3] and we transform the spin-wave (SW) polarizations $a_{\mathbf{r}i}$ and $a^*_{\mathbf{r}i}$ with respect to any complete orthonormal basis $\phi_k(\mathbf{r},i)$, indexed by label k

$$a_{\mathbf{r}i}=\sum_k a_k\phi_k(\mathbf{r},i),\quad a^*_{\mathbf{r}i}=\sum_k a^*_k\phi^*_k(\mathbf{r},i). \tag{3}$$

The quadratic part W_2 of the energy density is then

$$W_2=\sum_{12}A_{12}a^*_1a_2+\tfrac{1}{2}\left(\sum_{12}B^*_{12}a_1a_2+\text{c.c.}\right) \tag{4}$$

where, defining g as a gyromagnetic ratio,

$$A_{12}=\frac{gM_0}{2VN}\sum_{i,j}\int d\mathbf{r}\,d\mathbf{r}'\Big[\phi^*_1(\mathbf{r},i)\phi_2(\mathbf{r}',j)$$
$$\times(\hat{G}^{++}_{\mathbf{r}\mathbf{r}'ij}+\hat{G}^{--}_{\mathbf{r}'\mathbf{r}ji})(1+\delta_{ij})-2\delta(\mathbf{r}-\mathbf{r}')$$
$$\times\delta_{ij}\left(\sum_j\int d\mathbf{r}'\hat{G}^{zz}_{\mathbf{r}\mathbf{r}'ij}+\frac{H}{M_0}\right)\Big], \tag{5}$$

$$B_{12}=\frac{gM_0}{VN}\sum_{i,j}\int d\mathbf{r}\,d\mathbf{r}'\phi_1(\mathbf{r},i)\phi_2(\mathbf{r}',j)$$
$$\times\hat{G}^{+-}_{\mathbf{r}\mathbf{r}'ij}(1+\delta_{ij}). \tag{6}$$

Here indices 1 and 2 stand for k_1 and k_2, and the superscripts $+$, $-$, and z denote the corresponding components of the interaction tensor in terms of $M^{\pm}=M^x\pm iM^y$ and M^z.

To choose the orthonormal basis $\phi_k(\mathbf{r},i)$ we assume that: (i) the interlayer interaction is weak, so that the SW modes of a single layer (SWSL) do not differ significantly from the corresponding modes S_n of a single magnetic film;[3] and (ii) the individual layers are thin enough for the different SWSLs to be well separated in frequency. With these two assumptions the SW modes of a multilayer can be represented as SW composite modes (SWCM) of the following form:

$$\phi_k(\mathbf{r},i)\equiv\phi_{\mathbf{k}nQ}(\mathbf{r},i)=L_{niQ}S_n(\xi_i)\exp(-\mathbf{k}\cdot\rho), \tag{7}$$

where $\mathbf{k}$ is the in-plane wave vector, and ξ_i is the spatial coordinate perpendicular to the layers measured from the center of layer i. The orthonormality condition is

$$\sum_{nj}L^*_{njQ}L_{njQ'}=N\delta_{QQ'}. \tag{8}$$

 0021-8979/94/76(10)/6549/3/$6.00 © 1994 American Institute of Physics

We now substitute the above expressions into Eqs. (5) and (6) to obtain A_{12} and B_{12} in terms of the coefficients L_{njQ}, which we take to have the form

$$L_{njQ}=R_{nQ}\exp(-iQ_j)+T_{nQ}\exp(iQ_j), \tag{9}$$

where Q, which generally depends on the mode number n, is a (dimensionless) superlattice Bloch wave number for the SWCM.

By analogy to the single film case,[3,5] the values of R_{nQ}, T_{nQ}, and Q depend on the effective "macroscopic pinning" at the top and bottom magnetic layers of the multilayer structure. These macropinning parameters may depend on the different effective anisotropy fields in the top, bottom, and bulk layers as well as on the anisotropy of interlayer exchange. Details will be given elsewhere,[6] but in the simple case of no multilayer boundary anisotropy we get

$$L_{njQ}=(2-\delta_{0m})^{1/2}\cos\left[\frac{\pi m}{N}\left(j-\frac{1}{2}\right)\right], \tag{10}$$

where $Q\equiv\pi m/N$, and $m=0,1,2,\ldots,N-1$. For any given $\mathbf{k}$ and n, we can eventually rewrite the coefficients A and B and the lowest nonhybridized SWCM frequencies ω_{knQ} as

$$A_{kn,QQ'}=\delta_{QQ'}[\omega_H+\alpha\omega_M(\mathbf{k}^2+q_n^2)+(\beta Q^2/2\tilde{L})]+\tfrac{1}{4}\omega_M U_{kn,QQ'}, \tag{11}$$

$$B_{kn,QQ'}=\tfrac{1}{4}\omega_M U_{kn,QQ'}, \tag{12}$$

$$\omega_{knQ}^2=A_{kn,QQ}^2-|B_{kn,QQ}|^2=\Omega_{knQ}(\Omega_{knQ}+\tfrac{1}{2}\omega_M U_{kn,QQ}). \tag{13}$$

Here $\omega_M=4\pi gM_0$, $\omega_H=g(H-4\pi M_0)\equiv gH_i$, q_n is the single-film transverse wave number for mode n, and

$$\Omega_{knQ}=\omega_H+\alpha\omega_M[\mathbf{k}^2+q_n^2+(\beta Q^2/2\tilde{L})], \tag{14}$$

$$U_{kn,QQ'}=\frac{1}{N}\sum_{i,j}L_{niQ}^{*}L_{njQ'}P_{nnij}(\mathbf{k})+P_{nn}(\mathbf{k}L)\delta_{QQ'}. \tag{15}$$

The dipole matrix elements $P_{nnij}(\mathbf{k})$ and $P_{nn}(\mathbf{k}L)$ are defined analogously to the single film case.[3] The following factorization is possible:

$$P_{nnij}(\mathbf{k})=\mathcal{G}_{\mathbf{k}}(i,j)P_n(kL), \tag{16}$$

where $P_n(kL)$ depends only on the single-layer parameters and

$$\mathcal{G}_{\mathbf{k}}(i,j)=\frac{k}{2}\exp(-k\tilde{L}|i-j|) \tag{17}$$

is a discrete analog of the dipole Green function[3] (denoting $k\equiv|\mathbf{k}|$). For $N\gg1$ we can write[6] $U_{kn,QQ}\sim P_{QQ}(\mathbf{k}\tilde{L}N)P_n(kL)$ where the function P_{QQ} is given by the same formal expression as the matrix element P_{nn} for a single film.[3]

Now, using Eqs. (11)–(15), we can calculate the frequencies of the nonhybridized composite modes in a similar way to the single film case. Equations (13)–(15) constitute a description of the multilayer in an effective-medium approximation. In particular, Eq. (13) has the same form as for a single film, but with renormalized parameters. By analogy with the single-film results we conclude that, if the multilayer has no "macrosurface" anisotropy, i.e., the interaction between the first (or last) layer and its neighboring one is the same as for any adjacent layers in the bulk, there are no pseudosurface ($\mathrm{Im}\,Q>0$) composite modes. In this case the lowest frequency excitation will be the uniform precession (constant L_{njQ}) mode, which also will be the only one excited in FMR experiments. If there is a macrosurface anisotropy on the edges of a multilayer, the consistency equation to determine the composite modes transverse wave numbers Q will be similar to that for a film:[1,3]

$$(Q^2-D_1D_2)\tan(QN\tilde{L})=Q(D_1+D_2) \tag{18}$$

with the parameters D_1 and D_2 characterizing the boundary-layer anisotropy of the interlayer exchange. The solutions of Eq. (18) for Q with imaginary values correspond to the pseudosurface excitations while real values produce the pseudobulk solutions.

We first relate the above results to some recent FMR measurements.[7] The two branches of FMR can be associated with the hybridized pseudosurface and first pseudobulk composite modes. The hybridization occurs as the spacer thickness becomes greater than 5 Å and is due to mixing of the branches with different q_n but close SWCM frequencies. We expect low value of macropinning constant as the first pseudobulk composite mode has relatively small resonance amplitude. We assume that $D_2=0$ and $D_1\equiv D$, which roughly matches assumptions in Refs. 7 and 8. Using Eq. (18) we can write that far from the hybridization area for small D

$$\frac{\Delta\omega}{\omega_M}=\frac{\alpha}{2N\tilde{L}}[\pi^2+4D+\pi(\pi^2+4D)^{1/2}]. \tag{19}$$

Equation (19) enables the value of D to be deduced from the experimental values of $\Delta\omega$. Although our approach is capable of predicting the behavior of the FMR dispersion relationships, there is no simple way to include hybridization in our formalism. The reason is that the possible mechanism for hybridization is mixing of single film modes with different transverse wave vectors but close frequencies, occurring due to the micropinning dependence on the spacer thickness. It would be worth developing a numerical perturbation theory of the kind used in Refs. 9 and 10 that would use our analytical expressions as a zero-order approximation.

For the case of Brillouin light scattering (BLS) experiments, where $k\sim10^5\ \mathrm{cm}^{-1}$, the above-mentioned effects will be much less important as the main role in the hybridization will be played by dipole interlayer interaction. Hence we apply the SWCM formalism to Fe/spacer multilayers with the parameters: $\alpha=1.15\times10^{-13}\ \mathrm{cm}^2$, $4\pi M_0=21$ kOe, $H=22.5$ kG, $L=100$ Å, spacer thickness 10 Å, and zero macro- and micropinning. It is straightforward to confirm numerically that for these parameters there is no noticeable hybridization of the modes with different n. In Fig. 1 we display the boundaries of the bulk bands for multilayers with $\beta=10^5\ \mathrm{cm}^{-1}$ and different values of N. One of the boundaries (at $Q=\pi$), is independent of N within the given $\mathbf{k}$ interval. This can be explained by the vanishing of the dipolar

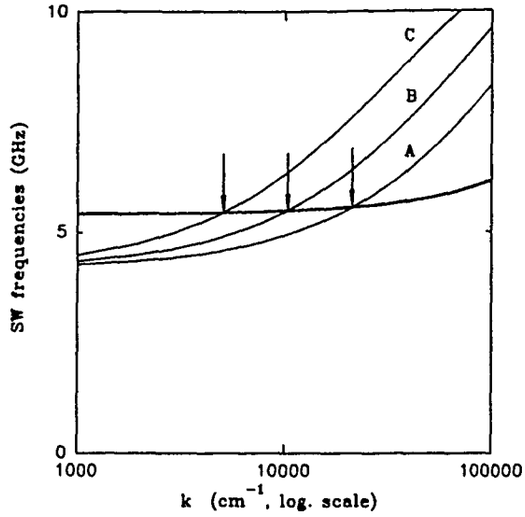

FIG. 1. Dispersion relationships for Fe/spacer multilayers with number of layers $N=10$ (A), 20 (B), and 40 (C). The flat curve represents the purely exchange branch ($Q=\pi$); curves A, B, and C represent the purely dipole branch ($Q=0$). $\beta=10^5$ cm^{-1}. See the text for the other parameters.

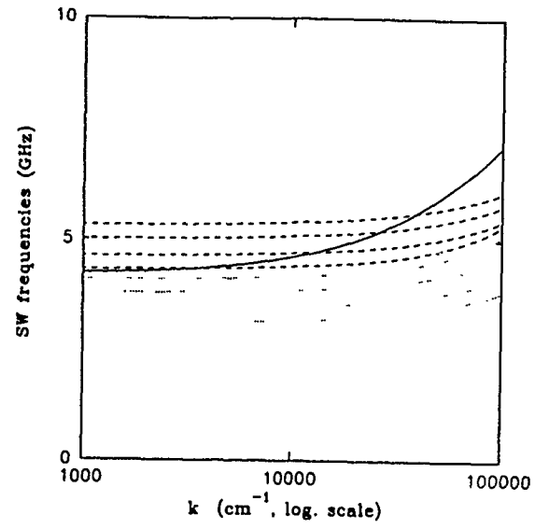

FIG. 2. The dispersion relationships for a five-layer structure. The solid line corresponds to the purely dipole branch, while the dashed and broken lines refer to $\beta=10^5$ and -10^5 cm^{-1}, respectively.

contribution for the modes with high Q. The other boundary (at $Q=0$) does not depend on the interlayer exchange. The dipolar contribution to this branch is significant and it depends on N. From our analysis we expect a scaling behavior with the dimensionless universal variable being $k\tilde{L}N$. Indeed, in Fig. 1 we see that the crossings, denoted by arrows are equidistant in the logarithmic k scale. In Fig. 2 we show the dispersion branches for Fe/spacer multilayers with $N=5$ and different values of β corresponding to ferromagnetic and antiferromagnetic interlayer exchange. The branch separation for the low k region, which is directly measurable from the BLS spectrum, is directly proportional to $|\beta|$. This provides a convenient way of measuring β.

The extension of the above to obtain the BLS intensities follows a well-established procedure, generalizing our results[1,2] for thin films and double layers. Basically, the scattering cross section can be expressed in terms of a weighted summation over magnetization-dependent Green functions $\langle\langle m^{\mu}_{n\mathbf{k}}; m^{\nu}_{n'\mathbf{k}}\rangle\rangle$ with $\mu,\nu=x,y$. The weighting factors depend on temperature, magneto-optical coupling, electric-field polarizations, scattering geometry, and optical transmission coefficients at the various surfaces and interfaces. Once the appropriate Green functions have been calculated from the formalism described earlier (by linear-response methods), it is straightforward to determine the BLS intensities associated with the various SWCM modes. Details will be presented elsewhere.[6] In general, it is necessary to take account of the various internal multiple reflections of the incident and scattered light at the surfaces and interfaces of the sample,[1,2] but we avoid this difficulty by restricting attention to the case where the optical penetration depth of the light in the sample is smaller than L (e.g., as would be typically in the case of Fe/spacer multilayers).

[1] I. Rojdestvenski, M. G. Cottam, and A. Slavin, Phys. Rev. B **48**, 12768 (1993).
[2] A. Slavin, I. Rojdestvenski, M. G. Cottam, J. Appl. Phys. **75**, 6443 (1994).
[3] B. A. Kalinikos and A. N. Slavin, J. Phys. C **19**, 7013 (1986).
[4] T. Holstein and H. Primakoff, Phys. Rev. **58**, 1040 (1940).
[5] P. E. Wigen, C. F. Kooi, and M. R. Shanabarger, Phys. Rev. Lett. **9**, 206 (1962).
[6] I. Rojdestvenski, M. G. Cottam, and A. Slavin (unpublished).
[7] Z. Zhang, P. E. Wigen, and S. S. P. Parkin, J. Appl. Phys. **69**, 5649 (1991).
[8] Z. Zhang, P. E. Wigen, and T. Suzuki, J. Magn Soc. Jpn. **17**, 119 (1993).
[9] B. Hillebrands, Phys. Rev. B **41**, 530 (1990).
[10] M. Vohl, J. Barnas, and P. Grunberg, Phys. Rev. B **39**, 12 003 (1989).

Spin wave spectra in semi-infinite magnetic superlattices with nonuniaxial single-ion anisotropy

E. L. Albuquerque
Departamento de Física, Universidade Federal do Rio Grande do Norte, 59072-970-Natal, RN, Brazil

A microscopic theory, based on the Heisenberg model, is employed to investigate the spin wave spectra in a semi-infinite superlattice made up of two ferromagnetic materials, where the constituents may present both the uniaxial and nonuniaxial components of the single-ion anisotropy. Our calculations are carried out for the exchange-dominated regime, and a transfer-matrix approach is used to simplify the algebra, which otherwise could be quite heavy. The calculated spectra show that, in addition to bulk spin wave modes, there may be surface modes associated with the truncation of the superlattice.

I. INTRODUCTION

As a result of recent advances in fabrication techniques, there has been a continuing interest in investigating the properties of spin waves that propagate in multilayer magnetic microstructures. Many of these works have been concerned with these excitations at the low-temperature regime, where at least one of the components is a ferromagnetic or an antiferromagnetic material (for a review see Ref. 1). Further, depending on the relative importance of the magnetic dipole-dipole and exchange interactions, different models for the magnetic behavior can be employed. For instance, for sufficiently small values of the excitation wave vector, dipolar effects are dominant and magnetostatic modes should propagate in such superlattices.[2–4] On the other hand, at large excitation wave vectors typically greater than 10^8 m^{-1} in a ferromagnet, exchange interaction, which is the restoring force for spin waves, will be dominant.[5–10]

In this article we are concerned with the spin wave spectra in exchange-dominated magnetic superlattices. We intend to extend previous work[7,11,12] by considering surface effects in a semi-infinite magnetic superlattice, whose constituents have nonuniaxial ("easy-plane") single-ion anisotropy, besides the uniaxial ("easy-axis") single-ion anisotropy. Nonuniaxial anisotropy exists in many magnetic materials, like the ferromagnet $CrBr_3$ and the antiferromagnet NiO, and it can be different at a surface or interface because the crystalline electric fields are different there. We employ a microscopic theory to investigate the spin wave spectra based on the Heisenberg model, together with a transfer-matrix approach. This method was used with success in dealing with the theory of superlattice plasmon-polaritons (for a review see Ref. 13), and it leads to a compact expression for the spin wave dispersion relation of the magnetic superlattice. Experimental systems are likely to be more complicated than the model described here, with less simple crystal structures and possible different ordering at interface layers.[14] However, these details would influence only the detailed form of the transfer matrix, and neither the general method nor the qualitative form of the dispersion relations should be affected.

II. THEORY

As indicated in Fig. 1, we consider a superlattice in which n_a layers of material A alternate with n_b layers of material B. Both materials are taken to be simple cubic nonuniaxial Heisenberg ferromagnets, having bulk exchange constants J_A and J_B with nearest-neighbor exchange interaction. The size of the superlattice unit cell is $L=(n_a+n_b)a$, where a is the lattice constant of both materials. A static applied magnetic field $\mathbf{H}_0$ is assumed to be in the z direction. The superlattice is truncated at $z=0$, with vacuum occupying the region $z<0$.

The two materials are characterized by single-ion uniaxial anisotropy parameters D_A and D_B, as well as single-ion nonuniaxial anisotropy parameters F_A and F_B. At the interfaces, between constituents, these values are D_{SJ} and F_{SJ} ($J=A$ or B), while at the free surface (material A), defined by $z=0$, we have D_0 and F_0, respectively. The exchange constant across each interface A-B is equal to I.

The Heisenberg Hamiltonian for a bulk specimen of component $J=A$ or B is

$$H=-(1/2)\sum_{i,j} J_J \mathbf{S}_i\cdot\mathbf{S}_j - g\mu_B H_0 \sum_i S_i^z + H_{\text{anis}} \tag{1}$$

with

$$H_{\text{anis}}=-\sum_i D_J (S_i^z)^2 - \sum_i F_J[(S_i^x)^2-(S_i^y)^2]. \tag{2}$$

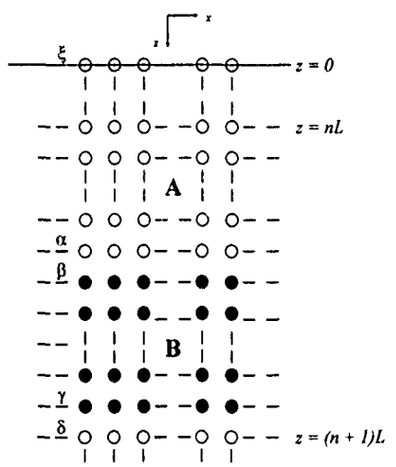

FIG. 1 The semi-infinite nonuniaxial ferromagnetic superlattice discussed in this article.

 0021-8979/94/76(10)/6552/3/$6.00 © 1994 American Institute of Physics

Here, $\mathbf{S}_i$ denotes the spin operator at magnetic site i, g is the usual Landé factor, and μ_B is the Bohr magnetron.

The dispersion equation for a bulk spin wave in medium J is found within the random-phase-approximation (RPA) from the equation of motion for the operator $S_i^{\pm}=S_i^x \pm iS_i^y$. This equation is

$$(\pm\hbar\omega-\Delta_J)S_i^{\pm}=S\sum_J J_J(S_i^{\pm}-S_j^{\pm})+2F_JS\eta^{1/2}S_i^{\mp}, \quad (3)$$

where we have made a Fourier transform to frequency ω. Also, $\eta=[1-(2S)^{-1}]$, and S is the RPA approximation for S_i^z. The value of Δ_J is

$$\Delta_J=g\mu_BH_0+2D_JS\eta. \quad (4)$$

Considering plane-wave solution for the operators $S_i^{\pm}$, and either by diagonalizing the Hamiltonian (1) or by solving Eq. (3) directly, we can find that the spin-wave dispersion relation in a nonuniaxial ferromagnet J is[15]

$$\cos(k_za)=(\Delta_J/2J_JS)+[3-\gamma(\mathbf{k}_p)] \pm[(\Omega_J/2)^2+F_J^2\eta/J_J^2]^{1/2}. \quad (5)$$

Here, $\Omega_J=\hbar\omega/J_JS$ and $\gamma(\mathbf{k}_p)=\cos(k_xa)+\cos(k_ya)$, with $\mathbf{k}_p=(k_x,k_y)$.

We now turn to the semi-infinite magnetic superlattice depicted in Fig. 1. At nonzero temperature the equilibrium configuration must exhibit the analog of surface reconstruction. This implies that the mean spin S in both materials is a function of its distance from the nearest A-B interface. However, although this effect is important, we can overcome it by restricting our attention to the low temperature regime, that is $T\ll T_c$, at which the spins are fully ordered. The spin wave dispersion equation can then be found by solving the RPA equations of motion for the spin operators $S_J^{\pm}$. A spin that is not in an interface layer, labeled α, β, γ, δ and ξ in Fig. 1, has the same nearest-neighbor environment and therefore the same equation of motion as a spin in the corresponding bulk medium. Thus, the spin wave amplitudes should be given, within each bulk material, by a linear combination of the positive- and negative-going solutions, i.e.,

$$S_J^+=\zeta_{1J}+F_{JJ}\zeta_{2J}, \quad (6)$$

$$S_J^-=Q_{1J}F_{JJ}\zeta_{1J}+Q_{2J}\zeta_{2J}, \quad (7)$$

where

$$\zeta_{1J}=A_1^n\exp(ik_{1J}z)+A_2^n\exp(-ik_{1J}z) \quad (8)$$

and ζ_{2J} is equal to ζ_{1J} provided we replace A_1^n, A_2^n, and k_{1J} by A_3^n, A_4^n, and k_{2J}. Also, ($J=A$ or B):

$$F_{JJ}=F_J\eta_J^{1/2}/J_J, \quad (9)$$

$$Q_{1J}=-2[\Omega_J+(\Omega_J^2+4F_{JJ}^2)^{1/2}]^{-1}=-(Q_{2J})^{-1}. \quad (10)$$

The wave vectors k_{1J} and k_{2J} are related to Ω_J by Eq. (5).

The equations of motion for layers α and β relate the amplitudes A_j^n, ($j=1-4$) of medium A with the corresponding amplitudes B_j^n ($j=1-4$) of medium B. Similarly, the equations of motion for layers γ and δ relate the amplitudes A_j^{n+1} ($j=1-4$) of medium A with the corresponding amplitudes B_j^n ($j=1-4$) of medium B. If one defines the column vectors $|A^n\rangle$, $|B^n\rangle$ and $|A^{n+1}\rangle$ formed by the corresponding undetermined amplitudes A_j^n, B_j^n and A_j^{n+1} ($j=1-4$), these equations can be cast in matrix forms as

$$\mathbf{M_A}|A^n\rangle=\mathbf{N_B}|B^n\rangle$$

and (11)

$$\mathbf{N_A}|A^{n+1}\rangle=\mathbf{M_B}|B^n\rangle,$$

where the 4×4 matrices $\mathbf{M}$ and $\mathbf{N}$ can be found elsewhere.[16]

Now, making use of the transfer-matrix treatment and Bloch's theorem, as in previous works,[7,12] we find that

$$\mathbf{T}|A^n\rangle=\exp(iQL)|A^n\rangle, \quad (12)$$

where Q is the Bloch wave vector, and the 4×4 transfer matrix $\mathbf{T}$ is defined by

$$\mathbf{T}=\mathbf{N_A}^{-1}\mathbf{M_B}\mathbf{N_B}^{-1}\mathbf{M_A}. \quad (13)$$

Also, as $\mathbf{T}$ is a unimodular matrix, the eigenvalues of Eq. (12) occur in pairs (t_i,t_i^{-1}), $i=1, 2$, and they are related to the two Bloch waves vectors Q_i by $t_i=\exp(iQ_iL)$. Thus, once $\mathbf{T}$ is evaluated, the required eigenvalues can be determined in a standard way. This calculation generalizes those presented in a previous paper,[12] where we discussed two limiting cases, namely first the nonuniaxial parameter F in each medium has the same value at the interface as in the bulk, and second the nonuniaxial anisotropy is considered only at the interfaces.

Now we consider the truncation of the superlattice at the plane $z=0$, with vacuum occupying the half space $z<0$. This allows us to investigate the occurrence of surface spin waves for this superlattice structure. For these modes Eq. (12) still holds, provided we replace the Bloch wave vector Q by $i\beta$, with $\mathrm{Re}(\beta)>0$ to guarantee a localized mode. Further we should take into account the equations of motion (3) for layer ξ at $z=0$, considering the single-ion anisotropy parameters D_0 and F_0. This provides an implicit dispersion relation for the surface spin waves and in fact, once the equations are solved, we can obtain a value of β which satisfies Eq. (12), with $\mathrm{Re}\,(\beta)>0$. The details of this calculation can be found elsewhere.[16]

III. NUMERICAL RESULTS AND DISCUSSIONS

In Fig. 2 we show the spin wave spectra for the surface and bulk modes which can propagate in a semi-infinite nonuniaxial ferromagnetic superlattice. We have plotted a reduced frequency $\Omega_A=\hbar\omega/J_AS_A$ against a reduced wave number k_xa across the whole Brillouin zone. The wave vector $\mathbf{k_p}=(k_x,k_y)$ is taken in the [10] direction.

The bulk superlattice bands of spin waves are shaded and they are bounded by the curves $QL=0$ and π. There are frequency gaps where no bulk superlattice modes exist, and the locations and widths of these gaps are influenced by the nonuniaxial anisotropy, being more pronounced for small values of k_xa where exchange effects are small. As a consequence, surface modes may propagate in these forbidden region, and indeed, as shown dashed in Fig. 2, there are surface spin waves occurring as discrete branches to the spectrum, in the gap regions between the continuum bulk mode bands. It is important to notice that some of the surface modes emerge

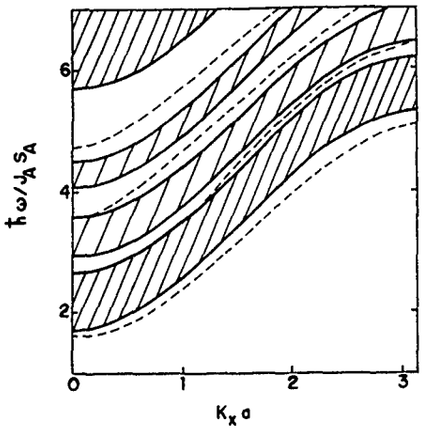

FIG. 2. Surface (dashed lines) and bulk (shaded bands) spin wave superlattice modes. The physical parameters used here are $J_A=2J_B=0.8I$, with $g\mu_B H_0=J_A$, and the spin average $S_A=S_B=1$. The anisotropy parameters were taken to correspond to $D_J/J_J=0.9$, $F_J/J_J=0.6$, while $D_{SJ}/I=0.9$, $F_{SJ}/I=0.6$, for $J=A$ or B. At the outermost interface we took $D_0/F_0=1.2$.

from the bulk continuum at a nonzero wave vector. For instance, the second and third surface spin-wave branch emerge from the bulk bands at the values of $k_x a$ equal to 0.12 and 1.2, respectively. For large values of $k_x a$, all surface modes tend to merge with the bulk bands.

Appropriate experimental technique for studying the superlattice spin waves would include light scattering spectroscopy of Raman and Brillouin type, and magnetic resonance. They have previously been successfully applied to surface and bulk spin waves in various magnetic microstructures.[1]

We also have extended the present ferromagnetic theory to take into account systems in which there is an antiparallel magnetization between the ferromagnetic materials.[16] High quality antiferromagnetic superlattices have recently been fabricated,[17] and we have also interest to extent the present theory to Heisenberg antiferromagnets.

ACKNOWLEDGMENT

This research was partially financed by the Brazilian Research Council CNPq.

[1] M. G. Cottam and D. R. Tilley, *Introduction to Surface and Superlattice Excitations* (Cambridge University Press, Cambridge, 1989).
[2] R. E. Camley, T. S. Rahman, and D. L. Mills, Phys. Rev. B **27**, 261 (1983).
[3] P. Grünberg and K. Mika, Phys. Rev. B **27**, 2955 (1983).
[4] R. E. Camley and M. G. Cottam, Phys. Rev. B **35**, 189 (1987).
[5] L. L. Hinchey and D. L. Mills, Phys. Rev. B **33**, 3329 (1986).
[6] L. L. Hinchey and D. L. Mills, Phys. Rev. B **34**, 1689 (1986).
[7] E. L Albuquerque, P. Fulco, E. F. Sarmento, and D. R. Tilley, Solid State Commun. **58**, 41 (1986).
[8] L. Dobrzynski, B. Djafari-Rouhani, and H. Puszkarski, Phys. Rev. B **33**, 3251 (1986).
[9] J. Barnas, J. Phys. C **21**, 1021 (1988).
[10] W.-Z. Shen and Z.-Y. Li, J. Phys.: Condens. Matter **4**, 5873 (1992).
[11] E. L. Albuquerque and M. G. Cottam, Phys. Rev. B **46**, 14543 (1992).
[12] E. L. Albuquerque and M. G. Cottam, Solid State Commun. **89**, 249 (1994).
[13] E. L. Albuquerque and M. G. Cottam, Phys. Rep. **233**, 67 (1993).
[14] J. Kwo, E. M. Gyorgy, D. B. McWhan, M. Hong, F. J. DiSalvo, C. Vettier, and J. E. Bower, Phys. Rev. Lett. **55**, 1402 (1985).
[15] S. Gopalan and M. G. Cottam, Phys. Rev. B **42**, 624 (1990).
[16] E. L. Albuquerque (to be published).
[17] C. A. Ramos, D. Lederman, A. R. King, and V. Jaccarino, Phys. Rev. Lett. **65**, 2913 (1990).

Ground state of antiferromagnetic systems in a magnetic field and in the presence of surfaces

L. Trallori, P. Politi, and A. Rettori
Dipartimento di Fisica dell'Università di Firenze, I-50125 Firenze, Italy

M. G. Pini
Istituto di Elettronica Quantistica, Consiglio Nazionale delle Ricerche, I-50127 Firenze, Italy

J. Villain
Departement de Recherche Fondamentale sur la Matière Condensée, C.E.N.G., 85X, 38041 Grenoble Cédex, France

We determine the ground state of semi-infinite uniaxial antiferromagnets and films, in terms of a two-dimensional area-preserving map, where the surfaces are introduced as appropriate boundary conditions. For the film, the ground state is calculated in a very rapid and accurate way for any value of N, the number of planes. For the semi-infinite system, we show that the so-called surface spin-flop state does not exist, while a non-homogeneous ground state is found in the bulk spin-flop phase.

Recently, new materials made of ferromagnetic films antiferromagnetically coupled, were synthetized. Using Kerr and SQUID magnetometry, sharp cusps in dM/dH were detected for such an $N=22$ multilayer of Fe/Cr(211) with a magnetic field applied parallel to the easy axis.[1] The peak at the higher field H_B was attributed to the bulk spin-flop (BSF) transition, and the peak at the lower field H_S to the surface spin-flop (SSF) transition.[1]

For a semi-infinite antiferromagnet with the surface spins *antiparallel* to the magnetic field ($AF_{\uparrow\downarrow}$), the presence of the SSF instability was inferred some years ago,[2,3] by noting that the $k=0$ surface mode softens for $H=H_S\simeq H_B/\sqrt{2}$. In the SSF state, the spins were predicted[2] to turn by nearly $\pi/2$ near the surface and asymptotically reach the $AF_{\uparrow\downarrow}$ configuration in the bulk. It was also suggested[4] that the extension of the region of turned spins should increase with increasing H, until the onset, for $H=H_B$, of a uniform bulk spin-flop state, with all the spins rotated by nearly $\pi/2$. In contrast, for a semi-infinite system with the surface spins *parallel* to the field ($AF_{\uparrow\uparrow}$),[3] the only instability was found at $H=H_B$, as in the infinite system, in correspondence to the softening of a bulk mode.

A doubtful point of this description is that, in the semi-infinite system, the same uniform BSF phase would be achieved in different ways, depending on the parallel or antiparallel orientation of the surface spins with respect to H.

For a film with a finite number of planes, N, one finds an analogous behavior of the excitations. For N even, there are two surface modes, and for $H=H_S$ only the one localized at the surface with the spins antiparallel to H shows a complete softening.[5] For N odd, if the excitations are calculated with respect to the AF ground state with the spins on both the two surfaces parallel to the field, the only instability is found at $H=H_B$.[5]

In this article, the determination of the ground state of both the semi-infinite system and the film is formulated as a two-dimensional area-preserving map[6–8] where the surfaces are introduced with appropriate boundary conditions.[9] The mapping is characterized by the fixed points and the orbits of the infinite sistem, but the spin structures relevant for our problem are only those which satisfy the previous conditions, a very selective constraint. In this way we are able to calculate the inhomogeneous ground state very rapidly and with a high accuracy (within machine double precision). For films with zero anisotropy, so that $H_B=0^+$, we recover the results obtained by numerical self-consistent methods.[10]

For the semi-infinite system, we show that the SSF state does not exist; for $H<H_B$, the stable ground state is always the $AF_{\uparrow\uparrow}$ one. We show that the $AF_{\uparrow\downarrow}$ state is metastable for $H<H_S$, while for $H_S<H<H_B$ it is unstable with respect to the formation of a Bloch wall which makes the surface spins turn from antiparallel to parallel to the field. For $H>H_B$, a nonuniform bulk spin-flop ground state is found.

For a film with even N, if $H<H_S$, the ground state is the AF one, with zero magnetization. For $H_S<H<H_B$, the lowest free energy is accomplished by an inhomogeneous configuration carrying a finite magnetization. In fact, it consists of a domain wall separating two nearly antiferromagnetic regions, with the spins on the two surfaces almost parallel to the applied field. In contrast, for a film with odd N, the ground state is the AF one with the spins on both the two surfaces parallel to H for any $H<H_B$. This explains why a peak in dM/dH was observed[1] at $H=H_S$ only for films with an even number of planes. For $H>H_B$, in both cases one has a nonuniform BSF configuration, owing to the surfaces effect.

The energy of the system is given by

$$\frac{E}{N_{\parallel}S}=\sum_n \left[H_E\cos(\phi_n-\phi_{n-1})-H_A\cos^2\phi_n - 2H\cos\phi_n\right], \tag{1}$$

where H_E and H_A are the exchange and anisotropy fields, respectively; n is the plane index, with $n\in\mathbb{Z}$ for the infinite system, $n\in\mathbb{N}$ for the semi-infinite one, and $n=1,2,\ldots,N$ for a film. By derivation we obtain

 0021-8979/94/76(10)/6555/3/$6.00 © 1994 American Institute of Physics

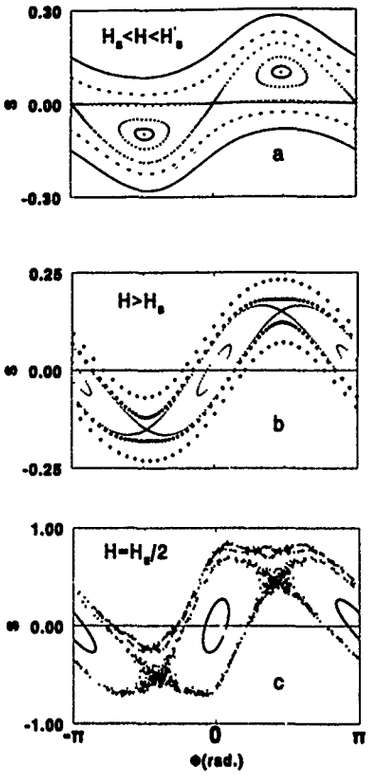

FIG. 1. Phase portraits obtained from mapping (3) for $H_A=0.9$ kG, $H_E=100$ kG ($\zeta=0.009$). (a) $H=10$ kG, (b) $H=15$ kG; full circles denote two nonhomotopic to zero trajectories pertinent to films with $N=20$ and $N=50$, respectively, (c) $H=50$ kG.

$$\sin(\phi_{n+1}-\phi_n)+\sin(\phi_{n-1}-\phi_n)+2\xi\sin\phi_n+\zeta\sin 2\phi_n=0 \quad \text{(infinite)}, \tag{2a}$$

$$\sin(\phi_{n+1}-\phi_n)+(1-\delta_{1,n})\sin(\phi_{n-1}-\phi_n)+2\xi\sin\phi_n+\zeta\sin 2\phi_n=0 \quad \text{(semi-infinite)}, \tag{2b}$$

$$(1-\delta_{N,n})\sin(\phi_{n+1}-\phi_n)+(1-\delta_{1,n})\sin(\phi_{n-1}-\phi_n)+2\xi\sin\phi_n+\zeta\sin 2\phi_n=0 \quad \text{(film)}, \tag{2c}$$

where $\xi\equiv H/H_E$ and $\zeta\equiv H_A/H_E$. We first consider Eq. (2a), valid for the infinite system. Introducing[8] $s_n=\sin(\phi_n-\phi_{n-1})$, it can be written as a two-dimensional mapping

$$\phi_{n+1}=\phi_n+\sin^{-1}(s_{n+1}), \tag{3a}$$

$$s_{n+1}=s_n-2\xi\sin\phi_n-\zeta\sin 2\phi_n. \tag{3b}$$

The mapping is area preserving (because the Jacobian is $J\equiv 1$), and invariant with respect to the transformation $(\phi,s)\rightarrow(-\phi,-s)$. Trajectories in (ϕ,s) space are associated with equilibrium configurations. In general, from the mapping (3) we obtain phase portraits [see Figs. 1(a)–1(c)] characterized by inflowing and outflowing orbits connecting the hyperbolic fixed points, elliptic orbits which encircle the homonymous fixed points and, finally, nonhomotopic to zero curves (i.e., curves which cannot be reduced to a point by a continuous deformation). The fixed points correspond to uniform ground states of the infinite system, and are second-order ones owing to its antiferromagnetic nature. Carrying out a stability analysis, it results that the AF fixed points $P_-^{AF}=(0,0)$, $P_+^{AF}=(\pi,0)$ are hyperbolic for $H\leqslant\sqrt{2H_EH_A+H_A^2}\equiv H_B$ [see Fig. 1(a)] and elliptic for higher fields [see Figs. 1(b) and 1(c)]. On the contrary, the BSF fixed points $P_-^{BSF}=(-\tilde{\phi},-\sin\tilde{\phi})$, $P_+^{BSF}=(\tilde{\phi},\sin\tilde{\phi})$, where $\cos\tilde{\phi}=H/(2H_E-H_A)$, are hyperbolic for $H\geqslant\sqrt{2H_EH_A-3H_A^2}\equiv H_B'$ [see Figs. 1(b) and 1(c)] and elliptic for lower fields[11] [see Fig. 1(a)].

In order to take care of the presence of surfaces in the film [see Eq. (2c)], we introduce two fictitious planes for $n=0$ and $n=N+1$, so that the boundary conditions are given by

$$s_1=\sin(\phi_1-\phi_0)=0, \tag{4a}$$

$$s_{N+1}=\sin(\phi_{N+1}-\phi_N)=0. \tag{4b}$$

For the semi-infinite system, only one fictitious plane must be introduced for $n=0$ [see Eq. 2(b)], and the boundary condition is given by Eq. 4(a). Among all trajectories obtained from the mapping (3), only those satisfying Eqs. (4) represent equilibrium configurations for the system in presence of surfaces. This is a very selective constraint; e.g., for a film, the physical trajectories must have two intersections with the $s=0$ line, separated by exactly N steps of the recursive mapping.

From the analysis of the phase portrait at different values of the field, we have found the ground state configurations for the semi-infinite system and for a film with even N.

(1) For $H<\sqrt{H_EH_A+H_A^2}\equiv H_S$, the phase portrait does not show peculiar features: the ground state is the $AF_{\uparrow\uparrow}$ one for the semi-infinite system, and the AF one for the film.

(2) For $H_S<H<H_B'$ [see Fig. 1(a)], the surface spin-flop state is not an equilibrium one for the semi-infinite system. This happens because none of the inflowing orbits, converging to one of the hyperbolic fixed points, P_-^{AF} and P_+^{AF}, is found to cross the line $s=0$ at $\phi\neq 0,\pi$.[5] It will be shown later, by energetic arguments, that the configuration assumed by the semi-infinite system in this field regime is the $AF_{\uparrow\uparrow}$ one. For the film, the ground state configuration is provided by one of the non homotopic to zero curves, since they are the only ones crossing the $s=0$ line in two different points which are not fixed points. In Fig. 2 we show the ground state configuration of an $N=50$ film for different values of H. It results that there is only one trajectory which is able to satisfy the boundary conditions (4), and the corresponding energy turns out to be smaller than that of the AF one. For $H_S<H<H_B'$, we find an inhomogeneous configuration consisting of a domain wall separating two nearly antiferromagnetic regions, with the spins on the two surfaces almost parallel to the applied field. Thus for $H=H_S$, the magnetization of a film with an even number of planes presents a jump from zero to a finite value. Such a field-induced phase transition was experimentally revealed as a peak in dM/dH in Fe/Cr multilayers.[1]

(3) For $H>H_B$ [see Fig. 1(b)], the uniform bulk spin-flop state is never an equilibrium one since the hyperbolic fixed points, P_-^{BSF} and P_+^{BSF}, do not lie on the line $s=0$, as

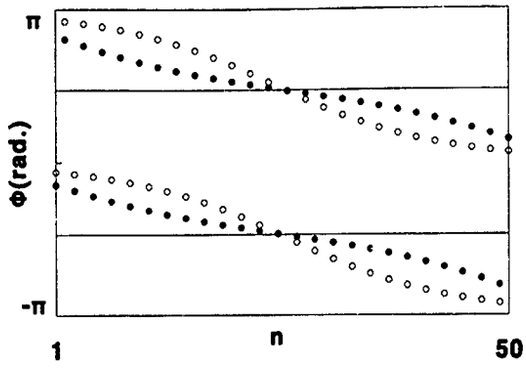

FIG. 2. Ground state configuration for an $N=50$ film with $H_A=0.9$ kG, $H_E=100$ kG. Open circles: $H=10$ kG. Full circles: $H=15$ kG. The solid horizontal lines show the canting angles for an infinite system in the bulk spin-flop phase fo $H=15$ kG.

required by the boundary conditions. For the semi-infinite system, an inhomogeneous ground state is found since all the inflowing orbits, converging to one of the hyperbolic BSF fixed points, intersect the $s=0$ line. For the film, the nonhomotopic to zero trajectories giving the ground state configuration, are closer and closer to $P_{\pm}^{\mathrm{BSF}}$ as N increases: then, for $H>H_B$ and moderate fields, only the middle planes present a configuration similar to the BSF one, while the spins in the planes near the surfaces are rotated by angles significantly different from $\pi/2$ (see Fig. 2). For $H>H_B$ and high fields ($H\gtrsim H_E/2$), the phase portrait becomes chaotic [see Fig. 1(c)]. It is important to note that evidence for chaotic behavior is also found[5] for those high values of the H_A/H_E ratio ($\zeta=0.25$) pertinent to Fe/Cr multilayers.[1]

At this point we put forward an energetic, though approximate, argument to confirm that for the semi-infinite system in the field range $H_S<H<H_B$, the SSF state (or any other nonuniform configuration) cannot exist. We rewrite Eq. (1) as

$$\frac{E}{N_{\|}S}=\sum_{n=1}^{\infty}\left[H_E\cos(\phi_n-\phi_{n-1})-H_A\cos^2\phi_n\right]$$

$$-H\sum_{n=1}^{\infty}\left[\cos\phi_n+\cos\phi_{n+1}\right]-H\cos\phi_1. \qquad (5)$$

Only systems in which $(\cos\phi_n+\cos\phi_{n+1})$ goes to 0 when n goes to ∞ will be considered. It is so both in the $AF_{\uparrow\downarrow}$ state and in the $AF_{\uparrow\uparrow}$ state, since $(\cos\phi_n+\cos\phi_{n+1})$ is identically zero for any n in both cases. Therefore, in both states, the Zeeman energy reduces to $-H\cos\phi_1$ which is minimum in the $AF_{\uparrow\uparrow}$ state, but maximum in the $AF_{\uparrow\downarrow}$ state! Since the $AF_{\uparrow\downarrow}$ state is not the ground state, but it is stable with respect to spin waves for $H<H_S$, we conclude that it is metastable for $H<H_S$. However, for $H_S<H<H_{\mathrm{BSF}}$ the situation is different. We are going to argue that the $AF_{\uparrow\downarrow}$ state is unstable with respect to the formation of a Bloch wall which will form at the surface and sink into the bulk, thus transforming the system in its $AF_{\uparrow\uparrow}$ state. Performing in Eq. (5) a $T=0$ decimation procedure in order to eliminate the even spins,[12] we obtain, for small H_A and H

$$\frac{E}{N_{\|}S}=\sum_{n=1}^{\infty}\left[\frac{H_E}{4}(\phi_{2n-1}-\phi_{2n+1})^2\right.$$

$$\left.-\left(2H_A-\frac{H^2}{H_E}\right)\cos^2\phi_{2n-1}\right]-H\cos\phi_1, \qquad (6)$$

where the last term is due to the existence of a free surface at $n=1$. Equation (6) has the well-known sine-Gordon form. In order to investigate the transformation of the $AF_{\uparrow\downarrow}$ state into the $AF_{\uparrow\uparrow}$ state, and also the stability of the SSF state, it is of interest to minimize this energy for a given value of ϕ_1 and for fixed $\cos\phi_{2n+1}=-1$ at $n=\infty$. The solution of this problem is given by the Euler–Lagrange equation of a domain wall

$$\frac{H_E}{2}(2\phi_{2n+1}-\phi_{2n+3}-\phi_{2n-1})$$

$$+\left(2H_A-\frac{H^2}{H_E}\right)\sin 2\phi_{2n+1}=0. \qquad (7)$$

Inserting its solution into Eq. (6), we have

$$\frac{E}{N_{\|}S}=\sqrt{(2H_AH_E-H^2)}(\cos\phi_1+1)-H\cos\phi_1. \qquad (8)$$

For weak fields, the coefficient of $\cos\phi_1$ is positive, so that the energy presents a minimum for $\cos\phi_1=-1$ or $\phi_1=\pi$. Thus, the $AF_{\uparrow\downarrow}$ state is a metastable one, in agreement with the spin wave argument. In other words, if a Bloch wall is introduced into the $AF_{\uparrow\downarrow}$ state from the surface, the system expels it through the surface. This occurs if $H^2<H_AH_E$, i.e., if $H\lesssim H_S$. On the other hand, if $H_S\lesssim H<H_B$, the energy (8) is minimum for $\phi_1=0$. In this case, if a Bloch wall is introduced into the $AF_{\uparrow\downarrow}$ state from the surface, the system swallows it and transforms progressively into the $AF_{\uparrow\uparrow}$ state. In particular, the SSF state corresponds to $\cos\phi_1=0$, and it is unstable, in agreement with the mapping argument.

[1] R. W. Wang, D. L. Mills, E. E. Fullerton, J. E. Mattson, and S. D. Bader, Phys. Rev. Lett. **72**, 920 (1994).
[2] D. L. Mills, Phys. Rev. Lett. **20**, 18 (1968).
[3] D. L. Mills and W. M. Saslow, Phys. Rev. **171**, 488 (1968); **176**, 760(E) (1968).
[4] F. Keffer and H. Chow, Phys. Rev. Lett. **31**, 1061 (1973).
[5] L. Trallori, P. Politi, A. Rettori, M. G. Pini, and J. Villain, Phys. Rev. Lett. **72**, 1925 (1994); L. Trallori *et al.* (unpublished).
[6] S. Aubry, in *Solitons and Condensed Matter Physics*, edited by A. R. Bishop and T. Schneider (Springer, New York, 1979).
[7] P. Bak, Phys. Rev. Lett. **46**, 791 (1981).
[8] P. I. Belorov, V. V. Beloshapkin, G. N. Zaslavskii, and A. G. Tret'yakov, Zh. Eksp. Teor. Fiz. **87**, 310 (1984) [Sov. Phys. JETP **60**, 180 (1984)].
[9] R. Pandit and M. Wortis, Phys. Rev. B **25**, 3226 (1982).
[10] F. C. Nörtemann, R. L. Stamps, A. C. Carriço, and R. E. Camley, Phys. Rev. B **46**, 10847 (1992).
[11] The difference between H_B' and H_B is related to the metastability region in the first order BSF phase transition.
[12] J. Villain and J. M. Loveluck, J. Phys. **38**, L77 (1977).

Magnetoresistance of ultrathin Co films grown in UHV on Au(111): Crossover from granular to continuous film behavior versus Co thickness (abstract)

C. Dupas, E. Kolb, J. P. Renard, and E. Vélu
Institut d'Electronique Fond, Université Paris-Sud, 91405 Orsay, France

M. Galtier, M. Mulloy, and D. Renard
Institut d'Optique Théorique et Appliquée, Université Paris-Sud, 91405 Orsay, France

Co/Au(111) is a model system for magnetoresistance (MR) studies due to abrupt interfaces without intermixing between Co and Au and perpendicular magnetization of Co films for Co thickness below nine atomic monolayers (AL). The high quality of Co/Au(111) multilayers is revealed by highly contrasted MR oscillations versus Au spacer thickness.[1] We report here a detailed study of the effect of cobalt thickness done to 0.2 AL on the MR of various Au/Co structures. Experiments were performed on single Co layer sandwiched between two Au(111) films, Au/Co/Au, and on double Co films, Au/Co/Au/Co/Au, in the T range 1.5–300 K and in magnetic fields up to 10 T. For the sandwiches, two series were studied, each including eight samples grown in UHV in a single run, with Co thicknesses t_{Co} from 0.2 to 1.6 and from 1.4 to 4 AL. The MR in the perpendicular and transverse configurations show that the easy magnetization axis is perpendicular to the films, even for low t_{Co}. The MR value increases with t_{Co} to the high value of 5% at low temperatures for a noncontinuous Co film and decreases afterwards, clearly evidencing the transition from islandlike to continuous-like character of the Co film. In the islandlike regime, the magnetic domain size is limited by the island size and is thus smaller than in the continuous Co films, leading to higher MR values. In the double Au/Co/Au/Co/Au samples, different Au spacer thicknesses were chosen in order to ensure either FM or AFM coupling between the magnetic layers, and t_{Co} was varied up to 10 AL. We did not observe coupling oscillations versus t_{Co}. Moreover, the lack of any significant variations of the MR value shows that the electronic mean free path in Co is larger than 10 AL at any T.

[1] V. Grolier *et al.*, Phys. Rev. Lett. **71**, 3023 (1993).

 0021-8979/94/76(10)/6558/1/$6.00 © 1994 American Institute of Physics

The micromagnetics of periodic arrays of defects in trilayers with interlayer exchange coupling (abstract)

H. A. M. van den Berg
Siemens A G, Erlangen, P.O. Box 3220, Germany

A significant loss in the giant magnetoresistive signal of magnetic stacks with antiferromagnetic coupling across nonmagnetic intermediate layers is caused by regions with a ferro- rather than an antiferromagnetic coupling. The impact of these ferromagnetic coupling regions extends itself into the lateral direction due to the bulk exchange coupling. The present micromagnetic model provides a tool by which a detailed quantitative evaluation of the impact of periodic arrays of parallel line defects is possible. These defects have deviating exchange-coupling constants, and/or anisotropy constants or directions, bulk exchange constants, saturation magnetization, etc., in specific regions. Previously, we developed a phenomenological model of trilayers with two magnetic films separated by a nonmagnetic interlayer[1] that contains one such defect. This model, with a relatively small number of free parameters, allows one to trace complete hysteresis curves. A large number of mode branches reveal themselves and jumpwise transitions between these modes frequently occur along the hysteresis loops. The present micromagnetic model requires a sufficiently accurate assessment of the starting magnetization configuration in order to get a convergence of the code. In general, the micromagnetic code is not capable of overcoming the above irreversible mode conversions. The mode branches evaluated by the phenomenological model are applied to provide the micromagnetic model with appropriate starting configurations after meeting a situation of nonstability. The micromagnetic theory of Brown[2] constitutes the basis of the present approach. The micromagnetic effective field is calculated at grid points and the torque exerted by it on the magnetic dipole is made zero at each grid side by an iteration scheme. The long ranging magnetostatic fields are given by convolution integrals and are evaluated in the Fourier space by using two-dimensional fast Fourier transforms. The single defect is micromagnetically studied by zero padding techniques. Depending on the course of the external field, two different wall regions reveal themselves, to wit, the wall core and the so-called Néel tails. These tails were not incorporated into the phenomenological model. Provided that the defects are sufficiently wide spaced, the agreement between both models is rather good in the core regions. The impact on the GMR signal, in particular of the Néel tails, will be discussed with emphasis on systems with weak interlayer coupling, e.g., the decoupled systems.

[1] H. A. M van den Berg *et al.*, IEEE Trans. Magn. L9, 3099 (1993).
[2] W. F. Brown, *Micromagnetics* (Krieger, New York, 1978).

 0021-8979/94/76(10)/6559/1/$6.00 © 1994 American Institute of Physics

FMR doublet in two-layer iron garnet films (abstract)

A. M. Grishin, V. S. Dellalov, E. I. Nikolayev, V. F. Shkar, and S. V. Yampolskii
Donetsk Phystech, Donetsk 340114, Ukraine

Multilayer epitaxial iron garnet films have been investigated very intensively in the recent past. The dipole and exchange couplings of spins lying in different layers results in the existence of new types of oscillations in these structures and give rise to the characteristic resonance properties of them.[1,2] Resonance microwave absorption in two-layer iron garnet films, of which one layer is in a saturated state and the other is in a demagnetized state, is investigated. The films were prepared by the epitaxial method on a gallium-gadolinium substrate with (111) orientation. The first layer on the substrate was the doped iron yttrium garnet with the easy plane magnetization. The second easy axis layer was the bubble domain layer. The resonant field of the first layer FMR line versus the external in-plane magnetic field was investigated. It was determined that the FMR line is doubled when the external field is applied along the [112]-type axes. The lines of the FMR doublet merge into a single line and the resonance intensity is doubled if the magnetic field is oriented in the [110] directions. It was established that the FMR line splitting is conditioned by the layer exchange interaction, the cubic anisotropy, and the domain dissipative field. The magnetic and anisotropy of the resonance fields agrees with the model of an isolated layer magnetized by the domains of the neighboring layer.

[1] A. M. Grishin *et al.*, Phys. Lett. A **140**, 133 (1989).
[2] V. F. Shkar, I. M. Makmak, and V. V. Petrenko, JETP Lett. **55**, 330 (1992).

Influence of the dipole interaction on the direction of the magnetization in thin ferromagnetic films (abstract)

A. Moschel and K. D. Usadel
Theoretische Tieftemperaturphysik, Universität Duisburg, Lotharstrasse 1, 47048 Duisburg, Germany

The magnetization of thin films depends in a very sensitive way on surface anisotropy fields which often favor a perpendicular orientation and on the dipole interaction which favors an in-plane magnetization. A temperature driven transition from one to the other orientation has been observed experimentally.[1] In order to understand this behavior theoretically we performed detailed calculations of the magnetization of very thin films (thickness of up to 5 layers) within a quantum mechanical mean field approach. A surface anisotropy that favors a perpendicular orientation and a long range dipole interaction were taken into account. It is shown that these competing interactions for certain values of the parameters may result in a temperature driven switching transition from an out-of plane to an in-plane ordered state. Varying the strength of the dipole interaction we found that the switching temperature is a very sensitive function of the ratio of these two competing interactions. A perpendicular ground state magnetization of the film is only found for values of the surface anisotropy which are larger than a critical surface anisotropy value. The reorientation of the magnetization vector has its physical origin in an entropy increase of the system when going from a perpendicular to an in-plane ordered state.

This work was supported by the Deutsche Forschungsgemeinschaft through Sonderforschungsbereich 166.

[1] D. P. Pappas, K.-P. Kamper, and H. Hopster, Phys. Rev. Lett. **64**, 3179 (1990).

 0021-8979/94/76(10)/6560/1/$6.00 © 1994 American Institute of Physics

Coercivity and switching field of single domain γ-Fe_2O_3 particles under consideration of the demagnetizing field

Paul L. Fulmek and Hans Hauser
Institut für Werkstoffe der Elektrotechnik, Technische Universität Wien Gusshausstrasse 27-29, A-1040 Vienna, Austria

The coherent rotation of the spontaneous polarization in ellipsoidal ferromagnetic single domain particles is calculated under consideration of the magnetocrystalline anisotropy and the true, inner field. Magnetization curves and switching fields are computed for uniaxial and cubic magnetocrystalline and shape anisotropy. Considering only the magnetic energy inside the particle, the resulting switching fields are lower than those predicted by the Stoner–Wohlfarth theory, and they are qualitatively and quantitatively comparable to the results of other models. The comparison to measurements on isolated γ-Fe_2O_3 particles shows excellent agreement.

I. INTRODUCTION

The idealized particles discussed are small, perfect single crystals of exactly ellipsoidal shape. They consist of one single domain only.[1] The magnetization process happens by coherent rotation of the spontaneous polarization. This rotation need not happen continuously, switching occurs for critical field strengths.[2]

It is further assumed that all processes happen at temperatures far below the Curie temperature, where the spontaneous polarization of the material is constant. The analysis assumes static and isothermal ferromagnetism. Effects associated with the time rate of change of magnetization are not considered.

The coherent rotation of the spontaneous polarization is determined by the behavior of the minima of the total energy density. Therefore, only anisotropic contributions have an influence. The energies taken into account are the magnetocrystalline energy E_c and the energy of the fields in connection with the applied field $\mathbf{H}_a$ and the demagnetizing field $\mathbf{H}_d$. All other energies are neglected. As single domain particles are always in the state of saturation, the demagnetizing field has a strong influence on the true field and on the energy due to the field. Stoner–Wohlfarth (SW) calculations demand that the particle does not interact with surrounding magnetic material. Completely neglecting the field outside the particle, however, yields results that agree perfectly with measurements on single γ-Fe_2O_3 particles.

Magnetization curves are calculated by tracing the minima of the energy areas (the three-dimensional space variation of the total energy) as the applied field is changed continuously.[2–6]

II. ANISOTROPIC ENERGIES

To calculate magnetization curves we have to find the minimum energy configuration for a given applied field. Only the direction of $\mathbf{I}_s$ can vary. Under this assumption the energy is a function of only two variables, of the direction of $\mathbf{I}_s$. For searching the minima we have to take into account only anisotropic energies.

In crystalline ferromagnetic materials $\mathbf{I}_s$ prefers certain directions of the crystal lattice to minimize the *magnetocrystalline energy* E_c. For cubic crystal structures (bcc, fcc) we use a series expansion of the directional dependence (direction cosines α_i) with respect to the crystal axes

$$E_c = K_0 + K_1(\alpha_1^2\alpha_2^2 + \alpha_1^2\alpha_3^2 + \alpha_2^2\alpha_3^2) + K_2\alpha_1^2\alpha_2^2\alpha_3^2. \quad (1)$$

Three coefficients $K_{0,1,2}$ are sufficient to describe this property. Uniaxial magnetocrystalline anisotropy is described by

$$E_u = K_{u0} + K_{u1}\sin^2\varphi + K_{u2}\sin^4\varphi, \quad (2)$$

where φ is the angle between the easy axis and $\mathbf{I}_s$.

The general expression for the power density of the magnetic field in any material, especially in nonlincar and anisotropic materials,[8] is

$$P_m = \frac{\partial E_m}{\partial t} = \mathbf{H}\frac{\partial \mathbf{B}}{\partial t}. \quad (3)$$

The time integral supplies the general formula for the energy density of any general magnetic field configuration[9,10]

$$E_m = \int \mathbf{H}d\mathbf{B}. \quad (4)$$

The true $\mathbf{H}$ acting in the material is the vectorial sum of the applied field $\mathbf{H}_a$ and the demagnetizing field $\mathbf{H}_d$. In the special case of a specimen surface of second order (e.g., a general ellipsoid) all fields in the volume of the specimen are homogeneous, and therefore, the demagnetizing field can be determined by a demagnetizing matrix $\underline{N}$

$$\mathbf{H}_d = -\frac{1}{\mu_0}\underline{N}\mathbf{I}_s, \qquad \mathbf{H} = \mathbf{H}_a + \mathbf{H}_d = \mathbf{H}_a - \frac{1}{\mu_0}\underline{N}\mathbf{I}_s. \quad (5)$$

Demagnetizing factors are determined in the directions of the axes of the ellipsoid.[11] This diagonal matrix has to be transformed for general ellipsoids in arbitrary orientations.

 0021-8979/94/76(10)/6561/3/$6.00 © 1994 American Institute of Physics

The induction $\mathbf{B}$ in the specimen results from the vacuum induction of the magnetic field $\mathbf{H}$ and the polarization of the material:

$$\mathbf{B}=\mu_0\mathbf{H}+\mathbf{I}_s=\mu_0\mathbf{H}_a+(\underline{1}-\underline{N})\mathbf{I}_s. \tag{6}$$

As an approximation for the total energy we integrate Eq. (4) with Eqs. (5) and (6) over the volume of the specimen only. The variation of the energy density is due to the variation of the polarization vector $\mathbf{I}_s$ only. The energy density of the material is therefore reduced by

$$-E_m=-\int \mathbf{H}\left(\frac{\partial\mathbf{B}}{\partial\mathbf{H}_a}\,d\mathbf{H}_a+\frac{\partial\mathbf{B}}{\partial\mathbf{I}_s}\,d\mathbf{I}_s\right)$$

$$=(\underline{1}-\underline{N})\left(-\mathbf{H}_a\mathbf{I}_s+\frac{1}{2\mu_0}(\underline{N}\mathbf{I}_s)\mathbf{I}_s\right). \tag{7}$$

For a given applied field the energy can be expressed as a function of two variables, the direction of $\mathbf{I}_s$. A minimum energy for constant $\mathbf{H}_a$ yields stable solutions of $\mathbf{I}_s(\mathbf{H}_a)$. Two interesting properties of the magnetization curve will be discussed here. The point of magnetization reversal—the coercive force—and the point(s) of instability—the switching field strength. As single domain particles are always in the state of saturation, we have to define the magnetization curve as projection of $\mathbf{I}_s$ in the applied field $\mathbf{H}_a$ versus the value of the applied field H_a.

III. UNIAXIAL CALCULATIONS

For comparison to other models it is convenient to calculate the coercive force and the critical field (switching field) in the case of simple uniaxial anisotropies (magnetocrystalline and shape anisotropy, $K_{u2}=0$) for prolate ellipsoids. The polar axis of the ellipsoid is identical to the axis of uniaxial magnetocrystalline anisotropy. The angles α of the applied field and φ of the polarization are denoted with respect to the axis of uniaxial anisotropy.

As we need the energy expressions Eqs. (2) and (7) to find the minimum energy only, we can reduce the total energy E to E^*

$$E=E_u-E_m\rightarrow E^*=\sin^2\varphi-h\left[\cos\alpha\cos\varphi+\frac{1}{2}\left(\frac{1+N}{1-N}\right)\sin\alpha\sin\varphi\right], \tag{8}$$

$$h=H_a\frac{1}{K_{u1}/[I_s(1-N)]+I_s(1-3N)/(8\mu_0)}, \tag{9}$$

$$\frac{dE^*}{d\varphi}=\sin(2\varphi)-h\left[-\cos\alpha\sin\varphi+\frac{1}{2}\left(\frac{1+N}{1-N}\right)\sin\alpha\cos\varphi\right], \tag{10}$$

$$\frac{d^2E^*}{d\varphi^2}=2\cos(2\varphi)+h\left[\cos\alpha\cos\varphi+\frac{1}{2}\left(\frac{1+N}{1-N}\right)\sin\alpha\sin\varphi\right]. \tag{11}$$

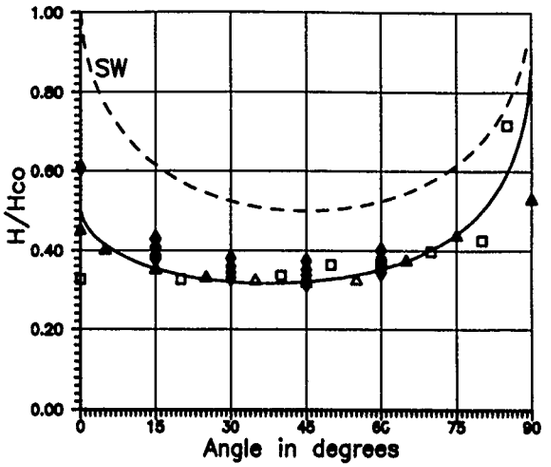

FIG. 1. Switching field of prolate ellipsoids (aspect ratio 4:1:1) with vanishing magnetocrystalline anisotropy. The dashed line gives H_c according to SW theory. All H_c values are related to SW$-H_{c0}=138$ kA/m. □ Measurements γ-Fe_2O_3 particles (Ref. 13); △ Micromagnetic calculations (parallelepiped) (Ref. 12); ◇ calculations for additional cubic anisotropy ($K_1=-4600$ kJ/m^3).

In the SW model the influence of shape and magnetocrystalline anisotropy can be included as an *anisotropy field* $H_A\rightarrow h=H_a/H_A$. This reduction is impossible for our calculations. To find a direction φ for the polarization with minimum energy, we have to find the value for h [Eq. (9)] that gives $\partial E^*/\partial\varphi=0$ [Eq. (10)]. With a second derivative Eq. (11) greater than zero, h gives a stable minimum, a stable point on the magnetization curve. When Eq. (11) is zero, the corresponding field is a critical field; the solution is an unstable one. This critical, switching field strength is important for magnetic storage.

Figure 1 shows the switching field strength depending on the direction of the applied field calculated by the formulas from above. In comparison to our results Fig. 1 shows the switching field curve according to SW calculations, results from a micromagnetic approach by Yan and Della Torre using a parallelepiped as model geometry (aspect ratio 6:1:1, length 300 nm, uniaxial magnetocrystalline anisotropy),[12] and measurements of the switching field on small isolated γ-Fe_2O_3 particles (aspect ratio ≈4:1:1) by Knowles.[13]

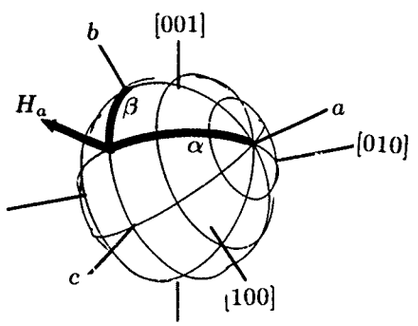

FIG. 2 Coordinate system for magnetocrystalline anisotropy ⟨100⟩, shape anisotropy (a,b,c), and the direction of the applied field (α,β)

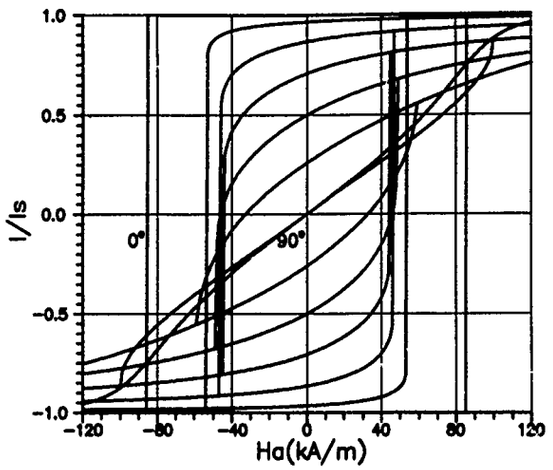

FIG. 3. Magnetization curves for γ-Fe_2O_3 particles (aspect ratio 4:1:1) in dependence of the angle α (β=0) of the applied field with respect to the easy axis of shape and cubic magnetocrystalline anisotropy. α is varied from 0° to 90° in steps of 15°.

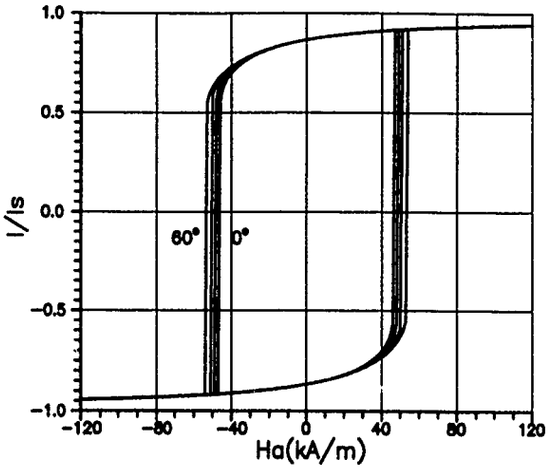

FIG. 4. Magnetization curves for γ-Fe_2O_3 particles (aspect ratio 4:1:1) in dependence of the angle β for α=30°.

For uniaxial considerations, we did our calculations for γ-Fe_2O_3 particles with I_s=0.45 T, K_{u1}=0, and an ellipsoid shape with an aspect ratio of 4:1:1. The demagnetizing factor in the direction of the longer axis is N=0.075.

For an angle of the applied field of 0°, our calculations yield exactly half the value for the switching field of SW when the uniaxial anisotropy constant K_{u1} is zero. In this case are both angles $\alpha=\varphi=0$

$$E^*_{SW}=\sin^2\varphi-h_{SW}\cos(\alpha-\varphi),$$
$$h_{SW}=4H_a\mu_0/[I_s(1-3N)], \qquad (12)$$
$$h/h_{SW}=2\rightarrow H_c/H_{c0}=0.5.$$

IV. CUBIC CALCULATIONS

For cubic anisotropies the two-dimensional minimum search on the surface of the energy areas was realized by a numerical algorithm implemented on a computer.

The calculations have been carried out for elongated ellipsoids of γ-Fe_2O_3 with an aspect ratio of 4:1:1. We assume that the long axis of the ellipsoid lies in the [111] direction of the crystal lattice.[4] The material parameters are: I_s=0.45 T, $K_1=-4600$ J/m^3, K_2=0 J/m^3.[14]

As we calculate magnetization curves for cubic anisotropies, we have to consider two angles of the applied field with respect to the axes of the ellipsoid. The angles are denoted according to the angles in a spherical-coordinate system with the long axis of the ellipsoid as polar axis (i.e., the [111] direction). The first angle α is always the angle between the direction of the applied field and the long axis of the ellipsoid. The second angle β is the angle between the $(1\bar{1}0)$ plane and the field vector (see Fig. 2).

Figure 3 shows the resulting magnetization curves when the direction of the applied field is changed in the $(1\bar{1}0)$ plane by 15° steps (α=0°···90°, β=0). The magnetization curve for α=0° calculated by SW theory would have a coercivity of 138 kA/m. For $\alpha<60°$ the switching field is identical to the coercivity.

The influence of the second angle β is shown in Fig. 4: the angle α between the applied field and the easy polar axis of the ellipsoid is constant 30°. The coercive force varies by 15%, as the secondary angle β changes from 0° to 90°.

Values of the coercive force variation due to the cubic anisotropy are plotted in Fig. 1 in comparison to pure uniaxial shape anisotropy. The values of switching fields for $\alpha>60°$ could not be determined precisely, as with increasing angle the continuous rotation yields steeper slopes of the magnetization curve, numerically indistinguishable from a real instability (compare Fig. 3).

[1] C. Kittel, Phys. Rev. **70**, 965 (1945).
[2] E. C. Stoner and E. P. Wohlfarth, Philos Trans. R Soc. London Ser A **240**, 599 (1948).
[3] H. Lawton and K. H. Stewart, Proc. R. Soc. London Ser. A **193**, 72 (1948).
[4] C. E. Johnson, Jr. and W. F. Brown, Jr., J. Appl. Phys. **30**, 320 (1959).
[5] P. L. Fulmek and H. Hauser, Appl. Electromagn Mater. **5**, 323 (1994)
[6] H. Hauser and P. L. Fulmek, IEEE Trans. Magn **28**, 1815 (1992)
[7] H J. Richter, IEEE Trans. Magn. **29**, 2185 (1993).
[8] H. Hofmann, *Das Elektromagnetische Feld* (Springer, New York, 1982).
[9] J. A. Stratton, *Electromagnetic Theory* (McGraw-Hill, New York, 1941).
[10] E. A. Guggenheim, Proc. R. Soc. London **155**, 49 (1936).
[11] J. A Osborn, Phys. Rev. **64**, 351 (1945).
[12] Y. D. Yan and E. Della Torre, J. Appl. Phys. **66**, 320 (1989)
[13] J. E. Knowles, IEEE Trans. Magn. **MAG-14**, 858 (1978).
[14] M. E. Schabes, J. Magn. Magn Mater. **95**, 249 (1991)

Structural and magnetic characterization of Co particles coated with Ag

J. Rivas, R. D. Sánchez, A. Fondado, C. Izco, A. J. García-Bastida, J. García-Otero, J. Mira, and D. Baldomir
Departamento Física Aplicada, Universidad de Santiago de Compostela, Spain

A. González, I. Lado, and M. A. López Quintela
Departamento de Química-Física, Universidad de Santiago de Compostela, Spain

S. B. Oseroff
San Diego State University, San Diego, California 92182

Co fine particles coated with Ag have been synthesized through the microemulsion method in an inert atmosphere. The size of the particles is controlled by the water droplets of the microemulsions. Fine particles prepared by this method, consist of a magnetic core of Co covered by a layer of Ag. Samples containing from 3.3 to 40.5 vol % Co have been prepared. The average size of the particles obtained is in the nanometer range. The magnetic properties were studied by dc magnetization at 77 K and room temperature. The data show a strong dependence of the magnetic properties on the annealing temperature.

I. INTRODUCTION

Single domain magnetic particles show very interesting properties, such as high coercivity and remanence, which are of special interest to several applications in magnetic recording and permanent magnets. Different methods can be used in order to obtain small particles in the submicrometric range. Among these, chemical reactions and vacuum deposition are the most usual ones. Most studies of ultrafine metallic particles have been performed on granular materials in nonmetallic matrices.[1–3] Interest in single domain particles immersed in a nonmagnetic metallic matrix has increased recently.[4,5] The interest in granular materials, such as Fe-Ag, Co-Ag, $Ni_{81}Fe_{19}$-Ag, etc., is because they present a giant magnetoresistance (GMR).[6,7] Although much effort has been devoted during the last years studying the origin of their properties, a quantitative understanding of the phenomenon is still lacking.[8,9]

In this work we describe a new chemical method for the preparation of ultrafine Co particles covered by metallic silver. This method consists in mixing two water-in-oil (W/O) microemulsions containing the reactants dissolved in the aqueous phase in order to produce the Co core. The reaction takes place inside the droplets, which controls the final size of the particles. Subsequently, silver ions are adsorbed onto these particles and finally are reduced to produce a silver metallic shell.

II. EXPERIMENT

The microemulsions employed in the production of the particles were composed of *n*-heptane, aqueous solution, and aerosol-OT (AOT, sodium dodecylsulfosuccinate). The droplet size of these microemulsions was controlled by the ratio $R=[H_2O]/[AOT]$. This ratio was set to 10. The whole process for obtaining the particles, that was carried out in an inert glove box, can be divided into two stages.

(1) Formation of the magnetic cores: To carry out this first stage, two different microemulsions were prepared. The first one consisted in an aqueous solution of $Co(NO_3)_26H_2O$ (0.1 M) and the second one contained $NaBH_4$ (0.2 M). The two microemulsions were mixed and the magnetic particles were formed inside the microdroplets. The microparticles, separated from the microemulsion by ultracentrifugation, were washed later with *n*-heptane and ethanol several times and finally dried with acetone.

(2) Coating with Ag: The magnetic particles were redispersed with AOT in an aqueous solution containing $AgNO_3$ and EDTA (ethylendiaminetetracetic). Silver ions were then absorbed on the particles which acted as nucleation centers. This solution was later irradiated with UV light during 30 min to obtain a metallic cover of silver on the magnetic particles.[10] The amount of EDTA and $AgNO_3$ used depends on the Ag/Co ratio to be obtained. The coated microparticles were separated again from the solution by ultracentrifugation, washed several times with *n*-heptane and ethanol in order to remove the AOT surfactant, and finally dried with acetone. Then, the microparticles were examined before and after annealing in flowing Ar.

Most of the organic impurities were eliminated after annealing, followed by a process of oxidation and reduction. These were observed by differential thermogravimetric analysis measurements.

The samples were characterized analytically by inductive coupled plasma-atomic emission spectroscopy and the final composition of Co, Ag, and impurities were determined. The structural characterization was carried out by x-ray powder diffraction. These measurements were performed at room temperature, and matched with diffraction patterns from the total access diffraction database. In order to determine the size distribution, measurements of transmission electron microscopy (TEM) and dynamic light scattering (DLS) were carried out. For both TEM and DLS measurements, particles were dispersed in water using AOT. The average crystallite sizes were calculated from the shape of the x-ray diffraction peaks using the Debye–Scherrer formula. The magnetic properties of the samples were measured with a vibrating sample magnetometer in the temperature range of 80 K$<T<$300 K. The powder was introduced, loosely packed, in a cylindrical sample holder.

 0021-8979/94/76(10)/6564/3/$6.00 © 1994 American Institute of Physics

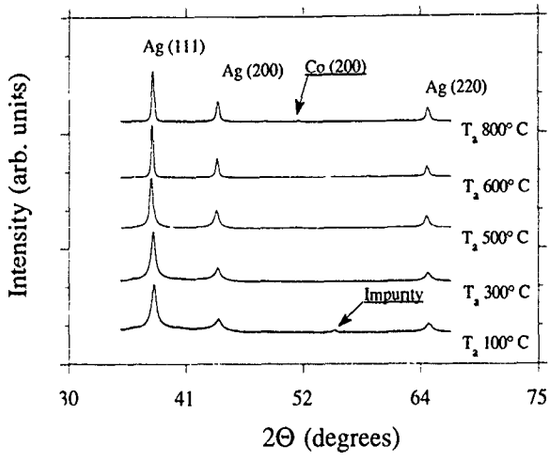

FIG. 1. X-ray diffraction pattern for $Co_{0.5}Ag_{0.5}$ after annealing at different temperatures. The arrows show the position of cobalt reflections.

III. RESULTS AND DISCUSSION

A. Structural characterization

X-ray diffraction on as-prepared Co particles (first chemical stage) shows a typical amorphous spectrum. Figure 1 shows the x-ray diffraction pattern for a typical Co/Ag sample at five temperatures of annealing (T_A=100, 300, 500, 600, and 800 °C). Long measurement times, counting times of 20 s per 0.002° step in 2θ, were needed in order to observe cobalt peaks in samples with high concentration of Co and high treatments of temperature. Only one Co peak is visible (200) because the others overlap with those due to silver. In Fig. 1 it can be observed how the width decreases with annealing temperature. Studies of the width of Ag (111) and Ag (220) peaks done as a function of annealing temperature yields the size of the Co/Ag particles grows from 15 to 60 nm.

Figure 2 shows the TEM electron micrograph for the sample with x=0.12 of Co_xAg_{1-x} treated at 500 °C. To obtain the micrograph, the samples were dispersed in water and then deposited onto Cu grid substrates. The average diameter was of about 30 nm, similar to the results obtained by DLS.

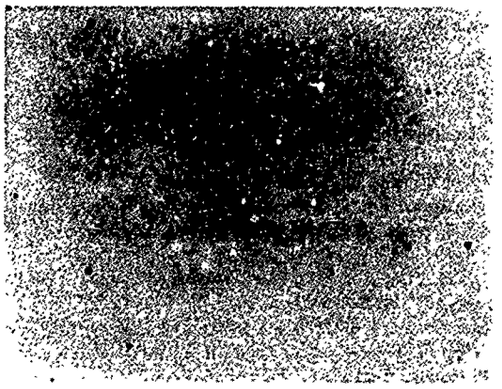

FIG. 2. TEM microphotograph of a sample of $Co_{0.12}Ag_{0.88}$.

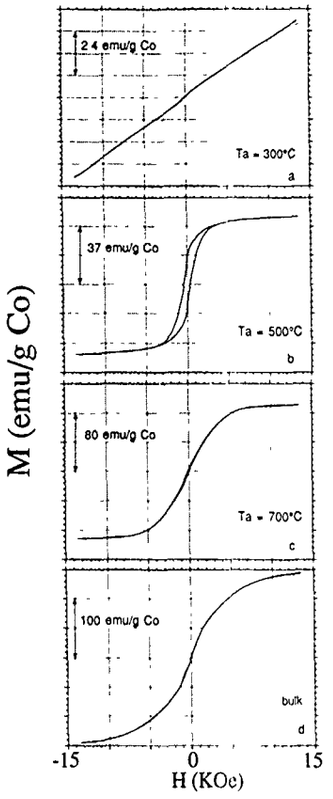

FIG. 3. In plane M-H loops at room temperature of Co_xAg_{1-x} with $x \approx 0.12$ at different annealing temperatures in series A. (a) T_A=300 °C, (b) T_A=500 °C, (c) T_A=700 °C, and (d) bulk Co.

B. Magnetic properties

The temperature dependence of the magnetization has been measured after cooling in zero magnetic field (ZFC) and also after cooling in a field (FC). The M-T data show a splitting between the FC and ZFC curves. For the as-prepared samples, this splitting occurs close to room temperature (RT). For annealed samples, the sizes of cobalt cores grow and this splitting point is shifted towards higher temperature.

The magnetic hysteresis loops have been measured in three series of Co_xAg_{1-x} (A, B, and C). Series A and B are two separate fabrication runs with the same Co concentration (x=0.12±0.02) but with different annealing temperatures, 100 °C<T_A<800 °C. Series C are samples of different compositions, from x=0 to x=0.66 annealed at T_A=500 °C. Figure 3 shows magnetization (M) as function of magnetic field (H) at RT for T_A=300 °C [Fig. 3(a)], 500 °C [Fig. 3(b)], and 700 °C [Fig. 3(c)]. Figure 3(d) is the M for cobalt powder (d<250 μm) and reflects the bulk properties of the material. The coercive field (H_c) as function of T_A is plotted in Fig. 4(a). The squareness, SQ, defined as M_r/M_s where M_r is the remanence magnetization and M_s is the magnetization at H=13.5 kOe, vs T_A, is shown in Fig. 4(b).

According to Fig. 4, for series A and B, it is possible to define three regions of annealing temperature. The first for low T_A, between 100 and 300 °C, shows a reversible M-H behavior. The second region, for 300<T_A<600 °C shows a hysteresis loop [Fig. 3(b)]. The dramatic change of the mag-

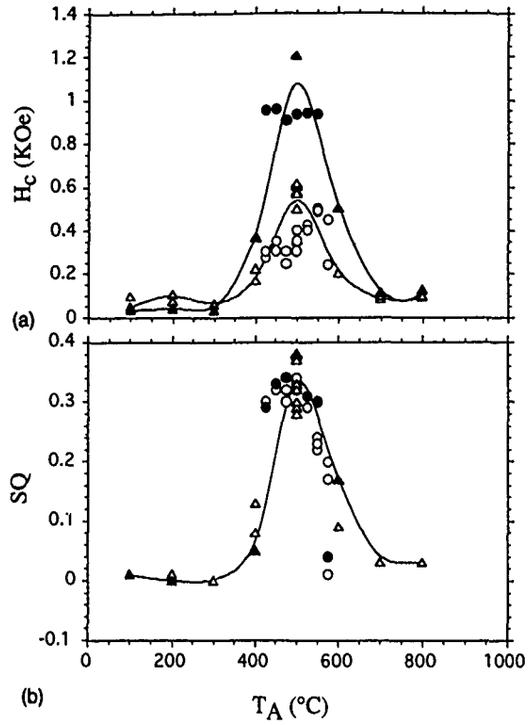

FIG. 4. (a) H_c vs T_A and (b) SQ vs T_A for two different runs of Co_xAg_{1-x} ($x\sim0.12$). Series A (△) RT, (▲) 77 K, series B (○) RT and (◔) 77 K.

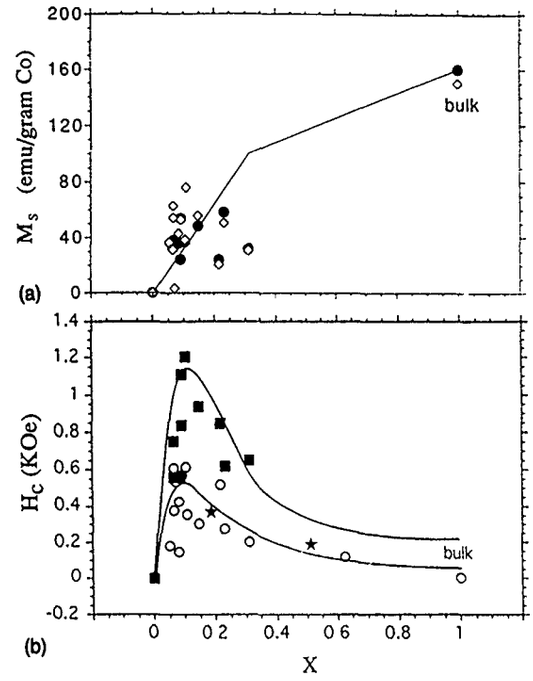

FIG. 5. Co_xAg_{1-x} samples (a) M_s vs x (experimental composition) after annealing at 500 °C (the solid line comes from Co_xCu_{1-x} in Ref. 5) and (b) H_c vs x. The solid lines are guides to the eye. Open and filled symbols show measurements at RT and 77 K, respectively. The filled stars are data from Ref. 11 of Co_xAg_{1-x} films.

netic properties in this range could be due to an increase of the Co nuclei and/or the crystallization of some amorphous portions of the Co cores as T_A increases. For $T_A\approx500$ °C, H_c and SQ have maximum, as seen in Fig. 4. This maximum is similar to the one found by other authors in $Co_{19}Ag_{81}$ and $Co_{50}Ag_{50}$ granular magnetic thin films.[11] The third region ($T_A>600$ °C) shows that the H_c and SQ decrease as T_A increases. The reason for it is that the interaction between the particles is strong and they are no longer single domains so their magnetic behavior approaches the one found for bulk Co.

Finally, in Fig. 5, we show M_s and H_c as function of experimental Co composition. The solid line is the data of Ref. 5 about Co_xCu_{1-x}. For the samples with low Co concentration ($x<0.12$), the magnetization does not saturate and the coercive field has a value close to zero. The long range magnetic order appears at high Co concentrations. For samples with $0<x<0.12$ the magnetization was found to saturate more easily and the systems exhibit a monotonic increase of H_c with increasing Co content. For $x>0.15$, the samples present a monotonic decrease of H_c with increasing x, which is consistent with a coupling effect of the Co particles.

IV. CONCLUSIONS

In summary, we have studied the structural and magnetic properties in a Co-Ag granular systems obtained by chemical reactions in microemulsions. The reaction takes place inside the droplets, which control the final size of the particles. By this method, magnetic ultrafine particles, in the nanometer range, of Co coated with Ag were obtained. From the x-ray analysis we observe that Ag crystallizes in the face centered cubic structure. The magnetic behavior of these samples after thermal treatments ($T_A\approx500$ °C) shows coercive fields as high as $H_c\approx600$ Oe at room temperature. These values are similar to those reported for granular materials which present GMR.[6,7] We are now in the process of measuring the MR in our samples.

ACKNOWLEDGMENTS

Research was supported in part by the Fundación Ramón Areces and the Xunta de Galicia (Spain), Nos. NSF-DMR 91172122 and NATO CRG 920255. R.D.S. was also by the Ministerio de Educación y Ciencia, Spain for a postdoctoral fellowship. The authors wish to thank to B. Rodríguez-González for the technical support in x rays.

[1] B. Abeles, Appl. Solid State Sci. **6**, 1 (1976).
[2] W. P. Halperin, Rev. Mod. Phys. **58**, 533 (1986).
[3] C. L. Chien, J. Appl. Phys. **69**, 5267 (1991).
[4] J. R. Childress, C. L. Chien, and M. Nathan, Appl. Phys Lett. **56**, 95 (1990).
[5] J. R. Childress and C. L. Chien, J. Appl. Phys. **70**, 5885 (1991).
[6] A. E. Berkowitz, J. R. Mitchell, M. J. Carey, A. P. Young, S. Zhang, F. E. Spada, F. T. Parker, A. Hutten, and G. Thomas, Phys. Rev. Lett. **68**, 3745 (1992).
[7] J. Xiao, J. S. Jiang, and C. L. Chien, Phys. Rev. Lett. **68**, 3749 (1992).
[8] S. Zhang and P. M. Levy. J. Appl. Phys. **73**, 5315 (1993).
[9] J. C. Slonczewski, J. Magn. Magn. Mater. **129**, L123 (1994).
[10] A. Fabrikanos, S. Athanassion, and K. H. Lieser, Z. Naturforsch. Teil B **18**, 612 (1963).
[11] S. H. Liou, S. Malhotra, Z. S. Shan, D. J. Sellmyer, S. Nafis, J. A. Woollam, C. P. Reed, R. J. de Angelis, and G M. Chow, J. Appl. Phys. **70**, 5882 (1991).

Magnetic properties of Fe clusters in NaY zeolite

J. A. Cowen
Department of Physics, Center for Fundamental Materials Research, Michigan State University, East Lansing, Michigan 46624

K. L. Tsai and J. L. Dye
Department of Chemistry, Center for Fundamental Materials Research, Michigan State University, East Lansing, Michigan 46624

Clusters of up to 28 Fe^0 atoms have been introduced into the "supercages" of NaY zeolite by ion exchange of Fe^{+2} for Na^+ followed by reduction to Fe^0 with solvated electrons and Na^{-1} ions. The temperature-dependent ac and dc susceptibilities, which exhibit Curie–Weiss behavior before reduction, change to something approximating superparamagnetic behavior afterwards. The blocking temperature, T_b, shows a strong dependence on magnetic field but weak dependence on frequency. There is at best a very weak remanence and coercive field while the onset of irreversibility occurs at temperatures well above T_b. In addition, the real and imaginary parts of the ac susceptibility show essentially similar temperature dependence. Some of this anomalous behavior can be attributed to a distribution of particle sizes. To the best of our knowledge these preliminary data—while poorly understood—represent the first measurements of the temperature, frequency, and field dependence of the magnetic properties of such small clusters.

I. INTRODUCTION

The study of the magnetic properties of small particles or clusters has been divided into two regimes. *Small clusters* consisting of between 10 and 600 atoms are produced in a "molecular" beam by laser vaporization. Particle size is selected by mass spectrometry and the magnetic properties are determined in a Stern Gerlach experiment.[1] *Large clusters*—nanocrystals—consisting of between 10^3 and 10^7 atoms are produced by sputtering, evaporation, or chemical techniques and are collected in quantity in an insulating matrix.[2] These larger particles can be characterized and their magnetic properties measured by using all of the standard techniques—x rays, extended x-ray-absorption fine structure, magnetic susceptibility, Mössbauer spectroscopy, NMR, electron spin resonance, etc.

By using conventional ion exchange methods, we have introduced up to 28 Fe^{+2} ions into NaY zeolite and reduced them to metallic Fe^0 particles that are presumably trapped in the supercages. According to the stoichiometry of this zeolite, an average of not more than 28 Fe^0 atoms can be present per supercage. We are thus able to measure for the first time the temperature, field and time dependence of the magnetic properties of such small clusters. Although these are preliminary measurements and the samples have not been completely characterized, our experimental results agree qualitatively with previous results on small clusters obtained at a single temperature and field. The overall magnetic behavior is quite complex and requires further experimental and theoretical study.

II. SAMPLE PREPARATION

Zeolites are alumino-silicates which are characterized by an open structure (about 50% of the volume is voids) in which charge unbalance in the structure is compensated for by the appropriate number of charged ions in the open holes or cages. NaY zeolite, with the chemical formula $Na_{56}Al_{56}Si_{134}O_{348}\cdot 240H_2O$ has an fcc structure in which "large" (1.2-nm-diam) "supercages" are connected by "small" (0.7-nm-diam) sodalite cages. The unit cell has a lattice parameter of 2.5 nm and contains one supercage and 56 Na^{+1} ions. These charges are balanced by negative charges produced by the substitution of Al^{+3} for Si^{+4} in the alumino-silicate framework.[3]

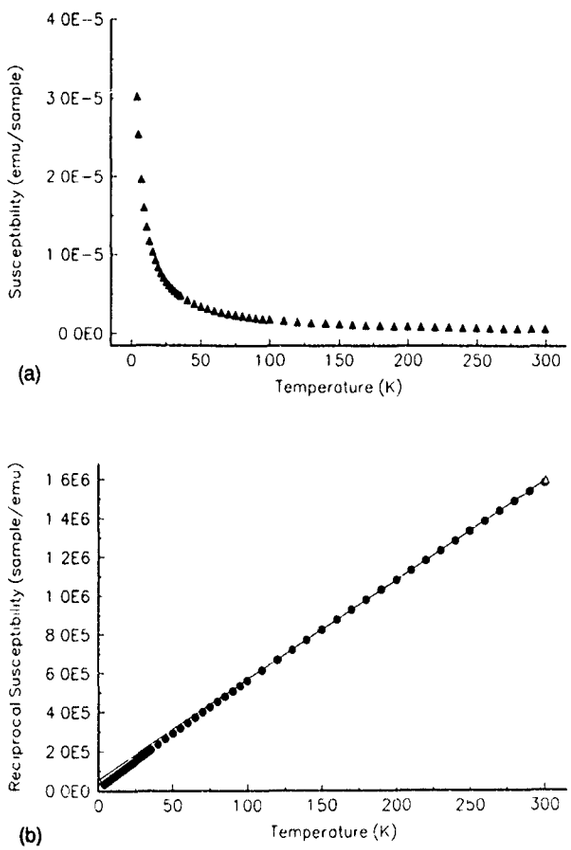

FIG. 1. (a) The dc susceptibility of an ion exchanged sample consisting entirely of Fe^{2+}. (b) The reciprocal susceptibility obtained from the data of (a)

 0021-8979/94/76(10)/6567/3/$6 00 © 1994 American Institute of Physics

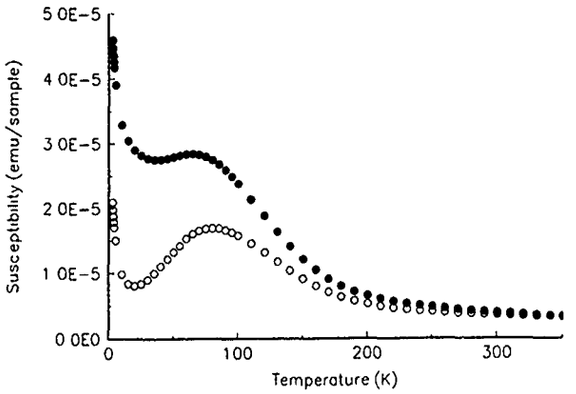

FIG. 2. The dc susceptibility of a sample after a single reduction to Fe^0 measured in a 10 G field. The upper curve is field cooled; the lower is zero field cooled.

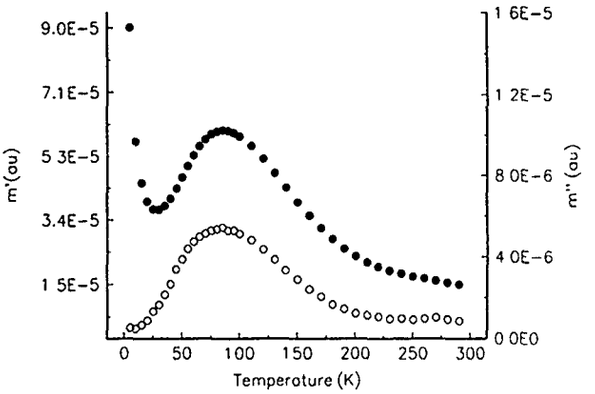

FIG. 4. The real (solid circles) and imaginary (open circles) parts of the ac magnetization of a reduced sample measured at 10 Hz.

By using conventional ion-exchange methods, we have introduced Fe^{+2} ions into the NaY zeolite and reduced it to Fe^0 with solvated electrons and Na^{-1} anions in an ether solvent.[4] The ion exchange process followed by the reduction is expected to yield iron clusters in the supercages with a maximum of 28 Fe atoms, with 56 K^{+1} and/or Na^{+1} ions reintroduced to maintain charge neutrality. Although we have tried to prevent exposure to oxygen we expect some oxidation of Fe atoms to occur yielding a mixture of Fe^0 and Fe^{+2} of unknown proportions. Although both multiple-exchange and multiple-reduction processes are possible, the samples used in these experiments were the result of one stage of each.

III. EXPERIMENTAL RESULTS

We are reporting here the temperature- and field-dependent dc susceptibility and the temperature- and frequency-dependent ac susceptibility which have been measured on a Quantum Design MPMS2 susceptometer. The dc magnetic susceptibility and reciprocal susceptibility of the zeolite sample after Fe^{2+} exchange but before reduction are shown in Fig. 1. The high temperature behavior is Curie—Weiss (CW) with $\Theta \approx 10$ K with small deviations from CW at low temperature.

The dc magnetic susceptibility measured after reduction to Fe^0 is shown in Fig. 2. The upper and lower curves are obtained from the field cooled (FC) and zero field cooled (ZFC) measurements, respectively. There are three interesting features in these data; the irreversibility which starts near 300 K, the peak near 100 K, and the Curie-like behavior at low temperatures. The Curie behavior arises from residual Fe^{+2} ions which were missed in the reduction process or were oxidized after reduction. Magnetic measurements made several months after sample preparation give essentially the same results implying no long term oxidation. The peak near 100 K can be attributed to a blocking temperature, T_b, associated with superparamagnetic behavior, although if this were a conventional superparamagnet the irreversibility would begin near T_b. Figure 3 shows the field dependence of the ZFC data for magnetic fields between 10 and 5000 G. The blocking temperature peak is first shifted to lower temperatures and then destroyed by fields of less than 1000 G. Hysteresis curves taken between T_b and the paramagnetic regime indicate remanence and coercive fields of about 1×10^{-6} and 5 G, respectively.

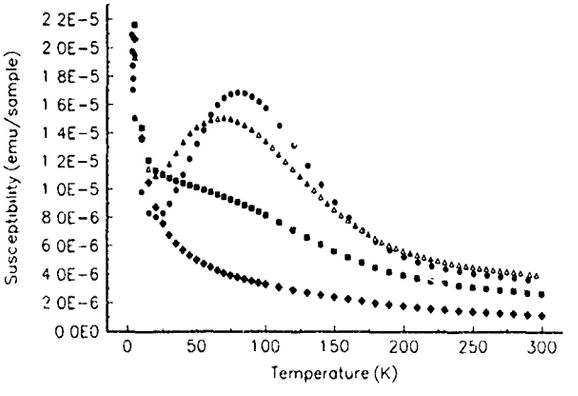

FIG. 3. The dc susceptibility of a reduced sample measured in. ●, 10, △, 100; ■, 500; and ◇, 5500 G.

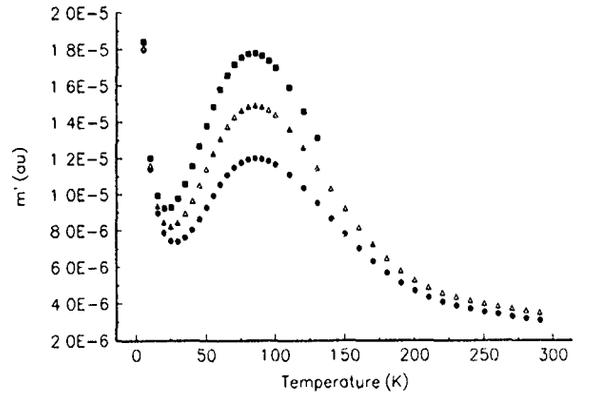

FIG. 5. The real part of the ac magnetization of a reduced sample measured at: ●, 0.1; △, 10; and ■, 100 Hz.

The real and imaginary parts of the ac susceptibility—χ' and χ'', respectively—were measured in an ac field of 1 G (with no static field) for frequencies between 0.1 and 1000 Hz. The temperature dependence of χ' and χ'' measured at 10 Hz is shown in Fig. 4. The absence of an imaginary component in the low temperature range confirms our suggestion that this is a paramagnetic regime—where there are essentially no losses. On the other hand, near the peak in the susceptibility of a superparamagnet (or a spin glass) where the measuring frequency and relaxation time are related by $\omega = 1/\tau$, the real part of the magnetization, χ', should have an inflection point while χ'' should have a maximum.[5] The data do not show this behavior at any measuring frequency. In addition there is a weak frequency dependence of T_b (Fig. 5).

IV. SUMMARY

The ion exchange and reduction techniques which we have developed to incorporate small clusters of Fe^0 into the supercages of NaY zeolite have produced novel samples whose magnetic properties can best be described as "nominally superparamagnetic." Some of the anomalous behavior which is observed is certainly due to a distribution of particle sizes or possibly to particles which consist of a mixture of Fe^0 and Fe^{+2} leading to a frustrated spin glass. Currently we are investigating the effects of multiple exchange and reduction on the magnetic properties and the use of Mössbauer spectroscopy to characterize the structure.

[1] W. A. de Heer, P. Milani, and A. Chatelain, Phys. Rev. Lett. **65**, 488 (1990).
[2] G. Xiao, S. H. Liou, A. Levy, J. N. Taylor, and C. L. Chien, Phys. Rev. B **34**, 7573 (1986).
[3] D. W. Breck, *Zeolite Molecular Sieves* (Wiley, New York, 1974).
[4] K. L. Tsai and J. L. Dye, Chem. Mater. **5**, 540 (1993).
[5] C. Y. Huang, J. Magn. Magn. Mater. **51**, 1 (1985).

Preparation and microwave characterization of spherical and monodisperse $Co_{20}Ni_{80}$ particles

G. Viau, F. Ravel, and O. Acher
Commissariat à L'Energie Atomique, BP 12, 91680, Bruyères le Châtel, France

F. Fiévet-Vincent and F. Fiévet
Laboratoire de Chimie des Matériaux Divisés et Catalyse, Université Paris 7-Denis Diderot, 2 Place Jussieu, 75251 Paris, Cedex 05, France

Spherical and monodisperse $Co_{20}Ni_{80}$ particles were prepared, in the micrometer and submicrometer size range, by the polyol process. X-ray diffraction showed crystalline particles with a fcc structure. From electron probe microanalysis a fairly homogeneous distribution of both elements within each particle was observed. Microwave properties of metal particles/dielectric matrix composites were studied in the 0.1–18 GHz range for different filler concentrations. The intrinsic permeability of the metal powders was obtained using the Bruggeman effective medium theory. The control of the particle size allowed the study of its effect upon dynamic permeability. Whereas micrometer size particle permeability presents a single resonance band at low frequencies which can be correlated to the low magnetocrystalline anisotropy of the particles, submicrometer size particle permeability exhibits an original behavior, never reported before, with several resonance bands.

I. INTRODUCTION

One way to make electromagnetic absorbers is to disperse ferromagnetic powders in an insulating matrix. Previous studies[1,2] showed that the microwave properties of such materials depend on particle shape and granulometry. Spherical particles present an advantage in minimizing permittivity level of the composites whereas the maximum of the imaginary part of permeability decreases when the particle size increases.

The polyol process is a method for preparing fine metallic powders which has been developed over the last few years.[3] This process which applies to cobalt and nickel allowed the elaboration of spherical and monodisperse particles with an accurate control of the particle mean diameter in the micrometer and submicrometer size range.[4] Our aim was to adapt the polyol process to the preparation of fine bimetallic cobalt-nickel particles. We focused the study on the $Co_{20}Ni_{80}$ composition which corresponds to low magnetocrystalline anisotropy in bulk alloys. Composites were made with the $Co_{20}Ni_{80}$ powders and their microwave permeability was measured.

II. EXPERIMENTAL METHODS

A. General description of the polyol process

Finely divided metal powders (Co,Ni,Cu,Pb, precious metals) are obtained by precipitation in hot liquid polyols. The reaction proceeds according to the following scheme: progressive dissolution of a suitable powdered metallic compound (precursor), reduction of the dissolved species by the polyol itself; nucleation and growth of the metal particles from the solution.[4]

In standard conditions the metallic nuclei are formed spontaneously (homogeneous nucleation). However this homogeneous nucleation can be replaced by an heterogeneous one by the formation of seed particles acting as foreign nuclei. More generally, the kinetic control of the nucleation and growth steps allows the synthesis of powders made up of particles with a well-defined shape, a controlled size, and a narrow size distribution.[5]

B. Preparation of $Co_{20}Ni_{80}$ particles

CoNi particles were prepared as follows: cobalt and nickel acetate hydrate were used as precursors, they were dissolved in a NaOH-ethylene glycol solution; the NaOH concentration was in the range 0.5–2 mol dm^{-3}, the precursor concentration was typically 0.2 mol dm^{-3} with a Co/Ni molar ratio: 20/80. The solution was stirred and heated up to 195 °C; the water and the volatile organic products of the reaction were distilled off while the polyol was refluxed. After a few hours the metal was quantitatively precipitated from the solution, the metal particles were recovered by centrifugation, washed with ethanol, and dried in air at 50 °C. The use of a basic solution of ethylene glycol shortens the reaction time and allows one to obtain, by homogeneous nucleation, monodisperse particles more easily. CoNi particles were also obtained by heterogeneous nucleation, the seed particles being tiny metallic silver particles formed *in situ* by the admixture of silver nitrate dissolved in ethylene glycol to the original reactant solution.

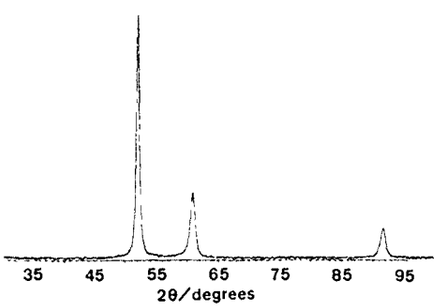

FIG. 1 XRD pattern of a $Co_{20}Ni_{80}$ powder obtained by reduction of Co and Ni acetate in NaOH-ethylene glycol solution (Co $K\alpha$ radiation).

 0021-8979/94/76(10)/6570/?/$6.00 © 1994 American Institute of Physics

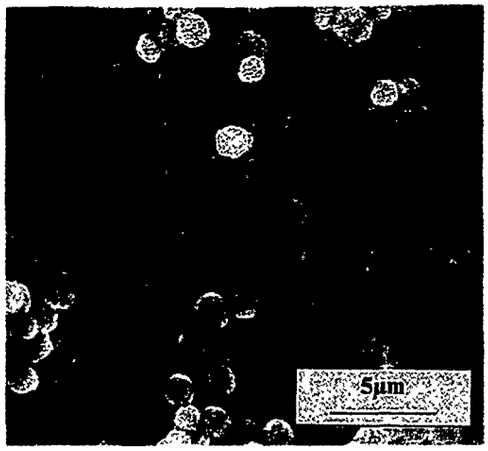

(a)

(b)

FIG. 2. (a) Micronic size $Co_{20}Ni_{80}$ monodisperse particles obtained by homogeneous nucleation (d_m=1.4 μm, σ=0.2 μm). (b) Submicronic size $Co_{20}Ni_{80}$ monodisperse particles obtained by heterogeneous nucleation (d_m=0.33 μm, σ=0.05 μm).

C. Characterization techniques

Phase analysis was performed by x-ray diffraction (XRD) using a C.G.R. x-ray powder diffractometer (Co $K\alpha$ radiation). The form and the size of metallic particles were determined by scanning electron microscopy (Philips 505). The average diameter and the standard deviation were estimated from image analysis of ~250 particles. The distribution of the two elements within isolated particles was studied by energy dispersive x-ray spectrometry (EDS), the microprobe being associated with a scanning transmission electron microscope (STEM). Magnetization saturation of powders and composites were measured by a vibrating sample magnetometer.

Particles were randomly dispersed in epoxy resin with concentration ranging from 30% to 50% by volume. Particle concentrations were determined by saturation magnetization measurements. Microwave properties of composites were measured in 0.1–18 GHz frequency range with an APC7 coaxial line associated with a network analyzer.

III. RESULTS AND DISCUSSION

$Co_{20}Ni_{80}$ powders obtained are well crystallized as evidenced by XRD (Fig. 1). The pattern can be indexed as a fcc lattice. It is well known[6] that nickel crystallizes with a fcc lattice (a=0.352 38 nm) and that there are two cobalt polymorphs: Co(α) with a hexagonal lattice and Co(ϵ) with a fcc one (a=0.354 47 nm). From Fig. 1 it can be inferred that there is no Co(α) polymorph but it is not possible to ascertain if $Co_{20}Ni_{80}$ powders are solid solutions or mixtures of cobalt and nickels fcc phases owing to the very close values of the cell parameters of these two phases.

Typical examples of $Co_{20}Ni_{80}$ powders obtained by the polyol process are provided by the scanning electron microscopy micrographs in Fig. 2. The first sample [Fig. 2(a)] was obtained by homogeneous nucleation from a 2 mol dm^{-3} NaOH-ethylene glycol solution. The particles are quasispherical with a mean diameter d_m=1.4 μm, a narrow size distribution (standard deviation σ=0.2 μm), and a low degree of agglomeration. The second sample [Fig. 2(b)] was obtained by heterogenous nucleation (Ag/Co+Ni atomic ratio: 5×10^{-5}). The particles are smaller (d_m=0.33 μm, σ=0.05 μm). Heterogeneous nucleation gives particles in the submicrometer size range and allows their mean diameter to be controlled by varying the amount of $AgNO_3$ used to form the silver seed particles.

The Co/Ni ratio in the final metal powder is the same as in the starting solution: 20/80. Chemical analysis shows that the main impurities are carbon and oxygen at a level lower than 0.5% by weight.

The global composition $Co_{20}Ni_{80}$ is found again for each isolated particle analyzed by energy dispersive spectroscopy

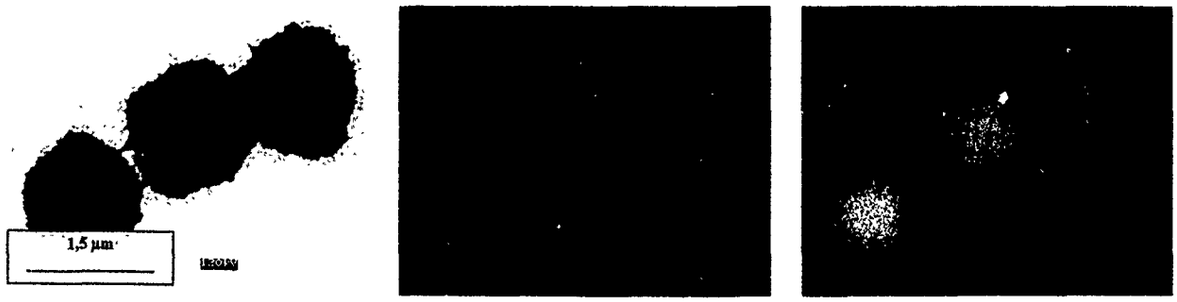

(a) (b) (c)

FIG 3 Qualitative analysis of element distribution in $Co_{20}Ni_{80}$ particles with EDS microprobe (a) STEM micrograph, repartition map for (b) nickel, (c) cobalt.

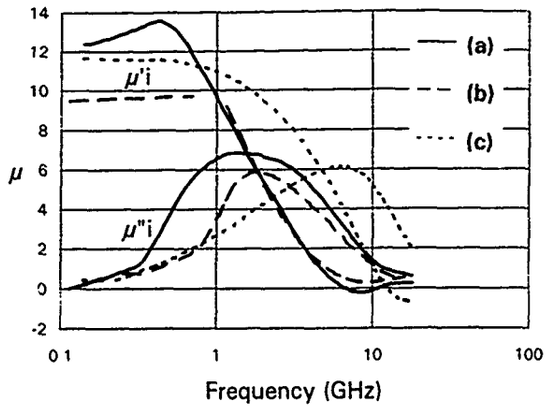

FIG. 4. Intrinsic permeability $[\mu_i'(\omega),\mu_i''(\omega)]$ for (a) $Co_{20}Ni_{80}$ powder (d_m=1.5 μm); (b) Ni powder (d_m=1.4 μm); (c) Co powder (d_m=1.9 μm).

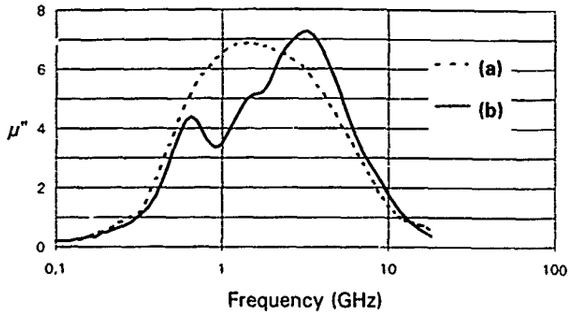

FIG. 5. Comparison of $\mu_i''(\omega)$ for two $Co_{20}Ni_{80}$ powders of different granulometry (a) d_m=1.5 μm; (b) d_m=0.3 μm.

(EDS). Moreover, the distribution of each element within one particle appears fairly homogeneous (Fig. 3). However, a small concentration gradient can be observed from the heart to the outer part of the particle, the heart being slightly poorer in nickel than the outer part. This difference in composition which cannot be estimated quantitatively is related to different kinetics of reduction and precipitation for the two metals.

Saturation magnetization values were typically 75 and 72 emu/g for micrometer and submicrometer size particles, respectively. These values are very close to bulk metal value and corroborate the low level of impurities.

Dynamic permeability of $Co_{20}Ni_{80}$ powders-epoxy resin composite materials presents a resonance in the 0.1–18 GHz range. The composite permeability $\mu_e(\omega)$ depends on the ferromagnetic particle concentration. It has been shown recently[1,2] that a homogenization law adapted from Bruggeman theory[7] can describe this effect. According to these studies intrinsic permeability $\mu_i(\omega)$ of our powders was inferred from composite permeability measurements. For a given powder the values $\mu_i(\omega)$, computed from $\mu_e(\omega)$ measurements for several composites of different volume fraction, were found weakly dependent on the volume fraction. Thus, $\mu_i(\omega)$ may be considered as an intrinsic property of the powders.

Figure 4 shows $\mu_i(\omega)$ for $Co_{20}Ni_{80}$, Ni, and Co powders of comparable granulometry in the micrometer range. The maximum of $\mu_i''(\omega)$ appears at 1.4, 1.8, and 6.5 GHz for $Co_{20}Ni_{80}$, Ni and Co powders, respectively. The shift of resonance bands observed with chemical composition can be correlated to a variation of the magnetocrystalline anisotropy. In the case of a monodomain and monocrystalline sphere Kittel[8] linked the resonance frequency to the magnetocrystalline anisotropy field: $f_r=(\gamma/2\pi)H_a$. H_a values computed from resonance frequency measurements by Kittel formula present a variation with chemical composition in qualitative agreement with the variation of the anisotropy constants reported for Ni, Co, and NiCo alloys.[9]

Effect of particle size upon microwave permeability were studied by Berthault *et al.* with permalloy particles in the 4–16 μm size range.[1] It was shown that the variation of the dynamic permeability with granulometry could be interpreted by the eddy current effects. We present here a comparison between $\mu_i''(\omega)$ for two $Co_{20}Ni_{80}$ samples of different granulometries in the micrometer and submicrometer size range (Fig. 5). Whereas micrometer size particles (d_m=1.5 μm) exhibit a permeability curve with a single resonance band the submicrometer size particles (d_m=0.3 μm) exhibit an original behavior with three resonance bands. This unexpected phenomena for particles exhibiting uniformity of shape, size, and composition, can be clearly related to their small size. Actually, we have observed a similar behavior with ferromagnetic fine particles of different composition but with a similar mean diameter. Results will be reported elsewhere.[10] To our knowledge such a phenomena has never been reported before. It can be tentatively related either to the magnetic domain structure of small particles or to a surface effect similar to the effect responsible for spin wave resonance in thin ferromagnetic films.

IV. CONCLUSION

The intrinsic permeability $\mu_i''(\omega)$ of $Co_{20}Ni_{80}$ particles having controlled and well-defined morphological characteristics have been measured. A size effect has been clearly evidenced. For particles in the micronic size range a single resonance band has been observed at low frequency as expected for a material with a low magnetocrystalline energy. Particles in the submicron range exhibit an original behavior, never reported before, with several resonance bands.

[1] A. Berthault, D. Rousselle, and G. Zerah, J. Magn. Magn. Mater. **112**, 477 (1992).
[2] L. Olmedo, G. Chateau, C. Deleuze, and J. L. Forveille, J. Appl. Phys. **73**, 6992 (1993).
[3] M. Figlarz, F. Fiévet, and J. P. Lagier, European Patent No. 0113281; USA Patent No. 4539041; Fin. Patent No. 74416; Japan Patent No. 04024402.
[4] F. Fiévet, J. P. Lagier, and M. Figlarz, Mater. Res. Soc. Bull. **14**, 29 (1989).
[5] F. Fiévet, J. P. Lagier, B. Blin, B. Beaudoin, and M. Figlarz, Solid State Ion. **32/33**, 198 (1989).
[6] X ray powder data file J.C.P.D.S. No. 4-850, No. 15-806.
[7] D. A. G. Bruggeman, Ann. Phys. (Leipzig) **24**, 636 (1935).
[8] C. Kittel, Phys. Rev. **73**, 155 (1948).
[9] *Landolt-Bornstein II band, 9 teil, Magnetic properties I* (Springer, Berlin, 1962), pp. 1–119.
[10] G. Viau, F. Ravel, O. Acher, F. Fiévet-Vincent, and F. Fiévet, presented at International Conference on Magnetism, Warsaw, August 1994, J. Magn. Magn Mater. (to be published).

Coercivity of Fe-SiO_2 nanocomposite materials prepared by ball milling

Anit K. Giri, C. de Julián, and J. M. González
Departamento de Propiedades Ópticas, Magnéticas y de Transporte, Instituto de Ciencia de Materiales de Madrid—CSIC, c/Serrano 144, 28006 Madrid, Spain

Samples containing Fe nanoparticles dispersed in SiO_2 were prepared by high energy ball milling. We have studied the variation with the milling time of both the saturation magnetization and the coercive force of these samples. The rapid increase of coercivity with the decrease of temperature observed in the low temperature range suggested the presence of superparamagnetic particles in the samples. Nevertheless, our experimental data were in poor agreement with the well-known $T^{1/2}$ law describing the coercive force of superparamagnetic particles. Coercivities as high as 540 and 850 Oe were obtained for samples with $x=0.3$ at room temperature and at 1.7 K, respectively. From the analysis of the temperature dependence of the saturation magnetization the spin wave stiffness constant was obtained. This quantity evidenced the enhancement of the thermal demagnetization associated with the reduction in size.

I. INTRODUCTION

The high coercivity values (up to 1 kOe) measured for Fe nanoparticles embedded in insulating or conducting matrix have induced a lot of research work on the preparation and characterization of this kind of nanocomposite materials.[1] Most of these materials were prepared by sputtering technique.[1] Although some bulk preparational methods such as high energy ball milling have been successfully used to prepare nanostructured materials, only a few results have been reported regarding the properties of metal nanoparticles prepared by this technique. Recently, using high energy ball milling, Ambrose *et al.*[2] prepared Fe nanoparticles in an Al_2O_3 matrix and obtained coercivities of 600 Oe at 5 K and 230 Oe at room temperature. In this paper we report on the preparation and detailed characterization of the magnetic properties of Fe-SiO_2 nanocomposities prepared by high energy ball milling.

II. PREPARATION OF SAMPLES AND EXPERIMENTAL TECHNIQUES

Samples of the series $Fe_x(SiO_2)_{1-x}$ with Fe volume fraction x in the range $0.1 \leq x \leq 0.65$ were prepared by high energy ball milling. The starting materials consisted of -325 mesh Fe powders and silica gel prepared by the conventional method[3] of hydrolysis and polycondensation of silicon tetraethoxide in water and ethanol solutions under acidic medium. The gel was dried in air at 333 K for 15 days. The amorphous nature of silica gel was confirmed by x-ray diffraction (XRD). Appropriate amounts of Fe and SiO_2 gel were placed in a hardened stainless steel vial with four hardened stainless steel balls so that the ratio of the weight of the balls to that of the powder was 14:1. The vial was sealed in an inert atmosphere to prevent oxidation. These materials were then milled for up to 70 h. The as-milled samples were characterized by XRD and transmission electron microscopy (TEM). Magnetic measurements were carried out in pressed powder samples by means of vibrating sample magnetometer, superconducting quantum interference device, and an ac susceptometer.

III. RESULTS AND DISCUSSIONS

XRD patterns of the samples revealed along with the presence of Fe peaks that the samples were free from the oxides of Fe down to the resolution of the technique. The average Fe grain size was evaluated from the width at half-maximum of the (110) reflection after making the correction due to the instrumental broadening. Figure 1 shows the milling time dependence of the average grain size as measured in the sample with $x=0.3$. From Fig. 1 a rapid decrease of the average grain size down to a saturation value of 9 nm is apparent. In the inset of Fig. 1 we plotted the saturation (70 h milling) average grain size of samples as a function of compositions. Particle size and dispersion were examined by TEM. Figure 2 presents a picture taken in a $x=0.3$ sample (milled for 70 h). From this picture it was possible to evaluate the average particle size as 11 ± 2 nm and to observe the excellent degree of dispersion of the particles. For all the samples comparison of the average grain and particle size showed reasonable agreement and led us to identify both parameters. In Fig. 3 we present, for the different compositions studied, the variation of the magnetization with the milling time corresponding to an applied field of 10 kOe. In all the cases the magnetization decreased down to a composition-dependent saturation value. The milling time dependence of the as-milled room temperature coercive force is presented in Fig. 4. This parameter increased with milling

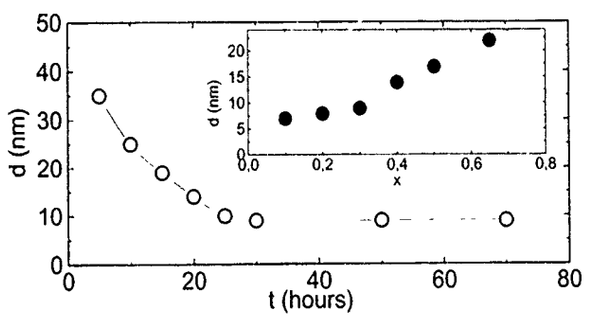

FIG. 1. Typical plot of the average grain size (d) vs the milling time (t) for the $Fe_{0.3}(SiO_2)_{0.7}$ sample. In the inset a plot of d vs Fe volume fraction (x) (samples milled for 70 h) is presented.

 0021-8979/94/76(10)/6573/3/$6.00 © 1994 American Institute of Physics

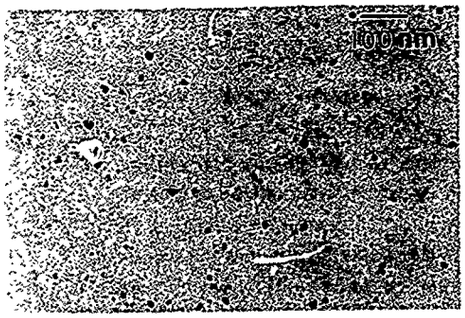

FIG. 2. Typical TEM micrograph of the sample with $x=0.3$.

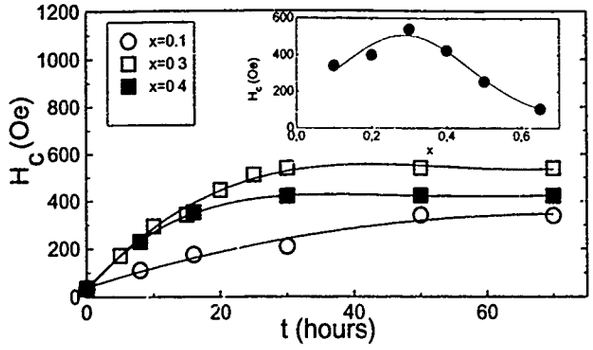

FIG. 4. Plot of the coercive force (H_c) vs the milling time (t). The inset shows a plot of H_c vs x for the 70 h milled samples.

time up to a maximum (saturation) value which was achieved after 30 h of milling. The correlation of these results with the milling time evolution of the particle size allowed us to conclude that both the decrease in saturation magnetization and the increase of coercive force were originated by the reduction of particle size. Regarding the first quantity this correlation suggests the presence of superparamagnetic particles in the samples. As for the coercive force the values we obtained are larger than the anisotropy field of Fe which evidences that an interaction different from the bulk magnetocrystalline anisotropy rules magnetization reversal. The inset in Fig. 4 presents the compositional evolution of the coercive force of samples milled for 70 h. Interestingly a maximum is obtained for $x=0.3$ which evidences the occurrence of interparticle interaction since this value is clearly lower than the percolation concentration.

In Fig. 5(a) we present results corresponding to the temperature dependence of the magnetic moment, m, for the sample with $x=0.3$ milled for 70 h. These results represent the behavior of all the samples studied. The magnetic moment was measured after zero field cooling (ZFC) and field cooling (FC) with two different applied fields (20 kOe and 75 Oe). Our data evidence the presence of a fraction of superparamagnetic particles in the samples. Nevertheless, magnetometric measurements did not allow us to distinguish any variation of the blocking temperature either with the composition of the samples or with the milling time (blocking temperatures close to 4 K were observed in all the cases). In order to clarify this point we measured the temperature dependence of the ac (1 kHz) susceptibility [see Fig. 5(b) where results corresponding to $x=0.3$ milled for 70 h are presented]. From these results we obtained the blocking temperature, T_B, plotted in the inset of Fig. 5(b). The values obtained are in quantitative agreement with the magnetometric results, considering the typical measuring time characteristic of both techniques. We can conclude that the average volume of the superparamagnetic fraction of the samples was not influenced very much by the preparation parameters. Considering the evolution with these parameters (and also with the composition) of the average particle size (XRD and TEM) we can conclude that the superparamagnetic particles corresponded to the tails of the size distribution and therefore were only small minority. Going back to thermal evolution of the magnetic moment of the samples [Fig. 5(a)] it is worth

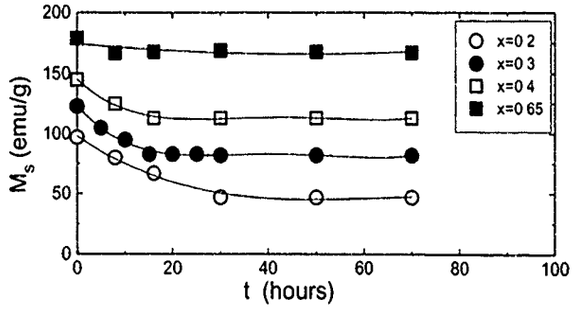

FIG. 3. Plot of the saturation magnetization (M_s) vs the milling time (t).

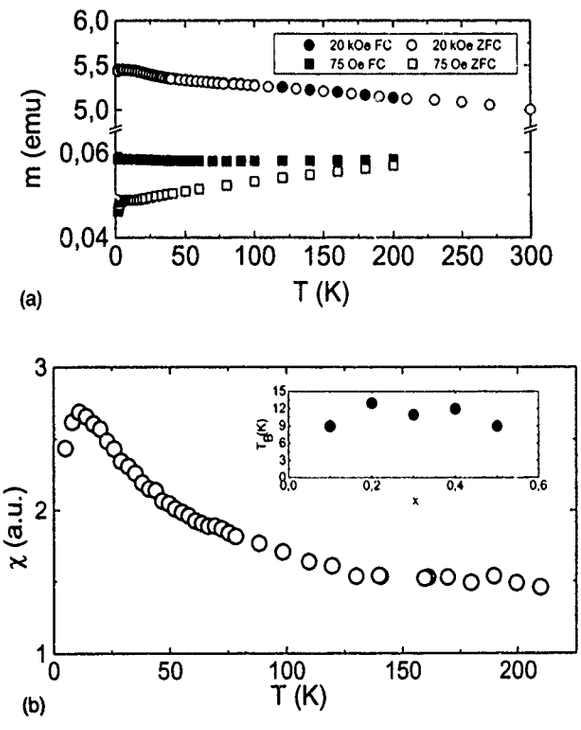

FIG. 5. (a) Plot of the magnetic moment (m) vs temperatures (T) for the sample with $x=0.3$ milled for 70 h (see the text). (b) Plot of the ac susceptibility (χ) vs temperature (T) for sample with $x=0.3$ milled for 70 h. Inset: Plot of the blocking temperature (T_B), as obtained from ac susceptibility measurements, vs Fe volume fraction (x).

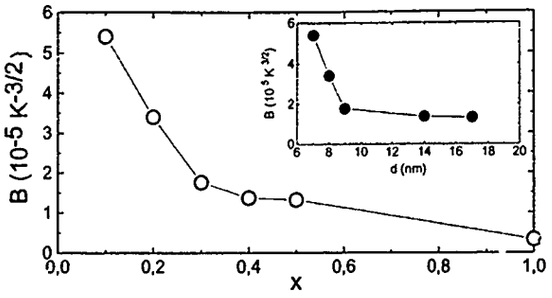

FIG. 6. Plot of the spin wave stiffness constant (B) against Fe volume fraction (x) for the samples milled for 70 h (inset). Plot of B against the average grain size (d) for the samples milled for 70 h.

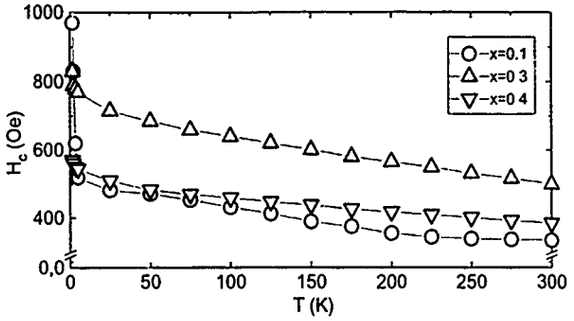

FIG. 7. Plot of coercive force (H_c) vs temperature (T)

pointing out that the increase in magnetic moment with the increase of temperature observed in the low field curves can be understood as corresponding to a decrease of the magnetic anisotropy with the increase of temperature, which originates the alignment with the field of the moments of a larger number of particles. From the high field $m(T)$ curve it was possible to obtain the thermal evolution of the magnetic moment using Bloch's law given by $m(T)=m(0)(1-BT^{3/2})$ where B is spin wave stiffness constant, $m(T)$ and $m(0)$ are the moments at temperatures T and 0 K, respectively. For that purpose we considered a temperature range clearly above the blocking temperature of the superparamagnetic particles. Our results are presented in Fig. 6 where we have plotted the values of B obtained from the fits of the straight line plots of $m(T)/m(0)$ vs $T^{3/2}$ as a function of the composition and average grain size (inset, for the samples milled for 70 h). The occurrence of the enhanced thermal demagnetization in the small particles (compared to the equivalent bulk process) is apparent from Fig. 6. Also it is interesting to note that our B values are of the order of those obtained in samples of similar composites prepared by sputtering.[1] The enhanced demagnetization results from the influence of size in the electronic properties of the materials and has been related to the occurrence of a cutoff frequency in the spin wave spectrum.[1]

The temperature dependence of the coercive force (Fig. 7) also suggested the presence of superparamagnetic particles to which the rapid increase of this parameter with the decrease of temperature could be ascribed. This effect is more clear for the sample with $x=0.1$ where the coercive force increased up to 970 Oe at 1.7 K. The temperature dependence of the coercive force of our samples does not obey the $T^{1/2}$ law[4] which can be ascribed to the occurrence of interparticle dipolar interactions (evidenced by the compositional dependence of the coercive force).

IV. CONCLUSIONS

We have studied the effect of particle size on the magnetization and coercive force of Fe nanoparticles dispersed in silica-gel matrix prepared by ball milling. Reduction in particle size originated a decrease of the saturation magnetization and an increase in both coercivity and spin wave stiffness constant. It is worth remarking that our room temperature coercive force values were of the same order as those obtained in Fe-SiO_2 nanocomposites prepared by sputtering.[1]

ACKNOWLEDGMENTS

The authors acknowledge Fundación Domingo Martínez for financial support. A.K.G. thanks the Ministerio de Educación y Ciencia, Government of Spain for a postdoctoral fellowship.

[1] C. L. Chien, *Science and Technology of Nanostructured Magnetic Materials*, edited by G. C. Hadjipanayis and G. A. Prinz (Plenum, New York, 1991), p. 477, and references therein.
[2] T. Ambrose, A. Gavrin, and C. L. Chien, J. Magn. Magn. Mater. **116**, L311 (1992).
[3] D. M. Krol and J. G. Lierop, J. Non-Cryst. Solids **126**, 52 (1990).
[4] E. F. Kneller and F. E. Luborsky, J. Appl. Phys. **34**, 656 (1963).

Nuclear magnetic resonance study of the magnetic behavior of ultrafine Co clusters in zeolite NaY

Y. D. Zhang,[a] W. A. Hines, and J. I. Budnick
Department of Physics and Institute of Materials Science, University of Connecticut, Storrs, Connecticut 06269

Z. Zhang[b] and W. M. H. Sachtler
Ipatieff Laboratory and Department of Chemistry, Northwestern University, Evanston, Illinois 60208

^{59}Co spin-echo nuclear magnetic resonance (NMR) experiments have been carried out at 1.3 and 4.2 K, for external magnetic fields up to 9 kOe, in order to study 6–10 Å, single-domain Co clusters isolated inside zeolite NaY supercages. The magnetic behavior is characterized by a superparamagnetic blocking temperature, relaxation time behavior for increasing and decreasing fields, and a dependence on the magnetic history. The observed NMR spectra are broad with structural features characteristic of both fcc- and hcp-like short-range order. Unlike bulk materials, the application of fields up to 9 kOe causes a dramatic increase in the signal intensity. The results are discussed in terms of the particle-size distribution and crystalline anisotropy, and their relationship to the temperature and field dependence of the superparamagnetic/ferromagnetic behavior.

I. INTRODUCTION

In an earlier work, it was demonstrated how information concerning the size and location of Co clusters in zeolite NaY could be obtained by ^{59}Co spin-echo NMR measurements.[1] In particular, the superparamagnetic blocking temperature was used to obtain an estimate for the average Co cluster size in Co/NaY samples which were prepared using different thermal treatments. Also, a selective chemical treatment with triphenylphosphine was used to determine the location of the clusters. It was found that preparation of Co/NaY under "mild" conditions (decomposition and annealing carried out at 200 °C) resulted in the production of Co clusters with an average diameter of 6–10 Å inside the NaY supercages, while preparation of Co/NaY under "extreme" conditions (decomposition and annealing carried out at 500 °C) resulted in larger clusters outside the NaY cages.

This work focused on the interested magnetic behavior which characterizes the 6–10 Å, single-domain Co clusters isolated inside the zeolite NaY supercages.[1] In order to study this behavior, detailed ^{59}Co spin-echo NMR experiments have been carried out at 1.3 and 4.2 K, for magnetic fields up to 9 kOe. The observed spectra are broad with a primary peak and a secondary peak characteristic of fcc- and hcp-like short-range order, respectively. Unlike bulk materials, the application of a magnetic field causes a dramatic increase in the NMR signal intensity which is reversible. As described below, in addition to a superparamagnetic blocking temperature which occurs within this temperature range, the magnetic behavior is characterized by relaxation time effects for increasing and decreasing fields, and a dependence on the magnetic history. [More precisely, the superparamagnetic relaxation is blocked in the time window of the NMR measurement (5 ns).] These results are discussed in terms of the particle-size distribution and crystalline anisotropy, and their relationship to the temperature and field dependence of the superparamagnetic/ferromagnetic behavior.

II. EXPERIMENTAL APPARATUS AND PROCEDURE

Zeolite NaY (Linde LZY-52) was dehydrated at 500 °C for 2 h in Ar, followed by $Co_2(CO)_8$ vapor absorption at room temperature in CO atmosphere. The yellow colored sample was then thermally treated at 200 °C for 1 h in H_2 to remove the carbonyl ligands. The adsorbed hydrogen was subsequently removed by purging with Ar gas at 200 °C for 1 h. The Co/NaY sample was evacuated and then sealed in a Pyrex tube. The final Co loading was approximately 1 wt %.

Spin-echo NMR measurements were carried out on a commercial Matec model 7700 pulse modulator and receiver (mainframe), with matching Matec model 765 rf pulsed oscillator plug in (90–300 MHz and 500 W). The spectrometer system was matched with a Varian model V3400 electromagnet and Fieldial regulated power supply capable of fields up to 9 kOe. Operation at liquid helium temperatures was possible with a conventional glass double-dewar system and pumping system. The measured echo amplitude was normalized and divided by the first power of the frequency in the usual manner. Additional details concerning the sample preparation procedure, pulsed NMR apparatus, data acquisition, and spectral analysis can be found in the previous report.[1]

III. RESULTS AND ANALYSIS

Figure 1 shows the ^{59}Co spin-echo NMR spectrum obtained from the Co/NaY sample described above at 4.2 and 1.3 K, for zero external magnetic field. As illustrated in Fig. 1, no NMR signal was observed at 4.2 K (solid diamonds); however, as the temperature was lowered to 1.3 K, a broad spectrum with a central peak at 212 MHz dramatically appeared (open circles). A secondary peak in the spectrum exists at approximately 222 MHz. As indicated in the earlier work,[1] a consideration of the signal-to-noise ratio indicates that this is indeed the result of a blocking of the superparamagnetic relaxation, and not just an increase in the signal

[a]On leave from Lanzhou University, Lanzhou, Ganzu, P. R. China.
[b]Present address: AKZO Chemical Inc, 1 Livingston Ave., Dobbs Ferry NY 10522.

 0021-8979/94/76(10)/6576/3/$6.00 © 1994 American Institute of Physics

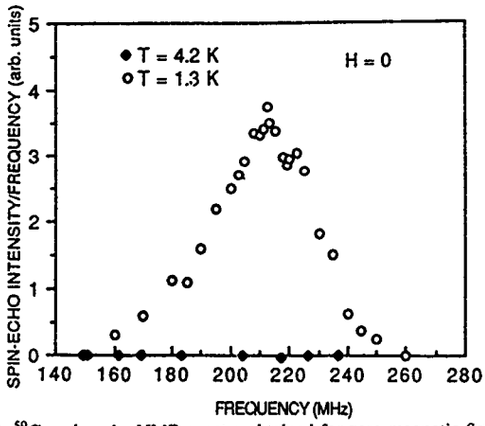

FIG. 1. ^{59}Co spin-echo NMR spectra obtained for zero magnetic field from 6 to 10 Å clusters inside zeolite NaY supercages; solid diamonds, T=4.2 K (no signal observed); open circles, T=1.3 K. The sample was initially cooled from room temperature to 4.2 K and then 1.3 K in zero field.

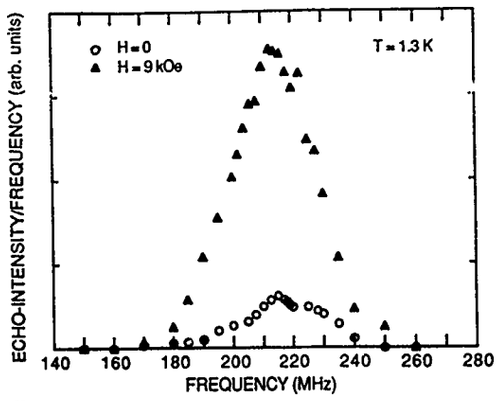

FIG. 2. ^{59}Co spin-echo NMR spectra obtained at 1.3 K from 6 to 10 Å Co clusters inside zeolite NaY supercages; solid triangles, H=9 kOe; open circles, H=0. The sample was initially cooled from room temperature to 1.3 K in zero field.

intensity due to the Boltzmann factor. The existence of a superparamagnetic blocking temperature in this temperature range along with an approximate value for the crystalline anisotropy for small Co particles resulted in an estimate of the average cluster diameter between 6 and 10 Å.[1] This is supported by the fact that a chemical treatment with triphenylphosphine does not change the observed spectrum, indicating that the clusters must be protected by being located inside the NaY supercages. Consequently, an upper limit of 12 Å, which is the diameter of the supercages, is established for the clusters. The principal peak at 212 MHz and secondary peak at 222 MHz are characteristic of fcc- and hcp-like short-range order, respectively. These values are lower than the corresponding bulk cobalt values by about 7 MHz. This tentative assignment seems reasonable in view of a similar spectrum which was obtained from a Co/NaY sample that was prepared under "extreme" conditions (decomposition and annealing carried out at 500 °C), resulting in larger clusters outside of the NaY cages.[1] The larger Co clusters were characterized by a spectrum which was similar in shape to that presented in Fig. 1, although about 25% narrower. The two peak frequencies were quite close to the bulk values.

Figure 2 shows the ^{59}Co spin-echo NMR spectrum obtained from the Co/NaY sample at 1.3 K for external magnetic fields of H=9 kOe (solid triangles) and H=0 (open circles). The spectra illustrated in Fig. 2 were obtained by cooling the sample in zero field from room temperature to 1.3 K, measuring the H=0 spectrum, increasing the field to H=9 kOe, and then remeasuring the spectrum. It is significant to note that, unlike bulk materials, the application of magnetic fields up to 9 kOe causes a dramatic increase in the signal intensity which is reversible. This is illustrated in Fig. 3 which shows the spin-echo intensity (echo height) obtained at 1.3 K and 215 MHz as a function of the external magnetic field. The open circles are for increasing field and the solid triangles represent decreasing field. As discussed below, the variation of the NMR signal intensity with magnetic field is also characterized by (different) relaxation time behavior for both increasing and decreasing fields. The points illustrated in Fig. 3 were measured for times that were long compared to the corresponding relaxation time, and hence, can be considered as equilibrium values. Further, although it is not shown in either Figs. 1 and 2, the application of an external field of 9 kOe causes a reappearance of the NMR signal at 4.2 K. Finally, a careful comparison of the two spectra illustrated in Fig. 2 shows that the application of an external field of 9 kOe causes a downward shift of the spectrum by 2.5 ±0.5 MHz. Based on an analysis carried out by Gossard *et al.*[2] for single-domain Co particles, the shift observed here is about one-third that predicted from bulk behavior.

Figure 4 shows the ^{59}Co spin-echo intensity (echo height) obtained for the Co/NaY sample at 1.3 K and 210 MHz as a function of time for both increasing and decreasing external field. Here, the sample was first cooled in zero field from room temperature to 1.3 K. The field was quickly increased to 9 kOe and the time dependence of the signal intensity was measured (open circles). After coming to equilibrium at 9 kOe, the field was quickly reduced to 0 and the signal intensity was again measured as a function of time (solid triangles). Fitting the data in Fig. 4 to single exponentials resulted in values of 47 and 16 s for the relaxation time

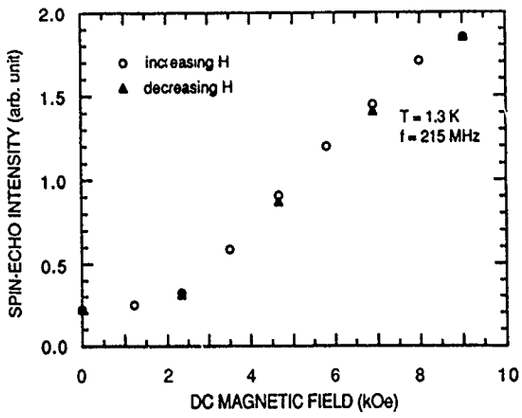

FIG. 3. ^{59}Co spin-echo NMR intensity (echo height) obtained at 1.3 K and 215 MHz from 6 to 10 Å Co clusters inside zeolite NaY supercages vs external magnetic field, H, in kOe; open circles, increasing field; solid triangles, decreasing field. The data points are characteristic of the equilibrium values.

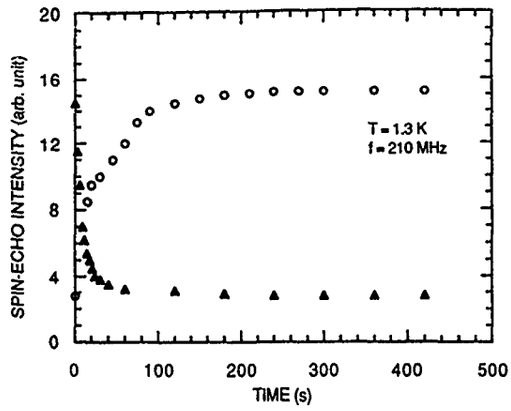

FIG. 4. ^{59}Co spin-echo NMR intensity (echo height) obtained at 1.3 K and 210 MHz from 6 to 10 Å Co clusters inside zeolite NaY supercages versus time, t, in s: open circles, field quickly increased from 0 to 9 kOe; solid triangles, field quickly decreased from 9 kOe to 0. The sample was initially cooled from room temperature to 1.3 K in zero field.

at 1.3 K characteristic of increasing and decreasing field, respectively. The corresponding values at 4.2 K were significantly smaller.

IV. DISCUSSION AND SUMMARY

The magnetic behavior of the small, single-domain Co clusters isolated inside zeolite NaY supercages is characterized by a superparamagnetic blocking temperature which occurs at liquid helium temperatures, relaxation time behavior for increasing and decreasing fields, and a dependence on the magnetic history. The ^{59}Co spin-echo NMR spectra are broad with a central peak at 212 MHz and a secondary peak at 222 MHz, which are attributed to fcc- and hcp-like short-range order, respectively. The application of fields up to 9 kOe results in a downward frequency shift of the spectrum which is approximately one-third that expected for bulk, single-domain Co. For bulk multidomain ferromagnetic materials, the application of an external magnetic field causes a decrease in the NMR signal intensity due to the disappearance of the domain walls. The dramatic increase in NMR signal intensity with applied field that is observed here for the small Co clusters is worthy of special mention.

For zero applied field, a single-domain ferromagnetic particle is magnetized along some easy crystallographic direction (for fcc cobalt, this is the [111] direction). The energy required to reverse the direction of the magnetization relative to the easy direction may be written as K_0V, where K_c is the crystalline anisotropy constant and V is the volume of the particle. (It is assumed that the particles are spherical and not stressed by external forces, so the shape and strain anisotropy can be neglected.) The single-domain particles will have thermal fluctuations in the magnetization direction and, at a given temperature T, there exists a finite probability that the magnetization vector will reverse its direction and the time that describes how rapidly this occurs may be written

$$\tau=(a\nu)^{-1}\exp(K_cV/k_BT), \tag{1}$$

where a is a geometrical factor and k_B is the Boltzmann constant.[3] The frequency factor ν is the Larmor frequency of the magnetization vector M_s in an effective field $H_{\text{eff}}=K_c/M_s$. The behavior of a magnetic particle depends on the experimental observation time τ_{obs}. For $\tau_{\text{obs}}\gg\tau$, the particle will appear to be superparamagnetic, while for $\tau_{\text{obs}}\ll\tau$, the superparamagnetic relaxation will be blocked and the particle will show ferromagnetic behavior. For the present NMR observations, $\tau_{\text{obs}}=1/\nu_L\approx5\times10^{-9}$ s, where ν_L is the resonance frequency (or Larmor frequency of the nuclear moment about the magnetic field at the nuclear site). Thus, if $1/\nu_L\ll\tau$ (i.e., ferromagnetic behavior), the nuclear Zeeman splitting caused by the hyperfine field at the nuclear site will be observed. Conversely, for $1/\nu_L\gg\tau$ (i.e., superparamagnetic behavior), the Zeeman splitting and, consequently, the NMR signal will disappear. A superparamagnetic blocking temperature can be defined as $T_B=K_cV/k_B$. Kündig *et al.*[4] have used the Mössbauer effect to study small particles of α-Fe_2O_3 and β-Co. They find that as the particles transform from ferromagnetic to superparamagnetic behavior (by varying the particle size or the temperature), the Mössbauer spectra shows a decrease in the Zeeman structure with a corresponding increase in the quadrupole structure. The relaxation time described above by Eq. (1) can also be influenced by the application of an external magnetic field, H. In this case, there will be a magnetic energy M_sHV in addition to the anisotropy energy K_cV which will contribute to the superparamagnetic blocking. This will cause more of the (smaller) particles to exhibit ferromagnetic behavior and, hence, contribute to the NMR signal intensity. Further, the application of an external magnetic field will cause the cluster moments to reorient such that the internal fields at the Co nuclei become more aligned perpendicular to the rf excitation field of the NMR spectrometer. Consequently, more nuclei undergo the appropriate transitions and the signal intensity is increased. It is even likely that the clusters are free to reorient such that the easy axes are aligned with the magnetic field in equilibrium. The change in magnetic field behavior shown in Fig. 3 provides an estimate for the anisotropy field of 2 kOe. For external magnetic fields in excess of the 9 kOe used here, the NMR signal intensity may eventually start to decrease due to a decrease in the domain enhancement factor. Work is currently in progress in an attempt to extract a quantitative description of the cluster size distribution from the field dependence of the NMR signal intensity.

[1] Z. Zhang, Y. D. Zhang, W. A. Hines, J. I. Budnick, and W. M. H. Sachtler, J. Ame. Chem. Soc. **114**, 4843 (1992).
[2] A. C. Gossard, A. M. Portis, M. Rubinstein, and R. H. Lindquist, Phys. Rev. **138**, A1415 (1965).
[3] L. Néel, Ann. Geophys. **5**, 99 (1949).
[4] W. Kündig, R. H. Lindquist, and G. Constabaris, *Proceedings of the International Conference on Magnetic Resonance and Relaxation*, Colloque Ampere XIV, Ljubljana, 1966 (North-Holland, Amsterdam, 1967), p. 1029.

Published without author corrections

Perfluorocyclobutane containing aromatic ether polymers as planarization materials for alternative magnetic media substrates

Donald J. Perettie
The Dow Chemical Company, 1702 Building, Midland, Michigan 48674

Jack Judy and Qixu Chen
University of Minnesota, 200 Union Street, S. E., Minneapolis, Minnesota 55455

Rick Keirstead
Nashua Corporation, 44 Franklin Street, Nashua, New Hampshire 03061

Perfluorocyclobutane aromatic ether polymers (PFCB) are being researched as planarization materials for alternative magnetic media substrates allowing smoother surfaces for lower head flying recording. The results of current work reported herein have shown that PFCB can be used to affect surfaces on canasite with R_A's less than 2 nm. In addition, magnetic media can be produced of a quality comparative to that obtained on standard NiP-coated Al as well as that produced on regular canasite with equivalent coercivities at about 1500–1600 Oe and squarenesses of 0.8 or better. In addition to the above magnetic properties the recording performance was excellent with signal-to-noise ratios of planarized media 3.5 dB higher than that on regular canasite.

I. INTRODUCTION

Alternative or nonaluminum magnetic media substrates have been the topic of numerous discussions as well as seminar series as presented by IDEMA[1] and the subject of a recent presentation by one of these authors at the Head and Media Technology Conference (1992) during Comdisk.[2] In addition to these presentations two recent publications by Perettie *et al.*[3,4] have focused on the use of benzocyclobutene (BCB) as a planarization resin for aluminum substrates with conceptually the same idea; the difference being that the BCB work required the coated substrates be cured in an inert atmosphere. A continuation of this effort is presented here with the resin being PFCB.

Perfluorocyclobutane aromatic ether polymers (PFCB) are being researched as planarization materials for alternative magnetic media substrates allowing smoother surfaces for lower head flying recording. Canasite is a glass ceramic material, and is being used as an alternative substrate for advanced magnetic thin film media. Even though the height of the automatically textured surface peaks of polished canasite are uniform, the large peak-to-valley heights are not. However, PFCB-coated canasite substrates have small and uniform peak-to-valley heights which should improve durability and recording performance. The properties of the materials and the surface roughness of the PFCB-coated canasite substrates are being reported here. The magnetic and recording performance of the thin film media deposited on PFCB-planarized substrates are compared with that on regular canasite.

II. EXPERIMENT

A. Substrates

The surface morphology of the substrates was characterized with an atomic force microscope (AFM).

B. Magnetic media

The deposition conditions of the C/CoCr (12 at. %) Ta (2 at. %)/Cr films are shown with Table I. The magnetic properties of the thin film media were measured using a digital vibrating sample magnetometer (VSM). The recording performance of the thin film media were tested using thin film heads with 0.4 μm gap width and 16.5 μm track width. The head wrote and read back an all ones pattern at a relative linear velocity of 10 m/s. The flying height was approximately 0.2 μm. The average signal output amplitude was determined by averaging digitized wave forms. The medium noise was obtained by subtracting the integrated noise power of the recording system from the total integrated noise power over a 20 MHz bandwidth.

TABLE I. Deposition conditions of C/CoCrTa/Cr thin film media.

Films	Sputter mode	Thickness (Å)	Ar pressure (mTorr)	Deposition rate K (Å/min)	Substrate bias (V)	Deposition temperature
Cr	dc magnetron	1000	1	1.8	0	Varied
CoCrTa	rf magnetron	500	3	1.42	−48	Varied
C	dc magnetron	300	8	0.3	0	Room temperature

 0021-8979/94/76(10)/6579/3/$6.00 © 1994 American Institute of Physics

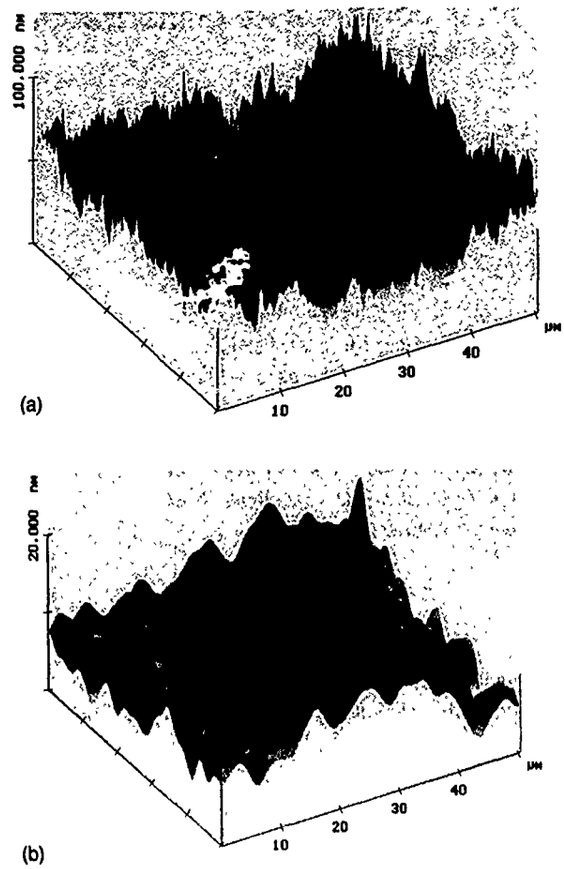

FIG. 1. Surface profile of regular canasite and PFCB-planarized canasite substrates measured with AFM.

III. RESULTS

Figure 1 shows the comparison of the surface topography of regular canasite and PFCB-planarized canasite substrates measured with AFM. Table II shows the calculated roughness of the two types of substrates using the data from AFM with R_A showing mean roughness and R_{max} indicating maximum height which is the difference in height between the highest and lowest points on the profile relative to the mean line over the length of the profile. It is obvious that the surface of PFCB-planarized canasite substrates is much smoother than that of regular canasite substrates.

The effect of sputtering parameters on magnetic properties of CoCrTa/Cr films deposited on NiP/Al substrates has been intensively investigated. For example, it was reported that in-plane coercivity increases and in-planes decrease as substrate temperature increases.[5] The same relative result is true for the CoCrTa/Cr films deposited on PFCB-planarized substrates. In addition, C/CoCrTa/Cr films were deposited on

TABLE II. Surface roughness of regular and PFCB-planarized canasite.

Scan size (μm)	1		50	
Substrates	Canasite	PFCB/canasite	Canasite	PFCB/canasite
R_A (nm)	1.0	0.48	6.5	1.9
R_{max} (nm)	14.9	10.2	76	22

TABLE III. Magnetic properties of C/CoCrTa/Cr films deposited on canasite and PFCB-coated canasite substrates.

Substrates	PFCB/canasite	Canasite	PFCB/canasite	Canasite
H_c (Oe)	1523	1329	1594	1457
MrT (mEMU/cm^2)	1.9	2.1	1.9	2.2
S	0.73	0.76	0.75	0.75
S^*	0.81	0.82	0.80	0.76
SFD	0.22	0.22	0.25	0.27
Preheat temperature	200 °C		300 °C	

pure canasite and PFCB-coated canasite substrates under identical deposition conditions but at different experimental runs. The magnetic properties of the films deposited on canasite substrates are not subject to the effect of the possible outgassing from PFCB polymer. The magnetic properties of the CoCrTa/Cr films are shown below in Table III.

The coercivity of the magnetic files deposited on PFCB-coated substrates is higher than those of films deposited on canasite substrates as shown above. Figure 2 also shows the comparison of signal-to-media noise ratio of C/CoCrTa/Cr films deposited at identical conditions on canasite and PFCB-coated canasite substrates, respectively.

The deposition conditions of these samples are shown in Table I. The preheat temperature was 200 °C with the magnetic properties of the samples shown in Table III. The media deposited on PFCB-coated canasite substrates exhibit about

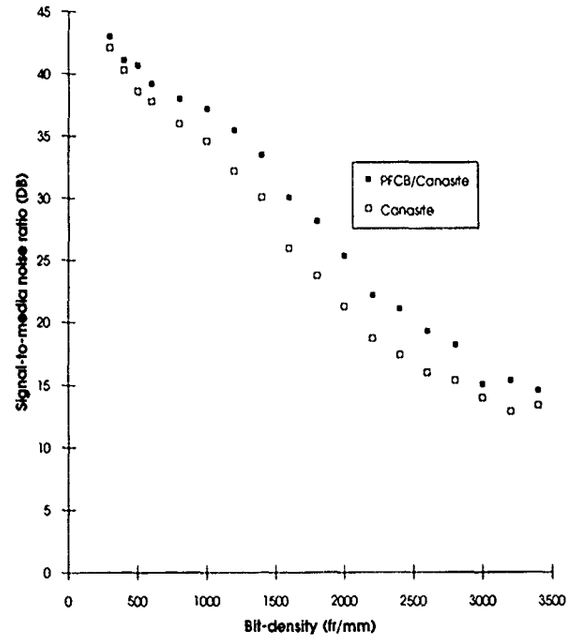

FIG. 2. Comparison of signal-to-media noise ratio of C/CoCrTa/Cr films deposited on canasite and PFCB-coated canasite substrates, respectively. (Preheat temperature is 200 °C.)

3.5 dB higher signal-to-media noise ratio than the films on canasite substrates. The films deposited at 300 °C also show the similar results.

IV. CONCLUSION

PFCB polymer films can be used to affect a surface smooth on canasite with R_A's less than 2 nm in 50 μm scan size. CoCrTa/Cr thin film media deposited on PFCB-coated canasite exhibited higher coercivity and a 3.5 dB higher signal-to-noise ratio over a wide range of recording densities in comparison to media deposited on regular canasite substrates.

[1] Alternative Substrates presented at IDEMA Seminar, 1993 and 1994.
[2] Head and Media Technology Conference, November 1992.
[3] J. Magn. Soc. Jpn. **15**, Supplement, No. S2 (1991).
[4] IEEE Trans. Magn. **MAG-27**, 5175 (1991).
[5] M. Lu *et al.*, IEEE Trans. Magn. **MAG-28**, 3255 (1992).

Anomalous perpendicular magnetoanisotropy in Mn_4N films on Si(100)

K. M. Ching, W. D. Chang, T. S. Chin, and J. G. Duh
Department of Materials Science and Engineering, Tsing Hua University, Hsinchu, Taiwan, Republic of China

H. C. Ku
Department of Physics, Tsing Hua University, Hsinchu, Taiwan 30043, Republic of China

Ferrimagnetic Mn_4N films were deposited on Si (100) substrate by dc reactive magnetron sputtering from sintered Mn target. Highly (002) textured Mn_4N ordered phase is formed *in situ* at studied substrate temperatures of 150–250 °C without further annealing. Anomalous perpendicular magnetoanisotropy exists in these face-centered cubic films with larger coercivity measured perpendicular to the film (2000–3000 Oe) than that parallel (1100–1300 Oe), as is the remanence. Coercivity in either direction decreases, while the saturation flux density (from 240 to 610 G) increases with increasing substrate temperature. The anomalous perpendicular magnetoanisotropy is attributed to (1) the stress-induced anisotropy due to in-plane tensile stress coupled with a reverse magnetostriction, and (2) the shape anisotropy due to columnar grain structure.

I. INTRODUCTION

In 1932 Ochsenfeld observed that manganese takes up nitrogen at about 1100 °C and gives it off again at 1300–1320 °C, and that the nitrided product has a Curie point of about 500 °C, a coercive force, Hc, of 200 Oe, an intrinsic induction of 200 G under an applied field of 600 Oe, and a remanence, Br, of 110 G.[1]

Although there was an argument that Mn_4N is ferromagnetic,[1,2] according to the result of neutron diffraction in 1962, the Mn_4N compound was identified to be a ferrimagnetic material,[3] which can be formulated as $Mn(I)NMn(II)_3$. It crystallizes in a perovskite-derived structure ABX_3: A is Mn(I) at the corner position, B is N at the body center, and X is Mn(II) at face centers of the cubic cell. Mn(I) has a large moment (3.53 μ_B at 300 K) with antiparallel spin alignment with respect to Mn(II) (−2.89 μ_B at 300 K), leading to a ferrimagnetic order of the lattice with a total magnetization at 300 K of 0.86 μ_B per formula unit.[3]

It is arduous to synthesize Mn_4N powder by traditional ceramic processes, because it requires high temperature (>925 K), long reaction time (>200 h), and precise atmosphere control.[4] However, through the assistance of technology like sputtering, it is possible to obtain such films much more easily, because high temperature phases could be successfully deposited at low substrate temperatures. On the other hand, Mn_4N films were rarely studied. One report studied Mn_4N films prepared by facing target reactive sputtering and obtained a film with saturation flux density of 510 G and coercivity of less than 900 Oe.[5] It is interesting to investigate again other synthesis methods and magnetic properties of such films. In this study, Mn_4N films have been prepared by dc reactive magnetron sputtering at low substrate temperatures on Si (100) substrate. Structure and magnetic properties of the films were studied.

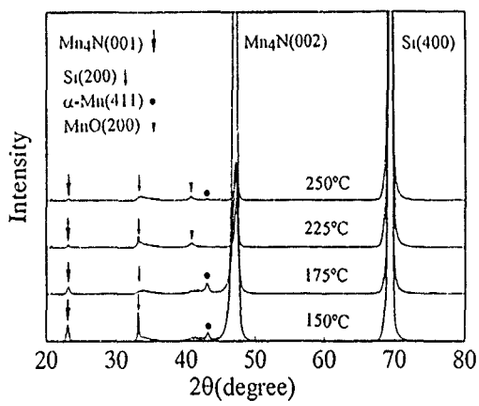

FIG. 1. X-ray diffraction patterns of as-deposited Mn_4N films at various substrate temperatures shown.

II. EXPERIMENT

The Mn_4N films were prepared by dc reactive magnetron sputtering from sintered Mn (99.9%) target. The substrates used were Si (100). The vacuum system was pumped to the base pressure of 5×10^{-5} Torr. Ultrahigh purity Ar and N_2 gases were first mixed at a ratio of 80:40 sccm, and the total pressure during deposition was set at 3 mTorr, controlled by a needle valve. The substrate temperature was varied from 150 to 250 °C. Distance between the target and the substrate was 3.5 cm.

The resultant films were examined by x-ray diffractometry (XRD) using Cu-$K\alpha$ radiation at a scanning speed of 1°/min for phase identification. Hysteresis loop both perpendicular and parallel to the film plane were measured at room temperature by using a vibrating sample magnetometer with a maximum applied field of 20 kOe. The sign of magnetostriction coefficient was measured by a strain gauge. Microstructure of the films was observed by means of a scanning electron microscope (SEM). Stress of the films was mea-

TABLE I. Magnetic properties of Mn_4N vs substrate temperature (T_s, in °C). S is the squareness ratio, H_c in Oe, B_s in G.

Sample	T_s	$H_{c\parallel}$	$H_{c\perp}$	B_s	$S_\parallel$	$S_\perp$
A1	150	1333	3048	240	0.40	0.56
A2	175	1143	2476	260	0.35	0.43
A3	225	1143	2381	530	0.38	0.61
A4	250	1153	2020	610	0.37	0.59

 0021-8979/94/76(10)/6582/3/$6.00 © 1994 American Institute of Physics

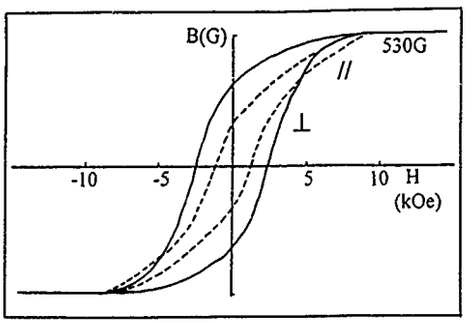

FIG. 2. Hysteresis loops measured perpendicular (⊥) and parallel (∥) to the film plane of a Mn_4N film deposited at 225 °C.

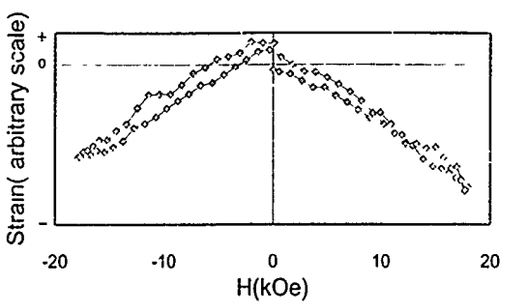

FIG. 3. Typical magnetostriction vs applied field of a Mn_4N film.

sured by a film stress measurement apparatus (FSM). Thickness of the films was measured by means of a stylus method.

III. RESULTS AND DISCUSSION

Films of fixed 1.2 μm thickness, as monitored by *ex situ* thickness measurements, were deposited on Si (100) at substrate temperature (T_s) of 150, 175, 225, and 250 °C, respectively, with a controlled deposition rate of 27 nm/min. Figure 1 shows the XRD patterns of films deposited on Si(100) substrates. The films exhibit a strong Mn_4N (002) texture with distinguishable (001) superlattice reflection. The degree of ordering, estimated from the peak height ratio between (001) and (002) diffractions, is practically the same for all T_s. There are contaminative phases, MnO and α-Mn. The amount of MnO increases with T_s due to higher oxidation tendency for α-Mn on the substrate with residual oxygen. While the amount of α-Mn decreases with increasing T_s due to oxidation.

Magnetic properties of the films are shown in Table I. For an fcc structure, large magnetic anisotropy is not usually anticipated. However, it is not true for the deposited Mn_4N films. Comparing the hysteresis loops of the films measured parallel (∥) to the film plane with those perpendicular (⊥) (see Fig. 2) the perpendicular coercivity ($Hc_\perp$) and remanence ($Br_\perp$), hence the perpendicular squareness ($S_\perp$) are always much larger than $Hc_\parallel$, $Br_\parallel$, and $S_\parallel$, for all substrate temperatures (T_s). Specifically, $Hc_\perp$ can be 1.8–2.3 times higher than $Hc_\parallel$. Due to much higher Hc values and larger squareness ratio in the perpendicular direction, the films deposited on Si(100) show apparently perpendicular magnetic anisotropy. Also it is found that saturation flux density (Bs) increases with increasing T_s. The film deposited at 250 °C has a Bs of 610 G, which is 34% of the theoretical value (1770 G). This discrepancy should arise from impurity phases (e.g., Mn and MnO) embedded in the films.

By FSM measurement, it was found that films show in-plane tensile stress, which increases with increasing substrate temperature, as shown in Table II. Further, by measuring with a strain gauge bonded on the film, it was confirmed that films deposited on Si(100) at various substrate temperatures have negative magnetostriction coefficient λ in the film plane, as shown in Fig. 3. However, precise magnetostriction was not possible by this method. Magnetoelastic anisotropy constant Ku can be calculated by the following formula:[6]

$$Ku = -(3/2)\lambda\sigma \tag{1}$$

since σ of the films is positive, the reverse magnetostriction makes a positive Ku, that is the perpendicular magnetoanisotropy.

Besides, microstructure observation of the films by SEM, as shown in Fig. 4, reveals that films are in fact composed of columnar grain structure which gives rise to the shape anisotropy that is proportional to the square of saturation magnetization. For the grain shown in Fig. 4, the aspect ratio is estimated to be 5.6, giving rise to a shape anisotropy constant Ks of, assuming the grain structure is perfect having a theoretical saturation magnetization,

$$Ks = (Na - Nc)Ms^2 = 1.1 \times 10^5 \text{ ergs/cm}^3. \tag{2}$$

TABLE II. The in-plane stress of the films vs substrate temperature (T_s, in °C).

Sample	T_s	Stress (MPa)
A1	150	622
A2	175	648
A3	225	667
A4	250	730

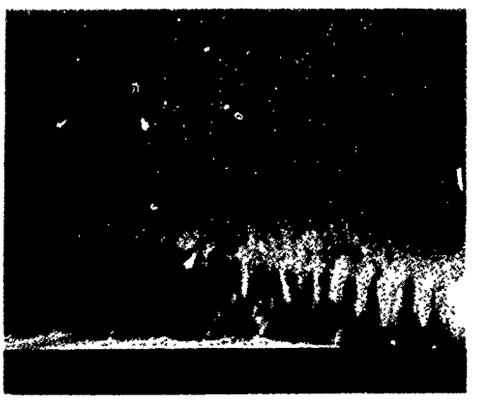

FIG. 4. A typical SEM micrograph of a Mn_4N film showing cross-sectional view of the film structure.

The contribution of the shape anisotropy to coercivity would be as high as 760 Oe, which is within the reasonable increment range as comparing the perpendicular coercivity to that parallel.

IV. CONCLUDING REMARKS

(1) Ferrimagnetic Mn_4N films with ordered structure and (002) texture can be successfully deposited at low substrate temperatures from 150 to 250 °C by using dc magnetron reactive sputtering from sintered Mn target onto Si(100) substrate without any further annealing.

(2) Anomalous perpendicular anisotropy exists in these films. The coercivity measured perpendicular to the film plane (2000 to 3000 Oe) is 1.8–2.3 times that measured parallel. The perpendicular magnetoanisotropy is attributed to the combined effects of (a) the stress-induced anisotropy caused by in-plane tensile stress coupled with a reverse magnetostriction, and (b) the shape anisotropy caused by columnar grain structure.

ACKNOWLEDGMENT

This work was sponsored by the National Science Council of the Republic of China under Grant No. NSC82-0208-M007-144.

[1] R. M. Borzorth, *Ferromagnetism* (IEEE, New York 1993), p. 338.
[2] I. Pop, M. Andrecut, I. Burda, R. Munteanu, and H. Criveanu, Mater. Chem. Phys. **37**, 52 (1994).
[3] W. J. Takei, R. R. Heikes, and G. Shirane, Phys. Rev. **125**, 1893 (1962)
[4] J. Garcia, J. Bartolomé, and D. González, J. Chem. Thermodyn. **15**, 465 (1983).
[5] S. Nakagawa and M. Naoe, J. Appl. Phys. **75**, 6568 (1994).
[6] M. Langlet and J. C. Joubert, J. Appl. Phys. **64**, 780 (1988).

Formation kinetics of polycrystalline $Eu_{2-x}Ce_xCuO_{4-y}$ obtained from a sol-gel precursor

P. A. Suzuki[a] and R. F. Jardim
Instituto de Física, Universidade de São Paulo, CP 20516, 01452-990 São Paulo, SP, Brazil

S. Gama
Instituto de Física Gleb Wataghin, Universidade Estadual de Campinas, Campinas, SP, Brazil

Polycrystalline samples of $Eu_{2-x}Ce_xCuO_{4-y}$ ($0.0 \leq x \leq 0.18$) were prepared from a sol-gel precursor and sintered in air at different temperatures. From the x-ray diffraction results, the beginning of $Eu_{2-x}Ce_xCuO_{4-y}$ phase formation is observed by increasing the sintering temperature up to 500 °C, as indicated by the presence of very broad Bragg reflections belonging to the desired phase. At 700 °C, $Eu_{2-x}Ce_xCuO_{4-y}$ coexists with Eu_2O_3, CeO_2, and CuO. Additional sintering at 950 °C in air for 20 h results in single phase materials. The effectiveness of Eu replacement by Ce in the Eu_2CuO_4 pristine phase has been confirmed by a decrease in the lattice parameter c with increasing x. Also, the solubility limit of Ce in these series was found to be higher than $x=0.15$. The results of thermal analysis reveal that the eutectic temperature $T_e \approx 1020$ °C is Ce independent. On the other hand, the peritectic temperature T_p increases significantly with increasing Ce concentration. It is close to $T_p \approx 1180$ °C for Eu_2CuO_4 and $T_p \approx 1195$ °C for $Eu_{1.82}Ce_{0.18}CuO_{4-y}$. Thermogravimetric analysis performed during the heating process in all samples studied revealed a weight loss of $\approx 1.5\%$ at the peritectic temperature. This weight loss has been attributed to an oxygen removal which is partially recovered during the cooling process.

I. INTRODUCTION

Since the discovery of electron-doped superconductors by Tokura, Uchida, and Takagi[1] many investigations towards the new class of $Ln_{2-x}Ce_xCuO_{4-y}$ (Ln=Pr, Nd, Sm, Eu; $0.0 \leq x \leq 0.20$) based materials have been carried out in order to better understand the relationship between their crystallographic structure and physical properties.[2,3] Compounds of $Ln_{2-x}Ce_xCuO_{4-y}$ crystallize in the so-called T' (Nd_2CuO_4) structure, but their physical properties strongly depend on the host Ln and the substituent Ce or Th.[2,3] In fact, this is mirrored in the observed superconducting critical temperature T_c: it is almost constant ≈ 23 K for Ln=Pr, Nd, and Sm, and it decreases significantly for Eu ($T_c \approx 13$ K). In addition, when Ln is replaced by heavier Gd, although the T' structure is preserved, the material does not reveal superconducting properties for x up ≈ 0.15.[3,4] Some authors have proposed that $Gd_{2-x}Ce_xCuO_{4-y}$ should show superconductivity for x higher than the Ce solubility limit, which is close to 0.15. This upper limit should be related to the structural instability originated by the growth of the intraplanar stresses.[5] Compounds of $Eu_{2-x}Ce_xCuO_{4-y}$ are on the frontier of this problem involving crystallographic properties and the appearance of superconducting properties. Up to now, few studies have been carried out on the crystallographic and physical properties of $Eu_{2-x}Ce_xCuO_{4-y}$ compounds.[2,3,6]

The conventional procedure used to obtain polycrystalline samples of $Ln_{2-x}Ce_xCuO_{4-y}$ compounds utilizes simple oxides as starting materials and subsequent heat treatments to promote Ce diffusion into the T' structure. Usually, these heat treatments are carried out at temperatures above the eutectic temperature T_e, which involves the presence of a liquid phase.[7,8] On the other hand, it is desirable that sintered materials should be as homogeneous as possible. This implies samples sintered without the presence of a liquid phase, provided that an appropriate Ce diffusion also occurs. Among several processes available in the literature, the sol-gel route allows homogeneous samples and complete Ce diffusion at sintering temperatures well below the eutectic temperature.[9]

In this work we focus on the preparation of polycrystalline $Eu_{2-x}Ce_xCuO_{4-y}$; $0.0 \leq x \leq 0.18$, starting from a sol-gel precursor. All samples were heat treated in air and at different temperatures up to 950 °C. The formation of the desired phases were accompanied by x-ray diffraction measurements and thermal analysis. We have also determined either the eutectic temperature T_e or the peritectic temperature T_p in all samples studied.

II. EXPERIMENTAL DETAILS

Powders of $Eu_{2-x}Ce_xCuO_{4-y}$; $x=0.0$, 0.05, 0.10, 0.15, and 0.18, were prepared as described below. Initially, appropriate amounts of high purity Eu_2O_3 were dissolved in 75 ml of water and 10 ml of 65% HNO_3 in a beaker to form ≈ 3.5 g of the desired phase. The solution was heated on a hot plate at ~50 °C under magnetic stirring. After the complete dissolution of the Eu_2O_3, stoichiometric amounts of $(NH_4)_2Ce(NO_3)_6$ and $Cu(NO_3)_2$ were slowly added to the solution. Ethylene glycol (~40 ml) and 7.6 g of citric acid were also dissolved in the mixture. The resultant blue solution was heated at $T \sim 100$ °C and magnetically stirred to evaporate water in order to form a homogeneous mixture. A brown NO_2 gas evolution during the heating process was frequently observed. Then, the solution was heated until it initiates a process of polymerization through a transformation into a green gel. The product was then transferred to an alumina crucible, and subjected to a continuous heating up to 150 °C. When the product dried, it reacted by spontaneous

[a]Permanent address: Faculdade de Engenharia Química de Lorena, CP 16, 12600 Lorena, SP, Brazil.

 0021-8979/94/76(10)/6585/3/$6.00 © 1994 American Institute of Physics

ignition, transforming into a fine brown powder. This powder was heat treated in air in a muffle furnace at temperatures of 300, 500, 700, and 950 °C for 22 h.

In order to characterize these powders, x-ray diffraction measurements (XRD) and thermal analysis were performed. The XRD measurements were taken in a Jena–Zeiss URD-6 diffractometer with Ni filtered Cu$K\alpha$ radiation. All samples were measured between $10° \leq 2\Theta \leq 70°$ with angular scanning of 0.05°. All measurements were made at ambient temperature. Lattice parameters were obtained through the refinement of the corrected peak positions utilizing a least-square program.

The XRD reflections belonging to polycrystalline samples of $Eu_{2-x}Ce_xCuO_{4-y}$, $0.0 \leq x \leq 0.18$, were indexed according to the symmetry of the tetragonal T' phase, namely the $I4/mmm$ space group.[10,11] A computer simulated pattern was generated by using the experimentally calculated lattice parameters and by replacement of Ln by Eu and Ce on the atomic coordinates of the T' structure.[10,11] The simulated and the experimental patterns were in good agreement, with typical deviation $\leq 3\%$ for the intensity of the Bragg reflections.

Differential thermal analysis and thermogravimetric analysis (TG) were performed in air by using Al_2O_3 as the reference. The temperature T ranged between 20 °C $\leq T \leq$ 1400 °C. Heating and cooling rates of 10 °C/min have been employed in these measurements.

III. RESULTS AND DISCUSSIONS

While the as-dried precursors revealed low crystallinity, Fig. 1 displays XRD patterns measured on polycrystalline samples of $Eu_{1.85}Ce_{0.15}CuO_{4-y}$ heat treated at several higher temperatures: 500 °C (a), 700 °C (b), and 950 °C (c). In Fig. 1(a), the XRD pattern of the heat-treated powder at 500 °C shows very broad reflections which are strong evidence for low crystallinity. Some of these broad peaks have been identified as belonging to CuO and Eu_2O_3. All the reflections belonging to CeO_2 are probably overlapped with those of Eu_2O_3. A few reflections attributed to $Eu_{2-x}Ce_xCuO_{4-y}$ phases are also identified. Additional sintering at 700 °C [Fig. 1(b)] promoted the crystallization process of the desired phase. However, vestiges of reflections belonging to Eu_2O_3, CuO, and CeO_2 were still present. The lattice parameters obtained for sintered samples at 700 °C showed that they have intermediate values between Eu_2CuO_4 and $Eu_{1.85}Ce_{0.15}CuO_{4-y}$, suggesting a partial Ce diffusion at this temperature.

Finally, sintering at $T = 950$ °C for 20 h [Fig. 1(c)] resulted in almost single phase material for $Eu_{1.85}Ce_{0.15}CuO_{4-y}$. A very small unidentified peak at ~29.0° has been detected in all samples studied and it is the object of future work. Similar XRD patterns as those shown in Fig. 1 were obtained for other x values, except for $x = 0.0$. For this particular concentration and sintered samples at 500 °C, the XRD patterns showed additional peaks (not shown), which were attributed to Ce-free complexes formed during the ignition of the mixture.

By comparing the diffractograms obtained in heat-treated samples at 950 °C with different Ce concentrations,

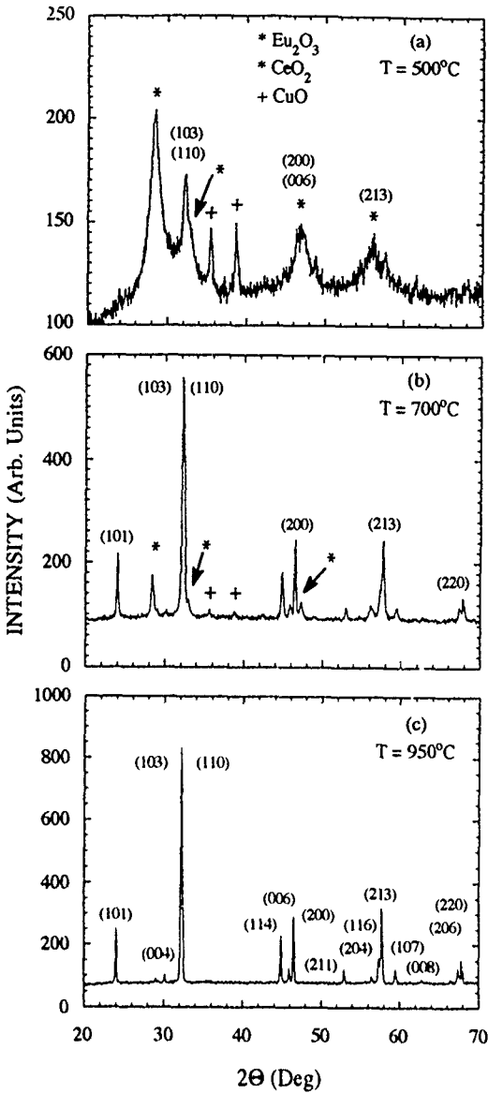

FIG. 1. XRD patterns of heat-treated polycrystalline samples of $Eu_{1.85}Ce_{0.15}CuO_{4-y}$ at different temperatures: 500 °C (a), 700 °C (b), and 950 °C (c). The desired phase is marked with Miller's indexes.

the lattice parameter evolution has been followed. This can be made by monitoring the observed shift in the (006) peak in samples with different x. It shifts to higher 2Θ angles with increasing x, while the (200) peaks are almost constant since the lattice parameter a shows small changes with increasing Ce concentration. Another perceptible evidence of Eu replacement by Ce is the observed enlargement of the (103)–(110) peak separation with increasing Ce concentration. Following this analysis, the lattice parameters a and c have been calculated from several reflections and the relevant data are shown in Fig. 2. The lattice parameter c decreases with increasing Ce concentration, while the lattice parameter a is almost constant for all the range studied. The decrease in the lattice parameter c with increasing Ce concentration strongly suggests that Ce^{+4} ions, with an effective ionic radius 0.97 Å, replaces Eu^{+3}, with an effective ionic radius 1.066 Å, in these series. The calculated lattice parameters were $c = 11.902(2)$ Å for Eu_2CuO_4 and $c = 11.834(3)$ Å for $Eu_{1.82}Ce_{0.18}CuO_{4-y}$.

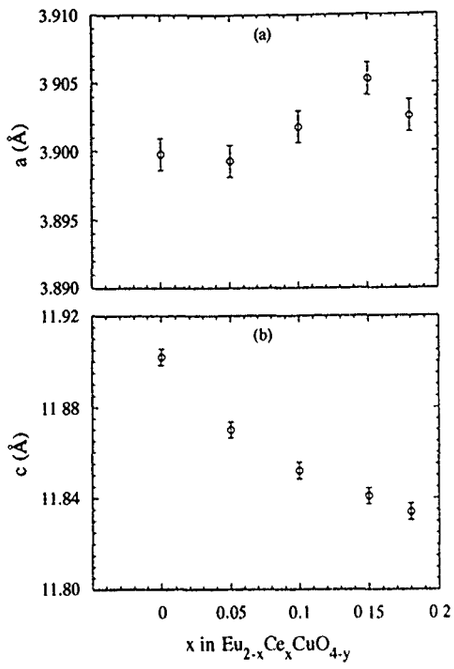

FIG. 2. Lattice parameters a and c as a function of Ce concentration of polycrystalline samples of $Eu_{2-x}Ce_xCuO_{4-y}$.

The results of differential thermal analysis performed on the as-grown powders (not shown) revealed a broad endothermic peak in the range of temperatures between 260 and 530 °C with a prominent maximum at ~400 °C. Such a peak has been associated with the desired phase formation. At higher temperatures, we also have observed two endothermic peaks: one of them close to the temperature $T_e \approx 1020$ °C and the other one close to temperature $T_p \approx 1190$ °C. The first one has been attributed to a eutectic temperature T_e and the other one to the peritectic temperature T_p. We have obtained these temperatures for all the samples studied and the relevant data are shown in Table I. It is worthwhile to mention that a small variation $\Delta T < 5$ °C has been found in the determination of the eutectic temperature for all samples studied. Similar behavior has been not observed at the peritectic temperature which increases with increasing Ce concentration. For example, it is close to 1178 °C for Eu_2CuO_4 and it is close to 1195 °C for $Eu_{1.82}Ce_{0.18}CuO_{4-y}$. Similar behavior in the peritectic temperature as a function of Ce content has also been observed by Oka and Unoki[12] in isomorphic series of $Nd_{2-x}Ce_xCuO_{4-y}$, $0.0 \leq x \leq 0.3$.

TABLE I. Eutectic temperature (T_e) and peritectic temperature (T_p) measured in polycrystalline samples of $Eu_{2-x}Ce_xCuO_{4-y}$, $0.0 \leq x \leq 0.18$. These temperatures were obtained from differential thermal analysis measurements performed in air.

x	T_e (°C)	T_p (°C)
0.0	...	1178(5)
0.05	1021(3)	1188(3)
0.10	1018(3)	1190(3)
0.15	1023(3)	1191(3)
0.18	1025(3)	1195(3)

The results of TG (not shown) revealed a large weight loss, about 25% of the total mass, during the reaction of the formation of the phases. This weight loss, which occurs at temperatures between 250 °C $\leq T \leq$ 550 °C, is believed to be related to the decomposition of the complexes into simple oxides as Eu_2O_3, CeO_2, and CuO. Another weight loss, which is of the order of 1.2%, near the peritectic temperature $T_p \approx 1190$ °C, has been also observed, during the heating process. However, this weight loss was found to be reversible during the cooling process. Such a weight loss was then attributed to the oxygen removal from the T' structure. This point is now being explored.

From these results and the preliminary discussion made above, one can surmise that, in samples prepared through the sol-gel process, the Ce diffusion into the T' structure occurs even at low temperatures ($T \leq 950$ °C). Such a complete diffusion can be explained by invoking features of the precursor material as a higher contact surface that improves the diffusion at low sintering temperatures, etc.

In summary, the formation of polycrystalline $Eu_{2-x}Ce_xCuO_{4-y}$, $0.0 \leq x \leq 0.18$, prepared from a sol-gel precursor, has been investigated. The desired phase has been obtained at sintering temperatures up to 700 °C, but the complete Ce diffusion only occurs at ≈950 °C. This temperature is well below the eutectic temperature of ≈1020 °C. The Ce solubility limit was found to be higher than $x = 0.15$ in these series. Thermogravimetric analysis showed a small weight loss near the peritectic temperature. This weight loss was found to be reversible and it was attributed to an oxygen removal from the T' structure.

ACKNOWLEDGMENTS

This work was supported by the Brazilian Agency FAPESP under Grant No. 93/4204-4 and FINEP. One of us (P.A.S.) was supported by a fellowship under the RHAE/CNPq (Brazil) program and R.F.J. acknowledges support from the Brazilian Agency CNPq under Grant No. 304647/90-0.

[1] Y. Tokura, H. Takagi, and S. Uchida, Nature **337**, 345 (1989).
[2] J. T. Markert, E. A. Early, T. Bjornholm, S. Ghamaty, B. W. Lee, J. J. Neumeier, R. D. Price, C. L. Seaman, and M. B. Maple, Physica C **158**, 178 (1989).
[3] S. L. Seaman, N. Y. Ayoub, T. Bjornholm, E. A. Early, S. Ghamaty, B. W. Lee, J. T. Markert, J J. Neumeier, P. K. Tsai, and M. B. Maple, Physica C **159**, 391 (1989).
[4] R. F. Jardim, C. H. Westphal, C. C. Becerra, and A. Paduan-Filho, Phys. Rev. B **45**, 10 485 (1992).
[5] Y. T. Zhu and A. Manthiram, Phys. Rev. B **49**, 6293 (1994).
[6] H. Itoh and M. Kusuhashi, Physica C **185–189**, 919 (1991).
[7] E. Wang, J. M. Tarascon, L. H. Greene, G. W. Hull, and W. R. McKinnon, Phys. Rev. B **41**, 6582 (1990).
[8] R. J. Cava, H. Takagi, R. M. Fleming, J. J. Krajewski, W. F. Peck, Jr., P. Bordet, M. Marezio, B. Batlogg, and L. W. Rupp, Jr, Physica C **199**, 65 (1992).
[9] R. F. Jardim, L. Ben-Dor, and M. B. Maple, J. Alloys Compounds **190**, 105 (1993)
[10] I. Mangelshots, N. H. Anderson, B. Lebech, A. Wisniewski, and C. S. Jacobsen, Physica C **203**, 369 (1992).
[11] Y. Xu, C. Jin, G Pan, D. Dai, Y. Yao, and W. Wang, Physica C **204**, 288 (1993).
[12] K. Oka and H. Unoki, Jpn. J. Appl. Phys. **29**, L909 (1990).

Thermal decay of N coupled particles

Ivo Klik and Ching-Ray Chang
Department of Physics, National Taiwan University, Taipei, Taiwan, China

Jyh-Shinn Yang
Division of General Education, National Taiwan Ocean University, Keelung, Taiwan, China

A periodic chain of N magnetostatically coupled uniaxial particles is considered within the nearest-neighbor approximation of weak coupling. The time-dependent magnetization of the ensemble, which relaxes thermally in constant reversing field, is calculated using a master equation approach. It is found that at very small applied fields the net magnetization relaxes via simple exponential decay while at large reversing fields its relaxation becomes multiexponential. It is conjectured that at large N this effect gives rise to field induced logarithmic decay.

In a recent work[1] we analyzed the evolution of an array of N identical interacting uniaxial particles whose magnetization reverses by thermally activated coherent rotation. Such an array has up to $\mathcal{N}=2^N$ distinct metastable configurations and its evolution may then be given by the master equation

$$dn_i/dt=-\sum_{k=1}^{\mathcal{N}} K_{ik}n_k, \tag{1}$$

where n_i is the probability that the system finds itself in the ith configuration and K_{ik} is the matrix of transition probabilities between these configurations. By conservation of probability $\Sigma_i n_i=1$ and hence $\Sigma_i K_{ik}=0$ for every k. Zero is thus an eigenvalue of K to which there corresponds the stationary state of thermal equilibrium. We shall address first the formal properties of Eq. (1): If K is independent of time (constant applied field H and temperature T) and if it has no degenerate eigenvalues then the solution of Eq. (1) assumes the simple form $n_i(t) = \Sigma_k c_k u_i^{(k)} e^{-r_k t}$ where $\mathbf{u}^{(k)}$ is the eigenvector corresponding to the eigenvalue r_k ($r_1=0$ and $u^{(1)}$ is the thermal equilibrium probability distribution) while the integration constants c_k are to be determined from initial conditions. Let further $M_i=m_i M_s$, M_s is saturation magnetization, be the magnetization of the ith configuration whose reduced magnetization is m_i. The nonequilibrium magnetization then becomes

$$M(t)=M_s\sum_{k=1}^{\mathcal{N}} w_k e^{-r_k t}, \tag{2}$$

where the weights w_k are defined as $w_k = N^{-1}c_k\Sigma_{i=1}^{\mathcal{N}} m_i u_i^{(k)}$. Equation (2) may be viewed as an average, $M(t)=M_s\langle e^{-rt}\rangle_w$, over a discrete distribution w normalized by initial conditions, $M(0)/M_s=\Sigma_k w_k$, equilibrium magnetization, $M_{eq}=M_s w_1$. The time dependence of $M(t)$ is determined by the index function w_k and one may encounter simple exponential, multiexponential, or logarithmic decay. In either case one may write

$$S(t)=-dM(t)/d\ \ln(t/t_a)=M_s\sum_{k=1}^{\mathcal{N}} w_k r_k t e^{-r_k t} \tag{3}$$

(t_a is an arbitrary time scale). Logarithmic decay is observed[2] if the the sum $S(t)$ maintains its peak value over long periods of time. The distribution of relaxation rates within the sample is usually attributed to a distribution of activation volumes or nucleation fields[2,3] but Eq. (1) shows that a similar effects may occur also due to the presence of interparticle coupling. This conclusion has been reached previously, within a mean field theory, by Lottis *et al.*[4]

The determination of the matrix K poses a major problem. We have analyzed[1,5] the case of two magnetostatically coupled particles described recently by Chen *et al.*[6] The easy axes of the two particles are aligned with applied field and their bond angle $\beta=0$ or $\pi/2$. To the first order of small coupling strength ρ (defined below) the magnetization reversal of the particle pair takes place[1,6] by single particle switching events during which one particle remains frozen at the metastable minimum while the other particle reverses in magnetostatic field. At larger ρ both particles deviate initially from the metastable minimum, but only one of them overcomes the energy barrier while the other returns back[6] and at even larger ρ both particles reverse simultaneously.[6]

We consider here a chain of N identical uniaxial particles with individual energies $E_i=KV(\sin^2\theta_i-2h\cos\theta_i)$ where K is the anisotropy constant, V is the activation volume, and θ_i is the angle spanned by the applied field $\mathbf{H}=H\mathbf{k}$ and the magnetization of the ith particle. The reduced field $h=H/H_n$, $H_n=2K/M_s$. Following Chen *et al.*[6] we write $E_{int}=2KV\rho[\boldsymbol{\alpha}_i\cdot\boldsymbol{\alpha}_j-3(\mathbf{r}\cdot\boldsymbol{\alpha}_i)(\mathbf{r}\cdot\boldsymbol{\alpha}_j)]$ for the interaction energy of two particles at a distance R from each other, $\rho=M_s^2V/(2KR^3)$ is the coupling constant, $\boldsymbol{\alpha}_i$ is a unit vector in the direction of the magnetization of the ith particle, and $\mathbf{r}=\sin\beta\mathbf{i}+\cos\beta\mathbf{j}$, $\beta=0$ or $\pi/2$. We assume here the weak

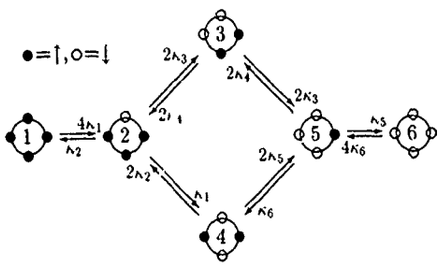

FIG. 1. A schematic representation of the transition matrix K for $N=4$ particles, $\rho=6$, with periodic boundary conditions. Labeled arrows represent transitions between individual configurations and their respective rates.

 0021-8979/94/76(10)/6588/3/$6.00 © 1994 American Institute of Physics

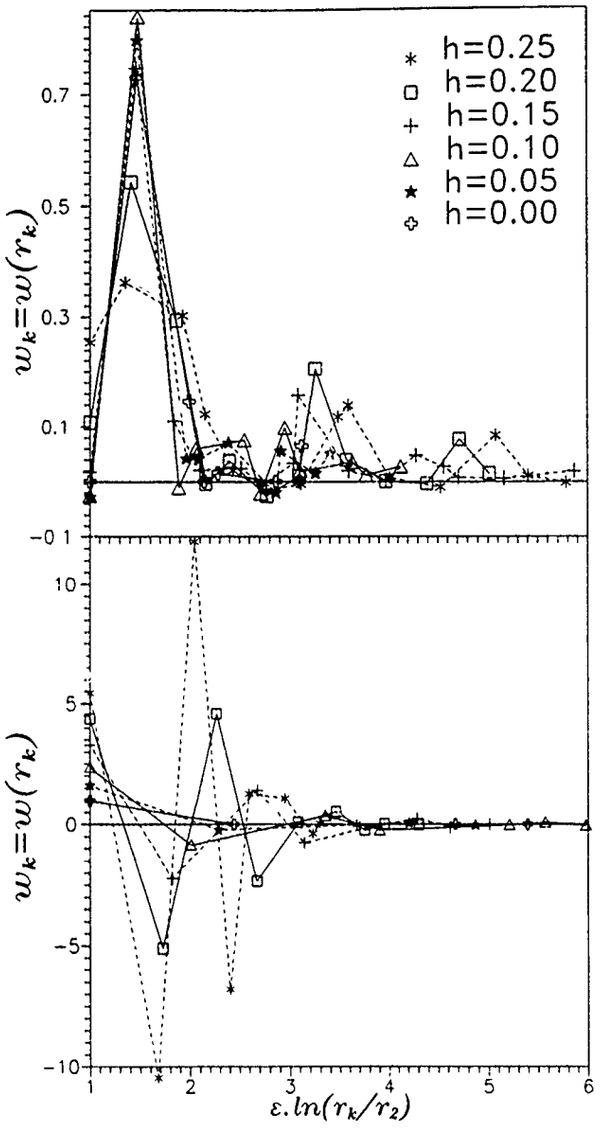

FIG. 2. The weights w_k for $N=8$ at selected values of reversing applied field h. The system was initially saturated and $\Sigma_k w_k=1$. Coupling strength $\rho=0.03$ for $\beta=\pi/2$ and $\rho=0.05$ for $\beta=0$. The scaling factor $\epsilon|_{\beta=0}=1.5$ and $\epsilon|_{\beta=\pi/2}=1$. $r_2=r_2(\rho,h)$ is the smallest nonzero eigenvalue of K.

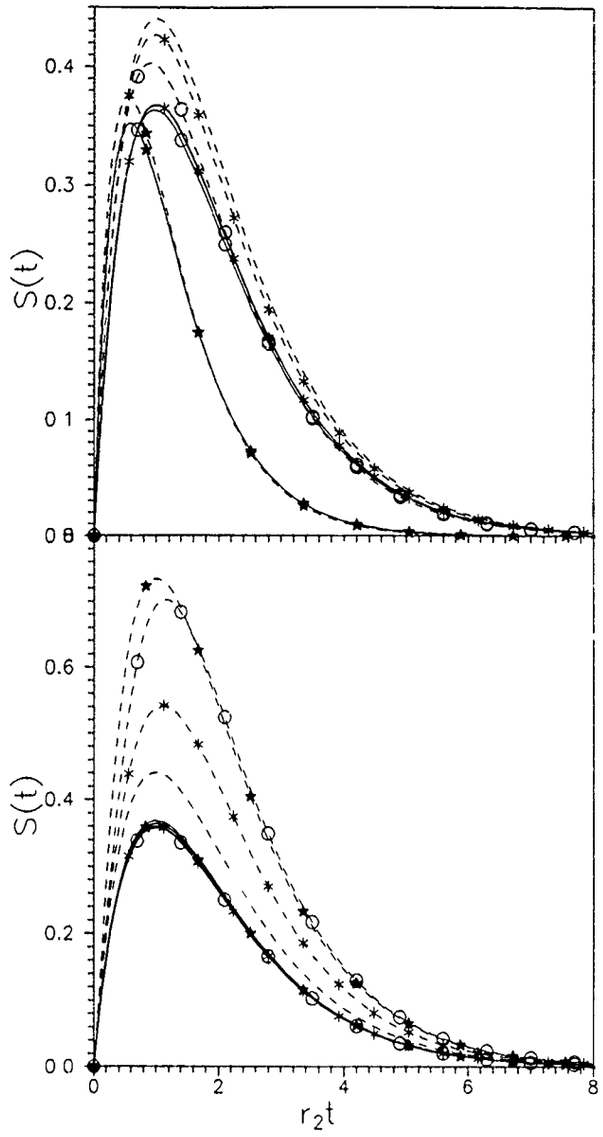

FIG. 3. The derivative $S(t)$ plotted vs the scaled time tr_2, $r_2=r_2(\rho,h)$ $N=8$, $\beta=\pi/2$ (top), and $\beta=0$ (bottom). Applied field $h=0$ (solid lines) and $h=0.05$ (dashed lines). Coupling strength $\rho=0$ (no marks), $\rho=0.01$ (*), $\rho=0.03$ (○), and $\rho=0.06$ (*) if $\beta=\pi/2$; $\rho=0.05$ (*), $\rho=0.1$ (○), and $\rho=0.15$ (*) if $\beta=0$.

coupling limit of single particle reversals, periodic boundary conditions, and nearest-neighbor interactions. There exist[1] then only six independent relaxation rates

$$\uparrow\uparrow\uparrow \xrightarrow{\kappa_1} \uparrow\downarrow\uparrow \xrightarrow{\kappa_2} \uparrow\uparrow\uparrow, \tag{4}$$

$$\downarrow\uparrow\uparrow \xrightarrow{\kappa_3} \downarrow\downarrow\uparrow \xrightarrow{\kappa_4} \downarrow\uparrow\uparrow, \tag{5}$$

$$\downarrow\uparrow\downarrow \xrightarrow{\kappa_5} \downarrow\downarrow\downarrow \xrightarrow{\kappa_6} \downarrow\uparrow\downarrow, \tag{6}$$

where $\kappa_{2l+1} = f_0 \exp[-q(1+h_{\rm eff}^{(i)})^2]$ and $\kappa_{2l+2} = f_0 \exp[-q(1-h_{\rm eff}^{(i)})^2]$, $h_{\rm eff}^{(0)}=h+\epsilon(\beta)$, $h_{\rm eff}^{(1)}=h$, and $h_{\rm eff}^{(2)}=h-\epsilon(\beta)$, with $\epsilon(0)=4\rho$ and $\epsilon(\pi/2)=-2\rho$. For the prefactor we take the value[7] $f_0=e^{25}$ Hz and we set $q=KV/k_BT=25$ throughout. All possible metastable configurations of four particles ($N=6$) are schematically shown in Fig. 1. Here $K_{11}=4\kappa_1$, $K_{12}=-\kappa_4$, $K_{21}=-4\kappa_1$, $K_{22}=\kappa_2+2\kappa_3+\kappa_1$, etc. For large N we use a separate program which classifies all configurations and writes down the FORTRAN code for $K=K(\kappa_i)$ which is sparse and the initial value problem (1) is fairly easily solved[8] even for large N.

The associated eigenvalue problem is numerically much more demanding since K is not symmetric and its eigenvalues are not necessarily real though Re $r_k \geq 0$ by construction. In order to gain some insight into the problem we shall restrict ourselves here to a small number of particles, $N \leq 8$, $\mathcal{N} \leq 27$, where the eigenvalue problem is easily solvable. In all cases $M(0)=M_s$ and $n_1(0)=1$ (see Fig. 1). Then all eigenvalues are real[9] and for $N=8$ we show the weights w_k in Fig. 2 and the corresponding functions $S(t)$ in Fig. 3. The

two bond angles share a common feature: At very small h only a single eigenstate is excited and one observes simple exponential decay regardless of the coupling strength and the $h=0$ curves are thus almost identical. The exception is the $\beta=\pi/2$, $\rho=0.06$ curve and we ascribe its irregular behavior to a breakdown of the weak coupling limit. With growing h ever higher eigenstates are excited so that the system, which at zero field exhibited simple exponential decay, relaxes multiexponentially. The two graphs of Fig. 2 are unlike in their character: At zero bond angle the weights are highly oscillatory (also note the scale) while at $\beta=\pi/2$ they resemble, in particular at higher fields, a smooth distribution. This leads us to conjecture that at very large N and sufficiently large reversing fields the weights w_k may assume the aspect of a real distribution function and give rise to a field-induced magnetic viscosity which vanishes if the applied field is removed.

The finding that the number of open relaxation channels depends, in interacting systems, on the magnitude of applied field is the main result of this work which was sponsored by the National Science Council of ROC under Grant No. NSC-82-0208-M002-35.

[1] I. Klik, C. R. Chang, and X. X. Yang (unpublished).

[2] I. Klik and C. R. Chang, Phys. Rev. B **47**, 9091 (1993); I. Klik, C. R. Chang, and J. Lee, J. Appl. Phys. **75**, 5505 (1994).

[3] M. El-Hilo, S. H. Uren, K. O'Grady, J. Popplewell, and R. W. Chantrell, IEEE Trans. Magn. **MAG-26**, 244 (1990).

[4] D. K. Lottis, R. M. White, and E. Dan Dahlberg, Phys. Rev. Lett. **67**, 362 (1991).

[5] I. Klik, C. R. Chang, and J. S. Yang (these proceedings).

[6] W. Chen, S. Zhang, and H. N. Bertram, J. Appl. Phys. **71**, 5579 (1992).

[7] D. P. E. Dickson, N. M. K. Reid, C. Hunt, H. D. Williams, M. El-Hilo, and K. O'Grady, J. Magn. Magn. Mater. **125**, 345 (1993).

[8] W. H. Press, B. P. Flannery, S. A. Teukolsky, and W. T. Vetterling, *Numerical Recipes. (FORTRAN VERSION)* (Cambridge University Press, Cambridge, 1990), Sec. 15.6.

[9] For $N\geq 12$ we find some complex eigenvalue pairs $r_k=r_k^{(1)}\pm ir_k^{(2)}$, $r_k^{(2)}\ll r_k^{(1)}$, which correspond to attenuating oscillations between closely spaced levels.

Influence of size and magnetocrystalline anisotropy on spin canting anomaly in fine ferrimagnetic particles

D. H. Han, J. P. Wang, Y. B. Feng, and H. L. Luo
State Laboratory for Magnetism, Institute of Physics, Chinese Academy of Sciences, Beijing 100080, China

Fine equiaxed γ-$Co_xFe_{2-x}O_3$ (x=0, 0.06) particles with a diameter ranging from 200 to 1000 Å were prepared by chemical precipitation. The average crystallite sizes were determined from x-ray line broadening measurements. The saturation magnetization and magnetocrystalline anisotropy of the particles were determined by using the approach to saturation. An empirical linear dependence of the specific saturation magnetization σ_s on the specific surface area S_a of the fine crystallites was obtained in the form of $\sigma_s(S)=\sigma_s(\infty)(1-AS_a)$. The slope A which reflects the surface spin canting anomaly is different for γ-Fe_2O_3 and γ-$Co_{0.06}Fe_{1.94}O_3$ particles. Under the supposition of the fine crystallite consisting of two parts, i.e., the surface layer, whose magnetic moment cannot be turned entirely along the direction of the applied field, but makes an average canting angle with the field, and the inner part, whose magnetic moment can be aligned along the direction of the applied field, the above formula can be interpreted well. The different slope A for γ-Fe_2O_3 and γ-$Co_{0.06}Fe_{1.94}O_3$ particles may be caused by the different anisotropies of the two series particles.

I. INTRODUCTION

More recently the spin canting anomaly and its origin in fine ferrimagnetic particles have experienced a renaissance of fresh research activities.[1,2] The surface spin canting anomaly in fine ferrimagnetic particles was demonstrated more than two decades ago,[3] and it was found that the smaller the particles, the larger the reduction of the saturation magnetization.[4] However, the results of the specific saturation magnetization decreasing with the reduction of the particles or crystallites size have not been explained yet. The origin of this phenomenon is still a matter of dispute.[2,5] As Co-γ-Fe_2O_3 particles or crystallites have become the fundamental structural units of very high density magnetic recording media, it is necessary to study the dependence of the specific saturation magnetization (σ_s) on the specific surface area (S_a) of the fine crystallites in detail.

In this article, the relationship between σ_s and S_a of the crystallites of equiaxed γ-$Co_xFe_{2-x}O_3$ (x=0,0.06) particles with various sizes are studied. An empirical formula of $\sigma_s(S)=\sigma_s(\infty)(1-AS_a)$ was obtained. The results are well explained with the assumption of the surface spin canting. The different slope A may be caused by the different anisotropies of the two series particles.

II. EXPERIMENT

The equiaxed γ-$Co_xFe_{2-x}O_3$ (x=0,0.06) particles with the diameter from 200 to 1000 Å were prepared by chemical precipitation. The samples with x=0 are denoted, in the following, as series F, and the ones with x=0.06 as series C, respectively. The crystal structure of the particles was determined by using a SRA M18XHF x-ray diffractometer. The average crystallite sizes were determined from x-ray diffraction line broadening measurements by using the Scherrer formula.[6] The morphology of the particles was determined by using a Hitachi H-700 transmission electron microscope. The magnetic properties and magnetocrystalline anisotropy of the particles were measured at 295 and 79 K by using a LDJ vibrating sample magnetometer with a maximum field of 20 kOe. The saturation magnetization of the particles was obtained by a $1/H$ extrapolation to infinite field.

III. RESULTS AND DISCUSSION

All the particles were determined with the structure of γ-Fe_2O_3 with a crystalline lattice parameter a_0=8.35 Å, and no other phase was found.[7] The particles are equiaxed with a small size distribution. The dependence of σ on $1/H$ for series C, measured at 295 and 79 K are shown in Figs. 1(a) and 1(b), from which σ_s can be obtained by extrapolation to infinite field. As the result, the average crystallite size D, S_a under the assumption of cubic crystallites, as well as σ_s are listed in Table I. The dependence of σ_s on S_a of series C and F at 295 and 79 K are shown in Figs. 2(a) and 2(b), respectively. It can be seen clearly that for the two series σ_s decreases linearly with the increasing S_a at both 295 and 79 K. These results are very similar to that of Mollard *et al.*[4] and

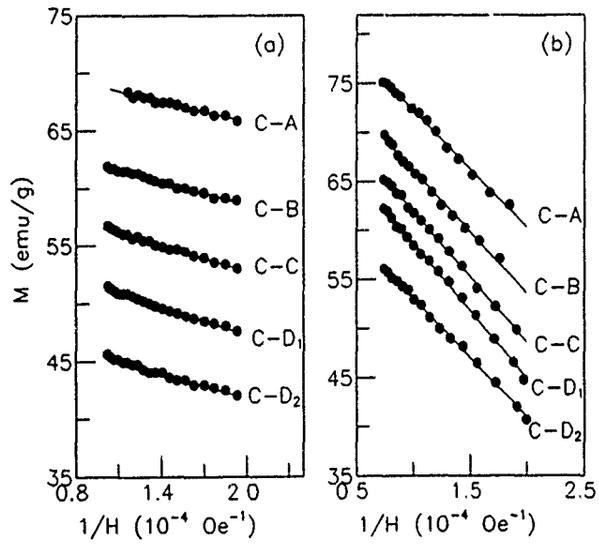

FIG. 1. The dependence of σ on $1/H$ of series F at (a) 295 and (b) 79 K.

 0021-8979/94/76(10)/6591/3/$6.00 © 1994 American Institute of Physics

TABLE I. The measured D, S_a, and σ_s at 295 and 79 K of series F and C

Sample	D (Å)	S_a (m^2/g)	σ_s (emu/g) 79 K	σ_s (emu/g) 295 K
F-A	431	28.4	71.3	66.0
F-B	305	40.2	70.1	63.5
F-C	151	81.1	67.4	58.9
F-D	119	103.3	66.2	57.6
F-E	103	119.1	62.7	53.8
C-A	768	15.9	84.2	71.8
C-B	231	53.1	78.8	65.3
C-C	159	76.8	75.4	60.5
$C-D_1$	106	115.3	72.5	55.6
$C-D_2$	91	134.3	65.2	49.2

also to that of the estimated data from Berkowitz *et al.*[9] These dependencies can be expressed as the following empirical linear formula:

$$\sigma_s(S_a)=\sigma_s(\infty)(1-AS_a), \tag{1}$$

where $\sigma_s(S_a)$ is the specific saturation magnetization of the particles composed of the crystallites with an average diameter D, $\sigma_s(\infty)$ the specific saturation magnetization when S_a approaches zero, and A the slope of the straight line. The values of $\sigma_s(\infty)$ and $[\sigma_s(\infty)A]$ by linear regression of $\sigma_s(S_a)$ vs S_a for series F and C are listed in Table II.

Various assumptions have been proposed to explain the decrease of the saturation magnetization with the decrease of particles and/or crystallites size. Some of them are, (1) the magnetization is actually reduced by adsorbed water and a noncollinear spin arrangement;[3] (2) the nonmagnetic grain boundary may instead be a magnetic boundary in which the spin suffers considerable canting, and at 4.2 K the random-angle assumption is equivalent to an average canting angle of

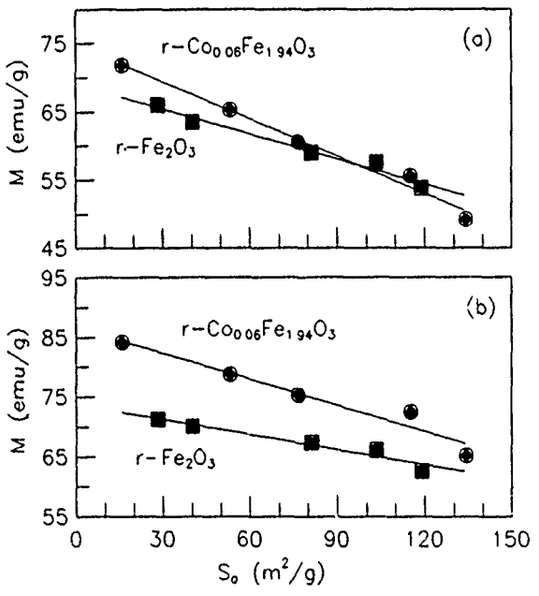

FIG. 2. The dependencies of σ_s on S_a of series F and C measured at (a) 295 and (b) 79 K.

TABLE II. The values of $\sigma_s(\infty)$ and $[\sigma_s(\infty)A]$ by linear regression of $\sigma_s(S_a)$ vs S_a for series F and C at 295 and 79 K.

Sample	$\sigma_s(\infty)$ (emu/g) 295 K	$\sigma_s(\infty)$ (emu/g) 79 K	$[\sigma_s(\infty)A]$ (emu/m^2) 295 K	$[\sigma_s(\infty)A]$ (emu/m^2) 79 K
F	69.1	73.8	−0.12	−0.08
C	73.9	86.1	−0.17	−0.14

54.5°,[8] which is consistent with the results of Coey *et al.*;[3] (3) the crystallites in acicular γ-Fe_2O_3 particles are separated by a nonmagnetic grain boundary on the order of 6 Å wide;[9] (4) in small particles below the superparamagnetic blocking temperature, the magnetization direction fluctuates around an average minimum corresponding to an easy direction of magnetization with average angle $\langle\cos\theta\rangle_T$.[10]

In order to analyze the effects of the fluctuation on the magnetization reduction of the particles, the coercivities, measured at 79 K, of samples F–D (242 Oe) and C–D_2 (2737 Oe) were first taken into Eq. (2)[10]

$$H_c=\frac{2K}{M_s}\left[1-\left(\frac{25k_BT}{KV}\right)^{1/2}\right], \tag{2}$$

to calculate the effective anisotropy constant K, and then estimate $\langle\cos\theta\rangle_T$, respectively. The results are listed in Table III. From the large differences between the calculated $\langle\cos\theta\rangle_{T,C}$ values and the measured ones $\langle\cos\theta\rangle_{T,M}$ [measured from the curves of 79 K for samples F–D and C–D_2 in Fig. 2(b) and Table II, respectively], one knows that the magnetization reduction with the increasing S_a cannot be explained by the magnetization thermal fluctuation.

We assume that the fine crystallite consists of two parts. The first part is the noncollinear surface layer with a thickness t, whose magnetic moment cannot be turned entirely along the direction of the applied magnetic field, but makes an average canting angle α with respect to the field direction. The second one is the inner part, whose magnetic moment can be aligned along the direction of the applied magnetic field. Under this circumstance the measured σ_s of the samples is actually contributed by the effective magnetic volume V_{eff}, not by the geometric volume V_0, i.e.,

$$\frac{V_{\text{eff}}M_s}{V_0\rho}=\sigma_s(S_a), \quad \frac{V_0M_s}{V_0\rho}=\sigma_s(\infty), \tag{3}$$

where ρ is the density of the corresponding materials and in this article it is taken as 4.9 g/cm^3 for both γ-Fe_2O_3 and γ-$Co_{0.06}Fe_{1.94}O_3$ particles.

According to this model and neglecting the small values of higher powers of t, the relationship between σ_s and S_a can be deduced as

TABLE III. The measured H_c, V, $\langle\cos\theta\rangle_{T,M}$, and the calculated K, $\langle\cos\theta\rangle_{T,C}$ of samples F-D and C-D_2 at 79 K.

Sample	H_c(Oe)	V(cm^3)	K(erg/cm^3)	$\langle\cos\theta\rangle_{T,C}$	$\langle\cos\theta\rangle_{T,M}$
F-D	242	8.8×10^{-19}	3.1×10^5	0.98	0.85
$C-D_2$	2737	3.9×10^{-19}	1.4×10^6	0.99	0.76

TABLE IV. The measured A, assumed α and calculated t of series F and C.

Sample	T (K)	A ($m^{-2}g$)	σ(deg)	t(Å)
F	79	1.14×10^{-3}	54.7	6
F	295	1.77×10^{-3}	54.7	8
C	79	1.62×10^{-3}	54.7	8
C	295	2.34×10^{-3}	54.7	11
γ-Fe_2O_3[c]	4.2	···	54.5[a]	4–7[a]
γ-Fe_2O_3[d]	4.2	2.63×10^{-3} [b]	54.7	13[b]
γ-Fe_2O_3[e]	293	1.26×10^{-3}	54.7	6

[a]Measured from Mössbauer effect.
[b]Measured from the relation of σ_s vs the average particles' size.
[c]Reference 8.
[d]Reference 4.
[e]Reference 9.

$$\frac{\sigma_s(S_a)}{\sigma_s(\infty)}=\frac{V_{\text{eff}}}{V_0}=1-(1-\cos\alpha)\rho t S_a. \tag{4}$$

Comparing Eq. (4) to Eq. (1), one knows that the measured linear dependence of $\sigma_s(S_a)$ on S_a has the same form to that of the deduced one with an equation of

$$A=(1-\cos\alpha)\rho t. \tag{5}$$

Therefore according to the measured A in Eq. (1) and the assumed α in Eq. (5) one can calculate the thickness t of the noncollinear surface layer.

It is worthy to point out that in Figs. 2(a) and 2(b) there are obvious differences in slope A between series F and C at the same temperature and between 295 and 79 K for one series. At a certain temperature, as shown in Figs. 2(a) and 2(b), γ-$Co_{0.06}Fe_{1.94}O_3$ particles show a larger slope than that of γ-Fe_2O_3 particles. And for a certain series the slope is larger at 79 K than that at 295 K. According to Eq. (5) the slope of the straight line is affected by two independent factors α and t. If one factor is measured or assumed, then the other one can be calculated from Eq. (5). Morrish *et al.*[8] have assumed that for γ-Fe_2O_3 particles α is 54.5°. If assuming α for both γ-Fe_2O_3 and γ-$Co_{0.06}Fe_{1.94}O_3$ particles and at both 79 and 295 K to be 54.7°, then we can obtain the thickness t of the noncollinear surface layer.

The measured A, assumed α and calculated t for series F and C are listed in Table IV. As a reference, the results of Morrish *et al.*,[8] Mollard *et al.*,[4] as well as Berkowitz *et al.*[9] are also listed in Table IV. From this table one knows that the measured relationship between $\sigma_s(S_a)$ and S_a can be explained with the simple model of the fine crystallite being consisted of the spin collinear core and the spin canted surface layer. Under the assumption of the same σ, γ-$Co_{0.06}Fe_{1.94}O_3$ crystallites show a larger t, 8 and 11 Å at 295 and 79 K, respectively, than those of γ-Fe_2O_3 crystallites, 6 and 8 Å at the above two temperatures. The different slopes of the different straight lines for series F and C may be caused by the different effective anisotropies of the two series particles. The magnetocrystalline anisotropy constants K_1 were determined by using the approach to saturation at 295 K to be 2.2×10^5 ergs/cm^3 for series C and 4.4×10^4 ergs/cm^3 for series F, respectively. The larger thickness t of the surface spin canting layer for series C, comparing to that of series F, may be caused by the larger effective magnetocrystalline anisotropy of the particles.

IV. CONCLUSION

The specific saturation magnetizations of both γ-Fe_2O_3 and γ-$Co_{0.06}Fe_{1.94}O_3$ particles decrease linearly with the increasing specific surface area of the fine crystallites. The results can be explained with the model of the spin canted surface layer. The fine crystallites consist of two parts, i.e., the surface layer, whose magnetic moment cannot be turned entirely along the direction of the applied field, but make an average canting angle with the field, and the inner part, whose magnetic moment can be aligned along the direction of the applied field. With this assumption, the empirical linear formula of σ_s and S_a can be interpreted. The different thickness t of the surface spin canting layer between series F and C may be caused by the different effective anisotropies of the two series particles.

ACKNOWLEDGMENT

This work was supported by the National Science Foundation of China.

[1] F. T. Parker and A. E. Berkowitz, Phys. Rev. B **44**, 7437 (1991).
[2] Q. A. Pankhurst and R. J. Pollard, Phys. Rev. Lett. **67**, 248 (1991).
[3] J. M. D. Coey and D. Khalafalla, Phys. Status Solidi A **11**, 229 (1972).
[4] P. Mollard, P. Germi, and A. Rousset, Physica B **86–88** 1393 (1977).
[5] S. Linderoth *et al.*, J. Appl. Phys. **75**, 6583 (1994).
[6] B. E. Warren, *X-Ray Diffraction* (Addison–Wesley, Reading, MA, 1980), p. 253.
[7] D. H. Han, J. W. Ping, and H. L. Luo, J. Magn. Magn. Mater. (in press).
[8] A. H. Morrish and K. Haneda, J. Phys. **41**, C1-171 (1980).
[9] A. E. Berkowitz, W. J. Schuele, and P. J. Flanders, J. Appl Phys. **39**, 1261 (1968).
[10] S. MøRup, H. TopsøE, and J. Lipka, J. Phys. **37**, C6-287 (1976).

Magnetic properties of nanometer-sized Fe_4N compound (abstract)

Y. B. Feng
State Key Laboratory of Magnetism, Institute of Physics, Chinese Academy of Sciences, P.O. Box 603, Beijing 100 080, China

Nanometer-sized magnetic materials have attracted a lot of attention because of their potential applications in the fields of ferrofluids, high density magnetic recording, and magnetic refrigeration. The sol-gel method[1] has been considered to be effective for creating dispersions of small metal particles in nonmetallic materials. In this work, nanometer-sized Fe-N compound particles were prepared by nitrogenating the iron-boron oxide glass powders, which were synthesized by the sol-gel method from ethylene glycol gel. The magnetic properties of nanometer-sized iron nitride were measured by a vibrating sample magnetometer (VSM). The specific magnetic moment σ is equal to 132 emu/g and the coercivity H_c is 150 Oe. The phase composition was determined by using an x-ray diffractometer (XRD). The diffraction pattern shows that the sample consisted of a main phase of Fe_4N and a small α-Fe phase. The crystallite size d of the Fe_4N particles was estimated by Scherrer's formula, and is about 12 nm. The nanometer-sized Fe-N compound was also studied by using Mossbauer spectroscopy. The Mossbauer absorption pattern consisted of a ferromagnetic component superimposed on a superparamagnetic doublet. The ratio of superparamagnetic fraction to ferromagnetic is about 13%. It is shown that the sol-gel technique could be used to prepare ultrafine particles of Fe-N compound.

[1]K. Yamaguchi *et al.*, IEEE Trans. Magn. **MAG-25**, 3321 (1989).

 0021-8979/94/76(10)/6594/1/$6.00 © 1994 American Institute of Physics

Theory of the negative magnetoresistance of ferromagnetic-normal metallic multilayers (invited)

L. M. Falicov and Randolph Q. Hood
Department of Physics, University of California, Berkeley, California 94720-7300 and Materials Sciences Division, Lawrence Berkeley Laboratory, Berkeley, California 94720

Transport properties for a system consisting of a ferromagnetic-normal metallic multilayer are theoretically examined. The in-plane conductance of the film is calculated for two configurations; the ferromagnetic layers aligned (i) parallel and (ii) antiparallel to each other. The results explain the giant negative magnetoresistance encountered in these systems when an initial antiparallel arrangement is changed into a parallel configuration by application of an external magnetic field. The calculation depends on (a) geometric parameters (the thicknesses of the layers); (b) intrinsic metal parameters (number of conduction electrons, magnetization and effective masses in the layers); (c) bulk sample properties (conductivity relaxation times); and (d) interface scattering properties (diffuse scattering versus potential scattering at the interfaces). It is found that a large negative magnetoresistance requires, in general, considerable asymmetry in the interface scattering for the two spin orientations. All qualitative features of the experiments are reproduced. Quantitative agreement can be achieved with sensible values of the parameters. The effect can be conceptually explained based on considerations of phase-space availability for an electron of a given spin orientation as it travels through the multilayer sample in the various configurations.

I. INTRODUCTION

Ferromagnetic-normal metallic superlattices and sandwiches[1,2] display several interesting properties, such as a varying interlayer magnetic coupling[3] and a negative, sometimes very large magnetoresistance (MR) effect.[4–15] A few examples include $(Co/Cu)_n$, $(Fe/Cr)_n$, $(Fe/Cu)_n$, $(Co/Ru)_n$, (NiFe/Cu/NiFe), and (NiFe/Ag/NiFe). In these systems the magnetic moment of each ferromagnetic layer is arranged with respect to that of the neighboring ferromagnetic layers either in a parallel or an antiparallel fashion, depending on the thickness of the metal spacers and on the quality of the interfaces.

When the consecutive moments are arranged antiparallel to each other, the application of an external magnetic field to the sample rearranges the moments into a completely parallel arrangement for fields of the order of 1 T. Also, the resistance of the sample decreases—negative MR—in all directions (in-plane in particular). The MR can vary from a few percent to as large as 55% (for Co/Cu at liquid-helium temperatures).[13] A decrease by more than 20% is generally known as the *giant magnetoresistance effect* (GMR).

Spin-dependent interfacial scattering plays an important role in the MR in many different ferromagnetic-normal metallic multilayers. Experiments by Fullerton *et al.*[16] indicate that increased interfacial roughness enhances the GMR in $(Fe/Cr)_n$. Parkin[17] found that the addition of thin Co layers at the interfaces of $(NiFe/Cu)_n$ enhanced the MR. The MR increased monotonically as the Co layer increased to 4 Å, then become insensitive to the thickness of the Co layer with a MR similar to that of $(Co/Cu)_n$ despite the presence of the NiFe layers sandwiched between thin Co layers. Baumgart *et al.*[18] have found that ultrathin layers of elements (V, Mn, Ge, Ir, or Al) deposited at the Fe/Cr interface lead to changes in the MR which correlate with the ratio of spin-up and spin-down resistivities arising from spin-dependent impurity scattering of these elements when alloyed with Fe. This result is in agreement with the suggestion of Baibich *et al.*[4] that the spin dependence of impurity scattering at the interfaces is related to that observed[19] in alloyed ferromagnetic metals such as Fe, Co, and Ni.

Further confirmation of the importance of the interface in the MR effect was provided by Barthélémy *et al.*[20] who point out that the experimental data they obtained for epitaxially grown Fe(001)/Cr(001) multilayers seem to be in agreement with a variation of the MR of the form

$$\exp(-t_{Cr}/\lambda^*),$$

where t_{Cr} is the thickness of Cr layer and λ^* is a length of the order of the mean-free path. Such a variation of the MR with layer thickness is expected from spin-dependent interface scattering.

It is important to distinguish clearly between the concepts of spin-flip scattering and spin-dependent scattering. The first refers to an event in which, during scattering, an electron reverses its spin orientation; such a phenomenon is normally caused by spin-orbit effects and/or by scattering from impurities with a localized magnetic moment. Spin-flip scattering is neglected in this contribution. The second one refers to the fact that electrons with different spin orientations experience different potentials and have different phase-space distributions. Consequently, they have very different scattering cross sections both in the bulk and at the interfaces. The latter is extremely relevant for the purposes of this study.

 0021-8979/94/76(10)/6595/6/$6.00 © 1994 American Institute of Physics

The aim of this contribution is to present a model that incorporates spin-dependent interfacial scattering in a more realistic way. While the model presented here is similar in many respects to that of Camley and Barnaś[21,22] it does not suffer from the shortcomings encountered there in the description of interfacial scattering. Utilization of a more accurate description of the interface permits a study and separation of the various scattering mechanisms and their relevance in the MR effect.

The present model, an extension of the Fuchs–Sondheimer theory,[23,24] uses a Stoner description[25] of the itinerant ferromagnetic layers; it introduces different potentials for majority and minority spins. Band-structure and electron-density effects are included only by means of a constant, metal- and spin-dependent potential, and an isotropic effective mass for each spin in each layer. The different potentials in neighboring layers result in coherent potential scattering (i.e., refraction) of electrons as they traverse the interface. The angular-dependent effects are treated by a quantum-mechanical matching of the electron wave functions at the interfaces. Scattering at the interfaces from impurities and interfacial roughness are also a source of spin-dependent scattering, and they contribute to the present model through a spin-dependent function, in a way similar to that used by Camley and Barnaś.

The model predicts the dependence of the MR on the quality of the samples (mean-free path), on the quality (roughness) of the interfaces, and on the thickness of the layers.

II. THE MODEL

The in-plane conductivity was calculated for a multilayer consisting of alternating layers of a ferromagnet (F) of thickness d_F, and a spacer layer of thickness d_s. The coordinate system is chosen with the z axis perpendicular to the layers. There is complete isotropy in the (x,y) plane.

For each structure the conductivity was calculated for both an antiparallel alignment, denoted $\sigma\uparrow\downarrow$, and for a parallel alignment, denoted $\sigma\uparrow\uparrow$, of the moments of successive F layers. The structure repeats itself after four layers ($\cdots/F\uparrow/s/F\downarrow/s/\cdots$) in the antiparallel arrangement. In the parallel arrangement the period consists of two layers ($\ldots/F\uparrow/s/\ldots$). Application of a sufficiently large magnetic field to a sample in the antiparallel arrangement results in a parallel alignment of the magnetic moments. The magnetoresistance ($\Delta\rho/\rho$), is defined by

$$\frac{\Delta\rho}{\rho}\equiv\frac{\rho\uparrow\downarrow-\rho\uparrow\uparrow}{\rho\uparrow\downarrow}=\frac{\sigma\uparrow\uparrow-\sigma\uparrow\downarrow}{\sigma\uparrow\uparrow}, \tag{1}$$

where $\rho_{\mu,\nu}=(\sigma_{\mu,\nu})^{-1}$. Note that this quantity varies between zero and one (or 0% and 100%) whenever the resistance decreases upon the application of an external magnetic field.

For both alignments the conductivity is obtained by adding the contributions of the spin-up and the spin-down electrons, calculated separately. This is the two-current model,[19] which provides a good description of electron transport in magnetic $3d$ metals. As mentioned above spin-flip processes, which mix the two currents, are neglected. Their effect is know to be small at low temperatures.

The electrons involved in transport are considered as free-electron-like with spherical Fermi surfaces. Within each layer the electrons move in a constant potential $V_{i\sigma}$ which depends on the particular layer i and the spin σ of the electron.

The electron distribution function is written in the form

$$f_{i\sigma}(\mathbf{v},z)=f^0_{i\sigma}(\mathbf{v})+g_{i\sigma}(\mathbf{v},z), \tag{2}$$

for each layer i and for each spin σ, which is independent of x and y by symmetry. The first term $f^0_{i\sigma}(\mathbf{v})$ is the equilibrium distribution in the absence of an electric field and $g_{i\sigma}(\mathbf{v},z)$ is the deviation from that equilibrium in the presence of the electric field. For an electric field of magnitude E in the $\hat{x}$ direction, the Boltzmann equation in the relaxation-time approximation reduces to

$$\frac{\partial g_{i\sigma}}{\partial z}+\frac{g_{i\sigma}}{\tau_{i\sigma}v_z}=\frac{|e|E}{m_{i\sigma}v_z}\frac{\partial f^0_{i\sigma}}{\partial v_x}, \tag{3}$$

where $\tau_{i\sigma}$ is the relaxation time in layer i for spin σ, and e is the charge of the electron. The second-order term, proportional to the product $(E\cdot g_{i\sigma})$, has been discarded since nonlinear effects (deviations from Ohm's law) are neglected. The Lorentz-force term, proportional to $(\mathbf{v}\times\mathbf{H}/c)$, has also been dropped from the Boltzmann equation since it gives an effect which is orders of magnitude smaller than those considered here.[21]

Because of the nature of the boundary conditions it is useful to divide $g_{i\sigma}$ into two parts: $g^+_{i\sigma}(\mathbf{v},z)$ if $v_z\geq 0$ and $g^-_{i\sigma}(\mathbf{v},z)$ if $v_z<0$. The boundary conditions for the potential (nondiffusive) scattering at the (i,j) interface then take the form

$$\begin{aligned} g^-_{i\sigma}&=S_{ij;i;\sigma}R_{ij,\sigma}g^+_{i\sigma}+S_{ji;i;\sigma}T_{ji;\sigma}g^-_{j\sigma},\\ g^+_{j\sigma}&=S_{ji,j;\sigma}R_{ji;\sigma}g^-_{j\sigma}+S_{ij;j;\sigma}T_{ij;\sigma}g^+_{i\sigma}. \end{aligned} \tag{4}$$

Here $S_{ij;k;\sigma}$, which varies between zero and one, is a factor that indicates the degree of potential scattering at the interface (i,j) for an electron of spin σ arriving at the interface from the layer i and being scattered into the layer k. The scattering is completely diffusive when $S=0$ and follows the reflection–refraction laws when all $S=1$. The notation used for the transmission T and the reflection R coefficients is the following: $T_{ij;\sigma}\equiv$ probability for an electron of spin σ in layer i to be transmitted (refracted) into layer j; $R_{ij,\sigma}\equiv$ probability for an electron of spin σ in layer i with a velocity directed towards layer j to be reflected back into layer i. The equations and boundary conditions, as written, satisfy all necessary conservation laws.

The functional dependence of the transmission and reflection coefficients was determined[26] by matching the free-electron-like (plane-wave) functions and their derivatives at each interface. The solution to this problem, which is identical to that encountered in optics for an interface between two media with different index of refraction, is illustrated in Fig. 1.

The current density along the electric field in each layer i for electrons with spin σ is given by

$$J_{xi\sigma}(z)=-|e|\left(\frac{m_{i\sigma}}{h}\right)^3\int v_x g_{i\sigma}(\mathbf{v},z)d^3\mathbf{v}, \tag{5}$$

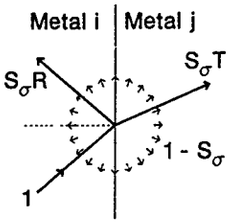

FIG. 1. Schematic diagram of the scattering process at the metal–metal interface. The parameter S_σ defines the fraction controlled by the potentials; $S_\sigma R$ is the probability of specular scattering; $S_\sigma T$ is the probability of transmission (refraction) into the other metal.

where h is Planck's constant. The conductivity of the multilayer is obtained by averaging over the whole film

$$\sigma = \frac{1}{E d_{\text{film}}} \sum_{i} \sum_{\sigma=\uparrow,\downarrow} \int J_{xi\sigma}(z) dz.$$

The MR, $(\Delta\rho/\rho)$, is found by calculating independently the conductivities $\sigma\uparrow\downarrow$ and $\sigma\uparrow\uparrow$. Many parameters are necessary to characterize a structure. Associated with the electrons in the F layers are the minority (denoted using a small subscript m) and the majority (denoted using a capital subscript M) spins with effective masses m_m and m_M, relaxation times τ_m and τ_M, and potentials V_m and V_M. In the spacer layer s the spin-up and spin-down electrons move in a potential V_s with an effective mass m_s and relaxation time τ_s. At the interfaces, the functions $S_{ij;k;\sigma}$, which vary with angle of incidence, describe the interfacial scattering of the majority and the minority spins.

The values of the potentials are determined by treating all of the valence s and d electrons as being in a single free-electron-like band with an isotropic effective mass. In general the effective mass is taken to be larger than the electron mass, since the d electrons, which contribute to the density of electrons, are in narrower bands than the free-electron-like s electrons. Within the F layers the bands for the minority and the majority spins are shifted by a k-independent exchange potential, yielding two different spin-dependent, constant potentials, V_m and V_M. The value of the exchange splitting is chosen so that the difference in the density of the majority and the minority electrons yields the net magnetic moment of the bulk ferromagnetic material.

III. RESULTS

As developed thus far, the theory includes 11 parameters and eight angular functions:

three effective masses m_M, m_m, and m_s;
three constant potentials V_M, V_m, and V_s;
three relaxation times τ_M, τ_m, and τ_s;
two thicknesses d_F, and d_s;

and

eight interface scattering functions $S_{F,s,F;M}$, $S_{F,s,F,m}$, $S_{F,s,s,M}$, $S_{F,s,s,m}$, $S_{s,F;s,M}$, $S_{s,F;s,m}$, $S_{s,F;F,M}$, and $S_{s,F,F,m}$.

The results presented here include only the cases for which the *relaxation times* are identical $\tau \equiv \tau_m = \tau_M = \tau_s$. (Note that the *mean-free paths* of the minority and the majority spins within the F layers and for the spacer metal are different, since the Fermi velocities are different.) The interfaces are treated in two different ways. In the first approach the angular dependence of the functions $S_{ij;k;\sigma}$ is neglected and the eight functions are replaced by two constants

$$S_{F,s,F,M} = S_{F,s,s;M} = S_{s,F;s;M} = S_{s,F;F,M} = S_M,$$

$$S_{F,s;F;m} = S_{F,s;s;m} = S_{s,F;s,m} = S_{s,F;F;m} = S_m.$$

In this approach the system is defined by 11 constants.

In the second approach the different angular dependences in various $S_{ij;k;\sigma}$ are explicitly included.

Results are presented for two different multilayer systems, $(\text{Fe/Cr})_n$ and $(\text{Fe/Cu})_n$. In these three metals the isotropic effective mass is assumed to be independent of the material and spin orientation with a value $m_M = m_m = m_s = 4.0\times$ free-electron mass. With this effective mass the potentials, with respect to the Fermi energy E_F chosen to be at $E_F = 0$, are

$$V_M = -8.23 \text{ eV}, \quad V_m = -5.73 \text{ eV for Fe};$$

$$V_s = -5.77 \text{ eV for Cr};$$

$$V_s = -8.54 \text{ eV for Cu}.$$

The parameters that remain to be specified for each case—$(\text{Fe/Cr})_n$ and $(\text{Fe/Cu})_n$—in the constant-S approximation are altogether five: (a) one relaxation time τ, which depends on bulk sample properties; (b) two geometric parameters d_F and d_s; and (c) two interface scattering parameters S_M, S_m (diffuse scattering versus potential scattering at the interfaces for the majority and the minority spins, respectively).

Even with these simplifications, the phenomena under consideration are complicated functions of the five variables, and the task of describing these dependencies is not simple. In general terms, and with exceptions, it is found that $(\Delta\rho/\rho)$ is a strong function of the interface parameters S_M and S_m, and a relatively weak function of the thicknesses and the mean-free path. For example, as S_M and S_m independently vary between 0 and 1, the calculated $(\Delta\rho/\rho)$ varies between 0% and 92.7% for $(\text{Fe/Cr})_n$ and 0% and 94.4% for $(\text{Fe/Cu})_n$, when values of $d_F = 20.0$ Å; $d_s = 10.0$ Å and $\tau = 5.0\times10^{-13}$ s are chosen. Figure 2 shows the regions in the two-dimensional parameter space $(S_M - S_m)$, where $(\Delta\rho/\rho)$ is greater than 20% for these values of d_F, d_s, and τ. With this choice of τ, the mean-free paths are (i) 4250 Å for the majority-spin electrons and 3540 Å for the minority-spin electrons in Fe; (ii) 3560 Å for electrons in Cr; and (iii) 4330 Å for electrons in Cu. These values correspond to all mean-free paths which are orders of magnitude larger than the film thicknesses, i.e., the clean-film limit, where interface effects are supposed to be paramount.

Some of the interesting results of the calculations are illustrated in Figs. 2–6. It was found in general that:

(a) $(\Delta\rho/\rho)$ is only a few percent when $S_M = S_m$, except[27] when both parameters are close to 1 (see Figs. 2 and 3).

(b) $(\Delta\rho/\rho)$, as a function of d_F, exhibits a variety of behaviors that include (i) a monotonic decrease with increas-

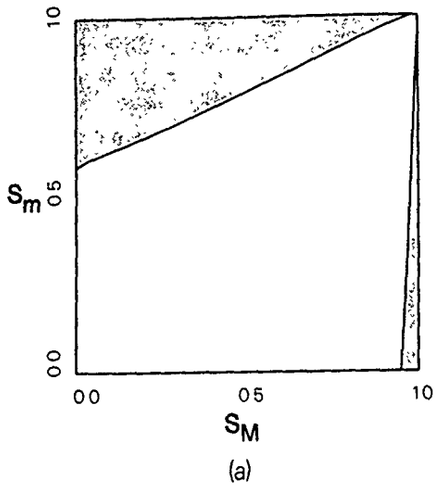

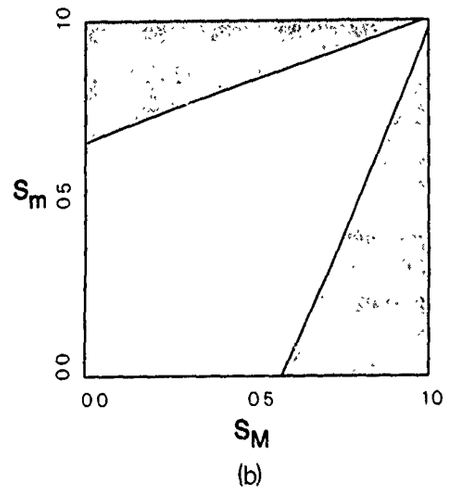

FIG. 2. The region in the two-dimensional parameter space (S_M, S_m), where $(\Delta\rho/\rho)>0.2$ for $d_F=20$ Å, $d_s=10$ Å, and $\tau=5.0\times10^{-13}$ s. (a) Potential parameters corresponding to $(Fe/Cr)_n$. (b) Potential parameters corresponding to $(Fe/Cu)_n$.

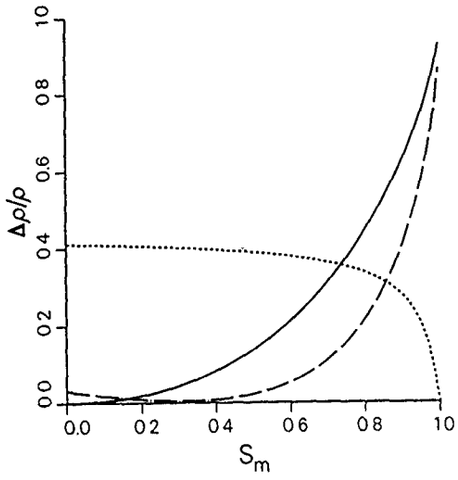

FIG. 3. Variation of $(\Delta\rho/\rho)$ as a function of S_m for the parameters of $(Fe/Cr)_n$, $\tau=5.0\times10^{-13}$ s, $d_F=d_s=10$ Å and three values of S_M: (1) dashed curve $S_M=1$; (2) chain-dotted curve $S_M=0.5$; and (3) solid curve $S_M=0$.

ing d_F; and (ii) an initial increase followed by a decrease (a single maximum); in all cases the asymptotic value as $d_F\to\infty$ is zero (see Fig. 4).

(c) $(\Delta\rho/\rho)$, as a function of increasing d_s, exhibits either (i) a continuous monotonic decrease, or, more commonly, (ii) a single maximum at a value of d_s of the order of d_F; the asymptotic value as $d_s\to\infty$ is also zero (see Fig. 5).

(d) $(\Delta\rho/\rho)$, as a function of the relaxation time τ, either (i) increases monotonically and saturates at a maximum value, or, more commonly, (ii) increases to a maximum, and then *very gradually* decreases (see Fig. 6).

Figure 2 contains information on how the quality of the interfaces influences the MR, for specific values of d_F, d_s, and τ. From the figure it is evident that the region of large MR is close either to the line $S_M=1$, or to the line $S_m=1$, and away from the line $S_M=S_m$. There is a very large asymmetry between S_M and S_m in $(Fe/Cr)_n$, but considerably less so in $(Fe/Cu)_n$.

A more realistic approach to the diffuse-versus-potential scattering at the interface requires the full angular dependence of the eight functions $S_{ij;k;\sigma}$. In general[28–31] the diffuse scattering is considerably larger for electrons impinging upon the interface in directions close to the normal. Grazing-angle electrons are less effectively scattered, and they tend to be almost completely internally reflected. A common (first-order) approximation to these functions[28–31] is

$$S_{ij;i;\sigma}=S_\sigma \exp[-4\eta^2(k_{i\sigma}\cos\Theta_i)^2], \tag{6}$$

$$S_{ij;j;\sigma}=S_\sigma \exp[-\eta^2(k_{i\sigma}\cos\Theta_i-k_{j\sigma}\cos\Theta_j)]. \tag{7}$$

Here, η is a parameter which depends on the roughness of the interface as well as the strength and physical distribution of the scattering centers at the interface, $k_{i\sigma}$ is the magnitude of the k vector at the Fermi sphere of the spin-σ electrons in layer i, and Θ_i is the angle between the electron velocity and

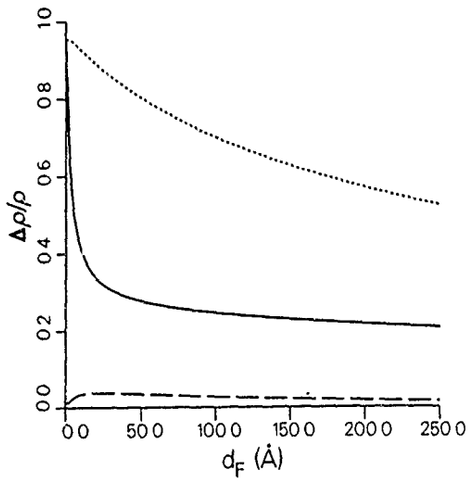

FIG. 4. Variation of $(\Delta\rho/\rho)$ as a function of d_F for the parameters of $(Fe/Cr)_n$, $d_s=10$ Å, $\tau=5.0\times10^{-13}$ s and three different values of S_M and S_m: (1) chain-dotted curve $S_M=S_m=0.8$; (2) dashed curve $S_M=0$, $S_m=1$; and (3) solid curve $S_M=1$, $S_m=0$.

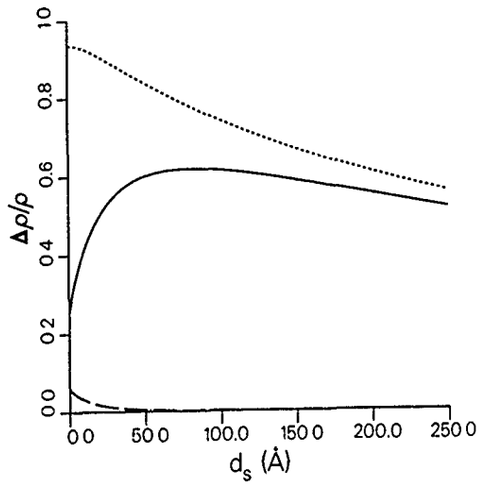

FIG. 5. Variation of $(\Delta\rho/\rho)$ as a function of d_s for the parameters of $(Fe/Cr)_n$, $d_F=20$ Å, $\tau=5.0\times10^{-13}$ s and different values of S_M and S_m: (1) solid curve $S_M=1$, $S_m=0$; (2) dashed curve $S_M=0$, $S_m=1$; and (3) chain-dotted curve $S_M=S_m=0.9$.

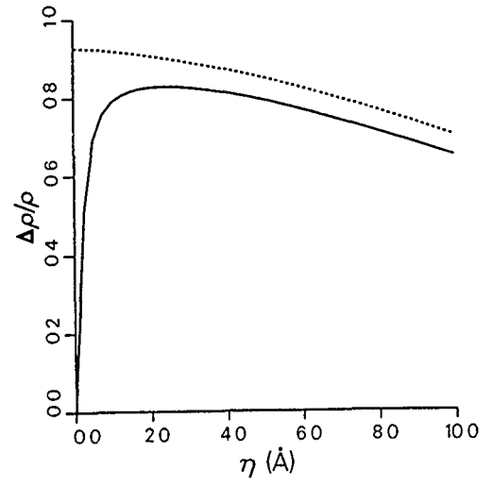

FIG. 7. Variation of $(\Delta\rho/\rho)$ as a function of η for the parameters of $(Fe/Cr)_n$, $d_s=10$ Å, $d_F=20$ Å and two different values of S_σ in Eqs. (6) and (7): (1) solid curve $S_M=S_m=1$; and (2) dashed curve $S_M=0$, $S_m=1$.

the normal to the interface; S_σ is the overall diffuse scattering strength at grazing angle $\Theta=\pi/2$. It should be noted that the limit $\eta=0$ reduces the approximation to the one previously discussed.

The influence of this angular dependence on the MR is shown in Fig. 7. As η increases, the MR in general decreases, except for the case in which S_M and S_m are very close in value; in the latter, the difference in k vector between the two spins, and the nonvanishing η produce an asymmetry in the diffuse interface scattering between the spins in the F layers, and thus increases the MR.

IV. DISCUSSION AND CONCLUSIONS

Figure 2(a) shows a marked asymmetry in the dependence of $(\Delta\rho/\rho)$ for $(Fe/Cr)_n$ on S_M and S_m, i.e., the majority- and minority-spin interface scattering have a very different effect on the MR. For this system

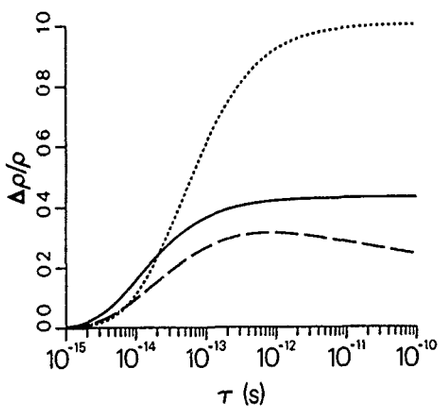

FIG. 6. Variation of $(\Delta\rho/\rho)$ as a function of τ for the parameters of $(Fe/Cr)_n$, $d_s=10$ Å, $d_F=20$ Å, and three different values of S_M and S_m: (1) chain-dotted curve $S_M=0$ and $S_m=0.7$; (2) dashed curve $S_M=0.5$ and $S_m=1$; and (3) solid curve $S_M=1$ and $S_m=0$.

$$|V_M|<|V_s|\approx|V_m|.$$

By contrast, a large asymmetry is not present in $(Fe/Cu)_n$, Fig. 2(b). Here,

$$|V_s|\approx|V_M|<|V_m|.$$

This difference in V_s has a large effect on the MR, as can be seen in plots of the in-plane current distribution across the layers.[26] Often when $(\Delta\rho/\rho)$ is very large, the current distribution responsible for the large value of $\sigma\uparrow\uparrow$ is such that it is highly concentrated in one type of layer, either in the ferromagnet or in the spacer. This effect, which can be called *channeling*, appears frequently when there is a GMR. When the channeling is in the spacer layer it occurs *only when there is parallel alignment*. Channeling in the FM layers, on the other hand, occurs (in one type of F layer for each electron spin orientation) for both the parallel and the antiparallel configurations. From these considerations the channeling in the spacer layer should be more intimately connected with a GMR. It should emphasized that channeling is present when the potentials are different; GMR requires, in addition, asymmetric values of S_σ. Channeling and GMR are strongly correlated.[32]

The experimentally observed values of MR in $(Fe/Cr)_n$ and $(Fe/Cu)_n$ multilayers can be obtained by the calculation with a proper choice of the parameters. However, the model in its present form, which considers all of the valence s and d electrons as comprising a single band with a single isotropic effective mass, yields effective resistivities $\rho\uparrow\uparrow$ and $\rho\uparrow\downarrow$ which are about an order of magnitude smaller than those measured in multilayer structures. The effective resistivities are too small because the model has too many free-electron-like conduction electrons: 8 in Fe, 6 in Cr, and 11 in Cu. Proper consideration must be taken of the fact that, in these metals, s and d electrons contribute very differently to the transport properties. The narrow character of the d bands has been accounted for in the single-band approach by a single, large, isotropic effective mass, four times larger than the

free-electron mass. A better approach to the problem would be to include a realistic band structure with its 12 bands, wide and narrow, as well as the hybridization and spin polarization. Such a treatment would make the calculations much more difficult.

Within the confines of a single-band model a simple, natural way to decrease the number of conduction electrons is by reducing the density of the electrons in each layer by a constant scaling factor, γ, independent of the material and the spin of the electron. It should be stressed that the introduction of such a scaling factor does not change the form of the results found above. The number of electrons and the magnetization decreases by a factor of γ. The resistivities $\rho\uparrow\uparrow$ and $\rho\uparrow\downarrow$ increase by a factor of about γ, and $(\Delta\rho/\rho)$ decreases by a factor of about $\gamma^{1/3}$. A value of $\gamma=8$ was chosen for making comparisons with experimental data. With this value the number of effective free-electron-like conduction electrons are 1.00 in Fe, 0.5 in Cr, and 1.38 in Cu. Calculations were able to yield values of the MR and the resistivities, $\rho\uparrow\uparrow$ and $\rho\uparrow\downarrow$, similar to those measured experimentally.

Baibich *et al.*[4] found that a multilayer of (Fe 30 Å/Cr 9 Å)$_{60}$, prepared by molecular beam epitaxy, had $(\Delta\rho/\rho)\approx0.46$ and a absolute resistivity change of about 23 $\mu\Omega$ cm. With $S_M=0.23$, $S_m=0.98$, $d_F=30$ Å, $d_s=9$ Å, and $\tau=1\times10^{-13}$ s values of $\rho\uparrow\uparrow=30.6$ $\mu\Omega$ cm and $\rho\uparrow\downarrow=56.6$ $\mu\Omega$ cm were calculated, which corresponds to $(\Delta\rho/\rho)=0.46$ for the MR. Experimental values of ρ are between 20 and 80 $\mu\Omega$ cm. With this choice of γ, τ, and effective mass (i.e., an effective mass of four times the electron mass), the bulk mean-free paths are 425 Å for the majority-spin electrons and 354 Å for the minority-spin electrons in Fe; and 356 Å for the electrons in Cr.

Pétroff *et al.*[14] report that a multilayer (Fe 15 Å/Cu 15 Å)$_{60}$ made by sputtering, had the following characteristics: $\rho\uparrow\uparrow=24.8$ $\mu\Omega$ cm, $\rho\uparrow\downarrow=27.8$ $\mu\Omega$ cm, and $(\Delta\rho/\rho)=0.108$. With $S_m=0.71$, $S_M=0.92$, $d_F=d_s=15$ Å and $\tau=1\times10^{-13}$ s values of $\rho\uparrow\uparrow=25.2$ $\mu\Omega$ cm and $\rho\uparrow\downarrow=28.3$ $\mu\Omega$ cm were calculated, which correspond to $(\Delta\rho/\rho)=0.11$. Here, the bulk mean-free paths are 425 Å for the majority-spin electrons and 354 Å for the minority-spin electrons in Fe; and 433 Å for the electrons in Cu.

As seen above, a large MR requires, in general, a large difference in interface scattering for the different spins. When $S_M=S_m$ the MR is found to be not more than a few percent. Therefore, a large MR cannot be explained as being caused solely by different densities of electrons with different spins, which vary from layer-to-layer. What is required is a spin imbalance *and* a spin-dependent scattering mechanism at the interface, i.e., $S_M\neq S_m$. When such a spin-dependent scattering mechanism exists, for example when magnetic impurities are present at the interfaces, the MR is profoundly influenced by spatial variations in the density of electron spins. This is the main cause of the GMR effect in ferromagnetic multilayers.

ACKNOWLEDGMENTS

This research was supported, at the Lawrence Berkeley Laboratory, by the Director, Office of Energy Research, Office of Basic Energy Sciences, Materials Science Division, U.S. Department of Energy, under Contract No. DE-AC03-76SF00098.

[1] *Thin Film Growth Techniques for Low-Dimensional Structures*, edited by R. F. C. Farrow, S. S. P. Parkin, P. J. Dobson, J. H. Neave, and A. S. Arrott (Plenum, New York, 1987).
[2] *Synthetic Modulated Structures*, edited by L. L. Chang and B. C. Giessen (Academic, New York, 1985); *Metallic Superlattices: Artificially Structured Materials*, edited by T. Shinjo and T. Takada, Studies in Physical and Theoretical Chemistry, Vol. 49 (Elsevier, Amsterdam, 1987); B. Y. Jin and J. B. Ketterson, Adv. Phys. **38**, 189 (1989).
[3] S. S. P. Parkin, Phys. Rev. Lett. **67**, 3598 (1991).
[4] M. N. Baibich, J. M. Broto, A. Fert, F. Nguyen Van Dau, F. Pétroff, P. Etienne, G. Creuzet, A. Friederich, and J. Chazelas, Phys. Rev. Lett. **61**, 2472 (1988).
[5] S. S. P. Parkin, N. More, and K. P. Roche, Phys. Rev. Lett. **64**, 2304 (1990).
[6] G. Binasch, P. Grünberg, F. Saurenbach, and W. Zinn, Phys. Rev. B **39**, 4828 (1989).
[7] B. Dieny, V. S. Speriosu, S. S. P. Parkin, B. A. Gurney, D. R. Wilhoit, and D. Mauri, Phys. Rev. B **43**, 1297 (1991).
[8] A. Chaiken, P. Lubitz, J. J. Krebs, G. A. Prinz, and M. A. Harford, J. Appl. Phys. **70**, 5864 (1991).
[9] B. Dieny, V. S. Speriosu, S. Metin, S. S. P. Parkin, B. A. Gurney, P. Baumgart, and D. R. Wilhoit, J. Appl. Phys. **69**, 4774 (1991).
[10] A. Chaiken, T. M. Tritt, D. J. Gillespie, J. J. Krebs, P. Lubitz, M. Z. Harford, and G. A. Prinz, J. Appl. Phys. **69**, 4798 (1991).
[11] A. Chaiken, G. A. Prinz, and J. J. Krebs, J. Appl. Phys. **67**, 4892 (1990).
[12] T. Miyazaki, T. Yaoi, and S. Ishio, J. Magn. Magn. Mater. **98**, L7 (1991).
[13] S. S. P. Parkin, Z. G. Li, and D. J. Smith, Appl. Phys. Lett. **58**, 2710 (1991).
[14] F. Pétroff, A. Barthélémy, D. H. Mosca, D. K. Lottis, A. Fert, P. A. Schroeder, W. P. Pratt, Jr., and R. Loloee, Phys. Rev. B **44**, 5355 (1991).
[15] W. P. Pratt, Jr., S. F. Lee, J. M. Slaughter, R. Loloee, P. A. Schroeder, and J. Bass, Phys. Rev. Lett. **66**, 3060 (1991).
[16] E. E. Fullerton, D. M. Kelly, J. Guimpel, I. K. Schuller, and Y. Bruynseraede, Phys. Rev. Lett. **68**, 859 (1992).
[17] S. S. P. Parkin, Phys. Rev. Lett. **71**, 1641 (1993).
[18] P. Baumgart, B. A. Gurney, D. R. Wilhoit, T. Nguyen, B. Dieny, and V. Speriosu, J. Appl. Phys. **69**, 4792 (1991).
[19] A. Fert and I. A. Campbell, J. Phys. F Metal Phys. **6**, 849 (1976); I. A. Campbell and A. Fert, in *Ferromagnetic Materials*, edited by E. P. Wohlfarth (North-Holland, Amsterdam, 1982), Vol. 3, p. 769.
[20] A. Barthélémy, A. Fert, M. N. Baibich, S. Hadjoudj, F. Pétroff, P. Etienne, R. Cabanel, S. Lequien, F. Nguyen Van Dau, and G. Creuzet, J. Appl. Phys. **67**, 5908 (1990).
[21] J. Barnaś, A. Fuss, R. E. Camley, P. Grünberg, and W. Zinn, Phys. Rev. B **42**, 8110 (1990).
[22] R. E. Camley and J. Barnaś, Phys. Rev. Lett. **63**, 664 (1989).
[23] K. Fuchs, Proc. Cambridge Philos. Soc. **34**, 100 (1938).
[24] E. H. Sondheimer, Adv. Phys. **1**, 1 (1952).
[25] E. C. Stoner, Proc. R. Soc. London Ser. A **165**, 372 (1938).
[26] R. Q. Hood and L. M. Falicov, Phys. Rev. B **46**, 8287 (1992).
[27] The particular result $(\Delta\rho/\rho)=0$ is valid for $S_M=S_m=1$ and for any combination of geometric and intrinsic metal parameters as long as $\tau_{i\sigma}=\tau_\sigma$, i.e., the relaxation times for each spin is *the same* in all layers of the system.
[28] S. B. Soffer, J. Appl. Phys. **38**, 1710 (1967).
[29] V. Bezák and J. Krempaský, Czech. J. Phys. B **18**, 1264 (1968).
[30] V. Bezák, M. Kedro, and A. Pevala, Thin Solid Films **23**, 305 (1974).
[31] R. Q. Hood, L. M. Falicov, and D. R. Penn, Phys. Rev. B **49**, 368 (1994).
[32] It should be noted that the channeling effect, *per se*, does not necessarily lead to a GMR, as can be seen from the case shown in Fig. 3 [$(\Delta\rho/\rho)=0$ for $S_M=S_m=1$; the current distribution is nevertheless concentrated in the ferromagnetic layers]. The GMR appears when, in the parallel arrangement, there is channeling for *only one spin* and diffuse interface scattering for the other one. In that case, in the antiparallel arrangement, both spins partake in the diffuse scattering, and the long electron trajectories (and the channeling) are lost.

Giant magnetoresistance in Co/Cu multilayers after annealing

T. R. McGuire, J. M. Harper, C. Cabral, Jr., and T. S. Plaskett[a)]
IBM Research Division, Thomas J. Watson Research Center, P.O. Box 218, Yorktown Heights, New York 10598

Multilayer films of [Co 10 Å/Cu(t)]$_{64}$ with copper thicknesses from $t=10$ to 29 Å annealed for 1 h at temperatures about 350 °C showed a decrease in sample resistivity at 4.2 K. The giant magnetoresistance (GMR) maximums for as-deposited films at $t=10$ Å and $t=23$ Å shifted with annealing. The GMR decreased for $t=10$ Å and $t=23$ Å but increased for $t=19$ Å and $t=29$ Å indicating a complex behavior with annealing. Similarities with granular films are discussed.

I. INTRODUCTION

It is known that both granular Cu-Co films[1–3] and multilayer films[4,5] undergo large changes in giant magnetoresistance (GMR) with annealing. Hylton *et al.*[4] found that sputtered multilayers of $Ni_{80}Fe_{20}$/Ag have no significant magnetoresistance in the as-prepared state but after annealing at just above 300 °C a GMR of over 5% at room temperature is observed. This GMR is attributed to the breakup of NiFe layers because of diffusion of the Ag layer into grain boundaries and cracks in the NiFe layers. A discontinuous magnetic layer is created with a distribution of magnetization directions which increases the spin-dependent electron scattering causing GMR.

For the Cu-Co system consider first the granular films where annealing precipitates Co particles from the Cu matrix. These particles cause large GMR from conduction electron spin-dependent scattering attributed mainly at the interface of the Co particle with the Cu matrix. In addition resistivity (ρ) decreases in annealed granular Cu-Co films because of the increased purity of the Cu matrix as the Co precipitates out.

Annealed multilayers of Cu/Co have been studied by Zhang *et al.*[5] They find for a series of films with varying Cu thickness that there is a decrease in resistivity with increasing annealing temperature (T) up to 300 °C. There is also a decrease in GMR at 300 °C but in some cases an increase is found at lower T. The GMR results are mainly for room temperature.

It is the objective of the present work to study a similar series of films as reported by Zhang *et al.*[5] with emphasis on low temperature measurements where the GMR is largest. Data are given in units of specific resistivity (ρ) and volume magnetization (M) to help in interpretation and for comparison with previous work.

II. EXPERIMENTAL RESULTS AND DISCUSSION

Our multilayer films are deposited on glass substrates by magnetron sputtering in a 3 m Torr Ar atmosphere. Multilayer structures are made[6,7] using computer control where substrates at ambient temperature are moved sequentially over each gun to deposit the Co or Cu layer. The films have the form Cu 10 Å/[Co 10 Å/Cu(t)]$_{64}$ where the Cu thickness t has values ranging from 10 to 29 Å. We previously reported[6] that Co/Cu multilayer films studied by high angle x-ray and transmission electron microscopy were found to be polycrystalline with a (111) texture and the Co had the fcc structure.

The films are annealed in a vacuum furnace at 350 °C. This temperature was based on that used in other studies[3,4] as well as from a continuous *in situ* measurement of ρ vs T for the multilayer film (Co 10 Å/Cu 23 Å)$_{64}$ which showed a linear rise in ρ up to 235 °C followed by a strong decrease at higher temperatures. Two films for each Cu thickness are annealed; a rectangular one for M and a disc sample for ρ. They were both measured prior to annealing.

Magnetic measurements are made with a "quantum design" superconducting quantum interference device magnetometer with the applied field H parallel to the plane of the film. The film is initially cooled in a -20 kOe field and then measured over the range $H=\pm 20$ kOe. The total volume of Co is determined from the rectangular area (approximately 0.55×1.2 cm^2) and Co thickness which is 640 Å for this series of films. Measured values of saturation volume magnetization M at 4.2 K are listed in the Table I. The saturated value for bulk Co at 4.2 K is $M_0=1430$ emu/cm^3, the listed values are scattered about the bulk value. Because of this variation of M we could not determine if there was any

TABLE I. Data at 4.2 K for as-deposited (d) and annealed (a) [Co 10 Å/Cu(t)]$_{64}$ films.[a]

Films Cu(t)	ρ_{max} ($\mu\Omega$ cm)	ρ_{min} ($\mu\Omega$ cm)	GMR (%)	w (kOe)	M_0 (emu/cm^3)
10 Å d	24.5	18 8	36.3	2.6	1350
a	15.8	14.0	12.9	3.5	1350
19 Å d	14.1	13.1	7.4	0.5	1450
a	9.4	6.9	36.8	0.9	1470
21 Å d	15.9	12.4	28.0	0.3	1360
a	10.1	8.8	14.8	0.5	1360
23 Å d	12.8	9.0	42.0	0.7	1430
a	6.0	5.0	20.0	0.8	1460
25 Å d	10.8	8.6	26.0	0.6	1430
a	7.4	6.0	23.0	0 8	1360
29 Å d	8.9	8.1	9.9	0.4	1440
a	9.0	7.6	18.0	0.8	1440

[a]The films are annealed in a vacuum furnace at 350 °C.

[a)]Also at Instituto de Engenharia de Sistemas e Computadores, 1000 Lisbon, Portugal.

 0021-8979/94/76(10)/6601/3/$6.00 © 1994 American Institute of Physics

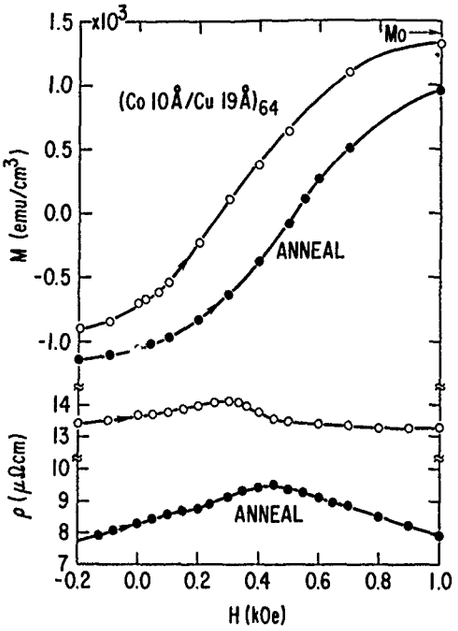

FIG. 1. Magnetization M and resistivity ρ at 4.2 K of as-deposited and annealed multilayer film (Co 10 Å/Cu 19 Å)$_{64}$ as a function of applied field H. The saturation value M_0 for Co is marked by an arrow.

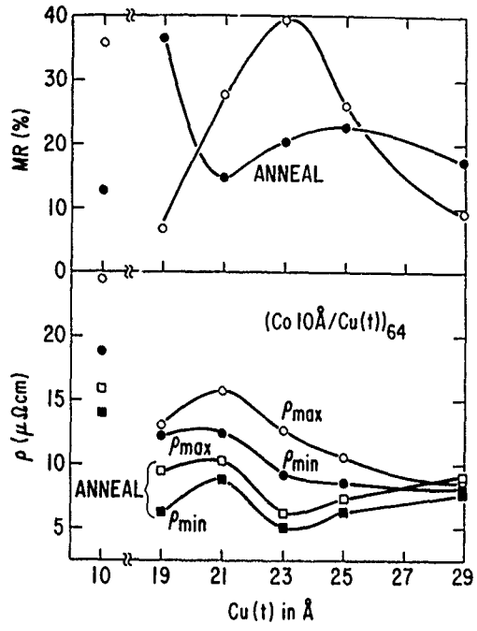

FIG. 3. Resistivity at 4.2 K for various Cu(t) thicknesses. GMR is calculated from $(\rho_{max}-\rho_{min})/\rho_{min}$.

change in saturation M before and after annealing.

Figures 1 and 2 shows M vs H plots at low values of H taken from a complete magnetization curve for as deposited and annealed films with $t=19$ Å and Fig. 2 for $t=23$ Å. These plots illustrate a general feature that the annealed samples all saturate more slowly and have a slightly higher coercive field (H_c) than the as-deposited samples. At

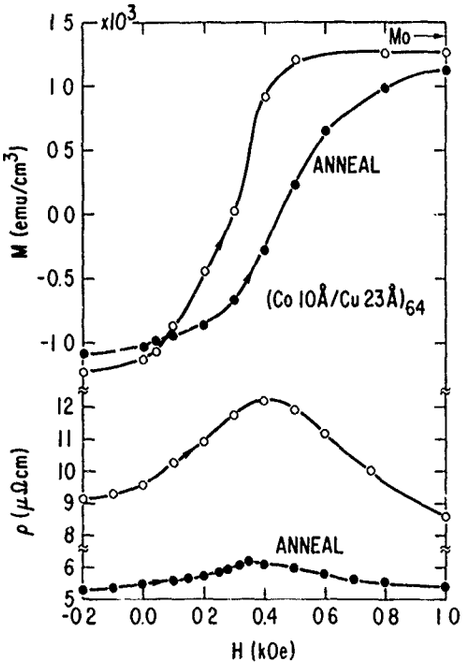

FIG. 2. Magnetization M and resistivity ρ at 4.2 K of as-deposited and annealed multilayer film (Co 10 Å/Cu 23 Å)$_{64}$ as a function of applied field H. The saturation value M_0 for Co is marked by an arrow.

$H=1000$ Oe the as-deposited multilayer film has almost reached saturation while the annealed film is several percent below saturation.

Figures 1 and 2 also show resistivity as a function of field for the respective compositions and annealed state. Resistivity is measured on a disc sample using the van der Pauw method over the range $H=\pm 18$ kOe. In both Figs. 1 and 2 the maximum in resistivity (ρ_{max}) is approximately at H_c. Both ρ_{max} at H_c and ρ_{min} at $H=18$ kOe are listed in the Table I. The ratio $(\rho_{max}-\rho_{min})/\rho_{min}$ gives the GMR and this is tabulated as MR(%). We note that MR(%) increases with annealing for the $t=19$ Å but MR% decreases for $t=23$ Å. The annealed magnetization curves, however, look about the same for both thicknesses. Figure 3 shows ρ_{max}, ρ_{min}, and MR(%) vs Cu(t). Compositions $t=10$ Å and $t=23$ Å correspond to the first two peaks[4,7] in GMR as a function of t for as-deposited films. As seen in Fig. 3 the peaks in GMR are shifting with annealing.

Another change that takes place during annealing is the width of the ρ vs H curve. As shown on Figs. 1 and 2 the width of the maximum region in the annealed films has increased somewhat. We define the half-width (w) of the ρ vs H curve as that width in kOe midway between ρ_{max} and ρ_{min}. We find that w increases at 4.2 K from about 2.6 to 3.5 kOe for $t=10$ Å and 0.7 to 0.8 kOe for $t=23$ Å with annealing as listed in Table I. This increase in w is opposite to that found by Hylton *et al.*[4] in NiFe/Ag multilayers where w narrowed with annealing.

The decrease in ρ in Cu/Co multilayers has been attributed in part to grain growth by Zhang *et al.*[4] We suggest also there is the possibility that any mixing of the Cu and Co at the interface in the as-prepared film is now changed in some way by Co precipitation from annealing as found in granular films. Since the spin-dependent scattering of the conduction

electrons is chiefly involved with the interface[8] this could cause a change in GMR depending on initial conditions of the as-deposited film and the annealing temperature. Zhang *et al.* found that room temperature GMR increased at annealing temperatures of 250 °C in some of their compositions. It appears that the annealing has a complex behavior and that there may exist a sensitive threshold of temperatures which gives the best interface conditions for large GMR.

In addition we had previously pointed out[6] that the shape of the ρ vs H curve for [Co 10 Å/Cu 10 Å]$_{64}$ is within a few percent identical with granular Cu-Co films.[2] This similarity suggests that as-deposited multilayer [Co 10 Å/Cu(t)]$_n$ may have noncontinuous Co layers that act like a granular particulate. After annealing the discontinuities in the Co layer are no longer the same size and GMR is decreased but in some cases an optimum is reached in terms of discontinuities as well as interface conditions and GMR is increased. A series of annealing temperatures for each composition are needed to determine the best T to give maximum GMR.

III. SUMMARY

(a) The peak value of GMR with Cu thickness shifts with annealing at 350 °C.

(b) There is a decrease of film resistivity as much as 50% with annealing at 350 °C.

(c) The half-width of the magnetoresistance vs field curve increases with annealing and this increase correlates with the slower increase in films magnetization with field.

[1] J. X. Xiao, J. S. Jiang, and C. L. Chien, Phys. Rev. Lett. **68**, 3749 (1992).
[2] A. E. Berkowitz, M. J. Carey, J. R. Michell, A. P. Young, S. Zhang, F. E. Spada, F. T. Parker, A. Hutten, and G. Thomas, Phys. Rev. Lett. **68**, 3745 (1992).
[3] R. J. Gambino, T. R. McGuire, J. M. Harper and C. Cabral, J. Appl. Phys. **75**, 15 May (1994).
[4] T. L. Hylton, K. R. Coffey, M. A. Parker, and J K. Howard, Science, **261**, 1021 (1993).
[5] H. Zhang, R. W. Cochrane, Y. Huai, Ming. Mao, X. Blan, and W. B. Muir, J. Appl. Phys. **75**, 15 May (1994).
[6] T. S. Plaskett and T. R. McGuire, J. Appl. Phys. **73**, 6378 (1993).
[7] T. R. McGuire and T. S. Plaskett, IEEE Trans. Magn. **MAG-28**, 2748 (1992).
[8] P. M. Levy, S. Zhang, and A. Fert, Phys. Rev. Lett. **65**, 1643 (1990).

Magnetoresistance and magnetization oscillations in Fe/Cr/Fe trilayers

R. Schad, C. D. Potter, P. Belien, G. Verbanck, V. V. Moshchalkov, and Y. Bruynseraede
Laboratorium voor Vaste-Stoffysika en Magnetisme, K.U. Leuven, Celestijnenlaan 200 D, B-3001 Leuven, Belgium

M. Schäfer, R. Schäfer, and P. Grünberg
IFF-FZ, Kernforschungsanlage Jülich, Postfach 1913, D-52425 Jülich, Germany

The 2-ML (monolayer) oscillation period has been observed in the magnetization as well as in the magnetoresistance of Fe/Cr/Fe trilayers. Kerr effect measurements were performed in order to verify the periodicity and determine the kind of the coupling between the Fe layers. The magnetoresistance loops show characteristic steps at magnetic field values at which the size of the magnetization changes.

I. INTRODUCTION

Magnetic multilayers have attracted much attention since they display a wide variety of interesting physical properties.[1–11] In the Fe/Cr system, the coupling between adjacent Fe layers was found to switch between ferromagnetic and antiferromagnetic depending on the thickness of the Cr interlayer.[1] This was seen first in a giant magnetoresistance, the amplitude of which oscillated with the thickness of Cr with a period of 18 Å.[2,3] Magneto-optic Kerr effect measurements (MOKE) confirmed this period for the coupling between Fe layers.[5] With improvements in the layering quality, an additional short period oscillation was seen in Fe/Cr/Fe trilayers, probed by scanning electron microscopy with spin polarization analysis (SEMPA).[9] The short period oscillation was found to have a length of two monolayers and be commensurate with the spin density wave found in bulk Cr.[12,13] However, the SEMPA and MOKE studies were performed on trilayers which were grown on Fe whiskers or thick metallic buffer layers, making these samples unsuitable for electrical transport studies.

We report here on electrical transport and magneto-optical studies performed on Fe/Cr/Fe trilayers grown epitaxially on MgO(100) substrates without any buffer layer. Both the magnetoresistance (MR) and the MOKE measurements clearly display the existence of the short period oscillation. At the same time the MOKE measurements are used to identify the nature of the coupling between the Fe layers. This also allows the direct comparison of the Kerr loops with the magnetic field dependence of the MR. The magnetoresistance displays steps at values of the magnetic field at which the absolute value of the magnetization of the sample changes.

II. SAMPLE PREPARATION

The Fe/Cr/Fe trilayers were prepared in a Riber molecular beam epitaxy (MBE) deposition system (base pressure 2×10^{-11} mbar) equipped with two electron-beam guns and four Knudsen cells. Fe and Cr (both starting materials of 99.996% purity) were *e*-beam evaporated at a rate of 1 Å/s on MgO (100) substrates held at 150 °C. A homemade feedback control system using Balzers quadrupole mass spectrometers was utilized to stabilize the rate to within 1%. *In situ* reflection high-energy electron diffraction (RHEED) was used to monitor the quality of the substrate, the epitaxial relationship and the quality of the growth.

The Fe thickness of the top and bottom layers was 50 Å and the Cr thickness varied, respectively, from 4 to 20 Å and from 0 to 40 Å with slopes of 1 and 2 Å of Cr per mm for the two samples. The wedges were prepared using a computer controlled movable shutter. The wedge direction was chosen parallel to the [010] direction of the Fe/Cr layers (the [011] direction of the MgO) in order to facilitate alignment with the magnetic field during the MOKE and MR experiments. The trilayer was then covered with 30 Å of Ag as protection against oxidation of the Fe.

First, MOKE experiments were performed at room temperature, using a Kerr effect configuration which is sensitive for the longitudinal Kerr effect. The field was applied parallel to the easy [010] axis of the Fe layers. A micrometer screw was used to move the wedged sample through the laser beam, with an alignment accuracy of 10 μm. The coupling strength between the Fe layers was estimated from the saturation field of the Kerr rotation.

Subsequently, one sample was patterned using standard photolithographic techniques to produce a stripe pattern. The stripes used for transport measurements were 80 μm wide and about 1 cm long and separated from each other by about 30 μm. Each stripe has a Cr thickness variation of 0.2 Å, due to the wedge itself and any possible misalignment during the lithography procedure. To measure the MR, leads were attached to the sample by ultrasonic wire bonding. Four-probe measurements were performed at 4.2 K in a cryostat equipped with a superconducting magnet. Since the signal was relatively small, a Linear Research bridge was used to measure the resistance versus field data. The sample was aligned in such a way that the Fe [010] direction was parallel to the field.

In the following the magnetoresistance is defined as the ratio $\Delta\rho/\rho_s$, with $\Delta\rho=\rho_0-\rho_s$, where ρ_0 is the resistivity at $H=0$ Oe and ρ_s is the saturation resistivity at $H=3$ kOe. We define the magnetization saturation field as the field, H_s at which the Kerr signal reaches its saturation value.

III. RESULTS AND DISCUSSION

Figure 1 shows a plot of H_s from the MOKE measurements and the MR of the transport measurements versus Cr

 0021-8979/94/76(10)/6604/3/$6.00 © 1994 American Institute of Physics

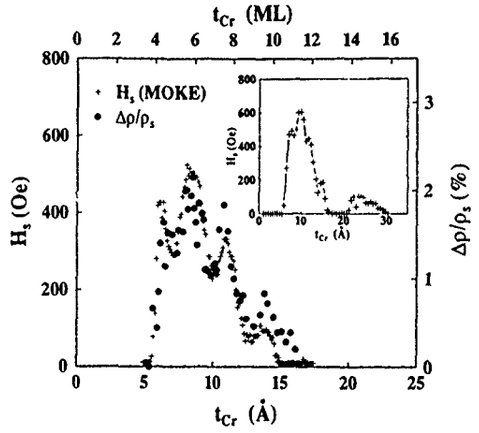

FIG. 1. The saturation field H_s (crosses, scale at left) for the Kerr rotation, and MR (filled circles, scale at right) for the magnetoresistance vs Cr interlayer thickness in angstroms and monolayers. The inset shows a plot of the saturation fields obtained from the MOKE measurements over a wider range of t_{Cr}.

thickness in both angstroms and monolayers. Both sets of data clearly show four peaks in the range 4 to 10 ML (monolayers). This 2-ML oscillation period is in agreement with the value reported from SEMPA measurements.[9] The inset in Fig. 1 shows a plot of the saturation fields over a wider range of t_{Cr} determined from the MOKE measured on a sample with a larger variation in t_{Cr}. The oscillation with the period of 18 Å in t_{Cr} is clearly visible.

Figure 2 shows typical MR and MOKE hysteresis curves for different values of t_{Cr}. With increasing t_{Cr} the nature of the coupling changes from biquadratic coupling [at about t_{Cr}=7 Å, see Fig. 2(a)], over to a combination of bilinear and biquadratic coupling [around t_{Cr}=8.5 Å, see Fig. 2(b)] to again biquadratic coupling [at t_{Cr}=13 Å, see Fig. 2(c)]. The arrows on the figures indicate the orientation of the magnetization of the top and bottom Fe layers.

In the case of biquadratic coupling, there is a remnant field at zero applied field and the magnetization vectors in the layers of Fe are not parallel, but differ by 90°. As the field increases, the magnetization of the layers becomes aligned parallel at the saturation field. The sample with t_{Cr}=8.5 Å is antiferromagnetically coupled at zero field, and switches to 90° coupling at a higher field before being saturated at H_s. The 90° coupling is explained in terms of biquadratic coupling possibly due to a roughness at the interfaces of 1 ML monolayer.[14] In all cases, the total strength of the coupling is well described by the saturation field. The surface energy per unit area as a function of the individual coupling strengths is given by

$$E_s = -J_1 \cos\theta - J_2 \cos^2\theta,$$

where J_1 and J_2 are the bilinear and biquadratic coupling strengths and θ is the angle between the magnetization vectors in the two Fe layers. From the MOKE measurements, J_1 and J_2 can be determined. For example, at t_{Cr}=8.5 Å, J_1 and J_2 were found to be, respectively, -0.46 mJ/m^2 and -0.20 mJ/m^2.

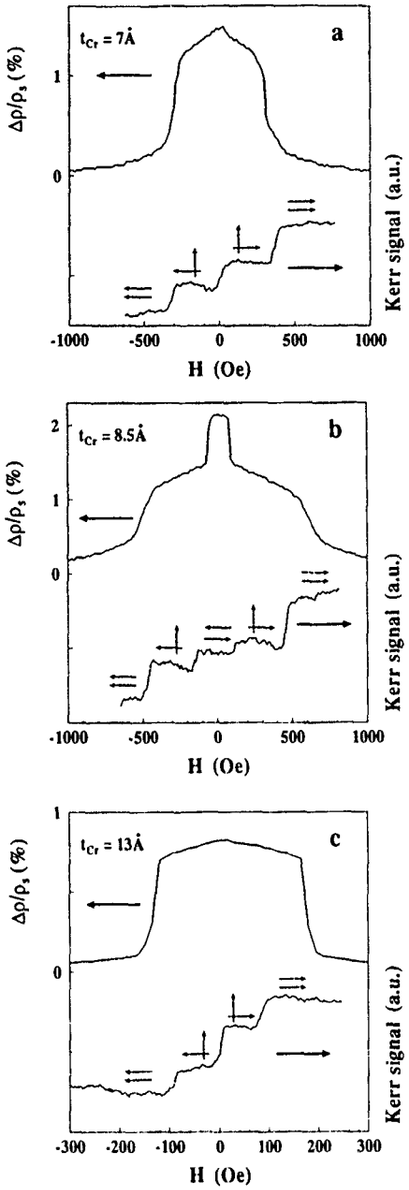

FIG. 2. MR at 4.2 K and Kerr effect at 300 K over applied magnetic field of Fe/Cr/Fe trilayers for three different values of t_{Cr}: (a) t_{Cr}=7 Å, showing biquadratic coupling; (b) t_{Cr}=8.5 Å, showing a combined bilinear and biquadratic coupling; (c) t_{Cr}=13 Å, showing biquadratic coupling. The arrows indicate the direction of magnetization of the two Fe layers. The corresponding MR loops show steps at field values at which the size of the magnetization changes.

Figure 2 also shows the measured MR loops for the different values of t_{Cr}. In the case of biquadratic coupling [Figs. 2(a) and 2(c)] the MR displays steps at values of the magnetic field at which the 90° coupling is saturated. The reversal of the sign of the magnetization at zero field produces only a step in the Kerr loop but not in the MR. This can be easily explained by the fact that the MR is sensitive only to changes in the size of the magnetization but is not sensitive to changes of its orientation.

In Fig. 2(c) the magnetic field values of the steps in the Kerr effect (measured at 300 K) and the MR (measured at 4.2 K) do not match, a fact which is likely due to the tem-

perature dependence of the coupling constants. This temperature dependence is changing with t_{Cr},[15] which is in qualitative agreement with the decrease of H_s with increasing temperature at t_{Cr}=13 Å [Fig. 2(c)].

The MR loop at t_{Cr}=8.5 Å [Fig. 2(b)], corresponding to the maximum of the MR oscillations, reproduces all four steps visible in the magnetization. Each of the steps in the magnetization corresponds to a change in its absolute value and accordingly causes a change in the magnetoresistance. Small differences in the values of the switching fields can be explained by the different coupling strength due to the different measuring temperature.

The MR curves of Fe/Cr superlattices do not display sharp steps but have more bell-shaped or triangular-field dependencies[2,16,17] This may be due to an averaging effect over many layers which have different coupling strengths. A bell-shaped MR curve would correspond to either biquadratic coupling as in Fig. 2(a) or to bilinear coupling which should naturally produce a similar shape. The triangular shape would be a reminiscent of the combined bilinear and biquadratic coupling as in Fig. 2(b).

IV. CONCLUSION

We have observed the 2-ML period in the oscillations of the magnetoresistance in Fe/Cr/Fe trilayers. This periodicity arises from the antiferromagnetism of the Cr interlayer. MOKE measurements indicate that the Fe layers can be aligned parallel, antiparallel, or 90° degrees off. The magnetoresistance displays characteristic steps at values of the applied magnetic field at which the amplitude of the magnetization changes.

This work is financially supported by the Belgian Concerted Action (GOA) and Interuniversity Attraction Poles (IUAP) programs. RS, CDP, and GV are Research Fellows supported by respectively the European Community, the Research Council of the Katholieke Universiteit Leuven and the Interuniversity Institute for Nuclear Science.

[1] P. Grünberg, R. Schreiber, Y. Pang, M. B. Brodsky, and H. Sowers, Phys. Rev. Lett. **57**, 2442 (1986).
[2] M. N. Baibich, J. M. Broto, A. Fert, F. Nguyen Van Dau, F. Petroff, P. Etienne, G. Creuzet, A. Friederich, and J. Chazelas, Phys. Rev. Lett. **61**, 2472 (1988).
[3] S. S. P. Parkin, N. More, and K. P. Roche, Phys. Rev. Lett. **64**, 2304 (1990).
[4] J. J. Krebs, P. Lubitz, A. Chaiken, and G. A. Prinz, J. Appl. Phys. **67**, 5920 (1990).
[5] P. Grünberg, J. Barnas, F. Saurenbach, J. A. Fuss, A. Wolf, and M. Vohl, J. Magn. Magn. Mater. **93**, 58 (1991).
[6] A. Barthélémy, A. Fert, M. N. Baibich, S. Hadjoudj, F. Petroff. P. Etienne, R. Cabanel, S. Lequien, F. Nguyen Van Dau, and G. Creuzet, J. Appl. Phys. **69**, 969 (1990).
[7] S. S. P. Parkin, Phys. Rev. Lett. **67**, 3598 (1991).
[8] S. Demokritov, J. A. Wolf, and P. Grunberg, Europhys. Lett. **15**, 881 (1991).
[9] J. Unguris, R. J. Celotta, and D. T. Pierce, Phys. Rev. Lett. **67**, 140 (1991).
[10] W. F. Egelhoff, Jr. and M. T. Kief, Phys. Rev. B **45**, 7795 (1992).
[11] L. Piraux, A. Fert, P. A. Schroeder, R. Laloee, and P. Etienne, J. Magn. Magn. Mater. 110, L27 (1993).
[12] E. Fawcett, Rev. Mod. Phys. **60**, 209 (1988).
[13] J. Unguris, R. J. Celotta, and D. T. Pierce, Phys. Rev. Lett. **69**, 1125 (1992).
[14] J. C. Slonczewski, Phys. Rev. Lett. **67**, 3172 (1991).
[15] J. A. Wolf, Q. Leng, R. Schreiber, P. A. Grunberg, and W. Zinn, J. Magn. Magn. Mater. **121**, 253 (1993).
[16] E. E. Fullerton, M. J. Conover, J. E. Mattson, C. H. Sowers, and S. D. Bader, Phys. Rev. B **48**, 15 755 (1993).
[17] W. Folkerts, W. Hoving, and W. Coene, J. Appl. Phys. **71**, 362 (1992).

Structural and magnetic properties of Co/Ag multilayers

E. A. M. van Alphen, P. A. A. van Heijden, and W. J. M. de Jonge
Department of Physics, Eindhoven University of Technology, P.O. Box 513, 5600 MB Eindhoven, The Netherlands

The structural properties and growth of sputtered Co/Ag multilayers were studied with nuclear magnetic resonance. For samples with a nominal Co thickness of less than 10 Å the Co grows in three-dimensional islands. If the nominal Co thickness is larger than 10-Å continuous Co layers are formed. The relation of the structural properties with magnetization and magnetoresistance is discussed.

Currently Co/Ag multilayers and Co-Ag alloys are widely studied because of their giant magnetoresistance (MR) effects.[1–3] Since the magnetoresistance and the magnetic properties are strongly related to the structure of the magnetic layer and the topology of the interfaces, the present paper focuses on the structural information as can be obtained from ^{59}Co nuclear magnetic resonance (NMR) studies. We also discuss the influence of annealing on the magnetoresistance. The strain in these Co/Ag multilayers has been studied previously.[4]

The Co/Ag multilayers were made by magnetron sputtering on Si [100] at the Michigan State University. The deposition rate was 4 Å/s for Co and 8 Å/s for Ag. The Ag layer thickness was 20 Å for all the samples, the Co thickness varied between 4 and 100 Å. The number of repetitions was 100. X-ray diffractometry confirmed the superlattice modulations and showed [111] texture.

The NMR experiments were performed with a coherent spin echo spectrometer at a temperature of 1.5 K. Magnetic fields, larger than the saturation field, were applied parallel to the film plane. The hyperfine field B_{hf} was obtained from the resonance field B_r and the frequency f using the relation $2\pi f=\gamma(B_{hf}-B_r)$, where γ is the ^{59}Co nuclear gyromagnetic ratio ($\gamma/2\pi=10.054$ MHz/T).[5] The transverse magnetoresistance was measured at room temperature in fields up to 1.3 T using a standard four-probe method.

Figure 1 shows the NMR spectra of the $100\cdot(x$ Å Co+20 Å Ag) multilayers with $x=4$, 8, 10, 12, and 15 Å Co. The integral of the intensity is normalized to the nominal Co thickness. Apart from the intensity which arises from bulk Co nuclei around 21 T, a clear contribution at lower fields can also be observed. This intensity at lower fields is believed to originate from Co atoms at or near the interfaces (Co atoms with one or more Ag neighbors). The maximum at 17.5 T probably arises from Co atoms at locally flat (111) interfaces. Both the interface and the bulk lines are much broader than the lines found in Co/Ni and Co/Cu multilayers were the structure of the Co is mainly fcc.[5] This is because the Co in Co/Ag multilayers is a mixture of fcc Co, hcp Co, and Co in stacking faults.

Figure 2 gives a survey of the different contributions to the spectrum as a function of the Co thickness. The intensities are obtained by dividing the spectra in two parts and integration of these parts (interface part 15–19.5 T, bulk part 19.5–23 T). Changing the boundary between the bulk and the interface part a little bit, as well as comparing the height of the interface and the bulk line, give similar results.

Remarkable is the presence of the bulk Co signal for the sample with a nominal thickness of 4 Å (2 monolayers) Co (Fig. 1). The presence of this signal demonstrates that the Co did not grow in the layer-by-layer mode but in three-dimensional islands, becuase in the case of layer-by-layer growth every Co atom would have Ag neighbors. If the Co layer thickness is increased from 4 to 8 to 10 Å both the interface and the bulk intensity increases and the relative increase is approximately the same for both. Consequently, this implies that the volume to surface ratio remains constant [see Fig. 2(c)]. This behavior can only be understood if, in the nominal Co thickness range 4–10 Å, the growth mode is such that the number of three-dimensional islands increases or the islands become larger. (This last option is only possible when the influences of the edges of the islands are negligible.) The bulk intensity [Fig. 2(b)] increases from 4 to 10 Å Co with a certain slope. The fact that this line extrapolates approximately to zero also indicates that the growth cannot be layer-by-layer [such a growth would result in a straight line with a positive intersection with the Co thickness axis; 4 Å for perfectly smooth layers and more than 4 Å for layers with a certain roughness (Ref. 5)].

For Co thicknesses increasing from 10 to 15 Å the intensity of the interface remains approximately constant [Fig. 2(a)] while the amount of Co atoms in the bulk increases [Fig. 2(b)]. The constant intensity of the interface shows that for Co thicknesses larger than 10 Å apparently a continuous Co layer is formed and the islands mentioned before have merged and cover the whole layer at a nominal thickness of 10 Å. This implies that the Co layers are build with clusters of Co with a thickness of about 5 ML (monolayers) in the nominal range up to 10 Å Co. As an additional check on this conclusion we can compare the interface to bulk ratio of the spectra of 4, 8, and 10 Å Co. Clusters with a Co thickness of 5 ML would have at least 2-ML Co at the interface and at most 3 ML bulk Co resulting in a bulk to interface intensity ratio of at most 3/2 (if the interfaces are sharp and the islands are relatively large). Roughness as well as a finite lateral size would result in a ratio smaller than 3/2. The measured bulk/interface ratio of about 1 [Fig. 2(c)] fits reasonably in this model. If we assume that the islands are cubes or cylinders with a thickness of 10 Å and implement the experimental bulk to interface ratio of 1, we can estimate the lateral dimensions of the islands. This approximation results in typical lateral length scales of about 50 Å. Roughness would decrease this number.

In this same (simple) growth model we can also predict

 0021-8979/94/76(10)/6607/3/$6.00 © 1994 American Institute of Physics

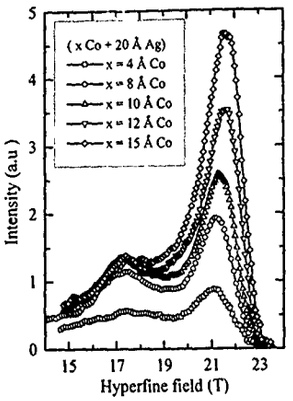

FIG. 1. NMR spectra measured at 1.5 K of 100·(x Å Co+20 Å Ag) multilayers. The integral (between 15 and 23 T) of the spectra are normalized to the nominal Co thickness. The spectra are corrected for enhancement.

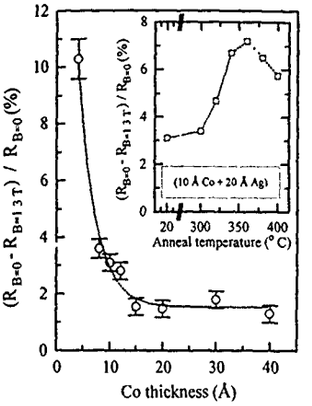

FIG. 3. Magnetoresistance as a function of the nominal Co thickness. The inset shows the MR of (10 Å Co+20 Å Ag) as a function of the anneal temperature. All MR measurements were performed at room temperature with the applied field parallel to the film plane.

the increase of the bulk to interface ratio above the nominal thickness of 10 Å since in our model all Co above this thickness contributes to the bulk intensity. The resulting prediction is shown by the solid line in Fig. 2(c) and fits remarkably well with the data for Co thicknesses just above 10 Å. If the Co thickness is further increased (t_{Co}>15 Å) the increase of the interface intensity [Fig. 2(a), interfaces become rougher] brings about a deviation of the data with this theoretical line.

The growth mode of the Co/Ag multilayers observed in the present experiments is in accordance with the expectations based on a comparison of the surface energies of Co and Ag.[6] Because the surface energy of Co is much larger than the surface energy of Ag and because the atomic interaction between the Co and the Ag atoms is weak,[7] Co is expected to grow in three-dimensional islands on Ag (Volmer–Weber mode) and Ag is expected to grow in the layer-by-layer mode on Co. Earlier reflection high-energy electron diffraction (RHEED) studies on molecular beam epitaxy (MBE) grown Co/Ag multilayers[8] yielded, for some growth temperatures, similar results, although in this paper no information is given about the size of the clusters.

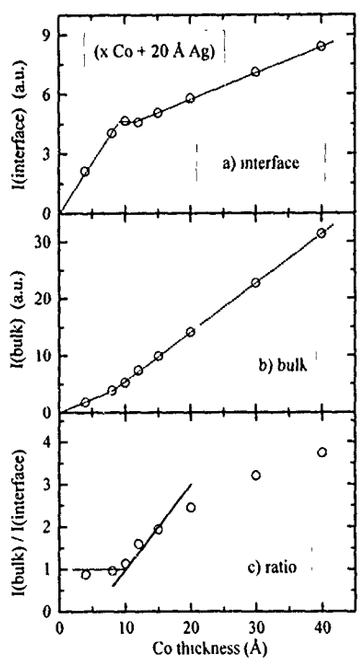

FIG. 2. Intensity of the interface part (a), the bulk part (b), and the ratio between the bulk and the interface part (c), as a function of the nominal Co thickness. The dotted lines are guides to the eye, the solid line in Fig. 2(c) is in accordance with the model discussed in the text.

The magnetoresistance as well as the magnetization of the present series of samples has been investigated.[9] We will restrict ourselves here to a few general comments specifically in relation to the structural data observed by NMR.

The magnetoresistance of these Co/Ag multilayers, defined as $(R_{B=0} - R_{B=1.3\ T})/R_{B=0}$, is shown in Fig. 3. The MR increases strongly for nominal Co thicknesses smaller than 10 Å. As we have seen this is the regime in which the Co layers are discontinuous. For nominal Co thicknesses larger than 10 Å (continuous Co layers) the MR is small and almost independent of the Co thickness. The larger MR for the discontinuous Co layers might be caused by mechanisms similar as reported by Hylton *et al.*[10] for the NiFe/Ag system; isolation of pinholes or interlayer magnetostatic coupling. One difference between the present Co/Ag system and the NiFe/Ag system is that now the transition from continuous to discontinuous layers is not achieved by annealing but is already present in the as deposited state (for t_{Co}<10 Å).

The restoration of interlayer (AF) coupling as deduced from the decrease of the remanent magnetization (M_r) in NiFe/Ag does not seem valid for Co/Ag. Although we observed in (Co/20 Å Ag) a strong decrease of M_r in the nominal t_{Co} range below 10 Å (when discontinuous layers are formed), we also found an identical decrease in a (6 Å Co+40 Å Ag) multilayer, where the interlayer coupling (if any) is weak. In our analysis the behavior of M_r is brought about by the change of anisotropy (magnetostatic as well as surface) when the continuous layer breaks up in (noninteracting) clusters. This ultimately results in almost isotropic

magnetization for the 4-Å Co system and an increase in MR due to the transition from a ferromagnetic layer system to an assembly of decoupled clusters. This effect is enhanced upon annealing as is corroborated by NMR.

A similar dependence of the MR on the Co thickness for Co/Ag multilayers is reported by Araki.[2] As a reason for the strong increase of the MR properties below 10 Å of Co an increase of the fcc phase of Co for thin Co layers is suggested. In Fig. 1, however, we can see that the line shape of the bulk part does not change when the Co layers become thinner. From this we can conclude that, for the present Co/Ag multilayers, the changes in the MR cannot be explained by change in the structure of the Co.

The inset of Fig. 3 shows the magnetoresistance of the Co/Ag multilayer with 10 Å Co and 20 Å Ag as a function of the anneal temperature. When the multilayer is annealed the MR first increases (from 3% to 7%), while for anneal temperatures higher than about 360 °C the MR decreases upon annealing. This behavior agrees with earlier results of Tosin *et al.*.[11]

In summary, we have shown with NMR that the growth of sputtered Co/Ag multilayers starts with a three-dimensional island growth of Co. For nominal Co thicknesses larger than 10-Å continuous Co layers are formed. The strong increase in the magnetoresistance for nominal Co thicknesses smaller than 10 Å is related to the transition from continuous to discontinuous Co layers in this thickness range. A more detailed paper on the MR of Co/Ag multilayers with discontinuous Co layers is planned.[9]

The authors gratefully acknowledge the Michigan State University, where the Co/Ag multilayers were produced in the sputtering system funded by the U.S. National Science Foundation under Grant No. DMR-9122614, and the MSU Center for Fundamental Materials Research.

[1] W. P. Pratt, Jr., S. F. Lee, J. M. Slaughter, R. Loloee, P. A. Schroeder, and J. Bass, Phys. Rev. Lett. **66**, 3060 (1991).
[2] S. Araki, J. Appl. Phys. **73**, 3910 (1993).
[3] J. A. Barnard, S. Hossain, M. R. Parker, A. Wakins, and M. L. Watson, J. Appl. Phys. **73**, 6372 (1993).
[4] E. A. M. van Alphen, S. G. E. te Velthuis, H. A. M. de Gronckel, K. Kopinga, and W. J. M. de Jonge, Phys. Rev. B (to be published).
[5] H. A. M. de Gronckel and W. J. M. de Jonge, *Magnetism and Structures in Systems of Reduced Dimension*, edited by R. F. C. Farrow *et al.* (Plenum, New York, 1993).
[6] E. Bauer and J. H. van der Merwe, Phys. Rev. B **33**, 3657 (1986).
[7] F. R. de Boer, R. Boom, W. C. M. Mattens, A. R. Meidema, and A. K. Niessen, *Cohesion and Structure* (North-Holland, Amsterdam, 1988), Vol. 1.
[8] K. Sakai and T. Kingetsu, J. Cryst. Growth **126**, 184 (1993).
[9] E. A. M. van Alphen and W. J. M. de Jonge (unpublished).
[10] T. L. Hylton, K. R. Coffey, M. A. Parker, and J. K. Howard, Science **261**, 1021 (1993).
[11] G. Tosin, L. F. Schelp, M. Carara, J. E. Schmidt, A. A. Gomes, and M. N. Baibich, J. Magn. Magn. Mater. **121**, 399 (1993).

Published without author corrections

Magnetic states of magnetic multilayers at different fields

P. A. Schroeder, S.-F. Lee, P. Holody, R. Loloee, Q. Yang, W. P. Pratt, Jr., and J. Bass
Department of Physics and Astronomy, and Center for Fundamental Materials Research, Michigan State University, East Lansing, Michigan 48824-1116

The resistance of an as-sputtered magnetic multilayer in zero applied magnetic field can be considerably different from the maximum resistance measured after the multilayer has been cycled to above its saturation field. We examine the relation between these two resistances in some Ag/Co, Cu/Co, and Cu/NiFe multilayers, and its implications for interpreting giant magnetoresistance.

The magnetoresistance (MR) of a magnetic multilayer composed of alternating thin layers of a ferromagnetic (F) and a nonmagnetic (N) metal is defined as $\mathrm{MR}(H)=[R(H)-R(H_s)]/R(H_s)$, where H_s is the in-plane magnetic field at which the resistance $R(H)$ saturates at its lowest value. This quantity can be measured with the current parallel (CIP-MR) or perpendicular (CPP-MR) to the layer planes. Figure 1 shows the resistance in CIP and CPP geometries, along with the total magnetization M parallel to the layer planes, for a Cu(6 nm)/Co(6 nm) multilayer as a function of H. We see that there are two different states of locally maximal MRs: one, labeled H_0, the as-grown state at $H=0$, which might be associated with the demagnetized state of the multilayer; and one at H_p, the state of maximum resistance after cycling to above H_s. H_p is close to the coercive field, H_c, where $M=0$. In this article, we provide some new experimental information about $\mathrm{MR}(H_0)$ and $\mathrm{MR}(H_p)$, to stimulate more thought about the significance of both quantities.

The largest MRs in magnetic multilayers occur when the N-metal layer thickness, t_N, is such that the magnetizations of neighboring F layers are aligned antiparallel (AP) to each other in zero field—antiferromagnetic (af) coupling. In this case, H_p is essentially zero, and $\mathrm{MR}(H_0)\approx\mathrm{MR}(H_p)$. This is the situation that is standardly modeled, because the magnetic states of the system are known at both limits of the MR. Unfortunately, af coupling gives large values of H_s, which make such multilayers unsuitable for most applications. There is thus interest in understanding the MR when there is only weak coupling between F layers, such as that illustrated in Fig. 1. From studies of oscillatory behavior in magnetic multilayers, we take this regime as $t_N \geq 6$ nm.[1,2]

The most direct attack upon the "weak coupling" regime was made by Zhang and Levy,[3] who proposed modeling the $H=H_c$, $M=0$ state as a superposition of statistically uncorrelated (SU) magnetic configurations that satisfy the condition $\Sigma M_i=0$. (M_i is the magnetization of individual layers.) They noted that the CPP-MR should be the same for the SU and AP states, but that the CIP-MR should be smaller for the SU than the AP state.

In the weak coupling regime, the CIP-MR has usually been evaluated at H_p, both because this state is reproducible after cycling to above H_s and because it occurs near H_c—i.e., near $M=0$. Zhang and Levy[3] have analyzed such data in terms of a SU state, and argued that such a state is needed to explain why the CPP-MR is usually so much larger than the CIP-MR. [We note that our experiments suggest that H_p is not identical to H_c, and $M(H_p)$ may be an appreciable fraction of $M(H_s)$.]

For the CPP-MR, in contrast, we have focused upon H_0[4,5] as the $M=0$, SU state, for two reasons: (1) $\mathrm{MR}(H_0)$ is usually larger than $\mathrm{MR}(H_p)$—and one expects the AP and SU states to have the highest possible MRs. (2) It fits better a data analysis[6] involving extrapolation from the af regime to the completely uncoupled regime, that we now describe. We and others have shown[5,7,8] that a two-current model, in which spin up and spin down electrons carry current independently through the multilayer, gives a good description of a wide range of CPP-MR data on Ag/Co,[5,6,9] Cu/Co,[6,9] and Cu/NiFe.[10] For multilayers in the AP or SU configurations, with fixed F metal thickness t_F and fixed total thicknesses t_T, this model predicts that the plot of the total resistance R_T versus number of bilayers N, should be a straight line with an intercept on the ordinate axis that can be independently determined. This straight line should pass through the data for AP states and for uncoupled SU states, but not those for which significant ferromagnetic coupling is present. Experimentally we find that such a line fits the data for H_0 much better than the data for H_p in Cu/Co,[6] where the differences between the two sets of data are large. The H_0 data for Cu/NiFe also fits this pattern but the distinction between the H_0 and H_p data is small.[11]

With this background we now turn to a more detailed examination of the ratio $\mathrm{MR}(H_0)/\mathrm{MR}(H_p)$ in our sputtered multilayers than has hitherto been presented. We first examine the ratio under different conditions in different multilayer systems, and then describe some preliminary tests we have made to see whether the H_0 states can be restored by demagnetizing a sample.

In Figs. 2(a), 2(b) we plot the ratio $\mathrm{MR}(H_0)/\mathrm{MR}(H_p)$ for a series of Ag/Co, Cu/Co, and Cu/NiFe samples with fixed $t_F=6$ nm, and with $t_F=t_N$, respectively.

For "uncoupled" samples, $t_N \geq 6$ nm, we see that most of the Ag/Co and Cu/Co data lie in a band around a ratio of 1.5 in Fig. 2(a) and around 2 in Fig. 2(b). Importantly, most of the CIP-MR data for Ag/Co behave very similarly to the CPP-MR data for both Ag/Co and Cu/Co. For these "uncoupled" samples, H_0 and H_p thus seem to have similar significance for the CPP- and CIP-MRs. This similarity rules out the possibility that the H_0 and H_p states are AP and SU states, respectively. For while in CIP this would result in $R(H_0)/R(H_p)>1$, in CPP the ratio would be 1. The situation for Cu/NiFe is more complex, with some data falling close to the data for Ag/Co and Cu/Co, and other data falling around

 0021-8979/94/76(10)/6610/3/$6.00 © 1994 American Institute of Physics

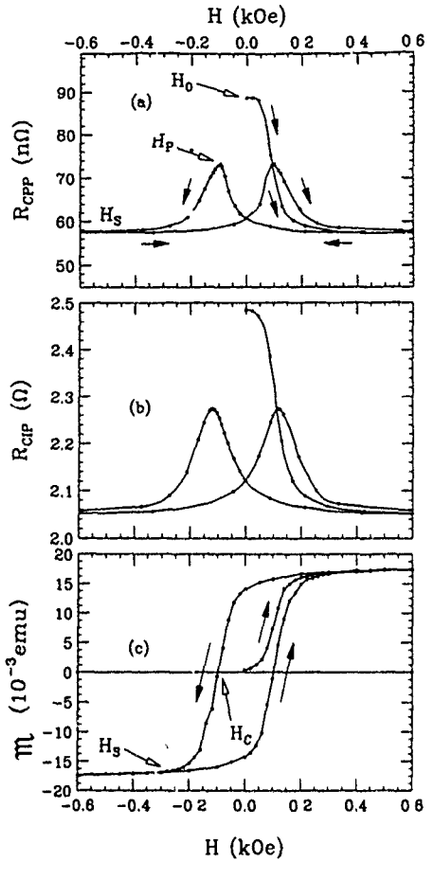

FIG. 1. (a) and (b) give the resistances of a [Cu(6 nm)/Co(6 nm)]×60 multilayer in the CPP and CIP geometries, respectively. (c) shows the magnetization of the same sample.

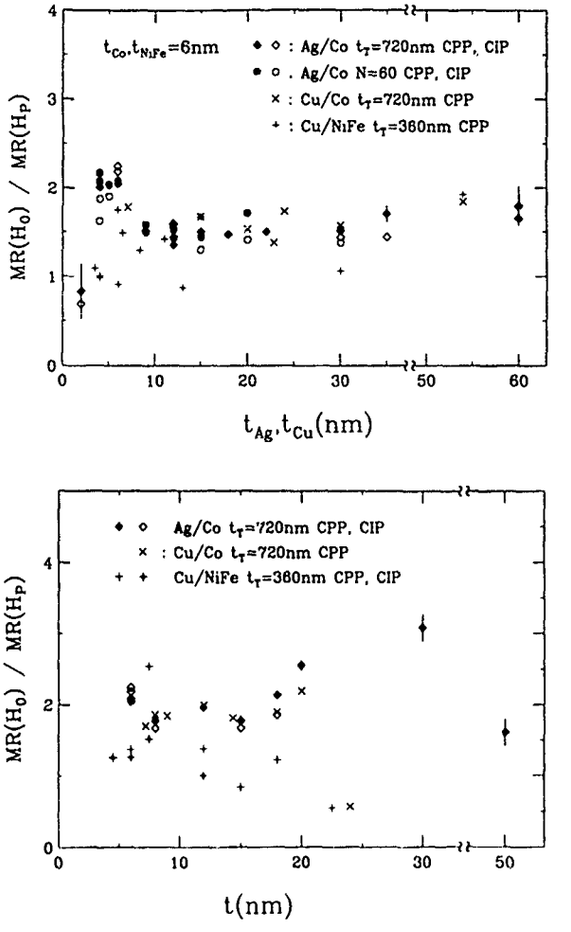

FIG. 2. (a) MR(H_0)/MR(H_p) plotted against thicknesses of Ag and Cu for a variety of multilayers with constant t_F=6 nm (b) MR(H_0)/MR(H_p) plotted against t, the thickness of both the F and N layers, for samples with $t=t_F=t_N$.

1. The reasons for these variations are not yet understood, but it should be noted that the uncertainties in the Cu/NiFe ratios are large partly because the MRs themselves are smaller than those for equivalent Ag/Co and Cu/Co samples.

For the samples with the thinnest Ag layers in Figs. 2(a) and 2(b), we find MR(H_0)/MR(H_p)<1. Values of this ratio below 1 have been found rather generally in Ag/Co samples with t_{Ag}<3 nm, as we will show elsewhere.[12] This may indicate ferromagnetic bridging between the Co layers. Apparently the values ~1.5–2 shown in Figs. 2(a) and 2(b) are representative only of weakly coupled samples.

If, as suggested at the beginning, we wish to associate the H_0 state with a demagnetized state, then we could hope to restore this state by demagnetizing the sample by cycling it through steadily decreasing fields. In Table I we give MRs evaluated for H for the states H_0, H_p, and H_0'' which is the zero field state after demagnetization. The first sample is strongly af coupled, and the second is f coupled. Here, exchange forces dominate coercive effects and the MRs are not dramatically different. The third sample is weakly af coupled and the remaining samples are uncoupled, and now there are significant differences. For Cu(9 nm)/Co(6 nm), MR(H_0'') is appreciably greater than MR(H_p) but much less than MR(H_0). This result supports our assumption that the H_0 state is the best candidate to date for the AP state. For Cu/NiFe, on the other hand, for t_{Cu}<10 nm, MR(H_0)<MR(H_p), and MR(H_0'') is larger than both. Here, MR(H_0'') is probably the best available experimental estimate for the AP state.

For the Cu/Co and Ag/Co systems, both H_0 and H_p seem to be rather well-defined states, in the sense that their properties vary systematically with other parameters in the system. In the uncoupled region, the H_0 state seems to correspond better with the AP state. Once a sample has passed

TABLE I. MR(H_0), and MR(H_0'') are the MRs (in percent) of the multilayers in zero field as prepared, and after demagnetization, respectively. MR(H_p) is the peak MR after cycling to H_s. Layer dimensions are given in nm.

System		MR(H_0)	MR(H_p)	MR(H_0'')
[Cu(0.8)/NiFe(6)]×53	CIP	35	34	34
[Cu(3)/NiFe(6)]×40	CPP	1.3	1.3	1.3
[Cu(2.0)/Co(1.5)]×143	CPP	68	58	64
	CIP	12	8.2	9.3
[Cu(9.0)/Co(6.0)]×49	CPP	61	37	44
[Cu(5.7)/NiFe(1.5)]×50	CPP	17	26	33
[Cu(3.3)/NiFe(1.5)]×75	CPP	23.6	35	39
	CIP	7.6	8.0	10.5

through a complete hysteresis cycle, we have not succeeded in restoring the original H_0 state by demagnetization at 4.2 K. For our "uncoupled" sputtered multilayers of Ag/Co and Cu/Co, the ratio $MR(H_0)/MR(H_p)$ is rather stable at ≈ 1.6 or 2 for multilayers with fixed t_F or $t_F = t_N$, respectively. For "uncoupled" Cu/NiFe with $t_{Cu} < 10$ nm, on the other hand, larger resistances at zero field can generally be obtained by demagnetizing at 4.2 K; here, the H_0 state cannot be the AP state.

We conclude that H_p is unlikely to closely represent the SU state. Further study is needed to establish how close H_0 comes to the AP state in different systems. In hopes of clarifying this issue, we are making CPP-MR measurements on spin-valve multilayers, in which alternating layers of F_A and F_B have values of H_c different enough that they should give an AP state for $H_{cA} < H < H_{cB}$.

This research was supported in part by the US NSF under Grant No. DMR 91-22614, by the MSU CFMR, and by the Ford Motor Company.

[1] S. S. Parkin *et al.*, Phys. Rev. Lett. **64**, 2304 (1990); **66**, 2152 (1991).
[2] D. H. Mosca *et al.*, J. Magn. Magn. Mater. **94**, L1 (1991).
[3] S. Zhang and P. M. Levy, Phys. Rev. B **47**, 6776 (1993).
[4] W. P. Pratt, Jr. *et al.*, Phys. Rev. Lett. **66**, 3060 (1991); S.-F. Lee *et al.*, Phys. Rev. B **46**, 548 (1992).
[5] S.-F. Lee *et al.*, J. Magn. Magn. Mater. **118**, L1 (1993).
[6] P. A. Schroeder *et al.*, NATO ASI Series B **309**, 129 (1993).
[7] S. Zhang and P. A. Levy, J. Appl. Phys. **69**, 4786 (1991).
[8] T. Valet and A. Fert, Phys. Rev. B **48**, 7099 (1993).
[9] W. Pratt *et al.*, J. Magn. Magn. Mater. **126**, 406 (1993).
[10] P. A. Schroeder *et al.*, MRS Symposium Proc. **313**, 47 (1993).
[11] P. Holody *et al.* (to be published).
[12] R. Loloee *et al.*, Physica (to be published).

Investigation of the magnetic structures in giant magnetoresistive multilayer films by electron microscopy

L. J. Heyderman and J. N. Chapman
Department of Physics and Astronomy, Glasgow University, Glasgow, G12 8QQ, United Kingdom

S. S. P. Parkin
IBM Research Division, Almaden Research Centre, 650 Harry Road, San Jose, California 95120-6099

The magnetic structures which occur in $(Co/Ni_{81}Fe_{19}/Co)/Cu$ multilayer films showing giant magnetoresistance have been investigated using electron microscopy. Rather similar fine domains, with sub-μm dimensions, were found in films comprising 14 and 6 magnetic layers. Whilst the observed structure depended greatly on the magnetic history of the sample, a combination of differential phase contrast imaging and low angle diffraction allowed an estimate to be made of the extent to which neighboring magnetic layers were aligned antiparallel to each other. For both samples typically two layers were found to have parallel alignment leading to the possibility that departures from the expected antiferromagnetic behavior are more prevalent at the surfaces rather than in the bulk of the multilayer.

I. INTRODUCTION

In a recent paper the magnetic structures present in giant magnetoresistive $(Co/Ni_{81}Fe_{19}/Co)/Cu$ multilayer films with 14 magnetic layers were investigated using various Lorentz modes of transmission electron microscopy.[1] The films, which gave magnetoresistance ratios of up to 18% at room temperature, displayed distinct and rather complex small-scale magnetic structures at zero field that were incompatible with complete antiparallel alignment of the magnetization in adjacent layers. Whilst Lorentz microscopy is one of the few techniques with the ability to image submicron domain structures, a detailed interpretation of the images is made difficult in this instance because information is provided only on the projection of the in-plane component of magnetic induction averaged through the multilayer stack. In the present work we have gained further insight into the magnetic structures by comparing observations in the 14-layer sample with those in a sample of identical composition but which comprised only six magnetic layers. Furthermore, low angle electron diffraction (LAD) has been introduced to provide quantitative data on the degree of magnetic alignment throughout the multilayer stack.

The multilayer material was chosen to ensure that films were soft whilst retaining high magnetoresistance (MR) values,[2] its composition being substrate |30ÅRu|5ÅCo|11ÅNiFe|5ÅCo|$n\times${19.5Cu|5ÅCo|11ÅNiFe|5ÅCo|}|50ÅRu|. $n+1$ is the number of magnetic layers in the multilayer stack. The magnetic structures were observed by Fresnel imaging and differential phase contrast (DPC) microscopy. The former is an out-of-focus technique suitable for domain observations during magnetization reversal. Large *in situ* perpendicular fields were available using the objective lens field[3] and, on tilting the sample, an in-plane field component of up to 1000's Oe could be applied. DPC imaging was used to look in more detail at structures of particular interest and processed DPC image pairs yielded vector maps of the magnetic induction averaged through the magnetic layers.[4] LAD was employed to quantify the total Lorentz deflection suffered by the electrons as they passed through the magnetic layers of the multilayer films and, as such, gave a direct measure of the net magnetization alignment in the multilayer stack. The LAD patterns were recorded from sample areas $\approx$20 μm in diameter and the patterns were calibrated by reference to a standard diffraction grating specimen.

II. RESULTS

A Fresnel image of a typical fine domain structure in the 14-layer sample at near-zero field is given in Fig. 1 (the applied field orientation is given by the double headed arrow). This is the highest magnetic contrast state during magnetization reversal. For comparison, some features of interest during magnetization reversal in the six-layer sample are shown in Fig. 2. As the field was reduced from saturation, fine striations which are similar to magnetization ripple were observed [Fig. 2(a)]. Reduction of the applied field to zero followed by a small increase in the reverse sense [Figs. 2(b) and 2(c)] led to an increase in the magnetic contrast and the formation of an irregular submicron domain structure similar to that observed in the original 14-layer film (Fig. 1). Thus the generic form of the domain structure formed during magnetization reversal from a saturated state did not change when the number of magnetic layers was reduced to six.

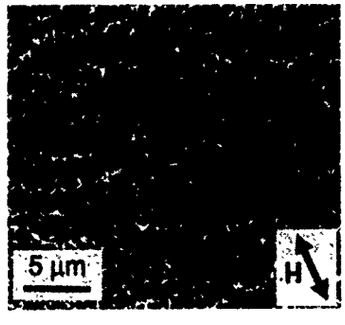

FIG. 1. Fresnel image of the near-zero field domain structure ($H=4$ Oe) in the 14-layer sample.

 0021-8979/94/76(10)/6613/3/$6.00 © 1994 American Institute of Physics

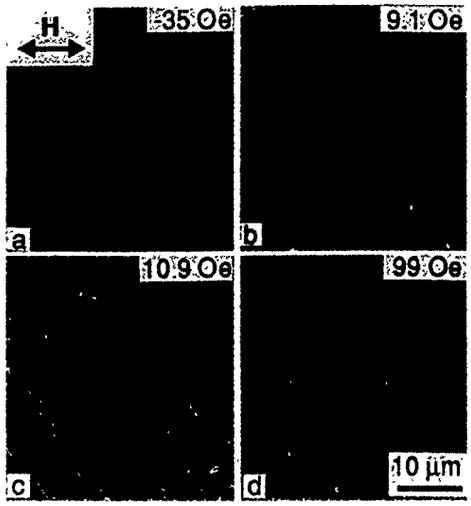

FIG. 2. Fresnel images of magnetization reversal in the six-layer sample.

Application of higher fields to the six-layer sample, however, introduced further complexities. In the presence of a greater reverse field, a high density of 360° wall structures formed as the irregular domain structure collapsed [Fig. 2(d)]. Annihilation of these 360° wall structures required field values in excess of 350 Oe. These observations should be contrasted with what happened when the sample was demagnetized along a minor hysteresis loop for maximum field values between 20 and 30 Oe. Under these circumstances much larger domains were nucleated [Fig. 3(a)]. Whilst increasing the field from this state once again led to the formation of 360° loops, these spanned much larger areas than those in Fig. 1(d) as a consequence of their originating from the larger domains. Figure 3(b) shows such 360° wall structures after the field was removed. Thus substantially different magnetic structures could be induced in the sample dependent on its magnetic history.

We have investigated the small and large domain structures discussed above [Figs. 2(c) and 3(a)] using DPC microscopy. One of a pair of DPC images for each of the small and large domain structures at zero field are given in Figs. 4(a) and 4(b). While the large domains [Fig. 4(b)] are ≈ 1 μm across, the dimensions of the small domains [Fig. 4(a)] are $\ll 1$ μm. Using pairs of DPC images sensitive to orthogonal induction components, the vector maps corresponding to

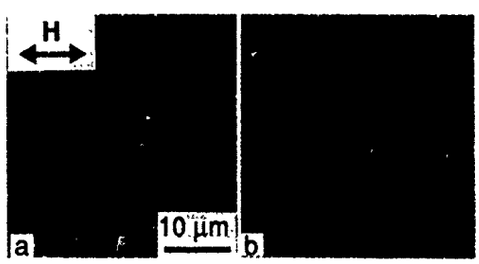

FIG. 3. (a) Large domains induced in the six-layer sample and (b) resulting 360° wall structures.

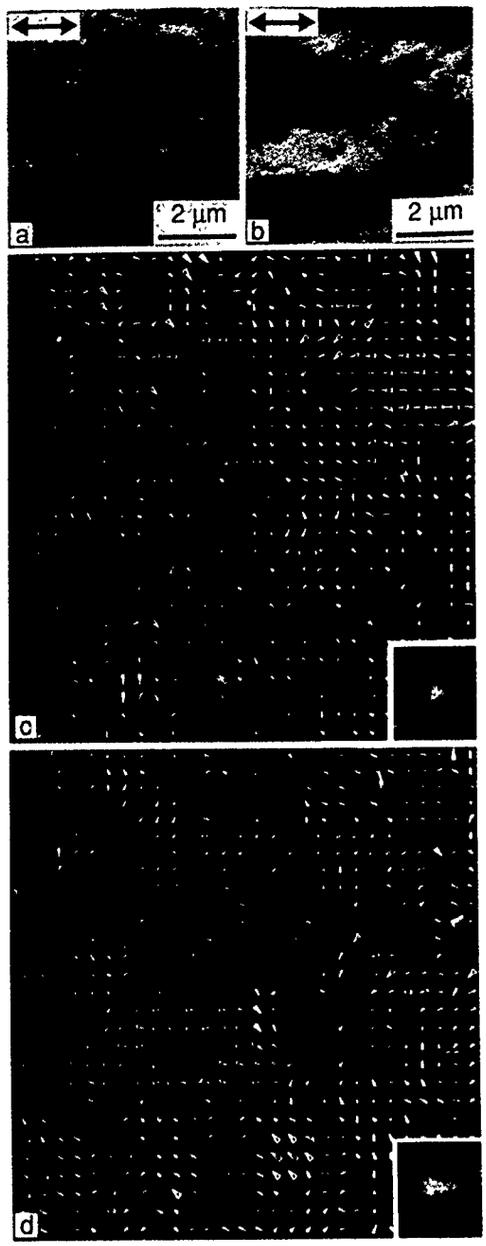

FIG. 4. DPC images of (a) small and (b) large domain structures in the six-layer sample mapped along directions given by the double headed arrow. (c) and (d) are vector maps for the regions in (a) and (b), each with a scattergram inset.

the regions shown in Figs. 4(a) and 4(b) were formed. These are given in Figs. 4(c) and 4(d) and clearly show spatial variations in magnetization orientation and magnitude on a sub-μm scale. The inset in each vector map is a scattergram which can be thought of as a two-dimensional histogram of the in-plane induction components within each area mapped.[4] The scattergram in Fig. 4(c) indicates that all orientations of the projected induction and magnitudes below a certain limit (defined by the width of the scattergram) are present. The elongation of the scattergram in Fig. 4(d) is consistent with the horizontal directionality of Fig. 4(b) but it is clear that, as before, all magnitudes for the projected in-

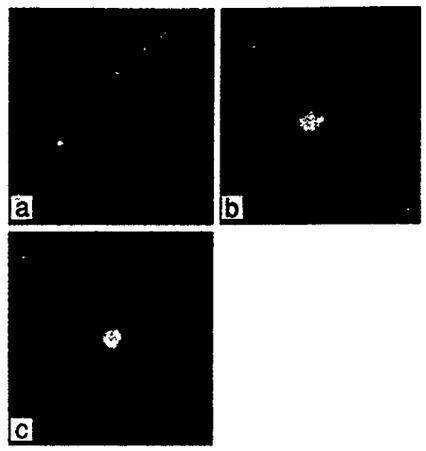

FIG. 5. LAD patterns for (a) a 14-layer ferromagnetically coupled sample at a region of near-180° domain walls; the fine domain states of (b) the 14-layer sample and (c) the 6-layer sample.

duction from the maximum observed value down to zero are present. Similar observations were made on the 14-layer sample.[1]

Quantitative information on the magnitude of the projected induction were obtained using LAD. For comparison purposes, an LAD pattern for a 14-layer sample containing magnetic layers of the same thickness but with intervening Cu interlayers of reduced thickness, thereby favoring parallel alignment of the magnetic layers,[1] is given in Fig. 5(a). This pattern is typical of one from a simple ferromagnetic film supporting in-plane magnetization and containing domains separated by ≈180° walls. The two lobes in the LAD pattern correspond to the two almost anitparallel domain magnetization orientations and the circumferential spread in the lobes is an indication of the magnetization dispersion in the sample. The expected Lorentz deflection, β_L, for a multilayer supporting parallel magnetization alignment is given by $\beta_L=(e\lambda/h)\int B_0\,dt$, where B_0 is the magnetic induction of the material, λ is the electron wavelength, and the integral is evaluated over the thickness of the magnetic layers. Assuming saturation magnetization values appropriate to bulk Co and permalloy, the expected value of β_L was calculated to be 26 μrad. This compares reasonably with the experimental value of 23 μrad.

The LAD patterns seen in Figs. 5(b) and 5(c) are very different to that in Fig. 5(a). They were taken from the fine domain structures seen in the 14- and 6-layer samples and closely resemble the scattergram of Fig. 4(c). Furthermore, despite the fact that the number of layers in the two samples differs markedly, the extent of the LADs are remarkably similar and substantially less than that of Fig. 5(a). Indeed most of the intensity in the diffraction patterns is within an angular radius of 6 μrad. This corresponds to ≈25% of the maximum deflection angle that would be obtained for the 14-layer sample if the magnetization in adjacent layers was always parallel and ≈60% of the corresponding quantity for the 6-layer sample. More significantly the observed distributions resemble what would be observed if, in different areas of the multilayer film, zero, two, and occasionally up to four layers were aligned parallel rather than antiparallel to each other.

III. DISCUSSION AND CONCLUSIONS

We have shown that complex domain structures, dependent on the magnetic history of the sample, exist in multilayer films with a composition that ensures a high value of MR and relatively low switching fields. In general, the magnetic contrast is rather low but neither it, nor the geometry of the structures, differs substantially in films comprising both 14 and 6 magnetic layers. A combination of DPC imaging and LAD has shown that whilst local areas exist within the films where the net magnetic deflection is zero, in most regions, the electrons suffer a small deflection as they pass through. This is consistent with an incomplete antiparallel alignment of magnetization in adjacent layers throughout the multilayer stack. Furthermore, using LAD we have made a quantitative estimate of the extent to which parallel alignment is present and have shown that the parallel alignment is usually between two layers, and rarely exceeds four magnetic layers. As similar results are found for both 14- and 6-layer samples, rather than there being a scaling with the number of layers, it is possible that parallel alignment is most frequently found near one or both film surfaces. Further investigations involving smaller numbers of layers should help to clarify this. We conclude that a contribution of electron imaging and diffraction techniques provides information on magnetization processes in complex multilayer structures that would not be accessible by other experimental techniques.

[1] L. J. Heyderman, J. N. Chapman, and S. S. P. Parkin, J. Phys D **27**, 881 (1994).
[2] S. S. P. Parkin, Appl. Phys. Lett. **61**, 1358 (1992).
[3] J. N. Chapman, R. P. Ferrier, L. J. Heyderman, S. McVitie, W A. P. Nicholson and B. Bormans, Inst. Phys. Conf. Ser. No. 138, Sec 1 (IOP, Bristol, 1993), pp. 1–8.
[4] J. Zweck, J. N. Chapman, S. McVitie, and H. Hoffmann, J. Magn. Magn. Mater. **104-107**, 315 (1992).

Distribution of current in spin valves (abstract)

Bruce A. Gurney, Virgil S. Speriosu, Harry Lefakis, and Dennis R. Wilhoit
IBM Research Division, Almaden Research Center, 650 Harry Road, San Jose, California 95120-6099

We present a model describing the distribution of spin up and spin down currents within the layers of spin valve structures. With this model and experimentally determined bulk mean free paths we successfully describe a variety of experimental results, including the variation of resistance and magnetoresistance with both ferromagnetic and nonferromagnetic layer thicknesses, and the current-induced field acting on the ferromagnetic layers versus overall current. Our model is based on an approximate path integral solution of the Boltzmann equation for in-plane transport in a multiply layered structure. For a given orientation of the magnetizations it calculates the current density $j^{\sigma}(\mathbf{r})$ at each point $\mathbf{r}$ for each spin σ throughout the structure. From $j^{\sigma}(\mathbf{r})$ it is straightforward to obtain the current in each layer for parallel versus antiparallel magnetizations, or of the current density near interfaces relevant to electromigration. Included in our model are both spin dependent bulk scattering as well as scattering at interfaces, which are treated as thin layers. For example, in order to obtain quantitative agreement with experiments with permalloy based structures it is essential to include spin independent scattering arising from Fe and Ni atoms rendered nonferromagnetic next to the spacer due to interfacial intermixing. Our results bear directly on the fundamentals of GMR by successfully describing transport in spin valves using the measured bulk spin dependent mean free paths of the individual layers. Our results are also of technological interest because they predict how current affects the MR response to an external field.

A comparison of the giant magnetoresistance and anisotropic magnetoresistance in Co/Cu sandwich films (abstract)

B. H. Miller, E. Youjun Chen,[a] Mark Tondra, and E. Dan Dahlberg
School of Physics and Astronomy, University of Minnesota, 116 Church Street SE, Minneapolis, Minnesota 55455

By a systematic variation of structures, recent measurements conclude the scattering associated with the high resistance giant magnetoresistance (GMR) state occurs within 0.25 nm of the magnetic interface.[1] We have accomplished a similar measurement that does not require such stringent control of the sample structure. Instead, the present work uses measurements of the anisotropic magnetoresistance (AMR) in both the high resistance and low resistance GMR states. The samples are sandwiches of Co/Cu/Co/CoO with Co thicknesses ranging from 1 to 10 nm and Cu thickness of approximately 2.5 nm. The AMR is measured with the Co magnetizations aligned parallel to one another (the low resistance GMR state) and with the Co magnetizations aligned antiparallel to one another (the high resistance GMR state). The data show that the AMR in the antiparallel configuration is less than that in the parallel configuration. An analysis that relates the reduced AMR to the magnetic interfacial region giving rise to the high resistance GMR state indicates the scattering occurs within approximately 0.5 nm of the interface.

Supported by AFOSR under Grant No. AF/FA 9620-92-J-0185.
[a]Currently at Nonvolatile Electronics, 11403 Valley View Road, Eden Prairie, MN.

[1]S. S. P. Parkin, Phys. Rev. Lett. **71**, 1641 (1993).

 0021-8979/94/76(10)/6616/1/$6.00 © 1994 American Institute of Physics

Enhanced magnetoresistance in chromium doped Fe/Cr multilayers (abstract)

Noa M. Rensing and Bruce M. Clemens
Department of Applied Physics and Department of Materials Science and Engineering, Stanford University, Stanford, California 94305-2205

We report enhanced room temperature magnetoresistance of up to 11.4% in sputter deposited Fe/Cr multilayers when the iron layers are doped with additional chromium. To our knowledge, this is the largest room temperature magnetoresistance in polycrystalline Fe/Cr multilayers reported to date. In comparison, the magnetoresistance was 7.5% in a similar, undoped sample made at the same time. The magnetoresistance of antiferromagnetically coupled Fe/Cr multilayers has been the subject of considerable study in the past five years. We have investigated the possibility of doping the Fe layers with additional chromium, in order to increase the magnetoresistance by enhancing the spin dependent scattering. In one series of samples, the chromium dopant was concentrated into thin layers within the Fe layer. A 1 Å layer of chromium ($\frac{1}{2}$ monolayer) was deposited at a depth of 4, 8, or 15 Å into the 30-Å-thick iron layers of the multilayers. The magnetoresistance was enhanced in all of the samples, to 8% when the doping layer was at 4 Å and to 10.5% in the others. In the second series of samples the iron layers were alloyed with between 1.5% and 50% chromium. The maximum magnetoresistance was 11.4%, observed in the sample with 20% chromium in the Fe layers. This is larger than the magnetoresistance in any of the samples where the Cr was concentrated in a thin layer within the Fe layer, but a given amount of chromium appears to be more effective in increasing magnetoresistance when it is concentrated in a layer rather than distributed as an alloy. A 1 Å layer of Cr is roughly equivalent to a 3% alloy, but the alloyed sample only showed 8% magnetoresistance, in comparison to up to 10.5% in the samples with layered doping.

Low field giant magnetoresistance and oscillatory interlayer exchange coupling in polycrystalline and (111)-oriented permalloy/Au multilayers (abstract)

S. S. P. Parkin, T. A. Rabedeau, R. F. C. Farrow, and R. Marks
IBM Research Division, Almaden Research Center, San Jose, California 95120-6099

The existence of oscillatory interlayer exchange coupling of ferromagnetic layers via (111)-oriented noble metal spacer layers is controversial. We present evidence from magnetic and giant magnetoresistance studies for well-defined antiferromagnetic interlayer coupling in single crystalline (111) permalloy/Au multilayers. Four oscillations in the coupling are observed as the Au spacer layer thickness is increased. The oscillation period is $\simeq$10 Å which is significantly shorter than the period of $\simeq$11.5 Å predicted in Ruderman–Kittel–Kasuya–Yosida based models. Similar oscillatory interlayer coupling is found in polycrystalline permalloy/Au multilayers prepared by dc magnetron sputtering. The interlayer coupling strength is significantly weaker in the polycrystalline as compared to the (111)-oriented crystalline samples. In both cases the coupling strength is weaker than in comparable structures containing Ag, for which the coupling is weaker than in similar structures containing Cu. The weakness of the antiferromagnetic interlayer coupling via Au leads to very low saturation fields, lower than for all other noble and transition metals. Indeed, the saturation fields are as low as just a few Oersted for sufficiently thick Au layers. Consequently, we find giant magnetoresistance values of $\simeq$1%/Oe or greater at room temperature in polycrystalline permalloy/Au multilayers. These values are the highest values yet reported in multilayer structures and are comparable to or greater than those recently reported in discontinuous permalloy/Ag multilayers.

 0021-8979/94/76(10)/6617/1/$6.00 © 1994 American Institute of Physics

Giant magnetoresistance at low fields in $[(Ni_xFe_{1-x})_yAg_{1-y}]$/Ag multilayers prepared by molecular beam epitaxy (abstract)

R. F. C. Farrow, R. F. Marks, A. Cebollada, M. F. Toney, D. Dobbertin, R. Beyers, and S. S. P. Parkin
IBM Research Division, Almaden Research Center, 650 Harry Road, San Jose, California 95120-6099

T. A. Rabedeau
Stanford Synchrotron Radiation Laboratory, Stanford, California 94305

The structural changes that accompany the development of GMR (giant magnetoresistance) at low ($\lesssim$10 Oe) fields in annealed magnetic multilayers[1] are of current interest because of potential applications of such structures in sensors. In this paper we report a study of the development of GMR in [111]-oriented multilayers comprising ferromagnetic films of a mixture of Ag and permalloy (Ni_xFe_{1-x}, $x\sim0.8$) alternating with Ag spacer films. The multilayers were grown by molecular beam epitaxy (MBE) on Pt(111) seed films on sapphire (0001) substrates at temperatures in the range 20 to 200 °C. The structure of the multilayers was investigated using x-ray diffraction and electron microscopy. For a series of multilayers grown with nominally identical ferromagnetic and spacer layer thicknesses, the magnetoresistance is found to be strongly dependent on both growth temperature and subsequent annealing temperature. The multilayers exhibited a negative magnetoresistance in the as-grown state which more than doubled when the growth temperature was increased from 20 to 100 °C. However, the highest magnetoresistance (peak 5.6%; maximum slope 0.4% per Oe) was obtained by annealing (at 400 °C) multilayers grown at 100 °C. Transmission electron microscopy studies of such multilayers showed no evidence for discontinuities or penetration of the ferromagnetic films by Ag along grain boundaries. Thus, we conclude that discontinuous or granular multilayers with complete phase separation are not necessary for GMR with low saturation fields.

The full article appeared in the 15 September 1994 issue of Journal of Applied Physics on p. 3688.

[1]T. L. Hylton, K. R. Coffey, M. A. Parker, and J. K. Howard, Science **261**, 1021 (1993).

 0021-8979/94/76(10)/6618/1/$6.00 © 1994 American Institute of Physics

Effects of domains on magnetoresistance (abstract)

Shufeng Zhang and Peter M. Levy
Department of Physics, New York University, New York, New York 10003

Our present understanding of the giant magnetoresistance observed in magnetic multilayered structures is based on the premise that the layers are either monodomains or that the sizes of the domains are much larger than all other length scales (mean free path, spin-diffusion length, and layer thickness) relevant to the magnetoresistance. We extend our theory of magnetoresistance to include multilayers with small in-plane domains where there is the possibility that their size may be limited by columnar growth.[1] We study magnetoresistance in the presence of in-plane domains both for the current parallel and perpendicular to the plane of layers. The domain boundaries introduce additional scattering and the direction of the internal current will be different from that of the driven current. In the presence of spin-dependent scattering, a transverse spin current develops so that the current in each of the spin channels is "mixed" even without spin-flip processes. Analytical expressions will be given for limiting cases where the mean free path is either much larger or much smaller than the layer thickness and the domain size. We find that the domain size is a relevant length scale and contributes to the spin diffusion length λ_{sdl} in the equations that govern the spin diffusion attendant to charge transport in magnetic multilayers. If one does not know the domain structure, nor the amount of spin-flip scattering, both mechanisms are equally plausible for producing spin diffusion which suppresses the magnetoresistance for the current perpendicular to the plane of the layers.

Research sponsored by the Office of Naval Research.

[1] J. Bass (private communication).

 0021-8979/94/76(10)/6619/1/$6.00 © 1994 American Institute of Physics

The synthesis, structure, and characterization of α''-$Fe_{16}N_2$ (invited)

K. H. Jack
University of Newcastle upon Tyne and the Cookson Group plc., United Kingdom

Controversy about the magnetic properties of α''-$Fe_{16}N_2$ thin films makes it desirable to examine bulk material. In the original preparation and crystal structure determination of α'' in 1951, N-austenite (γ) prepared by nitriding α-iron powder at 700–750 °C was quenched to give N-martensite (α') which then gave $\alpha+\alpha''$ on long tempering at 120 °C. The final product was a mixture of either $\alpha+\alpha''$ or $\alpha+\alpha''+\gamma$ with less than 50%α''. Recent repetitions of this preparative method in three different laboratories have given mixtures with varying amounts of α'', again never greater than 50%, and with magnetic moments of α''—assessed from measurements made on the mixtures—that show considerable variation. Studies of α' tempering by XRD, and of α'' precipitation from supersaturated N ferrite (α) by high-resolution TEM, both show that slow ordering of N atoms to produce α'' occurs only after localized regions of α' and α reach the Fe_8N composition by a clustering process. Thus α'-Fe_8N can be obtained with a tetragonality c/a equal to that of α'', but without the complete N ordering that is characteristic of $Fe_{16}N_2$. This might explain some of the variability in magnetic properties. The inhibiting effect of oxygen and other impurities on the nitriding of iron is emphasized, the existence of the α''-carbonitride $Fe_{16}(C,N)_2$ is noted, and possible methods for 100% production of bulk α'' are suggested.

I. INTRODUCTION

α''-$Fe_{16}N_2$ was discovered and its crystal structure determined in 1951,[1] but its magnetic properties remained unexplored until 1972 when Kim and Takahashi[2] reported an abnormally high magnetization in films obtained by evaporating iron onto a glass substrate in low-pressure nitrogen. The major phase was α'', and from the experimentally determined volume fraction its polarization was calculated as 2.76 T, corresponding to an average moment of 2.9 μ_B per Fe atom. This discovery, neglected for nearly two decades, has inspired much recent activity. Various techniques have been used to produce films on a variety of substrates with very variable results;[3–6] see Table I. Most remarkably, Sugita and co-workers[4,5] claim single-crystal α'' films, prepared by MBE on $Ga_{0.8}In_{0.2}As$ substrates, with a moment per Fe atom of 3.2 μ_B at room temperature. At the other extreme, Takahashi and his colleagues more recently report[6] that films produced both by plasma evaporation and by sputtering show no abnormally large magnetization. A "giant magnetic moment" seems incompatible with band theory; three independent calculations[7–9] based on the structure of α''-$Fe_{16}N_2$ give an average moment of 2.4 μ_B per Fe atom, i.e., only about 10% higher than that of α-iron.

Because of the controversy engendered by these widely different observations, it seems essential to measure the properties of pure, bulk samples of α''-$Fe_{16}N_2$. So-far, this has been attempted in three different laboratories,[10–12] but again with different results. Reasons for the variability of products and possible methods of meeting the objective are suggested in the present paper.

II. ORIGINAL PREPARATION AND CHARACTERIZATION OF α''-$Fe_{16}N_2$

α''-$Fe_{16}N_2$ was first prepared during an investigation of the Fe-N system. The solubility of molecular nitrogen in iron is negligible and so Fig. 1 is not a true equilibrium diagram because the nitrogen is not at one atmosphere pressure. Different phases and exact compositions within a phase are readily obtained by nitriding with NH_3:H_2 gas mixtures in which the N potential, $a_N = k.p_{NH_3}/p_{H_2}^{3/2}$, can be precisely controlled.

N-austenite (γ) exists above 590 °C and is a fcc arrangement of Fe atoms with N randomly occupying up to one in ten of the octahedral interstices. The γ' nitride Fe_4N also has a fcc Fe-atom arrangement but with one in four of the octahedral holes occupied in a perfectly ordered manner; see Figs. 2 and 3.

When γ is quenched rapidly from above 600 °C the Fe-atom arrangement changes from fcc to approach that of bcc

TABLE I. Magnetic properties of α'' thin films.

Reference	Method	σ_s ($J\,T^{-1}\,kg^{-1}$) (emu g^{-1})	J_s (T) (10^4 G)	μ_B per Fe atom
2	sputtering	296±14	2.76±0.13	2.9±0.2
3	N ion implantation	256	2.40	2.5
4,5	MBE	310±10	2.9±0.1	3.2±0.1
6	(i) sputtering	218	2.0	···
	(ii) plasma	235	2.2	···
α-Fe		220	2.15	2.2

 0021-8979/94/76(10)/6620/6/$6.00 © 1994 American Institute of Physics

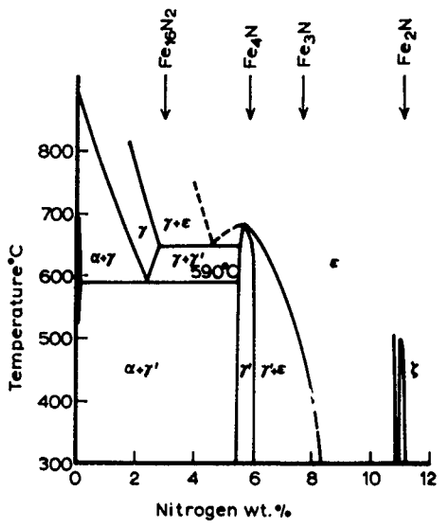

FIG. 1. The Fe-N phase diagram.

α-Fe. However, the N atoms have insufficient time to move from the interstices they occupied in the austenite and the extra holes created by the fcc–bcc transition remain empty. The result is a bc tetragonal martensite (α') of the same composition as the parent austenite, and where up to a maximum of one in ten of the holes at the midpoints of the c edges and the centers of the C faces are occupied by N (the N^z sites). Figure 4 shows a variable position for the Fe atoms; where a hole is occupied, the Fe atoms are pushed apart in the c direction; when the hole is empty the Fe-atom positions are the same as in α-Fe. Dimensions of unfilled and filled octahedra are shown by Fig. 5.

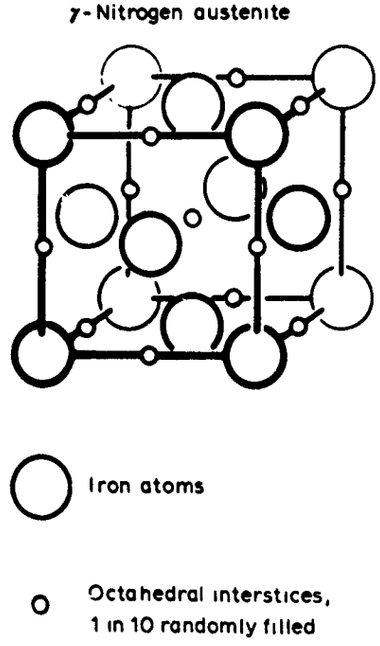

FIG. 2. γ phase, N-austenite.

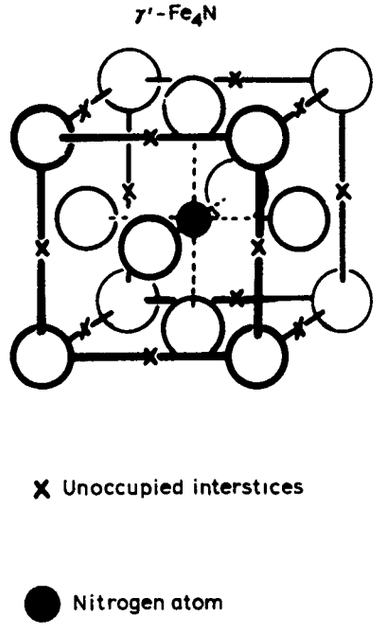

FIG. 3. γ phase, Fe_4N.

When N-martensite (α'), obtained by quenching γ, is tempered below 590 °C, the phase diagram indicates that the products should be $\alpha+\gamma'$. Instead they are $\alpha+\alpha''$. The $Fe_{16}N_2$ unit cell (Fig. 6) consists essentially of eight ($2\times2\times2$) distorted bcc cells of α-Fe with N atoms occupying 2 of the 48 octahedral interstices in a perfectly ordered manner, i.e., 2 of the 16 N^z sites with 16 N^x and 16 N^y sites com-

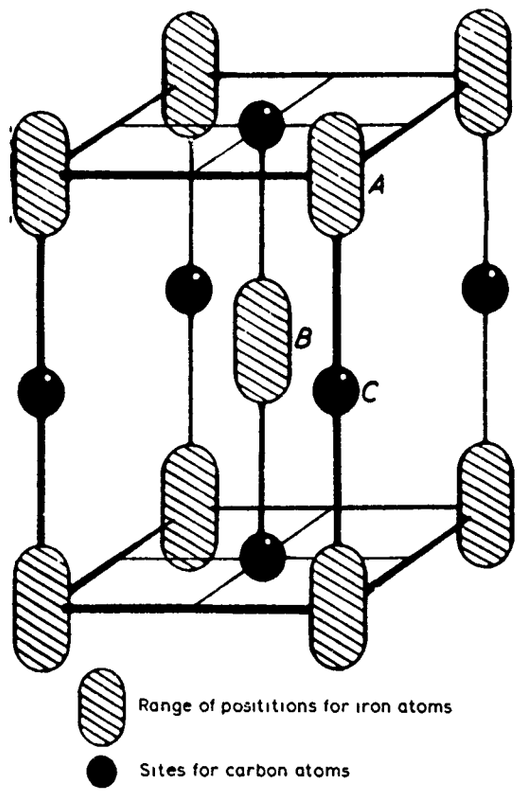

FIG. 4. α' phase, N-martensite.

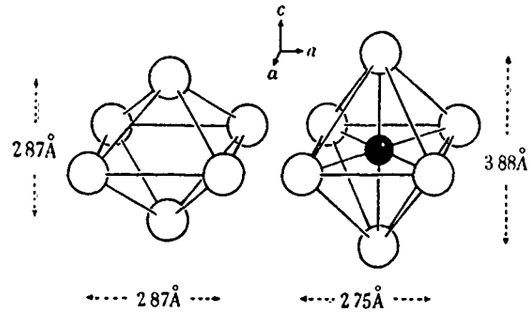

FIG. 5. Unfilled and filled octahedra in bcc α-Fe.

pletely empty. The Fe atoms are in three different crystallographic sites: $4(e)$ and $8(h)$ which form the octahedra coordinating the two N atoms and which, within experimental error, are all equidistant from a N atom; and sites $4(d)$ which have no nearest N-atom neighbors.

Figure 7 shows that α'' viewed along [110] is a distorted $\gamma'Fe_4N$ with alternate N atoms missing. Thus, in both structure and composition, $Fe_{16}N_2$ ($=Fe_4N_{0.5}$) is midway between bcc α-Fe and fcc γ'-Fe_4N. In all the Fe-N phases (α, α', α'', γ, and γ') the filled octahedra (NFe_6) are all the same size; only their numbers and distribution change.

III. THE FORMATION OF α' AND α'' PHASES

Figure 8 shows x-ray powder photographs of N-martensites (α') prepared by quenching austenites (γ). As the N content increases, the increasing tetragonality of α' is shown by the increasing separation of the component reflexions of the "tetragonal pairs" $M2$, $M4$, $M6$, and $M8$, i.e., (101) and (110), (002) and (200), etc. The maximum N content of γ, and hence of the α' that forms from it, is $\gtrsim$10 N/100 Fe and so it never reaches Fe_8N (12.5 N/100 Fe). Even the highest N-martensite must give α-Fe+α'' on tempering; it can never give pure α''. Further, α' is not produced isothermally from γ. It is formed only during cooling, and

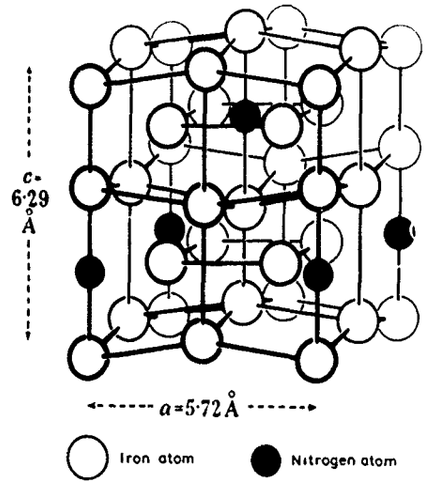

FIG. 6. Structure of α''-$Fe_{16}N_2$.

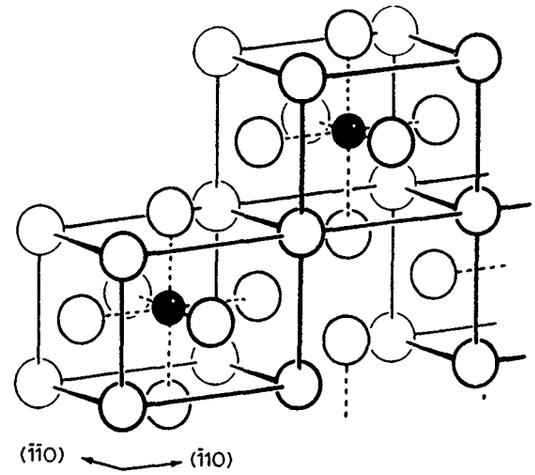

FIG. 7. The structure of α'' considered as a distorted fcc lattice.

the M_s temperature—the temperature at which transformation starts—decreases as the N concentration increases. For high-N contents which might be expected to produce high-N α' phases and hence purer $Fe_{16}N_2$, M_s is at subzero temperatures. Also, the stresses set up when γ transforms to α' inhibit further transformation and the effect increases as M_s decreases.

To summarize, low-N-content austenites produce, by quenching and then tempering, a mixture of $\alpha+\alpha''$ with only a small proportion of α''. High-N austenites produce more α'', up to perhaps 50%, but with some α and a large amount of nonmagnetic retained austenite (γ).

It is also important to appreciate that when α' is tempered at low temperatures, the α'' does not form instantaneously. The N atoms in localized regions gradually cluster together to produce a martensite of higher N content and hence of greater tetragonality with concurrent formation of ferrite. Figure 9 shows x-ray photographs of N martensite (2.0 wt % N; 8.1 N/100 Fe) aged at 80 °C. With increasing time, the separation of the paired reflections $M2$, $M4$, ..., $M10$ gradually increases, showing increasing tetragonality and hence increasing N concentration of α'; compare Fig. 8. Even when the tetragonality c/a reaches that of α'', corre-

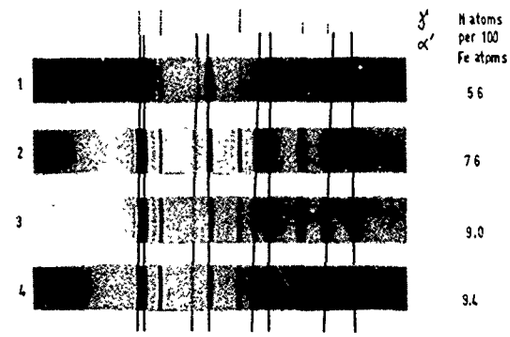

FIG. 8. X-ray powder photographs of N martensites (with retained γ) with increasing N content.

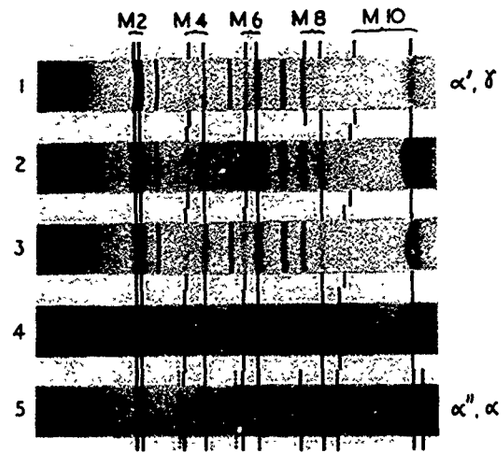

FIG. 9. X-ray powder photographs of N martensites (2.0 wt % N=8.1 N/100 Fe) aged at 80 °C for increasing times.

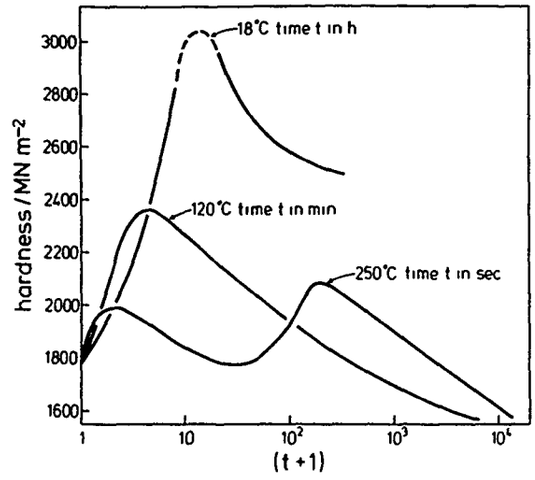

FIG. 11. Hardness curves for quench-aged N ferrite, 0.07 wt % N.

sponding to an α' composition Fe_8N, weak reflections due to N-atom ordering that are characteristic of the $Fe_{16}N_2$ structure are not observed; these appear only after further prolonged tempering.

IV. AGING NITROGEN FERRITE

Another way of producing α''-$Fe_{16}N_2$ is by precipitation from supersaturated N ferrite. The solubility of N in α-Fe is a maximum at 590 °C, 0.1 wt %=0.4 at. %. On quench aging α containing ~0.07 wt % N, the phase diagram of Fig. 10 indicates that γ'-Fe_4N should be precipitated. Instead, optical and electron micrography, XRD, and electron-diffraction evidence, together with the hardness curves of Fig. 11, show that at 250 °C α'' is first precipitated within seconds and then dissolves and is replaced by equilibrium γ'. At 120 °C the α'' remains and is transformed to γ' only after very long times. After 10 h aging at room temperature the quenched ferrite shows a remarkably high hardness for such a small N concentration with no evidence from optical microscopy of any precipitation. Only an electron micrograph at a magnification of ~0.5×10^6 reveals a structure identical with the classical Guinier–Preston zones in Al:4 wt % Cu; see Fig. 12.

A combination of techniques, (i) x-ray measurements of unit-cell dimensions, (ii) internal friction, (iii) transmission electron microscopy, and x-ray and electron diffraction, allows the complete quantitative characterization of nitrogen in iron and iron alloys; see Jack[13] and references therein. Nitrogen in the aged N ferrite (α) of Fig. 12 is clustered as a nonrandom solid solution of disc-shaped GP zones. Figure 13 is an (002) lattice image of α containing 0.05 wt % N, i.e., $Fe_{500}N$, after aging for 15 h at 23 °F. The (002) interplanar spacing of 1.49 Å within the cluster corresponds with a composition $Fe_{20}N$ whereas the adjacent ferrite with which the cluster is completely coherent has the N-free spacing of α-Fe, i.e., 1.43 Å. Further aging continues to increase the N content in the localized clustered regions until, after reaching Fe_8N, N ordering slowly occurs to give α''-$Fe_{16}N_2$. The 1.57 Å spacing shown in Fig. 14 is not unequivocal evidence of α'' even though this is the d value for (004) of α'' for which $c=6.28$ Å. The same d value is shown by the (002) planes

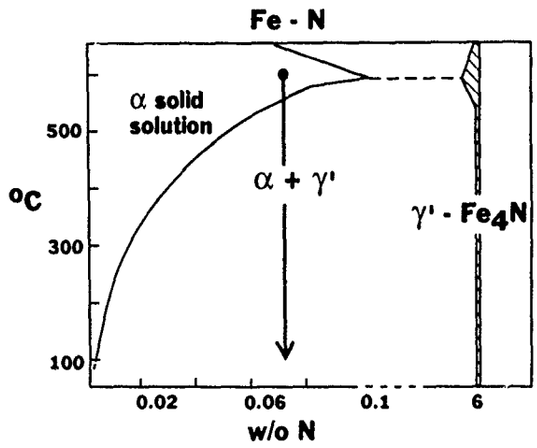

FIG. 10. Part of the Fe-N system.

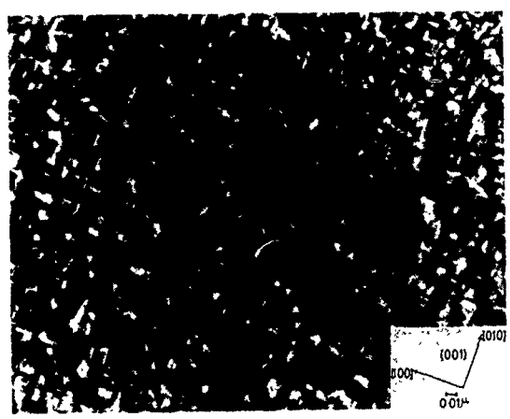

FIG. 12. TEM of Fe:0.07 wt % N quench-aged 16 h at 21 °C; foil normal [001].

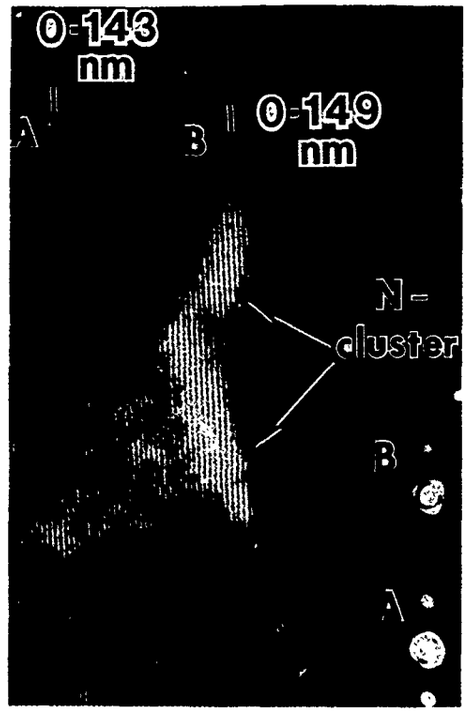

FIG. 13. (002) lattice image of a N cluster ($Fe_{20}N$) in Fe:0.05 wt % N ($Fe_{500}N$) aged 15 h at 23 °C.

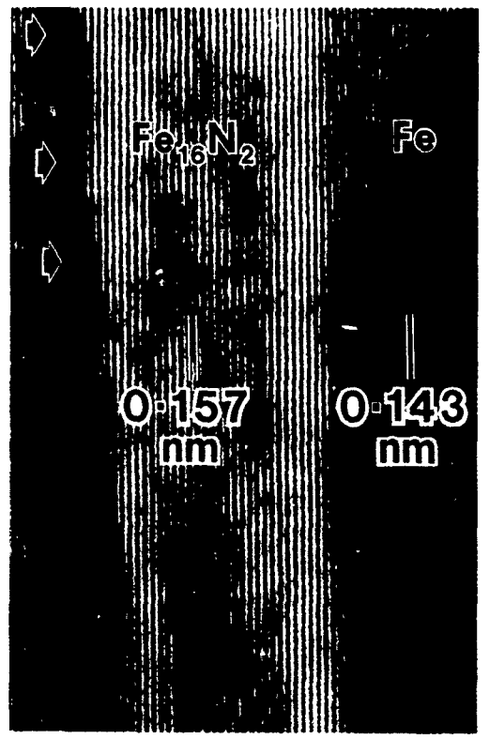

FIG. 14. (004) lattice image of α''-$Fe_{16}N_2$ in Fe:0.05 wt % N aged 46 h at 100 °C.

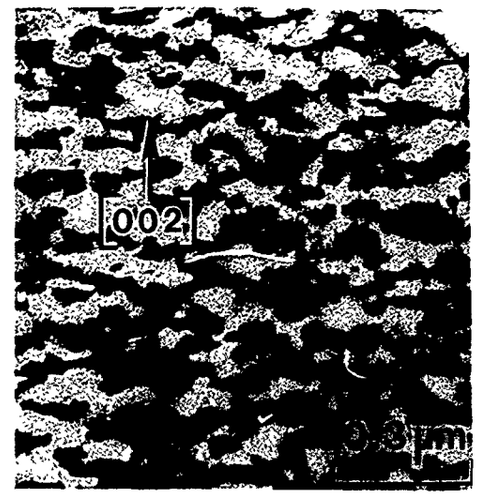

FIG. 15. Stress-oriented N-atom clusters in aged Fe:0.06 wt % N.

of α'-Fe_8N and evidence of the N-atom ordering characteristic of α''-$Fe_{16}N_2$ comes from additional reflections in the electron- and x-ray-diffraction patterns.

It is worth noting that aging under an applied mechanical stress produces clusters and then α'' platelets in only one preferred cube orientation. As shown in Fig. 15, the plane of the plates is perpendicular to the applied extensive stress.

The aging of N ferrite fully supports the evidence of N-martensite tempering that α'-Fe_8N is obtained in a penultimate stage with a tetragonality c/a equal to that of α'' but without the N-ordering characteristic of $Fe_{16}N_2$.

V. BULK α''-$Fe_{16}N_2$

The production of bulk α'' as powders or foils has followed essentially the 1951 preparative method via γ and α'. For reasons given in Sec. III, all three laboratories have produced mixtures, the phase compositions of which have been determined by either XRD[10] or Mössbauer spectroscopy.[11,12] Huang *et al.*[10] claim 56% α'' with $J_s = 2.65 \pm 0.15$ T corresponding to 2.95 ± 0.15 μ_B per Fe atom—a 34% increase over that of α-Fe. Coey *et al.*[11] produce >40% α'' with smaller magnetization values of $J_s = 2.3 \pm 0.2$ T and 2.45 ± 0.15 μ_B at ~0 K; these are only about 10% higher than for α-Fe but are in broad agreement with the band-structure calculations. Bao *et al.*[12] start from hydrogen-reduced Fe_2O_3 and convert up to 30% into α''. They claim that the measured moment is in agreement with a "dramatically large magnetization," i.e., $\sigma_s = 310$ emu g^{-1}, but the experimental evidence for this is not convincing.

VI. DISCUSSION AND CONCLUSIONS

The limited work so far carried out on bulk α''-$Fe_{16}N_2$ has not resolved the controversy concerning the existence of a giant magnetic moment iron nitride. This is partly due to preparative limitations whereby less than 50% of the product mixture is α''. The variation in the magnetic properties of thin films is explicable by differences in N-atom ordering,

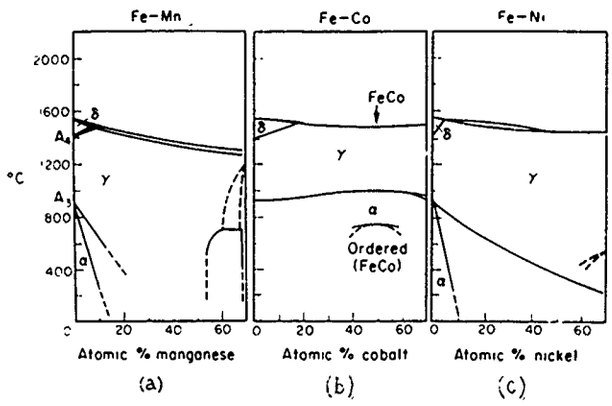

FIG. 16. Phase diagrams: (a) Fe-Mn, (b) Fe-Co, (c) Fe-Ni.

and the existence of α'-Fe_8N which, superficially, is indistinguishable from α''-$Fe_{16}N_2$ but which might have different magnetization values.

Bulk preparation of 100% α'' is essential. By the conventional route this is possible by extending the N content of γ until it includes Fe_8N. Only three elements, Mn, Co, and Ni, are γ stabilizers and extend the γ-phase field. From the phase diagrams of Figs. 16(a)–16(c), additions to Fe of Mn and Ni reduce markedly the M_s temperature but Co does not. Although detailed phase relationships in the Fe-Co-N system are not known, it is suggested that small alloying additions of Co would extend the γ-phase limit to include $(Fe,Co)_8N$. The M_s temperature will not thereby be lowered and it is not expected that Co additions will reduce the magnetization of the final α'' phase.

It is well established[14] that alloying elements which lower the activity coefficient of N in Fe (i.e., f_N^X where, for example, X is Mo, Mn, Ta, Cr, Nb, V, and Ti) also stabilize the transformation stages of the homogeneous precipitation to temperatures higher by about 500 °C. Small additions of these elements might be expected to stabilize α''-$(Fe,X)_{16}N_2$ to temperatures of 600–700 °C.

It is also established that both the quench aging of carbon-nitrogen ferrite[15] and the tempering of carbon-nitrogen martensite[16] give an α''-$Fe_{16}(C,N)_2$ carbonitride phase. The effects of carbon on the properties and stability of α'' are not known.

These observations suggest that there is ample scope for a wide exploration of α'' alloy phases that might be more easily prepared and have greater thermal stability than the pure α''-Fe-N phase.

The possibility of nitriding at low temperatures by mechanical alloying is attractive but, although a supersaturated bcc Fe-N phase with up to 14.5 at. % N is claimed[17] in Japan by ball-milling iron powder in NH_3 at room temperature, there is no trace of α'' and the magnetization decreases rapidly as the N concentration increases. Similar negative results were obtained by Foct[18] in France.

At temperatures where α'' is relatively stable (≯250 °C), its nitrogen activity a_N is higher than that of the more stable γ'-Fe_4N and so a higher nitrogen potential is required to produce it by gaseous nitriding; surface nucleation of γ' must be avoided. By the conventional $\gamma \rightarrow \alpha' \rightarrow \alpha''$ route, low-N-content austenite transforms completely to low N-martensite which, on tempering, gives $\alpha''+\alpha$. If this mixed phase, prepared as a finely divided (10 μm) powder, is then nitrided in the appropriate NH_3:H_2 gas mixture at <250 °C the α'' regions will act as nuclei and will grow at the expense of α, eventually producing 100% α''. In nitriding, the slowest rate-controlling step is at the surface, and so it is essential to maintain a scrupulously clean surface and clean grain boundaries. Adsorped oxygen or other active species (e.g., sulfur) will inhibit completely the nitriding reaction. Even at 200 °C the diffusivity of N in Fe is high enough to ensure homogeneity of 10 μ powder particles provided that surfaces are perfectly clean. It is now suggested that this quench tempering of low-N-content γ, followed by low-temperature gaseous nitriding, should also be explored to produce 100% α''-$Fe_{16}N_2$.

[1] K. H. Jack, Proc. R. Soc. London, Ser. A **208**, 200 (1951).
[2] T. K Kim and M. Takahashi, Appl. Phys. Lett. **20**, 492 (1972)
[3] K. Nakajima and S. Okamoto, Appl. Phys. Lett. **56**, 92 (1990).
[4] M. Komuro, Y. Kozono, M. Hanazono, and Y. Sugita, J. Magn. Soc. Jpn. **13**, 301 (1989).
[5] Y. Sugita, K. Mitsuoka, M. Komuro, H. Hochiya, Y. Kozono, and M. Hanazono, J. Appl. Phys. **70**, 5977 (1991).
[6] M. Takahashi, H. Shoji, H. Takahashi, T. Wakiyama, M. Kinoshita, and W. Ohta, IEEE Trans. Magn. **29**, 3040 (1993).
[7] A. Sakuma, J. Magn. Magn. Mater. **102**, 127 (1991).
[8] S. Matar, Z. Phys. B **87**, 91 (1992).
[9] R. Coehoorn, G. H. O. Daalderop, and H. J. F. Jansen, Phys. Re **48**, 3830 (1993).
[10] M. Q. Huang, W. E. Wallace, S. Simizu, and S. G. Sankar (these proceedings).
[11] J. M. D. Coey, K. O'Donnell, Q. Qinian, E. Touchais, and K. H. Jack, J. Phys. Condens. Matter **6**, L23 (1994).
[12] X. Bao, R. M. Metzger, and M. Carbucicchio (these proceedings).
[13] K. H. Jack, in *High Nitrogen Steels*, edited by J. Foct and A. Hendry (The Institute of Metals, London, 1989), pp. 117–135.
[14] K. H. Jack, in *Heat Treatment '73* (The Metals Society, London, 1975), pp. 39–50.
[15] P. Ferguson and K. H. Jack, in *Heat Treatment '81* (The Metals Society, London, 1983), pp. 158–163.
[16] P. Ferguson and K. H. Jack, Scr. Metall. **18**, 1189 (1984).
[17] T. Koyano, C. H. Lee, T. Fukunaga, and U. Mizutani, in *Materials Science Forum* (Trans. Tech. Publications, Switzerland, 1992), Vols. 88–90, pp. 809–816.
[18] J. Foct (private communication).

Magnetism of α''-$Fe_{16}N_2$ (invited)

Robert M. Metzger and Xiaohua Bao
Department of Chemistry and Center for Materials for Information Technology, University of Alabama, Tuscaloosa, Alabama 35487-0336

Massimo Carbucicchio
Department of Physics, Università di Parma, Viale delle Scienze, I-43100 Parma, Italy

The metastable α''-$Fe_{16}N_2$ phase may have a magnetic moment up to 50% higher than that of pure bulk α-Fe. This article addresses the following issues. (i) Can epitaxial films of α''-$Fe_{16}N_2$ be prepared phase pure? Yes, but there are some doubts. (ii) Can powders of α''-$Fe_{16}N_2$ be prepared phase pure? Not yet. (iii) Is the Mössbauer spectrum due to α''-$Fe_{16}N_2$, to martensite, or to something else? Most assign it to α''-$Fe_{16}N_2$. (iv) What is the specific saturation magnetic moment of α''-$Fe_{16}N_2$? Some claim it is close to that of α-Fe, most claim that it is much larger. (v) Is the high moment due to α''-$Fe_{16}N_2$, or to some other phase?

I. INTRODUCTION

In 1950 Jack first reported[1,2] the metastable phase α -$Fe_{16}N_2$ in a study of the Fe-N phase diagram, which resembles the Fe-C phase diagram.[3] The α''-$Fe_{16}N_2$ phase is formed from α'-*N*-martensite Fe_xN with $6<x<11$, in the temperature range $150\,°C<T<300\,°C$ by a nitriding, quenching, and tempering process.[2] It also precipitates at the strain boundaries of supersaturated "nitrogen ferrite" (α-Fe_xN) and during the normal aging of α'-*N*-martensite.[4]

Kim and Takahashi reported a high magnetic moment (saturation magnetic flux density $B_s=2.58$ T) in a polycrystalline Fe-N film, deposited by Fe evaporation in N_2 on a glass substrate, and attributed these dramatically large values to the partial presence of α''-$Fe_{16}N_2$ (estimated $B_s=2.83$ T);[5] this synthesis could not be replicated [6] This B_s for α''-$Fe_{16}N_2$ was about 30% larger than that of bulk α-Fe ($B_s=2.20$ T).[7]

Sugita and co-workers[8,9] formed thin films of α''-$Fe_{16}N_2$ by molecular beam epitaxy on Fe(100)|GaAs(100); B_s was largest (2.66 T) for the thinnest (7 nm) films.[9] B_s rose to 2.8 T for 100 nm films.[10] Nakajima and Okamoto implanted N_2^+ in epitaxial α-Fe|MgO(100), to get partially ordered α'-*N*-martensite and α''-$Fe_{16}N_2$; annealing in vacuum at 150 °C increased the α''-$Fe_{16}N_2$ fraction from 16 to 24 wt %, but the magnetic moments were not dramatic.[11]

Gao and Doyle formed α''-$Fe_{16}N_2$ on sputtered single layer Fe-N films, with a specific saturation magnetic moment of 247 emu g^{-1}.[12] An effort to get α''-$Fe_{16}N_2$ from α-Fe and γ'-Fe_4N at 300 °C failed.[13] Takahashi and co-workers reported on sputtered films containing α''-$Fe_{16}N_2$, but the magnetic moments were low.[14]

A practical synthesis of α''-$Fe_{16}N_2$ has been sought in acicular[15] or equant[16] small particles, in larger particles,[17–19] and in large particles and foils.[7] Opinions differ on the large reported magnetic moment: Coey wonders whether one is looking "at revolutionary results or egregious errors."[20]

II. SYNTHESIS

α''-$Fe_{16}N_2$ was first made by nitriding Fe, quenching, then tempering[3] (Table I). One can start with γ-Fe_2O_3 (obtained from goethite γ-FeOOH), reduce it to α-Fe by H_2 gas at 450 °C, nitride under H_2:NH_3 gas (volume ratio 7:1 to 10:1) at 650–700 °C, quench the resulting γ-*N*-austenite to 77 K, thus forming α'-*N*-martensite, then temper the sample under N_2 gas at 120–200 °C for several hours, yielding α''-$Fe_{16}N_2$.[15] There is a time-to-temperature (TTT) diagram for its formation.[21]

A second approach is to strain or age α'-*N*-martensite: oriented needles of α''-$Fe_{16}N_2$ grow at the strain boundaries.[22–25] A third method is to grow Fe films epitaxially, under a low-pressure NH_3-N_2 gas, by molecular beam epitaxy (MBE), on GaAs(100)[9] or on $In_{0.2}Ga_{0.8}As$(100).[26] A fourth way is to grow an Fe film on MgO(100), and then implant N_2^+ ions.[11] The first and second methods cannot usually provide phase-pure α''-$Fe_{16}N_2$; the third and fourth methods can yield better purity, but in impractically small samples.

III. PHYSICAL PROPERTIES

α''-$Fe_{16}N_2$ crystallizes in the tetragonal space group *I*4/*mmm*, with three unique Fe positions[2] (Table II). Table III lists the x-ray reflections of α''-$Fe_{16}N_2$ and of other phases (α-Fe, γ-*N*-austenite, γ'-Fe_4N, or α'-*N*-martensite) at the N mol fractions X_N at which the phases are stable closest to the theoretical $X_N=0.111$ of α''-$Fe_{16}N_2$. Many reflections are overlapped.

The structure evolves from α-Fe to α'-*N*-martensite to α''-$Fe_{16}N_2$, as one adds N atoms gradually in the structure and tempers it.[2,3] In pure α-Fe (bcc), one should consider the "empty" octahedron of four next-nearest neighbor Fe atoms in the *ab* plane ("equatorial" Fe-Fe distance=2.866 Å), plus two body-centered Fe atoms along **c** above and below that plane ("axial" Fe-Fe distance=2.866 Å, axial Fe-equatorial Fe distance=2.482 Å): in its center is the "octahedral hole." In the solid solution of N in Fe called α'-*N*-martensite, the entry of an N atom into this hole distorts the octahedron: for $X_N=0.0859$, there is a contraction in what becomes the martensitic $a_{\alpha'}b_{\alpha'}$ plane (equatorial Fe-Fe distance=2.75 Å), and a dilation in the $c_{\alpha'}$ direction (axial Fe-Fe distance=3.88 Å); these empty and "filled" octahedra occur randomly along the three axes, to yield a tetragonal unit cell with sides $a_{\alpha'}=b_{\alpha'}=2.850$ Å, $c_{\alpha'}=3.091$ Å for $X_N=0.0859$.[3] The martensitic nearest-neighbor Fe-N distance (octahedral coordination of Fe around N) is 1.94 Å.[3,36]

 0021-8979/94/76(10)/6626/6/$6.00 © 1994 American Institute of Physics

TABLE I. Synthesis conditions (Lab. code: CAM=University of Cambridge, CMU=Carnegie–Mellon U., DUT=Delft University of Technology, HIT =Hitachi Research Laboratory, LBL=Lawrence Berkeley Laboratory, NAG=Nagaoka University of Technology, TCD=Trinity College Dublin, TOU =Tohoku University, UAL=University of Alabama).

Lab. code (Ref)	Starting material	Sizes μm	Heating temp./°C [time] (NH_3: H_2)	Quench temp./°C	Tempering temp./°C [time] atmosphere
CAM (3)	α-Fe powder[a]	<53 μm	700–750[?] (1:5–1:20)	25	120 [7–19 d]
CMU(17)	α-Fe powder	6–9 μm	660–670 [2–3 h]	−196,−269	120–150 [0.5–2 h] vac
DUT(4)	α-Fe foil	t=200 μm	742–877	−196	200[?]
LBL(27)	α-Fe foil	t=100 μm	590 (1:9)	−50	<200[?]
TCD(7)	α-Fe powder	30 μm	760 [several h]	···	120 [7 d]
	α-Fe foils	t=25, 100 μm	760 [several h]	···	120 [7 d]
UAL(15)	γ-Fe_2O_3	300×60×60 nm	650–700 (1:7–1:10)	−196	120–200 [1–4 h] N_2
UAL(15)	$Fe_{0.85}Mn_{0.15}SO_4$	300×60×60 nm	650–700 (1:7–1:10)	−196	120–200 [1–4 h] N_2
UAL(16)	$Fe_{0.93}Mn_{0.07}(NO_3)_2$	70×70×70 nm	650–700 (1:8–1:10)	−196	150 [2–6 h] N_2

Lab.	Substrate	Thickness	Conditions
HIT(9)	Fe‖GaAs(100)	7–100 nm	MBE 30 nm Fe (0.5 Å/s, T=300 °C)+Fe(0.04 Å/s, T=150 °C)+N_2 5×10^{-4} Torr
HIT(28,29)	InGaAs(001)		MBE
HIT(30)	InGaAs(001)	50 nm	MBE: Fe(0.004 Å/s, T=150 °C+N_2: NH_3(4–9:1)10^{-5}–10^{-4} Torr
NAG(31)	Fe‖glass	200 nm	Sputt.; 150 keV N_2^+ implantation ($2–4\times10^{16}$ cm^{-2})
NAG(11,32,33)	Fe‖MgO(100)	200 nm	Sputt.; 80–150 keV N_2^+ impl. ($1–11\times10^{16}$ cm^{-2})+ann.
TOU(14)	MgO	200 nm	dc plasma evaporation; annealing at 150 °C for 2 h
TOU(14,34)	MgO	30–3000 nm	Sputtering; Ar+N_2; annealing at 150 °C for 2–20 h
TOU(35)	MgO	3000 nm	dc sputt. on MgO+5 nm Fe(001), Ar+N_2 air, ann.
UAL(12)	Glass	200–250 nm	rf sputtering Fe+N_2(15 sccm)+Ar(6 mTorr)

[a]Mn added to stabilize the γ-N-austenite phase at room temperature.

As tempering proceeds, a collective reorientation of the martensitic $c_{\alpha'}$ axes occurs, clusters or Guinier–Preston zones form, and finally, a full ordering ensues into the tetragonal α''-$Fe_{16}N_2$ structure: the unit cell axes become $a_{\alpha''}=b_{\alpha''}=5.72$ Å ($\approx 2a_\alpha$), and $c_{\alpha''}=6.30$ Å.[37] In α''-$Fe_{16}N_2$, the N atom is surrounded by a distorted octahedron of Fe atoms: four equatorial Fe3 atoms at 2.01 Å, two axial Fe2 atoms at 1.95 Å. Atom Fe1, at Wyckoff site 4d, does not have close N atoms, and should most resemble Fe in α-Fe. Atom Fe2 (4e) has a distorted octahedron of neighbors: one axial N, four equatorial Fe3, and one axial Fe2. Atom Fe3 (8h) has seven closest neighbors: one N, two Fe2, and four Fe1. The inclusion of N causes very close Fe-Fe distances (Fe2-Fe2 and Fe2-Fe3). One can designate Fe2 as 1nn, Fe3 as 2nn, and Fe1 as 3nn: this indicates the first, second, and third nearest-neighbor Fe atoms to the N atom. In α'-N-martensite the Fe-N distance is quite different for 1nn than 2nn, while in α''-$Fe_{16}N_2$ they are very close. The paucity of diffraction data for α''-$Fe_{16}N_2$ gave only approximate values of the parameters z/c (Fe2), and x/a (Fe3).[2] α''-$Fe_{16}N_2$ is most likely a daltonide, or "line phase," with precise N stoichiometry.[2,3]

The 002 and 006 reflections have been seen for epitaxial and sputtered thin films[10,12,33,35,38] but not in powder samples.[2]

One can determine the uptake of N in γ-N-austenite or α'-N-martensite from the unit cell constants,[17,36] using the equations in Table III. One can assess the mol fractions of the various phases by calculating[17,18] x-ray line profiles from the solved crystal structures.[39]

For epitaxial films, the relative crystal orientation is α''-$Fe_{16}N_2$(110)‖Fe(001), and α''-[001]‖Fe [110],[9,30] and α''-$Fe_{16}N_2$(001)‖InGaAs(001).[29,30] For sputtered films on MgO, the orientations are α''-$Fe_{16}N_2$(001)‖MgO(001) and α'' [110]‖MgO [100], or α''(211)‖MgO(101) and α'' [011]‖MgO [001].[14]

TEM diffraction patterns for 7 nm films of α''-$Fe_{16}N_2$‖Fe‖GaAs show the less intense reflections 200, 020, 0$\bar{2}$0, $\bar{2}$00; and the more intense ones: 1$\bar{1}$0, 220, 040, 2$\bar{2}$0, $\bar{2}$20, 040, $\bar{2}\bar{2}$0, and $\bar{4}$00.[9] Similar results were seen for films of α''-$Fe_{16}N_2$‖Fe(001)‖InGaAs(001),[29] and for sputtered films.[12] TEM of α''-$Fe_{16}N_2$ has been seen in fine powders.[16]

Spin-polarized linearized muffin-tin orbital calculations yield magnetic moments at the three sites of α''-$Fe_{16}N_2$

TABLE II. Crystal structure of α''-$Fe_{16}N_2$: body-centered tetragonal (a=5.72 Å, c=6.29 Å, space group $I4/mmm$, #139) (Refs. 1,2).

Site	Site symm.	x/a	y/b	z/c	First [second] coordination	Fe-N
N	2a(4/mmm)	0	0	0	2 Fe2 @ 1.95 Å, 4 Fe3 @ 2.01 Å [8 Fe1 @ 3.24 Å]	···
Fe1	4d($\bar{4}$m2)	0	1/2	1/4	8 Fe3 @ 2.55 Å [4 Fe2 @ 2.86 Å] 2 N @ 3.26 Å	3nn
Fe2	4e(4mm)	0	0	0.31	1 N @ 1.95 Å, 4 Fe3 @ 2.33 Å, 1 Fe2 @ 2.39 Å [4 Fe3 @ 2.80 Å, 4 Fe1 @ 2.86 Å]	1nn
Fe3	8h(mm)	0.25	0.25	0	1 N @ 2.01 Å, 2 Fe2 @ 2.33 Å, 4 Fe1 @ 2.55 Å [2 Fe2 @ 2.80 Å, 4 Fe3 @ 2.84 Å]	2nn

TABLE III. X-ray reflections (d) at the specified mol fraction of nitrogen X_N, phase codes (F,4,8,A,M), relative intensities (to different scales), and Miller indices hkl, for the phases α-Fe (*code: F*; a=2.866 45 Å) (Ref. 40), γ'-Fe_4N (*code: 4*; a=3.795 Å) (Ref. 41), α''-$Fe_{16}N_2$ (*code: 8*; a=5.72 Å, c=6.29 Å) (Ref. 2), γ-*N*-austenite (*code: A*; $a=3.646$ for $X_N=0.0868$ using $a=3.5718+0.472\ 48X_N+4.3627X_N^2$ recalculated from Ref. 3; stability range X_N=0.0–0.0868 or 0.106) (Refs. 3,42,43), and α'-*N*-martensite (*code: M*; a=2.850, c=3.090 for X_N=0.0868 using $a=2.8659-0.002\ 69X_N-2.0943X_N^2$ and $c=2.8665+2.965\ 15X_N-4.524\ 34X_N^2$ recalculated from Ref. 3; stability X_N=0.0–0.0868 or 0.1064) (Refs. 3,42,43).

d/Å	X_N	Phase (Rel. int.)	hkl	d/Å	X_N	Phase (Rel. int.)	hkl
3.145[a]	0.111	8(−)	002	1.241)[b]	0.111	8(28)	224)
2.483	0.111	8(*w*)	112	1.239)[b]	0.111	8(28)	332)
2.191	0.20	4(100)	111	1.229	0.111	8(−)	105
2.105	0.0868	*A*(≈90)	111	1.226	0.0868	*M*(31)	112
2.116	0.111	8(−)	202	1.191	0.0868	*M*(100)	211
2.027	0.0	*F*(100)	110	1.187)	0.111	8(86)	314)
2.022	0.111	8(61)	220	1.185)	0.111	8(86)	422)
1.968	0.111	8(*w*)	103	1.170	0.0	*F*(30)	211
1.898	0.20	4(77)	200	1.144	0.20	4(83)	311
1.823	0.0868	*A*(≈51)	200	1.099	0.0868	*A*(≈100)	311
1.626[b]	0.111	8(8)	213	1.096	0.20	4(38)	222
1.573)[b]	0.111	8(11)	004)	1.058)[b]	0.111	8(43)	404)
1.568)[b]		8(11)	312)	1.057)[b]	0.111	8(43)	512)
1.545	0.0868	*M*(22)	002	1.053	0.0868	*A*(≈44)	222
1.466	0.111	8(−)	114	1.048[a]	0.111	8(−)	006
1.433	0.0	*F*(20)	200	1.015)	0.111	8(61)	116)
1.430	0.111	8(25)	400	1.011)	0.111	8(61)	440)
1.425	0.0868	*M*(68)	200	1.013	0.0	*F*(10)	220
1.342	0.20	4(67)	220	0.986)[b]	0.111	8(46)	325)
1.289	0.0868	*A*(≈48)	220	0.984)[b]	0.111	8(46)	206)
1.265	0.111	8(6)	323	0.949	0.20	4(44)	200
				0.906	0.0	*F*(12)	310

[a]Seen only in thin films (Refs. 10, 12, 14, 33, 35, and 38).
[b]α''-$Fe_{16}N_2$ reflections that are fairly intense and do not overlap badly with other reflections.

(Table IV), and moments close to experiment for Fe_3N and for γ'-Fe_4N.[7,44] An augmented spherical wave calculation has been done.[45] The maximum magnetic moment is assigned to site Fe1. The average calculated values are considerably below the large experimental thin-film values.

There are qualitative similarities between the Fe-N and Fe-C phase diagram. In the Fe-N diagram, the ordered N-Fe compounds (line phases, with narrow ranges of X_N) are γ'-Fe_4N and ζ-Fe_2N; α''-$Fe_{16}N_2$ is a metastable line phase; the phases γ and ϵ are stable for wide ranges of X_N; α'-*N*-martensite is metastable over a moderate range of X_N.

The name α''-$Fe_{16}N_2$ denotes the occupancy of the unit cell and its evolution from α-Fe and α'-*N*-martensite. An alternate name Fe_8N has been used.[13,15,45,48]

The Mössbauer data for α''-$Fe_{16}N_2$ are collected in Table V, together with comparable data for other phases of interest (α-Fe, α'-*N*-martensite, γ'-Fe_4N).

The Mössbauer spectrum of α''-$Fe_{16}N_2$ differs from that of α'-*N*-martensite. The three sextets seen for α''-$Fe_{16}N_2$ can be assigned with certainty to the three sites Fe1, Fe2, Fe3 of Table II only if the expected 4:4:8 relative intensities are obtained[49] (which identifies the 8*h* site Fe3) and if the signs of all the electric field gradients are known. The Mössbauer hyperfine fields H_{hf}=296, 316, and 399 kOe[49] were first assigned to Fe2 (site 4*e*, 1*nn*), Fe1 (site 4*d*, 3*nn*), and Fe3 (site 8*h*, 2*nn*), respectively.[50] This assignment is customary for iron alloys and for α'-*N*-martensite: H_{hf} (relative to α-Fe) decreases for the first nearest neighbors, increases dramatically for the second, then converges from above to the pure α-Fe value for third, fourth, etc., nearest neighbors.[50]

For α''-$Fe_{16}N_2$ this assignment is not supported by the relative Mössbauer line intensities[2,15,16,38,49] or by the band structure results, which assign the highest moment to site Fe1.[7,44,45] The new assignments in Table V give the largest

TABLE IV. Calculated magnetic moments (in Bohr magnetons μ_B) at sites in the α''-$Fe_{16}N_2$ lattice (Refs. 7, 44, 45), and distances from the N atom.

Site (symmetry)	Fe-N distance/Å	Fe-N	Calculated μ_{Fe}/μ_B (Ref)		
Fe1 (4*d*−4̄m2)	3.26	3*nn*	2.83(44)	2.81(7)	2.74 or 2.89[a](45)
Fe2 (4*e*−4*mm*)	1.95 or 1.93[a]	1*nn*	2.25(44)	2.21(7)	2.30 or 2.29[a](45)
Fe3 (8*h*−*mm*)	2.01 or 1.79[a]	2*nn*	2.27(44)	2.39(7)	2.37 or 2.21[a](45)
Average			2.41	2.45(7)	2.45 or 2.40[a](45)

[a]Uses z=0.3060 for position 4*e*, x=0.222 for position 8*h* (Ref. 45).

TABLE V. Mössbauer spectral parameters (hyperfine magnetic fields H_{hf}, quadrupole splittings ΔE_Q, and isomer shifts IS against pure α-Fe at room temperature) for α''-$Fe_{16}N_2$, and relative population (Fe atom %). Data for other phases (α-Fe, α'-*N*-martensite, γ'-Fe_4N) are given for comparison

H_{hf} kOe	ΔE_Q mm/s	IS mm/s	Fe%	H_{hf} kOe	ΔE_Q mm/s	IS mm/s	Fe%	H_{hf} kOe	ΔE_Q mm/s	IS mm/s	Fe%	$\langle H_{hf} \rangle$ kOe	Ref.
α''-$Fe_{16}N_2$(three sextets)													
Fe1 (4*d*)*mm*2 (3*nn*)[a]					Fe2 (4*e*) 4*mm* (1*nn*)[a]				Fe3 (8*h*) *mm* (2*nn*)			Ave.	
418(1)	+0 27(2)	−0.08(2)		302(2)	+0.14(5)	−0.15(5)		325(5)	0.3(1)	0.1(1)		342	50
372.8				297.9				315.9				325.6	31
400.2	0.15	−0.06	13.9(3)	289.8	0.04	−0.10	19.4(4)	321.7	0.16	0.06	47.2(9)	333.3	38
399	0.12	−0.07	17.9	296	−0.07	−0.09	18.7	316	0.25	0.06	34.9	332	33,49
397	−0.04	0.07	9.7	292	−0.17	0.01	9.7	317	0 15	0.10	15.8	331	15
397(2)	−0.12(3)	0.03(4)	8.5(5)	289(2)	−0.17(2)	−0.11(3)	7.3(3)	318(2)	0.14(3)	0.29(4)	21.8(1.5)	331	16
406	0.25	−0.18		307	0.05	−0.49		316	0.21	0.21		336	7
391	0.26	−0.05	12.5	289	0.16	−0.05	20.6	316	0.32	0.04	37.7	328	34
α''-$Fe_{16}N_2$ (single sextet) (Refs. 29,30,47)				α-Fe (single sextet)[c] (Refs. 14,50)				γ-austenite (paramagnetic) (Ref. 15)					
(460)[b,c]				341	0.0	0.0			0	−0.04			
330[d]				330	−0.09	0.0			0.37	0.07			
326				335	0.17	−0.07							
α'-*N*-martensite (three sextets)													
1*nn*				2*nn*				3*nn* and 4*nn*					
314(2)	−0.01(5)	−0.12(5)		356(2)	+0.01(5)	0.01(5)		348(2)	+0.08(5)	0.02(5)			50
γ'-Fe_4N (three sextets)													
Fe1 or 1*a*				Fe2 or Fe2*A* or 3*c*-*A*				Fe2*B* or 3*c*-*B*					
345(10)	0.30(8)			215(10)	0.45(6)								52
340.6	0.0	0.24		215.5	−0.22	0.52		219.2	0.43	−0.15			53
366				235				235					51

[a]These two assignments are uncertain, and could be interchanged.

[b] This datum is considered incorrect (Ref. 54).

H_{hf} to Fe1, the smallest to Fe2, and the value closest to α-Fe to Fe3.

From the Mössbauer hyperfine fields, the magnetic moments have been estimated at the sites Fe1, Fe2, and Fe3 as either 3.8, 1.3, and 2.5 μ_B,[33,49] or as 2.98, 2.01, and 2.25 μ_B,[51] respectively. The average H_{hf} of the three sites of α''-$Fe_{16}N_2$ (weighted 4:4:8 for Fe1:Fe2:Fe3), shown as $\langle H_{hf} \rangle$ in Table V, is essentially identical to H_{hf} of α-Fe.[14] For the epitaxial thin films of α''-$Fe_{16}N_2$ on GaAs, one single Mössbauer line is reported:[29,30,47] is this due to low resolution, or to a different species?[2,14]

An important technological goal is to produce macroscopic samples of 100% phase-pure α''-$Fe_{16}N_2$. Table VI shows the estimated Fe at. % contributions from various samples. High mol fractions of α''-$Fe_{16}N_2$ were achieved by epitaxy on GaAs[9] or by topotactical N_2^+ implantation.[49] Nitriding thin foils in NH_3:H_2 yields 40%.[7] Large particle powders (6–9 μm) yield 50%.[17] For small particles, at most 38% conversion was reached.[15,16] For small particles, 7–15 at. % Mn was needed,[16] while for larger particles Mn was unnecessary.[7,17] One cannot achieve X_N=0.1111 in γ-*N*-austenite, so by quenching and annealing, one cannot get 100% α''-$Fe_{16}N_2$.[51] Ways to obtain phase-pure α''-$Fe_{16}N_2$ have been proposed.[55]

The magnetic data for various samples, and the inferred values for the α''-$Fe_{16}N_2$ fraction, are summarized in Table VII. The first few benchmark entries are for bulk and powder α-Fe, and γ'-Fe_4N, and for recently measured powder samples (6–9 μm) of α'-*N*-martensites with different N contents.[17,18] The dependence of the high moment on the N atom concentration is very roughly linear.[29] As the 002 x-ray reflection of α''-$Fe_{16}N_2$ grows in intensity, the saturation volume magnetization M_s increases to a maximum of 2307 emu cm^{-3}.[47]

The inferred values of the specific saturation magnetization σ_s for α''-$Fe_{16}N_2$ depend on the reliability of the estimates of the mol fractions of all the magnetic constituents. In small powder samples exposed to air, the moment due to pure bulk α-Fe (218 emu g^{-1}) is reduced by passivation of the surface to maybe 140 emu g^{-1}. This passivation is less important for very large particles and epitaxial films, so the bulk value can be used.

For some laboratories, tempering the nitrided sample at 150–200 °C increases the sample magnetization, e.g., from 177 to 189 emu g^{-1},[16] or from 182 to 189 emu g^{-1};[17] other laboratories report no increase,[34,35,38] or only a modest increase, e.g., from 218 to 226 emu g^{-1}.[34]

The coercivities H_c for α''-$Fe_{16}N_2$ are small; shape anisotropy was sought by growing acicular particles.[15]

If α''-$Fe_{16}N_2$ is heated at 160 °C for 21 days, it decomposes to α-Fe and γ'-Fe_4N;[2] a similar decomposition occurs if one heats it to 200 °C for one week.[60] For α''-$Fe_{16}N_2$ particles (35 at. % Fe; 15 at. % Mn) kept at room temperature for six months the Mössbauer spectrum did not change.[60]

The high magnetization observed for epitaxial films of α''-$Fe_{16}N_2$ on GaAs or InGaAs(001) decreases reversibly with increasing temperature between −269 °C (B_s=3.1 T, μ=3.4 μ_B) and +400 °C (B_s=1.0 T), with a Curie temperature of 540 °C; above 400 °C this magnetization decreases irreversibly.[29] By annealing a rf sputtered film at 500 °C for 1 h, the moment density increases from about 225 to 253 emu g^{-1}, and the x-ray lines due to α''-$Fe_{16}N_2$ sharpen, while

TABLE VI. Composition (Fe at. %, estimated by X=x-ray diffraction, M=Mössbauer spectroscopy) of nitrided Fe or Fe+Mn films, powders and foils (laboratory codes as in Table I).

Lab. form	Est.	α-Fe	γ-*N*-aust	γ'-Fe_4N	α'-N-mart.	α''-$Fe_{16}N_2$	Ref
CMU 6–9 μm powder	*X*	13	31	0	0	56	17,19
HIT 7–100 nm‖GaAs(100)	*X*	15	0	0	0	85	9
NAG 200 nm film‖glass	*M*,*X*	65	0	0	0	35	31
NAG 200 nm film‖MgO	*X*	40	0	0	36	24	11
NAG 200 nm film‖MgO	*X*	30	0	0	62	8	32
NAG 200 nm film‖MgO	*X*,*M*	28.5	0	0	0	71.5	49
TCD 30 μm powder	*M*	61	7	4	0	28	7
TCD 100 μm foil	*M*	52; 59	5; 11	11; 10	0	32; 20	7
TCD 25 μm foil	*M*	55; 51	11; 9	0; 0	0	34; 40	7
TOU sputt. film	*X*	27	0	0	0	73 ($\alpha'+\alpha''$)	34
UAL sputt. film	*X*	82	0	0	0	18	12
UAL 0.6 μm powd.+15 wt % Mn	*M*	29	36	0	0	35	15
UAL 70 nm powd.+7 wt % Mn	*M*	55	7	0	0	38	16

TABLE VII. Magnetic properties of reference compounds, of samples containing α''-$Fe_{16}N_2$, and for pure α''-$Fe_{16}N_2$: saturation volume magnetization M_S (emu/cc=emu cm^{-3}), saturation magnetic flux density B_S (T), specific saturation magnetization σ_S (emu/g=J/T kg), magnetic moment of the average Fe site μ_{Fe} (μ_B=Bohr magneton), coercivity H_c (Oe).

Overall sample properties					Inferred α''-$Fe_{16}N_2$ contribution					
M_S emu/cc	B_S T	σ_S emu/g	μ_{Fe} μ_B	H_c Oe	M_S emu/cc	B_S T	σ_S emu/g	μ_{Fe} μ_B	H_c Oe	Morphology (Ref.)
Reference data:										
1717	2.16	218.0	2.18	···	···	···	···	···		Pure bulk α-Fe (56)
···	···	≈140	···	···	···	···	···	···	···	Powder α-Fe
1392	1.75	193	2.05	···	···	···	···	···	···	Pure bulk γ'-Fe_4N (57)
···	···	180	···	600	···	···	···	···	···	Powder γ'-Fe_4N (58)
···	···	160	···	1000	···	···	···	···	···	Powder γ'-Fe_4N (13)
···	2.35	250±10	···	···	···	···	···	···	···	α'-*N*-martensite (inf.) (17,18)
···	···	257	···	···	···	···	···	···	···	Sputt. α'-*N*-mart. film (32,33,38)
Film obtained by molecular beam epitaxy:										
2050	2.58	···	···	···	2250	2.83	298	3.0	···	55 nm epitax. film (5)
···	2.66	···	···	···	···	3.0	315	3.2	···	7 nm epitax. film (9)
···	···	233	···	···	···	···	···	···	···	200 nm epitax. film (31)
···	2.9	···	3.2	···	···	2.9	···	3.2	50	50 nm epitax. film (30)
···	···	···	···	···	2390	···	···	···	···	Epitax. film ‖$In_{0.2}Ga_{0.8}As$ (26)
···	···	···	···	···	2300	···	···	···	···	Epitax. film ‖$In_{0.2}Ga_{0.8}As$ (46)
2307	2.9	···	···	···	···	···	···	···	···	Epitax. film ‖$In_{0.2}Ga_{0.8}As$ (47)
Foils										
···	···	205	···	···	···	2.52	271[a]	2.34	···	100 μm foil+NH_3H_2 (7)
···	···	208	···	···	···	···	238[a]	2.62	···	25 μm foil+NH_3:H_2 (7)
Sputtered or plasma evaporated films:										
···	···	247	··	···	···	···	315	···	···	250 nm film‖glass (12)
···	···	233	···	···	···	···	···	···	···	200 nm sputt film+N_2^+‖glass (31)
···	···	245	···	···	···	···	257	···	···	200 nm sputt., N_2^+‖MgO (32,33,38)
2000	···	···	···	···	<1	···	···	···	···	Sputter. films (2 at. % N) (59)
···	···	235	···	···	···	···	···	···	···	Plasma evap. ‖Fe‖MgO (14)
···	···	218	···	···	···	···	···	···	···	Sputt. ‖Fe‖MgO (14)
···	···	232	···	···	···	···	237[a]	···	···	Sputt. ‖Fe‖MgO (34)
···	···	220	···	300	···	···	225[a]	···	···	Sputt. ‖Fe‖MgO (35)
Powders large or small:										
···	···	210	···	···	···	···	241[a]	2.40	···	30 μm powd. (7)
···	···	189	···	···	···	···	285[a]	···	···	6–9 μm powd. (17)
···	···	210	···	···	···	2.66	286[a]	2.94	···	6–9 μm powd. (18,19)
···	···	170	···	200	···	···	310[a]	···	200	300×60×60 nm powd.+0.15 Mn (15)
··	···	189	···	210	···	···	300[b]	···	···	70×70×70 nm powd.+0.07 Mn (16)

[a]Using 218 or 220 emu g^{-1} for α-Fe.
[b]Using 140 emu g^{-1} for small particles of α-Fe.

for another sample the same treatment decreases the moment from 247 to 212 emu g^{-1}, and the α''-$Fe_{16}N_2$ lines disappear.[12] For films made by sputtering or by evaporation the moment drops when the temperature reaches 200–250 °C.[14]

Since α''-$Fe_{16}N_2$ powders are not stable above about 200 °C,[2,60] it has been speculated that epitaxial films with large magnetic moments contain a different phase.[14]

IV. CONCLUSIONS

α''-$Fe_{16}N_2$ is a fascinating magnetic system. The evidence for a very large moment (>280 emu g^{-1}) for α''-$Fe_{16}N_2$ comes from epitaxial thin films,[5,9,26,30,31,46,47] from some sputtered films,[12] and from medium[17,18] and small particle[15,16] studies. Already, α'-*N*-martensite has a moment considerably higher than that of α-Fe.[18,32,33] The high magnetization of the epitaxial films has even been ascribed to some unknown phase.[14]

The "dissenting" evidence against large moments comes from foils,[7] large particles,[7] N_2^+ ion-implanted films,[31,32,33,38] some sputtered films,[14] and from theoretical studies.[7,44,45,51] It is tempting to dismiss the theoretical results, since theory often fails us. All these arguments, pro and con, rest on x-ray or Mössbauer estimates of the magnetic constituents present in the samples, and on how well the samples resist to air oxidation.

To answer Coey's challenge,[20] many are convinced that we are facing a "real value," not an "egregious error."

ACKNOWLEDGMENTS

The authors are very grateful to Dr. Yutaka Sugita and Migaku Takahashi, and to Professors J. M. D. Coey, William D. Doyle, Kenneth H. Jack, and W. Edward Wallace for illuminating discussions. The work has been supported by the Advanced Research Projects Agency, funneled through the Advanced Tape Project of the National Storage Industry Consortium.

[1] K. H. Jack, Acta Cryst. **3**, 392 (1950).
[2] K. H Jack, Proc. R. Soc. London Ser. A **208**, 216 (1951).
[3] K. H. Jack, Proc. R. Soc. London Ser. A **208**, 200 (1951).
[4] A. Van Gent, F C. Van Doorn, and E. J Mittemejer, Metall. Trans. **16A**, 1371 (1985).
[5] T. K. Kim and M. Takahashi, Appl. Phys. Lett. **20**, 492 (1972).
[6] M. Takahashi, IEEE Trans J. Magn. Jpn. **6**, 1024 (1991).
[7] J. M. D. Coey, K. O'Donnell, Q. Qi, E. Touchais, and K. H. Jack, J Phys. CM **6**, L23 (1994).
[8] M. Komuro, Y. Konozono, M. Hanazono, and Y. Sugita, J. Magn Soc. Jpn. **13**, 301 (1989).
[9] M. Komuro, Y. Kozono, M. Hanazonc, and Y. Sugita, J Appl. Phys. **67**, 5126 (1990).
[10] Y. Sugita, K Mitsuoka, M Komuro, H. Takahashi, and A Sakuma, Proceedings of the Second International Symposium on the Physics of Magnetic Materials, ISPMM'92, Beijing, China, 2–7 July 1992, edited by S. Zhang (unpublished), p. 190.
[11] K. Nakajima and S. Okamoto, Appl. Phys. Lett. **54**, 2536 (1989).
[12] C. Gao, W D Doyle, and M. Shamsuzzoha, J. Appl. Phys. **73**, 6579 (1993).
[13] X. Bao, R. M. Metzger, and W. D. Doyle, J. Appl Phys. **73**, 6734 (1993).
[14] Migaku Takahashi, H. Shoji, H. Takahashi, T. Wakiyama, M. Kinoshita, and W. Ohta, IEEE Trans. Magn. **MAG-29**, 3040 (1993).
[15] X Bao, R. M Metzger, and M. Carbucicchio, J. Appl. Phys. (in press).
[16] X. Bao, M. Shamsuzzoha, R. M. Metzger, and M. Carbucicchio, IEEE Trans. Magn. (in press).
[17] M. Q. Huang, W. E. Wallace, S. Simizu, A. T. Pedziwiatr, R. T. Obermyer, and S. G. Sankar, J. Appl. Phys. (in press).
[18] M. Q. Huang, W. E. Wallace, S. Simizu, and S. G. Sankar, J. Mag. Magn. Mater. (in press).
[19] W. E. Wallace and M. Q. Huang (these proceedings)
[20] J. M. D. Coey, Phys. World **6**, 25 (1993).
[21] K. Abiko and Y. Imai, Trans. Jpn. Inst. Metals **18**, 113 (1977).
[22] A. Sato, Y. Watanabe, and T. Mura, J. Phys. Chem. Solids **49**, 529 (1988).
[23] Y. Watanabe, A. Sato, and T. Mura, J. Phys. Chem. Solids **50**, 957 (1989).
[24] Y. Watanabe, A. Nakano, and A Sato, Mater. Sci. Eng. A **146**, 1251 (1991).
[25] Y. Watanabe, H. Nozaki, M. Kato, and A. Sato, Acta Metall. Mater. **39**, 3161 (1991).
[26] M. Komuro, H. Hoshiya, K. Mitsuoka, Y. Kozono, M. Hanazono, and Y. Sugita, Mater. Res Soc. Symp. Proc. **232**, 147 (1991).
[27] U. Dahmen, P. Ferguson, and K. H. Westmacott, Acta Metall. **35**, 1037 (1987).
[28] Y. Kozono, M. Komuro, M. Hanazono, and Y. Sugita, J. Magn. Soc. Jpn. **15**, 59 (1991).
[29] Y. Sugita, K. Mitsuoka, M. Komuro, H. Hoshiya, Y. Kozono, and H. Hanazono, *Proceedings of the International Symposium on Third Transition Semi-Metal Thin Films*, Sendai, Japan, 5–8 March 1991 (Japan Soc. Prom. Sci. Committee 131-Thin Films), p. 12
[30] Y. Sugita, K. Mitsuoka, M. Komuro, H. Hoshiya, Y. Kozono, and M. Hanazono, J. Appl. Phys. **70**, 5977 (1991).
[31] K. Nakajima, S. Okamoto, and T. Okada, J. Appl. Phys. **65**, 4357 (1989).
[32] K. Nakajima and S. Okamoto, Appl. Phys. Lett. **56**, 92 (1990).
[33] K. Nakajima and S. Okamoto, in Ref. 29, p. 21.
[34] Migaku Takahashi, H. Shoji, H. Takahashi, H. Nashi, T. Wakiyama, M. Doi, and M. Matsui (these proceedings).
[35] Migaku Takahashi, H. Shoji, H. Takahashi, and T. Wakiyama, Mater. Res. Soc. Symp. Proc. (in press).
[36] D. H. Jack and K. H. Jack, Mater. Sci. Eng. **11**, 1 (1973).
[37] K. H. Jack, in *High-Nitrogen Steels*, edited by J. Fogt and A. Hendry (The Institute of Metals, Metals Park, OH, 1989), p. 117.
[38] K. Nakajima and S. Okamoto, IEEE Trans. J. Magn. Jpn. **6**, 45 (1991) [J Magn. Soc. Jpn. **14**, 271 (1990)].
[39] B. D. Cullity, *Elements of X-ray Diffraction* (Addison–Wesley, Reading, MA, 1978), p. 411.
[40] ASTM p. 6-0696, Swanson, NBS Circular 539, Vol 4, part 3, 1955.
[41] K. H. Jack, Proc. R. Soc. London Ser. A **195**, 34 (1948).
[42] H. A. Wriedt, N. A. Gokcen, and R. H. Nafziger, Bull. Alloy Phase Diagr. **8**, 355 (1987).
[43] Y. Imai, M. Izumiyama, and M. Tsuchiya, Sci. Rept. Res. Inst. Tohoku Univ. A **17**, 173 (1965).
[44] A. Sakuma, J. Magn. Magn. Mater. **102**, 127 (1991).
[45] S. Matar, Z. Phys. B **87**, 91 (1992)
[46] H. Takahashi, K. Mitsuoka, M. Komuro, and Y. Sugita, J. Appl. Phys. **73**, 6060 (1993).
[47] H. Takahashi, M. Komuro, K. Mitsuoka, and Y. Sugita, Digest of the 17th Annual Conference on Magnetics in Japan, 1993 (unpublished), Abstract 11aB-11, p. 152.
[48] W. Pies and A. Weis, in *Landolt-Bornstein Numerical Data and Functional Relationships in Science and Technology, New Series*, edited by K.-H. Hellwege (Springer, Berlin, 1978), Vol. 7, Part c1, p. 78.
[49] K. Nakajima, T Yamashita, M. Takata, and S. Okamoto (unpublished).
[50] T. Moriya, Y. Sumitomo, H. Ino, F. E. Fujita, and Y. Maeda, J. Phys. Soc. Jpn. **35**, 1378 (1973).
[51] J. M. D. Coey (these proceedings).
[52] G. Shirane, W. J. Takei, and S. L. Ruby, Phys. Rev. **126**, 49 (1962).
[53] A. J. Nozik, J. C. Wood, Jr., and G. Haacke, Solid State Commun. **7**, 1677 (1969).
[54] Y. Sugita (private communication).
[55] K. H. Jack (these proceedings).
[56] R. M. Bozorth, *Ferromagnetism* (Van Nostrand, Princeton, NJ, 1951).
[57] K. Tagawa, E. Kita, and A. Tasaki, Jpn. J. Appl Phys. **21**, 1596 (1982).
[58] S. F. Matar, G. Demazeau, and B. Siberchicot, IEEE Trans. Magn. **MAG-26**, 60 (1990).
[59] M. A. Russak, C. V. Jahnes, E. Klohkolm, J.-W. Lee, M. E. Re, and B. C. Webb, J. Appl. Phys. **70**, 6427 (1991).
[60] X. Bao, R. M. Metzger, and M Carbucicchio (unpublished results).

The magnetization of bulk $\alpha''Fe_{16}N_2$ (invited)

J. M. D. Coey
Physics Department, Trinity College, Dublin 2, Ireland

Evidence for giant magnetic moments in the metastable nitride $\alpha''Fe_{16}N_2$ is reviewed, with reference to the related stable nitride $\gamma'Fe_4N$ and αFe. It is concluded from a survey of electronic structure calculations, Mössbauer spectra, and magnetization measurements on bulk multiphase samples that the average iron moment in $\alpha''Fe_{16}N_2$ at $T\sim0$ lies in the range 2.3–2.6 μ_B. A significantly larger moment of about 2.9 μ_B appears on the $4d$ sites which have no nitrogen neighbors.

I. INTRODUCTION

Alpha-iron is a weak ferromagnet with an incompletely filled $3d^{\uparrow}$ subband. The electronic configuration is approximately $3d^{\uparrow 4.4}3d^{\downarrow 2}4s^{0.6}4p^{0.8}$, giving a magnetic moment per atom $\mu_{Fe}=2.2\ \mu_B$. It is actually the saturation polarization J_s, related to the magnetic moment per unit volume M_s by $J_s=\mu_0 M_s$, which is important for technical applications; J_s for iron at room temperature is 2.15 T. There is scope for increasing the moment by modifying the density of states and moving the position of the Fermi level in the d band, but if they are to improve the magnetization, these changes must be accomplished with as little increase as possible in lattice volume.

The greatest polarization that has been achieved in iron-based substitutional alloys is $J_s=2.45$ T, in $Fe_{65}Co_{35}$. Iron ions with atomic moments as high as 5 μ_B for the $3d^{\uparrow 5}$ configuration of Fe^{3+} are obtained by charge transfer in ionic compounds, yet J_s in ferrites does not exceed 0.6 T because the order is ferrimagnetic and most of the volume is occupied by nonmagnetic O^{2-}.

The quest for greater iron magnetization is currently focused on interstitial compounds, particularly those where nitrogen is accomodated in octahedral voids in the iron lattice. Nitrogen in cubic $\gamma'Fe_4N$ occupies the $1b$ body-center site in an fcc lattice, so the $1a$ cube corner and $3c$ face-center iron sites become inequivalent. The ordered, metastable iron nitride $\alpha''Fe_{16}N_2$ discovered by Jack in 1951[1] has a related structure where only half of these octahedral interstices are occupied by nitrogen (Fig. 1). The tetragonal cell contains eight bcc units, and the structure can be regarded as lying midway between αFe and $\gamma'Fe_4N$.[1] The $4d$ site in $\alpha''Fe_{16}N_2$ is analogous to the $1a$ site in $\gamma'Fe_4N$ and the $4e$ and $8h$ sites in $\alpha''Fe_{16}N_2$ are analogous to the $3c$ sites in $\gamma'Fe_4N$, except that they have only one nitrogen neighbor instead of two.

The magnetic properties of $\alpha''Fe_{16}N_2$ remained unexplored until 1972 when Kim and Takahashi produced thin films where αFe was the major phase by evaporating iron in nitrogen. Some of these films were found to have a polarization as high as 2.64 T, and the polarization of pure $\alpha''Fe_{16}N_2$ was inferred to be 2.76 T, corresponding to an average iron moment of 3.0 μ_B.[2] In recent years, other Japanese groups have made films containing $\alpha''Fe_{16}N_2$ by different methods, with quite variable results.[3–10] Most remarkable are those of Sugita and co-workers at Hitachi, who produced films by molecular-beam epitaxy on $(Ga_{0.8}In_{0.2})As$ substrates where the polarization of $Fe_{16}N_2$ was found to be 2.9 T.[5] They have corroborated their result by a ferromagnetic-resonance experiment.[9] The corresponding average moment per iron atom μ_{av} is 3.2 μ_B at room temperature, rising to 3.5 μ_B at $T\sim0$. Other workers, however, report values of magnetization of their thin films which are much closer to that of αFe.[8]

Here we review the evidence of electronic structure calculations, Mössbauer spectra and bulk magnetization measurements regarding the site and average moments in αFe, $\alpha''Fe_{16}N_2$, and $\gamma'Fe_4N$. Experimental investigations of $\alpha''Fe_{16}N_2$ have been hindered by the lack of bulk, single-phase samples of the metastable α'' phase.

II. ELECTRONIC STRUCTURE CALCULATIONS

Self-consistent spin-polarized electronic structure calculations have now developed to the point where it is routinely possible to deduce the ground-state spin moments in iron-group ferromagnetic alloys to within about 0.1 μ_B. The moment of iron itself is accurately reproduced.[11] Linearized muffin-tin orbital (LMTO) calculations for $\alpha''Fe_{16}N_2$ and other iron nitrides were carried out by Sakuma[12–14] and many others,[15–21] varying the unit cell volume, c/a ratio, and special position parameters. These LMTO calculations are based on the atomic spheres approximation, which is well

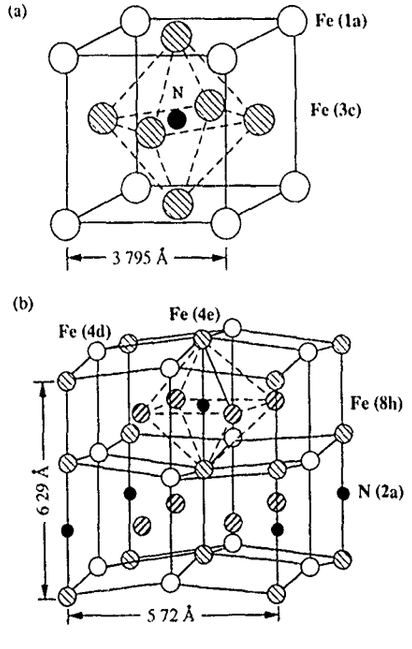

FIG 1. Crystal structures of (a) $\gamma'Fe_4N$ and (b) $\alpha''Fe_{16}N_2$.

 0021-8979/94/76(10)/6632/5/$6.00 © 1994 American Institute of Physics

TABLE I. Calculated data and experimental results on local and averaged magnetic moments and hyperfine fields in $\gamma'Fe_4N$.

Methods	μ (μ_B/Fe)			B_{hf}(T)			Ref.
	Fe(1a)	Fe(3c)	$\langle\mu\rangle$	Fe(1a)	Fe(3c)	$\langle B_{hf}\rangle$	
LMTO-ASA	3.07	2.03	2.29	...	...	...	12,14
LMTO-ASA	3 09	2.11	2.36	−32.8	−24.5	−26 6	17
LMTO-ASA	3.10	1.94	2.23	−32.8	−24.2	−26.4	15
LMTO-ASA	3.22	2.01	2.32	−36.0	−24.7	−27.6	19,20
ASW	2.98	1.79	2.09	...	...	...	23
FLAPW	2.98	2.23	2.41	−36.3	−21.7	−25.4	22
Average(calculation)	3 07	2.02	2.28	−34.5	−23.8	−26.5	...
Measurements	2.98	2.01	2.25	...	...	...	27
	...	...	...	−36.6	−23.6	−26.9	21

justified by the charge-density distributions obtained by Coehoorn *et al.* using a first-principles full potential (FLAPW) approach.[22] Matar has used the augmented spherical wave (ASW) method[23,24] and there have also been some cluster calculations.[25,26] Results of these calculations for $\gamma'Fe_4N$ and $\alpha''Fe_{16}N_2$ are summarized in Tables I and II, respectively.

It can be seen in Table I that the calculations for $\gamma'Fe_4N$ give average and site moments which agree quite well with those measured experimentally by magnetization and neutron diffraction (2.98 μ_B/Fe on 1a, 2.01 μ_B/Fe on 3c, μ_{av}=2.25 μ_B/Fe).[27] In the case of $\alpha''Fe_{16}N_2$, the atomic positions depend on two special position parameters,[1] which have not been determined precisely. However, these parameters and the c/a ratio can be varied over a reasonable range in the computer. When this is done, there are small variations in the site moments, but in no case does the average moment per iron atom exceed 2.50 μ_B. An exception is the cluster calculation of Li,[25] which gives an average moment of 3.3 μ_B/Fe, but this method greatly overestimates the moment of α-Fe, and it cannot be regarded as quantitatively reliable. Larger moments are also reported in an "LDA+U" calculation which involves an on-site Hubbard interaction U,[44] but the approach does not appear to have been tested on α Fe or γ' Fe_4N.

In $\alpha''Fe_{16}N_2$, $\gamma'Fe_4N$ and other interstitial iron nitrides[20,28] there is a tendency for all iron moments to increase as the lattice is expanded by interstitial nitrogen. This is counteracted to some extent by sp-d hybridization at those iron sites which have nitrogen neighbors. However, iron atoms which are next-nearest neighbors of nitrogen see their moments increased. The local density of states for 4d sites in $\alpha''Fe_{16}N_2$ and 1a sites in $\gamma'Fe_4N$ indicates strong ferromagnetism at these sites. The increase of the next-nearest-neighbor iron moments in nitrides was explained by Kanamori,[29] by analogy with the increase of iron moment in $Fe_{65}Co_{35}$.[29] The iron neighbors of nitrogen hybridize with the nitrogen sp orbitals, which decreases the spin splitting and lowers the effective iron potential, especially for the 3$d\downarrow$ states. These iron atoms then have some of the character of cobalt in the Fe-Co alloys. Interaction with iron atoms which are next-nearest neighbors of nitrogen increases the amplitude of wave functions at the latter in the antibonding states of the 3$d\downarrow$ band whereas it will decrease the amplitude of the

TABLE II. Calculated data and experimental results on local and averaged magnetic moment and hyperfine fields in $\alpha''Fe_{16}N_2$.

Methods	μ (μ_B/Fe)				B_{hf}(T)				
	Fe(4e)	Fe(8h)	Fe(4d)	$\langle\mu\rangle$	Fe(4e)	Fe(8h)	Fe(4d)	$\langle B_{hf}\rangle$	Ref
LMTO-ASA	2.27	2.25	2.83	2 39	...	...	...	...	12
LMTO-ASA	2.30	2.27	2.82	2.42	...	...	...	...	13
LMTO-ASA	1.96	2.41	2.91	2.42	−24.1	−25.0	−33.7	−27.0	15
LMTO-ASA	2.13	2.50	2.85	2 50	...	...	...	...	16
LMTO-ASA	2.01	2.45	2.99	2.34	...	...	...	...	18
LMTO-ASA	2.30	2.37	2.86	2.48	−24.3	−25.4	−33.7	−26.9	19,20
ASW	2.30	2.37	2.74	2.44	...	...	...	...	24
	2 29	2.21	2.89	2.40	...	...	...	...	24
FLAPW	2.04	2.33	2.82	2.37	−24.3	−24.1	−33.4	−26.5	22
(DV)-X_α cluster	1.98	2.09	2.82	2 25	...	...	...	...	26
Average (calculation)	2.16	2.32	2.85	2.41	−24.2	−24.8	−33.6	−26.9	...
Measurement	(2.33)	(2 45)	(3.05)	(2 57)	...	...	...	...	...
	...	...	...	...	−30.7	−32.3	−41.2	−33.7	21

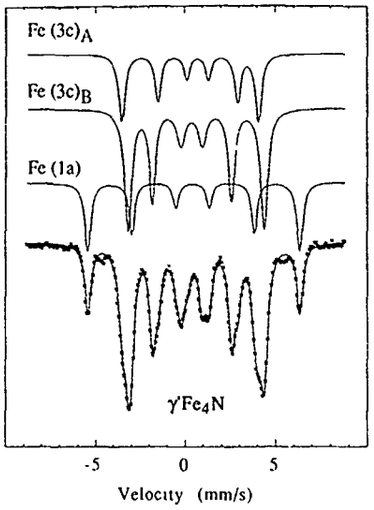

FIG. 2. The ^{57}Fe Mössbauer spectrum of $\gamma'Fe_4N$ measured at 15 K.

bonding states of the $3d\downarrow$ band. The decrease of occupied states in the $3d\downarrow$ band is compensated by a shift in spectral weight to occupied states in the $3d\uparrow$ band. Hence the moment of the next-nearest-neighbor iron is raised.

Large iron moments in $\alpha''Fe_{16}N_2$ can be achieved in LMTO calculations by expanding the lattice. Ishida *et al.*[15] show that the average iron moment reaches 3.0 μ_B when the lattice volume is increased by 50%, but the polarization of the expanded lattice is only 2.0 T.

III. MÖSSBAUER SPECTRA

Before considering the Mössbauer spectrum of $\alpha''Fe_{16}N_2$, it is useful to look at those of αFe and $\gamma'Fe_4N$, whose interpretation in unambiguous. Alpha-iron has a single site with cubic symmetry where the hyperfine field is 33.8 T at $T\sim0$. The spectrum of $\gamma'Fe_4N$ (Fig. 2) exhibits two clearly resolved subspectra with hyperfine fields of 36.6 and 23.5 T in an intensity ratio 1:3 which are identified with the $1a$ and $3c$ sites, respectively. (The $3c$ spectrum is split into two barely resolved components with a 2:1 intensity ratio because the field gradient axis may lie parallel or perpendicular to the magnetization direction.[17,30,31]) The calculated Fermi contact hyperfine fields agree well with the measurements (Table I).

The distinctive feature of the Mössbauer spectrum of $\alpha''Fe_{16}N_2$ is the hyperfine component with B_{hf}=41 T,[21,32-38] which is attributed to iron in $4d$ sites. The subspectra of iron in $4e$ and $8h$ sites, which form an octahedron around the nitrogen interstitial, have hyperfine fields of 31 and 32 T, respectively. This assignment is in accord with that of Nakajima *et al.*, based on conversion-electron spectra of ion-implanted films,[37] and with previous work on bulk samples.[19,32,38] It also agrees with the order of the hyperfine fields calculated by Coehoorn *et al.* using a full potential linearized augmented plane-wave method.[22] Moriya *et al.*[33] assigned the highest field to the $8h$ site, but their interpretation is inconsistent with the expectation that $8h$ and $4e$ sites,

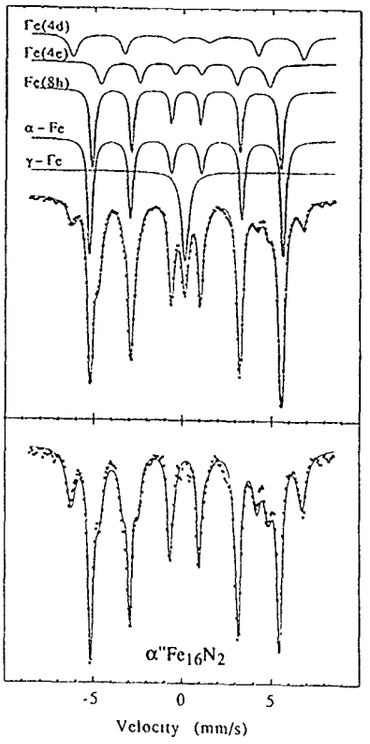

FIG. 3. The ^{57}Fe Mössbauer spectra of (a) a sample containing 40% $\alpha''Fe_{16}N_2$ measured at 15 K and (b) the spectrum of $\alpha''Fe_{16}N_2$ after stripping to remove αFe and γFe absorption.

each with one nitrogen neighbor, should have similar hyperfine fields.[38] The spectrum of $\alpha''Fe_{16}N_2$ obtained after stripping off the other constituents is shown in Fig. 3. Fitted hyperfine parameters are given in Table III.

TABLE III Mössbauer parameters of αFe, $\gamma'Fe_4N$, and $\alpha''Fe_{16}N_2$, including hyperfine field (B_{hf}), quadrupole splitting (QS), and isomer shift (IS) relative to metallic iron at room temperature. RA is the percent of the relative area.

Nitride	Temp (K)	Sites	B_{hf} (T)	IS (mm/s)	QS (mm/s)	RA (%)
αFe	293	Fe(2a)	33.0	0.00	0.00	100
	15	Fe(2a)	33.8	0.12	0.00	100
$\gamma'Fe_4N$	293	Fe (1a)	33.9	0.25	0.02	25
		Fe $(3c)_A$	21.7	0.32	−0.40	25
		Fe $(3c)_B$	21.4	0.32	0.19	50
	15	Fe (1a)	36.6	0.40	0.02	25
		Fe $(3c)_A$	23.6	0.46	−0.45	25
		Fe $(3c)_B$	23.5	0.46	0.22	50
$\alpha''Fe_{16}N_2$	293	Fe (4d)	39.5	0.07	−0.15	7.9
		Fe (4e)	30.1	−0.08	0 53	7.9
		Fe (8h)	31.2	0.09	0.22	15.8
		αFe	33.0	0.00	0.00	64.7
		γFe	0.0	−0.04	0.24	3.7
	15	Fe (4d)	41.2	0.30	−0.13	7 9
		Fe (4e)	30.7	0.01	−0.46	7.9
		Fe (8h)	32 3	0.26	0 27	15.7
		αFe	33.8	0.12	0.00	60.8
		γFe	0.0	0.09	0 25	7.7

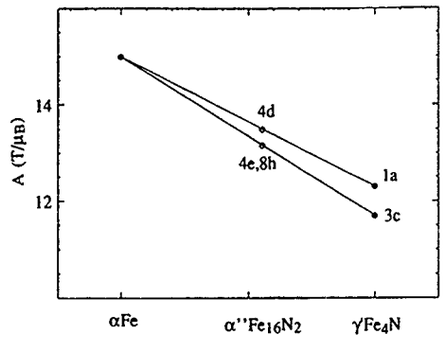

FIG. 4. The relation between iron site moment and hyperfine field for $\alpha''Fe_{16}N_2$ interpolated from data on $\gamma'Fe_4N$ and αFe.

It is not a straightforward matter to infer the site moments from the hyperfine fields. Writing $B_{hf}=A\mu_{Fe}$, the "constant" A is -15 T/μ_B for αFe, but values lying anywhere from -11 to -17 T/μ_B can be found for different iron sites in iron-rich alloys. (Mössbauer data usually give the magnitude, but not the sign of the hyperfine fields.) There are several different contributions to B_{hf} which have different dependences on μ_{Fe}.

$$B_{hf}=B_{cp}+B_{val}+B_{orb}+B_{dip}. \quad (1)$$

The leading term B_{cp} due to spin polarization of the $1s$, $2s$, and $3s$ core orbitals is strictly proportional to the $3d$ spin moment, with $A=-11.3$ T/μ_B. It is the contribution of the valence electrons B_{val} which depends on the chemical bonding that varies most with the compound or the sites considered. The orbital contribution B_{orb} is often neglected because the orbital moment is quenched in itinerant ferromagnetic iron alloys (typically it is less than 0.1 μ_B). The classical dipolar field B_{dip} at the nucleus is also small (<1 T). Evaluations of the hyperfine fields due to spin moments in electronic structure calculations reproduce the observed trends, but tend to underestimate B_{hf} by up to 5 T.[22] The calculations

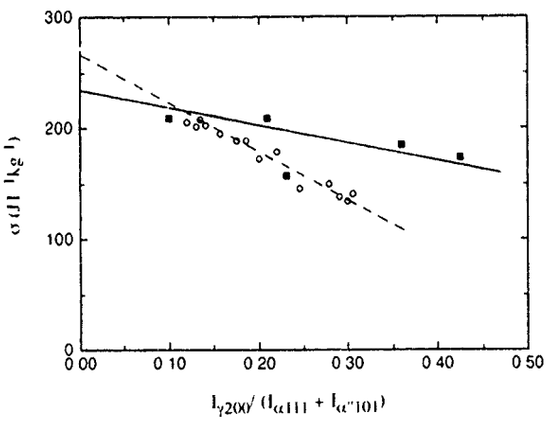

FIG. 5. Extrapolations to deduce the magnetic moment of pure $\alpha''Fe_{16}N_2$ using x-ray intensities for phase analysis. Experimental data sets are those of Huang *et al.* (see Ref. 41), circles and dashed line and Coey *et al.* (see Ref. 19), squares and solid line.

give the first two terms in Eq. (1), known as the Fermi contact interaction, which depend on the unpaired spin density at the nucleus.

Here we adopt an empirical approach to evaluate the factor A at the three sites in $\alpha''Fe_{16}N_2$. It can be deduced for $1a$ and $3c$ sites in $\gamma'Fe_4N$, from the site moments measured by neutron diffraction,[27] and the hyperfine fields in Table II. The values for $\alpha''Fe_{16}N_2$ are then deduced by interpolation between αFe and γFe_4N, as shown in Fig. 4. The site moments and the average iron moment shown in parentheses on the bottom line of Table II are obtained. Note the large moment of 3.0 μ_B/Fe on $4d$ sites, but the average value is only 2.6 μ_B/Fe.

IV. MAGNETIC MEASUREMENTS

Mitsuoka *et al.*[39] estimated the magnetic moment of bulk $\alpha''Fe_{16}N_2$ some years ago as 2.6 μ_B/Fe. There have been several recent reports of magnetic measurements on samples containing a significant proportion (<~50%) of $\alpha''Fe_{16}N_2$.[19,36,40,41] All materials were prepared by the $\gamma\rightarrow\alpha'\rightarrow\alpha''$ route originally used by Jack,[1] and described by him in more detail in a preceding paper.[42] Nitrogen has a solubility range extending up to 10 N/100 Fe in austenite (γFe) which is stable above 590 °C. Nitrogen austenite can be prepared by heating iron powders or foils in an atmosphere of flowing NH_3/H_2 at about 700 °C for several hours, then rapidly quenching to yield nitrogen martensite, thereby avoiding decomposition into the equilibrium phases, $\alpha Fe+\gamma'Fe_4N$. Prolonged annealing of the martensite at 120 °C for 7 days yields samples composed of αFe, γFe, and $\alpha''Fe_{16}N_2$ in varying proportions. Pure $\alpha''Fe_{16}N_2$ cannot be obtained by this method because the solubility of nitrogen in austenite is less than the required 12.5 N/100 Fe. Furthermore, the martensitic transformation is depressed to lower temperatures as the nitrogen content increases, so the nitrogen-rich samples tend to contain retained austenite, whereas the nitrogen-poor ones are mostly αFe.

The magnetization of these bulk samples is easily measured,[19,36,39–41] but *none has been found to possess a magnetization greater than that of αFe.* If $\alpha''Fe_{16}N_2$ really has a magnetization σ_s in excess of 300 J T^{-1} kg^{-1}, one would expect the nitrogen-poor samples at least to exhibit a magnetization greater than 220 J T^{-1} kg^{-1}, the value for αFe.

The inference of the magnetization of the α'' phase from measurements on phase mixtures relies on (i) quantitative analysis of the phases present and (ii) knowledge of the magnetization of each one. The phase analysis can be obtained from x-ray diffraction[41] or Mössbauer spectra.[19,36] Huang *et al.* use x-ray diffraction to deduce σ=272–286 J T^{-1} kg^{-1} at room temperature, corresponding to $\mu_{Fe}=2.94$ μ_B whereas Coey *et al.* base their quantitative phase analysis on the absorption areas of Mössbauer spectra taken at 15 K and deduce σ=225–270 J T^{-1} kg^{-1} corresponding to μ_{Fe}=2.3–2.6 μ_B and J=2.1–2.5 T. The Mössbauer method of phase analysis has the advantage that it probes all the iron in the sample, not just a surface region as is the case for x-ray diffraction. Bao *et al.* find that the magnetization of a single sample is consistent with a large magnetization for the α''

phase.[36] Sakamoto[40] deduces from annealing experiments that the magnetization of $Fe_{16}N_2$ has a higher value than that of pure iron.

A problem for inferring the α'' moment from γ-rich material is that the magnetic properties of nitrogen-austenite are not entirely clear. A broadened peak appears as the room-temperature Mössbauer spectrum, but it is uncertain that the broadening is exclusively due to the distribution of quadrupole splitting. A small magnetic hyperfine ·tion with B_{hf}~2 T might contribute. Electronic structu. ..ulations indicate the possibility of very weak ferromagnetism in expanded γFe before the transition to a high-moment state.

V. CONCLUSIONS

Most data on bulk $\alpha''Fe_{16}N_2$ indicate that the average iron moment lies in the range 2.3–2.6 μ_B. None of the results we have reviewed provide support for an average iron moment of 3.0–3.5 μ_B, as has been claimed for certain thin films.

The sites which carry the largest moments of ~3.0 μ_B in the interstitial iron nitrides are those ($1a$ in γFe_4N, $4d$ in $\alpha''Fe_{16}N_2$) which are *next*-nearest neighbors of the nitrogen. The moments on the nearest-neighbor sites are much influenced by hybridization with the nitrogen *sp* orbitals.

The discrepancy with the results on the thin films of the Hitachi group in particular is unexplained. Extensive studies by Takahashi and co-workers[43] on films prepared by reactive sputtering and plasma evaporation indicate a value of σ_s of 230–240 J T^{-1} kg^{-1}. Possible considerations are surface effects and nitrogen order. Surface enhancement of magnetization might arise in very thin films. It is doubtful whether disordering the nitrogen can increase the moment, in view of results on mechanically alloyed material[21] and the increase of magnetization which accompanies annealing the nitrogen martensite.[36,40] However, one might imagine an ordered phase containing less nitrogen which contains more of the high-moment iron sites.

Although there may be no giant moment, the data indicate that $\alpha''Fe_{16}N_2$ is closer to strong ferromagnetism than αFe and they encourage further efforts to prepare the α'' phase in a pure form[42] and investigate alloy additions in order to optimize the properties for those applications that call for ferromagnetic material with the greatest possible polarization.

ACKNOWLEDGMENTS

The author is grateful to many co-workers who have participated in our investigations of metastable iron nitrides, particularly Dr. Qinian Qi, Kathy O'Donnell, Emmanuelle Touchais, and James O'Sullivan. He has benefitted greatly from the advice and encouragement of Professor K. H. Jack.

[1] K. H. Jack, Proc. R. Soc. London, Ser. A **208**, 200 (1951).
[2] T. K. Kim and M. Takahashi, Appl. Phys. Lett. **20**, 492 (1972).
[3] A. Hano, N. S. Kazama, H. Fujimori, and T. Takahashi, J. Appl. Phys. **53**, 8332 (1982).
[4] K. Nakajima and S. Okamoto, Appl. Phys. Lett. **56**, 92 (1990).
[5] M. Komuro, Y. Kozono, M. Hanazono, and Y. Sugita, J. Appl. Phys. **67**, 5126 (1990).
[6] Y. Sugita, K. Mitsuoka, M. Momuro, H. Hoshiya, Y. Kozono, and M. Hanazono, J. Appl. Phys. **90**, 5977 (1991).
[7] M. Matsuoka, K. Hoshino, and K. Ono, in Proceedings of the International Symposium on 3d Transition Metal Thin Films, Sendai 1991 (unpublished), p. 29.
[8] M. Takahashi, H. Shoji, H. Takahashi, T. Wakiyama, M. Kinoshita, and W. Ohta, IEEE Trans. Magn. **29**, 3040 (1993).
[9] H. Takahashi, M. Mirsuoka, M. Komuro, and Y. Sugita, J. Appl. Phys. **73**, 6060 (1993).
[10] M. A. Russak, C. V. Jahnes, E. Klokholm, J. W Lee, M. E. Re, and B. C. Webb, J. Appl. Phys. **70**, 6427 (1991).
[11] J. Janak and A. R. Williams, Phys. Rev. B **14**, 4199 (1976); O. K. Andersen, J. Madsen, U. K. Poulsen, O. Jepsen, and J. Kollar, Physica **86–88B**, 249 (1977); J. Kübler, Phys. Lett. **81A**, 81 (1981); T. Jarborg and M. Peter, J. Magn. Magn. Mater. **42**, 89 (1984); H. S. Greenside and M. A. Schluter, Phys. Rev. B **27**, 3111 (1983); D. Bagayoko and J. Callway, Phys. Rev. B **28**, 5412 (1983).
[12] A. Sakuma, J. Magn. Magn. Mater. **102**, 127 (1991).
[13] A. Sakuma, J. Phys. Soc. Jpn. **61**, 223 (1992).
[14] A. Sakuma, J. Phys. Soc. Jpn. **60**, 2007 (1991).
[15] S. Ishida and K. Kitawatase, J. Magn. Magn. Mater. **104–107**, 1933 (1992); S. Ishida, K. Kitawatase, S. Fujii, and S. Asano, J. Phys. Condens. Matter **4**, 765 (1992).
[16] B. I. Min, Phys. Rev. B **46**, 8232 (1992).
[17] C. A. Kuhnen, R. S. de Figueiredo, V. Drago, and E. Z. da Silva, J. Magn. Magn. Mater. **111**, 95 (1992).
[18] H. Sawada, A. Nogami, and T. Matsumiya, in *Computer Aided Innovation of New Materials*, edited by M. Doyama, J. Kihara, M. Tanaka, and R. Yamamoto (Elsevier Science, New York, 1993), p. 213.
[19] J. M. D. Coey, K. O'Donnell, Q. Qi, E. Touchais, and J. H. Jack, J Phys. Condens. Matter **6**, L23 (1994).
[20] Q. Qi, Ph.D. thesis, University of Dublin, 1994.
[21] Q. Qi, K. O'Donnell, E. Touchais, and J. M. D. Coey, Hyperfine Interactions (in press).
[22] R. Coehoorn, G. H. O. Daalderop, and H. J. F. Jansen, Phys. Rev. B **48**, 3830 (1993).
[23] S. Mater, P. Mohn, G. Demazeau, and B. Siberchicot, J. Phys. (Paris) **49**, 1761 (1988).
[24] S. Mater, S. Z. Phys. B **87**, 91 (1992).
[25] Z. Q. Li, J. Phys. Condens. Mater **5**, 1411 (1993).
[26] K. Miura, S. Imanaga, and Y. Hayafuji (in press).
[27] B. C. Frazer, Phys. Rev. **112**, 751 (1958).
[28] T. Beuerle and M. Fähnle, Phys. Status Solidi B **174**, 257 (1992).
[29] J. Kanamori, Prog. Theor. Phys. Suppl. **101**, 1 (1990).
[30] A. J. Nozik, J. C. Wood, Jr., and G. Haacke, Solid State Commun. **7**, 1677 (1969); M. J. Clauser, *ibid.* **8**, 781 (1970).
[31] J. C. Wood, Jr., and A. J. Nozik, Phys. Rev. B **4**, 2224 (1971).
[32] N. de Cristofaro and R. Caplow, Metal Trans. A **8**, 35 (1977).
[33] T. Moriya, Y. Sumitomo, H. Ino, and F. E. Fujita, J. Phys. Soc. Jpn. **35**, 1378 (1973).
[34] K. Nakajima, S. Okamoto, and K. Okada, J. Appl. Phys. **65**, 4357 (1989).
[35] K. Nakajima and S. Okamoto, in Proceedings of the International Symposium on 3*d* Transition Metal Thin Films, Sendai, 1991 (unpublished), p. 21.
[36] X. Bao, R. M. Metzger, and M. Carbucicchio, J. Appl. Phys. **73**, 6734 (1993).
[37] K. Nakajima, T. Yamashita, M. Takata, and S. Okamoto, J. Appl. Phys. **70**, 6033 (1991).
[38] J. Foct, J. Phys. (Paris) **35**, C6-487 (1974); P. Rochegude and J. Foct, Phys. Status Solidi A **88**, 137 (1985).
[39] K. Mitsuoka, H. Miyajima, H. Ino, and S. Chikazumi, J. Phys. Soc. Jpn. **53**, 2381 (1984).
[40] M. Sakamoto, Proceedings of the Second International Symposium on Physics of Magnetic Materials, Peking, 1992 (unpublished), p. 7.
[41] M. Q. Huang, W. E. Wallace, S. Simizu, R. T. Obermyer, and S. G. Sankar, J. Appl. Phys. **75**, 6574 (1974); M. Q. Huang, W. E. Wallace, S. Simizu, and S. G. Sankar, J. Magn. Magn. Mater. **135**, 226 (1994).
[42] K. H. Jack, J. Appl. Phys. (these proceedings).
[43] M. Takahashi (private communication); M. Takahashi, H. Shoji, H. Takahashi, H. Nashi, T. Wakiyama, M. Doi, and M. Matsui, J. Appl. Phys. (these proceedings).
[44] W. Y. Lai, Q. Q. Zheng, and W. Y. Hu, J. Phys. Condens. Matter **6**, L259 (1994).

Magnetic and Mössbauer studies of single-crystal $Fe_{16}N_2$ and Fe-N martensite films epitaxially grown by molecular beam epitaxy (invited)

Yutaka Sugita, Hiromasa Takahashi, and Matahiro Komuro
Central Research Laboratory, Hitachi, Ltd., Kokubunji, Tokyo 185, Japan

Katsuya Mitsuoka
Data Storage and Retrieval Systems Division, Hitachi, Ltd., Odawara, Kanagawa 256, Japan

Akimasa Sakuma
Magnetic and Electronic Materials Research Laboratory, Hitachi Metals, Ltd., Kumagaya, Saitama 360, Japan

Single-phase, single-crystal $Fe_{16}N_2(001)$ films and Fe-11 at. %N martensite films of 200–900 Å thickness have been epitaxially grown on $In_{0.2}Ga_{0.8}As(001)$ substrates by evaporating Fe in an atmosphere of mixed gas of N_2 and NH_3, followed by annealing. The saturation magnetizations $4\pi M_s$'s for $Fe_{16}N_2$ and Fe-N martensite films have been measured to be around 29 and 24 kG at room temperature, respectively, and almost constant in the above thickness range by using a vibrating sample magnetometer. $4\pi M_s$ for Fe-N martensite films has been increased with ordering of N atoms caused by annealing and finally reached around 29 kG for $Fe_{16}N_2$. Mössbauer spectra have been measured for those films. The spectrum for Fe-N martensite films was a superposed one with hyperfine fields of 360, 310, and 250 kOe, similar to those previously reported for martensite. While the spectrum became simpler with ordering, finally reaching a single hyperfine field of 330 kOe for $Fe_{16}N_2$. $4\pi M_s$ of 29 kG for $Fe_{16}N_2$ (3.2 μ_B/Fe atom) and $4\pi M_s$ of 24 kG for martensite (2.6 μ_B/Fe atom) has not been explained based on the conventional band theory of $3d$ metal magnetism. Behaviors of Mössbauer spectra could not be understood based on the conventional concept either. Thus a new physical concept is likely to be needed for clarification of giant magnetic moments and Mössbauer spectra for $Fe_{16}N_2$ and Fe-N martensites.

I. INTRODUCTION

In 1972, Kim and Takahashi[1] found that Fe-N films, evaporated in a N_2 gas atmosphere, exhibit 25.8 kG for the saturation magnetization $4\pi M_s$ at room temperature, which is higher than that of pure Fe by 17%. Furthermore, they confirmed that the Fe-N films are polycrystalline, consisting of Fe and $Fe_{16}N_2$ crystallites and estimated the $4\pi M_s$ of $Fe_{16}N_2$ to be 28.3 kG from the volume fraction of $Fe_{16}N_2$ in the films. $Fe_{16}N_2$ is a metastable Fe-N compound with a bct structure, which was discovered by Jack[2] in 1951.

Quite recently, Komuro *et al.*[3,4] and Sugita *et al.*[5] have grown single-phase, single-crystal $Fe_{16}N_2$ films of around 500 Å thickness epitaxially on $In_{0.2}Ga_{0.8}As(001)$ substrates by using molecular-beam epitaxy (MBE) and found that the $4\pi M_s$ of $Fe_{16}N_2$ films is around 29 kG at room temperature and around 32 kG at 5 K. Those values are equivalent to the average magnetic moments of 3.2 and 3.5 μ_B per Fe atom at room temperature and 5 K, respectively. These are truely giant magnetic moments, much greater than the Slater–Pauling curves.[6]

More recently, $4\pi M_s$ of Fe-N films and powders formed by sputtering,[7–11] ion implantation,[12] and ammonia nitrification,[13–15] have been intensively investigated. In many cases, significant increases in $4\pi M_s$ for Fe-N or $Fe_{16}N_2$ have been found,[7,8,11–13] although the values are different. In contrast to these, Takahashi *et al.*[10] reported that a significant increase in $4\pi M_s$ is not observed for $Fe_{16}N_2$ films epitaxially grown on MgO substrates by reactive plasma sputtering. The reasons for the above different results of $4\pi M_s$ for $Fe_{16}N_2$ and Fe-N films remain to be clarified.

In this study, the effect of ordering of N atoms on $4\pi M_s$ and the film thickness dependence of $4\pi M_s$ have been investigated in detail for single-crystal $Fe_{16}N_2$ and Fe-N martensite films epitaxially grown on $In_{0.2}Ga_{0.8}As$ substrates by MBE. Also, the Mössbauer spectra have been measured for those films.

II. EXPERIMENT

A. Sample preparation

$Fe_{16}N_2$ and Fe-N films were prepared in an atmosphere of mixed gas of N_2 and NH_3 by using an MBE apparatus equipped with electron-beam evaporation sources. $In_{0.2}Ga_{0.8}As(001)$ single-crystal wafers were used as substrates because the lattice matching between $In_{0.2}Ga_{0.8}As$ (5.71 Å) and the a axis of $Fe_{16}N_2$ (5.72 Å) is very good. The substrates were etched by using 5:1:0.3 solution of H_2SO_4:H_2O:H_2O_2. After that, the substrates were mounted on a stainless-steel block with indium bonding and cleaned by heating at 675 °C for 5 min in the MBE chamber ($<1\times10^{-9}$ Torr). The temperatures of the samples were measured at the backside of the stainless block. The purity of Fe used as the deposition source was 99.999%.

The deposition conditions are listed in Table I. Those conditions were selected based on the trade off between epitaxial growth and introduction of around 11 at. % N into deposited films for forming $Fe_{16}N_2$. Among these, the deposition rate and the gas pressure were most critical. Film thicknesses were 200–900 Å.

 0021-8979/94/76(10)/6637/5/$6.00 © 1994 American Institute of Physics

TABLE I. Deposition conditions of Fe-N and Fe films on InGaAs(001) substrates.

	Fe-11 at. % N	Fe
Base pressure (Torr)	1×10^{-9}	←
Gas	N_2+20%NH_3	vacuum
Substrate temperature (°C)	200	250
Deposition rate (Å/s)	0.02–0.03	0.1
Pressure during deposition (Torr)	$1–2\times10^{-4}$	5×10^{-7}

Pure Fe films were prepared on $In_{0.2}Ga_{0.8}As(001)$ substrates in vacuum of 5×10^{-7} Torr for comparison with Fe-N films and reference for measurements.

B. Characterization

Nitrogen concentrations in those films were measured by using x-ray photoelectron spectroscopy (XPS) and Auger electron spectroscopy (AES). Figure 1 shows the intensity ratio of N 1*s* to Fe 2*p* peaks of XPS versus N concentration curve used as calibration. The relationship was obtained using standard Fe-N powder samples with various concentrations. Concentrations of Fe-N films used in this study were around 10–11 at. % N as shown in Fig. 1. The depth profile of the concentration was obtained by AES.

The film thicknesses were measured routinely by using a needle contact feeler gauge. Some of the obtained values were checked by comparing with the thicknesses measured by using the cross-sectional transmission electron microscopy (TEM) images as shown in Fig. 2. The agreement between both data is very good, suggesting an error of measurement of less than ±3% with the exception of one point.

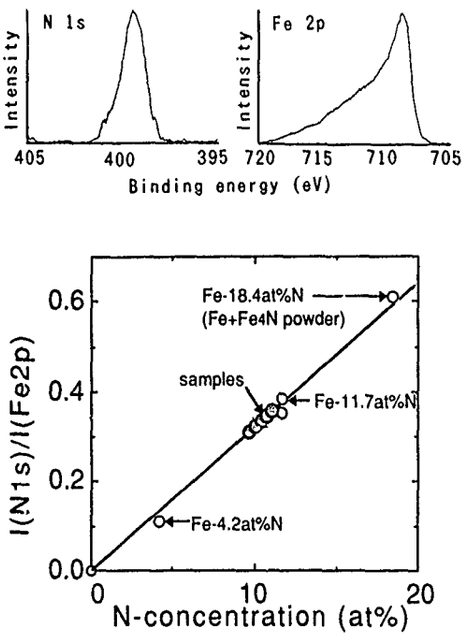

FIG. 1. The intensity ratio of N 1*s* to Fe 2*p* peaks of XPS as a function of N atom concentration in standard Fe-N powder samples along with Fe-N films used in this study.

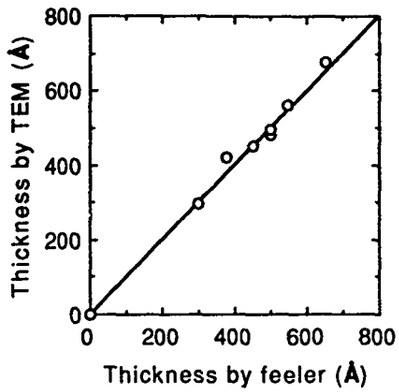

FIG. 2. Comparison between film thicknesses measured with a cross-sectional TEM and a needle contact feeler gauge.

The crystal structures of the samples were investigated by the x-ray-diffraction (XRD) method using monochromatic Cu $K\alpha$ radiation. Also, the crystallinity of the films was evaluated with reflection high-energy electron-diffraction (RHEED) analysis.

The saturation magnetizations $4\pi M_s$'s of the films were measured with a vibrating sample magnetometer (VSM). Samples were circular plates of 8 mm diameter which were formed very accurately by using photolithography and etching using HNO_3. Therefore the measurement error of $4\pi M_s$ obtained was likely to be less then ±5% (sample volume ±3%, VSM ±2%).

Mössbauer spectra were measured by using a conversion electron-type apparatus. Samples were coated with around 100 Å thick Au layers for protection against oxidation. Before and after the Mössbauer measurements, $4\pi M_s$ was measured and made sure to remain the same by a VSM.

III. RESULTS AND DISCUSSION

A. Effect of ordering of N atoms on $4\pi M_s$

Fe-11 at. % N films of around 500 Å thickness were prepared with changing annealing time after the deposition of the films. Annealing was carried out at 200 °C in vacuum of 10^{-8} Torr. Figures 3(a)–3(c) show XRD patterns for unannealed, annealed (40 h), and fully annealed (90 h) samples. In Fig. 3(a), peaks for $Fe_{16}N_2(\alpha'')$ are not seen, but only the (002) peak for Fe-N martensite (α') is seen at 58.1°. This shows that N atoms are located in disorder. In this case also, a RHEED pattern of straight fine streaks is seen, which suggests that the film is a high quality single crystal. In Fig. 3(b), the α''(002) peak appears at around 28.1°, but it is much smaller than the peak at 58.1° corresponding to α'(002) and α''(004). The ratio is around 0.04. Taking into consideration that the ratio of the peak intensity of α''(002) to α''(004) is calculated to be 0.125 for $Fe_{16}N_2$, the film is considered to be a mixture of α' and α''; that is, ordering of N atoms occurs partially. In Fig. 3(c), the α''(002) peak becomes stronger and the intensity ratio of two peaks is around 0.1, showing that the film is single-phase $Fe_{16}N_2$ with full ordering of N atoms in a bct structure. This is confirmed by a RHEED pattern of fine streaks with half period of pure Fe.

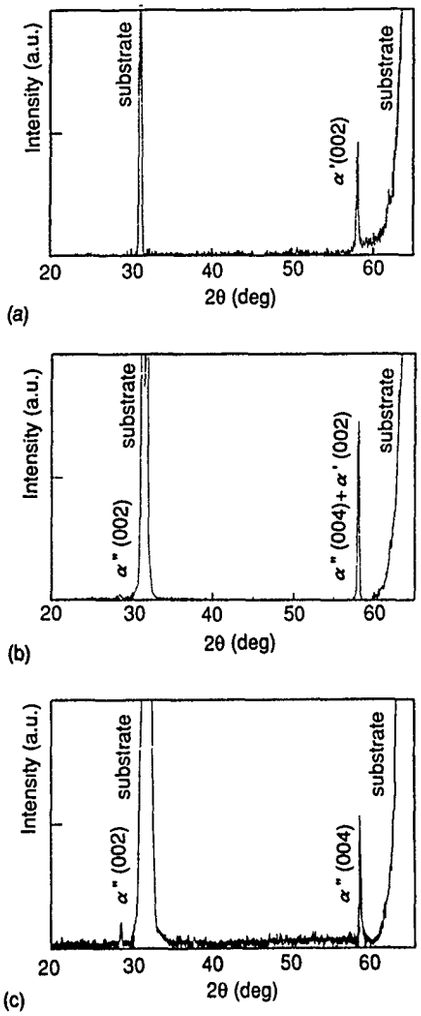

FIG. 3. XRD patterns for unannealed and annealed Fe-11 at. % N films. (a) Unannealed, Fe-N martensite (α'); (b) annealed at 200 °C for 40 h, $\alpha'+\alpha''$; and (c) annealed at 200 °C for 90 h, $Fe_{16}N_2(\alpha'')$.

Thus the ratio of $\alpha''(002)$ peak to $\alpha''(004)$ and $\alpha'(002)$ peaks can be a measure of ordering N atoms in Fe-N films. The lattice parameters for α'' are 6.33 Å (c axis) and 5.71 Å (a axis), which are close to previously reported values.[2]

Magnetization curves for the above samples measured with a VSM are shown in Fig. 4. $4\pi M_s$ for an Fe-N martensite (α') film is 24 kG and that for an $Fe_{16}N_2(\alpha'')$ film is 29 kG. For an intermediate film, $4\pi M_s$ is 27 kG, an intermediate value of α' and α''. The relationship between $4\pi M_s$ and ordering of N atoms is shown in Fig. 5. $4\pi M_s$ is increased monotonically from 24 kG for α' up to 29 kG for α'' with ordering of N atoms or the intensity ratio of $\alpha''(002)$ peak to $[\alpha''(004)+\alpha'(002)]$ peaks. The deviation of data is rather large. This is due to inaccuracy of measurement of weak $\alpha''(002)$ peak intensities. However, the above relationship is clear.

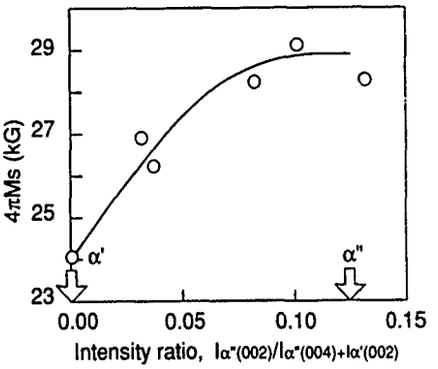

FIG. 5. The relationship between $4\pi M_s$ and ordering of N atoms expressed by $I\alpha''(002)/I[\alpha''(004)+\alpha'(002)]$.

As shown in Fig. 4, all samples exhibit low remanence. Possibly stripe domains are formed by strong perpendicular anisotropy;[16] that is, the magnetization tilts upwards and downwards from the films plane periodically.

B. Film thickness dependence of $4\pi M_s$

$4\pi M_s$'s for $Fe_{16}N_2$ and Fe-N martensite films are shown as a function of the film thickness from 200 to 900 Å in Fig. 6. For comparison, the data for epitaxially grown Fe films of the same thickness range measured in the exactly same way are shown.

$4\pi M_s$ for $Fe_{16}N_2$ films is around 29 kG and does not depend on the film thickness in this range at all. This means that the giant magnetization for $Fe_{16}N_2$ originates from the bulk properties of $Fe_{16}N_2$, not from the surface. $4\pi M_s$ for Fe-N martensite films is around 24 kG and also does not depend on the film thickness. Quite large deviations are seen in the thinner thickness region, but this is due to the difficulty of detecting partial formation of small amount of

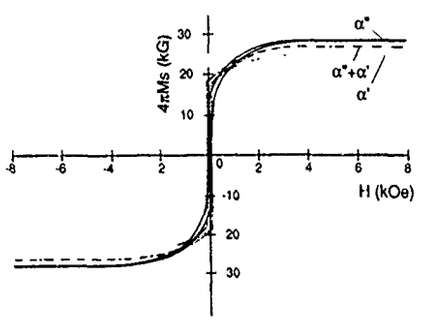

FIG. 4. Magnetization curves for unannealed and annealed Fe-11 at. % N films as shown in Fig. 3. α', dotted line; $\alpha'+\alpha''$, dashed line; α'', solid line.

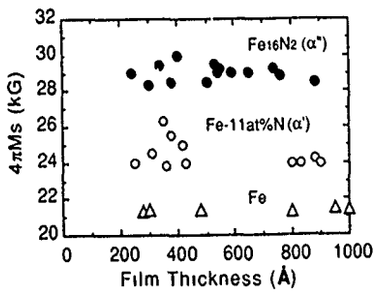

FIG. 6. Film thickness dependence of $4\pi M_s$ for $Fe_{16}N_2$ and Fe-N martensite films along with Fe films.

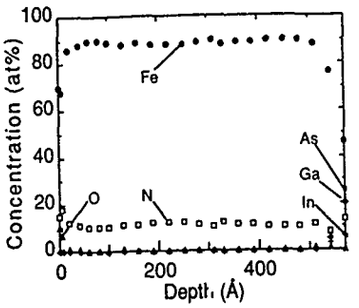

FIG. 7. AES profile for an $Fe_{16}N_2$ film.

$Fe_{16}N_2$ in Fe-N martensites. Here it should be noticed that $4\pi M_s$ for pure Fe films is around 21.5 kG over the thickness range, which is very similar to the bulk value previously reported. This confirms that the accuracy of the measurement of $4\pi M_s$ of films in the thickness range is very high and the obtained $4\pi M_s$'s for $Fe_{16}N_2$ and Fe-N martensite are correct. Furthermore, $4\pi M_s$ for $Fe_{16}N_2$ was confirmed to be 28 kG also by FMR[16] independently of VSM measurements.

Figure 7 shows a typical AES profile for a 550 Å thick $Fe_{16}N_2$ film. The concentrations of Fe and N atoms are just around 89 and 11 at. % for $Fe_{16}N_2$, respectively, through the film thickness, except for 10–20 Å thick regions of the top and bottom surfaces of the film. This is consistent with the above data of $4\pi M_s$ independence on the film thickness. The concentrations of impurities such as oxygen atoms are much smaller than 1% except for the top surface of the film.

C. Mössbauer spectra

Mössbauer spectra for Fe-N martensite, intermediate, and $Fe_{16}N_2$ films are shown in Fig. 8. As shown in Fig. 8(a), the spectrum for an Fe-N martensite film with $4\pi M_s$ of 24 kG is a complicated one, being superposed with three kinds of hyperfine fields of 360, 310, and 250 kOe. This is substantially similar to previously reported data[17,18] for Fe-N martensite foils. The spectrum for a film of partial ordering with $4\pi M_s$ of 27 kG becomes simpler as shown in Fig. 8(b). The spectrum is still a superposed one, but a hyperfine field of around 330 kOe appears clearly. For an $Fe_{16}N_2$ film with $4\pi M_s$ of 29 kG, the spectrum becomes very clear with the single hyperfine field of 330 kOe as shown in Fig. 8(c). The same spectra are observed for five different $Fe_{16}N_2$ samples prepared at different times. The spectrum is quite different from previously reported data for $Fe_{16}N_2$ precipitates formed from Fe-N martensite powders[19] by 100 °C annealing and N ion implanted Fe-N films including $Fe_{16}N_2$.[20] The previous data are rather similar to that for martensite or intermediate ones as shown above.

The hyperfine field of 330 kOe for $Fe_{16}N_2$ is very similar to that for pure Fe. Apparently it seems contradictory that the hyperfine fields are almost the same, although the magnetic moments are very different. However, the relationship between the magnetic moment and the hyperfine field is very complicated and not definite, since the magnetic moment originates from the polarization of $3d$ electrons, while the

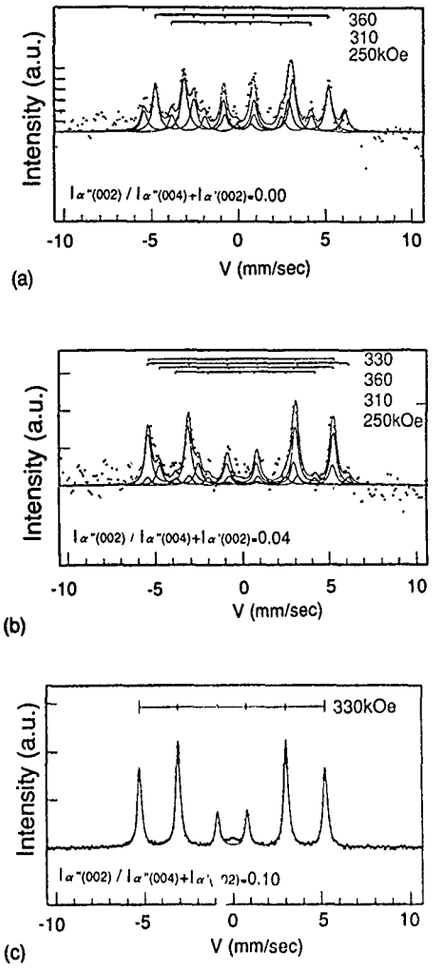

FIG. 8. Mössbauer spectra for unannealed and annealed Fe-11 at. % N films. (a) Fe-N martensite (α'), (b) Fe-N intermediate ($\alpha'+\alpha''$), and (c) $Fe_{16}N_2(\alpha'')$.

hyperfine field comes from that of $1s$, $2s$, and $3s$ electrons. Therefore the above experimental results cannot be said to be contradictory based on the simple linear relationship.

D. Origin of giant magnetic moment

The magnetic moment for $Fe_{16}N_2$ has been calculated using the local spin-density functional approach by Sakuma[21] first and then by several scientists.[22–26] All the calculated average magnetic moments are around 2.4–2.5 μ_B per Fe atom. These are much smaller than the experimental value of 3.2 μ_B per Fe atom for $Fe_{16}N_2$ and smaller than 2.6 μ_B per Fe atom even for Fe-N martensite. Therefore the conventional theoretical approach is inadequate for discussion on the issue of the giant magnetic moment. In the above calculations, the volume expansion effect and the charge-transfer effect between Fe sites due to the introduction of N atoms are treated automatically. Therefore some other new effects of N atoms such as local binding between Fe and N atoms should be taken into consideration in addition to the above-mentioned two effects. In discussing the issue, it is important to notice that the magnetic moment increases with ordering of N atoms from 2.6 to 3.2 μ_B per Fe atom, al-

though the bct structure remains the same. Also, it should be noticed that the hyperfine field for $Fe_{16}N_2$ is 330 kOe and the same for three kinds of Fe sites with different distances to N atoms.

As for the different values of $4\pi M_s$ and Mössbauer spectra for $Fe_{16}N_2$ and Fe-N reported by different authors, it is likely that some of them come from the difference in ordering and/or concentration of N atoms. Also, some impurities such as oxygen atoms might suppress the enhancement of magnetic moment in some cases. However, the reasons for this remain unclear yet.

IV. CONCLUSIONS

Single-crystal $Fe_{16}N_2$ and (Fe- around 11 at. % N) martensite films of 200–900 Å thickness have been grown epitaxially on $In_{0.2}Ga_{0.8}As(001)$ substrates by MBE. $4\pi M_s$'s for $Fe_{16}N_2$ and Fe-N martensite films have been confirmed to be around 29 and 24 kG at room temperature, respectively. $4\pi M_s$ for Fe-N martensite films has been found to increase with increase in ordering of N atoms by annealing and finally reach around 29 kG for $Fe_{16}N_2$.

$4\pi M_s$'s for $Fe_{16}N_2$ and Fe-N martensite films were almost constant in the range of the film thickness from 200 to 900 Å.

Mössbauer spectrum for Fe-N martensite films was found to be a superposed one with hyperfine fields of 360, 310, and 250 kOe. The spectrum became simpler with increase in ordering, finally reaching a spectrum with a single hyperfine field of 330 kOe.

$4\pi M_s$ of 29 kG for $Fe_{16}N_2$ (3.2 μ_B/Fe atom) and 24 kG for Fe-N martensite (2.6 μ_B/Fe atom) has not be explained based on the conventional band theory of $3d$ metal magnetism. Behaviors of Mössbauer spectra could not be understood either. Thus a new physical concept is concluded to be needed for clarification of giant magnetic moments and Mössbauer spectra for $Fe_{16}N_2$ and Fe-N martensite.

ACKNOWLEDGMENTS

The authors would like to thank Dr. H. Awano and Dr. M. Igarashi of Central Research Laboratory, Dr. R. Imura, Dr. Y. Hirai, and Dr. T. Uda of Advanced Research Laboratory, Hitachi, Ltd., for their valuable discussions on preparation and characterization of $Fe_{16}N_2$. They thank also Dr. R. Suzuki and Dr. M. Fuyama of Central Research Laboratory, Hitachi, Ltd., for their encouragement throughout this study.

[1] T. K. Kim and M. Takahashi, Appl. Phys. Lett. **20**, 492 (1972).
[2] K. H. Jack, Proc. R. Soc. London, Ser. A **208**, 216 (1951).
[3] M. Komuro, Y. Kozono, M. Hanazono, and Y. Sugita, J. Appl. Phys. **67**, 5126 (1990).
[4] M. Komuro, H. Hoshiya, K. Mitsuoka, Y. Kozono, M. Hanazono, and Y. Sugita, Mater. Res. Soc. Symp. Proc. **232**, 147 (1991).
[5] Y. Sugita, K. Mitsuoka, M. Komuro, H. Hoshiya, Y. Kozono, and M. Hanazono, J. Appl. Phys. **70**, 597 (1991).
[6] R. M. Bozorth, *Ferromagnetism* (Van Nostrand, New York, 1951), p. 441.
[7] M. A. Russac, C. V. Jahnes, E. Klokholm, J. Lee, M. E. Re, and B. C. Webb, J. Appl. Phys. **70**, 6427 (1991).
[8] C. Gao and W. D. Doyle, J. Appl. Phys. **73**, [illegible] .993).
[9] C. Gao and M. Shamsuzzoha, IEEE Trans Magn. **29**, 3046 (1993).
[10] M. Takahashi, H. Shoji, H. Takahashi, T. Wakiyama, M. Kinoshita, and W. Ohta, IEEE Trans. Magn. **29**, 3040 (1993).
[11] S. Okamoto, O. Kitagami, and Y. Shimada (unpublished).
[12] K. Nakajima and S. Okamoto, Appl. Phys. Lett. **56**, 92 (1990).
[13] M. Q. Huang, W. E. Wallace, S Simizu, and S. G. Sankar, J. Magn. Magn. Mater. **135**, 226 (1994).
[14] X. Bao and R. M. Metzger, J. Appl. Phys. **75**, 58 (1994).
[15] J. M. D. Coey, K. O'Donnell, Q. Qinian, E Touchais, and K. H. Jack, J. Phys. Condens. Matter **6**, L23 (1994).
[16] H. Takahashi, K. Mitsuoka, M. Komuro, and Y. Sugita, J. Appl. Phys. **73**, 6060 (1993).
[17] T. Moriya, Y. Sumitomo, H. Ino, F. E. Fujita, and Y. Maeda, J. Phys. Soc. Jpn. **35**, 1378 (1973).
[18] K. Mitsuoka, H. Miyajima, H. Ino, and S. Chikazumi, J. Phys. Soc. Jpn. **53**, 2381 (1984).
[19] N. De Cristofaro and R. Kaplow, Metal Trans. **8A**, 36 (1977).
[20] K. Nakajima, T. Yamashita, M. Takata, and S. Okamoto, J. Appl. Phys. **70**, 6033 (1991).
[21] A. Sakuma, J. Magn. Magn. Mater. **102**, 127 (1991).
[22] S. Ishida, K. Kitawatase, S. Fujii, and S. Asano, J. Phys. Condens. Matter **4**, 765 (1992).
[23] B. I. Min, Phys. Rev. B **46**, 8232 (1992).
[24] S. Matar, Z. Phys. B **87**, 91 (1992).
[25] R. Coehoorn, G. H. O. Daalderop, and H. J. F. Jansen, Phys. Rev. B **48**, 3830 (1993).
[26] A. Sakuma and Y. Sugita, Mater. Res. Soc. Symp. Proc. **313**, 257 (1993).

Magnetic moment of α''-$Fe_{16}N_2$ films (invited)

Migaku Takahashi, H. Shoji, H. Takahashi, H. Nashi, and T. Wakiyama
Department of Electronics Engineering, Tohoku University, Sendai 980-77, Japan

M. Doi and M. Matsui
Department of Materials Science, Nagoya University, Nagoya 464-01, Japan

In order to determine the value of the intrinsic magnetic moment of the α'' phase, the films of nitrogen-martensite with various N content were fabricated under various reactive sputtering conditions. The magnetic moment of $(\alpha''+\alpha')$-$Fe_{16}N_2$ films is discussed in connection with the change of the unit-cell volume of the bct structure and the degree of N site ordering in nitrogen-martensite. As a result, it is found that (1) the same structure as bulk α''-$Fe_{16}N_2$ is realized in the present films, (2) the saturation magnetization σ_s of the α' phase increases about 4% with increasing unit-cell volume of the α' phase, (3) the degree of N site ordering from α' to α''-$Fe_{16}N_2$ does not much affect σ_s, and (4) the experimentally obtained maximum value of σ_s for the $(\alpha''+\alpha')$-$Fe_{16}N_2$ film was 232 emu/g. The intrinsic value of σ_s in the α'' phase (in the perfectly ordered state) is proposed to be no more than 240 emu/g at 300 K.

I. INTRODUCTION

Recently, the present authors have established synthesizing processes for α''-$Fe_{16}N_2$ compound films on MgO (100) single-crystal substrates by using both reactive sputtering and plasma evaporation methods.[1,2]

However, the magnitude of the saturation magnetization σ_s for $(\alpha''+\alpha')$-$Fe_{16}N_2$ films with stoichiometric N content showed 226 emu/g for sputtered films and 232 emu/g for plasma evaporated films, respectively. The films thus fabricated did not show any giant magnetic moment, even though clear formation of $(\alpha''+\alpha')$-$Fe_{16}N_2$ phase was achieved. These values of σ_s in $(\alpha''+\alpha')$-$Fe_{16}N_2$ films agree well with the result of the recent theoretical band calculation,[3] and are completely different from the earlier results reported by various groups.[4–7]

Up to now, reported values of σ_s of the α'' phase (about 257–315 emu/g) were estimated ones (not directly measured) except for the films synthesized by MBE[7] (2.9 T directly measured, α'' single phase). The estimation of the value of σ_s in the α'' phase was carried out by using experimentally determined volume-averaged values of σ_s (240–260 emu/g)[4–6] after fixing the volume fraction of the α'' phase in whole films which consist of phase mixtures of α-Fe+α''-$Fe_{16}N_2$ and/or $\alpha+\alpha'+\alpha''+\gamma'$-$Fe_4N+\cdots$.

There still exist some physical problems concerning σ_s of the α''-$Fe_{16}N_2$ phase, especially for the multiphase films, namely, (1) the big difference among reported values of σ_s in the α'' phase, from 257 to 315 emu/g at RT, and (2) quantitative evaluation for fixing the volume fraction of the α'' phase in whole film. These physical situations lead to a conclusion that the intrinsic magnetic moment of σ_s in the α'' phase is still unknown.

On the other hand, for the single-crystal films with a single α'' phase prepared by the MBE method,[7] there also exists some physically contradictive problems: (1) No clear superlattice lines from the lattice planes including the a axis in the α'' phase were detected, even though a perfect site ordering of N atoms was realized;[8] (2) the hyperfine field Hi of the α'' phase was nearly equal to that of α-Fe (330 kOe) and no splitting of Hi due to three different Fe sites in the α''-$Fe_{16}N_2$ structure was observed,[8] even though σ_s showed 2.9 T ($\simeq$315 emu/g, assuming ρ=7.4 g/cm^3 for α''-$Fe_{16}N_2$); (3) σ_s of the fully ordered α''-$Fe_{16}N_2$ films changed reversibly within the temperature range up to 400 °C and an irreversible change of σ_s due to the phase transformation from α'' to $\alpha+\gamma'$ was not observed.[8] According to the experiment by Jack using powder, the α'' phase is metastable and it must decompose into $\alpha+\gamma'$ phases at about 200 °C.[10]

These experimental results lead to a physical conclusion that the appearance of the giant magnetic moment in α''-$Fe_{16}N_2$ films proposed by Kim and Takahashi and Komuro *et al.* are not simply attributable to the conventional α''-$Fe_{16}N_2$ structure. Therefore the origin of the giant magnetic moment arising from the nitrogen-martensite structure is still under question.

In the present study, in order to determine the value of the intrinsic magnetic moment of the α'' phase, nitrogen-martensites with various N content were systematically fabricated under various sputtering conditions. Also, the magnetic moment of $(\alpha''+\alpha')$-$Fe_{16}N_2$ film is discussed in connection with the change of the unit-cell volume of the body-centered tetragonal (bct) structure and the degree of N site ordering in nitrogen-martensites.

II. EXPERIMENTAL PROCEDURE

Fe-N films were fabricated by a facing target-type dc sputtering system under the selected plasma condition (Te =0.2 eV, Ne$\simeq 1\times10^{10}$ cm^{-3}). The base pressure of the sputtering chamber was below 3×10^{-7} Torr. An Ar-N_2 mixture was introduced to the sputtering chamber at 5 sccm (standard cc/min) with controlling N_2 flow ratio (0%–30%) under a fixed total pressure (1–10 mTorr).

MgO (100) and (110) single-crystal substrates were used. Before the film fabrication, substrates were baked at 200 °C for 2 h and cooled down to RT. This heat treatment was carried out in the evacuated sputtering chamber ($\simeq 2\times10^{-6}$ Torr).

Prior to the fabrication of Fe-N films, an α-Fe underlayer with thickness of 50 Å was deposited on MgO (deposition rate=33 Å/min; Ar pressure P_{Ar}=5 mTorr). Successively, an

 0021-8979/94/76(10)/6642/6/$6.00 © 1994 American Institute of Physics

Fe-N film with a thickness of 3000 Å was deposited onto the α-Fe underlayer (deposition rate=33–240 Å/min; pressure of Ar-N_2 mixture P_{total}=1–10 mTorr).

Annealing of the films after an air exposure was carried out at 150 °C for 2–20 h in a vacuum atmosphere below 5×10^{-6} Torr.

Values of the saturation magnetization σ_s of the films were determined by a vibrating sample magnetometer (VSM) measurement. Conversion electron Mössbauer (CEM) spectra were obtained at RT. The velocity was referred to the pure α-Fe.

Structure analysis of the films were made with a Co $K\alpha$ x-ray diffractometer (XRD) equipped with a graphite monochrometer and a pole figure attachment. Schultz's reflection method was used for the determination of lattice constants and preferred orientation of grains. Contents of nitrogen atoms in the films were determined by electron spectroscopy for chemical analysis (ESCA). Calibration of nitrogen contents were made by using the value obtained from ϵ-$Fe_{2-3}N$ foil (24.2 at. % N) for a standard sample.

N contents in the films increased with increasing N_2 flow ratio. In the case of the film deposited at P_{total} of 5 mTorr and N_2 flow ratio of 18%, the N content was found to be about 11 at. %, which is the same value as the stoichiometric N content of the α''-$Fe_{16}N_2$ phase.

III. RESULTS AND DISCUSSION

A. Structure

According to Jack,[10,11] in the α' phase, N atoms occupy randomly the octahedral interstices at the midpoints of the c edges of the bct cell (0, 0, $\frac{1}{2}$), and the centers of the C faces, ($\frac{1}{2}$, $\frac{1}{2}$, 0). As a result, the lattice constant c of the α' phase is elongated from 2.866 to 3.195 Å and the lattice constant a is shortened from 2.866 to 2.832 Å, respectively, depending on the N content.

The α'' phase has an ordered N site location of the octahedral interstices. The unit cell of the α'' phase contains eight of the expanded bct pseudo-unit cells and has dimensions $a'=2a$ and $c'=2c$, where a and c are the lattice constants of the pseudocell. In the larger true unit cell, the symmetry is also bct, since the α'' phase can be identified by observing reflections from this larger true unit cell for which $(h+k+l)$, Miller's index, is even. Based on this structural knowledge, phase identification is carried out in the present films.

In the case of a MgO(100) single-crystal substrate, a diffraction line from the (002) plane of the α'' phase, $\alpha''(002)$, which is expected to appear around 33° for 2θ, was not observed in an as-deposited state. Only $\alpha'(002)$ was clearly observed in the high angle region. The peak position of $\alpha'(002)$ shifted from 75° to 68° for 2θ with increasing N_2 flow ratio. This shift to lower angle of 2θ is simply explained by the elongation of the c axis of the bct structure of the α' phase. By taking into account the N concentration dependence on lattice constants a and c in nitrogen-martensite,[11] the N content of the α' phase in the present films was found to increase with increasing N_2 flow ratio. This result agrees well with that of ESCA measurements.

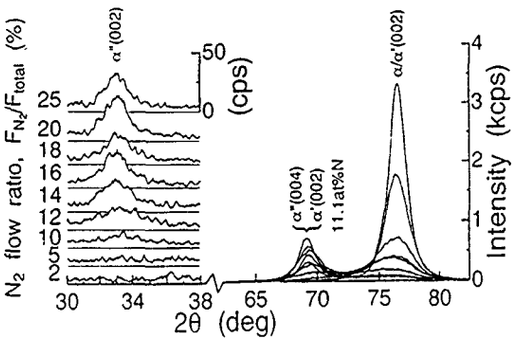

FIG. 1. X-ray diffraction patterns for the films fabricated under P_{total}=5 mTorr, deposition rate=240 Å/min after annealing at 150 °C for 2 h.

In Fig. 1, typical changes of XRD patterns of the films after annealing are shown. After annealing, $\alpha'(002)$, which had been observed in an as-deposited state, split into two diffraction lines. One corresponds to $\alpha''(004)$ and/or $\alpha'(002)$ with satisfying stoichiometric N content of α''-$Fe_{16}N_2$ (11 at. % N). The other corresponds to $\alpha(002)$ of slightly deformed α-Fe. Furthermore, simultaneously at around 33° for 2θ, $\alpha''(002)$, which is the diffraction line from the larger true unit cell of the α'' phase, came to be clearly observed. This fact means that the ordering of N atoms was promoted by annealing while retaining the bct structure and the α'' phase with stoichiometric N content was synthesized.

The unique diffraction patterns from (103), (105), (112), (114), and (213) planes of the α'' phase, including the a axis for ($\alpha''+\alpha'$)-$Fe_{16}N_2$ film, are shown in Fig. 2. As seen in the

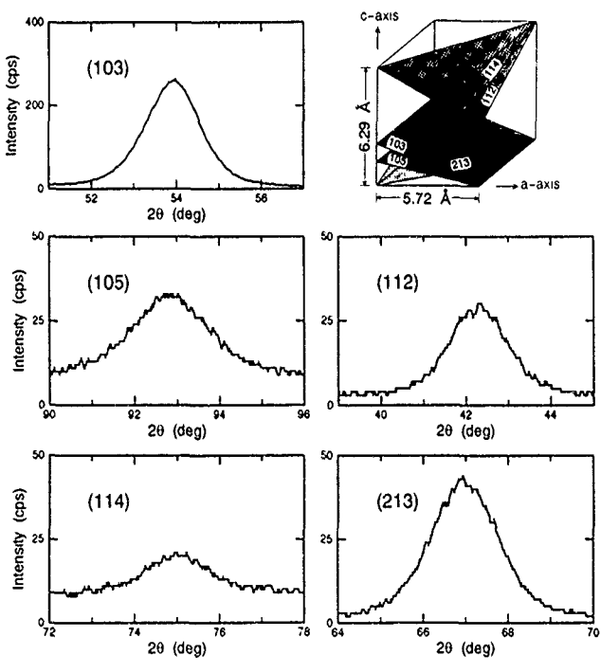

FIG. 2. The unique diffraction patterns from (103), (105), (112), (114), and (213) planes of the α'' phase including the a axis for ($\alpha''+\alpha'$)-$Fe_{16}N_2$ film fabricated under P_{total}=10 mTorr, F_{N_2}=12%, deposition rate=33 Å/min, and annealed at 150 °C for 2 h.

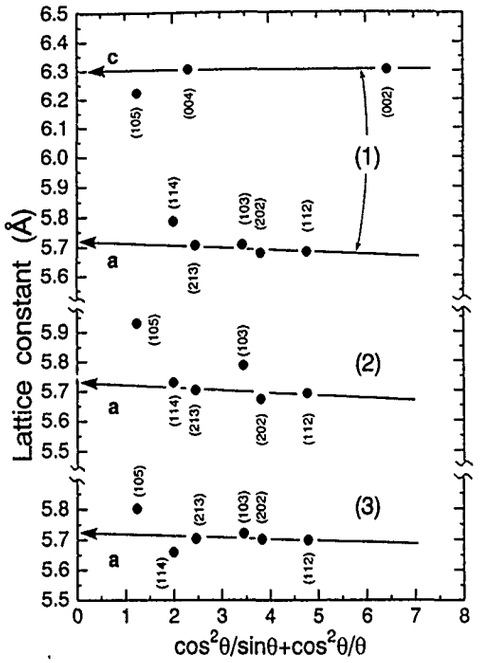

FIG. 3. The lattice constants a and c of the α'' phase, determined by various unique diffraction lines of the α'' phase, plotted against the Nelson–Riley function. Fabrication conditions of the films: (1) P_{total}=10 mTorr, F_{N_2}=16%, deposition rate=240 Å/min, annealed at 150 °C for 2 h; (2) the same as (1) annealed for 20 h; (3) P_{total}=10 mTorr, F_{N_2}=12%, deposition rate=33 Å/min, annealed at 150 °C for 2 h.

figure, the existence of the α'' phase was reconfirmed by these clear unique diffraction lines. In order to determine accurate lattice constants a and c of the α'' phase, the lattice constants a calculated from each plane are plotted against the Nelson–Riley function[12] ($\cos^2\theta/\sin\theta+\cos^2\theta/\theta$) in Fig. 3. In the figure, the reflections marked (3) correspond to the film shown in Fig. 2, and those marked (1) and (2) correspond to $(\alpha''+\alpha')$-$Fe_{16}N_2$ films prepared by different experimental conditions. As a reference, the lattice constant c calculated from $\alpha''(002)$ and $\alpha''(004)$ is also shown as (1). Each extrapolated value of the lattice constants a and c of the present films coincided with that of the α''-$Fe_{16}N_2$ precipitates in bulk powder reported by Jack.[10] Therefore it is concluded that the α'' phase formed in sputtered films has the same structure as the bulk α'' phase.[13]

While in the case of a MgO(110) single-crystal substrate, a preferred grain orientation of (211) and (112) of the α' phase was found in an as-deposited state. By annealing, unique diffraction lines of the α'' phase, $\alpha''(211)$, and $\alpha''(112)$, were observed. Therefore it was found that the α'' phase with a preferred orientation of (211) of the α'' phase can also be synthesized even on MgO(110) substrates. Through the whole result, relationships concerning the crystal orientation between α''-$Fe_{16}N_2$ structure and MgO are shown in Table I.

TABLE I. Crystal orientation relations between α''-$Fe_{16}N_2$ and MgO.

MgO(100)	MgO(110)
$\alpha''(001)\|\|MgO(001)$	$\alpha''(211)\|\|MgO(101)$
$\alpha''[110]\|\|MgO[100]$	$\alpha''[011]\|\|MgO[001]$

B. Magnetic moment

1. Dependence of magnetic moment on N_2 flow ratio

Values of σ_s in an as-deposited state increased slightly with increasing N_2 flow ratio, and took a maximum of 220 emu/g around a N_2 flow ratio of 15%. The N content of the films, which showed the broad maximum in σ_s, was nearly equal to the stoichiometric N content of $Fe_{16}N_2$ (11 at. %). The values of σ_s for annealed film with stoichiometric N content of $Fe_{16}N_2$ (11 at. %) ranged from 213 to 226 emu/g. The average values of σ_s for Cu-coated films were 228 emu/g for the film consisting of the α' phase and 232 emu/g for the film consisting of $(\alpha''+\alpha')$-$Fe_{16}N_2$ phases. The difference of the value of σ_s between coated and noncoated ones may mainly be caused by the surface oxidation due to the adsorbed oxygen at the film surface introduced by venting the chamber with air. In the case of films deposited on a MgO(110) substrate, the value of σ_s in $(\alpha''+\alpha')$-$Fe_{16}N_2$ was 210 emu/g (non-Cu-coated). As a whole, maximum values of σ_s of about 232 emu/g were obtained for $(\alpha''+\alpha')$-$Fe_{16}N_2$ films in the present study. This experimentally determined value was definitely smaller than the value reported as a giant magnetic moment of 2.9 T.[7]

2. Dependence of magnetic moment on unit-cell volume

Figure 4 shows the changes of σ_s against unit-cell volume of the α' phase with various N contents in an as-deposited state. In the figure, 1/8 of the unit-cell volume of the bulk α''-$Fe_{16}N_2$ is indicated. Filled marks correspond to

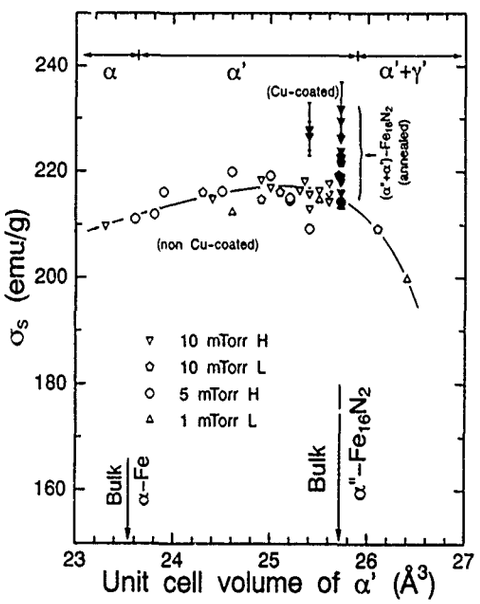

FIG. 4. The changes of σ_s against unit-cell volumes: (1) α' phase with various nitrogen contents in an as-deposited state, and (2) annealed $(\alpha''+\alpha')$-$Fe_{16}N_2$ films with and without Cu coating. H and L correspond to high (240 Å/min) and low (33 Å/min) deposition rates, respectively

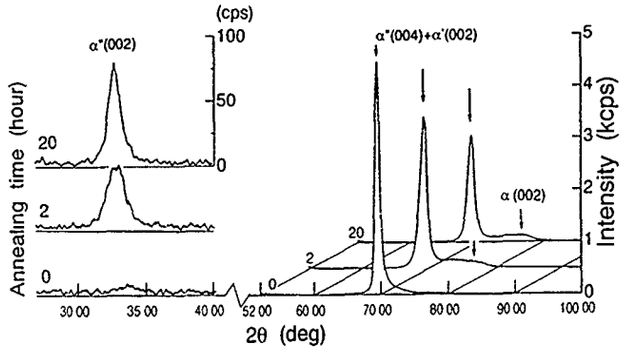

FIG. 5. The change of x-ray profiles against annealing time for the film with stoichiometric N content of the α'' phase (11 at. %) sputtered under P_{total}=10 mTorr, F_{N_2}=10%, and deposition rate=33 Å/min.

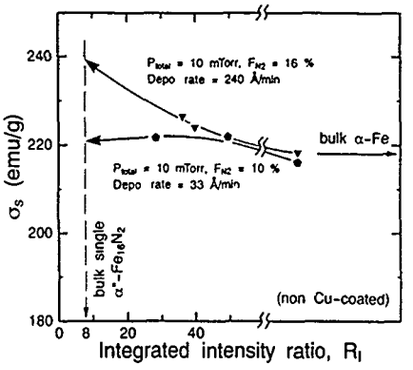

FIG. 6. The change of σ_s against the integrated intensity ratio R_I for the films sputtered under P_{total}=10 mTorr, deposition rate=33 and 240 Å/min, F_{N_2}=10% and 16%, non-Cu-coated.

the annealed $(\alpha''+\alpha')$-$Fe_{16}N_2$ films with stoichiometric N content. In the same figure, σ_s for the Cu-coated films are also shown.

For the films consisting of α' single phase (in an as-deposited state), the values of σ_s increased slightly with the increment of the unit-cell volume. At the unit-cell volume of about 25.5 Å^3 (α' phase with 11 at. % N), σ_s showed 228 emu/g on average (Cu-coated) and this value was about 4% higher compared to that of bulk α-Fe.

In the case of annealed $(\alpha''+\alpha')$-$Fe_{16}N_2$ films (Cu-coated), the value of σ_s showed 232 emu/g on average, and were about 2% larger than that of each as-deposited film, while the unit-cell volume of the α'' phase is always constant and coincided with that of the bulk α'' phase (see Fig. 3). The unit-cell volume of the α'' phase with 11 at. % N is equal to that of the α''-$Fe_{16}N_2$ phase within the accuracy of this experiment. Therefore the change of σ_s by annealing in nitrogen-martensite with 11 at. % N content cannot be discussed as a function of the change of unit-cell volume of a bct structure caused by the phase transformation from α' to α'' phase. In the next section, as a second physical factor the degree of N site ordering in nitrogen-martensite will be discussed in connection with the change of σ_s.

3. Dependence of magnetic moment on N site ordering

To evaluate the degree of N site ordering in the bct structure of nitrogen-martensite, two factors should be taken into account. One is the change of the integrated intensity of the $\alpha''(002)$ line which is the unique superlattice diffraction from the α'' phase. Another is the integrated intensity ratio of $\alpha''(004)+\alpha'(002)$ to $\alpha''(002)$, R_I, namely

$$R_I \equiv [I^{\alpha''}{}_{(004)}+I^{\alpha'}{}_{(002)}]/I^{\alpha''}{}_{(002)}.$$

The calculated value of R_I is about 8 for the ideal structure of the α'' phase.[14]

Figure 5 shows the change of XRD profiles against annealing time for the film with stoichiometric N content of the α'' phase (11 at. %). From these profiles, the intensity of $\alpha(200)$ was relatively very weak and any diffraction lines from the γ' phase were not observed. After annealing for 2 h, $\alpha''(002)$ came to be observed clearly. By annealing further for 20 h, the integrated intensity of $\alpha''(002)$ increased about 20% compared to that of 2 h. On the other hand, the experimentally determined value of R_I changed from 50 to 28 with the increase of annealing time.

Therefore, from these experimental results (1) the increase of the integrated intensity of $\alpha''(002)$ and (2) the change of R_I approaching to the ideal value of 8, the increase of degree of N site ordering in nitrogen-martensite, which directly corresponds to the increase of the volume fraction of the α'' phase in the films, is strongly promoted by annealing.

In Fig. 6, the changes of σ_s in $(\alpha''+\alpha')$-$Fe_{16}N_2$ films by isothermal annealing at 150 °C are shown against the integrated intensity ratio R_I. For one film σ_s increases slightly from 218 (as deposited) to 226 emu/g at R_I=36.4 (20 h). On the other hand, for another film, σ_s takes the value of about 222 emu/g at R_I=49 (2 h) and keeps a constant value even though R_I approaches to the value of 8. From these experimental facts, it was found that the degree of N site ordering in nitrogen-martensite does not much affect the increment of σ_s. The expected values of σ_s at R_I=8 (perfect ordered state in α''-$Fe_{16}N_2$) estimated by the simple extrapolation with using the data points of σ_s against R_I are no more than 222–240 emu/g, a value which is definitely smaller than the giant magnetic moment of 2.9 T.

4. Dependence of magnetic moment on temperature

Figure 7 shows the temperature dependence of σ_s in $(\alpha''+\alpha')$-$Fe_{16}N_2$ films with stoichiometric N content deposited on MgO (100) and (110) substrates, respectively. Heating and cooling were at 60 °C/h. On heating, the value of σ_s gradually decreased with increasing temperature. Around 200 °C a sudden discontinuous decrease of σ_s from 200 to 170 emu/g was observed. With further increasing temperature, σ_s decreased monotonously and reached about 130 emu/g at 400 °C, while on cooling, the change of σ_s with respect to temperature was completely different from that of heating, and no sudden change of σ_s was observed. The sudden discontinuous change of σ_s observed around 200 °C is considered to correspond to the phase change from $\alpha''+\alpha'$ to $\alpha+\gamma'$. Therefore the hysteresis in the σ_s-T curve is caused by this irreversible phase decomposition from

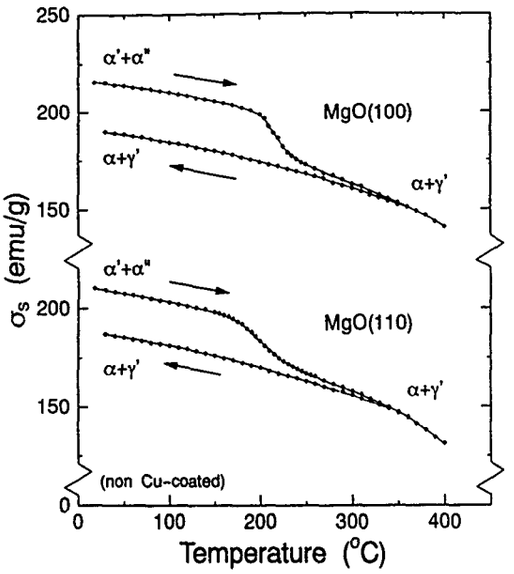

FIG. 7. The temperature dependence of σ_s in the films consisting of the α'' phase deposited on MgO (100) and (110) substrates fabricated under P_{total}=10 mTorr, deposition rate =240 Å/min, and F_{N_2}=16% after an initial anneal at 150 °C for 2 h.

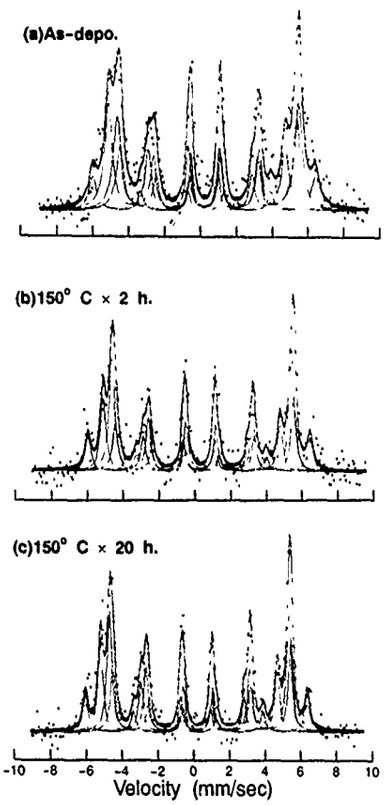

FIG. 8. Mössbauer spectra of $(\alpha''+\alpha')$-$Fe_{16}N_2$ film (non-Cu-coated) measured at R.T. (a) As-deposited, (b) annealed at 150 °C for 2 h, and (c) annealed at 150 °C for 20 h, respectively. The film was deposited under P_{total}=10 mTorr, deposition rate=240 Å/min, and F_{N_2}=16%.

TABLE II. Mössbauer parameters of the film deposited under P_{total}=10 mTorr, F_{N_2}=16%, deposition rate=240 Å/min. *Hi* is the hyperfine field, *I.S.* the isomer shift, *e.q.Q.* the quadrupole splitting, *Hwid* the distribution of *Hi*, and area the relative intensity, respectively.

Site	*Hi* (kOe)	*I.S.* (mm/s)	*e.q.Q.* (mm/s)	*Hwid* (kOe)	Area (%)
Fe(I)	289	0.01	−0.05	7.00	21.3
Fe(II)	316	0.17	0.04	7.00	31.3
Fe(III)	391	0.11	−0.05	7.00	11.2
α-Fe	335	0.02	−0.007	7.00	36.1
(As-deposited)					
Fe(I)	289	0.01	−0.05	4.00	17.8
Fe(II)	316	0.17	0.04	4.00	41.8
Fe(III)	391	0.11	−0.05	4 00	13.1
α-Fe	335	0.02	−0.007	4.00	27.3
(Annealed at 150 °C for 2 h)					
Fe(I)	289	0.01	−0.05	3.00	20.6
Fe(II)	316	0.17	0.04	3.00	37.7
Fe(III)	391	0.11	−0.05	3.00	12.5
α-Fe	335	0.02	−0.007	3.00	29.3
(Annealed at 150 °C for 20)					

$\alpha''+\alpha'$ to $\alpha+\gamma'$. The temperatures of this phase decomposition for the present films were good agreement with that of the α''-$Fe_{16}N_2$ precipitates in bulk powder reported by Jack.[10] The temperature dependence of σ_s observed in present experiments is found to be quite different from that of Gao and Komuro.[15,16]

C. Mössbauer spectrum

Figure 8 shows the change of Mössbauer spectra of the $Fe_{16}N_2$ film with stoichiometric N content by annealing. The spectrum in each film can be fitted into four hyperfine field interactions *Hi* of α phase, Fe(I), Fe(II), and Fe(III) of the $(\alpha''+\alpha')$-$Fe_{16}N_2$ phase. The fitted Mössbauer parameters are listed in Table II. As seen in the table, the large value of *Hi*, about 390 kOe, due to the Fe(III) site in nitrogen-martensite was detected in each film. Half widths of the peaks become narrower with increasing annealing time. This result corresponds to the promotion of N site ordering in nitrogen-martensite caused by annealing, and is in good agreement with the change of R_I and also the result of ion-implanted films reported by Nakajima.[14]

For the films examined presently, the average value of *Hi* was about 325 kOe, which was nearly equal to that of *Hi* of α-Fe. Therefore the value of σ_s in $(\alpha''+\alpha')$-$Fe_{16}N_2$ film of about 232 emu/g determined by VSM was consistent with the result of Mössbauer spectrum analysis. Based on the fitted Mössbauer parameters, the volume fraction of α-Fe was estimated to be 27% and 73% for the $(\alpha''+\alpha')$-$Fe_{16}N_2$ phase in annealed films. Using these values, the value of σ_s in the $(\alpha''+\alpha')$-$Fe_{16}N_2$ phase, $\sigma_{Fe_{16}N_2}$, is estimated by the following equation:

$$232^{exp}=\sigma_{Fe_{16}N_2}\times 0.73+\sigma_{\alpha\text{-}Fe}\times 0.27,$$

where $\sigma_{\alpha\text{-}Fe}$ is 218 emu/g. The obtained value of $\sigma_{Fe_{16}N_2}$ is 237 emu/g. Considering this calculated result and the result of the dependence of σ_s on R_I, the value of saturation mag-

netization of the α'' phase (perfect ordered state) should be no more than 240 emu/g, while the site population of the $(\alpha''+\alpha')$-$Fe_{16}N_2$ phase determined in this study was about 4:9:3, which is slightly different from the ideal ratio of 4:8:4 determined uniquely from the structure of α''-$Fe_{16}N_2$.

IV. SUMMARY

(i) $(\alpha''+\alpha')$-$Fe_{16}N_2$ films were synthesized on MgO single-crystal substrates by the reactive sputtering method. The result of the structural analysis using XRD and CEM revealed that the same structure as bulk α''-$Fe_{16}N_2$ is realized in the present films.

(2) The intrinsic value of saturation magnetization of the α'' phase (perfect ordered state) is proposed to be no more than 240 emu/g ($\simeq$2.4 μ_B per Fe atom in average) at 300 K.

[1] M. Takahashi, H. Shoji, H. Takahashi, T. Wakiyama, M. Kinoshita, and W. Ohta, IEEE Trans. Magn. **29**, 3040 (1993)

[2] M. Takahashi, H. Shoji, H. Takahashi, and T. Wakiyama, Proc. MRS (in press).

[3] A. Sakuma, J. Magn. Magn. Mater. **102**, 127 (1991).

[4] T. K. Kim and M. Takahashi, Appl. Phys. Lett. **20**, 492 (1972).

[5] K. Nakajima and S. Okamoto, Appl. Phys. Lett. **56**, 92 (1990).

[6] C. Gao and W. D. Doyle, J. Appl. Phys. **73**, 6579 (1993).

[7] M. Komuro, Y. Kozono, M. Hanazono, and Y. Sugita, J. Appl. Phys. **67**, 5126 (1990).

[8] Y. Sugita, K. Mitsuoka, M. Komuro, H. Takahashi, and A. Sakuma, Proc. ISPMM **1**, 190 (1992).

[9] H. Takahashi, M. Komuro, K. Mitsuoka, and Y. Sugita, Digests of the 17th Conference on Magnetics in Japan 1993 (Magnetics Society of Japan, Tokyo, 1993), p. 152.

[10] K. H. Jack, Proc. R. Soc. London, Ser. A **208**, 216 (1951).

[11] K. H. Jack, Proc. R. Soc. London, Ser. A **208**, 200 (1951).

[12] J. B. Nelson and D. P. Riley, Proc. Phys. Soc. London **57**, 126 (1945).

[13] The values of lattice constant a of the α'' phase reported by the present authors was previously determined only by using $\alpha''(004)$ and $\alpha''(202)$, which are duplicated with $\alpha'(002)$ and $\alpha'(101)$, respectively. Therefore the discrepancy for the value of lattice constant a between the present and earlier results is caused by the difference of the determination methods.

[14] K. Nakajima, Ph.D. thesis, Nagaoka Institute of Technology, 1990.

[15] C. Gao and W. D. Doyle, IEEE Trans. Magn. **29**, 3046 (1993).

[16] Y. Sugita, K. Mitsuoka, M. Komuro, H. Hoshiya, Y. Kozono, and M. Hanazono, J. Appl. Phys. **70**, 5977 (1991).

Enhanced Fe moment in nitrogen martensite and $Fe_{16}N_2$ (invited)

W. E. Wallace and M. Q. Huang
Department of Materials Science and Engineering, Carnegie Mellon University, Pittsburgh, Pennsylvania 15213

Nitrogen martensite was prepared by treating fine Fe powder with NH_3/H_2 gas mixtures at temperatures around 665 °C. Upon quenching to a temperature T_q, the γ phase which had formed at the elevated temperature undergoes a martensitic transformation to form nitrogen martinsite (α' Fe-N alloy), a tetragonal material. Heat treating this material for 1–2 h at 140±10 °C produced the α'' phase $Fe_{16}N_2$. The α' phase occurred along with γ Fe-N. From x-ray line intensities, the amount of α' phase was ascertained. The α' phase exhibits a room-temperature moment of 250±10 emu/g. $Fe_{16}N_2$ is formed along with α Fe and also there is retained N-austenite. Using XRD and conventional magnetic measurement procedures, one obtained 280±10 emu/g for the saturation moment of $Fe_{16}N_2$. The experimental Fe moment, 2.88 μ_B, is in excellent agreement with the most recent band-structure calculations, 2.85 μ_B. The ternary systems $(Fe,M)_{16}N_2$ were studied with M=Mn or Ni. γ Fe-Mn nitride readily forms, but it does not undergo the $\gamma \rightarrow \alpha'$ transformation. The α' phase and possibly the α'' phase form in the Fe-Ni nitride.

I. INTRODUCTION

Iron nitrides have been known for many years.[1] Nitrogen cannot be introduced into Fe by treating it with nitrogen at normal pressures (i.e., 1–100 atm). However, iron can be nitrogenated to form the γ FeN phase by treating it with a mixture of 90 mol % H_2 and 10 mol % NH_3 at temperatures ranging from about 900 to 975 K. At these temperatures NH_3 is unstable with respect to its constituent elements by ~47 kJ. With a suitable catalyst, NH_3 will decompose and generate N_2 at pressures in the thousands of atmospheres at temperatures between 900 and 1000 K. For example, at 665 °C (938 K), the equilibrium pressure of N_2 is ~2400 atm. It is well known that Fe and its alloys are effective synthetic NH_3 catalysts and hence under the experimental conditions cited, N_2 is generated at high pressures, sufficiently high to force N atoms into the Fe lattice. This was shown many years ago in a study by Lehrer.[2]

Nitrogenation of Fe leads to a variety of phases: α, γ, γ', ϵ, ζ, α', α''. Fe-N is the terminal solid solution based on α Fe and it is a simple bcc. The γ phase, often called nitrogen austenite, is cubic. The Fe atoms in the γ phase are in a fcc arrangement with N partially and randomly occupying the octahedral interstices.[3] α' and α'' are phases derived from the γ phase by a martensitic transformation. Both α' and α'' are tetragonal materials[4] with $c/a \sim 1.1$. The ϵ phase is one in which the Fe atoms are in a cph arrangement.[5] The ζ phase is orthorhombic.[5] Very recently, Suzuki *et al.*[6] have reported the formation of FeN by reactive sputtering and have stated that it exists in the zinc-blende structure. Of the eight known Fe-N phases, the present paper is concerned primarily with only the γ, α', and α'' phases for reasons brought out below.

Introduction of nitrogen into the Fe lattice produces striking changes in the magnetism of phases in which Fe is magnetic. For example, the Curie temperature, shown in Fig. 1, in the ϵ phase varies from 300 to −250 °C as the concentration is varied, passing though a maximum at the composition $Fe_{78}N_{22}$. Another startling feature is the difference in magnetic properties of the γ and γ' phases. The former is nonmagnetic, whereas the latter is strongly magnetic with σ_{sat}=186 emu/g and $T_c \sim 761$ K. In each case the N atoms partially occupy the octahedral interstices in the Fe lattice. The principal structural difference between the γ and γ' phases is that the nitrogens are disordered in γ FeN but are ordered in γ' FeN (i.e., Fe_4N). How ordering of the (nonmagnetic) nitrogens can generate strong ferromagnetism in this material is not immediately evident. It undoubtedly originates with an altered band structure brought on by ordering of the nitrogens. Japanese workers have shown[7,8] that nitrogenation of Fe to form the $Fe_{16}N_2$ phase leads to a significant rise in magnetization. This has greatly intensified interest in the magnetism of Fe-N alloys.

In previous publications from this laboratory[9,10] it has been shown that nitrogen austenite can be formed by the method of Lehrer[2] and Jack,[3–5] i.e., by treating Fe powder with an NH_3/H_2 gas mixture at temperatures around 950 K. In the classic work of Jack, it was shown that upon quench-

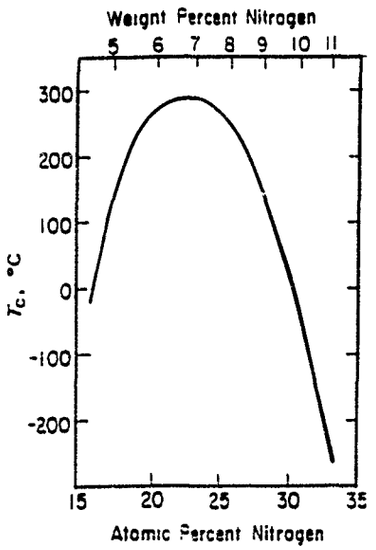

FIG. 1. T_c vs composition in ϵ Fe-N alloys, taken from H. A. Wriedt, N. A. Gokcen, and R. H. Nofzinger, Bull. Alloy Phase Diagrams **8**, 355 (1987).

 0021-8979/94/76(10)/6648/5/$6.00 © 1994 American Institute of Physics

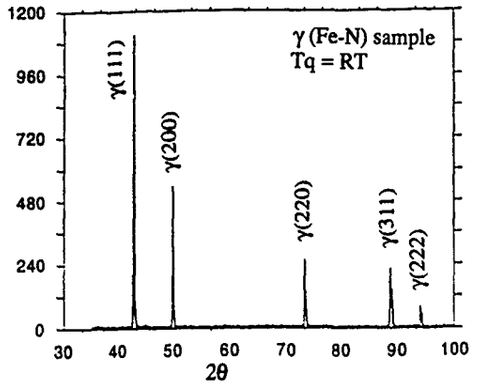

FIG. 2 X-ray-diffraction pattern of the Fe-N alloy containing 10.7 at. % nitrogen which has been quenched to room temperature. The pattern is characteristic of a single-phase fcc material. This indicates that by this treatment a single-phase alloy is produced. No α' Fe-N alloy is produced by this procedure.

ing, γ FeN undergoes a transition into the nitrogen analog of martensite (the α' phase). Jack also found that with heat treatment at temperatures ranging from 150 to 200 °C the α' phase transforms into the α'' phase, an alloy with the composition $Fe_{16}N_2$.

In previous work in this laboratory,[9,10] results were obtained that were similar but not identical to those obtained by Jack. The principal difference lay in the quenching procedures necessary to effect the $\gamma \rightarrow \alpha'$ transformation. In the work of Jack, quenching to room temperature was all that was needed to bring about the martensitic transformation, whereas the experience in this laboratory is that cryogenic temperatures are required, particularly for high N concentrations.

This dependence of conversion efficiency on quenching temperature and the necessity to quench to cryogenic temperatures was also observed by Bao *et al.*[11]

In the present work, the α' and α'' phases have been synthesized and studied magnetically. Results obtained for these alloys are reported herein, as well as those for ternary alloys in which 10–15 wt % of the Fe has been replaced by M, where M=Cr, Mn, Co, Ni, Cu, Ti, or Al.

II. FORMATION AND CHARACTERIZATION OF THE α' AND α'' Fe-N PHASES

A. Experimental details and results obtained for α' Fe-N alloys

A mixture of NH_3 and H_2 in the ratio $H_2/NH_3 \sim 9$ was flowed over 6–9 μm Fe powder at a temperature of 660–670 °C. The samples were then quenched to temperatures ranging from room temperature to liquid-helium temperature. The Cu radiation diffraction pattern for the sample containing 10.7 at. % N[12] is shown in Fig. 2. The material consists entirely of γ phase within the detection limit of this technique, perhaps 3%–5%. Upon cooling to liquid-nitrogen or liquid-helium temperatures, transformation of a substantial fraction of the material into the α' form occurs. Examples of the extent of the transformations and the conditions needed are given in Table I. The magnetization versus temperature behavior (see Fig. 3) is used to follow the $\gamma \rightarrow \alpha'$ transformation. The rise in magnetization upon cooling below 150 K is occasioned by the transformation of nonmagnetic γ Fe-N into the strongly magnetic α' phase.

TABLE I. α' phase formation by quenching γ Fe-N and moment for α' Fe-N.

Composition of alloy	T_q (K)[a]	wt % α' phase	Moment of α' Fe-N (emu/g)
at. % N			
6.4	RT[b]	87	240
8.1	RT	72	246
···	LN	82	···
10.7	RT	0	···
···	LN[b]	51	260
···	LHe[b]	56	···

[a] T_q=quench temperature.
[b] RT=room temperature ~20 °C; LN and LHe represent liquid N_2 and liquid He, respectively.

The data of Table I indicate that the $\gamma \rightarrow \alpha'$ transformation occurs at higher temperatures when the nitrogen concentration is low. The XRD pattern for the alloy containing 10.7 atoms of N per 100 atoms of Fe is shown in Fig. 4; this is for the sample (see Table I) which had been quenched to liquid-helium temperature. This alloy is a two-phase mixture consisting of the retained austenite phase (γ phase) and the martensitic (α' phase). The phase composition can be estimated from the observed line intensities of the two strongest peaks. There is a complication in that the γ (111) and α' (101) lines overlap at $2\theta \sim 43°$. The contribution of the α' (101) line to this line can be evaluated by conventional x-ray-diffraction theory. Using the methodology and nomenclature employed by Cullity,[13] $I_{\alpha'(110)}/I_{\alpha'(101)} = B_{\alpha'(110)}/B_{\alpha'(101)}$, where $I_{\alpha'(110)}$ and $I_{\alpha'(101)}$ are the intensities of the (110) and (101) lines of the α' phase and the B's are the quantities used by Cullity.

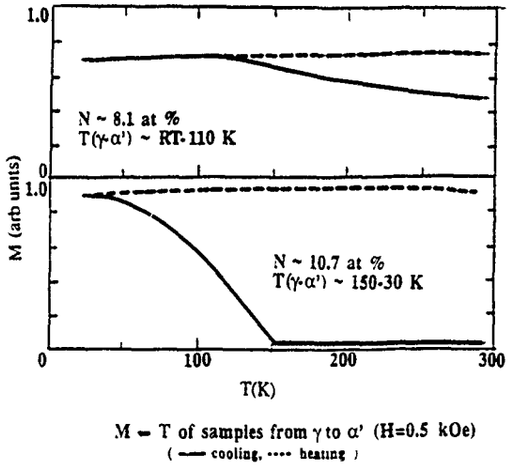

FIG 3. Two representative magnetization-temperature plots showing the rise in magnetization at low temperatures. The rise is due to the $\gamma \rightarrow \alpha'$ transformation, viz., the conversion of the nonmagnetic γ phase into the strongly ferromagnetic α' phase. The solid and dashed lines are for cooling and heating, respectively.

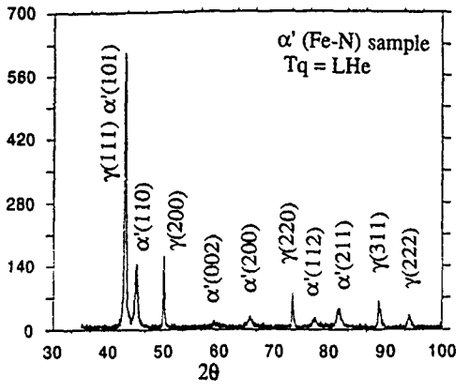

FIG. 4. X-ray-diffraction pattern for the γ alloy in Fig. 2 after cooling to liquid-He temperatur. lines appear which are characteristic of the α' Fe-N phase. Thus this alloy is a mixture of the γ and α' phases.

The B's involve the structure factor (F_{hkl}), multiplicity, and the Lorentz polarization. Using the expression and the measured value of $I_{\alpha'(110)}$, one can calculate $I_{\alpha'(101)}$. Knowing this, one can readily evaluate $I_{\gamma(111)}$, the contribution of the γ phase to the intensity of the peak at $2\theta \sim 43°$. Once this is known, one can evaluate the volume fraction V of the α' phase in the mixture from the expression:

$$I_{\alpha'(101)}/I_{\gamma(111)} = VB_{\alpha'(101)}/(1-V)B_{\gamma(111)}.$$

One can also make this calculation using other lines, $\gamma(200)$, $\alpha'(211)$, etc.

The volume fractions calculated by this procedure can be combined with the known densities to find the wt % of the phases present in γ, α' two-phase alloy. Up to 87% of the γ phase has been transformed (see Table I).

Results for several samples and involving different quenching conditions are shown in Table I. The moment calculated for α' Fe-N is 250 ± 10 emu/g.

B. Experimental details and results obtained for α'' Fe-N alloys

The procedure to form α'' Fe-N is as follows: (1) α' is first formed by the procedure described above. (2) It is then heat treated at 140 ± 10 °C (i.e., tempered) for 1–2 h, at which temperature the N atoms become sufficiently mobile to redistribute ' :r the interstitial sites and convert the N-martensite into $Fe_{16}N_2$.

A number of samples containing the α' phase were heat treated in this fashion to form the α'' phase. Typical and characteristic XRD lines, (213) and (004) of the α'' phase, were observed after the tempering treatment (Fig. 5). This sample contained 10.0 at. % N. The original alloy was Fe rich compared to $Fe_{16}N_2$; hence, as the α'' phase formed, α Fe precipitates out. Thus there are four indications of the $\alpha' \rightarrow \alpha''$ conversion: (1) the appearance of lines characteristics of α Fe in the XRD pattern (see Ref. 9), (2) the development of the (213) line for the α'' phase, (3) shifts of other diffraction lines[9]—(202), (220), (400), (224), and (422)—with respect to the positions of the lines in the original martensite phase, and (4) the rise in moment during tempering.

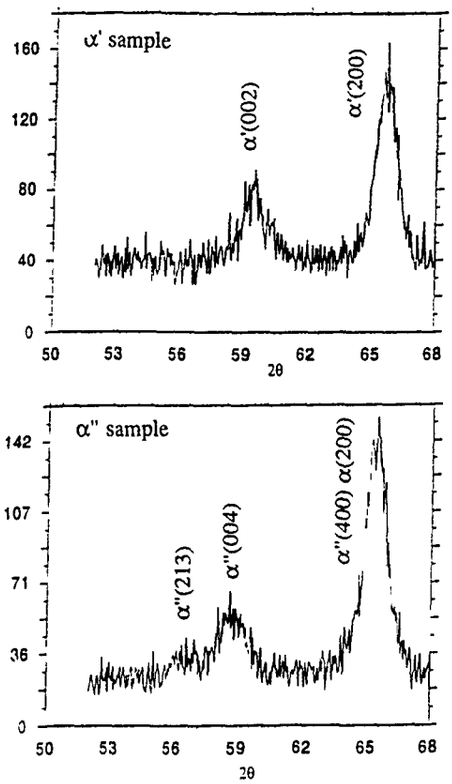

FIG. 5. Segments of the XRD patterns for α' and α'' phases. Lines are shifted and a new peak (213) appears. These changes and the rise in magnetism are indicative of the $\alpha' \rightarrow \alpha''$ transformation.

The lattice constants a and c are very close to those reported by Jack, $a = 5.718$ Å and $c = 6.290$ Å. The magnetic moment of the three-phase mixture increases from 182 to 189 emu/g as the α' phase transforms to α''. To evaluate the α'' moment, it is necessary to know the phase composition of the alloy. This information is obtained by the procedure described in detail in Ref. 9. A representative sample was estimated to contain 56% α'', 13% α Fe, and 31% γ. The estimated moment is ~285 emu/g for α''. The enhanced Fe moment of α'' Fe-N was observed in many samples. Results are summarized in Table II. It seems well established that Fe in $Fe_{16}N_2$ has an enhanced moment 30% larger than that for α Fe.

TABLE II. Phases in tempered α' Fe-N and the moment of $Fe_{16}N_2$. Two independent samples were studied for the 9.4 and 10.7 samples and three independent samples were studied for the 10.0 sample.

Composition of γ phase (at. % N)	wt % of phases			$Fe_{16}N_2$ magnetic moment (emu/g)
	γ	α	α''	
8.1	16	35	49	272
9.4	25	23	52	280
	25	27	48	283
10.0	30	11	59	283
	31	13	56	286
	35	13	52	283
10.7	45	7	48	283
	53	8	39	286

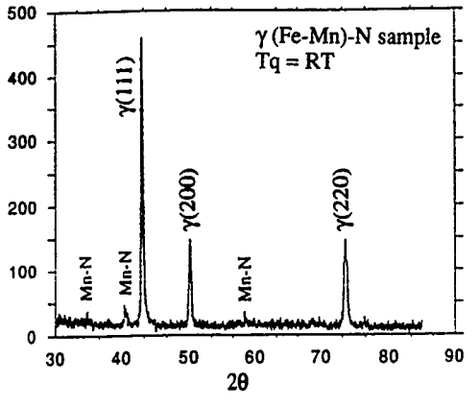

FIG. 6. XRD pattern of the nitride of Fe-Mn (15 wt %). Impurity peaks are noted at 2θ=34.5°, 40.5°, and 58.5°, which are identified as originating with Mn nitride.

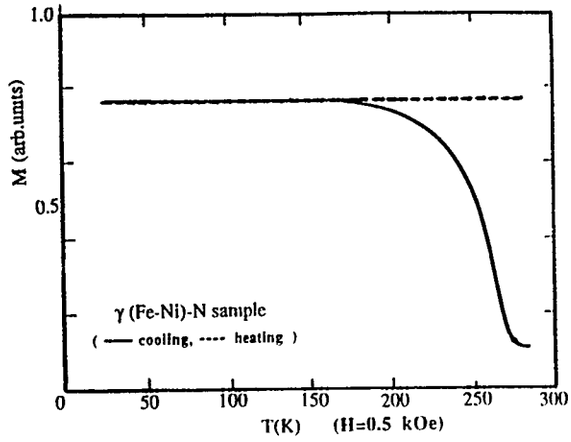

FIG. 8. TMA of the sample in Fig. 7. Irreversible transformation of $\gamma \rightarrow \alpha'$ begins at about 275 K.

III. MAGNETISM OF $(Fe,M)_{16}N_2$ WITH M=Mn OR Ni

Experiments have been carried out to prepare and characterize $(Fe,M)_{16}N_2$ in which M=Cr, Mn, Co, Ni, Cu, Ti, or Al. Because of space limitations, only results for the system in which M=Mn or Ni will be presented.

A. Experimental details

Fe-M (15 wt %) with M=Mn or Ni was prepared by mechanical alloying using a high-energy SPEX 800 ball mill. The milled powders were heat treated for 20 min at temperatures of 300–800 °C. The original powders were 100–300 mesh. The procedures for nitriding and magnetically characterizing the samples were as those used for Fe powder, except that higher temperatures for nitriding were employed. The nitrogen contents were estimated from the measured lattice parameters of the nitride.[9]

B. Results for Fe-Mn nitrides

Fe-Mn (15 wt %) was nitrided at 700–720 °C and then quenched to room temperature. Figure 6 shows the XRD pattern of one of the Fe-Mn nitrides. Analysis of the pattern shows the majority phase to be fcc. Three small impurity peaks at 2θ~34.5°, 40.5°, and 58.5° originate from Mn nitride, as was confirmed by making the Mn nitride and studying it by XRD. The magnetic moment of this sample was ~13 emu/g. There was no evidence of the α' or α'' phase. According to Bozorth,[14] Fe-Mn alloys in the γ region are nonmagnetic. Therefore we conclude the moment of this sample is due to a very small amount of the bcc Fe-Mn impurity phase.

The Fe-Mn (15 wt %) nitride was cooled to 10 K in an effort to induce the $\gamma \rightarrow \alpha'$ transformation. This effort was unsuccessful, as evidenced by the facts that (1) the XRD pattern was unchanged and (2) the moment was unaffected; there was no effect comparable to that in Fig. 3. This observation is not in conflict with the findings of Jack.[3]

C. Results for the Fe-Ni nitride

1. Formation of the α' phase

The situation here is more interesting than that for Fe-Mn nitrides. Figure 7 shows the diffraction pattern for Fe-Ni (15 wt %) nitride. This is a nitrogen austenite with a=3.601 Å. This material was obtained by nitriding the alloy powder (made by mechanical alloying) at 710–720 °C

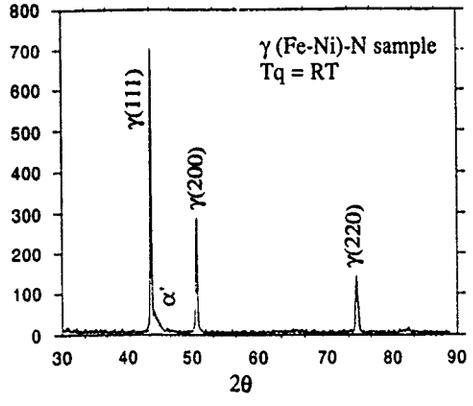

FIG. 7. XRD pattern of the nitride of $Fe_{0.85}Ni_{0.15}$, showing it to be an austenite.

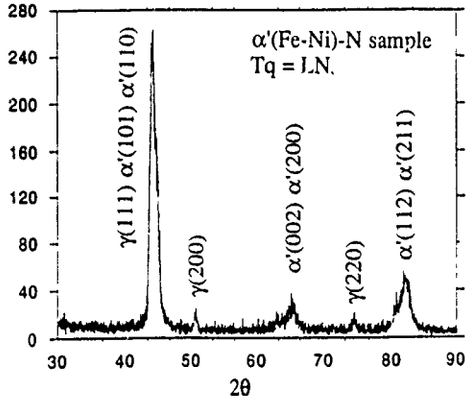

FIG. 9. XRD pattern of $Fe_{0.85}Ni_{0.15}$ nitride.

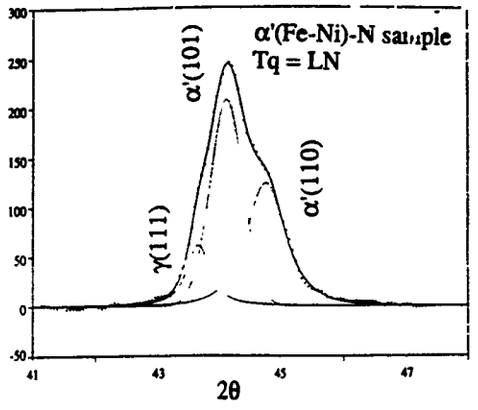

FIG. 10. Enlarged regions of the XRD pattern for the sample in Fig. 9.

and quenching to room temperature. This sample exhibited a moment of 48 emu/g. This moment is ascribed to the presence of a small amount of α' phase in the sample. Upon cooling to 10 K, the magnetism of the sample increases strikingly and irreversibly at temperatures 275–200 K (see Fig. 8). It appears that upon cooling to low temperatures the $\gamma \rightarrow \alpha'$ phase transformation is taking place. The measured moment rises to 186 emu/g. XRD (Figs. 9 and 10) confirms the formation of the α' phase. Its axial ratio is lower than that of Fe_8N. For α', $c=2.952$ Å, $a=2.855$ Å, and $c/a \sim 1.03$.

2. Possible formation of the α'' phase

Low-temperature heat treatment produced a further rise in moment. Heat treating 1 h at 120 and 150 °C gave moments of 193 and 197 emu/g, respectively. This provides suggestive evidence that under these conditions α' is being transformed into α''. However, this postulate was not confirmed by diffraction measurements. The characteristic α'' (213) line was not detected.

IV. CONCLUDING REMARKS

The magnetism of Fe-N alloys present many interesting features. The divergent magnetic behavior of the γ and γ' phases was referred to above. γ is nonmagnetic, where γ' is strongly ferromagnetic and yet, these alloys are structurally very similar, differing only in the way the (nonmagnetic) nitrogens are arranged in the interstitial sites. The fact that systems dilute in nitrogen undergo the martensitic transformation at higher temperatures is counterintuitive. A possible explanation for this surprising behavior is related to the existence of Fe_4N, the γ' phase, which is quite stable. As the nitrogen content increases, the γ phase becomes more like the γ' phase and becomes more stable. It is more resistant to the martensitic transformation, requiring lower temperature to bring on the $\gamma \rightarrow \alpha'$ transformation.

At present, information is lacking as to T_c and the anisotropy of the α' and α'' phases. In regard to T_c, as temperature is increased α' and α'' transform into α Fe and γ', making evaluation of T_c difficult, if not impossible. The presence of large amounts of α Fe in the α'' preparation obscures the true anisotropic features of $Fe_{16}N_2$. Efforts are under way to prepare α'' Fe-N which is freer of γ and α Fe.

One disconcerting feature of the studies of $Fe_{16}N_2$ has been that band-structure calculations have failed to indicate an enhanced Fe moment. See, for example, the results obtained by Sakuma.[15] however, a very recent treatment by Lai *et al.*,[16] including electron correlation effects, gives an Fe moment of 2.85 μ_B for $Fe_{16}N_2$. This is in excellent agreement with experiment as obtained in the present study, viz. 2.88 μ_B.

Strong evidence emerges from this study that Fe in $Fe_{16}N_2$ has a 30% enhanced moment compared to α Fe.

[1] See, for example, W. B. Pearson, *A Handbook of Lattice Spacings and Structures of Metals and Alloys* (MacMillan, New York, 1948), p. 984.
[2] E. Lehrer, Z. Elektrochem. **36**, 383 (1930).
[3] K. H. Jack, Acta Crystallogr. **3**, 392 (1950); Proc. R. Soc. London, Ser. A **208**, 200 (1951).
[4] K. H. Jack, Proc. R. Soc. London, Ser. A **208**, 216 (1951).
[5] K. H. Jack, Acta Crystallogr. **5**, 404 (1952).
[6] K. Suzuki, H. Morita, T. Kaneko, H. Yoshida, and H. Fujimori, J. Alloys Compounds **201**, 11 (1993).
[7] T. K. Kim and M. Takahashi, Appl. Phys. Lett. **20**, 492 (1972).
[8] M. Komuro, Y. Kozono, M. Hanazono, and Y. Sugita, J. Appl. Phys. **69**, 5126 (1990); **70**, 5977 (1991).
[9] M. Q. Huang, W. E. Wallace, S. Simizu, A. T. Pedziwiatr, R. T. Obermyer, and S. G. Sankar, J. Appl. Phys. **75**, 6574 (1994).
[10] M. Q. Huang, W. E. Wallace, S. Simizu, and S. G. Sankar, J. Magn. Magn. Mater. **135**, 226 (1994).
[11] X. Bao, R. M. Metzger, and M. Carbucicchio, J. Appl. Phys. **75**, 5870 (1994).
[12] Concentration in this case is number of nitrogen atoms per 100 atoms of Fe. For simplicity, this is termed at. %.
[13] B. D. Cullity, *Element of X-ray Diffraction* (Addison-Wesley, Reading, MA, 1978), p. 411.
[14] R. M. Bozorth, *Ferromagnetism* (Van Nostrand, New York, 1951), p. 234
[15] A. Sakuma, J. Magn. Magn. Mater. **102**, 127 (1991).
[16] W. Y. Lai, Q. Q. Zheng, and W. Y. Hu, J. Phys. Condens. Matter **6**, L259 (1994).

Enhancement of the formation of $Fe_{16}N_2$ on Fe films by Co additions (invited)

Yoshiharu Inoue, Shigeto Takebayashi, and Toshio Mukai
Advanced Materials and Technology Research Laboratories, Nippon Steel Corporation, 1618 Ida, Nakahara-ku, Kawasaki 211, Japan

Effects of Co additions on the formation of $Fe_{16}N_2$ have been investigated by observing nitrides formed on thin-film surfaces. Thin films of Fe-Co alloys with a (100) surface sputter-deposited on MgO(100) substrates are exposed to a mixed gas of NH_3 and H_2. The 16:2 nitride was observed to form on a surface of Fe-10 at. % Co film at a nitriding temperature of 500 °C. The formation temperature is 50 °C higher than for pure iron. The amount of the formed 16:2 nitride has been found to be 3× larger for Fe-10 at. % Co than for pure iron.

I. INTRODUCTION

There has been much attention to $Fe_{16}N_2$ since reconfirmation of its giant magnetization (2.9 T) by Kom.uro *et al.*,[1] which was stimulated by Kim and Takahashi's pioneering work.[2] $Fe_{16}N_2$ (16:2 nitride) is a metastable compound as discovered by Jack.[3] The crystal structure is body-centered tetragonal (bct) consisting of eight bcc cells distorted by interstitial N atoms. There are number of studies on the structure of nitrided ion-based alloys such as Fe-Ti, Fe-Mo, and Fe-Ni.[4] However, the enhancement of formation of the 16:2-type nitride by the third element additions has not been reported so far.

The purpose of the present paper is to show the first experimental evidence that Co enhances the 16:2 nitride formation. The following two points are considered to choose Co as the third element. The first point is that Fe maintains a bcc structure even after alloying with the third element; this is essential because $Fe_{16}N_2$ has an analogous bct structure.[3] The second point is that the third element does not undergo preferential nitridation; its chemical affinity for N is weaker or comparable to that of Fe. Co meets the above two requirements.

A surface-nitriding method is used for this investigation. The formation of iron nitrides on bulk iron surfaces on NH_3 gas-nitriding was studied by Inokuchi *et al.*[5] They reported that needle-shaped $Fe_{16}N_2$ precipitates form on the (100) surface. The present paper demonstrates that the Co-contained 16:2 nitride is granular and its amount is larger than the pure iron case.

II. EXPERIMENT

Fe-Co alloy films with a (100) surface were prepared as follows. First, Fe was deposited onto a MgO(100) single-crystal substrate and successively Co was deposited onto the Fe layer. Sputtering was performed with an Ar gas using an ECR made for Fe and a usual magnetron for Co. The total film thickness is 500 nm. The composition of Co was changed up to 30 at. % by changing the film thickness of Co. Alloying was performed by annealing at 750 °C for 120 min in a flowing H_2 gas. X-ray diffraction showed that the (100) orientation of the film is maintained after annealing.

The films were exposed to a mixed gas of 75% NH_3 and 25% H_2. The nitriding temperature was ranged from 450 to 550 °C. Annealing and nitriding were performed sequentially in an infrared furnace. The heat pattern is shown in Fig. 1. The structure of the nitride was determined by x-ray diffraction using Cu $K\alpha$ radiation. The morphology of the nitrides was observed through an optical microscope and a scanning electron microscope. Detailed analyses were performed by transmission electron microscopy (TEM) using a Hitachi 200 kV electron microscope with EDS (energy dispersion spectroscopy). TEM foils were prepared by ion milling. The samples were milled from the substrate side in order to reveal the surface structure.

III. RESULTS AND DISCUSSION

Figure 2 shows the x-ray-diffraction patterns for pure iron and Fe-10 at. % Co nitrided at 450–550 °C for 30 min. For pure iron, the $Fe_{16}N_2$ peaks were observed at a nitriding temperature of 450 °C, as shown in Fig. 2(a). At a nitriding temperature of 500 °C, the Fe_4N peak appeared instead of the $Fe_{16}N_2$ peak, as shown in Fig. 2(b). In the case of a nitriding temperature of 550 °C, the intensity of the Fe peak drastically decreased and the intensity of the Fe_4N peak increased as compared to the case of 500 °C, as shown in Fig. 2(c). This result indicates that the pure iron film is almost converted to a Fe_4N film.

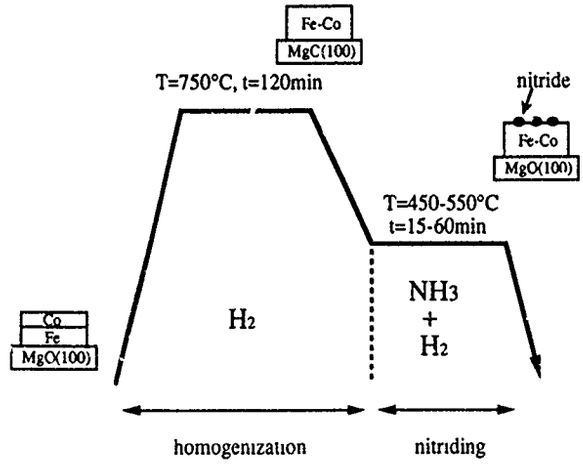

FIG. 1. Heat pattern for alloying and nitriding.

 0021-8979/94/76(10)/6653/3/$6.00 © 1994 American Institute of Physics

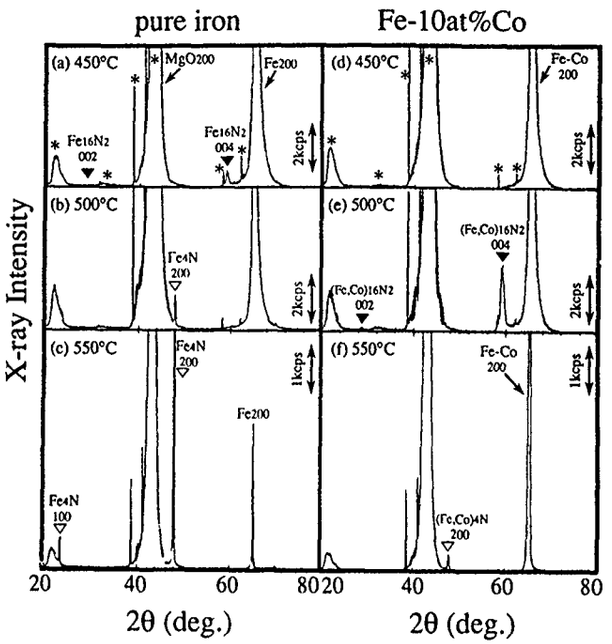

FIG. 2. X-ray-diffraction patterns for pure iron and Fe-10 at. % Co nitrided. The nitriding temperatures are (a) 450, (b) 500, and (c) 550 °C for pure iron and (d) 450, (e) 500, and (f) 550 °C for Fe-10 at. % Co. The nitriding time is 30 min. The mark (*) indicates the peaks from the MgO substrate.

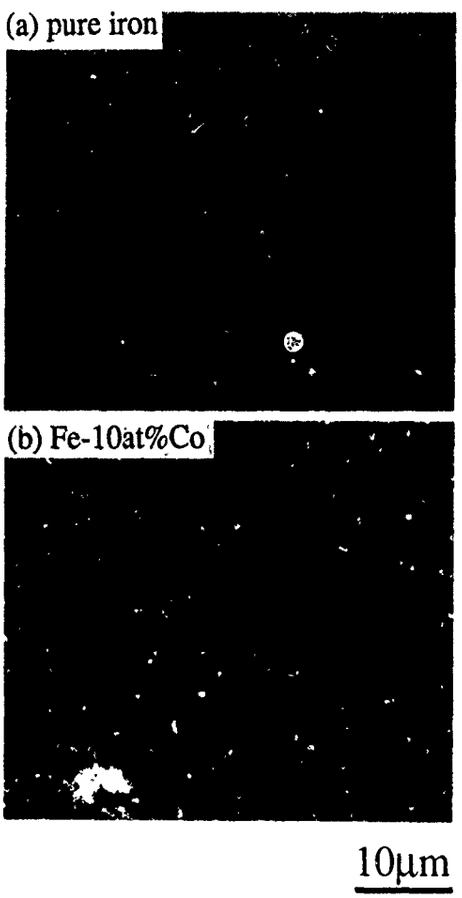

FIG 3. Scanning electron microscope images of the 16:2 nitride formed on (a) a pure iron film nitrided at 450 °C for 30 min and (b) a Fe-10 at. % Co film nitrided at 500 °C for 30 min.

FIG. 4. Bright field image of a granular precipitate on a Fe-10 at. % Co film nitrided at 500 °C for 30 min and the corresponding electron-diffraction pattern. The indices of the 16:2 nitride are also shown in the diffraction pattern.

For Fe-10 at. % Co, no nitride peaks were observed at a nitriding temperature of 450 °C as shown in Fig. 2(d). At a nitriding temperature of 500 °C, a strong 004 peak of the 16:2 nitride was observed. The 002 peak of the 16:2 nitride, which is an order reflection peak of the 16:2 nitride, was apparently observed [see Fig. 2(e)]. At a nitriding temperature of 550 °C, the 16:2 nitride peaks disappeared, as shown in Fig. 2(f). The intensity of the 4:1 nitride 200 peak is very weak as compared to that of the pure iron, indicating that the formation of the 4:1 nitride is suppressed by Co additions.

The nitridation behavior for the 16:2 nitride is different in the following two points. The formation temperature of the 16:2 nitride is 50 °C higher for Fe-10 at. % Co than for pure iron. The amount of the formed 16:2 nitride, which was calculated from the x-ray peak intensities, is 3× larger for Fe-10 at. % Co than for pure iron.

Figures 3(a) and 3(b) show the scanning electron microscope images of the 16:2 nitride which formed on a pure iron film nitrided at 450 °C and a Fe-10 at. % Co film nitrided at 500 °C, respectively. For the pure iron case, the morphology of the nitride is needle shaped. For the Fe-10 at. % Co case, granular precipitates were observed. From the x-ray-diffraction pattern in Fig. 2(e), the granular precipitate is assumed to be the 16:2 nitride.

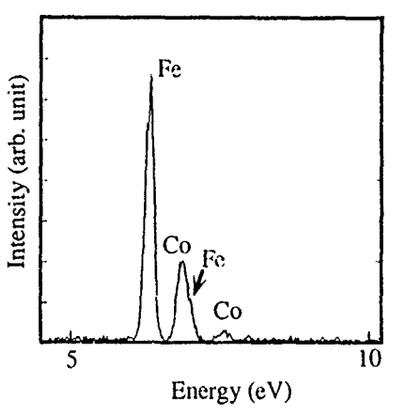

FIG. 5. EDS spectrum taken from a granular precipitate of the 16:2 nitride formed on a Fe-10 at. % Co film (the same precipitate as shown in Fig. 4).

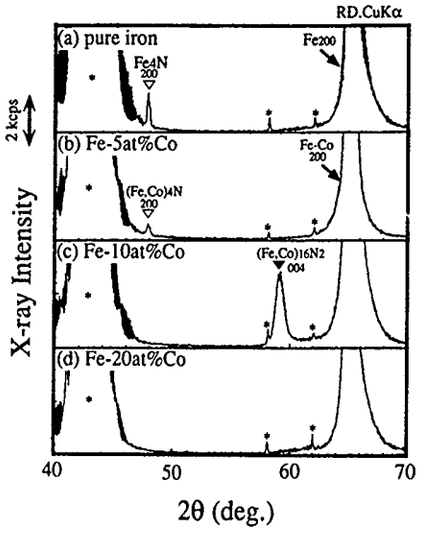

FIG. 6. X-ray-diffraction patterns of Fe-Co films with various Co contents nitrided at 500 °C for 30 min. The film compositions are (a) pure iron, (b) Fe-5 at. % Co, (c) Fe-10 at. % Co, and (d) Fe-20 at. % Co. The mark (*) indicates the peaks from the MgO substrate.

TEM observations were performed for the granular precipitate formed on Fe-10 at. % Co film. Figure 4 shows a bright field image of the granular precipitate and the corresponding electron-diffraction pattern. As shown in the diffraction pattern, we can observe weak spots at the midpoints between 000 and 400 spots. These spots are indexed by the 200 order reflections of the 16:2 nitride. Figure 5 shows an EDS analysis spectrum taken from the granular precipitate. The Co content of the precipitate was determined to be almost the same as that of the matrix bcc phase. From these results, the granular precipitate is determined to be a Co-contained 16:2 nitride, which can be denoted by $(Fe,Co)_{16}N_2$.

Figure 6 shows the x-ray-diffraction patterns for Fe-Co films with various Co contents nitrided at 500 °C for 30 min. For pure iron, only the Fe_4N peak was observed. As the Co content increases, the intensity of the 4:1 nitride peak decreases. At Fe-10 at. % Co, the 4:1 nitride peak disappeared and instead a strong 16:2 nitride peak appeared. Further increase in the Co content results in no nitride peaks, indicating harder nitridation for higher Co contents.

The stability of the Co-contained 16:2 nitride is discussed as follows. Due to a 10 at. % Co substitution, the lattice parameter of the bcc Fe-Co phase increases by 0.16% relative to that of the bcc pure Fe.[6] Assuming that the atomic volume of Co is the same as that of Fe, we presume that the interstitial sites are wider in the Fe-Co lattice than in the Fe lattice. This idea is supported by the fact that the solubility of nitrogen is increased by Co additions.[7] The 16:2 nitride is considered to be a nitrogen-ordered form of the tetragonal Fe-N solid solution, which is derived without changing the basic arrangement of Fe atoms in the bcc structure. Therefore, it can be speculated that the Co-contained 16:2 nitride also forms with less strain energy, leading to a higher stability. The observed enhancement of formation of the 16:2 nitride by Co additions can be related to the improvement of the stability of the 16:2 structure. Suppression of the 4:1 nitride formation by Co additions, as described in Fig. 2, may also benefit the 16:2 nitride formation.

IV. SUMMARY

We have newly found that Co additions enhance the formation of the 16:2 nitride. Granular 16:2 nitrides were confirmed to form on a (100) surface of Fe-10 at. % Co alloy. The formation temperature is 500 °C, which is 50 °C higher than that for pure iron. The amount of the 16:2 nitride is 3× larger than for pure iron. It is suggested that Co stabilizes the 16:2 structure.

ACKNOWLEDGMENT

The authors are greatly indebted to Dr. Okumura of Nippon Steel Corporation for his helpful discussion.

[1] M. Komuro, Y. Kozono, M. Hanazono, and Y. Sugita, J. Appl. Phys. **67**, 5130 (1990).
[2] T. K. Kim and M. Takahashi, Appl. Phys. Lett. **20**, 492 (1972).
[3] K. H. Jack, Proc. R. Soc. London, Ser. A **208**, 216 (1951).
[4] K. H. Jack, Proceedings of the International Conference on High Nitrogen Steels 88, 1989, p. 117.
[5] Y. Inokuchi, N. Nishida, and N. Ohashi, Met. Trans. **6A**, 773 (1975).
[6] W. B. Pearson, A Handbook of Lattice Spacings and Structures of Metals and Alloys (1958).
[7] V. Raghavan, Phase Diagrams of Ternary Iron Alloys (1987), Part 1, p. 167.

Published without author corrections

Properties and measurement of scanning tunneling microscope fabricated ferromagnetic particle arrays (invited)

A. D. Kent[a)]
IBM Research Division, T. J. Watson Research Center, P. O. Box 218, Yorktown Heights, New York 10598

S. von Molnár
Florida State University, Center for Materials Research and Technology, 406 Keen Building, Tallahassee, Florida 32306

S. Gider and D. D. Awschalom
Department of Physics, University of California, Santa Barbara, California 93106

The low temperature magnetic properties of arrays of scanning tunneling microscope (STM) fabricated ferromagnetic particles have been studied as a function of their dimension using a novel high sensitivity Hall magnetometer. Iron deposits with controlled shape and nanometer scale diameters (~25 nm) are formed using a STM to decompose a metalorganic precursor [$Fe(CO)_5$] in the active area of the measurement device. The hysteresis loops change significantly in going from nearly isotropic to oriented high aspect ratio (6:1 length to diameter) filamentary particles. In particles of intermediate aspect ratio and diameter the largest coercive field of 2.7 kOe is observed. This b· r as well as the characteristics of the Hall magnetometer (spin sensitivity of 10^{-14} emu/$Hz^{1/2}$) . ribed.

I. INTRODUCTION

The physical properties of ferromagnetic particles continue to be an active area of fundamental experimental and theoretical research. Advances in lithographic and measurement techniques are now permitting some of the basic tenets in the field of small particle classical magnetism to be critically tested. For example, measurements of a single acicular γ-Fe_2O_3 particle[1] and electron beam fabricated rectangular permalloy particles[2] are not consistent with the Néel–Brown[3] theory of thermally assisted magnetization reversal over a simple potential barrier. Usually this theory is the starting point in the analysis of more complex particulate media which have a distribution of sizes, shapes, and interactions. Magnetization reversal in elongated particles has also recently been re-examined theoretically. In idealized filaments Braun[4] finds that spatially localized magnetization fluctuations increase the switching rates and hence reduce the measured coercivities at finite temperature relative to the Néel–Brown theory. Real samples, of course, contain defects, ends, and surfaces that are not considered in this work but which are expected to play an important, if not dominant, role in the physics of magnetization reversal. Of fundamental interest is the mechanism of reversal in real particles—whether it is a classical coherent (Néel–Brown, Braun) or incoherent mode or, alternatively, heterogeneous nucleation and growth.[5] We have set out to study smaller noninteracting particles in which the competing effects can be highlighted by systematically varying the particle dimensions.

It is the purpose of this article to show how this is accomplished in scanning tunneling microscope (STM) nanolithographically produced small particle systems. STM and chemical vapor deposition techniques have been used to fabricate nanometer scale diameter (~25 nm) iron particles with a range of shapes from nearly isotropic to filamentary. Deposits are fabricated directly in the active area of a newly developed high sensitivity Hall magnetometer. With this device hysteresis loops of dilute particle arrays comprising 100–600 particles ($<10^{-11}$ emu) have been measured at low temperature. Moreover, the magnetic characteristics have been studied for a variety of particles sizes and shapes. In particles of intermediate aspect ratio (2.2:1 height:diameter) and diameter the largest coercive force is observed. This observation is not consistent with the well-known classical coherent or incoherent modes of reversal.[3,6] Further, from the hysteresis loops and array geometry we estimate the particle magnetization and interparticle interaction strength.

We begin with a brief review of the materials fabrication technique and characterization.[7] This is followed by a discussion of the magnetic measurements and analysis on particles of systematically varied geometry.

II. FABRICATION

Iron particles are formed by using a STM to decompose iron pentacarbonyl [$Fe(CO)_5$] which is metered into the mi-

[a)]Present address: Department of Physics, New York University, 4 Washington Place, New York, NY 10003.

 0021-8979/94/76(10)/6656/5/$6.00 © 1994 American Institute of Physics

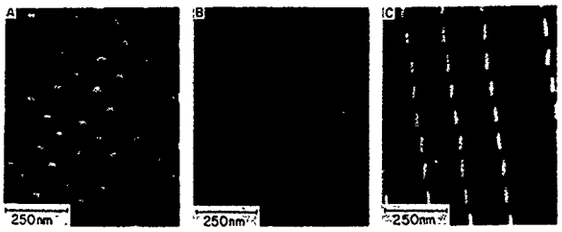

FIG. 1. Scanning electron micrographs (at a 45° tilt) show the particle and array geometry of a subset of samples we have fabricated and measured: (A) diameter 42±7 nm, height/diameter (c/a) 1.3±0.3, (B) diam. 29±2 nm, c/a 2.2±0.3, (C) diam. 17±1 nm, c/a 5.8±0.5.

croscope's ultrahigh vacuum chamber ($P=2\times10^{-10}$ T). To initiate the growth the substrate-tip bias is raised to 15 V and a current of 50 pA maintained in the presence of 30 μTorr of $Fe(CO)_5$. The STM feedback loop is *active* and maintains a constant current and thus constant height between the tip and growing deposit. When the deposit has reached the desired height above the surface the tip is retracted to stop the growth. The tip is moved to another location and the process repeated to form arrays.

Characterization by both Auger electron spectroscopy (AES) and transmission electron microscopy (TEM) indicate that relatively pure iron deposits are formed under these conditions. TEM shows that these consist of a polycrystalline bcc iron interior surrounded by a contamination coating in which the grain size is approximately the inner core diameter. AES reveals greater than 70 at. % Fe with a carbon remainder. The fact that the bcc phase is formed is evidence for greater purity of the deposits in their interior since the equilibrium phase of the Fe-C system above 0.4% carbon is fcc.[8]

The scanning electron micrographs in Figs. 1(A) and 1(C) show the extremes in dimensions we have fabricated and studied. The particle geometry, with the long axis perpendicular to the substrate surface, is highlighted in the oblique view presented in the micrograph. Note that from Figs. 1(A) and 1(C) the particle diameters progressively decrease from 42 to 17 nm while the ratios of height to diameter increase from 1 to 6. Although these measurements serve as a basis for comparing particle dimensions, contamination built up during observation as well as the finite resolution of the SEM cause systematic overestimates of the actual particle size.[9] The interparticle distance is approximately 130 nm and was chosen to minimize, as much as possible, the effect of interparticle interactions while building up enough overall moment for measurement. Magnetic measurements have been made on these samples as well as on some of intermediate dimensions.

III. MEASUREMENTS

Measurements were made using a novel high sensitivity magnetometer based on the Hall response in a semiconductor heterostructure. In contrast to integrated superconducting quantum interference device microsusceptometers,[10] this device allows for systematic investigations over a wide range of applied fields and temperatures. A high mobility

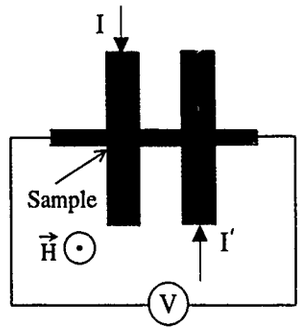

FIG. 2. Schematic of the Hall magnetometer showing the device layout and bridge measurement circuit. The sample is deposited into one Hall cross while the other serves as a reference. I and I' are independent current sources that float with respect to one another.

GaAs/$Ga_{0.7}Al_{0.3}As$ two-dimensional hole gas sample [$n_{2D}=3\times10^{11}$ cm^{-2}, $\mu(5\text{ K})=10^5$ cm^2/V s)] was wet chemically etched into the form depicted in Fig. 2 and a thin (30 nm) gold gate deposited over the active area of the device. The linewidths for the current and voltage probes ranged from 1 to 10 μm and the heterointerface was 100 nm below the surface. STM deposits were subsequently grown in the active area of one of the Hall crosses. The difference in Hall voltage between this sample cross and a closely spaced reference is measured using a bridge circuit (Fig. 2). With the bridge properly balanced, the resulting output voltage V is proportional to the sample contribution to the magnetic induction. This contribution can then be calculated using the measured Hall coefficient so that $\Delta B=V/RI$ where R is the Hall coefficient (~0.2 Ω/G) and I is the measurement current. Typically we use a 6.5 Hz ac current (~1 μA/rms) and lock-in detect the difference signal V.

In practice, a difference voltage is present even in the absence of a magnetic sample due to small variations in the Hall crosses (typically ~0.1%). This imbalance results in a signal proportional to the applied magnetic field which is minimized by adjusting the ratio I to I' at high field ($H\gg H_c$, the coercive field).

The large Hall response (~0.2 μV/G) in combination with good coupling of small samples to the device results in an excellent spin sensitivity. For example, the observed field noise of 0.1 G/Hz$^{1/2}$ (at 0.1 Hz, 5 K) in a 2 μm^2 device implies a spin sensitivity of 10^{-14} emu/Hz$^{1/2}$. Typically, signals from the STM arrays are 10 times this noise level. In addition, the sensor works over a large range of magnetic field and temperature. At low temperature, ballistic transport (on the scale of the magnetic arrays) reduces the responsivity. The quantum Hall effect and the associated nonlinear dependence of Hall voltage on magnetic field also changes the response at low temperature and high fields. Both the decreasing hole mobility and thermally activated switching of defects in GaAs cause the noise to increase with temperature. We have successfully used this magnetometer from 1 to 80 K with some decrease in performance with increasing temperature ($T>50$ K).

An array of particles of intermediate size [those in Fig. 1(B), referred to as sample (B)] placed in the active area of

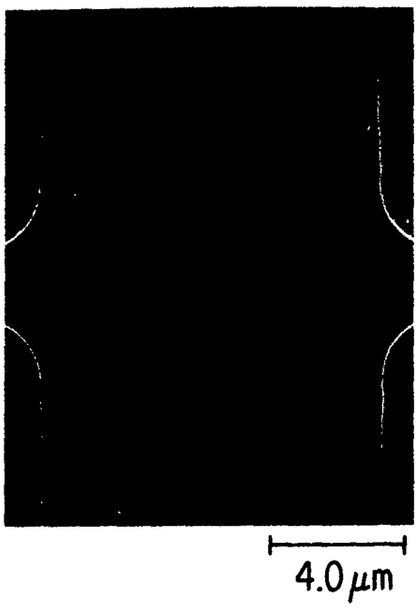

FIG. 3. SEM micrograph of a STM fabricated array [sample (B)] placed in the 10 μm×2.5 μm active area of a Hall magnetometer.

the magnetometer is shown in Fig. 3. An external field is applied perpendicular to the plane of the device and hence parallel to the long axis of the particles. Hysteresis loops are measured starting from a saturating field, ramping at a constant rate to the opposite field polarity and then back. Figure 4 shows the difference in induction, which is proportional to the sample magnetization, plotted versus the external field. Measurements were made at different temperatures and ramp rates. Under these conditions the coercive field has only a slight dependence on the measurement time and temperature

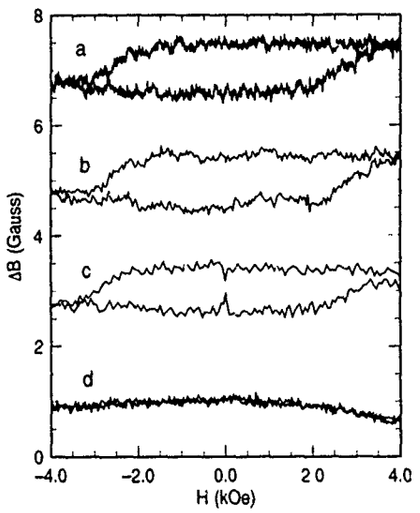

FIG. 4. Hysteresis loops for sample (B) measured from negative to positive saturation and back showing the difference in induction, which is proportional to the sample magnetization, versus external field. (a) 15 K, dH/dt =250 Oe/min, (b) 15 K, 1 kOe/min, (c) 5 K, 1 kOe/min, and (d) the difference between two reference crosses with no sample 5 K, 1 kOe/min. Plots are offset for clarity.

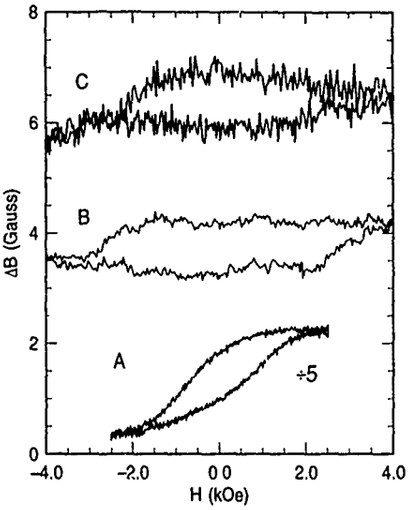

FIG. 5. Hysteresis loops as a function of particle dimensions. Measurements on sample (A) 5 K, 250 Oe/min, (B) 15 K, 1 kOe/min, and (C) 5 K, 500 Oe/min. These variations in measurement time and temperature do not affect the curves on the scale presented (as seen in Fig. 4). The increased noise in (C) is due to the smaller dimensions of the Hall cross (2 μm^2). In this case, the sample consists of only 100 particles with a total moment of $\sim 2\times10^{-13}$ emu.

and is approximately 2.7 kOe. The magnetization reversal occurs over a range ±0.4 kOe about the value. In Fig. 4(d), as a check, the same measurement was made using two reference crosses, neither of which contained a sample. This shows no hysteresis and only a small deviation from a constant value.

Magnetic measurements were made on arrays (A), (B), and (C) in Fig. 1 in order to study the dimensional dependence of the magnetic properties (Fig. 5). The shapes of the hysteresis loops change significantly in going from the nearly isotropic particles of sample (A) to the filamentary particles in (C). Most notably, the loops are increasingly square with more abrupt magnetization transitions. The change in sample magnetization also decreases due both to the geometry of the samples as well as to the decreasing moment per particle. The coercivity initially increases in more anisotropic particles [(A) to (B)]. Surprisingly, this is followed by a decrease in the more filamentary particles of sample (C). Samples intermediate in dimensions to (B) and (C) appear to confirm this trend.

The loop shape for sample (A) is close to that expected from the Stoner–Wohlfarth theory[11] for noninteracting uniaxial particles with randomly oriented easy axes. For instance, the remanence is 0.46 times the saturation magnetization close to the 0.5 predicted by SW. The coercivity is 640 Oe. Within this model the anisotropy field is $H_c/0.48$ or 1.33 kOe. Small deviations from isotropic shape would account for this entire anisotropy although a crystailine contribution might also be present (bcc Fe[6]~540 Oe). The demagnetization factors of a prolate ellipsoid of iron with axial ratio 1.17 is sufficient to explain this and within the range of measured particle asymmetries [$c/a=1.3\pm0.3$, Fig. 1(A)]. For the oriented elongated particles [samples (B) and (C)] increasingly

TABLE I. Summary of particle properties.

Sample	No. of particles	diam (nm)	c/a	m (emu/particle)	H_c (Oe)	diam (nm)[b]
A	500	42 ± 7	1.3 ± 0.3	1.0×10^{-14}	1324[a]	21
B	600	29 ± 2	2.2 ± 0.3	5.4×10^{-15}	2700	9
C	100	17 ± 1	5.8 ± 0.5	1.6×10^{-15}	2050	4

[a]Anisotropy field determined from the measured coercivity and the SW model.
[b]Magnetic core diameter inferred from the magnetic moment and particle shape.

square hysteresis curves are also expected on the basis of the SW theory. In contrast to sample (A), these particles' easy axes are not randomly oriented but expected to be aligned with their long axes.

From the change in induction in going from positive to negative saturation the magnetic moment per particle can be estimated. In the dipole approximation this change in B field perpendicular to the heterointerface averaged over the sensor area is given by

$$\Delta B = \frac{2m}{S} \sum_i \int_S d\mathbf{r} \frac{1}{[z^2+(\mathbf{r}-\mathbf{r}_i)^2]^{3/2}} \times \left(1 - \frac{3z^2}{[z^2+(\mathbf{r}-\mathbf{r}_i)^2]}\right), \quad (1)$$

where m, the magnetic moment per particle, is the quantity of interest; $\mathbf{r}$ is a vector in the plane of the surface; $\mathbf{r}_i$ the position of the ith particle; S the surface of the Hall cross, and z the distance from the dipole's center to the heterointerface. The integral over the rectangular surface S of the Hall cross can be performed analytically and then summed over particles numerically to solve for m. This calculation approximates the actual nonuninform field distribution from the array geometry and position in the Hall bar by a spatially homogeneous average field in estimating the moment. For sample (B), we find $m=5.4\times10^{-15}$ emu. This is a factor of approximately 10 smaller than an estimate based on the bulk moment of Fe and our observations of the particle size. As previously mentioned, it seems appropriate to assume that the magnetic volume is smaller than that found from SEM measurements. Taking the measured magnetization of bcc Fe (1700 emu/cm^3) gives a magnetic volume of 3×10^{-17} cm^3 or equivalently a magnetic core only 9 nm in diameter, compared to the 29 nm diam measured from Fig. 1(B). This interior size is consistent with TEM observations on similar deposits.[9] Within this analysis, the aspect ratio of the magnetic volume would also be greater than the measured value. The results for the other samples are summarized in Table I.

From the particle moment the strength of the dipolar interactions between particles can be estimated. For a square lattice of oriented dipoles with spacing a, the interparticle interaction field due to nearest neighbors is $4m/a^3$. For sample (A) this is 20 G. Substantial contributions result from the long range nature of the dipole interactions. Including oriented neighbors out to four lattice spacings (48 particles) results in a field of 40 G. This is still much less than the anisotropy field and will play a role only in the tails of the magnetization transition. Interactions are less important in samples (B) and (C) due to their smaller moment per particle.

IV. DISCUSSION

Changes in the coercive force with dimensionality, notably the decrease in high aspect ratio smaller diameter particles, are not consistent with conventional coherent[10] or incoherent modes of spin reversal.[6] For instance, the curling mode, which is applicable only in larger diameter particles, predicts an increase in coercive field with decreasing diameter. In both coherent reversal and fanning models the coercive field increases with aspect ratio. For reference, coherent reversal in an iron particle of axial ratio 2.2 [like sample (B)], would require a field of 5.7 kOe—twice the observed value. Fanning, which postulates decoupled grains, at least can account for the magnitude of the observed switching field.

Recently, Braun has considered the role of nonuniform magnetization fluctuations in reducing the coercivity at finite temperature in elongated particles.[4] It is therefore worth estimating whether this theory applies to our measurements. Fluctuation effects are important when the thermal energy is comparable to the barrier height. For uniform coherent reversal, at zero field, the barrier is KV, the anisotropy volume product. To be specific, for sample (C) this is 10^4 K. At low temperature this implies that such reversal cannot occur until the applied field is very close to the intrinsic (zero temperature) coercivity. For example, at 5 K the particles switch when $H/H_c \sim 0.9$, with our measurement times. In Braun's theory, the energy is no longer proportional to the volume but the cross-sectional area of the particle, $8\sqrt{JK/c}\ A$. This is the energy density of a domain wall times the cross-sectional area, A. J is the exchange constant and c the lattice spacing. An estimation of this energy for sample (C) is also 10^4 K. Thus spatially nonuniform reversal requires the same amount of thermal energy as the uniform case due both to the large exchange and anisotropy energies. Only in far more filamentary particles does the nonuniform mode dominate. These estimations suggest that fluctuations cannot account for the observed reduction in coercivity.

As an alternative to the above models, the particle ends, surfaces, and defects might play an important role in determining the magnetic properties. For example, large demagnetization fields such as occur at the particle ends would favor a heterogeneous nucleation and growth of reversed domains as occurs in bulk ferromagnets.[5] Reversal would con-

sist of either the localized nucleation of a reversed domain and its subsequent propagation or the movement of an existent closure domain through the particle. Moreover, defects, such as grain boundaries, lower the barrier to domain nucleation. As the energy of a domain wall is proportional to its area these scenarios are qualitatively consistent with the observed decrease in coercive force in smaller diameter particles.

In summary, we have demonstrated the ability to fabricate and measure nanometer scale ferromagnets. Magnetic structures with well-defined geometries have been coupled to an electronic system. This is the basis for a novel high sensitivity magnetometer which relies on the Hall effect in a semiconductor heterostructure. In addition to investigations of magnetic nanostructures, this combination enables studies of the effect of local magnetic interactions on electronic properties and transport in semiconductors.

ACKNOWLEDGMENTS

We would like to thank D. DiVincenzo and H.-B. Braun for helpful discussions and P. F. Hopkins and A. C. Gossard for providing the molecular beam epitaxy material. This work was supported in part by the Air Force Office of Scientific Research Grant No. F49620-93-1-0117 and the NSF Science and Technology Center for Quantized Electronics Structures Grant No. DMR 91-20007.

[1] M. Lederman, R. O'Barr, M. Ozaki, and S. Schultz, J. Appl. Phys. (in press).
[2] M. Lederman, G. A. Gibson, and S. Schultz, J. Appl Phys **73**, 6961 (1993).
[3] W. F. Brown, Phys. Rev. **130**, 1677 (1963)
[4] H.-B. Braun, Phys. Rev. Lett. **71**, 3557 (1993).
[5] A. E. Berkowitz, IEEE Trans. Magn. **MAG-22**, 466 (1986).
[6] See for example A. H. Morrish, *The Physical Principles of Magnetism* (Wiley, New York, 1965).
[7] A. D. Kent, T. M. Shaw, S. von Molnár, and D. D. Awschalom, Science **262**, 1249 (1993).
[8] See for example, *Binary Alloy Phase Diagrams*, 2nd ed., edited by T. B. Massalski (Scott, Materials Park, 1990), pp. 842–848.
[9] See the TEM photo in Fig. 3 of Ref. 7.
[10] D. D. Awschalom, M. A. McCord, and G. Grinstein, Phys. Rev. Lett. **65**, 783 (1990).
[11] E. C. Stoner and E. P Wohlfarth, Philos. Trans. R. Soc. London, Ser. A **240**, 599 (1948).

Magnetic properties of amorphous nanocolumns created by heavy ion irradiation of paramagnetic YCo_2 thin films (invited)

D. Givord, J. P. Nozières, and M. Ghidini
Laboratoire Louis Néel, C.N.R.S., BP166X 38042 Grenoble Cedex, France

B. Gervais
CIRIL, BP5133, 14040 Caen Cedex, France

Y. Otani
KEIO University, Yokohama 223, Japan

Recent studies have demonstrated the possibility of inducing amorphous latent tracks in metallic materials by GeV heavy ion irradiation. In the present work, 0.880 GeV ^{238}U beams have been used to induce ferromagnetic amorphous nanocolumns in nonmagnetic crystalline YCo_2 films. The loss of crystallinity deduced by x-ray analysis is in good agreement with the one determined by magnetic measurements. The Co magnetic moment in the columns is approximately equal to 1 μ_B, as in bulk amorphous YCo_2, but the ordering temperature (150 K) is strongly reduced with respect to the bulk. Magnetization measurements reveal the nanocolumns to be single domain. A perpendicular anisotropy is observed in samples irradiated at the smallest fluencies, which is interpreted to be due to shape anisotropy. A progressive decrease of the anisotropy with increasing fluence is observed and qualitatively described in terms of dipolar interactions between columns. At low temperature, the coercive field reaches 650 Oe. A simple nonuniform magnetization reversal process is suggested.

I. INTRODUCTION

The formation of defects by GeV heavy ion irradiation through inelastic scattering with the target electrons has recently been demonstrated for amorphous or crystalline metallic materials.[1–4] In particular, it has been shown that above an electronic stopping power threshold, the target could be locally amorphized. Two models have been proposed to describe the formation of amorphous latent tracks, based either on the mutual repulsion of highly ionized atoms (Coulomb explosion model[5]) or the heat transfer via phonons (thermal spike model[6]). Transmission electron microscopy (TEM) observations have revealed that under certain conditions, the irradiation-induced defects were stabilized in the form of cylindrical amorphous tracks along the ion path (latent tracks), with diameters in the range 20–50 Å.[7–9] In this study, we show that in Y-Co alloys it is possible to induce amorphous ferromagnetic nanocolumns in a nonmagnetic crystalline matrix. This allows magnetization reversal processes to be studied in an assembly of nanocolumns with a relatively well-defined size and shape, in which the amplitude of the dipolar interactions can be varied through the total fluence of the ion beam.

The formation of ferromagnetic columns in a nonmagnetic matrix is possible due to the fact that the magnetic properties of the binary Y-Co alloys depend drastically on whether the material is crystalline or amorphous. It is well known that in Y-Co compounds, the Co magnetic moment decreases as the Y content is increased through electron transfer into the $3d$ band and $3d$-$4d$ hybridization[10] (Fig. 1). As a result, Co-rich crystalline compounds are ferromagnets, whereas compounds richer in Y then YCo_2 are Pauli paramagnets. However, amorphous Y-Co alloys are ferromagnetic up to an Y:Co ratio of the order of 1:1.[11] This is due to the higher localization of the $3d$ electrons in the amorphous state when compared to the crystalline state, as a result of atomic disorder and of the relatively weaker density. In addition, the surrounding of a given Co atom is Co richer in the amorphous state where atoms are more or less distributed at random, as compared to the crystalline state where Y—Co bonds, chemically favored with respect to Co—Co bonds, can better be formed.

Crystalline thin films of YCo_2 were prepared and subsequently irradiated by U heavy ions in an attempt to induce amorphous tracks. The results of structural and magnetic analyses performed prior to and after irradiation are presented in the following.

II. EXPERIMENT

The samples were deposited at room temperature by dc sputtering with a deposition pressure of $1–3\times10^{-3}$ Torr. Two sets of films were prepared with the following compositions: Si(100)/Ta 1000 Å/YCo_2 1.5 μm/Ta 1000 Å (samples A) and Si(100)/Ta 500 Å/YCo_{11} 2300 Å/Ta 500 Å (samples

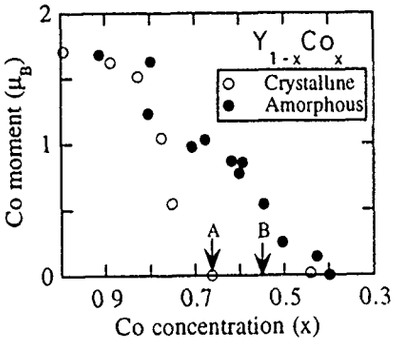

FIG. 1 Co atomic magnetic moment as a function of Co concentration in Y-Co binary alloys (after Ref. 11). The arrows labeled A and B indicate the stoichiometry of the series of samples A and B, respectively.

 0021-8979/94/76(10)/6661/6/$6.00 © 1994 American Institute of Physics

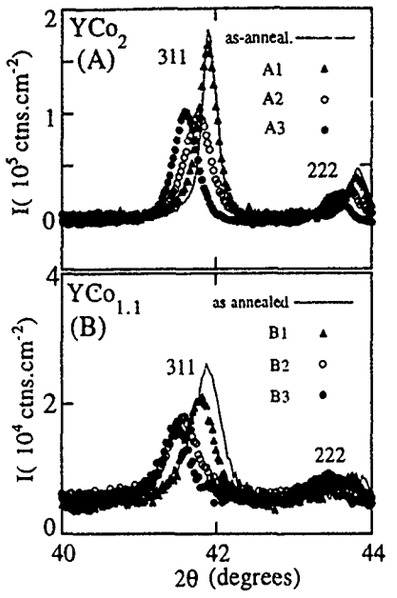

FIG. 2. Detailed view of the XRD patterns showing the 311 and 222 most intense reflections in the irradiated samples. The symbols refer to samples irradiated at fluence: A1 and B1 at 10^{12} ions/cm^2, A2 and B2 at 5×10^{12} ions/cm^2, A3 and B3 at 2×10^{13} ions/cm^2. For reference, the XRD patterns of the as-annealed samples are also shown (full line).

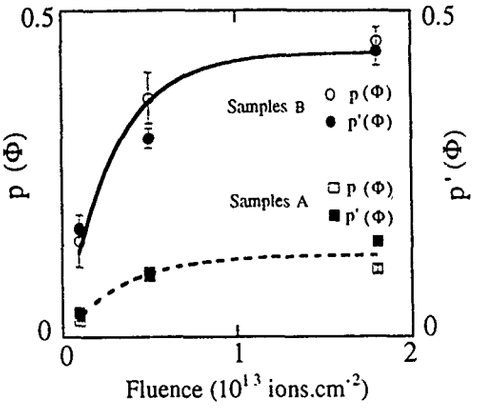

FIG. 3. Amorphous fraction as deduced by XRD [$p(\phi)$: open symbols] and by magnetic measurements [$p'(\Phi)=M_s(\phi)/M_s^{(a)}$: closed symbols]. $M_s^{(a)}$ is the spontaneous magnetization of bulk amorphous YCo_2. Data are fitted according to Eq. (2).

B). The compositions and thicknesses of the films were determined by Rutherford backscattering (RBS) and transmission electron microscopy (TEM). The as-deposited films were subsequently vacuum annealed at 550–600 °C for 1 h in order to crystallize the YCo_2 phase. The samples were then irradiated by 0.880 GeV ^{238}U ion beams at the GANIL accelerator in Caen, France. Three ion fluencies were selected: 10^{12} ions/cm^2 (samples A1 and B1), 5.10^{12} ions/cm^2 (samples A2 and B2) and 2×10^{13} ions/cm^2 (samples A3 and B3). Structural characterization was performed by quantitative x-ray diffraction analysis (XRD) on a θ-2θ diffractometer with Cu K_α wavelength. The magnetic properties were determined between 4.2 K and room temperature using either a VSM or a SQUID magnetometer.

III. STRUCTURAL CHARACTERIZATION

XRD and TEM analyses revealed the as-deposited films to be amorphous and the annealed films to be crystalline. The latter showed the diffraction pattern of the fcc YCo_2 Laves phase.[12] Samples A appeared to be single phase while in samples B, apart from the YCo_2 Bragg reflections, some additional peaks corresponding to a phase which could not be unambiguously identified were observed. However, considering the mean stoichiometry of the alloy ($YCo_{1.1}$) and the phase diagram of the Y-Co binary alloys,[13] one can infer that this phase could most likely be Y_9Co_7 and estimate the fraction of YCo_2 to be about 30% of the total volume. Y_9Co_7 is nonmagnetic in both the amorphous and the crystalline states.[12]

A detailed view of the YCo_2 311 and 222 peaks is represented in Fig. 2 for both sets of samples. When the irradiation fluence is increased, the peaks are broadened and their integrated intensities are decreased. We ascribe this loss of crystallinity to the appearance of irradiation-induced amorphous regions. A shift of the peaks toward smaller Bragg angles is also observed, which we ascribe to irradiation induced stresses. A detailed analysis of this effect is reported elsewhere.[14] The percentage $p(\Phi)$ of amorphized YCo_2 in the irradiated samples can be deduced by comparing the peak integrated area of the 311 Bragg reflection for each series of samples to the one measured before irradiation (Fig. 3). The equation describing the kinetics of defect creation can be expressed as:[15]

$$\frac{dv}{d\Phi}=\sigma_1(V_t-v)-\sigma_2 v, \tag{1}$$

where σ_1 is the amorphization cross section, σ_2 is the exclusion cross section, v is the amorphized volume and V_t the total sample volume. The exclusion cross section accounts for the fact that an ion track can be recrystallized if an incoming ion happens to hit a ring around it. This exclusion ring implies that a complete amorphization of the samples is impossible. In particular, it defines a minimum separation distance between the amorphous columns. Solving Eq. (1) leads to

$$p(\Phi)=\frac{v}{V_t}=\frac{\sigma_1}{\sigma_1+\sigma_2}\left(1-e^{-(\sigma_1+\sigma_2)\Phi}\right). \tag{2}$$

Assuming that defects consist of latent tracks expanding across the film thickness, σ_1 and σ_2 can be expressed as

$$\sigma_1=\frac{\pi D_1^2}{4}$$

$$\sigma_2=\frac{\pi(D_2^2-D_1^2)}{4}, \tag{3}$$

where D_1 is the diameter of the amorphous latent tracks and D_2 the diameter of the exclusion ring. Equations (2) and (3) were fitted to the experimentally deduced $p(\phi)$ enabling D_1 and D_2 to be determined. The fit yielded D_1=25 Å and D_2=50 Å for samples A and D_1=50 Å and D_2=60 Å for

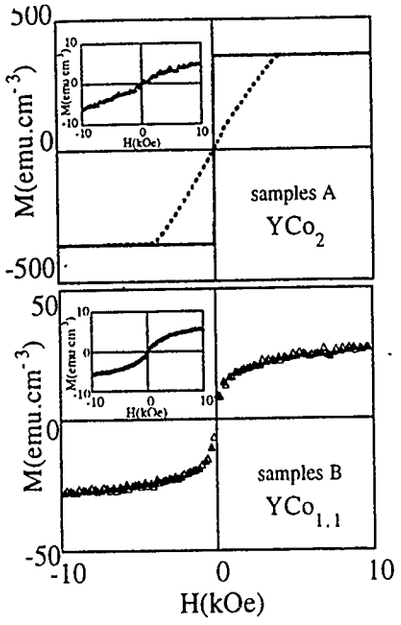

FIG. 4. (a) Magnetization curves of the as-deposited samples A measured in an applied field perpendicular (dashed line) and parallel (full line) to the film plane. Inset: magnetization curves of the same samples after heat treatment. (b) Magnetization curves of the as-deposited samples B measured in an applied field perpendicular (open symbols) and parallel (closed symbols) to the film plane. Inset: magnetization curves of the same samples after heat treatment.

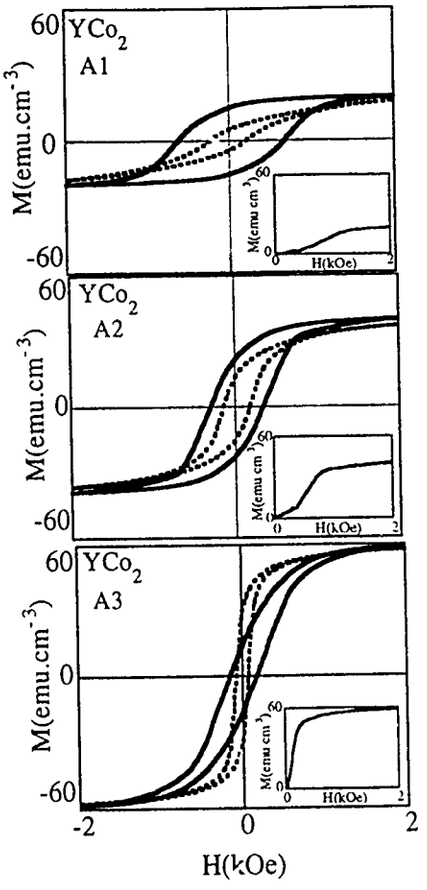

FIG. 5. Hysteresis loops measured in samples A in applied fields perpendicular (full line) and parallel (dashed line) to the film plane. Insets: first magnetization curves measured along the easy directions. (a) Sample A1 irradiated at 10^{12} ions/cm^2, (b) sample A2 irradiated at 5×10^{12} ions/cm^2, (c) sample A3 irradiated at 2×10^{13} ions/cm^2.

samples B. The reasons for the difference in the track diameters for both series of samples, as well as for the reduced recrystallization effects in samples B [revealed by the linearity of $p(\Phi)$ up to higher fluencies] remain unclear. Differences in the microstructure of the specimens could play a role. A smaller average grain size, for example, can reasonably be expected to influence the processes involved in defect creation and annealing. TEM observations are in progress.

IV. MAGNETIZATION MEASUREMENTS

A. Magnetization measurements of unirradiated films

Magnetization measurements at 10 K have been carried out on both the amorphous as-deposited A and B samples as shown in Fig. 4. For samples A, a large susceptibility is obtained when the field is applied in the film plane. The spontaneous magnetization is 360 emu/cm^3, corresponding to approximately 1 μ_B/Co in agreement with the value already reported for bulk a-YCo_2.[11] When the field is applied perpendicular to the film plane, the magnetization varies accordingly to the demagnetizing field slope, which indicates that magnetocrystalline anisotropy may be neglected with respect to shape anisotropy. After the crystallization heat treatment in-plane magnetization measurements of the same sample yield a very small residual magnetization of the order of 5 emu/cm^3 (inset of Fig. 4). This residual ferromagnetic contribution can either originate from residual amorphous material or from the presence of magnetic crystallized phase, richer in Co than YCo_2 which could result from Y oxidation through the Ta capping layer.

In samples B, the spontaneous magnetization of the as-deposited amorphous films is weak (25 emu/cm^3). This is a consequence of the large Y content (see Fig. 1). The magnetization curves measured in-plane and out-of-plane are similar. A significant susceptibility is present up to 10 kOe. This is ascribed to superimposed paramagnetism, in agreement with the fact that the alloy stoichiometry is close to the critical concentration for the disappearance of magnetism. After heat treatment, the spontaneous magnetization is further reduced to 5 emu/cm^3, a value similar to that measured in annealed samples A.

B. Magnetization measurements on irradiated samples

After irradiation, magnetization measurements were initially performed on thermally demagnetized samples. The susceptibility of the virgin magnetization curve measured at 10 K along the easy direction is shown in the insets of Figs. 5 and 6. In all samples, the initial susceptibility is weak until the field reaches values of the order of the coercive field

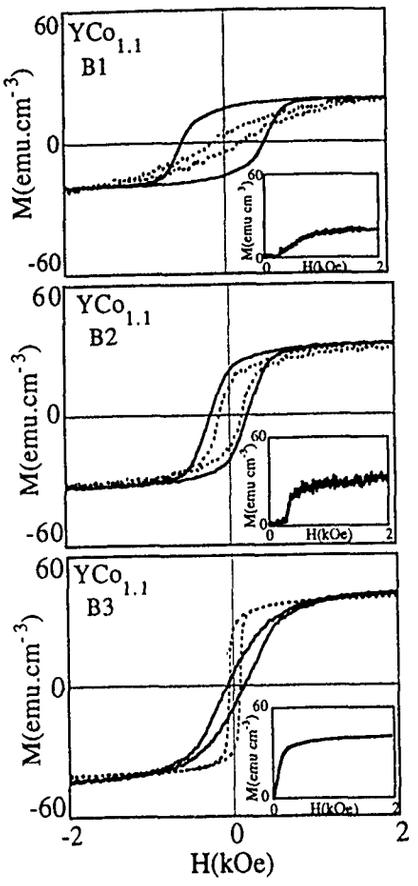

FIG. 6. Hysteresis loops measured in samples B in applied fields perpendicular (full line) and parallel (dashed line) to the film plane. Inset: first magnetization curves measured along the easy directions. (a) Sample B1 irradiated at 10^{12} ions/cm^2, (b) sample B2 irradiated at 5×10^{12} ions/cm^2, (c) sample B3 irradiated at 2×10^{13} ions/cm^2.

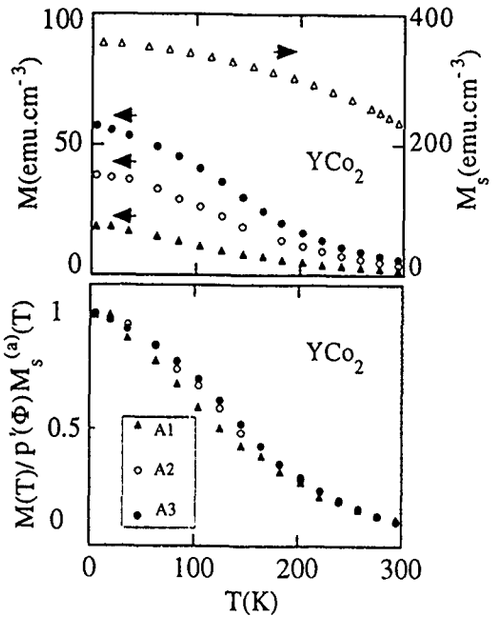

FIG. 7. (a) Temperature dependence of the magnetization $M(T)$ in a field $H=10$ kOe for samples A. (b) Temperature dependence of $M(T)/p'(\Phi)M_s^{(a)}(T)$. The prefactor $1/p'(\Phi)$ is used to normalize the data to bulk YCo_2.

measured on the hysteresis cycles. Considering the small size of the nanocolumns deduced from the analysis in the above section, this can be attributed to single domain behavior.

The magnetization loops measured at 10 K are reported in Figs. 5 (samples A) and 6 (samples B). The magnetization increases as the fluence is increased. This confirms the formation of amorphous ferromagnetic YCo_2 through irradiation. The fraction of amorphized film in samples A, $p'(\Phi)$, deduced from the variation with the ion fluence of the spontaneous magnetization $M_s(\Phi)$ and normalized with the ion fluence and normalized to the magnetization of bulk amorphous YCo_2, $M_s^{(a)}$, is reported in Fig. 3. $p(\phi)$ is in good agreement with the values of $p(\Phi)$ deduced from XRD analysis. Assuming continuous amorphous columns with diameter D_1 one deduces that the Co moment is $\mu_s=1.0\pm0.2$ μ_B/Co in all samples. This agrees with the value measured in the as-deposited amorphous films. A similar analysis can be carried out for samples B. However, because the sample is not single phase, the measured magnetization normalized to bulk YCo_2, $M_s(\Phi)/M_s^{(a)}$ must be multiplied by a factor α to match with $p(\Phi)$ values deduced from XRD. A value $\alpha=4$ is obtained. $1/\alpha$ represents the volume fraction of the YCo_2 phase in the whole sample; it is in fairly good agreement with the value of 30% estimated in Sec. III.

The temperature dependence of the magnetization measured in a field of 10 kOe for the A samples is shown in Fig. 7(a). This large field value was chosen to minimize possible superparamagnetic contributions. The magnetization decreases rapidly with temperature. An average ordering temperature can be located at about 150 K. The curves $M(T)/p'(\Phi)M_s^{(a)}(T)$, which compare the temperature dependence of the nanocolumns magnetization in the different samples, normalized through the factor $p'(\Phi)$ to account for the different proportions of amorphous phase in each sample, are identical [Fig. 7(b)]. However, there are serious differences with the temperature dependence of the magnetization in bulk amorphous YCo_2: The rate of decrease of $M(T)$ is enhanced and the Curie temperature is decreased ($T_c=380$ K for amorphous YCo_2). This can be ascribed to the reduced dimensionality of the nanocolumns.

C. Anisotropy in irradiated samples

The comparison of hysteresis cycles obtained for H applied, respectively, in-plane and out-of-plane shows that in samples irradiated at the lowest fluence (A1 and B1) the magnetization tends to be perpendicular to the film plane. This is consistent with the formation of elongated magnetic columns by irradiation since shape anisotropy favors the magnetization to lie along the column's long dimension. A remanent magnetization, which amounts to 0.2 M_s, is however obtained for the in-plane hysteresis loop, which reveals that the magnetization is not perfectly perpendicular to the film plane. This can be due either to the tracks not being

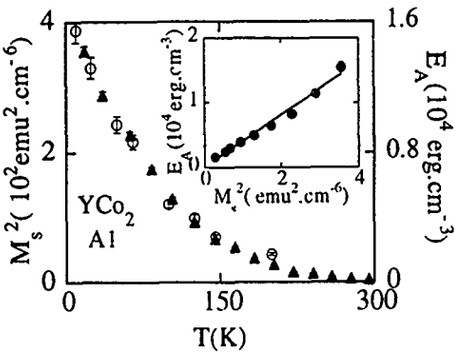

FIG. 8. Thermal variation of the anisotropy energy $E_A(T)$ in sample A1 (open symbols) compared to the square of the magnetization (closed symbols). Inset: variation of E_A as a function of M_s^2.

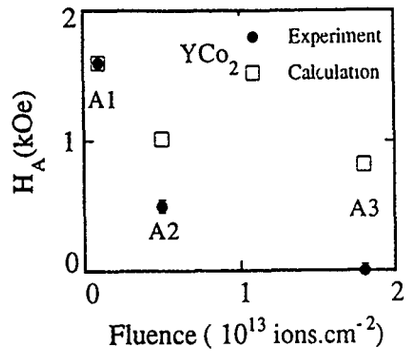

FIG. 9. Calculated (open symbols) and experimental (closed symbols) values of the mean anisotropy field as a function of the ion beam fluence (samples A).

exactly perpendicular to the film plane or to the magnetization deviating of the column axis. Further microstructural studies will be required to clarify this point.

The anisotropic behavior of samples A may however be discussed by neglecting to first approximation the deviation of the magnetization from the perpendicular direction. At 10 K, the anisotropy energy for the sample A1 is $E_A = 1.55 \times 10^4$ erg/cm^3 and the deduced mean anisotropy field is $H_A = 1.6$ kOe. The temperature dependence of the anisotropy energy is identical to that of M_s^2 (Fig. 8). This confirms that the anisotropy of the magnetic columns is dominated by shape anisotropy. Magnetocrystalline bulk or surface anisotropy may be neglected, in agreement with the low anisotropy value observed in the as-deposited Y-Co amorphous films (see Sec. II B).

To analyze the properties of sample A1, the total energy for a single column can be written as

$$E = 2\pi N_{\parallel} M_s^{(a)2} \cos^2\theta + 2\pi N_{\perp} M_s^{(a)2} \sin^2\theta + 2\pi p(\Phi) M_s^{(a)2} \cos^2\theta - 2\pi N_{\perp} p(\Phi) M_s^{(a)2} \sin^2\theta - M_s^{(a)} H \sin\theta, \quad (4)$$

where $N_{\parallel}$ and $N_{\perp}$ are the demagnetizing field coefficients, respectively, along the column's long dimension (perpendicular to the film plane) and perpendicular to it (parallel to the film plane), and θ is the angle between the magnetization direction and the film normal. The two first terms in Eq. (4) represent the particle self-dipolar energy, the two next terms represent the interparticle dipolar energy (see further) expressed in the continuous medium approximation [i.e., equivalent to the demagnetizing field created by a continuous film of magnetization $p(\Phi)M_s^{(a)}$] and the last term is the Zeeman energy. From Eq. (4), the anisotropy may be related to the demagnetizing field coefficients through

$$H_A = 4\pi\{N_{\perp}[1 - p(\Phi)] - N_{\parallel} - p(\Phi)\}M_s. \quad (5)$$

From Eq. (5) and with $N_{\parallel} + 2N_{\perp} = 1$, the values $N_{\parallel} \approx 0.1$ and $N_{\perp} \approx 0.45$ are obtained. These values suggest that the nanocolumns in sample A1 are not ideally elongated. The same feature has been reported for $NiZr_2$ alloys in which discontinuous elongated latent tracks were observed.[7] TEM observations are in progress in order to reveal the exact morphology of the tracks in our systems.

The anisotropy was also measured in samples A2 and A3, irradiated at higher fluences. When the fluence is increased to 5×10^{12} ions/cm^2 (sample A2) the magnetization curves are approximately identical whatever the direction of the applied field is. When the fluence is further increased to 2×10^{13} ions/cm^2 (sample A3), the easy magnetization direction lies in-plane. From the identical temperature dependence of the reduced magnetization in the three samples [Fig. 7(b)], one can assume that the columns are identical whatever the fluence is. The variation of the anisotropy field with the ion fluence must then originate from the rise of interactions between columns. Exchange interactions are generally isotropic in nature and it is thus legitimate to first order to consider dipolar interactions only. However, such dipolar interactions depend drastically on the initial zero-field magnetic configuration which in turn depends on exchange interactions between particles. For amorphous YCo_2 columns embedded in a Pauli paramagnetic matrix of crystalline YCo_2, exchange interactions between columns may be mediated by itinerant $3d$ electrons of the matrix. The very strong decrease in anisotropy observed with increasing ion fluence suggests that large dipolar interactions develop as the density of tracks in increased. This implies ferromagnetic coupling between neighboring columns, i.e., the formation of correlated regions with large average magnetization. This justifies the formulation used in Eq. (4) to express dipolar interactions.

The anisotropy field variation calculated for samples A according to Eq. (5) is reported in Fig. 9. It accounts for only half the total anisotropy variation. This suggests that the continuous medium approximation is not valid, especially at large ion fluencies. Statistical fluctuations in the column's distribution function, which would locally increase the dipolar interactions may have to be considered. Another possibility is that irradiation in recrystallized regions induces the formation of magnetic columns whose shape anisotropy is not as large as that of columns formed during first irradiation.

A discussion of the anisotropic behavior in samples B

leads to a very similar conclusion. It is not included in this article.

D. Coercivity

The low-temperature value of the coercive field reaches H_c=650 Oe in sample A1, that is half the value of the mean anisotropy field. It is known that for coherent rotation H_c is equal to H_A. However, in the case where shape anisotropy is involved, nonuniform magnetization processes, such as curling, are, in general expected to occur and to reduce the coercive field to values much lower than 1/2 H_A. The rather large value of the coercive field in the present case can be understood by considering that, as a consequence of the small diameter of the magnetic columns, curling cannot occur. A simple nonuniform process can be considered, consisting in a progressive reversal and rotation of the magnetization about the column axis. To the very first approximation, the dipolar energy is reduced by a factor of 4 with respect to a uniform magnetization perpendicular to the column axis (coherent rotation). The exchange energy is

$$E_{\text{Exch}}=\int_z A\left(\frac{d\theta}{dz}\right)^2 dz=\frac{A\Pi^2}{l}, \tag{6}$$

where A is the exchange constant, θ the angle between adjacent moments, and l the length over which rotation occurs. l is obtained by minimizing the exchange energy with respect to the dipolar energy. One obtains

$$l=\sqrt{\frac{2\pi}{N_\perp}}\sqrt{\frac{A}{M_s^2}}\,. \tag{7}$$

With $A=5\times10^{-7}$ erg/cm[16] and $M_s^{(a)}$=360 emu/cm^3, the domain wall length is l=600 Å.

The coercive field can be estimated from the above by expressing that for $H=H_c$, the Zeeman energy MH_cl is equal to the sum of the dipolar and exchange energies. This yields H_c=800 Oe, which is in reasonable agreement with the experimental value. For the samples A2 and A3 the coercive field is reduced to 300 and 150 Oe, respectively. This abrupt decrease can be explained by considering that magnetostatic interactions will produce an additional demagnetizing field expressed in the continuous medium approximation as $4\pi p(\Phi)M_s$. Comparison between the experimental and the estimated values of the coercive fields is shown in Fig. 10. It is somehow surprising that the variation of coercivity with fluence can be correctly described by this simple model whereas the same type of analysis does not properly account for the anisotropy field variation.

V. CONCLUSIONS

The original properties of magnetic nanocolumns produced by heavy ion irradiation have been discussed. The observed anisotropy in these systems has been attributed to shape anisotropy. A magnetization reversal process has been discussed in which dipolar interactions are not fully minimized because of the very small diameter of the magnetic columns. Further microstructural analysis and new irradiation experiments on other intermetallic compounds containing magnetic rare-earth elements are needed to allow a better understanding of the underlying mechanisms at the origin of anisotropy and coercivity.

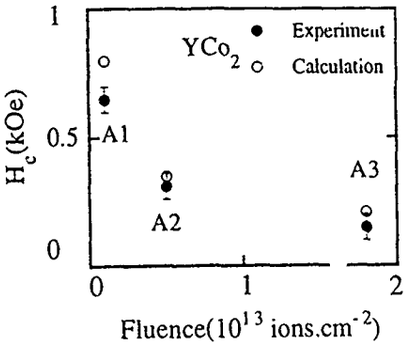

FIG. 10. Calculated (open symbols) and experimental (closed symbols) values of the coercive field as a function of the ion beam fluence (samples A).

[1] S. Klaumunzer, M.-d. Hou, and G. Schumacher, Phys. Rev. Lett. **57**, 850 (1986).
[2] A. Audouart, E. Balanzat, G. Fuchs, J. C. Jousset, D. Lesueur, and L. Thomé, Europhys. Lett. **5**, 241 (1988).
[3] A. Dunlop, D. Lesueur, J. Morillo, J. Dural, R. Spohr, and J. Vetter, C. R. Acad. Sci. Paris **309**, 1277 (1989).
[4] A. Audouart, E Balanzat, S. Bouffart, J. C. Jousset, A. Chamberod, A. Dunlop, D. Lesueur, G. Fuchs, R. Spohr, J. Vetter, and L Thomé, Phys. Rev. Lett. **65**, 875 (1990).
[5] R. L. Floeischer, P. B. Price, and R. M. Walker, J. Appl. Phys. 36, 3645 (1965).
[6] M. Toulemonde, E. Paumier, and C. Dufour, Radiat. Eff. Defects Solids **126**, 201 (1993).
[7] A. Barbu, A. Dunlop, D Lesueur, and S. Averback, Europhys. Lett. **15**, 37 (1991).
[8] G. Fuchs, F. Studer, E. Balanzat, D. Groult, M. Toulemonde, and J. C. Jousset, Europhys. Lett. **3**, 321 (1987).
[9] M. Toulemonde and F. Studer, Philos Mag A **58**, 799 (1988).
[10] K. H. J Buschow, in *Ferromagnetic Materials*, edited by E. P. Wohlfarth (North-Holland, Amsterdam, 1980), Vol. 1.
[11] K. Moorjani and J. M. D. Coey, in *Magnetic Glasses*, edited by S. P. Wolsky and A W. Czanderna (Elsevier, New York, 1984).
[12] E. Burzo, A. Chelkowski, and H. R. Kirchmayr, in *Numerical Data and Functional Relationships in Science and Technology* (Landolt-Börnstein) edited by O. Madelung (Springer, Berlin, 1992), Vol. 19, p. 2.
[13] R. P. Elliott, in *Constitution of Binary Alloys* (McGraw-Hill, New York, 1965).
[14] M. Ghidini, J. P. Nozières, D. Givord, and B. Gervais (unpublished).
[15] V. Chailley, E. Doorhye, S. Bouffart, and E. Balanzat, Nucl. Instrum. Methods B (to be published).
[16] B. Dieny, D. Givord, and J. M. B. Ndjaka, J. Magn. Magn. Mater. **93**, 503 (1991).

Magnetic wire and box arrays (invited)

Atsushi Maeda, Minoru Kume, Takashi Ogura, and Kazuhiko Kuroki
New Materials Research Center, Sanyo Electric Co., Ltd., 1-1 Dainichi-higashimachi, Moriguchi, Osaka 570, Japan

Takashi Yamada, Madoka Nishikawa, and Yasoo Harada
Microelectronics Research Center, Sanyo Electric Co., Ltd., 1-18-13 Hashiridani, Hirakata, Osaka 573, Japan

Ferromagnetic wire and box arrays with widths and spacings in the range of 2–0.6 μm were successfully fabricated utilizing high-resolution electron-beam lithography and lift-off techniques. The box arrays possessed a unique magnetic switching mechanism. As the magnetic field decreased, the magnetic coherency between the boxes which are in a row first disappeared. Domain wall motion in each box occurred in the next step. The demagnetizing fields observed in the wire arrays with short spacings were different from those calculated by a model, in which the wires are isolated from each other. Ferromagnetic resonance measurement implied the appearance of interwire dipole-dipole interaction. Multilayered wire arrays were also prepared to study the magnetoresistive characteristics.

I. INTRODUCTION

The physical properties of materials with an artificial superstructure have attracted much attention.[1,2] This is because the effects from the periodicity and size are expected to be significantly different from those in the bulk states. In the past study, we have shown that metallic superlattices prepared by molecular-beam epitaxy possess unique structural[3] and magnetic[4] characteristics. An artificial periodicity along the film normal plays an important role in this uniqueness. Therefore, two- or three-dimensional composition modulation in materials should be proposed as the next research target. Though atomic-level control is still not possible in the preparation of such artificial structures, fine patterning in submicron size can be made using various lithography techniques. In the field of magnetism, microscopic arrays of ferromagnetic particles are prepared to study the basic problems, such as demagnetization process and interparticle interaction.[5,6]

In the present study, periodic arrays of ferromagnetic wires and boxes are fabricated as the first step toward two- or three-dimensional modification. The magnetic properties are discussed on the basis of results obtained from hysteresis loops, Bitter patterns, and ferromagnetic resonance (FMR) measurement. As one of the applications of the artificial structure, magnetoresistive characteristics of multilayered wire arrays are also studied.

II. EXPERIMENT

The wire and box arrays were fabricated utilizing high-resolution electron-beam lithography and lift-off techniques. 1-μm-thick poly(methyl methacrylate) resist films coated on Si (100) wafers were directly exposed by an electron beam with acceleration voltages between 25 and 50 kV. The typical exposure area (equivalent to sample size) was 10×10 mm^2. After baking at 473 K under N_2 atmosphere for 20 min, they were developed using methyl isobutyl ketone. Next, $Ni_{80}Fe_{20}$ alloys (wt %) which form simple wire or box arrays were deposited at the room temperature on to a lithographic resist mask. Ion beam sputtering was used for the preparation of $Ni_{80}Fe_{20}$/Co/Cu/Co multilayered wire arrays. The resist portions were finally removed with acetone. In order to study the effect of the interwire or interbox interactions, arrays with various widths (w) and spacings (s) between 0.6 and 2 μm were prepared. The artificial periodic structures formed were observed by scanning electron microscopy (SEM). Other structural characterization was done by x-ray diffraction (XRD) with CuKα radiation. Magnetic hysteresis loops were measured at room temperature using a vibrating sample magnetometer. Bitter patterns were observed under magnetic fields less than 55 G. The FMR measurements were made with an electron spin resonance spectrometer operated on the X band at 300 K. Magnetoresistance (MR) was measured at room temperature in a four-terminal geometry with a direct current (J).

III. RESULTS AND DISCUSSION

A. Structural characteristics of $Ni_{80}Fe_{20}$ arrays

All $Ni_{80}Fe_{20}$ wires and boxes prepared in this study have a thickness of 50 nm. Figure 1(a) shows the SEM images of the wire arrays with various widths and spacings. It is found that the widths are equal to the spacings as designed. The linearity and edge structure of each wire are good enough to discuss the physical properties. In the present study, we confirmed that the specimen with a width and a spacing of 0.6 μm possesses a sharp artificial structure. Though the box arrays also showed a clear periodic structure, the shape of each box rounded with increasing the exposure resolution, as shown in Fig. 1(b). The XRD patterns of the $Ni_{80}Fe_{20}$ arrays showed no peaks in the middle-angle region. The measurement system used possesses sufficient sensitivity to detect the diffraction from the arrays. Therefore, the crystallinity of the $Ni_{80}Fe_{20}$ wires and boxes is concluded to be low.

B. Magnetic characteristics of $Ni_{80}Fe_{20}$ arrays

The hysteresis loops obtained for the $Ni_{80}Fe_{20}$ box array with a width and a spacing of 1 μm are shown in Fig. 2. When the magnetic field (H) was applied parallel to a side of

 0021-8979/94/76(10)/6667/4/$6.00 © 1994 American Institute of Physics

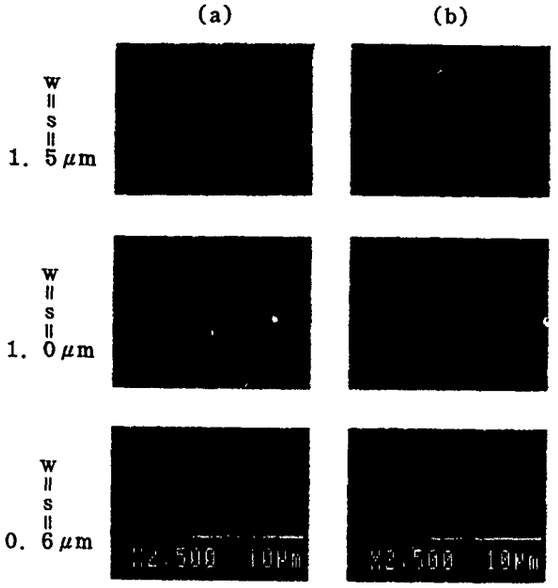

FIG. 1. SEM images of $Ni_{80}Fe_{20}$ (a) wire and (b) box arrays with various widths (w) and spacings (s).

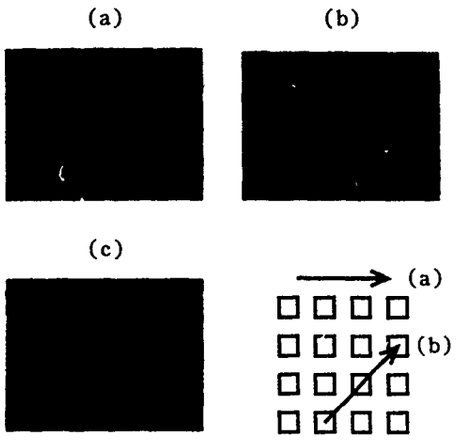

FIG. 3. Bitter patterns of $Ni_{80}Fe_{20}$ box arrays with a width and a spacing of 2 μm under (a), (b) 55 G and (c) zero field. The applied field direction is described.

the square (see Fig. 3). The magnetization (M) increased and/or decreased in two steps. The same behavior was also observed in the M-H curves measured under the condition where the magnetic field was applied at an angle of 45° to a side of the square. These observations suggest the presence of two kinds of magnetization switching mode in the box arrays. Figure 3 shows the Bitter patterns of the box array with a width and a spacing of 2 μm. Under 55 G, only a dim pattern was observed in each box, indicating the incomplete saturation. In contrast, under the same field, some patterns were linearly present between the boxes which are in a row. This indicates that magnetic coherency was induced in the box arrays. As shown in Figs. 3(a) and 3(b), the coherence direction was in accordance with that of the applied field. Here, no coherent patterns were observed in the box arrays with large spacings. Consequently, the interbox distance is expected to be responsible for the appearance of the magnetic coherency. Whether the boxes interact with each other or whether they are isolated from each other is a most interesting problem in the magnetism of the arrays. From this point of view, the above results are important. With decreasing field, the patterns between the boxes disappeared and the domain structure in each box became clear [see Fig. 3(c)]. Therefore, the demagnetization process observed in the box arrays can be understood as follows. As the first step, the magnetic coherency between the boxes disappears with decreasing magnetic field. The linear change of the magnetization, which is in the second step, reflects the wall motion in each box.

Figure 4 shows the M-H curves obtained at room tem-

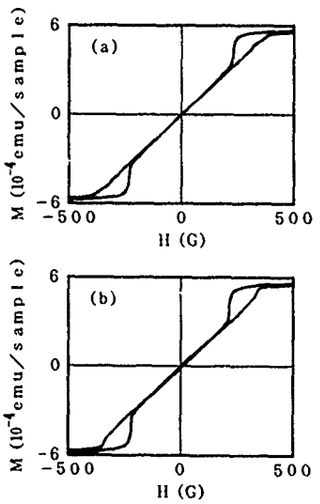

FIG. 2. M-H curves of $Ni_{80}Fe_{20}$ box arrays with a width and a spacing of 1 μm. (a) and (b) were measured under the condition where the H was applied parallel and at an angle of 45°, respectively, to a side of the square.

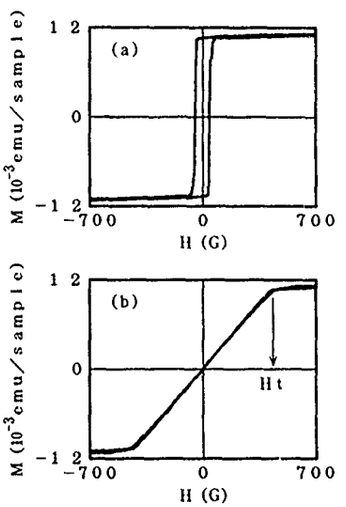

FIG. 4. M-H curves of $Ni_{80}Fe_{20}$ wire arrays with a width and a spacing of 1 μm. (a) and (b) were measured under the condition where the H was applied parallel and perpendicular, respectively, to the stripes.

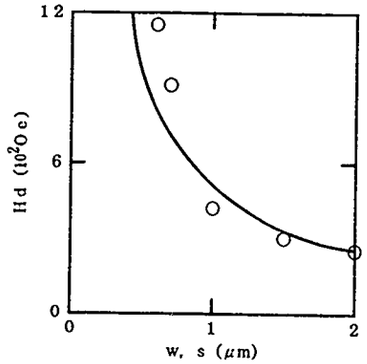

FIG. 5. Experimental (O) and calculated (–) H_d values of $Ni_{80}Fe_{20}$ wire arrays with various widths (w) and spacings (s).

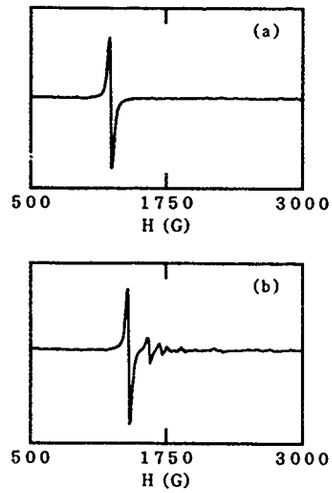

FIG. 6. FMR spectra of $Ni_{80}Fe_{20}$ wire arrays with a width and a spacing of 1 μm. (a) and (b) were measured under the condition where the static field was applied parallel and perpendicular, respectively, to the stripes.

perature for the $Ni_{80}Fe_{20}$ wire arrays with a width and a spacing of 1 μm. Rectangular loops were observed when the magnetic field was applied parallel to the stripes. The hysteresis feature indicates that the magnetization switching is attributable to only domain wall motion. The coercive field increased with decreasing wire width. Under the condition where the magnetic field was applied normal to the stripes, the magnetization linearly changed with increase and/or decrease in the magnetic field. The feature shows that only magnetization rotation is responsible for the switching process. Based on the magnetic data described above, the shape anisotropy is found to be induced in each wire, resulting in a magnetic easy-axis along the stripes. Here, no MR change was observed when the magnetic field was applied parallel to the stripes. Consequently, the induced anisotropy is concluded to be extremely strong. This prompted us to prepare multilayered wire arrays as described in Sec. III C. The demagnetizing fields (H_d) in the wire arrays were studied as the function of the width and spacing. Since the total field (H_t) for hard-axis saturation as noted in Fig. 4(b) is the algebraic sum of the anisotropy field (H_k) and the H_d,[7] the H_d value was experimentally determined by using Eq. (1)

$$H_d = H_t - H_k. \tag{1}$$

In the present study, 5 Oe, which has been obtained for a $Ni_{80}Fe_{20}$ thin film with no patterns, was used as the H_k value. In contrast, the H_d of the wire arrays, in which the wires are isolated from each other, can be calculated from the geometry and the saturation magnetization[8]

$$H_d = tM_s/w, \tag{2}$$

where t is the thickness (50 nm), M_s the saturation magnetization of the $Ni_{80}Fe_{20}$ (10 000 G), w the wire width. As shown in Fig. 5, H_d exponentially increased as the w and s values decreased. Here, it is worth noting that the difference between the experimental and calculated data increases with decreasing width and spacing. This suggests that the wires interact with each other. However, the observation does not prove it because both of the w and s values are parametrized. Therefore, a FMR measurement was carried out on the wire arrays. The samples were in a uniform rf field at 9.224 GHz in a TE_{011} cavity. A static magnetic field was applied perpendicular to the rf field. As shown in Fig. 6(a), when the static field was applied parallel to the stripes, uniform precessional mode was observed. On the other hand, under the condition where the magnetic field was applied normal to the stripes and parallel to the array plane, multiple resonances were observed at higher field than the main resonance. Such multiple resonances are similar to that corresponding to spin wave excitation.[9] However, the thickness of each wire is smaller than the wavelength of the spin wave. In addition, the multiple resonances observed in the present study were strongly dependent on the width and spacing in the wire arrays, as shown in Fig. 7. Therefore, some other mechanism must be proposed for the wire arrays. In this context, we note the role

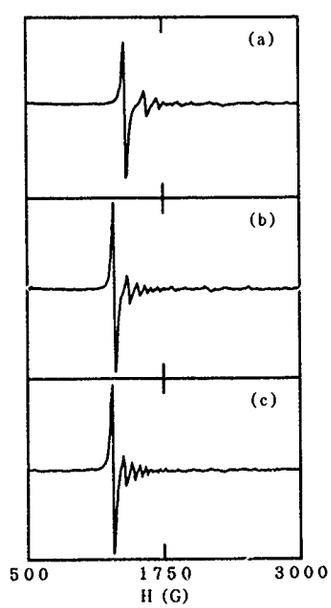

FIG. 7. FMR spectra of $Ni_{80}Fe_{20}$ wire arrays measured under the condition where the static field was applied perpendicular to the stripes. The width and spacing were (a) 1.0, (b) 1.5, and (c) 2.0 μm.

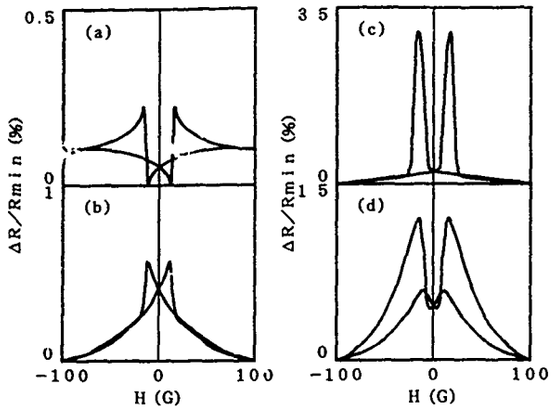

FIG. 8. MR curves of $Ni_{80}Fe_{20}$ (6.0 nm)/Co (0.6 nm)/Cu (2.3 nm)/Co (4.0 nm) multilayered wire array (a), (b) and film (c), (d). (a), (c) and (b). (d) were measured under the condition where the magnetic field was applied parallel and perpendicular, respectively, to the easy axis.

of dipole-dipole interactions in the stripes. This is because the dipolar coupling is effective over a long range. In the pioneering work by Nakatani, it has been suggested that magnetic dipolar standing waves are excited in the wire arrays.[10]

C. Magnetoresistive characteristics of $Ni_{80}Fe_{20}$/Co/Cu/Co multilayered arrays

Various multilayered materials containing "spin valves" display a large negative MR change when the moments of adjacent ferromagnetic layers are turned from antiparallel to parallel.[11–13] However, the magnetic moment is expected to form an angle of several degrees with another one in the plane. Therefore, we note the strong anisotropy induced in the wire structure as shown in Fig. 4. The shape anisotropy makes the magnetic antiparallel and parallel alignments in the multilayers complete. Figures 8(a)–8(d) show the MR curves of the $Ni_{80}Fe_{20}$ (6.0 nm)/Co(0.6 nm)/Cu(2.3 nm)/Co(4.0 nm) multilayered wire array and film. Here, the multilayered film sample was coprepared with the wire array. When the magnetic field was applied along the easy axis, the difference in the shape of the MR curves between the array and the film was distinct [see Figs. 8(a) and 8(c)]. Since the film sample possesses a normal MR change associated with the different coercive fields, the uniqueness is probably due to the wire structure. On the other hand, under the condition where the magnetic field was applied normal to the easy axis, the MR change in the wire array was likely steeper than that in the film, as shown in Figs. 8(b) and 8(d). The relation between the MR change and the demagnetization process of these samples is currently under investigation.

IV. SUMMARY

Wire and box arrays of $Ni_{80}Fe_{20}$ with widths and spacings in the range of 2–0.6 μm were successfully fabricated utilizing high-resolution electron-beam lithography and lift-off techniques. Bitter patterns of the box arrays indicated that magnetic coherency is induced between the boxes which are in a row under the magnetic field. Two kinds of magnetization switching modes were present in the box arrays. The demagnetizing fields of the wire arrays with short spacings were larger than those calculated by a model, in which the wires are isolated from each other. The multiple resonances observed in the wire arrays implied the appearance of inter-wire dipole-dipole interaction. The magnetoresistive characteristics of the $Ni_{80}Fe_{20}$/Co/Cu/Co multilayered wire array were preliminarily studied.

[1] L. L Chang and B. C. Giessen, *Synthetic Modulated Structures* (Academic, New York, 1985)

[2] T. Shinjo and T. Takada, *Metallic Superlattices* (Elsevier, Amsterdam, 1987).

[3] A. Maeda, T. Satake, T. Fujimori, and H. Kuroda, J. Appl. Phys. **68**, 3246 (1990); **69**, 6417 (1991).

[4] A. Maeda, T. Satake, T. Fujimori, H. Tajima, M. Kobayashi, and H. Kuroda, J. Appl. Phys **65**, 3845 (1989); A. Maeda, T. Satake, T. Fujimori, and H. Kuroda, J. Phys.: Condens. Matter **2**, 245 (1990); **3**, 1967 (1991); A. Maeda, T. Satake, and H. Kuroda, *ibid.* **3**, 5241 (1991); Phys. Lett. A **157**, 178 (1991).

[5] J. F. Smyth, S. Schultz, D. R. Fredkin, D. P. Kern, S. A. Rishton, H. Schmid, M. Cali, and T. R. Koehler, J. Appl. Phys. **69**, 5262 (1991).

[6] O. Geoffroy, D. Givord, Y. Otani, B Pannetier, and F. Ossart, J. Magn. Magn. Mater. **121**, 223 (1993).

[7] P. Ciureanu and H. Gavrila, *Magnetic Heads for Digital Recording* (Elsevier, Amsterdam, 1990).

[8] D. Thompson, L. Romankiw, and A. Mayadas, IEEE Trans. Magn. **MAG-11**, 1039 (1975).

[9] C. Kittel, Phys. Rev. **110**, 1295 (1958); R. Weber, IEEE Trans. Magn. **MAG-4**, 1 (1968).

[10] I. Nakatani, in Digests of the INTERMAG Conference, Stockholm, Sweden, April, 1993 (unpublished).

[11] M. N. Baibich, J. M. Broto, A. Fert, F. Nguyen van Dau, F. Petroff, P. Etienne, G. Creuzet, A. Friederich, and J. Chazelas, Phys. Rev Lett. **61**, 2472 (1988).

[12] T. Shinjo and H Yamamoto, J. Phys. Soc. Jpn. **59**, 3061 (1990).

[13] B. Dieny, P. Humbert, V. S. Speriosu, S. Metin, B. A. Gurney, P. Baumgart, and H. Lefakis, Phys. Rev. B **45**, 806 (1992).

Ferromagnetic filaments fabrication in porous Si matrix (invited)

Sergey A. Gusev, Natalia A. Korotkova, Dmitry B. Rozenstein,[a] and Andrey A. Fraerman
Institute for Physics of Microstructures, Russian Academy of Sciences, 46 Ul'janova St., 603600 Nizhny Novgorod, Russia

We have fabricated Ni filaments by nickel precipitation into a porous silicon matrix, making Ni filaments of about 200 Å in diameter and 30 μm in length separated by ~500 Å silicon walls. This composite material demonstrates strong magnetic anisotropy perpendicular to the surface due to shape anisotropy of the Ni filaments.

I. INTRODUCTION

When a silicon wafer is electrochemically etched by anodization in hydrofluoric acid solutions a porous silicon (PS) layer is formed. Choosing appropriate etching conditions (electrolyte composition and current densities) which is specific for each silicon type, one can get a PS structure with cylindrical micropores oriented perpendicular to the surface. The remarkable properties of PS that are pertinent here are that its pores are very uniform in diameter and length, that the pores are parallel and the pore density, pore length and diameter can be controlled rather easily by varying electrochemical parameters and silicon doping.[1]. Typical pore diameters which could be obtained are in the range of 10–1000 Å and pore length is practically unlimited and controlled only by etching time. We used PS as a matrix to form ferromagnetic filaments by electrodepositing nickel into the pores. Starting the research we assumed this material to have a large perpendicular anisotropy due to shape anisotropy of ferromagnetic filaments. Some properties of small anisotropic magnetic particles in nonmagnetic matrix have been previously reported for Fe needles into Al_2O_3 matrix[2,3] and for Co rods in the same matrix.[4,5] In the present article we report on our experiments on the Ni filaments in porous Si matrix.

II. EXPERIMENT AND RESULTS

A. Anodization

We have anodized a *n*-type Sb-doped 0.01 Ω cm silicon substrate in the HF:ethanol (1:1) solution at 18–20° C with a dc current (100 mA/cm^2) for 5 min, getting the PS layer of 30 μm thickness. A JEM 2000 EXII electronic microscope was used to study PS structure. Scanning electron microscopy (SEM) observations of the sample split (Fig. 1) revealed that the pore diameter and the average separation between pores are ~200 and ~500 Å, respectively.

B. Nickel precipitation

After PS formation, nickel was electrodeposited into the pores using ac electrolysis in an electrolyte of the following composition: $NiCl_2 \cdot 6H_2O$ 185g/ℓ; boric acid 45 g/ℓ; *p*H ≃3.0. Nickel precipitation was carried out at 1-3 V, 50 Hz, and 18–20° C with nickel counterelectrode. The nickel concentration profile were studied by x-ray microanalysis with a LINK analyzer mounted on the electronic microscope, scanning along the sample split in the pore direction by the electronic spot. The Si $K\alpha$ and Ni $K\alpha$ lines intensity distribution (corresponding with the elements concentration profiles) along the sample depth are presented in Fig. 2.

C. Magnetic properties

To investigate magnetic properties of the obtained medium a ferromagnetic resonance (FMR) study of samples was carried out with electron paramagnetic resonance (EPR) spectrometer PS100X at rf 9.45 GHz in the magnetic fields up to 7 kOe. The angular anisotropy along the nickel filaments with the value in the range 300–2000 Oe depending on the sample structure. A representative angular dependence corresponding to 800 Oe uniaxial anisotropy is shown in Fig. 3.

The hysteresis curves for this sample were measured by vibrating sample magnetometer (VSM) and are presented in

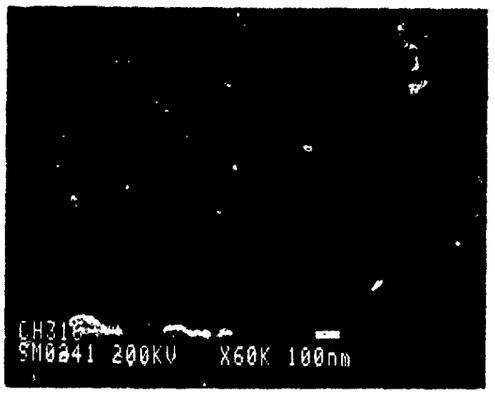

FIG. 1. SEM image of the porous silicon sample split along the pores. Substrate: *n*-type Si 0.01 Ω cm; electrolyte: HF:ethanol (1:1); etching current: 100 mA/cm^2. Average pore diameter, length 200 Å, 30 μm.

[a]E-mail: rozen@imp.nnov.su

 0021-8979/94/76(10)/6671/2/$6.00 © 1994 American Institute of Physics

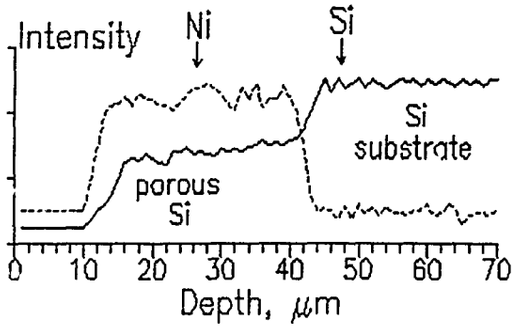

FIG. 2. The Si $K\alpha$ and Ni $K\alpha$ lines intensity distribution (corresponding with elements concentration profiles) of metalliized porous layer determined by x-ray microanalysis.

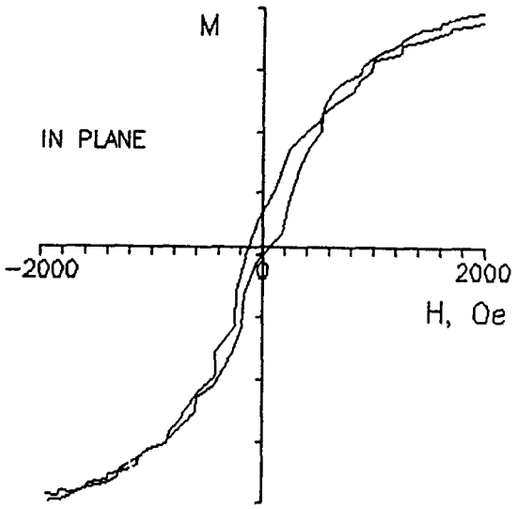

Fig. 4. The difference between the perpendicular and in-plane loops confirms the presence of perpendicular magnetic anisotropy.

III. CONCLUSION

The carried out magnetic measurements shows the perpendicular anisotropy material fabrication. Our investigation of this medium structure revealed that this material represents a set of nickel filaments with diameters $\leqslant 200$ Å and length ~ 30 μm separated by 500 Å silicon walls. It is known, that in a ferromagnetic cylinder with radius less than the exchange length magnetization is uniform along the radius.[5] The calculated exchange length for nickel is about 300 Å. So one can expect quasi-one-dimensional magnetic properties for the obtained Ni filaments with smaller diameters ~ 200 Å).

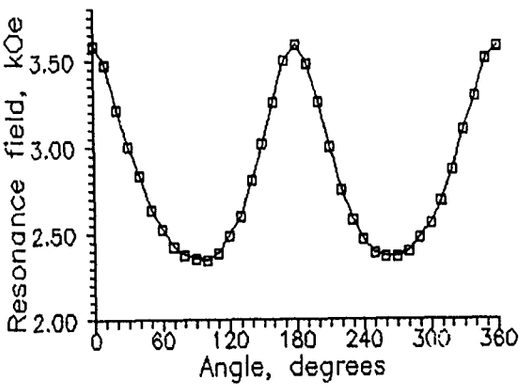

FIG 3. FMR resonant field angular dependence. (Zero angle corresponds with in-plane external magnetic field.) Corresponding perpendicular anisotropy ~800 Oe.

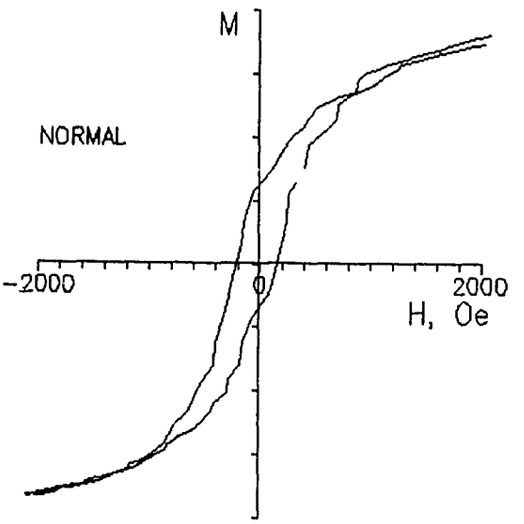

FIG. 4. Perpendicular (a) and in-plane (b) hysteresis loops measured by VSM for a Ni-filled porous Si sample.

ACKNOWLEDGMENTS

The authors are grateful to Dr. Nickolay S. Perov for the VSM measurements and to Dr. Vladimir G. Shenguro[v] for a helpful discussion.

[1] R. L. Smith and S. D. Collins, J. Appl. Phys. **71**, R1 (1992).
[2] D. AlMawlawi, N. Coombs, and M. Moskovits, J. Appl. Phys. **70**, 4421 (1991).
[3] A. Liberatos, R. W. Chantrell, E. R. Sterringa, and J C. Lodder, J. Appl. Phys. **70**, 4431 (1991).
[4] M. Abe, M. Gomi, and F. Yokoyama, I. Appl. Phys. **57**, 3909 (1985).
[5] W. F. Brown, *Micromagnetics* (Wiley, New York, 1963), Chap. 6.

Published without author corrections

Single-domain magnetic pillar array of 35 nm diameter and 65 Gbits/in.^{2} density for ultrahigh density quantum magnetic storage

Stephen Y. Chou, Mark S. Wei, Peter R. Krauss, and Paul B. Fischer
Department of Electrical Engineering, University of Minnesota, Minneapolis, Minnesota 55455

Using electron beam nanolithography and electroplating, arrays of Ni pillars on silicon that have a uniform diameter of 35 nm, a height of 120 nm, and a period of 100 nm were fabricated. The density of the pillar arrays is 65 Gbits/in.^{2}—over two orders of magnitude greater than the state-of-the-art magnetic storage density. Because of their nanoscale size, shape anisotropy, and separation from each other, each Ni pillar is single domain with only two quantized perpendicular magnetization states: up and down. Each pillar can be used to store one bit of information, therefore such nanomagnetic pillar array storage offers a rather different paradigm than the conventional storage method. A quantum magnetic disk scheme that is based on uniformly embedding single-domain magnetic structures in a nonmagnetic disk is proposed.

I. INTRODUCTION

Perpendicular magnetic recording media have been considered by many as the media that will offer the largest storage density. Previously, several perpendicular recording media were developed and investigated. These include Co-Cr thin films with vertical grains,[1,2] barium ferrite powder with a perpendicular c axis,[3] and vertical ferromagnetic pillars plated through porous Al films[4] or plastics films with nuclear radiated tracks.[5] In all these media, the diameter of magnetic grains and the magnetization direction have a broad continuous distribution; the spacing between the grains varies and is uncontrollable; and each bit of information is stored over at least several magnetic grains.

In order to explore the ultimate size of a magnetic bit and the ultimate spacing between neighboring magnetic bits (therefore storage density), to improve understanding of the fundamental magnetics, and to develop new magnetic devices of high speed and high density, we have fabricated ultrahigh density arrays of single-domain nickel pillars using electron beam nanolithography and electroplating. The unique advantage of nanolithography is that the dimension of each pillar as well as the spacing between the pillars can be well controlled and uniform. Due to small size and shape anisotropy, each pillar is a single domain with magnetization perpendicular to the substrate. Moreover, each magnetic pillar can be used to store one bit of information. In this article we will discuss the fabrication process, magnetic force microscope (MFM) measurements, and the possibilities of a novel new recording paradigm offered by these pillars.

II. FABRICATION OF MAGNETIC PILLAR ARRAYS

A schematic of our fabrication process is shown in Fig. 1. A thin gold plating base was deposited or a silicon substrate. A high resolution electron beam resist, polymethyl methacrylate (PMMA), was then spun onto the substrate. Depending upon the desired pillar height, the thickness of the PMMA is typically 130 nm; however, 720 nm thick PMMA was also used in some cases. Dot arrays with diameters from 35 to 40 nm and spacings from 50 to 1000 nm were exposed in the PMMA using a high resolution electron beam lithography system with a beam diameter of 4 nm. The exposed PMMA was then developed in a cellosolve and methanol solution creating a template for the electroplating process. The sample was immersed in a nickel sulfamate type plating bath and nickel was electroplated into the template openings until the nickel thickness was near the template thickness. The plating rate, which is a function of plating current, template diameter, and template thickness, was well calibrated and was fixed at 45 nm/min for our work. After electroplating, the PMMA template was removed.

After fabrication, the pillars were examined using a scanning electron microscope (SEM) to verify the pillar dimensions. The resulting nickel pillars are uniform and have desired shape anisotropy. Figure 2 shows a SEM micrograph of a pillar array having a diameter of 35 nm, a height of 120 nm, and therefore an aspect ratio of 3.4. The pillar array has a period of 100 nm, and thus has a magnetic storage density of 65 Gbits/in.^{2} which is two orders of magnitude higher than the state-of-the-art storage. The pillars have a cylindrical shape with very smooth sidewalls.

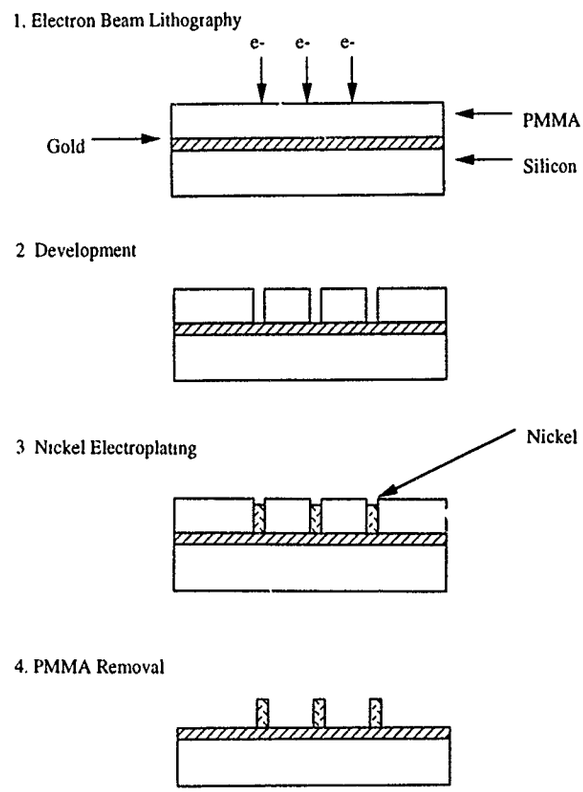

FIG. 1. Schematic of nanomagnetic pillar array fabrication process.

 0021-8979/94/76(10)/6673/3/$6.00 © 1994 American Institute of Physics

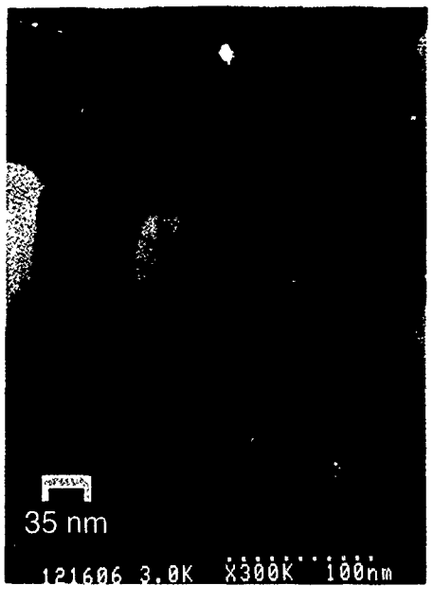

FIG. 2. SEM image of Ni pillar array of 35 nm diameter, 120 nm height, and a 100 nm spacing. The density is 65 Gbits/in.^{2} and the aspect ratio is 3.4.

Figure 3 shows a SEM micrograph of a second sample that was fabricated using 720 nm thick PMMA to obtain taller nickel pillars. These pillars have an average diameter of 75 nm, a height of 700 nm (therefore an aspect ratio of 9.3), and a period of 100 nm. Compared with the pillars in Fig. 2, these tall pillars have a cone shaped sidewall with an angle of 1.6° from vertical. Such cone shape results from the fact that during the plating, the Ni pillars conformed with the PMMA template that has a cone shape due to significant electron scattering in the thicker PMMA during the lithography.

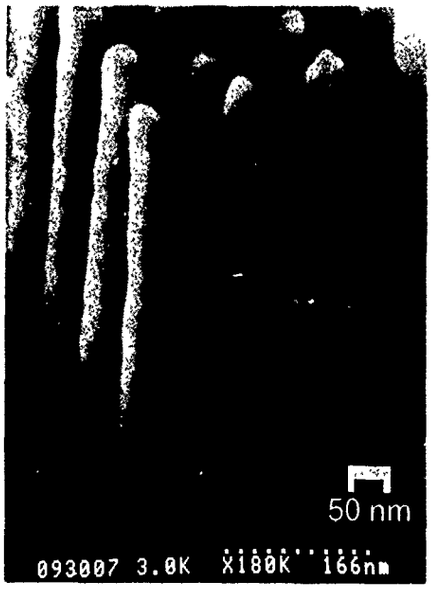

FIG. 3 SEM image of Ni pillar array of average 75 nm diameter, 700 nm height, and a 100 nm spacing. The density is 65 Gbits/in.^{2} and the aspect ratio is 9.3.

III. THEORETICAL ANALYSIS

We discuss the theoretical analysis of the nickel pillar arrays here and the characterization in the next section. First, theoretical calculation indicates that each nickel pillar should be single domain. Using Aharoni's formulas, the diameter for a prolate nickel spheroid with an aspect ratio of 3.4 to be single domain should be 52 nm or smaller.[6] In our case, the pillar diameter is 35 nm and therefore should be single domain.

Second, if each pillar is used to store one bit of information, such nanoscale pillar array storage has a rather different paradigm than the conventional storage. In conventional storage, each bit of information is stored over a number of magnetic grains which have a broad distribution in grain size, spacing, and magnetization direction. These distributions will result in the variation of the total magnetization of each bit stored and give rise to noise in reading. In the single-domain pillar array on the other hand, each bit is stored in a pillar which has only two quantized magnetization values: up or down in direction but equal in magnitude. Therefore, noise for each bit should be small. Certainly development of fabrication processes for these nanomagnetic pillar arrays is just the first step towards realization of this paradigm; methods for writing and reading information in such a media still need to be developed.

IV. CHARACTERIZATION

We have attempted to use a high resolution magnetic force microscope (MFM) operating at 300 mTorr to examine these ultra-high density pillar arrays, but were unsuccessful. The primary reason is that since the topology image and magnetic image are intertwined in MFM, the aspect ratio of our nanomagnetic pillars is so large that the topology image completely masks the magnetic image. Despite the difficulty in characterizing these nanomagnetic pillars, MFM measurements showed that horizontal nanomagnetic bars of 35 nm thickness and nanoscale widths are single domain, supporting our theoretical estimation that the nanomagnetic pillars should be single domain as well.[7]

Two other possible methods may be able to characterize the nanoscale magnetic pillars: scanning electron microscopy with polarization analysis (SEMPA) and magnetooptical Kerr effect microscopy (MOKE). Currently, we are pursuing these two studies. SEMPA analysis forms images by scanning a focused electron beam across a sample and detecting the spin polarization of secondary electrons. The magnitude and direction of the secondary electron's spin polarization is directly proportional to the magnitude and direction of the magnetization of the sample being scanned. MOKE analysis measures the magnetization of the pillars versus the magnetic field by detecting the rotation of polarization state of light reflected from a ferromagnetic sample. We have built a detection system that can detect a signal-to-noise ratio near 10^{-8} and are building a special probe station that will enable us to focus the laser beam to a diameter of 3–4 μm and position the beam to a specific location of the sample within 2 μm accuracy.

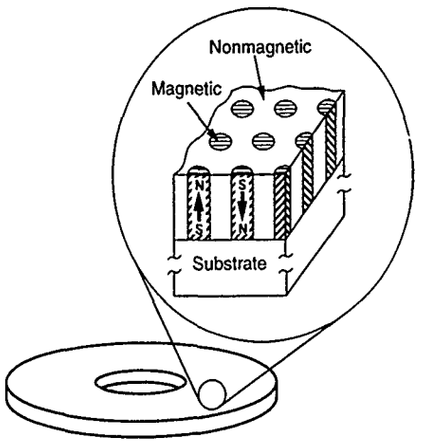

FIG. 4. Schematic of a quantum magnetic disk which consists of prepatterned single-domain magnetic structures embedded in a nonmagnetic disk.

V. QUANTUM MAGNETIC DISK

Based on these artificially patterned single-domain magnetic structures, we propose a new paradigm for ultra-high density magnetic disk: Quantum Magnetic Disk.[8] As shown in Fig. 4, a quantum magnetic disk consists of prepatterned single-domain magnetic structures embedded in a nonmagnetic disk. Each bit in the quantum magnetic disk is represented by a prefabricated single domain magnetic structure that has a uniform and well-defined shape, a prespecified location, and most importantly, a quantified magnetization that has only two states: the same in value and opposite in direction. In other words, the shape, magnetization, and location for each bit in a quantum magnetic disk are all quantized and predefined during the disk manufacturing. On the contrary, in a conventional magnetic disk where a bit is not defined at disk fabrication, the shape and magnetization of each bit have a broad distribution and the location of a bit can be anywhere on the disk. The quantum magnetic disk also differs from discrete track disk[9,10] and discrete segment disk[11,12] where the magnetization (both value and direction) of each bit can have a continuous and broad distribution.

The advantages of quantum magnetic disks over the conventional disks are apparent. First, the writing process in the quantum disk is greatly simplified, resulting in much lower noise and lower error rate and allowing much higher density. In the quantum disk, the writing process does not define the location, shape, and magnetization value of a bit, but just simply flips the quantized magnetization orientation of a prepatterned single-domain magnetic structure. The writing can be perfect, even though the head slightly deviates from the intended bit location and partially overlaps with other bits, as long as the head flips only the magnetization of the intended bit. But in the conventional magnetic disk, the writing process must define the location, shape, and magnetization of a bit. If the head deviates from the intended location, the head will write part of the intend bit and part of the neighboring bits.

Second, the quantum disk can track every bit individually, but the conventional disk cannot track all of its bits. This is because that in quantum disk each bit is separated from others by nonmagnetic material, but in the conventional disk many bits are connected. The individual-bit-tracking ability allows precise positioning, lower error rate, and therefore ultrahigh density storage.

Finally, reading in the quantum disk is much less jitter than that in the conventional disk. The reason is that in the conventional disk the boundary between bits is ragged and not well defined, but in the quantum disk each bit is defined with nanometer precision (can be less than the grain size) and is well separated from each other.

VI. SUMMARY

Using electron beam nanolithography and electroplating, arrays of Ni pillars on silicon that have a uniform diameter of 35 nm, a height of 120 nm, and a period of 100 nm were fabricated. The density of the pillar arrays is 65 Gbits/in.^{2}—over two orders of magnitude greater than the state-of-the-art magnetic storage density. Because of their nanoscale size, shape anisotropy, and separation from each other, each Ni pillar is single domain with only two quantized perpendicular magnetization states: up and down. Each pillar can be used to store one bit; such nanoscale pillar array storage offers a rather different paradigm than the conventional storage method. Certainly development of fabrication processes for such magnetic recording media is just the first step towards realization of this paradigm; methods for writing and reading information with such a media still need to be developed. MFM characterization of these pillars is unsuccessful at the moment due to large aspect ratio. Characterization using SEMPA and MOKE is in progress. Finally, based on the artificially patterned single-domain magnetic structures, a new paradigm for ultrahigh density magnetic recording media—the quantum magnetic disk is proposed.

ACKNOWLEDGMENTS

We thank J. G. Zhu for very helpful discussion and information. We also thank Robert Guibord for his technical assistance. This work was partially supported by ONR and ARPA.

[1] S. Iwasaki and K. Ouchi, IEEE Trans. Magn. **MAG-14**, 849 (1978).
[2] K. Ouchi, IEEE Trans. Magn. **MAG-26**, 24 (1990).
[3] T. Fujiwara, IEEE Trans. Magn. **MAG-23**, 3125 (1987).
[4] N. Tsuya, T. Tokushima, M. Shiraki, Y. Wakui, Y. Saito, H Nakamura, and Y. Harada, IEEE Trans. Magn. **MAG-24**, 2661 (1988)
[5] T. M. Whitney, J. S. Jiang, P. C. Searson, and C L. Chien, Scienc **261**, 1316 (1993).
[6] A. Aharoni, J. Appl. Phys. **63**, 5879 (1988).
[7] P. R. Krauss, P. B. Fischer, and S. Y. Chou, J. Vac. Sci. Technol. (to be published).
[8] S. Y. Chou (private communication, May, 1994).
[9] L. F. Shew, IEEE Trans., Broadcast Tel. Receivers **BTR-9**, 56 (1963).
[10] S. E. Lambert, I. L. Sander, A. M. Patlach, and M. T. Krounbi, IEEE Trans. Magn. **MAG-23**, 3690 (1987).
[11] K. A. Belser, T. Makansi, and I. L. Sanders, US Patent No. 4,912,585, March 27, 1990.
[12] S. E. Lambert, I. L. Sanders, A. M. Pattan, M. T. Krounbi, and S. R. Hetzler, J. Appl. Phys **69**, 4724 (1991).

Magnetic properties of nanostructured thin films of transition metal obtained by low energy cluster beam deposition

V. Dupuis, J. P. Perez, J. Tuaillon, V. Paillard, P. Mélinon, and A. Perez
Département de Physique des Matériaux, Université Lyon, I-69622 Villeurbanne Cédex, France

B. Barbara and L. Thomas
Laboratoire de Magnétisme Louis Néel, CNRS BP166X-38042 Grenoble Cédex, France

S. Fayeulle
Département Matériaux Mécanique Physique, Ecole Centrale de Lyon, BP 163-69131 Ecully, France

J. M. Gay
CRMC2, Campus de Luminy, CNRS-13397, Marseille Cédex 13, France

Clusters of iron, cobalt, and nickel are produced in a laser vaporization source. The size distributions of the incident clusters are checked by time-of-flight mass spectrometry before deposition at low energy. Studying the near threshold photoionization, Co_n and Ni_n clusters exhibit an icosahedral structure while for iron, no clear structure emerges. Neutral clusters were deposited on different substrates at room temperature with thicknesses up to 100 nm in view to determine their structure and magnetic properties. A limited coalescence of the clusters is observed from high-resolution transmission electron microscopy. No icosahedron has been observed but cuboctahedron and interface twins between adjacent particles have been clearly identified in Ni films. Grazing incidence x-ray diffraction experiments reveal a classical phase with grain size around 6 and 4 nm for Fe and Ni films, respectively but an anomalous fcc phase for Co films and a very low grain size of 2 nm. The density of films determined by x-ray reflectivity was estimated to represent only 60%–65% of the bulk density. Magnetic behaviors studied by ferromagnetic resonance and SQUID magnetization measurements have been interpreted using the correlated spin glass model. Mössbauer spectra performed on Fe films at zero field revealed the presence of 20% of iron in the form of thin nonmagnetic oxide skin surrounding Fe grains which allow to find 2.2 μB per magnetic iron atom in agreement with macroscopic magnetic measurements. Nevertheless we found an anomalous reduced atomic moment for Ni film.

INTRODUCTION

Recently, magnetic properties such as exchange coupling or giant magnetoresistance mainly observed in metallic multilayers have been detected in other nanostructured systems. For example, Berkowitz *et al.*[1] and Xiao *et al.*[2] observed giant magnetoresistances in ultrafine Co-rich precipitate particles in a Cu-rich matrix. These samples were prepared by coevaporation taking advantage of the low solubility of Cu in Co. However, though this technique is limited to nonmiscible components, the adjustable cluster diameter is a new parameter in addition to the distance between particles as in thin film layers. Thus, studies on clusters and cluster assembled materials are of increasing interest.

The laser vaporization source of the laboratory[3] allows the obtention of an intense cluster beam of any size distribution (from few to a thousand atoms per cluster) and the synthesis of cluster assembled materials, even of the most refractory and of the most complex ones. The cluster size distribution is checked by time-of-flight mass spectrometry before deposition. Our source producing cold clusters with low kinetic energy, incident clusters do not fragment on the substrate and may conserve their intrinsic structures. Thus we succeeded in the stabilization of very small size fullerenes (C_{20}-C_{32}), never previously observed experimentally. We clearly evidenced that deposited carbon clusters presented the in flight-clusters fingerprint.[3]

Our challenge in depositing transition metal clusters is to synthesize new phases where the anomalous crystallographic structures of free clusters would be kept and to study the specific magnetic behavior of these weakly correlated entities on a substrate. Once more, we show that our technique leads to a random compact cluster stacking (RCCS).[3] Thus magnetic results could be interpreted by random anisotropy model with a scale law and in terms of localization of spin waves.

EXPERIMENT

Our cluster source is based on the technique of laser vaporization.[3–5] Roughly, a plasma is created in a vacuum cavity by Nd-YAG laser light. Synchronized with the laser, a high pressure (5 bars) helium pulse, injected in the cavity by a nozzle, thermalizes the plasma and cluster growth occurs. The nascent clusters are then rapidly quenched during the following isentropic expansion into vacuum (10^{-7} Torr).

Cluster size distributions are analyzed in a time-of-flight mass spectrometer. Studying the near threshold photoionization (performed with a frequency-doubled tunable dye laser pumped by a XeCl excimer laser), mass spectra of Co_n and Ni_n clusters exhibit oscillations and a series of magic numbers ($n=13,55,147,309,561,\ldots$) corresponding to an icosahedral or cuboctahedral atomic shell structure in the obtained mass range (50–800 atoms per cluster). A finer analy-

 0021-8979/94/76(10)/6676/3/$6.00 © 1994 American Institute of Physics

sis allows us to conclude for the icosahedral structure.[6] For iron clusters, the results are not so simple, indicating a competition between different regimes.[6]

Then, free neutral clusters are deposited with a kinetic energy in the 10–20 eV range on different substrates at room temperature with thicknesses up to 100 nm in view to determine their structure and magnetic properties.

SAMPLE CHARACTERIZATION

The typical size of supported clusters obtained from high-resolution transmission electron microscopy (HRTEM) was about 2–6 nm for an initial size distribution centered around 150 atoms for Fe and 300 atoms for Co and Ni clusters, respectively. No icosahedron was observed but cuboctahedra and interface twins between adjacent particles was clearly identified in Ni films. Quasispherical grain morphology existed in Fe film which could correspond to a bcc rhombic dodecahedron [110] according to the Wulff's theorem.[7] Grazing incidence x-ray diffraction (GIXD) experiments exhibit a classical bcc phase for Fe films but a fcc phase for both Co and Ni with a grain size extracted from the peak width of about 6, 4, and 1.5 nm, respectively, in agreement with electronic diffractions and TEM observations. The classical structure of cobalt being hcp, the fcc phase observed in Co films might be related to the icosahedral structure of the incident cluster beam. In fact, the icosahedron is expected to be the precursor of the fcc crystal. The small grain size and the reminiscence of a free cluster structure confirm the limited coalescence process due to a weak diffusion of metallic clusters on the substrate even at room temperature.

Rutherford backscattering spectroscopy showed that these porous films are composed of 20%–30% of oxygen for 70%–80% of metals. The density of the films, determined by x-ray scattering at very low angle in $\theta/2\theta$ mode and from rocking curve around the critical angle of the total reflectivity, was estimated to represent only 60%–65% of the bulk density.[8]

MAGNETIC PROPERTIES

Mössbauer spectra performed at room temperature on Fe films without magnetic field revealed the presence of the sextet of the metallic iron (with hyperfine field around 332 KOe and representing 80% of the signal) and of two doublets corresponding to 20% of ferric oxide (Fig. 1). Whereas the common isomer shift of both nonmagnetic signals is equal to 0.4 mm/s compared to the metallic iron, the quadrupolar splittings respectively equal to 0.9 and 2.4 mm/s allow us to differ two types of oxide. The first one is identified as a thin layer of nonstoechiometric Fe_3O_4 or/and a mixture of stoechiometric Fe_3O_4 and γ-Fe_2O_3 phases[9] (in agreement with the GIXD experiments on the most oxidized films[10]). The second one, not identified so far could be related to a free-cluster oxidation. These results allow to describe the supported clusters as pure iron core surrounded by a thin skin (2 or 3 monolayers[7]) of non-magnetic oxide. On the other hand, the intensity ratio of the sextuplet (321123) evidences a random spatial distribution of the magnetization at zero field.

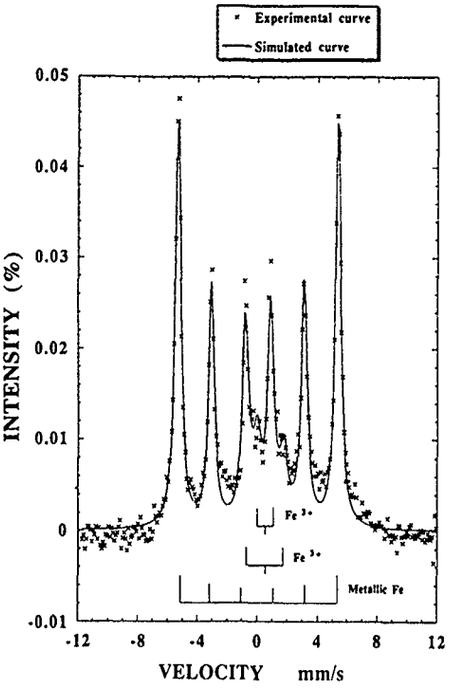

FIG. 1. Mössbauer spectra obtained on a Fe_{150} film at 300 K.

The macroscopic magnetic behavior of our films has been studied using ferromagnetic resonance (FMR) and magnetization measurements (SQUID). FMR curves roughly traduced a thin film behavior[11] but revealed several resonance magnetic fields due to anchorage of spin waves at the surface (when the applied field is perpendicular to the surface of the film). The coercive field at 300 K is about 100 Oe for cobalt, 50 Oe for iron, and lower than 10 Oe for nickel and increases at 10 K up to 1000 and 500 Oe for Co and Fe films, respectively. The value of the saturation magnetization was related to the density value and to the quantities of oxides. For iron in agreement with Mössbauer results, the classical atomic moment of 2.2 μB per magnetic iron atom is retrieved. On the contrary we found a strongly reduced value in Ni film. The atomic moment per Ni atom has been estimated to be equal to 1/4 of the bulk value (taking into account the film density). By extrapolating the magnetization curve versus temperature, the Curie temperature T_c has been found to be around 350–400 K. Thus the magnetization reduction can not be uniform, otherwise T_c would be much more reduced. This could be due to the presence of dead magnetic layers similar to that observed in Fe films and/or to antiferromagnetic coupling between Ni particles via Ni shell. Magnetoresistance measurements and magnetization under high magnetic field are in progress in view to see respectively an important negative magnetoresistance and a second transition of the saturation magnetization.

We fitted the approach to saturation of the magnetization using the Chudnovsky model.[12,13] The experimental law of approach to saturation in magnetic systems is perfectly fitted by the formalism of the random-anisotropy amorphous magnets. In the Chudnovsky's model,[12] a physical parameter is defined

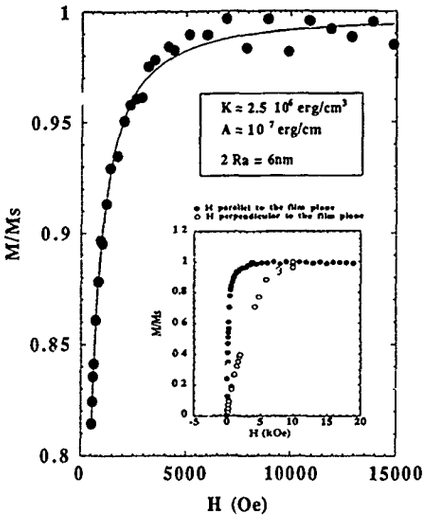

FIG. 2. Magnetization law in approaching saturation obtained on a Fe_{150} film at 300 K.

$$\lambda = \left(\frac{2}{15}\right)^{1/2} \frac{K R_a^2}{A},$$

where R_a is the distance over which the local anisotropy axes are correlated and A is the exchange constant. The parameter λ is the critical boundary between the correlated spin glass (CSG) regime ($\lambda<1$) and the speromagnetic state ($\lambda>1$). One can define the ferromagnetic correlation length $R_f=R_a/\lambda^2$. The best fit[10,13] of the curve on Fe films (Fig. 2) gives respectively, $2R_a=6$ nm, $K\sim 2.5 10^6$ erg/cm^3 (in agreement with FMR fits, to compare to 5×10^5 erg/cm^3 in the bulk), $A\sim 10^{-7}$ erg/cm, therefore $\lambda=0.66$ and $R_f=8$ nm. Let us underline that in amorphous alloys, R_a is always of the order of the inter-reticular distance (e.g., in rare earth-Fe compounds $R_a=0.5$ nm[14].) In our case we note that R_a exactly corresponds to the supported particles size and that the R_f value shows the ferromagnetic correlation limited to the first neighbors. However, if the ferromagnetic domain was strictly limited to the R_f value, the film should be superparamagnetic. That confirms the definition of R_f in the CSG model where it represents an exponential decay coupling. We thus showed that RCCS films can be described as an amorphous with an adjustable parameter R_a. In our case, R_a is great enough to reach experimental fields larger than the crossover field[11] $H_{co}=2A/M_sR_a^2$ which separates the region with and without random anisotropy fluctuations (determined around 3 kOe in Fe films). In Ni films (Fig. 3) we clearly see two regimes for the low field ($\Delta M/M_s$) variation versus temperature (maybe correlated to a $T_{Néel}$ of Ni oxide). At low temperature the random anisotropy fluctuations dominate (with a H^{-2} law) whereas at high temperature the exchanges dominate (with a $H^{-1/2}$ law), the transition occurring around 200 K.

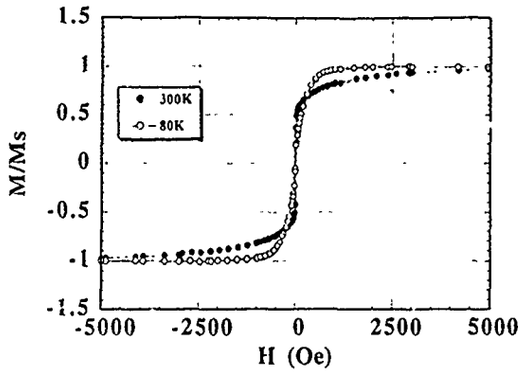

FIG. 3. Magnetization vs temperature obtained on a Ni_{300} film.

In conclusion, these first results lead us to pursue this study to elucidate some other characteristic magnetic parameters of the layers (T_c, e.g., antiferromagnetic coupling in Ni films, and complete magnetic study on promising Co films). In particular, x-ray absorption measurements will allow us to locally describe crystallographic and magnetic atomic environment in view to explain the anomalous atomic moment in Ni films. Experiments with cooled substrates are in progress to attempt to stabilize the icosahedral structure which is expected to lead to specific magnetic properties.

[1] A. E. Berkowitz, J. R. Mitchell, M. J. Carey, A. P. Young, S. Zhang, F. E. Spada, F. T. Parker, A. Hutten, and G. Thomas, Phys. Rev. Lett. **68**, 3745 (1992).
[2] J. Q. Xiao, J. S. Jiang, and C. L. Chien, Phys. Rev. Lett. **68**, 3749 (1992).
[3] V. Paillard, P. Mélinon, V. Dupuis, J. P. Perez, A. Perez, and B. Champagnon, Phys. Rev. Lett. **71**, 4170 (1993).
[4] R. E. Smalley, Laser Chem. **2**, 167 (1983).
[5] P. Milani and W. A. de Heer, Rev. Sci. Instrum. **61**, 1835 (1990).
[6] M. Pellarin, B. Baguenard, J. L. Vialle, J. Lermé, M. Broyer, J. Miller, and A. Perez, Chem. Phys. Lett. **217**, 349 (1994).
[7] R. V. Hardeveld and F. Hartog, Surf. Sci. **15**, 189 (1969).
[8] J. M. Gay, P. Stocker, and F. Rethore, J. Appl. Phys. **73**, 8169 (1993).
[9] K. Haneda and A. H. Morrish, Surf. Sci. **77**, 584 (1978).
[10] J. P. Perez, V. Dupuis, V. Paillard, P. Mélinon, A. Perez, and J. Tuaillon, Revue de Métallurgie-CIT/Sci. Gén. des Mat. **9**, 1198 (1993).
[11] J. P. Perez, V. Dupuis, J. Tuaillon, A. Perez, V. Paillard, P. Mélinon, M. Treilleux, L. Thomas, B. Barbara, and B. Bouchet, J. Magn Magn. Mat. (submitted).
[12] D. L. Griscom, J. J. Krebs, A. Perez, and M. Treilleux, Nuc. Instrum. Methods Phys. Res. B **32**, 272 (1988).
[13] E. M. Chudnovsky, J. Appl. Phys. **64**, 5570 (1988).
[14] J. Filippi, V. S. Amaral, and B. Barbara, Phys. Rev. B **44**, 2842 (1991).
[15] J. J. Rhyne, IEEE Trans. Magn. **MAG-21**, 1990 (1985).

Published without author corrections

Size effects on switching field of isolated and interactive arrays of nanoscale single-domain Ni bars fabricated using electron-beam nanolithography

Mark S. Wei and Stephen Y. Chou
Department of Electrical Engineering, University of Minnesota, Minneapolis, Minnesota 55455

Isolated nanoscale Ni bars with a length of 1 μm, a width from 15 to 300 nm, and interactive bar arrays with a spacing from 200 to 600 nm were fabricated using electron-beam lithography and were studied using magnetic force microscopy. The study showed that the virgin magnetic state of bars with a width smaller than 150 nm was single domain and otherwise multidomain. It also showed that the switching field of isolated bars initially increases with decreasing bar width, then reaches a maximum switching field of 740 Oe at a width of 55 nm, and afterwards decreases with further bar width reduction. Furthermore, it was found that the switching field of the interactive bars decreases almost linearly with reduction of the spacing between the bars.

I. INTRODUCTION

Understanding the behavior of a single domain magnetic particle and the interaction between the particles is very important, because these particles are the basic constituents of many magnetic recording materials. However, previously most experimental studies of magnetic particles were made in an ensemble of such particles and the properties of a single particle were inferred only through extrapolation. Due to large variation in particle dimensions, randomness of magnetization and unavoidable interaction, detailed information about single particles and their interaction is smeared out.

Due to advance in nanofabrication technology, now it is possible to nanoscale magnetic particle arrays with precise sizes, shapes, and spacing. This opens up new opportunities to understand the fundamentals of micromagnetics and develop new magnetic materials. Recently, the first reported study of nanoscale permalloy bars fabricated using electron beam lithography was carried out by a joint team from the University of California at San Diego and IBM.[1,2] In that study, isolated bars had a fixed length of 1 μm and a fixed width of 133 nm and interactive bar arrays had a fixed spacing with the strongest coupling along the bars' long axis.

In this article, we present the fabrication and investigation of isolated Ni bars with a width varying from 15 to 300 nm and interactive Ni bar arrays with a spacing varying from 200 to 600 nm with the strongest coupling in the bars' short axis. Furthermore, we report and discuss the effects of bar width and spacing on the switching field of these isolated and interactive bars.

II. FABRICATION OF NANOMAGNETIC BAR ARRAYS

The isolated and interactive nanomagnetic nickel bars were fabricated using electron-beam nanolithography and a lift off process. In the fabrication, a resist, polymethyl methacralate (PMMA), was first spun onto a silicon substrate. A high resolution electron beam lithography system with a beam diameter of 4 nm was used to expose bar arrays in the PMMA. The exposed PMMA was developed in a cellosolve and methanol solution to form a resist template on the substrate. A nickel film, 35 nm thick, was evaporated onto the entire sample. In the lift off, the sample was submersed in acetone which dissolved the PMMA template and lifted off the nickel on its surface, but not the nickel on the substrate. After fabrication, bar widths were determined using a scanning electron microscope (SEM) and the bar width presented here is the measured bar width.

For isolated bars, the bar length was fixed at 1 μm, but the bar width varied from 15 to 300 nm. The spacing between isolated bars is 10 μm. Figure 1 shows a scanning electron micrograph of a Ni bar with a 15 nm width.

For interactive bar arrays, the bar width and length were fixed at 100 nm and 1 μm, respectively. The spacing between bars along the long axis is 2 μm, but the spacing between the bars along the short axis varies from 200 to 600 nm. Therefore the interaction between bars is primarily along the short axis, and the bar arrays can be regarded as isolated rows of one dimensional interactive arrays. This is very different from that in Ref. 1 where the bars were coupled primarily along the long axis. To illustrate the fabrication resolution

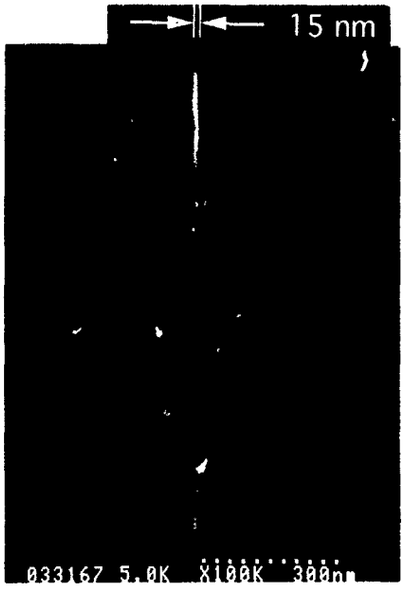

FIG. 1. SEM image of a high aspect ratio isolated Ni bar that is 1 μm long and 15 nm wide.

 0021-8979/94/76(10)/6679/3/$6.00 © 1994 American Institute of Physics

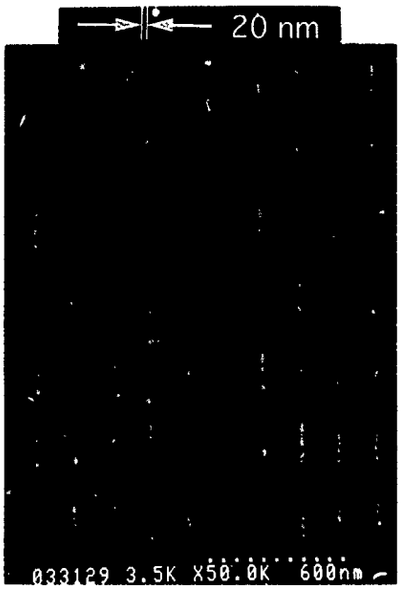

FIG. 2. SEM image of interactive bar arrays. Each bar is 200 nm long, 20 nm wide and 35 nm thick.

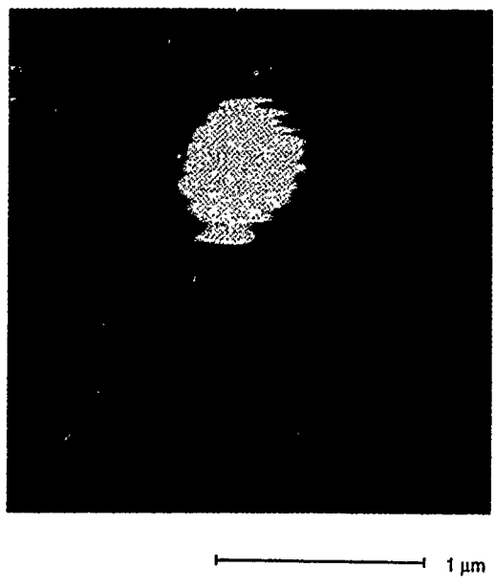

FIG. 3. MFM image of a Ni bar which is 1 μm long and 100 nm wide. The bright spot stands for the north pole and the dark spot stands for the south pole.

and uniformity, Fig. 2 shows a large array of Ni bars which are 200 nm long, 20 nm wide, and 150 nm apart along the short axis and 100 nm apart along the long axis, despite the fact that such dense bar arrays were not able to be resolved in our magnetic force microscopy (MFM) study.

III. MFM MEASUREMENTS

The nanomagnetic bars were studied using a custom built MFM that was modified from a commercial atomic force microscope (AFM). The MFM was operated in amplitude detection mode at ~200 mTorr vacuum for a high sensitivity. The MFM tips are the ordinary AFM cantilevers coated with 30 nm of cobalt and have a resonance frequency of 18 kHz. These soft tips give better sensitivity but poorer resolution than that of a harder tip.

In measuring the switching field of the isolated bars, the sample was first saturated in a fixed direction along its easy axis using a 2000 Oe magnetic field and a MFM image was taken to determine its magnetization. Then a test field was applied in the opposite direction and returned to zero. The sample was examined under MFM again to see if its magnetization flipped. If the bar flipped, a smaller test field was applied in next measuring cycle, otherwise a large field was applied. This process continued until the switching field of a nickel bar was located within 10 Oe.

IV. DATA AND ANALYSIS

A. Isolated bars

Before the isolated bars were put into any magnetic field, MFM images of the sample were taken. These images showed that for bars of a width smaller than 150 nm, the virgin magnetic state is single domain with magnetization along the direction of its easy (i.e., long) axis; and the bars of wider width are multidomain. A MFM image of a 100 nm wide isolated bar is shown in Fig. 3.

It was found that the magnetization switching field of an isolated bar is a strong function of width, as shown in Fig. 4. The switching field first increases with decreasing bar width, reaches a maximum switching field of 740 Oe at a bar width of 55 nm, then decreases with further reduction of the bar width. The initial increase in the switching field is because the bar is changing from multidomain to single domain. The later decrease is likely due to the fact that thermal energy becomes comparable to magnetization switching energy.[4]

Compared to the study in Ref. 2, where the permalloy bars of a width 133 nm had a switching field greater than 400 Oe, the Ni bar with the same width studied here has a switching field about 100 Oe less. This could be due to two reasons. First, nickel film on Si surface has significant stress, so there

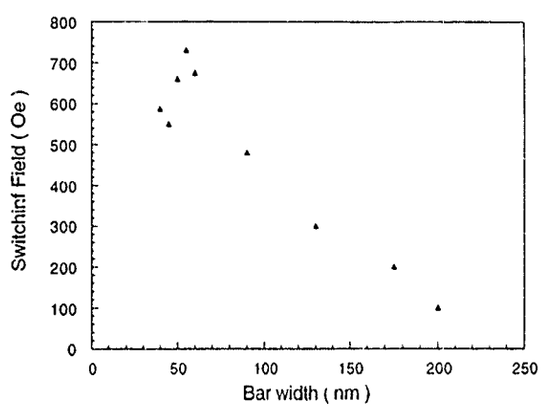

FIG. 4. Switching field of isolated bars vs bar width The maximum switching field is 740 Oe for 55 nm wide bars. The bars are 1 μm long and actual bar width was measured using SEM

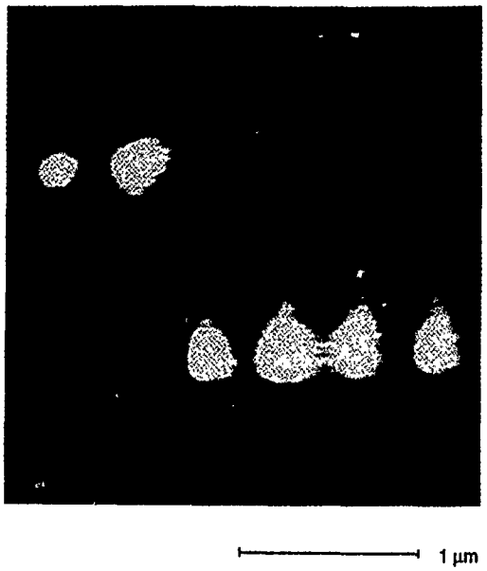

FIG. 5. MFM image of one-dimensional interactive bar arrays with 400 nm spacing.

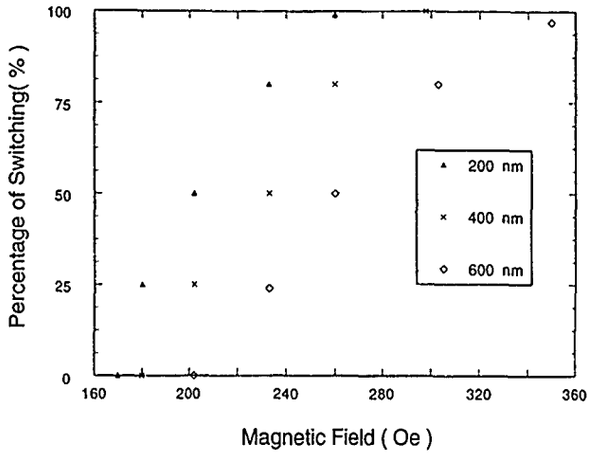

FIG. 6. Percentage of bars that switched vs the applied magnetic field for interactive bars with a spacing along the short axis of 200, 400, and 600 nm.

may be a magnetostriction effect which decreases the net anisotropy. Second, Ni has strong crystalline anisotropy but permalloy does not.

The critical width for superparamagnetism can be estimated from the switching field vs size curve. The switching field of a particle of volume V, can be described by the equation $h_{ci}=1-(V_p/V)^{0.5}$, where h_{ci} is reduced coercivity and V_p is the volume below which the particle is superparamagnetic. The equation can be rewritten in terms of the bar width W:$h_{ci}=1-(W_p/W)^{0.5}$. By fitting the switching field of the bars with a width smaller than 55 nm, W_p is found to be 18 nm.

B. Interactive nanomagnetic bars

The interactive bar arrays that were studied using MFM have a bar width of 100 nm and a spacing between bars of 0.2, 0.4, and 0.6 μm, respectively, along the short axis. Figure 5 shows a MFM image of these bar arrays. The switching field distribution was measured and is shown in Fig. 6. In this measurement, an average of about 30 bars were counted for each data point and the bars at the end of each row were not counted. Figure 6 shows three facts. First, the smaller the spacing, the smaller the switching field. The switching field for 100 nm wide isolated bar is 300 Oe. But due to interaction, the mean value of switching field (i.e., the field at which 50% of bars can flip) is 205, 232, and 260 Oe for a spacing of 0.2, 0.4, and 0.6 μm, respectively. Second, the switching field decreases with the reduction of spacing at a rate 15 Oe per 100 nm. This behavior is due to the fact that as the spacing decreases, the demagnetization field generated by neighbor bars increases and will help a bar to flip. Third, the broadness of the switching field distribution is about 100 Oe which is due to bar interaction as well as size variations.

V. CONCLUSION

We have fabricated nanoscale isolated magnetic bars with different bar widths as well as interactive bar arrays with different spacing.[5] The switching field was measured using MFM. The SEM micrographs show that these Ni bars have good uniformity and very high aspect ratio. The MFM studies show that bars with a width smaller than 150 nm were single domain and the switching field depends strongly on the width (therefore the aspect ratio) of the bar. The switching field of the isolated bars first increases with decreasing bar width, then reaches the maximum switching field of 740 Oe with 55 nm wide bars, and afterwards decreases with further reduction of bar width. The switching field of interactive bars decreases almost linearly with the reduction of spacing. The broadness of switching field distribution for interactive bar arrays is 100 Oe.

ACKNOWLEDGMENTS

We would like to thank Peter Krauss and Bob Guibord for their technical assistance in fabrication and J. G. Zhu for useful discussion. This work was partially supported by ARPA and ONR.

[1] J. F. Smyth, S. Schultz, D. R. Fredkin, T. Koehler, I. R. McFaydlin, D. P. Kern, and S. A. Rishton, J. Appl. Phys. **63**, 4237 (1988).
[2] G. A. Gibson, J. F. Smith, S. Schultz, and D. P. Kern, IEEE Trans. Magn. **MAG-27**, 5187 (1991).
[3] D. Rugar, H. J. Mamin, P. Guethner, S. E. Lambert, J. E. Stern, I. McFadyen, and T. Yogi, J. Appl. Phys. **68**, 1169 (1990).
[4] B. D. Cullity, *Introduction to Magnetic Materials* (Addison–Wesley, Reading, PA, 1972).
[5] P. B. Fisher and S. Y. Chou, Appl. Phys. Lett. **62**, 2989 (1993).

Itinerant electron metamagnetism and related phenomena in Co-based intermetallic compounds (invited)

T. Goto and H. Aruga Katori
Institute for Solid State Physics, University of Tokyo, Roppongi, Minato-ku, Tokyo 106, Japan

T. Sakakibara and H. Mitamura
Department of Physics, Faculty of Science, Hokkaido University, Sapporo 060, Japan

K. Fukamichi and K. Murata
Department of Materials Science, Faculty of Engineering, Tohoku University, Sendai 980, Japan

Susceptibility and high field magnetization have been measured for $Y(Co_{1-x}M_x)_2$ (M=Al, Fe, and Ni). YCo_2 exhibits a metamagnetic transition at 69 T. Ni doping in YCo_2 increases the critical field (B_c), while Fe doping decreases it. These changes can be elucidated with the band picture of metamagnetism. B_c of YCo_2 exhibits a positive shift proportional to the square of temperature. In the paramagnetic region of $Y(Co_{1-x}Al_x)_2$ with $x \leqslant 0.11$, the susceptibility is enhanced with Al and a sharp metamagnetic transition with lower B_c is observed. The susceptibility becomes maximum at a finite temperature T_{max}. B_c in the ground state is proportional to T_{max}. These experimental results are discussed with a new theory based on a spin fluctuation model. The susceptibility and the metamagnetic transition are found to be very sensitive to pressure.

I. INTRODUCTION

Ultrahigh magnetic fields over 100 T are now available for fundamental research on magnetism. One of the most interesting subjects in ultrahigh magnetic fields is itinerant electron metamagnetism, that is, a first-order field-induced transition from the paramagnetic to the ferromagnetic state in a d-electron system. Since this phenomenon was predicted to occur by Wohlfarth and Rhodes,[1] many theoretical and experimental studies have been made to elucidate it.

We have systematically studied the magnetization process of various Co-based Laves phase compounds in magnetic fields up to 120 T. We observed clear metamagnetic transitions in $Y(Co,Al)_2$ (Refs. 2 and 3), $Y(Co,Fe)_2$ (Ref. 4), $Sc(Co,Al)_2$ (Ref. 5), $Lu(Co,Al)_2$ (Refs. 6 and 7), $Lu(Co,Sn)_2$ (Ref. 8), $Lu(Co,Si)_2$ (Ref. 9), $Lu(Co,Ga)_2$ (Ref. 10), YCo_2 (Refs. 11 and 12), and $LuCo_2$.[12] Adachi *et al.* found a metamagnetic transition in the paramagnetic pyrite $Co(S,Se)_2$.[13]

All of the above compounds have characteristics of a strongly exchange-enhanced Pauli paramagnet: the electronic specific heat coefficient and the magnetic susceptibility are very large. Moreover, the temperature dependence of susceptibility $\chi(T)$ is anomalous: $\chi(T)$ increases with temperature and then decreases through a maximum at a finite temperature $T=T_{max}$. These facts suggest that the itinerant electron metamagnetism and the appearance of a maximum in $\chi(T)$ come from the same origin. Itinerant metamagnetism is considered to originate from a special shape of the density-of-states (DOS) curve for a d-electron system in the vicinity of the Fermi level.[1] On the other hand, the origin of the unusual behavior of $\chi(T)$ observed in a strongly exchange-enhanced paramagnet is not well understood. However, the above facts imply that the behavior of $\chi(T)$ also originates from the special shape of the DOS.

Thermodynamical properties of an itinerant electron magnet are dominated by the effect of spin fluctuations. In fact, magnetic properties of a weakly ferromagnetic metal at finite temperatures are successfully elucidated with the spin-fluctuation theory developed by Moriya.[14] However, the relation between the temperature dependence of susceptibility for an exchange-enhanced paramagnet with metamagnetism and its magnetization process remains unknown.

In the present study, we have studied the magnetization process and susceptibility for a typical metamagnetic compound YCo_2 and pseudobinary systems $Y(Co_{1-x}M_x)_2$ (M =Al, Fe, and Ni) to clarify the origin of the transition and the anomaly of $\chi(T)$. The metamagnetic transition is expected to be very sensitive to pressure.[15] We have also examined the effect of pressure on the magnetization process and the susceptibility of the $Lu(Co_{1-x}Ga_x)_2$ system.

II. EXPERIMENTAL PROCEDURE

The Laves phase compounds $Y(Co_{1-x}M_x)_2$ (M=Al, Fe, and Ni) and $Lu(Co_{1-x}Ga_x)_2$ were prepared by arc melting in an argon atmosphere, followed by annealing at 900–950 °C for a week. All the specimens are confined to be single phase with the cubic Laves phase structure by x-ray diffraction. The obtained ingots were powdered for magnetic measurements.

High magnetic fields up to 42 T were produced using a wire-wound pulse magnet with a duration time of about 10 ms. Ultrahigh magnetic fields up to 120 T were generated by means of a fast capacitor discharge into a single-turn coil

 0021-8979/94/76(10)/6682/6/$6.00 © 1994 American Institute of Physics

with a 100 kJ capacitor bank. Duration time of the pulse field is about 7 μs.

The magnetization in pulsed high and ultrahigh magnetic fields was measured using an induction method with a set of compensated pickup coils. For the magnetization measurement in ultrahigh magnetic fields, the powder sample was molded into a rod of 1.5 mm diameter and 5 mm length with epoxy resin (Stycast #1266) to avoid an eddy current effect. The magnetization under high pressure was measured using an extraction-type magnetometer, with a high pressure clamp cell made of Cu-Ti alloy, in steady magnetic fields up to 7 T. The specific heat was measured at low temperatures in magnetic fields of 0, 6, 10, and 14.6 T using a conventional heat pulse method with a mechanical heat switch. The temperature was measured with a carbon-glass resistor thermometer calibrated in magnetic fields.

III. RESULTS AND DISCUSSION

First we show the magnetization of YCo_2 (Refs. 11 and 12) and $LuCo_2$ (Ref. 12) at low temperatures in ultrahigh magnetic fields up to about 100 T. Sharp metamagnetic transitions can clearly be seen around 70 T with small hysteresis. In $ScCo_2$, however, we could not find a transition up to 120 T. The critical field of the transition in the ground state (B_{c0}) is determined to be 69 T for YCo_2 and 74 T for $LuCo_2$. Here, we define B_{c0} from the average of two positions at which the differential susceptibility dM/dB becomes maximum in the increasing and decreasing field scans. The values of magnetization in the paramagnetic and ferromagnetic phases at B_{c0} are 0.17 and 0.44 μ_B/Co for YCo_2, and 0.15 and 0.64 μ_B/Co for $LuCo_2$. The magnetization jump due to the transition is $\Delta M = 0.27$ μ_B/Co for YCo_2, which is apparently smaller than $\Delta M = 0.49$ μ_B/Co for $LuCo_2$. The high field susceptibility for both compounds is still large in the ferromagnetic phase. This indicates that the magnetization is not completely saturated by the metamagnetic transition.

Yamada *et al.*[16] estimated the magnetization in the ground state as a function of magnetic field for $ScCo_2$, YCo_2, and $LuCo_2$ by calculating the electronic structure of d-electrons in magnetic fields. They assumed that the volume does not change in magnetic fields. The calculated magnetization process exhibits an itinerant metamagnetic transition at 120, 89, and 94 for $ScCo_2$, YCo_2, and $LuCo_2$, respectively. A sharp peak being just below the Fermi level in DOS plays an important role in these transitions. The peak comes mainly from the d component of Co atoms. As the external field is increased, the Fermi level for the minority spin band approaches the peak of DOS and eventually a transition to a larger moment state occurs at a certain field. The estimated B_{c0} for YCo_2 and $LuCo_2$ is larger by 20 T than the observed ones. Yamada and Shimizu[15] have suggested that a magnetovolume effect reduces the value of B_{c0}. The reduction is roughly evaluated to be -13 T for YCo_2. The evaluated B_{c0} becomes very close to the observed one by considering the magnetovolume effect.

In order to get further information to support the band picture for the observed metamagnetic transition, we examined the change of B_{c0} produced by the shift of the Fermi level.[17] A small amount of 3d transition metals Fe and Ni are substituted for Co in YCo_2. Fe substitution shifts the Fermi level to the lower energy side, while the Ni substitution shifts it to the higher energy side.

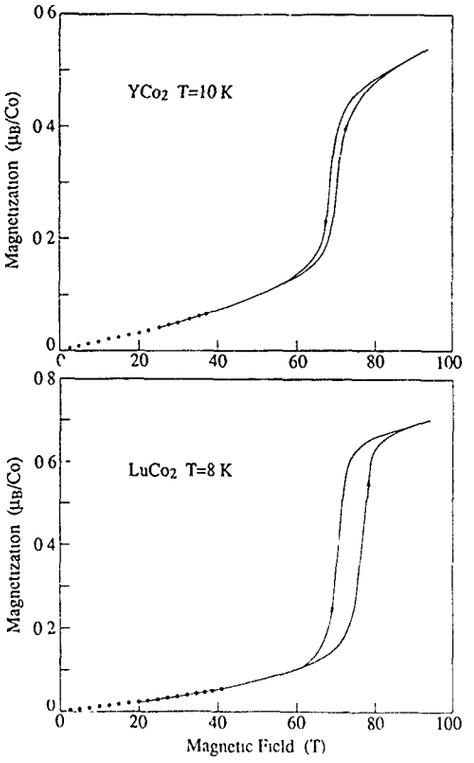

FIG. 1. Magnetization process for YCo_2 and $LuCo_2$ in ultrahigh magnetic fields up to 100 T.

As an example, we show in Fig. 2 the dM/dB curve of $Y(Co_{1-x}Ni_x)_2$ in an increasing field scan. The B_{c0} of YCo_2 obtained in this study is 72 T, which is slightly higher than that shown in Fig. 1. The position of B_{c0} rapidly moves to the higher field side with increasing Ni content. In addition to the movement of B_{c0}, significant broadening of the tran-

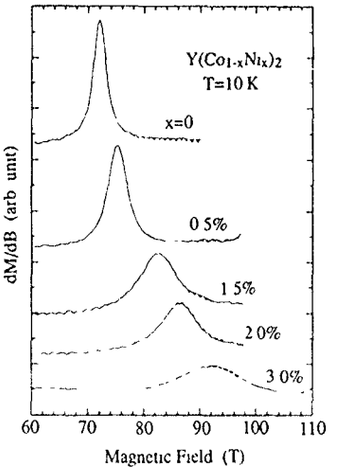

FIG. 2. Differential susceptibility dM/dB of $Y(Co_{1-x}Ni_x)_2$ measured in an increasing field scan.

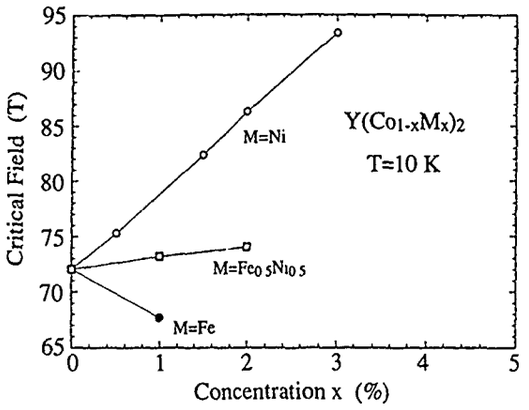

FIG. 3. Concentration dependence of the critical field for the substituted compounds $Y(Co_{1-x}M_x)_2$ (M=Fe, Ni, and $Fe_{0.5}Ni_{0.5}$).

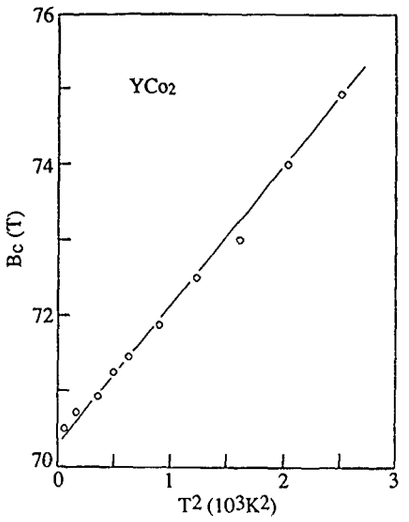

FIG. 5. Critical field of YCo^2 in an increasing field scan as a function of temperature.

sition becomes apparent in the concentration region of $x>0.015$.

The values of B_{c0} obtained for $Y(Co_{1-x}Ni_x)_2$ and $Y(Co_{1-x}Fe_x)_2$ are plotted in Fig. 3. Ni substitution results in a linear increase of B_{c0} in the investigated concentration region $x\leqslant 0.03$. In the case of Fe substitution, on the other hand, B_{c0} decreases. The observed change of B_{c0} due to Ni and Fe substitution can easily be understood with the band model of metamagnetism. Since excess d-electrons produced by Ni substitution increase the distance between the Fermi level and the peak position of DOS, the condition for the metamagnetic transition is satisfied at a higher field. On the contrary, a decrease of B_c is expected by Fe substitution. The change of B_c can qualitatively be explained with a simple rigid band model. However, the magnitude of the observed change in B_c is apparently different for these two systems. We obtain $|dB_{c0}/dx|=7.2$ T/%Ni for Ni substitution and $|dB_{c0}/dx|=4.5$ T/%Fe for Fe substitution. This fact seems to be contradictory to the rigid band model, in which symmetrical changes are expected at least for small doping. In the case of simultaneous doping with equal amounts of Fe and Ni, no change of B_{c0} is expected from the model. However, an appreciable increase of 2 T is observed for $x=2\%$ in $Y(Co_{1-x}(Fe_{0.5}Ni_{0.5})_x)_2$ as shown in Fig. 3. It should be noted that the volume change due to the substitution is negligibly small and gives no effect to B_{c0}. A theoretical study on the change of B_{c0} due to the substitution is now in progress.

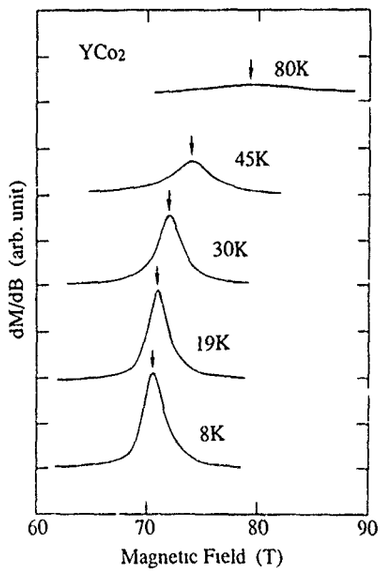

FIG. 4. Differential susceptibility dM/dB of YCo_2 for several temperatures measured in an increasing field scan.

At finite temperatures, spin fluctuations are excited in a metamagnetic compound. The metamagnetic transition is affected by the spin fluctuations. Figure 4 shows the dM/dB curve of YCo_2 at several temperatures for an increasing field scan. The metamagnetic transition is very sharp at low temperatures, but it broadens rapidly with increasing temperature. We determine the temperature, at which the first-order metamagnetic transition becomes second order (hysteresis in the magnetization curve disappears), as $T_0=100\pm10$ K. The critical field $B_c(T)$ shows a positive shift proportional to T^2 at low temperatures, as shown in Fig. 5.

In RCo_2 (R:magnetic rare-earth element) compounds, the Co site is exposed to an exchange field from the R sublattice. As the temperature decreases, ferromagnetic or ferrimagnetic ordering is realized in RCo_2 and is accompanied with a metamagnetic transition of the d-electron system (the Co sublattice). The Curie temperature T_c corresponds to the metamagnetic transition point. If T_c is lower than T_0, the magnetic transition of RCo_2 should be first order. In fact, the transitions of $ErCo_2$ ($T_c=30$ K) and $HoCo_2$ ($T_c=76$ K) are first order and those of $TbCo_2$ ($T_c=232$ K) and $GdCo_2$ ($T_c=405$ K) are second order.[18]

The positive shift of $B_c(T)$ suggests that the entropy of the d-electron system is reduced by the metamagnetic transition. The entropy reduction comes from the suppression of spin fluctuations by the transition, leading to a decrease in the coefficient γ for the electronic specific heat. Here, we evaluate the decrease of γ from the temperature dependence

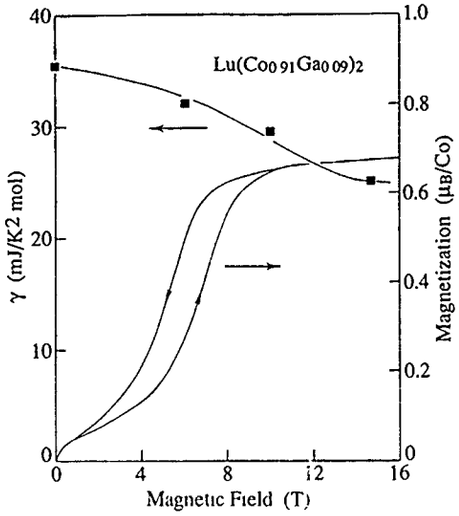

FIG. 6. Magnetization and γ value for $Lu(Co_{0.91}Ga_{0.09})_2$ as a function of field.

of the critical field. On the first-order phase boundary, the Clausius–Clapeyron relation is satisfied

$$\frac{dH_c(T)}{dT} = -\frac{\Delta S}{\Delta M}, \tag{1}$$

where ΔS and ΔM are changes in entropy and magnetization across the phase boundary. Since $H_c(T)$ $[=B_c(T)/\mu_0]$ is proportional to T^2, ΔS is proportional to T. This indicates that γ is discontinuously decreased by the metamagnetic transition. Using the experimental values of $dB_c/dT = 1.85\times10^{-3}$ T/K^2 and $\Delta M = 0.27$ μ_B/Co, we obtain the decrease of γ for YCo_2, $\Delta\gamma = -11$ mJ/K^2 mol.

In order to confirm directly the reduction of γ caused by the metamagnetic transition, we measured the specific heat of $Lu(Co_{0.91}Ga_{0.09})_2$ with low B_{c0} in steady magnetic fields.[8] Figure 6 shows the specific heat together with the magnetization as a function of magnetic field. The γ value, which is 35.5 mJ/K^2 mol in zero field, decreases during the metamagnetic transition and becomes 25 mJ/K^2 mol in the ferromagnetic state. The decrease of γ due to the transition, $\Delta\gamma = -10.5$ mJ/K^2 mol, is consistent with that estimated from $B_c(T)$ of YCo_2.

The resistivity of the metamagnetic compounds YCo_2, $LuCo_2$, and $ScCo_2$ shows a temperature dependence of $\rho(T) = \rho_0 + AT^2$ at low temperatures.[19] The coefficients A and γ for these compounds are very large compared with isostructural compounds with small susceptibility, such as $ZrCo_2$ and $HfCo_2$. Baranov *et al.*[19] have found that YCo_2, $LuCo_2$, and $ScCo_2$ satisfy the Kadowaki–Woods relation (Ref. 20), $A/\gamma^2 = 1.0\times10^{-5}$ $\mu\Omega$ cm(K mol/mJ)^2, as well as heavy fermion compounds. This relation can be explained in terms of spin fluctuation theory.[21] These results indicate that the resistivity of metamagnetic compounds is dominated by spin fluctuations. In RCo_2 the resistivity is also very large above T_c, but it is abruptly reduced at T_c.[22] The abrupt reduction mainly comes from the suppression of spin fluctuations due to the metamagnetic transition, as suggested by the decrease of γ observed in YCo_2 and $Lu(Co_{0.91}Ga_{0.09})_2$.

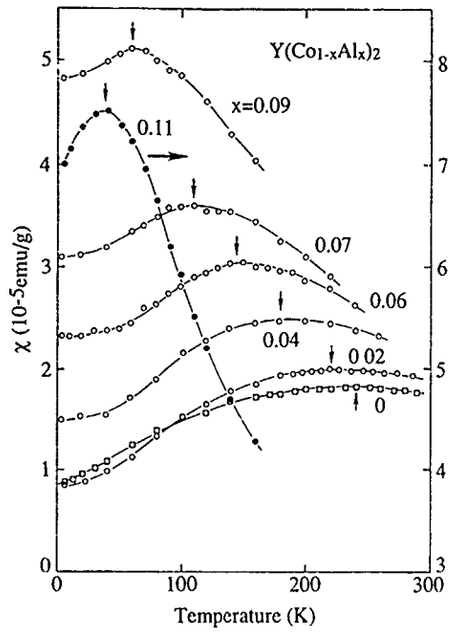

FIG. 7. Temperature dependence of susceptibility for $Y(Co_{1-x}Al_x)_2$. Small arrows indicate the position of T_{max}.

As already described in the introduction, we have found the fact that every metamagnetic compound has a maximum in $\chi(T)$. We examined the relation between the susceptibility and the magnetization process using the $Y(Co_{1-x}Al_x)_2$ system.[3] We show $\chi(T)$ for this system in Fig. 7. $\chi(T)$ of YCo_2 increases with temperature and becomes maximum around 240 K. At higher temperature it obeys a Curie–Weiss law. With increasing x, $\chi(0)$ is more enhanced. Compounds with $x \leq 0.11$ exhibit behavior typical of a strongly exchange-enhanced paramagnet like YCo_2. Above $x = 0.12$, the compound becomes weakly ferromagnetic.[23] The temperature at

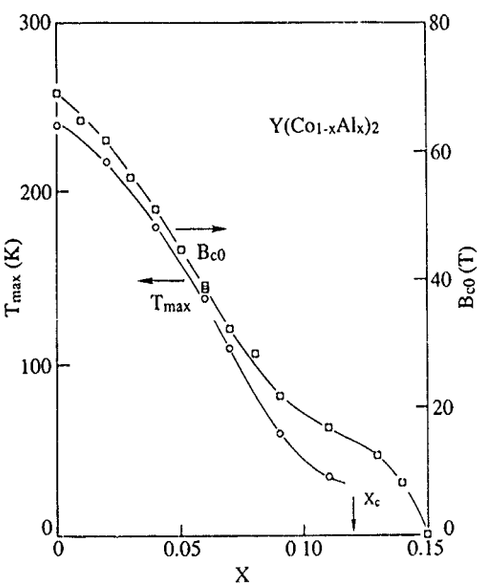

FIG. 8. Values of B_{c0} and T_{max} for $Y(Co_{1-x}Al_x)_2$ as a function of x. x_c indicates the critical concentration for the onset of ferromagnetism.

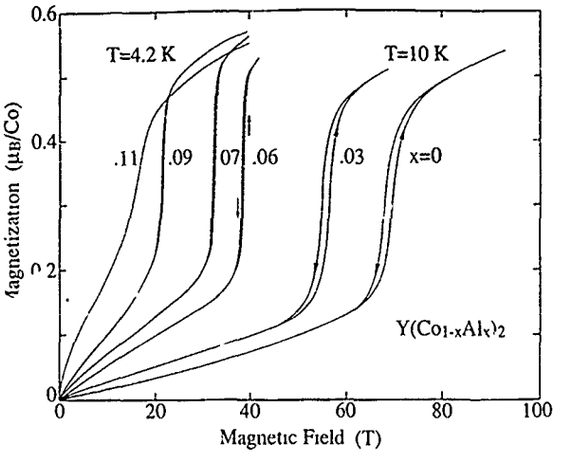

FIG. 9. Low temperature magnetization process of $Y(Co_{1-x}Al_x)_2$.

which the susceptibility becomes maximum, T_{max}, decreases rapidly in accordance with the enhancement of $\chi(0)$. The concentration dependence of T_{max} is indicated in Fig. 8. T_{max} systematically decreases as x increases.

Figure 9 shows the low temperature magnetization of the $Y(Co_{1-x}Al_x)_2$ system.[3] All the compounds with $x \leq 0.09$ exhibit sharp metamagnetic transitions. The critical field B_{c0} is plotted together with T_{max} in Fig. 8. B_{c0} decreases nearly linearly with increasing x. Above $x=0.08$, however, B_{c0} exhibits an anomalous change. In the weakly ferromagnetic phase $0.12 \leq x < 0.15$, ferromagnetism and metamagnetism coexist. This may come from heterogeneity of the system. The critical concentration, at which the critical field becomes zero, is estimated to be $x_c=0.12$ from the x dependence of B_{c0} in the concentration range $x \leq 0.08$. This x_c coincides with the onset of ferromagnetism. It should be noted that the concentration dependence of B_{c0} is very similar to that of T_{max}. We plot B_{c0} against T_{max} in Fig. 10. In the

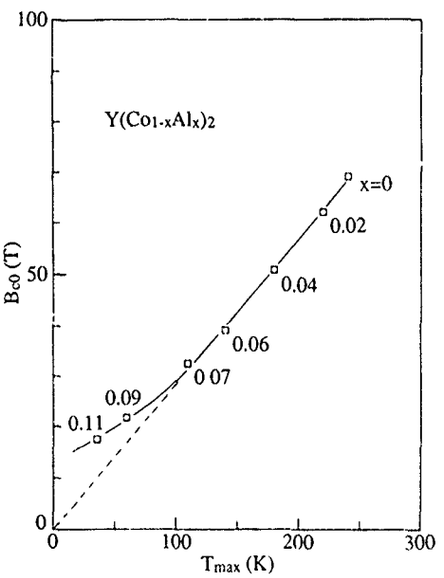

FIG. 10. Critical field B_{c0} vs T_{max} for $Y(Co_{1-x}Al_x)_2$.

$Y(Co_{1-x}Al_x)_2$ system, a simple linear relation $B_{c0}/T_{max}=0.29$ T/K is satisfied. Similar relations are found in some pseudobinary systems such as $Lu(Co_{1-x}Al_x)_2$,[7] and $Hf(Co_{1-x}Fe_x)_2$.[24] These facts suggest that the appearance of a maximum in $\chi(T)$ is strongly related to the occurrence of metamagnetism and both phenomena have the same origin: the susceptibility maximum is also associated with a special shape of the DOS curve in the vicinity of the Fermi level.

Recently, Yamada[25] developed a theory of the itinerant electron metamagnetism at finite temperatures based on the spin fluctuation model. Characteristics of the itinerant metamagnet at finite temperatures are examined by the theory. The equation of state for the itinerant system is written in the ground state as

$$H(M)=aM+bM^3+cM^5, \tag{2}$$

where a is the inverse susceptibility. The coefficients b and c are expressed in terms of the density of states and its derivatives at the Fermi level. The condition for the occurrence of a metamagnetic transition[26] is given by

$$a>0, \quad b<0, \quad c>0, \quad \text{and} \quad \frac{3}{16}<\frac{ac}{b^2}<\frac{9}{20}. \tag{3}$$

At finite temperatures, the coefficients are renormalized by thermal spin fluctuations. The coefficient a is transformed into

$$A(T)=\chi(T)^{-1}=a+\tfrac{5}{3}\,b\xi_p(T)^2+\tfrac{35}{9}\,c\xi_p(T)^4, \tag{4}$$

where $\xi_p(T)^2$ is the thermal average of the square of the fluctuating magnetic moment in the paramagnetic state. $\xi_p(T)^2$ is a monotonically increasing function and is proportional to T^2 at low temperatures. Under the condition (3), the susceptibility $\chi(T)=A(T)^{-1}$ has a maximum at a finite temperature $T=T_{max}$ due to thermal excitation of spin fluctuations. This means that both the metamagnetic transition and the maximum of $\chi(T)$ originate from the electronic structure of d electrons. The temperature dependence of the critical field is expressed as

$$B_c(T)=B_{c0}+\alpha\xi_p(T)^2, \tag{5}$$

where α is a function of b and c. This indicates that $B_c(T)$ is increased by the effect of spin fluctuations, consistent with the observed $B_c(T)$ for YCo_2. The linear relation between $B_c(T)$ and T_{max}, B_{c0}/T_{max}=const, is derived by the theory. This is also consistent with the relation between B_{c0} and T_{max} observed in the $Y(Co_{1-x}Al_x)_2$ system. Moreover, the temperature T_0, at which the first-order metamagnetic transition disappears, can be estimated using the experimental values of T_{max} and $\chi(0)/\chi(T_{max})$. The estimated T_0 is 104 K for YCo_2 with $T_{max}=240$ K and $\chi(0)/\chi(T_{max})=0.50$. This value is in good agreement with the experimental result of $T_0=100\pm10$ K. The observed characteristics of the itinerant metamagnet are successfully elucidated with this theory based on the spin fluctuation model.

Finally, we show the pressure effect on the magnetization process and the susceptibility of $Lu(Co_{1-x}Ga_x)_2$. Itinerant metamagnetism is expected to be very sensitive to high pressure since it comes from the shape of the DOS curve in the vicinity of the Fermi level. Figure 11 shows the pressure

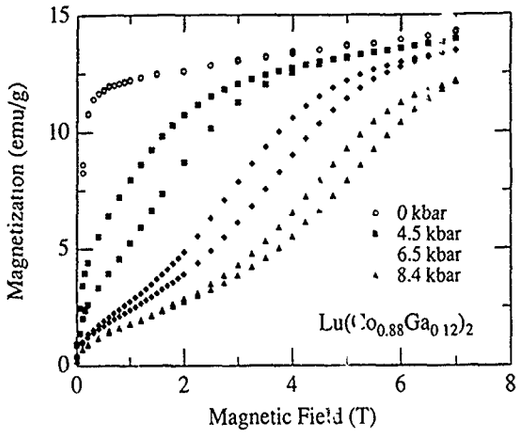

FIG. 11. Pressure effect on the magnetization process of $Lu(Co_{0.88}Ga_{0.12})_2$ at 4.2 K.

dependence of the magnetization process for $Lu(Co_{0.88}Ga_{0.12})_2$ at 4.2 K. This compound shows ferromagnetic behavior at 0 kbar. With increasing pressure, a metamagnetic transition appears and the critical field increases linearly. We obtain $dB_{c0}/dP = 1.0$ T/kbar. The DOS curve of $LuCo_2$ also has a sharp peak just below the Fermi level, which gives the metamagnetism.[16] In the $Lu(Co_{1-x}Ga_x)_2$ system, the peak becomes very broad due to hybridization between Co d and Ga p bands and the peak position approaches the Fermi level.[27] This may cause the decrease of the critical field in the Ga-substituted system. The application of high pressure increases the band width and the distance between the Fermi level and the peak position. These effects increase the critical field.

Figure 12 shows the temperature dependence of susceptibility for $Lu(Co_{0.92}Ga_{0.08})_2$ at high pressures. The application of pressure decreases the susceptibility and increases T_{max}. We obtain $dT_{max}/dP = 2.1$ K/kbar. According to Yamada's theory, T_{max}^2 is proportional to the inverse of $\chi(0)$.[25]

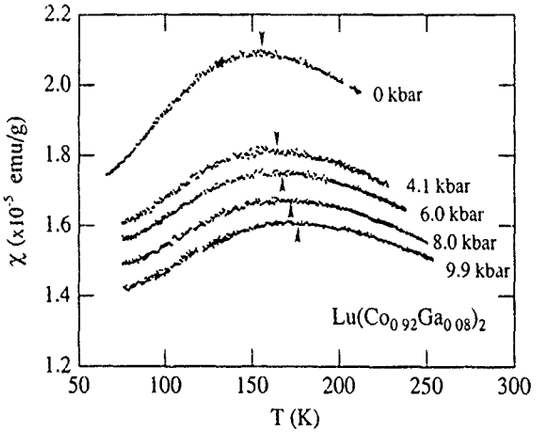

FIG. 12. Pressure effect on the susceptibility of $Lu(Co_{0.91}Ga_{0.08})_2$. Arrows indicate the position of T_{max}.

The observed increase of T_{max} indicates that the pressure effect decreases both DOS at the Fermi level and the enhancement factor. The large reduction of $\chi(T_{max})$ suggests that the spin fluctuations are much suppressed by the application of pressure. In the present study we cannot determine the relation between $B_{c0}(P)$ and $T_{max}(P)$ under high pressure with the same sample. However, the simple relation $B_{c0}(P)/T_{max}(P) = \text{const}$ may be satisfied.

In conclusion, we have successfully observed metamagnetic transitions in YCo_2 and $LuCo_2$ at $B_{c0} = 69$ and 74 T. The change of B_{c0} due to Ni and Fe doping in YCo_2 suggests that the transition originates from a special shape of the DOS curve around the Fermi level. $B_c(T)$ of YCo_2 shows a positive shift proportional to T^2 at low temperatures. In the $Y(Co_{1-x}Al_x)_2$ system, we have found the relation $B_{c0}/T_{max} = \text{const}$. These experimental results can be explained by theory based on a spin fluctuation model. We have observed the suppression of spin fluctuations due to metamagnetic transition. The metamagnetic transition and susceptibility are sensitively changed by pressure.

[1] E. P. Wohlfarth and P. Rhodes, Philos. Mag. **7**, 1817 (1962).
[2] T. Sakakibara, T. Goto, K. Yoshimura, M. Shiga, and Y. Nakamura, Phys. Lett. A **177**, 243 (1986)
[3] T. Sakakibara, T. Goto, K. Yoshimura, and K. Fukamichi, J. Phys. Condens. Matter **2**, 3381 (1990).
[4] K. Yoshimura, Y. Yoshimoto, M. Mekata, T. Sakakibara, and T. Goto, J. Magn. Magn. Mater. **70**, 147 (1987).
[5] K. Ishiyama, K. Endo, T. Sakakibara, T. Goto, K. Sugiyama, and M. Date, J. Phys. Soc. Jpn. **56**, 29 (1987).
[6] T. Sakakibara, T. Goto, K. Yoshimura, M. Shiga, Y. Nakamura, and K. Fukamichi, J. Magn. Magn. Mater. **70**, 126 (1987).
[7] M. Iijima, K. Endo, T. Sakakibara, and T. Goto, J. Phys. Condens. Matter **2**, 10069 (1990).
[8] K. Murata, K. Fukamichi, K. Komatsu, T. Sakakibara, and T. Goto, J Phys. Condens. Matter **3**, 2515 (1991).
[9] K. Murata, K. Fukamichi, T. Goto, H. Aruga Katori, T. Sakakibara, and K. Suzuki (Physica B, to be published).
[10] K. Murata, K. Fukamichi, T. Sakakibara, T. Goto, and K. Suzuki, J. Phys. Condens. Matter **5**, 1525 (1993).
[11] T. Goto, K. Fukamichi, T. Sakakibara, and H Komatsu, Solid State Commun. **72**, 945 (1989).
[12] T. Goto, T. Sakakibara, K. Murata, H. Komatsu, and K. Fukamichi, J. Magn. Magn. Mater. **90** and **91**, 700 (1990).
[13] K. Adachi, M. Matsui, Y. Ohshima, H. Mollymoto, M. Motokawa, and M. Date, J. Phys. Soc. Jpn. **47**, 675 (1979).
[14] T. Moriya, *Spin Fluctuations in Itinerant-Electron Magnetism* (Springer, Berlin, 1985).
[15] H. Yamada and M. Shimizu, Physica B **161**, 179 (1989).
[16] H. Yamada, T. Tohyama, and M. Shimizu, J. Magn. Magn. Mater. **70**, 44 (1987).
[17] T. Sakakibara, H. Mitamura, and T. Goto, Physica B (1994, in press).
[18] R. Minakata, M. Shiga, and Y. Nakamura, J. Phys. Soc. Jpn. **41**, 1435 (1976).
[19] N. Baranov, E. Bauer, E. Gratz, R. Hauser, A. Markosyan, and R. Resel, *Proceedings of the International Conference on the Physics of Transition Metals*, Darmstadt, 1992 (World Scientific, Singapore, 1993), p. 370.
[20] K. Kadowaki and S. B. Woods, Solid State Commun. **58**, 507 (1986).
[21] H. Wada, N. Shimamura, and M. Shiga, Phys. Rev. B **48**, 10221 (1993).
[22] N. H. Duc, V. Sechovsky, D. T Hung, and N. H. Kim-Ngan, Physica B **179**, 111 (1992).
[23] K. Yoshimura and Y. Nakamura, Solid State Commun. **56**, 767 (1985).
[24] T. Sakakibara, T. Goto, and Y. Nishihara, J. Phys. Coll. C **8**, 263 (1988).
[25] H. Yamada, Phys. Rev. B **47**, 11211 (1993).
[26] M. Shimizu, J. Physique **43**, 155 (1982).
[27] M. Aoki and H. Yamada, J. Magn. Magn. Mater. **78**, 377 (1989)

Local and nonlocal density functional studies of FeCr

David J. Singh
Complex Systems Theory Branch, Naval Research Laboratory, Washington, DC 20375

Local spin density approximation and generalized gradient approximation calculations are reported for ferromagnetic $B2$ FeCr. Both shear elastic constants are found to be positive, indicating metastability of the $B2$ structure. Both the moments of the Fe and Cr layers are ferromagnetically aligned, with the Fe moment being considerably depressed. This is in contrast to the behavior for thicker films. The evolution of the behavior as a function of the layer thickness is addressed using supercell calculations. It is found that Fe monolayers in bcc Cr are ferromagnetically aligned with the neighboring Cr moments, while thicker Fe layers are antiferromagnetically aligned with the adjacent Cr layers.

INTRODUCTION

Fe/Cr multilayers have become the focus of intense investigation over the past few years in part because of the discovery of oscillatory interlayer coupling and giant magnetoresistance (GMR) in this system. Although CsCl ($B2$) structure FeCr does not exist in the Fe-Cr phase diagram,[1] the system is of interest not only because of the possibility of growing it layer by layer with molecular beam epitaxy (MBE) but also because it may be viewed as alternating (001) layers of Fe and Cr, thus forming the low thickness limit in the Fe/Cr/Fe multilayer family.

This article reports local spin density approximation (LSDA) and generalized gradient approximation (GGA) calculations used to investigate the electronic, magnetic, structural, and elastic properties of this phase. The results are in general accord with an earlier LSDA linearized muffin-tin orbital (LMTO) calculation of the electronic structure, lattice parameter, and bulk modulus for this phase.[2] Enhanced bonding, reduced Fe moments, and an unexpected parallel alignment of the Fe and Cr spins is found. This alignment is opposite to that observed in multilayers. Calculations were performed for several multilayers with different Fe and Cr layer thicknesses in order to understand the parallel alignment and the regime in which it occurs.

METHOD

The present self-consistent calculations were performed using the general potential linearized augmented planewave (LAPW) method[3,4] with a local orbital extension[5] to relax the linearization of the $3d$ bands. Unlike the LMTO calculations of Ref. 2, this method imposes no shape approximations on the charge density or potential. LAPW sphere radii of 2.25 a.u. were used with well converged basis sets derived from an interstitial cutoff of 16 Ry. The Brillouin zone sampling were performed using a 16^3 special **k**-points mesh, which yielded 120 points in the irreducible 1/48 wedge of the simple cubic zone. The multilayer calculations were performed using a 12^3 mesh in the cubic zone which was folded down into the appropriate tetragonal zones. The LSDA calculations were performed using the Hedin–Lundqvist[6] functional with the von Barth–Hedin spin scaling;[7] GGA calculations used the recent Perdew–Wang functional.[8]

$B2$ FeCr: STRUCTURAL AND ELASTIC PROPERTIES

Spin polarized LSDA and GGA total energy and electronic structure calculations were performed for lattice parameters between 5.20 and 5.45 a.u. Lattice parameters and bulk moduli were obtained by fitting these to the Birch equation of state. This procedure yielded an LSDA lattice parameter of $a=5.23$ a.u. or 2.77 Å and a bulk modulus of 297 GPa. The present lattice parameter is 1.3% smaller than the 5.30 a.u. obtained by Moroni and Jarlborg using the LMTO method,[2] while the bulk modulus is 10% larger. Converged LSDA calculations for $3d$ magnets typically give lattice parameters that are 2% to 3% smaller than experiment and bulk moduli that are 25% to 40% too large, even though elastic and other properties when calculated at the experimental lattice parameter are in close agreement with experiment.[9] In contrast GGA calculations typically yield lattice parameters and bulk moduli in much better agreement with experiment for these materials. The calculated GGA lattice parameter for FeCr is $a=5.33$ a.u. which is approximately 2% larger than the LSDA value, but still 2% smaller than is obtained by applying Vegard's rule to bcc Fe and Cr; this suggests enhanced bonding in FeCr. The GGA bulk modulus is 256 GPa. Elastic constants were calculated within the LSDA but are the likely more realistic GGA lattice parameter, using the procedure of Mehl *et al.*[9] This results in fairly stiff shear elastic constants, $c_{44}=150$ GPa and $c_{11}-c_{12}=230$ GPa. These large values, which suggest strong bonding, suggest that $B2$ FeCr is a metastable phase, and therefore that this phase may be grown epitaxially to large thicknesses.

$B2$ FeCr: ELECTRONIC AND MAGNETIC PROPERTIES

The LSDA band structure and electronic density of states (DOS) are presented in Figs. 1 and 2, respectively. The Fermi energy falls in a peak in the majority spin DOS, perhaps related to the fact that the $B2$ phase is thermodynamically unstable. Both the minority and majority spin d bands are partially occupied. The similarity of the Fe and Cr projections of the DOS is remarkable. This reflects hybridization between the Fe and Cr d orbitals. This is also seen in the magnetic moments. At $a=5.33$ a.u., Fe and Cr spin moments of 1.21 μ_B and 0.61 μ_B were obtained within the LSDA. The interstitial polarization is very small as expected. Moroni and Jarlborg[2] report LSDA values at their calculated lattice parameter of 5.30 a.u. At that lattice parameter, I obtain mo-

 0021-8979/94/76(10)/6688/3/$6.00 © 1994 American Institute of Physics

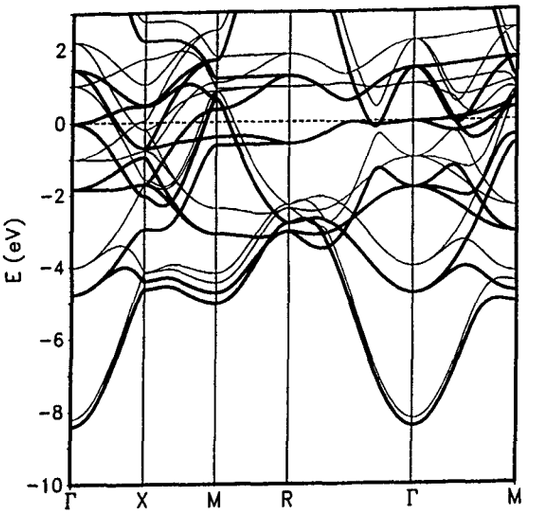

FIG. 1. LSDA band structure of $B2$ FeCr. Majority (minority) spin bands are denoted by heavy (light) lines. The dashed horizontal line denotes the Fermi energy.

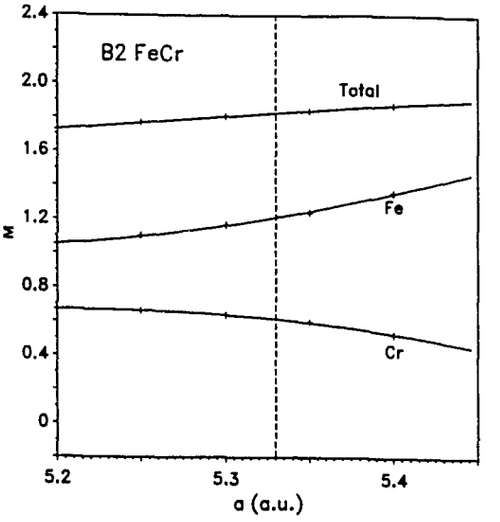

FIG. 3. Total and projected spin magnetization in μ_B per formula unit vs lattice parameter for $B2$ FeCr.

ments of 1.164 μ_B and 0.635 μ_B for Fe and Cr, respectively. These values are 0.06 μ_B larger for Fe and 0.05 μ_B smaller for Cr than for those of Ref. 2. The Cr moment is only slightly enhanced relative to bcc Cr, while the Fe moment is strongly reduced. Further, the Fe and Cr moments are aligned in FeCr (coincidentally the total spin moment of 1.82 μ_B is what would be expected if the Fe and Cr moments were antiparallel and were close to their bulk elemental values). This is in sharp contrast to what is known about the interface between thicker Fe and Cr layers where the Fe and Cr moments are antiparallel.[10,11] As shown in Fig. 3, the moments vary slowly over the entire volume range studied and in particular the parallel alignment of the Fe and Cr moments persists. This result, which is qualitatively in accord with the earlier calculations of Moroni and Jarlborg[2] and also holds in GGA calculations, can be rationalized in terms of the electronic structure. In the $B2$ structure each Fe atom is surrounded by eight Cr atoms and vice versa—a favorable environment for d bonding. As mentioned, the electronic structure shows strong Fe-Cr hybridization as reflected in the similar projected DOS for the two species. This similarity arises in three ways, a charge transfer from the Fe to the Cr atoms, parallel alignment of the spin moments, and a strong reduction in the Fe moment. Evidently, the bonding energy is sufficient to bring these things about in $B2$ FeCr.

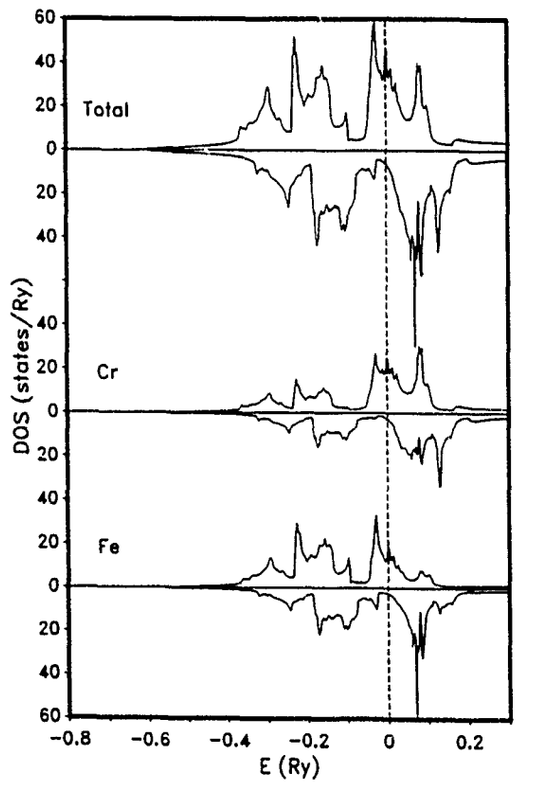

FIG. 2. Total and projected DOS of $B2$ FeCr. Majority (minority) spin contributions are shown above (below) the axis. The dashed vertical line denotes the Fermi energy.

FeCr MULTILAYERS

Regarding FeCr as a stack of single (001) Fe and Cr layers, one may consider the effects of changing the layer thicknesses. For thicker Fe layers, each interface Fe atom would be coordinated by four Cr atoms and four Fe atoms in the next layer, which depending on the layer thickness would be interior or interface Fe atoms. Similarly, one may consider changing the Cr layer thickness. In order to study these situations, LSDA supercell calculations at the bulk Fe lattice parameter were performed for several such stacks, as shown in Table I. These are denoted as Fe_nCr_m, where n is the thickness of the Fe layers and m is the thickness of the Cr layers. GGA calculations, which, were performed for the stacks containing four and fewer layers yielded similar results but with larger Cr moments consistent with previous GGA calculations for bulk Cr.[12]

The results show that thickening the Cr layer does not change the parallel interface alignment provided that the Fe

TABLE I. Projected spin moments in μ_B/atom of Fe_nCr_m (001) stacks. The projections are onto the LAPW spheres. The alignment of the spin moments is given by the sign. In cases where there are more than one inequivalent Fe or Cr atom, the moments are given in order of the distance from the interface; Fe_1 and Cr_1 are the interfacial atoms.

n	m	$M(Fe_1)$	$M(Fe_2)$	$M(Fe_3)$	$M(Cr_1)$	$M(Cr_2)$
1	1	1.36	···	···	0.52	···
1	3	1.33	···	···	0.30	−0.27
2	1	2.09	···	···	−0.41	···
3	1	1.92	2.49	···	−0.35	···
5	1	1.99	2.44	2.36	−0.42	···

remains a single atomic layer thick. In fact, the Fe spin moment changes little when additional Cr layers are added. The Cr layers are, however, antiferromagnetically aligned with neighboring Cr atoms as expected, and a reduction in the interfacial Cr moment is found when the Cr layer is thickened. On the other hand, adding even a single Fe layer leads to a reversal of the interfacial alignment and an increase in the Fe moment to near the bulk Fe value, which persists as additional Fe layers are added. Thus parallel alignment of the interfacial moments in Fe-Cr multilayers is dependent on having single atomic layer thick Fe layers so that each Fe atom is coordinated by eight Cr atoms. This prediction may perhaps be verified experimentally by growing, with MBE, a single atomic layer of Fe between two Cr layers and measuring the alignment of the Fe moment with its Cr neighbors.

CONCLUSIONS

Total energy and electronic structure calculations have been reported for $B2$ FeCr and for Fe-Cr multilayers. It is found that FeCr is elastically stable and is likely a metastable phase. A parallel alignment of the Fe and Cr moments is found; this may be understood in terms of strong hybridization apparent in the electronic structure. Calculations for Fe-Cr multilayers show that the interfacial Fe and Cr moments remain antiparallel, except in the case when the Fe is a single atomic layer thick, in which case a novel parallel alignment is found.

ACKNOWLEDGMENTS

Computations were performed at the Cornell National Supercomputer Facility. Work at the Naval Research Laboratory is supported by the Office of Naval Research.

[1] T. S. Massalski, *Binary Alloy Phase Diagrams*, 2nd ed. (American Society of Metals, Metals Park, OH, 1990).
[2] E. G. Moroni and T. Jarlborg, Phys. Rev. B **47**, 3255 (1993).
[3] O. K. Andersen, Phys. Rev. B **12**, 3060 (1975).
[4] S. H. Wei and H. Krakauer, Phys. Rev. Lett. **55**, 1200 (1985); D. J. Singh, *Planewaves, Pseudopotentials, and the LAPW Method* (Kluwer Academic, Boston, 1994), and references therein.
[5] D. Singh, Phys. Rev. B **43**, 6388 (1991).
[6] L. Hedin and B. I. Lundqvist, J. Phys. C **4**, 2064 (1971).
[7] U. von Barth and L. Hedin, J. Phys. C **5**, 1629 (1972).
[8] J. P. Perdew, J. A. Chevary, S. H. Vosko, K. A. Jackson, M. R. Pederson, D. J. Singh, and C. Fiolhais, Phys. Rev. B **46**, 6671 (1992).
[9] M. J. Mehl, D. J. Singh, and D. A. Papaconstantopoulos, Mater. Sci. Eng. A **170**, 49 (1993); Equation (9) should read: $e_6=x$; $e_3=x^2/(4-x^2)$.
[10] J. Unguris, R. J. Celotta, and D. T. Pierce, Phys. Rev. Lett. **67**, 140 (1991).
[11] B. V. Reddy, S. N. Khanna, P. Jena, M. R. Press, and J. J. Jaswal, J. Magn. Magn. Mater. **130**, 255 (1994), and references therein.
[12] D. J. Singh and J. Ashkenazi, Phys. Rev. B **46**, 11 570 (1992).

Temperature-dependent electronic structure and ferromagnetism of bcc iron

W. Nolting
Humboldt-Universität, Lehrstuhl Festkörpertheorie, Invalidenstrasse 110, 10115 Berlin, Germany

A. Vega
Departamento de Física Teórica, Universidad de Valladolid, 47011 Valladolid, Spain

The influence of electron correlations on the temperature dependence of the electronic structure of ferromagnetic bcc iron is investigated by the use of a many-body evaluation of a generalized model of magnetism. The one-particle part of the model Hamiltonian is taken from an LDA band-structure calculation. The model contains only two parameters, an intraband Coulomb interaction U, and an interband exchange J. With $U=1.8$ eV and $J=0.2$ eV the self-consistent model solution yields a $T=0$ moment of about 2.04 μ_B and an exact Curie temperature of 1044 K. Details of the magnetic behavior of Fe can be traced back to a striking temperature variation of the quasiparticle density of states. Typical differences in the magnetic behavior of Fe and Ni are worked out.

I. INTRODUCTION

Decisive features of band ferromagnets like Fe, Co, and Ni can be traced back to electron-correlation effects in the relatively narrow $3d$ subbands, which only weakly hybridize with the $4s$ and $4p$ bands. The Fe valence band contains eight electrons, about seven of them have predominantly d character. Current state-of-the-art band structure calculations within the "local spin density approach" (LSDA) are able to account for ground state properties of Fe quite reasonably. However, up to now a convincing theory does not exist for the temperature-dependent electronic structure, from which magnetic key quantities, such as the Curie temperature, the magnetization curve, and the exchange splittings can be derived.

II. THEORETICAL MODEL

Although prototypical magnetic materials like Fe, Co, Ni, Gd, EuO, NiO,..., belong to rather different classes of magnetism, they should be describable by one and the same theoretical model and by use of very similar approaches to the sophisticated many-body problem. Our model Hamiltonian

$$H=H_0+H_1 \tag{1}$$

has already been applied in preliminary works to some of the above-mentioned materials.[1–3] The single-particle part reads

$$H_0=\sum_{ij\sigma} T_{ij}(m)c^+_{im\sigma}c_{jm\sigma}=\sum_{\mathbf{k}m\sigma}\varepsilon_m(\mathbf{k})c^+_{\mathbf{k}m\sigma}c_{\mathbf{k}m\sigma}. \tag{2}$$

The indices i,j mark the lattice sites and σ marks the spin projection. In the case of Fe the band index m runs over the $3d$ subbands. It is commonly accepted that the important aspects of band ferromagnetism are sufficiently well accounted for by intraatomic direct ($U_{mm'}$) and exchange ($J_{mm'}$) terms only. These terms can be rearranged in the following illustrative way:[2]

$$H_1=H_U+H_J+H_{\tilde{U}}. \tag{3}$$

H_U is an intraband Coulomb interaction of Hubbard-type ($U_{mm}+J_{mm}\rightarrow U\ \forall m$)

$$H_U=\frac{1}{2}U\sum_{i m\sigma} n_{im\sigma}n_{im-\sigma}. \tag{4}$$

The second term is an interband exchange interaction ($J_{mm'}\equiv J\ \forall m\neq m'$), which has exactly the same structure as the interaction part of the $sf(sd)$ model

$$H_J=-J\sum_{i,m}\boldsymbol{\sigma}_{im}\cdot\mathbf{S}_{im}. \tag{5}$$

$\boldsymbol{\sigma}_{im}$ is the electron spin operator [$\sigma^+_{im}=c^+_{im\uparrow}c_{im\downarrow}$, $\sigma^-_{im}=c^+_{im\downarrow}c_{im\uparrow}$, $\sigma^z_{im}=0{,}5(n_{im\uparrow}-n_{im\downarrow})$]. $\mathbf{S}_{im}$ is a fictitious spin, "seen" by an electron from subband m and built up by electron spins from all the other subbands

$$\mathbf{S}_{im}=\sum_{m'}^{\neq m}\boldsymbol{\sigma}_{im'}. \tag{6}$$

The third term in Eq. (3) is a spin-independent direct Coulomb interaction between electrons from different subbands ($\tilde{U}=0{,}5(U_{mm'}-0{,}5J_{mm'})\ \forall m\neq m'$)

$$H_{\tilde{U}}=\frac{1}{2}\tilde{U}\sum_{i,m,m'}^{m\neq m'} n_{im}n_{im'};\quad n_{im}=\sum_{\sigma} n_{im\sigma}. \tag{7}$$

Since there is no direct spin dependence in $H_{\tilde{U}}$, this partial Hamiltonian will not execute a direct influence on typical magnetic phenomena. We therefore neglect it in the treatment of Fe.

We believe that H_1 contains all the interactions which are vital for the magnetic correlations and the temperature dependence of the electronic structure. For a realistic comparison to experimental data, however, we have to reintroduce the influence of all the *other* interactions by a proper renormalization of the single-particle energies. This is done by an LSDA-band-structure calculation.

$$\varepsilon_m(\mathbf{k})\rightarrow\varepsilon_m^{\mathrm{LSDA}}(\mathbf{k}). \tag{8}$$

 0021-8979/94/76(10)/6691/3/$6.00 © 1994 American Institute of Physics

We perform this LSDA calculation along the line given in Ref. 4, for *paramagnetic* Fe in order to avoid a double counting of the magnetic interactions which are already covered by the model-Hamiltonian part H_1. A more detailed justification is given in Ref. 7. Starting from an s,p,d basis we pick out the five eigenstates with highest d character and number them according to increasing single-particle energy by $m=1,2,...,5$ $[\varepsilon_1(\mathbf{k})\leq\cdots\leq\varepsilon_5(\mathbf{k})]$. The energies $\varepsilon_m(\mathbf{k})$ for all $\mathbf{k}$ from the first Brillouin zone form the mth subband. In this way the $3d$ band is decomposed into five nondegenerate subbands.

The many-body problem posed by our model Hamiltonian is not exactly solvable. However, the decomposition (3) of the interaction part can conveniently be exploited, since the partial operators H_U and H_J are well known from simpler models of magnetism. The starting point is the retarded one-electron Green function

$$\langle\langle c_{\mathbf{k}m\sigma};c^{+}_{\mathbf{k}m\sigma}\rangle\rangle_E=\frac{\hbar}{E-\varepsilon_m^{\mathrm{LDA}}(\mathbf{k})-\Sigma_{\mathbf{k}m\sigma}(E)} \tag{9}$$

the formal solution of which can be written in terms of the fundamental self-energy $\Sigma_{\mathbf{k}m\sigma}(E)$.

Via the definition

$$\langle\langle[c_{\mathbf{k}m\sigma},H_{U,J}];c^{+}_{\mathbf{k}m\sigma}\rangle\rangle(E)\equiv M^{(U,J)}_{\mathbf{k}m\sigma}(E)\langle\langle c_{\mathbf{k}m\sigma};c^{+}_{\mathbf{k}m\sigma}\rangle\rangle_E \tag{10}$$

the self-energy parts $M^{(U,J)}_{\mathbf{k}m\sigma}(E)$ of the full self-energy

$$\Sigma_{\mathbf{k}m\sigma}(E)=M^{(U)}_{\mathbf{k}m\sigma}(E)+M^{(J)}_{\mathbf{k}m\sigma}(E) \tag{11}$$

may be introduced. In the next step we define "effective" single-particle energies

$$\eta^{(x)}_{m\sigma}(\mathbf{k},E)=\varepsilon_m^{\mathrm{LDA}}(\mathbf{k})+M^{(y)}_{\mathbf{k}m\sigma}(E)\quad(x,y=U,J;\ x\neq y) \tag{12}$$

for an "effective medium" Hamiltonian

$$H^{(x)}_{\mathrm{eff}}=\sum_{\mathbf{k}m\sigma}\eta^{(x)}_{m\sigma}(\mathbf{k};E)c^{+}_{\mathbf{k}m\sigma}c_{\mathbf{k}m\sigma}+H_{\lambda}\,. \tag{13}$$

In general $H^{(x)}_{\mathrm{eff}}$ will be energy dependent and non-Hermitian, but the resulting Green function is the same as in Eq. (9). The advantage lies in the fact that the "effective-medium" Hamiltonian poses a formally simpler many-body problem than the "original" model Hamiltonian (1). For each $x(x=U,J)$ we try to find a reasonable approach to the corresponding "effective" Green function. This means that for $x=U$ we solve the "Hubbard problem," for which we use the self-consistent moment method from Ref. 5. For $x=J$ one meets the "sf problem," which we approximate by use of the moment-conserving decoupling procedure, developed in Ref. 4. The resulting self-energy parts

$$M^{(U,J)}_{\mathbf{k}m\sigma}(E)=F[E;\eta^{(U,J)}_{\mathbf{k}m\sigma}(E);\langle\cdots\rangle] \tag{14}$$

depend via η on the respective other self-energy part. Furthermore they will contain several thermodynamic expectation values, indicated in Eq. (13) by $\langle\cdots\rangle$. It is the main requirement of our procedure that all these averages can be represented in terms of the full self-energy, so that a closed set of equations is guaranteed, which can be solved self-consistently for the quantities of interest.

III. RESULTS

The two model parameters U and J have been fitted to get a self-consistent ferromagnetic solution with a phase transition of second order at T_C, and a $T=0$ magnetic moment as realistic as possible ($U=1.8$ eV; $J=0.2$ eV). In the same spirit we determined in Ref. 1 U and J for Ni.

It turns out that the possibility of a ferromagnetic ground state is mainly due to the intraband Coulomb interaction U, while the exchange J influences the actual values of the magnetic quantities. To realize ferromagnetism the coupling parameter U/W_m (W_m: width of the mth $3d$ subband), the electron density n_m ($0\leq n_m\leq 2$), as well as the hole density, $2-n_m$, have to exceed certain critical values, which depend on the given lattice structure. Furthermore, an upper limit for U/W_m appears, above which the magnetic phase transition is of first order.[5]

The $m=1,2$ subbands are completely filled and therefore magnetically inactive. The $m=3$ and 5 subbands $[n_3(T=0)=1.346,\ n_5(T=0)=0.704]$ have convenient occupations for a ferromagnetic ground state (Fig. 1). The $m=4$ subband, however, is for all temperatures exactly half filled ($n_4=1$, Fig. 1) and has therefore a strong tendency to antiferromagnetism, which competes with the ferromagnetic tendency of the $m=3$ and 5 subbands. According to our model solution for bcc iron the ferromagnetism of the $m=3$ and 5 subbands dominates and forces the in principle antiferromagnetic $m=4$ band by interband exchange (J) into a ferromagnetic order. So, the situation is very much more complicated than in Ni, where only the uppermost $m=5$ subband is magnetically active,[1] because the $m=1,2,3$ bands are fully occupied and the $m=4$ band contains only very few holes.

All magnetic properties of the band ferromagnet Fe can be understood as direct consequences of the temperature-dependent quasiparticle density of states (QDOS)

$$\rho_{m\sigma}(E)=-\frac{1}{\pi}\sum_{\mathbf{k}}\mathrm{Im}\langle\langle c_{\mathbf{k}m\sigma};c^{+}_{\mathbf{k}m\sigma}\rangle\rangle_E\,, \tag{15}$$

which is plotted in Fig. 1 for four different temperatures, and separately for the five $3d$ subbands. The total QDOS is of course nothing else than the sum of the five partial densities. The T dependence of the two lowest subbands ($m=1,2$) is exclusively due to interband exchange with the magnetically active $m=3,4,5$ subbands. In the latter two different correlation effects are produced by the intraband interaction U. There is a splitting into two quasiparticle subbands, which persists for all temperatures, and an additional spin splitting of each of these bands, which disappears for $T\rightarrow T_c$. The latter is still enhanced by the interband exchange. The weight ("area") of the lower σ-quasiparticle band scales with the probability for the propagating electron to find a lattice site, which is not preoccupied by a $(-\sigma)$ electron of the same subband. This probability is zero for fully occupied bands. Therefore the $m=1,2$ subbands do not split. The weight of the upper quasiparticle subband is proportional to the probability that the σ electron does meet a $(-\sigma)$ electron of the same subband. A special case is the $m=4$ subband, which is half filled and at $T=0$ fully spin polarized. So a $\uparrow$ electron has no chance to meet a $\downarrow$ electron, and a $\downarrow$ electron, brought

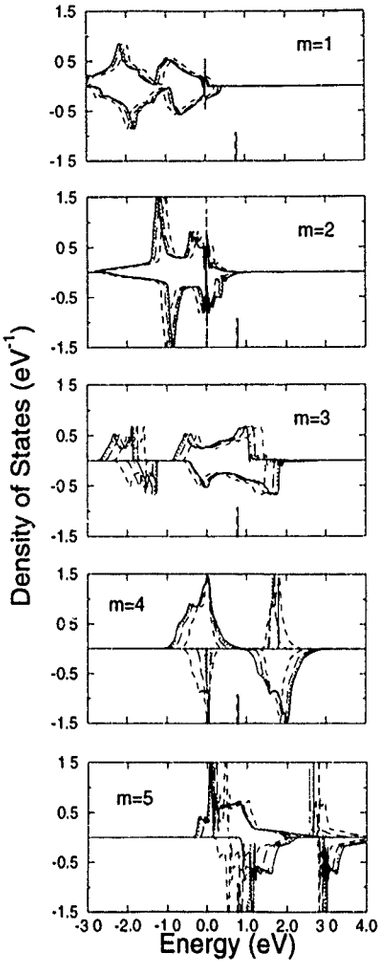

FIG. 1. Quasiparticle density of states $\rho_{m\sigma}$ of the five $3d$ subbands as a function of energy for four different temperatures [$T=0$ K: solid line; $T=900$ K: dotted line; $T=1025$ K: broken line (large bars); $T=1044$ K$=T_c$: broken line (small bars)]. Upper halves for $\sigma=\uparrow$, lower halves for $\sigma=\downarrow$. Bars on the energy axis mark the chemical potential μ.

into the system, cannot avoid a double occupancy. Consequently, the upper $\uparrow$- and the lower $\downarrow$-quasiparticle subbands disappear at $T=0$. For finite temperature collective spin excitations become dominant for this subband, introducing a spin disorder. An electron, picked out of the sample by a photoemission experiment, is then with finite probability a $\downarrow$ electron. This causes the appearance of a lower $\downarrow$-quasiparticle band. For analogous reasons there grows out an upper $\uparrow$ band for $T>0$. Above T_c the spin asymmetry disappears, but the splitting into a lower and an upper subband persists. This explains the "noncollapsing exchange splitting" in the Fe band structure, observed in spin-resolved photoemission.[6] It is interesting to compare these features to the Ni spectrum.[1] In Ni only the uppermost $m=5$ subband is partially filled, and therefore magnetically active. The first

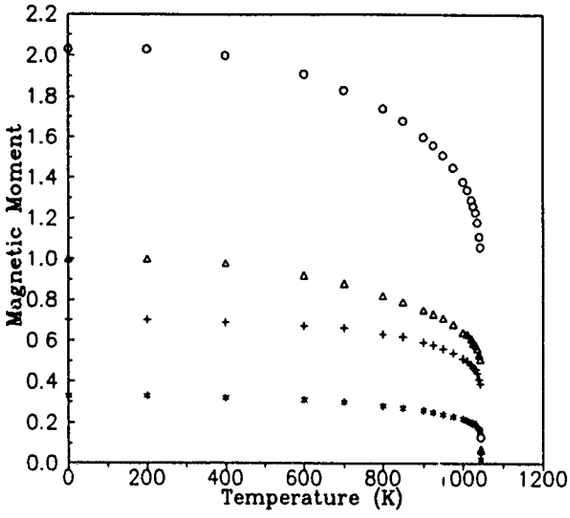

FIG. 2. Magnetic moment of ferromagnetic iron as a function of temperature (circles). Partial contributions from the subbands are also indicated ($m=3$: stars; $m=4$: triangles; $m=5$: crosses).

four subbands behave like the $m=1$ and 2 bands of Fe. They do not split, because the spectral weight of the lower quasiparticle subband is zero. Only the $m=5$ band shows the quasiparticle splitting which persists for all temperatures and is of order U. Because $U=6$ eV in Ni, the lower quasiparticle subband of the $m=5$ band lies some 6 eV below the chemical potential μ and is nothing else than the famous "Ni 6 eV satellite." In principle, the $m=3$, 4, and 5 subbands in Fe exhibit the same behavior as the Ni $m=5$ band. Because of the smaller U, however, all the quasiparticle subbands are melting together avoiding therewith a feature which could be denoted as "satellite." On the other hand, the "quasiparticle splitting" gives rise to a "noncollapsing" exchange splitting above T_c.

The T dependence of the magnetic moment, plotted in Fig. 2, follows directly from the respective T dependence of the QDOS. The model solution reproduces exactly the experimental value for the Curie temperature $T_c=1044$ K. The $T=0$ moment amounts to 2.035 μ_B, being therewith only slightly smaller than the experimental value (≈ 2.2 μ_B). The actual value of the moment depends sensitively on the total number of d electrons, which is not uniquely established. We took $n_{3d}=7.05$ from Ref. 4. Another choice can slightly alter the calculated $T=0$ moment.

[1] W. Nolting, W. Borgiel, V. Dose, and Th. Fauster, Phys. Rev. B **40**, 5015 (1988).
[2] W. Nolting, T. Dambeck, and G. Borstel Z. Phys. B **94**, 409 (1994).
[3] W. Nolting, L. Haunert, and G. Borstel, Phys Rev. B **46**, 4426 (1992).
[4] D. A. Papaconstantopoulos, *Handbook of the Band Structure of Elemental Solids* (Plenum, New York, 1986).
[5] W. Nolting and W. Borgiel, Phys. Rev. B **39**, 6962 (1989)
[6] E. Kisker, K. Schröder, W. Gudat, and M Campagna, Phys. Rev. B **31**, 329 (1985).

Theory for itinerant electrons in noncollinear and incommensurate structured magnets (invited)

J. Kübler, L. M. Sandratskii, and M. Uhl
Institut für Festkörperphysik, Technische Hochschule, D-64289 Darmstadt, Germany

Itinerant-electron systems are described that can form a variety of magnetic-moment arrangements. These are dealt with quantitatively by using energy-band theory and the local density-functional approximation; the theoretical and computational basis is briefly reviewed and results are presented for quite general collinear and noncollinear moment arrangements and states having incommensurate helical order characterized by a wave vector **q**. Some examples presented here are Fe_3Pt-Invar, fcc-iron precipitates, and tetragonal iron. Furthermore, finite-temperature effects become tractable; the magnetovolume effect in Fe_3Pt-Invar serves as an example. Finally, the problem of biquadratic exchange in Fe-Cr multilayers will be discussed briefly.

I. INTRODUCTION

This overview is intended to demonstrate how we use the local density-functional approximation[1,2] to do *ab initio* calculations for magnetic properties of materials possessing a variety of magnetic-moment arrangements like ferromagnets, collinear and noncollinear antiferromagnets, and incommensurate spiral or helical magnets. Our treatment of the electronic and magnetic properties of these itinerant-electron systems has grown out of a long development connected with the work of Korenman and Prange, Heine, Moriya, and many others.[3-10] This is not the place to discuss the similarities and differences in our work compared with the many previous theories. Let it be said that Korenman[11] treated the vector nature of the magnetic moments formed by the itinerant electrons like we do. But unlike Korenman's, our calculations are self-consistent concerning the charge and spin densities and—if desired—the interatomic magnetic moment arrangements.

Our theory was applied previously to a number of cases some of which are the noncollinear magnetic states of Mn_3Sn (Ref. 12), the problem of fcc-Fe (γ-Fe) (Ref. 13), the case of Fe_3Pt-Invar (Ref. 14), and the problem of $ThMn_2$ (Ref. 15) which is an antiferromagnet on a frustrated lattice.

After a brief description of the theoretical background in Sec. II we will highlight the problem of Fe_3Pt-Invar in Sec. III where we point out that transverse spin fluctuations contribute in an essential way to the formation of the Invar anomaly; this leads to an understanding of the Invar effect that, though it relies on the existence of high-spin and low-spin states, does not require them to be near degenerate. Thus our results yield a magnetovolume anomaly without the somewhat artificial near degeneracy that was thought to be so essential in previous theories (for a review concerning the latter see, e.g., Refs. 16, 17). In connection with the problem of γ-Fe we will then discuss some new estimates concerning tetragonal Fe that is produced today by epitaxial growth. We will close our overview with a discussion of some new but preliminary results concerning the observed[18-20] magnetization steps and biquadratic coupling in Fe-Cr multilayers.

II. THEORETICAL BACKGROUND

The Euler–Lagrange equations that minimize the total energy as a functional of the density matrix define an effective single-particle Hamiltonian[1,2] which for spin-polarized electrons forming a noncollinear magnetic order may be written in bispinor form as[21]

$$\hat{\mathbf{H}}(\mathbf{r}) = -\nabla^2 \mathbf{1} + \sum_{j\nu} \mathbf{U}^{+}(\theta_{j\nu},\phi_{j\nu})\mathbf{V}_{\nu}(\mathbf{r}_{j\nu})\mathbf{U}(\theta_{j\nu},\phi_{j\nu}). \quad (1)$$

Here $\mathbf{U}(\theta_{j\nu},\phi_{j\nu})$ is the standard spin-$\frac{1}{2}$-rotation matrix

$$\mathbf{U}(\theta_{j\nu},\phi_{j\nu}) = \begin{pmatrix} \cos(\theta_{j\nu}/2)\exp(i\phi_{j\nu}/2) & \sin(\theta_{j\nu}/2)\exp(-i\phi_{j\nu}/2) \\ -\sin(\theta_{j\nu}/2)\exp(i\phi_{j\nu}/2) & \cos(\theta_{j\nu}/2)\exp(-i\phi_{j\nu}/2) \end{pmatrix}, \quad (2)$$

which describes the transformation between a global and a local spin coordinate system to be defined subsequently. We use the label j to designate the unit cell and the label ν the basis atom. The polar angles $\theta_{j\nu},\phi_{j\nu}$ give the direction of the local magnetization, in Cartesian coordinates

$$\mathbf{m}_{j\nu} = m_{\nu}\cdot(\cos\phi_{j\nu}\sin\theta_{j\nu},\ \sin\phi_{j\nu}\sin\theta_{j\nu},\ \cos\theta_{j\nu}), \quad (3)$$

with respect to a global coordinate system and

$$\mathbf{V}_{\nu}(\mathbf{r}_{j\nu}) = \begin{pmatrix} v_{\nu\uparrow}(\mathbf{r}_{j\nu}) & 0 \\ 0 & v_{\nu\downarrow}(\mathbf{r}_{j\nu}) \end{pmatrix} \quad (4)$$

is the spin-polarized potential of the atom at site $(j\nu)$ in the local frame of reference. The potential is unambiguously given by functional derivatives of the total energy in the local density approximation;[12,22] it is centered at $\mathbf{r}_{j\nu} = \mathbf{r} - \boldsymbol{\tau}_{\nu} - \mathbf{R}_j$ and is assumed to vanish outside its atomic sphere, $\Omega_{j\nu}$. The local frame of reference is defined as follows; designating by $\boldsymbol{\rho}_{j\nu}$ the density matrix integrated over

 0021-8979/94/76(10)/6694/6/$6.00 © 1994 American Institute of Physics

the atomic sphere $\Omega_{j\nu}$, i.e., $\rho_{j\nu} = \int_{\Omega_{j\nu}} \Sigma_{i\in occ}\, \psi_i(\mathbf{r})\psi_i^+(\mathbf{r})d^3r$, where the $\psi_i(\mathbf{r})$ are solutions of the Schrödinger equation with the Hamiltonian given by Eq. (1), we define the local frame of reference by those polar angles for which $\mathbf{U}(\theta_{j\nu},\phi_{j\nu})\rho_{j\nu}\mathbf{U}^+(\theta_{j\nu},\phi_{j\nu})$ is diagonal. Strictly speaking, one should make this transformation at every point in space and Korenman *et al.*[3] show what this entails. But we believe the essential physics is obtained by making an atomic-sphere approximation, thus averaging over the local directions in each sphere this way replacing a fine-grained mesh by a coarse-grained mesh given by the atomic spheres. When the polar angles are chosen to render the integrated density matrix diagonal we call the angles self-consistent.

The polar angles $\theta_{j\nu}$ and $\phi_{j\nu}$ can now be chosen to model any desired collinear or noncollinear moment arrangement. However, to guarantee translational invariance most general types of order require larger magnetic unit cells (supercells) than the crystallographic (chemical) unit cell. This can quickly lead to an insurmountable numerical problem. Fortunately there exists a type of magnetic order that does not require such large supercells. It is a helical or spiral order that was, to our knowledge, first described by Herring.[23] Here the direction of the magnetic moment of each atom in the unit cell rotates around the z axis with a particular wave vector $\mathbf{q}$ which is defined by specifying the polar angles as $\theta_{j\nu}=\theta_\nu$, $\phi_{j\nu}=\phi_\nu+\mathbf{q}\cdot\mathbf{R}_j$. Herring introduced a generalized translation operator which combines a spin rotation with a space translation; it is constructed such that it commutes with the Hamiltonian forming an Abelian group, isomorphic with the group of ordinary space translations. Therefore a generalized Bloch theorem for the eigenfunctions exists which may be labeled by a $\mathbf{k}$ vector as usual. This means that for any choice of the vector $\mathbf{q}$ it is the chemical Brillouin zone that constitutes the domain for the $\mathbf{k}$ vectors to be used for sampling the elements of the density matrix. Details can be found in Refs. 23, 24, 13, and 14.

Using the generalized Bloch theorem we expand the wave functions $\psi_k(\mathbf{r})$ in terms of the atomic bispinor functions $\phi_{k\nu L\sigma}(\mathbf{r})$ in the following form:

$$\psi_k(\mathbf{r})=\sum_{\nu L\sigma} C_{\nu L\sigma}(\mathbf{k})\mathbf{U}_\nu^+\phi_{\mathbf{k}\nu L\sigma}(\mathbf{r}). \tag{5}$$

Here the coefficients $C_{\nu L\sigma}(\mathbf{k})$ are obtained by minimizing the expectation value of the Hamiltonian using the variational method and for the basis functions, $\phi_{\mathbf{k}\nu L\sigma}(\mathbf{r})$, we employ augmented spherical waves (ASW)[25] defined in the local frame of reference; details may again be found in Refs. 13 and 14.

At this stage we can calculate the total energy as a function of the volume and a given type of magnetic order, most notably of the wave vector $\mathbf{q}$, whereas the value of the local magnetic moment normally is the result of a self-consistent calculation. However it is advantageous to know the total energy, as a function of the volume, the $\mathbf{q}$ vector, and the magnetic moment (comparable to a thermodynamic potential). For a ferromagnet this was achieved in the past by the so-called fixed-spin-moment method, see, for instance, Refs. 26–28, where the total energy, $E(m)$, of the state having a magnetic moment m per unit cell is obtained from a constrained variation.

For a general noncollinear spin structure the constrained variation must be formulated as

$$E(\{\mathbf{m}_\mu\})=\min\left\{E[\mathbf{m}(\mathbf{r})] + \sum_\nu \mathbf{b}_\nu\left(\int_{\Omega_\nu}\mathbf{m}(\mathbf{r})d^3r-\mathbf{m}_\nu\right)\right\}, \tag{6}$$

where on the left-hand side $\{\mathbf{m}_\mu\}$ is the set of desired moments at the sites (μ). On the right-hand side the vector parameters $\mathbf{b}_\nu$ can be treated as magnetic fields acting on the spin densities of the corresponding atoms. The component of $\mathbf{b}_\nu$ parallel to $\mathbf{m}_\nu$ stabilizes the magnitude of the moment and the perpendicular component counteracts the torque that is produced by the nondiagonal density matrix. In self-consistent spin arrangements the density matrix by definition is diagonal in the local frame of reference; thus in Eq. (6) the vectors $\mathbf{m}(\mathbf{r}),\mathbf{m}_\nu,\mathbf{b}_\nu$ are parallel and we may drop the vector symbols. These conditions apply to our calculations when we use planar spin spirals which are defined by $\theta_\nu=90°$ for all sites (ν).

The variation of Eq. (6) yields the Hamiltonian

$$\hat{\mathbf{H}}(\mathbf{r})=-\nabla^2 1+\sum_{j\nu}\mathbf{U}^+(\theta_{j\nu},\phi_{j\nu}) \times[\mathbf{V}_\nu(\mathbf{r}_{j\nu})+\sigma^z b_\nu(\mathbf{r}_{j\nu})]\mathbf{U}(\theta_{j\nu},\phi_{j\nu}). \tag{7}$$

Here the constraining fields $[b_\nu(\mathbf{r}_{j\nu})=b_\nu$ inside the sphere (ν) and zero outside] must be adjusted such that the resulting moments coincide with the those wanted: $\int_{\Omega_\nu} m(\mathbf{r})d^3r = m_\nu$. We emphasize that the Hamiltonian, Eq. (7), is not diagonal in the spin quantum numbers, a fact that leads to spin-hybridized energy bands.[10,13,29] Therefore the concept of two Fermi energies for bands with different spin indices cannot be applied here. Instead, to do the actual constrained calculations for noncollinear configurations one proceeds iteratively as described in detail in Ref. 14.

III. RESULTS AND DISCUSSION

We will begin with the case of Fe_3Pt-Invar stating some very basic facts first. It crystallizes in the Cu_3Au structure and is ordered such that Pt occupies the cube corners and Fe the face centers. The atomic-sphere approximation used in our calculations requires the choice of sphere radii for the constituents which were such that the atomic spheres were neutral to within about 0.2 electrons per sphere. To a good approximation this leads to a minimum in the total energy at a given volume and is found to require equal sphere radii for all volumes and states of magnetic order considered.

The ground state of Fe_3Pt is calculated to be ferromagnetic for a sphere radius, S, of $S=2.79$ a.u. possessing magnetic moments of $m_{Fe}=2.67\ \mu_B$ and $m_{Pt}=0.27\ \mu_B$. The corresponding lattice constant is $a=3.77$ Å which is somewhat larger than the experimental lattice constant of $a=3.73$ Å.[30] The calculated magnetic moment corresponds to $m=2.07\ \mu_B$

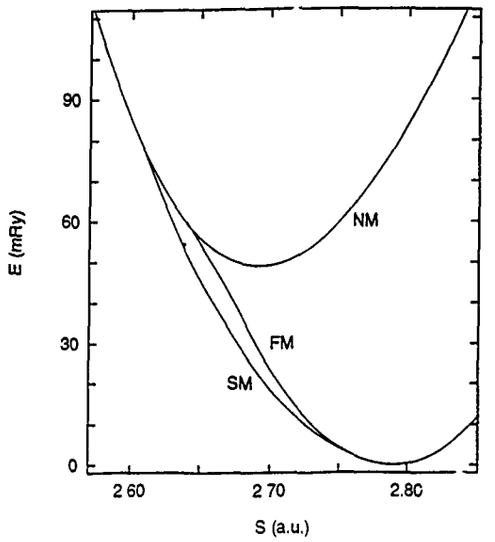

FIG. 1. Total energy per unit cell of Fe_3Pt as a function of the Wigner–Seitz radius, S. NM: nonmagnetic, FM: ferromagnetic, and SM: spiral magnetic.

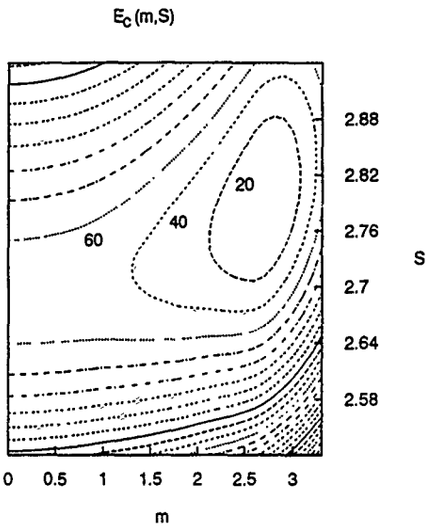

FIG. 2. Contours for Fe_3Pt of the collinear contribution to the total energy, E_c, see Eq. (8), in mRy per unit cell. S: Wigner–Seitz radius in atomic units and m: magnitude of the magnetic moment in μ_B.

per atom which is slightly smaller than the experimental value of $m=2.16\ \mu_B$ per atom quoted by Shimizu.[31] Our results differ somewhat from the results of previous calculations[32] (see also Ref. 17) in particular in the numerical values of the total energy difference between the ferromagnetic and nonmagnetic states, the values of the equilibrium lattice constant, and the equilibrium magnetic moment. This is so because our calculations are not relativistic in contrast to the older calculations where the scalar-relativistic wave equation (SRWE)[33] was used. In the earlier stages of these calculations we noticed that results for Fe_3Pt obtained without relativistic corrections were closer to experimental ground-state properties than those obtained with the SRWE. We thus purposely dropped the relativistic corrections. This is our only justification for the approach used here.

Continuing with the discussion of our results we find that spin-spiral states having $\theta_\nu=90°$ for all sites (ν) possess the lowest total energy for a wide range of volumes smaller than the calculated equilibrium volume. Furthermore, the collinear antiferromagnetic state is higher in energy than the ferromagnetic state. The total energy as a function of the atomic-sphere radius is shown in Fig. 1 for the nonmagnetic, ferromagnetic, and spin-spiral states. The lowest energy for a wide range of volumes is obtained approximately for $q=0.25$. This can be translated into the angle between the moments of two neighboring ferromagnetic planes obtaining about 90°.

Numerical experiments showed that the total energy can be written as

$$E(v,m,\mathbf{q})=E_c(v,m)+\alpha(v)E_q(m,\mathbf{q}). \tag{8}$$

Here $\alpha(v)$ is a slowly varying scaling factor which for the volume range investigated is $\alpha(v)\simeq(v_0/v)^4$, where v_0 is the equilibrium volume. The first term on the right-hand side, E_c, we may call the collinear and the second, E_q, the noncollinear contribution to the total energy. This empirical relationship greatly facilitates the discussion, so we show in Fig. 2 the collinear and in Fig. 3 the noncollinear contribution to the total energy. Here, from Fig. 3 we find for a given local moment, m, the value of q corresponding to the state with the lowest total energy and from Fig. 2 the relevant value of the volume, v. Figure 3 shows that for $m>2.6\ \mu_B$ the energy is lowest in ferromagnetic order and for $m<2.6\ \mu_B$ the energy is minimized by a spin-spiral structure with values of q lying in the interval from 0.2 to 0.3. Note that the

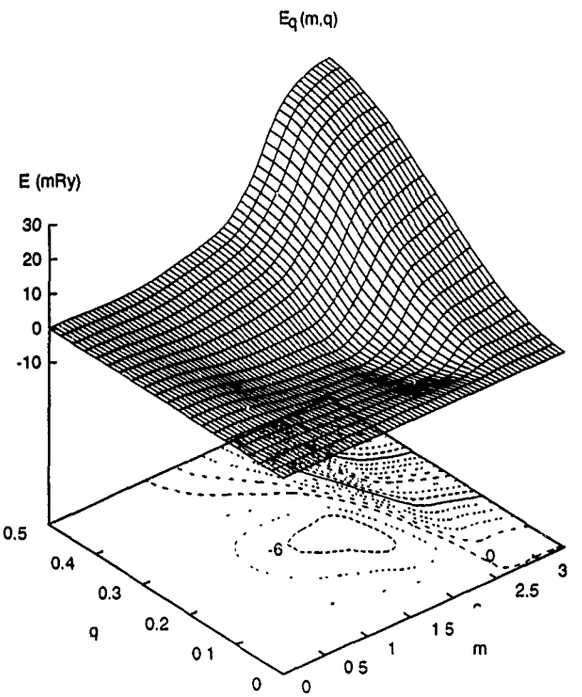

FIG. 3. Contours and surface for Fe_3Pt of the noncollinear contribution to the total energy, E_q, see Eq. (8), in mRy per unit cell. m: magnitude of the magnetic moment in μ_B and q: magnitude of the spiral vector in units of $2\pi/a$ along the (1,1,1) axis.

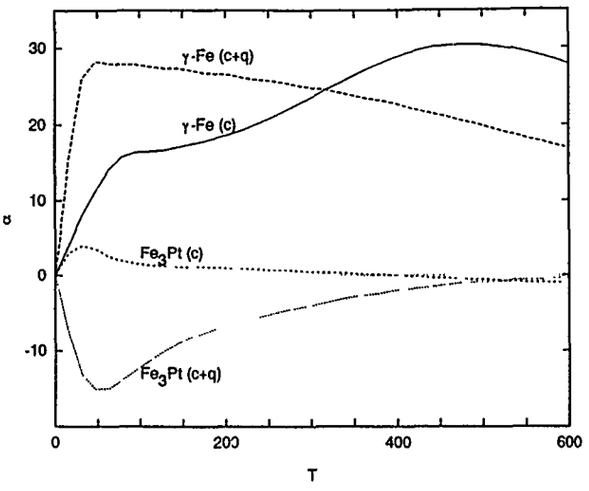

FIG. 4. Expansion coefficient α as a function of temperature T calculated for γ-Fe and Fe_3Pt; (I) using only collinear states (c) and (II) including collinear and noncollinear states ($c+q$).

noncollinear portion of the total energy $E_q(m,q)$ has a clear tendency to increase for large m, see Fig. 3. In particular the noncollinear contribution, $E_q(m,q)$, is negative for states with small moments, ($m<2.6\ \mu_B$), and positive for states with large moments, ($m>2.6\ \mu_B$). If we assume that the calculated energy surfaces are also realized at finite temperatures, this contribution upon heating leads to a preferable occupation of noncollinear states having local magnetic moments smaller than the ground-state value of $m_0=2.67\ \mu_B$.

In Ref. 14 we described a rather simple-minded scheme for statistical averages showing that the excited states modeled above give indeed important contributions to thermodynamic properties. We do not, however, claim to have a consistent scheme that enables us at the present stage to compute thermodynamic potentials and the magnetic phase transition. Still, using the computed energy surfaces we calculate the temperature dependence of the magnetic contribution to the expansion coefficient, $\alpha(T)$, from the derivative with respect to the temperature of the average value of the specific volume $\langle v(t)\rangle$. The calculations were done with and without taking into account noncollinear states and the result is shown in Fig. 4 which also contains results for γ-Fe to be discussed shortly. It is seen that with the use of only collinear magnetic states the coefficient $\alpha(T)$ is positive at very low temperatures and nearly zero for higher temperatures. Inclusion of noncollinear configurations leads to a negative sign of $\alpha(T)$ over a wide temperature range; this is one of the most prominent effects associated with Invar. The thermal expansion coefficient due to magnetic effects has been obtained experimentally.[34] Its sign and order of magnitude are in agreement with our results, although the functional form, especially an experimental peak slightly below T_C, is not brought out by our calculations.

The information on the total energy of spiral structures can also be used for a rough estimate of both the Curie temperature, T_C, and the spin-wave stiffness constant, D. The Curie temperature T_C can be estimated within the mean field approximation to the Heisenberg Hamiltonian. Neglecting the magnetic contribution of platinum, the Curie temperature is given by $T_C=J(0)(m_0+2)/3m_0$. Here the exchange parameter $J(0)$ is calculated by

$$J(0)=\Omega_{BZ}^{-1}\int_{BZ} d^3q\,\Delta E(\mathbf{q}),$$

where $\Delta E(\mathbf{q})=[E(v_0,m_0,\mathbf{q})-E(v_0,m_0,0)]/3$ is the total energy per Fe atom counted from the ground state and Ω_{BZ} is the volume of the Brillouin zone. Our calculations give $T_C=435$ K, which is in good (probably fortuitous) agreement with the experimental value of ordered Fe_3Pt, $T_C=430$ K.[17] We hasten to point out that we do not imply here that the localized-electron picture is appropriate for a description of the magnetovolume effects.

To estimate the spin-wave stiffness constant D we use the following expression (Ref. 35): $D=(4/m_0)\times\lim_{q\to 0}\Delta E(\mathbf{q})/|\mathbf{q}|^2$, with $\Delta E(\mathbf{q})$ defined above, we obtain the value of $D=135$ meV Å^2 which should be compared with the value of $D=80$ meV Å^2 for $Fe_{72}Pt_{28}$.[17,36]

Let us now briefly turn to the case of γ-Fe which was discussed in great detail in Ref. 13 and 14. Here it suffices to point out that the magnetic structures that can occur with low total energy depend sensitively on the volume. In agreement with older work[37–39] we find that there exist ferromagnetic states having high magnetic moments at volumes larger than the bcc-equilibrium volume. New in our calculations is the occurrence of spiral magnetic states at volumes larger than the equilibrium volumes but having lower total energies than the ferromagnetic states. We could show that these states are being measured by neutron diffraction experiments on γ-Fe precipitates in copper.[40] Since these states occur at large volumes (in contrast to Fe_3Pt where they occur at small volumes, see Fig. 1) they are responsible for the large positive thermal expansion coefficient that is shown in Fig. 4.

The object of these previous calculations was either iron in the bcc structure (α-Fe) or in the fcc structure (γ-Fe). Since at constant atomic volume the bcc structure can be continuously deformed to the fcc structure, the latter appearing as a body centered tetragonal with a value of $c/a=\sqrt{2}$, we now describe results of new calculations in which we focus our attention on the possible magnetic states of tetragonal iron with $1\leq c/a\leq\sqrt{2}$. These states may occur in epitaxially grown iron, but we remind the reader that our calculations are for bulk materials and not for surfaces. Thus, in view of possible effects due to lowered dimensionality, our results should be understood to describe real cases perhaps only semiquantitatively. In Fig. 5 we show the total energy counted from some suitable but arbitrary origin and the local magnetic moment for three different volumes labeled by the Wigner–Seitz radius R_{WS} as a function of the spiral $\mathbf{q}$ vector. The value of $R_{WS}=2.646$ corresponds to the equilibrium volume of bcc iron and it is seen that bcc Fe ($c/a=1$) is stable for $q=0$ which is the ferromagnetic state; up to about $c/a=1.2$ iron is ferromagnetic, but fcc Fe at this volume is nonmagnetic at $q=0$ having a metastable spiral magnetic state with a reduced magnetic moment at about $q=0.6$. At a somewhat larger volume ($R_{WS}=2.67$) the range of stable ferromagnetic states is increased, $1\leq c/a<1.3$, but fcc Fe still appears to have a spiral magnetic state. For a large volume

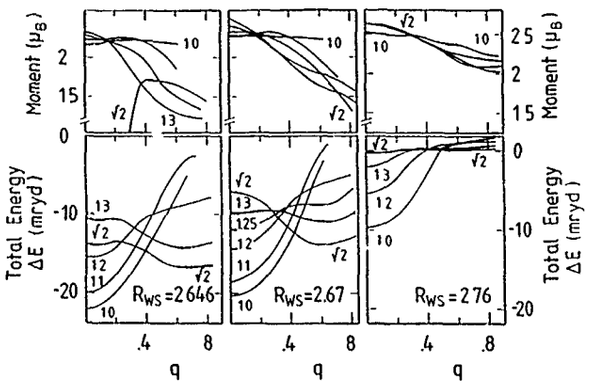

FIG. 5. Total energy and local magnetic moment of iron as a function of q, the magnitude of the spiral vector in units of $2\pi/a$, for three different volumes labeled by the Wigner–Seitz radius, R_{WS}; the parameters labeling the different curves give the values of c/a, $c/a=1$: bcc Fe, $c/a=\sqrt{2}$: fcc Fe, values in between: tetragonal iron.

corresponding to $R_{WS}=2.76$ fcc Fe is now barely stable in a ferromagnetic state, but we may speculate that its Curie temperature could be rather low because the flatness of the total energy as a function of q signals small interatomic exchange constants.

We will close this section by discussing new but preliminary results for Fe-Cr multilayers. This modern topic has received considerable attention recently by many research groups whose work, unfortunately, we have no space to cite here properly. Concentrating instead on the work of only the Jülich group[18–20] and only on a few salient facts we may state that depending on the spacer (chromium) thickness, iron layers experimentally appear to be coupled ferromagnetically, antiferromagnetically, or in a 90° configuration. One therefore postulates that the exchange coupling between Fe layers can be written as $H_c=-A_1\cdot\cos\theta-B_1\cdot\cos 2\theta$ where the second term on the right-hand side is the biquadratic coupling term. This type of coupling among other things shows up in hysteresis loops as steps in the magnetization. To our knowledge it is still not clear whether this coupling is intrinsic or extrinsic.[41]

A simple multilayer was simulated[42] by continuing periodically two closed packed (CP) layers of Fe, two CP layers of Cr, and two CP layers of Fe. The two Fe layers were found to be coupled antiferromagnetically by the chromium spacer. Next a magnetic field in the global frame of reference is turned on and increased slowly iterating the system to self-consistency at each chosen value of the magnetic field until eventually the field has aligned the Fe moments ferromagnetically. We find that the reorientation of the magnetic moments happens in steps first at about 120° then at about 30° between the Fe moments. The steps, however, are not as pronounced as in the experimental hysteresis curves. The total energy calculated was fitted to H_c above by separately taking care of the Zeeman energy. The result was $B_1/A_1\simeq 0.16$ which is in fair agreement with the value $B_1/A_1\simeq 0.13$ quoted in Ref. 18. We add, however, that the separate values of A_1 and B_1 are obtained to be about one order of magnitude larger than the experimental estimates. Furthermore we emphasize that in our calculations the spin-orbit coupling, i.e., the magnetocrystalline anisotropy, and any roughness between the layers were neglected. Therefore, even though our results are tentative at best and our simulated multilayer may not really represent reality, we conclude that the biquadratic coupling is an intrinsic property that is due to certain features in the electronic structure of the Fe-Cr layers that still need to be clarified.

IV. CONCLUSION

For itinerant-electron magnets we succeeded in describing the vector nature of the magnetic moments whose magnitude and direction are treated in noncollinear constrained moment calculation as independent variables for an *ab initio* calculation of the total energy. This supplies the energetics of spin fluctuations and enabled us to make a step—although crude—in the direction of determining finite-temperature properties. Our calculations describe the magnetovolume properties of Fe_3Pt and the results agree with experimental facts in a semiquantitative way, notably with the Invar behavior. On first sight it does not appear surprising that in Fe_3Pt with increasing temperature the magnetic moment and thus the specific volume decrease. One should bear in mind, however, that the decreasing magnetic moment is not the usual decreasing thermal average but is brought about by longitudinal spin fluctuations that are triggered by transverse fluctuations.

Furthermore, we discussed the possible states of tetragonal iron and estimated the volume at which fcc Fe is ferromagnetic by studying the total energy as a function of the spiral **q** vector. Finally we calculated the energetics of reorienting antiferromagnetically coupled Fe layers in Fe-Cr and estimated the ratio of the bilinear and biquadratic exchange constants concluding that the biquadratic coupling might be of intrinsic origin.

ACKNOWLEDGMENTS

This work was partially supported by the Deutsche Forchungsgemeinschaft through SFB 252 Darmstadt, Frankfurt, Mainz.

[1] W. Kohn and L. J. Sham, Phys. Rev. A **140**, 1133 (1965).
[2] U. von Barth and L. Hedin, J. Phys. C **5**, 1629 (1972).
[3] V. Korenman, J. L. Murray. and R E Prange, Phys. Rev. B **16**, 4032 (1977).
[4] T. Moriya, J. Magn. Magn. Mater. **14**, 1 (1979).
[5] M. V. You and V. Heine, J. Phys. F **12**, 177 (1982)
[6] T. Oguchi, K. Terakura, and N. Hamada, J. Phys. F **13**, 145 (1983).
[7] A. J. Pindor, J. Staunton, G. M. Stocks, and H. Winter, J. Phys. F **13**, 979 (1983).
[8] B. L. Gyorffy, A. J. Pindor, J. Staunton, G. M. Stocks, and H Winter, J. Phys. F **15**, 1337 (1985).
[9] A. I Liechtenstein, M I Katsnelson, V P. Antropov, and V. A. Gubanov, J. Magn. Magn. Mater. **67**, 65 (1987).
[10] L. M. Sandratskii and P. G. Guletskii, J. Magn. Magn. Mater. **79**, 306 (1989).
[11] V Korenman, *Metallic Magnetism*, edited by H. Capellmann (Springer, Berlin, 1987)
[12] J Sticht, K.-H. Hock, and J Kubler, J. Phys. Condens. Matter **1**, 8155 (1989).

[13] M. Uhl, L. M. Sandratskii, and J. Kübler, J. Magn. Magn. Mater. **103**, 314 (1992).
[14] M. Uhl, L. M. Sandratskii, and J. Kübler, Phys. Rev. B **50**, 291 (1994).
[15] J. Kübler, M. Uhl, and L. Sandratiskii, Phys. B **186–188**, 863 (1993).
[16] E. F. Wassermann, Phys. Scr. T **25**, 209 (1989).
[17] E. F. Wassermann, in *Ferromagnetic Materials*, edited by K. H. J. Buschow and E. P. Wohlfarth (North-Holland, Amsterdam, 1990), Vol. 5.
[18] M. Rührig, R. Schäfer, A. Hubert, R. Mosler, J. A. Wolf, S. Demokritov, and P. Grünberg, Phys. Status Solidi A **125**, 635 (1991).
[19] U. Köbler, K. Wagner, R. Wichers, A. Fuss, and W. Zinn, J. Magn. Magn. Mater. **103**, 236 (1992).
[20] P. Grünberg, S. Demokritov, A. Fuss, R. Schreiber, J. A. Wolf, and S. T. Purcell, J. Magn. Magn. Mater. **104–107**, 1734 (1992).
[21] L. M. Sandratskii, Solid State Commun. **75**, 527 (1990).
[22] J. Kubler, K.-H. Höck, J. Sticht, and A. R. Williams, J. Appl. Phys. **63**, 3482 (1988).
[23] C. Herring, in *Magnetism IV*, edited by G. Rado and H. Suhl (Academic, New York, London, 1966).
[24] L. M. Sandratskii, Phys. Status Solidi B **135**, 167 (1986).
[25] A. R. Williams, J. Kubler, and C. D. Gelatt, Jr., Phys. Rev. B **19**, 6094 (1979).
[26] A. R. Williams, V. L. Moruzzi, J. Kübler, and K. Schwarz, Bull. Am. Phys. Soc. **29**, 278 (1984).
[27] V. L. Moruzzi, P. M. Marcus, K. Schwarz, and P. Mohn, Phys. Rev. B **34**, 1784 (1986).
[28] P. H. Dederichs, S. Blügel, R. Zeller, and H. Akai, Phys. Rev. Lett. **53**, 2512 (1984).
[29] L. M. Sandratskii and J. Kübler, Phys. Rev. B **47**, 5854 (1993).
[30] J. Hesse, G. Nölle, and H. Körner, Solid State Commun. **46**, 721 (1983).
[31] M. Shimizu, Rep. Prog. Phys **44**, 329 (1981).
[32] M. Podgorny, Phys. Rev. B **43**, 11 300 (1991).
[33] D. D. Koelling and B. N. Harmon, J. Phys. C **10**, 3107 (1977).
[34] N. L. Sedov, *Antiferromagnetism Gamma-Shelesa / Problema Invara* (Nauka, Moscow, 1987).
[35] A. J. Holden and M. V. You, J. Phys. F **12**, 195 (1982).
[36] Y. Ishikawa, K. Tajima, Y. Noda, and N. Wakabayashi, J. Phys. Soc. Jpn. **48**, 1097 (1980).
[37] J. Kübler, Phys. Lett. A **81**, 81 (1981).
[38] K. Schwarz and P. Mohn, J. Phys. F **14**, L129 (1984).
[39] C. S. Wang, B. M. Klein, and H. Krakauer, Phys. Rev. Lett. **54**, 1852 (1985).
[40] Y. Tsunoda, J. Phys. Condens. Matter **1**, 10 427 (1989).
[41] J. C. Slonczewski, Phys. Rev. Lett. **67**, 3172 (1991).
[42] J. Teichmann, Diplomarbeit, Darmstadt (unpublished 1994).

Verwey transition in magnetite: Mean-field solution of the three-band model

S. K. Mishra, Z. Zhang,[a] and S. Satpathy
Department of Physics and Astronomy, University of Missouri, Columbia, Missouri 65211

The nature of the Verwey transition in magnetite (Fe_3O_4) within a three-band spinless model Hamiltonian is examined. These bands, which arise from the minority-spin t_{2g} orbitals on the Fe(B) sublattice, are occupied by half an electron per Fe(B) atom. The Verwey order–disorder transition is studied as a function of the ratio of the intersite Coulomb repulsion U_1 and the bandwidth W. It is found that the electrons are ordered beyond the critical value of $U_1/W \approx 0.25$ in essential agreement with the results of the one-band Cullen–Callen model. For larger values of U_1/W, a Verwey-like order is exhibited where the electrons occupy alternate (001) planes. The model predicts a transition from the metallic to the semiconducting state with the band gap increasing linearly with U_1 beyond the transition point.

I. INTRODUCTION

The Verwey transition in magnetite[1–3] is a well-known metal–insulator transition characterized by a decrease of two orders of magnitude in conductivity as temperature is decreased below the Verwey temperature of $T_v \sim 120$ K. The transition is accompanied by an order–disorder transition, where in the simplest ionic picture, Fe^{2+} and Fe^{3+} ions order on the B sublattice of the spinel structure, interacting via Coulomb forces. Examining this picture quite early on, Anderson[4] pointed out the remarkable property of the spinel B sublattice that the short-range part of the Coulomb interaction is minimized by $\sim(3/2)^{N/2}$ different configurations of the ions where N is the number of sites on the B sublattice. The long-range part of the Coulomb interaction, on the other hand, is minimized only by a few of these configurations. The Verwey transition may therefore be interpreted as a loss of long-range order (LRO) above T_v with no abrupt change in the short-range order (SRO). This interpretation is consistent with the entropy change at the Verwey transition obtained from specific heat measurements.

This ionic picture, while providing a reasonable description of the order–disorder transition, does not provide any quantitative description of the transition from metal to insulator. Issues unaddressed include questions such as: What are the charge carriers in magnetite? Is the conductivity via motion of ions or does one has to think of itinerant electrons? In fact, subsequent to Anderson's work, a number of models have been proposed to describe the mechanism of electrical conduction and simultaneously the order–disorder transition. These include the itinerant one-band electron model of Cullen and Callen,[5] and the molecular polaron or bipolaron pictures of Yamada and Chakraverty,[6] etc.

The itinerant electron model of Cullen and Callen describes the Verwey transition in terms of motion of electrons on the B sublattice. The Hamiltonian consists of a nearest-neighbor hopping integral t and the intersite Coulomb interaction U_1 between nearest neighbors. In a seminal work,[5] Cullen and Callen studied this model and in fact found an order–disorder transition below a critical value of $U_1/t \sim 2.2$. However, there was no justification for the origin of such a model and, since there was no reliable estimate for U_1/t until our recent work,[7] the applicability of the Cullen–Callen model to magnetite remained unclear.

Recently we have examined the electronic structure of magnetite using density-functional methods with the local spin-density approximation (LSDA).[7] Based on this work, we have obtained a three-band electronic Hamiltonian for the motion of electrons on the B sublattice of magnetite. In this article, we discuss the results of a mean-field solution of the three-band model. We find that both (a) the order–disorder transition and (b) the metal–insulator transition can be described within the three-band model.

II. THE MODEL HAMILTONIAN

The crystal structure of magnetite consists of three sublattices, viz., the oxygen sublattice and the Fe(A) and the Fe(B) sublattices. The magnetic moments within each Fe sublattice are aligned in the same direction, while the two sublattices are aligned antiferromagnetically. Since there are twice as many atoms on the B sublattice as on A, there is a net magnetic moment with a magnitude of 4.1 μ_B per Fe_3O_4 formula unit.

In our earlier work,[7] we have calculated the density-functional spin-polarized electronic structure of magnetite, which is schematically shown in Fig. 1. As seen from the figure, the majority-spin bands are semiconducting, while the minority-spin bands are metallic, a picture also obtained by Yanase and Siratori from independent calculations.[8] The presence of only the minority-spin electrons at the Fermi energy is consistent with the spin-polarized photoemission experiments of Alvarado *et al.*[9]

The t_{2g} orbitals of the Fe(B) atoms form the electron bands at the Fermi energy E_f with the t_{2g} bands occupied by half an electron per Fe(B) atom. The electron count is such that the presence of these "extra" electrons makes the valency of half the B site atoms Fe^{+2} and the other half B site atoms have the valency of Fe^{+3}. The picture that emerges then is that the "extra" electrons move on the background of Fe^{+3} atoms on the B sublattice in agreement with the traditional view of charge transport in magnetite.[4]

The electronic structure provides justification for the conventional picture of conduction via Fe(B) electrons moving on the B sublattice. However, unlike the one-band pic-

[a]Present address: Department of Physics, North Carolina State University, Raleigh, NC 27695.

 0021-8979/94/76(10)/6700/3/$6.00 © 1994 American Institute of Physics

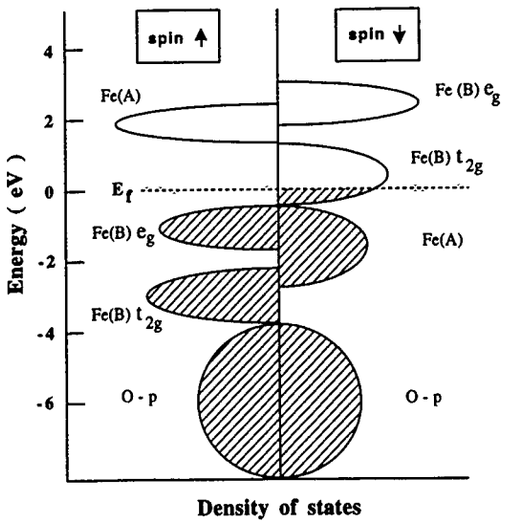

FIG. 1. Schematic picture of the electronic structure in magnetite as obtained from the density-functional band calculation (Ref. 7). The minority spin t_{2g} electrons on the Fe(B) sublattice play the key role in charge transport.

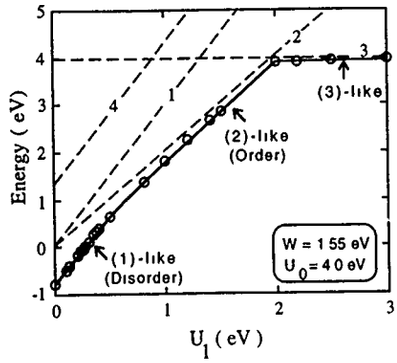

FIG. 2. Ground-state energy as a function of U_1. The dashed curves correspond to energies in the limit of zero hopping (no kinetic energy term) for various configurations. The configurations are characterized by the mean occupation of the xy,yz,zx orbitals on the four Fe(B) atoms, viz., (1) {1/2,0,0; 1/2,0,0; 1/2,0,0; 1/2,0,0}, (2) (1,0,0; 1,0,0; 6∗0}, (3) {1,1,0; 9∗0}, and (4) {12∗1/6}. The Coulomb energy of the four configurations are (1) $E=3U_1$, (2) $E=2U_1$, (3) $E=U_0$, and (4) $E=U_0/3+3U_1$. Even though the Coulomb energy of configuration (1) is relatively high, the large kinetic energy gain for this configuration makes it the ground state for lower values of U_1. Configuration (2) wins beyond the transition point of $U_1\approx0.38$ eV because of its lower Coulomb energy.

ture of Cullen and Callen, we now have the three t_{2g} bands (xy, yz, and zx), which leads to a three-band electron model on the B sublattice

$$H=\sum_{\langle ij\rangle}\sum_{\mu,\nu=1}^{3} t_{\mu,\nu}a_{i\mu}^{+}a_{j\nu}+\sum_{ij}\sum_{\mu,\nu=1}^{3} U_{i\mu,j\nu}n_{i\mu}n_{j\nu}. \quad (1)$$

Here $a_{i\mu}^{+}(a_{i\mu})$ are the creation (annihilation) operators of the electron on the B sublattice with i, μ being the site and orbital indices (xy,yz,zx), respectively, $n_{i\mu}$ is the corresponding number operator, and $\langle ij\rangle$ denotes summation over nearest neighbors (NN). The Hamiltonian (1) consists of a tight-binding NN hopping term (the band-structure term) plus the Coulomb interaction term.

The values of the electronic parameters in the Hamiltonian (1), calculated from "constrained" density-functional methods,[7] have the following values for magnetite: (a) the hopping integrals $t_{dd\sigma}=-0.41$ eV, $t_{dd\pi}=0.05$ eV, and $t_{dd\delta}=0.12$ eV, resulting in an average $t\approx-0.13$ eV and a bandwidth of $W=1.55$ eV and (b) the Coulomb parameters $U_0=4.1\pm0.5$ eV, $U_1=0.3$–0.4 eV, and $U_2\approx0.05$–0.1 eV. Here the on-site Coulomb repulsion is denoted by U_0 and the first and the second NN Coulomb terms are denoted by U_1 and U_2, respectively. Since U_0 is much larger than U_1 and $t_{\mu\nu}$, double site occupancy is prevented in view of the fact that there are half as many electrons as the B sites. Although a small value of U_2 is necessary to stabilize[10] the experimentally observed "Mizoguchi structure" at low temperatures,[11] a structure where the unit cell is doubled, U_2 is an unimportant parameter for our purpose here. In our study below, we choose the values of $U_0=4$ eV and $U_2=0$, leaving thereby the only relevant parameter U_1/W in the Hamiltonian.

III. MEAN-FIELD SOLUTION

We study the Verwey transition by solving the Hamiltonian (1) in the mean-field approximation. We retain the periodicity of the spinel structure, which means the electrons can occupy any of the twelve orbitals [four Fe(B) atoms × three orbitals/atom] in the unit cell. In the standard mean-field approximation, we have

$$n_{i\mu}n_{j\nu}\cong\langle n_{i\mu}\rangle n_{j\nu}+n_{i\mu}\langle n_{j\nu}\rangle-\langle n_{i\mu}\rangle\langle n_{j\nu}\rangle. \quad (2)$$

Incorporating the first two terms in the band-structure part of Eq. (1), the total energy may then be written as a sum over the occupied one-electron eigenvalues ε_i minus the Coulomb energy

$$E=\sum_{i}^{\varepsilon_F}\varepsilon_i-E_{\text{Coulomb}}. \quad (3)$$

The mean electron occupations $\langle n_{i\mu}\rangle$ are calculated from the eigenfunctions of the Hamiltonian (1), which in turn depends on $\langle n_{i\mu}\rangle$. These are then determined self-consistently. The procedure is thus to diagonalize the 12×12 Hamiltonian matrix for each k point in the Brillouin zone and find the $\langle n_{i\mu}\rangle$ from the eigenvectors of the occupied states. We then go back and find the eigenvalues and eigenvectors taking these new values of $\langle n_{i\mu}\rangle$ in the Hamiltonian. The process is repeated until $\langle n_{i\mu}\rangle$ values have converged, which then corresponds to the minimum energy configuration. We performed the eigenvalue summation in the expression (3) with 216 k points in the full Brillouin zone.

The calculated ground-state energy is shown in Fig. 2 as a function of the parameter U_1. The dashed curves refer to the energies of selected configurations without the band-structure term, i.e., in the limit of zero bandwidth. Without the band-structure term, the ordered phase, denoted by configuration (2) in Fig. 2, has the lowest energy for all values of $U_1\leq2$ eV. This phase has the electron configuration where two of the four sites in the unit cell have an electron each and the other two sites are empty. However, with the inclusion of

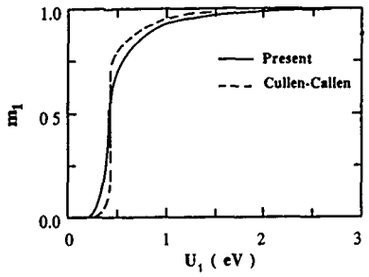

FIG. 3. The calculated Cullen–Callen order parameter m_1 as a function of the nearest-neighbor Coulomb energy U_1.

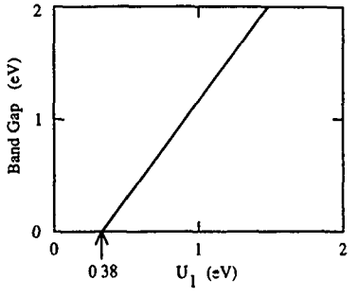

FIG. 4. Band gap as a function of the nearest-neighbor Coulomb energy U_1. A metal–insulator transition is seen at the value of U_1=0.38 eV.

the band-structure term, the disordered phase, viz., configuration (1), with half an electron on each site, has the lowest energy for the smaller values of U_1. For higher values of U_1, the Coulomb energy of configuration (1) becomes progressively larger and the ordered phase, configuration (2), wins over thereby resulting in a structural phase transition as indicated in the figure. Thus the transition is a result of the competition between the kinetic energy (band-structure energy) and the Coulomb energy.

The ordered phase is similar to the Verwey order with electrons occupying alternate (100) planes in the cubic structure. The so-called "Mizoguchi" structure,[11] inferred to be the structure of magnetite at low temperatures, where the unit cell has doubled compared to the cubic cell, is not reproduced in our calculation because we have restricted ourselves to the cubic unit cell of the spinel structure. To study the nature of the transition, we define the order parameters following earlier authors:[5]

$$m_1=(n_1+n_2-n_3-n_4)/2,$$
$$m_2=(n_1-n_2+n_3-n_4)/2, \tag{4}$$
$$m_3=(n_1-n_2-n_3+n_4)/2,$$

and

$$n=(n_1+n_2+n_3+n_4)=2.$$

Here $n_i=\Sigma_{\mu=1}^{3}\langle n_{i\mu}\rangle$. For perfect order $m_1=1$, while for perfect disorder $m_1=0$.

The calculated order parameter m_1 as a function of the Coulomb parameter U_1 is shown in Fig. 3, where we also reproduce the results of the one-band Cullen–Callen model. There is a rather sharp transition around the value of $U_1\approx0.38$ eV in both the Cullen–Callen model and the present three-band model. The order parameters m_2 and m_3 are zero everywhere except the transition region corresponding to "multiple order,"[5] an issue we have not examined yet in any detail.

We have also calculated the mean-field electronic eigenvalues (band structure). The bands are metallic until the transition point beyond which a band gap develops with the gap value increasing linearly with U_1 as shown in Fig. 4.

IV. CONCLUSION

In conclusion, we have studied the three-band model for the Verwey transition in magnetite in the mean-field approximation. The Verwey transition is described in terms of the order–disorder transition of the t_{2g} "extra" electrons on the B sublattice. Whether these electrons are ordered or not depends on the relative strengths of the Coulomb energy and the kinetic energy, characterized by the Coulomb parameter U_1 and bandwidth W, respectively. For lower values of the Coulomb parameter, a disordered state is favored, while a larger value results in an ordered state with the crossover taking place at the ratio $U_1/W\approx0.25$. The ordered state in our calculation has a Verwey-like order, where alternate (001) planes on the B sublattice are occupied by the "extra" electrons. We have shown earlier[10] that given the degree of freedom (larger unit cell) the kinetic energy term destabilizes the Verwey order into the experimentally observed Mizoguchi order. Finally, even though the Verwey transition occurs as temperature is changed, our present results pertain to zero temperature with the Verwey transition taking place as electronic parameters are varied. We are currently studying the Verwey transition within a finite-temperature mean-field theory. Preliminary results indicate that our model can explain the experimentally observed Verwey transition as a function of temperature.[12]

[1] N. F. Mott, *Metal-Insulator Transitions* (Taylor & Francis, London, 1964).
[2] E. J. W. Verwey, Z. Krist. **91**, 65 (1935); E. J. W. Verwey and P. W. Haayman, Physica **8**, 979 (1941); E. J. W. Verwey, P. W. Haayman, and F. C. Romeijn, J. Chem. Phys. **15**, 181 (1947).
[3] For an overview of the Verwey transition in magnetite, see Philos. Mag. **42**, 327 (1980).
[4] P. W. Anderson, Phys. Rev. **102**, 1008 (1956).
[5] J. R. Cullen and E. R. Callen, Phys. Rev. B **7**, 397 (1973).
[6] Y. Yamada, Philos. Mag. B **42**, 377 (1980); B. K. Chakraverty, Solid State Commun. **15**, 1271 (1974).
[7] Z. Zhang and S. Satpathy, Phys. Rev. B **44**, 13 319 (1991).
[8] A. Yanase and K. Siratori, J. Phys. Soc. Jpn. **53**, 312 (1984).
[9] S. F. Alvarado, W. Eib, F. Meier, D. T. Pierce, K. Sattler, H. C. Siegmann, and J. P. Remeika, Phys. Rev. Lett. **34**, 319 (1975).
[10] S. K. Mishra and S. Satpathy, Phys. Rev. B **47**, 5564 (1993).
[11] M. Mizoguchi, J. Phys. Soc. Jpn. **44**, 1512 (1978).
[12] M. Samiullah *et al.* (to be published).

Wannier states in magnetite

Trao Her and Carel Boekema
Physics Department, San Jose State University, San Jose, California 95192-0106

Magnetite exhibits the well-known metal–insulator transition at the Verwey temperature (T_V) near 123 K. Neither the physical origin nor the conduction process above T_V is well understood. Using the Cullen and Callen tight-binding Hamiltonian, the "extra" fully spin-polarized $3d$ conduction electrons in the B sublattice are described. By introducing a covalency parameter Γ, the Wannier states for these conduction electrons can be characterized. Only for the lower singlet subband, does the Γ value point toward delocalization. The results reveal that the Wannier states in magnetite are a mixture of localized and delocalized electron states.

I. INTRODUCTION

The debate on the origin of the Verwey phase transition in magnetite (Fe_3O_4) and its unusual physical properties observed above this transition still continue.[1] Fe_3O_4 is a mixed-valence oxide material that undergoes a metal-to-insulator transition at the Verwey temperature (T_V) near 123 K. Several models, ranging from electron hopping to broadband conduction, have been proposed for the conduction mechanism above T_V. The local-magnetic-field anomaly[2] in Fe_3O_4 observed at twice T_V (T_W) has provided new stimulus in magnetite studies, and clearly marked the temperature interval $[T_V, T_W]$, for which precursor effects related to the Verwey transition occur.

Fifteen years ago, Mott and others[1a] suggested that above T_V Fe_3O_4 behaves like a Wigner glass, in which the "extra" $3d$ electrons ($3d^*$) randomly occupy one-half of the B sites. According to Mott,[3] the electric properties of such a glass are best described by a narrow (polaron) band. Furthermore, combined experimental evidence involving muon-spin research (μSR), Moessbauer effect spectroscopy, and neutron scattering studies strongly support this picture of phonon-assisted electron hopping above T_V.[2a] Direct experimental proof of the Mott–Wigner glass state in Fe_3O_4 has been provided by the observation of the μSR cross-relaxation effect at T_W.[2]

Despite the progress made in recent years, additional study is needed. Some questions still remain: Are these $3d^*$ electrons localized and, is the Hubbard approach as performed by Ihle and Lorentz[4] justified? A study of the Wannier states of these "hopping" $3d^*$ electrons could provide answers to these questions and shed light on the origin of the Verwey phase transition. We have used the established Cullen and Callen (CC) Hamiltonian[5] as a starting point of our Wannier study of magnetite.

II. TIGHT-BINDING METHOD

Magnetite, which can be well described by $(Fe^{3+})_A[Fe_2^{3+}e^{-1}]_BO_4$, is a ferrimagnet and has an inverse spinel structure. The Fe ions at the A sites do not play a role in the conduction mechanism. The Fe ions in the B sites are surrounded by six oxygens in an octahedral environment. The unit cell has two molecules and thus four B sites. These four B sites share two $3d^*$ conduction electrons and are half occupied. The ferrimagnetic Neel temperature of 858 K and Hunds's rules impose that these $3d^*$ electrons are fully spin polarized below RT. In the trigonally distorted octahedron, the $d_{3(z')^2-r^2}$ electron state is the lowest in energy; z' being parallel to the $\langle 111\rangle$ axis. At the corners of a cube, the four B sites form a tetrahedron, the unit of the B sublattice. For this atomic unit, the quadruplet (available for the two $3d^*$ electrons) will split into a singlet and a higher triplet electron state, when considering an attractive potential at the B sites.

Cullen and Callen (CC) introduced the following one-band Hamiltonian for these $3d^*$ electrons in the B sublattice:[5]

$$H_{\alpha\beta}=H\{1+\exp(2i\mathbf{k}\tau_{\alpha\beta})\},\quad \alpha,\beta=0,1,2,\text{ or }3 \tag{1}$$

and

$$H_{\alpha\alpha}=0,\quad \alpha=0,1,2,\text{ and }3, \tag{2}$$

where α and β are B sites in the atomic unit, H is a negative constant transfer integral and is of the order of -0.05 eV,[2a,2b] and $\tau_{\alpha\beta}$ is a vector between sites α and β. In case the obtained Wannier states show substantial *de*localization, we may need to use the three-band Hamiltonian as proposed by Zhang and Satpathy.[1b] The total Bloch function $\Phi(\mathbf{r})$ for the $3d^*$ electrons reads

$$\Phi=\sum_{\alpha=0}^{3} c_\alpha(\mathbf{k})\Psi_\alpha, \tag{3}$$

where

$$\Psi_\alpha=N^{-1/2}\sum_{j}^{N}\{\exp(i\mathbf{k}\mathbf{R}_j)\}\psi(\mathbf{r}-\mathbf{R}_j-\mathbf{t}_\alpha). \tag{4}$$

$\mathbf{R}_j$ is the B sublattice vector and $\mathbf{t}_\alpha$ is the B site vector within the atomic unit.

The Wannier function W is defined as

$$W(\mathbf{r}-\mathbf{R}_i)=N^{-1}\sum_{\mathbf{k}}\sum_{j}\sum_{\alpha}\exp\{i\mathbf{k}(\mathbf{R}_j-\mathbf{R}_i)\}c_\alpha(\mathbf{k})\psi_{\alpha,j}. \tag{5}$$

The Wannier states are then evaluated to be

 0021-8979/94/76(10)/6703/2/$6.00 © 1994 American Institute of Physics

$$W^*W=\sum_{\mathbf{k}}\sum_{\alpha}\sum_{\beta} c_\alpha^*(\mathbf{k})c_\beta(\mathbf{k})\psi_\alpha^*\psi_\beta. \tag{6}$$

The $c_\alpha(\mathbf{k})$ are determined from solving

$$\sum_{\beta=0}^{3}\{H_{\alpha\beta}-EV(\mathbf{k})\delta_{\alpha\beta}\}c_\beta=0, \quad \alpha=0,1,2, \text{ and } 3, \tag{7}$$

where the eigenvalues $EV(\mathbf{k})$ are obtained from the determinant equation

$$|H_{\alpha\beta}-E(\mathbf{k})\delta_{\alpha\beta}|=0. \tag{8}$$

In nearest neighbor (nn) approximation, we then have

$$W^*W=\sum_{\mathbf{k}}\sum_{\alpha}|c_\alpha(\mathbf{k})|^2|\psi_\alpha|^2 + \sum_{\mathbf{k}}\sum_{\alpha\alpha'}^{\text{nn}}\sum c_\alpha^*(\mathbf{k})c_{\alpha'}(\mathbf{k})\psi_\alpha^*\psi_{\alpha'}. \tag{9}$$

In order to describe electron overlap and transfer, we introduce the mixing parameter Γ for each subband

$$\Gamma=\{\sum_{\mathbf{k}}\sum_{\alpha\alpha'}^{\text{nn}}\sum c_\alpha^*(\mathbf{k})c_{\alpha'}(\mathbf{k})\}\Big/\{\sum_{k}\sum_{\alpha}|c_\alpha(\mathbf{k})|^2\}. \tag{10}$$

When the covalency parameter Γ is negative or zero, antibonding and/or localization are indicated; when positive, more covalency and delocalization are present in the Wannier states.

III. CALCULATIONS AND RESULTS

Solving for the eigenvalues $EV(\mathbf{k})$'s of the CC Hermitian matrix $H_{\alpha\beta}$ is straightforward, and can be performed analytically. An important feature is that for all $\mathbf{k}$ directions a degenerate doublet exists *in*dependent of $\mathbf{k}$; this doublet was part of the triplet (see above) at $\mathbf{k}=0$. The obtained eigenvalues fully agree with the literature values.[5] The broadening of the upper singlet (departing from the $\mathbf{k}=0$ triplet) and the lower singlet is in the order of $|3H|$ (an estimate could be between 0.1–0.2 eV). To solve for the eigenvectors $c_\alpha(\mathbf{k})$, we have transformed the 4×4 Hermitian into a real symmetric 8×8 matrix following a standard recipe. In this way, Mathematica provides the eigenvectors in a convenient and correct way.

In Table I, the results on Γ and other relevant information are given.

TABLE I. Results on Γ.

$3d^*$ bands	Γ parameter	W^*W state	Occupancy 0 K	Broadening
Doublet	-1.4_5	very localized	0	0
Upper singlet	−0.0	localized	1	$<\|2H\|$
Lower singlet	+2.9	delocalized	1	$<\|2H\|$

The estimated values for Γ have been obtained by summing over 150 $\mathbf{k}$ points; these are estimates because complete convergence for the $\mathbf{k}$ sums has not been obtained. As one can see from the table, only one state has become delocalized. When the temperature increases from 0 K, this state is being emptied. However, the available (excited) empty states, especially the doublet state, are localized in this CC description. Therefore, we see no need to use a three-band Hamiltonian (see above); for now, the CC $H_{\alpha\beta}$ appears to be sufficient, and approximately correct.

IV. DISCUSSION AND CONCLUSIVE REMARKS

As $T\to 0$ K, only the lower and upper singlet bands will be occupied. Only at X (1,0,0) in the Brillouin zone, these singlets touch; otherwise, a gap exists having an effective width of the order of $|H|$. Thus, at sufficiently high temperatures of about T_V or T_W (when thermal energies are in the order of 0.01–0.02 eV), a localized behavior of the $3d^*$ states is predicted. The upper singlet and doublet (narrow) bands are primarily responsible for the conduction process; this is consistent with the Mott–Wigner glass description. Above T_W, our Wannier picture supports the idea of (phonon-assisted) electron hopping. However, this depiction is incomplete: the strong localization indicates the necessity to take into account Hubbard-like terms, as has been done (in the extreme limit) by Ihle and Lorentz[4] to describe the Coulombic $3d^*$-electron interactions. Also, Mishra and Satpathy[1c] have used Hubbard-like terms (together with the CC $H_{\alpha\beta}$) to study the atomic charge ordering below T_V.

Our present results reveal that the Wannier states in magnetite are a mixture of localized and delocalized electron states. Evidence for such a mixture is also exhibited in the electronic properties of the high-T_c cuprates. Similarities between the electronic and geometrical structures of Fe_3O_4 and $LiTi_2O_4$ and CuO-based superconductors suggest Wannier studies may provide substantial clues on the conduction mechanisms of these transition-metal oxides. Further work is in progress.

ACKNOWLEDGMENTS

This work is supported in part by Research Corporation. We thank Fay Sharifi and Stephen P. Weathersby for their assistance, stimulus, and discussions.

[1] (a) See Conference Proceedings of the International Cavendish Meeting (September 1979), Philos. Mag. B **42**, 327 (1980); (b) Z. Zhang and S. Satpathy, Phys. Rev B **44**, 13319 (1991), (c) S K. Mishra and S Satpathy, *ibid.* **47**, 5564 (1993); (d) E. De Grave *et al.*, *ibid.* **47**, 5881 (1993); (e) J H. Park *et al.*, APS Bull. **39**, 204 (1994); T. Her *et al.*, *ibid.* **39**, 205 (1994); S. Satpathy *et al.*, *ibid.* **39**, 850 (1994).
[2] (a) C. Boekema *et al.*, Phys. Rev. B **33**, 210 (1986) and references therein, (b) Hpf. Int. **31**, 487 (1986); (c) Philos. Mag. B **42**, 409 (1980).
[3] N. F. Mott, *Metal–Insulator Transitions* (Taylor & Francis, London, 1974).
[4] D. Ihle and B. Lorentz, Philos. Mag. B **42**, 337 (1980).
[5] J. R. Cullen and E. R. Callen, Phys. Rev. B **7**, 397 (1973).

Orbital ordering and magneto-optical effects in CeSb

V. P. Antropov and B. N. Harmon
...s Laboratory-U.S. Department of Energy, Iowa State University, Ames, Iowa 50011

A. I. Liechtenstein
Max-Planck-Institut für Festkörperforschung, D-70506 Stuttgart, Germany

The influence of on-site Hubbard correlations on electronic structure and magneto-optical spectra of CeSb have been studied. As the new key mechanism to produce the large magneto-optical signal is linked to the interaction between the anisotropy of the Coulomb matrix and m-dependent p-f hybridization, this effect suggests a systematic search for materials with large magneto-optical effects.

Cerium monopnictides with the NaCl-type of structure are prototypical materials belonging to strongly correlated low-carrier-density systems which have attracted attention for their unusual spectral and magnetic properties and the difficulties in explaining them. There are controversial interpretations of the double peak structure of valence-band photoemission spectra,[1] different explanations for the de Haas–van Alphen (dHvA) data,[2] and limited understanding of the nature of the structural phase transitions for these systems.[3] Among the pnictides CeSb has a special position. In addition to the anomalies inherent to all monopnictides, CeSb has a large magnetic anisotropy together with a small crystal field splitting,[4] an extremely complicated magnetic phase diagram, including a type of Devil's staircase at low temperature,[5] and the largest known Kerr angle.[6] It turns out that the widely used local spin density approximation (LSDA) fails to predict many of the ground and excited state properties: the value of the equilibrium magnetic moment, the additional orbits found in de Haas–van Alphen experiments, the small density of states at the Fermi level, and the magneto-optics.[2,7]

In this communication we have used the so-called LDA+U method in rotation-invariant form[8] to describe the ground state electronic structure and the anomalies of the magneto-optical spectra of CeSb. Some details of the method were published in Ref. 9. It turns out that the results of the self-consistent band structure of CeSb are similar to those of the empirical p-f mixing model[10,11] and leads to improvement in the description of the magneto-optical (MO) spectra.

We used the full-potential scalar-relativistic linear muffin-tin orbital (LMTO) method[12] to calculate the self-consistent band structure of ferromagnetically ordered CeSb (this corresponds to the high field state obtained in MO experiments) with the LDA+U functional (1) and the atomic sphere approximation (ASA) LMTO[10] method with spin-orbital coupling in the second-order variational step to investigate the magneto-optical spectra. The integration over the Brillouin zone has been done by the tetrahedron method with 69 **k** points for the self-consistent field (SCF) calculation and about 1000 **k** points in the $\frac{1}{16}$ BZ for optical matrix elements. The low temperature experimental crystal structure for CeSb with a 0.2% tetragonal distortion was used.[3]

Without spin-orbital coupling it was found that the Hartree–Fock-like one-electron $4f$ spin "up" states with predominantly $m=3$ and $m=-3$ character have the lowest total energy. This is in agreement with the first and second of Hund's rules, with energy differences among the $4f$ configurations arising from anisotropic Coulomb and crystal field effects. One should note that the symmetry of such orbitals is not cubic anymore, and that Jahn–Teller tetragonal distortions give a lower energy. The spin-orbital coupling (~0.5 eV) lifts the degeneracy of the $m=\pm 3$ states according to Hund's third rule and the lowest energy corresponds to the $|-3\uparrow\rangle$ one-electron state. The spin and orbital moments are equal to $-0.92\ \mu_B$ and $2.86\ \mu_B$, respectively, yielding a total magnetic moment of $1.94\ \mu_B$, which is close to the experimental value obtained for the antiferromagnetic (AFM) ground state ($2.10\pm0.04\ \mu_B$).[5]

In this article we consider only the one-determinant LDA+U singlet ground state. The ground state band structure of CeSb (with spin-orbital coupling) is shown in Fig. 1. The f bands are split by approximately 6 eV, and the singly occupied f band is located at 2.3 eV below the Fermi level. All unoccupied f bands are at approximately 3.7 eV above E_F and the broadbands which cross the Fermi level are formed by Sb p states. This picture of the CeSb electronic structure is in agreement with the phenomenological p-f mixing model.[10,11]

The density of states (DOS) is shown in Fig. 2(a) and is quite different from the LSDA DOS [Fig. 2(b)]. There is a large reduction of the density of states at the Fermi level with our LDA+U value of $N(E_F)=6.5$ st/Ry^{-1} compared to the LDA value of about 150 st/Ry^{-1}. The occupied f band with mostly $m=-3$ character interacts in a very anisotropic way with the Sb p bands (see Fig. 3) and even pushes one of the p states (mostly $m=1$ character) above the Fermi level along

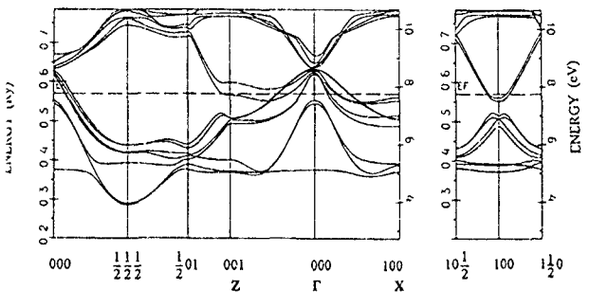

FIG. 1. Band structure of ferromagnetically ordered CeSb. Both rydberg and electronvolt scales are shown.

 0021-8979/94/76(10)/6705/3/$6.00 © 1994 American Institute of Physics

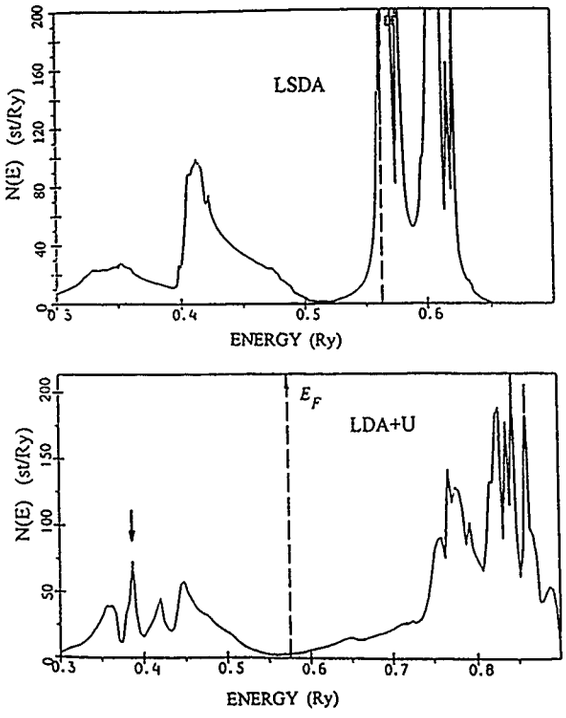

FIG. 2. (a) Total density of states of ground state for the ferromagnetically ordered CeSb in LDA+U. The narrow peak at 0.38 Ry is predominantly $l=3$, $m=-3$, and $\sigma=+1$ in character. The Fermi level is shown by the arrow. (b) Total density of states of ground state for the ferromagnetically ordered CeSb in usual LSDA. The two large peaks correspond to $4f$ "up" and "down" states.

the Γ-Z direction, but not in the Γ-X direction. The anisotropic p-f interaction helps explain the anomalous magnetic properties of CeSb (Ref. 13) with strong magnetic anisotropy in the ferromagnetically ordered phase {our calculated value of magnetic anisotropy as the total energy difference with the magnetic field along [001] and [110] directions is 2.4 meV (standard LSDA calculations give 0.54 meV)}. Such anisotropic p-f mixing for different m subbands near the Fermi

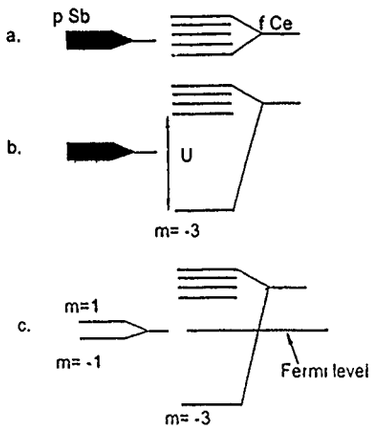

FIG. 3. Schematic picture of Hubbard-induced anisotropy formation in frame of LDA+U for CeSb. (a) Normal LDA structure of p and f bands in CeSb. (b) A shift of one f state of Ce (predominantly with $m=-3$ character). (c) The results of strong p-f hybridization and the creation of a highly polarized structure of p states of Sb.

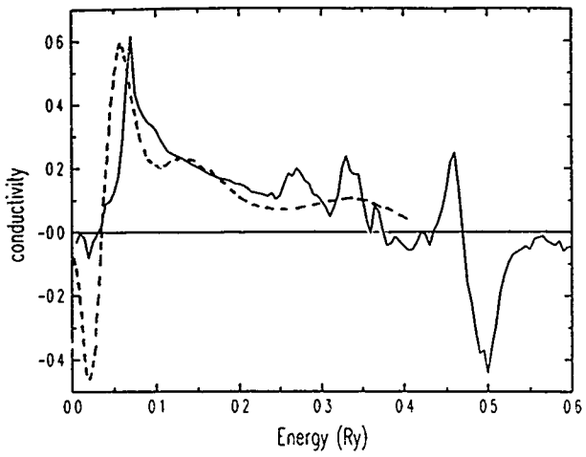

FIG. 4. Interband off-diagonal optical conductivities of CeSb (in 10^{15} s^{-1}). The theoretical curve does not include broadening from quasiparticle lifetime effects or experimental resolution.

level, together with the large spin-orbital coupling of Sb p states (~0.6 eV) leads to particularly strong MO effects.

The nondiagonal part of the conductivity tensor (Fig. 4) is in better agreement with experimental MO spectra[6,14] than the LDA result[7] which qualitatively disagrees with experiment. A serious problem however is the small magnitude of the negative peak at 0.3 eV in comparison with the experimentally predicted MO spectra. This particular peak is of interest because the small value of the diagonal conductivity near this energy helps produce the largest measured Kerr angle of any material. The theoretical θ_k of 5° (at 0.3 eV) is large, but still smaller than the predicted value (>15°) or measured value (of about 14° at 0.5 eV).

Analysis of MO matrix elements shows that the main contribution to the peaks in $\sigma_{xy}(\omega)$ at 0.3 and 0.9 eV comes from the transitions from p to d bands near the Fermi level. Among those states the radial functions consist of an atomic-like p orbital around the Sb site and tails of states from surrounding sites which have some d-like symmetry within the Sb sphere. These are exactly the p bands which interact strongly with the occupied Ce f band and are pushed above E_F along the Γ-Z direction and stay below E_F along Γ-X. One of the interesting consequences of such anisotropy [which comes from the symmetry breaking nature of the LDA+U approach (see Fig. 3)] is that the orbital angular character (m quantum numbers) is further separated than would occur from just the spin-orbit coupling alone. Especially large contributions to $\sigma_{xy}(\omega)$ may be predicted for systems with such a big anisotropy of the f electron angular momentum density. For CeSb there is strong hybridization of one particular f orbital and one p orbital with significant energy shifts near the Fermi level where spin-orbital splitting of p states is also large. With the same mechanism it may be possible to produce strong MO effects using f-d anisotropic hybridization (with materials like CePt, CePtSb, and so on). In any case anisotropy induced contributions to MO may affect significantly the off-diagonal conductivity (but not the diagonal part), and may be another consideration for increasing the MO effect in searching for new MO materials.

ACKNOWLEDGMENTS

This work was carried out at the Ames Laboratory, which is operated for the U S. Department of Energy by Iowa State University under Contract No. W-7405-82. This work was supported by the Director for Energy Research, Office of Basic Energy Sciences of the U.S. Department of Energy.

[1] A. Franciosi, J. Weaver, N. Martensson, and M. Goft, Phys. Rev. B **24**, 3658 (1981).

[2] H. Kitazawa, T. Suzuki, M. Sera, Z. Oguro, A. Yanase, A. Hasegawa, and T. Kasuya, J. Magn. Magn. Mater. **31–34**, 421 (1983).

[3] F. Hillinger, M. Landolt, H. R. Ott, and R. Schmelczer, J. Low Temp. Phys. **20**, 269 (1975).

[4] H. Heer, A. Furrer, W. Halg, and O. Vogt, J. Phys. C **12**, 5207 (1979); H. Bartholin, D. Florence, W. Tcheng-Si, and O. Vogt, Phys. Status Solidi A **24**, 631 (1974).

[5] P. Fisher, B. Lebech, G. Meier, B. D. Rainford, and O. Vogt, J. Phys. C **11**, 345 (1978); G. Meier, P. Fisher, W. Hály, B. Lebech, B. D. Rainford, and O. Vogt, *ibid.* **11**, 1173 (1978); J. Rossat-Mignod, J. M. Effantin, P. Burlet, T. Chattopadhyay, L. P. Regnault, H. Baltholin, O. Vogt, and D. Ravot, J. Magn. Magn. Mater. **52**, 111 (1985).

[6] J. Schoenes, in *High Density Digital Recording*, edited by K. H J. Buschow *et al.* (Kluwer, Amsterdam, 1993), p. 377; W. Reim and J. Schoenes, in *Ferromagnetic materials*, ed. by K. H. J. Buschow and E. P. Wohlfarth (Elsevier, New York, 1990), Vol. 5, p. 165.

[7] S. P. Lim, D. L. Price, and B. R. Cooper, IEEE Trans. Magn. **27**, 3648 (1991).

[8] V. I. Anisimov, J. Zaanen, and O. K. Andersen, Phys. Rev. B **44**, 943 (1991); V. I. Anisimov, and O. Gunnarsson, *ibid.* B **43**, 7570 (1991); V. I. Anisimov, I. V. Solovyev, M. A. Korotin, M. T. Czyzyk, and G. A. Sawatzky, *ibid.* B **48**, 16929 (1993).

[9] A. I. Liechtenstein, V. P. Antropov, and B. N. Harmon, Phys. Rev. B **49**, 2556 (1994).

[10] T. Kasuya, O. Sakai, J. Tanaka, H. Kitazawa, and T. Suzuki, J. Magn. Magn. Mater. **63–64**, 9 (1987).

[11] T. Kasuya, O. Sakai, H. Harima, and M. Ikeda, J. Magn Magn. Mater. **76–77**, 46 (1988).

[12] S. Savrasov and D. Savrasov, Phys. Rev. B **46**, 12181 (1992).

[13] O. Sakai, H. Takahashi, M. Takeshige, and T. Kasuya, Solid State Commun. **52**, 997 (1984); K. Takegahara, H. Takahashi, A. Yanase, and T. Kasuya, *ibid.* **39**, 857 (1981).

[14] J. Schoenes and W. Reim, J. Less Common Metals **112**, 19 (1985); J. Schoenes (unpublished).

Magnetic properties of $Sm_2(Fe,V)_{17}N_y$ coarse powder

Shunji Suzuki, Shinya Suzuki, and Masahito Kawasaki
Minebea Co., Ltd., R&D Center, 1743-1 Asaba, Iwata-Gun, Shizuoka-Ken 437-11, Japan

Magnetic properties and crystal structures of $Sm_2(Fe,V)_{17}N_y$ alloys were studied. Crystal structures of $Sm_2Fe_{17-x}V_x$ alloys varied from Th_2Zn_{17} ($x=0$–1) to $TbCu_7$ ($x=1.5$), and $ThMn_{12}$-type ($x=2$) as a function of vanadium content (x). The alloys were nitrogenated at 823 K for 4 h, and in all cases resulted in the expansion of the crystal lattice. The nitrogenated and annealed $Sm_2Fe_{15.5}V_{1.5}N_y$ coarse powders with 20–74 μm particles showed H_{cJ} of 342 kA/m (4.3 kOe) without fine grinding. It is supposed that one of the reasons of the high coercivity is due to the microstructures of the particles.

INTRODUCTION

Since the discovery of $Sm_2Fe_{17}N_{3-\delta}$ compounds,[1] a number of studies concerning their application for permanent magnets have been reported.[2,3] It is well known that fine grinding, nanostructures, and zinc bonding methods for those alloys improve the coercivity. High energy products around 160 MJ/m^3 (20 MGOe) for bonded magnets have been obtained by compacting an anisotropic fine powder with a resin.[4,5] However, very high compaction pressures are required to achieve the above value. Because of that reason, coarse powders are more advantageous for preparing high performance magnets.

In this study, the nitrogenation of $Sm_2Fe_{17-x}V_x$ alloys were performed and their magnetic properties were investigated in detail. It was found that $Sm_2Fe_{15.5}V_{1.5}N_y$ coarse powder showed the highest coercivity among those alloys and was suitable for bonded magnet materials.

EXPERIMENT

$Sm_2Fe_{17-x}V_x$ ($x=0,0.5,1,1.5,2$) alloys were prepared by induction melting and homogenizing at 1373 K for 12 h, and ground to 20–150 μm in particle size. These powders were nitrogenated at 773–873 K for 4 h under 0.8 MPa of N_2 atmosphere, and some were subsequently annealed at 823 K for 2–16 h. Nitrogenated $Sm_2Fe_{15.5}V_{1.5}$ alloy powders were studied in detail as these showed the highest coercivity compared to other alloy powders. Crystal structures and magnetic properties of these powders were measured by x-ray diffraction with Cu K_α radiation and vibrating sample magnetometry (VSM), respectively. The nitrogen content of alloy powders after a nitrogenation was calculated by the mass change and calibrated from a LECO analyzer (TC-436). A scanning electron microscope (SEM) and an electron probe microanalyzer (EPMA) were also used for the analysis of microstructures of alloy powders.

RESULTS AND DISCUSSION

Figure 1 shows x-ray diffraction patterns of $Sm_2Fe_{17-x}V_x$ ($x=0,0.5,1,1.5,2$) alloys. Crystal structures of the main phase for the alloys varied from Th_2Zn_{17} ($x=0$–1) to $TbCu_7$ ($x=1.5$), and $ThMn_{12}$ type ($x=2$), with the increase of vanadium content. A negligible amount of α-iron is observed in all alloys of $x=0$–2, and the $SmFe_2$ phase is observed for alloys of $x=1.5$ and 2. This is explained by the fact that iron-rich $TbCu_7$ and $ThMn_{12}$ phases compared to the Th_2Zn_{17} phase appear with accompanying samarium-rich $SmFe_2$ phase in highly vanadium substituted alloys. The composition of the $TbCu_7$-type phase for the $Sm_2Fe_{15.5}V_{1.5}$ alloy is estimated to be $Sm_{10.1}(Fe,V)_{89.9}$ from the analysis by EPMA, and is found to be nearly the same as that reported elsewhere.[6] $Sm_2Fe_{17-x}V_x$ alloys were all nitrogenated at 823 K for 4 h, resulting in the expansion of the crystal lattice without a change in structure.

Figure 2 shows the coercivity of nitrogenated $Sm_2Fe_{17-x}V_xN_y$ alloy powders as a function of x value. It is found that H_{cJ} is strongly dependent on the value of x for these alloys. The value of 120 kA/m is obtained for the powder of $x=1.5$ which is not finely ground. In particular, the nitrogenation conditions for $Sm_2Fe_{15.5}V_{1.5}$ alloys were varied in order to study their magnetic properties.

Figure 3 shows x-ray diffraction patterns of $Sm_2Fe_{15.5}V_{1.5}N_y$ alloys nitrogenated at 773–848 K for 4 h. Nitrogen contents of these alloys are also shown in the fig-

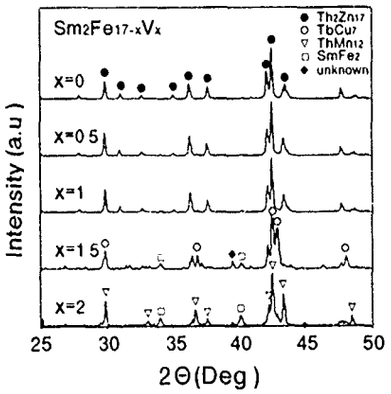

FIG. 1. X-ray diffraction patterns of $Sm_2Fe_{17-x}V_x$ ($x=0,0.5,1,1.5,2$) alloys

0021-8979/94/76(10)/6708/3/$6.00
© 1994 American Institute of Physics

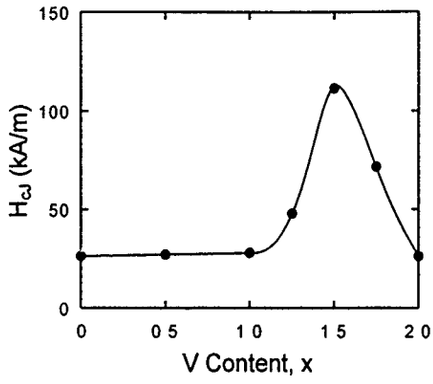

FIG. 2. Coercivity of $Sm_2Fe_{17-x}V_xN_y$ alloy powders nitrogenated at 823 K for 4 h as a function of x value.

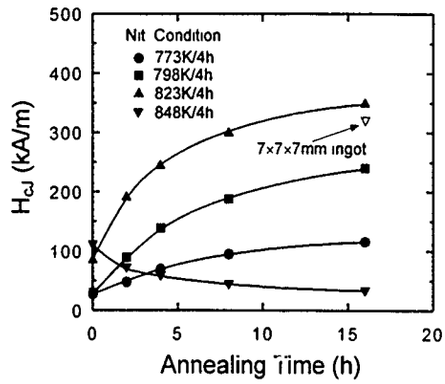

FIG. 4. Coercivity of $Sm_2Fe_{15.5}V_{1.5}N_y$ powders annealed at 823 K for 2–16 h after nitrogenation at 773–848 K for 4 h.

ure. Reflection peaks of the $TbCu_7$-type phase are shifted toward the lower angle and are broadened with increasing temperatures and the peaks of the $SmFe_2$ phase are suppressed by the nitrogenation. Nitrogen contents of these alloys are considerably higher than those of $Sm_2Fe_{17}N_{3-\delta}$ alloys nitrogenated by N_2 gas. In addition, it was found that nitrogen contents of an ingot of 7×7×7 mm in dimension were as high as those of powders prepared by similar nitrogenation conditions. Nitrogen atoms are thought to be diffused into the lattice and crystal boundaries. Heat treatment is performed in order to help diffusions of nitrogen atoms, because the distribution of nitrogen atoms in coarse powders compared to fine powders is thought to be heterogeneous.[7]

Figure 4 shows the coercivity of $Sm_2Fe_{15.5}V_{1.5}N_y$ powders annealed at 823 K for 2–16 h after nitrogenation at 773–848 K for 4 h. It is found that annealing after nitrogenation remarkably enhances the coercivity. H_{cJ} of nitrogenated powders before annealing increases with increasing nitrogenation temperatures and has a value of 116 kA/m for 848 K, where the x-ray diffraction peaks are fairly broadened and the crystal perfection is lowered as shown in Fig. 3. The annealing time also affects the coercivity which increases with time. The highest value in H_{cJ} of 330 kA/m is obtained for the powder annealed at 823 K for 16 h after nitrogenation at 823 K for 4 h. High H_{cJ} is also obtained for the 7×7×7 mm ingot as denoted by ∇ in the figure. The reason for the decrease in H_{cJ} after the annealing of the powder nitrogenated at 848 K is due to an acceleration of a decomposition of the principal $TbCu_7$ phase. The distribution of nitrogen atoms in particles by EPMA observation showed little change during annealing. The effect of annealing on the coercivity is now under study.

Figure 5 shows the hysteresis loop and magnetization curve of anisotropic $Sm_2Fe_{15.5}V_{1.5}N_y$ powder with 20–74 μm particles nitrogenated at 823 K for 4 h and annealed at 823 K for 16 h. As shown in the figure, H_{cJ} of 342 kA/m (4.3 kOe) and a remanence of 1.08 T are obtained from the coarse powder. Little change in particle size of the powder after the nitrogenation was observed, however, a few cracks on the surface of the particles were observed by SEM. A feature characteristic of pinning is observed in the magnetization curve of the present compound. This is distinct from the behavior of $Sm_2Fe_{17}N_3$ although the reason for this distinction is not yet clear.

Figure 6 shows the dependence of H_{cJ} for $Sm_2Fe_{15.5}V_{1.5}N_y$ and $Sm_2Fe_{17}N_3$ powders on particle size. $Sm_2Fe_{15.5}V_{1.5}N_y$ particles were prepared by sieving the nitrogenated and annealed powders with 20–150 μm particles, while 1–3 μm particles were prepared by grinding using a

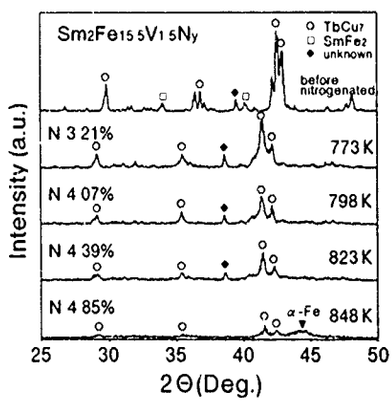

FIG 3 X-ray diffraction patterns of $Sm_2Fe_{15.5}V_{1.5}N_y$ alloys nitrogenated at 773–848 K for 4 h

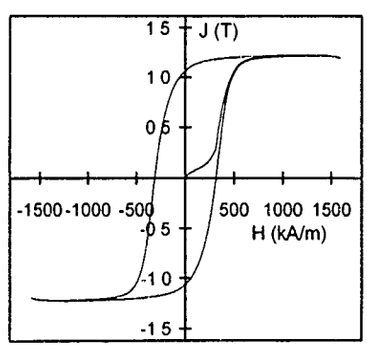

FIG. 5. Hysteresis loop and magnetization curve of anisotropic $Sm_2Fe_{15.5}V_{1.5}N_y$ powder nitrogenated at 823 K for 4 h and annealed at 823 K for 16 h.

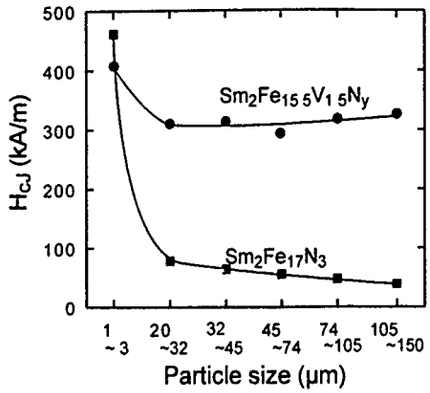

FIG. 6. Dependence of H_{cJ} of $Sm_2Fe_{15.5}V_{1.5}N_y$ and $Sm_2Fe_{17}N_3$ powders on particle size.

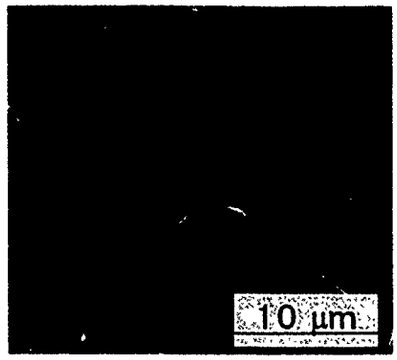

FIG. 7. SEM picture of nitrogenated and annealed $Sm_2Fe_{15.5}V_{1.5}N_y$ powder.

jet mill after annealing. The data of $Sm_2Fe_{17}N_3$ particles prepared by the authors were reproduced from Ref. 8. Both powders show high coercivity for particles of 1–3 μm. An increase in H_{cJ} for the fine particles can be explained by the behavior of single magnetic domain particles.[9] On the other hand, the values of H_{cJ} for $Sm_2Fe_{15.5}V_{1.5}N_y$ are several times higher than those for $Sm_2Fe_{17}N_3$ for the particles of 20–150 μm, and are not affected by particle size.

Figure 7 shows the microstructure of nitrogenated and annealed $Sm_2Fe_{15.5}V_{1.5}N_y$ powder as observed by SEM. The particles have polycrystalline structure with 10–30 μm grains, and show laminated structures with submicron spaces which are not observed before nitrogenation. These microstructures are one possible reason of the high coercivity.

CONCLUSION

Crystal structures of $Sm_2Fe_{17-x}V_x$ alloys changed as a function of vanadium content (x). Among nitrogenated $Sm_2Fe_{17-x}V_xN_y$ alloys, $Sm_2Fe_{15.5}V_{1.5}N_y$ alloy powder with $TbCu_7$-type structure absorbed more than 4 wt % of nitrogen, and showed H_{cJ} of 342 kA/m (4.3 kOe) without fine grinding. A feature characteristic of pinning was observed in the magnetization curve of the coarse powder, although this kind of pinning could not be observed in the behavior of $Sm_2Fe_{17}N_3$.

ACKNOWLEDGMENT

The authors thank Professor H. Yamamoto of Meiji University for valuable discussions for this study.

[1] J. M. D. Coey and H. Sun, J. Magn. Magn. Mater. **87**, L251 (1990).
[2] K. Schnitzke, L. Schultz, J. Wecker, and M. Katter, Appl. Phys. Lett. **57**, 2853 (1990).
[3] Y. Otani, A. Moukarika, H. Sun, and J. M. D. Coey, J. Appl. Phys. **69**, 6735 (1991).
[4] T. Iriyama, K. Kobayashi, N. Imaoka, T. Fukuda, H. Kato, and Y. Nakagawa, IEEE Trans. Magn. **28**, 2326 (1992).
[5] S. Suzuki, T. Miura, and M. Kawasaki, IEEE Trans. Magn. **29**, 2815 (1993).
[6] M. Katter, J. Wecker, and L. Schultz, J. Appl. Phys. **70**, 3188 (1991).
[7] J. M. D. Coey, *Proceedings of the 6th International Conference on Ferrites, Japan* (Japan Society of Powder and Powder Metallurgy, Kyoto, 1992), p. 1064.
[8] S. Suzuki and T. Miura, IEEE Trans. Magn. **28**, 994 (1992).
[9] K. Kobayashi, T. Iriyama, T. Yamaguchi, H. Kato, and Y. Nakagawa, J. Alloys Comp. **193**, 235 (1993).

Mössbauer study of $R_2Fe_{17}C_x$ (R=Tb,Dy) as-quenched intermetallics compounds

Hua-Yang Gong,[a] Bao-Gen Shen, Lin-Shu Kong, Lei Cao, Wen-Shan Zhan, Zhao-Hua Cheng, and Fang-Wei Wang

State Key Laboratory for Magnetism, Institute of Physics, Chinese Academy of Science, 100080 Beijing, People's Republic of China

Intermetallics compounds $Dy_2Fe_{17}C_x$ (x=1.5,2.0,2.5,2.8) and $Tb_2Fe_{17}C_x$ (x=1.5,2.0,2.5) have been successfully prepared by the melt-spinning method. The x-ray-diffraction patterns and the thermomagnetic curves show that they are single phase with the rhombohedral Th_2Zn_{17}-type structure, except for $Dy_2Fe_{17}C_{2.8}$ and $Tb_2Fe_{17}C_{2.5}$ which have a small percentage of α-Fe. ^{57}Fe Mössbauer spectra were measured at 12 K and room temperature to study both the magnetic properties of $R_2Fe_{17}C_x$ on a local scale and the effect of the interstitial C atom on the Fe atoms. It is found that the effective hyperfine fields of the various Fe sites decrease in the order $6c>18f>18h>9d$. The average effective hyperfine fields H_{eff} at 12 and 293 K do not change much with C concentration x in agreement with the moment of the Fe atoms obtained by magnetic measurements at 1.5 K. It can be concluded that the effect of C is to enhance the exchange interaction between Fe-Fe atoms, which is sensitive to the distance of Fe-Fe atoms. The C has little influence on the moments of Fe atoms.

I. INTRODUCTION

Introduction of interstitial nitrogen or carbon atoms into R_2Fe_{17} intermetallic compounds results in a significant improvement of the magnetic properties of these compounds. The carbides $R_2Fe_{17}C_x$ ($x\approx2.5$), prepared by a gas-solid reaction, have unit-cell volumes about 6.5% larger, Curie temperatures of 760 K, and room-temperature anisotropy fields of 15±0.5 T.[1] These carbides are promising new materials for applications as permanent magnets, however, their drawback is high-temperature unstability. In our previous work we have discovered that the carbides $R_2Fe_{17}C_x$ with high carbon concentration can be prepared by melt spinning. The melt-spun $R_2Fe_{17}C_x$ compounds were found to be stable at high temperature and to retain the Th_2Zn_{17}-type or Th_2Ni_{17}-type structure up to at least 1273 K. We have successfully obtained the melt-spun $R_2Fe_{17}C_x$ (R=Y, Gd, Tb, Ho, Er, and Tm; x=0–3.0) compounds and systematically studied their structure and magnetic properties.[2–5] In this article, we report the Mössbauer effect spectra of $R_2Fe_{17}C_x$ (R=Tb, Dy, x=1.5,2.0,2.5,2.8) compounds prepared by melt spinning.

II. EXPERIMENT

Iron and carbon were first arc melted into Fe-C alloys, and then R, Fe, and Fe-C alloy were melted, by arc melting in an argon atmosphere of high purity, into homogeneous buttons with the compositions $R_2Fe_{17}C_x$ (R=Tb, Dy, $1.5\leqslant x\leqslant2.8$). For homogeneity the ingots were melted several times. The purities of the elements used were at least 99.9% After arc-melting, the ingots were melt spun under a high-purity argon atmosphere on the surface of a rotating copper wheel. The quenching rate was varied by changing the surface velocity of the copper wheel between 0 and 47 m/s. The ribbons obtained were about 1 mm wide and 20–30 μm thick.

X-ray-diffraction measurements were performed on the melt-spun ribbons using Co$K\alpha$ radiation to identify the phase components and determine the crystallographic structure. The Curie temperatures were determined from the temperature dependence of the magnetization measured in a vibrating sample magnetometer in a magnetic field of 1 kOe.

The ^{57}Fe Mössbauer spectra were recorded using a constant-acceleration spectrometer (Oxford MS-500) in transmission geometry with a ^{57}Co source. Temperature control to better than ±0.1 K was achieved by the use of a proportional temperature controller. The data were analyzed using a least-squares-fitting program.

III. EXPERIMENTAL RESULTS AND ANALYSIS

X-ray-diffraction experiments show that the cast compounds $R_2Fe_{17}C_x$ (R=Tb, Dy, $1.5\leqslant x\leqslant2.8$) are single phase with the rhombohedral Th_2Zn_{17}-type structure. Table I lists the lattice parameters, unit-cell volumes, Curie temperatures, and M_s. The addition of C to the R_2Fe_{17} leads to an expansion of the unit cell. The $Tb_2Fe_{17}C_{2.5}$ compound has a unit-cell volume about 5.6% larger than that of Tb_2Fe_{17}. For $Dy_2Fe_{17}C_{2.8}$ the unit-cell volume expansion is about 6.3% compared with the carbon-free compound. The T_c of these compounds is found to increase with increasing C concentration. It is commonly assumed that the Curie temperature of rare-earth–iron compounds is determined by the Fe-Fe, R-Fe, and R-R interactions. In general, the Fe-Fe interaction is dominant, the R-R interaction is negligible, and the influence of R-Fe interaction yields the difference in T_c among the different rare-earth compounds. The increase in Curie temperature of the carbides or nitrides is mainly due to the increase in the Fe-Fe ferromagnetic interaction which results from the increased interatomic distance produced by the carbon or nitrogen.

[a]Also with Iron and Steel Research Institute of Wuhan Iron and Steel Co., 430080 Wuhan, People's Republic of China.

 0021-8979/94/76(10)/6711/3/$6.00 © 1994 American Institute of Physics

TABLE I. Structure and magnetic data for $Tb_2Fe_{17}C_x$ and $Dy_2Fe_{17}C_x$.

Compounds	a (Å)	c (Å)	V (Å^3)	$\Delta V/V$ (%)	T_c (K)	M_s (μ_B)
Dy_2Fe_{17}[a]	8.767	8.312	516.0		367[b]	
$Dy_2Fe_{17}C_{1.5}$	8.621	12.454	804.6	4.0	578	15.4
$Dy_2Fe_{17}C_{2.0}$	8.645	12.449	814.6	5.2	626	16.1
$Dy_2Fe_{17}C_{2.5}$	8.669	12.585	820.1	6.0	680	15.0
$Dy_2Fe_{17}C_{2.8}$	8.667	12.613	822.5	6.3	676	17.0
Tb_2Fe_{17}[a]	8.473	8.323	517.5		404[b]	
$Tb_2Fe_{17}C_{1.5}$	8.643	12.465	806.4	3.9	610	16.4
$Tb_2Fe_{17}O_{2.0}$	8.664	12.536	814.9	5.0	656	17.4
$Tb_2Fe_{17}O_{2.5}$	8.680	12.559	819.5	5.6	698	23.6

[a]Reference 6.
[b]Reference 7.

The ^{57}Fe Mössbauer spectra of $Dy_2Fe_{17}C_x$ (x=1.5,2.0, 2.5,2.8) and $Tb_2Fe_{17}C_x$ (x=1.5,2.0,2.5) at 12 and 293 K are shown by dots in Figs. 1 and 2. There are four crystallographically nonequivalent Fe sites, denoted in Wyckoff notation by 6c, 9d, 18f, and 18h for the Th_2Zn_{17} structure type. However, when the easy magnetization direction is perpendicular to the c axis, the spectra consist of more than four independent subspectra. Owing to differences in angle between the magnetization direction and the direction of the principal axis of the electric-field gradient tensor, the crystallographically equivalent iron atoms of a given subgroup will become magnetically nonequivalent.[8] In addition, the magnetic dipolar fields also make the situation complex. According to a calculation of the field gradients by means of a point charge model and calculations of the magnetic dipole field, the 2:17 compounds with magnetization direction perpendicular to the c axis should be analyzed in terms of seven independent subspectra. However, for $Dy_2Fe_{17}C_{2.8}$ and $Tb_2Fe_{17}C_{2.5}$ we use eight subspectra to count in the α-Fe contribution.

For $Dy_2Fe_{17}C_x$ and $Tb_2Fe_{17}C_x$ a further subdivision of the 18f, 18h, 9d sites into two groups with a relative intensity ratio of 1:2 is assumed. The relative intensity ratios for each of the spectral components were constrained to 6:6:12:6:12:3:6, corresponding to 6c, 18f_1, 18f_2, 18h_1, 18h_2, 9d_1, and 9d_2 in the crystal structure. Relative areas of the lines in each sextet were constrained in the ratio 3:2:1:1:2:3, as is required for a randomly oriented power sample. Different linewidths were used for the inner, middle, and outer pairs lines. To assign the subspectra to the various sites, we refer to our previous ^{57}Fe Mössbauer studies of $Er_2Fe_{17}C_2$. Below the spin-reorientation temperature T_{sr},[9] it was found that acceptable fits can be obtained by assuming that the hyperfine fields decrease in the order of 6c>18f >18h>9d. Therefore, we analyzed the spectra of $Dy_2Fe_{17}C_x$ and $Tb_2Fe_{17}C_x$ in the same way.

The results of the fitting procedure are shown by the solid curves in Figs. 1 and 2. The average hyperfine fields are weighted by the contribution of the various sites. The average hyperfine fields of $Dy_2Fe_{17}C_x$ and $Tb_2Fe_{17}C_x$ at 12 and 293 K are plotted as a function of C content in Fig. 3 which illustrates that the hyperfine fields are almost independent of C content. For $Dy_2Fe_{17}C_x$, H_{eff} even shows a small decrease as the C concentration increases. It has been found that the

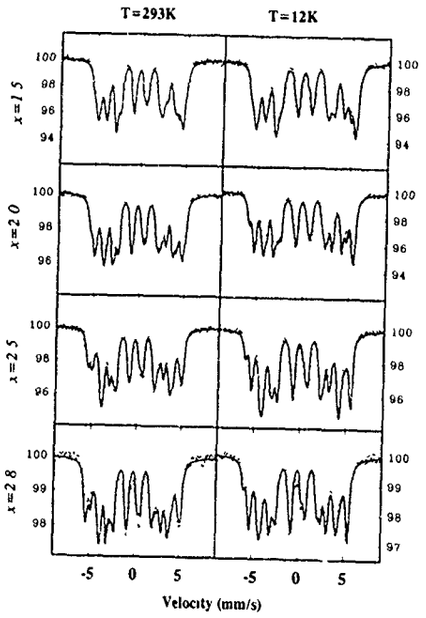

FIG 1. ^{57}Fe Mossbauer spectra of $Dy_2Fe_{17}C_x$ at 12 and 293 K. The solid curves are fits to the spectra

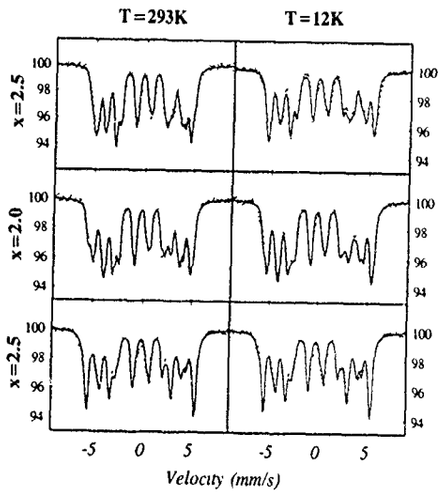

FIG. 2. ^{57}Fe Mossbauer spectra of $Tb_2Fe_{17}C_x$ at 12 and 293 K. The solid curves are fits to the spectra.

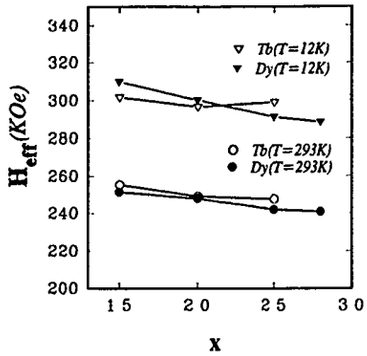

FIG. 3. Dependence on C content x of the average hyperfine field for $Dy_2Fe_{17}C_x$ and $Tb_2Fe_{17}C_x$.

average hyperfine fields are nearly proportional to the average iron moment.[10] This indicates that the interstitial C atom has little influence on the iron moment. This conclusion agrees with our previous magnetic studies on the $R_2Fe_{17}C_x$ compounds, which showed that the saturation magnetization M_s, at 1.5 K does not change much with increasing C concentration. This situation is different for $R_2Fe_{17}N_x$ obtained by gas-solid interaction, in which interband electron transfer is believed to occur,[11] the iron moments increase with the nitrogen, and the average hyperfine fields are approximately 4 T larger in the parent alloy. This indicates that the influence of interstitial C atoms on the Fe sublattice is different from that of N atoms due to their different electronic configuration. Nitrogen has a larger electronegativity than that of carbon.

ACKNOWLEDGMENTS

This work was supported by the State's Science and Technology Commission and the National Natural Science Foundation of China.

[1] L.-X. Liao, X. Chen, Z. Altounian, and D. H. Ryan, Appl. Phys. Lett. **60**, 129 (1992).
[2] B.-G. Shen, L.-S. Kong, and L. Cao, Solid State Commun. **83**, 753 (1992).
[3] L.-S. Kong, L. Cao, and B.-G. Shen, J. Magn. Magn. Mater. **115**, L137 (1992).
[4] L. Cao, L.-S. Kong, and B.-G. Shen, J. Phys. Condens. Matter **4**, L515 (1992).
[5] L.-S. Kong, L. Cao, and B.-G. Shen, J. Alloys Compounds **191**, 301 (1993).
[6] K. H. J. Buschow, R. Coehoorn, D. B. de Mooij, K. de Waard, and T. H. Jaccobs, J. Magn. Magn. Mater. **92**, L35 (1990).
[7] H. Sun, J. M. D. Coey, Y. Otani, and D. P. F. Hurley, J. Phys. Condens. Matter **2**, 6465 (1990).
[8] W. Steiner and R. Haferl, Phys. Status Solidi A **42**, 739 (1977).
[9] L.-S. Kong, B.-G. Shen, L. Cao, H.-Y. Gong, and Y.-L. Chen, Solid State Commun. **85**, 1011 (1993).
[10] K. H. J. Buschow, in *Ferromagnetic Materials. A Handbook on the Properties of Magnetically Ordered Substances*, edited by E. P. Wohlfarth and K. H. J. Buschow (North-Holland, Amsterdam, 1988), Vol. 4, p. 60.
[11] B.-P. Hu, H.-S. Li, H. Sun, and J. M. D. Coey, J. Phys. Condens. Matter **3**, 3983 (1991).

Magnetic properties of $Tm_2Fe_{17}C_x$ ($0 \leq x \leq 2.8$) compounds prepared by melt spinning

Bao-Gen Shen, Lin-Shu Kong, Lei Cao, Hua-Yang Gong, Fang-Wei Wang, Zhao-Hua Cheng, and Jian-Gao Zhao
State Key Laboratory of Magnetism, Institute of Physics, Chinese Academy of Sciences, P.O. Box 603, Beijing 100080, People's Republic of China

The formation, structure, and magnetic properties of $Tm_2Fe_{17}C_x$ compounds with $x=0$, 0.5, 1.0, 1.5, 2.0, 2.5, and 2.8 were studied. The samples with $x \leq 1.0$ were arc melted and heat treated at 1370 K for 14 h. The carbides were prepared by melt spinning at appropriate quenching rates of $v_s=10$–20 m/s for $1.5 \leq x \leq 2.5$ and by the crystallization from corresponding amorphous for $x=2.8$. X-ray diffraction and thermomagnetic measurements show that all samples studied are single phase with the hexagonal Th_2Ni_{17}-type structure except for $Tm_2Fe_{17}C_{2.8}$, which contains a few percent of α-Fe. The lattice parameters a,c and the unit-cell volumes v increase as the carbon concentration x increases. The Curie temperature is found to rise with x from 260 K for $x=0$ to 669 K for $x=2.8$. The saturation magnetization M_s at 1.5 K is found to be 92.2–97.1 emu/g as x varies from 0 to 2.8, and the carbon concentration dependence of the Fe moment is approximately constant ($2.12 \pm 0.04 \mu_B$). The spin-reorientation transitions are observed. The spin-reorientation temperature is found to increase with the carbon concentration for $x \leq 1.5$, and then has a slight decrease with x for $x>1.5$.

I. INTRODUCTION

In previous works[1–3] we have shown that the interstitial carbides $R_2Fe_{17}C_x$ with higher carbon concentration can be prepared by the melt-spinning method. These carbides are found to be single phase up to carbon concentration $x=2$ for R=Y and Gd and $x=2.8$ for R=Dy, Ho, and Er. As compared with the carbon-free parent compounds, the unit-cell volume expansion in the carbide with $x=2.8$ is about 6%–7% and the Curie temperature increase is about 400 K, which are comparable to those of corresponding nitrides or carbides produced by solid-gas reaction. It is notable that the $R_2Fe_{17}C_x$ compounds obtained by melt spinning are stable at high temperatures at least up to 1000 °C.[1–3] We have reported the formation, structure, and magnetic properties of $R_2Fe_{17}C_x$ (R=Y, Gd, Tb, Dy, Ho, and Er) compounds.[1–5] For $Tm_2Fe_{17}C_x$ with $x \leq 1.4$, a number of investigations have been made, however, when the carbon concentration x is higher than 1.5, the carbides have not been investigated in detail because the interstitial carbon concentration is limited to about $x=1.5$ by arc melting and is not well controlled by a gas-solid-phase interstitial modification. In this article, the structure, intrinsic magnetic properties and spin reorientation are reported for melt-spun $Tm_2Fe_{17}C_x$ compounds with the higher carbon concentration of up to $x=2.8$.

II. EXPERIMENT

Iron (99.9% in purity), thulium (99.9%), and Fe-C alloy (99.8%) were melted by arc melting in an argon atmosphere of high purity into homogeneous buttons with composition $Tm_2Fe_{17}C_x$ ($x=0$, 0.5, 1.0, 1.5, 2.0, 2.5, and 2.8). The alloys were melted several times to ensure homogeneity. After melting, the ingots with $x \leq 1.0$ were then annealed in a steel tube in a highly purified argon atmosphere at 1370 K for 14 h, resulting in the formation of single-phase compounds of the 2:17-type structure, while for $x \geq 1.5$ the ingots of about 3 g were melt spun on the outside of a copper wheel rotating with the surface speeds of 0–47 m/s. Ribbons about 1 mm wide and 20–30 μm thick were produced. X-ray-diffraction measurements were made to determine the single-phase and crystallographic structure. The magnetizations at 1.5 and 300 K were measured by using an extracting sample magnetometer with a field up to 65 kOe. The Curie temperatures were determined from the temperature dependence of the magnetization measured by using a vibrating sample magnetometer under a field of 1 kOe. The spin-reorientation temperatures were determined from the ac susceptibility versus temperature curves measured at an ac magnetic field of less than 1 Oe.

III. RESULTS AND DISCUSSION

X-ray-diffraction measurements show that the arc-melted ingots $Tm_2Fe_{17}C_x$ with $x \leq 1$ are single phase with a hexagonal Th_2Ni_{17}-type structure. When the carbon concentration x is greater than 1.5, the $Tm_2Fe_{17}C_x$ ingots show a multiphase structure with α-Fe coexisting with the rare-earth carbides and the 2:17 phases. The amounts of α-Fe phase increase with increasing carbon concentration and become a majority for $x \geq 2.0$; however, the single phase of $Tm_2Fe_{17}C_x$ with $1.5 \leq x \leq 2.5$ can be obtained by melt spinning. The as-quenched samples revealed a hexagonal Th_2Ni_{17} structure. It is found that the formation of the single-phase $Tm_2Fe_{17}C_x$ is sensitive to the quenching rates. The optimal quenching rates are only a relatively narrow range of 10–20 m/s. For $x=2.8$, the preparation of single-phase compound is difficult by direct quenching; however, the sample of almost single phase can be obtained by the crystallization from a corresponding amorphous $Tm_2Fe_{17}C_{2.8}$ alloy prepared at a speed of 47 m/s. Figure 1 shows the example of the x-ray-diffraction patterns with Co$K\alpha$ radiation for the $Tm_2Fe_{17}C_x$ compounds with $x=0.5$, 1.5, and 2.8.

 0021-8979/94/76(10)/6714/3/$6.00 © 1994 American Institute of Physics

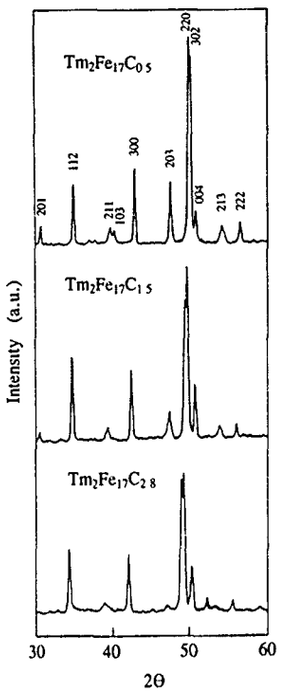

FIG. 1. X-ray-diffraction patterns of $Tm_2Fe_{17}C_x$ with $x=0.5$, 1.5, and 2.8.

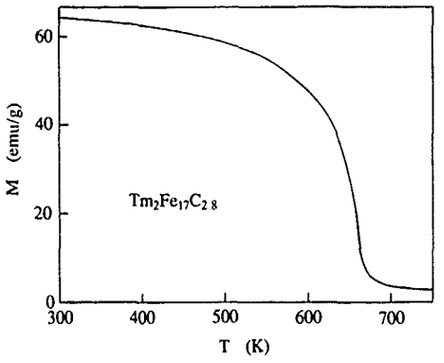

FIG. 2. Temperature dependence of the magnetization measured in a field of 1 kOe for $Tm_2Fe_{17}C_{2.8}$.

The lattice constants and unit-cell volumes of $Tm_2Fe_{17}C_x$ compounds are listed in Table I. Both lattice parameters a and c, and the volumes v dilate upon carbonation and rise monotonically with increasing carbon concentration, which is consistent with the reported results for the melt-spun $R_2Fe_{17}C_x$ with R=Dy, Ho, and Er.[1–3] The relative cell volume increase $\Delta v/v$ is 1.0%–6.8% as x increases from 0.5 to 2.8, also shown in Table I. For $x=2.8$ the value of $\Delta v/v$ is comparable to that of the corresponding nitrides or carbides produced by gas-solid reaction.[6]

Curie temperature T_c of $Tm_2Fe_{17}C_x$ were determined from the temperature dependence of magnetization measured at a field of 1 kOe. As an example, the magnetization versus temperature curve for $x=2.8$ is shown in Fig. 2. Values of T_c are listed in Table I. T_c is found to rise remarkably with increasing carbon concentrations. When $x=2.8$, T_c is about 400 K higher than that of the parent compound Tm_2Fe_{17}. In rare-earth Fe-rich compounds, the Curie temperature depends mainly on the exchange interactions between Fe-Fe atoms, which is sensitive to the distance between Fe-Fe atoms. The increase of Curie temperature with x demonstrates that the introduction of interstitial carbon atoms results in the increase of Fe-Fe interactions in $Tm_2Fe_{17}C_x$. It seems reasonable to suggest that the volume expansion has an essential effect on the Curie temperature.[4]

The saturation magnetizations M_s(1.5 K) and M_s(300 K) measured by using an extracting sample magnetometer in a field of 65 kOe at 1.5 and 300 K, respectively, are also summarized in Table I. The M_s(1.5 K) of $Tm_2Fe_{17}C_x$ is found to be 92.2–97.1 emu/g, as x varies from 0 to 2.8. A small effect of the interstitial carbon atoms on the M_s(1.5 K) is observed. The antiparallel coupling between the rare-earth spin moment and the Fe moment for heavy-rare-earth compounds leads to ferrimagnetism. For $Tm_2Fe_{17}C_x$, the saturation moment μ_s can be expressed as

$$\mu_s = 17\mu_{Fe} - 2\mu_{Tm}, \tag{1}$$

where μ_{Fe} and μ_{Tm} are the Fe and Tm magnetic moments, respectively. The μ_{Tm} can be assumed to be $7\mu_B$, which is the moment of a free Tm^{3+}. According to Eq. (1), the Fe magnetic moment is obtained, as shown in Table I. The μ_{Fe} is found to be $2.12\pm0.04\mu_B$, being almost independent of carbon concentration.

The room-temperature saturation magnetization M_s(300 K) is found to increase with increasing carbon concentration for $x\leqslant1.5$, then has an approximately constant value of 123.4 emu/g for $x\geqslant1.5$. The increase of the M_s(300 K) at lower carbon concentration is due to the enhancement of the Curie temperature which shifts the thermomagnetization curve to higher temperature.

TABLE I. Structure and magnetic parameters of $Tm_2Fe_{17}O_x$ with $0\leqslant x\leqslant2.8$.

Composition	a (Å)	c (Å)	v (Å^3)	$\Delta v/v$ (%)	T_c (K)	M_s(300 K) (emu/g)	M_s(1.5 K) (emu/g)	μ_s (μ_B)	μ_{Fe} (μ_B)	T_{sr} (K)
Tm_2Fe_{17}	8.422	8.278	510.9		260	80.7	92 7	21.36	2.08	
$Tm_2Fe_{17}C_{0.5}$	8.469	8.308	516.0	1.0	432	108.0	95 6	22.13	2.13	144
$Tm_2Fe_{17}C_{1.0}$	8.499	8 341	521.8	2.1	517	111 0	97.1	22.59	2 15	178
$Tm_2Fe_{17}C_{1.5}$	8.546	8.351	528.2	3.4	558	124.0	94.7	22.13	2.13	216
$Tm_2Fe_{17}C_{2.0}$	8.567	8.348	532.9	4 3	604	123 1	93.8	22.02	2.12	221
$Tm_2Fe_{17}C_{2.5}$	8.617	8.406	540.5	5.8	624	123 9	92.2	21.74	2.10	209
$Tm_2Fe_{17}C_{2.8}$	8.640	8.443	545.8	6.8	669	122.7	95.4	22.55	2.15	208

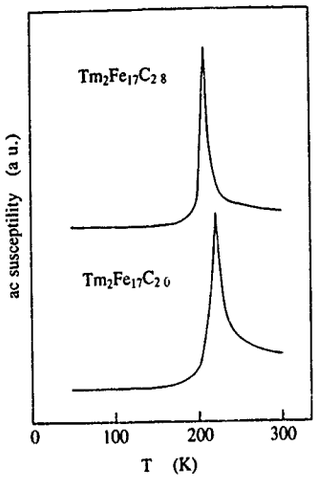

FIG. 3. Temperature dependence of the ac susceptibility of $Tm_2Fe_{17}C_x$ with $x=2.0$ and 2.8.

The spin reorientation in $Tm_2Fe_{17}C_x$ is observed from the measurements on ac susceptibility versus temperature curves. Examples of these measurements are shown in Fig. 3. The spin-reorientation temperatures T_{sr} are summarized in Table I and Fig. 4. Figure 4 also presents the experimental data reported by Zhao *et al.*[7] and Gubbens *et al.*[8] for comparison. It is known that the spin reorientation in the rare-earth–iron compounds generally results from the competing anisotropies with different temperature dependence for the rare-earth and iron sublattices. The introduction of carbon atoms ($x \leq 1.5$) into Tm_2Fe_{17} leads to the enhancement of spin-reorientation temperature. This demonstrates that the Tm sublattice anisotropy has a strong enhancement for $x \leq 1.5$. When the carbon concentration x is richer than 1.5, the T_{sr} is found to decrease slightly, indicating that the Tm sublattice anisotropy has a little change at higher carbon concentration.

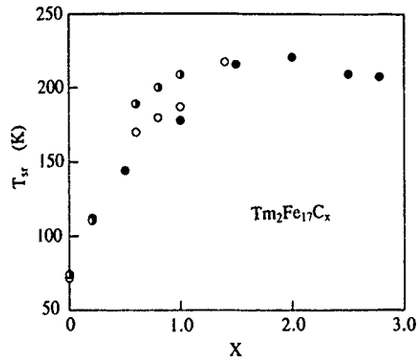

FIG. 4. The spin-reorientation temperature of $Tm_2Fe_{17}C_x$ as a function of carbon concentration x: (●) present results; other data are taken from (○) Zhao *et al.* (Ref. 7) and (◑) Gubbens *et al.* (Ref. 8).

ACKNOWLEDGMENTS

This work was supported by the State's Sciences and Technology Commission and The National Natural Science Foundation of China.

[1] B.-G. Shen, L.-S. Kong, and L. Cao, Solid State Commun. **83**, 753 (1992).
[2] L.-S. Kong, L. Cao, and B.-G. Shen, J. Magn. Magn. Mater. **115**, L137 (1992).
[3] L. Cao, L.-S. Kong, and B.-G. Shen, J. Phys. Condens. Matter **4**, L515 (1992).
[4] L.-S Kong, L. Cao, and B.-G. Shen, J. Alloys Compounds **191**, 301 (1993).
[5] L. Cao, L.-S. Kong, and B.-G. Shen, J. Phys. Condens. Matter **5**, 2001 (1993).
[6] L.-X. Liao, X. Chen, Z. Altounian, and D. H. Ryan, Appl. Phys. Lett. **60**, 129 (1992).
[7] T.-S. Zhao, X.-C. Kou, R. Grössinger, and H. R. Kirchmayr, J. Appl. Phys. **73**, 6041 (1993)
[8] P. C. M. Gubbens, A. M. van der Kraan, T H. Jacobs, and K. H. J. Buschow, J. Magn. Magn. Mater. **80**, 265 (1989).

Kerr microscopy observation of carbon diffusion profiles in $Sm_2Fe_{17}C_x$

J. Zawadzki,[a] P. A. P. Wendhausen, B. Gebel, A. Handstein, D. Eckert, and K.-H. Müller
Institut für Festkörper und Werkstofforschung Dresden, D-01171 Dresden, Germany

The effect of carbon diffusion from CH_4 gas into coarse Sm_2Fe_{17} powder on the magnetic domain structure (MDS) was studied at room temperature by means of the magneto-optical polar Kerr effect. The diffusion occurs initially along preferential paths and then through the bulk. A gradual variation in the MDS through incompletely carburized grains was observed, which reflects local changes in spontaneous magnetization and magnetic anisotropy. This suggests the existence of smooth "bathtublike" carbon concentration profiles. An acceleration of the carburization process caused by cracking of grains during the diffusion was observed. The diffusivity R of carbon in Sm_2Fe_{17} at 450 °C was estimated to be 2.5×10^{-16} m^2/s. For $Sm_2Fe_{17}C_{2.2}$ the domain-wall energy density is $\gamma=3.1\times10^{-2}$ J/m^2, the domain-wall thickness $\delta=3.3$ nm, the single-domain particle size $D_c\approx0.3$ μm, and the exchange constant $A=8.1\times10^{-12}$ J/m.

I. INTRODUCTION

Recently much attention has been focused on the ternary interstitial $Sm_2Fe_{17}Z_x$ (Z=N,C) phases with rhombohedral Th_2Zn_{17}-type crystallographic structure. $Sm_2Fe_{17}Z_x$ compounds can be formed, e.g., by melting processes in the case of carbon[1] or by heating Sm_2Fe_{17} powder in nitrogen- or carbon-containing gases at elevated temperatures. They have excellent intrinsic magnetic properties, which can exceed those of $Nd_2Fe_{14}B$.[2–5] For instance, by absorbing carbon the Sm_2Fe_{17} compound changes its magnetic anisotropy from planar to uniaxial, connected with an anisotropy field up to about 16 T.[4] Simultaneously, a substantial increase of the Curie temperature from 389 K up to about 700 K is observed. Nitrogen has a similar or even more pronounced effect on the magnetic properties of Sm_2Fe_{17}. Understanding of the coercivity mechanism in $Sm_2Fe_{17}C_x$ materials requires the knowledge of their microstructure as well as their magnetic domain structure (MDS). Fundamental parameters controlling the nucleation as well as the pinning mechanism are the domain-wall width δ, the wall energy density γ, and the single-domain particle size D_c. Until now, however, no information on the MDS of $Sm_2Fe_{17}C_x$ has been available.

This article focuses on the MDS in the $Sm_2Fe_{17}C_x$ series and its evolution during the carburization process.

II. EXPERIMENTAL DETAILS

The Sm_2Fe_{17} alloy was prepared by melting elemental Fe with Fe-50 wt % Sm master alloy under argon in an induction furnace. The cast ingots were homogenized at 1000 °C for one week in a sealed glass ampoule filled with argon. The structure and phase composition were examined by x-ray diffraction (XRD) using Co $K\alpha$ radiation as well as by metallographic techniques. The homogenized ingots were coarsely crushed. Powder fractions with particle sizes from 160 to 500 μm and 30 to 60 μm were used. The powder was then exposed to CH_4 gas at a pressure of 0.6 bar. The coarse powder was carburized at 450 °C for 40, 160, and 200 h. For comparison finer powder was carburized at 500 °C for 96 h to get a high carbon content. After these heat treatments the following nominal carbon contents were obtained: $x\approx0.8$, 1.2, 1.3, and $x\approx2.2$ (x being the number of carbon atoms per formula unit). The amount of absorbed carbon was checked by the combustion method with CO_2 determination. After carburization the powders were examined by XRD. An additional phase analysis of the carburized powders was also performed by thermomagnetic measurements. For magneto-optic investigations powders were embedded in epoxy resin. These specimens were polished using emery papers and diamond pastes. The MDS observations were performed at room temperature with polarized light in a Jenapol microscope equipped with a high-resolution camera and an image analyzer. The domain contrast was provided mainly by the magneto-optical polar Kerr effect, which depends on the component of magnetization normal to the surface.

III. RESULTS AND DISCUSSION

Figure 1 shows the typical temperature dependence of magnetic polarization (measured at a small magnetic field) for $Sm_2Fe_{17}C_x$ samples with different carbon contents x. For medium values of x the sharp magnetic transition of Sm_2Fe_{17} at 120 °C is diminished and a small step appears near 400 °C. For $Sm_2Fe_{17}C_{2.2}$ only one sharp transition is observed at 415 °C. Therefore, it can be assumed that in par-

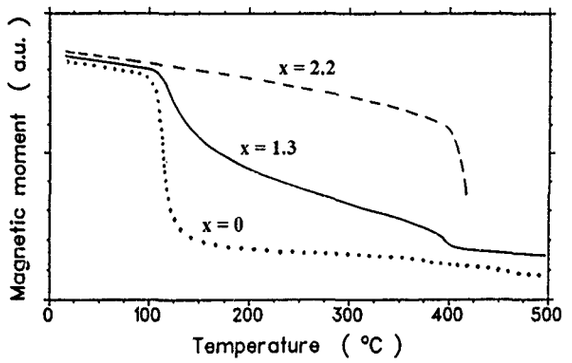

FIG. 1. Thermomagnetic analysis of $Sm_2Fe_{17}C_x$ for different values of x (Applied field $\mu_0H=0.1$ T, temperature sweep $dT/dt=20$ K/min)

[a]On leave from. Institute of Physics, Polish Academy of Sciences, Al Lotników 32/46, 02-668 Warsaw, Poland.

 0021-8979/94/76(10)/6717/3/$6.00 © 1994 American Institute of Physics

FIG. 2. Development of carbon diffusion layers in Sm_2Fe_{17} after carburization for 40 h (nominal composition of the sample is $Sm_2Fe_{17}C_{0.8}$). The laminar magnetic domains with strong Kerr contrast show the distribution of the uniaxial phase.

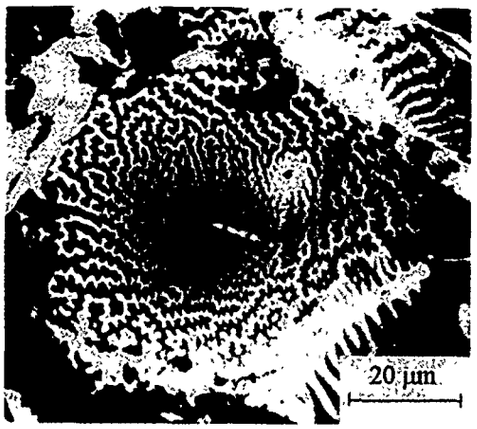

FIG. 4. Gradual change of the domain structure in a partially carburized grain (nominal composition of the sample is $Sm_2Fe_{17}C_{1.2}$).

tially carburized powders thin surface layers of the grains have a composition near to that of $Sm_2Fe_{17}C_{2.2}$.

The photographs show typical MDS for $Sm_2Fe_{17}C_x$ with nominal carbon contents $x \approx 0.8$ (Fig. 2), $x \approx 1.2$ (Figs. 3 and 4), $x \approx 1.3$ (Fig. 5), and $x \approx 2.2$ (Fig. 6). Obviously the carbon absorption has a strong influence on the MDS. In carburized regions the MDS is that of a magnetically uniaxial compound with a large anisotropy field. Simple wavy or complex starlike MDS with spikelike closure domains (see, for instance, Figs. 3 and 5) were observed in some grains. This indicates that the c axis (magnetically easy direction in the carburized phase) is oriented nearly perpendicularly to the polished surface in these grains. Laminar or wedge domains appear in the carburized regions of grains with the c axis parallel or nearly parallel to their surface (upper-left-hand-side part of Fig. 3). The pure Sm_2Fe_{17} phase reveals sometimes a coarse irregular domain pattern typical for basal plane anisotropy magnets. The characteristic feature of the MDS in $Sm_2Fe_{17}C_x$ series is that the carburized regions show a very strong Kerr contrast in opposition to the noncarburized ones, where only a relatively weak contrast was observed.

The distribution of domains characteristic for the uniaxial phase suggests that the carburization process is initially controlled by grain-boundary diffusion and then by diffusion into the bulk of the grains. In the sample of nominal composition $Sm_2Fe_{17}C_{0.8}$ carburized regions were observed mainly along cracks and grain boundaries (see Fig. 2). At this stage, the grains consist of a carburized outer shell and a noncarburized core. Because of the higher diffusion rate close to sharp edges of the grains compared to round ones, the internal rim of the carburized shell became oval after some time. It shrinks then to the center, gradually decreasing the Sm_2Fe_{17} core and finally results in carburization of the whole grain (see Fig. 4). The inhomogeneous carbon diffusion can induce mechanical stress and strain resulting in cracks or even in decrepitation (see Figs. 2 and 3). This increases the surface area of the powder and makes the diffusion process more effective. For instance, Fig. 5 shows often-observed circular microcracks arising from inhomogeneous stress profiles.

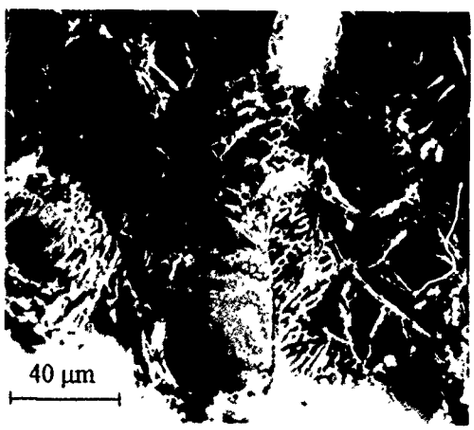

FIG. 3. Typical domain patterns observed for the nominal composition $Sm_2Fe_{17}C_{1.2}$ showing fully and partially carburized grain regions (carburization time 160 h).

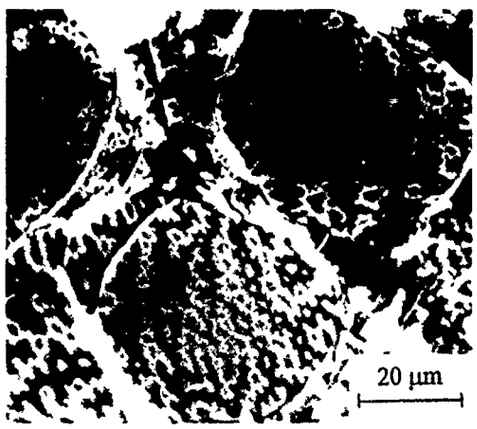

FIG. 5. Circular cracks caused by inhomogeneous stress profiles during carburization (nominal composition of the sample is $Sm_2Fe_{17}C_{1.3}$).

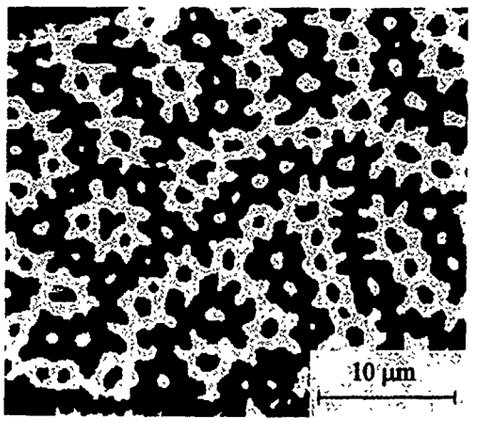

FIG. 6. Starlike domain structure in a large grain with the magnetically easy direction perpendicular to the polished surface (nominal composition is $Sm_2Fe_{17}C_{2.2}$).

Our observations of the MDS in $Sm_2Fe_{17}C_x$ series suggest also that the carbide is rather a single gas-solid solution with a continuous range of carbon contents than a two-phase mixture of carbon-poor and carbon-rich phases. A gradual change of the MDS across the grains was observed in the Sm_2Fe_{17} powders heated under CH_4 atmosphere for 160 and 200 h. For instance, Fig. 4 shows the domain pattern in a grain with the c axis perpendicular to its polished surface. As can be seen the MDS becomes finer as the distance from the grain boundary increases. According to models of the MDS, developed for uniaxial materials,[6] assuming a constant crystallite thickness, the main domain width is approximately proportional to $\gamma^{1/3}J_s^{-2/3}$, where J_s is the saturation polarization. The domain-wall energy can be expressed as $\gamma=4(AK_1)^{1/2}$,[7] where A and K_1 are exchange and anisotropy constants, respectively. Therefore, the decrease of the main domain width can be attributed to a diminution of A or K_1 in the regions with smaller carbon content.

By determination of the carburized layer thickness d at initial stages of carburization the estimation of the diffusion rate is possible. The diffusivity R of carbon atoms of 450 °C was calculated according to the equation for the average displacement x of diffusing particles with the Brownian movement: $R=x^2/2t$,[8] where t is the carburization time. In our estimation we assumed $x\cong d$. In order to avoid the influence of geometrical effects of the grain size on the $Sm_2Fe_{17}C_x$ layer thickness, we considered only very big grains with flat edges. The value obtained is $R=(2.5\pm0.5)\times10^{-16}$ m^2/s, which is of the same order of magnitude as that reported in Ref. 2 for nitrogen.

The wall energy density γ was determined for a $Sm_2Fe_{17}C_{2.2}$ sample, in which all the grains were homogeneously carburized. For this purpose the MDS in large grains with the easy axis normal (or almost normal) to the polished grain surface was analyzed. The Bodenberger–Hubert approach[9] was used for the analysis of the characteristic starlike surface domain patterns like those in Fig. 6. It can be shown that the average surface domain width w in the basal plane (perpendicular to the easy axis) for large grains in polycrystalline material is independent of the grain size and is given by $w=\mu_0\beta\gamma/J_s^2$, where β is a geometrical factor depending on the type of surface domain structure. We adopted the value of β as determined for uniaxial highly anisotropic materials in Ref. 9. We obtained an average surface domain width w of (0.93 ± 0.09) μm. Using a value of 1.43 T for the saturation polarization J_s, this yields a wall energy γ of $(3.1\pm0.3)\times10^{-2}$ J/m^2. From this, the single-domain particle size, $D_c=5.6\pi\mu_0\gamma/J_s^2$, is $D_c\approx0.3$ μm. The standard continuum model for a domain wall[7] gives in a first approximation the relations $A=\gamma/16K_1$ for the exchange constant and $\delta=\pi\gamma/4K_1$ for the domain-wall thickness. Using the anisotropy constant $K_1=7.4$ MJ/m^3 calculated from demagnetization curves[10] we obtained $A=8.1\times10^{-12}$ J/m and $\delta=3.3$ nm.

[1] R. B. Helmhodt and K. H. J. Buschow, J. Less-Common Matter **155**, 15 (1985).
[2] J. M. D. Coey, H. Sun, and Y. Otani, in Proceedings of the Sixth International Symposium on Magnetic Anisotropy and Coercivity in Rare-Earth–Transition-Metal Alloys, Pittsburgh, 1990, p. 36.
[3] J. M. D. Coey, H. Sun, Y. Otani, and D. P. F. Hurley, J. Magn Magn. Mater. **98**, 76 (1991).
[4] H. Sun, Y. Otani, and J. M. D. Coey, J. Magn. Magn. Mater. **104-107**, 1439 (1992).
[5] J. M. D. Coey, R. Skomski, and S. Wirth, IEEE Trans. Magn. **MAG-28**, 2332 (1992).
[6] R. Szymczak, Acta Phys. Polon. A **43**, 571 (1973).
[7] S. Chikazumi, *Physics of Magnetism* (Wiley, New York, 1964).
[8] G. E. R. Schulze, *Metallphysik* (Akademie, Berlin, 1967).
[9] R. Bodenberger and A. Hubert, Phys. Status Solidi A **56**, 637 (1979).
[10] K.-H. Müller, D. Eckert, P. A. P. Wendhausen, A. Handstein, S. Wirth, and M. Wolf, IEEE Trans. Magn. **MAG-30**, 586 (1994).

Neutron-diffraction study on the structure of $Nd(TiFe)_{12}N_x$ and $Nd(TiFeCo)_{12}N_x$ alloys

Shu-Ming Pan
General Research Institute for Nonferrous Metals, CNNC, Beijing 100088, People's Republic of China

Hong Chen, Zu-Xiong Xu, and Ru-Zhang Ma
Department of Materials Physics, University of Science and Technology Beijing, Beijing 100083, People's Republic of China

Ji-Lian Yang and Bai-Sheng Zhang
Institute of Atomic Energy, Beijing 102413, People's Republic of China

De-Yan Xue, and Qiang Ni
Shatoujiao New Materials Factory, Shenzhen 518081, People's Republic of China

The preference of nitrogen atoms in $Nd(FeTi)_{12}N_x$ and $Nd(FeTiCo)_{12}N_y$ alloys have been studied by neutron diffraction. The results show that Ti atoms are preferentially to occupy the 8*i* sites, but Co atoms enter the 8*f* rather than the 8*i* site. Nitrogen atoms occupy the 2*b* sites in $Nd(FeTi)_{12}N_x$ and $Nd(FeTiCo)_{12}N_y$.

I. INTRODUCTION

A ternary Fe-rich $R(MFe)_{12}$ (M=stabilizing elements) alloy with tetragonal $ThMn_{12}$ structure has been studied extensively.[1,2] The Curie temperature of $SmTiFe_{11}$ is lower than that of $Nd_2Fe_{14}B$ and its lower saturation magnetization leads to the theoretical $(BH)_{max}$ of $SmTiFe_{11}$ only half that of $Nd_2Fe_{14}B$.[3] It is shown that Curie temperature, iron moment, and magnetocrystalline anisotropy increase drastically with the addition of nitrogen atoms.[4,5] $RTiFe_{12}N_x$ compounds have been observed to possess different intrinsic magnetic properties from their original counterparts $RTiFe_{11}$.[6] It has been shown that the Curie temperature of $RTiFe_{11}N_x$ increases by about 150–170 K and the Fe moment increases by 17%. In particular, $RTiFe_{11}N_x$ has an easy axis with a strong anisotropy field at room temperature for R=Nd, Tb, and Dy. Owing to the fact that the easy uniaxial anisotropy is a prerequisite for a magnetic material with high coercive force, to understand the effects produced by nitriding it is necessary to investigate the crystallographic structures of these nitrides. The determination of the site occupation of nitrogen atoms is a key prerequisite to the calculation of the electronic structure or crystal-field interactions in the nitrides. For this reason, we have carried out a neutron-diffraction and Mössbauer spectra study on the $Nd(FeTi)_{12}N_x$ and $Nd(FeTiCo)_{12}N_y$ alloys.

II. EXPERIMENTAL DETAILS

The samples used were prepared by arc melting of the high-purity (99.9%) primary materials under purified argon atmosphere. The buttons were melted at least three times to achieve homogeneity. Then the alloy buttons were smashed into powders. Nitrides were prepared by passing puried nitrogen gas at atmospheric pressure over finely ground powder samples at 500 °C for 3 h and at sufficiently high rates of flow to ensure enough absorption of nitrogen, followed by rapidly cooling to room temperature. X-ray diffraction analysis was used to detect phase structure. Neutron-diffraction data were collected at room temperature.

III. RESULTS AND DISCUSSION

All the samples are of single phase except for a very little amount of α-Fe coexistence found by x-ray diffraction analysis. The nitrides of $RTiFe_{11}$ were found to maintain their original tetragonal structure, space group $I4/mmm$, but with slight increases in cell volumes. This increase in lattice parameters is highly anisotropic (mainly in the basal plane).

Neutron-diffraction measurements were performed on $Nd(FeTi)_{12}N_x$ and $Nd(FeTiCo)_{12}N_y$ alloys to determine the site occupation of nitrogen atoms. The results obtained from neutron diffraction data fit are listed in Tables I and II. It can be seen from Tables I and II that Ti atoms still prefer to occupy the 8*i* sites in agreement with Ref. 6, but Co atoms enter the 8*f* site rather than the 8*i* site. The occupation of nitrogen atoms in $NdTi_{1.12}Co_{0.94}N_y$ is the same as that in $Y(TiFe)_{12}N_x$, in which nitrogen atoms enter the 2*b* site. The quantities of nitrogen atoms entering interstitial position are $x=0.43$ and $y=0.395$ for $Nd(FeTi)_{12}N_x$ and $Nd(FeTiCo)_{12}N_y$ alloys, respectively. The position of the N atom was found to correspond to the 2*b* site of the tetragonal space group, which gives rise to noticeable displacements of the 8*j* metal

TABLE I. The structural parameters of $Nd(FeTi)_{12}N_x$ from neutron-diffraction data The atomic coordinate parameters (in units of the cell constants *a* and *c*) are *x*, *y*, *z*, *n* is the number of atoms on different sites; K_z is the moment value (μ_B) in the *z* direction; *R* is the consistent factor; R_N and R_M are quality-of-fit indices for the nuclear and magnetic scattering, respectively; X^2 is the residual value.

Atom site	*x*	*y*	*z*	*n*	$K_z(\mu_B)$
Nd (2*a*)	0.0000	0.0000	0.0000	2.000	0.976
Fe (8*i*)	0.3544	0.0000	0.0000	5.754	2.120
Ti (8*i*)	0.3544	0.0000	0.0000	2.246	0.000
Fe (8*j*)	0.2661	0.5000	0.0000	8.000	1.920
Fe (8*f*)	0.2500	0.2500	0.2500	8.000	1.720
N (2*b*)	0.0000	0.0000	0.5000	0.860	0.000
R (%)				0.98	
R_N (%)				0.98	
R_M (%)				0.89	
X_2				1.87	

 0021-8979/94/76(10)/6720/2/$6.00 © 1994 American Institute of Physics

TABLE II. The structural parameters of $NdTi_{1.12}Co_{0.94}Fe_{9.94}N_y$ from neutron-diffraction data.

Atom site	x	y	z	n	K_Z (μ_B)
Nd (2*a*)	0.0000	0.0000	0.0000	2.00	1.20
Fe (8*i*)	0.3582	0.0000	0.0000	5.58	1.70
Ti (8*i*)	0.3582	0.0000	0.0000	2.42	0.00
Fe (8*j*)	0.2837	0.0000	0.0000	8.00	1.50
Fe (8*f*)	0.2500	0.2500	0.2500	6.12	1.30
Co (8*f*)	0.2500	0.2500	0.2500	1.88	0.00
N (2*b*)	0.0000	0.0000	0.5000	0.79	0.00
R (%)				1.60	
R_N (%)				1.59	
R_M (%)				1.74	
X^2				1.08	

positions. The increase in T_c and cell volume are in good agreement with the values reported in Refs. 2 and 7–9. The short metal-metal distances (between the 8*f* sites) remain almost unchanged after N insertion and can be derived directly from cell parameters.

IV. CONCLUSION

Neutron-diffraction analysis of Nd-(FeTi)-N and Nd-(FeTiCo)-N alloys has been performed. It was found that Ti atoms still prefer to occupy the 8*i* site, but Co atoms enter the 8*f* rather than the 8*i* site. The nitrogen atoms prefer to occupy the 2*b* site.

ACKNOWLEDGMENTS

This work was partly supported by the National Natural Science Foundation of China and the State Key Laboratory of Magnetism, Institute of Physics, Chinese Academy of Sciences.

[1] Y.-C. Yang, B. Kebe, W. J. James, J Deportes, and W B. Yelon, J. Appl. Phys. **52**, 2077 (1981).
[2] K. H. J. Buschow, J. Appl. Phys. **63**, 3130 (1988).
[3] Y.-C. Yang, X.-D. Zhang, S.-L. Ge, Q. Pan, L.-S. Kong, H.-L. Li, J.-L. Yang, B -S. Zhang, Y.-F. Ding, and C.-T. Ye, J. Appl. Phys. **70**, 6001 (1991).
[4] J. M. D. Coey and H. Sun, J. Magn. Magn. Mater. **87**, L251 (1991).
[5] Y.-C. Yang, X.-D. Zhang, L.-S. Kong, Q. Pan, S.-L Ge, in Proceedings of the 11th International Workshop on Rare Earth Magnets and their Applications, Pittsburgh, PA, October, 1990, Vol. 2, p. 190.
[6] K. H. J. Buschow, in CEAM Report, edited by I. V. Mitchell, 1989.
[7] M Pnagnostou, C. Christides, and D Niarchos, Solid State Commun. **78**, 681 (1991).
[8] Th. Sinnemann, K. Erdmann, M. Rosenberg, and K. H. J. Buschow, Hyperfine Interactions **50**, 675 (1989).
[9] O. Moze, L. Pareti, M. Solzi, and W. L. David, Solid State Commun. **66**, 465 (1989).

Synthesis and magnetic properties of $PrFe_{12-x}Mo_x$ and $PrFe_{12-x}Mo_xN_y$ ($0.5 \leq x \leq 1.0$, $y \approx 1$)

O. Kalogirou, V. Psycharis, L. Saettas, and D. Niarchos
National Center for Scientific Research "Demokritos," Institute of Materials Science, 153 10 Ag. Paraskevi, Attiki, Greece

A series of iron-rich ternary intermetallics $PrFe_{12-x}Mo_x$ ($x=0.5$, 0.75, 1.0) and their nitrides have been prepared by arc melting, annealing at 1273–1393 K and water quenching. A single-phase structure of the $ThMn_{12}$ type has been obtained for $x=1.0$ when annealed at 1345 K (with α-Fe<5%). The lattice constants are $a=8.5978(2)$ Å, $c=4.7795(3)$ Å. The alloys exhibit planar anisotropy, a Curie temperature of 498 K, and a room-temperature magnetization of 120.4 A m^2/kg prior to the nitrogenation. After nitrogenation the anisotropy changes to uniaxial, the Curie temperature increases to 681 K, and the room-temperature magnetization becomes 136 A m^2/kg. A lattice expansion corresponding to 2.4% of the cell volume is observed. In the $x=0.5$ and $x=0.75$ alloys, a secondary 2:17 phase is also present, besides the 1:12-type structure. The peritectic decomposition temperature is 1393 K for all samples.

I. INTRODUCTION

The ternary Fe-rich R-Fe-M alloys related to the tetragonal $ThMn_{12}$-type structure, and especially their nitrides, have been extensively studied during the past few years as potential candidates for permanent magnet applications due to their relatively high Curie temperature, saturation magnetization, and favorable magnetocrystalline anisotropy.[1] The tetragonal phase can be stabilized only by replacing iron with a small amount of a third element such as M=Ti, Mo, V, Cr, etc.[1]

One significant result of introducing nitrogen into the 1:12 phase is the observed change in the magnetocrystalline anisotropy from planar for non-nitrided compounds to uniaxial for nitrided ones[2] due to the change of the second-order crystal-field parameter A_{20} from negative to positive as in the case of Nd.[3] Among the light-rare-earth elements Pr has a negative a_J like Nd. Thus the magnetic properties of $Pr(Fe,Mo)_{12}$ and $Nd(Fe,Mo)_{12}$ nitrides are expected to be similar; however, since it has been reported that Pr does not form the 1:12 phase[4] no attention has been paid to the synthesis of this compound. Recently Yang *et al.*[5] have reported the preparation of $PrFe_{10.5}Mo_{1.5}$ and its nitride. Sun *et al.*[6] have reported that the solubility range in the $YFe_{12-x}Mo_x$ system is $0.5 \leq x \leq 4.0$. On the other hand, it has been shown that the intrinsic magnetic properties of $RFe_{12-x}Mo_xN_y$ improve with decreasing Mo concentration.[6,7] Thus, we examined the existence range of $PrFe_{12-x}Mo_x$ between $0.5 \leq x \leq 1.0$ and have succeeded in synthesizing at least the $x=1.0$ member of the series in the form of the $ThMn_{12}$-type structure. The structural and magnetic properties of the parent $PrFe_{11}Mo$ compound and the related nitride have also been studied.

II. EXPERIMENT

The $PrFe_{12-x}Mo_x$ ($x=0.5$, 0.75, 1.0) samples were synthesized by arc melting, with ≥99.9% pure constituents, in an argon atmosphere. The ingots were wrapped in tantalum foil, annealed in vacuum at various temperatures between 1273 and 1393 K for 3 days and then water quenched. Nitrides were formed by heat treating fine powders (<37 μm) of the alloys in purified N_2 gas at 723 K for 12 h. The samples were characterized by x-ray powder diffraction (XRD) (Siemens D500, Cu$K\alpha$ radiation with a diffracted-beam monochromator), Rietveld analysis, and thermomagnetic analysis (TGM). The magnetocrystalline anisotropy was studied by means of x-ray powder diffraction on magnetically aligned powder samples. Magnetization curves were measured using a Quantum Design superconducting quantum interference device (SQUID) magnetometer with a maximum field of 5 T at room temperature.

III. RESULTS AND DISCUSSION

Alloys with the composition $PrFe_{11}Mo$ ($x=1.0$) can be prepared by arc melting and annealing at 1273, 1348, or 1373 K. All annealed alloys present the $ThMn_{12}$-type structure with some α-Fe impurity (less than 10%). At 1393 K the 1:12 phase almost disappeared due to α-Fe precipitation indicating that 1393 K exceeds the peritectic decomposition temperature of $PrFe_{11}Mo$. The lowest α-Fe content was obtained after annealing at 1348 K for 3 days and was calculated to be 5% by the Rietveld analysis. For this sample a complete crystallographic analysis was performed. The crystal structure parameters (unit-cell dimensions, atom positions) for the sample with nominal composition $PrFe_{11}Mo$ were determined by applying the Rietveld refinement method[8] and using as starting structural parameters the ones given in Refs. 9 and 10. Following the procedure described in Ref. 9, it was concluded that the Mo atoms occupy the 8*i* site. The Mo atoms per formula unit were calculated as 0.92(7), very close to the nominal value of $x=1.0$. The isotropic thermal parameters B were kept constant during the refinement and equal to the values given in Ref. 10. The calculated α-Fe content is 5% wt. The lattice constants, atomic positions, and bond distances are listed in Table I. The Rietveld diffraction patterns (observed, calculated, and difference patterns) are shown in Fig. 1.

The Curie temperature of $PrFe_{11}Mo$ as determined by TGM was 498 K. No other ordering temperature was observed, except that of α-Fe. The room-temperature magneti-

 0021-8979/94/76(10)/6722/3/$6.00 © 1994 American Institute of Physics

TABLE I. Crystallographic data for $PrFe_{11}Mo$ compound (space group: $I4/mmm$). Unit-cell dimensions: a=8.5978(2) Å, c=4.7795(3) Å, and V=353.31 Å^3. Agreement indexes (R factors): R_p=6.67, R_{wp}=11.65, R_B=8.46, and R_{expt}=3.91%.

Atom	Site	x	y	z	Occupancy
Pr	2a	0.0	0.0	0.0	1.0
Fe_i/Mo_i	8i	0.3618(3)	0.0	0.0	0.77(1)/0.23(1)
Fe_j	8j	0.2720(4)	0.5	0.0	1.0
Fe_f	8f	0.25	0.25	0.25	1.0

Bond distances

Pr-Fe_i×4	3.111(3)	F_j-Fe_j×2	2.772(3)
Pr-Fe_j×8	3.091(2)	-Fe_f×4	2.467(1)
Fe_i-Fe_i×1	2.376(4)	Fe_f-Fe_f×2	2.391(4)
-Fe_i×4	2.921(1)		
-Fe_j×2	2.623(3)		
-Fe_j×2	2.652(2)		
-Fe_f×4	2.640(1)		

zation at 5 T of $PrFe_{11}Mo$ is 120.4 A m^2/kg. This value was deduced taking into account the α-Fe content, 5%, as calculated from the Rietveld analysis. After nitrogenation the Curie temperature increased by about 180 K reaching 681 K. The room-temperature magnetization of the nitride at 5 T reached a value of 136 A m^2/kg (Fig. 2). Nitrogenation resulted in an increase of α-Fe content. The given magnetization value was calculated considering the α-Fe content, 15%, as found from preliminary Mössbauer spectroscopy. The unit-cell dimensions for the nitrided compound are a=8.649(2) Å, c=4.835(3) Å, and V=361.70 Å^3. The unit-cell expansion is 2.4% comparable to the other 1:12 nitrides leading to a value of $y \approx 1$. The magnetization values confirm recent experimental observations that a lower Mo concentration improves the magnetic properties of $RFe_{12-x}Mo_x$ and their nitrides.[6,7] The Curie temperatures of $PrFe_{11}Mo$ and $PrFe_{11}MoN_y$ are 43 and 41 K higher than those of $PrFe_{10.5}Mo_{1.5}$ and $PrFe_{10.5}Mo_{1.5}N_y$, respectively.[5] A similar improvement is observed in the saturation magnetization, i.e., 8.4 and 15.1 A m^2/kg higher than those of $PrFe_{10.5}Mo_{1.5}$ and $PrFe_{10.5}Mo_{1.5}N_y$, respectively.[5]

In Fig. 3 the XRD spectra of the non-nitrided and nitrided $PrFe_{11}Mo$ compounds and the corresponding spectra of magnetically aligned powders, bounded on double-side tape with a magnetic field normal to the plane of the sample holder are shown. As shown in Fig. 3(b) the intensity of the (0 0 2) reflection of the aligned non-nitrided sample decreases and the intensities of the (2 4 0), (0 3 1), (2 3 1), and (1 4 1) increase indicating planar anisotropy. The opposite behavior of the corresponding reflections was observed in the nitrided sample indicating uniaxial anisotropy [Fig. 3(d)]. Such a change from planar anisotropy for the parent compound to uniaxial for the nitrided one has been observed in the case of the x=1.5 compound as well.[5] This is probably due to the sign change of the second-order crystal-field coefficient in the Pr site by analogy to Nd.[3,4]

The $PrFe_{12-x}Mo_x$ alloys with x=0.5 and x=0.75 were annealed at 1273, 1348, 1368, and 1393 K. As found by both

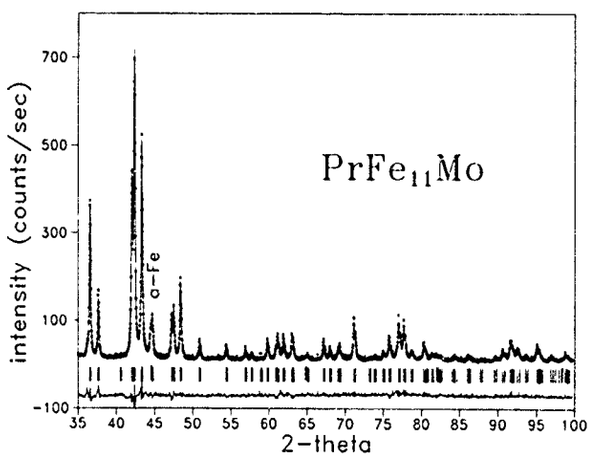

FIG 1. Rietveld refinement patterns for the $PrFe_{11}Mo$ compound. The observed intensities are shown by dots and the calculated ones by the solid line. The position of the Bragg reflections are shown by small vertical lines below the pattern The line at the bottom indicates the intensity difference between the experimental and the refined patterns.

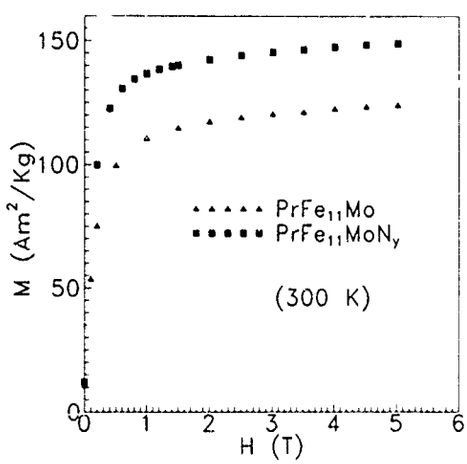

FIG. 2. Room-temperature magnetization curves of randomly aligned powders of $PrFe_{11}Mo$ before and after nitrogenation

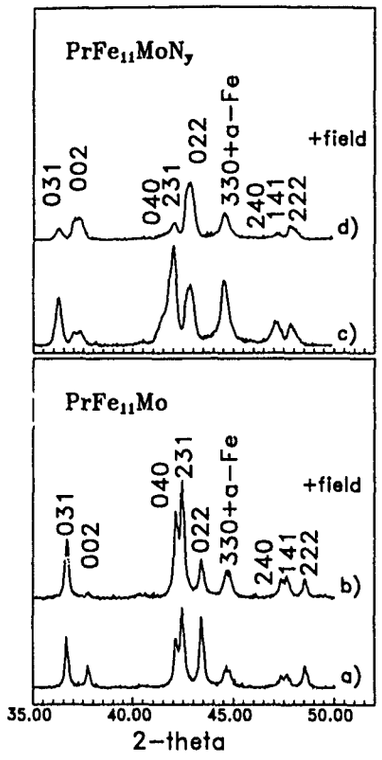

FIG. 3. XRD spectra for (a) parent non-nitrided compound ($PrFe_{11}Mo$), (b) magnetically aligned compound (field normal to the plane), (c) nitrided compound ($PrFe_{11}MoN_y$), and (d) magnetically aligned nitrided compound (field normal to the plane).

XRD and TGM all annealed samples presented a mixture of the 1:12, 2:17, and α-Fe phases. Best results, i.e., minimum 2:17 and α-Fe content, were observed at 1348 K and at 1368 K for the $x=0.5$ and $x=0.75$ samples, respectively. After nitrogenation a mixture of 1:12 and 2:17 nitrides and α-Fe was observed. As in the case of the $x=1.0$ samples, annealing at 1393 K of the $x=0.5$ and $x=0.75$ samples resulted in the precipitation of α-Fe. It was concluded that the peritectic decomposition temperature of $PrFe_{12-x}Mo_x$ is around 1390 K.

IV. CONCLUSION

This work has demonstrated that useful properties of the derivatives of the $ThMn_{12}$-type structure alloys such as $PrFe_{11}Mo$ studied in this work can be obtained by proper heat treatment and second transition-metal concentration. As in other $ThMn_{12}$-type alloys nitrogenation enhances further the magnetization, Curie temperature, and anisotropy. To our knowledge this is the first time that the $PrFe_{11}Mo$ ($x=1.0$) and the related nitride have been synthesized and characterized. It is expected that further improvement can be obtained concerning the system $PrFe_{12-x}Mo_xN_y$ ($0.5 \leqslant x \leqslant 1.0$, $y=0,1$) by proper heat treatment and is part of our current work.

ACKNOWLEDGMENT

This work was partially supported by the B/E-CT91-405 project of the EU.

[1] K. H. J. Buschow, J. Magn. Magn. Mater. **100**, 79 (1991).
[2] Y.-C. Yang, X.-D. Zhang, L.-S. Kong, Q. Pan, and S.-L. Ge, Appl. Phys. Lett. **58**, 2042 (1991).
[3] H.-S. Li and J. M. Cadogan, J. Magn. Magn. Mater. **109**, L153 (1992).
[4] B.-P. Hu, H.-S. Li, J. P. Gavigan, and J. M. D. Coey, J. Phys. Condens. Matter **1**, 755 (1989).
[5] Y.-C. Yang, Q. Pan, X.-D. Zhang, J. Yang, M.-H. Zhang, and S.-L. Ge, Appl. Phys. Lett. **61**, 2723 (1992).
[6] H. Sun, M. Akayama, K. Tatami, and H. Fujii, Physica B **183**, 33 (1993).
[7] Y.-Z. Wang, B.-P. Hu, X.-L. Rao, G.-C. Liu, L. Yin, W.-Y. Lai, W. Gong, and G. C. Hadjipanayis, J. Appl. Phys. **73**, 6251 (1993).
[8] D. A. Wiles and R. A. Young, J. Appl. Cryst. **14**, 149 (1981).
[9] V. Psycharis, M. Anagnostou, C. Christides, and D. Niarchos, J. Appl. Phys. **70**, 6122 (1991).
[10] O Moze, L. Pareti, M. Solzi, and W. I. F. David, Solid State Commun. **66**, 465 (1988).

Study of permanent magnetic properties of the 1-12 nitrides with Nd and Pr

Ying-Chang Yang, Qi Pan, Ben-Pai Cheng, Xiao-Dong Zhang, Zun-Xiao Liu, and Yun-Xi Sun
Department of Physics, Peking University, Beijing 100871, People's Republic of China

Sen-Ling Ge
Beijing University of Posts and Communications, People's Republic of China

The permanent magnetic properties of isotropic and anisotropic powders of $R(Fe,Mo)_{12}N_x$ compounds, where R=Pr and Nd, were investigated by using mechanical alloying and a conventional milling process. For the isotropic magnetic powders, a coercive force of up to 9 kOe and a maximum energy product of 6.6 MGOe were obtained in Nd compounds, while with the anisotropic powders a maximum energy product of 12 MGOe was achieved. In the isotropic $Pr(Fe,Mo)_{12}N_x$ compounds the best result were 4.5 MGOe for $(BH)_{max}$ and 6.0 kOe for ${}_iH_c$. The temperature dependence of coercive force has been investigated in a temperature range between 300 and 500 K, and the results are reported in a comparison with that of Nd-Fe-B magnets.

I. INTRODUCTION

Findings of the nitrogenation effect on the magnetic properties of rare-earth intermetallic compounds have recently made a great progress in the field of hard magnetic materials. These important developments in magnetism and magnetic materials have shown that great improvements in the magnetic properties can be achieved by introducing interstitial nitrogen or/and carbon atoms. This is particularly important for permanent magnet materials, which require large values of magnetization, uniaxial anisotropy, high Curie temperature T_c, and coercivity at or above room temperature. In 1990 the nitrides $Sm_2Fe_{17}N_x$ and $Nd(Fe,M)_{12}N_x$, where M=Ti, V, Mo, W, etc., were discovered,[1,2] and the studies of the new hard magnetic materials based on RE-Fe nitrides spread worldwide. We have reported that for the RE-Fe nitrides having the $ThMn_{12}$-type structure the interstitial nitrogen atoms not only have a crucial effect of increasing Curie temperature and saturation magnetization, but also give rise to a profound change in magnetocrystalline anisotropy. Due to these effects, $Nd(Fe,M)_{12}N_x$ and $Pr(Fe,M)_{12}N_x$ became well-known candidates for permanent magnet applications.[3–6] Compared to the case of 2-17 nitrides, because of the difficulty in stabilizing the 1-12 phase with a light rare earth, more problems have been encountered in developing high-performance magnets based on the 1-12 nitrides. However, from an economic point of view, the 1-12 compounds present special interest due to the lower price of Nd than Sm. In addition, the 1-12 nitrides have a lower ratio of rare earth to transition metal than the 2-17 nitrides. Accordingly, it is worth studying the 1-12 nitrides concerning the formation conditions of good single phase, improvement on the intrinsic magnetic properties, and creation of high coercivity. As we know, a strong easy-axial anisotropy is the origin of a large coercive force, however, the coercivity is a very sensitive property and depends on microstructure formed by the processing treatment. In this work we have succeeded in preparing the single phase of $NdFe_{10.5}Mo_{1.5}$ and $PrFe_{10.5}Mo_{1.5}$, as well as their nitrides. The key problems dealing with magnet manufacture and the prospect of the 1-12 nitrides in the permanent magnet development are discussed.

II. EXPERIMENTS

Alloys were prepared by arc melting of 99.9% pure materials in an argon atmosphere, followed by a heat treatment around 1000 °C for 1 week. The nitrogenation was carried out at 400–600 °C for 2–4 h in high-purity N_2 gas at atmospheric pressure. The nitrogenated powder was then further pulverized into fine powder by a ball mill. The hysteresis loops of the samples were measured by vibrating sample magnetometer (VSM) with a field of up to 20 kOe in a temperature range from room temperature to 600 K. Some samples were magnetized with a pulse field of up to 40 and 100 kOe.

Mechanically alloyed powders were produced in a high-energy ball mill, starting with Pr-Mo-Fe and Nd-Fe-Mo alloy powders. Magnetic amorphous powders were made by milling process for 1–10 h under argon atmosphere. The powders were then heat-treated in the temperature 750–950 °C for 40 min to form the crystallized 1-12 phase, in a vacuum of 10^{-3} Pa. Nitrides were prepared by passing purified nitrogen gas over the crystallized 1-12 phase at atmospheric pressure at 500 °C for 1–4 h.

Anisotropic magnets based on $Nd(Fe,Mo)_{12}N_x$ nitrides were prepared by a conventional milling process. The powder samples of cylindrical shape ($\Phi 3\times 4$ mm) were aligned with a magnetic field of 10 kOe and fixed in epoxy resin.

III. RESULTS AND DISCUSSIONS

All the samples were found to crystallize in the $ThMn_{12}$-type structure, and, no second phase was observed before and after nitrogenation. As an example, the x-ray-diffraction patterns of $PrFe_{10.5}Mo_{1.5}$ and their nitrides are shown in Fig. 1.

A. Isotropic powders

Isotropic magnetic powders based on $Pr(Mo,Fe)_{12}N_x$ and $Nd(Mo,Fe)_{12}N_x$ were prepared by using a mechanical milling process. In both cases of $Nd(Mo,Fe)_{12}$ and $Pr(Mo,Fe)_{12}$, the x-ray-diffraction patterns and thermomagnetic curves show that there are no other magnetic phases (such as α-Fe). It is important to mention that in order to obtain a desirable co-

 0021-8979/94/76(10)/6725/3/$6.00 © 1994 American Institute of Physics

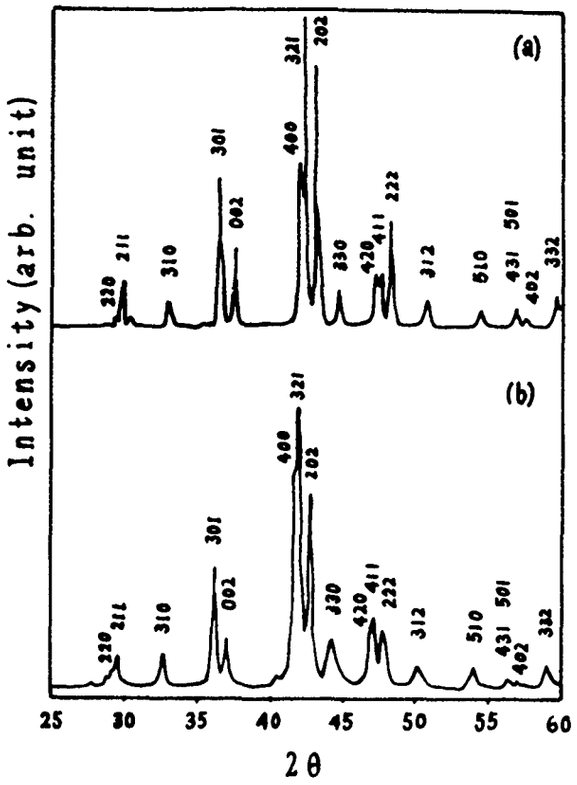

FIC 1. X-ray-diffraction patterns of (a) $PrFe_{10.5}Mo_{1.5}$ and (b) $PrFe_{10.5}Mo_{1.5}N_x$.

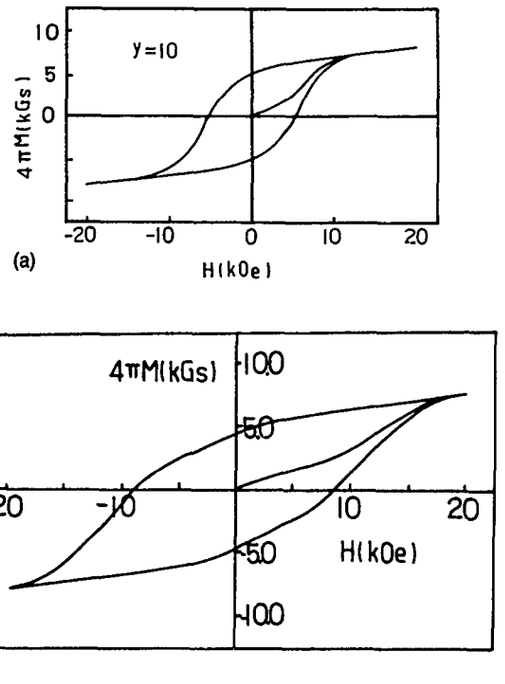

FIG. 3. The magnetic hysteresis loops of different composition powders (a) $Pr(Mo_{0.13}Fe_{0.87})_{10}N_x$, (b) $Nd(Fe,Mo)_{12}N_x$, which were obtained at an annealing temperature of 770 °C for 40 min, measured at room temperature.

ercivity, no α-Fe second phase associated with the starting alloys is required. Figure 2 shows the variations of coercive force, saturation magnetization, and remanence as a function of crystallized temperature of $Pr(Mo_{0.13}Fe_{0.87})_{10}N_x$. From the figure it can be seen that intrinsic coercive force depends sensitively on crystallization temperature with the optimum crystallization temperature 770 °C.

A coercive force of 6.0 kOe is obtained for the Pr nitrides with a crystallization temperature of 770 °C for 40 min and a nitrogenation treatment at 500 °C for 2 h. Figure 3(a) indicates the magnetic hysteresis loop which was obtained at an annealing temperature of 770 °C for 40 min and followed by a heat treatment at 500 °C under N_2 atmosphere for 2 h. The best results were obtained in $Pr(Mo_{0.13}Fe_{0.87})_{10}N_x$, which has a large coercive force combined with a high remanent magnetization. A higher coercive force, e.g., ${}_iH_c$=8.9 kOe, is achieved for $Nd(Fe,Mo)_{12}N_x$ with the same process and is seen in Fig. 3(b). As in the case of the mechanically allowed powders, no sensitive orientation effect is observed. Thus, the mechanically alloyed powders are isotropic. From the virgin magnetization curves an obvious jump is observed, which is characteristic of a pinning mechanism for the coercive force. The critical field at which the jump occurs corresponds to the value of the coercive force. This behavior suggests that the coercive force in the case of mechanical alloying is determined by a domain-wall pinning. For the

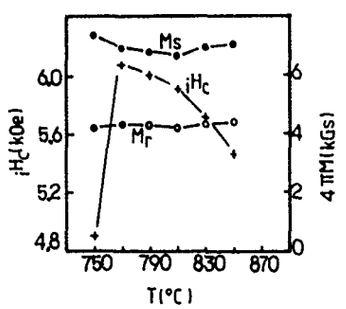

FIG. 2 The variations of coercive force ${}_iH_c$, saturation magnetization M_s, and remanence M_r as a function of crystallized temperature for $Pr(Mo,Fe)_{12}N_x$ samples.

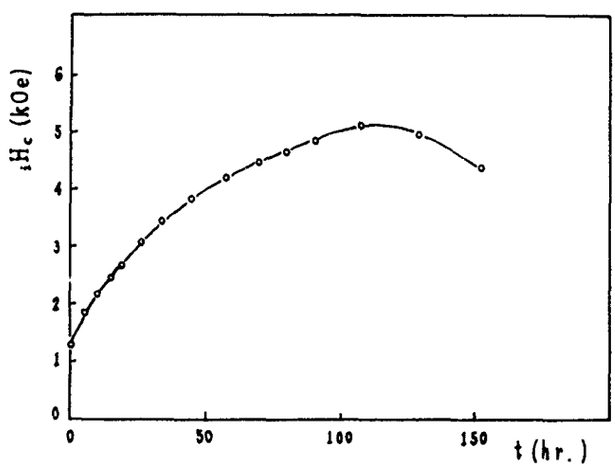

FIG 4. The variation of coercive force as a function of milling time for $Nd(Fe,Mo)_{12}N_x$ powder samples

TABLE I. Coercive force $_iH_c$ vs magnetizing field H_m of $Nd(Fe,Mo)_{12}N_x$.

Mill time (h)	19	49	59	64	107
$_iH_c$ (kOe)[a]	2 558	3.880	4.133	4.326	5.171
$_iH_c$ (kOe)[b]	3 894	5.168	5.209	5.561	6.305

[a]Samples were magnetized and measured at H=20 kOe
[b]Samples were magnetized at H=100 kOe and measured at H=40 kOe.

isotropic samples, the theoretical values of square ratio should be 0.5; our results are larger than this value indicating that the samples are far from saturation at the applied field of 20 kOe.

B. Anisotropic powders

Figure 4 indicates the variation of coercive force as a function of milling time for $Nd(Fe,Mo)_{12}N_x$. It is clear that the coercive force depends sensitively on particle size of the powders, i.e., it increases with grinding time, reaching a maximum, then decreases after prolonged milling. The intrinsic coercive force $_iH_c$ of the powders prepared by the milling process exhibits a large dependence of the magnitude of the magnetic field H_m applied before the coercive force measurements. Table I shows $_iH_c$ for the same sample under different magnetizing field. For the powders with the optimum milling time, a coercive force of 5.2 and 6.3 kOe was obtained by using a magnetizing field of 20 and 100 kOe, respectively. The magnetizing-field dependence of $_iH_c$ is characteristic of domain nucleation. This behavior is different from that of mechanical alloying powders mentioned above. Anisotropic magnets can be made by using the powders prepared by milling methods; however, the saturation magnetization and remanence were found to degrade with milling. Thus, the optimum values of coercive force and remanence cannot be obtained simultaneously. Figure 5 is related with a larger remanence, but a smaller coercive force for $Nd(Fe,Mo)_{12}N_x$. Their permanent magnetic properties are summarized below, respectively: $_iH_c$=2.6 kOe, B_r=9.1 KG, $(BH)_{max}$=12.0 MGOe. All these measurements were made with a magnetizing field of 20 kOe. The coercive force is larger when using a higher applied field as indicated in Table I. Figure 6 plots the temperature dependence of coercive force for three kinds of samples: One was prepared by milling process, the other two by using mechanical alloying. In a temperature range from room temperature to 100 °C the temperature coefficient of coercive force for both samples is −0.5%/K. For a comparison, the temperature dependence of coercive force of $Nd_2Fe_{14}B$ magnets is presented also in Fig. 6. The temperature coefficient of $_iH_c$ for the latter is −0.6%/K. Among the 1-12 nitrides the Curie temperature of $Nd(Fe,Mo)_{12}N_x$ and $Pr(Fe,Mo)_{12}N_x$ is lower. Thus, it may be expected to improve the temperature stability of the magnets based on the 1-12 nitrides by a substitution of Mo with another element, such as Ti, V, etc.

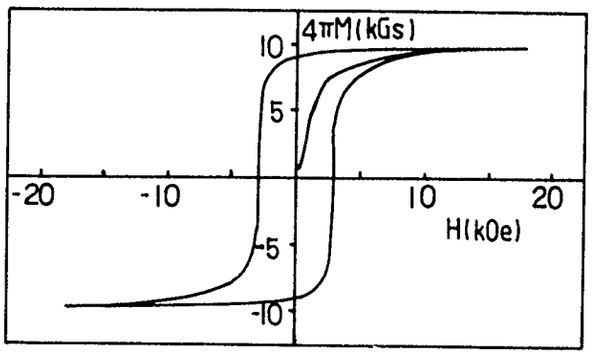

FIG. 5. Hysteresis loops of $NdFe_{10.5}Mo_{1.5}N_x$ powders for 20 h milling.

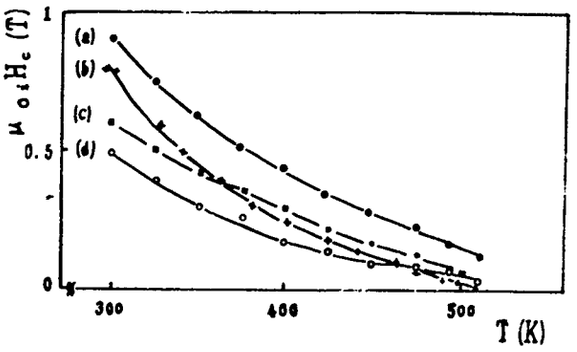

FIG. 6. Temperature dependence of coercive force: (a) $_iH_c$ of $NdFe_{10.5}Mo_{1.5}N_x$ mechanical alloy powders; (b) $_iH_c$ of $Nd_2Fe_{14}B$; (c) $_iH_c$ of $Pr(Mo_{0.13}Fe_{0.87})_{10}N_x$ mechanical alloy powders; (d) $_iH_c$ of $NdFe_{10.5}Mo_{1.5}N_x$ anisotropic powders

[1] J. M. D. Coey and H. Sun, J. Magn. Magn. Mater **87**, L251 (1990).
[2] Y.-C. Yang, S.-L. Ge, X.-D. Zhang, L.-S. Kong, and Q. Pan, in *Proceedings of the Sixth International Symposium on Magnetic Anisotropy and Coercivity in Rare Earth Transition Metal Alloys*, edited by S. G. Sankar (Carnegie Mellon University Press, Pittsburgh, 1990), p. 190.
[3] Y-C. Yang, X.-D. Zhang, L.-S. Kong, Q. Pan, and S -L. Ge, Appl. Phys. Lett. **58**, 2042 (1991)
[4] G. Wei and G. C. Hadjipanayis, IEEE Trans. Magn. **MAG-28**, 2563 (1992).
[5] M. Endoh, K. Nakamura, and H. Mikami, IEEE Trans Magn. **MAG-28**, 2560 (1992).
[6] Y.-C. Yang, Q. Pan, X.-D. Zhang, J. Yang, M.-H. Zhang, and S.-L. Ge, Appl. Phys. Lett. **61**, 2723 (1992).

Structural and magnetic properties of $Ce(Fe,M)_{12}N_x$ interstitial compounds, M=Ti, V, Cr, and Mo

Qi Pan, Zun-Xiao Liu, and Ying-Chang Yang
Department of Physics, Peking University, Beijing 100871, People's Republic of China

Stabilizing the 1-12 phase with cerium was possible using a special heat treatment. The structural and magnetic properties of $Ce(Fe,M)_{12}$ and their nitrides, for M=Ti, V, Cr, Mo, etc., were investigated using x-ray-diffraction and magnetic measurements. The effects of interstitial nitrogen atoms on lattice parameters, Curie temperature, saturation magnetization, and magnetocrystalline anisotropy are reported. A profound change was found on the magnetocrystalline anisotropy. As an example, in the case of $CeMo_2Fe_{10}N_x$, the easy magnetization direction changes from c axis to the basal plane depending on the nitrogen content x.

I. INTRODUCTION

During the last few years, a lot of work dealing with the rare-earth (RE)–Fe nitrides having the $ThMn_{12}$-type structure has been conducted for the purpose of permanent magnet development.[1,2] Because of the difficulties in forming the 1-12 phase with cerium, few reports were concerned with cerium compounds. The cerium ion often possesses a relatively higher valence (Ce^{4+}) in the RE-iron intermetallics.[3] Generally, the Ce-Fe compounds have smaller lattice parameters, lower Curie temperatures T_c and less spontaneous magnetization than other rare-earth compounds; thus, it is expected that the interstitial nitrogen atoms may have more significant effects on magnetic properties of the Ce compounds. In addition, Ce^{4+} is nonmagnetic, and it is hoped to obtain useful information associated with the iron sublattice behavior. A study on the Ce nitrides is not only of significance for basic research, but there is also a potential technical application. Since there is a lot of cerium in inexpensive mischmetal, an investigation on the formation and magnetic properties of Ce nitrides might be useful for developing low-cost magnetic materials.

In this work we succeeded in stabilizing the $Ce(FeM)_{12}$ compounds and their nitrides, where M=Ti, V, Cr, and Mo. The effects of interstitial nitrogen atoms on lattice parameters, Curie temperature, saturation magnetization, and magnetocrystalline anisotropy are reported.

II. EXPERIMENT

The samples were prepared by arc melting 99.5% pure materials in a purified argon atmosphere, followed by a heat treatment at 600–1000 °C for 1 week. Nitrides were prepared by passing purified nitrogen gas at atmospheric pressure over finely ground powder samples at 400–600 °C for 1–5 h, followed by rapidly cooling to room temperature. X-ray diffraction and chemical analysis were made to determine the structure and the weight percentage of nitrogen. The powder samples of cylindrical shape were aligned in a 10 kOe field and fixed in epoxy resin. Magnetization curves were measured on aligned powder samples with a field of up to 70 kOe K by using an extracting sample magnetometer. The Curie temperature was determined from σ-T curves which were measured by a vibrating sample magnetometer in the temperature range from 300 to 1000 K.

III. RESULTS AND DISCUSSIONS

A. Crystallographic structure

The samples before nitrogenation were found to be crystallized in single $ThMn_{12}$-type phase for M=Ti, V, Mo. The only exception is Cr, which contained a little 2-17 phase. After nitrogenation, the $Ce(M,Fe)_{12}N_x$ maintains the same structure, but with an increase in the lattice parameters. The lattice parameters a and c, unit-cell volume V, and relative change in unit-cell volume upon nitrogenation $\Delta V/V$ of $Ce(M,Fe)_{12}N_x$, in comparison with $Ce(M,Fe)_{12}$, are all listed in Table I. As an example, x-ray-diffraction patterns of $CeTiFe_{11}$ are illustrated in Fig. 1(a). The unit-cell volumes increase from 2.7% to 3.5% compared with their original counterparts.

B. Curie temperature and saturation magnetization

The Curie temperature T_c, saturation magnetization σ_s, anisotropy field H_A, and easy magnetization direction (EMD) of $Ce(M,Fe)_{12}$ and their nitrides are summarized in Table II. The interstitial nitrogen atoms have an effect of increasing the Curie temperature. The T_c of $CeTiFe_{11}N_x$ is raised from 485 to 710 K by introducing the nitrogen atoms into the $CeTiFe_{11}$ compounds. This effect may be due to the expansion of the unit-cell volume after nitrogenation.

The effect of the interstitial nitrogen atoms on the enhancement of saturation magnetization is significant. The molecule moment is increased from 17.4 μ_B to 21.88 μ_B with M=Ti, or from 13.6 μ_B to 18.6 μ_B with M=V in the $Ce(M,Fe)_{12}$, etc. Since Ce^{4+} is nonmagnetic, the increase of

TABLE I. The lattice parameters a and c, unit-cell volume V, and relative change in unit-cell volume upon nitrogenation $\Delta V/V$ of $Ce(M,Fe)_{12}N_x$, in comparison with $Ce(M,Fe)_{12}$.

Compounds	a (Å)	c (Å)	V (Å^3)	$\Delta V/V$ (%)
$CeTiFe_{11}$	8.542	4.779	348.7	···
$CeTiFe_{11}N_x$	8.574	4.872	358.2	2.7
CeV_2Fe_{10}	8 503	4.758	344.0	···
$CeV_2Fe_{10}N_x$	8.646	4.761	355.9	3.46
$CeMo_{1\,5}Fe_{10\,5}$	8 535	4 766	347.2	···
$CeMo_{1\,5}Fe_{10\,5}N_x$	8.617	4.821	358.1	3.2
$CeMo_2Fe_{10}$	8.585	4.799	353 7	···
$CeMo_2Fe_{10}N_{0\,8}$	8.674	4 842	364.3	3.0

 0021-8979/94/76(10)/6728/3/$6.00 © 1994 American Institute of Physics

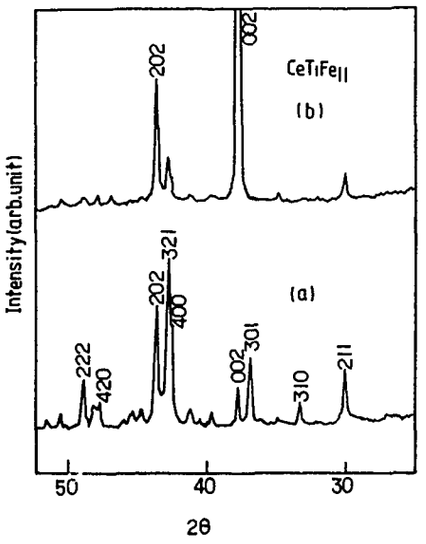

FIG 1. X-ray-diffraction patterns of $CeTiFe_{11}$: (a) nonaligned; (b) aligned

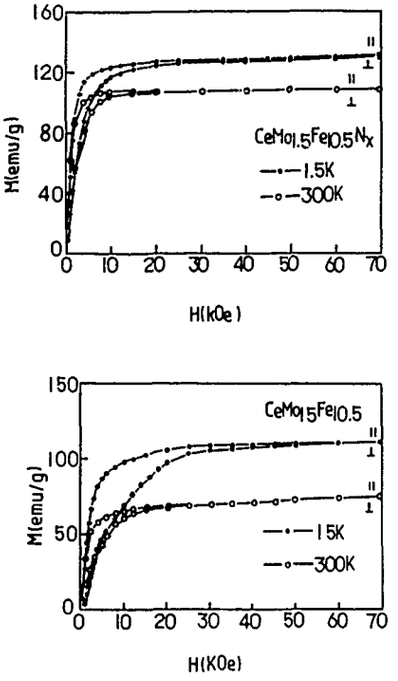

FIG. 2. Magnetization curves along and perpendicular to the origination direction at 1.5 K and room temperature between $CeMo_{1.5}Fe_{10.5}$ and $CeMo_{1.5}Fe_{10.5}N_x$.

the saturation magnetization represents an increase in the iron atomic moment.[4] So far, the increases of T_c and the magnetic moments have been regarded as being attributed mainly to the volume expansion (about 3% in average), as a magnetovolume effect, but, that is not enough. The nitrogen atoms enhance the Fe moments not only through lattice expansion but also by changing the electronic bonding nature, which was calculated by Sakuma.[5]

C. Magnetocrystalline anisotropy

In the most rare-earth compounds, 4 f electrons are expected to be well localized compared with the d and s electrons in the transition-metal compounds. So the single-ion model is used effectively dealing with the magnetocrystalline anisotropy in the rare-earth-ion sublattice. In the case of iron sublattice, owing to the itinerant properties of 3d electrons, the situation becomes more complicated. It is not easy to calculate the changes in magnetocrystalline anisotropy theoretically before or after nitrogenation. So the experimental results are even more important in obtaining information about the iron sublattice behavior.

On the basis of the x-ray-diffraction patterns on aligned samples, we can obtain the magnetocrystalline anisotropy of $Ce(M,Fe)_{12}$ and their nitrides. The x-ray-diffraction patterns of magnetically aligned powder samples of $CeTiFe_{11}$ are shown in Fig. 1(b): a drastic increase in (002) reflections and diminution of ($hk0$) lines reveals that it has an easy axial. Figures 2 and 3 are the comparison of magnetization curves along, and perpendicular to, the origination direction at 1.5 K and room temperature between $CeMo_{1.5}Fe_{10.5}$ and $CeMo_{1.5}Fe_{10.5}N_x$, $CeTiFe_{11}$, and $CeTiFe_{11}N_x$. It can been seen that after nitrogenation the anisotropy is decreased. In

TABLE II. The Curie temperature T_c, saturation magnetization σ_s, anisotropy field H_A, and easy magnetization direction (EMD) of $Ce(M,Fe)_{12}$ compounds and their nitrides.

Compounds	T_c (K)	σ_s (emu/g)		H_A (kOe)		EMD
		T=1.5 K	T=300 K	T=1.5 K	T=300 K	T=300 K
$CeTiFe_{11}$	485	129.586	108.245	35	15	axis
$CeTiFe_{11}N_x$	710	151.006	135.743			
CeV_2Fe_{10}	425	99.209	75.515	20	10	axis
$CeV_2Fe_{10}N_x$	725	128.304	116.292			weak axis
$CeCr_2Fe_{10}$	433	95.139	59.999	12	8	axis
$CeCr_2Fe_{10}N_x$	685	132.546	111.514			plane
$CeMo_{1.5}Fe_{10.5}$	386	111.256	76 044	23	10	axis
$CeMo_{1.5}Fe_{10.5}N_x$	612	131 56	108.758			
$CeMo_2Fe_{10}$	340	64.697	40.608			axis
$CeMo_2Fe_{10}N_{0.8}$	500	97.427	75.880			plane

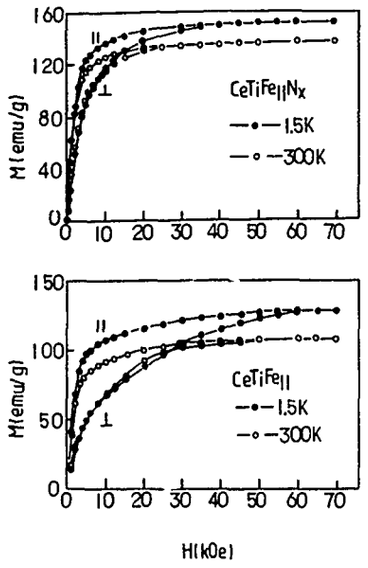

FIG. 3. Magnetization curves along and perpendicular to the origination direction at 1.5 K and room temperature between $CeTiFe_{11}$ and $CeTiFe_{11}N_x$

the compounds with Ce, iron is the only magnetic atom, so the behavior of $CeMo_{1.5}Fe_{10.5}N_x$ anisotropy represents changes in the anisotropy on the iron sublattice.

In order to determine the effect of interstitial nitrogen atoms on the magnetocrystalline anisotropy of the iron sublattice we made samples of $CeMo_2Fe_{10}N_x$ where $x=0$, 0.2, 0.5, 0.8. The x-ray diffraction patterns of $CeMo_2Fe_{10}N_x$ are plotted in Fig. 4: (a) $x=0$ nonaligned samples; (b) $x=0$ aligned samples; (c) $x=0.2$ aligned samples; (d) $x=0.5$ aligned samples; (e) $x=0.8$ aligned samples. The x-ray-diffraction pattern on aligned samples of $CeMo_2Fe_{10}$ in Fig. 4(b) shows that the EMD is along the c axis due to the drastic increase in (002) reflection and diminution of ($hk0$) lines. After the absorption of a certain quantity of nitrogen, the EMD deviates from the c axis, as indicated in Fig. 4(c) for $CeMo_2Fe_{10}N_{0.2}$ because the relative intensity of the (202) line is larger rather than the (002) line. As expected, a profound change was found on the magnetocrystalline anisotropy upon nitrogenation. With the increases of nitrogen content, the drastic increases in ($hk0$) reflections and decreases in (001) lines reveal that when almost all the 2b sites are occupied by nitrogen atoms, the EMD changes to basal plane for $CeMo_2Fe_{10}N_{0.8}$, which is shown in x-ray-diffraction pattern Fig. 4(e). It is clear that the changes in the magnetocrystalline anisotropy of the iron sublattice is observed from the c axis to basal plane with increasing the nitrogen content x.

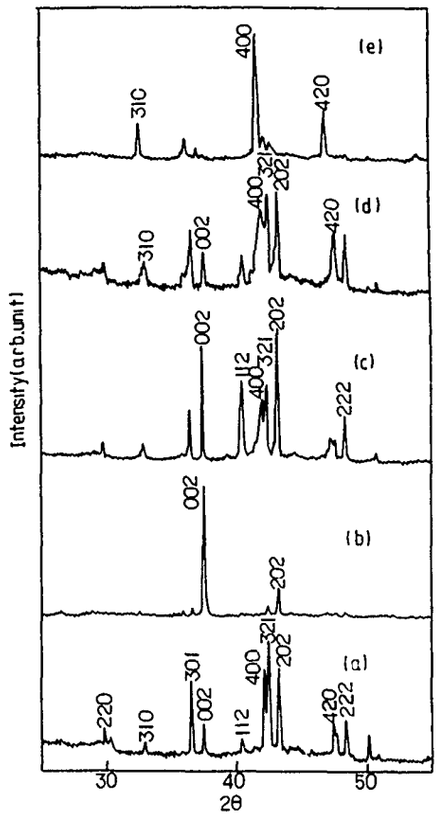

FIG. 4. The x-ray-diffraction patterns of $CeMo_2Fe_{10}N_x$: (a) $x=0$ nonaligned samples; (b) $x=0$ aligned samples; (c) $x=0$ 2 aligned samples; (d) $x=0.5$ aligned samples; (e) $x=0.8$ aligned samples.

IV. CONCLUSION

We have succeeded in forming $Ce(M,Fe)_{12}$ compounds and their nitrides with $ThMn_{12}$-type structure. The nitrides increases both the Curie temperature and spontaneous magnetization, and makes significant changes in magnetocrystalline anisotropy which depends on the nitrogen content x. The experimental results indicate that at room temperature the easy magnetization direction for $CeMo_2Fe_{10}N_{0.8}$ is in the basal plane, contrary to the $CeMo_2Fe_{10}$ compounds.

ACKNOWLEDGMENT

This work was supported by the National Natural Science Foundation of China.

[1] Y.-C. Yang, Q. Pan, X.-D. Zhang, J Yang, M.-H. Zhang, and S.-L. Ge, Appl. Phys. Lett. **61**, 2723 (1992).
[2] L. Schultz, K. Schnitzke, J. Wecker, and C Kuhrt, J. Appl. Phys. **70**, 6339 (1991).
[3] K. A. Gschneider and R. Smoluchowski, J. Less-Common Met **5**, 374 (1963)
[4] Y.-C. Yang, X.-D Zhang, Q Pan, and S.-L. Ge, J. Appl. Phys. **70**, 6001 (1991).
[5] A. Sakuma, J. Phys. Soc. Jpn. **61**, 4119 (1992).

Neutron-diffraction and Mössbauer effect study of the $Tb_2Fe_{17-x}Al_x$ solid solutions

G. K. Marasinghe, S. Mishra, and O. A. Pringle
Department of Physics, University of Missouri-Rolla, Rolla, Missouri 65401-0249

Gary J. Long
Department of Chemistry, University of Missouri-Rolla, Rolla, Missouri 65401-0249

Z. Hu and W. B. Yelon
University of Missouri Research Reactor and the Departments of Chemistry and Physics, University of Missouri-Columbia, Columbia, Missouri 65211

F. Grandjean
Institute of Physics, B5, University of Liège, B-4000 Sart-Tilman, Belgium

D. P. Middleton and K. H. J. Buschow[a)]
Philips Research Laboratories, P.O. Box 80000, NL-5600 JA Eindhoven, The Netherlands

The magnetic properties of a series of $Tb_2Fe_{17-x}Al_x$ solid solutions, with nominal x compositions of 0, 2, 3, 4, 5, 6, 7, and 8, have been studied by neutron diffraction and Mössbauer spectroscopy. Neutron-diffraction data indicate that the compounds all crystallize with the Th_2Zn_{17} structure and that the aluminum atoms are excluded from the $9d$ site and show a distinct preference for the $6c$ site only for an aluminum content greater than 6. The unit-cell volume increases by approximately 1% per aluminum atom substituted in the formula unit. The magnetic moment per formula unit, measured at 295 K, shows very little change for x less than or equal to 4, but decreases rapidly with increasing aluminum content for higher values of x. Mössbauer spectral results indicate that all the samples are ferromagnetically ordered at 85 K. However, at 295 K $Tb_2Fe_9Al_8$ is paramagnetic and $Tb_2Fe_{10}Al_7$ is either paramagnetic or has at most very small ferromagnetic moments. An analysis of the magnetic spectra with a basal magnetic model is successful for x values of 5 or less; however, at higher x values an axial model for the magnetization is required, indicating the presence of a spin reorientation with increasing aluminum content and decreasing temperature. The weighted average hyperfine field decreases approximately linearly by 21 kOe per substituted aluminum atom at 85 K and more rapidly at 295 K. As expected, the isomer shifts increase with increasing aluminum content as a result of interatomic charge transfer and intraatomic iron $4s$-$3d$ electronic redistribution.

The discovery[1] that the addition of interstitial nitrogen could dramatically increase the Curie temperature of R_2Fe_{17} and, in some cases, change the magnetic anisotropy from basal to axial has led to a renewed interest in these compounds. The primary reason for the increased T_C is the expansion of the lattice caused by the interstitial nitrogen.[2] The lattice may also be expanded by partially substituting the iron by other elements,[3] and an investigation of such partially substituted compounds may lead to a better understanding of the magnetization process and consequently to solid solutions possessing better magnetic properties. In the $R_2Fe_{14-x}Al_xB$ solid solutions,[4,5] aluminum causes both the coercive and the anisotropic fields to increase with only slight decreases in the magnetization and T_C. Partial substitution of iron atoms by aluminum in Ce_2Fe_{17}, Y_2Fe_{17}, Nd_2Fe_{17}, Dy_2Fe_{17}, and Ho_2Fe_{17} causes the unit cell to expand and the T_C to increase with aluminum content at lower aluminum concentrations.[3,6-8] In $Tb_2Fe_{14}B$ the terbium magnetic moments are aligned antiparallel[9] with the iron moments and a similar antiparallel magnetic structure is expected in $Tb_2Fe_{17-x}Al_x$. It has been reported[10,11] that $Tb_2Fe_{17-x}Al_x$ crystallizes in the hexagonal Th_2Ni_{17} structure at aluminum concentrations up to an x of 3.8 and in the rhombohedral Th_2Zn_{17} structure at higher concentrations. Furthermore, its T_C increases with increasing aluminum content at low aluminum concentrations.[10]

The $Tb_2Fe_{17-x}Al_x$ samples were prepared from 99.9% pure elements by arc melting followed by annealing at 900 °C for more than 3 weeks. The phase purity of the samples was checked by x-ray diffraction which indicated that the $Tb_2Fe_{17-x}Al_x$ samples with nominal x values of 2 and higher crystallized with the rhombohedral Th_2Zn_{17} structure. This limiting composition for the rhombohedral phase is considerably lower than that reported by Oesterreicher and Boller[10-12] and may be due to the higher annealing temperature used for the samples in our study.

The neutron-diffraction patterns were measured[6] and refined[13,14] by the same methods as reported earlier. The Mössbauer spectra were measured[6] and fit[15-17] as reported earlier. The spectra that indicated ferromagnetic ordering were fit with four or seven magnetic sextets corresponding to the four or seven magnetically inequivalent iron sites expected for an axial or basal orientation of the magnetization and the site point symmetry.

The Curie temperature of the $Tb_2Fe_{17-x}Al_x$ solid solutions increases with increasing aluminum content at lower aluminum concentrations and reaches a maximum at an x ~3.[18] The results of the refinement of the 295 K neutron-diffraction patterns of these solid solutions are given in Table

[a)]Present address. Van der Waals–Zeeman Laboratory, University of Amsterdam, NL-1018 XE Amsterdam, The Netherlands.

 0021-8979/94/76(10)/6731/3/$6.00 © 1994 American Institute of Physics

TABLE I. The lattice and positional parameters, site occupancies, and moments in $Tb_2Fe_{17-x}Al_x$ as measured by neutron diffraction at 295 K.

Compound	$Tb_2Fe_{15}Al_2$	$Tb_2Fe_{14}Al_3$	$Tb_2Fe_{13}Al_4$	$Tb_2Fe_{12}Al_5$	$Tb_2Fe_{11}Al_6$	$Tb_2Fe_{10}Al_7$	$Tb_2Fe_9Al_8$
x refined	1.98	3.14	4.08	5.10	6.06	7.16	8.12
a (Å)	8.5768(2)	8.6011(2)	8.6212(1)	8.6625(1)	8.6942(1)	8.7482(1)	8.7874(1)
c (Å)	12 5191(4)	12.5549(3)	12.5872(2)	12.6307(3)	12.6501(2)	12.6988(3)	12.7270(3)
c/a	1.460	1.460	1.460	1.458	1.455	1.452	1.448
V (Å^3)	797.5	804.4	810.2	821.3	828.1	841.6	851.1
Tb, 6c, z	0.3413(4)	0.3409(3)	0.3406(3)	0.3433(2)	0.3417(3)	0.3458(2)	0.3480(2)
Fe/Al, 6c, z	0.0958(3)	0	0.0941(2)	0.0962(2)	0.0993(1)	0.1002(3)	0.1028(4)
Fe/Al, 18f, x	0 2964(2)	0.2 [illegible]	0.2896(1)	0.2893(1)	0.2920(1)	0.2905(2)	0.2928(2)
Fe/Al, 18h, x	0.1676(1)	0.1684(1)	0.1690(1)	0.1697(1)	0.1681(1)	0.1683(1)	0.1677(1)
Fe/Al, 18h, z	0.4921(2)	0.4920(1)	0.4895(1)	0.4895(1)	0.4882(1)	0.4905(1)	0.4904(1)
%Al, 6c	14.4	21.0	24.6	32.9	41.3	72.4	94.0
%Al, 9d	0.0	0.0	0.0	0.0	0.0	0.0	0.0
%Al, 18f	9.8	18.8	23.4	31.4	41.4	57.6	68.8
%Al, 18h	18.4	26 6	36.4	42.6	45.8	37.6	35.2
R factor	5.88	5.24	5.26	5.09	4.46	4.84	4.97
R_w factor	6.80	6.10	5.95	6.17	5.46	5.73	5.78
R_m factor	10.1	8.23	5.07	8.48	9.67	14.0	···
χ^2	2.57	2.49	2.56	2.61	2.62	2.50	2.54
μ, Tb, 6c (μ_B)	−4.5(1)	−4.3(1)	−4.1(1)	−4.1(1)	−3.5(1)	−0.6(1)	···
μ, Fe, 6c (μ_B)	2.7(2)	3.0(1)	3.1(1)	3.3(1)	32.3(1)	0.6(1)	···
μ, Fe, 9d (μ_B)	1.9(1)	1.9(1)	2.0(1)	1.8(1)	1.7(1)	0.6(1)	···
μ, Fe, 18f (μ_B)	1.9(1)	2.0(1)	2.1(1)	2.0(1)	1.9(1)	0.6(1)	···
μ, Fe, 18h (μ_B)	1.5(1)	1.8(1)	1.6(1)	1.6(1)	1.1(1)	0.6(1)	···
μ/cell (μ_B)	56.7	57.6	55.5	46.2	34.5	14.1	···
μ/formula (μ_B)	18.9	19.2	18.5	15.4	11.5	4.7	···
$\mu(z)/\mu(x)$	0.0	0.0	0.0	0.0	1.2	infinite	···

I. The lattice parameters increase approximately linearly with x as was found[19] to be the case for the related $Nd_2Fe_{17-x}Al_x$ solid solutions, but the increase differs from the behavior found for the c lattice parameter in $Tb_2Fe_{17-x}Ga_x$, which increases up to an x of 6 and then remains constant at higher values. The unit-cell volume of $Tb_2Fe_{17-x}Al_x$ increases linearly by 8.9 Å^3 per aluminum, a value which is similar to that of the gallium solid solutions.[20]

As is shown in Fig. 1, the aluminum completely avoids the 9d crystallographic site, the site expected to have the smallest Wigner–Seitz cell volume.[19] In contrast, at [illegible]t up to an x of 6, the aluminum somewhat favors the 18h site and occupies the 6c and 18f sites almost randomly. At x values above 6 these trends change and aluminum highly favors the 6c and 18f sites. A rather similar occupation has been observed[19] in the $Nd_2Fe_{17-x}Al_x$ solid solutions and explained on the basis of the differing near-neighbor environments of the different sites.

The compositional dependence of the magnetic moments derived from the neutron-diffraction[9] scattering is given in Table I, and shown in Fig. 2. As expected on the basis of the terbium crystal field,[20] the terbium magnetic moments are antiferromagnetically exchange coupled to the iron moments which are in the basal plane of the unit cell for x values of 5 and less. At larger x values a spin reorientation occurs such that, in $Tb_2Fe_{10}Al_7$, the magnetization is axial. Unfortunately, $Tb_2Fe_9Al_8$ is paramagnetic, at least at 295 K. The iron moment on the 6c site increases gradually for x values up to 6, whereas the other iron moments remain approximately constant for x between 0 and 6.

The Mössbauer spectra of the $Tb_2Fe_{17-x}Al_x$ solid solutions have been measured at 85 and 295 K. The spectra were initially fit with either four or seven broadened magnetic sextets which represent the expected number of magnetic

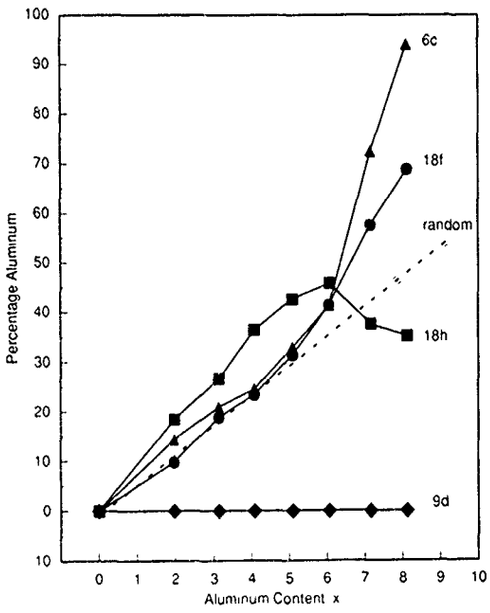

FIG. 1. The percentage of aluminum found by neutron diffraction on each of the four crystallographic iron sites in the $Tb_2Fe_{17-x}Al_x$ solid solutions. The dashed line represents random occupation by aluminum.

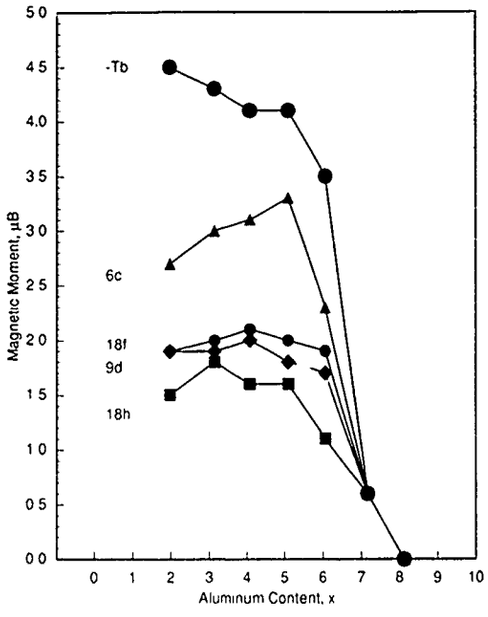

FIG. 2. The iron and terbium magnetic moments at 295 K in the $Tb_2Fe_{17-x}Al_x$ solid solutions. The terbium moments are aligned antiparallel to the iron moments.

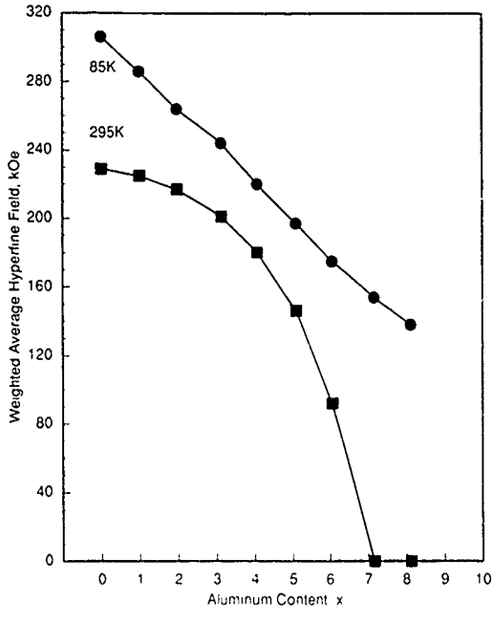

FIG. 3. The area weighted average hyperfine fields in the $Tb_2Fe_{17-x}Al_x$ solid solutions.

sextets in the axially or basally magnetized R_2Fe_{17} materials.[15,21] In agreement with the neutron-diffraction results, it was found that all the 295 K magnetic Mössbauer spectra could only be fit with the basal magnetization model, except for $Tb_2Fe_{11}Al_6$, for which a better fit with the simpler axial model was obtained. The low-temperature spectra for the samples with x values of 6, 7, and 8 were successfully fit with an axial model. This spin reorientation is also apparent in the quadrupole shift changes with increasing x and decreasing temperature. The fitting model, which does not take into account the near-neighbor environment of each iron site, is quite successful in reproducing the observed spectral absorption, but some problems with intensity do occur. A more detailed analysis of these spectra in terms of a binomial distribution of the near-neighbor aluminum environments will be reported elsewhere.[22] Because of the approximations involved in the spectral fits, only the weighted average hyperfine parameters are discussed herein.

The weighted average isomer shifts increase linearly with increasing aluminum content with variations of 0.0257 and 0.0185 mm/s per aluminum at 295 and 85 K, respectively. These increases are typical of those found upon the substitution of either aluminum[19] or gallium[20] for iron to form R_2Fe_{17} solid solutions. The increase may be attributed to an interatomic charge transfer between the iron and aluminum and a subsequent $3d$-$4s$ intraatomic iron electronic redistribution.[23–25] The weighted average hyperfine fields at 295 and 85 K, as a function of aluminum content, are shown in Fig. 4. As expected the hyperfine field at 85 K decreases almost linearly by 21 kOe per aluminum atom with the increasing replacement of magnetic iron with diamagnetic aluminum and the decrease is even more rapid at 295 K; however, the observed hyperfine fields are higher than those observed in the $Nd_2Fe_{17-x}Al_x$ solid solutions, even though the unit-cell volumes of the former are smaller.

[1] J. M. D. Coey and H. Sun, J. Magn. Magn. Mater. **87**, L251 (1990).
[2] Q. Qi, H. Sun, R. Skomski, and J. M. D. Coey, Phys. Rev. B **45**, 12 278 (1992).
[3] T. H. Jacobs, K H. J. Buschow, G.-F. Zhou, X. Li, and F. R. de Boer, J Magn. Magn. Mater. **116**, 220 (1992).
[4] Y.-C. Yang, W. J. James, X.-D. Li, H.-Y. Cheng, and L.-G. Xu. IEEE Trans. Magn. **MAG-22**, 757 (1986).
[5] Y.-C. Yang, D. E. Tharp, G. J. Long, O A Pringle, and W. J. James, J. Appl. Phys. **61**, 4343 (1987).
[6] W. B. Yelon, H. Xie, G J. Long, O. A. Pringle, F. Grandjean, and K. H. J. Buschow, J. Appl. Phys. **73**, 6029 (1993).
[7] T. H. Jacobs, K. H. J. Buschow, G. F. Zhou, and F. R. de Boer, Physica B **179**, 177 (1992).
[8] D. P. Middleton and K. H. J. Buschow, J. Alloys Compounds **203**, 217 (1994).
[9] J. F. Herbst, C. D. Fuerst, and W. B. Yelon, J Appl. Phys. **74**, 5884 (1993)
[10] H. Oesterreicher, J. Less-Common Met. **40**, 207 (1975).
[11] H. Boller and H. Oesterreicher, J. Less-Common Met **45**, 103 (1976).
[12] H. Oesterreicher, J. Less-Common Met. **46**, 127 (1976).
[13] FULLPROF Rietveld refinement code written by J. Rodriguez-Carjaval, Institute Laue Langevin, Grenoble, France.
[14] J. F. Herbst, J. J. Croat, and R W. Lee, J. Appl. Phys. **53**, 250 (1982).
[15] G. J. Long, O. A. Pringle, F. Grandjean, W. B. Yelon, and K. H J. Buschow, J. Appl. Phys. **74**, 504 (1993).
[16] G. J. Long and F. Grandjean, in *Supermagnets, Hard Magnetic Materials*, edited by G. J. Long and F. Grandjean (Kluwer, Dordrecht, 1991), p 355
[17] F. Grandjean and G. J. Long, in *Interstitial Intermetallic Alloys*, edited by F. Grandjean, G. J. Long, and K. H. J. Buschow (Kluwer, Dordrecht, 1994), p. 463.
[18] T. H. Jacobs, D. P. Middleton, and K. H. J. Buschow (unpublished results).
[19] G. J. Long, G. K. Marasinghe, S. Mishra, O A Pringle, Z. Hu, W. B. Yelon, D. P. Middleton, K. H. J. Buschow, and F. Grandjean, J Appl Phys. **76**, 5383 (1994)
[20] Z. Hu, W. B. Yelon, S. Mishra, G. J. Long, O. A Pringle, D. P. Middleton, K. H. J. Buschow, and F. Grandjean, J. Appl. Phys. **76**, 443 (1994).
[21] G. J. Long, O. A. Pringle, F. Grandjean, and K. H. J Buschow, J. Appl. Phys **72**, 4845 (1992).
[22] S. Mishra, G. J. Long, G. K. Marasinghe, O. A. Pringle, Z. Hu, W. B. Yelon, D P. Middleton, K. H. J. Buschow, and F Grandjean (unpublished).
[23] A. M van der Kraan and K. H J. Buschow, Physica B **138**, 55 (1986)
[24] J. W. C. de Vries, R. C. Thiel, and K. H. J. Buschow, J. Phys. F **14**, 2403 (1985).
[25] J. Pszczola, J. Zukrowski, J. Suwalski, Z. Kucharski, and M. Lukasiak, J. Magn Magn. Mater. **40**, 197 (1983)

Structure and magnetic anisotropy of $Sm_2Fe_{17-x}Al_xC$ (x=2–8) compounds prepared by arc melting

Zhao-Hua Cheng, Bao-Gen Shen, Jun-Xian Zhang, Fang-Wei Wang, Hua-Yang Gong, Wen-Shan Zhan, and Jian-Gao Zhao
State Key Laboratory of Magnetism, Institute of Physics, Chinese Academy of Sciences, P.O. Box 603, Beijing 100080, People's Republic of China

In previous work it was discovered that the 2:17-type rare-earth–iron compounds with high carbon concentration could be formed by the substitution of Ga, Si, or Al, etc., for Fe in $R_2Fe_{17}C_x$. The effect of Al substitution for Fe on the structure and magnetic anisotropy of $Sm_2Fe_{17}C$ has been investigated. Alloys with the composition of $Sm_2Fe_{17-x}Al_xC$ (x=2, 3, 4, 5, 6, 7, and 8) were prepared by arc melting. The carbides are single phase with rhombohedral Th_2Zn_{17}-type structure except for $Sm_2Fe_{17}C$ which contains a small amount of α-Fe. The addition of Al results in an approximately linear increase in the lattice constants and the unit-cell volumes. The Curie temperature T_c is found to increase slightly when $x \leqslant 3$, then decrease rapidly with increasing Al concentration, while the room-temperature saturation magnetization decreases monotonically with the addition of aluminum. X-ray-diffraction and magnetization measurement studies of magnetic-field-oriented powders demonstrate that the samples with $x \leqslant 6$ exhibit an easy c-axis anisotropy at room temperature and the room-temperature anisotropy field increases from 5.3 T for x=0 to about 11 T for x=2. Further substitution decreases the anisotropy field. For the sample with x=2, the room-temperature anisotropy field is higher than that of $Nd_2Fe_{14}B$, and the saturation magnetization is about 110 emu/g. In this alloy, the substitution of a small amount of other elements, such as Co, Ni, etc., may yield a further improvement in its magnetic properties. Thus, it is possible that these carbides can be used as the starting materials for producing high-performance 2:17-type sintered permanent magnets.

I. INTRODUCTION

The interstitial rare-earth–iron compounds based on the rhombohedral Th_2Zn_{17}-type or hexagonal Th_2Ni_{17}-type structure are found to have an excellent intrinsic magnetic properties;[1] however, the poor high-temperature stability of $Sm_2Fe_{17}C_x$ and $Sm_2Fe_{17}N_x$ compounds prepared by gas-solid reaction methods restricts the possible application of these materials as permanent magnets. Our previous studies have shown that the heavy-rare-earth–iron compounds $R_2Fe_{17}C_x$ with high carbon concentration ($x \approx 3.0$) could be obtained from melt spinning.[2–4] Their intrinsic magnetic properties are comparable to those of the corresponding carbides prepared by gas-solid reaction. It was noteworthy that they could be stabilized at high temperature (above 1000 °C). It was, however, still difficult to synthesize $Sm_2Fe_{17}C_x$ with $x \geqslant 1.5$. Recently, it was discovered that highly stable $Sm_2Fe_{17}C_x$ with $x \leqslant 3.0$ can be formed by the substitution of Al, Ga, or Si.[5–7] In this work, the effect of the substitution of Al on the structure and magnetic anisotropy of $Sm_2Fe_{17}C$ is reported.

II. EXPERIMENT

Iron and carbon were first melted together in an induction furnace to form Fe-C alloy with a lower melting temperature. Then Fe, Sm, Al, and Fe-C alloys were melted by arc melting in a high-purity argon atmosphere. Elements used were at least 99.9% pure. An excess of 10%–20% Sm was added to compensate the evaporation during melting. The ingot alloys were melted at least four times to ensure homogeneity, then annealed under an argon atmosphere at 1400 K for 5 days followed by quenching into water. Ingots were then ground to yield powders and oriented in an applied field of 2 T in an epoxy resin. X-ray-diffraction (XRD) experiments were performed on powder samples using Co$K\alpha$ radiation to determine the phase structure as well as lattice constants and unit-cell volume. The Curie temperature T_c was derived from the temperature dependence of magnetization $\sigma(T)$ curves measured by a vibrating sample magnetometer in a field of 700 Oe. The anisotropy fields H_A were obtained from the magnetization curves measured along and perpendicular to the aligned direction by using the magnetometer with a magnetic field up to 7 T. The saturation magnetization at 300 K was obtained from fitting the experimental data for $M(H)$ vs H using the law of approach to saturation.

III. RESULTS AND DISCUSSIONS

The XRD study demonstrates that all Al-containing alloys are single-phase compounds with the rhombohedral Th_2Zn_{17}-type structure and no significant diffraction from impurity phases, especially bcc α-Fe, is observed. For example, Fig. 1(a) shows the typical XRD pattern of $Sm_2Fe_{11}Al_6C$; however, $Sm_2Fe_{17}C$ contains a few percent α-Fe of impurity phase. This fact implies that the addition of Al can help the formation of the 2:17-type carbides with high carbon concentration.

The lattice constants a,c and the unit-cell volume v of $Sm_2Fe_{17-x}Al_xC$ compounds are summarized in Table I. It can be seen that these both show a linear dependence on Al concentration as we would excepted on the basis of a simple model involving atomic volumes. To a good approximation,

 0021-8979/94/76(10)/6734/3/$6.00 © 1994 American Institute of Physics

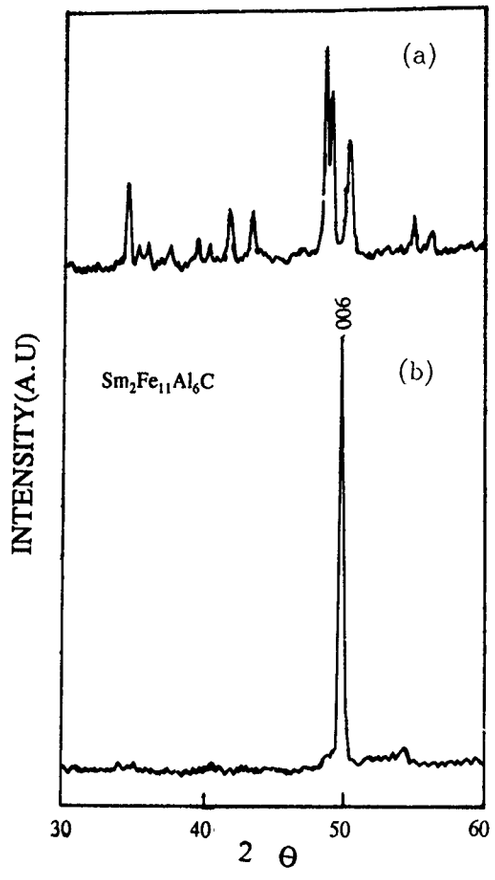

FIG. 1. Co$K\alpha$ radiation x-ray-diffraction patterns of $Sm_2Fe_{11}Al_6C$ prepared by arc melting: (a) unoriented powders, and (b) oriented powders.

therefore, the substitution of larger Al atoms for Fe merely produces an expansion of the lattice. This result is consistent with that of $R_2Fe_{17-x}Al_x$ with R=Y, Ho,[8] and Sm.[9] The fact that the ratio c/a is, within experimental uncertainty, independent of the Al content of these carbides indicates that the expansion of the lattice caused by the substitution of larger Al atoms for smaller Fe atoms is essentially an isotropic process.

The Curie temperature T_c of $Sm_2Fe_{17-x}Al_xC$ versus Al concentration is shown in Fig. 2. For comparison, the T_c of $Sm_2Fe_{17-x}Al_x$ is also presented in this figure.[9] For the carbides, T_c is found to increase slightly when $x \leqslant 3$, then decrease rapidly with increasing Al concentration, while the T_c

TABLE I. Structural parameters for $Sm_2Fe_{17-x}Al_xC$ compounds.

Compounds	a (Å)	c (Å)	v (Å^3)	c/a
$x=0$	8.644[a]	12.476[a]	807.3	1.443
$x=2$	8.674	12.506	814.0	1.441
$x=3$	8.709	12.575	826.0	1.444
$x=4$	8.716	12.617	830.0	1.447
$x=5$	8.755	12.664	840.2	1.447
$x=6$	8.764	12.723	846.2	1.451
$x=7$	8.806	12.787	858.7	1.452
$x=8$	8.816	12.809	862.1	1 451

[a]Reference 11.

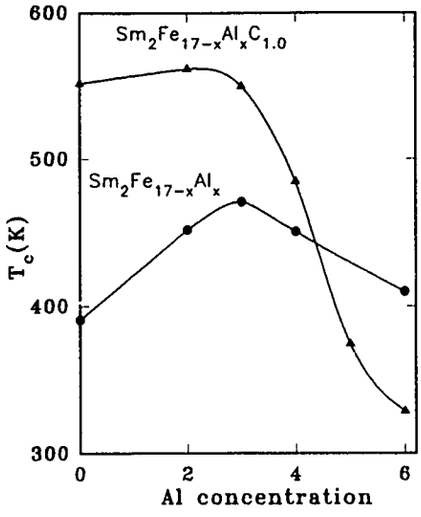

FIG. 2. The Curie temperature of $Sm_2Fe_{17-x}Al_xC$ and $Sm_2Fe_{17-x}Al_x$ as a function of Al concentration.

of $Sm_2Fe_{17-x}Al_x$ increases more sharply when $x \leqslant 3$. It is commonly assumed that the magnetic ordering temperature in rare-earth–iron compounds is determined by the Fe-Fe exchange interactions. The generally low values of T_c in R_2Fe_{17} compounds result from the relatively small Fe-Fe distance in these materials. The increase in Curie temperature corresponds to an increase in the positive Fe-Fe exchange coupling as a result of increased interatomic distance. Jacobs *et al.* have shown that this coupling increases with increasing Al content up to about $x=3$ in $R_2Fe_{17-x}Al_x$ with R=Y, and Ho;[8] however, for the carbides, the interstitial carbon atoms have already enlarged the interatomic distance. Both C and Al atoms will influence the Curie temperature and the effect of Al atoms on the Curie temperature is not significant.

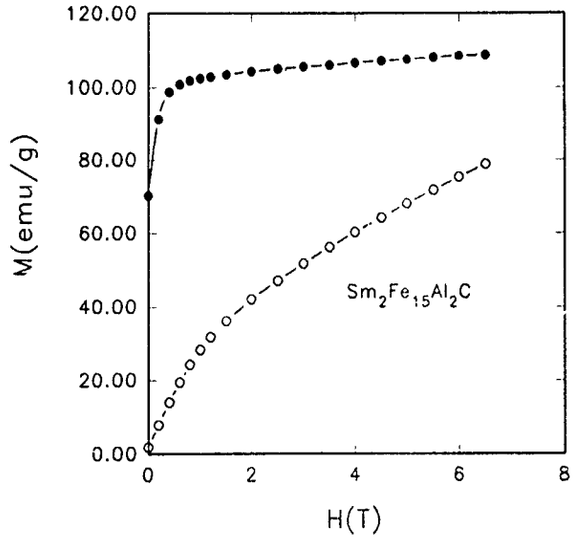

FIG. 3. Magnetization curves of $Sm_2Fe_{15}Al_2C$ at 300 K along and perpendicular to aligned direction, solid and open circles are for parallel and perpendicular to the aligned direction, respectively.

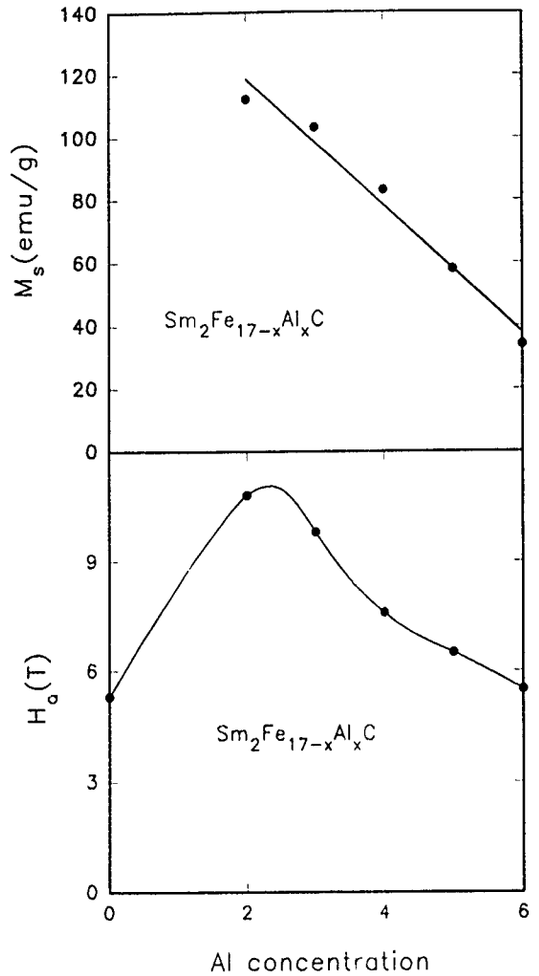

FIG. 4. The saturation magnetization M_s and anisotropy field at room temperature as a function of the Al concentration.

In order to study the effect of Al on the magnetocrystalline anisotropy in $Sm_2Fe_{17}C$ compounds, XRD and magnetization measurements have been carried out on the magnetic-field-aligned powder samples. XRD studies of magnetic-field-oriented powders can provide information concerning the magnetocrystalline anisotropy on the basis of the diffraction peaks present in each of the patterns. Figure 1(b) presents the room-temperature diffraction patterns of oriented $Sm_2Fe_{17-x}Al_xC$ powders with $x=6$. A uniaxial anisotropy occurs for all compounds as evidenced the fact of a drastic increase in the (0,0,6) reflection and the disappearance of $(h,k,0)$.

Figure 3 shows an example of the magnetization curves measured parallel and perpendicular to the aligned direction at room temperature for the sample with $x=2$. The anisotropy field H_A estimated from the measurement curves and the saturation magnetization M_s of $Sm_2Fe_{17-x}Al_xC$ as a function of the Al concentration is plotted in Fig. 4. The room-temperature saturation magnetization decreases monotonically with increasing Al content, while the room-temperature anisotropy field of $Sm_2Fe_{17-x}Al_xC$ is found to increase from 5.3 T,[10] for $x=0$, to 10.8 T for $x=2$. Further substitution decreases the anisotropy field. This means that the addition of Al in $Sm_2Fe_{17-x}Al_xC$ has a very significant influence on the magnetocrystalline anisotropy. Earlier reports indicated that the addition of Al in Sm_2Fe_{17} compounds can develop a room-temperature uniaxial anisotropy when $x\geq 2$,[6,9] without the need to introduce interstitial nitrogen or carbon atoms. For the sample with $x=2$, the Curie temperature is about 560 K, the room-temperature saturation magnetization is about 110 emu/g, and the anisotropy field at room temperature is 10.8 T. The value of H_A is much higher than that of $Sm_2Fe_{17}C$ and $Nd_2Fe_{14}B$ (8 T), but the saturation magnetization is somewhat lower than that of the Al-free compound. In this alloy, the substitution of a small amount of other elements, such as Co, Ni, etc., or the reduction of the Al concentration may yield a further improvement in the hard magnetic properties. Thus, it is possible that these carbides can be used as the starting materials for producing high-performance 2:17-type sintered permanent magnets.

In summary, single-phase $Sm_2Fe_{17-x}Al_xC$ compounds with $2\leq x\leq 8$ have been prepared by arc melting. The addition of Al in these materials can not only help the formation of the 2:17-type rare-earth–iron compounds with high carbon concentration, but also improve the hard magnetic properties. For the samples with $x=2$, the Curie temperature is about 180 K higher than that of Sm_2Fe_{17} and comparable with that of $Nd_2Fe_{14}B$, and the anisotropy field is much higher than that of $Nd_2Fe_{14}B$ and $Sm_2Fe_{17}C$. The present work suggests that $Sm_2(Fe,Al)_{17}C_x$ magnets with appropriate carbon concentration can be a starting material for sintered permanent magnets.

ACKNOWLEDGMENTS

The authors wish to express their gratitude to T. S. Ning and M. Hu for their assistance with x-ray-diffraction experiments. This work is supported by the National Natural Science Foundation of China and State's Sciences and Technology Commission.

[1] J. M. D. Coey and H. Sun, **87**, L251 (1990).
[2] B.-G. Shen, L.-S. Kong, and L. Cao, Solid State Commun. **83**, 753 (1992).
[3] L.-S. Kong, L. Cao, and B.-G. Shen, J. Magn. Magn. Mater. **115**, L137 (1992).
[4] L. Cao, L.-S. Kong, and B.-G. Shen, J Phys. Condens Matter **4**, L515 (1992).
[5] B -G. Shen, L -S. Kong, F.-W. Wang, and L. Cao, Appl. Phys. Lett. **63**, 2288 (1993).
[6] Z.-H. Cheng, B.-G. Shen, F.-W. Wang, J.-X. Zhang, H.-Y. Gong, and J -G Zhao, J. Phys. Condens. Matter **6**, L185 (1994).
[7] B.-G. Shen, F.-W. Wang, L -S. Kong, L Cao, and W -S Zhan, J Appl. Phys. **75**, 6253 (1994).
[8] T. H. Jacobs, K. H J Buschow, G -F. Zhou, X. Li, and F R. de Boer, J. Magn. Magn. Mater. **116**, 220 (1992)
[9] Z Wang and R A. Dunlap, J. Phys. Condens. Matter **5**, 2407 (1993).
[10] X. C. Kou, R Grossinger, T H. Jacobs, and K. H. J Buschow, J Magn. Magn Mater **88**, 1 (1990).
[11] X -P Zhong, R. J. Radwanski, F. R. de Boer, T H Jacobs, and K H J. Buschow, J. Magn. Magn. Mater. **86**, 333 (1990)

Uniaxial magnetic anisotropy in Fe-rich 2:17 compounds with *sp* substitutions

R. A. Dunlap and Z. Wang
Department of Physics, Dalhousie University, Halifax, Nova Scotia B3H 3J5, Canada

M. Foldeaki
Département de Physique, Université du Québec à Trois-Rivières, Trois-Rivières, Québec G9A 5H7, Canada

The magnetic properties of single-phase 2:17 compounds of the composition $Sm_2Fe_{17-x-y}Co_yM_x$ with M=Al and Ga and x and y in the range 0–5 are reported. The Curie temperature is found to increase for the $y=0$ samples with increasing x up to a maximum at $x=3$ for M=Al and $x=4$ for M=Ga and a monotonic increase with increasing y for all x and M. Samples with $x<2$ showed an easy-plane magnetic anisotropy at room temperature while samples with $x>2$ showed a single-phase uniaxial anisotropy. The addition of Co is seen to increase the saturation magnetization and the anisotropy field.

I. INTRODUCTION

The rare-earth–iron compounds of the composition R_2Fe_{17} are of potential commercial interest as they possess good thermal stability and the large Fe content yields high saturation magnetization; however, two severe drawbacks have limited the practical application of these compounds as hard magnetic materials; (1) the relatively low values of the Curie temperature[1,2] and (2) the lack of a room-temperature uniaxial anisotropy. While many rare-earth–cobalt compounds do not suffer from these drawbacks, they are certainly not as attractive for commercial applications from an economic standpoint.

Recent studies concerning methods by which the technical magnetic properties may be improved have been concerned with the preparation of materials with either substitutional or interstitial impurities. Results have shown that the substitution of Co, Ni, Al, and Si, for Fe, at least up to a certain point, increases the Curie temperature (see, e.g., Refs. 1–3) and recent evidence has indicated that the substitution of sufficient quantities of Al or Ga for Fe can induce a room-temperature anisotropy in these materials.[4,5] Interstitial hydrogen, carbon, and nitrogen can yield substantial increases in the Curie temperature (see, e.g., Refs. 6 and 7). Although C and N interstitials favor the formation of a uniaxial anisotropy,[7,8] the presence of interstitial H has been shown to be detrimental in this respect.[8] In the present work an investigation of the effects of *sp* (i.e., Al and Ga) substitutions on Sm-based compounds is reported.

II. EXPERIMENTAL METHODS

Samples of $Sm_2Fe_{17-x-y}Co_yM_x$, with M=Al and Ga and x and y in the range of 0–5 were prepared by arc melting components followed by grinding to a powder with an average particle size of about 20 μm. Powders were annealed under argon at 1273 K for 72–100 h and water quenched. Structural properties were investigated using a Siemens D500 scanning x-ray diffractometer. Room-temperature magnetic anisotropy was determined from x-ray-diffraction patterns of powder samples which were mixed with epoxy resin and aligned in a magnetic field of 1.0 T. Curie temperatures were obtained by calorimetric techniques. Magnetization curves were obtained at 10 K with a standard induction magnetometer in applied fields up to 3.0 T.

III. RESULTS

X-ray-diffraction studies indicate that all compounds are of the rhombohedral Th_2Zn_{17} structure. A typical pattern is illustrated in Fig. 1(a) and cell volumes are given in Table I. The measured magnetic anisotropies and Curie temperatures are also given in the table. The presence of a uniaxial anisotropy observed in some of the samples is illustrated in Fig. 1(b). The unit-cell-volume dependence of the Curie temperature is illustrated in Fig. 2 for the Sm-Fe-Al and SM-Fe-Ga compounds. The magnetic properties of the Sm-Fe-Co-Al compounds are summarized in Fig. 3. ΔM_0 is defined as the difference between the easy- and hard-axis magnetization extrapolated to zero applied field and is a measure of the strength of the magnetic anisotropy field.

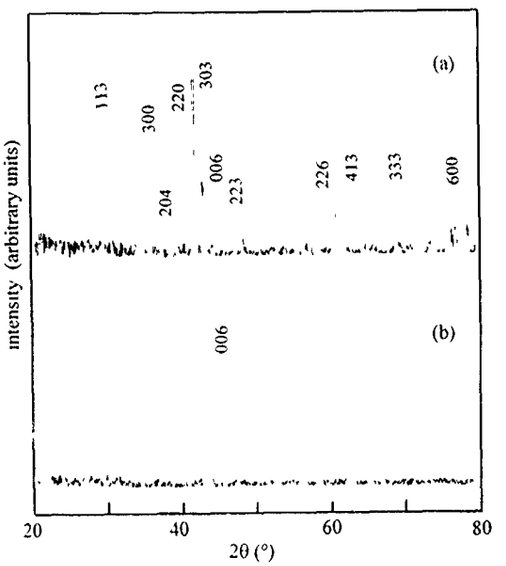

FIG 1 Room-temperature CuK x-ray-diffraction patterns for $Sm_2Fe_{14}Al_3$ (a) nonoriented and (b) field oriented

 0021-8979/94/76(10)/6737/3/$6 00 © 1994 American Institute of Physics

TABLE I. Unit-cell volumes, magnetic anisotropies, and Curie temperatures of the series of $Sm_2Fe_{17-x-y}Co_yM_x$ compounds with the Th_2Zn_{17} structure.

M	x	y	V (Å^3)	Anisotropy	T_c (K)
...	...	0	788	planar	391
Al	1	0	798	planar	417
Al	2	0	805	mixed	452
Al	3	0	809	uniaxial	471
Al	4	0	818	uniaxial	451
Al	3	1	810	uniaxial	533
Al	3	2	807	uniaxial	578
Al	3	3	803	uniaxial	625
Al	3	4	800	uniaxial	663
Al	3	5	798	uniaxial	698
Ga	1	0	795	planar	468
Ga	2	0	802	mixed	540
Ga	3	0	809	uniaxial	570
Ga	4	0	817	uniaxial	580
Ga	5	0	823	uniaxial	555
Ga	3	3	804	uniaxial	712

IV. DISCUSSION AND CONCLUSIONS

The value of the Curie temperature in these materials[2] is primarily dependent on the magnitude of the exchange coupling between transition-metal (TM) atoms J_{TT}. This becomes more positive and increases T_c as larger nonmagnetic atoms are substituted for Fe. Beyond a certain point, however, a decrease in J_{TT} and T_c results from either the further dilution of the magnetic species or the further increase in Fe-Fe neighbor distances or both. The rare-earth–transition-metal (RE-TM) coupling[3] J_{RT} and the RE-RE coupling J_{RR} are substantially smaller than J_{TT} and are relatively independent of interatomic distances. As illustrated in Fig. 2, the changes in T_c as a function of atomic volume which result from the substitution of Al are substantially less than those which result from the substitution of Ga. As this difference is not expected on the basis of atomic volume, it is presumably due to the $3d$ coupling between Ga and Fe, which is not a factor for the Al-containing compounds. The substantial increase in Curie temperature with the substitution of Co for Fe is indicative of a strong Ferromagnetic Fe-Co coupling.

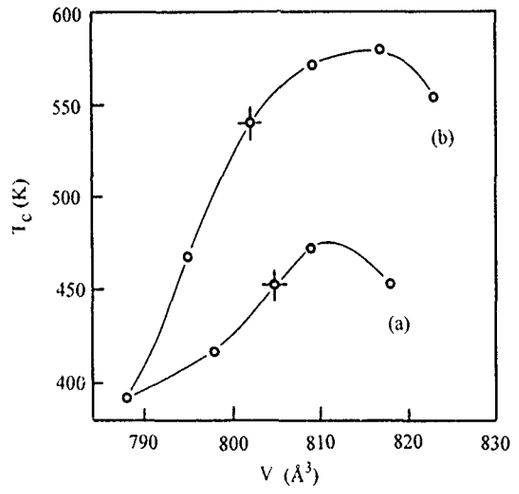

FIG 2 Measured cell volume dependence of the Curie temperature for $Sm_2Fe_{17-x}M_x$ compounds for (a) M=Al and (b) M=Ga.

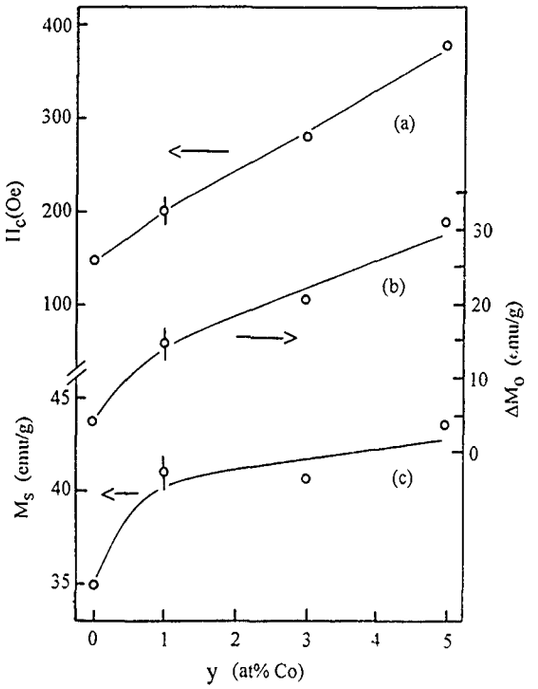

FIG. 3. Composition dependence of the magnetic properties of $Sm_2Fe_{14-y}Co_yAl_3$ compounds: (a) coercivity at 10 K, (b) ΔM_0=difference between easy- and hard-axis magnetization at 10 K, and (c) M_s (saturation magnetization) at 10 K and 1.0 T.

In contrast to earlier reports[2] that the substitution of Al or Ga for Fe in Sm_2Fe_{17} does not alter the planar anisotropy, the present results clearly show that in compounds with $x>2$, a uniaxial anisotropy is observed. The net magnetic anisotropy is determined from the sum of the Fe and the rare-earth sublattice anisotropies. The rare-earth sublattice anisotropy is determined by the product of the second-order Stevens coefficient α_J, which reflects the form of the $4f$ charge distribution and the second-order crystal-field parameter. A_2^0 is negative in the 2:17 compounds,[6,9,10] and a negative product $\alpha_J A_2^0$ gives a uniaxial contribution, it is in cases where α_J is positive, as for Sm, that an easy-axis anisotropy is favored. The present studies indicate that increasing the sp content (at least up to $x=5$) increases the uniaxial contribution from the Sm sublattice as a result of an increase in the magnitude of the negative A_2^0.[4] These changes can be understood in terms of the electronic structure of the RE environment.[11] The principal contribution to the electric-field gradient experienced by the Sm $4f$ shell results from the details of the RE $5d$ and $6p$ electron charge density which must match that of the neighboring atoms on the Wigner–Seitz (WS) boundary. These are the $18f$ TM sites which lie in the basal plane of the Th_2Zn_{17} structure as illustrated in Fig. 4. The existence of sp atoms in those sites in Al- and Ga-substituted compounds has been demonstrated by Weitzer *et al.*[12,13] The large electron density at the WS boundary of the $18f$ sp atoms is analogous to the case of N or C interstitials in the basal plane and yields a large negative A_2^0.

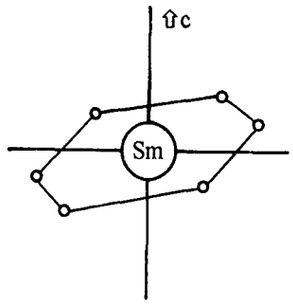

FIG. 4. 18*f* site configuration around the Sm atoms in the rhombohedral Th_2Zn_{17} structure.

The hysteretic properties of the uniaxial materials studied here show several characteristic features: (1) large distinction between the magnetization measured along the easy axis and along the hard axis; (2) large values of the saturation magnetization; and (3) moderate values of the coercivity. These properties are illustrated in Fig. 3 for $Sm_2Fe_{14-y}Co_yAl_3$. Even very small concentrations of Co are beneficial in improving the technical magnetic properties, including an increase in the saturation magnetization and Curie temperature as given in Table I.

Numerous RE-TM compounds have been studied with the idea of utilizing their hard magnetic properties for permanent magnet applications. The RE_2Fe_{17} compounds are attractive because of their low cost. The present work shows that a room-temperature uniaxial anisotropy and an increase in Curie temperature can be achieved by *sp* substitution for Fe. As well, the saturation magnetization in these materials is high and can be further improved by the substitution of a small quantity of Co for Fe. Further investigation of sample preparation methods such as e.g., ball milling is required in order to achieve improvement in coercivity. The properties for the materials prepared in the present work are consistent with the requirements for perpendicular recording materials and are comparable to commercially viable materials such as CoCr films. The present compounds also have the advantage of allowing for the design of materials with specific characteristics which are tailored to particular recording applications. Further investigation of these materials for this application is warranted and will enable compositions and processing techniques to be refined.

ACKNOWLEDGMENTS

This work was funded by NSERC (Canada) and the Faculty of Graduate Studies, Dalhousie University.

[1] K. S. V. L. Narasimhan, W. E. Wallace, and R. D Hutchens, IEEE Trans Magn. **MAG-10**, 729 (1974).
[2] B.-P. Hu, X.-L. Rao, J.-M. Xu, G.-C. Liu, X -L. Dong, H. Li, L. Yin, and Z.-R. Zhao, J. Magn. Magn Mater. **114**, 138 (1992).
[3] T. H. Jacobs, K. H. J. Buschow, G.-F. Zhou, X Li, and F. R. de Boer, J. Magn. Magn. Mater. **116**, 220 (1992).
[4] Z. Wang and R A. Dunlap, J. Phys Condens. Matter **5**, 2407 (1993).
[5] Z. Wang and R. A. Dunlap, Philos. Mag. B **69**, 103 (1994).
[6] X.-C. Kou, R. Grossinger, T. H Jacobs, and K. H. J. Buschow, Physics B **168**, 181 (1991).
[7] M. Katter, J. Wecker, C. Kuhrt, L. Schultz, and R Grossinger (these proceedings).
[8] R. A. Dunlap and Z. Wang, Can. J. Phys **71**, 574 (1994).
[9] J. M. D. Coey, H. Sun, Y. Otani, and D. P. F. Hurley, J Magn. Magn. Mater. **98**, 76 (1991).
[10] K. H. J. Buschow, Rep. Prog Phys. **40**, 1179 (1977).
[11] J. M. D. Coey, H. Sun, and D. P. F. Hurley, J. Magn. Magn. Mater **101**, 310 (1991).
[12] F. Weitzer, H. Klesnar, K. Hiebl, and P. Rogl, J Appl. Phys **67**, 2544 (1990).
[13] F. Weitzer, K. Hiebl, and P. Rogl, J. Appl. Phys **65**, 4963 (1989).

Magnetic properties of $R_2Fe_{17-x}Ga_x$ compounds (R=Y, Ho)

J. L. Wang, R. W. Zhao, N. Tang, W. Z. Li, Y. H. Gao, and F. M. Yang
Magnetism Laboratory, Institute of Physics, Chinese Academy of Sciences, P.O. Box 603, Beijing 100080, People's Republic of China

F. R. de Boer
Van der Waals-Zeeman Laboratory, University of Amsterdam, Valckenierstraat 65, 1018 XE Amsterdam, The Netherlands

Structural and magnetic properties of the $R_2Fe_{17-x}Ga_x$ compounds (R=Y, Ho, $0 \leq x \leq 6$) have been investigated. All investigated $Ho_2Fe_{17-x}Ga_x$ compounds with $x>2.5$ crystallize in the Th_2Zn_{17}-type structure and the others in the Th_2Ni_{17}-type structure. The substitution of Ga for Fe leads to an increase in lattice constants a, c, and unit-cell volume, a decrease of the average Fe moment, and a maximum of the Curie temperature as a function of the Ga concentration at $x=3$, for both $Y_2Fe_{17-x}Ga_x$ and $Ho_2Fe_{17-x}Ga_x$ compounds. The high magnetic field leads to a spin phase transition from the ferromagnetic to the canted phase. The critical field B_c of the transition decreases with increasing Ga concentration. The exchange interaction constants J_{TT} between Fe–Fe spins and J_{RT} between R–T spins have been derived from a mean field analysis of Curie temperature. It has been found that J_{TT} increases at first, going through a maximum at $x=3$, then decreases with increasing x, whereas J_{RT} is almost independent of the Ga content, which is consistent with the result obtained from a mean field analysis of the high field magnetization curves of the $Ho_2Fe_{17-x}Ga_x$.

I. INTRODUCTION

Since Coey and Sun reported that the introduction of nitrogen leads to a remarkable improvement in the magnetic properties of R_2Fe_{17} compounds,[1] which makes these compounds interesting materials for permanent magnets, the structural and magnetic properties of the interstitial nitrides have attracted much attention. In order to fully understand the interaction in these nitrides, it is necessary to first understand the exchange interaction of the R–T and T–T spins in their parent compounds. Previous studies of these interactions have shown improvement in the properties of these compounds by substituting other atoms for Fe or R.[2,3] In this paper, the influence of the substitution of Ga for Fe on the magnetic properties of $R_2Fe_{17-x}Ga_x$ (R=Ho, Y) compounds has been studied. The exchange interaction of the R–T and T–T spins in these compounds has been calculated based on a mean field analysis of the Curie temperature of $R_2Fe_{17-x}Ga_x$ (R=Y, Ho), which are then compared with the results obtained by the mean field analysis of the high field magnetization curves of $Ho_2Fe_{17-x}Ga_x$.

II. EXPERIMENT

The $Ho_2Fe_{17-x}Ga_x$ ($x=0$, 0.25, 1.0, 2.5, 4.0, and 6.0) and $Y_2(Fe_{1-x}Ga_x)_{17}$ ($x=0$, 0.06, 0.12, 0.20, 0.30, and 0.40) compounds were prepared by arc melting the constituent elements of 99.9 wt % purity or better, and followed by annealing in an argon atmosphere at 1473 K for 4 h. X-ray diffraction was performed on powdered samples using Cu-$K\alpha$ radiation. Magnetization measurements at 4.2 K have been performed in the High Magnetic Field Installation at the University of Amsterdam.[4] The measurements were done on powder particles about 30 μm, which are sufficiently small to regard them as monocrystalline. During the magnetization measurement, the particles are free to rotate in the sample holder, so that they can orient their magnetic moments into the direction of the applied field. Magnetization versus temperature curves were measured in a field of 500 Oe by means of the vibrating sample magnetometer (VSM) between temperatures from 300 K to 800 K. The Curie temperature were derived by σ^2 vs T plot.

III. RESULT AND DISCUSSION

X-ray diffraction patterns showed that the $Ho_2Fe_{17-x}Ga_x$ compounds for $x \leq 2.5$ crystallize in Th_2Ni_{17}, and for $x>2.5$ crystallize in Th_2Zn_{17}, as shown in Fig. 1. The substitution of a larger radius Ga atom for the Fe atom makes the Th_2Ni_{17}-type structure unstable. The values of lattice parameters a and c are given in Table I. The substitution of Ga for Fe results in a linear increase of the lattice constants in $Ho_2Fe_{17-x}Ga_x$ compounds, reflecting the larger radius of the Ga atom.

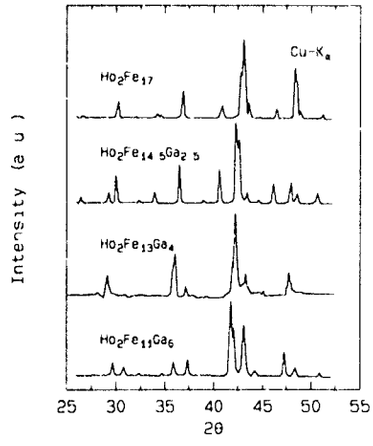

FIG. 1. The x-ray diffraction patterns of $Ho_2Fe_{17-x}Ga_x$, $x=0$, 2.5, 4.0, and 6.0

 0021-8979/94/76(10)/6740/3/$6.00 © 1994 American Institute of Physics

TABLE I. The lattice constants (a and c), Curie temperature (T_c), saturation magnetization Ms (Am^2/kg), and average iron magnetic moment (μ_{Fe}) for $Ho_2Fe_{17-x}Ga_x$ and $Y_2Fe_{17-x}Ga_x$ compounds The data between parentheses a and c (± 0.005 Å); T_c (± 5 K); Ms (± 0.1 Am^2/kg); μ_{Fe} ($\pm 0.02\mu_B$/Fe).

x	a (Å)	c (Å)	T_c (K)	M_s (Am^2/kg)	μ_{Fe} (μ_B/Fe)
Y_2Fe_{17}	8.492	8.315	337	166.6	1 98
$Y_2(Fe_{0.94}Ga_{0.06})_{17}$	8 522	8.332	426	152 0	1.94
$Y_2(Fe_{0.88}Ga_{0.12})_{17}$	8.559	8.348	475	137.8	1.91
$Y_2(Fe_{0.80}Ga_{0.20})_{17}$	8.601	8.369	513	119.7	1 85
$Y_2(Fe_{0.70}Ga_{0.30})_{17}$	8.650	8.392	484	99.5	1.79
$Y_2(Fe_{0.60}Ga_{0.40})_{17}$	8.706	8.412	379	81.0	1.74
Ho_2Fe_{17}	8.431	8.303	360	69.4	2 11
$Ho_2Fe_{16.75}Ga_{0.25}$	8.458	8.314	380	66 8	2.11
$Ho_2Fe_{16.0}Ga_{1.0}$	8.482	8 325	425	58.5	2.10
$Ho_2Fe_{14}Ga_{2.5}$	8.520	8.352	505	43 7	2.09
$Ho_2Fe_{13.0}Ga_{4.0}$	8.584	8.392	518	20.4	1.91
$Ho_2Fe_{11.0}Ga_{6.0}$	8.639	8.434	450	0.4	1.83

The Curie temperature T_c of the $Ho_2Fe_{17-x}Ga_x$ and $Y_2Fe_{17-x}Ga_x$ rises rapidly at first with x, going through a maximum at about $x=3$, and falls quickly with x, as shown in Fig. 2. The values of Tc for these compounds are also listed in Table I. The Curie temperature is mainly determined by the Fe–Fe exchange interaction, which is sensitive to the Fe–Fe distance. Therefore the increase of Tc for the compounds with $x<2$ with x may be partially associated with the lattice expansion upon the substitution of Ga for Fe. On the other hand, it has previously been found that Ga, like Al in $Y_2Fe_{17-x}Al_x$ compounds, preferentially occupies the $6c$ sites.[5–7] Therefore the substitution of Ga for Fe may decrease the negative exchange interaction between Fe–Fe at $6c$ sites and increase the Curie temperature of these compounds. The decrease of the Curie temperature for the compounds with $x>3$ increasing with the Ga concentration is due to the decrease of the average iron magnetic moment and the reduced iron concentration.

The saturation moment of $Ho_2Fe_{17-x}Ga_x$ and $Y_2Fe_{17-x}Ga_x$ decreases with increasing Ga concentration. The average iron magnetic moment μ_{Fe} was derived on the basis of the saturation magnetization σ_s measured at 4.2 K. The σ_s values have been corrected for the contribution of α-Fe impurity phase to the magnetization, which could be deduced from the high temperature magnetization measurements. In the evaluation of the magnetic moment per iron, it was assumed that the moment of Ho is independent of the Ga content, and the value is the same as that of the free Ho ion ($10\mu_B$). It can be found that the average Fe ion moment decreases with increasing Ga content, as shown in Table I.

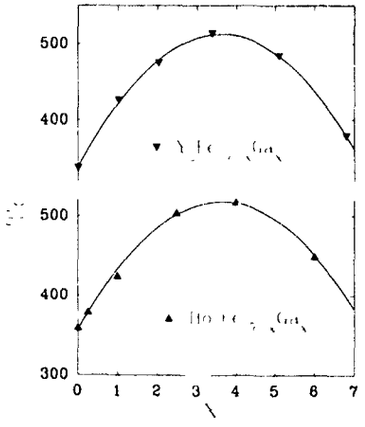

FIG. 2. Ga content dependence of the Curie temperature T_c of $Y_2Fe_{17-x}Ga_x$ and $Ho_2Fe_{17-x}Ga_x$.

In the rare earth-transition metal intermetallics, there are three types of the interactions, namely the R–R interactions between the magnetic moments within the R sublattice, the T–T interactions between the magnetic moments of T sublattice, and the R–T intersublattice interactions. Among them, the T–T interaction is the strongest and the R–R interaction is the weakest, and is usually neglected.[8] According to the mean field analysis of Curie temperature,[8] J_{RT} and J_{FeFe} can be expressed by

$$J_{RT}=g_R g_T \mu_B{}^2 N_T n_{RT}/2Z_{RT}(g_R-1)(g_T-1), \tag{1}$$

$$3kT_c=a_{FeFe}+(a_{FeFe}{}^2+4a_{RFe}a_{FeR})^{1/2}, \tag{2}$$

where

$$a_{FeFe}=Z_{FeFe}J_{FeFe}s_{Fe}(s_{Fe}+1), \tag{3}$$

$$a_{RFe}a_{FeR}=Z_{RFe}Z_{FeR}s_{Fe}(s_{Fe}+1)(g-1)^2J(J+1)J_{RFe}{}^2, \tag{4}$$

$$J_{FeFe}=a_{FeFe}/Z_{FeFe}s_{Fe}(s_{Fe}+1), \tag{5}$$

where a_{ij} is the microscopic exchange coupling parameters, J_{ij} is $i-j$ exchange constants, n_{RT} expresses the macroscopic molecular field coefficients, $g_R=8$ and $j=\frac{5}{4}$ for Ho, the orbital moment of the Fe atom is assumed to be quenched, so one takes $g_T=2$, $J_T=s_T$, and $s_T=\mu_{Fe}/2$. Z_{ij} is the number of the nearest j neighbors of the i ion, N_i is the numbers of the i atom per formula unit. The J_{FeFe} and J_{RFe} were calculated using Eqs. (1)–(5). The values of J_{FeFe} and J_{RFe} as a function of Ga content are shown in Fig. 4. It can be seen that J_{RFe} is almost unchanged with x; however, J_{TT} increases with the Ga content for $x<3$, going through a maximum at about $x=3$, and then decreases for $x>3$, as shown in Fig. 4. The J_{RT} can also be calculated from a mean field analysis of the high field magnetization curves.[9] For ferrimagnetic R–T in-

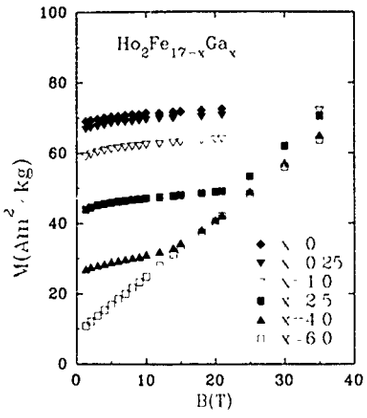

FIG. 3. The high field magnetization curves of $Ho_2Fe_{17-x}Ga_x$.

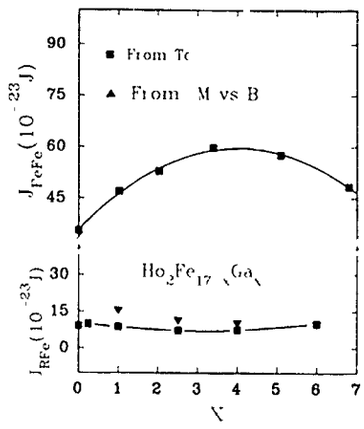

FIG. 4. Ga content dependence of the exchange interaction constants J_{FeFe} and J_{RFe} in $Ho_2Fe_{17-x}Ga_x$.

termetallics, in the fields beyond a critical field strength $B_{cr,1}=n_{RT}|M_T-M_R|$ (M_T and M_R are the magnetization of the R and T sublattice, respectively), the exactly antiparallel R and T moments start to bend toward each other. The total magnetization is described by $M=B/n_{RT}$ and thus

$$\frac{dM}{dB}=[n_{RT}]^{-1}, \tag{6}$$

where $M=[M_R{}^2+M_R{}^2+2M_RM_T\cos(\alpha)]^{1/2}$.

The parameter n_{RT} can be derived from the high field slopes for $B>B_{cr,1}$. We can see in Fig. 3 that the critical field $B_{cr,1}$ decreases with increasing Ga concentration because of the decrease of M_T. J_{RFe} was also calculated using the obtained values of n_{RT} and Eq. (1), and the values of J_{RT} are also shown in Fig. 4. They are in agreement with the results obtained by the mean field analysis of the Curie temperature.

IV. CONCLUSION

The substitution of Ga for Fe results in an increase in lattice constants and a transformation from the Th_2Ni_{17}-type structure to the Th_2Zn_{17} structure. A maximum of the Curie temperature with Ga concentration is due to the change of Fe–Fe and R–Fe exchange interaction and the decrease of average iron magnetic moment μ_{Fe}. The exchange interaction constants J_{TT} between Fe–Fe spins and J_{RT} between R–T spins have been derived, based on the mean field analysis of Curie temperature. It has been found that J_{TT} increases at first, going through a maximum at $x=3$, then decreases with increasing x, whereas J_{RT} is almost independent of the Ga content, which is consistent with the result obtained from a mean field analysis of the high field magnetization curves of the $Ho_2Fe_{17-x}Ga_x$. J_{FeFe} is about four times J_{RFe}. The critical field $B_{cr,1}$ decreases with increasing Ga concentration.

ACKNOWLEDGMENT

This study was supported by the National Natural Science Foundation of China.

[1] J. M. D. Coey and H. Sun, J. Magn. Magn. Mater. L251 87 (1990)
[2] X. Li, N. Tang, Z. Lu, T. Zhao, W. G. Lin, R. Zhao, and Fu-m. Yang, J. Appl. Phys. **73**, 5890 (1993).
[3] Q. A. Li, G. F. Zhou, F. R. de Boer, and K. H. J. Bushow, Physica B **190**, 121–125 (1993).
[4] R. Gersdorf, F. R. de Boer, J. W. Wolfrat, F. A. Muller and L. W. Roeland, in *High-Field Magnetism*, edited by M. Date (North-Holland, Amsterdam, 1983), p. 277.
[5] K. S. V. Li. Narasimhan and W. E. Wallace, AIP Conf. Proc. **18**, 1248 (1974).
[6] D. Plusa, R. Pfranger, B. Wyslock, and T. Mydlarz, J. Less-Common Met. **120**, 1 (1986).
[7] F. Weitzer, K. Hiebl, and P. Rogl, J. Appl. Phys. **65**, 4963 (1989).
[8] N. H. Duc, T. D. Jien, D. Givord, J. J. M. Franse, and F. R. de Boer, J. Magn. Magn. Mater. **124**, 305–311 (1993).
[9] R. Verhoef, F. R. de Boer, J. J. M Franse, C. J M. Denissen, T. H. Jacods, and K. H. J. Buschow, J. Magn. Magn. Mater. **80**, 41 (1989).

Magnetic properties of $Sm_2(Fe_{1-x}Ga_x)_{17}$ ($x=0-0.5$) compounds and their nitrides

W.-Z. Li, N. Tang, J.-L. Wang, and Fuming Yang
Magnetism Laboratory, Institute of Physics, Chinese Academy of Sciences, P.O. Box 603, Beijing 100080, People's Republic of China

Y. W. Zeng and J. J. Zhu
Department of Physics, Beijing Normal University, Beijing, 100875, People's Republic of China

F. R. de Boer
Van der Waals–Zeeman Laboratory, University of Amsterdam, 1018XE Amsterdam, The Netherlands

Magnetic properties of $Sm_2(Fe_{1-x}Ga_x)_{17}$ compounds and their nitrides have been studied. Substitution of Ga for Fe leads to an increase in lattice constants. Introduction of nitrogen results in a further increase in lattice constants. Substitution of Ga for Fe causes a dramatic change of the Curie temperature of the $Sm_2(Fe_{1-x}Ga_x)_{17}$ compounds. When $x=0.2$ the Curie temperature is enhanced by about 200 K. X-ray-diffraction patterns of aligned samples of $Sm_2(Fe_{1-x}Ga_x)_{17}$ compounds show that alloys with $x=0.15$, 0.20, and 0.25 exhibit uniaxial anisotropy at room temperature. The introduction of nitrogen made the samples with $x\leqslant 0.4$ exhibit uniaxial anisotropy at room temperature. The Curie temperature of the nitrides decreases with the Ga concentration. The anisotropy fields of the nitrides derived from the high-field magnetization. The changes of the magnetic anisotropy, saturation magnetization, and the moment of the Fe atoms in the nitrides and their parent compounds with Ga concentration are discussed.

I. INTRODUCTION

Recently many studies on improving the magnetic properties of R_2Fe_{17} compounds have been performed. The most striking improvements, the strong enhancements of the Curie temperature and uniaxial anisotropy, have been achieved by absorption of nitrogen.[1] The magnetic ordering temperature and other magnetic properties can also be improved by uptaking hydrogen or carbon as well as by substituting some elements such as Al, Si, and Co for Fe in R_2Fe_{17} compounds.[2–7]

In the present work we have focused our attention on the crystal structure and magnetic properties of $Sm_2(Fe_{1-x}Ga_x)_{17}$ ($x=0-0.5$) compounds and their nitrides, especially on magnetization and magnetocrystalline anisotropy. The effects of Ga substitution for Fe and of the introduction of interstitial nitrogen on the Curie temperature, the magnetic anisotropy, and the saturation magnetization have been determined.

II. EXPERIMENTAL METHODS

All $Sm_2(Fe_{1-x}Ga_x)_{17}$ host compounds with $x=0$, 0.01, 0.02, 0.04, 0.07, 0.1, 0.15, 0.2, 0.25, 0.3, 0.35, 0.4, and 0.5 were prepared by arc melting. The nitrides were formed by heating the powder samples of $Sm_2(Fe_{1-x}Ga_x)_{17}$ compounds in a mixture of NH_3 gas and H_2 gas under a pressure of 1 atm at 720 K for 20 min.

X-ray diffraction was employed to determine the structure, phase composition, the lattice parameters, and the anisotropy of aligned samples. The thermomagnetic σ-T curves were measured by means of a vibrating sample magnetometer in a field of 0.05 T. The Curie temperatures T_c were derived from σ^2-T plots.

The high-field magnetization curves were measured at 4.2 K in high fields up to 21 and 35 T for the host compounds and their nitrides, respectively, at the University of Amsterdam.[8] The anisotropy fields of the nitrides were derived from the intersection point of the high-field magnetization curves measured with the field applied parallel and perpendicular to the aligned direction. The saturation magnetization was deduced from σ_s-$1/B$ plots.

III. RESULTS AND DISCUSSION

Based on x-ray powder diffraction, all the investigated $Sm_2(Fe_{1-x}Ga_x)_{17}$ compounds and their nitrides crystallize in the Th_2Zn_{17}-type structure. A small amount of impurity was found in a few samples. Ga substitution for Fe does not change the structure of Sm_2Fe_{17}, but leads to an expansion of the unit cell (Fig. 1). This result may be ascribed to the larger atomic radius of Ga atom compared to Fe. After introduction of nitrogen, the volume of the unit cell further increases; but, the magnitude of increase is smaller than that resulting from the Ga substitution. The nitrogen content introduced into the compounds, determined by weighing, decreases linearly with Ga concentration from 2.6 for $x=0$ to 1 for $x=0.5$. One can conclude that the substitution of Ga for Fe prevents the introduction of nitrogen.

The Curie temperatures of $Sm_2(Fe_{1-x}Ga_x)_{17}$ compounds and their nitrides are shown in Fig. 2. This figure clearly displays that the Curie temperature of $Sm_2(Fe_{1-x}Ga_x)_{17}$ compounds first goes up, passes through a maximum at about $x=0.2$, then decreases with increasing Ga content. The initial increase of T_c is mainly due to the volume expansion. At higher Ga concentration, the average iron magnetic moment decreases dramatically and causes a decrease in T_c.[6] This variation of T_c may also be associated with preferential substitution of Ga atoms for Fe atoms.[9] Ga atoms preferentially substitute for Fe atoms at the sites responsible for negative exchange interaction. The Curie temperature of the nitrides decreases monotonically with Ga concentration.

 0021-8979/94/76(10)/6743/3/$6.00 © 1994 American Institute of Physics

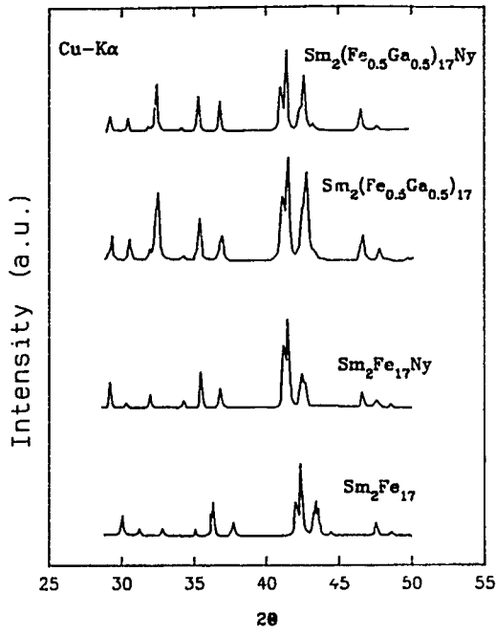

FIG 1. X-ray-diffraction patterns of $Sm_2(Fe_{1-x}Ga_x)_{17}$ compounds and their nitrides with $x=0.0$ and 0.5.

When $x \leqslant 0.2$, the Curie temperature of the nitrides is higher than that of their parent compounds, this indicates that the introduction of N atoms results in an enhancement of the exchange interaction.[10]

X-ray-diffraction patterns at room temperature with Co$K\alpha$ radiation for the aligned samples of $Sm_2(Fe_{1-x}Ga_x)_{17}$ show that the samples with $x=0.15$, 0.20, and 0.25 exhibit uniaxial anisotropy; the others are planar [Fig. 3(a)]. X-ray-diffraction patterns of $Sm_2(Fe_{1-x}Ga_x)_{17}N_y$ [Fig. 3(b)] show that the samples with $x \leqslant 0.3$ exhibit uniaxial anisotropy at room temperature. Ga substitution for Fe in $Sm_2(Fe_{1-x}Ga_x)_{17}$ compounds enhances the transition temperature of the anisotropy from easy plane to easy c axis.

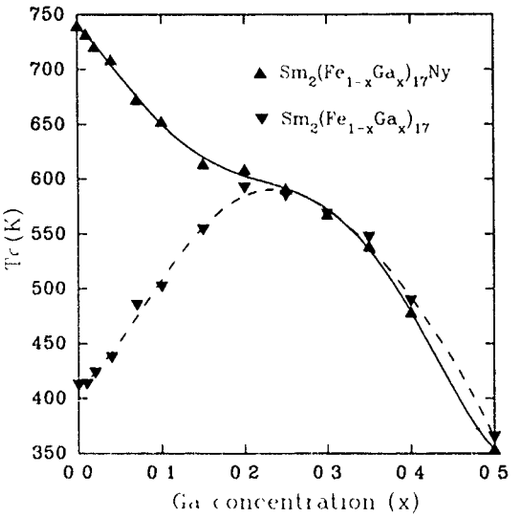

FIG. 2. Ga concentration dependence of the Curie temperature for $Sm_2(Fe_{1-x}Ga_x)_{17}$ compounds and their nitrides.

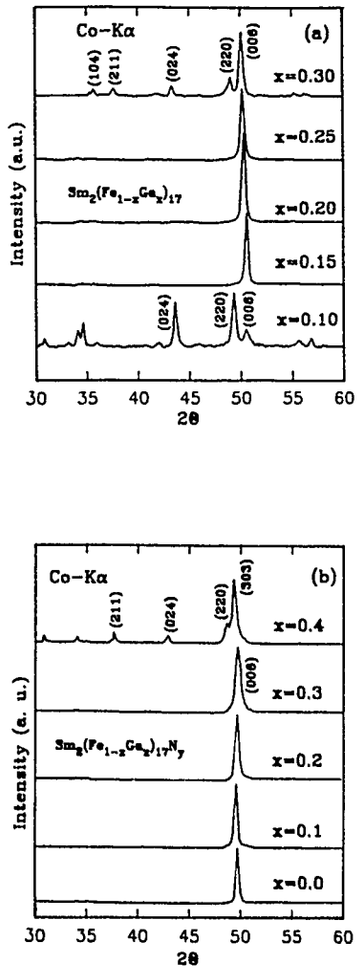

FIG. 3. (a) X-ray-diffraction patterns with Co$K\alpha$ radiation for aligned samples of $Sm_2(Fe_{1-x}Ga_x)_{17}$ compounds with $x=0.10$, 0.15, 0.20, 0.25, and 0.30, (b) x-ray-diffraction patterns with Co$K\alpha$ radiation for aligned samples of $Sm_2(Fe_{1-x}Ga_x)_{17}N_y$ compounds with $x=0$, 0.1, 0.2, 0.3, and 0.4.

This may be attributed to a change of the second crystal-field coefficients A_{20} at the rare-earth sites in $Sm_2(Fe_{1-x}Ga_x)_{17}$ compounds toward a more negative values. After the uptake of the N atoms, the A_{20} becomes more negative,[11,12] which makes the samples of $Sm_2(Fe_{1-x}Ga_x)_{17}N_y$ with $x \leqslant 0.3$ have uniaxial anisotropy at room temperature.

The saturation magnetization of $Sm_2(Fe_{1-x}Ga_x)_{17}$ and their nitrides decreases monotonically with Ga concentration. In order to get more information about the influence of Ga substitution on the magnetization, the average iron magnetic moment μ_{Fe} was calculated on the basis of the saturation magnetization measured at 4.2 K. In the process of evaluating μ_{Fe}, it was assumed that the magnetic moment of the Sm ion is independent of the Ga concentration, and that its magnetic moment was same as that of free Sm ion. Our results imply that both in the nitrides and in the parent compounds the iron moment μ_{Fe} decreases monotonically with Ga concentration. The average iron moment decreases with Ga concentration from $2.11\mu_B$ for $x=0$ to $1.51\mu_B$ for $x=0.5$ for the nitrides and from $1.96\mu_B$ for $x=0$ to $1.54\mu_B$ for $x=0.5$ for the parent compounds. This is a reduction of the Fe moment

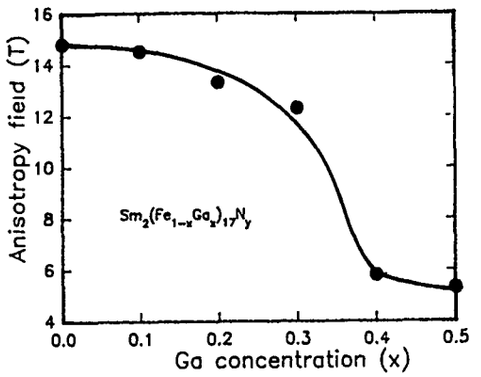

FIG. 4. Magnetic anisotropy field B_a for $Sm_2(Fe_{1-x}Ga_x)_{17}N_y$ compounds as a function of Ga concentration.

due to the substitution of Ga, which is very similar to the case of Al substitution for Fe in $Sm_2(Fe_{1-x}Al_x)_{17}$.[4]

Introduction of nitrogen leads to a change of the magnetic anisotropy of Sm_2Fe_{17} from planar to uniaxial in the whole temperature range up to T_c. Substitution of Ga for Fe also a significantly influences the anisotropy of the nitrides. Figure 4 shows the anisotropy field B_a as a function of Ga concentration for the $Sm_2(Fe_{1-x}Ga_x)_{17}N_y$ compounds. For $x \leq 0.3$, B_a decreases very slowly with Ga concentration. Obviously there is a contribution to the uniaxial anisotropy resulting from the substitution of Ga for Fe. for $x>0.3$, B_a decreases quickly. B_a becomes zero at $x=0.4$, which is in good agreement with the results of the x-ray diffraction mentioned above. It is well known[13] that in $Sm_2Fe_{17}N_y$ compounds the N atoms preferentially occupy $9e$ sites which are the nearest to the Sm atoms. The N atoms influence the crystal field at the Sm sites resulting in a significant increase of A_{20} of the Sm atoms,[11,12] so that the uniaxial anisotropy of the Sm sublattice increases. Ga substitution for Fe prevents the introduction of N atoms, so that the anisotropy field of $Sm_2(Fe_{1-x}Ga_x)_{17}N_y$ decreases with Ga concentration.

ACKNOWLEDGMENTS

The present investigation was partly supported by the National Natural Science Foundation of China and has been carried out within the scientific exchange program between China and The Netherlands.

[1] J. M. D. Coey and H. Sun, J. Magn. Magn. Mater. **87**, L251 (1990).
[2] D. McNeely and H. Oesterreicher, J. Less-Common Met. **44**, 183 (1976).
[3] H. Oesterreicher and D. McNeely, J. Less-Common Met. **53**, 245 (1977).
[4] X.-W. Li, N. Tang, Z.-H. Lu, T.-Y. Zhao, W.-G. Li, R.-W. Zhao, and F.-M. Yang, J. Appl. Phys. **73**, 5890 (1993).
[5] B.-P. Hu, X.-L. Rao, J.-M. Xu, G.-C. Lu, X.-L. Dong, H. Li, L. Yin, and Z.-R. Zhao, J. Magn. Magn. Mater. **114**, 138 (1992).
[6] T. H. Jacobs, K. H J. Buschow, G.-F. Zhou, X. Li, and F. R. de Boer, J. Magn. Magn. Mater. **116**, 220 (1992).
[7] Z. Wang and R. A. Dunlap, J. Phys. Condens. Matter **5**, 2407 (1993).
[8] R. Gersdorf, F. R. de Boer, J. W. Wolfrat, F. A. Muller, and L. W. Roeland, in *High-Field Magnetism*, edited by M. Date (North-Holland, Amsterdam, 1983), p. 227.
[9] K. S. K. C. Nardsimban and W. E. Wallace, AIP Conf. Proc. **18**, 1248 (1974).
[10] H. Sun, J. M. D. Coey, Y. Otani, and D. P. F. Hurley, J. Phys. Condens. Matter **2**, 6465 (1990).
[11] H.-S. Li and J. M. Cadogan, Solid State Commun **80**, 905 (1991).
[12] H.-S. Li and J. M. Cadogan, J. Magn. Magn. Mater. **103**, 53 (1992).
[13] J. M. D. Coey, J. F. Lawler, H. Sun, and J. E. M. Allan, J. Appl. Phys. **69**, 3007 (1991).

Structure and magnetic properties of arc-melted $Sm_2(Fe_{1-x}Co_x)_{14}Ga_3C_2$ compounds

Bao-gen Shen, Lin-shu Kong, Fang-wei Wang, Lei Cao, Bing Liang,
Zhao-hua Cheng, Hua-yang Gong, Hui-qun Guo, and Wen-shan Zhan
State Key Laboratory of Magnetism, Institute of Physics, Chinese Academy of Sciences, P.O. Box 603, Beijing 100080, People's Republic of China

The effects of the substitution of Co for Fe on the formation, structure, and magnetic properties of $Sm_2Fe_{14}Ga_3C_2$ compounds were studied. Alloys with composition $Sm_2(Fe_{1-x}Co_x)_{14}Ga_3C_2$ ($x=0$, 0.1, 0.2, 0.3, 0.4, and 0.5) were prepared by arc melting. X-ray diffraction shows that these alloys are single phase compounds of the rhombohedral Th_2Zn_{17}-type structure. The lattice constants a and c, and the unit cell volumes v of $Sm_2(Fe_{1-x}Co_x)_{14}Ga_3C_2$ compounds decrease monotonically with increasing cobalt concentration. It is found that the Curie temperature increases from 615 K for $x=0$ to 666 K for $x=0.5$. Room-temperature saturation magnetization is 90.3 emu/g for $x=0$, and it decreases to 79.6 emu/g at $x=0.5$. All compounds of $Sm_2(Fe_{1-x}Co_x)_{14}Ga_3C_2$ studied in this work exhibit an easy axis anisotropy at room temperature. The anisotropy field is higher than 90 kOe for $x\leq 0.2$, and it decreases slightly with $x\geq 0.3$.

I. INTRODUCTION

In our previous work,[1-3] it was found that the partial substitution of Ga, Al, or Si for Fe in $R_2Fe_{17}C_x$ helps the formation of high-carbon rare-earth iron compounds with a 2:17-type structure. It is found that the high-carbon $R_2Fe_{17}C_x$ compounds by the substitution of Ga, Al, or Si exhibit a high thermal stability, in contrast with the carbides or nitrides produced by the gas–solid reaction. We have prepared successfully single-phase compounds of $R_2(Fe,M)_{17}C_x$ (R=Y, Nd, Sm, Gd, Tb, Dy, Ho, Er, and Tm; M=Ga, Al, or Si; and $x\leq 3.0$), with the rhombohedral Th_2Zn_{17}-type or hexagonal Th_2Ni_{17}-type structures by arc melting, and studied their formation, structure, and magnetic properties.[1-4] It was found that the arc-melted $Sm_2(Fe,M)_{17}C_x$ compounds with $x\geq 1.5$ and relatively lower M concentration have a Curie temperature of higher than 600 K, and exhibit an easy c-axis anisotropy at room temperature and have an anisotropy field of higher than 90 kOe. The $Sm_2(Fe,M)_{17}C_x$ compounds are novel hard magnetic materials for sintering permanent magnets. A high-coercivity of 15 kOe at room temperature was obtained in the $Sm_2(Fe,Ga)_{17}C_x$ compounds by melt spinning.[1,5] In this paper, the structure and magnetic properties of $Sm_2(Fe_{1-x}Co_x)_{17}C_2$ ($0\leq x\leq 0.5$) compounds prepared by arc melting are reported.

II. EXPERIMENT

The $Sm_2(Fe_{1-x}Co_x)_{14}Ga_3C_2$ alloys with $x=0$, 0.1, 0.2, 0.3, 0.4, and 0.5 were prepared by arc melting in an argon atmosphere of high purity. The raw materials of the Sm, Fe, Co, Ga, and Fe–C alloy were at least 99.9% pure. The ingots were melted at least four times to ensure homogeneity. An excess of 4.5% Sm was added to compensate for the evaporation of Sm during melting. X-ray diffraction measurements on powder samples were performed using Co K_α radiation to identify the single phase and determine the crystallographic structure. The room-temperature saturation magnetization was measured by an extracting sample magnetometer in a field of 65 kOe. The Curie temperatures were determined from the temperature dependence of magnetization measured by a vibrating sample magnetometer and a magnetic balance in a magnetic field of 1 kOe. The aligned samples for anisotropy field measurements were prepared by mixing the powder with epoxy resin and then aligning in a magnetic field of 10 kOe. The anisotropy field was determined from magnetization curves measured along and perpendicular to the orientation direction by using the extracting sample magnetometer with a magnetic field of up to 65 kOe at room temperature.

III. RESULTS AND DISCUSSION

X-ray diffraction measurements show that the $Sm_2(Fe_{1-x}Co_x)_{14}Ga_3C_2$ alloys with $x\leq 0.2$ prepared by arc melting are single phase with the rhombohedral Th_2Zn_{17}-type structure. No significant diffraction from the impurity phase is observed. For $x>0.2$, the samples exhibit a predominant 2:17 phase and a few percent α-Fe as a second phase. However, the single-phase compounds with $x>0.2$ were obtained by melt spinning at a speed of 20 m/s. Both of the arc-melted and melt-spun $Sm_2(Fe_{1-x}Co_x)_{14}Ga_3C_2$ carbides are found to be stable at high temperature. The stability of the samples results from the substitution of Ga, which helps the formation of the high-carbon rare-earth iron compounds with a 2:17-type structure.[1,2,4]

The lattice constants a and c, and the unit-cell volumes v obtained from the x-ray diffraction patterns of $Sm_2(Fe_{1-x}Co_x)_{14}Ga_3C_2$ compounds with $0\leq x\leq 0.5$ are shown in Fig. 1 as a function of Co concentration. The substitution of Co for Fe in the $Sm_2Fe_{14}Ga_3C_2$ leads to a reduction of the unit-cell volume. An approximately linear decrease of the unit-cell volume with x is observed. For $x=0.5$, the unit-cell volume reduction is about 2.8%, compared with the cobalt-free compound. A similar result was also observed in other Fe–Co-based compounds.

The saturation magnetization M_s of $Sm_2(Fe_{1-x}Co_x)_{14}Ga_3C_2$ compounds is shown in Fig. 2(a) as

 0021-8979/94/76(10)/6746/3/$6.00 © 1994 American Institute of Physics

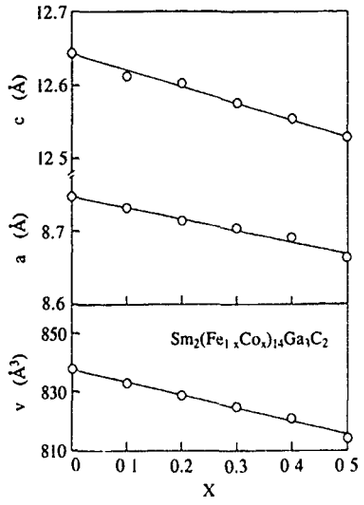

FIG. 1. The lattice constants a and c, and the unit cell volumes v of $Sm_2(Fe_{1-x}Co_x)_{14}Ga_3C_2$ compounds as a function of Co concentration.

a function of Co concentration x. The room temperature saturation magnetization of these compounds is essentially constant at 90 emu/g for $x \leq 0.3$. However, higher Co concentration ($x > 0.3$) decreases M_s.

Figure 2(b) shows the Co-concentration dependence of the Curie temperature T_c of $Sm_2(Fe_{1-x}Co_x)_{14}Ga_3C_2$ compounds. The T_c is found to increase monotonously from 615 K for $x=0$ to 666 K for $x=0.5$. In a previous study, it was shown that the introduction of interstitial carbon[6] or the substitution of Ga for Fe[7] in the Sm_2Fe_{17} compound results in the strong increase of Curie temperature. The enhancement of T_c can be suggested to be mainly due to the lattice expansion induced by the introduction of carbon atoms and the addition of Ga atoms. However, the increase of the Curie temperature with increasing x in $Sm_2(Fe_{1-x}Co_x)_{14}Ga_3C_2$ is observed, although the substitution of Co results in a monotonic decrease of the unit cell. In general, the Fe–Fe interaction is dominant in the Fe-rich rare-earth iron compounds. In the Fe-based compounds by the substitution of cobalt, the Curie temperature is mainly determined by the Fe–Fe, Fe–Co, and Co–Co interactions. It has been shown previously that the exchange interaction between Fe–Co atoms is stronger than those between Fe–Fe or Co–Co atoms, resulting in the increase of T_c.[8]

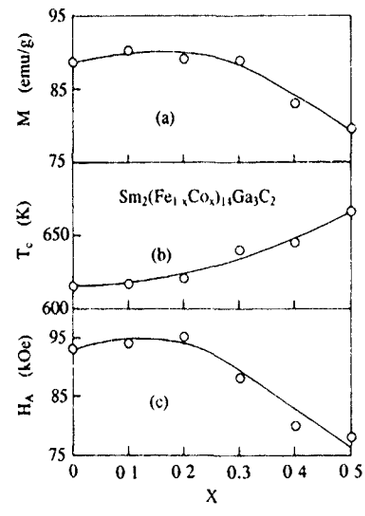

FIG. 2. The room-temperature saturation magnetization M_s (a), the Curie temperature T_c (b), and the room-temperature anisotropy field H_A (c) of $Sm_2(Fe_{1-x}Co_x)_{14}Ga_3C_2$ compounds as a function of Co concentration.

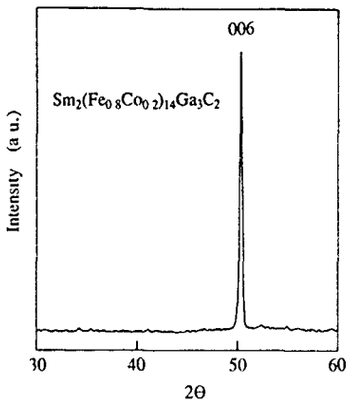

FIG. 3. X-ray diffractions pattern of magnetically aligned $Sm_2(Fe_{1-x}Co_x)_{14}Ga_3C_2$ powder samples, with $x=0.2$

All compounds studied in this work exhibit an easy c-axis anisotropy at room temperature. Figure 3 shows the x-ray diffraction patterns of magnetically aligned powder samples of $Sm_2(Fe_{1-x}Co_x)_{14}Ga_3C_2$, with $x=0.2$. A strong (0,0,6) reflection and the absence of $(h,k,0)$ indicates the characteristics of an uniaxial magnetocrystalline anisotropy. Figure 4 shows the magnetization curves of $Sm_2(Fe_{1-x}Co_x)_{14}Ga_3C_2$ ($x=0.2$) compound measured along and perpendicular to the aligned directions at room temperature. The magnetocrystalline anisotropy field H_A estimated from magnetization curves is shown in Fig. 2(c) as a function of Co concentration x. The H_A is found to be greater than 90 kOe for $x \leq 0.2$, and it decreases slightly with increasing Co concentration. The anisotropy field of $Sm_2(Fe_{1-x}Co_x)_{14}Ga_3C_2$ ($x \leq 0.5$) is comparable with that of $Nd_2Fe_{14}B$.

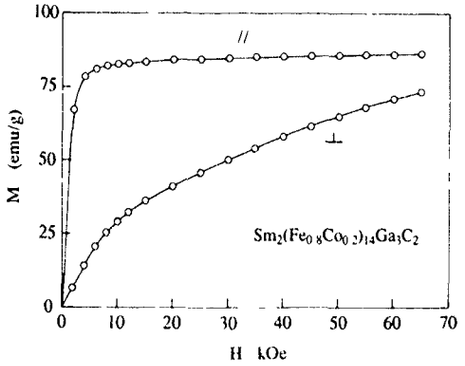

FIG. 4. The magnetization curves of the oriented $Sm_2(Fe_{1-x}Co_x)_{14}Ga_3C_2$ ($x=0.2$) sample measured along and perpendicular to the aligned directic s

ACKNOWLEDGMENTS

This work was supported by the State's Sciences and Technology Commission, the Chinese Academy of Sciences, and The National Natural Science Foundation of China.

[1]B. G. Shen, L S. Kong, F. W. Wang, and L. Cao, Appl. Phys. Lett. **63**, 2288 (1993).
[2]B. G. Shen, F. W. Wang, L. S Kong, L. Cao, and W. S. Zhan, J. Appl. Phys. **75**, 6253 (1994).
[3]Z. H. Cheng, B. G. Shen, F. W. Wang, J. X. Zhang, H. Y. Gong, and J. G. Zhao, J. Phys Condens. Matter **6**, L185 (1994).
[4]B. G. Shen, F. W. Wang, L. S. Kong, L. Cao, and H. Q. Guo, J. Magn. Magn. Mater. **127**, L267 (1993).
[5]L. S. Kong, B. G. Shen, F. W. Wang, L. Cao, H. Q. Guo, and T. S. Ning, J. Appl. Phys. **75**, 6250 (1994).
[6]J. M. D. Coey and D P. F. Harley, J. Magn. Magn. Mater **104–107**, 1098 (1992).
[7]B. G. Shen, F. W. Wang, L. S. Kong, and L Cao, J. Phys. Condens. Matter **5**, L685 (1993).
[8]B. G Shen, L. Y. Yang, J. Z. Liang, and H. Q. Guo, J. Phys Condens. Matter **4**, 7247 (1992)

Neutron diffraction and Mössbauer effect study of the structure of $DySi_xFe_{11-x}CoN$ alloys

Shu-ming Pan
General Research Institute for Nonferrous Metals, CNNC, Beijing 100088, People's Republic of China

Hong Chen, Den-ke Liu, Zu-xiong Xu, and Ru-zhang Ma
Department of Materials Physics, University of Science and Technology Beijing, Beijing 100083, People's Republic of China

Ji-lian Yang and Bai-sheng Zhang
Institute of Atomic Energy, Beijing 102413, People's Republic of China

De-yan Xue and Qiang Ni
Shatoujiao New Materials Factory, Shenzhen 518081, People's Republic of China

$DySi_xFe_{11-x}Co$ (x=0.5, 1.0, and 1.5) alloys and their nitrides are studied by x-ray diffraction, Mössbauer effect and neutron diffraction experiments. The results show that both Si and Co atoms can occupy the $8f$ and $8j$ sites, and more preferentially occupy the $8f$ sites. Nitrogen atoms as interstitial atoms enter into the $2b$ site. The nitrides have high Curie temperatures. The results of Mössbauer spectroscopy indicate that nitriding increases the hyperfine fields of all Fe sites.

I. INTRODUCTION

$ThMn_{12}$-type Fe-rich ternary compounds $R(Fe,T)_{12}$, in which R is a rare-earth element and T is a stabilizing element like Ti, V, Cr, Si, *et al.*,[1–4] have a high iron content and a large a/c ratio, and high values for saturation magnetization, Curie temperature, and magnetocrystalline anisotropy can be expected. The Sm-containing compounds especially show uniaxial anisotropy with an anisotropy field of up to 90 KOe, but the coercivity of samples prepared by standard powder metallurgy techniques does not exceed 1 KOe. The application of mechanical alloying or rapid quenching is more successful in achieving high coercivity, but the saturation magnetization of the samples is no higher than $1.35T$. Coey[5] and Yang *et al.*[6] discovered that the magnetic properties can be improved by introducing nitrogen atoms into the lattice interstitially. This work reports on such a study, by means of neutron diffraction and Mössbauer spectroscopy of the structure and magnetic properties of novel intermetallic compounds in which Fe is substituted by Co and Si atoms and nitrogen atoms are introduced interstitially.

II. EXPERIMENTAL DETAILS

Samples of $DySi_xFe_{11-x}Co$ (x=0.5, 1.0, and 1.5) were prepared by arc melting together with the raw elements with purities of Dy(99.9%), Fe(99.8%), Co(99.5%), and Si(99.999%). Melting was carried in a high purity argon atmosphere. The ingots were crushed into powder (<100 μm) in C_2H_5OH. Nitriding was carried out by heating powder samples at 500 °C for 1 h in nitrogen atmosphere. The phase detection was carried out by x-ray diffraction. Curie temperatures and saturation magnetizations were measured on a vibrating sample magnetometer (VSM). Neutron diffraction was used for analyzing the structure and the lattice occupation of N atoms. Mössbauer spectra were collected using a conventional constant acceleration spectrometer with a ^{57}Co (in Pd) source. The velocity scale was calibrated using an α-Fe absorber at room temperature.

III. RESULTS AND DISCUSSIONS

The x-ray diffraction patterns indicated that $DySi_xFe_{11-x}Co$ alloys were nearly single phase with the tetragonal $ThMn_{12}$-type structure. The nitrided alloy had high Curie temperature with T_c=450 °C and high saturation magnetization with δ=146 A M^2/kg.

The neutron diffraction experiment was carried out at room temperature and the neutron diffraction pattern is shown in Fig. 1. Table I shows the parameters for the crystal and magnetic structures of $DySiFe_{10}CoN_{0.42}$ alloys. Co atoms preferentially occupy the $8f$ and the $8j$ sites and N atoms enter into the $2b$ site. The Si atoms occupy the $8f$ and $8j$ sites as previously reported for $SmFe_{12-x}Si_x$ compounds in Refs. 2, 8, and 9.

Mössbauer spectra were obtained for $DySi_xFe_{11-x}Co$ (x =1.0 and 1.5) and their nitrides. The distribution of the Si atoms over the different lattice sites changes the near-neighbor environment of the Fe atoms and broadens the lines of the subspectra. Fitting of the Mössbauer spectra was done assuming that the Si atoms preferentially occupy $8j$ and $8f$ sites. For x=1.0 and 1.5, overall intensity ratios of 7.7:7.2:7.2 and 7.7:6.2:6.2 for $8i$:$8j$:$8f$ were imposed, respectively. The assignment takes into account the nearest-

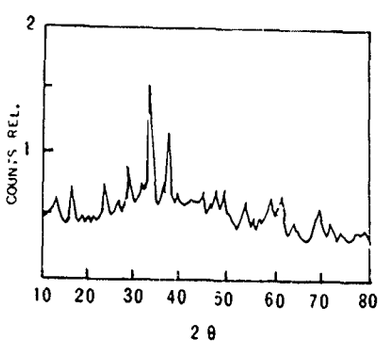

FIG. 1. The neutron diffraction pattern of $DySiFe_{10}CoN_{0.42}$ at 300 K.

 0021-8979/94/76(10)/6749/2/$6.00 © 1994 American Institute of Physics

TABLE I. The structural parameters of $DySiFe_{10}CoN_{0.42}$ obtained from neutron diffraction data at 300 K. x,y,z are atomic coordinate parameters, N is the atomic number on the different lattice sites, K_Z is the magnetic moment value in the z direction; R is the consistent factor; R_N is the consistent factor for nuclear diffraction, R_M is the consistent factor for magnetic diffraction, x^2 is the residual value.

Atom site	x	y	z	N	$K_Z(\mu_B)$
Dy ($2a$)	0.0	0.0	0.0	2.0	−4.471
Fe ($8i$)	0.2989	0 0	0.0	7.226	1.511
Si ($8i$)	0.2989	0.0	0.0	0.004	0.0000
Fe ($8j$)	0.2789	0.5	0.0	7.284	1.132
Si ($8j$)	0.2789	0.5	0.0	0.744	0.000
Co ($8j$)	0.2789	0.5	0.0	0.672	1.132
Fe ($8f$)	0.25	0.25	0.25	5.490	1.012
Si ($8f$)	0.25	0.25	0.25	1.182	0.000
Co ($8f$)	0.25	0.25	0.25	1.328	1.012
N ($2b$)	0.0	0.0	0.5	0.835	
$R\%$				4.37	
$R_N\%$				4.27	
$R_M\%$				6.19	
X^2				1.44	

neighbor environment of each respective site and the Fe-Fe distance. We considered that the largest H_{hf} corresponds to the site ($8i$), which had the largest TM coordination. The lowest H_{hf} was attributed to the $8f$ sites which had the same coordination number as the $8j$ site but the shortest mean Fe-Fe nearest-neighbor distance. The outer lines of the spectra in Si-containing compounds were much narrower than the inner ones, indicating the presence of a distribution of H_{hf}. The Mössbauer spectra showed that nitriding makes the hyperfine fields of all Fe sites increase.

IV. CONCLUSIONS

(1) The neutron diffraction study of $DySiFe_{10}CoN_{0.42}$ shows that the Si and Co atoms preferentially occupy the $8f$ site and N atoms enter into $2b$ site.

(2) Nitriding increases the hyperfine fields of all Fe sites.

ACKNOWLEDGMENTS

This work was partially supported by the National Natural Science Foundation of China and the State Key Laboratory of Magnetism, Institute of Physics, Chinese Academy of Sciences.

[1] K. Ohasi, T. Yokohama, R. Osuga, and Y. Tawara, IEEE Trans. Magn **MAG-23**, 3101 (1987).
[2] K. H. Buschow, J. Appl. Phys. **63**, 3130 (1988).
[3] B. de Mooij and K. H. J. Buschow, Philips J. Res. **42**, 246 (1987).
[4] P. Stefanski and A. Wrzeciono, J Magn. Magn. Mater. **82**, 125 (1989).
[5] J. N. D. Coey, H. Sun, and Y. Otani, in Proceedings of the Sixth International Symposium on Magnetic Anisotropy and Coercivity in Rare-Earth-Transition Metal Alloys, Pittsburgh, PA, October 25, 1990, p. 36
[6] Y. C. Yang, L. J. Kong, S. H. Sun, D M. Gu, and B. P. Cheng, J. Appl. Phys. **63**, 3702 (1988).
[7] Y. C. Yang, X. D. Zhang, L J. Kong, and Q. Pan, Solid State Commun. **78**, 317 (1991).
[8] Th. Sinnemann, K. Erdmann, M. Rosenberg, and K. H. J. Buschow, Hyp. Inter. **50**, 675 (1989).
[9] O. Moze, L. Pareti, M. Solzi, and W. I. David, Solid State Commun. **66**, 465 (1988).

A full electron LMTO-ASA study of electronic band structure and magnetic properties for $RFe_{11}TiN_x$ (R=Y, Nd, Sm; x=0,1)

W. Y. Hu, J. Z. Zhang, and Q. Q. Zheng
Institute of Solid State Physics, Chinese Academy of Sciences, Hefei 230031, China

C. Y. Pan
Department of Physics, Utah State University, Logan, Utah, 84332

The band structure and magnetic properties are studied for $RFe_{11}TiN_x$ (R=Y, Nd, Sm; x=0,1) rare-earth iron intermetallic compounds using the linear muffin tin orbital with the atomic sphere approximation (LMTO-ASA) method. In order to elucidate the role played by the rare-earth atoms in these compounds, a full electron calculation is performed using a semirelativistic spin-polarized LMTO-ASA method in the local spin density approximation (LSDA) regime. The $4f$ electrons of the rare-earth atoms are considered to be valence electrons in the self-consistent calculations. For $NdFe_{11}TiN$, a calculation in which the $4f$ electrons are treated as core-frozen states is also performed, and is compared with the full electron calculation. The effects of N atoms in these compounds are also discussed.

I. INTRODUCTION

The rare-earth iron ternary intermetallic compounds have attracted great attention as promising new permanent magnetic materials. Theoretical first-principle calculations regarding these materials are few, because of the complexity of these systems and the presence of the rare-earth $4f$ electrons. In early works, band structure calculations of the electronic structure of these materials often focused on the Y compounds. For instance, Jaswal *et al.*[1] and Sakuma[2] have calculated the electronic structure of $Y_2Fe_{17}N_x$ (x=0,3) and $YFe_{11}TiN_x$ (x=0,1), respectively, using the LMTO-ASA band method. Choosing Y rather than the rare-earth atoms avoids the trouble of considering $4f$ electrons, but these systems differ from the realistic materials that have applied prospects. These results using Y may only provide some qualitative discussion about the rare-earth iron compounds. It is better to perform the electronic structure calculations for realistic systems. Jaswal[3] has used a simple method in which the $4f$ states were treated as frozen-core states for $Nd_2Fe_{14}B$. Hummler *et al.*[4] have studied $R_2Fe_{14}B$ (R=Gd, Tb, Dy, Ho, and Er) using a so-called "open core" approximation in which $4f$ electrons are not allowed to hybridize with other valence electrons. The latter approximate method can only consider the effects on the $4f$ energy level by the crystal field and the possible hybridization and charge transfer are neglected. Recently, Asano *et al.*[5] have studied the electronic structure of $RFe_{12}A$ (R=Y, Ce, Gd; A=N, C), and the $4f$ electrons were treated as valence electrons. Their results indicate that the calculation of the electronic structure can explain the experimental results in the frame of the Stoner–Wohlfarth theorem. In their work, the role of N or C atoms are not discussed sufficiently. Zeng *et al.*[6] have calculated the electronic structure of $R_2Fe_{17}N_{3-\delta}$ (R=Sm, Nd, and Gd; δ=0,3) using the cluster method. Their results imply that there are relatively strong hybridizations between $4f$ and other valence electrons. Many experiments also show that there exist differences in the properties of R–Fe–A compounds for different rare earths, especially for light rare earths. This difference cannot be attributed to the de Gennes factors completely. Hence, treatment of the $4f$ electrons as valence electrons in the band calculations is necessary.

In this work, the full-electron self-consistent spin-polarized band calculation for $RFe_{11}TiN_x$ (R=Y, Nd, and Sm; x=0,1) has been performed using the semirelativistic LMTO-ASA method. The frozen core approximation is used for the inner close shells for simplification. The maximum l is taken as l_{max}=3 for R, l_{max}=2 for Y, Fe, Ti, and l_{max}=1 for N. The crystal structure of $RFe_{11}TiN_x$ is as shown in Ref. 2 and the lattice parameters are from Refs. 2 and 8. The ratio of the atomic sphere radius is $r_R:r_{Fe}:r_{Ti}$=1.23:1.00:1.10 for $RFe_{11}Ti$ and $r_R:r_{Fe}:r_{Ti}:r_N$=1.40:1.15:1.25:1.00 for $RFe_{11}TiN_x$. As a comparison, a calculation of electronic structure for $NdFe_{11}TiN$ is also performed, with the $4f$ electrons of Nd in a frozen core approximation.

II. RESULTS AND DISCUSSION

A. Magnetic moments

The magnetic moments of R, Fe, and N (for x=1) atoms in $RFe_{11}TiN_x$ compounds are listed in Table I. In the case of x=0, the Fe($8i$) atoms have the highest moments and the Fe($8f$) atoms have the lowest ones. The average moment of Fe atoms is 2.14μ_b, 2.23μ_b, and 2.15μ_b for $YFe_{11}Ti$, $NdFe_{11}Ti$, and $SmFe_{11}Ti$, respectively. These results are similar to those of Asano *et al.* for $YFe_{11}Ti$[5] and those of Jaswal for $NdFe_{11}Ti$.[8] The calculated magnetic moments are slightly higher than the experimental values. This discrepancy seems to possess a systematic character and is insensitive to the radius of atomic sphere used in different works. It is interesting to note that the magnetic moments may slightly depend on the number of k points used in the band calculation. There are 126 k points in the irreducible Brillouin zone in our self-consistent calculation, which is smaller than the 215 k points used by Asano *et al.*[5] but larger than the six k points used by Jaswal.[8] The calculated total magnetic moments of transition metal atoms are 22.60μ_b, 23.57μ_b, and 22.76μ_b for $YFe_{11}Ti$, $NdFe_{11}Ti$, and $SmFe_{11}Ti$, respectively. In the LMTO calculation, the nonzero contribution of the orbital moment for rare-earth atoms was not evaluated. Due to the

 0021-8979/94/76(10)/6751/3/$6.00 © 1994 American Institute of Physics

TABLE I. Calculated local and total magnetic moments (in μ_b/atom and μ_b/f.u., respectively) for R[illegible]iN_x(R=Y, Nd, and Sm, x=0,1).

	$YFe_{11}TiN_x$		$NdFe_{11}TiN_x$		$SmFe_{11}TiN_x$	
	x=0	x=1	x=0	x=1	x=0	x=1
R(2a)	−0.42	−0.34	2.73	2 89	5.19	−5.69
	(0.00)	(0.00)	(2 71)	(1.38)	(0.55)	(−0.28)
Fe(8j)	2.25	2.25	2 33	2.25	2 25	2.18
Fe(8f)	1 72	2.17	1.88	2.11	1 77	2.05
Fe(8i)	2.54	2.62	2.56	2.61	2.51	2.62
Ti(8i)	−0.94	−1.02	−0.96	−0.99	−0.89	−1 03
N(2b)	···	0.10	···	0.07	···	0 09
Fe	2.14	2.32	2.23	2.30	2 15	2.25
(aver.)	(1.69)	(1 98)	(1.69)	(1.98)	(1.69)	(1.98)
Total	22.14	24.28	26.29	27.24	27.91	18.15
	(18.57)	(21.75)	(21.27)	(23.22)	(19.12)	(21.23)

[a]The bracketed data are experimental data from Ref. 12, f.u. denotes the formula unit, and Fe (aver.) represents the average Fe magnetic moment.

magnetic anisotropy, the magnetic moments of the rare-earth and iron atoms may be not collinear. In Table I, only the spin moments are listed for the rare-earth atoms. The moment of each Y atom is $-0.42\mu_b$, which comes from the polarization of the 4d, 5s electr[illegible]s. The spin moment of Nd and Sm in $RFe_{11}Ti$ is $2.73\mu_b$ [illegible] μ_b, respectively. Due to the neglecting of spin orbit coupling and the orbital moment in our semirelativistic LMTO-ASA calculations, one cannot compare the spin moments directly with experimental magnetic moments of rare-earth ions. However, our calculations will describe the coupling of moments between Fe and rare-earth atoms. The self-consistent calculations reveal a ferromagnetic coupling between the spin of Fe and Nd (or Sm) in Nd (or Sm) $Fe_{11}Ti$ compounds. The moment of each Ti atom is $-0.94\mu_b$, $-0.96\mu_b$, and $-0.89\mu_b$ for Y, Nd, and Sm compounds, respectively, which is antiferromagnetically coupled with the Fe moments. This antiferromagnetic coupling between Fe and Ti is similar to that of YFe_8T_4 discussed by Coehoorn.[9]

The magnetic moment of Fe atoms are increased by the uptake of nitrogen, which is in agreement with experiments. The largest Fe moments are still associated with the Fe(8i), but the largest increment of moments are associated with the Fe(8f) atoms, which is $0.55\mu_b$, $0.23\mu_b$, and $0.28\mu_b$ for $YFe_{11}TiN$, $NdFe_{11}TiN$, and $SmFe_{11}TiN$, respectively. The moments of Fe(8j) atoms, which are the nearest neighbors of N atoms, are not changed for $YFe_{11}TiN$, and even show a small reduction for $NdFe_{11}TiN$ and $SmFe_{11}TiN$. The moments of Ti are still antiferromagnetically coupled to the Fe sublattice, and have a $\sim 0.1\mu_b$ increment. There is a moment of $0.1\mu_b$ on N atoms due to the spin polarization of s,p electrons. The average moment of Fe atoms is $2.32\mu_b$, $2.30\mu_b$, and $2.25\mu_b$ for Y, Nd, and Sm compounds, respectively. It seems to be a general trend that the magnetic moment of Fe in iron nitride depends on the distance from neighboring N atoms. The results of Fe_4N, $Fe_{16}N_2$,[10] $R_2Fe_{17}N_3$,[6] and $RFe_{11}TiN$ show that the lowest magnetic moment of Fe always corresponds to the nearest neighbor of a N atom. The moments of Nd in Nd compounds and that of Sm in $SmFe_{11}Ti$ are ferromagnetically (FM) coupled to the moments of Fe. This coupling becomes antiferromagnetic (AFM) for the $SmFe_{11}TiN$ compound. This fact is qualitatively in agreement with the measurement results of Yang *et al.*[11]

B. Density of states

The calculated partial density of states (PDOS) of $YFe_{11}Ti$ and $YFe_{11}TiN$ are similar to that of Sakuma.[2] After uptaking N, the 3d band of Fe atoms become narrower, due to the increased distance between Fe atoms. The PDOS of majority moment of the 3d band is slightly low, which produces an enhancement of the moment of Fe and a reduction of the DOS at Fermi surface E_f. Then the reduction of $N(E_f)$ is responsible for the increase of Tc in these compounds. There is explicit hybridization between 3d of Fe(8j) and N 2p at an energy about 6 eV below E_f. The effect of the presence of N atoms is not only changing the crystalline field, but also producing a hybridization between electrons of N, Fe(8j), and Y.

The PDOS of $SmFe_{11}TiN_x$ (x=0,1) are shown in Fig. 1. The essential situation is similar to that of Y compounds, except for the PDOS of the rare-earth atoms. These facts confirm that the discussion based on the calculated results of Y compounds can give a qualitatively correct conclusion about magnetic moments. From these figures, the spin polarization of the N 2p band in these magnetic materials is small. The main contribution of the N 2p band is around the energy of −4.5−−8.0 eV. It is worthwhile to point out that the difference between the full electron and frozen 4f calculation reveals the effect of interaction among the 4f electrons of rare-earth atoms, 3d of Fe(8j), and 2p of N atoms. The hybridization is taking place among not only N 2p, Fe(8j) 3d and 4s, R(Nd, Sm) 5d and 6s, but also 4f of Nd or Sm. It is interesting to point out that, for the case of $SmFe_{11}TiN$, although we begin with a ferromagnetic coupling between moments of R and Fe, the self-consistent calculation gives an antiferromagnetic coupling between Fe sublattice moments and a Sm 4f moment, which is in agreement with the experiments of Yang *et al.*[11] It is well known that the spin–orbit

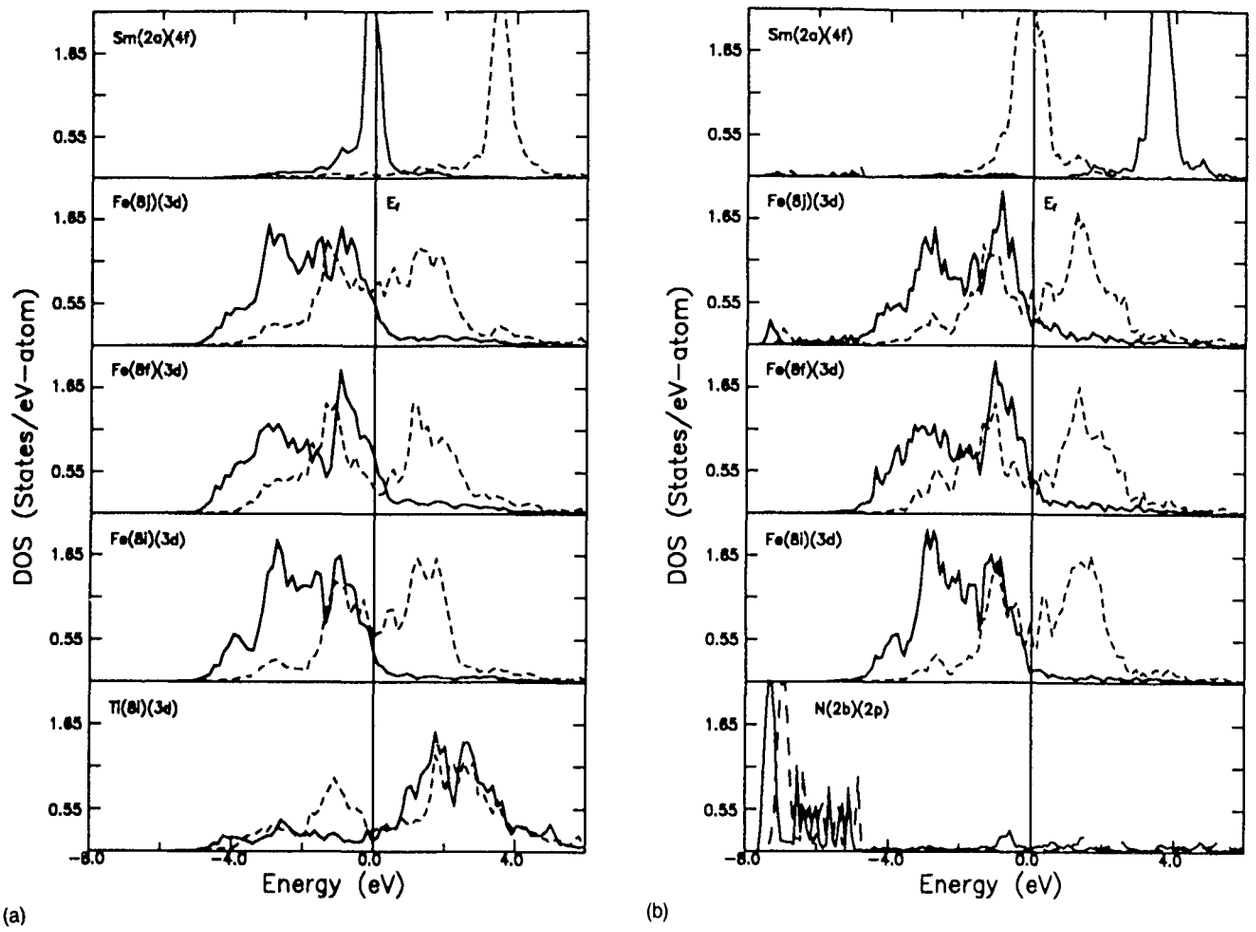

FIG. 1. The PDOS of (a) $SmFe_{11}Ti$, (b) $SmFe_{11}TiN$; the full and dotted curves show the up and down spin states, respectively

coupling is important for the rare-earth atoms. The spin–orbit interaction, together with the crystalline field, is the source of magnetic anisotropy of rare-earth atoms in these compounds. In this stage, the calculation including spin–orbit coupling may be important for a quantitative comparison.

In conclusion, we have studied the electronic structure of permanent magnetic materials $RFe_{11}TiN_x$ (R=Y, Nd, and Sm; $x=0,1$) using the LMTO-ASA band method. By comparing our full electron calculation with that for Y compounds, or using the frozen core approximation, the main conclusions can be summarized as (1) studies for Y compounds can give correct results of the magnetic moment of Fe atoms; (2) the $4f$ electrons of the rare-earth atoms do have hybridization with other valence electrons to some degree; and (3) a full electron calculation can give the correct relation of moments between rare-earth and iron atoms.

ACKNOWLEDGMENT

This work is supported by the National Nature Science Foundation of China under Grants No. 19174057 and No. LWTZ-1289 of the Chinese Academy of Sciences.

[1] S. S. Jaswal, W. B Yelon, G. C Hadjipanayis, Y. Z. Wang, and D J Sellmyer, Phys Rev. Lett. **67**, 644 (1991)
[2] A. Sakuma, J Phys Soc. Jpn. **61**, 4119 (1992).
[3] S. S. Jaswal, Phys. Rev B **41**, 9697 (1990)
[4] K Hummler and M. Fahnle, Phys. Rev. B **45**, 3161 (1992)
[5] S. Asano, S. Ishida, and S Fujii, Physica B **190**, 155 (1993)
[6] Z. Zeng and Q. Q. Zheng, J. Appl. Phys **73**, 6916 (1993).
[7] Y. C Yang, X. D. Pei, H. L Li, X. D. Zhang, L. S. Kong, Q Pan, and M H. Zhang, J. Appl Phys. **70**, 6574 (1991)
[8] S. S. Jaswal, Phys. Rev. B **48**, 6156 (1993).
[9] R. Coehoorn, Phys. Rev B **41**, 11 790 (1990).
[10] W. Y. Hu, Z. Zeng, Q. Q Zheng, and W. Y Lai (to be published)
[11] Y. C Yang, X D. Zhang, L S Kong, Q. Pan, and S L Ge, Solid State Commun **78**, 317 (1991)

Magnetic properties and molecular field theory analysis of $RFe_{10}Mo_2$ alloys

Xie Xu and S. A. Shaheen
Department of Physics and Center for Materials Research and Technology (MARTECH), Florida State University, Tallahassee, Florida 32306

The $RFe_{10}Mo_2$ compounds (R=Y, Nd, Gd, Dy) with $ThMn_{12}$ type structure have been synthesized, and their magnetizations have been investigated in the temperature range from 2 to 800 K using a SQUID magnetometer. The Curie temperature, saturation moments, and measurements, as well as molecular field analysis of the temperature dependence of the magnetization are reported. Our work demonstrates that the molecular field analysis based on a two-sublattice model is capable of quite accurately describing the temperature dependence of the magnetization for the $RFe_{10}Mo_2$ compounds. The results also suggest that the moments of the R and Fe sublattices are nearly collinear in a large temperature range. According to the calculated molecular field coefficients, we find that the magnetic interactions are dominated by exchange between iron $3d$ electrons, and, on the other hand, the strength of the R–R interaction has even the same order as that of the R–Fe interaction.

I. INTRODUCTION

The Fe-rich ternary compounds $RFe_{1-x}TM_x$ (R=rare earth or yttrium, TM=Ti, V, Cr, Mo, Si, etc.; $x=1$ or 2)[1–5] have attracted much attention as possible candidates for permanent magnet applications. They crystallize in the tetragonal $ThMn_{12}$ type structure with space group I4/mm.[1] In this structure, the R atoms occupy the crystallographic $2a$ site and the $3d$ atoms occupy the $8i$, $8j$, $8f$ sites. The molecular field theory (MFT) is commonly used to describe the temperature dependence of magnetization in the R–T compounds, and it has been shown to be quite successful.[2–6] In this paper, we present studies of the $RFe_{10}Mo_2$ series with R=Y, Nd, Gd, and Dy. The molecular field theory based on a two sublattice model[2] was used to analyze the experimental data.

II. EXPERIMENT

Samples for this investigation were prepared by arc melting appropriate amounts of Fe, Mo, and rare earth elements (Y, Nd, Gd, and Dy) under a purified argon atmosphere. As cast samples were vacuum annealed at 1000 °C for a week. All samples are almost single phase, as determined by both x-ray powder diffraction and thermomagnetic analysis. A Quantum Design SQUID magnetometer with an external field up to 5.5 T was used to measure the magnetization of powdered samples in a temperature range from 2 K to their Curie temperatures. The experimental values of the Curie temperatures (T_C) were determined by means of the linear relationship $M^2(T)\propto(1-T/T_C)$ near the $T_C(T\leq T_C)$.

III. ANALYSIS AND RESULTS

According to the two sublattice MFT, the molecular field acting on the R sublattice and Fe sublattice is separated, and can be expressed, respectively, as follows:

$$H_R(T)=H+d[n_{RR}M_R(T)+10n_{RF}M_F(T)], \tag{1}$$

$$H_T(T)=H+d[10n_{FF}M_F(T)+n_{RF}M_R(T)], \tag{2}$$

where H is the applied field, $M_R(T)$ and $M_{Fe}(T)$ represent the magnetic moment per rare earth ion and per Fe ion, respectively, at temperature T. The factor d converts the moment per $RFe_{10}Mo_2$ in μ_B to Gauss: $d=N_A\mu_B\rho/A$, where N_A is Avogadro's number, ρ is the density of $RFe_{10}Mo_2$ in g/cm^3, and A is the formula weight of $RFe_{10}Mo_2$. n_{RR}, n_{RF}, and n_{FF} are the molecular field coefficients, which describe the R–R, R–Fe, and Fe–Fe magnetic interactions, respectively.

The temperature dependence of each sublattice magnetization is governed by a Brillouin function:

$$M_R(T)=M_R(0)B_{J_R}\left(\frac{M_R(0)H_R(T)}{k_BT}\right), \tag{3}$$

$$M_F(T)=M_F(0)B_{J_F}\left(\frac{M_F(0)H_F(T)}{k_BT}\right), \tag{4}$$

where $M_R(0)$ and $M_F(0)$ are the magnetic moments of R and Fe at zero temperature, respectively. J_R and J_F are the individual R and Fe angular moments.

In the calculations, the free ion moment is used for the rare earth ion, i.e., $M_R(0)=g_JJ_R$, and $M_F(0)$ can be deduced from the observed low temperature moment:

$$M_F(0)=[M_{exp}(0)\pm M_R(0)]/10, \tag{5}$$

where "−" applies for the light rare earths Nd and Y, and "+" applies for the heavy rare earths Gd and Dy.

The coefficients n_{ij} are determined by numerically solving Eqs. (1)–(4), under the condition that the calculated total moments,

$$M_{tot}(T)=M_R(T)\pm 10M_F(T), \tag{6}$$

correspond best with the experimental data. This is done by minimizing the percentage deviation,

$$R=100\,\frac{\Sigma|M_{exp}(T_i)-M_{tot}(T_i)|}{\Sigma M_{exp}(T_i)}, \tag{7}$$

where $M_{exp}(T_i)$ is the magnetization observed at temperature T_i. No other constraints are imposed. From Eqs. (3) and (4), the Curie temperature in the zero field is related to the n_{ij} by

 0021-8979/94/76(10)/6754/3/$6.00 © 1994 American Institute of Physics

TABLE I. Density ρ, rare earth gyromagnetic ratio g_J, and total angular momentum J_R used in MFT calculations. n_{FF}, n_{RF}, and n_{RR} are the computed molecular field coefficients The MFT calculated T_C and experimental T_C are listed. R% is the quality-of-fit index defined by Eq. (7).

R	ρ (g/cm^3)	g_J	J_R	$M_R(0)$ (μ_B)	$M_{Fe}(0)$ (μ_B)	n_{FF}	n_{RF}	n_{RR}	R% (%)	T_C (K) cal.	T_C (K) exp.
Y	8.03	...	...	...	1.73	4562	...	...	3.5	327	350
Nd	7 60	$\frac{8}{11}$	$\frac{9}{2}$	$\frac{36}{11}$	1.53	8780	2000	1900	4.0	445	420
Gd	8.0	2	$\frac{7}{2}$	7	1.65	6300	−2500	2300	4.0	465	480
Dy	7.83	$\frac{4}{3}$	$\frac{15}{2}$	10	1.61	6120	−1100	1000	3.0	383	390

$$T_C = \frac{(n_{FF}\alpha + n_{RR}\beta) + \sqrt{(n_{FF}\alpha + n_{RR}\beta)^2 - 4\alpha\beta(n_{FF}n_{RR} - n_{RF}^2)}}{2\alpha\beta}, \tag{8}$$

where

$$\alpha \equiv [3JR/(JR+1)][kB/\mu Bd]MR2(0);$$

$$\beta \equiv \frac{[3J_T/(J_T+1)][k_B/\mu_B d]}{10M_T^2(0)}. \tag{9}$$

For compounds with R=Y, we have

$$T_C = \frac{n_{FF}}{\beta} = 10n_{FF}M_T^2(0)[(J_T+1)/3J_T][\mu_B d/k_B]. \tag{10}$$

Table I summarizes the experimental information, such as low temperature magnetization $M_s(0)$ and Curie temperature T_C of $RFe_{10}Mo_2$ intermetallics. The low temperature magnetization $M_s(0)$ was measured at 2 K in a field of 3 T by means of a SQUID magnetometer. The parameters used in the calculations and the MFT coefficients for each $RFe_{10}Mo_2$ compound by solving Eqs. (1)–(7) numerically are also summarized in Table I. The moment of an Fe atom at 0 K is about $1.7\mu_B$ in these compounds. We chose $J_F=1.0$ in the calculations.

In Figs. 1–4, the temperature dependence of the magnetization for four $RFe_{10}Mo_2$ compounds is plotted. The data are represented by circles, while the MFT calculation results for total moment $M_{tot}(T)$, rare earth sublattice moment $M_R(T)$, and Fe sublattice moment $M_{Fe}(T)$ are indicated by solid, dashed, and dot–dashed lines, respectively. MFT with a single coefficient (n_{FF}) provides a quite reasonable description of the temperature dependence of the magnetization for $YFe_{10}Mo_2$, as Fig. 1 shows. The percentage deviation between the measured and calculated values is $R=3.5\%$, and $T_C^{cal}=327$ K is about 6% lower than the observed Curie temperature of 350 K.

Figures 3 and 4 show that the two-sublattice model with the assumption of ferrimagnetically coupled R and Fe moments yields results in excellent correspondence with the data for $GdFe_{10}Mo_2$ and $DyFe_{10}Mo_2$. The Curie temperatures calculated are consistent with the experimental values.

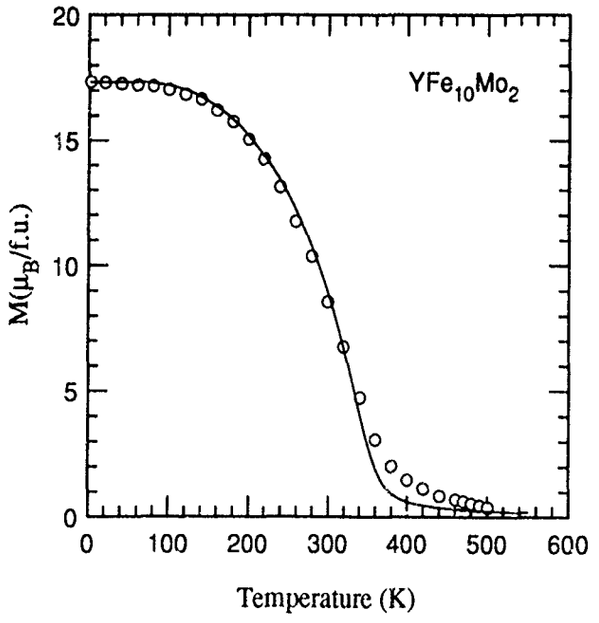

FIG. 1 The temperature dependence of the magnetization of $YFe_{10}Mo_2$ Circles represent the experimental data and the solid line represents the MFT results

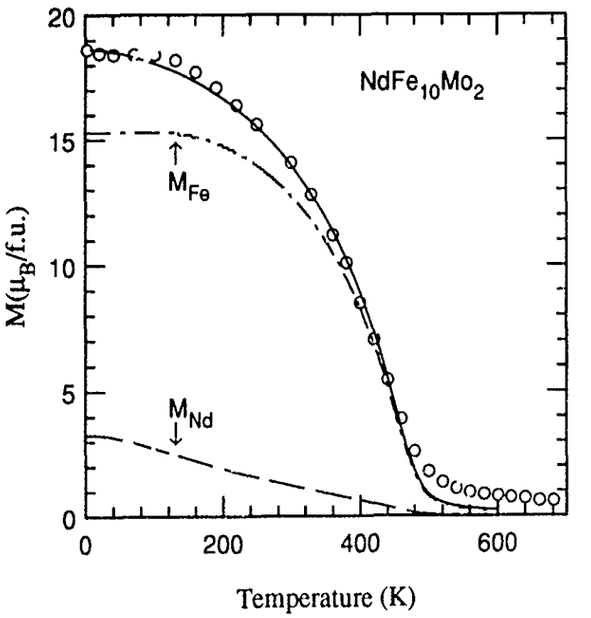

FIG 2 The temperature dependence of the magnetization of $NdFe_{10}Mo_2$ Circles represent the experimental data. Lines represent the MFT results

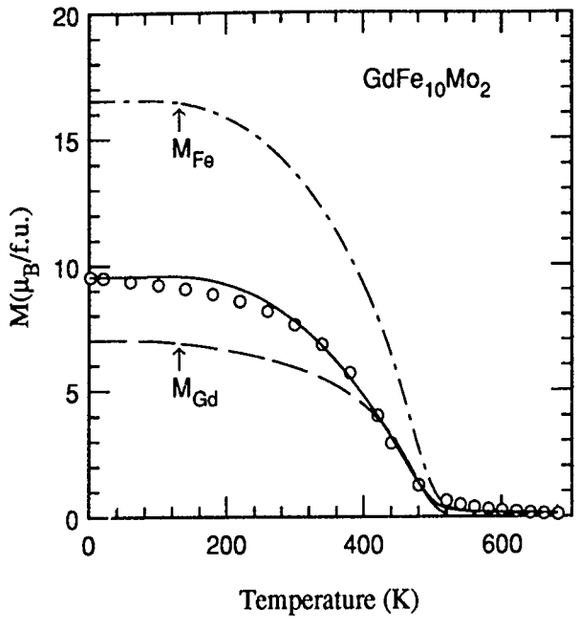

FIG 3 The temperature dependence of the magnetization of $GdFe_{10}Mo_2$. Circles represent experimental data. Lines represent MFT results.

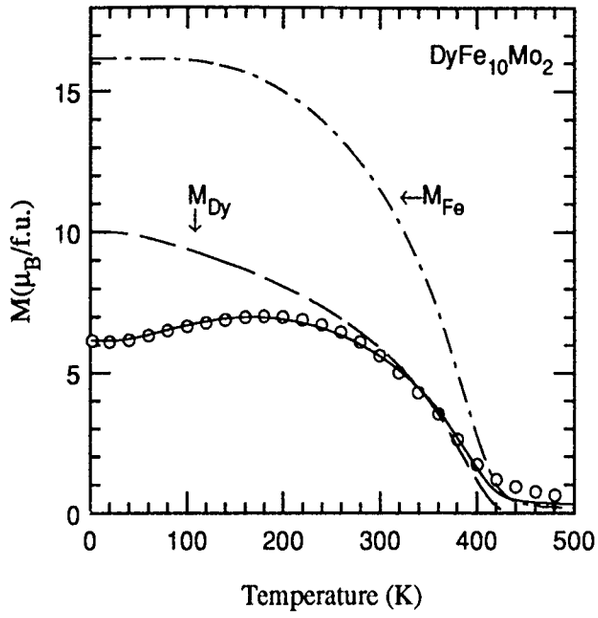

FIG 4. The temperature dependence of the magnetization of $DyFe_{10}Mo_2$ Circles represent experimental data. Lines represent MFT results.

Our calculations demonstrate that the two-sublattice MFT is quite successful in describing the temperature dependence of magnetization in the $RFe_{10}Mo_2$ series. The results also suggest that the moments of R and Fe sublattices are nearly collinear. In all instances, we found that n_{FF} is the largest of the computed molecular field coefficients (cf. Table I). This implies that the magnetic interactions are dominated by the exchange between $3d$ electrons. On the other hand, the strength of the R–R interaction cannot be neglected, as it has nearly the same magnitude as that of the R–Fe interaction. Such behavior seems to a common feature in a number of R–T compounds, for example, RFe_3,[2] R_2Co_{17},[5] $RFe_{10}V_2$,[7] and $R_2Fe_{14}B$.[8] These observations suggest that, in order to obtain a more realistic account of magnetic behavior in R–T intermetallic compounds, one may have to consider the effect of crystal field interactions on the R sites.

[1] K. Ohashi, T. Yokoyama, R Osugi, and Y. Tawara, IEEE Trans. Magn. **MAG-23**, 3101 (1987).
[2] J F. Herbst and J. J. Croat, J. Appl. Phys. **53**, 4304 (1982).
[3] E Belorizky, J. Appl. Phys **61**, 3971 (1987)
[4] Z. Liu, J. Magn Magn. Mater. **87**, 63 (1990)
[5] H S. Li, Z W. Zhang, and M. Z. Dang, J. Magn Magn. Mater. **75**, 159 (1988).
[6] Q. H. Qiao, Q Wang, X. P. Zhong, and H. L. Luo, J. Magn Magn. Mater. **110**, 170 (1992).
[7] H. Rui-Wang, Z. Zhong-Wu, H. Bin, K. Jian-Dong, Z. Zhi-Dong, X K Sun, and Y. C. Chuang, J. Magn Magn Mater. **119**, 180 (1993).
[8] L Huai-Shan, Z. Zhong-Wu, and D Mei-Zhen, J. Magn. Magn. Mater. **71**, 355 (1988).

Magnetic alignment in powder magnet processing

S. Liu
University of Dayton Research Institute, Dayton, Ohio 45469-0170

A strong magnetic field is used to align single-crystal powder particles in the process of producing sintered powder permanent magnets, including hard ferrites and rare-earth permanent magnets. The applied magnetic field aligns the easy direction of magnetization of each particle, owing to strong crystalline anisotropy. Shape anisotropy, existence of particles containing multigrains, and physical interlock between particles reduce the degree of alignment. This study provides a quantitative analysis of magnetic alignment in powder magnet processing. We assume (1) the powder particle is a single crystal; (2) it has the shape of an oblate spheroid and its short axis is the easy direction of magnetization; and (3) the applied magnetic field is strong enough to overcome the resistance of alignment. By applying the minimum-energy principle, it was concluded that the necessary and sufficient condition for a complete magnetic alignment is that the magnetocrystalline anisotropy constant K_1 of the particles is greater than its shape anisotropy constant K_s, provided the applied magnetic field is strong enough. When $K_s > K_1 + 2K_2$, the angle between the short axis of the oblate particle and the direction of applied magnetic field is 90°, and when $K_1 \leq K_s \leq K_1 + 2K_2$, the angle is $\arcsin\sqrt{(K_s - K_1)/2K_2}$.

The fabrication of powder magnet materials involves a complicated multistep process. For example, the production of high performance sintered $Sm_2(Co,Fe,Cu,Zr)_{17}$ permanent magnets involves seven major steps: melting and casting, homogenization, crushing and milling, magnetic alignment and compacting, sintering, solid solution treatment, and aging. Each step includes three or more process variables. A quantitative analysis of each step in powder magnet processing would lead to an insight into the physical and/or chemical processes involved in each step. This is not yet possible for all steps in the processes due to the complexity of the problem. Magnetic alignment is perhaps the simplest step in the whole processing procedure for producing powder magnets; therefore, it is possible to explore this step in some detail.

The most useful magnets are anisotropic with a single preferred axis of magnetization, requiring that the c axes of all grains in the sintered magnet are aligned parallel. This is achieved by applying a magnetic field strong enough to align the particles against the frictional force, and then compacting to immobilize them in this state. The crystal texture is maintained through the subsequent sintering and homogenizing if properly conducted.[1] Magnetic alignment is used to produce all types of anisotropic powder permanent magnets, including hard ferrites, $SmCo_5$, Sm_2TM_{17}, and Nd–Fe–B magnets.

If all particles are perfect single-crystal spheres, or if the long axes of all particles happen to be the easy direction of magnetization, then perfect alignment can be obtained, provided the applied magnetic field is strong enough. Obviously, the real case is more complicated. Shape anisotropy (if the long axis of a particle does not happen to be the easy direction of magnetization), the existence of particles containing multigrains, and the physical interlock between particles reduce the degree of alignment.

Assume (1) the powder particle is a single crystal; (2) it has the shape of an oblate spheroid and its short axis is the easy direction of magnetization; and (3) the applied magnetic field is strong enough to overcome the resistance of alignment. These assumptions are appropriate for several reasons. First, the size of the powder particle used for powder magnet production is usually in the range of 1–5 μm, far smaller than the grain size of the starting materials. Therefore, most powder particles can be considered single-crystal particles. Second, all powder magnet materials are of uniaxial crystal structure (hexagonal, rhombohedral, or tetragonal), and the basal plane is the most densely packed crystal plane. Breaking into particles having a shape similar to an oblate spheroid with its c axis to be the short axis rather than a prolate spheroid with its c axis to be the long axis during crushing and milling is an energetically favorable process. Actually, needle-like particles (prolate spheroid) are seldom observed for either hard ferrites or rare earth-transition metal alloys. Third, in practice, the applied magnetic field for powder alignment is either a dc magnetic field of 20–30 kOe or a pulse field of 70–100 kOe. These fields are proved strong enough to overcome any resistance of alignment.

When a magnetic field is applied, the shape anisotropy tends to align the long axis (a axis) parallel with the direction of the applied field. On the other hand, the crystalline anisotropy tends to align the short axis (c axis) parallel with the applied field. Obviously, the orientation of the particle in a given applied field is determined by the balance between the shape anisotropy energy and the crystalline anisotropy energy, rather than simply by the strength of the field. Suppose the angle between the c axis of the oblate particle and the direction of applied field H is ϕ, as shown in Fig. 1, the shape anisotropy energy, E_s, and the crystalline anisotropy energy, E_c, of the particle are

$$E_s = K_s \sin^2(90 - \phi) = K_s \cos^2 \phi, \tag{1}$$

$$E_c = K_1 \sin^2 \phi + K_2 \sin^4 \phi, \tag{2}$$

respectively, where K_s is the shape anisotropy constant and K_1 and K_2 are the crystalline anisotropy constants of a uniaxial crystal, which all powder magnets, including hard ferrites and rare earth magnets, belong to. The total energy of the system is

 0021-8979/94/76(10)/6757/3/$6 00 © 1994 American Institute of Physics

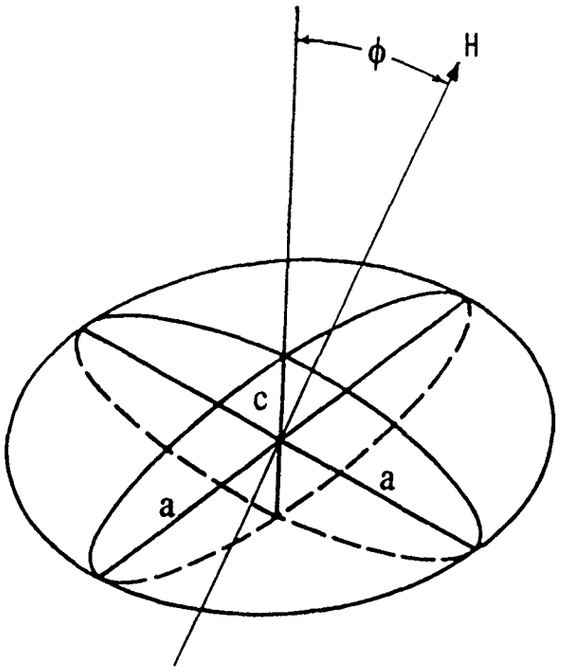

FIG. 1. Orientation of an oblate spheroid in a magnetic field.

$$E=E_c+E_s, \tag{3}$$

and the minimum energy condition requires

$$\frac{dE}{d\phi}=0. \tag{4}$$

Let us determine the angle ϕ corresponding to the minimum energy condition by the following two steps.

Step I. Considering only a single anisotropy constant, K_1.

In this case, Eq. (3) becomes

$$E=K_1 \sin^2 \phi+K_s \cos^2 \phi. \tag{5}$$

For the minimum energy condition, we have

$$\frac{dE}{d\phi}==K_1 \sin 2\phi-K_s \sin 2\phi=(K_1-K_s)\sin 2\phi=0. \tag{6}$$

If $K_1=K_s$, ϕ can have any value (but not only 45°, as common sense may lead to). If $K_1\neq K_s$, then $dE/d\phi=0$ when $\sin 2\phi=0$ or $\phi=0$ or 90°. In order to determine ϕ, corresponding to the minimum energy condition, the second derivative,

$$\frac{d^2E}{d\phi^2}=2(K_1-K_s)\cos 2\phi, \tag{7}$$

should be positive. If $K_1>K_s$, when $\phi=0°$, $\cos 2\phi=1$, and thus $d^2E/d\phi^2>0$. Therefore, E has the minimum value. If $K_1<K_s$, when $\phi=90°$, $\cos 2\phi=-1$, $d^2E/d\phi^2>0$, E also has the minimum value, as shown in Table I.

Step II. Taking into consideration both K_1 and K_2.

In this case, Eq. (3) becomes

$$E=(K_1-K_s)\sin^2 \phi+K_2 \sin^4 \phi+K_s. \tag{8}$$

TABLE I. Angle ϕ corresponding to the minimum energy condition.

K_2	Relation among K_s, K_1, and K_2	ϕ For minimum energy
$K_2=0$	$K_s=K_1$	any ϕ
	$K_s>K_1$	90°
	$K_s<K_1$	0°
$K_2>0$	$K_s>K_1+2K_2$	90°
	$K_s<K_1$	0°
	$K_1\leq K_s\leq K_1+2K_2$	$\arcsin\sqrt{(K_s-K_1)/2K_2}$

For a minimum energy condition, we have

$$\frac{dE}{d\phi}=(K_1-K_s)\sin 2\phi+2K_2 \sin^2 \phi \sin 2\phi=0. \tag{9}$$

It is obvious that the first two solutions of Eq. (9) are $\phi_1=0°$ and $\phi_2=90°$. In order to determine ϕ corresponding to the minimum energy, we calculate the secondary derivative,

$$\frac{d^2E}{d\phi^2}=2(K_1-K_s)\cos 2\phi+2K_2(\sin^2 2\phi +2 \sin^2 \phi \cos 2\phi). \tag{10}$$

If $K_1>K_s$, when $\phi=0°$, we have $\cos 2\phi=1$, $\sin 2\phi=0$, and $\sin^2 \phi=0$. So, $d^2E/d\phi^2>0$. Therefore, E has a minimum value. Substituting $\phi=90°$ into Eq. (10) yields

$$\frac{d^2E}{d\phi^2}=2[K_s-(K_1+2K_2)], \tag{11}$$

when $K_s>K_1+2K_2$, $d^2E/d\phi^2>0$. Thus, E has a minimum value.

If $\phi\neq0°$, $\phi\neq90°$, and $0°<\phi<90°$, then $\sin 2\phi\neq0°$, and Eq. (9) becomes

$$\frac{dE}{d\phi}=(K_1-K_s)+2K_2 \sin^2 \phi=0 \tag{12}$$

or

$$\sin^2 \phi=(K_s-K_1)/2K_2, \quad \phi=\arcsin\sqrt{(K_s-K_1)/2K_2}, \tag{13}$$

and obviously K_s must not be smaller than K_1, and K_s-K_1 must not be greater than $2K_2$. The secondary derivative of E, with respect to ϕ, should be evaluated at the angle ϕ for which $dE/d\phi=0$. It is obvious from Eq. (12) that

$$\frac{d^2E}{d\phi^2}=2K_2 \sin 2\phi. \tag{14}$$

When $0°<\phi<90°$ and $K_2>0$, $d^2E/d\phi^2>0$; thus E has a minimum value. The above results are summarized in Table I.

It is obvious that increasing the strength of the applied magnetic field only helps to overcome the resistance of alignment caused by the physical interlock between particles, but cannot align the powders unless $K_s<K_1$. In other words, the necessary and sufficient condition for a complete magnetic alignment is $K_s<K_1$, provided the applied magnetic field is strong enough. This conclusion was supported by our

TABLE II. Data summary for crystalline anisotropy constants of $(Sm_{1-x-y}Pr_xNd_y)_2(Co_{1-v}Fe_v)_{17}$ (10^6 erg/cm^3).

x	y	v	K_1	K_2	Reference
0	0	0	32		3
0	0	0.2	43		3
0	0	0.3	35	1.4	4
0	0	0.4	14		3
0	0.1	0.2	29		5
0	0.3	0.2	16		5
0	0.5	0.2	15		5
0	0.5	0.3	11		5
0.3	0	0.3	17		5

experiments of Nd, Pr substituted Sm_2TM_{17} permanent magnets. Table II summarizes crystalline anisotropy constant values for $(Sm_{1-x-y}Pr_xNd_y)_2(Co_{1-v}Fe_v)_{17}$. Table III lists the calculated demagnetizing factors and shape anisotropy constants for a oblate spheroid with various a/c ratios, r. Equations used for these calculation are as follows:[2]

$$N_c=4\pi r^2/(r^2-1)[1-\sqrt{1/(r^2-1)}\ \sin^{-1}\ \sqrt{r^2-1}/r, \tag{15}$$

$$N_a=0.5(4\pi-N_c), \tag{16}$$

$$K_s=0.5(N_c-N_a)M^2. \tag{17}$$

It can be seen from comparing Tables II and III that for magnet alloys of $(Sm_{1-x-y}Pr_xNd_y)_2(Co_{1-v}Fe_v)_{17}$ in most cases, $K_1 \gg K_s$. This means that crystalline anisotropy dominates. However, with further extensive increasing Fe substitution for Co, or with further extensive increasing Pr and/or Nd substitution for Sm, it is possible for K_1 to drop to a level lower than K_s. This would decrease the degree of alignment and reduce values of remanence, B_r, and the maximum energy product, $(BH)_{max}$, of the magnets. For powder permanent magnet materials with uniaxial crystal structure, the demagnetizing curves in the first quadrant are more or less like a straight line, and the slope of this line reflects the degree of powder alignment. What happens in the first quadrant demagnetizing process is that the magnetization vector in every grain (each individual grain was developed from one or more

TABLE III. Calculated demagnetizing factors and shape anisotropy constants (for $M=1000$ G).

r	N_c	N_a	K_s (10^6 rg/cm^3)
1.5	5.60	3 48	1 06
2	6 63	2.97	1.83
3	7.98	2.29	2.85
5	9.43	1.57	3.93
10	10.82	0 87	4.97
50	12.18	0.19	5.99
100	12 37	0.10	6 14
∞	4π	0	6.28

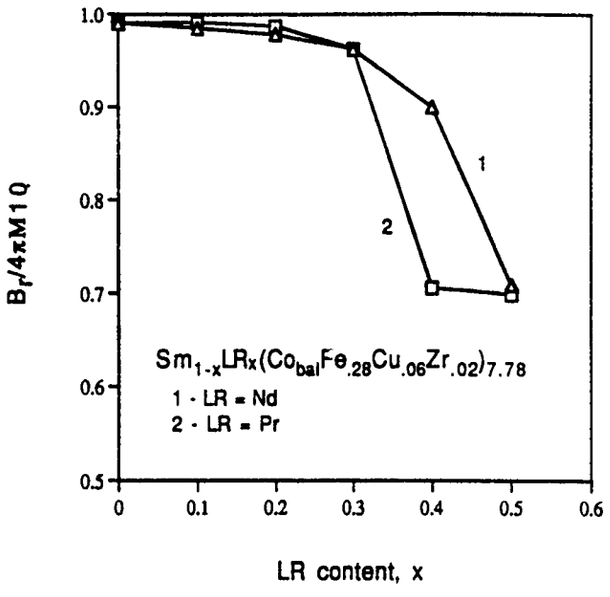

FIG. 2. Dependence of $B_r/4\pi M_{10}$ on LR content, x.

powder particles during the sintering process) turns back to the nearest easy magnetization direction. If the powder particles are perfectly aligned and this crystal texture is maintained during the sintering process, then the demagnetization curve in the first quadrant would be a straight line parallel to the horizontal axis, and the ratio of $B_r/4\pi M_s$ would be equal to 1. In another extreme, if the powder particles are of a completely random distribution, then, according to Chikazumi's calculation,[6] $B_r/4\pi M_s$ would be equal to 0.5. Therefore, for a material with uniaxial crystal structure, the ratio of $B_r/4\pi M_s$ should have a value ranging from 0.5 (corresponding to a completely random distribution) to 1.0 (corresponding to a perfect alignment). So, $B_r/4\pi M_s$ can serve as a good measure for the degree of particle alignment.

In practice, $4\pi M_{10}$, the magnetization value in a 10 kOe applied magnetic field, is a good approximation to $4\pi M_s$. Figure 2 shows the dependence of $B_r/4\pi M_{10}$ upon the light rare earth (LR) content, x, for $Sm_{1-x}LR_x(Co_{bal}Fe_{0.28}Cu_{0.06}Zr_{0.02})_{7.78}$ with LR=Nd or Pr. It can be seen from Fig. 2 that $B_r/4\pi M_{10}$ drops sharply when x exceeds 0.3. The author believes this indicates that the crystalline anisotropy constant K_1 is no longer greater than its shape anisotropy K_s when $x>0.3$ for this particular magnet composition.

[1] K. J. Strnat, in *Ferromagnetic Materials*, edited by E. P. Wohlfarth and K. H. J. Buschow (Elsevier, New York, 1988), Vol. 4, p. 180.
[2] B. D. Cullity, *Introduction to Magnetic Materials* (Addison–Wesley, Reading, MA, 1972), pp. 57, 243.
[3] R. S. Perkins, S. Gaffi, and A. Menth, IEEE Trans. Magn. **MAG-11**, 1431 (1975).
[4] R. W. Lee, IEEE Trans. Magn. **MAG-15**, 1762 (1979).
[5] C. J. Willman and K. S. V. L. Narasimhan, IEEE Trans. Magn. **MAG-21**, 1976 (1985).
[6] S. Chikazumi, *Physics of Magnetism* (Wiley, New York, 1964), p. 249

Sputter synthesis of $TbCu_7$ type Sm(CoFeCuZr) films with controlled easy axis orientation

H. Hegde, P. Samarasekara, R. Rani, A. Navarathna, K. Tracy, and F. J. Cadieu
Department of Physics, Queens College of CUNY, Flushing, New York 11367

Single phase $TbCu_7$ type films of Sm(CoFeCuZr) have been sputter synthesized for a range of sputter gas pressure, deposition temperature, and two different gas species: Ar and Ar50%Xe. The magnetic and crystallographic properties of these films as a function of sputter deposition parameters have been studied. Films synthesized at temperatures near their crystallization temperatures at sputter gas pressures exceeding 60 mTorr of Ar50%Xe, had a strong c-axis in-plane texture. The remanent magnetization ratio for measurement perpendicular to the film plane versus in plane was close to zero for such films. X-ray diffraction patterns of these films showed only (hk0) type reflections. At gas pressures around 30 mTorr predominant reflection was (111) type. The perpendicular to the in-plane B_R ratio for such films was around 0.55. For films with in-plane c-axis texture, in-plane B_r of 9.0 kGauss and coercivities in the range 3–10 kOe were possible. Pressures of Ar and Ar50%Xe correlated roughly in the ratio 1:2 for the synthesis of films, with comparable crystallographic and magnetic properties.

I. INTRODUCTION

Permanent magnets based on the $Sm_2(CoFeCuZr)_{17}$ rhombohedral 2-17 type structure are extremely attractive because of their high temperature stability, fairly high saturation moment, and energy product.[1,2] Such magnets consist of a cellular structure of 2-17 regions with $SmCo_5$ based grain boundaries to enhance the coercivity.[3] The magnetic properties of such two phase cellular structures are very sensitive to thermal treatments. In contrast to this, $TbCu_7$ type single phase film magnets that exhibit a high degree of in-plane c-axis texture and energy product have been sputter synthesized in recent years.[4] The $TbCu_7$ type films are single phase, whereas bulk samples of similar composition exhibit the cellular structure. The magnetic properties of the single phase sputtered film samples exhibit optimal magnetic properties as deposited and are very insensitive to subsequent thermal treatments. Such films are extremely important in applications involving magnetic biasing of magnetoresistive, magneto-optic, microwave devices, etc.[5–7] We have now studied the texture change and resultant change in magnetic properties of these permanent magnet $TbCu_7$ type films, as a function of their sputter deposition parameters.

II. EXPERIMENT

The films in the study were sputter synthesized from commercially available 2-17 bulk magnets of the type $Sm_2(CoFeCuZr)_{17}$. The films were deposited on polycrystalline Al_2O_3 substrates. The film thickness were generally in the 2 μ range. The deposition temperatures for all films in this study exceeded the minimum temperature required for their crystallization, so that they were directly crystallized as deposited, with no post deposition heat treatments required. Two varieties of sputter gases were used, 100% Ar, and equal mixtures of Ar and Xe referred to henceforth as Ar50%Xe. For all films in this study, the target to substrate distance was held constant at 5 cm. The crystal phase and film texture were determined with Cu K_α radiation by x-ray diffractometer measurements using a Si(Li) solid state detector to allow fluorescence discrimination. Magnetic measurements were performed using a VSM for fields up to 18 kOe. Film compositions were determined by electron excited x-ray fluorescence using a PGT System 4 Plus unit coupled to a scanning electron microscope.

III. RESULTS AND DISCUSSION

The Sm concentrations in the films were dependent on sputter gas species, pressure, and deposition temperature due to the high volatility of Sm and the preferential scattering of the low mass TM atoms out of the sputtered atom beam.[7] However, the relative concentrations of the TM atoms in the films were fairly constant, at 24, 9, 3, and 1 for Co, Fe, Cu, and Zr, respectively. These TM relative concentrations were about the same as in the target.

All films in this study exhibited the $TbCu_7$ type disordered crystalline phase, even though the target magnets were a 2-17 cellular based structure. For the deposition temperature range, 300 °C–475 °C, and Fe concentration used, the ordered 2-17 phase was not formed.[8] The crystallite c-axis orientation was found to depend on the deposition temperature, as shown in Fig. 1. At lower temperatures, the films were strongly c-axis in-plane textured. As the temperature was raised, the degree of in-plane texturing was reduced. Even with a modest increase in temperature of 55 °C, from the initial temperature of 345 °C, crystallites with the c axis oriented away from the film plane were observed, as indicated by (hkl) reflections, $l \neq 0$, in Fig. 1. As the net easy axis direction deviates from the film plane, the ratio of the remanent magnetic moments, in directions perpendicular to the film plane versus in-plane increases.[9] This is clearly seen from Fig. 3(a). For Ar50%Xe, at 60 mTorr pressure, this ratio is only 0.07 for a deposition temperature of 345 °C, increasing to 0.40 at 450 °C. However, for 100%Ar, at 60 mTorr pressure, the degree of the c-axis in-plane texturing was rather poor for all deposition temperatures tried. The texture change with pressure is shown in Fig. 2. At deposition temperature of 345 °C for sputter gas Ar50%Xe, the films could be formed with the c-axis in-plane texture at pressures of 60

 0021-8979/94/76(10)/6760/3/$6.00 © 1994 American Institute of Physics

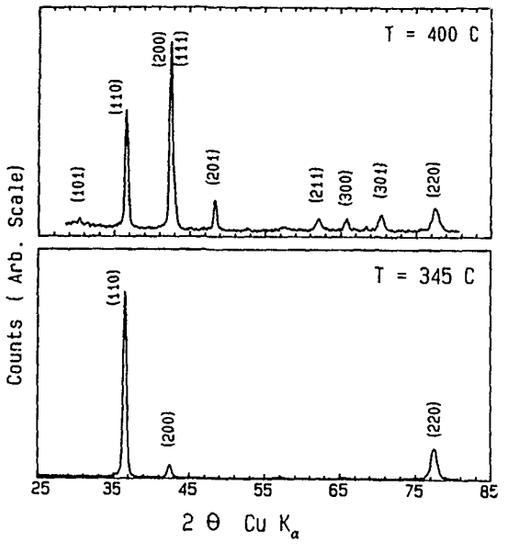

FIG. 1. The texture change with deposition temperature, for films synthesized in Ar50%Xe at 60 mTorr pressure. X-ray diffraction is using CuK_α radiation.

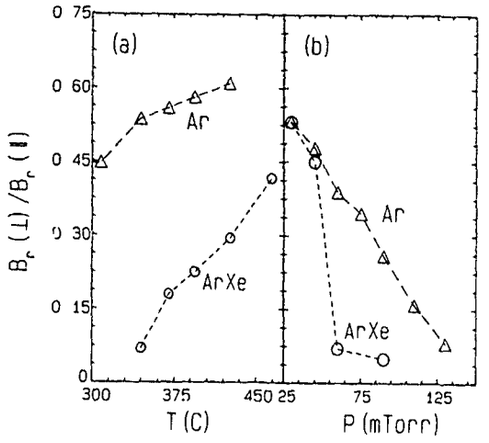

FIG. 3. Variations of ratios of remanent magnetizations perpendicular to the film plane to that in plane for films synthesized in 100%Ar and Ar50%Xe. (a) Variation with temperature at 60 mTorr pressure. (b) Variation with pressure at temperature 345 °C.

mTorr and above. For sputter gas 100%Ar, a similar pure in-plane texture could only be obtained at pressures exceeding 120 mTorr. In terms of texture control, this suggests that 60 mTorr of Ar50%Xe is equivalent to about 120 mTorr of Ar.

The film magnetic properties and their Sm at. % are shown in Fig. 4 and Fig. 5. The coercivities of the films are found to be strongly correlated to the film Sm concentration. This is attributable to the increase in the magnetocrystalline anisotropy of the 1-7 phase with Sm concentration. However, a fairly significant departure in the correlated behavior of Sm at. % and coercivity is observable for films formed at pressures below 45 mTorr, Fig. 5. This is due to defects caused by increased energy bombardment of the growing film at lower pressures. Previous calculations have shown that to completely thermalize the sputtered atoms, the pressures required are around 60 mTorr of Ar50%Xe.[10] The rather sharp deviation of coercivity from its correlated behavior with Sm at. %, in Fig. 4, below 345 °C, is attributable to incomplete crystallization of the film. High resolution SEM studies of the films have not revealed any type of cellular structure, as observed in bulk 2-17 type magnets.

No attempt to saturate the film magnetization was made, due to the large fields required. However, the $4\pi M_s$ values of the films are expected to decrease with increased Sm concentration. For films sputtered in Ar50%Xe, the film Sm at. % is given in Fig. 4, and Fig. 5, as a function of deposition temperature at 60 mTorr pressure and as a function of gas pressure at a deposition temperature of 345 °C. Figure 4 and Fig. 5 also show the remanance B_r, energy product

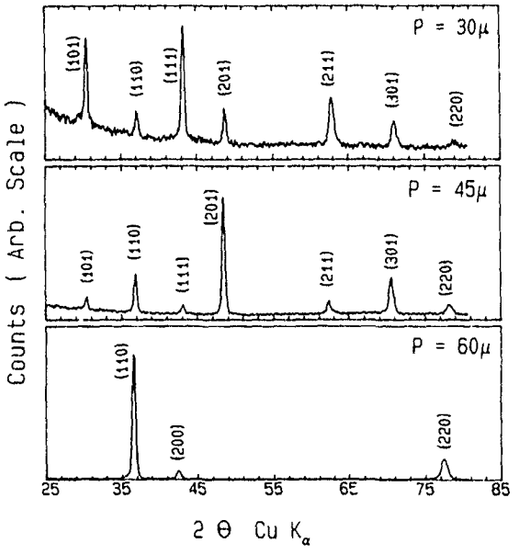

FIG. 2. The texture change with pressure, for films synthesized in Ar50%Xe at 345 °C. X-ray diffraction is using Cu K_α radiation.

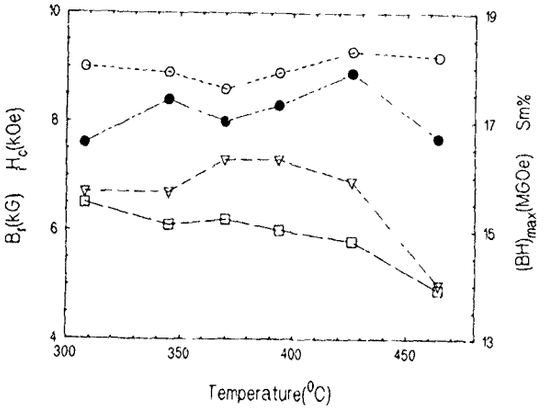

FIG. 4. Variation with deposition temperature, of remanent magnetization B_R (open circle), coercivity H_c (triangle), energy product BH_{max} (shaded circle), and Sm at. % (square) Magnetic measurements are in the film plane Films synthesized in Ar50%Xe, at 60 mTorr.

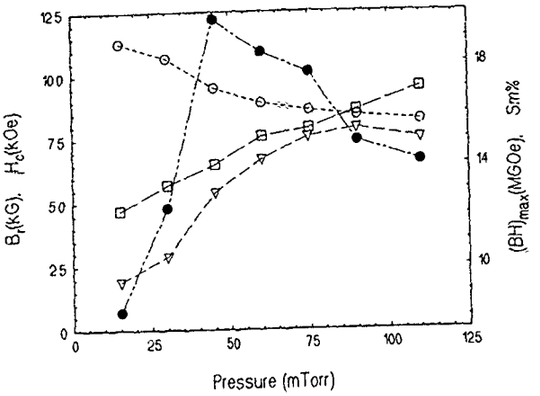

FIG. 5. Variation with pressure, of remanent magnetization B_R (open circle), coercivity $_iH_c$ (triangle), energy product BH_{max} (shaded circle), and Sm at. % (square). Magnetic measurements are in the film plane. Films synthesized in Ar50%Xe, at 345 °C.

BH_{max}, and coercivity $_iH_c$, for magnetic measurements made in the film plane. From Fig. 4, the remanance is seen to be fairly constant, with respect to deposition temperature. It appears that at higher deposition temperatures, the increase in the saturation moment is offset by the lower degree of in-plane c-axis texturing. The energy product BH_{max} is seen to be fairly constant at a reasonably large value around 18 MGOe, for the entire temperature range at this pressure. The energy product, BH_{max}, of the films is sharply dependent on the gas pressure, Fig. 5. In fact, the best energy products, in excess of 18 MGOe, are obtainable in only a narrow pressure range from 45 to 75 mTorr.

For films sputtered in Ar at pressures around 120 mTorr, the general variation of texturing with temperature was similar to that of films sputtered at 60 mTorr of Ar50%Xe, showing the pressure equivalence of these different gas species, in terms of their thermalization efficiency.

In conclusion, the magnetic properties and texture control of sputter synthesized $TbCu_7$ type permanent magnet films have been studied in terms of their sputter deposition parameters. The sputtering parameters for the best in-plane c-axis texture, the optimum energy products, and coercivity have been identified. The pressure equivalence of two types of gas species in terms of their thermalization efficacy has been established

ACKNOWLEDGMENT

This work was supported by the AFOSR.

[1] K. Kumar, J. Appl. Phys. **63**, R13 (1988).
[2] R. K. Mishra, G. Thomas, T. Yoneyama, A. Fukuno, and T. Ojima, J. Appl. Phys. **52**, 2517 (1981).
[3] G. C. Hadjipanayis, J. Appl. Phys **55**, 2091 (1984)
[4] F. J. Cadieu, H. Hegde, and K Chen, J Appl. Phys. **67**, 4969 (1990).
[5] H. Hegde, S. U. Jen, K Chen, and F. J Cadieu, J Appl. Phys. **73**, 5926 (1993).
[6] M. Levy, R. Scarmozzino, R. M. Osgood, Jr., R. Wolfe, F. J. Cadieu, H Hegde, C. J. Gutierrez, and G. A. Prinz, J. Appl. Phys. **73**, 5926 (1994).
[7] F. J. Cadieu, H. Hegde, E. Schloemann, and H J. Van Hook, Paper AB-11 (these proceedings).
[8] H. Hegde, K. Chen, and F. J Cadieu, J Appl. Phys. **69**, 5850 (1990)
[9] F. J. Cadieu, *Permanent Magnet Thin Films*, Physics of Thin Films, Vol 16 (Academic, San Diego, 1992).
[10] F. J. Cadieu, H. Hegde, and K. Chen, Thin Solid Films **193/194**, 875 (1990).

Metastable $Nd_2(Fe_{1-x}Co_x)_{23}B_3$ ($0 \leq x \leq 1.0$) compounds with the 2:23:3-type structure

Bao-gen Shen, Bo Zhang, Fang-wei Wang, Jun-xian Zhang, Bing Liang, Wen-shan Zhan, Hui-qun Guo, and Jian-gao Zhao
State Key Laboratory of Magnetism, Institute of Physics, Chinese Academy of Sciences, P.O. Box 603, Beijing 100080, People's Republic of China

Amorphous $Nd_2(Fe_{1-x}Co_x)_{23}B_3$ ($0 \leq x \leq 1.0$) alloys were prepared by melt spinning at a speed of 47 m/s. When the amorphous samples were annealed at 900 K for 20 min, they crystallized to the metastable 2:23:3 single phase for all x. A detailed study of structure and magnetic properties of metastable $Nd_2(Fe_{1-x}Co_x)_{23}B_3$ compounds has been made by x-ray diffraction and magnetization measurements. They are body-centered cubic, and the lattice constant decreases linearly from $a=14.16$ Å for $x=0$ to 13.86 Å for $x=1.0$. The Fe atom moment $\bar{\mu}_{Fe}$ for $Nd_2(Fe_{1-x}Co_x)_{23}B_3$ was found to increase with x from $2.02\mu_B$ for $x=0$ to $2.17\mu_B$ for $x=0.8$, when the Co atom moment $\bar{\mu}_{Co}$ is assumed to be constant, as made in previous papers for crystalline Fe–Co alloys. The Curie temperature T_c is found to increase monotonically with increasing x from 659 K for $x=0$ to about 1218 K for $x=1.0$. The thermomagnetic measurements showed that when the $Nd_2(Fe_{1-x}Co_x)_{23}B_3$ compounds were heated to certain temperatures, they decomposed to $Nd_2(Fe,Co)_{14}B$ and α-(Fe,Co) phases. The decomposition temperature of metastable compounds was about 990±15 K, and was almost independent of the Co concentration x.

I. INTRODUCTION

Since the discovery of the Nd–Fe–B permanent magnet materials, a number of investigations on rapidly quenched Nd–Fe–B ternary alloys systems have been reported. Most of these studies focus on their hard magnetic properties, while the investigations on crystallization behaviors and magnetic properties of amorphous Nd–Fe–B alloys are relatively fewer. Buschow *et al.*[1] studied the crystallization of amorphous alloys of Fe-rich composition in the Nd–Fe–B system, and found a novel ternary compound $Nd_2Fe_{23}B_3$. The compound is metastable magnetic. Its crystal structure is body-centered cubic, space group $I\bar{4}3d$, the lattice constant $a=14.19$ Å.[2] Shen *et al.*[3] have prepared amorphous alloys in a wide composition range of the Nd–Fe–B system, and studied the phase diagram of crystallization and magnetic properties of the metastable phase. A study of crystalline phases of amorphous $Nd_2Fe_{23}B_3$ and the formation and magnetic properties of metastable $Nd_2Fe_{23}B_3$ compound has been made using x-ray diffraction and magnetization measurements.[4] Gou *et al.*[5] have reported the powder neutron diffraction study of magnetic structure of metastable $Nd_2Fe_{23}B_3$ compound. In order to obtain more information about the structure and magnetic properties of metastable compound, we have studied the effect of the substitution of Co for Fe on the crystal structure and magnetic properties of $Nd_2Fe_{23}B_3$ compound. In this paper, some results of the investigation are reported.

II. EXPERIMENTAL

Iron (purity, 99.9%), cobalt (purity, 99.9%), neodymium (purity, 99.9%) and Fe–B alloy (purity, 98.6%) were melted by arc melting in an argon atmosphere of high purity into homogeneous buttons with the compositions $Nd_2(Fe_{1-x}Co_x)_{23}B_3$ ($x=0$, 0.2, 0.4, 0.6, 0.8, and 1.0). Amorphous ribbons about 1 mm wide and 20 μm thick were prepared by melt spinning in an argon atmosphere in a polished Cu drum of 20 cm diam with a speed of about 47 m/s and were then annealed in a steel tube in a vacuum of 10^{-5} Torr at different temperatures and times.

X-ray diffraction measurements were performed on the annealed ribbons using Co K_α radiation to identify the phase components and determine the crystallographic structure. The Curie temperature T_c of the compounds were determined from the temperature dependence of magnetization. High-field magnetization measurements at 1.5 K were made on these samples using an extracting sample magnetometer in fields ranging from 0 to 65 kOe.

III. RESULTS AND DISCUSSION

The $Nd_2(Fe_{1-x}Co_x)_{23}B_3$ alloys prepared at a speed of 47 m/s were amorphous, and its x-ray diffraction pattern exhibited a diffuse broad maximum. The amorphous ribbons annealed at different temperatures of higher than their crystallization temperature produced different crystalline phases. For the annealing temperature of about 900 K, the amorphous samples crystallized to the metastable $Nd_2(Fe,Co)_{23}B_3$ phase. When the annealing temperature was higher than 925 K, the α-(Fe,Co) phase appeared, coexisting with the $Nd_2(Fe,Co)_{23}B_3$ phase.

Figure 1 shows an example of the x-ray diffraction patterns of $Nd_2(Fe_{1-x}Co_x)_{23}B_3$ ($x=0.2$ and 1.0) after annealing at 900 K for 20 min. It is found that with increasing Co concentration, the diffraction line was shifted to higher angles, indicating that the lattice constants decrease with x. The present study shows that the substitution of Co for Fe in the $Nd_2Fe_{23}B_3$ compound does not change its crystal structure. The complete substitution obtains a new single-phase compound of $Nd_2Co_{23}B_3$. The crystal structure of the $Nd_2(Fe,Co)_{23}B_3$ compound is body-centered cubic, space group $I\bar{4}3d$. The lattice constant calculated from the x-ray

 0021-8979/94/76(10)/6763/3/$6.00 © 1994 American Institute of Physics

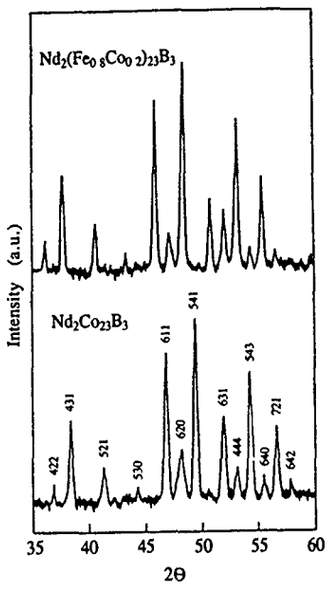

FIG. 1. X-ray diffraction patterns of metastable $Nd_2(Fe_{1-x}Co_x)_{23}B_3$ compounds with $x=0.2$ and 1.0.

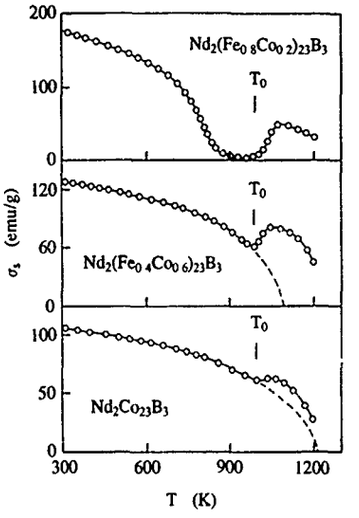

FIG. 2. Temperature dependence of the saturation magnetization σ_s of $Nd_2(Fe_{1-x}Co_x)_{23}B_3$ compounds with $x=0.2$, 0.6, and 1.0.

diffraction patterns are found to decrease linearly from $a=14.16$ Å for $x=0$ to 13.86 Å for $x=1.0$, as shown in Table I.

X-ray diffraction and thermomagnetic measurements showed that the $Nd_2(Fe,Co)_{23}B_3$ compounds obtained by the crystallization from corresponding amorphous alloys were metastable. When the compounds were heated to certain temperature T_0, as shown in Fig. 2, they decomposed to $Nd_2(Fe,Co)_{14}B$ and α-(Fe,Co) phases. The decomposition temperature of the metastable compounds was about 990 ± 15 K, and was almost independent of the Co concentration x.

Figure 3 shows the magnetization σ of metastable $Nd_2(Fe_{1-x}Co_x)_{23}B_3$ compounds at 1.5 K as a function of the external field H. The spontaneous magnetization $\sigma_s(1.5)$ at 1.5 K were obtained by a liner extrapolation of magnetization curves to $H=0$. The $\sigma_s(1.5)$ shows a monotonic decrease with increasing Co concentration from 184 emu/g to 113 emu/g as x increases from 0 to 1.0, as shown in Table I. A similar result was observed in other Fe–Co-based alloys.[6]

The magnetic moment per unit formula μ_s of $Nd_2(Fe_{1-x}Co_x)_{23}B_3$ compounds is shown in Fig. 4(a) as a function of Co concentration x. The μ_s is found to decrease from $52.9\mu_B$ for $x=0$ to $33.9\mu_B$ for $x=1.0$. If the magnetic moment of the Nd atom $\bar{\mu}_{Nd}$ is suggested to be $3.27\mu_B$, which is the moment of a free Nd^{3+} ion, the average magnetic moment $\bar{\mu}_{Fe+Co}$ per Fe+Co atom can be obtained, according to $\mu_s=23\bar{\mu}_{Fe+Co}+2\bar{\mu}_{Nd}$. The composition dependence of the average moment $\bar{\mu}_{Fe+Co}$ may be written as $\bar{\mu}_{Fe+Co}=\bar{\mu}_{Fe}(1-x)+\bar{\mu}_{Co}x$, where $\bar{\mu}_{Fe}$ and $\bar{\mu}_{Co}$ are the effective magnetic moments per the Fe atom and the Co atom, respectively. A study of Collins *et al.*[7] on the crystalline Fe–Co alloys using polarized neutron diffraction demonstrated that the average moment $\bar{\mu}_{Fe}$ per Fe atom increases with increasing Co concentration, and the average moment $\bar{\mu}_{Co}$ per Co atom remains an essential value. Similar results were found in other Fe–Co-based alloys.[8] If $\bar{\mu}_{Co}$ of $Nd_2(Fe_{1-x}Co_x)_{23}B_3$ is assumed to keep the constant value of $1.20\mu_B$ (the value of $\bar{\mu}_{Co}$ in $Nd_2Co_{23}B_3$ compound), the $\bar{\mu}_{Fe}$ is found to rise with increasing Co concentration from $2.02\mu_B$ for $x=0$ to $2.17\mu_B$ for $x=0.8$.

TABLE I. The lattice constant a, saturation magnetization σ_s at 1.5 K and the Curie temperature T_c of $Nd_2(Fe_{1-x}Co_x)_{23}B_3$ compounds.

x	a (Å)	σ_s (emu/g)	T_c (K)
0.0	14.16	184	659
0.2	14.11	177	831
0.4	14.06	162	~978
0.6	13.99	146	~1097
0.8	13.90	129	~1156
1.0	13.86	113	~1218

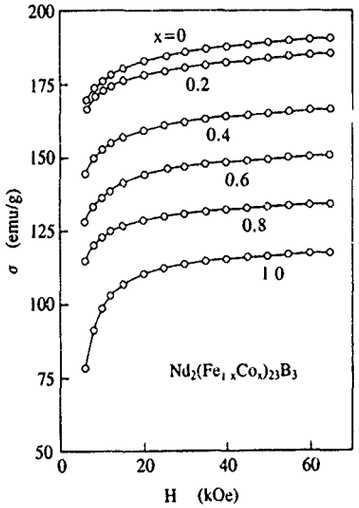

FIG. 3. Magnetization curves of $Nd_2(Fe_{1-x}Co_x)_{23}B_3$ compounds.

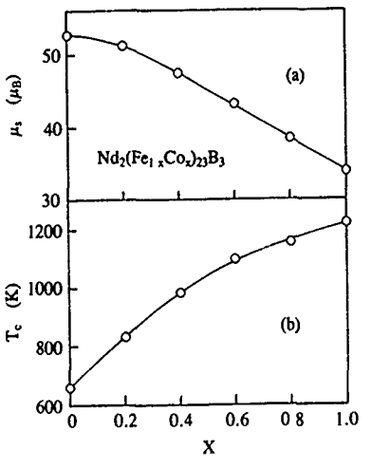

FIG. 4. The magnetic moment per unit formula μ_s at 1.5 K (a) and the Curie temperature T_c (b) of $Nd_2(Fe_{1-x}Co_x)_{23}B_3$ compounds as a function of Co concentration x.

The temperature dependence of the saturation magnetization σ_s of $Nd_2(Fe_{1-x}Co_x)_{23}B_3$ compounds with $x=0.2$, 0.6, and 1.0 is shown in Fig. 2. For $x \geq 4$, the Curie temperature T_c of the metastable compounds was higher than the decomposition temperature. The T_c of the samples was obtained by linear extrapolation of the squared magnetization σ_s^2 versus temperature curves to $\sigma_s^2=0$. Figure 4(b) and Table I show the Curie temperature of $Nd_2(Fe_{1-x}Co_x)_{23}B_3$ compounds as a function of Co concentration. The T_c was found to increase monotonically from 659 K for $x=0$ to about 1218 K for $x=1.0$. The variation of T_c with x was different from that of the crystalline Fe–Co alloys and some amorphous Fe–Co-based alloys,[6,8] in which T_c showed a maximum value. According to the average molecular-field model, the Curie temperature is directly proportional to the exchange interactions between magnetic atoms and the number of nearest-neighbor magnetic atoms. For $Nd_2(Fe_{1-x}Co_x)_{23}B_3$, the T_c depends mainly on Fe–Fe exchange interactions for the Fe-rich region or Co–Co exchange interactions for the Co-rich region. The strong increase of T_c with x for $Nd_2(Fe_{1-x}Co_x)_{23}B_3$ compounds indicated that the contribution of the exchange interactions between the Co–Co atom on T_c was much larger than that between Fe–Fe atoms.

ACKNOWLEDGMENT

This work was supported by the National Natural Science Foundation of China.

[1] K. H. J. Buschow, D. B. de Mooij, and H. M. van Noort, J. Less-Common Met. **125**, 135 (1986).
[2] D. B. de Mooij and K. H. J Buschow, Philips J. Res. **41**, 400 (1986).
[3] B. G. Shen and L. Y. Yang, Prog. Nat. Sci. **3**, 130 (1993).
[4] B. G. Shen, L. Y. Yang, L. Cao, H. Y. Yang, J. G Zhao, and F. M. Yang, J. Magn. Magn. Mater. **104–107**, 1281 (1992).
[5] C. Gou, Z. X. Cheng, D. F. Chen, S. W. Niu, Q. W. Yan, P. L. Zhang, B. G. Shen, and L. Y. Yang, J. Magn. Magn. Mater. **128**, 26 (1993).
[6] B. G. Shen, L. C. Cao, and H. Q. Guo, J. Appl. Phys. **73**, 5730 (1993).
[7] M. F. Collins and J. B. Forsyth, Philos. Mag. **8**, 401 (1963).
[8] B. G. Shen, L. Y. Yang, J. Z. Liang, and H. Q. Guo, J. Phys. Condens. Matter **4**, 7247 (1992).

Magnetic properties of $(Nd_{0.9}R_{0.1})_5Fe_{17}$ with R=Sm, Gd, and Y

Cong-Xiao Liu, Yun-Xi Sun, Zun-Xiao Liu, and Chin Lin
Department of Physics, Peking University, Beijing, People's Republic of China

Magnetic properties of $(Nd_{0.9}R_{0.1})_5Fe_{17}$ have been investigated. Samples were prepared by arc melting and annealed at 600 °C for 48 days. X-ray diffraction and thermomagnetic analyses showed that the samples are almost single phase with the Nd_5Fe_{17} structure when R=Sm, Gd, and Y, but this structure cannot be formed when R=Pr. The effects of R substitution on saturation magnetization, Curie temperature, and lattice parameters are reported. X-ray diffraction analyses of aligned powders suggests that these samples have basal plane anisotropy. The magnetization does not fully saturate along the field in a field up to 70 kOe although the magnetization curves show the characteristic behavior of a soft ferromagnetic material.

I. INTRODUCTION

Recently, a revised Nd–Fe phase diagram, including the new stable phase Nd_5Fe_{17}, was reported.[1] The crystal structure of Nd_5Fe_{17} belongs to the hexagonal space group $P6_3/mcm$, with 12 formula units per cell.[2–4] Magnetic measurements[5,6] showed that Nd_5Fe_{17} is a ferromagnet with T_c=503 K and saturation magnetization 162 emu/g at 4.2 K. Mossbauer spectra[5] were fitted with five Fe sites, yielding an average B_{eff}=30.7 T at 10 K, from which an average Fe moment of 2.12 μ_B is deduced. X-ray diffraction analyses of magnetically aligned powders suggest basal plane anisotropy. This compound is not considered to be a promising permanent magnetic material.[6] On the other hand, a high coercivity Sm–Fe–Ti phase was produced by sputtering,[7,8] mechanical alloying,[9] and melt spinning.[10] This Sm–Fe–Ti phase was identified as having the Nd_5Fe_{17} structure by x-ray indexing.[4] The substitution of V and Ti for approximately 10% of Fe yields a systematic expansion of the unit-cell volume.[11] Binary Sm_5Fe_{17} was also synthesized.[11] Because the Stevens factor α_J is of a different sign for Sm and for Nd, Sm_5Fe_{17} has uniaxial anisotropy. Magnetically hard $Sm_5(Fe, Co, Ti)_{17}$ phases have been synthesized by a conventional powder metallurgical method.[12] $Sm_5(Fe_{0.94}Ti_{0.06})_{17}$ showed a room-temperature coercivity $_jH_c$=21.5 kOe. In this work, we substitute 10% of Nd in Nd_5Fe_{17} by other rare earth elements and investigate their structural and magnetic properties.

II. EXPERIMENT

Samples were prepared by arc melting $(Nd_{0.9}R_{0.1})$ and Fe in the proportion of 1 to 3 under a purified argon atmosphere, with R=Nd, Pr, Sm, Gd, and Y. The samples were annealed in vacuum at 600 °C for 48 days. Structural analyses were carried out on powdered samples with a Rigaku D/MAX-RB diffractometer using Cu K_α radiation. X-ray diffraction and thermomagnetic analyses showed that the samples are almost single phase with the Nd_5Fe_{17} structure when R=Nd, Sm, Gd, and Y. Small amounts of metallic rare earth elements and R_2Fe_{17} were found in some samples. The Nd_5Fe_{17} structure could not formed when 10% of the Nd was substituted by Pr.

Magnetic measurements were performed with an extraction magnetometer, in a field up to 70 kOe on bulk polycrystalline samples. Powdered samples were aligned in a field of 10 kOe at room temperature and fixed in epoxy resin. The easy magnetization direction was determined by x-ray diffraction analyses of aligned powders. Thermomagnetic

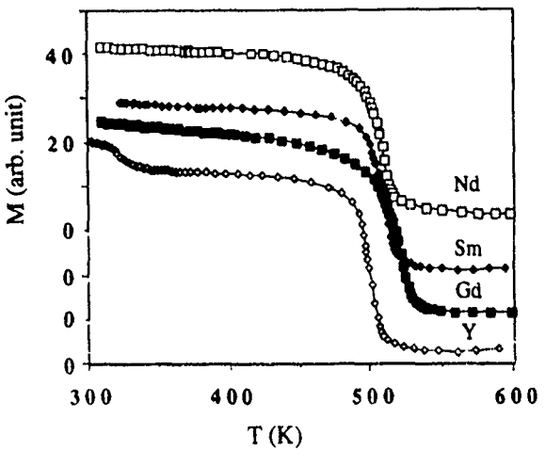

FIG. 1. Thermomagnetic curves of $(Nd_{0.9}R_{0.1})_5Fe_{17}$ with R=Nd, Sm, Gd, and Y.

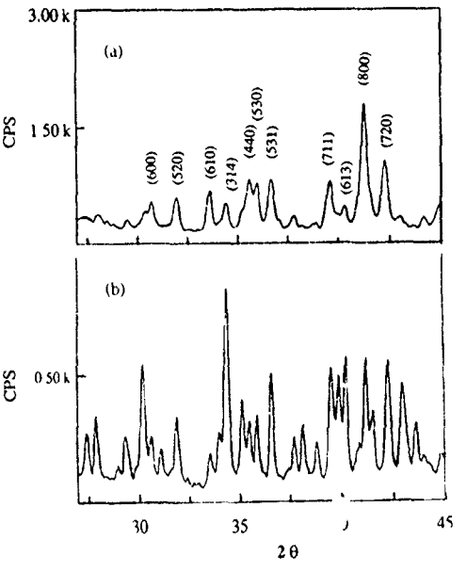

FIG. 2 X-ray diffraction patterns of $(Nd_{0.9}Sm_{0.1})_5Fe_{17}$ (a) Magnetically aligned, (b) random powder.

 0021-8979/94/76(10)/6766/3/$6.00 © 1994 American Institute of Physics

TABLE I. Lattice parameters, Curie temperature and saturation magnetization at 1.5 K.

	a(Å)	c(Å)	T_c(K)	$M_s(\mu_B/fu)$
Nd_5Fe_{17}	20.207	12.341	507	48.2
$(Nd_{0.9}Sm_{0.1})_5Fe_{17}$	20.204	12.354	508	48.9
$(Nd_{0.9}Gd_{0.1})_5Fe_{17}$	20.226	12 348	526	43.7
$(Nd_{0.9}Y_{0.1})_5Fe_{17}$	20.207	12 354	499	47.5

curves at temperatures higher than room temperature were measured by a vibrating sample magnetometer operating at a low field. The Curie temperature was determined by plotting M^2 vs T near T_c and extrapolating the linear part to $M=0$. It may be slightly higher than that determined by the "kink-point" method.[2]

III. RESULTS AND DISCUSSION

Thermomagnetic curves of $(Nd_{0.9}R_{0.1})_5Fe_{17}$ with R=Nd, Sm, Gd, and Y are shown in Fig. 1. Gd substitution increases T_c slightly and Y substitution decreases T_c. A small amount of R_2Fe_{17} is observed in the Y-substituted sample. X-ray diffraction patterns of magnetically aligned and random powder $(Nd_{0.9}Sm_{0.1})_5Fe_{17}$ are shown in Figs. 2(a) and 2(b), respectively. The intensity of the (314) reflection, which is the strongest in random powders, is reduced in aligned powders. The intensities of (hkl) with $l=0$ are enhanced. The (004) and (006) reflections are still weak. This suggests that the sample has basal plane anisotropy. Similar results were obtained for Gd and Y substituted samples. Lattice parameters and Curie temperatures of these samples are listed in Table I.

The initial composition of these samples is off-stoichiometric. However, considering that there is negligible loss in weight in the arc melting, the materials should have rare earth metals, as in the starting composition. Nd, Sm, and Gd are antiferromagnetic ordering at 1.5 K. Their contributions to magnetization are negligible in our experiments, so that the magnetizations of $(Nd_{0.9}R_{0.1})_5Fe_{17}$ are deduced from the measured values. The magnetization curve and the magnetic hysteresis loop in the second quadrant for Nd_5Fe_{17} at

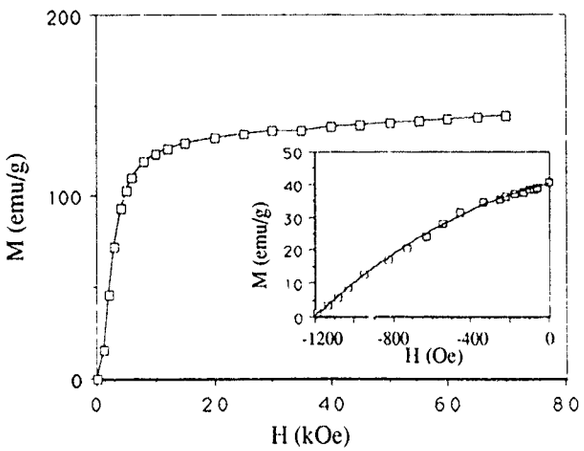

FIG. 3. Magnetization curve at 1.5 K for Nd_5Fe_{17}. The inset is the magnetic hysteresis loop in the second quadrant.

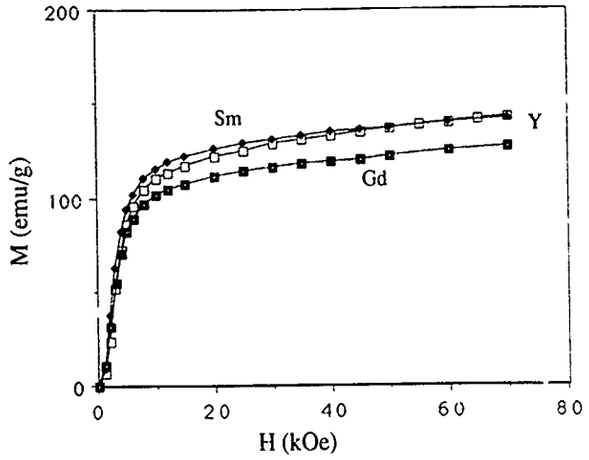

FIG. 4. Magnetization curves at 1.5 K for $(Nd_{0.9}R_{0.1})_5Fe_{17}$, with R=Sm, Y, and Gd.

1.5 K are shown in Fig. 3. Magnetization curves at 1.5 K for $(Nd_{0.9}R_{0.1})_5Fe_{17}$ with R=Sm, Y, and Gd are shown in Fig. 4. The samples do not fully saturate along the field in a field up to 70 kOe, due to the large in-plane magnetocrystalline anisotropy. The saturation magnetization M_s was deduced by fitting the data to a law of the type

$$M=M_s(1-a/H-b/H^2).$$

The results are also listed in Table I. Y has no magnetic moment. The magnetic moment of Gd is $7\mu_B$. If we take the average Fe moment to be $2.17\mu_B$,[5] and Nd moment $2.44\mu_B$, the effects of Y and Gd substitution are in agreement with the calculated values of M_s.

Our results show that although only 10% of the Nd is substituted, the effects are evident. The substitution of Pr destroys the Nd_5Fe_{17} structure. Y lowers the stability of the structure, the R_2Fe_{17} phase appears. Gd has the largest de Gennes factor. It enhances T_c but decreases magnetization, due to the antiferromagnetic coupling between Gd and Fe. The formation of quasibinary $(Nd,Sm)_5Fe_{17}$ reveals a possibility that a uniaxial anisotropy could be obtained by increasing the substitution of Sm for Nd. Further investigations are in progress.

ACKNOWLEDGMENTS

The project is supported by the National Natural Science Foundation. We are grateful to Professor Shun-Ying Chen for x-ray diffraction experiments.

[1] F. J. G. Landgraf, G. Schneider, V. Villas-Boas, and F. P. Missell, J. Less-Common Met. **163**, 209 (1990).
[2] G. Schneider, F. J. G Landgraf, V Villas-Boas, G. H. Bezerra, F. P. Missell, and A. E. Ray, Mater. Lett. **8**, 472 (1989).
[3] J. M. Moreau, L. Paccard, J. P. Nozieres, F. P. Missell, G. Schneider, and V. Villas-Boas, J. Less-Common Met. **163**, 245 (1990)
[4] H. H. Stadelmaier, G. Schneider, E.-Th. Henig, and M. Ellner, Mater. Lett. **10**, 303 (1991).
[5] J. P. Nozieres and H. R. Rechenberg, Solid State Commun. **79**, 21 (1991).
[6] F. J. G. Landgraf, F. P. Missell, H. R. Rechenberg, G. Schneider, V. Villas-Boas, J. M. Moreau, L. Paccard, and J. P. Nozieres, J Appl. Phys. **70**, 6125 (1991).

[7]N. Kamprath, N. C. Liu, H. Hegde, and F J. Cadieu, J. Appl. Phys. **64**, 5720 (1988).
[8]N. Kamprath, X. R. Qian, H. Hegde, and F. J. Cadieu, J. Appl. Phys. **67**, 4948 (1990).
[9]K. Schnitzke, L. Schultz, J. Wecker, and M. Katter, Appl. Phys. Lett. **56**, 587 (1990).
[10]M. Katter, J. Wecker, and L. Schultz, Appl. Phys. Lett. **56**, 1377 (1990).
[11]F. J. Cadieu, H. Hegde, R Rani, A. Navarathna, and K. Chen, Mater. Lett. **11**, 284 (1991).
[12]M. Q. Huang, S. Simizu, K. Miller, and W. E. Wallace, J. Appl. Phys. **73**, 5902 (1993).

New permanent magnetic MnBiDy alloy films

Fang Ruiyi, Fang Qingqing, Zhang Sheng, Peng Chubing, and Dai Daosheng
Department of Physics, Peking University, Beijing 100871, China

We have studied the magnetic properties of MnBiDy films fabricated by the thermal coevaporation method and annealed subsequently in a vacuum oven at temperatures of 350 °C–425 °C. The thicknesses of these films are in the range from 60 to 1200 nm. X-ray diffraction analyses have confirmed that those samples have an hcp structure. Magnetic measurements revealed that the saturation magnetization σ_s=46–78 emu/g, remanence ratio R=0.67–0.98, coercive force μHc=2.2–7.3 kOe, and magnetic energy product $(BH)m$=3.3–14.3 MGOe. These values are sensitive to the film thicknesses. It was found that μHc reaches a maximum at $d\approx$400 nm.

I. INTRODUCTION

Recently, studies on the permanent magnet films are concentrated on rare earth-transition metal compounds and alloys. The films of $SmCo_5$ and SmCo-based systems exhibit very high in-plane anisotropy, and high magnetic energy products about 21 MGOe.[11] In Sm–Co 2:17-type films, the energy product can reach 20 MGOe.[2] NdFeB films have a high intrinsic coercive force with an energy product about 12 MGOe,[3] but with a relatively low Curie temperature. The Sm_1Fe_{12}-type allow films exhibit a perpendicular anisotropy with energy product 20.7 MGOe.[4] Generally, these films are deposited at very high substrate temperatures of 500 °C–700 °C and are necessary to apply an external magnetic field (~2 kOe) during the process of deposition for controlling the growth of out-plane texture.

We have prepared new permanent magnet films of MnBi doped with rare earth elements Dy and Sm by using the vacuum deposition method. In this paper the magnetic properties are reported.

II. SAMPLE PREPARATION AND MEASUREMENT

MnBi films doped with Dy or Sm were fabricated by using thermal evaporation at a vacuum of 1×10^{-6} Torr. First a Bi buffer layer of suitable thickness was deposited onto a glass substrate cooled by liquid nitrogen; then Mn, Bi, and Dy (or Sm), with an atomic ratio of 2:1:0.10 were simultaneously deposited onto the buffer layer with a different thickness, ranging from 60 to 1200 nm. Finally, a SiO_2 overlayer of about 300 nm was deposited to prevent samples from oxidation. The as-deposited samples were annealed in a vacuum oven (2×10^{-6} Torr) at different of temperatures 350 °C, 375 °C, 400 °C, and 425 °C for 4 h. The composition of all samples were analyzed by electron probe and an Auger profile. These results show that the samples exhibit the component ratio of Mn:Bi:Dy of about 1:1:0.10.[5] So we refer to these samples as MnBiDy. The crystal structure of the prepared films was analyzed by x-ray diffraction. It shows that the films have the NiAs structure with their c axes perpendicular to the film plane. The magnetic hysteresis loops at room temperature were measured with a VSM (LDJ 9500).

III. RESULTS AND DISCUSSIONS

Figure 1 shows the hysteresis loops of MnBiDy films for several film thickness (d=60, 257, 377, 622, 913, and 1200 nm) at the external magnetic field He=0–2.0 T. The saturation magnetizations of the MnBiDy films for all annealing temperatures decreases as d increases for d<300 nm. This can be explained by the increase in the amount of free Bi and Bi_3Mn_2 phases as the film thickness increases. This is confirmed by the x-ray diffraction analysis. The intrinsic coercive force μHc as a function of d is shown in Fig. 3. μHc increases with d for d<400 nm. This may be caused by the nucleation. Then μHc decreases as d increases for d>400 nm; this is due to the domain rotation during the demagnetizing process. The reasons are given as follows.

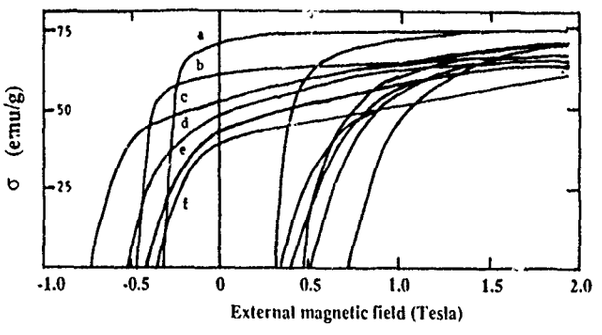

FIG 1. Hysteresis loops as a function of film thicknesses d=60 nm (a), d=257 nm (b), d=377 nm (c), d=622 nm (d), d=913 nm (e), and d=1200 nm (f) for MnBiDy films.

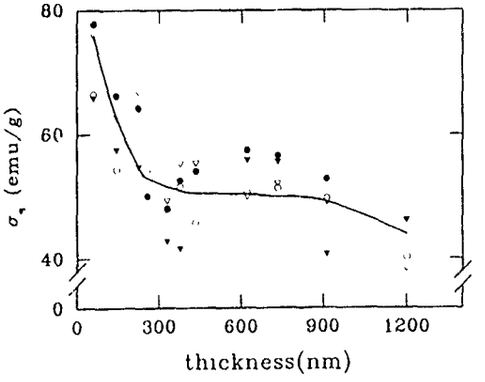

FIG. 2. Thickness dependence of the saturation magnetization of MnBiDy films annealed at 350 °C (○), 375 °C (●), 400 °C (▼), and 425 °C (▽) for 4 h.

 0021-8979/94/76(10)/6769/3/$6.00 © 1994 American Institute of Physics

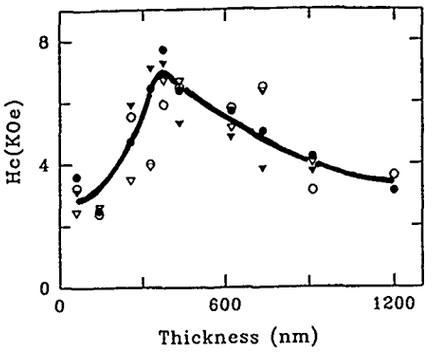

FIG. 3. Thickness dependence of the intrinsic coercive force of MnBiDy films annealed at 350 °C (○), 375 °C (●), 400 °C (▼), and 425 °C (▽) for 4 h.

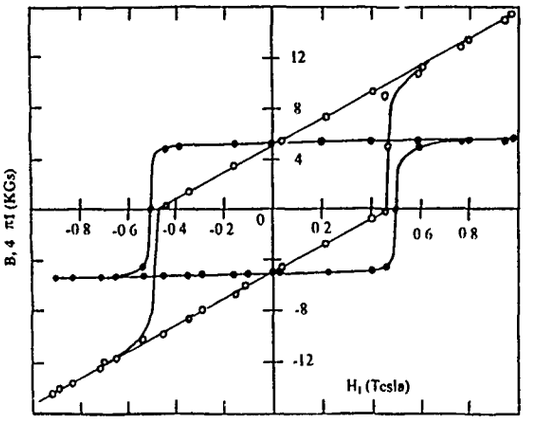

FIG. 5. The $4\pi M$-Hi and B-Hi hysteresis loops of the MnBiDy film annealed at 375 °C for 4 h. d=230 nm, μHc=5 kOe, $_{13}Hc$=4.7 kOe, and $(BH)m$ 8.3 MGOe.

The intrinsic coercive force may result from three irreversible magnetization processes: (a) nucleation and growth of the reverse domain; (b) domain wall pinning; and (c) irreversible domain rotation. In order to identify which process the Hc comes from for MnBiDy films, we also measured the magnetic hysteresis loops for those films under various magnetic fields, as shown in Fig. 4. Evidently, as $d=60$ and 143 nm, the Hc value increases with the applied field, but the magnetization does not vary with the field when the field is high. This feature reveals that Hc results from the nucleation and growth. This is also confirmed by the observation of nucleation processes using polarized light microscopy patterns. As $d=622$ and 913 nm, the shape of hysteresis loops is completely different from those for $d=60$ nm, indicating that the coercivity does not result from the nucleation and growth. Hence, we suggest that it results from the domain rotation. According to the domain rotation model for films with uniaxial anisotropy, the value of Hc is estimated to be about 3.7 kOe for the $d=913$ nm sample, which is nearly equal to the experimental data (about 4.0 kOe at the magnetic field of 2 T).

According to the measured data of the hysteresis loops, we can obtain the magnetization $4\pi M$ and magnetic induction B as a function of the intrinsic magnetic field Hi (see Fig. 5) by using the relations Hi=He-NM and B=Hi+$4\pi M$, when N is the demagnetizing factor ($N=4\pi$ for films when He is perpendicular to the plane, and the effective anisotropy field is neglected). Then, the maximum magnetic energy product $(BH)m$ as a function of film thickness d, which is shown in Fig. 6, can be obtained. It decreases quickly as d increases for $d\leqslant 350$ nm, and then remains as a constant for $d>350$ nm. This can be understood due to the behaviors related to thickness dependence of the μHc and magnetization of these films.

In conclusion, we have prepared MnBiDy permanent magnet films with a large magnetic energy product and also studied the saturation magnetization, coercive force and $(BH)m$ as a function of film thicknesses for these films.

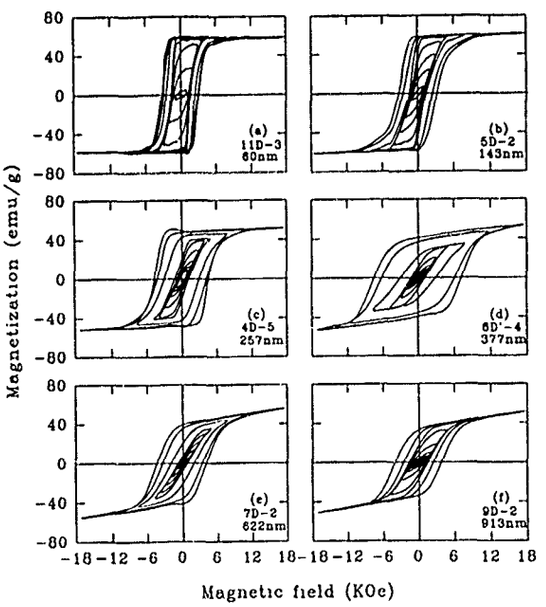

FIG. 4 Hysteresis loops of MnBiDy film with different thicknesses (a) 60 nm, (b) 143 nm, (c) 257 nm, (d) 377 nm, (e) 622 nm, and (f) 913 nm. The applied fields are 1, 2, 3, 4, 5, 8,12, and 18 kOe from the inner to exterior.

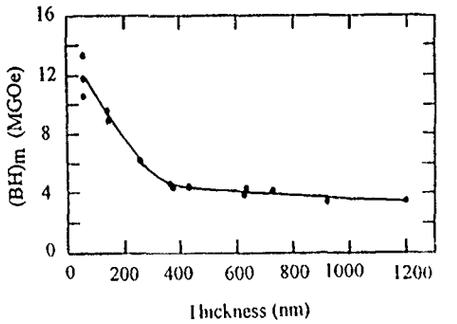

FIG 6. Thickness dependence of the $(BH)m$ of MnBiDy films

ACKNOWLEDGMENTS

We acknowledge useful discussions with Professor Zhong Wending and Professor Yang Yingchang. This work was supported by the NSFC, the State Key Laboratory of Magnetism, and The Measurement Center of the Zhong Guan Cun area.

[1] T. D. Cheung, L. Wichramasekara, and F. J. Cadieu, J. Appl. Phys. **57**, 3598 (1985).
[2] F. J. Cadieu and H. Hadge, IEEE Trans. Magn. **MAG-25**, 3788 (1989).
[3] K. D. Aylesworth, Z. R. Zhao, and D. J. Sellmyer, J. Appl. Phys. **64**, 5742 (1988).
[4] F. J. Cadieu *et al.*, Appl. Phys. Lett. **59**, 875 (1991).
[5] D. S. L. *et al.*, J. Magn. Magn. Mater. **115**, 66 (1992).

Published without author corrections

Neutron scattering studies of the vortex lattice in niobium and ℜ123 superconductors (invited)

N. Rosov, J. W Lynn,[a] and T. E. Grigereit[a]
Reactor Radiation Division, National Institute of Standards and Technology, Gaithersburg, Maryland 20899

The magnetic flux lattice undergoes a melting transition not only in high-T_c oxide superconductors, but also in conventional superconductors, as recently observed in superconducting niobium films. Small-angle neutron scattering was used to investigate the properties of the magnetic flux lattice in a large, high-quality single crystal of niobium. The small London penetration depth of niobium gives a large magnetic scattering signal, and the use of a high-quality single crystal eliminates other unwanted scattering (from twin boundaries, voids, etc.). The signal-to-noise ratio is therefore improved by several orders of magnitude over the best available measurements of high-T_c oxide superconductors. A sixfold hexagonal pattern of peaks is observed in the mixed state ($H_{c1}<H<H_{c2}$) at all temperatures. These peaks are resolution limited below the irreversibility line; above it, the width in the transverse direction increases with temperature due to the vortex dynamics. Close to H_{c2}, the radial widths of the peaks also broaden. The increase in broadening is a direct observation of a transition to a disordered phase. Nevertheless, the basic hexagonal pattern of peaks is maintained throughout the mixed state, indicating that a correlated flux fluid exists in the reversible regime. Some results on the vortex lattice in superconducting $DyBa_2Cu_3O_7$ are presented and some of the possible exotic states resulting from the coexistence of antiferromagnetic order and superconductivity are described.

I. INTRODUCTION

The melting of the flux lattice in high-temperature oxide superconductors is currently a subject of great fundamental and practical interest. The early discovery of an irreversibility line[1] in the cuprate superconductors suggested that the basic vortex behavior was quite different from previously known superconductors, perhaps due to the much higher critical temperature T_c. Neutron scattering studies of the melting process to probe the exact nature of the melting transition would be most interesting, especially since techniques such as Bitter decoration are restricted to low fields. Unfortunately, the very nature of the high-T_c superconductors makes observing such a melting transition via neutrons extremely difficult. The London penetration depth λ_L in the oxide superconductors is a factor of 4 or 5 larger than for niobium (for which $\lambda_L \approx 350$ Å). As a result, the neutron scattering intensity from the flux lattice, which goes as λ_L^{-4}, is much smaller for the high-T_c materials. An additional technical difficulty is that presently available large single crystals of 123 superconductors have grain boundaries, twin boundaries, and various other defects that give rise to scattering in the same small-angle region as the vortex scattering. This dramatically reduces the signal-to-noise ratio for the vortex scattering, and makes the vortex scattering pattern much more difficult to study.

Irreversibility lines have also been recently observed in niobium, which is an ideal candidate for neutron studies of the vortex lattice, with the combined benefits of large signal and low background due to the availability of large, high-quality single crystals. Pure, defect-free niobium has a Ginzburg–Landau parameter κ of 0.77, just slightly greater than the minimum value ($1/\sqrt{2}$) for type II behavior. In addition, niobium is a material for which κ can be dramatically increased by the influence of defects such as grain boundaries or by the introduction of impurities. Neutron diffraction experiments on the flux line lattice in niobium have been performed over the last thirty years, beginning with a study by Cribier *et al.*[2] that explicitly demonstrated the existence of a triangular vortex lattice, and continuing with much more detailed work by groups at Jülich[3] and Oak Ridge.[4] The subsequent work focused on the interaction of the flux lattice with the crystalline lattice, concentrated mainly on the region of the phase diagram well below the upper critical field $H_{c2}(T)$. The work[5] that we review here extends the measurements to the $H_{c2}(T)$ line.

In the first part of this article we describe the basics of the neutron scattering experiments and the features of the vortex lattice over the (H,T) plane in niobium. We continue with a description of our detailed measurements of the melting of the vortex lattice in niobium and conclude with a description of some recent work on rare-earth 123 superconductors.

[a]Also at the Center for Superconductivity Research, Department of Physics, University of Maryland, College Park, MD.

 0021-8979/94/76(10)/6772/6/$6.00 © 1994 American Institute of Physics

II. EXPERIMENT

A. Neutron scattering

The bulk of the experimental results described here were obtained on the 30 m small-angle neutron scattering (SANS) spectrometers of the Cold Neutron Research Facility at the National Institute of Standards and Technology. Both spectrometers operate in the same way: A beam of neutrons moderated by a cold source is incident on a neutron velocity selector, which produces a triangular wavelength distribution of neutrons with $\Delta\lambda/\lambda \approx 15\%$. The neutrons pass down a long ($\lesssim$15 m) variable-length flight path with a pinhole collimator at each end, which fixes the incident neutron momentum $\mathbf{k}_i$. After the sample there is another variable-length flight path to a multidetector, which allows the simultaneous collection of data over some range of momentum transfer $\mathbf{Q}=\mathbf{k}_i-\mathbf{k}_f$.

Our sample is a 95 g single crystal of niobium, 9 cm in length, with a diameter of 1.25 cm. The cylinder axis is the [110] crystallographic axis, which was oriented perpendicular to the applied field. The neutron beam illuminated a section of approximately 1 cm diameter near the midpoint of the cylinder. Initial measurements were performed in a flow cryostat with an Al vacuum shroud and 77 K heat shield that was mounted in an electromagnet with holes for the neutron beam drilled through the pole pieces. Later measurements were performed in a horizontal superconducting magnet cryostat specially designed for SANS measurements, with single-crystal sapphire windows along the beam path to reduce unwanted cryostat scattering.

At low temperatures a crystalline vortex lattice is formed, and the scattering pattern of neutrons from the flux lattice directly reveals the reciprocal lattice. Our experimental configuration involved applying the magnetic field nearly along the incoming neutron direction $\mathbf{k}_i$. In this case, the possible momentum transfers for all six 10 reflections are approximately parallel to the plane of the detector, so a pattern such as Fig. 1 will appear on the detector. The simultaneous appearance of all six spots in this case results from some domain structure in the formation of the lattice. If the lattice is formed carefully, it is possible to observe a single diffraction spot as in Fig. 1(bottom).

This pattern [Fig. 1(top)] was collected in two minutes. In comparison, a similarly sized single crystal of $YBa_2Cu_3O_7$ (Ref. 6) requires the subtraction of a zero-field cooled background scan from the applied field scan, each of which takes several hours counting time. The excellent quality of the Nb single crystal—with an almost complete lack of sample-dependent small-angle scattering, incoherent scattering, and absorption—not only allowed the rapid collection of data in the low-temperature regime, but in fact permitted the analysis of the behavior near the H_{c2} phase boundary, where the signal is drastically reduced.

The reciprocal lattice of a triangular lattice with lattice constant a is a self-similar triangular lattice with lattice constant $a^*=4\pi/\sqrt{3}a$. Since the flux quantum $\phi_0=2.068\times10^{-15}$ T m^2 and the area per flux quantum is $\sqrt{3}a^2/2$, we can relate the internal magnetic field B to the lattice parameter by $\phi_0=\sqrt{3}Ba^2/2$. The position in reciprocal

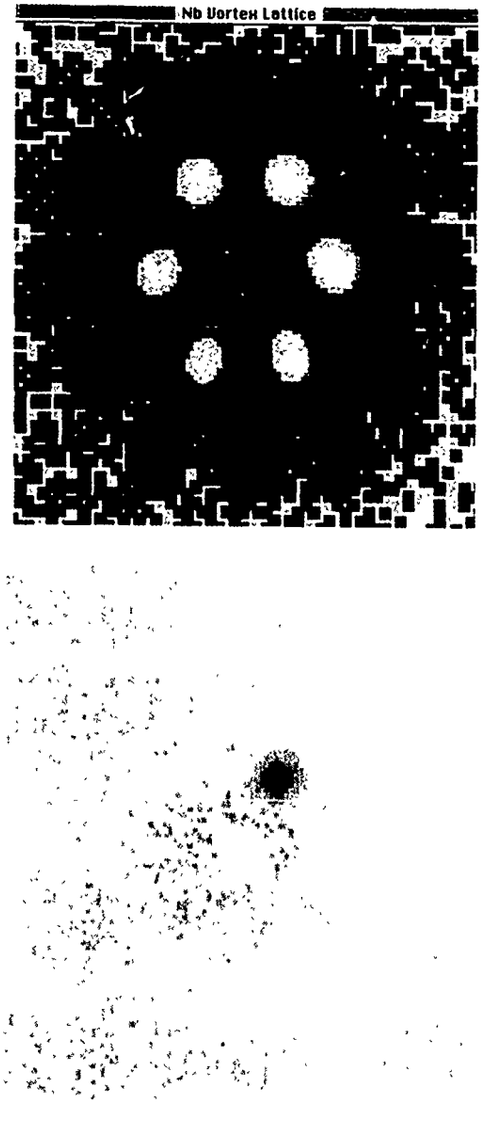

FIG. 1. (Top) Sixfold scattering pattern as observed on the two-dimensional multidetector from single crystal niobium at $T=4.5$ K and $\mu_0H=0.12$ T. The gray-scale image is logarithmically scaled. (Bottom) Pattern of a single diffraction spot obtained at 6.85 K and $\mu_0H=0.12$ T. Here the gray scale is linear.

space of the 10 reflection, which occurs at a momentum transfer $Q_{10}=a^*$, is

$$Q_{10}=2\pi\sqrt{2B/\sqrt{3}\phi_0}. \tag{1}$$

In the $\mathbf{H}\|\mathbf{k}_i$ configuration, there are a number of ways to view the data. One way is a "radial scan," which is performed by summing the scattering at a particular Q around a portion, or all, of the detector [see Fig. 2(a)]. These scans (or sums, in this case) determine the translational correlations between the flux lines in the lattice. Another possibility is a "transverse scan," a sum of the scattering over a small range of Q as a function of angle ϕ around the detector [see Fig. 2(b)], which gives the angular correlations between the flux lines. Finally, we can perform rocking scans [see Fig. 2(c)], where the intensity in a particular region of the detector is

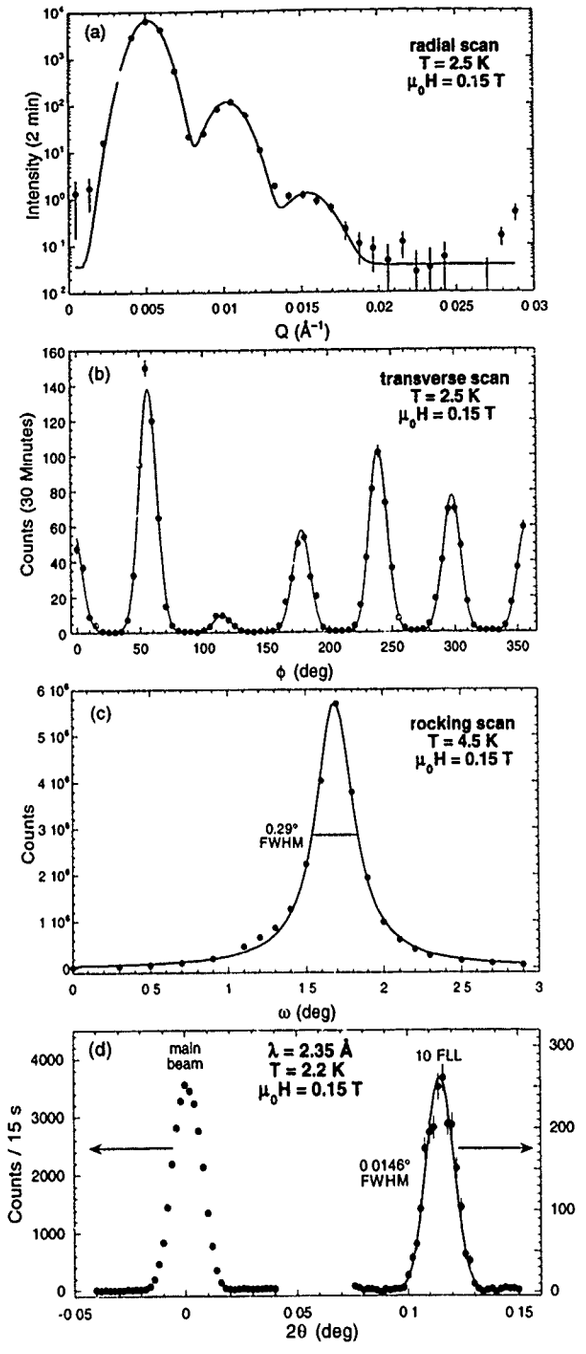

FIG. 2. Various summations of the Fig. 1(top) pattern: (a) Radial and (b) transverse scans at $T=2.5$ K and $\mu_0 H=0.15$ T. (c) Rocking curve of Nb as collected on the SANS spectrometer total intensity in the peak as a function of magnet angle. (d) Radial scan of 10 peak with improved resolution performed on the BT-7 reflectometer.

recorded as a function of magnet rotation angle ω. In this configuration, the rocking scans primarily determine the straightness of the flux lines.

B. The flux line lattice in Nb

In the Meissner state, the magnetic field in the sample must vanish, i.e., $\mathbf{B}=0$. The magnetization $\mathbf{M}$ of the sample then depends directly on the applied magnetic field $\mathbf{H}_{app}$ to produce the required cancellation. The boundary conditions on the field imply a demagnetizing field, due to the sample magnetization, that opposes the applied field, and so

$$\mathbf{H}=\mathbf{H}_{app}-\eta\mathbf{M}, \tag{2}$$

where η is the demagnetization factor. In the case of an infinite right cylinder with a field applied perpendicularly to the cylinder axis $\eta=1/2$, the H inside the sample is actually $2H_{app}$ in the Meissner state. For the internal field to reach the lower critical field H_{c1}, a field $H_{app}=\frac{1}{2}H_{c1}$ needs to be applied.

For $H_{app}\geq\frac{1}{2}H_{c1}$, flux will penetrate the sample. The competition between the short-range repulsion and long-range attraction of the fluxoids initially causes the formation of domains of flux lines with a density B_0 determined by the strength of the long-range attraction. In this intermediate mixed state (IMS), the sample magnetization is $\mathbf{M}=f\mathbf{B}_0/\mu_0-\mathbf{H}$, where f is the fraction of the sample in the vortex state. As the applied field is $\mathbf{H}_{app}=\mathbf{H}+\eta\mathbf{M}$, in the IMS the relation between the applied field and the internal fields is

$$\mathbf{H}_{app}=(1-\eta)\mathbf{H}+f\eta(\mathbf{B}_0/\mu_0). \tag{3}$$

In our experimental configuration, f increases linearly from 0 at $H_{app}=\frac{1}{2}H_{c1}$ to 1 at $H_{app}=\frac{1}{2}H_{c1}+\frac{1}{2}B_0/\mu_0\equiv H_2$. With further increase of H_{app} above H_2, the flux lattice density increases throughout the sample. Just below H_{c2} the flux lattice achieves its highest density, and ultimately, at $H_{app}=H_{c2}$, the sample magnetization goes to zero and the sample is no longer superconducting.

We thus expect to observe the following behavior as a function of field in a SANS measurement: For $H_{app}<\frac{1}{2}H_{c1}$ the sample is in the Meissner state and there is no scattering. Just above $\frac{1}{2}H_{c1}$ flux penetrates the sample and is confined to regions with constant flux density B_0; elsewhere in the sample, the flux density is zero. At this point, a scattering pattern can be observed, with a lattice spacing corresponding to the flux density B_0,

$$a_0=\sqrt{\frac{2}{\sqrt{3}}\frac{\Phi_0}{B_0}}. \tag{4}$$

This lattice spacing remains constant while the scattering intensity increases linearly with field, until $H_{app}=H_2$, where the flux lattice fills the entire sample. Above H_2, the flux density increases, but the scattering intensity decreases as the fluxoids overlap each other and the contrast is consequently reduced. The sample magnetization is $\mathbf{M}=\mathbf{B}/\mu_0-\mathbf{H}$, so the flux density is then $B=\mu_0[H_{app}-(1-\eta)H]/\eta$. Exactly this behavior has been observed for niobium by Christen *et al.*[4]

We can also make the SANS measurements as a function of temperature in a constant applied field. Since $H=-M+B/\mu_0$, then

$$B=\mu_0(H_{app}+\tfrac{1}{2}M) \tag{5}$$

for our experimental configuration. As the magnetization is negative and approaches zero near the superconducting phase boundary, the flux density increases as the phase boundary is approached, and so the diffraction peaks move out from their low-temperature position. Since the magneti-

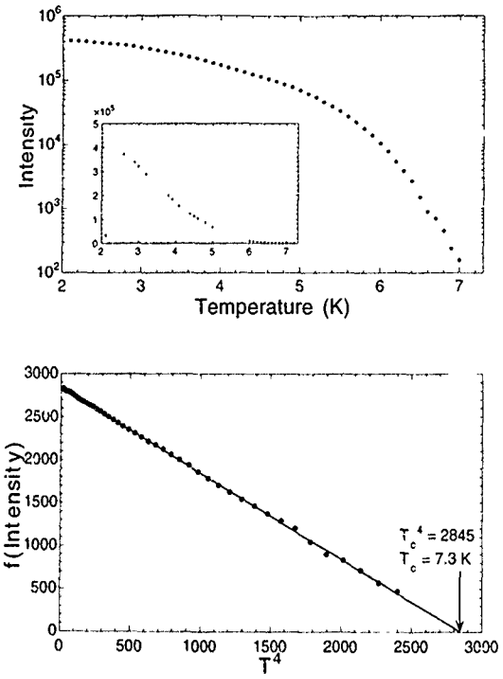

FIG. 3. (a) Intensity of the 10 peak as a function of temperature and (b) linearized plot of $f(I)$ vs T^4, showing the extrapolation to obtain $T_c(H)$.

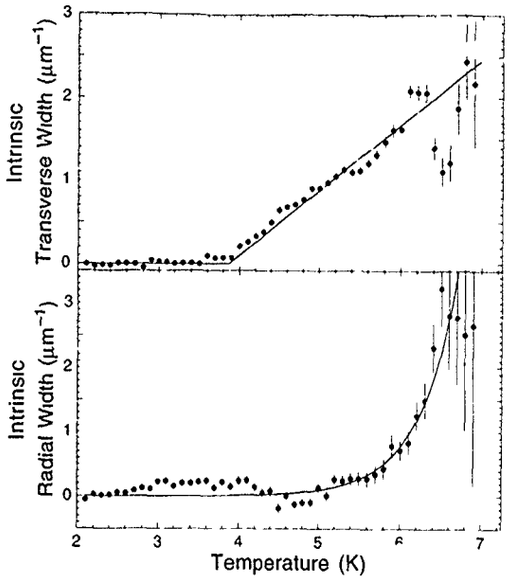

FIG. 4. Intrinsic transverse (top) and radial (bottom) widths as a function of T.

zation goes to zero at H_{c2}, the demagnetization factor does not affect the determination of the upper critical field, and the magnetic scattering will disappear at $H_{app}=H_{c2}$.

III. MELTING OF THE FLUX LATTICE IN NIOBIUM

The observation of irreversibility lines and the implication of melting phenomena occurring in the flux lattice of the high-T_c superconductors prompted a reexamination of "conventional" superconductors to see if similar phenomena were possible in these systems. Drulis *et al.*[7] observed irreversibility effects from flux depinning in vibrating reed measurements on cold-rolled niobium foils. Later work by Schmidt *et al.*[8] demonstrated the existence of a magnetic irreversibility line in sputtered Nb films that followed the expectations for a melting line.

One would naively expect that the melting of the flux line lattice might be manifested by a sudden transition from the low-temperature hexagonal pattern of Fig. 1 to an isotropic ring of scattering on the detector, indicative of an isotropic liquid state. We therefore performed field cooling measurements, starting well above the superconducting transition at constant H_{app}, and then slowly (<0.1 K/5 min and even slower near the H_{c2} line) lowered the temperature, collecting scattering patterns at various temperatures. Care was taken to avoid overshooting the new temperature set point on changing the temperature. From our discussion above, we expect the intensity to appear just below $T_c(H)$, as the magnetic contrast appears, and this is in fact what happens [see Fig. 3(a)]. We note that since κ is small for our niobium sample, the two-fluid model does not exactly apply; however, we have used the T^4 behavior of the London model to guide us in linearizing the temperature dependence of the scattering intensity, and so allow the extrapolation of the intensity to zero and the determination of $T_c(H)$ [Fig. 3(b)]. From our temperature scans we were able to determine the H_{c2} phase boundary. In addition, we immediately noticed that (i) the temperature dependence of the scattering was smooth, with no discontinuities; (ii) the scattering intensity was not lost until just below the extrapolated H_{c2} line; and (iii) we always had a sixfold pattern—no ring of scattering ever appeared. Not only did the scattering from the vortices maintain its hexagonal symmetry at all fields and temperatures in the mixed state, but it was locked by the crystalline anisotropy, since we consistently observed the same orientation for the sixfold diffraction pattern over many different experimental configurations.

If, however, we examined the widths of the peaks in the radial and transverse directions as a function of temperature, we found (see Fig. 4) that at some temperature $T_t(H)$ well below $T_c(H)$, an intrinsic width developed in the transverse direction. This width determines the degree of orientational correlations. The radial width remained resolution limited until some higher temperature $T_r(H)$, whereupon it also developed an intrinsic width. We also measured the scattering pattern from the vortex lattice on the NIST BT-7 reflectometer. The spectrometer resolution here is a factor of 3 better for radial scans than the corresponding SANS resolution [see Fig. 2(d)]. We observed the radial width increase above the resolution limit with the reflectometer at the same temperature as we had observed on the SANS, and this therefore lends confidence the intrinsic radial widths develop at higher temperatures than the intrinsic transverse widths.

To further clarify the nature of these two transitions, we performed isothermal field sweeps and found that the peak intensities and widths were reversible above the T_t line and hysteretic below. The restoration of the reversible behavior above T_t leads us to believe that we have observed the onset of a correlated flux fluid state above T_t. This state may not

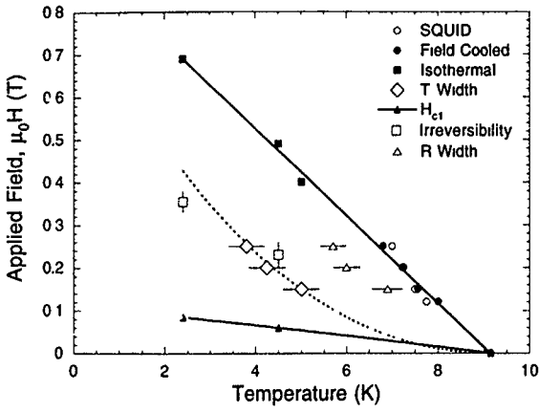

FIG. 5. Phase diagram H vs T for Nb as determined by neutron scattering. The H_{c1} and H_{c2} boundaries are indicated, as are the points where the radial and transverse widths broaden.

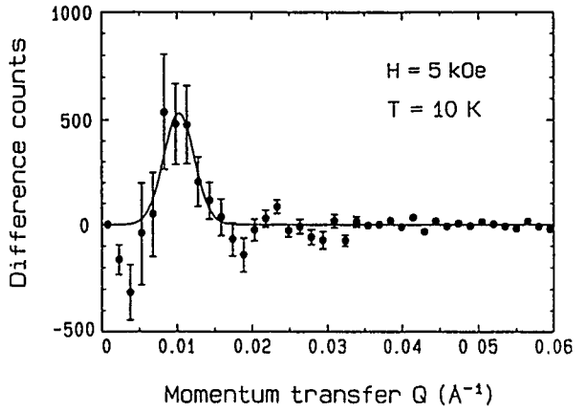

FIG. 6. Radial sum of the difference pattern between field-cooled and zero-field cooled Dy123 at $T=10$ K and $\mu_0 H=0.5$ T. The peak position indicates that the lattice is close to triangular.

be a hexatic phase, since in hexatic systems both the transverse and radial widths appear to be coupled and therefore the intrinsic widths would be expected to develop together.[9]

Figure 5 displays the experimentally determined phase diagram for our niobium crystal. The lower and upper critical fields have been determined via neutrons by the respective onset and loss of scattering from the flux lattice. We can estimate from the two-fluid model that $\kappa \approx \sqrt{H_{c2}/H_{c1}} \approx 2$. This is larger than the value of $\kappa \approx 0.8$ obtained for high purity and defect-free niobium.[4,10] Our sample and those of Drulis *et al.*[7] and Schmidt *et al.*[8] are high purity niobium; however, the various preparation methods created samples with varying defect and grain boundary concentrations, as reflected by the value of κ. Those samples with larger κ have a larger $H_{c2}(T)$: the $\kappa \approx 7$ cold-rolled foil[7] higher than our sample and the $\kappa \approx 10$ sputtered film[8] still larger. The phase diagram also shows $T_r(H)$, $T_t(H)$, and the irreversibility line $T_{irr}(H)$. The irreversibility line and $T_t(H)$, which we identify with a melting curve, are well below that reported for the cold-rolled foils,[7] which is lower again than the melting curve for the sputtered niobium films.[8] This supports the reasonable expectation that T_{irr} depends on the pinning strength and defect density.

The broadening is definitely dynamic in origin, and there are two possibilities for the behavior which we observe. The first possibility is that the onset of broadening in the transverse width indicates a transition to an orientationally disordered phase and that the broadening of the radial width at a higher temperature is associated with the loss of translational order. In this case, the low-temperature phase is crystalline, the transition to an orientationally disordered phase occurs at $T_t(H)$, and a correlated flux fluid exists above $T_r(H)$.

The second possibility is that the transverse broadening is "lattice dynamical" in origin, associated with the same soft shear mode of the vortex lattice that would be involved in melting. This would imply that if much higher instrumental resolution were available, we would see wings of inelastic scattering on the sides of an elastic Bragg peak. The present (best available) resolution would convolve the elastic and inelastic scattering into a single broadened peak. In this case, we would be observing the effect of the inelastic scattering on the linewidth at T_t, and the lattice would not melt until the intrinsic radial width begins to develop.

Given the correlation between the onset of irreversibility in the isothermal scans and the abrupt onset of an intrinsic transverse width in the constant field scans, we believe that the first explanation is the correct one. We cannot entirely rule out the second; however, in either case we observe a correlated flux fluid, due to the non-negligible interactions of the crystal with the vortices. It is interesting to note that broadening in the radial and transverse widths, similar to what we have observed for this two-dimensional system, has also been observed in melting transitions in two-dimensional colloidal suspensions.[11]

IV. THE FLUX LINE LATTICE IN MAGNETIC ℜ123 SUPERCONDUCTORS

The coexistence of antiferromagnetism and superconductivity poses the question: What is the effect of an underlying magnetic order on the vortex lattice? The high-T_c compounds $DyBa_2Cu_3O_7$ and $ErBa_2Cu_3O_7$ are already known to have a very well-defined zero-field ordering of the rare-earth moments at low temperatures ($T_N \approx 1$ K) (Ref. 12) without significant detriment to the superconductivity. We have observed the flux line lattice in a 250 mg single crystal of $DyBa_2Cu_3O_7$, at 10 K in a 5 T applied field (see Fig. 6), well above any temperature where one would expect any effects from the ordering of the rare-earth sublattice. The 10 peak appears at $Q_{10}=0.0105$ Å^{-1}, which is expected for a vortex lattice that is close to triangular, as has been observed by Keimer *et al.*[13] in $YBa_2Cu_3O_7$.

At lower temperatures there are several possible interesting behaviors. Above the onset of long-range order, the enhanced susceptibility of the rare-earth moments would allow a variation of the rare-earth moment alignment that would decorate the vortices. Since the total magnetic flux must be quantized, the addition of the Dy magnetization M_{Dy} will then give a new momentum transfer for scattering from the vortex lattice

$$Q_{M10}=2\pi\sqrt{2\mu_0(H+M_{Dy})/\sqrt{3}\phi_0}. \quad (6)$$

The measured saturated Dy moment is approximately 7 μ_B, which implies that $\mu_0 M_{Dy} \approx 1$ T. In a 0.1 T applied field, we would then expect that the vortex density would increase by roughly a factor of 3 due to the saturated alignment of the Dy moments.

Below T_N, the Dy magnetization will be close to zero at modest applied fields, and so we would return to the original behavior for the flux lattice. However, another possible behavior below T_N could be observed by applying a field strong enough to put the Dy moments through a metamagnetic or spin-flop transition. If the sample has a nonzero demagnetization factor, there would then be coexistence of "paramagnetic" domains that have a net magnetization, with reflections as described by Eq. (6), and "antiferromagnetic" domains where there is no net magnetization, as described by Eq. (1).[14] Another possibility proposed by Buzdin *et al.* is the existence of two-quanta vortices in metamagnetic superconductors, which could occur if the applied field for the metamagnetic or spin-flop transition is near H_{c1}. In this regime, because of the spatial variation of the vortex field, the metamagnetic transition could be localized to a region near the vortex core and substantially affect the structure of the vortex. Work is in progress to experimentally explore these possibilities.

ACKNOWLEDGMENTS

We thank H. Zhang and T. Clinton for assistance at the early stages of this work, J. Z. Liu and R. N. Shelton for the single crystal of $DyBa_2Cu_3O_7$, J. J. Rush for the Nb single crystal, C. Majkrzak for assistance with the BT-7 reflectometer measurements, and S. Krueger and C. Glinka for much assistance in the smooth operation of the SANS spectrometers. Research at Maryland is supported by the NSF, DMR 93-02380. The NG-3 30 m SANS spectrometer at the NIST Cold Neutron Research Facility is supported by the NSF, DMR 91-22444.

[1] K. A. Müller, M. Takashige, and J. G. Bednorz, Phys. Rev. Lett. **58**, 1143 (1987).
[2] D. Cribier, B. Jacrot, L. M. Rao, and B. Farmoux, Phys. Lett. **9**, 106 (1964).
[3] J. Schelten, H. Ullmaier, and W. Schmatz, Phys. Status Solidi B **48**, 619 (1971); J. Schelten, H. Ullmaier, and G. Lippmann, Z. Phys. **253**, 219 (1972); H. W. Weber, J. Schelten, and G. Lippmann, Phys. Status Solidi B **57**, 515 (1973); G. Lippmann, J. Schelten, R. W. Hendricks, and W. Schmatz, Phys. Status Solidi B **58**, 633 (1973); J. Schelten, G. Lippmann, and H. Ullmaier, J. Low Temp. Phys. **14**, 213 (1974).
[4] D. K. Christen, F. Tasset, S. Spooner, and H. A. Mook, Phys. Rev. B **15**, 4506 (1977); D. K. Christen, H. R. Kerchner, S. T. Sekula, and P. Thorel, *ibid.* **21**, 102 (1980).
[5] J. W. Lynn, N. Rosov, T. E. Grigereit, H. Zhang, and T. W. Clinton, Phys. Rev. Lett. **72**, 3413 (1994).
[6] B. Keimer, J. W. Lynn, R. W. Erwin, F. Doğan, W. Y. Shih, and I. A. Aksay (these proceedings).
[7] H. Drulis, Z. G. Xu, J. W. Brill, L. E. De Long, and J.-C. Hou, Phys. Rev. B **44**, 4731 (1991).
[8] M. F. Schmidt, N. E. Israeloff, and A. M. Goldman, Phys. Rev. Lett **70**, 2162 (1993); Phys. Rev. B **48**, 3404 (1993).
[9] J. D. Brock, R. J. Birgeneau, J. D. Litster, and A. Aharony, Contemp. Phys. **30**, 321 (1989).
[10] H. W. Weber, E. Seidl, C. Laa, E. Schachinger, M. Prohammer, A. Junod, and D. Eckert, Phys. Rev. B **44**, 7585 (1991).
[11] C. A. Murray and D. H. Van Winkle, Phys. Rev. Lett. **58**, 1200 (1987).
[12] See, for example, J. W. Lynn, in *High Temperature Superconductivity*, edited by J. W. Lynn (Springer, New York, 1991).
[13] B. Keimer, F. Doğan, I. A. Aksay, R. W Erwin, J. W. Lynn, and M. Sarikaya, Science **262**, 83 (1993).
[14] A. I. Buzdin, S. S. Krotov, and D. A. Kuptsov, Solid State Commun. **75**, 229 (1990).

Vortex structures in $YBa_2Cu_3O_7$ (invited)

B. Keimer
Department of Physics and Princeton Materials Institute, Princeton University, Princeton, New Jersey 08544 and National Institute of Standards and Technology, Gaithersburg, Maryland 20899

J. W. Lynn and R. W. Erwin
National Institute of Standards and Technology, Gaithersburg, Maryland 20899

F. Dogan
Princeton Materials Institute and Department of Chemical Engineering, Princeton University, Princeton, New Jersey 08544

W. Y. Shih
Princeton Materials Institute, Princeton University, Princeton, New Jersey 08544

I. A. Aksay
Princeton Materials Institute and Department of Chemical Engineering, Princeton University, Princeton, New Jersey 08544

Extensive small angle neutron scattering experiments have been conducted on the vortex system in $YBa_2Cu_3O_7$ in a magnetic field range of $0.5\ T \leq H \leq 5\ T$, and with various orientations of the magnetic field with respect to the crystallographic axes. For H parallel to the c axis, the vortex lattice is oblique with two nearly equal lattice constants and an angle of 73° between primitive vectors. One principal axis of the vortex lattice coincides with the (110) direction of the crystal lattice. It is shown that this structure cannot be explained in the framework of a purely electrodynamic (London) model, and that it is intimately related to the in-plane anisotropy of the superconducting coherence length. When the field is inclined with respect to the c axis, the uniaxial anisotropy due to the layered crystal structure of $YBa_2Cu_3O_7$ becomes relevant. The interplay between the square in-plane anisotropy and the uniaxial anisotropy leads to both a continous structural transition and a reorientation of the vortex lattice as a function of inclination angle. For the largest inclination angles, the vortex lattice decomposes into independent chains.

I. INTRODUCTION

The vortex system in the cuprate superconductors has received a high level of attention mostly because of its novel phase behavior inferred from transport experiments at high temperatures and high magnetic fields. Small angle neutron scattering (SANS) is applicable in high magnetic fields and capable of measuring the relevant correlation lenghts of the vortex lattice. SANS is therefore very promising as a tool to further elucidate this behavior. However, since the signal intensity at high temperatures is very small, these experiments are difficult. Our approach has therefore been to first develop a thorough experimental description of the vortex system at low temperatures as a function of field strength and field orientation with respect to the crystallographic axes, before studying thermal effects in detail. We have found that the behavior of the vortex lattice is very rich even at low temperatures. In particular, our experiments indicate a close relation between the structure of the vortex lattice and the microscopic electronic structure of $YBa_2Cu_3O_7$. The following is a preliminary summary of these studies.

II. EXPERIMENTAL DETAILS

Our sample is a disk-shaped single crystal of $YBa_2Cu_3O_7$ of volume $\sim 2.5\ cm^3$ and mosaicity $\sim 1.5°$. The sample is too large to fit into a superconducting quantum interference device (SQUID) magnetometer, but small pieces cut off from samples prepared under identical conditions showed sharp superconducting transitions at ~93 K. The microstructure of these samples has been extensively characterized by transmission electron microscopy. Prominent microstructural features are μm sized Y_2BaCuO_5 inclusions with a total volume fraction ~10%, twin boundaries of average separation ~900 Å extending in the (110) or $(1\bar{1}0)$ crystallographic directions, and stacking faults perpendicular to the (001) direction. The latter two features occur on length scales comparable to intervortex distances and therefore give rise to background small angle scattering in the experimentally relevant range of scattering angles. This (temperature independent) background is comparable to or larger than the magnetic scattering from the vortex lattice and must be subtracted from the raw data.

All experiments were performed on the NG-3 and NG-7 SANS spectrometers at the Cold Neutron Research Facility of the National Institute of Standards and Technology. We mostly used the standard horizontal-field scattering geometry[1] with the neutron beam almost parallel to the magnetic field. Horizontal magnetic fields of 0.5 T or less were generated by an electromagnet, larger fields were achieved in a horizontal-field superconducting magnet. For some experiments we also used a vertical-field electromagnet.

The experimental geometry is illustrated in Fig. 1. The x (horizontal) axis in this figure is the magnetic field direction. The scattered neutrons are collected as a function of the coordinates y and z perpendicular to the field by an area detector behind the sample. During the experiment the angle be-

 0021-8979/94/76(10)/6778/6/$6.00 © 1994 American Institute of Physics

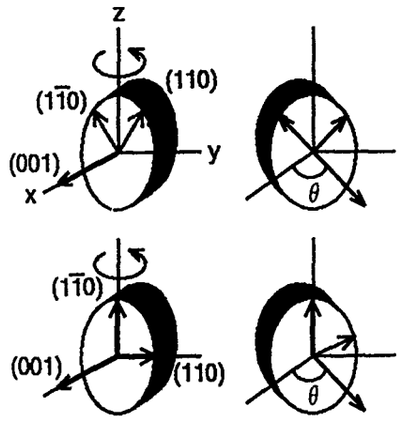

FIG. 1. Coordinate system illustrating the experimental geometry of our experiments. The x axis is the magnetic field direction. The neutron beam is almost parallel to the magnetic field (i.e., the scattering angle is small). The angle θ (rotation angle around $\hat{z}$ relative to the x axis) can be changed during the experiment. The orientation of the crystalline axes with respect to x,y,z is chosen by orienting the crystal outside the cryostat. Two different crystal orientations are shown: (top) (100) parallel to $\hat{z}$ and (bottom) (110) parallel to $\hat{z}$. The axes $\hat{y}$ and $\hat{z}$ perpendicular to the magnetic field are the horizontal and vertical axes in the diffraction patterns below.

tween the neutron beam and the magnetic field (i.e., the scattering angle ϑ) can be varied, and the sample can be turned around the vertical $\hat{z}$ axis without remounting the sample. We denote the angle between the crystalline (001) direction and the magnetic field by θ. The crystallographic direction coinciding with the $\hat{z}$ axis is selected by orienting the sample by x-ray and thermal neutron scattering outside the cryostat. We chose three different sample orientations: (i) (100) parallel to $\hat{z}$ (Fig. 1, top); (ii) (110) parallel to $\hat{z}$ (Fig. 1, bottom); and (iii) a low-symmetry crystallographic direction parallel to $\hat{z}$ (not shown). A uniform flux profile within the sample is achieved by field cooling the crystal for each crystal orientation. Typical counting times for high quality diffraction patterns are several hours.

In order to optimize both resolution and signal intensity, different spectrometer settings were chosen at each magnetic field. We mostly used neutrons of wavelengths 5 or 6 Å and wavelength spread $\Delta\lambda/\lambda=0.31$, source and sample apertures of 5 and 1.27 cm diameter, respectively, and source-to-sample distances between 11 and 13 m. A parameter of particular importance is the angular resolution in the plane of the area detector (yz plane in Fig. 1). At a given wavelength and source aperture (chosen to optimize the neutron flux on the sample), this quantity is primarily controlled by the distance between the sample and the detector.[2] For larger magnetic fields (corresponding to larger scattering angles), smaller sample-to-detector distances can be chosen, and the angular resolution is improved. On the other hand, because of the decreasing form factor the signal-to-background ratio becomes worse for larger fields. We found that data of optimal overall quality could be taken for $H=2$ T.

III. VORTEX LATTICE SYMMETRY AND ELECTRONIC STRUCTURE

Early SANS experiments on $YBa_2Cu_3O_7$ for $H=0.8$ T revealed a diffraction pattern with fourfold symmetry when

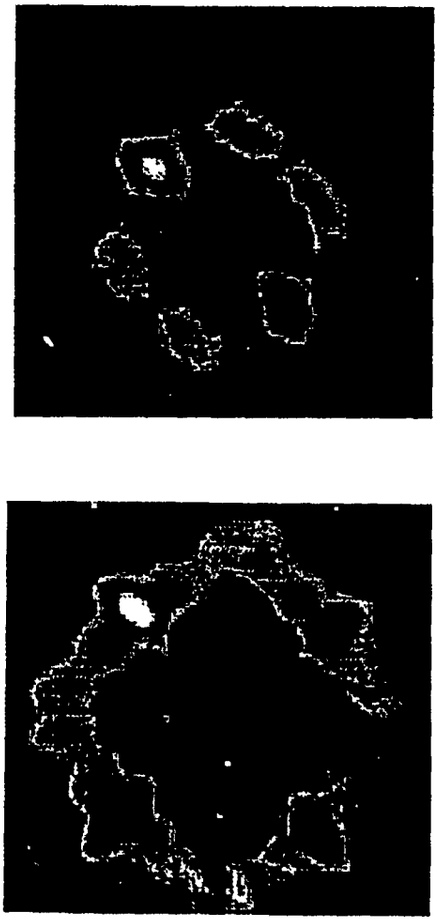

FIG. 2. Grey scale images of SANS diffraction patterns taken for (top) $H=0.5$ T, $\theta\sim10°$, obtained by rotating around a low-symmetry crystallographic direction and (bottom) $H=2$ T, $\theta=0$.

the magnetic field is aligned with the (001) crystalline direction.[3] This pattern was subsequently shown to consist of two sixfold symmetric patterns with 90° relative orientation.[4] However, the angular resolution of these patterns was not sufficient to determine the structure of the vortex lattice for this field orientation in detail. We have now used the improved angular resolution achievable in higher magnetic fields to resolve this issue definitively. The bottom panel of Fig. 2 shows that a total of 16 weak and 4 strong Bragg reflections can be resolved for fields of 2 T and above. (Note that all patterns shown here are for ϑ fixed. Since by Bragg's law each reflection corresponds to a different ϑ, not all of the 20 spots appear in a single pattern. The remaining spots can be moved into the resolution volume by adjusting ϑ appropriately.)

The real-space lattice corresponding to this diffraction pattern, shown in Fig. 3, can be regarded as intermediate between triangular (with an angle of $\beta=60°$ between primitive vectors) and square (corresponding to $\beta=90°$). In a high resolution measurement at $H=2$ T we obtained $\beta=(73\pm1)°$. We also found that the lattice constants differ by $(5\pm5)\%$; the unit cell area satisfies the flux quantization rule within the experimental accuracy. We can therefore not distinguish

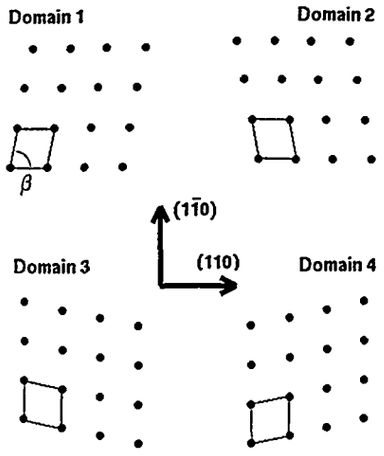

FIG. 3. Real-space structures corresponding to the diffraction patterns of Fig. 2. The top pattern of that figure is taken under conditions in which only two of the domains are populated (1 and 2, or 3 and 4). In the bottom pattern all four domains are populated.

experimentally between oblique (unequal lattice constants, space group $p2$) or rectangular (equal lattice constants, space group $c2mm$) vortex lattice symmetry. As the figure indicates, four domains with different orientations of the unit cell are observed. One of the nearest-neighbor directions of the vortex lattice coincides with either the (110) or the (1$\bar{1}$0) direction of the crystal lattice. Superposition of the diffraction patterns of these four domains results in the experimentally observed pattern of Fig. 2; the four strong reflections originate from two domains, the 16 weak reflections from one domain. A deconvolution of the patterns for $H=0.5$ T and $H=5$ T which takes the appropriate spectrometer resolution into account yields the same value for β. Note that with the spectrometer settings that had to be chosen for $H=0.5$ T two of the weak spots could not be resolved completely (Fig. 2, top).

When H is precisely aligned with the c axis, these four domains are degenerate and occupy equal fractions of the sample volume. However, the degeneracy between the domains is lifted even by a subtle inclination of the field with respect to the c axis. Tilting often favors two of the domains over the remaining two, as shown in Fig. 2. The mechanism for creation of this domain imbalance will be discussed in the next section.

The oblique structure we observe is manifestly different from the triangular lattice expected when the vortices interact purely electrodynamically. We have therefore evaluated the Gibbs free energies of vortex lattices with different β, taking the nonzero extent of the vortex core into account. In the London approximation, the Gibbs free energy density can be written as[5]

$$G=\frac{B^2}{8\pi}\left(\sum_Q \frac{1}{1+\lambda^2 Q^2}\right)-\frac{HB}{4\pi}, \tag{1}$$

where $\lambda\sim1500$ Å is the penetration depth, B is the magnetic induction, and the sum runs over all reciprocal lattice vectors Q. The finite extent of the vortex core is approximated by a circular "hard core" cutoff $Q_{max}=2\pi/\xi$, where $\xi\sim15$ Å is the in-plane coherence length. At each applied field H and for each β the magnetic induction, B, is computed by numerically evaluating $\partial G/\partial B=0$. While at low magnetic fields our calculation is insensitive to the size of the vortex core and reproduces the well-known free energy minimum at $\beta=60°$, $G(\beta)$ becomes extremely sensitive to the core cutoff in fields of several tesla. Typical numerical data are shown in Fig. 4. This means that the structure of the vortex core begins to have a significant influence on the structure of the vortex lattice in the field regime investigated in our experiments. The shape of the vortex core and the behavior of the superconducting order parameter near the core reflect the underly-

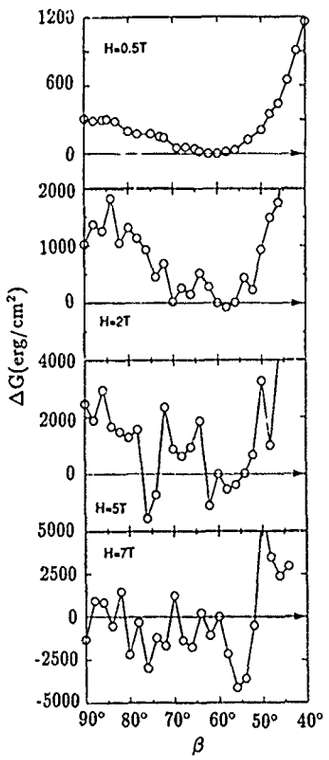

FIG. 4. Numerically computed Gibbs free energy density of a vortex lattice with space group $c2mm$ and angle β between primitive vectors (Fig. 3), relative to the triangular lattice ($\beta=60°$). The calculations are based on Eq. (1) with $\lambda=1500$ Å and $\xi=16$ Å. The numerical errors are much smaller than the symbol size.

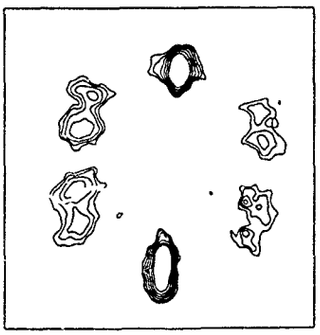

FIG. 5 Contour plot of SANS pattern for $H=2$ T, $\theta=20°$, obtained by rotating around (110).

ing microscopic electronic structure of the superconductor, in particular the spatial variation of the energy gap.

The link between the microscopic electronic structure and the mesoscopic structure of the vortex lattice is provided by the gap equation in a magnetic field. Even for an isotropic Bardeen–Cooper–Schrieffer (BCS) superconductor this equation is difficult to solve at a general magnetic field. Additional difficulties arise in the cuprates because the functional form of the gap equation is still under debate. However, as first shown by Abrikosov,[6] the equations simplify significantly near the upper critical field, where the magnetic induction is almost uniform. While for isotropic superconductors the equilibrium vortex lattice structure is the triangular lattice near H_{c2},[7] a $c2mm$ structure of the type we observe here has been observed before in the cubic superconductor Nb,[8] when the field is oriented in a fourfold crystallographic direction. This observation was explained theoretically by Takanaka,[9] who solved the gap equation of a superconductor with a cubic Fermi surface and found that in general structures of $c2mm$ symmetry have lower free energies than the triangular lattice. The angle β between primitive vectors depends on the degree of Fermi surface anisotropy through the parameter $\langle e^{i4\varphi}\rangle$, where φ is the azimuthal angle in the yz plane perpendicular to the magnetic field, and the brackets denote an average on the Fermi surface. We have parametrized the Fermi surface extracted from photoemission experiments[10] by two harmonics invariant under the point symmetry of the lattice

$$E_F(\varphi)=E_{F0}+E_{F1}\sin^2\varphi\cos^2\varphi, \tag{2}$$

with $E_{F1}\approx E_{F2}$, and obtain $\langle e^{i4\varphi}\rangle\approx E_{F1}/16E_{F0}$. According to the numerical calculations of Ref. 9, this value of $\langle e^{i4\varphi}\rangle$ corresponds to $\beta=63°$, much closer to 60° than the angle we observe. The origin of this discrepancy is likely to be an energy gap anisotropy contributed by the pairing interaction in the cuprates. It is already known that significant modifications to the standard gap equation are needed to account for the large directional variation of the energy gap observed in photoemission experiments on $Bi_2Sr_2CaCu_2O_{8+\delta}$.[11] Another possible origin of the quantitative discrepancy between theory and our observations is an in-plane penetration depth anisotropy, which various authors have determined to be between ~1.1 (Ref. 12) and ~1.5.[13] While a quantitative explanation of our data thus has to await more elaborate calculations based on realistic gap equations, it is remarkable that the symmetry of the vortex lattice is correctly predicted by an analysis whose only ingredient is the fourfold symmetry of the vortex core.

A more extensive treatment of anisotropic vortex lattices in type-II superconductors with a small ratio of penetration depth to coherence length has been given by Teichler,[14] who considered a cubic superconductor with an anisotropic pairing interaction. The resulting gap anisotropy leads to an attractive interaction between the vortices, in addition to the electrodynamic repulsion. The magnitude of the attractive interaction is largest in the direction of minimum energy gap, which is the (110) direction in $Bi_2Sr_2CaCu_2O_{8+\delta}$(Ref. 11) and presumably also in $YBa_2Cu_3O_7$. Teichler's analysis will likely need substantial modifications in the case of $YBa_2Cu_3O_7$. In particular, the energy gap in the (110) direction is extremely small and possibly zero, which may lead to a long range interaction between vortices. Nevertheless, the directional variation of the energy gap in the CuO_2 planes is a plausible explanation for the observed coupling between vortex lattice and crystal lattice orientations.

We[4] and others[3] had previously attributed this unique orientation of the vortex lattice to pinning by twin boundaries. However, the persistence of this orientation even as the field is inclined by up to 40° with respect to the twin boundaries is difficult to reconcile with this model. Moreover, the persistence of the same structure over an order of magnitude in magnetic field which we have now observed argues against a significant influence of twin boundaries on the vortex lattice structure and orientation. (Whereas at $H=0.5$ T the intervortex distance is comparable to the average twin boundary spacing, at $H=5$ T it is almost five times smaller.)

Since near H_{c1} the size of the vortex core is negligible compared to the intervortex distance, vortex core effects cannot play a role in determining the vortex lattice structure and orientation in very low magnetic fields. Indeed, Bitter decoration experiments near H_{c1} have revealed the expected triangular lattice with an orientation unrelated to any crystalline high-symmetry direction.[12,15] We thus expect a crossover between an orientationally degenerate triangular lattice and the oblique structure with unique orientation in an intermediate field range. There are some indications that this crossover actually occurs at a very low field, as expected for a large gap anisotropy: For $B\sim0.0065$ T, close to the largest field for which the Bitter decoration technique is applicable, Dolan *et al.*[13] observed a structure that is completely consistent with the one we observed (Fig. 3), except that $\beta=(65°\pm5°)$. Note that these measurements were taken in untwinned sections of $YBa_2Cu_3O_7$ crystals, further supporting our argument for an intrinsic origin of the coupling between the crystal lattice and vortex lattice. The field independence of β in the field range we have investigated suggests that β has already saturated at its H_{c2} value.

IV. TILT-INDUCED STRUCTURAL TRANSITION

We observe a potentially related structural transition as the magnetic field is inclined by an angle θ with respect to the c axis. This transition is superposed by an overall distortion of the vortex lattice due to the quasi two dimensionality of the electronic structure.[4,16] For inclination angles up to $\theta\sim60°$, the structure of the vortex lattice remains dominated by interactions within the CuO_2 sheets. The vortex lattice for small θ can thus be thought of as the projection of an isotropic two-dimensional lattice onto the field direction. This effect gives rise to an elliptical distortion of the vortex lattice; the semimajor axis of the ellipse coincides with $\hat{H}\times\hat{c}$, and the aspect ratio is $\cos\theta$ for small θ. (As three-dimensional interactions become relevant for larger θ, the aspect ratio becomes $\sqrt{\epsilon^2\sin^2\theta+\cos^2\theta}$, where $\epsilon\sim0.2$ is the penetration depth anisotropy.)

In addition to this overall anisotropy, we observe a continuous structural transition of the in-plane isotropic lattice as a function of θ: The angle $\beta=73°$ observed for $\theta\sim0$ de-

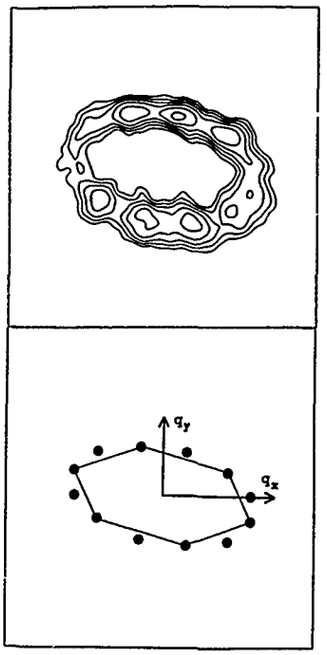

FIG. 6. (Top) contour plot of SANS pattern for $H=0.5$ T, $\theta=60°$, obtained by rotating around a low-symmetry crystallographic direction. (Bottom) projection of two isotropic triangular lattices in the CuO_2 layers onto the field direction for the same geometry. The lattices are oriented such that nearest-neighbor pairs point in either the (110) or the $(1\bar{1}0)$ direction. One of these domains is highlighted.

creases continuously and reaches $\beta=60°$, corresponding to the triangular lattice, for $\theta\sim50°$ (Fig. 6). The nearest-neighbor direction remains the in-plane (110) direction.

While the structural transition occurs for all three experimental geometries discussed in Sec. I, the domain structure of the observed lattice depends on the crystallographic direction chosen as the axis of rotation. If the field inclination is achieved by rotating around (100), all four domains of Fig. 3 continue to be populated. However, once β has reached 60°, domains 1 and 2, as well as domains 3 and 4, become identical. If the rotation axis is (110), a two-domain lattice is observed (Fig. 5). For the two observed domains, the projection of $(1\bar{1}0)$ is parallel to the direction $\hat{H}\times(\hat{H}\times\hat{c})$, i.e., the y axis in Fig. 1. [Note that the diffraction pattern can be obtained from the real lattice by a 90° rotation and rescaling, and that because of twinning (110) and $(1\bar{1}0)$ are superposed in our crystal.] This is the nearest-neighbor direction favored by the uniaxial anisotropy reflecting the quasi two-dimensional electronic structure.[17] The uniaxial anisotropy can thus lift the degeneracy between the domains.

We have also chosen an experimental geometry in which the inclination is achieved by rotating around a low-symmetry crystallographic direction such that (110) and $(1\bar{1}0)$ subtend identical angles with the rotation axis.[4] In this case we also observe a two-domain lattice for small θ, although the uniaxial anisotropy does not distinguish between the two domain pairs. However, the vortices in the two domain pairs subtend different angles with respect to both sets of twin boundaries.[4] Pinning interactions between vortices and twin boundaries favor the pair of domains subtending the smaller angle with respect to the twin boundaries, because the vortices have to bend less in order to gain advantage of the pinning energy. Although, as discussed above, the structure and orientation of the vortex lattice are determined by electronic energies that are presumably much larger than pinning energies, pinning effects appear to provide enough energy to select between otherwise degenerate domains.

It may not be coincidental that the triangular structure observed in inclined fields is just the structure expected in the London limit, since the in-plane vortex lattice is only sensitive to a reduced field component $H\cos\theta$ perpendicular to the CuO_2 sheets. Moreover, for large θ the effective core size shrinks because of the reduced coherence length in the c-axis direction. Electrodynamic effects should thus become more relevant for larger inclinations. Detailed numerical calculations to test these ideas are currently underway.

V. TILT-INDUCED REORIENTATION AND VORTEX CHAIN STATE

In agreement with this general scenario, we observe a reorientation of the vortex lattice into the unique orientation predicted by the anisotropic London model when the inclination is achieved by rotating around (100). In this case the orientation favored by the in-plane energy gap anisotropy is different from the orientation favored by the anisotropic electrodynamic interactions between the vortices. For small θ the electrodynamic energies favoring the $\hat{H}\times(\hat{H}\times\hat{c})$ direction as the nearest-neighbor direction are small,[17] and the in-plane anisotropy determines the vortex lattice orientation. As the shielding currents around the vortices begin to flow in the c-axis direction for large θ, in-plane anisotropy effects diminish and the electrodynamic effects associated with the uniaxial penetration depth anisotropy begin to dominate. The crossover between these two orientations is gradual and begins at $\theta\sim70°$ in this geometry, coming to completion for $\theta\sim80°$.

In the large-θ orientation, the vortex lattice can be considered as a collection of chains with locked periodicity extending in the $\hat{H}\times(\hat{H}\times\hat{c})$ direction. Because of the penetration depth anisotropy, the distance between the chains is much larger than the nearest-neighbor distance within the chains. Based on calculations in the London limit, an extremely small modulus for shear in the chain direction has been predicted,[18] thus causing a decoupling of the chains even for very weak pinning disorder or thermal fluctuations. This vortex chain state has indeed been observed in Bitter decoration experiments in very low magnetic fields.[19] We have observed the same instability in fields of 0.5 and 2 T. Its experimental signature is a continuous broadening of all Bragg reflections not exclusively associated with the distance between the chains. For $\theta=80°$ only the two reflections with Bragg planes parallel to the chain direction remain sharp and observable. Note that all of our diffraction patterns were taken after field cooling the sample to low temperatures. The disordered vortex chain state is thus presumably frozen in at high temperatures.

We have carefully measured the width of the "rocking curves" of the vortex chain state reflections at $H=0.3$ T, using a vertical-field electromagnet. This measurement pro-

vides direct information about the "straightness" of the vortices in the bulk of the sample. A temperature dependence of the rocking curve could thus herald dimensional crossover effects or thermal wandering of three-dimensional vortices. We find that the rocking curves, as well as the width of the reflections perpendicular to the field direction, remain resolution limited up to at least $T=80$ K. The signal-to-background ratio became too low to extract reliable information from measurements taken at higher temperatures. We plan to repeat these measurements in higher magnetic fields, where we expect the conditions to be more favorable

VI. CONCLUSIONS

In conclusion, we have demonstrated an unanticipated connection between the vortex lattice structure in magnetic fields of order 1 T and the microscopic electronic structure of $YBa_2Cu_3O_7$. As a result of the directional variation of the energy gap in the CuO_2 plane, the symmetry and orientation of the vortex lattice is coupled to the underlying crystal lattice when the field is applied in the c-axis direction. This coupling diminishes gradually as the field is inclined with respect to the c axis. As a function of increasing inclination angle we observe a two-step transition of the vortex lattice into the symmetry and orientation predicted by the London model with uniaxial anisotropy.

ACKNOWLEDGMENTS

We are grateful to C. Glinka and J. Rush for their support and advice, and to V. J. Emery, H. F. Hess, D. E. Moncton, N. P. Ong, and M. Yethiraj for helpful discussions. This work is based upon activities supported by the National Science Foundation under Agreement No. DMR-9122444. The work at Princeton was supported by the Advanced Research Projects Agency and the Air Force Office of Scientific Research under Grants AFOSR No. F49620-90-C-0079 and No. F49620-93-I-0259.

[1] G. Lippmann, J. Schelten, and W. Schmatz, Philos. Mag. **33**, 475 (1976).
[2] J. S. Pedersen, D. Posselt, and K. Mortensen, J. Appl Crystallogr. **23**, 321 (1990).
[3] E. M. Forgan *et al.*, Physica C **185–189**, 247 (1991); M. Yethiraj *et al.*, Phys. Rev. Lett. **70**, 857 (1993).
[4] B. Keimer *et al.*, Science **262**, 83 (1993)
[5] M. Tinkham, *Introduction to Superconductivity* (Krieger, Malabar, 1975).
[6] A. A. Abrikosov, Zh. Exp. Teor. Fiz. **32**, 1442 (1957); Sov. Phys. JETP **5**, 1174 (1957).
[7] W. H. Kleiner, L. M. Roth, and S. H. Autler, Phys. Rev. **133**, A1226 (1964).
[8] J. Schelten, G. Lippmann, and H. Ullmaier, J. Low Temp. Phys. **14**, 213 (1974).
[9] K. Takanaka, Prog. Theor. Phys. **46**, 1301 (1971); **49**, 64 (1973).
[10] J. C. Campuzano *et al*, Phys. Rev. Lett. **64**, 2308 (1990).
[11] Z.-X. Shen *et al.*, Phys. Rev. Lett **70**, 1553 (1993).
[12] G. J. Dolan *et al.*, Phys. Rev. Lett. **62**, 2184 (1989).
[13] K. Zhang and D A Bonn *et al*, preprint.
[14] H. Teichler, Philos. Mag. **30**, 1209 (1974); **31**, 789 (1975); K. Fischer and H. Teichler, Phys. Lett. A **58**, 402 (1976)
[15] P. L. Gammel, in *Phenomenology and Applications of High-Temperature Superconductors* (Addison–Wesley, New York, 1992).
[16] M. Yethiraj *et al.*, Phys. Rev. Lett. **71**, 3019 (1993).
[17] L. J. Campbell, M. M. Doria, and V. G. Kogan, Phys. Rev. B **38**, 2439 (1988); L J. Campbell and V. G. Kogan, Phys. Rev. Lett. **62**, 1552 (1989).
[18] B. I. Ivlev and N. B. Kopnin, Phys. Rev. B **44**, 2747 (1991); B. I. Ivlev, N. B. Kopnin, and M. M. Salomaa, *ibid.* **43**, 2896 (1991).
[19] P. L. Gammel *et al.*, Phys. Rev. Lett. **68**, 3343 (1992).

Small-angle neutron scattering study of the flux-line lattice in a single crystal of $Bi_{2.15}Sr_{1.95}CaCu_2O_{8+x}$ (invited)

M. Yethiraj and H. A. Mook
Oak Ridge National Laboratory, Solid State Division, MS 6393, Oak Ridge, Tennessee 37831-6393

E. M. Forgan, R. Cubitt, and M. T. Wylie
School of Physics and Space Research, University of Birmingham, Edgbaston, Birmingham B15 2TT, United Kingdom

D. M. Paul
Department of Physics, University of Warwick, Coventry CV4 7AL, United Kingdom

S. L. Lee
Physk-Institut der Universität Zürich, CH-8057 Zürich, Switzerland

J. Ricketts
Superconductivity Research Laboratory, ISTEC, Japan

P. H. Kes
Kammerlingh Onnes Laboratorium, Leiden University, P.O. Box 9506, 2300 RA, Leiden, The Netherlands

K. Mortensen
Physics Department, Risó National Laboratory, DK-4000, Roskilde, Denmark

A flux-line lattice (FLL) was observed in a single crystal of $Bi_{2.15}Sr_{1.95}CaCu_2O_{8+x}$ (BSCCO) using small-angle neutron scattering methods. The sample has a superconducting transition at 85 K. The flux-line lattice is observed to melt. evidenced by the rapid disappearance of diffracted intensity as the temperature is increased above a field-dependent melting temperature. Diffracted intensity due to the vortex lattice also falls off as the applied field is increased. It is believed that this is a manifestation of the transition of the three-dimensional flux lines into two-dimensional pancake vortices. The Bragg intensity of the FLL peak is inversely proportional to the fourth power of the London penetration depth (λ_L). Hence, the temperature (T) dependence of the order parameter can be measured quite accurately from the intensity of the Bragg spots at different temperatures. In BSCCO with an applied field of 50 mT, the measured T dependence appears linear. The low-T behavior is of great interest for an understanding of the underlying mechanism for superconductivity in these materials.

INTRODUCTION

In type-*I* superconductors, an applied field is completely screened till the field strength exceeds the critical field. A higher field causes the superconductor to become normal, that is, nonsuperconducting. In 1957, Abrikosov[1] in his theory of type-*II* superconductors predicted the existence of the "mixed" state, where flux carried by quantized flux lines or vortices penetrate the bulk material, causing parts of the superconducting material to become normal. This occurs for applied fields (B) such that $H_{c1}<B<H_{c2}$, where H_{c1} and H_{c2} are the lower and upper critical fields, respectively.

The interaction between vortices is repulsive, hence vortices form a lattice which maintains the maximum distance between them. Each vortex line contains a total flux equal to the flux quantum $\Phi_0=hc/2e$, where h is Planck's constant, c is the speed of light, and e the charge of an electron. Hence the total number of flux lines in the sample is determined by the external applied field.

The arrangement of flux lines was first observed in Bitter patterns or decoration experiments. When a thin layer of finely ground ferromagnetic particles are deposited on the surface of a superconductor which is then cooled in a field, the magnetic dust settles at the normal cores of the vortex. The resulting decoration reflects the underlying field distribution. Extremely clear decorations have been seen by a number of groups, both in the conventional as well as in the high-T_c materials. It is also the method by which defects in vortex lattices were first observed. More recently, scanning tunneling microscopes equipped with a magnetic tip have been used to look at the field distribution in conventional superconductors. The most serious limitation of both these techniques is that they probe only the surface. Also, the fields used to get a good decoration must be quite low to distinguish between the cores. To their advantage, samples can be quite small. Invariably, more perfect samples can be obtained when large size is not required.

The properties of the flux lattice as a function of field and temperature are important both for a better understanding of the nature of the interaction causing pair formation in high-T_c superconductors and also for applications of the material in devices. Using small-angle neutron scattering (SANS), the temperature (T) dependence of the London depth is vital information that can be measured. In the London model, the intensity of the Bragg peaks is proportional to the inverse fourth power of the London penetration depth; because of this strong dependence, this length can be accurately determined. Of all the high-T_c superconductors, $YBa_2Cu_3O_7$ (YBCO) is of particular interest in applications since the large pinning, due to twin plane defects, leads to

 0021-8979/94/76(10)/6784/4/$6.00 © 1994 American Institute of Physics

high critical currents. However, the transition mechanism in high-T_c superconductors is a topic of ongoing debate and the high density of the twin plane defects in the samples of YBCO that have been studied cast some doubt on whether or not the observed temperature dependence is intrinsic or due to the defects combined with the fact that the temperatures involved are quite high and thermal effects can be substantial. Hence, measuring the temperature dependence of the order parameter in a material with relatively few defects, such as our sample of $Bi_{2.15}Sr_{1.95}CaCu_2O_{8+x}$ (BSCCO), is quite important.

In addition, it has been clear for some time that YBCO and BSCCO behave quite differently. BSCCO is much more anisotropic than YBCO. A variety of vortex structures that have been suggested for high-T_c superconductors in general vortex lattice melting with increase in temperature and $3d$-$2d$ dissociation have been invoked to explain experimental data. Although this is expected in YBCO as well, the effects in BSCCO were larger and occurred at lower fields and temperatures because of its larger anisotropy. It was apparent that the B-T phase diagram for BSCCO was not dull.

The anisotropy of the high-T_c superconductors is, in general, nominally uniaxial since the a-b (basal plane) anisotropy is fairly small and the c axis is considerably larger. In BSCCO, the crystal structure is nearly tetragonal with the a/b ratio close to unity and $c \approx 5.5a$. Consequently, the high symmetry configuration for the observation of the vortex lattice is with the applied field parallel to the crystallographic c axis of the crystal. The information about the ratio of the in-plane effective mass to that out of plane is obtained from FLL's in the geometry where the applied field is at a large angle to the c axis of the crystal.

In the last few years, we have carried out SANS experiments in the high-T_c superconductors YBCO and BSCCO. In this article we discuss the measurements that we have made of the flux lattice in single-crystal samples of BSCCO both with the field parallel to the c axis and with the field at an angle of up to 15° from the c axis. We also discuss the experimental technique and the information that it gives in some detail.

EXPERIMENT

Small-angle neutron scattering experiments were first suggested by deGennes and Matricon.[2] (Since neutrons have a magnetic moment, they interact with the field modulation caused by an array of flux lines.) Shortly thereafter, a Bragg diffraction peak from a flux-line lattice corresponding to the predicted triangular arrangement was observed by Cribier and co-workers[3] in a single-crystal sample of niobium on which a magnetic field was applied. Since then, extensive measurements have been made in Jülich[4] and Oak Ridge,[5] on niobium as well as other conventional superconductors, probing the details of the lattice structure, the effect of defects, the exact nature of the form factor and of the temperature-dependent order parameter.

The d spacing, d, of the first-order reflection of a triangular isotropic lattice, determined solely by the applied field and the flux quantum, is given by

$$d = \left(\sqrt{\frac{2}{3}} \frac{\Phi_0}{B} \right)^{1/2}, \tag{1}$$

where B is the applied field and Φ_0 is the flux quantum. (The intervortex spacing, $a, = d/\cos 30.$) For an applied field of 100 mT, this distance is approximately 1350 Å, corresponding to a q value of 0.0047 $Å^{-1}$. Hence, the angles at which this scattering can be observed are small. The vortex is a line of magnetic flux; the lateral extent of the field distribution is determined by the London penetration depth, λ_L. The intensity of a diffraction peak, I_{hk}, is given by

$$\frac{I_{hk}}{I_0} = 2\pi \left(\frac{\mu}{4} \right)^2 \frac{1}{q_{hk}} \left(\frac{V\lambda_n^2}{\phi_0^2} \right)^2 \left(\frac{B}{1+q_{hk}^2\lambda_L^2} \right)^2, \tag{2}$$

where I_0 is the incident neutron flux, μ the neutron magnetic moment in Bohr magnetons ($\mu = 1.91$), V the sample volume, λ_n the neutron wavelength, λ_L the London penetration depth, B is the applied magnetic field, and Φ_0 is the flux quantum.

The London depth is approximately the half-width at half maximum of the field distribution of a single flux line, hence there is less contrast for larger λ_L. For niobium, $\lambda_L \approx 400$ Å, whereas for the high T_c materials, it is at least three times larger. The signal to be measured is therefore lower by approximately two orders of magnitude. Also, the signal for the first-order reflections, barring other complications, is relatively independent of the applied field except for a geometrical $1/q$ factor. On the one hand, there is less contrast between the peak and valley at a higher field due to larger number of flux lines; on the other, the number of scatterers is higher which balances the equation. However, there is considerable gain in utilizing a larger field in order to get away from the incident beam and the metallurgical scattering as much as possible in order to increase the signal to noise ratio.

In order to obtain the integrated intensity, the rocking curve (or mosaic width), $\Delta\theta$, of the Bragg scattering must be measured. This mosaic is a measure of the straightness of the flux lines along the applied field direction or a measure of the length over which they remain straight. If it is assumed that the mosaic is entirely due to finite sample size (i.e., flux-line length), the lower limit on this length is determined. A scattering object of finite size leads to an extended object in reciprocal space. If it is assumed that the flux lines are straight over length l, the Fourier width on reciprocal space is given by

$$\left(\frac{2\pi}{l} \right) \Big/ q = \Delta\theta, \quad \text{hence} \quad l = \frac{d}{\Delta\theta}. \tag{3}$$

Because the measured rocking width convolutes this length effect with any meandering of the flux lines away from the field direction, l is a lower limit on the length of the lines.

Data were taken on the small-angle spectrometer at Risø National Laboratory using an incident neutron wavelength of nearly 20 Å and a $\delta\lambda/\lambda$ of 18%. The lowest applied field was 200 mT.

The sample used for most of these measurements was a platelike single crystal weighing 180 mg. This sample had a (crystal) mosaic width of approximately 0.5°. Other samples were also studied briefly thus far; all had a nominal compo-

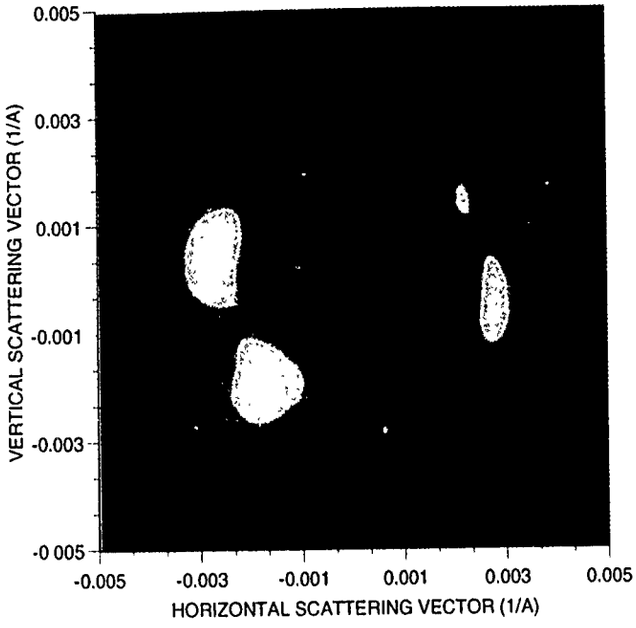

FIG. 1. The flux-lattice signal seen in a difference measurement between field-cooled (40 mT) and zero-field-cooled data.

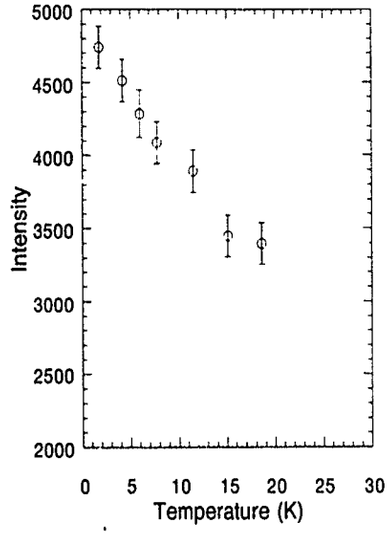

FIG. 2. The temperature dependence of the order parameter at low temperature.

sition given by $Bi_{2.15}Sr_{1.95}CaCu_2O_{8+x}$. The samples appear to be untwinned; front and back faces had the same relative orientation of the a axis in x-ray characterizations.

RESULTS AND DISCUSSION

At the lowest temperatures, with the applied field (50 mT) parallel to the c axis of the sample, the flux-line lattice was seen[6] in the difference signal between field-cooled and zero-field-cooled runs, shown in Fig. 1. The lattice has six-fold symmetry and is aligned with the crystalline b axis in all the samples measured. It is likely that the samples are untwinned since the flux lattice consists of only one domain. (A twinned crystal would give rise to a second domain rotated by 90°.) The mosaic width of this lattice was approximately 1.2(2)°, giving a minimum flux-line length of approximately 10 μm. From the integrated intensity, the London penetration depth obtained for BSCCO at the lowest temperatures is approximately 1800 Å, not significantly different from YBCO.

As the applied field was increased, the signal intensity decreased faster than expected from the $(1/q)$ factor. The signal intensity began to decrease as the field was raised above 50 mT and for fields above 100 mT, no flux lattice was observed at all. We believe this to be a manifestation of the dissociation of three-dimensional flux lines into $2d$ pancakes. This was also observed in μSR measurements[7] on samples prepared by the same method. The $3d$-$2d$ transition occurs at the same field that appears to be independent of temperature.

The intensity, which is inversely proportional to the fourth power of the London penetration depth, decreases linearly at low temperatures in BSCCO, as shown in Fig. 2. This is unlike conventional s-wave superconductors where intensity changes very little for T less than about $T_c/3$. Also, there appears to be no anisotropy within the measured errors in the plane. That is, the T dependence of the Bragg peaks aligned along b compared to the peaks 60° from b show no significant difference. However, it must be emphasized that the linear slope at low temperatures does not imply d-wave superconductivity, the interpretation of the T dependence is still an open question.

At a temperature that is dependent on the applied magnetic field, we observe the rapid decrease of the intensity associated with melting of the flux lattice. The melting occurs at the same temperature at which finite resistance appears within the the superconducting state. The melting line in the B-T phase diagram appears to coincide with measurements of the irreversibility line. The schematic B-T phase diagram from neutron scattering and magnetic measurements is shown in Fig. 3. The solid line in the figure is found by using the relation[8]

$$B_{3D}(T_m) \approx \frac{1}{\{[4\sqrt{2}-1)+1]^2 \pi \mu_0^2\}} \left[\frac{\phi_0 c_L^4}{[\gamma k_B T_c \lambda_{ab}^2(0)]^2}\right] \times \left[\frac{1-(T_m/T_c)^n}{T_m/T_c}\right]^2, \quad (4)$$

with the Lindemann melting parameter, $c_L=0.2$, the mass ratio, $\gamma^2=140^2$, the in-plane London penetration depth at zero temperature, $\lambda_{ab}(0)=1800$ Å, and $n=3.3$. This line is in good agreement with the observation of flux-lattice melting observed here as well as by the muon spin rotation measurements. It is reasonable to assume that this decrease in intensity represents the melting of the 3-d lattice. Careful analyses show no broadening or any other indication that the flux line is approaching the melting temperature. We do not see any signal at all above T_m even though a ring of scattering is expected, presumably because the disordered flux liquid is not a strong enough scatterer to give a measurable count. The coherent Bragg signal could not be seen in the raw data but only in a difference as stated earlier. Hence it is not unex-

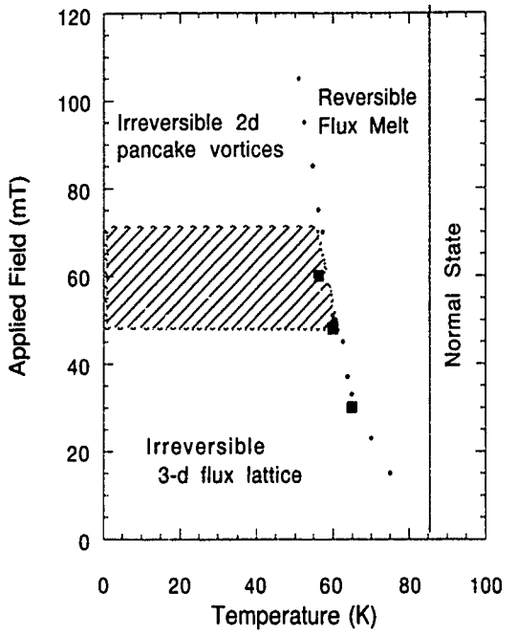

FIG. 3. The B-T phase diagram for BSCCO.

pected that a signal from a disordered liquid having the same total scattering contrast would be beyond what can be measured here in a reasonable time. Since the melting is associated with finite resistance, applications may not have advantages in using BSCCO. Materials with lower anisotropies and stronger pinning will probably make better candidates for devices.

In our earlier work[9] on YBCO, the effects of anisotropy were clearly seen as the angle between the applied field and c axis of the crystal, Θ, was increased and the effective mass ratio was determined. In BSCCO, an effort to measure this ratio resulted in very odd behavior. In this system, when the angle Θ was increased, the signal from the vortex lattice dropped sharply at a moderate applied field of 30 mT. In fact, by the time Θ was increased to 15°, no measurable scattering was observed. The loss of intensity could arise due to melting at a lower temperature when Θ is increased, but this is inconsistent with the μSR data[7] in which a three-dimensional lattice is clearly seen for larger angles at the same field. It is possible that the c axis is a preferred direction for the flux line (in a manner similar to YBCO, although twin plane defects are thought to cause the effect in that compound), perhaps because the currents prefer to flow in the a-b plane. To test this hypothesis, we searched for the scattering signal with the q vector perpendicular to the c axis but did not observe any. (NOTE: In the latter configuration, the field direction was Θ from the incident neutron direction and the c axis was now parallel to the incident neutrons.) More experiments are planned in order to elucidate this matter. Clearly, much more remains to be learned about these superconducting systems.

ACKNOWLEDGMENTS

This work was supported in part by the Division of Materials Sciences, US DOE under Contact No. DE-AC05-84OR21400 with Martin Marietta Energy Systems, Inc.

[1] A. A. Abrikosov, Zh. Eksper. Teor. Fiz. **32**, 1442 (1957); Sov Phys JETP **5**, 1174 (1957).
[2] P. G. deGennes and I. Matricon, Rev. Mod. Phys. **36**, 45 (1964).
[3] D. Cribier *et al.*, Phys. Lett. **9**, 106 (1964).
[4] Schelten *et al.*, Phys Status Solidi B **48**, 619 (1971).
[5] D. K. Christen *et al.*, Phys. Rev. B **15**, 4506 (1977)
[6] R. Cubitt, E. M. Forgan, G. Yang, S L. Lee, D McK. Paul, H. A. Mook, M. Yethiraj, P. H. Kes, T. W. Li, A. A. Menovsky, Z. Tarnawski, and K. Mortensen, Nature (London) **365**, 407 (1993).
[7] S. L. Lee *et al*, Phys. Rev. Lett. **71**, 3862 (1993).
[8] A. Houghton, R. A. Pelcovits, and A Sudbø, Phys Rev. B **43**, 130 (1991).
[9] M. Yethiraj *et al.*, Phys. Rev. Lett **71**, 3019 (1993).

Neutron diffraction from the vortex lattice in the heavy fermion superconductor UPt_3 (invited) (abstract)

R. N. Kleiman, G. Aeppli, D. J. Bishop, C. Broholm, E. Bucher, N. Stüchelli, and U. Yaron
AT&T Bell Laboratories, Murray Hill, New Jersey 07974

K. N. Clausen, B. Howard, K. Mortensen, and J. S. Pedersen
Risø National Laboratory, Roskilde, Denmark

The heavy fermion superconductor UPt_3 is thought to have a d-wave pairing ground state. The principal experimental evidence for this consists of the anisotropy of the power-law behavior observed in transverse ultrasound and μ^+ SR measurements. The observation of a complex phase diagram in the superconducting state in ultrasound, torsional oscillator, and specific heat measurements may be a further indication of an unconventional pairing state. Theoretical investigations suggest the possibility of vortex lattices that are unconventional in their symmetry, their quantization, or the structure of their composite vortex cores. Transitions between such exotic vortex lattices are in principle allowed and could explain the observed features at $\mathbf{H}\approx 0.6\,H_{c2}$ (for $H\|\hat{c}$) and $H\approx 0.3H_{c2}$ (for $\mathbf{H}\perp\hat{c}$). Neutron diffraction is an ideal bulk probe of the microscopic properties of the vortex lattice. We have studied the vortex lattice with $\mathbf{H}\perp\hat{c}$ and $T\approx 50$ mK in the field range $0.75<H<10$ kG. The structure of the vortex lattice and the quantization of the vortices, in addition to the London penetration depth, λ_L, the coherence length, ξ, and the effective mass anisotropy are all well determined by our measurements.[1] The lattice is oblique hexagonal with conventional quantization. Its anisotropy can be explained by considering a combination of Fermi surface and gap anisotropy. However, the lattice does not appear to change near the transition between superconducting phases identified by other techniques.

[1] R. N. Kleiman, C. Broholm, G. Aeppli, E Bucher, N. Stüchelli, D J Bishop, K. N. Clausen, K. Mortensen, J. S. Pedersen, and B. Howard, Phys. Rev. Lett. **69**, 3120 (1992).

 0021-8979/94/76(10)/6788/1/$6.00 © 1994 American Institute of Physics

Small angle neutron scattering from the vortex lattice in 2*H*-$NbSe_2$ (invited) (abstract)

P. L. Gammel, U. Yaron, D. A. Huse, R. N. Kleiman, B. Batlogg, C. S. Oglesby, E. Bucher, and D. J. Bishop
AT&T Bell Laboratories, Murray Hill, New Jersey 07974

T. E. Mason and K. Mortensen
Risø National Laboratories, 4000 Roskilde, Denmark

We report on small angle neutron scattering studies of the flux-line lattice in single crystal 2H-$NbSe_2$. For fields inclined with respect to the c axis, we find distortions and form factors consistent with Ginzburg–Landau corrections to the London equations with a mass anisotropy $\Gamma=10.1\pm0.9$. The flux lattice orientation, however, remains pinned to the crystal lattice for all tilts studied, in disagreement with the orientation defined by anisotropic London theory.[1] For fields below 2 kG parallel to the c axis, the peaks are no longer resolution limited. The correlation lengths extracted are history dependent, and show that the lattice is annealed when a current greater than the critical current is applied. This occurs both when a direct transport current is used, or an induced current in a zero field cooled experiment. The annealing is seen in both the transverse and longitudinal correlation lengths, and calls into question the relationship between the Larkin–Ovchinnikov correlation length and the measured critical currents in this system.

[1] P. L. Gammel *et al.*, Phys. Rev. Lett. **72**, 278 (1994).

 0021-8979/94/76(10)/6789/1/$6.00 © 1994 American Institute of Physics

Giant magnetoresistance in sputtered Cr-Fe heterogeneous alloy films

K. Takanashi, T. Sugawara, K. Hono, and H. Fujimori
Institute for Materials Research, Tohoku University Sendai 980-77, Japan

We have observed large negative magnetoresistance (MR) in Cr-Fe heterogeneous alloy films sputter deposited on heated substrates. The largest MR, 37.3% at 4.2 K and 14 T, appears around the Fe concentration of 20 at. %. While a large substrate temperature dependence of MR is observed when the Fe concentration is lower than 20 at. %, MR does not vary noticeably with changes in the substrate temperature when Fe concentration exceeds 20 at. %.

I. INTRODUCTION

Recently, giant magnetoresistance (GMR) in heterogeneous alloy films such as Cu-Co,[1,2] Ag-Co,[3,4] and Ag-Fe,[4-6] in which ferromagnetic particles of nanometer size are homogeneously distributed in the nonmagnetic matrix, has been attracting much interest. GMR was found in multilayered Cr/Fe for the first time;[7,8] however it has never been reported in Cr-Fe heterogeneous alloys. This is the first report on GMR behavior in sputtered Cr-Fe heterogeneous alloy films.

Cr-Fe has an isostructure two phase region below 475 °C but the solubility limit of Fe in Cr is considerable. The σ phase is present in the temperature range from 475 to 821 °C, which makes high temperature annealing for inducing phase separation without an appearance of σ phase difficult. Above 821 °C, Cr and Fe are entirely miscible.[9] These features are in contrast to the Cu-Co, Ag-Co, and Ag-Fe systems, in which GMR has been reported in the heterogeneous structure. In such alloy systems, the heterogeneous structure can been obtained upon annealing nonequilibrium solid solutions prepared by sputtering or rapid quenching. In the case of Cr-Fe, however, post-deposition annealing is not appropriate for phase separation because of the slow kinetics. Hence, in the present study, we have deposited Cr-Fe alloy films at elevated temperatures. Sputter deposition on heated substrates is expected to promote phase separation due to surface diffusion which is many orders of magnitude faster than the volume diffusion that would otherwise control the kinetics of the post-deposition annealing.[10]

II. EXPERIMENT

Cr-Fe heterogeneous alloy films were prepared by the rf sputtering method on Si substrates heated up to 200 °C. For comparison, Cr-Fe homogeneous alloy films were also prepared by rf sputtering on Si substrates cooled by liquid nitrogen. The composition of the alloy films was varied from 0 to 40 at. % Fe by the number of Fe sheets (10×10 mm^2) on a Cr target (ϕ100 mm). The composition of the films was determined by inductively coupled plasma (ICP) emission spectroscopy analysis. In this article, the sample with the Fe concentration of x at. % deposited at the heated/cooled substrate is denoted as h/c-$Cr_{1-x}Fe_x$. The background pressure of the sputtering chamber was approximately 1×10^{-6} Torr. Sputtering was carried out in an atmosphere of Ar gas at 5×10^{-3} Torr by applying a power of 500 W. The distance between the target and the substrate was 100 mm. The deposition rate was typically 1.5 Å/s, and the films were 1–2 μm thick. The microstructure of the samples was observed by a 120 kV transmission electron microscope (TEM), Philips CM12. TEM specimens were prepared by ion milling after mechanically grinding the substrate. The Ar ion current for ion milling was set to be 0.5 mA at 4 kV. Magnetoresistance (MR) was measured at 4.2 K by the conventional four-probe method. An electromagnet was used in a low field range of $\pm$0.6 T, and a superconducting magnet was used in high fields up to 14 T. Magnetization versus applied magnetic field (M-H) curves were measured at 4.5 K in the range of $\pm$5.5 T, using a SQUID magnetometer (Quantum Design, MPMS).

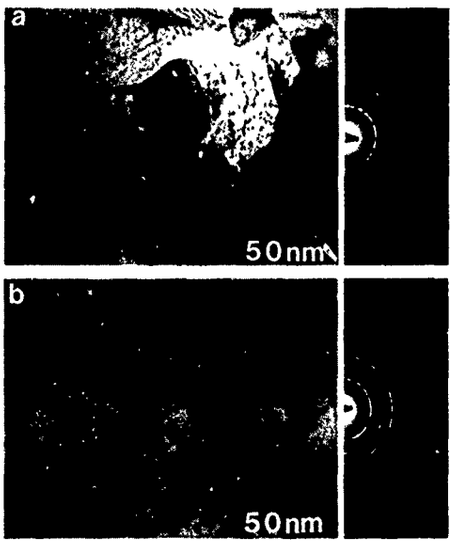

FIG. 1. Bright field TEM images and selected area diffraction patterns of (a) a $Cr_{83.9}Fe_{16.1}$ film sputtered on the heated substrate (h-$Cr_{83.9}Fe_{16.1}$) and (b) a $Cr_{83.1}Fe_{16.9}$ film sputtered on the cooled substrate (c-$Cr_{83.1}Fe_{16.9}$).

 0021-8979/94/76(10)/6790/3/$6.00 © 1994 American Institute of Physics

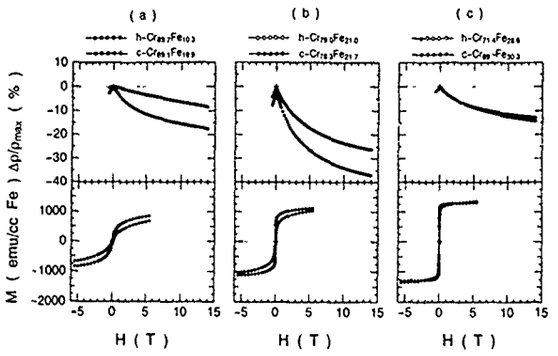

FIG. 2. MR (upper) and M-H (lower) curves of (a) a $Cr_{89.7}Fe_{10.3}$ film sputtered on the heated substrate (h-$Cr_{89.7}Fe_{10.3}$) and a $Cr_{89.1}Fe_{10.9}$ film sputtered on the cooled substrate (c-$Cr_{89.1}Fe_{10.9}$), (b) h-$Cr_{79.0}Fe_{21.0}$ and c-$Cr_{78.3}Fe_{21.7}$, and (c) h-$Cr_{71.4}Fe_{28.6}$ and c-$Cr_{69.7}Fe_{30.3}$. The MR curve is represented as the resistivity normalized by the maximum around zero field, $\Delta\rho/\rho_{max}$, as a function of applied field, H. In the M-H curves, the values per Fe volume are shown.

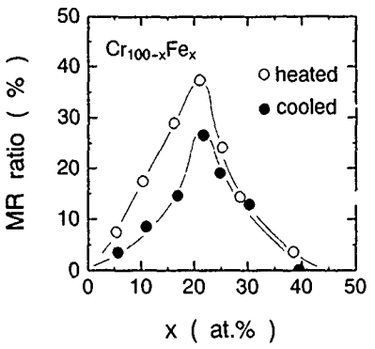

FIG. 3. Fe concentration, x, dependence of the MR ratio in $Cr_{1-x}Fe_x$ alloy films sputtered on the heated (open circles) and cooled (closed circles) substrates.

III. RESULTS AND DISCUSSION

Figures 1(a) and 1(b) show bright field images and their corresponding selected area diffraction patterns (SADP) of h-$Cr_{83.9}Fe_{16.1}$ and c-$Cr_{83.1}Fe_{16.9}$, respectively. The SADPs indicate that the films consist of a bcc phase. The average grain size is 200 nm for h-$Cr_{83.9}Fe_{16.1}$ and 70 nm for c-$Cr_{83.1}Fe_{16.9}$, respectively, indicating that cooling by liquid nitrogen reduces the grain size remarkably. For the h-$Cr_{83.9}Fe_{16.1}$ sample, small specks can be seen within a grain. The size of the specks is approximately 2 nm and these distribute homogeneously within the grain. Such specks are seen in many grains, although the appearance of the image varies depending on the orientation of the grains. This specklike contrast is probably due to the presence of Fe-rich ferromagnetic isostructural particles. The formation of these particles is considered to be a result of the phase separation which progressed during the film growth on the heated substrate.

Typical examples of MR and M-H curves are shown in Figs. 2(a)–2(c). The MR curves represent the normalized resistivity, $\Delta\rho/\rho_{max}$, as a function of applied magnetic field H. In the M-H curves, the values of magnetization are calculated per Fe volume. The results of two specimens with a similar composition but grown at different temperatures are displayed in the same figure. Negative MR is observed for all the samples. Interestingly, the maximum value of MR as large as 37.3% is observed in h-$Cr_{79.0}Fe_{21.0}$. However, MR does not saturate even at 14 T for all the samples. At the Fe concentrations of $x<10$ at. %, the resistivity for the films grown on the cooled substrate decreases almost linearly as a function of the magnetic field. On the other hand, the resistivity drops more steeply in the low field region for the films grown on the heated substrate. As the concentration of Fe increases, the discrepancy between the MR curves for the heated and cooled substrates diminishes and both are almost the same at $x>25$ at. %. A similar tendency is seen for the M-H curves. The magnetization for the heated substrate saturates more easily than that for the cooled substrate in the low x region, and the saturation of the magnetization for the cooled substrate becomes easier with increasing x. The concentration dependence of the MR ratio, $[\rho_{max}-\rho(H=14\ T)]/\rho_{max}$, is shown in Fig. 3. The MR ratio has a maximum around $x=20$ at. % for both heated and cooled substrates, similarly to other systems such as Ag-Fe.[5] However, the MR ratio for the cooled substrate is smaller than that for the heated substrate at $x<25$ at. %, and no difference is seen at $x>25$ at. %.

The negative MR behavior observed in samples grown on cooled substrates is considered to be equivalent to that reported for various spin glasses.[11–13] We have also prepared homogeneous bulk Cr-Fe alloys by the solution treatment, and confirmed a similar MR behavior.[14] In the spin glass state, single Fe atoms and/or small Fe clusters with a few Fe atoms distribute in a Cr matrix randomly. The magnetization vectors of the Fe atoms and clusters lie in different directions. Therefore, the MR and the magnetization do not saturate easily. By heating substrate phase separation may progress during the film growth. In this case, large ferromagnetic Fe particles, the average size of which is estimated to be 2 nm, are formed as shown in Fig. 1(a). Consequently, the MR and the magnetization for the heated substrate changes more steeply in low fields than those for the cooled substrate; the MR ratio for the heated substrate is larger than that for the cooled substrate. However, Figs. 2 and 3 indicate that the shape of the MR curve and the magnitude of the MR ratio do not depend on the substrate temperature at $x>25$ at. %. The reason for this is considered to be as follows: In a concentrated region, even if Fe atoms are randomly distributed in the Cr matrix, the density of Fe atoms is so high that a considerable amount of Fe atoms couple ferromagnetically to form a magnetic cluster.[15] The size of the magnetic clusters may be comparable to that of Fe particles precipitated by heating the substrate. Consequently, the difference between the MRs for the heated and cooled substrates disappears in the concentrated region. The fact that the MR has a maximum around $x=20$ at. % also suggests that ferromagnetic coupling of Fe atoms becomes dominant when x becomes larger than 20–25 at. %. In fact, by neutron diffraction, Burke *et al.*[15] showed that the onset of ferromagnetism was around 19 at. % Fe in bulk Cr-Fe alloys.

It should be noted that the MR does not saturate even at 14 T for any samples, irrespective of Fe concentrations and the substrate temperatures, while the magnetization reaches saturation at 5.5 T for $x>25$ at. % as shown in Fig. 2. We consider that this is due to spin glass behavior of Fe atoms contained in the Cr matrix. The values of magnetization are much smaller than that of pure bcc Fe, suggesting the phase separation is incomplete. Therefore, a large amount of Fe atoms is considered to be dissolved, forming a supersaturated solid solution in the Cr matrix. Regarding the absolute magnitude of the saturated MR it has been pointed out both theoretically and experimentally that the MR is larger as the size of magnetic clusters is smaller at a certain concentration of a magnetic element.[16–18] This may suggest that the saturated MR could be largest in the spin glass state. The unsaturated behavior of MR was also observed for other heterogeneous alloys.[4,6] We would like to remark here that the magnitudes of MR in heterogeneous alloys are not necessarily meaningful values because it varies depending on the magnetic field under which the MR is measured.

IV. CONCLUSION

We have investigated the GMR behavior of sputtered $Cr_{1-x}Fe_x$ heterogeneous alloy films. The MR ratio shows a maximum around $x=20$ at. % both for the heated and cooled substrates. However, the MR ratio for the cooled substrate is smaller than that for the heated substrate at $x<25$ at. %, and the discrepancy diminishes with increasing x. This suggests that in dilute regions, the samples sputtered on cooled substrates behave like spin glass, while in concentrated regions, ferromagnetic interaction becomes dominant even in the homogeneous solid solution.

ACKNOWLEDGMENTS

The authors would like to thank T. Hihara and Professor K. Sumiyama, IMR, Tohoku University, for their help in the high field measurements of MR. The authors also thank Professor Sakurai for his encouragement in this research and for the provision of laboratory facilities.

[1] A. E. Berkowitz, J. R. Mitchell, M. J. Carey, A. P. Young, S. Zhang, F. E. Spada, F. T. Parker, A. Hutten, and G. Thomas, Phys. Rev. Lett. **68**, 3745 (1992).
[2] J. Q. Xiao, J. S. Jiang, and C. L. Chien, Phys. Rev. Lett. **68**, 3749 (1992).
[3] J. Q. Xiao, J. S. Jiang, and C. L. Chien, Phys. Rev. B **46**, 9266 (1992).
[4] A. Tsoukatos, H. Wan, G. C. Hadjipanayis, and Z. G. Li, Appl. Phys. Lett. **61**, 3059 (1992).
[5] G. Xiao, J. Q. Wang, and P. Xiong, Appl. Phys. Lett. **62**, 420 (1993).
[6] S. A. Makhlouf, K. Sumiyama, K. Wakoh, K. Suzuki, K. Takanashi, and H. Fujimori, J. Magn. Magn. Mater. **126**, 485 (1993).
[7] M. N. Baibich, J. M. Broto, A. Fert, F. Nguyen Van Dau, F. Petroff, P. Etienne, G. Creuzet, A. Friedrich, and J. Chazelas, Phys. Rev. Lett. **61**, 2472 (1988).
[8] G. Binasch, P. Grüberg, F. Saurenbach, and W. Zinn, Phys. Rev. B **39**, 4828 (1989).
[9] *Binary Alloy Phase Diagram*, edited by T. B. Massalski, J. L. Murray, L. H. Bennett, and H. Baker (American Society for Metals, Metals Park, OH, 1986), p. 822.
[10] K. Hono, Y. Maeda, J.-L. Li, and T. Sakurai, IEEE Trans. Magn. **MAG-29**, 3745 (1994).
[11] A. K. Nigam and A. K. Majumdar, Phys. Rev. B **27**, 495 (1983).
[12] H. Rakoto, J. C. Ousset, S. Senoussi, and I. A. Campbell, J. Magn. Magn. Mater. **46**, 212 (1984).
[13] S. Banerjee and A. K. Raychaudhuri, J. Phys.: Condens. Matter **5**, L295 (1993).
[14] R. Okano, K. Hono, T. Takanashi, T. Sugawara, T. Sakurai, and H. Fujimori (unpublished).
[15] S. K. Burke, R. Cywinski, J. R. Davis, and B. D. Rainford, J. Phys. F: Met. Phys. **13**, 451 (1983).
[16] S. Zhang, Appl. Phys. Lett. **61**, 1855 (1992).
[17] Y. Asano, A. Oguri, J. Inoue, and S. Maekawa, Phys. Rev. B **49**, 12831 (1994).
[18] G. Xiao, J. Q. Wang, and P. Xiong, Proceedings of the Intermagnetic Conference, 1994 (to be published).

Origin of giant magnetoresistance effect in granular thin films

Atsushi Maeda, Minoru Kume, Satoru Oikawa, and Kazuhiko Kuroki
New Materials Research Center, Sanyo Electric Co., Ltd., 1-1 Dainichi-higashimachi, Moriguchi, Osaka 570, Japan

Though the demagnetization process of granular Co-Ag films became steep by adding permalloy layer, slow saturation in the magnetoresistance (MR) curves was maintained. In addition, the MR characteristics of granular Fe-Ag films prepared under a magnetic field, in which strong magnetic anisotropy was induced, were isotropic. The disagreement between the MR and magnetic characteristics implies that ferromagnetic granules are not responsible for the giant MR (GMR) effect. The MR ratio of the granular Fe-Ag films considerably increased at thicknesses less than 20 nm. In such ultrathin films, the features of the MR curves corresponded well with those of the magnetization curves with slow saturation and no hysteresis. These results suggest that the GMR effect in the granular systems is attributable to superparamagnetism.

I. INTRODUCTION

Giant magnetoresistance (GMR) effect in the Fe/Cr multilayer[1] has stimulated a great deal of investigation of the magnetotransport properties in the various multilayered and sandwiched materials. Since the interlayer diffusion strongly influences the physical properties of such structures, the origin of the GMR effect is believed to be an interfacial spin-dependent scattering.[2–5] Recently, it has been observed that the GMR effect is also present in granular materials comprising mutually insoluble magnetic and nonmagnetic metals and/or alloys.[6,7] These results demonstrated that the GMR effect is not restricted to multilayered structures and that additional opportunities exist for technological applications. However, the transport phenomena in the granular systems are not much understood. So far a few models have been used for an explanation of the GMR effect.[8,9] Though magnetization of the granular films is saturated at low fields, the MR curves show a slow saturation.[10] We consider that such disagreement between the MR and magnetic characteristics is a key in the understanding of the mechanisms for the GMR effect in the granular systems.

In the present study, based on the experimental results for Fe-Ag films prepared under a magnetic field, ferromagnetic granules are pointed out to be not responsible for the GMR effect in the granular systems. Detailed thickness dependence study suggests that the GMR effect is dominated by fine granules with superparamagnetic characteristics.

II. EXPERIMENT

To study the effects of the applied field, the Fe-Ag films were prepared by rf sputtering under a magnetic field H_{ex}=130 Oe. The thickness dependence was studied on the granular Fe-Ag films that were prepared under zero field. The details for the preparation have been described previously.[11] An electron probe microanalyzer (JEOL JXA-840) was used for the elemental analyses. Magnetization (M) and hysteresis loops were measured using a vibrating sample magnetometer (TOEI VSM-3S). The MR was measured at room temperature, about 293 K, in a four-terminal geometry with an in-plane direct current (J) between 0.01 and 1 mA. A magnetic field (H) up to 1.5 T was applied parallel to the current. In the present study, the MR ratio is displayed as follows:

$$\Delta \mathrm{MR} = \Delta R / R(1.5), \tag{1}$$

where ΔR is the MR change, $R_{\max} - R(1.5)$, and $R(1.5)$ is the MR at H=1.5 T.

III. RESULTS AND DISCUSSION

Very recently, we have indicated that the Co-Ag/permalloy double-layered structure possesses a steep magnetization change.[10] This occurred because the ferromagnetic granules in the granular Co-Ag layer were magnetically dragged by the Permalloy layer with a soft magnetic nature. However, saturation was not observed in the MR curves of the double-layered films with a steep demagnetization process. Such disagreement between the MR and magnetic characteristics is also observed in granular Fe-Ag films prepared under a magnetic field (H_{ex}=130 Oe) which was applied parallel to the film plane. Figure 1(a) shows the M-H curves measured under the condition where the H was applied par-

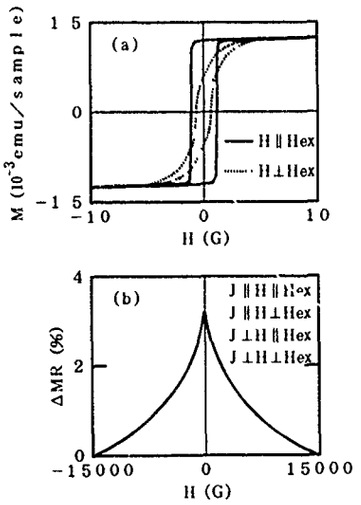

FIG. 1. M-H (a) and MR (b) curves at room temperature of 100-nm-thick $Fe_{48}Ag_{52}$ film prepared under a magnetic field.

 0021-8979/94/76(10)/6793/3/$6.00 © 1994 American Institute of Physics

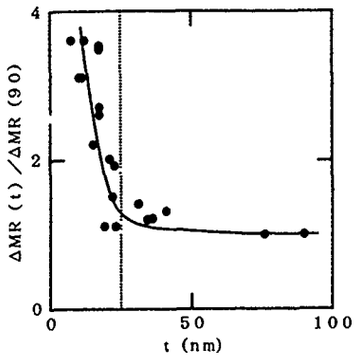

FIG. 2. MR ratios of $Fe_{48}Ag_{52}$ films with variou. thicknesses (t). The broken line indicates the critical diameter of Fe granule estimated by theoretical calculation.

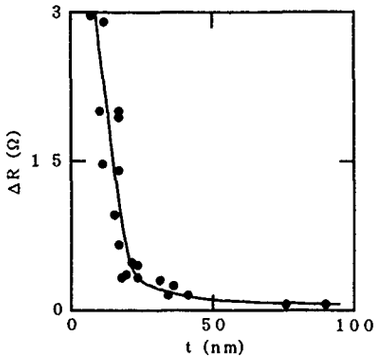

FIG. 3. MR changes of $Fe_{48}Ag_{52}$ films with various thicknesses (t).

allel ($H \| H_{ex}$) and perpendicular ($H \perp H_{ex}$) to the H_{ex} in the film plane. Here the thickness of the sample was 100 nm. It is found that magnetic anisotropy was induced in the prepared samples. This is probably because the applied field dominated the easy axis direction of the ferromagnetic granules. In contrast, the MR characteristics were independent on the arrangements between the J, H, and H_{ex}, as shown in Fig. 1(b). This indicates that the MR characteristics are maintained to be isotropic in the samples prepared under a magnetic field. These results for the Co-Ag/Permalloy double-layered films and the Fe-Ag films prepared under a magnetic field suggest that the GMR effect is not attributable to the ferromagnetic granules. In the granular systems, therefore, other magnetic components must be proposed as scattering centers. In this respect, we note small magnetic granules with superparamagnetic characteristics. Though the contribution of the superparamagnetic components are negligibly small in the magnetic properties of the granular materials, the transport properties are probably influenced by them.

The magnetic property of granules changes from ferromagnetic to superparamagnetic as the granule size decreases.[12] Therefore, the existing ratio of the superparamagnetic granules is expected to increase with decreasing the thickness of the granular films. This idea prompted us to prepare the granular "ultrathin" films. Figure 2 shows the thickness dependence of the MR ratio in $Fe_{48}Ag_{52}$ films that were prepared under zero field. Here the MR ratio is normalized relative to the MR ratio of the 90-nm-thick sample. The MR ratio considerably increased at thicknesses less than 20 nm. It is interesting that this thickness is close to the "critical diameter" of the Fe granule (25 nm), below which the Fe is theoretically estimated to be superparamagnetic.[13] Here the value of $R(1.5)$ necessarily increased with decreasing thickness. Therefore, it is noteworthy that the MR ratio increased in spite of the increase in the $R(1.5)$ value. This means that intrinsic change in the MR, which is estimated from ΔR in Eq. (1), is extremely large in the ultrathin films. From a quantitative study, it was found that the MR change is about 60 times as much as that in the "bulk" films which are thicker than 90 nm (see Fig. 3). As shown in Fig. 4, the $Fe_{48}Ag_{52}$ ultrathin films showed the M-H curves with slow saturation and no hysteresis. In addition, the features of the MR curves corresponded well with those of the M-H curves. This is in contrast to the disagreement between the MR and M-H data in the Co-Ag/Permalloy double-layered films and the Fe-Ag films prepared under a magnetic field. The above results indicate that the growth of the granules is restrained with decreasing the thickness as we expected. It is also suggested that the small granules with superparamagnetic characteristics mainly contribute to the GMR effect in the granular systems. Figure 5 shows the thickness dependence of saturation field (H_s) associated with the MR characteristics. Here the H_s is defined as the value of the magnetic field corresponding to the MR ratio at a value 80% below each MR ratio [see Fig. 5 in Ref. 11(b)]. The H_s decreased with increasing the MR ratio in the ultrathin films. Toward the application for thin-film sensor devices, it is extremely important that the MR ratio increases and H_s decreases with reducing the thickness in the granular systems.

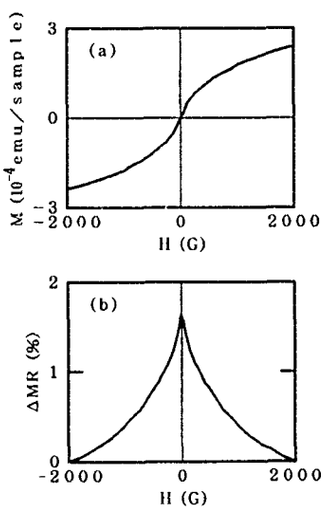

FIG. 4. M-H (a) and MR (b) curves at room temperature of 16-nm-thick $Fe_{48}Ag_{52}$ film.

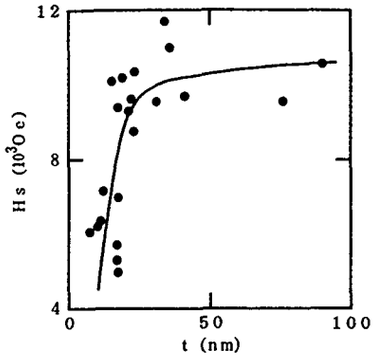

FIG. 5. H_s of $Fe_{48}Ag_{52}$ films with various thicknesses (t).

IV. SUMMARY

Though the interlayer magnetic coupling was induced in the Co-Ag/permalloy double-layered films, the MR change was maintained to be slow. In addition, the isotropic MR characteristics were observed in the granular Fe-Ag films prepared under a magnetic field. The MR ratio in the Fe-Ag system considerably increased at thicknesses less than 20 nm. In such ultrathin films, a slow saturation and no hysteresis were observed in the *M-H* curves, whose features corresponded well with those of the MR curves. These results suggest that the larger ferromagnetic particles are not as effective as the smaller superparamagnetic particles to the GMR effect in the granular systems. This is probably because of the small surface to volume ratio of the former.

[1] M. N. Baibich, J. M. Broto, A. Fert, F. Nguyen Van Dau, F. Petroff, P. Etienne, G. Creuzet, A. Friederich, and J. Chazelas, Phys. Rev. Lett. **61**, 2472 (1988).
[2] R. E. Camley and J. Barnas, Phys. Rev. Lett. **63**, 664 (1989).
[3] P. M. Levy, S. Zhang, and A. Fert, Phys. Rev. Lett. **65**, 1643 (1990).
[4] J. Inoue, A. Oguri, and S. Maekawa, J. Phys. Soc. Jpn. **60**, 376 (1991).
[5] E. F. Fullerton, D. M. Kelly, J. Guimpell, and I. K. Schuller, Phys. Rev. Lett. **68**, 859 (1992).
[6] A. E. Berkowitz, J. R. Mitchell, M. J. Carey, A. P. Young, S. Zhang, F. E. Spada, F. T. Parker, A. Hutten, and G. Thomas, Phys. Rev. Lett. **68**, 3745 (1992).
[7] J. Q. Xiao, J. S. Jiang, and C. L. Chien, Phys. Rev. Lett. **68**, 3749 (1992).
[8] S. Zhang, Appl. Phys. Lett. **61**, 1855 (1992).
[9] L. Xing and Y. C. Chang, Phys. Rev. B **48**, 4156 (1993).
[10] M. Kume, A. Maeda, S. Oikawa, and K. Kuroki, Jpn. J. Appl Phys. **33**, L520 (1994).
[11] (a) A. Maeda, M. Kume, S. Oikawa, Y. Shimizu, and M. Doi, J Phys.: Condens. Matter **5**, L189, 4641 (1993); (b) A. Maeda, M. Kume, S. Oikawa, T. Tanuma, Y. Shimizu, and M. Doi, *ibid.* **5**, 6745 (1993).
[12] W. H. Meiklejohn, Rev. Mod. Phys. **25**, 302 (1953).
[13] C. Kittel, Phys. Rev. **70**, 965 (1946); W. F. Brown, *ibid.* **105**, 1479 (1957).

Evolution of structure and magnetoresistance in granular Ni(Fe,Co)/Ag multilayers: Dependence on magnetic layer thickness

X. Bian, X. Meng, J. O. Ström-Olsen, Z. Altounian, W. B. Muir, and M. Sutton
Centre for the Physics of Materials and Department of Physics, McGill University, 3600 University Street, Montréal, Québec H3A 2T8, Canada

R. W. Cochrane
Département de Physique et Groupe de Recherche en Physique et Technologie des Couches Minces, Université de Montréal, C.P. 6128, Succ. Centre-Ville, Montréal, Québec H3C 3J7, Canada

Structural and magnetoresistance results on annealed sputtered ($Ni_{81}Fe_{19}$, $Ni_{66}Fe_{16}Co_{18}$)/Ag granular multilayers are presented. Structural evolution has shown that highly (111) textured, discontinuous layered structures can persist on annealing up to 400 °C. The average magnetic particle size is controlled by the annealing temperature and the initial magnetic layer thickness. No giant magnetoresistance was observed in the as-deposited films, while significant MR was found after annealing between 300 °C and 400 °C. Magnetoresistance over 30%, together with a small saturation field, was found at 4.2 K for a starting magnetic thickness of 4 Å. Increasing the magnetic layer thickness to 20 Å greatly improves the magnetic thermal stability, and leads to high magnetoresistive sensitivities of up to 0.35%/Oe in a field of 10 Oe at room temperature. The magnetization hysteresis, anisotropy, and magnetic interaction in such a granular multilayer are also discussed.

I. INTRODUCTION

Since the observation of giant magnetoresistance (GMR) first in antiferromagnetically coupled multilayers,[1,2] and later in uncoupled granular alloy films,[3,4] structural and magnetotransport properties have been intensely studied in a variety of artificially inhomogeneous structures. High negative GMR, which is essential for magnetoresistive sensor applications, is found in these system and is shown to be related to the interface spin-dependent scattering, and is associated with the reorientation of the magnetic moments in either a coupled multilayer structure or an immiscible granular alloy.[1,3] However, the magnetic fields required to achieve magnetic saturation and a significant magnetoresistive effect are generally too large to be useful in low-field device applications.

Annealed NiFe/Ag multilayers, however, have shown low-field GMR.[5–8] We have recently extended these studies by annealing NiFe/Ag multilayers containing ultrathin NiFe layers. Larger enhancements in GMR at 4.2 K were found for annealed multilayers and low saturation fields were also observed by controlling the size and shape of the magnetic precipitates.[9] In this paper, we report the magnetic layer thickness dependence of annealed (NiFe,NiFeCo)/Ag multilayers on the structural, magnetic, and transport properties.

II. EXPERIMENT

A series of ($Ni_{81}Fe_{19}$,$Ni_{66}Fe_{16}Co_{18}$)/Ag multilayers with individual magnetic layers, ranging from 4 to 20 Å and Ag layers of 20–40 Å were prepared by dc magnetron sputtering at room temperature from separate targets of $Ni_{81}Fe_{19}$, $Ni_{66}Fe_{16}Co_{18}$, and Ag onto both glass and oxidized Si substrates. The base pressure was less than 2×10^{-7} Torr. The deposition rates were typically 1.4–1.6 Å/s in 7.5 mTorr argon. The individual layer thicknesses of the magnetic alloys and Ag were adjusted to yield films of magnetic composition between 20 and 55 at. %. Total film thicknesses were 750–1200 Å. The heat treatment was carried out, either under a vacuum of better than 2×10^{-6} Torr or under a flow of 5% H_2 and 95% Ar.

The structural characterization of the samples were performed using low- and high-angle x-ray diffraction using Cu-K_α radiation and a transmission electron microscope. The film compositions, as determined by electron microprobe measurements, were found to be within 4% of the nominal values. The magnetoresistance measurements were carried out using a four-terminal geometry and a high-resolution ac bridge.[10] The current was in the plane of the film, with the magnetic field either in the film plane and perpendicular to the current (transverse ρ_T) or perpendicular to the plane (perpendicular $\rho_\perp$). Magnetic hysteresis data at 300 K were obtained using a magneto-optic Kerr effect (MOKE) magnetometer with the applied field in the plane of the film.

III. RESULTS AND DISCUSSIONS: $Ni_{81}Fe_{19}$/Ag MULTILAYERS

($Ni_{81}Fe_{19}t$/Ag20 Å)$_{30}$ multilayers with t_{NiFe}=4–20 Å were deposited on glass substrates and followed by annealing under vacuum. The low-angle x-ray reflectivity spectra reveal superlattice peaks for all the as-deposited samples, down to a bilayer thickness of Λ=24 Å (with a 4 Å layer of magnetic component), indicating a well-defined compositional modulation along the growth direction. The corresponding high-angle x-ray diffraction and electron diffraction for these samples show that the multilayer films have coherent interfaces and a highly textured structure with (111) orientations normal to the film plane. Figure 1 shows the high-angle x-ray diffraction patterns for a multilayer with t_{NiFe}=20 Å at different annealing temperatures. Highly textured Ag(111) and NiFe(111) structures can be seen in the

 0021-8979/94/76(10)/6796/3/$6.00 © 1994 American Institute of Physics

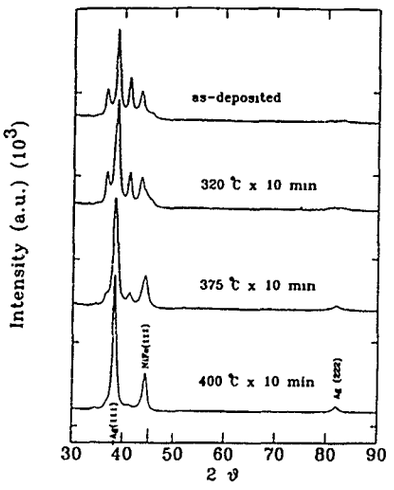

FIG. 1. High-angle x-ray data for the samples with form glass/(Ag20 Å/$Ni_{81}Fe_{19}$20 Å)$_{30}$/Ag20 Å, as-deposited and annealed at 320 °C, 375 °C, and 400 °C for 10 min.

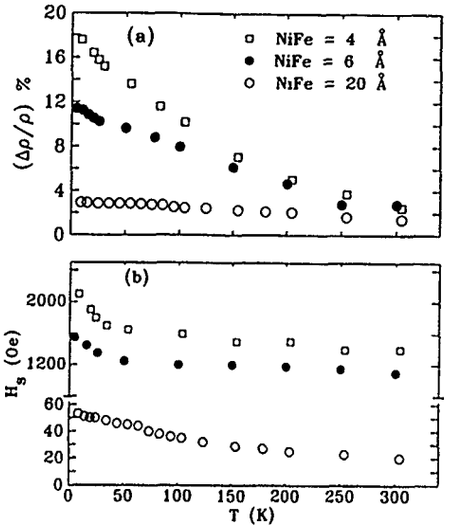

FIG. 2. Temperature dependencies of (a) $\Delta\rho/\rho$ and (b) saturation field H_S for three $Ni_{81}Fe_{19}$ samples with layer thicknesses, as indicated.

annealed samples. As illustrated in Fig. 1, superlattice coherence persists for samples annealed up to 400 °C. Further annealing above 450 °C, however, dissolved the superlattice structures, as shown by the disappearance of the satellite peaks around the two primary Bragg peaks, indicating significant interdiffusion during annealing. Similar structural changes in annealing, found from high-angle x-ray diffraction, were observed for all the NiFe thicknesses studied here. However, low-angle x-ray reflectivity data show that, except for very thin NiFe layers (4–6 Å), the compositionally modulated layer structures persist, even after annealing at 450 °C, indicating a well-spaced discontinuous multilayer structure. The average NiFe grain sizes, D, corresponding to different t_{NiFe}, estimated from the high-angle diffraction peak width, range from 60 to 250 Å for samples annealed at 450 °C, as shown in Table I. As the annealing temperature is increased, the high-angle NiFe (111) x-ray peak intensity increases and becomes sharper, indicating the growth of NiFe particles.[7]

For a wide range of NiFe thicknesses (4–20 Å) and Ag spacer 20 Å, the as-deposited multilayers show no GMR at room temperature. However, large MR was found for samples annealed between 300 and 450 °C at both 4.2 and 300 K. Data obtained at 4.2 K are shown in Table I. For the samples with ultrathin NiFe layers (~4–6 Å), which is considered as granular in nature, GMR as large as 30% was found in the samples annealed at 300 °C with a saturation field generally less than those observed in cosputtered granular films of similar compositions.[3,4] As t_{NiFe} increases to 20 Å, a substantial decrease of the GMR is observed. This result is expected, since for high NiFe concentrations, the surface to volume ratio decreases, thereby reducing the interfacial spin-dependent electron scattering.[11] However, the saturation field is greatly reduced as the magnetic layer thickness is increased. Similar behavior was found for samples annealed at 450 °C, except that the values of the GMR and H_S are lower, due to the growth of magnetic precipitates.

An important aspect of increasing t_{NiFe} is the improvement of the magnetic thermal stability. Figure 2 shows the temperature dependence of GMR and H_S. Cooling the samples down from 300 K to 4.2 K increased $\Delta\rho/\rho$ by a factor of 7 for the sample with t_{NiFe}=4 Å, but only by a factor of 2 for the sample with t_{NiFe}=20 Å. Interestingly, the MR values for these samples are comparable at 300 K. The saturation fields show behavior similar to those of GMR. A large increase of H_S for thinner NiFe samples are seen at temperatures below 50 K, compared to a relatively flat variation for the thickest NiFe sample. The strong temperature dependences of the GMR parameters for the samples with ultrathin NiFe layers were shown to be related to the superparamagnetic properties of the small magnetic precipitates.[9]

TABLE I. Dependence of magnetoresistance parameters on t_{NiFe} for samples annealed at 300 °C and 450 °C, data obtained at 4.2 K. ρ_0 and ρ_S are the resistivities at $H=0$ and $H=H_S$, respectively.

Sample	300 °C				450 °C				
t_{NiFe} (Å)	ρ_0 ($\mu\Omega$ cm)	$\Delta\rho$ ($\mu\Omega$ cm)	$\Delta\rho/\rho_S$ (%)	H_S (Oe)	ρ_0 ($\mu\Omega$ cm)	$\Delta\rho$ ($\mu\Omega$ cm)	$\Delta\rho/\rho_S$ (%)	H_S (Oe)	D (Å)
4	9.94	2.30	30.0	2000	5.95	0.945	18.8	1400	60.0
6	9.93	1.98	25.0	1700	5.76	0.630	12.3	1150	80.0
8	...	...	...	...	5.49	0.59	12.0	1050	95.0
20	10.93	0.296	2.8	50	...	...	...	...	250.0

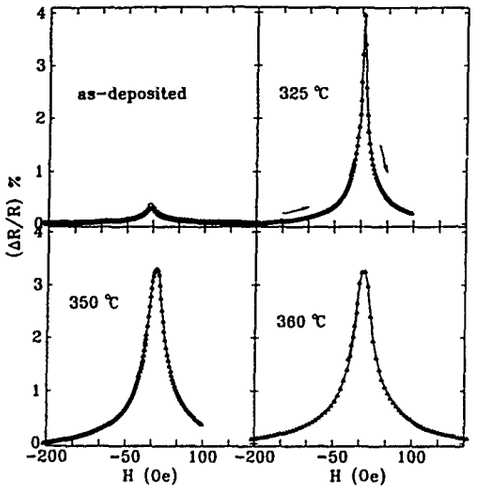

FIG. 3. Room temperature magnetoresistance for multilayers with the form SiO_2/Nb50 Å/Ag20 Å/NiFeCo20 Å(Ag40 Å/NiFeCo20 Å)$_4$/Ag20 Å/Nb100 Å, in different heat-treatment states, as indicated. The curves show one-half of the MR vs H cycle.

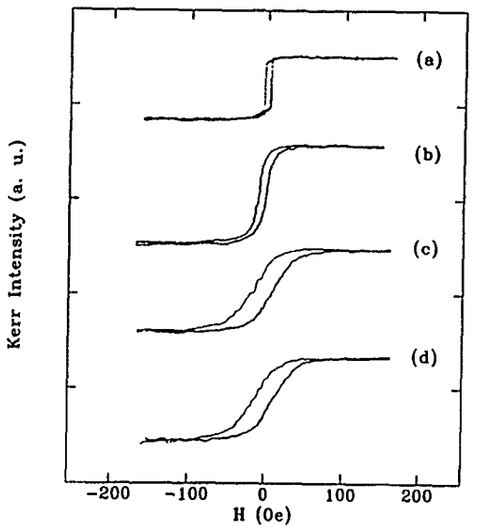

FIG. 4. Magneto-optic Kerr effect (MOKE) measurements for the samples shown in Fig. 3, (a) as-deposited, and annealed for 10 min at (b) 325 °C, (c) 350 °C, and (d) 360 °C.

IV. LOW-FIELD GMR STRUCTURE

Although large GMR values have already been obtained in a variety of multilayers and granular alloys, the magnetic fields required are usually large. In a multilayer structure, low saturation fields are possible by choosing a structure with small antiferromagnetic coupling.[12] A recent report has shown that very low field GMR is obtained in an annealed NiFe/Ag multilayer structure, with a typical magnetic layer thickness of 20 Å.[5] The large value of the magnetoresistive sensitivity, over 0.8%/Oe, was ascribed to the balance of magnetostatic and local antiferromagnetic interaction between the plate-like islands in the annealed layer structures. We have prepared similar structures by substituting the magnetic component by a magnetically soft $Ni_{66}Fe_{16}Co_{18}$ alloy. Figure 3 shows the room temperature magnetoresistance data for multilayer with form SiO_2/Nb50 Å/Ag20 Å/NiFeCo20 Å (Ag40 Å/NiFeCo20 Å)$_4$/Ag20 Å/Nb100 Å, at a different annealing temperature. No GMR was found for the as-deposited sample, while significant GMR was observed after annealing the samples between 300 °C and 400 °C. Values of $\Delta R/R=4\%$ and $(dR/dH)/R=0.35\%$/Oe were obtained for the sample annealed at 325 °C. It appears that the large increase in $\Delta R/R$ is dominated by the increase of ΔR, as the sheet resistances generally decrease by only 10%–15% after annealing. We also note that the MR parameters, particularly the saturation field are extremely sensitive to the annealing temperature. As a consequence, the annealing temperature needed for maximum sensitivity was found to lie within a very narrow window of a few degrees around 325 °C for this particular structure.

Finally, the magnetization hysteresis was studied using a MOKE magnetometer. Figure 4 shows the room temperature MOKE hysteresis loops for the same samples indicated in Fig. 3. A typical ferromagnetic characteristic is seen for the as-deposited sample with relatively small Kerr intensity. Upon annealing at a moderate temperature below 370 °C, the hysteresis loop gradually tilts and the remanence magnetization decreases, suggesting the formation of a fractional antiferromagnetic spin configuration. Annealing above 370 °C increases both the remanence and the coercivity; correspondingly, the GMR sensitivity decreases. Although a small in-plane anisotropy was found in the as-deposited sample, the hysteresis loop difference of the in-plane magnetic easy and hard axes vanishes after annealing above 300 °C. Therefore, one could conjecture that under a minimum in-plane anisotropy, low-field GMR and high sensitivity are promoted as the results of the balance of magnetostatic interaction and local antiferromagnetic coupling.[5]

ACKNOWLEDGMENTS

We wish to thank Yiming Huai for useful discussions. We acknowledge the financial support from the Natural Sciences and Engineering Research Council of Canada and Fonds FCAR du Québec.

[1] M. N. Baibich, J. M. Broto, A. Fert, F. Nguyen van Dau, F. Petroff, P. E Etienne, G. Creuzet, A. Friederich, and J. Chazelas, Phys. Rev. Lett. **61**, 2472 (1988).
[2] S. S. Parkin, P. Bhadra, and K. P. Roche, Phys. Rev. Lett. **66**, 2152 (1991).
[3] A. E. Berkowitz, M. J. Carey, J. R. Mitchell, A. P. Young, S. Zhang, F. E. Spada, F. T Parker, A. Hutten, and G. Thomas, Phys. Rev. Lett. **68**, 3745 (1992).
[4] J. Q. Xiao, J. S. Jiang, and C. L. Chien, Phys. Rev. Lett. **68**, 3749 (1992).
[5] T. L. Hylton, K. R. Coffey, M. A. Parker, and J. K. Howard, Science **261**, 1021 (1993).
[6] B. Rodmacq, G. Palumbo, and Ph. Gerard, J Magn. Magn. Mater. **118**, L11 (1993).
[7] M. Kitada, J. Magn. Magn. Mater. **123**, L18 (1993).
[8] X. Bian, A. Zaluska, Z Altounian, J. O. Ström-Olsen, Y. Huai, and R. W. Cochrane, Mater. Res. Soc. Symp. **313**, 405 (1993).
[9] X. Bian, Z. Altounian, J. O. Ström-Olsen, A. Zaluska, Y. Huai, and R. W. Cochrane, J. Appl. Phys. **75** 6560 (1994).
[10] Y. Huai and R. W. Cochrane, J. Appl. Phys. **72**, 2523 (1992).
[11] S. Zhang, Appl. Phys. Lett. **61**, 1855 (1992)
[12] X. Bian, B. D. Gaulin, J. O Strom-Olsen, Z. Altounian, C Stager, and J Avelar, Phys. Rev. B **50**, 3114 (1994).

Magnetoresistance in (Fe–Co)/Ag films

A. Tsoukatos,[a] D. V. Dimitrov, A. S. Murthy, and G. C. Hadjipanayis
Department of Physics and Astronomy, University of Delaware, Newark, Delaware 19716-2570

The structural and magnetotransport properties of $(Fe_yCo_{1-y})_{100-x}Ag_x$ films were studied as a function of composition. Giant magnetoresistance (GMR) values were measured in these granular films, with the best GMR obtained for the composition $(Fe_{0.33}Co_{0.67})_{27}Ag_{73}$, with values of 29% at 30 K and 11.7% at 300 K. XRD and TEM results have shown a fcc crystal structure with a relatively homogeneous microstructure. Magnetic data for the samples with the best GMR indicate a superparamagnetic behavior. The narrow peak in thermomagnetic data and low blocking temperature suggest a small and uniform size distribution of magnetic granules. A summary of the electrical transport properties is presented, in relation to the structural, microstructural, and magnetic properties.

I. INTRODUCTION

Giant magnetoresistance has been recently observed in transition metal multilayers,[1] composite films,[2,3] and in broken multilayers.[4] The origin of GMR is attributed to spin-dependent scattering at the interfaces between magnetic and nonmagnetic regions.[5–7] The highest GMR, of the order of 150%, was observed in multilayers,[8] but the highest sensitivity, about 1.2%/Oe, was found in broken multilayers.[4] Both of these systems require very stringent preparation techniques, which make them difficult to be used for practical applications. On the other hand, granular films are much easier to prepare, but the studies, to date, showed low sensitivity and high saturation fields. This study was performed in an effort to improve the sensitivity and lower the saturation field in (Fe–Co)/Ag films by investigating the dependence of these parameters on the composition, structure, size, and density of magnetic granules.

II. EXPERIMENTAL PROCEDURES

$(Fe_yCo_{1-y})_{100-x}Ag_x$ granular films with $y=0$–0.4 and $x=30$–80 were prepared using magnetron sputtering from Fe–Co and Ag targets on water cooled substrates. Carbon coated copper grids, Al foils, kapton, and glass were used as substrates. The predeposition pressure was 3×10^{-8} Torr, and sputtering was done in a 5 mTorr Ar pressure. X-ray diffraction (XRD) and transmission electron microscope (TEM) studies were used to determine the crystal structure and microstructure of the samples. A SQUID magnetometer, with a maximum applied field of 55 kOe, was used for the magnetic and the electrical transport measurements in the temperature range of 10–300 K. The four-probe technique with the field parallel to both the current and the film surface was used for the GMR measurements.

III. RESULTS AND DISCUSSION

The XRD (Fig. 1) and TEM results (Fig. 2) have shown a fcc crystal structure with uniform microstructure (grain size ranging from 5 to 50 nm), irrespective of the Ag or Fe–Co relative composition. All the observed selected area diffraction (SAD) reflections were solely due to Ag. The absence of diffraction rings characteristic of elemental Fe or Co or some FeCo structure is reminiscent of Co(Fe)/Ag granular films. In the latter system,[9] the absence of Co(Fe) reflections was attributed to the very small size of Co(Fe) granules (1 nm), which were observed only when high resolution TEM was used.

The dependence of GMR values on composition in (Fe–Co)/Ag is shown in Fig. 3. It is seen that for a fixed ratio between Fe and Co (y), the GMR values form a well-defined bell-shaped curve. All these curves show maxima that lie in the region of 65%–70% Ag. The magnitude of GMR drops significantly when the magnetic content becomes 50%, which corresponds to the theoretical estimation for the percolation point of granular solids.[10] For the samples with a small percent of magnetic material (less than 20%), the density of magnetic granules is small, giving rise to a small scattering surface area and a large separation between the granules, leading to small GMR values. Figure 3 also shows that the GMR values for Fe–Co/Ag films are consistently lower than those of the Co/Ag films prepared under identical conditions. However, for $y=0.33$ and $x=0.73$, comparable values were observed, with a maximum $\{[R(H)-R(0)]/R(0)\}$ of 29% at 30 K and 11.7% at 300 K. The prominent feature of all Fe–Co/Ag samples was the lower magnetic

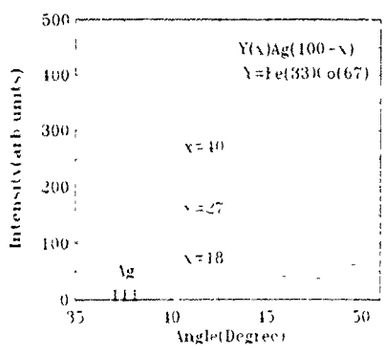

FIG. 1 X-ray diffraction patterns of samples with different Fe–Co content.

[a]Present address: Center for Materials Research and Analysis, 112 Brace Lab, University of Nebraska, P.O. Box 880113, Lincoln, NE 64588-0113.

 0021-8979/94/76(10)/6799/3/$6.00 © 1994 American Institute of Physics

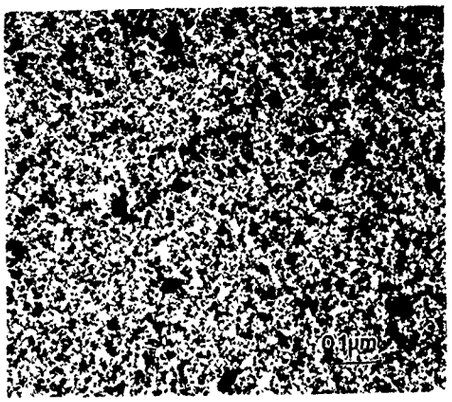

(a)

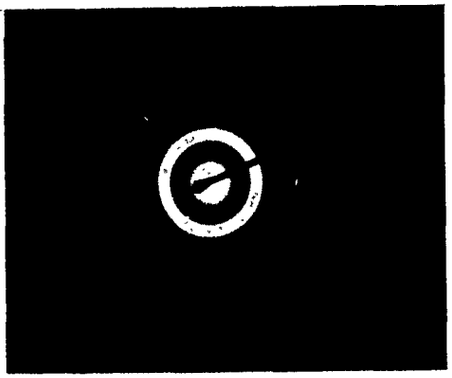

(b)

FIG. 2. (a) BF micrograph showing a fine uniform microstructure, (b) corresponding SAD pattern showing only the Ag rings.

fields required for the saturation of magnetoresistance, which results in sharper GMR (H) peaks compared to their Co/Ag counterparts. This point is clearly demonstrated in Fig. 4.

The GMR vs H curves taken for samples with different magnetic content (Fig. 5) show that for a small amount of the magnetic material, the magnitude of GMR smoothly increases with increasing field. For samples with a magnetic content of about 30%, it is seen that the magnetoresistance increases and the curve appears to have a peak at around $H=0$. The magnitude of the peak becomes smaller, and the

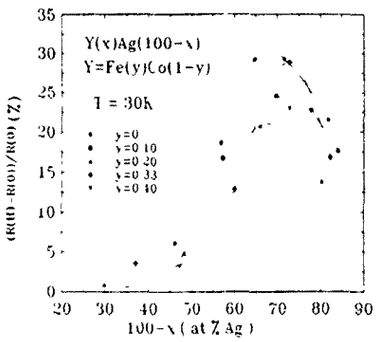

FIG. 3. Dependence of GMR on Ag content in $(Fe_yCo_{1-y})_xAg_{100-x}$ films.

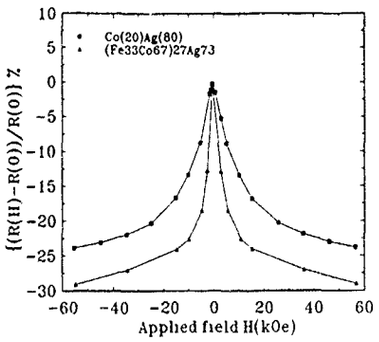

FIG. 4. Field dependence of GMR at 30 K.

slope of the curve decreases with a further increase of the magnetic content. The peak vanishes for the sample with 63% magnetic content. Magnetization curves (Fig. 6) taken on the samples with the best GMR, at different temperatures, show small coercivity (100 Oe at 20 K and a negligible value at 300 K) and lack of saturation, even for fields up to 55 kOe [the magnetization curve at 300 K seems to achieve saturation, because of the higher signal from the diamagnetic substrate (kapton)]. These results are indicative of the superparamagnetic behavior of the samples, having a small grain size. A notable feature here, however, is that although the magnetization does not show complete saturation, the magnetization at 10 kOe is 95% of the magnetization at 55 kOe. This is in contrast to the Co/Ag samples with the same percentage of magnetic material, which never approached saturation, even for fields as high as 55 kOe.[11]

The thermomagnetic data for the samples showing the highest GMR values (Fig. 7) confirm their superparamagnetic behavior. The low blocking temperature, of the order of 25 K, is suggestive of a very small size of the magnetic particles, which is consistent with the absence of SAD reflections and XRD peaks. The narrow peak is indicative of the uniform size distribution of magnetic particles.

IV. CONCLUSIONS

We observed high values of GMR in Fe–Co/Ag granular films with values of 29% at 30 K and 11.7% at 300 K. The GMR saturating fields are lower than those in Co/Ag. The

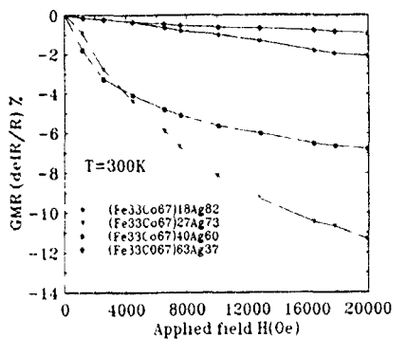

FIG. 5. Dependence of GMR on magnetic field and the amount of magnetic component.

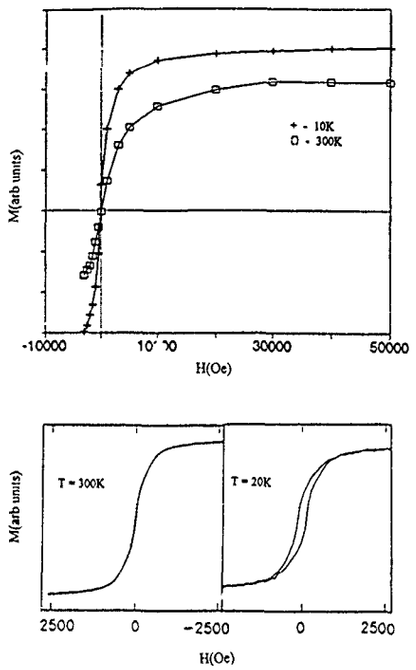

FIG. 6. Magnetization curves and hysteresis loops for $(Fe_{0.33}Co_{0.67})_{27}Ag_{73}$.

origin of GMR in these structures seems to be due to the spin-dependent scattering from the surfaces of the Fe–Co clusters. The percentage of the magnetic content and relative Fe and Co composition play a significant role in the magnitude of GMR and the saturation field.

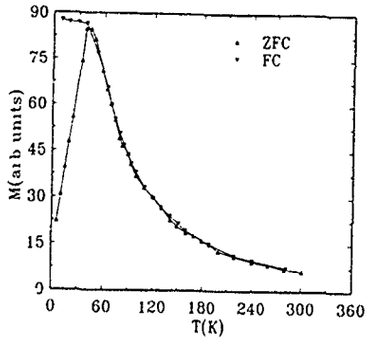

FIG. 7. Thermomagnetic data of $(Fe_{0.33}Co_{0.67})_{27}Ag_{73}$ on an applied field of 50 Oe.

ACKNOWLEDGMENT

This work was supported by National Science Foundation Contract No. DMR-9307676.

[1] M. N. Baibich, J. M. Broto, A. Fert, F. Nguyen van Dan, F. Petroff, P. Etienne, G. Grenzet, A. Friederich, and J. Chazeles, Phys. Rev. Lett. **61**, 2472 (1988).
[2] J. Q. Xiao, J. S. Jiang, and C. L. Chien, Phys. Rev. Lett. **68**, 3749 (1992).
[3] A. Berkowitz, J. M. Carey, J. R. Mitchell, A. P. Young, S. Zhang, F. E. Spada, F. T. Parker, A. Hutten, and G. R. Thomas, Phys. Rev. Lett. **68**, 3745 (1992).
[4] T. L. Hylton, K. R. Coffey, M. A. Parker, and J. K. Howard, Science **261**, 1021 (1993).
[5] R. E. Camley and J. Barnas, Phys. Rev. Lett. **63**, 664 (1989).
[6] P. M. Levy, S. Zhang, and A. Fert, Phys. Rev. Lett. **65**, 1643 (1990).
[7] B. L. Johnson and R. E. Camley, Phys. Rev. B **44**, 9997, (1991).
[8] S. S. P. Parkin, APS March Meeting, Pittsburgh, PA, 1994.
[9] H. Wan, A. Tsoukatos, G. C. Hadjipanayis, and Z. G. Li, Phys. Rev. B **49**, 1524 (1994).
[10] P. Sheng, Phys. Rev. Lett. **45**, 60 (1980).
[11] A. Tsoukatos, H. Wan, G. C. Hadjipanayis, and K. M. Unruh, J. Appl. Phys. **73**, 5509 (1993).

Interaction effects and magnetic ordering in GMR alloys

S. J. Greaves, M. El-Hilo, and K. O'Grady
Magnetic Materials Research Group, SEECS, UCNW, Bangor, Gwynedd LL57 1UT, United Kingdom

M. Watson
Centre for Data Storage Materials, Coventry University, Coventry CV1 5FB, United Kingdom

In this paper AgNiFe alloy films were examined both before and after annealing. Characterization of the samples and examination of interaction effects was carried out by measuring the temperature decay of remanence, initial susceptibility, and magnetoresistance. The temperature decay of remanence reveals that annealing widens the distribution of energy barriers, which is indicative of grain growth. The behavior of the initial susceptibility as a function of temperature is analogous to that found in spin glasses. From these measurements, it is believed that interaction effects in these systems are small.

I. INTRODUCTION

Recently, there has been a growing interest in giant magnetoresistance (GMR) materials, which are being considered for applications such as sensors and read/write heads in recording systems. Materials that exhibit GMR may be multilayers or alloys. In granular alloy films such as AgNiFe, the giant magnetoresistance arises from spin-dependent electron scattering within and at the boundaries of the grains contained within the Ag matrix. The size of these precipitates and the interactions between them affects the orientation of the spins, and hence the magnitude of the magnetoresistance.

In disordered magnetic materials, the first step in their characterization is the measurement of the energy barrier distribution. This measurement is made by cooling the sample in the zero field to the lowest temperature, where all the moments are blocked and unable to fluctuate over their energy barriers (ΔE). Then the saturation remanence of the magnetic compound is measured as a function of temperature, this variation is given by[1]

$$\tilde{M}_r(T)=\tilde{M}_r(0)\int_{y_{\rm crit}}^{\infty} f(y)dy, \tag{1}$$

where $\tilde{M}_r=M_r/M_s$ is the reduced remanence relative to the saturation magnetization of the system, $y=\Delta E/\overline{\Delta E}$ is the reduced energy barrier relative to the average barrier $\overline{\Delta E}$ and $f(y)$ is the distribution function of reduced energy barriers, which, in this formalism we assume to be independent of T. $y_{\rm crit}$ is the reduced critical barrier above which the moments are unable to fluctuate on a given time scale. Using this criterion of the critical barrier, $y_{\rm crit}$ is given by

$$y_{\rm crit}=\frac{\Delta E_{\rm crit}}{\overline{\Delta E}}=\frac{T}{\overline{T_B}}, \tag{2}$$

where $\Delta E_{\rm crit}=kT\ln(t_m f_0)$, t_m is the measuring time and f_0 is a frequency factor associated with these fluctuations. $\bar{T}_B$ is the average blocking temperature of the system, at which fluctuations are taking place over the average barrier. According to Eq. (1), the differential of the temperature decay of remanence curve shows directly the distribution of energy barriers $f(\Delta E/\overline{\Delta E}) \equiv f(T_B/\overline{T_B})$.

A second useful measurement is the variation of initial susceptibility with temperature. For a zero field cooled process this behavior is well known and gives a peak at a temperature $T=T_g$.[2] If the distribution of energy barriers originates from a distribution of precipitate sizes, then well above T_g and over a limited range of temperature, the initial susceptibility, χ_i is given by[3]

$$\chi_i(T)=\frac{bC_0}{T+T_{0\,\rm tot}}, \tag{3}$$

where $T_{0\,\rm tot}=T_{0\,\rm Bi}-T_{0i}$ is the total ordering temperature over that limited range of temperature. T_{0i} represents the contribution of interactions to $T_{0\,\rm tot}$ and $T_{0\,\rm Bi}=\gamma T_{B\,\rm eff}$ represents the correction for the blocking effects that arise, due to the fact that there is a distribution of blocking temperatures. Equation (3) was derived by fitting the tail of the distribution function to $f(y)=\alpha y^{-3}$ in the limited range of temperature examined, where $\gamma=\alpha/b$ and $b=\exp(-\sigma_y^2/2)$ and σ_y is the standard deviation of $f(y)$, since a lognormal distribution of energy barriers is assumed.

According to this analysis of the temperature variation of the initial susceptibility, and with the help of the energy barrier distribution data obtained via the decay of remanence measurement, the interaction effects in the AgNiFe alloy films can be examined.

II. EXPERIMENT

The films examined consisted of silver, which formed the bulk of the material, together with nickel and iron, the ferromagnetic components that form precipitates in the silver matrix. The size of these grains, and hence the GMR, may be controlled after deposition by annealing of the film, which causes growth of the grains.

The films were produced by rf sputtering onto glass substrates in 8 mTorr argon pressure from a base pressure of better than 2×10^{-7} Torr. The films were between 200–300 nm thick and the deposition time was 1 min. The film compositions were varied by changing the configuration of the sputtering target. Films were generally 78 ± 5 atomic percent silver, with the rest consisting of nickel and iron in a range of proportions. Annealing was carried out at three different temperatures: 600 °C, 650 °C, and 750 °C under vacuum, using halogen bulbs as heaters.

 0021-8979/94/76(10)/6802/3/$6.00 © 1994 American Institute of Physics

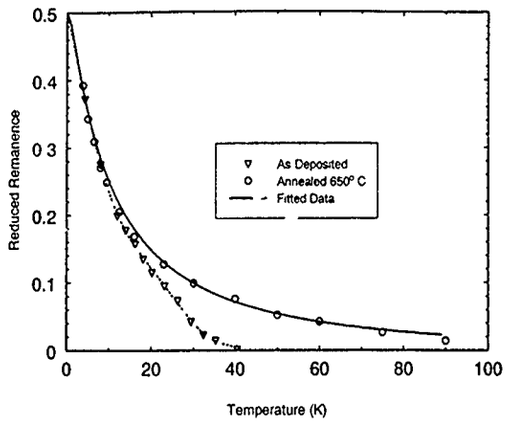

FIG. 1. Temperature decay of remanence data for the as-deposited and annealed films.

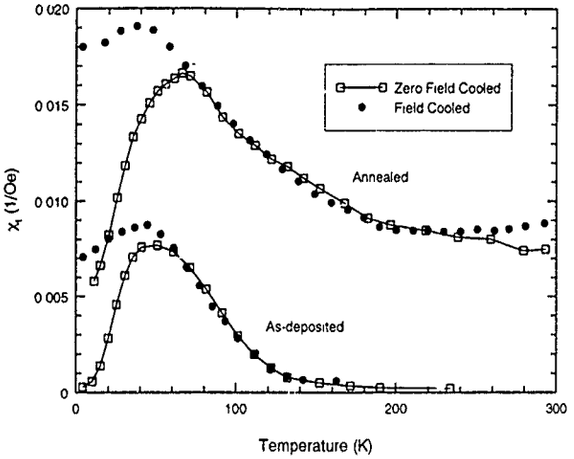

FIG. 3. Initial susceptibility, χ_i, for as-deposited and annealed samples after cooling in zero and 50 Oe fields.

Magnetic measurements were made with a PAR4500 VSM. Measurements of the initial susceptibility were made after zero field cooling using applied fields of ±50 Oe over a temperature range from room temperature to 4 K. The samples were cooled in zero field. Further susceptibility measurements were made at $T>T_g$ while cooling the sample in a 50 Oe field. Temperature decay of remanence measurements were made over the same temperature range, measurements of the remanence were made after saturating in a ±1.2 T field. Magnetoresistance was measured using a four point probe.

III. RESULTS AND DISCUSSION

Figure 1 shows the measured temperature decay of remanence curves for two films of composition 78.9% Ag, 11.3% Fe, and 9.7% Ni before and after annealing at 650 °C. We see that the value of $\bar{M}_r(0)$ can be extrapolated to 0.5, i.e., the Stoner–Wolfarth value for a system with randomly oriented easy axes.[4] Analysis of this data according to Eq. (1) gives the energy barrier distribution. Figure 2 shows the distribution of energy barriers or the distribution of blocking temperatures obtained from the decay of remanence curves. The energy barrier distribution for the as-deposited sample shows that there is some degree of bimodality that disappears when the sample is annealed. The data also shows that the distribution becomes broader after annealing, which may be due to precipitate growth arising from coagulation of neighboring precipitates or alloying. The analysis of the decay of the remanence curve for the annealed sample gives a value of $\bar{T}_B=10$ K and $\sigma_y=1.3$, however, it is difficult to fit the curve for the as-deposited sample, since a bimodal distribution is present.

Figure 3 shows the temperature variation of reduced initial susceptibility: $\bar{\chi}_i(T)=\chi_i(T)/M_s(T)$, where $M_s(T)$ is the saturation magnetization. Curves are shown for cooling in the zero applied field and cooling in a 50 Oe field. The samples exhibit typical spin-glass behavior. From the figure, the values of initial susceptibility for the annealed sample are larger than those of the as-deposited sample, and also the position of the peak in the zero field cooled curve is shifted to a higher temperature. This behavior can be attributed to

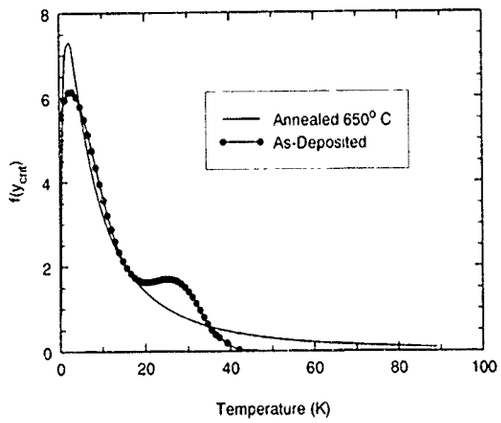

FIG. 2. The energy barrier distributions, $f(y_{crit})$, for the as-deposited and annealed films.

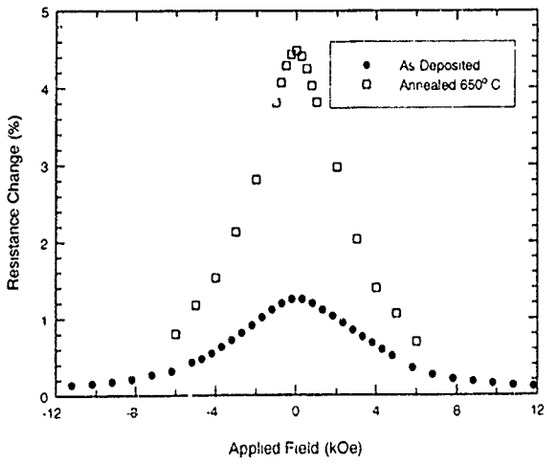

FIG. 4. Magnetoresistance for the two films.

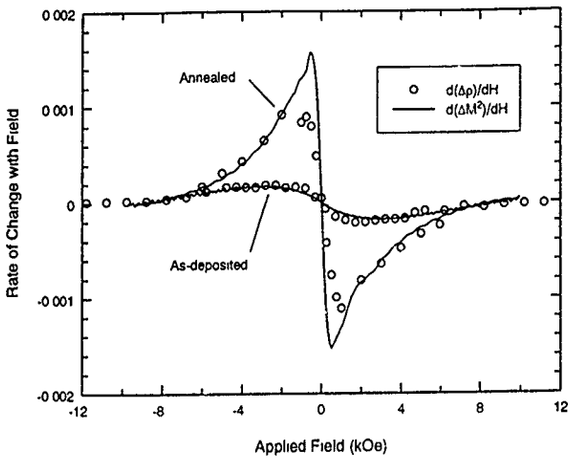

FIG. 5. Comparison of $d(\Delta\rho)/dH$ and $d(\Delta M^2)/dH$ for the annealed and as-deposited films.

the fact that the precipitates are larger in the annealed sample.

Analysis of χ_i^{-1} versus temperature for the annealed sample according to Eq. (3) gives a total ordering temperature of $T_{0\,\mathrm{tot}}=-50$ K. Using the data for the energy barrier distribution obtained for this sample, we calculate a value for $T_{0\,\mathrm{Bi}}$ of -55 K. Subtracting this from $T_{0\,\mathrm{tot}}$ gives a value for T_{0i} of 5 K that arises due to interaction effects. This value of T_{0i} indicates that the interaction effects in this sample are small.

Figure 4 shows the GMR curves measured at room temperature before and after annealing. We see that the GMR effects in the annealed sample with the larger precipitates are greater than in the as-deposited film, and $\Delta\rho$ increases from 1.3% to 4.7% as the sample is annealed to 650 °C.

Since neither samples exhibit remanence or coercivity at room temperature, we may compare the field dependence of $\Delta\rho(H)$ and $\Delta\bar{M}^2(H)$, where $\Delta\bar{M}^2=[\bar{M}(\infty)-\bar{M}(H)]^2$. This comparison is based on the model of Gittleman *et al.*,[5] describing the relationship between the magnetoresistance and the magnetization of the system. Figure 5 shows the rate of change of $\Delta\rho(H)$ and $\Delta\bar{M}^2(H)$ for both samples examined. The data clearly shows that the rate of change of $\Delta\rho(H)$ is greater for the annealed sample. This data also shows that for the as-deposited sample, the variation of $d[\Delta\rho(H)]/dH$ and $d[\Delta\bar{M}^2(H)]/dH$ is similar, whereas for the annealed sample the $d[\Delta\rho(H)]/dH$ curve deviates from the $d[\Delta\bar{M}^2(H)]/dH$ curve; this is particularly apparent at low fields. This result can be explained in terms of recent calculations,[6] in which, due to interaction effects, the $\Delta\rho(H)$ curve does not follow the $\Delta\bar{M}^2(H)$ curve at low fields. This is because the magnetoresistance is influenced by the short range correlation between neighboring precipitates, whereas the behavior of $\Delta\bar{M}^2$ is an average over the whole system. The data for the annealed sample shown in Fig. 5 shows that the deviation of the $d[\Delta\rho(H)]/dH$ curve from the $d[\Delta\bar{M}^2(H)]/dH$ curve is not large, which again suggests that interaction effects are small in this sample. This result is consistent with the magnitude of the ordering temperature $T_{0i}=5$ K, obtained from the initial susceptibility data.

IV. CONCLUSIONS

In this paper, a method of examining and characterizing interaction effects has been presented. The temperature decay of remanence is found to give useful information about the energy barrier distribution that can be used to examine interaction effects, in conjunction with initial susceptibility measurements. From the examination of the initial susceptibility data and a comparison of the resistivity and magnetization curves of the annealed sample, the effects of interactions are found to be small. These effects are believed to play a significant role in the increase in the GMR effect as the sample is annealed.

[1] D. P. E. Dickson, N. M. K. Reid, C. Hunt, H. D. Williams, M. El-Hilo, and K. O'Grady, J. Magn. Magn. Mater. **69**, 276 (1987).
[2] J. I. Gittleman, B. Abeles, and S. Bozowski, Phys. Rev. B **9**, 3891 (1974).
[3] K. O'Grady, M. El-Hilo, and R. W. Chantrell, EA03 INTERMAG 1993.
[4] E. C. Stoner and E. P. Wohlfarth, Philos. Trans. R. Soc. London Ser. A **240**, 599 (1948).
[5] J. I. Gittleman, Y. Goldstein, and S. Bozowski, Phys. Rev. B, **5**, 3609 (1971).
[6] M. El-Hilo, K O'Grady, and R. W. Chantrell (these proceedings).

Magnetic structure of the spin valve interface

D. M. C. Nicholson, W. H. Butler, and X.-G. Zhang
Oak Ridge National Laboratory, Oak Ridge, Tennessee 37831-6114

J. M. MacLaren
Department of Physics, Tulane University, New Orleans, Louisiana 70118

B. A. Gurney and V. S. Speriosu
IBM Almaden Research Center, 650 Harry Road, San Jose, California 95120

Nonferromagnetic atoms present at Ni/Cu and Permalloy/Cu interfaces in sputtered spin valve magnetoresistive layered structures have been shown to cause reduced magnetoresistance. Here we show that a model in which the moments on the Ni atoms in the interfacial region of Ni/Cu are reduced substantially by interdiffusion with Cu is consistent with the experimental results. In contrast, we believe that moments persist at the permalloy/Cu interface, which first principle total energy calculations suggest will be disordered at finite temperatures. These reduced or disordered moments are expected to significantly reduce the GMR.

I. INTRODUCTION

It is clear from experiments[1–4] that an understanding of the chemical, physical, and magnetic structure of the interfaces in magnetic multilayers is an important part of understanding the giant magnetoresistance (GMR) effect in these systems. Here we report on experiments and calculations aimed at elucidating the magnetic structure of these interfaces.

For some time, the moment as a function of the total amount of magnetic material deposited in Cu/Permalloy/Cu and Cu/Ni/Cu sandwiches, as well as Ni/Cu and Permalloy/Cu and other spin valves, has been measured,[1–3,5] and the moment found to be less than expected from the amount of Ni and Fe deposited. In particular, for nickel thicknesses less than T_{nf} (thickness nonferromagnetic) no moment was observed, but with a further increase in thickness, the moment increased linearly with a slope given by the bulk magnetization. This showed that a nonmagnetic region is formed at the interface, and that away from the interface relatively undisturbed ferromagnetic material is present. The thickness T_{nf} corresponded to roughly one atomic layer of $Ni_{0.8}Fe_{0.2}$ per interface for the "as deposited" sample and increased to approximately four atomic layers after annealing at 320 °C. For Ni/Cu, the missing moment was equivalent to approximately 2.5 atomic layers of bulk Ni. A direct correlation of T_{nf} with loss in GMR was observed, and was interpreted as arising from spin-independent scattering caused by the nonferromagnetic atoms near the interface. This scattering reduces the number of majority carrier electrons that can traverse the interface unhindered and penetrate into the ferromagnetic layer.[1,3,5]

The need to understand the magnetic structure of GMR interfaces takes on added importance in light of experiments in which atoms of third elements added to the interface greatly modify the GMR amplitude;[6] in particular, small amounts of Co at the Permalloy/Cu interface greatly increase the GMR effect.[4] Also, first principles calculations[7] predict an extremely large GMR effect for multilayer systems, such as Permalloy/Cu/Permalloy or Co/Cu/Co. This large calculated GMR arises, because the majority spin potentials (and majority d-wave phase shifts) of fcc Ni, Fe, and Co are all similar and close to that of Cu. As a consequence of this matching of potentials, interfaces in these materials that have no imperfections other than a substitutional intermixing of the constituent atoms are predicted to scatter majority spin electrons only weakly, whereas the scattering of the minority spin electrons at the interfaces (and in the bulk for Permalloy) is predicted to be very strong. The GMR arises in part because these majority carriers that carry most of the current do not scatter strongly at either interface for the case of ferromagnetic layer alignment, but scatter strongly off of one of the interfaces in the antiferromagnetic case. Another contribution to the GMR arises because of the difference in ferromagnet spin up and spin down mean-free paths, so that majority carriers that traverse the interface unhindered can travel a large distance before scattering, but minority carriers continue to be strongly scattered throughout the ferromagnetic layer.[8] In this paper, we attempt to present a coherent picture of the disorder present at the Cu/Ni and Cu/Permalloy interfaces and its effect on the GMR amplitude.

II. DIFFUSION MODEL OF NI/CU CONCENTRATION PROFILES

Ni differs from Fe and Co, in that it loses its moment as a substitutional impurity in Cu. At low temperature, the solid solution moment per atom is observed both experimentally[9] and theoretically[10] to decrease from its value of $0.6\mu_B$ in pure Ni at about $1\mu_B$ per atomic fraction Cu. This decrease is due both to the dilution of Ni by Cu and to the decrease of the Ni moment, which vanishes at around 60% Cu. At room temperature the moment decreases faster, vanishing at about 30% Cu.

We shall investigate a model in which Cu atoms migrate into the magnetic layer, where they reduce the nearby moments. To model interfaces with different amounts of intermixing, and to make connection to the annealing data, we consider initially abrupt interfaces that we allow to interdiffuse for increasing amounts of time, resulting in more intermixing. For Ni/Cu, the atoms are of similar size, and the equilibrium phase above 322 °C is a slightly clustering solid solution. Therefore, it is reasonable to assume that hopping

 0021-8979/94/76(10)/6805/3/$6 00 © 1994 American Institute of Physics

probabilities are species independent. Thus, the concentration on a layer should obey a one-dimensional diffusion equation of the form

$$\frac{dc_k}{dt}=\sigma_D\left(-c_k+\frac{1}{2}\left(c_{k+1}+c_{k-1}\right)\right), \tag{1}$$

where c_k is the concentration of Cu on the kth plane and σ_D is the number of out of plane jumps per second per site. This equation is easily solved in terms of the dimensionless time, $\tau=\sigma_D t$, for an initially perfect periodic multilayer consisting of n_{Cu} planes of Cu followed by n_{Ni} planes of Ni. Unfortunately σ_D is not available, and since the experimental deposition and annealing includes several successive temperatures, the mapping from τ to t is not even linear. However, the mapping should be independent of n_{Cu} and n_{Ni}. This allows us to qualitatively compare our calculated loss in moment and interfacial width with those obtained from magnetometry and x-ray reflectance.[11] Specifically, we calculate the concentration profile $c_k(\tau)$ as a function of τ for a periodic structure initially consisting of 25 [111] planes of Cu followed by n_{Ni} planes of Ni. As τ increases, mixing occurs and the concentration profile evolves.

We are interested in fcc [111] layers, where each atom has six neighbors in its plane and three neighbors in each of the two neighboring planes. To obtain a rough picture of the dependence of the moment on the thickness of the Ni layer, n_{Ni}, we approximate the moment on a Ni atom by the average Ni moment in a random alloy, with the same average number of Ni nearest neighbors as the Ni atom under consideration. With this assumption, the total moment can be determined as a function of intermixing, calculated from Eq. (1) for different numbers of Ni planes. In Fig. 1(a), we show the total moment per unit cell of a multilayer consisting of 25 Cu planes followed by n_{Ni} planes calculated as a function of τ using the room temperature data for the moment as a function of concentration.

These results show that, depending on τ (i.e., intermixing), when only a few Ni layers are present, there is no moment, but that as Ni layers are added, a point is reached when the moment appears; the moment then increases almost linearly. In Fig. 1(b), the net moment versus the number of Ni layers is plotted for $\tau=5$, along with room temperature (RT) measurements. The value, $\tau=5$, was chosen to give the best agreement with the measurements. Based on this qualitative agreement with experiment, we propose that our simple diffusion model provides a plausible description of the concentration profile, and may be the explanation for the missing moment at Cu/Ni interfaces. The intermixed region is predicted to be somewhat larger than the number of layers corresponding to the missing moment, in general agreement with x-ray measurements.[11]

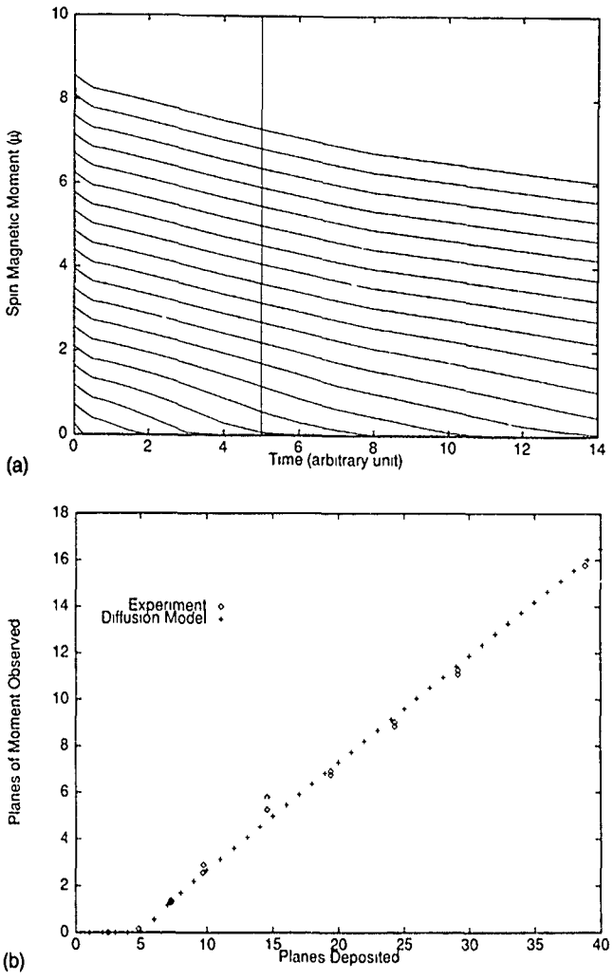

FIG. 1. (a) The total spin magnetic moment as calculated in the model is shown as a function of τ for various n_{Ni}. The number of Ni planes goes from 2 in the lower left corner to 20 at the top. (b) Magnetization (expressed in terms of an equivalent number of planes with bulk moments) vs the number of planes deposited. Calculated and experimental results are shown for Cu/Ni/Cu sandwiches.

III. PERMALLOY/CU INTERFACES

In the case of Permalloy ($Fe_{0.2}Ni_{0.8}$)/Cu interfaces, the situation is more complicated. Fe, which contributes as much to the total moment of Permalloy as Ni, is unlikely to have its moment reduced by mixing at the interface, since the moment of an Fe atom as an impurity in Cu is greater than that of an Fe atom in bulk Fe. This picture is confirmed by our calculation of the moments in Permalloy/Cu/Permalloy sandwiches with interfacial mixing, as shown in Table I. We find that the moment on Fe actually increases slightly for atoms in the nominally Cu layer, while the Ni moment decreases. Thus, although it may be possible to model the missing moment at Permalloy/Cu interfaces similarly to our treatment of the Ni/Cu interfaces, an alternative or additional explanation for the missing moment at Permalloy/Cu inter-

TABLE I. Calculated moments on Ni and Fe near Permalloy Cu interfaces. It is assumed that three layers have interdiffused with a simple linear diffusion profile.

Layer No.	%Ni	%Fe	%Cu	Ni moment (μ_B)	Fe moment (μ_B)
1	80	20	0	0.521	2.897
2	80	20	0	0.478	2.895
3	60	15	25	0.395	2.914
4	40	10	50	0.326	2.935
5	20	5	75	0.242	2.943

TABLE II. Calculated energy differences and moments for ferromagnetic and disordered-local-moment Permalloy and Permalloy 0.5Cu0.5.

System	Relative energy (mHa)	Ni moment (μ_B)	Fe moment (μ_B)
Ferromagnetic Ni0.8Fe0.2	0.00	0.570	2 59
Disordered local moment Ni0.8Fe0.2	1.70	0.050	2.55
Ferromagnetic Ni0.4Fe0.1Cu0.5	0.00	0.292	2.54
Disordered local moment Ni0.4Fe0.1Cu0.5	0.33	0.023	2.51

faces is that as an Fe atom becomes increasingly surrounded by Cu and very weakly magnetic Ni, its moment becomes increasingly decoupled from the moments of its neighboring magnetic atoms, i.e., the exchange interaction is substantially weakened and the spins disorder.

In order to test this hypothesis, we calculate the total energy of Ni, Permalloy, and a hypothetical Permalloy–Cu alloy, both in the ferromagnetic state and in a state with disordered local moments.[12] These calculations provide a rough idea of the relative energy cost for disordering the moments in the presence of the exchange coupling, which attempts to align them ferromagnetically. These calculations were performed using the local density approximation and the layer Korringa–Kohn–Rostoker coherent potential approximation technique.[13] Details of the calculations will be published elsewhere.

For bulk Permalloy, we find (Table II) that the ferromagnetic state is stable with respect to a state in which the moments are completely disordered by 1.7 mHa (1 mHa =0.0272 eV or 1 mHa/k_B=316 K). For a hypothetical Permalloy–Cu alloy, such as might form at the interface between Permalloy and Cu, we find that the exchange forces holding the moments in ferromagnetic alignment are much weaker. The energy difference ($\approx\frac{1}{3}$ mHa$\approx$100 K) between the ferromagnetic state and the disordered local moment state is smaller by a factor of 5 for the alloy.

It is unlikely that a sharp ferromagnetic transition will be observed from any disordered moments near the interfaces, since we expect that in most samples there will be a continuum of environments and local concentrations. We expect that even at zero temperature these very small exchange forces may be overcome by local perturbations due to strains, local fluctuations in concentration, crystal fields, etc. This is consistent with the temperature variation of T_{nf} observed for annealed Permalloy/Cu spin valves, where only about 10% of the moment lost at RT was recovered when cooling to 4 K.[3] The presence of disordered local moments and of decreased local moments near the interface is expected to cause a large reduction in the GMR effect, because it spoils the very close matching between the majority spin potentials and leads to greatly increased scattering.

The increased GMR observed[4] when Co is added to the Permalloy/Cu interface may also be explained in terms of the reduction of disorder in the moments at the interface. Since cobalt and Cu are mutually insoluble below 500 °C, cobalt may impede the mixing of the Permalloy and Cu near the interface. Probably more important, however, is the ability of cobalt to maintain its ferromagnetic alignment, even in the presence of dilution by Cu. To test this idea, we performed total energy calculations for an equiconcentration fcc cobalt–Cu alloy in its ferromagnetic state and in the disordered local moment state. The ferromagnetic state was more stable by 2.1 mHa. Thus, we predict that the ferromagnetic exchange interaction in fcc cobalt, even when diluted by 50% Cu, is stronger than in Permalloy with no dilution.

ACKNOWLEDGMENTS

Work was sponsored by the Department of Energy Assistant Secretary of Defense Programs, Technology Management Group, Technology Transfer Initiative under Contracts No. DEAC05-84OR21400 with Martin Marietta Energy Systems, Inc. and W7405-ENG-48 with Livermore National Laboratory, and at Tulane University by the Louisiana Educational Quality Support Fund under Grant No. LEQSF (1991–1994)-RD-A-30.

[1] V. S. Speriosu, J. P. Nozieres, and B. A. Gurney, Phys. Rev. B **47**, 11 579 (1993).
[2] B. A. Gurney, J. P. Nozieres, V. S. Speriosu, D. R. Wilhoit, and O. U. Need, in Symposium on Magnetic Ultra Thin Films, Multilayers, and Surfaces 7, 1992.
[3] J. P. Nozieres, V. S. Speriosu, B. A Gurney, B. Dieny, H. Lefakis, and T. C Huang, J. Magn. Mater. **121**, 386 (1993).
[4] S. S. P. Parkin, Phys. Rev. Lett. **71**, 1641 (1993).
[5] B. Dieny, P. Humbert, V. S. Speriosu, S. Metin, B. A. Gurney, P. Baumgart, and H. Lefakis, Phys. Rev. B **45**, 806 (1992).
[6] P. Baumgart, B A. Gurney, D. R. Wilhoit, T Nguyen, B. Dieny, and V. S. Speriosu, J. Appl. Phys. **69**, 4792 (1991).
[7] W. H. Butler, J. M MacLaren, and X.-G. Zhang, Mater. Res. Soc Symp Proc. **313**, 59 (1993).
[8] B. A. Gurney, V. S. Speriosu, J.-P. Nozieres, H. Lefakis, D. R. Wilhoit, and O. U. Need, Phys. Rev. Lett. **71**, 4023 (1993).
[9] S. A. Ahern and W. Sucksmith, Proc. Phys. Soc. B **69**, 1050 (1956), S. A Ahern, M. J. C. Martin, and W. Sucksmith, Proc. R Soc. London Ser. A **248**, 145 (1958); A. T. Alred, B. D. Ramford, T. J. Hicks, and J. S. Kouvel, Phys. Rev. B **7**, 218 (1973).
[10] Y. Wang, G. M. Stocks, D. M. C. Nicholson, and W. A. Shelton, *Alloy Modeling and Design*, edited by G. M. Stocks and P. E. A. Turchi (TMS, 1994), p. 75.
[11] T. C. Huang, J.-P. Nozieres, V. S. Speriosu, B. A. Gurney, and H Lefakis, Appl. Phys. Lett. **62**, 1478 (1993).
[12] J. B. Staunton, B. L. Gyorffy, D. D. Johnson, F. J. Pinski, and G. M. Stocks, *Alloy Phase Stability*, edited by G M. Stocks and A. Gonis (Kluwer, Dordrecht, 1989), p. 469.
[13] J. M. MacLaren, S. Crampin, D. D. Vvedensky, and J. B. Pendry, Phys Rev. B **40**, 12 164 (1989).

Theory of transport in inhomogeneous systems and application to magnetic multilayer systems

W. H. Butler, X.-G. Zhang, and D. M. C. Nicholson
Metals and Ceramics Division, Oak Ridge National Laboratory, Oak Ridge, Tennessee 37831-6114

J. M. MacLaren
Department of Physics, Tulane University, New Orleans, Louisiana 70118

A theory of the electrical conductivity of homogeneous random alloys based on the Korringa—Kohn—Rostoker coherent potential approximation (KKR-CPA) is generalized to treat an inhomogeneous alloy in which the concentrations of the constituent atoms can vary from site to site. A special case of such a system is an epitaxial multilayer system. We develop the theory for such systems and show how it can be implemented by using the layer Korringa—Kohn—Rostoker technique to calculate the electronic structure. Applications to magnetic multilayers and to the calculation of the giant magnetoresistance are discussed.

I. INTRODUCTION

Recently, there has been great interest in the transport properties of layered magnetic materials because of the discovery of a new form of magnetoresistance,[1,2] which may have important practical applications. The transport properties of layered materials have been the subject of several theoretical investigations already. Fuchs,[3] and later Sondheimer,[4] obtained a solution to the semiclassical Boltzmann equation with boundary conditions appropriate to a thin film. Barnás and co-workers[5] extended this approach to the case in which the film has several layers with differing scattering rates. Levy and co-workers[6–10] used the more rigorous Kubo–Greenwood theory,[11,12] which avoids certain conceptual difficulties associated with the semiclassical approach. The work described in this paper also starts from the Kubo–Greenwood linear response formula, but it is based on quantities calculable from first principles electronic structure theory. We do not assume that the scattering is weak or that the electron wave functions are those of free electrons. The only necessary inputs to our calculations are the atomic numbers and concentrations of the atoms in each layer.

Our approach is based on the Korringa–Kohn–Rostoker coherent potential theory for transport in homogeneous random alloys.[13] We first generalize this theory so that it can be applied to the case in which the concentrations of the constituent atoms can vary from site to site, then we treat the particular case of layered systems. Finally, we show how this theory can be implemented using the layer Korringa–Kohn–Rostoker technique.[14]

II. CONDUCTIVITY OF INHOMOGENEOUS ALLOYS

We define the nonlocal conductivity $\sigma^s_{\mu\nu}(\mathbf{r},\mathbf{r}')$ as the linear response of the current of electrons of spin s at point $\mathbf{r}$ in direction μ to the local applied field at point $\mathbf{r}'$ in direction ν,

$$J^s_\mu(\mathbf{r}) = \int d\mathbf{r}' \sum_\nu \sigma^s_{\mu\nu}(\mathbf{r},\mathbf{r}') E^s_\nu(\mathbf{r}'). \tag{1}$$

Here, "local applied field" means the change in the local electrostatic field that arises due to the application of a potential difference across the sample. For an inhomogeneous system, this may differ from the average applied field and it may be different for different spins.[8]

For a homogeneous random alloy, the current and applied field can be assumed to be uniform, so that one can define a single conductivity that is also uniform, $J^s_\mu = \Sigma_\nu \sigma^s_{\mu\nu} E_\nu$. This is the conductivity that is given by the Kubo–Greenwood formula[11,12]

$$\sigma^s_{\mu\nu} = \frac{\pi\hbar}{N\Omega} \left\langle \sum_{\alpha,\alpha'} \langle\alpha|j_\mu|\alpha'\rangle\langle\alpha'|j_\nu|\alpha\rangle \delta(\epsilon_F - \epsilon_\alpha) \times \delta(\epsilon_F - \epsilon_{\alpha'}) \right\rangle, \tag{2}$$

where j_μ is the current operator, $j_\mu \equiv (-i\hbar e/m_e)\partial/\partial r_\mu$, Ω is the volume per atom, and N is the number of atoms. The quantum states $|\alpha\rangle$ in Eq. (2) represent the exact eigenfunctions of a particular configuration of the random potential, and the large angle brackets indicate an average over configurations.

In order to define a nonlocal site-dependent conductivity, $\sigma^{ij,s}_{\mu\nu}$, we define the current density at site i for spin s as the average of the current density over the atomic cell at that site, $J^{i,s}_\mu = \Omega_i^{-1} \int_{\Omega_i} d\mathbf{r}\, J^s_\mu(\mathbf{r})$. We also assume that the local field, $E^s_\nu(\mathbf{r})$, is constant over each atomic cell. Thus, we write Ohm's law in a discrete form, in which the current at site i is related to the local electric field at site j through the two-point conductivity function, σ^{ij},

$$J^{i,s}_\mu = \sum_{j\nu} \sigma^{ij,s}_{\mu\nu} E^{j,s}_\nu. \tag{3}$$

The superscript s on the local field indicates that it can be spin dependent, as has been emphasized by Camblong *et al.*[8] The local field will be determined *after* the nonlocal conductivity is determined by the requirement of current continuity in the steady state, $\Sigma_\mu \partial J^s_\mu(\mathbf{r})/\partial r_\mu = 0$.

The intersite conductivity, $\sigma^{ij,s}_{\mu\nu}$, is given by Eq. (2), with the matrix element integrals $\langle\alpha|j_\mu|\alpha'\rangle$ and $\langle\alpha'|j_\nu|\alpha\rangle$ restricted to sites i and j, respectively, and can be seen to depend on

 0021-8979/94/76(10)/6808/3/$6 00 © 1994 American Institute of Physics

the *imaginary part* of Green's function, $\Sigma_\alpha|\alpha\rangle\langle\alpha|\delta(\epsilon_F-\epsilon_\alpha)$. It can be written in terms of the Green's function, $G(\mathbf{r},\mathbf{r}';\epsilon_F)$, by writing

$$\sigma_{\mu\nu}^{ij,s}=\frac{1}{4}\sum_{p,p'=\pm 1}(pp')\tilde{\sigma}_{\mu\nu}^{ij,s}(\epsilon_F+i\eta p,\epsilon_F+i\eta p'), \quad (4)$$

where η is infinitesimal, and where

$$\tilde{\sigma}_{\mu\nu}^{ij,s}(z_1,z_2)=\frac{-\hbar}{\pi\Omega_i}\int_{\Omega_i}d\mathbf{r}\int_{\Omega_j}d\mathbf{r}'\; j_\mu(\mathbf{r})G^s(\mathbf{r},\mathbf{r}';z_1)j_\nu(\mathbf{r}') \times G^s(\mathbf{r}',\mathbf{r};z_2). \quad (5)$$

Following Ref. 13, we write Green's function in terms of the scattering path operator of multiple scattering theory, $\tau_{LL'}^{ij,s}$, and the local solution to the Schrödinger equation on site i, $Z_L^{i,s}(\mathbf{r},z)$,

$$\frac{\hbar^2}{2m_e}G^s(\mathbf{r}_i,\mathbf{r}_j')=\sum_{L_1L_2}Z_{L_1}^{i,s}(\mathbf{r}_i)\tau_{L_1L_2}^{ij,s}Z_{L_2}^{j,s}(\mathbf{r}_j')+\text{S.T.} \quad (6)$$

The scattering path operator τ is a "representation" of Green's function within the angular momentum space, and depends on the atomic t matrices, $t_L^{i,s}$, calculated from the self-consistent atomic potentials, and on the structure constants, which depend only upon the positions of the atoms. The singular term in the Green function (S.T.), which involves the irregular solution to the local Schrödinger equation, can be omitted from the calculation of the conductivity because it does not contribute to Eq. (4). Thus, we write the conductivity in the form

$$\tilde{\sigma}_{\mu\nu}^{ij,s}(z_1,z_2)=\frac{-4m_e^2}{\pi\hbar^3\Omega_i}\sum_{L_1L_2L_3L_4} \times\langle M_{L_4L_1}^{i\mu,s}(z_2,z_1)\tau_{L_1L_2}^{ij,s}(z_1) \times M_{L_2L_3}^{j\mu,s}(z_1,z_2)\tau_{L_3L_4}^{ji,s}(z_2)\rangle, \quad (7)$$

where the dipole matrix element is given as

$$M_{L_1L_2}^{i\mu,s}(z_1,z_2)=\frac{-ie\hbar}{m_e}\int_{\Omega_i}d\mathbf{r}\; Z_{L_1}^{i,s}(\mathbf{r},z_1)\nabla_\mu Z_{L_2}^{i,s}(\mathbf{r},z_2). \quad (8)$$

So far, we have not made any serious approximations in evaluating the linear response to the applied field. Under certain circumstances, it may be computationally feasible to evaluate Eq. (7) directly, however, in this paper we use the coherent potential approximation (CPA) to put this equation into a more tractable form. The CPA is a technique for "self-consistently" averaging over the atomic configurations. The individual atomic t matrices, t_α^i are replaced in the CPA by "coherent" t matrices, t_c^i. The self-consistency condition for determining these "coherent" t matrices is $\Sigma_\alpha c_j^\alpha x^{\alpha j}=0$. Here $x^{\alpha j}$ describes the scattering caused by replacing a coherent t matrix by one for an atom of type α at site j, and is given by $x^{\alpha j}=\Delta m^{\alpha j}\,D^{\alpha j}$, where $\Delta m^{\alpha j}$ is the difference between the inverse of the coherent t matrix and the t matrix for an atom of type α on site j, $\Delta m^{\alpha j}=(t_c^j)^{-1}-(t_\alpha^j)^{-1}$, and $D^{\alpha j}$ is given by $D^{\alpha j}=(1-\tau_c^{jj}\,\Delta m^{\alpha j})^{-1}$.

We follow Rcf. 13 to average the two particle Green's function and obtain an expression for the conductivity of the form

$$\tilde{\sigma}_{\mu\nu}^{IJ}=\frac{-4m_e^2}{\pi\hbar^3\Omega_i}\sum_{L_4L_1}\bar{M}_{L_4L_1}^{i\mu}\mathscr{L}_{L_1L_4}^{ij\nu}, \quad (9)$$

where the function $\mathscr{L}$ is given by

$$\mathscr{L}_{L'L''}^{ij\nu}=\sum_{L_1L_2}\tau_{L'L_1}^{ci j}\bar{M}_{L_1L_2}^{j\nu}\tau_{L_2L'}^{cjt} +\sum_{L_i}\sum_{k\alpha}c_k^\alpha\tau_{LL_1}^{cik}x_{L_1L_2}^{\alpha k}\mathscr{L}_{L_2L_3}^{kj\nu}x_{L_3L_4}^{\alpha k}\tau_{L_4L'}^{ck\iota}, \quad (10)$$

where the second term is the vertex correction, and $\bar{M}_{LL'}^{i\mu}$ is a particular average over the matrix elements for the various types of atoms that may occupy site i,

$$\bar{M}^{i\mu}=\sum_\alpha c_i^\alpha\tilde{D}^{i\alpha}M^{i\alpha\mu}D^{i\alpha}. \quad (11)$$

Equations (9)–(11) are the generalization of the KKR-CPA theory of transport to an inhomogeneous alloy. The generalization from the results of Ref. 13 is straightforward because the CPA self-consistency condition is a single site condition and therefore can be applied independently on each site. For a general inhomogeneous alloy, this theory would be difficult to implement, because it would be hard to calculate the scattering path operators τ_c^{ij}. However, for a layered system that retains a two-dimensional periodicity, implementation is feasible, as we describe in the next section.

III. APPLICATION TO LAYERED SYSTEMS

In this section we consider a special case where the concentration of the alloy can vary from layer to layer, but is uniform within each layer. The CPA average is performed on the atomic sites to produce an effective layered system that has a two-dimensional periodicity. We use a notation in which a site labeled by i in Sec. II and representing any lattice site in the three-dimensional crystal acquires two labels: $i\rightarrow Ii$, where the upper case I distinguishes different *atomic* layers, and the lower case i labels a site within layer I. The probability of site Ii being occupied by an atom of type α depends only on the layer index, I. Thus, suppressing the angular momentum, Cartesian, and spin indices, we can write Eq. (9) as $\tilde{\sigma}^{IiJj}=(-4m_e^2/\pi\hbar^3\Omega_i)\bar{M}^{Ii}\mathscr{L}^{IiJj}$. The interlayer conductivity can then be written in the form $\tilde{\sigma}^{IJ}=N_I^{-1}\Sigma_{ij}\tilde{\sigma}^{IiJj}$, where N_I is the number of atoms per layer.

Because of the two-dimensional periodicity (after the CPA average), we can relate the scattering path operator that connects any two sites τ_c^{IiJj} to a scattering path operator that connects layers through an integral over the two-dimensional Brillouin zone, of area Ω_z,

$$\tau_c^{IiJj}=\Omega_z^{-1}\int_{\Omega_z}d^2q\;\tau_c^{IJ}(\mathbf{q})e^{i\mathbf{q}\cdot(\mathbf{R}_i-\mathbf{R}_j)}. \quad (12)$$

These layer scattering path operators τ_c^{IJ} can be calculated using the layer KKR formalism.[14]

The final expression for the conductivity is expressed in terms of matrices indexed by the layer numbers, $\tilde{\sigma}^{IJ}=(-4m_e^2/\pi\hbar^3\Omega_t)\tilde{M}^I\mathscr{L}^{IJ}$, where

$$\mathscr{L}^{IJ}=\Omega_z^{-1}\int_{\Omega_z} d^2q\ \tau_c^{IJ}(\mathbf{q})\tilde{M}^J\tau_c^{JI}(\mathbf{q}) + \sum_{K,\alpha} c_K^\alpha\Omega_z^{-1}\int_{\Omega_z} d^2q\ \tau_c^{IK}(\mathbf{q})x_K^\alpha\mathscr{L}^{KJ}x_K^\alpha\tau_c^{KI}(\mathbf{q}). \tag{13}$$

The local fields can be determined after σ^{IJs} is obtained, by using $J^{Is}=\Sigma_K\sigma^{IKs}E^{Ks}$, and the condition that the current for each spin must be continuous in the steady state. Two geometries are commonly discussed. If the field is applied parallel to the layers, sometimes referred to as "CIP" for "current in the plane," the local fields will be uniform by symmetry and equal to the average applied field. Thus, the overall conductivity will be given by $\sigma=t^{-1}\Sigma_{IKs}t_I\sigma^{IKs}$, where t_I is the thickness of layer I and t is the total film thickness. If the field is applied perpendicular to the layers, $J^{I,s}$, will be independent of I for each spin. Thus, $J^s=\Sigma_K\sigma^{IKs}E^{KS}$, and the local fields can be obtained by inverting σ^{IKs},

$$E^{Is}=\sum_K[(\sigma^s)^{-1}]^{IK}J^s=\sum_K\rho_s^{IK}J^s. \tag{14}$$

This allows the current to be expressed in terms of the voltage difference across the sample, ΔV, as $J^s=\Delta V/\Sigma_{IK}t_I\rho_s^{IK}$. In this case, the resistivity for each spin (neglecting spin-flip scattering) is given by $\rho_s=t^{-1}\Sigma_{IK}t_I\rho_s^{IK}$, and the conductivities of the two spin channels should be added to obtain the overall conductivity.

The giant magnetoresistance effect is observed in layered films in which ferromagnetic layers alternate with nonmagnetic spacer layers. If the moments on neighboring ferromagnetic layers are brought into alignment by the application of a magnetic field, the electrical resistance of the film may decrease. This giant magnetoresistance systems can be calculated directly using the results derived in this paper by calculating the conductivity for the case in which alternate ferromagnetic layers are aligned parallel or antiparallel. Calculations that we have performed for cobalt—copper—cobalt sandwiches using the formalism of this paper implemented within the layer-KKR technique in the "CIP" arrangement show that the major contributions to the magnetoresistance arise from terms, σ^{IJ}, in which I and J are atomic layers adjacent to the ferromagnetic–spacer interfaces, and are on opposite sides of the spacer layer. Details of these calculations will be published elsewhere.

ACKNOWLEDGMENTS

Work at Oak Ridge was sponsored by the Department of Energy Assistant Secretary of Defense Programs, Technology Management Group, Technology Transfer Initiative under Contract No. DEAC05-84OR21400 with Martin Marietta Energy Systems. Work at Tulane University was partially supported by the Louisiana Quality Education Support Fund under Grant No. LEQSF (1991–1994)-RD-A-30.

[1] M. N. Baibich, J. M. Broto, A. Fert, F. Nguyen Van Dau, F. Petroff, P. Etienne, G. Creuzet, A. Friederich, and J. Chaezelas, Phys. Rev. Lett. **61**, 2472 (1988).
[2] G. Binasch, P. Grünberg, F. Sauerbach, and W. Zinn, Phys. Rev. B **39**, 4828 (1989).
[3] K. Fuchs, Proc. Cambridge Philos. Soc. **34**, 100 (1938).
[4] E. H. Sondheimer, Adv. Phys. **1**, 1 (1952).
[5] J. Barnas, A. Fuss, R. E. Cameley, P. Grünberg, and W. Zinn, Phys. Rev. B **42**, 8110 (1990).
[6] P. M. Levy, S. Zhang, and A. Fert, Phys. Rev. Lett. **65**, 1643 (1990).
[7] S. Zhang, P. M. Levy, and A. Fert, Phys. Rev. B **45**, 8689 (1992).
[8] H. E. Camblong, S. Zhang, and P. M. Levy, Phys. Rev. B **47**, 4735 (1993).
[9] H. E. Camblong and P. M. Levy, Phys. Rev. Lett, **69**, 2835 (1992).
[10] H. E. Camblong and P. M. Levy, J. Appl. Phys. **73**, 5533 (1993).
[11] R. Kubo, J. Phys. Soc. Jpn. **12**, 570 (1957).
[12] D. A. Greenwood, Proc. Phys. Soc. London **71**, 585 (1958).
[13] W. H. Butler, Phys Rev. **31**, 3260 (1985).
[14] J. M. MacLaren, S. Crampin, D. D. Vvednsky, R. C. Albers, and J. B. Pendry, Comput. Phys. Commun. **60**, 365 (1990)

The effect of interactions on GMR in granular solids

M. El-Hilo and K. O'Grady
Magnetic Materials Research Group, SEECS, UCNW, Bangor, Gwynedd LL57 1UT, Great Britain

R. W. Chantrell
Department of Physics, Keele University, Keele, Staffs ST5 5BG, Great Britain

In this article the effects of dipolar and exchange interactions on the magnetoresistance curves in granular solids has been calculated using a generalized 3-*d* Monte Carlo model. This model allows the final configuration of magnetic moments to be calculated as a function of concentration, temperature, and magnetic field. The results show that interaction effects give rise to a finite resistivity in small magnetic fields. The magnitude of this finite magnetoresistance is found to increase with increasing concentration. Thus the maximum change in MR with field is found to be lowered by the interaction effects.

I. INTRODUCTION

The magnetoresistance phenomena have recently received major attention due to its potential application in magnetic sensors and recording heads. The first attempt to obtain a simple description for the magnetoresistance was made by Gittleman *et al.*[1] who showed that the change in resistivity with magnetic field is directly proportional to the moment to moment correlation of the neighboring grains averaged over all configurations

$$\rho(H) \propto \frac{\langle \boldsymbol{\mu}_i \cdot \boldsymbol{\mu}_j \rangle}{\mu^2}, \tag{1}$$

where $\boldsymbol{\mu}_i$ and $\boldsymbol{\mu}_j$ are the magnetic moments of the ith and jth neighboring grains, respectively.

For systems which contain uniform, noninteracting superparamagnetic particles (i.e., all the moments fluctuate thermally) the statistical average of $\langle \boldsymbol{\mu}_i \cdot \boldsymbol{\mu}_j \rangle / \mu^2$ along the field direction gives

$$\langle \boldsymbol{\mu}_i \cdot \boldsymbol{\mu}_j \rangle = \mu^2 [L(b)]^2 = \bar{M}^2, \tag{2}$$

where $\bar{M}[=M/M_s = L(b)]$ is the reduced magnetization of the system, $L(b)$ is the Langevin function with $b = \mu H / k_B T$, where H is the field acting on the grain, k_B is Boltzmann's constant, and T is the absolute temperature. In Ref. 1 interaction effects were represented by a mean-field term which was added to the applied field (H_a), i.e., $H \rightarrow H_a + \lambda M$. However, this way of representing interaction effects has always been criticized particularly when the problem is related to inhomogeneous systems and hence the strength of the interaction field is not directly proportional to M.

In general and particularly at low temperatures, the magnetoresistance curves exhibit hysteresis effects and plots of $\Delta\rho(H) = \rho(\infty) - \rho(H)$ as a function of field, give a peak near the coercivity, where $\rho(\infty)$ is the maximum resistivity in a saturating field.[2,3] In the case where no hysteresis is observed Eq. (2) has been adapted to analyze the MR curves and estimate the average volume of the cluster in Co-Ag granular systems.[4] In other Co-Ag systems the MR data are observed not to follow the $\bar{M}^2$ law particularly in the region of low fields which was attributed to different magnetic phases within the sample.[5] However in Ref. 5 and at low temperatures where hysteresis is observed, the value of $\Delta\rho(H = H_c)$ i.e., $\Delta\rho_{\max}$ was observed to be different from the value obtained at zero field (i.e., starting from a demagnetized state). This effect was attributed to interaction effects between the so-called active magnetic regions.

Thus, in order to provide an unambiguous explanation for the interaction effects on the behavior of MR in granular or quasigranular systems we have used a generalized 3-*d* Monte Carlo model in which the quantity $\langle \boldsymbol{\mu}_1 \cdot \boldsymbol{\mu}_2 \rangle$ can be examined directly as a function of temperature, field, and other variables.

II. MODEL

The model consists of a cubic cell in which the positions of the particles are generated randomly. The particle sizes were generated according to a log-normal distribution function and fitted randomly within the cell without their positions being overlapped. Anisotropy effects were also considered and the particles easy axes were generated randomly. According to this arrangement the axis system for any particle within the cell is described in Fig. 1 where the total energy of the ith particle is

$$E = KV_i \sin^2 \alpha - \boldsymbol{\mu}_i \cdot \mathbf{H}_T, \tag{3}$$

where K is the anisotropy constant (uniaxial) and $\mu_i = I_{sb} V$ is the magnetic moment of the particle, with I_{sb} the saturation magnetization of the bulk material, and V the particle volume. $\mathbf{H}_T(H_T, \theta_{HT}, \phi_{HT})$ is the total field that particle i experiences which is the vector sum of the applied field and the dipolar and exchange fields arising from neighboring particles j

$$\mathbf{H}_T = H_a \hat{z} + \sum_{i \neq j} \left[\frac{3(\boldsymbol{\mu}_j \cdot \mathbf{r}_{ij}) \mathbf{r}_{ij}}{d_{ij}^5} - \frac{\boldsymbol{\mu}_j}{d_{ij}^3} \right] + c^* \sum_{i \neq j} \boldsymbol{\mu}_j, \tag{4}$$

where the applied field (H_a) is chosen to be along the z axis. The second term of Eq. (4) represents the vector sum of the total dipolar fields arising from neighboring particles while the third term represents the vector sum of the exchange fields with C^* being the average exchange coupling between the grains whose surfaces lie within a distance comparable to the interatomic spacing ($\approx$10 Å). The range of the dipolar field is chosen to be at a distance of $3D_m$ from the particle under investigation where D_m is the median diameter of the particles. This range is chosen because the dipolar field aris-

 0021-8979/94/76(10)/6811/3/$6.00 © 1994 American Institute of Physics

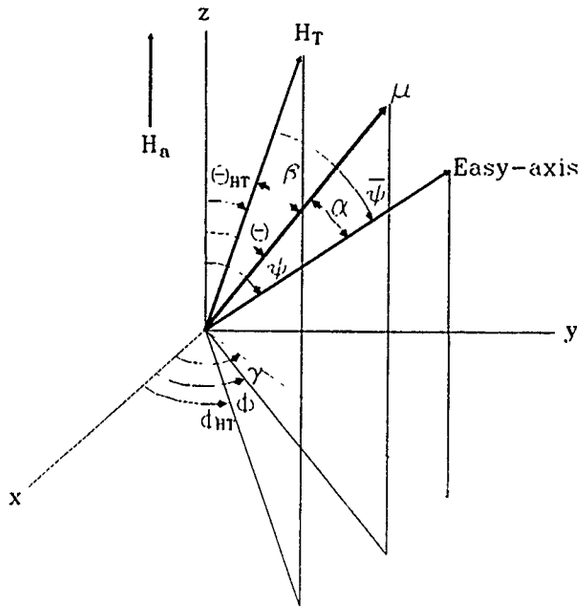

FIG. 1. Axis system for a particle within the cell.

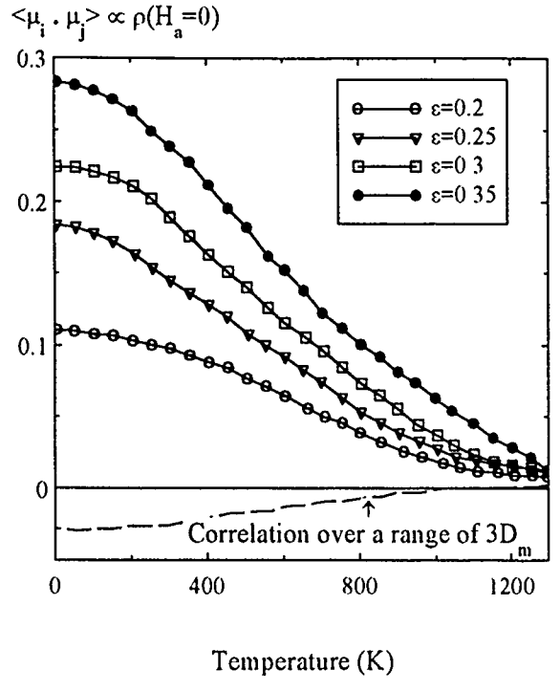

FIG. 2. The calculated short-range correlation of moments during the thermal demagnetization process.

ing from other particles located outside this range becomes very small (<4%). The calculation is based on the energy minimization of Eq. (3) where the final configuration of moments is obtained after several hundred iterations for θ and ϕ. Therefore, the magnetoresistance is calculated as $\rho \propto \langle \hat{\mu}_i, \hat{\mu}_j \rangle$ where the correlation range is taken over the neighboring particles, i.e., the short-range correlation. More details of this model and how the calculation is performed for both superparamagnetic and blocked particles are to be published elsewhere.[6]

III. RESULTS AND DISCUSSION

All the calculations were made using a primary cell which contained 400 particles. The particles generated were chosen to have a median diameter of D_m=60 Å with a standard deviation of σ=0.15 and an effective anisotropy constant of $K=2\times10^6$ erg/cc. These parameters were obtained for a fine particle system containing cobalt particles in previous experimental work.[7] For this system the MR curves were calculated as a function of concentration. One advantage of this study is that the distribution of particle sizes was invariant with particle concentration, thus any changes in the behavior was due entirely to interaction effects. However, in real alloy films the distribution will not be invariant with concentration and an extended report on this matter is in preparation.[6] In these calculations a value of C^*=0.05 was used in order to keep the exchange interaction effects small and the total interaction effect will then be dominated by dipolar interactions.

Before starting the calculation of the MR curve, the initial configuration of the magnetic moments (i.e., the demagnetized state) was achieved by thermal demagnetization. This technique produces demagnetized states which are equivalent to those obtained via an ac demagnetizing technique.[8] Thus the demagnetized state was achieved by taking the system to the Curie temperature and then cooling down slowly in zero applied field. Figure 2 shows the temperature variation of the short-range correlation of moments during the thermal demagnetization process. These data show that there is a finite positive correlation which increases with concentration due to the increase in the interaction strength within

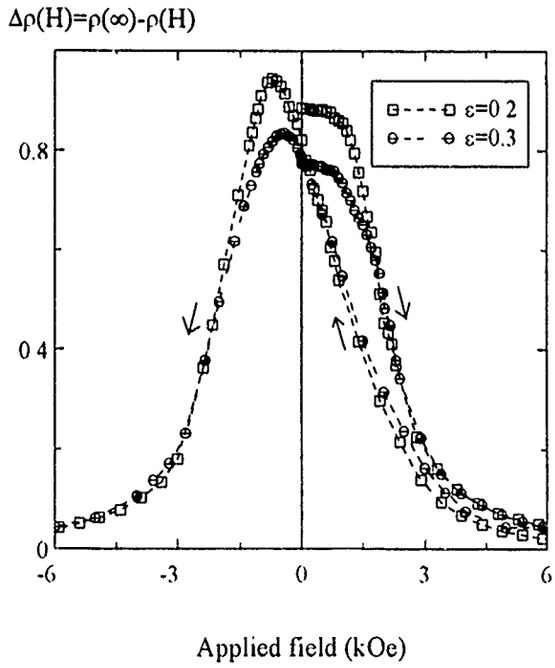

FIG 3. Calculated MR curves at T=5 K for Co particles

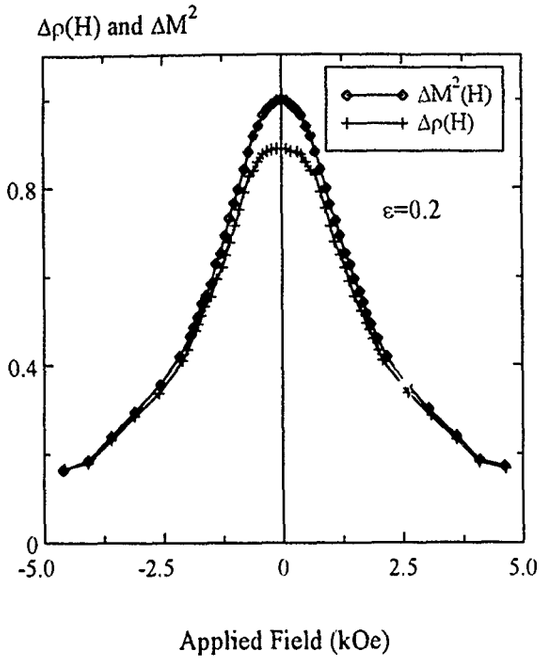

FIG. 4. Calculated room-temperature MR curves for Co particles.

the system. This result suggests that the moments have formed a vortex structure where the correlation over a short-range compared to the particle diameter is positive, whereas if this range is extended further a negative correlation is obtained (see the dotted line in Fig. 2 which represents the correlation of moments over a range of $3D_m$ where D_m is the average diameter of the system.

Figure 3 shows the calculated MR loops at $T=5$ K for concentrations $\epsilon=0.2$ and 0.3, starting from the demagnetized state and increasing the field to positive saturation and then to negative saturation. These data for $\Delta\rho(H)$ are typical and show that the value of $\Delta\rho(H=0)$ is lower than that for $\Delta\rho(H)_{\max}$ due to the fact that there is a finite positive correlation of moments in the demagnetized state. Also, these data show that as the concentration increases $\Delta\rho(H)_{\max}$ decreases which indicates that interaction effects in random systems depress the MR values and then decrease the maximum change in magnetoresistance for the system. Figure 3 also shows that due to interaction effects the peak in the $\Delta\rho(H)$ curve is shifted to lower fields and becomes more rounded.

Figure 4 shows the MR curves at room temperature ($T=300$ K) for the sample with $\epsilon=0.2$. In this case all the particles are superparamagnetic and the system exhibits no remanence and coercivity. Also on the same figure $\Delta\bar{M}^2$ data are shown where $\Delta\bar{M}^2=\bar{M}^2(\infty)-\bar{M}^2(H)$ and $\bar{M}$ is the reduced magnetization of the system. It is clear from the data that the $\Delta\rho(H)$ curve starts to deviate from the $\Delta\bar{M}^2$ curve as the field is reduced and at low fields the $\Delta\rho(H)$ exhibits a flat region which is lower than $\Delta\bar{M}^2$. This result can be understood since $\Delta\bar{M}^2$ is a measure of the average correlation over the whole system whereas the $\Delta\rho(H)$ data give the degree of short range correlation between the neighboring particles. At low fields the short-range correlation is insensitive to field changes and only gives small changes in the magnetoresistance. These results also shows that even at room temperature the short-range correlation is still significant which indicates that interaction effects in random systems decrease the values of $\Delta\rho(H)_{\max}$.

IV. CONCLUSIONS

In this article the effects of interactions on the behavior of GMR in idealized granular systems is examined using a generalized 3-*d* Monte Carlo model. Calculations of the short-range correlation of moments as a function of field are partially consistent with the observed MR curves in random systems. These calculations show that due to interaction effects the $\Delta\rho(H=0)$ is different from that for $\Delta\rho(H)_{\max}$. Also, when there is no hysteresis the $\Delta\rho(H)$ does not follow an M^2 law due to the fact that MR depends on the short-range order whereas the magnetization is an average over the whole system.

[1] J. I Giteleman, Y Goldstein, and S. Bozowski, Phys. Rev. B **9**, 3609 (1972).
[2] J. Q. Xiao, J. S. Jiang, and C. L. Chien, Phys. Rev. Lett. **68**, 3749 (1992).
[3] A. E. Berkowitz, J. R. Mitchell, M. J. Carey, A. P. Young, D. Rao, A. Star, S. Zang, F. E. Spada, F. T. Praker, A. Hutten, and G. Thomas, J. Appl. Phys. **73**, 5320 (1993).
[4] M. R. Parker, J. A. Barnard, D. Seale, and A. Waknis, J. Appl. Phys. **73**, 5512 (1993).
[5] J. F. Gregg, S. M. Thompson, S. J. Dawson, K. Ounadjela, C. R. Staddon, J. Hamman, C. Fermon, G. Saux, and K O'Grady, Phys. Rev. B **49**, 1064 (1994).
[6] M. El-Hilo, K. O'Grady, and R. W. Chantrell (unpublished).
[7] K. O'Grady, R. W. Chantrell, J. Popplewell, and S. W. Charles, IEEE Trans. Magn. **16**, 1077 (1980).
[8] C. Dean, A Hart, D. A. Parker, R W. Chantrell, and J. J. Miles, IEEE Trans. Magn. **27**, 4769 (1991).

Giant magnetoresistance in spinodally decomposed Cu–Ni–Fe films

L. H. Chen
Department of Electrical Engineering, Kaohsiung Polytechnic Institute, Kaohsiung, Taiwan

S. Jin and T. H. Tiefel
AT&T Bell Laboratories, Murray Hill, New Jersey 07974

T. C. Wu
Department of Materials Science, University of Cornell, Ithaca, New York 14853

We report the observation of the GMR effect in spinodally decomposed Cu–20Ni–20Fe thin films. A $\Delta R/R$ value as high as 6.5% was observed at room temperature. In contrast to the commonly observed temperature-dependent behavior of $\Delta R/R$ increasing at low temperature; thin film shows a decrease in $\Delta R/R$ at 4.2 K. The dependence of the GMR effect on various deposition parameters, such as substrate temperature has been studied. The observed giant magnetoresistance behavior in Cu–20Ni–20Fe films is most likely related to the field-induced decrease in electron scattering in a pseudosuperparamagnetic material, as well as the spin-dependent scattering at the two-phase interface and in the ferromagnetic phase.

Giant magnetoresistance (GMR) type ferromagnetic/nonmagnetic superlattice structure was first discovered in a Fe/Cr system,[1] and later in other systems, including Co/Cu, Fe/Cu, Co/Ag, etc.[2,3] Recently, negative magnetoresistance in granular alloys, consisting of ferromagnetic particles dispersed in a nonmagnetic matrix, was also found in Cu–Co thin films,[4,5] as well as in other thin film systems, for example, Ag–Co, Cu–Fe, and Au–Co.[5–7] While many combinations of ferromagnetic–nonmagnetic phases are possible in granular alloys, the systems that exhibit the GMR effect are restricted to those that are essentially not soluble to each other in the solid state.

In our previous reports, giant negative magnetoresistance was created in spinodally decomposed Cu–Ni–Fe bulk alloys with artificial layer-like structures, in both the ferromagnetic–nonmagnetic and ferromagnetic–ferromagnetic two-phase states.[8,9] The superlattice-like structure with a size scale of 10–30 A was obtained, either by anisotropic deformation or by proper heat treatment of spinodally decomposed Cu–20Ni–20Fe alloys. In this study, the creation of the ultrafine and spinodally decomposed microstructure of Cu–20Ni–20Fe thin films by triode magnetron sputtering is reported, and the giant magnetoresistance and magnetization results are presented.

The Cu–20Ni–20Fe (wt.%) alloy thin films were prepared by dc magnetron triode sputtering from a 57 mm diam target. The films with a thickness of 1000–5000 Å were sputtered onto Si(100) single crystal substrate under various sputtering conditions. The substrate temperatures during sputtering were changed from 77 to 500 K. Various accelerating bias voltages, applied between the target and the substrate, ranging from 75 to 250 V were used in the sputtering.

The film thickness was determined by Rutherford Backscattering Spectrometry (RBS). The crystal structure and texture of the deposited films were investigated by x-ray diffraction (XRD) using K_α (Cu) radiation. The magnetoresistance (MR) measurement were made using the conventional four-point probe method with a magnetic field applied in the film plane. The measurements were carried out at various temperatures (4.2 K–295 K) and fields up to 60 KOe. The magnetic properties were studied by using a vibrating sample magnetometer. The microstructure of thin films was studied by high resolution transmission electron microscopy (TEM) using JEOL 4000 microscope operated at 400 kV, after sample thinning by ion milling at 77 K.

The Cu–20Ni–20Fe film was first deposited onto a substrate at a temperature of 77 K with an Ar accelerating bias of 200 V and under a pressure of 4 mTorr. Figure 1 shows the room temperature and 4.2 K magnetoresistance (MR) ratio versus the applied magnetic field for this film. The MR ratio was defined here as $\Delta\rho_m/\rho_s$ or $\Delta R_m/R_s$, where ρ_s (or R_s) is the electrical resistivity or resistance near the saturation field. The electrical resistivity of the film in zero field is about 24 $\mu\Omega$ cm at room temperature and 14 $\mu\Omega$ cm at 4.2 K. As the field strength is increased, the electrical resistivity of the film decreases continuously. The as-deposited sample exhibits a negative room temperature magnetoresistance ratio of about 6.5% at H=60 KOe. The MR ratio versus H curve is not saturated at the maximum applied field, and hence the maximum magnetoresistance ratio attainable must

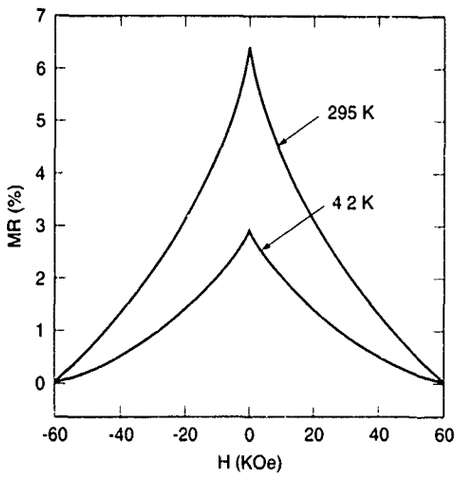

FIG. 1. MR ratio vs H curves at room temperature and 4 2 K in a Cu–20Ni–20Fe thin film.

 0021-8979/94/76(10)/6814/3/$6.00 © 1994 American Institute of Physics

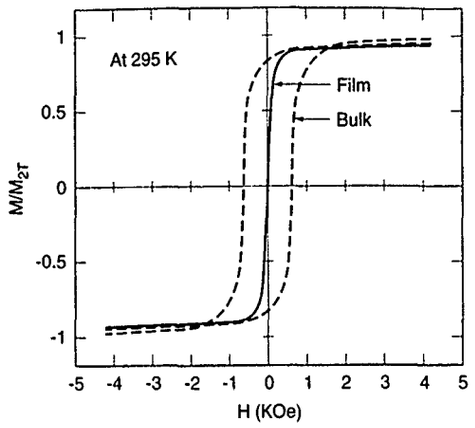

FIG. 2. M–H loops for the as-deposited film and bulk Cu–20Ni–20Fe alloy.

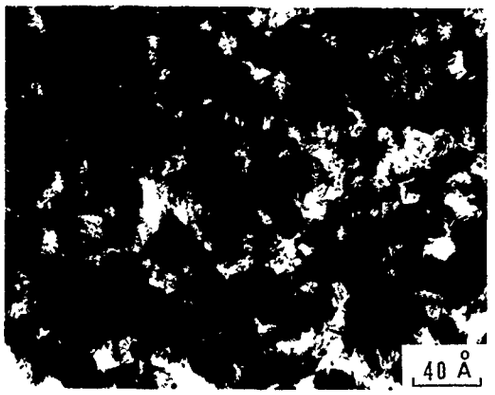

FIG. 3. Spinodally decomposed microstructure in the as-deposited Cu–Ni–Fe film.

be higher than 6.5% measured at the field of 6 T. The magnetoresistance ratio of the sample in Fig. 1 was also measured with magnetic fields up to 2 T, applied perpendicular to the film surface. When the demagnetizing field is taken into consideration, essentially the same magnetoresistance behavior as for the in-plane field orientation was observed. Thus, the possibility of significant anisotropic magnetoresistance contribution is eliminated.

Shown in Fig. 2 is the M–H magnetization hysteresis loop at room temperature, measured with the maximum field of 2 T for the as-deposited film. The M–H loop for the bulk Cu–20Ni–20Fe alloy sample is also shown as a dotted curve for comparison. The as-deposited film exhibits a relatively small hysteresis with a relatively lower coercivity (Hc) of less than ~20 Oe, a remanence ratio (M_r/M_s) of ~0.2, and a saturation (M_s) of 130 emu/cm^3, which suggests a film microstructure with very fine particle size of the ferromagnetic phase, almost close to the superparamagnetic regime. However, the bulk sample with particle size of ~500 Å has a coercivity of 620 Oe, a remanence ratio of 0.87, and saturation of 200 emu/cm^3. Essentially, similar M–H behavior is observed at 4.2 K, except with slightly larger hysteretic behavior for both samples.

The x-ray diffraction study indicates that the main diffraction peak in the XRD pattern of this as-deposited film are, respectively, (111), (200), and (220) in the order of integral intensity for both the Cu-rich and the (Fe, Ni)-rich phases, as their lattice parameters are very close to each other and the peaks overlap due to the slight shift and broadening of the peaks. This suggests that polycrystalline structure exists in this as-deposited Cu–20Ni–20Fe film, and the composition fluctuation and phase separation in it is small, as indicated by diffraction peaks without significant splitting. Figure 3 shows the decomposition structure with a ~30 Å size composition modulation in the as-deposited Cu–Ni–Fe film. The Moire fringes in the TEM image suggests that the (Fe, Ni)-rich phase (the darker phase in Fig. 3) has a lattice parameter slightly different from that of Cu-rich matrix. The relative volume of the two phases is approximately 50% each. The particle size in the present film is comparable to the layer thickness, and the interlayer spacing between the ferromagnetic layers in GMR-type superlattice films, which is on the order of 10–30 A. Thus, the observed giant magnetoresistance in the as-deposited Cu–Ni–Fe film is attributed to the extremely fine-scale spinodally decomposed structure, the presence of which is further confirmed by magnetization measurement, as well as by XRD and TEM. The bulk spinodally decomposed Cu–20Ni–20Fe alloy (Cunife 1, a common permanent magnet material) with a particle size of ~500 Å was found to exhibit a magnetoresistance ratio of only about 0.6% at room temperature, with fields up to 6 T in our previous report.[8] Here we show that the promotion of the magnetoresistance effect in the spinodally decomposed Cu–Ni–Fe alloy could be achieved through microstructure modification by a sputtering process, in addition to the anisotropic deformation or heat treatment methods reported in the previous papers.

Upon cooling from room temperature to 4.2 K, the film exhibits a decrease of electrical resistivity by a factor of 1.7 (from 24 to 14 $\mu\Omega$ cm). In contrast to the resistivity, the $\Delta\rho_m$, defined as $(\rho_0-\rho_s)$, decreases by a factor of 3.3 (from 1.4 to 0.4 $\mu\Omega$ cm). The net result is that the room temperature MR ratio is higher than that at 4.2 K as shown in Fig. 4, which is opposite to the commonly observed tendency of MR ratio increasing at lower temperatures.

Comparing the MR ratio versus H curve to the M–H curve, the saturation field for the M–H curve appears to be

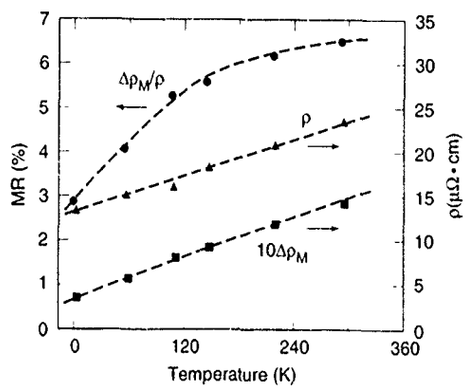

FIG. 4. MR ratio and resistivity vs temperature.

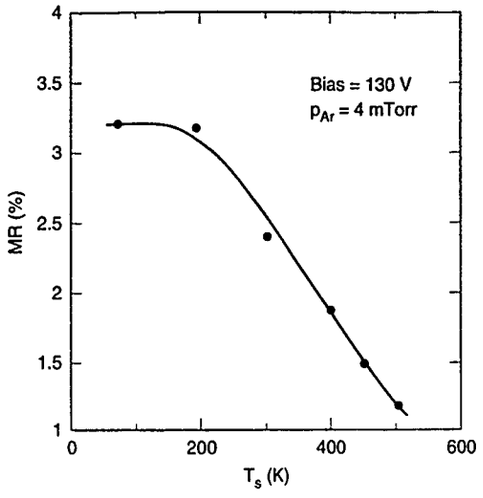

FIG. 5. Substrate temperature dependence of the MR ratio (for H=2 T) for the Cu–20Ni–20Fe film.

significantly lower than that for the corresponding magnetoresistance curve (Fig. 1). Although the exact mechanisms not fully understood are still obscure, the GMR behavior is believed to be related to the spin-dependent scattering, which is reduced when the angle between the magnetization of adjacent layers of magnetic grains (domains) is decreased. It is thus expected that the GMR and magnetization will be directly related.

However, in view of the much lower saturation field for the M–H curve than that for the magnetoresistance curve, as well as the abnormal temperature dependence of MR, it is speculated that the GMR mechanism in the present film may be qualitatively different from the general feature described by previous investigators. Similar to the as-deformed Cu–Ni–Fe alloy wire, the observed MR, as well as its temperature dependence, could be explained in terms of the mechanism proposed by Dieny *et al.*[10] The magnetic excitations in the nearly superparamagnetic film, which is supported by the M–H curve data, as well as the XRD and TEM observation, lead to strong, but not necessarily spin-dependent, electron scattering. Such excitations are reduced by an applied field, and lead to the observed MR behavior. At lower temperatures, they are significantly reduced, and hence the field-related decreasing of resistivity becomes smaller than at higher temperatures. This gives the negative temperature dependence of the MR ratio for the film. However, the contribution of spin-dependent scattering at the two-phase interface and in the ferromagnetic phase to the GMR phenomenon could not be ruled out in this study. Further studies are necessary to verify the exact role of various mechanisms involved.

Figure 5 describes the substrate temperature (T_s) dependence of the MR ratio measured at room temperature in Cu–20Ni–20Fe thin film samples, prepared with an accelerating bias of 130 V and under Ar pressure of 4 mTorr. The MR ratio versus T_s curve shows a strong dependence of MR ratio on T_s. It increases from 1.2% to 3.2% after the substrate temperature is lowered down to 200 K or below. The measurement at room temperature indicates that higher coercivity, magnetization (at H=2 T) and remanence magnetization ratio (M_r/M_s) are obtained for the films deposited at higher T_s. For example, the magnetization for the film deposited at 500 K is ~380 emu/cm^3 at room temperature, which is about 2.5 times that for the film deposited at 77 K. In general, the films deposited at higher temperatures show more significant hysteresis behavior of M–H loops.

Higher substrate temperatures tend to increase the particle size (or wavelength in a spinodally decomposed structure) and compositional segregation. The Cu–20Ni–20Fe film deposited at low T_s below 300 K is composed of small particles (clusters) with comparatively smaller compositional variation, and gives small coercivity and a remanence magnetization ratio, which indicates a superparamagnetic-like behavior at the measurement temperatures. For the substrates at higher T_s, the larger driving force for the sputtered particles to diffuse and coalesce in the film enhances the particle growth, and phase separation. It is noteworthy that the energy (and mobility) of the impinging atoms on substrate surface during sputter deposition is much higher than that of bulk materials at nominally the same temperature as T_s. The magnetoresistance ratio (measured at H=2 T) is substantially reduced from 3.2% for the film with T_s=77 K to 1.2% for the film with T_s=500 K. This is most likely due to the particle coarsening at higher T_s, which will raise the superparamagnetic blocking temperature (T_b) for the (Fe, Ni)-rich clusters and reduce the degree of superparamagnetic fluctuation.

We are greatly thankful for the partial financial support from the National Science Council of Republic of China under Contract No. of NSC 83-0208-M007-083PC. We also acknowledge the assistance in RBS measurement provided by Dr. S. Y. Hou at AT&T Bell Laboratories.

[1] M. N. Baibich, J. M. Broto, A. Fert, F. Nguyen Van Dau, F. Petroff, P. Etienne, G. Creuzet, A. Friederich, and J. Chazelas, Phys. Rev. Lett. **61**, 2472 (1988).
[2] S. S. P. Parkin, R. Bhadra, and K. P. Roche, Phys. Rev. Lett. **66**, 2152 (1991).
[3] W. P. Pratt, Jr., S.-F. Lee, J. M. Slaughter, R. Loloee, P. A. Schroeder, and J. Bass, Phys. Rev. Lett. **66**, 3060 (1991).
[4] A. E. Berkowitz, J. R. Mitchell, M. J. Carey, A. P. Young, S. Zhang, F. E. Spada, F. T. Parker, A. Hutten, and G. Thomas, Phys. Rev. Lett. **68**, 3744 (1992).
[5] J. Q. Xiao, J. S. Jiang, and C. L. Chien, Phys. Rev. Lett. **68**, 3749 (1992).
[6] M. J. Carey, A. P. Young, A. Starr, D. Rao, and A. E. Berkowitz, Appl. Phys. Lett. **61**, 2935 (1992).
[7] R. Von Helmolt and J. Wecker, Appl. Phys. Lett. **64**, 791 (1994).
[8] L. H. Chen, S. Jin, T. H. Tiefel, and R. Ramesh, Appl. Phys. Lett. **64**, 1039 (1994).
[9] L. H. Chen, T. H. Tiefel, S. Jin, S. H. Chang, and R. Ramesh, Phys. Rev. B **49**, 9194 (1994).
[10] B. Dieny, S. R. Teixera, B. Rodmacq, C. Cowache, S. Huffret, and J. Pierre, J. Mag. Magn. Mat. **130**, 197 (1994).

Relaxation of magnetoresistance and magnetization in granular $Cu_{90}Co_{10}$ obtained from rapidly quenched ribbons

P. Allia, C. Beatrice,[a] M. Knobel,[a] P. Tiberto,[a] and F. Vinai[a]
Dipartimento di Fisica, Politecnico di Torino, I-10129 Torino, Italy

Bulk granular $Cu_{90}Co_{10}$ systems displaying a negative giant magnetoresistance (GMR) were produced by submitting melt-spun ribbons to conventional annealing and dc joule heating in order to induce diverse microstructures. Room-temperature GMR values up to 9% at 20 kOe were found in samples produced using both kinds of thermal treatments. An evolution from a superparamagnetic towards a ferromagnetic behavior has been observed in samples submitted to different heat treatments. A long-time, nearly logarithmic relaxation of the magnetic remanence has been measured after fast removal of a magnetic field of 10 kOe. The progressive randomization of the magnetic moments also gives rise to a corresponding increase in the zero-field electrical resistance.

I. INTRODUCTION

A strong negative magnetoresistance has been observed in certain granular magnetic materials where clusters of a ferromagnetic metal such as Co or Fe are dissolved in a metallic matrix such as Cu or Ag.[1,2] Although the interest for these granular magnetic systems is obviously enhanced by the possible applications of the giant magnetoresistance effect (GMR), a great research effort is being focused on a number of open problems concerning their fundamental properties.[3,4] The magnetoresistance behavior of these heterogeneous alloys was first observed in deposited thin films.[5,6] Melt-spinning techniques have been successfully exploited to produce bulk metastable solid solutions where superparamagnetic and ferromagnetic clusters may be developed by effect of suitable annealing treatments.[7,8]

The technique of joule heating under a direct electrical current, where the temperature of a metallic ribbon strip is dramatically increased by the joule effect, has recently proven to be a most effective method to produce nanostructured ferromagnets starting from compositionally homogeneous, melt-spun ribbons.[9]

In this article, we report on the magnetic and transport properties of a set of CuCo granular bulk systems obtained by submitting the rapidly quenched alloy either to conventional annealings, or to dc joule heating under different currents for the same time. The latter technique allows one to easily produce materials with GMR comparable to the ones found in conventionally annealed materials. The superparamagnetic component of the considered granular magnetic materials is particularly evidenced by a significant relaxation of the magnetic remanence. In correspondence of this gradual reduction in the magnetic order, the zero-field electrical resistance of the samples is observed to steadily increase with time.

II. EXPERIMENT

A rapidly quenched $Cu_{90}Co_{10}$ alloy was obtained in ribbon form by planar flow casting in controlled atmosphere on a CuZr drum. Strips cut from the ribbon (width 5×10^{-3} m, thickness 5×10^{-5} m) were submitted either to furnace annealing in Ar atmosphere at T_a=440 and 500 °C for 1 h, or to dc joule heating *in vacuo*. The latter treatment was performed by clipping the samples between copper electrodes (electrode distance 1×10^{-1} m), and subsequently applying an electrical current I of constant intensity for 60 s. The electrical resistance R was continuously monitored by measuring the voltage drop across a standard resistor, in order to detect thermal and structural changes occurring in the samples.[10] A detailed description of the technique is given elsewhere.[11]

Room-temperature measurements of magnetization curves and magnetoresistance were performed on both as-quenched and annealed ribbon strips. The magnetic moment of each sample was measured as a function of the applied field H by means of a vibrating sample magnetometer (LDJ/VSM model 9500) up to H=10 kOe. The field behavior of the electrical resistance was measured up to H=20 kOe in the same magnetometer through a conventional four-contact technique. The magnetic field was applied either in the ribbon's plane, perpendicular to the bias current (transverse configuration), or normally to the ribbon plane (perpendicular configuration).

III. RESULTS AND DISCUSSION

Hysteresis loops give information about the development of Co clusters. The values of magnetic remanence (M_r) and coercivity (H_c) of selected samples are reported in Table I along with the saturation magnetization M_s determined by

TABLE I. Magnetic hysteresis parameters of various granular $Cu_{90}Co_{10}$ samples. Treatment times: joule heating 60 s; furnace annealing: 3600 s. The GMR ratio is defined in the text.

Treatment	H_c (Oe)	M_r (emu/g)	M_s (emu/g)	GMR (%)
As-quenched	42	0.12	7.7	−1.7
7 A (2.8×10^7 A/m^2)	141	0.53	10.0	−6.3
8 A (3.2×10^7 A/m^2)	185	1.4	10.9	−5.5
9.25 A (3.7×10^7 A/m^2)	198	1.4	15.2	−6.2
10 A (4×10^7 A/m^2)	208	4.6	13.0	−0.5
440 °C	187	1.2	12.5	−7.3
500 °C	203	1.9	14.8	−8.9

[a]Istituto Elettrotecnico Nazionale Galileo Ferraris, C.so Massimo D'Azeglio 42, I-10125 Torino, Italy.

 0021-8979/94/76(10)/6817/3/$6.00 © 1994 American Institute of Physics

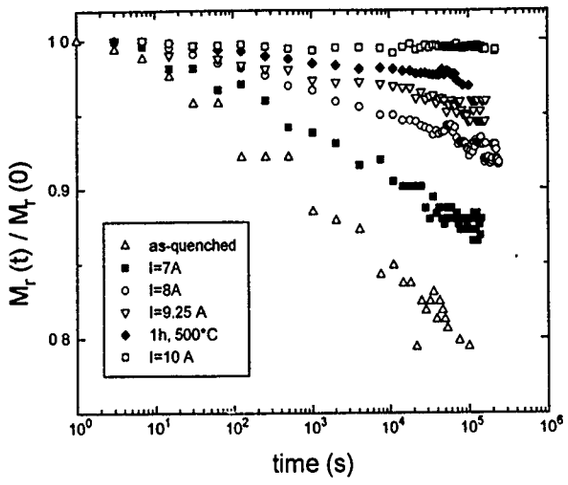

FIG. 1. Time behavior of the reduced magnetic remanence $M_r(t)/M_r(0)$ in joule heated and conventionally annealed $Cu_{90}Co_{10}$ samples.

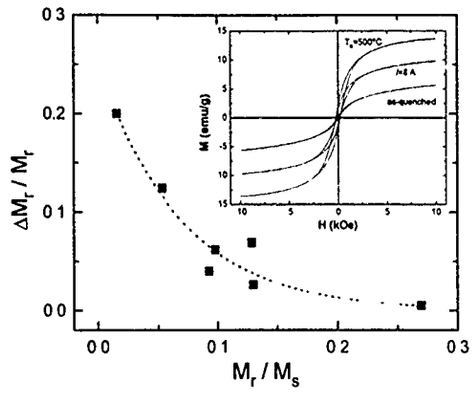

FIG. 2. Intensity of the remanence relaxation, $\Delta M_r/M_r \equiv [M_r(0) - M_r(10^5\ \text{s})]/M_r(0)$, as a function of the ratio M_r/M_s for the samples of Fig. 1. Inset: selected hysteresis loops up to $H=10$ kOe.

extrapolation of the experimental curves to $H \rightarrow \infty$ through a multiple-Langevin function fit. This fitting procedure allows one to assign values of the cluster radii ranging between 2 and 6 nm. The values of M_r and H_c of the as-quenched sample show that the starting material is not an ideal solid solution, although the size of quenched-in clusters is so small that the system nearly behaves as a superparamagnet. Table I shows that all annealing treatments induce a growth of H_c with increasing either the current density or the annealing temperature. Usually, the value of H_c may be taken as a measure of the average size of the ferromagnetic clusters once the value of the magnetic anisotropy constant of the precipitates is known.[12] This is however not the case for granular systems produced by high heating rates, where both the crystalline structure and the shape of the Co clusters are still unknown. The evolution of the product KV (V being the average cluster volume) with changing the annealing parameters is responsible for the magnetic behavior of this set of samples. A particularly large value of KV is possibly responsible for the peculiar magnetic and transport properties of the sample submitted to 4×10^7 A/m^2 joule heating.

A significant isothermal relaxation of the magnetic remanence was observed in all samples. This effect was measured by first applying to each sample a high magnetic field (10 kOe) for a fixed time (1 h), and subsequently measuring the time behavior of the magnetic moment in the range $1-10^6$ s after sudden removal of the field (stabilized in ≈5 s). The relaxation of $M_r/M_r(0)$ is reported in Fig. 1 for different samples. The curve for the specimen treated at $T_a=440$ °C is not shown because it is identical to the one observed in the sample submitted to joule heating at $I=8$ A. The relaxation kinetics is roughly of logarithmic type in all samples. However, the intensity of relaxation is strongly influenced by the thermal treatment, being highest in the as-quenched material, where Co clusters are very small and finely dispersed in the Cu matrix.[13] In this case the magnetic field is effective in orienting the magnetic moments, which are progressively randomized by thermal fluctuation when the field is removed. The increase in the average cluster size brings about both an increase in the ferromagnetic character of the hysteresis loops (Table I) and a reduction in the relaxation intensity, as evidenced in Fig. 2, where $M_r(0)-M_r(10^5\ \text{s})/M_r(0)$ is reported as a function of the ratio M_r/M_s for the considered set of samples.

The magnetoresistance (MR) ratio is defined here as $[R(H)-R_{max}]/R_{max}$, where R_{max} is the maximum resistance value obtained in each hysteresis loop. For as-quenched samples the MR value obtained for a maximum field of 20 kOe is about 1.7%. After a proper furnace annealing or joule-heating treatment, the room-temperature MR ratio can reach values as high as 9%, comparable to the highest GMR values obtained in granular solids.[1,2] Figure 3 shows two representative GMR curves, obtained for a conventionally annealed sample (curve a, $T_a=440$ °C) and for a current-heated ribbon (curve b, $I=6\,A$). The differences between the curves of Fig. 3 mainly arise from a different experimental procedure. Curve a was measured by waiting until complete stabilization of the resistance value was obtained for each value of H (≈15 s per point). Curve b was instead obtained during a continuous hysteresis loop (total time 5 min). The curves do not saturate up to 20 kOe, indicating the presence, in both samples, of a superparamagnetic phase responsible for the

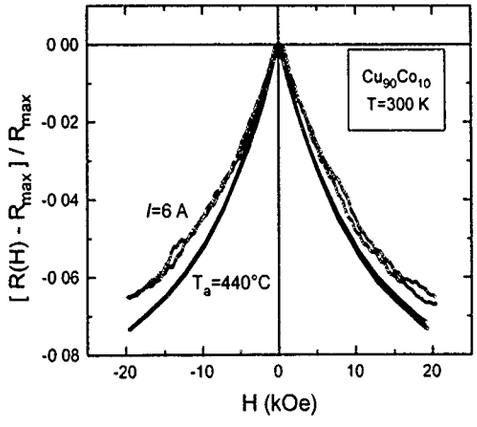

FIG. 3. Room-temperature giant magnetoresistance in a conventionally annealed and a joule-heated sample of granular $Cu_{90}Co_{10}$.

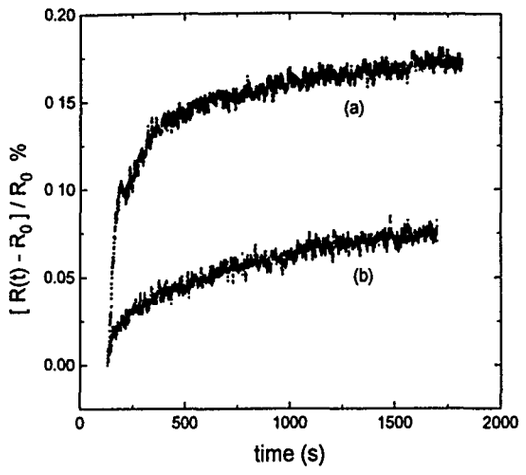

FIG. 4. Time behavior of the zero-field electrical resistance after applying a transversal (curve a) or perpendicular (curve b) field of 20 kOe for 120 s on a joule-heated sample (I=6 A, 60 s).

giant MR effect. In agreement with Wecker *et al.*,[7] we also verified that the $R(H)$ data obtained in a loop are always different from the ones obtained on the virgin curve.

Owing to the close relation existing between the magnetoresistance and the magnetic order within the material, a change in the electrical resistance should be measured along with the relaxation of M_r. In order to study this effect, we tried to follow the same procedure adopted for the remanence relaxation. However, we noticed that the resistance values are extremely sensitive to very small variations in temperature and/or magnetic history of the sample (the temperature coefficient of resistivity being as high as 9×10^{-4} K^{-1} in this granular material), and therefore extrinsic thermal effects dominate over the true relaxation of R. In order to overcome this difficulty, we applied a field of 20 kOe for 2 min only. The ratio $[R(t)-R_0]/R_0$, where R_0 is measured after suddenly removing the field, is reported in Fig. 4 as a function of the measurement time for a joule-heated sample (I=6 A) in both the transverse (curve a) and perpendicular (curve b) field configurations. Although the effect is very small, the gradual randomization of the magnetic moments induces an increase in the conduction-electron scattering and in the electrical resistance, as expected. The relaxation of R is about two orders of magnitude lower than the relaxation of M_r, as one should expect considering that the effect of a change in the magnetic order must have only a minor effect on the overall sample resistance. Owing to the reduced magnitude of the observed effect, the differences found between the two measurement configurations can have several origins, including anisotropic magnetoresistance,[1] ordinary magnetoresistance of Cu, or even the lack of complete sphericity of the clusters, as proposed by Xiao *et al.*[5]

In conclusion, the present results confirm that the joule-heating technique can be adopted as a reliable, fast, and easy-to-use treatment to produce granular magnetic materials. In fact, this treatment allows one to produce a variety of microstructures in the $Cu_{90}Co_{10}$ system, dependent on the value of the joule-heating current, and characterized by very small clusters displaying a magnetic behavior gradually evolving from the nearly superparamagnetic to a more ferromagnetic character. By properly choosing the treatment conditions, not only very similar MR curves, but also nearly identical magnetic parameters may be obtained through conventional annealing and joule heating, indicating that the same microstructures are generated independently of the rate of heating involved in the thermal treatments. Finally, the observed relaxations in both M_r and R, although detrimental to perspective applications of granular magnetic systems, are intrinsically very interesting and worthy of more detailed investigation in the near future.

ACKNOWLEDGMENT

M. K. acknowledges the financial support by FAPESP (Brazil).

[1] A. E. Berkowitz *et al.*, J. Appl. Phys. **73**, 5320 (1993).
[2] C. L. Chien, J. Q. Xiao, and J. S. Jiang, J. Appl Phys. **73**, 5309 (1993).
[3] J. F. Gregg *et al.*, Phys. Rev. B **49**, 1064 (1994).
[4] M. B. Stearns and Y. Cheng, J. Appl. Phys. **75**, 6894 (1994).
[5] J. Q. Xiao, J. S. Jiang, and C. L. Chien, Phys. Rev. Lett. **68**, 3749 (1992).
[6] A. E. Berkowitz *et al.*, Phys. Rev. Lett. **68**, 3745 (1992).
[7] J. Wecker, R. von Helmolt, L. Schultz, and K. Samwer, Appl. Phys. Lett **62**, 1985 (1993); IEEE Trans. Magn. **29**, 3087 (1993).
[8] B. Dieny *et al.*, J. Magn. Magn. Mater. **126**, 433 (1993).
[9] P. Allia, P. Tiberto, M. Baricco, and F. Vinai, Appl. Phys. Lett. **63**, 2759 (1993).
[10] P. Allia, M. Baricco, P. Tiberto, and F. Vinai, Phys. Rev. B **47**, 3118 (1993).
[11] P. Allia, P. Tiberto, M. Baricco, and F. Vinai, Rev. Sci. Instrum **64**, 1053 (1993).
[12] B. D. Cullity, *Introduction to Magnetic Materials* (Addison–Wesley, Reading, MA, 1972), p. 415.
[13] V. G. Harris, B. N. Das, M. Rubinstein, J. L. Goldberg, W. T. Elam, and N. C. Koon, IEEE Trans. Magn. **29**, 2616 (1993).

Magnetic and magnetotransport properties of granular $Cu_{85}Fe_{15}$ prepared by mechanical alloying

Siddharth S. Saxena and Jinke Tang
Department of Physics, University of New Orleans, New Orleans, Louisiana 70148

Young-Sook Lee and Charles J. O'Connor
Department of Chemistry, University of New Orleans, New Orleans, Louisiana 70148

The magnetic and magnetotransport properties of granular $Cu_{85}Fe_{15}$ prepared by mechanical alloying have been investigated. The sample was prepared by grinding fine powders of copper and iron in a high energy ball mill. Zero field cooled and field cooled susceptibilities showed a behavior that is typical of a superparamagnet. The blocking temperature T_B of 20 K was determined from ac susceptibility. The magnetoresistance reached 5.5% at 4.5 K in a field of 5 T. It was increased to 7.6% after the sample was annealed at 300 °C for 20 min. The hysteresis loop was measured for both magnetization and magnetoresistance. There was a clear correlation between the two. The magnetoresistance is due to the scattering associated with iron nanoparticles present in the samples and its dependence on particle size is discussed.

INTRODUCTION

The discovery of negative giant magnetoresistance (GMR) in Fe-Cr magnetic multilayers by Baibich *et al.*[1] and the subsequent finding that GMR occurs in many other multilayer ultrathin magnetic film systems[2–5] have attracted much attention. Recently, GMR was also found in granular structures where metallic ferromagnetic nanoparticles are dispersed in a nonmagnetic metal matrix.[6,7] Not only have these discoveries provided new opportunities for studying the fundamental issues of spin-dependent electrical transport phenomena but they may also have an enormous impact on the information storage technologies due to the potential device applications of these materials in magnetic read heads.[8] The fact that GMR also exists in some granular systems has provided opportunities to explore other preparation methods which are capable of producing the granular systems and are less expensive and more reliable than, for example, the commonly used sputtering techniques. Wecker *et al.*[9] have applied the melt-spinning method to produce bulk Cu-Co alloys by rapid solidification. For the optimally annealed samples the GMR was found to be 36% at 30 K. Ounadjela *et al.* have studied GMR in the Ag-Co granular system prepared by mechanical alloying.[10] GMR of 7.7% at 5 K was observed in their bulk mechanically alloyed $Ag_{70}Co_{30}$ sample. In this article, we report the magnetic and magnetoresistive properties of granular $Cu_{85}Fe_{15}$ prepared by mechanical alloying.

EXPERIMENTAL DETAILS

$Cu_{85}Fe_{15}$ was prepared by mechanical alloying using a high energy Spex 8000 mixer/mill. The starting materials were fine powders of copper and iron of 99.9% purity. Stoichiometric amounts of the powders were sealed in a grinding vial made of hardened steel under argon atmosphere. Also sealed in the vial were two hardened steel balls. The weight ratio of ball to sample was approximately 2:1. After 30 h of grinding, the product was shiny, almost colorless and in the form of small spherical dots. A SCINTAG x-ray powder diffractometer with Cu $K\alpha$ radiation was used for x-ray diffraction examinations. The sample was cold pressed into pellets, and some of those were annealed at low temperatures (T=300 and 550 °C) for 20 min in order to study the effects of such annealing on the interested physical properties.

The magnetic susceptibility of the mechanically alloyed sample was measured as a function of temperature under both zero field cooled (ZFC) and field cooled (FC) conditions, and measured with an ac field using a Quantum Design SQUID susceptometer (Model MPMS-5S). The blocking temperature of the superparamagnetic iron nanoparticles embedded in the copper matrix was determined from the data. Magnetization (M vs H) and hysteresis loop of the sample were examined at 4.5 K. Magnetoresistance measurements were carried out, using a four-point technique, at both room temperature and low temperatures as a function of applied field. Magnetoresistive hysteresis was also studied and compared with the magnetic hysteresis.

RESULTS AND DISCUSSION

The x-ray diffraction pattern of the $Cu_{85}Fe_{15}$ sample which was mechanically alloyed for 30 h showed only broad peaks from fcc copper. No peak from bcc α iron was observable. The diffraction peaks of the mechanically alloyed sample were slightly shifted toward lower angles relative to those of pure copper. This indicated an increase in the lattice constant a of the mechanically alloyed sample as compared to that of pure copper, which implies that a certain amount of iron has been dissolved in the fcc copper matrix. This result is consistent with the finding that mechanical alloying induces fcc solid solution $Cu_{1-x}Fe_x$ for $x<0.6$.[11–13] However, as will be discussed later, magnetic measurements indicated that our sample also contained undissolved iron particles. The reason that peaks from the iron were absent in the x-ray pattern is probably attributed to the extremely small sizes of the iron particles.

Figure 1 shows the magnetic susceptibility of the 30 h mechanically alloyed $Cu_{85}Fe_{15}$ measured under both field-cooled (FC) and zero-field-cooled (ZFC) conditions. What is obvious is the irreversibility indicated by the deviation be-

 0021-8979/94/76(10)/6820/3/$6.00 © 1994 American Institute of Physics

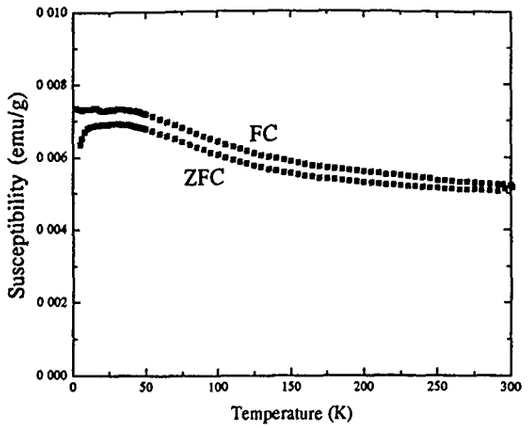

FIG. 1. dc magnetic susceptibilities of the as-mechanically alloyed $Cu_{85}Fe_{15}$ measured under both ZFC and FC conditions The measuring field is 2000 Oe.

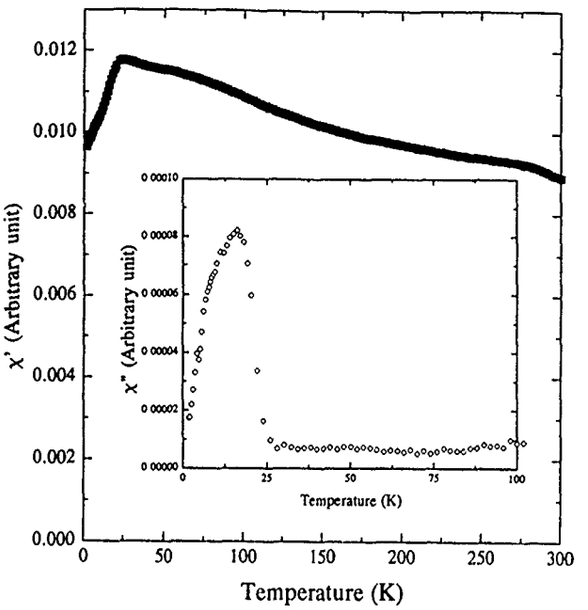

FIG. 2. The real part of the ac susceptibility χ' of the as-mechanically alloyed sample and imaginary part of the ac susceptibility χ'' (inset). Only the low-temperature portion of the χ'' is shown.

tween FC and ZFC susceptibilities. There is a broad maximum in the ZFC susceptibility at 20–30 K. This maximum can be caused by either a spin-glass-type transition or superparamagnetic iron particles. For a spin-glass transition, the peak in the ZFC susceptibility is normally very sharp and all irreversibility effects disappear just above the freezing temperature. On the other hand, in a superparamagnet, the maximum is broad and irreversibility persists well above the blocking temperature.[14] Therefore, we believe the observed irreversibility and broad maximum in the ZFC susceptibility of our sample is caused by an assembly of superparamagnetic iron particles dispersed in the copper matrix. In addition, the absolute value of susceptibility is quite high even at room temperature, which suggests that there is a wide distribution of particle size with blocking temperatures ranging from very low temperature to above room temperature. Figure 2 shows the real part of the ac (f=32 Hz) susceptibility χ' of the same sample. The inset shows the imaginary part χ'' in the low-temperature region. The average blocking temperature T_B determined from the peak in the ac susceptibility χ' is 20 K. As seen, χ'' shows a corresponding loss peak near the same temperature.

The magnetoresistance was measured as a function of applied field up to 5 T at 4.5, 77, and 300 K, respectively. Figure 3 shows such magnetoresistance, defined as $[\rho_{(H)}-\rho_{(0)}]/\rho_{(0)}$, versus applied field plots. The magnetoresistance reaches 5.5% at 4.5 K in a field of 5 T. It is reduced to 3.8% at 77 K and less than 0.2% at 300 K. The observed magnetoresistance shows no indication of saturation in a field of 5 T at all temperatures.

The as-mechanically alloyed sample was subsequently annealed for 20 min at 300 and 550 °C, respectively. Figure 4 is the magnetoresistance versus field plots at 4.5 K for samples annealed at these temperatures. The as-mechanically alloyed sample is also shown for comparison. The heat treatment at 300 °C results in an increase in magnetoresistance to 7.6% from 5.5% of the not-annealed sample. This is attributed to the precipitation of additional iron particles from the copper matrix, which contribute to the spin-dependent scattering process. As the annealing temperature is further increased to 550 °C, the sizes of the iron particles grow and become sufficiently large such that the GMR decreases significantly. The effects of annealing at the mentioned temperatures on the particle size have been well documented, for example, see Ref. 15.

Shown in Fig. 5 are the hysteresis loops for magnetization and magnetoresistance measured at 4.5 K. Only data below H=3500 Oe are shown. A clear correlation between the two hysteresis loops exists. The coercivity H_c (at which magnetization becomes zero) is about 500 Oe, and as can be seen, it is also the field at which magnetoresistance becomes zero.

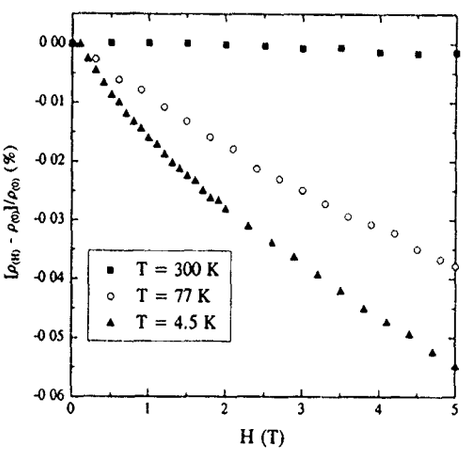

FIG. 3 Magnetoresistance of the as-mechanically alloyed sample vs applied field measured at 4 5, 77, and 300 K.

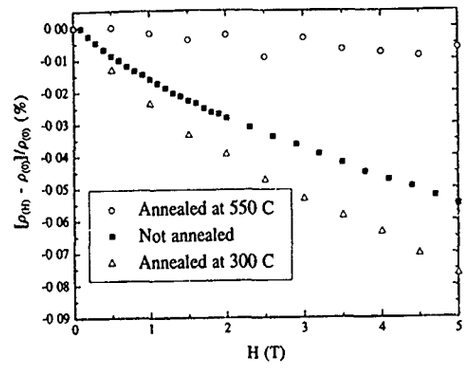

FIG. 4. Magnetoresistance as a function of applied field at 4.5 K for the as-mechanically alloyed sample and subsequently annealed at 300 and 550 °C samples.

CONCLUSIONS

The magnetic and magnetoresistive properties of granular $Cu_{85}Fe_{15}$ prepared by mechanical alloying have been studied. The presence of magnetic iron nanoparticles in the as-mechanically alloyed sample is demonstrated by both zero-field-cooled and field-cooled susceptibilities. The superparamagnetic behavior is also shown in its ac susceptibility from which a blocking temperature T_B of 20 K is derived. There is a clear correlation between the hysteresis loops of magnetization and magnetoresistance. The magnetoresistance is 5.5% at 4.5 K in a field of 5 T. It is increased to 7.6% after the sample was annealed at 300 °C for 20 min. The effect of such heat treatment is to let more iron particles precipitate out of the copper matrix. Further annealing at higher temperature has a deteriorating effect on the magnetoresistance. The largest magnetoresistance of 7.6% found in our sample is smaller than reported elsewhere using other preparation methods.[6,7] Improvement should be possible by optimizing parameters like grinding time, composition, and annealing temperature. As mentioned earlier, x-ray diffraction data indicate that a part of iron is dissolved in the fcc copper matrix in the as-mechanically alloyed sample, therefore the actual composition of the granular portion of the sample which contributes to GMR is not $Cu_{85}Fe_{15}$ but probably contains less iron. It is interesting to note that another granular system prepared by mechanical alloying $Ag_{70}Co_{30}$ exhibits MGR of 7.7% at 5 K, which is almost identical to the value found in our sample.

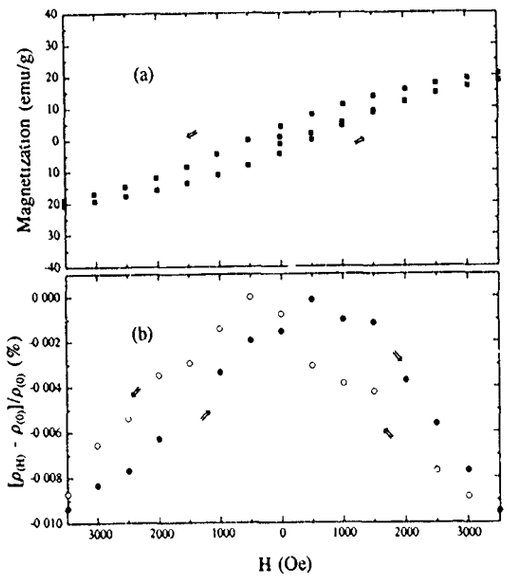

FIG 5. Hysteresis loops of magnetization (a) and magnetoresistance (b) measured at 4 5 K.

ACKNOWLEDGMENTS

Acknowledgment is made to the Donors of The Petroleum Research Fund, administrated by the American Chemical Society (PRF No. 25865-B3), and to the Louisiana Education Quality Support Fund [LEQSF(RF/1993-94)-ENH-TR-60], for partial support of this research.

[1] M. N. Baibich, J M. Broto, A. Fert, F. Nguyen van Dau, F. Petroff, P. Etienne, G. Creuzet, A. Friederich, and J. Chazeles, Phys. Rev. Lett. **61**, 2472 (1988)
[2] S. S. P. Parkin, R. Bhadra, and K. P. Roche, Phys. Rev Lett. **66**, 2152 (1991).
[3] F. Petroff, A. Barthelemy, D. H. Mosca, D. K. Lottis, A. Fert, P. A. Schroeder, W. P. Pratt, Jr., R. Loloee, and S. Lequien, Phys. Rev B **44**, 5355 (1991).
[4] W. P. Pratt, Jr., S. F. Lee, J. M. Slaughter, R. Loloee, P. A. Schroeder, and J. Bass, Phys. Rev. Lett. **66**, 3060 (1991).
[5] E. E. Fullerton, D M. Kelly, J. Guimpel, I. K. Schuller, and Y. Bruynseraede, Phys. Rev. Lett. **68**, 859 (1992).
[6] J. Q. Xiao, J. S. Jiang, and C. L. Chien, Phys Rev. Lett. **68**, 3749 (1992).
[7] A. E. Berkowitz, J. R. Mitchell, M. J. Carey, A. P. Young, S. Zhang, F. E. Spada, F. T. Parker, A Hutten, and G. Thomas, Phys Rev. Lett. **68**, 3745 (1992)
[8] L M. Falicov, D. T. Pierce, S. D. Bader, R. Gronsky, K. B. Hathaway, H. J. Hopster, D. N. Lambeth, S. S P. Parkin, G. Prinz, M. Salamon, I. K. Schuller, and R. H. Victora, J. Mater. Res **5**, 1299 (1990)
[9] J. Wecker, R. von Helmolt, L Schultz, and K. Samwer, Appl. Phys. Lett. **62**, 1985 (1993)
[10] K. Ounadjela, J M. D. Coey, A. Fagan, C. R. Staddon, D. Daniel, J. F Gregg, S. M Thompson, A. Herr, R. Poinsot, K. O'Grady, and S Greaves, J. Appl. Phys. **75**, 6921 (1994).
[11] K. Uenishi, K. F. Kobayashi, S. Nasu, N. Hatano, K Ishihara, and P. H. Shingu, Z. Metallkd. **83**, 132 (1992).
[12] J. Eckert, R. Birringer, J. C. Holzer, C. E. Krill III, and W. L Johnson, MRS Symp. Proc. **238**, 739 (1992); J. Appl. Phys. **73**, 2794 (1993).
[13] E Ma, M. Atzmon, and F. E. Pinkerton, J. Appl Phys. **74**, 955 (1993).
[14] J. L. Tholence, *Magnetic Susceptibility of Superconductors and Other Spin Systems*, edited by R. A. Hein, T. L. Francavilla, and D. H. Liebenberg (Plenum, New York, 1991), pp. 503
[15] C. L. Chien, J. Q. Xiao, and J. S. Jiang, J Appl. Phys **73**, 5309 (1993).

Granular giant magnetoresistive materials and their ferromagnetic resonances (abstract)

M. Rubinstein, B. N. Das, N. C. Koon, D. B. Chrisey, and J. Horwitz
U.S. Naval Research Laboratory, Washington, DC 20375-5000

Ferromagnetic resonance (FMR) can reveal important information on the size and shape of the ferromagnetic particles which are dispersed in granular giant magnetoresistive (GMR) materials. We have investigated the FMR spectra of three different types of granular GMR material, each with different properties: (1) melt-spun ribbons of $Fe_5Co_{15}Cu_{80}$ and $Co_{20}Cu_{80}$, (2) thin films of $Co_{20}Cu_{80}$ produced by pulsed laser deposition, and (3) a granular multilayer film of [Cu(50 Å)/Fe(10 Å)]×50. We interpret the linewidth of these materials in as simple a manner as possible, as a "powder pattern" of noninteracting ferromagnetic particles. The linewidth of the melt-spun ribbons is caused by a completely random distribution of crystalline anisotropy axes. The linewidth of these samples is strongly dependent upon the annealing temperature: the linewidth of the as-spun sample is 2.5 kOe (appropriate for single-domain particles) while the linewidth of a melt-spun sample annealed at 900 °C for 15 min is 3.8 kOe (appropriate for larger, multidomain particles). The linewidth of the granular multilayer is attributed to a restricted distribution of shape anisotropies, as expected from a discontinuous multilayer, and is only 0.98 kOe with the magnetic field in the plane of the film.[1]

[1]M. Rubinstein, B. N. Das, N. C. Koon, D. B. Chrisey, and J. Horwitz, Phys. Rev. B **50**, 184 (1994).

 0021-8979/94/76(10)/6823/1/$6 00 © 1994 American Institute of Physics

Magnetoresistance of granular Cu-(Co,Fe) and Cu-Co-B (abstract)

R. v. Helmolt
Siemens AG, Research Laboratories, 91052 Erlangen, Germany and Institute of Physics, University of Augsburg, 86159 Augsburg, Germany

J. Wecker
Siemens AG, Research Laboratories, 91052 Erlangen, Germany

K. Samwer
Institute of Physics, University of Augsburg, 86159 Augsburg, Germany

Giant magnetoresistance (GMR) is known to occur in alloys consisting of superparamagnetic precipitates in a metallic matrix. This had been demonstrated for the first time for Cu-Co prepared as co-sputtered thin films[1] and later for rapidly quenched alloys.[2] For Cu-Fe no GMR has been reported even in multilayer systems. In order to study the transition from Cu-Co to Cu-Fe in more detail we prepared quasibinary $Cu_{90}Co_{10-x}Fe_x$ ribbons by conventional melt spinning followed by an annealing treatment to precipitate Co-Fe clusters in the Cu matrix. The particle sizes of the ferromagnetic phase have been determined by fitting the magnetization and magnetoresistance curves with a Langevin function. The saturation magnetization increases with increasing Fe content x for $x \leqslant 4$ as expected from the Slater–Pauling curve. However, a strong decrease of the magnetization is observed at high Fe contents. The GMR effect continuously decreases with increasing Fe content and for $x > 0.7$ no GMR is observed, similar to Cu-Fe multilayers. Small B additions were added to Cu-Co in order to improve the homogeneity of the as-quenched ribbons. For these samples the magnetoresistance is suppressed even by small B additions below 3 at. %. This is different from the Au-Co system, where B additions of up to 20% enhance the GMR effect.[3]

This work was supported by the German Ministry for Research and Technology (BMFT).

[1] J. Q. Xiao, J. S. Jiang, and C. L. Chien, Phys. Rev. Lett. **68**, 3749 (1992).
[2] J. Wecker, R. v. Helmolt, L. Schultz, and K Samwer, Appl Phys Lett. **62**, 1985 (1993).
[3] R. v. Helmolt, J. Wecker, and K. Samwer, Appl. Phys. Lett. **64**, 791 (1994).

 0021-8979/94/76(10)/6824/1/$6.00 © 1994 American Institute of Physics

Evolution of recombination in a solid HDDR processed $Nd_{14}Fe_{79}B_7$ alloy

N. Martinez, D. G. R. Jones, and O. Gutfleisch
School of Metallurgy and Materials, The University of Birmingham, Birmingham, United Kingdom

D. Lavielle and D. Peré
Rhône Poulenc, Centre de Recherches d'Åubervilliers, France

I. R. Harris
School of Metallurgy and Materials, The University of Birmingham, Birmingham, United Kingdom

A high-resolution scanning electron microscope was used to study the microstructural changes occurring during the desorption and recombination stages in a cast $Nd_{14}Fe_{79}B_7$ alloy HDDR processed at 780 °C. Phase identification was based on backscattered electron contrast. In the early stages of desorption, the disproportionated structure in the matrix coarsens to produce a mixture of Nd-rich (NdH_2 and/or Nd) and Fe-rich (αFe and/or Fe_2B) clusters. At the center of the specimen, regions of recombined multicrystalline $Nd_2Fe_{14}B$ phase are observed associated with Nd- and Fe-rich clusters. When desorption of hydrogen is almost complete, the microstructure consists of a $Nd_2Fe_{14}B$ matrix with a few remaining Nd- and Fe-rich clusters. The subsequent completion of recombination results in a multigrained $Nd_2Fe_{14}B$ structure, some grains being separated by Nd-rich material. The magnetic properties of the $Nd_{14}Fe_{79}B_7$ alloy have been measured at significant stages during the desorption/recombination process at 600 °C, the stages being deduced from electrical resistivity measurements. Initially, the material is noncoercive with a high magnetization at 1100 kA/m, reflecting the high proportion of αFe in the sample. As recombination proceeds, the magnetization drops and the coercivity increases as the fine-grained $Nd_2Fe_{14}B$ develops and the αFe disappears.

I. INTRODUCTION

The Hydrogenation–Disproportionation–Desorption and Recombination process (HDDR)[1,2] transforms a coarse-grained ingot (cast or homogenised) into a friable, powdered material with submicrometer grain size. The first stage results in the hydrogenation and decrepitation of the ingot (HD process).[3] The disproportionation reaction occurs at elevated temperature and produces an intimate mixture[2,4] of αFe, Nd hydride, and Fe_2B. Recombination occurs on hydrogen desorption at high temperature. The main potential of these coercive powders is to produce polymer bonded[1] and hot pressed[5] magnets.

It is possible to disproportionate solid blocks of Nd-Fe-B based alloys without decrepitating them by using very high heating rates under hydrogen[6] or introducing hydrogen at high temperature.[7] It has been observed that, in $Nd_{16}Fe_{76}B_8$, the disproportionation process begins at the grain boundaries at the Nd hydride/$Nd_2Fe_{14}B$ interface and then progresses into the matrix phase.[8,9] The block does not decrepitate as in the HD process. The process is referred to as "solid HDDR" and can be usefully employed to study the development of the HDDR microstructure because of the modified reaction kinetics.

II. EXPERIMENTAL PROCEDURE

Differential thermal analysis (DTA) was carried out in order to determine the starting temperatures of disproportionation in a hydrogen atmosphere and recombination under vacuum. The solid HDDR was carried out at 780 °C in an initial hydrogen pressure of 1 bar. Hydrogen was evacuated, and the samples held under vacuum for 20, 40, and 70 min at 780 °C. Finally, the samples were quenched in order to fix the recombined structure. The observations were carried out with a high-resolution field-emission scanning electron microscope (Hitachi 4000) using the backscattered electron mode.

An electrical resistivity monitoring method[8] was used to follow the average state of three samples during recombination at 600 °C under vacuum, after disproportionation at 700 °C in an initial hydrogen pressure of 0.7 bar. These low temperatures were chosen in order to slow the reaction and study only the transformations occurring in the matrix phase by avoiding the desorption and melting of the intergranular Nd-rich phase.[10] Intrinsic coercivity and magnetization at 1100 kA/m were measured with a vibrating sample magnetometer (VSM).

III. RESULTS AND DISCUSSION

A. Determination of the desorption temperature

Figure 1 represents the DTA graph showing the desorption of hydrogen from the disproportionated material with increasing temperature. The first peak starting at ≈100 °C corresponds to the transformation from NdH_{2+x} to NdH_2 that takes place within the disproportionated matrix and Nd-rich intergranular phase. The two peaks, starting at ≈600 °C, represent first, desorption of hydrogen from the disproportionated matrix and also recombination and second, from the Nd-rich grain-boundary phase.[11]

B. Microstructures of samples desorbed at 780 °C

During solid hydrogenation and disproportionation, a disproportionated front moves from the edges towards the

 0021-8979/94/76(10)/6825/3/$6.00 © 1994 American Institute of Physics

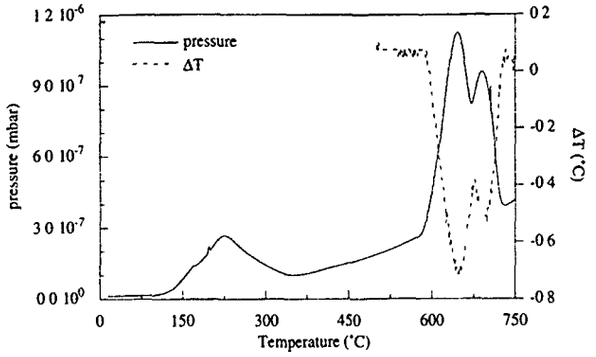

FIG. 1. ΔT and pressure traces vs temperature of the hydrogen desorption of the disproportionated $Nd_{14}Fe_{79}B_7$ material.

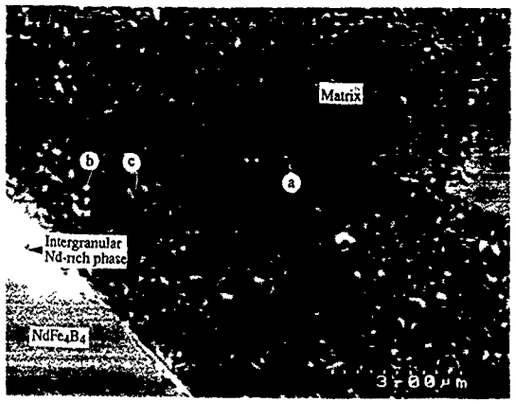

FIG. 2. Backscattered electron picture of a $Nd_{14}Fe_{79}B_7$ sample desorbed at 780 °C for 20 min. (a) colonies of lamellae, (b) Nd-rich cluster, (c) Fe-rich cluster.

center of the specimen. Because of the hydrogen diffusion during absorption and desorption, the microstructure of a solid disproportionated and recombined sample, at a given temperature and initial hydrogen pressure, depends on the region observed in the specimen and also the position considered in the original $Nd_2Fe_{14}B$ grains. The evolution of the microstructure with time, during the solid HDDR process, also depends upon the total volume of the specimen. Times given in the present work must therefore be considered in the light of these factors. It should also be noted that at $T \geqslant 655$ °C, the Nd-rich material melts as soon as the transformation of NdH_2 into metal Nd occurs.[12]

In the specimen, desorbed for 20 min, the distribution of the original grain boundaries, most of which contain $NdFe_4B_4$ and Nd-rich phases, has not been altered by this process and appears to be the same as in the cast material. Residual free-iron dendrites, present in the cast state, could also be observed. The colony-type structure,[8,9] observed in the matrix of disproportionated samples, has coarsened as shown in Fig. 2. The microstructure of the matrix, between the edges and the center of the sample, consists of small colonies of (a) lamellae, which are broader than those of a fully disproportionated matrix, indicating that coarsening has occurred, thus lowering the total interfacial energy. This microstructure corresponds to the stage where the desorption reaction is dominant. At the center of the specimen, the recombination of the $Nd_2Fe_{14}B$ phase has begun and Fig. 3 illustrates the formation of (d) the recombined, multicrystalline $Nd_2Fe_{14}B$ phase from the surrounding (e) Nd-rich and (f) Fe-rich particles. This microstructure is only located at the center of the sample occupying a very small volume fraction of the total volume. The specific identification of αFe and Fe_2B has not been possible so far by SEM studies.

Figure 4 shows the microstructure of a sample desorbed for 40 min. The structure is different from that shown in Fig. 2, as the matrix consists now of (g) a multicrystalline $Nd_2Fe_{14}B$ phase but still contains some remaining (h) Nd-rich and (i) Fe-rich clusters. This microstructure is similar to that of the $Nd_2Fe_{14}B$ region shown in Fig. 3 and was also observed by Nakayama and Takeshita.[13] The scale of clear regions indicates multicrystalline $Nd_2Fe_{14}B$ phase but individual crystallites cannot be imaged. Powder x-ray-diffraction analysis revealed that this sample consists predominantly of the $Nd_2Fe_{14}B$ phase.

Fully recombined samples were obtained after 70 min of desorption. This microstructure consists of submicrometer grains, some of which are delineated because they are surrounded by Nd-rich phase.

C. Desorption and recombination at 600 °C

Figure 5 represents the variation of normalized electrical resistivity [$\rho(0)$=resistivity at 600 °C before desorption] and hydrogen pressure with desorption time at 600 °C. Approximately three different stages could be identified during recombination, although in the bulk samples the various stages will overlap. When the temperature is lower than the melting point of Nd metal and the Nd-rich phase, it is possible to follow the recombination as a completely solid-state reaction occurring exclusively in the matrix phase and thus much less dependent upon the state and proportion of the intergranular Nd-rich phase. Thus, during desorption and recombination at 600 °C, the Nd-rich phase remains in the hydrided state. In the first stage (stage I in Fig. 5), the desorption of hydrogen

FIG. 3. Backscattered electron picture of a $Nd_{14}Fe_{79}B_7$ sample desorbed at 780 °C for 20 min. (d) region of recombined $Nd_2Fe_{14}B$, (e) Nd-rich cluster, (f) Fe-rich cluster

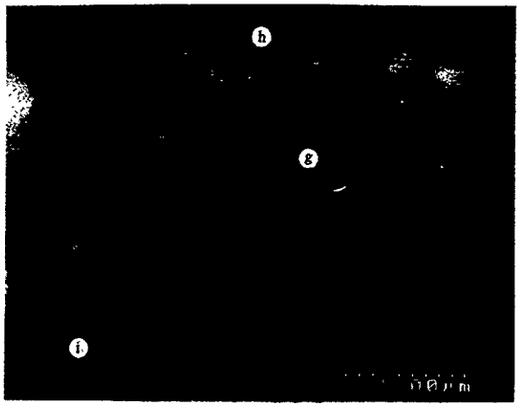

FIG. 4. Backscattered electron picture of a $Nd_{14}Fe_{79}B_7$ sample desorbed at 780 °C for 40 min. (g) $Nd_2Fe_{14}B$ phase, (h) Nd-rich cluster, (i) Fe-rich cluster.

from NdH_2, within the disproportionated structure, is the dominant reaction and is responsible for the resistivity drop as this reaction transforms semiconducting NdH_2 into metallic Nd.[7] The subsequent increase in resistivity (stage II in Fig. 5) is due to the consumption of αFe as the recombination reaction proceeds. In order to study the mechanism of the recombination reaction, samples were obtained by quenching in vacuum at three stages (A, B, and C in Fig. 5) of the desorption and recombination process (stage II in Fig. 5). Their magnetic properties were measured and compared with those of a specimen fully disproportionated at 700 °C.

Figure 6 shows the demagnetization traces of the fully disproportionated specimen and the partially and fully desorbed samples. It can be seen that the magnetization of the fully disproportionated material at 1100 kA/m is the highest and its coercivity is the lowest, as expected from the presence of αFe and the absence of the $Nd_2Fe_{14}B$ phase. These results are in accordance with those reported by Book *et al.*[14]

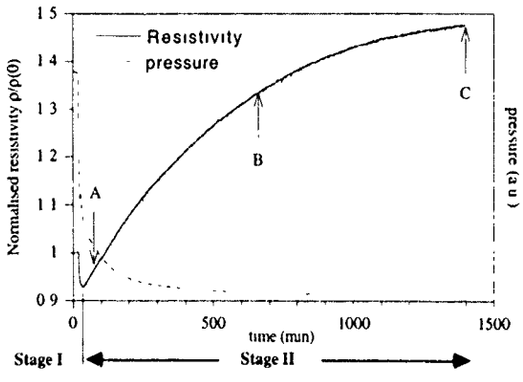

FIG. 5. Electrical resistivity and pressure vs desorption time at 600 °C for a $Nd_{14}Fe_{79}B_7$ alloy Stage I: desorption of hydrogen from the matrix is the dominant reaction, stage II recombination is dominant and consists of three substages, A, B, and C.

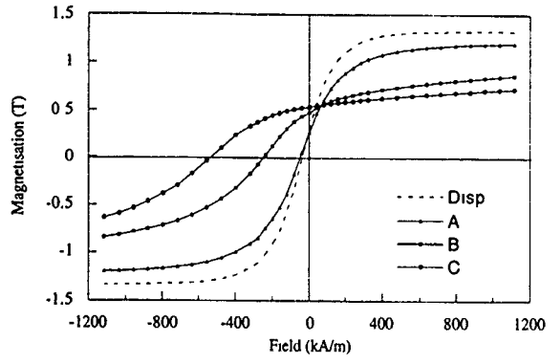

FIG. 6. VSM traces of disproportionated (Disp) and partially desorbed (A,B,C) $Nd_{14}Fe_{79}B_7$ samples.

At stage A, when the specimen is partially desorbed and recombined, the coercivity has not been modified significantly and the magnetization has decreased but is still high compared to that of the fully recombined sample. This indicates that the recombined $Nd_2Fe_{14}B$ phase coexists with αFe. The second curve represents the demagnetization curve of a sample quenched at stage B, when the specimen is almost desorbed but still partially recombined. The coercivity has improved and the magnetization at 1100 kA/m has decreased significantly, thus indicating that the proportion of recombined phase is much larger compared to stage A. At stage C, when the sample is fully desorbed and recombined, the coercivity has improved considerably, whereas the magnetization at 1100 kA/m has decreased slightly compared to that of the previous sample. This indicates that the remaining αFe was removed between stages B and C. The microstructures of all these specimens are currently under investigation and will be reported at a later date.[15]

[1] T. Takeshita and R. Nakayama, Proceedings of the 10th International Workshop on Rare-Earth Magnets and their Applications, Kyoto, 1989, p. 551.
[2] P. J. McGuiness, X. J. Zhang, X. J. Yin, and I. R. Harris, J. Less-Common Met. **158**, 359 (1990a).
[3] I. R. Harris, J. Evans, and P. S. Nyholm, UK Patent No. 1554384 (October 1979).
[4] P. J. McGuiness, X. J Zhang, H. Forsyth, and I. R Harris, J. Less-Common Met. **162**, 379 (1990b).
[5] P. J. McGuiness, C. Short, A. F. Wilson, and I. R. Harris, J. Alloys Comp. **184**, 243 (1992).
[6] X. J. Zhang, P. J. McGuiness, and I. R. Harris, J. Appl Phys **69**, 5838 (1991).
[7] O. Gutfleisch, M. Verdier, I. R. Harris, and A. E. Ray, IEEE Trans. Magn. **29**, 2872 (1993).
[8] O. Gutfleisch, N. Martinez, M. Verdier, and I. R. Harris, J. Alloys Comp. **204**, L21 (1994).
[9] O. Gutfleisch, N. Martinez, M. Verdier, and I. R. Harris, J. Alloys Comp. (in press).
[10] D. Book and I. R. Harris (unpublished).
[11] A. J. Williams, P. J. McGuiness, and I. R. Harris, J. Less-Common Met. **171**, 149 (1991).
[12] P. J. McGuiness, O. Gutfleisch, L Ruiz de Angulo, and I. R. Harris (unpublished).
[13] R. Nakayama and T. Takeshita, J. Appl. Phys. **74**, 2719 (1993).
[14] D. Book and I. R. Harris, IEEE Trans. Magn. **28**, 2145 (1992).
[15] N. Martinez and I. R. Harris (unpublished).

Effects of HDDR treatment conditions on magnetic properties of Nd-Fe-B anisotropic powders

H. Nakamura, R. Suefuji, S. Sugimoto, M. Okada, and M. Homma
Department of Materials Science, Faculty of Engineering, Tohoku University, Sendai 980, Japan

It is reported that Nd-Fe-B magnetic powders prepared by utilizing the HDDR (hydrogenation, disproportionation, desorption, and recombination) phenomena exhibit high coercivity, and the addition of Co, Ga, and Zr induces magnetic anisotropy in these powders. HDDR phenomena are caused by the heat treatment in hydrogen (H treatment) and subsequently in vacuum (V treatment). Present works describe the effects of V-treatment conditions on magnetic properties of $Nd_{12.6}Fe_{bal}Co_xB_{6.0}$ (x=0–17.4) alloys. The powders V-treated at lower temperature show lower remanence and no noticeable magnetic anisotropy. V treatment at higher temperature enhances remanence and increases the differences of remanence between the powders aligned with and without magnetic field. Higher values are obtained in Co added alloys. This result suggests that a selective grain growth of $Nd_2Fe_{14}B$ grains during V treatment plays an important role for the inducement of magnetic anisotropy in HDDR-treated powders. The temperature for complete recombination reaction under evacuating condition decreases with increasing Co content. It can be said that Co addition enhances recombination reaction and results in acceleration of grain growth.

I. INTRODUCTION

Hydrogenation, disproportionation, desorption, and recombination (HDDR) phenomena[1,2] in Nd-Fe-B alloys are caused by the heat treatment in hydrogen (H treatment) and further treatment in vacuum (V treatment). $Nd_2Fe_{14}B$ compound disproportionates into a mixture of NdH_2, α-Fe, and Fe_2B at an elevated temperature of around 800 °C in H treatment. Removal of hydrogen in the mixture by subsequent V treatment reforms the $Nd_2Fe_{14}B$ compound with homogeneous and fine grains of about 0.3 μm in diameter, which is close to the single domain size of $Nd_2Fe_{14}B$. This results in high coercivity in HDDR-treated Nd-Fe-B powders.

Since it has been reported that Co, Ga, Zr, and Nb addition induces magnetic anisotropy through this phenomena,[3] Nd-Fe-B powders produced by utilizing HDDR phenomena have been candidates as powders for high performance bonded magnets. But the mechanism for inducement of magnetic anisotropy is still unclear. One of the proposed mechanisms has been reported, in which the role of Co is to depress the disproportionation reaction during H treatment especially at high temperature. The origin of anisotropy is due to the undecomposed fine particles which inherit a crystallographic relationship with newly formed grains.[4] These works are only concerned with H treatment conditions on magnetic properties and microstructure. But the magnetic anisotropy might be varied not only with H treatment but with V treatment. Then the purpose of this study is to investigate the effects of V-treatment temperatures on magnetic anisotropy in $Nd_{12.6}Fe_{81.4-x}Co_xB_{6.0}$ (x=0–17.4) alloys.

II. EXPERIMENTAL PROCEDURE

The diagram of the experimental procedure is shown in Fig. 1(a). The compositions of studied alloys were $Nd_{12.6}Fe_{81.4-x}Co_xB_{6.0}$ (x=0,5.8,11.6,17.4). The alloys were induction-melted from high-purity elements under an Ar atmosphere and then were homogenized at 1100 °C for 20 h. The homogenized ingots were ground into powders of <63 μm and pressed into compacts. These compacts were used for investigating the hydrogen absorption and desorption characteristics, which were measured by monitoring the difference between the flow rate in front and in the rear of the furnace (called ΔQ hereafter). Details on ΔQ measurement are described elsewhere.[5] H treatment and further V treatment (referred to as HV treatment) was performed on crushed ingots and sintered bodies which were magnetically anisotropic. The process of HV treatment is schematically illustrated in Fig. 1(b) and details of HV treatment are described elsewhere.[5] H treatment was carried out at 850 °C for 2 h which was the same condition as used in Ref. 1. Subsequent V treatment was made at 700–950 °C for 1 h.

HV-treated samples were ground into powders of <63 μm by hand milling. These powders were mixed with molten paraffin and were solidified with or without applying a magnetic field of 12 kOe. Magnetic properties were measured by a vibrating sample magnetometer with the maximum applied field of 15 kOe after applying a pulsed field of 50 kOe to the sample.

X-ray diffractions with Fe $K\alpha$ radiation were carried out.

III. RESULTS AND DISCUSSION

The characteristics of hydrogen absorption and desorption of $Nd_{12.6}Fe_{81.4-x}Co_xB_{6.0}$ (x=0,11.6,17.4) on heating at a rate of 400 °C/h are shown in Fig. 2. It consists of two

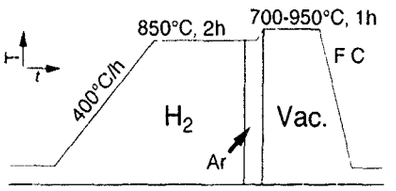

FIG. 1 (a) Diagram of experimental procedure and (b) schematic illustration of the process of HV treatment

 0021-8979/94/76(10)/6828/3/$6.00 © 1994 American Institute of Physics

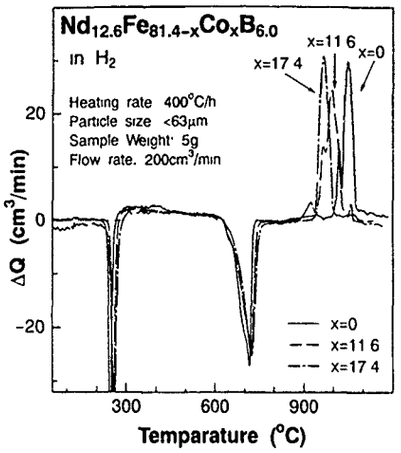

FIG. 2. Hydrogen absorption and desorption characteristics of $Nd_{12.6}Fe_{81.4-x}Co_xB_{6.0}$ (x=0,11.6,17.4) on heating at a rate of 400 °C/h.

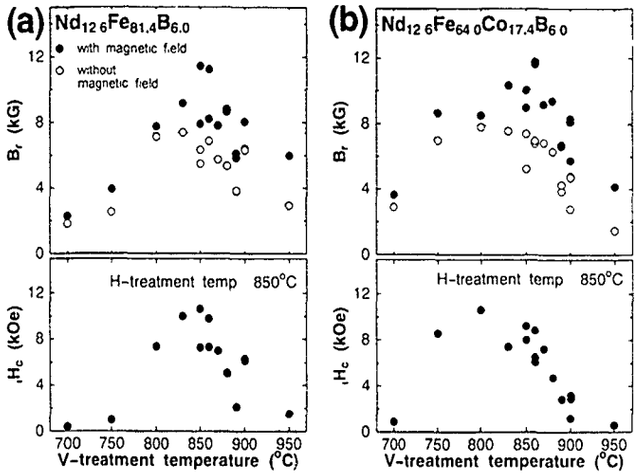

FIG. 3. V-treatment temperature dependence in magnetic properties of HV-treated $Nd_{12.6}Fe_{81.4-x}Co_xB_{6.0}$ where (a) x=0, (b) 17.4. (Dotted line indicates half values of saturation magnetization of each homogenized alloy)

absorption peaks and two desorption peaks. X-ray-diffraction analysis reveals that the characteristics of hydrogen absorption and desorption correspond to the phase changes during the heat treatment in hydrogen, and that the peaks indicate the reaction as follows: Absorption peaks at around 250 °C correspond to interstitial hydrogen uptake to form $Nd_2(Fe,Co)_{14}BH_x$, and the desorption peaks covering 250–650 °C indicate hydrogen atoms leaving the interstitial site. Hydrogen absorption peaks at around 700 °C, corresponding to a disproportionation reaction into a mixture of NdH_2, α-(Fe,Co), and $(Fe,Co)_2B$ phases. The desorption peaks observed above 900 °C correspond to the recombination reactions to the original compound. The results described above are in good agreement with the reported ones by Harris[6] and Takeshita.[7] The shape of the peaks corresponding to the disproportionation reaction is narrow in both alloys with and without Co. Co added alloys show the recombination reaction at lower temperature. It can be considered that the disproportionation reactions are very drastic in the both alloys. It can also be said that the Co contained disproportionated mixture is less stable under an atmospheric pressure of hydrogen, and tends to form $Nd_2(Fe,Co)_{14}B$ compounds at lower temperature.

Figure 3 shows the V-treatment temperature dependence in magnetic properties of HV-treated $Nd_{12.6}Fe_{81.4-x}Co_xB_{6.0}$. Coercivities increase with increasing V-treatment temperature and exhibit maximum values at 850 and 800 °C in the alloys without and with Co, respectively. Co added alloys show higher coercivity at lower V-treatment temperature than the alloys without Co. In both alloys, remanence increases with increasing temperature and shows highest values at 850–860 °C, which then decreases at above 880 °C. The alloys aligned with a magnetic field exhibit higher remanence than the half values of saturation magnetization of each homogenized alloy, which correspond to the remanence of isotropic alloys and are shown by the dotted lines in Fig. 3, in the temperature range between 800 and 900 °C. The differences of remanence between the alloys aligned with and without a magnetic field become larger at above 800 °C. Judging from the magnetic properties shown in Fig. 3, the inducement of anisotropic aspect proceeds by the V treatment above 800 °C.

Figure 4 shows x-ray-diffraction patterns of $Nd_{12.6}Fe_{81.4-x}Co_xB_{6.0}$ (x=0, 11.6, 17.4) alloys V-treated at 700 °C, which is a relatively low temperature of V treatment. X-ray reflections from NdH_2 and α-Fe phases are dominant in $Nd_{12.6}Fe_{81.4}B_{6.0}$ powders. The intensity of reflections from the $Nd_2(Fe,Co)_{14}B$ phase increases with increasing Co content. It can be said that Co added alloys tend to form $Nd_2(Fe,Co)_{14}B$ compound under evacuation condition. This results in higher coercivity at lower temperature in Co added alloys.

Figure 5 shows x-ray-diffraction patterns of HV-treated $Nd_{12.6}Fe_{81.4}B_{6.0}$ powders which were pressed with a magnetic field of 12 kOe. The x-ray-diffraction pattern of the

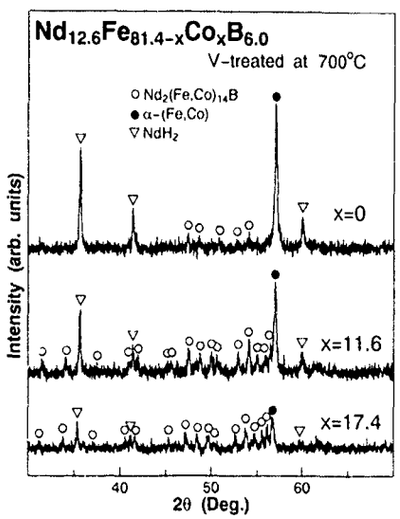

FIG. 4. X-ray-diffraction patterns of $Nd_{12.6}Fe_{81.4-x}Co_xB_{6.0}$ (x=0,11.6,17.4) V-treated at 700 °C.

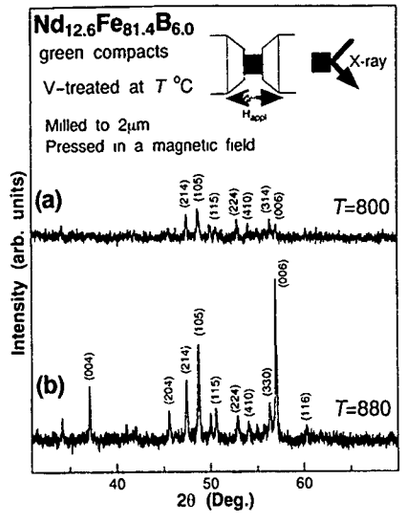

FIG. 5. X-ray-diffraction patterns of $Nd_{12.6}Fe_{81.4}B_{6.0}$ V-treated at (a) 800 and (b) 880 °C, which were milled to 2 μm and then pressed in a magnetic field.

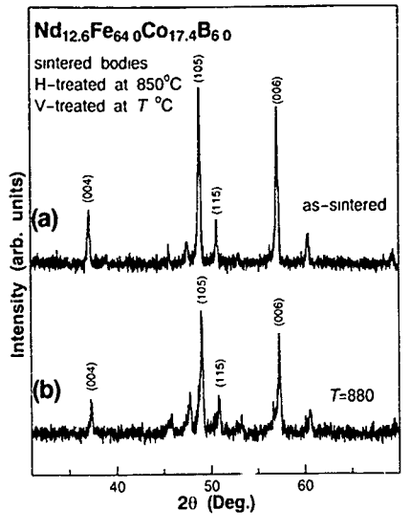

FIG. 6. X-ray-diffraction patterns of $Nd_{12.6}Fe_{64.0}Co_{17.4}B_{6.0}$ sintered bodies (a) before HV treatment, and (b) after V treatment at 880 °C.

V-treated green compact at 800 °C, where remanence equals to the value of isotropic alloy and exhibits no difference between the alloys aligned with and without magnetic field, shows isotropic characteristics. But the V-treated one at 880 °C exhibits intensive reflection from (006) which indicates alignment of grains in the powders. This feature is closely related to the difference in remanence at higher temperature shown in Fig. 3 and it would be due to grain alignment.

In order to investigate the texture change during V treatment, x-ray diffraction was performed on anisotropic sintered bodies after HV treatment. X-ray-diffraction patterns of $Nd_{12.6}Fe_{64}Co_{17.4}B_{6.0}$ sintered bodies (a) before HV treatment and (b) after V treatment at 880 °C are shown in Fig. 6. The diffraction pattern of an as-sintered sample shows an anisotropic characteristic since intensive reflections from (006) and (105) are observed in Fig. 6(a). High intensities of reflections from (006) and (105) are also observed in the sample after V treatment at 880 °C shown in Fig. 6(b). It is considered that the V-treated powders at higher temperatures tend to form the same texture as the original samples before HV treatment.

Taking account of the results shown in Fig. 5, it can be said that magnetic anisotropy in HV-treated powders is induced by high-temperature V treatment. It suggests that inducement of magnetic anisotropy proceeds through a selective grain growth of $Nd_2Fe_{14}B$ grains. Uehara *et al.* concluded that residual $Nd_2Fe_{14}B$ grains among the disproportionated mixture after H treatment are the nuclei of recombination during V treatment and Co makes this tendency noticeable.[4] Since the disproportionation reaction is very drastic and no difference can be observed in hydrogen absorption and desorption characteristics below 900 °C in all the studied alloys from Fig. 2, it is anticipated that no residual $Nd_2Fe_{14}B$ phase exists after H treatment at 850 °C. If the oriented nucleation had been dominant, magnetic anisotropy would be induced by V treatment at lower temperatures. But in our results, shown in Fig. 3, the remanence of $Nd_{12.6}Fe_{81.4}B_{6.0}$ powders V-treated at 800 °C and solidified with a magnetic field is almost the same as that without a magnetic field. The main effect of Co addition is to enhance the recombination reaction.

[1] T. Takeshita and R. Nakayama, Proceedings of the 10th International Workshop on Rare Earth Magnets and Their Applications, Kyoto, 1989, (unpublished), Vol. I, p. 551.

[2] P. J. McGuiness, X. J. Zhang, X. J. Yin, and I. R. Harris, J. Less-Common Met. **158**, 359 (1990).

[3] T. Takeshita and R. Nakayama, Proceedings of the 12th International Workshop on Rare Earth Magnets and Their Applications, Canberra, 1992 (unpublished), p. 670.

[4] M. Uehara, H. Tomizawa, S Hirosawa, T. Tomida, and Y. Maehara, IEEE Trans. Magn. **29**, 2770 (1993).

[5] H. Nakamura, S. Sugimoto, M. Okada, and M. Homma, Mater. Chem. Phys **32**, 280 (1992).

[6] T. Takeshita and R. Nakayama, Proceedings of the 11th International Workshop on Rare Earth Magnets and Their Applications, Pittsburgh, 1991, Vol. I (unpublished), p. 49.

[7] I. R Harris, Proceedings of the 12th International Workshop on Rare Earth Magnets and Their Applications, Canberra, 1992 (unpublished), p. 347.

The use of polytetrafluoroethylene in the production of high-density bonded Nd-Fe-B magnets

C. Tattam, A. J. Williams, J. N. Hay, and I. R. Harris
School of Metallurgy and Materials, University of Birmingham, Birmingham B15 2TT, United Kingdom

S. F. Tedstone and M. M. Ashraf
Penny and Giles Blackwood, Ltd., Blackwood, Gwent NP2 2YD, United Kingdom

Rotary forging has been used to produce high-density bonded magnets from rapidly quenched Nd-Fe-B based ribbons [MQP-D, of nominal composition 28%Nd-56%Fe-15%Co-1%B (wt %)]. Polytetrafluoroethylene (PTFE), when used as an additive (5%–15% by volume) has been found to act as an effective binder and greatly enhances the forgeability of the MQI, allowing higher forging pressures to be used. Densities of up to 98% of the fully dense composite have been achieved. The forging process can be undertaken in air at room temperature. Magnetically, the compacts are comparable to conventional epoxy resin bonded MQI, with energy products of up to 84 kJ/m^3. Equivalent volume fractions of MQI (~83.5 vol %) have been achieved in the compacts with increased PTFE content due to the displacement of pores by the PTFE. The effect of PTFE content on the mechanical strength of the compacts has been assessed and it has been found that strength increases with increasing PTFE content, consistent with the reduction in porosity.

I. INTRODUCTION

There are two principal methods used for processing Nd-Fe-B alloys into permanent magnets. The first is a conventional powder metallurgy process which is similar to that employed for the production of rare-earth cobalt magnets.[1,2] The second involves the rapid quenching of the alloy from the melt.[3,4] The ribbons that result from rapid quenching have a high coercivity which can be attributed to the extremely fine grained microstructure. Magnets can be produced using rapidly quenched material by grinding, mixing with a binder, and then pressing. Various binders have been employed for this purpose including epoxy resins,[5] and more recently, polytetrafluoroethylene (PTFE).[6]

It has been shown that high-density magnets can be produced by rotary forging MQI with or without a soft metal binder.[7,8] MQI compacts forged with no binder were found to have poor mechanical integrity. PTFE was chosen as an additive to enhance the flow of the flakes, due to its low coefficient of friction, during forging. The PTFE was subsequently found to act as an effective binder as well as allowing the forging of ribbon in air, where previously it was necessary to forge in an inert atmosphere.[8]

It has been shown[6] that densities of 6.2 g/cm^3 can be achieved by the compression moulding of anisotropic Nd-Fe-B powder (prepared by the hydrogen decrepitation of hot deformed overquenched ribbon) with 2.1 wt % PTFE at a temperature of 250 °C under an argon atmosphere. The subject of this paper is the formation by rotary forging, in air at room temperature of high-density compacts of isotropic melt spun ribbon using PTFE as a binder.

II. EXPERIMENT

Melt spun flake material was mixed with 5, 10, and 15 vol % PTFE powder using a powder blender. 15 g batches were loaded into the die cavity of a rotary forging machine (Fig. 1). The contact area between the upper tool and the workpiece rotates around the top surface, producing a shearing action. The relatively small contact area means that lower overall loads are required to produce a given compaction compared with uniaxial pressing. The forging pressure in the hydraulic ram was varied to ascertain the optimum conditions with respect to compact density. Ejection of the compacts from the die was facilitated by the presence of PTFE.

The magnetic properties were measured by demagnetizing the compacts in a permeameter. The second quadrant demagnetization loop was obtained after pulse magnetizing the sample in a field of 4.5 T. The mechanical strength of the compacts was assessed using a method based on the ball on ring test.[9] Samples were supported around the edge of their base by a ring of 15 mm diameter while a load was applied to the center of the top surface via a steel sphere of 11 mm

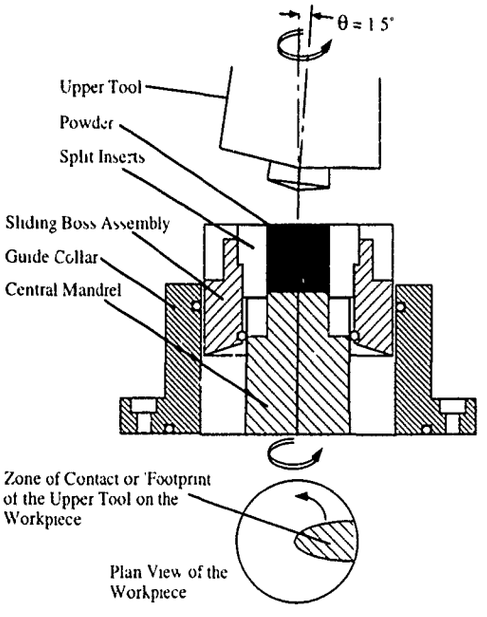

FIG. 1. A schematic representation of the rotary forging process.

 0021-8979/94/76(10)/6831/3/$6.00 © 1994 American Institute of Physics

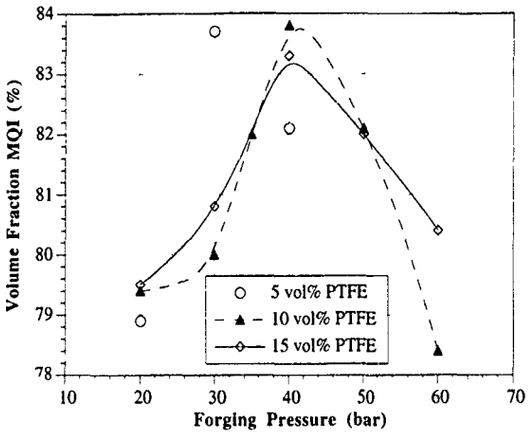

FIG 2. The effect of forging pressure on the volume fraction of MQI.

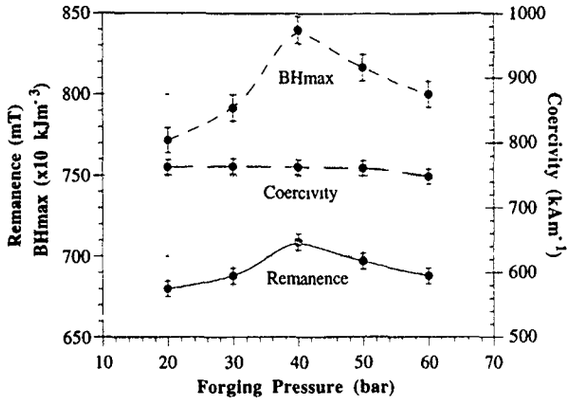

FIG. 4. The variation of magnetic properties with forging pressure for MQI+15 vol % PTFE compacts.

diameter. The cross head speed employed was 0.05 cm/min. The load required for fracture of the specimen was recorded on a chart recorder.

III. RESULTS AND DISCUSSION

The effect of varying the forging pressure on the volume fraction of MQI within the compact is shown in Fig. 2. Relative densities were determined by dividing the actual density by the theoretical maximum and converting to a percentage. The volume fraction of MQI was then calculated by multiplying the relative density by the volume fraction of MQI in the original composition. It can be seen from Fig. 2 that there is little difference in the maxima obtained for these three compositions, the largest MQI content being 83.8±0.5% for 10 vol % PTFE and the lowest being 83.3±0.5% for 15 vol % PTFE.

For all three compositions, to the left of the maxima, the lower volume fraction of MQI is due to the lower forging pressure, producing compacts of lower density and hence higher porosity. The porosity within the compacts for the three compositions as a function of forging pressure is shown in Fig. 3. At forging pressures higher than those at which the maxima in volume fraction occur, values decrease due to the onset of cracking at these pressures. The presence of cracks means that, despite the probability of there being regions of higher density within the compact, the overall density is lower than the maximum.

The traces shown in Fig. 3 are consistent with the data shown in Fig. 2. It can be seen that the higher the PTFE content, the lower the porosity. This displacement of the pores by PTFE during forging accounts for the near-equivalent volume fractions of MQI being obtainable in compacts with higher PTFE content. From these investigations it appears that the optimum forging pressure for MQI+5 vol % PTFE samples is 30 bars and for 10 and 15 vol % PTFE, 40 bars.

The effect of varying the forging pressure on the magnetic properties of MQI+15 vol % PTFE compacts is shown in Fig. 4. It can be seen that, as expected, the remanence curve follows the same trend as the volume fraction of MQI curve obtained for these compacts. Variations in the forging pressure appear to have little effect on the coercivities of the compacts. The maximum energy products are also shown and it can be seen that the highest $BH(\max)$ obtained was ~84 kJ/m^3 for samples forged at 40 bars.

A typical demagnetization loop for an MQI+15 vol % PTFE magnet is shown in Fig. 5. A curve for an epoxy bonded magnet of equivalent density is included for comparison. Both magnets have comparable remanences but it can be seen that the epoxy bonded sample has a somewhat lower coercivity. This trend has been observed in all the magnets tested, and could be due to possible modification of the ribbon microstructure during forging.[8] The energy product of the PTFE bonded magnet is slightly higher, 84±1 kJ/m^3 compared to 81±1 kJ/m^3 for the epoxy bonded magnet.

Table I shows the load required for mechanical failure of PTFE, zinc, and epoxy bonded compacts. An MQI+15 vol % PTFE compact was also produced by compression moulding at 3 tons/cm^2 but this crumbled prior to testing, exhibiting a much inferior mechanical integrity compared with that of the rotary forged compacts. The zinc bonded sample was fabricated using an identical procedure to that of

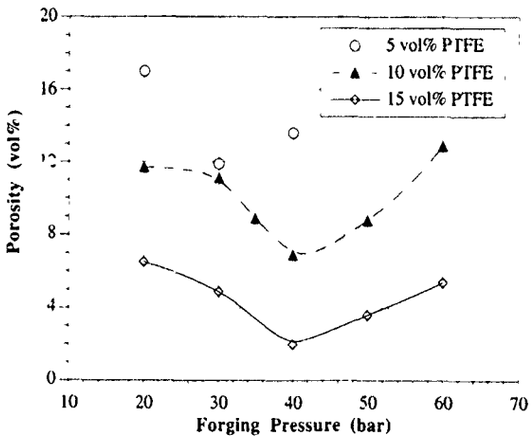

FIG. 3. The effect of forging pressure on the porosity content.

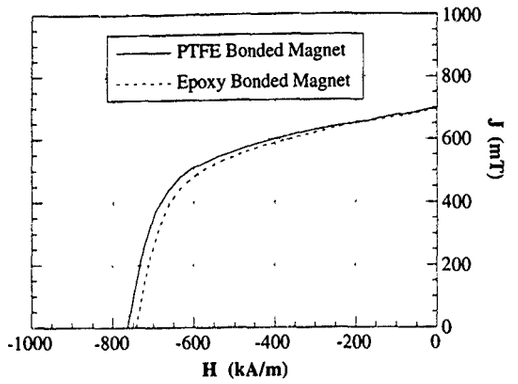

FIG. 5. Demagnetization curves for PTFE and epoxy bonded magnets.

the rotary forged PTFE bonded samples and the epoxy bonded sample was fabricated using a compression moulding technique and a low viscosity resin. All compacts tested had the same thickness.

It can be seen that the load required for fracture increases almost linearly with increasing PTFE content. Both zinc and epoxy bonded compacts required a higher load to fail; indeed the epoxy bonded sample appears to be over 6× as strong as the MQI+15 vol % PTFE sample. However. a subsequent heat treatment of the PTFE bonded samples can substantially improve their mechanical integrity.[10]

TABLE I. Load required for the fracture of various compacts.

Sample	Load to fracture/*N*
MQI+5 vol % PTFE	88
MQI+10 vol % PTFE	177
MQI+15 vol % PTFE	284
MQI+15 vol % zinc	373
Heat treated MQI+15 vol % PTFE	726
MQI+15 vol % epoxy	1766

IV. CONCLUSIONS

When PTFE is present during the rotary forging of MQI, it greatly increases the forgeability and also acts as a binder. The PTFE content can be increased without loss of MQI content due to the displacement of pores by the PTFE. Densities of up to 98% of the fully dense composite can be achieved resulting in energy products of up to 84 kJ/m^3 for the isotropic ribbon.

The mechanical testing of compacts indicates that by increasing the PTFE content the mechanical integrity increases. The non-heat-treated compacts, however, are not as strong as either zinc or epoxy bonded compacts. Heat treatment of the PTFE bonded samples improves substantially their mechanical strength.

ACKNOWLEDGMENTS

Thanks are due to both F. Biddlestone and A. Rogers for their technical assistance. The financial support of the SERC and Eureka is gratefully acknowledged.

[1] M. Sagawa, S. Fujimura, N. Togawa, H. Yamamoto, Y. Matsuura, and K. Hirage, IEEE Trans. Magn. **MAG-20**, 1584 (1984).
[2] M. Sagawa, S. Fujimura, N. Togawa, H. Yamamoto, and Y. Matsuura, J. Appl. Phys. **55**, 2083 (1984).
[3] J. J. Croat, J. F. Herbst, R. W. Lee, and F. E. Pinkerton, Appl. Phys. Lett. **44**, 148 (1984).
[4] J. F. Herbst, J. J. Croat, F. E. Pinkerton, and W. B Yelon, Phys Rev. B **29**, 4176 (1984).
[5] R. W. Lee, E. G. Brewer, and N. A. Shaffel, IEEE Trans Magn. **MAG-21**, 1958 (1985).
[6] V. Panchanathan, A. T. McMullen, J. J. Croat, M. Doser, and R. W. Ribitch, J. Appl. Phys. **70**, 6465 (1991).
[7] N Rowlinson, M. M. Ashraf, and I. R. Harris, J. Magn. Magn. Mater. **80**, 93 (1989).
[8] N. Rowlinson, M. M. Ashraf, and I. R Harris, J. Magn. Magn. Mater. **87**, 93 (1990)
[9] S. Timoshenko and S. Wainsky-Kreiger, *Theory of Plates and Shells* (McGraw-Hill, New York, 1959), p. 71.
[10] C. Tattam, A. J. Williams, J. N. Hay, S. F. Tedstone, M M. Ashraf, and I. R. Harris, *Proceedings of the 13th International Workshop on Rare Earth Magnets ad Their Applications* (The University of Birmingham, Birmingham, 1994), p. 573.

Evidence of domain-wall pinning in W-doped (NdDy)(FeCo)B sintered magnets

T. Y. Chu
Materials Research Laboratories, Industrial Technologies Research Institute, Chutung, 310 Taiwan, Republic of China

T. S. Chin, C. H. Lin, and J. M. Yao
Department of Materials Science and Engineering, Tsing Hua University, Hsinchu, 300 Taiwan, Republic of China

Addition of tungsten (1–2 at. %) is very effective in improving coercivity of (Nd,Dy)-(Fe,Co)-B sintered magnets both at room temperature and elevated temperatures in addition to improving thermal stability. Transmission electron microscopy shows that there exists a WFeB precipitate phase inside the $Nd_2Fe_{14}B$ (2-14-1) matrix grain. The WFeB phase is plateletlike, and occasionally appears to have its largest dimension running parallel to the *c* axis of the 2-14-1 matrix phase. The orientation relationship between the WFeB precipitate and the matrix is found to be $(102)_{WFeB}\|(220)_{2\text{-}14\text{-}1}$, and $[010]_{WFeB}\|[002]_{2\text{-}14\text{-}1}$. Domain walls jump from a position alongside the WFeB particles to a new position alongside others upon turning on magnetic field of the objective lens, as evidenced by Lorentz microscopy, denoting the ability of domain-wall pinning by the strain field around the WFeB precipitate. As a result, this provides extra hindrance to domain-wall motion and leads to enhanced coercivity and thermal stability, particularly at elevated temperatures.

I. INTRODUCTION

The high-temperature properties of Nd-Fe-B magnets have been found to improve dramatically by doping with some elements.[1–4] When alloying both Co and Dy in the Nd-Fe-B magnets, addition of a third element such as Al, Ga, Nb, V, or Mo has been studied extensively and was shown to be effective in improving high-temperature magnetic properties of Nd-Dy-Fe-Co-B magnets.[4–6] The Nb-rich precipitates dispersed in the matrix were suggested to be responsible for the coercivity increase of Nb-containing magnets.[7] The combined substitutions of (Nb,Ga) or (Nb,Al) for partial Fe content are effective in reducing the irreversible thermal loss and the temperature coefficient of remanence.[8] Sagawa *et al.* and Hirosawa *et al.* have shown that the addition of V or Mo is effective in improving the thermal stability of sintered Nd-Fe-B magnets, and a working temperature of over 200 °C may be possible.[5,6]

The effect of W addition on magnetic properties of Nd-Dy-Fe-Co-B magnets have been reported by us in a previous paper.[9] The observation of W-rich inclusions and precipitates in W-containing Nd-Fe-B magnets has also been reported elsewhere.[10] However, the crystallographic relationship between these precipitates and the matrix phase has never been studied. In this paper, the results of microstructure study of W-containing magnets are presented and the reason for enhanced coercivity is delineated.

II. EXPERIMENT

Alloy ingots of $Nd_{14}Dy_{1.5}Fe_{71-x}Co_6W_xB_{7.5}$ ($x=0$ or 2) were prepared by induction melting under Ar protection, then made into sintered magnets (sintering at 1090 °C for 1 h) and heat treated (at 900 °C for 2 h then 550 °C for 1 h) under Ar atmosphere by conventional powder metallurgy processes as described in the previous paper.[9] Magnetic properties of sintered specimens were isothermally measured at temperatures between 25 and 150 °C by a B-H tracer after specimens were magnetized by a 5 T pulse field. The microstructure was studied by transmission electron microscopy in a JEOL 2000 FX scanning transmission electron microscope (STEM) equipped with a LINK AN10000 energy dispersive x-ray analyzer.

III. RESULTS AND DISCUSSION

Figure 1 shows coercivity versus temperature, up to 150 °C, for the optimally heat-treated $Nd_{14}Dy_{1.5}Fe_{71-x}Co_6W_xB_{7.5}$ ($x=0$, the blank, and $x=2$) magnets. The W-containing alloy shows remarkable intrinsic coercivity (iHc) as compared to the blank alloy. Furthermore, iHc values of the W-containing alloy are twice as large as that of blank alloy even at temperatures higher than 100 °C.

It was speculated that the increased coercivity and thermal stability might be due to an intrinsic enhancement of

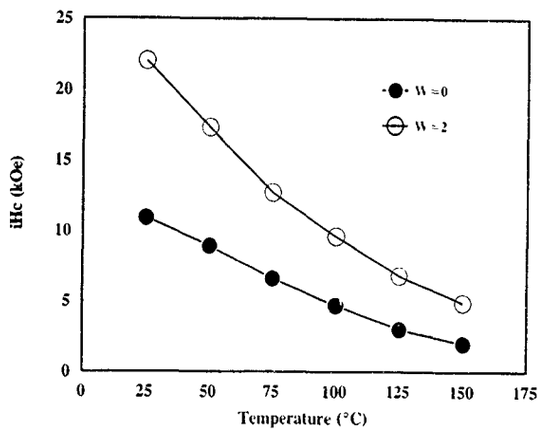

FIG. 1. Coercivity of sintered $Nd_{14}Dy_{1.5}Fe_{71-x}W_xCo_6B_{7.5}$ magnets ($x=0$, the blank alloy, and $x=2$) vs temperature.

 0021-8979/94/76(10)/6834/3/$6.00 © 1994 American Institute of Physics

FIG. 2. WFeB platelet precipitates dispersed in $Nd_2Fe_{14}B$ matrix of a 2 at. % W-containing sintered magnet, the inset is the microdiffraction pattern (the marker=200 nm).

FIG. 3. Large inclusion phase on the grain boundary (the marker=2 μm).

magnetocrystalline anisotropy field (H_A) arising from W alloying. However, experiments on H_A for both the blank and the 2% W-containing alloys showed the same value of 7.8 T. That is to say, the improvement might be due to extrinsic reasons.

It has been reported that W is not completely dissolved into the matrix 2-14-1 phase, and W-rich inclusions and precipitates exist in the W-containing magnets.[9,10] In other reports in which V- or Mo-containing Nd-Dy-Fe-Co-B alloys were studied, V_2FeB_2 or Mo_2FeB_2 phases were observed, respectively.[11,12]

Figure 2 shows the platelet precipitates dispersed inside the 2-14-1 matrix grains of W-containing magnet. Since the precipitates are generally smaller than 200 nm in thickness, the microdiffraction method, in which a focused electron probe is used to acquire the diffraction patterns, was performed in order to reduce the contribution from the surrounding 2-14-1 matrix phase. The precipitates were indexed as orthorhombic W-Fe-B (1-1-1) phase with lattice parameters $a=0.582$ nm, $b=0.316$ nm, and $c=0.681$ nm. A diffraction pattern is shown as the inset of Fig. 2. By analyzing diffraction patterns taken from the junction between the precipitate and matrix phase, it is found that there exists an orientation relationship between them, that is

$$(1\ 0\ 2)_{\mathrm{WFeB}} \| (2\ 2\ 0)_{2\text{-}14\text{-}1}. \tag{1}$$

$$[0\ 1\ 0]_{\mathrm{WFeB}} \| [0\ 0\ 2]_{2\text{-}14\text{-}1}. \tag{2}$$

Crystallographically, the platelet precipitate is found to be identical to the larger W-containing inclusions present at grain boundaries, even though their dimension is one order of magnitude larger and their morphologies are quite different from each other. The inclusions on the grain boundaries are usually equiaxed as shown in Fig. 3. These two kinds of particles are suggested to appear at different stages in the manufacturing processes. The inclusions are the broken bits of W-rich dendrite in the cast ingot as evidenced by an optical microscope. The platelets inside the matrix grains are believed to precipitate out of supersaturated W-containing matrix phase during the heat-treatment stage (900–550 °C).

It was occasionally observed that the largest dimension of these precipitates runs parallel to the c axis of the 2-14-1 phase, as identified by the electron-diffraction pattern taken from the matrix phase near the precipitate (Fig. 4). The preferred orientation of the precipitate thus results in aligning their largest dimension parallel to the domain wall, as shown in Fig. 5(a). Therefore the precipitates can very effectively act as domain-wall-pinning sites, as clearly shown by the Lorentz microscopy micrographs in Figs. 5(a) and 5(b). In the micrograph shown in Fig. 5(a), taken with the TEM specimen experiencing virtually no externally applied field, the domain wall (white line in the middle of the micrograph) is straight and sits alongside two precipitates (arrowed). The micrograph in Fig. 5(b) is taken after turning on the objective lens of the electron microscope; the domain-wall jumps left over the middle larger precipitate and bowed around the other precipitates (arrowed). Thus the dispersed platelet precipitates are effective as domain-wall-pinning sites. How-

FIG. 4. The electron-diffraction pattern taken from the matrix phase near the WFeB precipitate (the marker=200 nm).

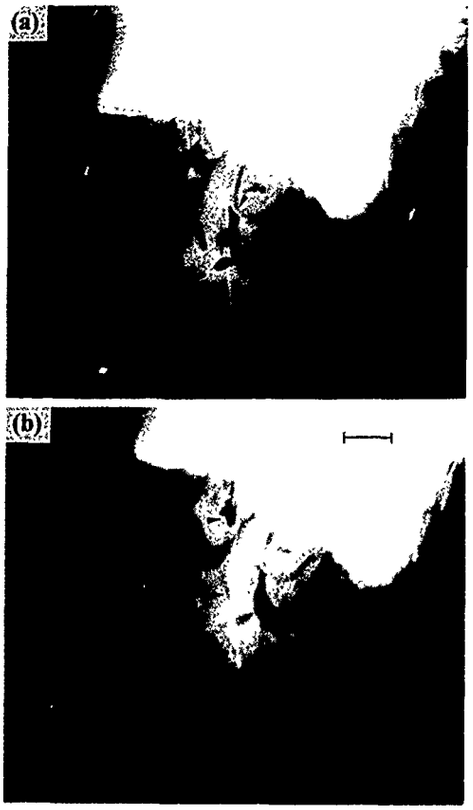

FIG. 5. Lorentz microscopy showing domain-wall motion nearby WFeB precipitates. (a) A straight domain-wall site alongside arrowed precipitates, without external field, (b) the domain-wall jump to the left and rest alongside other arrowed precipitates upon turning on an external field (the marker=1 μm).

ever, the WFeB phase, being nonmagnetic, is not able to interact with domain wall itself. It is believed that the strain field around the fine coherent precipitates inside the 2-14-1 grains are responsible for the pinning action to the domain walls.

For a sintered Nd-Fe-B magnet, it is proposed that nucleation of reverse domain prevails and the domain wall of a reverse domain, once nucleated, can sweep across the grain without difficulty.[13] The fine WFeB precipitate provides extra hindrance to domain-wall motion across the grain through the strain field around them, hence is responsible for the extremely high coercivity and thermal stability of the W-containing magnets. On the other hand, but to a lesser extent, the W-rich inclusions present on the grain-boundary regions might impede the grain growth of the 2-14-1 phase during sintering, giving rise to a fine grain structure which is also essential for high coercivity. Since the refractory WFeB phase is thermally stable at elevated temperatures, the ability of acting as domain-wall-pinning sites sustains to high temperature.

IV. CONCLUSIONS

Coercivity of (Nd,Dy)-(Fe,Co)-B sintered magnets, both at room temperature and elevated temperatures, and thermal stability can be very effectively improved by the addition of tungsten (1–2 at. %). Transmission electron microscopy studies show that there exists a WFeB precipitate phase inside the $Nd_2Fe_{14}B$ (2-14-1) matrix grain. The WFeB phase is plateletlike, and occasionally appears to have its largest dimension running parallel to the c axis of the 2-14-1 matrix phase. The orientation relationship between the WFeB precipitate and the matrix is found to be $(102)_{WFeB}\|(220)_{2\text{-}14\text{-}1}$, and $[010]_{WFeB}\|[002]_{2\text{-}14\text{-}1}$. Domain walls jump from a position alongside the WFeB particles to a new position alongside other WFeB particles upon turning on magnetic field of the objective lens, as evidenced by Lorentz microscopy, denoting the ability of domain-wall pinning by the strain field around the WFeB precipitate. Consequently, this refractory precipitate provides extra hindrance to domain-wall motion and leads to enhanced coercivity and thermal stability, particularly at elevated temperatures.

ACKNOWLEDGMENTS

The support of this work partly from the Ministry of Economic Affairs and partly from the National Science Council (Grant No. NSC83-0405-E007-14) of the Republic of China is gratefully acknowledged.

[1] J. J. Herbst, J. J. Croat, F. F. Pinkerton, and W. B. Yelon, Phys. Rev. B **29**, 4176 (1984)
[2] M. Sagawa, S. Fujimura, M. Togawa, and Y. Matsuura, J. Appl. Phys. **55**, 2083 (1984).
[3] B. M. Ma and K. S. V. L. Narasimhan, IEEE Trans. Magn. **22**, 1081 (1986).
[4] T. Mizoguchi, I. Sakai, H. Niu, and K. Inomata, IEEE Trans. Magn. **22**, 919 (1986).
[5] M. Sagawa, P. Tenaud, F. Vial, and K. Hiraga, IEEE Trans. Magn. **26**, 1957 (1990).
[6] S. Hirosawa, H. Tomizawa, S. Mino, and A. Hamamura, IEEE Trans. Magn. **26**, 1960 (1990).
[7] S. F. H. Parker, P. J. Grundy, and J. Fidler, J. Magn. Magn. Mater. **66**, 74 (1987).
[8] G F. Zhou, M.S. thesis, Institute of Metal Research, Academia Sinica, Shenyang, P.R. China, 1989.
[9] C. H. Lin, T. S. Chin, Y H. Huang, J. M. Yau, K. H. Cheng, and T. Y. Chu, IEEE Trans. Magn. **29**, 2785 (1993).
[10] J. Bernardi, J. Fidler, and F. Fodermayr, IEEE Trans. Magn. **28**, 2127 (1992).
[11] P. Tenaud, F. Vial, A. Barzasi, A. Duchene, and M. Sagawa, Proceedings of the 11th International Workshop on Rare Earth Magnets and their Applications, Pittsburgh, PA, 1990 (unpublished), Vol. 1, pp 123–135.
[12] S Hirosawa, S. Mino, H. Tomizawa, and K. Tokuhara, Proceedings of the 11th International Workshop on Rare Earth Magnets and their Applications, Pittsburgh, PA, 1990 (unpublished), Vol. 1, pp. 136–147.
[13] S. Hirosawa, K Tokuhara, Y. Matsuura, H. Yamamoto, S. Fujimura, and M. Sagawa, J. Magn. Magn Mater. **61**, 363 (1986).

Magnetic properties of rare-earth compounds of the $RCo_{10}Mo_2$ type

D. C. Zeng
Van der Waals-Zeeman Laboratory, University of Amsterdam, Valckenierstraat 65, 1018 XE Amsterdam, The Netherlands, and Institute of Metal Research, Academia Sinica, Shenyang 110015, China

N. Tang
Van der Waals-Zeeman Laboratory, University of Amsterdam, Valckenierstraat 65, 1018 XE Amsterdam, The Netherlands, and Institute of Physics, Academia Sinica, Beijing 100080, China

T. Zhao
Van der Waals-Zeeman Laboratory, University of Amsterdam, Valckenierstraat 65, 1018 XE Amsterdan, The Netherlands, and Institute of Metal Research, Academia Sinica, Shenyang 110015, China

Z. G. Zhao, K. H. J. Buschow, and F. R. de Boer
Van der Waals-Zeeman Laboratory, University of Amsterdam, Valckenierstraat 65, 1018 XE Amsterdam, The Netherlands

The magnetic properties of the tetragonal $ThMn_{12}$-type $RCo_{10}Mo_2$ compounds have been investigated by means of magnetic measurement and x-ray diffraction. It is found that the Co moment is roughly the same in all $RCo_{10}Mo_2$ compounds (0.9 μ_B/Co), excepting $CeCo_{10}Mo_2$ (0.7 μ_B/Co). It is also found that the Co sublattice displays easy c-axis magnetization. Nonaxial behavior at room temperature is observed only for $SmCo_{10}Mo_2$, whereas in $ErCo_{10}Mo_2$ a spin reorientation occurs from axial to planar magnetization upon cooling below $T_{sr}=125$ K. These results suggest that the A_2^0 term, mainly responsible for the rare-earth-sublattice anisotropy has the same sign as in the $R_2Fe_{14}B$ series ($A_2^0>0$). This is in contrast to other $ThMn_{12}$-type compounds ($RFe_{10}V_2$, $RFe_{11}Ti$) where it is generally assumed that $A_2^0<0$. The intersublattice coupling of $ErCo_{10}Mo_2$ has been determined by means of the high-field free-powder method.

I. INTRODUCTION

Many novel Fe-rich rare-earth-based permanent-magnet materials have comparatively low Curie temperatures and hence require Co substitution for Curie temperature enhancement. Well-known examples are $Nd_2Fe_{14}B$, $SmFe_{11}Ti$, and $SmFe_{10}Mo_2$. In order to study the effect of Co substitution on Curie temperature, magnetization, intersublattice-coupling constant, and anisotropy field in $RFe_{10}Mo_2$ compounds, we have studied the magnetic properties of the $RCo_{10}Mo_2$ series in pure form.

II. EXPERIMENT

The compounds of the $RCo_{10}Mo_2$ type were prepared by arc-melting stoichiometric mixtures of the metallic constituents of at least 99.9% purity. After arc melting, the polycrystalline specimens were wrapped in tantalum foil, sealed into evacuated quartz tubes, and annealed at 1000 °C for 4 weeks. The samples were quickly cooled to room temperature after annealing by breaking the quartz tubes under water. Subsequently, the samples were investigated by x-ray powder diffraction and found to be approximately single phase. The x-ray patterns were indexed on the basis of the $ThMn_{12}$-type of structure. For each compound, the free-powder magnetization was measured at 4.2 K as a function of applied magnetic fields up to 35 T, using the High-Field Installation at the University of Amsterdam.[1] In order to investigate the presence of spin-reorientation transitions between 4.2 K and room temperature, ac-susceptibility measurements were made on several compounds in the $RCo_{10}Mo_2$ series.

III. EXPERIMENTAL RESULTS

From x-ray-diffraction experiments on magnetically aligned powders, it was derived that at room temperature the easy-magnetic direction in the $RCo_{10}Mo_2$ compounds is parallel to the c-axis. The only exception is $SmCo_{10}Mo_2$ where the easy-magnetization direction is perpendicular to the c-axis. These results confirm earlier observations by Xu and Shaheen.[2]

ac-susceptibility measurements show no temperature-induced spin reorientations except in $ErCo_{10}Mo_2$ and $Er_{0.8}Y_{0.2}Co_{10}Mo_2$ (see Fig. 1). The sharp cusp observed for

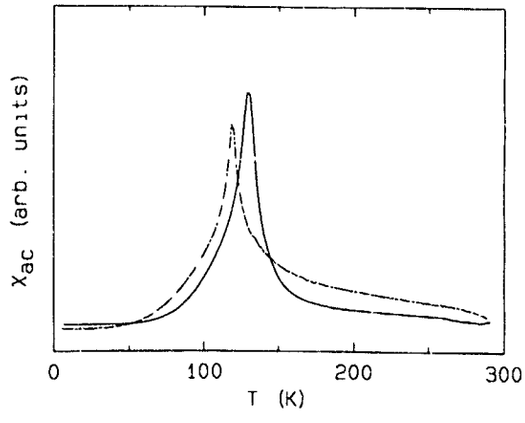

FIG. 1. Temperature dependence of the ac susceptibility for $ErCo_{10}Mo_2$ (solid line) and $Er_{0.8}Y_{0.2}Co_{10}Mo_2$ (dashed line)

 0021-8979/94/76(10)/6837/3/$6.00 © 1994 American Institute of Physics

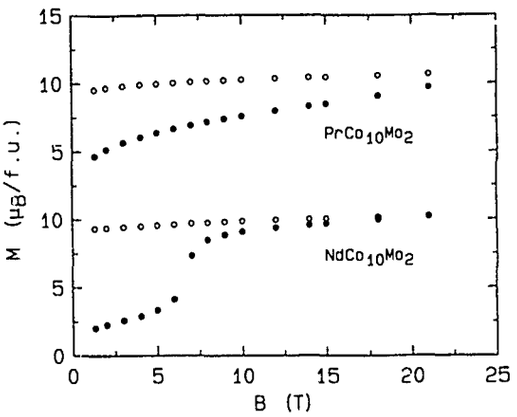

FIG. 2. Magnetic isotherms at 4.2 K measured on magnetically aligned powders of $PrCo_{10}Mo_2$ and $NdCo_{10}Mo_2$. Open circles correspond to the field parallel to the alignment direction and filled circles to perpendicular to the alignment direction.

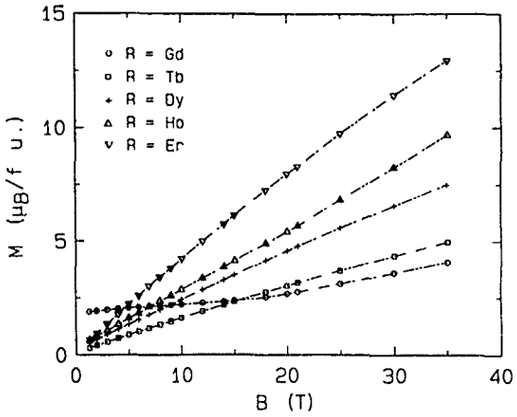

FIG. 3. Magnetic isotherms at 4.2 K of $RCo_{10}Mo_2$ compounds (R=Gd, Tb, Dy, Ho, and Er) measured on powder particles that are free to rotate in the sample holder.

both materials is taken as evidence of spin reorientations from $M \perp c$ (at low temperature) to $M \| c$ (at high temperature), at 125 K in $ErCo_{10}Mo_2$ and at 115 K in $Er_{0.8}Y_{0.2}Co_{10}Mo_2$. From the magnetic measurements on $RCo_{10}Mo_2$ compounds by Xu and Shaheen,[2] it can be derived that the moments of the light rare earths couple parallel to the Co moments and that the moments of the heavy rare earths couple antiparallel to the Co moments, as is usually observed.[3] Therefore no information on the intersublattice-coupling strength can be derived by means of the high-field free-powder (HFFP) method[4,5] for the compounds with the light-rare-earth elements. The isotherms of these compounds were therefore studied only in fields up to 20 T.

The magnetization at 4.2 K of magnetically aligned powders of $PrCo_{10}Mo_2$ and $NdCo_{10}Mo_2$ is shown in Fig. 2. The anisotropy field B_A for $PrCo_{10}Mo_2$ equals approximately 25 T. In $NdCo_{10}Mo_2$ there is a field-induced change of the magnetization direction, the critical field being equal to 6.5 T.

The saturation moments $M(0)$ at 4.2 K were derived from the free-powder magnetization curves by extrapolation to $B=0$. These values ar listed in Table I. The anisotropy in $CeCo_{10}Mo_2$ and $GdCo_{10}Mo_2$ is predominantly that of the Co sublattice since Ce is tetravalent and Gd is an S-state ion. The deviating valence of Ce follows from the lattice constants.

In order to obtain experimental information on the intersublattice-coupling strength we have studied how the low-field ferromagnetic state is affected by an applied field by measuring the magnetization of free single-crystalline powder particles of the compounds formed with the heavy rare earths in applied fields up to 35 T. Results obtained on the $RCo_{10}Mo_2$ compounds with R=Gd, Tb, Dy, Ho, and Er are shown in Fig. 3. The observation that the magnetic isotherms pass almost through the origin for the compounds with R=Tb, Dy, Ho, and Er means that the R-sublattice magnetization M_R and the Co-sublattice magnetization M_{Co} are nearly equal to each other in these materials.

In practically all R-T intermetallics previously investigated by means of the HFFP method,[5] the T-sublattice anisotropy is much smaller than the R-sublattice anisotropy. In these cases, the former can be ignored and the R-sublattice magnetization can be parallel to the easy-magnetization direction and to remain so during the bending process. The free energy is given by

$$E = E_R^{an} + E_{Co}^{an} + n_{RCo} M_R M_{Co} \cos\alpha - BM. \quad (1)$$

The magnetization M is given by $M=(M_R^2+M_{Co}^2+2M_R M_{Co}\cos\alpha)^{1/2}$.

In deriving the magnetization by minimizing the free energy, only the last two terms in Eq. (1) need to be taken into consideration. In this case, the intersublattice-coupling constant n_{RT} can be obtained straightforwardly from the magnetization in the region where the bending process from the ferrimagnetic configuration to the forced ferromagnetic state occurs ($n_{RT}=[M/B]^{-1}$).

In the $RCo_{10}Mo_2$ compounds, however, it is no longer legitimate to neglect the Co-sublattice anisotropy. If only the first-order anisotropy constants K_1^R and K_1^{Co} are taken into account, the free-energy expression reads

TABLE I. Magnetic properties of $RCo_{10}Mo_2$ compounds

Compounds	$M(0)$	M_R	M_{Co}
$YCo_{10}Mo_2$	8.5	0	8.5
$CeCo_{10}Mo_2$	6.5	0	6.5
$PrCo_{10}Mo_2$	11.2	3.2	8.0
$NdCo_{10}Mo_2$	10 6	3.2	7.4
$SmCo_{10}Mo_2$	9 5	0.7	8 8
$GdCo_{10}Mo_2$	1.9	7.0	7.0±1.9
$TbCo_{10}Mo_2$	0.1	9.0	9 0±0.1
$DyCo_{10}Mo_2$	0.3	10.0	10.0±0.3
$HoCo_{10}Mo_2$	0.3	10.0	10.0±0.3
$Er_{0.8}Y_{0.2}Co_{10}Mo_2$	1.4	7.2	7 2±1 4
$ErCo_{10}Mo_2$	0.0	9.0	9.0

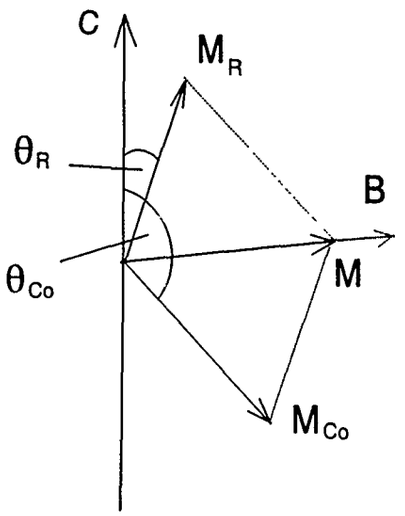

FIG. 4. Schematic representation of the orientations of M_R and M_{Co} in an external field for a free single crystal.

$$E=K_1^R \sin^2\theta+K_1^{Co} \sin^2(\theta+\alpha)+n_{RCo}M_R M_{Co} \cos\alpha-BM. \quad (2)$$

The angles θ and α are defined in Fig. 4. Due to the presence of the two anisotropy terms in Eq. (2) neither of the two sublattice magnetizations will remain oriented along the corresponding easy-axis direction during the process that the two sublattice magnetizations bend towards each other under influence of the external field. This leads to a nonlinear behavior of the magnetic isotherm.[10,11]

By minimizing the free energy given in Eq. (2), the following expression for the magnetization can be derived:

$$\frac{B}{M}=n_{AB}-\frac{2K_1^A K_1^B}{M_A M_B |K|}\cos\alpha, \quad (3)$$

with

$$|K|=[(K_1^A)^2+(K_1^B)^2+2K_1^A K_1^B \cos 2\alpha]^{1/2}.$$

By fitting the experimental magnetization curves to this expression, details about n_{RCo} and the anisotropy constants can be obtained.

As an example we analyzed the magnetization curve of $ErCo_{10}Mo_2$. The result of the fitting procedure is shown in Fig. 5. The parameters obtained ar $K_1^{Er}=-4.32\times10^{-22}$ J/f.u., $K_1^{Co}=1.13\times10^{-22}$ J/f.u., and $n_{ErCo}=3.06\times10^{23}$ T f.u./A m^2, $M_{Er}=9.0\ \mu_B$/f.u., and $M_{Co}=8.35\ \mu_B$/f.u. When expressed by means of the Hamiltonian $H=2\ J_{ErCo}\mathbf{S}_{Er}\cdot\mathbf{S}_{Co}$, the value of $-J_{ErCo}/k$ is equal to 6.7 K. One can see in Fig. 5 that the Er- and Co-sublattice moments will become parallel at about 60 T. In the bending process, the Er-sublattice moment oscillates around its easy direction (basal plane).

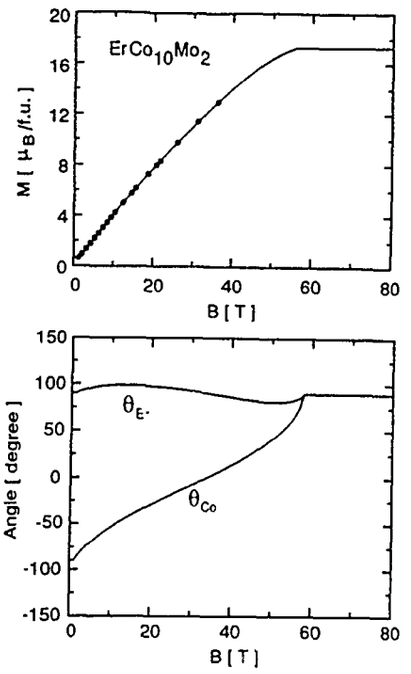

FIG. 5. (a) Comparison of the experimental and calculated magnetizations of $ErCo_{10}Mo_2$ (b) calculated field dependence of the orientations of the Er- and Co-sublattice moments.

It should be mentioned that in order to obtain the information about the magnetic coupling between R and Co sublattices for the other $RCo_{10}Mo_2$ compounds, all the magnetization curves shown in Fig. 2 should be analyzed taking into account the anisotropy of the two sublattices. This analysis which presently is carried out may be very different for the different rare-earth ions. For instance, for R=Ho, high-order anisotropy constants have to be taken into account.

[1] R. Gersdorf, F. R de Boer, J. W. Wolfrat, F. A. Muller, and L. W. Rocland, in *High-field Magnetism*, edited by M. Date (North-Holland, Amsterdam, 1983), p. 277.
[2] X Xu and S. A Shaheen, J. Magn. Magn. Mater. **118**, L6 (1993)
[3] J. J M. Franse and R. J. Radwanski, in *Magnetic Materials*, edited by K. H. J. Buschow (Elsevier Science, Amsterdam, 1993), Vol. 7, p. 308.
[4] R. Verhoef, P. H. Quang, J. J. M. Franse, and R. J Radwanski, J. Magn Magn. Mater. **74**, 43 (1988).
[5] J. P. Liu, F. R. de Boer, P. F. de Châtel, R. Coehoorn, and K. H. J. Buschow, J. Magn. Magn Mater (in press).
[6] L. M Garcia, R. Burriel, F. Luis, E. Palacios, J. Bartolome, E. Tomey, D. Fruchart, J. L Soubeyroux, and D. Gignoux, IEEE Trans Magn.
[7] E. Belorizky, M. E. Fremy, J. P. Gavigan, D. Givord, and H. S Li, J. Appl. Phys **61**, 3971 (1987).
[8] M. S. S. Brooks and B. Johansson, in *Magnetic Materials*, edited by K H J. Buschow (Elsevier Science, Amsterdam, 1993), vol. 7, p 139
[9] N. H. Duc, Phys. Status Solidi B **164**, 545 (1991).
[10] Z. G. Zhao, Thesis, University of Amsterdam, 1994.
[11] Z. G. Zhao, X. Li, J. H V. J Brabers, P F de Châtel, F. R. de Boer, and K. H J. Buschow, J. Magn. Magn. Mater. **123**, 74 (1993)

Published without author corrections

Magnetic hardening by crystallization of amorphous precursors using very high heating rates

C. de Julián and J. M. González
Instituto de Ciencia de Materiales de Madrid—CSIC, c/Serrano 144, 28006 Madrid, Spain

C. Morón
Facultad de Ciencias Físicas, Universidad Complutense, Avda. Complutense s/n, 28040 Madrid, Spain

The dependence of the treatment parameters of the coercivity of PrNdFeB samples prepared by crystallization of melt spun amorphous precursors is investigated. The crystallization treatments were carried out at high temperatures and using very high heating rates ("flash crystallization"). From the analysis of the temperature dependence of the critical field of the samples, it is concluded that this kind of crystallization treatment leads to very fine and homogeneous microstructures which result in a significant enhancement of the hard magnetic properties.

I. INTRODUCTION

The crystallization of amorphous alloys is usually described by specifying the fraction of material which is transformed either after a certain time at a given temperature (isothermal crystallization) or after a certain time when the material is heated up at a constant rate (continuous heating crystallization).[1] Nevertheless, for a given percentage of transformed material and depending on the concrete values of the treatment parameters, both the phase distribution and especially the microstructure of the crystallization product can be significantly different.[2] This is due to the different kineti 's of the elemental processes (i.e., nucleation and grain growth) involved in the crystallization and has a very interesting consequence: the possibility of optimizing the hysteretic properties of the crystallized material, which depend very sensitively on the microstructure. As it is shown in a previous work,[2] the use of high heating rates up to the treatment temperature allowed, in the case of NdDyFeB melt spun samples, optimizes the phase distribution of the crystallization product through the inhibition of the precipitation of the excess of α-Fe. Also, the accomplishment of crystallization at high temperatures favors the increase of the nucleation, which results in homogeneous microstructures.[1] In the present work, the coercivity of amorphous melt spun PrNdFeB samples crystallized by using a high heating rate and short-time anneals ("flash crystallization") is experimentally studied and correlated to the treatment parameters.

II. EXPERIMENTAL RESULTS AND DISCUSSION

Samples with nominal composition $Nd_9Pr_6Fe_{76}B_9$ were prepared by means of the single roller melt spinning technique (tangential speed of the roller, 20 m s^{-1}). According to x-ray diffraction (XRD) the as-quenched samples were amorphous. From differential scanning calorimetry (DSC) thermograms carried out at 160 °C min^{-1}, two consecutive crystallization stages, respectively, taking place at 620 and 690 °C were observed. The crystallization product consisted of a majority 2:14:1 phase.

The flash crystallization treatments were carried out by sandwiching some flakes of the amorphous precursor in between two ribbons of resistive alloy through which it was possible to flow electric current pulses (see Fig. 1). Current densities J_x, typically in the range from 1.6 to 1.9×10^3 A cm^{-2} and pulse time widths t_x, going from 1 to 12 s, were used. In order to protect the samples, and also to improve the homogeneity of the temperatures distribution, the flakes of the amorphous precursors were wrapped in a Ta foil which, in turn, was electrically isolated from the heating elements by means of mica foils. The whole setup was maintained under dynamic Ar atmosphere.

In Fig. 2 we present the time evolution of the temperature of the samples (measured by means of a low-mass thermocouple which was in good thermal contact with the Ta foil) when 16 A current pulses flow through the heating elements (cross section 0.01 cm^2) for different pulse widths t_x. The maximum temperature T_M achieved for the different treatments increased with the width of the current pulse (up to 1200 °C in the case of the 8 s, 19 A pulse). The maximum heating rate (approximately 15 000 °C min^{-1}) was achieved 2.5 s after the beginning of the pulse. The inset in this figure presents, as a function of the pulse width t_x, the total time t_{700} for which the temperature of the sample was above 700 °C (slightly above the temperature of the peak associated to the second crystallization stage as measured from DSC thermograms carried out at 160 °C min^{-1}). Since, due to the dissipation characteristics of the system, the T vs t curves of all the different treatments showed the same the initial heating regime, in the following we will use t_{700} in addition to J_x (or, equivalently, the current intensity I_x) to characterize our flash crystallization treatments.

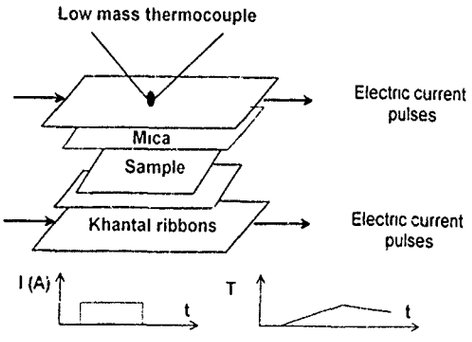

FIG. 1. Setup used for the flash crystallization treatments

 0021-8979/94/76(10)/6840/3/$6.00 © 1994 American Institute of Physics

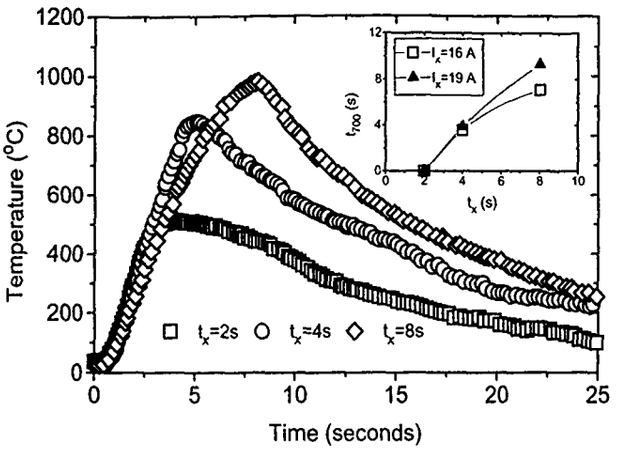

FIG. 2. Temperature of the samples vs time obtained with $I_x=16$ A and different pulse widths t_x.

The microstructure of the crystallized samples was dependent on the treatment parameters. For short-time, low intensity pulses, the samples were partially crystalline (according to the XRD) as one would expect from the increase with increasing heating rate of the crystallization processes.[3] A scanning electron micrograph (SEM) of a typical fresh fracture surface taken in the sample crystallized by using 16 A for 4 s is shown in Fig. 3(a). In it an inhomogeneous two-phase microstructure characterized by the presence of voids and domes can be observed. In contrast with this, the samples treated by means of longer pulses were fully crystallized, a homogenous microstructure [similar to that shown in Fig. 3(b)] being observed.

The study of the hysteretic properties of the samples was carried out by means of a SQUID magnetometer. Since our samples were isotropic, some reversible demagnetization occurred along the branches of the hysteresis loops corresponding to the first and second quadrants. Then, and in order to characterize the irreversible demagnetization, we considered the so-called critical field H_{crit}, defined as the demagnetization field for which the maximum susceptibility is observed. In Fig. 4 we have plotted the dependence on t_{700} of the room-temperature critical field. From this figure it is possible to observe that the critical field of the fully crystallized samples decreases with the increase of t_{700}. The deterioration of the critical field was basically related to the α-Fe segregation (which increases with T_M). Slightly lower values of the critical field than those achieved for the samples treated with $t_{700}\approx 4$ s were obtained for the samples crystallized by means of the shortest current pulses, which were only partly crystalline.[4] The optimum magnetic hardness corresponded to the samples treated with $t_{700}=4$ s, which were completely crystallized and presented a critical field of 22 kOe.

The temperature dependence of the critical field of the samples is shown in Fig. 5. We have analyzed these data in terms of the law proposed by Kromüller,[5]

$$H_{crit}=\alpha_\Psi \alpha_K H_K(T)-N_{eff}M_s(T), \qquad (1)$$

where $H_K(T)$ and $M_s(T)$ are, respectively, the anisotropy

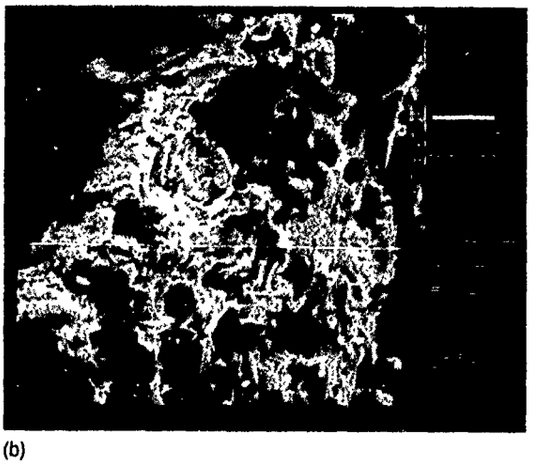

FIG. 3. (a) SEM micrograph of the fresh fracture surface of a sample treated for $t_x=4$ s with $I_x=16$ A. (b) SEM micrograph of the fresh fracture surface of a sample treated for $t_x=12$ s with $I_x=16$ A.

field and the saturation magnetization of the samples at a given temperature; α_Ψ reflects the influence on coercivity of the easy axes misalignment; α_K is related to the local reduction of anisotropy at the defects and N_{eff} gives the magnitude of the stray fields originated by the inhomogeneities in the distribution of magnetization. In samples with strong inter-

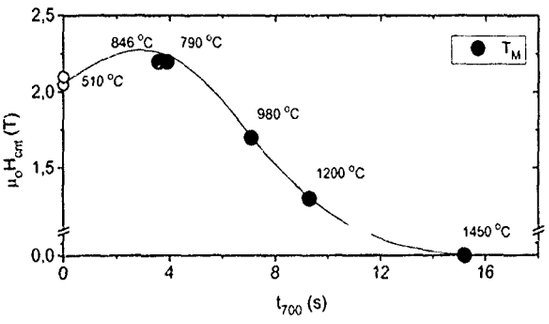

FIG. 4. Dependence of the room-temperature critical field vs t_{700} for the samples with optimum magnetic hardening.

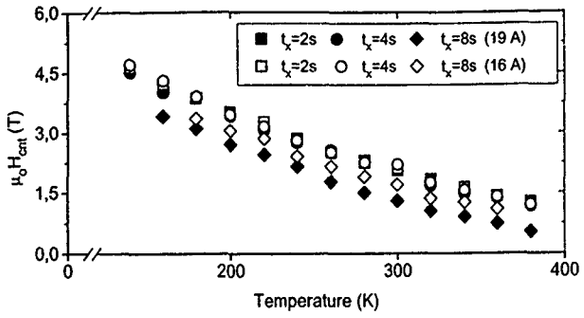

FIG. 5. Temperature dependence of the critical field of the samples.

granular coupling, tl magnetization reversal proceeds from those grains whose orientation with respect to the applied field has associated the lowest critical field. In this case α_Ψ can be replaced by its minimum value $\alpha_{\Psi_{min}}$ which depends on the anisotropy constants as reported in Ref. 5. Considering this, from the fits of the experimental results for $H_{crit}(T)$ to Eq. (1) the parameters α_K and N_{eff} can be obtained. Figure 6 presents the results of these fits for the samples crystallized by means of I_x=19 A. These plots were carried out by taking into account the temperature dependence of the anisotropy field and magnetization of the $Nd_2Fe_{14}B_1$ and $Pr_2Fe_{14}B_1$ phases reported in Refs. 5 and 6.

The dependence of our results for α_K and N_{eff} on t_{700} is shown in Figs. 7(a) and 7(b), respectively. It is interesting to see how α_K presents a maximum value [only slightly lower than the ideal value of Eq. (1) in the case of the samples with optimum properties]. Also, and according to these results, the

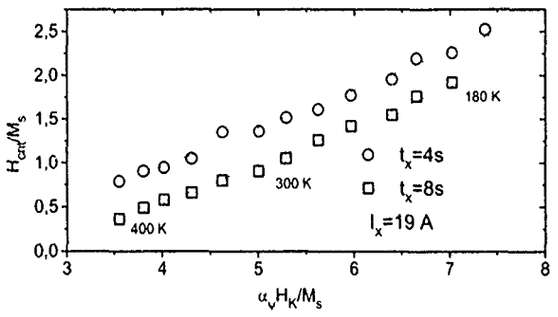

FIG. 6. Plot of the experimental $H_{crit}(T)$ data in terms of Eq. (1).

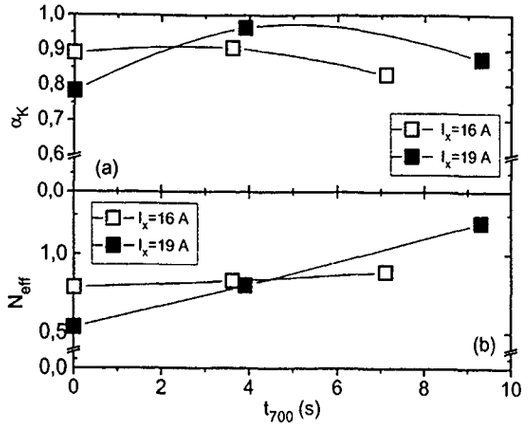

FIG. 7. (a) Variation of α_K with t_{700}. (b) Variation of N_{eff} with t_{700}.

treatments carried out by using 16 A current originated larger deteriorations of the local anisotropy than those corresponding to treatments carried out by means of 19 A pulses.

Finally, N_{eff} increases with t_{700}, which reflects the progressive evolution in shape of the hard phase grains[2] from rounded original nucleus (predominant in the partly crystallized samples) to the well developed polyhedral grains with edges and corners which can be observed[2] in fully crystallized samples. Also, the inhomogeneities of the microstructure arising from the precipitation, for long t_{700} values, of α-Fe contribute to the increase of that parameter.

To summarize, we can say that optimum critical fields (larger than those achieved in as-quenched crystalline melt spun samples) can be obtained by flash crystallizing amorphous precursors using treatment times (t_{700}) of the order of a few seconds (long enough to complete the crystallization and short enough to avoid significant α-Fe segregation).

[1]M. T. Clavaguera-Mora, M. D. Baró, S. Suriñach, J. A. Diego, J. M. González, and F. Cebollada, J. Magn. Magn. Mater. **104–107**, 1179 (1992).
[2]V. E. Martín, J. Bernardi, J. Fidler,, F Cebollada, and J. M. González, J. Alloys Compounds **191**, 127 (1993).
[3]S. Suriñach, M. D. Baró, M. T. Clavaguera-Mora, and N. Clavaguera, J Non-Cryst. Solids **58**, 1201 (1993).
[4]J. M. González, F. Cebollada, V E Martín, M. Leonato, D. Koeler, and M. Seeger, J. Magn. Magn. Mater. **101**, 397 (1991).
[5]H. Kronmuller, in *Science and Technology of Nanostructured Magnetic Materials*, edited by G. C. Hadjipanayis and G. A. Prinz (Plenum, New York, 1991)
[6]D. W Taylor, Ph.D. thesis, INP Grenoble, 1992.

Magnetic phase diagrams of YCo_4B-based components

Z. G. Zhao, R. de Boer, and K. H. J. Buschow
Van der Waals-Zeeman Laboratory, University of Amsterdam, Valckenierstraat 65, 1018 XE Amsterdam, The Netherlands

Y. P. Ge and J. Y. Wang
Shenyang College of Architectural Engineering, Shenyang 110015, China

The magnetic properties of $(Y,Nd)Co_4B$, $Y(Co,Fe)_4B$, and $YCo_4(B,C)$ compounds have been investigated. The spin-reorientation temperature of YCo_4B increases with substitution of Nd for Y and Fe for Co, but decreases with the replacement of B for C. The Curie temperature of YCo_4B decreases upon substitution of Nd for Y and C for B, whereas it increases upon the introduction of Fe. The magnetic phase diagrams are given for $(Y,Nd)Co_4B$, $Y(Co,Fe)_4B$, and $YCo_4(B,C)$. The results show that the temperature range of the easy-axis anisotropy in YCo_4B is increased by C substitution, and decreased by Nd and Fe substitution. The saturation magnetization of YCo_4B increases by the introduction of Nd and Fe. Substitution of C for B changes the magnetic moment of Co only slightly. The magnetic anisotropy is increased by substitution of C for B.

I. INTRODUCTION

YCo_4B and the corresponding pseudoternary compounds crystallize in the $CeCo_4B$-type structure, which is derived from the $CaCu_5$ structure by partial substitution of B for Co in every two Co layers.[1] The structure and the magnetic properties of both Fe- and Co-based compounds of the $CeCo_4B$ type have been studied extensively in the past few years because of their potential of being used in permanent magnets.[2–8] Previous results have shown that in YCo_4B the Co-sublattice anisotropy is complex at low temperature.[5,8] In this compound, a spin-orientation occurs at about 150 K which has been attributed to a change of the easy-magnetization direction of the Co sublattice from c axis at high temperature to basal plane at low temperature. Another anomaly is observed at about 60 K, the origin of which is still unknown. In order to understand the magnetic behavior of the Co sublattice in this type of compound, we have performed a detailed study of the magnetic phase diagrams of $(Y,Nd)Co_4B$, $Y(Co,Fe)_4B$, and $YCo_4(B,C)$.

II. EXPERIMENTAL PROCEDURE

The compounds $Y_{1-x}Nd_xCo_4B$ (x=0.0,0.1,0.2,0.3), $YCo_{4-x}Fe_xB$ (x=0.0,0.1,0.2,0.3,0.4), and $YCo_4B_{1-x}C_x$ (x=0.0,0.1,0.2,0.3), were prepared by melting in an arc furnace in an argon atmosphere, followed by annealing in an atmosphere of highly purified argon at 900 °C for 2 weeks. Subsequently, the materials were quenched into ice water. X-ray-diffraction results showed that only negligible amounts of impurity phases were present.

The temperature dependence of the a.c. susceptibility was measured on bulk samples in the temperature range from 4.2 to 600 K. The high-field magnetization was measured at 4.2 K in the high-field facility at the University of Amsterdam on magnetically aligned samples. These samples were prepared by mixing fine powder of the compound with epoxy resin and letting the mixture subsequently solidify in a field of about 1 T.

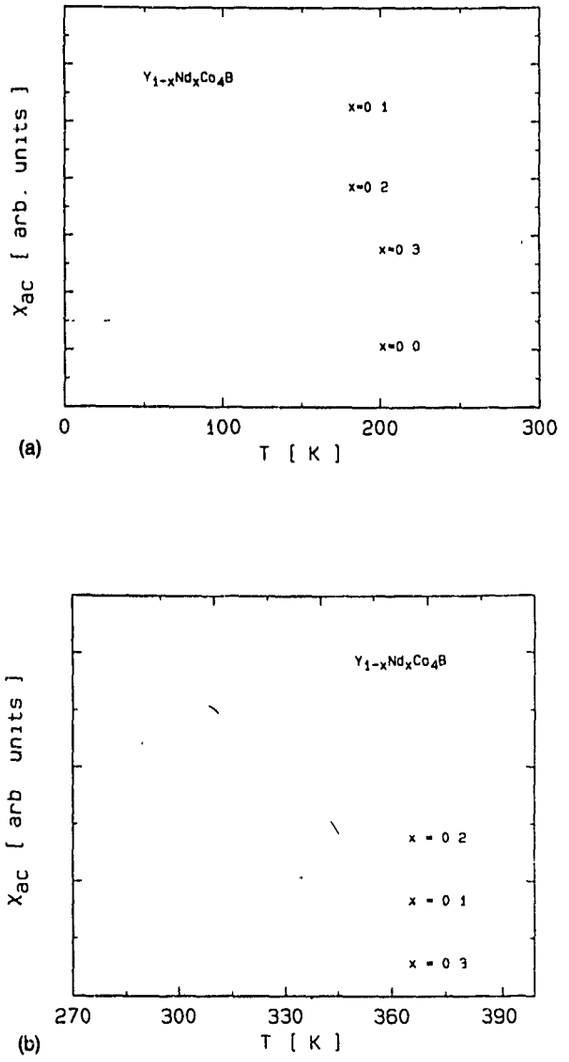

FIG. 1. Temperature dependence of the a.c. susceptibility of $Y_{1-x}Nd_xCo_4B$ compounds between (a) 4 2 and 300 K, and (b) 270 and 400 K.

 0021-8979/94/76(10)/6843/3/$6.00 © 1994 American Institute of Physics

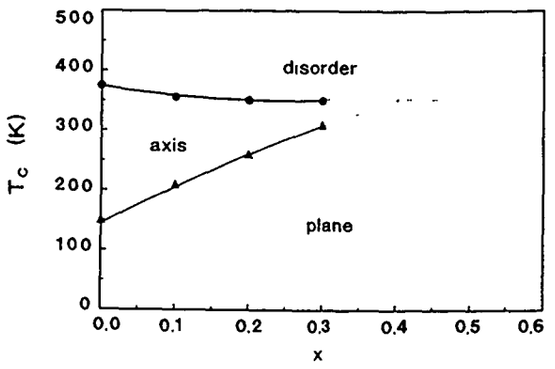

FIG. 2. Magnetic phase diagram of $Y_{1-x}Nd_xCo_4B$ compounds.

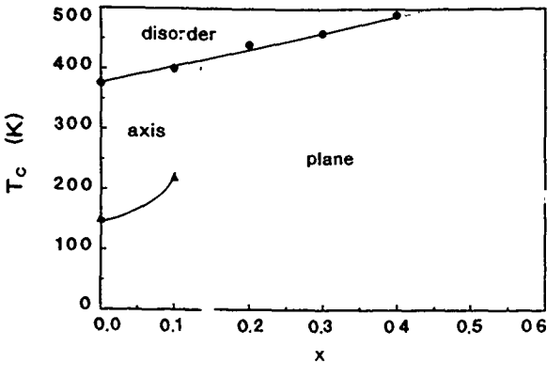

FIG. 4. Magnetic phase diagram of $YCo_{4-x}Fe_xB$ compounds

III. EXPERIMENTAL RESULTS AND DISCUSSION

A. $Y_{1-x}Nd_xCo_4B$

Substitution of Nd for Y markedly affects the anisotropy of YCo_4B. Figure 1 shows the temperature dependence of the a.c. susceptibility of the $Y_{1-x}Nd_xCo_4B$ compounds. The spin reorientation at 150 K in YCo_4B and the anomaly around 60 K are both strongly influenced by the introduction of Nd. The spin-reorientation temperature is found to increase with increasing Nd content. In the sample with $x=0.3$, the transition even occurs above room temperature, at 310 K. The anomaly at 60 K shifts to lower temperatures in a rather random way. The high-temperature parts of the a.c. susceptibility show that the Curie temperature of YCo_4B slightly decreases from 375 K for YCo_4B to 350 K for $Nd_{0.3}Y_{0.7}Co_4B$.[5] Since $NdCo_4B$ has easy-plane magnetization at room temperature,[6] the magnetization in the Nd-containing compounds can also be expected to change from easy axis at high temperature to easy plane at low temperature. Therefore we tentatively conclude from the composition dependence of the spin-reorientation temperature in the $Y_{1-x}Nd_xCo_4B$ system that the transition at 150 K in YCo_4B is also an axis-to-plane transition. The magnetic phase diagram of the (Y,Nd)Co_4B system constructed on the basis of these experimental results is shown in Fig. 2. The easy-axis region is only found in the Y-rich part and its width decreases strongly with increasing Nd content.

B. $YCo_{4-x}Fe_xB$

Substitution of Fe for Co in YCo_4B strongly influences the magnetic anisotropy of the 3d sublattice. Figure 3 shows the temperature dependence of the a.c. susceptibility of $YCo_{4-x}Fe_xB$ compounds between 4.2 and 300 K. The spin-reorientation temperature increases with increasing Fe content and for $x=0.2$, no spin reorientation is observed up to the Curie temperature. As YFe_4B also has easy-plane magnetization at room temperature,[7] this composition dependence of the transition temperature can be taken as evidence that the transition is from easy axis at high temperature to easy plane at low temperature. Substitution of Fe for Co strongly enhances the easy-plane anisotropy. With increasing Fe content, the Curie temperature increases strongly from 375 K for YCo_4B to 490 K for $YCo_{3.6}Fe_{0.4}B$.[7] This means that the $3d$–$3d$ exchange interaction is strongly increased

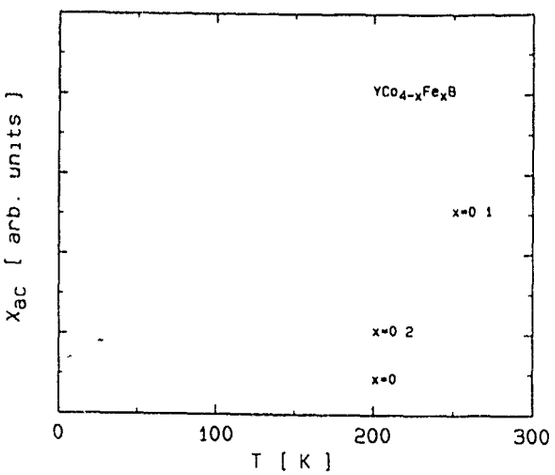

FIG. 3. Temperature dependence of ac susceptibility of $YCo_{4-x}Fe_xB$ compounds between 4.2 and 300 K.

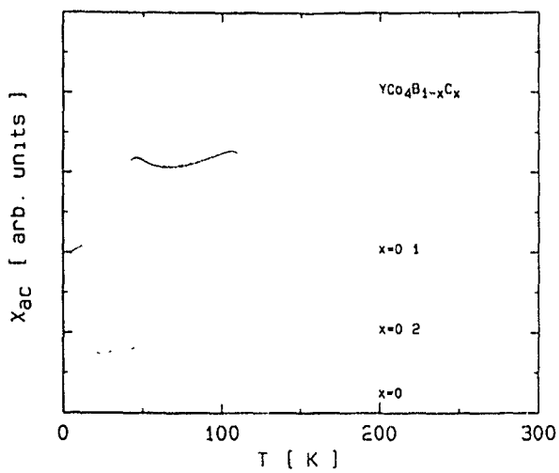

FIG. 5 Temperature dependence of the a c. susceptibility of $YCo_4B_{1-x}C_x$ compounds between 4.2 and 300 K.

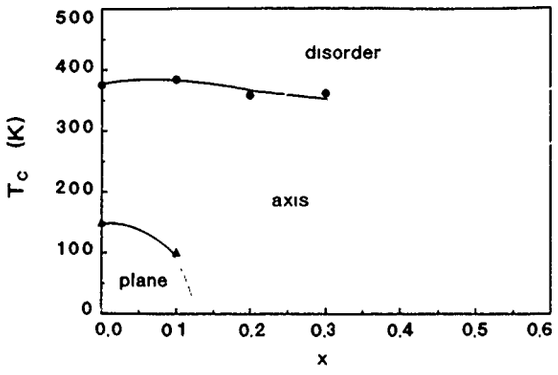

FIG. 6. Magnetic phase diagram of $YCo_4B_{1-x}C_x$ compounds.

upon the introduction of Fe. The magnetic phase diagram in Fig. 4 shows that the easy-axis region is small and restricted to the Co-rich part.

C. $YCo_4B_{1-x}C_x$

The magnetic properties of the Co sublattice for YCo_4B are also affected by substitution of C for B. Figure 5 shows the temperature dependence of the a.c. susceptibility of $YCo_4B_{1-x}C_x$ compounds with $x=0.0$, 0.1, and 0.2. Both transitions in the compound with $x=0.0$ at 60 and 150 K move to lower temperatures for $x=0.1$ and then disappear for $x=0.2$. In contrast to the types of substitution discussed before, substitution of C and B enlarges the temperature range of easy-axis magnetization, which is favorable for applications. Substitution of C for B in YCo_4B causes the Curie temperature to first slightly increase for $x=0.1$ and then to decrease for $x>0.1$. The phase diagram of the $YCo_4(B,C)$ system is shown in Fig. 6.

The magnetization curves are shown in Fig. 7. From the planar diagram shown in Fig. 6 one would have expected that the magnetic moment of the compound with $x=0.1$ when measured in low fields applied parallel to the alignment direction would have been lower than the moment measured perpendicular to the alignment field (as for $x=0$). It is possible that this latter situation is realized in applied fields lower than those considered here with an intersection point between the isotherm below 1.3 T. It can be seen from Fig. 7 that the saturation magnetization of the compound changes only slightly with x. This is similar to what has been observed in the $Nd_2Co_{14}(B,C)$ system.

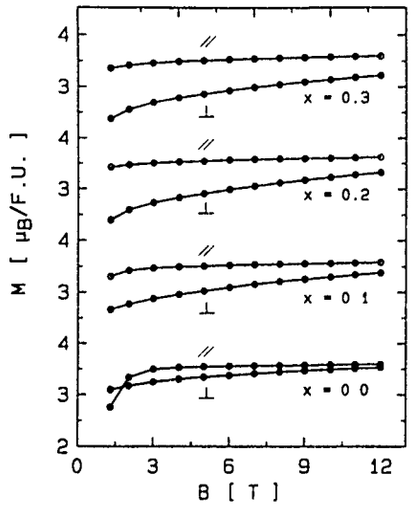

FIG. 7. Magnetization of $YCo_4B_{1-x}C_x$ compounds at 4.2 K for the field parallel (○) and perpendicular (●) to the alignment direction.

[1] Yu. B. Kuzma and N. S. Bilonizhko, Kristallographia **18**, 710 (1973).
[2] T. T. Dung, N. P. Thuy, N. M. Hong, and T. D. Hien, Phys. Status Solidi A **106**, 201 (1988).
[3] H. Ido, W. E. Wallace, T. Suzuki, S. F. Cheny, V. K. Sinha, and S. G. Sankar, J. Appl. Phys. **67**, 4635 (1990).
[4] H. Ido, K. Konno, S. F. Cheng, W. E. Wallace, and S. G. Sankar, J. Appl. Phys. **67**, 4638 (1990).
[5] Z. G. Zhao, Y.-P. Ge, J.-Y. Wang, X. K. Sun, and Y. C. Chuang, J. Magn. Magn. Mater. **98**, L231 (1991).
[6] J.-Y. Wang, Z.-G. Zhao, Y.-P. Ge, X. K. Sun, and Y. C. Chuang, Phys. Status Solidi A **127**, K61 (1991).
[7] Y.-P. Ge, Z.-B. Zhao, J.-Y. Wang, X. K. Sun, and Y. C. Chuang, Phys. Status Solidi A **126**, K177 (1991).
[8] Z. G. Zhao, S. J. Collocott, J. B. Dunlop, F. R. de Boer, X. K. Sun, and Y. C. Chuang, J. Appl. Phys. **73**, 5920 (1993).

Published without author corrections

A systematic study on stability of flux in Nd-Fe-B magnets consolidated by direct joule heating

H. Fukunaga and H. Tomita
Faculty of Engineering, Nagasaki University, Nagasaki 852, Japan

M. Wada, F. Yamashita, and T. Toshimura
Matsushita Electric Industry, Co., Ltd., Daito, Osaka 574, Japan

Magnetic aftereffect and irreversible flux loss at elevated temperatures were studied for fully dense isotropic and anisotropic Nd-Fe-Co−B magnets consolidated from rapidly quenched powder by direct joule heating. The consolidation process and the subsequent alignment of c axis do not affect the aftereffect constant S_v and the prepared magnets have roughly the same S_v as a bonded magnet, independent of coercivity at room temperature (650–1200 kA/m), exposure temperature (60–120 °C), and anisotropy of the magnets. Thus the magnitude of the aftereffect is determined mainly by the magnitude of the irreversible susceptibility χ_{irr}. It was also clarified empirically that the irreversible flux loss FL is proportional in magnitude to χ_{irr}. However, the slopes of the FL vs χ_{irr} line for isotropic magnets are much larger than those for the anisotropic ones. Thus FL can be reduced by decreasing χ_{irr} and/or making magnets anisotropic.

I. INTRODUCTION

Although Nd-Fe-B based magnets have superior hard magnetic properties, the thermal stability of their magnetic properties is poor compared with that of Sm-Co magnets because of their low Curie temperature.[1] Improvements in the thermal stability have been studied by many authors,[2] and it has been clarified that rapidly quenched powder has smaller temperature dependences of coercivity and remanence.[3] Therefore utilization of rapidly quenched powder would be one of the methods of improving their stability. Recently, two of the authors have developed a new method of preparing fully dense Nd-Fe-B magnets from rapidly quenched powder by direct joule heating.[4] The developed magnets, which consist of fine grains, exhibit smaller temperature variation of coercivity than conventional sintered magnets.[4,5]

Thus, in this study, the magnetic aftereffect and the flux loss due to exposure at elevated temperatures were investigated for Nd-Fe-Co-B magnets (H_c=650–1200 kA/m) prepared by the above-mentioned method.

II. EXPERIMENT

Fully dense anisotropic and isotropic magnets with a variety of coercivities were consolidated from $Nd_{14}Fe_{73}Co_7B_6$ rapidly quenched powder. Details of the preparation method have been reported in the previous papers.[4,6] Cylindrical specimens, 5 mm diam×6.6 mm long and 5 mm diam×4.1 mm long, were cut out of them. In this paper, anisotropic and isotropic specimens are designated as "ANISO" and "ISO," respectively, and long and short specimens as "L" and "S," respectively. Thus "ANISO-L" means a long anisotropic specimen.

The specimens were first premagnetized in a pulse magnetic field of 4 MA/m and were exposed at an elevated temperature T_a (60–120 °C). Then the decrease in magnetization ΔI due to magnetic aftereffect was measured with a flux meter as a function of the exposure time t_a [Fig. 1(a)]. The irreversible flux loss FL due to the exposure was determined by

$$FL=(\Phi_0-\Phi_1)/\Phi_0, \tag{1}$$

where Φ_0 and Φ_1 are the flux values measured at room temperature before and after the exposure, respectively [Fig. 1(b)]. Hysteresis loops were traced with a computer-aided hysteresis tracer and the demagnetizing effect was corrected by using a Ni cylinder. The coercivity H_c(RT) and the remanence M_r(RT) at room temperature are listed for the obtained magnets in Table I. The irreversible susceptibility χ_{irr} at a working point was calculated by subtracting the reversible susceptibility from the total susceptibility χ_{total}.

III. RESULTS AND DISCUSSION

Typical ΔI observed in our specimens is shown in Fig. 2 for an anisotropic magnet with H_c(RT)=990 kA/m. The magnetization decreases nearly linearly with the logarithm of t_a between 0.2 and 10 h and a unique slope $d(\Delta I)/d(\ln t_a)$ can be defined for each T_a. Figure 3 shows typical variation of $d(\Delta I)/d(\ln t_a)$ as a function of H_c(RT) for ISO-S and ANISO-S specimens. The slope of the anisotropic specimens at each T_a is smaller at H_c(RT)=1200 kA/m than that of the

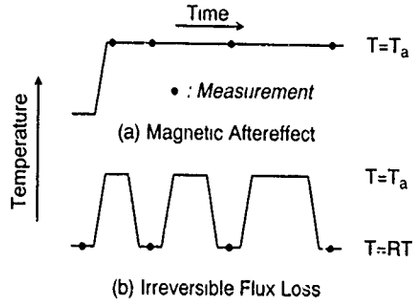

FIG. 1. Schematic representation of measuring procedures of magnetic aftereffect and irreversible flux loss.

 0021-8979/94/76(10)/6846/3/$6.00 © 1994 American Institute of Physics

TABLE I. Remanence and coercivity at room temperature of investigated magnets.

Specimens	Remanence (T)	Coercivity (kA/m)
ISO No. 1	0.76	680
ISO No. 2	0.82	950
ISO No. 3	0.84	1200
ANISO No. 1	1.24	650
ANISO No. 2	1.22	990
ANISO No. 3	1.20	1200

isotropic ones. However, it increases markedly with a decrease in H_c(RT) and then becomes larger at H_c(RT)=1000 kA/m than that of isotropic ones when T_a=100 and 120 °C. This behavior can be attributed to the fact that the working point of the anisotropic specimen with low H_c(RT) moves abruptly to a steep part of demagnetization curve from its flat part with increasing T_a.

It has been proposed that ΔI can be expressed[7,8] for specimens with a demagnetizing factor N as

$$\Delta I = S_v \chi_{irr} (\ln t_a - A)/(1+\chi_{total} N/\mu_0), \quad (2)$$

where S_v and A are the aftereffect constant and the constant related to the initial value of the magnetization, respectively. In general, S_v and χ_{irr} depend on material, T_a, and the magnetization state of a specimen. In order to clarify which of S_v and χ_{irr} is the dominant factor in affecting the magnitude of ΔI, $(1+\chi_{total}N/\mu_0)d(\Delta I)/d(\ln t_a)$ is plotted in Fig. 4 as a function of χ_{irr}. Figure 4 includes results obtained for isotropic as well as anisotropic specimens with various H_c(RT) (650–1200 kA/m), T_a (60–120 °C), and lengths (4.1 and 6.6 mm). As clearly seen in the figure, $(1+\chi_{total}N/\mu_0)d(\Delta I)/d(\ln t_a)$ has strong correlation with χ_{irr} and all the plotted points are near the one straight line indicated by the solid line. Since the slope of the line corresponds to the value of S_v as indicated in Eq. (2), this result suggests that S_v of our specimens is nearly constant, independent of H_c, T_a, the alignment of c axis, and the length of the specimens. Thus the magnitude of magnetic aftereffect is determined mainly by χ_{irr}.

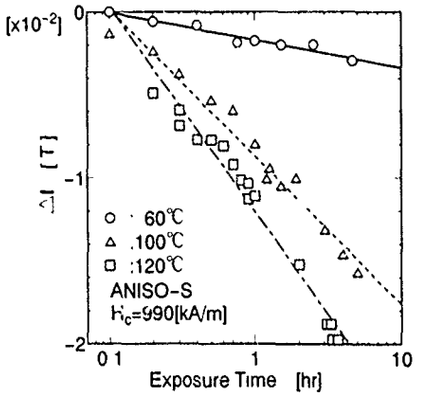

FIG. 2. Typical variation of magnetization ΔI due to magnetic aftereffect as a function of exposure t_a

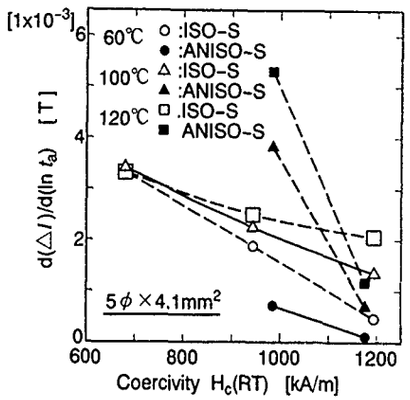

FIG. 3. Typical variation of $d(\Delta I)/d(\ln t_a)$ as a function of coercivity at room temperature H_c(RT).

Previously Nishio and Yamamoto[9] have reported that S_v of a $Nd_{12.2}Fe_{77}Co_{5.4}B_{5.4}$ compression bonded magnet, which has nearly the same composition as ours, is between 2.6 and 3.1 kA/m in the temperature range of 20–125 °C. The lines corresponding to these values of S_v are also shown in the figure by broken lines. Our measured data roughly agree with the broken lines, which suggests that the consolidation of rapidly quenched powder and the subsequent alignment of c axis do not affect S_v remarkably and that the prepared fully dense magnets preserve the value of S_v of rapidly quenched powder.

The irreversible flux loss FL due to 1 h exposure at T_a is shown in Fig. 5 as a function of χ_{irr}. From an empirical point of view, FL is proportional in magnitude to χ_{irr} at each T_a. Thus a decrease in χ_{irr} reduces FL. Irreversible flux loss can be attributed to magnetization reversals based on magnetic aftereffect and a reduction in H_c at an elevated temperature. As the magnetization reversal due to magnetic aftereffect has strong correlation with χ_{irr}, the reversal due to a reduction in H_c is also expected to correlate with χ_{irr}.

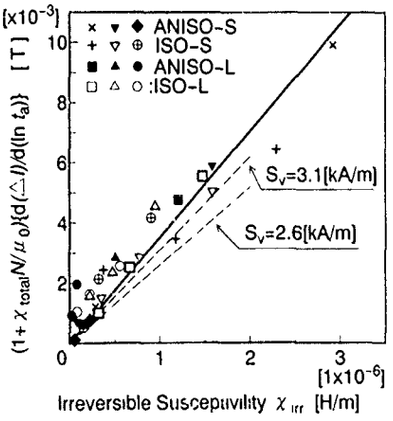

FIG 4. $(1+\chi_{total}N/\mu_0)d(\Delta I)/d(\ln t_a)$ for isotropic as well as anisotropic specimens with various H_c(RT), T_a, and lengths, as a function of χ_{irr}. Solid line. best-fit line for measured data, broken lines. lines corresponding to S_v=2.6 and 3.1 kA/m. The slopes of lines correspond to the values of S_v

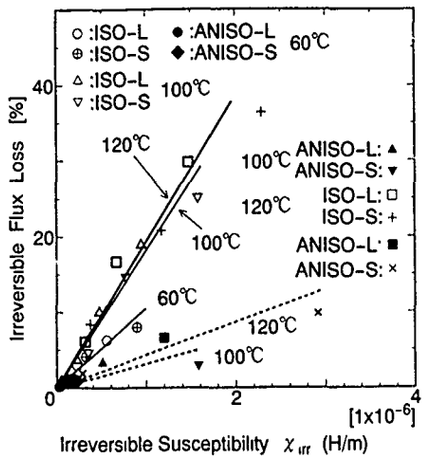

FIG. 5. Irreversible flux loss FL due to exposure for 1 h at elevated temperatures as a function of χ_{irr}. Solid lines: isotropic specimens, broken lines: anisotropic specimens.

It is also seen that FL can be reduced by making the magnets anisotropic. Large M_r(RT) of the anisotropic magnets is partly responsible for this improvement because FL is expressed after the zation by the initial value of flux as indicated by Eq.

IV. CONCLUSIONS

Stability of flux at elevated temperatures was studied for fully dense isotropic and anisotropic Nd-Fe-Co-B magnets consolidated from rapidly quenched powder by direct joule heating. Although the magnitude of aftereffect varied with coercivity, exposure temperature, anisotropy, and the shape of specimens, the unique aftereffect constant S_v was observed independently of these parameters. In addition, the observed S_v agreed roughly with that reported previously for a bonded magnet. These results suggest that the consolidation process and the subsequent alignment of c axis do not affect S_v and that the magnitude of the aftereffect is determined mainly by the irreversible susceptibility χ_{irr}.

The irreversible flux loss FL due to exposure at an elevated temperature was also proportional in magnitude to χ_{irr} which depends on the coercivity and the shape of specimens. However, FL of the anisotropic specimens was much smaller than that of isotropic ones. Therefore FL is expected to be reduced by decreasing χ_{irr} and/or making magnets anisotropic.

[1] D. Li, H. F. Mildrum, and K. J. Strnat, J. Appl. Phys. **57**, 4140 (1984)
[2] For example, M. Tokunaga, N. Meguro, M. Endoh, S. Tanigawa, and H. Harada, IEEE Trans. Magn. **MAG-21**, 1964 (1985).
[3] J. J. Croat, J. F. Herbst, R W. Lee, and F. E. Pinkerton, J. Appl Phys. **55**, 2074 (1984).
[4] M. Wada and F. Yamashita, IEEE Trans. Magn. **26**, 2601 (1990)
[5] H Fukunaga, T. Yoshimura, M. Wada, and F Yamashita, Digests of 14th Annual Conference of the Magnetic Society of Japan, 11pE-12, 1990 (unpublished).
[6] F. Yamashita and M. Wada, Digests of 14th Annual Conference of the Magnetic Society of Japan, 11pE-11, 1990 (unpublished).
[7] L. Néel, J. Phys. Rad. **11**, 49 (1950).
[8] O. Yamada, Electrotechn. J. Jpn. **4**, 119 (1958).
[9] H. Nishio and H. Yamamoto, J. Magn. Soc. Jpn. **16**, 131 (1992)

Studies of Mössbauer spectrum on $Sm_2(Fe,Ga)_{17}C_{1.5}$ alloy

Hong Chen, Zu-xiong Xu, and Ru-zhang Ma
Department of Materials Physics, University of Science and Technology, Beijing, Beijing 100083, People's Republic of China

Shu-ming Pan
General Research Institute for Nonferrous Metals, CNNC, Beijing 100088, People's Republic of China

Bao-gen Shen
Institute of Physics, Academia Sinica, Beijing 100080, People's Republic of China

De-yan Xue and Qiang Ni
Shatoujiao New Materials Factory, Shenzhen 518081, People's Republic of China

X-ray-diffraction patterns and Mössbauer spectra of $Sm_2(Fe,Ga)_{17}C_{1.5}$ alloys have been studied. The results of x-ray-diffraction patterns and Mössbauer spectra indicate that little α-Fe and carbonides appear in $Sm_2(Fe,Ga)_{17}C_{1.5}$ alloys. The addition of a few Ga atoms show that the thermal stability in $Sm_2(Fe,Ga)_{17}C_{1.5}$ alloys is getting better. Structural analyses indicate C atoms as interstitial atoms occupying the $9d$ site. Ga atoms seem to substitute partially for Fe atoms and occupy preferentially the $18h$ site.

I. INTRODUCTION

The binary R_2Fe_{17} compounds are not suitable for permanent magnetic materials because of their low Curie temperature and plane-preferred magnetocrystalline anisotropy. It has been recently shown that the presence of the interstitial C atoms in R_2Fe_{17} compounds gives rise to an increase of the Curie temperature by more than 100 K compared with their counterparts without carbon.[1,2] In particular, in the case of $Sm_2Fe_{17}C_x$, a relatively high uniaxial crystal anisotropy and an anisotropy field of about 6 T were found at room temperature for $x=1$.[3] But the carbon concentration was well below $x=2$ in $R_2Fe_{17}C_x$ compounds achieved by arc melting.[4,5] Liao *et al.*[6] reported that high carbon-containing $R_2Fe_{17}C_x$ ($x=2.5$) compounds were obtained by solid–gas phase reaction. Unfortunately, these carbides will decompose into the equilibrium phases RC and α-Fe on heating to 700 °C.[7] Recently, Shen and co-workers[8] have obtained $R_2Fe_{17}C_x$ ($x=0$–3.0) compounds by means of the melt-spinning method. These carbides are highly stable at least at high temperature up to 1100 °C. Shen's results shows that a few Ga, Si, and Al atoms substitutions for Fe can enhance the thermal stability in $Sm_2Fe_{17}C_x$ alloys. In order to better understand the influence of carbon and substitution atoms on the structure in $Sm_2Fe_{17}C_x$ alloys, we performed Mössbauer spectra study of melt-spun $Sm_2(Fe,Ga)_2C_{1.5}$ alloys.

II. EXPERIMENTAL DETAILS

The alloy $Sm_2Fe_{17-x}Ga_xC_{1.5}$ ($x=1$–6) was prepared by melting of 99.9%-pure primary elements in argon atmosphere. The buttons were melted at least three times to achieve homogeneity. Then the alloy buttons were annealed at 1000–1200 °C in vacuum for 50 h. $Sm_2(FeGa)_{17}C_{1.5}$ alloy buttons were melted and then made into ribbons by the melt-spinning technique. The obtained ribbons were about 1 mm wide and 20–30 μm thick. X-ray-diffraction experiments with Cu K_α radiation were made to determine the crystallographic structure. The ^{57}Fe Mössbauer spectra for $Sm_2Fe_{15}Ga_2C_{1.5}$ compounds (a natural abundance Fe used) at room temperature were collected using a constant acceleration spectrometer with a source of ^{57}Co (in Pd). The velocity scale was calibrated using an α-Fe absorber at room temperature.

III. RESULTS AND DISCUSSIONS

X-ray-diffraction patterns indicated that the main phases of all the samples is the 2:17 structure. $Sm_2(FeGa)_{17}C_{1.5}$ compounds crystallize in the rhombohedral Th_2Zh_{17}-type structure ($R3m$). The substitution of Fe with Ga results in a increase in the lattice constants. The results of x-ray diffraction show the unit-cell volume of $Sm_2(FeGa)_{17}C_{1.5}$ linearly increases with increasing Ga concentration.

For some samples in $Sm_2Fe_{17}C_x$ compounds with high carbon concentration, the α-Fe also has to be taken into account. But here, the x-ray pattern (Fig. 1) shows a slight trace of α-Fe in the $Sm_2(FeGa)_{17}C_{1.5}$ compound. That is to say, the addition of the few Ga atoms in $Sm_2(FeGa)_{17}C_{1.5}$ compounds will help to enhance a single phase in the carbides of $Sm_2(FeGa)_{17}C_{1.5}$.

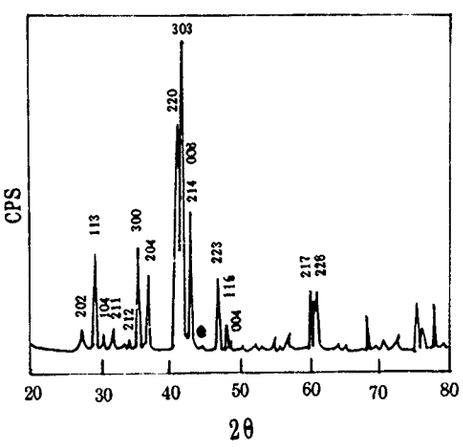

FIG. 1. X-ray-diffraction pattern of $Sm_2Fe_{15}Ga_2C_{1.5}$ compound (● α-Fe)

 0021-8979/94/76(10)/6849/2/$6.00 © 1994 American Institute of Physics

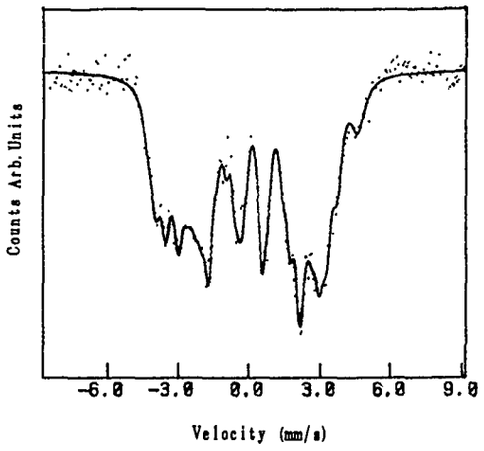

FIG. 2. Mossbauer spectrum of $Sm_2Fe_{15}Ga_2C_{1.5}$ compound.

The addition of the Ga atoms leads to an increase of axis anisotropies. At the optimal quenching rate, the intrinsic coercivity obtained is iH_c=14 kOe.

There are four nonequivalent types of Fe sites in the Th_2Zn_{17} unit cell ($6c$, $9d$, $18h$, and $18f$), and the C atoms could be statistically distributed over the $9d$ site in this structure.[9,10]

For the C-containing compounds, because of their uniaxial anisotropy, the Mössbauer subspectra for $18h$ and $18f$ sites have to be split into two subspectra with the intensity ratio of 1:2,[11] so that six subspectra were used in order to fit the Mössbauer spectrum of the $Sm_2Fe_{15}Ga_2C_{1.5}$ compound (Fig. 2).

During the fitting of the Mössbauer spectrum, six Ga atoms are regarded as entering into $18h$ and $18f$ sites with equivalent ratio, so an overall intensity constant of 6:9:(10:5):(10:5) for $6c$:$9d$:$18f$:$18h$ was imposed. We used the fitting procedure written by one author (Zu-xiong Xu) of this paper, which can impose the restricted condition of the above-mentioned intensity ratios to the fitting. The hyperfine fields for each crystallographic site of the $Sm_2Fe_{15}Ga_2C_{1.5}$ compound are listed in Table I.

TABLE I. Hyperfine fields for each crystallographic site of the $Sm_2Fe_{15}Ga_2C_{1.5}$ compound

$6c$ (T)	$9d$ (T)	$18f_1$ (T)	$18f_2$ (T)	$18h_1$ (T)	$18h_2$ (T)
27.6	23.5	20.9	16.8	18.8	14.0

There is no doubt that the $6c$ dumbell site should have the largest hyperfine field since it has the most Fe atoms, and the fewest rare-earth neighbors. Similarly, the $18f$ site has a larger hyperfine field than the $18h$ site. The $9d$ site can be distinguished by its intensity from the $18f$ and $18h$ sites. Hence we find hyperfine fields for the different Fe sites that decrease in the order $6c>9d>18f>18h$.

ACKNOWLEDGMENT

This project was supported by the State Key Laboratory of Magnetism Institute of Physics, Academia Sinica.

[1] R. B. Helmholdt and K. H. Buschow, J. Less-Common Met. **155**, 15 (1989).
[2] D. B. de Mooij and K. H. J. Buschow, J. Less-Common Met. **142**, 349 (1988).
[3] K. H. J. Buschow, T. H. Jacobs, and W. Coene, Proceedings of INTERMAG'90, April 17–20, 1990 (unpublished).
[4] X. P. Zhong, R. J. Radwanshi, F. R. de Boer, T. H. Jacobs, and K. J. Buschow, J. Magn. Magn. Mater. **86**, 333 (1990).
[5] T. H. Jacobs, M. W. Dirken, R. C. Thiel, L. J. de Jongh, and K. H J. Buschow, J. Magn. Magn. Mater. **83**, 293 (1990).
[6] L. X. Liao, X. Chen, Z. Altounian, and H. Ryan, Appl. Phys. Lett. **60**, 129 (1992).
[7] C. Kuhrt, M. Katter, J. Wecker, K. Schnitgke, and L. Schultz, Appl. Phys. Lett. **60**, 2029 (1992).
[8] L. S. Kong, L. Cao, and B.–G. Shen, J. Magn. Magn. Mater. **115**, L137 (1992).
[9] R. J. Zhou, Th. Sinnemann, M. Rosenberg, and K. H. J. Buschow, J. Less-Common Met. **171**, 263 (1991).
[10] J. Ding and M. Rosenberg, J. Less-Common Met. **168**, 335 (1991)
[11] B. P. Hu, H. S. Li, H. Sun, and J. M. D. Coey, J. Phys. Condens. Matter **3**, 3983 (1991).

Low-temperature behavior of thermopower in rare-earth iron borides $R_2Fe_{14}B$ (R=Nd, Sm, Gd, Tb, Dy, Ho, Er)

R. P. Pinto, M. E. Braga, M. M. Amado, and J. B. Sousa
Centro de Física da Universidade do Porto and IFIMUP–IMAT, Praça Gomes Teixeira, 4000 Porto, Portugal

K. H. J. Buschow
Philips Research Laboratories, 5600 JA Eindhoven, The Netherlands

Recently it was shown that the electrical resistivity behaves anomalously both at low temperatures and near the Curie point in rare-earth iron borides due to the subtle interplay between $4f$ and $3d$ transition elements. Here a systematic experimental study on the behavior of the thermoelectric power (S) of $R_2Fe_{14}B$ compounds with heavy (R=Gd, Tb, Dy, Ho, Er) and light (Nd, Sm) rare-earth elements is presented. Data for $La_2Fe_{14}B$, in the temperature range 10 K$<T<$350 K, is also included for comparison. The results are consistent with the spin-mixing model for electron scattering, with an intrinsic thermopower contribution related to Fe and a spin dependent impurity scattering term related to the rare-earth magnetic ions. From the interplay of both terms we can get maxima in S (for R=Td, Dy, Ho, Er samples) or minima (Gd, Nd, Sm) at low temperatures. The data indicates the ultimate dominance of impurity scattering at low temperatures, producing a linear variation in the magnetic thermopower (S). In $La_2Fe_{14}B$, only the intrinsic effect is observed, and $S(T)$ does not follow a linear temperature dependence.

I. INTRODUCTION

Studies on R-Fe-B compounds generally deal with their magnetic properties for applications at room temperature and above. These compounds, however, exhibit interesting effects in other physical properties, namely in transport phenomena, due to the subtle interplay between $4f$ and $3d$ transition elements. Recently, we have shown that the electrical resistivity behaves anomalously both at low temperatures and near the Curie point.[1,2] The results on the behavior of the thermoelectric power of $R_2Fe_{14}B$ compounds is here reported, for the case of heavy (R=Gd, Tb, Dy, Ho, Er) and light (Nd, Sm) rare earths, over the temperature range 10 K$<T<$350 K. For comparison we also include the data for $La_2Fe_{14}B$.

II. RESULTS AND DISCUSSION

As shown in Figs. 1 and 2, the thermoelectric power (S) is negative at high temperatures, exhibiting a flat curve from about 250 up to 350 K, with relatively large values, e.g., $S\cong -15\ \mu V\,K^{-1}$ for R=Gd and $S\cong -17\ \mu V\,K^{-1}$ for R=Sm.

Below ~200 K the thermopower rises rapidly with the decrease of temperature, exhibiting characteristic maxima at intermediate temperatures. For example, in $Er_2Fe_{14}B$ we observe $S_{max}=10.5\ \mu V\,K^{-1}$ at $T=37.5$ K.

In the heavy rare-earth samples with R=Tb, Dy, Ho, Er (Fig. 2), and also in $LaFe_{14}B$, the thermoelectric power decreases monotonically from such maxima, towards vanishing values at the lowest temperatures. In contrast, in the samples with R=Gd, Sm, Nd, a more complex behavior occurs, leading to the appearance of a negative minimum at lower temperatures. For example, in $Gd_2Er_{14}B$ we have $S_{min}=-2\ \mu V\,K^{-1}$ at $T=27$ K.

We have also measured the electric resistivity in the same samples, which enabled us to obtain the normalized quantity $S(T)/\rho(T)$ for each sample. As can be seen from the phenomenological transport equations, such quantity depends only on the cross-transport coefficient L_{10}, which is responsible for the appearance of any finite thermoelectric power:[3]

$$\frac{S(T)}{\rho(T)} \simeq \frac{L_{10}(T)}{T}.$$

As shown in Fig. 3, all the S/ρ high-temperature data closely approaches a common curve, indicating a similar behavior for all the samples in this temperature range. This quantity affords a more direct comparison with simpler theoretical expressions, obtained after the discarding of several scattering mechanisms which do not contribute to L_{10} although they give important effects in ρ.

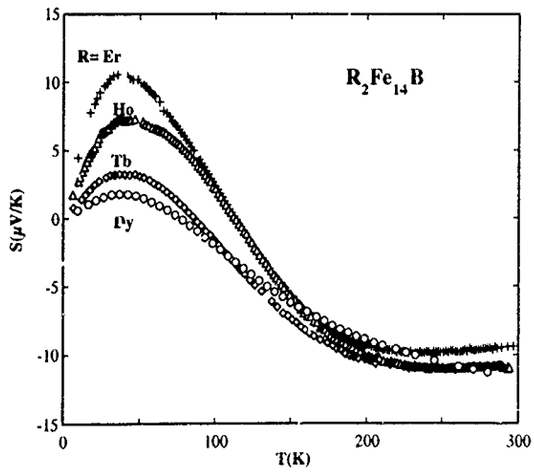

FIG. 1. Temperature dependence of the thermoelectric power for $R_2Fe_{14}B$ (R=Tb, Dy, Ho, Er) and $La_2Fe_{14}B$.

 0021-8979/94/76(10)/6851/2/$6.00 © 1994 American Institute of Physics

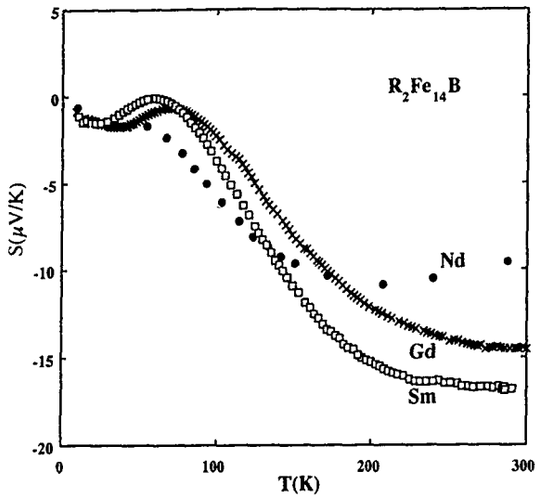

FIG. 2. Temperature dependence of the thermoelectric power for $R_2Fe_{14}B$ (R=Nd, Sm, Gd).

The low-temperature data shows a rapid rise of S with the increase of temperature, quickly reaching a maximum with relatively high values; for example, we have $S \cong 11$ $\mu V\,K^{-1}$ in $Er_2Fe_{14}B$ when $T \sim 35$ K. These effects are not due to the normal scattering mechanisms which invariably lead to small values, $S \sim (k/e)\,(kT/E_F)$ or $S \sim (k/e)\,(\Delta/E_F)$, since both the thermal (kT) and exchange (Δ) energies are much smaller than the Fermi energy.

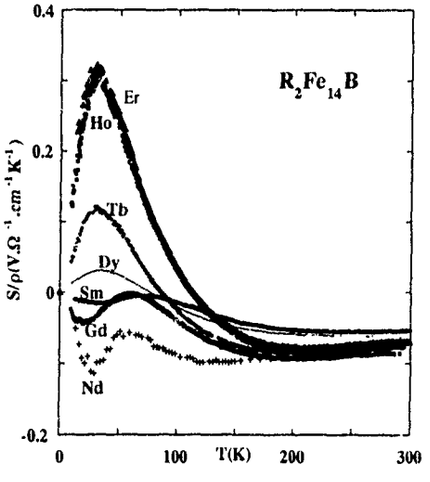

FIG. 3. Temperature dependence of S/ρ for $R_2Fe_{14}B$ (R=Nd, Sm, Gd, Tb, Dy, Ho, Er).

Large values of S at low temperatures, with sizable maxima or minima before fading away at high temperatures, occur frequently in ordered magnets caused by magnon scattering (spin-flip relaxation time $\tau_{\uparrow\downarrow}$) in the particular cases where impurity scattering leads to *different* electron collision times for spin-up or -down directions ($\tau_\uparrow \neq \tau_\downarrow$).[4–6]

If the concentration of impurities is sufficiently large so that relaxation of the electrons with respect to momentum (causing electrical resistivity) occurs on the impurities, while only energy relaxation occurs on the magnons, it can be shown that:[5,6]

$$S \propto (\tau_\uparrow - \tau_\downarrow) T,$$

$$S \propto (\tau_\uparrow - \tau_\downarrow) \frac{1}{T},$$

where the first regime ($S \propto T$) holds at low temperatures where $\tau_\uparrow$, $\tau_\downarrow \ll \tau_{\uparrow\downarrow}$ (when a cutoff exists for electron-magnon scattering, an exponential decrease of S takes over at still lower temperatures). The second regime ($S \propto T^{-1}$) occurs when the magnon scattering dominates over impurity scattering, $\tau_{\uparrow\downarrow} \ll \tau_\uparrow$, $\tau_\downarrow$. The absolute value of S should then go through a maximum at intermediate temperatures, when $\tau_{\uparrow\downarrow} \sim \sqrt{\tau_\uparrow \tau_\downarrow}$.

The $\tau_\uparrow \neq \tau_\downarrow$ asymmetry, which is absolutely necessary to produce large effects in S,[5–9] usually arises from the presence of impurities causing *spin-dependent s-s* electron scattering, such as magnetic impurities or transition-metal impurities.[10–12] In addition, the intrinsically spin transitions at temperatures below the Curie point, caused by magnons as well as by phonons, can play a role similar to the magnetic impurities.[6]

[1] J. B. Sousa, M. M. Amado, R. P. Pinto, V S. Amaral, and M E. Braga, J. Phys. Condens. Matter **2**, 7543 (1990).
[2] J. B. Sousa, M. M. Amado, R. P. Pinto, M. A. Salgueiro, M E. Braga, and K. H. J. Buschow, J. Phys. Condens. Matter **3**, 4119 (1991).
[3] See, e.g., J M Ziman, *Electrons and Phonons* (Oxford University Press, New York, 1960), Chap. VII.
[4] T. Farrel and D. Greig J Phys. C **3**, 138 (1970).
[5] J. Ya Korenblit and Yu. P. Lazarenko, JETP Lett. **11**, 236 (1979).
[6] I. Ya. Korenblit and Yu P. Lazarenko, Sov. Phys. JETP **33**, 837 (1971).
[7] L. Piraux, A. Fert, P A. Schroeder, R. Loloee, and P. Etienne, J. Magn. Magn. Mater. **110**, L247 (1992).
[8] T. Kasuya, Prog. Theor. Phys. **22**, 227 (1959).
[9] L. É. Gurevich and G M. Nedlin, Sov. Phys. JETP **18**, 396 (1964).
[10] T Farrel and D Greig, J. Phys. C **1**, 1359 (1968).
[11] A. Fert and I. A. Campbell, J. Phys. F **6**, 849 (1976).
[12] A. Fert, J. Phys. C **2**, 1784 (1969).

Effects of field orientation on field uniformity in permanent magnet structures

J. H. Jensen and M. G. Abele
Department of Radiology, New York University School of Medicine, New York, New York 10016

The effects of magnetic-field orientation are investigated for permanent magnet structures designed for the generation of highly uniform fields. The structures considered are based on closed cavities that produce exactly uniform internal fields. An open structure with an approximately uniform field is obtained by removing part of the wall from such a cavity. This paper explores how the magnetic-field uniformity depends on the field orientation relative to the opening. A yokeless, cylindrical cavity that is opened at both ends is considered in detail with the field oriented both perpendicular to and parallel to the cylinder's axis. The field uniformity is shown to be substantially better for the perpendicular orientation. The leakage field outside the magnet is also contrasted for the two cases.

I. INTRODUCTION

A general approach for designing open permanent magnet structures that generate highly uniform magnetic fields is to begin with a closed structure that generates an exactly uniform field in an internal cavity.[1] From the infinite variety of such closed structures, one may be selected to meet particular design criteria. To open the structure, which is necessary to allow access to the field, magnetic material is removed from the cavity wall. This paper examines how the character of the resulting approximately uniform field depends on the orientation of the field relative to the opening.

A yokeless, cylindrical structure (Fig. 1) is used as a prototype. If the cylinder is closed at both ends, the magnetization can be chosen, without changing the structure's geometry, to produce a perfectly uniform magnetic field inside the cavity oriented either perpendicular or parallel to the axis of the cylinder and with no magnetic field outside the cylinder. If the cylinder is then opened at both ends, the field will be approximately uniform in the center of the structure, but highly perturbed near the ends. There will also be a leakage field outside.

The degree of uniformity in the center, the nature of the perturbation at the end of the cylinder, and the amount of leakage field is shown to be substantially different for the two orientations. In particular, the perpendicular orientation gives a more uniform central field, better end behavior, and less leakage field. These advantages of the perpendicular orientation follow from general considerations and apply also to structures of direct practical interest.

II. DESCRIPTION OF MODEL

Consider first an infinitely long cylinder of inner radius r_1 and outer radius r_2. Assume magnetic material filling the region between r_1 and r_2 and having a magnetic polarization density $\mathbf{J}(r,\psi,z)$, where (r,ψ,z) are conventional cylindrical coordinates taken relative to the cylinder's symmetry axis. There is a unique choice of $\mathbf{J}$ that produces a uniform magnetic field $\mathbf{H}$ of specified magnitude and orientation in the region $r<r_1$ and zero magnetic field for $r>r_2$, and that obeys the constraints $\nabla\cdot\mathbf{J}=0$, $\nabla\times\mathbf{J}=0$, and $\int\mathbf{J}\cdot d\mathbf{a}=0$, where the integral is taken over the inner surface of the cylinder. The three constraints on $\mathbf{J}$ select, from the distributions producing the specified field, the one with the greatest possible figure of merit.

A perpendicular orientation, corresponding to the choice $\mathbf{H}=H_0(\sin\psi\hat{\mathbf{r}}+\cos\psi\hat{\boldsymbol{\psi}})$ for $r<r_1$, yields the distribution

$$\mathbf{J}=\mu_0 H_0\frac{2r_1^2r_2^2}{r^2(r_2^2-r_1^2)}(\sin\psi\hat{\mathbf{r}}-\cos\psi\hat{\boldsymbol{\psi}}), \tag{1}$$

while the parallel orientation $\mathbf{H}=H_0\hat{\mathbf{z}}$ produces

$$\mathbf{J}=\mu_0 H_0\left\{\frac{z}{r\ln(r_2/r_1)}\hat{\mathbf{r}}-\left[\frac{1}{(r_2/r_1)^2-1}+\frac{\ln(r_2/r)}{\ln(r_2/r_1)}\right]\hat{\mathbf{z}}\right\}. \tag{2}$$

By truncating the cylinder at $z=\pm z_0$, an open structure, shown in Fig. 1, is obtained, having an approximately uniform internal field.[2] This structure can also be properly considered the result of opening a finite closed cylinder, since end caps for the truncated cylinder can be designed that restore the perfect uniformity of the field.

III. RESULTS

Since $\nabla\cdot\mathbf{J}=0$, the magnetic charge density σ for the structure is nonzero only on it's surface and is readily found, for the two orientations, from Eqs. (1) and (2) using the expression $\sigma=\mathbf{J}\cdot\mathbf{n}$, where $\mathbf{n}$ is an outward pointing unit vec-

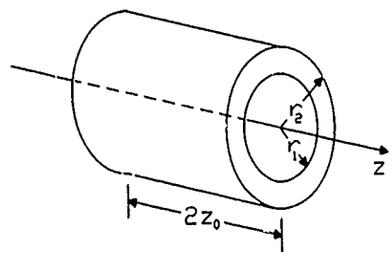

FIG. 1. Yokeless, cylindrical magnetic structure of length $2z_0$. Magnetic material fills the region between $r=r_1$ and $r=r_2$

 0021-8979/94/76(10)/6853/3/$6.00 © 1994 American Institute of Physics

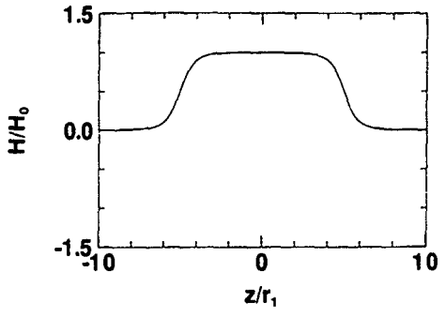

FIG. 2. H/H_0 on the z axis vs z/r_1 for $r_2/r_1=2.0$ and $z_0/r_1=5.0$. The uniformity of the central field is better for the perpendicular orientation (solid line) than for the parallel orientation (dotted line).

tor perpendicular to the surface.[1] The magnetostatic scalar potential Φ at a point $\mathbf{x}$ is computed from the integral

$$\Phi(\mathbf{x})=\frac{1}{4\pi\mu_0}\int_S \frac{\sigma(\mathbf{x}')}{|\mathbf{x}-\mathbf{x}'|}\,da', \tag{3}$$

taken over the surface of the structure, and the magnetic field is calculated from $\mathbf{H}=-\nabla\Phi$.

Figure 2 shows the magnetic field on the z axis, for the two orientations, with $r_2/r_1=2.0$ and $z_0/r_1=5.0$. For the perpendicular case, the perpendicular component is plotted, and for the parallel case the parallel component is plotted. The central field for the perpendicular orientation is significantly stronger and more uniform than for the parallel orientation. Moreover, the field for the parallel case varies rapidly near the end of the structure, acquiring large negative values, while the field for the perpendicular case falls monotonically to zero.

In Fig. 3, the magnitude of the field at the center of the structure is given as a function of z_0/r_1 for $r_2/r_1=2.0$, showing that the field approaches its asymptotic value of H_0 much more slowly for the parallel orientation. In Fig. 4, equipotential lines near the structure's end, in the two-dimensional cross section corresponding to $\psi=\pi/2$, are illustrated for the two orientations. For the parallel orientation a saddle point occurs near $(r/r_1=0.0,\ z/r_1=4.0)$.

Both inside and outside the cylinder, the potential can be expanded in spherical harmonics. Introducing spherical coordinates (ρ,θ,ψ), where ρ is the radial coordinate and θ is the angle to the z axis, the potential has the expansion, for $\rho<r_1$,

$$\Phi=\sum_{l=0}^{\infty}\rho^{l}\left\{a_{l0}P_l(\cos\theta)+\sum_{m=1}^{\infty}[a_{lm}\cos(m\psi)+b_{lm}\sin(m\psi)]P_l^m(\cos\theta)\right\}, \tag{4}$$

and for $\rho>(z_0^2+r_2^2)^{1/2}$,

$$\Phi=\sum_{l=0}^{\infty}\rho^{-(l+1)}\left\{c_{l0}P_l(\cos\theta)+\sum_{m=1}^{\infty}[c_{lm}\cos(m\psi)+d_{lm}\sin(m\psi)]P_l^m(\cos\theta)\right\}, \tag{5}$$

where P_l and P_l^m are Legendre functions. Using symmetry arguments, all the coefficients for the parallel case can be shown to vanish except the a_{l0} and c_{l0} with odd l. In Ref. 1, it is demonstrated for the perpendicular case that the only nonzero coefficients are the b_{l1} with odd l and the d_{l1} with odd l and $l\neq 1$.

Tables I and II show expansion coefficients for $l=1$, 3, and 5 with $r_2/r_1=2.0$ and $z_0/r_1=5.0$. For an exactly uniform field, the only nonzero coefficients would be $b_{11}=H_0$, for the perpendicular case, and $a_{10}=-H_0$, for the parallel case. Deviations from these values represent perturbations caused by the opening.

Aside from the b_{11} and a_{10}, the magnitudes of corresponding coefficients having the same l value are much

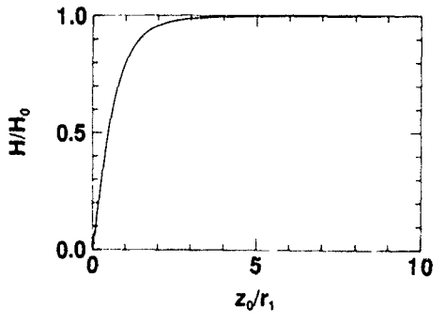

FIG. 3 H/H_0 at the center of the magnet vs z_0/r_1 for $r_2/r_1=2.0$. H/H_0 approaches its asymptotic value of 1.0 more rapidly for the perpendicular orientation (solid line) than for the parallel orientation (dotted line).

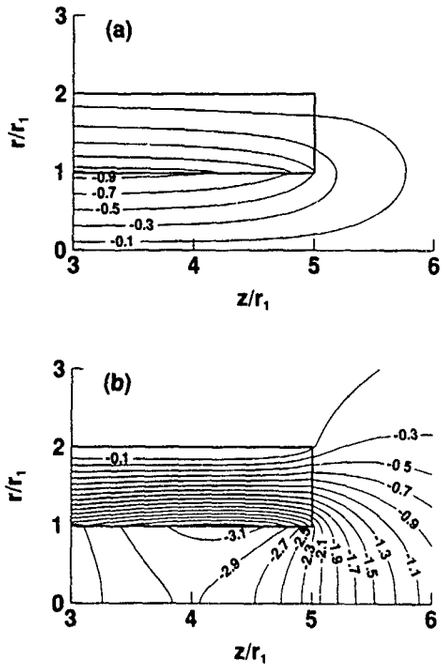

FIG. 4. Equipotential lines for (a) the perpendicular orientation and (b) the parallel orientation near the end of the magnet ($\psi=\pi/2$). The lines are labeled with the value of Φ/H_0r_1.

TABLE I. Expansion coefficients for perpendicular orientation ($r_2/r_1=2.0$, $z_0/r_1=5.0$).

l	m	$b_{lm}r_1^{(l-1)}/H_0$	$d_{lm}/[H_0r_1^{(l+2)}]$
1	1	0.998	0
3	1	-1.2×10^{-4}	5.0
5	1	-5.2×10^{-6}	2.4×10^{2}

greater for the parallel orientation than for the perpendicular orientation. In particular, the coefficients show that the uniformity in the central region is about 40× better for the perpendicular case. In addition, since the d_{11} coefficient vanishes for the perpendicular orientation, the leakage field has an octupole character and decays as ρ^{-5}, while the field for the parallel case is of dipole character and decays as ρ^{-3}.

IV. DISCUSSION

The magnetic fields for the the parallel and perpendicular orientations are different in three basic ways. First, the field for parallel orientation changes sign near the opening and becomes larger in magnitude than the field at the center of the structure. In contrast, the field for the perpendicular orientation decreases monotonically at the opening. Second, the distortion of the central field is much greater for the parallel case, as indicated by the spherical harmonic expansion coefficients. Third, the leakage field decays as an octupole for the perpendicular case, but only as a dipole for the parallel case.

The change in sign of the field for the parallel orientation is due to the fact that well inside the cylinder the magnitude of the potential on the z axis increases with z, as required by a parallel field, while outside the cylinder, the potential must decrease in magnitude. Thus, somewhere in between, the potential has an extremum where its derivative, the magnetic field, changes sign. Moreover, because the rate of change of the potential is most rapid, as is reasonable, near the opening, the magnitude of the field there exceeds the value at the center of the structure.

TABLE II Expansion coefficients for parallel orientation ($r_2/r_1=2.0$, $z_0/r_1=5.0$).

l	m	$a_{lm}r_1^{(l-1)}/H_0$	$c_{lm}/[H_0r_1^{(l+2)}]$
1	0	−0.923	−5.41
3	0	5.1×10^{-3}	-3.9×10^{2}
5	0	2.3×10^{-4}	-1.4×10^{4}

Since end caps designed to close the structure and restore the perfect field uniformity would have to generate a stronger near field for the parallel orientation than for the perpendicular orientation, it should be expected that the far field from such end caps also be stronger for the parallel case. Thus the greater distortion found in the central region for the parallel case may be regarded as a consequence of orienting the field in the parallel direction.

The vanishing of the dipole moment for the perpendicular orientation is not unique to the model considered here, but occurs generally for any cylindrical, yokeless structure where $\mathbf{J}$ is independent of z and perpendicular to $\hat{\mathbf{z}}$. Since these conditions can only be met for a perpendicularly oriented field, the zero dipole moment obtained for the perpendicular case can, in a sense, be attributed to the field's orientation.

Field orientation effects similar to those demonstrated for the truncated cylinder of this paper should also apply to other yokeless structures of similar geometry. Examples of practical interest include cylindrical structures generating perpendicular[3] and parallel[4–6] fields and structures of polygonal cross section made from uniformly magnetized polyhedra.[1]

V. SUMMARY

The effects of magnetic-field orientation have been investigated for a cylindrical permanent magnet structure opened at both ends and designed to generate a uniform central field. Fields oriented primarily perpendicular and parallel to the cylinder's axis have been compared. The distribution of magnetic polarization for both cases is chosen to maximize the figure of merit. It is found that: (1) The main component of the field decreases monotonically near the structure's end for the perpendicular orientation, but changes sign for the parallel orientation; (2) the field in the center of the structure is more uniform for the perpendicular orientation; 3) the leakage field for the perpendicular case is smaller due to a vanishing of the dipole moment.

[1] M. G. Abele, *Structures of Permanent Magnets* (Wiley, New York, 1993).
[2] A detailed discussion of the truncated cylinder with the magnetic polarization density of Eq. (1) is given in Ref. 1, pp. 275–286.
[3] K. Halbach, Nucl. Instrum. Methods **169**, 1 (1980).
[4] W. Neugebauer and E M. Branch, Technical Report, Microwave Tube Operations, General Electric, Schenectady, 15 March, 1972 (unpublished).
[5] J. P. Clarke and H A Leupold, IEEE Trans Magn. **MAG-22**, 1063 (1986)
[6] H A. Leupold and E. Potenziani II, IEEE Trans. Magn. **MAG-22**, 1078 (1986).

Lightweight, distortion-free access to interiors of strong magnetic field sources

H. A. Leupold, E. Potenziani, II, and A. S. Tilak
U. S. Army Research Laboratory, AMSRL-EP-EC-H, Fort Monmouth, New Jersey 07703-5601

A permanent magnet structure has been designed to provide field distortion-free access to large magnetic fields in cylindrical and spherical cavities without the unacceptably large mass increases usually incurred to provide it. For example, a spherical shell that produces a 1.2-T field in a spherical cavity of 2-cm radius has a mass of about 2.3 kg if material of 12.2-kOe coercivity and 12.2-kG remanence is used. If the sphere is compensated for distortion-free equatorial access, its mass must rise to 23 kg to maintain the same field in the cavity. If the geometry is altered by the new technique to maintain field integrity under access, the mass is only 1.7 kg. Some applications are discussed that afford, up to this time, unviable devices.

I. INTRODUCTION

The so-called "magic" rings and spheres[1,2] are capable of generating unusually high magnetic fields in their inner chambers and therefore afford a considerable expansion of the applicability of permanent magnets to technology. Since many of the new applications require access tunnels of diameter sufficient to significantly distort the internal working fields, the authors devised a method to greatly reduce such distortions[3] Figure 1 shows how this is done for a ring. In effect, each segment of the ring is given a magnetization which is the result of a uniform magnetization, which has no effect on the generated field, and the original ring magnetization which produces that field.

The uniform component of magnetization may be in any direction and of any magnitude so that it can be chosen to render the required magnetization zero in any desired segment, thereby making that segment dispensable and affording distortion-free access through it. Figure 1(a) shows a ring in which such access is provided at the poles and Fig. 1(b) where the access is at the equator. In the structure in Fig. 1(a), the magnetization is radial everywhere in direction while in Fig. 1(b) it is transverse in direction. The same procedure may be used in "magic spheres."

II. COMPACTION OF DISTORTION-FREE STRUCTURES

An often serious drawback of the described procedure is that it requires materials of double the remanence of those available if the maximum available remanence is used in the original unaltered sphere. If the original field is to be maintained in the distortionless configuration, its radius, and hence its mass must be increased considerably. For example, a "magic" sphere of 1.2-T remanence, B_r and 1.2-T cavity flux density, has an outer radius of 4.25 cm if its inner cavity is 2.0 cm in radius. An altered sphere would behave as a regular sphere with only 0.6-T remanence. For the altered sphere to produce the same internal field of 1.2 T, its outer radius r_o' must be increased according to the relation:[2]

$$\frac{\ln(r_o'/r_i)}{\ln(r_o/r_i)}=\frac{B_r}{B_r'}=\frac{1.2}{0.6}=2, \tag{1}$$

where r_o and r_i are the original outer and inner radii, respectively. This is a consequence of the expression for the flux density in the cavity of a "magic" sphere, viz: $B=(4/3)B_r \ln(r_o/r_i)$. Substituting $r_i=2.0$ and $r_o=4.25$, we obtain $r_o'=9$ cm and the resulting mass increase would be from 2.3 to 24 kg, a factor of more than ten.

The magnitude of remanence of an altered "magic" ring or sphere varies with the polar angle as

$$\begin{aligned} B_r&=2B_0 \sin\theta \quad \text{polar access} \\ B_r&=2B_0 \cos\theta \quad \text{equatorial access,} \end{aligned} \tag{2}$$

so that maximum remanence is required only at the poles in a spheroid designed for equatorial access or at the equator for those with polar access. This suggests that if the remanence was the maximum available everywhere, it might be possible to pare the local radius in compensation where maximum remanence is in excess of that specified and to augment the local radius only where the maximum remanence falls short of that required. In this way, the net addition of material to spheres to make them distortion-free would be minimized.

The field in the cavity of a "magic" ring or sphere arises from three sources: the poles σ on the inner and outer surfaces of the spheroidal or cylindrical shell and the volume polar distribution ρ. The surface pole contribution is zero for

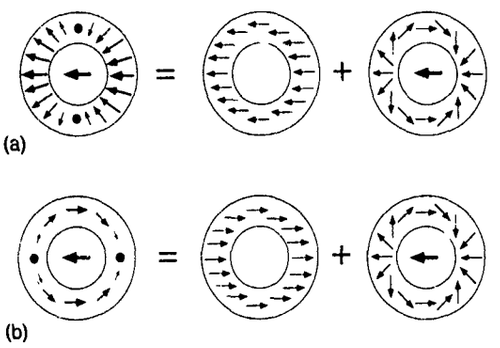

FIG. 1 Alteration of magnetization (small arrows) of "magic rings" and "spheres" to provide distortion-free access at the poles (a) and at the equator (b) The resultant magnetizations are transverse for polar access A and radial for equatorial access B The large central arrows represent the internal fields, the smaller arrows in the shell the remanences and the dots the regions of zero remanence.

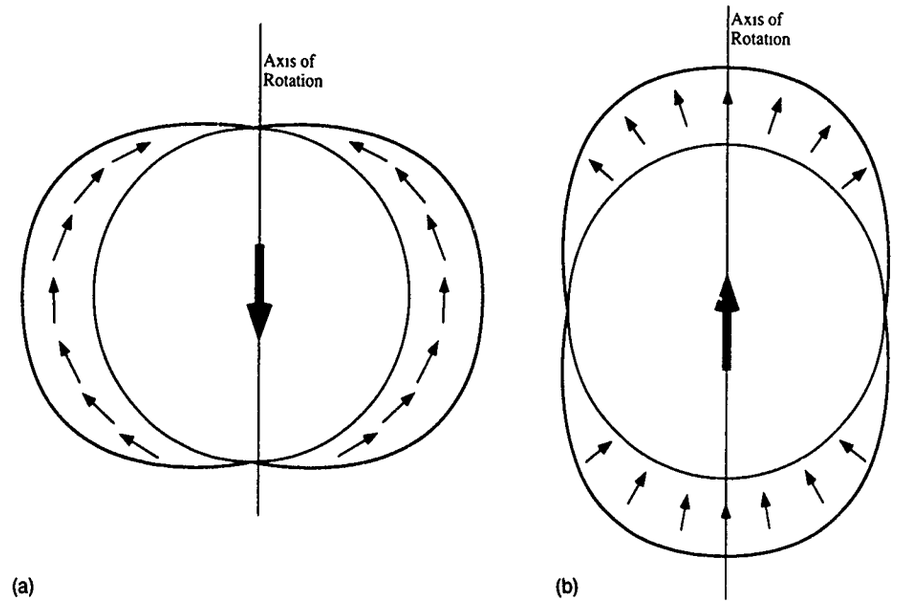

FIG 2. Cross sections and outer surfaces of (a) oblate and (b) prolate distortion-free structures.

structures of this type and the volumic distribution of poles is given by the divergence of the magnetization. For "magic" spheres and cylinders, ρ is equal to $4M\cos\theta/r$ and $2M\sin\theta/r$, respectively. This is true for both the conventional and distortion-free structures because the two differ only by a constant uniform magnetization which has no divergence and hence gives rise to no poles.

If in the cylinder the value of ρ is substituted into Coulomb's Law and the integration over r is performed, we have for the contribution of a segment at θ

$$dB = 4\int_0^{2\pi} M[\ln r_o/r_i]\sin^2\theta\, d\theta. \tag{3}$$

We note that if M is a function of θ as in the distortion-free cylinder (DFC) and if one wishes, as we do, to keep M constant at the maximum available value, we can do so by giving $r_o(\theta)$ the functional form that would leave the product $M(\theta)\ln[r_o(\theta)/r_i]$ the same as before. This is accomplished when

$$M_{\max}\ln r_o(\theta) = M_{\mathrm{DFC}}\ln(r_o)_{\mathrm{DFC}}. \tag{4}$$

Since for the polar access

$$\mu_0 M_{\mathrm{DFC}} = B_{\mathrm{DFC}} = 2B_0\sin\theta$$
$$\ln r_o = 2\sin\theta\ln(r_o)_{\mathrm{DFC}}. \tag{5}$$

If this procedure is applied to a sphere with polar access, the resulting spheroid of revolution is that in Fig. 2(a). For the same field and working space specifications as the spheres already discussed, the mass of the new structure is only 12.7 kg or about half that of the distortion-free sphere of varied remanence.

Even greater mass savings are obtainable for spheres compensated for equatorial access. In that case, our spheroid of uniform remanence construction yields the pinched-equator-prolate structure of Fig. 2(b) with a mass of 1.7 kg which is actually less than that of the unaltered parent sphere. This is because the paring of radius occurs where the azimuthal circles are large and the radius augmentation where they are small. The reverse is true for the "polar dimpled," apple-shaped oblate structure of Fig. 2(a).

III. APPLICATIONS

Many electron-beam microwave sources require strong, uniform magnetic fields parallel to the beam direction to focus the electrons. Often bulky, energy consuming solenoids are used. Recently, much more compact permanent magnet solenoids were developed for this purpose but they are limited to fields of about one-half the magnetic remanence or less.[4] For higher fields, the "magic spheres" are attractive alternatives. Often, electron beam tubes require access ports large enough to seriously distort the working fields in their vicinities. Also, electron beams are subject to abrupt field reversals upon transits through tunnels in the shells of standard "magic spheres." The new structures adequately solve both problems in many applications. Figure 3 compares the axial field profile of a standard with that of an oblate structure, both of which have large (25% of cavity diameter) axial access tunnels at the poles. The latter is seen to maintain its field to the tunnel entrance while that of the former drops to about one-half of the peak field. If desired, the "bumps" near the ends of the curve for the oblate spheroid can be smoothed out by a judicious tailoring of the local remanence[4] or by placement of axially magnetized toroidal correcting rings.[5]

For medical MRI devices, prolate structures would afford similarly improved transverse field profiles for equatorial access. Other potential applications are in Faraday rota-

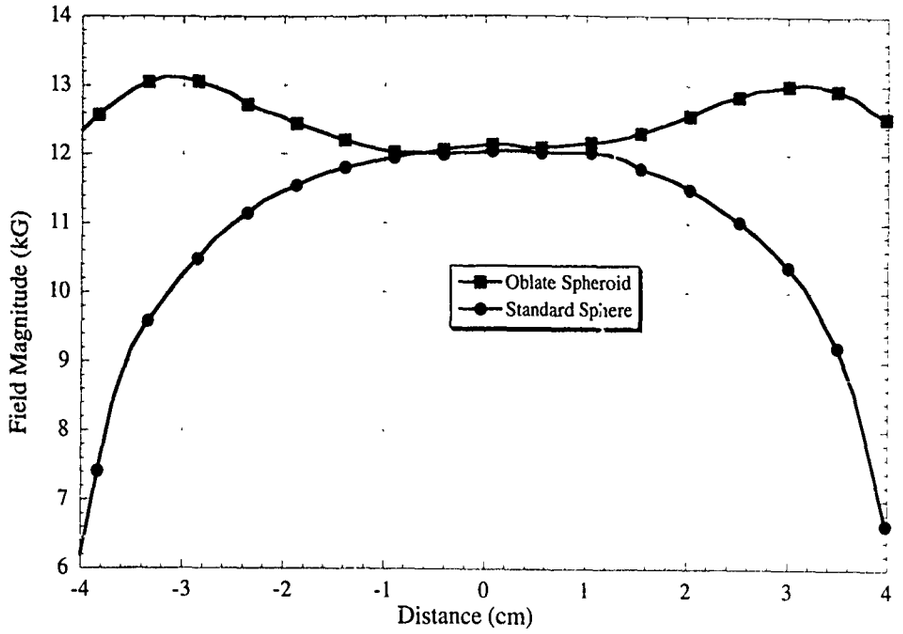

FIG. 3. Axial field profiles of (●) standard sphere and (■) oblate spheroid

tors, mass spectrometers, free-electron lasers, and wherever else access to large, uniform fields is needed.

IV. SUMMARY AND CONCLUSIONS

If a "magic sphere" with undistorting polar access is required, considerable mass savings are realized by uniform remanence, variable radius construction. Some configurations with equatorial access may actually have less mass than the unaltered spheres. It might seem that manufacture would be unduly complex and expensive, but both problems can be solved by a simple manufacturing procedure discussed in a companion article in this issue of the Journal of Applied Physics.

[1] K. Halbach, *Proceedings of the 8th International Workshop on Rare Earth Cobalt Permanent Magnets* (University of Dayton Press, Dayton, OH, 1985), p. 123.
[2] H. A. Leupold and E. Potenziani II, IEEE Trans. Magn. **MAG-23**, 3628 (1987).
[3] H A. Leupold and E. Potenziani II, J Appl. Phys. **70**, 6621 (1991)
[4] H. A. Leupold, E. Potenziani II, and A. S. Tilak, IEEE Trans. Magn. **MAG-28**, 3045 (1992).
[5] H. A. Leupold, E. Potenziani II, D J. Basarab, and A. Tilak, J. Appl. Phys. **67**, 4650 (1990).

Laminar construction of spheroidal field sources with distortion-free access

H. A. Leupold, A. S. Tilak, and E. Potenziani, II
U.S. Army Research Laboratory, AMSRL-EP-EC-H, Fort Monmouth, New Jersey 07703-5601

Certain high-field permanent magnet structures in the forms of spheroidal and cylindrical shells can be altered so that access ports through specified areas of the shells have minimal detrimental effect on the field integrity in the internal working space. This can be effected either parametrically or geometrically. Both approaches result in an increase of fabricational complexity; the former because it entails components with a variety of magnetizations and the latter because it requires a variety of geometric dimensions. This article describes how simplifying approximations to either type of structure can be obtained by an assembly of laminar pieces cut from sheets or slabs of permanent magnet materials with their magnetization oriented parallel to their principal faces.

INTRODUCTION

Several variants of the high-field permanent magnet sources sometimes known as "magic" rings, spheres, or cylinders have been designed recently[1–3] to meet the demands of miscellaneous applications. Some of these are illustrated in Fig. 1 from which it can be seen that each has complexities of shape or distribution of magnetization that might make its fabrication seem unduly difficult and expensive. However, all such structures can be made from sheets or slabs of material that are uniformly magnetized parallel to their faces.

STANDARD RINGS, CYLINDERS, AND SPHERES

One can cut circular rings "cookie-cutter" style from a uniformly magnetized slab and then, as shown elsewhere,[4] divide the ring into the desired number of sectional segments. Each segment is then rotated about its local radius to form the "magic ring" as shown in Fig. 2(a). Such rings can be stacked congruently to form dipolar cylinders[5] or beveled to form melonlike components of a "magic sphere" and bounded together [Fig. 2(b)].

The discs cut from the centers of the ring shells can be used either to make smaller "magic" rings or spheres or to be formed into cylindrical or spherical dipoles for possible use for field defect compensation as in MRI systems.[5] The cylindrical versions could even be turned into adjustable-strength dipoles by a cutting of the center of the cylinder to form a smaller nested cylinder in a shell of equal dipole strength [Fig. 2(c)], then, by rotation of the two with respect to each other, any dipole strength from zero to plus/minus the maximum is obtainable.

SPHERES AND CYLINDERS WITH DISTORTION-FREE ACCESS

In these structures, the required magnetizations in the circular or spherical segments vary in magnitude and are always either radial or transverse in direction depending upon where zero magnetization is desired, so that distortion-free access holes can be drilled there.[6] If access is to be at the poles, magnetization is transverse or tangential, whereas if access and zero magnetization are to be at the equator, it is radial.

Such structures [Figs. 1(b) and 1(c)] also can be fabricated from uniformly magnetized sheets but then a variety of sheets with different magnitudes of magnetization are necessary. The closer the approximation to an ideal continuous

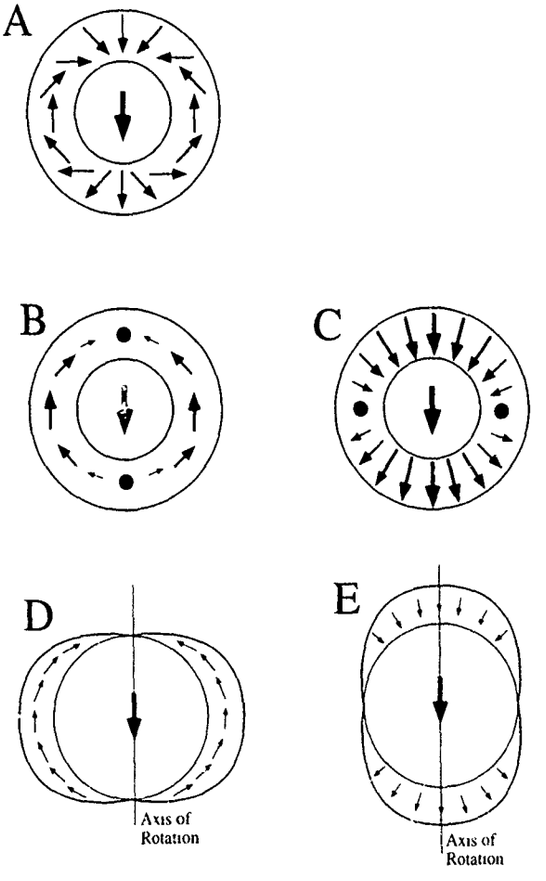

FIG. 1. Cylindrical or spheroidal permanent magnet cross sections: (a) standard, (b) for distortion-free access (DFA) at the poles, (c) for DFA at the equator, (d) full remanence DFA at the poles, (e) full remanence DFA at the equator Arrow sizes indicate relative magnetizations.

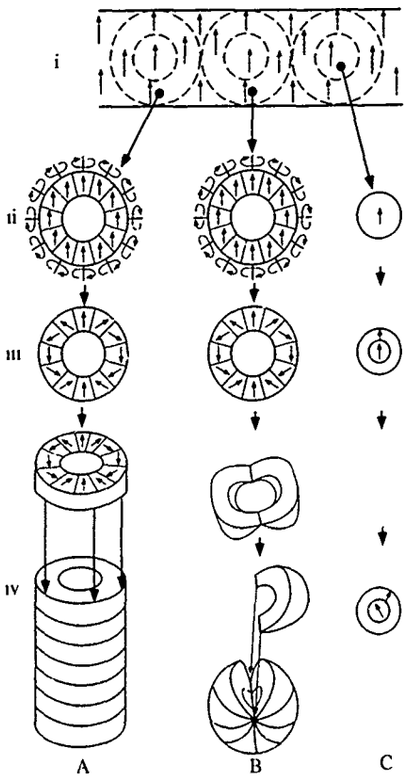

FIG. 2. Assembly of a (a) "magic cylinder," (b) "magic sphere," and (c) adjustable dipole.

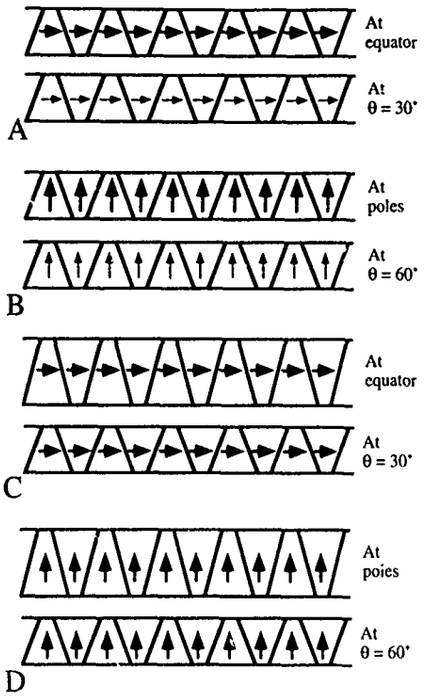

FIG. 4. Cutting of uniformly magnetized slabs to produce structures of Fig. 3. (a) Segments for structure of circular cross section with polar access; (b) segments for structure of circular cross section with equatorial access; (c) segments for oblate structure with polar access; (d) segments for prolate structure with equatorial axis. Arrow sizes are indicative of relative magnetizations.

structure, the more different magnetizations will be needed. Thus, the ideal structure can be approximated as closely as desired by substitution of the circular segments with trapezoids as in Figs. 3(a) and 3(b).

All of the segments of a given latitude have the same magnitude of magnetization and so can be fabricated entirely from a single uniformly magnetized slab. The pieces are cut from it in trapezoidal form with the ratio of lengths of the parallel sides equal to the ratio of the outer to inner radius of the finished structure. Figure 4 shows the cutting pattern for structures of Fig. 4(a) polar access and Fig. 4(b) equatorial access. Note that in the latter case, there are two kinds of segments: oriented inward and outward. Both are needed in equal numbers as produced by the cutting patterns of Fig. 4(b). In all cases, the final two-dimensional rings can be beveled to form segments of spheroids as already mentioned for the case of the standard "magic ring."

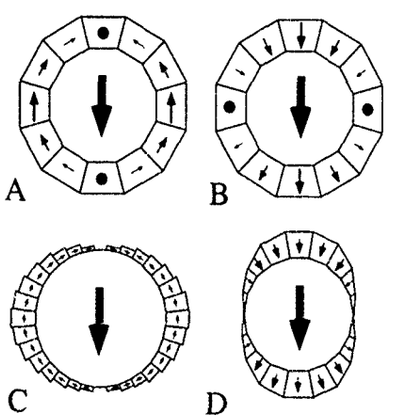

FIG. 3. Approximations to structures of Fig. 1 with trapezoidal segments. Arrow sizes indicate relative magnetizations

SPHEROIDS AND CYLINDERS WITH ONLY ONE MAGNITUDE OF MAGNETIZATION

The manufacture of structures of the previous section is complicated by the necessity of having a variety of magnetizations in the standardized sheets or slabs from which the segments are cut. Minimum-distortion access can also be effected by use of constant magnetization and segments whose radial dimension has the same angular dependence as does the magnetization in the circular cylindrical and spheroidal structures [Figs. 1(d) and 1(e)]. These are cut and assembled in the same way except that in the present case, the width of the cut zig–zag patterns varies instead of their magnetization [Figs. 4(c) and 4(d)].

SUMMARY AND CONCLUSIONS

"Magic" rings and spheres and all their uniform field variants can be manufactured by the proper cutting up of uniformly magnetized laminas and the subsequent reassembly of the resulting pieces.

[1]K. Halbach, *Proceedings of the 8th International Workshop on Rare Earth-Cobalt Permanent Magnets* (University of Dayton, Dayton, OH, 1985), p. 123.
[2]H. A. Leupold and E. Potenziani, II, IEEE Trans. Magn. **MAG-23**, 3628 (1987).
[3]H. A. Leupold and E. Potenziani, II, J. Appl. Phys. **70**, 6621 (1991).
[4]H. A. Leupold, E. Potenziani, II, J. P. Clarke, and D. J. Basarab, Proc. Mater. Res. Soc. **96**, 279 (1987).
[5]M. G. Abele, R Chandra, H. Rusinek, H. A. Leupold, and E. Potenziani, II, IEEE Trans. Magn. **25**, 3904 (1989).
[6]H. A. Leupold and E. Potenziani, II, J. Appl. Phys. **70**, 6621 (1991).

Effect of magnetization profiles on the torque of magnetic coupling

Der-Ray Huang and Gwo-Ji Chiou
Opto-electronics and System Laboratory, ITRI, Hsinchu 310, Taiwan, Republic of China

Yeong-Der Yao
Department of Physics, National Chung Cheng University, Chiayi 621, Taiwan and Institute of Physics, Academia Sinica, Taipei 115, Taiwan, Republic of China

Shyh-Jier Wang
Opto-electronics and System Laboratory, ITRI, Hsinchu 310, Taiwan, Republic of China

The torque of magnetic coupling is sensitive to the number of magnetic poles, the magnetization profiles, the magnetic field strength of magnets, and the separation distance between the magnets of the coupling. For different multipole magnetic couplings with the same magnetic field strength, the torque of magnetic coupling is proportional to the number of magnetic poles at small separation distance, but it is inversely proportional to the number of magnetic poles as the separation distance becomes large. The theoretically calculated values of the torque of magnetic coupling are in excellent agreement with the experimentally measured values.

Magnetic coupling devices transmit torque between a primary driver and a secondary follower, without any mechanical contact. They can operate in gas or liquids, and can transmit torque through a separation wall. The magnetic coupling can also be used as an overload protection device or to transmit instrument readings from a vacuum or pressure enclosure.[1,2] From both fundamental and applied viewpoints, magnetic coupling devices are of considerable interest.[3–5]

The axial magnetic coupling device for this study was constructed by using a pair of hard ferrite ring magnets that were magnetized with a multipole configuration along the axial direction. For example, Fig. 1 shows a 10-pole magnetic coupling device. All ring magnets used in this study have an outer radius of 56 mm, an inner radius 40 mm, and a thickness of 9 mm. The magnetization profiles with 6, 8, and 10 poles were used to analyze the variation of magnetic coupling. The magnetic field distributions of the ring magnets were measured by placing a Hall probe over the surface of the magnets. The torque between the two magnets was measured by using a Kowa–Giken torque meter.

The torque and force between these two coaxial ferrite rings are functions of several variables including the number of pole pairs, dimensions, separation distance, material properties, the relative angular offset of the magnets, etc. Recently, a three-dimensional theoretical analysis has been developed by Furlani for computing the transmitted force and torque of an ideal magnetic coupling.[6,7] Therefore, the effect of magnetization profiles on the torque of magnetic coupling can be studied by both experimental measurement and theoretical calculation.

For the theoretical analysis, it is assumed that the magnetization profiles of the magnetic rings are uniform throughout the magnets, and it is characterized by a uniform polarization. The concept of this theoretical analysis is to represent one of the magnetic rings as a distribution of equivalent currents, and to consider the field due to the other

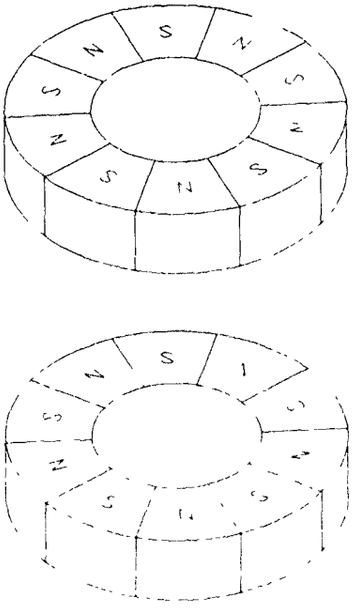

FIG. 1. Magnetic coupling with 10-pole magnets.

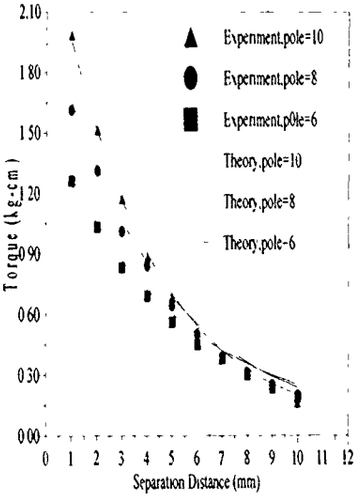

FIG. 2 The torque of magnetic coupling vs separation distance.

0021-8979/94/76(10)/6852/3/$6.00
© 1994 American Institute of Physics

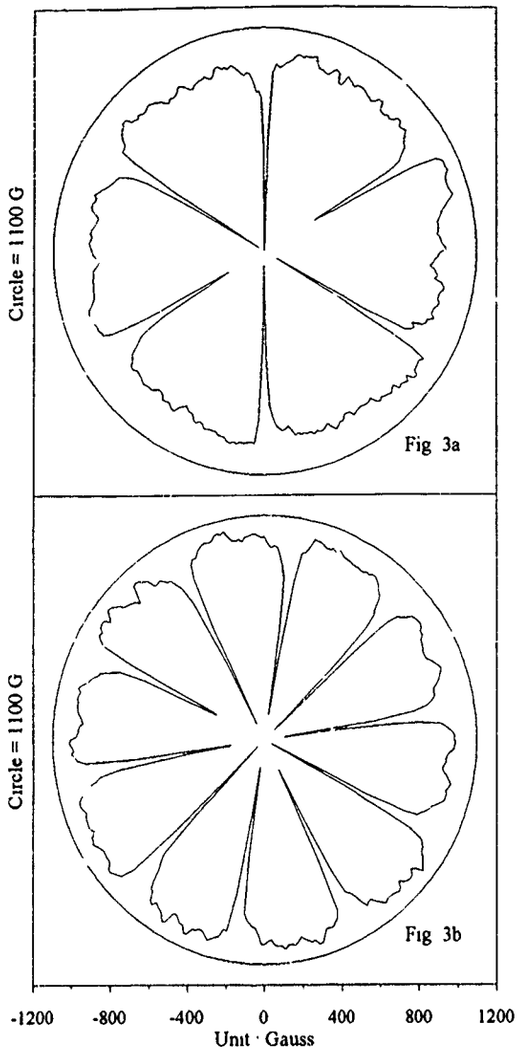

FIG 3. The magnetic field distribution of the magnet measured at a distance of 0.3 mm above the magnet: (a) 6-pole magnet, (b) 10-pole magnet.

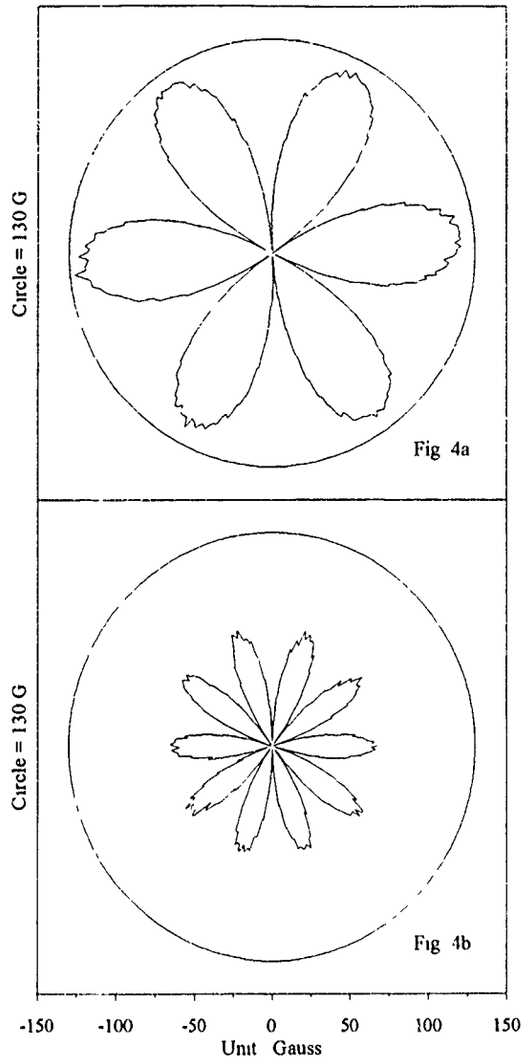

FIG. 4. The magnetic field distribution of the magnet measured at a distance of 10 mm above the magnet: (a) 6-pole magnet, (b) 10-pole magnet

magnet as an external field. After mathematical derivation, the torque can be obtained by summing the contributions from all of the sectors and surfaces of the magnets. The final form of the formula for the torque $T_{z,\text{total}}(\theta)$ of a magnetic coupling is[7]

$$T_{z,\text{total}}(\theta) = \frac{\mu_0}{4\pi} M^2 N_{\text{pole}} \left[\frac{\pi(R_2^2 - R_1^2)}{N_{\text{pole}} N_r N_\theta} \right]^2 \sum_{i=1}^{N_r} \sum_{j=1}^{N_\theta} \sum_{i'=1}^{N_r} \sum_{j'=1}^{N_\theta} \sum_{n=1}^{N_{\text{pole}}} \sum_{m=0}^{2} \times \frac{(-1)^{(n+m)} \alpha_m r_i r_{i'} \sin(\theta_j - \theta_{j'})}{[r_i^2 + r_{i'}^2 - 2 r_i r_{i'} \cos(\theta_j - \theta_{j'}) + h^2]^{3/2}},$$

where N_{pole} is the number of poles, M is the uniform magnetization, R_1 is the inner radius of the magnet, R_2 is the outer radius of the magnet, and N_r and N_θ are the number of radial and angular mesh divisions, respectively, of the sectors used for calculation. The variables h_m and α_m are given by $h_m = h + m t_m$ and $\alpha_m = -m^2 + 2m + 1$, where t_m is the thickness of magnets, h is the separation distance, and $m = 1$ for this study. The theoretically predicted torque numerically evaluated using the above torque equation can easily be compared with the experimental torque measurements.

Figure 2 shows the torque of magnetic coupling as a function of the separation distance d of magnets that are magnetized with 6, 8, and 10 poles. The torque of magnetic coupling decreases quickly as d is increased at a small separation distance. This means that the rate of decrease of the torque at small d is a function of the number of poles. However, it becomes roughly the same value for large d. For different multipole magnetic couplings, under the same magnetic field strength of magnets, the magnitude of the torque is proportional to the number of poles at separation distances of magnets within a certain range, but it becomes inversely proportional to the number of poles as the separation increases outside of that range. For example, the torque of a 10-pole magnetic coupling is greater than that of a 6-pole magnetic coupling at d less than 8 mm, but the torque is inversely proportional to the number of poles at d over 8 mm. This

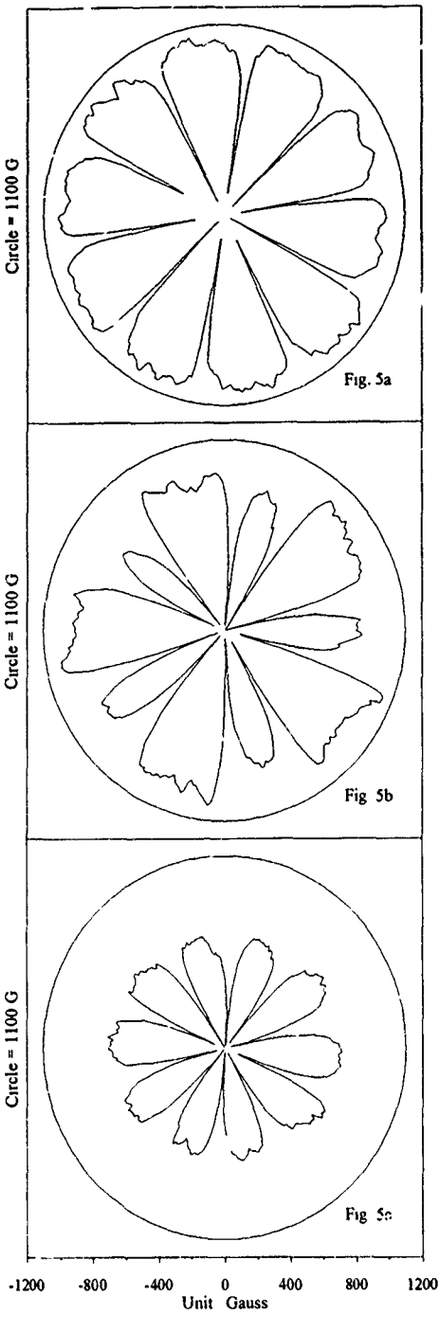

FIG. 5. The magnetic field distribution of the magnet measured at a distance of 0.3 mm above the magnet. (a) big square wave profile, (b) hybrid wave profile, (c) small wave profile.

phenomenon can be explained by analyzing the magnetic field distribution of the magnets used in the magnetic coupling. Figure 3 shows the magnetic field distribution of a 6-pole magnet and a 10-pole magnet at a distance 0.3 mm over the magnet. The average magnetic field strength is about 1 kG for both the 6-pole and 8-pole magnetic couplings. However, if we measure the magnetic field distribution of a 6-pole and a 10-pole magnet at a distance 10 mm over the magnet, the magnetic field strength is about 129 G

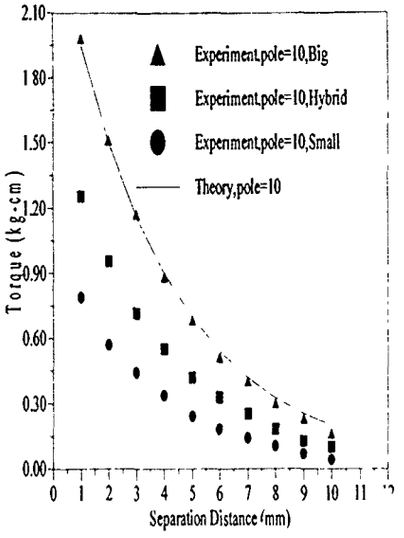

FIG. 6. The torque of magnetic couplings using different magnetization profiles

for the 6-pole magnet, but it is about 70 G for the 10-pole magnetic coupling, as shown in Fig. 4. This indicates that the magnetic field strength of the 10-pole magnet is less than that of the 6-pole magnet because the magnetic circuit loop of the 10-pole magnet is smaller than that of the 6-pole magnet at separation distance greater than 8 mm. Therefore, the torque of the 6-pole magnetic coupling is greater than that of the 10-pole magnetic coupling at separations greater than 8 mm. Considering the theoretical calculation, the torque of magnetic coupling at small separation distances matches well with the experimental data, as shown in Fig. 2.

The magnetization profiles of the multipole magnets can affect the torque of magnetic coupling markedly. Different magnetization profiles can be controlled by the design of the magnetizing fixtures. Figure 5 shows different magnetization profiles with a big square wave, hybrid wave, and small wave for a 10-pole magnet. The maximum magnetic field strength of the big square wave profile is about 1 kG as shown in Fig. 5(a), and the maximum magnetic field strength of the small wave profile is about 700 G as shown in Fig. 5(c). The magnetic field of the hybrid wave profile shown in Fig. 5(b) is a combination of the wave profiles from Figs. 5(a) and 5(c). The torque curves of the 10-pole magnetic coupling with different magnetization profiles are shown in Fig. 6. The torque of magnetic coupling with the big square wave profile is greater than that of the hybrid wave profile, and the torque of magnetic coupling with the hybrid wave profile is greater than that of the small wave profile.

[1] J. P. Yonnet, Proceedings of the 12th International Workshop on RE Magnets and their Applications (University Western Australia, Nedlands, 1992), p. 608–617.
[2] J. P. Yonnet, IEEE Trans. Magn. **17**, 1159 (1981).
[3] R. J. Parker, *Advances in Permanent Magnetism* (Wiley, New York, 1990).
[4] J. P. Yonnet, IEEE Trans. Magn. **17**, 2291 (1981).
[5] S. A. Nasar and G. Xiong, IEEE Trans. Magn. **24**, 2038 (1988).
[6] E. P. Furlani, IEEE Trans. Magn. **29**, 4165 (1993).
[7] E. P. Furlani, IEEE Trans. Magn. **29**, 2295 (1993).

A magnetic coupling without parasitic force for measuring devices

Jean-Paul Yonnet and Jérôme Delamare
Laboratoire d'Electrotechnique de Grenoble (URA 355 au CNRS), ENSIEG, B.P. 46, 38402 Saint Martin d'Heres Cedex, France

Original structures of permanent magnet couplings have been studied. They can transmit a torque without creating forces or stiffnesses between the driver and the driven part. Except for torque, the two parts are in indifferent equilibrium. These couplings have been designed for measuring devices in which they exert no force on the bearings but they can be used in other domains.

I. INTRODUCTION

Permanent magnet couplings (PMC) are synchronous devices which allow a torque to be transmitted through a partition wall. Two types of PMC are commonly used, the coaxial type operating with a cylindrical separation wall, and the face-type coupling which has a plane airgap.[1] Other types of PMC exist for specific applications. In this article, we shall present PMC configurations which are well-adapted to measuring devices. The main characteristic of these couplings is to transmit angular information without disturbing the measuring system.

In a PMC, magnet interaction allows torque transmission, but it also creates forces in the axial and radial direction. The stiffnesses, which are the force variations, are also very high. These forces have to be supported by the mechanical bearings, which produce frictional torque. Special configurations allow a torque to be transmitted without any force and stiffness,[2] but they are not well-adapted to large airgaps and only operate correctly with a high pole number.

The couplings presented in this article have been designed for measuring devices. They do not create any force between the two halves, even if the driver part is submitted to axial or radial displacement. Consequently, the friction on the mechanical bearings is reduced and does not disturb the accuracy and the sensitivity of the measurement. Moreover, these couplings operate with a large airgap, and have a reduced pole number, 2 or 4.

II. MAGIC CYLINDER COUPLING

A cylindrical magnet with rotating distribution of the magnetization direction creates a very homogeneous field in its central part.[3] This device is often called a "magic cylinder."[4] For a two-pole system, a constant dipole field is produced in the interior cylindrical cavity of magnitude

$$H_m = J_1 \ln(R_{ext}/R_{int}),$$

where J_1 is the magnet polarization in tesla, R_{ext} and R_{int} are the outer and the inner radii of the annular magnet.

This magic cylinder is the driver part of the coupling. The driven part is made of a small magnet in the middle of the hole (Fig. 1). Since the small magnet is situated inside an almost perfect homogeneous transversal field, it is not submitted to any force or stiffness, but it can transmit a torque whose maximum value is given by

$$\Gamma_{max} = J_2 v H_m,$$

where v is the volume of the driven magnet and J_2 its polarization.

To obtain perfect insensitivity to the radial and axial displacement of one part from the other, a relatively long magic cylinder has to be used. The end effects produce a field distortion at a depth d which is about

$$d \approx 0{,}7(R_{ext}+R_{int});$$

consequently, the length of the cylinder L must be at least twice its diameter.

Figure 2 presents a four-pole version of the magic cylinder coupling. The end effects are reduced in this configu-

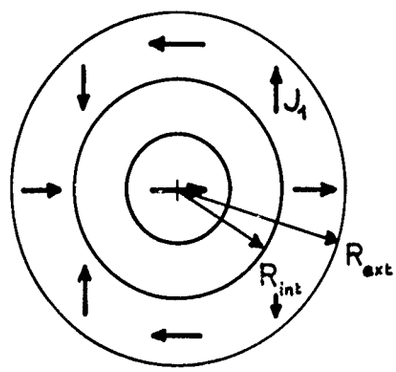

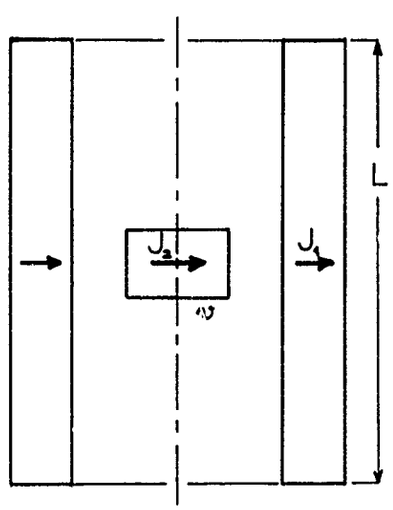

FIG. 1 A magic cylinder coupling.

 0021-8979/94/76(10)/6865/3/$6.00 © 1994 American Institute of Physics

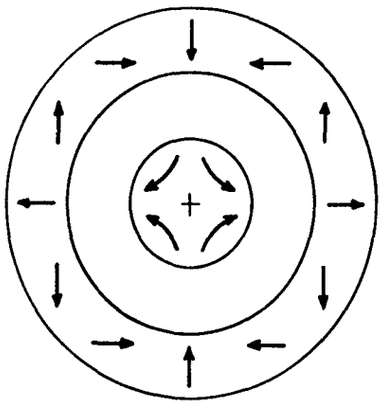

FIG. 2. A four-pole magic cylinder coupling.

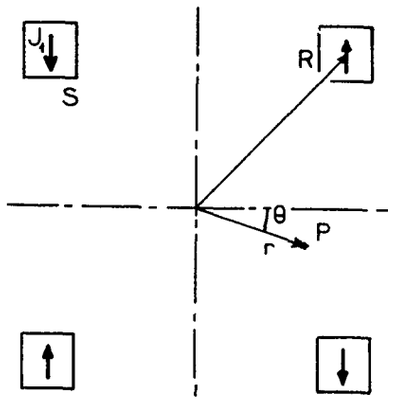

FIG. 4. Measurement of the field intensity in the four bar-shaped magnet coupling.

ration. A prototype has given very good results: the maximum torque transmitted was relatively high (2×10^{-2} Nm) and the absence of forces in a large domain of radial and axial displacements has been verified.

Several other configurations have been investigated. An interesting one uses a driver part made with four bar-shaped magnets.

III. BAR-SHAPED MAGNET COUPLING

The driven part is equipped with four bar-shaped magnets which are parallel to the rotation axis (Fig. 3). This system takes the place of the previous magic cylinder, and can be seen as an incomplete cylinder. The bar length is equivalent to the cylinder height L, and the end effects are identical.

In comparison with the magic cylinder system, the four bar-shaped magnet coupling has a lighter driver part which reduces the inertia of the measuring device. The volume of very good homogeneity of the magnetic field is smaller, especially in the radial direction. Consequently, the domain of null forces and stiffnesses is reduced, but it remains sufficient.

The maximum transmissible torque can be easily calculated by simplified expressions since the airgap is relatively large. By using the following notations:

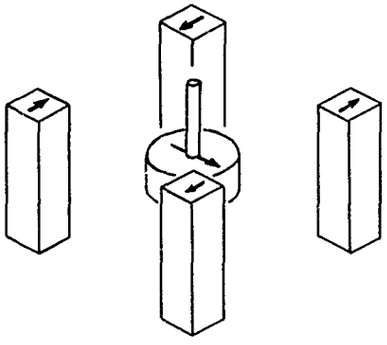

FIG. 3. The four bar-shaped magnet coupling.

(a) for the driver part;
S section of each bar,
L length of the bar,
J_1 magnet polarization,
R average distance between the center and each bar.
(b) for the driven part;
v magnet volume,
J_2 magnet polarization (in tesla).
The intensity of the magnetic field (H_{4b}) is given by

$$H_{4b}=\frac{2}{\pi\mu_0}J_1\frac{S}{R^2}$$

and the maximum torque is obtained by

$$C_{\max}=J_2 v H_{4b}=\frac{2}{\pi\mu_0}J_1 J_2\frac{Sv}{R^2}.$$

IV. EXPERIMENTAL STUDY

A prototype designed for a gas meter has been built. The following dimensions have been chosen
(a) for the driver part;
$S=9$ mm^2 (3 mm$\times$3 mm),
$L=20$ mm,
$R=10$ mm,
$J_1=0{,}4$ T (anisotropic ferrite magnets).
(b) for the driven part;
$r_2=5$ mm,
$h_2=4$ mm,
$v=314$ mm^3,
$J_2=1{,}20$ T (NdFeB magnet).

The domain of uniform field between the four bars has been investigated. In the center, we have measured a field H_{4b} of 18 kA/m.

We have studied variations of intensity of the field H_{4b} as a function of the distance from the center r and the direction θ (Fig. 4). The results are presented in Fig. 5. The homogeneity is very good for a radial distance lower than 2 mm. After, the field slowly increases when moving toward a bar magnet and decreases between two bars.

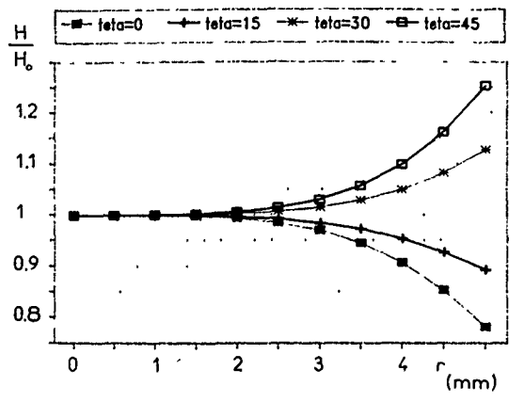

FIG. 5. Field variation around the centered position. In the center, $H_0=18$ kA/m.

The forces and stiffnesses have not been measured precisely because they are too small around the centered position. The magnetic interaction between the two parts creates very low parasitic forces.

The torque has a sinusoidal variation with the internal angle. Its maximum value is 6.3×10^{-3} Nm (63 g cm). It agrees correctly with the calculated value of 6.8×10^{-3} Nm.

V. CONCLUSION

Two unconventional types of permanent magnet couplings have been studied. They can transmit a torque without creating forces or stiffnesses between the two parts of the coupling. The first one uses the specific property of field homogeneity inside a magic cylinder. A magnet situated in this field can exert a torque, but it is not submitted to any force. The second one is built with four bar-shaped magnets. It is lighter and has lower inertia. For these two couplings, the measurements on prototypes are in good agreement with the calculated characteristics.

These couplings have been designed for measurement devices where they can be used to transmit a torque without creation of forces and friction on the mechanical bearings. They can have other applications, like for example vibration insulators.

[1] J.-P. Yonnet, Proceedings of the 12th International Workshop on Rare Earth Magnets and their Applications, Canberra, July 1992, p. 608–617.
[2] J.-P. Yonnet, IEEE Trans. Magn. **MAG-17**, 2991 (1991).
[3] K. Halbach, Proceedings of the Fifth International Workshop on Rare Earth Cobalt Magnets and their Applications, Roanoke, Virginia, June 1981, p. 73–80.
[4] H.-A. Leupold, E. Potenziani, and J.-P. Clarke, Proceedings of the 9th International Workshop on Rare Earth Magnets and their Applications, Bad Soden, Germany, September 1987, pp. 109–123.
[5] J.-P. Yonnet, IEEE Trans. Magn. **MAG-17**, 1169 (1981).

Accurate determination of permanent magnet motor parameters by digital torque angle measurement

M. A. Rahman and Ping Zhou
Faculty of Engineering and Applied Science, Memorial University of Newfoundland, St. John's, Newfoundland A1B 3X5, Canada

This article presents a novel test method to determine the important load dependent reactance parameters X_d, X_q, and magnet-excited voltage E_0 of permanent magnet (PM) motors. The results bring forward a clear picture of the impact of the previous assumption of constant E_0 on the value of X_d. As improved accuracy and fast data sampling are required for online control, the traditional method for measuring torque angle is deficient. To this end, a new microprocessor-based digital torque angle measurement system was designed and built. At the same time, a scheme for accurately positioning the zero torque angle is proposed without referring to the interior structure of a motor. The proposed techniques have been successfully employed for a 1 hp laboratory permanent magnet motor.

INTRODUCTION

The effects of saturation for PM motor are profound. It was recognized that saturation would cause d-axis reactance X_d and q-axis reactance X_q to vary with load and supply voltage.[1,2] What is perhaps easily overlooked is the assumption that the E_0 is constant for all loads. In addition, the d-q axis quantities are no longer independent due to saturation. The significance of these effects has been clearly mentioned in the previous works from the simulation point of view.[3,4] The investigation from a testing point of view has been characterized by Miller's early work.[5] The load test method proposed by Miller is to determine X_d from the stator d-axis voltage component and X_q from the q-axis voltage component, respectively, under the assumption of constant E_0. The failure to consider the variation of E_0 with load is due to the fact that effects of the permanent magnet excitation voltage E_0 and the d-axis armature reaction are inherently linked together by the stator d-axis voltage component, and usually cannot be separated. In this article, a modified load test method is proposed to determine these load-dependent parameters, X_d, X_q, and E_0 more accurately for practical use.

It is necessary to properly measure the torque angle δ at any load condition for performance prediction. In addition, torque angle is also an important control parameter for variable frequency inverter driven PM motors. It is necessary that the measurement is conducted within an interval of time that should be very small compared to the mechanical time constant of the machine. With increasing emphasis on online digital control, it has also become necessary to obtain the quantities of torque angle in digital form, and the conventional stroboscopic method is no longer suitable for such applications. To this end, a fast-response microprocessor-based torque angle measurement system has been designed and built.

Due to the characteristics of PM motor, the precision of measured torque angle is highly related to the accuracy of the positioning of zero torque angle $\delta=0$. However, for a PM motor under normal voltage supply, the no-load operation is at $\delta=\delta_0$ and therefore cannot be used to position the zero torque angle. Usually, some approximate methods[5] are employed to determine the position of $\delta=0$. Therefore, it is desirable to find a way which can accurately locate the zero torque angle position for precision measurement and control purposes.

MODIFIED TORQUE TEST METHOD

Because the parameters X_d, X_q, and E_0 tend to vary widely with loads, their values must be quoted together with the load and voltage conditions under which they were determined. From the phasor diagram of a PM motor[4] one can get

$$E_t \sin \delta_i = I_1 \sin \beta X_q, \tag{1}$$

$$E_t \cos \delta_i = E_0 + I_1 \cos \beta X_d. \tag{2}$$

It is noted that once the data of applied voltage V, current I_1, input power P_1, and torque angle δ are known from the load test, other quantities in Eqs. (1) and (2) can be easily obtained as

$$\varphi = \arccos \frac{P_1}{3I_1 V}, \tag{3}$$

$$\beta = \frac{\pi}{2} + \delta - \varphi, \tag{4}$$

$$E_t = \sqrt{(V \sin \delta + I_1 r_1 \cos \beta)^2 + (V \cos \delta - I_1 r_1 \sin \beta)^2}, \tag{5}$$

and

$$\delta_i = \arctan \frac{V \sin \delta + I_1 r_1 \cos \beta}{V \cos \delta - r_1 I_1 \sin \beta}. \tag{6}$$

From Eq. (1), the X_q can be easily obtained. However, from Eq. (2), it is inadequate to evaluate the two unknown quantities E_0 and X_d. To this end, a small change of the load is exerted to obtain another set of test data and get the following equation as

$$E_t' \cos \delta_t' = E_0 + I_1' \cos \beta' X_d. \tag{7}$$

The solution of the simultaneous algebraic Eqs. (2) and (7) would give the saturated values E_0 and X_d for any operating point. In practice, the procedure is simply to produce three curves $E_t(\beta)$, $\delta_i(\beta)$, and $I_1(\beta)$ by curve fitting from re-

 0021-8979/94/76(10)/6868/3/$6.00 © 1994 American Institute of Physics

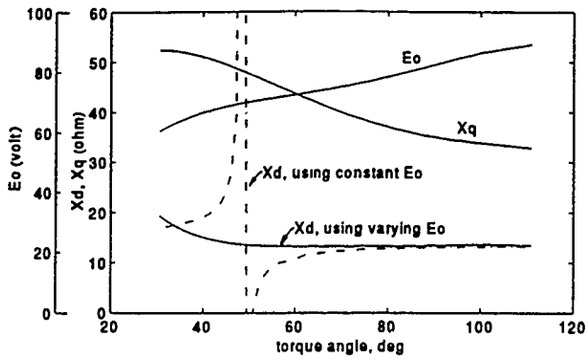

FIG. 1. Test results of X_d, X_q, and E_0 with torque angle δ.

corded data which cover the entire range of different loads. Then, the required information for both Eqs. (2) and (7) can be obtained from these curves.

Figure 1 shows the values of X_d, X_q, and E_0 for a 1 hp, 4-pole interior-type PM synchronous motor by using the above-proposed modified load test method. The effect of assuming constant E_0, as made in the original load test method,[1,5] on the value of X_d can be clearly seen from the dashed-line curve in Fig. 1. Over a load range around δ=47° where the armature reaction in d axis is changing from magnetizing to demagnetizing mode, the value of X_d becomes extremely irregular. This phenomenon was also observed in references.[5,6] This irregularity is mainly due to the assumption of constant E_0 which, in fact, is dependent on the saturation level, particularly in the region of ferromagnetic bridges. It is evident from Fig. 1 that E_0 is load dependent.

MICROPROCESSOR-BASED LOAD ANGLE MEASUREMENT

The torque angle of a synchronous machine is defined as the angular displacement between the excitation voltage E_0 and the terminal voltage V. For motoring operation, when the zero crossing of any one of the three phase terminal voltages as the reference to initiate a pulse and the zero crossing of the magnet excitation voltage in the same phase winding to terminate the pulse are used, the resulting pulse width will then represent the instantaneous torque angle. For generating mode, the reverse will happen.

The signal representing the excitation voltage is derived from a transducer consisting of a rotor shaft-mounted disc with an equispaced hole drilled on the circumference for each pole pair and a stator frame-fixed photocoupler. This photocoupler can produce a pulse whenever any one of the holes cuts across the photocoupler governed by the rotation of the shaft. This arrangement can always provide one pulse per cycle of the terminal voltage when the shaft rotates at synchronous speed. The produced chain of low voltage pulses are then amplified to TTL level using voltage comparator as shown in the block diagram of Fig. 2.

The reference phase voltage signal is derived through a step-down transformer. Before the reduced sinusoidal voltage is converted into a 5-V rectangular pulse by a zero-crossing detector, a phase-lag shifter with a range of 0°–180° is employed to provide an approximate means for positioning the zero torque angle. It is intended to ensure that the photopulse at point a in Fig. 2 will align with the terminal voltage pulse at point b at no-load operation by adjusting the variable resistor of the phase shifter. A compensator is then used to make the phase shifter work in both phase lead and phase lag.

It is noted that for the motoring mode, the pulses at point b in Fig. 2 have to be taken as reference; while for generating mode, the pulses at point a have to be taken as reference. Therefore, a multiplexer circuit is employed to enable this measurement device to be applicable to both the motoring and generating modes.

If the output gate pulse of the phase detector at d is combined with the 1-MHz clock pulses at f, a chain of the clock pulses at g are produced through an AND gate, and the number of these clock pulses is a measure of the torque angle. However, when these clock pulses are used to drive a 16-bit BCD counter, occasionally, false counting may occur. The reason is that in the case of high machine speed and heave load, the next output gate pulse at d may start before

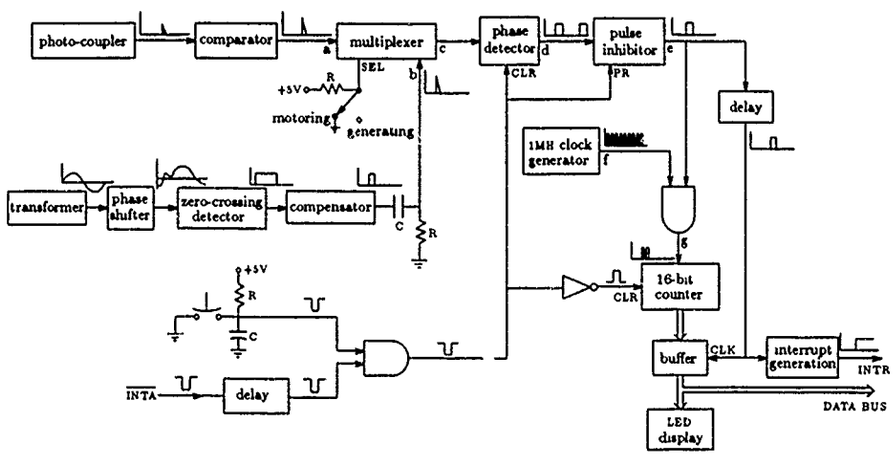

FIG 2. Block diagram for torque angle measurement.

the final settled number of the counting is latched to the buffer and counter is cleared. To avoid this undesirable operation, a pulse inhibitor is employed to ensure that no further gate pulses would pass to the AND gate until the reset signal is issued, which comes from the reset switch or interrupt acknowledgment signal ($\overline{INTA}$) from the microprocessor as indicated in Fig. 2.

Since 1-MHz clock frequency is employed, for a 60-Hz power supply system, there are 8333 pulses corresponding to 180° electrical, which is the maximum torque angle to be measured. Thus, a resolution of 0.02 electrical degree per pulse is obtained. To obtain a stable reading, the buffer is enabled after the counting is over and hold the information until the arrival of next count. The output of the buffer is further fed into a microprocessor using 8255 programmable parallel port as the interface. At the same time, the buffered data are also decoded by display driver into 7-segment LED display. The clock signal for latching the buffer and the interrupt signal can be derived from the output of the pulse inhibitor through a delay element to account for the propagation delay of the 16-bit cascade counter. The interrupt signal is produced using a JK flip–flop whose output goes high once the delay is over.

The above-mentioned torque angle measurement system was designed, built and tested on the 1 hp, 4-pole PM motor which is coupled to a conventional synchronous generator. The measurement system functioned properly as desired and was also found to be very stable over the entire range of operating conditions.

DETERMINATION OF ZERO TORQUE ANGLE POSITION

From the above discussion, it is noted that the signal representing the excitation voltage can be errorless only if the holes on the disc are aligned with the d axis of the rotor and the photocoupler is positioned at the axis of that stator phase winding whose applied voltage is taken as the reference signal. However, unless special marks were made on the rotor during assembly, there is no obvious reference to determine the position of the d axis. In order to overcome this difficulty, a scheme is introduced to find out the positions of the d axis of the rotor and the axis of the reference stator phase winding without the need to concern the interior structure of the motor. The procedure is described as follows:

(1) Mount the disc with an equispaced hole for each pole pair on the rotor shaft and fix the photocoupler to the stator frame, both at any position. Then, take any one of three phase voltages, e.g., phase A to provide the referenced phase voltage signal for the primary of the step-down transformer.

(2) Turn on the three-phase power supply and run the PM motor at no-load. By reversing the leads of the phase A power supply to the primary of the transformer and interchanging the three phase power supply leads A, B, and C to the three phase stator windings, find out the connection which would lead to a minimum torque angle reading. Under this connection, the stator winding connected to the phase A power supply is then the phase A stator winding.

(3) Run the motor first in one direction and get the torque angle reading, then do the same at the reverse direction by interchanging the phase B and phase C power supply. Assuming that the photocoupler was just positioned at the axis of phase A winding of the stator, then both the torque angle readings should be the same if the holes on the disc were aligned with the d axis of the rotor. This suggests that the disc has to be moved towards the rotating direction which has given the larger torque angle reading if both readings are not the same. This adjustment is repeated until the two readings corresponding to forward and backward rotating directions are reasonably close.

(4) In the step 3, it is assumed that the arbitrary positioning of the photocoupler was aligned with the axis of phase A winding. Generally speaking, it is not true. Hence, an adjustment is needed to relocate the position of the axis of phase A winding. It can be done by applying a low dc voltage between phase A and the shorted point of phases B and C of 3-phase Y-connected stator windings. What happens is that the disc will rotate in such a way that the holes on the disc, which represents the d axis of the rotor, should move to the axis of phase A winding. As a result, one can easily relocate the photocoupler to the position as indicated by the holes.

Due to the adjustment of photocoupler position in step 4, the holes on the disc have to be positioned again by repeating step 3. This iteration process is continued until no further adjustment is made in step 4. Practical application shows that only few iterations are required for both the holes on the disc and the photocoupler to converge to its desired position.

By using the proposed scheme, the initial torque angle for the 1 hp laboratory test PM motor was 29.6°; while using the approximate method, the initial torque angle was 22.2°. It can be seen that the error caused by the approximate method is quite significant.

CONCLUSION

In this article, a novel load test method is proposed to determine the saturated parameters X_d, X_q, and E_0. This method not only takes into account the variation of E_0 with load and the interaction between d-q axis quantities, but is also convenient to use for practical applications. The developed microprocessor-based torque angle measurement system can provide fast transient response with adequate resolution for measuring and control purposes. A prototype system was successfully built and tested in a 1 hp laboratory PM synchronous motor.

[1] V. B. Honsinger, IEEE Trans. Power Appar. Syst. **PAS-101**, 867 (1982).
[2] B. J. Chalmers, S. A. Hamed, and G. D. Baines, Proc. IEE **132B**, 117 (1985).
[3] M. A. Rahman and P. Zhou, IEEE Trans. Magn. **MAG-27**, 3947 (1991).
[4] P. Zhou, M. A. Rahman, and M. A. Jabbar, IEEE Trans. Magn. **MAG-28**, 1350 (1994).
[5] T. J. E. Miller, IEEE Ind. Appl Soc. Ann. Conf Rec. **CH1678-2**, 494 (1981).
[6] K. Miyashita, S. Yamashita, S. Tanabe, T. Shimozu, and H. Sento, IEEE Trans. Power Appar. Syst. **PAS-99**, 2175 (1980).

A three-material passive *dI/dt* limiter

S. J. Young, F. P. Dawson, and A. Konrad
Department of Electrical and Computer Engineering, University of Toronto, Toronto M5S-1A4, Canada

This article introduces and examines a composite magnetic device (called a *dI/dt* limiter) which functions as a bilevel inductor. For dc currents below a designed threshold level, the inductance and resistance of the device is quite low. However, the inductance of the device increases dramatically for all currents greater than the threshold level. In this article a set of performance equations are derived which describe the inductance of the *dI/dt* limiter as a function of current. The data obtained from these performance equations are compared to the results of a set of finite element simulations.

I. INTRODUCTION

In our earlier work,[1,2] we have examined a composite magnetic device which could function as a protective unit in voltage source fed circuits. This device, called a cylindrical *dI/dt* limiter, functions as a bilevel inductor. It has a low inductance value for all currents below a designed threshold level, and a dramatically increased inductance when the current in the device increases beyond the threshold level. This *dI/dt* limiter would limit the rate of current change in voltage source circuits during overcurrent fault conditions, while having only a modest effect on the circuits normal operation. During a fault it may also be possible to maintain the current in the *dI/dt* limiter, and hence in the series connected external circuit, at a nondestructive level long enough for the nature of the fault to be determined. Once determined, the appropriate actions would be taken to correct the source of the fault without the need for shutting down the circuit as a tripped fuse or breaker would.

This article examines a three-material square geometry *dI/dt* limiter which uses corner blocks of a high permeability material to bend the magnetic flux around the corners of the device. The result is that the flux density within the core and magnet materials is made more uniform, and the radial dependence of flux density is eliminated. Thus, not only is the transition region largely eliminated, but many of the other limitations associated with the cylindrical geometry are addressed as well.

II. THREE-MATERIAL *dI/dt* LIMITER

Stripped to its essential components, the three-material *dI/dt* limiter is shown in Fig. 1. This device consists of four coils with cores composed of alternating slices of a soft-core material, and a permanent magnet material. These solenoids are joined at the corners of the device by blocks of another type of soft-core material which has both a high permeability and a saturation flux density which is significantly higher than that of the sandwiched core material.

With zero coil current flowing, the permanent magnet slices cause a magnetic flux to flow through the permanent magnet and core materials with sufficient intensity to saturate the sandwiched core material. The corner pieces provide a low reluctance path for the magnetic flux, and so the flux exists in a closed path confined mainly to the device. Since the sandwiched core material is saturated, the incremental inductance (rate of change of flux linkage with respect to current) of the device is low. For all negative currents, and positive currents smaller than the designed threshold level, the core remains in saturation, and the incremental inductance of the *dI/dt* limiter is low. Still larger coil currents reduce the flux density in the core region below the saturation level and into the high permeability region. In this state the reluctance of the flux path is low, which causes the incremental inductance of the device to be greatly increased. It is this large device inductance which reduces the rate of current change in voltage-source-fed circuits.

III. DERIVATION

The flux density versus magnetic field intensity (B vs H) relationships of the core and permanent magnet materials are approximated by linear equations. The permanent magnet material is described by

$$B_{\text{mag}} = -B_m + \mu_0 \mu_m H_{\text{mag}}. \tag{1}$$

This may be either the natural recoil line of the magnetic material, or the result of stabilization. The linear approximation to the core's B versus H curve is given by

$$\text{In saturation } B_{\text{core}} = -B_c + \mu_0 \mu_{\text{sat}} H_{\text{core}}, \tag{2}$$

$$\text{Out of saturation } B_{\text{core}} = \mu_0 \mu_{\text{unsat}} H_{\text{core}}. \tag{3}$$

The analysis begins with Ampere's circuital law

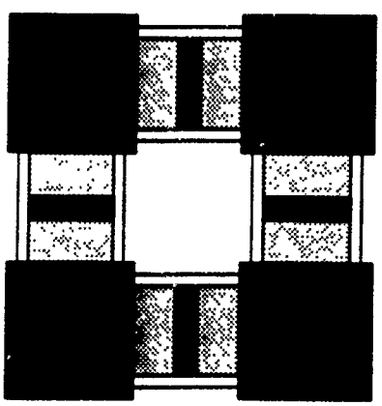

FIG 1 A three material *dI/dt* limiter: permanent magnet material (black); high permeability high saturation flux density material (dark gray); high permeability low saturation flux density material (light gray). The four coils (white) each surround a core.

 0021-8979/94/76(10)/6871/3/$6.00 © 1994 American Institute of Physics

$$\oint H \cdot dl = I_{\text{enclosed}}. \tag{4}$$

It will be assumed that the mmf drop within the corner pieces is negligible in comparison with the other mmf drops around the magnetic circuit. Thus, within the core and magnet materials

$$H_{\text{mag}} l_{\text{mag}} + H_{\text{core}} l_{\text{core}} = NI. \tag{5}$$

In Eq. (5), l_{mag} and l_{core} are the total magnetic path lengths through the magnet and core materials, respectively.

While the core material is saturated, the flux density within the core material is approximately described by

$$B_{\text{core}} = \frac{-B_m \mu_{\text{sat}} l_{\text{mag}} - \mu_m l_{\text{core}} B_c + \mu_0 \mu_m \mu_{\text{sat}} NI}{\mu_{\text{sat}} l_{\text{mag}} + \mu_m l_{\text{core}}}. \tag{6}$$

The flux linkage (Λ) within the dI/dt limiter is $\Lambda_{\text{sat}} = NB_{\text{core}} A_{\text{core}}$, and while the core is in saturation, the inductance of the dI/dt limiter is

$$L_{\text{sat}} = \frac{d\Lambda_{\text{sat}}}{dI} = \frac{N^2 A_{\text{core}} \mu_0 \mu_m \mu_{\text{sat}}}{\mu_{\text{sat}} l_{\text{mag}} + \mu_m l_{\text{core}}}. \tag{7}$$

When the core is operating in the high permeability region, the flux density within the core material is

$$B_{\text{core}} = \frac{-B_m l_{\text{mag}} \mu_{\text{unsat}} + \mu_0 \mu_m \mu_{\text{unsat}} NI}{l_{\text{mag}} \mu_{\text{unsat}} + \mu_m l_{\text{core}}}, \tag{8}$$

the flux linkage is given by $\Lambda_{\text{unsat}} = NB_{\text{core}} A_{\text{core}}$ and the inductance of the dI/dt limiter is

$$L_{\text{unsat}} = \frac{d\Lambda_{\text{unsat}}}{dI} = \frac{N^2 A_{\text{core}} \mu_0 \mu_m \mu_{\text{unsat}}}{l_{\text{mag}} \mu_{\text{unsat}} + \mu_m l_{\text{core}}}. \tag{9}$$

Let the intersection between Eqs. (2) and (3) be labeled B_x, then let the coil current required to achieve a flux density of B_x within the core material be called I_{knee}.

$$I_{\text{knee}} = \frac{-B_c (l_{\text{mag}} \mu_{\text{unsat}} + \mu_m l_{\text{core}}) + B_m l_{\text{mag}} (\mu_{\text{unsat}} - \mu_{\text{sat}})}{N \mu_0 \mu_m (\mu_{\text{unsat}} - \mu_{\text{sat}})}. \tag{10}$$

I_{knee} is the demarcation point between the low inductance region $I < I_{\text{knee}}$, and the high inductance region $I > I_{\text{knee}}$.

It can be shown that the volume of permanent magnet material required for a given I_{knee} and L_{unsat} is

$$\text{Magnet volume} = A_{\text{mag}} l_{\text{mag}} = \frac{\mu_0 \mu_m L_{\text{unsat}} I_{\text{knee}}^2}{\left(B_m - B_c \frac{A_{\text{core}}}{A_{\text{mag}}} \right)^2}. \tag{11}$$

IV. DESIGN OF A THREE-MATERIAL *dI/dt* LIMITER

The design process usually begins with a specification of the required fault inductance L_{unsat}, and the threshold current level I_{knee}. For the device pictured in Fig. 1, $A_{\text{core}} = A_{\text{mag}}$, and so the volume of permanent magnet material is determined by Eq. (11).

For most practical core and magnet materials $\mu_{\text{sat}} \approx \mu_m$, rearranging Eqs. (7) and (9) yields

$$\frac{L_{\text{unsat}}}{L_{\text{sat}}} = 1 + \frac{\text{core volume}}{\text{magnet volume}}. \tag{12}$$

TABLE I. Physical dimensions of six dI/dt limiters.

	$1+\frac{l_{\text{core}}}{l_{\text{mag}}}$	10	20
$N=100$	Square edge D_s (m)	0.1826	0.1826
	Solenoid length l_s (m)	0.0275	0.0550
	Resistance R_s (Ω)	0.057	0.053
$N=150$	Square edge D_s (m)	0.1491	0.1491
	Solenoid length l_s (m)	0.0412	0.0825
	Resistance R_s (Ω)	0.071	0.066
$N=250$	Square edge D_s (m)	0.1155	0.1155
	Solenoid length l_s (m)	0.0687	0.1374
	Resistance R_s (Ω)	0.095	0.087

Since the magnet volume is fixed by Eq. (11), for a given L_{unsat} and I_{knee}, the ratio $L_{\text{unsat}}/L_{\text{sat}}$ is increased at the expense of an increase in the volume and mass of the core material. Increasing A_{mag} reduces l_{mag}, for a given volume of magnet. This results in a decreased flux path reluctance; thus fewer winding turns are required in order to achieve the necessary L_{unsat}. With fewer turns, the resistance of the dI/dt limiter is reduced and the mass of the copper windings is lessened. However, increasing A_{mag} also increases the volume of the four corner blocks (which are proportional to $A_{\text{mag}}^{3/2}$); achieving the desired balance between device resistance and mass will determine the area A_{mag}.

Table I summarizes a set of dI/dt limiter designs in which $L_{\text{unsat}} = 40$ mH and $I_{\text{knee}} = 50$ A; Table II provides a breakdown of the mass of each of the Table I designs. It is assumed that the core and magnet cross sections are square, the length of each side being $D_s = (A_{\text{core}})^{1/2}$. The symbol l_s is simply the length of each core from one corner block to the next. The material constants for the core and magnet materials are $B_c = 0.4$ T, $\mu_{\text{sat}} = 1.0$, $\mu_{\text{unsat}} = 1000$, $B_m = 1.0$ T, and $\mu_m = 1.05$. The density of the permanent magnet material is 7.4×10^3 kg/m^3, and the density of both the sandwiched core material, and the corner block material is 4.9×10^3 kg/m^3.

TABLE II. Mass of various dI/dt limiter components.

	$1+\frac{l_{\text{core}}}{l_{\text{mag}}}$	10	20
$N=100$	Magnet mass (kg)	2.713	2.713
	Core mass	16.17	34.13
	Corner mass	228.1	228.1
	Coil mass	16.82	15.97
	Total mass	263.8	280.9
$N=150$	Magnet mass	2.713	2.713
	Core mass	16.17	34.13
	Corner mass	124.1	124.1
	Coil mass	21.08	19.97
	Total mass	164.1	180.7
$N=250$	Magnet mass	2.713	2.713
	Core mass	16.17	34.13
	Corner mass	57.71	57.71
	Coil mass	28.18	26.04
	Total mass	104.8	120.6

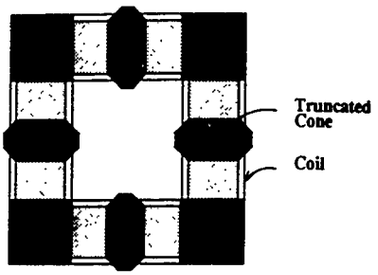

FIG. 2. A modified three-material dI/dt limiter in which $A_{mag}>A_{core}$. This device uses eight coils instead of four.

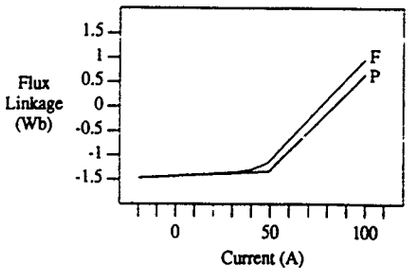

FIG. 3. Flux linkage (Λ) vs current (I) graph of the three material dI/dt limiter. Graph F was obtained from a finite element simulation, and curve P is from the performance equations of Sec. III.

As Table II shows, at low values of N, the mass of the corner pieces dominates the total device mass, and spoil what would otherwise be a promising design. A modification to the three-material dI/dt limiter which addresses this problem is shown in Fig. 2. In this modification, truncated cones of the high permeability, high saturation flux density material used for the corner pieces are employed to focus the flux from a large diameter magnet through a smaller diameter core material. Although a lack of space does not allow a complete analysis of this device, Table III shows that considerable savings in material mass and device dimensions can be achieved by using this modified design.

TABLE III. Three modified dI/dt limiter designs: $A_{mag}=4A_{core}$, $N=100$ $L_{unsat}=40$ mH, and $I_{knee}=50$ A.

$1+\frac{\mu_{mr}A_{mag}l_{core}}{\mu_{sat}A_{core}l_{mag}}$	10	20	100
Core diameter (m)	0.0841	0.0841	0.0841
Magnet diameter	0.1682	0.1682	0.1682
Solenoid length l_s	0.0899	0.0942	0.1291
Resistance (Ω)	0.053	0.035	0.021
Magnet mass (kg)	1.21	1.21	1.21
Core mass	0.428	0.903	4.70
Corner mass	15.52	15.52	15.52
Coil mass	18.16	11.85	7.26
Cone mass	21.36	21.36	21.36
Total mass	56.68	50.85	50.06

The flux linkage versus current graph for the $N=250$, l_{core}/l_{mag} device is shown in Fig. 3, along with the resulting curve from a finite element simulation. The slope of these curves is the incremental inductance of the dI/dt limiter.

V. CONCLUSIONS

This article examined a device which has the potential to function as a selective rate of current change (dI/dt) limiter. For currents below a designed threshold level, it was shown that the inductance of this device could be designed to be quite small; above this threshold level, the inductance of the device increases dramatically to another much larger designed value. A simple first-order analysis of the dI/dt limiter was favorably compared to a set of finite element simulations.

A modification to the basic dI/dt limiter was shown in which the flux from a large area permanent magnet was focused through a smaller diameter core material. The effect of this was to significantly reduce the total mass of the dI/dt limiting device.

ACKNOWLEDGMENT

The authors would like to acknowledge the generosity of Infolytica Corp. of Montreal, Canada for the use of their finite element software package MagNet.

[1] S. J. Young, F. P. Dawson, and A. Konrad, IEEE Trans. Magn. **28**, 3051 (1992).
[2] S. J. Young, F. P Dawson, and A. Konrad, IEE Jpn. Ind. Appl. Soc. E **1991**, 105.

An extended magnet in a passive *dI/dt* limiter

S. J. Young, F. P. Dawson, and A. Konrad
Department of Electrical and Computer Engineering, University of Toronto, Toronto M5S-1A4, Canada

This article examines a composite magnetic device which has the potential to function as a rate of current change (dI/dt) limiter. A possible application of such a device is to protect voltage-source-fed systems, either ac or dc, from overcurrents during fault situations. The operation of this dI/dt limiter is discussed, and performance equations are derived. Results obtained from this analysis are compared to a set of finite element simulations. An improvement to the basic design is suggested, in which the permanent magnet slices are extended in order to decrease the amount of leakage flux surrounding the dI/dt limiter.

I. INTRODUCTION

In all but the most trivial of electric circuits, some form of overcurrent protection must be provided. Although overcurrent protection has traditionally been provided by breakers and fuses, there are numerous applications where some additional method is needed in order to guarantee circuit and component security. This is especially true of certain semiconductor devices, which have a very low tolerance to overcurrents due to the very low thermal capacity of the thin semiconductor wafers from which these devices are made.

This article examines a device, called a cylindrical dI/dt limiter,[1,2] which could be placed in series with the fuse, and which for normal circuit operation would appear to the circuit as a low impedance conductor, but which would transform itself into a large inductance when the circuital currents exceeded some designed threshold level.

II. CYLINDRICAL *dI/dt* LIMITER

Stripped to its essential components, the cylindrical dI/dt limiter is shown in Fig. 1(a). In essence, it is a hollow cylinder made up of alternating slices of a soft saturable core material (dark gray) and a permanent magnet material (black). This cylinder is then surrounded by a coil having in general N turns.

The dI/dt limiter functions as follows: With zero coil current, the wedges of a permanent magnet cause a magnetic flux to flow in a near-circular path through the magnet and core materials with sufficient intensity to saturate the core. In this state, the incremental inductance (rate of change of flux linkage with respect to current) is low.

A positive coil current creates a magnetomotive force (mmf) which opposes the mmf of the permanent magnets. As long as the current does not exceed the designed threshold level, the mmf of the permanent magnets is sufficient to maintain the core material in saturation, and the incremental inductance of the device remains low. Larger positive coil currents reduce the flux density in the core region below the saturation level and into the high permeability region. In this state, the incremental inductance of the device is high. It is this increased device inductance which reduces the rate of current change in voltage-source-fed circuits.

The mmf due to negative currents supports the mmf of the magnets; the core is forced deeper into saturation, and the incremental inductance of the dI/dt limiter remains low.

III. MODEL OF THE CYLINDRICAL *dI/dt* LIMITER

A two-dimensional model of the dI/dt limiter is used as the basis for analysis. In essence, it neglects the end effects due to the finite length of the dI/dt limiter, and it assumes that the magnetic flux flows in circular paths through the device.

The flux density versus magnetic field intensity (B vs H) relationships of the core and permanent magnet materials are approximated by linear equations of the type shown below.

$$B_{\text{mag}} = -B_m + \mu_0 \mu_m H_{\text{mag}}. \tag{1}$$

This may be either the natural recoil line of the magnetic material or the result of stabilization. The linear approximation to the core's B vs H curve is shown in Fig. 2:

$$\text{In saturation} \quad B_{\text{core}} = -B_c + \mu_0 \mu_{\text{sat}} H_{\text{core}}, \tag{2}$$

$$\text{Out of saturation} \quad B_{\text{core}} = \mu_0 \mu_{\text{unsat}} H_{\text{core}}. \tag{3}$$

IV. DERIVATION OF FLUX LINKAGES AND INCREMENTAL INDUCTANCE

Applying Ampere's circuital law

$$\oint H \cdot dl = I_{\text{enclosed}} \tag{4}$$

to the two-dimensional dI/dt limiter model shown in Fig. 3 yields a set of equations which describe the static or low frequency flux linkages (Λ) within the dI/dt limiter. By low frequency, it is meant that the effects of eddy currents are not taken into account.

The operation of the dI/dt limiter is divided into three modes of operation determined by the state of the core. The state of the core is determined by the coil current. The total

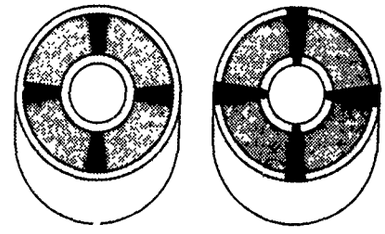

FIG. 1. The cylindrical dI/dt limiter (left-hand side) and the extended magnet version (right-hand side).

 0021-8979/94/76(10)/6874/3/$6.00 © 1994 American Institute of Physics

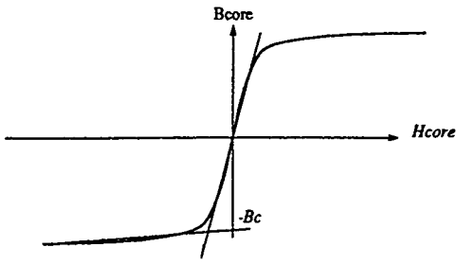

FIG. 2. The piecewise linear representation of the core material.

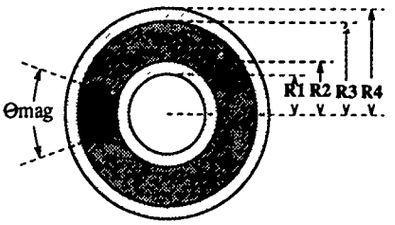

FIG. 3. The two-dimensional model of the dI/dt limiter.

flux linkage has three components: Λ_{in} is due to the inner conductor, Λ_{out} is due to the outer conductor, and the remaining component is due to the flux in the core.

Region 1: $NI<R_2\beta$; The core is completely saturated.

$$\Lambda_{SAT}=\Lambda_{in}+\Lambda_{sat}+\Lambda_{out}. \tag{5}$$

Region 2: $R_2\beta\leqslant NI\leqslant R_3\beta$; The core is partially saturated. This is a transition region.

$$\Lambda_{TRANS}=\Lambda_{in}+\Lambda_{trans}+\Lambda_{out}. \tag{6}$$

Region 3: $NI\geqslant R_3\beta$; The core is completely out of saturation.

$$\Lambda_{UNSAT}=\Lambda_{in}+\Lambda_{unsat}+\Lambda_{out} \tag{7}$$

$$\beta=\frac{B_m\theta_{mag}(\mu_{unsat}-\mu_{sat})-B_c((2\pi-\theta_{mag})\mu_m+\theta_{mag}\mu_{unsat})}{\mu_0\mu_m(\mu_{unsat}-\mu_{sat})}. \tag{8}$$

The incremental inductance ($L=d\Lambda/dI$) of the basic dI/dt limiter has a constant value L_{UNSAT} in the fault region, and a lower constant value L_{SAT} in the normal operating region. It is only in the transition region that the incremental inductance is a function of current. In the following equations, the symbol "Length" is the axial length of the three-dimensional device.

$$\Lambda_{in}=\frac{\mu_0N^2I\text{Length}}{2\pi}\left[\frac{R_2^2-3R_1^2}{4(R_2^2-R_1^2)}+\frac{R_1^4\ln(R_2/R_1)}{(R_2^2-R_1^2)^2}\right] \tag{9}$$

$$\Lambda_{out}=\frac{\mu_0N^2I\text{Length}}{2\pi}\left[\frac{R_3^2-3R_4^2}{4(R_4^2-R_3^2)}+\frac{R_4^4\ln(R_4/R_3)}{(R_4^2-R_3^2)^2}\right] \tag{10}$$

$$\Lambda_{sat}=N\text{Length}\times\left[\frac{-B_m\theta_{mag}\mu_{sat}-B_c(2\pi-\theta_{mag})\mu_m}{\theta_{mag}\mu_{sat}+(2\pi-\theta_{mag})\mu_m}(R_3-R_2)+\frac{\mu_0\mu_m\mu_{sat}NI}{\theta_{mag}\mu_{sat}+(2\pi-\theta_{mag})\mu_m}\ln\left(\frac{R_3}{R_2}\right)\right] \tag{11}$$

$$\Lambda_{trans}=N\text{Length}\left[\frac{-B_m\theta_{mag}\mu_{unsat}}{\theta_{mag}\mu_{unsat}+(2\pi-\theta_{mag})\mu_m}(R_x-R_2)+\frac{\mu_0\mu_m\mu_{unsat}NI}{\theta_{mag}\mu_{unsat}+(2\pi-\theta_{mag})\mu_m}\ln\left(\frac{R_x}{R_2}\right)\right]+N\text{Length}\left[\frac{-B_m\theta_{mag}\mu_{sat}-B_c(2\pi-\theta_{mag})\mu_m}{\theta_{mag}\mu_{sat}+(2\pi-\theta_{mag})\mu_m}(R_3-R_x)+\frac{\mu_0\mu_m\mu_{sat}NI}{\theta_{mag}\mu_{sat}+(2\pi-\theta_{mag})\mu_m}\ln\left(\frac{R_3}{R_x}\right)\right] \tag{12}$$

$$R_x=NI/\beta. \tag{13}$$

R_x is the dividing radius between the unsaturated core region (inside this radius) and the saturated core region (outside the radius).

$$\Lambda_{unsat}=N\text{Length}\times\left[\frac{-B_m\theta_{mag}\mu_{unsat}}{\theta_{mag}\mu_{unsat}+(2\pi-\theta_{mag})\mu_m}(R_3-R_2)+\frac{\mu_0\mu_m\mu_{unsat}NI}{\theta_{mag}\mu_{unsat}+(2\pi-\theta_{mag})\mu_m}\ln\left(\frac{R_3}{R_2}\right)\right]. \tag{14}$$

Table I summarizes the physical dimensions of three example dI/dt limiters. Each device has a low inductance region extending up to $I_{knee}=50$ A, and each has a fault inductance $L_{UNSAT}\approx 45$ mH. In these examples, the material constants for the core and magnet material are: $\mu_{sat}=1.0$, $\mu_{unsat}=1000$, $B_c=0.4$ T, $\mu_m=1.05$, and $B_m=1.0$ T. The coil is made of square No. 4 wire ($A_{wire}=39\,842.5$ mil^2), which has a dc resistance of 0.686Ω/1000 mil at 25 °C and a mass of 0.2335 kg/m.

In Fig. 4, the flux linkage versus current graph for the $\theta_{mag}=2\pi/20$ device of Table I is shown along with the results from a set of finite element simulations. The only difference between the 16 and 64 segment devices is the number of permanent magnet wedges that the magnetic angle θ_{mag} is divided into. Many thin wedges tend to reduce the amount of leakage flux outside the device, i.e., more of the flux is confined to the core. Hence, the transition from the low to high inductance state is sharpened as the number of wedges increases. However, large numbers of core and magnet wedges may be undesirable from a cost and construction perspective.

In Fig. 1(b), a modified device is depicted in which the permanent magnet wedges are extended to the outer edge of

TABLE I. Physical characteristics of three dI/dt limiters.

θ_{mag}	$\frac{2\pi}{10}$	$\frac{2\pi}{20}$	$\frac{2\pi}{100}$
R_1	0.2998	0.3964	0.6960
R_2	0.3241	0.4083	0.6983
R_3	0.3565	0.4491	0.7681
R_4	0.3771	0.4596	0.7702
Length	0.06482	0.08166	0.1397
N	1852	1167	399
Magnet mass (kg)	3.33	3.33	3.33
Core mass	19.8	41.8	217.9
Coil mass	122.9	78.95	39.86
Total mass	146.0	124.1	261.1
Resistance (Ω)	0.36	0.23	0.12
L_{SAT} (mH)	6.22	2.51	0.43
L_{UNSAT} (mH)	46.0	44.0	40.3
$\frac{L_{UNSAT}}{L_{SAT}}$	7.4	17.5	93.1

the conductors. Extending the magnets helps to maintain a more uniform flux density in the core material. Thus, fewer magnetic wedges are required to achieve a sharp transition from the low to high inductance state of the device.

It can be shown, that for the cylindrical dI/dt limiter, the combined volume of the core and permanent magnets is

$$\text{Volume} > \frac{2\pi\mu_0\mu_m I_{knee}^2 L_{UNSAT}}{\theta_{mag}(B_m - B_c)^2}. \tag{15}$$

This is an unavoidable characteristic of the cylindrical dI/dt limiter which tends to result in a fairly heavy device for large values of I_{knee} and L_{UNSAT}, or small values of θ_{mag}. For instance, the mass of the $2\pi/20$ device is 124.1 kg, of which 3.33 kg is due to the permanent magnets, 41.8 kg is due to the ferrite core, and 78.95 kg is due to the copper conductors. For smaller values of L_{UNSAT} and I_{knee}, the weight of the device is more reasonable, and the simplicity of the cylindrical device makes it attractive.

V. CONCLUSIONS

This article examined a device which has the potential to function as a selective rate of current change (dI/dt) limiter.

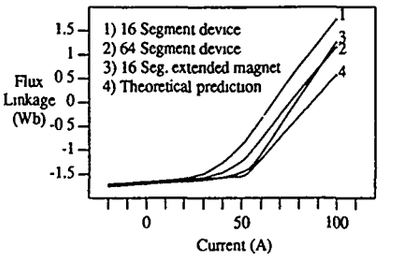

FIG. 4. Flux linkage vs current graphs for the $\theta_{mag}=2\pi/20$ device of Table I. The "theoretical prediction" line was obtained from the performance equations. The remaining curves are from a set of finite element simulations.

For currents below a designed threshold level, it was shown that the inductance of this device could be designed to be quite small; above this threshold level, the inductance of the device increases dramatically to another much larger designed value.

A modification to the basic dI/dt limiter was shown in which the permanent magnet wedges were extended to the outer edge of the current conductors. The effect of this was to reduce the number of wedges required to achieve acceptable device performance.

It was also seen that at larger values of threshold current and device inductance that the volume and mass of the device could be considerable, thus the cylindrical dI/dt limiter would likely only be practical for applications in which $I_{knee}^2 L_{UNSAT}$ is small.

ACKNOWLEDGMENT

The authors would like to acknowledge the generosity of Infolytica Corp. of Montreal, Canada for the use of their finite element software package MagNet.

[1] S. J. Young, F. P. Dawson, and A. Konrad, IEEE Trans. Magn. **28**, 3051 (1992).
[2] S. J. Young, F. P. Dawson, and A. Konrad, IEE Jpn. Ind. Appl. Soc. E 105 (1991).

Effects of additives on magnetic properties of sheet Sr-Ba ferrite magnets

Young Jei Oh, In Bo Shim, and Hyung Jin Jung
Division of Ceramics, Korea Institute of Science and Technology, Seoul 130-650, Korea

Jae Yun Park
Department of Materials Science and Engineering, University of Inchon, Inchon 402-749, Korea

Seung Iel Park, Young Rang Um, Young Jong Lee, Seung Wha Lee, and Chul Sung Kim
Department of Physics, Kookmin University, Seoul 136-702, Korea

$Sr_{0.75}Ba_{0.25}Fe_{12}O_{19}$ hexagonal ferrite has attracted much attention due to its large $(BH)_{MAX}$ values and workability. We have prepared sheet magnets by the Dr. Blade method. To examine the effects of additives, such as SiO_2, TiO_2, Al_2O_3, and Cr_2O_3, on magnetic properties of sheet magnets, we used VSM magnetometer, x-ray diffraction, and Mössbauer spectrometer. The crystal structure is found to be a magnetoplumbite of typical M-type hexagonal ferrite, but the α-Fe_2O_3 phase develops with increasing additives concentration. Using our refined computer program, we have analyzed the Mössbauer spectra in the temperature range from 13 to 800 K. The Mössbauer spectra indicate that the line intensity for the 12k site is reduced with increasing SiO_2 concentration, which is different from the reports of Fe-substituted Ba ferrite. This suggests that the developing α-Fe_2O_3 phase is related to 12k sites. The isomer shifts show the charge states of Fe ions is ferric. When the additives concentrations increase, the Curie temperatures, T_c go down. One sextet for α-Fe_2O_3 phase still persists above T_c, so it suggests that the high-T_c values do not result from α-Fe_2O_3. While Al_2O_3 and Cr_2O_3 additives increase coercive force H_c, the other additives reduce it.

I. INTRODUCTION

The hexagonal ferrite of the M-type $(Ba,Sr)Fe_{12}O_{19}$, have attracted much attention as permanent magnets, perpendicular magnetic recording media, and microwave device materials.[1-3] They are widely used because of their high coercivity and low cost. Besides, they are very stable and have electrical resistivity.[4] In optimizing hard ferrites for permanent magnet applications, a compromise is usually struck between obtaining a high remanence value or a high coercivity, which is dependent on microstructural features.

The remanence Br is a strong function of density, chemistry, and orientation, while the coercive force, H_c is related to grain size. The problem is to achieve fine grain size and high density simultaneously. It has been reported that some additives such as SiO_2,TiO_2, Ba_2O_3, Cr_2O_3, and Ga_2O_3 are active ingredients that definitely influence the microstructure.[5-7]

Additives play a role as an activator and inhibitor. The method of addition and amounts are also very important techniques. Kools[5] has found that SiO_2 in the correct proportion inhibited grain growth by forming a second phase at the grain boundaries. Okumura[8] has found Bi_2O_3 improves the reaction rate and increases the density of barium, strontium, and lead ferrites. Seok[9] noticed that Al_2O_3 reduces the size of unit cell of barium ferrite, raises the coercive force, lowers the saturation magnetization, remanence, Curie temperature, and rate of growth of the crystallites. On the other hand, Wolski[7] has investigated the influence of the admixtures (Al_2O_3, Ga_2O_3, B_2O_3) upon the magnetic properties of the strontium-barium ferrite $Sr_{0.75}Ba_{0.25}Fe_{12}O_{19}$.

In this work, the effects of trivalent base oxides (Al_2O_3, Cr_2O_3) and tetravalent base oxides (TiO_2, SiO_2) on magnetic properties of the Sr-Ba ferrite are discussed. There has not

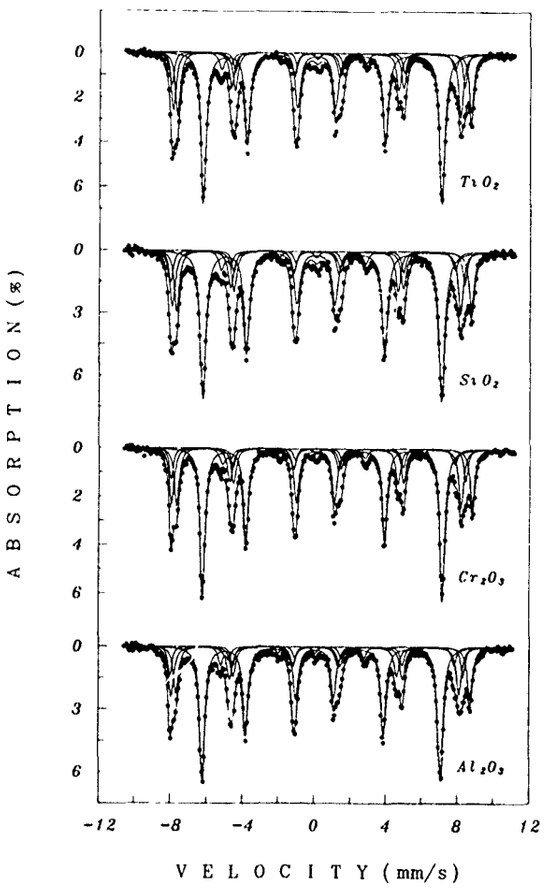

FIG. 1. Mossbauer spectra of Sr-Ba ferrites with 1.0-wt % additives at room temperature.

 0021-8979/94/76(10)/6877/3/$6.00 © 1994 American Institute of Physics

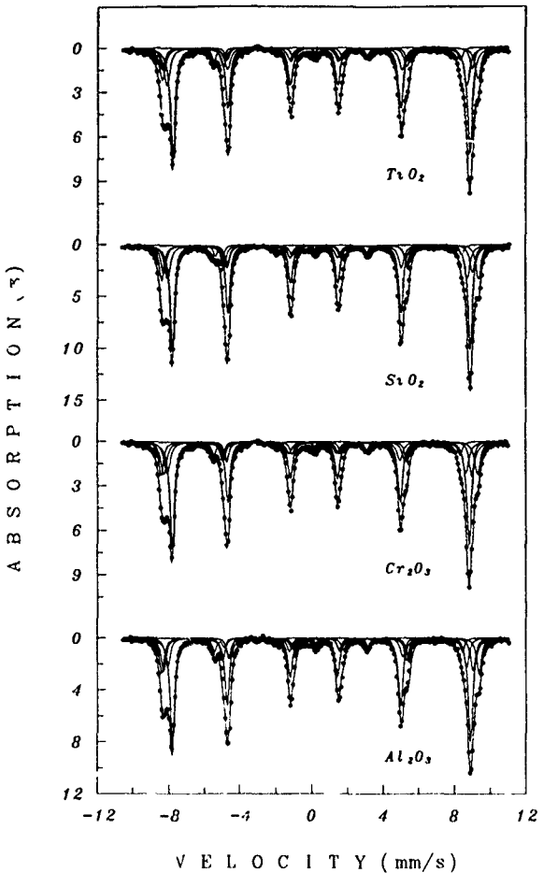

FIG. 2. Mossbauer spectra of Sr-Ba ferrites with 1.0-wt % additives at 13 K.

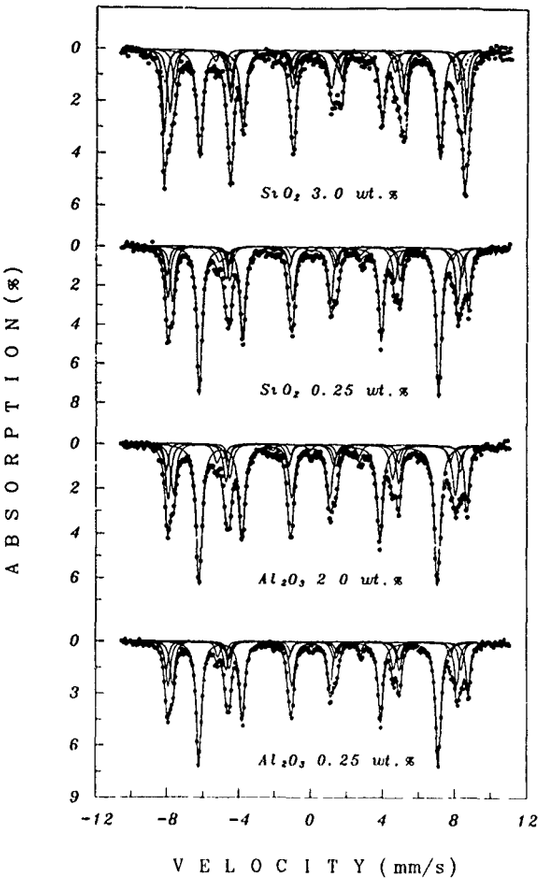

FIG. 3. Mössbauer spectra of Sr-Ba ferrites with admixed with Al_2O_3 and SiO_2 at room temperature. The dashed line indicates the α-Fe_2O_3.

been an exploration of the effects of substituting part of Fe^{3+} with the cations of additives by Mössbauer spectroscopy.

II. EXPERIMENT

Strontium-barium ferrite $Sr_{0.75}Ba_{0.25}Fe_{12}O_{19}$ was prepared by the citric sol–gel method. The starting materials were $Sr(NO_2)_2$, $Ba(NO)_2$, $Fe(NO_3)\cdot 9H_2O$ of 99% purity. After grinding and drying citrate gel, the ferrite powder was reacted by calcining it at 850 °C for 2 h. The green sheets of $Sr_{0.75}Ba_{0.25}Fe_{12}O_{19}$ to which additives oxides were introduced were made by Dr. Blade. Sintering was done at 500 °C for 1 h and for the second time at 1200 °C for 2 h.

Mössbauer spectra were recorded using a conventional Mössbauer spectrometer of the electromechanical-type[10] with a ^{57}Co source in a rhodium matrix.

III. RESULTS AND DISCUSSION

The x-ray diffraction patterns of the samples showed that the crystal structure was a typical magnetoplumbite of the *M*-type hexagonal. The lattice constants of $Sr_{0.75}Ba_{0.25}Fe_{12}O_{19}$ were found to be $a=5.875$ Å, $c=23.03$ Å. Adding oxides has no appreciable effect on the dimensions of unit cell. In the case of SiO_2, the a axis of the hexagonal cell is almost unchanged, while the c axis seems to decrease slightly. α-Fe_2O_3 phase appear above 2.0 wt % of SiO_2 additives. The effect of substituting part of the Fe^{3+} with oxides was not noticed in powder diffraction patterns.

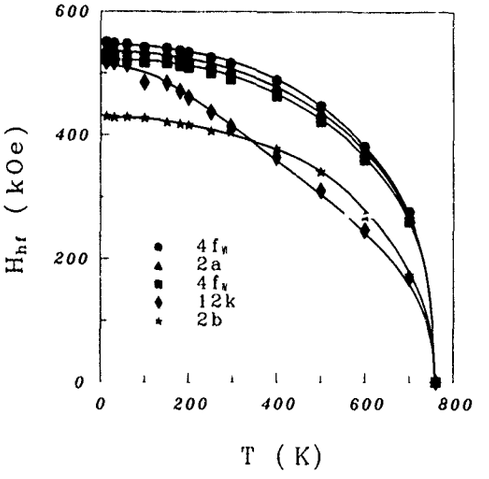

FIG. 4. Temperature dependence of magnetic hyperfine fields of Sr-Ba ferrite with 1.0-wt % TiO_2 additives.

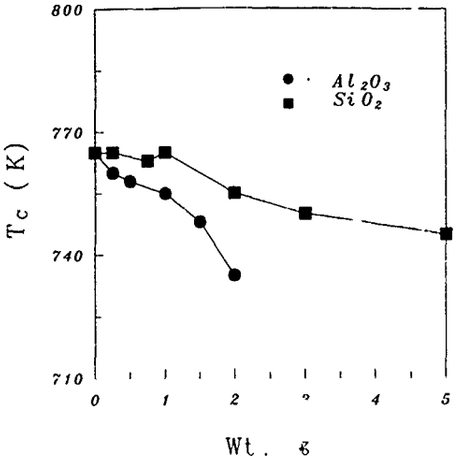

FIG. 5. Dependence of Curie temperature, T_c upon the concentration of additives Al_2O_3 and SiO_2.

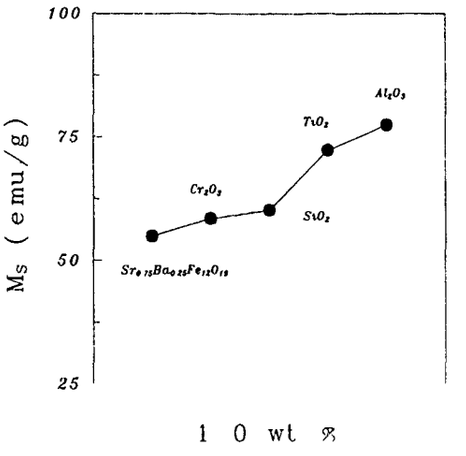

FIG. 6 Saturation magnetization M_w of Sr-Ba ferrites with and without admixtures.

Mössbauer spectra of Sr-Ba ferrite with 1.0-wt % SiO_2, TiO_2, Al_2O_3, and Cr_2O_3 are shown in Figs. 1 and 2. Each sites contributes a magnetic hyperfine sextet, in proportion to site population times the recoil-free fraction, to the total Mössbauer spectrum. With the assignments shown in Figs. 1 and 2, peaks of five sites may be identified visually. They are a typical Mössbauer spectra of the Sr-Ba ferrite.[11] The isomer shifts at room temperature are in the range of 0.18–0.27 mm/s relative to Fe metal,[12] which means that the ionic state of iron ions with respect to five sites is ferric. The effects of Fe^{3+} substitution with trivalent and tetravalent cation of additive is not found in the Mössbauer spectra.

The quadrupole splittings of sublattice as a function of temperature show no abrupt change near 80 K. Kreber[13] had proposed a model in which Fe^{3+} occupies randomly one of the two equivalent sites of 4*e* instead of 2*b* at low temperature. Figure 3 show Mössbauer spectra of Sr-Ba ferrites with changing weight percent of the additives Al_2O_3 and SiO_2.

When the portion of additives is increased, the Mössbauer spectra of the Sr-Ba ferrite with Al_2O_3 admixture is almost unchanged, while that of SiO_2 is obviously changed. The line intensity of the 12*k* site is reduced with the addition of SiO_2, which indicates that Fe^{3+} substitutes for Si^{4+}. As shown in Fig. 4, the variation of magnetic hyperfine fields of Sr-Ba ferrite with the use of 1.0-wt % TiO_2 additives is similar to that of the typical Sr ferrite.

The variation of Curie temperatures with the weight percent of additives are shown in Fig. 5. When the weight percent of additives of samples increase, the Curie temperatures T_c decreases, but remain high, and one sextet for α-Fe_2O_3 still persists about T_c. It suggests that this high value of the Curie temperature T_c due to additive oxides may be explained as the small substitution of Fe^{3+} on 2*b* or 12*k* sites by the trivalent or tetravalent cation, which effects changes in the distance or the angle between Fe-O-Fe involved in superexchange interaction, however changes of Mössbauer spectra due to these ions are not detectable below the Curie temperature.

It is noted in Fig. 6 that additives increase the saturation magnetization. Of all the additives Al_2O_3 has the greatest effect on M_s in the range of 1.0 wt %. However, an increase in additives reduces the saturation magnetization. The coercive force, H_c is increased with the addition of the admixture Al_2O_3 and Cr_2O_3, but is decreased with the other additives.

In general, H_c and M_s partly depend upon density and grain size, and it has been shown that the coercive force, H_c depends on the anisotropy field which is related to five Fe^{3+} sites, but any effects due to the replacement of trivalent by tetravalent cations in Mössbauer spectra was not observed.

In conclusion, it may be said that when the concentration of additives is less than 5 wt % the magnetic properties such as H_c, M_s, and M_r depend more on microstructure characteristics than on the additives. Additives can also play a role as inhibitor or activator when the cation concentration is less than 5 wt %.

ACKNOWLEDGMENT

The present studies were supported by the Nondirected Research Fund, Korea Research Foundation, 1994.

[1] H. Kojima, *Ferromagnetic Materials*, edited by E. P. Wolfarth (North-Holland, Amsterdam, 1982), Vol. 3, p. 205.
[2] G. K. Thompson and B. J. Evans, J. Appl. Phys. **73**, 6295 (1993).
[3] G. F. Dionne and J. F. Fitzgerald, J. Appl. Phys. **70**, 6140 (1991).
[4] P. Cavallotti, R. Roberti, and G. Caironi, J. de Phys. C**1**, Suppl. 4, c1-333 (1977).
[5] F. Kools, Adv. Ceram. **15**, 177 (1985).
[6] A. Yazaki, D. Endo, T. Uchida, Y. Nagata, and K. Ohta, Proc. ICF **6**, 385 (1992).
[7] W. Wolski and J. Kowalewska, Jpn. J. Appl. Phys **9**, 711 (1970).
[8] T. Okumura, H. Kojima, and S. Watanabe, Sci. Rep. RITU A **7**, 411 (1955).
[9] J. H. Seok, J. H. Kim, and S. H. Cho, Proc. ICF **6**, 1126 (1992).
[10] C. S. Kim, D. Y. Kim, H. M. Ko, J. K. Kim, and J. Y. Park, J. Appl. Phys. **73**, 6986 (1993).
[11] X. Z. Zhou, A. H. Morrish, Z. W. Li, and Y. K. Hong, IEEE Trans. Magn. **MAG-27**, 4654 (1991).
[12] C. S. Kim, H. M. Ko, W. H. Lee, and C. S. Lee, J. Appl Phys. **73**, 6298 (1993).
[13] E. Kreber, D. Gonser, and A. Trautwein, J. Phys. Chem. Solids **36**, 263 (1975).

Critical scattering of electromagnetic waves on spin fluctuations in nonsaturated magnetic films under acoustic pump

I. E. Dikshtein, R. G. Kryshtal, and A. V. Medved
Institute of Radioengineering & Electronics of Russian Academy of Sciences, Mokhovaya, Moscow GSP-3, Russia 103907

The theoretical and experimental investigation of the microwave (MW) combination scattering on spin fluctuations (SF) in the yttrium iron garnet film under acoustic pump were pursued. MW frequency $f \cong 3.5-4.1$ GHz was well above spin wave spectrum at a preassigned magnetic field. At the external magnetic field range $H_0 \cong 5-40$ Oe one (or more) intensity peaks of MW scattering were observed. The positions of these peaks do not depend on MW and surface acoustic wave (SAW) amplitudes and frequencies and depend heavily on the magnetic field directions in a film plane. Because these phenomena were closely associated with the domain walls (DW) reorientation or at the domain structure transformations, e.g., at the flexural instability of DW, one may speculate that critical scattering of MW on SAW and SF was observed. Cross section for such scattering was calculated. In nonsaturated magnetic films the phenomena of MW scattering on SAW and spin fluctuations at high amplitudes of the MW and SAW were investigated as well. In the area of external magnetic fields $H_0 \geqslant 250$ Oe a stepped dependence of intensity of scattering MW was observed. There is no appropriate explanation of this effect now.

Experimental investigations of nonelastic scattering of magnetostatic waves (MSW) by a surface acoustic wave (SAW) in yttrium iron garnet (YIG) films were shown to be rather useful methods for measuring MSW propagation parameters,[1-3] as well as for studying MSW nonlinear peculiarity.[4] The experimental procedure in this case consists mainly of measuring the output microwave (MW) signal level of frequency $f+F$ (or $f-F$) as a function of the input microwave signal frequency f at fixed SAW frequency F and external magnetic field H_0. Usually under nonelastic scattering of MSW by a SAW the maximum level of the output signal takes place at a certain input MW signal frequency f_0, when the phase synchronism conditions of nonelastic scattering are satisfied.

Recently, when investigating nonlinear MSW scattering by a SAW in YIG films we observed that the output signal of the $f \pm F$ frequency may have, under a certain condition, rather essential level in relatively wide input signal frequency range which is far away from the phase synchronism frequency f_0 and even outside the MSW frequency spectrum. Furthermore, such a signal appears also in nonsaturated YIG films at low external magnetic fields and its behavior as a function of input microwave signal power shows a steplike dependence.

We have no reliable explanation of these experimental results now, and we would like to present here some of these results and discuss one of the possible hypotheses which may probably serve as an approach for explaining these results.

The experimental setup is similar to that used by us for surface MSW (SMSW) nonelastic scattering by SAW investigations.

Figure 1 shows the experimental setup and the configuration of a gadolinium gallium garnet (GGG)–YIG film samples used for studying of the SMSW scattering by SAW phenomenon as well in our latest experiments. For excitation and reception of SMSW use was made of ordinary transducers, i.e., planar conductor antennas deposited on the surface of Y-Z $LiNbO_3$ plates and YIG film was placed on the top of these antennas, a very thin layer of vacuum oil being between the surface of $LiNbO_3$ plates and that of YIG film, providing rather good acoustic contact. SAW was excited by interdigital transducers (IDT). The insertion loss of such a SAW device was no higher than 20 dB at 15–40 MHz SAW frequencies in 50-Ω-measurement circuit. The dimensions of the antennas were $5 \times 0.025 \times 0.002$ mm^3.

We used 3–30 μ thick YIG films fabricated on ⟨111⟩ GGG substrates by the liquid phase epitaxy method. The structures under investigation were installed between the poles of an electromagnet as shown in Fig. 1.

At a certain input MW signal frequency f_0 at which the

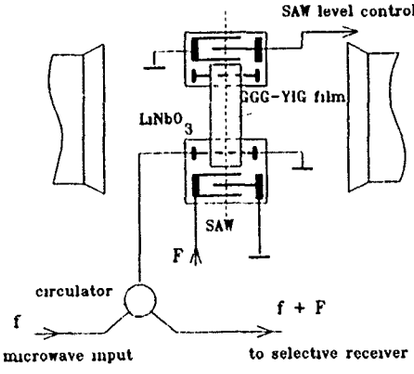

FIG. 1. Schematic of the experimental setup and the configuration of YIG film–GGG samples under investigation.

 0021-8979/94/76(10)/6880/3/$6.00 © 1994 American Institute of Physics

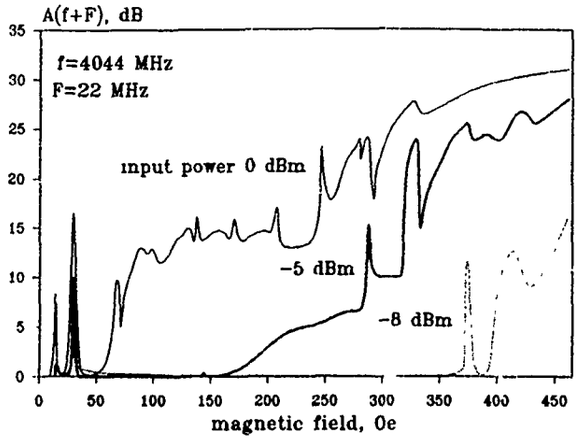

FIG. 2. The output signal level A of frequency $(f+F)$ as a function of the external magnetic field at three values of he input cw microwave powers. SAW—in pulse regime, pulse duration 10 μs, repetition rate 200 kHz. YIG film thickness 5 μ, planar dimensions of the samples 4×10 mm^2.

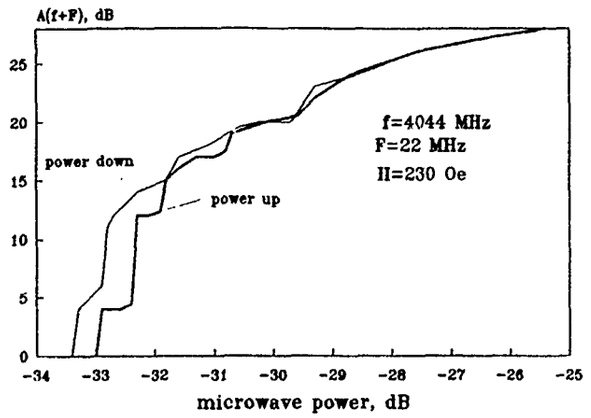

FIG. 4. Output signal level as a function of the input signal level for a 5-μ YIG film sample. $H=230$ Oe, SAW pulse power 50 mW. -30 dB in horizontal axis corresponds to 0 dBm.

phase synchronism conditions for the scattering are satisfied and at sufficient SAW power a substantial decreasing in the output MW signal level (transmitting SMSW level) is observed in the sample. This decreasing is proportional to the SAW power in a relatively wide range of SAW power variation. In this case a reflected (scattered) SMSW also can be observed. The reflected SMSW frequency in the case of the SMSW and SAW propagating in the same direction is less and in the counter-propagation case is higher than the frequency of the incident SMSW by the SAW frequency, F. The signal corresponding to the reflected SMSW may be taken from the input antenna with the help of a circulator as is shown in Fig. 1 and measured by a selective receiver tuned to $(f_0\pm F)$ frequency. It should be noted that such a technique is rather sensitive, because no problems connected with interference between the output signal of frequency $(f\pm F)$ and the input MW signal of frequency f arise.

When investigating SMSW scattering by SAW the input MW power usually did not exceed -20 dBm and experimental results were in good agreement with the theory.[1,3,5] At higher MW powers we observed the output signal of $(f\pm F)$ frequency at low external magnetic fields when the input signal frequencies f did not correspond to the scattering phase synchronism conditions and even were outside the MSW spectra for a given value of the external magnetic field. The measured output signal level of $(f+F)$ frequency as a function of external magnetic field H at three different values of the input signal powers is presented in Fig. 2 for 5-μ-thick YIG film (magnetic field was parallel to the antennas). One can see two relatively narrow peaks at low magnetic fields (one at 5–15 Oe and the second at 25–40 Oe). It should be noted that the power level of these peaks is directly proportional to the input MW signal power, though the output signal level at higher magnetic fields is essentially nonlinear function of the input power. The experimental results presented in Fig. 2 were obtained at 4044 MHz. Our investigations have shown that qualitatively similar dependences, including these two peaks, take place also at other frequencies in the range from 3500 MHz up to 4100 MHz.

In relatively thick YIG films (thicker than 20 μ) a series of two or more peaks at the 5–15 Oe position was observed, while only one peak was at 25–40 Oe as in the thin film case.

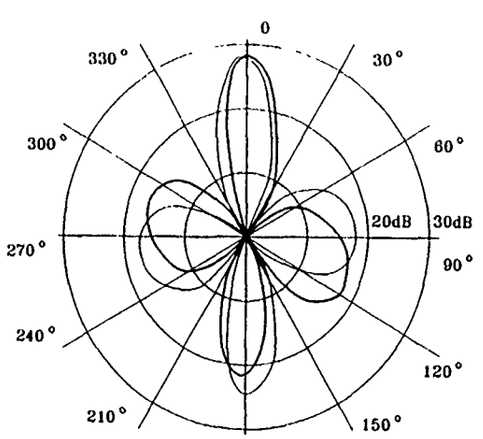

FIG. 3. The output signal level of $(f+F)$ frequency as a function of the angle between the external magnetic field vector and the direction of SAW propagation. $f=4044$ MHz, $F=22$ MHz, input microwave power 5 dBm, SAW power 20 dBm (pulse regime, 10-μs pulse duration), $H=37$ Oe.

Figure 3 represents the angular dependence of the output signal level measured for 5-μ YIG sample at 37-Oe magnetic field (the second peak in Fig. 2) at 0-dBm input power when the sample was turned around its vertical axes between the magnet poles. Zero degrees corresponds to a sample position when the direction of magnetic field is parallel to the antennas (see Fig. 1). The thick line in Fig. 3 represents the measurement result when a sample was rotated clockwise from 0° to 360°; the thin line represents the result when the sample was rotated in the opposite direction from 360° to 0°. Curves of the angular dependences of the output signal level measured at higher magnetic fields differed from these in Fig. 3 and were stretched along the 90° and 180° directions, when antennas were perpendicular to the magnetic field vector.

Measured output signal level as a function of the input microwave power for a 5-μ YIG film sample at 230-Oe magnetic field value is presented in Fig. 4. This measurement

was produced at magnetic field directed parallel to the antennas. SAW power was 50 mW. A steplike dependence and a hysteresis are clear seen in this picture.

It should be noted that a stripe domain structure (DS) with 120° blocks was observed in all our YIG film samples under investigation without external magnetic field. This DS was reconstructing under the action of external magnetic field.

We are coming now to the theoretical investigation of the MW combination scattering by spin fluctuations (SF) under acoustic pump in nonsaturated magnetic films at the first- and second-order phase transitions (PT) accompanied by the stripe DS transformations. The equilibrium orientation of domain walls (DW) depends on a DW type, the magnetic anisotropy and a direction of a magnetization field H_0 in a film plane. At the specific values H_0 the first- and second-order PT of DW reorientation type takes place in a film. On the other hand, as a magnetization field changes a DS with fixed period d can become unstable with respect to a sinusoidal (or zigzag) disturbance of a DW profile.[6] A long-order parameter of such PT is a displacement field amplitude $u(\mathbf{r},t)$ of DW points about their positions in a regular DS. Soft modes corresponding to the order parameter are DW flexural vibrations.

The intensity of the MW scattering U can be represented in the following form

$$U=(\omega^4/32\pi^4c^2)(e_\beta)^2V\ \mathrm{Re}\ i\int d\mathbf{k}'\langle\langle\Delta\epsilon_{\alpha\beta}(\mathbf{k}'-\mathbf{k},\omega-\omega')\Delta\epsilon_{\alpha\beta}(\mathbf{k}'-\mathbf{k},\omega-\omega')\rangle\rangle, \quad (1)$$

where V is a scattering volume, ω (ω') and $\mathbf{k}$ ($\mathbf{k}'$) are a frequency and a wave vector of falling (scattering) MW, respectively; wave vector $\mathbf{k}$ ($\mathbf{k}'$) is determined in a film plane (x,y); e is an intensity of the electric field of falling MW; $\Delta\epsilon_{\alpha\beta}(\mathbf{r},t)$ is a difference between the local and equilibrium value of dielectric permeability of ferromagnet; c is a MW speed; $\langle\langle...\rangle\rangle$ denotes the average over the statistical ensemble and over film thickness.

We will be further interested in the microwave scattering on the order parameter fluctuations. Therefore, it will be considered the corrections to the tensor of the dielectric permeability in the form

$$\Delta\epsilon_{\alpha\beta}=\Gamma_{\alpha\beta\gamma\delta\nu\sigma ik}U_{\gamma\delta}M_\nu\partial^2M_\sigma/\partial x_i\partial x_k, \quad (2)$$

where $\hat{\Gamma}$ is a magneto-optoelastic tensor, $U_{\gamma\delta}$ is the elastic deformation tensor induced by SAW; $U_{\alpha\beta}=U^0_{\alpha\beta}\times\exp i(\mathbf{k}_A\mathbf{r}_\perp-\omega_At)$; $\mathbf{k}_A$ and ω_A are a frequency and a wave vector of SAW, respectively; a tensor $\hat{U}$ corresponds to the Love waves.

Substituting Eq. (2) into Eq. (1) we find the intensity of the scattering microwave on the frequency interval $d\omega'$ and on the solid angle interval $d0$ in the form

$$dU=(V/16\pi)\times(\epsilon_0^{1/2}/c^2d^2)\omega^4(\Gamma_{\alpha\beta\gamma\delta\nu\sigma ik}Q_iQ_kU_{\gamma\delta}M_\nu M_\sigma e_\beta)^{2*}\times\langle\langle|u(\mathbf{Q},\omega)|^2\rangle\rangle d\omega'\ d0, \quad (3)$$

where a correlator of order parameter fluctuations is

$$\langle\langle|u(\mathbf{Q},\omega)|^2\rangle\rangle\propto 2\gamma T\Omega[(\Omega^2-\omega_s^2)^2+4\gamma^2\Omega^2]^{-1}, \quad (4)$$

a frequency of the DW flexural vibrations is $\omega_s(\mathbf{Q})=(S_x^2Q_x^2+S_y^2Q_y^2)^{1/2}$, S is a velocity of the DW flexural vibrations, γ is the DW flexural vibrations damping, $\Omega=\omega'-\omega-\omega_A$, $\mathbf{Q}=\mathbf{k}-\mathbf{k}'-\mathbf{k}_A$. The following relations for frequencies and wave vectors: $\omega\approx\omega'\gg\omega_A\gg\Omega$, $k\approx k'\ll k_A\approx Q$ take place.

Generally, the magnitude of dU is negligibly small. Situation reverses in the vicinity of the second-order PT point H_c when DS loses stability with respect to the DW reorientation or with respect to the sinusoidal disturbance of a DW profile. Then the projection of the velocity of the DW flexural vibrations on the DW direction (for definiteness sake we denote this projection S_x) tends to zero ($S_x\propto|H_0-H_c|^{1/2}$). In that case, when the conditions $\Omega=\omega_s(\mathbf{Q})$, $\mathbf{Q}=\mathbf{k}'-\mathbf{k}-\mathbf{k}_A$ are fulfilled, the MW scattering intensity increases abruptly and the scattering effect can be accessible to observation. MW scattering intensity depends heavily on the direction of MW and SAW propagation in a film plane. It has a maximum $dU\propto(\gamma\omega_s)^{-1}\propto|H_0-H_c|^{-1/2}$ for $\mathbf{k}\parallel\mathbf{k}_A\parallel\mathbf{x}$.

At the first-order PT point a discontinuous jump of the DW direction or DW profile disturbance of finite amplitude takes place. In that case a correlator $\langle\langle|u(\mathbf{Q},\omega)|^2\rangle\rangle$ has δ-shaped peculiarity. In real crystals even a weak dispersion of magnetic parameters of a film leads to blurring of such a peculiarity and decreasing of MW scattering intensity peak. So the intensity peak has a finite width and can be accessible to observation.

Thus we suppose a hypothesis for explaining the formation of intensity peaks of the MW scattering in the weak magnetic fields. In line with it we observed the MW combination scattering by SF under acoustic pump in nonsaturated magnetic films at the first- and second-order PT accompanied by DS transformations. This hypothesis gives the reasonable qualitative explanation of the following experimental results: (1) the linear dependence of the MW scattering intensity on MW and SAW power; (2) a weak dependence of the positions of peaks of the MW scattering intensity on MW and SAW frequencies; (3) abrupt increase of the MW scattering power $dU\propto|H_0-H_c|^{-1/2}$ in the vicinity the PT field $H_0=H_c$; (4) the strong dependence of the MW scattering power on the direction of a magnetization field in a film plane.

There is no appropriate explanation of effects of high MW scattering far away from the phase synchronism fre quency range. For the calculation of these effects it is necessary to take into account the high order processes involving MW, SAW, and SF. Jumps of MW scattering intensity can be associated with the DS transformation in the high MW fields.

[1] R. G. Kryshtal and A. V. Medved, Sov. J. Tech. Phys. **57**, 1936 (1987).
[2] R. G. Kryshtal *et al.*, Sov. J. Tech. Phys. **58**, 2315 (1988).
[3] R. G. Kryshtal and A. V. Medved, Sov. J. Tech. Phys. **59**, 82 (1989).
[4] R. G. Kryshtal and A. V. Medved, Sov. Phys. Solid. State **34**, 335 (1992).
[5] A. F. Popkov, Radiotekh. Elektron. **27**, 1366 (1982).
[6] I. E. Dikshtein *et al.*, Sov. Phys. JETP **73**, 114 (1991).

Light scattering from spin waves in MnF_2

M. G. Cottam
Physics Department, University of Western Ontario, London, Ontario, Canada N6A 3K7

V. P. Gnezdilov,[a] H. J. Labbé, and D. J. Lockwood
National Research Council, Ottawa, Ontario, Canada K1A 0R6

Measurements of the weak one-magnon light scattering in the antiferromagnet MnF_2, including Stokes and anti-Stokes scattering, as a function of temperature are reported. From the theoretical analysis of the temperature and polarization dependences of the integrated Raman intensities, values are deduced for the ratio of quadratic and linear magneto-optical coupling coefficients.

The observation of one-magnon light scattering in the tetragonal, insulating antiferromagnet MnF_2(T_N=68 K, S=5/2) was reported earlier.[1] However, experimental difficulties due to the low frequency of the spin waves and their weak light scattering intensity precluded an accurate study of their temperature dependence. The advent of a high-resolution spectrometer with high stray-light rejection has now enabled a detailed study of the Stokes and, for the first time, the anti-Stokes scattering as a function of temperature. The magnon frequency in zero-applied magnetic field renormalized from 8.7 cm^{-1} at low temperature [consistent with antiferromagnetic resonance results (Ref. 2)] to 4.8 cm^{-1} at 57 K, while the linewidth increased slightly from about 0.6 to 0.8 cm^{-1} over the same temperature range. The magnon Raman integrated intensity exhibited a pronounced polarization dependence in both Stokes and anti-Stokes scattering. The measured temperature and polarization dependences of the Stokes and anti-Stokes intensities has enabled a theoretical study to be carried out for the magneto-optical coupling in MnF_2.

The MnF_2 crystal used in this study has been described elsewhere.[1] The sample was mounted in a Janis DT cryostat for the low-temperature measurements and the sample temperature was controlled and measured to within ±0.1 K. The magnon Raman spectrum was excited with 800 mW of argon laser light at 476.5 nm, which resulted in little laser heating of the sample[1] (the temperatures quoted have been corrected for a 1.0-K laser heating). The light scattered at 90° was analyzed with a SOPRA DMDP2000 double monochromator, which has the high-resolution capability (better than 0.03 cm^{-1}) and high stray-light rejection needed for this experiment,[3] and detected with a cooled Hammamatsu R928P photomultiplier. In the analysis of the scattered light polarization, the X,Y,Z labels refer to the a,b,c crystallographic axes, respectively. A typical anti-Stokes–Stokes Raman spectrum is shown in Fig. 1.

The relevant theories for the temperature dependence of the magnon frequencies and the one-magnon Raman intensities are already well established for antiferromagnets with the rutile crystal structure of MnF_2 (see, e.g., Refs. 1, 4, and 5). Here, we test the theories by comparing with the experimental data and, from the analysis, we deduce results for the nature of the magneto-optical coupling in MnF_2.

The Raman peak positions for the temperature dependence of the magnon frequency are shown in Fig. 2, combining results from Stokes and anti-Stokes scattering in several polarizations. The peak frequencies were measured to within ±0.05 cm^{-1} for the stronger lines. Comparisons are made with two types of theory, as described before.[1] The broken and solid lines refer, respectively, to predictions of a linear spin-wave theory and a perturbation theory. The latter includes effects of magnon–magnon interactions and is valid over a limited range of temperature (up to $\sim 0.6T_N$ in this case). We assumed J=2.49 cm^{-1} for the dominant exchange interaction (neglecting the small effect of the other exchange interactions for the zone-center magnons excited by Raman scattering) and $g\mu_B H_A$=0.75 cm^{-1} for the uniaxial anisotropy at low temperatures, consistent with neutron scattering data.[6] The temperature dependence of the anisotropy is conventionally introduced by writing $H_A \propto \langle S^z \rangle^n$, where $\langle S^z \rangle$ is the sublattice spin average and n is a positive index[1] with a value depending on the physical origin of the anisotropy. If the neighboring spins are considered as being either completely uncorrelated (implying $\langle S_i S_j \rangle = \langle S_i \rangle \langle S_j \rangle$ for sites $i \neq j$ as in mean-field theory) or strongly correlated, then this would lead to n=1 and n=2, respectively, as limiting values. In Figure 2 we show the theory curves for n=1 and n=2. On

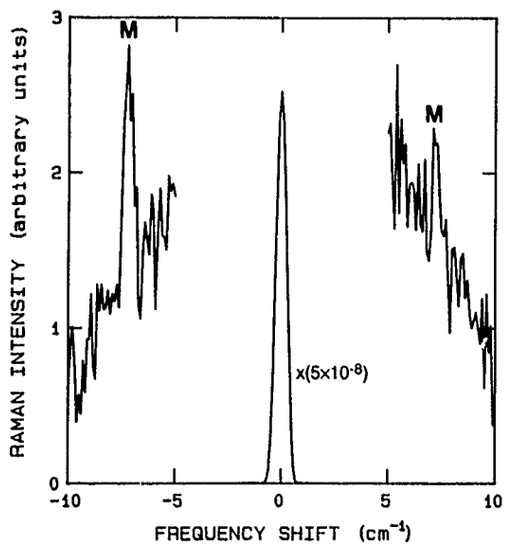

FIG. 1. One-magnon (M) Raman spectrum of MnF_2 at 41 K in $X(ZX)Y$ polarization with a spectral resolution of 0.53 cm^{-1}.

[a]Permanent address: Institute for Low Temperature Physics and Engineering, Ukrainian Academy of Sciences, 310164 Kharkov, Ukraine.

 0021-8979/94/76(10)/6883/3/$6.00 © 1994 American Institute of Physics

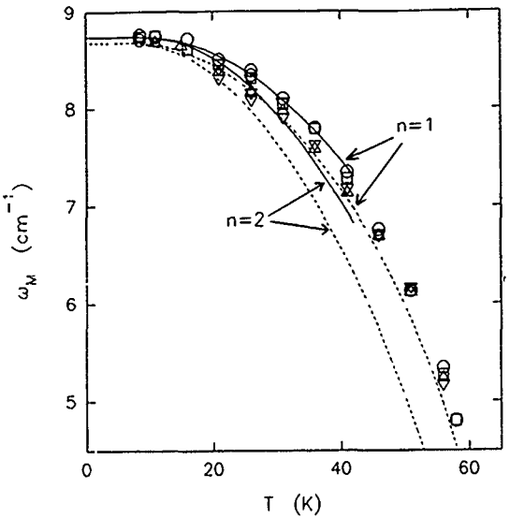

FIG. 2. Comparison of experiment and theory for the temperature dependence of the magnon frequency. The data points refer to ○, Stokes scattering in (XZ) polarization; □, Stokes scattering in (YZ) polarization; △, anti-Stokes scattering in (ZX) polarization; ▽, anti-Stokes scattering in (ZY) polarization. The broken and solid lines refer to linear and interacting spin-wave theories, respectively (see text).

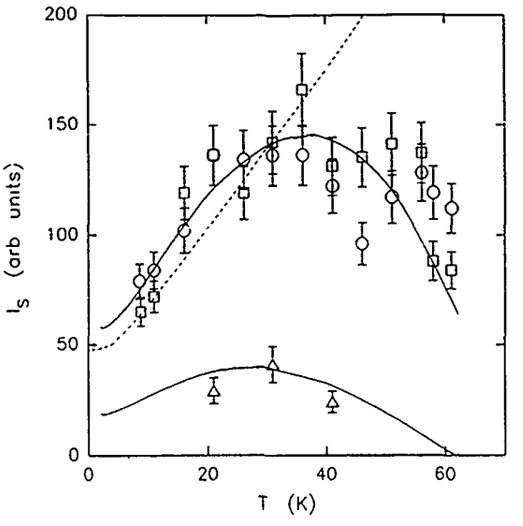

FIG. 3. Experiment and theory for the temperature dependence of the integrated intensity for Stokes scattering in several polarizations. The experimental points refer to ○, (XZ) polarization; □, (YZ) polarization; △, (ZX) polarization. The theory curves are for $G_+/K_+=0$ (broken line) and $G_+/K_+=0.08$ (solid lines).

comparing with the experimental data, which are more detailed and extend to higher temperatures than in Ref. 1, we see that taking $n=1$ provides a clearly better fit in the case of the linear theory and a marginally better fit also in the case where spin-wave interactions are included.

We next discuss the results for the light-scattering intensities. Data have been obtained for both Stokes and anti-Stokes scattering in $X(ZX)Y$ and $Z(YZ)Y$ polarizations, for Stokes scattering in $Z(XZ)Y$ polarization, and for anti-Stokes scattering in $Y(ZY)Z$ polarization. Some results for the temperature dependences of the Stokes and anti-Stokes integrated intensities, I_S and I_{AS}, are shown in Figs. 3 and 4, respectively, and will be discussed later. The units are arbitrary, but are consistent between the two figures. According to theory, I_S for Stokes scattering takes the general form[1,4]

$$I_S=A\langle S^z\rangle(n_M+1)(F_{in}+F_{out})/\omega_M, \quad (1)$$

where the overall factor A is independent of the temperature T and the scattering geometry, ω_M is the magnon frequency, and $n_M=[\exp(\hbar\omega_M/k_BT)-1]^{-1}$ is the corresponding Bose factor. The quantities F_{in} and F_{out} refer to the in-phase and out-of-phase contributions, respectively, to the scattering from the two sublattices of the antiferromagnet. Their explicit expressions are given in Ref. 1 and include the effects of a magneto-optic coupling that is quadratic in the spin operators as well as the usual linear magneto-optical coupling.[1,4] The quadratic magneto-optical coupling is known to be important in another rutile-structure antiferromagnet[4,5] FeF_2, and it is of interest to determine its effect in MnF_2. The possibility of an out-of-phase term in I_S arises because the two sublattices in FeF_2 are not equivalent (due to the coordination of the F^- ions). Hence, the theoretical model involves four magneto-optical coefficients that are independent of temperature and light scattering geometry. Following Ref. 1, these are denoted by K_+ and G_+ for the linear and quadratic magneto-optical coupling for in-phase scattering, while K_- and G_- are the corresponding coefficients for out-of-phase scattering.

The expression for the anti-Stokes intensity I_{AS} is similar to Eq. (1) provided the factor (n_M+1) is replaced by n_M. Also F_{in} and F_{out} are replaced by $\tilde{F}_{in}$ and $\tilde{F}_{out}$, respectively, obtained by making the substitutions[4] $K_+\rightarrow -K_+$ and $K_-\rightarrow -K_-$ in the definitions of F_{in} and F_{out}. In general, $F_{in}\neq\tilde{F}_{in}$ and $F_{out}\neq\tilde{F}_{out}$ (except in the limits of linear magneto-optical coupling only or quadratic magneto-optical

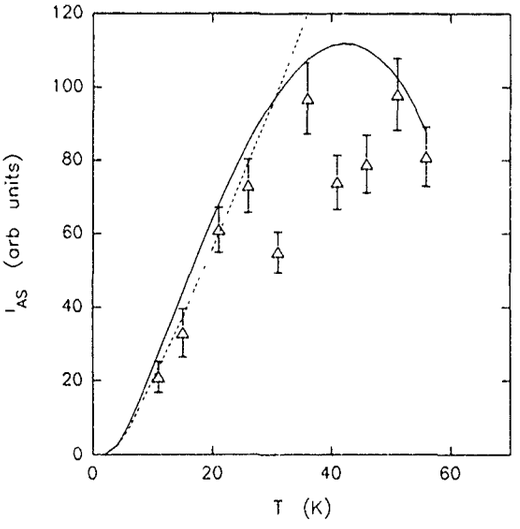

FIG. 4. Experiment and theory for the temperature dependence of the integrated intensity for anti-Stokes scattering. The experimental points (△) refer to (ZX) polarization. The theory curves are for $G_+/K_+=0$ (broken line) and $G_+/K_+=0.08$ (solid line).

coupling only), and consequently the intensity ratio I_{AS}/I_S differs from the usual thermal factor $n_M/(n_M+1)$ when both types of magneto-optical couplings apply. Also the individual temperature dependences of I_S and I_{AS} are modified and depend on the polarization, e.g., as confirmed experimentally for FeF_2 (see Ref. 5).

In making preliminary comparisons of theory with experiment for the Raman integrated intensities in MnF_2, we have assumed for simplicity that in-phase scattering is dominant. This would be expected because the deviation from tetragonal symmetry at a Mn^{2+} site is relatively small. For the Stokes data in Fig. 3, the theory predicts that $I_S(XZ)=I_S(YZ)$ at any given temperature, whatever the values are for K_+ and G_+, whereas $I_S(ZX)$ will be different (unless $G_+/K_+=0$). It is seen that the intensity data points (allowing for an experimental uncertainty of 10% to 20% typically) broadly confirm this prediction and allow us to make a rough estimate for the ratio G_+/K_+. First, we note that in the absence of any quadratic coupling ($G_+/K_+=0$), the intensities for all three polarizations would be described by the broken curve in Fig. 3, which provides an inadequate fit to the data. A much better fit is provided if G_+/K_+ is small and positive, as illustrated by the solid lines for $G_+/K_+=0.08$ in Fig. 3, where the upper line refers to (XZ) and (YZ) polarizations and the lower line to (ZX) polarization.

Similarly, for the anti-Stokes data, the role of quadratic coupling is to enhance the intensities in certain polarizations (making it easier to study experimentally) and to modify the temperature dependence. In Fig. 4 it can be seen that the variation of $I_{AS}(ZX)$ is much better described by the solid theory curve for $G_+/K_+=0.08$ than by the broken curve for $G_+/K_+=0$. Further evidence that $G_+/K_+\neq 0$ is provided by the intensity ratio I_{AS}/I_S in (ZX) polarization, where we have measurements at three different temperatures. Overall, from the T dependences of I_S and I_{AS} and from the behavior of I_{AS}/I_S, we deduce that G_+/K_+ lies approximately in the range 0.05 to 0.1.

In conclusion, we have presented new experimental data for the Stokes and anti-Stokes light scattering in MnF_2. From a preliminary analysis for the dependence of the integrated intensities on temperature and polarization, we obtain good agreement between theory and experiment. The results indicate that, while the linear magneto-optical coupling coefficient K_+ for in-phase scattering is dominant, there is an important contribution due to the quadratic in-phase coefficient G_+. A more detailed comparison between theory and experiment will be undertaken to determine if out-of-phase scattering is significant.

[1] D. J. Lockwood and M. G. Cottam, Phys. Rev. B **35**, 1973 (1987).
[2] F. M. Johnson and A. H. Nethercot, Phys. Rev. **114**, 705 (1959).
[3] D. J. Lockwood, Surf. Sci. **267**, 438 (1992).
[4] M. G. Cottam, J. Phys. C **8**, 1933 (1975).
[5] M. G. Cottam and D. J. Lockwood, *Light Scattering in Magnetic Solids* (Wiley, New York, 1986).
[6] A. Okazaki, K. C. Turberfield, and R. W. H. Stevenson, Phys. Lett. **8**, 9 (1964).

Controlling high frequency chaos in circular YIG films

D. W. Peterman, M. Ye, and P. E. Wigen
Department of Physics, The Ohio State University, Columbus, Ohio 43210

High power ferromagnetic resonance experiments involving thin circular YIG films produce chaotic oscillations with broad band frequency spectra in the 0.5–25 MHz range. To eliminate chaotic oscillations, a delayed feedback of the ac component of the ferromagnetic resonance signal was used to modulate one of the system parameters, the applied static magnetic field. The chaotic oscillations were converted to oscillations of reduced periodicity, and ultimately the quiescent state, as the gain in the feedback loop was increased. Similar results have been obtained in numerical simulations.

I. INTRODUCTION

The ability to control chaos has generated much experimental and theoretical interest.[1–6] Chaos in nonlinear dynamic systems can be controlled by applying small perturbations to an accessible system parameter to stabilize an unstable periodic orbit of the system's chaotic attractor. Using the method proposed by Ott, Grebogi, and Yorke (OGY),[1] the discrete perturbations to the chaotic system are calculated from the dynamic properties of the chaotic system near the unstable fixed point on the Poincare map corresponding to the periodic orbit onto which the system is going to be stabilized. This method of controlling chaos has been used successfully in a number of different experimental systems.[2–4]

In high power ferromagnetic resonance (FMR) experiments involving thin films, interactions between magnetostatic modes give rise to the observed nonlinear effects.[7,8] Above some threshold of the rf pumping power, instability oscillations in the absorption signal are observed. With increasing pumping power, the oscillations bifurcate from periodic to chaotic oscillations through period doubling.[9,10] The fundamental frequencies of chaotic oscillations in the absorption signals are typically in the range of 0.5–4.0 MHz. The high frequency dynamics in the FMR experiments make it difficult to control the chaos using discrete perturbations such as the OGY method. Consequently, for controlling chaos at high frequencies, a time delayed feedback method has been developed, in which the chaotic signal detected from the sample was time delayed and amplified before it was used to perturb a system parameter, the bias magnetic field of the sample. An advantage of this analog continuous feedback method is that no detailed calculation is necessary, allowing unstable orbits with submicrosecond periods to be controlled. In addition to stabilizing unstable periodic orbits of the attractor, the total suppression of auto-oscillations, the quiescent state, can be obtained by using this method as well. Suppression of chaos, resulting in periodic oscillations in experimental FMR using external sinusoidal modulation of the applied field has been previously reported.[11,12]

II. EXPERIMENT

The experiments were performed on circular disks of yttrium iron garnet (YIG) film roughly 2 mm in diameter and about 1 μm thick. A static magnetic field of about 2000 Oe was applied perpendicular to the film plane. The sample was excited into resonance by an rf pumping field of around 1.2 GHz which was produced by a slotline structure and oriented perpendicular to the static field.[13] Radio frequency absorption of the sample was detected by a diode. Under high rf pumping power, the absorption signals of the sample were observed to show periodic or chaotic oscillations with typical frequencies of a few MHz. The emergence of the oscillations is a function of the frequency and power of the rf pumping field, and the magnitude of the static bias field.[7,8]

In the experiments, the static field and rf power were chosen to produce a chaotic absorption signal from the sample. The ac component of the oscillating signal at the diode was fed into a delay line and then to a voltage to current converter amplifier. The current from the amplifier was used to drive a 20 turn coil 5 mm in diameter, approximately 1 mm above the YIG sample. The coil plane was adjusted to be parallel to the sample plane. The magnetic field produced by the coil perturbed the static magnetic field. The delay time and the gain of the feedback loop could be adjusted to achieve the control of chaos. Only the ac component in the output current from the amplifier was used for the perturbations. This was done to prevent a dc component that could bias the system out of the chaotic state by the application of a constant term to the bias field. This also allowed the perturbation to the system to approach zero as the oscillation amplitude in the rf absorption signal was reduced due to the effect of the perturbations.

Figure 1 shows an experimental result of controlling chaos. In this case the chaotic absorption signal of the sample was time delayed by 470 ns. As the feedback gain was increased, the absorption signal from the sample was converted to a period-4 oscillation by the perturbation fields of the coil. Further increase of the feedback gain resulted in a period-2, period-1, and finally the quiescent state, where only dc absorption was present in the FMR signal even though the pumping field was sufficient to maintain a chaotic state without the control. Delay coordinate plots of the data presented in Fig. 1 were used to construct attractors for the controlled and uncontrolled signals. From visual inspection of these attractors in delay coordinate space, it is apparent that the stabilized period-4 and period-2 orbits are unstable orbits of the unperturbed chaotic attractor. In the quiescent state, the amplitudes of the frequency components in the Fourier spectrum were found to be 20–30 dB less than those of the chaotic spectrum. A chaotic signal reemerged from the quiescent state when the gain was increased even further. Other samples show similar behavior.

 0021-8979/94/76(10)/6886/3/$6 00 © 1994 American Institute of Physics

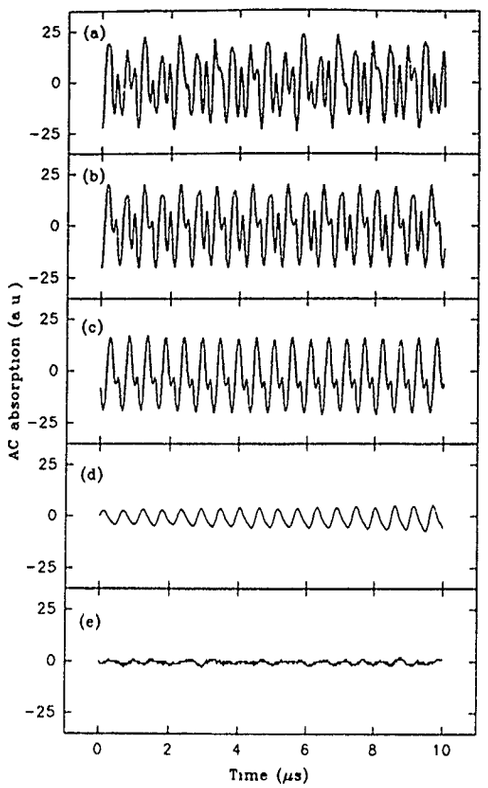

FIG. 1. Experimental results for controlling chaos in FMR using the time delayed feedback method. (a) Chaotic oscillation of FMR signal without perturbation. (b) Controlled period-4 oscillation (gain=0.45 arbitrary units). (c) Controlled period-2 oscillation (gain=0.80 a.u.). (d) Controlled period-1 oscillation (gain=5.50 a.u.). (e) The quiescent state (gain=6.50 a.u.), in which all oscillations were extinguished.

The amplitudes of the perturbation field required to maintain the periodic oscillations were in the range of 0.01–0.1 Oe. In preserving the quiescent state, the coil produced fields of less than 0.01 Oe. Thus, the ratio of perturbation field to the static magnetic field was about 10^{-4} for controlling periodic oscillations. The ratio was less than 10^{-5} for maintaining the quiescent state. Removal of the perturbation field caused the system to revert back to the chaotic state. It was possible to stabilize periodic orbits for several values of the feedback gain, but quiescence was only achievable with a delay time of around 470 ns.

Figure 2 shows another example of controlling chaos using time delayed feedback. However, in this example, the derivative of the sample absorption signal was time delayed before it was used to perturb the static field. Although the quiescent state has not yet been achieved, this example also shows a debifurcation route with increasing feedback gain, as seen in Fig. 1. With increasing rf power, the sample displayed a period doubling route to chaos. Applying time delayed feedback led to the stabilization of period-2 and period-1 orbits as the feedback gain was increased. In this example, the perturbation fields ranged from 0.1 to 0.5 Oe and the delay time used was 390 ns. In addition, the system attractors of both the controlled and uncontrolled signals in a delayed coordinate plot indicate that the controlled orbits were unstable orbits of the unperturbed chaotic attractor.

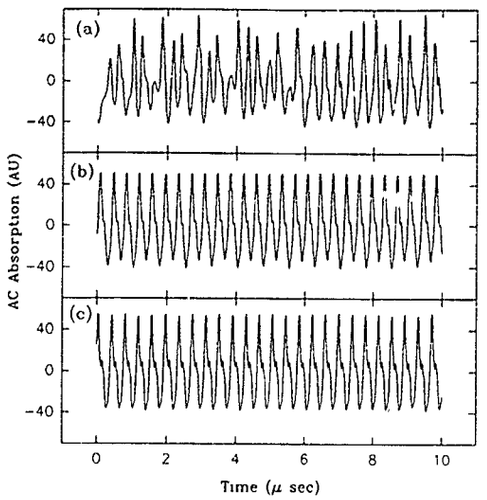

FIG. 2. Experimental results for controlling chaos in FMR using time delayed derivative feedback method. (a) Chaotic oscillation of FMR signal without perturbation. (b) Controlled period-2 oscillation (gain=2.4 a.u.). (c) Controlled period-1 oscillation (gain=4.2 a.u.).

III. SIMULATION

In the numerical simulations for controlling chaos in FMR using the time-delayed feedback method, the theoretical model developed by McMichael and Wigen was used.[8] The normal modes in thin circular YIG films are the magnetostatic modes, which have the form of Bessel functions. By integrating the equations of motion for the complex amplitude of these modes, the dynamic behavior of the system could be simulated. The FMR signal in the model, $S(t)$ was proportional to the sum of the imaginary parts of the mode amplitudes. This corresponded to the absorption signals measured in experiments. To simulate the time delay feedback, the static magnetic field H_0 in the equations of motion was modulated by the ac component of the FMR signal

$$H_{\text{total}}(t)=H_0+K[S(t-\delta)-\overline{S(t-\delta)}].$$

Here δ is the delay time and K is proportional to the gain of the feedback loop in the experiment. The dc component of the FMR signal $\overline{S(t-\delta)}$ is subtracted so that only the ac component in $S(t)$ is used for perturbation. The debifurcation route caused by increasing the feedback gain observed in the experiments is predicted in the simulations for both direct and derivative time delayed feedback. Also, the values and sensitivity of the delay times used in the model are similar to those observed in the experiment.

IV. CONCLUSION

In conclusion, through use of time delayed feedback, very high frequency chaotic absorption signals of FMR have been controlled by perturbing the static magnetic field continuously. In using this time delayed feedback method for controlling chaos, no detailed analysis of the system's attractor needs to be made. It is suitable for controlling the chaos in complicated systems which show high frequency oscillations. All that is required is the alteration of some system parameter by a time delayed signal of the system's output.

Another advantage of this method is that the chaotic state can be converted to the periodic state as well as the quiescent state. Finally, a mixture of the derivative signal and the original signal of the system's output can be used in this time delayed feedback method to control the chaos. Experiments using these techniques have shown promise and the work is ongoing.

ACKNOWLEDGMENT

The authors wish to acknowledge funding from the National Science Foundation, Grant Number DMR-9017223.

[1] E. Ott, C. Grebogi, and J. Yorke, Phys. Rev. Lett. **64**, 1196 (1990).
[2] W. Ditto, S. Rauseo, and M. Spano, Phys. Rev. Lett. **65**, 3211 (1990).
[3] E. Hunt, Phys. Rev. Lett. **67**, 1953 (1991).
[4] R. Roy, T. Murphy, T. Maier, Z. Gills, and E. Hunt, Phys. Rev. Lett. **68**, 1259 (1992).
[5] K. Pyragas and A. Tamasevicius, Phys. Lett. A **180**, 99 (1993).
[6] K. Pyragas, Phys. Lett. A **170**, 421 (1992).
[7] R. McMichael and P. Wigen, Phys. Rev. Lett. **64**, 64 (1990).
[8] R. McMichael and P. Wigen, Phys. Rev. B **42**, 6723 (1990).
[9] M. Ye and H. Dötsch, Phys. Rev. B **44**, 9458 (1991)
[10] P. E. Wigen, H. Dötsch, Y. Ming, L. Baselgia, and F. Waldner, J. Appl. Phys. **63**, 4157 (1988).
[11] A. Azevedo and S. M. Rezende, Phys. Rev. Lett. **66**, 1342 (1991).
[12] M. Ye, D. Jones, and P. Wigen, J. Appl. Phys. **73**, 6822 (1993).
[13] B. Lührmann, M. Ye, H. Dötsch, and A. Gerspach, J. Magn. Magn. Mater. **96**, 237 (1991).

Study of spin wave resonance in a superconductor with paramagnetic impurities

I. A. Garifullin, Yu. V. Goryunov, and G. G. Khaliullin
Kazan Physical-Technical Institute, Kazan 420029, Russia

The spin dynamics of paramagnetic impurities in a superconductor in the presence of external magnetic field has been studied both theoretically and experimentally. Long-wave excitations ($q \leqslant \xi^{-1}$, where ξ is the coherence length) are shown to have coherent spin-wave nature even in a paramagnetic phase. This effect is caused by the long-range ($R \sim \xi$) indirect exchange interaction between localized spins in a superconductor. The spin-wave effects in EPR of Er^{3+} ions in the superconducting (SC) $La_{1-x}Er_x$ thin films have been observed. An additional absorption at the high field side of the main resonance line which leads to its distortion has been found. Satisfactory description of all features of observed spectra was obtained by simulating the spectra with account for the microwave absorption by spin-wave excitations. The spin stiffness coefficient and the temperature dependence of the spin susceptibility of the SC lanthanum has been determined.

I. INTRODUCTION

Previous study of EPR of Er^{3+} ions in the superconductor[1] revealed anomalous behavior of the EPR linewidth ΔH which contrasted strongly with the expected change in ΔH. Instead of increasing due to the coherence effects the EPR linewidth narrowed sharply at the transition to the SC state. This effect was attributed to a new long-range exchange coupling of local moments in the SC phase due to correlations in Cooper condensate. This idea on additional indirect interaction was previously proposed by Anderson and Suhl[2] when they discussed the magnetic ordering in the SC phase.

The exchange-coupling integral in a superconductor[3] can be represented approximately as a sum of two parts $J_n(R)+J_s(R)$, the first one, acting at short distances,

$$J_n(R) \approx (J_0 v_0/4\pi R^3)\cos(2k_F R), \tag{1}$$

being the conventional *RKKY* interaction, and the second one

$$J_s(R) \approx (J_0 v_0/4\pi\xi^2 R)\,\delta\chi(T)\exp(-R/\xi), \tag{2}$$

being the SC correction. In Eqs. (1) and (2) v_0 is the volume per lattice site, and k_F is the Fermi momentum. The quantity

$$\delta\chi(T) = (\chi_p - \chi_s)/\chi_p \leqslant 1 \tag{3}$$

characterizes the decrease in the spin susceptibility χ_s of conduction electrons in the singlet BCS state as compared with the Pauli susceptibility χ_p. The constant $J_0 = J_{sf}^2 \rho(\epsilon_F) v_0/2$ is determined by the $s-f$ coupling constant J_{sf} and the electron density of states $\rho(\epsilon_F)$.

The additional interaction (2) is of an antiferromagnetic character. Its contribution to the total molecular field is of the same order of magnitude as the normal RKKY contribution (1). Furthermore, even when the concentration x of magnetic impurities is low, the number of spins $N \approx x\xi^3/v_0$ in the interaction region is anomalously high, since ξ is much larger than the lattice constant a. This introduces a new feature into spin dynamics: the long-wave excitations in an external magnetic field exhibit spin-wave behavior.

This report is devoted to the investigations of the spin-wave excitations of paramagnetic impurities in a superconductor in an external field.

II. THEORY

We calculated the dynamic susceptibility $\chi_{\omega,q}$ of local moments using the method of nonequilibrium statistical operator.[4] We obtained the following spin excitation spectrum at $q \leqslant \xi^{-1}$

$$\omega_q = \epsilon_q - i(\gamma_q^{ex} + \gamma_q^{dd}). \tag{4}$$

Here the spin excitation energy ϵ_q and its damping due to the exchange fluctuations (γ_q^{ex}) and dipole-dipole coupling (γ_q^{dd}) can be written as

$$\epsilon_q = g\beta H_0 - D'' q^2, \quad D'' \approx x\langle S^x\rangle \delta_\chi J_0 \xi^2, \tag{5}$$

$$\gamma_q^{ex} = D' q^2, \quad D' \approx x^{1/3}\langle S^x S^x\rangle^{1/2} J_0 a^2/4, \tag{6}$$

$$\gamma_q^{dd} = \frac{3}{5}(2\pi)^{5/2}\frac{x\langle S^x S^x\rangle^{1/2}}{J_0}\left(\frac{g^2\beta^2}{v_0}\right)^2. \tag{7}$$

$\langle S^x\rangle$ in Eq. (5) is the local moment polarization induced by magnetic field H_0, g being g value. Note that the q-dependent part of Eq. (5) is mainly contributed by the SC correction (2). It is precisely the long-range potential (2) which produces the transverse stiffness and real dispersion of spin excitations. Comparing the the energy (5) and the damping (6) we find that the condition for the existence of coherent spin motion

$$\frac{D''}{D'} \approx \left(\frac{\xi}{r_{av}}\right)\frac{g\beta H_0}{k_B T} \gg 1 \tag{8}$$

is easily satisfied in superconductors with the large coherence length ξ (compared with the average distance between impurities r_{av}) in magnetic fields of the order of several kilogauss and at liquid-helium temperatures. For $q > \xi^{-1}$ spin excitations are incoherent. The negative sign in the dispersion relation (5) reflects the antiferromagnetic nature of the potential (2); as the temperature decreases, the spectrum ϵ_q softens and magnetic order appears at nonzero wave vectors $q \sim \xi^{-1}$, as predicted by Anderson and Suhl.[2] For small q the damping is determined by the dipole contribution γ_q^{dd}. A "window" for spin-wave excitations exists if

$$x\langle S^x\rangle(\delta_\chi) J_0 > \gamma_q^{dd}. \tag{9}$$

 0021-8979/94/76(10)/6889/3/$6.00 © 1994 Amer.can Institute of Physics

This condition can also be satisfied, since exchange coupling in metals is usually stronger than the dipole-dipole interaction. Thus when the conditions (8) and (9) are satisfied, the long-wave spin dynamics has a magnon character. Of course, the contribution of these excitations to the thermodynamic parameters is negligible; the main fraction of the spectral density of spin fluctuations is incoherent and is determined by the short-range RKKY potential. Spin waves can only appear in the long-wave magnetic response of a superconductor.

We present below the experimental evidence for spin-wave effects in a superconductor with magnetic impurities, obtained in EPR studies performed in $La_{1-x}Er_x$ thin films.

III. EXPERIMENT

Films of $La_{1-x}Er_x$ with $x=0.008-0.02$ and thickness $L=2500-5000$ Å were prepared by separate thermal evaporation of the components from tantalum crucibles. The prepared film was coated immediately by a protective silicon monooxide layer of 3000 Å thickness.

X-ray structural analysis showed that all prepared films have mainly an face-centered-cubic structure. Measurements of the electrical resistivity, of the SC critical parameters, and of the magnetization in the SC state have been performed in addition to the EPR measurements. These data will be used in the discussion of our EPR results.

EPR experiments were carried out at 9.4 GHz in a rectangular TE_{102} cavity in the temperature range from 1.5 to 20 K. The out-of-plane angular dependencies of the spectra were observed with the microwave field lying in the film plane.

In the normal state we observed EPR line of Er ions which was just similar to that previously observed in bulk samples.[1] A change in the angle between the plane of the sample and the direction of the dc magnetic field had no effect on the position and shape of the EPR line [Fig. 1(a)]. Upon transition to the SC state in perpendicular orientation of the film to the direction of dc magnetic field the line shape did not change [Fig. 1(d)]. In a longitudinal magnetic field, however, the shape of the signal became drastically distorted as the temperature was lowered [see Figs. 1(b) and 1(c)]. The degree of distortion of the high field wing of absorption signal was dependent on thickness of film and erbium concentration in the sample (Fig. 2). These effects are illustrated by the EPR spectra shown in Figs. 1 and 2.

IV. ANALYSIS OF RESULTS

It is unlikely that the unusual behavior of the EPR spectrum in the studied films could be attributed to a magnetic field distribution in a vortex lattice which differs from that found in a bulk sample. The amplitude of the magnetic field variation and the value of the London penetration depth λ, which we estimated from our measurements of the critical field and the SC moment of the films, turned out to be on the order of 50 Oe and 600 Å, respectively. These values are essentially the same as those obtained for the bulk samples.[1]

We believe that the shape of the signal is distorted because of the additional absorption of the microwave energy

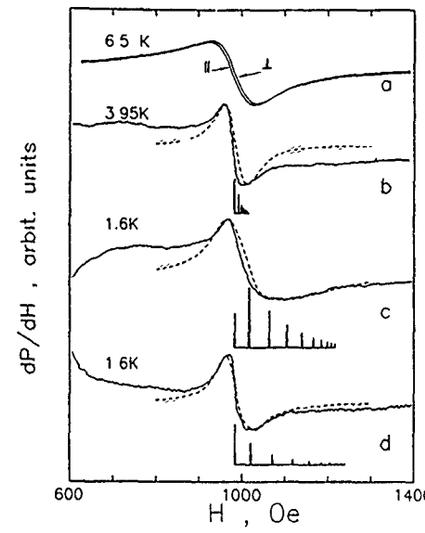

FIG. 1. EPR spectra for the sample with $L=4800$ Å, $x=0.014$ and critical temperature $T_c=5.0$ K at different temperatures: in a normal state with magnetic field oriented parallel and perpendicular to the plane of the film (a) and in the SC state with magnetic field oriented parallel (b) and (c) and perpendicular (d) to the plane of the film. The dashed lines are the computed spectra. The relative intensities and arrangement of the spin-wave resonance lines in the computed spectra are indicated below each spectrum.

by the nonuniform spin-wave excitations discussed above. The resonance field H_n for excitation of a magnon with momentum q_n can be approximately written as

$$H_n=H_0+H_0\frac{xJ_0\delta\chi(T)}{k_BT}\frac{S(S+1)}{3}\frac{(\xi q_n)^2}{1+(\xi q_n)^2}. \tag{10}$$

The intensity of the spin-wave satellites is determined by the boundary conditions at the surface of the film and the degree of nonuniformity of the microwave field $H_1(z)$. In the case of symmetric excitation

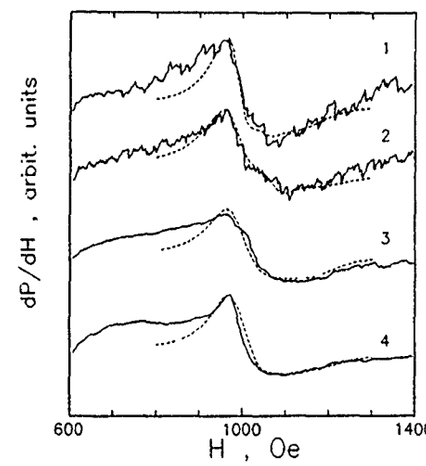

FIG. 2. EPR spectra for the samples No. 1 ($L=2500$ Å, $x=0.014$, and $T_c=5.0$ K)-1, No. 2 ($L=3380$ Å, $x=0.02$, and $T_c=4.8$ K)-2, No. 3 ($L=4030$ Å, $x=0.009$, and $T_c=5$ 2 K)-3, No. 4 ($L=4800$ Å, $x=0$ 014, and $T_c=5.0$ K)-4 at a temperature of 1.6 K with the magnetic field oriented parallel to the surface of the film. The dashed lines were computed.

$$H_1(z)=H_1\frac{ch(k_0z)}{ch(k_0L/2)},\quad k_0^2=i\frac{4\pi\omega}{c^2}\sigma(\omega), \tag{11}$$

where H_1 is the amplitude of the incident wave and $\sigma(\omega)$ is the complex conductivity at the resonance frequency. It is well known that in type-II superconductors with a vortex lattice the conductivity is anisotropic and depends strongly on the relative orientation of the dc magnetic field H and of the electric component E_1 of the microwave field in the sample.[5] It can be shown that the penetration depth of the microwave field is much smaller for parallel orientation of the film. Therefore, the distribution of microwave field in the SC state is most inhomogeneous in this geometry and in this case the best demonstration of spin-wave effects would be expected. To calculate the spectra it is necessary to know the parameters of the studied samples: the coherence length ξ and the inverse penetration depth k_0 of the microwave field. These values were estimated from our measurements of the critical field H_{c2}, of the diamagnetic susceptibility, and of the integral intensity of the EPR signal. The obtained values of $\xi(0)=200$ Å and $\lambda(0)=600$ Å give the possibility to fit all spectra as it is shown in Figs. 1 and 2. Some discrepancy between the calculated and experimental spectra at low field wing is caused by nonresonant absorption of microwave power by superconductor which has been observed earlier for bulk samples.[1] The only fitting parameter was

$$A=J_0S(S+1)\delta_\chi/3, \tag{12}$$

which entered in expression (10) and was fitted for each spectrum independently. The obtained temperature dependence of A value is shown in Fig. 3. This figure actually reflects the temperature behavior of $\delta_\chi(T)$. The solid curve corresponds to the temperature dependence of δ_χ in a BCS superconductor. By knowing A it is possible to determine the spin stiffness coefficient $D''=0.04$ cm^2/s at $T=1.6$ K and

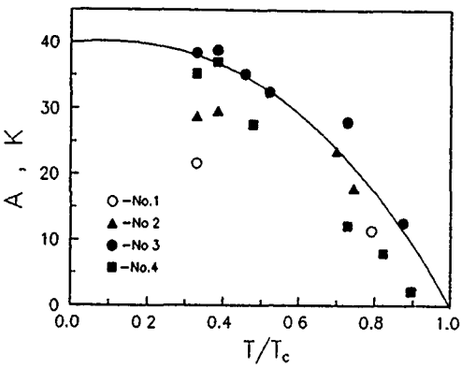

FIG. 3. The parameter A as a function of the reduced temperature for the samples No. 1–4. The solid line corresponds to $\delta_\chi(T)$ of a BCS superconductor.

$x=0.01$. Thus we have shown experimentally that in a superconductor in an external magnetic field weakly damped spin waves exist. These excitations resulted from the nonlocal nature of spin susceptibility of the superconductor. Their observation is the direct evidence of the existence of a long-range exchange interaction between impurities. Previously, spin waves in paramagnetic spin systems have been observed in two particular cases: first the spin waves in the Fermi liquid[6] and second the nuclear spin waves in magnetics.[7]

[1] N. E. Alekseevskii, I. A. Garifullin, B. I. Kochelaev, and E. G. Kharakhash'yan, Sov. Phys. JETP **45**, 799 (1977).
[2] P. W. Anderson and H. Suhl, Phys. Rev. **116**, 898 (1959).
[3] B. I. Kochelaev, L. R. Tagirov, and M. G. Khusainov, Sov. Phys. JETP **49**, 291 (1979).
[4] D. N. Zubarev, *Nonequilibrium Statistical Thermodynamics* (in Russian) (Nauka, Moscow, 1971).
[5] C. Caroli and K. Maki, Phys. Rev. **159**, 306 (1967).
[6] S. Schultz and G. Dunifer, Phys. Rev. Lett. **18**, 283 (1967).
[7] P. G. de Gennes, P. A. Pincus, E. Hurtman-Boutron, and M. Vinter, Phys. Rev. **129**, 1105 (1963).

Published without author corrections

Two-magnon absorption in Nd_2CuO_4

V. L. Sobolev[a)]
Department of Physics, National Taiwan University, Taipei, Taiwan, 10764, Republic of China

Yu. G. Pashkevich
Donetsk Physicotechnical Institute, Academy of Sciences of Ukraine, Donetsk, 340114 Ukraine

H. L. Huang
Department of Physics, National Taiwan University, Taipei, Taiwan, 10764, Republic of China

I. M. Vitebskii and V. A. Blinkin
Institute for Single Crystals, Academy of Sciences of Ukraine, Kharkov, 310001 Ukraine

The two-magnon absorption of the electromagnetic waves in the exchange noncollinear magnetic phase of four-sublattice antiferromagnet Nd_2CuO_4 has been considered. The spin-wave density of states and the frequency dependencies of the absorption coefficient have been calculated. It is shown that the intensity of the two-magnon absorption by exchange magnons in exchange-noncollinear magnets is substantially larger than in magnets collinear in the exchange approximation.

I. INTRODUCTION

The two-magnon absorption (TMA) phenomenon consists in the decay of a quantum of the electromagnetic radiation into two magnons. The intensity of the TMA proportional to the density of magnon states. Thus, it will be higher for those regions of the spectrum which correspond to the flattened portions of the dispersion curves. In the case of the three-dimensional magnets the flattening of the dispersion curves takes place only for the exchange magnons due to the changes of the spectrum under the action of a constant external magnetic field.[1] The TMA has been investigated in two-sublattice quasi-two-dimensional antiferromagnets.[2–4] The TMA by the exchange magnons was studied for the first time in the three-dimensional antiferromagnet in Ref. 1 and then in the quasi-two-dimensional one in Ref. 5. The magnets collinear in the exchange approximation have been considered. In these magnets the TMA is due to the interaction of the magnetic component of the electromagnetic wave with the crystal. The TMA in exchange-noncollinear magnets has not been considered.

The exchange-noncollinear four-sublattice antiferromagnet Nd_2CuO_4 is unique from the point of view of the experiment: First, because its magnon spectrum has quasi-two-dimensional character for some particular directions of the wave vector;[6] second, due to the special magnetic and crystal symmetry of this compound the TMA is electro-dipole active in the exchange approximation.

II. SPIN-WAVE SPECTRUM OF Nd_2CuO_4

The detailed information about the crystal and magnetic symmetry and possible magnetic phases of Nd_2CuO_4 can be found in Ref. 7. The magnon spectrum in noncollinear phase has four branches, three of which are acoustic, while the fourth is the exchange spin wave.[6] In the case $\mathbf{k}\|[001]$ (the fourfold axis of the tetragonal crystal) the energies of the acoustic modes A_1 and A_2 are degenerate and do not depend on $\mathbf{k}$. This particular case of the pure two-dimensional behavior of the A_1 and A_2 branches is connected with the specific crystal and magnetic symmetry. As to the exchange E mode, it has a very weak dispersion and its dispersion relation has also a quasi-two-dimensional character.

In the case when $\mathbf{k}$ has components in the plane parallel to CuO_2 layers (the crystal planes normal to [001]) the magnon dispersion relations are typical for the three-dimensional magnet. As in all parent compounds of the high-temperature superconductors the intralayer exchange interaction is much greater than the others.

The parameters describing the copper magnetic subsystem of Nd_2CuO_4 may be roughly estimated on the basis of the results of Refs. 8–10 (see also Ref. 6). The frequencies of the homogeneous vibrations are as follows;[6,7] $\omega_{A_1,A_2} = 16S\sqrt{J|a_2|}$; $\omega_{A_3} = 16S\sqrt{J|a_2-a_4|}$ and $\omega_E = 16S\sqrt{JD}$, where J is approximately equal to intralayer exchange; a_i ($i=2, 4, 6, 8$) are the anisotropy constants (see Ref. 7 for details). The value of $J\approx 870$ cm^{-1} was obtained in Ref. 8 and it is supposedly the largest of the exchange parameters. Using experimental results[9,10] one can get $|a_2|\approx 2.87\times10^{-4}$ cm^{-1} and $|a_2-a_4|\approx 3.32\times10^{-5}$ cm^{-1}. The other anisotropy constants have to be of the same order of magnitude.[6,7] The values of the four-site D and of the interlayer I exchange interactions are unknown at present. The results of the estimations allow us to suppose that $J\gg D\gg A$, where A is the combinations of the anisotropy constants.

Numerical calculations will be done for the I and D values related to the known value of J with $I=10^{-1}J$, and $D=10^{-3}J$. The corresponding magnon spectrum can be found in Ref. 6.

III. TMA OF ELECTROMAGNETIC WAVES

The interaction Hamiltonian with a uniform external electromagnetic field is

$$H_{\text{int}} = \sqrt{N}[-g_{ij}\mu_B h_i F_j(0) + e_j P_j(0)], \tag{1}$$

where h_i and e_i are the components of the magnetic and electric vectors of the electromagnetic wave, $i, j = x,y,z$, the x, y and z axes, are oriented along the [100], [010], and [001] crystal axes, respectively; g_{ij} is the g-factor tensor; $F_i(0)$ and $P_i(0)$ are the zero Fourier components of the magnetization vector $\mathbf{F}=\sum_{\alpha=1}^{4}\mathbf{S}_\alpha$ (see Ref. 7 for details) and the

[a)]On leave from: Institute for Single Crystals, Academy of Sciences of Ukraine, Kharkov, 310001, Ukraine.

 0021-8979/94/76(10)/6892/3/$6.00 © 1994 American Institute of Physics

electric dipole moment associated with the pair of spins,[11] respectively. Magnetic symmetry allows the existence of the electric dipole moment, associated with the pair of spins, having an exchange nature

$$P_j(0)=\sum_{\alpha,\beta;\mathbf{k}} \pi^{j}_{\alpha\beta}(\mathbf{k})S_\alpha(-\mathbf{k})S_\beta(\mathbf{k}). \tag{2}$$

The tensors $\pi^{j}_{\alpha\beta}(0)$ are nonzero for those pairs of the Cu^{2+} ions that cannot be permuted by the inversion operation and also for the ions whose group of positional symmetry does not contain an inversion. That is why for the crystal symmetry under consideration the tensor $\pi^{j}_{\alpha\beta}(0)$ is equal to zero in case the lattice structural distortions are absent (see Ref. 7 for details). The other mechanisms that contribute to **P** are not considered here.

The part of the expression (1), which is quadratic with respect to the magnon creation and annihilation operators, may be obtained with the help of quantization of the spin-system Hamiltonian described in Ref. 6. We have

$$H^{(m,e)}_{\text{int}}=\sum_{\mathbf{k}} [\Phi^{(m,e)}_{A_1A_3}(\mathbf{k})\xi^{+}_{\mathbf{k}A_1}\xi^{+}_{-\mathbf{k}A_3} + \Phi^{(m,e)}_{A_2E}(\mathbf{k})\xi^{+}_{\mathbf{k}A_2}\xi^{+}_{-\mathbf{k}E}+\text{h.c.}], \tag{3}$$

where the amplitudes $\Phi^{(m,e)}_{\sigma,\nu}$ are calculated in the nearest-neighbor approximation; the superscripts m and e denote the magneto-dipole and electro-dipole channels of the TMA, respectively. Expression (3) corresponds to the case of h_x component of the magnetic vector or e_x component of the electric vector of electromagnetic wave. In the case of h_y or e_y one has to change $A_2 \Leftrightarrow A_1$ in (3). For the orientation of the magnetic component of the electromagnetic wave along the z axis the TMA will not take place in the approximation considered. The exchange magnon taking part in the absorption process is always accompanied by the acoustic spin wave. In contrast to the three-dimensional magnets[1] collinear in the exchange approximation the amplitudes $\Phi^{(m,e)}_{AE}$ do not contain any small parameter. The TMA leading to the generation of the magnons corresponding to the same branches of spectrum is absent.

The separation of the electro-dipole and magneto-dipole channels of the TMA may be carried out by the proper choice of the orientation of the polarizations of the electromagnetic-field components and the propagation direction of the incident radiation. For example, in the case when $\mathbf{k}\|0y$ and $\mathbf{e}\|0z$ only magneto-dipole absorption by the A_1, A_3 and E, A_2 magnons takes place. For the magneto-dipole absorption by the A_1 and A_3 branches in the frequency region $\omega \ll \epsilon_{ex}=8SJ$, one can obtain

$$K^{(h)}_{A_1,A_3}(\omega)\propto \frac{(g\mu_B)^2}{4\omega^2_{ex}\omega^2}\int_{t_0(\omega)}^{1}\frac{[\omega_4^2\ \text{sign}(a_4)+\omega_E^2(1-t)]^2}{\sqrt{1-t^2}}\,dt. \tag{4}$$

where (and henceforth) the notations $\omega_i = 16S\sqrt{J|a_i|}$ and $\omega_{ij} = 16S\sqrt{J|a_i-a_j|}$ $(i=2, 4, 6, 8)$ are used. The electro-dipole contribution to the TMA is as follows:

$$K^{(e)}_{A_1,A_3}(\omega)\propto \frac{(S\pi_{12})^2}{16\omega^2_{ex}\omega^2}\int_{t_0(\omega)}^{1}[\omega^2+\omega_4^2\ \text{sign}(a_4) + \omega_E^2(1-t)]^2 t(1-t^2)^{-1/2}\,dt. \tag{5}$$

The limiting value $t_0(\omega)$ in Eqs. (4) and (5) is determined by the relations

$$t_0(\omega)=\begin{cases}(\omega_E^2-\omega^2+\omega_4^2\ \text{sign}(a_4)+2\omega\omega_{A_1})\omega_E^{-2}, \\ \quad \text{at}\ \ \omega_0\leqslant\omega\leqslant\omega_1 \\ 0 \quad \text{at}\ \ \omega_1\leqslant\omega,\end{cases}$$

in which $\omega_0=\omega_{A_3}+\omega_{A_1}$ and $\omega_1=\omega_{A_1}+\sqrt{\omega_E^2+\omega_{A_3}^2}$. The coefficients of the magneto-dipole and electro-dipole absorption by the A_2 and E modes may be represented by the expressions

$$K^{(h)}_{A_2,E}(\omega)\propto \frac{(g\mu_B)^2}{4\omega^2_{ex}\omega^2}\int_0^{t_0(\omega)}\frac{[\omega_6^2\ \text{sign}(a_6)+\omega_E^2(1+t)]^2}{\sqrt{1-t^2}}\,dt \tag{6}$$

and

$$K^{(e)}_{A_2,E}(\omega)\propto \frac{(S\pi_{12})^2}{16\omega^2_{ex}\omega^2}\times\int_0^{t_0(\omega)}\frac{[\omega^2+\omega_6^2\ \text{sign}(a_6)+\omega_E^2(1+t)]^2 t}{\sqrt{1-t^2}}\,dt, \tag{7}$$

respectively. In these formulas

$$t_0(\omega)=\begin{cases}(\omega^2-\omega_6^2-\omega_E^2-2\omega\omega_{A_2})\omega_E^{-2} & \text{at}\ \ \omega_0\leqslant\omega\leqslant\omega_1, \\ 1 \quad \text{at}\ \ \omega_1\leqslant\omega,\end{cases}$$

and

$$\omega_0=\omega_{A_2}+\sqrt{\omega_E^2+\omega_{62}^2\ \text{sign}(a_6-a_2)},$$

$$\omega_1=\omega_{A_2}+\sqrt{2\omega_E^2+\omega_{62}^2\ \text{sign}(a_6-a_2)}.$$

Following from Eq. (4),(5), and (6),(7), $K^{(e)}_{\mu\nu}(\omega)$ increase with increasing frequency whereas the frequency dependence of $K^{(h)}_{\mu\nu}(\omega)$ is nonmonotonic. Such a behavior is connected with specific features of the spin-wave spectrum and the structure of $\Phi^{(m)}_{\mu\nu}(\mathbf{k})$. The quasi-two-dimensionality of the spin-wave spectrum leads to different behavior in the amplitudes of magnon normal modes in two regions of the wave vector **k** space. These amplitudes of magnon normal modes enter the expressions for $\Phi^{(m,e)}_{\mu\nu}(\mathbf{k})$. In the first region $(ka_0) \ll \sqrt{(D+A)J^{-1}}$ (a_0 is the lattice parameter in the basal plane) these amplitudes do not depend or depend weakly on the k_z component of the wave vector which varies from 0 to π/c_0. So, in this region of the wave vectors they are approximately equal to their values at $\mathbf{k}=0$. The second region is determined by $\sqrt{(D+A)J^{-1}} \ll (ka_0) \ll 1$. In this region $\Phi^{(m)}_{\mu\nu}(\mathbf{k})$ is proportional to the inverse square of the frequency. The frequency dependencies of the coefficients $K^{(h)}_{A_1,A_3}(\omega)$ and $K^{(e)}_{A_1,A_3}(\omega)$ are presented in Fig. 1. The curves are obtained by the numerical integrations of the correspondent expressions using the values of the parameters of the copper subsystem given in the previous section. The dependencies of the coefficients $K^{(h)}_{A_2,E}(\omega)$ and $K^{(e)}_{A_2,E}(\omega)$ are

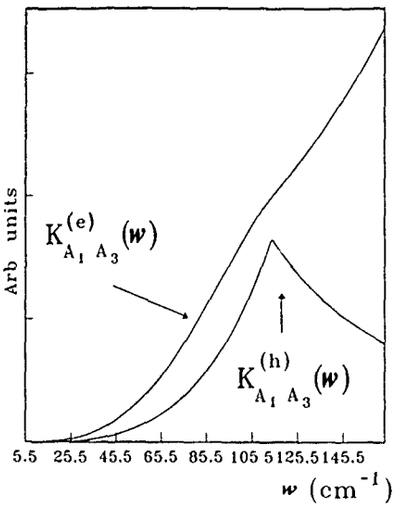

FIG. 1. The frequency dependencies of the absorption coefficients $K^{(h)}_{A_1,A_3}(\omega)$ and $K^{(e)}_{A_1,A_3}(\omega)$.

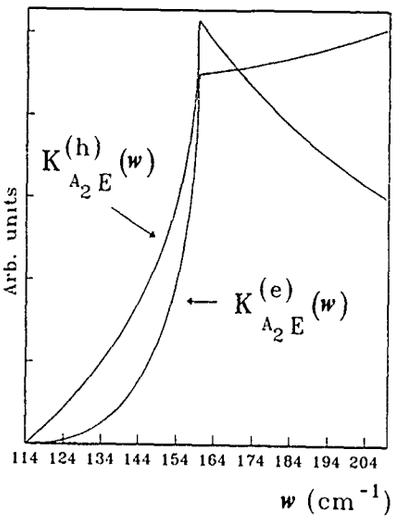

FIG. 2. The frequency dependencies of the absorption coefficients $K^{(h)}_{A_2,E}(\omega)$ and $K^{(e)}_{A_2,E}(\omega)$.

given in Fig. 2. The dependence of the coefficient of magneto-dipole absorption does not follow the frequency dependence of the density of magnon states in the low-frequency region. This discrepancy in the frequency dependencies of the absorption coefficient and the spin-wave states density is caused by the structure of the $\Phi^{(m)}_{\mu\nu}(\mathbf{k})$ amplitude discussed above.

The TMA by the exchange mode has the main peculiarities similar to that of the absorption by the acoustic magnons. They are the nonmonotonic behavior of $K^{(h)}_{A,E}(\omega)$ in the region of the frequencies near the activation energy of the exchange and acoustic magnon and monotonic behavior of $K^{(e)}_{A_2,E}(\omega)$ in the same region. It is important to note that the peak height of the magneto-dipole absorption by the exchange mode is of the same order of magnitude as the peak height of the magneto-dipole absorption by the acoustic modes. Thus, the TMA, by the exchange modes in exchange noncollinear magnets in the absence of the external magnetic field, has substantially larger intensity than in many-sublattice magnets collinear in exchange approximation. It is caused by the fact that at $\omega \ll \omega_{ex}$ the heights of the step of the density of magnon states for the exchange and acoustic modes coincide with each other.

It is necessary to note an interesting peculiarity of the TMA originated from the structure of the H_{int}. In the case when the radiation is propagated along the z axis the absorption coefficient does not depend on the orientation of the polarization of the incident electromagnetic wave with respect to the x and y axes. It is connected with the fulfillment of the relations.

$$\omega_{A_1}(k_x,k_y,k_z)=\omega_{A_2}(k_y,k_x,k_z),$$
$$\omega_{A_3}(k_x,k_y,k_z)=\omega_{A_3}(k_y,k_x,k_z). \tag{8}$$

From relation (8) and explicit form of $\Phi_{\mu\nu}(\mathbf{k})$ it follows that

$$K^{(h_x)}_{A_1,A_2}(\omega)=K^{(h_y)}_{A_2,A_3}(\omega), \quad K^{(e_x)}_{A_1,A_3}(\omega)=K^{(e_y)}_{A_2,A_3}(\omega). \tag{9}$$

During the experimental investigations of the TMA with the scheme of the experimental setup using the fixed frequency of the generator the absorption channels A_1,A_3 and A_2,A_3 will be undistinguishable with respect to the energy. Thus, for the case $\mathbf{k}\|0z$ and arbitrary polarization $h_x=h\cos\varphi$, $h_y=h\sin\varphi$ the combined absorption coefficient observed in the experiments does not depend on φ. The combined absorption coefficient

$$K(\omega)=K^{(h)}_{A_1,A_3}(\omega)+K^{(e)}_{A_1,A_3}(\omega)$$

contains the contributions which are determined by formulas (5) and (6). The same phenomenon takes place for the case of the absorption by the exchange mode E because relations (8) and (9) are valid at the interchange $A_3 \Rightarrow E$.

ACKNOWLEDGMENT

This research is supported by the NSC of the Republic of China through Grant No. NSC-82-0212-M002-172.

[1] V. V. Eremenko, S. A. Zvyagin. Yu. G. Pashkevich, V. V. Pishko, V. L. Sobolev, and S. A Fedorov, Sov. Phys. JETP **66**, 1184 (1987).
[2] L. A. Prozorova and A. I. Smirnov, Pis'ma Zh. Eksp. Teor. Fiz. **23**, 148 (1976).
[3] Yu. V. Pereverzev and A. A. Stepanov, Fiz. Nizk. Temp. **3**, 502 (1977).
[4] A. G. Anders, A. I. Zvyagin, and A. I. Petunin, Fiz. Nizk. Temp. **3**, 237 (1977).
[5] A. L. Alistratov, V. N. Krivoruchko, and D. A. Yablonskii, Fiz. Nizk. Temp. **14**, 374 (1988).
[6] V. L. Sobolev, H. L. Huang, Yu. G. Pashkevich, M. M. Larionov, I. M. Vitebskii, and V. A. Blinkin, Phys. Rev. B **49**, 1170 (1994).
[7] V. A. Blinkin, I. M. Vitebskii, O. D. Kolotii, N. M. Lavrinenko, V. P. Seminozhenko, and V. L. Sobolev, Sov. Phys. JETP **71**, 1179 (1990).
[8] P. E. Sulevsky, P. A. Fleury, K. B. Lions, S.-W. Cheong, and Z. Fisk, Phys. Rev. B **41**, 225 (1990).
[9] A. A. Stepanov, M. I. Kobets, V. A. Pashchenko, A. I. Zvyagin, D. I. Zhigunov, and S. N. Barilo, Sov. Phys. Low Temp. Phys. **17**, 416 (1991).
[10] A. I. Smirnov, S. N. Barilo, and D. I. Zhigunov, Sov. Phys. JETP **73**, 734 (1991).
[11] T Moriya, J. Appl. Phys. **39**, 1042 (1968).

Surface precession solitons (surface "Magnetic drops") in uniaxial magnetics (abstract)

Yurij Bespyatykh, Igor Dikshtein, and Sergey Nikitov
Institute of Radioengineering & Electronics of the Russian Academy of Sciences, Moscow, Russia 103907

Surface spin waves, localizing near the surface of magnets as a consequence of nonlinear properties of material, have been studied in Ref. 1. According to the Lighthill criterion this wave is modulationally unstable. This can lead to the creation of nonunidimensional surface states. In this work, a new class of nonlinear exitations in a pure exchange-coupled uniaxial ferro- and antiferromagnets is considered. These exitations are 3D surface precession solitons or "magnetic drops" localized near the surface of a crystal. Such solitons are the space localized solutions of the Landau–Lifshits equation of motion for magnetization field with appropriate boundary conditions for the spins on the surface of magnetics. They keep their dynamic structure during the motion in space. The conditions of their stability are found. The problem of soliton motion is considered. It is shown that energy and precession frequency for surface 3D solitons is less than for volume 3D solitons, which was studied in Ref. 2. The possibility of experimental registration of such solitons is discussed.

[1] Yu. I. Bespyatykh and I. E. Dikshtein, Sov. Phys. Solid State **35**, 1175 (1993).
[2] A. M. Kosevich, B. A. Ivanov, and A. S. Kovalev, Phys. Rep. **194**, 117 (1990).

Nonlinear self-localized surface spin waves in ferromagnets (abstract)

Alan Boardman
Salford University, Salford M54WT, United Kingdom

Yurij Bespyatykh, Igor Dikshtein, and Sergey Nikitov
Institute of Radio Engineering and Electronics of the Russian Academy of Sciences, Moscow 103907, Russia

It is well known that in linear theory, surface spin waves (SW) do not exist in a pure exchange-coupled ferromagnet for the case of free spins at the surface. However, in these approximations of the linear theory the plane volume spin waves (VW), propagating along the surface of a ferromagnet, satisfies not only the Landau–Lifshitz equation for the magnetization motion, but the boundary conditions for the free surface spins. Such VW can be unstable and can be transformed into SW under small changes of a magnetic medium, e.g., if the surface spins are partly pinned. In the present work a new type of self-localized SW in the ferromagnet has been considered. The existence of such waves is conditioned entirely by the nonlinear properties of a ferromagnet. The penetration length of such SW is proportional to 1/A, where A is a maximum of the magnetization amplitude on the surface of the crystal. The dispersion equations have been obtained for pure exchange and dipole-exchange nonlinear SW. In the latter case the influence of the second harmonic generation on the wave propagation at the fundamental frequency was studied. The conditions when the SW excites the VW, carrying the energy into the volume of the crystal, are derived. The nonlinear Schrödinger equation for the SW envelope amplitude was derived and its solitonic solutions are obtained. The estimations of threshold values for the wave numbers of the propagating waves are provided.

 0021-8979/94/76(10)/6895/1/$6.00 © 1994 American Institute of Physics

Spin wave dispersion in ferromagnetic nickel (abstract)

J. M. Rejcek, J. L. Fry, and N. G. Fazleev[a)]
Department of Physics, University of Texas at Arlington, Arlington, Texas 76019-0059

The spin wave dispersion in ferromagnetic nickel has been computed in random phase approximation using the wave vector and frequency dependent magnetic susceptibility including many body enhancement effects. The latter were included using an orbital basis to invert the susceptibility matrices that are encountered in a local density, first principles version of a Stoner-like theory of many body enhancements. The complicated computer codes employed in the calculation were tested by computing numerically the wave vector and frequency dependent spin and orbital magnetic susceptibility of the uniform electron gas and comparing with known analytic expressions. Numerical work was done using the analytic tetrahedron method. For nickel the theory was simplified by introducing a single adjustable parameter in lieu of calculation of complicated integrals involving the band structure. The parameter was adjusted to yield agreement with a long wavelength spin wave neutron scattering measurement. With the fit parameter, good agreement with the experimental dispersion of spin waves in nickel was obtained for other wavelengths as well.

Research supported by the National Research Council, the Robert A. Welch Foundation, and Texas Advanced Research Program.
[a)]Permanent address: Kazan University, Kazan 420008, Russia.

 0021-8979/94/76(10)/6896/1/$6.00 © 1994 American Institute of Physics

Ferromagnetic resonance and Brillouin light scattering from epitaxial Fe_xSi_{1-x} films on Si(111) (abstract)

M.. Mendik,[a] Z. Frait,[b] H. von Känel, and N. Onda
Laboratorium für Festkörperphysik, ETH, 8093 Zürich, Switzerland

The magnetic properties of epitaxial Fe_xSi_{1-x} films on Si(111) have been determined by means of ferromagnetic resonance (FMR) and Brillouin light scattering (BLS). The investigated films are (111) oriented, with thicknesses $h=150$ Å, 250 Å, 710 Å, and Fe concentrations $x=0.75$, 0.79, and 0.75, respectively.[1] All experiments have been carried out at room temperature. For BLS, the frequencies of both surface and bulk magnons have been measured as a function of the external in plane field **H** and the in plane direction of magnon propagation versus the main crystallographic axis. Moreover, the wave vector dependence has been used to identify the surface and bulk magnons present in the thicker films. FMR has been used in the parallel configuration (PC) and normal configuration (NC), where the external applied field lies in the sample plane and normal to the sample, respectively. Several waveguide setups were used to cover the frequency range from 18 to 92 GHz. For the numerical analysis we used the resonance conditions for a thin single crystalline film grown in the (111) plane. From our fits we obtained for the Landé g value 2.1, for the saturation induction $4\pi M_s=8.8$ kG, 10.7 kG, 13.7 kG for $h=150$ Å, 710 Å, and 250 Å, respectively. The magnetic parameters have been found to depend strongly on the Fe concentrations and Fe_xSi_{1-x}-Si substrate interface interdiffusion. The magnetic parameters of epitaxial Fe_xSi_{1-x} films are in agreement with the data obtained from single crystals by Hines *et al.*[2] The Landau–Lifshitz FMR relaxation constant is very small, ranging from 5 to 8×10^7 rad/s.

---

[a]Present address: Department of Physics, Colorado State University, Fort Collins, CO 80523.
[b]Institute of Physics, Na Slovance 2, Praha 8, 18040, Czech Republic.

[1]N. Onda, H. Sirringhaus, S. Goncalves-Conto, C. Schwarz, S. Zehnder, and H. von Känel, Appl. Surf. Sci. **73**, 124 (1993).
[2]W. A. Hines, A. H. Menotti, and J. I. Budnick, J. Magn. Mater. **39**, 223 (1983).

 0021-8979/94/76(10)/6897/1/$6 00 © 1994 American Institute of Physics

Nuclear secondary echo in ferromagnets caused by quadrupole and Suhl–Nakamura interactions

V. I. Tsifrinovich
Physics Department, Polytechnic University, Six Metrotech Center, Brooklyn, New York 11201 and Bramson ORT Technical Institute, 321 Avenue N, Brooklyn, New York 11230

The formation of the secondary nuclear spin echo signals in ferromagnets has been investigated taking into consideration the quadrupole and Suhl–Nakamura interactions. It is assumed that the inhomogeneous distribution of the quadrupole frequency $\omega_Q+\delta\omega_Q$ is independent of the distribution of nuclear magnetic resonance frequency $\omega_n+\delta\omega_n$, and a characteristic size of these inhomogeneities is small in comparison to the correlation radius of the exchange interaction in the electron ferromagnetic system. It is shown that the quadrupole interaction causes the formation of the secondary echo signals at $t=(2k+1)\tau$, $1\leqslant k\leqslant I-1/2$, where I is the nuclear spin, the time t is measured from the second rf pulse, and τ is the time interval between the rf pulses. The spectrum of the spin echo signal with maximum at $t=t_E$ contains $(2I+1-t_E/\tau)$ frequencies. The Suhl–Nakamura interaction causes the additional echo signals with maximum at even values t/τ.

INTRODUCTION

It is well known that in ferromagnets after the action of two pulses with the nuclear magnetic resonance (NMR) frequency one can observe not only the usual Hahn's nuclear spin echo but also the secondary echo signals.[1] This article is dealing with the investigation of these signals.

First of all we note that the secondary echoes may be caused by two "external" circumstances. (1) High frequency of the pulse pairs repetition in the real experiments. If the period of repetition is small in comparison with the time of longitudinal relaxation, then the secondary echoes may be caused by the influence of previous pairs. (2) If the connection between the magnetic system of a sample and a measuring circuit is strong enough, the currents in the circuit, that are induced by the first echo signal, act on a sample and cause the additional echo signal, etc. Furthermore, we will suggest that these situations are eliminated, so we will consider internal mechanisms of a secondary echo formation.

QUADRUPOLE INTERACTION

The Hamiltonian of a nuclear system with the quadrupole interaction is

$$H=-\hbar\{(\omega_n+\delta\omega_n)I_z+(1/2)(\omega_Q+\delta\omega_Q)I_z^2+(1/2)\times[q_1(t)+q_2(t)][I_+\exp(i\omega t)+\text{C.C.}]\},\quad(1)$$

where I is the nuclear spin, $\omega_n+\delta\omega_n$ is the inhomogeneous NMR frequency, $\omega_Q+\delta\omega_Q$ is the inhomogeneous quadrupole frequency, and $q_p(t)$ is the envelope of the pth rf pulse. The evolution of nuclear spins is described by the equation of motion for the density matrix ρ

$$i\hbar\dot{\rho}=[H,\rho].\quad(2)$$

To describe the echo signals we calculated the average transverse component of a nuclear spin

$$\langle I_+\rangle=\int_{-\infty}^{\infty}\int g(\delta\omega_n,\delta\omega_Q)\mathrm{Tr}(I_+\rho)d(\delta\omega_n)d(\delta\omega_Q),\quad(3)$$

where $g(\delta\omega_n,\delta\omega_Q)$ is a distribution function.

The secondary echo formation depends on values $\langle|\delta\omega_n|\rangle\tau$ and $\langle|\delta\omega_Q|\rangle\tau$, where τ is the time interval between the rf pulses, $\langle|\delta\omega_n|\rangle$ and $\langle|\delta\omega_Q|\rangle$ are characteristic inhomogeneities of NMR and quadrupole frequencies. The situation $\delta\omega_n=0$ that is typical for nonmagnetic substances was first considered by Solomon.[2] The opposite situation $\delta\omega_Q=0$ was considered by Abe *et al.*[1]

We have considered another realistic situation

$$\langle|\delta\omega_n|\rangle\tau,\langle|\delta\omega_Q|\rangle\tau\gg 1.\quad(4)$$

In this case the nuclear spin system acquires an inhomogeneous phase caused by the inhomogeneity in both $\delta\omega_n$ and $\delta\omega_Q$. For the signal formation this inhomogeneous phase must be canceled after the second rf pulse. For analytical calculations we used the Symbolic Formulas method.[3] The results of calculations depend sufficiently on correlation between inhomogeneities of $\delta\omega_n$ and $\delta\omega_Q$. We have considered the situation when inhomogeneities of $\delta\omega_n$ and $\delta\omega_Q$ were independent. According to our calculations the echo signals appear at

$$t=(2k+1)\tau,\quad 0\leqslant k\leqslant I-1/2,\quad(5)$$

where t is measured from the end of the second pulse. (The usual Hahn's signal corresponds to the value $k=0$).

If $\omega_Q>\langle|\delta\omega_Q|\rangle$, i.e., the NMR spectrum is a quadrupole split one, then the spectra of echo signals are essentially different. The spectrum of the spin echo with maximum at $t=t_E$ contains $(2I+1-t_E/\tau)$ frequencies. The echo spectrum at $t=\tau$ has $2I$ frequencies that coincide with the quadrupole split NMR spectrum, the echo spectrum at $t=3\tau$ has

 0021-8979/94/76(10)/6898/2/$6 00 © 1994 American Institute of Physics

$(2I-2)$ frequencies and so on. For half-integer spin I the spectrum of the echo at $t=t_E$ consists of frequencies ω

$$\omega=\omega_n\pm q\omega_Q, \quad 0\leqslant q\leqslant I-t_E/2\tau. \tag{6}$$

For integer spin I we have received

$$\omega=\omega_n\pm\omega_Q(q+1/2), \quad 0\leqslant q\leqslant I-1/2-t_E/2\tau. \tag{7}$$

In particular for $I=3/2$ the spectrum of the echo at $t=\tau$ contains frequencies $\omega=\omega_n,\omega_n\pm\omega_Q$, and the spectrum of the echo at $t=3\tau$ has only one frequency $\omega=\omega_n$. This result is in agreement with experiments of Abelyashev *et al.*[4]

The mechanism of formation of secondary echo signals and their frequencies may be explained with the symbolic formulas.[3] For example, the latest echo signal for half-integer spin I is described by symbolic formulas

$$(1_{jj}^{1i}-2_{1i}^{k+1,k}), \qquad i=2I+1, \quad k=i/2. \tag{8}$$

This means that under the action of the first pulse the initial matrix elements ρ_{jj} are transformed into the off-diagonal element ρ_{1i} that oscillates with the frequency $\omega_{1i}=-2I(\omega_n+\delta\omega_n)$. In a time interval τ between the rf pulses the quantity ρ_{1i} acquires an inhomogeneous phase $-2I(\omega_n+\delta\omega_n)\tau$. The second pulse transforms ρ_{1i} into $\rho_{k+1,k}$, that oscillates with the frequency $\omega_{k+1,k}=\omega_n+\delta\omega_n$. So, the advance of the inhomogeneous phase Φ continues, and we obtain

$$\Phi=-2I(\omega_n+\delta\omega_n)\tau+(\omega_n+\delta\omega_n)t. \tag{9}$$

Consequently, at time $t=2I\tau$ the inhomogeneous phase Φ has the same value for all the spins, and the spin echo signal appears with a carrier frequency ω_n.

SUHL–NAKAMURA INTERACTION

To take into consideration the Suhl–Nakamura interaction we used the half-classical theory of motion for nuclear spins in ferromagnets.[5] The half-classical Hamiltonian of the Suhl–Nakamura interaction may be written as

$$H_{SN}=-(1/2)\hbar\omega_p s I_- + \text{C.C.}, \tag{10}$$

where ω_p is the parameter of the interaction which coincides with the frequency pulling for homogeneous nuclear system,[6]

$$s=\langle I_+\rangle/\langle I_z^0\rangle, \tag{11}$$

$\langle I_z^0\rangle$ is the equilibrium value of $\langle I_z\rangle$. We regard a characteristic size of the inhomogeneity in the nuclear system as a small one in comparison with the correlation radius of the exchange interaction in the electron spin system.

Putting $H+H_{SN}$ into (2) we receive the integrodifferential equations for the nuclear density matrix that include $\rho(\delta\omega_n,\delta\omega_Q)$ and $\int\int\rho g d(\delta\omega_n),d(\delta\omega_Q)$. Integral terms describe the Suhl–Nakamura interaction which is "turned on" only at those time intervals when the average transverse nuclear spin $\langle I_+\rangle$ has a sufficiently large value. This effect is caused by a small characteristic size of nuclear inhomogeneity: the electron spins interact with the average nuclear spin $\langle I_+\rangle$.

In the linear approximation to the Suhl–Nakamura interaction we have received the additional echo signals that have maximum at

$$t=2p\tau, \quad 1\leqslant p\leqslant N, \tag{12}$$

where $N=2I$ for he half-integer spin, and $N=2I-1$ for the integer spin. For example, the mechanism of formation of the echo signal with maximum at $t=2\tau$ is described by symbolic formulas

$$(1_{jj}^{i,i+1}-2_{i,i+1}^{mm}-E_{mm}^{i+1,i}). \tag{13}$$

Here the first pulse transforms the diagonal matrix elements into $\rho_{i,i+1}$. In a time interval τ between the pulses the quantity $\rho_{i,i+1}$ acquires an inhomogeneous phase $\omega_{i,i+1}\tau$. The second pulse again transforms $\rho_{i,i+1}$ to diagonal elements ρ_{mm} that do not change a phase between the second pulse and the first echo signal. When the first echo signal is formed, the average transverse nuclear spin $\langle I_+\rangle$ has the maximum value. Consequently, the Suhl–Nakamura interaction is "turned on," and it transforms ρ_{mm} into $\rho_{i+1,i}$. The inhomogeneous phase advance Φ is

$$\Phi=\omega_{i+1,i}[-\tau+(t-\tau)], \tag{14}$$

and the spin echo appears at $t=2\tau$.

In conclusion we note that for $\omega_Q=0$ all secondary signals except the signal at $t=2\tau$ disappear. It means that other signals at even values t/τ are caused by both the Suhl–Nakamura and the quadrupole interactions.

[1] H. Abe, H. Yasuoka, and A. Hirai, J. Phys. Soc. Jap. **21**, 77 (1966).
[2] I. Solomon, Phys. Rev. **110**, 61 (1958).
[3] V. I. Tsifrinovich, Sov. Phys. JETP **68**, 1413 (1988).
[4] G. N. Abelyashev, V. N. Berzharskij, and N. A. Sergeev, Phys. Lett. A **133**, 263 (1988).
[5] V. I. Tsifrinovich, Sov. Phys. JETP **65**, 783 (1987).
[6] P. G. De Gennes, P. A. Pincus, F. Hartmann-Boutron, and J. M. Winter, Phys. Rev. **129**, 1105 (1963).

A Mössbauer effect study on the acicular cobalt ferrite particles

J. G. Na
Korea Institute of Science and Technology, Sungbuk, Seoul 136-791, Korea

D. H. Han, J. G. Zhao, and H. L. Luo
State Key Laboratory of Magnetism, Institute of Physics, CAS, Beijing 100080, People's Republic of China

The causes of the coercivity enhancement and the coercivity instability of acicular cobalt ferrite particles containing 0–9.2 wt % Fe^{2+} ions under the influence of magnetic field and temperature were investigated by means of transverse magnetic field annealing, torque, and Mössbauer experiments. The coercivity enhancement and the instability of Co modified iron oxide particles are closely related to the uniaxial magnetic anisotropy. A Fe^{2+}-CO^{2+} pair model was proposed to explain the uniaxial magnetic anisotropy of Co modified iron particles. To verify the nature of the Fe^{2+}-Co^{2+} pair, the probability of one or more Co ions appearing in the neighborhood of a B site Fe^{2+} ion was calculated using the chemical composition, the Mössbauer parameters, Pi(Fe_2^+) and Pi(Fe^{+3}) and discussed conditions for forming the pair between the nearest-neighbor Co^{2+} and Fe^{2+} ion.

I. INTRODUCTION

Cobalt modified iron oxide particles are the predominant materials for use in video tapes and disks for high density digital recording density, but there are still some problems to be addressed. For cobalt body doped iron oxide particles, the coercivity decreases irreversibly with temperature and time in a magnetic field. On the other hand, the coercivities of cobalt surface doped or adsorbed iron oxide particles cannot increase significantly, usually from 600 to 800 Oe, compared to 2000 Oe for cobalt body doped ones.[1,2] Therefore, it is important to investigate the mechanism of the coercivity enhancement and the coercivity instability of cobalt modified iron oxide particles.

In this article, a Co^{2+}-Fe^{2+} model was proposed to explain the results of the transverse magnetic field annealing and the torque experiments of cobalt modified iron oxide particles. Also calculated was the probability of one or more Co^{2+} ions appearing in the neighborhood of a B site Fe^{2+} ion using Mössbauer parameters, Pi(Fe^{+}) and Pi(Fe^{+3}) to verify the nature of the Co^{2+}-Fe^{2+} pair.

II. EXPERIMENTAL PROCEDURE AND RESULTS

A. Preparation of samples

Cobalt body doped iron oxide particles were prepared by coating acicular γ-Fe_2O_3 particles (an average length of 0.5 μm, an aspect ratio of 10) with about 3.5 wt % Co^{2+} and different Fe^{2+} contents by the usual chemical coprecipitation method and then heated at 390 °C in N_2 atmosphere for 2 h for diffusing Co^{2+} and Fe^{2+} ions into the core of γ-Fe_2O_3 particles. The powders were mixed with the organic resin ink and coated on a plastic film in the presence of external magnetic field at room temperature (denoted A_1–A_6). A magnetic field of 2 kOe applied an in-plane direction of the sheets and the direction was fixed during magnetic drying. For comparison to the body doped particles, surface epitaxial iron particles were also prepared. Detailed procedures for preparing these particles were described elsewhere.[3] Magnetic tapes using these particles were made by the same process above except the heating (denoted B).

Table I represents the composition of samples A_1–A_6 and B analyzed by an inductive coupled plasma method.

B. Magnetic measurement

Magnetic properties of samples were measured using a vibrating sample magnetometer (Princeton model 155).

The coercivity instability of the sheets was measured using the method proposed by Eiling.[2] The oriented particulate magnetic sheets were put in a magnetic field of 3 kOe perpendicular to the sheet plane and annealed at 85 °C for 12 h (denoted $A_1' - A_6'$ and B'). The coercivities measured parallel to the orientation direction of the samples before and after the transverse magnetic annealing (TMA) were denoted as $H_{c\parallel}$ and $H_{c'\parallel}$ and that perpendicular to the plane of the samples as $H_{c\perp}$ and $H_{c'\perp}$, respectively. The results are listed in Table II.

The torque curves of the sheets were measured using a TOEI torque magnetometer. The detailed procedure to measure the uniaxial magnetic anisotropy constant, K_u and the crystalline magnetic anisotropy constant, K_l of the acicular cobalt ferrite particles is presented elsewhere.[4] Table III represents the K_u and K_l before and after TMA.

C. Mössbauer spectrum measurement

The Mössbauer equipment used is an electromagnetically driven, constant acceleration Mössbauer spectrometer. The radioactive source is Co(Rh) of 20 mCi. The γ-ray propagation direction was perpendicular to the plane of the samples. The Mössbauer curves of the samples before and after TMA were taken at room temperature. The Mössbauer parameters were deduced from the Mössbauer spectra by the

TABLE I. The content of Fe^{2+} and Co^{2+} ions of cobalt modified iron particles.

Sample	A_1	A_2	A_3	A_4	A_5	A_6	B
Co^{2+} (wt %)	3.6	3.5	3.4	3.3	3.3	3.2	3.1
Fe^{2+} (wt %)	0	2.8	5.0	6.4	8.5	9.2	9.1

 0021-8979/94/76(10)/6900/3/$6.00 © 1994 American Institute of Physics

TABLE II. The coercivity changes of magnetic sheets before (A) and after (A') TMA.

Sample	$H_{c\parallel}$ (Oe)	$H_{c\perp}$ (Oe)	Sample	$H_{c'\parallel}$ (Oe)	$H_{c'\perp}$ (Oe)
A_1	969	604	A_1'	703	608
A_2	845	611	A_2'	719	642
A_3	939	637	A_3'	717	712
A_4	1001	630	A_4'	749	781
A_5	1130	671	A_5'	744	875
A_6	1164	653	A_6'	750	889
B	648	548	B'	514	625

usual least-squares fitting techniques, using a computer. The spectra were fitted assuming two magnetic components: Fe^{+3} on the A sites, Fe^{+2} and Fe^{+3} on the B sites.

The Mössbauer spectra of sample A_4, and B were taken because the Fe^{2+} ion content of these samples is significantly different. Figure 1 shows the Mössbauer spectra of sample A_4, and B and Table IV represents the Mössbauer parameters deduced from these spectra. The Mössbauer spectra of samples before TMA are presented in Fig. 1 because there were no significant differences between the spectra of samples before and after TMA.

According to the theory of the hyperfine field of transition metal ions[5,6] and the Mössbauer parameters given in Table IV the value of $\langle N_d\rangle_{exp}$, $Pi(Fe^{+2})$ and $Pi(Fe^{+3})$ can be calculated from the following equations

$$\langle N_d\rangle = \langle N_d\rangle_{Fe^{3+}}(H_F)_{exp}/H_F(Fe^{3+}), \quad (1)$$

where $\langle N_d\rangle_{exp}$ is the local average number of the d electron with unpaired spins, $\langle N_d\rangle_{Fe^{3+}}$ unpaired d-electron number of Fe^{3+} ions, which is 5, $H_f(Fe^{3+})$ the hyperfine field of Fe^{3+} ions, which is equal to 517 kOe.[6]

$$(H_F) = P(Fe^{2+})H_F(Fe^{2+}) + P(Fe^{3+})H_F(Fe^{3+}), \quad (2)$$

where $Pi(Fe^{+2})$ and $Pi(Fe^{+3})$ are normalized probabilities for the admixture of Fe^{2+} and Fe^{3+} ions.

The calculated $\langle N_d\rangle$ and Pi are also given in Table IV.

III. DISCUSSION

From Tables I and II, it may be seen that the coercivity of cobalt body doped iron particles (A_i) increased linearly with increasing Fe^{2+} content, although the Co content of these samples was the same at about 3.5 wt %. The K_u of samples A_i increased with increasing Fe^{2+} content, while K_l of these samples decreased, as seen in Table III. These results are in good agreement with that of Wang *et al.*[7] They reported that the H_c of cobalt body doped particles increased with increasing Fe^{2+} content, which was attributed to the increase of K_u.

From the changes of the coercivities and the magnetic anisotropies of the before (A) and after (A') TMA, given in Tables II and III, one can see that the $H_{c\parallel}$ of samples decreases significantly with increasing Fe^{2+} content, while the $H_{c\perp}$ increases slightly with TMA, and this is mainly attributed to the decrease of K_u with TMA. From the above experiments, one may understand that the coercivity and the coercivity instability of cobalt modified iron particles are strongly dependent on the uniaxial anisotropy and are closely related to the Fe^{2+} ions as well as the Co^{2+} ions. These results cannot be explained by the model proposed by Kishimoto[8] and Sharrock.[9] They reported that the uniaxial

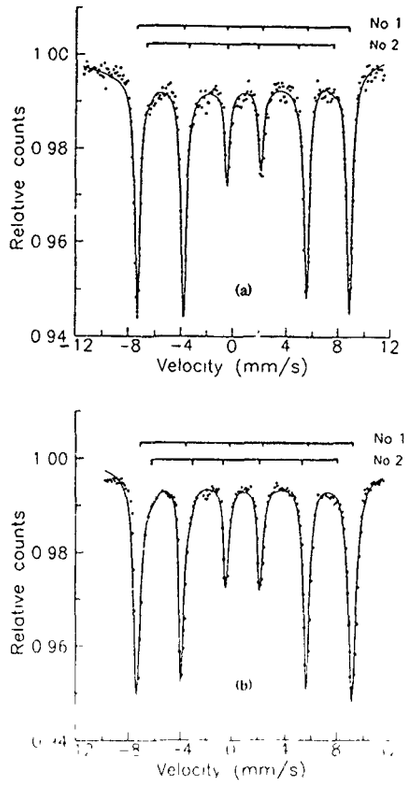

FIG. 1. Mössbauer spectra for sample A_4 (a) and B A (b). No 1 and No. 2 represent A and B sites, respectively

TABLE III. The changes of magnetic anisotropy constant of magnetic sheets before(A) and after(A') TMA.

Sample	K_u ($\times 10^5$ erg/cc)	K_l($\times 10^5$ erg/cc)	Sample	K_u ($\times 10^5$ erg/cc)	K_l ($\times 10^5$ erg/cc)
A_1	7.6	12 6	A_1'	7.6	12.6
A_2	11.0	11.4	A_2'	8.9	10.1
A_3	13.9	7.6	A_3'	10.1	8.3
A_4	14 9	7.0	A_4'	10.9	8.5
A_5'	16.0	6 6	A_5'	11.2	8 1
A_6	19.2	4.6	A_6'	11.1	5.4

TABLE IV. Mössbauer parameters $\langle N_d\rangle_{exp}$ and P_i of magnetic sheet A_4 and B before TMA.

Mössbauer subspectrum	IS (mm/s)	H_F (kOe)	Area ratio (%)	$\langle N_d\rangle_{exp}$	$P(Fe^{2+})$	$P(Fe^{3+})$
$A_4(A)$	0.34	502	92.3	4.9	0.9	0.1
$A_4(B)$	0.43	444	7.7	4.3	0.4	0.6
$B(A)$	0.36	501	91.3	4 9	0.8	0.1
$B(B)$	0.60	441	8.7	4.3	0.4	0.6

anisotropy of cobalt ferrite powders was closely related to the coercivity instability but induced by the migration of Co^{2+} ions in a spinel lattice, and Fe^{2+} ions facilitated the migration of cobalt ions only.

On the basis of these results, we suggest that the uniaxial magnetic anisotropy of cobalt modified iron particles would be originated from the arrangement of Fe^{2+} ions with Co^{2+} ions, i.e., Fe^{2+}-Co^{2+} pair.

The Mössbauer parameters of magnetic sheets A_4 and B before TMA, given in Table IV, are comparable to those of other's works.[9] There is no significant change in the $\langle N_d \rangle_{exp}$, Pi($Fe^{+2}$) and Pi($Fe^{+3}$) between samples A_4 and B except the values of Pi(Fe^{+2}) and Pi(Fe^{+3}) in the A site. The difference of these values may be attributed to the different Fe^{2+} content of samples A_4 and B. From the values of Pi(Fe^{+2}) and Pi(Fe^{+3}) of subspectra, it may be deduced that the subspectra (A) of samples are mainly attributed to Fe^{3+} ions and the subspectra (B) to Fe^{2+} and Fe^{3+} ions. The higher the value of IS and area ratio in the B subspectrum of sample B than those of A_4, is attributed to the higher the Fe^{2+} content of sample B than that of A_4.

The probability of n-Fe ions appearing in the neighborhood of a B site Fe ion may be calculated from the following equation[10]

$$P(n) = {}_6C_n C^n (1-C)^{6-n}, \tag{3}$$

where C is the concentration of Fe ions on B sites in the spinel lattice.

Substituting $C=0.91$ in Eq. (5), the concentration of Fe in sample A_4, $P(n)$ for $N=6$, 5, 4, and 3 were obtained. $P(n)$ was calculated as 0.57, 0.34, 0.08, and 0.01 for $n=6$, 5, 4, and 3, respectively. The probability of one or more Co^{2+} ions appearing in the neighborhood of a B site Fe ion is 0.43 and that of a B site Fe^{2+} ion is about 0.25, calculated using the values of Pi(Fe^{+2}) and Pi(Fe^{+3}) in the B subspectrum of sample A_4. We did not calculate the probability for sample B because sample B was prepared using Co surface epitaxial particles. However, the probability of this sample might be higher than that of sample A_4, because of the higher Fe^{2+} content and confinement of Co^{2+} and Fe^{2+} ions to surface epitaxial layer of iron particles of sample B.

It is thought that these Co^{2+}-Fe^{2+} arrangements may form the Co^{2+}-Fe^{2+} pairs, but the appearance of Co ions in the neighborhood of the B site Fe^{2+} is only a requisite condition for forming the Co^{2+}-Fe^{2+} pair because more than a Co ion can appear in the neighborhood of a B site Fe^{2+} ion and more than a Fe^{2+} ion can also appear in the neighborhood of a Co^{2+} ion. Therefore, there may be another condition for forming the Co^{2+}-Fe^{2+} pair between the nearest-neighbor Co^{2+} and Fe^{2+} ion. These may include the ion-configuration around a Co^{2+} ion as well as that of a Fe^{2+} ion, and that distance between the nearest-neighbor Co^{2+} and Fe^{2+} because that is not the same due to the crystalline field.[11] Additional study on these points is suggested.

IV. CONCLUSIONS

(1) The coercivity enhancement and instability of Co modified iron oxide particles containing 0–9.2 wt % Fe^{2+} ions are closely related to the uniaxial magnetic anisotropy from the transverse magnetic annealing and torque experiments.

(2) The Fe^{2+}-Co^{2+} pair model was proposed to explain the uniaxial magnetic anisotropy of the magnetic particles.

(3) To verify the nature of the Fe^{2+}-Co^{2+} pair, the probability of one or more Co ions appearing in the neighborhood of a B site Fe^{2+} ion was calculated using the chemical composition, the Mössbauer parameters, Pi(Fe^{+2}) and Pi(Fe^{+3}).

[1] M. P. Sharrock, IEEE Trans. Magn. **MAG-25**, 4375 (1989).
[2] A. Eiling, IEEE Trans. Magn. **MAG-23**, 16 (1987).
[3] K. Sun, J. H. Xu, M. X. Lin, G, M. Chen, and H. L. Luo, J. Magn. Magn. Mater. **87**, 260 (1990).
[4] M. Kishimoto, M. Amemiya, and F. Hayama, J. Appl. Phys. **55**, 2272 (1984).
[5] A. J. Freeman and R. E. Watson, Phys. Rev. Lett. **5**, 498 (1960).
[6] H. Franke and M. Rosenberg, J. Magn. Magn. Mater. **4**, 186 (1977).
[7] G. H. Wang, X. P. Zhong, H. C. Yang, H. l. Luo, and R. Y. Lu, Proceedings of the 6th International Conference on Ferrites, 1992, p. 1434.
[8] M. Kishimoto, IEEE Trans. Magn. **MAG-15**, 906 (1979).
[9] M. P. Sharrock, P. J. Picone, and A. H. Morrish, IEEE Trans. Magn. **MAG-19**, 1446 (1983).
[10] G. A. Sawatzky, F. Der Woude, and A. H. Morrish, Phys Rev. **187**, 747 (1969).
[11] J. C. Slonczewski, Phys. Rev. **110**, 1343 (1958).

X-ray photoelectron spectroscopy and Mössbauer study of $Ho(Fe_{1-x}Mn_x)_2$ compounds

Y. J. Tang, Y. B. Feng, and H. L. Luo
Institute of Physics, Academia Sinica, Beijing, People's Republic of China

S. M. Pan
General Research Institute for Non-Ferrous Metals, CNNC, Beijing, People's Republic of China

Cubic Laves compounds $Ho(Fe_{1-x}Mn_x)_2$ ($x=0$, 0.1, 0.2, 0.3) were investigated by XPS and Mössbauer measurements. It was found that the binding energy (BE) of compounds obtained by XPS remains almost the same for all the compounds and no chemical shift (δ) of the core-electron binding energy was found, which implies that no charge transfer takes place from Mn atoms to Fe atoms due to Mn substitution. Mössbauer study has shown that the average hyperfine fields and the deduced Fe moment decrease with increasing Mn content. It is considered that the variation of isomer shift (IS) due to Mn substitution obtained by Mössbauer measurement is mainly due to the size effect since the isomer shift (δ) for the compounds are almost linearly dependent on the volume; electron transfers seem to be of minor importance.

I. INTRODUCTION

In recent years much research has been carried out on the magnetic and magnetostrictive properties of $R(Fe_{1-x}T_x)_2$ (R=rare earth elements, T=Mn, Al, B, Ga, Si...) pseudobinary cubic Laves compounds in order to examine the substitution effect.[1-3] It was found from Mössbauer study that the isomer shift (IS) in $Dy(Fe_{1-x}T_x)_2$ (T=Al, B) compounds increases with increasing x value, which was ascribed to the $2p$ or $3p$ electrons of B or Al atoms are transferred into the $3d$ band of Fe atoms.[3] However since it was also found that the isomer shift (IS) in $R(Fe_xNi_{1-x})_2$ (R=Dy, Ho) compounds are linearly dependent on the volume of the variation of the isomer shift (IS) and was suggested to be mainly due to the size effect and is not related to the increase of the electron concentration of the system.[4] A better knowledge of these phenomena can lead to a better understanding of the substitution effect for transition metals on magnetic and magnetostrictive properties in RFe_2 compounds. X-ray and photoelectron spectroscopy (XPS) analysis can provide useful information about the energy shift of the core-electron binding energies. These energy shifts are related to the potential at the nucleus, which is approximately a function of the valence electron population and the potential due to the atoms of the environment, so detailed study on $R(Fe_{1-x}T_x)_2$ compounds by XPS can provide direct information about the charge transfer due to substitution. By Mössbauer study, the charge density $\rho(0)$ at the nucleus is measured through the isomer shift (IS). Mössbauer studies on ^{57}Fe for RFe_2 compounds have shown that even though these compounds have an identical crystallographic structure, they present several types of spectra.[5] With the direction of easy magnetization (n) along the [100] axis all iron atoms are equivalent and a simple six-line spectrum is obtained, as was observed for $HoFe_2$ and $DyFe_2$. If n is along the [111] or [110] direction, there are two magnetically inequivalent iron sites, giving rise to a spectrum superposed by two six-line patterns with population ratios 1:3 or 2:2, as observed for YFe_2, $TbFe_2$, $ErFe_2$, and $TmFe_2$ or $SmFe_2$ at low temperature. For $R(Fe_{1-x}T_x)_2$ compounds the spectrum become more complex when Fe was substituted with other elements, which is due to the existence of a range of hyperfine fields in the material occasioned by the random distribution of Fe and T atoms over the transition metal sublattice.

In the present study the chemical shift (δ) obtained by XPS and isomer shift (IS) measured by ^{57}Fe Mössbauer for $Ho(Fe_{1-x}Mn_x)_2$ ($x=0-0.3$) compounds were examined in order to reveal the substitution effect.

II. EXPERIMENT

$Ho(Fe_{1-x}Mn_x)_2$ ($x=0$, 0.1, 0.2, 0.3) compounds were arc melted in an arc furnace under high pure argon atmosphere, and annealed at 900 °C for a week under a purified argon atmosphere. The x-ray analysis showed that all samples were a single phase of cubic Laves structure ($C15$), and the lattice constant were calculated by using the (440) peak of x-ray spectra for the compounds. The Mössbauer spectra were recorded at room temperature with a conventional constant acceleration spectrometer with a ^{57}Co source in a Pd matrix. The record time for each sample is about two days and the velocity was calibrated with an α-Fe foil of 25-μm thickness. The x-ray photoelectron spectra (XPS) were obtained by an ESCALAB5 ESCA spectrometer equipped with an Al radiation source $E(K\alpha)=1486.6$ eV and with a resolution of 0.5 eV. The samples were supported in the appropriate sample holders and mounted on high vacuum feedthroughs, then argon sputtered for 15 min to ensure clean surface for examination.

III. RESULTS AND DISCUSSION

The lattice constants of $Ho(Fe_{1-x}Mn_x)_2$ ($x=0$, 0.1, 0.2, 0.3) compounds are obtained by the x-ray method and listed in Table I. They increase with increasing Mn content. The binding energy (BE) calculated from the XPS spectra are also listed in Table I. For metals, the binding energy is the minimum energy required to excite a core electron to an available unoccupied state above the Fermi level and is in-

 0021-8979/94/76(10)/6903/3/$6.00 © 1994 American Institute of Physics

TABLE I. Lattice constant, binding energy, hyperfine parameters, and magnetic moment μ_{Fe} in $Ho(Fe_{1-x}Mn_x)_2$ ($x=0$, 0.1, 0.2, 0.3) compounds at room temperature.

X	a (Å)	Binding energy (eV) Fe2$p_{1/2}$	Fe2$p_{3/2}$	Mn2$p_{3/2}$	H_{hf} (kOe)	IS (mm/s)	SQ (mm/s)	μ_{Fe} (300) (μ_B/Fe)
0	7.333	706.8	719.8	···	195.4	−0.121	0.038	1.43
0.1	7.343	706.6	719.4	639.2	179.6	−0.135	0.063	1.31
0.2	7.361	706.7	719.5	639.1	138.1	−0.084	0.072	1.01
0.3	7.381	706.6	719.6	639.3	130.3	−0.022	0.058	0.96

fluenced by the chemical environment. According to charge potential model,[6] the ionization energy of a core subshell (i_A) is approximated by

$$I(i_A)=k_i^A q_A+eV_A, \tag{1}$$

where q_A is the partial charge on the atom A, k_i^A, is an adjustable parameter, and V_A is the potential of atom A due to the other atoms B in the system. With a simple point-charge approximation

$$V_A=\sum_{B\neq A}\frac{q_B}{4\pi\epsilon_0 R_{AB}}, \tag{2}$$

where the R_{AB} are internuclear distances. From analyzing the binding energy of Fe $2p_{1/2,3/2}$ and of Mn $2p_{3/2}$ listed in Table I we found that the binding energy (BE) of compounds remains almost the same value for all the compounds and no chemical shift of the core-electron binding energy was found. This implies that no charge transfer takes place from Mn atoms to Fe atoms due to Mn substitution.

The Mössbauer spectra present in Fig. 1 were analyzed using a standard computer procedure. Depending on the shape of the spectrum one to five independent six-line patterns with unrestricted intensities, hyperfine fields, quadruple splitting, and isomer shift were fitted in order to reproduce the broadening of the spectra with increasing Mn content. The half-width of all the six-line patterns was kept constant. The spectrum of $HoFe_2$ was fitted as one six-line pattern, indicating that the magnetic moment is directed along the [100] axis.[5] It is obvious that Mn substitution has a great influence on the hyperfine interaction, as can be seen from Fig. 1. The Mössbauer absorption spectra for $x>0$ compounds indicate the existence of the wide hyperfine field distribution because of the random distribution of Mn atoms in transition metal sublattice. The broadening of spectra was also found in other $R(Fe_{1-x}T_x)_2$ compounds due to substitution and was explained, for $R(Fe_{1-x}Al_x)_2$ compounds,[2] on the basis of the local environment effect which supposes that the hyperfine fields distribution for a given iron atom has a proportionality relation with the number of Fe nearest- and next-nearest-neighbors calculated from the binomial formula. However, no reasonable results can be obtained in the present study when the same procedure, as used for $R(Fe_{1-x}Al_x)_2$ compounds, was employed to fit the spectra of $Ho(Fe_{1-x}Mn_x)_2$ compounds, which means that no definite conclusion can be drawn about the existence of the local environment effect in $Ho(Fe_{1-x}Mn_x)_2$ compounds. Through fitting the spectra, the average hyperfine field H_{hf}, isomer shift (IS), and quadruple splitting (QS) are obtained and listed in Table I. It is clearly seen from Table I that the average hyperfine field decreases with increasing Mn content. It has been shown[7] from combined NMR and Mössbauer investigation that the average iron hyperfine field and average iron moment are proportional to each other

$$H_{hf}=a\mu_{Fe}. \tag{3}$$

The proportionality constant a equals 145 kOe/μ_B for Y-Fe compounds[7] and 125 kOe/μ_B was used for $Dy(Fe_{1-x}B_x)_2$ compounds.[3] Here we consider $a=137$ kOe/μ_B for $Ho(Fe_{1-x}Mn_x)_2$ compounds, which was deduced from the hyperfine field and iron moment for $HoFe_2$ in the present study. The Fe moments calculated from Eq. (3) were listed in Table I. The decrease of μ_{Fe} with increasing Mn content is evident which means that Fe moment is strongly influenced by Mn atoms.

From Table I it can also be seen that the average isomer shift (IS) shows a weak concentration dependence, which is the characteristic of these compounds. We note that the IS for the compounds are almost linearly dependent on the volume, as can be seen from Fig. 2. Taking the XPS results for the compounds into account we suggest that the variation of IS

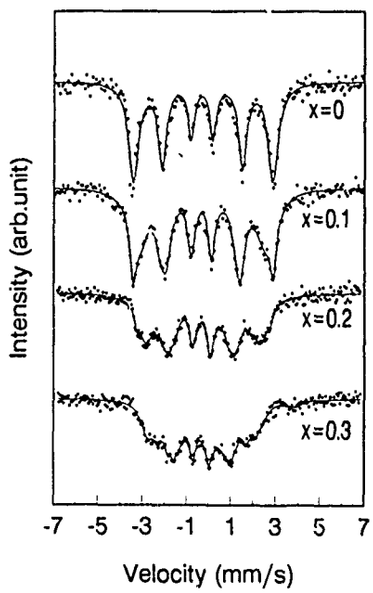

FIG 1. Mossbauer spectra of $Ho(Fe_{1-x}Mn_x)_2$ compounds ($x=0$, 0.1, 0.2, 0.3) at room temperature.

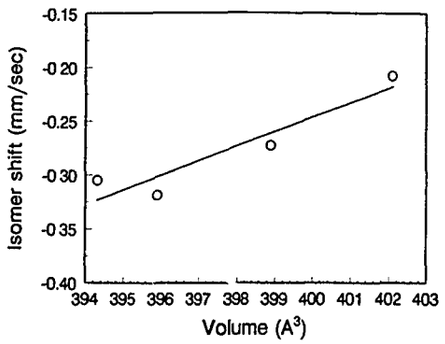

FIG. 2. Volume dependence of the isomer shift in $Ho(Fe_{1-x}Mn_x)_2$ compounds.

due to Mn substitution is mainly due to size effects; electron transfers seems to be minor importance.

IV. CONCLUSION

In conclusion, we would like to point out that for $Ho(Fe_{1-x}Mn_x)_2$ ($x=0$, 0.1, 0.2, 0.3) compounds:

(1) From the XPS measurement it was found that the binding energy (BE) of compounds remains almost the same value for all the compounds and no chemical shift (δ) of the core-electron binding energy was found, which implies that no charge transfer takes place from Mn atoms to Fe atoms due to Mn substitution.

(2) From the Mössbauer study it was found that the average hyperfine fields and the deduced Fe moment decrease with increasing Mn content. The variation of the IS due to Mn substitution is mainly due to size effects; electron transfers seem to be of minor importance.

[1] T. Funayama, T. Kobayashi, I. Sakai, and M. Sahashi, Appl. Phys Lett. **61**, 114 (1992)
[2] W. Steiner, M. Reissner, W. Schäfer, and G. Will, Physica B **130**, 426 (1985).
[3] W. D. Zhong, J. Lan, Z. X. Liu, F. S. Li, D S. Xue, R. J. Zhou, S. H. Ge, and Y. D. Zhang, J. Magn. Magn. Mater. **79**, 202 (1989).
[4] E. Burzo, Phys. Rev. B **17**, 1414 (1978).
[5] G. J. Bowden, D. ST. P. Bunbury, A. P. Guimarâes, and R. E. Snyder, J. Phys. C **1**, 1376 (1968).
[6] A. F. Orchard, *Handbook of X-ray and Ultraviolet Photoelectron Spectroscopy*, edited by D. Briggs (Heyden, London, 1977), p. 1.
[7] A. S. Schaafsma, M. J. Besnus, I. Vincze, and F. van der Woude, J. Magn. Magn. Mater. **15–18**, 1149 (1980).

Hyperfine fields of mercury in single-crystalline cobalt

J. G. Marques, J. G. Correia,[a] A. A. Melo, and J. C. Soares
CFNUL, Av. Prof. Gama Pinto 2, 1699 Lisboa Codex, Portugal

E. Alves and M. F. da Silva
Physics Department, ICEN/INETI, E.N. 10, 2685 Sacavém, Portugal and ISOLDE Collaboration, CERN, CH-1211 Geneva, Switzerland

The combined hyperfine interaction of mercury in a hexagonal close-packed cobalt single crystal was measured using the $e^- - \gamma$ perturbed angular correlation technique with the ^{197}Hg and ^{199}Hg probes, without applied magnetic field. The magnetic and quadrupole coupling constants of the $5/2^-$ levels in both ^{197}Hg and ^{199}Hg were measured with extremely high precision, ω_L(^{197}Hg)=951(9) Mrad/s, ω_L (^{199}Hg)=1039(10) Mrad/s, υ_Q (^{197}Hg)=3.7(5) MHz and υ_Q (^{199}Hg)=32(2) MHz. Using the well-known g factors and quadrupole moments of the respective levels, the magnetic hyperfine field, $|H_{hf}(\underline{\text{Hg}}\text{Co})|$=581(12) kG, and the electric field gradient, $|V_{zz}(\underline{\text{Hg}}\text{Co})|$ $=2.0(3)\times10^{17}$ V/cm^2, were derived. The importance of using these hyperfine probes for studying the microscopic structure of cobalt-based multilayers is introduced and discussed.

I. INTRODUCTION

The potential applications of the giant magnetoresistance effect in recent years led to a considerable interest of magnetic multilayers consisting of a magnetic material, usually cobalt, separated by a thin nonmagnetic spacer. The optimization of the effect depends on the thickness, structure, and interface properties of the spacer and Co layers. Using the ^{111}Cd nucleus from the decay of ^{111}In as a probe implanted in Co/Re and Co/Cu multilayers,[1,2] the perturbed angular correlation (PAC) technique proved to be sensitive for the microscopic characterization of structural and point defects, phases, and interfaces in magnetic multilayers. The application of this technique is, however, limited to suitable probes. In the present work, it is shown that the ^{197m}Hg and ^{199m}Hg isotopes are appropriate for these studies: the hyperfine fields are higher and the substitutional fraction of Hg implanted in Co is a factor of three higher than in the Cd case, with no need to perform annealing treatments after the implantation.

The magnetic hyperfine interaction of Hg in Co has been previously studied by Krien and co-workers.[3] Their measurement could not, however, explain if the Hg atoms are at different sites in the Co lattice or if a combined hyperfine interaction is responsible for the observed modulation, since a quadrupole interaction is expected for the Co hexagonal close-packed (hcp) phase. To clarify this problem, new results are reported here, using the $e^- - \gamma$ PAC technique with the ^{197m}Hg and ^{199m}Hg isotopes, in a Co single crystal. The lattice site location of the Hg atoms has also been studied by a high precision channeling experiment performed after the radioactive decay on the same sample.

II. EXPERIMENTAL DETAILS

The ^{197m}Hg and ^{199m}Hg isotopes were implanted into a Co single crystal at 60 keV, using the ISOLDE facility at CERN, to doses of 5×10^{13} and 5×10^{12} at./cm^2, respectively. The mean-Hg range profile value is 11 nm.

The PAC experiments were performed using the 165–134 keV cascade from the decay of the 23.8-h isomeric state of ^{197}Hg, and the 374–158 keV cascade from the decay of the 43-min isomeric state of ^{199}Hg. The first transitions in these cascades are strongly converted, α_L(165 keV, ^{197}Hg)=173 and α_K(374 keV, ^{199}Hg)=3.5, which makes them ideal for e^--γ measurements. The calculated anisotropies are b_2A_{22}(^{197}Hg)=0.213 and b_2A_{22}(^{199}Hg)=0.235.[4]

The experimental setup consists of two magnetic β spectrometers of the Siegbahn type[5] for detection of conversion electrons and two BaF_2 scintillators for γ detection, arranged in a plane. Each lens makes 90° with one γ detector and 180° with the other. The time resolution (FWHM) of the setup for the ^{197m}Hg and ^{199m}Hg cascades was 1.0 ns. Four coincidence spectra were recorded, corresponding to the combinations of each magnetic lens with a γ detector. From these spectra the usual time differential anisotropy $R(t)=2\,[N(180°, t)-N(90°,t)]/[N(180°,t)+2\,N(90°,t)]$ was calculated.

The theoretical $R(t)$ function was calculated numerically taking into account the full Hamiltonian for a combined hyperfine interaction, as described by Barradas and co-workers.[6] In the calculation, independent fractions f_i of probe nuclei were considered, each experiencing a Larmor frequency, $\omega_L=-g\mu_N H_{hf}/\hbar$ and a quadrupole frequency, $\upsilon_Q=eQV_{zz}/h$. H_{hf} is the magnetic hyperfine field and V_{zz} is the main component of the electric field gradient (EFG) tensor at the nucleus. Q and g are, respectively, the quadrupole moment and g factor of the $I=5/2$ intermediate state of the cascade. For ^{197}Hg and ^{199}Hg these parameters are well known, $Q_{5/2^-}$ (^{197}Hg)=0.057(7) b, $Q_{5/2^-}$(^{199}Hg)=0.674(77) b,[7,8] $g_{5/2^-}$(^{197}Hg)=0.342(6), and $g_{5/2^-}$(^{199}Hg)=0.352(13).[9] Lattice imperfections, impurities, or defects cause a damping of the $R(t)$ function, described by a Lorentzian distribution with relative width δ, centered at a given ω_L.

No external magnetic field was necessary to orient the magnetic domains, since below 525 K the spins of the hcp Co lattice are aligned along the c axis. This is also the direction of the main component of the EFG tensor. For each isotope, experiments were performed on two complementary

[a]Current address. PPE Division, CERN, CH-1211 Geneva, Switzerland.

 0021-8979/94/76(10)/6906/3/$6.00 © 1994 American Institute of Physics

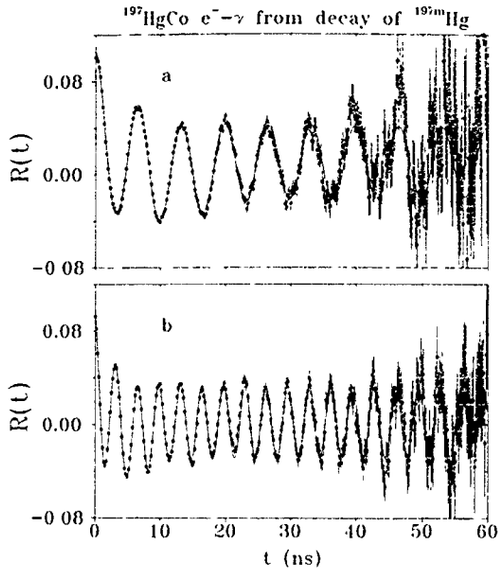

FIG. 1. Anisotropy ratios obtained with ^{197}Hg for (a) single crystal with c axis on the detectors' plane at 45°; (b) with c axis perpendicular to the detectors' plane.

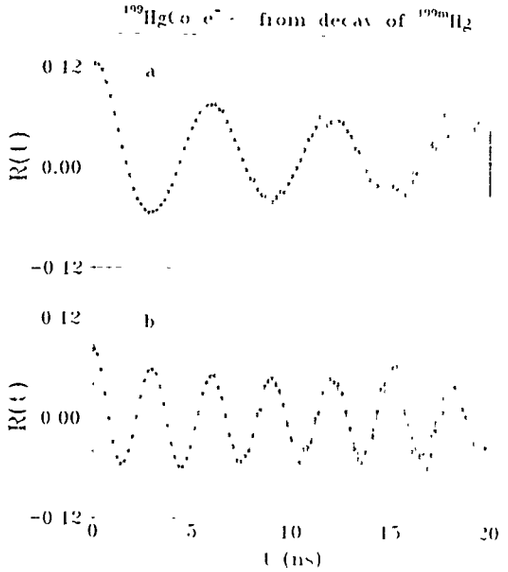

FIG. 2. Anisotropy ratios obtained with ^{199}Hg for (a) single crystal with c axis on the detectors' plane at 45°; (b) with c axis perpendicular to the detectors' plane.

geometries. In geometry G1 the c axis of the Co-single crystal lies on the detectors' plane at an angle of 45° with the detectors, and in geometry G2 it is perpendicular to that plane. For a collinear interaction, only the $\omega_L \pm 2\omega_0$ and $2\omega_L \pm \omega_0$ frequencies ($\omega_0 = 3\pi\upsilon_Q/10$) have observable amplitudes in geometries G1 and G2, respectively.

Complementary RBS/channeling experiments were carried out after the ^{197m}Hg decay in the channeling line of the 2.5-MeV Van de Graaff of INETI, Sacavém, using a 1.6-MeV He^+ beam. The backscattered particles were detected at angles of 140° and 180° using two silicon surface barrier detectors with resolutions of 13 and 18 keV, respectively.

III. RESULTS

Figures 1(a) and 1(b) show the anisotropy ratios $R(t)$ obtained with the ^{197m}Hg implanted sample in geometries G1 and G2, respectively. The measurements have been performed at room temperature. Assuming the Hg ions are substitutional in the Co lattice they would experience only one combined interaction, described by a theoretically predicted modulation. However, to obtain a satisfactory least-squares fit to both geometries, it was necessary to consider that the Hg atoms are located in three nonequivalent Co lattice sites. The results are shown in Table I. Parameter f_1 gives the percentage of Hg atoms described by a theoretical function assuming well-defined magnetic and electric frequencies. Parameter f_2 corresponds to Hg atoms characterized by the same values for the frequencies, but with a small Lorentzian distribution on the magnetic frequency. The remaining Hg atoms are described by a strongly damped frequency distribution, characterized by a large value of δ.

Figures 2(a) and 2(b) show the corresponding anisotropy ratios, $R(t)$, obtained with the ^{199m}Hg implanted sample. Again, it was necessary to consider three fractions of Hg atoms in the Co lattice. The results are shown in Table II.

Figure 3 shows the angular scans obtained for the (0001) plane (c plane) and for the $\langle 11\bar{2}0\rangle$ and $\langle 10\bar{1}0\rangle$ axes along that plane. From the minimum yields of the Hg and Co signals, a fraction of 70% of Hg atoms in regular positions in the Co single crystal is obtained. The slight narrowing of the Hg signal, clearly seen in the (0001) plane and in the $\langle 10\bar{1}0\rangle$ axis, indicates a fraction of Hg ions deviated from the substitutional positions. The continuous line in Fig. 3 is a Monte Carlo simulation of these scans, using a modified version of the FLUX program,[10] assuming a 50% substitutional fraction, a 20% slightly deviated fraction, and a 30% random fraction. The errors in the determination of these fractions are of the order of 10%.

TABLE I. ^{197}HgCo fit parameters.

	Fraction (%)	ω_L (Mrad/s)	δ	υ_Q(MHz)
f_1	33(3)	951(9)	0	3.7(5)
f_2	38(3)	951(9)	0.12(2)	3.7(5)
f_3	29(3)	300(30)	0.5(1)	0

TABLE II. ^{199}HgCo fit parameters.

	Fraction (%)	ω_L (Mrad/s)	δ	υ_Q (MHz)
f_1	53(3)	1039(10)	0	32(2)
f_2	29(3)	1039(10)	0.15(2)	32(2)
f_3	18(3)	510(40)	0.6(1)	0

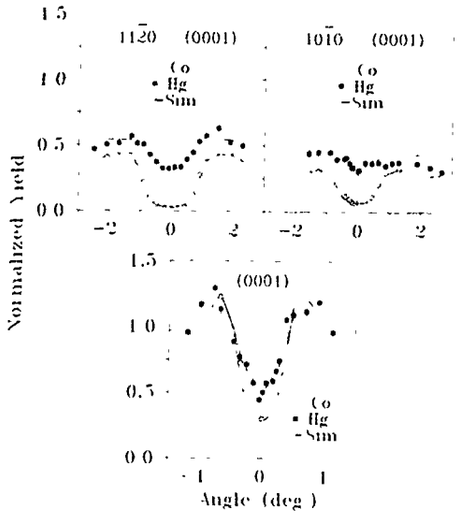

FIG. 3. Channeling scans for the (0001) plane and the $\langle 11\bar{2}0\rangle$ and $\langle 10\bar{1}0\rangle$ axes along that plane. The continuous line is a Monte Carlo simulation.

IV. DISCUSSION AND CONCLUSIONS

The PAC experiments show the surprising result that about 75% of the implanted probe atoms (fractions f_1 and f_2) stop at regular sites, and the channeling experiment proves that the Hg atoms are substitutionally located in the Co matrix. The observed frequency distribution of fraction f_2 is small and the modulation could be followed for about eight half-lives of the intermediate state of the cascades. This is due to the fact that the magnetic coupling constant is much higher than the quadrupole coupling constant.

Although the quadrupole coupling constants are very small, as a consequence of the small deviation for Co of the c/a=1.6228 ratio from the ideal value (c/a=1.633), in this work they were derived very accurately: υ_Q (^{197}HgCo)=3.7(5) MHz and υ_Q (^{199}HgCo)=32(2) MHz. From the value of υ_Q(^{199}Hg Co) and the corresponding quadrupole moment, the derived EFG is $|V_{zz}$(Hg Co)|=2.0(3)$\times 10^{17}$ V/cm^2. According to known trends[11] its sign should be negative. In Ref. 3, the ionic EFG produced by the Co ions at the Hg-probe nucleus has been calculated as $V_{zz}^{\text{ion}}=+1.14\times 10^{17}$ V/cm^2. The enhancement of the ionic EFG by the conduction electrons is usually described by a factor K, as $V_{zz}=(1-K)\ V_{zz}^{\text{ion}}$. For the present case we deduce $K=2.8$ which is of the same order as for most cases.

An important result of this work is the derivation of a more precise value for the magnetic hyperfine coupling constant measured by the Larmor frequency ω_L(^{197}Hg Co)=951(9) Mrad/s. Due to the high statistics obtained in these measurements, the errors in the magnetic frequencies are limited only by the 1% uncertainty of the time calibration. Using the known g factor, $g_{5/2}$-(^{197}Hg)=0.342(6),[9] the derived magnetic hyperfine field is $|H_{hf}$(HgCo)|=581(12) kG, which fits very well in the systematic of hyperfine fields in Co.[12]

In conclusion, the ^{197}Hg and ^{199}Hg are very attractive probes for the study of Co-based structures using the PAC technique, due to the high substitutionality in Co achieved after implantation at room temperature. Additionally, the availability of two isotopes with quadrupole moments differing by one order of magnitude allows a great flexibility for the study of EFGs. Since the EFGs at the Hg site in the interfaces, or at the Co site with trapped defects or impurities, are normally much higher than the EFG of Hg in Co, a large range of values can be measured selecting the appropriate probe, ^{197}Hg or ^{199}Hg, for the high or low range of EFGs. These advantages are currently being explored at ISOLDE/CERN due to the high yields for the production of these isotopes.

ACKNOWLEDGMENTS

This work has been partially funded by JNICT (Portugal) under CERN Project 982/92. J.G.M. acknowledges a grant from JNICT, under "Fundo CERN".

[1] N. P. Barradas, J. L. Leal, H. Wolters, M. F. da Silva, A. A. Melo, J. C. Soares, L. V. Melo, P. P. Freitas, B. Swinnen, and M. Rots, J. Magn. Magn. Mater. **121**, 80 (1993).
[2] P. P. Freitas, I. G. Trindade, L. V. Melo, J. L. Leal, N. P. Barradas, and J. C. Soares, J. Appl. Phys. **73**, 5527 (1993).
[3] K. Krien, A. G. Bibiloni, K. Freitag, J. C. Soares, and R. Vianden, Phys. Rev. B **8**, 2248 (1973).
[4] R. S. Hager and E. C. Seltzer, Nucl. Data A **4**, 397 (1968).
[5] P. Kleinheinz, L. Samuelsson, R. Vucanovic, and K. Siegbahn, Nucl. Instrum. Methods **32**, 1 (1965)
[6] N. P. Barradas, M. Rots, A. A. Melo, and J. C. Soares, Phys. Rev. B **47**, 8763 (1993).
[7] P. Herzog, K. Krien, K. Freitag, M. Reuschenbach, and H. Walitzki, Nucl. Phys. **A337**, 261 (1980).
[8] W. Tröger, T. Butz, P. Blaha, and K. Schwarz, Hyperfine Interact. **80**, 1109 (1993).
[9] K. Krien, K. Kroth, H. Saitovitch, and W. Thomas, Z. Phys. **283**, 337 (1977).
[10] P. J. M. Smulders and D. O. Boerma, Nucl. Instrum. Methods B **29**, 471 (1987).
[11] E. Bondenstedt, Hyperfine Interact. **15-16**, 1061 (1983)
[12] G. N. Rao, Hyperfine Interact. **26**, 1120 (1985).

Simulation of nuclear magnetic resonance spin echoes using the Bloch equation: Influence of magnetic field inhomogeneities

J. A. Nyenhuis and O. P. Yee
School of Electrical Engineering, Purdue University, West Lafayette, Indiana 47907

There are a number of low cost nuclear magnetic resonance (NMR) applications that are based on measurements of spin-spin (T_2) and spin-lattice (T_1) relaxation times. Pulsed rf magnetic fields are typically used to flip the nuclear spins in these measurements. The ability to perform these measurements in relatively nonuniform magnetic fields is a factor in minimizing costs. In this work, we explore the limitations of field inhomogeneity on spin echo techniques for measuring relaxation times. Using a computer model that was developed for this study, we numerically integrate the Bloch equation to simulate spin echo peaks for CPMG and other pulse sequences. We quantify how higher intensity rf pulses result in increased amplitudes of spin echo peaks in an inhomogeneous static magnetic field. An rf amplitude which is five times the maximum inhomogeneity in the static field results in less than 0.5% attenuation between even numbered peaks in a CPMG sequence.

I. INTRODUCTION

Numerous applications of nuclear magnetic resonance (NMR) have been developed; for example, it has been proposed that NMR be used to sort fruits and vegetables,[1] to measure the percentage of saturated fats in vegetable oils,[2] and for the early detection of osteoporosis in humans.[3]

NMR techniques have several advantages over other methods of experimental analysis; they are neither destructive nor invasive to the sample under study. Ultimately, however, it is cost and not these advantages, which will determine whether NMR can compete with experimental methods already in place. A major factor affecting the cost of a NMR system is the magnet. Magnets that produce highly uniform magnetic fields are difficult to manufacture and, correspondingly, are expensive.

This paper investigates the effects of nonuniform magnetic fields on spin echo techniques for measuring relaxation times. We seek to answer the question: how uniform must the fields be in order to achieve good measurements?

II. SIMULATION MODEL

A computer model, written in FORTRAN, of NMR phenomena was developed for this study. The assumptions made in this model are (1) a one-dimensional model is used, (2) the sample is magnetically homogeneous, (3) the applied rf fields are uniform across the sample, and (4) diffusion effects are ignored. These assumptions are made in order to isolate the effects of nonuniform magnetic fields and are not limitations of the computer model.

In the simulation model the sample is divided into regions of magnetization $\mathbf{M}_i=(M_x,M_y,M_z)$, which represent the vector sum of all magnetic moments in the region.

The number of regions used in the simulations was 2499, although a choice as low as 99 regions would yield comparable results. For a sufficiently large number of regions, the solutions are basically independent of the number of regions, because the magnetization in each region is independent of that in another region; however, if diffusion is included in the model, magnetization in one region is coupled to adjoining regions, and the accuracy of solutions improves by increasing the number of regions. The number of regions chosen must be large enough, however, to obtain a good sampling of the dephased spins in an inhomogeneous magnetic field.

An rf field of carrier frequency ω_0 with only x and y components is assumed: $\mathbf{h}_{\rm rf}=(h_x,h_y)$. The static field is assumed to lie in the z direction and has an amplitude $H_0+\Delta H_i$, where $H_0\equiv\omega_0/\gamma$, with γ being the nuclear gyromagnetic constant. H_0 is thus the field for which the resonance frequency is equal to the rf frequency and ΔH_i accounts for inhomogeneity in the static field.

The time evolution of each region's M_i in response to the static and rf magnetic fields is given by the Bloch equation

$$\frac{d\mathbf{M}_i}{dt}=\gamma\{\mathbf{M}_i\times[(H_0+\Delta H_i)\hat{\mathbf{z}}+\mathbf{h}_{\rm rf}]\}-\frac{M_{x,i}}{T_{2,i}}\hat{\mathbf{x}}-\frac{M_{y,i}}{T_{2,i}}\hat{\mathbf{y}}-\frac{M_{z,i}-M_{0,i}}{T_{1,i}}\hat{\mathbf{z}}, \tag{1}$$

where $M_{0,i}$ is the saturation magnetization in the presence of the static field.

In Eq. (1), the subscript i indicates that the Bloch equation is applied separately to each region in the sample.

The normalized magnetization in a region is expressed as $\mathbf{m}_i=\mathbf{M}_i/M_{0,i}$, where $M_{0,i}$ is the saturation magnetization in that region. Magnetic fields are normalized to the value of static field for which the nuclear spins have resonance frequency ω_0, e.g., $\tilde{\mathbf{h}}_{\rm rf}=\mathbf{h}_{\rm rf}/H_0$. Time is normalized to cycles of the rf field, e.g., $\tilde{t}=\omega_0 t/(2\pi)$.

Transforming Eq. (1) into a coordinate frame[4] that rotates at the rf field frequency ω_0, and letting $\tilde{H}_{{\rm eff},i}\equiv\Delta H_i/H_0$, the normalized Bloch equation in component form for each region is

$$\begin{aligned}
\frac{dm_{x,i}}{d\tilde{t}}&=2\pi(\tilde{H}_{{\rm eff},i}m_{y,i}-\tilde{h}_{y,i}m_{z,i})-\frac{m_{x,i}}{\tilde{T}_{2,i}},\\
\frac{dm_{y,i}}{d\tilde{t}}&=2\pi(\tilde{h}_x m_{z,i}-\tilde{H}_{{\rm eff},i}m_{x,i})-\frac{m_{y,i}}{\tilde{T}_{2,i}},\\
\frac{dm_{z,i}}{d\tilde{t}}&=2\pi(\tilde{h}_{y,i}m_{x,i}-\tilde{h}_{x,i}m_{y,i})-\frac{m_{z,i}-1}{\tilde{T}_{1,i}}.
\end{aligned} \tag{2}$$

 0021-8979/94/76(10)/6909/3/$6.00 © 1994 American Institute of Physics

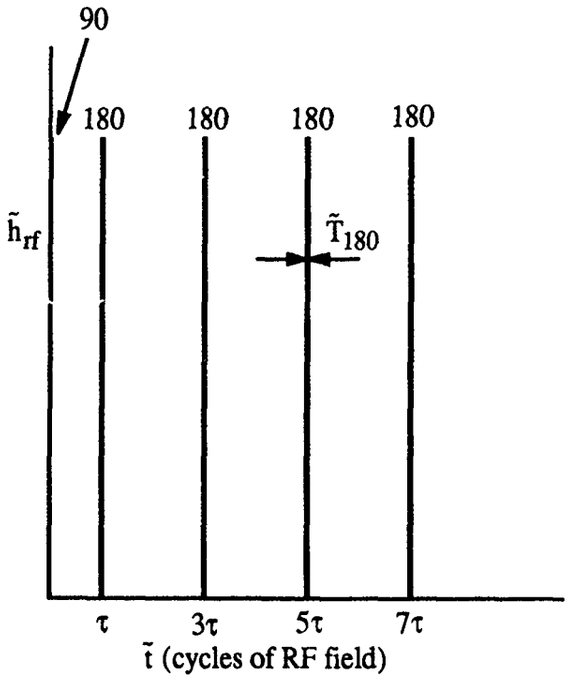

FIG. 1. rf pulse sequence used in the spin echo simulations.

The Bloch equation is now in the form of three first-order differential equations that are solved numerically for each region in the sample. The simulations implement the fourth-order Runge–Kutta method with a step time of five cycles of the rf field. This step time was chosen because it was a large enough step that excessive computing time was not required and at the same time the solutions would converge to five decimal places.

For the case when the rf signal is turned off, simple closed form expressions[5] for the magnetization components exist, which reduces the computational time of the simulations.

After each time step in the simulation, the transverse magnetization components, $m_{x,i}$ and $m_{y,i}$, are summed vectorially over all the regions in the sample. The receiver coils in a NMR system will detect signals proportional to the transverse magnetization of the sample. The receiver flux, normalized to the maximum possible value when all the spins are in phase, is then

$$\text{Normalized receiver response} = \left(1 \Big/ \sum_i M_{0,i}\right) \times \sqrt{\left(\sum_i M_{0,i} m_{x,i}\right)^2 + \left(\sum_i M_{0,i} m_{y,i}\right)^2}. \quad (3)$$

III. SIMULATION RESULTS AND DISCUSSION

The rf pulse sequence used in the simulations is shown in Fig. 1. A 90° rf pulse cants the nuclear magnetization from the z direction into the transverse plane. 180° pulses are used to generate the spin echoes, which result from refocusing of the spins after the 180° pulse. The 90° rf pulse is taken to be in the x direction in the rotating frame. For a Carr–Purcell–Meiboom–Gill[6] (CPMG) pulse sequence, the 180° pulses are in the y direction, while they are in the x direction for a Carr–Purcell[7] (CP) pulse sequence. With the 180° pulses depicted, spin echoes occur near times 2τ, 4τ, 6τ, and 8τ. Amplitude $\tilde{h}_{rf}$ and durations $\tilde{T}_{90}$ and $\tilde{T}_{180}$ of the rectangular rf pulses were varied for different simulations. From Eq. (2), it can be shown that for a 90° flip $\tilde{T}_{90}=1/4\tilde{h}_{rf}$ and $\tilde{T}_{180}=2\tilde{T}_{90}$.

A linear inhomogeneity was assumed for the simulation results presented here:

$$\Delta H_i = \Delta H_{max} x_i / L \quad -L \leq x_i \leq L. \quad (4)$$

For the results presented here, the normalized inhomogeneity $\Delta\tilde{H}_{max}=\Delta H_{max}/H_0$ was 5×10^{-4}, i.e., 500 ppm. This inho-

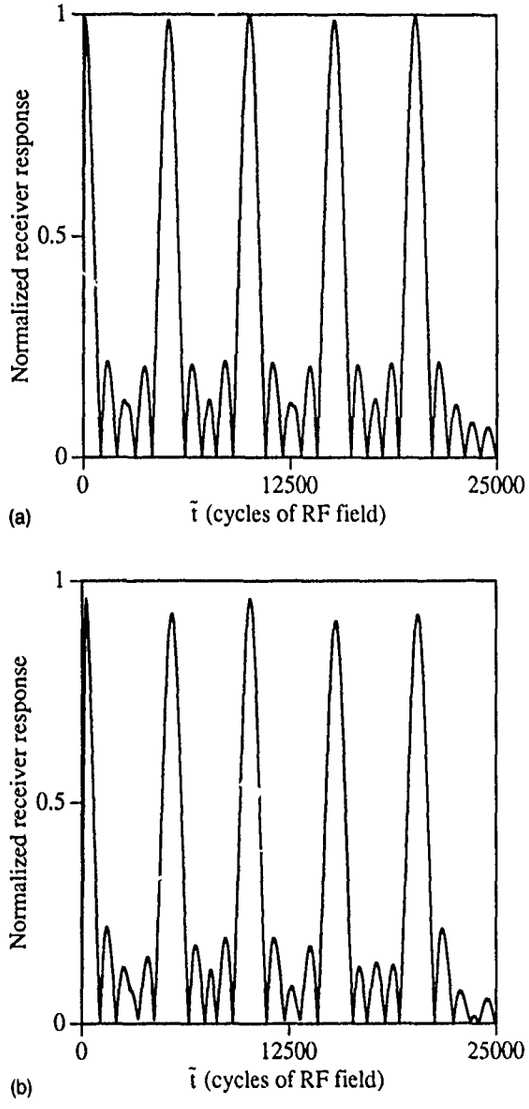

FIG. 2. Effect of rf amplitude on spin echo amplitudes. A CPMG rf pulse sequence was used for a linear inhomogeneity with $\Delta\tilde{H}_{max}=500$ ppm and $\tau=2500$ cycles. $\tilde{T}_1=\tilde{T}_2=10^{12}$ cycles of rf field in the model. (a) $\tilde{h}_{rf}=2.5\times10^{-3}$ and $\tilde{T}_{180}=2\tilde{T}_{90}=200$ cycles. Response peaks are 0.9933, 0.9873, 0.9985, 0.9873, and 0.9946. (b) $\tilde{h}_{rf}=10^{-3}$ and $\tilde{T}_{180}=500$ cycles of rf field. Response peaks are 0.9610, 0.9260, 0.9590, 0.9087, and 0.9236.

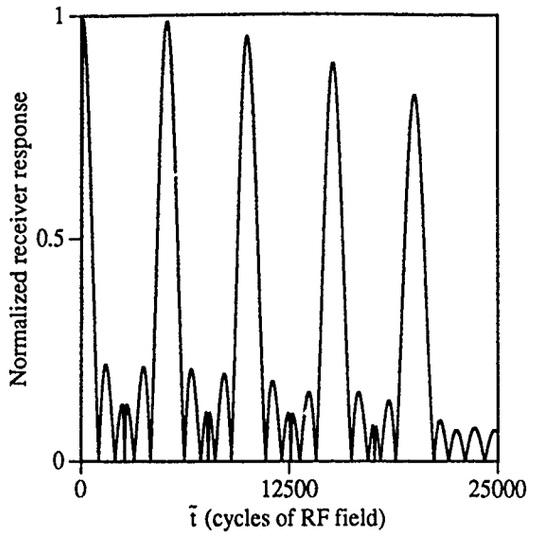

FIG. 3. Effect of using CP rf pulse sequence on spin echo simulations. rf pulse amplitude $\tilde{h}_{rf}=2.5\times10^{-3}$ ($\tilde{T}_{90}=100$ cycles of rf field) and a linear inhomogeneity with $\Delta\tilde{H}_{max}=500$ ppm was used. $\tau=2500$ cycles and $\tilde{T}_1=\tilde{T}_1=10^{12}$ cycles of rf field. Response peaks are 0.9933, 0.9864, 0.9514, 0.8905, and 0.8195.

mogeneity is of the order of magnitude that is experienced in low cost NMR applications. However, spectrometers and medical imagers use magnets with much better homogeneity. The normalized relaxation times $\tilde{T}_1$ and $\tilde{T}_2$ were arbitrarily set to a large value of 10^{12} cycles. With the effects of nuclear relaxation essentially removed from the calculations, we could focus on the effects of inhomogeneity in the static field on the spin echo response.

In Fig. 2, we evaluate the effect of rf amplitude on the echo peaks for a CPMG sequence. In Fig. 2(a) a rf field with amplitude $\tilde{h}_{rf}=2.5\times10^{-3}$ is used, which results in a normalized duration $\tilde{T}_{180}=200$ cycles. As is expected for the CPMG pulse sequence, even echo peaks have the greatest height, and the fourth peak in the sequence has normalized amplitude 0.9946. In Fig. 2(b), the rf field amplitude has been reduced to $\tilde{h}_{rf}=10^{-3}$, and the 180° pulse has a duration of 500 cycles. Compared to the case for $\tilde{h}_{rf}=2.5\times10^{-3}$, the echo peaks have a smaller amplitude, with the fourth peak having an amplitude of 0.9236.

The reduction between even numbered peaks in a spin echo sequence is used to determine T_2 in a CPMG sequence: normalized receiver response $\propto\exp(-t/T_2)$. For an accurate T_2 measurement, we would like the attenuation, due to magnetic field inhomogeneity, between even peaks to be much less than the attenuation due to spin-spin relaxation. For Fig. 2(a), the reduction in signal between the even peaks corresponds to an effective spin-spin relaxation time $\tilde{T}_{2,eff}$ of 2.6×10^6 cycles, whereas in Fig. 2(b) $\tilde{T}_{2,eff}$ is 0.27×10^6 cycles. Thus, the higher intensity rf field results in a more accurate T_2 measurement. Less effect of the inhomogeneity could also be achieved by increasing τ. For instance, increasing τ to 5000 cycles, but maintaining the other conditions of Fig. 2(a), results in $\tilde{T}_{2,eff}$ of 6.2×10^6 cycles. For $\tau=7000$ cycles, $\tilde{T}_{2,eff}=8.5\times10^6$ and for $\tau=9000$ cycles, $\tilde{T}_{2,eff}=10.6\times10^6$.

An intuitive argument can be made to explain why shorter (i.e., higher intensity) rf pulses result in higher echo peaks in a CPMG sequence. With inhomogeneity in the static field, nuclear spins will have precession frequencies different from the frequency of the rotating rf field. Assume that the direction of the rf field is fixed in the rotating frame. The azimuthal angle of the nuclear magnetization will rotate at frequency $\Delta\omega=\gamma\Delta H_t$ with respect to the direction of the rf field. Let $\Delta\phi_{180}$ represent the change in angle during the 180° pulse between the rf field and the transverse component of nuclear magnetization:

$$\Delta\phi_{180}=\Delta\omega T_{180}=\gamma\Delta H_{max}T_{180}$$
$$=2\pi\Delta\tilde{H}_{max}\tilde{T}_{180}=\pi\Delta\tilde{H}_{max}/\tilde{h}_{rf}. \quad (5)$$

If there is significant change in angle between the rf field and the nuclear spins during a rf pulse, the flip angle will not have the desired value. For spin echo peaks with maximal value, we thus expect $\Delta\phi_{180}\ll1$. For $\tilde{h}_{rf}=2.5\times10^{-3}$ in Fig. 2(a), $\Delta\phi_{180}=0.63$ and for $\tilde{h}_{rf}=10^{-3}$ in Fig. 2(b), $\Delta\phi_{180}=1.57$.

Figure 3 shows a spin echo sequence using the same conditions as in Fig. 2(a), except that both the 90° and 180° pulses are in the x direction. For this CP sequence, the echo peaks progressively decrease in amplitude, with the fourth peak having an amplitude of 0.8195. Comparison of Figs. 2(a) and 3 clearly shows the advantage of the CPMG over the CP sequence in an inhomogeneous field. In the CMPG sequence, deviations from the ideal flip between successive 180° pulses are partially compensated, whereas errors in flip angle accumulate in the CP sequence.[8]

The CPMG sequence is forgiving of imperfections in rf pulse duration. The parameters of Fig. 2(a) were maintained, but $\tilde{T}_{90}$ and $\tilde{T}_{180}$ were independently made 10% too long. The amplitudes of the fourth echo peaks were then respectively 0.9829 and 0.9840, only slightly less than those shown in Fig. 2(a).

ACKNOWLEDGMENTS

We thank the U.S. Department of Energy, the Southeastern Egg and Poultry Association, and the National Live Stock and Meat Board for financial support. We also thank J. Marks, M. Morgan, D. Rellinger, J. Schmidt, R. Stroshine, and W. Wai for fruitful discussions.

[1] S. I. Cho, G. W. Krutz, H. G. Gibson, and K. Haghighi, Trans. ASAE **33**, 1043 (1990).
[2] F. D. Gunstone, J. Am. Oil Chem. Soc. **70**, 361 (1993).
[3] C. E. Brown J. H. Battocletti, R. Srinivasan, J. R. Allaway, J. Moore, and P. Sigmann, Clin. Chem. **34**, 1431 (1988).
[4] T. C. Farrar and E. D Becker, *Pulse and Fourier Transform NMR* (Academic, New York, 1971), p. 9.
[5] P. Meakin and J. P. Jesson, J. Magn. Res. **10**, 290 (1973).
[6] H. Y. Carr and E. M. Purcell, Phys. Rev **94**, 630 (1954).
[7] S. Meiboom and D. Gill, Rev. Sci. Instrum. **29**, 688 (1958).
[8] T. C. Farrar and E. D. Becker, *Pulse and Fourier Transform NMR* (Academic, New York, 1971), p. 27.

Correlation of magneto-volume effects and local properties of the Fe_2Ti-laves phase (abstract)

J. Pelloth, R. A. Brand, and W. Keune
Laboratorium für Angewandte Physik, Universität Duisburg, D-47048 Duisburg, Germany

Magneto-volume effects have been calculated[1] and shown to exist[2,3] in Fe_2Ti alloys. Since Mössbauer spectroscopy provides insight into local magnetic properties we have performed such measurements in the temperature range 4.2 K$<T<$800 in $B_{ext}=0$ and $\neq 0$ on $Fe_{2+x}Ti_{1-x}$ powder samples with $x=-0.05$ to $+0.1$. The spectra of Fe_2Ti at 4.2 K show two subspectra, one belonging to the antiferromagnetically coupled $6h$ sites, and the other one to the paramagnetic $2a$ sites, in agreement with Ref. 4. A detailed analysis shows that the electric field gradient of the $6h$ sites changes in sign and value when going from the antiferromagnetic to the paramagnetic state at 310 K. Moreover, the isomer shift values of the two sites are found to be different at 4.2 K, while they are equal above 310 K. Both changes suggest a change in the local electronic band structure between the paramagnetic and antiferromagnetic states. An increase of the linewidth is observable in the temperature region of 200 K$<T<$310 K that could be caused by a distribution of hyperfine fields on the $6h$ sites or by spin fluctuations during the lifetime of the excited state of the Mössbauer nucleus. For $x>0$ and 4.2 K, an additional magnetically split subspectrum appears that is associated with $6h$ sites and neighboring Fe antisite atoms. For $x<0$ the spectra are similar to those of Fe_2Ti.

This work was supported by the Deutsche Forschungsgemeinschaft (SFB 166).

[1] S. Asano and S. Ishida, J. Magn. Magn. Mater. **70**, 39 (1987).
[2] Y. Muraoka, M. Shiga, and Y. Nakamura, J. Phys. Soc. Jpn. Lett. **40**, 905 (1976).
[3] E F. Wassermann, B. Rellinghaus, M. Pasek, J. Kriegel, and W Pepperhoff, Phys. Rev. B (to be published).
[4] G. K. Wertheim, J. H. Wernick, and R. C. Sherwood, Solid State Commun. **7**, 1399 (1969).

 0021-8979/94/76(10)/6912/1/$6.00 © 1994 American Institute of Physics

Giant magnetoresistance effects in intermetallic compounds (invited)

V. Sechovský and L. Havela
Department of Metal Physics, Charles University, Ke Karlovu 5, CZ 121 16 Praha 2, The Czech Republic

K. Prokeš, H. Nakotte, F. R. de Boer, and E. Brück
Van der Waals-Zeeman Laboratory, University of Amsterdam, Valckenierstraat 65, NL 1018XE Amsterdam, The Netherlands

Giant magnetoresistance (GMR) effects are observed in several classes of bulk magnetic materials. The resistance changes at metamagnetic transitions connected with reorientation of $4f$ moments are only moderate due to the relatively weak coupling of the $4f$ and conduction electrons. Much larger GMR effects can be achieved by mechanisms involving the d states (RhFe, RCo_2), though the most spectacular resistance variations are connected with metamagnetic transitions in U-intermetallic antiferromagnets. This phenomenon can be interpreted as due to Fermi surface gapping (due to magnetic superzones) and/or due to spin-dependent scattering in analogy with magnetic multilayers.

I. INTRODUCTION

During the dramatic development in the research of magnetic multilayers, the magnetoresistance has become one of the frequently reported quantities. This originated by the discovery a large ("giant") magnetoresistance (GMR) in Fe/Cr multilayers.[1] Since then, further multilayer systems exhibiting GMR have been reported. One of the most impressive effects has been observed in Co/Cu multilayers, in which the electrical resistivity at low temperatures is reduced in magnetic field to half of its zero-field value.[2] The strong interest in GMR effects is closely connected with promising industrial applications in magnetoresistive reading heads and similar elements.

Magnetic multilayers are artificial superlattices in which the layers of atoms carrying magnetic moments are separated by nonmagnetic layers. The nonmagnetic layers mediate exchange interactions between the magnetic ones. In systems exhibiting GMR, these exchange interactions are, as a rule, antiferromagnetic. As a result we obtain antiparallel interlayer coupling. These exchange interactions are relatively weak and can be easily overcome by magnetic field and a ferromagnetic alignment of spins can be achieved in a relatively low field. A pronounced reduction of the electrical resistivity can be observed due to this transition, because the resistance in the ferromagnetic aligned is much smaller than in the antiferromagnetic case. The occurrence of GMR effects in multilayer systems is usually ascribed to the spin-dependent scattering.[3]

Magnetic-field-induced transitions in antiferromagnets have been studied in bulk materials for decades. These transitions are called metamagnetic in analogy to the metastable (metamagnetic) state which sets in above the critical field. They take place in a magnetic field sufficient to overcome the antiferromagnetic interactions and to modify the magnetic structure. The modification of the magnetic structure is frequently connected with a change of the translational symmetry and is usually accompanied by a noticeable change of the electrical resistivity.

Another type of metamagnetic transition, which is also reflected in the electrical resistivity, can be found in itinerant electron materials, which are close to a magnetic instability. This class of materials can be well represented by the RCo_2 compounds (R=rare-earth metal). Here a sufficiently large magnetic field can induce magnetic moment on Co sites[4,5] and, simultaneously, the system undergoes a transition from the paramagnetic to a magnetically ordered state.

Note that the magnetoresistance is usually defined by the expression

$$\Delta\rho/\rho=[\rho(T,H)-\rho(T,0)]/\rho(T,0), \tag{1}$$

where $\rho(T,H)$ and $\rho(T,0)$ are the resistivities at a given temperature in the actual and zero magnetic field, respectively. For the transition from the antiferromagnetic to the ferromagnetically aligned state with the resistivities ρ_{AF} and ρ_F, respectively:

$$\Delta\rho/\rho=(\rho_{AF}-\rho_F)/\rho_{AF}. \tag{2}$$

In the multilayer research it is customary to use a modified expression:

$$\Delta\rho/\rho=\{\rho_{AF}-\rho_F\}/\rho_F, \tag{3}$$

which provides naturally much more spectacular values. Unless especially mentioned, we will use the representations (1) and (2).

Here, we review the magnetoresistance effects in different classes of bulk magnetic materials with a special emphasis on single-crystal data available only very recently for lower symmetry materials. We want to demonstrate that the GMR effects are frequently observed especially in $5f$ electron intermetallics and discuss the origin of these phenomena. We will discuss also required model parameters of an intermetallic system to achieve GMR effects at conditions desirable for practical applications.

 0021-8979/94/76(10)/6913/6/$6.00 © 1994 American Institute of Physics

II. RESISTANCE IN METALLIC SYSTEMS

For simplicity, the resistance in metallic systems can be discussed as due to independent scattering mechanism (i.e., supposing the validity of the Mathiessen's rule):

$$\rho=\rho_0+\rho_{e-p}+\rho_{spd}. \tag{4}$$

Both the temperature independent term ρ_0 due to crystal structure imperfections and the electron-phonon scattering term ρ_{e-p} are present in all materials. In magnetic materials the scattering of conduction electrons on magnetic moments should be taken into account. This is reflected in the spin-disorder resistivity term ρ_{spd}. In the paramagnetic range, where the magnetic correlations are absent, electrons are scattered on entirely disordered magnetic moments. The spin-disorder resistivity originates in the exchange interactions acting on the conduction-electron spin and scales therefore with the De Gennes factor $(g-1)^2J(J+1)$ and with the square of the coupling parameter $\mathscr{J}$.[6] For a system with stable magnetic moments, ρ_{spd} is constant above the magnetic ordering temperature. In ferromagnets below T_C, ρ_{spd} decreases with temperature in a way characteristic for the type of magnetic excitation in a particular system. Finally, it should vanish in the low temperature limit. For low temperatures, a quadratic temperature dependence of ρ_{spd} can be derived[7,8] and is frequently observed experimentally.

The situation is less clear in antiferromagnets, in which the magnetic periodicity can be different from the crystallographic one. This leads to creation of new Brillouin zone boundaries (superzone boundaries) and, consequently, gaps can appear on the Fermi surface. In this case, the effective number of charge carriers is reduced leading to initial increase of the resistivity with decreasing temperature below the Néel temperature T_N.[9] Such effect can be found both in itinerant antiferromagnets[10] and in rare-earth local-moment systems.[9] The resistivity can be described as

$$\rho=\frac{\rho_0+\rho_{e\text{-}p}+\rho_{spd}}{1-gm(T)}, \tag{5}$$

where $m(T)$ is a normalized sublattice (staggered) magnetization. The truncation parameter g characterizes the effective reduction of the number of conduction electrons as a consequence of the Fermi level gapping. It is evident that this factor enhances the resistivity even in the low temperature limit. The difference between ρ_F (resistance in the ferromagnetic state) and ρ_{AF} (resistance in the antiferromagnetic state) depends on the width of the gap in the electron energy spectrum, which scales with the exchange coupling parameter $\mathscr{J}$. Therefore, the magnetoresistance effect connected with the metamagnetic transition (between the antiferromagnetic state and the state with "ferromagnetically" aligned magnetic moments) should scale approximately with ρ_{spd}, which is governed by similar parameters.

In compounds based on regular rare-earth metals, the ρ_{spd} values are, however, rather modest despite large ionic magnetic moments. The reason is apparently a weak coupling of the conduction electron spin and the ionic spin moment S. Much larger ρ_{spd} values can be expected in materials where a strong coupling can be expected. This situation is likely in actinide and transition metal intermetallic compounds, as will be demonstrated on several examples.

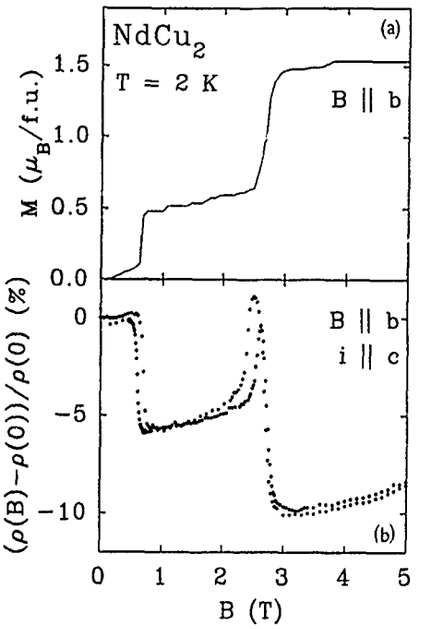

FIG. 1. (a) Magnetization and (b) transversal magnetoresistance vs magnetic field applied along the b axis measured on $NdCu_2$ single crystal at 2 K (data taken from Ref. 11).

III. EXAMPLES OF GMR IN BULK MATERIALS

As an example of one of the largest magnetoresistance effects in regular-rare-earth intermetallic compounds, we show in Fig. 1 the magnetoresistance of $NdCu_2$ which is antiferromagnetic below 6.3 K.[11,12] By applying the magnetic field along the b axis two metamagnetic transitions can be induced leading to a step-wise increase of the magnetization in $\cong$0.6 and $\cong$2.8 T. Both transitions are associated with pronounced changes of the resistance leading to $\Delta\rho/\rho \cong -10\%$ in 3 T. The increase of $\Delta\rho/\rho$ with the approaching critical field can be attributed to the enhanced scattering due to intersite fluctuations.[13,14]

The large magnetoresistance changes in $NdCu_2$ are confined to very low temperatures because of the low value of T_N. Therefore, $SmMn_2Ge_2$, which is antiferromagnetic between $\cong$100 and 150 K and ferromagnetic outside this range,[15,16] might be more attractive for applications. The transition from the antiferromagnetic state to a low-resistance ferro-state can be induced by moderate fields (below 1 T), but the reduction of the resistivity does not exceed 10%.

A similar situation can be found in $Ce(Fe_{1-x}Co_x)_2$, with ~10% cobalt substitution. This material first becomes ferromagnetic below ~180 K, and with further lowering temperature a transition to the low-temperature antiferromagnetic state appears at $\cong$80 K.[17,18] This transition manifests in a dramatic increase of the electrical resistivity.[19] The ferromagnetic (and presumably the low-resistance) state can be then recovered by application of a sufficient magnetic field.[19] Similar loss of ferromagnetism at low temperatures can also

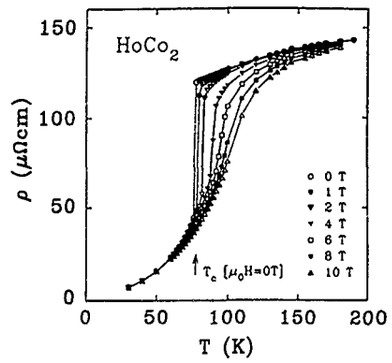

FIG. 2. Temperature dependence of the electrical resistivity in $HoCo_2$ in several magnetic fields (see Ref. 4).

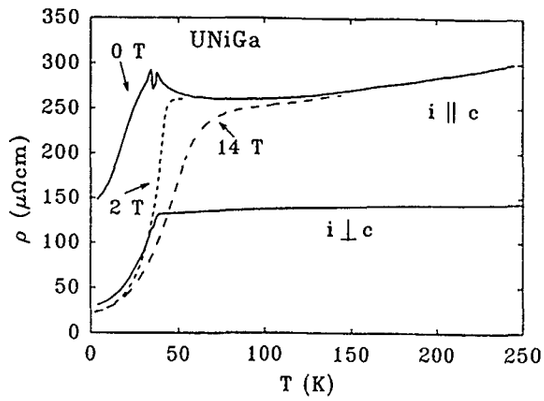

FIG. 3. Temperature dependence of the electrical resistivity in the UNiGa single crystal for $i \| c$ and $i \perp c$. For $i \| c$ also results measured in 2 and 14 T ($B \| c$) are displayed.

be observed for small substitutions of Fe (in $CeFe_2$) by Al,[20] Si,[21] Ru, Ir, and Os,[22] which could also lead to large magnetoresistance.

Significantly larger effects can be observed in materials, where the external magnetic field assists in the stabilization of magnetic moments. This situation can be followed, e.g., in RCo_2 compounds. For some rare earths, the Co moments are formed from the highly susceptible matrix of the $3d$ states by the concerted action of ordered rare earth moments at the Curie temperature T_C, which thus becomes a first order transition. Above T_C, the large resistivity is affected not only by disordered rare-earth moments, but the strong spin-fluctuations in the Co $3d$-electron subsystem contribute, as well. The electron-spin fluctuation scattering is removed in the transition by a sudden drop of a considerable absolute value (e.g., $\cong 80\ \mu\Omega$ cm in $DyCo_2$ and $HoCo_2$).[4,5,23] The effect of exchange fields of the $4f$ subsystem on the $3d$ one can be naturally assisted by the external magnetic field, which shifts the transition towards higher temperatures. Thus, for a particular temperature from a limited range above T_C, the resistivity can be reduced drastically. A typical example of $HoCo_2$ can be seen in Fig. 2. Qualitatively similar behavior also occurs in $DyCo_2$, $ErCo_2$, and $TmCo_2$.[4,5,23] Although present in compounds containing rare earths, the effect is clearly due to the onset of $3d$ magnetism in this case.

There are also purely d systems with a large magnetoresistance. One case known for many years is the equiatomic ordered FeRh compound.[24] It is antiferromagnetic below 340 K, where it undergoes a transition to the ferromagnetic state. At lower temperatures, the ferro-state can be achieved by the magnetic field, which increases from 0 T at 340 K to about 30 T at 4.2 K (the critical field is 4 T at room temperature). As the resistivity increases strongly at 340 K due to the $F \rightarrow AF$ transition, the suppression of antiferromagnetism in the field leads to a dramatic reduction of the resistivity. As the residual resistivity in the ferromagnetic state can be rather small, the relative drop of its value is largest—by the factor of 20—in the low temperature limit ($\Delta\rho \cong 20\ \mu\Omega$ cm). Recent calculations[25] yield the electron structure in both phases. The Fe atoms display local moments of $\cong 3\mu_B$, while the Rh local moments are zero in the antiferromagnetic configuration and $1\mu_B$ for the ferromagnetic configuration. This means that the Rh magnetic moment is induced by the $AF \rightarrow F$ transition similar to the onset of the Co magnetic moment at the ordering temperature in some RCo_2 compounds. Then both the spin-flip transition of Fe magnetic moments and the onset of Rh magnetism can be accounted for by the large magnetoresistance change in FeRh. Large magnetoresistance changes accompanying the magnetic-phase transitions in the transition metal sublattice have also been observed in the $La(Fe_xAl_{1-x})_{13}$ system.[26]

Much larger MR effects occur in systems with uranium, a most thoroughly studied light actinide. We will review some experimental data on UTX compounds, which are formed in several types of crystal structures. The compounds crystallizing in the hexagonal ZrNiAl structure have been studied most thoroughly. This structure consists of U-T and T-X basal-plane layers alternating along the c axis. The stronger U-U coupling within the plane leads to a very strong magnetic anisotropy confining the U moments in the c direction. The magnetic interactions along c are much weaker and in some cases antiferromagnetic with various propagation vectors. The electrical resistivity in antiferromagnetic compounds shows qualitatively different behavior for the current along the basal plane and along the c axis (see Fig. 3). A typical example is UNiGa,[27] which orders antiferromagnetically below 40 K. The ground state can be characterized by the sequence of $(++--+--)$ orientation of equal U magnetic moments of $1.4\mu_B$. The ferromagnetic configuration is reached in ~0.8–1 T (at 4.2 K). As shown in Fig. 4, the first-order metamagnetic transition is accompanied by a drastic decrease of the resistivity of about 120 $\mu\Omega$ cm ($\Delta\rho/\rho = 86\%$).[28] Knowing the complex magnetic phase diagram of UNiGa, one can gain some insight into the magnetoresistance effect by inspection of the $\rho(T)$ dependencies in various magnetic fields (Fig. 3). In high magnetic fields sufficient to suppress the antiferromagnetic correlations, $\rho(T)$ behaves as in a ferromagnet, with a resistance drop below the ordering temperature. Thus the anomalies in $\rho(T)$ found between 35 and 40 K, which are connected with several different antiferromagnetic phases existing in zero field, totally disappear in the field of 2 T. The slower increase of the resistivity in the ferromagnetic phase means that the largest

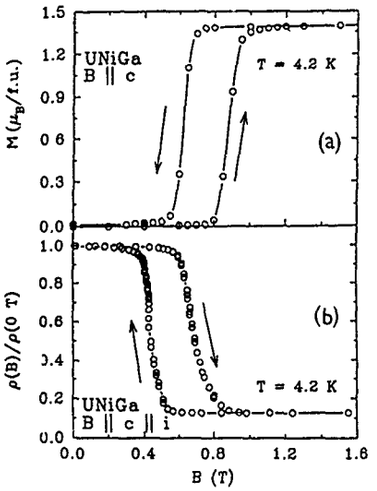

FIG. 4. (a) Magnetization and (b) relative electrical resistivity for $i \| c$ vs magnetic field applied along the c axis measured on UNiGa single crystal at 4.2 K.

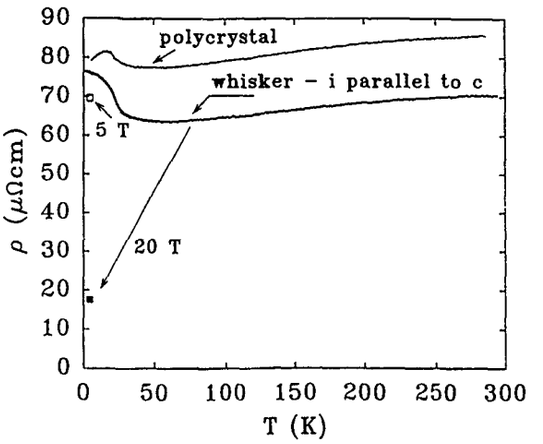

FIG. 6. Temperature dependence of the electrical resistivity of a UPdIn polycrystal and a single-crystalline whisker for $i \| c$ The two additional points indicate the value to which the resistance of the whisker drops in applied fields above the two metamagnetic transitions seen in Fig. 7.

drop $\Delta\rho \cong 200\ \mu\Omega$ cm is found at 25 K. Around this temperature a two-step metamagnetic process is observed (see Fig. 5). For current perpendicular to the c axis, which is sensing essentially the ferromagnetic ordering of U moments within the basal-plane sheets, the $\rho(T)$ dependence resembles that of a ferromagnet already in the zero-field phase, but the field applied along c still reduces the residual resistivity from ~30 to ~10 $\mu\Omega$ cm.

The second compound of this type of structure is UPdIn, where the layers of the U moments of $1.5\mu_B$ are stacked along c in the sequence $(++-+-)$, which gives a net ground-state magnetization of $1/5\mu_U$. As can be seen in Fig. 6, an increase of the resistivity is found at low temperatures for current along the c axis.[29] Below the inflection point in $\rho(T)$ at 20 K, which coincides with the ordering temperature, a gradual saturation to $\rho_0 \cong 80\ \mu\Omega$ cm is observed. For current perpendicular to the c axis, a more regular behavior with a low temperature decrease of the resistivity appears. In a field of 4 T along the c axis, the magnetic structure transforms into the $(++-)$ stacking, and the full parallel alignment of moments is achieved in 16 T. Both metamagnetic transitions (Fig. 8) are accompanied by a drop in the resistivity. The major part of the magnetoresistance effect (total drop of 60 $\mu\Omega$ cm) is concentrated into the latter transition. From these two examples with $\Delta\rho \gg \rho_0$, it is evident that the magnitude of $\Delta\rho/\rho$ at low temperatures is strongly dependent on the residual resistivity ρ_0 in a "ferromagnetic" state, which is essentially related to crystal imperfections. Inspecting the temperature dependence of $\Delta\rho/\rho$, we note that this parameter should decrease at high T even in cases where electron-phonon scattering is not of primary importance. The reason is the increase of the resistivity due to magnetic ex-

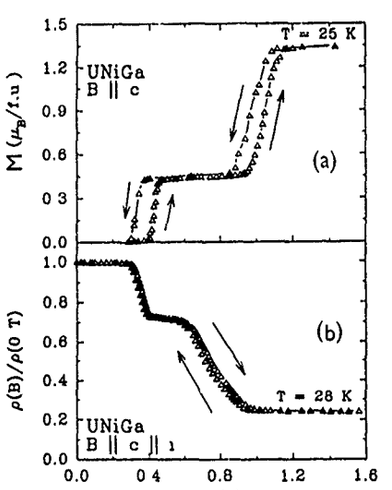

FIG. 5. (a) Magnetization and (b) relative electrical resistivity for $i \| c$ vs magnetic field applied along the c axis measured on UNiGa single crystal at 25 and 28 K, respectively.

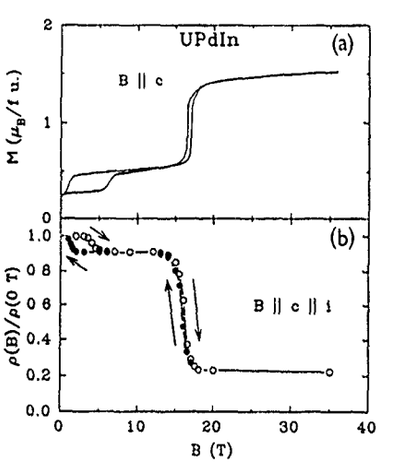

FIG. 7. (a) Magnetization and (b) relative electrical resistivity for $i \| c$ vs magnetic field applied along the c axis measured on UPdIn single crystal at 4.2 K.

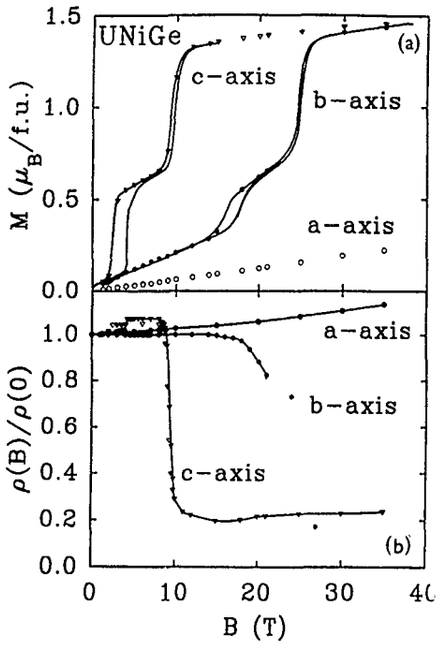

FIG. 8. (a) Magnetization and (b) relative electrical resistivity for $i \| c$ vs magnetic field applied along the three principal crystallographic axes measured on UNiGe single crystal at 4.2 K.

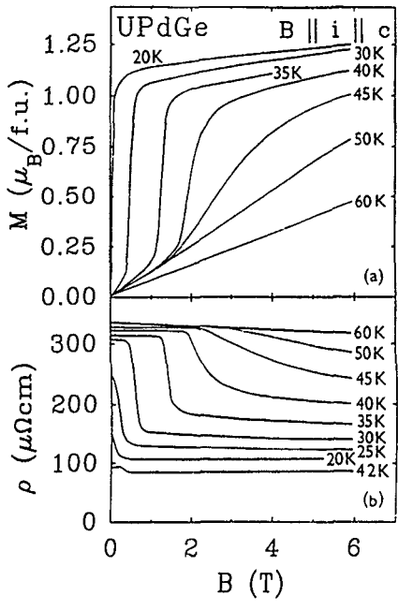

FIG. 9. (a) Magnetization and (b) electrical resistivity for $i \| c$ vs magnetic field applied along the three principal crystallographic axes measured on UPdGe-single crystal at different temperatures.

citations, which affects $\rho(T)$ progressively with raising temperature up to the ordering temperature.

UNiGe[30] crystallizes in the orthorhombic TiNiSi structure type. Below 41.5 K, this compound orders antiferromagnetically with a propagation vector (0,1/2,1/2). Applying the magnetic field along the c axis, one first induces (in approximately 4 T) another magnetic structure with the propagation vector (0,1/3,1/3) and a net magnetic moment corresponding to the stacking $(++-)$. The parallel alignment of U moments is achieved above 10 T. In the longitudinal geometry $(i \| c, B \| c)$, we find that ρ is reduced by a similarly large relative value as in the compounds mentioned above (Fig. 8). The absolute value of the resistivity decrease is about 80 $\mu\Omega$ cm. However, in contrast to the previous cases, $\rho(B)$ first increases by the transition from the ground-state phase $(+-)$ to the one with the $(++-)$ stacking.

UPdGe[31] is formed within the same structure type. Unlike UNiGe, it is ferromagnetic below $T_C = 28$ K. The antiferromagnetic ordering (long wavelength modulated structure) existing between 28 and 50 K, can be suppressed by a moderate magnetic field applied along the c axis (see Fig. 9). The transition field can be tuned by temperature variations, and the maximum size of the drop of ρ can reach about 150 $\mu\Omega$ cm.

IV. DISCUSSION AND CONCLUSIONS

The examples presented above show unambiguously an additional contribution to the electrical resistivity due to the antiferromagnetic coupling of magnetic moments, which can be removed by forcing the moments to orient parallel to each other. This contribution does not vanish in the low-temperature limit, and at low temperatures it can contribute a substantial part of the total resistivity.

Concerning possible mechanisms by which the antiferromagnetic ordering influences the electrical resistivity, one should also consider the spin-dependent scattering, which can play an important role besides the Fermi-surface gapping, and which is often considered in the context of multilayers. In this concept the electrons with different spin orientation are supposed to experience different potentials and have a different k-space distribution. The origin of the spin-dependent scattering can be understood if we consider the different scattering amplitude for electrons with spin parallel or antiparallel to ionic magnetic moments in a local moment case. In band magnetism, the asymmetry of the scattering is given due to significantly different partial densities of states at E_F for each subband (spin-up or spin-down). In both cases, the increment of the resistivity in the AF state is dependent on a concentration of $+-$ interfaces. It is worth systematic experimental effort to check whether it is really the case, i.e., whether the larger resistivity in the AF state is due to an additional scattering mechanism, or if the explicit parameter is the modification of the effective conduction-electron concentration. In a case such as this there should be a proportionality between ρ_{AF} and ρ_F irrespectively of, e.g., the ρ_0 value. The unique proportionality constant given by the truncation factor mentioned above should be observed at least in the low-T, limit, where different excitations in antiferromagnetic and "ferromagnetic" states can be neglected. The size of the magnetoresistance effect should scale more with the size of the AF unit cell in this case.

Keeping in mind an applicability potential, future effort should focus on materials with exchange interactions strong enough to guarantee ordering in the room temperature range.

As shown in the example of FeRh, this need not lead to extremely high metamagnetic fields in compounds with competing ferro- and antiferro-interactions. The orientation on artificial multilayers or cluster systems is apparently not the only promising stream of GMR research.

ACKNOWLEDGMENTS

This work has been supported by the "Stichting voor Fundameteel Onderzoek der Materie (FOM), the Grant Agency of the Czech Republic (Grant No. 202/94/0454), and by the Charles University Grant Agency (Grant No. 312).

[1] M. N. Baibich, J. M. Broto, A. Fert, F. Nguyen Van Dau, F. Petroff, P. Etienne, G. Creuzert, A. Friedrich, and J. Chazelas, Phys. Rev. Lett. **61**, 1979 (1988).
[2] S. S. P. Parkin, Z. G. Li, and D. J. Smith, Appl. Phys. Lett. **58**, 2710 (1991).
[3] For a review see; R. E. Camley and R. L. Stamps, J. Phys.: Condens. Mat. **5**, 3727 (1993).
[4] J. M. Fournier and E. Gratz, "Transport Properties of Rare Earth and Actinide Intermetallics," in *Handbook of the Physics and Chemistry of Rare Earths*, Vol. 17, edited by K. A. Gschneidner, L. Eyring, G. R. Choppin, and G. H. Lander (North-Holland, Amsterdam, 1993), pp. 409–537.
[5] N. V. Baranov and A. I. Kozlov, J. Alloys and Compounds **190**, 83 (1992).
[6] A. J. Dekker, J. Appl. Phys. **36**, 906 (1965).
[7] T. Kasuya, Prog. Rep. Phys. (Kyoto) **16**, 227 (1959).
[8] D. L. Mills and P. Lederer, J. Phys. Chem. Solids **27**, 1805 (1966).
[9] R. J. Elliot and F. A. Wedgwood, Proc. Phys. Soc. **81**, 846 (1963).
[10] See, e.g., S. Arajs, R. V. Colvin, and M. J. Marcinkowski, J. Less-Common Metals **4**, 46 (1962).
[11] P. Svoboda, M. Diviš, A. V. Andreev, N. V. Baranov, M. I. Bartashevich, and P. E. Markin, J. Magn. Magn. Mater. **104–107**, 1329 (1992).
[12] N. V. Baranov, P. E. Markin, A. I. Kozlov, and E. V. Sinitsin, J. Alloys and Compounds **200**, 43 (1993).
[13] H. Yamada and S. Takada, J. Phys. Soc Jpn. **34**, 51 (1973).
[14] H. Yamada and S. Takada, Prog. Theor. Phys. **49**, 1401 (1973).
[15] R. B. van Dover, E. M. Gyorgy, R. J. Cava, J. J. Karjewski, R. J. Felder, and W. F. Peck, Phys. Rev. B **47**, 6134 (1993).
[16] J. H. V. J. Brabers, K. Bakker, H. Nakotte, F. R. de Boer, S. K. J. Lenczowski, and K. H. J. Buschow, J. Alloys and Compounds **199**, L1 (1993).
[17] A. K. Rastogi and A. P. Murani, *Proceedings of the International Conference on Valence Fluctuations* (Plenum, Bangalore, 1987), p. 437
[18] S. J. Kennedy, A. P. Murani, B. R. Coles, and O. Moze, J. Phys. F **18**, 2499 (1988).
[19] A. K. Rastogi, G. Hilscher, E. Gratz, and N. Pillmayr, J. Phys. (Paris) **C8**, 277 (1988).
[20] Y. Nishihara, M. Tukumoto, Y. Yamaguchi, and G. Kido, J. Magn. Magn. Mater. **70**, 173 (1987).
[21] A. K. Grover, R. G. Pillay, V. Balasubramanian, and P N. Tandon, J. Phys. (Paris) **C8**, 281 (1988).
[22] S. B. Roy, S. J. Kennedy, and B. R. Coles, J. Phys. (Paris) **C8**, 271 (1988).
[23] E. Gratz, E. Bauer, R. Hauser, M. Maikis, P. Haen, and A. Markosyan, *Proceedings of the International Conference on the Physics of Transition Metals*, Darmstadt, 1992, edited by P. M. Oppeneer and J. Kübler (World Scientific, Singapore, 1993), p. 366.
[24] C. J. Schinkel, R. Hartog, and F. H. A. M. Hochstenbach, J. Phys. F: Metal Phys. **4**, 1412 (1974).
[25] V. L. Moruzzi and P. M. Marcus, Phys. Rev. B **46**, 14198 (1992).
[26] T. T. M. Palstra, G. J. Nieuwenhuys, J. A. Mydosh, and K H J Buschow, Phys. Rev. B **31**, 4622 (1985).
[27] V. Sechovsky, L. Havela, F. R. de Boer, E. Bruck, T. Suzuki, S. Ikeda, S. Nishigori, and T Fujita, Physica B **186–188**, 775 (1993).
[28] V. Sechovsky, L. Havela, L. Jirman, W. Ye, T. Takabatake, H. Fujii, E. Brück, F. R. de Boer, and H. Nakotte, J. Appl. Phys. **70**, 5794 (1991).
[29] H. Nakotte, E. Bruck, F. R. de Boer, A. J. Riemersma, L. Havela, and V. Sechovsky, Physica B **179**, 269 (1992).
[30] K. Prokes, H. Nakotte, E. Brück, F. R. de Boer, L. Havela, V. Sechovsky, and P. Svoboda, IEEE Trans. Magn. **MAG-30**, 1214 (1994).
[31] S. Kawamata, H. Iwasaki, N. Kobayashi, K. Ishimoto, Y. Yamaguchi, and T. Komatsubara, J. Magn. Magn. Mater. **104–107**, 53 (1992).

Giant magnetoresistance related transport properties in multilayers and bulk materials (invited)

H. Sato, H. Henmi, Y. Kobayashi, and Y. Aoki
Department of Physics, Tokyo Metropolitan University, Hachioji-shi, Tokyo 192-03, Japan

H. Yamamoto
Functional Devices Research Laboratory, NEC Corporation, Kawasaki, Kanagawa 216, Japan

T. Shinjo
Institute for Chemical Research, Kyoto University, Uji, Kyoto-fu 611, Japan

V. Sechovsky
Department of Metal Physics, Charles University, Ke Karlovu 5, 121 16 Praha 2, Czech Republic

A systematic comparison of magnetoresistance, Hall effect, thermal conductivity, and thermoelectric power has been made on systems exhibiting giant magnetoresistance (GMR), Co/Cu/Ni(Fe) multilayers, and AgCo granular alloys, for examples. Each property exhibits field dependence characteristic of the GMR and justifies its own merit in characterizing the conduction-electron scattering responsible for the GMR. The comparison was extended to intermetallic compounds such as $REGa_2$ and $RECo_2$ (RE: rare earth element) which also show a large magnetoresistance.

I. INTRODUCTION

The GMR in magnetic multilayers[1] is one of the most attractive subjects. Most of experimental works focus mainly on the magnetoresistance (MR).[2] To characterize the conduction electron scattering responsible for the GMR, it is best to study the Hall effect, thermoelectric power, and thermal conductivity simultaneously on the same sample and under the same experimental geometry.[3] From thermal conductivity measurements, it can be judged whether the scattering responsible for the GMR is large angle in nature or not. Such works on magnetic multilayers and granular alloys are still scarce.[4,5] Thermoelectric power measurements give information on the density of electron states at E_F. Thermoelectric power measurements on magnetic multilayers and granular alloys[6–8] reveal common main mechanism of conduction-electron scattering. The extraordinary part of the Hall resistivity contains information about the left-right asymmetry of conduction-electron scattering.[9] Several reports[10–13] correlate the anomalous behavior of the extraordinary Hall resistivity correlated with the GMR.

The large resistance change in UNiGa (Ref. 14) and $SmMn_2Ge_2$,[15] at their metamagnetic transition has a close similarity to multilayers. First of all, they have geometrical similarity, i.e., the neighboring magnetic layers are coupled antiferromagnetically at zero field, and are aligned ferromagnetically under magnetic fields.

We describe here the systematic comparison of the transport properties correlated with the GMR in both metallic superlattices and in magnetic granular films. For the multilayer, we chose a typical noncoupled one, Cu/Co/Cu/Ni(Fe), in which the large resistance state is attained utilizing the large difference of the coercive field of the two ferromagnetic components. AgCo was selected as an example of granular alloys with the largest MR ratio We further extend the comparison to the with $REGa_2$ and $RECo_2$.

II. EXPERIMENT

The multilayer samples are Cr(30 Å)/[Co(20 Å)/Cu(40 Å)/Ni(Fe)(20 Å)/Cu(40 Å)]$_{50}$ (sample ML-1) and Cr(30 Å)/[Co(20 Å)/Cu(40 Å)/Co(1 Å)/Ni(Fe)(20 Å)/Co(1 Å)/Cu(40 Å)]$_{50}$ (sample ML-2). AgCo granular samples containing two different Co concentrations of 27.2 at. % (GL-1) and 42 at. % (GL-2) have a total thickness of 5000 Å. Both systems were evaporated in ultrahigh vacuum on glass substrates at room temperature. Samples for the Hall effect and the MR were made with a mask suitable for transport measurements. Samples for thermal measurements were evaporated on thin glass substrates (~80 μm) in order to reduce the thermal shunt effect. $REGa_2$ (RE:Nd, Pr, and Sm) single crystals were grown in a triarc furnace by the Czochralski pulling method. Polycrystalline $RECo_2$ (RE: Ho and Dy) were melted in an arc furnace from elements with a purity of at least 99.9%, and were annealed 100 h at 900 °C.

III. RESULTS AND DISCUSSION

A. Magnetic multilayers and granular alloys

The larger MR ratio is desirable for investigating the influence of the GMR effect on other transport properties. The MR ratios at 4.2 K for ML-1 and GL-1 (annealed at 240 °C) are 51% and 84% for the field in-plane, respectively. The MR ratio is defined as $MRR_s=(\rho_{max}-\rho_s)/\rho_s$ (ρ_{max} and ρ_s are a maximum value of the electrical resistivity ρ and ρ at maximum applied field, respectively).

The result of the field dependence of the thermoelectric power (S) for ML-2 is shown in Fig. 1 along with the corresponding MR curves. The resemblance of the field dependence to that of MR is clear, including the anisotropy, which suggests that the conduction-electron scattering responsible for GMR plays a major role also in the $S(H)$ dependence. In the spin-split density of states (DOS) model given by Shi *et al.*,[16] S is a linear function of $\rho(0)/\rho(H)$. which was reported to hold well for Co/Cu multilayers and for AgCo granular alloys.[16,17] The corresponding plot for ML-2 is

 0021-8979/94/76(10)/6919/6/$6 00 © 1994 American Institute of Physics

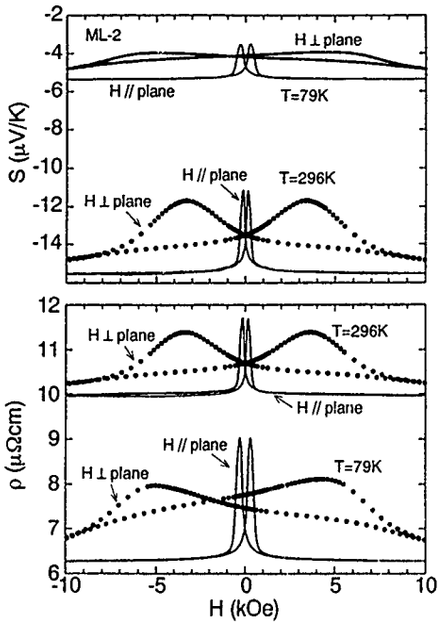

FIG. 1. The field dependence of the thermoelectric power (S) and the resistivity (ρ) in ML-2 for the fields parallel and perpendicular to the film.

shown in Fig. 2. The data points are also on a line regardless of the field direction. Recently, Tsui *et al.* reported a more restricted scaling relation of S, i.e., the plots of $S(H)/T$ vs $\rho(0)/\rho(H)$ for $T=78$, 113, and 161 K in Co/Cu superlattices are all on a single line. For the present multilayers, however, the data plotted in the same procedure at 79 and at 296 K are on different lines, which indicates that the scaling relationship by Tsui *et al.* is not a universal one for GMR systems.

Thermoelectric power measurements on AgCo granular alloys were reported by Piraux *et al.*[5] and Shi *et al.*[16] The dependence $S(T)$ in the two works is roughly similar; however, two different characteristics have been found at lower temperatures. Shi *et al.*[16] reported that S changes sign from negative at high temperatures to positive below about 25 K. In Ref. 5, on the other hand, the sign is always negative and a small negative peak near 70 K was found. We also measured S vs T on an as-grown sample and on one annealed at

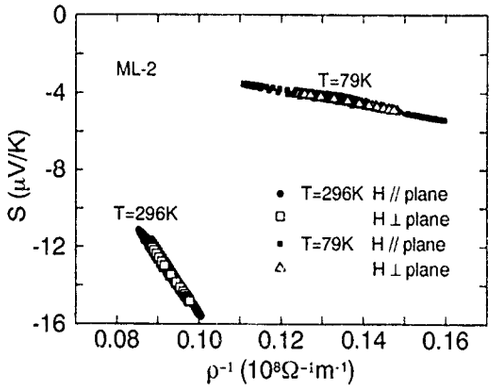

FIG 2. $S(H)$ vs $1/\rho(H)$ plots for ML-2 obtained from the data in Fig. 1

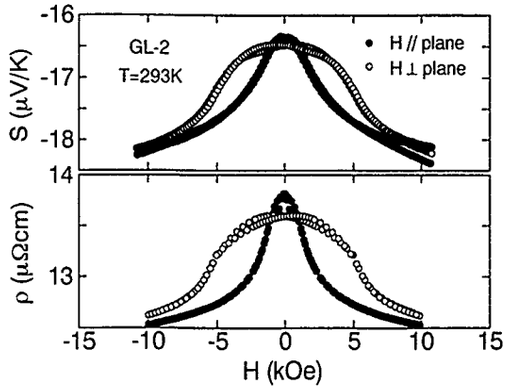

FIG. 3. The field dependence of S and ρ of GL-2 for the fields parallel and perpendicular to the film.

310 °C (not shown). Overall, our result is similar to that in Ref. 5, although we have found neither the sign change nor the negative minimum. The sign change might not be intrinsic in AgCo granular samples since it has not been found in either the present work or in Ref. 5. The anisotropy observed in the MR is also clearly reflected in the $S(H)$ dependence as shown in Fig. 3. The figure shows that the scattering responsible for GMR dominates also in the $S(H)$ dependence in AgCo granular alloys although there is a slight discrepancy for the H//plane curve due to the thermal delay effect.

We have reported the field dependent thermal conductivity correlated with GMR for the first time on Co/Cu/Ni(Fe)/Cu multilayers.[4] Piraux *et al.* reported the extensive investigation of thermal conductivity on Co 20 vol % (27.2 at. %) AgCo granular alloys.[5] In order to measure the absolute value of thermal conductivity, their method of using very thick and substrate free films has a considerable advantage. However, we can obtain data as reliable as them even on a thinner sample with a substrate for the field dependent part of thermal conductivity $\Delta\kappa(H)$ as[4]

$$\Delta\kappa(H)=K_{TS}(l/S)DT(H)/\Delta T_S, \tag{1}$$

where K_{TS} is the total thermal conductance of a sample including the substrate at saturation field, l the sample length, and S the sample cross section; $DT(H)/\Delta T_S$ is the ratio of the field dependent change of the temperature gradient to that at saturation field. Figure 4 shows typical examples of the field dependent part of thermal conductivity $\Delta\kappa(H)$ for ML-1 and GL-1 along with the calculated $\kappa(H)$ from the field dependence of $\rho(H)$ measured on the same samples based on the Wiedemann–Franz law (W-F-L),

$$\kappa(H)=L_0T/\rho(H), \tag{2}$$

assuming the Lorenz number of $L_0=2.45\times10^{-8}$ W Ω/K^2. Present experiments show that the W-F-L is well obeyed at least for the field dependent part of thermal conductivity both for the multilayer and for the granular samples within a 5% accuracy. It agrees with the result of Piraux *et al.* where the absolute value of thermal conductivity on the granular AgCo samples fulfills the W-F-L within a 10% accuracy. These results suggest that the conduction-electron scattering re-

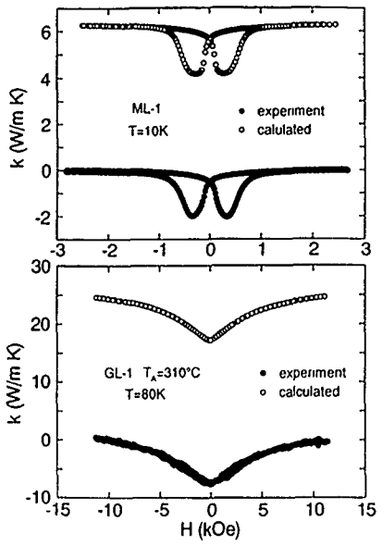

FIG. 4. The field dependence of the thermal conductivity. The calculated curves from $\rho(H)$ based on the W-F-L are also given for comparison.

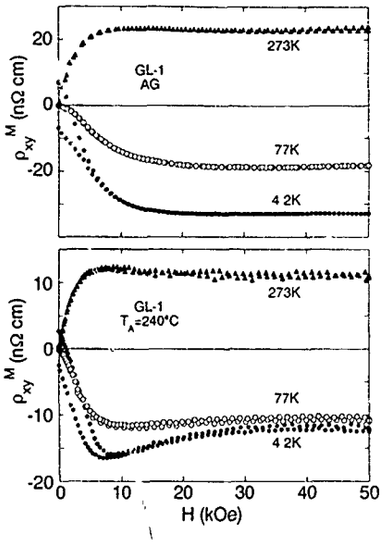

FIG. 5. The $\rho_{xy}(H)$ dependence for GL-1

sponsible for GMR in AgCo granular alloys is large angle in nature as well as in the magnetic multilayers.

The Hall effect in magnetic multilayers and granular alloys is still controversial.[11–13] The key issue is the field dependence of R_S, which has not been taken into account by most researchers.[11,13] The Hall resistivity ρ_{xy} is described as the sum of the two terms, the normal part proportional to magnetic field H and the extraordinary one ρ_{xy}^M proportional to magnetization M as

$$\rho_{xy}=R_0H+4\pi R_SM, \tag{3}$$

where R_0 and R_S are the normal and the extraordinary Hall coefficient,[9] respectively. In most experiments on ordinary ferromagnetic films and on multilayer samples[9,12] with a small MR ratio, $\rho_{xy}(H)$ has been described fairly well by Eq. (3), assuming a field independent R_S. In this case $\rho_{xy}(H)$ is a simple superposition of a linear normal part and an anomalous term that mimics the $M(H)$ dependence. During recent experiments on magnetic multilayers exhibiting the GMR, Fe/Cr,[10,12] and Co/Cu (Ref. 18) multilayers, an anomalous peak in the field dependence of $\rho_{xy}(H)$ has been found. It can never be explained by a field independent R_S since M increases monotonously with increasing field. This suggests that R_S, representing the magnitude of asymmetric scattering of conduction electrons, is no longer a field-independent constant in GMR systems. R_S is known to originate from two different asymmetric scattering mechanisms, i.e., the skew scattering and the side-jump mechanisms.[9]

$$R_S=a\rho+b\rho^2, \tag{4}$$

where a and b represent the magnitudes of the skew-scattering and the side-jump components, respectively. Taking into account the $\rho(H)$ dependence, Eq. (3) has been successfully applied to reproduce the anomalous $\rho_{xy}(H)$ dependence. For both Fe/Cr (Ref. 12) and Co/Cu (Ref. 18) multilayers, the experimental data R_S/ρ vs ρ are nearly on a line, which means that the parameters a and b are independent of magnetic field strength. In other words, the scattering responsible for the GMR has the same characteristics as that of the residual scattering at saturation fields from the viewpoint of left-right asymmetry.

We cannot properly explain the Hall effect on large GMR samples without taking into account the field dependent decrease of conduction-electron scattering. Granular systems cannot be a exception. For AgCo granular samples at 4.2 K, Xiong *et al.*[11] reported an experimental correlation $\rho_{xy}\propto\rho^{3.7}$ conflicting with the existing theory given by Eq. (3) without taking into account the field dependence of ρ. In order to clarify the origin of the discrepancy, we carefully measured the field dependence of ρ_{xy} simultaneously with MR. M was also measured in the same geometry, i.e., the $H\perp$ film plane. Figure 5 shows the $\rho_{xy}(H)$ dependence on an as-grown sample (denoted as AG) and a sample annealed at 240 °C (T_A=240 °C) for 15 min, where R_0 was already subtracted using the linear slope at higher fields. It is negative at 4.2 K and the overall behavior is basically the same as that of Xiong *et al.*[11] The field dependence for the as-grown sample resembles that of M in Ref. 11, including the hysteresis. ρ_{xy}^M shifts to a positive direction with increasing temperature, and the sign is always positive at 273 K.

The most salient feature is the peak below 10 kOe for T_A=240 °C. The dependence is close to that reported for Fe/Cr (Ref. 12) and Co/Cu (Ref. 18) multilayers exhibiting the large GMR. Xiong *et al.*[11] asserted the independence of R_S on H based on the fact that the field dependence of ρ_{xy}^M resembles that of M. However, the resemblance exists only on heat treated samples at low temperatures. Even for these samples, the resemblance is only approximate (see Fig. 6). For the samples annealed at higher temperatures in the both experiments, however, ρ_{xy}^M shows a peak or more complex structures below 1 T. If Fig. 1 in Ref. 11, T_A=330 °C, for example, is re-examined carefully, one can clearly identify a peak of similar magnitude to our data, i.e., the magnitude of the peak is about 150% of the saturation value of ρ_{xy}^M if the

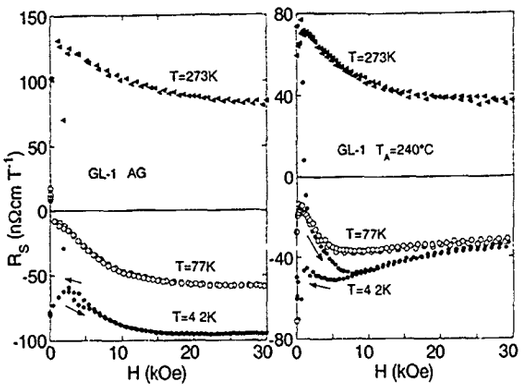

FIG. 6. The $R_S(H)$ dependence for GL-1 calculated from $\rho_{xy}^M(H)$ and $M(H)$ measured in the same geometry.

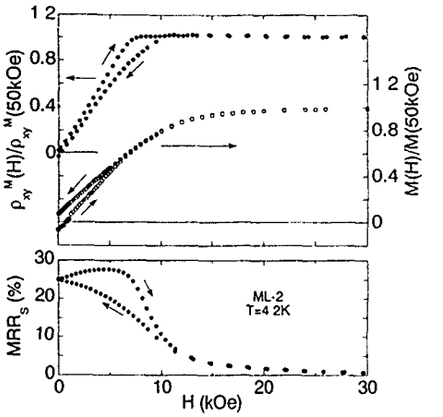

FIG. 7. The field dependence of the normalized Hall resistivity, M, and MR for ML-2 in the same geometry

normal part were properly subtracted. It must be pointed out that one must determine the extraordinary part of Hall resistivity (not the total Hall resistivity) within the required precision in order to discuss the influence of the GMR effect on the left-right asymmetry of conduction-electron scattering.

Starting from Eq. (3), the peak in ρ_{xy}^M indicates that R_S decreases with increasing H since M increases monotonously. Due to the competition between the increasing M and the decreasing R_S, a peak may appear in the field dependence of ρ_{xy}^M. It seems very natural since the magnitudes of the two terms in Eq. (4) decrease with increasing H for constants a and b. Of course, there is no guarantee that a and b are constant since the character of conduction-electron scattering might change with field and temperature. In order to see the field dependence more clearly, $R_S(H)=\rho_{xy}^M(H)/[4\pi M(H)]$ is plotted against H in Fig. 6. The dependence of R_S on H is far beyond the experimental error. The field dependence at 273 K is relatively simple since the predominant side-jump component with positive sign decreases monotonously with increasing H in the same manner as the MR. The dependence is not simple at lower temperatures since both the negative skew-scattering and the positive side-jump one compete. At low fields, R_S initially decreases with H since the decrease of the positive side-jump component with ρ^2 dependence overcomes the increase of the negative skew-scattering component with ρ dependence. R_S has a peak at a field where the change of the two components becomes equal. Additional details of the AgCo system will be published elsewhere.[19]

In the noncoupled multilayers, ρ_{xy}^M looks different, as shown in Fig. 7. No peak can be seen against H; however, it does not mean that R_S is independent on ρ. If R_S is constant, the field dependence of ρ_{xy}^M and M must be exactly alike. However, ρ_{xy}^M becomes nearly constant above 10 kOe while M is still increasing. Above 10 kOe, the increasing contribution to the second term in Eq. (3) from M is canceled out by the decreasing R_S correlated to the negative MR in Fig. 7. The hysteresis is also largely different between ρ_{xy}^M and M: i.e., we find the largest difference between the increasing and the decreasing field curves near zero field for M while it is near 7 kOe for ρ_{xy}^M. That can be also understood as due to the field dependence of R_S since the largest difference in the MR ratio is near 7 kOe as is also shown in Fig. 7. It must also be noted that the arrows given to the hysteresis curves for ρ_{xy}^M and M are directed inversely. The present Hall effect measurement proves that the reduction of conduction-electron scattering associated with the GMR undoubtedly affects the field dependence of the extraordinary Hall resistivity both in the magnetic multilayers and in granular alloys. Furthermore, it gives a clue that some change in the scattering character with field strength (the field dependence of a and b) is larger in granular alloys compared to ordinary multilayers such as Fe/Cr (Ref. 12) and Co/Cu.[18]

B. Intermetallic compounds

In rare earth intermetallic compounds, the large MR effect associated with metamagnetic transitions is not exceptional. We first list the characteristics to compare to the magnetic multilayers and granular alloys.

(1) The effect has a magnetic origin.

(2) The MR ratio is larger than 10% with negative sign.

(3) The dimensionality of magnetic layers plays an important role.

(4) Different conduction electron mean free paths of two spin-split bands play an essential role.

(5) The magnitude of each magnetic moment does not change under the magnetic field.

Of these, (1) and (2) are taken as necessary conditions as the starting point. Both the UNiGa (Ref. 14) and $SmMn_2Ge_2$ (Ref. 15) have the characteristic (3), which is not a necessary condition for granular alloys but is for the multilayer samples. Characteristics (4) and (5) seem to be key issues to the usual GMR effect.

Recently many RE- or U-intermetallic compounds have been investigated and few compounds have been found to possess the above characteristics except for characteristic (4). An example is $NdGa_2$, although the definite magnetic structure is not clear yet.[20] For most RE, $REGa_2$ has an antiferromagnetic ground state and shows several step metamagnetic transition. $PrGa_2$ shows two peaks in the MR near the spin-flip transition as was already reported for $ErGa_2$ (Ref. 21),

while $SmGa_2$ shows a steplike increase of MR at each metamagnetic transition.[22] The field dependence of the MR for $NdGa_2$, which resembles that of UNiGa, is shown in Fig. 8 along with M and ρ_{xy} at 4.2 K. Clear resistivity drops can be seen associated with metamagnetic transitions. $NdGa_2$, we do not discuss in depth here, but it can be stressed that a large negative MR over 40% is obtainable on a compound without the characteristics of (4).

YCo_2 exhibits a typical itinerant metamagnetism at high magnetic fields.[23,24] When Y is replaced by magnetic RE ions, the exchange field from the ions splits the d band and a ferrimagnetic state is stabilized below T_C. The transition is of the first order for Er, Ho, and Dy with a large and sudden change of resistivity.[25] Recently $HoCo_2$ and $ErCo_2$ have been reported to show a drastic resistivity decrease under magnetic fields above T_C.[26] The decrease may be caused by the suppression of spin-fluctuation scattering due to the field-induced transition.

This system has no characteristic (3) but has (4), on the same level as magnetic multilayers and granular alloys. The temperature dependence of the Hall coefficient, the resistivity, and the magnetic susceptibility are shown in Fig. 9 for $HoCo_2$ and $DyCo_2$. Overall, $\rho(T)$ is close to those reported by Gratz *et al.*[25] R_H is always positive for $HoCo_2$ while for $DyCo_2$ it changes sign depending on T, which suggests that the two components in Eq. (4) have a different sign in $DyCo_2$.

Figure 10 shows the field dependence of MR, ρ_{xy}, and M in the same geometry. The magnitude of the transverse MR in polycrystalline $HoCo_2$ is nearly the same as was reported for the longitudinal MR in the single crystal. For $DyCo_2$, a MR ratio over 25% has been observed at 138 K, despite the fact that the large spin-fluctuation scattering already exists below T_C and the sample quality is not satisfactory. The main source of the resistance drop may be the suppression of spin-fluctuation scattering due to field-induced band splitting.[26]

From the band structure calculation on YCo_2,[23,24] on the other hand, we naturally expect that the s-d scattering contribution similar to the usual GMR effect in the magnetic multilayer also plays a role. In a paramagnetic state, the valence band structure of $HoCo_2$ and $DyCo_2$ is similar to YCo_2. Under that condition, the s-d Mott mechanism may reduce the mean free path of s-like conduction electrons since the Fermi level is just at the dropping part of the d band where the density of the d-like states is still high, close to the Stoner criterion.[23,24] In a field induced ferrimagnetic state, the majority d band is put under the Fermi level, as was previously determined for a ferromagnetic YCo_2.[23] The mean free path of s electrons becomes longer compared to that of a paramagnetic state due to the disappearance of the s-d scattering in the majority band. As a result, the total resistivity decreases at the field-induced transition to the ferrimagnetic state. This mechanism resembles that responsible for the GMR effect in magnetic multilayers.[3] Starting from the low resistivity ferromagnetic (ferrimagnetic) state, the difference between the two systems is how the mean free path of conduction electrons is suppressed in the low filed high resistive state. For the state in magnetic multilayers the

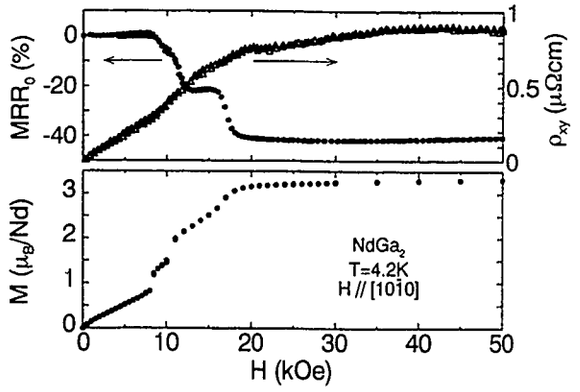

FIG. 8. The field dependence of the MR ratio, ρ_{xy}^M, and M for $NdGa_2$.

suppression is made by the averaging the conduction electron mean free path in the two spin bands over successive magnetic layers with the reverse magnetic moment, while for the paramagnetic state in $RECo_2$, the mean free paths in the both spin bands are suppressed by the s-d Mott mechanism which disappears for the majority band in the field-induced ferrimagnetic state. In other words, the s-d scattering averaged over more than two ferromagnetic layers in antiferromagnetically aligned multilayers is, in effect, similar to that in the paramagnetic state with a high d-electron density of states at E_F. Of course, for the $RECo_2$ system, band splitting apparently reduces the spin-fluctuation scattering which may be the main mechanism of the resistance drop in this system. However, we cannot ignore the possible contribution of the s-d mechanism to the MR at this stage.

For both compounds, the field dependence of ρ_{xy} resembles that of M below T_C. Above T_C, the field dependence is clearly different from that in ordinary ferromagnetic films. ρ_{xy} shows a clear decrease at higher fields, especially at 90 K for $HoCo_2$ and at 138 K for $DyCo_2$, whereas M is still increasing in the same fields. The decrease cannot be

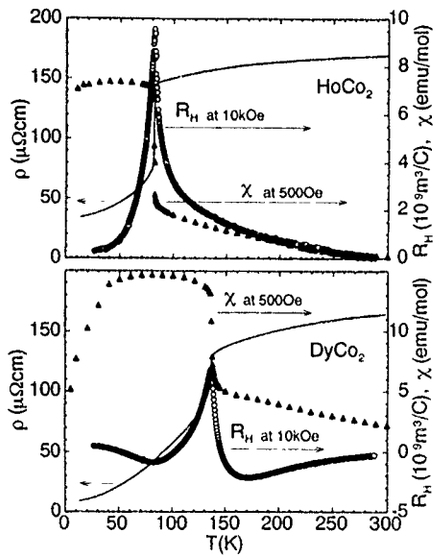

FIG. 9. The temperature dependence of ρ, R_H, and χ for $HoCo_2$ and $DyCo_2$.

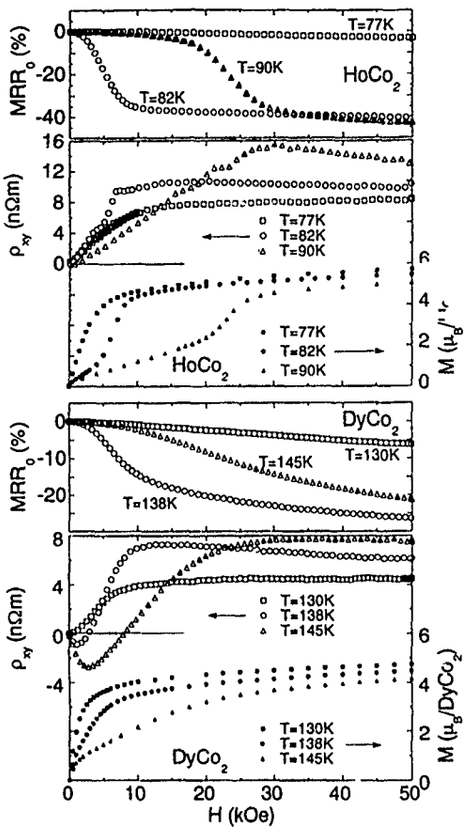

FIG. 10. The field dependence of the MR ratio, ρ_{xy}, and M for $HoCo_2$ and $DyCo_2$. The measurements were done for the increasing field direction.

due to the normal part of ρ_{xy} since ρ_{xy} in the ferrimagnetic state is nearly constant at high fields. The source of the decrease may be the same as that in the magnetic multilayers and granular alloys, i.e., reduction of left-right asymmetric scattering associated with negative MR. At lower fields, ρ_{xy} deviates to positive for $HoCo_2$ and to negative for $DyCo_2$ compared to the field dependence expected from the magnetization curves. For $DyCo_2$, ρ_{xy} even changes its sign. This can be understood if we take into account the field-induced transition from para- to ferrimagnetic states. The side-jump component in Eq. (4) is effective only in the ferromagnetic or ferrimagnetic state whereas the skew-scattering component also contributes in paramagnetic state. For $HoCo_2$ both components are positive while for $DyCo_2$ the skew component is negative and the side-jump one is positive, which was already shown in Fig. 9. In the low field paramagnetic range, the skew term dominates the whole sign.

Compared to magnetic multilayers and granular alloys, the Hall resistivity in $RECo_2$ system shows both a similarity and a difference. The decrease at higher fields correlated to the decreasing resistivity is the similarity while the strange dependence at lower fields is the later and probably related to characteristic (5) described earlier.

To summarize: (1) The effects correlated to the GMR appeared in all the transport properties and for all the materials investigated. (2) Simultaneous measurements of the different transport properties revealed both a difference and a similarity in the character of conduction electron scattering. (3) The existence of neither itinerant magnetic electrons nor two dimensional ferromagnetic layers is a necessary condition for the GMR effect in intermetallic compounds.

ACKNOWLEDGMENTS

This work was supported by a Grant-in-Aid for Scientific Research from the Ministry of Education, Science and Culture, by a Fund for Special Research Project at Tokyo Metropolitan University, by the Yamada Science Foundation and the Grant Agency of the Czech Republic (project No. 94/202/0454).

[1] M. N. Baibich, J. M. Broto, A. Fert, F. Nguyen Van Dau, F. Petroff, P. Etienne, G. Creuzet, A. Friederich, and J. Chazelas, Phys. Rev. Lett. **61**, 2472 (1988).
[2] Author, J. Magn. Magn. Mater. **126**, 406 (1993).
[3] J. Inoue, H. Itoh, and S. Maekawa, J. Phys. Soc. Jpn. **61**, 1149 (1992).
[4] H. Sato, Y. Aoki, Y. Kobayashi, H. Yamamoto, and T. Shinjo, J. Phys. Soc. Jpn. **62**, 431 (1993); H. Sato *et al.*, Jpn. J. Appl. Phys. (in press).
[5] L. Piraux, M. Cassart, J. S. Jiang, J Q. Xiao, and C. L. Chien, Phys. Rev. B **48**, 638 (1993); L. Piraux *et al.*, J. Magn. Magn. Mater. (in press).
[6] J. Sakurai, M. Horie, S. Araki, H. Yamamoto, and T. Shinjo, J. Phys. Soc. Jpn. **60**, 2522 (1991).
[7] M. J. Conover, M. B. Brodsky, J. E. Mattson, C. H. Sowers, and S. D. Bader, J. Magn. Magn. Mater. **102**, 15 (1992).
[8] L. Piraux, A Fert, P. A. Schroeder, R. Loloee, and P. Etienne, J Magn Magn. Mater **110**, L247 (1992).
[9] L. Berger and G. Bergmann, in *The Hall Effect and Its Applications*, edited by C. L. Chien and C. R. Westgate (Plenum, New York, 1980), p. 180; see also A. Fert and A. Hamizic, *ibid.*, 77 and C. M. Hurd, *ibid.*, p. 1.
[10] S. N. Song, C. Sellers, and J. B. Ketterson, Appl. Phys Lett. **59**, 479 (1991).
[11] P. Xiong, G. Xiao, J. Q. Wang, J. Q. Xiao, J. S. Jiang, and C. L Chien, Phys. Rev. Let. **69**, 3220 (1992); J. Q. Wang, P. Xiong, and G. Xiao, Phys. Rev. B **47**, 8341 (1993).
[12] H. Sato, T. Kumano, Y. Aoki, T. Kaneko, and R Yamamoto, J. Phys. Soc. Jpn. **62**, 479 (1993); Y. Aoki *et al.*, in Ref. 2, p. 448.
[13] F. Tsui, B. Chen, D. Barlett, R. Clarke, and C. Uher, Phys. Rev. Lett. **72**, 740 (1994).
[14] H. Fujii, T. Takabatake, T Suzuki, T. Fujita, J. Sakurai, and V. Sechovsky, Physica B **192**, 219 (1993).
[15] R. B. van Dover, E. M. Gyorgy, R. J. Cava, J. J. Krajewski, R. J. Felder, and W. F. Peck, Phys. Rev. B **47**, 6134 (1993).
[16] J. Shi, E. Kita, L. Xing, and M. B. Salamon, Phys. Rev B **48**, 16119 (1993).
[17] J. Shi, S. S. P. Parkin, L. Xing, and M B. Salamon, J Magn. Magn. Mater **125**, L251 (1993)
[18] Y. Kobayashi, H. Sato, Y Aoki, and A. Kamijo (unpublished).
[19] H. Sato, Y. Kobayashi, Y. Aoki, and H. Yamamoto (unpublished).
[20] A. R. Ball, D. Gignoux, and D. Schmitt, Physica B **180&181**, 58 (1992).
[21] N. V. Baranov, A. V. Deryagin, P. E. Markin, and E. V. Sinitsyn, Sov. J. Low Temp. Phys **10**, 400 (1984).
[22] H. Henmi, Y. Aoki, T. Fukuhara, I. Sakamoto, and H. Sato, Physica B **186-188**, 655 (1993).
[23] H. Yamada, J. Inoue, K. Terao, S. Kanda, and M. Shimizu, J. Phys. F **14**, 1943 (1984).
[24] M. Cryot and M. Lavagna, J. Phys. (Paris) **40**, 763 (1979).
[25] E. Gratz, H. Sassik, and H. Nowotny, J Phys. F **11**, 429 (1981).
[26] N. V. Baranov and A I. Kozlov, J. Alloys Compounds **190**, 83 (1992).

Intrinsic giant magnetoresistance of mixed valence La-A-Mn oxide (A=Ca,Sr,Ba) (invited)

R. von Helmolt[a] and J. Wecker
Siemens AG, Research Laboratories, 91052 Erlangen, Germany

K. Samwer
Institute of Physics, University of Augsburg, 86159 Augsburg, Germany

L. Haupt and K. Bärner
IV Physics Institute, University of Göttingen, 37073 Göttingen, Germany

A large intrinsic magnetoresistance has been found near the ferromagnetic transition of metallic manganese oxides with perovskite-type crystal structure. The magnetic and transport properties were measured on bulk and thin-film $La_{1-x}A_xMnO_{3+\delta}$ with A=Ca,Sr,Ba. Assuming the double-exchange model proposed by Zener [Phys. Rev. **81**, 440 (1951); **82**, 403 (1951)], the strong dependence of the transport properties on the magnetic field and also on the chemical composition is attributed to the mixed Mn^{3+}/Mn^{4+} valence.

I. INTRODUCTION

Much interest has been focused on giant magnetoresistance (GMR) since the first observation of it in metallic multilayers consisting of ferromagnetic layers which are separated by nonmagnetic spacer layers.[1] Meanwhile, resistance changes $\Delta R/R(H=0)$ of up to 60% at 10 K,[2] or 40% at room temperature,[3] have been reported. Beside multilayers, the effect has also been found in heterogeneous alloys with superparamagnetic precipitates embedded in a nonmagnetic metallic matrix. Spin-dependent scattering near the interface between the ferromagnetic and the nonmagnetic phase is the physical origin of the magnetoresistance in these systems, whereas the "conventional" anisotropic magnetoresistance (MR) of ferromagnets and also the isotropic MR which is attributed to magnetic impurity scattering are intrinsic properties of the material.

Although today's interest in GMR mainly focuses on the heterogeneous systems with ferromagnetic/nonmagnetic interfaces, one has to keep in mind the very high intrinsic MR of some materials, which is possible if the electronic transport is strongly related to the spin order, especially in those cases of coincidence of a magnetic and a metal-semiconductor transition. Such an intrinsic GMR has, e.g., been reported for some ferromagnetic Eu-chalcogenide alloys (T_C=6 K). In the ferromagnetic region, the resistance could be lowered by more than four orders of magnitude by applying a magnetic field of less than 1 T.[4] It has been shown by several authors (e.g., Refs. 5–7), that the intrinsic GMR is not restricted to low temperatures if a system with a suitable high transition temperature is chosen. One example is the mixed-valence perovskite-type $La_{2/3}Ba_{1/3}MnO_{3+\delta}$, for which we found a lowering of the resistance of $\Delta R/R(H=0)>60\%$ at room temperature.[7] Leaving out for a moment the very high magnetic field of 7 T which is necessary, these numbers are still higher than those reported for multilayer systems.

In this article we first review magnetic properties of Mn-oxides with distorted perovskite-type structure. Then the effect of spin disorder on the transport properties is discussed. In Sec. IV also some results on "doped" bulk samples are reviewed, where chemical impurities have been introduced by partially substituting Cu for Mn.[8] The effect of an external field on the resistance is then reported in Sec. V for various thin-film samples, and we will finally conclude with a short summary.

II. EXPERIMENTS

The bulk samples were prepared by standard ceramic techniques from oxides, carbonates, or acetates either from an acid solution as described earlier[9] or just by repeated grinding and annealing in air, which finally resulted in black, compact sintered pellets. Using some of these samples as laser targets, thin films with thicknesses between 100 and 500 nm were grown on $SrTiO_3$ 10×10 mm^2 substrates in (100) and (110) orientation by laser deposition as described elsewhere.[10] The substrate temperature had to have a temperature range around T_S=600 °C to obtain epitaxial growth. The sample quality was controlled by x-ray diffraction and also by reflection high-energy electron-diffraction (RHEED) measurements. A higher substrate temperature resulted in polycrystalline films, which did not differ in their electric properties from the epitaxial ones. Since we did not carry out chemical analysis, the exact oxygen content of our samples is uncertain and thus we assume an oxygen excess δ.

III. MAGNETIC Mn-OXIDES WITH PERVOSKITE STRUCTURE

Early investigations on magnetic oxides with distorted perovskite-type structure[11] showed that antiferromagnetic, insulating $LaMnO_3$ can be driven into the metallic state by replacing a certain amount of the trivalent La by divalent Ca, Sr, or Ba. At the same time as electric transport becomes possible, the antiferromagnetic spin order changes via a canted spin structure or an antiferromagnetic spiral arrangement into a ferromagnetic state. The crystal symmetry changes from tetragonal, monoclinic, or rhombohedral toward cubic symmetry. The electric and magnetic properties are also very sensitive on the preparation parameters, which

[a]Also with. Institute of Physics, University of Augsburg, 86159 Augsburg, Germany.

 0021-8979/94/76(10)/6925/4/$6.00 © 1994 American Institute of Physics

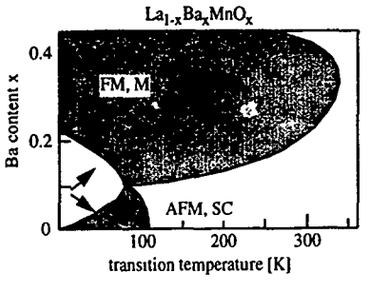

FIG. 1. Schematic phase diagram of $La_{1-x}Ba_xMnO_3$. Antiferromagnetic (AFM), semiconducting (SC) $LaMnO_3$ becomes ferromagnetic (FM) and metallic (M) if trivalent La is substituted by divalent Ba. Similar phase diagrams can be drawn for Sr and Ca substitution (Ref. 11).

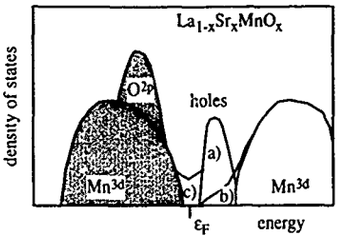

FIG. 2. Schematic diagram of the band structure of $La_{1-x}Sr_xMnO_{3+\delta}$ (Ref. 19). The initial bandgap of about 1.3 eV is reduced by the hole states (a) due to Sr doping and (b) due to excess oxygen. (c) States at ϵ_F are probably introduced by band broadening in the ferromagnetic region for high Sr content $x>0.15$ (Ref. 20).

is mainly the annealing temperature.[7,11–13] A schematic magnetic phase diagram for $La_{1-x}Ba_xMnO_3$ is shown in Fig. 1.

The antiferromagnetic coupling between Mn^{3+} ions in the undoped parent compound $LaMnO_3$ is believed to be transferred by superexchange via the intermediate oxygen, leading to a layered spin structure with antiferromagnetic coupling between adjacent layers and ferromagnetic order within the layers.[14] Weak (or parasitic) ferromagnetism is observed even in the undoped compound and is interpreted as an intrinsic property[15] or to result from an excess of oxygen δ.[11]

Zener was the first to develop the mechanism of double exchange to understand the occurrence of ferromagnetism together with metallic conductivity, if a portion of the La is substituted by a divalent metal.[16] A corresponding number of formerly triply charged Mn must then become quadruply charged, and the displacement of these holes increases the conductivity and at the same time provides a mechanism for ferromagnetic interaction. The double-exchange model proceeds from a resonance valence-bond description of the Mn $3d$ electrons and O $2p$ electrons. While no electron transfer is possible from a Mn^{3+} to another Mn^{3+} ion, this changes by introducing some Mn^{4+} ions, and in this case the bond between Mn ions of different oxidation state can be described as a resonance hybrid between the two states,

$$\Psi_1: \ Mn^{3+}O^{2-}Mn^{4+}, \quad \Psi_2: \ Mn^{4+}O^{2-}Mn^{3+}.$$

A fluctuation of the electron is energetically favored and, as it has been shown for such a simplified physical model,[17,18] the transfer integral for one electron becomes

$$t_{ij}=b_{ij}\cos(\theta_{ij}/2),$$

with some constant b_{ij}, when θ_{ij} is the angle between the two ionic spins. This dependence of the carrier energy on θ_{ij} is, together with the competing antiferromagnetic superexchange interaction, the reason for either a canted spin arrangement with two sublattices in the ferromagnetic region, or a spiral arrangement, which is stable in a certain range of the dopant concentration x.

IV. MAGNETIC AND CHEMICAL DISORDER

While all of the Zener carriers participate in double exchange, at least at low concentrations x, only a small fraction of them is involved in the conduction process.[18] This peculiarity of the conduction band was recently confirmed in a spectroscopic investigation by Chainani, Mathew, and Sarma:[19] Their x-ray photoelectron spectroscopy (XPS) and ultraviolet photoemission spectroscopy (UPS) spectra of sintered $La_{1-x}Sr_xMnO_3$ showed only a negligible intensity at the Fermi level even in the metallic region $x>0.2$, and thus the authors conclude that the energy gap (or a pseudogap with a low density of states) of the "pure" semiconducting compound $LaMnO_3$ survives even if chemical holes are doped by introducing Sr. Figure 2 shows the schematic band structure as suggested by these authors. A theoretical study of $La_{1-x}Sr_xMnO_3$, which extends the double-exchange model by including band-structure effects, predicts a band broadening at the ferromagnetic transition, which reduces the gap or even closes it, thus leading to increased or metallic conductivity in the ferromagnetic region[20] and activated conductivity above T_C. This might explain the activated behavior we observed above T_C also in the metallic ferromagnets (Figs. 3 and 4).

As a consequence of this interplay between spin order and the small number of mobile charge carriers, the conduc-

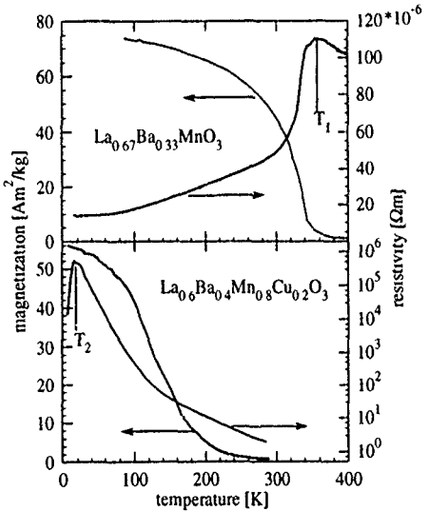

FIG. 3. Magnetization (under an applied field of $\mu_0 H=0.4$ T) and resistance vs temperature of sintered $La_{0.67}Ba_{0.33}MnO_3$ [upper figure (a)] and $La_{0.6}Ba_{0.4}Mn_{0.8}Cu_{0.2}O_{3+\delta}$ [lower figure (b)]. Data taken from Ref 8.

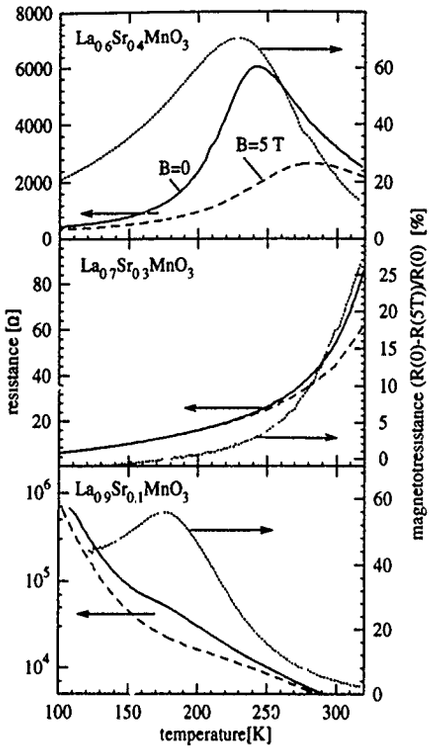

FIG. 4. Temperature dependence of the resistivity at zero field (solid line, left-hand-side axis) and under an applied field of $\mu_0 H = 5$ T (dashed) for thin films of $La_{0.9}Sr_{0.1}MnO_{3+\delta}$ $La_{0.8}Sr_{0.3}MnO_{3+\delta}$ and $La_{0.6}Sr_{0.4}MnO_{3+\delta}$. The dotted curves (right-hand-side axis) represent the relative MR effect MR $=[R(0T)-R(5T)]/R(0T)$.

tivity is strongly affected by perturbations of the spin lattice. This leads in some cases even to an Anderson type of localization and, therefore, semiconducting behavior.[21] Figure 3(a) shows the temperature dependence of the magnetic moment and the resistance of the metallic ferromagnet $La_{0.67}Ba_{0.33}MnO_3$. At low temperature $T \ll T_C$, metallic behavior is observed, i.e., a positive temperature coefficient of resistivity, $\rho^{-1} d\rho/dT > 0$, down to the lowest temperature of 4.2 K. Near T_C, a very prominent spin-disorder scattering leads to a strong increase of resistivity. The resistance reaches a maximum at $T_1 \approx 355$ K, and then decreases, i.e., activated behavior is observed above the ferromagnetic transition.

If 20% of the Mn is replaced by Cu, we obtain the curves of Fig. 3(b). Beside the lowered T_C, the saturation magnetization differs significantly from the calculated spin-only values of the $3d$ elements, thus indicating a global or local canting of spins. The resistivity is increased by several orders of magnitude, compared to Fig. 3(a), and exhibits activated behavior also in the ferromagnetic region. The transition to metallic conduction takes place at a much lower temperature $T_2 \approx 20$ K. The high resistance in the region of activated conduction has been explained by a reduced mobility or even localization due to "frozen-in" magnetic disorder.[8] Further Cu doping breaks the long-range magnetic order, and spin-glass behavior occurs. The resistivity of the spin-glass samples shows activated behavior in the whole examined temperature range.

In order to explain the very strong dependence of the resistance on spin order in a material with such a low density of states in the conduction band, some authors suggested a magnetic polaron model[5,22,23] i.e., the spin of a conducting electron induces a local distortion of the spin lattice and moves on surrounded by this spin polarization. The transport properties at low temperature should then be dominated by a hopping process. Indeed we find that the resistivity data of Fig. 3(b) and also those obtained on spin-glass samples follow a $\ln \rho \sim T^{-1/4}$ law at temperatures $T \ll T_C$,[8,12] thus suggesting variable-range hopping of spin polarons in a disordered spin lattice.[21,24]

The conception of spin polarons is supported by infrared measurements, which were obtained on sintered samples of $La_{1-z}A_zCu_{1-x}Mn_xO_{3+\delta}$ (A=Sr, Ba).[12,25] A broad peak in optical conductivity at around 2000 cm^{-1} is observed, which is attributed to polaron transport effects. This peak becomes more pronounced as spin disorder is increased by doping of Cu, thus indicating the increased effect of spin polarization on the mobility. Experimental evidence for magnetic polarons above T_C was found by spin-polarized neutron scattering for the very similar compound $Nd_{0.5}Pd_{0.5}MnO_3$.[5]

V. MAGNETORESISTANCE IN THE FERROMAGNETIC REGION

The dependence of the conductivity on the spin order and thus on the magnetization implies a high magnetoresistance in the ferromagnetic region. The highest values should be expected near T_C, because here we find the highest change of saturation magnetization under an applied magnetic field.

Figure 4 shows the temperature dependence of the resistance and magnetoresistance of $La_{1-x}Sr_xMnO_{3+\delta}$ thin films for three compositions $x=0.4$, 0.3, and 0.1. Again we find a cusp in the zero-field resistance (solid line in Fig. 4) at a temperature near T_C, with metallic behavior below and activated behavior above this temperature. The application of an external magnetic field of $\mu_0 H = 5$ T decreases the resistance (dashed line), and the difference to the zero field values is shown by the MR curve (dotted line), which is normalized to the zero-field resistance. The highest MR value is found near to the cusp in resistivity, and the cusp itself becomes smaller and shifts towards higher temperature as the field is increased. Magnetoresistance curves of $La_{0.6}Sr_{0.4}MnO_{3+\delta}$ films at various temperatures are shown in Fig. 5. The MR is normalized to the zero-field values again since no saturation was achieved, but one should notice that, if normalized to the resistance at high field, as is usually done for GMR multilayers, the MR at 230 K exceeds 400% in the 7 T field range.

Films prepared from a $La_{0.67}Ca_{0.33}MnO_3$ target even show an intrinsic GMR of more than 2 orders of magnitude (i.e., 10^4 %) at $T=120$ K. The $R(T)$ curve of this sample, measured at zero field, shows a very high peak near this temperature, which can be completely suppressed by applying a magnetic field of 5 T. At lower temperature ($T<100$ K), we observe spin-glass-like behavior in the magnetization and also in the magnetoresistance. Details about this will be published elsewhere.

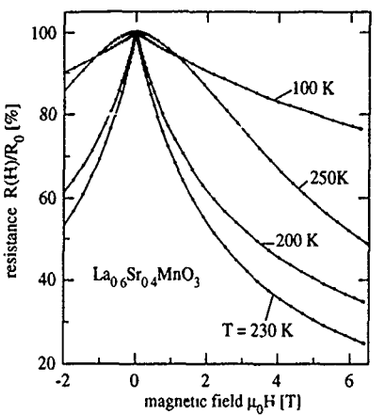

FIG. 5. Magnetoresistance of $La_{0.6}Sr_{0.4}MnO_{3+\delta}$ thin films at various temperatures, normalized to the resistance at $H=0$.

The MR seems not to depend on the relative orientation between magnetic field, electric current, and crystal axes, if one takes into account the different demagnetization factors, thus indicating that the contribution of anisotropic MR can be neglected. At low temperature $T \ll T_C$, the MR decreases again. This is consistent with the conception of a spin-disorder-dependent conductivity which cannot be changed by an applied field if the spin lattice is ordered at zero field.

VI. SUMMARY

In some ferromagnets with composition in the vicinity of a metal-semiconductor transition, an intrinsic GMR effect is possible which by far can be higher than the GMR of metallic multilayers or heterogeneous alloys. This intrinsic GMR occurs in the temperature range around the ferromagnetic transition, and it is not restricted to low temperature, as has been shown for samples with sufficiently high Curie temperature. Zener's model of double exchange gives an impressive imagination of the interplay between magnetic and electric properties. Both are very sensitive to chemical or magnetic disorder, which sometimes can even lead to a localization of charge carriers. The existence of magnetic polarons which determine the transport properties in the ferromagnetic region seems to be a plausible explanation for the observed temperature dependence of the resistance and magnetoresistance.

ACKNOWLEDGMENTS

We thank B. Holzapfel and U. Sondermann for useful discussions. R. v. H., L. H., and K. B. acknowledge partial support by the Deutsche Forschungsgemeinschaft (DFG), and R. v. H., J. W. and K. S. by the German Ministry for Research and Technology (BMFT).

[1] M. N. Baibich, J. M. Broto, A. Fert, F. Nguyen Van Dau, F. Petroff, P. Etienne, G. Creutzet, A. Friederich, and J. Chazelas, Phys. Rev. Lett. **61**, 2472 (1988).
[2] E. E. Fullerton, M. J. Conover, J. E. Mattson, C. H. Sowers, and S. D Bader, Appl. Phys. Lett. **63**, 1699 (1993).
[3] S. S. P. Parkin, Z. G. Li, and D. J. Smith, Appl. Phys Lett. **58**, 2710 (1991).
[4] S. von Molnar and S. Methfessel, J. Appl. Phys **38**, 959 (1967).
[5] R. M. Kusters, J. Singleton, D A. Keen, R. McGreevy, and W Hayes, Physica B **155**, 362 (1989).
[6] K. Chahara, T. Ohno, M Kasai, and Y. Kozono, Appl. Phys Lett. **63**, 1990 (1993).
[7] R. von Helmolt, J. Wecker, B. Holzapfel, L. Schultz, and K. Samwer, Phys. Rev. Lett. **71**, 2331 (1993).
[8] R. von Helmolt, L. Haupt, K. Bärner, and U Sondermann, Solid State Commun. **82**, 693 (1992)
[9] R. von Helmolt, L. Haupt, K. Barner, and U. Sondermann, Solid State Commun. **80**, 865 (1991).
[10] B. Holzapfel, B. Roas, L. Schultz, P. Bauer, and G Saemann-Ischenko, Appl. Phys. Lett **61**, 3178 (1992).
[11] G. H. Jonker and J. H. van Santen, Physica **16**, 337 (1950); G. H. Jonker, *ibid.* **22**, 707 (1956).
[12] L. Haupt, R. von Helmolt, U. Sondermann, K. Barner, Y. Tang, E. R Griessinger, E. Ladizinsky, and R. Braunstein, Phys. Lett A **165**, 473 (1992).
[13] J. Cho, M. Gomi, and M. Abe, Jpn. J. Appl. Phys. **29**, 1686 (1990).
[14] E. O. Wohllan and W. C. Kohler, Phys. Rev. **100**, 545 (1955).
[15] G. Matsumo, J. Phys. Soc Jpn. **29**, 606 (1970).
[16] C. Zener, Phys. Rev., **81**, 440 (1951); **82**, 403 (1951).
[17] P. W. Anderson and H. Hasegawa, Phys. Rev. **100**, 675 (1955).
[18] P. G. de Gennes, Phys. Rev. **118**, 141 (1960).
[19] A. Chainani, M. Matthew, and D. D Sarma, Phys. Rev. B **47**, 15 397 (1993).
[20] J Mazzaferro, C. A. Balseiro, and B. Alascio, J. Phys. Chem Solids **46**, 1339 (1985).
[21] N. F. Mott and E. A. Davies, *Electronic Processes in Noncrystalline Materials* (Clarendon, Oxford, 1979).
[22] S. Methfessel, M. Freiser, B Petit, and J C. Suits, J. Appl Phys **38**, 1501 (1967).
[23] T. Kasuya and A. Yanase, Rev. Mod. Phys. **40**. 648 (1968).
[24] A. S. Ioselevich, Phys. Rev Lett. **71**, 1067 (1993).
[25] Y. Tang, I. Shaltout, R. Braunstein, R. von Helmolt, L. Haupt, and K Barner, Phys Status Solidi B **182**, 509 (1994).

Colossal magnetoresistance in La-Ca-Mn-O ferromagnetic thin films (invited)

S. Jin, M. McCormack, and T. H. Tiefel
AT&T Bell Laboratories, Murray Hill, New Jersey 07974

R. Ramesh
Bellcore, Redbank, New Jersey 07701

A colossal magnetoresistance effect with more than a thousandfold change in resistivity ($\Delta R/R_H$=127 000% at 77 K, H=6 T) has been obtained in epitaxially grown La-Ca-Mn-O thin films. The effect is negative and isotropic with respect to the field orientations. The magnetoresistance is strongly temperature dependent, and exhibits a sharp peak that can be shifted to near room temperature by adjusting processing parameters. Near-room-temperature $\Delta R/R_H$ values of ~1300% at 260 K and ~400% at 280 K have been observed. The presence of grain boundaries appears to be detrimental to achieving very large magnetoresistance in the lanthanum manganite films. The orders of magnitude change in electrical resistivity could be useful for various magnetic and electric device applications.

I. INTRODUCTION

Perovskite-like oxide of lanthanum manganite ($LaMnO_3$) exhibits both strong ferromagnetism and metallic conductivity when La ions (3+ valence) are partially substituted with 2+ valence ions such as Ca, Ba, Sr, Pb, and Cd. This results in a Mn^{3+}/Mn^{4+} mixed valence state creating mobile charge carriers and canting of Mn spins.[1–10] The unit cell of a perovskite ABO_3 is shown in Fig. 1, where A at the corners represents a large ion such as La^{3+}, Nd^{3+}, Ca^{2+}, Sr^{2+}, Ba^{2+}, Pb^{2+}, B at the center of the cube stands for a small ion such as Mn^{3+}, Mn^{4+}, Cr^{3+}, Fe^{3+}, Ti^{4+}, and O at the center of the faces represents O^{2-}. The ionic radii of the elements pertinent to the manganites are listed in Table I. These elements form either simple $AMnO_3$-type or mixed (A+A′) (B+B′) MnO_3-type perovskites following Goldschmidt's perovskite stability criterion on ionic radii, i.e., the ratio $(r_A+r_O)/(r_B+r_O)\sqrt{2}$ should be approximately unity.[1] (r_A, r_B, r_O represent the radii of ions A, B, and O, respectively.)

Thin films of La-manganite thin films have recently been prepared and their magnetoresistance (MR) behavior has been reported for La-Ba-Mn-O (Ref. 11) (with the MR ratio of ~150% at room temperature) and La-Ca-Mn-O (Ref. 12) (MR ratio of ~110% at 220 K and near zero at room temperature). The MR ratio is defined here as $\Delta R/R_H = (R_H - R_0)/R_H$ where R_0 is the zero-field resistance and R_H is the resistivity in the applied magnetic field, e.g., H=6 T. These oxide films exhibited large magnetoresistance comparable to the higher end of the values for the so-called "giant-magnetoresistance(GMR)"-type materials of metallic multilayer or heterogeneous films[13–20] with the MR values typically in the range of 5–150%.

In this article we report the electrical, magnetic, and magnetoresistance behavior in epitaxial La-Ca-Mn-O films with extraordinary MR values in excess of 100 000%, about three orders of magnitude greater than were previously reported for the GMR-type or La-manganite films. Some potential applications of the material are also discussed.

II. EXPERIMENTAL PROCEDURE

Thin films of La-Mn-Ca-O, ~1000 Å thick, were deposited on (100) $LaAlO_3$ substrates by pulsed laser deposition (PLD). The substrate temperature was 650–700 °C, and the oxygen partial pressure in the chamber was maintained at 100–300 mTorr. The nominal target composition was $La_{0.67}Ca_{0.33}MnO_x$. The chemical composition of the depos-

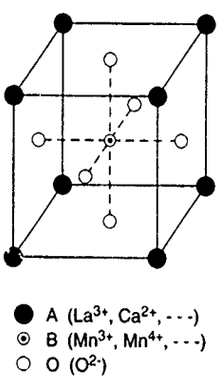

FIG. 1. Unit-cell structure of perovskite.

TABLE I. Ionic radii of elements involved in perovskitelike manganites.

Ion	Radius (Å)
La^{3+}	1.22
Pr^{3+}	1.16
Nd^{3+}	1.15
Sm^{3+}	1.13
Gd^{3+}	1.11
Y^{3+}	1.06
Ca^{2+}	1.06
Sr^{2+}	1.27
Ba^{2+}	1.43
Cd^{2+}	1.03
Pb^{2+}	1.32
Mn^{3+}	0.70
Mn^{4+}	0.52
O^{2-}	1.32

 0021-8979/94/76(10)/6929/5/$6.00 © 1994 American Institute of Physics

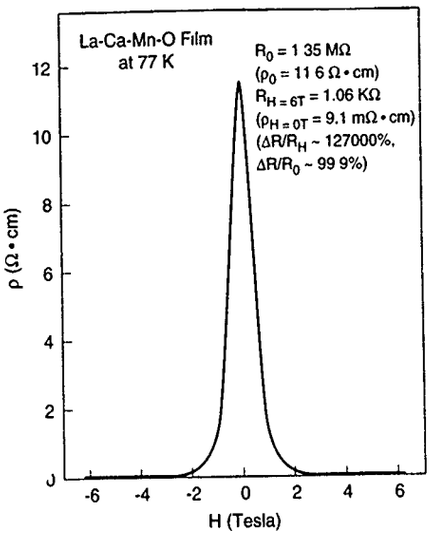

FIG. 2. Magnetoresistance behavior of the epitaxial La-Ca-Mn-O films (900 °C/30 min heat treated).

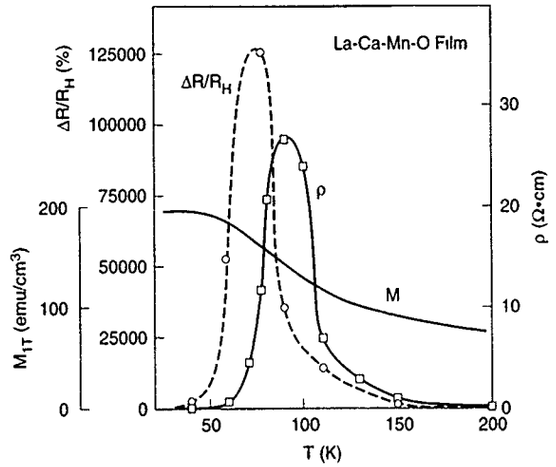

FIG. 3. ρ, $\Delta R/R_H$, and M vs T curves for the epitaxial La-Ca-Mn-O film

ited film was found to be similar to that of the bulk target used for the deposition, as indicated by scanning electron microanalysis and Rutherford backscattering analysis. X-ray-diffraction and rocking angle analysis indicate that the films have the perovskite-type cubic structure with a lattice parameter of $a=3.89$ Å (or $a=7.78$ Å from the crystallographic point of view) and grow epitaxially on the $LaAlO_3$ substrate ($a=3.79$ Å).

The electrical resistance and magnetoresistance of the films were measured as a function of temperature and magnetic field by the four-point technique (using a constant current) in a superconducting magnet with the maximum applied field of $H=6$ T. For most of the films the field direction was parallel to the current direction. Some of the measurements were carried out with the field applied perpendicular to the current direction in the film (using either in-plane field or perpendicular field). The MR behavior in the La-Ca-Mn-O films is almost always negative and essentially isotropic with respect to the field direction if the demagnetizing factor is taken into consideration. The M-H loops were obtained by using a vibrating sample magnetometer with the maximum field of $H=1$ T. The transmission electron microscopy (TEM) was carried out by using JEOL 4000 microscope operated at 400 kV. The samples were thinned by ion milling.

III. RESULTS AND DISCUSSION

The La-Ca-Mn-O films in the as-deposited condition exhibit low MR ratios of typically less than ~500% over a broad temperature range of 50–300 K (low MR only in a relative sense as this is still quite impressive). It has been found that a post-heat treatment of the deposited films is essential in order to maximize the MR behavior.[21] The highest MR ratio so far has been obtained by heat treatment at 900 °C/30 min. in an oxygen atmosphere (3 atm oxygen). As shown by the R vs H curves in Fig. 2 the La-Ca-Mn-O film exhibits a very large magnetoresistance value of 127 000% at 77 K (more than a thousandfold decrease in resistivity). The zero-field resistivity of the film, $\rho\sim11.6$ Ω cm ($R=1.35$ MΩ for the sample size ~1000 Å thick×2 mm wide×4 mm long), decreased in the presence of applied field $H=6$ T to ~9.1 mΩ cm ($R=1.06$ KΩ). The 77 K data indicate that the most significant portion of the resistivity drop occurs at $H<2$ T. The 127 000% MR value in this film is colossal when compared to the 5%–150% magnetoresistance in the GMR multilayer films. As this particular film has been heat treated so as to exhibit the peak MR value near the liquid-nitrogen temperature (77 K), other measurement temperatures gave lower MR ratios, e.g., 14 400% at a higher temperature of 110 K and 54 100% at a lower temperature of 60 K as shown in Fig. 2.

Shown in Fig. 3 are the temperature dependence characteristics of ρ, $\Delta R/R_H$, and M of the La-Ca-Mn-O film. As is evident in the figure, the ρ vs T curve exhibits a relatively sharp cusp at ~95 K with the film showing semiconductor behavior (i.e., a negative $d\rho/dT$) above and metallic behavior (a positive $d\rho/dT$) below this temperature. The temperature at which the magnetoresistance ($\Delta R/R_H$) of the film is maximum is almost invariably located in the metallic-behavior region on the left-hand (low-temperature) side of the resistivity peak. It is interesting to note that the magnetoresistance peak occurs at the temperature where the resistivity is roughly one-half of the peak resistivity or near the inflection point of the curve.

Also shown in Fig. 3 is the magnetization M (at $H=1$ T) versus temperature curve for the La-Ca-Mn-O film. It is evident that the film is strongly ferromagnetic with $M\sim200$ emu/cm^3 at 50 K and $M\sim100$ emu/cm^3 at 150 K. The M-H loops measured at various temperatures are given in Fig. 4. The loops exhibit magnetic hysteresis with coercivity H_c of about 30–50 Oe.

The mechanism(s) responsible for the very large magnetoresistance observed in the La-Ca-Mn-O films appear(s) to be related to the semiconductor-to-metal transition, however, the exact mechanism(s) are not clearly understood at the moment. Previous reports suggested the possibility of spin-disorder scattering, magnetic polaron hopping, or critical magnetic scattering for the relatively small MR effect present

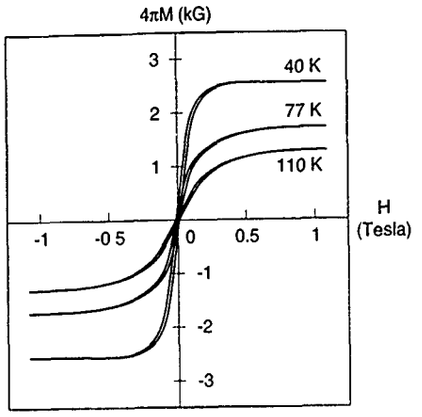

FIG. 4. Magnetization loops for the La-Ca-Mn-O film.

in their La-manganite films.[11,12] However, the fact that the peak in magnetoresistance in the present La-Ca-Mn-O film occurs, not near the magnetic transition temperature where M is near zero, but in the temperature region where M is still substantial (Fig. 3), indicates that spin-disorder scattering is not likely to be the major contributing factor. X-ray-diffraction analysis of the La-Ca-Mn-O film of Fig. 3 at various temperatures shows that there is no change in the cubic crystal structure (no phase transition) in the range of 10–300 K. The resistivity behavior near the temperature of peak MR suggests that the very large magnetoresistances observed are related to the semiconductor-to-metal transition. Further study is required to elucidate the underlying mechanisms for the colossal magnetoresistance in the present La-Ca-Mn-O film.

If the as-deposited film is heat treated for a longer time, e.g., 900 °C/3 h/3 atm O_2, the temperature of peak magnetoresistance is shifted to a higher temperature of ~100 K with a somewhat diminished MR value of $\Delta R/R_H \sim 11\,000\%$ at $H=6$ T. At 77 K and at a lower field, e.g., $H=1000$ Oe, the MR ratio is ~28%. A crude experiment to estimate the local-field-sensing capability of this film has been carried out at the liquid-nitrogen temperature as follows. A magnetic pen (a small Nd-Fe-B magnet attached at the end) was brought to within about 1 mm vertically of the La-Ca-Mn-O film (2 mm×3 mm×1000 Å thick). The magnetic field from the pen at this distance was ~1000 Oe; however, because of the near-perpendicular orientation of the field and the associated demagnetizing factor, the actual effective field on the film is estimated to be much lower than ~900 Oe. The film has the resistance $R=15.9$ kΩ (or $\rho=106$ mΩ cm) at 77 K. The change in voltage output in the film by the approaching field was measured by the four-point technique using a constant current of 1 mA. The zero-field voltage of 15.9 V was altered to 14.6 V when the magnetic pen came near the film with the significant sensor voltage signal ΔV of 1.3 V (or ~8% change). At room temperature a measurement with a similarly sized film with slightly modified composition of $La_{0.55}Ca_{0.25}Sr_{0.08}MnO_x$ ($\rho \sim 1.4$ mΩ cm, $R \sim 280$ Ω) gave a sensor voltage output ΔV of ~13 mV (or ~4.6% change), a sufficient signal for many sensor applications. As the ΔV signal in the sensor is expected to decrease with the distance

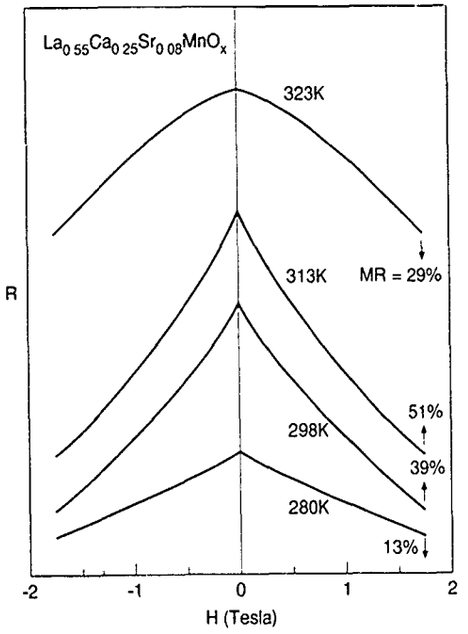

FIG. 5. R vs H curves for the La-Ca-Sr-Mn-O film.

away from the sensor, the magnetoresistive sensor (or an array of sensors) can be used as a position sensing device.

The substantially higher electrical resistivity in the La-Ca-Mn-O films, typically 2–4 orders of magnitude higher than the metallic magnetoresistive materials such as the 80Ni-20Fe Permalloy, could be an advantage for field sensing as the sensor voltage output ($\Delta V/\Delta H$ or $\Delta R/\Delta H$) is that much larger. The R vs H curve for this La-Ca-Sr-Mn-O film at room temperature is approximately linear for a relatively wide range of applied field,[22] as shown in Fig. 5. Thus, the MR ratio of 4.6% at $H \sim 1000$ Oe is equivalent to about 0.046% MR for a lower field of ~10 Oe (this is about the level of field strength of interest for magnetic recording read head). However, as the electrical resistance of this oxide film is about two orders of magnitude higher than that of the Permalloy (with the MR ratio on the order of 3% for $H=10$ Oe), the field-sensing output voltages turn out to be comparable for the two materials at the same level of sensor current. For a constant current of 1–10 mA, the ΔV voltage signal from this unoptimized film for $H=10$ Oe would be 0.13–1.3 mV, comparable to the ΔV value from the Permalloy film with the same dimension.

The magnetoresistive properties of the La-manganite films can be used for a number of other applications. An example is a magnetoresistive microphone design[23] such as schematically illustrated in Fig. 6. A small, La-Ca-Sr-Mn-O–type MR sensor, about 2×4 mm^2 in size, was mounted on a plastic diaphragm. As sound waves with varying intensity hit the diaphragm and make it vibrate, the MR sensor is moved in relation to the magnet that supplies a gradient field. The resulting change in the magnetic-field intensity on the sensor causes a change in resistivity, which in turn changes the output voltage ΔV. Shown in Fig. 7 is a schematic diagram illustrating a circuit configuration for the microphone device. The sensor signal, many mV even in the unamplified condi-

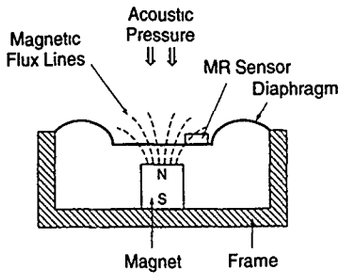

FIG. 6. A magnetoresistive microphone design.

tion, Fig. 8, decreases with the distance from the sound source as is expected.

The MR behavior of the La-Ca-Mn-O film depends not only on the specifics of post-heat treatment but also on a number of other composition and processing details including various film deposition conditions. For example, a higher oxygen partial pressure p_{O_2} during deposition tends to produce films with higher temperature of peak resistance. The magnetization especially near room temperature also increases noticeably with p_{O_2}. A film deposited at p_{O_2}~300 mTorr gives near-room-temperature magnetoresistance values of $\Delta R/R_H$~1300% at 260 K and ~470% at 280 K as shown in Fig. 9. (Because of the cryostat operation in the superconducting magnet used, the MR measurement at 300 K was difficult.) The film is strongly magnetic at these temperatures with $4\pi M$ in excess of 2000 G. The exact nature of this change in MR behavior with the oxygen partial pressure is not clearly understood. Further investigations are underway to find out if it is caused by the change in chemistry (e.g., oxygen or cation stoichiometry) or structure (e.g., degree of epitaxy, lattice parameter, nature and density of defects, etc.).

It is not clearly understood why our La-Ca-Mn-O films exhibit the magnetoresistance effect as much as three orders of magnitude larger than was reported previously on similar La-manganite films.[11,12] It may be attributable to a number of differences in composition and processing details. The presence of grain boundaries appears to be very detrimental to achieving high MR values, based on the following observations: (i) Polycrystalline bulk La-Ca-Mn-O samples of similar composition exhibit low MR values of ~100% or less between 4.2 and 300 K; (ii) nonepitaxial (nonsingle-

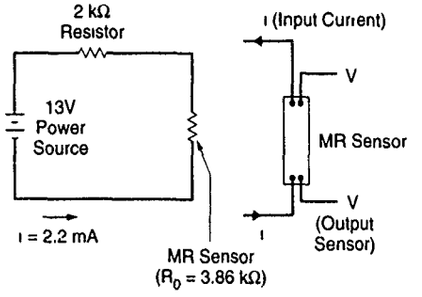

FIG. 7. Schematic diagram illustrating a circuit configuration for the microphone device.

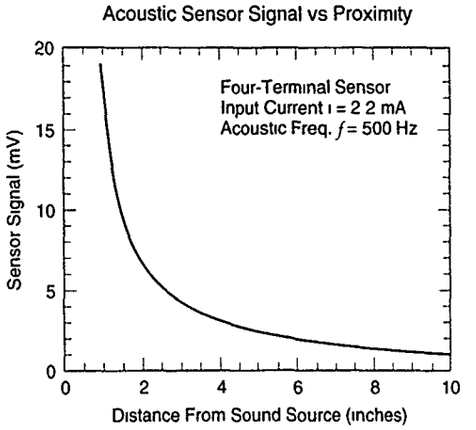

FIG. 8. Sensor signal vs proximity to the sound source for the microphone device of Fig. 6.

crystalline) films deposited on substrates with a greater lattice mismatch [such as Si, (100)MgO] or on polycrystalline substrates (such as yttria-stabilized zirconia) also yield low MR values of less than ~200%. The data previously reported on La-manganite films[11,12] all fall in the similarly low MR value regime. It is also noteworthy that no major difference in MR values was observed between the film and bulk, polycrystalline La-Ba-Mn-O, both exhibiting low MR values.[11] These observations strongly suggest that single crystallinity (a high degree of epitaxy and the absence of grain boundaries), such as shown by TEM analysis over large area and x-ray analysis for the La-Ca-Mn-O film, is a necessary condition for obtaining the very large magnetoresistance such as reported in this work. The single-crystalline nature of the film as well as the near-perfect epitaxy across the $LaAlO_3$/La-Ca-Mn-O interface is evident from Fig. 10.

The possible effect of grain boundaries on MR behavior is a very interesting subject for further investigation. In the La manganites, high electrical resistivity is a prerequisite to the occurrence of large magnetoresistance. The bulk, polycrystalline La-Ca-Mn-O material is too conductive (ρ<50 mΩ cm at 4.2–200 K) to exhibit very large magnetoresistance. Whether the grain boundaries in the La manganites

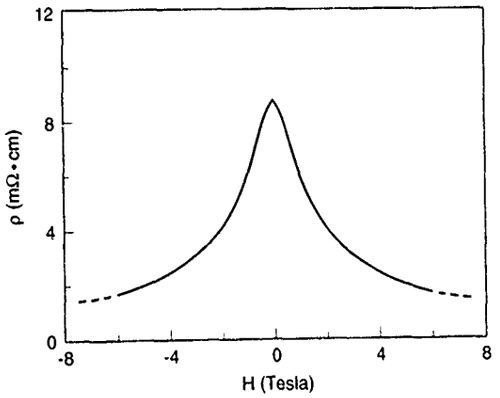

FIG. 9. ρ vs H curve (La-Ca-Mn-O film) at 280 K.

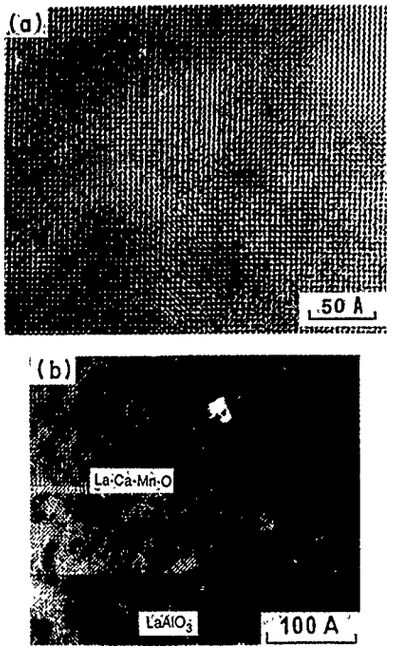

FIG. 10 High-resolution TEM micrographs for the La-Ca-Mn-O film: (a) top view; (b) cross-sectional view.

behave like "weak links" that short out the intragranular, high MR regions and, if so, what the underlying cause behind such a behavior is, needs to be investigated.

IV. SUMMARY

Colossal magnetoresistance in excess of 100 000% at 77 K and 1300% near room temperature has been obtained in epitaxially grown, single-crystalline La-Ca-Mn-O films. These values are orders of magnitude higher than those previously reported for the GMR multilayer films and La-manganite films. The magnetoresistance behavior appears to be related to the semiconductor-to-metal transition. The fact that the electrical resistivity of the material can be manipulated by applied field to a value orders of magnitude different could be exploited for various technical applications.

[1] G. H. Jonker and J. H. van Santen, Physica **16**, 337 (1950).
[2] E. O. Wollan and W. C. Koehler, Phys. Rev. **100**, 545 (1955).
[3] P. G. deGennes, Phys. Rev. **118**, 141 (1960).
[4] C. Zener, Phys. Rev. **82**, 403 (1951).
[5] J. B. Goodenough, Phys. Rev **100**, 564 (1955).
[6] B. C. Tofield and W. R. Scott, J. Solid State Chem. **10**, 183 (1974).
[7] J. B. Goodenough, in *Progress in Solid State Chemistry*, edited by H. Reiss (Pergamon, New York, 1971), Vol. 5, Chap. 4, p. 325.
[8] R. M. Kusters, J. Singelton, D. A. Keen, R. McGreevy, and W. Hayes, Physica B **155**, 362 (1989).
[9] L. K. Leung, A. H. Morrish, and C. W. Searle, Can. J. Phys. **47**, 2697 (1969).
[10] C. W. Searle and S. T. Wang, Can. J. Phys. **48**, 2023 (1970).
[11] R. von Hemlolt, J. Wecker, B. Holzapfel, L. Schultz, and K Samwer, Phys. Rev. Lett. **71**, 2331 (1993).
[12] K. Chahara, T. Ohno, M. Kasai, and Y. Kozono, Appl. Phys. Lett. **63**, 1990.
[13] S. S. P. Parkin, R. Bhadra, and K. P. Roche, Phys. Rev. Lett. **66**, 2152 (1991).
[14] B. Dieny, P. Humbert, V. S. Speriosu, S. Metin, B. A. Gurney, P. Baumgart, and H. Lefakis, Phys. Rev. B **45**, 806 (1992).
[15] E. E. Fullerton, M. J. Conover, J. E. Mattson, C H. Sowers, and S. D Bader, Appl. Phys. Lett. **63**, 1699 (1993).
[16] L. H. Chen, T H. Tiefel, S Jin, R. B. van Dover, E. M. Gyorgy, and R. M. Fleming, Appl. Phys. Lett. **63**, 1279 (1993).
[17] A. E. Berkowitz, J. R. Mitchell, M. J. Carey, A. P. Young, S. Zhang, F. E. Spada, F. T. Parker, A. Hutten, and G. Thomas, Phys. Rev. Lett. **68**, 3744 (1992).
[18] P. M. Levy, Science **265**, 972 (1992)
[19] L. H. Chen, S. Jin, T. H. Tiefel, and R. Ramesh, Appl. Phys Lett **64**, 1039 (1994).
[20] T. L. Hylton, K. R. Coffey, M. A. Parker, and J K. Howard, Science **261**, 1021 (1993).
[21] S. Jin, T. H. Tiefel, M. McCormack, R. A. Fastnacht, R. Ramesh, and L H. Chen, Science **264**, 413 (1994).
[22] M. McCormack and S. Jin (unpublished)
[23] L. A. Marcus, M. McCormack, and S. Jin (unpublished)

Giant magnetoresistance in *f*-electron systems (invited) (abstract)

Tadao Kasuya and Takashi Suzuki
Physics Department, Tohoku University, Sendai 980, Japan

Various kinds of giant magnetoresistance have been observed. In the present report, we concentrate on the f-electron systems, particularly on rare earth compounds, and summarize the results by classifying according to mechanisms. One important category is concerning the magnetic impurity state in a doped magnetic semiconductor with a fairly wide band gap. A typical classical example is EuO with O vacancies, in which two conduction electrons with opposite spin directions are trapped at each vacancy. The applied field aligns the spin direction, induces magnetic polaron, expands the extension of the impurity state, and causes a large decrease in resistivity. Another typical example is $Gd_{3-x}S_4$, with x near $\frac{1}{3}$ namely, near Gd_2S_3, in which only a small amount of conduction electrons exists below or around the mobility edge. This system is characteristic in the sense that a strong band tail exists nearly independently on the number of doped carrier. A strong tendency to form magnetic polaron exists and various anomalous properties including giant magnetoresistance is observed. Recently, we performed an extensive study on this material to reveal the fundamental mechanism. Some details will be reviewed. Another category is the intrinsic character, even though it is modified substantially by defects in the real materials. A typical prototype is EuB_6, a typical narrow gap magnetic semiconductor. Applied field causes a ferromagnetic alignment of $4f$ spins, which causes overlapping between the up spin conduction band and the up spin valence band through the d-f exchange and p-f mixing interaction causing the system into a semimetallic state. This further accelerates the $4f$ spin alignment. To see the real intrinsic mechanism, the sample should be very pure and the most suitable samples for this purpose are Ce and Yb monopnictides. Recently, we performed an extensive investigation on a series of the above materials and found various novel characteristic properties, including both giant positive and negative magnetroresistances. A detailed summary is planned.

 0021-8979/94/76(10)/6934/1/$6.00 © 1994 American Institute of Physics

Theory of spin dynamics in the metallic cuprates (invited)

Qimiao Si
Department of Physics, University of Illinois, 1110 West Green Street, Urbana, Illinois 61801

Yuyao Zha and K. Levin
James Franck Institute, University of Chicago, 5640 South Ellis Avenue, Chicago, Illinois 60637

The spin dynamics in the metallic cuprates are studied theoretically. In the normal state, it is demonstrated that the interplay of correlation effects and fermiology lead to a natural understanding of the contrasting wave vector dependences in the neutron scattering cross sections of the two best characterized cuprates: LaSrCuO and YBaCuO, as well as the anomalous frequency and temperature dependences in the neutron scattering cross sections and in the NMR relaxation rates $1/T_1$ and $1/T_{2G}$. In the superconducting state, the compatibility of the d-wave pairing state with magnetic data is explored.

I. INTRODUCTION

In order to address the origin of high temperature superconductivity, it is essential to understand the nature of the low lying excitations in the metallic cuprates. In this article, we focus on the spin excitations. In conventional metals, the spin dynamics are described by an itinerant picture based on the particle-hole excitation spectrum and the dynamical spin susceptibility is given by the Lindhard function. Such a simple picture does not apply in the copper oxides.

We start the discussion with the stoichiometric compounds such as La_2CuO_4 and $YBa_2Cu_3O_6$. They are insulators with a charge gap of the order of 2 eV. The insulating behavior is unexpected from the one-electron picture since the outermost copper band is half filled. Furthermore, it is unusual compared to band insulators in that spin excitations are not gapped. In fact, an antiferromagnetic ordering is developed at low temperatures.[1] In the paramagnetic phase, the spin dynamics have been studied using both low energy and high energy inelastic neutron scattering, nuclear quadrupole resonance (NQR), and Raman scattering experiments.[1–4] These data have been successfully analyzed in terms of interacting spin waves in the two-dimensional Heisenberg model on a square lattice.[5] In this picture, spins are localized at the copper sites within each CuO_2 layer, and are coupled with each other through essentially a nearest-neighbor Heisenberg coupling. These features are characteristic of a Mott (charge-transfer) insulator and explicitly establish the existence of a strong on-site Coulomb repulsion among the copper d electrons.

As the system is doped away from half filling, the magnetic order quickly vanishes, and an insulator to metal (superconductor) transition sets in. In the metallic cuprates, antiferromagnetic fluctuations have also been observed, mainly through NMR/NQR and inelastic neutron scattering experiments.[6,1] In the context of a conventional theory of spin fluctuations in simple metals, the NMR/NQR data appear to be highly anomalous: (a) The copper-site spin-lattice relaxation rate, $(1/T_1)_{Cu}$, is strongly enhanced in magnitude. Its temperature dependence deviates strongly from the usual linear behavior.[6] Such an anomalous temperature dependence is also reflected in the Gaussian component of the transverse relaxation rate, $1/T_{2G}$.[7] (b) At the same time, the oxygen-site spin-lattice relaxation rate, $(1/T_1)_O$, is almost linear in temperature, and has a nominal Korringa ratio of order 1.[8] The neutron scattering data are also puzzling: (c) The momentum dependences in the two best-characterized cuprates, YBaCuO and LaSrCuO, are quite different. In YBaCuO, antiferromagnetic spin fluctuations are commensurate. The commensurate peaks are broad, with essentially temperature-independent widths.[9,10] In LaSrCuO, spin fluctuations are sharply peaked at incommensurate wave vectors $\mathbf{Q}^*$;[11,12] (d) Within the lightly doped nonsuperconducting LaSrCuO system[13] the cross sections are found to scale with ω/T. Systematic studies of the temperature and frequency dependences of the cross sections for systems closer to optimal doping have, however, revealed low energy scales in YBaCuO.[9,10] Comparable experiments are still under way for the normal state of superconducting LaSrCuO.

Given that the conduction electrons in the cuprates are strongly interacting with each other, it is perhaps not surprising that the magnetic data appear to be anomalous compared to conventional metals. However, the exact nature of the spin excitations in a doped Mott–Hubbard system is not known. In particular, it is not clear *a priori* whether doped holes leave the localized spins of the half filled cuprates intact leading to a frustrated spin system, or they manage to convert the localized spins into renormalized quasiparticles. Therefore, an analysis of the spin dynamical data of the metallic cuprates can help clarify the nature of these spin excitations and the residual magnetic coupling. It also allows us to discuss their implications of magnetic data for the nature and the origin of superconductivity. This brief review summarizes our own work[14–18] in this area and is not intended to be comprehensive.

II. DYNAMICAL SPIN SUSCEPTIBILITY

The inelastic neutron scattering cross section is directly related to the spin structure factor $S(\mathbf{q},\omega)$,

 0021-8979/94/76(10)/6935/6/$6.00 © 1994 American Institute of Physics

$$d^2\sigma/d\Omega_q\, d\omega \sim S(\mathbf{q},\omega). \tag{1}$$

$1/T_1$ is the rate at which the nuclear magnetization relaxes towards equilibrium and is given by

$$\left(\frac{1}{T_1}\right)_r \sim \sum_{\mathbf{q}} A_r^2(\mathbf{q}) S(\mathbf{q},\omega_N \to 0), \tag{2}$$

where ω_N represents the nuclear resonance frequency which is essentially zero compared to typical electronic energies, and $A_r(\mathbf{q})$ is the hyperfine coupling constant for nuclei r (copper or oxygen). Through the fluctuation-dissipation theorem, $S(\mathbf{q},\omega)=\chi''(\mathbf{q},\omega)/(1-e^{-\omega/T})$, where $\chi''(\mathbf{q},\omega)$ is the imaginary part of the dynamical spin susceptibility. Finally, the Gaussian component of the Cu-site spin-echo decay rate, $1/T_{2G}$, is determined by the coupling between the copper nuclear spins. Through the usual Ruderman–Kittel–Kasuya–Yosida (RKKY) mechanism, the indirect contribution can be related to the static spin susceptibility $\chi(\mathbf{q})$ and is given approximately by[19]

$$\frac{1}{T_{2G}} \sim \left[\sum_{\mathbf{q}} F(\mathbf{q})^4 \chi(\mathbf{q})^2 - \left(\sum_{\mathbf{q}} F(\mathbf{q})^2 \chi(\mathbf{q}) \right)^2 \right]^{1/2}, \tag{3}$$

where $F(\mathbf{q})$ is the out of plane component of $A_{\mathrm{Cu}}(\mathbf{q})$.

In conventional metals, $\chi''(\mathbf{q},\omega)$ has the Lindhard form, $\chi''(\mathbf{q},\omega) \sim \Sigma_{\mathbf{k}}[f(E_{\mathbf{k}+\mathbf{q}}) - f(E_{\mathbf{k}})]\delta(E_{\mathbf{k}} - E_{\mathbf{k}+\mathbf{q}} - \omega)$. This implies that (a) the $\mathbf{q}$ dependence in the neutron scattering cross section at low energies reflects the geometry of the Fermi surface. Physically, only single-particle states close to the Fermi level can contribute to the low energy spin fluctuations; (b) the energy scale for the temperature and frequency dependences is determined by the Fermi energy which is of the order of eV or 10 000 K; (c) $1/T_1$ is linear in temperature, and satisfies the Korringa law, $1/T_1 T\chi^2 = 1$, where χ is the static uniform magnetic susceptibility. (Here, for simplicity, dimensionless units are used.) Physically, the number of electrons available to flip the nuclear spin is proportional to $TN(E_F)$, and each electron contributes a relaxation rate proportional to $N(E_F)$, where $N(E_F)$ is the density of states at the Fermi level which is also proportional to χ.

To derive the appropriate form of the dynamical susceptibility for the metallic cuprates,[14] we consider the extended Hubbard model defined in a CuO_2 layer

$$H = \sum_{i\sigma} \epsilon_d^0 d_{i\sigma}^\dagger d_{i\sigma} + \sum_i U n_{d,i\uparrow} n_{d,i\downarrow} + \sum_{il\sigma} V_{pd}(d_{i\sigma}^\dagger p_{l\sigma} + \text{h.c.})$$

$$+ \sum_{l_1 l_2 \sigma} t_{l_1 l_2}(p_{l_1\sigma}^\dagger p_{l_2\sigma} + \text{h.c.}). \tag{4}$$

The copper d electrons have an energy level ϵ_d^0 and an on-site interaction U. The oxygen p electrons have a dispersion determined by the hopping matrix elements t_{pp} (nearest neighbor) and t'_{pp} (next nearest neighbor). The two bands are coupled through the hybridization matrix element V_{pd} (nearest neighbor).

At half filling, this model has a Mott (charge-transfer) insulating solution when both the Coulomb repulsion U (taken as infinity here) and the level separation $\epsilon_p - \epsilon_d^0$ are large. The low energy configurations correspond to each copper site occupied by a spin, and each oxygen site fully occupied by electrons, or equivalently, empty of holes. The exchange interaction among the copper spins comes from the superexchange mechanism. Among the excited states that can be virtually occupied, the lowest ones correspond to holes occupying the oxygen orbitals. Since there is only nearest-neighbor hybridization between copper and oxygen orbitals, the dominant contribution to the exchange interaction among the copper spins comes from the nearest neighbor term. Therefore

$$J(\mathbf{q}) = J_0[\cos(q_x) + \cos(q_y)]. \tag{5}$$

This result is quite insensitive to the oxygen dispersion, so long as the (bare) oxygen levels are well separated from the copper level. Such a nearest-neighbor form for $J(\mathbf{q})$ is supported by high energy spin wave measurements on the insulating state.[2]

In the metallic cuprates, one of the key experimental results is the observation of a large Fermi surface with a volume satisfying Luttinger's theorem.[20] This implies that, when a sufficient number of holes are doped into the insulator to make a metallic phase, these holes convert the localized copper spins into itinerant quasiparticles at low energies. Such a picture is also supported by various numerical calculations of the single-particle spectral functions in Hubbard-like models. This picture can be formally implemented in terms of the widely used large N approach to the extended Hubbard Hamiltonian equation (4) (here N is the spin degeneracy). Within the mean field theory, the constraint that there be no double occupancy of a copper site, as a consequence of strong Coulomb interactions, is manifested in the renormalization of the hybridization matrix element, $V_{pd} \to V_{pd}^*$, as well as of that of the copper level, $\epsilon_d \to \epsilon_d^*$. The quasiparticles of the system are described by the renormalized band. Compared to the noninteracting case, the renormalized band has an enhanced mass, and the density of states of the antibonding band has a large asymmetry with respect to the Fermi level.

We have chosen the bare band parameters so that (a) the plasma frequencies of the renormalized band fit those experimentally derived from the Drude-fitted optical conductivity.[21] This constraint assures that the band widths are reasonable; and (b) the correct Fermi surfaces are obtained for both LaSrCuO and YBaCuO. The Fermi surface in YBaCuO is rotated by 45° relative to the diamond shape expected in a nearest-neighbor tight binding, one band model.[20,22] The Fermi surface in LaSrCuO retains a diamond-like shape, though it is somewhat distorted so that the nearly flat regions are closer to the Γ point.[22] While the origins of these differences are not well understood, we are able to arrive at the correct Fermi surfaces through effectively modeling the oxygen dispersion appropriately. Such a modeling of the oxygen dispersion is expected to be reasonable for the discussion of the spin dynamics in the large U limit, since the spin degrees of freedom are mainly associated with the copper states. Finally, our renormalized band structure shows logarithmically divergent van Hove singularities in the single-particle density of states at $(\pm\pi,0)$ and $(0,\pm\pi)$. The separation of the energy at these wave vectors

from the Fermi energy introduces a van Hove energy, ω_{VH}. Due to the different shapes of the Fermi surfaces, ω_{VH} is found to be larger in YBaCuO, of the order of 25 meV, than that in LaSrCuO, which is less than 5 meV.

At a formal level, the superexchange interaction of the metallic phase can be established through analyzing the corrections to the mean field theory, beyond the leading order in $1/N$ expansion.[14] We found that, while the quasiparticle dispersion is determined by the renormalized copper level, ϵ_d^*, and the renormalized hybridization, V_{pd}^*, the relevant quantities for the calculation of the dominant superexchange interaction are the corresponding bare parameters, ϵ_d^0 and V_{pd}. This is not surprising since the superexchange interaction arises from the *virtual* occupancy of the high-lying excited states. A separation of energy scales, therefore, remains and the dominant antiferromagnetic interaction is insensitive to the oxygen dispersion and continues to have the nearest-neighbor form of Eq. (5) for both YBaCuO and LaSrCuO systems, despite their very different Fermi surface shapes.

The dynamical spin susceptibility is found to have the generalized random-phase approximation (RPA) form

$$\chi(\mathbf{q},\omega)\sim\frac{\chi_0(\mathbf{q},\omega)}{1+J(\mathbf{q})\chi_0(\mathbf{q},\omega)}, \tag{6}$$

where $\chi_0(\mathbf{q},\omega)$ is the Lindhard function associated with the renormalized quasiparticle energy dispersion $E(\mathbf{k})$. It should be noted that, this form of the dynamical susceptibility describes the contribution to the spin susceptibility due to the coherent (quasiparticle) part of the single-particle excitation spectra. The incoherent contribution becomes increasingly important at high energies where local-moment behavior is evidenced.

III. SPIN DYNAMICS IN THE NORMAL STATE

A. Wave vector dependence of the inelastic neutron scattering cross sections

In two-dimensional systems, the (dynamical) Kohn anomaly leads to peaks in the imaginary part of the Lindhard function at wave vectors $\mathbf{q}=2\mathbf{k}_F$.[15,23–25] In LaSrCuO, such a Kohn anomaly, along with the nesting enhancement, leads to incommensurate peaks at $\mathbf{Q}^*=\pi(1\pm\delta,1)$, $\pi(1,1\pm\delta)$ (Ref. 26) away from, but close to, $\mathbf{Q}_{AF}=(\pi,\pi)$, as is illustrated in the inset to Fig. 1(a). Since $-J(\mathbf{q})$ is peaked at $\mathbf{Q}_{AF}$, it enhances $\chi''(\mathbf{q},\omega)$ and hence $S(\mathbf{q},\omega)$ around an extended region in the Brillouin zone near $\mathbf{Q}_{AF}$. For moderate values of J_0/J_c (where J_c is the strength of the interaction which gives rise to an actual magnetic instability in the system), the four peak structure is enhanced with overall shape unchanged, as is clearly seen in Fig. 1(a). When projected along two of the four peaks, our results can be favorably compared to the experimental results of Refs. 11 and 12. We have also carried out a detailed analysis of the behavior of the incommensurability as a function of the doping concentration. The large value, together with the strong doping dependence, of the incommensurability observed experimentally[11] can be understood only when strong Coulomb interactions as well as a finite nearest-neighbor oxygen–oxygen hopping matrix element t_{pp} are included.

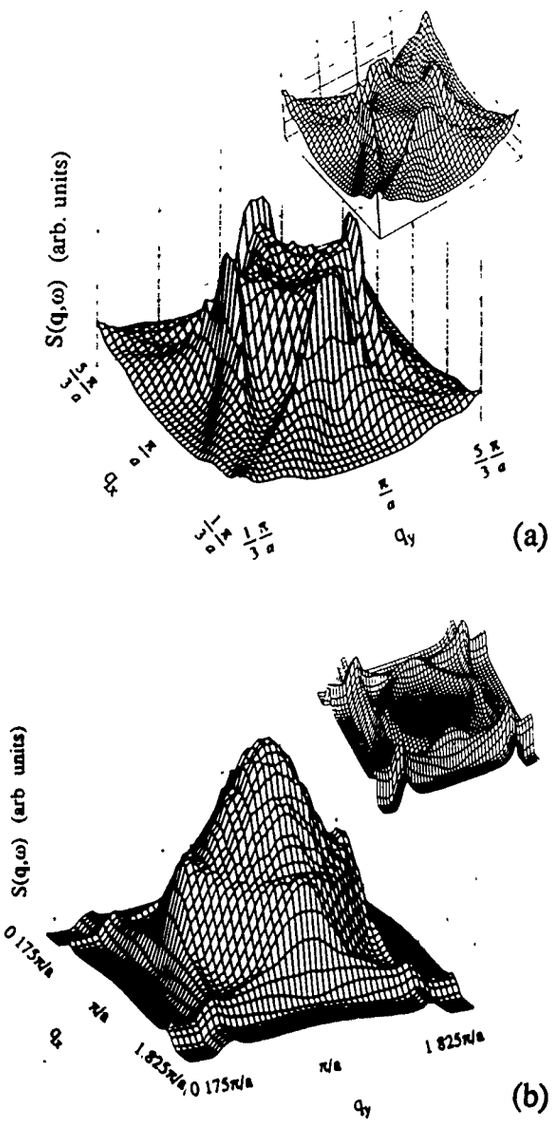

FIG. 1. Calculated $S(\mathbf{q},\omega)$ vs (q_x,q_y) (a) for $YBa_2Cu_3O_{6.7}$ with $J_0/J_c=0.7$ and (b) for $La_{1.82}Sr_{0.18}CuO_4$ with $J_0/J_c=0.6$. The insets give the corresponding results with $J_0=0$. Here the temperature and frequency are 1 and 10 meV, respectively.

We now study the spin dynamics in the YBaCuO family. The $\mathbf{q}$ structure of the Lindhard susceptibility corresponding to the appropriate renormalized band structure with a rotated Fermi surface is shown in the inset to Fig. 1(b). Because of the Fermi surface rotation, the Kohn anomaly induced—and nesting enhanced—peaks are far away from the antiferromagnetic wave vector $\mathbf{Q}_{AF}=(\pi,\pi)$. Therefore, the dynamical susceptibility is essentially featureless near $\mathbf{Q}_{AF}$. The antiferromagnetic interaction enhances the amplitude of $S(\mathbf{q},\omega)$ or $\chi''(\mathbf{q},\omega)$ in the region surrounding $\mathbf{Q}_{AF}$, leading to an essentially commensurate peak shown in Fig. 1(b). When projected along the diagonal direction, our results can be compared favorably to the experimental results of Refs. 9 and 10. Experimentally, in the fully oxygenated system, the half widths correspond to magnetic correlation lengths of around one lattice spacing[27,10] and in the deoxygenated case

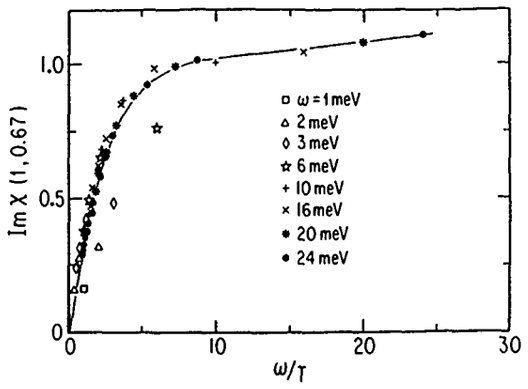

FIG. 2. Normalized $\chi''(\mathbf{q},\omega)$ as a function of ω/T for $La_{1.82}Sr_{0.18}CuO_4$ at the peak wave vector. The solid line represents the scaling curve.

$(YBa_2Cu_3O_{6,7})$ the corresponding length is around two lattice spacings.[9,10] Furthermore, the **q**-integrated structure factor is found to have essentially the same temperature dependence as that of the structure factor at $\mathbf{Q}_{AF}$.[9] In our theory, the fact that J is not particularly close to a magnetic instability yields a relatively broad peak whose width is essentially independent of temperature. This is in contrast with other theories in which longer and strongly temperature-dependent correlation lengths are assumed.[28,29]

The contrasting **q** dependences of the dynamical susceptibilities in LaSrCuO and YBaCuO, therefore, provide direct evidence that the particle-hole continuum associated with the renormalized quasiparticles gives the dominant contribution to the spin dynamics at low energies.

B. Temperature and frequency dependences of the dynamical spin susceptibility

The frequency and temperature dependences of the dynamical susceptibility in the present theory are discussed extensively in Ref. 17. The lowest energy scale is manifested as a weak peak in the frequency dependence of the neutron structure factor, and is found to correspond to the van Hove singularity energy ω_{VH}. Magnetic interactions of moderate strength lower the position of this peak, and considerably enhance the low energy spin fluctuation spectra. These low energy scales can also be illustrated in a scaling plot of the susceptibility in terms of ω/T. In Fig. 2, such a scaling plot is shown for susceptibilities calculated for LaSrCuO at the incommensurate peak position. Since ω_{VH} is small in LaSrCuO, we find that the dynamical susceptibility scales with ω/T until very low temperature and frequency. In YBaCuO system, ω_{VH} is considerably larger, $\omega_{VH}\sim 25$ meV. A deviation from scaling is predicted[16] for YBaCuO, when the frequency is smaller than ω_{VH} *and* the temperature smaller than $T_{VH}\sim\frac{1}{4}\omega_{VH}$. Recent experimental results from Ref. 9 seem to be consistent with this prediction for the case of YBaCuO.

C. NMR/NQR relaxation rates

We now turn to the analysis of the NMR/NQR data. Shown in Fig. 3(a) is the calculated temperature dependence of $1/T_1T$ at the copper site in deoxygenated YBaCuO. The

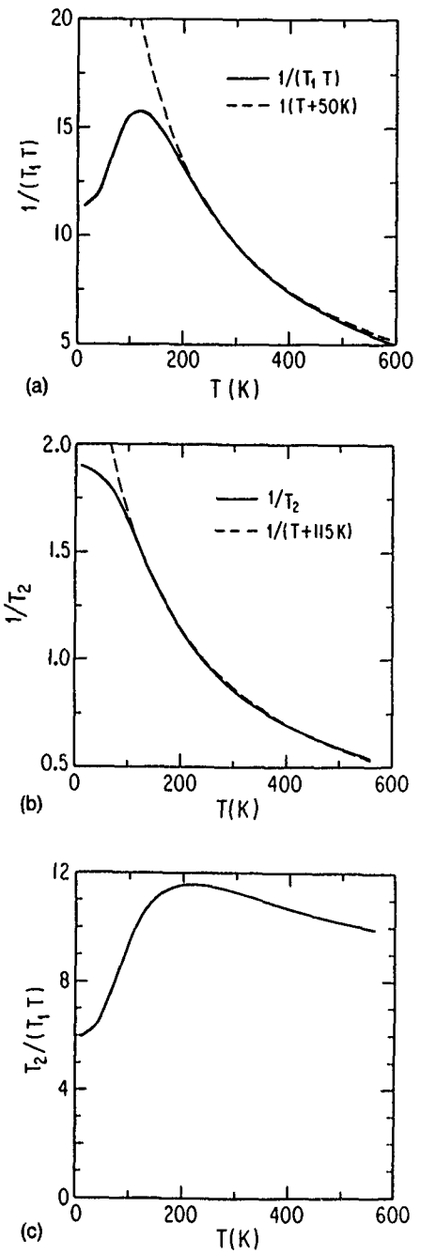

FIG. 3. Calculated temperature dependence of NMR relaxation rates in $YBa_2Cu_3O_{6.7}$: (a) $1/T_1T$; (b) $1/T_{2G}$; and (c) T_{2G}/T_1T. The vertical axes are in arbitrary units.

downturn at low temperatures reflects the van Hove energy scale ω_{VH}. (By contrast, this downturn is not present in the normal state of LaSrCuO since ω_{VH} is much smaller.) At high temperatures $1/T_1$ starts to saturate and $1/T_1T$ exhibits a Curie–Weiss temperature dependence. This temperature dependence is in reasonable agreement with experimental data, as is the enhanced magnitude. We emphasize that, within our analysis, the strong Coulomb correlations lead to two effects. They renormalize the quasiparticle energy spectrum, and induce residual exchange interactions between the quasiparticles. Because of this Coulomb-induced renormalization, we find that there is sufficient spin fluctuation spectral weight to explain the enhanced magnitude in $1/T_1$, without making the

assumption of proximity to a magnetic instability. In this way, we are able to explain both the neutron scattering and the Cu-site NMR results. In LaSrCuO system, this is consistent with the recent results of Walstedt and co-workers.[30] These authors have demonstrated that $(1/T_1)_{Cu}$ measured in the NMR experiments are in quantitative agreement with their counterparts calculated from the incommensurate peaks derived from the neutron scattering experiments.[11] As shown earlier, the incommensurate peaks arise from the the quasiparticle contributions; this quantitative agreement, therefore, reinforces the conclusion that low energy spin dynamics are dominated by quasiparticle contributions.

We have also calculated $1/T_{2G}$. As is seen in Fig. 3(b), a high temperature Curie--Weiss dependence is also reflected in $1/T_{2G}$, consistent with experimental results.[7] The Curie–Weiss behavior for both $1/T_1T$ and $1/T_{2G}$ also implies that the ratio T_{2G}/T_1T is weakly temperature dependent at high temperatures, as is seen in Fig. 3(c). The qualitative behavior is quite similar to the corresponding experimental plot of Takigawa.[7] In our calculations, the high temperature Curie–Weiss behavior for $1/T_1T$ and $1/T_{2G}$ results from the Curie–Weiss behavior for both $\chi'(\mathbf{q},\omega\rightarrow 0)$ and $\lim_{\omega\rightarrow 0}\chi''(\mathbf{q},\omega)/\omega$ over an extended region in the Brillouin zone around $\mathbf{Q}_{AF}=(\pi,\pi)$. The temperature scale is set by the fraction of the Fermi energy further lowered by the exchange enhancement factor. In this way, it reflects the proximity to Mott localization [which is incorporated in $\chi_0(\mathbf{q},\omega)$] *combined with* moderate magnetic interaction effects. By contrast, weak coupling calculations[29] assume that the system is very close to a magnetic instability; this soft spin fluctuation frequency then leads to these very low energy scales, as well as large magnitudes in $1/T_1$. Our result is also in contrast with the essentially temperature independent $1/T_{2G}$ calculated by Littlewood *et al.*[23] within a marginal Fermi liquid framework, in which the magnetic interaction between the quasiparticles is assumed to be zero.

In the strong coupling limit, the renormalized quasiparticle description is in essence a low temperature expansion. At sufficiently high temperatures, this description should break down; instead, the single particle excitations become incoherent, and the spin dynamics should cross over to a local-momentlike behavior. In this way a temperature-independent $1/T_1$ is expected at high temperatures. This physical picture is consistent with recent measurements of $1/T_1$ in LaSrCuO.[3] The situation is very similar to the spin dynamics in heavy fermion metals.[31,32] The precise local-moment dynamics for the cuprates are not known. Recently, based on the phase diagram for the 2D quantum nonlinear sigma model,[5] suggestions have been made that the high temperature local-moment dynamics in the metallic cuprates may show a universal behavior controlled by a zero temperature critical point.[33,34] In particular, a temperature-independent T_{2G}/T_1T has previously been shown to arise within this scheme.[34] In general, it is important to determine, in a given temperature regime, how much of the spin fluctuations can be attributed to the quasiparticle-quasihole continuum contribution, and how much to the local-moment contributions. Neutron scattering results at higher frequencies and temperatures should help clarify this issue, as the dynamical susceptibilities associated with these different contributions are expected to have different forms.

The situation for the oxygen site NMR relaxation rate is more complex. Because the peaks in the dynamical spin susceptibility are strongly *incommensurate* in LaSrCuO, and have a *broad* half-width in YBaCuO, a perfect oxygen form-factor cancellation, based on the transfer-coupling Hamiltonian,[35] is not expected in either system. In the present calculations, within the transfer-hyperfine coupling model, $(1/T_1)_O$ shows considerable deviation from a linear temperature dependence. In the context of the LaSrCuO system, similar conclusions have also been reached.[30] At present, it is not clear whether this means that our understanding about the hyperfine coupling associated with the oxygen nucleus is not complete or an important piece of physics is still missing.

To summarize, the contrasting spin dynamics in LaSrCuO and YBaCuO, and the consistency of the spin fluctuation spectral weights inferred from the neutron scattering cross sections and (Cu-site) NMR relaxation rates, lead us to conclude that, at low temperatures and frequencies the dominant spin fluctuations are described in terms of a particle-hole excitation spectrum associated with renormalized quasiparticles, which interact with each other through an antiferromagnetic interaction of moderate strength. At higher temperatures and frequencies, the relative contributions of the quasiparticle (coherent) part and the local-moment (incoherent) part remain to be determined.

IV. SPIN DYNAMICS IN THE SUPERCONDUCTING STATE

The application of Eq. (6) below T_c is straightforward. We have found that[18] the anomalous temperature dependences at low frequencies observed in neutron measurements[11,12,9] of $S(\mathbf{q},\omega)$ may be compatible with a $d_{x^2-y^2}$ pairing state in both LaSrCuO and YBaCuO. However there are problems with the wave vector dependences of $S(\mathbf{q},\omega)$. Of the two cases, the effects are more striking in YBaCuO. At the lowest temperatures all that contributes to the cross section are processes in which the Lindhard function is not fully "gapped out." These correspond to node-to-node scattering and because the nodal positions are unrelated to the Fermi surface nesting, these low T peaks will not be in the same position as their counterparts in the normal state. In this way the peaks in the structure factor move with decreasing T, from their high T positions to incommensurate positions along the zone diagonal. Similar observations were made first in Ref. 36. The failure of current experiments[11,12,9] to observe this shift in the peak position is thus not consistent with a (clean) d-wave picture.

Recently, similar calculations[37] were performed in the context of a weak-coupling Hubbard Hamiltonian with only first nearest-neighbor hopping integrals. In this case, the real part of $\chi_0(\mathbf{q},\omega)$ and, hence, the exchange enhancement, are strongly peaked at $\mathbf{Q}^*$ both for $T>T_c$ and for $T<T_c$. Therefore, the peak shifts will not occur; rather, the four peaks in the normal state are expected to become sharper. This is illustrated in Fig. 4(a). Such a sharpening of the peaks, however, is not seen experimentally.[11] Furthermore, we have

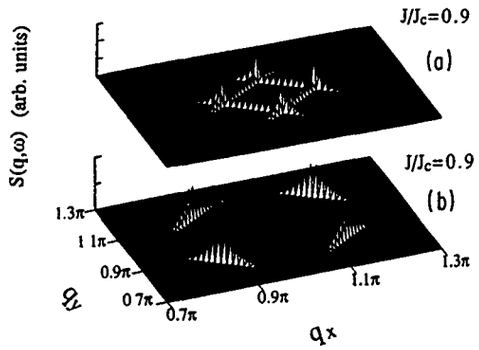

FIG. 4. Calculated $\chi''(\mathbf{q},\omega)$ vs (q_x,q_y) for the tight-binding band (a) with nearest-neighbor hopping only, $t'=0$, and $J/J_c=0.9$; and (b) with additional nonzero next-to-nearest-neighbor hopping term $t'=0.2t$ and $J/J_c=0.9$. Here $T=3$ K and $2\Delta_0/kT_c\sim 3$ 5.

found that this result is dependent on the specific features of the band structure. Our studies of this model and its three band extension reveal that, when moderately strong second nearest-neighbor hopping integrals are included, the exchange enhancement is no longer sharply peaked at $\mathbf{Q}^*$, and a shift in the position of the $\mathbf{q}$ dependent peaks occurs no matter how strong the exchange enhancements are. Such a second nearest-neighbor hopping matrix is necessary to arrive at more realistic Fermi surface shapes, correct Hall coefficient as well as to explain the large value of the incommensurability in the normal state.[17] In Fig. 4(b) we have plotted the corresponding result for $t'=0.2t$ with a very strong exchange enhancement, $J/J_c=0.9$; a shift of the peak positions is evident.

On this basis, it may be argued that magnetic data are not fully consistent with the d-wave picture. Nevertheless, one can not rule out the effects of impurity scattering which may smear the density of states and thereby affect the position of the $\mathbf{q}$-dependent peaks. It should be noted, however, that impurity effects in an anisotropic superconductor give rise to pair breaking and thereby a significant depression of T_c.[38] Furthermore, they should also be incorporated in the theoretical interpretations[36,39] of the Cu and O NMR data in $YBa_2Cu_3O_7$,[40] which have been argued to give strong support for a $d_{x^2-y^2}$ pairing state. Whether one can arrive at a "dirty d-wave" scenario for neutron and NMR data which at the same time leaves T_c unchanged has not yet been established.

ACKNOWLEDGMENTS

We thank A. Millis and M. Takigawa for helpful communications on the T_2 data. We acknowledge earlier collaboration with J. P. Lu and Ju Kim, and useful discussions with A. Chubukov, T. Imai, G. Kotliar, and A. Sokol. This work was supported by NSF DMR 91-20000

[1] R. J. Birgeneau and G. Shirane, in *Physical Properties of High Temperature Superconductors*, edited by D. M. Ginsberg (World Scientific, Singapore), Vol. I, p. 151.
[2] S. M. Hayden *et al.*, Phys. Rev. Lett. **67**, 3622 (1991).
[3] T. Imai *et al.*, Phys. Rev. Lett. **70**, 1002 (1993).
[4] R. R. P. Singh *et al.*, Phys. Rev. Lett. **62**, 2736 (1989).
[5] S. Chakravarty, in *High Temperature Superconductivity* edited by K. S. Bedell *et al.* (Addison–Wesley, New York, 1990), p. 136.
[6] C. H. Pennington and C. P. Slichter, in Ref. 1, Vol. II, p. 269.
[7] T. Imai *et al.*, Phys. Rev. B **47**, 9158 (1993); M. Takigawa, Phys. Rev. B **49**, 4158 (1994).
[8] M. Takigawa *et al.*, Physic: C **162–164**, 853 (1989)
[9] B. J. Sternlieb *et al.*, Phys Rev. B **47**, 5320 (1993), J. M. Tranquada *et al*, Phys. Rev. B **46**, 5561 (1992).
[10] J. Rossat-Mignod *et al*, Physica C **185–189**, 86 (1991); B **180–181**, 383 (1992).
[11] T. E. Mason *et al.*, Phys. Rev. Lett. **71**, 919 (1993); S -W. Cheong *et al.*, *ibid.* **67**, 1791 (1991).
[12] T. Thurston *et al.*, Phys. Rev. B **46**, 9128 (1992).
[13] B. Keimer *et al.*, Phys. Rev. Lett. **67**, 1930 (1991); S. M. Hayden *et al.*, *ibid.* **66**, 821 (1991).
[14] Q. Si, J. P. Lu, and K. Levin, Phys. Rev. B **45**, 4930 (1992), Physica C **162–164**, 1467 (1989).
[15] J. P. Lu, Q. Si, J. H. Kim, and K. Levin, Phys. Rev. Lett. **65**, 2466 (1990); Physica C **179**, 191 (1991).
[16] Y. Zha, Q. Si, and K. Levin, Physica C **201**, 289 (1992); **212**, 413 (1993).
[17] Q. Si, Y. Zha, K Levin, and J. P. Lu, Phys. Rev. B **47**, 9055 (1993).
[18] Y. Zha, K. Levin, and Q. Si, Phys. Rev. B **47**, 9124 (1993).
[19] C. Pennington and C. P Slichter, Phys. Rev. Lett. **66**, 381 (1991); D. Thelen and D. Pines, Phys. Rev. B **47**, 3528 (1993).
[20] J. C. Campuzano *et al.*, Phys Rev. Lett. **64**, 2308 (1990); R. Liu *et al.*, Phys. Rev. B **45**, 5614 (1992).
[21] J. Orenstein *et al.*, Phys. Rev. B **42**, 6342 (1990); M. Suzuki, in *Strong Correlation and Superconductivity*, edited by H. Fukuyama *et al.* (Springer, New York, 1989).
[22] J. H. Xu *et al.*, Phys. Lett. A **120**, 489 (1987); W. E. Pickett, R. E. Cohen, and H. Krakauer, Phys. Rev. B **42**, 8764 (1990).
[23] P. B. Littlewood, J. Zaanen, G. Aeppli, and H. Monien, Phys. Rev. B **48**, 487 (1993).
[24] P. Benard, L. Chen, and A.-M. S. Tremblay, Phys. Rev. B **47**, 15217 (1993).
[25] T. Tanamoto, H. Kohno, and H. Fukuyama, J. Phys. Soc. Jpn. **61**, 1886 (1992).
[26] H. J. Schulz, Phys. Rev. Lett. **64**, 1445 (1990)
[27] H. A. Mook *et al.*, Phys. Rev. Lett. **70**, 3490 (1993).
[28] A. J. Millis, H. Monien, and D. Pines, Phys. Rev. B **42**, 167 (1990).
[29] N. Bulut, D. Hone, D. J. Scalapino, and N. E. Bickers, Phys. Rev Lett. **64**, 2723 (1990); N. Bulut and D. J. Scalapino, *ibid.* **67**, 2898 (1991).
[30] R. E. Walstedt, B S. Shastry, and S.-W. Cheong, Phys. Rev. Lett **72**, 3610 (1994).
[31] K. Asayama, Y. Kitaoka, and Y. Kohori, Physica B **171**, 226 (1991)
[32] Q. Si, J. H Kim, J. P. Lu, and K. Levin, Phys Rev. B **42**, 1033 (1990).
[33] A. V. Chubukov and S. Sachdev, Phys. Rev. Lett. **71**, 169 (1993).
[34] A. Sokol and D. Pines, Phys. Rev. Lett. **71**, 2813 (1993).
[35] B. S. Shastry, Phys. Rev Lett. **63**, 1288 (1989).
[36] J. P. Lu, Phys. Rev. Lett. **68**, 125 (1992); Mod. Phys. Lett. B **6**, 547 (1992).
[37] N. Bulut and D. J. Scalapino, preprint (1993).
[38] R. J. Radtke *et al.*, Phys. Rev. B **48**, 653 (1993); similar results have been obtained by P. Monthoux and D. Pines.
[39] N. Bulut and D. J. Scalapino, Phys. Rev. Lett. **68**, 706 (1991).
[40] J. A. Martindale *et al.*, Phys. Rev. Lett. **68**, 702 (1992).

Hydrostatic pressure on $HgBa_2CaCu_2O_{6+\delta}$ and $HgBa_2Ca_2Cu_3O_{8+\delta}$

F. Chen, L. Gao, R. L. Meng, Y. Y. Xue, and C. W. Chu
Department of Physics and Texas Center for Superconductivity, University of Houston, Houston, Texas 77204-5932

The superconducting transition temperature T_c and its pressure dependence dT_c/dP of $HgBa_2CaCu_2O_{6+\delta}$ (Hg-1212) and $HgBa_2Ca_2Cu_3O_{8+\delta}$ (Hg-1223) were measured up to 17 kbar. T_c increases with pressure approximately linearly for both compounds before oxidation. However, the nonlinearity in the T_c-P correlation shows up after oxidation in both compounds. For Hg-1212, the average dT_c/dP decreases as oxygen doping increases, while it increases in Hg-1223. These observations are in conflict with the modified pressure-induced charge-transfer model, but might be attributed to the possible existence of fine electronic structure. These observations suggest that a T_c much higher than 140 K might be achievable in Hg-1223 by means of higher physical or chemical pressure.

I. INTRODUCTION

Previous pressure studies on high T_c cuprates at various oxidation states show that the T_c changes linearly at pressures between 0 and 20 kbar.[1] This can usually be explained by pressure-induced charge-transfer,[2] i.e., dT_c/dP decreases with the carrier concentration n, which increases with oxidation. Soon after the discovery of the superconducting homologous series $HgBa_2Ca_{n-1}Cu_nO_{2n+2+\delta}$ [Hg-12(n-1)n],[3] band-structure calculations showed that the electronic structure of these compounds was strongly affected by the van Hove singularity and evolved with doping rather abnormally,[4] suggesting that their pressure effect dT_c/dP might be unusual. After samples of these compounds with different oxygen stoichiometry became available, we systematically studied their pressure dependence.

A positive dT_c/dP was observed in all $HgBa_2CaCu_2O_{6+\delta}$ (Hg-1212) and $HgBa_2Ca_2Cu_3O_{8+\delta}$ (Hg-1223) samples. For the as-prepared Hg-1212 samples with $T_c \sim 112$ K, T_c increased linearly with pressure at a rate $dT_c/dP = 0.22 \pm 0.02$ K/kbar throughout our pressure range. For oxygenated Hg-1212 samples with $T_c \sim 119$ K, T_c increases with pressure at a similar rate below ~4 kbar, but the rate of increase decreases to 0.11 ± 0.02 K/kbar thereafter. Although the nonlinear T_c-P correlation is rather unusual, the smaller average dT_c/dP after oxygenation is consistent with the charge-transfer model,[2] which suggests that the average dT_c/dP decreases with the carrier concentration n. The dT_c/dP of several Hg-1223 samples was also measured. The dT_c/dP of vacuum-annealed and as-synthesized samples was independent of P. However, the T_c vs P of oxygenated Hg-1223 shows positive curvature above 12 kbar. Unlike that for Hg-1212, the overall dT_c/dP for Hg-1223 increases with oxidation, which is in direct conflict with the modified charge-transfer model.[2]

II. EXPERIMENT

High quality samples were prepared using the controlled vapor/solid reaction (CVSR) technique.[5] The samples are ~90% pure with ~10% $CaHgO_2$ and $Ba_2Cu_3O_{5+\delta}$ impurities. Structure characterization was carried out by x-ray diffraction using a Rigaku D-MAX/BII powder diffractometer. The dc magnetic susceptibility (χ_{dc}) of samples at ambient pressure was measured by a quantum design superconducting quantum interference device (SQUID) magnetometer. A standard inductance bridge, operated at 16 Hz in an ac field of ~5 Oe peak to peak, was employed to determine the ac magnetic susceptibility (χ_{ac}) under pressures. The standard four-lead measurement was applied to measure resistivity. Hydrostatic pressure up to 18 kbar was generated at room temperature inside a Teflon cup housed in a Be-Cu high pressure clamp,[6] using 3M Fluorinert as the pressure medium. The pressure was determined by a Pb-manometer placed next to the sample. The temperature was measured by an alumel-chromel thermocouple above 30 K and a Ge thermometer below 30 K.

III. RESULTS AND DISCUSSION

Four samples of Hg-1212 were characterized. Samples A and C were as synthesized with $T_c \sim 112$ K. Samples B and D were annealed in 1 atm O_2 at 300 °C for 30 h with $T_c \sim 119$ K and were determined to be overdoped. The χ_{dc} of samples A, B, and D are shown in Fig. 1. The transition is quite sharp and the superconducting volume fraction is large (especially for sample D). The onset and midpoint of T_c (T_{co} and T_{cm}) as determined by ac-susceptibility measurements at various pressures are shown in Fig. 2. The T_{co}'s of sample A and C have the same trend as the T_{cm}'s although they are not shown in the figure. The T_{cm} of sample D is not well defined due to poor grain coupling and thus not shown. T_c increases linearly with P at a rate of 0.22 ± 0.02 K/kbar for samples A and C. For samples B and D, T_c increases at a rate of ~0.23 K/kbar below 4 kbar. The rate fell to 0.11 ± 0.03 K/kbar above 4 kbar. As proposed by the modified charge-transfer model,[2] the overall dT_c/dP decreases as oxidation increases.

Five samples from two different batches of Hg-1223 were also examined. Sample V was as synthesized with $T_c \sim 117$ K. Sample W, with $T_c \sim 79$ K, was obtained by high vacuum annealing at 450 °C for 1 day. Samples X, Y, and Z were annealed in flowing oxygen at 300 °C for 1 day, with $T_c \sim 135$ K. Figure 3 shows T_c versus pressure for Hg-1223. The T_c's for samples V, X, Y, and Z were measured resistively. Although we only plotted T_{cm} for these samples, the behavior of T_{co} and T_{cz} (zero point of the transition) is similar. A long tail in the superconducting transition was ob-

 0021-8979/94/76(10)/6941/3/$6.00 © 1994 American Institute of Physics

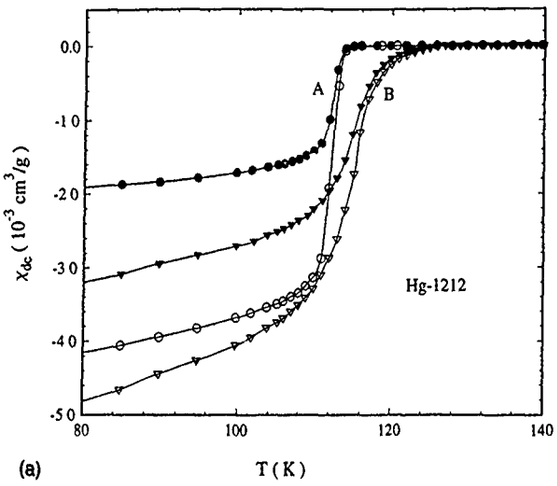

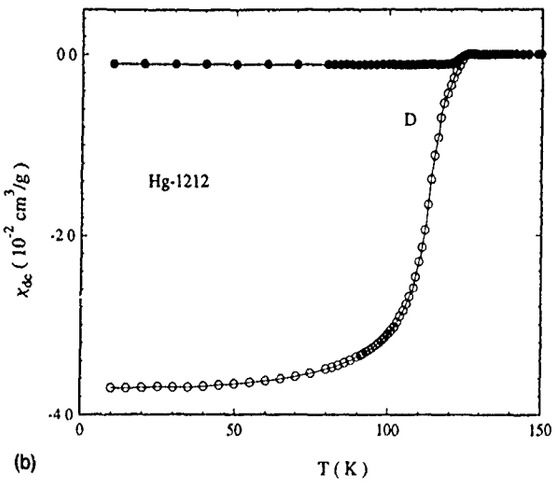

FIG. 1. (a) χ_{ac} vs T for Hg-1212 sample A and B. (b) χ_{dc} vs T for Hg-1212 sample D. Filled symbol: field cooling; open symbol: zero-field cooling.

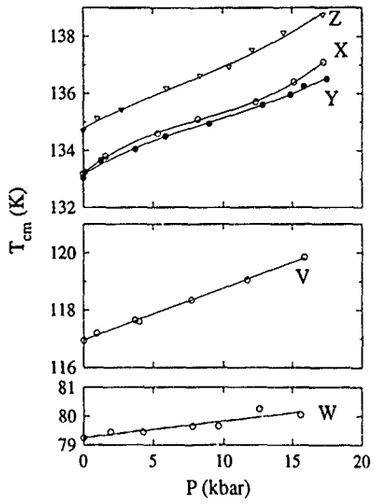

FIG. 3. T_{cm} vs P for Hg-1223 samples V, W, X, Y, and Z.

served for the sample W, which might be due to damage caused to the grain boundaries during annealing. Therefore, the T_c of this sample was measured magnetically and T_{cm} was obtained from the peak of $d\chi_{ac}/dT$. We can see clearly that the average dT_c/dP increases with oxidation. From thermoelectric measurements, we extracted the carrier concentration n by an empirical law.[7] Figure 4 shows the average dT_c/dP vs n for Hg-1212 and Hg-1223.

Recently, a study[2] of combined effects of pressure and doping on $(Y,Ca)(Ba,Ca)_2Cu_3O_{7-\delta}$ compounds shows that pressure-induced charge-transfer alone cannot explain the observed results and an "intrinsic" pressure effect on T_c is included. This term, $dT_{c,\max}/dP$, is assumed to be independent of P and n. Thus, the empirical modified pressure-induced charge-transfer model can be written as

$$T_c(n,P) = T_{c,\max}(n_{\text{optimal}},0) + (dT_{c,\max}/dP)\times P + A\times[(n-n_{\text{optimal}}) + (dn/dP)\times P]^2,$$

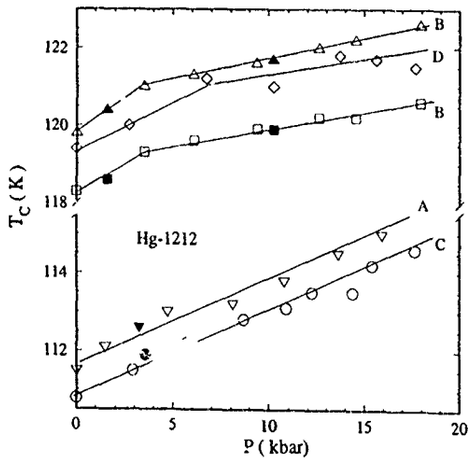

FIG. 2. T_c vs P for Hg-1212. △: T_{co} for sample B, ◇: T_{co} for sample D; □: T_{cm} for sample B, ▽. T_{cm} for sample A; ○· T_{cm} for sample C. Filled symbol obtained on pressure reduction.

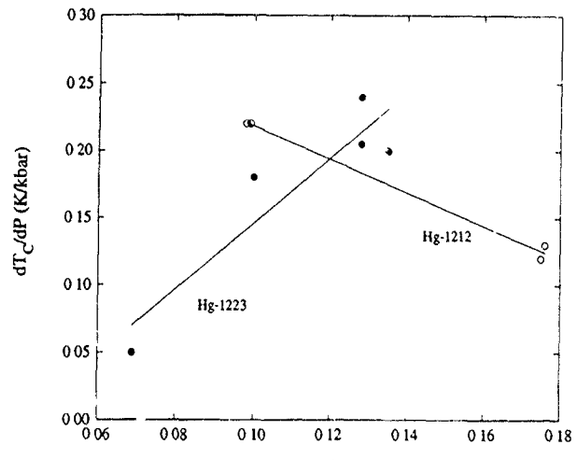

FIG. 4. dT_c/dP vs n for Hg-1212 and Hg-1223.

where A is a negative compound-dependent constant. By ignoring higher order contributions, the pressure effect on T_c becomes

$$dT_c/dP = dT_{c,\max}/dP + 4A \times dn/dP \times (n - n_{\text{optimal}}),$$

which should decrease with n (oxidation), since $dn/dP > 0$ (which has been demonstrated by the negative $d\rho/dP$, positive dR_H/dP;[8] where ρ is normal state resistivity and R_H is the Hall coefficient). However, the average dT_c/dP increases with n in Hg-1223, despite the negative $d\rho/dP$ over the whole P range. This is in direct conflict with the model[2] and suggests that $dT_{c,\max}/dP$ should be P and/or n dependent. The ever increasing dT_c/dP with P after oxidation (cf. Fig. 3) suggests that the T_c of Hg-1223 can be enhanced further by applying pressures up to 500 kbar.[9]

In summary, we investigated the pressure effect on samples of Hg-1212 and Hg-1223 with different oxygen contents. We found that the pressure effect becomes rather nonlinear after oxidation. Although a modified charge-transfer model can explain the pressure effect on Hg-1212, it is in direct conflict with the observation on Hg-1223. The positive dT_c/dP for all the samples suggests that high T_c is optimistic.

ACKNOWLEDGMENTS

This work is supported by NSF Grant No. DMR 91-22043, USAFOSR Grant No. F49620-93-1-0310 from BMDO, ARPA Grant No. MDA 972-90-J-1001, the State of Texas through the Texas Center for Superconductivity at the University of Houston, and the T. L. L. Temple Foundation.

[1] J. S. Schilling and S. Klotz, in *Physical Properties of High Temperature Superconductors III*, edited by D. M. Ginsberg (World Scientific, Singapore, 1992), p. 84.
[2] J. J. Neumeier and H. A. Zimmermann, Phys. Rev. B **47**, 8386 (1993).
[3] S. N. Putilin, E. V. Antipov, O. Chmaissem, and M. Marezio, Nature **362**, 226 (1993).
[4] D. L. Novikov, V. A. Gubanov, and A. J. Freeman, Physica C **210**, 301 (1993); D. L. Novikov and A. J. Freeman, Physica C **216**, 273 (1993).
[5] R. L. Meng, L. Beauvais, X. N. Zhang, Y. Y. Sun, J. Kulik, Y. Y. Xue, and C. W. Chu, Physica C **216**, 21 (1993).
[6] C. W. Chu, Phys. Rev. Lett. **33**, 1283 (1974).
[7] S. D. Obertelli, J. R. Cooper, and J. L. Tallon, Phys. Rev. B **46**, 14928 (1992).
[8] C. Murayama, Y. Iye, T. Enomoto, A. Fukushima, N. Môri, Y. Yamada, and T. Matsumoto, Physica C **185-189**, 1293 (1991).
[9] L. Gao, Y. Y. Xue, F. Chen, Z. J. Huang, R. L. Meng, and C. W. Chu, Nature **365**, 323 (1993).

Magnetoconductivity of $Bi_2Sr_2Ca_{1-x}Y_xCu_2O_{8+\delta}$ in fluctuation regime

C. P. Dhard and S. N. Bhatia
Department of Physics, Indian Institute of Technology, Bombay 400 076, India

P. V. P. S. S. Sastry and J. V. Yakhmi
Chemistry Division, Bhabha Atomic Research Centre, Bombay 400 085, India

A. K. Nigam
Tata Institute of Fundamental Research, Bombay 400 005 India

The magnetoconductivity of polycrystalline $Bi_2Sr_2Ca_{1-x}Y_xCu_2O_{8+\delta}$, $x=0$, 0.05 and 0.20 samples in the magnetic field of 4 T was measured. The excess conductivity has been analyzed in the light of Aronov–Hikami–Larkin and Bieri–Maki formalisms together with Thompson's correction of the Zeeman term of both theories. The later theory was found within the clean limit to describe the data adequately and yielded the estimate for the phase braking time $\tau_\phi \simeq 1\times10^{-13}$ s. The Maki–Thompson–Zeeman contribution ($\Delta\sigma_{MTZ}$) in these samples is found to be negligible.

The short coherence length coupled with the high transition temperature provide an excellent opportunity to study the rounding of the transition in the oxide superconductors. The fluctuation enhanced conductivity, i.e., excess conductivity ($\Delta\sigma$) in zero field is representable by the Aslamazov–Larkin (AL) and Maki–Thompson (MT) terms.[1] The magnetic field affects the excess conductivity through the orbital angular momentum giving rise to AL-orbital ($\Delta\sigma_{ALO}$) and MT-orbital ($\Delta\sigma_{MTO}$) terms and through the spin angular momentum yielding AL-Zeeman ($\Delta\sigma_{ALZ}$) and MT-Zeeman ($\Delta\sigma_{MTZ}$) terms. Aronov, Hikami, and Larkin[2] (AHL) have derived the expressions for these terms from the standard theory in the dirty limit. However this theory is not applicable to high T_c superconducting (HTSC) materials as they fall within the clean limit with the mean free path $l \geqslant \xi_{ab}(0)$ [$l \simeq 100$ Å and $\xi_{ab}(0) \simeq 15$ Å for $YBa_2Cu_3O_7$ (YBCO)]. Later Bieri and Maki[3] (BM) proposed another theory of $\Delta\sigma(H)$ which was valid for the clean limit but it gave results identical to the AHL theory. Both AL contributions are not sensitive to the mean free path of the electrons. Therefore, their values remain essentially unchanged in both dirty and clean limits. However the MT contribution depends sensitively on l since the vertex renormalization is essentially controlled by l in the clean limit. The expressions obtained by Bieri and Maki[3] in this limit for all the four terms are identical to the AHL expressions with the difference that the terms $\Delta\sigma_{ALZ}$ and $\Delta\sigma_{MTZ}$ had $(\omega_s/4\pi kT)^2$ instead of $(\omega_s/4\pi kT_c)^2$ as their prefactors and δ was defined by $\delta = 1.203[l/\xi_{ab}(0)]\delta_{AHL}$, where δ_{AHL} is given by (Ref. 2) $\delta_{AHL} = 16\xi_c^2(0)kT\tau_\phi/\pi d^2\hbar$. Later it was pointed out by Thompson[4] that both these theories were wrong in treating the Zeeman splitting energy, correction to this leaves the three terms, viz., $\Delta\sigma_{ALO}$, $\Delta\sigma_{MTO}$, and $\Delta\sigma_{ALZ}$ unchanged but modifies the fourth $\Delta\sigma_{MTZ}$.

Experimentally almost all the attention appears to have been focused on YBCO only and to the best of our knowledge no attempt has been made to study the $Bi_2Sr_2CaCu_2O_{8+\delta}$ (BSCCO) system in this light. Earlier Matsuda *et al.*[5] analyzed the magnetoconductivity of YBCO thin films in terms of AHL formalism without Thompson correction. All four contributions were required giving the value of the phase breaking time $\tau_\phi \simeq 10^{-13}$ s at 100 K. However Semba *et al.*[6] found no evidence for the $\Delta\sigma_{MTZ}$ in their data on single crystals of YBCO. They found $\tau_\phi \simeq 5\times10^{-14}$ s which is the shortest time reported so far. Sugawara *et al.*[7] have analyzed their $\Delta\sigma(H)$ data measured on chemical vapor deposition (CVD) films of YBCO in BM theory with Thompson's correction[8] (BMT), and find the $\Delta\sigma_{MTZ}$ term to be essential in both the $\Delta\sigma(H)$ vs $\epsilon[=(T-T_c^{mf})/T_c^{mf}, T_c^{mf}$ is the mean field transition temperature] as well as $\Delta\sigma(H)$ vs H data. In polycrystalline YBCO Matsuda *et al.*[9] also found vanishing values of $\Delta\sigma_{MTZ}$ using uncorrected AHL expressions. And our recent analysis on similar samples in the light of corrected AHL/BM expressions support these results.[10]

We have measured the magnetoconductivity of polycrystalline $Bi_2Sr_2Ca_{1-x}Y_xCu_2O_{8+\delta}$ samples with $x=0$, 0.05, and 0.20 and find the $\Delta\sigma_{MTZ}$ contribution to be negligible.

The samples were prepared by the matrix precursor method by reacting Bi_2O_3 with a $Sr_2CaCu_2O_8$ precursor in the presence of O_2 at 900–950 °C. All the samples were confirmed to be of single phase by x-ray diffraction (XRD). dc conductivity was measured by the four probe method on bar shaped samples.[1] The current density used was typically 0.1 A/cm^2. Samples were so oriented that the measuring current was perpendicular to the applied field. The sample temperature was measured with a Si diode/CGR thermometer placed in contact with the sample in a copper holder, and was raised at the rate of 2 K/h. The data were taken at the interval of 20 mK within the transition region.

At high temperatures ($T \geqslant 2T_c$) the zero field and the field data coincide for all the samples implying negligible magnetoresistance to be present in the normal state and below T_c^{mf} the transition broadens in the field. A field of 4 T was used because for the higher fields the orbital terms show deviations from the H^2 behavior predicted by the above theories.[2,3] In zero field, a single sharp peak in $d\rho/dT$ is symmetrical about the temperature T_{max} of its maximum, whereas in the field this curve spreads towards lower temperatures. This spread is around 35 K for $x=0$ and increases further with the Y concentration.

We have analyzed the total fluctuation conductivity $\Delta\sigma_f(H) = [\sigma(H,T) - \sigma_n(H,T)]$ where $\sigma_n(H,T) = 1/\rho_n(H,T)$ is the background conductivity. $\Delta\sigma_f(H)$ contains the zero field conductivity (Ref. 11) $\Delta\sigma(0)$ and the modifications produced in it by the magnetic field. The esti-

 0021-8979/94/76(10)/6944/3/$6 00 © 1994 American Institute of Physics

TABLE I. Various fitted physical parameters for BSCCO samples in the clean and dirty limit. τ_ϕ, τ, and l are calculated at 100 K. In BM, $\xi_c(0)$ and $\xi_{ab}(0)$ are constants, whereas in BMT-d(dirty) and BMT-c(clean) these are temperature dependent.

	$\xi_c(0)$ (Å)	$\xi_{ab}(0)$ (Å)	τ_ϕ (10^{-13} s)	τ (10^{-14} s)	l (Å)
$x=0$					
AHL	1.9	10.0	1.0	1.0	
BM	2.3	9.1	1.3	5.3	
BMT-d	1.8	9.9	0.81	0.13	9.8
BMT-c	1.8	8.9	0.11	5.3	52.5
$x=0.05$					
AHL	2.5	11.4	4.0	1.1	
BM	2.6	10.2	1.7	5.3	
BMT-d	1.8	9.9	0.86	0.16	11.0
BMT-c	1.8	8.6	0.12	5.3	58.6
$x=0.20$					
AHL	3.2	12.8	6.0	1.3	
BM	3.1	11.8	2.0	5.3	
BMT-d	1.9	10.4	0.86	0.18	11.5
BMT-c	1.9	10.4	0.12	5.3	61.2

mation of background conductivity $\sigma_n(H,T)$ have been discussed in detail in Ref. 1.

The experimental data of $\Delta\sigma_f(H,T)$ of $x=0$ was first fitted to the combined expressions of zero field AL and MT terms and field dependent AHL expressions of AL and MT terms with Thompson's correction by taking $\xi_c(0)$, $\xi_{ab}(0)$, and τ_ϕ as the adjustable parameters. τ_ϕ was assumed to vary as $\tau_\phi=\tau_{\phi 0}/T$ where $\tau_{\phi 0}$ is a constant. The values of fitted parameters are shown in Table I. Good agreement can be obtained with $\xi_c(0)=1.9$ Å, $\xi_{ab}(0)=10.0$ Å, and $\tau_\phi=1\times10^{-13}$ s. The value of $\xi_c(0)$ agreed with that obtained from the zero field data.[1] The agreement further improved when BM equations with Thompson's correction were used and the mean free path l was allowed to vary with temperature as $l=l_0/T$ where l_0 is a constant. Here in the clean limit $\xi_c(0)$, $\xi_{ab}(0)$, and $l_0\tau_{\phi 0}$ were taken as the free parameters. $\xi_c(0)$ slightly increased to 2.3 Å and $\xi_{ab}(0)$ decreased to 9.1 Å. We obtained $l_0\tau_{\phi 0}=6.8\times10^{-8}$ Å s. To get an estimate of τ_ϕ from this product, we note that $l=\tau v_F=\tau_0 v_F/T$ (i.e., $l_0=\tau_0 v_F$) where τ is the transport relaxation time and v_F the Fermi velocity of the carriers. The later is estimated as $(0.6-1.6)\times10^7$ cm/s from the relation $\xi_{ab}(0)=\hbar v_F/\pi\Delta$ with the in-plane energy gap parameter given[12] by $2\Delta/kT_c=3.5-8$. Now assuming $\tau_\phi\simeq\tau$ this product yields τ_ϕ (100 K)$\simeq1.3\times10^{-13}$ s for the lowest estimate of v_F, i.e., $v_F=0.6\times10^7$ cm/s. This compares well with the value obtained by Sugawara *et al.*[7] Batlogg,[12] from the resistivity data, has obtained $\tau=\hbar/1.35kT=5.4\times10^{-12}/T$. With $v_F\simeq10^7$ cm/s, this yields $\tau_\phi(100\ K)\simeq5\times10^{-14}$ s from our estimates of $l_0\tau_{\phi 0}$ and the τ_ϕ/τ comes out to be $\simeq2.3$.

BMT[8] have further also assumed $\xi_c(0)$ and $\xi_{ab}(0)$ to be temperature dependent along with l, for both dirty and clean limits. Assuming these temperature variations, values of the parameters obtained are listed in Table I. Both the limits give identical values of $\xi_c(0)$ as 1.8 Å whereas $\xi_{ab}(0)$ works out to be $\simeq9$ Å and $\simeq10$ Å for the dirty and clean limits, respectively, at 100 K. These values agree with those obtained by BMT on single crystals of YBCO. Our analysis yields $\tau_\phi/\tau=0.2$ and $v_F=7\times10^6$ cm/s for the clean limit using the Batlogg's[12] value of τ. This is the clean limit τ and therefore

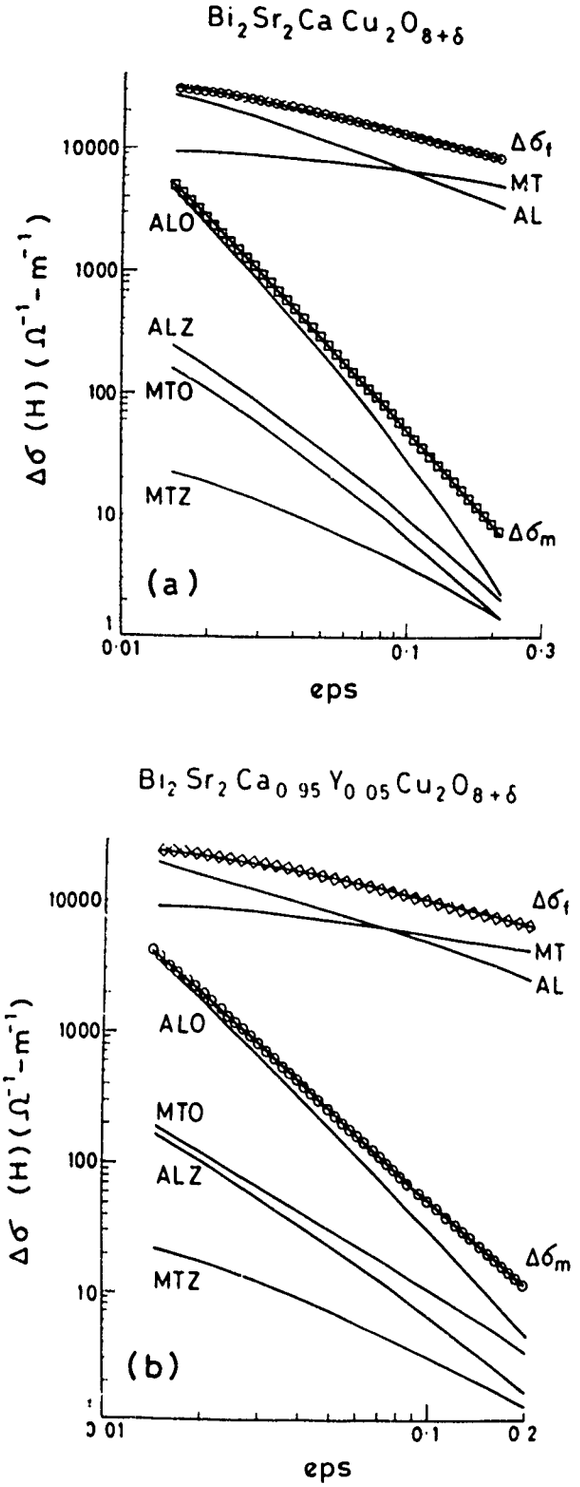

FIG. 1. Fluctuation and magnetoconductivity of BSCCO $x=0$ and 0.05 in (a) and (b). In (a) $\xi_c(0)$ and $\xi_{ab}(0)$ are temperature dependent while in (b) they are constants. Note the change in relative order of ALZ and MTO contributions in (a) and (b). All the four contributions to $\Delta\sigma(H,T)$, i.e., ALO, MTO, ALZ, and MTZ and the excess magnetoconductivity $\Delta\sigma_m$ displayed here, are negative in magnitude.

cannot be used in the dirty limit as has been used conventionally. To estimate τ in the dirty limit we assumed $v_F=1\times10^7$ cm/s. We get $\tau_\phi\simeq1\times10^{-13}$ and τ in this limit$=\tau_d=1.3\times10^{-15}$ s. Thus $\tau_\phi/\tau_d\simeq62$. This ratio is too large. τ_d appears to be too small, its reasonable value should be a smaller fraction of τ. If v_F is reduced further the ratio τ_ϕ/τ also gets reduced but it still remains too high. In the case of AHL τ is also very small. As this theory is valid for the dirty case, l will be $\simeq\xi_{ab}(0)$. With $v_F\simeq10^7$ cm/s this yields $\tau_d\simeq1\times10^{-14}$ s and $\tau_\phi/\tau_d\simeq10$.

Two points are to be noted about this analysis. The data has been fitted over the range $0.01\leqslant\epsilon\leqslant0.2$ and the nonlocal effects have not been included. These effects apparently become visible at $\epsilon\geqslant0.25$ as shown by BMT.

The magnetoconductivity obtained by subtracting $\Delta\sigma_{AL}(0)$ and $\Delta\sigma_{MT}(0)$ from $\Delta\sigma_f(H,T)$ is displayed in Fig. 1(a) along with the calculated values of the four field dependent contributions. $\Delta\sigma_{MTZ}$ has the smallest value over the entire ϵ range, being less than 1% of the total $\Delta\sigma_f(H,T)$. The fit does not deteriorate when the term $\Delta\sigma_{MTZ}$ is dropped altogether. However the rms deviation jumps when the next larger term $\Delta\sigma_{ALZ}$ is dropped. This result is in conformity with our previous conclusion[10] on polycrystalline YBCO (measured at 4 T) and with Semba *et al.*[6] and Matsuda *et al.*[9] who also found $\Delta\sigma_{MTZ}$ to be negligible in their magnetoconductivity of single crystal and polycrystalline YBCO, respectively, measured at 1 T. However Sugawara *et al.*[7] found this term to be present as a substantial fraction of the total magnetoconductivity at 13 T. Since the BMT equations predict each of the four contributions to be proportional to $-H^2$, the relative magnitude of $\Delta\sigma_{MTZ}$, i.e., the ratio $\Delta\sigma_{MTZ}/(\Delta\sigma_{ALO}+\Delta\sigma_{MTO}+\Delta\sigma_{ALZ}+\Delta\sigma_{MTZ})$ will not increase with H and will be a function of ϵ and τ_ϕ only. In actual practice since $\Delta\sigma_{ALO}$ and $\Delta\sigma_{MTO}$ show some saturation at high fields near T_c(at $\epsilon\leqslant0.015$) the ratio may increase at such fields. For the present data the equations predict the ratio to be less than 1% over the entire ϵ range of the data, i.e., for $0.05\leqslant\epsilon\leqslant0.2$, and to remain at negligible levels even when τ_ϕ is increased to $\simeq10^{-13}$ s. The anisotropy ratio $(\Delta\sigma_{MTZ}+\Delta\sigma_{ALZ})/(\Delta\sigma_{ALO}+\Delta\sigma_{MTO}+\Delta\sigma_{ALZ}+\Delta\sigma_{MTZ})$ works out to be 5.6 at $\epsilon=0.05$ and $\Delta\sigma_{MTZ}$ forms 10% of this ratio.

The magnetoconductivity of the $x=0.05$ and 0.20 samples behaves identically. The plot for $x=0.05$ is shown in Fig. 1(b). $\Delta\sigma_{MTZ}$ here is also negligible and the neglect of this term does not alter the fits in any of these samples. Though the AHL theory gives reasonable estimates of τ_ϕ, it underestimates τ thus yielding a very large value for the ratio τ_ϕ/τ. This ratio is similarly overestimated in the BMT dirty limit and underestimated in its clean limit. Only when $\xi_c(0)$ and $\xi_{ab}(0)$ are taken as temperature independent does this theory yield reasonable estimates of τ_ϕ/τ. The values are listed in Table I. All the parameters, viz., τ_ϕ, $\xi_c(0)$ and $\xi_{ab}(0)$, etc., increase systematically with Y concentration. τ_ϕ shows a slight increase with Y doping but still $\Delta\sigma_{MTZ}$ remains negligible. However this increase in τ_ϕ increases the magnitude of the $\Delta\sigma_{MTO}$ relative to those of the other two. Instead of being the smallest term as in the Y-free sample, it over takes $\Delta\sigma_{ALZ}$ and becomes the second largest term.

In summary our analysis of the magnetoconductivity of Y-doped polycrystalline BSCCO suggests the absence of $\Delta\sigma_{MTZ}$ contributions for the fields up to 4 T. The other three terms $\Delta\sigma_{ALO}$, $\Delta\sigma_{MTO}$, and $\Delta\sigma_{ALZ}$ all contribute significantly. Due to the absence of $\Delta\sigma_{MTZ}$ the validity of the Thompson correction could not be verified. Though BMT theory appears to agree with experiments, for a better estimate of τ_ϕ prior knowledge of some of the parameters, $\xi_c(0)$, $\xi_{ab}(0)$, or v_F, will be useful. Data further appear to favor the temperature independent value of $\xi_c(0)$ and $\xi_{ab}(0)$ and discard their functional forms given by the BMT equations.

[1] S. N. Bhatia and C. P. Dhard, Phys. Rev. B **49**, 12206 (1994).
[2] A. G. Aronov, S. Hikami, and A. I. Larkin, Phys. Rev. Lett **62**, 965 (1989); **62**, 2336(E) (1989).
[3] J. B. Bieri and K. Maki, Phys. Rev. B **42**, 4854 (1990)
[4] R. S. Thompson, Phys. Rev. Lett. **66**, 2280 (1991).
[5] Y. Matsuda, T. Hirai, S. Komiyama, T. Terashima, Y Bando, K. Iijima, K. Yamamoto, and K. Hirata, Phys. Rev. B **40**, 5176 (1989).
[6] K. Semba, T. Ishii, and A. Matsuda, Phys. Rev Lett. **67**, 769 (1991).
[7] J. Sugawara, H. Iwasaki, N. Kobayashi, H. Yamane, and T. Hirai, Phys. Rev. B **46**, 14 818 (1992).
[8] J. B. Bieri, K. Maki, and R. S. Thompson, Phys. Rev. B **44**, 4709 (1991)
[9] A. Matsuda and K. Semba, Physica C **185–189**, 797 (1991).
[10] S. N. Bhatia and C. P Dhard, Physica C (to be published)
[11] S. Hikami and A. I. Larkin, Mod. Phys. Lett. B **2**, 693 (1988).
[12] B. Batlogg, in *High Temperature Superconductors*, edited by K. S Bedell *et al.* (Addison–Wesley, Redwood City, 1990), p 37.

Straightened voltage effect in high-T_c superconductors

A. Grishin
Department of Condensed Matter Physics, The Royal Institute of Technology, S-100 44 Stockholm, Sweden

J. Niska and B. Loberg
Department of Engineering Materials, Luleå University of Technology, S-971 87 Luleå, Sweden

H. Weber
Department of Physics, Luleå University of Technology, S-971 87 Luleå, Sweden

A new effect called "*ac-current straightening*" has been observed in ceramic (Bi,Pb)-2223 slabs carrying ac current $I_{dc}+I_{ac}\cos(\omega t)$. The current-voltage ($I$-$V$) characteristics of the ceramic were measured at 77 K at frequencies ranging from 50 to 20 000 Hz. A spectrum analyzer showed a series of high harmonics in the voltage signal as well as a constant voltage drop. The full set of experimental data has been explained theoretically using the Bean–Kim critical state model with a magnetic field dependent critical current $j_c(H)=j_c(0)/(1+H/H_0)$. A low transport ac current gives a voltage linearly proportional to the frequency and quadratically proportional to the ac-current amplitude I_{ac}. It consists of odd harmonics only. If a bias dc current is switched on, then even harmonics and a dc-voltage drop appear. Their amplitudes are proportional to the small parameter I_{ac}/cH_0 and depend on the I_{dc}/I_{ac} ratio.

One of the main features of high-T_c superconductors is the very wide interval of magnetic field and temperature in the H-T diagram between the two critical fields $H_{c1}(T)$ and $H_{c2}(T)$ conditioned by extremely small coherence length. Due to this fact and the great anisotropy of the samples, magnetic vortices cause the strong nonlinearity of magnetic and transport properties in the mixed state for high-T_c superconductors even at very low magnetic fields and current densities. Strong magnetic field dependence of susceptibility and aharmonic diamagnetic response manifest this behavior (see, for example, Ref. 1). In the present article we report experimental observations and a theoretical explanation for a new effect in current transport properties. Pinning of vortices results in odd harmonics in the voltage response for sinusoidal ac currents. Field dependence of the critical current causes even harmonics and a dc-voltage drop if a bias dc-transport current or a dc-magnetic field violate the symmetry $t\rightarrow -t$.

Bulk samples of (Pb,Bi)-2223 were prepared by sintering a commercial 2212+oxides precursor powder, regrinding and pressing it into nominally 10 mm wide bars. dc-testing lead to the conclusion that the critical current is limited by the magnitude of the magnetic self-field at the surface of the bar.[2] A dc-voltage signal was detected when testing using ac+dc currents.[3] The frequency dependence of the effect was examined by using an audio amplifier to increase the current from a frequency generator. Necking and a reduction in the size of the specimens were done in some cases to reduce the transport current required to reach the critical magnitude. A four point probe test circuitry was used with a HP 3478A microvolt multimeter to detect the dc voltage across the center contacts. Additional details of the nature of the voltage signals were observed after amplification with a high gain operational amplifier and a storage oscilloscope and the harmonics were found using a HP 3580A spectrum analyzer.

A pure sinusoidal ac current gives a sinusoidal voltage signal from the voltage contacts until the transport current exceeds the dc critical current magnitude I_c. Far above I_c the shape of the voltage signal wave form changes to a more triangular shape due to the odd harmonics in the voltage signal. If a dc offset current I_{dc} is added, then asymmetry can be observed in the $V(t)$ curve as evidence of even harmonic frequencies (Fig. 1, harmonics above and below I_c). Another effect is a dc offset, so that the curve progressively shifts away from the zero axis (on the oscilloscope) as the current is increased further. The dc voltage observed on a multimeter for a dc offset current, is seen to primarily depend on a shift of the voltage curve from the zero axis, since the deformation of the wave form is not as large (Fig. 2). The transition for ac plus dc current testing occurs at approximately the same total current as for dc alone, when using the rms ac current and if $I_{dc}\geq I_{ac}$. This would indicate a common mechanism generating the voltage signals. To examine for frequency dependence in the effect, the frequency of the ac current was varied in the audio frequency range of 50–20 000 Hz by the use of an audio power amplifier. Visible changes in the I-V characteristics were not observed. A VOM was used to measure the critical current at the transition for a triangle, sine, and square wave input. The resistive transition occurred first for the triangle wave, then the sine, and last for the square wave. The VOM uses a fixed resistor and a constant to give the expected current, rather than measuring the voltage and current and the phase angle as in an ac watt meter. Therefore, the ratio of the peak voltage to power is lower for the same current for a square wave input than for a triangular wave form, and the transition sequence follows a decreasing ratio.

We use the critical state model[4] to calculate the distributions of local magnetic field h and current in an infinite superconducting slab (Fig. 3) carrying a transport current $I_{tr}(t)=I_{dc}+I_{ac}\cos(\omega t)$ (the magnetic susceptibility for samples carrying dc+ac transport current has been experimentally studied in Ref. 5). Kim's expression

$$j_c(h)=\frac{j_c(0)}{1+(|h|/H_0)} \tag{1}$$

 0021-8979/94/76(10)/6947/3/$6.00 © 1994 American Institute of Physics

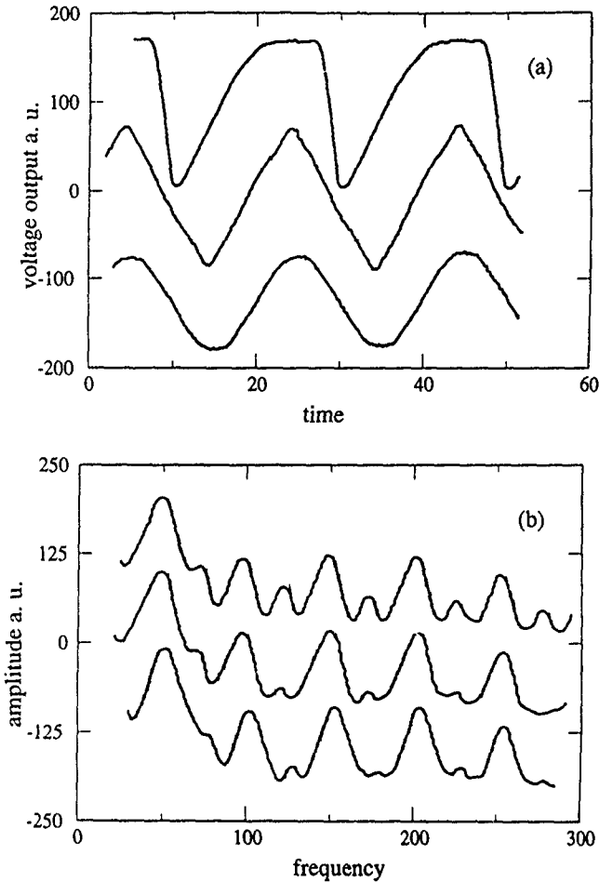

FIG. 1. $V(t)$ for 50 Hz ac-transport currents as a function of time (ms) and the associated harmonic frequencies present (plotted as log I vs frequency ω). The lower curve in (a) is for $I=2.85$ A rms and shows mostly odd harmonics in the superconducting state. Increasing the current to $I=3.51$ A rms, middle curve in (a), distorts the wave form due to flux penetration but symmetry is maintained. A dc-bias current of 0.6 A dc to the middle curves case gives an asymmetric wave form and increases the even harmonics upper curve. In (b) the associated harmonic frequencies to the curves in (a) are shown.

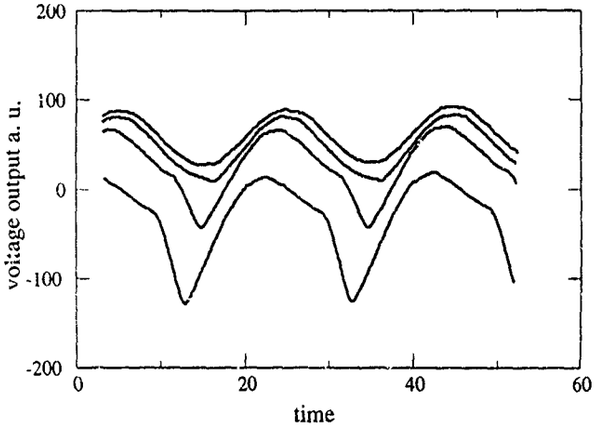

FIG. 2. $V(t)$ wave form for increasing 50 Hz ac currents, while holding I_{dc} nearly constant at 0.9 A Sinusoidal wave form symmetry is gradually lost as I_{ac} is increased in steps 4.04 A (upper curve), 4.51 A, 5.04 A, and finally 5.30 A (rms)

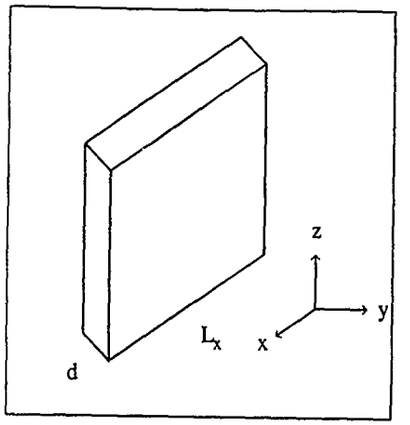

FIG. 3. Experimental setup showing the superconducting slab. The current is driven in the z direction.

is used to define the field dependence of the critical current. Here the parameter H_0 characterizes the reduction of the critical current by magnetic field, and $j_c(0)$ is a function of temperature. Maxwell's equation

$$\frac{\partial h_x}{\partial y}=\pm\frac{4\pi}{c}j_c(h) \tag{2}$$

is solved with a standard boundary condition

$$h_x(d/2)=-(2\pi/c)I_{tr}(t). \tag{3}$$

Signs $\pm$ in Eq. (2) depend on the time-dependent phase of the transport current, and d is the slab thickness. Here and later on we use the linear density of transport current $I=J/L_x$, normalized to the unit of slab width L_x.

The quasistatic solutions of Eq. (2) may be classified for three different cases. The first is a *critical state* realized for low transport currents

$$I_{tr}\leqslant(cH_0/2\pi)[\sqrt{1+[4\pi dj_c(0)/cH_0]}-1]. \tag{4}$$

In this case magnetic field and supercurrents exist near the slab surface only. If the inequality (4) transforms to strict equality, then the magnetic field reaches the center of the slab. Higher transport currents give

$$(cH_0/2\pi)[\sqrt{1+[4\pi dj_c(0)/cH_0]}-1]\leqslant I_{tr}\leqslant j_c(0)d \tag{5}$$

for the *intermediate state*. In this case the supercurrent density is not enough to support the total transport current in the slab. The slab interior is occupied by supercurrent, as before, but near the slab surface the normal state occurs with a uniform normal current density higher than $j_c(h)$. If the transport current continues to increase, then the boundary between critical and normal states reaches the center of a sample and

$$I_{tr}\geqslant j_c(0)d, \tag{6}$$

which is the *normal* state in the entire slab.

We present here the final results in the limiting case using the *critical state* (4), and a low bias dc component in the transport current

$$I_{dc}\leqslant I_{ac},$$
$$2\pi|I_{tr}|/cH_0\ll 1. \tag{7}$$

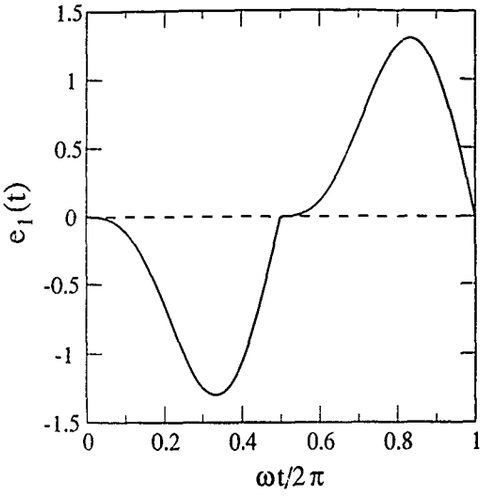

FIG. 4. Graph of the function $e_1(t)$ in Eq (8). The dashed line represents the zero level.

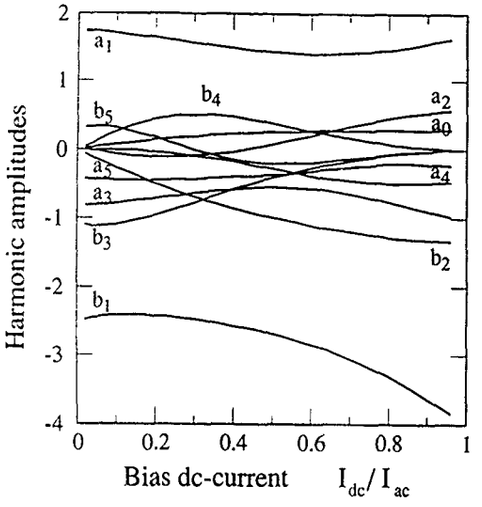

FIG. 5. The Fourier amplitudes a_0-a_5 and b_1-b_5 used in the evaluation of $e_2(t)$ in Eq. (8). $e_2(t)$ describes the additional voltage caused by the field dependence of critical current vs bias dc current.

For these conditions the electric field into the slab may be presented as a sum of two terms

$$E(t)=\frac{\pi I_{ac}^2\omega}{4c^2 j_c(0)}\left[e_1(t)+\frac{\pi I_{ac}}{cH_0}e_2(t)\right],$$

$$e_1(t)=-\sin(\omega t)+|\sin(\omega t)|\cos(\omega t)$$

$$=-\sin(\omega t)+\frac{4}{\pi}\sum_{k=0}^{\infty}\frac{\cos[(2k+1)\omega t]}{4-(2k+1)^2}, \qquad (8)$$

$$e_2(t)=a_0+\sum_{k=1}^{\infty}[a_k\cos(k\omega t)+b_k\sin(k\omega t)],$$

where $e_1(t)$ is the main ac-voltage signal. The shape of the function is presented in Fig. 4. As can be seen from Eq. (8) it contains odd harmonics only. And an additional term $e_2(t)$ appears because of the dependence of the critical current on the local magnetic field.[1] Its contribution to $E(t)$ in Eq. (8) is small, since the parameter $(2\pi|I_{tr}|)/(cH_0)\ll 1$ [Eq. (7)]. It contains both odd and even harmonics. The dependences of the Fourier amplitudes a_0, a_k, and b_k on the parameter I_{dc}/I_{ac} are presented in Fig. 5. All even harmonic amplitudes go to zero with $I_{dc}\to 0$. The item a_0 in Eq. (8) corresponds to the "straightened voltage drop." It appears only when a bias dc current I_{dc} appears. It is remarkable that the straightened voltage magnitude in $E(t)$ is linearly proportional to frequency and quadratically in the low (and cubically in the high) ratio of the I_{dc}/I_{ac} case for the ac-current amplitude, since no frequency dependence was seen experimentally.

In summary, a new effect called ac-current straightening has been observed experimentally and explained theoretically. Strong nonlinear dependence of shielding supercurrents from external magnetic fields causes the occurrence of high harmonics in the voltage signal. The field dependence of the critical current leads to stratification of the sample into a critical state interior and a normal state exterior. Even harmonics and dc-voltage drop appear for bias dc-transport currents or dc-magnetic fields.

ACKNOWLEDGMENTS

This work is supported by the Swedish funding agencies NUTEK and NFR.

[1] R. B. Goldfarb, M Lelental, and C. A. Thompson, *Magnetic Susceptibility of Superconductors and Other Systems*, edited by R. A. Hein, T. L. Francavilla, and D. H. Liebenberg (Plenum, New York, 1992).
[2] B. Loberg, J Niska, and P. Rubin, Appl. Supercond. **1**, 1757 (1993).
[3] J. Niska and B. Loberg, J Supercond. **6**, 255 (1993).
[4] C P. Bean. Phys. Lett **8**, 250 (1962)
[5] A. N Ulyanov, V. N. Korenivski, K V. Rao, and A. M Grishin, Appl. Supercond. **1**, 971 (1993).

Long-time magnetic relaxation measurements on a quench melt growth YBCO superconductor

L. H. Bennett, L. J. Swartzendruber, M. J. Turchinskaya, J. E. Blendell, and J. M. Habib
NIST, Gaithersburg, Maryland 20899

H. M. Seyoum
Department of Physics, University of the District of Columbia, Washington, DC 20008

The decay of magnetization with time is recorded for a quench-melt-growth processed $YBa_2Cu_3O_{7-x}$ sample. The vortex-glass and collective pinning theories fit the data quite well over all time regimes with an exponent, μ, value of 0.78. The normalized logarithmic magnetic relaxation rate, S, attains a plateau value of 0.05, considerably higher than a variety of samples which fall within a universal plateau curve.

INTRODUCTION

The understanding of the pinning mechanism is essential for the improvement of the critical current in high-temperature superconductors. A key component that determines the critical current density J_c and the relaxation rate of the magnetization S is the pinning energy $U(J)$. Measurement of the magnetic relaxation $M(t)$ has been one of the most popular means of investigating pinning phenomena in high-temperature superconductors. The relaxation of magnetization is usually interpreted within the framework of the thermally activated flux flow (TAFF) over an average energy barrier U. In the simplified model, first proposed by Anderson,[1,2] U is assumed to vary linearly with the current density J. In general, however, a number of different competing mechanisms govern the interaction of flux lines and defects.[3–7]

A number of articles have proposed varying forms of $U(J)$, resulting in magnetization relaxation with time that obeys a logarithmic law,[2] a power law,[4] or an exponential law.[5] These analytical expressions can describe well the experimental data over a limited time window. Our various YBCO samples show dependencies of $M[(\ln t)]$ that deviate from straight lines at long times. More complex models, such as the collective pinning (CP) theory of Fiegel'man *et al.*[8,9] and the vortex-glass (VG) theory of Fisher *et al.*,[10] predict an interpolation formula of the form

$$M(t)=M(0)[1+(\mu kT/U_0)\ln(t/t_0)]^{-1/\mu}. \quad (1)$$

Phenomenologically, this implies a potential barrier of the form

$$U(J)=(U_0/\mu)[(J_{c0}/J)^{\mu}-1], \quad (2)$$

where U_0 and J_{c0} are, respectively, temperature dependent barrier height and critical current density in the absence of flux creep. The value of the exponent μ is controversial. Its value has been reported to vary from 0.2 to 2.5, and others have even reported it to be dependent on temperature and applied field.[11–15]

In the study reported here, we have investigated the pinning mechanism by measuring the kinetics of magnetization in a crystalline sample of $YBa_2Cu_3O_{7-x}$ (YBCO or 123) prepared by the quench-melt-growth (QMG) process.[16] The sample is similar to one whose relaxation rates are described elsewhere.[17] The QMG sample was produced by melting a solid-state sintered YBCO superconductor precursor powder at 1450 °C, holding for 5 min before quenching the liquid onto a copper plate. The resultant glass was rapidly reheated to 1150 °C and cooled to 1000 °C at 200 °C/h. The samples were then cooled at a very slow rate (1 °C/h) to 940 °C in order to go slowly through the peritectic temperature. Below the peritectic temperature, the reaction Y_2BaCuO_5 (211)+liq =123 occurs, forming the superconducting YBCO phase. The main difference between the present sample and the earlier one[16] is that better temperature control was achieved during processing of the present sample, and the microstructures of the two samples are very different. The earlier sample contained areas of inclusion-free single crystal 123, but containing parallel arrays of microcracks. During the rapid reheating of the earlier sample, there were temperature oscillations above 1150 °C by as much as 25 °C. The oscillations occurred during the first minute of reheating. The higher temperature may have caused dissolution of the 211 particles in the melt. In contrast, for the present sample the temperature did not exceed 1150 °C and although it contains porous regions, 211 and CuO inclusions, it has inclusion-free single crystal 123 regions which are not microcracked.

EXPERIMENTAL METHODS

Measurements of the isothermal magnetization M were carried out for a set of temperatures T between 10 and 70 K using superconducting quantum interference device (SQUID) magnetometry. The samples were first cooled to the measuring temperature in zero magnetic field (ZFC). A magnetic field of 0.4 T was then applied, and the magnetization, $M(t)$, was recorded as a function of time. Measurements of the decay of the remanent magnetization M_{rem} were also carried out, but are not reported in this article. The results for M_{rem} were similar to those obtained for the ZFC procedure.

 0021-8979/94/76(10)/6950/3/$6.00 © 1994 American Institute of Physics

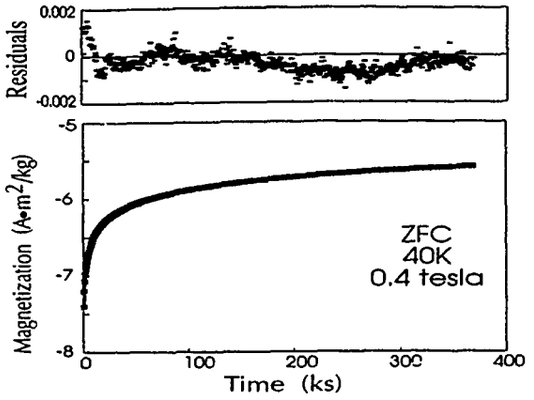

FIG. 1. Decay of zero-field-cooled magnetization vs time for $T=40$ K and $H=0.4$ T (lower figure). Squares represent data and the dotted line is the fit using Eq. (1), with $\mu=7/9$. The top figure shows the residuals between the data and the fit.

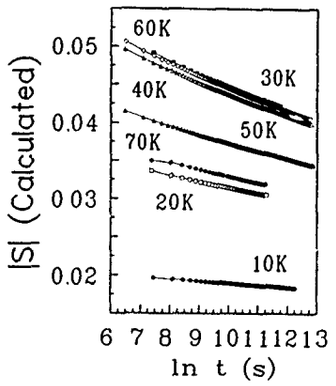

FIG. 3. The time variation of the normalized logarithmic rate, $|S|$, for various temperatures.

RESULTS AND DISCUSSION

A typical result of the decay of the magnetization M versus time at $T=40$ K and $H=0.4$ T is displayed in Fig. 1. This curve (and the curves at all the other temperatures) shows deviations from a logarithmic law or an exponential law at the long times ($1.4 \leq t \leq 400$ ks). The normalized logarithmic rate $\mathbf{S}=|d[\ln M]/d[\ln t]|$ versus temperature is shown in Fig. 2, for a time of $\cong 1.4$ h after the field was turned on. The time variation of $|\mathbf{S}|$ is shown in Fig. 3. The sample is small enough for complete field penetration (verified by Meissner measurements) and the values of **S** are a suitable measure to compare the pinning properties of different crystals. For most YBCO samples, there is a universal curve in which $|\mathbf{S}|$ values attain a plateau within the range of 0.022 to 0.038 (shaded area of Fig. 2) for the temperature interval ≈ 30–60 K.[18] Crystals containing only small defects show a low and constant **S** with temperature. By comparison, our QMG sample has a plateau with a high value of $S \approx 0.05$ which lies outside the universal plateau curve. A high value of S is usually associated with the existence of extended defects.[19]

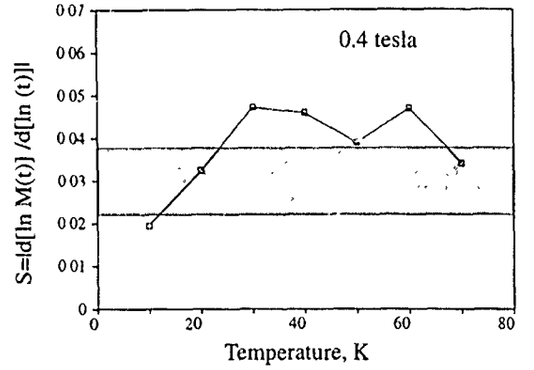

FIG 2. Normalized logarithmic rate $S=|d[\ln(M)]/d[\ln(t)]|$ vs temperature, evaluated at $t=5$ ks The shaded area represents data obtained from Refs. 17 and 18

The VG and CP models fit the data quite well over the entire measured time range. Results obtained by fitting the data to Eq. (1) (see Fig. 1) indicate that μ lies between 0.7 to 0.9 in the temperature interval 10–70 K, similar to the values observed by Ren and de Groot[14] for a flux-grown YBCO single crystal which is described as being heavily twinned and containing many defects. In contrast, for highly proton-irradiated YBCO single crystals,[11] and for melt-textured samples of YBCO Ref. 20, μ was found to be 0.5 at $T=10$ K, reach a peak of 1.4 at $T=30$ K, and then drop back to a low value at $T=60$ K.

The VG theory of Fisher *et al.* predicts that μ is a universal exponent less than 1. The CP model of Fiegel'man *et al.* assumes weak pinning and proposes three different regimes of current density J and thus three different values of μ depending on the flux bundle size. In the three dimensional case, $\mu=1/7$ for the high current region, $\mu=3/2$ for intermediate J, and $\mu=7/9$ for much lower J values. The values of μ obtained for our QMG sample have an average value near 7/9 for $10 \leq T \leq 70$. Assigning a μ value from 0.7 to 0.9 does not significantly affect the goodness of fit (correlation coefficient $r^2 \approx 0.998$) for any of the temperatures. We therefore analyzed all of our data for a fixed value of 7/9. This value of μ is consistent with the VG and CP models associated with large vortex bundles. QMG samples can be considered as nearly bulk superconductors with weak links.[10] The pinning energy, U_0, obtained from our fits is approximately constant at 0.043 eV for the temperature interval 10 to 30 K, and rises to over 0.1 eV at 70 K. This behavior is different than that found[3,21] for single crystals where U_0 continued to decrease as the temperature was lowered below 30 K.

In summary, we have measured the magnetic relaxation of a QMG-processed YBCO crystal. We have found that CP and VG models fit our data quite well. The value of μ is controversial, with the different μ values found in the literature appearing to depend on the technique of measurement and method of sample preparation. The data obtained here over a wide temperature range from either $M(t)$ and $M_{\text{rem}}(t)$ is in agreement with $\mu=7/9$ for our sample, as predicted by the collective pinning theory, and is consistent with the VG model for large vortex bundles.

ACKNOWLEDGMENT

We wish to thank H. Brown for technical aid with the SQUID measurements and data reduction.

[1] P. W. Anderson and Y. B. Kim, Rev. Mod. Phys. **36**, 39 (1964).
[2] M. R. Beasley, R. Labusch, and W. W. Webb, Phys. Rev. **181**, 682 (1969).
[3] D. Shi and S. Salem-Sugui, Jr., Phys. Rev. B **44**, 7647 (1991).
[4] M. E. Smith, Donglu Shi, S. Sengupta, and Z. Wang, Appl. Supercond. **1**, 151 (1993).
[5] E. Zeldov, N. M. Amer, G. Koren, A. Gupta, M. W. McElfresh, and R. J. Gambino, Appl. Phys. Lett. **56**, 680 (1990).
[6] A. M. Campbell and J. E. Evetts, Adv. Phys. **21**, 199 (1972).
[7] S. Sengupta, D. Shi, Z. Wang, M. E. Smith, and P. J. McGinn, Phys. Rev. B **47**, 5165 (1993).
[8] M. V. Feigel'man, V. B. Geshkenbein, A. I. Larkin, and V. M. Vinokur, Phys. Rev. Lett. **63**, 2303 (1989).
[9] M. V. Feigel'man, V. B. Geshkenbein, and V. M. Vinokur, Phys. Rev. B **43**, 6263 (1991).
[10] D. S. Fisher, M. P. A. Fisher, and D. A. Huse, Phys. Rev. B **43**, 130 (1991).
[11] J. R. Thompson, Y. R. Sun, L. Civale, A. P. Malozemoff, M. W. McElfresh, A. D Marwick, and F. Holtzberg, Phys. Rev. B **47**, 14440 (1993).
[12] C. Dekker, W. Eidelloth, and R. H. Koch, Phys. Rev. Lett. **68**, 3347 (1992).
[13] Y. Y. Xue, L. Gao, Y. T. Ren, W. C. Chan, P. H. Hor, and C W. Chu, Phys. Rev. B **44**, 12029 (1991).
[14] Y. Ren and P. A. J. de Groot, Cryogenics **33**, 357 (1993).
[15] V. Calzona, M. R. Cimberle, C. Ferdeghini, E. Giannini, G. Grasso, M. Putti, A. S. Siri, and F. Licci, Supercond. Sci. Tech. **6**, 771 (1993).
[16] J. M. Habib, H. M. Seyoum, L. H. Bennett, L. J. Swartzendruber, and J. E. Blendell, Mod. Phys. Lett. B **8**, 351 (1994).
[17] M. Turchinskaya, L H. Bennett, L J. Swartzendruber, A Roitburd, C. K. Chiang, M. Hill, J. E. Blendell, and K. Savano, Mater. Res. Soc. Symp. Proc. **169**, 931 (1990).
[18] A. P. Malozemoff and M. P. A. Fisher, Phys. Rev. B **42**, 6784 (1990).
[19] H. G. Schnack, R. Griessen, J. G. Lensink, C. J. van der Beek, and P. H. Kes, Physica C **197**, 337 (1992).
[20] Y. R. Sun, J. R. Thompson, Y. J. Chen, D. K. Christen, and A Goyal, Phys. Rev. B **47**, 14481 (1993).
[21] Y. Xu, M. Suenaga, A. R Moodenbaugh, and D. O. Welch, Phys. Rev. B **40**, 10882 (1989).

Surface barriers and two-dimensional-collective pinning in single crystal $Nd_{1.85}Ce_{0.15}CuO_{4-\delta}$ superconductors

F. Zuo and S. Khizroev
Department of Physics, University of Miami, Coral Gables, Florida 33124

Xiuguang Jiang, J. L. Peng, and R. L. Greene
Department of Physics and Center for Superconductivity Research, University of Maryland, College Park, Maryland 20742

We report detailed magnetization studies on a single crystal $Nd_{1.85}Ce_{0.15}CuO_{4-\delta}$ superconductor in the magnetic field parallel to the c-axis direction. Two characteristic peaks are observed in the magnetization data, corresponding to surface barriers and two-dimensional (2-D) collective pinnings. The critical currents corresponding to the maximum and minimum widths in the hysteresis loops increases with decreasing temperature exponentially. We propose that the fishtail magnetization in this compound is due to the presence of a surface barrier and the pinning of collective 2-D vortices. The initial peak in magnetization is due to the presence of Bean–Livingston surface barriers and the larger peak in M at higher H corresponds to 2-D pinning.

The study of vortex pinning in the high T_c cuprate systems is of great interest in terms of both fundamental physics involved and application of these materials as current-carrying devices. One of the many interesting features observed in these compounds is the so-called fishtail magnetization.[1] The critical current defined as the width of a hysteresis loop at a given temperature increases with increasing field. This effect has been observed in several high T_c materials, including YBCO, BISCO, and a Tl compound.[1-3] However, the mechanism for this behavior is still controversial.

In this work, we report extensive magnetic measurements performed on a low T_c single crystal $Nd_{1.85}Ce_{0.15}CuO_{4-\delta}$ superconductor. The magnetization (M) measured as a function of field shows a similar fishtail characteristics in $H\|c$-axis direction. At high temperatures, M is nearly zero for a certain range of fields in the descending branch of a hysteresis loop. At low temperatures, pinning becomes increasingly important. The critical currents defined at the minimum and maximum widths of the magnetization loop can be well fit with an exponential temperature dependence, $J_c = J_0 \exp(-T/T_0)$. We propose that the anomalous fishtail magnetization is due to surface barriers and pinning of the collective two-dimensional (2-D) vortices.

Single crystals of $Nd_{1.85}Ce_{0.5}CuO_{4-\delta}$ are grown using a directional solidification technique.[4] Several crystals are used in the measurement, with average dimensions of $1\times1\times0.02$ mm. Extensive measurements were made on one crystal with a T_c of 21 K. The magnetic transition width measured at 1 G with zero-field cooling is about 1 K. Measurements are performed using a Quantum Design magnetometer with low field options. After de-Gaussing and magnet resetting (quenching), the remanent field is typically 5–10 mG. Measurements reported here are for the $H\|c$-axis configuration.

Shown in Fig. 1 are magnetic hysteresis loops taken at constant temperatures, $T=17$, 13, and 7 K, respectively. The overall shapes are similar to each other, but some differences are clearly visible. At $T=17$ K, shown in Fig. 1(a), the magnetization loop forms a complete fishtail. Three characteristic regimes are clearly observed in the field ascending branch. In the first regime, the magnetization decreases linearly with the field initially (the Meissner state); in the second regime, M increases sharply toward zero from the Meissner state and is followed by an almost constant magnetization for 50 G$<H<$100 G; in the third regime, M decreases again with increasing H, followed by an eventual increase to almost zero with an increasing field. In the field descending branch, three field ranges with almost-mirror-imaged magnetization are observed. However, in the corresponding second regime, the magnetization is almost zero, rather than a constant, as seen in the field increasing direction. At low field, the magnetization increases monotonically with the decreasing field.

At a lower temperature, $T=13$ K, as shown in Fig. 1(b), the magnetization curve is somewhat different from that of 17 K. The maximum sweeping field is increased to 1 kG. The relatively sharp peak in the third regime in Fig. 1(a) is replaced by a broader $M(H)$ dependence at this temperature. The magnetization in the second regime in the field descending branch remains close to zero, followed by increasing M at a lower field. At very low temperature $T=7$ K, shown in Fig. 1(c), the differences are more pronounced. The magnetization at field up to 2 kG is very broad. In the descending branch, the minimum M is finite rather than close to zero.

To quantify the anomalous field dependence of the magnetization, we define several characteristic parameters. For each hysteresis loop, there are two well-defined critical currents. One critical current J_{max} corresponds to the maximum width at H_{max} in the third regime. The other J_{min} can be defined, corresponding to the minimum width in the second regime. The critical current can be obtained by using the standard expression $J=\Delta M/(2r)$ where $\Delta M=|M_-(H)-M_+(H)|$ and r is the effective radius of the specimen. In the following discussion, we will use $J\propto\Delta M$ and obtain the temperature dependence of J from ΔM directly. The temperature dependence of these two widths are plotted in Fig. 2. The solid lines are fits to the expression of $J=J_0\exp(-T/T_0)$, where J_0 is the zero temperature critical current and $1/T_0$ is the slope of the fit. The values obtained for T_0 are 4 and 2 K for maximum and minimum width, respectively. The zero temperature critical values are the

 0021-8979/94/76(10)/6953/3/$6 00 © 1994 American Institute of Physics

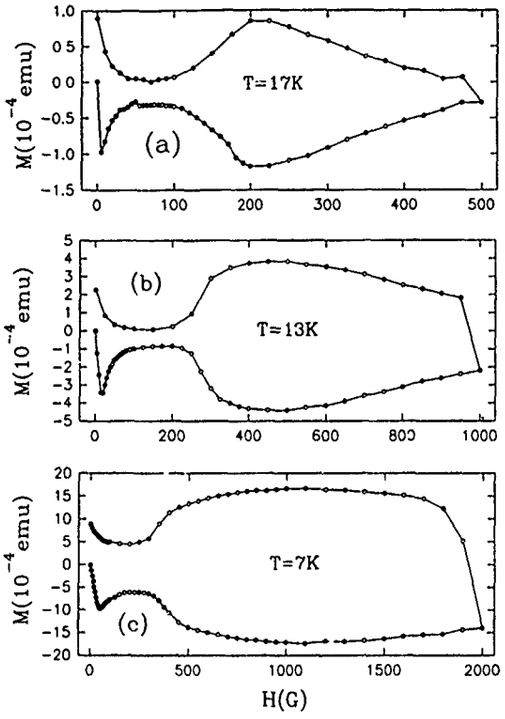

FIG. 1. Magnetization hysteresis loop at (a) $T=17$ K; (b) $T=13$ K, and (c) $T=7$ K in the $H\|c$-axis configuration.

same within the experimental errors. The inset shows the temperature dependence of the maximum peak field. The solid line is a fit to $\ln H_{max}=\ln H_0-T/T_1$, with $H_0=3$ kG and $T_1=7$ K.

The crossover from the minimum to maximum magnetization can be characterized by a crossover field H_x when M is in the middle of M_{min} and M_{max}. The data is very close to each other in both branches. The temperature dependence of H_x is plotted in Fig. 3. At high temperature, H_x increases with decreasing T; at lower temperatures, H_x tends to saturate. The solid line is a two-variable fit to $H_x=H_x(0)[1-(T/T_x)^2]$. The fit gives a $H_x(0)=440$ G and $T_x=21$ K, which is exactly the same as the T_c determined from magnetic and transport measurements. The same T_x is obtained from a linear extrapolation of the high temperature data.

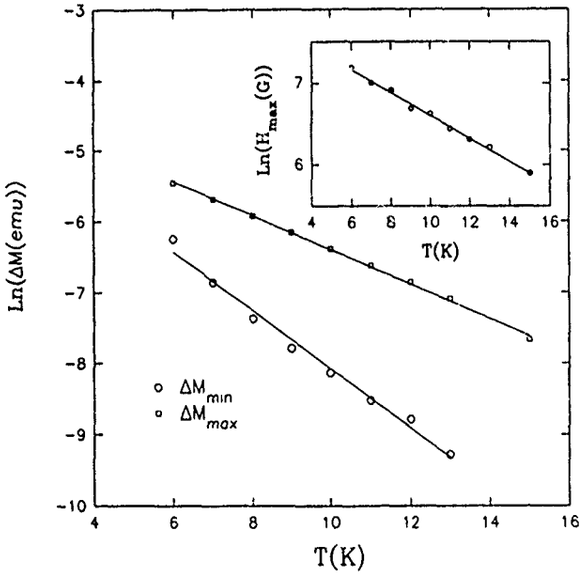

FIG 2. $\ln \Delta M$ as a function of temperature for both ΔM_{max} and ΔM_{min} The lines are fits to $\ln \Delta M=\ln \Delta M_0-T/T_0$ The inset is a plot of $\ln H_{max}$ vs T and the line is a fit to $\ln H_{max}=\ln H_0-T/T_1$

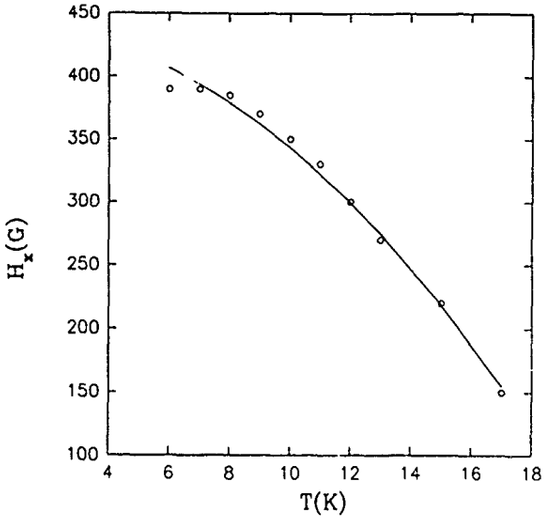

FIG. 3. H_x as a function of temperature. The solid line is a fit to $H_x(T)=H_x(0)[1-(T/T_x)^2]$

The exponential temperature dependence of J is of interest here. The result is consistent with a general collective pinning theory, with the current near its critical state.[5,6] The theory predicts a nonlinear logarithmic time decay of the current density, $j(t)=j_c[1+(\mu T/U_c)\ln(1+t/t_0)]^{-1/\mu}$, where j_c is the zero temperature critical current, U_c is the barrier height, t is the experimental measuring time, and $1/t_0$ is a characteristic frequency. In a typical SQUID measurement, $t=100$ s and $t/t_0\sim10^{10}$. In the single vortex pinning regime, $1/\mu=7$ and $j(t)\simeq j_c\exp(-T/T_0)$, with $T_0\simeq U_c/\ln(t/t_0)$. The exponential dependence is only expected when $j\simeq j_c$. If $j\ll j_c$, the current density has a power-law dependence on temperature, $j(t)\sim j_c[(T/U_c)\ln(t/t_0)]^{-1/\mu}$. We have also tried to fit the critical currents with the power-law dependence; we obtain the exponent $1/\mu$ to be 2 and 3.8 for J_{max} and J_{min}, respectively. However, it is noticed that power-law fit is not as good as that of $\exp(-T/T_0)$.

The collective pinning theory predicts $1/\mu=7$ in the single vortex regime; $\frac{2}{3}$ in the small vortex bundle regime; and $\frac{5}{7}$ in the large vortex regime. It has been proposed recently that the fishtail magnetization is due to the crossover of different pinning regimes.[3] The small M is due to the fast relaxation of single vortices, and large M is due to slow relaxation in the vortex bundle regimes. However, our data clearly indicate lack of correspondence in the exponents $1/\mu$ with the theory. The discrepancy suggests the inadequacy of

applying the model to explain the fishtail shape of magnetization.

The anomalous magnetization can also be derived from a model where the order parameter is reduced substantially at the high field. For example, a region of lower T_c phase can become a strong pinning site once the external field is of order of H_{c2} of that low T_c phase. This can be realized in the YBCO system, where T_c depends strongly on local oxygen stoichiometry. In the low T_c $Nd_{1.85}Ce_{0.15}CuO_{4-\delta}$ compound, T_c does not change appreciably with oxygen content. The local T_c fluctuation model is not appropriate here. This picture is supported by the temperature dependence of the crossover field H_x. If the large peak at high field were due to another lower T_c phase, H_x should be of order of H_{c2}. The temperature dependence of H_x would determine the T_c of this phase. In this case, the fitted T_x being exactly the same as that of the bulk T_c indicates the absence of spurious low T_c structures in this crystal. The temperature dependence of peak field H_{max} is in sharp contrast with the "lattice matching" model, where a peak in M occurs when the vortex density is matched with that of defects. However, in this model the peak field should not change with temperature. The exponential T dependence of H_{max} excludes the lattice matching effect.

We propose that the fishtail magnetization is a result of surface barriers and the pinning of correlated 2-D pancakes. The effects of surface barriers have been considered by Chikomoto and Kopylov earlier.[1,2] The difference between this model and the previous model is that we believe the 2-D nature is very important here. The minimum magnetization in the second regime is due to the combination of surface barriers and fast relaxation of single vortex lines. The increasing magnetization with increasing field is due to the slow relaxation and large pinnings of correlated 2-D vortices.

The presence of surface barrier is evident from high temperature hysteresis loop measurements.[7] The rapid decrease in magnetization in the second regime in the H-ascending direction is consistent with a surface barrier model, where $4\pi M = H - \sqrt{H^2 - H_p^2}$ for $H > H_p$.[8,9] At low T, finite pinning has to be considered to evaluate M. The penetration field H_p increases with decreasing T. The data can be fit with $H_p = H_0 \exp(-T/T_0)$. The result implies that the magnetic penetration is in the form of 2-D pancakes rather than 3-D flux lines. At small field, vortices penetrate the surface barriers in the form of 2-D pancakes. The Josephson and magnetic interaction align the pancakes in different planes once they are inside. Magnetic relaxation is determined by the combination of surface barriers and single vortex line pinning. At high field, the collective pinning lengths in the plane L_{ab} increases with field. If L_{ab} is greater than the Josephson length, the motion of vortices will be dominated by 2-D collective pinnings. The collective pinning will increase the number of pinning centers, thus, the pinning energy and the effective critical current. Measurements of magnetic relaxation as a function of field at a given temperature confirms the different relaxation mechanisms at different fields.[7] We attribute the rising of magnetization at high field to large collective pinning of 2-D vortices and their slow relaxation from a critical state.

In summary, we have reported detailed magnetization studies on a single crystal $Nd_{1.85}Ce_{0.15}CuO_{4-\delta}$ superconductor. The magnetization in the H parallel to c direction shows the anomalous fishtail field dependence. The temperature dependence of characteristic critical currents J_{min}, J_{max}, and the crossover field H_x rules against the 3-D collective pinning model, as well as the oxygen deficiency model. We suggest that the fishtail magnetization is due to the combined effect of surface barriers and collective pinning of 2-D vortices.

[1] M. Daeumling, J. M. Seuntjens, and D. C. Larbalestier, Nature **346**, 332 (1990); V. N. Kopylov, A. E. Koshelev, I. F. Schegolev, and T. G. Togoniaze, Physica C **170**, 291 (1990); M. S. Osofsky, J. L. Kohn, E. F. Skelton, M. M. Miller, R. J. Soulen, Jr., S. A. Wolf, and T. A. Vanderah, Phys. Rev. B **45**, 4916 (1992); G. Yang, P. Shang, I. P. Jones, J. S. Abell, and C. E. Gough, *ibid.* **48**, 4054 (1993); M. Xu, D. K. Finnemore, V. M. Vinokur, G. W. Crabtree, K. Zhang, B. Dabrowski, and D. G. Hinks, *ibid.* **48**, 10 630 (1993); Y. Yeshurun, N. Bontemps, L. Burlachkov, and A. Kapitulnik, *ibid.* **49**, 1548 (1994).

[2] N. Chikumoto, M. Konczykowski, N. Motohira, and A. P. Malozemoff, Phys. Rev. Lett. **69**, 1260 (1992).

[3] L. Krusin-Elbaum, L. Civale, V. M. Vinokur, and F. Holtzberg, Phys. Rev. Lett. **69**, 2280 (1992).

[4] J. L. Peng, Z. Y. Li, and R. L. Greene, Physica C **177**, 79 (1991).

[5] G. Blatter, M. V. Feigel'man, V. B. Geshkenbein, A. I. Larkin, and V. M. Vinokur, "Vortices in high temperature superconductors," Rev. Mod. Phys. (in press).

[6] M. V. Feigel'man, V. B. Geshkenbein, and V. M Vinokur, Phys. Rev. B **43**, 6263 (1991); M. V. Feigel'man, V. B. Geshkenbein, A. I. Larkin, and V. M. Vinokor, Phys. Rev. Lett. **20**, 2303 (1989); T. Nattermann, *ibid.* **64**, 2454 (1990).

[7] F. Zuo, S. Khizroev, X. Jiang, J. L. Peng, and R. L. Greene, Phys. Rev. B **49**, 12 326 (1994); F. Zuo *et al.* (unpublished).

[8] C. P. Bean and J. D. Livingston, Phys. Rev. Lett. **12**, 14 (1964).

[9] J. R. Clem, *Proceedings of Low Temperature Physics-LT 13*, edited by K. D. Timmerhaus *et al.* (Plenum, New York, 1974), Vol. 3, p. 102.

On vector generalization of the critical state model for superconducting hysteresis

I. D. Mayergoyz
Department of Electrical Engineering and Institute for Advanced Computer Studies, University of Maryland, College Park, Maryland 20742

The critical state model for superconducting hysteresis is based on an analytical study of the penetration of electromagnetic fields into hard superconductors. In the literature, this study has been carried out for linear and circular polarizations of electromagnetic fields. In the paper, the attempt is made to extend this study to arbitrary electromagnetic field polarizations, which can be treated as perturbations of circular polarizations. Another distinct feature of our work is that this extension is carried out for gradual resistive transitions described by the "power law."

Most of the literature on the critical state model is concerned with scalar superconducting hysteresis. This is because the study of vector hysteresis requires the investigation of penetration of electromagnetic fields into superconductors for the case when these fields are not *linearly* polarized. This is a very difficult analytical problem that requires the solution of coupled nonlinear partial differential equations. This problem has been solved only for *circular* polarization in the case of ideal (sharp) resistive transition,[1] as well as in the case of gradual resistive transition[2] described by the "power law."

In this paper, we consider vectorial polarizations of electromagnetic fields that can be treated as perturbations of circular polarizations. We also consider gradual resistive transitions that are usually described by the following "power law:"

$$E=(J/k)^n \quad (n>1). \tag{1}$$

Here E is an electric field, J is an electric current density, and k is some parameter that coordinates the dimensions of both sides in Eq. (1).

In the vectorial form, the power law can be written as follows:

$$J_x=k(\sqrt{E_x^2+E_y^2})^{1/n-1}E_x, \quad J_y=k(\sqrt{E_x^2+E_y^2})^{1/n-1}E_y. \tag{2}$$

The exponent "n" is a measure of the sharpness of the resistive transition and it may vary in the range 4–1000. At first, the power law was regarded only as an empirical description of the resistive transition. Recently, there has been a considerable research effort to theoretically justify the power law. The related discussion can be found in Refs. 3–5. In this paper, the power law is used as a constitutive equation for hard superconductors.

To start the discussion, consider a plane electromagnetic wave penetrating superconducting half-space $z>0$. The magnetic field on the boundary of this half-space is specified as follows:

$$\begin{aligned} H_x(0,t)&=H_m[\cos(\omega t+\gamma)+\epsilon f_x(t)],\\ H_y(0,t)&=H_m[\sin(\omega t+\gamma)+\epsilon f_y(t)], \end{aligned} \tag{3}$$

where ϵ is some small parameter, while $f_x(t)$ and $f_y(t)$ are given periodic functions of time. It is apparent that this plane wave can be construed as a perturbation of the circularly polarized plane wave. By using the Maxwell equations, we find that the distribution of electric field in half-space $z>0$ is governed by the following coupled nonlinear partial differential equations:

$$\frac{\partial^2 E_x}{\partial z^2}=\mu_0\frac{\partial J_x(E_x,E_y)}{\partial t}, \quad \frac{\partial^2 E_y}{\partial z^2}=\mu_0\frac{\partial J_y(E_x,E_y)}{\partial t}, \tag{4}$$

subject to the boundary conditions

$$\frac{\partial E_x}{\partial z}(0,t)=-\mu_0 H_m[\omega\cos(\omega t+\gamma)+\epsilon f_y'(t)], \tag{5}$$

$$\frac{\partial E_y}{\partial z}(0,t)=-\mu_0 H_m[\omega\sin(\omega t+\gamma)+\epsilon f_x'(t)], \tag{6}$$

$$E_x(\infty)=E_y(\infty)=0. \tag{7}$$

Next, we shall look for the periodic solution of the boundary value problem (4)–(7) in the following form:

$$\begin{aligned} E_x(z,t)&=E_x^0(z,t)+\epsilon e_x(z,t),\\ E_y(z,t)&=E_y^0(z,t)+\epsilon e_y(z,t). \end{aligned} \tag{8}$$

By substituting expressions (8) into Eqs. (4) and boundary conditions (8), and equating the terms of like powers of ϵ, we arrive at the following boundary value problems for E_x^0, E_y^0 and e_x, e_y:

$$\frac{\partial^2 E_x^0}{\partial z^2}=\mu_0\frac{\partial J_x(E_x^0,E_y^0)}{\partial t}, \quad \frac{\partial^2 E_y^0}{\partial z^2}=\mu_0\frac{\partial J_y(E_x^0,E_y^0)}{\partial t}, \tag{9}$$

$$\begin{aligned} \frac{\partial E_x^0}{\partial z}(0,t)&=-\omega\mu_0 H_m\cos(\omega t+\gamma),\\ \frac{\partial E^0}{\partial z}(0,t)&=-\omega\mu_0 H_m\sin(\omega t+\gamma), \end{aligned} \tag{10}$$

$$E_x^0(\infty)=E_y^0(\infty)=0, \tag{11}$$

and

$$\frac{\partial^2 e_x}{\partial z^2}=\mu_0\frac{\partial}{\partial t}\left(\frac{\partial J_x}{\partial E_x}(E_x^0,E_y^0)e_x+\frac{\partial J_x}{\partial E_y}(E_x^0,E_y^0)e_y\right), \tag{12}$$

$$\frac{\partial^2 e_y}{\partial z^2}=\mu_0\frac{\partial}{\partial t}\left(\frac{\partial J_y}{\partial E_x}(E_x^0,E_y^0)e_x+\frac{\partial J_y}{\partial y}(E_x^0,E_y^0)e_y\right), \tag{13}$$

 0021-8979/94/76(10)/6956/3/$6.00 © 1994 American Institute of Physics

$$\frac{\partial e_x}{\partial x}(0,t)=-\mu_0 H_m f_y'(t), \quad \frac{\partial e_y}{\partial z}(0,t)=\mu_0 H_m f_x'(t), \tag{14}$$

$$e_x(\infty)=e_y(\infty)=0. \tag{15}$$

The boundary value problem (9)–(11) describes the penetration of a circularly polarized plane wave into the superconducting half-space. The solution of this problem has been found in Ref. 2. For the case when the initial phase, γ, is such that the initial phase of $\mathbf{E}^0$ on the boundary ($z=0$) is equal to zero, this solution is given by the following expressions:

$$E_x^0(z,t)=E_m\left(1-\frac{z}{z_0}\right)^{\alpha'} \cos[\omega t+\theta(z)], \tag{16}$$

$$E_y^0(z,t)=E_m\left(1-\frac{z}{z_0}\right)^{\alpha'} \sin[\omega t+\theta(z)], \tag{17}$$

$$z_0=\frac{\sqrt[4]{2n(n+1)(3n+1)^2}}{\sqrt{\omega\mu_0\sigma_m}(n-1)}, \quad \sigma_m=kE_m^{1/n-1}, \tag{18}$$

$$\theta(z)=\alpha'' \ln(1-z/z_0), \tag{19}$$

$$\alpha'=\frac{2n}{n-1}, \quad \alpha''=\frac{\sqrt{2n(n+1)}}{n-1}, \tag{20}$$

and E_m can be found from the equation

$$H_m=\frac{|\alpha'+i\alpha''|}{\omega\mu_0 z_0}E_m. \tag{21}$$

By substituting (16) and (17) into Eqs. (12) and (13) and by using expressions (2), after simple but somewhat lengthy transformations we arrive at the following equations for e_x and e_y:

$$\frac{\partial^2 e_x(z,t)}{\partial z^2}=\mu_0\sigma_m\left(1-\frac{z}{z_0}\right)^2\frac{\partial}{\partial t}\left[\left(\frac{1+n}{2n}+\frac{1-n}{2n}\cos[2\omega t+2\theta(z)]\right)e_x(z,t)+\frac{1-n}{2n}\sin[2\omega t+2\theta(z)]e_y(z,t)\right], \tag{22}$$

$$\frac{\partial^2 e_y(z,t)}{\partial z^2}=\mu_0\left(1-\frac{z}{z_0}\right)^2\frac{\partial}{\partial t}\left[\frac{1-n}{2n}\sin[2\omega t+2\theta(z)]e_x(z,t)+\left(\frac{1+n}{2n}-\frac{1-n}{2n}\cos[2\omega t+2\theta(z)]\right)e_y(z,t)\right]. \tag{23}$$

Equations (22) and (23) are coupled linear partial differential equations of parabolic type with a variable in time and space coefficients. We would like to find the periodic solutions of these equations, subject to the boundary conditions (14) and (15). To this end, we introduce new complex valued state variables:

$$\varphi(z,t)=e_x(z,t)+ie_y(z,t),$$
$$\psi(z,t)=e_x(z,t)-ie_y(z,t). \tag{24}$$

By using these state variables, and some simple transformations, we can represent Eqs. (22) and (23) in the following form:

$$\frac{\partial^2\varphi}{\partial z^2}=\mu_0\sigma_m\frac{1-n}{2n}\left(1-\frac{z}{z_0}\right)^{-2}\frac{\partial}{\partial t}\left[\frac{1+n}{1-n}\varphi+\left(1-\frac{z}{z_0}\right)^{i2\alpha''}e^{i2\omega t}\psi\right], \tag{25}$$

$$\frac{\partial^2\psi}{\partial z^2}=\mu_0\sigma_m\frac{1-n}{2n}\left(1-\frac{z}{z_0}\right)^{-2}\frac{\partial}{\partial t}\left[\frac{1+n}{1-n}\psi+\left(1-\frac{z}{z_0}\right)^{-i2\alpha''}e^{-i2\omega t}\varphi\right]. \tag{26}$$

Assuming that functions $f_x(t)$ and $f_y(t)$ in boundary conditions (14) are function of half-wave symmetry (the case that is usually of the most practical interest), we conclude that $e_x(z,t)$ and $e_y(z,t)$ will also be the functions of half-wave symmetry. For this reason, we will use the following Fourier series for $\varphi(z,t)$ and $\psi(z,t)$:

$$\varphi(z,t)=\sum_{k=-\infty}^{\infty}\varphi_{2k+1}(z)e^{i(2k+1)\omega t}, \tag{27}$$

$$\psi(z,t)=\sum_{k=-\infty}^{\infty}\psi_{2k+1}(z)e^{i(2k+1)\omega t}. \tag{28}$$

It is clear from (24), (27), and (28) that

$$\varphi_{2k+1}^*(z)=\psi_{-2k-1}(z), \quad \psi_{2k+1}^*(z)=\varphi_{-2k-1}(z), \tag{29}$$

where the superscript "*" means a complex conjugate quantity.

By substituting (27) and (28) into (25) and (26), and by equating the terms with the same exponents, after simple transformations we derive

$$\left(1-\frac{z}{z_0}\right)^2\frac{d^2\varphi_{2k+1}}{dz^2}=i\chi_{2k+1}\left[a\varphi_{2k+1}-\left(1-\frac{z}{z_0}\right)^{i2\alpha''}\psi_{2k-1}\right], \tag{30}$$

$$\left(1-\frac{z}{z_0}\right)^2\frac{d^2\psi_{2k-1}}{dz^2}=i\chi_{2k-1}\left[a\psi_{2k-1}+\left(1-\frac{z}{z_0}\right)^{-i2\alpha''}\varphi_{2k+1}\right] \quad (k=0,\pm1,\pm2,\ldots), \tag{31}$$

where we have introduced the following notations:

$$a=\frac{1+n}{1-n}, \quad \chi_{2k+1}=(2k+1)\omega\mu_0\sigma_m\frac{1-n}{2n}. \tag{32}$$

Thus, we have reduced the problem of integration of partial differential equations (25)–(26) to the solution of infinite set of ordinary differential equations with respect to Fourier coefficients φ_{2k+1} and ψ_{2k-1}. The remarkable property of these simultaneous equations is that they are only coupled by pairs. It allows one to solve each pair of these coupled equations separately. After φ_{2k+1} and ψ_{2k-1} are found, we can compute $\varphi(z,t)$ and $\psi(z,t)$, and then $e_x(z,t)$ and $e_y(z,t)$. Another simplification is that according to (29) it suffices to solve coupled equations (30) and (31) only for non-negative values of k.

We shall seek a solution of the coupled equations (30) and (31) in the form

$$\varphi_{2k+1}(z)=A_{2k+1}\left(1-\frac{z}{z_0}\right)^{\beta},$$
$$\psi_{2k-1}=B_{2k-1}\left(1-\frac{z}{z_0}\right)^{\beta-i2\alpha''}. \tag{33}$$

By substituting (33) into (30) and (31), we end up with the following simultaneous homogeneous equations with respect to A_{2k+1} and B_{2k-1}:

$$(\beta^2-\beta-i\chi_{2k+1}z_0^2a)A_{2k+1}-i\chi_{2k+1}z_0^2B_{2k-1}=0, \tag{34}$$

$$-i\chi_{2k-1}z_0^2A_{2k+1}+[(\beta-i2\alpha'')^2-(\beta-i2\alpha'')-i\chi_{2k-1}z_0^2a]B_{2k-1}=0. \tag{35}$$

The above homogeneous equations have a nonzero solution for A_{2k+1} and B_{2k-1} if and only if the corresponding determinant is equal to zero. This yields the following characteristic equation for β:

$$(\beta^2-\beta-i\chi_{2k+1}z_0^2a)[(\beta-i2\alpha'')^2-(\beta-i2\alpha'')-i\chi_{2k-1}z_0^2a]+\chi_{2k+1}\chi_{2k-1}z_0^4=0. \tag{36}$$

From expressions (32) and (18), we find

$$\chi_{2k+1}z_0^2a=\frac{(2k+1)(3n+1)(n+1)}{(n-1)^2}\sqrt{\frac{n+1}{2n}}, \tag{37}$$

$$\chi_{2k+1}\chi_{2k-1}z_0^4=\frac{(4k^2-1)(3n+1)(n+1)}{(n-1)^2}\sqrt{\frac{n+1}{2n}}. \tag{38}$$

From the last two expressions, we conclude that the coefficients of the characteristic equation (36) depend on the exponent, n, of the power law and k. Consequently, the roots of this equation also depend only on n and k. It can be proven that the above characteristic equation has two roots $\beta_1(n,k)$ and $\beta_2(n,k)$ with positive real parts. After these roots are found, the solution of coupled equations (30) and (31) can be represented in the form

$$\varphi_{2k+1}(z)=A_{2k+1}^{(1)}\left(1-\frac{z}{z_0}\right)^{\beta_1}+A_{2k+1}^{(2)}\left(1-\frac{z}{z_0}\right)^{\beta_2}, \tag{39}$$

$$\psi_{2k-1}(z)=B_{2k-1}^{(1)}\left(1-\frac{z}{z_0}\right)^{\beta_1-i2\alpha''}+B_{2k-1}^{(2)}\left(1-\frac{z}{z_0}\right)^{\beta_2-i2\alpha''}, \tag{40}$$

where, for the sake of notational simplicity, we have omitted the dependence of β_1 and β_2 on n and k.

From boundary conditions (14) and expressions (24) and (34), we obtain the following equations for $A_{2k+1}^{(1)}$, $A_{2k+1}^{(2)}$, $B_{2k-1}^{(1)}$, and $B_{2k-1}^{(2)}$:

$$\beta_1z_0A_{2k+1}^{(1)}+\beta_2z_0A_{2k+1}^{(2)}=\mu_0H_m(-f'_{y,2k+1}+if'_{x,2k+1}), \tag{41}$$

$$(\beta_1-i2\alpha'')z_0B_{2k-1}^{(1)}+(\beta_2-i2\alpha'')z_0B_{2k-1}^{(2)}=\mu_0H_m(-f'_{y,2k-1}-if'_{x,2k-1}), \tag{42}$$

$$(\beta_1^2-\beta_1-i\chi_{2k+1}z_0^2a)A_{2k+1}^{(1)}-i\chi_{2k+1}z_0^2B_{2k-1}^{(1)}=0, \tag{43}$$

$$(\beta_2^2-\beta_2-i\chi_{2k+1}z_0^2a)A_{2k+1}^{(2)}-i\chi_{2k+1}z_0^2B_{2k-1}^{(2)}=0, \tag{44}$$

where $f'_{x,2k+1}$ and $f'_{y,2k+1}$ are complex Fourier coefficients of f'_x and f'_y.

By solving simultaneous equations (41)–(44), we can find coefficients $A_{2k-1}^{(1)}$, $A_{2k+1}^{(2)}$, $B_{2k-1}^{(1)}$, and $B_{2k-1}^{(2)}$. Then, by using (39), (40), (27)–(28), and (24), we can determine perturbations $e_x(z,t)$ and $e_y(z,t)$, which, in turn, can be used in (8) to compute the total electric field.

In conclusion, consider the particular case when

$$f_x(t)=\cos\omega t, \quad f_y=\sin\omega t. \tag{45}$$

This case corresponds to elliptical polarization of the incident field. It is easy to see that in this case, the right-hand sides of Eqs. (41) and (42) are equal to zero for all k except $k=1$. This means that only first and third harmonics are not equal to zero. We have reached this conclusion, because we have considered only first-order perturbations with respect to ϵ. If we consider higher-order perturbations with respect to ϵ, we shall recover higher-order harmonies of the electric field.

From the purely mathematical point of view, it is remarkable that the solution of coupled equations (22)–(23), corresponding to the boundary conditions (14), (15) and (45), contains only the first and third harmonics. Probably, this is because the coupled PDE's (22) and (23) have inherited some symmetry properties from the unperturbed problem, corresponding to the circular polarization of the incident wave.

Finally, we note that in the limiting case of $n\to\infty$, we obtain from the presented formulas the distribution of electromagnetic fields for ideal (sharp) resistive transition.

ACKNOWLEDGMENT

The reported research is supported by the U.S. Department of Energy, Engineering Research Program.

[1] C. P. Bean, J. Appl. Phys. **41**, 2482 (1970).
[2] I. D. Mayergoyz, J. Appl. Phys. **75**, 6963 (1994).
[3] C. S. Nichols and D. R. Clarke, Acta Metall. Matter **39**, 995 (1991).
[4] J. W. Elkin, Cryogenics **2**, 603 (1987).
[5] C. J. G. Plummer and J. E. Evetts, IEEE Trans. Magn. **23**, 1179 (1987).

Proximity effect in MBE-grown superconducting/spin-glass multilayers

Carlos W. Wilks, Brad N. Engel, and Charles M. Falco
Department of Physics and the Optical Sciences Center, University of Arizona, Tucson, Arizona 85721

We have grown epitaxial superconductor/spin-glass multilayers, Nb/CuMn, as well as complimentary nonmagnetic Nb/Cu multilayers by molecular beam epitaxy. To probe the interaction of superconductivity and magnetism, we measured the resistivity and ac susceptibility as a function of temperature for multilayers of nominally constant Nb thickness and varying normal-metal thickness. The reduction of the transition temperature of the Nb/Cu multilayers with increasing Cu thickness is in excellent agreement with the de Gennes–Werthamer proximity effect theory. The inclusion of Mn in the Cu causes a significant additional suppression of the transition temperatures relative to the Nb/Cu multilayers. The extension of the de Gennes–Werthamer theory to include the effects of random magnetic impurities agrees well with the data from the Nb/CuMn multilayers for small CuMn layer thicknesses. However, deviations occur at the largest CuMn thicknesses studied. These deviations between the data and theory may be due to a decoupling of the Nb layers, as a result of the spin-glass ordering, causing a three-dimensional to two-dimensional crossover.

I. INTRODUCTION

The coexistence of superconductivity and magnetism has been the focus of many studies over the years, because magnetism is, in general, detrimental to the superconducting state. Nonetheless, ferromagnetism and antiferromagnetism have been shown to coexist with superconductivity.[1,2] Superconductivity can also coexist with spin-glass materials in which the localized impurity spins interact through the conduction electrons. Below the spin-glass freezing temperature, the spins can be considered frozen in the random direction of the local magnetic field instead of forming any long-range magnetic order.

While most of the work to date on the interaction of magnetism and superconductivity has been on bulk alloys with magnetic impurity substitutions, there has been some more recent work on artificial structures, namely, multilayers.[3] To date, the majority of the superconducting/magnetic multilayers have been fabricated in high vacuum systems (10^{-7}–10^{-8} Torr) using sputtering, electron beam, and/or thermal evaporation. Our work utilizes molecular beam epitaxy (MBE) techniques (10^{-10}–10^{-12} Torr) in order to fabricate high-quality multilayers with improved properties.

We chose to study the interaction of magnetism and superconductivity in the Nb/CuMn multilayer system, where CuMn is a well-studied spin-glass system. Due to finite size effects,[4] the spin-glass freezing temperature, T_f, where the magnetic moments locally align, scales with the thickness of the CuMn film. The Nb transition temperature also depends on film thickness, decreasing from the bulk value as the film thickness is reduced. These two effects allow us to tailor the multilayer system, such that either T_c or T_f is higher. This allows the interplay of the two phenomena to be studied. Work on sputtered Nb/CuMn multilayers has been recently reported.[5,6] We have also deposited the complementary Nb/Cu multilayer system as a nonmagnetic baseline reference for comparison.

II. EXPERIMENTAL PROCEDURES

The multilayers were grown in a Perkin-Elmer 433-S MBE system with a base pressure of $\sim 5\times10^{-11}$ Torr. *In situ* reflection high-energy electron diffraction (RHEED) and low-energy electron diffraction (LEED) were used for structural characterization. The Nb and Cu are deposited using separate electron beam guns, while the Mn is deposited from an effusion cell. The multilayers are grown on Si(111) wafers. The wafers are first dipped in a 2% HF acid solution and then immediately annealed to 850 °C in the MBE system. RHEED is performed on the substrate to check the quality of the resultant 7×7 Si(111) reconstruction. The reconstruction is a good indication of a high-quality impurity free surface. We then grow a 40 Å epitaxial fcc Cu(111) buffer layer on the Si wafer once it has cooled to room temperature. The buffer layer is a necessary seed to grow bcc Nb(110). Using this technique, the Nb and the Cu layers grow epitaxially with their densest packed planes parallel to the substrate. RHEED is again employed during the growth of the buffer layer to monitor crystal quality.

During all depositions, the substrate is rotated at 10 rpm about its normal to enhance the uniformity of the films. The pressure in the MBE system during the multilayer deposition is in the $2\text{–}5\times10^{-9}$ Torr range. The Nb is deposited first at a rate of 0.6 Å/s followed by a Cu deposition at a rate of 0.3 Å/s. For Nb/CuMn, the CuMn layers are formed by a codeposition of Cu at a rate of 0.3 Å/s and Mn at 0.021 Å/s, resulting in a spin-glass having seven at. % Mn. Again, we use RHEED to probe the top surface of the multilayer to confirm epitaxial growth. All the multilayers consist of ten bilayers, in which the thickness of the Nb layers was constant at nominally 230 Å and the normal-metal thickness was varied. The actual layer thicknesses of each of the multilayers was determined from the Rutherford backscattering spectroscopy (RBS). In Table I, we present the measured layer thicknesses, the expected spin-glass freezing temperatures and the measured multilayer transition temperatures for this series of multilayers.

 0021-8979/94/76(10)/6959/3/$6.00 © 1994 American Institute of Physics

TABLE I. Multilayers design parameters.

	d_s (Å)	d_n (Å)	T_f (K)	T_c (K)
Nb/CuMn	232	3.3	2.6	8.57
	220	7.25	5.1	7.79
	245	9.6	6.1	7.59
	217	19.6	11.4	5.69
	223	29.2	15.2	4.69
	239	53	20.2	4.62
	231	84.3	23.8	4.53
	230	106.5	26.7	4.85
Nb/Cu	278	8.4		9.19
	257	24		8.93
	247	61		8.49

Low temperature measurements were performed using a charcoal-pumped ^{3}He cryostat. Both the resistance and the ac susceptibility measurements were simultaneously measured using ac lock-in techniques. A calibrated Ge thermometer in close thermal contact to the samples was used to measure the temperature. The superconducting transition temperatures of the multilayers are determined upon cooling from the onset of the susceptibility transition.

III. RESULTS AND DISCUSSION

High and low angle x-ray diffraction are performed on each multilayer. From the high angle x-ray diffraction scans, we find the Nb grows in the (110) orientation, and the Cu or CuMn grows in the (111) orientation, as expected. We present, in Fig. 1(a), the high angle x-ray scan, and in Fig. 1(b), the low angle x-ray scan for a Nb(239 Å)/CuMn(53 Å) multilayer. The high angle scan is representative for all the multilayers made. From the peak positions in the high angle scans, we find the Nb lattice constant is compressed by less than 2% relative to bulk Nb, while the Cu lattice constant is expanded by less than 1% relative to bulk Cu. Low angle x-ray diffraction was also performed as a check on the multilayer quality and to obtain an additional measure of the bilayer thickness. This value was then compared to the results obtained from RBS. Multilayer Bragg peaks are seen in the low angle scans for multilayers with a Cu or CuMn thickness of 9 Å or greater. Fitting of the low angle x-ray scans to a Fresnel-type optical model yields values for the interfacial roughness of less than 8 Å. This agrees well with the maximum top layer roughness, as determined by atomic force microscopy.

The relevant theory to describe the superconducting properties of our Nb/Cu multilayers is the de Gennes–Werthamer[7] theory. It applies to the case when the materials in the superconducting/normal-metal sandwich are in the dirty limit. This theory requires the coherence length, ξ_i, of each material be smaller than the layer thickness, d_i, and the mean-free paths, l_i, of each material be smaller than the coherence length. The extension of this theory to include magnetic impurities in the normal metal was done by Hauser, Theuerer, and Werthamer.[8] The equations that relate the physical parameters of the individual materials to the transition temperature, T_c, of the multilayer are given in the paper by Banerjee.[9]

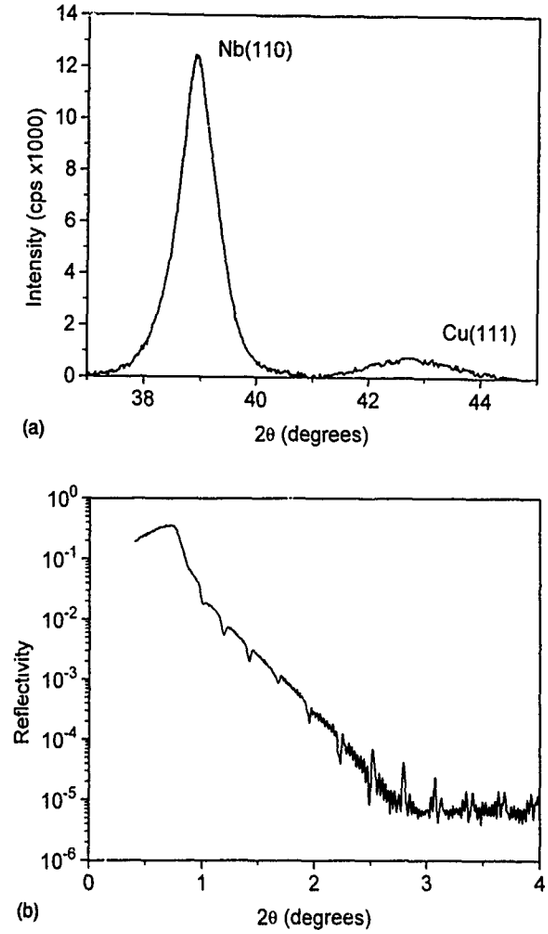

FIG. 1. (a) High angle and (b) low angle x-ray scans of the Nb(239 Å)/CuMn(53 Å) multilayer.

As a verification of our Nb film quality, a thick Nb film was grown and T_c determined. For an 860 Å Nb film grown on a 40 Å Cu buffer layer, $T_c = 9.27$ K, in good agreement with the transition temperature of bulk Nb. Thus, we can rule out the possibility of localization effects[10] and lifetime broadening of the density of states[11] as a cause of the reduction in T_c in our multilayers.

In Fig. 2, we show the transition temperature of our multilayer series as a function of normal-metal thickness. The upper data set (squares) is for the Nb/Cu multilayers, while the middle set (diamonds) is for the Nb/CuMn series. Applying the de Gennes–Werthamer theory to the Nb/Cu multilayers yields excellent agreement between the measured and calculated values for T_c with no adjustable parameters. The calculated values are within 0.02 K of the measured T_c values for all three of the Nb/Cu multilayers. The inclusion of Mn in the Cu layers causes a dramatic decrease of the transition temperature of the Nb/CuMn multilayers, as expected for these magnetic atoms.

When a dilute concentration of randomly oriented and distributed magnetic moments are included in the normal-metal, the equation relating T_c to the relevant physical parameters is modified by the inclusion of an electron relaxation time due to the magnetic pair breaking. Strictly speak-

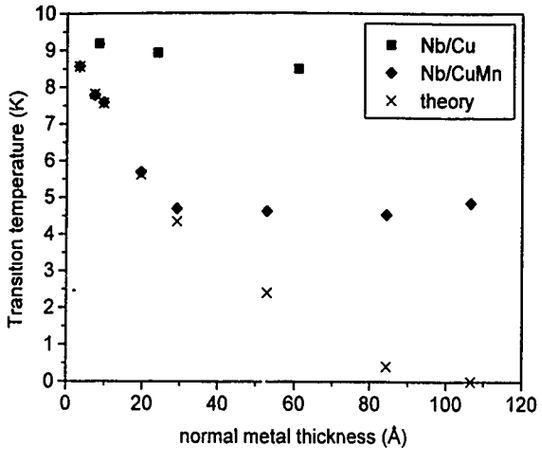

FIG. 2. Transition temperatures of the multilayers as a function of normal-metal thickness.

ing, the extension of the de Gennes–Werthamer theory to include random magnetic impurities should not apply to our multilayers with thick CuMn layers, where the Mn moments locally order. Applying the theory to the multilayer with a CuMn layer thickness of 3.3 Å, where $T_f < T_c$, and where the theory is most likely to be valid, yields a reasonable value for the electron relaxation time, τ_s, of 9.6×10^{-15} s. Using this value of τ_s as an input for the theory, we can calculate T_c values for the other multilayers. This yields the cross points marked theory in Fig. 2. The theory is in good agreement for the first four data points (the theory is set equal to the first data point), but then falls well below the measured values at larger thicknesses. Clearly the magnetic extension of the Werthamer theory fails to describe all the data.

For those multilayers with $T_f > T_c$, where the Mn moments are in a locally more ordered state, one would expect a greater suppression of T_c than predicted by the random magnetic impurity model. This is not the case. It is interesting to note that the deviation between the data and the theory begins near the CuMn thickness, where T_f becomes larger than T_c. In addition, as the CuMn layer thickness is increased, a three-dimensional to two-dimensional crossover decoupling the Nb layers is expected. Further work is needed to determine if the deviations from the theory are a result of a dimensional crossover or are driven by the spin-glass ordering of the CuMn. Parallel critical field measurements are now underway to investigate at what normal-metal thickness the three-dimensional to two-dimensional crossover takes place.

IV. CONCLUSION

We have grown epitaxial spin-glass/superconductor multilayers of Nb and CuMn, as well as the nonmagnetic Nb/Cu multilayers using MBE. The suppression of T_c for the Nb/Cu multilayers is in excellent agreement with the de Gennes–Werthamer proximity effect theory, without the complication of localization or lifetime broadening of the density of states. At small CuMn thicknesses, the additional depression of T_c caused by the inclusion of Mn in the Cu can be described by the extension of the de Gennes–Werthamer theory for random magnetic impurities. The data and theory disagree for the larger CuMn layer thicknesses. This may be due to a three-dimensional to two-dimensional crossover decoupling the Nb layers, and is currently under investigation.

ACKNOWLEDGMENTS

We gratefully acknowledge J. Leavitt and L. Macintyre for the RBS measurements. This work was supported by the Office of Naval Research under Contract No. N00014-92-J-1159.

[1] M. Ishikawa and Ø. Fisher, Solid State Commun. **23**, 37 (1977).
[2] W. A. Fertig, D. C. Johnston, L. E. Delong, R. W. McCallum, M. B. Maple, and B. T. Matthias, Phys. Rev. Lett. **38**, 987 (1977).
[3] B. Y. Jin and J. B. Ketterson, Adv. Phys. **38**, 189 (1989).
[4] G. G. Kenning, J. M. Slaughter, and J. A. Cowen, Phys. Rev. Lett. **59**, 2596 (1987).
[5] M. L. Wilson and J. A. Cowen, Phys. Rev. B **49**, 6228 (1994).
[6] C. Attanasio, L. Maritato, B. Engel, and C. M. Falco, Physica B **194–196**, 1721 (1994).
[7] N. R. Werthamer, Phys. Rev. **132**, 2440 (1963).
[8] J. J. Hauser, H. C. Theuerer, and N. R. Werthamer, Phys. Rev. **142**, 118 (1966).
[9] I. Banerjee, Q. S. Yang, C. M. Falco, and I. K. Schuller, Solid State Commun. **41**, 805 (1982).
[10] C. C. Koch, J. O. Scarbrough, and D. M. Kroeger, Phys. Rev. B **9**, 888 (1974).
[11] S. I. Park and T. H. Geballe, Physica B **135**, 108 (1985).

Heterodyne microwave mixing in a superconducting $YBa_2Cu_3O_{7-x}$ coplanar waveguide circuit containing a single engineered grain boundary junction

R. G. Seed and C. Vittoria
Department of Electrical and Computer Engineering, Northeastern University, Boston, Massachusetts 02115

A. Widom
Department of Physics, Northeastern University, Boston, Massachusetts 02115

The purpose of this work was to utilize the nonlinear current-voltage properties of induced grain boundaries in high temperature superconducting $YBa_2Cu_3O_{7-x}$ thin films to fabricate a planar microwave mixer. The experiment involved constructing a coplanar waveguide microwave circuit, the center conductor of which had a constriction patterned in it containing a single high angle grain boundary, thus forming a weak link junction. Analysis was provided by use of the resistively shunted junction model with excess current.

I. INTRODUCTION

Sufficient precedent exists, as a result of previous work in years past on low temperature superconducting mixers, which provides the motivation for conducting extensive research in microwave and millimeter wave mixers using high temperature superconductors. For example, theoretical calculations on lower bounds on noise temperature have been determined for superconducting-insulator-superconducting (SIS) mixers employing quasiparticle tunneling.[1] These theoretical limits have been approached experimentally, providing noise temperatures below those currently available in semiconductor devices.[2] At least one experimental result has demonstrated a positive conversion gain using low temperature superconducting tunnel junctions.[3]

Since the introduction of high temperature superconductors, several reports of mixing have appeared. Some of these measurements were performed using the transition resistance occurring above the temperature at which the dc resistance falls to zero.[4] Other successful experiments in mixing have been reported using materials other than $YBa_2Cu_3O_{7-x}$ (YBCO).[5] Microwave mixing using YBCO and employing weak link effects, have been reported. These devices contain weak links involving polycrystalline materials with multiple randomly oriented grain boundaries or involving step edge junctions.[6–9] Some of these devices, indeed, have shown remarkable results in terms of conversion loss in mixing at microwave frequencies.[10]

The purpose here has been to construct truly planar superconducting YBCO mixers employing artificially induced grain boundaries with predictable angles, and to characterize these grain boundary mixers by employing suitable physical models.

II. EXPERIMENTAL DETAILS

The starting material was an epitaxial YBCO thin film, which was grown by laser ablation deposition on a bicrystalline $SrTiO_3$ substrate.[11] This substrate was composed of two crystals joined together with an interface that formed a 36.8° angle.

The coplanar waveguide circuit was patterned on this thin film, such that a 30 μm wide microbridge was formed, which spanned the bicrystal boundary, and thereby induced a single grain boundary in the microbridge, as is evident in the mixer circuit depicted schematically in Fig. 1. The pattern was obtained by conventional wet etching.

This procedure resulted in circuits with constrictions that would contain a single grain boundary with an angle of 36.8°. Such circuits exhibit greatly reduced critical current densities and weak link properties.[12,13]

The etched circuit was mounted on an acrylic block, and the coplanar waveguide was connected to 50 Ω cables by means of SMA to microstrip launchers. The dc probes for applying bias current and measuring the voltage were composed of stainless steel spring loaded contacts, which mated with the surface of the center conductor in the circuit. This configuration is also shown in Fig. 1.

Output from the two microwave sources used for mixing could be independently adjusted in power and frequency. The signals were combined in a directional coupler, and then passed through a dc block and into the device. The output signal passed through the output launcher from the device and through a second dc block into a high gain spectrum

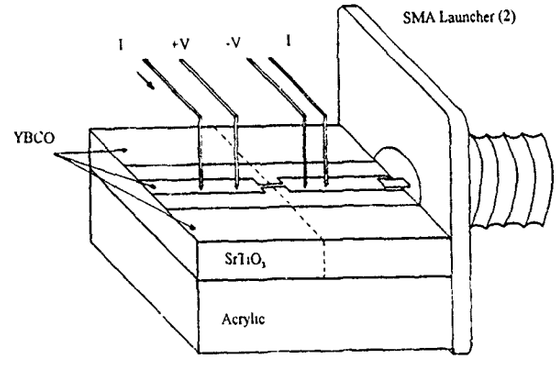

FIG. 1. Schematic drawing of coplanar waveguide YBCO mixer circuit showing the substrate bicrystal interface, the location of the microbridge constriction with respect to the bicrystal interface, the bias contacts, and the microwave SMA launchers

 0021-8979/94/76(10)/6962/3/$6.00 © 1994 American Institute of Physics

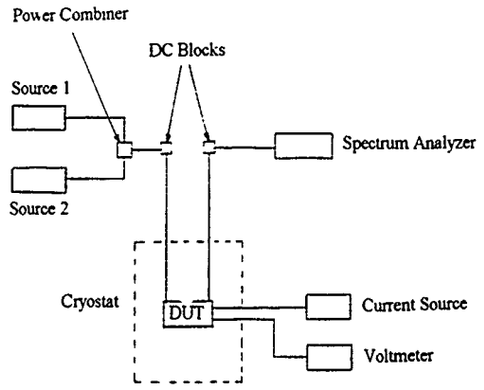

FIG. 2. Schematic diagram of the experimental microwave mixer test apparatus.

analyzer. The experimental apparatus is depicted in Fig. 2.

First, current versus voltage characteristic curves were obtained for the junction, in the absence of microwave energy, and recorded. When the junction was driven by the local oscillator, with microwave energy, current steps were produced in the current voltage characteristic curve. These steps appeared at voltages that were integral multiples of the flux quantum times the frequency. Both characteristic curves are overlaid in Fig. 3. The current steps, evident in Fig. 3, were the basis for adjustments of the current bias levels, and were the nonlinear contribution of the circuit, which was utilized for down-conversion mixing.

III. THEORETICAL MODELING

Modeling of the coplanar waveguide circuit involved the use of some approximations of the standard equations.[14] Approximate values for the transmission line characteristic impedances were obtained using the value of $\epsilon_r=9190$, obtained from published data[15] and a value of tan $\delta=0.03$ obtained from literature.[16] From the characteristic impedances, together with the transmission line dimensions, and by using transmission line matrix methods, it was possible to calculate the input impedance of the transmission line at the signal frequency and the local oscillator frequency. The value obtained was found to be $Z_{IN,S}=1.368-j0.116$ and $Z_{IN,LO}=1.396+j0.144$. Using the input impedances and the transmission line matrices, together with the knowledge of the input signal power and input local oscillator power, it was possible to estimate the respective currents on the microbridge portion of the transmission line. This was found to be $I_S=-555.8\times10^{-6}-j562.4\times10^{-6}$ A and $I_{LO}=483.8\times10^{-6}+j187.5\times10^{-6}$ A.

With an estimated value of the currents due to the two input microwave signals, and a knowledge of the bias current, a calculation for the output current level was obtained using the following two equations:

$$I=I_c \sin \phi \tag{1}$$

and

$$-\frac{\hbar}{q}\frac{d\phi}{dt}=R_N(I_B+I_{LO}\cos \omega_{LO}t+I_S \cos \omega_S t-I_0 - I_c \sin \phi). \tag{2}$$

Equations (1) and (2) are recognized as the Josephson relations used in the resistively shunted junction model for the shunted Josephson junction, with excess current, I_0,[17] I_B is the dc bias current, I_0 is the superconducting excess shunt current, R_N is the normal mode resistance obtained from the characteristic curves, and q is the superconducting pair charge. These equations were solved numerically using the technique of Runge–Kutta in double precision and then subject to a discrete Fourier transform to extract the harmonic content. These calculations yielded the result for the magnitude of $I_{i.f.}$, the current of the intermediate frequency at the junction, which was $I_{i.f.}=4.25\times10^{-6}$ A$=3.00\times10^{-6}$ A (rms). The calculated value of $I_{i.f.}$ was then used again in the matrix representation of the transmission line using impedances determined at the intermediate frequency. The result was an output power of -82 dB m.

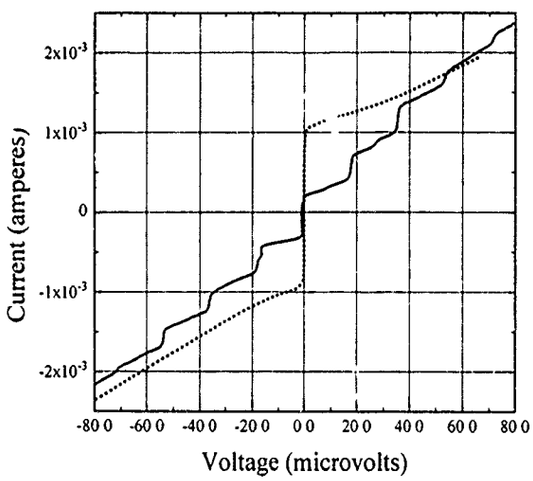

FIG. 3. Current voltage characteristic curves for YBCO grain boundary weak link junction. Dotted line is without rf signal. Solid line with rf energy at 8.7 GHz.

IV. RESULTS AND DISCUSSION

When the circuit was dc current biased near any one of the current steps, and when both the microwave local oscillator and the microwave signal were applied, an intermediate frequency was observed at the difference frequency. In the experiments, the local oscillator was at 8.7 GHz and the signal frequency was at 7.7 GHz, therefore the difference frequency was measured at 1.0 GHz. The input signals are shown as an inset in Fig. 4 and output intermediate frequency is shown in Fig. 4.

It was determined that the conversion loss of the mixer was dependent upon the input power and the bias current. Approximate relative values of conversion gain are shown in Fig. 5. It was evident during the experiment that mixing was absent for bias values between steps, whereas the i.f. signal was maximum when the bias current was located within the

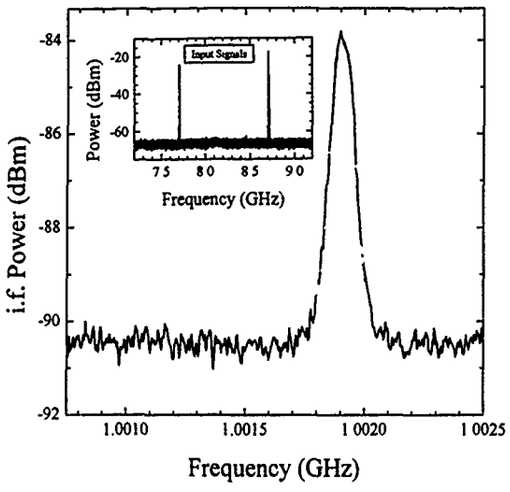

FIG. 4. Output intermediate frequency, i.f., signals at temperature 45 K, with dc current bias of 0.78 mA. Input microwave signals are shown in the inset.

range of values of the current steps. The smallest conversion loss appeared at current values corresponding to the $n = \pm 1$ steps.

The bias current levels were theoretically and experimentally observed to provide mixing when biased at the steps. The measured conversion loss agrees with the theoretical calculation to within 3 dB.

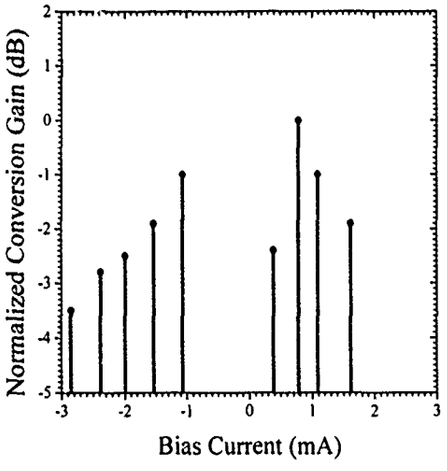

FIG. 5. Approximate experimental values of conversion gain for YBCO grain boundary mixer at $T = 45$ K vs bias current. Values are relative to the minimum conversion loss at 0.78 mA bias current.

V. CONCLUSION

The coplanar waveguide geometry allowed the fabrication of a high frequency transmission line in one plane. This eliminated the need for copper grounding blocks, and allowed the circuit to be fabricated using standard wet etch technology. Thus, there is potential use in monolithic microwave integrated circuits.

The use of engineered grain boundary junctions provided the opportunity to characterize the intrinsic operation of the weak link junctions used as mixers. It allowed the reproducible fabrication and testing of weak link junctions with similar results, since the grain boundary angles could be assured during their construction. However, by using $SrTiO_3$ substrates, the resulting embedding impedances limited the amount of i.f. power efficiently coupled to the output.

Using the resistively shunted junction model with excess current, it was possible to mathematically model the operation of superconducting grain boundary mixers using the coplanar waveguide configuration. The calculations are in excellent agreement with the measured results, and should provide insight in further developments.

ACKNOWLEDGMENTS

This work was supported in part by TRW Inc. and the NSF. The authors would like to thank Rick Verrault of M/A-COM for providing several microwave components and to thank Dr. Paul Dorsey at the Naval Research Laboratory for several useful contributions.

[1] M. J. Wengler and D. P. Woody, IEEE J. Quantum Electron. **23**, 613 (1987).
[2] W. R. McGrath, P. L. Richards, D. W. Face, D. E. Prober, and F. L. Floyd, J. Appl. Phys. **63**, 2477 (1988).
[3] Y. Taur, J. H. Claasen, and P. L. Richards, Appl. Phys. Lett. **24**, 101 (1974).
[4] J. Konopka, R. Sobolowski, G. Jung, W. Kula, P. Gierlowski, A. Konopka, and S. J. Lewandowski, IEEE Trans. Microwave Theor Tech. **38**, 160 (1990).
[5] H. K. Olsson, W. R. McGrath, T. Claeson, S. Eriksson, and L. G. Johansson, J. Appl. Phys. **62**, 4923 (1987).
[6] K. Y. Constantinian, L. E. Amatuni, A. A. Hakhumian, R. B. Hayreptian, and R. M. Martirossian, Physica B **173**, 313 (1991).
[7] Y. Fukumoto, H. Kajikawa, R. Ogawa, and Y. Kawate, Jpn. J. Appl. Phys. **31**, L1239 (1992).
[8] Y. Yoshisato, M. Takei, K. Niki, S. Yoshikawa, T. Hirano, and S. Nakano, IEEE Trans. Magn. **27**, 3073 (1991).
[9] P. H. Wu, Y. Xu, and C. Heiden, Appl. Phys. Lett. **57**, 1265 (1990).
[10] D. P. Butler, J. Wang, A. Bhandari, and Z. Celik-Butler, IEEE Trans. Appl. Sup. **3**, 2269 (1993).
[11] R. G. Seed, P. C. Dorsey, H. How, A. Widom, and C. Vittoria, IEEE Trans. Magn. **29**, 3568 (1993).
[12] P. Chaudhari J. Mannhart, D. Dimos, C. C. Tsuei, J. Chi, M. M. Oprysko, and M. Scheuermann, Phys. Rev. Lett. **60**, 1653 (1988).
[13] R. Gross, P. Chaudhari, D. Dimos, A. Gupta, and G. Koren, Phys. Rev. Lett. **64**, 228 (1990).
[14] K. C. Gupta, R. Garg, and I. J. Bahl, *Microstrip Lines and Slotlines* (Artech House, Dedham, MA, 1979).
[15] G. A. Samara, Phys. Rev. **151**, 378 (1966).
[16] J. Talvacchio, G. R. Wagner, and S. H. Talisa, Microwave J. **34**, 105 (1991).
[17] R. G. Seed, C. Vittoria, and A. Widom, J. Appl. Phys. **75**, 8195 (1994).

Superconducting $YBa_2Cu_3O_{7-x}/Y_4Ba_3O_9$ multilayers: Field independent critical current and dimensional crossover (abstract)

Jun-Hao Xu, A. M. Grishin, and K. V. Rao
Department of Condensed Matter Physics, Royal Institute of Technology, S-100 44 Stockholm, Sweden

A new class of c-axis-oriented $YBa_2Cu_3O_{7-x}/Y_4Ba_3O_9$ (YBCO/YBO) multilayer films with YBCO and YBO individual thicknesses ranging from 24 to 156 Å have been fabricated by a single target on-axis biased rf magnetron sputtering technique on $LaAlO_3$ (001) substrates. SQUID dc magnetic measurements reveal a striking feature of magnetic field independent critical current $j_c(T)$ from 5 K to almost near superconducting transition T_c. For thin YBCO layer thickness the magnitude of j_c is found to decrease as $(1-T/T_c)^2$, and exponentially with the thickness of the isolating spacer YBO. It is distinctly shown that $j_c(T)$ in the (**a**,**b**) plane is determined by interlayer Josephson current. All the SQUID data for the temperature dependencies of magnetization for a few families of multilayers with thin YBCO layers are shown to scale and collapse into a single universal behavior consistent with a model of "slipped out pancake vortices in Josephson coupled heterostructures." On approaching T_c, the characteristics of critical current j_c change gradually from the field independent behavior to another dependence similar to an ordinary $H^{-1/2}$ dependence typical for collective pinning of the vortex lattice in the YBCO single layer film. This suggests that a dimensional crossover takes place when the quantum coherence between individual YBCO layers sets. The crossover temperature is found to depend on the multilayer period and individual thicknesses of superconducting and isolating layers while a linear temperature dependence of j_c appears for multilayers with thick YBCO layers.

Schematic frictional model for interacting vortices in an isotropic superconducting plate (abstract)

J. S. Kouvel[a] and S. J. Park
Department of Physics, University of Illinois, Chicago, Illinois 60680

In the simple model proposed, repulsive intervortex forces are balanced by containing forces produced by the external field (H) and by frictional forces representing the effects of pinning on displaced vortices. For the field-cooled (FC) state, whose vortex density is presumably uniform, the empirical fact that the average flux density ($\bar{B}$) in nearly equal to H yields an operational inverse-square dependence of the intervortex force on the intervortex spacing. For both the FC and zero-field-cooled (ZFC) states, expressions are derived for $\bar{B}$ vs H (including the remanences at $H=0$) and for the profiles of B across the sample thickness. Calculations of these properties are compared with experiment and with the macroscopically related critical-state model, revealing again that the pinning forces are strongly dependent on H. The frictional interacting-vortex model is also used in deriving the critical current as a transport property of the FC and ZFC states.

[a]Work supported in part by the NSF (DMR-92-21901).

 0021-8979/94/76(10)/6965/1/$6.00 © 1994 American Institute of Physics

Spin-polarized photoemission from quantum well and interface states (invited)

C. Carbone, E. Vescovo, R. Kläsges, and W. Eberhardt
IFF/KFA Jülich, D-52425 Jülich, Germany

O. Rader and W. Gudat
BESSY, D-14195 Berlin, Germany

We examine the role of quantum well and interface states in mediating the coupling between magnetic films. We have studied with spin- and angle-resolved photoemission the electronic structure of Cu on Co(100) and Ag on Fe(100). Noble metal states of *sp*-derived character are found to be spin-polarized upon contact with the magnetic materials. In Cu films up to 10 monolayer thickness polarized states have been observed. These observations are well described within the framework of one-dimensional quantum-well states, for film thicknesses above a few monolayers. In the low coverage regime, the hybridization with the magnetic states of the substrate strongly influences the character and the dispersion of the conduction bands.

I. INTRODUCTION

The origin of the indirect exchange coupling[1] between magnetic layers separated by a nonmagnetic spacer is related to the Fermi surface of the spacer material, in a Ruderman–Kittel–Kasuya–Yasida (RKKY) picture[2] as well as in a quantum well picture.[3] The oscillatory and long range character of the indirect exchange coupling in magnetic multilayers can be explained within the framework of RKKY interactions. Studies based on the RKKY coupling scheme identify the experimentally found oscillations as a Fermi surface effect within the nonmagnetic spacer material.

A full understanding of the coupling mechanisms should require however a detailed description of the conduction band states, explicitly including the modification due to the reduced dimensionality and to the exchange interaction. In interface systems with one magnetic component, the bonding at the interface often induces a polarization in the nonmagnetic material through a spin-dependent electronic hybridization.[4,5] The resulting moment in transition metal overlayers on magnetic substrates depends primarily on the extent of the *d*-*d* hybridization. For a noble metal on a 3*d* ferromagnet the calculated interface moment is very small ($<0.1\ \mu_B$)[4] because of the small degree of overlap between the *d* states of the two metals.

The induced magnetization of the *d* electrons of a nonmagnetic material typically becomes negligible a few atomic layers away from the interface.[4,5] On the other hand, the spin-polarization induced on the more delocalized *sp* states can extend over several layers. Therefore, those states provide a way of mediating the long range indirect coupling among magnetic layers through a wide class of nonmagnetic materials, including transition and noble metals. The recent quantum well approach relates the coupling to *sp*-derived electronic states observable in electron spectroscopies.[6–8] Ortega *et al.*[6] found that the *sp*-derived electronic states of ultrathin noble metal films present some characteristic features of one-dimensional quantum-well states. In addition, their wave vector can be related within a simple picture to the wave vectors of the RKKY coupling in the asymptotic high coverage limit. This unusual set of properties suggested that polarized quantum-well states could provide the coupling through nonmagnetic layers.

Here we review some of our recent experimental results on quantum-well and interface states of noble metal films on magnetic substrates. We applied spin- and angle-resolved photoemission spectroscopy, being directly sensitive to magnetic information, to systems which have shown oscillatory coupling and which can be grown epitaxially on (100) single crystal surfaces. Results from spin-resolved photoemission are presented to clarify some aspects of the oscillatory magnetic coupling through the noble metals, Cu and Ag. The experiments comprise (i) the asymptotic limit of the coupling, where the bulk electronic structure of the nonmagnetic material has developed, and (ii) the low coverage limit, where the hybridization with the magnetic interface is the determining factor.

II. EXPERIMENT

The spin- and angle-resolved photoemission apparatus[9] consists of a spherical energy analyzer coupled to a 100 keV Mott detector for spin analysis. The spectra were measured with monochromatic synchrotron radiation from the storage ring BESSY in Berlin. The experimental geometry allows for a component of the electric field vector perpendicular to the surface plane. Photoemission spectra were measured with photon energies between 10 and 80 eV on the TGM5 and the TGM1 beamlines.

The growth of Cu on Co(100) and Ag on Fe(100) has been characterized by several methods.[10] A full account of our preparation and characterization procedures can be found

 0021-8979/94/76(10)/6966/6/$6.00 © 1994 American Institute of Physics

in our recent and forthcoming publications.[7,11] The measurements presented here were performed on Cu/Co/Cu(100) and Ag/Fe/Ag(100) three-layered systems. The single-crystal substrates were prepared by sputtering and annealing cycles. Epitaxial films were deposited *in situ* by e-beam evaporation. A 20 monolayer thick fcc Co film was grown on Cu at 100 °C. Ultrathin Cu layers were subsequently deposited on Co at room temperature. Similarly, we grew a 10 monolayer thick Fe films on Ag(100), by evaporation on the substrate at room temperature. We produced an overlayer of Ag on Fe by annealing the sample at 250 °C for 30 min. Temperature and time of the annealing were chosen in order to achieve a complete monolayer coverage, as indicated by the saturation of the Ag $4d$/Fe $3d$ intensity ratio in the photoemission spectra. The system prepared in this way, consisting of a Ag(1 ML)/Fe(10 ML)/Ag(100), is stable upon further heating and upon cooling to room temperature. The binding energy of Ag-related spectral features corresponds to those obtained by Brookes *et al.*[12] for an evaporated Ag monolayer on Fe(100).

We observe a sharp low-energy electron diffraction (LEED) pattern with low background at all stages of the epitaxial growth. The distinct and intense "quantum-well states" observed in the photoemission spectra, shown in Sec. III, also demonstrate the good quality of the overlayer structure. According to Ortega *et al.*[6] these states provide a very strict test for the smoothness and crystalline order of the overlayer. The Co and Fe substrates have been magnetized along the in-plane ⟨011⟩ and ⟨001⟩ directions, respectively, which are the easy axes of these ferromagnetic thin films. Photoemission spectra have been measured in magnetic remanence. The sample magnetization was aligned parallel to the spin-sensitive direction of the spin detector.

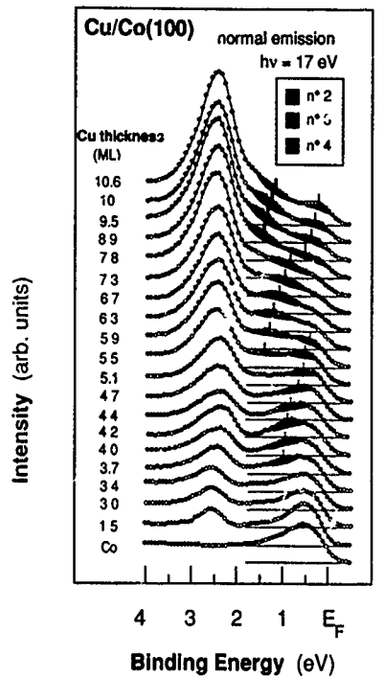

FIG. 1. Angle-resolved photoemission spectra of Cu films on Co(100). The spectra are measured for normal emission with 17 eV photon energy. The emission from Cu sp-derived states is shown by the gray-shadowed areas. These states are labeled according to the definitions in Ref. 6.

III. RESULTS AND DISCUSSION

A. Cu on Co(100): Spin-polarized quantum-well states

For Cu on Co(100) we have explored the sp-derived quantum-well states up to large thicknesses, where the electronic structure of the spacer layer is believed to be largely independent of that of the ferromagnetic substrate (asymptotic limit). The spin-integrated photoemission spectra in Fig. 1 show the development of the valence band states for increasing thickness of the Cu film. These data have been measured for normal electron emission. This geometry probes states with initial state $k_{\parallel}=0$, where $k_{\parallel}$ is the component of the wave vector parallel to the surface plane. The sp-derived Cu states give rise to new and well-defined structures easily observed above the Cu $3d$ band edge, within 2 eV binding energy from the Fermi level.

The energy dispersion of the sp-derived Cu states as a function of film thickness, shown in Fig. 1, resembles that of quantum-well states. It can be satisfactorily modeled assuming discretization of bulklike states due to the finite size of the layer, as proposed by Ortega *et al.*[6] In Fig. 2(a) we compare the dependence of the sp-state binding energy on the film thickness with the predictions based on the bulk band structure. Above a film thickness of about 5 monolayers the experimental data follow rather closely the expectations of a simple quantum-well picture. Our results are similar to those reported by Ortega *et al.*[6] and by Garrison *et al.*[8] Noble metal films display a similar development of sp-derived quantum-well states also on other magnetic[6] and nonmagnetic substrates.[13]

The capability of quantum-well states to mediate the indirect exchange interactions in multilayers depends on their coupling to the magnetic substrate. The interface boundary conditions and the hybridization with substrate levels will in general be different for states of opposite spin. For this reason the electronic structure of the thin film might develop spin-polarized bands, for which the spin degeneracy has been lifted. We have experimentally established that quantum-well states of Cu on Co(100) are magnetically polarized, by measuring the spin polarization of the photoelectrons. The results of the spin-resolved measurements are presented in Fig. 3, for several film thicknesses. In correspondence to the quantum-well states discussed above, the spectra exhibit spin-polarized spectral features. The quantum-well states shown in Fig. 3 are spin-polarized up to a Cu thickness of at least 10 monolayers. They are predominantly of spin-down (minority) character. Furthermore, weak spin-up (majority) states appear, separated by an exchange splitting (in average 0.2 eV) from the more intense spin-down states.

Pairs of spin-up and spin-down features gradually shift with increasing coverage to lower binding energy [see Fig. 2(b)]. By varying the film thickness, polarized states at a given energy periodically appear and disappear. This causes a modulation of the photoemission intensity [Fig. 2(c)] and of the spin polarization at the Fermi level [Fig. 2(d)]. Both have a similar periodicity, with an oscillation period of 5–6 monolayers, corresponding to the main RKKY wave vector

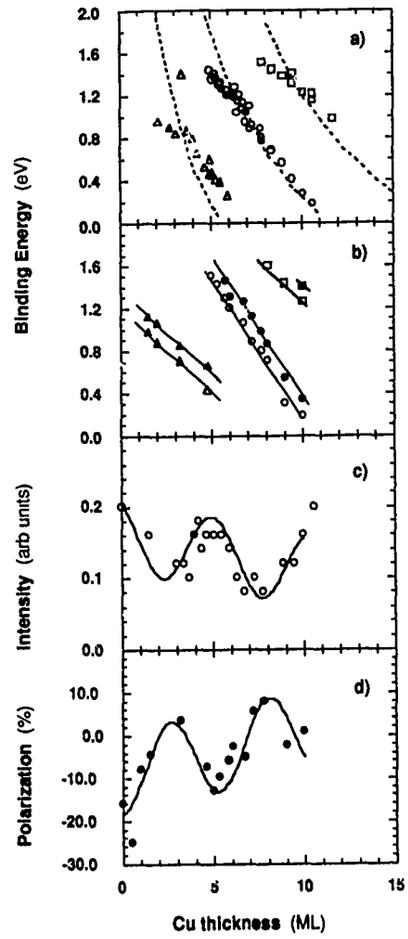

FIG. 2. (a) Binding energy of the Cu sp-derived states as a function of the film thickness, as determined from spin-integrated photoemission spectra. (b) Binding energy of the spin-polarized Cu-derived states as a function of film thickness, as determined from spin-resolved spectra. (c) Intensity at the Fermi level as a function of film thickness, after subtraction of the substrate emission. (d) Spin polarization at the Fermi level as a function of film thickness.

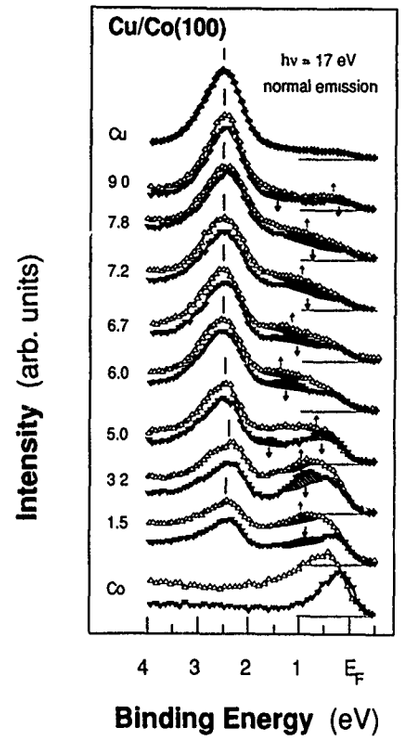

FIG. 3. Spin- and angle-resolved photoemission spectra of Cu on Co(100). The spectra are measured for normal emission with 17 eV photon energy, as in Fig. 1. Open symbols correspond to spin-up emission, full symbols to spin-down emission.

along the ⟨100⟩ direction. In brief, the results directly show that the interaction with the magnetic substrate induces a spin polarization on the Cu sp states. These levels are spin-split into two separated sub-bands, both displaying a dispersion close to that expected for quantum-well states.

It should be noticed that quantum-well states, intended as discrete states strictly confined within the overlayer, can only form in correspondence to a band gap in the substrate electronic structure. In Co(100) there is no band gap for states near E_F (Ref. 14) with $k_\parallel=0$. A complete confinement within the overlayer should thus not be expected, because of the coupling to degenerate bulk states (of proper symmetry) of the substrate. In fcc Co these states are the strongly dispersive Δ_1 subbands of both spin characters, which cross the Fermi level along the Γ-X direction. A Δ_1 symmetry-projected energy gap of the spin-down bands is located in fcc Co between 1 and 2 eV binding energy. In fact, in this energy region most intense quantum-well structures are observed in the spin-down channel. However, the reflectivity due to the interface may also partially confine within the film sp states that are degenerate with the substrate levels.[6] In this way, narrow resonance states[15] rather than discrete quantum-well states appear in the overlayer. It is thus ultimately a departure from an ideal quantum-well behavior that determines the role of the sp states in the magnetic coupling through Cu(100). The coupling to the substrate polarizes the s-derived states but at the same time reduces their degree of confinement within the overlayers.

For a comprehensive understanding of the polarization effects in the Cu films the coupling to the Co states will still have to be analyzed experimentally and theoretically in more detail. For example, the role of (modified) surface states and interface states localized near the magnetic substrate still needs to be examined. In the case of Ag on Fe(100),[12] Pd on Fe(100),[5] and Fe on Pd(100),[16] it has been shown that interface states can convey the magnetization in nonmagnetic layers. Furthermore, recent measurements of the x-ray magnetic circular dichroism at the Cu $L_{2,3}$ edge in multilayers have detected an induced moment in the Cu $3d$ levels.[17] This moment is largely localized at the interface but it might also present weak long-range oscillation. On the basis of tight binding calculations Garrison *et al.*[8] suggest that the polarization of the quantum well states results from the hybridization between the Cu s- and d-derived states. Recent first principle calculations,[15] which emphasize the scattering nature of quantum well states using a Korringa–Kohn–Rostoker (KKR)–Green's function method, account for their

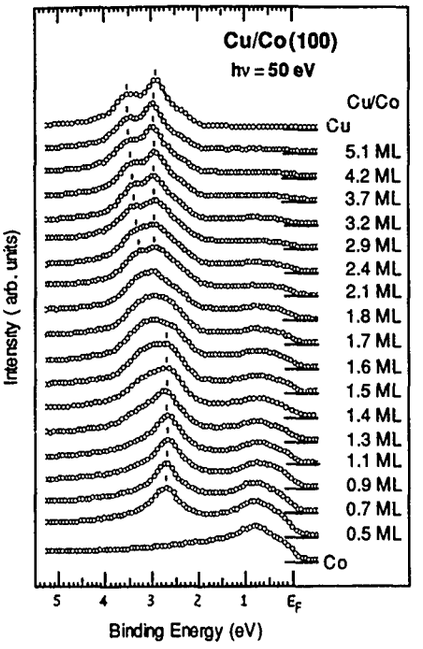

FIG. 4. Angle resolved photoemission spectra of Cu films on Co(100). The data are obtained with 50 eV photon energy for normal electron emission. The development of the Cu 3*d* bands, below 2 eV binding energy, is displayed as a function of the film thickness.

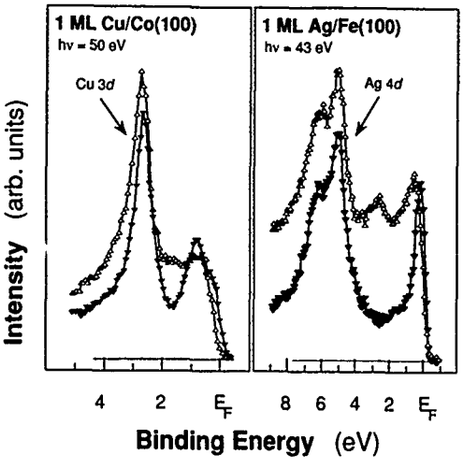

FIG. 5. Spin- and angle-resolved photoemission spectra of a Cu monolayer on Co(100), (left panel), and an Ag monolayer on Fe (100). Open symbols correspond to spin-up emission, full symbols to spin-down emission. The noble metal *d* states appear as intense features, at binding energies below 2 eV in Cu and below 4 eV in Ag. The strongly polarized emission closer to the Fermi level is mainly due to the magnetic 3*d* states of the substrate.

dispersion as a function of Cu thickness and for a small spin splitting between spin-up and spin-down states. These calculations predict a very small exchange splitting for the Cu 3*d* bands, in accord with the weak spin-dependence of the Cu 3*d* emission in the photoemission spectra of Fig. 3.

The experimental results presented above show that polarized electronic states related to the long range exchange coupling in multilayer systems, either of *s* or *d* character, can be directly investigated by spectroscopic methods. Further photoemission studies are now in progress in order to assess the connection between spectroscopically accessible conduction band properties (such as the Fermi surface and its modification in ultrathin layers) and the magnetic coupling phenomena. We present in the next section new results for the low coverage limit (i.e., noble metal films 1–2 monolayers thick), where the hybridization with the magnetic interface is the determining factor.

B. Cu on Co(100) and Ag on Fe(100): Approaching the monolayer limit

Deviations from a simple quantum-well behavior, based on the quantization of bulklike states, or from the RKKY scheme are expected to become evident for small thicknesses of the nonmagnetic film. Approaching the monolayer limit, the electronic structure can be strongly modified by the interaction with the substrate as well as by the reduced atomic coordination. This is manifested for example in the photoemission spectra of the relatively highly localized Cu 3*d* states up to about 4 ML.

The spectra in Fig. 4 display the developments of the Cu 3*d* states with increasing coverage, for initial states with $k_{\parallel}=0$ (the $\bar{\Gamma}$ point of the two-dimensional Brillouin zone). Similar results are obtained at other emission angles and photon energies. Up to 1 ML coverage we obtain a single narrow peak. With the second monolayer the spectra develop a broader structure still without a corresponding structure in the Cu bulk spectra. At 1 and 2 ML coverages the Cu 3*d* states do not show any dispersion with varying photon energy, as expected for two-dimensional states. With the formation of the third monolayer the Cu 3*d* bands begin to develop the spectral features of three-dimensional Cu. Only with the fourth monolayer the binding energy of most Cu 3*d* states becomes close to that of the bulk, although the (relative) spectral intensities still differ in some cases considerably from the bulk case.

In order to test the importance of the spin dependent hybridization with the magnetic substrate in determining the evolution of the Cu 3*d* bands, we have measured the monolayer spectrum also with spin resolution. The results, shown in Fig. 5, indicate that the exchange splitting of those 3*d* states is smaller than 0.1 eV. We also show in Fig. 5 the spin-polarized spectrum corresponding to the $\bar{\Gamma}$ point for an Ag monolayer on Fe(100). Similarly to the case of Cu, the data suggest that these Ag 4*d* states, between 4 and 7 eV binding energy, exhibit only a very small exchange splitting, of less than 0.1 eV. Although other point in *k* space might present a larger splitting, calculations on noble metal monolayers and interfaces coupled with magnetic materials[4,17] show that it should not exceed a few tenths of an eV. For this reason, we believe that the development of the 3*d* spectral features described above reflects primarily a transition from quasi-two-dimensional bands to a bulklike electronic structure.

The convergence to a bulklike band structure can be expected to occur at even larger thicknesses for the extended *sp*-conduction states. Indeed, as mentioned already in the previous section, below about 5 ML the experimental bind-

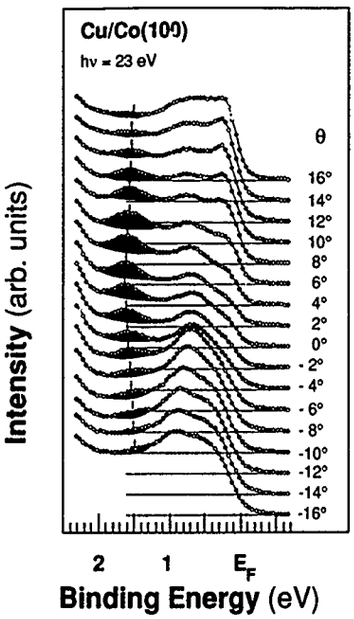

FIG. 6. Angle-resolved spectra of 2 Cu monolayers on Co(100), probing the dispersion along the $\bar{\Gamma}$-$\bar{X}$ direction. The spectra are measured at 23 eV for various emission angles. The noble metal induced features are indicated by gray shadowed areas.

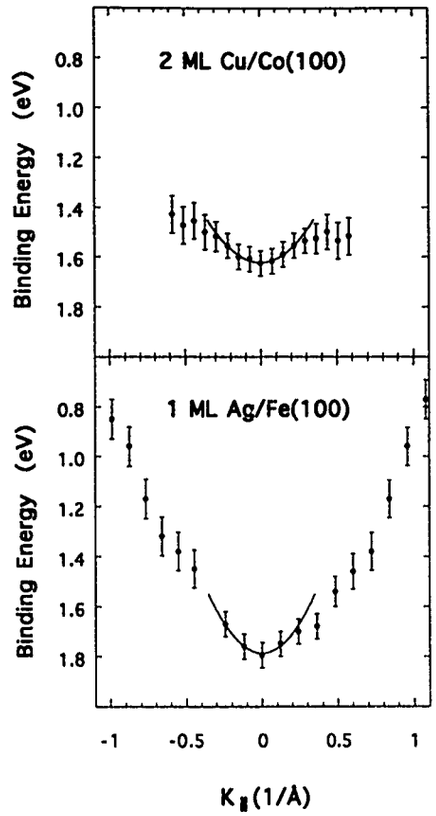

FIG. 8. Experimentally determined band dispersion as a function of the parallel wave vector for 2 Cu monolayers on Co (100) (upper panel) and 1 Ag monolayer on Fe(100) (lower panel). The dispersion is measured along the $\bar{\Gamma}$-$\bar{X}$ symmetry direction. The solid lines indicate free electron-like dispersion corresponding to an electron effective mass of 2.7 (upper panel) and 2 (lower panel).

ing energies of the *sp* states differ systematically from those expected for quantized bulklike states, in Cu on Co(100)[6,7] and in other noble metal films.[6] The discrepancy can originate from two effects: (i) in the monolayer regime the bands are altered by the reduced atomic coordination and lowered symmetry, as seen above for the *d* states, (ii) the hybridization with the substrate states further modifies the overlayer states in a way that depends on the spin, wave vector and symmetry of the band. We examine here how the *sp*-derived

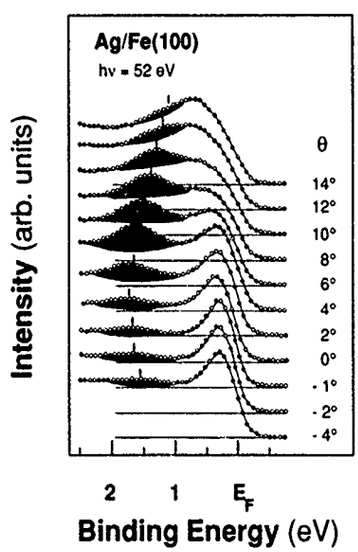

FIG. 7. Angle-resolved spectra of an Ag monolayers on Fe(100), probing the dispersion along the $\bar{\Gamma}$-$\bar{X}$ direction. The spectra are measured at 52 eV for various emission angles. The noble metal induced features are indicated by gray shadowed areas.

states form at low coverages two-dimensional magnetic bands, which eventually develop the simple behavior of quantum-well states in thicker films. We have studied the system Cu on Co (100) as well as an Ag monolayer on Fe (100).

The spectra in Figs. 6 and 7 show the band dispersion for an Ag monolayer on Fe(100), and for two Cu monolayer on Co(100) along the $\bar{\Gamma}$-$\bar{X}$ symmetry direction. The gray shadowed areas indicate the noble metal-induced features which appear superimposed to the 3*d* emission of the substrate. In both cases the features we have followed correspond to the first and most intense spectral structure induced by the overlayer, apart from the strong *d*-emission at higher binding energy. For Cu on Co the peak at 1.6 eV is prominent in the 23–30 eV photon energy spectra but hardly discernible at lower photon energy. The *s*-related character of these states is indicated by tight binding calculations.[8,12] In both cases spin-resolved photoemission reveals that these structures have predominantly spin-down character.[8,11,12] These states are thus well suited for studying the preasymptotic limit as they can be looked upon as the precursor of spin-polarized quantum-well states. We do not detect a dispersion of these features upon changing the photon energy, consistently with a two-dimensional character. By varying the emission angle we can determine the dispersion of these bands as a function

of the parallel wave vector $\mathbf{k}_{\parallel}$. The initial state wave vector is given by the projection on the surface plane of the photoelectron momentum as measured outside the solid.

The experimentally determined band dispersion in Fig. 8 summarizes the results presented above. The spin-down band between 1 and 2 eV induced by the noble metal display the expected symmetric behavior with respect to the center of the Brillouin zone. The dispersion of these bands is considerably weaker than for nearly free-electron-like states. Assuming a simple parabolic dispersion in the proximity of the zone center $\bar{\Gamma}$ we obtain an electron effective mass of about 2 for the Ag bands and about 2.7 for the Cu-derived bands. This strong departure from a free-electron-like dispersion becomes in both cases even more evident away from $\bar{\Gamma}$. This behavior indicates the importance at low coverage of the hybridization of Cu 4*s* states with other and more localized levels. For an Ag monolayer on Fe(100) tight binding band structure calculations identify the state at 1.7 eV as a spin-polarized interface states. Recent *ab initio* calculations describe well the experimental dispersion,[11] showing that a true spin polarized interface states derived from the Ag 5*s* levels is shared by both the constituents. Consistently with the experimental results reported above, the calculated bands[11] present an increasingly admixture with Fe 3*d* states on moving from $\bar{\Gamma}$-$\bar{X}$. In summary the *s*-derived states in the low thickness limits show a significant departure from a simple quantum-well model. This is not only due to the reduced dimensionality of the system but also to the hybridization with the magnetic states of the substrate.

IV. CONCLUSIONS

By spin- and angle-resolved photoemission we have investigated the electronic structure of Cu on Co(100) and Ag on Fe(100), in order to clarify the origin of the indirect exchange coupling through noble metals. We find that the *sp*-derived electronic states of the noble metals are spin-polarized upon contact with the magnetic materials. For film thicknesses above a few monolayers, a quantum-well picture, based on the quantization of bulklike states, describes the development of the *sp* states. In the low coverage regime, the conduction electron bands are instead strongly modified by hybridization with the states of the magnetic substrate.

[1] P. Grunberg, R. Schreiber, Y. Pang, M. B. Brodsky, and H. Sowers, Phys. Rev. Lett. **57**, 2442 (1986); C. Carbone and S. F. Alvarado, Phys. Rev. B **36**, 2433 (1987); S. S. P. Parkin, N. More, and K. P. Roche, Phys. Rev. Lett. **64**, 2304 (1990); S. S. P Parkin, R. Bhandra, and K. P. Roche, *ibid.* **66**, 2152 (1991).

[2] P. Bruno and C. Chappert, Phys. Rev. Lett. **67**, 1602, 2592 (1991); R. Coehoorn, Phys. Rev. B **44**, 9331 (1991); D. M. Edwards, J. Mathon, R. B. Muniz, and M. S. Phan, Phys. Rev. Lett. **67**, 493 (1991).

[3] M. van Schilfgaarde, and W. A. Harrison, Phys. Rev. Lett. **71**, 3870 (1993); B. A. Jones and C. B. Hanna, *ibid.* **71**, 4253 (1993).

[4] M. Weinert and S. Blügel, in *Magnetic Multilayers*, edited by L. H. Bennett and R. E. Wabon (World Scientific, Singapore, 1993).

[5] O. Rader, C. Carbone, W. Clemens, E. Vescovo, S. Blügel, W. Eberhardt, and W. Gudat, Phys. Rev. B **45**, 13 823 (1992); T. Kachel, W. Gudat, C. Carbone, E. Vescovo, U. Alkemper, S. Blügel, and W. Eberhardt, *ibid.* **46**, 12 888 (1992).

[6] J. Ortega and F. J. Himpsel, Phys. Rev. Lett. **69**, 844 (1992); J. Ortega, F. J. Himpsel, G. J. Mankey, and R. F. Willis, Phys. Rev. B **47**, 1540 (1993).

[7] C. Carbone, E. Vescovo, O. Rader, W. Gudat, and W. Eberhardt, Phys. Rev. Lett. **71**, 2805 (1993).

[8] K. Garrison, Y. Chang, and P. D. Johnson, Phys. Rev. Lett. **71**, 2801 (1993).

[9] E. Kisker and C. Carbone, in *Angle Resolved Photoemission*, edited by S. D. Kevan (Elsevier, Amsterdam, 1992).

[10] See for example: J. de Miguel, A. Cebollada, J. M. Gallego, R. Miranda, C. M. Schneider, P. Schuster, and J. Kirschner, J. Magn. Magn. Mat. **93**, 673 (1990); Z. Q. Qiu, J. Pearson, and S. D. Bader, Phys. Rev. B **46**, 8659 (1992); W. F. Egelhoff, Jr. and I. Jacob, Rev. Lett. **62**, 921 (1989); H. Li, Y. S. Li, J. Quinn, D. Tian, J. Sokolov, F. Jona, and P. M. Marcus, Phys. Rev. B **42**, 9195 (1990).

[11] E. Vescovo, O. Rader, J. Redinger, S. Blügel, and C. Carbone (to be published).

[12] N. Brookes, Y. Chiang, and P. D. Johnson, Phys. Rev. Lett. **67**, 354 (1991).

[13] T. Miller, A. Samsavar, G. E. Franklin, and C. T. Chiang, Phys. Rev. Lett. **61**, 1404 (1988).

[14] W. Clemens, T. Kachel, O. Rader, E. Vescovo, S. Blugel, C. Carbone, and W. Eberhardt, Solid State Commun. **81**, 739 (1992); J. Noffke and L. Fritsche (private communication).

[15] L. Nordström, P. Lang, R. Zeller, and P. H. Dederichs (to be published).

[16] O. Rader, E. Vescovo, J. Redinger, S. Blugel, C. Carbone, W. Eberhardt, and W. Gudat, Phys. Rev. Lett. **72**, 2247 (1994).

[17] M. G. Samant, J. Stöhr, S. S. P. Parkin, G. A. Held, B. D. Hermsmeier, F. Herman, M. van Schilfgaarde, L. -C. Duda, D. C. Mancini, N. Wassdahl, and R. Nakajima, Phys. Rev. Lett. **72**, 1112 (1994).

Recent progress in the theory of interlayer exchange coupling (invited)

P. Bruno[a)]
Institut d'Électronique Fondamentale, CNRS URA, 22 Bât. 220, Université Paris-Sud, F-91405 Orsay, France

Recent progress in the theory of interlayer exchange coupling is presented. The interlayer coupling is described in terms of quantum interferences in the spacer layer, due to reflections of Bloch waves on the spacer boundaries. This approach is used to discuss (i) the coupling variation with respect to *ferromagnetic layers thickness*, and (ii) the coupling across a *nonmetallic* spacer layer.

I. INTRODUCTION

In the past few years, the intense research activity on interlayer exchange coupling, both experimental and theoretical, has been essentially focussed on the oscillations of the interlayer coupling with respect to *spacer thickness*, in systems with *metallic* spacer layers.[1,2] Recently, the interest in this field has been renewed by (i) the theoretical prediction[3,4] and experimental confirmation[5,6] of oscillations of the coupling with respect to *ferromagnetic layers thickness*, and (ii) the discovery of interlayer exchange coupling across *nonmetallic* spacer layers,[7] which, furthermore, may be *thermally induced*[8] or *photoinduced*.[9,10]

In this article, I address the above mentioned new aspects of the problem of interlayer exchange coupling. This study relies on a formalism developed previously,[11] in which the interlayer coupling is described in terms of quantum interferences in the spacer, due to reflections of Bloch waves on the spacer boundaries. This approach, which has been rederived subsequently by Stiles,[12] has the virtue of being physically transparent, and also provides a suitable starting point for quantitative calculations, either for models, or for realistic systems. A heuristic presentation of this approach is given in Sec. II.

As pointed out in Ref. 4, it becomes almost obvious, in the light of the "quantum interferences" formulation, that one may expect oscillations of the coupling versus ferromagnetic layers thickness, as a consequence of the interferences associated with the multiple internal reflections in a magnetic layer of finite thickness, in analogy with the reflection oscillations in an optical Pérot–Fabry cavity. This problem is discussed in detail in Sec. III.

In contrast to the important theoretical literature devoted to interlayer coupling across metal spacer, the magnetic coupling across insulators has attracted very little attention on the theoretical point of view. A notable exception is Slonczewski's model of coupling, at $T=0$, through a tunneling barrier:[13] the coupling, in this case is non-oscillatory, and decays exponentially with spacer thickness. In a recent paper,[14] I discussed this problem within the quantum interferences approach: at $T=0$, one recovers the results of Slonczewski; on the other hand, the coupling is found to *increase* with increasing temperature, in contrast to the metal spacer case. This study is presented in Sec. IV.

In view of pedagogical clarity, the free-electron model will be used in Secs. III and IV. For this simple case, the calculations can be performed analytically, thus providing a physically transparent illustration of the various aspects of the problem. The model is sketched in Fig. 1: the zero of energy is taken at the bottom of the majority band of the ferromagnetic layers; the potential of the minority band is given by the exchange splitting Δ, while the spacer, of thickness D, has a potential equal to U. The ferromagnetic layers, F_A and F_B, have a thickness L ($L=\infty$ stands for semiinfinite magnetic layers), and their magnetizations are at an angle θ with respect to each other. According to the position of the Fermi level, this model describes the case of a metallic spacer (for $\epsilon_F > U$), or of an insulating spacer (for $\epsilon_F < U$).

II. QUANTUM INTERFERENCES AND INTERLAYER EXCHANGE COUPLING

In this section, I shall present a heuristic presentation of the interlayer coupling in terms of quantum interferences in the spacer layer; the emphasis will be on physical transparency rather than on mathematical strictness.

Inside the paramagnetic layer, a conduction electron experiences essentially the same potential as in the bulk material; deviations from the bulk potential are confined to the interface regions, and, of course, to the regions occupied by the ferromagnetic material. Thus, the electrons propagate through the spacer like in the bulk material; the effect of potential deviations as they encounter the interface with the ferromagnetic material make them being (partly) reflected towards the paramagnet. Because of the spin polarization of the ferromagnetic material, the potential deviation at the interface is spin dependent, and so is the reflection coefficient.

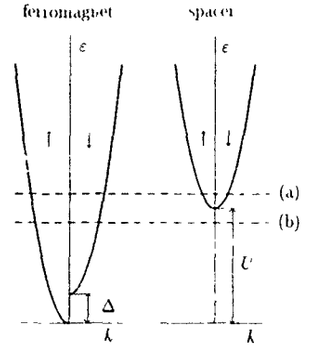

FIG. 1. Sketch of the free-electron model; the dashed line indicates the position of the Fermi level, (a) for the metallic spacer case, (b) for the insulating spacer case.

a)E-mail: bruno@ief-paris-sud.fr

 0021-8979/94/76(10)/6972/5/$6.00 © 1994 American Institute of Physics

Since the in-plane translational invariance is maintained, the in-plane component $\mathbf{k}_\parallel$ of the wave vector is a good quantum number, i.e., it is conserved under reflection. For an incident electron of wave vector $\mathbf{k}^i=(\mathbf{k}_\parallel,k_\perp)$, the reflected wave vector is $\mathbf{k}^r=(\mathbf{k}_\parallel,-k_\perp)$ and the corresponding complex reflection coefficient for spin parallel (antiparallel) to the magnetization in the ferromagnet is $r^{\uparrow(\downarrow)}$; the module of the reflection coefficient gives the amplitude of the reflected wave, while its argument ϕ gives the phase shift due to the reflection. We also define

$$\bar{r}\equiv\frac{r^\uparrow+r^\downarrow}{2} \quad \text{and} \quad \Delta r\equiv\frac{r^\uparrow-r^\downarrow}{2}, \tag{1}$$

respectively, the spin-average and spin-asymmetry of the reflection coefficients.

In the paramagnetic spacer, the electrons are reflected on both interfaces (F_A and F_B), so that interferences take place due to the multiple reflections. Let us consider a wave of vector $\mathbf{k}=(\mathbf{k}_\parallel,k_\perp)$, with $k_\perp>0$; the phase change of the wave function after a round trip in the spacer (one reflection on F_A and one reflection on F_B) is

$$\phi_{AB}=2k_\perp D+\phi_A+\phi_B; \tag{2}$$

if the interferences are constructive (respectively, destructive), i.e., if

$$\begin{aligned}\phi_{AB}&=2n\pi\\&=(2n+1)\pi \ \text{(respectively)},\end{aligned} \tag{3}$$

with n integer, the density of states is enhanced (respectively, lowered) in the spacer layer. Taking these interferences into account, the wave function in the spacer may be written as

$$\psi(\mathbf{r})\sim e^{i\mathbf{k}_\parallel\cdot\mathbf{r}}e^{ik_\perp z}(1+|r_Ar_B|e^{i(2k_\perp D+\phi_A+\phi_B)}), \tag{4}$$

where higher order interference terms have been neglected. The corresponding contribution to the ($\mathbf{k}_\parallel$ projected) density of states is

$$n(\mathbf{k}_\parallel,\epsilon)\sim\frac{dk_\perp}{d\epsilon}\int_0^D dz|\psi|^2, \tag{5}$$

where the integral gives the contribution of one state $(\mathbf{k}_\parallel,k_\perp)$ and the prefactor $dk_\perp/d\epsilon$ gives the number of states in an energy interval $[\epsilon,\epsilon+\delta\epsilon]$.

Here, we are interested essentially in the part of $n(\mathbf{k}_\parallel,\epsilon)$ which is associated with the interferences, i.e.,

$$\begin{aligned}\Delta n(\mathbf{k}_\parallel,\epsilon)&\sim 2D\frac{dk_\perp}{d\epsilon}|r_Ar_B|\cos(2k_\perp D+\phi_A+\phi_B)\\&\sim\mathrm{Im}\left(2iD\frac{dk_\perp}{d\epsilon}r_Ar_Be^{2ik_\perp D}\right).\end{aligned} \tag{6}$$

The total change of in the density of states per unit area is obtained by summing over in-plane wave vectors and over the spin, yielding

$$\Delta n_F(\epsilon)\sim\mathrm{Im}\int d\mathbf{k}_\parallel 2iD\frac{dk_\perp}{d\epsilon}(r_A^\uparrow r_B^\uparrow+r_A^\downarrow r_B^\downarrow)e^{2ik_\perp D}, \tag{7}$$

for the ferromagnetic configuration, and similarly,

$$\Delta n_{AF}(\epsilon)\sim\mathrm{Im}\int d\mathbf{k}_\parallel 2iD\frac{dk_\perp}{d\epsilon}(r_A^\uparrow r_B^\downarrow+r_A^\downarrow r_B^\uparrow)e^{2ik_\perp D}, \tag{8}$$

for the antiferromagnetic configuration.

The interlayer exchange coupling per unit area (at $T=0$) may be expressed as

$$E_F-E_{AF}\equiv\int_{-\infty}^{\epsilon_F}(\epsilon-\epsilon_F)[\Delta n_F(\epsilon)-\Delta n_{AF}(\epsilon)]d\epsilon; \tag{9}$$

integrating by parts, we get for the interlayer exchange coupling (for large D)

$$\begin{aligned}E_F-E_{AF}&\sim-\mathrm{Im}\int d\mathbf{k}_\parallel\int_{-\infty}^{\epsilon_F}d\epsilon(r_A^\uparrow r_B^\uparrow+r_A^\downarrow r_B^\downarrow-r_A^\uparrow r_B^\downarrow\\&\quad-r_A^\downarrow r_B^\uparrow)e^{2ik_\perp D}\\&\sim-\mathrm{Im}\int d\mathbf{k}_\parallel\int_{-\infty}^{\epsilon_F}d\epsilon\,4\Delta r_A\Delta r_Be^{2ik_\perp D}.\end{aligned} \tag{10}$$

As appears clearly from Eq. (10), the coupling depends on (i) the wave vectors $k_\perp$ in the spacer layer, and (ii) the spin-asymmetries Δr_A and Δr_B of reflection coefficients at the paramagnetic-ferromagnetic interfaces; the former determine the oscillation periods of the coupling, while the latter determine its strength.

So far I have implicitely considered that the incident and reflected waves are usual propagative Bloch waves (with $k_\perp$ real); these are the states which are allowed in bulk materials. However, in a slab of finite thickness, evanescent states [with $\mathrm{Im}(k_\perp)$ nonvanishing] are also present and contribute to the density of states. Thus, evanescent states contribute to the coupling in Eq. (10) on an equal footing; in particular, they are found in gaps of the bulk band structure. The rôle played by these states will be discussed in Sec. IV.

An exact derivation, using Green's functions formalism, yields, for the interlayer coupling energy per unit area,[11]

$$E_{AB}(\theta)=J_0+J_1\cos\theta+J_2\cos^2\theta+\cdots \tag{11}$$

with the Heisenberg coupling constant

$$\begin{aligned}J_1=&-\frac{1}{4\pi^3}\mathrm{Im}\int d^2\mathbf{k}_\parallel\int_{-\infty}^{+\infty}d\epsilon\,f(\epsilon)\\&\times\frac{2\Delta r^2e^{2ik_\perp D}}{1-2\bar{r}^2e^{2ik_\perp D}+(\bar{r}^2-\Delta r^2)^2e^{4ik_\perp D}},\end{aligned} \tag{12}$$

where $f(\epsilon)$ is the Fermi–Dirac distribution, and where the indices A and B have been dropped, since $r_A^{\uparrow(\downarrow)}=r_B^{\uparrow(\downarrow)}$.

III. VARIATION OF THE COUPLING WITH RESPECT TO MAGNETIC LAYERS THICKNESS

I consider here the case of ferromagnetic layers of finite thickness L. For simplicity, I shall restrict myself to the case of a metallic spacer; more precisely, I take $U=0$; thus, the magnetic layer is *transparent* for electrons of spin parallel to the majority spins, i.e., $r^\uparrow=0$ and $\bar{r}=-\Delta r=r^\downarrow/2$.

In the case of a layer of finite thickness, like in Pérot–Fabry cavity, all the waves associated with the multiple re-

flections inside the magnetic layer contribute to the net reflection coefficient. The summation is easily carried out, and one gets

$$r^{\downarrow}=r_{\infty}^{\downarrow}\frac{1-\exp[2ik_{\perp}^{\downarrow}L]}{1-r_{\infty}^{\downarrow 2}\exp[2ik_{\perp}^{\downarrow}L]}, \tag{13}$$

where $k_{\perp}^{\downarrow}$ is the minority-spin wave-vector in the magnetic layer, and $r_{\infty}^{\downarrow}$ the reflection coefficient for a semi-infinite magnetic layer. Clearly, the variation of $r^{\downarrow}$ with respect to L is oscillatory or exponential, according to the nature—propagative or evanescent—of the state of wave vector $k_{\perp}^{\downarrow}$. The interlayer coupling is governed essentially by the states lying at the Fermi level. Thus, if $k_F^{\downarrow}$ is real, one can expect oscillations of the interlayer coupling vs. magnetic layers thickness to show up. The oscillations are due to the quantum interferences inside the magnetic layers: when the interferences are constructive (respectively, destructive), the coupling strength is enhanced (respectively, reduced). Below, I consider only the former case, i.e., $k_F^{\downarrow}$ real.

In the limit where both L and D are large, the expression of the coupling (at $T=0$) reduces to[4]

$$J_1=\frac{1}{4\pi^2D^2}\frac{\hbar^2k_F^2}{2m}\,\mathrm{Im}\left\{\frac{r_{\infty}^{\downarrow 2}}{2}e^{2ik_FD}\times\left[1-2(1-r_{\infty}^{\downarrow 2})\left(1+\frac{k_F}{k_F^{\downarrow}}\frac{L}{D}\right)^{-2}e^{2ik_F^{\downarrow}L}\right]\right\}. \tag{14}$$

Clearly, the interlayer exchange coupling oscillates versus L, with a period equal to $\pi/k_F^{\downarrow}$. The amplitude of these oscillations decays essentially as L^{-2}. To illustrate this behavior, I have performed numerical calculations for the free-electron model with $\epsilon_F=7.0$ eV, $U=0$, and $\Delta=1.5$ eV; these calculations use the exact expression (12), not the asymptotic one (14). The results are displayed in Fig. 2: the coupling variation versus magnetic layer thickness L, for several value of the spacer thickness D. The oscillatory behavior of period $\pi/k_F^{\downarrow}$, and the L^{-2} decay appear clearly. A striking feature is that, in contrast to the oscillations of J_1 vs D, the oscillations are not necessarily around zero: instead, J_1 may oscillate around a positive, or a negative value, depending on the choice of the spacer thickness D. This point is also obvious from Eq. (15).

On the other hand, for large D and small L, one has

$$J_1=\frac{1}{4\pi^2D^2}\frac{\hbar^2k_F^2}{2m}\,\mathrm{Im}(-2k_F^{\downarrow 2}L^2r_{\infty}^{\downarrow 2}e^{2ik_FD}). \tag{15}$$

The fact that the coupling varies like L^2 at low magnetic layers thickness is obvious from the analogy with optics: the reflection coefficient for a thin layer is proportional to its thickness.

Until recently, it was generally believed that the coupling is essentially independent of the magnetic layers thickness. This point has been studied experimentally in the case of Co/Cu/Co(001) by Qiu *et al.*,[15] who found no dependence of the coupling versus Co thickness; however, only three different Co thicknesses have been used in this study. On the theoretical point of view, oscillations of the coupling versus magnetic layers thickness have been first reported by Barnaś[3]

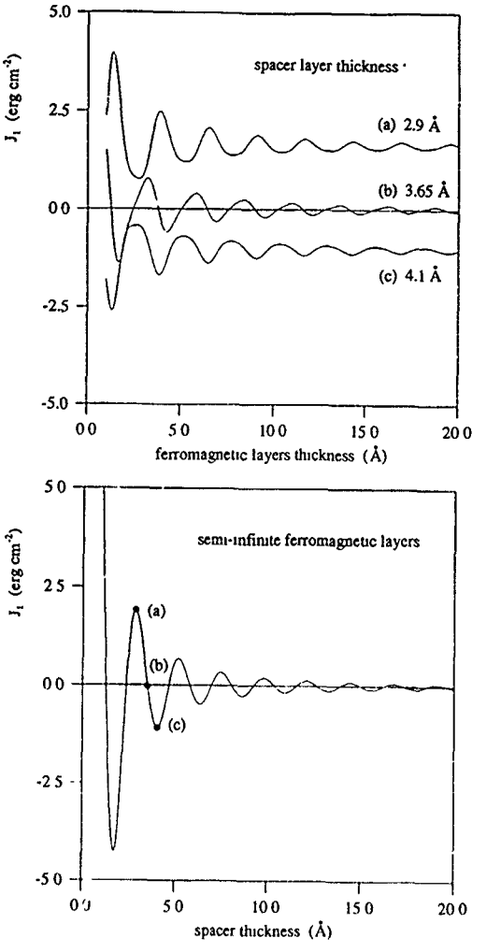

FIG. 2. Interlayer exchange coupling constant J_1, calculated as a function of the spacer thickness D, for semi-infinite ferromagnetic layers (lower panel), and as a function of the ferromagnetic layers thickness L, for various values of the spacer thickness D (upper panel).

from numerical calculations for the free-electron model. The explanation of this behavior on the basis of the quantum interferences picture has been given in Ref. 4; in this article, I also estimated the oscillation period versus Co thickness in Co/Cu/Co(001) to be about 3.5 atomic layers (ALs).

The predictions of Ref. 4 have been confirmed recently by Bloemen *et al.*,[5] who succeeded in observing oscillations of the coupling versus Co thickness in Co/Cu/Co(001); the observed period is about 3.5 ALs, in very good agreement with the predicted one. Further confirmation has been given by Okuno and Innomata,[6] who observed oscillations of interlayer coupling versus Fe thickness in Fe/Cr(001) multilayers.

IV. METALLIC VERSUS INSULATING SPACER

In this section, I discuss the coupling behavior, in particular its spacer thickness and temperature dependence, for a nonmetallic spacer ($\epsilon_F<U$), in comparison with the case of a metallic spacer ($\epsilon_F>U$). For simplicity, I take $L=\infty$.

Because of the abrupt variation of the Fermi–Dirac distribution at the Fermi energy, the interlayer coupling is determined by the neighborhood of the Fermi level. Thus, the

nature of the states present at the Fermi level controls the physical behavior of the coupling. In the case of a metallic spacer, one has propagative states at Fermi energy, and this leads to the oscillatory character of coupling vs. spacer thickness. For an insulating spacer, on the other hand, the states with Fermi energy are evanescent waves, so that we expect a monotonic exponential decay of the interlayer coupling with spacer thickness.

In the limit of large spacer thickness and low temperature, Eq. (12) becomes[14]

$$J_1=\frac{1}{4\pi^2}\frac{\hbar^2k_F^2}{mD^2}\,\mathrm{Im}(\Delta r^2 e^{2ik_FD})\frac{2\pi k_BTDm/\hbar^2k_F}{\sinh(2\pi k_BTDm/\hbar^2k_F)} \tag{16}$$

with

$$k_F=[2m(\epsilon_F-U)/\hbar^2]^{1/2}, \tag{17a}$$

$$k_F=i[2m(U-\epsilon_F)/\hbar^2]^{1/2}, \tag{17b}$$

respectively, for a metallic and an insulating spacer.

Of course, the coupling behavior is completely different in both cases. While it is oscillatory for a metal spacer, it decreases exponentially with spacer thickness in the insulator case. Another striking difference concerns the temperature dependence, which is given by the last factor in Eq. (16). For a metal spacer the coupling decreases with increasing temperature.[2] On the other hand, when we consider the insulating spacer case, where k_F is imaginary, the exchange coupling *increases* with temperature for an insulating spacer, because $\sinh(ix)/ix \equiv \sin(x)/x$ is an increasing function. Physically, this behavior may be understood easily: when the temperature increases, the contribution of states below the Fermi level is lowered, at the expense of states above the Fermi level; since the penetration length of the latter is larger than the one of the former, the exchange coupling is thereby enhanced.

To illustrate the above results more quantitatively, we have performed numerical calculations of the exchange coupling for the free electron model, with $\epsilon_F=10.0$ eV, $\Delta=1.5$ eV, and $U-\epsilon_F=0.1$ eV; the calculation uses the exact expression (12), not the asymptotic result (16). The results are displayed on Fig. 3. With the above choice of parameters, the coupling at large spacer thicknesses is antiferromagnetic ($J_1>0$). One clearly observes the strong temperature increase of the coupling; as expected from Eq. (16), the relative thermal variation increases with increasing thickness.

One should be careful when comparing the results with experimental observations of coupling across no-metallic spacers: indeed, the latter concern materials that are disordered or even amorphous, whereas the theory presented here pertains to ordered systems; the importance of disorder for the *thermally induced* coupling remains to be clarified. Nevertheless, the finding of a positive temperature coefficient for the exchange coupling through an insulating spacer provides a plausible explanation for the experimental observations of *thermally induced* exchange coupling.[8] Note that the latter result is not restricted to the free-electron case, and may be shown to hold for any insulating spacer material.

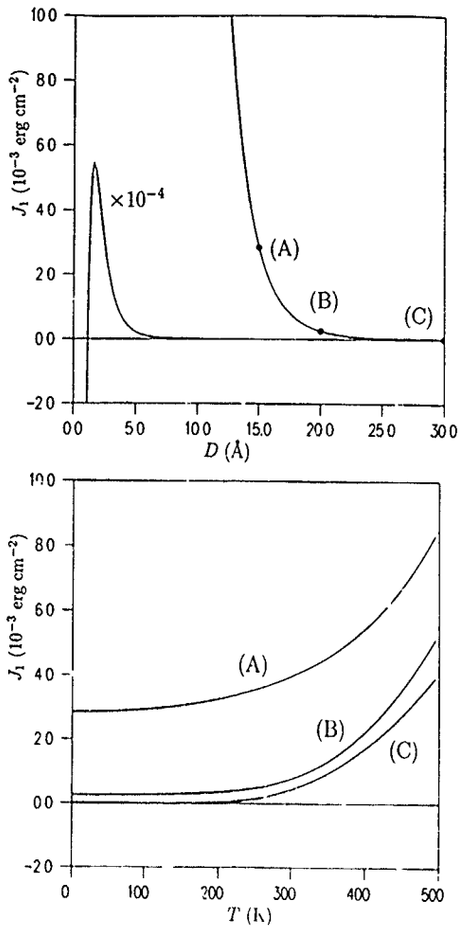

FIG. 3. Calculated interlayer exchange coupling across an insulating spacer; (upper panel) exchange coupling versus spacer thickness at $T=0$; (lower panel) exchange coupling vs. temperature for various spacer thickness, corresponding to the solid points: (A) 15.0 Å, (B) 20.0 Å, and (C) 30.0 Å.

V. CONCLUDING REMARKS

In this article, I have discussed various new aspects of the problem of interlayer exchange coupling, on the basis of the quantum interference approach, is which the coupling is expressed in terms of reflection coefficients at the boundaries of the spacer layer.

This approach provides a physically transparent description of the phenomenon of interlayer exchange coupling. When applied to simple models, such as the free-electron model, the calculations can be performed almost completely analytically.

I have shown that the interlayer coupling me be expected to exhibit oscillations versus ferromagnetic layers thickness, a prediction which has been confirmed recently by experiments. For the case of an insulating spacer, the expression of the coupling is formally similar to the metallic spacer case; however, the evanescent character of the states with Fermi energy leads to a completely different physical behavior: in contrast to the metal spacer case, the coupling has a monotonic exponential decay with respect to spacer thickness, and increases with temperature. This result provides a plausible explanation for recent experimental observations.

[1] S. S. P. Parkin, N. More, and K. P. Roche, Phys. Rev. Lett. **64**, 2304 (1990).
[2] P. Bruno and C. Chappert, Phys. Rev. Lett. **67**, 1602, 2592E (1991); Phys. Rev. B **46**, 261 (1992).
[3] J. Barnaś, J. Magn. Magn. Mat. **111**, L215 (1992).
[4] P. Bruno, Europhys. Lett. **23**, 615 (1993).
[5] P. J. H. Bloemen, M. T. Johnson, M. T. H. van de Vorst, R. Coohoern, J. J. de Vries, R. Jungblut, J. aan de Stegge, A. Reinders, and W. J. M. de Jonge, Phys. Rev. Lett. **72**, 764 (1994).
[6] S. N. Okuno and K. Inomata, Phys. Rev. Lett. **72**, 1553 (1994).
[7] S. Toscano, B. Briner, H. Hopster, and M. Landolt, J. Magn. Magn. Mat. **114**, L6 (1992).
[8] S. Toscano, B. Briner, and M. Landolt, in *Magnetism and Structure in Systems of Reduced Dimensions*, edited by R. F. C. Farrow, B. Dieny, M. Donath, A. Fert, and B. D. Hermsmeier, NATO ASI Ser. B 309 (Plenum, New York, 1993), p. 257.
[9] J. E. Mattson, S. Kumar, E. F. Fullerton, S. R. Lee, C. H. Sowers, M. Grimsditch, S. D. Bader, and F. T. Parker, Phys. Rev. Lett **71**, 185 (1993).
[10] B. Briner and M. Landolt, Z. Phys. B **92**, 135 (1993).
[11] P. Bruno, J. Magn. Magn. Mat. **121**, 248 (1993).
[12] M. D. Stiles, Phys. Rev. B **39**, 7238 (1993).
[13] J. C. Slonczewski, Phys. Rev. B **39**, 6995 (1989).
[14] P. Bruno, Phys. Rev. B **49**, 1323 (1994).
[15] Z. Qiu, J. Pearson, and S. D. Bader, Phys. Rev. B **46**, 8659 (1992).

Exchange anisotropy in films, and the problem of inverted hysteresis loops

Amikam Aharoni[a)]
Department of Electronics, Weizmann Institute of Science, 76100 Rehovoth, Israel

The inverted hysteresis loop is claimed to be possible, in an exchange-coupled bilayer, when a magnetically soft material is affected by the demagnetizing field of the hard material. These demagnetizing fields are caused by the charge on the surfaces, neglected in all the theories that assume a strictly one-dimensional structure, in an *infinite* material. For these one-dimensional models, an analytic solution is presented, which reduces the computation from a numerical integration of a set of differential equations to the solution of an *algebraic*, transcendental equation (which contains elliptic functions) for fitting only the boundary conditions. It may then be feasible to introduce at least an approximation for the demagnetizing effect of the surfaces in a finite sample.

I. INTRODUCTION

Inverted hysteresis loops have been observed[1,2] in some exchange-coupled multilayers. In the decreasing part of such loops the magnetization becomes negative when the applied field is still positive, while in the increasing part the magnetization becomes positive when the applied field is still negative (see Fig. 2). No explanation is known for this unusual phenomenon. The attempt[1,2] to relate it only to the exchange coupling at the interface failed, in the sense that the theory did not produce anything similar to the observed loops.

Unlike the exchange coupling, which acts on the boundary layer only, magnetostatic interaction between the layers acts on the whole volume of the film, and is thus more effective and more likely to produce inverted loops. However, the magnetostatic interaction is complicated and difficult to take into account, and is just neglected in most theoretical studies. To illustrate the complexity, two cases of such exchange-coupled layers are shown schematically in Fig. 1.

In case (a) the magnetic field is in the film plane, and the magnetization of the hard component, A, is pointing to the right. A simple-minded calculation assumes an *infinite* film, with no demagnetizing effect. However, these films do end *somewhere* and there is a charge on that surface. This charge (shown schematically as the pluses) creates a field (shown schematically by the two field lines), which points to the left when the applied field is to the right. The field acting on the soft material, B, is the difference between these fields, and can be negative in a positive applied field.

In case (b) the applied field, and the magnetization in the film, are pointing upwards. There should be no demagnetizing effects besides the overall demagnetization, which is easy to take into account. However, if the films are not continuous, and one material "penetrates" through the other one, a surface charge can be created, as seen in Fig. 1, and the effect is the same as in case (a).

These effects are not easy to estimate, because they depend on the fine details of the layer structure; but they are *not* negligible, because the magnetostatic self-energy is usually very large. A rather crude theory will be given in Sec. II, which demonstrates the main physics of the present suggestion for the origin of the inverted hysteresis loop. A method for advancing to a more realistic approximation will be proposed in Sec. III.

II. SIMPLE THEORY

The earliest theory[3] of exchange coupling in a geometry of an infinite slab used an oversimplified picture of the CoO layer as being infinitely hard, so that the direction of its magnetization could not be changed by any applied field. The softer, cobalt, layer was assumed to be sandwiched between such CoO layers, and the coupling to these layers gave the boundary conditions for the energy minimization. For this model the differential equation could be solved analytically, and the reduced magnetization in the field direction was shown[3] to be

$$j=\langle M_H\rangle/M_s=-1+2E(k)/K(k), \tag{1}$$

where K and E are the complete elliptic integrals of the first and second kind, respectively, and k is a parameter, related to the reduced applied field,

$$h=H/(2\pi M_s), \tag{2}$$

by

$$-\pi S^2 h=[K(k)]^2, \quad S=aM_s/\sqrt{A}. \tag{3}$$

Here $A=C/2$ is the exchange constant, and a is the Co film thickness.

Two changes are made in this theory for using it here.

(1) In a sufficiently large field the CoO layer reverses its

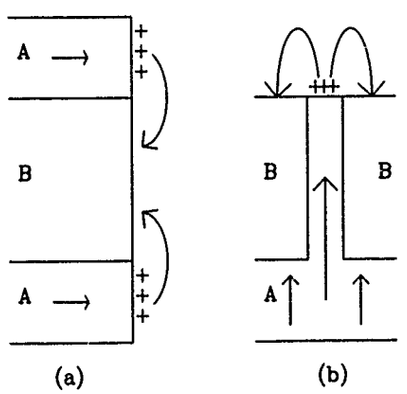

FIG. 1. Schematic representation of a soft magnetic layer, "B" being demagnetized by the field due to the surface charge on a hard layer, "A" magnetized parallel (a), or perpendicular (b) to the layer plane.

a)E-mail: a.aharoni@ieee.org

 0021-8979/94/76(10)/6977/3/$6.00 © 1994 American Institute of Physics

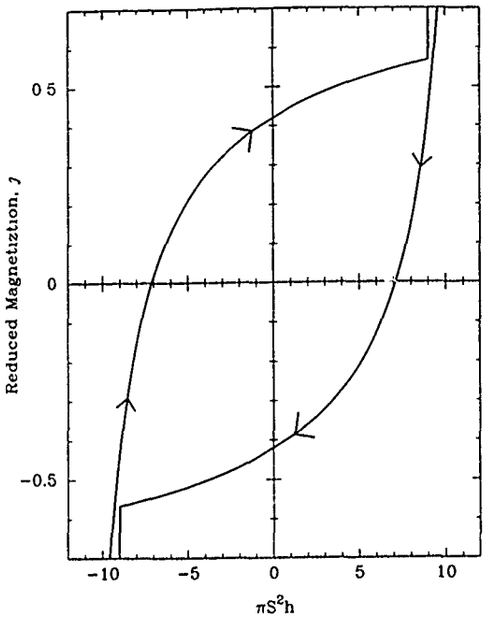

FIG. 2. An inverted hysteresis loop computed from Eqs. (1) and (4), with $\pi S^2 h_D = 12.5$.

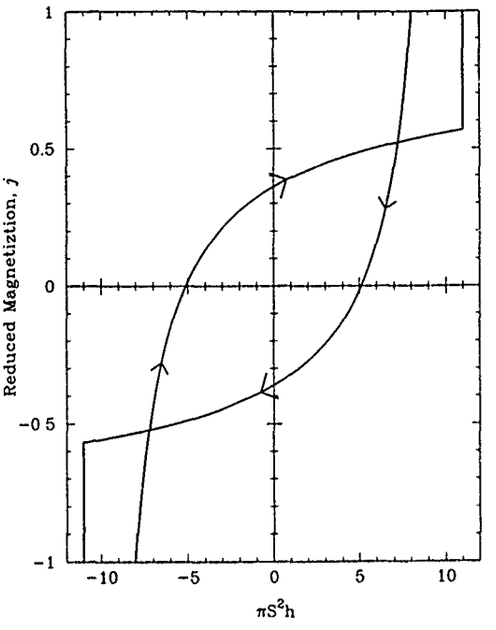

FIG. 3. As in Fig. 2, only with $\pi S^2 h_D = 10.5$. Note that the scales are different.

magnetization into the field direction. Effectively, boundary conditions no longer require the surface magnetization to be always parallel to $+z$. At a large negative field it becomes parallel to $-z$.

(2) A demagnetization is added by replacing Eq. (3) by

$$-\pi S^2(h-h_D)=[K(k)]^2. \tag{4}$$

Of course, these assumptions are oversimplified, because the CoO is not magnetized abruptly, and the demagnetization is not a *constant*, h_D. However, this simple model contains all the physics of the assumed mechanism, and it can produce the experimental curves. A typical hysteresis curve, computed from Eqs. (1) and (4) and plotted in Fig. 2, contains all the features of, and is qualitatively very similar to, the observed[1,2] inverted hysteresis loops.

The plot in Fig. 2 is sensitive to the value used for h_D. For a smaller value the increasing and decreasing part of the hysteresis curve cross, approaching the shape of the curves computed[2] with no demagnetization. An example is plotted in Fig. 3. This result is not inconsistent with the experimental observation[1,2] that the loops are not always inverted. It must mean that the geometrical details of the demagnetization are important.

It should be emphasized that the curve in Fig. 2 is *not* a true minor loop. If the decreasing-field part in Fig. 2 is stopped and reversed at, say, $\pi S^2 h = -7$, the magnetization will climb back on the *same* branch, and not on the increasing part. Changing between the two branches occurs only in a highly positive or highly negative field, where energy has to be spent on reversing the *hard* component. Presumably, the same is also true for the observed inverted loops, although this point is not specified in the published[1,2] accounts. Otherwise, the negative resistance of the minor loop could be used to create a perpetual motion machine, thus violating the second law of thermodynamics. Actually, the energy gain in small fields is more than balanced by the energy loss in higher fields, as is the case for an electronic circuit with a negative resistance in *part* of the V-I cycle.

III. ONE-DIMENSIONAL THEORY

The crude approximations of Sec. II do not allow for a magnetization distribution in the hard magnetic component, take the demagnetizing field as a constant, and do not take into account the demagnetizing of the hard by the soft component. These approximations can be much improved by a slight modification of the theory which was used[4] for bilayers of NiFe-TbCo, but which is *qualitatively* the same for any other pair of materials. It should be particularly noted that this theory contains as particular cases all the other one-dimensional models which were developed separately, e.g., when each film is taken as a "single domain," without[5] or with[6] a transition wall between them.

This theory[4] considers a soft layer whose magnetization is at an angle $\theta_1(z)$ to the axis of induced anisotropy, taken as the x axis, in the region $-t_1 \leq z \leq 0$; and a hard layer whose magnetization is at an angle $\theta_2(z)$ to x, in the region $0 \leq z \leq t_2$. For the soft and the hard films, the saturation magnetization is M_j, the uniaxial anisotropy constant is K_j, and the exchange constant is A_j, with $j=1, 2$, respectively. It is only assumed here that the soft film interacts with a field $H_A - H_{D1}$, and the hard film with $H_A - H_{D2}$, instead of just with the applied field, H_A. Here H_{D1} should *eventually* be taken as proportional to the average of $\cos\theta_2$, and H_{D2} as proportional to the average of $\cos\theta_1$, which should be a reasonably good approximation to many real physical situations. This part will be published elsewhere. The following notations are used for short:

$$h_1=(H_A-H_{D1})M_1/K_1, \quad h_2=(H_A-H_{D2})M_2/K_2,$$
$$q^2=K_b^2\sin^2(2\theta_b)/(4A_2K_2), \quad \theta_b=\theta_2(t_2), \tag{5}$$
$$\theta_0=\theta_1(-t_1), \quad Q=\sqrt{q^2+(h_2/2+\cos\theta_b)^2},$$

where K_b is[4] the surface anisotropy.

Smith and Cain[4] solved numerically the two *second-order* differential equations which minimize the energy. However, it is known[7,8] and has been pointed out[9] again, that *all* the equations of one-dimensional micromagnetics can be integrated at least once, if not twice. After the first integration, these equations become

$$(A_1/K_1)(d\theta_1/dz)^2=h_1[\cos(\theta_0-\theta_H)-\cos(\theta_1-\theta_H)] +\sin^2\theta_1-\sin^2\theta_0, \tag{6a}$$

$$(A_2/K_2)(d\theta_2/dz)^2=h_2[\cos(\theta_b-\theta_H)-\cos(\theta_2-\theta_H)] +q^2+\sin^2\theta_2-\sin^2\theta_b. \tag{6b}$$

Here θ_H is the angle between the applied field and the x axis. It can be checked that Eqs. (6) are indeed first integrals of the second-order equations[4] *and* that they fulfill two of the boundary conditions, which require the z derivatives of θ_1 and of θ_2 to vanish on $z=-t_1$ and $z=t_2$, respectively. It should be noted, though, that θ_0 and θ_b are known at this stage only as the boundary values of θ_1 and θ_2. They still need to be evaluated.

One of the remaining boundary conditions is that the derivative is continuous,

$$d\theta_1/dz=d\theta_2/dz, \quad \text{on } z=0. \tag{7a}$$

The other one was taken[4] as a certain *discontinuity* of the angle at $z=0$, thus introducing unnecessarily another, *unknown* parameter, K_t. It is better to take the limit $K_t\to\infty$, because the exchange is the largest force over short distances. Other micromagnetics studies do not allow a discontinuity because the exchange is so strong, and having an exchange coupling between two *different* materials cannot change this argument. In the studies of nucleation at crystalline imperfections, with an abrupt[10] or a gradual[11] or a periodic[12] change in the anisotropy, and in the study[13] of domain wall pinning, or wall motion[14] in a material with a variable exchange, the angle was assumed to be continuous. There is no reason to assume anything else here, and the second boundary condition is that the angle is also continuous,

$$\theta_t=\theta_1(0)=\theta_2(0). \tag{7b}$$

Analytic integration of these equations is possible in many cases, but there are different types of functions depending on the values of the physical parameters involved. The following solution is only an example, for the particular case of an in-plane field, $\theta_H=0$

$$1-\cos\theta_1=\frac{1-\cos\theta_0}{1-\frac{k_1^2}{2}(1+\cos\theta_0)\mathrm{sn}^2\left(\frac{z+t_1}{t_1}u_1,k_1\right)}, \tag{8a}$$

$$1-\cos\theta_2=\frac{1-Q+h_2/2}{1-\frac{k_2^2}{2}\left(1+Q-\frac{h_2}{2}\right)\mathrm{sn}^2(U_2,k_2)}, \tag{8b}$$

$$k_1^2=\frac{2(h_1+2\cos\theta_0)}{(1+\cos\theta_0)(1+h_1+\cos\theta_0)}, \tag{8c}$$

$$k_2^2=\frac{4Q}{(1+Q)^2-(h_2/2)^2}, \tag{8d}$$

$$u_1=\frac{t_1}{2}\sqrt{\frac{K_1}{A_1}}\sqrt{(1+\cos\theta_0)(1+h_1+\cos\theta_0)}, \tag{8e}$$

$$U_2=u_0+\frac{z-t_2}{t_2}u_2, \quad u_2=\frac{t_2}{k_2}\sqrt{\frac{K_2}{A_2}}Q, \tag{8f}$$

$$\mathrm{sn}^2(u_0,k_2)=\frac{q^2}{2Q}\left(\frac{1}{Q+\cos\theta_b+h_2/2}+\frac{1}{1-\cos\theta_b}\right), \tag{8g}$$

where sn is the Jacobian elliptic function, and where the integration constants have already been chosen so that $\theta_1=\theta_0$ on $z=-t_1$, and $\theta_2=\theta_b$ on $z=t_2$. It can be checked by differentiation that Eqs. (8) solve the differential Eqs. (6). Therefore Eqs. (8) are a legitimate solution, provided the parameters are such that

$$0<k_1^2<1 \quad \text{and} \quad 0<k_2^2<1. \tag{9}$$

If either k_1 or k_2 is not in this region, standard transformations to other elliptic functions may be used.

The problem has thus been reduced to finding θ_0 and θ_b that will fulfill the boundary conditions of Eqs. (7).

Once this problem is solved, the average magnetization in each region,

$$\langle\cos\theta_1\rangle=\frac{1}{t_1}\int_{-t_1}^{0}\cos\theta_1\,dz, \tag{10a}$$

$$\langle\cos\theta_2\rangle=\frac{1}{t_2}\int_{0}^{t2}\cos\theta_2\,dz, \tag{10b}$$

is a standard elliptic integral of the third kind. The reduced total magnetization is then

$$j=\frac{M_1t_1\langle\cos\theta_1\rangle+M_2t_2\langle\cos\theta_2\rangle}{M_1t_1+M_2t_2}. \tag{11}$$

[1] C. Gao and M. J. O'Shea, J. Magn. Magn. Mater. **127**, 181 (1993).
[2] M. J. O'Shea and A.-L. Al-Sharif, J. Appl. Phys. **75**, 6673 (1994).
[3] A. Aharoni, E. H. Frei, and S. Shtrikman, J. Appl. Phys. **30**, 1956 (1959).
[4] N. Smith and W. C. Cain, J Appl. Phys. **69**, 2471 (1991).
[5] K. O. Legg, W. D. Doyle, and M. Prutton, Phys. Status Solidi A **12**, 499 (1972).
[6] D. Mergel, J. Appl. Phys. **74**, 4072 (1993).
[7] A. Aharoni, Phys. Rev. **123**, 732 (1961).
[8] A. Aharoni, CRC Crit. Rev. Solid State Sci. **2**, 121 (1971).
[9] A. Aharoni, Phys. Rev. B **47**, 8296 (1993).
[10] A. Aharoni, Phys. Rev. **119**, 127 (1960).
[11] C. Abraham and A. Aharoni, Phys. Rev. **1120**, 1576 (1960).
[12] A. Aharoni, J. Appl. Phys. **32**, 245S (1961).
[13] H. R. Hilzinger, Appl. Phys. **12**, 253 (1977).
[14] E. Della Torre and C. M. Perlov, J. Appl. Phys. **69**, 4596 (1991).

Ruderman–Kittel–Kasuya–Yosida polarizations in inhomogeneous media

W. Baltensperger and J. S. Helman
Centro Brasileiro de Pesquisas Físicas (CBPF), Rua Dr. Xavier Sigaud 150, Rio de Janeiro, RJ 22290, Brazil

An analytical treatment of the Ruderman–Kittel–Kasuya–Yosida polarization in inhomogeneous media is possible for some simple models. This is exemplified with the half-spaces and slabs in one and three dimensions, and with an especially chosen potential barrier in one dimension.

I. INTRODUCTION

Experiments with films and with layered structures require information on the Ruderman–Kittel–Kasuya–Yosida (RKKY) polarization in inhomogeneous situations. This work deals with especially simple situations for which a calculation can be made analytically. The aim is to get familiar with effects that appear in idealized situations rather than to study a model that incorporates many features of actual experimental conditions.

As in the classical papers on RKKY polarization[1] we shall assume the electron gas to be ideal and fully degenerate. At a position **a** the electron spins are subject to a point field leading to a perturbing Hamiltonian

$$H' = -\gamma\delta^3(\mathbf{r}-\mathbf{a})\,\frac{\sigma_z}{2}. \tag{1}$$

The coupling constant γ has the dimension energy volume, **r** is the electron position, and σ_z the Pauli spin matrix for the z direction. In the homogeneous case plain waves $\phi_{k,s} = 1/\sqrt{\pi}e^{i\mathbf{k}\cdot\mathbf{r}}|s\rangle$, with $s=\pm\frac{1}{2}$ the spin quantum number, and which belong to the energy $\epsilon(\mathbf{k})=\hbar^2k^2/2m$, form a complete set of unperturbed one particle states. It can be shown by an extension of Yosida's argument[2] to inhomogeneous situations, Eq. (33), that the first-order perturbed wave functions

$$\psi_{k,s} = \phi_{k,s} + \int d^3\mathbf{k}'\,\frac{\langle\phi_{k',s'}|H'|\phi_{k,s}\rangle}{\epsilon(\mathbf{k}')-\epsilon(\mathbf{k})}\,\phi_{k',s}, \tag{2}$$

lead to the correct spin polarization which has z direction:

$$P(\mathbf{x}) = \frac{1}{(2\pi)^3}\int_{k<k_F} d^3\mathbf{k}\,\psi^*_{k,s}(\mathbf{x})\,\frac{\sigma_z}{2}\,\psi_{k,s}(\mathbf{x}). \tag{3}$$

k_F is the Fermi wave vector

II. THE SEMISPACE

Consider an ideal electron gas confined to the half-space with coordinate $x>0$. This is obviously not a realistic model for a surface of a true metal. However, it has the virtue that again a simple set of one particle functions can be written down. In the one-dimensional case they can be taken to be $1/\sqrt{2}\sin(kx)|s\rangle$. The electron density and therefore the polarization vanishes at the surface. Mathematically the whole change is a sine function in place of an exponential. In the unlimited one-dimensional space the spin polarization is[3,4]

$$R_1(|x-a|) = \frac{\gamma}{4\pi}\,\frac{2m}{\hbar^2}\left(\frac{\pi}{2} - \mathrm{Si}(2k_F|x-a|)\right). \tag{4}$$

For the half-line the calculation[5] gives

$$P_{1h}(x) = R_1(|x-a|) + R_1(x+a) - 2R_1[|x-a|/2 + (x+a)/2]. \tag{5}$$

The first term is the polarization in a homogeneous medium due to a point field at position a, and the second is the same expression centered around the mirror point $-a$. At the surface, $x=0$, the two terms have the same value. In this sense the second term is not a reflected wave. It is the third term, which depends on the average distance to the source and to its mirror point, which compensates the first two terms at the surface. P_{1h} is shown in Fig. 1.

When the half-space has more than one dimension, a complete set of one particle wave functions which vanish at the boundary $x=0$ is

$$\phi_{k,K,s}(x,\mathbf{R}) = \sqrt{2}\,\sin(kx)e^{i\mathbf{K}\cdot\mathbf{R}}|s\rangle, \tag{6}$$

where $k>0$, and **R** and **K** are orthogonal to the x direction. In two dimensions the authors were unable to perform the integrations analytically. For a three-dimensional half-space the polarization P_h can again be expressed[5] in terms of the usual RKKY function

$$R(x) = \frac{\gamma k_F^4}{4\pi^3}\,\frac{2m}{\hbar^2}\,\frac{\sin(x)-x\,\cos(x)}{x^4} \tag{7}$$

as

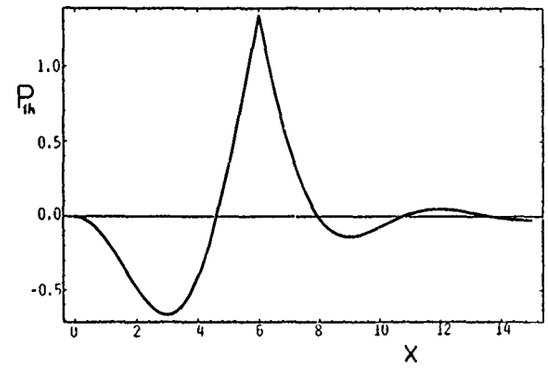

FIG. 1. The spin polarization $P_{1h}(x)$ in a half-line for a point field at $a=6$. Distances are in units of $1/(2k_F)$ and P_{1h} is in units of $\gamma 2m/(4\pi\hbar^2)$

 0021-8979/94/76(10)/6980/3/$6.00 © 1994 American Institute of Physics

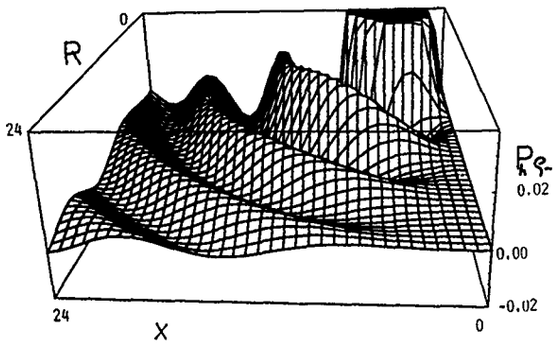

FIG. 2. Polarization in half-space due to a point field at $a=4$. $P_h(x,R)\rho_-$ is shown, where the factor ρ_-, the distance to the point source, suppresses the divergence of P_h at the source and emphasizes the oscillations. Distances are in units of $1/(2k_F)$ and P_h is in units of $\gamma k_F^4 2m/(4\pi^3\hbar^2)$.

$$P_h = R(2k_F\rho_-) + R(2k_F\rho_+) - \frac{(\rho_- + \rho_+)^2}{(2\rho_-\rho_+)} R[k_F(\rho_- + \rho_+)]. \tag{8}$$

Here

$$\rho_\mp = \sqrt{(x \mp a)^2 + R^2}, \tag{9}$$

so that ρ_- is the distance to the source and ρ_+ to its mirror point. The first two terms are spherical waves, while the third term depends on $\rho_+ + \rho_-$ and compensates the first two at the surface. See Fig. 2.

III. THE SLAB

In the one-dimensional case, i.e., for the finite line of length L, a closed expression for the polarization $P_{1f}(x)$ has been derived.[5] The plot in Fig. 3 assumes an even number of electrons N, so that the highest occupied level is designated by $n_F=N/2$. In three dimensions, for the slab of width L, the polarization $P_f(x,R)$ can be written as a rapidly converging series.[5] Here, x, with $0<x<L$, and R are coordinates of a circular cylinder with the source at $x=a$, $R=0$. Figure 4

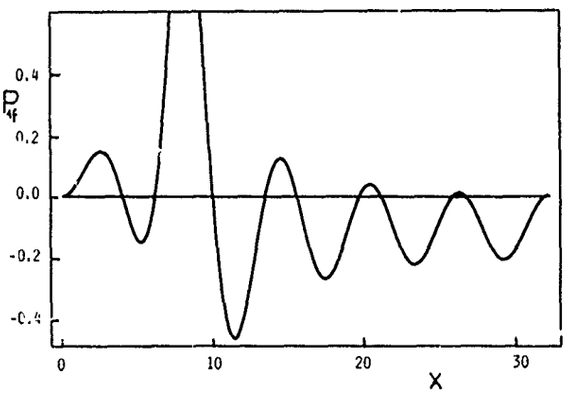

FIG. 3. Polarization in a finite line of length $L=32$ due to a point field at $a=8$. $n_F=5$. Units are as in Fig. 1. The precise position a determines whether the positive polarization near a is compensated by a negative one mostly to the right or to the left of a.

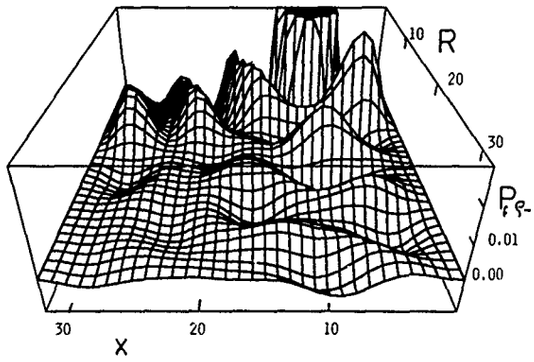

FIG. 4. The spin polarization $P_f(x,R)\rho_-$ in a slab of width $L=32$. $a=12$. Units are as in Fig. 2.

shows $P_f\rho_-$, where ρ_- is the distance from the source. $n_F=\mathrm{Int}(\pi k_F/L)=5$ designates the band at the Fermi level.

IV. POLARIZATION ACROSS A POTENTIAL WELL

A potential also creates an inhomogeneity in an electron gas. A square well leads to wave functions with somewhat complicated coefficients which inhibit a further analytical treatment. A numerical calculation has been performed by Jones and Hanna.[6] Here we discuss a one-dimensional model with a particular localized potential which lends itself to analytic treatment.

The electrons are subject to a localized potential of width λ

$$V(x) = -V_0 \operatorname{sech}^2(\lambda x) \tag{10}$$

$$V_0 = 2\lambda^2\hbar^2/(2m), \tag{11}$$

where m is the mass of an electron. With Eq. (11) the potential has the remarkable property of being reflectionless.[7] Note that Eqs. (10) and (11) imply that the depth and width of the potential cannot be varied independently. This potential has been chosen for the simplicity of its wave functions and spectrum. This consists of a continuous part

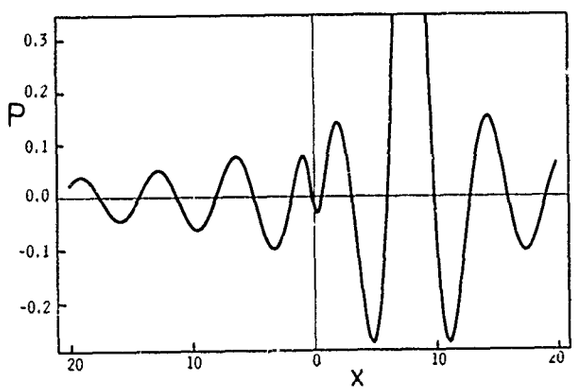

FIG 5. Spin polarization due to a point source at $a=3$ in the presence of a potential, Eq. (23) with $\lambda=1$, near $x=0$. Units are as in Fig 1.

$$\phi_{k,s}(x)=\frac{-ik+\lambda\tanh(\lambda x)}{\sqrt{k^2+\lambda^2}}e^{ikx}|s\rangle,\quad E_k=\frac{\hbar^2k^2}{2m},\tag{12}$$

and one bound state

$$\phi_{b,s}(x)=\sqrt{\frac{\lambda}{2}}\,\mathrm{sech}(\lambda x)|s\rangle,\quad E_b=-\frac{\hbar^2\lambda^2}{2m}.\tag{13}$$

With

$$z=|x-a|,\tag{14}$$

$$T=\tanh(\lambda x)\tanh(\lambda a),\tag{15}$$

$$S=|\tanh(\lambda x)-\tanh(\lambda a)|,\tag{16}$$

$$C_k=\frac{(k^2+\lambda^2T)\cos(kz)-k\lambda S\,\sin(kz)}{k^2+\lambda^2},\tag{17}$$

the polarization becomes

$$P(x,a)=-\frac{2m}{\hbar^2}\frac{\gamma}{4\pi}\left\{-\frac{\pi}{2}T^2+\int_0^{k_F}\frac{dk}{k}\frac{1}{(k^2+\lambda^2)^2}\{[(k^2+\lambda^2T)^2-(k\lambda S)^2]\sin(2kz)+2\lambda Sk(k^2+\lambda^2T)\right.$$
$$\times\cos(2kz)\}+2\lambda[e^{-\lambda z}(T-1-S)+\mathrm{sech}(\lambda x)\mathrm{sech}(\lambda a)]\int_0^{k_F}dk\,\frac{C_k}{(k^2+\lambda^2)}-\frac{\pi}{2}\,\mathrm{sech}(\lambda x)$$
$$\left.\times\mathrm{sech}(\lambda a)e^{-\lambda z}[T+1+\lambda z(T-1-S)]\right\}.\tag{18}$$

This still contains an integration to be performed numerically (Fig. 5).

As a limiting case let both x and a be on the same side of the potential and far away from it, i.e.,

$$x,a\gg\lambda,\quad\text{or}\quad -x,-a\gg\lambda.\tag{19}$$

In this case $T=1$ and $S=0$. Thus $P(\mathbf{x},\mathbf{a})\approx R_1(|\mathbf{x}-\mathbf{a}|)$ of Eq. (4). Note that the terms that were neglected were exponentially small. This result conforms with the reflection free property of the potential. In general $P(a,a)=\gamma 2m/(4\pi\hbar^2)$ independent of a and λ.

V. INTEGRATED POLARIZATION

The validity of the procedure used by Ruderman and Kittel to derive the polarization induced by a point field was demonstrated by Yosida. This can be extended to situations in which the electron gas is subject to boundary conditions and spin independent potentials. Let $\phi_{\kappa,\nu}(\mathbf{x})$, $\epsilon(\kappa,\nu)$ represent the orbital wave functions and energies of the continuous part of the spectrum, where κ is a continuous quantum number while ν labels the bands. Then it can be shown that the polarization satisfies

$$\int P(\mathbf{x},\mathbf{a})d^3x=\frac{\gamma}{(2\pi)^2}\sum_\nu\int_{S_{F,\nu}}\frac{dS_{\kappa,\nu}}{4\pi}\frac{|\phi_{\kappa,\nu}(\mathbf{a})|^2}{|\nabla_\kappa\epsilon(\kappa,\nu)|},\tag{20}$$

where the integration extends over the Fermi surfaces $S_{F,\nu}$ of all bands that are partially filled. The right-hand side can be interpreted as counting the spin flips at the Fermi energy due to the point field. However the formula is derived using perturbed wave functions and the unperturbed occupation of states. The bound states contribute only indirectly, through the orthogonality to the continuous states. Apart from justifying our method of calculation, Eq. (20) provides a shortcut to obtain the integrated polarization.

[1] C. Kittel, *Quantum Theory of Solids* (Wiley, New York, 1963).
[2] Kei Yosida, Phys. Rev. **106**, 893 (1957).
[3] C. Kittel, *Solid State Physics*, edited by F. Seitz, D. Turnbull, and H. Ehrenreich (Academic, New York, 1968), Vol. 22, p. 11.
[4] Y. Yafet, Phys. Rev. B **36**, 3948 (1987).
[5] J. S. Helman and W. Baltensperger, Phys. Rev. B (in press).
[6] Barbara A. Jones and C. B. Hanna, Phys. Rev. Lett. **71**, 4253 (1993)
[7] L. D. Landau and E. M. Lifshitz, *Quantum Mechanics, Nonrelativistic Theory*, Course of Theoretical Physics Vol. 3 (Pergamon, Oxford, 1977), pp 73 and 81.

Spin reversal in Co/Au(111)/Co trilayers

V. Grolier, J. Ferré, M. Galtier,[a] and M. Mulloy[a]
Laboratoire de Physique des Solides, Bât. 510, Université Paris-Sud, 91405 Orsay Cedex, France

In Co/Au(111)/Co trilayers exhibiting oscillatory interlayer coupling, we show how the nature and the strength of this interaction modify the magnetization reversal. In the case of antiferromagnetic (AF) coupling the magnetic domain patterns observed by Faraday microscopy differ drastically according to the amplitude of the coupling. This effect can be understood on the basis of the fluctuations of the effective field acting on a layer produced by the roughness of the Au interlayer. Among the ferromagnetically (F) coupled layers slighter differences are visible that can be accounted by changes of the anisotropy energy.

INTRODUCTION

Widely observed in systems with planar anisotropy, the oscillatory interlayer coupling has been detected in few systems with perpendicular anisotropy.[1,2] Among them Co/Au(111)/Co is particularly attractive in view to study the magnetization reversal and the corresponding domain patterns, because much of the work has been devoted to simple Au/Co/Au sandwiches.[3,4] The purpose of this article is to show how the spin reversal near the coercive field(s) is affected by the interlayer coupling and its oscillatory nature and to understand this behavior in light of what is already known about Au/Co/Au monolayers.

SAMPLES AND EXPERIMENTAL TECHNIQUES

The samples are Co/Au(111)/Co trilayers grown by thermal evaporation in ultrahigh vacuum on a polycrystalline fcc Au(111) buffer. Details about the growth conditions and the structural properties of the samples are reported elsewhere.[1]

The Au interlayer has a stepped-wedge shape, with eight different thicknesses, from 2 to 9 atomic layers (AL). The two Co films have the same thickness—0.8 nm—and comparable roughness (1 AL) in this range of Au interlayer thickness, as was shown by AFM and RHEED experiments.[5] Therefore, for the thinnest samples ($t_{Co} \leqslant 3$ AL), we can expect that in the absence of coupling the top and the bottom layers have almost the same intrinsic coercive field and exhibit similar domain patterns during the reversal of magnetization.

All the samples have perpendicular anisotropy and their magnetization was deduced from sensitive Faraday ellipticity measurements. At a more microscopic scale a Faraday microscope with an objective of high numerical aperture (0.85) was used to observe domain patterns.

RESULTS

The hysteresis loops (Fig. 1) measured in perpendicular field confirm the oscillatory nature of the interlayer coupling: for $t_{Au}=5$ AL and 9 AL we observe two successive jumps of magnetization at different fields, thus revealing AF coupling. For the other interlayer thicknesses, only one steep reversal is visible, occurring at a smaller coercive field for the thinnest interlayers ($t_{Au}=2$ AL and 3 AL).

In the case of AF coupling, the two coercive fields are different enough to enable the observation of the domains in each Co layer separately. For strong AF interaction, the time evolution of the domain structures after premagnetizing the sample in a large negative field are shown Fig. 2. The first layer exhibits a dendritic growth of domains starting from a few nucleation centers. The situation is completely different in the second layer: a great amount of small domains are nucleated and very limited propagation of their walls is visible afterwards.

For small AF coupling ($t_{Au}=9$ AL), if the reversals occur at different fields, the corresponding evolutions of the domain patterns (Fig. 3) are identical: a domain wall is moving across the sample with a reduced deformation of its shape by pinning centers.

Among the F coupled samples the less strongly coupled ones ($t_{Au}=4$, 6, 8 AL) form an homogeneous group with the same coercive field and identical domain patterns. The strongly F coupled films ($t_{Au}=2$, 3 AL) behave differently, which appear clearly on magnetic after-effect curves. For these samples, one has to notice that beside the regular RKKY coupling a direct exchange interaction exists. Figure 4 illustrates the influence of the strength of the F coupling on relaxation curves obtained for $t_{Au}=2$ and 4 AL. Both the bias fields and the shape of the relaxation are different: for $t_{Au}=4$ AL we get a typical reversal dominated by domain wall propagation, whereas for $t_{Au}=2$ AL, the nucleation process plays a more important role and the needed applied fields are smaller.

INTERPRETATION

Bruno and Chappert,[4] first have pointed out in this system the importance of the inhomogeneities in the determination of the coercivity via domain wall movement. In the case of coupled films, the effective field acting on each layer is

$$H_{eff}=H_{appl}+H_{int},$$

where H_{appl} and H_{int} are the applied and interaction fields, with $H_{int}>0$ for AF coupling. Therefore, to the inhomogeneities due to the structural roughness of each Co layer the ones produced by the fluctuations of H_{eff} due to the roughness of the interlayer are added.

[a]Institut d'Optique Théorique et Appliquée, Bât. 503, Université Paris-Sud, 91405 Orsay Cedex, France.

 0021-8979/94/76(10)/6983/3/$6.00 © 1994 American Institute of Physics

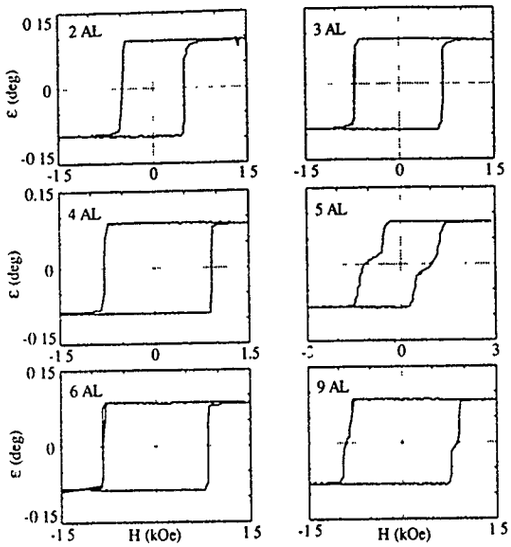

FIG. 1. Hysteresis loops measured by magneto-optical Faraday ellipticity for different values of the Au interlayer thickness.

When t_{Au}=5 AL, the coupling is AF but its amplitude and its sign are very sensitive to the Au layer thickness.[1] In that case, taking into account a realistic roughness of the interlayer of 1 AL, islands of F coupled zones exist in a majority of AF coupled regions. It must be noted that this picture of islands is reasonable when the mean interlayer thickness is smaller than the so-called cutoff thickness equal to 5 AL in this system.[6] For the first Co layer, nucleation occurs where the effective field is the highest (AF zones) and the F islands act as obstacles to be avoided by the moving wall, which explains the dendritic shape of the walls. In the second Co layer, nucleation occurs in F zones and very rapidly, the domain wall reaches an AF region which stops its motion.

For t_{Au}=9 AL, we are beyond the cutoff thickness and the fluctuations of the coupling are much smaller than near the first AF peak, namely 0.05 erg cm^{-2} for a change of the interlayer thickness of 1 AL. Besides, the variation of the anisotropy energy due to the roughness of each Co film is 0.1 erg cm^{-2} when t_{Co}=0.8 nm. Therefore, in this case, the AF

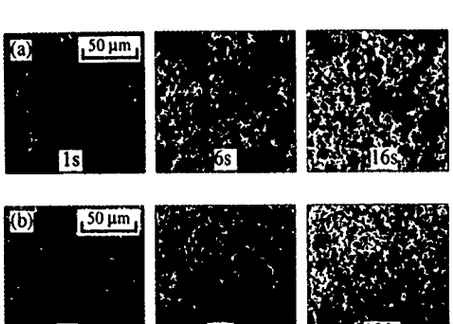

FIG. 2. Co(0.8 nm)/Au(5 AL)/Co(0.8 nm): time evolution of the magnetic domain structure in the first Co layer (a) at H=336 Oe and in the second one (b) at H=1008 Oe.

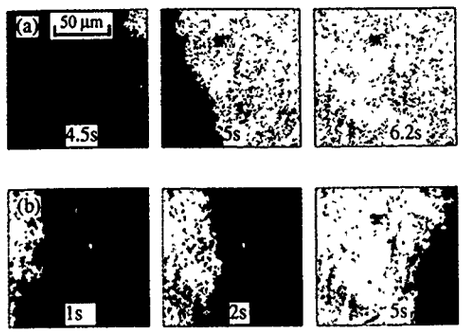

FIG. 3. Co(0.8 nm)/Au(9 AL)/Co(0.8 nm): time evolution of the magnetic domain structure in the first Co layer (a) at H=624 Oe and in the second one (b) at H=768 Oe.

coupling just shifts the magnetization reversals with respect to one another, but does not alter their mechanisms as compared to a single Au/Co/Au sandwich with t_{Co}=0.8 nm.

When the coupling is F another effect accounts for the differences observed between weakly and strongly coupled Co layers. The magnetic anisotropy of the above-mentioned samples (t_{Au}=2 and 4 AL) was compared to the one of a Au/Co/Au sandwich (t_{Co}=0.8 nm). For this purpose, the magnetic field is applied to 25° with respect to the sample plane and the variation of the perpendicular component of the magnetization is recorded as a function of the field amplitude.[7] The results are shown Fig. 5.

Whereas the sample with t_{Au}=4 AL is similar to the single Co film from the point of view of magnetic anisotropy, the strongly coupled one (t_{Au}=2 AL) is softer and is comparable to a single 1.2-nm thick Co layer.

Therefore, the differences observed in Fig. 4 can be understood on the basis of the effective thickness deduced from the anisotropy measurements. They correspond to the trends

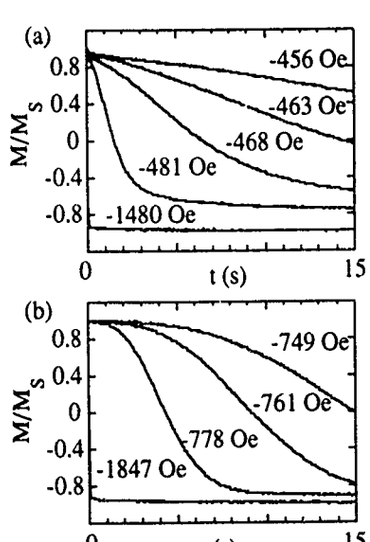

FIG. 4. Magnetic after effect for t_{Au}=2 AL (a) and t_{Au}=4 AL (b) for different values of the applied field.

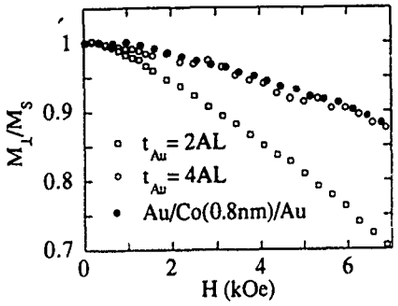

FIG. 5. Variation of the normal component of the magnetization under application of a magnetic field at 25° with respect to the film plane for two trilayers with t_{Au}=2 AL and t_{Au}=4 AL and for a 0.8-nm-thick Co monolayer.

observed for Au/Co/Au sandwiches: decrease of the coercive field, importance of the nucleation process when the Co thickness is increased.[8]

CONCLUSIONS

As for Co monolayers, the fluctuations play an important role in the dynamics of the magnetization reversal but contrary to the former case these fluctuations are not due to the own roughness of the Co films but results from the one of the Au interlayer. This effect is enhanced by the sensitivity of the coupling to the Au thickness, especially near the first AF peak. At lower thicknesses (strong F coupling), the differences originate from the decrease of the magnetic anisotropy for thin Au interlayers.

[1] V. Grolier, D. Renard, B. Bartenlian, P. Beauvillain, C. Chappert, C. Dupas, J. Ferré, M. Galtier, E. Kolb, M. Mulloy, J. P. Renard, and P. Veillet, Phys. Rev. Lett. **71**, 3023 (1993); C. Cesari, J. Faure, G. Nihoul, K. Le Dang, P. Veillet, and D. Renard, J. Magn. Magn. Mater. **78**, 296 (1989); S. Ould-Mahfoud, R. Mégy, N. Bardou, B. Bartenlian, P. Beauvillain, C. Chappert, J. Corno, B. Lécuyer, G. Sczigel, P. Veillet, and D. Weller, Mater. Res. Soc. Symp. Proc. **313**, 251 (1993).
[2] W. R. Bennett, W. Schwarzacher, and W. F. Egelhoff, Phys. Rev. Lett. **65**, 3169 (1990).
[3] P. Bruno, G. Bayreuther, P. Beauvillain, C. Chappert, G. Lugert, D. Renard, J. P. Renard, and J. Seiden, J. Appl. Phys. **68**, 5759 (1990).
[4] J. Pommier, P. Meyer, G. Pénissard, J. Ferré, P. Bruno, and D. Renard, Phys. Rev. Lett. **65**, 2054 (1990).
[5] D. Renard and C. Marlière (private communication).
[6] P. Bruno and C. Chappert, Phys. Rev. Lett. **67**, 1602 (1991); 2592(E) (1991); P. Bruno and C. Chappert, Phys. Rev. B **46**, 261 (1992).
[7] V. Grolier, J. Ferré, A. Maziewski, E. Stefanowicz, and D. Renard, J. Appl. Phys. **73**, 5939 (1993).
[8] V. Grolier, Ph.D. thesis, 1994 (unpublished).

Effect of coupling on magnetic properties of uniaxial anisotropy NiFeCo/TaN/NiFeCo sandwich thin films

T. Yeh, L. Berg, P. Witcraft, J. Falenschek, and J. Yue
Honeywell, Solid State Electronics Center, Plymouth, Minnesota 55441

The coercivity of the coupled NiFeCo thin films is a function of nickel-iron-cobalt (NiFeCo) film thickness and tantalum nitride (TaN) intermediate layer thickness. This can be attributed to the variation of energy and magnetization gradients of a domain wall. The magnetization gradient can be affected by a thickness-induced coupling effect associated with altering the exchange and magnetostatic interactions between the two NiFeCo films. Decreasing the exchange coupling and increasing the magnetostatic coupling between the coupled NiFeCo films tends to decrease the energy and magnetization gradients of domain walls and results in decreased coercivity.

INTRODUCTION

The success of utilizing coupled magnetic films as magnetic sensors or memories largely depends upon a better understanding and control of the magnetic coupling between the coupled magnetic films. One of the most striking effects of sandwich magnetic films, as compared to that of a single film, is the reduction of coercivity, which is attributed to reduced domain wall energy.[1–4] Theoretical calculation showed that the domain wall energy of coupled films can be significantly changed through the exchange and magnetostatic coupling of the coupled films by varying the thickness of magnetic and nonmagnetic films.[2,5,6] In this article, the manner in which the magnetic properties of coupled NiFeCo films are affected by pure tantulum (Ta) and reactive-sputter TaN films is examined, and the magnetic properties of sandwich NiFeCo/TaN/NiFeCo films as a function of TaN and NiFeCo film thicknesses are investigated. Also, the correlation between the coercivity of the coupled films and the domain wall is discussed.

EXPERIMENT

Because of the nature of short-range interaction, the exchange coupling of coupled films may be very sensitive to the thickness of the nonmagnetic interlayer and the interlayer material. The experiments for this article were performed as follow. First, the effect of Ta and TaN intermediate layers on magnetic properties of 150-Å-thick coupled NiFeCo films was investigated. Second, how the nonmagnetic intermediate layer thickness affects the magnetic properties of the coupled films was studied. In this portion of the study, the 150-Å-thick NiFeCo film was used with the intermediate TaN film thickness varying from 0 to 105 Å. Third, in an attempt to study the magnetostatic coupling effect on the magnetic properties of the sandwich films, the NiFeCo films were varied from 150 to 600 Å with the intermediate TaN film held constant at 50 Å.

Samples of NiFeCo/TaN/NiFeCo sandwich films were sputter deposited on a 4-in. silicon wafer coated with a thin sputtered silicon nitride film. rf sputtering was used to deposit the NiFeCo films while the TaN was deposited by a dc reactive-sputter process with an Ar and N_2 mixture sputtering gas and a pure Ta target producing the NiFeCo/TaN/NiFeCo sandwich. The deposition rates of the films were carefully characterized while the thickness of the films was controlled by varying the sputtering time.

Subsequent to the deposition, the film properties were characterized by a B-H looper using a maximum 100-Oe applied field. The sheet resistance and B's of the films were used to monitor the thickness of the NiFeCo films. The magnetic properties of the films, such as skew, dispersion α_{90}, anisotropy field H_K, and coercivity $H_{c//}$, were determined by the B-H looper measurements. Atomic force microscopy (AFM) was used to characterize the surface topography of the sandwich films.

The magnetic properties of the sample films are summarized in Tables I, II, and III. The skew and dispersion α_{90} data demonstrate that all the sample films exhibit in-plane magnetic unaxial anisotropy with easy and hard axes perpendicular to each other. A typical easy and hard axis hysteresis loop of the sandwich film is shown in Fig. 1. The anisotropy field H_K of the film was measured to be approximately 20 Oe, showing results of the easy and hard axes hysteresis loops to be consistent with the skew and dispersion α_{90} measurements.

RESULTS AND DISCUSSION

Before reporting and discussing the experimental results, we will first derive the relationship between coercivity and the domain wall energy of the coupled films. Because of the coupling effect in the configuration of two ferromagnetic films separated by a nonmagnetic film, the domain wall structure differs markedly from those observed in single ferromagnetic films. One of the most striking properties of coupled magnetic films is the modification of domain wall reversal properties by comparison with those of single films. The coercivity is a quantitative measure of the magnetic field required to reverse the magnetization direction in the film. Local energy gradients constitute a generalized force tending to hinder the magnetization reversal process of a ferromagnetic film.[7] However, for a magnetic uniaxial anisotropy film, the local energy gradients of domain walls are the dominant hindrance of the magnetization reversal process. If we call the domain wall energy γ, the coercivity is related to the derivative of this energy with respect to position $d\gamma/dx$, the energy gradient.[8]

 0021-8979/94/76(10)/6986/3/$6.00 © 1994 American Institute of Physics

TABLE I. Magnetic properties of the coupled NiFeCo films with different nonmagnetic intermediate layers.

NiFeCo thickness (Å)	Interlayer thickness (Å)	B_s (nW)	Skew (degree)	Dispersion (degree)	H_K (Oe)	H_{cl} (Oe)
150	50 (TaN)	2.41	0.52	0.7	20.0	0.45
150	50 (pure Ta)	2.34	−0.23	0.8	20.0	1.38

The total energy of the wall configuration is given by the sum of magnetostatic, anisotropy, and exchange terms, assuming that the domain wall is Néel and quasi-Néel type and the wall is thick compared to the total thickness of the sandwich film.[2,5,9] Therefore, the coercivity of the coupled films can be derived to be:[2]

$$H_{c//}=\left.\frac{d\gamma}{dx}\right|_{\max}=2\pi D\left(\frac{1}{2}b+\frac{1}{3}D\right)\left(\frac{dM_x}{dx}\right)^2+K\cos^2\varphi+A\left(\frac{d\varphi}{dx}\right)^2, \quad (1)$$

where D and d are thicknesses of the magnetic films and the nonmagnetic interlayer, respectively, K is the effective anisotropy constant, and A is the exchange constant. One may note that the coercivity $H_{c//}$ is a function of dM_x/dx and $d\varphi/dx$, the magnetization gradients, with lower magnetization gradient resulting in lower coercivity. Also, a domain wall with lower magnetization gradient implies a wider domain wall width. In other words, the domain wall width would be wider for the coupled film with lower coercivity due to lower magnetization gradient. The width of the domain wall appears to be inverse proportional to the square root of the coercivity $H_{c//}$.

Now, we move to a discussion of the effect of different intermediate layers on magnetic properties of the coupled NiFeCo films. The coercivity of the coupled NiFeCo films separated by a 50-Å thick Ta film is measured to be 1.38 Oe, while the coercivity is reduced to 0.45 Oe when the coupled films are separated by a 50-Å thick reactive-sputter TaN film. No effect from the anisotropy field H_K on the coercivity would be expected because of the same H_K were obtained in the two sample films. The coercivity reduction of the coupled NiFeCo films with a TaN intermediate layer could be attributed to the TaN film inducing a lower energy and magnetization gradient of the domain wall by altering the exchange and magnetostatic interactions between the magnetic films.

TABLE II. Magnetic properties of the coupled NiFeCo films as a fuction of TaN thickness (Fig. 3).

NiFeCo thickness (Å)	TaN thickness (Å)	B_s (nW)	Skew (degree)	Dispersion (degree)	H_K (Oe)	H_{cl} (Oe)
150	0	2.42	0.45	0.8	22.2	2.16
150	17	2.39	−0.03	0.7	19.9	0.55
150	35	2.39	−0.77	0.6	19.9	0.48
150	50	2.41	0.52	0.7	20.0	0.45
150	70	2.42	0.34	0.9	19.9	0.63
150	88	2.39	−0.31	1.0	20.2	1.06
150	105	2.37	0.74	1.0	20.0	1.21

TABLE III. Magnetic properties of the coupled NiFeCo films as a function of NiFeCo film thickness (Fig. 4).

NiFeCo thickness (Å)	TaN thickness (Å)	B_s (nW)	Skew (degree)	Dispersion (degree)	H_K (Oe)	H_{cl} (Oe)
150	50	2.41	0.52	0.7	20.0	0.45
200	50	3.26	0.52	0.7	21.2	0.38
250	50	4.06	0.54	0.6	21.6	0.34
600	50	10.12	0.54	0.5	23.6	0.25

The coercivity reduced by the intermediate TaN film may also have an impact on the domain wall structure of the coupled film.

The magnetic properties of coupled 150-Å NiFeCo films with varying TaN film thickness are summarized in Table II. The coercivity of the film with no TaN interlayer is measured to be 2.16 Oe, but when the film is separated by a 17-Å TaN film, the coercivity decreases to 0.55 Oe. The anisotropy field H_K decreases from 22.2 Oe for the film with no TaN interlayer to 19.9 Oe for the film separated by a 17-Å TaN film. This decreasing in H_K implies that the anisotropy constant K of the film separated by a 17-Å TaN film is 10% lower, but the 10% decrease in the anisotropy constant alone cannot explain the four times reduction of the coercivity. The

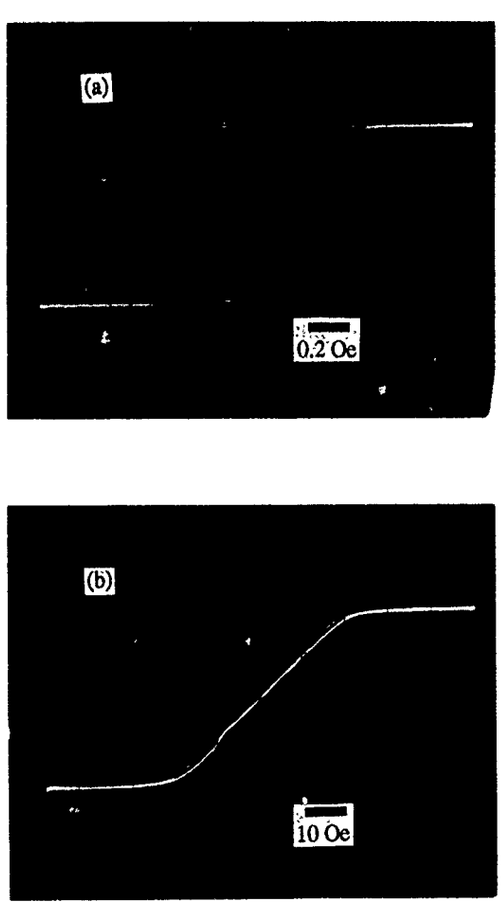

FIG. 1 Typical (a) easy axis (b) hard axis hysteresis loops of NiFeCo/TaN/NiFeCo sandwich film.

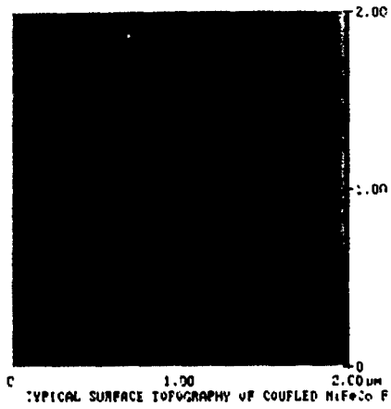

FIG. 2. The surface topography of the coupled film (rms roughness=3.4 Å).

coercivity reduction may be attributed to lowering the magnetization gradient of the domain wall induced by the 17-Å intermediate TaN film. The intermediate TaN film may induce the magnetostatic coupling and decouple the exchange interaction between the two NiFeCo films. The surface topography of the sample film shown in Fig. 2 demonstrates very smooth surface roughness. The surface roughness of the film indicates that a 17-Å thick intermediate TaN film is thick enough and continuous enough for the exchange coupling between the magnetic films to be weak or negligible, and for the magnetostatic interaction between the separated films to be appreciable which results in reducing the coercivity.

The coercivity as a function of the TaN intermediate layer thickness is shown in Fig. 3. As the TaN interlayer thickness increases, the coercivity decreases due to degradation of the exchange coupling between the magnetic films when the coercivity reaches a minimum at 50 Å. When the exchange interaction is degraded, the magnetostatic interaction between the two magnetic films comes to play a dominant role in determining the coercivity. While increasing the intermediate TaN thickness further, the magnetostatic interaction between the coupled NiFeCo films decreases and results in increasing the coercivity.

The dependence of coercivity on TaN thickness could be caused by variation of the energy and magnetization gradi-

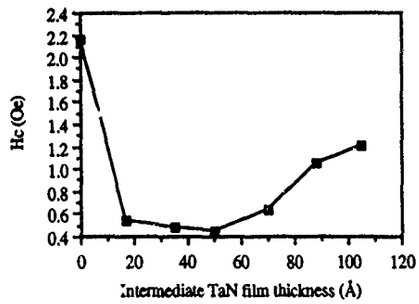

FIG. 3. The coercivity of the coupled films as a function of TaN thickness (Table II).

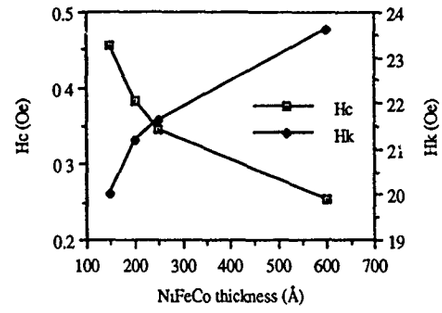

FIG. 4. The coercivity and anisotropy field of the coupled films as a function of NiFeCo thickness (Table III).

ents induced by varying the intermediate TaN thickness. Both the exchange and magnetostatic coupling between the coupled film could play a dominant role in different thickness regimes. The intermediate TaN film thickness may also have an effect on the domain wall structure.

Table III summarizes the effect of magnetostatic coupling on the magnetic properties of coupled films when varying the NiFeCo film thickness. The coercivity and anisotropy field of the coupled films as a function of NiFeCo film thickness is plotted in Fig. 4. The coercivity was found to decrease when increasing the thickness of the NiFeCo film, while the anisotropy field H_K increased when increasing the NiFeCo film thickness. This increasing of the anisotropy field can be attributed to the NiFeCo film thickness-induced magnetostatic coupling. Increasing the magnetostatic coupling between the uniaxial anisotropy coupled films tends to increase the coupling strength along the easy axis and results in lowering the energy state. For this reason, the anisotropy field increased when increasing the thickness of NiFeCo film. A higher anisotropy field H_K of the film would cause the coercivity to increase; therefore, the reduction of the coercivity is not due to increasing the anisotropy field. In this case, the coercivity can be related to the energy and magnetization gradients of the domain wall being decreased by increasing the magnetostatic coupling due to the thicker NiFeCo film.

In summary, decreasing the energy and magnetization gradients of a domain wall through altering the exchange and magnetostatic interactions between the coupled magnetic films is responsible for the reduction of the coercivity of the coupled films.

[1] S. Middelhoek, Z. Angew Phys. **18**, 524 (1965).
[2] J. C. Slonczewski and S. Middelhoek, Appl. Phys. Lett. **6**, 139 (1965).
[3] E. Feldtkeller, Z. Angew. Phys. **18**, 532 (1965).
[4] H. Niedoba, A. Hubert, B. Mirecki, and I. B. Puchalska, J. Magn. Magn. Mater. **80**, 379 (1989).
[5] F. J. Friedlaender, E. Kneller, and L. F. Silva, IEEE Trans. Mag. **MAG-1**, 251 (1965).
[6] J. C. Slonczewski, IBM J. Res. Dev. **10**, 377 (1966).
[7] T. Yeh, J. M. Sivertsen, and J. H. Judy, J. Magn. Magn. Mat. **104-107**, 1879 (1992).
[8] A. Yelon, Phys. Thin Films **6**, 238 (1971).
[9] S. Middelhoek, J. Appl. Phys. **37**, 1276 (1966).

Antiferromagnetic versus ferromagnetic coupling in Fe/Cr(107) and Cr/Fe(107)

A. Vega,[a] H. Dreyssé, and C. Demangeat
Institut de Physique et Chimie des Materiaux (IPCMS-GEMME), CNRS-Université Louis Pasteur, 67037 Strasbourg Cedex, France

A. Chouairi
Laboratoire de Physique des Solides, Université de Nancy I, BP 239, Vandoeuvre-les-Nancy, France

L. C. Balbás
Departamento de Física Teórica, Facultad de Ciencias, Universidad de Valladolid, 47011 Valladolid, Spain

We have calculated the local magnetic moments and magnetic order for a Fe(Cr) monolayer adsorbed on a stepped Cr(Fe)(107) substrate. The electronic structure at $T=0$ K has been self-consistently determined within the unrestricted Hartree–Fock approximation of the Hubbard Hamiltonian in the framework of a real-space tight-binding method. In the Cr/Fe(107) system, two magnetic arrangements have been obtained, the more stable being the less frustrated as obtained in the case of V overlayers on vicinal substrates of Fe. An analysis of both solutions in terms of the total energy calculation and the different degree of frustration is presented. For Fe/Cr(107), a two-step periodicity is obtained. The sign of the magnetization at the Fe overlayer changes from step to step. This spin-flop transition is consistent with the two-layer period oscillation recently observed in Fe/Cr/Fe wedge structures, and with the total magnetization determined from *in situ* magnetometer measurements during growth of ultrathin Fe films on Cr(001).

Considerable attention has been devoted for 15 years to the study of a possible enhancement of the spin polarization at the surface of Fe and Cr[1–6] and, more recently, to a physically transparent explanation of the exchange coupling of adjacent Fe layers across a Cr spacer. Antiferromagnetic exchange coupling of adjacent Fe layer magnetizations through Cr layers was found by Grünberg *et al.*[7] through light scattering and by Baibich *et al.*[8] through magnetoresistance experiments. Besides oscillations from ferromagnetic (FM) to antiferromagnetic (AFM) exchange couplings with a long period, Unguris, Celotta, and Pierce[9] and Purcell *et al.*[10] have discovered oscillations with a period of two Cr monolayers when the crystallographic quality of the Fe/Cr interface is extremely good. The coupling was measured on a sample consisting on a Fe(100) single-crystal whisker substrate, a Cr wedge deposited by molecular beam epitaxy and covered by the Fe overlayer. As discussed in those papers,[9,10] the sign of the polarization of the Fe overlayer changes from step to step.

There is agreement between most of the theoretical calculations concerning the Fe/Cr systems, whereas the experimental results indicate the possibility of complex magnetic behaviors in some cases. In a recent work, Turtur and Bayreuther[11] have used an *in situ* alternating gradient magnetometer (AGM) to continuously monitor the magnetic moment in ultrathin Cr films on Fe(100) during growth in ultrahigh vacuum with submonolayer sensitivity. They have reported an evident deviation from layered-AF order in the first two–three Cr monolayers, a very strong moment enhancement in submonolayer Cr films, and a complex magnetic order of Cr moments close to the Fe substrate. From these results the necessity of further band and total-energy calculations for corresponding model structures in these Fe/Cr systems is obvious.

It is the aim of this communication to explore the experimental results obtained by Unguris *et al.* and Purcell *et al.* for the Fe/Cr wedge structure, and to investigate the possible magnetic arrangements one can find at Cr monolayers deposited on nonideal substrates of Fe, as a first step for understanding the complex behaviors one can expect for thicker coverages.

In the following we present and discuss the results (local magnetic moments and magnetic order) obtained for the monolayer of Cr adsorbed on the stepped (107) substrate of Fe and for the monolayer of Fe on Cr(107). For this study, we have calculated the spin-polarized electronic-charge distribution for the valence $3d$ electrons using a self-consistent tight-binding real-space model within the unrestricted Hartree–Fock approximation of the Hubbard Hamiltonian. This method has been recently applied to describe the spin polarization at the Fe/V interface[12] and at vicinal surfaces of Cr.[13] Instead of going into detail, we refer the reader to these works.

In Fig. 1 we show the two magnetic arrangements obtained for Cr/Fe(107). In both cases, a periodicity of one step is obtained, together with AF coupling between most of the Cr atoms and the Fe substrate. Moreover, the Cr atoms at the edge of the step and at the kink positions are antiferromagnetically coupled. This result, which is consistent with the tendency of Cr to present AF coupling between nearest neighbors, gives an indication of the importance of the short-range-order interactions in these materials. These two solutions differ, however, in the degree of frustration. The main qualitative difference between them arises from a change of the sign of the local magnetization at the Cr atoms located at the kink and edge of the step. In the solution (a), the Cr at the edge displays a magnetic moment of $-1.51\mu_B$, and the Cr

[a]On leave from Departamento de Física Teórica, Facultad de Ciencias. Universidad de Valladolid, 47011 Valladolid, Spain.

 0021-8979/94/76(10)/6989/3/$6.00 © 1994 American Institute of Physics

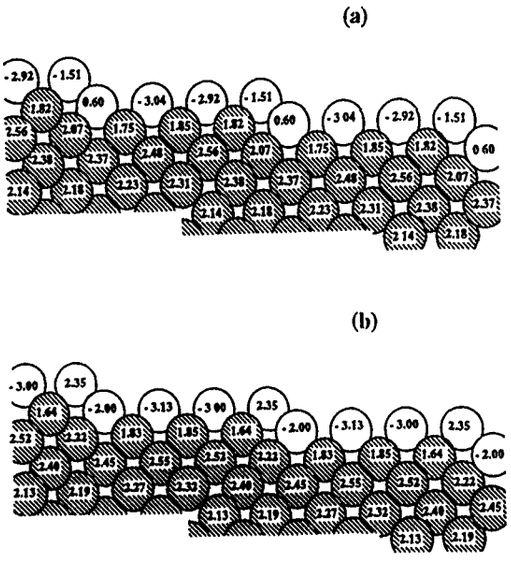

FIG. 1. Magnetic moment μ (in units of μ_B) per atom for the two solutions (a) and (b) obtained for the Cr monolayer adsorbed on the stepped (107) substrate of Fe. Open circles represent the Cr atoms whereas the filled circles represent the Fe atoms. The figure is given by projection in the (010) plane.

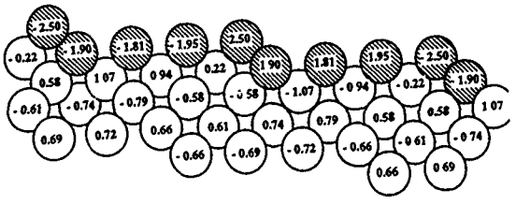

FIG. 2. Magnetic moment μ (in units of μ_B) per atom obtained for the Fe monolayer adsorbed on the stepped (107) substrate of Cr.

atom at the kink, a moment of $0.60\mu_B$, which is ferromagnetically coupled with four nearest-neighbor Fe atoms of the subsurface layer. Since Fe and Cr nearest neighbors tend to couple antiferromagnetically, strong frustration is present in the surrounding of the defect for solution (a). In contrast, in the solution (b), only the Cr atom at the edge (which displays a moment of $2.35\mu_B$) is ferromagnetically coupled with two nearest-neighbor Fe atoms of the subsurface layer. Thus, the degree of frustration is lower in solution (b) and the local magnetization around the defect results larger than in the solution (a). A total-energy calculation for the two magnetic arrangements gives a difference of 0.009 eV per atom within the cell of Fig. 1, which stabilizes the less frustrated solution (b). The same magnetic arrangement has been obtained as the more stable one in vanadium overlayers on vicinal substrates of iron.[14] A detailed inspection of the energy contribution of each atom within the system shows that most of the difference in the energy comes from the surrounding of the defect (kink and edge atoms) up to second nearest neighbors, indicating that the different degree of frustration plays an important role in the stabilization of solution (b) (a similar behavior has been obtained in the same kind of calculations for an infinite step[15]). However, the small difference of energy between them and the fact that experiments are performed at finite temperatures permit us to speculate about the possible coexistence of both solutions at finite temperature. Furthermore, the perfect layered-AF structure of Cr is broken as a consequence of the defect, since atoms at the kink in solution (a) and at the edge in solution (b) display a local moment opposite to the rest of Cr atoms belonging to the same plane. Complex magnetic order of Cr moments close to the Fe substrate has been pointed out by Turtur and Bayreuther in recent experiments on ultrathin Cr films on Fe(100).[11]

In Fig. 2, the results are shown for the most stable magnetic arrangement obtained in the Fe/Cr(107) system. In this case, F coupling between the kink and edge atoms of the Fe overlayer is obtained, in agreement with the tendency between nearest neighbors of Fe. Moreover, a periodicity of two steps is imposed by the AF Cr substrate, as can be seen in Fig. 2. Thus, the sign of the magnetization at the Fe overlayer oscillates from step to step. This spin flop gives support to the fact that the two-layer period oscillation of the exchange coupling between Fe layers observed in Fe/Cr/Fe wedge structures[9,10] is favored by the AF order of the Cr substrate, particularly for large Cr thickness. Furthermore, the total magnetic moment at the Fe overlayer results in zero, in agreement with the total moment measurements of Bayreuther[16] for Fe overlayers on Cr. Frustration effects are also present in this case, since the Fe atom at the edge is ferromagnetically coupled with two nearest-neighbor Cr atoms at the subsurface layer. Another two (less stable) magnetic arrangements are present for this system. One of them appears when Fe atoms at the kink and edge change the sign of their local magnetization.[13] In the third solution, the local magnetic moment in all Fe atoms points in the same direction, so that an F iron overlayer is obtained. However, the strong frustration present in this case give rise to a difference in energy of 0.004 eV per atom with respect to the most stable one.

The present work shows that if a steplike defect is considered at the surface or interface of these materials, various magnetic configurations can be found and, in some cases, with small differences in energy between them. Due to the strong environment dependence of the magnetic properties, one expects the surface reconstruction of the presented stepped systems to have an important influence in the magnetic arrangement. Thus, for a full understanding of the experimental observations,[11,16] the geometrical structure has to be treated in the same level as the electronic structure in the model calculations. Here, we have studied the effect of the steps, b t other phenomena like the mentioned reconstruction, interdiffusion, or local inclusions of other surface orientations deserve to be also analyzed. Calculations along these lines are in progress.

This work has been partly supported by DGICYT (Spain) and Junta de Castilla y León (Spain). A. V. would like to acknowledge Ministerio de Educación y Ciencia (Spain) for a post-doctoral grant.

[1]G. Allan, Phys. Rev. B **19**, 4774 (1979).
[2]L. E. Klebanoff, S. W. Robey, G. Liu, and D. A. Shirley, Phys. Rev. B **30**, 1048 (1984); L. E. Klebanoff, R. H. Victora, L. M. Falicov and D. A. Shirley, *ibid.* B **32**, 1997 (1985).
[3]R. H. Victora and L. M. Falicov, Phys. Rev. B **31**, 7335 (1985).
[4]C. L. Fu and A. J. Freeman, Phys. Rev. B **33**, 1755 (1986).
[5]S. Ohnishi, A. J. Freeman, and M. Weinert, Phys. Rev. B **28**, 6741 (1983).
[6]A. J. Freeman and C. L. Fu, J. Appl. Phys. **61**, 3356 (1987).
[7]P. Grünberg, R. Schreiber, P. Yang, M. B. Brodsky, and H. Sowers, Phys. Rev. Lett. **57**, 2442 (1986).
[8]M. N. Baibich, J. M. Broto, A. Fert, F. Nguyen van Dau, F. Petroff, P. Etienne, G. Creuzet, A. Friedrich, and J. Chazelas, Phys. Rev. Lett. **61**, 2472 (1988).
[9]J. Unguris, R. J. Celotta, and D. T. Pierce, Phys. Rev. Lett. **67**, 140 (1991).
[10]S. T. Purcell, W. Folkerts, M. T. Johnson, N. W. E. McGee, K. Jager, J. aan de Stegge, W. B. Zeper, and W. Honig, Phys. Rev. Lett. **67**, 903 (1991).
[11]C. Turtur and G. Bayreuther, Phys. Rev. Lett. **72**, 1557 (1994).
[12]A. Vega, L. C. Balbás, H. Nait-Laziz, C. Demangeat, and H. Dreyssé, Phys. Rev. B **48**, 985 (1993).
[13]A. Vega, L. C. Balbás, A. Chouairi, C. Demangeat, and H. Dreyssé, Phys. Rev. B **49**, 12 797 (1994).
[14]A. Vega, L. C. Balbás, H. Dreyssé, and C. Demangeat, Czech. J. Phys. **43**, 1045 (1993).
[15]D. Stoeffler (private communication, 1994).
[16]G. Bayreuther, in the International Symposium on Theoretical Physics: Magnetic Multilayers and Low Dimensional Magnetism, Ekaterinburg, Russia, 1994 (unpublished).

Influence of Cr growth on exchange coupling in Fe/Cr/Fe(100) (invited) (abstract)

Joseph A. Stroscio, D. T. Pierce, J. Unguris, and R. J. Celotta
Electron Physics Group, National Institute of Standards and Technology, Gaithersburg, Maryland 20899

The giant magnetoresistance and the interlayer exchange coupling between magnetic layers separated by nonmagnetic spacer layers are sensitive to the roughness at the interfaces in multilayer magnetic structures. We present scanning tunneling microscopy (STM) measurements of the thickness fluctuations in Cr films grown at different temperatures on near-perfectly flat Fe(100) whiskers and correlate these results with our scanning electron microscopy with polarization analysis (SEMPA) measurements of the oscillations of the exchange coupling in Fe/Cr/Fe(100) structures grown at similar temperatures. Layer-by-layer growth was observed by STM for Cr deposition on an Fe substrate at deposition temperatures greater than 300 °C. The SEMPA measurements of the Fe overlayer magnetization as a function of Cr spacer layer thickness for Cr growth at this temperature could be simulated well by oscillatory coupling with periods $2.105 \pm 0.005d$ and $12 \pm 1d$, where d is the layer spacing. Rougher Cr growth, limited by diffusion kinetics, is observed at lower temperatures, giving a distribution of thicknesses in the growth front. We modeled the Fe magnetization for lower temperature Cr growth by assuming that the exchange coupling at each discrete Cr thickness is the same as found for layer-by-layer growth. The total coupling at each average Cr spacer layer thickness was determined by adding the weighted contribution to the coupling from each Cr layer thickness contributing to the average thickness. Very good agreement was obtained with the SEMPA measurement of the Fe overlayer magnetization for Cr growth at lower temperatures without including other consequences of roughness at the interface, such as the breakdown of translational invariance.

This work was supported by the Office of Technology Administration of the Department of Commerce and by the Office of Naval Research.

 0021-8979/94/76(10)/6992/1/$6.00 © 1994 American Institute of Physics

Exchange magnetic coupling through nonmagnetic insulator spacers (abstract)

Shufeng Zhang
Department of Physics, New York University, New York, New York 10003

Interlayer magnetic coupling has been found in magnetic multilayers with nonmetallic spacers.[1,2] In metallic spacers the coupling is provided by electrons at the Fermi sphere; in nonmetallic spacers the coupling is either due to localized states or to thermally activated conduction electrons (or by other external means, e.g., photon exposure). We calculate this coupling by extending the RKKY-like interaction to insulator bands at finite temperatures. Since the length scale $1/k_F$ (where k_F is the Fermi wave vector) that governs the oscillatory behavior of coupling for metallic spacers does not appear in the present case, the form of the coupling with respect to the thickness and temperature is quite different for metallic and for nonmetallic spacers. We study the interlayer coupling for two types of spacers, crystalline, and noncrystalline (amorphous) semiconductors. For the former, the conduction (or valence) bands are well-defined and the calculation of the coupling is rather straightforward. The coupling at room temperature oscillates from ferromagnetic to antiferromagnetic and back to weakly ferromagnetic as the thickness of the spacer layer increases. The antiferromagnetic coupling only exists in a narrow range of the thickness of the spacer layer. For an amorphous semiconductor spacer, the coupling can be expressed in terms of localized states. Within the variable range hopping picture, one can relate these localized states to the localization length. We discuss the range and temperature dependence of the coupling for amorphous spacers. Our calculations are in good agreement with experimental results.

This research was sponsored by the Office of Naval Research.

[1] S. Toscano *et al.*, J. Magn. Magn. Mater. **114**, L6 (1992).
[2] J. E. Mattson *et al.*, Phys. Rev. Lett. **71**, 185 (1993).

 0021-8979/94/76(10)/6993/1/$6.00 © 1994 American Institute of Physics

Fabrication of magnetostrictive actuators using rare-earth (Tb,Sm)-Fe thin films (invited)

T. Honda
Materials Research Laboratory, Tokin Corporation, 6-7-1 Koriyama, Taihaku-ku 982, Japan

K. I. Arai and M. Yamaguchi
Research Institute of Electrical Communication, Tohoku University, 2-1-1 Katahira, Aoba-ku Sendai 980-77, Japan

A new concept is proposed for the microactuation based upon magnetostriction. Magnetostrictive bimorph cantilever actuators and a traveling machine, composed of the magnetostrictive amorphous Tb-Fe and Sm-Fe thin films on a polyimide substrate, were fabricated. These actuators moved without power supply cables. The 3-mm-long cantilever actuator exhibited the large deflection above 100 μm in as low a magnetic field as 300 Oe and above 500 μm at resonant frequency in an alternating magnetic field of 300 Oe. Such unique characteristics suggest that magnetostriction is useful as the driving force of the microactuator.

I. INTRODUCTION

A high-performance microactuator is required for the microelectromechanical system (MEMS). Several driving principles for the microactuator such as electrostatic force, electromagnetic force, piezoelectric effect, thermal expansion, and shape memory effect have been proposed up to now. In principle, electrostatic force devices are favorable for the μm-size actuators,[1] but some practical applications require larger mechanical forces than those obtained by electrostatic forces.

On the other hand, the electromagnetic force, which is predominant in a macroworld, had been considered to be unsuitable for the microactuator because it is a body force; however, recent developments of the three-dimensional micromachining techniques have enabled magnetic microstructures having enough volume to generate large mechanical forces. As a result, some magnetic microactuators have been demonstrated.[2,3] In the future, the magnetic microactuator is expected to play an important part of the MEMS.

In this article we propose a new concept for the microactuation based upon magnetostriction. The advantages of the magnetostrictive actuator are as follows: (1) The combination of a positive magnetostrictive material and a negative one enables a large deflection; (2) no power supply cable is required for its actuation because it is driven by external magnetic fields.

In spite of these advantages, only an in-pipe mobile robot made of a "bulk" magnetostrictive material has so far been reported.[4] Taking account of miniaturization and integration with other microelements, a magnetostrictive "thin film" should be used for the microactuator. In order to develop such thin-film actuators, we needed magnetic thin films with large magnetostriction in low magnetic fields. Here we used amorphous Tb-Fe thin films having positive magnetostriction and amorphous Sm-Fe thin films having a negative one. Both films exhibited a large magnetostriction of above 10^{-4} in low magnetic fields.[5,6]

In this article we fabricated two kinds of magnetostrictive "bimorph" cantilever actuators of different sizes and a traveling machine using the Tb-Fe and Sm-Fe thin films. We examined their basic properties and discussed their merits for the microactuators.

II. MAGNETOSTRICTIVE MATERIALS

The magnetostriction of the conventional materials such as Ni, Fe-Al, and amorphous Fe-Si-B is only $30–40\times10^{-6}$. On the other hand, some of rare-earth–transition-metal (RE-TM) crystalline alloys have very large magnetostriction above 10^{-3}. In particular, $TbFe_2$ has the largest positive magnetostriction and $SmFe_2$ has the largest negative one;[7] however, they have very large magnetocrystalline anisotropies and in general need large magnetic fields to saturate the magnetostriction. In order to reduce the magnetocrystalline anisotropy, two methods can be used: One is to alloy positive and negative magnetocrystalline materials such as

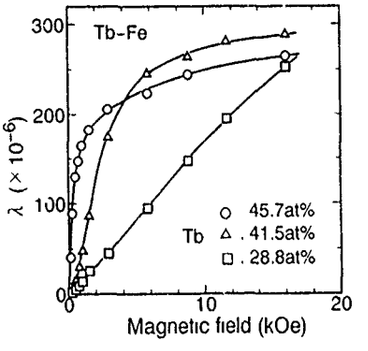

FIG. 1. Applied magnetic-field dependence of the magnetostriction for Tb-Fe thin films

 0021-8979/94/76(10)/6994/6/$6.00 © 1994 American Institute of Physics

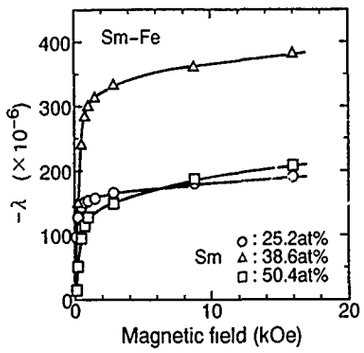

FIG. 2. Applied magnetic-field dependence of the magnetostriction for Sm-Fe thin films.

$(Tb,Dy)Fe_2$ and the other is to prepare amorphous state materials. In our study we applied the latter, because amorphous RE-TM thin films are easily obtained by a sputtering technique.

Details of the magnetic properties of the amorphous Tb-Fe and Sm-Fe thin films have been already reported in our previous articles.[5,6] In this section, we explain the outline.

Figure 1 shows the applied magnetic-field dependence of the magnetostriction for the Tb-Fe thin films having different compositions. The magnetostriction at 16 kOe exhibited large values above 250×10^{-6} in a wide composition range for 28–46 at. % Tb; however, the low-magnetic-field characteristics largely depended on the film composition because of the composition dependence of the magnetic anisotropy.

The films with 18–40 at. % Tb content had perpendicular magnetic anisotropy and needed high magnetic fields to saturate in-plane magnetization. On the other hand, the films with above 45 at. % Tb content had in-plane magnetic anisotropy. In this case, the in-plane magnetization increased rapidly in low magnetic fields, and accordingly the magnetostriction increased in the same manner. The saturation magnetostriction decreased with increasing Tb content above 50 at. % Tb; therefore, we used the 45–50 at. % Tb-Fe thin films for further examinations.

Figure 2 shows the applied magnetic-field dependence of the magnetostriction for the Sm-Fe thin films having different compositions. The magnetostriction increased rapidly in low fields regardless of Sm content because Sm-Fe thin films always had in-plane magnetic anisotropy. The maximum absolute values of $250–300\times10^{-6}$ at 1 kOe and $300–400\times10^{-6}$ at 16 kOe were obtained at 30–40 at. % Sm. In this experiment we chose the 30–40 at. % Sm-Fe films for the fabrication of actuators.

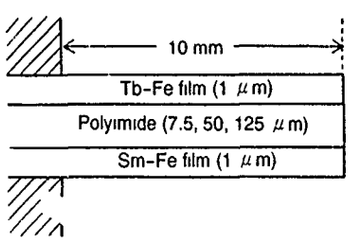

FIG. 3. Side view of the cantilever actuator.

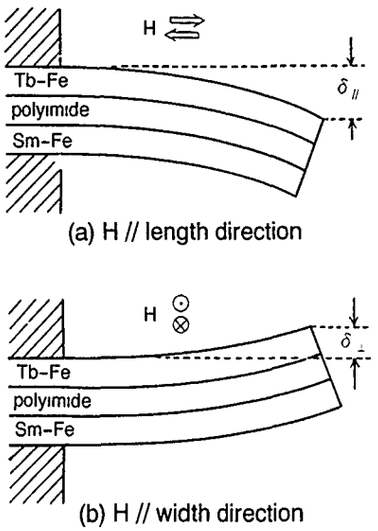

FIG. 4. Actuation behavior of the magnetostrictive bimorph cantilever.

III. DEVICE CONCEPT

Figure 3 shows the side view of the magnetostrictive bimorph cantilever. On a surface of a polyimide substrate, which has low elastic stiffness and high thermal stability, the Tb-Fe film is sputtered and on the opposite surface the Sm-Fe thin film is sputtered.

Figure 4 shows the actuation behavior of the magnetostrictive bimorph cantilever. When a magnetic field is applied along the cantilever length direction, the Tb-Fe film expands and the Sm-Fe film contracts in the length direction and as a result the cantilever deflects downward [Fig. 4(a)]. Next, when a magnetic field is applied along the cantilever width direction, the Tb-Fe film contracts and the Sm-Fe film expands in the length direction and then the cantilever deflects upward [Fig. 4(b)].

A bending behavior for the cantilever with composite structure such as a thermally excited bimetal cantilever[8] and a piezoelectric bimorph cantilever[9] has been analyzed using a classical method. Therefore, we applied this theory to the magnetostrictive cantilever and described below.

For the cantilever of total thickness h and length L, let the z direction be the thickness dimension and a neutral axis be located at $z=0$. We defined n $(0<n<1)$ to satisfy the condition that the upper surface and the lower one are located at $z=nh$ and $z=(n-1)h$, respectively. The neutral axis can be found from

$$\int_{(n-1)h}^{nh} E(z)z\,dz=0, \tag{1}$$

where $E(z)$ is Young's modulus as a function of thickness. In this article we assume that Tb-Fe and Sm-Fe films have the

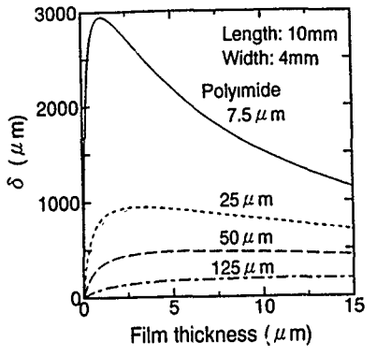

FIG. 5. Calculated deflection of magnetostrictive bimorph cantilevers as a function of thickness of each magnetic layer.

same Young's modulus and thickness; therefore, the neutral axis is located in the geometric center for a bimorph structure, that is, $n=0.5$.

When a magnetic field is applied along the length direction, the radius of bending curvature R caused by magnetostriction can be expressed by

$$R=\frac{\int_{(n-1)h}^{nh}E(z)z^2\,dz}{\int_{(n-1)h}^{nh}E(z)\lambda(z)z\,dz}, \tag{2}$$

where $\lambda(z)$ is the strain in the length direction caused by magnetostriction as a function of thickness and magnetic field. The tip deflection of the cantilever δ is

$$\delta=R[1-\cos(L/R)]. \tag{3}$$

In our study, R is much larger than L. Therefore, Eq. (3) can be approximated by

$$\delta=L^2/2R. \tag{4}$$

This equation indicates that the deflection decreases strongly with decreasing the cantilever length.

Next, when a magnetic field is applied along the width direction, we approximated that the strain in the length direction by magnetostriction is $-\lambda(z)/2$. Accordingly, the cantilever deflects in the opposite direction and the tip deflection is a half of that expressed in Eq. (4). When the cantilever is driven in rotating in-plane magnetic fields, the total deflection is the sum of the deflection caused by a magnetic field along the length direction and that by a magnetic field along the width direction.

Figure 5 shows the calculated tip deflection for the bimorph cantilever with a length of 10 mm as a function of thickness of each magnetic film layer when it is driven in a rotating in-plane magnetic field. In this calculation, we assumed the magnetostriction values of $\lambda_{Tb\text{-}Fe}=150\times10^{-6}$ for Tb-Fe films and $\lambda_{Sm\text{-}Fe}=-250\times10^{-6}$ for Sm-Fe films. These are typical experimental values obtained at 1 kOe on a glass substrate. The calculated deflection increases with decreasing the substrate thickness and that each substrate has the optimum thickness of the magnetic film to exhibit the maximum deflection. This calculation excludes the stress and strain in the width direction and the magnetic torque described later, but is effective to estimate the brief operation of the cantilever.

IV. FABRICATION

The amorphous Tb-Fe and Sm-Fe thin films were prepared by the rf magnetron sputtering method. They were deposited to a thickness of 1 μm on each surface of a rectangular polyimide substrate. The sputtering target used was composed of a pure Fe plate (3 in. diameter) and small Tb or Sm chips. The film composition was 45–50 at. % Tb for the Tb-Fe films and 30–40 at. % Sm for the Sm-Fe films as mentioned above. rf input power was 200 W, and Ar gas pressure was 4–10 mTorr for the Tb-Fe films and 10 mTorr for the Sm-Fe films. During sputtering, the substrate was water cooled. In order to prevent the oxidation of the magnetostrictive thin films, SiO_2 films with a thickness of 0.05–0.1 μm were coated on them.

After deposition, we clamped one end of the substrate and then obtained the magnetostrictive cantilever actuators as shown in Fig. 3. In this experiment, we fabricated two kinds of the cantilever actuators. One was a 10-mm-long cantilever using a commercial polyimide film with a thickness of either 7.5, 50, or 125 μm. The other was a microcantilever with a length of 3 mm using a 3-μm-thick polyimide film. This very thin substrate was made from 7.5-μm-thick polyimide by reactive-ion etching (RIE) using O_2 gas. The tip deflection of the cantilever was measured by both a three-terminal capacitance method[10] and direct observation using the optical microscope.

V. RESULTS AND DISCUSSION

A. Magnetic properties on a polyimide substrate

Before fabrication of the actuators, we investigated the magnetic properties of the Tb-Fe and Sm-Fe films sputtered on the polyimide substrate.

Figure 6 shows the magnetization curves of (a) Tb-Fe thin films on the glass substrate, (b) the 50-μm-thick polyimide substrate, and (c) the 3-μm-thick polyimide substrate. The 3-μm-thick substrate was the thinnest for our present techniques. The in-plane magnetization on the glass substrate increased rapidly in low magnetic fields, while that on the 50-μm-thick polyimide required high magnetic fields to saturate. This result suggests that we could not obtain the large magnetostriction in low magnetic fields when the 50-μm-thick polyimide was used. This change of the magnetic properties was caused by the large compressive stress in the Tb-Fe film with large positive magnetostriction. We think that this compressive stress was generated by the difference of the thermal expansion and/or the thermal contraction of the polyimide during sputtering; however, the magnetic properties on the 3-μm-thick polyimide was similar to those on the glass substrate. The stress in the Tb-Fe film from the substrate decreased with decreasing the thickness of the polyimide substrate.

On the other hand, the magnetic properties of the Sm-Fe films were less dependent on the substrate material, compared with those of Tb-Fe films. It seems that the compressive stress hardly influenced the magnetic properties of the Sm-Fe film because of negative magnetostriction.

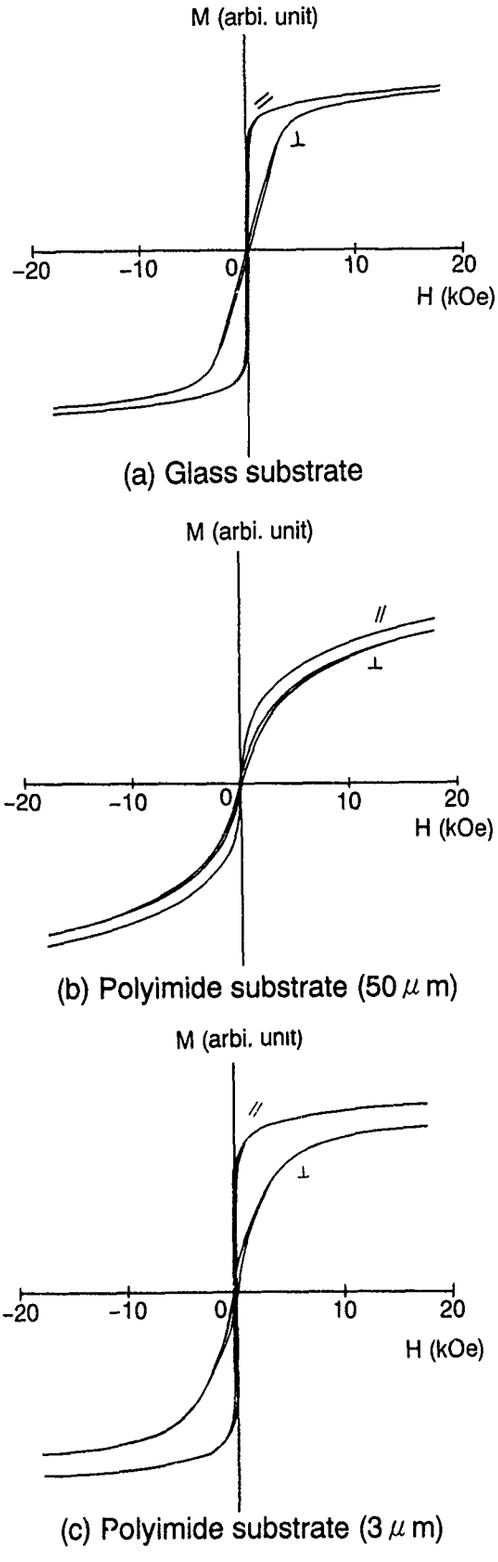

FIG. 6. Magnetization curves of Tb-Fe films

Generally, magnetic properties of the magnetostrictive material are greatly influenced by the stress. It is necessary to pay attention to the stress generated during the deposition and the micromachining process.

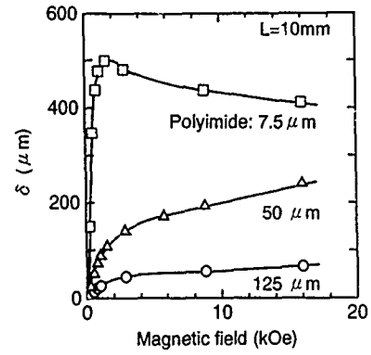

FIG. 7. Applied magnetic-field dependence of the deflection for 10-mm-long cantilevers.

B. 10-mm-long cantilever

In this subsection we examined the basic properties of the magnetostrictive cantilever. The cantilevers were 10 mm long and 4 mm wide.

Figure 7 shows the applied magnetic-field dependence of the deflection, when the cantilevers were driven in a rotating in-plane magnetic field. It is seen that each cantilever exhibited the large deflection in relatively low magnetic fields and that the deflection increased with decreasing the substrate thickness. The deflection of the cantilever using a 7.5-μm-thick polyimide exhibited the maximum value of approximately 500 μm at 1–1.5 kOe.

In the case of using the 7.5-μm-thick polyimide, however, the deflection decreased at high magnetic fields above 2 kOe. This was due to the magnetic torque generated by the large directional difference between the magnetic moment in the films and the applied magnetic field, when a high magnetic field was applied along the length direction as shown in Fig. 4(a). We must design the magnetostrictive actuator, taking account of both the amplitude and the direction of the applied magnetic field.

C. Microcantilever

From the results of the magnetic properties on the polyimide substrate and the 10-mm-long cantilever, we found that a thinner substrate was effective to obtain the large de-

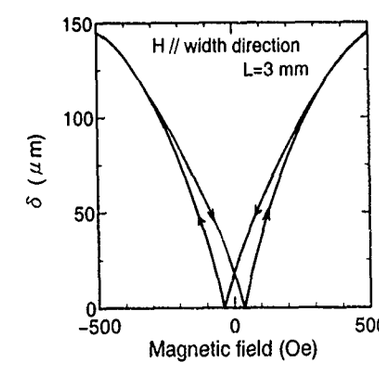

FIG. 8. Applied magnetic-field dependence of the deflection for a 3-mm-long cantilever.

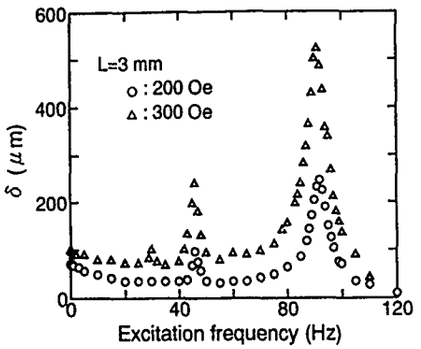

FIG. 9. Excitation frequency dependence of the deflection.

flection. Therefore, we fabricated a trial microcantilever using a 3-μm-thick polyimide substrate. The cantilever was 3 mm long and 0.5 mm wide. In this experiment we examined its hysteresis and dynamic behavior.

Figure 8 shows the hysteresis curve of the tip deflection of the microcantilever when a magnetic field was applied along the width direction, where the deflection was little influenced by the magnetic torque. It exhibited a large deflection above 100 μm at as low a field as 300 Oe. This deflection was equivalent to more than 1 mm of the 10-mm-long cantilever as seen from Eq. (4); besides, this microcantilever had relatively small hysteresis. Such characteristics of the cantilever actuator were suitable for application as a micropositioning device.

Figure 9 shows the excitation frequency dependence of the deflection when alternating magnetic fields of 200 and 300 Oe were applied along the width direction. Note that the vibrational frequency was double the excitation frequency because the cantilever deflected in the same direction for both positive and negative magnetic fields. The cantilever exhibited the maximum deflection above 500 μm at an excitation frequency of 92 Hz, where the vibrational frequency agreed with its mechanical resonant frequency. This maximum deflection was five times as large as that in a static field. Two small peaks observed around 30 and 45 Hz were caused by the harmonics of the vibration.

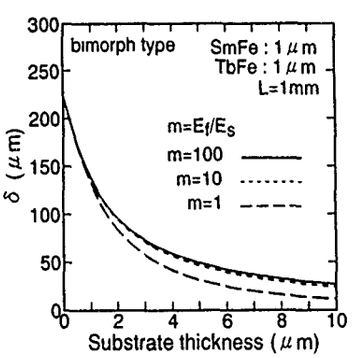

FIG. 10. Calculated deflection of the 1-mm-long cantilever as a function of the substrate thickness.

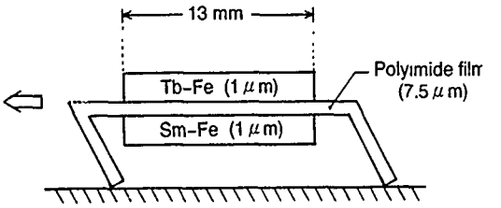

FIG. 11. Schematic view of a traveling machine.

We describe the future direction of the actuator design on the basis of Eq. (3). Figure 10 shows the calculated deflection of the bimorph cantilever with a length of 1 mm as a function of the substrate thickness when it is driven in a rotating in-plane magnetic field. E_f and E_s are the Young's modulus of the magnetostrictive films and substrate, respectively. Note that the deflection was a function of ratio of E_f/E_s. In our experiment, E_f/E_s is about 12 and the magnetostrictive films were supposed to be 1 μm thick and have magnetostriction as in the case of Fig. 5. The deflection increased gradually with decreasing the substrate thickness, and when substrate thickness is zero, that is, a "bimetal" structure composed of the Tb-Fe film and the Sm-Fe film, the predicted deflection exhibits the maximum value of 225 μm.

D. Traveling machine

We fabricated a traveling machine using the magnetostrictive bimorph actuator with 7.5-μm-thick polyimide as shown in Fig. 11. Its two legs at both ends were inclined so that it could travel in one direction. When an alternating magnetic field was applied, it vibrated and traveled in the arrow direction on disk planes as well as inside a quartz tubes (6.5 mm in diameter).

Figure 12 shows the excitation frequency dependence of the average traveling velocity when an alternating magnetic field of 300 Oe was applied along the machine width direction. The traveling machine needed the excitation frequency

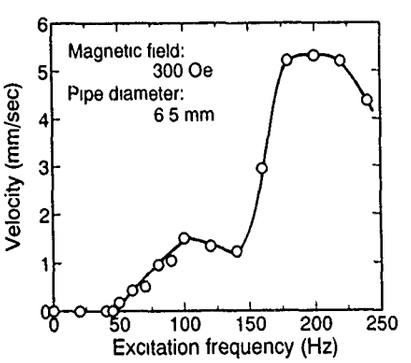

FIG. 12. Excitation frequency dependence of the average traveling velocity.

above 50 Hz to begin to travel and exhibited the maximum speed of approximately 5 mm/s around the mechanical resonant frequency of 200 Hz.

This magnetostrictive traveling machine requires no power supply cables which disturb its actuation in a microworld; therefore, magnetostriction is suitable for the driving force of the traveling micromachine.

VI. CONCLUSIONS

We fabricated cantilever actuators and a traveling machine using magnetostrictive Tb-Fe and Sm-Fe thin films and examined their basic properties. They showed unique characteristics such as large deflection and wireless driving. These results indicate that the magnetostrictive actuation is useful as the driving force of microactuators.

[1] W. S. N. Trimmer, Sensors and Actuators **19**, 267 (1989).
[2] C. H. Ahn, Y. J. Kim, and M. G. Allen, in Proceedings of the IEEE MEMS'93 Workshop, 1993, p. 1.
[3] H. Guckel, T. R. Christenson, K. J. Skrobis, T. S. Jung, J. Klein, K. V. Hartojo, and I. Widjaja, in Proceedings of the IEEE MEMS'93 Workshop, 1993, p. 7.
[4] T. Fukuda, H. Hosono, H. Ohyama, H. Hashimoto, and F. Arai, in Proceedings of the IEEE MEMS'91 Workshop, 1991, p. 210.
[5] Y. Hayashi, T. Honda, K. I. Arai, K. Ishiyama, and M. Yamaguchi, IEEE Trans. Magn. **MAG-29**, 3129 (1993).
[6] T. Honda, Y. Hayashi, K. I. Arai, K. Ishiyama, and M. Yamaguchi, IEEE Trans. Magn. **MAG-29**, 3126 (1993).
[7] A. E. Clark, in *Ferromagnetic Materials*, edited by E. P. Wohlfarth (North-Holland, Amsterdam, 1980), p. 531.
[8] S. Timoshenko, J. Opt. Soc. Am. **11**, 233 (1925).
[9] M. A. Marcus, Ferroelectrics **57**, 203 (1984).
[10] D. W. Forester, C. Vittoria, J. Schelling, and P. Lubitz, J. Appl. Phys. **49**, 1966 (1978).

Preparation and applications of magnetostrictive thin films

E. Quandt, B. Gerlach, and K. Seemann
Kernforschungszentrum Karlsruhe GmbH, Institute of Materials Research I, D-76021 Karlsruhe, Germany

Amorphous magnetostrictive films of the binary compound Sm_xFe_{1-x} as well as of the ternary compound $(Tb_yDy_{1-y})_xFe_{1-x}$ were prepared by rf or dc magnetron sputtering using either a multitarget arrangement with pure element targets or cast composite-type targets. The magnetostrictive properties of $(Tb_{0.3}Dy_{0.7})_{0.4}Fe_{0.6}$ and $Sm_{0.4}Fe_{0.6}$ films were investigated in relation to their preparation conditions. Depending upon these conditions (especially upon the deposition rate, the bias voltage, and the Ar sputtering pressure) amorphous films with a giant magnetostriction of about 250 ppm (−220 ppm) at 0.1 T and 400 ppm (−300 ppm) at 0.5 T for the TbDyFe (SmFe) and an in-plane magnetic easy axis could be prepared. In view of applications in microsystem technologies (e.g., pumps, valves, positioning elements) these films have been tested in a simple cantilever arrangement and the predicted deflection of a magnetostrictive actuated membrane has been calculated.

I. INTRODUCTION

Giant magnetostriction in thin films is thought to be a promising actuator mechanism for microactuators. Due to the interest in such applications, research has focused upon materials exhibiting low-field magnetostriction and soft-magnetic properties. During the last few years various attempts have been made to improve the low-field magnetostrictive properties of amorphous rare-earth–Fe films. Successful approaches were to increase the total rare-earth content compared to that of the crystalline phases,[1] to alloy different rare earths to compensate the anisotropy,[2] to adjust the preparation conditions in order to induce tensile film stresses,[3] and to add small amounts of B to change the amorphous state of the films.[4,5]

The present article describes the influence of preparation conditions (sputtering power, Ar sputtering pressure, bias voltage) on the composition, microstructure, and in-plane magnetostrictive properties. Functioning tests and calculations are then discussed which show the behavior of possible actuator components based on these films.

II. EXPERIMENTAL WORK

The binary systems TbFe and SmFe were dc magnetron sputtered by the multitarget arrangement with pure element targets.[1] For the rf or dc magnetron sputtering of the TbDyFe films a cast composite-type target (Degussa AG/Leybold Materials) was used. The Tb/Dy ratio of this target, $(Tb_{0.3}Dy_{0.7})_{0.42}Fe_{0.58}$, was chosen in accordance with results on the rare-earth anisotropy compensation composition at room temperature[6] and its total rare-earth content according to results that have been reported previously.[1] Typical deposition rates, with an Ar sputtering pressure of 0.4 Pa, are 3 μm/h for the multitarget arrangement at a distance of 100 mm and 16 μm/h for the composite-type target at 300 W and a distance of 50 mm.

Composition was determined by wavelength-dispersive x-ray microanalysis (WDX), and depth profiles were obtained using Auger electron spectroscopy (AES). The microstructures were investigated by x-ray diffraction (XRD) and transmission electron microscopy (TEM). In-plane magnetostriction was measured by the common cantilevered substrate technique, polarization by a vibrating sample magnetometer (VSM), and Curie temperature by a superconducting quantum interference device (SQUID) magnetometer. The film stress was calculated by measuring the difference of the curvature of the uncoated and coated Si substrate using a long-scan profiler.

III. RESULTS

A. Materials

The magnetron sputtering deposition of the rare-earth–Fe films onto unheated SiO_2, Si, or metal substrate resulted in amorphous, dense films with thicknesses ranging between 1 and 15 μm. A dependence of the magnetostriction upon film thickness was not observed within this range. The time-dependent oxidation was investigated at room temperature for TbFe and TbDyFe films. Although both these films have the same total rare-earth content, they exhibited slightly different oxidation dependencies (Fig. 1). AES depth profiles indicated that the rare-earth oxide formed at the film surface, which would tend to slow further oxidation within the sample, is more stable in the case of the TbFe compared to

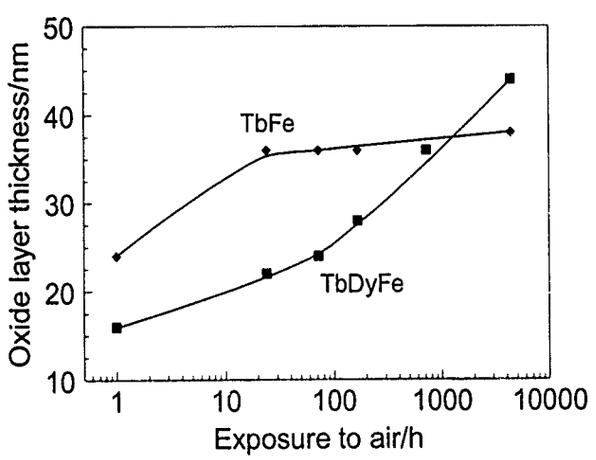

FIG. 1 Time dependence of the oxidation zone thickness obtained by AES depth profiling.

 0021-8979/94/76(10)/7000/3/$6.00 © 1994 American Institute of Physics

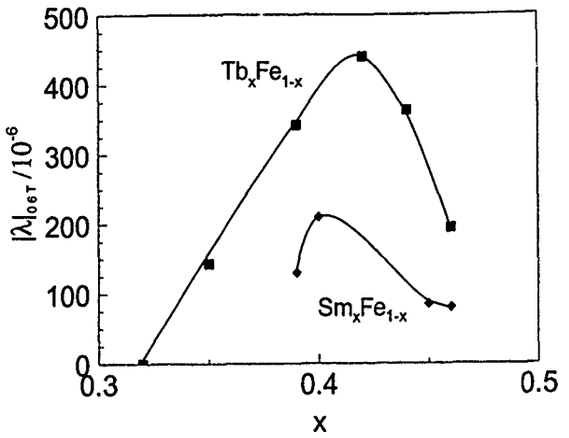

FIG. 2. Magnetostriction measured at an external field $\mu_0 H = 0.6$ T applied parallel to the film plane vs the rare-earth content of amorphous Tb_xFe_{1-x} and Sm_xFe_{1-x} films.

the TbDyFe film. Small-angle XRD revealed a crystalline nature for the oxidized region. This is in contrast to results reported previously.[7]

As was the case with the Tb_xFe_{1-x} films,[1] the maximum of the magnetostriction of the Sm_xFe_{1-x} films was found to be at a rare-earth content of about 40 at. % (Fig. 2). Compared to the TbFe films, however, the rare-earth anisotropy is significantly lower. This results in a higher low-field magnetostriction. The influence of the sputtering parameters has been investigated with the composite-type target $[(Tb_{0.3}Dy_{0.7})_{0.42}Fe_{0.58}]$ in more detail. Dramatic changes in the magnetostriction were observed in the low-field region (up to 0.15 T) which is of special interest for applications in microsystem technology. At 0.5 T all these films show a comparable magnetostriction of about 400 ppm. Best results were obtained for dc as opposed to rf magnetron sputtering, an Ar sputtering pressure of 0.4 Pa [Fig. 3(a)], an rf bias of 160 V [Fig. 3(b)], and a sputtering power of 300 W [Fig. 3(c)]. The results illustrated the dominant influence of the bias voltage on low-field magnetostrictive properties, which was also observed for the multitarget sputtering of $Sm_{0.4}Fe_{0.6}$ films (Fig. 4) even if the low-field improvement is less pronounced compared to TbDyFe films. The variations of the sputtering parameters have almost no influence on the chemical composition and on the Curie temperature of about 350 K. Although XRD and TEM investigations also give no evidence of a changed microstructure—due to temperature-annealing ongoing deposition as a result of the altered sputter conditions—the Ar-ion bombardment related with the applied bias voltage changes the magnetic anisotropy. This results in an in-plane magnetic easy axis for the optimized TbDyFe films (Fig. 5) whereas TbDyFe films sputtered without bias show perpendicular anisotropy.[1] In comparison to dc-sputtered TbDyFe films[3] the thermal induced stress is comparably low (100 GPa) and further reduced to about 40 GPa as a result of the applied bias voltage of 160 V. In this case the magnetoelastic energy due to the film stress is lower than the form anisotropy energy leading to an in-plane easy magnetization.

B. Applications

Sputtering deposition of magnetostrictive thin films in combination with microstructuring by etching or sputtering through masks provides a promising method for the integra-

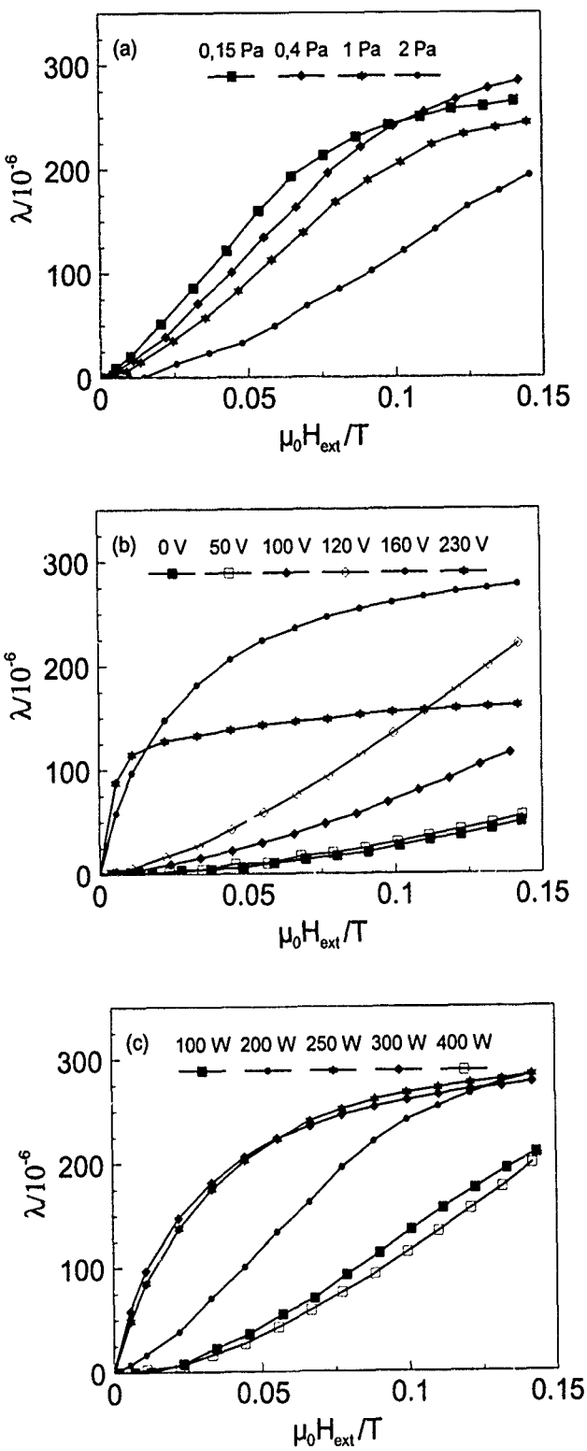

FIG. 3. Low-field magnetostriction of amorphous TbDyFe films vs the magnetic field applied in the film plane as a function of (a) the Ar sputtering pressure (160 V rf bias, 200 W); (b) the rf bias (0.4 Pa Ar, 300 W); and (c) the dc sputtering power (0.4 Pa Ar, 160 V rf bias).

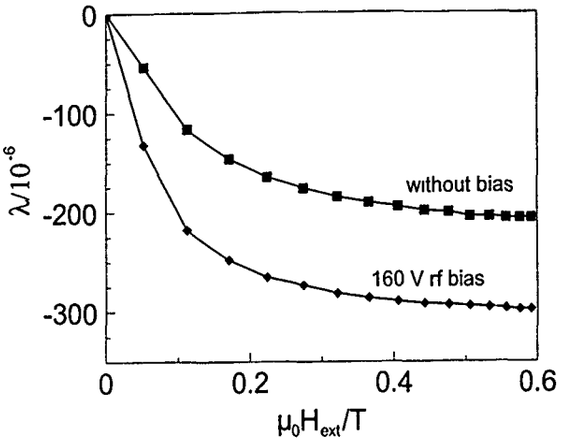

FIG. 4. Magnetostriction of SmFe films vs the magnetic field applied in the film plane.

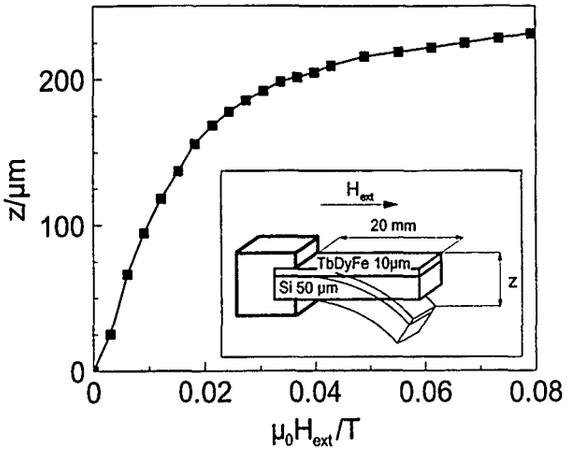

FIG. 6. Deflection of a TbDyFe/Si ⟨100⟩ cantilever vs the magnetic field applied in the film plane.

tion of actuator components in microsystems by batch processes. With this in mind, materials relevant to microengineering applications as Si and various metals suitable for the lithography, electroforming, and plastic molding (LIGA)[8] process were chosen as substrates for prototype components. Using the optimized TbDyFe film of 10 μm thickness a deflection of a Si (100) cantilever (20 mm×5 mm×50 μm) of about 200 μm at a field of 0.05 T could be obtained (see Fig. 6). This low-field deflection is considerably greater than that reported for 50-μm-thick polyimide samples.[9] For micropump and microvalve applications membranes, in addition to cantilevers, are important components. Finite-element-method (FEM) calculations of a magnetostrictive coated metal membrane predict a maximum deflection of 75 μm for a 12.5-mm-diam membrane with both 4 μm thickness of the membrane and the coating. Using the optimized films the required magnetostriction of 200 ppm already is obtainable in a field of 0.05 T.

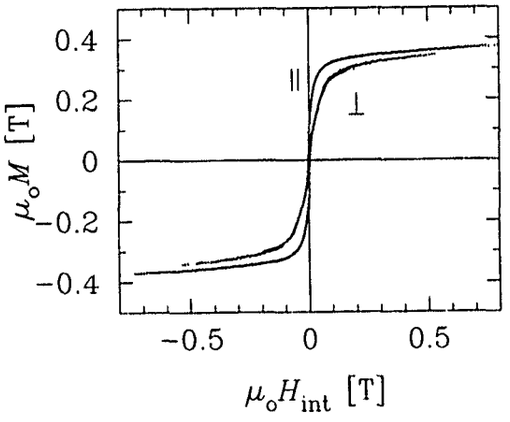

FIG. 5. Polarization vs external field applied parallel (||) and perpendicular (⊥) to the film plane for an optimized TbDyFe film.

ACKNOWLEDGMENTS

This research is supported by the European Commission within the Brite EuRam II program. We would like to thank M. Bernemann for the T_c measurements, M. Schnell (MPI für Metallforschung, Stuttgart) for the VSM and film stress measurements, and A. Skokan for the WDX analysis.

[1] E. Quandt, J. Appl. Phys. **75**, 5653 (1994).
[2] F. Schatz, M. Hirscher, G. Flik, and H. Kronmüller, Phys. Status Solidi A **137**, 197 (1993).
[3] G. Flik, M. Schnell, F. Schatz, and M. Hirscher, in Proceedings of Actuator 94, Bremen, Germany, p. 232.
[4] J. Y. Kim, J. Appl. Phys. **74**, 2701 (1993).
[5] H. Fujimori, J. Y. Kim, S. Suzuki, H. Morita, and N. Kataoka, J. Magn. Magn. Mater. **124**, 115 (1993).
[6] A. E. Clark, in *Ferromagnetic Materials*, edited by E. P. Wohlfarth (North-Holland, Amsterdam, 1980), Vol. 1, p. 531.
[7] R. B. van Dover, E. M. Gyorgy, R. P. Frankenthal, M. Hong, and D. J. Siconolfi, J. Appl. Phys. **59**, 1291 (1986).
[8] E. W. Becker, W. Ehrfeld, P. Hagmann, A. Maner, and D. Munchmeyer, Microelectron. Eng **4**, 35 (1986).
[9] T. Honda, K. I. Arai, and M. Yamaguchi, in Proceedings of IEEE MEMS 1994, Oiso, Japan, p. 51.

Magnetostriction in TbDyFe thin films

P. J. Grundy, D. G. Lord, and P. I. Williams
Joule Physics Laboratory and Science Research Institute, University of Salford, Greater Manchester M5 4WT, United Kingdom

Magnetization and magnetostriction in amorphous binary TbFe and DyFe and amorphous and polycrystalline, ternary $(Tb_xDy_{1-x})_yFe_{100-y}$ thin films have been investigated. The measurements reflect the compositional dependence of the easy direction of magnetization in the films. In plane magnetostrictions of over 300×10^{-6} were measured for some of the amorphous TbFe and TbDyFe films and values greater than 750×10^{-6} were obtained in polycrystalline TbDyFe films near to the Terfenol composition.

I. INTRODUCTION

Rare-earth–transition-metal (RE-TM) alloy films deposited from the vapor are usually amorphous, and postdeposition annealing or deposition onto a heated substrate is required to effect crystallization. Films containing heavy rare earths (e.g., Tb, Dy) are ferrimagnetic and can exhibit perpendicular anisotropy, magnetization compensation, and large coercivities. In common with others[1–3] we find that these interesting characteristics in the binary alloys are complemented by exceptional magnetostrictive properties at relatively low magnetic fields. We also find that very large magnetostrains are obtained in some ternary TbDyFe alloys in both the amorphous and crystalline forms.

II. EXPERIMENT

The films were deposited from a triode source in a cryopumped sputter-deposition system. The target consisted of a $150\times50\times6$ mm^3 rectangular Fe plate containing 33 10-mm-diam holes. With the holes occupied by Tb, Dy, or Fe inserts this arrangement allowed for the deposition of a continuous range of RE_xTM_{100-x} alloys with $5<x<50\%$. The deposition rate was typically 50 nm min^{-1} and the thickness of the resulting films was ~1 μm. Crystalline films were obtained by deposition onto heated glass substrates. The magnetic properties of the films were obtained by vibrating sample magnetometry (VSM) (up to 1000 kA m^{-1}) and their magnetostrictions were measured on an optical cantilever system with a sensitivity of 10^{-7} in fields up to 350 kA m^{-1} (Ref. 4). Young's modulus values for the films (in zero field) were calculated from load/indentation curves obtained on a sensitive microhardness instrument.

III. RESULTS AND DISCUSSION

The compositions of the films were obtained from Rutherford backscattering and x-ray microanalysis measurements. They were found to be near to the designed composition and to be uniform to better than 1 at. % over the area of the film (20×5 mm^2); however, a small composition gradient was measured through the thickness of the films, typically 2 at. % μm^{-1}. This gradient was probably caused by a gradual decrease in the sputtering yield from the RE inserts with time.

Amorphous alloy films in the two binary series Tb_xFe_{100-x} and Dy_xFe_{100-x} and the ternary $(Tb_xDy_{1-x})_{33}Fe_{67}$ and $(Tb_xDy_{1-x})_{43}Fe_{57}$ series were deposited. The ternary $RE_{33}Fe_{67}$ series was chosen because the equivalent bulk polycrystalline compositions are known to show interesting magnetic behavior. The ternary $RE_{43}Fe_{57}$ films were also deposited because of the large magnetostrictions found in the amorphous phase.[5] It was observed that an excess of RE was necessary for the formation of crystalline $REFe_2$; i.e., $Tb_{0.27}Dy_{0.73}Fe_2$, when deposited onto a heated (350 °C) substrate.

Figure 1 gives the compositional dependence of magnetization for amorphous Tb_xFe_{100-x} films. The results agree reasonably well with published data.[6–8] The different symbols indicate the effective easy direction in the films which varied with composition. In the range $15<x<40$ the strong perpendicular anisotropy and low magnetization ensured an easy direction of magnetization normal to the film plane. As expected, the coercivity peaks at the room-temperature compensation composition (RTCC). The compositional dependence of magnetization and coercivity in Dy_xFe_{1-x} follows the same pattern with generally smaller values of these two parameters.[5]

The magnetizations of the amorphous ternary $(Tb_xDy_{1-x})_{33}Fe_{67}$ and $(Tb_xDy_{1-x})_{43}Fe_{57}$ (i.e., $\simeq REFe_2$ and RE_3Fe_4) alloys are shown in Fig. 2 as a function of composition x. The easy direction of magnetization of the amorphous $RE_{33}Fe_{67}$ films was normal to the film plane; its value increases as the proportion of Tb increases. The $RE_{43}Fe_{57}$ alloys are at compositions well away from the RTCC and were almost magnetically equiaxed; their magnetization also varied linearly with x but with a greater rate of increase. Also shown is the compositional dependence of M_s for polycrystalline films which contained randomly oriented Laves $REFe_2$ crystallites, and small grains of Fe, excess RE, and RE oxides at concentrations of a few percent.[4] In the case of the crystalline film there is a departure from linearity with an apparent maximum in the magnetization for $25<x<35$. This is associated with the anisotropy minimum at $x=0.27$ (Ref. 9) near the composition of bulk Terfenol

The magnetostrictions of the films were calculated from the bending of the film+substrate cantilever using bending-beam theory.[4,10] Measurements of the magnetostrains λ from fields applied along $\lambda_\parallel$ and at right angles λ_n to the cantilever length can be related, with particular assumptions,[4] to the saturation magnetostriction λ_s as $\lambda_s=2(\lambda_\parallel-\lambda_n)/3$. Figure 3 shows $\lambda_\parallel$ for the amorphous Tb_xFe_{100-x} binary alloys. Values in the range $15<x<35$ are limited by the difficulty of

 0021-8979/94/76(10)/7003/3/$6.00 © 1994 American Institute of Physics

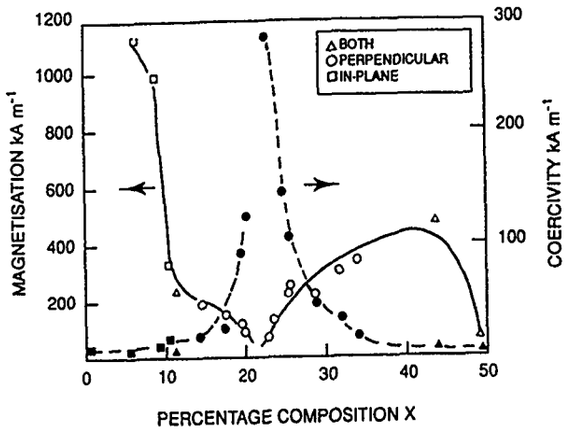

FIG. 1. The magnetization (open symbols) and coercivity (solid symbols) of amorphous Tb_xFe_{100-x} films as a function of x measured with the field applied normal to, in the film plane, and in either direction.

magnetizing the films to saturation in the modest fields used ($\approx$350 kA m^{-1}). For $x>35$, $\lambda_{\|}$ increases to a maximum and then decreases towards the composition ($x\approx50$) with a Curie point below room temperature. We include data from several other investigations.[1,2,11] The general trend of the results is the same; the scatter arises from many factors, such as different deposition techniques, film thickness, and methods of characterization. Magnetostriction values for the Dy_xFe_{100-x} films are much smaller and peak at a value of 60×10^{-6} at $x\approx30$. They agree reasonably well with published data.[3]

Magnetostrains in the amorphous ternary $RE_{33}Fe_{67}$ alloys were found to be small and of the order of $20-40\times10^{-6}$ with no obvious compositional trend. This was possibly accounted for by the inability of the maximum applied field to

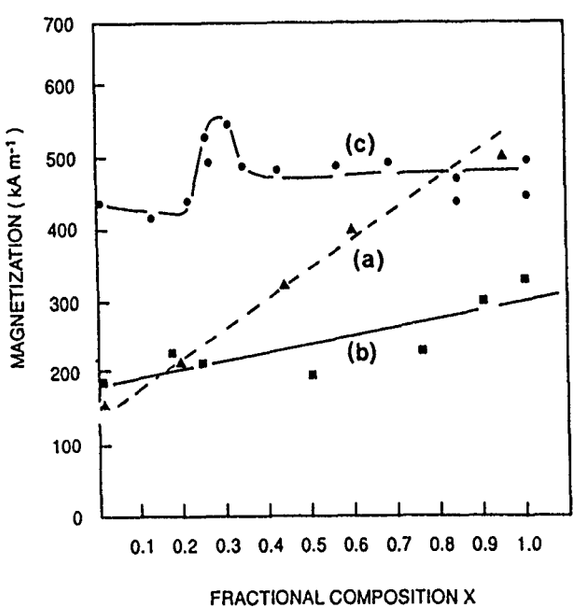

FIG. 2. The compositional dependence of magnetization of (a) amorphous $(Tb_xDy_{1-x})_{43}Fe_{57}$ films and (b) and (c) amorphous and polycrystalline $(Tb_xDy_{1-x})_{33}Fe_{67}$ films.

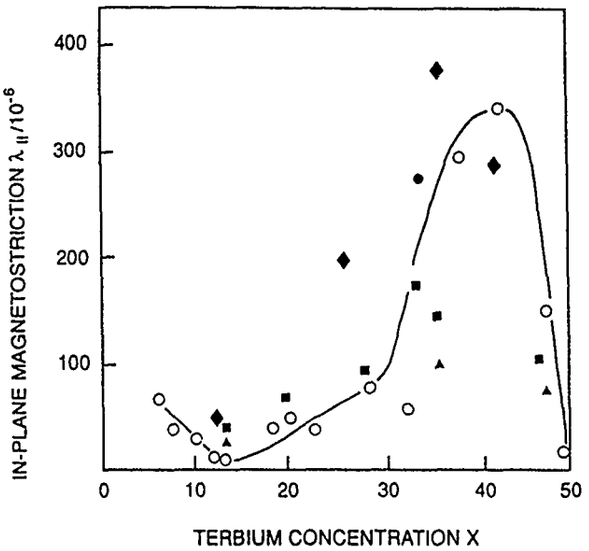

FIG. 3. In-plane magnetostriction values for amorphous Tb_xFe_{100-x} films (at 350 kA m^{-1}). Open symbols this investigation, (▲) and (■) Ref. 1 at 320 and 1280 kA m^{-1}, (●) Ref. 10, and (♦) Ref. 2.

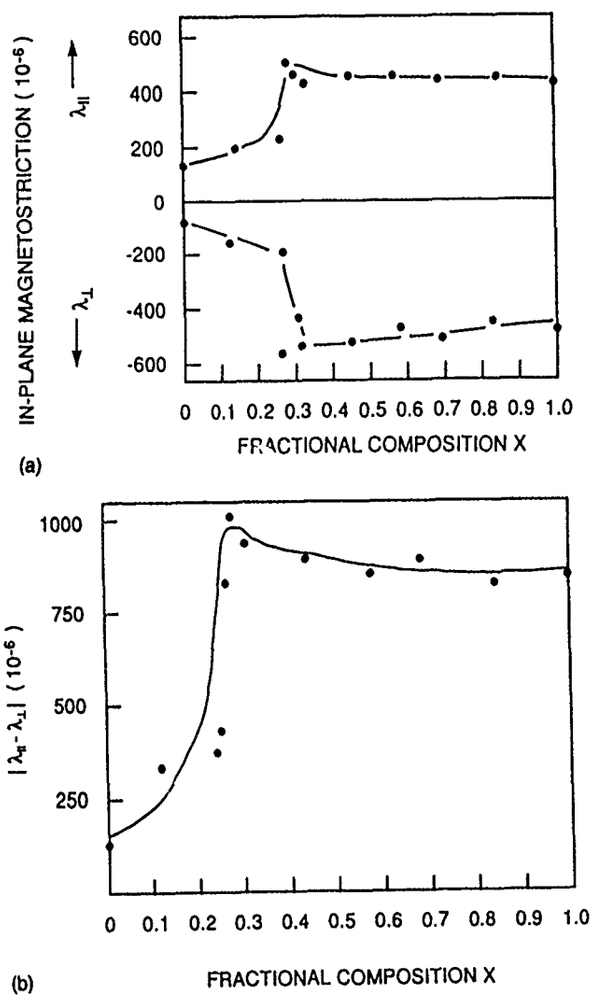

FIG. 4. Compositional dependence of (a) parallel $\lambda_{\|}$ and normal λ_n magnetostrictions and (b) in-plane magnetostrictions for polycrystalline $(Tb_xDy_{1-x})_{33}Fe_{67}$ films.

saturate in plane these films with perpendicular anisotropy. The potential of the amorphous alloy equivalent in composition to crystalline Terfenol could, therefore, not be tested. The $RE_{43}Fe_{57}$ alloys could be magnetized in plane although not to saturation. Values of $\lambda_{\parallel}$ show an increase from the Dy binary to the Tb binary composition with the maximum value of $\simeq 350\times10^{-6}$ obtained for $Tb_{43}Fe_{57}$ ($x=1$) being very close to the peak value shown in Fig. 3.

Parallel and normal magnetostrictions, $\lambda_{\parallel}$ and λ_n, for polycrystalline films containing $(Tb_xDy_{1-x})Fe_2$ phases are shown in Fig. 4(a). The fact that $\lambda_{\parallel} \neq -2\lambda_n$ implies a stress-induced alignment of domains along the cantilever length on deposition. This departure from a random alignment of domains results in a relatively large λ_n because domains are rotated through a larger angle in the transverse field. The general features of both curves, in particular the rise to a maximum or negative minimum at $x \simeq 0.3$ and the plateaux to $x=1$, are reflected in Fig. 4(b) which gives the planar magnetostriction $|\lambda_{\parallel}-\lambda_n|$. The planar magnetostriction is, in principle, equal to $3\lambda_s/2$, but not here as the films were not saturated. The maximum and minimum occur in the region of anisotropy compensation, and the plateau, rather than a rise, in magnetostriction from $x=0.3$ onward is possibly due to a varying value of E_f (Young's modulus) for the nlm. E_f is included in the formula for calculating λ and a positive ΔE_f near $x=0.3$ would reduce our calculated value of λ. The magnitude of ΔE_f ($\Delta E_f \propto \lambda^2$) can be quite large and a value of $\simeq 140\%$ has been reported[9] for bulk Terfenol over the range of applied field used in this investigation. Notwithstanding these uncertainties, the results presented here show that the planar magnetostriction of polycrystalline TbDyFe thin-film alloys reaches considerable values in fairly small magnetizing fields, with a maximum of $\simeq 1000\times10^{-6}$ for $Tb_{10}Dy_{23}Fe_{67}$ ($\equiv Tb_{0.3}Dy_{0.7}Fe_2$).

ACKNOWLEDGMENTS

The support of this research by the Johnson-Matthey Technology Centre and by SERC is acknowledged.

[1] Y. Hayashi, T. Honda, K. I. Arai, K. Ishiyama and M. Yamaguchi, in INTERMAG '93, April 13–16, Stockholm, Sweden.
[2] H. Takagi, S. Tsunashima, and S. Uchiyama, J. Appl. Phys. **50**, 1642 (1979).
[3] S. Yoshino, H. Takagi, S. Tsunashima, M. Masuda, and S. Uchiyama, Jpn. J. Appl. Phys. **23**, 188 (1984).
[4] P. I. Williams, D. G. Lord, and P. J. Grundy, J. Appl. Phys. **75**, 1 (1994).
[5] P. I. Williams and P. J. Grundy, J. Phys. D: Appl. Phys. **27**, 897 (1994).
[6] Y. Mimura, N. Imamaura, and T. Kobayashi, J. Appl. Phys. **47**, 368 (1976).
[7] F. Hellman and E. M. Gyorgy, Phys. Rev. Lett. **68**, 1391 (1992).
[8] P. J. Grundy, E. T. M. Lacey, and C. D. Wright, IEEE Trans. Magn. **MAG-23**, 2632 (1987).
[9] A. E. Clark, in *Ferromagnetic Materials*, edited by E. P. Wohlfarth (North-Holland, Amsterdam, 1980), Vol. 1, p. 531.
[10] A. C. Tam and H. Schroeder, J. Appl. Phys. **64**, 5422 (1988)
[11] D. W. Forester, C. Vittoria, J. Schelling, and P. Lubitz, J. Appl. Phys. **49**, 1966 (1978).

Application of the ratio d/χ to the investigation of magnetization processes in giant-magnetostrictive materials

A. R. Piercy, S. C. Busbridge, and D. Kendall[a)]
Department of Mathematical Sciences, University of Brighton, Brighton, East Sussex BN2 4GJ, United Kingdom

The change in magnetostriction $\Delta\lambda$ with change in magnetization ΔM for domain-wall motion is shown to depend only on the wall type, the magnetostriction constants, and the saturation magnetization and not on the field required to effect the change. The quantity $\Pi=\Delta\lambda/\Delta M$ (or the dynamic equivalent d/χ) is therefore a valuable parameter for use in investigating magnetization processes. Theoretical values of Π are given for different wall processes in $\langle 111\rangle$ and $\langle 100\rangle$ easy materials and used to interpret experimental measurements in different (Tb, Dy, Ho)Fe_2 materials. It is shown that Π vs M curves are more sensitive to the detail of the magnetization process than λ vs M curves. In $\langle 111\rangle$ easy compositions the processes are found to be complex with the combination of wall motion processes changing continuously with increasing magnetization and no region where a single process dominates. In contrast, for $\langle 100\rangle$ easy materials, there is an extended region in which 90° wall processes dominate. In both cases, quasistatic and dynamic processes are shown to be equivalent, independent of temperature, and independent of the frequency and magnitude of the drive field.

I. INTRODUCTION

The magnetic properties of giant-magnetostrictive rare-earth–iron alloys have been extensively investigated for applications as transducer materials. The early work was summarized by Clark[1] and subsequent developments have been reviewed by Jiles.[2] However, relatively little is known about the magnetization processes in these materials and Jiles[2] concludes that study of the processes is a requirement for their further development. This article aims to show that the ratio $\Delta\lambda/\Delta M$, of the change in magnetostriction λ to change in magnetization M, is a valuable parameter for use in investigating magnetization processes.

It is widely accepted that the task of identifying magnetization processes from curves of M (or λ) against applied field H is intractable because of extrinsic effects which limit rotation and domain-wall motion. These effects are generally not only unknown but also vary from point to point in a real polycrystalline material and consequently the field required to effect a change in M or λ is both unknown and nonuniform. Such extrinsic effects do, however, exert a similar influence on both magnetization and magnetostriction and curves of λ vs M have sometimes been used in attempts to infer magnetization processes. We show that the application of such curves is limited because they are relatively insensitive to different model processes and, in addition, their measurement is limited to quasistatic or very low-frequency variations. Conversely, $\Delta\lambda/\Delta M$ is more sensitive and its practical determination is not limited to low frequencies. We have previously reported[3,4] use of $\Delta\lambda/\Delta M$ for the investigation of magnetization processes in giant-magnetostrictive materials and this article aims to provide more detail and to expand its application to a range of conditions and compositions.

II. THEORETICAL VALUES FOR $\Delta\lambda/\Delta M$

We limit consideration to domain-wall motion processes involving walls separating domains having their magnetizations in directions 1 and 2 specified by the direction cosines l_1,m_1,n_1 and l_2,m_2,n_2, respectively, with the magnetostriction being measured in the direction 0 specified by l_0,m_0,n_0. The usual situation with the rare-earth–iron alloys is that the measurement direction is the axis of a rod-shaped specimen of material with preferred orientation such that $\langle 112\rangle$ is parallel to this axis. We are concerned with the ratio $\Delta\lambda/\Delta M$ for which we use the symbol Π, and note that under conditions of alternating excitation $\Delta\lambda/\Delta M$ is equivalent to d/χ, the ratio of the magnetomechanical d coefficient ($d_{33}=\partial\lambda/\partial H$) to the susceptibility ($\chi=\partial M/\partial H$).

When a domain wall moves through a small fraction F_v of the sample in response to a small change in field ΔH, the direction of the magnetization in the volume swept out changes from 1 to 2 so that the change in sample magnetization is

$$\Delta M=F_v M_s(\cos\theta_2-\cos\theta_1),$$

where θ_1 is the angle between directions 1 and 0 so that $\cos\theta_1=(l_1l_0+m_1m_0+n_1n_0)$ and similarly for θ_2. The corresponding change in magnetostriction is

$$\Delta\lambda=F_v(\lambda_{2,0}-\lambda_{1,0}),$$

where $\lambda_{1,0}$ is the saturation magnetostriction measured in direction 0 when the magnetization lies in direction 1 and is given by

$$\lambda_{1\,0}=(3\lambda_{100}/2)(l_1^2l_0^2+m_1^2m_0^2+n_1^2n_0^2-\tfrac{1}{3})+3\lambda_{111}(l_1m_1l_0m_0+m_1n_1m_0n_0+n_1l_1n_0l_0),$$

Π is then given by

$$\Delta\lambda/\Delta M=(\lambda_{2,0}-\lambda_{1,0})/M_s(\cos\theta_2-\cos\theta_1),$$

[a)]Present address: DRA, Holton Heath, Poole, BH16 6JU, UK

0021-8979/94/76(10)/7006/3/$6.00
© 1994 American Institute of Physics

TABLE I. Theoretical values of Π for ⟨111⟩ easy material with measurements made in ⟨112⟩.

Wall type	$\theta_2 \rightarrow \theta_1$	Equiv. No.	Example	$\Pi/(\lambda_{111}/M_s)$
180°	118.1°→61.9°	2	$[\bar{1}1\bar{1}]$-$[1\bar{1}1]$	0
	160.5°→19.5°	1	$[\bar{1}1\bar{1}]$-[111]	0
71°	118.1°→61.9°	2	$[1\bar{1}\bar{1}]$-$[1\bar{1}1]$	0
	90°→61.9°	2	$[\bar{1}11]$-$[1\bar{1}1]$	0.707
	90°→19.5°	1	$[11\bar{1}]$-[111]	1.414
	61.9°→19.5°	2	$[1\bar{1}1]$-[111]	2.123
109°	90°→61.9°	2	$[11\bar{1}]$-$[1\bar{1}1]$	0.707
	118.1°→19.5°	2	$[1\bar{1}\bar{1}]$-[111]	0.707
	90°→19.5°	1	$[\bar{1}11]$-[111]	1.414

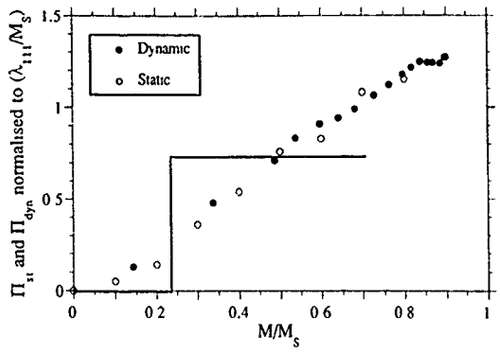

FIG. 1. Variation of Π_{st} and Π_{dyn} with magnetization for $Tb_{0.20}Ho_{0.80}Fe_2$. The solid line corresponds to the model in Fig. 2.

which is independent of both F_v and ΔH (and therefore of all extrinsic effects) and depends only on the saturation magnetization, the magnetostriction constants, and the wall type (determined by the directions 1 and 2). The resulting values of Π, normalized to (λ_{111}/M_s), are given for different wall types for ⟨111⟩ easy materials in Table I and for ⟨100⟩ easy materials, with Π normalized to (λ_{100}/M_s), in Table II. In both cases it is assumed that the materials have ⟨112⟩ orientation and only those wall movements that give rise to positive values are included (equivalent negative values also occur).

III. COMPARISON WITH EXPERIMENT

Tables I and II show that only a very few definite values of Π can be measured if domain walls of only one type move. In general it is to be expected that wall motion of several different types will occur and in that case values of Π intermediate between those of Table I (or II) are expected. In comparing these theoretical values of Π with measured values, we refer to Π_{dyn} (for d/χ) for values determined under dynamic (alternating) conditions and to Π_{st} (for $\Delta\lambda/\Delta M$) for those determined under quasistatic conditions.

Quasistatic measurements of (differential) permeability and d coefficient yield values considerably greater than those obtained under alternating excitation and it is not clear, *a priori*, whether these arise from the same, or different, magnetization processes. Figure 1 gives Π_{st} and Π_{dyn} as a function of M for $Tb_{0.20}Ho_{0.80}Fe_2$, which is ⟨111⟩ easy at 20 °C, and clearly shows that the static and dynamic processes are equivalent. It is equally clear that there is no sustained region where walls of only one type move (i.e., where Π is constant at one of the values in Table I) and moreover that the combination of wall processes changes continuously, giving a steadily increasing value of Π.

The corresponding λ vs M curve for this sample is shown in Fig. 2 to illustrate the greater sensitivity of the Π vs M curve. The solid line in Fig. 2 represents a possible theoretical model process in which it is assumed that, initially, all domain directions are equally populated and magnetization proceeds first by 180° domain-wall motion for $M<0.236M_s$, followed by 109° wall motion up to $0.707M_s$. This model appears to provide an approximate fit to the experimental points in Fig. 2 for $M<0.707M_s$ (above this it is necessary to invoke rotation to obtain a fit); however, the variation in Π for this model is that shown by the solid line in Fig. 1 from which it is clear that the model gives a completely inadequate description.

Figure 3 compares Π_{st} and Π_{dyn} for $Tb_{0.27}Dy_{0.73}Fe_2$ at 20 and 70 °C and shows that the static and dynamic processes are similar and are essentially independent of temperature. It is found that the variation of Π with M is qualitatively similar for different (Tb, Dy, Ho)Fe_2 compositions, with zero stress bias, in the ⟨111⟩ easy regime, as shown by Figs. 1 and 3. In contrast, for ⟨100⟩ easy compositions the variation of Π with M is very different, as illustrated for $HoFe_2$ in Fig. 4, although the static and dynamic processes are again equivalent. The broken line in Fig. 4 gives the value

TABLE II. Theoretical values of Π for ⟨100⟩ easy material with measurements made in ⟨112⟩.

Wall type	$\theta_2 \rightarrow \theta_1$	Equiv No.	Example	$\Pi/(\lambda_{100}/M_s)$
180°	114.1°→65.9°	2	$[\bar{1}00]$-[100]	0
	144.7°→35.3°	1	$[00\bar{1}]$-[001]	0
90°	114.1°→65.9°	2	$[0\bar{1}0]$-[100]	0
	114.1°→35.3°	2	$[\bar{1}00]$-[001]	0.612
	65.9°→35.3°	2	[100]-[001]	1.837

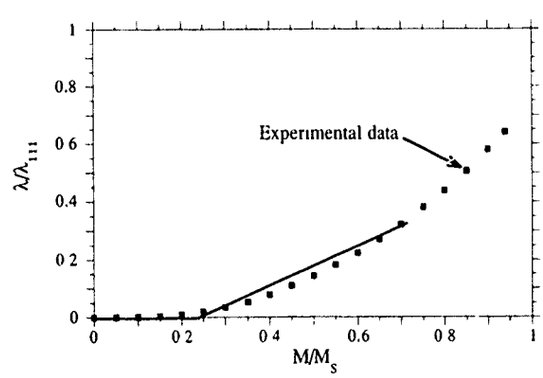

FIG. 2 Variation of magnetostriction λ with magnetization M for $Tb_{0.20}Ho_{0.80}Fe_2$ The solid line represents a possible model process

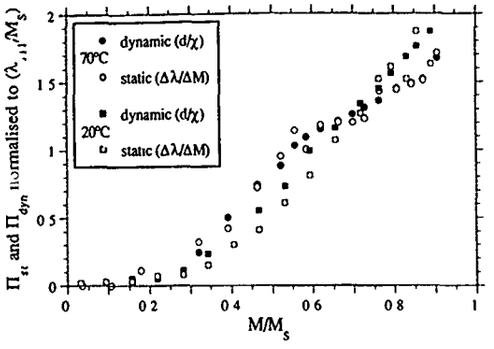

FIG. 3. Comparison of Π_{st} and Π_{dyn} at different temperatures for $Tb_{0.27}Dy_{0.73}Fe_2$.

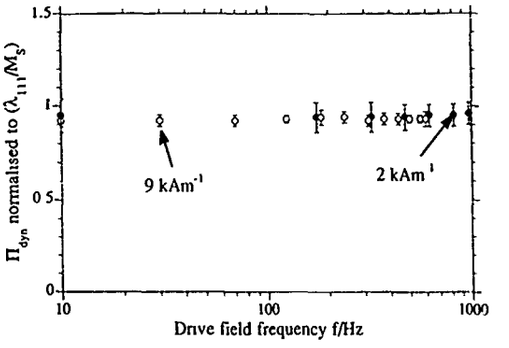

FIG. 5. Variation of Π_{st} and Π_{dyn} with drive field frequency and magnitude for $Tb_{0.27}Dy_{0.73}Fe_2$.

$\Pi=0.612\lambda_{100}/M_s$ (where λ_{100} has been taken as $-\lambda_{111}/3$) appropriate to one type of 90° wall motion and indicates that there is, in this case, an extended region where one domain process dominates. For magnetizations above $0.68M_s$ it is necessary to include rotation processes, as confirmed by domain studies,[5] to explain the observed values of Π.

The technique is also useful for investigating the drive field dependence of the magnetization processes and Fig. 5 shows that Π_{dyn} and, therefore, the magnetization processes are independent of both drive field frequency and magnitude.

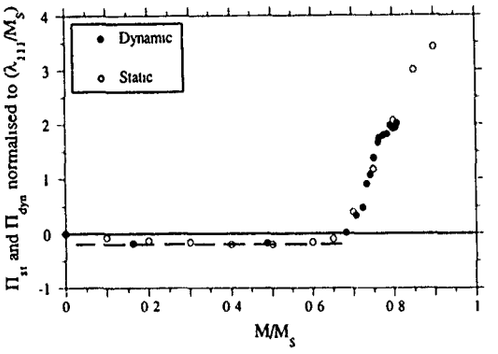

FIG. 4. Variation of Π_{st} and Π_{dyn} with magnetization for ⟨100⟩ easy $HoFe_2$. The broken line gives the value of Π for one type of 90° wall motion.

This frequency independence of Π_{dyn} is found to continue to well above the critical frequency at which eddy-current effects become significant even though, at these higher frequencies, the d coefficient and permeability are diminished.[4]

IV. CONCLUSIONS

It has been demonstrated that the ratio d/χ is a valuable parameter for use in investigating magnetization processes. Comparison of theoretical and measured values of d/χ for ⟨111⟩ and ⟨100⟩ easy giant-magnetostrictive materials has shown that the magnetization processes are generally complex, involving more than one domain-wall process, that quasistatic and dynamic processes are equivalent, independent of temperature and of drive field frequency and magnitude.

ACKNOWLEDGMENT

This work has been carried out with the support (D.K.) of the DRA (Maritime Division), U.K.

[1] A. E. Clark, in *Ferromagnetic Materials*, edited by E. P. Wohlfarth (North-Holland, Amsterdam, 1980), Vol. 1, Chap. 7.
[2] D. C. Jiles, J. Phys. D **27**, 1 (1994).
[3] D. Kendall and A. R. Piercy, IEEE Trans. Magn. **MAG-26**, 1837 (1990).
[4] D. Kendall and A. R. Piercy, J. Appl. Phys. **73**, 6174 (1993).
[5] S. C. Busbridge and A. R. Piercy, J. Appl. Phys **73**, 5354 (1993).

Magnetization, Young's moduli, and magnetostriction of rare-earth–iron eutectic alloys with $R=Tb_{0.6}Dy_{0.4}$

A. E. Clark, M. Wun-Fogle, J. P. Teter, J. B. Restorff, and S. F. Cheng
Naval Surface Warfare Center, Code R34, Silver Spring, Maryland 20903-5640

Rare-earth–iron alloys, $R_{0.9}Fe_{0.1}$, $R_{0.72}Fe_{0.28}$, and $R_{0.42}Fe_{0.58}$ ($R=Tb_{0.6}Dy_{0.4}$), containing the R/RFe_2 eutectic composition were prepared by Bridgman and free-standing zone-melting techniques. Magnetization measurements were made in fields up to 800 kA/m between 55 and 300 K. A huge increase in magnetization below 210 K occurs as the R component becomes ordered. At low applied magnetic fields there is clear identification of both the ferromagnetic ordering temperature T_C and the Néel spiral ordering temperature T_N of R. (For $Tb_{0.6}Dy_{0.4}$, $T_C=165$ K, $T_N=210$ K.) Magnetization and magnetostriction measurements reveal very large magnetocrystalline anisotropies for both the R and the RFe_2 components. Unexpectedly, at 77 K, were the rare-earth component of the eutectic system is ordered and the magnetostriction is large ($\lambda^{hy}>0.6\%$), the magnetostriction is largest in the samples containing the largest amount of the RFe_2 phase. Young's modulus measurements reveal the reduction in the stiffness with the addition of the softer rare earth to the stiff RFe_2 compound.

The rare earths Tb and Dy are the elemental components of many giant magnetostrictive materials. In the hexagonal binary alloys, $Tb_xDy_{1-x}(1\leq x\leq 1)$, basal plane magnetostrictions $\lambda^{\gamma 2}$ reach ~1% at 0 K and 0.6 % at 77 K.[1] Although the individual basal plane anisotropies K of Tb and Dy are very large ($K>0$ for Tb; $K<0$ for Dy), K can be minimized and the $\lambda^{\gamma 2}/K$ ratio maximized in the binary Tb_xDy_{1-x} alloy.[2] At 77 K anisotropy compensation occurs for $x\cong 0.6$, the value of x selected for this study. A second important class of materials is the cubic $Tb_xDy_{1-x}Fe_2$ (Terfenol) compounds. For this compound λ_{111} is very large over a wide temperature range.[3] In the Tb-Fe and Dy-Fe alloy systems, a eutectic composition consisting of a rare-earth phase and a rare-earth–Fe_2 phase occurs near 28 at. % Fe.[4] In this article we report magnetic, elastic, and magnetorestrictive properties of the eutectic-containing alloys.

For this study, samples of R, $R_{0.9}Fe_{0.1}$, $R_{0.72}Fe_{0.28}$, $R_{0.42}Fe_{0.58}$, and RFe_2 ($R\equiv Tb_{0.6}Dy_{0.4}$) were prepared into rod shapes by both Bridgman and free-standing zone-melting (FSZ) techniques.[5] Magnetization measurements were made on disk samples but normal to the growth direction in fields up to 800 kA/m using a commercial vibrating sample magnetometer. Young's moduli were measured by two methods. In the first method, static stress-strain curves were taken on rod samples (~3 cm × 0.3 cm diam.) at room temperature in the absence of a magnetic field. The strain was measured by multiple strain gauges affixed to the sample and the stress was measured using a conventional load cell. In order to determine the extent of the magnetomechanical hysteresis, measurements were taken by applying both increasing and decreasing stresses. For the $R_{0.42}Fe_{0.58}$ alloy and for the RFe_2 compound, Young's moduli were also measured as a function of magnetic field up to 160 kA/m at fixed compressive stresses of ~15 MPa at room temperature and 77 K using standard strain-gauge techniques. These moduli were measured under the two limiting magnetic conditions of (1) fixed magnetic field and (2) fixed magnetic induction. Magnetostriction measurements were made in fields up to 160 kA/m at room temperature and 77 K using strain-gauge and LVDT techniques. Magnetization measurements were made concurrently by integrating the voltage of a pickup coil wound around the samples.

In all samples, the magnetization process consists of two regions: (1) a region of nonmagnetostrictive 180° wall motion, resulting in a rapid rise in magnetization at low fields; and (2) a magnetostrictive noncollinear wall motion and magnetization rotation region resulting in a smaller magnetization change and approach to saturation. The magnetization curves of Fig. 1 reflect this process. At room temperature, only the RFe_2 component of the alloy is magnetic. Thus, as the weakly paramagnetic $Tb_{0.6}Dy_{0.4}$ alloy is added to RFe_2 to form the eutectic samples, the magnetization decreases. The coercive force is largest for the $R_{0.72}Fe_{0.28}$ sample. At 77 K the rare-earth component R has the larger magnetic moment. Therefore, as expected, as R is added to RFe_2, the magnetization increases. Again a maximum in the

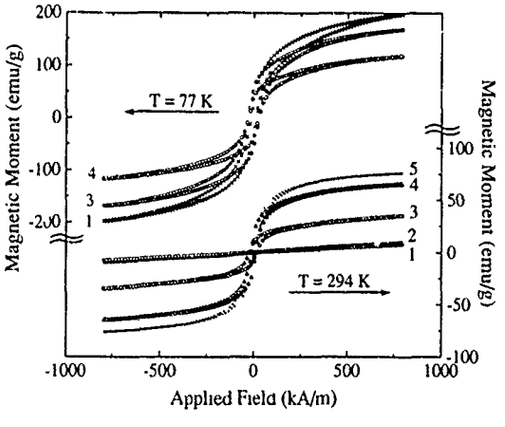

FIG 1. Magnetic moment in emu/g as a function of applied field at 77 K (upper set of curves) and 294 K (lower set of curves) for Bridgman-prepared samples: (1) $Tb_{0.6}Dy_{0.4}$ and (2) $(Tb_{0.6}Dy_{0.4})_{0.9}Fe_{0.1}$ and free-standing zone-melt samples (3) $(Tb_{0.6}Dy_{0.4})_{0.72}Fe_{0.28}$, (4) $(Tb_{0.6}Dy_{0.4})_{0.42}Fe_{0.58}$, and (5) $(Tb_{0.6}Dy_{0.4})_{0.33}Fe_{0.67}$.

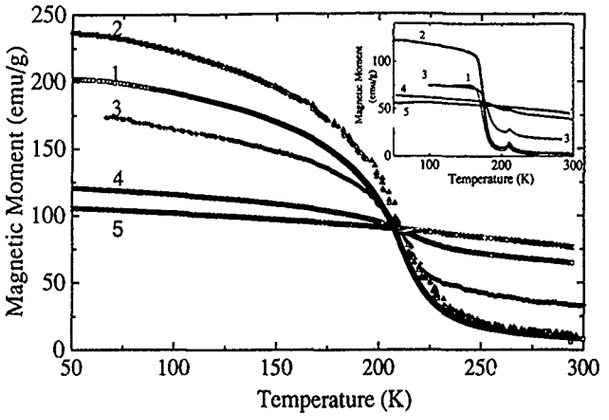

FIG 2 Magnetic moment in emu/g as a function of temperature at applied fields of 800 and 80 kA/m (see inset) for Bridgman-prepared samples: (1) $Tb_{0.6}Dy_{0.4}$ and (2) $(Tb_{0.6}Dy_{0.4})_{0.9}Fe_{0.1}$ and free-standing zone-melt samples: (3) $(Tb_{0.6}Dy_{0.4})_{0.72}Fe_{0.28}$, (4) $(Tb_{0.6}Dy_{0.4})_{0.42}Fe_{0.58}$, and (5) $(Tb_{0.6}Dy_{0.4})_{0.33}Fe_{0.67}$.

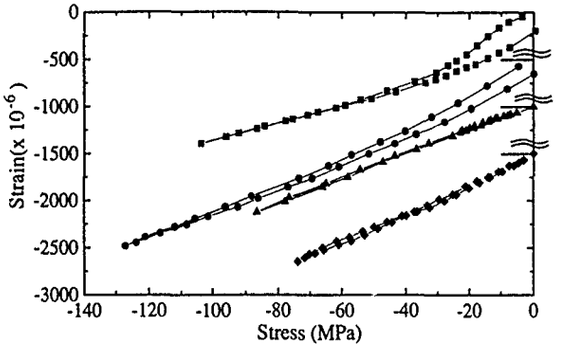

FIG. 3. Room-temperature stress-strain relationships in the absence of an applied magnetic field for Bridgman-prepared samples: (♦) $(Tb_{0.6}Dy_{0.4})_{0.9}Fe_{0.1}$; (▲) $(Tb_{0.6}Dy_{0.4})_{0.72}Fe_{0.28}$; (●) $(Tb_{0.6}Dy_{0.4})_{0.42}Fe_{0.58}$; and (■) $(Tb_{0.6}Dy_{0.4})_{0.33}Fe_{0.67}$ (Note that the zero position of three of the data sets has been shifted for display purposes only)

coercive force is observed for the eutectic composition $R_{0.72}Fe_{0.28}$.

Because of the very large uniaxial anisotropy in the hexagonal rare earths Tb and Dy, the polycrystalline R and alloys containing R are difficult to saturate at low temperatures. The magnetization versus temperature curves for these alloys are shown in Fig. 2. The full magnetic moment of the R component is not reached at 800 kA/m. As expected, a large increase in magnetization below 200 K occurs as the R component becomes ordered. The change in the slope of the curves, even of the $R_{0.42}Fe_{0.58}$ sample, which contains only 14% R, is clearly detected. A striking feature of the magnetization versus temperature curve is the appearance of a peak in the magnetization of $T \cong 210$ K for small applied fields. It is well known that a basal plane spiral magnetization structure exists in the Tb_xDy_{1-x} alloy system.[6] We observe that the coexistence of the RFe_2 component in the eutectic does not significantly alter T_N. Thus, the spiral structure of $Tb_{0.6}Dy_{0.4}$ remains essentially unchanged in the eutectic structure, and we conclude that the contributions to the magnetization from the individual R and RFe_2 phases within the eutectic are simply additive.

For most applications utilizing magnetostrictive materials, it is important to know the mechanical stiffness. We report measurements of Young's moduli at room temperature and at 77 K. In Fig. 3 we illustrate the stress-strain relationships at room temperature for the Bridgman-prepared samples in the absence of an applied magnetic field. The addition of the R component to the RFe_2 compound consists of two major features: (1) a reduction of the stiffness with the addition of the softer rare-earth binary alloy; and (2) a large magnetically induced hysteresis in the RFe_2 and the eutectic containing alloy richest in RFe_2. In these two cases, the moduli strongly depend upon the magnetic history of the sample. For RFe_2 and $R_{0.42}Fe_{0.58}$, Young's moduli measurements were taken with the samples premagnetized parallel to the rod axis to achieve the maximum magnetic moment rotation in an applied magnetic field. As the compressive stress is applied to these samples, the magnetization in the domains rotates from parallel to perpendicular to the rod axis, yielding a softening of the sample and the well-known ΔE effect. As the magnetic moments become nearly perpendicular to the rod axis ($\sigma > 60$ MPa), both samples become significantly harder. The fraction of RFe_2 is small in the samples richer in R and the hysteresis becomes negligible. The pure eutectic $R_{0.72}Fe_{0.28}$ alloy and those richer in R are also more ductile and deform under stresses greater than ~100 MPa. Young's moduli, calculated from the high-stress slopes of Fig. 3, are 110, 83, 77, and 72 GPa for RFe_2, $R_{0.42}Fe_{0.58}$, $R_{0.72}Fe_{0.28}$, and $R_{0.9}Fe_{0.1}$, respectively.

The effect of magnetic field on the moduli is shown in Fig. 4 for RFe_2 and $R_{0.42}Fe_{0.58}$ at room temperature and 77 K ($\sigma \cong 15$ MPa). When an axial magnetic field is applied to a positive magnetostriction material under a preexisting compressive stress, the magnetic moments again rotate, but now from perpendicular to parallel to the rod axis. As this rotation process takes place in the applied magnetic field, the elastic moduli at first decreases and then increases as the rotation process becomes complete. For the RFe_2 compound, the

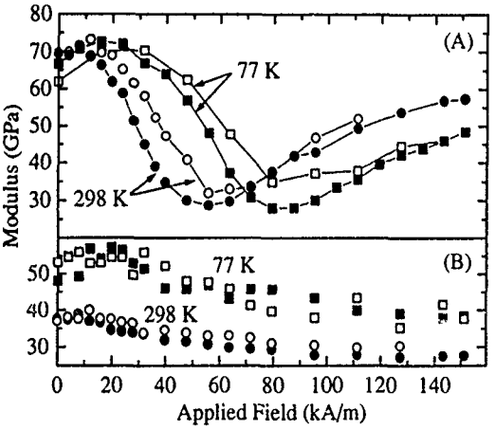

FIG. 4. Modulus under constant-field conditions Y^H and under constant induction Y^B vs applied field for Bridgman-prepared samples: (A) $(Tb_{0.6}Dy_{0.4})_{0.33}Fe_{0.67}$ at 15.8 MPa and (B) $(Tb_{0.6}Dy_{0.4})_{0.42}Fe_{0.58}$ at 15.4 MPa [(□) Y^B at 77 K, (■) Y^H at 77 K, (○) Y^B at 298 K, and (●) Y^H at 298 K]

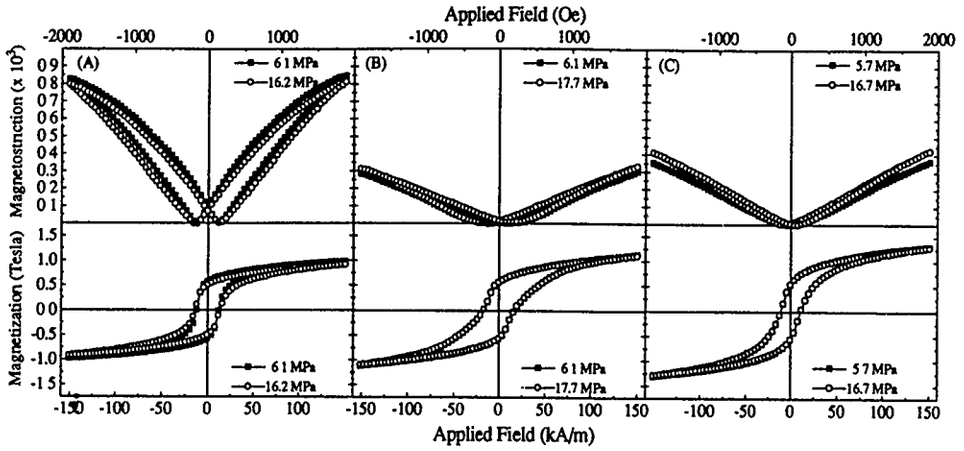

FIG. 5. Field dependencies of the magnetization and magnetostrictions for Bridgman-prepared samples: (A) $(Tb_{0.6}Dy_{0.4})_{0.42}Fe_{0.58}$; (B) $(Tb_{0.6}Dy_{0.4})_{0.72}Fe_{0.28}$, and (C) $(Tb_{0.6}Dy_{0.4})_{0.9}Fe_{0.1}$ at two compressive stresses.

easiest rotation takes place near 85 kA/m at 77 K (55 kA/m for room temperature). For the sample containing the smallest amount of eutectic, $R_{0.42}Fe_{0.58}$, the easiest rotation process occurs at a field higher than 160 kA/m. To evaluate the effect of 180° domain-wall motion in creating the nonmagnetostrictive magnetization process, measurements were taken under both constant magnetic field H and constant magnetic induction B. In these samples, both Y^B and Y^H decrease with applied field. Thus, even when the total induction is kept fixed, the domains redistribute themselves in such a way that yields some magnetization rotation and magnetostriction. Thus, the accepted conventional relationship between the coupling factor and Young's moduli, $k^2=1-Y^H/Y^B$, is not valid here.

At room temperature the magnetization and magnetostriction decrease rapidly with the addition of R to the RFe_2 compound. In this section we report the magnetization and magnetostriction at 77 K in magnetic fields up to 160 kA/m. Figure 5 illustrates the field dependencies for the $R_{0.42}Fe_{0.58}$, $R_{0.28}Fe_{0.72}$, and $R_{0.9}Fe_{0.1}$ alloys at compressive stresses σ of ~6 and ~17 MPa for the Bridgman-prepared samples. Similar results are observed for the FSZ samples, but not reported here. The expected σ dependencies of the magnetization and magnetostriction, characteristic of both R and the RFe_2 compound, are not seen. Here, little or no stress dependence was observed. Also striking is the large reduction in the magnetostriction with the addition of a small amount of the R component to the RFe_2 compound. In the RFe_2 compound (not shown), the magnetostriction reaches 2200×10^{-6} at 160 kA/m. As observed in Fig. 5(a), the magnetostriction of $R_{0.42}Fe_{0.58}$ is only $\sim800\times10^{-6}$. With samples richer in R, the magnetostriction decreases still further, even though the magnetostriction of the R is much higher than that of RFe_2. These unexpectedly low magnetostriction values are shown in Figs. 5(b) and 5(c) along with their corresponding magnetizations. Note the hysteresis is largest for the pure eutectic, $R_{0.72}Fe_{0.28}$. The conclusion reached is that the high c-axis texture of the rod samples, with the large uniaxial anisotropy, inhibits the large magnetization rotations required for giant magnetostrictions. In the R-rich samples, the magnetostrictions reach only $\sim400\times10^{-6}$, compared with the huge $\sim6000\times10^{-6}$ previously reported for the basal plane oriented $Tb_{0.6}Dy_{0.4}$ single crystals.[1]

The Néel and Curie temperatures of R ($=Tb_{0.6}Dy_{0.4}$) were clearly observed in all of the eutectic-containing alloys. Thus, the presence of RFe_2 component in the eutectic does not noticeably affect the magnetic properties of the R component, even its magnetic structure. On the other hand, the giant magnetostriction of the R component of the eutectic was not realized. Because of the highly textured nature of the Bridgman and FSZ samples and a strong R uniaxial anisotropy, the magnetostriction (for $H<160$ kA/m) is found to decrease as the portion of the highly magnetostrictive R component of the alloy is increased. Finally, Young's modulus decreases as the R/RFe_2 ratio in R_xFe_{1-x} ($0.33\leq x\leq1$) increases. The modulus in the $R_{0.42}Fe_{0.58}$ alloy is highly hysteretic and does not exhibit the large ΔE effect of the single-phase RFe_2 compound.

Research on magnetostrictive intermetallic alloys at the Naval Surface Warfare Center is sponsored by the Navy Independent Research Program.

[1] A. E Clark, M. Wun-Fogle, J. B. Restorff, and J. F. Lindberg, IEEE Trans Magn. **MAG-28**, 3156 (1992).
[2] M. B. Spano, A. E. Clark, and M Wun-Fogle, IEEE Trans. Magn. **MAG-25**, 3794 (1989).
[3] A. E. Clark, in *Ferromagnetic Materials*, edited by E. P. Wohlfarth (North-Holland, Amsterdam, 1980), Vol 1, p. 531.
[4] *Binary Phase Diagrams*, edited by T. R. Massalski (ASM, Metals Park, OH, 1986).
[5] Samples were prepared by Edge Technologies, Inc., ETREMA Div, Ames, IA.
[6] W. C. Koehler, in *Magnetic Properties of Rare Earth Materials*, edited by R. J. Elliot (Plenum, London, 1972), p 81

Published without author corrections

Theory of magnetostriction with application to Terfenol-D

R. D. James
Department of Aerospace Engineering and Mechanics, University of Minnesota, Minneapolis, Minnesota 55455

D. Kinderlehrer
Center for Nonlinear Analysis and Department of Mathematics, Carnegie Mellon University, Pittsburgh, Pennsylvania 15213

A mechanism for magnetostriction in the highly magnetostrictive material Terfenol-D is explained in detail. This mechanism is based on a theory of magnetostriction [R. D. James and D. Kinderlehrer, Philos. Mag. B **68**, 237 (1993)] that is particularly suited to predictions of the macroscopic behavior of materials that exhibit large magnetostriction. Some experiments that test these predictions are proposed.

I. INTRODUCTION

A theory of magnetostriction that is adapted to the description of large magnetostriction is given by the authors in Ref. 1. The theory is a micromagnetic in nature and follows the pattern established by Brown.[2] The focus is on an exact specification of the potential wells of the anisotropy energy.

For large specimens such as those encountered in usual actuator applications, the presence of complicated domain structures has hindered the usefulness of micromagnetic theories that seek to incorporate magnetostriction. In recent years new methods of calculating energy minimizers for this situation have emerged, partly as a result of advances in the analysis of the microstructure of martensite and partly as a result of related developments on the design of optimal composites. Using these ideas, the authors[1] found compatible energy minimizing domain structures for the theory specialized to a growth-twinned specimen of $Tb_xDy_{1-x}Fe_2$, $x \approx 0.3$ (Terfenol-D).

The patterns found in Ref. 1 consist of laminates which meet at the growth twin boundary; see, e.g., Fig. 1. Each layer of the laminate has a constant deformation gradient and a substructure of magnetic domains. The motivation for looking at laminates as energy minimizers arose from the observations of Lord *et al.*[3] Analyzing all possible compatible energy-minimizing laminates that meet at the growth twin boundary, we found five distinct energy minimizing microstructures, pictured in Fig. 1, one of which agreed with the photomicrograph of Lord *et al.* Subsequently, all of the other four patterns were observed (Lord[4]), with good agreement of the geometry and even (in the cases available) of the magnetic substructure.

Each of these structures is kinematically compatible and energy minimizing for all values of the volume fraction γ. As γ changes from 0 to 1 the sample experiences a macroscopic strain in the direction $[-211]$, the typical axial direction of a Terfenol-D rod; however, the amount of strain differs for the different laminates. It might then be inferred that, after a few cycles, the rod would be likely to choose the domain structure that yields the maximum magnetostrictive strain, because there is certainly an energy barrier to changing the whole pattern.

A more refined prediction suggests that something different might occur. There are actually two kinds of laminated microstructures predicted by the theory. In the first kind, analogous to "semicoherent" interfaces in the literature on martensite, the laminates are separated by a transition layer, which of course contains some energy. The value of this energy is proportional to the twin spacing, so it can be reduced as close to zero as desired by refining the twins. The second kind of laminate has no transition layer; it is "exactly compatible." The property of being exactly compatible versus approximately compatible is predicted by the theory; it is not just based on microscopic examination. With exchange energy present, it is clear that exactly compatible laminates are energetically preferred over those which have a transition layer.

Exactly compatible laminates have another interesting feature: The volume fraction γ can change with position along the growth twin boundary, giving them some additional freedom to meet remote conditions.

When we went back and checked the different laminates, we found that the laminate which achieves maximum magnetostrictive strain is not exactly compatible. This suggests that there may possibly be a drastic change in the domain pattern, and as explained herein, this would be favored by compressive stress. These predictions are explained in more detail below. They suggest some interesting experiments, now in progress (Tickle[5]).

These considerations apply to a specimen with parallel growth twins, such as one that is obtained by float-zone processing. Bridgman-grown specimens contain a significant number of grain boundaries and sometimes several different growth twin systems, which surely would rule out simple laminated energy minimizers.

II. THEORY OF TERFENOL-D

We give a brief description of the theory specialized to Terfenol-D. The basic unknown functions of the theory are the deformation $\mathbf{y}(\mathbf{x})$ and magnetization $\mathbf{m}(\mathbf{y})$. These are minimizers or relative minimizers of the total free energy

$$E(\mathbf{y},\mathbf{m}) = \int_\Omega \varphi\{\nabla \mathbf{y}(\mathbf{x}), \mathbf{m}[\mathbf{y}(\mathbf{x})]\} d\mathbf{x} + \tfrac{1}{2}\int_{R^3} |\nabla u(\mathbf{z})|^2 \, d\mathbf{z}. \tag{1}$$

Here Ω is the reference configuration of the specimen, φ is the anisotropy energy, and the magnetostatic potential u is determined from $\mathbf{m}$ by solving the magnetostatic equation

$$\operatorname{div}(-\nabla u + \mathbf{m}) = 0 \quad \text{on } R^3. \tag{2}$$

In solving this equation it is understood that $\mathbf{m}=0$ outside of $\mathbf{y}(\Omega)$, the deformed configuration. The theory is geometri-

 0021-8979/94/76(10)/7012/3/$6.00 © 1994 American Institute of Physics

cally exact, to allow it to apply for arbitrarily large deformations. In fact, the elasticity could be linearized. and then the theory would be similar to that of Clark,[6] but it is no more difficult to calculate the energy minimizers for the geometrically exact theory. The energy (1) is appropriate to a single-crystal specimen. Supposing that Ω is divided in two by a growth twin on the plane $\mathbf{x}\cdot\mathbf{m}_1=0$, so that $\Omega=\Omega_1\cup\Omega_2$ with $\Omega_1=\Omega\cap(\mathbf{x}\cdot\mathbf{m}_1>0)$ and $\Omega_2=\Omega\cap(\mathbf{x}\cdot\mathbf{m}_1<0)$, then the appropriate expression for the energy is

$$E_{gt}(\mathbf{y},\mathbf{m})=\int_{\Omega_1}\varphi\{\nabla\mathbf{y}(\mathbf{x}),\mathbf{m}[\mathbf{y}(\mathbf{x})]\}d\mathbf{x}+\int_{\Omega_2}\varphi\{\nabla\mathbf{y}(\mathbf{x})\mathbf{R}_0,\mathbf{m}[\mathbf{y}(\mathbf{x})]\}d\mathbf{x}+\frac{1}{2}\int_{R^3}|\nabla u(\mathbf{z})|^2\,d\mathbf{z}, \tag{3}$$

where $\mathbf{R}_0$ is a 180° rotation about $\mathbf{m}_1$. Here $\mathbf{m}_1$ is proportional to (111) and expression (3) takes into account the observed crystallography of the type-I growth twins of Terfenol-D. When minimizing Eq. (3), compatibility at the growth twin boundary is automatically taken into account by the assumption that $\mathbf{y}(\mathbf{x})$ is continuous on Ω. Finally, expressions (2) and (3) are appropriate for no applied field or loads.

The key feature about the anisotropy energy φ is its potential-well structure. For Terfenol-D it is assumed to have minima on the set

$$\{\mathbf{RU}_1,\pm\mathbf{Rm}_1\}\cup\{\mathbf{RU}_2,\pm\mathbf{Rm}_2\}$$
$$\{\mathbf{RU}_3,\pm\mathbf{Rm}_3\}\cup(\mathbf{RU}_4,\pm\mathbf{Rm}_4\}, \tag{4}$$

where $\mathbf{m}_1=\alpha[111]$, $\mathbf{m}_2=\alpha[-111]$, $\mathbf{m}_3=\alpha[1-11]$, $\mathbf{m}_4=\alpha[11-1]$, $\mathbf{U}_i=\eta_1\mathbf{1}+(\eta_2-\eta_1)\hat{\mathbf{m}}_i\otimes\hat{\mathbf{m}}_i$, $\hat{\mathbf{m}}_i=\mathbf{m}_i/|\mathbf{m}_i|$, $i=1,...,4$, and $\mathbf{R}$ is an arbitrary proper 3×3 rotation matrix. The scalar constant of proportionality α is $1/\sqrt{3}$ of the saturation magnetization, η_2-1 is the saturation strain along [111], and η_1-1 is the saturation strain along $[1-10]$. The notation $\mathbf{a}\otimes\mathbf{b}$ denotes the matrix with components a_ib_j and $\mathbf{1}$ is the identity matrix. Thus, the linear transformation $\mathbf{U}_1$ transforms a cube (aligned with the cubic axes in Ω) by stretching its [111] diagonal with a strain η_2-1 while contracting every direction perpendicular to [111] with a strain η_1-1. This can be seen by applying $\mathbf{U}_1$ to unit vectors in the various directions. We shall say that the specimen is in variant i at a point $\mathbf{x}\in\Omega_1$ if $[\nabla\mathbf{y}(\mathbf{x}),\mathbf{m}(\mathbf{x})]$ has the form $\{\mathbf{QU}_i,\pm\mathbf{Qm}_i\}$ for some rotation matrix $\mathbf{Q}$. A different notation is appropriate for the region Ω_2; that is, because of the presence of $\mathbf{R}_0$ in Eq. (3), the potential wells are modified there. Hence, we say that the specimen is in variant i' at a point $\mathbf{x}\in\Omega_2$ if $[\nabla\mathbf{y}(\mathbf{x}),\mathbf{m}(\mathbf{x})]$ has the form $\{\mathbf{QR}_0\mathbf{U}_i\mathbf{R}_0,\pm\mathbf{QR}_0\mathbf{m}_i\}$ for some rotation matrix $\mathbf{Q}$.

III. ENERGY-MINIMIZING COMPATIBLE DOMAIN STRUCTURES

The energy minimizers computed in Ref. 1 consist of laminates above and below the growth twin boundary. All possible compatible laminates were considered; that is, it was assumed that $\nabla\mathbf{y}$ oscillated between two values on Ω_1 and two different values on Ω_2, with possibly a transition layer in between. To be energy minimizing, these values necessarily have to come from the potential wells (4), the energy in the transition layer has to be reducible to zero by refining the layers, and the substructure of magnetic domains has to be arranged to make the field energy arbitrarily small (see Ref. 1 for the details of how this was done).

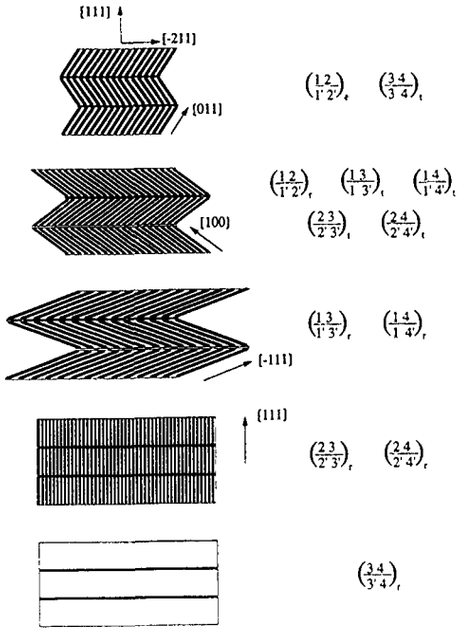

FIG 1 Appearance of the predicted laminates on the (0-11) plane with light and dark denoting the individual layers within a laminate. The magnetic substructure is not shown.

To summarize the results of these calculations, we use the notation

$$\left\langle\frac{ij}{k'l'}\right\rangle_{\text{subscript}} \tag{5}$$

to denote a minimizer which uses variants i and j on Ω_1 and k' and l' on Ω_2. The subscript can take the value t ("twin") or r ("reciprocal twin") which refers to which of the two kinematically compatible interfaces ({100} or {110}, respectively) is used in making the laminate; this choice also affects the rotations involved. Using this notation, all compatible variants are shown in Fig. 1. This figure shows only the domains of distortion [as would be revealed by differential interference contrast (DIC) microscopy, for example], not the magnetic substructure. Energy minimization gives one additional restriction: The volume fraction above and below the growth twin boundary is necessarily the same.

As mentioned in Sec. I, some of these laminates are exactly compatible. Exact compatibility is most easily explained by Fig. 2. An approximately compatible laminate has the property that the energy in the transition layer can be reduced to zero by refining the layers. Exchange energy imposes a limit to how much the laminates can be refined, and the ultimate fineness is determined by a compromise between the energy in the transition layer and the total interfacial energy. Exactly compatible laminates have no transition layer and, therefore, can be coarse or fine, and the tendency would be toward coarseness since the only energy present is exchange.

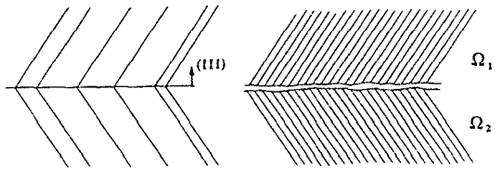

FIG. 2 Exactly compatible configuration (left-hand side) and approximately compatible configuration (right-hand side) laminates.

The exactly compatible laminates are[1]

$$\frac{23}{3'3'} \quad \frac{34}{3'4'} \quad \frac{24}{2'4'}. \tag{6}$$

IV. MECHANISM OF MAGNETOSTRICTION

If we imagine a unit line segment drawn on the specimen in the $[-211]$ direction above the Curie point (i.e., in the reference configuration), this line will become a zig-zag line when evaluated for any of these laminates. It will never "break," as we have assumed kinematic compatibility [i.e., the continuity of $\mathbf{y}(\mathbf{x})$]. For such a line that is long compared to the layer width, the length of the line depends only on the volume fraction γ and the choice of the laminate. A line in the $[-211]$ direction will have the same length whether it is placed above or below the growth twin boundary, by compatibility. It is easy to calculate the maximum and minimum lengths of such lines, as γ goes from 0 to 1, for all the laminates, and the result is given in Table I. (The right-hand-side column is an evaluation of these lengths for material constants η_1 and η_2 appropriate for Terfenol-D, obtained by using surface relief measurements of Al-Jiboory and Lord.[7]) It is seen from Table I that the maximum strain $\Delta l/l$ is obtained using the variants 1 2; however, from Eq. (6) these variants do not achieve exact compatibility. Another look at Table I shows that the reason that the variants 1 2 give the maximum magnetostrictive strain is that they give both the shortest (0.9992) and the longest (1.001 33) length; but, in fact, the variant pairs 2 3 and 2 4, both of which are exactly compatible, have the same maximal length (1.001 33) as 1 2 but their minimum length is longer.

TABLE I. The minimum and maximum macroscopic lengths of a line oriented along $[-211]$ which in the reference configuration had unit length.

Variants	Length	Length with $\eta_1=0.9992$, $\eta_2=1.0016$
1 2	$\min \eta_1$	0.9992
	$\max[\eta_1^2+\frac{8}{9}(\eta_2^2-\eta_1^2)]^{1/2}$	1 001 33
1 3	$\min \eta_1$	0.9992
	$\max[\eta_1^2+\frac{2}{9}(\eta_2^2-\eta_1^2)]^{1/2}$	0.999 73
1 4	$\min \eta_1$	0.9992
	$\max[\eta_1^2+\frac{2}{9}(\eta_2^2-\eta_1^2)]^{1/2}$	0 999 73
2 3	$\min[\eta_1^2+\frac{2}{9}(\eta_2^2-\eta_1^2)]^{1/2}$	0 9997
	$\max[\eta_1^2+\frac{8}{9}(\eta_2^2-\eta_1^2)]^{1/2}$	1 001 33
3 4	$\min\left(\eta_1^2+\frac{2}{9}(\eta_2^2-\eta_1^2)-\frac{(\eta_1^2-\eta_2^2)^2}{3(2\eta_2^2+\eta_1^2)}\right)^{1/2}$	0 999 47
	$\max[\eta_1^2+\frac{2}{9}(\eta_2^2-\eta_1^2)]^{1/2}$	0 999 73
(3 4),	$\min=\max=[\eta_1^2+\frac{2}{9}(\eta_2^2-\eta_1^2)]^{1/2}$	0.999 73
2 4	$\min[\eta_1^2+\frac{2}{9}(\eta_2^2-\eta_1^2)]^{1/2}$	0.999 73
	$\max[\eta_1^2+\frac{8}{9}(\eta_2^2-\eta_1^2)]^{1/2}$	1 001 33

Computations with applied field and load using the present theory are in progress,[8] but are not yet available; however, as far as the effect of small or moderate loads and fields is concerned, it is likely that they will reveal that compressive stress will favor variants yielding the shortest length, while applied fields in the direction $[-211]$ will favor variants yielding the longest length (This comes from a closer examination of the magnetic subdomain structure.)

Putting these assumptions together with the idea that exactly compatible variants are preferred, we can arrive at a proposal for what might happen. With no compressive stress or applied field, variants 2 3, 2 4, or perhaps 3 4 would be preferred. Still in the absence of stress but with a $[-211]$ field applied, 2 3 and 2 4 are then preferred, even up to large fields, because they give maximum extension and they are exactly compatible; however, upon application of compressive stress, there is clearly a preference for 1 2 (or 1 3 or 1 4, which, however, would not seem to survive cycling the stress, because they achieve only modest maximal lengths).

V. PROPOSED EXPERIMENTS

This proposal suggests some relatively simple experiments. Since the domains of distortion discussed above are observed by making use of surface relief, it is important to polish the specimen in the single-domain state. Failure to do this will result in the possibility of seeing false domain boundaries at places where leveled domain boundaries existed during polishing. Since it is difficult to polish above the Curie temperature, it is reasonable to use stress to do this. According to the results of the theory, a compressive stress favors the single-domain state consisting of variant 1, and a reasonably large compressive stress is advised, to overcome barriers associated with the inevitable defects. A fixture has been built to do this.

With domains of distortion revealed, the experiment consists of observing the effects of applied field and compressive stress on the domain pattern and macroscopic magnetostriction, as indicated in the last paragraph of Sec. IV. The switch from variants 2 3 to 1 2 should be accompanied by a significant change of both the geometry and the fineness.

ACKNOWLEDGMENTS

The authors thank ONR, AFOSR, ARO, and NSF for support through N/N0014-91-J-4034, AFOSR-91-0301, DAAL03-92-G-003, and NSF/DMS-9111572.

[1] R. D. James and D. Kinderlehrer, Philos. Mag. B **68**, 237 (1993)
[2] W F. Brown, Jr., *Magnetoelastic Interactions*, Springer Tracts in Natural Philosophy 9 (Springer, Berlin, 1966).
[3] D. G. Lord, V Elliot, A E Clark, H. T Savage, J. P. Teter, and O. D. McMasters, IEEE Trans. Magn. **MAG-24**, 1716 (1988)
[4] D. G. Lord (personal communication).
[5] R Tickle, M.S. thesis, University of Minnesota, 1994
[6] A E. Clark, in *Ferromagnetic Materials*, edited by E. P Wohlfarth (North-Holland, Amsterdam, 1980), Vol. 1, Chap. 7.
[7] M Al-Jiboory and D G Lord, IEEE Trans Magn **MAG-26**, 2583 (1990).
[8] D Kinderlehrer and L Ma, IEEE Trans. Magn. (to be published)

Recent developments in modeling of the stress derivative of magnetization in ferromagnetic materials

D. C. Jiles and M. K. Devine
Ames Laboratory, Iowa State University, Ames, Iowa 50011

The effect of changing stress on the magnetization of ferromagnetic materials leads to behavior in which the magnetization may increase, or decrease, when exposed to the same stress under the same external conditions. A simple empirical law seems to govern the behavior when the magnetization begins from a major hysteresis loop. The application of the law of approach, in which the derivative of the magnetization with respect to the elastic energy supplied dM/dW is proportional to the magnetization displacement $M_{an}-M$, is discussed.

Previous work on the development of model theories of the magnetization processes in ferromagnetic materials have concentrated on the description of hysteresis[1,2] and the changes in hysteresis curves which result from constant applied stress.[3–5] The magnetomechanical effect, which is defined as the change in magnetization of a magnetic material resulting from a changing applied stress under a constant applied field, has been reported occasionally,[6,7] but the effects have appeared to be very complex. For example, in the closely related works of Craik and Wood[8] and of Birss, Faunce, and Isaac,[9] the experimental results were obtained by applying different stresses to various polycrystalline magnetic materials in the presence of a small constant magnetic field. As noted by Craik and Wood, there were many features in the results which cannot be reconciled with the previous theory of Brown.[10]

Birss,[11] Schneider and Charlesworth,[12] and Finbow[13] have mentioned the prediction of Brown's theory that the changes in magnetization should be independent of the sign of the stress (i.e., symmetric with stress), which is contrary to the experimental results presented in these articles. The "wall pressure" theory developed by Brown, and later by Brugel and Rimet,[14] predicts that the magnetization remains constant as the stress is reduced from its maximum amplitude. This was termed the "horizontal fly-back" by Birss and co-workers,[9] which is known to be at variance with experimental observations, as shown by Schneider and Richardson[15] and Schneider and Semcken,[16] as well as in the results of Craik and Wood,[8] Birss and co-workers,[9] and Jiles and Atherton.[17]

Following the observation by Bozorth and Williams[6] that the magnetization curve of Permalloy 68, obtained after application of a magnetic field followed by stress of 39 MPa (4 kg mm^{-2}), was "as closely as it was possible to tell, identical to the anhysteretic magnetization curve," it was suggested[17] that the main effect of stress cycling on the magnetization causes it to approach the anhysteretic.

The concept of the law of approach was tested by Pitman[18] and later by Maylin and Squire.[19] The results, according to Pitman, seemed to confirm the law of approach, with the results from positive and negative remanence being mirror images of each other, while the amplitude of the change in magnetization was found to be much reduced when the point on the initial magnetization curve was close to the demagnetized state.

The results Maylin and Squire substantiated these results for locations beginning from the major loop; however, for locations beginning on a minor (i.e., asymmetric) loop, the law of approach, if it was operative, did not seem to pertain to the principal anhysteretic magnetization.

There are probably three factors which determine the magnitude and sign of the magnetomechanical effect: (i) how far the prevailing magnetization is above or below the anhysteretic (the displacement): (ii) how sensitive this displacement is to stress (the rate of decay); and (iii) how the anhysteretic changes with stress.

As described in previous work,[3] an applied uniaxial stress acts on a multidomain polycrystalline material like an applied magnetic field operating through the magnetostriction, and this additional "effective field" can be described by

$$H_\sigma=\frac{3}{2}\frac{\sigma}{\mu_0}\left(\frac{d\lambda}{dM}\right)_\sigma. \tag{1}$$

Therefore, if the magnetostriction λ can be described as a function of magnetization and stress, the anhysteretic magnetization at field H and stress σ becomes identical to the anhysteretic at field $H+H_\sigma$ and zero stress,

$$M_{an}(H,\sigma)=M_{an}(H+H_\sigma,0)=M_{an}\left[H+\frac{3}{2}\frac{\sigma}{\mu_0}\left(\frac{d\lambda}{dM}\right)_\sigma,0\right], \tag{2}$$

where the effects of stress have been incorporated into the effective field. A reasonable first approximation to the magnetostriction of iron can be obtained by using the series expansion

$$\lambda=\sum_{i=1}^{\infty}\gamma_i M^{2i}, \tag{3}$$

which enables the derivative $d\lambda/dM$ to be calculated.

The stress dependence of the magnetostriction curve $\lambda(M,\sigma)$ can be described from the stress dependence of the coefficients γ_i. Using a Taylor series expansion,

$$\gamma_i(\sigma)=\gamma_i(0)+\sum_{n=1}^{\infty}\frac{\sigma^n}{n!}\gamma_i^n(0), \tag{4}$$

where $\gamma_i^n(0)$ is the nth derivative of γ_i with respect to stress at $\sigma=0$.

The stress dependence of the anhysteretic magnetization curve can be determined from

 0021-8979/94/76(10)/7015/3/$6.00 © 1994 American Institute of Physics

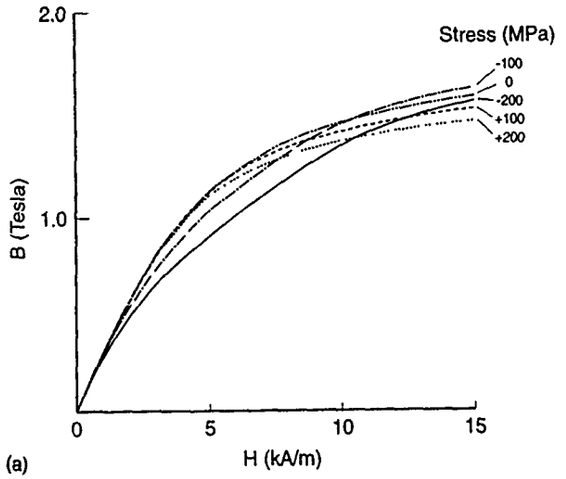

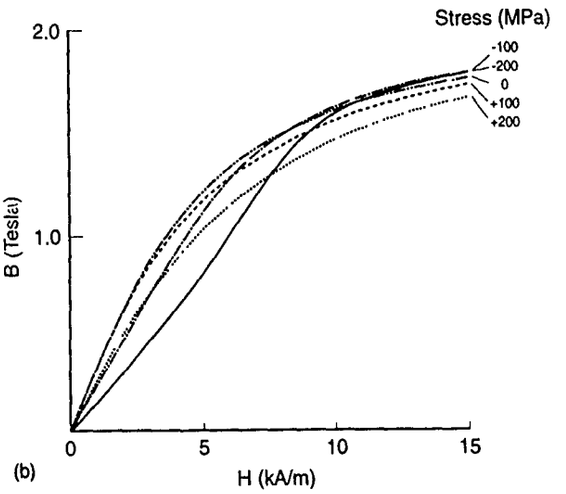

FIG. 1. (a) Measured variation of the anhysteretic magnetization with stress, as reported by Jiles and Atherton (Ref. 17); (b) modeled variation of the anhysteretic magnetization curve for various levels of stress together with the following values of the coefficients: $M_s=1.7\times10^6$ A/m, $a=100$ A/m, $k=1000$ A/m, $\alpha=0.001$, $c=0.1$, $\gamma_1=4\times10^{-18}-(3\times10^{-26})\sigma$ A^{-2} m^2, and $\gamma_2=2\times10^{-30}-(5\times10^{-39})\sigma$ A^{-4} m^4.

$$M_{an}(H,\sigma)=M_s\left[\coth\left(\frac{H+H_\sigma+\alpha M}{a}\right)-\frac{a}{H+H_\sigma+\alpha M}\right]. \tag{5}$$

The predictions of the present mode equation for the stress dependent anhysteretic are shown in Fig. 1 for selected values of the model parameters. It is clear from these results that there is good agreement with the experimental results of Jiles and Atherton.

The magnetization may increase or decrease when exposed to the same stress under the same external conditions. This indicates that the phenomenon is dependent on more than simply the external effects of stress and field. In fact the behavior depends on the magnetization history of the specimen.

We have now two factors to consider: the displacement from the anhysteretic and the change in elastic energy. The proposition which we wish to test is that the derivative of the magnetization with the change in elastic energy supplied W obeys a law of approach,

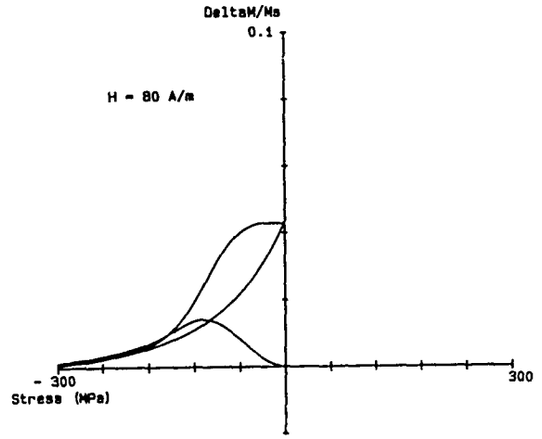

FIG. 2. Variation of magnetization with applied stress at a field strength of 80 A m^{-1} close to the anhysteretic magnetization curve and slightly below it. The right-hand-side half of the diagram shows the behavior in tension and the left-hand-side half shows the behavior in compression. The values of the quantities used were: $\epsilon=100\times10^6$ Pa, $\gamma_1=4\times10^{-18}-(3\times10^{-26})\sigma$ A^{-2} m^2, and $\gamma_2=2\times10^{-30}-(5\times10^{-39})\sigma$ A^{-4} m^4.

$$\frac{dM}{dW}=\frac{1}{\xi}(M_{an}-M), \tag{6}$$

where now ξ is a decay coefficient which has units of J m^{-3}. The change in elastic energy supplied to the material when the stress is changed from σ_0 to σ is

$$W=\frac{1}{E}(\sigma-\sigma_0)^2, \tag{7}$$

where E is the elastic modulus. Therefore, substituting

$$dW=\frac{2}{E}(\sigma-\sigma_0)d\sigma \tag{8}$$

into Eq. (6) gives

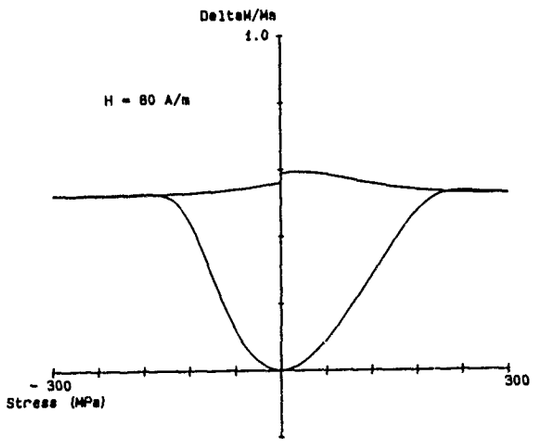

FIG. 3. Variation of magnetization with stress at 80 A m^{-1} along the lower loop of the magnetization curve after reducing from a field amplitude of -5000 A m^{-1}. The values of the quantities used were. $\epsilon=100\times10^6$ Pa, $\gamma_1=4\times10^{-18}-(3\times10^{-26})\sigma$ A^{-2} m^2, and $\gamma_2=2\times10^{-30}-(5\times10^{-39})\sigma$ A^{-4} m^4.

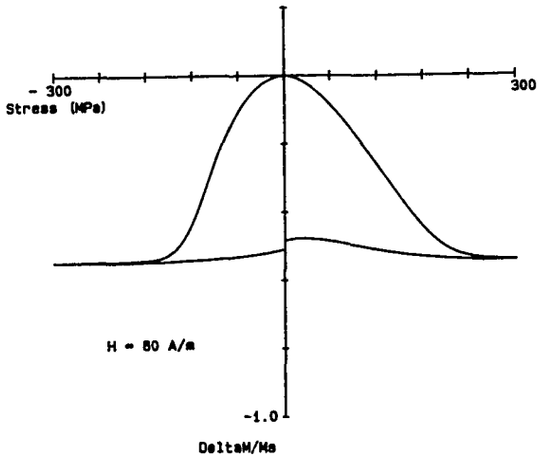

FIG. 4. Variation of magnetization with stress at 80 A m^{-1} along the upper loop of the magnetization curve after reducing from a field amplitude of 5000 A m^{-1}. The values of the quantities used were: $\epsilon=100\times10^6$ Pa, $\gamma_1=4\times10^{-18}-(3\times10^{-26})\sigma$ $A^{-2}m^2$, and $\gamma_2=2\times10^{-30}-(5\times10^{-39})\sigma$ $A^{-4}m^4$.

$$dM=\frac{2}{\epsilon^2}(\sigma-\sigma_0)(M_{an}-M)d\sigma, \tag{9}$$

where $\epsilon^2=E\xi$, and ϵ has units of Pa.

Rearranging Eq. (9) and integrating,

$$\int \frac{dM}{M-M_{an}}=-\frac{2}{\epsilon^2}\int(\sigma-\sigma_0)d\sigma, \tag{10}$$

and consequently

$$M_{an}-M(\sigma)=[M_{an}-M(\sigma_0)]\exp\left[-\left(\frac{\sigma-\sigma_0}{\epsilon}\right)^2\right], \tag{11}$$

which, on subtraction from $M_{an}-M(\sigma_0)$, gives the change in magnetization ΔM,

$$\Delta M=M(\sigma)-M(\sigma_0)$$
$$=[M_{an}-M(\sigma_0)]\left\{1-\exp\left[-\left(\frac{\Delta\sigma}{\epsilon}\right)^2\right]\right\}, \tag{12}$$

where $\Delta\sigma=\sigma-\sigma_0$. This gives the symmetric dependence of magnetization on stress.

However, if M_{an} is stress dependent, as is generally the case, then this stress dependence needs to be incorporated, as shown in Eq. (2), which leads to a more complicated integration. In practice, it has been found best under all conditions to simply evaluate Eq. (9) numerically using computer techniques.

Experimental results of Pitman[18] exhibit the principal feature of interest, which is the ΔM vs $\Delta\sigma$ locus under compression (first an increase, and at higher compressive stress a decrease in M, under conditions close to, but slightly below, the anhysteretic). Then positive, or negative, changes in M with the same compressive stress, and under the same applied field, depending on whether the magnetization began well below, or well above, the anhysteretic.

The results of Craik and Wood[8] were more diverse than those of Pitman, and in particular their results showed the essential asymmetry of the magnetization versus stress curves at higher stress levels. At small stress amplitudes of up to about ±0.5 kg mm^{-2} ($=4.9\times10^6$ Pa), the change in magnetization with stress was almost symmetric. Even up to ±2 kg mm^{-2} (19.6×10^6 Pa), the sign of the change was positive under both tension and compression; but, beyond ±3 kg mm^{-2} (29.4×10^6 Pa), the change of magnetization with stress was negative under compression but positive under tension. A wide range of different behaviors of magnetization under stress was reported by Craik and Wood, showing asymmetry under tension or compression, and in which the amplitude of the changes was dependent on the strength of the constant applied magnetic field; however, because Craik and Wood did not measure the anhysteretic magnetization, the physical significance of the observed changes was not clear from their work.

In the work of Birss[11] it was found that for small changes in magnetization the magnetization versus stress curves were symmetric with respect to stress. For larger changes in magnetization, Birss reported similar findings to Craik and Wood: namely, a change in sign of the stress derivative under compression, leading to an asymmetric behavior.

The results of model calculations are shown in Figs. 2–4. It can be seen from the results of Fig. 2 at a field strength of 80 A/m that the slope of the curve of ΔM vs $\Delta\sigma$ changes sign in the compressive region at about -100 MPa. This result is similar in behavior to the data of Craik and Wood,[8] Birss and co-workers,[9] and Pitman.[18] The results in Figs. 3 and 4 show that the change in magnetization is positive or negative, depending on whether the initial magnetization state is below or above the anhysteretic, respectively. The resultant curves here are in excellent agreement with the reported results of Pitman.[18]

This work was supported by the U.S. Department of Energy, Office of Basic Energy Sciences under Contract No. W-7405-Eng-82.

[1] D. C. Jiles and D. L. Atherton, J. Magn. Magn. Mater. **61**, 48 (1986)
[2] D. C. Jiles, J. B. Thoelke, and M. K. Devine, IEEE Trans Magn. **MAG-28**, 27 (1992).
[3] M. J. Sablik, G. L. Burkhardt, H. Kwun, and D. C. Jiles, J. Appl. Phys. **63**, 3930 (1988).
[4] M. J. Sablik and D. C. Jiles, IEEE Trans. Magn. **MAG-29**, 2113 (1993).
[5] J. J. Sablik, S. W Rubin, L. A. Riley, D. C. Jiles, D. A. Kaminski, and S B Biner, J. Appl. Phys. **74**, 480 (1993).
[6] R. M. Bozorth and H. J. Williams, Rev. Mod. Phys. **17**, 72 (1945).
[7] L. Lliboutry, Ann. Phys. (Paris) **12**, 47 (1951).
[8] D. J. Craik and M. J. Wood, J. Phys. D **3**, 1009 (1970)
[9] R. R. Birss, C. A. Faunce, and E D. Issac, J. Phys. D **4**, 1040 (1971).
[10] W. F. Brown, Phys. Rev. **75**, 147 (1949).
[11] R. R. Birss, IEEE Trans. Magn. **MAG-7**, 113 (1971).
[12] C. S. Schneider and M. Charlesworth, J. Appl. Phys. **57**, 4198 (1985)
[13] D. C Finbow, Phys. Status Solidi A **3**, 743 (1970).
[14] L. Brugel and G. Rimet, J. Phys Radium **27**, 589 (1966).
[15] C. S. Schneider and J. M. Richardson, J Appl. Phys **53**, 8136 (1982)
[16] C. S. Schneider and E. A. Semcken, J. Appl. Phys. **52**, 2425 (1981).
[17] D. C. Jiles and D. L. Atherton, J. Phys. D **17**, 1267 (1984).
[18] K. C Pitman, IEEE Trans. Magn. **MAG-26**, 1978 (1990).
[19] M. G. Maylin and P. T. Squire, J. Appl Phys. **73**, 2948 (1993).

Magnetization and magnetostriction curves from micromagnetics

Antonio DeSimone[a)]
Center for Nonlinear Analysis, Carnegie Mellon University, Pittsburgh, Pennsylvania 15213

The macroscopic behavior of magnetostrictive materials results from domain evolutions, often occurring at a microscopic scale. It is shown how to compute magnetization and magnetostriction curves by appraising the behavior of the underlying microstructures. The method hinges on an averaging device (Young measures), which allows one to pass from the microscopic to the macroscopic scale. The kinematical constraints on the accommodation of elastic effects are taken into account, and the role of material symmetry in the selection of energetically optimal microstructures is highlighted. Moreover, the effect of magnetoelastic coupling on the computation of magnetization curves is discussed.

I. INTRODUCTION

Specimens of magnetostrictive materials exhibit magnetic and elastic domains, which evolve under the action of applied magnetic fields and loads. Analyzing the mechanisms that govern these domain evolutions is a key step to understand the macroscopic response of magnetostrictive materials: The macroscopic deformations induced on these materials by applied magnetic fields result precisely from domain rearrangements, often occurring at a microscopic scale. In fact, the size of magnetic and elastic domains is typically rather small as compared to the size of the body in which they appear. As a consequence, domain patterns may result in complex geometries. Micromagnetics provides us with a rationale for the occurrence of fine domain patterns, based on energy minimization. Moreover, at least in principle, it could be used to predict the most energetically favored configurations under given applied fields and loads and, hence, for quantitative predictions of the macroscopic response of magnetostrictive materials. In practice, this program fails due to the complexity of the configurations to be computed.

In this article we report on recent progress in applying micromagnetics to predict virgin magnetization and magnetostriction curves. Our method, inspired by the work of James and Kinderlehrer,[1] is based on a simple idea: Only a few average properties of domain patterns are needed to compute magnetization and magnetostriction curves, and not all of the geometric details of domain patterns are needed to exactly quantify their energetics. We focus precisely on those features of domain patterns which are needed to select the energetically optimal ones, and to describe them in enough detail so that the macroscopic response can be characterized. Our analysis bears close similarities with those based on the classical article of Néel,[2] but there are also some significant differences. In particular, we do take into account the effect of magnetoelastic coupling on the prediction of magnetization curves.

II. MICROMAGNETICS

We adopt the large-body limit formulation of micromagnetics,[3] in which exchange energy is omitted. Following Clark,[4] we use the framework of linear elasticity, and we measure deformations through the linear strain $\mathbf{E}(x)=(\frac{1}{2})[\nabla\mathbf{u}(x)+\nabla^T\mathbf{u}(x)]$, where $\mathbf{u}(x)$ denotes the displacement of the point x of a body Ω. Moreover, we restrict our attention to an unloaded specimen (the case of applied surface tractions has been considered in Ref. 5). The state of Ω is described by a magnetization-deformation pair $(\mathbf{m},\mathbf{E})$, and we look for minimizers of the energy functional

$$G_{\mathbf{h}}(\mathbf{m},\mathbf{E})=\int_\Omega\{\varphi_{\mathrm{TOT}}[\mathbf{m}(x),\mathbf{E}(x)]-\mathbf{h}\cdot\mathbf{m}(x)\}dx + \frac{1}{2}\int_{\mathbb{R}^3}|\nabla u_{\mathbf{m}}(x)|^2\,dx. \tag{1}$$

Here $\mathbf{h}$ is a constant external magnetic field, while $-\nabla u_{\mathbf{m}}$ is the magnetic field generated by $\mathbf{m}$, defined as the solution of Maxwell equation $\mathrm{div}(-\nabla u_{\mathbf{m}}+\tilde{\mathbf{m}})=0$, where $\tilde{\mathbf{m}}$ is the extension of $\mathbf{m}$ to $\mathbb{R}^3$ which vanishes outside Ω. Moreover, we write

$$\varphi_{\mathrm{TOT}}(\mathbf{m},\mathbf{E})=\varphi(\mathbf{m})+\tfrac{1}{2}[\mathbf{E}-\mathbf{E}_0(\mathbf{m})]\cdot\mathbf{C}[\mathbf{E}-\mathbf{E}_0(\mathbf{m})], \tag{2}$$

where φ is the anisotropy energy density, $\mathbf{C}$ is the fourth-order tensor of elastic moduli, and $\mathbf{E}_0(\mathbf{m})$ is the stress-free strain corresponding to $\mathbf{m}$, i.e., the second-order tensor which, for given $\mathbf{m}$, is such that $\varphi_{\mathrm{TOT}}[\mathbf{m},\mathbf{E}_0(\mathbf{m})]\leq\varphi_{\mathrm{TOT}}(\mathbf{m},\mathbf{E})$ for every $\mathbf{E}$.

Crucial to our analysis are some properties of φ and $\mathbf{E}_0(\mathbf{m})$ dictated by material symmetry. Denoting by $\mathscr{P}$ the group of material symmetries of the material at hand, i.e., the set of orthogonal matrices $\mathbf{Q}$ such that $\varphi_{\mathrm{TOT}}(\mathbf{Qm},\mathbf{QEQ}^T)=\varphi_{\mathrm{TOT}}(\mathbf{m},\mathbf{E})$ for every $\mathbf{m}$ and $\mathbf{E}$, we have

$$\varphi(\mathbf{Qm})=\varphi(\mathbf{m}),\quad\text{and}\quad\mathbf{E}_0(\mathbf{Qm})=\mathbf{QE}_0(\mathbf{m})\mathbf{Q}^T,\quad\forall\mathbf{Q}\in\mathscr{P}. \tag{3}$$

We also remark that, in view of Eq. (2), $G_{\mathbf{h}}$ is the sum of a non-negative term (the energy due to magnetoelastic coupling), and of the energy

$$R_{\mathbf{h}}(\mathbf{m})=\int_\Omega\{\varphi[\mathbf{m}(x)]-\mathbf{h}\cdot\mathbf{m}(x)\}dx + \frac{1}{2}\int_{\mathbb{R}^3}|\nabla u_{\mathbf{m}}(x)|^2\,dx, \tag{4}$$

which would be associated with the magnetized body, were it to be considered rigid.

[a)]On leave from Dip Ing. Civile, Università di Roma "Tor Vergata," 00133 Rome, Italy.

 0021-8979/94/76(10)/7018/3/$6.00 © 1994 American Institute of Physics

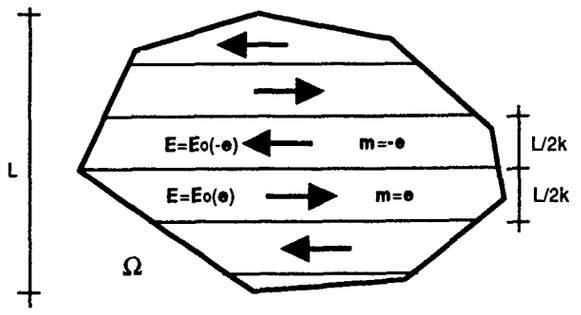

FIG. 1. The kth element of an energy-minimizing sequence for an unloaded specimen of uniaxial material under zero applied field.

III. MICROSTRUCTURES

The starting point of our analysis is the observation that the infimum of $G_{\mathbf{h}}$ may be unattainable in the space of admissible magnetization-deformation pairs. We illustrate this with an argument due to James and Kinderlehrer. We set $\mathbf{h}=0$, and we consider a uniaxial material with easy axis $\mathbf{e}$. Figure 1 shows the kth element of an energy minimizing sequence of magnetization-deformation pairs (note that the sequence is parametrized by the width of the layers, that the magnetization is always directed along the easy direction, and that the deformation is constant and it corresponds to a stress-free strain everywhere in Ω). By refining the width of the layers, we can drive the energy to its infimum I, which is $\varphi(\mathbf{e})$ times the volume of Ω. However, since there is no divergence-free magnetization field which takes only the values $\pm\mathbf{e}$, there is no configuration whose energy is exactly I. Thus, strictly speaking, the proposed minimization problem has no solution. In spite of this, the example gives a clear indication of how to proceed: a minimizer of G_0 should be described by the asymptotic behavior of an infinitely refining minimizing sequence, i.e., in a descriptive language, by a microstructure.

The notion of Young measure allows us to give a precise description of some of the asymptotic features of an infinitely refining sequence. Essentially, Young measures provide the precise mathematical description of the mixtures of magnetic phases introduced by Néel in Ref. 2. Indeed, the Young measure ν_x generated by a sequence of magnetizations $(\mathbf{m}_k)$, $k=1,2,...$, gives, at each point x of the body, the limiting distribution of the values of $\mathbf{m}_k$ in a vanishingly small neighborhood of x. For example, the Young measure generated by the sequence $(\mathbf{m}_k)$ of Fig. 1 is in fact independent of x and it can be written as

$$\nu=\tfrac{1}{2}\delta_{\mathbf{e}}+\tfrac{1}{2}\delta_{-\mathbf{e}}, \tag{5}$$

where $\delta_{\pm\mathbf{e}}$ is a Dirac mass centered at $\pm\mathbf{e}$. The physical meaning of Eq. (5) is the following: In the limit $k\to\infty$, $\mathbf{m}_k$ represents a microscopic arrangement of domains with the property that at every point of the body only domains with magnetization $\pm\mathbf{e}$ are present, and with equal volume fractions. The first moment of a Young measure generated by a sequence of magnetizations gives the average magnetization in a neighborhood of x, and its average over Ω gives the average magnetization of the whole specimen. For Eq. (5) we obtain zero, i.e., ν describes a demagnetized state. Similar arguments can be applied to sequences of deformations $\mathbf{E}_k$ and, in essence, our approach to the computation of magnetization and magnetostriction curves consists of a systematic application of the line of reasoning described above to cases in which an applied magnetic field is present. In particular, we note that if we are given a minimizing sequence $(\mathbf{m}_k,\mathbf{E}_k)$ of $G_{\mathbf{h}}$ for each value of the applied field $\mathbf{h}$, then the knowledge of the Young measures generated by the sequences $\mathbf{m}_k$ suffices to compute the corresponding magnetization curve.

Two remarks are in order. To clarify the physical meaning of infinitely refining sequences, we recall that the theory presented here is a limit theory for large specimens. Typically the ratio between the size of the domains and the size of the body in which they appear tends to zero as the latter increases. Since in the present theory this limiting process is represented on a reference body of fixed size, infinite refinement ensues. Our second remark concerns the problem of computing the energy of a microstructure. Put simply, the knowledge of the magnetic phases present in a microstructure, and of the corresponding volume fractions, does not provide enough information to compute its energy (in the example above, we carefully chose the orientation of the domain interfaces, and we also checked that no extra energy contributions arose from the magnetoelastic coupling). Thus, a model for magnetostrictive materials in which microstructures are described only through these quantities may lead to inaccurate predictions (see following section). It is indeed possible to characterize the energetics of microstructures without resolving them in their finest details. For this purpose, one needs not only Young measures, but also the H measures of Tartar.[6] The selection of optimal microstructures can thus be reduced to a minimization problem over Young measures and H measures. Here we follow the technically simpler alternative of computing minimizing sequences directly, and we use Young measures only to describe those of their features which are relevant for the computation of magnetization and magnetostriction curves. In this process, we do not neglect any energy contribution: In particular, we take into account both the magnetostatic and the magnetoelastic energy that may arise from jumps of the magnetization across adjacent domains.

IV. APPLICATIONS AND DISCUSSION

We illustrate our approach on a sample application. We consider a spherical specimen of uniaxial material, with anisotropy energy $\varphi(\mathbf{m})=\kappa[1-(\mathbf{m}\cdot\mathbf{e})^2]$ (we assume $|\mathbf{m}|=1$ and $\kappa>0$), under an applied field at 45° from the easy axis $\mathbf{e}$. We rely on the results of Ref. 3, where the corresponding minimization problem for $R_{\mathbf{h}}$ has been solved. The interesting regime is that of low field strengths, where minimizers of $R_{\mathbf{h}}$ are microstructures. Examples of the relevant minimizing sequences are shown in Fig. 2. They consists of layers, in each of which the magnetization takes one of two possible values (which depend on the applied field), say, $\mathbf{m}_1$ and $\mathbf{m}_2$. We obtain the minimizing sequences for $G_{\mathbf{h}}$ by setting every-

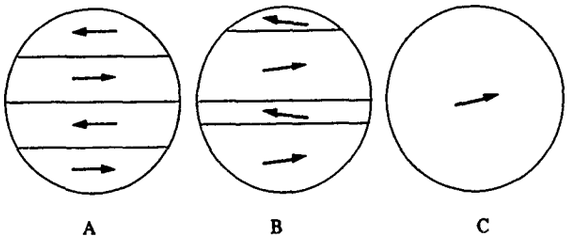

FIG. 2. Minimizing sequences for a spherical specimen of uniaxial mater. with applied field at 45° from the (horizontal) easy axis. A,B,C correspond to increasing field strengths.

where in the specimen $\mathbf{E}(x)=\mathbf{E}_0[\mathbf{m}(x)]$. This leads to a discontinuous deformation field, which is, however, kinematically compatible if

$$\mathbf{E}_0(\mathbf{m}_1)-\mathbf{E}_0(\mathbf{m}_2)=\tfrac{1}{2}(\mathbf{a}\otimes\mathbf{e}_\perp+\mathbf{e}_\perp\otimes\mathbf{a}), \tag{6}$$

for some vector $\mathbf{a}$ (here $\mathbf{e}_\perp$ denotes the normal to the layer interfaces, while $\mathbf{a}\otimes\mathbf{b}$ denotes the matrix with components $a_i b_j$). This is indeed the case, and it is not hard to check. The "structural" reason behind this result is that $\mathbf{m}_2=\mathbf{R}\mathbf{m}_1$, where $\mathbf{R}$ is a 180° rotation about $\mathbf{e}_\perp$, and hence it is an element of $\mathscr{P}$. Thus, by Eq. (3), $\mathbf{E}_0(\mathbf{m}_2)=\mathbf{R}\mathbf{E}_0(\mathbf{m}_1)\mathbf{R}^T$.

We can conclude that, in the example considered, the minimizers of G_h correspond to stress-free states. Thus, if $(\mathbf{m},\mathbf{E})$ is a "minimizer" (possibly a microstructure) of G_h, then $\mathbf{m}$ is a "minimizer" of R_h (in fact, the unique minimizer of R_h, as shown in Ref. 3). These observations give rise to a strategy for computing magnetization and magnetostriction curves: The computation of the magnetization curve is reduced to the computation of the minimizers of R_h, and the magnetostriction curve is obtained by considering the stress-free strains associated with the minimizers of R_h. This is a standard procedure, and we have thus shown that, in the example considered, it is justified as an exact consequence of micromagnetics.

In spite of the fact that similar results can be proved for a surprisingly large class of materials,[7] the validity of the procedure outlined above is not universal. A simple example is that of iron, when an external field applied in the [111] direction. It is interesting to note that, close to saturation, the magnetization curve computed from the minimization of R_h differs substantially from the experimental measurements. In this regime the minimizers of R_h consist of mixtures of four magnetic "phases" which are not symmetry related, and whose associated stress-free strains cannot give rise to kinematically compatible deformations (a proof will appear in Ref. 7). We conjecture that, by taking into account the energy contribution due to the magnetoelastic coupling, a more realistic prediction of the magnetization curve can be obtained: Indeed, in order to compensate for the elastic energy stored in a stressed configuration, higher field strengths should be necessary to sustain a given average magnetization.

ACKNOWLEDGMENTS

Several useful discussions with G. Friesecke and, at early stages of this research, with R. D. James, are gratefully acknowledged.

[1] R. D. James and D. Kinderlehrer, Cont. Mech. Therm. **2**, 215 (1990)
[2] L. Néel, J. Phys. Rad. **5**, 241 (1944).
[3] A DeSimone, Arch. Rat. Mech. Anal. **125**, 99 (1993).
[4] A E. Clark, in *Ferromagnetic Materials*, edited by E. P. Wohlfarth (North-Holland, Amsterdam, 1980), Vol. 1.
[5] A. DeSimone, in *Smart Structures and Materials 1994*, SPIE Proc. 2192, edited by H. T. Banks (Society of Photo-Optical Instrumentation Engineers, Bellingham, WA, 1994)
[6] L. Tartar, Center for Nonlinear Analysis Research Report 92-NA-002, Carnegie Mellon University, 1992.
[7] A. DeSimone (to be published).

Magnetostriction of melt-spun Dy-Fe-B alloys

S. H. Lim, T. H. Noh, and I. K. Kang
Magnetic Materials Laboratory, Korea Institute of Science and Technology, 136-791, Seoul, Korea

S. R. Kim and S. R. Lee
Department of Metallurgical Engineering, Korea University, 136-701, Seoul, Korea

The magnetostriction of melt-spun ribbons of $Dy_x(Fe_{1-y}B_y)_{1-x}$ ($x=0.2$, 0.25, 0.3; $0 \leq y \leq 0.2$) alloys is systematically investigated as a function of the wheel speed during melt quenching. As the wheel speed increases from 10 to 50 m/s, the magnetic softness improves with the wheel speed rather continuously for the alloys with the Dy content $x=0.2$ and 0.25 but it exhibits a maximum at the wheel speed of 30 or 40 m/s for the alloys with the highest B content ($x=0.3$). The softness also improves with the B content for a fixed wheel speed. Homogeneous and ultrafine grain structure is observed for the first time even in the as-spun state when the ribbons of the alloy $Dy_{0.3}(Fe_{0.8}B_{0.2})_{0.7}$ are fabricated at the wheel speed of 30 m/s. The ribbon having the ultrafine grain structure exhibits good magnetic softness together with a high strain.

I. INTRODUCTION

Giant magnetostrictive rare-earth (R) -transition-metal (TM) -based alloys such as $TbFe_2$ were developed more than 2 decades ago.[1,2] The saturation magnetostriction λ_s, of $TbFe_2$ compound at room temperature is as large as 1753×10^{-6} (or 1753 ppm);[3] however, since the magnetocrystalline anisotropy of the alloys is also very large, a large magnetic field is usually required to obtain a large strain. In the practical point of view it is important to have a large magnetostriction at a low magnetic field. In an early effort in this direction, many workers attempted to reduce the magnetocrystalline anisotropy through alloy design, one notable example being the investigation of pseudobinary (R_1,R_2)-TM compounds. One main outcome from the investigation was the development of $Tb_{0.3}Dy_{0.7}Fe_2$ compound commercially known as Terfenol-D.[4]

Recently, attempts have been made to improve the softness of R-TM compounds by suitably controlling the microstructure of the compounds.[5–10] The main route to microstructural modification is rapid quenching from the melt. It has been reported by many workers that the grain refinement or amorphization by this method improves the softness of the alloys although, in some cases, this improvement has been done at the expense of reduced λ_s.[7,8] Very recently, R-TM alloys of thick-film type were also fabricated by sputtering and were reported to show good magnetic softness.[9,10] It is clear from these later studies that the softness of R-TM alloys is sensitively affected by the microstructure, although it is felt that not much systematic work has been done so far.

In order to see how the microstructure and hence the softness of R-TM alloys is affected by fabrication conditions, we systematically investigate the magnetostriction of melt-spun ribbons of R-Fe-B alloys. In the present work, the alloys selected were $Dy_x(Fe_{1-y}B_y)_{1-x}$ ($x=0.2$, 0.25, 0.3; $0 \leq y \leq 0.2$). Similar work on Tb- and Sm-based alloys is in progress. The element B was added to the R-TM alloys, since it is known to affect the microstructure of as-spun ribbons.

II. EXPERIMENTAL DETAILS

The Dy-Fe-B alloys were arc melted in an Ar atmosphere. Subsequent melt spinning was carried out also in an Ar atmosphere. In the present experiments we fixed all the fabrication parameters except for the wheel speed which was varied over a wide range from 10 to 50 m/s. The melt temperature was maintained at just above the melting point of the respective alloys. The orifice diameter was about 0.5 mm and the chamber and ejecting Ar pressures were 2.1×10^{-2} and 1.85×10^{-1} MPa, respectively. The magnetostriction was measured by a three-terminal capacitance method at room temperature and at magnetic fields H up to 8 kOe. The microstructure was mainly examined by x-ray diffraction and, in some cases, by transmission electron microscopy (TEM).

III. RESULTS AND DISCUSSION

For the $Dy_{0.2}(Fe_{1-y}B_y)_{0.8}$ alloy system, it is observed from the results for λ vs H plots, not shown here due to space limitation, that λ increases very slowly with H at low fields, when ribbons of low-B alloys are fabricated at low wheel speeds (usually 30 m/s or less); however, the magnetic softness improves substantially with the increasing wheel speed and/or B content. These λ-H results are well explained by the x-ray-diffraction results. In low-B alloys, sharp diffraction peaks are seen at low wheel speeds indicating that crystalline phases with coarse grains exist, but, at high wheel speeds, the peaks are broadened indicative of the formation of finer grains. In high-B alloys, an amorphouslike broad pattern is observed even at low wheel speeds indicating that the glass-forming ability is increased by B addition. The value of λ in this alloy system is low, ranging from 30 to 60 ppm at 8 kOe. The crystalline phase is identified to be mainly Dy_6Fe_{23} compound with a small amount of $DyFe_3$.

For the alloy series $Dy_{0.25}(Fe_{1-y}B_y)_{0.75}$, the magnetic softness is observed to improve with the wheel speed, as is clearly demonstrated by the λ-H plots obtained at different wheel speeds for the $y=0.1$ alloy, as an example, shown in Fig. 1(a). The diffraction patterns for the same alloy are given in Fig. 1(b). Although the results are not shown here, the alloys with the other B content, except for the $y=0.2$ alloy, exhibit a similar λ-H behavior. This progressive improvement in the softness with the wheel speed is completely matched by the x-ray-diffraction patterns as shown in Fig. 1(b) from which it is observed that the peak intensity decreases and the peak width broadens continuously with the

 0021-8979/94/76(10)/7021/3/$6.00 © 1994 American Institute of Physics

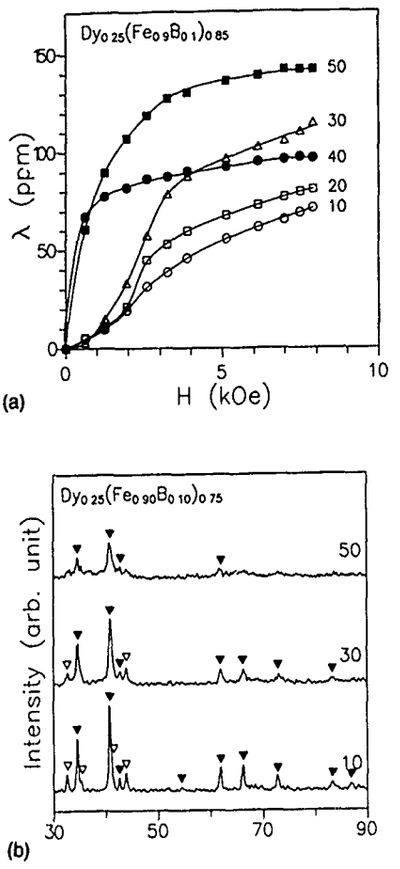

FIG. 1. (a) The λ-H plots for the alloy $Dy_{0.25}(Fe_{0.9}B_{0.1})_{0.75}$. (b) The x-ray-diffraction patterns for the same alloy as in (a). The $DyFe_2$ and $DyFe_3$ phases are indicated by the solid and open triangles, respectively. The numbers on the curves denote the wheel speed in m/s.

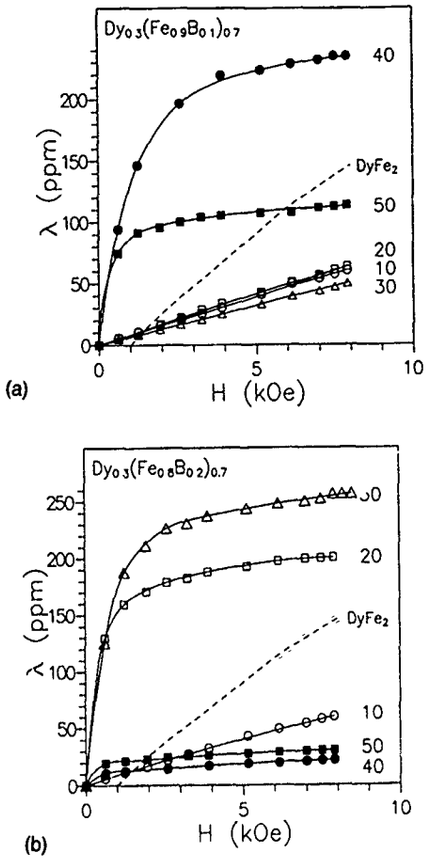

FIG. 2. The λ-H plots for the alloys (a) $Dy_{0.3}(Fe_{0.9}B_{0.1})_{0.7}$ and (b) $Dy_{0.3}(Fe_{0.8}B_{0.2})_{0.7}$. Also shown are the λ-H results for a bulk crystalline $DyFe_2$ for comparison (Ref. 3) (broken line). The numbers on the curves denote the wheel speed in m/s.

wheel speed. In the case of the $y=0.2$ alloy, the value of λ for the ribbons fabricated at the wheel speeds of 10 and 20 m/s is higher than that for the ribbons produced at the higher wheel speeds. The reason for this was originally thought to be due to the fact that, even at low wheel speed of 10 or 20 m/s, crystalline grains fine enough to result in good magnetic softness are formed at the large B content. The observed x-ray-diffraction patterns, however, do not seem to clearly support the assumption, since the peak intensity and the degree of line broadening do not vary greatly with the B content at the fixed wheel speed of 10 or 20 m/s. Further experiments are required to properly explain the high-λ values at the low wheel speeds in this high-B alloy.

The crystal structure of the $Dy_{0.25}(Fe_{1-y}B_y)_{0.75}$ series, which is determined by the x-ray-diffraction patterns, is observed to vary with the B content. Mostly the $DyFe_3$ phase exists in the B-free alloy and the $DyFe_2$ phase exists in the highest-B ($y=0.2$) alloy, and, in the alloys with the intermediate B content, the $DyFe_3$ and $DyFe_2$ phases coexist.

For the alloy system with the highest Dy content $Dy_{0.3}(Fe_{1-y}B_y)_{0.7}$, λ increases with the wheel speed, shows a maximum at the wheel speed of 40 m/s (30 m/s for the $y=0.2$ alloy), and then decreases with the further increase in the wheel speed. Some of the λ-H results are shown in Fig. 2(a) (for the alloy $y=0.1$) and Fig. 2(b) (for the alloy $y=0.2$). Although x-ray results are not shown here, the way in which the intensity and width of the x-ray peaks vary with the wheel speed is similar to that observed for the $Dy_{0.25}(Fe_{1-y}B_y)_{0.75}$ alloy system. The crystalline phase is determined to be mainly $DyFe_2$, a small amount of $DyFe_3$ being also observed for the alloys $y=0$ and 0.05. Also shown in Figs. 2(a) and 2(b) are the λ-H results for a bulk crystalline $DyFe_2$ for comparison.[3] No appreciable increase in λ of the bulk $DyFe_2$ is observed until $H=1$ kOe, after which λ increases with H almost linearly.

The decrease in λ at the high wheel speed of 40 or 50 m/s may be related to the presence of an amorphous phase. It is reported that the λ_s value of amorphous $DyFe_2$ is very low (38 ppm),[3] which is much lower than the value of 433 ppm at 25 kOe for the crystalline counterpart[3] as well as that of the present melt-spun ribbons fabricated at the optimum condition. It is therefore quite likely that λ decreases significantly by the formation of an amorphous phase. An amorphous phase can also be formed at the high wheel speed for the $Dy_{0.25}(Fe_{1-y}B_y)_{0.75}$ alloy system; however, since the main crystalline phase in $Dy_{0.25}(Fe_{1-y}B_y)_{0.75}$ is mainly $DyFe_3$ or a mixture of $DyFe_3$ and $DyFe_2$ (except for the high-B alloy where mainly $DyFe_2$ phase exists), as was already discussed, and the λ_s value of amorphous $DyFe_3$ is reported to be high (130 ppm),[5] which is similar to that for the ribbons fabricated

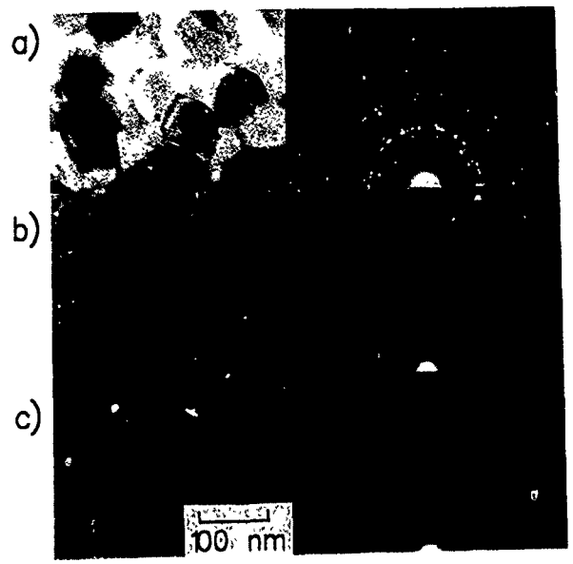

FIG. 3. Transmission electron micrographs (the bright-field images) and selected-area-diffraction patterns for the alloy $Dy_{0.3}(Fe_{0.8}B_{0.2})_{0.7}$ at the wheel speeds of (a) 10 m/s, (b) 30 m/s, and (c) 50 m/s.

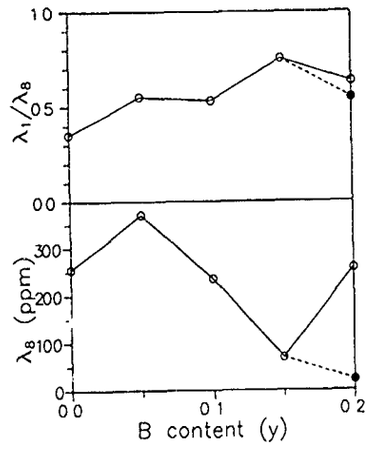

FIG. 4. The values of λ_1/λ_8 and λ_8 (where λ_1 and λ_8 are the values of λ at 1 and 8 kOe, respectively) as a function of the B content y in the alloy system $Dy_{0.3}(Fe_{1-y}B_y)_{0.7}$. The data with the open circles are for the wheel speeds which yielded the largest λ_1 (40 m/s for the alloys $y \leq 0.15$ and 30 m/s for the alloy $y=0.2$). In the $y=0.2$ alloy, the results at the wheel speed of 40 m/s are also shown and are indicated by the solid circles.

at the optimum wheel speed, the presence of an amorphous phase will not greatly affect the λ value. The assumption that the decrease in λ at the high wheel speed is related to the amorphous phase is supported by the present x-ray results, since amorphouslike patterns appear to be seen together with crystalline peaks at the high wheel speed. Amorphouslike patterns become clearer as the B content increases.

In order to examine the microstructure further, TEM experiments were conducted and some of the results are shown in Fig. 3 for the $Dy_{0.3}(Fe_{0.8}B_{0.2})_{0.7}$ alloy. From the TEM results, two important points can be noted: First, an amorphous phase is observed by TEM, as is evidenced by the halo pattern at the wheel speed of 50 m/s; second, the more important point is that, at the wheel speed of 30 m/s, homogeneous and ultrafine crystalline grains are formed. The grain size is estimated to be 10–20 nm. This is the first observation of homogeneous and ultrafine grains, to our knowledge, in the as-spun state, although similar ultrafine grains were previously observed for the Tb-Fe-B alloy system by annealing precursor amorphous alloy ribbons.[8]

In order to see how the magnetic softness and the value of λ vary with the B content, the results for λ_1/λ_8 (where λ_1 and λ_8 are the values of λ at 1 and 8 kOe, respectively) and λ_8 as a function of the B content are shown in Fig. 4 for the $Dy_{0.3}(Fe_{1-y}B_y)_{0.7}$ alloy system. The ratio λ_1/λ_8 is used to measure the degree of magnetic softness. For each B content, we plot data for that wheel speed which yielded the highest strain at 1 kOe (largest λ_1), which was obtained at the wheel speed of 40 m/s for the alloys with the composition $y \leq 0.15$ and the wheel speed of 30 m/s for the $y=0.2$ alloy. In the $y=0.2$ alloy, the results at the wheel speed of 40 m/s are also shown in the figure in order to compare the results for the ribbons fabricated at the same wheel speed. The reason for the highest λ_1/λ_8 ratio at $y=0.15$ is related to the presence of a magnetically soft amorphous phase. The high ratio, however, is achieved at the cost of very low λ_8 value. With the same reasoning, the λ_1/λ_8 ratio of the $y=0.2$ alloy at the wheel speed of 40 m/s is expected to be large but it is observed to be small. This is because the value of λ itself is so low that the contribution from the volume magnetostriction after saturation becomes appreciable, even though the value of volume magnetostriction (which is usually indicated by the slope $d\lambda/dH$ after the saturation) is similar to each other. The ribbon having the ultrafine grain structure ($y=0.2$) exhibits good magnetostrictive properties; good magnetic softness ($\lambda_1/\lambda_8=0.66$) and a high strain ($\lambda_8=260$ ppm).

IV. CONCLUSION

In conclusion, λ-H behavior of the melt-spun ribbons of Dy-Fe-B alloys is investigated as a function of the wheel speed and alloy composition. The homogeneous and ultrafine grain structure is observed for the first time even in the as-spun state when the ribbons of the alloy $Dy_{0.3}(Fe_{0.8}B_{0.2})_{0.7}$ are fabricated at the wheel speed of 30 m/s. The ribbons having the ultrafine grain structure are observed to exhibit good magnetostrictive properties.

[1] N. C. Koon, A. Schindler, and F. Carter, Phys. Lett. A **37**, 413 (1971).
[2] A. E. Clark and H. Belson, Phys. Rev. B **5**, 3642 (1972).
[3] A. E. Clark, in *Ferromagnetic Materials*, edited by E. P. Wohlfarth (North-Holland, Amsterdam, 1980), Vol. 1, p. 531.
[4] A. E. Clark, in *Proceedings of the 19th Conference on Magnetism and Magnetic Materials*, AIP Conf. Proc. No. 18 (American Institute of Physics, New York, 1974), p. 1015.
[5] S. Ishio and S. Kadowaki, J. Magn. Magn. Mater. **79**, 358 (1989).
[6] R. D. Greenough, T. J. Gregory, S. J. Clegg, and J. H. Purdy, J. Appl. Phys. **70**, 6534 (1991).
[7] S. Kikuchi, T. Tanaka, S. Sugimoto, M. Okada, M. Homma, and K. Arai, J. Magn. Soc. Jpn. **17**, 267 (1993).
[8] T. Ooike, S. Ishio, and T. Miyazaki, J. Magn. Soc. Jpn. **17**, 271 (1993).
[9] H. Fujimori, J. Y. Kim, S. Suzuki, H. Morita, and N. Kataoka, J. Magn. Magn. Mater. **124**, 115 (1993).
[10] J. Y. Kim, J. Appl. Phys. **74**, 2701 (1993).

Magnetic properties and magnetostriction in grain-oriented $(Tb_xDy_{1-x})(Fe_{1-y}Mn_y)_{1.95}$ compounds

T. Kobayashi, I. Sasaki, T. Funayama, and M. Sahashi
R&D Center, Toshiba Corporation, 1 Komukai, Toshiba-cho, Saiwai-ku, Kawasaki-210, Japan

The magnetic properties and magnetostriction in grain-oriented $(Tb_xDy_{1-x})(Fe_{1-y}Mn_y)_{1.95}$ compounds with $0.3 \leq x \leq 0.5$, $0 \leq y \leq 0.2$ prepared by the Bridgman method have been investigated. It is confirmed that the Mn substitution not only lowers the spin reorientation temperature but also enhances $\lambda\langle 100\rangle$. This large $\lambda\langle 100\rangle$ is contradictory to the single-ion model. For $Tb_{0.5}Dy_{0.5}(Fe_{0.9}Mn_{0.1})_{1.95}$ compound, no spin reorientation, which induces the sharp drop in the magnetostriction is seen in the temperature range from 77 to 400 K. In addition, by choosing the appropriate compressive stress, the quite excellent thermal stability and the large magnetostriction of 2000 ppm in the low applied field can be realized in the $Tb_{0.5}Dy_{0.5}(Fe_{0.9}Mn_{0.1})_{1.95}$ compound. These features make $Tb_{0.5}Dy_{0.5}(Fe_{0.9}Mn_{0.1})_{1.95}$ a promising material applicable to the various giant magnetostrictive actuators.

I. INTRODUCTION

The Laves phase compounds, rare earth with iron (RFe_2), are well known for their giant magnetostriction. In the pseudobinary compounds, $Tb_xDy_{1-x}Fe_2$, the spin reorientation takes place at a specific temperature. For $Tb_{0.27}Dy_{0.73}Fe_2$, the spin reorientation takes place near room temperature. In the compounds with cubic symmetry, the easy magnetization direction lies along the crystallographic axis $\langle 111\rangle$ at higher temperature, while $\langle 100\rangle$ is the easy magnetization direction at lower temperature.[1,2] Because the magnetostriction constant along $\langle 111\rangle$, $\lambda\langle 111\rangle$, is much larger than that along $\langle 100\rangle$, $\lambda\langle 100\rangle$, a large change in magnetostriction occurs around the spin-reorientation temperature.

On the other hand, the Mn substitution for Fe in $(TbDy)Fe_2$ enhances its magnetostriction at room temperature and also lowers its spin-reorientation temperature by changing the magnetocrystalline anisotropy.[3] Furthermore, the Mn-containing compound has the larger magnetostriction constant $\lambda\langle 100\rangle$ than the Mn free compounds;[4] however, the detailed behavior of the magnetostriction and the related phenomena is still ambiguous due to the lack of data obtained from the single crystals. The purpose of this article is to investigate the magnetocrystalline anisotropy and magnetostriction based on the data obtained from the $(TbDy)(FeMn)_2$ single-crystal samples and to discuss the spin-reorientation phenomena and the related magnetostriction behaviors.

II. EXPERIMENT

$Tb_xDy_{1-x}(Fe_{1-y}Mn_y)_{1.95}$ samples with $0.3 \leq x \leq 0.5$, $0 \leq y \leq 0.2$ were prepared by the Bridgman method. In preparing samples, a h-BN crucible was used. The solidification rate was 29 mm/h. The samples were heat treated in vacuum at 950 °C for 5 h. The crystallographical direction of the samples was determined by the Laue method. The metallographic observation were carried out by the scanning electron microscope (SEM).

The torque measurements were carried out in the temperature range from 77 to 400 K, using a torque magnetometer. The magnetic field was applied up to 1.7 T. The (110) plane, which contains all of the principal crystallographic axis, was chosen for the torque measurements. The magnetostriction along the $\langle 111\rangle$ and $\langle 100\rangle$ crystallographic direction was measured by a standard strain gauge technique, using $\phi 3 \times 0.5$ mm (disk) and $\phi 6 \times 10$ mm (cylindrical rod). The cylindrical samples were provided for the magnetostriction measurements under static compressive stress from 0.8 to 20.2 MPa with the applied field up to 0.4 T. Magnetostriction along the $\langle 111\rangle$ and $\langle 100\rangle$ without the compressive stress were measured with the applied field up to 1.7 T, using the disk samples.

III. RESULTS AND DISCUSSIONS

The metallographic observation by SEM shows that the samples prepared by the Bridgman method have regular platelet microstructures. Their crystallographic $\langle 111\rangle$ axis tilt about 10°–20° from their rod axis. The prepared samples have enough qualities for the torque measurements with one exception. In the Mn-free and high-Tb-content case of $Tb_{0.5}Dy_{0.5}Fe_2$, a planar dendrite microstructure is partially observed and the crystallographic direction deviates part by part in the prepared sample, while $Tb_{0.5}Dy_{0.5}(Fe_{0.9}Mn_{0.1})_{1.95}$ dose not show such a disorder. This suggests that the Mn substitution modifies the phase diagram and leads to the change in the solidification process and the microstructure of the sample, particularly in the high-Tb-content region. Figure 1 shows the temperature dependencies of the magnetostrictions at 0.1 T for the Mn-containing and Mn-free polycrystal materials.[5] In the figure the magnetostrictions are normalized by their room-temperature values. For $Tb_{0.3}Dy_{0.7}Fe_{1.93}$ and $Tb_{0.3}Dy_{0.7}(Fe_{0.8}Mn_{0.2})_{1.93}$, sharp magnetostriction drops can be seen around the spin-reorientation temperature, where the easy magnetization direction changes from $\langle 111\rangle$ to $\langle 100\rangle$; but, it starts at 300 K for $Tb_{0.3}Dy_{0.7}Fe_{1.93}$ while it starts at 220 K for $Tb_{0.3}Dy_{0.7}(Fe_{0.8}Mn_{0.2})_{1.93}$. So, the Mn substitution for Fe lowers the spin-reorientation temperature. It is also noted that the magnetostriction of $Tb_{0.3}Dy_{0.7}(Fe_{0.8}Mn_{0.2})_{1.93}$ in the lower-temperature region is larger than that of $Tb_{0.3}Dy_{0.7}Fe_{1.93}$. For the high-Tb-content $Tb_{0.5}Dy_{0.5}(Fe_{0.9}Mn_{0.1})_{1.93}$, such a magnetostriction drop is never seen in the temperature range from 77 to 400 K.

 0021-8979/94/76(10)/7024/3/$6.00 © 1994 American Institute of Physics

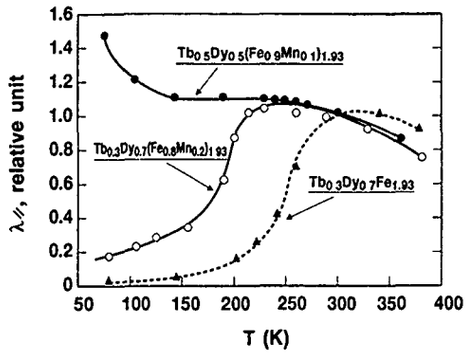

FIG. 1. Temperature dependences of the magnetostriction at 0.1 T for the Mn-containing and Mn-free polycrystal materials.

Figure 2 shows the temperature dependence of the free-energy difference between the magnetization along the ⟨111⟩ axis and that along ⟨100⟩ axis for $Tb_xDy_{1-x}(Fe_{0.9}Mn_{0.1})_{1.95}$ with $x=0.3$, 0.4 and 0.5. With decreasing temperature the energy difference increases at first and then it decreases. Its minimum corresponds to the spin-reorientation temperature. From this result we can confirm that the increase of the Tb content decreases the spin-reorientation temperature and that the spin reorientation does not take place in the temperature range from 77 to 400 K for $Tb_{0.5}Dy_{0.5}(Fe_{0.9}Mn_{0.1})_{1.95}$. Figure 3 shows the temperature dependence of the magnetostriction λ⟨111⟩ and λ⟨100⟩ for $Tb_{0.4}Dy_{0.6}Fe_{1.95}$ and $Tb_{0.4}Dy_{0.6}(Fe_{0.8}Mn_{0.2})_{1.95}$. The temperature is normalized by the Curie temperature T_c. In Fig. 3(a) the magnetostriction λ⟨111⟩ of both $Tb_{0.4}Dy_{0.6}Fe_{1.95}$ and $Tb_{0.4}Dy_{0.6}(Fe_{0.8}Mn_{0.2})_{1.95}$ behaves in almost the same manner. The drop of magnetostriction of both samples takes place around $T/T_c=0.2$ under the applied magnetic field of 0.2 T; however, the behavior of the λ⟨100⟩ is quite different. As can be seen in Fig. 3(b), λ⟨100⟩ of $Tb_{0.4}Dy_{0.6}Fe_{1.95}$ shows little temperature dependence although a little jump of the λ⟨100⟩ is seen around $T/T_c=0.2$ due to the change in the easy magnetization direction from ⟨111⟩ to ⟨100⟩. This indicates that the intrinsic magnetostriction along ⟨100⟩ axis is small for $Tb_{0.4}Dy_{0.6}Fe_{1.95}$. To the contrary the jump of the λ⟨100⟩ is

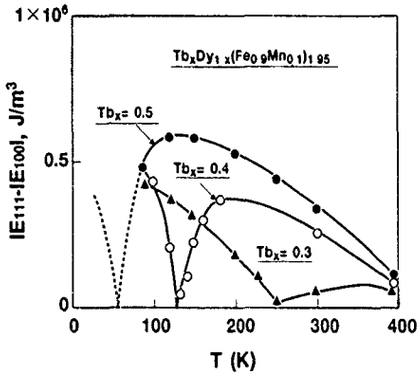

FIG. 2. Temperature dependence of the free-energy difference between the magnetization along ⟨111⟩ axis and that along ⟨100⟩ axis for $Tb_xDy_{1-x}(Fe_{0.9}Mn_{0.1})_{1.95}$ with $x=0.3$, 0.4 and 0.5.

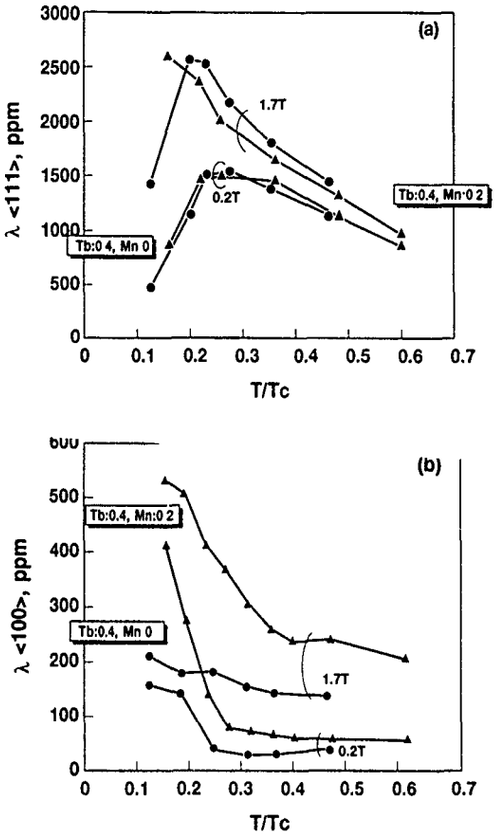

FIG 3. Temperature dependence of the magnetostriction λ⟨111⟩ and λ⟨100⟩ for $Tb_{0.4}Dy_{0.6}Fe_{1.95}$ and $Tb_{0.4}Dy_{0.6}(Fe_{0.8}Mn_{0.2})_{1.95}$: (a) λ⟨111⟩ and (b) λ⟨100⟩.

very large for $Tb_{0.4}Dy_{0.6}(Fe_{0.8}Mn_{0.2})_{1.95}$. Its λ⟨100⟩ reaches 500 or 600 ppm in the low-temperature region. This result suggests that the intrinsic magnetostriction along ⟨100⟩ axis is very large for $Tb_{0.4}Dy_{0.6}(Fe_{0.8}Mn_{0.2})_{1.95}$ and that the enhancement of λ⟨100⟩ results from the Mn substitution. The single-ion model proposed by Cullen and Clark[6] predicts the small λ⟨100⟩ by neglecting the transition-metal contributions. This is confirmed to be true for the Mn-free samples in our experiments, but the Mn-containing case is contradictory. This result suggests the importance of constructing a model to include the transition-metal contributions for explaining the behavior of the giant magnetostrictive materials properly.

Figure 4 shows the temperature dependence of λ⟨111⟩ at 1360 kA/m (17 kO) for $Tb_{0.3}Dy_{0.7}Fe_{1.95}$ and $Tb_{0.5}Dy_{0.5}(Fe_{0.9}Mn_{0.1})_{1.95}$. As the easy magnetization direction changes from ⟨111⟩ to ⟨100⟩, λ⟨111⟩ of $Tb_{0.3}Dy_{0.7}Fe_{1.95}$ decreases with decreasing temperature. On the other hand, λ⟨111⟩ of $Tb_{0.5}Dy_{0.5}(Fe_{0.9}Mn_{0.1})_{1.95}$ monotonically increases with decreasing temperature owing to the spin-reorientation-free characteristics. Its λ⟨111⟩ is 1500 ppm at the room temperature and reaches as high as 3250 ppm at 77 K. The high λ⟨111⟩ value and the spin-reorientation-free characteristics leading to the high thermal stability are very desirable for the applications of this giant magnetostrictive material.

Figure 5 shows the magnetostriction under the compressive stress of 0.8, 8.3, and 20.2 MPa as a function of the applied field for $Tb_{0.5}Dy_{0.5}(Fe_{0.9}Mn_{0.1})_{1.95}$. Under the compressive stress of 0.8 MPa, $\Delta l/l\langle 111\rangle$ is 1200 ppm at the

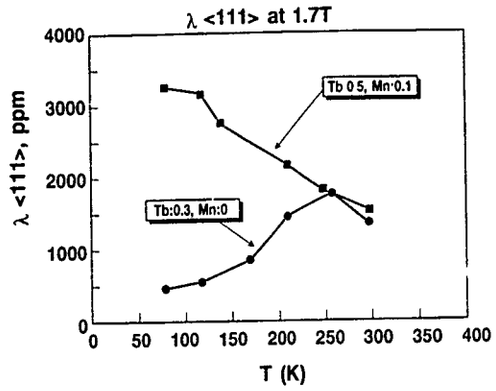

FIG. 4 Temperature dependence of λ⟨111⟩ at 1.7 T for $Tb_{0.3}Dy_{0.7}Fe_{1.95}$ and $Tb_{0.5}Dy_{0.5}(Fe_{0.9}Mn_{0.1})_{1.95}$.

room temperature [Fig. 5(a)]. When the compressive stress is increased to 8.3 MPa, $\Delta l/l\langle 111\rangle$ reaches to 2000 ppm even in the low-magnetic-field region. At 77 K [Fig. 5(b)], λ⟨111⟩ becomes as large as 1700 ppm under the compressive stress of 0.8 MPa; however, the $\Delta l/l\langle 111\rangle$ versus the applied field curve changes little under the compressive stress of 8.3 MPa compared to that at the room temperature. Therefore, by choosing the appropriate compressive stress the very good thermal stability of the magnetostriction can be obtained in $Tb_{0.5}Dy_{0.5}(Fe_{0.9}Mn_{0.1})_{1.95}$. The thermal stability as well as the large magnetostriction in the low applied field region makes $Tb_{0.5}Dy_{0.5}(Fe_{0.9}Mn_{0.1})_{1.95}$ a promising candidate applicable to the various giant magnetostrictive actuators.

In this connection, the hysteresis in the magnetostriction curve of $Tb_{0.5}Dy_{0.5}(Fe_{0.9}Mn_{0.1})_{1.95}$ is a little larger than that of $Tb_{0.3}Dy_{0.7}Fe_2$.[7] This is probably due to its higher Tb content which increases the magnetocrystalline anisotropy. So, this feature should be taken into consideration when designing the actuators.

IV. CONCLUSION

Based on the data obtained from the single-crystal measurements, it is confirmed that the Mn substitution does not only lowers the spin-reorientation temperature but also enhances λ⟨100⟩. This large λ⟨100⟩ is contradictory to the single-ion model.

$Tb_{0.5}Dy_{0.5}(Fe_{0.9}Mn_{0.1})_{1.95}$ compound has no spin-reorientation temperature in the temperature range from 77 to 400 K. In addition, by choosing the appropriate compressive stress, the quite excellent thermal stability and the large

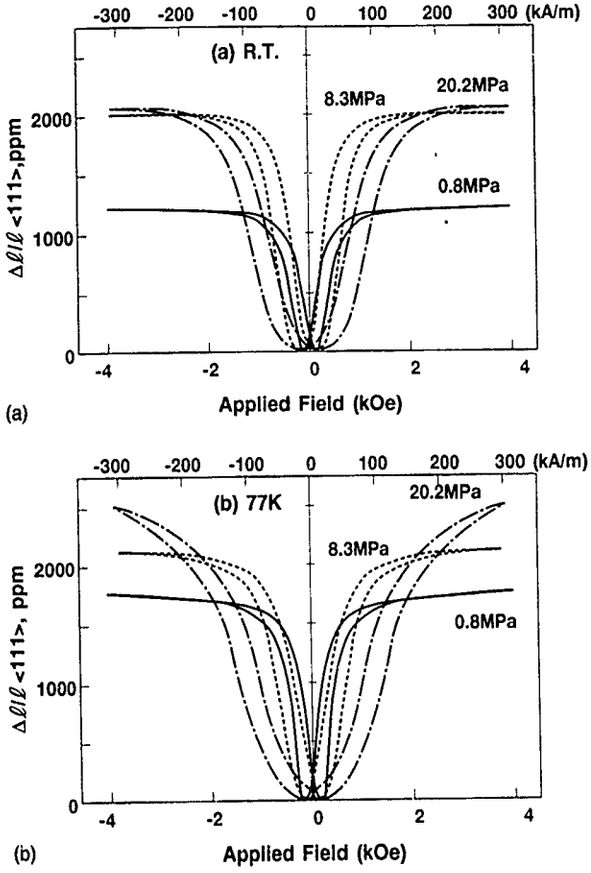

FIG. 5. Magnetostriction under the compressive stress of 0.8, 8.3, and 20.2 MPa as a function of the applied field for $Tb_{0.5}Dy_{0.5}(Fe_{0.9}Mn_{0.1})_{1.95}$ at (a) room temperature and (b) at 77 K.

magnetostriction of 2000 ppm in the low applied field can be realized in the $Tb_{0.5}Dy_{0.5}(Fe_{0.9}Mn_{0.1})_{1.95}$ compound. These features make $Tb_{0.5}Dy_{0.5}(Fe_{0.9}Mn_{0.1})_{1.95}$ a promising material applicable to the various giant magnetostrictive actuators.

[1] A. E. Clark, in *Ferromagnetic Materials*, edited by E. P. Wohlfarth (North-Holland, Amsterdam, 1980).
[2] A. E. Clark, J. P. Teter, and M. Wun-Fogle, J. Appl. Phys. **69**, 5771 (1991).
[3] M. Sahashi, T. Kobayashi, and T. Funayama, in Proceedings of 10th Workshop on Rare-Earth Magnets and their Applications, Kyoto, 1989, p. 347.
[4] T. Funayama, I. Sakai, T. Kobayashi, and M. Sahashi, Appl. Phys. Lett. **6**, 115 (1992).
[5] T. Kobayashi, I. Sakai, T. Funayama, and M. Sahashi, in Proceedings of the International Symposium on Giant Magnetostrictive Materials and their Applications, Tokyo, 1992, p. 163.
[6] J. R. Cullen and A. E. Clark, Phys. Rev. B **15**, 4510 (1977).
[7] J. P. Teter, A. E. Clark, M. Wun-Fogule, and O. D. McMasters, IEEE Trans. Magn. **MAG-26**, 1748 (1990).

Stress effect on the magnetization of Dy in the Dy/$DyFe_2$ eutectic

J. P. Teter, S. F. Cheng, and J. R. Cullen
NSWC-White Oak, Silver Sring, Maryland 20903-5640

The magnetization of the alloy $DyFe_{1.5}$ was studied as a function of temperature from 50 to 300 K in a range of magnetic field up to 10 kOe. Metallographic studies showed the existence of a eutectic phase containing both $DyFe_2$ and elemental Dy embedded in the $DyFe_2$ matrix. The presence of elemental Dy was observed in the magnetization data through a cusp in the temperature dependence of the magnetization at 178 K and an increase of the magnetization starting at 130 K and continuing to 80 K. While the first feature occurs at precisely the Néel temperature of bulk Dy, the second contrasts with the jump at the Curie temperature of 89 K observed in low fields in bulk single-crystal Dy. The more gradual increase in magnetization observed in the $DyFe_{1.5}$ alloy is attributed to variations in stress to which the Dy is subjected. The temperature dependence of the magnetic moment from 80 to 130 K is modeled as arising from a collection of Dy particles of varying Curie temperatures. This variation is in turn caused by the stress distribution. Curie temperature distributions are found for a range of magnetic fields and then are extrapolated to zero field in order to eliminate the effect of field. The calculations indicate that a significant amount of the Dy remains in the helimagnetic phase down to zero temperature.

I. BACKGROUND

Dy metal, which forms in the hexagonal close-packed structure, undergoes a transition from a paramagnetic to a helical phase at a temperature T_N=179 K. Below T_N, the magnetic moment spirals in the basal plane, with the propagation vector parallel to the c axis. The pitch angle of the spiral varies from 43.2° just below T_N to 26.5° at the transition temperature to ferromagnetism T_C. T_C is magnetic-field (H) dependent; it is equal to 89 K in zero field and rises to T_N at 10 kOe, completely erasing the helical phase at that field. At T_C, the magnetic moment is observed to abruptly increase. The jump in moment depends on the value of T_C; it decreases from a maximum of 300 emu/g at 89 K to zero at T_N.[1] T_C has also been observed to be stress dependent. Compressive stress applied in the basal plane of a single crystal of Dy increased T_C at a rate of 10 K/kbar.[2] In recent experiments on epitaxially grown Dy,[3] T_C increased with basal-plane compression at the same rate as was observed in the earlier stress measurements. On the other hand, T_C decreased more rapidly for Dy grown on increasingly expanded substrates,[4] so that the ferromagnetic state disappeared completely when the lattice-mismatch strain exceeded 10^{-3}, equivalent to a tensile stress of the order of 0.1 kbar.[4] This sensitivity to stress should manifest itself in materials in which elemental Dy is present in a disordered manner such as polycrystalline samples or as part of a multiphase material. Here we report our results of magnetic studies of $DyFe_{1.5}$, an alloy consisting of Laves-phase $DyFe_2$ and a eutectic phase containing both $DyFe_2$ and elemental Dy. An optical picture of the grain-boundary area of a polished sample is shown in Fig. 1. The central region shows the admixture of Dy and $DyFe_2$ surrounded by large crystals of primary $DyFe_2$ with random orientations. We interpret the temperature dependence of our magnetic moment measurements in terms of a model in which the Dy is assumed to exist in the eutectic as a randomly oriented set of particles of varying shapes, thereby subjected to stress of random strength, orientation, and sign. Guided by the results of Ref. 2–4, we expect that those particles which find themselves under a net basal-plane compression (or a c-axis tension) will display an enhanced T_C, and visa versa; however, other types of stresses are present in $DyFe_{1.5}$ and some of those will also change T_C. The magnetic moment data of themselves are not capable of distinguishing between the stress components; we extract only a probability per unit temperature that a particle will undergo a transition from the helimagnetic to the ferromagnetic phase at a given temperature. In the following, we briefly describe the experimental details. We then discuss the model and apply it to determine the probability distributions at zero field. In order to accomplish this, we extrapolate the distributions obtained at fields of 3, 2, 1, and 0.5 kOe to zero field.

II. MAGNETIZATION MEASUREMENTS

The magnetic moment of several disk-shaped samples with 0.5 cm diameter and 0.03 cm thickness cut from a rod

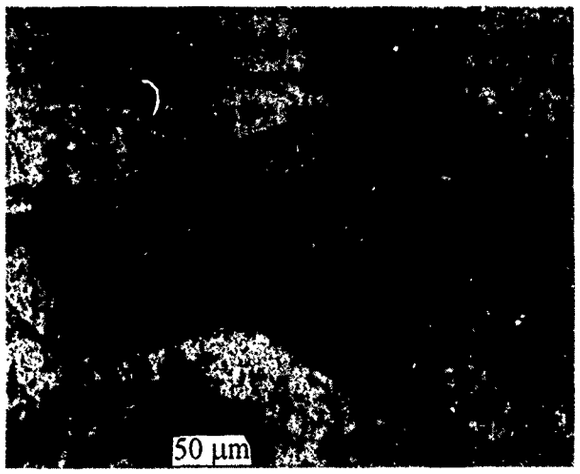

FIG 1. Optical photograph of $DyFe_{1.5}$. Surface was polished to $\frac{1}{4}$ μm The dark central region consists of elemental Dy intermixed with lighter colored $DyFe_2$ crystals. The outer region consists of the primary $DyFe_2$ phase with random crystallographic orientations.

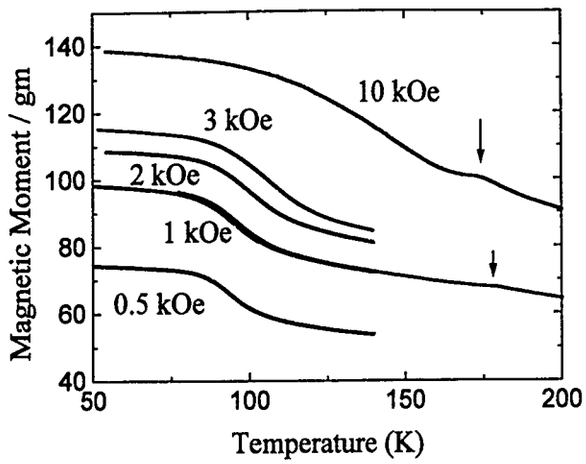

FIG. 2. Magnetic moment per gram of $DyFe_{1.5}$ vs temperature from 50 to 140 K or to 200 K. Each curve was taken at a constant applied magnetic field in the plane of the sample. Magnetic-field strengths were 10, 3, 2, 1, and 0.5 kOe (top to bottom). The arrows mark the onset of the helimagnetic phase at 10 and 1 kOe. The 1 kOe helimagnetic transition is at 178.5(±1) K.

of $DyFe_{1.5}$ was determined as a function of temperature T. The measurements were made as the samples were heated from 50 to 300 K. The moment was also measured as the temperature was held fixed at 50, 77, 256, and 300 K and H was swept between ±10 kOe. All measurements were made with the field in the plane of the disk. Plots of magnetic moment per gram versus T for $H=0.5$, 1, 2, 3, and 10 kOe are shown in Fig. 2. The onset of the Dy helimagnetic phase at $T=T_N$ is evident in all the data sets collected; shown are the 1 and 10 kOe plots in which it appears as a cusp at 178 K for $H=1$ kOe, the Néel temperature of bulk Dy. We interpret the rise in moment at lower T, progressively sharper as H decreases, as the onset of ferromagnetic order in Dy in the eutectic. The decrease in moment at 0.5 kOe results from the increase in the anisotropy of $DyFe_2$, which prevents its moment from saturating at low fields. We have observed an orientation dependence of the magnetization of our samples with respect to the direction of H, indicating the presence of texture. The maximum difference in moment is roughly 10% of the average moment. We therefore regard this as a small deviation from isotropy, and neglect texture in what follows.

III. DISCUSSION

Taking the $DyFe_{1.5}$ alloy as composed of elemental Dy and $DyFe_2$, we estimate that the Dy phase comprises 16.5% of the sample weight. The $T=0$ K saturation moment, using 350 and 140 emu/g as the moment, respectively, of Dy and $DyFe_2$,[5] is calculated to be 175 emu/g. To determine the theoretical remanent moment, we have assumed that the Dy moments all lie in the basal plane, while those of $DyFe_2$ all lie in ⟨100⟩ directions at remanence (see Table I). The value is then estimated to be 142.6 emu/g in comparison to 145 emu/g experimentally determined by extrapolating the 10 kOe curve of Fig. 2 to 0 K. The close agreement between these two values makes plausible the model of magnetically independent randomly oriented particles or crystallites of Dy

TABLE I. Remanent moments of polycrystals as a fraction of saturation moment.

Easy axis	Remanence	Crystal structure
[100][a]	0.831	cubic
[111]	0.866	cubic
$a(b)$	0.750	hexagonal
c	0.500	hexagonal
(a,b) plane[a]	0.785	hexagonal

[a]The cases assumed for calculating the remanent moments.

and $DyFe_2$. We now attempt to understand the temperature dependence of the moment for temperatures below the Néel point as follows. The random orientation and position of the Dy crystals in the eutectic places them under a distribution of stress which raises T_C for some, while reducing that of others. The probability that a given crystallite will undergo a spiral to ferromagnetic transition can be simply related to the temperature derivative of the moment. To do this, we imagine that, at a certain T and H a crystallite whose T_C is greater than T will have achieved the bulk moment consistent with that T and H. Thus, the moment per gram is

$$\sigma(T)\cong\Delta\sigma\int_0^{T_N} dT_C S(T-T_C)f(T_C)+\sigma_b, \tag{1}$$

where $S(T-T_C)=1$, $T-T_C\leq 0$; $S(T-T_C)=0$, $T-T_C>0$; and $f(T_C)dT_C$ is the probability of finding a Dy particle with that T_C in the range dT_C. $\Delta\sigma$ is the jump in the single-crystal moment. Then,

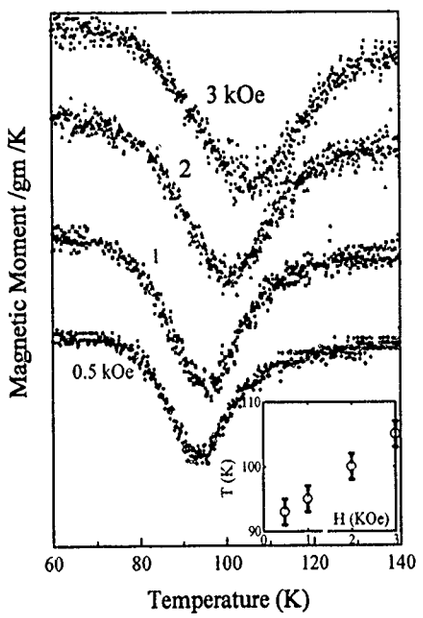

FIG. 3. Composite graph of the temperature derivative of the magnetic moment per gram of $DyFe_{1.5}$ at applied magnetic fields of 3, 2, 1, and 0.5 kOe (top to bottom). The vertical scale is shifted for each set of data. The 0.5 kOe curve was integrated from $T=0$ to $T=125$ K. The zero-derivative line in this case lies above the curve at low T, but decreases with increasing T, meeting the data at $T=125$ K. Each curve starts at near zero slope and minimizes at -0.7 magnetic moment/g/K. The inset is a plot of the estimated temperature minimum for each case, vs applied field.

$$\frac{d\sigma}{dT} = -\Delta\sigma f(T), \tag{2}$$

where we drop possible contributions to the derivative from the temperature dependence of $\Delta\sigma$ or σ_b, the background moment, the latter coming mainly from that of $DyFe_2$.

Plots of $d\sigma/dT$ taken from the moment measured on the disk at $H=0.5$, 1, 2, and 3 kOe are shown in Fig. 3. According to Eq. (2), they are proportional to $f(T)$, at the stated H. Ideally, to uncover the effects of stress alone on the Dy particles we need to eliminate the field effect entirely, and have $d\sigma/dT$ at $H=0$. Since the shapes of the curves in Fig. 3 do not change once H is <1 kOe, we take the 0.5 kOe curve as representative, except for an overall downward shift of 2 K, of $f(T)$. Using the single-crystal value of $\Delta\sigma$ times the weight percent of Dy in $DyFe_{1.5}$ (47.1 emu/g), and integrating the 0.5 kOe curve of Fig. 3 from 80 to 125 K, we obtain 0.25 as the probability of finding a particle with its T_C in that range of T. Since it is unlikely to find particles with higher T_C (T_C=130 K would require a compressive stress of 4 kbar) we conclude that 75% of the Dy particles have $T_C<80$ K. An estimate of the area under the same curve from 0 to 80 K gives another 25% of the particles in this range of T. Thus the remaining 50% of the Dy particles are in the helimagnetic phase, at all $T<T_N$.

IV. SUMMARY

We have discussed the temperature dependence of the magnetic moment of $DyFe_{1.5}$ below the Néel point as mainly due to a collection of Dy particles in the eutectic subjected to stresses which vary from particle to particle. The effect of the distribution of the stress is to spread the ferro- to helimagnetic transition over a range of temperatures. Our analysis of the data in terms of the model described above leads us to conclude that a significant number of the particles remain helimagnetic down to zero temperature. This accords with the result of measurements on epitaxial Dy, that basal-plane extensions of the order of 10^{-3} are sufficient to suppress the ferromagnetic phase. Such strains translate into stresses of 0.1 kbar, which are likely to be present in the $DyFe_{1.5}$ eutectic.

[1] S. Legvold, in *Ferromagnetic Materials*, edited by E P. Wohlfarth (North-Holland, Amsterdam, 1980).

[2] H. Bartholin, J Beille, D. Bloch, P. Boutron, and J. L. Feron, J Appl. Phys. **42**, 1679 (1971).

[3] F. Tsui and C. P. Flynn, Phys. Rev Lett. **71**, 1462 (1993).

[4] M. B. Salamon, S. Sinha, J. J. Rhyne, J E. Cunningham, R. W. Erwin, J. Borchers, and C. P. Flynn, Phys. Rev. Lett. **56**, 259 (1986)

[5] A. E. Clark, in *Ferromagnetic Materials*, edited by E. P. Wohlfarth (North-Holland, Amsterdam, 1980), Chap. 7

Direct measurements of magnetostrictive process in amorphous wires using a scanning tunneling microscope (abstract)

J. L. Costa, J. Nogués, and K. V. Rao
Department of Condensed Matter Physics, The Royal Institute of Technology, S-100 44 Stockholm, Sweden

We demonstrate a new and versatile method to measure, on a nanometric scale directly, the magnetostrictive properties during the magnetization process to saturation, using a modified scanning tunneling microscope (STM). Both positive and negative magnetostrictive amorphous as-quenched wires have been studied. The studied samples are *single* pieces of amorphous wires typically 125 μm in diameter and 10–15 mm long. The magnetostriction data are then correlated with the longitudinal magnetization process, measured by a conventional induction technique and by SQUID magnetometry. The longitudinal magnetization process measurements have been performed in the same wires used in the STM studies. The field dependence of the magnetostriction helps to discern the operative magnetization process in the wires. In a 12-mm-long Co-based amorphous wire we observe a continuous rotation of the magnetization from zero field to saturation. The field dependence of the magnetization is a linear process reaching a value of about 5100 G at 8 Oe applied field. The magnetostrictive process for the same wire measured with a STM shows a continuous shrinking of the samples as a function of the applied field, reaching a value of -2.0 Å for 8 Oe applied field. The obtained $\delta l/l|_{sat}$, -2.3×10^{-6}, agrees well with reported values of the saturation magnetostriction constant for this wire. In a 15-mm-long Fe-based amorphous wire we observe a more complicated field dependence of both the magnetization and the magnetostriction processes from zero-field to saturation. The longitudinal magnetization saturates at about 14000 G for 60 Oe applied field. The magnetostrictive process for the same wire measured with STM shows an elongation onset at about 1 Oe, pointing unambiguously to a 180° domain wall movement as the operative magnetization process below this field value. The field dependence of the magnetostriction saturates at about +5000 Å for 60 Oe applied field. The obtained $\delta l/l|_{sat}$, about $+3.3\times10^{-5}$, is again consistent with reported values of the saturation magnetostriction constant. Thus the STM approach to determine λ, on an Å length scale, gives us a distinct great advantage in studying the magnetization process towards saturation.

 0021-8979/94/76(10)/7030/1/$6.00 © 1994 American Institute of Physics

Tunable bistability from magnetostriction (abstract)

A. S. Arrott and J.-G. Lee
Simon Fraser University, Burnaby, British Columbia V5A 1S6, Canada

When a current passes along the axis of a [100] iron whisker in the presence of a field along the same axis, the magnetization in a central domain points along the field direction while the mangetization in four domains surrounding the central domain circulates about the axis, see Fig. 1. The size of the central domain grows with applied field, which overcomes the effect of the field from the current and the magnetostriction that favor the collapse of the central domain to an irreducible core. Depending on the current, the growth of the central domain can be a continuous or discontinuous process. At certain fields the energy is a double-well function of the size of the central domain, which determines the magnetization. The size of the energy barrier can be made arbitrarily small by suitable choice of the current. It is the ability to adjust the size of the barrier in such a clearly defined system that makes this an attractive experimental approach to understanding the role of fluctuations in magnetization processes. This structure has been verified using measurements of ac susceptibility.

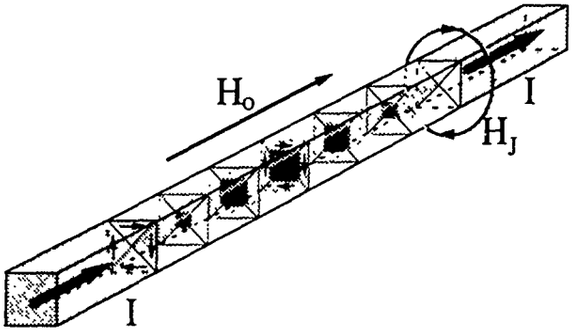

FIG. 1. Domain structure for an iron whisker with current leads (shaded).

 0021-8979/94/76(10)/7031/1/$6.00 © 1994 American Institute of Physics

Influence of Stoner-type excitations on the formation of magnetization and magnetic order in disordered metal-metalloid alloys

A. K. Arzhnikov, L. V. Dobysheva, and E. P. Yelsukov
Physics-Technical Institute, Kirov str. 132, Izhevsk 426001, Russia

The Rhodes–Wolfarth parameter and the ratio $T_c^{1/2}(x)/\bar{m}(x)$ have been analyzed on the basis of experimental data for disordered alloys Fe–Al, Fe–Si, Fe–P (T_c is the Curie temperature, $\bar{m}$ is the average magnetic moment, x is the concentration of non-magnetic impurity). The concentration dependences of these parameters show the possibility of considerable contribution of the Stoner excitations to the magnetic order formation. The analysis of the two-band Hubbard model shows that the Stoner excitations result in the turnover of the local magnetic moment at a certain temperature in the range of high concentration of nonmagnetic atoms.

For a long time the disordered alloys of metal–metalloid type (Fe–Al, Fe–Si, and Fe–P) have been attracting the attention of scientists. This interest is mainly due to the fact that these alloys are a good model object for studying the fundamental regularities of magnetic properties formation in disordered systems. The method of mechanical alloying makes it possible to widen the concentration range of a disordered state in these alloys.[1–5] Regularities of behavior of hyperfine field $\bar{H}$, isomeric shift $\bar{\delta}$, average magnetic moment $\bar{m}$, temperature of magnetic ordering T_c obtained in these papers,[1–5] combined with the data of other authors[6–8] and see references in Ref. 5, give the complete picture of the above characteristics behavior in the whole concentration range of magnetic order existence. Besides, the possibility of comparing the experiments on specimens obtained by different techniques, in particular, in amorphous and crystalline disordered states, has appeared. One can draw the following conclusions for the data available. The concentration dependences of $\bar{H}$, $\bar{\delta}$, $\bar{m}$, and T_c have the same qualitative peculiarities for all the above-mentioned alloys, that is, weak dependence on concentration x in the low concentration range (for Al—$x<30\%$, Si—$x<18\%$, P—$x<12\%$) changes into a sharper dependence in the range of high concentration of metalloid, and the local magnetic moments decrease with increasing the number of nonmagnetic atoms in the nearest environment.[1–4] This indicates that the main principles of magnetic moment formation in these alloys are similar. It is our opinion that the quantitative differences of concentration dependences of the alloys are dictated by different numbers of p electrons of a metalloid atom (Al—$n_p=1$, Si—$n_p=2$, P—$n_p=3$). While comparing the data for the amorphous and crystalline specimens, the conclusion can be made that the influence of topological disordering on the magnetic properties is weak, as compared to that of the compositional one.[5] A variety of models, for instance,[5–8] based on the Jaccarino–Walker model, where the average magnetic moment is defined by $\bar{m}=\Sigma_k P_k m_k$, were proposed for the phenomenological description of concentration dependences of $\bar{H}$, $\bar{\delta}$, and $\bar{m}$ of these alloys. The modification of the Jaccarino–Walker model put forward by one of the authors[1–4] provides a most successful description. This modification includes the interpolation of the dependence of the Fe magnetic moment on the number of nonmagnetic atoms in the nearest environment using the data available for ordered alloys, and the assumption that the probability of a configuration in the middle-concentration region $x_1<x<x_2$ looks like

$$P_k(x)=\sum_{n=0}^{6}\begin{bmatrix}6\\n\end{bmatrix}(1-x_{\rm rel})^{6-n}x_{\rm rel}^{n}\begin{bmatrix}8+n\\k\end{bmatrix}\times\left(1-\frac{x}{100}\right)^{8+n-k}\left(\frac{x}{100}\right)^{k},$$

where $x_{\rm rel}=(x-x_1)/(x_2-x_1)$, $x_1=25$, 15, 7 at. %, $x_2=55$, 33, 20 at. % for Fe–Al, Fe–Si, and Fe–P, respectively.

The justification of the modified Jaccarino–Walker model can be found in detail in Ref. 5. It should be mentioned that the Jaccarino–Walker models are conceptually closer to the localized models, whereas magnetism in Fe is the itinerant one.[9] This contradiction between the localized character of Jaccarino–Walker models and the itinerant magnetism of Fe has been removed after we had analyzed the disordered Hubbard model.[10] In addition, this model for the disordered alloys on the basis of the two-band Hubbard Hamiltonian proposed in Ref. 10 allowed us to explain the main qualitative regularities of the formation of the magnetic moment and isomeric shift of the magnetic atom under different impurities configurations in the ground state.

When analyzing the theoretical results, we have noted that the magnetic moment of magnetic atoms with many nonmagnetic atoms in the environment decreased drastically in magnitude, and the energy distribution of the electrons became flat, due to a strong $s-d$ hybridization. This shows the possibility of the great importance of Stoner excitations, even at low temperatures. In addition, we analyzed the experimental data for Fe–Si[2,11] for the Rhodes–Wolfarth (RW) relation M_c/M_s, where M_s is the saturation magnetic mo-

 0021-8979/94/76(10)/7032/2/$6.00 © 1994 American Institute of Physics

ment per magnetic atom and M_c is the effective moment per magnetic atom defined from the Curie constant, with the assumption of the existence of local moments (see Ref. 12, Chap. 7.1), and found that this parameter changes from 1.4 to 1.8 on changing the nonmagnetic component concentration from 0% to 28%. The large RW parameter testifies that the nature of the alloy magnetism becomes closer to "weak ferromagnetism" at high Si concentration (hereinafter this term means the magnetics with Stoner excitations[9]). Unfortunately, it is, in many cases, impossible to obtain the concentration dependence of the RW parameter because of technical difficulties of measuring the high-temperature Curie constant. In a wider concentration region, the experimental data available allow us to analyze the parameter $T_c^{1/2}(x)/\bar{m}(x)$ [T_c is the Curie temperature, $\bar{m}(x)$ is the magnetization at $T=0$]. As follows from our theoretical investigations of the Heisenberg model with nonmagnetic impurities,[13] such a parameter must decrease as the concentration tends to the percolation threshold. Contrastingly, this parameter in Fe–Al, Fe–Si, and Fe–P increases when the concentration of nonmagnetic impurities increases. As evidenced by all the above experimental estimations, the Stoner excitations may play a significant role in the formation of magnetization in these alloys at high metalloid concentration.

Finally, on the basis of the two-band Hubbard model proposed in Ref. 10, we carried out a theoretical investigation of the behavior of local magnetic moments under given configurations of the nearest environment, depending on the temperature. These calculations have been conducted in the middle-field approximation for the electron–electron interaction. A cluster of the predetermined configuration was placed in the effective medium calculated in the coherent potential approximation. The excitations of Stoner type were taken into account through the Fermi distribution, the self-consistence of the local magnetic moment being achieved at every temperature. As a result, we obtained the following. At low concentrations the influence of Stoner excitations becomes noticeable only at temperatures of $kT/W \simeq 0.2$–0.25 (W is the width of the d band), which corresponds to the usual results for "strong" ferromagnets of the Fe type (see Ref. 9). At concentrations near the critical one, the situation radically alters, and the Stoner excitations result in essential changes of magnetization, even at $kT/W \simeq 0.015$. For instance, at concentrations of the order of 0.6, there exists only one solution in the ground state for the configuration with four nonmagnetic atoms in the nearest environment, with a magnetic moment being opposed to the total magnetization (see Ref. 10). Along with this solution, the second one with a positively directed magnetic moment appears at $kT/W \simeq 0.01$, the energy of it being higher than that of the first solution. At temperature $kT/W \simeq 0.02$ the energies of these two states become equal, and further, when temperature increases the second state becomes preferable in energy. So at these temperatures, the local magnetic moment has to change from negative to positive. That is, the Stoner excitations cause the increase of the average magnetic moment with an elevation of temperature. Such changes of the magnetic moment due to the Stoner excitations can be an alternative to the explanation of the magnetization behavior by the excitations of a spin glass state. It is worth noting that although there is a latent antiferromagnetic ordering of the magnetic moments in our model, it is similar to Mattis' glasses ordering, and not to the spin glasses one.

So, as experimental and theoretical works show, in the range of high concentrations of nonmagnetic impurities in the Fe–Si, Fe–Al, and Fe–P alloys, the band character of the magnetism must fully manifest itself in the temperature dependences, and description of these alloys on the basis of the localized models of Heisenberg and Ising seems to be unjustified.

ACKNOWLEDGMENT

The authors are grateful to the George Soros Foundation for partial financial support.

[1] E. P. Yelsukov, E. V. Voronina, and V. A. Barinov, J. Magn. Magn. Mat. **115**, 271 (1992).
[2] E. P. Elsukov, G. N. Konygin, V. A. Barinov, and E. V. Voronina, J. Phys Condensed Matter **4**, 7597 (1992).
[3] E. P. Elsukov, Yu. N. Vorobev, and A. V. Trubachev, Phys Status Solidi A **127**, 215 (1991).
[4] E. P. Elsukov, Yu. N. Vorobev, T. I. Arbuzova, and I. S. Smolyak, J. Magn Magn. Mat. **130**, 44 (1994).
[5] E. P. Elsukov, Phys. Metals Metall. **76**, 451 (1993).
[6] T. M. Srinivasan, H. Claus, R. Viswanathan, P. A. Beck, and D. I. Bardos, in *Phase Stability in Metals and Alloys,* edited by P. S. Budman, J. Stringer, and R. I. Jaffe (McGraw-Hill, New York, 1967), p. 151.
[7] M. J. Besnus, A. Herr, and A. J. P. Al. Meyer, J. Phys. F: Met. Phys. **5**, 2138 (1975).
[8] V. A. Niculescu, T. J. Burch, and J. I. Budnick, J. Magn. Magn. Mat. **39**, 223 (1983).
[9] T. Moriya, *Spin Fluctuations in Itinerant Electron Magnetism* (Springer, New York, 1987).
[10] A. K. Arzhnikov and L. V. Dobysheva, J. Magn. Magn. Mat. **117**, 87 (1993).
[11] S. Arays, Phys. Status Solidi **11**, 121 (1965).
[12] P. R. Rhodes and E. P. Wolfarth, Proc. R. Soc. **273**, 274 (1963).
[13] A. K. Arzhnikov and A. V. Vedyaev, Theor. Math. Phys. **77**, 440 (1988) (in Russian).

Magnetic susceptibility studies in Gd_2CuO_4 below 300 K

J. Mira, J. Castro, J. Rivas, D. Baldomir, C. Vázquez-Vázquez, J. Mahía, and A. López-Quintela
Universidad de Santiago de Compostela, E-15706, Spain

D. Fiorani
ICMAT-CNR, Roma, Italy

R. Caciuffo and D. Rinaldi
Universita di Ancona, 60131 Ancona, Italy

T. Jones
NR&D, San Diego, California

S. B. Oseroff
San Diego State University, San Diego, California 92182

Measurements of the χ') part of the ac magnetic susceptibility have been performed on two polycrystalline Gd_2CuO_4 samples sintered at different temperatures, 850 °C and 1080 °C in the temperature range $10<T(K)<300$. Two well-defined maxima have been observed in the temperature dependence of χ'. One, located at about 20 K, that is frequency independent. The second is at about 280 K for the sample annealed at 1080 °C, and it is frequency independent. Instead, for the sample annealed at 850 °C the maximum appears at about 210 K, and it is frequency dependent. These results suggest the existence of magnetic domains, with their coherence lengths being a function of the thermal treatment.

I. INTRODUCTION

Rare earth cuprates R_2CuO_4 are characterized by the presence of long-range-order antiferromagnetism (AF) associated with the ordering of the magnetic moments of the Cu^{+2} ions. This AF ordering presents a three-dimensional/two-dimensional (3D/2D) transition at a temperature (T_N) between 250–280 K. The study of the magnetic properties of these compounds has initially led to their classification into two groups:[1] the first one with R=Pr, Nd, Sm, Eu, and the second with R=Gd and heavier rare earths. Both groups crystallize in the tetragonal T' structure, but, in the second group, a distortion of the oxygen in the CuO_2 planes in a direction perpendicular to the Cu–O–Cu bond[2,3] leads to an antisymmetric superexchange interaction that generates a weak ferromagnetic behavior.[4,5] Whereas for the former group superconductivity (SC) is achieved with Th or Ce doping,[6] for the latter superconductivity has not been observed.[7] The exclusion of weak ferromagnetism (WF) and SC has been recognized by several authors.[1]

A subdivision in the second group, revealing differences between Gd_2CuO_4 and the R_2CuO_4 (R=Tb, Dy, Ho, Er, and Tm) obtained at high pressure[8] (PO) has been suggested.[9] A difference is encountered in the temperature dependence of the ac magnetic susceptibility,[9] where Gd_2CuO_4 presents a double peak structure in the real part of the susceptibility at low temperatures, from $T\approx1$–20 K; while for the PO compounds only one peak, associated to the ordering of the R ions, appears in that range. The explanation of this difference has been sought in comparison between the R–R and R–Cu sublattice interactions. Differences have also been reported in the dynamic behavior of these compounds.[10] The mechanism leading to the observed dynamical behavior remains unclear, although spin-glass-like effects have been claimed.[10]

The aim of the present work is to perform a detailed study of the ac magnetic susceptibility of polycrystalline Gd_2CuO_4 in the temperature range $10<T(K)<300$. A comparison with ac magnetic susceptibility measurements of other weak ferromagnets of the R_2CuO_4 series is also presented.

II. EXPERIMENTAL TECHNIQUES

Gd_2O_3 and CuO oxides were used as starting materials for the ceramic synthesis of Gd_2CuO_4. Two methods were used to obtain the samples: (a) Stoichiometric amounts of the starting materials were milled for several hours and thermal treatments at 850 °C, with frequent intermediate millings were subsequently carried out. Around 400 h were required in order to obtain the pure Gd_2CuO_4 phase. We call this sample, sample I. (b) In the second method, the starting materials were sintered at 950 °C for 12 h. The product was milled again and resintered at 1000 °C for 20 h. Finally, it was sintered at 1080 °C for 24 h and slow cooled. The sample thus obtained is called sample II.

The structural characterization of the samples was performed by means of x-ray diffraction using a Philips PW-1710 diffractometer with Cu anode ($CuK_{\alpha1}$ radiation, $\lambda=1.540\,60$ A). The x-ray patterns showed a single phase with the same tetragonal structure for both samples. The analytic characterization was derived using inductively coupled plasma atomic emission spectroscopy (ICP-AES) with Ar plasma ICP (Perkin-Elmer 5000). The dc magnetic measurements were performed using a SQUID magnetometer (Quantum Design) in the $4<T(K)<300$ temperature range. The real and imaginary parts χ' and χ'', of the external complex ac susceptibility were measured during warming from $T=13$–300 K using a system with a concentric assembly consisting of a primary solenoid and two oppositely wound

 0021-8979/94/76(10)/7034/3/$6 00 © 1994 American Institute of Physics

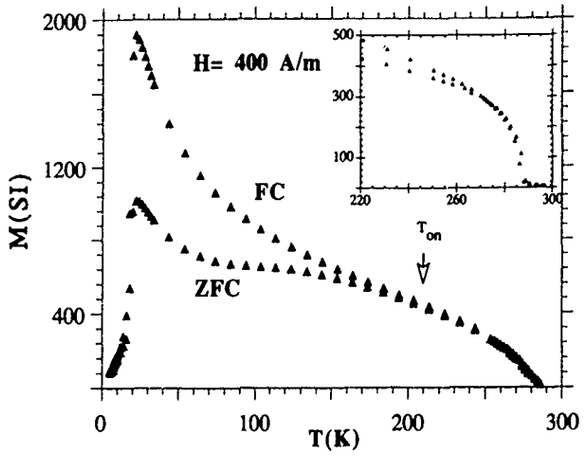

FIG. 1. FC and ZFC dc magnetization of the Gd_2CuO_4 sample I vs temperature, measured with an applied field of H_{appl}=400 A/m. The inset shows the dc magnetization for sample II.

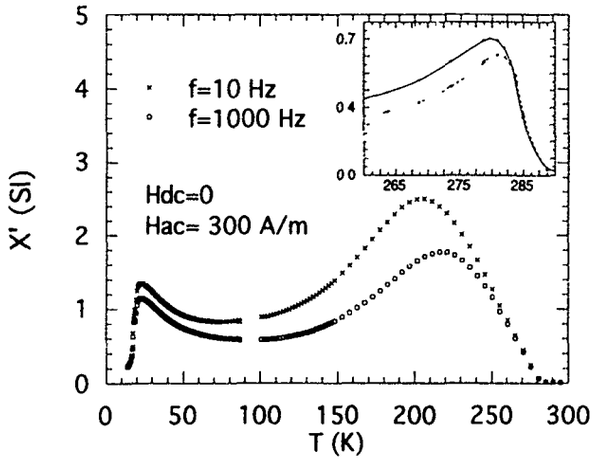

FIG. 2. The real part of the ac susceptibility, χ' of sample I, measured at frequencies of 10 and 1000 Hz in an ac magnetic field of H_{ac}=300 A/m. The inset shows the curve for sample II in the high temperature range.

sensing coils connected in series. A phase-sensitive detector is used to measure the output voltage that is proportional to the sample susceptibility. High sensitivity is obtained by moving the sample between the two sensing coils with high precision. The calibration was performed using a $Gd_2(SO_4)_3 \cdot 8H_20$ standard with the same shape and size as the investigated samples. Demagnetizing effects have been taken into account in the calculation of the internal susceptibility. For each run of measurements, the ac field was applied with a fixed amplitude of H_{ac}=300 A/m and fixed frequencies f, ranging from 5 to 1000 Hz. A dc field, H_{dc} from 0 to 800 A/m, was generated by applying a dc current to the primary coil. The temperature of the samples was controlled with an accuracy of about 0.1 K.

III. EXPERIMENTAL RESULTS

In Fig. 1, we display dc magnetization measurements for both Gd_2CuO_4 samples when they were (a) zero field cooled (ZFC) from 300 to 4 K (H_{cool}<80 A/m), and subsequently measured at increasing temperatures with an applied field, H_{appl}=400 A/m; and (b) field cooled (FC), i.e., measured at an applied field while cooling down from 300 K at $H_{cool}=H_{appl}$=400 A/m. The difference between the ZFC and FC curves indicates the onset of irreversibility for this field at a temperature $T_{irr}\approx$210 K for sample I and $T_{irr}\approx$280 K for sample II.

In Fig. 2, we show the temperature dependence of χ' at two different frequencies. We observe for both samples, two well-defined peaks. For sample I, one peak is centered at $\approx$210 K (T_{M1}) and the other at $\approx$20 K (T_{M2}). The high temperature peak is frequency dependent (it shifts to a higher temperature with an increasing frequency, as shown in Fig. 3). Instead, the low temperature peak is frequency independent. For sample II, the position and behavior of T_{M2} is similar to sample I. But T_{M1} is found at $\approx$280 K, and it is frequency independent.

Figure 4 shows the temperature dependence of χ' for sample I measured at the same ac field (H_{ac}) for different superposed dc fields (H_{dc}). We observe that the amplitude of the 210 K maximum decreases with increasing field and disappears for a dc field of about H_{dc}=800 A/m. The maximum onset temperature ($\approx$280 K) and the position of the maximum remains constant. For the 20 K peak, the dependence on the dc field is much weaker. It shifts slightly toward lower temperatures and decreases in amplitude with increasing field.

IV. DISCUSSION

The existence of WF in the R_2CuO_4 series is accompanied by the presence of irreversibility effects.[10,11] Differences are observed in the irreversible behavior of Gd_2CuO_4, depending on the thermal treatment. For the sample annealed at high temperature, sample II, the irreversibility appears at a temperature of the order of the AF 3D/2D ordering of the Cu^{+2} ions, $T_N\approx$270 K. Instead, for the sample annealed at a low temperature, sample I, T_{irr} and the temperature of the maxima of the real and imaginary parts of the susceptibility

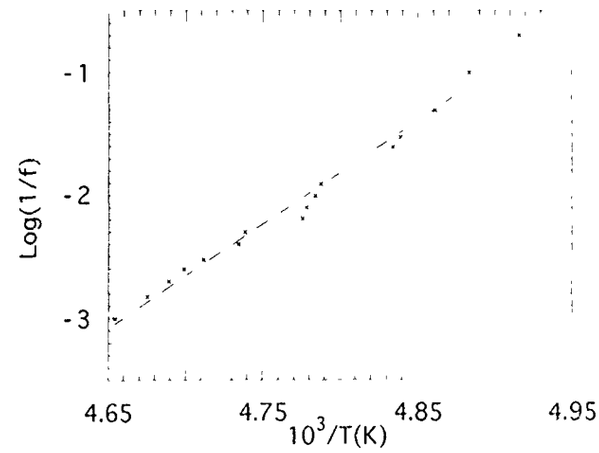

FIG. 3. Frequency dependence of the high temperature peak T_{M1} for sample I

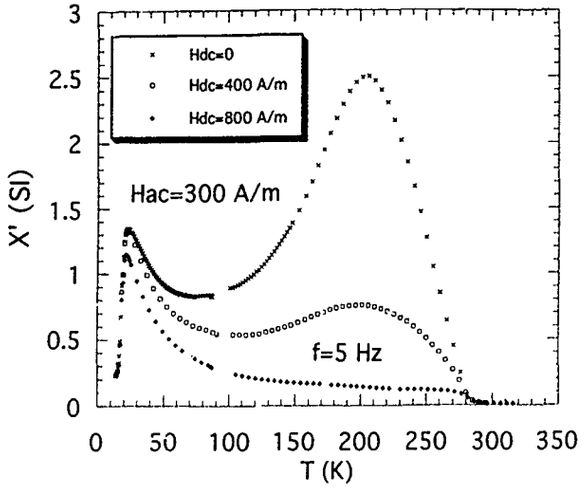

FIG. 4. Temperature dependence of χ' of sample I measured at the same ac magnetic field (H_{ac}=300 A/m) for different superposed dc fields (H_{dc}).

are located at $T \approx 210$ K, which is much lower than T_N. Another difference is that for sample I the position of the high temperature χ' maximum is frequency dependent. This dependence is not observed for sample II, as in the case of other weak ferromagnetic compounds treated at high temperature.[1]

The low temperature peak observed for both samples may be interpreted as due to a phase transition. Below this temperature, both the WF and the dynamic effects disappear, as seen in Fig. 5. This figure shows several isotherms of χ' versus the frequency. As we decrease the temperature below 20 K, the isotherms become frequency independent. The origin of this transition has been associated to the competition between the Gd–Gd and Gd–Cu interactions.[3]

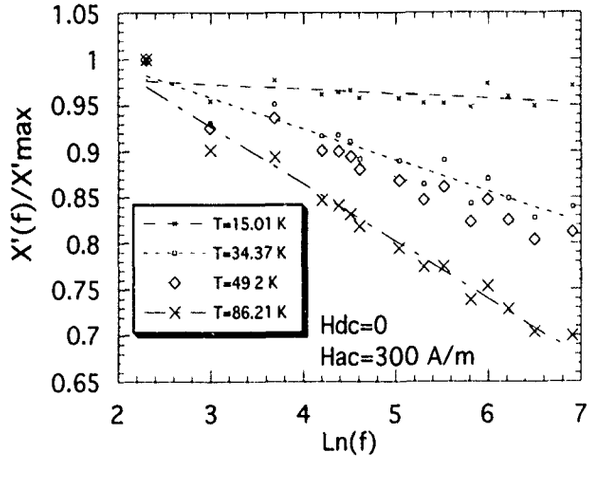

FIG. 5 χ' vs frequency at selected temperatures.

To analyze the frequency dependence of the high temperature maximum, we have plotted the data in an Arrhenius law form (Fig. 3). In the examined temperature range the relationship is linear. We have found that the Arrhenius law, predicted for independent fine particles or isolated clusters does not describe the observed dynamic properties, as a non-physical value was obtained for the pre-exponential factor τ_0 ($\tau_0 \approx 10^{-50}$ s). The observed frequency dependence could be associated to the existence of different magnetic domains (or large clusters). The domain size should be related to the coherence length of the oxygen distortion. This coherence length seems to be strongly dependent on the thermal treatment.

Finally, we discuss the effect of the superposition of a dc field on the ac measurements. The broadening of the 210 K maximum, and the decrease of its amplitude with increasing H_{dc} shows the effect of the field on the resulting WF and on the dynamical behavior of the magnetic domains. The small shift of the 20 K maximum to lower temperatures with the superposition of a dc field is consistent with the H–T phase diagram for Gd_2CuO_4 presented in Ref. 3.

ACKNOWLEDGMENTS

We wish to acknowledge financial support from the DGICYT, PB92-1086; Fundación Ramón Areces; NSF-DMR-01172122, and NATO, CRG920255. J. M. and C. V. also thank the Fundacion Segundo Gil Dávila and Xunta de Galicia for its financial support.

[1] S. B. Oseroff, D. Rao, F. Wright, D. C. Vier, S. Schultz, J. D Thompson, Z Fisk, S.-W. Cheong, M. F. Hundley, and M. Tovar, Phys. Rev. B **41**, 1934 (1990).
[2] T. Adelmann, R. Ahrens, G. Czjzek, G. Roth, H. Schmidt, and C. Steinleitner, Phys. Rev. B **46**, 3619 (1992).
[3] A. A. Stepanov, P Wyder, T. Chattopadhyay, P J. Brown, G. Filion, I. M. Vitebsky, A. Deville, G. Gaillard, S. N. Barilo, and D. I Zhigunov, Phys. Rev. B **48**, 12 979 (1993)
[4] I. Dyzaloshinskii, J. Phys. Chem. Phys. Solids **4**, 241 (1958)
[5] T. Moriya, Phys. Rev. **120**, 91 (1960).
[6] Y. Tokura, H. Takagi, and S Uchida, Nature **337**, 345 (1989); J T. Markert, E. A. Early, T. Bjornholm, S. Ghamaty, B. W. Lee, J. J. Nuemeier, R. D. Price, C. L. Seaman, and M. B Maple, Physica C **158**, 178 (1989).
[7] E. Moran, A. I. Nazzal, T. C. Huang, and J B. Torrance, Physica C **160**, 30 (1989).
[8] P Bordet, J. J. Capponi, C. Chaillout, D. Chateigner, J Chenavas, T. Fournier, J. L. Hodeau, M. Marezio, M. Perroux, G. Thomas, and A. Varela, Physica C **185**, 539 (1991).
[9] X. Obradors, P. Visani, M. A. De la Torre, M. B. Maple, M. Tovar, F. Pérez, P. Bordet, J. Chenavas, and D. Chateigner, Physica C **213**, 81 (1993).
[10] M. Tovar, X. Obradors, F. Prez, S. B. Oseroff, R. J. Duro, J. Rivas, D. Chateigner, P. Bordet, and J. Chenevas, Phys. Rev. B **45**, 4729 (1992).
[11] J. Mira, J. Castro, J. Mahía, C. Vázquez-Vázquez, M. A. López-Quintela, J. Rivas, and S. B. Oseroff, J. Non-Cryst. Solids (in press).

Cluster model studies on the electronic and magnetic properties of $LaCo_{13}$ and $La(Fe_xAl_{1-x})_{13}$ alloys

G. W. Zhang, X. G. Gong,[a] and Q. Q. Zheng,[a),b)]
Institute of Solid State Physics, Academia Sinica, 230031 Hefei, People's Republic of China

J. G. Zhao
Institute of Physics, Academia Sinica, 100080 Beijing, People's Republic of China

We present studies on both the electronic and magnetic properties of $LaCo_{13}$ and $La(Fe_xAl_{1-x})_{13}$ intermetallic compounds by cluster model calculations within the scheme of density-functional theory. The equilibrium structures of the isolated and embedded clusters, obtained by minimizing the total binding energy, are in good agreement with available experimental data and other theoretical results. The relative stability and formation of $LaCo_{13}$ and $La(Fe_xAl_{1-x})_{13}$ phases have been successfully explained. Interesting changes of magnetic properties in an Al doped Fe_{13} cluster have been obtained. The possible effect of Al on the magnetic phase diagram of $La(Fe_xAl_{1-x})_{13}$ is discussed.

The cubic $NaZn_{13}$-type alloys have long been the subject of much research. Recently, the successful fabrication of $LaCo_{13}$, $La(Fe_xAl_{1-x})_{13}$ alloys have enriched this family and attracted much experimental and theoretical interest.[1] Their structures are based on a faced-centered cubic lattice with the space group O_{h6}–F_{m3c} and eight molecular formulas in the unit cell. La atoms (e.g., for $LaCo_{13}$) are at the body centered positions. There are two nonequivalent positions for Co atoms. One of the important features of this structure is that Co_I is surrounded by 12 Co_{II} at the vertices of a regular icosahedron, and the La atom is at the center of a snub cube, with Co_{II} atoms at its 24 vertexes. It is well known that the icosahedral structures are very stable for many kinds of 13-atom clusters. The relative stability and electronic structure of the local icosahedral cluster may contribute to the formation of the characteristic $NaZn_{13}$-type structure. In experiments, it has been found that $LaCo_{13}$ alloy is stable, while the $LaFe_{13}$ alloys is not stable, but it can be stabilized by suitable doping with Al atoms. Many experiments show that $La(Fe_xAl_{1-x})_{13}$ alloys are only stable with the x range between 0.46 and 0.92.[2] Neutron diffraction experiments suggest that Fe and Al atoms not be randomly distributed in the alloys, the Co_I sites be completely occupied by Fe, Al atoms substitute Fe atoms in the Co_{II} sites.[3] The doping of Al in the icosahedral Fe_{13} cluster changes both relative stability and electronic structures of the local unit structure, which consequently favors the formation of $NaZn_{13}$-type alloys. The doping of Al also changes the magnetic properties of La–Fe alloys. The measurement of susceptibility reveals that $La(Fe_xAl_{1-x})_{13}$ alloys exhibit a unique magnetic diagram varying from the micromagnetic state to the ferromagnetic state and the antiferromagnetic state, with the increase of the Fe concentrations. The measurement of electrical resistivity and magnetization also suggest that local electronic and magnetic properties have played an important role in the properties of those alloys.[4] It is natural to ask why $LaCo_{13}$ alloys are stable, while $LaFe_{13}$ is only stable with some doping of Al, and also why the variant doping changes the magnetic and electronic properties? These problems are not been fully understood. In this paper, based on a cluster model, we have calculated the electronic structures and the total binding energies of $LaCo_{13}$ and $La(Fe_xAl_{1-x})_{13}$ alloys, trying to understand the relative stability of these alloys from a local structure point of view, and identify the role played by Al atoms in the $La(Fe_xAl_{1-x})_{13}$ alloys. We have used the icosahedral Co_{13}, Fe_{13}, and $Fe_{12}Al$ clusters to study the local properties of $LaCo_{13}$ and $La(Fe_xAl_{1-x})_{13}$ alloys. To take into account the effects of the crystal field, we also have studied the clusters embedded in the crystal. The calculations are performed using the density functional theory with a local spin density approximation.[5] The discrete variational method has been used to solve the Kohn–Sham equation.[6] In our calculations, the basis sets are the numerical atomic valence orbitals of $3d4s$ for Fe and Co atoms, and $3s3p$ for the Al atom, we have found that when including the more diffusive orbitals in the basis set, there were very small effects on equilibrium atomic distances and electronic structures. The inner orbitals are kept frozen in all the calculations. Group theory has been adopted to classify the molecular orbitals and consequently simplify the calculations. The equilibrium structures of all the calculated clusters are obtained by minimizing the total binding energies for several center to vertex distances, keeping the corresponding symmetry. The binding energy is defined by $E_b = E_{tot} - E_{ref}$, where E_{tot} is the total energy of the cluster and E_{ref} is the sum of the total energies of individual atoms. We have used the Mulliken population to get the occupation numbers for atomic orbitals.[7] The magnetic moments for each atom are the difference of electrons between spin-up and spin-down states.

In Table I, we have presented the calculated magnetic moments and the theoretical equilibrium distances from center to vertex for Co_{13}, Fe_{13}, and $Fe_{12}Al$ clusters, but for the embedded clusters, we have used the experimental atomic distances in the corresponding bulk phases. From Table I, we can see that the equilibrium distances of Co_{13} and Fe_{13} are almost the same, the small difference may come from the difference of atomic sizes for Co and Fe atoms. Actually, the

[a)]Also at CCAST (World Laboratory), Beijing 100080, People's Republic of China.
[b)]Also at The State Laboratory for Magnetism, Beijing 100080, People's Republic of China.

 0021-8979/94/76(10)/7037/3/$6.00 © 1994 American Institute of Physics

TABLE I. Some properties of all the calculated clusters. μ_c is the magnetic moments of Co_I sites. μ is the average magnetic moments per the Fe or Co atom of a cluster.

	Isolated clusters			Embedded clusters		
	Co_{13}	Fe_{13}	$Fe_{12}Al$	Co_{13}	Fe_{13}	$Fe_{12}Al$
d_0 (a.u.)	4.65	4.63	4.73	4.64	4.57	4.59
$\mu_c(\mu_B)$	2.38	3.25	2.97	2.94	3.85	4.20
$\mu(\mu_B)$	2.38	3.38	2.99	2.83	3.83	4.20

atomic size effects on the lattice constants can also be observed in $LaCo_{13}$ and $LaFe_{13}$ alloys, the distance between Co_I and Co_{II} in $LaCo_{13}$ is 4.64 a.u., similarly, the distance between Fe_I and Fe_{II} in $LaFe_{13}$ extrapolated from experimental data[2] is 4.57 a.u. The fact that the theoretical equilibrium distance for the icosahedral Co_{13} and Fe_{13} are very close to the experimental value in the LaM_{13} (M=Co,Fe) bulk phases suggest that the local icosahedral cluster will not be affected very much by the crystal environments. When substituting Fe with Al, we found an increase of equilibrium distance, which is in agreement with the experimental fact that the lattice constant increases with the increase of Al concentrations. This phenomenon can be easily understood, because the Al atoms have more diffusive electronic orbitals and hence a large atomic size. In Fig. 1, we show the calculated binding energies for all the clusters at the equilibrium center to vertex distance d_0. We obtained about ~45 eV binding energy for the Fe_{13} cluster, which is also in agreement with other theoretical calculations,[8] and the Co_{13} has about ~30 eV binding energy. On doping Al in the Fe_{13}, as shown in the figure, we found the binding energy of $Fe_{12}Al$ shifted up a little bit. We can expect that the binding energy will increase if the shifting Al atom outward deviated from a perfect icosahedron. In Fig. 2, we have plotted the eigenvalue spectra for all the calculated clusters. In the Co_{13} cluster, we obtained a fourfold degenerate G_g molecular orbital for the highest occupied state (HOMO), but the HOMO is not completely occupied and there are three electron deficiencies, so, in principle, the isolated icosahedral Co_{13} will not be stable, at least Jahn–Teller distortion will lower the total energy. But why are the $LaCo_{13}$ alloys with an icosahedral structural unit stable? This striking question can probably be understood as following. It is well known that the La atom has a strong tendency to lose three valence electrons. If La atom support Co_{13} with three electrons to fill the deficiency in HOMO, it makes the icosahedral Co_{13} stable with a closed electron shell. The large ion core of La atoms fills the space among icosahedral Co_{13} clusters. In this way, the icosahedral Co_{13} can be considered as superatoms, the complicated $LaCo_{13}$ alloys can be composed of a *superatom* Co_{13} and La atom. In fact, the idea of superatom that had been used successfully to explain the stability of icosahedral quasicrystals[9] is also applicable to many other systems. We have checked other Zn based AB_{13} alloys, we found the same explanation can be used. In the similar way, we can understand the stability of $LaFe_{13}$ alloys. In the Fe_{13} cluster, we obtain a five-fold degenerate H_g molecular orbital for the HOMO, but with only one electron in this orbital, and there is four-electron deficiency. So even though the La atom offers three electrons, the HOMO still cannot be completely filled like in Co_{13}, which means that the Fe_{13} cluster in

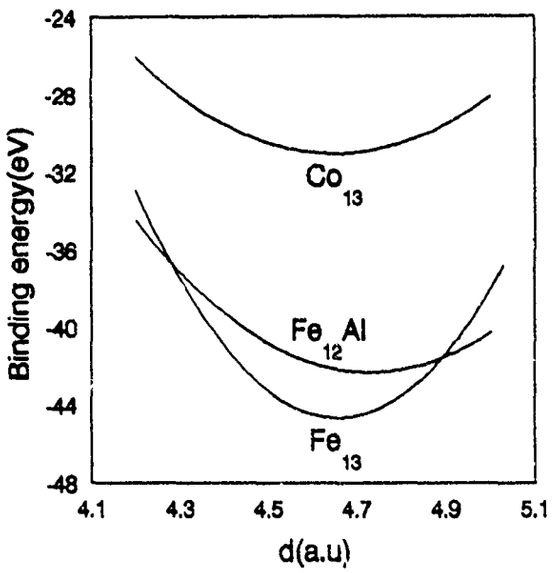

FIG. 1. The binding energy curves vs radial bond distance for Co_{13}, $Fe_{12}Al$, and $Fe_{11}Al_2$ clusters.

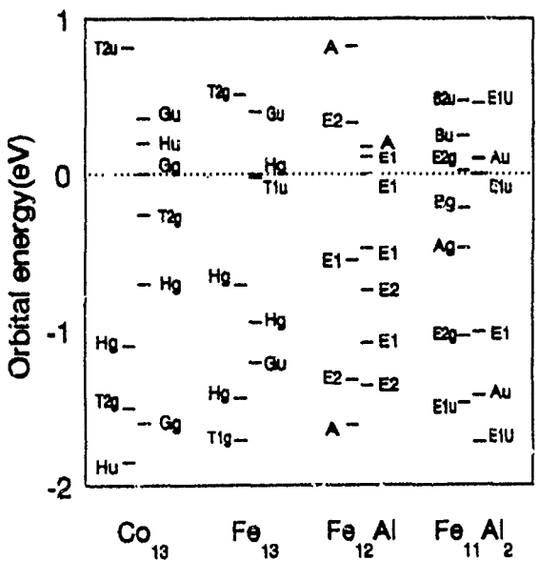

FIG. 2 Energy spectra c .he isolated Co_{13}, $Fe_{12}Al$, and $Fe_{11}Al_2$ clusters.

$LaFe_{13}$ alloy cannot be stable. All these results are consistent with experimental facts.[1,2] To see the influence of substituting Fe by Al on the stability and properties of $La(Fe_xAl_{1-x})_{13}$ alloys, we have studied the $Fe_{12}Al$ and $Fe_{11}Al_2$ clusters, which represent the alloys at the different region of a magnetic phase diagram. The experiments have already found that the Al atom did not occupy the center of the icosahedron,[3] so we chose $Fe_{12}Al$, with D_5 symmetry. From the eigenspectrum in Fig. 2, we can see the HOMO is two-fold degenerate, with only one electron in it, the two-fold degenerate lowest unoccupied molecular orbital (LUMO) is also very close to the HOMO, three electrons provided by the La atom can fill the one electron deficiency in HOMO and also fill the two-fold degenerate LUMO; consequently, the $Fe_{12}Al$ has a closed electron shell and becomes stable, which might be the reason why the experiment found the $Fe_{12}Al$ alloys stable. In a similar way, we can expect that the $Fe_{11}Al_2$ would be stable in the $La(Fe_xAl_{1-x})_{13}$ alloys.

In Table I, we have presented the magnetic moment for all calculated clusters, we have obtained the Co atom with $2.38\mu_B$ magnetic moments, which is in good agreement with other theoretical and experimental results.[10,11] We have also obtained a large average magnetic moment ($3.38\mu_B$) for the free icosahedral Fe_{13} clusters, and observed the magnetic moments for the atom at the center of the icosahedron are parallel to the magnetic moments for the atoms at the vertexes, which suggest that the ground state of the Fe_{13} cluster be ferromagnetic, in agreement with other theoretical calculations.[12] When doping with Al, we find the cluster expands and the magnetic moments decrease. This occurrence of decrease of the magnetic moments can be attributed to that more and more iron atoms will lose their magnetic moments when Fe concentration decreases. This is confirmed by our studies on the $Fe_{11}Al_2$ clusters with D_{5d} symmetry; we have found the magnetic moments for Fe atoms in $Fe_{11}Al_2$ are even smaller than that in $Fe_{12}Al$ cluster. Hence, based on the results of the present cluster model calculations, it can be expected to get Pauli paramagnetism when decreasing the iron concentration and consequently decreasing the magnetic interaction, which is in agreement with the complicated experimental magnetic phase diagram of $La(Fe_xAl_{1-x})_{13}$ alloys. In all the embedded clusters, we find a very similar eigenvalue spectra to the isolated clusters discussed above, so the same idea can be applied to stability of the embedded clusters, which have included the influence of the crystal field generated by 824 atoms. But we observed a small increase of magnetic moments with respect to the isolated clusters.

In summary, the electronic and magnetic properties of the four $NaZn_{13}$-type compounds, $LaCo_{13}$, $LaFe_{13}$, $LaFe_{12}Al$, and $LaFe_{11}Al_2$ have been studied by modeling those alloys by cluster on the basis of density functional theory. We found the relative stability as well as electronic structure of $NaZn_{13}$-type alloys can be explained according to its local icosahedral structural units. The main role of Al is to modify local electronic structure; this may facilitate the formation of the stable $NaZn_{13}$-type structure for the La–Fe alloys. In addition, the change of local magnetic properties with the change of Al concentrations bears resemblance to that of the alloys.

[1] T. T. M. Palstra, G. J. Nieuwenhuys, J. A. Mydosh, and K. H. J. Buschow, Phys. Rev. B **31**, 4623 (1985).
[2] R. B. Helholdt, T. T. M. Palstra, G J Nieuwenhuys, J. A. Mydosh, A. M. Van der Kraan, and R. H. J. Buschow, Phys. Rev. B **34**, 169 (1986).
[3] E Matsubara, Y. Waseda, T. H. Chiang, and K. Fukamichi, Mat. Trans JIM, **33**, 155 (1992).
[4] A. M. Van der Kraan, K. H. J. Buschow, and T. T. M Palstra, Hyperfine Interact. **15/16**, 717 (1983).
[5] P. Hohenberg and W. Kohn, Phys. Rev. B **136**, 864 (1964)
[6] D. E. Ellis and G. S. Painter, Phys Rev B **2**, 2887 (1970).
[7] R. S. Mulliken, J. Chem. Phys **23**, 1841 (1955).
[8] B. I. Dunlap, Phys. Rev. A **41**, 5691 (1990)
[9] X G. Gong and V Kumar (unpublished)
[10] Z. Q. Li and B. L. Gu, Phys. Rev. B **47**, 13 611 (1993)
[11] D. M. Cox, D. J. Trevor, R. L. Whetten, E. A. Rohlfing, and A. Kaldor, Phys. Rev. B **32**, 7290 (1993).
[12] O. B. Christensen and M. L Cohen, Phys Rev. B **47**, 13 643 (1993)

Structure, transport and thermal properties of UCoGa

A. Purwanto[a] and R. A. Robinson
LANSCE, Los Alamos National Laboratory, Los Alamos, New Mexico 87545

K. Prokeš, H. Nakotte, and F. R. de Boer
Van der Waals-Zeeman Laboratory, University of Amsterdam, 1018 XE Amsterdam, The Netherlands

L. Havela, V. Sechovský, and N. C. Tuan
Department of Metal Physics, Charles University, 12 116 Prague 2, Czech Republic

Y. Kergadallan, J. C. Spirlet, and J. Rebizant
European Commission, Joint Research Centre, Institute for Transuranium Elements, Postfach 2340, 76125 Karlsruhe, Germany

By means of neutron powder diffraction, we find that UCoGa crystallizes in the hexagonal ZrNiAl structure and orders ferromagnetically at low temperatures with magnetic moments stacked along the c axis. The magnetic-ordering temperature is reflected in anomalies in the temperature dependencies of the electrical resistivity and the specific heat at $T_C = 47$ K. Furthermore, the strong anisotropy in the electrical resistivity for $i \| c$ and $i \perp c$ indicates a significant contribution of the magnetic anisotropy to the electrical resistivity.

I. INTRODUCTION

UCoGa belongs to the large group of UTX compounds (T=transition metal, X=p-elec[illegible]metal), and is reported to crystallize in the hexagonal Zr [illegible]ucture.[1] Previous bulk magnetic investigations[2–4] revealed a magnetic order at about 47 K, but the results were inconclusive regarding whether the ground state is ferro- or antiferromagnetic.[4] The purpose of the present contribution is to determine the structural parameters and to clarify the type of ground state, as well as to investigate the bulk transport and thermal properties of single-crystalline UCoGa.

II. EXPERIMENTAL

For the present investigations, we have used two kinds of samples: polycrystalline material and a small single crystal. The polycrystal, which has been used in the neutron-diffraction experiments, was prepared by arc-melting appropriate amounts of the constituting elements with a purity of at least 99.99%. The small single crystal is the same as was used in a previous investigation.[4] Neither the polycrystal nor the single crystal have been annealed.

For neutron-diffraction experiments, the polycrystal was ground and enclosed with helium gas in a sealed vanadium tube, which was mounted on the cold finger of a closed-cycle refrigerator. This setup was installed in the High Intensity Powder Diffractometer (HIPD) at the Los Alamos spallation pulsed neutron source LANSCE. Data have been taken on six detector banks ($2\Theta = \pm 40, \pm 90, \pm 153$) at 60, 35, and 10 K. The diffraction patterns were analyzed using the Rietveld refinement program GSAS.[5] The magnetic intensities were also analyzed by extracting integrated intensities for individual peaks and fitting to models for the magnetic structure.

The temperature dependence of the electrical resistivity was measured between 4.2 and 300 K, with the standard four-point ac method on two small bar-shaped single crystals of typical size $0.5 \times 0.5 \times 2$ mm^3, where the largest distance coincides with the c axis for the first sample and is perpendicular to the c axis for the second one. The large error in the determination of the geometrical factor makes a reliable estimate of the absolute resistivity values impossible.

At 4.2 K, the field dependence of the electrical resistivity in magnetic fields up to 35 T has been measured in the Amsterdam High-Field Installation, with an $i \| B \| c$ axis.

The temperature dependence of the specific heat has been measured between 4.2 and 100 K, making use of both standard adiabatic and the relaxation-time method.

III. CRYSTAL AND MAGNETIC STRUCTURE

UCoGa crystallizes in the hexagonal ZrNiAl structure (space group: P$\bar{6}$2m). The structural parameters of UCoGa have been derived by neutron powder diffraction at 60 K, and the results of the refinement are listed in Table I. The absence of any unindexed reflection in the parent phase suggests that there is no impurity in the present sample. However, the reduced χ^2 drops by 5% when a slightly lower atomic fraction of Co and slightly higher fraction of Ga (of the order of 1% in both cases) are assumed. This result indicates a small deviation from the exact 1:1:1 stoichiometry. For UCoGa, the nearest interuranium distance d_{U-U} is found

TABLE I. Refined structural parameters for UCoGa at 60 K.

Space group:		P$\bar{6}$2m			
U	3g	x	0	$\frac{1}{2}$	x=0.580 018±0.000 026
Co_1	2c	$\frac{1}{3}$	$\frac{2}{3}$	0	
Co_2	1b	0	0	$\frac{1}{2}$	
Ga	3f	x	0	0	x=0.239 151±0.000 034
Lattice parameters				*R* factors	
a=666.456±0.010 pm				R_{wp}=3.00%	
c=392.653±0.006 pm				R_p=2.13%	
				reduced χ^2=3.53	

[a]Also at the Department of Physics, New Mexico State University, Las Cruces, New Mexico 88003.

 0021-8979/94/76(10)/7040/3/$6.00 © 1994 American Institute of Physics

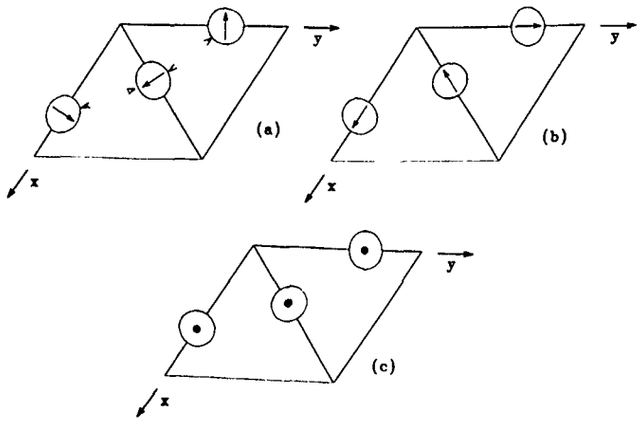

FIG. 1. The Shubnikov magnetic subgroup of P$\bar{6}$2m. In (a), the uranium moments are perpendicular to the mirror planes, while in (b) and (c), the moments are parallel to the mirror planes. Note that, in the models (a) and (b), the moments are located within the hexagonal basal plane, while in (c) they are ferromagnetically coupled along the c axis. For clarity, only uranium atoms are shown. The dashed lines with arrows indicate the nearest uranium–uranium links.

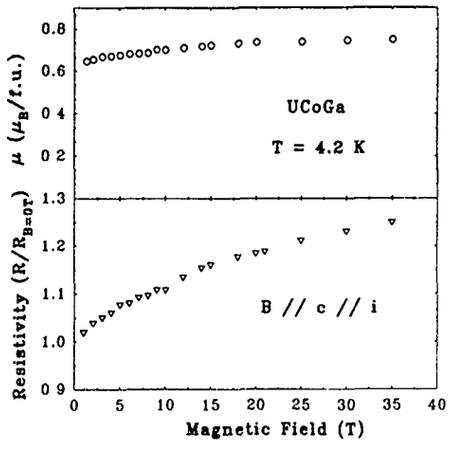

FIG. 2. Temperature dependence of the electrical resistivity of UCoGa for the $i\|c$ axis and $i\perp c$ axis normalized to the values at 300 K. In the inset, the low temperature detail for the $i\|c$ axis is shown in the representation $\rho/\rho_{300\text{ K}}$ vs T^2.

within the hexagonal basal plane (see Fig. 1), and is determined by $d_{U\text{-}U}=a\sqrt{(3x^2-3x+1)}$, where a is the lattice parameter and x is the U position parameter.

In order to clarify the magnetic structure, we have performed neutron-diffraction experiments at 35 and 10 K, well below the magnetic ordering temperature indicated by bulk magnetization results.[2–4] We do not observe any additional purely magnetic reflections at these temperatures, but an additional magnetic contribution to the nuclear reflections is found. This indicates that the magnetic unit cell is the same as the nuclear one, but antiferromagnetism is still possible in this structure. Possible magnetic structures have been derived using magnetic space-group analysis. U atoms in the unit cell lie in the mirror planes at $x=0$, $y=0$, and $x=y$ (note that x and y are at an angle of 120°). The moment corresponding to U in a certain mirror plane must be perpendicular or parallel to that mirror plane. The Shubnikov magnetic subgroups of P$\bar{6}$2m are shown in Fig. 1. Clearly, there are two antiferromagnetic noncollinear structures with moments in the basal plane, and only one ferromagnetic (collinear) model with U moments along the c direction. The fact that we do not observe any $00l$ magnetic contribution does not mean that the magnetic structure must be ferromagnetic, since the two noncollinear models also have no $00l$ magnetic contributions. This is easily understood, since the net moments in the $00l$ basal plane are zero for both noncollinear structures.

The integrated intensities have been corrected for the Lorentz factor[6] and for absorption. We find a significant magnetic contribution to the 110 reflection, which excludes structure 2(b), as this gives no intensity to this reflection. This is easily understood, since the net moments in the $hh0$ plane are perpendicular to that plane, which, in turn, gives zero magnetic contribution through the expression of $\sin\eta$, where η is the angle between the magnetic moment and the reciprocal lattice vector (in this case, $\eta=0$). On the other hand, both structures, 2(a) and 2(c), are possible and the lower reduced χ^2 of the ±90 detector banks suggests structure 2(c), the ferromagnetic one, to be more likely. However, the difference is only marginal, and, in fact, if the results obtained on the ±40 and ±153 detector banks are included into the refinement, structure 2(a) is slightly more likely. However, due to inconsistencies in the magnetic appearance in the + and − detector banks, which are less pronounced in the ±90 banks, we believe structure 2(c) to be the correct one, which is corroborated by the magnetization results. For the ferromagnetic structure 2(c), we deduce U magnetic moments of $0.74\pm0.03\mu_B$ per atom, which is in good agreement with the value of $0.78\mu_B$/f.u. obtained from the high-field magnetization.[4] Note that the Co moment is zero to within an experimental error of a $\pm0.1\mu_B$/atom. Also note that model 2(a) yields much larger U magnetic moments of about $1.04\pm0.04\mu_B$ per atom.

IV. TRANSPORT AND THERMAL PROPERTIES

The onset of magnetic ordering at $T_C=47$ K is reflected by a maximum in the temperature derivative of the electrical resistivity at this temperature (see Fig. 2) for both the $i\|c$ axis and $i\perp c$ axis. However, while for the $i\|c$ axis an appreciable reduction of the electrical resistivity with decreasing temperature is found, we observe an almost flat resistivity behavior for the $i\perp c$ axis. The observed strong anisotropy in the resistivity correlates well with the magnetic anisotropy found in bulk magnetization measurements. At 300 K, very rough estimates of resistivities yield values around 150 $\mu\Omega$ cm for the $i\|c$ axis, while twice as large values for the $i\perp c$ axis are found. Below 40 K, the electrical resistivity follow a quadratic temperature dependence for both orientations, which is shown for the $i\|c$ axis in the inset of Fig. 2. For UCoGa, we may roughly estimate the prefactors A to be about 0.216 and 0.138 $\mu\Omega$ cm/K^2 for the $i\|c$ axis and $i\perp c$ axis, respectively.

For this compound, we find at 4.2 K (Fig. 3) for the $i\|B\|c$ axis an increase of the electrical resistivity with an

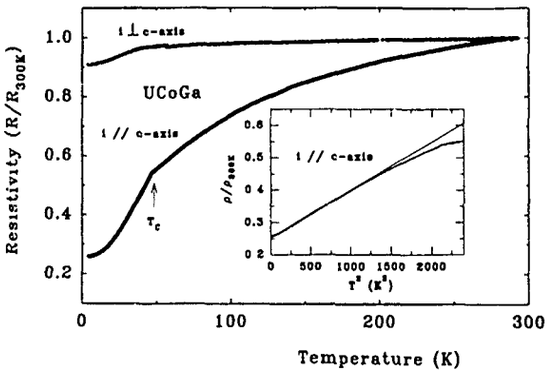

FIG 3. Field dependence of the electrical resistivity of UCoGa at 4.2 K in the configuration $i \| B \| c$ axis.

increasing magnetic field, which is in contrast to the large reduction of the electrical resistivity in the isostructural antiferromagnetic UTX compounds upon the application of sufficiently high magnetic fields.[7] The different behavior of UCoGa may be taken as a further support for a ferromagnetic ground state of this compound. At the highest fields applied, we observe a slight saturation tendency. In general, UCoGa reflects a more "normal" and expected magnetoresistance behavior, however, the total increase of the resistivity (about 27% in 35 T) is surprisingly large.

As can be seen in Fig. 4, the magnetic ordering of UCoGa is reflected in the specific heat by a maximum at T_C=47 K. After substraction of a phonon contribution determined by a Debye function with Θ_D=195 K, the magnetic entropy connected with ordering is considerably lower than

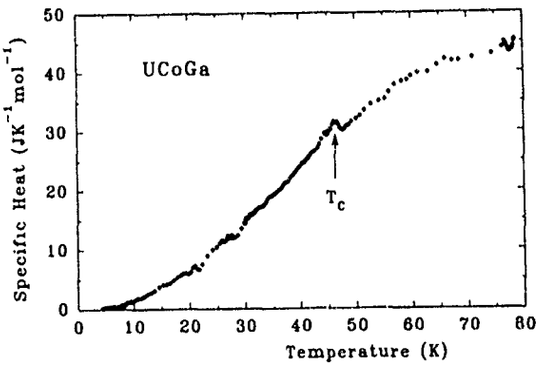

FIG. 4. Temperature dependence of the specific heat of UCoGa

R ln 9 or R ln 10, expected for the localized f^2 or f^3 configuration, respectively.

By linear extrapolation of C_p/T vs T^2 to T=0 K, we derived the coefficient γ of the electronic contribution to the specific heat, to be about 48 mJ/mol K^2.

V. CONCLUSIONS

UCoGa, which crystallizes in the hexagonal ZrNiAl structure, orders ferromagnetically below T_C=47 K with ordered $5f$ moments of about $0.74\mu_B$ stacked along the c axis. The rather low value of the ordered moments, which amounts to only half the values found in isostructural UNiX compounds,[9] confirms the expected trends arising from $5f-d$ hybridization,[10] and points to a larger delocalization of the $5f$ electrons in UCoGa. For UCoGa, a significant anisotropy in the temperature dependence of the electrical resistivity has been found. Strongly anisotropic transport properties have also been detected in other UTX compounds,[11] which suggests that they are caused by the general anisotropy due to the crystal structure and the Fermi-surface anisotropy.

ACKNOWLEDGMENTS

This work is part of the research programme of the "Stichting voor Fundamenteel Onderzoek der Materie" (FOM), which is financially supported by the "Nederlandse Organisatie voor Wetenschappelijk Onderzoek" (NWO). Part of the work was supported by the U.S.–Czech Joint Science Fund under Project No. 93039 and by the Grant Agency of the Czech Republic (No. 312). It was also supported in part by the division of Basic Energy Sciences of the U.S. Department of Energy.

[1] A. E. Dwight, in *Developments in the Structural Chemistry of Alloy Phases*, edited by B. C. Giessen (Plenum, New York, 1969), p. 181.
[2] A. V Andreev, L. Havela, M Zeleny, and J. Hrebik, Phys. Status Solidi A **82**, 191 (1984)
[3] A. V. Andreev, A. V. Deryagin, and R. Yu. Yumaguzhin, Sov. Phys. JETP **59**, 1082 (1984)
[4] H Nakotte, F. R. de Boer, L. Havela, P. Svoboda, V. Sechovsky, Y. Kergadallan, J C. Spirlet, and J. Rebizant, J. Appl. Phys **73**, 6554 (1993)
[5] A. C. Larson and R. B. Von Dreele, Los Alamos National Laboratory Report No. LA-UR-86-748, 1986.
[6] G. E. Bacon, in *Neutron Diffraction* (Cambridge University Press, Oxford, 1975).
[7] H Nakotte, K. Prokeš, E. Bruck, F. R. de Boer, V. Sechovsky, L. Havela, and H. Fujii, IEEE Trans Magn **30**, 1139 (1994).
[8] K. Kadowaki and S. B. Woods, Solid State Commun **58**, 507 (1986).
[9] V. Sechovsky and L. Havela, in *Ferromagnetic Materials*, edited by E P Wohlfarth and K. H. J. Buschow (North-Holland, Amsterdam, 1988), Vol 4, p. 309
[10] D. D. Koelling, B. D. Dunlap, and G W Crabtree, Phys. Rev. B **31**, 4966 (1985).
[11] L. Havela, V. Sechovsky, H Nakotte, E Bruck, and F R. de Boer, IEEE Trans Magn. **30**, 1130 (1994)

The effect of Mn on the magnetic properties of YFe_2

Jian-Wang Cai, Yuan-Bing Feng, and He-Lie Luo
State Key Laboratory of Magnetism, Institute of Physics, Academia Sinica, Beijing 100080, People's Republic of China

Zhi Zeng and Qing-Qi Zheng
Institute of Solid State Physics, Academia Sinica, Hefei 230031, People's Republic of China

The fully self-consistent discrete variational method within the local-spin-density framework has been employed to obtain the electronic structure and magnetic moments of the Mn-containing cubic Laves phase pseudobinary compound of YFe_2. The calculated results show that the substitution of Mn atoms on Fe sites weakens the ferromagnetism of this compound. The magnetic moments on distinct atomic sites were derived from the calculation. We found that when the Fe atom has one Mn atom in its nearest neighbor sites, its magnetic moment decreases rapidly, while the Mn moment is $0.71\mu_B$, parallel to the Fe moment. Based upon our results, the various experimental data have been satisfactorily explained.

I. INTRODUCTION

The cubic Laves phase pseudobinary compound $Y(Fe_{1-x}Mn_x)_2$ is a puzzling system. Quite a few attempts have been made to establish its magnetic properties.[1–7] As an antiferromagnet YMn_2 with Mn magnetic moment $2.7\mu_B$,[8] the ferromagnet YFe_2 can form complete solid solutions with it, while sustaining the cubic Laves phase structure.[9] Magnetization measurements[4] and Mössbauer data[7] show the consistent result that $Y(Fe_{1-x}Mn_x)_2$ keeps ferromagnetic until the breakdown of the magnetic order in $x=0.7$. As to the magnetic moments of Fe and Mn atoms in this pseudobinary, however, contrary results have been reported. Schaafsma *et al.*[7] suggested from Mössbauer experiments that Mn appear to carry either less than $0.1\mu_B$ or no magnetic moment at all; from the NMR spectra of ^{89}Y, Nagai *et al.*[5,6] made conclusions that Fe moments are hardly changed, and there are two kinds of Mn moments: one is antiparallel to the Fe moments with about $0.6\mu_B$ and the other is parallel to the Fe moments with about $2.8\mu_B$; While Besnus *et al.*[4] showed from magnetization, diffuse neutron scattering, Mössbauer measurements, and NMR studies that Mn atoms possess magnetic moments, which are ferromagnetically coupled with Fe moments, and that the mean Fe moments decrease strongly with increasing Mn concentration, while the Mn moments appear to be less concentration dependent.

From the theoretical point of view, the problem of the pseudobinary compound $Y(Fe_{1-x}Mn_x)_2$ has been put aside yet by theorists, due to its much more complex magnetic behavior. In this paper we present calculations of charge, spin, and density of states (DOS) for the Mn-containing pseudobinary compound of $Y(Fe_{1-x}Mn_x)_2$ using the well-developed discrete variational method within the local-spin-density framework. For transition metals and intermetallic compounds, it is now well recognized that the local magnetic properties and electronic structures are mostly determined by the nature of atoms involved and the local environments of these atoms. So, several embedded clusters are chosen to simulate the local environments of atoms in the Mn-substituted YFe_2 compound, and spin-polarized calculations on these clusters are performed to study the magnetic behavior of the Mn-containing pseudobinary compound of YFe_2. The computational procedure has been documented in detail elsewhere.[10]

II. RESULTS AND DISCUSSION

The cubic Laves phase compound YFe_2 has the cubic $MgCu_2$ C15 structure. There are eight YFe_2 formula units per simple cubic cell in this structure. The larger Y atoms occupy a cubic diamond lattice. Regular tetrahedra built of four smaller Fe atoms are centered at the fourfold-coordinated interstitial sites of the diamond structure. So the 26-atom cluster of $Fe_4Y_4Fe_{12}Y_6$, which consists of two distinct pairs of Fe and Y atoms, is chosen to represent the host compound YFe_2. While the cluster $Mn_4Y_4Fe_{12}Y_6$, with each Fe atom having one Mn atom in its nearest neighbor sites, is adopted to represent the pseudobinary compound $Y(Fe_{1-x}Mn_x)_2$ with low Mn concentration.

The DOS of the cluster $Mn_4Y_4Fe_{12}Y_6$, with a solid line, is depicted in Fig. 1. For comparison, we show the DOS of the host cluster $Fe_4Y_4Fe_{12}Y_6$ with a dashed line also in Fig. 1, which closely resembles the result obtained by the standard TBA method.[11] From these two curves, one can find that there is not a large change for the shape of the DOS when the Mn substitute at the Fe site of YFe_2, however, the positions of the peaks are changed. For majority-spin states, the main peaks below the Fermi level move to the direction of high energy, and meanwhile the peaks for minority-spin states move to low energy direction; thus the exchange splitting decreases with Mn diluting the Fe sublattice. As is well known, the origin of magnetism can be attributed to intraatomic and interatomic exchange interactions, and the Curie temperature is proportional to the exchange splitting, so the reduction of the exchange splitting gives rise to the decrease of the Curie temperature. Both the magnetization measurement and Mössbauer data show that the Curie temperature decreases almost linearly with the Mn content in the pseudobinary compound $Y(Fe_{1-x}Mn_x)_2$,[4,7] which is consistent with the above conclusion deduced from the electronic structure.

Table I lists the magnetic moments and electron occupation numbers of all atomic sites in the clusters $Fe_4Y_4Fe_{12}Y_6$ and $Mn_4Y_4Fe_{12}Y_6$. For comparison, let us first examine the result of the host cluster $Fe_4Y_4Fe_{12}Y_6$. It is noted that the

 0021-8979/94/76(10)/7043/3/$6.00 © 1994 American Institute of Physics

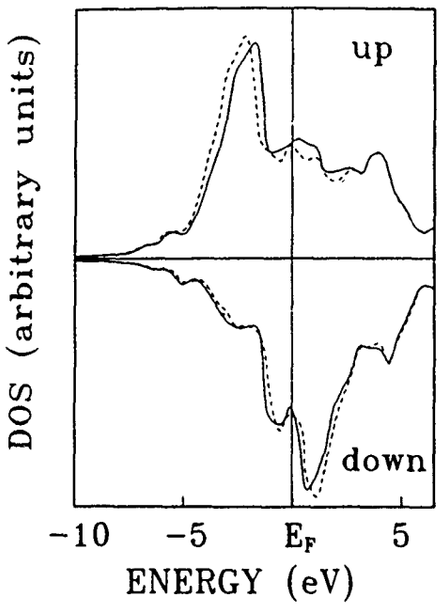

FIG. 1. Total density of states for the clusters $Mn_4Y_4Fe_{12}Y_6$ with a solid line and $Fe_4Y_4Fe_{12}Y_6$ with a dashed line. The spin-up and spin-down bands are normalized to the same scale for each cluster.

magnetic moments of Fe atoms are large and coupled ferromagnetically with small negative moments for Y atoms, which is consistent with the conclusion of the band calculation.[12]

By analyzing the result of the cluster $Fe_4Y_4Fe_{12}Y_6$ in Table I, one can see that the moments for both Fe and Y atoms tend to increase outwardly from inner sites due to the surface effect, which results from that the truncation of the cluster does not allow sufficient delocalization of the wave function in the solid to take place on the cluster surface. The surface effect is unavoidable for the present cluster calculation method, however, the atoms toward the central sites for a large cluster can reproduce the properties of the bulk solid.[13] In the present case, the calculated magnetic moment for the inner Fe atoms is $1.65\mu_B$, which is in fairly good agreement with the value of the band calculation,[12] while the moment of the inner Y atoms is $-0.58\mu_B$, a bit larger than the band calculated result, $-0.45\mu_B$, this difference is also attributed to the surface effect. It has been confirmed by many calculations that the cluster model tends to the same limit as band-structure methods when the cluster size increases, however, computation is too expensive for the larger cluster. For most physical properties, it has been observed that the three- to four-atom-shell cluster is sufficient.[14–16] For the magnetic moment, one can focus on trends instead of the absolute value.

TABLE I Electron occupation numbers and local magnetic moments in the different atomic sites of the clusters $Fe_4Y_4Fe_{12}Y_6$ and $Mn_4Y_4Fe_{12}Y_6$

	$Fe_4Y_4Fe_{12}Y_6$		$Mn_4Y_4Fe_{12}Y_6$	
Cluster	Charge	Spin (μ_B)	Charge	Spin (μ_B)
M(I) 3*d*	6.27	1.84	5.26	0.85
4*s*+4*p*	1.90	−0.19	1.88	−0.14
Net charge/spin	−0.17	1.65	−0.14	0.71
Y(I) 4*d*	1.56	−0.42	1.51	−0.32
5*s*+5*p*	1.12	−0.16	1.21	−0.13
Net charge/spin	0.32	−0.58	0.28	−0.45
Fe(II) 3*d*	6.14	3.46	6.17	2.92
4*s*+4*p*	2.12	0.34	2.06	0.17
Net charge/spin	−0.26	3.80	−0.23	3.09
Y(II) 4*d*	1.42	−0.51	1.39	−0.36
5*s*+5*p*	1.13	0.12	1.21	−0.10
Net charge/spin	0.45	−0.63	0.40	−0.46

The atoms of Y in the compound YFe_2 were assumed to be nonmagnetic before the spin-polarized calculations of its band structures. The cluster and band theory calculations on YFe_2 both show that the Y atoms are spin polarized with a small negative moment, which can be attributed to the hybridization between Fe 3*d* and Y 4*d* states. According to the band-structure calculations, the main part of the 4*d* bands for Y are just above the Fermi level,[17] while most of the states just above the Fermi level for Fe are the 3*d* minority-spin states. So the 4*d* states of Y mainly hybridize with the minority-spin 3*d* states of its neighbor Fe, which results in the minority-spin dominating for the occupied 4*d* bands of Y, and hence a negative moment develops on the Y atoms.

Now, we study the effect of Mn on the magnetic moment of the pseudobinary compound $Y(Fe_{1-x}Mn_x)_2$. From Table I, it is noted that the moments of Mn and Fe atoms both are positive for the cluster $Mn_4Y_4Fe_{12}Y_6$, which shows that Mn moments are coupled ferromagnetically with Fe moments in the pseudobinary compound $Y(Fe_{1-x}Mn_x)_2$ with a low concentration of Mn. Furthermore, one can see that the magnetic moment of Mn is $0.71\mu_B$ and the Fe moment, $3.09\mu_B$, much less than that of the corresponding Fe atom in the host cluster, $3.80\mu_B$. The calculated Mn magnetic moment is in excellent agreement with the measurement results by polarized neutron scattering and NMR studies for the pseudobinary compound with low Mn content,[4] while the Fe moment decreases rapidly with Mn substitution for Fe atoms, which is also in accord with the experimental results.[4] In addition, the Y magnetic moment also decreases. The Mn magnetic moment deduced by Nagai *et al.*[5,6] is opposite to our calculated result, which may result from their oversimplified assumptions that *Y* atoms in the pseudobinary compound have no magnetic moment and that the hyperfine field at ^{89}Y is strictly proportional to the magnetic moments of nearest neighbor atoms.

III. CONCLUSIONS

We have performed first-principles self-consistent-field calculations on several embedded clusters representing the Mn-containing cubic Laves phase pseudobinary compound of YFe_2. Our calculated results for the first time provide an insight into its complex magnetic properties. The following is a summary of our results.

(1) In the compound YFe_2, the magnetic moments of Fe atoms order ferromagnetically and cause small antiparallel moments at Y sites. Substitutions of Mn atoms on Fe sites reduce the exchange splitting of this compound, and hence weaken its ferromagnetism.

(2) When the Fe atom has one Mn atom in its nearest neighbor sites, its magnetic moment decreases rapidly, owing to the strong hybridizations between the minority-spin $3d$ bands of Fe and Mn, while the Mn moment is $0.71\mu_B$, parallel to the Fe moments, which is in fairly good agreement with the neutron-scattering data and NMR studies.

ACKNOWLEDGMENTS

This work was supported in part by the National Nature Science Foundation of China. Calculations were performed on a DEC-5200, at the Institute of Physics, Academia Sinica.

[1] E. Burzo, Z. Angew, Phys. **32**, 127 (1971).
[2] K. H. J. Buschow and A. M. van Diepen, Solid State Commun. **19**, 79 (1976).
[3] G. Hilscher and H. Kirchmayr, J. Phys. C **40**, 5-196 (1979).
[4] M. J. Besnus, A Herr, K. Le Dang, P. Veillet, A. S. Schaafsma, I. Vincze, F. van der Woude, F. Mezei, and G. H. M. Calis, J. Phys. F **12**, 2393 (1982).
[5] H Nagai, H. Yoshie, and A. Tsujimura, J. Phys. Soc. Jpn. **52**, 1122 (1983).
[6] H. Nagai, Hyperfine Interact. **51**, 1003 (1989).
[7] A. S. Schaafsma, M J. Besnus, I. Vincze, and F. van der Woude, J. Magn Magn. Mat. **15–18**, 1149 (1980).
[8] Y. Nakamura, M. Shiga, and S. Kawano, Physica B **120**, 212 (1983).
[9] G. Hilscher, J. Magn. Magn. Mat. **27**, 1 (1982).
[10] D. E. Ellis, Int. J. Quantum Chem Symp. **2**, 35 (1965), D. E Ellis and G P. Painter, Phys. Rev. B **2**, 2887 (1970).
[11] H. Yamada, J. Inove, K. Terao, S. Kanda, and M. Shimizu, J. Phys. F **14**, 1943 (1984).
[12] P. Mohn and K. Schwarz, Physica B **130**, 26 (1985).
[13] M. R. Press, F. Liu, S. N. Khanna, and P. Jena, Phys. Rev. B **40**, 399 (1989).
[14] D. Guenzburger and D. E. Ellis, Phys. Rev B **31**, 93 (1985)
[15] D. Guenzburger and D. E. Ellis, Phys. Rev. B **45**, 285 (1992).
[16] M. R. Press, S. N. Khanna, and P. Jena, Phys. Rev B **36**, 5446 (1987).
[17] V. L. Moruzzi, J. F. Janak, and A. R. Williams, *Calculated Electronic Properties of Metals* (Pergamon, New York, 1978)

Published without author corrections

Effects of Al substitution in Nd_2Fe_{17} studied by first-principles calculations

Ming-Zhu Huang and W. Y. Ching
Department of Physics, University of Missouri-Kansas City, Kansas City, Missouri 64110

We have studied the effect of Al substitution in Nd_2Fe_{17} compound by means of first-principles calculations. We first obtain the site-decomposed potentials for Fe from self-consistent calculation on Y_2Fe_{17} and the atomiclike potentials in the crystalline environment for Al and Nd. Calculations are carried out for a single Al substituting one Fe at four different Fe sites ($6c$), ($9d$), ($18f$), and ($18h$), two Al substituting two Fe ($18h$), and four Al substituting three Fe ($18h$) and one Fe ($18f$). Our results show that the Al moment is oppositely polarized to Fe. The average moment per Fe atom actually increases for Al substituting Fe ($18h$) and Fe ($18f$) is about the same for Al substituting Fe ($6c$), and is drastically reduced when replacing Fe ($9d$). Experimentally, Al is shown to be excluded from the ($9d$) sites because of the small Wigner–Seitz volume. When two Fe atoms are replaced by two Al atoms, the total moment is only slightly less than when only one Fe atom is replaced, and the M_s per Fe site actually increases, in agreement with the Mössbauer data. These results are analyzed in terms of the local atomic geometry and the charge transfer effect from the neighboring Fe to Al.

Recently, there has been a renewed interest in studying the substitutional effects in the R_2Fe_{17} intermetallic compounds (R represents a rare-earth element). The R_2Fe_{17} compounds in the rhombohedral Th_2Zn_{17} structure have high magnetic moments and are easy to process. However, none of the binary compounds exhibit uniaxial anisotropy at room temperature. The Curie temperature T_C is usually low, severely limiting their use as permanent magnets. Researchers soon discovered that interstitial doping by nitrogen and carbon can raise T_C substantially[1–4] and significantly modify the magnetocrystalline anisotropy of the R_2Fe_{17} compounds.

In the search for better and cheaper permanent magnets, elemental substitutions have also been explored in addition to interstitial doping, since it may also lead to an increase in Fe-Fe separation. The effects of elemental substitutions on the magnetic properties of R_2Fe_{17} compounds had been studied in the past.[5–8] More recently, Weitzer, Hiebl, and Rogl studied the magnetic behavior of Al and Ga substitution in R_2Fe_{17} compounds.[9] Yelon *et al.* carried out the neutron diffraction and Mössbauer effect studies of several $Nd_2Fe_{17-x}Al_x$ samples with x ranging from 0. to 9.4.[10] Li *et al.* studied the structural and magnetic properties of the combined effect of Al substitution and N doping.[11] These experiments demonstrate that Al has a preference to occupy the Fe ($18h$) sites when x is small and is excluded from the Fe ($9d$) sites at all concentrations.[10] The saturation moment and the T_C have a strong dependence on the Al concentration. Clearly, it is of fundamental interest to carry out theoretical calculations on the electronic structure and magnetic properties of the substituted compounds, and to trace the quantum mechanical origin of the improved magnetic properties.

In this report, we present the results of calculations on the electronic structure, local magnetic moment, charge, and spin density distribution for $Nd_2Fe_{17-x}Al_x$ ($x=0,1,2,4$). To our knowledge, there is not yet any theoretical calculation on the substitutional compounds of R_2Fe_{17}. For $x=1$, replacement of Fe by Al at each of the four Fe sites is studied even though the probability of Al occupation at certain Fe sites is almost zero. For $x=2$, we replace two Fe ($18h$) in the unit cell and for $x=4$, we replace three Fe ($18h$) and one Fe ($18f$). These proposed substitutional configurations are based on the neutron scattering data[10] which suggest Fe ($18h$) to be the most likely site for Al substitution, followed by the Fe ($18f$) site, and the occupation of the ($18h$) site tends to saturate at about half of the fraction. The lattice constants used in the calculation are from different sources,[10,12,13] and are listed in Table I. For simplicity, the experimental value for x has been rounded to the nearest integer. The calculated results are then correlated to the available experimental data.

We briefly outline the procedures of our calculation. We use the first-principles orthogonalized linear combination of the atomic orbitals method in the local spin density approximation (LSDA).[14] The computational details of this method have been described sufficiently elsewhere.[15] Since Nd contains localized $4f$ electrons for which the LSDA may not be a suitable theory, we start our calculation with Y_2Fe_{17} and $Y_2Fe_{17-x}Al_x$ but with the same lattice constants as for the corresponding $Nd_2Fe_{17-x}Al_x$ systems. We next obtain the site-decomposed Fe and Al potentials from these self-consistent calculations. Together with an atomiclike potential for Nd that has been used in the $Nd_2Fe_{17}B$ calculation,[16] we perform a series of spin-polarized calculations on $Nd_2Fe_{17-x}Al_x$. Interactions of the Nd-$4f$ orbitals with the neighboring atoms are taken into account with three of the Nd-$4f$ electrons fixed in the spin-up configuration.[16] Secular equations are solved for both spin cases at 11 special k points in the irreducible portion of the Brillouin zone to obtain the energy eigenvalues and wave functions. Spin-orbit couplings are neglected. Local spin magnetic moments are obtained from the wave functions and the overlap integrals using the Mulliken scheme.[17] In principle, for solid solutions of the type $Nd_2Fe_{17-x}Al_x$, a supercell calculation with sufficient statistical average over various possible configurations will be most desirable. However, such calculations will need a prohibitively large amount of computational time. For that reason, we limit our calculations to the original rhombohe-

 0021-8979/94/76(10)/7046/3/$6.00 © 1994 American Institute of Physics

TABLE I. Calculated site-decomposed spin moments (μ_B) in $Nd_2Fe_{17-x}Al_x$. An asterisk indicates the site is a nearest neighbor to the Al atom.

	$X=0$	$X=1$				$X=2$	$X=4$
Latt. Cont.							
a (Å)	8.5782 (Ref. 12)	8.612 (Refs. 10,12)				8.6569 (Ref. 10)	8.6882 (Ref. 13)
c (Å)	12.464	12.511				12.5782	12.6589
Atom site		(18h)	(18f)	(6c)	(9d)	2(18h)	3(18h),(18f)
1 Nd (c)	−0.43	−0.35	−0.41	−0.45	−0.50	−0.28	−0.16
2 Nd (c)		−0.41	−0.41	−0.45	−0.50	−0.33	−0.29
3 Fe (c)	2.00	2 21*	2.04*	1.83*	1.70*	2.38*	2.52*
4 Fe (c)		1.85	2.04*	···	1.71*	1.75	1.62*
Al				−0.32			
5 Fe (d)	1.55	1.71*	1.59*	1.56*	1.56	1 70*	1.85*
6 Fe (d)		1.55	1.66*	1.60*	1.57	1.82*	2.01*
7 Fe (d)		1.69*	1.55	1.55*	···	1.84*	1.79*
Al					−0.16		
8 Fe (f)	1.94	1.78	1.96*	1.93*	1.54*	2.06*	2.24*
9 Fe (f)		2.16*	2.01*	1.95*	1.54*	2.42*	2.37*
10 Fe (f)		2.09*	1.93	1 94*	1.59	2.01*	2 23*
11 Fe (f)		2.06*	1.89	1.92*	1.53*	2.30*	2 21*
12 Fe (f)		2 15*	1.91	1.94*	1.54*	2.05*	2.24*
13 Fe (f)		1.79	···	1.95*	1.58	2.00*	···
Al			−0 24				−0.22
14 Fe (h)	1.89	2.02*	1.91*	1.86*	1.66	2.23*	2.22*
15 Fe (h)		2.02*	1.82	1.79*	1.72*	1.94*	2.14*
16 Fe (h)		1.90	2.07*	2.05*	1.75*	2.20*	2.47*
17 Fe (h)		1.71	1 92*	1.82	1.65	1.66	···
18 Fe (h)		1.71	1.86*	1.81	1.71*	···	···
19 Fe (h)		···	2.03	2.04	1.75*	···	···
Al		−0.27				−0.28	−0.26
						−0.25	−0.26
							−0 23
Total (excluding Nd 4f)	30.79	29.36	28 72	28.32	24 95	29 18	26 49
Average Fe M_s	1.86	1.90	1.89	1.85	1.50	2.02	2.04

dral cell containing two Nd atoms and 17 Fe atoms with some of them substituted by Al as specified above. Lattice relaxation at the substituted sites is not considered, and all calculations are for a single configuration. Even with these limitations, we believe our results are meaningful for comparing the effect of substitution at different Fe sites and with different Al concentrations.

Table I lists the calculated magnetic moments at the two Nd and the 17 Fe (Al) sites for $Nd_2Fe_{17-x}Al_x$. For $x=0$, the moments on the Fe sites of the same symmetry type are the same. With Al substitution, the symmetry is lowered and the moments at all sites are different. To better understand these results, we put an asterisk on the moment number to indicate that this particular site is a nearest neighbor (NN) to a substituted Al atom. Oppositely polarized moments are listed as negative numbers. The main results of Table I can be summarized as follows. (1) The moments on the Nd and Al are oppositely polarized. (2) For a single Al substitution, the average Fe moments are 1.90, 1.89, 1.65, and 1.50 μ_B for Al at the (18h), (18f), (6c), and (9d) site, respectively. For $x=0$, the calculated average Fe moment is 1.86 μ_B. The average Fe moment becomes particularly low when the Fe(9d) is substituted by Al. Neutron diffraction data show the (9d) site is excluded from Al occupation. (3) For those sites which are NN to a substituted Al (with the exception of the Al at the 9d site), the moments tend to increase relatively, showing the influence of the Al on the neighboring Fe atoms. Effective charge calculation based on the Mulliken scheme[17] shows an average charge transfer of the order of 1.8 electrons from the Fe sites to the Al. (4) Although the total moment decreases as x increases, the average moment per Fe atom actually increases with x. Yelon *et al.*[10] found an increase in the occupation fraction at the (6c), (18f), and (18h) sites with an increase in x up to $x=9.4$. The fractional occupation for Fe (18h) saturates at $x=4$. On the other hand, the hyperfine field from the Mössbauer spectra reaches a maximum at $x=2$, and then decreases with increase in x.

The microscopic origin as to why the Fe moment is increased or decreased depending on the specific site of Al substitution is more difficult to pin down. It will require extensive analysis of local local geometry and interatomic distances in relation to the electronic structure. The extended

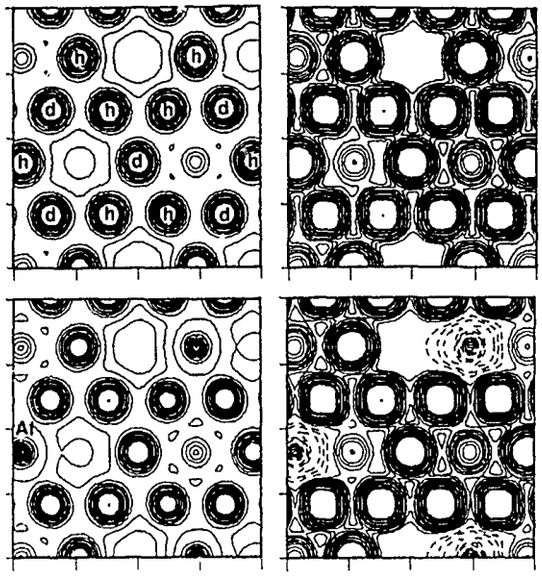

FIG. 1. Calculated charge density (left-hand panel) and spin density (right-hand panel) for Nd_2Fe_{17} (upper panel) and $Nd_2Fe_{16}Al_1$ (lower panel). The contour lines are: 0.01, 0.02, 0.04, 0.06, 0.08, 0.10, 0.15, 0.20, 0.25, 0.30, 0 40, 0.50 for charge density, and plus or minus of 0.001, 0.002, 0.003, 0 004, 0.006, 0 008, 0.01, 0.015, 0.020, 0.030, 0.040, 0 050 for the spin density. Negative numbers are indicated by dashed contours.

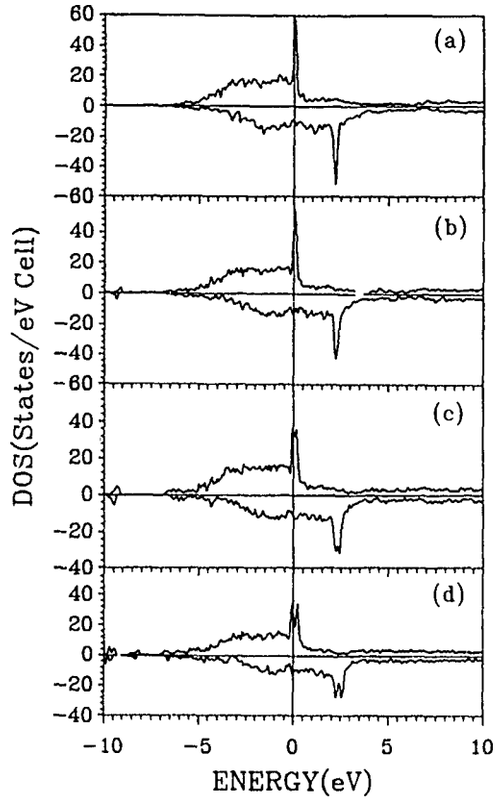

FIG. 2 Calculated total DOS for (a) Nd_2Fe_{17}; (b) $Nd_2Fe_{16}Al_1$; (c) $Nd_2Fe_{15}Al_2$, (d) $Nd_2Fe_{13}Al_4$. Positive values correspond to the majority spin band and negative values corresponds to the minority spin band.

nature of the Al-3s and Al-3p wave functions make it difficult to explain these rather complicated results based on simple arguments.

To further understand the calculated data in Table I and the role of Al atoms, we plot in Fig. 1, the charge and spin densities for Nd_2Fe_{17} and $Nd_2Fe_{16}Al_1$ with Al at the (18h) site. The plane of Fig. 1 is perpendicular to the c axis which contains the Fe (18h) atoms with the Fe (9d) atoms also very close to it and no Nd atoms. It is obvious that Al substitution breaks the local symmetry in the charge and spin distribution. The nonspherical and the negatively polarized spin density at the Al site are quite obvious. Similar distribution maps on other planes containing other Fe and Al sites are available but not shown. For Al substituting Fe (9d), charge- and spin-density maps reveal a much stronger interaction of Al with the nearby Fe atoms. This clearly indicates that the 9d site is small, hence unfavorable for Al occupation, in agreement with the conclusion of Ref. 10.

Figure 2 shows the total density of states (DOS) for $Nd_2Fe_{17-x}Al_x$ for $x=0$, 1, 2, and 4. The $x=1$ result is for Al substituting one Fe (18h). The Fermi energy is set at 0. The sharp peak near E_F for the majority spin band and at 2.5 eV for the minority spin band are from the Nd-4f states. The height of the Nd-4f peaks decreases as the Al concentration increases. The width of the occupied band is about 7 eV in all cases, but the total areas below E_F decrease because of reduced electron number as x increases. Partial DOS (not shown) indicates that Al-3p states are in the -4.5 to -4.7 eV range, and the split states near -9.5 eV originate from Al-3s. For $x=4$, Fig. 2(d) shows the splitting of the Nd-4f peaks and additional Al-3s states emerge at -8.5 eV. This simply reflects the fact that for $x=4$, Al replaces Fe atoms at two different sites, (18h) and (18f). The first-principles nature of the calculation accurately reflects the complicated interatomic interactions.

This work was supported by DOE Grant No. DE-FG02-84ER45170. M.-Z.H. was partially supported by a grant from the National Natural Science Foundation of China under Grant No. 188074.

[1] J. M. D Coey and H. Sun, J. Magn. Magn. Mater. **87**, L251 (1990)
[2] H. Sun, J. M D. Coey, Y. Otani, and D. P. F. Hurley, J. Phys. Condens. Matter **2**, 6465 (1990)
[3] X. P. Zhong, R. J. Radwanski, F. R. de Boer, T. H. Jacobs, and K. H. J. Buschow, J. Magn Magn. Mater. **86**, 333 (1990).
[4] Y. C. Yang, X. D. Zhang, L. S. Kong, Q. Pan, and S. I. Ge, Appl Phys. Lett. **58**, 204 (1991).
[5] K. S. V. L. Narasimhan and W. E. Wallace, AIP Conf Proc **18**, 1248 (1974).
[6] D McNeely and H. Oesterreicher, J. Less-Common Met. **44**, 183 (1976).
[7] D. Plusa, R. Pfaranger, and B. Wyslocki, J. Less-Common Met. **99**, 87 (1984).
[8] B. P. Hu and J. M. D. Coey, J. Less-Common Met. **142**, 295 (1988).
[9] F. Weitzer, K. Hiebl, and P Rogl, J. Appl. Phys **65**, 4963 (1989).
[10] W. B. Yelon, H. Xie, G. J. Long, O. A. Pringle, F. Grandjean, and K H J. Buschow, J. Appl. Phys. **73**, 6029 (1993).
[11] X. W. Li, N. Tang, Z. H. Lu, T. Y. Zhao, W. G. Lin, R W Zhao, and F. M Yang, J Appl. Phys. **73**, 5890 (1993)
[12] T. Kajitani *et al.*, J. Appl. Phys. **73**, 6032 (1993).
[13] W. B Yelon (private communication).
[14] W. Y Ching, J. Am. Ceram. Soc. **73**, 3135 (1990), W. Y. Ching, Y.-N Xu, B.-N. Harmon, J. Ye, and T C. Leung, Phys. Rev. B **42**, 4460 (1990).
[15] M.-Z. Huang and W. Y. Ching, J Appl Phys (submitted).
[16] Z Q Gu and W. Y Ching, Phys. Rev. B **36**, 8530 (1987).
[17] M. S Mulliken, J. Am. Chem. Soc. **23**, 1833 (1955).

Magnetic and crystallographic order in α-manganese

A. C. Lawson, Allen C. Larson, M. C. Aronson,[a] S. Johnson,[b] Z. Fisk, P. C. Canfield,[c]
J. D. Thompson, and R. B. Von Dreele
Los Alamos National Laboratory, Los Alamos, New Mexico 87545

We have made time-of-flight neutron diffraction measurements on α-manganese metal. Powder diffraction measurements were made at 14 temperatures between 15 and 305 K, and single crystal measurements were made at 15 and 300 K. We found that the crystal structure of α-Mn is tetragonal below its Néel point of 100 K, with crystal symmetry $I\bar{4}2m$ and magnetic (Shubnikov) symmetry $P_I\bar{4}2_1c$. In agreement with the earlier results of Yamada *et al.*, there are six independent magnetic atoms, and we found that their moments are weakly temperature dependent. The onset of magnetic order causes slight changes in the atomic positions and in the average atomic elastic constant.

I. INTRODUCTION

α-manganese has a surprisingly complex cubic crystal structure with 58 atoms per body-centered cell.[1] The complexity is surprising, because most elements have simple structures. In the case of Mn, the complexity is thought to arise from an instability of the $3d$ electron shell that gives rise to the formation of "self-intermetallic" compounds. In other words, elemental Mn is actually an intermetallic compound between Mn atoms in different electronic configurations. This possibility was first pointed out by Bradley and Thewlis.[1]

α-Mn becomes antiferromagnetic at 95 K. Given the crystal structure, the magnetic structure is necessarily complex. The structure was solved by Yamada *et al.*,[2] who used single crystal neutron diffraction data and first principles magnetostructural analysis of heroic proportions.[2–4] We wished to examine the magnetic ordering in more detail by obtaining structural data at a large number of temperatures. The multitemperature requirement dictated the use of powder neutron diffraction. However, we found that information from single crystal data was essential to the complete solution of the problem.

II. EXPERIMENTAL METHOD

α-Mn was prepared by heating Johnson-Matthey grade I electrolytic Mn in a turbomolecular pumped system in the β-phase region until outgassing was complete and then cooling slowly through the α–β transition. The material was cooled from 900 °C to 755 °C over 5 h, from 755 °C to 655 °C over 200 h, and finally furnace cooled to room temperature. Powder was prepared by grinding the resulting material. Small single crystals were cut from an arc-melted ingot that was prepared from this material and annealed for a long time below the α–β transition. Neutron powder diffraction data were taken on an α-Mn sample at 14 temperatures between 15 and 305 K. We used the high intensity powder diffractometer (HIPD) and the Manuel Lujan, Jr. Neutron Scattering Center (LANSCE) at the Los Alamos National Laboratory.[5] We also obtained single crystal diffraction data at 15 and 300 K on the single crystal diffractometer (SCD) at LANSCE. Powder data were analyzed by Rietveld analysis using the general structure analysis system (GSAS).[6] This refinement package allows for the refinement of magnetic reflections arising from structures that can be described by Shubnikov groups. Powder data from six detector bands were corefined in the analysis. Allowance was made for 0.90% (vol) of MnO that was present in the powder and for some weak aluminum lines from the cryostat. Single crystal data were also refined using GSAS. In this case, magnetic multidomain effects were treated as a twinning problem.

III. RESULTS AND DISCUSSION

Since there was no evidence for an incommensurate structure, our approach to the analysis of our data was guided by the use of Shubnikov groups.[7,8] These are magnetic space groups that are supergroups of the ordinary crystallographic space groups, with certain symmetry elements replaced by "anti"-elements. The antielements are the ordinary translations, mirror planes, etc., familiar from crystallography, except that the spatial symmetry operator is augmented by a time-reversal operator that reverses the microscopic current

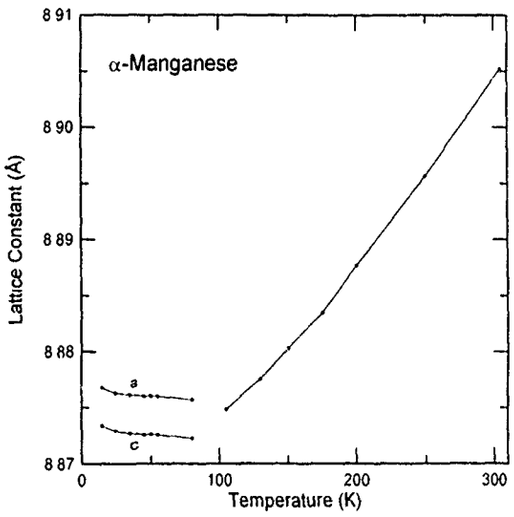

FIG. 1 Lattice constants vs temperature for α-Mn. The error bars are smaller than the plotted points.

[a]Present address Department of Physics, University of Michigan, Ann Arbor, Michigan.
[b]Deceased.
[c]Present address: Ames Laboratory, Iowa State University, Ames, Iowa 50011

 0021-8979/94/76(10)/7049/3/$6.00 © 1994 American Institute of Physics

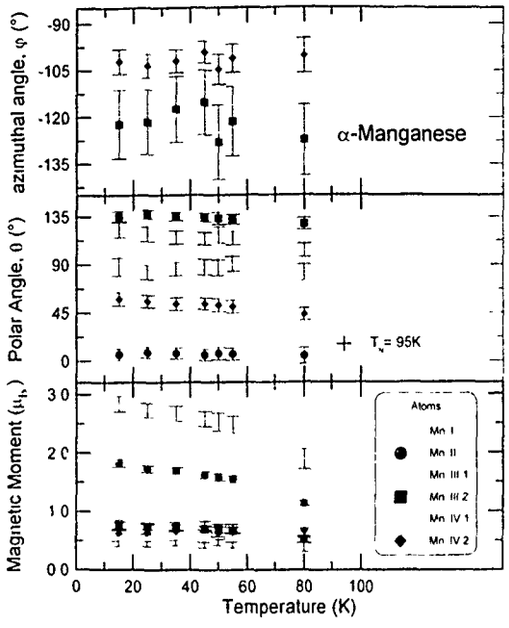

FIG. 2. Magnetic moments vs temperature for α-Mn.

driving the magnetic moment of the atom to which it is applied. In this way, 1651 magnetic space groups can be obtained from the original 230 ordinary space groups. Only commensurate magnetic structures are described by the Shubnikov groups.

The space group of α-Mn is $I\bar{4}3m$. The neutron diffraction data indicate a body-anti-centered lattice, so that the Shubnikov group $P_I\bar{4}3m$, or one of its subgroups, is indicated. The cubic and rhombohedral subgroups did not work, and we found that the best fit was obtained with the tetragonal Shubnikov group $P_I\bar{4}2'm' \equiv P_I\bar{4}2c$, which is a subgroup of the tetragonal space group $I\bar{4}2m$. This is equivalent to the magnetic model of Yamada *et al.*[2] The meaning of the symbol $P_I\bar{4}2'm'$ is the same as the ordinary space group symbol $I\bar{4}2m$, except that (1) the ordinary body-centering operator is replaced by an operator that flips the spin (reverses the current) as the body centering is applied; (2) the mirror planes are replaced by operators that reverse the current as a magnetic atom is reflected; and (3) the twofold axes are replaced by operators that flip the spin (reverse the current) as the dyad operation is applied to a magnetic atom. (The distinction between spin flipping and reversing the current is important only for improper symmetry operators, such as mirror planes.)

TABLE I. Atomic coordinates for α-Mn at 305 K.

	I	II	III	IV
x	0	0.318 36(5)	0.357 76(3)	0 090 81(4)
y	"	"	"	"
z	"	"	0 035 43(4)	0.282 76(5)

In addition to the group $P_I\bar{4}2'm'$, we also tried fits with $P_I\bar{4}2m$, $P_I\bar{4}'2m'$, and $P_I\bar{4}\ 2'm$. (Of these four, only the first does not exclude a magnetic moment on site I by symmetry.) The models with $P_I\bar{4}2m$ and $P_I\bar{4}'2m'$ can be excluded by the single crystal data, which clearly show the presence of (300), (500), etc. magnetic reflections, in agreement with Yamada *et al.*[2] This is indicative of the presence of the two-fold antiaxis 2′. These reflections are not directly observable in the powder data because of overlapping allowed reflections, so that powder data cannot distinguish between 2 and 2′.

The quality of the powder fits for $P_I\bar{4}2'm'$ and $P_I\bar{4}'2m'$ is very similar, so that single crystal data was essential for making this distinction. However, the use of powder data is the only practical way of making observations at a large number of temperatures in a reasonable amount of time. The combination of both types of experiment was necessary in this case.

Since the magnetic structure of α-Mn is tetragonal, a tetragonal nuclear (or chemical) structure is implied. This structure was found by Rietveld refinement. The space group is $I\bar{4}2m$, and there are six unique atoms in the tetragonal unit cell. Above the Néel point, the structure is cubic with four unique atoms in the cell. There are 58 atoms per unit cell in each case.

Figure 1 shows the lattice constants of α-Mn plotted versus temperature. We emphasize that no tetragonal splitting of the diffraction lines was observed directly; rather, the metric tetragonality was found by testing the powder data with Rietveld refinement. Simultaneous refinements of the strain broadening were well behaved, and sensible atomic positions were found, so we have some confidence in this result. The average of the tetragonal lattice constants agree with previous diffraction measurements for which the low-temperature structure was taken to be cubic.[9,10]

The magnetic moments are plotted versus temperature in Fig. 2. These were obtained from the powder refinements using the form factors for the $3d^5 4s^2$ state of neutral Mn determined by Freeman and Watson.[11] Thus, we did not allow for a variation of the form factor among the atoms, as

TABLE II. Atomic coordinates and magnetic moments (μ_B) for α-Mn at 15 K.

	I	II	III-1	III-2	IV-1	IV-2
x	0	0.3192(2)	0 3621(1)	0 3533(2)	0 0921(2)	0.0895(2)
y	"	"	"	0.0333(1)	"	0.2850(1)
z	"	0 3173(3)	0 0408(2)	0.3559(2)	0.2790(3)	0 0894(2)
m_x	0	0.14(12)	0.43(8)	−0 25(10)	0 27(8)	−0 08(4)
m_y	"	"	"	−0.25(10)	"	−0 45(8)
m_z	2.83(13)	1.82(06)	0.43(8)	−0.32(4)	−0.45(8)	0.48(5)

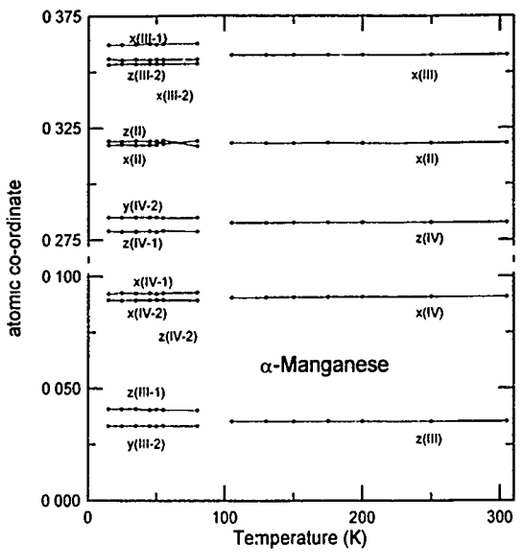

FIG. 3. Positional parameters for α-Mn. The error bars are smaller than the plotted points.

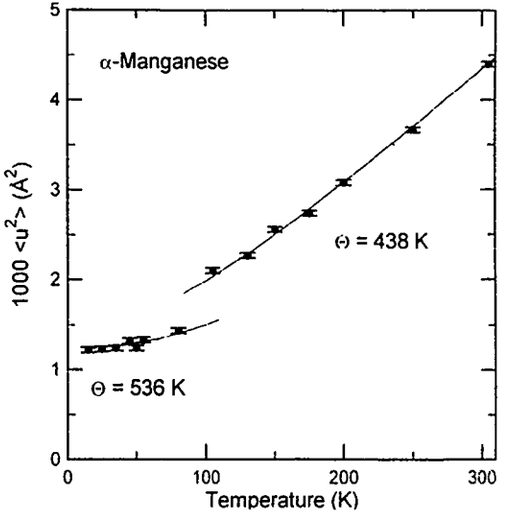

FIG. 4. Average mean square thermal displacement, $\langle u^2 \rangle$, vs temperature for α-Mn. The lines through the points are fits to a simple Debye–Waller formula. The fitted Debye–Waller temperatures are different above and below the Néel temperature.

did Yamada *et al.*[2] The moments we found are somewhat different from theirs, but the significant qualitative feature of groups of large and small moments is retained. The large moments on atoms I and II are somewhat temperature dependent, and the smaller moments on the remaining atoms are not.

The atomic positions also show the effects of magnetic ordering. Below the Néel temperature, the original four crystallographic sites of the cubic structure (Table I) split into the six sites of the tetragonal structure (Table II). The atomic positions obtained from the powder refinements are plotted versus temperature in Fig. 3. A diagram of the magnetic structure is given in the compilation by Wijn.[12] The Cartesian components of the magnetic moments at 15 K are given in Table II.

Magnetic ordering in α-Mn causes a stiffening of the lattice. Figure 4 shows the average mean-square thermal displacement, $\langle u^2 \rangle$, plotted versus temperature. The $\langle u^2 \rangle$ is obtained from the Debye–Waller factors from the Rietveld analysis of the powder data; it is averaged over atomic sites and direction.[13,14] We have made separate fits above and below the Néel temperature to the $\langle u^2 \rangle$ versus temperature data with a simple Debye model. The increase in Θ_{DW} observed at the Néel point (from 438 to 536 K) is quite large.

ACKNOWLEDGMENTS

This work was supported under the auspices of the United States Department of Energy. The Manuel Lujan, Jr. Neutron Scattering Center is a national user facility funded under Contract No. W-7405-ENG-36 by the United States Department of Energy, Office of Basic Energy Science. We wish to thank Professor Bryan R. Coles for the inspiration of his persistent interest in the structure of α-Mn.

[1] A. J. Bradley and J. Thewlis, Proc. R. Soc. London Ser. A **115**, 456 (1927).
[2] T. Yamada, N. Kunitomi, Y. Nakai, D. E Cox, and G. Shirane, J. Phys. Soc. Jpn. **28**, 615 (1970).
[3] T. Yamada, J. Phys. Soc. Jpn. **28**, 596 (1970).
[4] T. Yamada and S. Tazawa, J. Phys. Soc. Jpn. **28**, 609 (1970).
[5] A. C. Lawson, J. A. Goldstone, J. G. Huber, A. L. Giorgi, W. Conant, A. Severing, B. Cort, and R. A. Robinson, J. Appl. Phys. **69**, 5112 (1991).
[6] A. C. Larson and R. B. Von Dreele, Los Alamos National Laboratory Report No. LAUR 86-748 (1986).
[7] A. V. Shubnikov and N. V. Belov, *Colored Symmetry* (Wiley, New York, 1964), pp. 198–210.
[8] V. A Koptsik, *Shubnikov Groups* Izd., Moskovsk. Gos. Univ. Moscow, (1966), (in Russian).
[9] J. A. C. Marples, Phys. Lett. A **24**, 207 (1967).
[10] C.P. Gazzara, R. M. Middleton, R. J. Weiss, and E. O. Hall, Acta Crystallogr. **22**, 859 (1967)
[11] A. J. Freeman and R. E. Watson, Acta Crystallogr. **14**, 231 (1961)
[12] H. P. J. Wijn, *Magnetic Properties of Metals. d-Elements and Compounds* (Springer, New York, 1991), pp. 4–5.
[13] A. C. Lawson, A. Williams, J A. Goldstone, D. T. Eash, R. J Martinez, J. I. Archuleta, D. J. Martinez, B. Cort, and M. F. Stevens, J. Less-Common Met. **167**, 353 (1991).
[14] A. C Lawson, G. H. Kwei, J. A. Goldstone, B. Cort, R. I. Sheldon, E. Foltyn, J. Vaninetti, D. T. Eash, R. J. Martinez, and J.I. Archuleta, *Advances in X-Ray Analysis*, edited by V. Gilfrich *et al.* (Plenum, New York, 1993), Vol. 36, p. 577.

Magnetic field dependence of T_c of EuB_6 (abstract)

A. Lacerda and T. Graf
National High Magnetic Field Laboratory, Pulsed Facility, Los Alamos National Laboratory, Mail Stop E536, Los Alamos, New Mexico 87545

J. L. Sarrao, M. F. Hundley, D. Mandrus, J. D. Thompson, and Z. Fisk
Los Alamos National Laboratory, Mail Stop K764, Los Alamos, New Mexico 87545

We report measurements of resistivity and transverse magnetoresistance ($B \perp I$) on a single crystalline sample of EuB_6 in magnetic fields to 18 T in a temperature range from 4 to 100 K. The ferromagnetic transition (T_c) determined by resistivity versus temperature at constant field varies from 10 to 25 K at zero and 4 T, respectively. The transition is completely suppressed at 8 T. A very large and negative tranverse magnetoresistance is observed in the entire temperature range investigated: -5% at 4 K and -20% at 100 K at 18 T. Finally, the effect of high applied magnetic field on the transport properties is investigated in the temperature range below T_c.

Work supported under the auspices of the National Science Foundation.

 0021-8979/94/76(10)/7052/1/$6.00 © 1994 American Institute of Physics

Two- and three-dimensional calculation of remanence enhancement of rare-earth based composite magnets (invited)

T. Schrefl
Institut für Angewandte und Technische Physik, T. U. Wien, Wiedner Hauptstrasse 8, A-1040 Vienna, Austria, and Max-Planck-Institut für Metallforschung, Institut für Physik, Postfach 80 06 65, 70506 Stuttgart, Germany

R. Fischer
Max-Planck-Institut für Metallforschung, Institut für Physik, Postfach 80 06 65, 70506 Stuttgart, Germany

J. Fidler
Institut für Angewandte und Technische Physik, T. U. Wien, Wiedner Hauptstrasse 8, A-1040 Vienna, Austria

H. Kronmüller
Max-Planck-Institut für Metallforschung, Institut für Physik, Postfach 80 06 65, 70506 Stuttgart, Germany

Micromagnetic calculations using a finite element technique rigorously describe the magnetic properties of novel, isotropic rare-earth-based composite magnets. Numerical results obtained for a composite material of $Nd_2Fe_{14}B$, $SmCo_5$ or $Sm_2(Fe_{0.8}Co_{0.2})_{17}N_{2.8}$ and α-Fe particles show that remanence, coercivity, and coercive squareness sensitively depend on microstructural features. Interparticle exchange interactions enhance the remanence by about 60% with respect to noninteracting particles for a mean-grain size approaching the exchange length of the soft magnetic phase and a significant percentage of α-Fe. On the other hand, exchange interactions between the phases suppress the nucleation of reversed domains and thus preserve a high coercive field. Therefore, optimally structured, isotropic composite magnets show remarkably high energy products exceeding 400 kJ/m^3.

I. INTRODUCTION

Composite materials of magnetically hard and soft particles are excellent candidates for high performance permanent magnets. In composite permanent magnets soft magnetic grains cause a high magnetization and hard magnetic grains induce a large coercivity provided that the particles are small and strongly exchange coupled. Owing to remanence enhancement, nanostructured, composite magnets are expected to improve the maximum energy product of permanent magnets dramatically.[1] Coehoorn, Mooij, and Waard[2] found a considerably increased remanence in melt-spun Nd-Fe-B magnets of nominal composition containing a substantial fraction of soft magnetic Fe_3B grains. Recently, Ding, McCormick, and Street[3] reported a maximum energy product of more than $(BH)_{max}=200$ kJ/m^3 in mechanically alloyed, isotropic Sm_7Fe_{93}-nitride powders where exchange interactions between a soft magnetic α-Fe and a hard magnetic $Sm_2Fe_{17}N_x$ phase cause a significant enhancement of the remanence. A similar behavior was found in composite magnets of $Nd_2Fe_{14}B$ and α-Fe produced by rapid solidification.[4,5] The maximum possible energy product is an intrinsic quantity $(BH)^*_{max}=J_s^2/(4\mu_0)$,[6] depending only on the spontaneous magnetic polarization J_s. In order to reach this theoretical maximum, it is required that the magnet maintains saturated until the opposing field reaches the value $-(1/2)(J_s/\mu_0)$.[7] In real magnets the remanent polarization J_r rather than the spontaneous magnetic polarization will determine the maximum energy product, $(BH)_{max}$. Within the framework of the Stoner–Wohlfarth theory,[8] which assumes noninteracting single domain particles, the remanent magnetic polarization is given by

$$J_r=J_s\langle\cos\vartheta\rangle, \tag{1}$$

where ϑ is the angle between the saturation direction and the easy axes and $\langle\ \rangle$ denotes an ensemble average. According to (1) J_r/J_s is 0.5 for an assembly of noninteracting and randomly oriented particles, whereas J_r/J_s is $2/\pi=0.637$ for microstructures with in-plane random texture.

A theoretical treatment of remanence enhancement must take into account interactions of the grains. Using a one-dimensional micromagnetic model, Kneller and Hawig[9] estimated the optimum microstructure of composite magnets to consist of hard grains embedded in a magnetically soft matrix with the lateral dimensions of both phases about equal to the domain wall width of the hard magnetic phase. Grönefeld[10] numerically calculated the remanence of composite magnets, solving Poisson's equation for the magnetization distribution on a lattice of magnetically hard and soft moments. The results show that almost all the magnetic moments of the soft magnetic phase become aligned parallel to the saturation direction, which corresponds to the average direction of the easy axes of the neighboring hard magnetic grains. Nieber *et al.*[11] and Skomski *et al.*[1] explicitly derived the magnetic properties of multilayers being composed of

 0021-8979/94/76(10)/7053/6/$6.00 © 1994 American Institute of Physics

magnetically soft and hard layers. This article gives a quantitative treatment of the correlation between the microstructure and the magnetic properties of isotropic, rare-earth based composite magnets. In order to describe magnetization processes of realistic microstructures, the classical Stoner–Wohlfarth theory[8] has been extended to nonellipsoidal and interacting particles using a finite element technique.

Section II of this article introduces the micromagnetic concepts and the computational methods of the simulation model. Section III describes the two- and three-dimensional grain structures used for the calculations. Section IV presents the basic magnetic properties of nanocrystalline, composite magnets. Section V compares the demagnetization curves obtained for composite materials of $Nd_2Fe_{14}B$, $SmCo_5$, $Sm_2(Fe_{0.8},Co_{0.2})_{17}N_{2.8}$ and α-Fe particles.

II. MICROMAGNETIC AND COMPUTATIONAL BACKGROUND

Minimizing the total magnetic Gibb's free energy with respect to the magnetic polarization $\mathbf{J}_s$, subject to the constraint that $|\mathbf{J}_s|$ is constant, yields a stable equilibrium state of a magnetic structure. If one neglects magnetoelastic and surface anisotropy effects, the magnetic Gibb's free energy ϕ_t of a ferromagnetic specimen in an applied magnetic field is the sum of the exchange energy, the magnetocrystalline anisotropy energy, the stray field energy, and the magnetostatic energy of the $\mathbf{J}_s$ in an external field $\mathbf{H}_{ext}$.[12] For uniaxial magnetic materials, where the direction of $\mathbf{J}_s$ may be described by the angle α between $\mathbf{J}_s$ and the easy axis, ϕ_t is given by[13]

$$\phi_t = \int \{A[(\nabla\vartheta)^2+(\nabla\varphi)^2 \sin^2\vartheta]+K_1 \sin^2\alpha + K_2 \sin^4\alpha - \tfrac{1}{2}\mathbf{J}_s\cdot\mathbf{H}_d-\mathbf{J}_s\cdot\mathbf{H}_{ext}\}d^3r, \quad (2)$$

where K_1, K_2 are the anisotropy constants, and A is the exchange constant. Using the polar angle φ and the azimuth angle ϑ to represent $\mathbf{J}_s$, automatically fulfills the nonlinear constraint, $|\mathbf{J}_s|=J_s$, during minimization. All energy terms but the stray field energy, $\phi_s=-\frac{1}{2}\int\mathbf{J}_s\cdot\mathbf{H}_d d^3r$, depend only locally on the magnetic polarization $\mathbf{J}_s$. The demagnetizing field $\mathbf{H}_d$ follows from magnetic volume charges, $\nabla\cdot\mathbf{J}_s$, within the grains and magnetic surface charges, $\mathbf{J}_s\cdot\mathbf{n}$ ($\mathbf{n}$ denotes the surface normal) at the grain boundaries. Owing to these long-range contributions of $\mathbf{J}_s$ to $\mathbf{H}_d$, the direct evaluation of the total magnetic Gibb's free energy requires both large memory and long computation time. Introducing a magnetic vector potential to treat the demagnetizing field eliminates long-range interactions from the total Gibb's free energy.[14,15] Brown[16] showed that the stray field energy ϕ_s due to $\mathbf{J}_s(\mathbf{r})$ can be approximated by an upper bound, given by

$$\phi_s \leq W[\mathbf{J}_s,\mathbf{A}]=\frac{1}{2\mu_0}\int(\nabla\times\mathbf{A}-\mathbf{J}_s)^2 d^3r, \quad (3)$$

where $\mathbf{A}$ is an arbitrary continuous vector whose derivatives are also continuous everywhere. The functional W if minimized with respect to $\mathbf{A}$, makes $\mathbf{A}$ equal to the magnetic vector potential $\nabla\times\mathbf{A}=\mu_0\mathbf{H}_d+\mathbf{J}_s$. W itself reduces to the stray-field energy ϕ_s. Replacing the stray-field energy in Eq. (2) by $W[\mathbf{J}_s,\mathbf{A}]$ leads to an auxiliary functional whose local minima are in one-to-one correspondence to those of the total Gibb's free energy.[14] Fredkin and Koehler[17] originally applied a magnetic vector potential in micromagnetic finite element calculations, in order to investigate magnetization processes in irregular shaped particles.

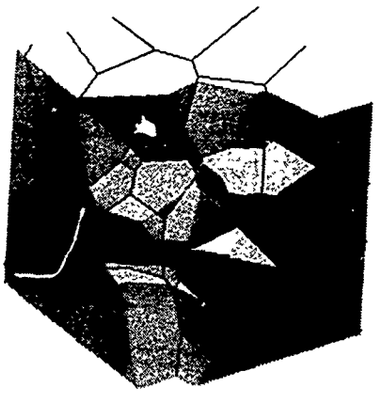

FIG. 1. Grains at the surface and in the interior of the cubic model magnet consisting of 64 irregularly shaped grains.

The linear interpolation of the magnetization angles and of the magnetic vector potential on triangular or tetrahedral elements gives an algebraic optimization problem. Since the magnetic polarization $\mathbf{J}_s$ and the magnetic vector potential $\mathbf{A}$ are two independent variables, the minimization can be performed simultaneously with respect to $\mathbf{J}_s$ and $\mathbf{A}$. Thus convergence difficulties of iterative techniques, which alternate between solving for a magnetic scalar potential for fixed magnetization and minimizing the total energy for fixed demagnetizing field, can be avoided. Among standard numerical minimization techniques, a preconditioned quasi-Newton conjugate gradient method[18] proved to be most efficient for minimizing the total Gibb's free energy of magnetic microstructures. The functional $W[\mathbf{J}_s,\mathbf{A}]$ is an integral not only over the magnetic particle but over the whole space. In principle, the finite element mesh has to be extended over a large region outside the particle. Applying spatial transformations to evaluate the integral reduces the size of the external mesh and provides an accurate approximation of the stray-field energy.[19,20]

III. MAGNETIC MICROSTRUCTURES

Modeling of grain growth yields realistic two- or three-dimensional microstructures. Starting from randomly located seed points, grains grow with constant growth velocity in each direction.[21]

Figure 1 shows a cut through a cubic model magnet consisting of 64 irregularly shaped particles. Figure 2 gives the distribution of the grain diameters. In order to describe composite magnets, material parameters of magnetically hard and soft phases are assigned to each grain. Beginning with the smallest grains, a fraction of the particles are considered to be magnetically soft. Thus the mean grain size of

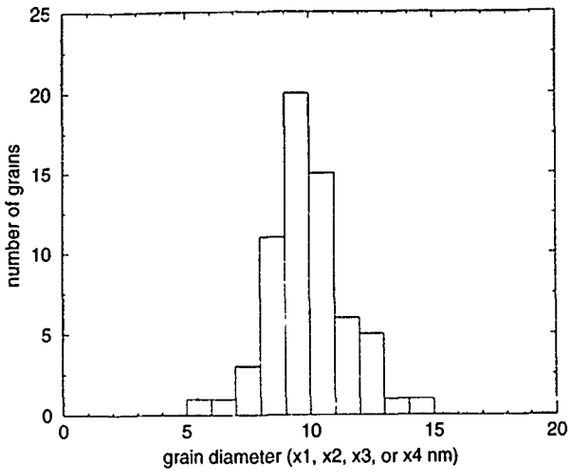

FIG. 2. Grain size distribution of the three-dimensional microstructure. The grain diameter is defined by the diameter of a sphere with equal volume.

the soft magnetic particles becomes smaller than that of the hard magnetic grains which has been been found in rapidly solidified, Nd-Fe-B based composite magnets.[5] The randomly oriented particles have direct contact and are coupled by short-range exchange and long-range magnetostatic interactions.

The basic magnetic properties of isotropic, composite magnets have been calculated for three-dimensional microstructures. However, the computational effort is much smaller in two-dimensional calculations where the magnetization is constrained in a plane and taken to be uniform in a direction perpendicular to this plane. The two-dimensional approximation of naturally three-dimensional magnetization processes does not severely influence the magnetic properties.[20] Thus, the comparison of the magnetic properties of various rare-earth-based composite magnets has been performed using two-dimensional microstructures. The two-dimensional grain structure consists of 30 grains with nearly hexagonal shape. Table I gives the intrinsic magnetic properties of the different materials used for the calculations.

IV. BASIC MAGNETIC PROPERTIES OF ISOTROPIC, COMPOSITE MAGNETS

Figure 3 shows the demagnetization curves of a $Nd_2Fe_{14}B$ and α-Fe magnet for increasing percentage of soft magnetic phases. The solid and the dashed line corresponds to the demagnetization curves for a mean grain size of 10 and 20 nm, respectively. For the calculations, the material parameters of $Nd_2Fe_{14}B$ and α-Fe at room temperature have been used. The numerical results clearly show that the magnetic properties of nanocrystalline, composite magnets drastically changes with the amount of α-Fe and with the average grain size.

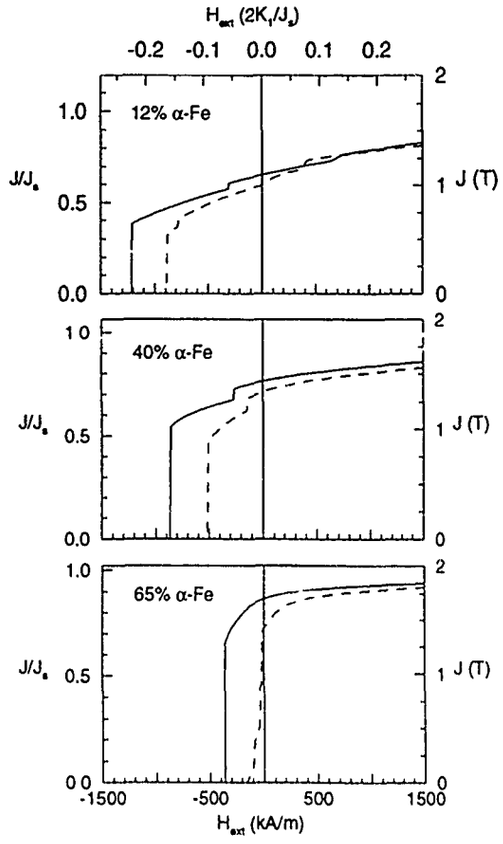

FIG. 3. Demagnetization curves of isotropic, $Nd_2Fe_{14}B$-based, composite magnets containing 12%, 40%, and 65% α-Fe. The different curves refer to 10 nm (solid line) and 20 nm (dashed line) mean grain size.

Figure 4 gives the remanence, the coercive field, and the maximum energy product of $Nd_2Fe_{14}B$-based composite magnets as a function of the amount of α-Fe for a mean grain size of 10 and 20 nm. The remarkably high remanence of nanocrystalline composite magnets has to be attributed to (1) the increased spontaneous magnetization of the soft magnetic phase and (2) remanence enhancement owing to interparticle exchange interactions. Figure 4 compares both con-

TABLE I. Intrinsic magnetic properties at $T=300$ K of hard and soft magnetic materials used for the calculations J_s, K_1, K_2, A, and T_c denotes the spontaneous magnetization, the first and second anisotropy constants, the exchange constant, and the Curie temperature, respectively.

	J_s (T)	K_1 (J/m^3)	K_2 (J/m^3)	A (J/m)	T_c (K)	Ref.
$Nd_2Fe_{14}B$	1.61	4.3×10^6	0.65×10^6	7.7×10^{-12}	588	27
$Sm_2(Fe_{0.8}Co_{0.2})_{17}N_{2.8}$	1.55	10.1×10^6	2.3×10^6	4.8×10^{-12}	842	28
$SmCo_5$	1.06	17.1×10^6		12.0×10^{-12}	1243	29
α-Fe	2.15	4.6×10^4	1.5×10^4	25.0×10^{-12}	1043	30

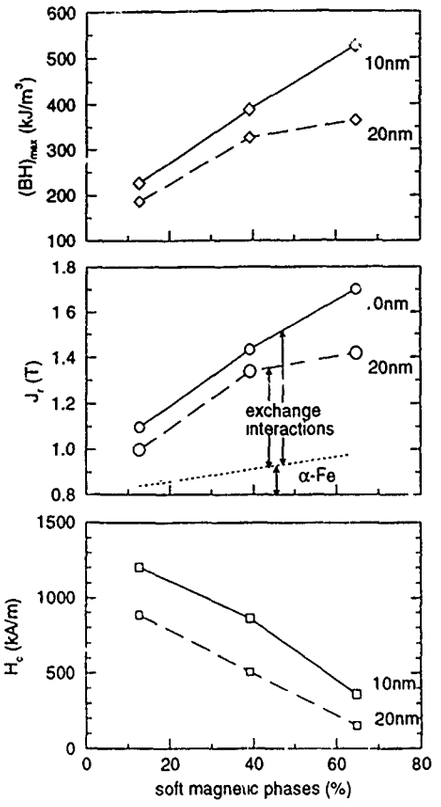

FIG. 4. Maximum energy product, remanence, and coercive field in isotropic, $Nd_2Fe_{14}B$-based, composite magnets as a function of the volume fraction of α-Fe. The different curves refer to 10 nm (solid line) and 20 nm (dashed line) mean grain size. The dotted line gives the remanence of the samples according to the Stoner–Wohlfarth theory.

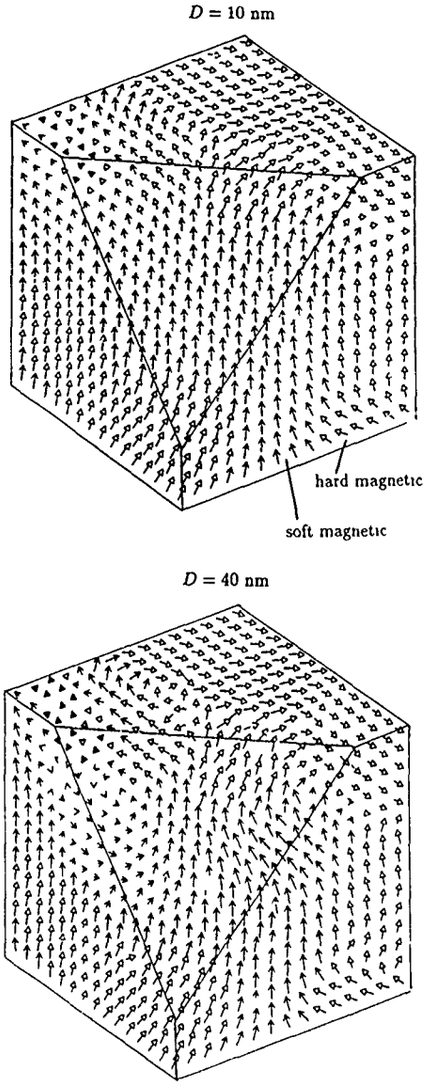

FIG. 5. Spin arrangements for zero applied field at the surface and in the interior of a composite magnet of 60% $Nd_2Fe_{14}B$ and 40% α-Fe for 10 and 40 nm mean grain size. The arrows with the closed heads denote the magnetic moments within hard magnetic grains, the arrows with the open heads denote the magnetic moments within soft magnetic grains.

tributions to the remanence. According to the Stoner–Wohlfarth theory,[8] an isotropic $Nd_2Fe_{14}B$ magnet has a remanence of $J_r = J_s/2 \approx 0.8$ T. The dotted line gives the remanence of the composite material assuming noninteracting particles. The remanence increases linearly with the percentage of α-Fe. The difference between the numerical results and the Stoner–Wohlfarth theory has to be entirely attributed to intergrain exchange interactions. In nanocrystalline materials exchange interactions align the magnetic moments parallel to the saturation direction and thus considerably increase the remanence. In soft magnetic particles exchange interactions override competitive micromagnetic effects to a greater extent than in hard magnetic grains. Therefore, remanence enhancement due to interparticle interactions increases with increasing amount of α-Fe.

The spin arrangements for zero applied field, given in Fig. 5 for a composite magnet of 60% $Nd_2Fe_{14}B$ and 40% α-Fe, demonstrate the effect of the particle size. For a mean grain size of 10 nm the exchange length of α-Fe, $l_{ex} = \pi\sqrt{A/(J_s^2/\mu_0)}$, approaches the particle diameter. Thus, almost all the magnetic moments of the soft magnetic phase are aligned parallel to the saturation direction. The ratio of the remanent to saturation polarization shows a remarkably high value of $J_r/J_s = 0.79$. For a mean grain size of 40 nm, stray field effects determine the direction of $\mathbf{J}_s$ within the soft magnetic phase. Exchange interactions influence the magnetization of the soft magnetic particles only near the interface between hard and soft magnetic phases. The ratio of the remanent to saturation polarization reaches only $J_r/I_s = 0.66$.

The coercive field decreases with increasing amount of α-Fe. Nevertheless, exchange interactions between the hard and soft magnetic phases preserve a high coercive field. As a consequence the maximum energy product resembles the behavior of the remanence. For a mean grain size of 10 nm and more than 50% α-Fe content, isotropic $Nd_2Fe_{14}B$-based composite magnets show maximum energy products exceeding 400 kJ/m^3. The self-demagnetizing field deteriorates the coercive squareness owing to reversible rotations or magnetization reversal within large soft magnetic regions. Thus, the increase of $(BH)_{max}$ with the increasing percentage of α-Fe is less significant for a grain size of 20 nm.

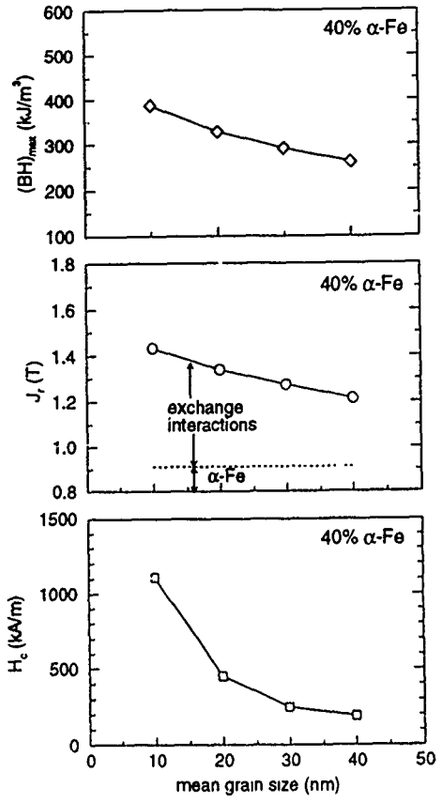

FIG. 6. Maximum energy product, remanence, and coercive field as a function of the mean grain size for a composite magnet consisting of 60% $Nd_2Fe_{14}B$ and 40% α-Fe. The dotted line gives the remanence of the samples according to the Stoner–Wohlfarth theory.

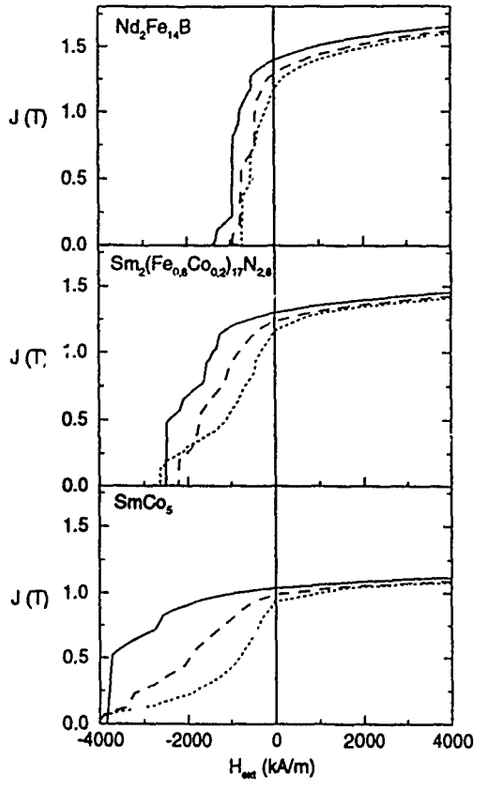

FIG. 7. Demagnetization curves of isotropic, rare-earth-based composite magnets containing 80% $Nd_2Fe_{14}B$, $Sm_2(Fe_{0.8}Co_{0.2})_{17}N_{2.8}$, or $SmCo_5$, and 20% α-Fe for an average grain diameter of 10 nm (solid line), 20 nm (dashed line), and 40 nm (dotted line).

Figure 6 shows the remanence, the coercive field, and the maximum energy product as a function of the mean grain size for a composite magnet of 60% $Nd_2Fe_{14}B$ and 40% α-Fe. Remanence and coercivity decrease with increasing grain size. In nanocrystalline, composite magnets two competitive effects determine the size dependence of coercivity: (1) Magnetic inhomogeneities owing to short-range exchange interactions between hard magnetic grains favor the nucleation of reversed domains. The nucleation field of hard magnetic grains coupled by short-range exchange interactions decreases with decreasing grain size.[22] (2) Exchange interactions between the different phases, suppress the nucleation of reversed domains within the soft magnetic particles. The nucleation field of a soft magnetic grain embedded within a hard magnetic phase decreases with increasing grains size.[23–26] The nucleation of reversed domains within the soft magnetic particles may cause magnetization reversal in neighboring hard magnetic grains, depending on the distribution of magnetically hard and soft phases, on the shape of the grains, and on the orientation of the easy axes. If the reversal of the soft magnetic particles initiates a cascade-type demagnetization process, the coercive field will be determined by the nucleation field of the soft magnetic particles and thus will decrease with increasing grain size.

V. COMPARISON OF ISOTROPIC RARE-EARTH-BASED COMPOSITE MAGNETS

Owing to a remarkably high magnetocrystalline anisotropy, novel nitrided intermetallic compounds have a large potential for composite permanent magnets. The demagnetization curves of Fig. 7 characterize the magnetic properties of novel, isotropic rare-earth-based composite magnets. Figure 7 compares the demagnetization curves for an average grain diameter of 10, 20, and 40 nm, obtained for composite magnets of 80% $Nd_2Fe_{14}B$, $Sm_2(Fe_{0.8}Co_{0.2})_{17}N_{2.8}$, or $SmCo_5$, and 20% α-Fe. The results clearly show that the coercive squareness decreases with increasing grain size for all materials. The demagnetization curves show a dip at the nucleation field of the soft magnetic phase. The comparison of the demagnetization curves for a mean grain size of 10 nm clearly shows that the nucleation field of the soft magnetic phase increases with increasing magnetocrystalline anisotropy of the hard magnetic phase. Exchange hardening becomes less effective with increasing grain size. Consequently, for a mean grain size of 40 nm, the nucleation field of the soft magnetic phase approaches nearly the same value for all composite materials. Nevertheless, the coercive field and the shape of the demagnetization curves differ drastically for the different materials. In $Nd_2Fe_{14}B$-based magnets the nucleation of reversed domains within the soft magnetic phase initiates a cascade-type demagnetization of neighbor-

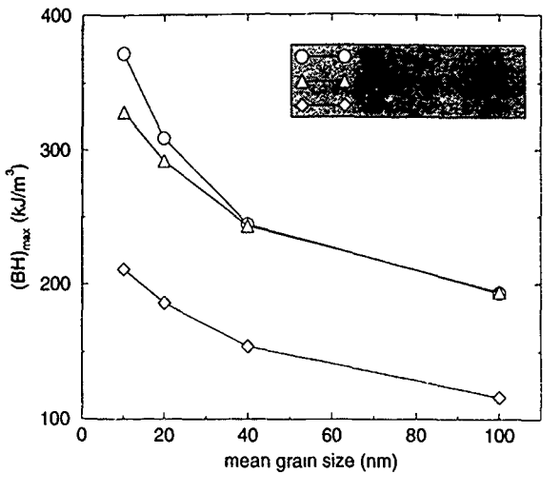

FIG. 8. Maximum energy product rare-earth-based composite magnets containing 20% α-Fe as a function of the mean grain size.

ing hard magnetic particles at a slightly increased external field. In composite magnets based on nitrided intermetallic compounds or $SmCo_5$, the elevated magnetocrystalline anisotropy of the hard magnetic phase preserves a high coercive field despite the reversal of the soft magnetic particles. However, the nucleation of reversed domains within the soft magnetic phase deteriorates the shape of the demagnetization curves.

Figure 8 compares the maximum energy product as a function of the grain size for composite magnets of 80% hard magnetic phase and 20% α-Fe. All materials but $SmCo_5$ show an energy product of about 300 kJ/m^3 for a mean grain size $D=20$ nm. Because of a high coercive field, $Sm_2(Fe_{0.8}Co_{0.2})_{17}N_{2.8}$-based composite magnets will show a better temperature stability and thus are superior to $Nd_2Fe_{14}B$-based magnets.

VI. CONCLUSIONS

Numerical micromagnetic calculations reveal the microstructural and micromagnetic conditions required for high remanent and high coercive composite magnets. The excellent hard magnetic properties of optimally structured composite magnets have to be attributed to intergrain exchange interactions. (1) Exchange interactions enhance the remanence by more than 40% as compared to the remanence of noninteracting particles. (2) Exchange hardening of the soft magnetic particles preserves a sufficiently high coercive field. The numerical studies show that remanence enhancement and exchange hardening are most effective for an average grain size comparable with the exchange length of the soft magnetic phase and a significantly high amount of soft magnetic particles.

[1] R Skomski and J. M. D. Coey, IEEE Trans Magn. **29**, 2860 (1994).
[2] R. Coehoorn, D. B. Mooij, and C. D. E. Waard, J. Magn. Magn. Mater. **80**, 101 (1989).
[3] J. Ding, P. G McCormick, and R. Street, J. Magn. Magn. Mater. **124**, 1 (1993).
[4] A. Manaf, R. A. Buckley, and H. A. Davies, J. Magn. Magn. Mater. **128**, 302 (1993).
[5] A. Manaf, M. Al-Khafaji, P. Z. Zhang, H. A. Davies, R. A. Buckley, and W. M. Rainforth, J. Magn. Magn Mater. **128**, 307 (1993).
[6] J. F. Herbst, Rev. Mod. Phys. **63**, 819 (1991).
[7] H. Zijlstra, in *Ferromagnetic Materials*, edited by E. P. Wohlfarth (North-Holland, Amsterdam, 1982).
[8] E C. Stoner and E. P. Wohlfarth, Philos. Trans. R. Soc. **240**, 599 (1948).
[9] E. F. Kneller and R. Hawig, IEEE Trans. Magn. **27**, 3588 (1991).
[10] M. G. Grönefeld, Ph.D. thesis, University of Stuttgart, Germany, 1990
[11] S. Nieber and H. Kronmuller, Phys. Status Solidi B **153**, 367 (1989).
[12] W. F. Brown, Jr., *Micromagnetics* (Wiley, New York, London, 1963)
[13] H. F. Schmidts and H. Kronmüller, J. Magn Magn. Mater **94**, 220 (1991).
[14] P. Asselin and A. A. Thiele, IEEE Trans. Magn **22**, 1876 (1986).
[15] A Aharoni, IEEE Trans. Magn. **27**, 3539 (1991).
[16] W. F. Brown, Jr., J. Phys. Soc. Jpn. Suppl. B-I **17**, 540 (1962).
[17] D. R. Fredkin and T. R Koehler, IEEE Trans. Magn. **23**, 3385 (1987).
[18] P. E. Gill, W. Murray, and M. H. Wright, *Practical Optimization* (Academic, London, New York, Toronto, 1981).
[19] X. Brunotte, G. Meunier, and J. F. Imhoff, IEEE Trans. Magn. **28**, 1663 (1992).
[20] T. Schrefl, J. Fidler, and H. Kronmuller, J. Magn. Magn Mater (in press).
[21] Y. Otani, H. Li, and J. M. D. Coey, IEEE Trans. Magn. **26**, 2658 (1990).
[22] T. Schrefl, J. Fidler, and H. Kronmuller, Phys. Rev B **49**, 6100 (1994).
[23] H. Kronmuller, Phys. Status Solidi B **144**, 385 (1987).
[24] H Fukunaga and T. Fukunda, Jpn. J. Appl. Phys **29**, 1711 (1990).
[25] A. Sakuma, T. Tanigawa, and M. Tokunaga, J. Magn. Magn. Mater. **84**, 52 (1990).
[26] T. Schrefl, H. Kronmuller, and J. Fidler, J. Magn. Magn. Mater. **127**, L273 (1993).
[27] S. Hock, Ph.D. thesis, University of Stuttgart, Germany, 1988.
[28] M. Katter, Ph.D. thesis, Technical University of Vienna, Austria, 1991.
[29] R. Kutterer, H. R. Hilzinger, and H. Kronmuller, J. Magn. Magn. Mater. **4**, 1 (1977)
[30] E. Kneller, *Ferromagnetismus* (Springer, Berlin, 1962).

Aligned two-phase magnets: Permanent magnetism of the future? (invited)

R. Skomski
Department of Pure and Applied Physics, Trinity College, Dublin 2, Ireland

Micromagnetic calculations are used to investigate coercivity and energy products of magnets consisting of an aligned hard-magnetic skeleton phase and a soft-magnetic phase with high saturation magnetization. Compared to the present-day theoretical limit of 516 kJ/m^3 for single-phase $Nd_2Fe_{14}B$, the energy product in suitable nanostructured $Sm_2Fe_{17}N_3/Fe_{65}Co_{35}$ composites is predicted to be as high as 1090 kJ/m^3. The influence of the skeleton's texture and shape is discussed, and aligned nanocrystalline two-phase magnets are compared with remanence-enhanced isotropic magnets. In particular it is shown how the nucleation-based analytical approach breaks down in the isotropic limit. Finally, we outline conceivable processing methods and discuss potential applications of "megajoule" magnets.

I. INTRODUCTION

A key figure of merit of permanent magnetic materials is the energy product $(BH)_{max}$, which describes the ability to store magnetostatic energy. Energy product increases with coercivity H_c and remanence M_r but can never exceed the value $\mu_0 M_r^2/4$ corresponding to an ideal rectangular hysteresis loop. Since $M_r \leq M_0$, the spontaneous magnetization M_0 yields an "intrinsic" limit $(BH)_{max} \leq \mu_0 M_0^2/4$, but if magnetization were the only consideration then α iron with $\mu_0 M_0 = 2.15$ T would be used for permanent magnets with energy products as high as 920 kJ/m^3. In fact, the coercivity of bcc iron is so low that energy products of iron magnets are only of order 1 kJ/m^3, and in the past it was necessary to resort to cumbersome bar and horseshoe shapes to avoid spontaneous demagnetization into a multidomain state by the magnet's own magnetostatic field. For this reason the quest for improved energy product has involved a search for compounds with a large magnetization combined with the strong uniaxial anisotropy needed to develop hysteresis.

In former years, the problem was to achieve the necessary anisotropy, but more recently the focus has shifted to the problem of enhancing the magnetization. Modern high-performance magnets such as $SmCo_5$, $Nd_2Fe_{14}B$, or the interstitial nitride $Sm_2Fe_{17}N_3$ consist of $3d$ atoms which are exchange coupled to rare-earth atoms which provide the uniaxial anisotropy required of a permanent magnet.[1–7] In reality, coercivity as high as 4.4 T has been achieved in $Sm_3Fe_{17}N_3$-based magnets,[8] but for practical purposes there is usually no call for coercivity very much greater than $M_0/2$. On the other hand, the magnetization is reduced due to the rare-earth and nonmagnetic elements. The light rare-earths' atomic moments are at best slightly larger than that of iron, but they occupy more than three times the volume. Nevertheless, it has been possible to use $Nd_2Fe_{14}B$ which has $\mu_0 M_0 = 1.61$ T and $\mu_0 M_0^2/4 = 516$ kJ/m^3 to achieve room-temperature energy products exceeding 400 kJ/m^3 in laboratory-scale magnets.[2] At about 200 °C, which is a technologically important temperature region, $Sm_2Fe_{17}N_3$ is potentially the best permanent magnetic material,[1,5] but here suitable processing methods have not yet been developed.

Energy product has doubled every twelve years since the beginning of the century, and much effort is being made to yield further quantitative and qualitative progress in the performance of permanent magnetic materials.[9] However, the outlook for discovering new ternary phases with magnetization significantly higher than that of those available, at present, is poor.[3] Permanent magnets based on the appearance of a new rare-earth iron intermetallic phase could offer better temperature stability, yet higher anisotropy field or improved corrosion resistance, but the scope for significant improvements in the spontaneous magnetization is very limited. For instance, interstitial modification with small atoms such as nitrogen or carbon is effective for enhancing Curie temperature and anisotropy,[1,5,10,11] but it has rather little effect on the magnetization—the moment increase is, on the whole, a zero sum game.[3]

In the case of isotropic magnets, which are often more easy to produce than oriented magnets, the comparatively low remanence $M_r \approx M_0/2$ reduces the theoretical energy product by a factor 4. However, the production of nanocrystalline composites such as $Nd_2Fe_{14}B/Fe_3BFe$ and $Sm_2Fe_{17}N_3/Fe$ by melt spinning[12] and mechanical alloying,[13] respectively, shows that it is possible to combine the high magnetization of soft-magnetic materials and the surplus anisotropy of rare-earth intermetallics. Soft magnetic phases such as bcc iron often reduce the energy product by degrading coercivity, but if the soft regions are small enough then exchange coupling stabilizes the magnetization direction of the soft phase. This kind of exchange coupling improves the low remanence of the isotropic hard phase,[12–16] but the energy product, though improved with respect to the isotropic single-phase rare-earth material, does not reach the level attained in oriented single-phase rare-earth magnets. In other words, new approaches are necessary if the energy product is ever to double again.

Recent work by Skomski and Coey[3,17,18] has shown how it should be possible to substantially increase the energy product in *oriented* nanostructured two-phase magnets by exploiting exchange coupling between hard and soft regions (Fig. 1). The idea behind these systems is to break out of the straightjacket of natural crystal structures by artificially structuring new materials. The concept is similar to that of the $4f$-$3d$ intermetallics themselves, but on a different scale, where the atoms are replaced by a mesoscopically structured hard-magnetic skeleton with surplus anisotropy and small soft-magnetic blocks. Based on analytical calculations, a

 0021-8979/94/76(10)/7059/6/$6 00 © 1994 American Institute of Physics

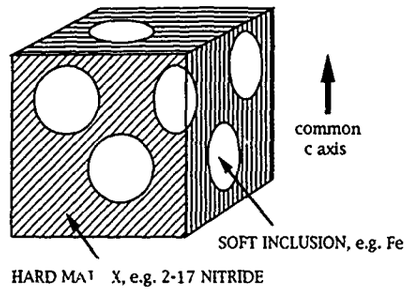

FIG. 1. Spherical soft inclusions in an aligned hard matrix.

well-defined and *realistic* upper limit to the energy product of permanent magnets has been established, and energy products of order 1 MJ/m^3 have been predicted for suitable multilayered and random structures.

Here, we summarize the background and results of these calculations, relate them to the problem of remanence enhancement in isotropic magnets, and draw conclusions with respect to future developments in permanent magnetism.

II. BACKGROUND

A. Micromagnetic free energy

To predict the performance of a permanent magnetic material we have to calculate the average magnetization $\langle \mathbf{M} \rangle$ as a function of the applied magnetic field $\mathbf{H}=H\mathbf{e}_z$. A convenient starting point is the (magnetic) free energy F, where the properties of the magnetic material enter as temperature-dependent parameters. Locally stable magnetic configurations are obtained by putting $\delta F/\delta \mathbf{M}(\mathbf{r})=0$, where $\delta .../\delta \mathbf{M}(\mathbf{r})$ denotes the functional derivative with respect to the magnetization $M(\mathbf{r})=M_0(\mathbf{r})\mathbf{s}(\mathbf{r})$ with $s^2=1$. Typically, the free energy of permanent magnets exhibits two or more metastable equilibrium states, and tracing the magnetic configuration $\mathbf{s}(\mathbf{r})$ as a function of an external field $\mathbf{H}=H\mathbf{e}_z$ is quite a demanding task.

On a mesoscopic level, i.e., assuming that the magnetization is a continuous variable, the free energy of a permanent magnet reads[19,20]

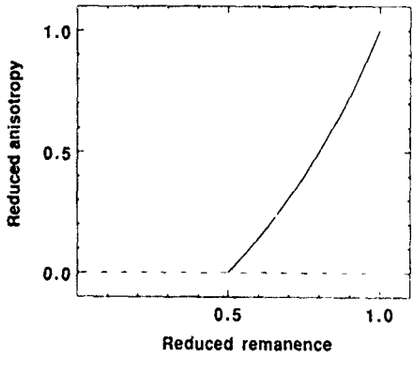

FIG. 2. Dependence of the reduced effective anisotropy constant $K_{\rm eff}/K_h$ on the reduced remanence M'/M_h. $M'/M_h=1/2$ and $M_r/M_h=1$ mean isotropic texture and complete alignment, respectively.

$$F=\int [\eta_{xc}(\mathbf{r})+\eta_a(\mathbf{r})+\eta_H(\mathbf{r})+\eta_{ms}(\mathbf{r})]d\mathbf{r}. \tag{1}$$

The contributions to the free-energy density are (i) the exchange free-energy density $\eta_{xc}=A(\mathbf{r})[\nabla \mathbf{s}(\mathbf{r})]^2$, where the exchange stiffness $A(\mathbf{r})$ describes the tendency towards parallel spin alignment, (ii) the energy density of the (uniaxial) anisotropy

$$\eta_a=-(K_1+2K_2+3K_3)(\mathbf{ns})^2+(K_2+3K_3)(\mathbf{ns})^4 -K_3(\mathbf{ns})^6, \tag{2}$$

where $\mathbf{n}$ is the unit vector of the local c-axis direction, (iii) the Zeeman energy density $\eta_H=-\mu_0 M_0(\mathbf{r})Hs_z(\mathbf{r})$, where $\mathbf{H}=H\mathbf{e}_z$ is the external magnetic field, and (iv) the magnetostatic dipole interaction

$$\int \eta_{ms}(\mathbf{r})d\mathbf{r}=-\frac{1}{2}\sum_{i,j=1}^{3}\int \mathrm{K}_{ij}(\mathbf{r}-\mathbf{r}') \times M_i(\mathbf{r})M_j(\mathbf{r}')d\mathbf{r}d\mathbf{r}', \tag{3}$$

with $\mathrm{K}_{ij}(\mathbf{r})=\mu_0(3r_ir_j-\delta_{ij}r^2)/(4\pi r^5)$ and $\mathbf{M}(\mathbf{r})=\Sigma_i M_i(\mathbf{r})\mathbf{e}_i$. Note that putting $\mathbf{n}(\mathbf{r})=\mathbf{e}_z$ in Eq. (2) is equivalent to the familiar expression $\eta_a=K_1\sin^2\theta+K_2\sin^4\theta+K_3\sin^6\theta$, where θ is the angle between magnetization and z direction.

B. Coercivity and energy product

Mechanical work to be done by a permanent magnet implies a magnetic hardness (coercivity) which keeps the magnetization in the desired direction. If the coercivity H_c is too small, or if the hysteresis loop has an unfavorable shape, then the energy product won't reach the theoretical value $\mu_0 M_0^2/4$ deduced from the saturation magnetization M_0.

Depending on the real structure of a permanent magnet, there are different hardening mechanisms. Here we treat aligned nanostructured two-phase magnets as nucleation-controlled magnets. The nucleation field $H_N=-H$ is defined as the (reverse) field at which the original state $\mathbf{s}(\mathbf{r})\approx\mathbf{e}_z$ becomes unstable. Mathematically, this requires the determinant of the continuous matrix $\delta^2F/\delta\mathbf{s}(\mathbf{r})\delta\mathbf{s}(\mathbf{r}')$ to vanish. Note, however, that the introduction of pinning centers is a potential way of improving the coercivity by inhibiting the propagation of the reversed nucleus, so $H_N\leq H_c$ is a lower limit to the coercivity.

The determination of H_N is a fairly demanding task,[19–21] and we have to introduce suitable approximations. Due to the long-range character of $\mathrm{K}_{ij}(\mathbf{r})$, the magnetostatic interaction is the most complicated one. A simple, though nontrivial, approximation is to replace the external magnetic field by $H_{\rm eff}=H-D\langle M_z\rangle$, where D is the demagnetizing factor. It has been shown quite generally[20–22] that for a homogeneous ellipsoid

$$H_c\geq\frac{2K_1}{\mu_0 M_0}-DM_0, \tag{4}$$

where the factor $D\,M_0$ arises from the gain in magnetostatic energy due to an incoherent rotation process. The $>$ sign in Eq. (4) indicates that incoherent rotation costs exchange en-

ergy, but the corresponding coercivity contribution scales as $A/(\mu_0 M_0 L^2)$, where L is the magnet's size, and is practically negligible. In the case of coherent rotation (the Stoner–Wohlfarth model), $H_N=2K_1/\mu_0 M_0-(1-3D)M_0/2$, and there is no influence of a "demagnetizing" field in spherical magnets where $D=1/3$. The result of the Stoner–Wohlfarth model is consistent with Eq. (4).

Equation (4) is called Brown's paradox, because real permanent magnets always seem to violate this inequality. This violation is due to the existence of inhomogenities in real magnets while Eq. (4) applies to homogeneous ellipsoids only.[21,22] In the following, we restrict ourselves to the so-called "intrinsic" $D=0$ hysteresis loop of macroscopic magnets, from which the energy product is determined.[23]

III. MODEL AND CALCULATION

To determine the nucleation field we assume ideal alignment of the hard phase, i.e., $\mathbf{n}(\mathbf{r})=\mathbf{e}_z$, and rewrite $\mathbf{s}(\mathbf{r})\approx\mathbf{e}_z$ as

$$\mathbf{s}=\sqrt{1-m^2}\mathbf{e}_z+\mathbf{m}, \quad \mathbf{m}=s_x\mathbf{e}_x+s_y\mathbf{e}_y, \quad m^2\ll 1. \tag{5}$$

Now series expansion of Eq. (1) yields the quadratic form

$$F=\int\left[A(\mathbf{r})\{\nabla\mathbf{m}\}^2+K_1(\mathbf{r})\mathbf{m}^2+\frac{1}{2}\mu_0 M_0(\mathbf{r})H\mathbf{m}^2\right]d\mathbf{r}. \tag{6}$$

Recall that K_2 and K_3 do *not* enter this expression,[19] so the nucleation field of ideally anisotropic hard magnets depends on K_1 only. The case of partially anisotropic and isotropic magnets will be discussed in Sec. IV. The equation of state $\delta F/\delta\mathbf{m}(\mathbf{r})=0$ is given by the identity

$$\frac{\delta F}{\delta\mathbf{m}(\mathbf{r})}=-\nabla\left(\frac{\partial\eta}{\partial\nabla\mathbf{m}(\mathbf{r})}\right)+\frac{\partial\eta}{\partial\mathbf{m}(\mathbf{r})}, \tag{7}$$

and reads

$$A(\mathbf{r})\nabla^2\mathbf{m}+\nabla A(\mathbf{r})\nabla\mathbf{m}-[2K_1(\mathbf{r})+\mu_0 M_0(\mathbf{r})H]\mathbf{m}=0. \tag{8}$$

Except for the $\nabla A(\mathbf{r})\nabla\mathbf{m}$ term (see Sec. IV), Eq. (8) is equivalent to Schrödinger's equation for a particle moving in a three-dimensional potential $2K_1(\mathbf{r})+\mu_0 M_0(\mathbf{r})H$, which allows us to apply ideas familiar from quantum mechanics to discuss micromagnetics. Note that the x and y components of $\mathbf{m}=m_x\mathbf{e}_x+m_y\mathbf{e}_y$ are decoupled and degenerate in Eq. (8), so the vector $\mathbf{m}(\mathbf{r})$ can be replaced by any unspecified nucleation mode $\Psi(\mathbf{r})$. It is, however, convenient to think of $\Psi(\mathbf{r})$ as the magnetization $m_x(\mathbf{r})$ in x direction.

Finally, for our inhomogeneous two-phase magnets we assume that the $\mathbf{r}$ dependence of the parameters A, K_1, and M_0 is given by A_h, K_h, M_h, and A_s, K_s, M_s for hard (index h) and soft (index s) regions, respectively. Let the volume fraction of the hard regions become f_h; the fraction of the soft regions is then given by $f_s=1-f_h$.

The nucleation field H_N is obtained as lowest eigenvalue of the Eq. (8). In the homogeneous "constant-potential" case, the ground-state eigenfunction is a plane wave with $\mathbf{k}=0$, and Eq. (8) reduces to the familiar form $H_N=-H=2K_1/\mu_0 M_0$. In the case of inhomogeneous magnets, the nucleation problem Eq. (8) can be solved by series expansion or an appropriate ansatz, which has been done for special one-, two-, and three-dimensional configurations.[17,19,24–27] An example is a spherical soft inclusion (diameter D, $K_s=0$) in a hard-magnetic matrix (cf. Fig. 1). Introducing spherical coordinates and using the interface boundary condition $A_s(\mathbf{e}\cdot\nabla)\Psi_s=A_h(\mathbf{e}\cdot\nabla)\Psi_h$ we obtain the eigenvalue equation[17]

$$\frac{A_s}{A_h}\left\{\frac{D}{2}\sqrt{\frac{\mu_0 M_s H_N}{2A_s}}\cot\left(\frac{D}{2}\sqrt{\frac{\mu_0 M_s H_N}{2A_s}}\right)-1\right\}+1 + \frac{D}{2}\sqrt{\frac{2K_h-\mu_0 M_h H_N}{2A_h}}=0, \tag{9}$$

which can be solved numerically. It turns out that the nucleation field reaches a high-coercivity plateau if the size of the soft inclusion is smaller than the Bloch wall thickness $\delta_h=\pi(A_h/K_h)^{1/2}$ of the hard phase. This plateau corresponds to complete exchange coupling. If the diameter D of the soft inclusion is too large, then the magnetization becomes unstable and the coercivity falls off as $1/D^2$.

For sufficiently small reverse fields $|H|<H_N(D)$ the single soft inclusion is perfectly aligned and slightly enhances the remanence provided $M_s>M_h$. On the other hand, when the distance between the soft inclusions is small, the magnetization modes can "tunnel" through the hard region which no longer acts as an effective potential barrier. In fact, this micromagnetic "exchange interaction" can reduce the nucleation field considerably when the thickness of the hard region is less than δ_h. To obtain physically reasonable nucleation fields, the complete $A(\mathbf{r})$, $K_1(\mathbf{r})$, and $M_0(\mathbf{r})$ profiles have to be taken into account.

IV. RESULTS

A. Coercivity

1. Plateau limit

In the plateau region, where the soft regions are very small, the problem can be treated in perturbation theory.[3,17,18] As in quantum mechanics, the lowest order eigenvalue correction is obtained by using the normalized unperturbed function Ψ_0. This yields the nucleation field

$$H_N=2\frac{f_s K_s+f_h K_h}{\mu_0(f_s M_s+f_h M_h)}. \tag{10}$$

Note that this result is independent of the shape of the soft and hard regions so long as the hard regions remain aligned.

2. Multilayer limit

It is comparatively easy to treat one-dimensional structures such as multilayers,[27] since the micromagnetic multilayer problem is analogous to the periodic multiple quantum well problem. For a multilayered structure of alternating soft and hard magnetic layers the nucleation field is given by the implicit equation[17]

$$\sqrt{\frac{2K_h-\mu_0 M_h H_N}{2A_h}}\tanh\left(\frac{l_h}{2}\sqrt{\frac{2K_h-\mu_0 M_h H_N}{2A_h}}\right) = \frac{A_s}{A_h}\sqrt{\frac{\mu_0 M_s H_N}{2A_s}}\tan\left(\frac{l_s}{2}\sqrt{\frac{\mu_0 M_s H_N}{2A_s}}\right), \tag{11}$$

where l_h and l_s denote the thicknesses of the hard and soft layers, respectively. Note, that this result does not depend on whether the orientation of the crystallographic c axis of the hard phase is perpendicular or longitudinal.

B. Energy product

Equation (10) implies an ideally rectangular hysteresis loop with energy product $\mu_0 M_r^2/4$, remanence $M_r = f_h M_h + f_s M_s$, and (minimum) coercivity $H_N = M_r/2$. Putting $K_s = 0$ in the plateau limit we obtain with $H_N = M_r/2$ the maximum energy product

$$(BH)_{\max} = \frac{1}{4}\mu_0 M_s^2 \left(1 - \frac{\mu_0 (M_s - M_h) M_s}{2K_h}\right). \tag{12}$$

Due to the large K_h, the second term in the bracket is small so the energy product approaches the ultimate value of $\mu_0 M_s^2/4$. The corresponding volume fraction of the hard phase is $f_h = \mu_0 M_s^2/4K_h$.

The intermetallic with the most favorable combination of magnetization and anisotropy is $Sm_2Fe_{17}N_3$. If we consider the $Sm_2Fe_{17}N_3/Fe$ system and assume values $\mu_0 M_s = 2.15$ T, $\mu_0 M_h = 1.55$ T, and $K_h = 12$ MJ/m^3, we obtain a theoretical energy product of 880 kJ/m^3 (110 MGOe) for a volume fraction of only 7% of the hard phase.[17] A further increase of the energy product is possible if iron is replaced by $Fe_{65}Co_{35}$ with $\mu_0 M_s = 2.43$ T—the theoretical energy product of the $Sm_2Fe_{17}N_3/Fe_{65}Co_{35}$ system might be as high as 1090 kJ/m^3 (137 MGOe), with $f_h = 9\%$. It is remarkable that these optimum magnets are almost entirely composed of $3d$ metals, with only about 2-wt % samarium.

Another possibility is a multilayered structure of alternating soft and hard magnetic layers. Assuming $A_s = 1.67 \times 10^{-11}$ J/m and $A_h = 1.07 \times 10^{-11}$ J/m we deduce from Eq. (11) that a $Sm_2Fe_{17}N_3/Fe_{65}Co_{35}$ "megajoule magnet" is obtained for layer thicknesses $l_h = 2.4$ nm and $l_s = 9.0$ nm. The macroscopic shape of the magnet must of course correspond to the optimum operating point on the BH curve; it should approximate an ellipsoid with c/a=0.55. Note that A is generally of order 10^{-11} J/m, so H_N and $(BH)_{\max}$ do not depend very much on the exchange-stiffness inhomogenity.

C. Texture

As we have seen, $K_2(\mathbf{r})$ and $K_3(\mathbf{r})$ do not influence the nucleation field so long as the unit vector in the easy axis direction $\mathbf{n}$ remains parallel to the field $\mathbf{e}_z$. The situation becomes much more difficult when the hard regions are only partially aligned or even isotropic. For instance, the components m_x and m_y of $\mathbf{m}$ [cf. Eq. (8)] are now coupled in a very complicated way. However, in lowest order perturbation theory the m_x and m_y decouple, and after some calculation we find that K_1 in Eq. (8) has to be replaced by

$$K_{\text{eff}} = -\tfrac{1}{2}(K_1 + 2K_2 + 4K_3) + \tfrac{3}{2}(K_1 + 4K_2 + 9K_3)\langle n_z^2\rangle - \tfrac{5}{2}(2K_2 + 3K_3)\langle n_z^4\rangle + \tfrac{21}{2} K_3 \langle n_z^6\rangle. \tag{13}$$

The ensemble average is defined as $\langle \ldots \rangle = \Omega^{-1} \int \ldots f(\theta) \sin\theta d\theta$ where $f(\theta)$ denotes the texture function of the hard phase. Note that Eq. (13) reduces to $K_{\text{eff}} = K_1$ in the ideally anisotopic limit $n_z = 1$.

To discuss the overall behavior of K_{eff} we use the single-parameter texture function $f(\theta) = (1+\nu)\cos^\nu \theta$[28] and restrict ourselves to the case $K_2 = K_3 = 0$. Using $n_z = \cos\theta$ we obtain

$$K_{\text{eff}} = K_h \left(\frac{2M' - M_h}{2M_h - M'}\right), \tag{14}$$

where M' is the remanence of the hard regions in the interaction-free limit, i.e., $M' = M_h$ for ideally anisotropic magnets and $M' = 0.5\, M_h$ for isotropic magnets. In lowest order perturbation theory the nucleation field is proportional to K_{eff}, so $H_N = 0$ for $M' = 0.5\, M_h$ in this approximation. This means, that the nucleation field vanishes in the isotropic limit if soft and hard regions are extremely small. An alternative interpretation is given by Eq. (12), where K_h has to be replaced by K_{eff}. The smallness of the $1/K_h$ correction term in Eq. (12) requires the effective anisotropy to be very large,[29] which is contradictory to $K_{\text{eff}} = 0$, and it is not possible to apply Eq. (12) to isotropic materials.

D. Isotropic magnets

In the case of an isotropic matrix with randomly oriented hard regions alternative methods have to be used to calculate the coercivity. An estimate is obtained from a simple model where two hard regions with $\mathbf{n}_1 = \mathbf{e}_z$ and $\mathbf{n}_2 = \pm\mathbf{e}_x$ are subject to an effective coupling A/R_{eff}^2. As it can be shown easily, the weak-coupling limit (isolated grains) yields $M_r = M_h/2$. In the case of strong exchange coupling the orientation of the grains is given by $\mathbf{s}_1 \approx \mathbf{s}_2 \approx \mathbf{e}_x/\sqrt{2} + \mathbf{e}_z/\sqrt{2}$, which yields the enhanced remanence $M_r = M_h/\sqrt{2}$. Note that the instability of the aligned $\mathbf{M}(\mathbf{r}) = M_h \mathbf{e}_z$ state implies $M_r < M_h$ for remanence-enhanced single-phase magnets.

On the other hand, exchange coupling destroys coercivity. For weak coupling we find $H_c = 2K_h/\mu_0 M_h$, while the strong-coupling coercivity $H_c = K_1^2 R_{\text{eff}}^2 (\sqrt{2}\mu_0 M_h A)^{-1}$ decreases with increasing exchange interaction. As expected, this result reduces to $H_c = 0$ in the "plateau limit" (infinitely large A or infinitely small R_{eff}).

V. DISCUSSION

A. Performance and processing

A conceivable way to exploit the surplus anisotropy in modern rare-earth permanent magnets is to use aligned two-phase magnets where the hard phase acts as a skeleton which keeps the magnetization of the soft phase in the desired direction. Micromagnetic analysis shows that the nucleation field in suitable nanostructured materials is proportional to the volume-averaged anisotropy.

Equation (12), which represents a hardness expansion with respect to the small parameter $\mu_0(M_s - M_h)M_s/K_1$, predicts the energy product of aligned nanostructured two-phase magnets to be nearly as high as the ultimate value $\mu_0 M_0^2/4$. From the point of view of exchange coupling, the

mechanism is similar to the remanence enhancement in isotropic magnets, but yields a saturation magnetization which is larger than that of the aligned hard phase.

The practical problem is to realize a structure where the soft regions are sufficiently small to avoid nucleation at small fields while having the hard regions crystallographically oriented. One conceivable solution is a disordered two-phase magnet with a common c axis throughout the hard regions. The energy product Eq. (12) is independent of the shape of the soft regions, so long as their size lies in the plateau region. However, soft regions much larger than this plateau size drastically reduce the nucleation field,[29] and it is difficult to see how the formation of large soft-magnetic clusters might be avoided in practice. Furthermore, the hard skeleton has to be aligned to avoid the anisotropy reduction described by Eq. (14). Note that remanence-enhanced *isotropic* two-phase magnets operate on a slightly larger length scale.

A more realistic possibility may be a multilayered structure of alternating soft- and hard-magnetic layers. Conceivable production methods are laser ablation deposition[30] or molecular-beam epitaxy. As discussed in Sec. IV, the permanent-magnetic performance of the multilayer is independent of whether the hard phase is perpendicularly or longitudinally aligned. It is worthwhile mentioning that permanent magnetic multilayers are one-dimensional systems, whose eigenmodes are subject to weak localization (Anderson localization). Weak localization in one-dimensional systems is caused by an arbitrarily small disorder,[31,32] and second-order perturbation theory[29] yields zero coercivity if the disorder is described by Gaussian or Poisson correlations. The reason for this coercivity breakdown is the small but finite probability of thick soft layers, since the coercivity is determined by the thickest soft layer around which the nucleation mode is localized. This means that weak localization does not destroy coercivity if there is an upper limit to the thickness of the soft layers.

Equation (1) is based on classical micromagnetic considerations; the sizes of the hard and soft regions must be large compared to atomic dimensions so that a continuum model can be applied. The model must break down when l_s or l_h is smaller than about 1 nm. However, due to the small prefactor $(M_s - M_h)/M_s$, 0.28 for the $Sm_2Fe_{17}N_3$/Fe system, the energy product is not much affected if the fraction of the hard phase is increased. We still have an energy product of almost 800 kJ/m^3 (100 MGOe) in the $Sm_2Fe_{17}N_3$/Fe system when $f_h \approx 30\%$, and we can use the extra hard material to outweigh quantum-mechanical size effects, to improve the thermal stability, suppress the effect of random stray fields and to create pinning centers.[17,29]

B. Outlook

Table I gives a tentative discussion of the question to what extent "giant-energy product" magnets will ever be exploited commercially. At present, the actual production of these structures represents a realistic but nevertheless extremely demanding challenge. In other words, the advantages of hypothetical "megajoule" magnets—very high energy product and low raw material costs—are largely outweighed by the complicated processing requirements. We therefore believe that the use of aligned nanostructured two phase magnets will be restricted to special applications such as micromechanics or thin-film electronics.

TABLE I. Permanent magnet processing and applications.

Material	Performance	Processing costs	Raw material price
Steel	low	low	low
Ferrites	moderate	moderate	low
$SmCo_5$	high	moderate	high
$Nd_2Fe_{14}B$	high	moderate	moderate
$Sm_2Fe_{17}N_3$	high	high	moderate
"MJ" magnets	very high	very high	low

Of course, this emphasis on processing is likely to be a feature of all future permanent magnets, even if we include "exotic" systems such as magnetically hard room-temperature superconductive currents or nanoscale magnetic clusters where the $>$ sign in Eq. (4) can be utilized.[9] Let us imagine, for example, that it is possible to produce a single-phase permanent magnet somewhat better than $Nd_2Fe_{14}B$ by quenching from a high-pressure equilibrium state. The processing of this material will almost certainly be much more expensive than that of $Nd_2Fe_{14}B$, leading to much less widespread commercial applications. In our opinion, singular events such as the discovery of $Nd_2Fe_{14}B$ are unlikely to happen again, and most future technological and scientific progress will be in directions other than improving the energy product.

VI. CONCLUSIONS

In conclusion, it is likely that substantial improvements in the energy product of permanent magnets can be achieved by exchange hardening in nanoscale combinations of a soft phase and an oriented hard phase, structured according to the principles we have outlined. For example, the maximum energy product of nanostructured $Sm_2Fe_{17}N_3/Fe_{65}Co_{35}$ multilayers is predicted to be as high as 1090 kJ/m^3 (137 MGOe). The high energy product, which is based on nucleation-controlled coercivity, breaks down in the limit of remanence-enhanced isotropic magnets. The actual production of the new material—a demanding but realistic aim—will be expensive, which restricts the potential use of 'giant-energy-product' magnets to special applications.

ACKNOWLEDGMENTS

The author is indebted to J. M. D. Coey for stimulating discussions and help in details. This work was supported by the BRITE/EURAM program of the European Commission. It forms part of the Concerted European Action on Magnets.

[1] J. M. D. Coey, Physica Scripta **T39**, 21 (1991).
[2] M. Sagawa, S. Hirosawa, H. Yamamoto, S. Fujimura, and Y. Matsuura, Jpn. J. Appl. Phys **26**, 785 (1987).
[3] J. M. D. Coey and R. Skomski, Physica Scripta **T49**, 315 (1993).
[4] M. Sagawa, S. Fujimura, N. Togawa, H. Yamamoto, and Y. Matsuura, J. Appl. Phys. **55**, 2083 (1984).
[5] J. M. D. Coey and H. Sun, J. Magn. Magn. Mater. **87**, L251 (1990).

[6]G. J. Long and F. Grandjean, *Supermagnets. Hard Magnetic Materials* (Kluwer, Dordrecht, 1991).
[7]J. J. Croat, J. F. Herbst, R. W. Lee, and F. E. Pinkerton, J. Appl. Phys. **55**, 2078 (1984).
[8]C. Kuhrt, K. O'Donnell, M. Katter, J. Wecker, K. Schnitzke, and L. Schultz, Appl. Phys. Lett. **60**, 3316 (1992).
[9]M. Sagawa and J. M. D. Coey, Europe-Japan Workshop on the Future of Permanent Magnetism, Connemara, Ireland, March 13–16, 1994 (to be published).
[10]Q.-N. Qi, H. Sun, R. Skomski, and J. M. D. Coey, Phys. Rev. **45**, 12278 (1992).
[11]R. Skomski, M. D. Kuz'min, and J. M. D. Coey, J. Appl. Phys. **73**, 6934 (1993).
[12]R. Coehoorn, D. B. de Mooij, J. P. W. B. Duchateau, and K. H. J. Buschow, J. Phys. **49**, C8-669 (1988).
[13]J. Ding, P. G. McCormick, and R. Street, J. Magn. Magn. Mater. **124**, L1 (1993).
[14]K.-H. Müller, J. Schneider, A. Handstein, D. Eckert, P. Nothnagel, and H. R. Kirchmayr, Mater. Sci. Eng. A **133**, 151 (1991).
[15]E. Kneller and R. Hawig, IEEE Trans. Magn. **27**, 3588 (1991).
[16]E. Callen, Y. J. Liu, and J. R. Cullen, Phys. Rev. B **16**, 263 (1977).
[17]R. Skomski and J. M. D. Coey, Phys. Rev. B **48**, 15812 (1993).
[18]R. Skomski and J. M. D. Coey, IEEE Trans. Magn. **29**, 2860 (1993).
[19]H. Kronmüller, Phys. Status Solidi B **144**, 385 (1987).
[20]W. F. Brown, *Magnetostatic Principles in Ferromagnetism* (Interscience, New York, 1962).
[21]A. Aharoni, Rev. Mod. Phys. **34**, 227 (1962).
[22]W. F. Brown, Rev. Mod. Phys. **17**, 15 (1945).
[23]Of course, the practical realization of $(BH)_{max}$ requires a shape which corresponds to the optimum operating point on the *BH* curve.
[24]R. Skomski, Phys. Status Solidi B **174**, K77 (1992).
[25]J.-F. Hu and H. Kronmüller, Phys. Status Solidi B **172**, 67 (1992).
[26]R. Skomski, K.-H. Müller, P. A. P. Wendhausen, and J. M. D. Coey, J. Appl. Phys. **73**, 6047 (1993).
[27]S. Nieber and H. Kronmüller, Phys. Status Solidi B **153**, 367 (1989).
[28]L. Jahn, K. Elk, and R. Schumann, J. Magn. Magn. Mater. **104-107**, 1439 (1992).
[29]R. Skomski and J. M. D. Coey, IEEE Trans. Magn. **30**, 607 (1994).
[30]M. Enrech, R. Skomski, J. M. D. Coey, and J. G. Lunney, J. Appl. Phys **73**, 6421 (1993).
[31]P. W. Anderson, Phys. Rev. **109**, 1492 (1958).
[32]P. A. Lee and T. V. Ramakrishnan, Rev. Mod. Phys. **57**, 287 (1985).

Nanocomposite $R_2Fe_{14}B$/Fe exchange coupled magnets

L. Withanawasam, A. S. Murphy, and G. C. Hadjipanayis
Department of Physics and Astronomy, University of Delaware, Newark, Delaware 19716

R. F. Krause
Magnetics International, Inc., 1111 North State Road 149, Burns Harbor, Indiana 46304

We have studied the crystallization, crystal structure, microstructure and magnetic properties of R-Fe-B (R=Nd,Pr,Dy,Tb) based melt-spun ribbons consisting of a mixture of $R_2Fe_{14}B$ and α-Fe phases. All the samples crystallize first to α-Fe and a metastable phase ($Y_3Fe_{62}B_{14}$ for R=Nd,Pr,Dy and $TbCu_7$ for R=Tb) before they finally transform to 2:14:1 and α-Fe. The highest values of coercivity and reduced remanence, 4.5 and 0.63 kOe, respectively, were obtained in a $Nd_{3.85}Tb_2(Fe\text{-}Nb\text{-}B)_{94.15}$ sample. These properties are the result of a fine grain microstructure consisting of a mixture of α-Fe and 2:14:1 having an average grain size of 30 nm.

INTRODUCTION

A high reduced remanence (M_r/M_s), greater than 0.5, in isotropic magnets is highly desirable for permanent magnet development. Remanence enhancement has been observed previously in isotropic $Nd_2Fe_{14}B$ magnets with small Al and Si substitutions,[1,2] and more recently,[3] in samples with a controlled microstructure. High values of magnetization and reduced remanence can also be achieved in samples with a microstructure consisting of a fine mixture of hard (high anisotropy) and soft (higher magnetization) phases.[4,5] Kneller and Hwaig[6] have shown that high remanence and relatively high coercivity could be expected in a fine two-phase microstructure where the small grains are exchange-coupled.

Previously, we have studied various mixtures of $Nd_2Fe_{14}B$ and α-Fe and observed a maximum coercivity of 4.0 kOe along with a remanent magnetization of 110 emu/g in a 50 wt % 2:14:1 and 50 wt % α-Fe mixture.[7] In this report, we extend our studies on nanocomposite magnets to other rare earth 2:14:1 phases.

EXPERIMENT

$R_x(Fe\text{-}Nb)_yB_z$ ingots with different composition with R=Nd, Pr, Dy and Tb ($4<x<6$, $88<y<93$, $4<z<6$) were prepared by arc melting the constituent elements in an argon atmosphere. Pieces of the ingot were melt-spun from a quartz tube having an orifice diameter of ~1 mm. A wheel speed in the range of 25–45 m/s was used. The resulting ribbons were studied using differential scanning calorimetry (DSC) and differential thermal analysis (DTA) for possible phase transformations. X-ray diffraction (Cu K_α) was used to identify the phases present. The hysteresis loops were measured in a vibrating sample magnetometer (VSM) with a maximum field of 20 kOe on long (7 mm) sample pieces to minimize demagnetization effects. Selected samples were also measured in a SQUID magnetometer with a maximum field of 55 kOe. The microstructure of samples having different coercivities was studied by transmission electron microscopy (TEM) using a Jeol JEM 2000FX.

RESULTS AND DISCUSSION

The melt-spun ribbons were found to be x-ray amorphous (or nanocrystalline) in structure. Calorimetric studies were performed on the as-spun samples using DSC and DTA to obtain transition temperatures, latent heats, and activation energies. Typical thermal scans consisting of two or more exothermic peaks are shown in Fig. 1 for Nd-Fe-B and Dy-Fe-B based samples. The first exotherm involves a latent heat of about 70–80 J/g along with activation energies in the range 280–380 kJ/mol (see Table I). The latter quantity was evaluated by plotting ln (rate/T_p) vs $1/T_p$ for different heating rates where T_p denotes the temperature of maximum transform.[8,9] In the case of Nd, Pr, Dy this exotherm corresponds to the transformation from amorphous to metastable $Y_3Fe_{62}B_{14}$ type structure in addition to α-Fe [see Fig. 2(a)]. Similar studies on Tb-Fe-B ribbons show a transition from amorphous to hexagonal $TbCu_7$-type structure and α-Fe. Structural information and the Curie temperatures of these metastable compounds are summarized in Table II. When the samples were heat treated at temperatures above the highest transition temperature, the metastable $Y_3Fe_{62}B_{14}$ structure was found to transform to 2:14:1 + α-Fe and the $TbCu_7$ structure to a mixture of 2:14:1, α-Fe, and probably to 2:17 phases as determined by x-ray diffraction. The temperature associated with the formation of 2:14:1 phase is higher in the samples with Tb or Dy.

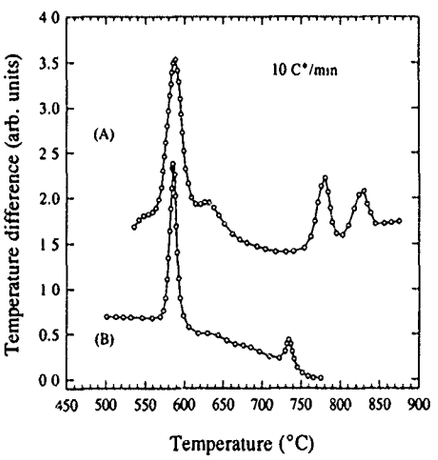

FIG. 1. DTA traces in (A) Dy-Fe-B and (B) Nd-Fe-B ribbon samples.

 0021-8979/94/76(10)/7065/3/$6.00 © 1994 American Institute of Physics

TABLE I. Transformation temperatures (T_i) and activation energies (E_i) associated with the phase transformations in R_6 (Fe-Nb-B)$_{94}$ ribbons (see text and Table II for details).

R	T_1 (°C)	E_1 (kJ/mol)	T_2 (°C)	E_2 (kJ/mol)
Nd	586	388	734	456
Pr	572	374	720	472
Dy	587	312	827	381
Tb	594	289	811	455

TABLE II. Structure type, lattice parameters and Curie temperatures of the phases formed after the first crystallization of R_6(Fe-Nb-B)$_{94}$ ribbons.

R	Structure type	a (nm)	c (nm)	T_c (°C)
Nd	bcc $Y_3Fe_{62}B_{14}$	1.231	...	200
Pr	same	1.234	...	200
Dy	same	1.235	...	210
Tb	hex. $TbCu_7$	4.801	4.225	240

The intensity distribution among the 2:14:1 peaks in these ribbon samples is similar to that of a $R_2Fe_{14}B$ powder diffraction pattern indicating the isotropic nature of the samples [Fig. 2(b)]. This was further confirmed by hysteresis loop measurements carried out along and transverse to the ribbon length.

Large coercivities were observed in the samples after annealing above the higher temperature (T_2 in Table I) exothermic peak. By varying the annealing temperature and time these coercivities were optimized. Hysteresis loops of two samples with optimum coercivity are shown in Fig. 3. Although these samples consist of two or more magnetic components, the smooth hysteresis loops are characteristic of a single component system but with high remanence values. The observation of high reduced remanence ($M_r/M_s>0.5$) and reversible demagnetization curves in these isotropic samples[7] indicates the behavior of exchange-coupled magnets.[6]

The highest coercivity of 4.5 kOe was observed in a sample containing a mixture of rare-earths ($Nd_{3.85}Tb_2$) compared to 4.0 kOe in the pure $Nd_{5.85}$(Fe-Nb-B)$_{94.15}$ sample. The slight asymmetry in these loops is believed to be a consequence of lack of saturation. However, the introduction of Tb lowers the magnetization of these ribbons from 155 emu/g in $Nd_{5.85}$(Fe-Nb-B)$_{94.15}$ to 130 emu/g. In Pr_6(Fe-Nb-B)$_{94}$ ribbons a maximum coercivity of 3.9 kOe and a remanent magnetization of 105 emu/g were observed. The coercivity of the pure Tb(Dy) samples is much lower (~1 kOe) despite the high anisotropy of the $R_2Fe_{14}B$ (R =Tb,Dy) phases. This is attributed to the formation of larger grains in these samples because of the higher annealing temperatures necessary to form the hard $R_2Fe_{14}B$ phase.

The values of the coercivities given previously correspond to a maximum magnetizing field of 20 kOe. To check whether the loops were not minor, higher magnetizing fields were used and the results are shown in Fig. 4 for the sample with largest coercivity. The coercive force does not saturate

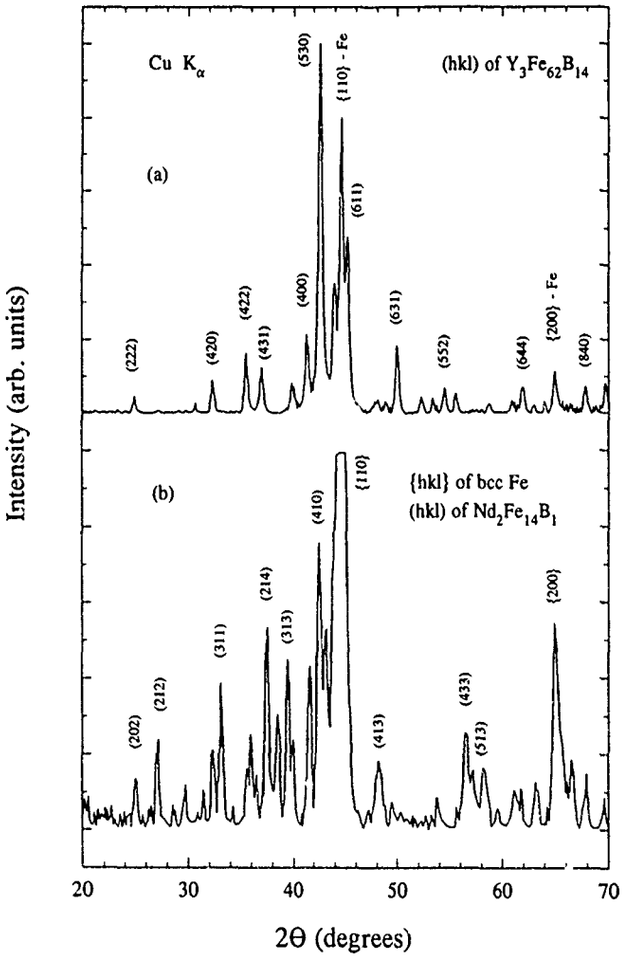

FIG. 2. X-ray diffraction patterns showing the (a) $Y_3Fe_{62}B_{14}$ and α-Fe structures and (b) $R_2Fe_{14}B$ + α-Fe observed in R_6(Fe-Nb-B)$_{94}$ ribbon samples with R=Nd, Pr, and Dy.

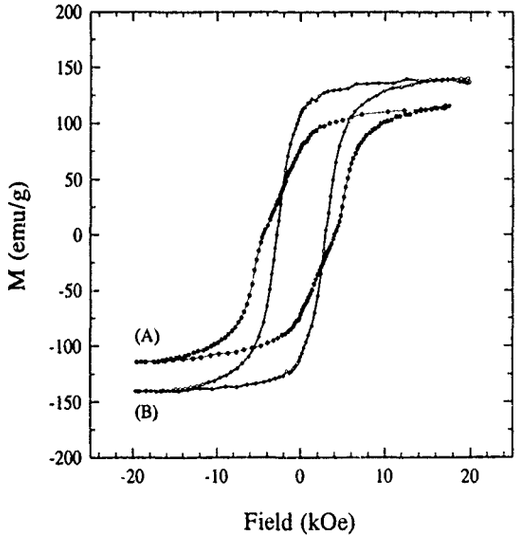

FIG. 3. Hysteresis loops of the coercivity optimized (A) $Nd_{3.85}Tb_2$(Fe-Nb-B)$_{94.15}$ and (B) $Nd_{3.2}Tb_1$(Fe-Nb-B)$_{95.8}$ samples.

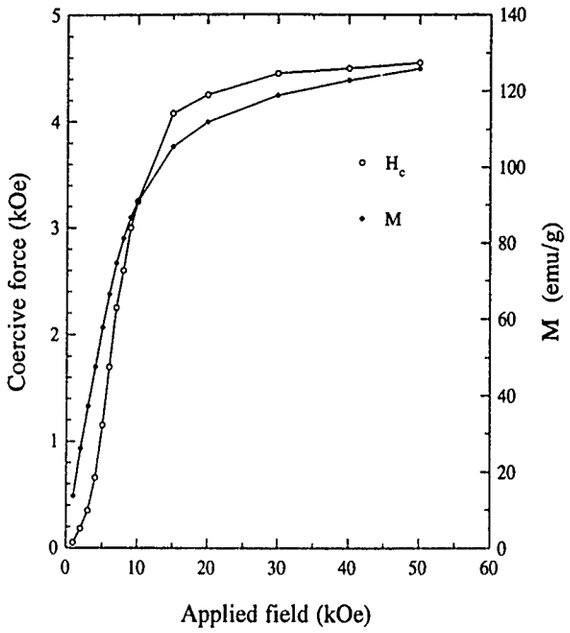

FIG. 4. The dependence of coercive force and magnetization on magnetizing field in a $Nd_{3.85}Tb_2(Fe\text{-}Nb\text{-}B)_{95.15}$ sample

for magnetizing fields lower than 30 kOe and the magnetization has a high field slope indicating lack of saturation.

Transmission electron microscopy was carried out to study the microstructure in samples exhibiting different coercive behavior. Figure 5 shows the bright-field images of two $Nd_6(Fe\text{-}Nb\text{-}B)_{94}$ samples annealed at 700 °C for 20 and 120 min. The samples annealed for a shorter period of 20 min showed a microstructure [Fig. 5(a)] consisting of a homogeneous mixture of α-Fe and 2:14:1 phases with an average grain size of about 30 nm. The hysteresis loops in the samples were similar to that of a single magnetic component. In samples annealed for 120 min, a microstructure consisting of clusters of α-Fe was observed in a matrix of 2:14:1 phase [Fig. 5(b)]. The hysteresis loops in these samples were representative of a two-component system.

CONCLUSIONS

The magnetic, structural, and microstructural properties of R-Fe-B based nanocomposite ribbons with R=Nd, Pr, Dy and Tb have been studied. A room-temperature coercivity of 4.5 kOe was observed in a sample containing Nd and Tb as compared to 4.0 kOe in the pure Nd samples. The optimum microstructure consists of a uniform mixture of 2:14:1 and α-Fe grains of about 30 nm. The coercivity of pure Tb or Dy samples is only in the 1 kOe range presumably due to the

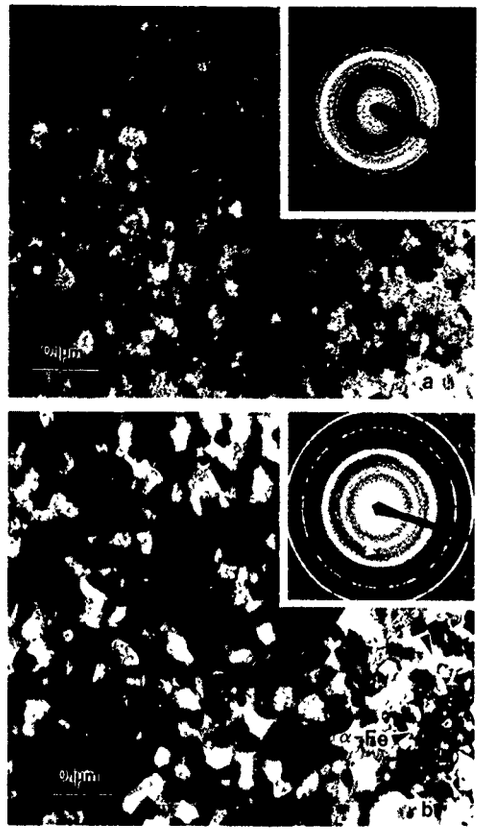

FIG. 5. Bright-field images in a $Nd_6(Fe\text{-}Nb\text{-}B)_{94}$ sample annealed at 700 °C for (a) 20 min, and for (b) 120 min. The diffraction patterns indicate a mixture of 2:14:1 and α-Fe phases

larger grains formed at the higher annealing temperatures (because of the higher transformation temperatures) associated with these alloys.

ACKNOWLEDGMENTS

The research was sponsored by U. S. Army and Magnetics International.

[1] R W. McCallum, A M Kadin, G B Clemente, and J. E Keem, J. Appl. Phys. **61**, 3577 (1987).
[2] G. C. Hadjipanayis and W. Gong, J. Appl. Phys. **64**, 5559 (1988)
[3] H. A. Davies, A. Manaf, and P. Z. Zhang, J Mater. Eng Perf. (to be published).
[4] R. Coehroon, D. B. De Mooji, and D De Waard, J Magn Mag. Mater. **80**, 101 (1989).
[5] J. Ding, P. G. McCormick, and R. Street, J. Magn. Mag. Mater. **124**, 1 (1993).
[6] E F. Kneller and R. Hawig, IEEE Trans. Magn **27**, 3588 (1991).
[7] L. Withanawasam, G C. Hadjipanayis, and R. F. Krause, J. Appl. Phys (to be published).
[8] F. G. Boswell, J. Therm. Anal. **18**, 353 (1980).
[9] J. A. Augis and J. D. Bennett, J. Thermal Anal. **13**, 283 (1978).

Influence of nitrogen content on coercivity in remanence-enhanced mechanically alloyed Sm-Fe-N

K. O'Donnell
Department of Pure and Applied Physics, Trinity College, Dublin 2, Ireland and Siemens AG, Research Laboratories, Erlangen, Germany

C. Kuhrt
Siemens AG, Research Laboratories, Erlangen, Germany

J. M. D. Coey
Department of Pure and Applied Physics, Trinity College, Dublin 2, Ireland

In nanostructured $Sm_2Fe_{17}N_x+\alpha$-Fe two-phase permanent magnets, exchange interactions between hard and soft magnetic phases result in remanence enhancement. With a starting composition of Sm_7Fe_{93}, mechanical alloying, annealing at 625 °C for 10 min and subsequent nitriding at 330 °C for 45 h results in hard magnetic powder with nanocrystallites of $Sm_2Fe_{17}N_3$ and α-Fe some 20 nm in size. There is a coercivity of $\mu_0 H_c = 0.4$ T and a remanence $J_r = 1.2$ T, after saturating in a field of 7.5 T. The deduced value of the remanence depends strongly on the choice of demagnetizing factor.

INTRODUCTION

Since the discovery of remanence enhancement in isotropic nanocrystalline $Nd_{4.5}Fe_{77}B_{18.5}$ in 1988 by Coehoorn *et al.*,[1] there has been much experimental and theoretical interest in this phenomenon. The idea of transmitting anisotropy by exchange coupling of hard and soft phases (the "exchange spring") was proposed by Kneller and Hawig.[2] There have been a number of papers on analytical calculations[3] and computer simulations[4] of these exchange hardened two-phase materials. Recent progress has been made to produce bonded magnets using the $Nd_{4.5}Fe_{77}B_{18.5}$ composition from melt spun ribbon realizing coercivities, $\mu_0 H_c$ of 0.36–0.44 T with remanences J_r of 0.89–0.80 T.[5]

The original material, $Nd_{4.5}Fe_{77}B_{18.5}$ consisted of exchange coupled grains of $Nd_2Fe_{14}B$, Fe_3B, and α-Fe in the ratio 15, 73, and 12 with crystallite sizes ranging from 10 to 30 nm. Related behavior is found in nanocrystalline, single phase, $Nd_2Fe_{14}B$ where the addition of 2 at. % Si refines the grain size to 20–30 nm.[6] Si is not a specific requirement,[7] as under certain processing conditions, which yield a grain size of 20–30 nm, a similar remanence enhancement could be obtained. This type of remanence enhancement has also been modeled using a computer simulation.[8]

Coercivities of 3 T have been obtained in $Sm_2Fe_{17}N_3$ produced by mechanical alloying,[9] but due to the isotropic nature of this nanocrystalline material the remanence was limited to a value of 0.75 T, half the saturation magnetization. Due to the rather low decomposition temperature of the $Sm_2Fe_{17}N_3$ phase (600 °C) it is not possible to apply the die upsetting method used in $Nd_2Fe_{14}B$ to produce anisotropy.

In 1993 Ding *et al.*[10] showed that a nanocrystalline two-phase mixture of $Sm_2Fe_{17}N_x$ and α-Fe produced by mechanical alloying exhibited remanence enhancement. The isotropic powders have $J_r = 1.4$ T and $\mu_0 H_c = 0.39$ T.

Theoretical modeling of such two-phase nanocrystalline materials, where a high magnetization soft phase is exchange coupled to a high anisotropy hard phase has yielded insight into the critical grain sizes and grain boundary requirements. To preserve coercivity in the nanocomposite, the size of the soft grains must be sufficiently small. The relevant length scale is the domain wall width of the hard phase. The analytical results of Skomski and Coey[3] and the computer simulations of Schrefl *et al.*[4] show that the size of the magneti-

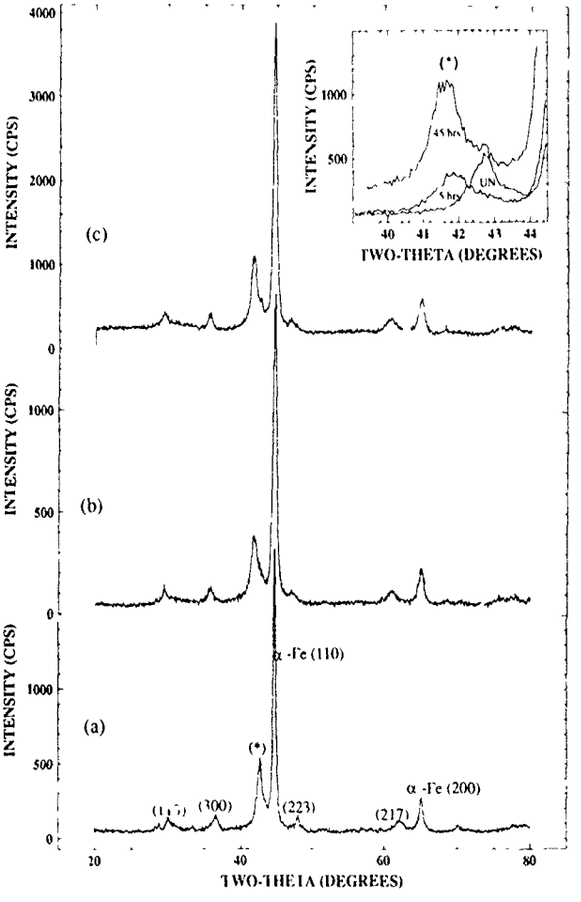

FIG 1. X-ray diffraction patterns of mechanically alloyed Sm_7Fe_{93}, annealed at 625 °C for 10 min, (a) before nitriding, (b) after 330 °C for 5 h in 1 bar of N_2 and (c) after 45 h at 330 °C. Inset shows the (220)/(303)/(214)/(006) peak under the same conditions. UN†=before nitriding (unnitrided)

 0021-8979/94/76(10)/7068/3/$6.00 © 1994 American Institute of Physics

TABLE I. Lattice parameters, magnetization, and weight gain results for mechanically alloyed Sm_7Fe_{93}, annealed at 625 °C for 10 min, and nitrided in 1 bar of N_2 for different temperatures and times.

Sample	a (Å)	c (Å)	V (Å)^3	$\Delta V/V$ (%)	$\mu_0 H_c$ (T)	J_r (T)	$\Delta W/W$ (%)
UN[a]	8.54±0.02	12.42±0.02	784±5	...	0.02	...	...
330, 5	8.66±0.01	12.75±0.04	828±3	5.6±1.0	0.35	1.12	1.7±0.1
330, 24	8.71±0.01	12.58±0.08	826±5	5.4±1.3	0.36	1.19	2.3±0.1
330, 45	8.73±0 01	12.68±0.06	837±4	6.7±1.2	0.38	1.17	2.4±0.1
330, 64	8.70±0.01	12.79±0.09	838±10	6.9±1.9	0.29	1.20	2.3±0.1
400, 475	8.73±0.01	12.72±0.15	839±10	7.0±2.0	0.28	1.20	2.4±0.1

[a]*UN*=before nitriding−unnitrided.

cally soft region should be roughly twice the domain wall width of the hard phase to stiffen the soft magnetic grains.

The domain wall width depends on the anisotropy according to the well-known formula $\delta_w = \pi(A/K_1)^{1/2}$. In the $Sm_2Fe_{17}N_x$ system, the anisotropy constant K_1 and the exchange parameter A increase with nitrogen content up to $x=3$.[11] Values for $x=3$ are $A=1.1\times10^{-11}$ J/m and $K_1=8$ MJ/m^3.[12] Here we investigate the influence of the nitriding conditions on the overall magnetic properties of two-phase exchange-hardened $Sm_2Fe_{17}N_x+\alpha$-Fe.

EXPERIMENT

Elemental Sm and Fe were mechanically alloyed in the ratio Sm_7Fe_{93} in a planetary ball mill. 20 g of the starting mixture was placed in hardened stainless-steel vials together with 400 g of 10-mm-diam stainless-steel balls. The as-milled powders were annealed at 625 °C for 10 min under vacuum. The subsequent nitriding was carried out in 1 bar of N_2 at 330 °C for times ranging from 5 to 64 h. Structural investigations were performed with a Siemens D500 x-ray diffractometer using Cu K_α radiation. The nanostructure of this two phase exchange-hardened material was characterized by transmission electron microscopy. Magnetization measurements were performed on powder samples dispersed in resin, with a packing density of about 30%, in a vibrating sample magnetometer in applied fields up to 7.5 T.

RESULTS AND DISCUSSION

The as-milled powders consisted of crystallites of α-Fe embedded in an amorphous matrix of Sm-Fe. Scherrer broadening of the x-ray reflections indicated these crystallites to be between 5 and 10 nm in size. Following crystallization of the Sm_2Fe_{17} phase there was a mixture of Sm_2Fe_{17} and α-Fe in the ratio 60:40 as determined from measurements of the saturation magnetization. Initially nitriding was carried out using 1 bar of N_2 at 400 °C for 2 h followed by 1 h at 475 °C. This resulted in a powder with a coercivity of 0.28 T. The weight gain on nitriding indicated complete nitrogenation. The nitriding temperature was then reduced to 330 °C and the time increased to 5 h. This yielded a better coercivity of 0.35 T even though both the weight gain and the x-ray diffraction pattern, shown in Fig. 1 suggest incomplete nitrogenation. The reason for the much improved results at the lower nitriding temperature of 330 °C is not yet clear. Using the formula for an activated interstitial diffusion process, $D=D_0\exp-(E_a/kT)$ with $D_0=1.02\times10^{-6}$ m^2/s and an activation energy $E_a=133$ kJ/mol,[13] the diffusion length for a temperature of 330 °C and a time of 5 h, is approximately 200 nm which is much less than the particle size (1–100 μm with an average of 20 μm) but greater than the size of the nanocrystallites which are only 20 nm in diameter. This suggests that nitrogen diffusion advances rapidly along the Sm_2Fe_{17}/Fe grain boundaries, but 5 h is insufficient to achieve complete nitrogenation of the particles.

Keeping a nitriding temperature of 330 °C samples were then nitrided for time periods of 24, 45, and 64 h and the

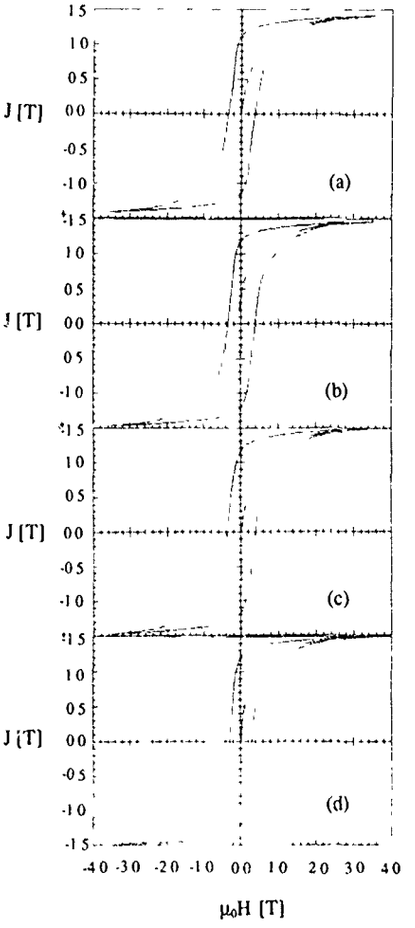

FIG. 2. Hysteresis loops of mechanically alloyed Sm_7Fe_{93}, annealed at 625 °C for 10 min after nitriding in 1 bar of nitrogen at 330 °C for (a) 5 h, (b) 24 h, (c) 45 h, and (d) 64 h.

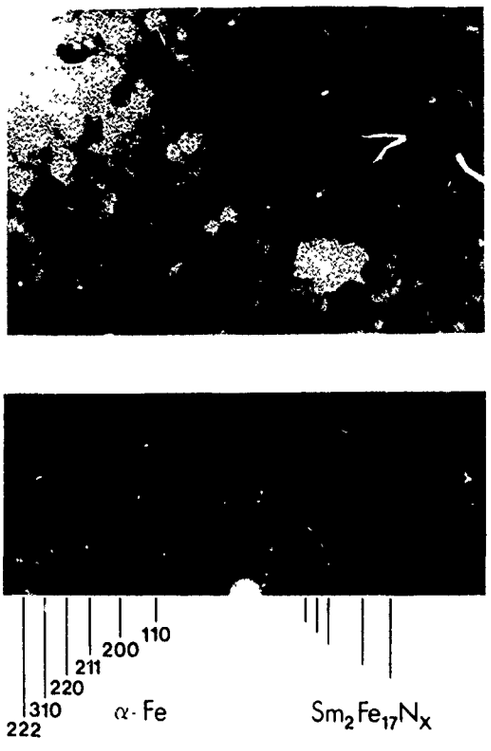

FIG. 3. (a) TEM bright-field micrograph of mechanically alloyed Sm_7Fe_{93} annealed at 625 °C for 10 min and nitrided in 1 bar of N_2 at 400 °C for 2 h followed by 1 h at 475 °C. (b) Electron diffraction pattern corresponding to the area in (a).

results are presented in Table I and Fig. 2. From the lattice parameters in Table I, it appears that after a nitriding treatment in 1 bar of N_2 at 330 °C for 24 h, the powder is completely nitrided. The coercivity increases from 0.36 to 0.38 T after nitrogenation at 330 °C for 45 h. Longer nitriding time leads to further increase in the lattice expansion, which may result from a value of x in the formula $Sm_2Fe_{17}N_x$, slightly greater than 3. The decrease in anisotropy field for $x>3$ (Ref. 14) is a possible explanation for the fall in coercivity from 0.38 to 0.29 T.

The coercivity and remanence values given in Table I were obtained in a field of 3.5 T. The A coercivity of 0.38 T increases to 0.40 T in a 7.5 T field. Remanence values are calculated using the theoretical powder density of 7.7 g/cm^3. In correcting the hysteresis loops of resin bonded powder samples for demagnetizing fields it is not sufficient to use the correction factor appropriate to the external shape of the sample. Due to the low packing density, there are internal demagnetizing fields which need to be taken into account. Samples measured in closed circuit using a BH loop tracer indicated strong internal demagnetizing fields, thus in each case a demagnetizing factor of 0.33 was used taking into account the roughly spherical shape of particles and the absence of magnetic interactions.

At annealing temperatures and times greater than 625 °C for 10 min, the hysteresis loop of the nitrided material showed a constriction, i.e., magnetic behavior indicative of two independent phases, one with a large coercivity and the other with a small coercivity. The α-Fe grains grow rapidly during annealing, and if they exceed a certain size the two phases tend to behave independently. Figure 3 shows a bright-field micrograph of the microstructure of an optimally annealed sample nitrided at 400 °C for 2 h followed by 475 °C for 1 h. Ultrafine grains with an average size of about 20 nm are visible. The electron diffraction pattern corresponding to that area is presented in the lower part of the figure. It reveals the presence of the two phases $Sm_2Fe_{17}N_x$ and α-Fe, which are both randomly oriented, indicated by the occurrence of complete diffraction rings. A high resolution image shows lattice fringes characteristic of the two phases.

The calculated domain wall width of $Sm_2Fe_{17}N_3$ is approximately 4 nm.[12] This implies that for most effective transfer of the hard magnetic properties to the soft magnetic grains, the size of the soft grains should not exceed approximately 8 nm. The milling and annealing conditions were systematically varied, but the end result, without the use of additions[15] was always that, the minimum size of the α-Fe grains after crystallization of the Sm_2Fe_{17} phase was about 20 nm. It should be investigated whether by lowering the anisotropy of the hard phase, $Sm_2Fe_{17}N_x$ by reducing x for example, the increase of the domain wall width δ_w would lead to a greater coercivity.

CONCLUSIONS

Complete nitrogenation at such a low temperature of the two-phase nanostructure is in contrast to that of nanocrystalline single phase $Sm_2Fe_{17}N_3$ prepared by a similar process. It suggests that nitrogen diffusion is particularly easy along Sm_2Fe_{17}/Fe grain boundaries. The activation energy for the diffusion of nitrogen in α-Fe is ~half that in Sm_2Fe_{17}. A homogeneous nanostructure is achieved by mechanical alloying, but the size of the soft, α-Fe regions is approximately 20 nm, which is about twice the size for optimum exchange hardening.

[1] R. Cochoorn, D. B. de Mooij, J. P. W. B. Duchateau, and K. H. J. Buschow, J. Phys. (Paris) **C8**, 669 (1988).
[2] E. F. Kneller and R. Hawig, IEEE Trans. Magn. **MAG-27**, 3588 (1991).
[3] R. Skomski and J. M. D. Coey, Phys. Rev. B **48**, 15 812 (1993).
[4] T. Schrefl, H. Kronmuller, and J. Fidler, J. Magn. Magn. Mater. **127**, L273–L277 (1993).
[5] S. Hirosawa, H. Kanekiyo, and M. Uehara, J. Appl. Phys. **73**, 6488 (1993).
[6] G. B. Clemente, J. E. Keem, and J. P. Bradley, J. Appl. Phys. **64**, 5299 (1988).
[7] A. Manaf, M. Leonowitz, H. A. Davies, and R. A. Buckley, Proceedings of the 12th International Workshop on RE Magnets and their Applications, Canberra, 1992, p. 1.
[8] H. Fukunaga and H. Inoue, Jpn. J. Appl. Phys. **31**, 1347 (1992)
[9] K. Schnitzke, L. Schultz, J. Wecker, and M. Katter, Appl. Phys. Lett. **57**, 2853 (1990).
[10] J. Ding, P. G. McCormick, and R. Street, J. Magn. Magn. Mater. **124**, L1 (1993).
[11] M. Katter, J. Wecker, C. Kuhrt, and L. Schultz, J. Magn. Magn. Mater **117**, 419 (1992).
[12] R. Skomski and P. A. P. Wendhausen, in *Interstitial Alloys for Reduced Energy Consumption and Pollution*, edited by G. J. Long, F. Grandjean, and K. H. J. Buschow (Kluwer, Dordrecht, in press)
[13] R. Skomski and J. M. D. Coey, J. Appl. Phys. **73**, 7602 (1993).
[14] T. Iriyama, K. Kobayashi, N. Imoaka, and T. Fukuda, IEEE Trans. Magn. **MAG-28**, 2326 (1992).
[15] K. O'Donnell, C. Kuhrt, and J. M. D. Coey, Proceedings of the 13th International Workshop on RE Magnets and their Applications, Birmingham, 1994, p. 851.

Coercivity of Ti-modified (α-Fe)-$Nd_2Fe_{14}B$ nanocrystalline alloys

J. M. Yao and T. S. Chin
Department of Materials Science and Engineering, Tsing Hua University, Hsinchu, 300, Taiwan, Republic of China

S. K. Chen
Department of Materials Science, Feng Chia University, Taichung, 400, Taiwan, Republic of China

Coercivity of Ti-modified nanocrystalline (α-Fe)-$Nd_2Fe_{14}B$ alloys with soft iron particles embedded in hard $Nd_2Fe_{14}B$ matrix was studied. The alloys were prepared by melt spinning and annealing. The grain size of $Nd_2Fe_{14}B$ is from 20 to 60 nm, while that of the soft iron particles is 11 to 30 nm. The coercivity of the annealed flakes decreased dramatically with increasing particle size of free iron, following the same tendency of a theoretical calculation by Schrefl *et al.* For the Ti-alloyed flakes, the 1 at. % Ti-containing ones show the highest coercivity of 11.1 kOe. Its $(BH)_m$ value is about 16 MGOe despite lower Nd and B contents than stoichiometric $Nd_2Fe_{14}B$. More Ti addition would deteriorate the coercivity.

I. INTRODUCTION

Rapidly quenched Nd-Fe-B flakes with Nd and B richer than the stoichiometric $Nd_2Fe_{14}B$ (2-14-1) composition have been extensively studied.[1,2] The high coercivity and energy product of the flakes primarily results from the magnetically hard $Nd_2Fe_{14}B$ phase. Recently, some researchers proposed a kind of nanostructured two-phase magnets with soft magnetic phase embedded in hard magnetic phase.[3–5] This material has been attracting much attention because it possesses high saturation magnetization with moderate coercivity, hence the maximum energy product can be greatly enhanced. In this study, we intend to precipitate fine soft iron particles within $Nd_2Fe_{14}B$ matrix in the α-Fe/$Nd_2Fe_{14}B$ psuedobinary system. The alloying effect of Ti element was also systematically studied.

II. EXPERIMENT

The studied alloy compositions are designated as shown in Table I. The samples were prepared first by arc-melting Nd, Fe, B, Ti elements of +99.5% purity under argon protection, then remelted by induction melting and rapid quenching at a wheel speed (V_s) of 40 m/s by using single-roller melt-spinning technique.[6,7] The as-spun flakes were annealed at different temperatures from 600 to 800 °C for 10 min. Differential thermal analysis (DTA) was used to determine the crystallization temperature and activation energy of crystallization of as-spun flakes. Magnetic properties were measured by a VSM with a maximum field of 20 kOe at room temperature. The crystal structure of the flakes was studied by x-ray diffractometry (XRD) using Cu $K\alpha$ radiation. The grain size of free α-Fe was calculated from the full width at half maximum (FWHM) data by using Schererr's formula. The microstructure was studied using a transmission electron microscope (TEM) with an energy dispersive spectroscopy (EDS) attachment.

TABLE I The designation of the studied alloy composition.

$Nd_{10.58}Fe_{84.11}B_{5.29}Ti_x$	$Nd_9Fe_{86.5}B_{4.5}Ti_x$	$Nd_8Fe_{88}B_4Ti_x$
N10T0 ($x=0$)	N9T0 ($x=0$)	N8T0 ($x=0$)
N10T1 ($x=1$)	N9T1 ($x=1$)	N8T1 ($x=1$)
...	N9T2 ($x=2$)	N8T3 ($x=3$)

III. RESULTS AND DISCUSSION

A. Crystallization behavior of as-spun flakes

The as-melt-spun amorphous flakes can be obtained by high-speed melt spinning even though they contain low B and Nd contents. These flakes show a glass transition temperature (T_g) of around 470 °C and a crystallization temperature (T_x) of around 600 °C. The T_x value increases with increasing amount of α-Fe and Ti, as shown in Table II. The activation energy (E_a) of crystallization is calculated using the Kissinger plot.[8] The N8T3 flakes show a higher-energy barrier of crystallization than N10T1 flakes, which is consistent with the crystallization temperature datum.

B. Magnetic properties of annealed flakes

The Ti-1 at. % alloyed flakes annealed at 750 °C for 10 min show the highest-energy product with an improved squareness of the demagnetization curve. The $(BH)_m$ value of 15.9 MGOe is higher than that of conventional MQI (tradename of flakes manufactured by Magnetquench, typically 14–15 MGOe) despite its lower Nd and B contents than stoichiometric $Nd_2Fe_{14}B$.

Figure 1 shows the dependence of Nd content on coercivity. The intrinsic coercivity (iHc) value increases linearly with Nd content. The increasing rate of iHc is 2.5 kOe at. % Nd. But the B_r value increases as decreasing Nd content due to the enhanced remanence effect as predicted by the theory.[3] For the Ti-containing samples, iHc of the 1 at. % Ti added

TABLE II. Crystallization temperature (T_x) and activation energy (E_a). T_x was measured at a heating rate of 10 °C/min, E_a calculated from the peak shift in DTA curves obtained at heating rates of 5, 10, and 15 °C/min.

Alloy	N10T1	N9T2	N8T3
T_x(°C)	576	590	605
E_a (kJ/mole)	73	..	119

 0021-8979/94/76(10)/7071/3/$6.00 © 1994 American Institute of Physics

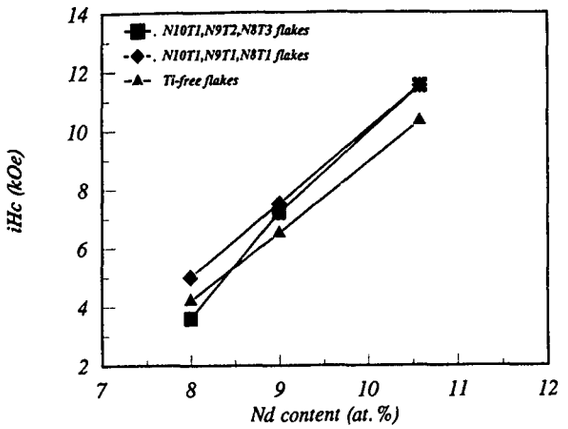

FIG. 1. Dependence of Nd content on iHc value of flakes annealed at 750 °C for 10 min.

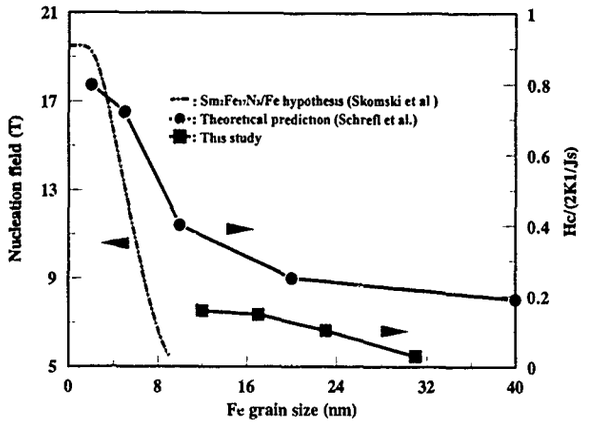

FIG. 3. Micromagnetic simulation (Ref. 5), Skomski's modeling (Ref. 3), and experimental data of the effect of α-Fe particle size on the coercivity of flakes annealed at 750 °C for 10 min.

samples is higher than Ti-free samples. However, more Ti addition would result in a rapid deterioration of iHc due to the growth of α-Fe. Figure 2 shows the effect of annealing temperature on iHc of the Ti-free, the 1% Ti and 2% Ti alloys. It is manifest that the optimum annealing temperature ranges from 700 to 750 °C. The optimum temperature increases with Ti content.

C. Microstructure features

The grain size of α-Fe is measured by the peak-broadening technique in XRD calibrated against a pure iron sample with large grains (about 10 μm). The coercivity of flakes decreased rapidly with increasing particle size of α-Fe precipitates. Figure 3 shows the relationship between α-Fe particle size and coercivity for the annealed Ti-containing flakes. The theoretical predictions proposed by Skomski and Coey[3] and Schrefl *et al.*[5] have delineated similar behavior, also shown in Fig. 3. There is a discrepancy between the experimental results and the theoretical calculation by Schrefl *et al.*[5] In the figure the normalized coercivity (normalized by the theoretical nucleation field, $2K_1/J_s$, of the hard magnetic phase) is twice as large as the experimental ones. This may arise from the fact that the theoretical modeling has the soft iron particles completely embedded within hard magnetic phase, while in the studied alloys, the free-iron particles are mostly free standing among $Nd_2Fe_{14}B$ grains and partly embedded (particularly for smaller ones), as shown in Fig. 4. Nevertheless, the tendency is correct that the coercivity does drop dramatically when α-Fe particles grow up. The comparison between the experimental results and Skomski's calculation is difficult because the size range is different.

Figure 4 is a TEM micrograph taken from N10T1 flakes annealed at 750 °C for 10 min. The flakes exhibit a fine grain structure with soft iron particles mostly free standing among and partly embedded in hard $Nd_2Fe_{14}B$ phase. The grain size of the $Nd_2Fe_{14}B$ phase ranges from 20 to 60 nm and the soft iron particles are generally less than 20 nm. It has proposed that fine $Nd_2Fe_{14}B$ grains significantly contribute to the coercivity by acting as the domain-wall-pinning sites. The free-iron particles are smaller than single domain, so when a domain wall sweep across it, large exchange anisotropy will be

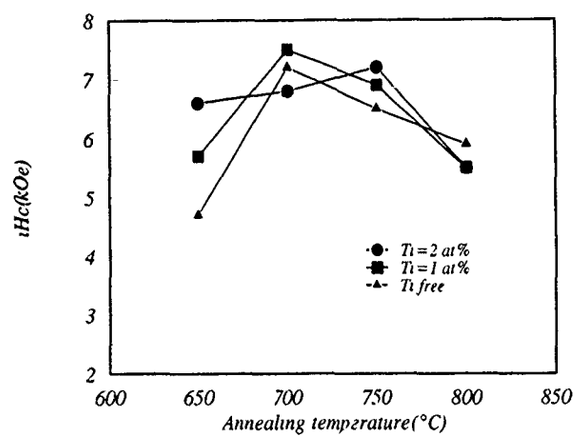

FIG 2. Annealing effect on the coercivity for $Nd_9Fe_{86.5}B_{4.5}Ti_x$ ($x=0-2$ at. %).

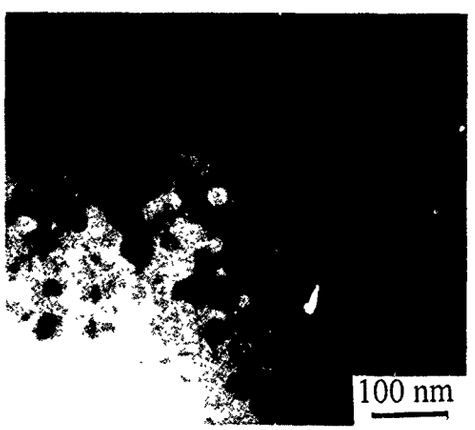

FIG. 4. TEM micrograph of a $Nd_{10.58}Fe_{84.11}B_{5.29}Ti$ flake annealed at 750 °C for 10 min.

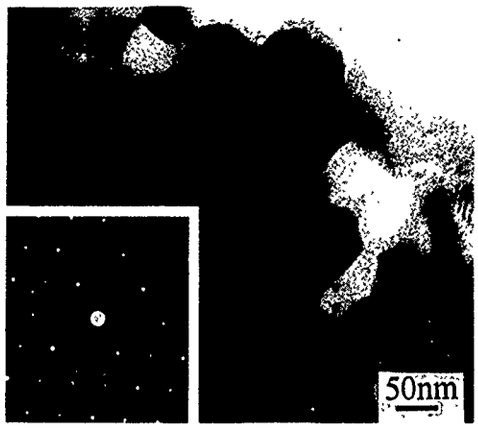

FIG. 5. A few larger grains found in annealed $Nd_{10.58}Fe_{84.11}B_{5.29}Ti$ flakes; inset is the SAD pattern showing the 2-14-1 phase.

encountered.[7] Similar results were also reported previously by Manaf *et al.*[4] When the particle size of α-Fe is further reduced, approaching the domain-wall width of hard $Nd_2Fe_{14}B$ phase, the exchange interaction would suppress the reversible rotation of magnetization in the soft iron particles and result in a significant rise of coercivity.[5] Figure 5 shows a few larger grains found in N10T1 flakes, probably due to a gas-pocket trapped between ribbon and wheel surface. The selected area diffraction pattern (the inset) of the larger grains demonstrates a $Nd_2Fe_{14}B$ phase structure. EDS analysis with an ultrafine electron probe (beam diameter ~10 nm) indicates that Ti atoms are homogeneously distributed between the $Nd_2Fe_{14}B$ matrix and α-Fe particles. The chemical composition of free-iron particles was analyzed to be Fe 93.2 at. %, and Ti 2.9 at. %.

IV. CONCLUDING REMARKS

Ti-modified (α-Fe)-$Nd_2Fe_{14}B$ nanocrystalline two-phase alloys with soft iron particles embedded in hard $Nd_2Fe_{14}B$ matrix were prepared by melt spinning and annealing. The grain size of $Nd_2Fe_{14}B$ is 20–60 nm while that of the soft iron particles is 11–30 nm. The coercivity of the annealed flakes decreased dramatically with increasing particle size of the free iron, following the same tendency of a theoretical calculation by Schrefl *et al.* The 1 at. % Ti-containing flakes show the highest coercivity of 11.1 kOe. Its $(BH)_m$ value is about 16 MGOe despite the lower Nd and B content than stoichiometric $Nd_2Fe_{14}B$.

ACKNOWLEDGMENT

The authors are grateful to the National Science Council of the Republic of China for sponsoring this work under Grant No. NSC83-0405-E007-14.

[1] J. J. Croat, J. F. Herbst, R. W. Lee, and F. E. Pinkerton, J. Appl. Phys. **55**, 2078 (1984).
[2] R. W. Lee, E. G. Brewer, and N. A. Schaffel, IEEE Trans. Magn. **MAG-21**, 1958 (1985).
[3] R. Skomski and J. M. D. Coey, Phys. Rev. B **48**, 15812 (1993).
[4] A. Manaf, R. A. Buckley, and H. A. Davies, J. Magn. Magn. Mater. **128**, 302 (1993).
[5] T. Schrefl, H. Kronmüller, and J. Fidler, J Magn. Magn. Mater. **127**, L273 (1993).
[6] T. S. Chin, S. H. Huang, and Y. S. Chen, J. Magn. Magn. Mater. **111**, 177 (1992).
[7] T. S. Chin, C. H. Lin, S. H Huang, J. M. Yao, T. Y. Chu, and C. D. Wu, Jpn. J. Appl. Phys. **31**, 3323 (1992).
[8] H. E. Kissinger, Anal. Chem. **29**, 1702 (1957).

Magnetization processes in remanence enhanced materials (invited) (abstract)

R. Street, P. Allen, J. Ding, E. Feutrill, L. Folks, P. A. I. Smith, and R. C. Woodward
Research Centre for Advanced Mineral and Materials Processing, Nedlands 6009, Australia

Isotropic assemblies of hard and soft magnetic phases in nanocrystalline form have been produced by high energy ball milling and melt spinning. These materials exhibit remanence enhancement, i.e., the remanence exceeds $0.5M_{sat}$, the value expected of an isotropic material. The phenomenon has been investigated using models in which interaction energy across the interfaces between magnetically hard and soft components is taken into account. An example of such a two-dimensional model will be discussed. Measurements have been made of the magnetic properties of SmFeN, Sm(Fe,Co), and NdFeB two phase nanocrystalline materials. All of them exhibit remanence enhancement. The time dependent behavior of materials exhibiting remanence enhancement is unusual. Magnetic viscosity occurs on both branches of recoil loops as well as on the initial magnetizing and demagnetizing curves.

 0021-8979/94/76(10)/7074/1/$6.00 © 1994 American Institute of Physics

Magnetic order and spin-flop transition in Co-Re multilayers

Z. Tun, W. J. L. Buyers, and I. P. Swainson
AECL Research, Chalk River, Ontario K0J 1J0, Canada

M. Sutton
Center for Physics of Materials and Department of Physics, McGill University, 3600 University Street, Montreal, Quebec H3A 2T8, Canada

R. W. Cochrane
Groupe de recherche en physique et technologie des couches minces et Departement de physique, Universite de Montreal, C.P. 6128, Succ. Centre Ville, Montreal, Quebec H3C 3J7, Canada

Polarized neutron reflectometry measurements were carried out on a thin-film Co-Re multilayer sample with Re thickness of 6 Å which is at the peak of the first oscillation of the magnetoresistance. Antiferromagnetic coupling between successive Co layers is observed at in-plane magnetic fields below 0.1 T. Towards the low field end of this regime, the axes of the antiferromagnetic domains are distributed relatively uniformly in the sample plane but at ~0.1 T the moments flop perpendicular to the applied field. As the field is increased further, the Co moments are pulled into the field direction producing a partial ferromagnetic alignment. At 0.5 T, the highest field where the measurements have been made, the antiferromagnetic to ferromagnetic transition was found to be only ~50% complete, indicating that the saturation field required for Co-Re system is much higher than that for Co-Cu multilayers of similar layer spacing.

I. INTRODUCTION

Multilayers composed of a ferromagnetic metal (Co, Fe, Ni)[1-5] separated by a nonmagnetic transition metal (such as Cu, Cr, Ru, and Ag) exhibit oscillatory interlayer magnetic coupling which has stimulated considerable fundamental and technological interest. In these materials, the coupling of adjacent magnetic layers oscillates between antiferromagnetic (AFM) and ferromagnetic (FM) alignment as a function of the nonmagnetic spacer thickness with a period about 10 Å for most systems.[3] This period can be understood in terms of the Ruderman–Kittell–Kasuya–Yosida interaction and the topological character of the Fermi surface of the nonmagnetic spacer layer.[6] Further, a strong negative magnetoresistance has been found in such multilayer films when the initial antiparallel magnetization alignment of adjacent layers is brought into parallel alignment by an external magnetic field.[1] As a result, the magnitude of the magnetoresistance oscillates with the nonmagnetic spacer thickness[2,3] and is attributed to spin-dependent scattering of the conduction electrons.[7]

We have recently demonstrated[8,9] that the magnetoresistivity of Co-Re multilayers also oscillates as a function of the Re layer thickness, with a small $\Delta R/R$ peak value of 1% and a large saturation field value near 1 T at low temperatures. Although the magnetoresistance is relatively small compared with other systems such as Co-Cu, the large fields required for the saturation of magnetoresistance are comparable with those in Co-Cu, indicating that the interlayer coupling is relatively strong for the Co-Re multilayers. In order to examine the interlayer magnetic coupling in detail, we have undertaken a series of polarized neutron reflectivity measurements on a sample with a Re layer thickness of 6 Å, chosen to be at the peak of the first oscillation of the magnetoresistance. Small angle spin-polarized neutron reflectometry is sensitive to both the nature of the interlayer coupling as well as the orientation of the internal magnetic axes with respect to the external applied magnetic field as has been shown for molecular-beam-epitaxy-grown (MBE) Co-Cu multilayers.[10]

II. EXPERIMENTAL DETAILS

The sample studied was taken from a series of samples[11] with layer structures substrate/Re(50 Å)/[Co(24 Å)/Re(t Å)]$_{\times 50}$/Re(10 Å) deposited on oxidized Si substrates using a modified single-source rf triode sputtering system. The additional 10 Å Re overlayer was included to inhibit oxidation of the Co layer immediately underneath. The deposition system was pumped to a base pressure $\sim 1\times 10^{-7}$ Torr before sputter deposition at a pressure of 4.0 mTorr argon and a rf power of 88 W. With a substrate-target distance of 5.5 cm, typical deposition rates were 2.1 Å/s for Co and 2.0 Å/s for Re. The structural characterization of the samples was performed by low- and high-angle x-ray diffraction measurements.[9] Low-angle reflectivity data show three superlattice peaks, confirming a well-defined composition modulation along the growth direction. In addition, high-angle x-ray diffraction data indicate coherent and highly textured structures with an hcp [002] direction normal to the film plane. X-ray linewidths suggest an in-plane grain size of about 200–300 Å for this sample.

The neutron reflectivity measurements were carried out at the NRU reactor, Chalk River, with the C5 spectrometer of the DUALSPEC facility. The spectrometer was fitted with a

 0021-8979/94/76(10)/7075/3/$6.00 © 1994 American Institute of Physics

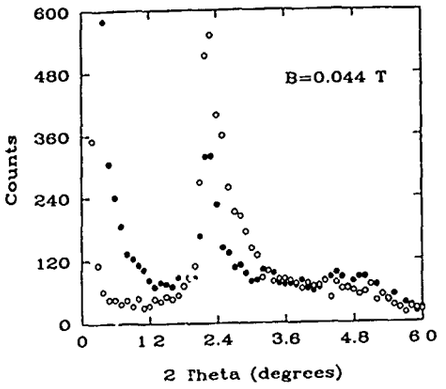

FIG. 1. Polarized neutron scattering intensity as a function of the scattering angle 2θ (2theta) at $B=0.044$ T. NSF scattering is plotted as filled circles and SF scattering as open circles.

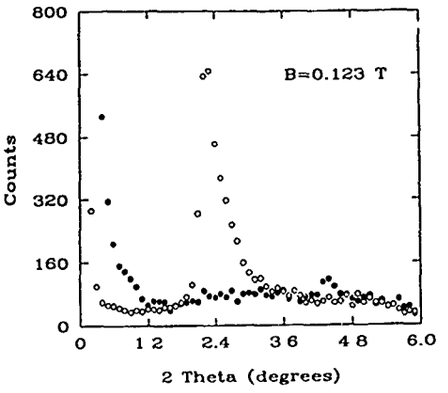

FIG. 2. Polarized neutron scattering intensity as a function of the scattering angle 2theta at $B=0.123$ T. NSF scattering is plotted as filled circles and SF scattering as open circles.

Cu_2MnAl Heusler alloy monochromator and analyzer, a pyrolytic graphite filter, and a Mezei-type spin flipper tuned for the selected neutron wavelength of 2.37 Å in the scattered beam. This setup allowed us to measure non-spin-flip (NSF) and spin-flip (SF) scattering of polarized neutrons by the sample. Since the Heusler alloy reflects only "spin down" neutrons the scattering processes correspond to $S(Q)_{down\text{-}down}$ and $S(Q)_{down\text{-}up}$. The sample was mounted in a cryostat with a horizontal magnetic field almost parallel to the multilayer planes. A small misalignment of the field of ~3° was required in order to avoid the neutron shadow caused by the liquid-helium feed tube for the lower part of the magnet. Specular reflectivity measurements were carried out at small glancing angles (<6°) with the scattering vector perpendicular to the multilayers. Sample temperatures were in the range from 4.2 to 250 K; only weak temperature dependences were observed and, in this paper, only low temperature data are presented.

III. RESULTS AND DISCUSSION

Magnetic neutron scattering is sensitive only to the components of the magnetic moment that are perpendicular to the scattering vector, i.e., that lie in the plane of the multilayer. Since the neutrons are polarized along the applied field B, the in-plane components of the moment parallel and perpendicular to B are observed as NSF and SF scattering, respectively.

Neutron reflectivity curves measured at three values of B are shown in Figs. 1–3. In general, resolved peaks are observed at three regions of scattering angle. The large peak at very small angles arises mostly from the unscattered neutrons. Additional small angle scattering is seen for the NSF channel due to finite critical angle for total external reflection. No total external reflection is seen for the SF channel. Additional peaks are found at $2\theta=4.5°$, arising from the structural period of 30 Å for this sample, and at $2\theta=2.3°$, corresponding to twice the structural period due to the AFM stacking of adjacent Co layers.

At the lowest applied field ($B=0.044$ T), specular peaks at $2\theta=2.3°$ are observed in both the NSF and SF scattering channels (Fig. 1), confirming that the interlayer magnetic order in the zero-field limit is AFM. The intensity ratio between the SF and NSF peaks in Fig. 1 is 2:1, indicating that in-plane AFM order is predominantly oriented perpendicular to B but approximately 30% of the moments remain parallel to B at this value of the field. For antiferromagnetically coupled layers in an applied field the magnetic energy is reduced if the moments are perpendicular rather than parallel to the field. The observation of AFM peaks in both scattering channels at $B=0.044$ T therefore indicates that there is a small amount of in-plane anisotropy present for the Co layers. A completely spin-flopped state of the sample, signaled by a purely SF scattering at the AFM peak position, is observed at 0.123 T (Fig. 2). Assuming the moment per unit area of each Co layer to be 3.5×10^{-4} G cm ($M\times t_{Co}\sim1446$ G×24 Å), we estimate the magnitude of the in-plane anisotropy to be ~0.4 erg/cm^2.

In Fig. 2 ($B=0.123$ T) the small NSF peak at $2\theta\sim4.5°$ is due to the establishment of a small net moment parallel to B. Note that the NSF signal in the corresponding range of Fig. 1 is undetectable above the background. More recent low-field measurements (to be published elsewhere)[12] show that there is indeed a very weak peak at this position of purely nuclear

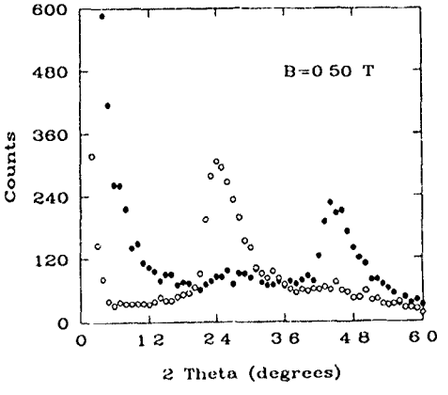

FIG. 3. Polarized neutron scattering intensity as a function of the scattering angle 2theta at $B=0.50$ T. NSF scattering is plotted as filled circles and SF scattering as open circles

origin [as confirmed by measurements of the two NSF cross sections, $S(Q)_{\text{up-up}}$ and $S(Q)_{\text{down-down}}$].

Measurements at fields ≥ 0.3 T reveal the development of a FM component at the expense of AFM order. At $B=$ 0.5 T the intensity of the FM peak is almost equal to that of AFM peak, indicating that the AFM to FM transition is halfway complete (Fig. 3). This result is consistent with the variation of transverse magnetoresistance in a similar sample with $t\sim 5$ Å, where $\Delta R/R$ is reduced to half of its zero-field value in an applied field of 0.5 T.[8]

IV. CONCLUSION

Antiparallel alignment of the Co layer moments at low fields, development of a spin-flop state at intermediate fields, and a gradual transition to parallel alignment at high fields indicate a classical AFM order with relatively strong interlayer coupling. Qualitatively similar behavior was found for MBE-grown Co-Cu multilayers[10] although significant FM order was also detected in AFM samples resulting from FM bridges due to pinholes in the films. Our sputtered Co-Re sample shows no low field FM order making it an ideal matrix for studying the spatial distribution of the magnetization in a system with antiferromagnetically coupled layers. Such an analysis is currently in progress.[12]

ACKNOWLEDGMENT

We would like to thank Dr. Yiming Huai for his assistance with the sample growth.

[1] M. N. Baibich, J. M. Broto, A. Fert, F. Nguyen van Dau, F. Petroff, P. Etienne, G. Creuzet, A. Friederich, and J. Chazelas, Phys. Rev Lett. **61**, 2472 (1988).

[2] S S. P. Parkin, N. More, and K. P. Roche, Phys. Rev. Lett. **64**, 2304 (1990); S. S. P. Parkin. R. Bhadra, and K. P. Roche, *ibid.* **66**, 2152 (1991).

[3] S. S. P. Parkin, Phys. Rev. Lett. **67**, 3598 (1991).

[4] D. H. Mosca, F. Petroff, A. Fert, P. A. Schroeder, W. P. Pratt, Jr., and R. Laloee, J. Magn. Magn Mat. **94**, L1 (1991).

[5] C. A. dos Santos, B. Rodmacq, M. Vaezzadeh, and B. George, Appl. Phys. Lett. **59**, 126 (1991).

[6] P. Bruno and C. Chappert, Phys. Rev. Lett. **67**, 1602 (1991); Phys. Rev. B **46**, 261 (1992).

[7] R. E. Camley and J. Barna, Phys. Rev. Lett. **63** 664 (1989); P. M. Levy, S. Zhang, and A. Fert, *ibid.* **65**, 1643 (1990).

[8] Y. Huai and R. W. Cochrane, J. Appl. Phys. **72**, 2523 (1992).

[9] Y. Huai, R. W. Cochrane, and M. Sutton, Phys. Rev. B **48**, 2568 (1993).

[10] A. Schreyer, K. Brvhl, J. F. Ankner, C. F. Majkrzak, Th. Zeidler, P. Bvdeker, N. Metoki, and H. Zabel, Phys. Rev. B **47**, 15334 (1993).

[11] Y. Huai, R. W. Cochrane, Y. Shi, H. E. Fischer, and M. Sutton, Mater. Res. Soc. Symp. Proc. **238**, 671 (1992).

[12] Z. Tun, W. J. L. Buyers, M. Sutton, and R. W. Cochrane (to be published).

Interlayer exchange coupling versus ferromagnetic layer thickness in asymmetric Co/Ru/Co trilayer films

L. Zhou, Z. Zhang, and P. E. Wigen
Department of Physics, The Ohio State University, Columbus, Ohio 43210

K. Ounadjela
23 rue du Loess, 67037 Strasbourg, Cedex, France

A dependence of the interlayer exchange coupling coefficient A_{12} on the Co layer thickness has been observed in asymmetric Co(32 Å)/Ru(t_{Ru})/Co(t_2) trilayer structures for several series within which t_{Ru} is a constant. As a function of the second Co layer thickness, the amplitude of A_{12} varies significantly but the sign of A_{12} does not change within each series. In both parallel and antiparallel coupled structures, the variation length Δt_2 between the maximum and the minimum coupling strength is rather large (about 10 Å) and consistent from series to series.

I. INTRODUCTION

Since the discovery of antiparallel coupling between Fe films across a Cr interlayer,[1] many studies have been done to evaluate the interlayer exchange coupling strength in various magnetic multilayer systems using ferromagnetic resonance (FMR) and Brillouin light scattering (BLS).[2–5] For a trilayer structure consisting of two ferromagnetic layers separated by a nonmagnetic spacer, the bilinear exchange coupling energy per unit surface area is defined as

$$A_{12}\frac{\mathbf{M}_1\cdot\mathbf{M}_2}{\mathbf{M}_1\times\mathbf{M}_2}, \tag{1}$$

where A_{12} is the exchange coupling coefficient and $\mathbf{M}_1$ and $\mathbf{M}_2$ are magnetization vectors in the first and second magnetic layers, respectively. The sign of A_{12} is chosen so that it is positive for an antiparallel coupled system and negative for a parallel coupled system.

While most work is devoted to the oscillation behavior of the interlayer exchange coupling with increasing interlayer thickness, little effort has been related to the dependence of the coupling on the thickness of the ferromagnetic layers. Recently, Bloemen *et al.*[6] have studied the coupling behavior in a (001) Co/Cu/Co trilayer structure with different Co layer thickness, and concluded that the interlayer coupling oscillates as a function of the Co layer thickness with a period of 6–7 Å. Their results are consistent with the prediction by Barnas[7] and Bruno.[8] Both the theoretical calculation by Barnas and Bruno and the experimental evidence by Bloemen *et al.* are done in symmetric trilayer systems (i.e., in each sample, the first Co layer thickness t_1 is equal to the second Co layer thickness t_2). In this paper we report the first experimental evidence for interlayer exchange coupling oscillations as a function of the Co layer thickness in asymmetric Co(32 Å)/Ru(t_{Ru})/Co(t_2) trilayer systems. The purpose for these series is (i) to observe the optic mode by creating an asymmetric anisotropy environment and (ii) to systematically investigate the variation of the interlayer exchange coupling with the magnetic layer thickness.

The interlayer coupling strength as well as the effective anisotropy energy within each magnetic layer has been evaluated using in-plane magnetization measurements and angular dependence of FMR measurements. In the antiparallel coupled in-plane magnetization curves, two transition fields $H_{cri,1}=A_{12}/\mathbf{M}_s\times(1/t_2-1/t_1)$ and $H_{cri,2}=A_{12}/\mathbf{M}_s\times(1/t_2+1/t_1)$ exist which separate the antiparallel, canted, and saturation states. The two transition fields can be used to evaluate the coupling coefficient A_{12}. However, the in-plane hysteresis loop for a parallel coupled system is degenerate with that of a noncoupled system and therefore cannot be used to evaluate the coupling strength. In contrast to the in-plane magnetization measurements, FMR can provide information of the exchange coupling strength and effective anisotropy energy for both parallel and antiparallel coupled systems.

II. EXPERIMENT

The Co(32 Å)/Ru(t_{Ru})/Co(t_2) structures were prepared in ultrahigh vacuum by evaporation on freshly cleaved mica substrates. In each of the four series, the Ru layer thickness is a constant (t_{Ru}=10, 12, 16, and 24 Å, respectively) while t_2 varies from 8 to 32 Å. Structure analysis using reflection high-energy electron diffraction and transmission electron microscopy indicates that the layers are grown epitaxially on the buffer layers, with good crystalline features and sharp interfaces.

It has been found that the magnetization vectors of the two Co layers are strongly antiparallel coupled in series I (t_{Ru}=10 Å) and series II (t_{Ru}=12 Å), parallel coupled in series III (t_{Ru}=16 Å), and antiparallel coupled in series IV (t_{Ru}=24 Å). This is similar to the coupling behavior observed in symmetric structures.[9] Series I and II are in the first antiparallel coupled region and series IV is in the second antiparallel coupled region while series III is in the parallel coupled region with respect to the Ru thickness. In-plane magnetization measurements were performed using a superconducting quantum interference device and alternating gradient force magnetometry magnetometers at room temperature. FMR measurements at both X-band (9.2 GHz) and K-band (23 GHz) frequencies have been performed at room temperature. The external field was rotated from the orientation parallel to the film plane, $\theta_H=90°$, to the orientation perpendicular to the film plane, $\theta_H=0°$, in 10° steps.

 0021-8979/94/76(10)/7078/3/$6 00 © 1994 American Institute of Physics

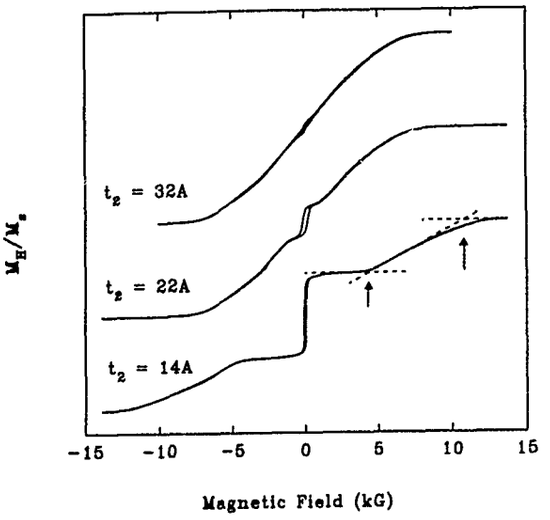

FIG. 1. Typical in-plane antiparallel coupled magnetization curves for the asymmetric series Co(32 Å)/Ru(10 Å)/Co(t_2) at room temperature. The arrows indicate the two transition fields.

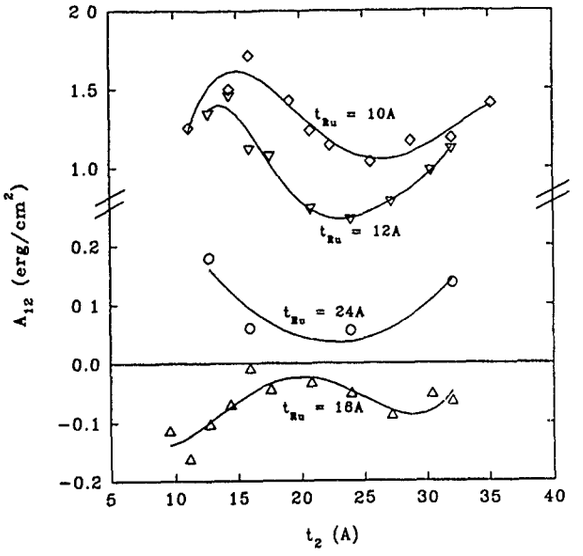

FIG. 2. The coupling coefficient A_{12} as a function of the second Co layer thickness, t_2, for four asymmetric series (I, II, III, and IV) having the structure of Co(32 Å)/Ru(t_{Ru})/Co(t_2) with t_{Ru}=10, 12, 16, and 24 Å, respectively. The curves indicated by ◇ and ▽ are calculated using in-plane magnetization measurements, and the curves indicated by ○ and △ are calculated using the FMR measurements. All results are at room temperature.

III. RESULTS AND DISCUSSIONS

All samples have an easy plane anisotropy energy when the second Co layer thickness $t_2 \geqslant 10$ Å. The saturation magnetization $\mathbf{M}_s$ per unit volume of Co is within 10% of the bulk Co value (1400 emu/cm^3) and is independent of the second Co layer thickness. No significant in-plane anisotropy field was found as expected for the hcp structure in the Co and Ru layers having the c axis normal to the film plane. Series I, II, and IV show typical antiparallel coupled magnetization curves, shown in Fig. 1. The in-plane saturation fields of ~16 kOe in these samples suggest that a very strong antiparallel coupling exists between the Co layers. Upon decreasing the second Co layer thickness t_2, the remanent magnetization increases and follows roughly the relation $\mathbf{M}_r/\mathbf{M}_s=(t_1-t_2)/(t_1+t_2)$ as expected. This shows the layer thickness is consistent from sample to sample. The well-defined shape of the hysteresis loops also indicates that the interlayer exchange coupling is quite uniform across the film plane. The coupling coefficient A_{12} in series I and II were calculated using the two transition fields $H_{cn,1}$ and $H_{cn,2}$ which can be obtained from the curves. In the parallel coupled system (series III), a nearly square hysteresis loop was obtained and the in-plane saturation field is less than 100 Oe for all of the samples in that series.

The FMR measurements of series I and II show only the acousticlike mode. But, both acoustic- and opticlike modes were observed in series III and IV. Therefore the angular dependence of resonance field was used to evaluate A_{12} for series III and IV. With increasing θ_H, one mode always stays on the low field side of the other mode. This is different from the behavior of a noncoupled trilayer structure unless the two layers have significantly different g values, which is not expected in these samples.

Figure 2 shows that the amplitude of A_{12} varies significantly as a function of the second Co layer thickness t_2, but the sign does not change within each series. In the antiparallel coupled systems (series I, II, IV), $|A_{12}|$ reaches maximum values (about 1.7, 1.5, and 0.18 ergs/cm^2 for series I, II, and IV, respectively) at $t_2 \sim 15$ Å, and minimum values (about 1.0, 0.6, and 0.06 ergs/cm^2 for series I, II, and IV, respectively) at $t_2 \sim 25$ Å. The variation amplitude, $|A_{12}^{max}|-|A_{12}^{min}|$, is on the same order as $|A_{12}|$ for each series which is larger than the theoretical predictions for the case of symmetric structure.[8] The variation length $\Delta t_2 \sim 10$ Å between maximum and minimum coupling strength is also much larger than the value obtained by Bloemen *et al.* in symmetric structures. In the parallel coupled system (series III), $|A_{12}|$ reaches extreme values at $t_2 \sim 20$ and 30 Å. $|A_{12}|$ is a minimum (about 0.01 ergs/cm^2) at $t_2 \sim 20$ Å, and a maximum (about 0.17 ergs/cm^2) occurs at $t_2 \sim 30$ Å.

From the FMR data the effective uniaxial anisotropy field $H_{u2,t}^{\text{eff}}$, which includes the demagnetization field $-4\pi\mathbf{M}_s$ and the perpendicular anisotropy field $2K_{u2,t}/\mathbf{M}_s$, was also evaluated for each Co layer. Figure 3 shows that $H_{u2,1}^{\text{eff}}$ for the 32 Å Co layer is a constant at −9.6 kG while $H_{u2,2}^{\text{eff}}$ for the second Co layer increases with decreasing t_2. The variation of $H_{u2,2}^{\text{eff}}$ can be expressed as using a bulk contribution $H_{\text{bulk}}^{\text{eff}}$ and a surface contribution H_s from each Co/Ru interface

$$t_2 \times H_{u2,2}^{\text{eff}} = t_2 \times H_{\text{bulk}}^{\text{eff}} + 2H_s, \tag{2}$$

where $H_{\text{bulk}}^{\text{eff}}$ is about −12.2 kG in these samples which agrees with the estimation using the demagnetization field (−17.6 kG) and the uniaxial anisotropy field (5.9 kG) of bulk Co. The surface anisotropy field H_s is quite large in these samples and corresponds to a surface anisotropy energy of $K_s \sim 0.40$ ergs/cm^2. A negative $H_{u2,2}^{\text{eff}}$ was obtained when t_2 is less than 10 Å, suggesting that the easy axis in the

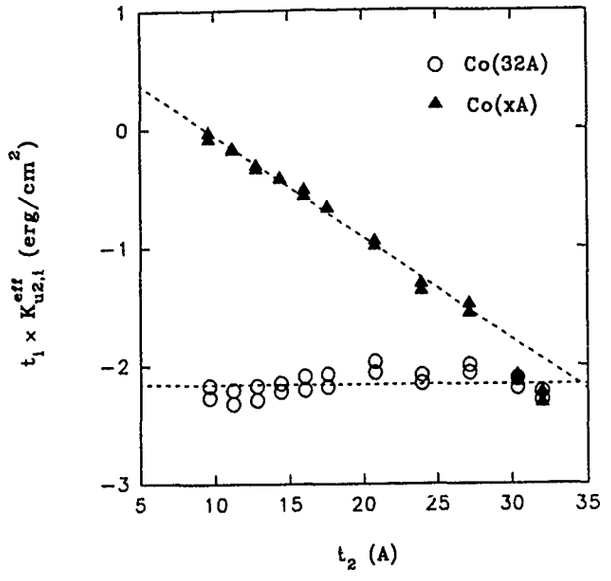

FIG. 3. The evaluation of $t_l \times K_{u2,l}^{\text{eff}}$ obtained from the FMR at 9.2 and 23 GHz as a function of the second Co layer thickness t_2 for the Co(32 Å)/Ru(16 Å)/Co(t_2) series at room temperature. The broken lines are the best fit using the expression described in the text.

second Co layer is in the normal film plane as expected from the in-plane and normal plane magnetization measurements in very thin films.

IV. CONCLUSION

The variation of the interlayer exchange coupling with the Co layer thickness in the asymmetric Co/Ru/Co trilayer structures has been investigated using the in-plane magnetization and angular dependence of FMR measurements. The results show that the coupling strength depends on the magnetic layer thickness. There is a significant variation of A_{12} on increasing the second Co layer thickness in both parallel and antiparallel coupled systems. This might be due to the different Fabry–Perot-like interference of electron Bloch waves within the individual magnetic layers. No change of the sign of A_{12} was observed in any of the series. The variation period between the maximum and minimum values of A_{12} is about 10 Å which is larger than the predicated value π/k_F from the free electron model, suggesting that the discreteness of the magnetic layer thickness and the moment distribution may have to be taken into account.[10]

The authors would like to thank Dr. R. Stamps for fruitful discussion and the North Atlantic Treaty Organization for support through Grant No. RG 930480.

[1] P. Grunberg, R. Schreiber, Y. Pang, M. B. Brodsky, and H. Sowers, Phys. Rev. Lett. **57**, 2442 (1986).
[2] J. J. Krebs, P. Lubitz, A. Chaiken, and G. A. Prinz, Phys. Rev. Lett. **63**, 1645 (1989).
[3] B. Heinrich, S. T. Purcell, J. R. Dutcher, K. B. Urquhart, J. F. Cochran, and A. S. Arrot, Phys. Rev. B **38**, 12879 (1988).
[4] J. F. Cochran, J. Rudd, W. B. Muir, B. Heinrich, and Z. Celinski, Phys. Rev. B **42**, 508 (1990).
[5] B. Hillebrands, A. Boufelfel, C. M. Falco, P. Baumgart, G. Guntherodt, E. Zirngiebl, and J. D. Thompson, J. Appl. Phys. **63**, 3880 (1988).
[6] P. J. H. Bloemen, M. T. Johnson, M. T. H. van de Vorst, R. Coehoorn, J. J. de Vries, R. Jungblut, J.aan de Stegge, A. Reinders, and W. J. M. de Jonge, Phys. Rev. Lett. **72**, 764 (1994).
[7] J. Barnas, J. Magn. Magn. Mater. **111**, L215, (1992); **128**, 171 (1994).
[8] P. Bruno, Europhys. Lett. **23**, 615 (1993).
[9] Z. Zhang, P. E. Wigen, and K. Ounadjela, IEEE Trans. Magn. **MAG-29**, 2717 (1993).
[10] P. Bruno and C. Chappert, Phys. Rev. Lett. **67**, 1602 (1991); Phys. Rev. B **46**, 261 (1992).

Magnetic layer thickness dependence of the interlayer exchange coupling in (001) Co/Cu/Co

P. J. H. Bloemen and M. T. H. van de Vorst
Department of Physics, Eindhoven University of Technology (EUT), 5600 MB Eindhoven, The Netherlands

M. T Johnson and R. Coehoorn
Philips Research Laboratories, Prof. Holstlaan 4, 5656 AA Eindhoven, The Netherlands

W. J. M. de Jonge
Department of Physics, Eindhoven University of Technology (EUT), 5600 MB Eindhoven, The Netherlands

A dependence of the strength of the antiferromagnetic coupling across Cu on the *Co layer thickness* has been observed. The Co thickness dependence displays two clear peaks consistent with the recently predicted oscillation period of 6.2 Å Co. Apart from the two peaks also several small peaks are visible on a scale of about 1 monolayer Co. Free-electron calculations indicate that these rapid variations in strength may result from slight differences between the slopes and starting points of the two Co wedges that were involved in the experiment.

Recent theoretical work by Bruno[1] and Barnaś[2] has shown that the interlayer exchange coupling between two ferromagnetic (FM) layers across a nonmagnetic (NM) metallic spacer layer may oscillate not only with the thickness of this spacer but also with the thickness of the ferromagnetic layers.

Systematic experimental studies investigating the detailed effect of the FM thickness upon the interlayer coupling are very scarce. Qiu *et al.*[3] and Chen *et al.*[4] studied the Co/Cu/Co (100) system for several Co thicknesses. However, their results were insufficient to reveal an oscillatory behavior. First experimental evidence for an oscillatory behavior as a function of the magnetic layer thickness was obtained by the present groups for a (001) Co/Ni/Co/Cu/Co/Ni/Co sandwich[5] and by Okuno and Inomata for Fe/Cr (100) multilayers.[6] In this article we summarize our experimental results[5] and discuss them using calculations based on the Bruno model.[1] Within the free-electron approximation, this model could be extended to include our experimental situation viz. a situation of, in principle, unequal FM layers which, in addition consist of multiple different FM layers (three in our case, Co/Ni/Co). To interpret or predict the behavior of these at first sight more complicated systems it is useful to recall the mechanism from which an oscillation with a FM layer thickness originates.

Bruno shows that the coupling problem can be described in terms of the reflection of electron waves at the potential steps at the various interfaces in the FM/NM/FM sandwich.[7] Here, the nonzero exchange spitting of the conduction bands in the FM layers is responsible for a difference in potential step heights for spin-up and spin-down electrons. This causes the reflection amplitude to be *spin dependent* resulting in a magnetic coupling. The coupling strength is larger for larger differences between the reflection amplitudes for spin-up and spin-down electrons. An oscillatory dependence of the coupling strength on the thickness of the FM layers is then, as Bruno argues, simply a result of multiple reflections of electron waves within the FM layers.[1] As in the case of light waves incident on a (multi)layer, the effective reflection amplitude of a layer (in our case a FM layer) is a result of the constructive and destructive interferences of the forward (transmitted) and backwards (reflected) traveling waves and depends upon the interplay between the layer thickness, the wavelength of the incident wave, and the wavelength within the reflecting medium. The latter is determined by the electronic structure of the FM layers and follows, in the large thickness limit, from the relevant extremal Fermi surface (FS) spanning vectors of the FM layer. From this "electron-optics" picture it is thus clear that if a FM layer is composed of, for example, a multilayer made of several different FM layers, the effective reflection amplitude of such a multilayer (and thus the coupling) will oscillate with the thickness of any of the constituent FM layers. This is exactly the case for our experimental system.

We have studied a molecular-beam-epitaxy-grown (001) Co/Ni/Co/Cu/Co/Ni/Co sandwich in which the two Co layers adjacent to the Cu spacer as well as the Cu spacer itself were deposited in the form of wedges oriented perpendicularly with respect to each other. This allowed for independent investigation of the Cu and Co layer thickness dependence of the coupling across Cu(001) in a single sample. In this way experimental artifacts are avoided that are related to changes in (i) deposition conditions, (ii) substrate quality, and (iii) layer thickness—changes that otherwise would have occurred in a series of separate samples. Especially slight changes in a presumably fixed Cu spacer layer thickness in an experiment of varying magnetic layer thickness would cause problems in our case since the coupling strength is extremely sensitive to the precise Cu thickness because of the presence of a short period oscillation with a period of about 2.6 ML Cu. Note that the latter problem was not encountered in the study of the sputtered Fe/Cr (100) samples of Okuno and Inomata[6] since only the long Cr period was present in their samples.

Two samples (referred hereafter as samples I and II) have been investigated. The typical composition of the magnetic layers in the samples was as follows: 30 Å Co/15 Å Ni/Co wedge (2.3 Å/mm). Further compositional details and information regarding the structure of the layers as obtained from low energy electron diffraction experiments can be found in Ref. 5.

The antiferromagnetic (AF) coupling behavior was in-

 0021-8979/94/76(10)/7081/3/$6.00 © 1994 American Institute of Physics

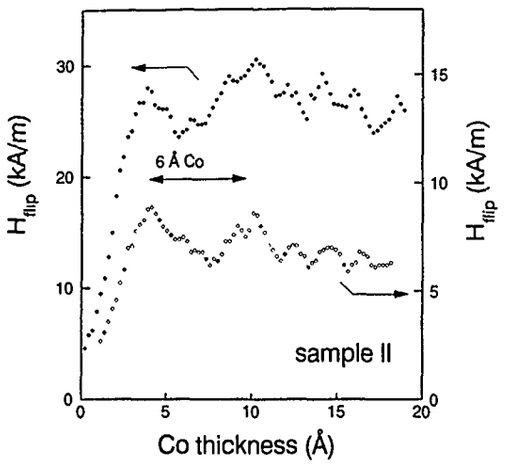

FIG. 1. The strength of the interlayer exchange coupling in the first and second AF peak as a function of the Co thickness for sample II.

vestigated by measuring hysteresis loops via the longitudinal magneto-optical Kerr effect. The behavior as a function of the Cu thickness displays a superposition of a long and a short period oscillation,[5] in accordance with earlier observations.[8,9] The presence of the short period in both samples indicates that these samples are of high structural quality. The dependence on the Co thickness of the strength of the first two AF maxima (at ≈9 Å Cu and ≈19 Å Cu) for sample II is shown in Fig. 1. An oscillatorylike behavior with an apparent period of 6–7 Å is observed in all experimental scans. From the electron-optics picture of Bruno it is immediately clear that this value is a property solely of Co. With varying Co thickness the effective reflection amplitude of the Co/Ni/Co FM layer (and thus the coupling) is modified in an oscillatory fashion with a period determined by the relevant wavelength in the Co layer. According to Bruno the latter is determined by the extremal spanning vector along the Γ-X line [(100) growth] in the spin-down FS of fcc Co. This vector yields a period of 3.5 ML or 6.2 Å Co which is in very good agreement with the present experiment. However, the functional shape of the experimentally obtained variation with Co thickness does not resemble a fully regular oscillatory behavior. Considering for example the behavior of the second AF peak, the lower curve in Fig. 1, two clear peaks are visible whereas around the position where the third peak is expected three smaller peaks occur with a spacing of about 2 Å. This behavior seems in contradiction with theory. In particular from the aliasing effect one would expect that because of the sampling at discrete Co planes, periodic variations in coupling strength should only occur on a scale larger than 2 ML (3.6 Å). This is true in the ideal situation. However, in the present experiment *two* Co wedges are involved which may not be identical but may differ slightly in, e.g., their slope. In this respect we remark that with scanning Auge. electron spectroscopy (AES) the slopes were determined to be equal within 10% accuracy. In order to evaluate the effect of unequal Co wedges on the experimentally observed behavior and in particular if it is possible to explain variations in coupling strength on a scale of 1 ML Co, we have extended the model of Bruno[1] to our experimental geometry and performed a number of simulations. Before proceeding with the results we briefly describe the steps that we have undertaken to adapt the model to our situation.

First, to account for unequal wedges Eq. (4) in Ref. 1 is generalized to the case of unequal FM layers. As is clear from Ref. 1 this can be performed by a Taylor expansion of the first Eq. in Ref. 1. In principle this step is sufficient to evaluate if rapid variations in coupling strength may arise from unequal wedges. Second, to account for the effect of the two additional FM layers which are coupled to the Co wedge the model is extended to the case that each FM layer is composed of an arbitrary number of layers, i.e., to describe the system $FM_1^a/FM_2^a/\cdots/FM_k^a/\text{spacer}/FM_1^b/FM_2^b/\cdots/FM_l^b$ with k and l integers denoting the number of FM layers of which FM layers a and b are composed, respectively. To our knowledge the latter step can only be made easily within the free-electron approximation. Within this approximation it is straightforward to calculate the effective reflection amplitude of each FM multilayer. Continuity of the wave functions (plane waves) and their derivative at the interfaces directly enables one to write down a recursion relation for the reflection amplitude of an arbitrary multilayer. Using this relation instead of the Fabry–Pérot formula given by Bruno [Eq. (5) in Ref. 1] allowed us to calculate the Co thickness dependence of the coupling for the situation in which the slopes of the Co wedges differ and their starting point do not coincide.

The results of several calculations for 19.86 Å Cu, i.e., for the strength of the second AF peak, are shown in Figs. 2(a)–2(c). The calculated coupling strengths are normalized to the limit of infinite Co wedge thickness. In Fig. 2(a) the behavior is shown for the ideal case of two identical Co wedges. Here the aliasing effect is demonstrated for the Co dependence. The fundamental period $\lambda=\pi/k_f^{\downarrow}=2.49$ Å pertaining to the Fermi wave vector $k_f^{\downarrow}$ of the spin-down fcc Co FS, yields after aliasing (with 1.805 Å Co ML thickness) a period of 6.1 Å. In Fig. 2(b) the ideal case is again calculated. However, for this calculation the situation that a Co layer consists of a nonintegral number of monolayers (incomplete coverage) is also calculated. This is done from a linear combination of the coupling across two independently patchy interfaces. Incomplete coverage is thus treated as follows: We define $J(n,m)$ as the coupling strength for the combination of n integral number of Co monolayers in Co wedge A and m monolayers in Co wedge B. The coupling $J'(t_A,t_B)$ for the situation that the thicknesses t_A and t_B at Co wedge A and B, respectively, are a nonintegral number of monolayers is calculated from

$$J'(t_A,t_B)=J(n,m)(1-f_A)(1-f_B)+J(n,m+1)\times(1-f_A)f_B+J(n+1,m)\times f_A(1-f_B)+J(n+1,m+1)f_Af_B.$$

Here, $f_{A(B)}$ represent the fractional coverages defined by $t_A=n+f_A$ and $t_B=m+f_B$ with $0\leq f_{A(B)}\leq 1$. Considering Fig. 2(b) it is clear that even for the ideal case of equal wedges, fractional coverages result in additional peaks like the small one between the third and fourth monolayer (±6 Å). Such features are a direct result of the asymmetric Co layer thick-

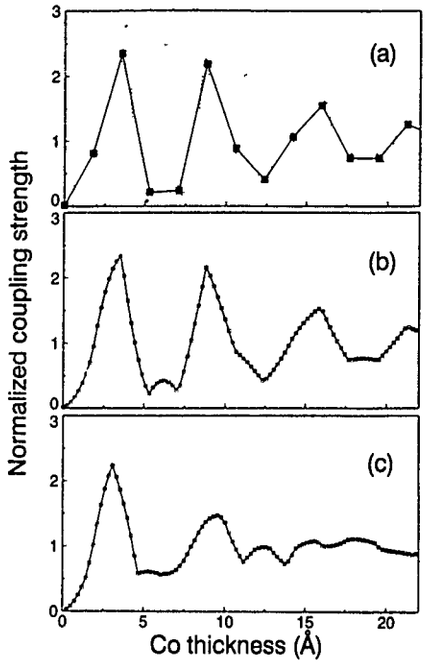

FIG. 2. Free-electron calculations of the Co thickness dependence of the coupling strength for 30 Å Co/15 Å Ni/Co/19.86 Å Cu/Co/15 Å Ni/30 Å Co. The values are normalized to the strength of infinite Co thickness limit. Calculation parameters are k_f^{Cu}=1.471 Å^{-1},$k_f^{\downarrow Co}$=1.261 Å^{-1}, $k_f^{\uparrow Co}$=1.363 Å^{-1}, $k_f^{\downarrow Ni}$=1.362 Å^{-1}, $k_f^{\uparrow Ni}$=1.389 Å^{-1} (Ref. 10).

ness combinations [$(n,n+1)$ and $(n+1,n)$]. It thus appears that for the present case in which two active layers are involved one is not allowed to make a linear interpolation [such as in Fig. 2(a)] between the situation in which both Co layers are n ML thick (n,n) and the situation in which both Co layers are $n+1$ ML thick [$(n+1,n+1)$]. The experimentally observed rapid variations in coupling strength may originate from this phenomenon. In an attempt to fit a free-electron calculation to the experimental strength dependence of the second AF peak (Fig. 1) we have tried a number of combinations for the wedge slopes and starting points of the Co wedges. Figure 2(c) shows a calculation in which the Co wedge slopes differed by about 10% from the AES determined value of 2.3 Å/mm viz. 2.5 Å/mm for Co wedge A and 2.1 Å/mm for Co wedge B. In addition wedge A has been given an offset of 0.5 Å with respect to wedge B. From the combinations we have tried it appeared that the first two peaks are relatively insensitive to modifications of the wedge parameters so that their separation remains a good measure for the oscillation period. The behavior at the larger Co thicknesses appears more susceptible. From Fig. 2(c) it is clear that the third and fourth peak may even disappear. Instead three smaller peaks appear with a spacing which is considerably smaller than the 6.2 Å oscillation period. The qualitative agreement with the experiment is striking, suggesting that the originally proposed interference/beating ef-

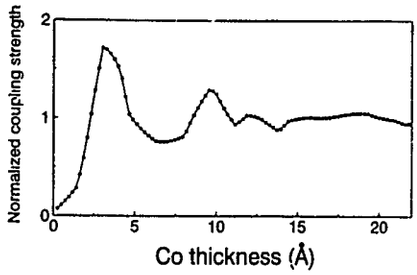

FIG. 3. Free-electron calculation of the Co thickness dependence of the coupling strength for the first AF peak, i.e., for 30 Å Co/15 Å Ni/Co/7.22 Å Cu/Co/15 Å Ni/30 Å Co. The values are normalized to the strength of infinite Co thickness limit.

fects in Ref. 5 may not be necessary to explain the behavior at the larger Co thicknesses. We did not attempt to obtain a better fit by varying more parameters, e.g., by introducing a difference in the thicknesses of the two Ni layers which were adjacent to the Co wedges. One should realize that the present model, although it explains many of the observed features, is a free-electron approximation and therefore seems inappropriate to make a comparison with the experiment on a detailed level. This is also reflected by the calculation shown in Fig. 3 representing the behavior for the *first* AF peak (calculation at 7.22 Å Cu). Here, the same Co wedge parameters were used as those to obtain the reasonable fit for the second AF peak [Fig. 2(c)]. The simulation does not display the smaller sharp features at the higher Co thicknesses such as observed in the experiment [the upper curve in Fig. 1]. Instead the variations are more gradual. What does agree are again the important features. Apart from the ones we already mentioned it is seen that the relative oscillation amplitude for the first AF peak is *smaller* than that for the second AF peak, (compare Figs. 3 and 2(c)). This is in agreement with the experiment where the peaks as afunction of the Co thickness are more pronounced for the second AF peak than for the first AF peak (Fig. 1).

The authors wish to express their gratitude to P. Bruno for explaining the application of the complex-path integration technique.

[1] P. Bruno, Europhys. Lett. **23**, 615 (1993).
[2] J. Barnaś, J. Magn. Magn. Mater. **111**, L215 (1992); **128**, 171 (1994).
[3] Z. Q. Qiu, J. Pearson, and S. D. Bader, Phys. Rev. B **46**, 8659 (1992)
[4] Q. Chen, M. Onellion, A. Wall, and P. A. Dowben, J. Phys. Cond. Matter **4**, 7985 (1992).
[5] P. J. H. Bloemen, M. T. Johnson, M. T. H. van de Vorst, R. Coehoorn, J. J. de Vries, R. Jungblut, J. aan de Stegge, A. Reinders, and W. J. M. de Jonge, Phys. Rev. Lett. **72**, 764 (1994).
[6] S. N. Okuno and K. Inomata, Phys. Rev. Lett. **72**, 1553 (1994).
[7] P. Bruno, J. Magn. Magn. Mater. **121**, 248 (1993).
[8] M. T. Johnson, S. T. Purcell, N. W. E. McGee, R. Coehoorn, J aan de Stegge, and W. Hoving, Phys. Rev. Lett. **68**, 2688 (1992).
[9] P. J. H. Bloemen, R. van Dalen, W. J.M. de Jonge, M. T. Johnson, and J. aan de Stegge, J. Appl. Phys **73**, 5972 (1993).
[10] We obtained these Fermi wave vectors from self-consistent ASW band-structure calculations.

Cumulative interface roughness and magnetization in antiferromagnetically coupled NiCo/Cu multilayers

X. Meng, X. Bian, R. Abdouche, W. B. Muir, J. O. Ström-Olsen, Z. Altounian, and M. Sutton
Centre for the Physics of Materials and Department of Physics, McGill University, 3600 University Street, Montréal, Québec H3A 2T8, Canada

Cumulative interface roughness and its influence on the magnetization process in antiferromagnetically coupled $(Ni_{80}Co_{20}/Cu)\times N$ multilayers is studied. In these multilayers, Cu and $Ni_{80}Co_{20}$ thicknesses are fixed at 20 and 15 Å, respectively, in order to obtain the antiferromagnetic coupling at the second oscillation peak of giant magnetoresistance (GMR) versus Cu thickness. Low-angle x-ray reflectivity measurements show that cumulative interface roughness increases with increasing bilayer number N. In-plane magnetization hysteresis measured with both SQUID and surface magneto-optic Kerr effect (SMOKE) magnetometers are compared. When the cumulative interface roughness is significant, SMOKE hysteresis loops, which are sensitive to the top 5 or 6 magnetic layers, display a nonlinear plateau region at small fields. Comparison of low-angle x-ray, and SMOKE results show that interfaces of relatively high quality in top layers only exist for sputtered multilayer with $N<10$.

INTRODUCTION

Reports of antiferromagnetic (AF) interlayer coupling and the associated giant magnetoresistance (GMR) in Cu-spaced ferromagnetic multilayers, such as Co/Cu,[1,2] NiFe/Cu,[3] NiFeCo/Cu,[4] and NiCo/Cu,[5,6] have stimulated great interest in these materials. Within each magnetic layer, demagnetizing fields due to the layer's shape anisotropy stabilize the in-plane easy axes. The AF coupling of neighboring magnetic layers results in net zero magnetization in the multilayers at zero field.[6] The application of in-plane fields align the magnetic moments through in-plane rotation. Below saturation in the absence of any in-plane anisotropy there is a linear relation between the magnetization M and the applied magnetic field H:[7]

$$M=\frac{M_s^2 t_M}{4J}H. \tag{1}$$

Where J is the AF coupling constant between two neighboring magnetic layers, t_M and M_s are, respectively, the thickness and saturation magnetization of each magnetic layer. Therefore, J can be obtained from magnetization hysteresis loops.

Theoretical analysis based on the RKKY model predicts that the AF coupling is weakened by the introduction of interface roughness,[8] whereas experiments explicitly show that interface roughness introduced by changing the sputtering parameters can enhance the GMR effect.[9] In this paper, we report specifically on the effects of cumulative interface roughness on the magnetic properties of AF-coupled multilayers. The cumulative interface roughness is the accumulation of small intrinsic interface roughness in each layer;[10] its effects become more pronounced when the number of bilayers increases. Magnetization measurements from a SQUID magnetometer, which measures the effects of the overall interface roughness, are compared to surface magneto-optic Kerr effect (SMOKE) measurements, which are sensitive only to the top few layers where the cumulative interface roughness reaches its maximum value. SMOKE measurements for multilayers with a different bilayer number can, therefore, show direct information on the effects of cumulative interface roughness on the magnetization process in AF-coupled multilayers.

EXPERIMENTAL RESULTS AND DISCUSSION

Previous experiments[5,6] have shown that $Ni_{80}Co_{20}/Cu$ multilayers exhibit an oscillatory GMR as a function of Cu spacer thickness and a well-defined simple AF ordering for Cu spacer thickness at 20 Å. In the present work $(Ni_{80}Co_{20}15$ Å$/Cu_{20}$ Å$)\times N$ multilayers with 50-Å $Ni_{80}Co_{20}$ buffer layer were deposited on Si wafers, by dc magnetron sputtering at room temperature. The base pressure before deposition was 2×10^{-7} Torr. With a sputtering pressure of 8.0 mT of argon, the deposition rates determined from the measured thickness of single films by low-angle x-ray reflectivity measurements were 1.5 Å/s for $Ni_{80}Co_{20}$ and 1.6 Å/s for Cu. A series of samples with N varying from 8 to 100 were prepared. Low-angle x-ray reflectivity measurements were performed for layer and interface characterizations and for estimating the cumulative interface roughness as a function of the bilayer number N. The room-temperature in-plane magnetization of the samples was measured using a SQUID magnetometer. The magnetization of the top few layers was studied using SMOKE magnetometer.

Figure 1 shows low-angle x-ray reflectivity results for the typical samples with different bilayer number N. All samples exhibit clear first-order superlattice Bragg peaks although the electronic contrast between the two constituent layers is very small. With increasing N, the second-order superlattice Bragg peaks are gradually damped, suggesting an increase of interface roughness.[11] Clear thickness oscillations (or lattice fringes) between superlattice Bragg peaks are observed for samples with $N<15$. For a finite thickness (<1000 Å) of the film, suppressing of the lattice fringes with increasing N is also partially correlated to the increased outer surface roughness.[12] The low-angle x-ray reflectivity has been analyzed using an optical model.[12] From the fit to the

 0021-8979/94/76(10)/7084/3/$6.00 © 1994 American Institute of Physics

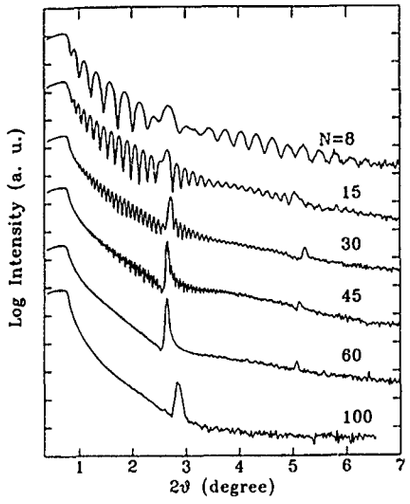

FIG. 1. Low-angle θ-2θ x-ray diffraction spectra of a selected series of ($Ni_{80}Co_{20}$ 15 Å/Cu 20 Å)×N multilayers. For clarity, the curves have been displaced vertically.

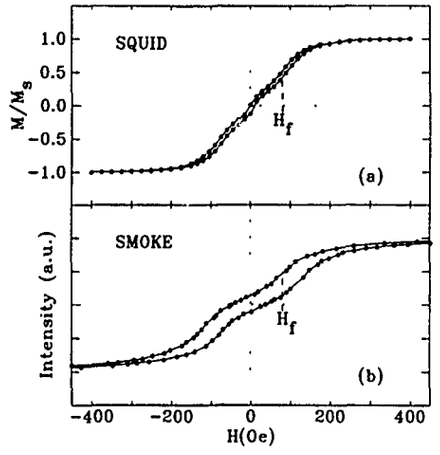

FIG 3. Magnetization of a typical ($Ni_{80}Co_{20}$ 15 Å/Cu 20 Å)×45 sample measured by (a) SQUID (normalized to M_s), and (b) SMOKE (arbitrary unit). It is indicated that the nonlinearity of the magnetization curve can be observed near a critical field H_f.

data the interface roughness and the outer surface roughness can be derived. Figure 2 shows that the outer surface roughness σ_s increases monotonically with increasing N. Intensities of second-order superlattice peaks, which decrease with increasing N, is also shown in Fig. 2.

Figure 3(a) shows the overall in-plane magnetization measured with a SQUID magnetometer for a ($Ni_{80}Co_{20}$15 Å/Cu_{20} Å)×45 multilayer having moderate cumulative interface roughness. Slight deviation from linear magnetization is observed near a critical field H_f. Figure 3(b) shows the magnetization of the top few layers measured using SMOKE. The deviation from a linear curve is more pronounced than it is for the SQUID curve which represents the average magnetization of the whole multilayer. Since SMOKE measurements were made using the 6328-Å He-Ne laser which has a penetration depth of approximately 200 Å, the SMOKE hysteresis loop typically represents the magnetic property of the top 5 or 6 bilayers of multilayer.

For samples with $N=8$ both SQUID and SMOKE measurements show linear $M-H$ relations below saturation fields. The saturation moment M_s of the 15-Å $Ni_{80}Co_{20}$ layer is about 620 emu/cm^3, which yields a value of $J\sim5.8\times10^{-3}$ erg/cm^2 for the second AF coupling peak in $Ni_{80}Co_{20}$/Cu multilayers.[6] This value is much smaller than the strength of the second AF coupling peaks found in other Cu-based multilayer systems,[2-4] indicating a very weak AF coupling between adjacent $Ni_{80}Co_{20}$ magnetic layers across 20-Å-thick Cu spacer layers. The M_s values measured with the SQUID magnetometer do not depend on N. This implies that the intermixing at the interfaces is not changing significantly with increased cumulative interface roughness.

Figure 4 shows SMOKE measurements for different bi

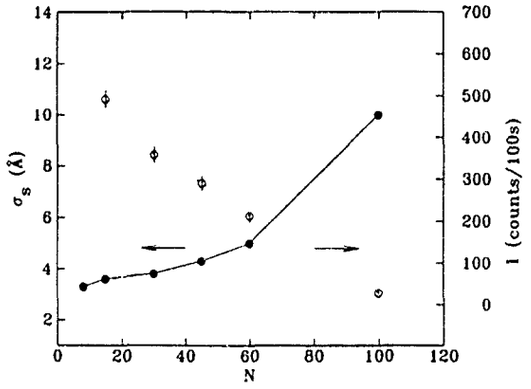

FIG 2. Dependence of σ_s and I on N Here σ_s is the outersurface roughness, and I the intensity of second-order superlattice Bragg peaks.

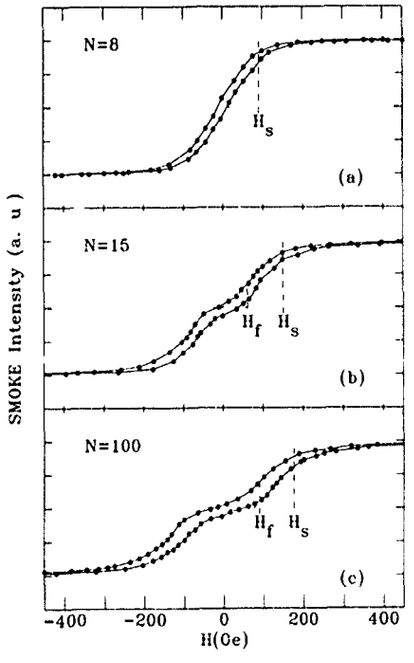

FIG. 4. SMOKE magnetization measurements of samples with different bilayer numbers. (a) $N=8$, (b) $N=15$, and (c) $N=100$ Two critical fields, i.e., saturation fields H_s and flip fields H_f, are indicated in the figures.

layer numbers. Figure 4(a) shows that the magnetization relation is nearly linear below saturation fields for the sample with $N=8$ where the interfaces are presumably flat. Figure 4(b) shows the result for the sample with $N=15$, where a plateau region with a relatively small slope is observed at low fields, and failure of the linear $M-H$ relation is clearly seen. As the bilayer number N increases up to 100, the cumulative interface roughness is considerably large, and the plateau region becomes more striking as indicated in Fig. 4(c). From low-angle x-ray reflectivity analyses and SMOKE measurements, we conclude that the nonlinear $M-H$ behavior in samples with large N are related to cumulative interface roughness which becomes significant as the bilayer stacking increases.

In some layered structures with nonideal interfaces, terraced interface roughness results in an extrinsic biquadratic coupling between ferromagnetic layers in the presence of intrinsic bilinear coupling.[13] Although the nonlinearity of the $M-H$ curve observed in $Ni_{80}Co_{20}$/Cu multilayers could, in principle, be explained by an additional biquadratic coupling term, a preliminary calculation indicates that the coefficient of this term is positive. However, previous studies have shown the sign of the biquadratic coupling to be negative.[13–15] In a multilayer with cumulative interface roughness, the profile correlation among consecutive interfaces increases toward the top of multilayer,[10] which distinguishes this type of roughness from other structural imperfections (e.g., the layer's terraced thickness fluctuation, etc.). We consider that such a cumulative roughness may produce a local magnetic anisotropy that is likely to be related to the interface and surface strains. Qualitatively, the two critical points (i.e., H_f and H_s) identified in an $M-H$ loop for a rougher sample, as illustrated in Fig. 4(c), should correspond to the strong- and weak-coupling limits of the exchange with respect to the anisotropy.[16] Modeling such an extrinsic roughness-related anisotropy is undertaken in order to interpret quantitatively the unusual magnetization behavior.

CONCLUSIONS

We have studied the cumulative interface roughness and its effect on magnetization in AF-coupled multilayers $(Ni_{80}Co_{20}15\ Å/Cu15\ Å)\times N$ using x-ray reflectivity and SMOKE. Both experiments show that interface roughness increases with an increasing number of bilayer period. SMOKE measurements are sensitive to the roughest region of the sample, namely the top several layers. Relatively flat interfaces only exist in sputtered multilayers with bilayer number $N<10$ for which SMOKE magnetization curves are linear below saturation fields as predicted from Eq. (1). As superlattice periods increase, deviation from linearity in $M-H$ curves gradually becomes large, which can be attributed to a roughness-related extrinsic anisotropy.

We acknowledge the financial support from the Natural Sciences and Engineering Research Council of Canada, and Fonds FCAR du Québec.

[1] S. S. P. Parkin, P. Bhadra, and K. P. Roche, Phys. Rev. Lett. **66**, 2152 (1991).
[2] D. H. Mosca, F. Petroff, A. Fert, P. A. Schroeder, W. P. Pratt, Jr., and R. Laloee, J. Magn. Magn. Mater **94**, L1 (1991).
[3] S. S. P. Parkin, Appl. Phys. Lett. **60**, 512 (1992).
[4] M. Jimbo, T. Kanda, S. Goto, S. Tsunashima, and S. Uchiyama, Jpn. J. Appl. Phys. **31**, L1348 (1992).
[5] X. Bian, J. O. Ström-Olsen, Z. Altounian, Y. Huai, and R. W. Cochrane, Appl. Phys. Lett. **62**, 3525 (1993).
[6] X. Bian, J. O. Ström-Olsen, Z. Altounian, B. D. Gaulin, C. V. Stager, and J. A. Avelar, Phys. Rev. B **50**, 3114 (1994).
[7] F. Nguyen Van Dau, A. Fert, P. Etienn, M. N. Baibich, J. M. Broto, G Creuzet, A. Friederich, S. Hadjoudj, H. Hurdequint, and J. Massies, J. Phys. (Paris) Colloq. **49**, C8-1633 (1988).
[8] R. Coehoorn, Phys. Rev. B **44**, 9331 (1991).
[9] E. E. Fullerton, D. M. Kelly, J. Guimpel, and I. K. Schuller, Phys. Rev. Lett. **68**, 859 (1992).
[10] A. P. Payne and B. M. Clemens, Phys. Rev B **47**, 2289 (1993).
[11] F. J. Lamelas, H. D. He, and R. Clark, Phys. Rev. B **43**, 12296 (1991)
[12] Y. Huai, R. W. Cochrane, and M. Sutton, Phys. Rev. B **48**, 2568 (1993).
[13] J. C. Slonczewski, Phys. Rev. Lett. **67**, 3172 (1991).
[14] M. Rührig, R. Schäfer, A. Hubert, R. Mosler, J. A. Wolf, S. Demokritov, and P. Gruberg, Phys. Status Solidi A **125**, 635 (1991).
[15] B. Rodmacq, K. Dumesnil, P. Mangin, and M. Hennion, Phys. Rev. B **48**, 3556 (1993).
[16] Z. Q. Qiu, J. Pearson, and S. D. Bader, J Appl. Phys. **73**, 5765 (1993)

Coercivity and magnetization process versus dipolar coupling in $Ni_{80}Fe_{20}$/Cu/Co/Cu spin valves

R. Kergoat and J. Miltat
Laboratoire de Physique des Solides, Université Paris Sud-CNRS, Orsay, France

T. Valet and R. Jerome
LCR-THOMSON, Laboratoire des Technologies Magnétiques, Orsay, France

The elaboration of four different sample types, namely, isolated NiFe or Co layers in their Cu environment and full, exchange decoupled, [Cu/NiFe/Cu/Co/Cu] periods with either the Co or NiFe layers in the vicinity of the free surface has allowed for a detailed study of the magnetization process of the constitutive layers of one period of a "hard–soft"-type spin valve. The domain distribution and magnetization fluctuations within domains have been monitored by Kerr microscopy. The experiments point to a strong influence of dipolar coupling on the properties of the soft permalloy layer, with a dramatic increase of the NiFe film coercive field with respect to the corresponding quantity in an isolated NiFe layer. The macromagnetization fluctuations detected in the NiFe layer appear most likely linked to fluctuations of low amplitude occurring in the Co layer in the vicinity of the NiFe coercive field.

I. INTRODUCTION

A recent study[1] of magnetization reversal in ferromagnetically exchange coupled [$Ni_{80}Fe_{20}$/Cu/Co] sputtered multilayers revealed the existence of strong magnetization fluctuations in the soft layers of those artificial stacks consisting of piled-up hard and soft magnetic layers separated by a nonmagnetic spacer. Fluctuations were ascribed to the existence of a random distribution of the cubic anisotropy axes in the polycrystalline Co layers.[2] On the other hand, previous experiments in exchange uncoupled, hard–soft-type, three-layer [PtCo/SiO_2/NiFe] structures[3] pointed to the influence of dipolar interactions on the magnetic properties of the soft layer. Moreover, a field dependent magnetostatic coupling was also found to operate between the two soft layers of a [NiFeCo/Au/NiFe] sandwich film and mediated by the rippling of magnetization.[4]

Since a significant increase of the Permalloy coercivity seems to be a common observation in the [$Ni_{80}Fe_{20}$/Cu/Co] system,[5,6] a property detrimental to the use of such systems as low field, high magnetoresistance sensors, the ultimate aim of this study is to weigh the respective influences of exchange and dipolar couplings on this phenomenon. The present work, however, is limited to an analysis of the magnetization process and coercivity under conditions of a sole magnetostatic coupling.

II. EXPERIMENT

Experiments carried out for this work include VSM magnetometry and Kerr optical microscopy. Two different types of samples have been studied. Samples of the first species are made of sputtered [50 Å Cu/M/30 Å Cu] layers grown over a 50 Å Cr buffer deposited on (100) Si substrates, where M is either a 100-Å thick $Ni_{80}Fe_{20}$ or a 50-Å Co layer. Such samples are useful to separately investigate the magnetic domain structures of a single layer, whether hard (Co) or soft (NiFe). In these reference samples, the environment of each isolated magnetic layer is identical to that found in the more complex stacks described hereafter. The two other samples are composed by one period of a spin valve, respectively [Si(100)/50 Å Cr/50 Å Cu/100 Å $Ni_{80}Fe_{20}$/100 Å Cu/50 Å Co/30 Å Cu] and the symmetrical stacking, i.e., [Si (100/50 Å Cr/50 Å Cu/50 Å Co/100 Å Cu/100 Å $Ni_{80}Fe_{20}$/30 Å Cu]. In these artificial structures, the Cu spacer thickness has been chosen to be sufficiently large in order to solely retain a dipolar coupling between the magnetic layers. Besides, since no magnetic field was applied during the sputtering process, virtually anisotropy-free samples were obtained.

For each sample, following the application of a saturation field along a selected in-plane direction, a domain pattern is first nucleated under reverse field **H**, the magnitude of which is stack dependent. The pattern is then observed under two different illumination conditions. For instance, in the figures labeled (a), the trace of the plane of incidence for the probing light is parallel to the saturation field. A first difference image (pattern minus saturated state) provides a picture of the domain distribution with a magnetization either parallel or antiparallel to **H**. A 90° rotation of the sample or of the plane of incidence followed by a second difference image (saturated state minus pattern) reveals, since the plane of incidence is now perpendicular to the average magnetization direction in each domain, the magnetization fluctuations within domains [figures labeled (b)].

In samples incorporating a single NiFe magnetic layer, magnetization reversal occurs through the nucleation of large lateral size domains, typically a few hundred microns wide. For instance, two domains with opposite magnetizations are shown in Fig. 1(a) ($H \approx -2$ Oe). The nonuniformity of the contrast in the domain with magnetization parallel to the saturated state (the white domain) already points to the existence of magnetization fluctuations within domains, a fact confirmed by the observations in Fig. 1(b). Due to the weak contrast observed in Fig. 1(b), the existence of only small amplitude fluctuations is inferred. The coercive field amounts to ≈ 1.5 Oe [Fig. 1(c)] whereas the tilted shape of the hysteresis loop may be ascribed to the existence of a range of nucleation fields within a sample with a fairly macroscopic lateral size (cm range) and/or correlated to the ripening of magnetization fluctuations.

 0021-8979/94/76(10)/7087/3/$6.00 © 1994 American Institute of Physics

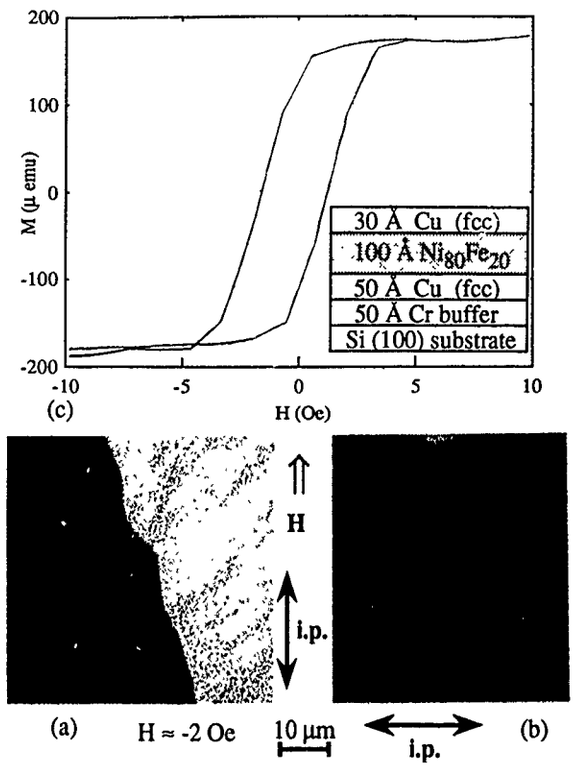

FIG. 1. Two similar domain structures generated under reverse **H** field ($H \approx -2$ Oe), observed in a single NiFe magnetic film bounded by two Cu layers. (a) Plane of incidence i.p.$\|$**H**; (b) i.p.$\perp$**H**; (c) is the corresponding hysteresis loop.

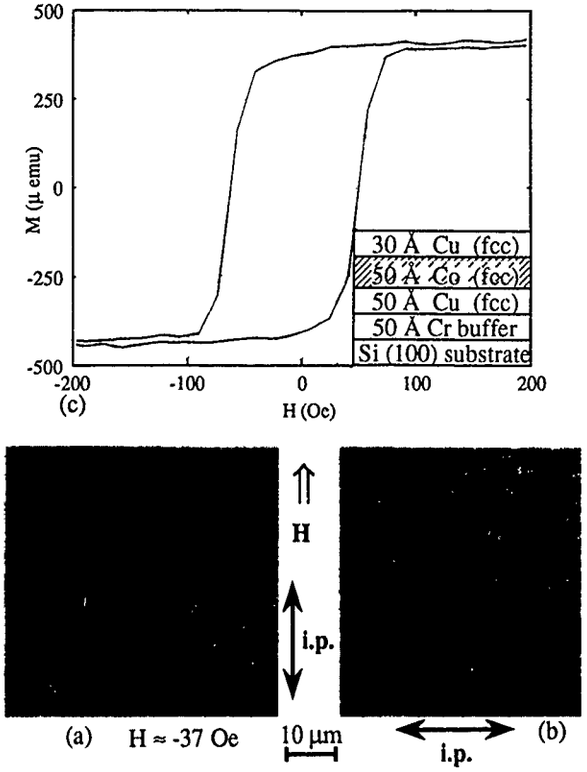

FIG. 2. Two similar domain structures generated under reverse **H** field ($H \approx -37$ Oe), observed in a single Co magnetic film bounded by two Cu layers. (a) Plane of incidence i.p.$\|$**H**; (b) i.p.$\perp$**H**; (c) is the corresponding hysteresis loop.

A much more irregular pattern is observed under reverse field in samples consisting of a single (fcc) Co magnetic layer [Fig. 2(a)]. Figure 2(b) exhibits the intensity modulations inside a domain of nonreverse magnetization [light grey shade domains in Fig. 2(a)], as recorded at the onset of magnetization reversal [≈ -37 Oe to be compared to $H_c \approx -60$ Oe: Fig. 2(c)]. When compared to Fig. 1(b), much more pronounced image intensity variations, hence wide amplitude magnetization fluctuations, are observed in the isolated Co layer. [The overall morphology of these fluctuations appears consistent with previous observations in ferromagnetically coupled multilayers,[1] although the spatial wavelength of the fluctuations proves to be smaller in the present case of a single Co layer.]

In samples made of a full spin-valve period, the thicknesses of the various layers have been tailored such as to solely gain information on the reversal of the top magnetic layer in a Kerr experiment (penetration depth of the light of the order of 200 Å). Conversely, VSM experiments are sensitive to both magnetic layers. Hysteresis loops measured from the symmetrical structures are qualitatively identical [Figs. 3(c) and 4(c)] although the coercive fields of the Co layers vary appreciably, probably a microstructure related phenomenon. The typical shapes of the hysteresis loops clearly indicate that the two magnetic layers are exchange uncoupled. Both VSM measurements and Kerr imaging experiments reveal strong changes in the magnetic properties of the NiFe layer. A significant increase of the NiFe coercive field is first detected (≥ 8 Oe, a value deduced from the minor hysteresis loop of Fig. 3c, to be compared to the 1.5 Oe value found in a single NiFe layer). Hence, independent of the variations in the Co layer coercive field, the coercive field of the NiFe layers amounts to 4–5 times the value typical of an isolated layer. Besides, Kerr imaging shows that magnetization reversal now takes place in the NiFe layer through the nucleation, under reverse field, of considerably smaller size domains. Domain nucleation proves quasihomogeneous, followed by some degree of domain collapse and merging whereas the typical domain size does not exceed a few microns. For instance, Fig. 3(a) exhibits in a $H \approx -14$ Oe reverse field, a finely subdivided domain pattern to be compared to the coarse structure in Fig. 1(a) pertaining to an isolated NiFe layer. Notwithstanding the change in the Co layers coercive field values, the domains observed in Fig. 3(a) prove to be still larger than those encountered in the hard (Co) layer of a full period [Fig. 4(a)]. The average domain size in a full stack always appears smaller than the corresponding quantity in a single Co layer [Fig. 2(a)]. The size of the smallest domains observed is comparable with the spatial resolution of the Kerr microscope, namely ≈ 3000 Å. Thus, they are made of only a few exchange coupled grains in these virtually untextured samples with grain sizes ranging from 500 to 1000 Å. Magnetization fluctuations of extremely high amplitude (as large as $\approx \pm 90°$) may be detected in the NiFe layer under proper illumination and polarization conditions [Fig. 3(b)]. The correlation between the patterns in Figs. 3(a) and 3(b) becomes more explicit when looking at Fig. 3(a) at glancing angle after rotating the Kerr micrograph by 90°. Magnetization fluctuations of very low amplitude are

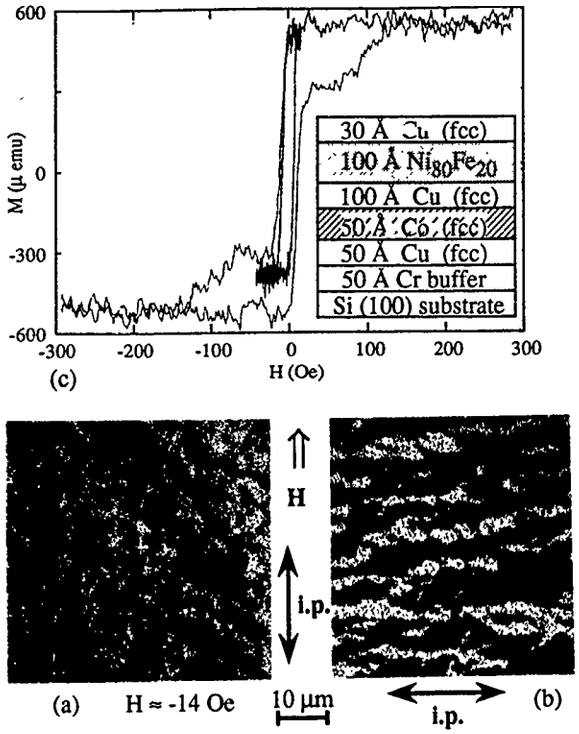

FIG. 3. Two similar domain structures generated under reverse **H** field ($H \approx -14$ Oe), observed in the NiFe layer of one spin-valve Cu/Co/Cu/NiFe/Cu full period. (a) Plane of incidence i.p.$\|\mathbf{H}$; (b) i.p.$\perp\mathbf{H}$; (c) is the corresponding hysteresis loop including the minor loop of the NiFe layer.

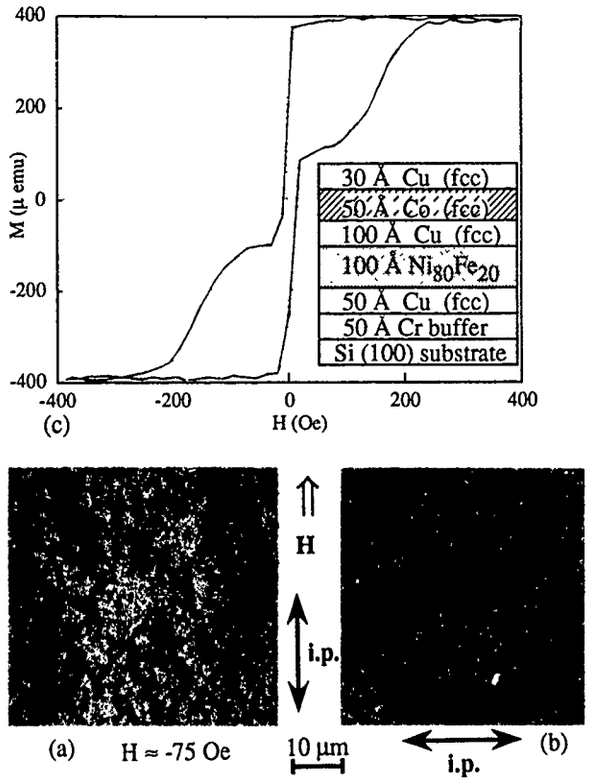

FIG. 4. Two similar domain structures generated under reverse **H** field ($H \approx -75$ Oe), observed in the Co layer of one spin-valve Cu/NiFe/Cu/Co/Cu full period. (a) Plane of incidence i.p $\|\mathbf{H}$, (b) i.p.$\perp\mathbf{H}$, (c) is the corresponding hysteresis loop.

first detected in the Co layer for applied field values as small as -15 Oe, a low value in comparison with the coercive field of the Co layer but close to the NiFe layer coercive field [≈ -14 Oe in Fig. 3(c)]. Fluctuations of higher amplitude are seen for larger field values, e.g., -75 Oe [Fig. 4(b)], a value close to the coercive field of the Co film.

III. DISCUSSION AND CONCLUSION

A clear increase of the coercivity of a "hard–soft"-type stack as a function of decreasing spacer thickness was brought into evidence by the work of Hill and McCullough.[3] For the system considered, any coupling effect seems to vanish for spacer thicknesses above ≈2000 Å. Such an experiment was not reproduced here. However, the thickness of the Cu spacer layers used in this work clearly lie above the threshold for indirect exchange coupling[6] and safely under the limit of dipolar coupling to be inferred from Ref. 3. It follows that the magnetization fluctuations detected in the NiFe layer may only be assumed to be linked to the fluctuations of moderate amplitude detected in the Co layer for field values close to the coercive field of the NiFe layer in a "hard–soft" environment. In more general terms, the observed phenomena appear to result from an interplay between microstructure and dipolar coupling across the 100-Å Cu spacer layer. A random 3D (2D) orientation of the cubic anisotropy axes in a nontextured ([111] textured) Co layer is bound to induce magnetization inhomogeneities in the hard layer, hence magnetization divergences which act as sources of stray field. One may be reminded that, at least in its hcp phase, the quality factor $K/2\pi M_s^2$ of cobalt is less than, but close to 1. Therefore, a regime of strong correlations between anisotropy driven magnetization fluctuations and dipolar interactions is anticipated to establish itself, even in a single Co film, as illustrated in Fig. 2.

In addition, the sputtering process promotes columnar growth, implying a high degree of coherence between the cubic axes of the fcc Co and fcc NiFe layers. Magnetization fluctuations in the soft layer thus should arise not only from magnetostatic interactions between the soft and hard layers, but also from the distribution of cubic anisotropy axes in the soft layer, with potentially different responses as a function of texturing.

Because of an anticipated strong correlation regime, perturbation approaches may hardly be considered as relevant. Although this work fails to provide some modeling of the observed phenomena, it clearly demonstrates the existence of macrofluctuations with a specific spatial wavelength range which appeals to a comparison with numerical simulation data in disordered, dipolar and/or exchange coupled media.

[1] R. Kergoat, M Labrune, J. Miltat, T. Valet, and J. C. Jacquet, J. Magn. Magn. Mat. **121**, 339 (1993).
[2] R. Kergoat, M. Labrune, J. Miltat, T. Valet, and J. C. Jacquet, IEEE Trans. Magn. **29**, 2533 (1993).
[3] E. W. Hill and A. M. McCullough, IEEE Trans. Magn **24**, 1707 (1988)
[4] M. Okon and H. Hoffmann, IEEE Trans. Magn. **9**, 563 (1973).
[5] T. Shinjo and H. Yamamoto, J. Phys. Soc. Jpn **59**, 3061 (1990).
[6] T. Valet, J. C Jacquet, P Galtier, J. M. Coutellier, L. G. Pereira, R. Morel, D. Lottis, and A. Fert, Appl. Phys. Lett. **61**, 3187 (1992).

Observation of large biquadratic coupling of FeCo through Mn (invited) (abstract)

M. E. Filipkowski,[a] C. J. Gutierrez,[b] J. J. Krebs, and G. A. Prinz
U. S. Naval Research Laboratory, Washington DC 20375-5000

A new system, exhibiting unusually large interlayer biquadratic exchange coupling, has been discovered, consisting of single crystal FeCo/Mn/FeCo sandwiches epitaxially grown on GaAs substrates. Normalized $m(H)$ curves yield a remanent moment of approximately 0.5 for all cases studied, with a number of examples having saturation fields as large as several Tesla. This implies a biquadratic coupling constant as large or larger than many known bilinear coupling constants. None of the normalized $m(H)$ data exhibits a remanence of less than 0.5, indicating the absence of comparable contributions from bilinear coupling. Angular dependent FMR at 9 GHz implies a fourfold anisotropy of opposite sign to that measured for single FeCo layers, whereas FMR at 35 GHz agrees in sign with the single layer anisotropy. Detailed analysis of this contradiction shows that this is an apparent anisotropy reversal which emerges within the theory of FMR in the presence of large biquadratic coupling, requiring values of the coupling constant in excess of $-j_2=2$ ergs/cm^2, where the coupling term in the energy is written $J_2[(\mathbf{m}_1\cdot\mathbf{m}_2)/m_1m_2]^2$. This large biquadratic coupling, together with the absence of bilinear coupling, appears to contradict existing theories of interlayer exchange.

Research supported by the Office of Naval Research.
[a]Office of Naval Technology, Postdoctoral Fellow.
[b]National Research Council, Postdoctoral Associate.

 0021-8979/94/76(10)/7090/1/$6 00 © 1994 American Institute of Physics

Magnetic dipole mechanism for biquadratic interlayer coupling (abstract)

S. Demokritov[a)]
Institute for Physical Problems, Moscow, Russia

E. Tsymbal, P. Grünberg, and W. Zinn
IFF, Forschungszentrum Jülich, Julich, Germany

Ivan K. Schuller
University of California, San Diego, La Jolla, California 92093

A mechanism resulting in biquadratic interlayer coupling is proposed and analyzed theoretically. This mechanism is connected with the magnetic dipole field, created by magnetic layers with roughness. This field decays exponentially with the distance from the layer, but it shows oscillating behavior in the lateral direction. The scale of both exponential and oscillating dependencies corresponds to the scale of the interface roughness and can reach 20–30 nm. The oscillating variation of the field makes 90° alignment of the magnetization energetically favorable in analogy to the Slonczewski's mechanism.[1] Computer simulations and estimates show that this mechanism can provide a coupling strength of the order of 0.01 erg/cm^2 for Fe films with 1 nm interlayer thickness. The part of the work done in Moscow and Jüelich was supported by Collaborative Research Grant CRG 921170 of the NATO Scientific Exchange Programmes. Work at UCSD was supported by the U. S. National Science Foundation. One of us (E.Ts.) is pleased to thank the Alexander von Humboldt Foundation for support.

[a)]Present address: IFF, Forschungszentrum Jülich, Jülich, Germany.

[1]J. C. Slonczewski, Phys. Rev. Lett. **67**, 3172 (1991).

 0021-8979/94/76(10)/7091/1/$6.00 © 1994 American Institute of Physics

Polarized neutron reflectivity studies of biquadratic coupling in [Fe/Cr] (100) and [Fe/Al] (100) superlattices and films (invited) (abstract)

J. F. Ankner
Missouri University Research Reactor, Columbia, Missouri 65211

A. Schreyer and H. Zabel
Fakultät für Physik und Astronomie, Ruhr Universität Bochum, D-44780 Bochum, Germany

J. A. Borchers and C. F. Majkrzak
National Institute of Standards and Technology, Reactor Radiation Division, Gaithersburg, Maryland 20899

M. Schäfer, J. A. Wolf,[a], and P. Grünberg
Forschungszentrum Jülich, D-52425 Jülich, Germany

M. E. Filipkowski, C. J. Gutierrez,[b] J. J. Krebs, and G. A. Prinz
Naval Research Laboratory, Washington, DC 20375

Sensitivity to magnetic atoms and low intrinsic absorption characterize the interaction of neutrons with matter. Consequently, polarized neutron reflectivity provides a unique means of performing depth-resolved vector magnetometry. We have used this technique to determine the magnetization depth profiles of Fe/Cr superlattices. Superlattices of bilayer composition [55 Å Fe/17 Å Cr], grown at 523 K, exhibit biquadratic coupling with large saturation fields (~3 kOe), while those grown at 293 K are ferromagnetically ordered. We have directly measured the evolution of the coupling angle between adjacent Fe layers as a function of applied field and will discuss how bilinear, biquadratic, and external field terms produce the observed order. The weaker coupling found in the Fe/Al system makes possible the investigation of a range of spin configurations at temperatures that do not endanger the sample. We have mapped the phase diagram of a [42 Å Fe/12 Å Al/39 Å Fe] (100) trilayer and find evidence of biquadratic coupling at low temperatures and fields (e.g., when $H=180$ Oe, the Fe layer spins relax away from ferromagnetic alignment below $T\approx170$ K). Our measurements agree qualitatively with energy minimization calculations and the results of bulk magnetometry.

---

[a]Present address: Naval Research Laboratory, Washington, DC 20899.
[b]Present address: Southwest Texas State University, San Marcos, Texas 78666.

 0021-8979/94/76(10)/7092/1/$6.00 © 1994 American Institute of Physics

Monte Carlo histogram calculation of the critical exponents of an $Fe_xMg_{1-x}Cl_2$ Ising model (invited)

Laura Hernández and H. T. Diep
Groupe de Physique Statistique, Université de Cergy-Pontoise, 49 Avenue des Genottes, B.P. 8428, 95806 Cergy-Pontoise Cedex, France

In a previous work, a realistic three-dimensional 3-D Ising model of $FeCl_2$ was studied. It consists of triangular lattice planes stacked along the c axis of the crystal, with the following interactions: a nearest neighbor (nn) ferromagnetic one competing with a next-nearest-neighbor (nnn) antiferromagnetic interaction, which causes some degree of frustration in the plane, the planes being weakly coupled by an antiferromagnetic interaction. In fact, the latter is a superexchange interaction, and we have taken into account all the equivalent superexchange paths in the sense of the Anderson rule, which amounts to 12 neighbors in each one of the adjacent planes. In this work we present the preliminary results of a study of the critical exponents of this model using the Monte Carlo histogram method and finite size scaling. The interest of such study lies in the layered structure of this system, which might have an effect on its effective dimensionality at the transition point, and also in the effects of frustration, as well as those of superexchange interactions on the critical exponents. We also show the results obtained by the same method, on the critical exponents of the diluted system in the zero and low magnetic field.

I. INTRODUCTION

$FeCl_2$ and $FeBr_2$ are prototype systems for the study of magnetic phase transitions since a long time ago. They show the outstanding feature of being associated to the different steps in the progress of the knowledge of this field. After the first results showing their metamagnetic character,[1] much effort has been done to describe their critical behavior. In particular, the experimental works of Jacobs and Laurence[2,3] and Vettier[6] have given a detailed description of their phase diagram in a magnetic field. Neutron scattering experiments[4–6] have provided us with the values of the relevant interaction constants.

Some theoretical Hamiltonian models showing this kind of metamagnetic phase transition have also been proposed. Harbus and Stanley[7] have performed a high temperature series expansion on a simple cubic lattice Ising model with in-plane ferromagnetic coupling and antiferromagnetic coupling of the planes (the "meta" model) and on the "nnn model"[8] consisting of a simple cubic Ising lattice with isotropic antiferromagnetic nearest neighbors (nn) and ferromagnetic next-nearest-neighbors (nnn) interactions.

Landau,[9] in a Monte Carlo study of antiferromagnetic Ising simple cubic and simple square lattices with nn antiferromagnetic and nnn ferromagnetic coupling, has also found a tricritical behavior.

However, all these models considered only the simplest lattice structures (square and simple cubic), without taking into account other features appearing in $FeCl_2$ and $FeBr_2$: high anisotropy, triangular lattice planes, superexchange paths along c axis, and in-plane frustration due to nnn antiferromagnetic interaction.

In 1979, Aharony and Fishman showed that an anisotropic antiferromagnetic system with bond dilution in a uniform magnetic field, has the same critical behavior as that of the random field Ising model (RFIM).[10] This statement was later extended by Cardy to anisotropic antiferromagnets with site dilution in a uniform magnetic field (DAFF).[11] This fact made $FeCl_2$ and $FeBr_2$ regain interest, as they constituted an excellent material for the experimental investigation of the RFIM.

Since then, a great experimental effort, as well as many theoretical studies, have been done. For instance, Soukoulis *et al.* and Grest *et al.* have tested the equivalence between DAFF's and RFIM in two and three dimensions[12,13] in simple square and simple cubic lattices with isotropic nn interactions. Diep *et al.*[14] and Galam *et al.*[15] have analyzed the existence of a tricritical point (TCP) as a function of dilution in a DAFF consisting of a simple cubic lattice with isotropic nn antiferromagnetic and nnn ferromagnetic interactions. Recently, a simulation on a highly diluted (50%) simple cubic lattice with isotropic antiferromagnetic nn interaction was performed by Nowak *et al.*,[16] with special attention paid to the high field region.

In spite of all this effort, many questions still remain open. For instance, while the existence of long range order (LRO) is admitted for a three-dimensional (3-D) RFIM,[17,18] it is still under discussion for some DAFF's because of the long relaxation times involved.[19–21]

Experimental studies show, in general, that the state of the system at a particular point of the temperature-field (T,H) space depends on the process used to take the system to that point. It seems reasonable to suppose that some of the unclear aspects found when comparing theoretical with experimental results may stem from the particularities of the real

 0021-8979/94/76(10)/7093/6/$6.00 © 1994 American Institute of Physics

system. For instance, the expected LRO as well as the shape of the magnetic domains (if any) formed while this (LRO) is being established, must be related to the kind of lattice considered, its spatial anisotropy, the existence of frustrated or competing interactions, its percolation threshold, etc.

In a previous work,[22] we have studied, by Monte Carlo simulations, the critical behavior of a $FeCl_2$ model. This model, though quite simple, kept the outstanding features of the system: high spatial anisotropy (triangular lattice planes stacked along the **c** axis), the superexchange paths for the interplane interaction, competing interactions, and frustration in the plane. The results we have obtained with such a model are in excellent qualitative and quantitative agreement with experimental ones.

Based on such a good description of the pure system, in a recent work we addressed our study to some of the experimental results on the diluted system that were not well understood. In particular, we studied the existence of a TCP and its behavior with dilution. We also studied the character of equilibrium temperature loops in a constant field (whether they are reversible or not) and the existence of a LRO for a field-cooling (FC) process. As mentioned above, irreversibilities in temperature loops have been experimentally reported. We have analyzed this fact by performing short simulations on our finite systems, showing that such irreversibilities correspond to a nonequilibrium effect. We have also investigated the experimental result stating that the magnetization issued from a FC process (m_{FC}) is greater than that issued from a field-heating (FH) one (m_{FH}).[20,21] We have determined the irreversibility line from the first temperature, where $m_{FC} > m_{FH}$ in a FC process, and we tried to elucidate the kind of magnetic domains formed in this irreversibility region that are responsible for that result.

We are now interested in determining the critical exponents of this system. Different questions may be asked on this topic. First, one may think that the layered structure of this system might affect its effective dimensionality, even in the pure case. Concerning the diluted system, the Harris criterion[23] states that when the specific heat exponent of the pure system is $\alpha > 0$, a small dilution may modify the critical behavior. In addition, renormalization group ϵ expansion treatments[24] show that a sharp transition may still exist, but with exponents different from those of the pure case. Finally, the application of a small uniform field to the diluted system in the strong concentration limit allows us to model an experimentally studied RFIM.

The article is organized as follows: in Sec. II we summarize the results obtained on these systems in our previous works; in Sec. III we describe the technical details concerning the present work; in Sec. IV we present the results on the critical exponents. Finally, in Sec. V we present our conclusions and discussions on forthcoming work.

II. PHASE DIAGRAM OF THE $Fe_x Mg_{1-x}Cl_2$ SYSTEM

A. Description of the model

Figure 1(a) shows the crystalline structure of the system determined by Wyckoff.[25] The Hamiltonian of the system may be written[26] as

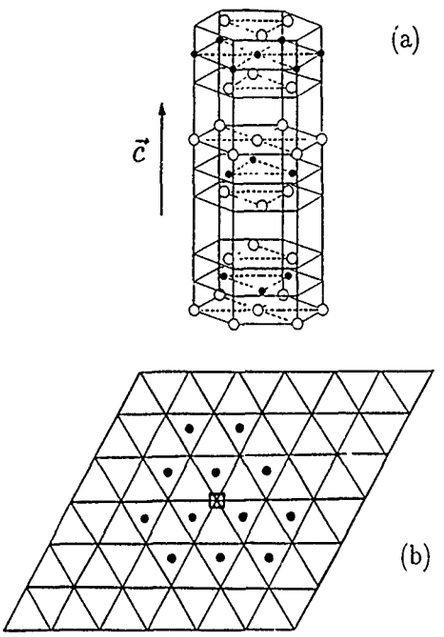

FIG. 1. (a) Crystalline structure of $FeCl_2$. (Ref. 25) ●, Fe^{2+}; ○, Cl^-. (b) Top view of the 12 neighbors of a Fe^{2+} ion □, the considered ion; ●, neighbors in the adjacent plane below.

$$\mathcal{H} = -J_1 \sum_{\langle nn \rangle} \eta_i \eta_j s_i s_j - J_2 \sum_{\langle nnn \rangle} \eta_i \eta_k s_i s_k - J' \sum_{\langle nn' \rangle} \eta_i \eta_l s_i s_l - g\mu_B H \sum_i \eta_i s_i , \quad (1)$$

where $s_i = \pm 1$ is an Ising spin; $\langle nn \rangle$ and $\langle nnn \rangle$ denote the sum over the nearest and next-nearest neighbors in the plane, respectively, and $\langle nn' \rangle$ indicates the sum over the interacting spins belonging to adjacent planes. As the latter is a superexchange one, we have taken into account all the equivalent magnetic paths for the coupling of iron planes via the chlorine ones. Following Anderson's rule, this leads to 12 neighbors in each one of the neighboring planes as is shown in Fig. 1.[22]

In order to simulate a given quenched disorder, we chose the sites at random and assigned to each site i one of the values of the corresponding occupation variable $\eta_i = 0,1$, with a probability $\mathcal{P}(\eta_i = 0) = p$, until we got $N_p = p \times N$ "vacancies" (N being the total number of sites and $p = 1 - x$ the desired amount of dilution).

The values of the interaction constants have been taken from Vettier's work.[6] As we have discussed in a previous work,[22] those values have been obtained fitting experimental data to a Hamiltonian that is different from Eq. (1). Thus, the relevant quantities are the ratios of the interaction constants, and not their absolute values. To simplify the comparison with experimental results on the diluted system, we have normalized these constants in the following way: we have performed simulations on the pure system, varying the values of the interaction constants but keeping their ratios fixed, until we reproduced the value of T_N given by Vettier.[6] Hence, we have a ferromagnetic nn interaction $J_1 = 6.74$ K, in com-

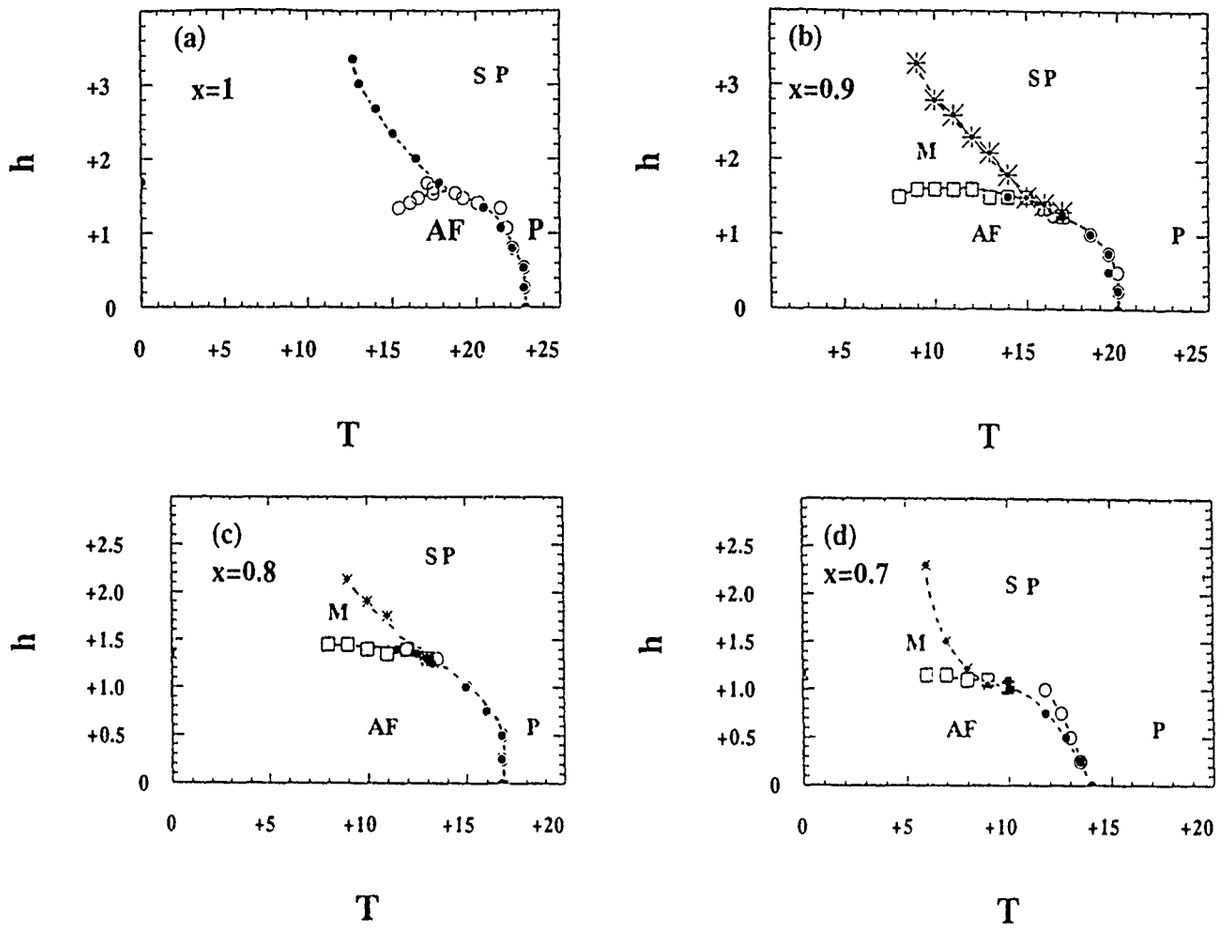

FIG. 2. Detailed cuts of the phase diagram along planes x = const. AF: antiferromagnetic phase; SP: saturated paramagnetic phase; P: paramagnetic phase; M: mixed region. (a) $x=1$, ● $h\uparrow$, ○$h\downarrow$. (b) $x=0.9$, ● FH, ○ FC, □ $h\downarrow$, ∗ h↑. (c) $x=0.8$, ●FH, ○ FC, ∗$h\uparrow$, □ $h\downarrow$. (d) $x=0=7$, ● FH, ○ irreversibility line, ∗$h\uparrow$, □ $h\downarrow$.

petition with a frustrated antiferromagnetic nnn one, $J_2=-1.01$ K, and a superexchange antiferromagnetic interplane interaction, $J'=-0.07$ K.

In the following we will use the notation

$$h=g\mu_B H / k_B .$$

B. Summary of previous results

In general, we studied the following quantities: global magnetization per site m; staggered magnetization along the c axis m_{st}; energy per site E; specific heat c; susceptibility χ; staggered susceptibility χ_{st}; and Edwards–Anderson order parameter q. We aiso keep the last configuration of the lattice obtained at each point of the (T,h,x) space for further analysis.

For the pure system, we have shown that the transition is continuous for low fields, but becomes first order at a tricritical temperature T_t that can be estimated as the temperature where hysteresis in field loops disappears. We have found the ratio between the TCP temperature and the Néel temperature to be $T_t/T_N=0.87$, in excellent quantitative agreement with the experimental value $T_t/T_N=0.886$.[6]

The diluted system was studied by means of simulations of loops in temperature (FC–FH) at a constant field and loops in the magnetic field at a constant temperature ($h\uparrow-h\downarrow$). We have determined the phase diagrams in the (T,h,x) space for concentrations $x=0.9,0.8,0.7$. Our results show the existence of a TCP that is shifted to low temperatures as dilution increases. The values obtained for T_t as well as those obtained for T_N, compare quite well with experimental

TABLE I. Variation of T_t and T_N as a function of dilution. Comparison with experimental values.

x	T_t^{exp}(K)[a]	T_t^{MC}(K)	T_N^{exp}(K)[b]	T_N^{MC}(K)
1	20.5	19.9	24	22.9
0.9	16.5	15	20.5	20
0.8	13	12	17.6	16.75
0 7	8	7	13.6	14

[a]Reference 27.
[b]Reference 28.

ones.[27,28] The width of the hysteresis cycle is also found to decrease with dilution.

Figure 2 summarizes these results. It shows cuts of the phase diagram for different values of concentration x.

Table I gives the comparison of our results with experimental ones obtained by Wood and Day[27] and Bertrand *et al.*[28]

We have also studied fast FH+FC cycles to simulate, on a finite system, the long relaxation times observed experimentally, and we have found that, for low fields, the cycle is still reversible, while for $h \sim h_0(x)$, irreversibilities appear giving rise to $m_{FC} > m_{FH}$, in agreement with experimental results.[21] The irreversibility line T_{irr}, defined as the highest temperature where $m_{FC}=m_{FH}$, is coincident with $T_c(h)$ for low fields, but lies above it as the field approaches $h_0(x)$, in agreement again with experimental measurements. This line is shown in Fig. 2 for the $x=0.3$ case.

We have also investigated the shape of the magnetic domains formed in the irreversible region. Here the domains look like distorted pipes that are placed one beside the other, trying to keep an antiferromagnetic order along the **c** axis. In each plane, clusters of opposite orientation are separated by vacancies in order to avoid losing exchange energy.[26]

III. CRITICAL EXPONENTS

A. Technical description

The Monte Carlo histogram method[29–31] is known to be a very accurate way to determine critical exponents. It does not need a previous knowledge of T_c with an overwhelming precision, as it was the case with traditional Monte Carlo calculations of critical exponents.

We have used our previous results on this system to locate the temperature T_0 where the Monte Carlo simulation is performed. We have calculated the following quantities: staggered magnetization,

$$m_{st}=\langle \mu_{st} \rangle, \tag{2}$$

$$\mu_{st}=\frac{1}{N_k}\sum_{k=1}^{N_k}(-1)^{k+1}\frac{1}{N_i N_j}\sum_{ij} s_{ijk}, \tag{3}$$

where i,j are the subscripts in the plane and k is the subscript corresponding to the **c** axis. In the following, we will consider systems of equal number of sites in each direction, and we will denote their sizes by $L \times L \times L$.

Energy per spin,

$$E=\langle \mathcal{H} \rangle;$$

specific heat,

$$c=\frac{1}{k_B T^2}(\langle \mathcal{H}^2 \rangle - \langle \mathcal{H} \rangle^2); \tag{4}$$

staggered susceptibility,

$$\chi_{st}=\frac{1}{k_B T}(\langle \mu_{st}^2 \rangle - \langle \mu_{st} \rangle^2); \tag{5}$$

first-order cumulant of the order parameter,

$$V_1=\left\langle \frac{\partial \ln m_{st}}{\partial(1/k_B T)} \right\rangle = \frac{\langle m_{st} E \rangle}{\langle m_{st} \rangle} - \langle E \rangle; \tag{6}$$

second-order cumulant of the order parameter,

$$V_2=\left\langle \frac{\partial \ln(m_{st}^2)}{\partial(1/k_B T)} \right\rangle = \frac{\langle m_{st}^2 E \rangle}{\langle (m_{st}^2) \rangle} - \langle E \rangle. \tag{7}$$

The mean values, which are functions of m_{st} and of powers of E, may be calculated as a continuous functions of temperature using the histogram obtained at T_0 as follows:[31]

$$\langle E^n f(m_{st}) \rangle = \frac{\Sigma_E E^n \langle f \rangle(E) H(E) \exp[-\Delta K\, E]}{\Sigma_E H(E) \exp[-\Delta K\, E]}, \tag{8}$$

where $H(E)$ is the histogram measured at T_0 and $\langle f \rangle(E)$ are the mean values of the corresponding function of m_{st} calculated at T_0 for each *fixed value of the energy*.

For large values of the system of linear size L, these quantities are expected to scale with L as follows:

$$V_1 \propto L^{-1/\nu}, \tag{9}$$

$$V_2 \propto L^{-1/\nu}, \tag{10}$$

$$c_{H_{max}} = C_0 + C_1 L^{\alpha/\nu} \tag{11}$$

$$\chi_{st\,max} \propto L^{\gamma/\nu}, \tag{12}$$

$$m_{st}[T_c(\infty)] \propto L^{-\beta/\nu}, \tag{13}$$

$$T_c(L) = T_c(\infty) + C_A L^{-1/\nu}. \tag{14}$$

Having a certain knowledge about the location of T_c helped us to neglect, in this first approach, corrections to scaling. In addition, as our smallest size is $L=12$, corrections to finite size scaling have also been neglected.

We have estimated ν independently from Eqs. (9) and (10). With these values, we calculate γ from Eq. (12). We have then estimated $T_c(\infty)$ by extrapolating Eq. (14) for each observable. Using this value of $T_c(\infty)$, we calculate β from Eq. (13). The Rushbrooke scaling law $\alpha+2\beta+\gamma=2$ allows us to obtain α. Finally, using the hyperscaling relationship, we can estimate the effective dimension of this model, $d=(2-\alpha)/\nu$.

B. Analysis of results

1. The pure system

We have performed a Monte Carlo histogram calculation for lattices of linear sizes $L=12$, 18, 24, and 30 at the temperature T_0 near the T_N obtained in our previous study. Figure 3(a) shows the finite size scaling study of staggered magnetization cumulants done over the first three lattices. The value obtained is $\nu=0.59\pm0.03$.

Figure 3(b) shows the fit of Eq. (12) to our data. We get a value $\gamma=1.19\pm0.08$.

The determination of β needs an estimation of the critical temperature of the infinite lattice. It has been extrapolated from the behavior of the extrema of different observables as a function of $L^{-1/\nu}$. We have found 23.12 ± 0.03 K. The fit shown in Fig. 3(c) gives $\beta=0.27\pm0.04$.

Using the Rushbrooke relationship, we obtain $\alpha=0.27\pm0.10$.

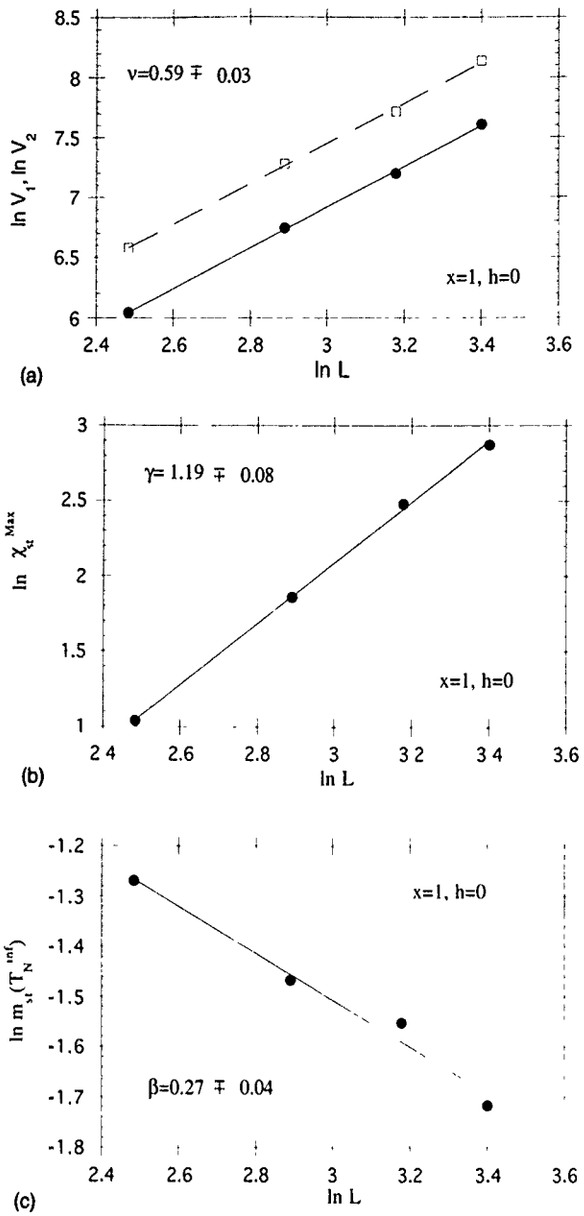

FIG. 3. $x=1$, $h=0$. (a) $\ln V_1$(●), $\ln V_2$(□) vs $\ln L$: determination of ν, (b) $\ln \chi_{st}$ vs $\ln L$: determination of γ. (c) $\ln m_{st}[T_N(\infty)]$ vs $\ln L$· determination of β.

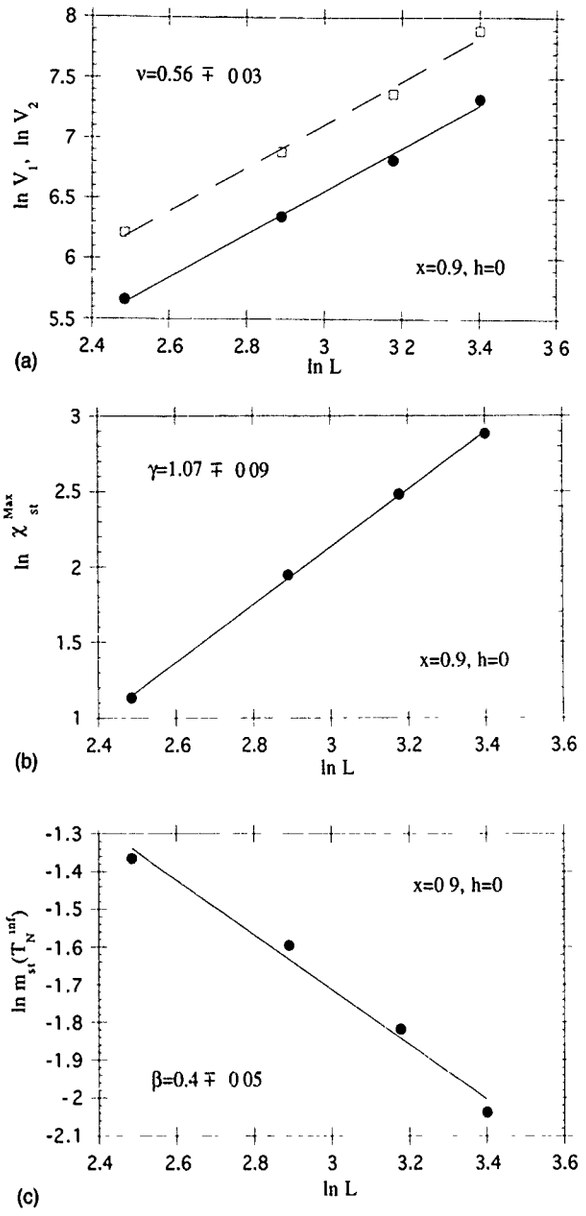

FIG. 4 $x=0.9$, $h=0$ (a) $\ln V_1$(●), $\ln V_2$ (□) vs $\ln L$. determination of ν, (b) $\ln \chi_{st}$ vs $\ln L$· determination of γ, (c) $\ln m_{st}[T_N(\infty)]$ vs $\ln L$: determination of β.

With these values, the hyperscaling relationship gives an effective dimensionality of $d_{\text{eff}}\sim 2.93$. This shows that the layered structure of the system does not affect its effective dimension, even in the case of a quite weak interlayer coupling.

The set of critical exponents obtained above does not exactly correspond to that of the 3-D Ising model,[24] although some of them are rather close to it within the error margin. Surprisingly, this set is found to be similar to the results obtained for the frustrated 3-D Heisenberg spin systems.[32,33]

2. The diluted system

In this first approach, we have studied a system with a small dilution $p=0.1$. The results shown have been obtained for systems of linear sizes $L=12$, 18, 24, and 30. The fit of V_1 and V_2, shown in Fig. 4(a) gives $\nu=0.56\pm0.03$, lower than the value obtained for the pure system.

From the fit shown in Fig. 4(b), we get $\gamma=1.07\pm0.09$, again lower than the value obtained above.

The extrapolated value for the temperature of the infinite diluted lattice is $T_N(\infty)=20.27\pm0.03$ K, which gives $\beta=0.36\pm0.07$ [Fig. 4(c)].

When applying a uniform magnetic field to the diluted system, the correlation length exponent is clearly increased. On the contrary, the other exponents are less affected, for the studied fields, $h=0.25$ K and $h=0.5$ K, which correspond to a quarter and a half of the corresponding threshold field for this dilution.

Figure 5(a) shows the fit of Eqs. (9) and (10), which gives $\nu=0.68\pm0.005$ for the case $h=0.25$ K. The fit of Eq.

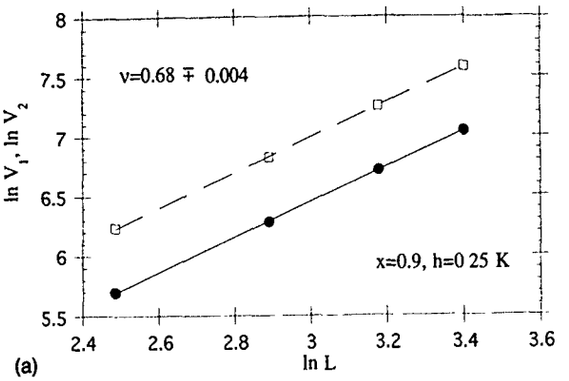

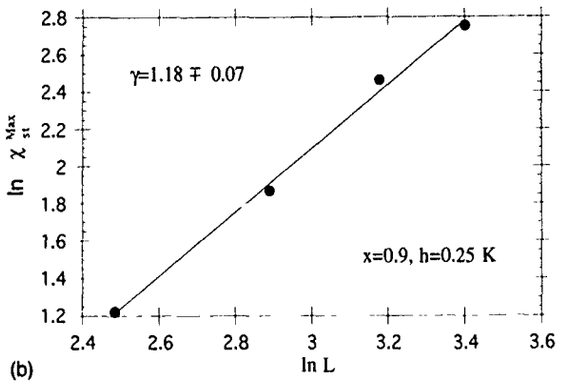

FIG. 5. $x=0.9$, $h=0.25$. (a) ln V_1 (●), ln V_2 (□) vs ln L. determination of ν, (b) ln χ_{st} vs ln L: determination of γ.

(12) [Fig. 5(b)] gives $\gamma=1.18\pm0.07$, which is similar within the error margin to the zero field case.

The determination of the remaining critical exponents proves to be more difficult in the nonzero magnetic field. In fact, the value of $T_N(\infty)$ obtained by extrapolation has a considerable uncertainty. We obtain $\beta=0.36\pm0.07$ and we derive from the Rushbrooke scaling law, $\alpha=0.1\pm0.04$ for $h=0.25$ K.

For $h=0.5$ K, the values of ν and γ remain unchanged (see Table II). As discussed above, the uncertainty on $T_N(\infty)$ is so large to prevent us from determining β.

IV. CONCLUSION

We have performed a preliminary study of the critical exponents of a $Fe_xMg_{1-x}Cl_2$ model. We have observed that the small degree of frustration due to nnn in-plane antiferromagnetic interaction and dominant nn in-plane interactions, as well as the superexchange between planes, are enough to cause a deviation of the critical exponents from those of the 3-D Ising model, even in the pure case. These exponents are closer to those of 3-D frustrated systems (antiferromagnetic stacked triangular lattices with Heisenberg spins) than those of the nonfrustrated 3-D Ising model.

We have also found that for this system of weakly coupled layers, the effective dimension remains 3. As soon as additional disorder is added to the system by means of simple dilution, critical divergences are reduced. This is seen by examining the values of ν, γ, and α given in Table II.

When applying a uniform magnetic field the diluted system is expected to behave like a RFIM. However, the results obtained do not correspond to those predicted for the 3-D RFIM.[35,36] This work shows that it is not obvious that the $Fe_xMg_{1-x}Cl_2$ system belongs to the RFIM universality class.

Further work concerning higher dilutions at different fields is in progress.

We summarize the previous results in Table II.

TABLE II. Summary of critical exponents for the four cases studied.

x	h	ν	γ	β	α
1	0	0.59(3)	1.19(8)	0.27(4)	0.27(10)
0 9	0	0.56(3)	1.07(9)	0.40(5)	0.13(2)
0.9	0.25	0.680(4)	1.18(7)	0.36(7)	0.10(4)
0.9	0.5	0.69(5)	1 15(18)	···	···

[1] C. Starr, F. Butter, and A. Kauffmann, Phys. Rev. **58**, 977 (1940).
[2] L. S. Jacobs and P. E. Lawrence, Phys. Rev. **164**, 866 (1967).
[3] L. S. Jacobs and P. E. Lawrence, J. Appl. Phys. **35**, 996 (1964)
[4] R. J Birgeneau, W. B. Yelon, E. Cohen, and J. Mackowski, Phys. Rev B **5**, 2607 (1972)
[5] W. B. Yelon and R. J. Birgenau, Phys. Rev. B **5**, 2615 (1972).
[6] C. Vettier, Phys. Rev. Lett. **31**, 1414 (1973).
[7] F. Harbus and H. E Stanley, Phys. Rev. B **8**, 1141 (1973).
[8] F. Harbus and H. E. Stanley, Phys. Rev. B **8**, 1156 (1973)
[9] D. P. Landau, Phys. Rev. Lett. **28**, 449 (1972).
[10] S. Fishman and A. Aharony, J. Phys. C **12**, L729 (1979).
[11] J. L. Cardy, Phys. Rev. B **29**, 505 (1984).
[12] C. M Soukoulis, G. Grest, C. Ro, and K. Levin, J. Appl. Phys. **57**, 3300 (1986).
[13] G. S Grest, C. M. Soukoulis, and K. Levin, Phys. Rev. B **33**, 7659 (1986)
[14] H. T. Diep, S. Galam, and P. Azaria, Europhys. Lett. **4**, 1067 (1987).
[15] S. Galam, P. Azaria, and H. T. Diep, J. Phys. Condens. Matter **1**, 5473 (1989).
[16] U. Nowak and K. D Usadel, Phys. Rev. B **44**, 7426 (1991).
[17] Y. Imry and S. K. Ma, Phys. Rev Lett. **35**, 1399 (1975).
[18] J. Z Imbrie, Phys Rev. Lett. **53**, 1747 (1984).
[19] H. Yosikawa and D. P. Belanger, Phys. Rev. B **30**, 5220 (1984).
[20] U. A. Leitaõ and W. Kleemann, Phys. Rev. B **35**, 8696 (1987).
[21] U. A. Leitaõ, W. Kleemann, and I. B. Ferreira, Phys. Rev. B **38**, 4765 (1988)
[22] L. Hernández, H. T. Diep, and D. Bertrand, Phys. Rev. B **47**, 2602 (1993).
[23] A B. Harris, J. Phys. C **7**, 1761 (1974).
[24] R. B. Stinchcombe, in *Phase Transitions and Critical Phenomena*, edited by C. Domb and J. L. Lebowitz (Academic, London, 1983), Vol. 7, Chap. 3, and references therein.
[25] R. W. G. Wyckoff, *Crystal Structures* (Interscience, New York, 1963).
[26] L. Hernandez, H T. Diep, and D. Bertrand, Phys. Rev. B **48**, 15 772 (1993).
[27] T. E Wood and P. Day, J. Magn. Magn. Mater. 782 (1980).
[28] D. Bertrand, F. Bensamka, A. R. Fert, J. Gélard, J. P. Redoulès, and S. Legrand, J. Phys. C **17**, 1725 (1984)
[29] A. M. Ferrenberg and R. H. Swendsen, Phys Rev. Lett. 2635 (1988).
[30] A. M. Ferrenberg and R. H Swendsen, Phys. Rev. Lett. 1195 (1989)
[31] A. M. Ferrenberg and D. P. Landau, Phvs. Rev. B **44**, 5081 (1991).
[32] H. Kawamura, J. Phys. Soc. Jpn. **61**, 1299 (1992), and references therein
[33] D Loison and H. T Diep, Phys. Rev. B (to be published)
[34] D Loison and H. T. Diep (unpublished).
[35] A P. Young and M. Nauenberg, Phys. Rev. Lett. **54**, 2429 (1985).
[36] D. P. Belanger, A. R. King, and V. Jaccarino, Phys. Rev. B **31**, 4538 (1985).

Published without author corrections

Simultaneous surface and bulk magnetic properties investigations by using simultaneous gamma, x-rays and conversion electron Mössbauer spectroscopy: Method and experimental results

A. S. Kamzin, L. A. Grigor'ev, and A. F. Ioffe
Physico-Technical Institute RAS, St. Petersburg 194021, Russia

The surface and bulk phase transitions in a microscopic antiferromagnetic Fe_3BO_6 crystal was investigated by means of new method: Simultaneous gamma rays, x-rays, and electron Mössbauer spectroscopy (A. S. Kamzin, V. P. Rusakov, and L. A. Grigor'ev, in Proceedings of the International Conference "Physics of transition metals," USSR-1988, Part 2, p. 271; A. S. Kamzin, and L. A. Grigor'ev, Pisma Zh. Tekh. Fiz. **16**, 38 (1990) [Sov. Tech. Fiz. Lett. **16**, 417 (1990)]), which makes it possible to study simultaneously the surface and volume properties of a bulk crystal.

I. INTRODUCTION

At the spin-reorientation phase transition (SRPT), it was observed that (1) the first-order SRPT transition in the volume of the crystal is accompanied by second-order reorientation of spins on the surface of crystal; (2) toward the surface of the crystal the temperature interval of the SRPT are increasing and no displacement of the center of the transition region is observed; (3) outside the SRPT region, the direction of the magnetic moments on the surface are different from in the volume of the crystals, and differences are increasing to the surface in the limit of the "transition" layer.

It was found that (1) the Neel temperature for the surface is lower than for the bulk; (2) there exists a surface layer of "critical" thickness, within which the transition temperature $T_N(L)$ increases with a distance from the surface and reaches at the lower (from the surface) boundary of the "critical" layer the value of Neel temperature for the volume of the crystal.

In order to understand surface phenomena, so as to determine how surface and bulk properties are related to each other, it is necessary to investigate the surface of bulk crystals in comparing with investigations of volume properties of that material, as well as the profiles of the properties (layer by layer analysis) of the surface layer. For this aim the experimental methods are very useful, which give us the possibility to study the surface and the bulk properties of massive crystals simultaneously. We have shown[1] that the Mössbauer effect measurements are simultaneous by detecting gamma rays in the transmission geometry, and conversion x-rays and conversion electrons in the backscattering mode are very suitable in each case.

In the present paper, we describe (1) new method (simultaneous gamma rays, x rays, and electron Mössbauer spectroscopy), which have been offered and used in Ref. 1 and that gives us the possibility to investigate the surface and bulk properties simultaneously; (2) results of investigations of the surface magnetic system behavior at the phase transitions (the Neel temperature as well as the spin-reorientation phase transition) in the bulk of crystal.

II. METHOD OF SIMULTANEOUS GAMMA RAYS, X RAYS, AND ELECTRON MÖSSBAUER SPECTROSCOPY

In the "classical" Mössbauer spectroscopy (MS) in the transmission mode (TMS) the γ rays permeating the sample are detected, thus giving information on the whole volume of the bulk samples. After absorption, the deexcitation radiation of nucleation in the absorber are the γ rays, the conversion, and Auger electrons (CED), and characteristic x rays (CX). Mössbauer spectroscopy CX (CXMS) allows us to study the properties of a few μm thick layer of a bulk crystal. In the case of Mössbauer spectroscopy with detection CE (CEMS), the information is extracted from a ~300 nm (for Fe^{57}) surface layer on the bulk sample.

The method of simultaneous gamma rays, x rays, and electron Mössbauer spectroscopy proposed in Ref. 1 combines these three modifications of Mössbauer effect measurements. The universal detector[2] and Mössbauer spectrometer constructed around the universal detector (Fig. 1) makes it possible to obtain the Mössbauer spectra immediately by detecting the γ rays, characteristic x rays, and secondary electrons, thereby simultaneously studying the properties of the

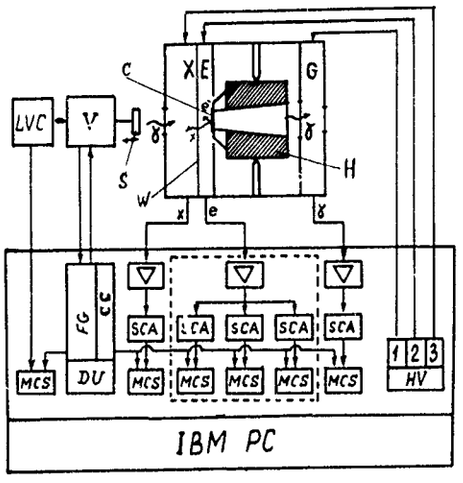

FIG. 1. Universal detector and block diagram of the system for the simultaneous gamma, x rays, and electron Mossbauer spectroscopy

 0021-8979/94/76(10)/7099/3/$6.00 © 1994 American Institute of Physics

volume and surface layers of bulk crystal. The γ rays emitted by a Mössbauer source (S) pass through the sample (C), through a hole in the heater (H), and are detected in chamber *G*. The sample is located in chamber *E*, and CE emitted from the sample are detected right in that chamber. The CX rays, after leaving the sample, pass through a beryllium foil (W) that separates counters *E* and *X*, and are detected in chamber *X*. Therefore chamber *E* detects only the conversion electrons, counter *X* detects only the conversion x rays, and chamber *G* detects only gamma quanta. This method of investigation was later called simultaneous triple radiation Mössbauer spectroscopy.[3]

It is known that the energy of an electron that has go out from the sample depends on the distance from the surface of the atom in which this electron was formed. Our electron counter has quite a good resolution, and by using discriminators (SCA in Fig. 1) we have the possibility to choose the electrons in a definite energy group.[4–6] Taking into account the probability that an electron reaches the surface of the crystal, it is possible to investigate the properties of a thin layer located at a definite depth from the surface. When a proportional detector is employed, the location of the layer and its thickness are not determined as accurately as with the electrostatic, or magnetic energy analyzer. However, a proportional detector is much more efficient, and thus has certain advantages.

It is not difficult to detect electrons at room temperature, but difficulties arises when the measurements are made above or below room temperature, because the sample is located inside counter E. In the universal detector, the furnace heats only the sample, but not the ambient gas. This is achieved by the multilayer heat insulation of the heater and also by its housing on needle supports. Liquid nitrogen vapor passes along the heat guide to take measurements at the region below room temperature. Thus, we have possibility for measurements in the interval from 100–750 K, with the accuracy of 0.03°–0.2°, depending on the measurements region.

To diminish the dead time of the storage system (MCS) we set the input pulse duration less than two buffer counters with checking before switching.[7] The form of motion of the Mössbauer source is controlled by the standard feedback (FG) signal. We have offered[7] to use an other optional controlling signal (CC), which is generated by adding the error signal averaged over 100–1000 periods to the current error signal. A given motion is provided with the accuracy of not greater than 0.03%.

The important advantage of the method, of simultaneous gamma rays, x rays, and electron Mössbauer spectroscopy[1] is that information from the bulk and surface of a macroscopic crystal is extracted: (1) simultaneously under identical conditions of the sample; (2) by using one method of investigation (the Mössbauer effect), which makes it possible to compare experimental results on surface and bulk properties strictly.

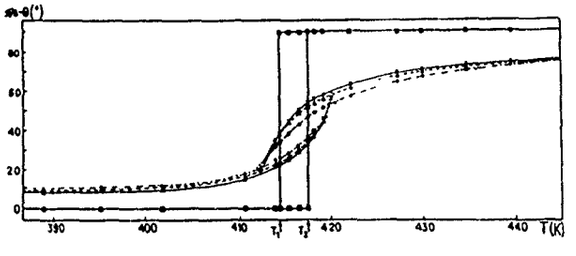

FIG 2. Experimental plots of the angle θ versus temperature in the volume (■) and surface layers of the Fe_3BO_6 crystal. Layer thickness (±10 nm): 0–40 nm (○); 50–90 nm (▽); and 150–200 nm (×).

III. INVESTIGATION OF THE SURFACE AND BULK SPIN-REORIENTATION PHASE TRANSITION IN ANTIFERROMAGNET Fe_3BO_6

We have studied the magnetic structure and SRPT in a surface layer and in a volume of a bulk crystal Fe_3BO_6 by using the new experimental method described above in Sec. II and in Ref. 1.

Surface studies were conducted on crystals chemically polished for ~50 h at room temperature in 1:1 mixtures of H_3PO_4 and H_2SO_4 acids. The experimental Mössbauer spectra obtained below and above the SRPT temperature $T_R = \sim 415$ K consist of two sextuplets, corresponding to iron ions in 8*d* and 4*c* positions. In the SRPT region, experimental spectra consist of the superposition of lines observed at the temperature below and above the SRPT temperature. The lines corresponding to different phases are well resolved, which makes it possible to investigate the behavior of the magnetic moments of each position and phase.[8]

The angle θ determining the direction of the magnetic moments, with respect to the wave vector of the γ rays, were found from the ratios of the intensities of the second and first (fifth and sixth) lines of the Zeeman sextuplets, using formula $I_{2,5}/I_{1,6} = (4\ \sin^2\theta)/3(1+\cos^2\theta)$. The temperature dependence of this angle is displayed in Fig. 2.

It is evident from Fig. 2 that the magnetic moments in the volume of the crystal are oriented only the two values, 0 or $\pi/2$. In the SRPT temperature range, these two phases coexist. This results prove convincingly that SRPT in the volume of Fe_3BO_6 crystals occurs as a first-order phase transition in a temperature range from T_1 up to T_2.

The magnetic moments on the surface layers outside the region of SRPT tilt away from the directions along which the moments are oriented in the volume of crystal. The tilting angle, increases as the surface or the SRPT is approached. In the SRPT region, in a surface layer, the angle θ varies continuously from one value to another.

The theoretical studying of the problem of a spin-reorientation phase transition (SRPT) on a surface showed that the shape of the temperature hysteresis loop must change.[9] Comparison with theoretical results[9] reveals that the experimental data are in good agreement.

IV. THE SURFACE AND BULK MAGNETIC PROPERTIES OF THE ANTIFERROMAGNET Fe_3BO_6 NEAR THE NEEL TEMPERATURE

Analysis of the experimental spectra of Fe_3BO_6 near the Neel temperature showed that they can be divided into four

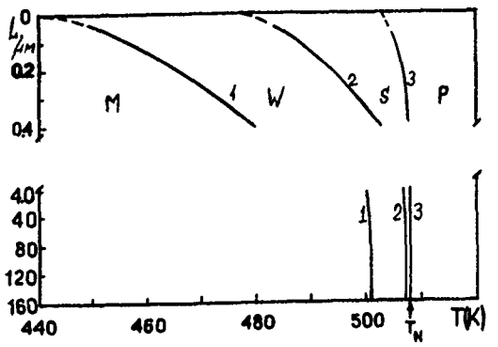

FIG. 3. Phase diagram of Fe_3BO_6 near the Neel temperature. One-boundary line $T_W(L)$; $2-T_s(L)$; and $3-T_N(L)$.

characteristic groups:[10] M, W, S, and P (see Fig. 3, where L is distance from the surface). The M spectra consist of two Zeeman sextuplets, P spectra—of two quadruple doublets. This means that the material in the M region is magnetic, in the P region—in the paramagnetic state. In region W, the widths of the outer lines of the sextuplets increases up to the $T_N(L)$, the width of the inner lines do not change. The experimental spectra observed in the S region consist of a superposition of lines of the paramagnetic doublets of the P phase on the spectra of the W phase. As the temperature increases from $T_c(L)$ to $T_N(L)$, the intensities of outer lines decrease and at the $T_N(L)$ these lines vanish. In those temperature intervals, intensity of inner lines increases.

In summary, analysis of the experimental results has shown that as the temperature increase in some sections paramagnetic regions arise directly on the surface of the crystal. As the crystal is heated further, the paramagnetic regions on the surface expand and penetrate deeper into the crystal. At a certain temperature below the Neel point for the bulk of the crystal, the entire surface becomes paramagnetic, and with increasing temperature, deeper layers transform into the paramagnetic phase. At the Neel point the magnetic order destroys the entire remaining volume of the crystal. Thus, there exist a surface layer of "critical" thickness, in which the transition temperature $T_N(L)$ increases with a distance L from the surface and reaches at the lower (from the surface) boundary of the "critical" layer the value of T_N, corresponding to the volume of the crystal.

[1] A. S. Kamzin, V. P. Rusakov, and L. A. Grigor'ev, "Physics of transition metals," Proceedings of the International USSR Conference, Part 2, p. 271.
[2] A. S. Kamzin and L. A. Grigor'ev, Pisma Zh. Tekh. Fiz. **16**, 38 (1990); A. S. Kamzin and L. A. Grigor'ev, Prib. Tekh. Eksp. **2**, 74 (1991).
[3] U. Gonser, P. Schaaf, and F. Aubertin, Hyperfine Interact. **66**, 95 (1991).
[4] A. S. Kamzin and L. A. Grigor'ev, Pisma Zh. Tekh. Fiz. **19**, 50 (1993); A. S. Kamzin and L. A. Grigor'ev, Pisma Zh. Tekh. Fiz. **19**, 32 (1993).
[5] M. Inaba, H. Nakagava, and Y. Ujihire, Nucl. Instrum. Methods **180**, 131 (1981).
[6] A. S. Kamzin and V. P. Rusakov, Prib. Tekh. Eksp. **5**, 55 (1988).
[7] A. S. Kamzin, S. M. Irkaev, Yu. N. Mal'tsev, and L. A. Grigor'ev, Prib. Tekh. Eksp. **1**, 80 (1993).
[8] A. S. Kamzin and L. A. Grigor'ev, Zh. Eksp. Teor. Fiz. **104**, 3489 (1993).
[9] M. I. Kaganov, Zh. Eksp. Teor. Fiz. **79**, 1544 (1980).
[10] A. S. Kamzin and L. A. Grigor'ev, Zh. Eksp. Teor. Fiz. **105** (1994).

Published without author corrections

Magnetic properties of Fe_xCu_{1-x} granular alloy films

Peng Chubing, Chen Haiying, Li Guozhong, and Dai Daosheng
Department of Physics, Peking University, Beijing 100871, People's Republic of China

The magnetic properties of the Fe_xCu_{1-x} granular system, as functions of iron particle size, were studied. Using high resolution transmission electron microscopy, iron particle size was determined to be ranged from 1–4 nm in as-deposited samples as $x=0.06$–0.34. Magnetic measurements revealed that samples exhibit superparamagnetic relaxation below 300 K as $x\leqslant 0.22$. At 1.5 K, the average magnetic moment per each iron atom is reduced as the average number N of iron atoms in a particle is less than 450, and approaches the value of bulk iron as $N\geqslant 600$. Moreover, the temperature dependence of magnetization for Fe–Cu granular alloys was found to obey the Bloch's $T^{3/2}$ law below 300 K as $x>0.22$. We suggest that spin wave excitations of long wavelength occur due to the weak exchange coupling among iron particles as $x>0.22$. This behavior was confirmed by the ferromagnetic resonance study.

I. INTRODUCTION

The studies of surface magnetism of ferromagnetic materials have discovered that the magnetic moment of surface atoms such as Fe(110) and Ni(111) is enhanced.[1,2] This behavior was also observed in multilayered thin films (e.g., Fe/Ag,[3,4] Co/Pd.[5] and Co/Pt[4,6]). It is very interesting whether magnetic moment of the ferromagnetic particles, such as Fe, Co, and Ni, is enhanced when its size is reduced. In recent experiments,[7–9] the magnetic behavior of Fe and Co clusters containing several tens to hundreds of atoms has been investigated by using the Stern–Gerlach method. It was found that the average effective moment in Fe and Co clusters was below that of bulk Fe and Co, respectively. Chien *et al.*[10] have studied the magnetic properties of iron particles in the Fe–SiO_2 granular films, and pointed out that the coercivity of those films was enhanced. It was also reported that the ferromagnetic, superparamagnetic, spin-glass, and cluster-glass behaviors exist in granular alloys.[11] In this paper, the magnetic properties of Fe_xCu_{1-x} granular films, including superparamagnetic behavior, effective exchange coupling, and the low-dimensional effect, were discussed.

II. EXPERIMENTS

Fe_xCu_{1-x} films were prepared by thermal co-evaporation method in a vacuum of 2×10^{-7} torr onto glass substrates cooled by liquid nitrogen. Thicknesses of films are about 500 nm. The iron volume fraction x was determined to be 0.06, 0.10, 0.13, 0.16, 0.20, 0.22, 0.24, 0.26, 0.28, 0.30, and 0.34 by electron energy spectrum analyses. The structure of films was characterized by electron diffraction and high resolution transmission electron micrograph (TEM). Magnetization curves for all samples at different temperatures were measured by a LDJ 9500 vibrating sample magnetometer (VSM). The ferromagnetic resonance measurements for samples with $x=0.16$ and 0.30 were carried out by using an electron paramagnetic resonance spectrometer working at x-band (9.8 GHz) at room temperature.

III. RESULTS AND DISCUSSIONS

Figure 1 displays the electron diffraction pattern and central dark-field micrograph for $Fe_{0.22}Cu_{0.78}$ film. In the diffraction pattern, (111), (200), (220), and (311) reflections of fcc Cu and (200), (211), and (220) reflections of bcc Fe appear, indicating that iron particles have precipitated from the film and form the bcc structure. In the TEM image, one can see that iron particles are very small, about 2.3 nm in diameter, and dispersed homogeneously in the film.

Figure 2 shows magnetization curves for Fe_xCu_{1-x} films with $x=0.10$, 0.16, and 0.22. It is seen that samples exhibit superparamagnetic relaxation below room temperatures as $x\leqslant 0.22$. In the superparamagnetic state, the effective magnetic moment μ_{eff} for Fe–Cu samples in the magnetic field H at temperature T is given by[10]

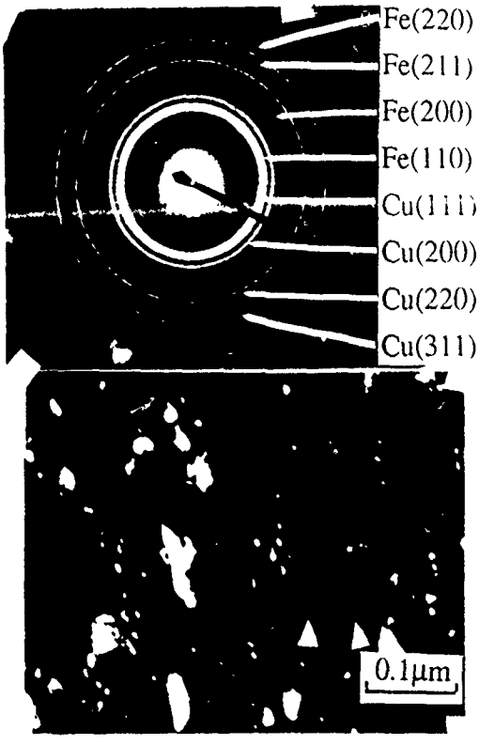

FIG. 1. Electron diffraction pattern and dark-field micrograph for as-prepared $Fe_{0.22}Cu_{0.78}$ film. The iron clusters are indicated by arrows.

 0021-8979/94/76(10)/7102/3/$6.00 © 1994 American Institute of Physics

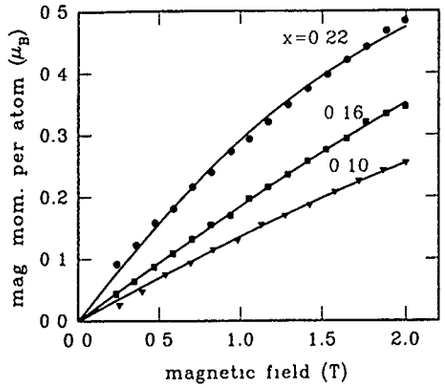

FIG. 2. Effective magnetic moment μ_{eff} per iron atom as a function of magnetic field for Fe–Cu films with $x=0.10$, 0.16, and 0.22 at $T=160$, 236, and 300 K, respectively. The solid lines are the theoretical curves obtained with Eqs. (1)–(2) with $\bar{D}=11.3$ Å, $\sigma=1.05$ for $x=0.10$; $\bar{D}=13.6$ Å, $\sigma=1.10$ for $x=0.16$ and $\bar{D}=22$ Å, and $\sigma=1.255$ for $x=0.22$.

$$\mu_{\text{eff}}=\int \mu L(v)f(v)dv, \tag{1}$$

where $L(v)$ is the classical Langevin function, $f(v)$ is the size distribution function, v is the volume of iron particles, and μ is the magnetic moment per iron atom in a cluster. For simplicity, the lognormal distribution function for spherical iron particles with diameter D is assumed,

$$f(D)=\exp[-(\ln D-\ln \bar{D})^2/2(\ln \sigma)^2]/\sqrt{2\pi}\ln \sigma. \tag{2}$$

By fitting the experimental data using Eqs. (1) and (2), the average diameter $\bar{D}$ and the width σ are estimated. For the $x=0.22$ sample, $\bar{D}=22$ Å and $\sigma=1.155$, in agreement with the TEM observation. From the $\bar{D}$ value, the average number N of iron atoms in a cluster for Fe–Cu samples can be determined and listed in Table I.

Figure 3 plots the average magnetic moment μ at 1.5 K as a function of the average number N for Fe–Cu samples. It can be seen that the magnetic moment of iron atoms increases rapidly with N as $N<450$, and approaches $2.2\mu_B$ as $N>600$. This reduction of μ as $N<450$ may result from the d–s electron hybridization on the interfaces between Fe particles and the Cu matrix.[12] Since the ratio of surface iron atoms to volume increases with the decreasing particle size, the average magnetic moment of iron clusters is hence reduced.

Figure 4 gives the temperature dependence of magnetization $\mu(T)$ for Fe_xCu_{1-x} samples with $x=0.10$, 0.13, 0.22, and 0.28. As $x\leqslant 0.22$, $\mu(T)$ decreases linearly with the increasing temperature below the blocking temperature. Such a linear dependence of magnetization is often associated with two-dimensional (2-D) magnetic behavior. At $x=0.28$, $\mu(T)$ can be fitted to the equation

TABLE I. The average number N of iron atoms in a cluster at each volume fraction x.

x	0.06	0.10	0.13	0.20	0.22	0.24	0.27	0.30	0.34
N	34	103	297	396	470	495	653	740	940

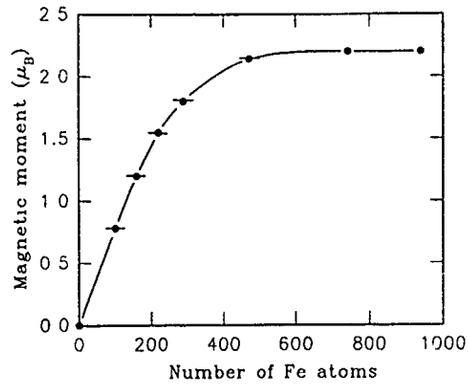

FIG. 3. The size dependence of the magnetic moment per iron atom for Fe–Cu film at $T=1.5$ K.

$$\mu(T)=\mu_0(1-BT^{3/2}), \tag{3}$$

which describes the thermal spin-wave excitations (Bloch's $T^{3/2}$ law). Obviously, it is hardly possible to excite a long-wavelength spin wave in an individual iron particle with size of about 3.0 nm. As iron concentration x is larger than about 0.24, a magnetic percolation effect sets in. By fitting the experimental data to Eq. (3), the Bloch constant B is obtained to be 1.34×10^{-4} $K^{-3/2}$. This B value is much larger than that for the bulk iron (about 3.5×10^{-6} $K^{-3/2}$). We suggest that an effective exchange interaction among single-domain iron particles appears for a Fe–Cu granular system with $x\geqslant 0.28$, leading to the excitation of a long-wavelength spin wave in the whole film. Since the Bloch constant is related to the exchange energy constant, then we deduce that the effective exchange constant is about one order less than that of the bulk iron. There is other evidence that may support the above suggestion. Figure 5 shows resonance field H_{res} vs the orientation ϕ_H of the applied dc magnetic for Fe–Cu samples, with $x=0.16$ and 0.28 at 300 K. For the $x=0.16$ sample, the magnitude of H_{res} is almost independent on the orientation, reflecting very little shape anisotropy. This very small angular variation of H_{res} results from the uniform precession of individual iron particles with spherical shape in the film. However, at $x=0.28$, the H_{res} value in-

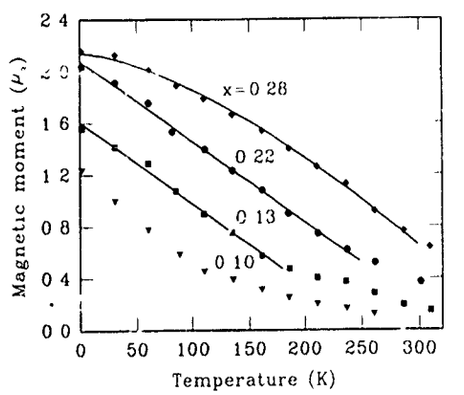

FIG. 4. The temperature dependence of the effective magnetic moment of iron clusters for Fe–Cu films with $x=0.10$, 0.13, 0.22, and 0.28. The solid lines are the fitted curves.

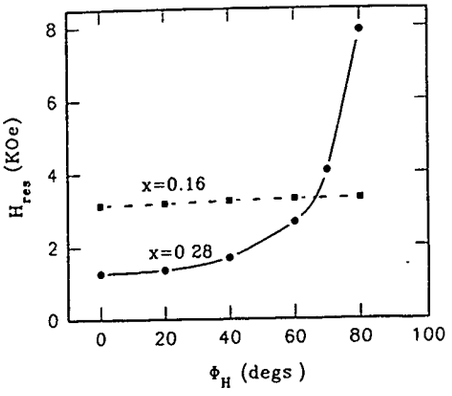

FIG. 5. The resonance field H_{res} as a function of angle ϕ_H between the dc magnetic field and the film plane for Fe–Cu granular films, with $x=0.16$ and 0.28.

creases rapidly with the ϕ_H value. This variation corresponds to the behavior of a ferromagnetic thin film dominated by shape anisotropy,[13] confirming the existence of effective exchange interaction among iron particles.

IV. CONCLUSIONS

The structural and magnetic properties of Fe_xCu_{1-x} granular alloys have been studied. The superparamagnetic behavior exists in a Fe_xCu_{1-x} granular system below 300 K as $x \leqslant 0.22$. At 1.5 K, the average magnetic moment of iron atoms decreases rapidly as iron particle size decreases. This behavior is understood by the hybridization of the $d-s$ electron on the surface of iron cluster. The appearance of long-wavelength spin wave excitations at low temperature and the ferromagnetic resonance experiment confirm that the weak exchange coupling exists among iron particles as $x>0.22$.

ACKNOWLEDGMENT

This work was supported by the NSFC, Doctoral Program Foundation of High Education, and State Key Laboratory of Magnetism.

[1] A. J. Freeman and Ru-q. Wu, J. Magn. Magn. Mat. **104–107**, 1 (1991).
[2] E. Tamura, R. Feder, D. Weller, and U. Gradmann, Phys. Status Solidi B **157**, 672 (1990), J. Magn. Magn. Mat. **100**, 481 (1191).
[3] J. Q. Xiao *et al.*, J. Appl. Phys. **67**, 5388 (1990).
[4] R. Krishnan and M. Tessier, J. Appl. Phys. **67**, 5391 (1990)
[5] K. Sparl and D. Weller, J. Magn. Magn Mat. **93**, 379 (1991).
[6] C J. Lin *et al.*, J. Magn. Magn. Mat. **93**, 194 (1991).
[7] W. A. de Heer, P. Milani, and A Chatelain, Phys. Rev. Lett. **65**, 488 (1990).
[8] J. Timinen, M. Manninenu, and P. Jena, Phys Rev Lett. **66**, 938 (1991).
[9] S. N. Khanna and S. Linderoth, Phys. Rev. Lett. **67**, 742 (1991)
[10] C. L Chien, J. Appl. Phys. **69**, 5267 (1991)
[11] B. Dieny *et al.*, J. Magn. Magn Mat **93**, 101 (1991)
[12] C L. Chien *et al.*, Phys. Rev. B **33**, 3247 (1986)
[13] C. Chappert, K. Le Deng, P Beauvillain, H. Hurdequint, and D. Renard, Phys. Rev. B **34**, 3194 (1986).

New possibilities offered by high resolution Fourier transform spectroscopy in studying magnetic phase transitions

M. N. Popova
Institute of Spectroscopy, Russian Academy of Sciences, 142092 Troitsk, Moscow Region, Russia

High resolution optical absorption spectra of an intrinsic R^{3+} ion or Er^{3+} probe were measured in cuprates $R_2Cu_2O_5$ and R_2BaCuO_5 related to high T_c superconductors of the 123 type and in low-dimensional nickelates R_2BaNiO_5. We have registered for the first time phase transitions, some of them not detectable by other methods, in R_2BaCuO_5 with R=Y, Lu, Nd, Dy, Yb, and Lu, in R_2BaNiO_5, with R=Nd, Sm, Eu, Dy, Ho, Tm, and Lu. Coexistence of two different magnetic phases in Y_2BaCuO_5 and Lu_2BaCuO_5 in a broad temperature range was demonstrated. Fine splitting of the low temperature magnetic phase transition, possibly caused by the interaction of critical fluctuations, has been observed in Dy_2BaCuO_5. Low-dimensional correlations at temperatures higher than the temperature of three-dimensional (3-D) magnetic ordering have been analyzed in quasi-2D compounds $R_2Cu_2O_5$ and quasi-1-D R_2BaCuO_5. We developed the method of the Er^{3+} probe in a series of isostructural $f-d$ compounds to select the right magnetic structure of an ordered d subsystem from several structures that fitted neutron scattering data equally well.

I. INTRODUCTION

The method of the rare earth (RE) spectroscopic probe has earlier been shown to complement substantially other methods of studying magnetic phase transitions (see, e.g., Ref. 1). The internal magnetic field that appears due to magnetic ordering in a system splits the Kramers doublets of a RE ion. The detection of an appropriate spectral line splitting versus temperature delivers information on a magnetic ordering in a system. Typically, the spectral resolution of grating spectrometers used for such studies is 0.5–1 cm^{-1} in the visible.[1] As we have shown recently,[2] inhomogeneous width of some RE spectral lines may be as small as 0.007 cm^{-1}. The most intense allowed in free ion optical transitions lie in the infrared and occupy broad spectral regions for a majority of RE^{3+} ions. It is advantageous to register such spectra by a Fourier transform spectrometer rather than by a classical one.[3]

In this paper, by the example of the RE–transition metal magnetic compounds related to high-T_c superconductors, we demonstrate that high resolution Fourier transform spectroscopy combined with some special technique proposed by us[4] broadens considerably the method of a RE spectroscopic probe and offers new possibilities in studying magnetic compounds. The work of the author's group is summarized.

II. SAMPLES AND EXPERIMENT

We have carried out the spectral studies of $R_2Cu_2O_5$[5,6] (here R stands for rare earth or yttrium), R_2BaCuO_5[8–12] and R_2BaNiO_5 (R=Lu,Yb)[13] magnetic cuprates and nickelates, which are related to high-T_c superconductors of the 123 type. It is interesting also to study these compounds in connection with the problem of low-dimensional magnetism. There are CuO planes in the structure of $R_2Cu_2O_5$ (R=Y,Tb–Lu,Sc,In), with intraplane Cu–Cu distances considerably smaller than interplane ones. The so-called "green phases" R_2BaCuO_5 (R=Y,Sm–Lu) and "brown phase" Nd_2BaCuO_5 of R–Ba–Cu–O superconducting ceramics contain isolated Cu^{2+} ions not interconnected by direct bonds through oxygen. Various Cu–O–O–Cu or Cu–O–R–O–Cu superexchange paths, low dimensional in particular, may dominate in these compounds, depending on a particular R^{3+} ion. R_2BaNiO_5 with R=Lu and Yb are isostructural to the green phases, while the other members of this family with R=Y, Nd–Gd, Dy–Tm (also studied by us[14,15]) have a completely different structure, containing isolated –Ni–O–Ni– chains.

Polycrystalline samples of the mentioned compounds, pure or with 1 at. % of erbium introduced as a spectral probe, were prepared from oxides by solid state reaction in air. The powder samples were carefully ground, mixed with ethanol, and put on the sapphire platelet directly before the window of the InSb detector. The whole assembly was inside an optical cryostat, either in liquid helium or in cold helium vapor. Near infrared spectra due to optical transitions in the intrinsic R^{3+} ion or Er^{3+} probe were registered at 2–120 K, with a spectral resolution down to 0.06 cm^{-1} employing the BOMEM DA3.002 Fourier transform spectrometer. In fact, we measured diffuse transmittance spectra. Absorption spectra were then calculated by the appropriate computer program. The width of some spectral lines in our samples at 2 K was as small as 0.1 cm^{-1}.

III. DETECTION OF MAGNETIC PHASE TRANSITIONS

High resolution spectrum of R^{3+} Kramers ion in a crystal is extremely sensitive to the changes of the local magnetic field at the place of this ion. This gives us a possibility to register unambiguously magnetic phase transitions, even those not detectable by other methods and, in some cases, to determine their nature. We have found, for the first time, magnetic ordering in Y_2BaCuO_5,[8] Lu_2BaCuO_5,[11] Nd_2BaCuO_5,[12] R_2BaNiO_5, with R=Lu, Nd, Sm, Eu, Dy, Ho, and Tm,[13–15] and specified the temperatures T_c of appropriate phase transitions. Spin reorientation first-order phase transitions not known before have been detected in Y_2BaCuO_5,[8,10] Dy_2BaCuO_5,[9] Lu_2BaCuO_5, and Yb_2BaCuO_5.[11]

 0021-8979/94/76(10)/7105/3/$6 00 © 1994 American Institute of Physics

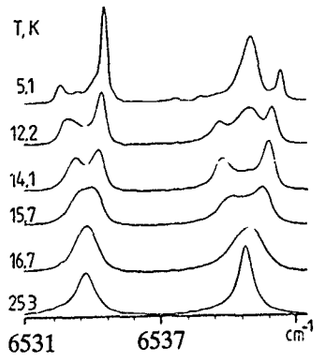

FIG. 1. Low-frequency part of the $^4I_{15/2} \rightarrow {}^4I_{13/2}$ absorption of the Er^{3+} probe in Y_2BaCuO_5 at different temperatures.

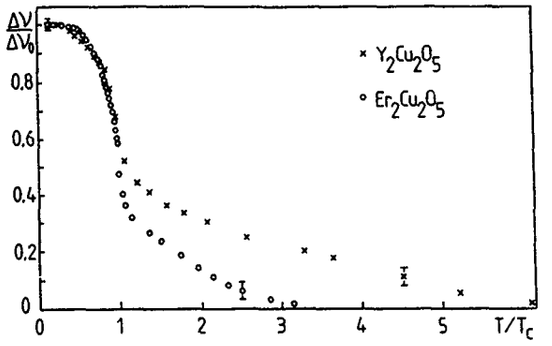

FIG. 2. Reduced splittings of the Er^{3+} probe spectral lines in $Y_2Cu_2O_5$ and $Er_2Cu_2O_5$.

On the other hand, our spectral method permits us to verify the interpretation of magnetic susceptibility (χ) and specific heat (c) measurements. Thus, we have shown that the maxima in $c(T)$ and $\chi(T)$ curves for Er_2BaCuO_5 and in the $\chi(T)$ curve for Er_2BaNiO_5, which had been attributed to phase transitions within the erbium magnetic subsystem, were, in fact, caused by the population changes within the ground Er^{3+} Kramers doublet split by an exchange interaction with an ordered d subsystem.[14,10]

IV. COEXISTENCE OF TWO DIFFERENT MAGNETIC PHASES

In the region of first-order spin reorientation phase transition, two magnetic phases coexist, usually, in a small interval of temperatures. The spectrum is a superposition of two different spectra with temperature-dependent relative intensities. High spectral resolution and precise temperature control ($\simeq$0.02 K) enabled us to separate these spectra and to register the temperature dependence of their intensities.[8–11]

We have found that in Y_2BaCuO_5 and Lu_2BaCuO_5, two different magnetic phases coexist in a broad range, starting from the temperature of spin reorientation transition T_R ($T_R \simeq 12$ K for Y_2BaCuO_5, $T_R \simeq 15$ K for Lu_2BaCuO_5), and down to the lowest measuring temperature of 2 K.[10,11] Evidently, various links Cu–O–O–Cu compete with each other in these compounds.

Figure 1, showing the lowest-frequency lines in the $^4I_{15/2} \rightarrow {}^4I_{13/2}$ spectral transition of the Er^{3+} probe in Y_2BaCuO_5 at different temperatures illustrates our research. The line splitting above 16.5 K manifests magnetic ordering of copper magnetic moments. At about 12.5 K, the spectrum changes abruptly. These changes are best seen for the high-frequency line in Fig. 1, namely, two components of the split line diminish in their intensity, while a new line appears between them. Such a behavior cannot be explained by population redistribution within the sublevels of the split Er^{3+} ground Kramers doublet, when changing the temperature. It clearly shows the appearance of a new magnetic phase with a different exchange field for the Er^{3+} probe. It is worth mentioning that neither magnetic susceptibility nor specific heat measurements suggested any magnetic phase transition in Y_2BaCuO_5.

V. SPECTRA OF Er^{3+} PROBE AND MAGNETIC STRUCTURE OF d SUBSYSTEM

We have shown that in the cuprates studied (1) the splittings of the Er^{3+} probe spectral lines are, mainly, due to the interaction with a d magnetic subsystem, while the interaction with f ions (RE ions) contributes little; (2) Er–Cu interactions are highly anisotropic. On these grounds, we proposed the method of the Er^{3+} probe in a series of isostructural f–d compounds to select the right magnetic structure of an ordered d subsystem from several structures that fitted neutron scattering data equally well. This method has been tested on $R_2Cu_2O_5$ cuprates,[6,7] where reliable neutron scattering data exist and applied to some of the R_2BaCuO_5 compounds.[11] The analogous work on the R_2BaNiO_5 chain nickelates is in progress now.

VI. LOW-DIMENSIONAL MAGNETIC CORRELATIONS AT $T > T_c$

For $T > T_c$ the splittings of spectral lines $\Delta\nu$ do not vanish—a "tail" is observed due to short range order. We have compared the dependences $\Delta\nu\ (T/T_c)$ for the Er^{3+} probe in two $R_2Cu_2O_5$ compounds with identical structure of copper magnetic moments μ_{Cu} (ferromagnetically ordered **ab** planes coupled antiferromagnetically with one another, μ_{Cu} aligned along the **b** axis), but with strongly different T_c temperatures, namely, in $Er_2Cu_2O_5$ ($T_c = 28$ K) and $Y_2Cu_2O_5$ ($T_c = 14$ K).[7,16] Figure 2 shows these dependences. Both dependences have a point of inflection at $T = T_c$, but the "tail" is about two times longer for the second one. This fact can be naturally explained if we assume that two-dimensional (2-D) magnetic correlations within isolated CuO planes take place below the same temperature in both compounds, while $Er_2Cu_2O_5$, where these planes interact through magnetic Er^{3+} ions orders three dimensionally at a two times higher temperature than $Y_2Cu_2O_5$ with nonmagnetic Y^{3+} ions.

We have observed in Nd_2BaCuO_5 an unusually long "tail" extending until about $10T_c$, and have explained it by quasi-1-D magnetism in this compound.[12] Such an explanation was confirmed later by the neutron scattering measurements.[17]

Various manifestations of low-dimensional magnetic correlations have been observed in the spectra of the erbium

probe in Ho_2BaCuO_5 and Er_2BaCuO_5,[10,16] Yb_2BaNiO_5, and Lu_2BaNiO_5.[13] Probably, the most interesting phenomenon is connected with different temperature behavior of the spectra from two different structural positions, Er1 and Er2 in these compounds. While the spectral lines of Er1 are markedly split only below T_c, those of Er2 demonstrate a long "tail" of residual splitting at $T \gg T_c$. We suppose that the Er2 ions are inside dominant magnetic chains and experience the establishment of short range order within a chain at $T \gg T_c$, while Er1 ions interconnect the chains and announce the 3-D ordering at T_c.

VII. SPLITTING OF MAGNETIC PHASE TRANSITION IN Dy_2BaCuO_5

Dy_2BaCuO_5 is a compound with well-separated temperatures for an ordering of d- and f-magnetic subsystems. While the magnetic subsystem of copper orders at $T_{N1}=20$ K, that of dysprosium—at $T_{N2}\simeq 11$ K. We have found[9] that the low temperature phase transition in Dy_2BaCuO_5 is split into two first-order transitions that follow one another with the interval of 0.2 K. Such a phenomenon may be caused by the interaction of critical fluctuations in a double $f-d$ system with a strongly different exchange for two subsystems.[18] To clarify the question, further experimental and theoretical work is necessary.

ACKNOWLEDGMENTS

The author would like to emphasize the decisive contribution of her collaborators, I. V Paukov, N. I. Agladze, Yu. A. Hadjiiskii, and G. G. Chepurko. The synthesis of the samples by B. V. Mill, Ja. Zoubkova, D. A. Kudrjavtsev, and E. P. Khlybov is greatly acknowledged.

[1] A. Hasson, R. M. Hornreich, Y. Komet, B. M. Wanklyn, and I. Yaeger, Phys. Rev. B **12**, 5051 (1975).
[2] N. I. Agladze, M. N. Popova, G. N. Zhizhin, V. J. Egorov, and M. A. Petrova, Phys. Rev. Lett. **66**, 477 (1991).
[3] M N. Popova, D. Sci. thesis, Institute of Spectroscopy, Russian Academy of Sciences, 1992.
[4] N. I. Agladze, G. G. Chepurco, E. P. Hlybov, and M N. Popova, in *Proceedings of the 7th International Conference of Fourier Transform Spectroscopy*, Fairfax, 1989 (SPIE, Bellingham, WA, 1989), Vol. 1145, p 321.
[5] G. G. Chepurko, I. V Paukov, M. N. Popova, and Ja. Zoubkova, Solid State Commun. **79**, 569 (1991).
[6] M. N. Popova and I. V. Paukov, Phys. Lett. A **159**, 187 (1991).
[7] M. N. Popova and I. V. Paukov, Opt. Spectrosc. **76**, 254 (1994).
[8] N. I. Agladze, M. N. Popova, E. P Khlybov, and G. G. Chepurko, JETP Lett. **48**, 45 (1988).
[9] M. N. Popova and G. G. Chepurko, JETP Lett. **52**, 562 (1990).
[10] M. N. Popova and I. V. Paukov, in *Proceedings of the 2nd International School on Excited States of Transition Elements*, Poland, September 1991, edited by W. Strek, W. Ryba-Romanowski, J. Legendziewicz, and B. Jezhowska-Trzebiatowska (World Scientific, Singapore, 1992), pp. 211–220.
[11] I. V. Paukov, M. N. Popova, and B. V. Mill, Phys. Lett. A **169**, 301 (1992).
[12] I. V. Paukov, M. N. Popova, and B. V. Mill, Phys. Lett. A **157**, 306 (1991).
[13] Yu A. Hadjiiskii, R. Z. Levitin, B. V. Mill, I. V. Paukov, M. N Popova, and V V. Snegirev, Solid State Commun. **85**, 743 (1993).
[14] G. G. Chepurko, Z. A. Kazei, D. A. Kudrjavtsev, R. Z. Levitin, B. V. Mill, M. N. Popova, and V. V. Snegirev, Phys. Lett. A **157**, 81 (1991).
[15] Yu. A. Hadjiiskii, I. V. Paukov, and M N Popova, Phys. Lett. A **189**, 109 (1994).
[16] I V Paukov, M. N. Popova, and J. Klamut, Phys Lett. A **189**, 103 (1994).
[17] I. V. Golosovsky, P. Böni, and P Fisher, Phys. Lett. A **182**, 161 (1993).
[18] V. L. Sobolev, I. M. Vitebsky, and A. A. Lisyansky, Phys Rev. B **47**, 8653 (1993).

How does mean-field theory work in magnetic multilayer systems?

Xiao Hu and Yoshiyuki Kawazoe
Institute for Materials Research, Tohoku University, 2-1-1 Katahira, Aoba-ku, Sendai 980, Japan

Phase transition and critical phenomena in magnetic multilayer systems are studied in terms of Ginzburg–Landau mean-field theory. Detailed calculations are carried out for a system consisting of a layer of finite thickness coupled to a semi-infinite bulk magnet. Correlation functions are derived and the shift in critical point with the overlayer thickness and coupling between the neighboring layer is evaluated. A new critical exponent $\tilde{\nu}=1$ is derived for the divergence of the effective extrapolation length at the interface with temperature and/or layer thickness.

I. INTRODUCTION

Magnetic multilayers are known to be very useful for magneto-optical recording.[1,2] The state-of-the-art technologies are so sophisticated as to resort to the difference among the critical points in the individual layers and the detailed temperature dependences of magnetization and anisotropy. Among the problems that have been raised from the experimental side in the recent years, we would like to call the attention to the shift of the critical point and new critical phenomena in magnetic multilayer structures coming from the finite thicknesses of the individual layers. For example, in the bilayer system for the magneto-optical recording, the thickness of the layer with in-plane anisotropy is typically of order of 100 Å.[2] Therefore, the thin layer can neither be treated simply as the surface to the bulk medium, nor be approximated as a semi-infinite bulk, both of which have been studied extensively.[3–8] One has to treat a system consisting of a layer with finite thickness coupled to a semi-infinite bulk.[9–12]

Since this structure is the simplest one that exhibits the most important aspects of multilayer structures, we concentrate on it in the present study. The geometry of the system is schematically shown in Fig. 1. The magnetic constants are taken to be uniform in the individual subsystems and to change abruptly at the interface.

II. FORMALISM AND RESULTS

The Ginzburg–Landau free-energy functional[3] for the present system under an external field can be given as

$$\frac{F}{T}=\int d\mathbf{x}_{\parallel}\int_0^L\left[\frac{1}{2}A_1m^2+\frac{1}{4}B_1m^4-H_{\mathrm{ext}}m+\frac{1}{2}C_1\left(\frac{\partial m}{\partial z}\right)^2\right]dz+\int d\mathbf{x}_{\parallel}\frac{1}{2}C_1\lambda^{-1}m^2(z=L)+\int d\mathbf{x}_{\parallel}\int_{-\infty}^0\left[\frac{1}{2}A_2m^2+\frac{1}{4}B_2m^4-H_{\mathrm{ext}}m+\frac{1}{2}C_2\left(\frac{\partial m}{\partial z}\right)^2\right]dz, \tag{1}$$

with the following interface condition:

$$m(\mathbf{x}_{\parallel},z=+0)=m(\mathbf{x}_{\parallel},z=-0). \tag{2}$$

The thickness L will be kept finite but large on the scale of the atomic lengths. The areas of the surfaces and the interface, on the other hand, are taken to be infinite. The coefficients of the quadratic terms are given by

$$A_1=A_1'(T-T_{c1}),\qquad A_2=A_2'(T-T_{c2}), \tag{3}$$

where T_{c1} and T_{c2} are the mean-field critical points for the layer in the infinite-thickness limit and the semi-infinite bulk, respectively, and A_1' and A_2' are positive constants. The coefficients B_i and C_i for $i=1$ and 2 are taken to be positive with weak temperature dependences. The parameter λ is adopted to describe the surface condition of the thin layer. In the present paper, we consider the case of $T_{c1}>T_{c2}$ and $\lambda>0$. The free-energy functional studied up to the present[4–6] can be obtained, putting $L=0$ in (1).

The differential equations for the correlation functions are derived from (1) and (2) as

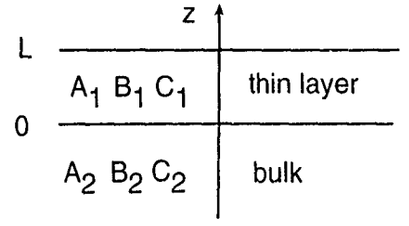

FIG. 1. Geometry of the present system: a thin layer coupled to a semi-infinite bulk.

 0021-8979/94/76(10)/7108/3/$6.00 © 1994 American Institute of Physics

$$\begin{cases} -\dfrac{\partial^2 S(\mathbf{Q}_\parallel;z,z')}{\partial z^2}+\gamma_1^2 S(\mathbf{Q}_\parallel;z,z')=\dfrac{1}{C_1}\,\delta(z-z'), & 0<z<L, \\ -\dfrac{\partial^2 S(\mathbf{Q}_\parallel;z,z')}{\partial z^2}+\gamma_2^2 S(\mathbf{Q}_\parallel;z,z')=0, & z<0, \end{cases} \tag{4}$$

for $z'>0$, and

$$\begin{cases} -\dfrac{\partial^2 S(\mathbf{Q}_\parallel;z,z')}{\partial z^2}+\gamma_1^2 S(\mathbf{Q}_\parallel;z,z')=0, & 0<z<L, \\ -\dfrac{\partial^2 S(\mathbf{Q}_\parallel;z,z')}{\partial z^2}+\gamma_2^2 S(\mathbf{Q}_\parallel;z,z')=\dfrac{1}{C_2}\,\delta(z-z'), & z<0, \end{cases} \tag{5}$$

for $z'<0$, where

$$S(\mathbf{r},\mathbf{r}')=\int \frac{d\mathbf{Q}_\parallel}{(2\pi)^{d-1}} S(\mathbf{Q}_\parallel;z,z')\exp[i\mathbf{Q}_\parallel\cdot(\mathbf{x}_\parallel-\mathbf{x}'_\parallel)], \tag{6}$$

$$\gamma_1^2\equiv\xi_1^{-2}+Q_\parallel^2\equiv\frac{A_1}{C_1}+Q_\parallel^2, \quad \gamma_2^2\equiv\xi_2^{-2}+Q_\parallel^2\equiv\frac{A_2}{C_2}+Q_\parallel^2. \tag{7}$$

The boundary conditions are

$$\begin{aligned} &\left.\frac{\partial S(\mathbf{Q}_\parallel;z,z')}{\partial z}\right|_{z=L}=-\lambda^{-1}S(\mathbf{Q}_\parallel;z,z')|_{z=L}, \quad \left.\frac{\partial S(\mathbf{Q}_\parallel;z,z')}{\partial z}\right|_{z=-\infty}=0, \\ &S(\mathbf{Q}_\parallel;z,z')|_{z=+0}=S(\mathbf{Q}_\parallel;z,z')|_{z=-0}, \quad \left.\frac{\partial S(\mathbf{Q}_\parallel;z,z')}{\partial z}\right|_{z=+0}=\left.\frac{\partial S(\mathbf{Q}_\parallel;z,z')}{\partial z}\right|_{z=-0}. \end{aligned} \tag{8}$$

It is not difficult to obtain the solutions to the above equations, and the correlation function is given explicitly for (4),

$$\begin{aligned} S(\mathbf{Q}_\parallel;z,z')=&\frac{1}{2C_1\gamma_1}\frac{(C_1\gamma_1-C_2\gamma_2)\exp(-\gamma_1 z)+(C_1\gamma_1+C_2\gamma_2)\exp(\gamma_1 z)}{(C_1\gamma_1+C_2\gamma_2)(\gamma_1+\lambda^{-1})/(\gamma_1-\lambda^{-1})-(C_1\gamma_1-C_2\gamma_2)\exp(-2\gamma_1 L)} \\ &\times\left\{\exp[-\gamma_1(2L-z')]+\frac{\gamma_1+\lambda^{-1}}{\gamma_1-\lambda^{-1}}\exp(-\gamma_1 z')\right\}, \end{aligned} \tag{9}$$

for $0\leq z, z'\leq L$.

At first glance, the above correlation function in the layer becomes singular at the critical point T_{c1}. One finds, however,

$$\begin{aligned} &\frac{1}{2\gamma_1}\frac{(C_1\gamma_1-C_2\gamma_2)\exp[-\gamma_1(2L+z-z')]}{(C_1\gamma_1+C_2\gamma_2)(\gamma_1+\lambda^{-1})/(\gamma_1-\lambda^{-1})-(C_1\gamma_1-C_2\gamma_2)\exp(-2\gamma_1 L)} \\ &=\int_{-\infty}^{\infty}\frac{dk}{2\pi}\frac{-\exp[ik(L+z-z')+i\theta_1+i\theta_2]}{(k^2+\gamma_1^2)2i\,\sin(kL+\theta_1+\theta_2)}+\frac{1}{2}\sum_{n=1,2,\ldots}\frac{\cos[k_n(z-z')]}{L+d\theta_1/dk+d\theta_2/dk}\times\frac{1}{k_n^2+\gamma_1^2}, \end{aligned} \tag{10}$$

and three other similar relations, where the summation is on the solutions of the following equation:

$$kL+\tan^{-1}\frac{k}{C_2'\gamma_2}+\tan^{-1}k\lambda=n\pi, \quad \text{for } n=1,2,\ldots, \tag{11}$$

graphically solved in Fig. 2, $\theta_1=\tan^{-1}(k/C_2'\gamma_2)$ and $\theta_2=\tan^{-1}(\lambda k)$. The integral terms, which show singularities at T_{c1}, cancel completely with each other, and thus the correlation function $S(\mathbf{Q}_\parallel;z,z')$ in (9) is equivalent to

$$\begin{aligned} &S(\mathbf{Q}_\parallel;z,z') \\ &=\frac{1}{C_1}\sum_{n=1,2,}\frac{\cos[k_n(z-z')]-\cos[k_n(z+z')+2\theta_1]}{L+d\theta_1/dk+d\theta_2/dk}\times\frac{1}{k_n^2+\gamma_1^2} \\ &=\frac{1}{C_1}\sum_{n=1,2,}\frac{\sin(k_n z+\theta_1)\sin(k_n z'+\theta_1)}{L+d\theta_1/dk+d\theta_2/dk}\times\frac{1}{k_n^2+\gamma_1^2}. \end{aligned} \tag{12}$$

The above complete cancellation among the integral terms is the mechanism responsible for the shift of critical point in the layer of finite thickness.

The correlation function in real space is then given as

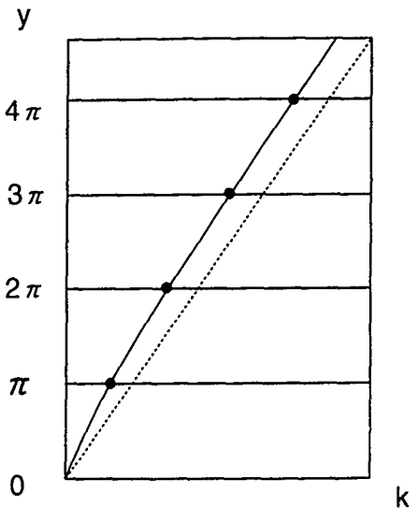

FIG. 2. Graphical solutions for (11): Solid curves are from (11); the dashed line is for $y=kL$.

$$S(\mathbf{r},\mathbf{r}')=\frac{2}{C_1}\sum_{n=1,2,\ldots}\frac{\sin(k_n z+\theta_1)\sin(k_n z'+\theta_1)}{L+d\theta_1/dk+d\theta_2/dk}\times G_{d-1}(\mathbf{x}_\parallel-\mathbf{x}'_\parallel,k_n^2+\xi_1^{-2}), \tag{13}$$

where the function $G_d(\mathbf{r},t)$ is defined in Ref. 6. The critical point is determined by $k_1^2+\xi_1^{-2}=0$ from (13). As $k_1^2>0$, it is now clear that $T_c<T_{c1}$.

Incorporating the definitions of the correlation lengths ξ_1 and ξ_2 in (7), one arrives at the following equation for the critical point T_c:

$$L\sqrt{\frac{-A_1}{C_1}}=\cot^{-1}\sqrt{\frac{-A_1C_1}{A_2C_2}}+\cot^{-1}\lambda\sqrt{\frac{-A_1}{C_1}}. \tag{14}$$

Comparing with (12) in Ref. 8, it becomes clear that the first term on the right-hand side in the above equation expresses the effect of interfacial coupling. Therefore, the shift of critical point of a layer depends on the magnetic properties of the neighboring layer to which it is coupled in a fashion given in the above relation. The critical point T_c is also the temperature at which spontaneous magnetic ordering occurs in the thin layer. We note that this coincidence is not trivial in the present inhomogeneous system.

As $L\to\infty$, the minimal pole k_1 approaches zero and the critical point is then restored to T_{c1}, as it should be by definition.

As for the correlation function within the semi-infinite bulk, it is found that the effect from the thin layer to the semi-infinite bulk can be expressed effectively by an extrapolation length $\xi_{\perp,e}$. The effective extrapolation length at the interface in the present system shows a clear temperature dependence, forming a contrast to the ones in previous studies[4–6] and that on the top surface of the present structure. Furthermore, it diverges with a new exponent $\tilde{\nu}$,

$$\xi_{\perp,2}\sim|1-T/T_*|^{-\tilde{\nu}},\quad T\to T_*, \tag{15}$$

with $\tilde{\nu}=1$, where $T_*<T_{c1}$ is given by

$$L\sqrt{A_1'(T_{c1}-T_*)/C_1}=\cot^{-1}\lambda\sqrt{A_1'(T_{c1}-T_*)/C_1}. \tag{16}$$

This critical exponent should be compared with the well-known $\nu=\frac{1}{2}$ for the correlation length.

The divergence of the effective extrapolation length can also be observed as the thickness of the layer increases, while the temperature is fixed. The critical exponent is also $\tilde{\nu}=1$ in the present mean-field theory.

It can be shown, within the present approach, that as the thickness L of the layer approaches infinity, the effective extrapolation length becomes $C_2\xi_1/C_1$. It diverges at $T=T_{c1}$ with the critical exponent $\nu=\frac{1}{2}$ for the correlation length. Therefore, the divergence of the interfacial extrapolation length with the exponent $\tilde{\nu}=1$ is a characteristic phenomenon in systems where a layer with finite thickness is coupled into the structure, such as the one discussed in the present paper.

III. SUMMARY

Magnetic multilayer structures are studied within the Ginzburg–Landau free-energy functional formalism. The shift of critical point is discussed, and the effects from the finiteness of layer thickness and from the coupling between neighboring layers are clarified for a system consisting of a magnetic overlayer on a bulk ferromagnet. The present result is expected to be important for the practical multilayer-disk design.

[1] M. Kaneko, K. Aratani, Y Mutoh, A. Nakaoki, K. Watanabe, and H. Makino, Jpn. J. Appl. Phys. Suppl **28-3**, 927 (1989).
[2] S. Ohnuki, K Shimazaki, N. Ohtar, and H. Fujiwara, J. Magn Soc. Jpn **15** Suppl. No. S **1**, 399 (1991).
[3] V. L. Ginzburg and L. D. Landau, Zh Eksp. Teor. Fiz. **20**, 1064 (1950)
[4] D. L. Mills, Phys Rev. B **3**, 3887 (1971).
[5] K. Binder and P C Hohenberg, Phys. Rev. B **6**, 3461 (1972); K Binder, in *Phase Transitions and Critical Phenomena*, edited by C. Bomb and J. L. Lebowitz (Academic, New York, 1983), p. 1; references therein.
[6] T C. Lubensky and M. H. Rubin, Phys. Rev. B **12**, 3885 (1975).
[7] A. Bray and M. A. Moore, J. Phys A **10**, 1927 (1977).
[8] M I. Kaganov and A. N. Omel'Yanchuk, Sov. Phys. JETP **34**, 895 (1972).
[9] X. Hu and Y. Kawazoe, Phys. Rev. B **49**, 3294 (1994).
[10] Y. Kawazoe, X. Hu, and S Honma, MRS Symp. Proc. **313**, 513 (1993).
[11] X. Hu, T. Yorozu, Y. Kawazoe, S. Ohmiki, and N. Ohta, IEEE Trans. Magn. **29**, 3790 (1993).
[12] X. Hu and Y. Kawazoe, J. Appl. Phys **75**, 6486 (1994)

Magnetic properties of the one-dimensional Heisenberg compounds (3-X-anilinium)$_8$[CuCl$_6$]Cl$_4$; X=Br, I

Gayatri Vyas and Leonard W. ter Haar[a)]
Department of Chemistry, University of Texas, El Paso, Texas 79968-0513

Recent x-ray diffraction studies have suggested that (3-Cl-anilinium)$_8$[CuCl$_6$]Cl$_4$ exhibits *compressed* [CuCl$_6$]$^{4-}$ octahedra. We report here the synthesis of the (3-Br-anilinium)$_8$[CuCl$_6$]Cl$_4$ and (3-I-anilinium)$_8$[CuCl$_6$]Cl$_4$ analogs. Their magnetic behavior is quite similar to one another, and in comparison to the *chloro* compound, the only similarity is that they all exhibit chain magnetism, as evidenced by their broad maxima in the region of 9–12 K. The *bromo* and *iodo* compounds do not exhibit the field dependence of the *chloro* compound, and in this respect, the *chloro* compound remains unique. For all three compounds, magnetic susceptibility data can be analyzed by the antiferromagnetic one-dimensional Heisenberg model.

I. INTRODUCTION

Bright yellow needle-like crystals with the composition (3-chloro-anilinium)$_8$CuCl$_{10}$ were first reported to consist of discrete [CuCl$_6$]$^{4-}$ ions in a tetragonal compressed octahedral coordination geometry.[1] We subsequently reported an independent x-ray structure determination at 298 K that reproduced this apparent compression, and provided structure determinations at 150 and 110 K, carried out in two independent laboratories, that revealed no significant changes concerning the compression versus elongation dilemma.[2] To date, all crystal structure determinations (293–110 K) have revealed a tetragonally *compressed* octahedron with four long Cu–Cl bonds of intermediate length (2.6 Å) and two short Cu–Cl bonds of 2.28 Å. The [CuCl$_6$]$^{4-}$ ions form a linear chain through axial Cl–Cl contacts (3.99 Å) between the [CuCl$_6$]$^{4-}$ ions, with the axis of tetragonal compression parallel to the axis of chain propagation.

In addition to the low-temperature structure determinations, we demonstrated with low-temperature (down to 1.7 K) single crystal magnetic susceptibility and EPR data that the material revealed a complex magnetic problem with several key questions concerning Jahn–Teller related lattice dynamics and disorder.[2] More recently, low-temperature electronic spectral data have been invoked in conjunction with the magnetic and EPR data to suggest that at the local level, each [CuCl$_6$]$^{4-}$ ion is tetragonally *elongated*, and that the axis of elongation is "antiferrodistortively" disordered over two possible sites, thereby leading to the crystallographically determined bond lengths that correspond to intermediate long bonds averaged over the unit cell and suggestive of *compressed* geometry.[3] These possibilities have stimulated additional synthetic, theoretical, spectroscopic, magnetic, and EPR studies. In this paper, we report the synthesis and magnetic characterization of (3-bromo-anilinium)$_8$CuCl$_{10}$ and (3-iodoanilinium)$_8$CuCl$_{10}$.

II. EXPERIMENT

(3-Br-anilinium)$_8$CuCl$_{10}$ and (3-I-anilinium)$_8$CuCl$_{10}$ were prepared by stoichiometric reaction of the appropriate 3-X-aniline with CuCl$_2\cdot$2H$_2$O in saturated 60/40 HCl/ethanol solutions. Second crops of crystals typically yielded higher quality product. Both products are bright yellow needle-like crystals. Elemental analysis, Atlantic Microlab: C$_{48}$H$_{56}$Cl$_{10}$Br$_8$N$_8$Cu, expected (actual) H 3.13 (3.08), C 31.99 (31.99), N 6.22 (6.21), Cl 19.67 (19.63), Br 35.47 (35.42); C$_{48}$H$_{56}$Cl$_{10}$I$_8$N$_8$Cu, expected (actual) H 2.59 (2.52), C 26.47 (26.51), N 5.14 (5.11), Cl 16.28 (16.30), I 46.61 (46.30).

All attempts to perform a single crystal x-ray structure determination have so far been unsuccessful. The habit of the acicular crystals is that of bundled fibers, thereby rendering most crystals as too small for diffraction, or too fragile with respect to cleavage when trying to cut the larger crystals to size. X-ray powder diffraction has been utilized to characterize the materials for comparison to the chloro derivative. Data were collected on a Rigaku D2000 and a Scintag XDS2000 at 293 K. Powder spectra for the bromo and iodo derivatives were superimposable and were fit to a tetragonal cell: (3-Br-anilinium)$_8$CuCl$_{10}$, $a=8.92$ Å, $c=11.38$ Å; (3-I-anilinium)$_8$CuCl$_{10}$, $a=8.92$ Å, $c=11.38$ Å.

Magnetic susceptibility measurements on freshly prepared powder samples were collected in the temperature range 1.7–300 K using a Quantum Design SQUID-based magnetometer utilizing modifications and procedures described elsewhere.[4] Data were corrected for temperature independent magnetism (X=Br: -1012×10^{-6} emu/mol; and X=I: -1124×10^{-6} emu/mol) using Pascal's constants for the diamagnetic components[5] and a T.I.P. per Cu(II) ion of 60×10^{-6} emu/mole. Figures in this paper are based on the molecular weights of 1802.3 g/mol (Br) and 2178.3 g/mol (I).

III. RESULTS AND DISCUSSION

All of the crystal structure determinations[1,2] of (3-Cl-anilinium)$_8$[CuCl$_6$]Cl$_4$ have indicated that discrete 3-chloroanilinium ions, uncoordinated chloride ions, and [CuCl$_6$]$^{4-}$ ions comprise the triclinic unit cell. The [CuCl$_6$]$^{4-}$ ions are linked into a quasilinear chain by way of axial Cl–Cl interactions; this lattice arrangement leads to the characteristic chain magnetism that has now been repeatedly verified.[1–3] Since we have only been able to collect powder diffraction data for the bromo and iodo derivatives, the notable observation is that the powder diffraction pattern of the

a)Author to whom all correspondence should be addressed.

 0021-8979/94/76(10)/7111/3/$6.00 © 1994 American Institute of Physics

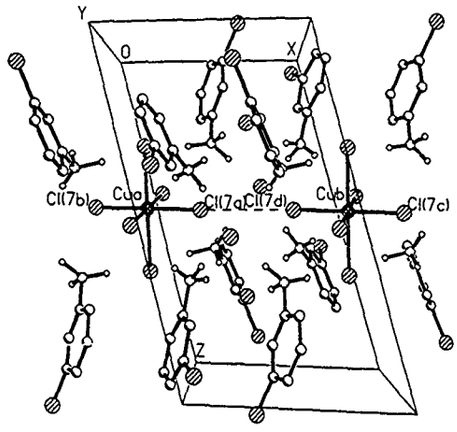

FIG. 1. View perpendicular to the chain structure in (3-X-anilinium)$_8$[$CuCl_6$]Cl_4; the superexchange pathway is the Cu–Cl···Cu–Cl contact.

chloro derivative (triclinic) is noticeably more complex than the diffraction patterns of the bromo and iodo derivatives (which are superimposable on one another within experimental error). In view of the elemental analyses, which confirm that the molecular composition of all three compounds corresponds to the general formula (3-X-anilinium)$_8$[$CuCl_6$]Cl_4, the tetragonal unit cell parameters for the bromo and iodo derivatives equate to a smaller unit cell with a smaller volume and a higher symmetry.

On this basis, the general packing arrangement of the $[CuCl_6]^{4-}$ ions in the bromo and iodo derivatives is expected to be similar to the chloro compound, i.e., a quasilinear chain arrangement similar to the chain structure of (3-Cl-anilinium)$_8$[$CuCl_6$]Cl_4, shown in Figs. 1 and 2. The copper–copper separation along the chain is 8.55 Å in the chloro compound. Antiferromagnetic superexchange interactions along such a chain arise from the –Cl(7′)–Cu–Cl(7)–Cl(7′)–Cu–Cl(7)–pathway, where the only close contact from an axial Cl(7) is to another axial Cl(7′) on a neighboring complex along the chain direction. This contact has been shown to be temperature dependent [3.995 (293 K)/3.805 (110 K)], as a result of thermal contraction of the unit

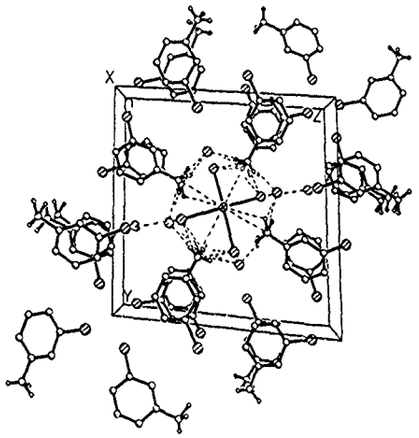

FIG. 2 Packing view along the chain axis in (3-X-anilinium)$_8$[$CuCl_6$]Cl_4.

cell,[2] and could very well lead to a temperature-dependent Heisenberg exchange. This distance is slightly greater than the van der Waal's contact of 3.60 Å.[6] The next closest contacts for the axial chlorides are to the uncoordinated chlorides at over 4.0 Å.

Since the structure of the $[CuCl_6]^{4-}$ ion may be a time-averaged structure in which the four "long" equatorial Cu–Cl bonds (of intermediate length, 2.6 Å) are actually an average of two long Cu–Cl bonds of 2.9 Å and two short bonds of 2.3 Å; then the crowded equatorial-coordinated-chloride to organo-chloro distance of 3.45 Å may be easily affected by chemical modification of the aniline metasubstituent. With the bromo and iodo derivatives, we have effected such a change. With the larger organo-halogens, the overall structure has clearly adjusted in order to accommodate the larger atoms. Given that the general nature of the lattice packing is preserved, the tetragonal a axis (8.92 Å) for both the bromo and iodo derivatives may reflect a Cu–Cu separation along the chain axis that is increased, relative to the 8.55 Å of the chloro compound. Precisely how the larger organo-halogens result in a structure of higher symmetry must await a complete structure determination.

The magnetic susceptibility data provide the strongest evidence that the quasichain structure in (3-Cl-anilinium)$_8$[$CuCl_6$]Cl_4 is also present in the bromo and iodo compounds. SQUID-based temperature-dependent magnetic susceptibility data were collected for the bromo and iodo derivatives, with applied magnetic fields in the range 0.1 mT to 1.0 T, and in the temperature range 1.7–300 K. Representative data for the bromo derivative are plotted in Fig. 3 as χ_m, $1/\chi_m$, and $\mu_{\text{eff}}=2.828(\chi_m T)^{1/2}$; the iodo data are nearly identical. Several dominant features are noteworthy. The χ_m of the bromo material exhibits a susceptibility maximum at a temperature of 11.5 K (iodo: 10.5 K) and μ_{eff} drops from near 1.8 B.M. at 300 K toward 0.4 B.M. near 2 K. These data are in qualitative agreement with the previous susceptibility studies on the chloro compound and suggest the presence of antiferromagnetic exchange interactions in a one-dimensional magnetic system.

In view of the observation that a quasichain structure is maintained for the bromo and iodo derivatives, it is reasonable to fit the susceptibility data to the uniform $S=\frac{1}{2}$ Heisenberg spin chain, given by the Hamiltonian

$$H=-2J_{ij}\sum_{i<j}\mathbf{S}_i\cdot\mathbf{S}_j,$$

where J_{ij} is the isotropic intrachain exchange parameter. The theoretical treatment of such a uniform chain was first provided by Bonner and Fisher.[7] Hall[8] later provided a useful analytical expression for the temperature dependence of the magnetic susceptibility as

$$\chi_{\text{BF}}=(Ng^2\mu_B^2/k_BT)[A+Bx+Cx^2]/[1+Dx+Ex^2+Fx^3], \quad (1)$$

where the coefficients[8] are given as $A=0.25$, $B=0.149\,95$, $C=0.300\,94$, $D=1.9862$, $E=0.688\,54$, $F=6.0626$, and $x=|J|/k_BT$; N is Avogadro's number, μ is the Bohr magneton, k is the Boltzmann constant, and g is the gyromag-

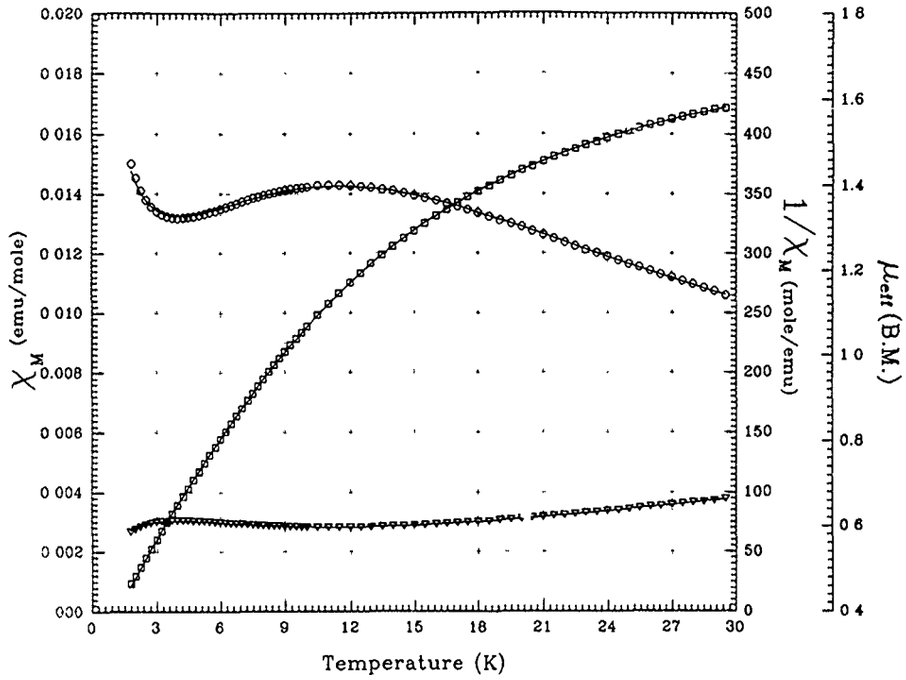

FIG. 3 Magnetic data for (3-Br-anilinium)$_8$[$CuCl_6$]Cl_4, curves are drawn using the best-fit parameters given in the text (○—χ_m, ▽—$1/\chi_m$, □—μ_{eff}).

netic ratio for the electron. Interchain interactions, denoted zJ', can be accounted for by applying a molecular field correction to the χ_{BF} expression, thus obtaining

$$\chi_{corr}=\chi_{BF}/(1-2zJ'\chi_{BF}/Ng^2\mu_B^2), \quad (2)$$

where J' is the interchain exchange parameter and z is the number of nearest neighbors. A best fit of the χ_{corr} expression to the χ_m data using nonlinear regression[9] yielded best-fit fitting parameters for *bromo*: $J=-6.9$ cm^{-1}, $zJ'=-1.64$ cm^{-1}, % impurity=0.20 and $g=2.13$; and for *iodo*: $J=-6.6$ cm^{-1}, $zJ'=-1.35$ cm^{-1}, % impurity=0.26 and $g=2.13$. The impurity fitting parameter was obtained by adding a monomeric Curie term to Eq. (2); this helps to account for the Curie tail evident in the data.

The solid line in Fig. 3 is generated with the best-fit parameters; it is in excellent agreement with the temperature dependence and the position of the maximum, as calculated according to the Bonner–Fisher model ($k_BT_{max}/|J|=1.2828$). The best-fit values for g are in excellent agreement with the EPR g value of 2.14. Unlike the chloro compound, the bromo and iodo derivatives do not exhibit magnetic field dependence below 10 K. They do, however, always exhibit the impurity tail clearly seen in Fig. 3. Several sample preparations have been used to demonstrate that the tail is essentially independent of the sample preparation technique or crystal quality. It has often been surmised that such effects can then be ascribed to finite chain effects because short finite chains with an odd number of spins would have a diverging susceptibility at low temperatures. It is clear however, that the magnitude of the bromo and iodo exchange energies are less than the -9.3 cm^{-1} found for the *chloro* compound, with that of the iodo material being slightly less than that of the bromo material. The decrease in the magnitude of the exchange energy corresponds well with the expected increased distance of the Cu–Cl···Cl–Cu superexchange pathway, given that the larger organo-halogens increase this distance, as suggested by the powder diffraction data. Single crystal studies continue to be addressed.

ACKNOWLEDGMENTS

Support from the Robert A. Welch Foundation and the National Science Foundation is gratefully acknowledged.

[1] D. A. Tucker, P. S. White, K. L. Trojan, M. L Kirk, and W. E. Hatfield, Inorg. Chem. **30**, 823 (1991).
[2] W. E. Hatfield, K. L. Trojan, P. S. White, O. Horner, L. W. ter Haar, D. J. Nelson, F. Cervantes-Lee, S. K. Hoffmann, W. Hilczer, J. Goslar, and M. A. Hitchman, Mol. Cryst. Liquid Cryst. **233**, 309 (1993).
[3] H. Stratemeier, B. Wagner, E. R. Krausz, R. Linder, H. H. Schmidtke, J. Pebler, W. E. Hatfield, L. W. ter Haar, D. Reinen, and M. A. Hitchman, Inorg. Chem. **33**, 2320 (1994).
[4] D. Nelson and L. W. ter Haar, Inorg. Chem. **32**, 182 (1992).
[5] E A. Boudreaux and L. N. Mulay in *Theory and Applications of Molecular Paramagnetism* (Wiley, New York, 1976).
[6] L. Pauling, *The Nature of the Chemical Bond*, 3rd ed. (Cornell Univ. Press, Ithaca, NY, 1960), p. 260.
[7] J. C. Bonner and M. E. Fisher, Phys. Rev. A **135**, 640 (1964).
[8] J. W. Hall, Ph.D. dissertation, University of North Carolina, 1977.
[9] Marquardt–Levenberg algorithm, SigmaPlot, MacIntosh Version 4.1, Jandel Scientific, 1992.

Comparison of two-dimensional Heisenberg and two-dimensional *XY* model behaviors in Pd(1.2 at. % Fe) films

J. D. McKinley
Physics Department and Rice Quantum Institute, Rice University, Houston, Texas 77251-1892

Multilayer Pd/Pd(1.2 at. % Fe)/Pd thin films were prepared by dc magnetron sputtering and characterized with dc SQUID magnetometry. Evidence for two-dimensional (2D) Heisenberg and 2D *XY* model behaviors was found in two different regions of temperature. In these temperature regimes, our data agree with the predicted form for magnetization M and susceptibility χ as functions of field and temperature. Both model's susceptibilities were found to fit our data. M and χ exhibit discontinuities at magnetic layer thickness-dependent temperatures which separate the different model behaviors.

I. INTRODUCTION

The Pd/Pd(1.2 at. % Fe)/Pd random quenched thin film trilayers were originally prepared as a model system for studying two-dimensional Heisenberg (2DH) model magnetism in a single magnetic layer.[1,2] We were motivated by previous studies of bulk dilute Fe-doped Pd alloys[3,4] showing Fe concentrations in Pd above 0.1 at. % to be 3D Heisenberg ferromagnets; dimensional reduction should result in two-dimensional behavior. Thick Pd layers provide good crystal growth, prevent oxidation in the Pd(Fe) layer, and ensure "bulk" lattice constants in the magnetic layer. The Pd(Fe) magnetic layer thickness L was varied over the range 5 Å$<L<$500 Å. Polycrystalline Pd(300 Å)/Pd(Fe) (L Å)/Pd(300 Å) films were grown on Si(111) substrates at room temperature using dc magnetron sputtering, at rates of ~1 Å/s in a UHV chamber in pressures $P\leqslant 5\times10^{-9}$ Torr. The films were characterized in a parallel applied field using a dc SQUID magnetometer. The 2DH model magnetic behaviors were observed in each film over a range of temperatures below the bulk Pd(Fe) $T_c\approx 40$ K.

The magnetic properties in the Pd(Fe) films indicate a phase transition or crossover to a different model behavior, possibly 2D *XY*,[1] at a thickness-dependent temperature. This behavior persists to an even lower temperature, where finite magnetizations and hysteresis loops are observed. We also observed peaks in the low-field magnetization versus temperature dependence.

It is well known[5] that there is no long-range ferromagnetic order in a fully isotropic 2DH ferromagnet. Real physical systems have anisotropies, which are often temperature dependent. The Pd(Fe) layer has a slightly smaller lattice constant[4] than the pure Pd layers, and this produces in-plane anisotropy.

The dimensional reduction of the Pd(Fe) layer also results in finite size[2] effects. At some temperature the percolating magnetic cluster in the Pd(Fe) layer reaches the finite thickness of the magnetic layer, constraining it to grow laterally at lower temperatures. Other finite sizes possibly affecting magnetic percolation are the crystallites from 100 to 300 Å in size, closely packed into islands with 0.1- to 0.2-μm lateral diameters, as determined from x-ray crystallography and transmission electron microscopy.

Finite field magnetization $M(H)$ data and susceptibility $\chi(T)$ data are presented for a 500-Å-thick Pd(Fe) layer film. Model predictions for 2DH and 2D *XY* behaviors are compared to these data in two separate regions of temperature.

II. 2D HEISENBERG AND 2D *XY* MODEL BEHAVIORS

The 2D Heisenberg and 2D *XY* models predict[6–10] similar field dependence of the magnetization and temperature dependence of the susceptibility, as shown below:

$$\chi_{2DH}(T)\sim\exp(B/T),\quad M_{2DH}(H)\sim A(T)\ln(H/H^*),$$

$$\chi_{2D\ XY}(\tau)\sim\exp(B'/\tau),\quad M_{2D\ XY}(H)\sim H^{1/\delta},\quad \delta=15.$$

where H is the externally applied field, H^* is a thickness-dependent constant, T the ambient temperature, and $\tau=(T-T_{KT})/T_{KT}$ is the reduced temperature using the Kosterlitz–Thouless temperature as the Curie temperature. The prefactor $A(T)$ is a function[7] of temperature T, and exponents B and B' depend on the magnetic layer thickness. Because the susceptibility model predictions are similar, the different model behaviors must be carefully distinguished. Physical reasons are given for interpreting the low- and high-temperature regions as corresponding to 2D *XY* (see below) and 2DH[1] behaviors, respectively. Interestingly, the 2D *XY* prediction for equation of state critical exponent $\delta=15$ is the same as for the 2D Ising model.

III. RESULTS AND DISCUSSION

In Figs. 1(a) and 1(b), the susceptibility data are fit to the 2DH and 2D *XY* predictions, respectively. Both models fit the whole range of data. In Fig. 1(a), the 2DH model $\chi_{2DH}(T)$ is plotted as $\ln(\chi)$ vs $1/T$. The high- and low-temperature regions are divided by a fairly sharp "kink" in the curve, as indicated by the lines drawn onto the data. The lines themselves are not the fits to the data, but separate fits to each region show that both portions are very linear, with correlation coefficients $R\sim0.999$. A line drawn from the intersection of the extrapolated fits indicates a kink temperature $T_{kink}\cong 36$ K. The 2D *XY* model $\chi_{2D\ XY}(\tau)$ is fitted to the data as $\ln(\chi)$ vs $\tau^{-1/2}$ in Fig. 1(b). Remarkably, for the 500-Å Pd(Fe) film data a single line can fit the susceptibility over the full range of temperatures. Two regions in the data can be determined with slightly different slopes, as the drawn lines indicate, but the differences are within uncertainties.

Magnetization data for the 500-Å-thick Pd(Fe) film is fitted to the 2DH model in Fig. 2(a) and to the 2D *XY* model

 0021-8979/94/76(10)/7114/3/$6.00 © 1994 American Institute of Physics

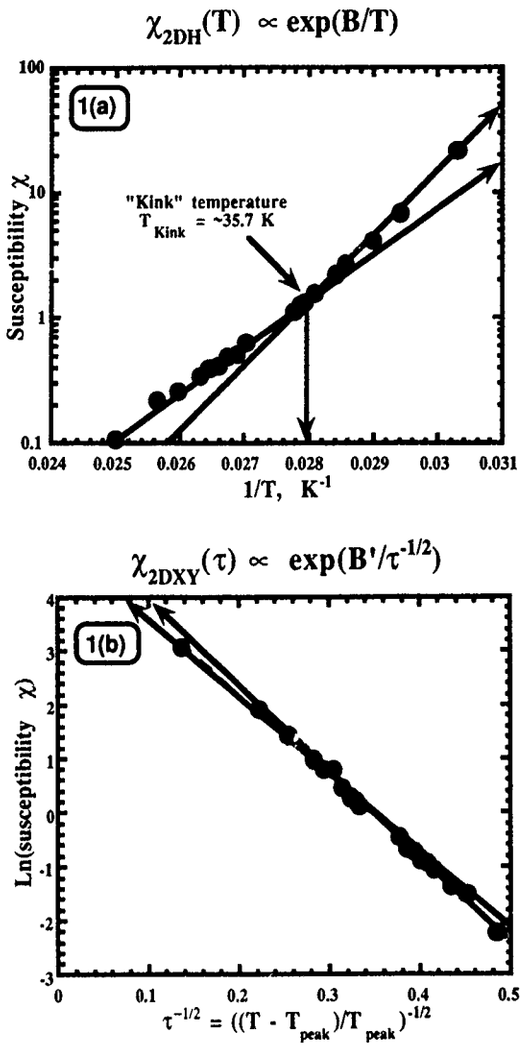

FIG. 1. Susceptibility χ vs temperature T plots for a 500-Å-thick Pd(Fe) magnetic layer. Plots (a) and (b), respectively, assume 2DH and 2D XY model behavior over the full range of temperatures from T_c [bulk Pd(Fe)] ≈40 K down to T_{peak}(500 Å)=32.4±0.2 K. Both linear regions in (a) fit the 2DH prediction well, with the slope merely increasing ~50% at the "kink" temperature T_{kink}≈36 K. The 2D XY assumption in plot (b) fits the entire temperature region; a slight change in slope near T_{kink} lies within the uncertainty of the 500-Å film data. The changes in the slope at T_{kink} are a function of magnetic layer thickness.

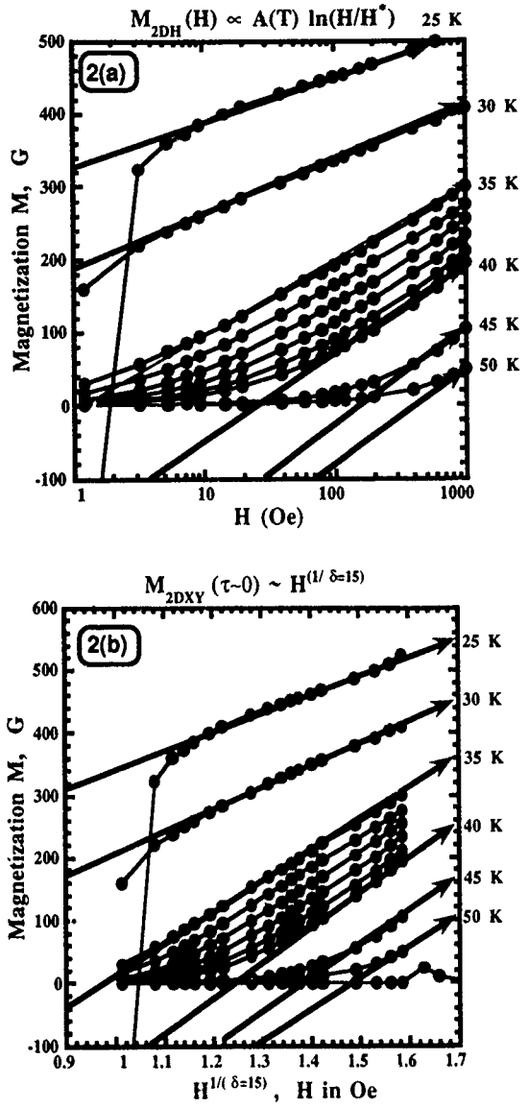

FIG. 2. Magnetization M vs applied field H plots for a 500-Å-thick Pd(Fe) magnetic layer. Plot (a) over temperatures $32.4 \leq T \leq 40.0$ K yields good agreement with 2DH behavior at finite fields. Plot (b) assuming 2D XY behavior indicates the onset of 2D XY behavior near T_{kink}≈36 K. Both model behaviors can be said to fit the data, but each seems to fit one temperature region slightly better

in Fig. 2(b). Here, differences between the two models are more apparent. The data were originally taken to study the 2DH behavior at higher temperatures, but enough data at lower temperatures was taken for a useful comparison. The 2DH prediction is only expected to apply for finite fields, and the Fig. 2(a) curves are linear at higher fields up to magnetic saturation. In lower fields, the magnetization is linear in the field, and was used to obtain the zero-field susceptibilities already discussed. The 2D XY model equation of state prediction (using the predicted critical exponent $\delta=15$) is shown in Fig. 2(b). It fits the data fairly well over the entire temperature range, but especially near the kink temperature. Despite the absence of intermediate data, the 30 and 35 K M vs H curves indicate a Kosterlitz–Thouless transition could have occurred between them.

The 2D XY model is consistent with the presence of magnetization versus temperature peaks observed in very small field measurements. A magnetization versus temperature peak for the 500-Å sample was observed around 32.4 to 33.0 K. Although the low fields were probably nonuniform, they were constant. Since the magnetization is proportional to the field in sufficiently low fields, a peak probably demonstrates a finite temperature susceptibility divergence. It is not prominent, and is superimposed on a large monotonically increasing magnetization curve. At present only the approximate location of the peak is reliable. An exponentially diverging shape is expected of a Kosterlitz–Thouless transition, instead of the usual power law divergence. Stronger evidence of such a peak shape is seen in data for the thinner films ($L<500$ Å), but consistent reproduction of the results will require a magnetometer measuring in controllably uniform low fields. Confirmation of the peak and peak shape,

coupled with demagnetization-limited susceptibility below T_{peak} would indicate 2D XY model behavior prevailing below the kink temperature.

IV. CONCLUSIONS

The 2D Heisenberg and 2D XY model behaviors are functionally similar. Consequently, magnetization $M(H)$ and susceptibility $\chi(T)$ for both models can be fitted to all the data. However, the model behaviors are distinguished by the kink in the 2DH plot of $\ln(\chi)$ vs $1/T$. Also, no susceptibility or magnetization peaks are seen at the temperature for which the susceptibility kink occurs, whereas a magnetization peak is observed at a lower temperature that could correspond to a Kosterlitz–Thouless transition.

For thinner films[1,2] the total range of temperature for both regions is greater and the behaviors are more easily distinguished, but the signal-to-noise ratios are proportionately worse, and low-temperature behavior in the thinnest films is more difficult to obtain experimentally. The 500-Å film also has the advantage of sufficient signal strength to observe its behavior up to and somewhat above the bulk Pd(1.2 at. % Fe) $T_c \approx 40$ K, thus connecting it to bulk Pd(Fe) results. The films described here were polycrystalline. Better film growth is currently being pursued, to increase the crystal size and determine if the boundaries between the different model behaviors become more sharply defined.

ACKNOWLEDGMENTS

I thank R. N. Shelton for the use of his dc SQUID magnetometer and P. Klavins for help in preparation of the Pd(Fe) targets and measurements of the films. This work represents an extension of my dissertation, and I thank my thesis advisor D. J. Webb for discussions and R. R. P. Singh for theoretical discussion of the 2D Heisenberg model.

[1] D. J. Webb and J. D. McKinley, Phys. Rev. Lett. **70**, 509 (1993).
[2] J. D. McKinley, Ph.D. dissertation, University of California, Davis, 1993.
[3] J. A. Mydosh and G. J. Nieuwenhuys, in *Ferromagnetic Materials*, edited by E. P. Wohlfarth (North-Holland, Amsterdam, 1980), p. 71.
[4] For some of the early work on Pd(Fe) and other dilute ferromagnetic alloys, see R. M. Bozorth, P. A. Wolff, D. D. Davis, V. B. Compton, and J. H. Wernick, Phys. Rev. **122**, 1157 (1961); A. M. Clogston, B. T. Matthias, M. Peter, H. J. Williams, E. Corenzwit, and R. C. Sherwood, *ibid.* **125**, 541 (1962); and J. Crangle and W. R. Scott, J. Appl. Phys. **36**, 921 (1965).
[5] N. D. Mermin and H. Wagner, Phys. Rev. Lett. **17**, 1133 (1966).
[6] Y. S. Karimov, Sov. Phys. JETP **38**, 129 (1974).
[7] S. B. Khokhlachev, Sov. Phys. JETP **44**, 427 (1976). This prediction indicates the prefactor A is proportional to T. The Pd(Fe) thin film data show a temperature dependence which is roughly linear over a restricted range of temperatures.
[8] A early review by V. L. Pokrovsky, Adv. Phys. **28**, 595 (1979).
[9] Recent 2D Heisenberg susceptibility calculations include M. Takahashi, Prog. Theor. Phys. **87**, 233 (1986); M. Takahashi, Phys. Rev. Lett. **58**, 168 (1987); D. P. Arovas and A. Auerbach, Phys. Rev. B **38**, 316 (1988).
[10] J. M. Kosterlitz, J. Phys. C **7**, 1046 (1974).

Published without author corrections

The effects of frustrated biquadratic interactions on the phase diagrams and criticality of the Blume–Emery–Griffiths model (abstract)

Daniel P. Snowman and Susan R. McKay
Department of Physics and Astronomy, University of Maine, Orono, Maine 04469

The Blume–Emery–Griffiths model, a spin-1 Ising model with bilinear (J), biquadratic (K), and the crystal field (Δ) terms, provides a general system for the study of both density and magnetic fluctuations. Previous work has shown that a rich variety of phase diagrams occurs in cases of positive[1] or negative[2] biquadratic coupling. In this study, we consider an exactly solvable system in which frustration is present due to competing biquadratic interactions. Thus, this calculation models a dilute ferromagnetic mate ial with two types of nearest neighbor site pairs, distinguished by whether or not simultaneous occupation is energetically favored. To determine the effects of this competition, we have constructed exactly solvable frustrated hierarchical models similar to those introduced to study spin glasses.[3] The resulting phase diagrams show that, when frustration is present, the dense disordered and dilute disordered phases can become separated by a phase with chaotic rescaling of K and Δ. In the $J=0$ plane, this chaotic rescaling is directly linked to that previously reported in spin glasses[3] via the Griffiths symmetry.[1,4]

[1]A. N. Berker and M. Wortis, Phys. Rev. B **14**, 4946 (1976)
[2]W. Hoston and A N. Berker, Phys. Rev. Lett. **67**, 1027 (1991).
[3]S R. McKay, A N. Berker, and S. Kirkpatrick, Phys. Rev. Lett. **48**, 767 (1982).
[4]R. B. Griffiths, Physica (Utr.) **33**, 689 (1967).

Magnetic phase transitions in $CsEr(MoO_4)_2$ and $KDy(MoO_4)_2$-chain-layered Ising compounds (abstract)

E. N. Khats'ko and A. S. Cherny
Institute for Low Temperature Physics & Engineering, Ukraine Academy of Sciences, 47 Lenin Avenue, Kharkov 310164, Ukraine

The crystals investigated belong to the family of the orthorhombic layered rare-earth double molybdates. These crystals have aroused interest because of the diversity of structural and magnetic phase transitions, which are due to the crystalline structure and the electron energy spectrum of rare-earth ions. These ions are distinguished for their Ising behavior. The magnetization and susceptibility measurements were performed at temperatures between 0.5 and 300 K in magnetic fields up to 0.4 T along three principal magnetic axes. The 3D magnetic ordering is found to occur at $T_c=0.84$ K for $CsEr(MoO_4)_2$ and $T_c=1.1$ K for $KDy(MoO_4)_2$. The magnetic properties are strongly anisotropic both above and below T_c. In the magnetic ordered state spin-orientation phase transitions were found in both of these compounds. For $CsEr(MoO_4)_2$ a typical metamagnetic transition was observed along one magnetic field direction (b). There is a more intricate situation in the case of $KDy(MoO_4)_2$. The spin-orientation phase transition has a rather complex character: it is anitferromagnetic along the a axis, and ferromagnetic along the b and c axes. The magnetic structures of these compounds were determined. In the case of $CsEr(MoO_4)_2$ a collinear two-sublattice structure of antiferromagnetically ordered ferromagnetic chains is realized. For $KDy(MoO_4)_2$, the magnetic structure is defined as a complicated noncollinear four sublattice structure with magnetic moments rotated 35° in the ac plane and 10° in the bc plane.

 0021-8979/94/76(10)/7117/1/$6.00 © 1994 American Institute of Physics

Na-doping effect on the magnetic properties of the YBCO ceramics

T. Nurgaliev, S. Miteva, I. Nedkov, A. Veneva, and M. Taslakov
Institute of Electronics, Bulgarian Academy of Sciences, 72 Blvd. Tzarigradsko Chaussee, 1784 Sofia, Bulgaria

The ac magnetization and the microwave surface resistance (at 12 GHz) were measured on a series of Na-doped YBCO ceramic samples at 77 K. Their magnetic behavior was explained on the basis of the modified critical state model by taking into account the existence of a field-dependent component J_{c1} (due to weakly linked grains) and a field-independent component J_{c0} (due to perfectly linked grains) in the bulk critical current density of the samples. The Na and Cu remaining after the heat treatment of the samples changed the intergranular medium parameters and impeded the correlation between the grains. As a result, an increase of the Na concentration led to a decrease of the specimens critical current density and an increase of their surface resistance. At small Na concentrations, a certain increase of J_{c1} was observed, which can be explained by taking into account the possibility of partial pinning of Josephson vortices in the "weakly seeded" places in the intergranular media.

I. INTRODUCTION

The magnetic behavior of the YBCO ceramics is largely dominated by processes in the intergranular medium, and described in the framework of the modified critical state model[1,2] by taking into account the field dependence of the mean intergranular critical current density J_c. A particular form for the field dependence is usually assumed, and then the fitting parameters, corresponding to the components of the critical current density and the scaling field, are obtained from a comparison of the model calculation with the measured data.[3,4] The microwave losses in such samples are mainly determined by intergranular coupling whose efficiency depends on the properties of the intergranular medium.[5,6] The presence of some metals during the YBCO synthesis affects the properties of the intergranular medium[7] of the end product. One should expect as a result a modification of the magnetic and microwave parameters of these samples as compared with the undoped ones.

This paper deals with experimental investigation and interpretation of the changes in the magnetic and microwave characteristics of YBCO ceramic samples prepared in the presence of a Na additive.

II. EXPERIMENTAL

The samples were produced using the general formula $Y_{1-0.2x}Ba_{2-0.2x}Na_{0.4x}Cu_{3+0.3x}O_y$, where x varies from 0 to 2.00, which allows an overstoichiometric presence of Na_2O and traces of CuO on the grain boundaries in the YBCO ceramics.

The presence of Na_2CO_3 during the sintering process enabled us to obtain a highly homogeneous structure with low grain size. The physical measurements were carried out on disk-shaped samples with a thickness of about 1 mm and a diameter about 9 mm. To study a sample's screening properties, we placed the sample in an ac magnetic field (1 kHz) and the response signal was registered by an almost flat coil (ϕ 1.5×0.5 mm^2) located at the center of the high-temperature superconducting (HTSC) pellet. The screening parameter N was found by taking the ratio of the signal's amplitude measured at superconducting ($T=77$ K) and normal ($T=295$ K) state of the specimen. The surface resistance at 77 K was measured by means of Cu resonator structures formed on a thin dielectric substrate, with the HTSC pellet serving as a ground plate.[7]

To perform the critical current measurements, ϕ 1×9 mm^2 cylinders were cut from HTSC disks. The pick-up coil was tightly wound around the sample, and a phase-sensitive device was used to record the response signal.

III. INTERPRETATION OF THE MAGNETIC BEHAVIOR

To interpret the magnetic behavior of the ceramic sample at low magnetic fields (≤3 mT) the existence of two kinds of the intergranular contacts in the sample must be taken into account.[1-9] The local macroscopic intergranular critical current density J_{c1} for the weakly coupled grains nearly exponentially decreases with increasing of the local magnetic field[3,4] H, while the local macroscopic "bulk" critical current density J_{c0} remains unchangeable for the perfectly coupled grains.[9] By taking into account this, we assumed the following field dependence for the critical current density J_c in our samples

$$J_c = J_{c0} + J_{c1}/ch(H/H_c), \tag{1}$$

where H_c is the scaling field. When the external magnetic field H_α decreases from its maximum H_m to its minimum $-H_m$, the following solution of the critical state equation can be obtained:

$$h_1 - h_m - C\ \ln[(e^{h_m}+A)(e^{h_1}+D)/(e^{h_m}+D)(e^{h_1}+A)] = J(x-1) \quad 0 \leq x \leq x_t, \tag{2}$$

 0021-8979/94/76(10)/7118/3/$6.00 © 1994 American Institute of Physics

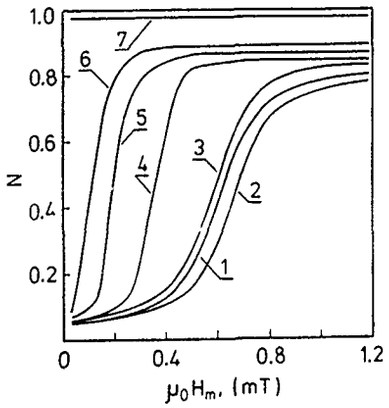

FIG. 1. The screening parameter N vs the magnetic field amplitude H_m for Na-doped YBCO pellets ($\phi 1\times 9$ mm^2) measured at 77 K. Curves 1–7 correspond to samples with initial Na concentrations $x=0$, 0.4, 0.75, 0.95, 1.2, 1.5, and 2, respectively.

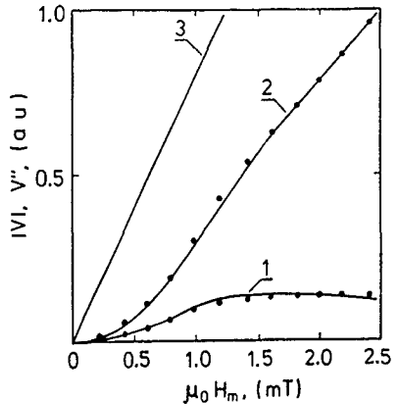

FIG. 2. Dependence of the response signal modulus (2) and the out-of-phase component (1) on the external-field amplitude H_m for a Na-doped ($x=0$ 4) YBCO sample ($\phi 1\times 9$ mm^2) measured at 77 K. The theoretical curves 1 and 2 (solid) are obtained by taking into account the J_c vs H dependence described by Eq. (1). The values of the fitting parameters are given in Table I. Curve 3 presents the $|V|$ vs H_m dependence for a sample in normal state (100 K).

$$h_2-h_\alpha-C\ \ln[(e^{h_\alpha}+A)(e^{h_2}+D)/(e^{h_\alpha}+D)(e^{h_2}+A)]$$
$$=-J(x-1)\quad x_i\leqslant x\leqslant 1, \tag{3}$$

where $h_1=H_1/H_c$ and $h_2=H_2/H_c$ are the dimensionless internal magnetic fields: $h_m=H_m/H_c$; $h_\alpha=H_\alpha/H_c$; $J=J_{c0}R/H_c$; $A=k+(k^2-1)^{1/2}$; $D=k-(k^2-1)^{1/2}$; $C=k/(k^2-1)^{1/2}$; $k=J_{c1}/J_{c0}>1$; $x=r/R$, r is the radial coordinate; $x_i=r_i/R$ is the dimensionless coordinate where the shielding current changes its direction and $H_1(x_i)=H_2(x_i)$. By solving Eqs. (2) and (3), one can find the magnetic field profile in the sample and calculate the total magnetic flux ϕ which penetrates it. For a harmonic external field $H_\alpha=H_m\cos(\omega t)$ (where ω is the angular frequency), the basic component of the total magnetic flux ϕ_ω can be expressed as follows:

$$\phi_\omega=\phi'_\omega\cos(\omega t)-\phi''_\omega\sin(\omega t)$$
$$=\pi R^2H_m(\mu'\cos(\omega t)-\mu''\sin(\omega t)$$
$$=\pi R^2H_m[(\chi'+1)\cos(\omega t)-\chi''\sin(\omega t)], \tag{4}$$

where ϕ'_ω and ϕ''_ω are the in-phase and out-of-phase components of the magnetic flux, which can be obtained from $\phi(t)$ by means of a Fourier transform; μ', μ'', χ', and χ'' are the real and imaginary components of the specimen's dynamic permeability and susceptibility. Signals proportional to $|\phi_\omega(H_m)|$, $\phi'_\omega(H_m)$, and $\phi''_\omega(H_m)$ are registered experimentally. Further, by comparing such theoretical and experimental dependences, one can find the optimal values of the parameters J_{c0}, J_{c1}, H_c corresponding to the real specimen characteristics.

IV. RESULTS AND DISCUSSION

Figure 1 presents the dependence of the screening coefficient N of HTSC pellets with various Na-additive amounts on the amplitude H_m of the external ac magnetic field. In specimens with small amounts ($x\leqslant 0.75$), the magnetic field begins to penetrate the intergranular medium at $\mu_0H\approx 0.5$ mT. A field of $\mu_0H\approx 1.0$ mT leads to a decrease in the intergranular critical current density and destroys the screening properties of the central zones of the pellet. At stronger fields $\mu_0H\geqslant 2.0$ mT, the screening effect is only due to the small number of "loops" consisting of perfectly linked grains and to the diamagnetism of the grains. The field starts penetrating the grains at $\mu_0H_g\geqslant 4.5$ mT. An estimate of the critical current density for the grains J_g using the above value for the field H_g (for YBCO at 77 K, the London penetration depth is ≈ 0.3 μm) yields $J_{cg}\sim H_g/\lambda\approx 10^6$ A/cm^2, a value typical for single-crystal YBCO samples. A worsening of the pellets screening properties is observed for higher initial Na concentrations ($x\geqslant 0.75$), but no noticeable drop of H_g is seen. This means that within the concentrations interval indicated ($0\leqslant x\leqslant 1.5$), the Na affects mainly the electrical parameters of the intergranular boundaries. At $x=2$, however, the sample becomes "transparent" to the magnetic field ($N\approx 0.97$) due to the strong suppression of the superconductivity in the grain themselves.

To determine the critical current density J_c, we used cylindrically shaped specimens with $R\approx 0.5$ mm. The dependences of the pick-up coil voltages modules $|V(H_m)|\sim|\phi_\omega(H_m)|$ and the out-of-phase component $V''(H_m)\sim\phi''_\omega(H_m)$ on the amplitude H_m of the external magnetic field was experimentally registered (Fig. 2). The values of the specimen's effective static permeability μ_c usually are 0.5–0.6. The initial value of J_{c0} was then found through fitting the theoretical dependence $|V(H_m)|$ (calculated for $J_{c1}=0$, the expressions are given in Ref. 8) to the experimental one measured at relatively large H_m values so that the contribution of the weak links current to the response signal is small but, at the same time, the field does not penetrate the grains. For the initial H_c value we assumed half of the field value which totally suppresses the weak link current. Further, the initial value of J_{c1} was obtained by fitting the theoretically calculated $|V(H_m)|$ dependence [Eqs. (1)–(4)] to the experimental one. The last procedure was then repeated with each of the parameters J_{c0}, J_{c1}, H_c varying within certain limits until good agreement was reached between the theo-

TABLE I. Characteristics of YBCO samples.

x	J_{c0} (A/cm^2)	J_{c1} (A/cm^2)	$\mu_0 H_c$ (mT)	R_s (mΩ) (f_0=12 GHz)
0	45	145	0.70	45
0.40	45	180	0.70	50
0.75	36	140	0.70	55
0.95	30	123	0.55	65
1.20	20	83	0.40	78
1.50	10	28	0.20	100

retical and experimental $|V(H_m)|$ and $V''(H_m)$ dependences. The sample characteristics found as described are presented in Table I.

Specimens with small Na-additive amounts ($x \approx 0.4$) exhibit some increase of the weak link critical current density J_{c1}, while the other two parameters J_{c0} and H_c stay practically unchanged. A further increase of the Na amount results in a decrease of all YBCO sample parameters and in their complete degradation at $x=2$. The behavior of the bulk sample electrical parameters is related to the properties of the intergranular boundaries. The critical current density J_c for a single-tunnel Josephson junction is proportional to the junction parameters Δ (the energy gap parameter) and R_n (the normal-state tunneling resistance).[6] $J_c \propto \Delta^2/R_n$. The R_n parameter is strongly affected by the distance between the junction boundaries.[6] After the heat treatment, the Na and Cu compounds are predominantly located on the surface of the YBCO grains and form a "surface layer" that can be characterized by a dielectric constant ϵ and a conductivity σ. A rise in the Na concentration leads to a drop in the critical current density at the expense of either an R_n increase (for an intergranular medium with $\sigma \approx 0$) or a gap parameter suppression (for an intergranular medium with $\sigma \gg 0$). Such a behavior of J_c, J_{c0}, and H_0 was in fact observed in YBCO for Na concentrations $x>0.75$. For small Na concentrations ($x \leqslant 0.75$), this "seeding" of the intergranular boundaries by Na compounds is insignificant. The small increases of the critical current density in the latter case can be explained by the possible pinning of Josephson vortices at the "seeded" points in the intergranular space.

The surface resistance R_s of the pellets increased with increasing x. If one assumes that the sample consists of weak links (i.e., the grain contribution to R_s is small), its surface resistance at weak fields will be proportional to $\omega^2\sigma/\lambda_J^3$, where λ_J is the Josephson penetration depth.[6] On the other hand, $\lambda_J \sim J_c^{-1/2}$, and, therefore, the surface resistance of the samples should increase as their critical current density decreases. Such a relationship is well observed experimentally in samples with $x \geqslant 0.75$; at smaller Na concentrations the R_s variation with x is not significant.

V. CONCLUSION

In the present work, the results are presented of measurements of the screening parameter N, the critical current density J_c, and the surface resistance R_s of YBCO samples prepared from initial batches containing various amounts of Na. The behavior of the intergranular critical current density J_c is interpreted by taking into account the presence of both weakly linked grains and of a small number of perfectly linked grains. The values of J_c and the behavior of its dependence on the field are determined by solving numerically the critical state equation and comparing the results with the experimental data. It is demonstrated that the Na and Cu compounds remaining in the samples after the heat treating process are predominantly located on the surface of the YBCO grains and impedes the correlation between the grains. As a result, an increase of the Na concentration leads to a decrease of the specimens' critical current density and an increase of their surface resistance. However, at low Na concentrations ($x<0.75$), a certain positive effect is observed in what concerns the critical current density J_c; this is probably related to the possibility of partial pinning of Josephson vortices in the "weakly seeded" places on the boundaries.

[1] H. Dersch and G. Blatter, Phys. Rev. B **38**, 11391 (1988).
[2] V. Calzona, M. R. Cimberle, C. Ferdeghini, M. Putti, and A. S. Siri, Physica C **157**, 425 (1989).
[3] T. B. Doyle and R. A. Doyle, Cryogenics **32**, 1019 (1992).
[4] G. E. Gough, M. S. Colclough, D. A. O'Connor, F. Wellhofer, N. McN. Alford, and T. W. Button, Cryogenics **31**, 119 (1991).
[5] N. McN Alford, T. W. Button, G. E. Peterson, P. A. Smith, L. E. Davis, S J. Penn, M. J. Lancaster, Z. Wu, and J. C. Gallop, IEEE Trans. Magn. **MAG-27**, Part II, 1510 (1991).
[6] K. K. Likharev, *Introduction to the Dynamic of the Josephson Junctions* [Moscow, "Nauka" (in Russian) 1985].
[7] I. Nedkov, A. Veneva, S. Miteva, T. Nurgaliev, and V. Lovchinov, IEEE Trans. Magn. **30**, 1187 (1994).
[8] R. B. Goldfarb, M. Lelental, and C. A. Thomson, *Alternating-Field Susceptometry and Magnetic Susceptibility of Superconductors* (Plenum, New York, 1992).

Properties of polycrystalline samples of $Nd_{2-x}Ce_xCuO_{4-y}$ obtained from a sol-gel precursor

V. B. Barbeta[a] and R. F. Jardim
Instituto de Física, Universidade de São Paulo, CP20516, 01452-990, São Paulo, SP, Brazil

L. Ben-Dor
Department of Inorganic and Analytical Chemistry, Hebrew University, Jerusalem 91904, Israel

M. B. Maple
Department of Physics and Institute for Pure and Applied Physical Sciences, UCSD, La Jolla, California 92093-0075

Polycrystalline samples of $Nd_{2-x}Ce_xCuO_{4-y}(0.0\leq x\leq 0.17)$ obtained from a sol-gel precursor were sintered below the eutectic temperature and reduced under different conditions. From the results of x-ray powder diffraction, the tetragonal T' structure is preserved for Ce content up to $x=0.17$. A decrease in the lattice parameter c and a small increase in the lattice parameter a are observed with increasing Ce concentration. Electrical resistance $R(T)$ measurements performed on reduced samples with $x\geq 0.12$ reveal superconducting behavior below $T\approx 25$ K. We also found that all reduced samples display a striking double resistive superconducting transition and that the zero resistance state is achieved through two distinct drops in $R(T)$ at upper and lower transition temperatures T_{ci} and T_{cj}. The upper transition temperature T_{ci} has a maximum for Ce concentration $x=0.14$, which is independent of the reduction process. The lower transition temperature T_{cj} is observed in reduced samples with Ce content $x\geq 0.14$ and decreases monotonically with increasing Ce concentration. Magnetic susceptibility measurements confirm bulk superconductivity in several reduced samples, and a significant diamagnetic contribution is only observed for temperatures below T_{cj}. The results are discussed within the framework of a granular superconductor model.

The discovery of superconductivity in compounds of $Ln_{2-x}M_xCuO_{4-y}$(Ln=Nd, Sm, Pr, Eu; M=Ce, Th)[1-5] has stimulated an intense effort in the study of their physical properties. Many features of these oxides are well known, although some fundamental aspects are either still not understood or controversial.

One of the doubts about these compounds concerns the quality of the samples studied. Usually, high quality samples with the same starting composition and subject to almost the same reduction process behave differently.[6] Some important questions regarding this situation are related to the doping process, i.e., the replacement of the Ln by Ce and the removal of oxygen which are necessary to induce superconductivity. As far as Ce doping is concerned, it is still somewhat controversial whether materials prepared in the range $0\leq x\leq 0.17$ actually form a solid solution. Based on x-ray diffraction analysis, Cava and collaborators[7] concluded that samples of $Nd_{2-x}Ce_xCuO_{4-y}$ $(0.0\leq x\leq 0.17)$ are true solid solutions. On the other hand, Lightfoot and collaborators[8] believe that there is only one superconducting phase in this range with a Ce content close to $x=0.165$.

Besides this structural issue, other points remain to be addressed. One of them is related to the nature of the double resistive superconducting transition which is frequently observed in $R(T)$ measurements and is identified by two sharp drops in the electrical resistivity before the zero resistance state is attained. It has been proposed by Peng *et al.*[9] that the double superconducting transition is due to the presence of two distinct superconducting phases, each with a different superconducting critical temperature. Another explanation for this feature assumes that the sample is composed of small superconducting islands connected through Josephson coupling.[10-12] By assuming this picture, the first transition is related to the intragrain transition while the second one is believed to be due to the coupling between the islands through Josephson junctions. The present work provides some new information regarding structural, magnetic, and transport properties of these electron-doped superconductors.

Polycrystalline samples of $Nd_{2-x}Ce_xCuO_{4-y}$ were prepared with a wide range of Ce concentrations $0.0\leq x\leq 0.17$ by means of the sol-gel process. Details of this chemical route for producing polycrystalline samples are discussed elsewhere.[12] The samples were sintered at 1000 °C, which is below the eutectic temperature of ≈1050 °C. Reduction was carried out under different conditions. This step is important in order to induce superconductivity in these materials, and it was performed in flowing He gas for 20 h at 950 °C, followed by fast cooling. We have prepared three different batches of samples: (1) unreduced samples, (2) samples cooled in 1 h after the reduction process, and (3) samples cooled in 2 h after the reduction process. Unreduced samples showed no evidence of superconductivity, while reduced samples showed superconductivity for Ce concentrations in the range $0.12<x<0.17$. All samples were analyzed by x-ray powder diffraction using a Rigaku RU-200B diffractometer. The x-ray patterns showed that the tetragonal T' structure (Nd_2CuO_4 type structure) is preserved for Ce content up to $x=0.17$ and no vestiges of additional phases have been found in any sample studied. The lattice parameters were obtained through the refinement of the corrected peaks utilizing a least-squares program. Magnetization measurements were performed using a commercial superconducting quantum interference device (SQUID) magnetometer from Quan-

[a]On a CNPq (Brazil) fellowship.

 0021-8979/94/76(10)/7121/3/$6.00 © 1994 American Institute of Physics

TABLE I. Lattice parameters a and c as a function of Ce concentration in polycrystalline samples of $Nd_{2-x}Ce_xCuO_{4-y}$, $0.0 \leqslant x \leqslant 0.17$.

x	a (Å)	c (Å)
0.00	3.948(1)	12.17(4)
0.05	3.948(9)	12.15(4)
0.08	3.949(4)	12.12(9)
0.10	3.949(7)	12.11(8)
0.14	3.950(4)	12.09(9)
0.15	3.950(6)	12.08(9)
0.17	3.950(9)	12.07(7)

tum Design. Electrical resistance measurements were performed with a Linear Research LR-400 ac impedance bridge operating at 16 Hz with variable excitation current.

The x-ray diffraction patterns for polycrystalline samples of $Nd_{2-x}Ce_xCuO_{4-y}$, $0.0 \leqslant x \leqslant 0.17$, showed, within our resolution, no vestiges of additional phases. The powder diffraction data have been used to extract the lattice parameters a and c for different Ce concentrations. These results are summarized in Table I. A careful observation of these results shows that the lattice parameter c decreases with increasing Ce content from $c=12.17(4)$ Å for Nd_2CuO_4 to $c=12.07(7)$ Å for the highest Ce concentration $x=0.17$. Also, from the results of Table I, one can see that the lattice parameter a is almost insensitive to the replacement of Nd by Ce. The dependence of the c lattice parameter on Ce concentration suggests that Ce substitutes for Nd in the T' structure. Such a replacement seems to be in complete agreement with the formation of a true solid solution and not, for example, with phase separation. This is supported by the fact that no drastic change in the lattice parameter c is observed, i.e., it decreases smoothly with increasing Ce content. This conclusion is in agreement with the proposition made by Cava *et al.*,[7] who have observed behavior similar to that shown in Table I for both lattice parameters. In addition, a very broad distribution of values for the lattice parameter c for $x \approx 0.15$ has been detected. If one assumes that there is no phase separation when Nd is replaced by Ce, as proposed by Lightfoot, *et al.*,[8] this means that the presence of the nonsuperconducting phases in these compounds needs to be explained by invoking another variable of these systems: the removal of oxygen. It is possible that the removal of oxygen of about 0.02 per formula introduces a defect structure in this series, generating two different regions within the samples, one of which is superconducting and the other of which is nonsuperconducting. Similar structural defects have been observed in polycrystalline samples of $La_{1.8}Sr_xCa_{1.2-x}Cu_2O_{6-y}$,[13] La_2NiO_{4-y},[14] and $La_2CuO_{4\pm y}$.[15]

The presence of at least one superconducting phase in these polycrystalline samples is somewhat reflected in macroscopic measurements such as electrical resistance and magnetic susceptibility. In order to place this in perspective, the temperature dependence of the electrical resistance and magnetic susceptibility has been measured in all samples described above. Typical curves of $R(T)$ and $\chi(T)$ are displayed in Fig. 1, which shows data for $Nd_{1.83}Ce_{0.17}CuO_{4-y}$ cooled in 2 h after the reduction process. It is evident that the $R(T)$ curve displays a double resistive superconducting transition in which the electrical resistance shows two abrupt drops in magnitude when the sample is cooled below 25 K. Such a feature has frequently been observed in these electron-doped superconductors[10–12] for samples with $x \geqslant 0.14$. For the sample shown in Fig. 1, the first drop in $R(T)$ occurs at an upper temperature $T_{c1} \approx 17$ K. At this temperature, a broad decrease of about 30% in the magnitude of $R(T)$ is observed down to a lower temperature $T_{cJ} \approx 6$ K, where a second sharper decrease in $R(T)$ occurs. This feature has been explained by assuming that these samples are comprised of two different phases: one which is superconducting and another one which is believed to be nonsuperconducting. When the temperature falls below T_{c1}, the superconducting transition takes place and a drop of about 30% in $R(T)$ is frequently observed. Below this temperature, the system does not attain the zero resistance state because the superconducting volume fraction is below the percolation threshold. In the temperature range between T_{c1} and T_{cJ} the samples are believed to be comprised of superconducting islands embedded in a nonsuperconducting host. At a lower temperature T_{cJ}, Josephson coupling takes place and the zero resistance state is usually achieved.[10–12]

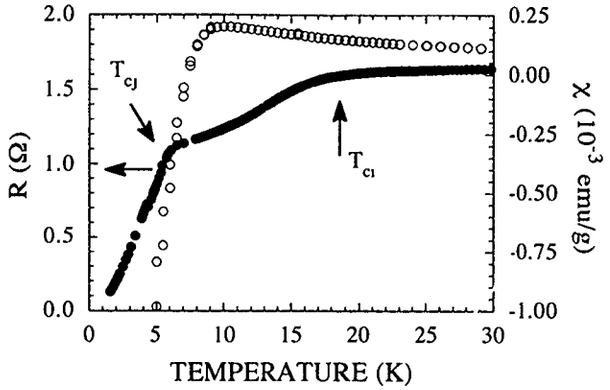

FIG. 1. Typical curves of $R(T)$ and $\chi(T)$ obtained on polycrystalline samples of $Nd_{2-x}Ce_xCuO_{4-y}$. These curves correspond to measurements performed on the sample with $x=0.17$ and cooled in 2 h after the reduction process. Arrows denote T_{c1} and T_{cJ} obtained from electrical resistance curves.

We believe that the brief discussion given above invalidates the presence of two superconducting phases in these electron-doped superconductors. If this were the case, the transition at T_{cJ} should not be very sensitive to changes in the excitation current and the application of a small magnetic field. However, several experimental results for these compounds reveal that below T_{cJ}, $\rho(T)$ is strongly dependent on these variables.[10–12] These results suggest that Josephson coupling develops at T_{cJ} and yield no evidence of two superconducting phases in this series.

Figure 1 is also useful for discussing the temperature dependence of the magnetic susceptibility in these compounds. Careful inspection of Fig. 1 reveals that significant diamagnetism only occurs below T_{cJ}. In fact, it is observed that the magnetic susceptibility is still increasing below T_{c1}, showing a paramagnetic-like behavior. When the temperature T_{cJ} is reached a transition occurs and the diamagnetic

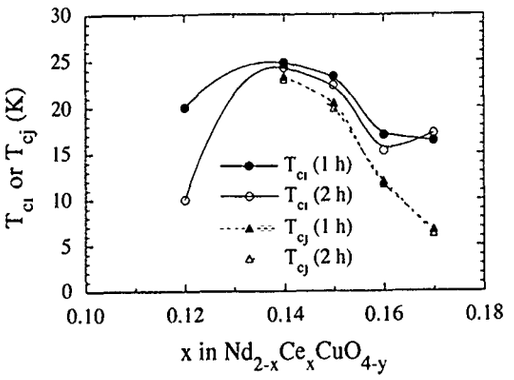

FIG. 2. Compositional dependence of T_{ci} and T_{cj} in a series of polycrystalline samples of $Nd_{2-x}Ce_xCuO_{4-y}$, $0.12 \leqslant x \leqslant 0.17$. The figure displays results obtained in two series cooled in either 1 or 2 h after the reduction process.

contribution becomes appreciable. The absence of appreciable diamagnetism between T_{ci} and T_{cj} indicates that superconducting properties must be confined to small regions, comparable with the London penetration depth. In fact, several results on polycrystalline samples of electron-doped superconductors are satisfactorily explained by assuming that superconducting properties are confined to small islands with typical size of 10–300 Å.[16–18]

Also of interest is the dependence of both T_{ci} and T_{cj} on Ce content in the $Nd_{2-x}Ce_xCuO_{4-y}$ series, $0.0 \leqslant x \leqslant 0.17$, which is shown in Fig. 2. From observations of Fig. 2 one can note that the transition temperature T_{ci} shows a maximum at $x=0.14$ and decreases at higher Ce concentration. It is also observed that T_{ci} is almost independent of cooling rate for $x \geqslant 0.14$ and is affected by the reduction process for $x=0.12$. On the other hand, the Josephson coupling temperature T_{cj} is almost insensitive to the reduction process in the Ce range studied. The qualitative behavior of T_{cj} obtained from electrical resistance measurements is in complete agreement with recent data of Singh *et al.*[19] even though they obtained T_{cj} from ac magnetic susceptibility measurements. This can be explained on the basis of the ac magnetic susceptibility data in this series that shows only one diamagnetic contribution which occurs at the Josephson coupling temperature.[16] In fact, our results for T_{ci} reveal remarkable differences with those of Ref. 19. They have observed from the electrical resistivity measurements that T_{ci} is almost constant for $0.14 \leqslant x \leqslant 0.17$. Our results show that T_{ci} has a maximum of ≈ 25 K at $x=0.14$ and decreases significantly for higher Ce content to 18 K for $x=0.17$. These discrepancies must be related to the sample preparation method used for making these materials.

From our results for $R(T)$ and $\chi(T)$ on polycrystalline samples of $Nd_{2-x}Ce_xCuO_{4-y}$, $0.0 \leqslant x \leqslant 0.17$, the behavior of these materials can be understood by using a model of a disordered array of small superconducting islands coupled through Josephson junctions. This is particularly evident from electrical resistivity measurements which show the striking double resistive superconducting transition. When the temperature decreases, the intergrain transition takes place and a drop in the magnitude of $R(T)$ is observed. This drop is not enough to drive the system to the zero resistance state, probably due to the very low superconducting volume. Additional decrease in temperature promotes the coupling of these superconducting islands below T_{cj}. At this temperature, the superconducting regions are believed to be coupled by Josephson effect and usually the system shows zero resistance. Due to the small size of these islands, comparable to the London penetration depth, an insignificant diamagnetic contribution to the susceptibility is observed between T_{ci} and T_{cj}. These superconducting islands become coupled together through Josephson junctions below T_{cj} and the diamagnetic contributions is appreciable.

In summary, we have performed x-ray powder diffraction, electrical resistance, and magnetic susceptibility measurements on polycrystalline samples of $Nd_{2-x}Ce_xCuO_{4-y}$, $0.0 \leqslant x \leqslant 0.17$, prepared from a sol-gel precursor. All of our x-ray results seem to agree with the proposition of Cava *et al.*,[7] since we have found no evidence of phase separation in this series. In addition, the macroscopic behavior of $R(T)$ and $\chi(T)$ can be fully explained by the assumption that all samples are comprised of small superconducting islands connected through Josephson junctions.

We have benefited from stimulating discussions with D. Stroud. This work was supported by the Brazilian Agency FAPESP Under Grants No. PD-EXT 91/2743-0 and 93/4204-4. Work at San Diego was supported by the DOE (USA) under Grant No. DE-FG03-86ER45230. One of us (RFJ) acknowledges support from the Brazilian Agency CNPq Under Grant No. 304647/90-0.

[1] Y. Tokura, H. Takagi, and S Uchida, Nature (London) **337**, 245 (1989).
[2] H. Takagi, S. Uchida, and Y Tokura, Phys. Rev. Lett. **67**, 1197 (1989).
[3] J T. Markert, E. A. Early, T. Björnholm, S. Ghamaty, B. W. Lee, J. J. Neumeier, R. D. Price, C. L. Seaman, and M. B. Maple, Physica C **158**, 178 (1989).
[4] J. T. Markert and M. B Maple, Solid State Commun. **70**, 145 (1989).
[5] E. A. Early, N. Y. Ayoub, J. Beille, J. T. Markert, and M. B. Maple, Physica C **160**, 320 (1989)
[6] C. Geibel, A. Vierling, P. V. Aken, R. Eichert, A Gravel, M. Rau, S. Horn, G. Weber, and F. Steglich, Physica C **185-189**, 591 (1991)
[7] R. J. Cava, H. Takagi, R. M. Fleming, J. J. Krajewski, W. F. Pech Jr., P. Bordet, M. Marezio, B. Batlogg, and L. W. Rupp, Jr., Physica C **199**, 65 (1992).
[8] P Lightfoot, D. R. Richards, B. Dabrowski, D. G Hinks, S. Pei, D. T. Marx, A. W. Mitchell, Y. Zheng, and J. D. Jorgensen, Physica C **168**, 627 (1990).
[9] J. L Peng, Z. Y. Li, and R. L Green, Physica C **177**, 79 (1991)
[10] E. A. Early, C. C. Almasan, R. F. Jardim, and M. B Maple, Phys. Rev. B **47**, 433 (1993).
[11] V B. Barbeta, C. H. Westphal, R. F. Jardim, M. B. Maple, and X. Obradors, J. Appl. Phys. **73**, 6639 (1993)
[12] R. F. Jardim, L Ben-Dor, and M B. Maple, J. Alloys Compounds **199**, 105 (1993)
[13] H. Shaked, J. D Jorgensen, B. A Hunter, R. L. Hitterman, K. Kinoshita, F Izumi, and T. Kamiyama, Phys Rev. B **48**, 12941 (1993).
[14] J. M. Tranquada, D J Buttrey, and D. E. Rice, Phys Rev. Lett. **70**, 445 (1993)
[15] P. G. Radaelli, J. D. Jorgensen, R. Kleb, B. A. Hunter, F. C Chou, and D. C. Johnston, Phys. Rev. B **49**, 6239 (1994).
[16] R F. Jardim, C. H. Westphal, C H. Cohenca, L. Ben-Dor, and M. B. Maple, J. Appl Phys. **75**, 6720 (1994).
[17] R. F Jardim, M. C. de Andrade, E. A. Early, M. B. Maple, and D. Stroud (unpublished).
[18] R. F Jardim, L. Ben-Dor, D Stroud, and M. B. Maple, Phys. Rev. B (in press).
[19] O. G. Singh, B. D. Padalia, O. Prakash, K Suba, A. V Narlikar, and L C. Gupta, Physica C **219**, 156 (1994)

Magnetic ordering of Pr in $Pb_2Sr_2PrCu_3O_8$

W. T. Hsieh, W-H. Li, and K. C Lee
Department of Physics, National Central University, Chung-Li, Taiwan 32054, Republic of China

J. W. Lynn
Reactor Radiation Division, National Institute of Standards and Technology, Gaithersburg, Maryland 20899

J. H. Shieh and H. C. Ku
Department of Physics, National Tsing Hua University, Hsinchu, Taiwan 300, Republic of China

The magnetic ordering of the Pr ions in $Pb_2Sr_2PrCu_3O_8$ has been studied using neutron-diffraction and ac-suspectibility measurements. An imperfect three-dimensional magnetic ordering of the Pr spins was observed at a temperature well below its Neel temperature of $T_N \approx 7$ K. The magnetic intensities observed at $T=1.4$ K can be explained by assuming long-range order in the *ab* plane with short-range correlations, of correlation length $\xi_c=20$ Å, along the *c* axis and a moment directed along the *c*-axis direction. The magnetic ordering is 2D in nature, and the basic magnetic structure consists of nearest-neighbor spins that are aligned antiparallel along all three crystallographic directions. The magnetic transition is also evident in the ac-susceptibility versus temperature measurements, where a cusp that is typical of antiferromagnetic ordering is clearly observed, which matches the T_N obtained by neutron diffraction.

Just like other high-T_c oxides, $Pb_2Sr_2PrCu_3O_8$ (Pr 2:2:1:3) also possesses a layered structure. From the crystallographic structural point of view, the major difference between Pr 2:2:1:3 and $PrBa_2Cu_3O_7$ (Pr 1:2:3) is the number of layers stacked along the *c*-axis direction. The structure of the former can be obtained by replacing the CuO-chain layer in the latter with two PbO layers and one Cu layer.[1] This replacement results in even more anisotropic physical properties for the 2:2:1:3 systems than for the 1:2:3 systems. The rare-earth atoms in the 2:2:1:3 systems form an orthorhombic sublattice, where $a \approx b$ and the nearest-neighbor distance along the *c* axis is more than four times that in the *ab* plane. It is thus clear that the crystallographic anisotropy naturally leads to highly anisotropic magnetic interactions, and two-dimensional (2D) behavior can be expected.

The 3D long-range ordering of the Pr spins has been observed in both the Pr 1:2:3 and $TlBa_2PrCu_2O_7$ (Pr 1:2:1:2) systems with anomalously high ordering temperatures.[2,3] Numerous observations have indicated that hybridization plays an important role in the Pr magnetism. If this is the case we should then expect the effect along the *c*-axis direction to be much reduced in the Pr 2:2:1:3 system compared to the Pr 1:2:3 and Pr 1:2:1:2 systems, simply because of its wider spacing along the *c* axis. The Pr 2:2:1:3 system is then a better candidate for observing the 2D character of the Pr ordering. In this paper we report an imperfect 3D ordering of the Pr spins observed in Pr 2:2:1:3. The Pr spins ordered at 7 K, nevertheless even at $T=1.4$ K, the correlations between the Pr spins along the *c*-axis direction are still short range. The basic magnetic structure consists of Pr spins that are aligned antiparallel along all three crystallographic directions. The antiferromagnetic ordering of the Pr spins is also evident in the ac-susceptibility versus temperature measurements, where a cusp, typical of antiferromagnetic ordering, in the χ_{ac} vs T curve is clearly evident.

A powder sample of $Pb_2Sr_2PrCu_3O_8$ was prepared by the standard solid-state reaction technique, and the details can be found elsewhere.[4] Both x-ray and high-resolution neutron diffraction were used to characterize the sample. The nearest-neighbor distances between the Pr atoms that we obtained at room temperature were 3.815(1) Å and 15.765(4) Å in the *ab* plane and along the *c*-axis direction, respectively. The nominal oxygen concentration determined from neutron profile refinement analysis was 8.01(2). During the course of the low-temperature neutron-diffraction experiment, the sample was sealed in a cylindrical holder filled with helium exchange gas to promote thermal conduction at low temperatures. A pumped ^{4}He cryostat was used to cool the sample, and the lowest temperature achieved was 1.4 K.

Neutron-diffraction measurements were performed at the Research Reactor at the U.S. National Institute of Standards and Technology. The data were collected using the BT-9 triple-axis spectrometer operated in double-axis mode. The incoming neutrons had a wavelength of 2.352 Å defined by a pyrolytic graphite PG(002) monochromator, with a PG filter placed after the monochromator position for suppressing higher-order wavelength contaminations. The angular collimations used were 40′ in front of the monochromator, and 48′-48′ before and after the sample position, respectively. No analyzer crystal was used in these measurements.

The magnetic signal was isolated from the nuclear one by subtracting the data collected at high temperatures from the data taken at low temperatures.[5] Figure 1 shows the magnetic Bragg peaks thus obtained at $T=1.4$ K, where the diffraction pattern taken at $T=15$ K, serving as the nonmagnetic "background," has been subtracted from the data. The indices shown are based on the Pr chemical unit cell. The underlying spin structure of Pr hence consists of the nearest-neighbor spins that are aligned antiparallel along all three crystallographic directions. This is the same type of spin structure found in Pr 1:2:3[2] and Pr 1:2:1:2.[3]

The widths of the observed magnetic peaks are much broader than the instrumental resolution, which indicates a short-range ordering of the Pr spins. Short-range correlations along the *c*-axis direction and long-range correlations within the *ab* plane can be expected, since the nearest-neighbor dis-

 0021-8979/94/76(10)/7124/3/$6.00 © 1994 American Institute of Physics

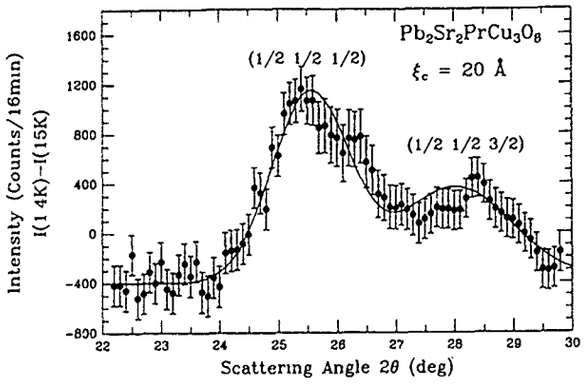

FIG. 1. Magnetic intensities observed in $Pb_2Sr_2PrCu_3O_8$ at $T=1.4$ K, where the indices shown are based on the Pr chemical unit cell. The Pr spins order antiferromagnetically along all three crystallographic directions. The solid curve is a fit to the data assuming long-range order in the *ab* plane and a short-range correlation length $\xi_c=20$ Å along the *c* axis.

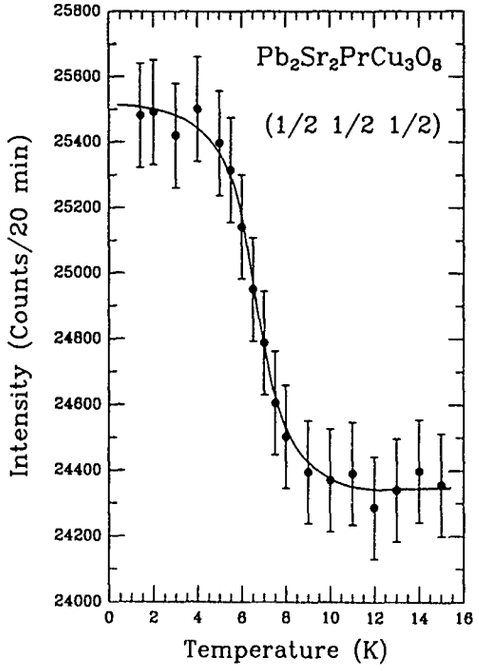

FIG. 2. Temperature dependence of the $\{\frac{1}{2}\frac{1}{2}\frac{1}{2}\}$ peak intensity. The data reveal a typical order parameter with an ordering temperature of $T_N\approx7$ K. The solid curve is only a guide to the eye.

tance along the *c* axis is more than four times that in the *ab* plane. The solid line shown in Fig. 1 is a fit to the theoretical curve, assuming long-range correlations in the *ab* plane and short-range correlations, with a correlation length $\xi_c=20$ Å, along the *c* axis and a moment pointed along the *c*-axis direction. In generating the fitted curve we adopt Warren's approach [6] of averaging the scattered intensity for a 2D powder sample over all possible orientations in reciprocal space, and in addition allow for the presence of finite correlations along the third axis.[7] In comparison with the Pr ordering in Pr 1:2:3 and Pr 1:2:1:2, the Pr-Pr coupling remains antiferromagnetic and the 2D character becomes more pronounced in Pr 2:2:1:3 likely due to the larger spacing between the Pr-Pr atoms along the *c* axis. This crystallographic character results in a reduction of the hybridization between the Pr ions that are mediated through the copper-oxygen layers between them.

Figure 2 shows the temperature dependence of the $\{\frac{1}{2}\frac{1}{2}\frac{1}{2}\}$ peak intensity, and reveals a typical order parameter with a Neel temperature of $T_N\approx7$ K. This ordering temperature of the Pr spins is a factor of 2 smaller than that found in Pr 1:2:3:7 ($T_N\approx17$ K) and is close to that found in Pr 1:2:1:2 ($T_N\approx8$ K). The ordering temperature of Pr is still much too high for purely dipolar interactions to explain.

The ac-susceptibility measurements were performed using a Lake Shore 7221 ac susceptometer. Data were collected with an alternating magnetic field of strength 1 Oe and frequency 250 Hz. A portion of the real part of the measured $\chi_{ac}(T)$ is shown in Fig. 3(a), and the temperature dependence of its derivative $d\chi_{ac}/dT$ is shown in Fig. 3(b). The magnetic transition is clearly seen with a $T_N\approx7$ K determined to be at the relative minimum in the $d\chi_{ac}/dT$ vs T plot. A cusp in the χ_{ac}-T curve, which is typical of antiferromagnetic ordering,[8] is also evident. These results are consistent with that obtained from neutron-diffraction measurements. We note that negative values for χ_{ac} were obtained on the high-temperature side shown in Fig. 3(a). This is due to the Meissner diamagnetism of the superconducting state present in the compound. The interplay between the Pr magnetism and superconductivity is the subject in a separate study.[9]

In conclusion, we have studied the magnetic ordering of the Pr spins in Pr 2:2:1:3 by neutron-diffraction and ac-susceptibility measurements. At $T=1.4$ K, which is well below the observed ordering temperature of $T_N\approx7$ K, an im-

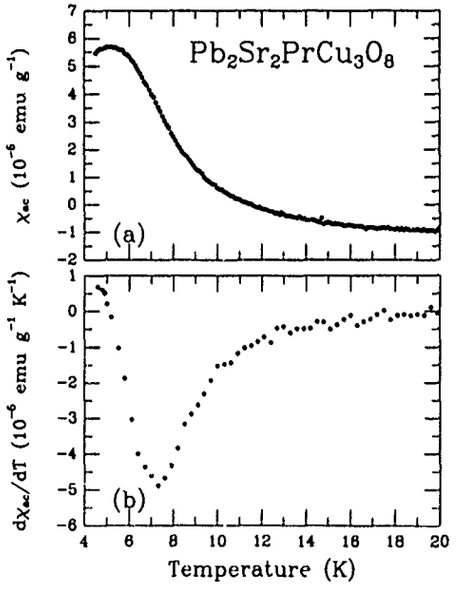

FIG. 3 A portion of the measured ac susceptibility $\chi_{ac}(T)$ and its temperature derivative $d\chi_{ac}/dT$ plotted against temperature. The transition temperature is determined to be at the relative minimum in the $d\chi_{ac}/dT$ vs T plot, which gives $T_N\approx7$ K. This T_N is consistent with the ordering temperature obtained from the data shown in Fig. 2.

perfect 3D ordering of the Pr spins was observed, with long-range correlations in the *ab* plane and short-range correlations along the *c* axis. The 2D behavior is believed to arise naturally from the crystallographic structure, and results in a reduction of the hybridization between the Pr ions in the present system. The ordering temperature observed is still much too high for purely dipolar and RKKY interactions may be anticipated.

The Tb ions in the isostructural compound Tb 2:2:1:3 were found[10] to order at $T_N \approx 5.5$ K. Even at $T = 1.4$ K the ordering of the Tb spins is still purely 2D without any correlation found along the *c* axis. It is then clear that, in the 2:2:1:3 system the coupling between the Pr atoms is much stronger than between the Tb atoms along all three crystallographic directions. Moreover, short-range correlations between the Pr spins have also been observed[11] in the $PrBa_2Cu_3O_{6.2}$ compound, which suggests that the oxygen concentration may also have important influence on the Pr hybridization along the *c* axis. A study of the effects of the oxygen concentration on the Pr ordering in the 2:2:1:3 system should give further information on the nature of the Pr hybridization.

The research at the NCU was supported by the National Science Council of the Republic of China under Grant No. NSC-83-0212-M-008-001, and was partially supported by the NCU Physics Department under Grant No. PHYS83-01. The research at the NTHU was supported by the National Science Council of the Republic of China under Grant No. NSC-83-0212-M-007-069.

[1] R. J. Cava, B. Batlogg, J. J. Krajewski, L. W. Rupp, L. F Schneemeyer, T. Siegrist, R. B. vanDover, P Marsh, W. F. Peck, Jr., P. K. Gallagher, S H. Glarum, J. H. Marshall, R. C. Farrow, J. V Waszczak, R Hull, and P. Trevor, Nature **336**, 211 (1988).
[2] W-H. Li, J. W. Lynn, S. Skanthakumar, T. W. Clinton, A. Kebede, C-S. Jee, J. E. Crow, and Mihalism, Phys Rev. B **40**, 5300 (1989)
[3] W. T. Hsieh, K. J. Chang, W-H. Li, K. C Lee, J. W. Lynn, and H C Ku, Phys. Rev. B **49**, 12200 (1994).
[4] H. C. Ku, C. C. Lai, J. H Shieh, J. W Liou, C. Y. Wu, and J. C. Ho, Physica B **199&200**, 252 (1994).
[5] G. E. Bacon, *Neutron Diffraction* (Oxford, Bristol, 1975).
[6] B. E. Warren, Phys. Rev. **59**, 693 (1941).
[7] H Zhang, J. W. Lynn, W-H. Li, T. W Clinton, and D. E. Morris, Phys. Rev. B **41**, 11229 (1990).
[8] C. Kittel, *Introduction to Solid State Physics* (Wiley, Singapore, 1986).
[9] W-H. Li, W. T. Hsieh S T Shyr, K C. Lee, J H Shieh, and H. C Ku, Physica B (to be published).
[10] S. Y. Wu, W. T. Hsieh, W-H Li, K. C. Lee, J. W. Lynn, and H. D. Yang, J. Appl. Phys. **75**, 6598 (1994).
[11] M Guillaume, P. Fischer, B. Roessli, A. Podlesnyak, J. Schefer, and A Furrer, Solid State Commun. **88**, 57 (1993)

Annealing temperature and O_2 partial pressure dependence of T_c in $HgBa_2CuO_{4+\delta}$

Q. Xiong, Y. Cao, F. Chen, Y. Y. Xue, and C. W. Chu
Department of Physics, Texas Center for Superconductivity at the University of Houston, Houston, Texas 77204-5932

Samples of $HgBa_2CuO_{4+\delta}$ (Hg-1201) were annealed under various conditions. After carefully controlling annealing time, annealing temperature (T_a), and O_2 partial pressure (P_0), we were able to find the reversible annealing conditions for Hg-1201. Under 1 atm O_2 at 260 °C$\leqslant T_a \leqslant$400 °C, the obtained T_c is nearly the same (~97 K). However, it decreases quickly with T_a>300 °C in high vacuum ($P_0 \sim 10^{-8}$ atm), and reaches zero at T_a=400 °C. On the other hand, T_c decreases with the decrease of T_a in high-pressure O_2 (~500 atm) and reaches ~20 K at about 240 °C. In the entire annealing region, the oxygen surplus varies significantly from 0.03 to 0.4, and a wide range of T_c variation (0→97 K→20 K) was obtained with anion doping alone.

Hg-1201 has a very simple crystal structure[1] and the highest T_c (~97 K at the optimal doping level) among all the single CuO_2-layer high-temperature superconductors (HTSs). Its simplicity makes it an ideal system for use in verifying theoretical models. For this purpose, doped samples with a wide T_c range to cover both the insulator-superconductor transition on the underdoped side and the superconductor-metal transition on the overdoped side are desirable. Many groups around the world raced to achieve that by annealing the as-synthesized samples in reduced or oxygenated gases. However, only limited results have been reported so far, partially due to Hg loss in this compound at elevated temperatures. Wagner *et al.*[2] reached T_c~50 K through reducing annealing in Ar at 500 °C. Itoh *et al.*[3] report at high-pressure O_2 annealing only produced a moderate change of T_c (~85 K on the overdoped side). The search for a wider T_c range has been obstructed by the decomposition of the compound above 500 °C. By studying the stability and the oxygen balance conditions, we explored a much wider annealing temperature-oxygen pressure region. The reversible annealing conditions were established. We obtained underdoped samples with T_c as low as zero (insulator) and heavily overdoped samples with T_c~20 K. In other words, the obtained samples cover nearly the whole insulator-superconductor-normal metal phase region. This enables us to further study the superconductivity of this compound in detail.

Hg-1201 samples were prepared by reacting a precursor pellet of Ba_2CuO_x and a composite Hg source. The precursor pellet is obtained by mixing appropriate amounts of BaO and CuO in an alumina crucible in a flowing mixed gas of Ar:O at a ratio of 4:1 at 930 °C for a total of 24 h with intermittent grinding once every 8 h. The composite Hg source used in this study was a prereacted Hg 1:2:0:1 pellet made by compacting the thoroughly mixed HgO and pulverized precursor powder. A small precursor pellet and a large composite Hg source are sealed inside an evacuated quartz tube, heated to about 810 °C and kept at this temperature for 8 h before being cooled to room temperature. Samples with different oxygen content were obtained by heating the as-synthesized samples at different temperatures and oxygen partial pressures for appropriate periods of time. Underdoped samples were prepared by heating the sample in vacuum at temperatures between 250 and 500 °C for 20–80 h. Overdoped samples were obtained by heating the as-synthesized compound for 10–240 h at temperatures between 240 and 400 °C and at an oxygen pressure that was between 1 and 500 bar. The structure was characterized by x-ray powder diffraction (XRD) and neutron powder diffraction (NPD). T_c were determined by both the dc magnetic susceptibility method using a Quantum Design superconducting quantum interference device (SQUID) magnetometer and the electrical resistivity method using the standard four-probe technique.

We knew beforehand that there are two things which may effect the T_c of Hg-1201, oxygen content and mercury loss. We tried to find annealing conditions which allowed any changes in sample structure and T_c to remain reversible. We found that long annealing times and high temperatures lead to mercury loss and sample decomposition. Figure 1(a)

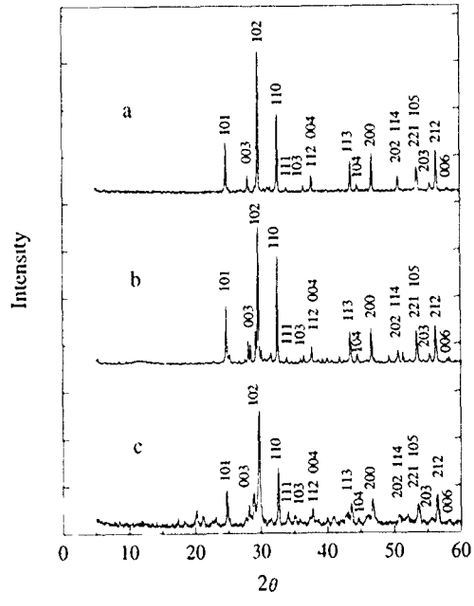

FIG 1 (a) The indexed x-ray powder diffraction pattern of a typical as-synthesized Hg-1201 sample (b) The XPD pattern of a Hg-1201 sample after 20 h of 500 °C Ar annealing (c) The XPD pattern of a Hg-1201 sample after four days of 500 °C Ar annealing.

 0021-8979/94/76(10)/7127/3/$6.00 © 1994 American Institute of Physics

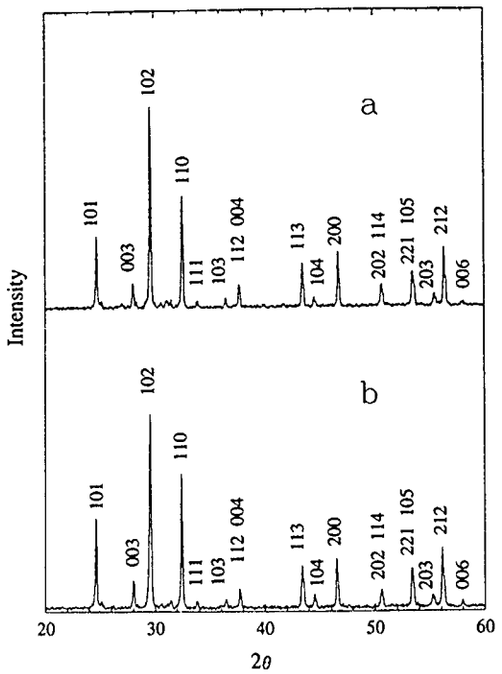

FIG. 2. (a) The XPD pattern of a Hg-1201 sample before annealing (b) The XPD pattern of a Hg-1201 sample after three days of vacuum annealing at 400 °C.

is the data taken from a sample immediately after it was synthesized. It is almost single phase. Figure 1(b) is data taken from a sample after annealing in Ar at 500 °C for 20 h. A small amount of impurities show up. Figure 1(c) is data taken from a sample after annealing in Ar at 500 °C for about four days. Many impurities now appear. After carefully controlling annealing time and temperature, we were able to find the reversible annealing conditions for Hg-1201. Some typical x-ray data are shown in Fig. 2. Figure 2(a) was taken before annealing and Fig. 2(b) was taken after three days of annealing in vacuum at 400 °C. These data indicate that the sample still had a single Hg-1201 phase after the anneal. The slight shift in the peaks was caused by the change in lattice parameters that arose from the change in oxygen content of the sample. It is clear that the change in structure is reversible under these conditions.

Figure 3 shows resistivity data for one of our samples. Line 1 is data taken from the sample immediately after it was synthesized. Line 2 is data taken after a 240 °C, high-pressure ($P=500$ bar) anneal. After this, we annealed the sample again in one atmosphere of oxygen at 300 °C. Resistivity data taken after this second annealing are plotted here as line 3. These data show that the change in T_c was reversible and the T_c drop was caused by oxygen doping alone. The small transition broadening and change in resistivity were probably due to mercury loss between boundaries. The Meissner effect of this sample, which is shown in the inset of Fig. 3, is also consistent with this point.

The reversible annealing conditions are summarized in Fig. 4. The annealing time t, which should be long enough to let oxygen reach an equilibrium state but avoid significant Hg loss, is about 10–240 h, depending on the annealing en-

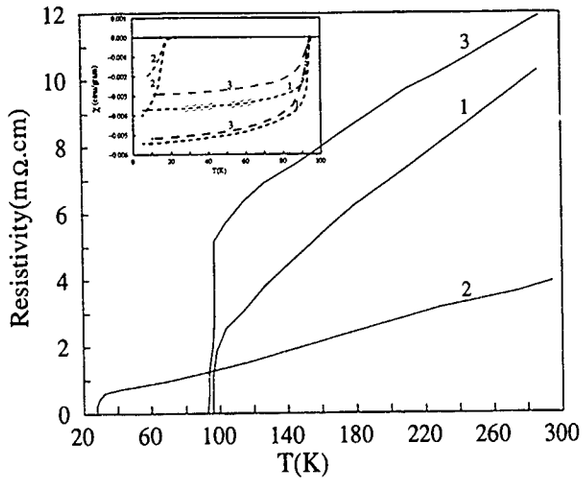

FIG. 3. Typical resistivity data taken from our Hg-1201 samples. Line 1 was taken immediately after the sample was synthesized. Line 2 shows data taken after a 240 °C, high-pressure ($P=500$ bar) anneal. Line 3 was taken after an anneal in 1 atm of oxygen at 300 °C.

vironment. The T_c corresponding to the desired T_a- $\log P_0$ conditions are obtained by interpolation. From the thermodynamic viewpoint an increase in annealing temperature should result in a decrease in oxygen content if the oxygen partial pressure is held constant. An increase in oxygen content should result from an increase in oxygen partial pressure if the annealing temperature is kept constant. When the sample is annealed in vacuum (10^{-8} atm) T_c decreases when the oxygen content decreases. This indicates that the sample is in its underdoped region. T_c increases with increasing annealing temperature when the sample is annealed in high-pressure oxygen ($5\times10^{+2}$ atm). This means that the sample is in the overdoped region. T_c is nearly the same over the range 250–400 °C in 1 atm of pure O_2. We were able to obtain T_c's ranging from 0 in the underdoped region to 97 K (optimal), then back down to 20 K in the overdoped region. According to an earlier study,[4] when the oxygen partial pressure is changed from 1 to 10^{-5} atm the oxygen content changes by about 0.4 for Y123. This means that the oxygen content is sensitive to the oxygen partial pressure in

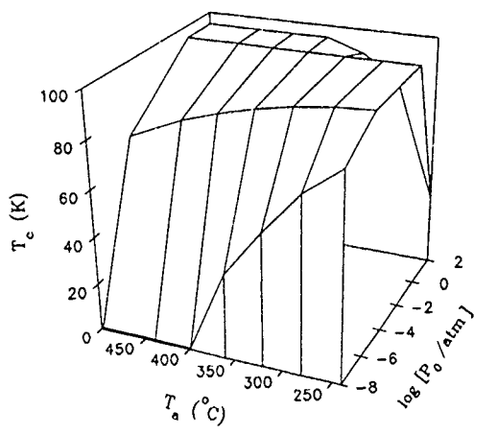

FIG. 4 3-D T_c vs (T_a, $\log P_0$) for Hg-1201.

$YBa_2Cu_3O_{7-\delta}$ (Y123). Comparing the annealing conditions with our thermogravimetric analysis and NPD results,[5] we found that when P_0 changes from $5\times10^{+2}$ to 10^{-8} atm, δ changes by about 0.4. This shows that the δ range is $0<\delta<0.4$, which is similar to that in Y123 but depends only weakly on P_0, which contrasts with Y123. The carrier concentration p has been determined, based on the room-temperature thermoelectric power and roughly follows $p\sim0.72\delta$; details will be published elsewhere.[5]

In summary, we have explored the reversible annealing conditions for Hg-1201 and obtained a T_c that covers the widest variation ever by anion doping only. Though the δ range in Hg-1201 is similar to that in Y123 we found that the sensitivity of δ to changes in oxygen partial pressure is much smaller than in Y123.

This work is supported by NSF Grant No. DMR-91-22043, NASA Grant No. NAGW-977, Texas Center for Superconductivity at the University of Houston, and the T.L.L. Temple Foundation.

[1] S. N. Putilin, E. V. Antipov, O. Chmaissem, and M. Marezio, Nature **362**, 226 (1993).
[2] J. L. Wagner, P. G. Radaelli, D. G. Hinks, J. D. Jorgensen, J. F. Mitchell, B. Dabrowski, G. S. Knapp, and M. A. Beno, Physica C **210**, 447 (1993).
[3] M. Itoh, A. Tokiwa-Yamamoto, S. Adachi, and H. Yamauchi, Physica C **212**, 271 (1993).
[4] T. B. Lindermer, J. F. Hunley, J. E. Gates, A. L Sutton, J. Brynestad, C. R. Hubbard, and P. K. Gallagher, J. Am. Ceram. Soc. **72**, 1775 (1989).
[5] Q. Xiong *et al.* (unpublished).

Penetration of electromagnetic fields into superconductors with gradual resistive transition

I. D. Mayergoyz
Electrical Engineering Department and Institute for Advanced Computer Studies, University of Maryland, College Park, Maryland 20742

The penetration of electromagnetic fields into superconductors is studied for the case of gradual resistive transition described by the "power law." Simple self-similar solutions are first found, which are then used to further generalize the Bean (critical state) model of superconducting hysteresis.

It is well known that models for superconducting hysteresis are based on the analytical study of penetration of electromagnetic fie! ıo hard superconductors. In the critical state model,[1,2] this study is performed under the assumption of ideal (sharp) resistive transition. However, actual resistive transitions are gradual and it is customary to describe them by the following power law:

$$E=\left(\frac{J}{k}\right)^n \quad (n>1), \tag{1}$$

where E is electric field, J is current density, and k is some parameter which coordinates the dimensions of both sides in expression (1).

The exponent "n" is a measure of the sharpness of the resistive transition and it may vary in the range 4–1000. Initially, the power law was regarded only as a reasonable empirical description of the resistive transition. Recently, there has been a considerable research effort to justify this law theoretically. As a result, models based on Josephson-junction coupling,[3] sausaging,[4] and spatial distribution of critical current[5] have been proposed. In the paper, the power law is used as a constitutive equation for hard superconductors. It is easy to show (by using Maxwell's equations) that this constitutive relation leads to the following nonlinear partial differential equation for the current density:

$$\frac{\partial^2 J^n}{\partial z^2}=\mu_0 k^n \frac{\partial J}{\partial t}. \tag{2}$$

We shall first consider the solution of this equation for the following boundary and initial conditions:

$$J(0,t)=ct^p, \quad (t\geq 0, p>0), \tag{3}$$

$$J(z,0)=0 \quad (z>0). \tag{4}$$

It is worthwhile to note here that the choice of the above boundary conditions is dictated by considerations of finding simple analytical solutions. It may seem at first that these boundary conditions are of very specific nature. However, it can be remarked that these boundary conditions do describe a wide class of monotonically increasing functions as p varies from 0 to ∞ (see Fig. 1). It will be shown below that for all these boundary conditions the profile of electric current density as a function of z remains practically the same. This observation will suggest to use the same profile of electric current density for arbitrary monotonically increasing boundary conditions. This will result in very simple analytical solutions.

The initial-boundary value problem (2)–(4) can be reduced to the boundary value problem for an ordinary differential equation. This reduction is based on the dimensionality analysis of Eqs. (2) and (3). This analysis leads to the conclusion that the following variable is dimensionless:

$$\zeta=\frac{z}{t^m\sqrt{k^{-n}\mu_0^{-1}c^{n-1}}}, \tag{5}$$

where

$$m=\frac{p(n-1)+1}{2}. \tag{6}$$

By using this dimensionless variable, we look for the self-similar solution of initial boundary value problem (2)–(4) in the form

$$J(z,t)=ct^p f(\zeta), \tag{7}$$

where $f(\zeta)$ is a dimensionless function of ζ. By substituting Eq. (7) into Eq. (2), after simple transformations we end up with the following ordinary differential equation:

$$\frac{d^2 f^n}{d\zeta^2}+m\zeta\frac{df}{d\zeta}-pf=0 \tag{8}$$

It is apparent that $J(z,t)$ given by expression (7) will satisfy boundary and initial conditions (3) and (4) if f satisfies the boundary conditions:

$$f(0)=1, \tag{9}$$

$$f(\infty)=0. \tag{10}$$

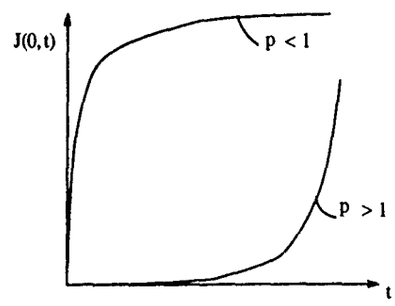

FIG. 1 Boundary conditions for the current density

 0021-8979/94/76(10)/7130/3/$6.00 © 1994 American Institute of Physics

Thus, the initial-boundary value problem (2)–(4) is reduced to the boundary value problem (8)–(10) for the ordinary differential Eq. (8). It can be proven that this nonlinear differential equation has the following group property: if $f(\zeta)$ is a solution to Eq. (8), then

$$F(\zeta)=\lambda^{-2/(n-1)}f(\lambda\zeta) \tag{11}$$

is also a solution to this equation for any constant λ. This property can be utilized as follows. Suppose that we have solution $f(\zeta)$ to Eq. (8) which satisfies the boundary condition (10), however

$$f(0)=a\neq 1. \tag{12}$$

Then, by using $\lambda=a^{n-1/2}$, we find that

$$f(\zeta)=\frac{1}{a}f(a^{(n-1)/2}\zeta) \tag{13}$$

is the solution to Eq. (8) which satisfies Eq. (10) as well as Eq. (9). Thus, we can first find a solution to Eq. (8) subject to boundary condition (10), then, by using transformation (11), we can map this solution into the solution which also satisfies the boundary condition (9).

It can be shown[6] that a solution to Eq. (8) satisfying the boundary condition (10) has the form

$$f(\zeta)=\begin{cases} b(1-\zeta)^{1/(n-1)}[1+b_1(1-\zeta)+b_2(1-\zeta)^2+\cdots], \\ \quad \text{if } 0\leq\zeta\leq 1, \\ 0, \quad \text{if } \zeta>1. \end{cases} \tag{14}$$

By substituting Eq. (14) into Eq. (8), after simple but lengthy transformations, we find

$$b=\left[\frac{m(n-1)}{n}\right]^{1/(n-1)}, \tag{15}$$

$$b_1=\frac{p(n-1)-m}{2mn(n-1)}, \tag{16}$$

$$b_2=-b_1\,\frac{1+\frac{1}{2}b_1[(2n-1)(3n-2)-4n]}{3(2n-1)}. \tag{17}$$

It is clear that

$$f(0)=b(1+b_1+b_2+\cdots)\neq 1. \tag{18}$$

This difficulty is overcome by using transformation (11) with

$$\lambda=[b(1+b_1+b_2+\cdots)]^{(n-1)/2}. \tag{19}$$

This leads to the following solution of the boundary value problem (8)–(10):

$$f(\zeta)=\begin{cases} (1-\lambda\zeta)^{1/(n-1)}\,\dfrac{1+b_1(1-\lambda\zeta)+b_2(1-\lambda\zeta)^2+\cdots}{1+b_1+b_2+\cdots}, \\ \quad \text{if } 0\leq\lambda\zeta<1, \\ 0, \quad \text{if } \lambda\zeta>1. \end{cases} \tag{20}$$

The last expression can be simplified by exploiting the fact that the exponent n in the power law is usually greater than 4. This simplification can be accomplished by using the following inequalities for b_1 and b_2 which can be easily derived from Eqs. (6), (16) and (17):

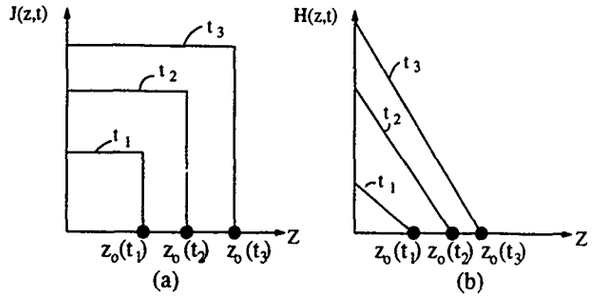

FIG. 2. Distributions of electric current density and magnetic field inside the superconducting half-space.

$$|b_1|\leq\frac{1}{2n(n-1)}, \tag{21}$$

$$|b_2|\leq\frac{1}{6(n-1)(2n-1)n}+\frac{1}{8(n-1)n}. \tag{22}$$

From the above inequalities, for $n\geq 4$ we find

$$|b_1|\leq 0.042, \quad |b_2|\leq 0.006. \tag{23}$$

This suggests the following simplification of solution (20):

$$f(\zeta)=\begin{cases} (1-\sqrt{m(n-1)/n}\,\zeta)^{1/(n-1)}, \\ \quad \text{if } 0\leq\zeta<\sqrt{n/m(n-1)}, \\ 0, \quad \text{if } \zeta>\sqrt{n/m(n-1)}. \end{cases} \tag{24}$$

By substituting Eq. (24) into Eq. (7) and taking into account Eq. (5), we end up with the following analytical expression for the current density:

$$J(z,t)=\begin{cases} ct^p\left(1-\dfrac{z}{dt^m}\right)^{1/(n-1)}, & \text{if } z\leq dt^m, \\ 0, \quad \text{if } z\geq dt^m, \end{cases} \tag{25}$$

where

$$d=\sqrt{(nc^{n-1})/[\mu_0 k^n m(n-1)]}\,. \tag{26}$$

The close examination of self-similar solution (25) leads to the following conclusion: in spite of the wide range of variation of boundary conditions (3) (see Fig. 1), the profile of electric current density $J(z,t)$ remains approximately the same. For typical values of n (usually $n\geq 7$), this profile is very close to a rectangular one. This suggests that the actual profile of electric current density will be close to a rectangular one for any monotonically increasing boundary condition $J_0(t)=J(0,t)$. Thus, we arrive at the following generalization of the critical state model.

Current density $J(z,t)$ has a rectangular profile with the height equal to the instantaneous value $J_0(t)$ of electric current density on the boundary of superconductor (see Fig. 2). Magnetic field $H(z,t)$ has a linear profile with a slope determined by instantaneous value of $J_0(t)$.

To better appreciate the above generalization, we remind that in the critical state model the current has a rectangular profile of constant (in time) height, while the magnetic field has a linear profile with constant (in time) slope.

For the zero front of the profile we have

$$z_0(t)=\frac{H_0(t)}{J_0(t)}. \tag{27}$$

However, $H_0(t)$ and $J_0(t)$ are not simultaneously known. For this reason, we intend to find $J_0(t)$ in terms of $H_0(t)$. To this end, we multiply Eq. (2) by z and integrate from 0 to $z_0(t)$ with respect to z and from 0 to t with respect to t. After simple transformations, we arrive at the following expression:

$$\mu_0 k^n \int_0^{z_0(t)} zJ(z,t)dz=\int_0^t J_0^n(\tau)d\tau. \tag{28}$$

By using in Eq. (28) the rectangular profile approximation for $J(z,t)$, we obtain

$$\frac{\mu_0 k^n}{2} J_0(t)z_0^2(t)=\int_0^t J_0^n(\tau)d\tau. \tag{29}$$

By substituting Eq. (27) into Eq. (29), we find

$$\frac{\mu_0 k^n}{2}\frac{d}{dt}\left[\frac{H_0^2(t)}{J_0(t)}\right]=J_0^n(t). \tag{30}$$

By introducing a new variable

$$\gamma(t)=\frac{H_0^2(t)}{J_0(t)}, \tag{31}$$

we can represent Eq. (30) as the following differential equation with respect to $\gamma(t)$:

$$\frac{d\gamma^{n+1}}{dt}=\frac{2(n+1)}{\mu_0 k^n} H_0^{2n}(t). \tag{32}$$

By integrating Eq. (32) and by using Eq. (31), we arrive at the following expression for $J_0(t)$:

$$J_0(t)=\frac{H_0^2(t)}{\{[(2(n+1)/\mu_0 k^n)]\int_0^t H_0^{2n}(\tau)d\tau\}^{1/(n+1)}}. \tag{33}$$

By substituting Eq. (33) into Eq. (27), we find the following expression for zero front $z_0(t)$ in terms of the magnetic field, $H_0(t)$, on th. boundary of superconductor:

$$z_0(t)=H_0(t)\left[\frac{2(n+1)}{\mu_0 k^n}\int_0^t H_0^{2n}(\tau)d\tau\right]^{1/(n+1)}. \tag{34}$$

This concludes our discussion of penetration of electromagnetic fields into superconductors with gradual resistive transition.

The reported research has been supported by the U.S. Department of Energy, Engineering Research Program.

[1] C. P. Bean, Phys. Rev. Lett. **8**, 250 (1962).
[2] H. London, Phys Lett. **6**, 162 (1963)
[3] C. S. Nichols and D. R. Clarke, Acta Metall. Matter **39**, 995 (1991)
[4] J. W. Elkin, Cryogenics **2**, 603 (1987).
[5] C. J. G. Plummer and J. E. Evetts, IEEE Trans. Magn. **MAG-23**, 1179 (1987).
[6] G. I. Barenblatt, Prikl. Math. Mekn (in Russian) **16**, 67 (1952).

Study of the frequency and low-field dependence of ac susceptibility in YBaCuO

M. Zazo, L. Torres, J. Iñiguez, C. de Francisco,[a] and J. M. Muñoz[a]
Departamento de Física Aplicada, Universidad de Salamanca, E-37071 Salamanca, Spain

The frequency dependence of the ac susceptibility in polycrystalline samples of YBaCuO has been studied at the ac field range 0.06–1.2 Oe. The curve of the real part of the susceptibility χ' exhibits two drops, the first one close to T_c and the other well below T_c which could correspond to screening behavior of the grains and grain boundaries, respectively. The imaginary part of the susceptibility shows only a peak below T_c which is related to hysteresis losses at the grain boundaries. The peak corresponding to intragrains hysteresis losses is very small and appears masked by the losses of the intergrains. In the range of 1–20 kHz, the onset temperature of χ' showed no frequency dependence. However, the width of the transition decreases lightly and there is a small shift in the peak of χ'' to higher temperature as the frequency increases. This behavior could be explained in terms of the thermally activated Anderson flux creep. The shift depends on the amplitude of the measuring field. The activation energy for flux creep ranges from 6.4 eV at 0.02 Oe to 3.23 eV at 1.2 Oe in the zero-field-cooled measurements and from 3.41 eV at 0.02 Oe to 1.41 eV at 1.2 Oe in the field-cooled measurements.

I. INTRODUCTION

The ac-susceptibility method is one of the conventional methods used to study the properties of high-T_c superconductors (HTCSs).[1–5] In this paper, we present measurements of the zero-field-cooled and field-cooled ac susceptibility of HTCS samples as a function of the temperature, frequency, and ac magnetic field amplitude. The real part of the susceptibility χ' shows two drops and the imaginary exhibits only a peak. This peak is attributed to hysteresis losses at the intergrains. The peak corresponding to the intragrain is masked by the intergrain losses or is negligibly small in the frequency and field measuring range. The susceptibility shows strong dependence with ac magnetic field as well as with the measuring frequency. There is a small shift in the peak towards higher temperatures with increasing frequency in the 1–20 kHz range. However, the peak shifts to lower temperatures when the ac magnetic field increases from 0.02 to 1.2 Oe. These properties seem related to the dynamics of magnetic field flux motion in HTCS materials which is not yet completely understood.

The variation of the susceptibility with the frequency could be explained in terms of the flux creep at the grain boundaries. We have studied the behavior with the frequency following the Anderson theory[6] for conventional type-II superconductors, in which a flux vortex can jump the pinning barrier (flux creep) by means of the thermally activated phenomena. This effect is thought to be small in conventional type II superconductors with lower critical temperature, but at the considerably higher temperatures of HTCS it can be important. We calculate the flux creep activation energies at the grain boundaries in polycrystalline YBaCuO by the Anderson's model. As a reference point for specifying the temperature shifts with the frequency and the field we have used the temperature of the peak in χ''.

[a]Dpto. de Electricidad, Univ. de Valladolid, E-47071 Valladolid, Spain.

II. EXPERIMENTAL DETAILS

Polycrystalline samples of $YBa_2Cu_3O_x$ were prepared by the usual solid-state sintering method using CuO, $BaCO_3$, and Y_2O_3 as precursor materials. The ac susceptibility was measured by the mutual inductance method with the applied ac magnetic field parallel to the long axis of the specimen by means of a controlled current of variable frequency in the coil (5). Secondary voltage of a mutual induction is related to the susceptibility χ of the sample under test. Both the real χ' and imaginary part χ'' components of the complex susceptibility can be determined from the coil signal by phase sensitive techniques, such as a lock-in amplifier detector. However, we have measured directly the complex mutual inductance by a LCZ bridge:

$$\overline{M} = \frac{|Z|}{\omega}\text{sen}\left(\varphi+\frac{\pi}{2}\right)+j\frac{|Z|}{\omega}\cos\left(\varphi+\frac{\pi}{2}\right), \tag{1}$$

where $|Z|$ is the module of the impedance and φ is the phase angle measured by the bridge, and ω is the angular frequency. We can derive the two components of the ac permeability as

$$\mu' = -\frac{|Z|}{\omega K}\text{sen}\ \varphi, \tag{2}$$

$$\mu'' = -\frac{|Z|}{\omega K}\cos\ \varphi, \tag{3}$$

where K is a calibration coefficient for the coil geometry. The ac permeability components are related to the susceptibility terms as $\mu' = 1+\chi'$ and $\mu'' = \chi''$.

Zero-field-cooled measurements were made by cooling the sample at 77 K without any field while in the field-cooled measurement the sample was cooled under dc magnetic field (220 Oe) parallel to the long axis of the specimen and then the field was switched off. In both cases the measurements were taken while warming up the sample from 77 K to temperature over T_c in an ac field ranging from 0.02 to 1.6 Oe for frequencies from 1 to 20 kHz.

 0021-3979/94/76(10)/7133/3/$6.00 © 1994 American Institute of Physics

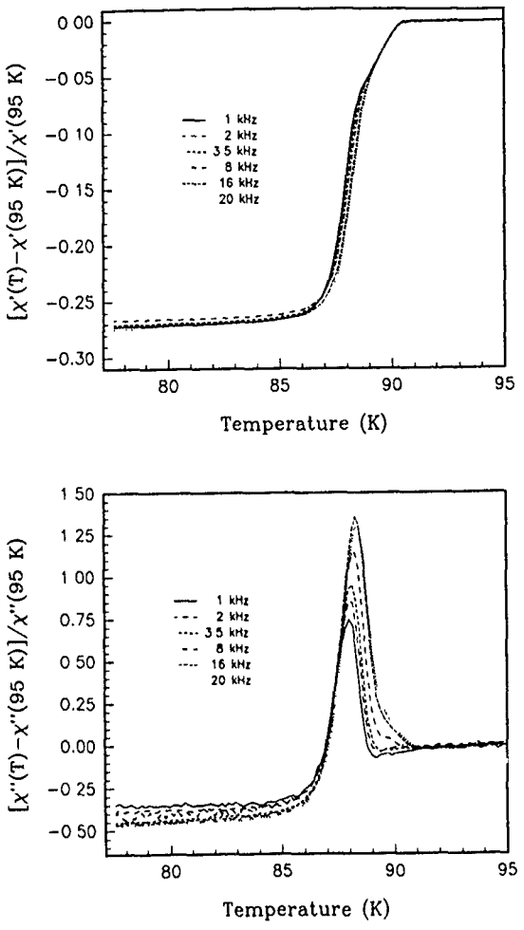

FIG. 1. χ vs temperature at different frequencies (h_{ac}=0.06 Oe).

III. RESULTS AND DISCUSSION

The susceptibility of the samples shows a typical dependence on temperature in which we can see two drops in the curve of the real part of the zero-field-cooled susceptibility χ_{zfc} (Fig. 1). In its turn, the curve of the imaginary part exhibits a peak corresponding to the drop in the lower-temperature region of χ_{zfc}, while the peak close to T_c associated with the intragrain losses is masked by the intergrain peak or it is very small (Fig. 1). The field-cooled susceptibility χ_{fc} presents similar results but the width of the diamagnetic transition in χ' increases, the peak broadens and the maximum of the χ'' shifts to lower temperatures.

Frequency dependence has been studied in the range 1–20 kHz at different ac magnetic fields parallel to the long axis of the specimen. The onset temperature of χ' was not modified by rising the frequency, however, the width of transition in χ' decreased lightly and there was a shift in the peak of χ'' to higher temperatures (Fig. 1). This seems a clear indication that the amount of magnetic flux penetrating the superconductor decreases with increasing frequency.

We have also studied the dependence with the ac magnetic field of the susceptibility of the samples in the range 0.02–1.2 Oe. The critical onset temperature of the diamagnetic transition does not change when increasing the magnetic field. However, the saturation of diamagnetic transition

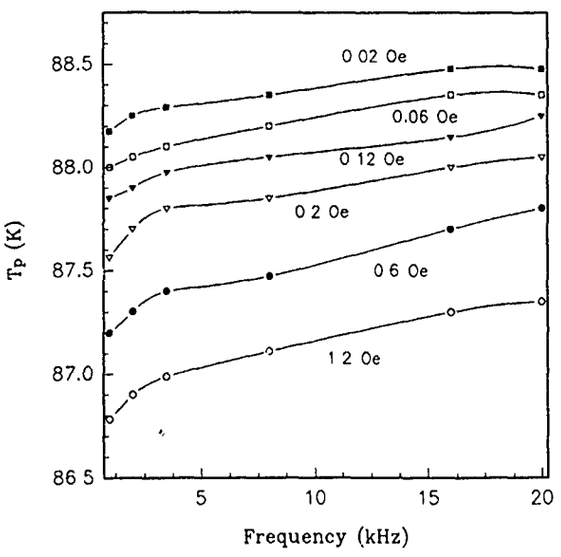

FIG. 2. T_p vs frequency at different ac magnetic fields.

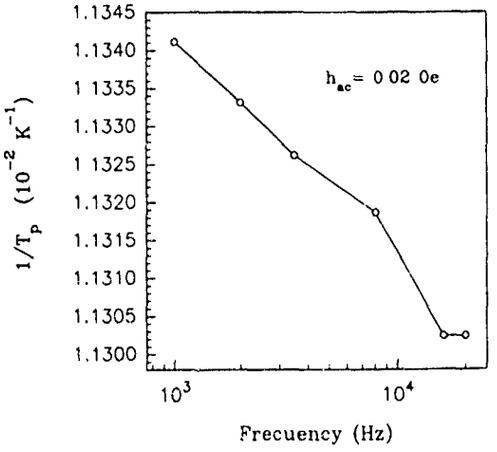

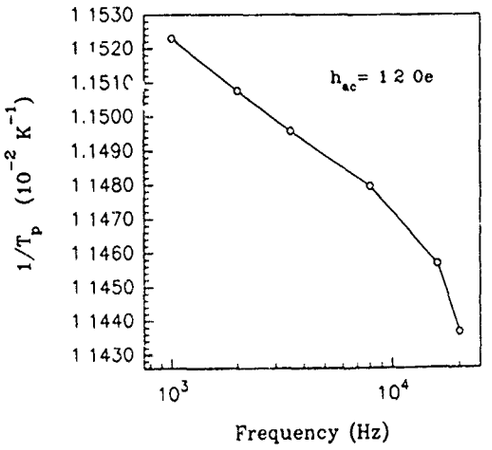

FIG 3. T_p^{-1} vs frequency at different ac magnetic fields

and the peak shift towards lower temperatures when the magnetic field increases, and furthermore the peak gets wider.

As was stated above, we have used the temperature of the peak (T_p) of χ'' for specifying the shifts with the frequency and ac magnetic field. Figure 2 shows the frequency dependence of T_p at different fields. T_p increases with the frequency and decreases with the magnetic field. This behavior could be explained by the thermally activated flux creep phenomenon proposed by Anderson for conventional type-II superconductors.[6] It is to be remarked that flux creep is thought to be a small effect in conventional type-II superconductor while in HTCS the thermally activated creep could have a significant effect.

According to the Anderson theory the jump over the pinning barriers is given by the usual Arrhenius expression

$$\nu = \nu_0 \exp(-U/k_B T), \tag{4}$$

where ν_0 is a characteristic frequency and U is an effective thermal activation energy, which includes a barrier height and a field-dependent force. Anderson and Kim[7] used the linear relation

$$U = U_0 - |\mathbf{F}| V a, \tag{5}$$

where U_0 was presumed to be the effective height of the energy barrier for thermally activated motion, $|\mathbf{F}|$ is the Lorentz force ($\mathbf{J}\times\mathbf{B}$), V is the activation volume, and a is the effective geometrical width of the energy barrier.

In Fig. 3 we plot $1/T_p$ vs ln ν for a field of 0.02 and 1.2 Oe, respectively. We have fitted these curves according to expression (4) to calculate the activation energy as a function of the magnetic field. The energies vary from 6.4 eV at 0.02 Oe to 3.23 eV at 1.2 Oe in the zero-field-cooled measurements. These values are comparable to those observed by Nikolo and Godfard[8] and by Dhingra and Das[9] with other measuring conditions. As the field increases, the Lorentz force ($\mathbf{J}\times\mathbf{B}$) increases, the thermal activation energy decreases and more flux vortices get depinned during the field cycle which is according to the Anderson–Kim model.

In a similar way we have measured the activation energy corresponding to χ_{fc}. In this case, the activation energy varies from about 3.41 eV at 0.02 Oe to 1.41 eV at 1.2 Oe. The activation energies are lower than in the zero-field-cooled measurements due to the effect of two contributions: the ac magnetic field and the dc magnetic flux trapped when the sample was cooled.

IV. CONCLUSIONS

The width of the diamagnetic transition decreases and the peak related with the intergrain losses shifts lightly to higher temperatures with increasing frequency. This could be demonstrative that the magnetic flux in the grain boundaries decreases with the increasing frequency. The shift of the peak in χ'' has been studied by means of the Anderson's theory of the flux creep. The activation energies take values in the range of 6.4–3.23 eV for applied field 0.02–1.2 Oe. These values of the activation energies decrease when the sample is cooled under a dc magnetic field.

[1] H. Kupfer *et al.*, in *High-T_c Superconductors*, edited by H. W. Weber (Plenum, New York, 1988), p. 293.
[2] D.-X. Chen *et al.*, J. Appl. Phys. **63**, 980 (1988).
[3] R. B. Flippen *et al.*, Physica C **201**, 391 (1992).
[4] X. C. Jin *et al.*, Phys. Rev. B **47**, 6082 (1993).
[5] M. Zazo *et al*, Appl. Phys. A **57**, 239 (1993).
[6] P. W. Anderson, Phys Rev. Lett. **9**, 309 (1962).
[7] P. W. Anderson and Y. B. Kim, Rev. Mod. Phys. **36**, 39 (1964).
[8] M. Nikolo and R. B. Goldfarb, Phys. Rev. B **39**, 6615 (1989).
[9] I. Dhingra and B. K. Das, Supercond Sci. Technol **6**, 765 (1993)

Effects of Ga doping on the magnetic ordering of Pr in $PrBa_2Cu_3O_7$

W-H. Li, C. J. Jou, S. T. Shyr, and K. C. Lee
Department of Physics, National Central University, Chung-Li, Taiwan 32054, Republic of China

J. W. Lynn
National Institute of Standards and Technology, Gaithersburg, Maryland 20899

H. L. Tsay and H. D. Yang
Department of Physics, National Sun Yat-Sen University, Kaohsiung, Taiwan 80424, Republic of China

Neutron-diffraction and ac-susceptibility measurements have been performed to study the effects of Ga doping on the magnetic ordering of the Pr in $PrBa_2(Cu_{1-x}Ga_x)_3O_7$. The Ga atoms preferentially replace the Cu atoms in the CuO-chain layers, and this substitution is found to decrease the antiferromagnetic ordering temperature as the Ga concentration is increased. In addition, the spin arrangement along the c axis is found to change from nearest neighbors being antiparallel for $x=0$ to nearest neighbors being parallel for $x=0.08$ (24% Cu chain substitution); for an intermediate x of 0.04 a mixture of the two spin structures is observed. The susceptibility results exhibit Curie–Weiss behavior above T_N, and departures from this behavior in the ordered state.

Among high-T_c oxides, $PrBa_2Cu_3O_7$ has attracted considerable attention because of its unexpected electric and magnetic properties. The introduction of Pr in $YBa_2Cu_3O_7$ suppresses superconductivity,[1,2] the Pr ions have a Neel temperature as high as 17 K, and an ordered moment as small as $0.74\mu_B$.[3] It is clear that interactions other than dipolar are responsible for the Pr magnetism. If superexchange is the dominant key, then those atoms located between the Pr atoms may also play important roles in Pr magnetism. An understanding of the coupling between the Pr atoms and the intermediate atoms located between them is then essential to a full understanding of the interactions involved.

There are three different types of layers of atoms that are located between the Pr atoms in $PrBa_2Cu_3O_7$: the CuO-chain layer, the CuO_2-plane layer, and the BaO layer. Metallic doping with Zn atoms, which substitutes for the Cu atoms located in the CuO_2-plane layers, causes the spin arrangement of Pr along the c axis to realign from antiparallel to parallel, without affecting its ordering temperature significantly.[4] On the other hand, a full replacement of the CuO-chain layers by TlO layers, i.e., $PrBa_2(TlCu_2)O_7$, does not alter the spin structure of Pr but reduces its ordering temperature by a factor of 2.[5]

In this paper we report neutron-diffraction and ac-susceptibility measurements made on the $PrBa_2(Cu_{1-x}Ga_x)_3O_{7-y}$ compounds to examine the effects of Ga doping on the ordering of the Pr spins. The Ga atoms replace the Cu atoms located in the CuO-chain layers. Two systems with $x=0.04$ and 0.08 (12% and 24% replacement, respectively) were studied, and we found that both the spin structure and the ordering temperature of Pr ions are sensitive to the presence of Ga atoms. The ordering temperature decreases with increasing Ga doping, and the nearest-neighbor spins along the c axis have the tendency to realign from antiparallel to parallel.

Powder samples of $PrBa_2(Cu_{1-x}Ga_x)_3O_{7-y}$ were prepared by the standard solid-state reaction technique, the details of the sample preparation techniques can be found elsewhere.[6] Both x-ray and high-resolution neutron diffractions were used to characterize the samples. The nominal oxygen concentration, determined from neutron profile refinement analysis,[7] is 6.98(4) and 6.96(4) for the $x=0.04$ and 0.08 compounds, respectively. Neutron-diffraction measurements were performed using the BT-9 triple-axis spectrometer at the Research Reactor at the U. S. National Institute of Standards and Technology. A pyrolytic graphite PG(002) monochromator was employed, with a PG filter placed after the monochromator position to suppress the higher-order wavelength contaminations. The energy of the incident neutrons was 14.8 meV (2.352 Å), and the angular collimations before and after the monochromator and after the sample were 40′, 48′, and 48′ full width at half maximum (FWHM), respectively. No analyzer crystal was used in these measurements. For the low-temperature experiments, the sample was mounted in a cylindrical aluminum can filled with helium exchange gas to facilitate thermal conduction. A pumped ^{4}He cryostat was used to cool the samples, and the lowest temperature obtained was 1.36 K.

A standard subtraction technique[8] was used to isolate the magnetic signal from the nuclear one, where the diffraction pattern taken at a temperature well above the ordering temperature was subtracted from the one taken at low temperature. Figures 1(a) and 1(b) show the magnetic Bragg peaks observed at low temperatures for the $x=0.04$ and 0.08 compounds, respectively. The indices shown are based on the chemical unit cell. Both the $\{\frac{1}{2}\frac{1}{2}0\}$ type and the $\{\frac{1}{2}\frac{1}{2}\frac{1}{2}\}$ type of reflections are needed in explaining the data shown in Fig 1(a). If only one reflection is assumed for the peak that occurs at around $2\theta=25°$, it turns out that not only the width of this peak is much too broad in comparison with the instrumental resolution but the peak position also would fit neither to the $\{\frac{1}{2}\frac{1}{2}0\}$ reflection nor to the $\{\frac{1}{2}\frac{1}{2}\frac{1}{2}\}$ reflection. In addition, the presence of the $\{\frac{1}{2}\frac{1}{2}1\}$ and $\{\frac{1}{2}\frac{1}{2}\frac{3}{2}\}$ reflections suggests the existence of the $\{\frac{1}{2}\frac{1}{2}0\}$ and $\{\frac{1}{2}\frac{1}{2}\frac{1}{2}\}$ reflections, respectively. The expected separation of the peak positions between the $\{\frac{1}{2}\frac{1}{2}0\}$ and the $\{\frac{1}{2}\frac{1}{2}\frac{1}{2}\}$ reflections is 0.7°, which is beyond our resolution limit. A calculation assuming the presence of both the $\{\frac{1}{2}\frac{1}{2}0\}$ type and the $\{\frac{1}{2}\frac{1}{2}\frac{1}{2}\}$ type of reflections gives excellent agreement for the peak positions and widths consistent with the instrumental resolution. The results of this calculation are

 0021-8979/94/76(10)/7136/3/$6.00 © 1994 American Institute of Physics

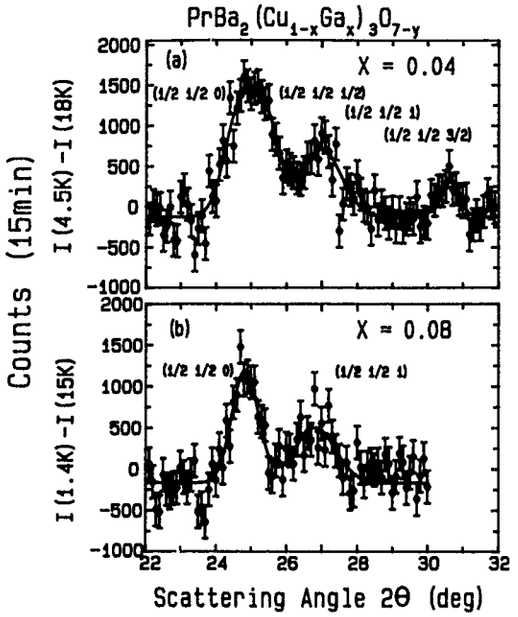

FIG. 1. Magnetic intensities in $PrBa_2(Cu_xGa_{1-x})_3O_7$ with (a) $x=0.04$ at $T=4.5$ K and (b) $x=0.08$ at $T=1.36$ K. Both the $\{\frac{1}{2}\frac{1}{2}0\}$ type and the $\{\frac{1}{2}\frac{1}{2}\frac{1}{2}\}$ type of reflections were observed in the $x=0.04$ compound, while only the $\{\frac{1}{2}\frac{1}{2}0\}$ type appeared in the $x=0.08$ compound.

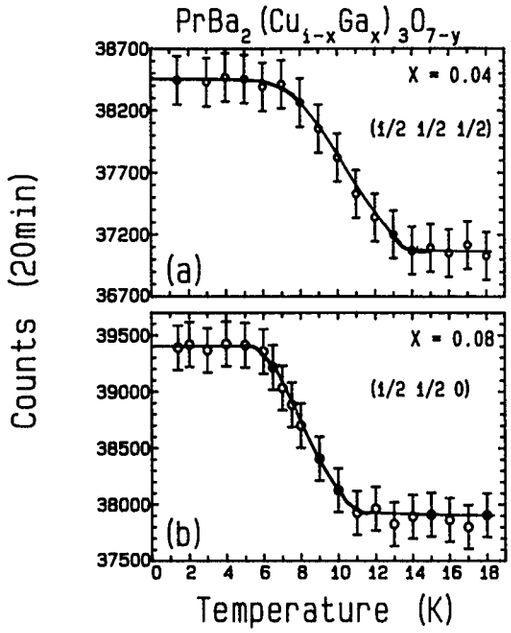

FIG. 2. Temperature dependence of the magnetic peak intensity The Neel temperatures are determined to be 14 and 10 K for the $x=0.04$ and 0.08 compounds, respectively. These data clearly show that the Ga doping effectively reduces the ordering temperature of the Pr spins.

shown as the solid lines in Fig. 1(a). No $\{\frac{1}{2}\frac{1}{2}\frac{1}{2}\}$ type of reflections were observed in the data shown in Fig. 1(b), and the solid lines are fits based on the presence of only the $\{\frac{1}{2}\frac{1}{2}0\}$ type of reflections.

The corresponding magnetic structure for the $\{\frac{1}{2}\frac{1}{2}\frac{1}{2}\}$ wave vector is that the spins are aligned antiparallel along all three crystallographic directions, and that for the $\{\frac{1}{2}\frac{1}{2}0\}$ wave vector is that nearest-neighbor spins along the c axis aligned parallel rather than antiparallel. Only the $\{\frac{1}{2}\frac{1}{2}\frac{1}{2}\}$ type of reflections was observed in the undoped system.[3,9] The observations shown in Fig. 1 then indicate that introducing Ga atoms into $PrBa_2Cu_3O_7$ causes the Pr spins along the c axis to change from antiparallel to parallel. A 12 at. % replacement of the Cu atoms located in the CuO-chain layers by Ga atoms partially reverses the Pr spins arrangement along the c axis, and a 24 at. % replacement complete this reverse.

The temperature dependence of the $\{\frac{1}{2}\frac{1}{2}\frac{1}{2}\}$ peak intensity of the $x=0.04$ compound is shown in Fig. 2(a), while that of the $\{\frac{1}{2}\frac{1}{2}0\}$ reflection of the $x=0.08$ compound is shown in Fig. 2(b). Both plots reveal a typical order parameter, that measures the square of the magnetization, for powder samples. The ordering temperatures determined from the data shown in Fig. 2 give $T_N \approx 14$ and 10 K for the $x=0.04$ and 0.08 compounds, respectively. We note that the T_N for the undoped system is 17 K. It is then clear that the ordering temperature of Pr is quite sensitive to the presence of Ga atoms.

The ordered moment can be obtained from a comparison of the magnetic intensities to the nuclear ones, while the spin direction was determined from the relative intensities of the magnetic reflections.[5] The saturated moment that we obtained for the $x=0.08$ compound using the data collected at $T=1.36$ K is $\langle \mu_z \rangle = 0.76 \pm 0.07 \mu_B$ with the moment directed along the c axis. This value of the ordered moment and the spin direction are the same as that found in the undoped system. Thus the Ga atoms do not alter the spin direction or the size of the ordered moment. Based on these results, the percentage in which the spin arrangement along the c axis has been reversed can be estimated by comparing the observed intensities between the $\{\frac{1}{2}\frac{1}{2}0\}$ type and the $\{\frac{1}{2}\frac{1}{2}\frac{1}{2}\}$ type of reflections. A calculation using the $\{\frac{1}{2}\frac{1}{2}0\}$ and $\{\frac{1}{2}\frac{1}{2}\frac{1}{2}\}$ intensities observed in the $x=0.04$ compound indicates that 80% of the sample has its Pr spins aligned parallel along the c axis. A calculation using the $\{\frac{1}{2}\frac{1}{2}1\}$ and $\{\frac{1}{2}\frac{1}{2}\frac{3}{2}\}$ reflections gives the same value.

The ac susceptibility was measured using the Lake Shore 7221 ac susceptometer. Portions of the real part of the measured ac susceptibility for both compounds are shown in Fig. 3. These data were taken with an alternating magnetic field of strength 3 Oe and frequency 300 Hz; data collected with a frequency as high as 10^4 Hz generated the same results. Above the Neel temperature of Pr, the data follow a Curie–Weiss law very well all the way up to the highest temperature studied of $T=320$ K. However, a small temperature-independent term χ_0 is also needed in describing the data. The solid lines shown in Fig. 3 are obtained by fitting the data to $\chi_0 + C/(T+\theta)$ for 30 K$<T<$320 K. The effects of the Pr ordering on the ac susceptibility are clearly seen. At low temperatures the data deviate from the fitted Curie–Weiss curves, and the temperatures at which these deviations begin agree very well with the T_N of Pr observed using neutron diffraction. However, no cusp on the χ_{ac}-T curve, typical of antiferromagnetic ordering, is observed.

The effective moment μ_{eff} that we obtained using the fitted values for the Curie–Weiss constants C are 3.39 and

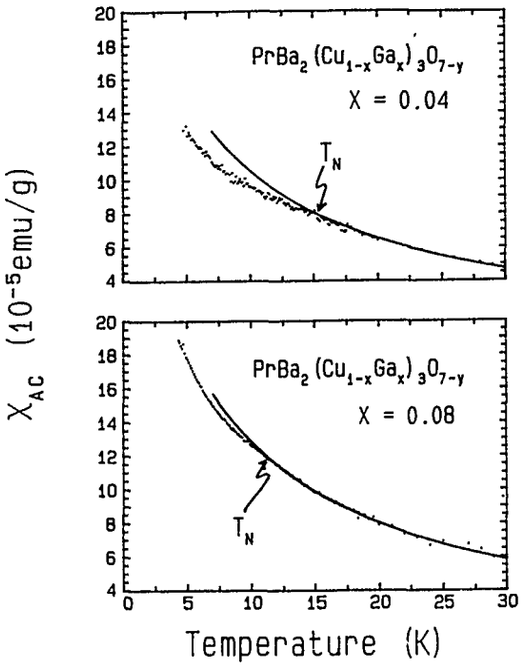

FIG. 3 Portions of the measured ac susceptibility as a function of temperature. The solid lines shown are fitted Curie–Weiss curves using data collected in the temperature range of 30 K<T<320 K. Departures from the fitted curves at low temperatures are clearly seen. The temperatures at which the departures begin match very well to the Neel temperature determined using neutron diffraction.

$3.01\mu_B$ for the x=0.04 and 0.08 compounds, respectively. These values are smaller than the value of $3.58\mu_B$ expected for free ions. We believe that the reduction of the effective moment is likely due to the crystalline electric field effects. As the Ga doping is increased the effect becomes more pronounced and hence the effective moment is much reduced.

In conclusion, the ordering temperature of the Pr spins is effectively reduced by Ga doping, while it is not affected by Zn doping.[4] The Ga atoms substitute into the CuO-chain layers, and the Zn atoms into the CuO_2-plane layers. It is then clear that the CuO-chain layers are more responsible than the CuO_2-plane layers for the high ordering temperature of Pr observed in $PrBa_2Cu_3O_7$.

The research at the NCU was supported by the National Science Council of the Republic of China under Grant No. NSC 83-0212-M-008-001, and was partially supported by the NCU Physics Department under Grant No. PHYS83-01. The research at the NSYSU was supported by the National Science Council of the Republic of China under Grant No. NSC 83-0212-M-110-028.

[1] C.-S. Jee, A. Kebede, D Nichols, J E. Crow, T. Mihalisin, G. H. Myer, I Perze, R. E Salomon, and P Schlottmann, Solid State Commun. **69**, 379 (1989).
[2] D. P. Norton, D. H. Lowmdes, B. C. Sales, J. D. Budai, B. C. Chakoumakos, and H. R. Kerchner, Phys. Rev. Lett. **66**, 1537 (1991)
[3] W-H. Li, J W Lynn, S. Shanthakumar, T. W. Clinton, A. Kebede, C-S. Jee, J. E. Crow, and T. Mihalisin, Phys Rev B **40**, 5300 (1989).
[4] W-H Li, K. J. Chang, W T. Hsieh, K C. Lee, J. W. Lynn, and H D Yang, Phys. Rev. B **48**, 519 (1993).
[5] W. T. Hsieh, K. J. Chang, W-H Li, K. C. Lee, J. W. Lynn, C C Lai, and H. C. Ku, Phys. Rev B **49**, 12200 (1994).
[6] H. D. Yang and M. W. Lin, Phys. Rev. B **44**, 5348 (1991).
[7] F. Beech, S. Miraglia, A. Santoro, and R. S. Roth, Phys Rev. B **35**, 8778 (1987).
[8] G E Bacon, *Neutron Diffraction*, 3rd ed (Clarendon, Oxford, 1975).
[9] M Guillaume, P. Fischer, B. Roessli, A. Podlesnyak, J. Schefer, and A. Furrer, Solid State Commun **88**, 57 (1993).

Galvanomagnetic properties of quasi-one-dimensional superconductors

K. Yu. Arutyunov and N. P. Danilova
Low Temperature Department, Physics Faculty, Moscow State University, Moscow 119899, Russia

A. A. Nikolaeva
Applied Physics Institute of Moldovian Academy of Sciences, Kishinev 277028, Moldovia

The transport properties of thin single-crystalline tin and indium filaments in glass cover were studied. The length of the samples was much greater than the quasiparticle relaxation length. The width of the resistive transition and the electron free path of the samples studied were comparable with the corresponding values of the perfect whiskers. The observed step-like current-voltage characteristic could be described by the model of noninteracting phase-slip centers.

I. INTRODUCTION

The sudden destruction of superconductivity by the transport current of a homogeneous bulk sample could be described by the model of a spreading "hot spot" when the normal phase nucleates within the region of reduced superconducting parameters. It is not obvious whether the above model could be applied to a homogeneous one-dimensional filament. A sample could be considered as a quasi-one-dimensional superconductor with a uniform current flowing in if the coherence length $\xi(T)$ and the field penetration depth $\lambda(T)$ are not small compared to the transverse dimensions. Due to strong temperature dependences of $\xi(T)$ and $\lambda(T)$ the requirement of quasi-one-dimensionality for clean I-type superconductors holds within few mK below T_c for the samples of several microns in diameter.

For small measuring currents the resistive transition curves $V(T)$ for thin whiskers is very small (~1 mK) and show the typical smooth shape of a fluctuation governed phase transition.[1] However, for high measuring currents the transition width rises and the voltage steps build up which become more distinct for larger fixed currents.[2] The voltage steps are also observed in the $V(I)$ characteristics at fixed temperatures few mK below the critical temperature T_c.[2]

At the present moment we may state that the step-like peculiarities of the voltage-current characteristics in quasi-one-dimensional superconductors could be qualitatively described by the essentially nonequilibrium process of the phase-slip centers (PSC) activation.[3] Still there are some questions which are not clear enough. One of them is the problem of the interaction of the PSC on a distances comparable with the length of quasiparticle charge imbalance relaxation.

In the present work we present the experimental study of galvanomagnetic properties of long tin and indium filaments in a glass cover. The process of filament drawing permits us to produce a homogeneous wire of hundred meters in length with highly uniform parameters. However, the existence of the glass cover along with considerable reinforcement of the metal core initiates several problems with the partial removal of the glass for voltage and current probes. That is why in the present work special attention is paid to contact effects.

II. EXPERIMENT

The filaments were prepared by drawing of molten metal in glass capillary.[4] Depending upon the metal, type of the glass, temperature, cooling, and speed of the wire spinning it is possible to produce filaments with diameter of metal core from 0.6 to 40 μm. X-ray analysis showed that all the wires studied are single crystals. The observation of the samples with the scanning electron microscope (SEM) displayed no cuts.

The filament with length ~1 cm was glued to a sapphire substrate excluding narrow ~20 μm regions for electrodes where the glass was removed with hydrofluoric acid. The current probes were prepared by direct placing silver paint or Wood's metal above the glass-free ends of the filament. The best results for potential probes were obtained by placing a 8 μm copper wire covered with a thin layer of conducting epoxy across the sample.

The samples were mounted inside a massive vacuum calorimeter with an internal heater. The temperature was stabilized with a double-level PID controller system with an accuracy ± 0.1 mK. All measurements were performed using a conventional four-probe method. External magnetic field was generated with a double-layer solenoid. The Earth magnetic field was reduced to ≤ 1 mOe by the superconducting shield.

III. THEORY

Soon after the experimental observation of a step-like $V(I)$ structure of tin whiskers[2] Scocpol, Beasley, and Tinkham (SBT) proposed a model[3] which can qualitatively describe the observed phenomena. The SBT model associates the voltage steps with activation of PSC along the one-dimensional superconductor. The PSC is a region of weakened superconductivity (S-S'-S boundary). The idea of PSC is related with the assumption that the phase $\varphi(r,t)$ of the superconducting order parameter $\Psi(r,t)=\Psi^2\exp[i\varphi(r,t)]$ is periodically reduced by 2π to compensate the monotonic growth of the time-dependent phase due to the existence of nonzero voltage across the PSC: $d\varphi/dt=2$ eV/h. In order the process could be stationary in time the period of the phase-slip events should be equal to $\tau_{slip}=h/(2e\langle V\rangle)$, where $\langle V\rangle$ is the time-averaged voltage across the PSC.

SBT postulated that the phase-slip event occurs within the range $\sim\xi(T)$ of the PSC core, while the nonequilibrium quasiparticles charge imbalance relax on a length scale $\Lambda=(1/3lv_F\tau_e)^{1/2}$, where l is the mean-free path, v_F the Fermi velocity, and τ_e is the elastic electron relaxation time.

 0021-8979/94/76(10)/7139/3/$6 00 © 1994 American Institute of Physics

The current-voltage characteristic of a single PSC could be described by[3]

$$V(I)=\frac{dV}{dI}(I-I_0), \tag{1}$$

where I_0 is the excess current and the differential resistance (dV/dI) is associated with the resistance of the normal-like section of length $L(1)=2\Lambda$.

Later, Tinkham[5] applied the ideas of SBT to describe the current-voltage characteristics of an ideal homogeneous filament. The resulting step-like $V(I)$ dependence was associated with successive activation of N independent PSC at critical currents $I_c=I_c(1)<I_c(2)<\cdots<I_c(N)$. The interaction of the PSC is reduced to the activation of the successive PSC midway between existing ones. For sufficiently long filament $L/2N\Lambda\gg 1$ the PSC are well separated and weakly interacting. The general spacing of the predicted steps is in a reasonable agreement with experimental results,[6] but the positions of the first steps are separated by inevitable inhomogeneities, which overwhelm the exponentially weak interaction of the ideal model.[5]

Kadin, Smith, and Scocpol (KSS) developed a detailed model of a charge imbalance wave equation for a PSC connected to a transmission line.[7] The KSS model includes the SBT as a limit of a diffusive decay of a charge imbalance. However, KSS showed that under some conditions the relaxation of charge imbalance results in propagating of charge-imbalance waves on the scales much greater than the Λ of the SBT model. Therefore, the KSS model predicts the long-distance interaction of the PSC.

Along with the models involving the phase-slip event[3,7] the generalized time-dependent Ginzburg–Landau (TDGL) model was introduced to describe the transport properties of one-dimensional superconductors.[8]

However, taking into account the inevitable inhomogeneities of the actual superconducting filaments and restricting attention to the first voltage steps of the $V(I)$ transition one can use the SBT model to rationalize the experimental results.

IV. RESULTS AND DISCUSSION

For all the samples studied the relation of resistance at room temperature R(room) to the one at 4.2 K $R(4.2)$ is used for calculation of the mean-free path l utilizing the well-known values for the product (ρl) and ρ(room) for tin and indium.[6] It was found that the mean-free path l monotonically increase with increasing of the filament diameter, reaching the maximum value of $l=6$ μm for 8 μm indium filament and $l=3.4$ μm for the thick 13 μm tin wire.

The width of the superconducting resistive transition ΔT_c varies from 0.01 to 0.15 K. Measuring the samples prepared from different parts of the same filament it was found that the broadening of the resistive transition is greatly determined by the quality of the contacts. An example of the wide resistive transition is shown in Fig. 1 for indium sample In-F1. It is clearly seen that there are at least two kinks on the $R(T)$ dependences at $H=0$. The form of the transition depends upon the direction of the temperature variation, displaying small hysteresis even for zero magnetic field. The kinks are related to the existence of weakened superconductivity in the locus of the potential probes. Joule heating leads to a small hysteresis. The application of the external magnetic field $H<H_c^{\text{bulk}}$ may efficiently suppress the weak superconductivity resulting in smooth $R(T)$ dependences at least at a high-temperature region. We suppose that the increase of number of kinks at a low-temperature limit is due to the generation of the intermediate state in the weakened region by the magnetic field. The suppression of superconductivity in the locus of contacts is a reversible process. Careful remounting of potential probes of the same sample may significantly smooth out the form and decrease the width ΔT_c of the resistive transition.

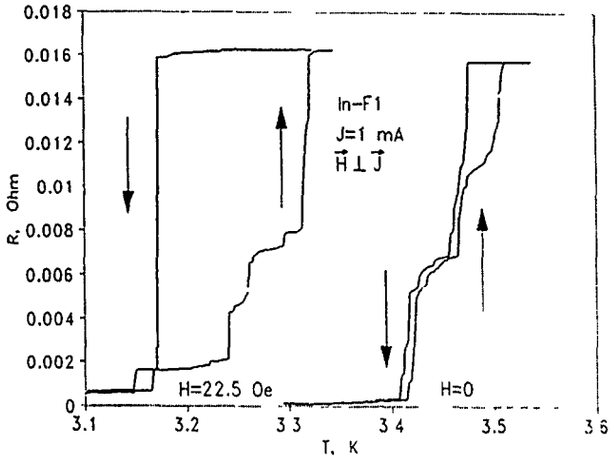

FIG. 1. Resistance vs temperature for the sample In-F1 for zero magnetic field and for applied transverse (H⊥J) magnetic field $H=22.5$ Oe. Arrows indicate the direction of the temperature variation.

However, along with the discussed above "contact" broadening of the $R(T)$ dependences, the increasing of measuring current increases the width of the resistive transition ΔT_c, displaying a step-like structure and hysteresis. We suppose that the observed phenomenon is related not only with the inevitable thermal heating,[9] but also with the details of nonequilibrium quasiparticle relaxation.[7]

The voltage-current characteristics at fixed temperatures display a wide transition with pronounced step-like structure (Fig. 2). Each $V(I)$ curve could be approximated by a set of voltage jumps $V(i)$ at currents $I_c(i)$ and linear plateaus with "constant" differential resistance $(dV/dI)_i$. The finite curvature of the actual $V(I)$ characteristics indicates the existence of heating. As one may expect, because of the existence of the glass cover, the heating effects are observable, but not so significant to smear out the step-like structure of the $V(I)$ transitions.

According to the model of noninteracting PSC[5] the increments of differential resistance for all voltage steps are equal: $(dV/dI)_i-(dV/dI)_{i-1}=(dV/dI)_1=\text{const}$. Due to the heating effects mentioned above, we cannot state that the above relation holds for all steps of $V(I)$ transition. But from Fig. 2 it can be clearly seen that $(dV/dI)_i$ increases with an increase of the transport current I.

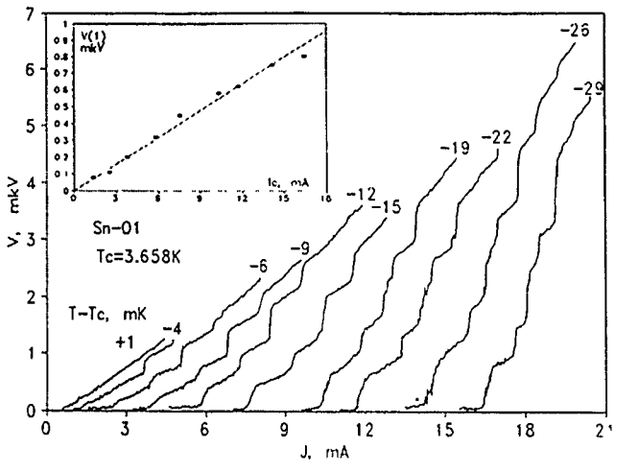

FIG. 2. Voltage-current characteristics of the sample Sn-O1 for fixed temperatures $\Delta T = T - T_c$. The inset shows the amplitude of the first voltage step $V(1)$ as a function of the critical current $I_c(1)$.

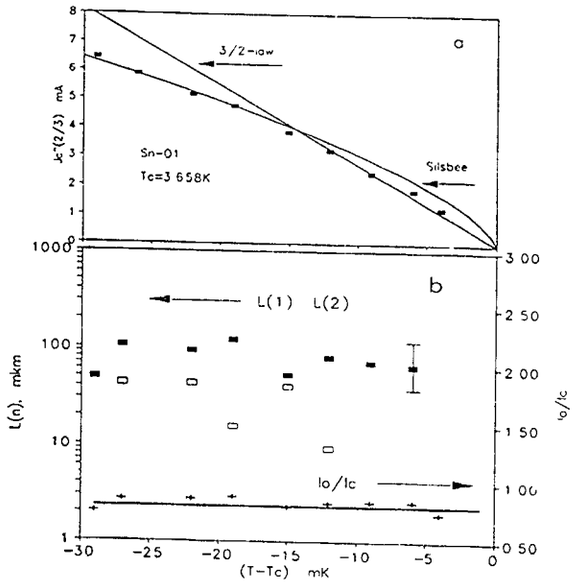

FIG. 3. (a) Critical current $I_c(1)^{2/3}$ as a function of the temperature $\Delta T = T - T_c$ for the sample Sn-O1. The lines are the theoretical calculations: the "3/2" law $I_c \sim (T_c - T)^{3/2}$ and the Silsbee rule $I_c \sim (T_c - T)^2$. (b) Relation I_0/I_c (+) and the normal-like lengths $L(1)$ (■), $L(2)$ (□) vs temperature $\Delta T = T - T_c$ for the sample Sn-O1. The solid line corresponds to the value $I_0/I_c = 0.8$

In the SBT model,[3] the quasilinear plateaus of the $V(I)$ transition are associated with activation of PSC with normal-like lengths $L(i) = 2\Lambda$:

$$L(i) = [(dV/dI)_i - (dV/dI)_{i-1}](L/R_N), \qquad (2)$$

where L is the length of the sample and R_N the normal resistance. Figure 3(b) shows the temperature dependences of $L(1)$ and $L(2)$ corresponding to $V(I)$ transition of Fig. 2. Significant dispersion of $L(i)$ experimental values is related with the problem of $(dV/dI)_i$ correct definition of the actually curved $V(I)$ plateaus. Within experimental errors no temperature dependence could be observed. The absence of temperature dependence and the values $L(i,T)$ correlate well with existing results for tin whiskers.[6]

It is remarkable that the height of the first voltage jump $V(1) = V[I_c(1)]$ follows a straight line (Fig. 2, inset), which holds for all tin and indium samples. Since according to Eq. (1), $V(1) = (dV/dI)_1[1 - I_0/I_c(1)]I_c(1)$ this observation indicates that the temperature dependence of $(dV/dI)_1$ and $[1 - I_0/I_c(1)]$ compensate each other so that their product is independent of the temperature and, therefore, is constant for different critical currents $I_c(1,T)$.

According to the SBT model[3] the relation of excess current to the critical value is a constant equal to $I_0/I_c \approx 0.6$. Within experimental errors our results give the value $I_0/I_c \approx 0.8$ for the first step [Fig. 3(b), right axis] which correlate with the TDGL model.[8]

The temperature dependence of the critical current $I_c(1,T)$ at temperatures close to critical value T_c follows the "3/2" law for a one-dimensional filament: $I_c(T) \sim (T_c - T)^{3/2}$ [Fig. 3(a)]. For low enough temperatures there are deviations from the "3/2" law and the $I_c(T)$ follows the Silsbee rule for a three-dimensional superconductor [Fig. 3(a)]. It is remarkable that, nevertheless, the sample displays qualitatively the same step-like $V(I)$ transition at low temperatures ($T_c - T \geq 20$ mK) being not one-dimensional (Fig. 2). The low-temperature behavior of superconducting filaments is a subject for future investigations.[10]

[1] W. W. Webb and R. J. Warburton, Phys Rev Lett. **20**, 461 (1968).
[2] J. D. Meyer, Appl Phys. **2**, 303 (1973).
[3] W. J. Skocpol, M. R. Beasley, and M. Tinkham, J Low Temp. Phys **16**, 145 (1974).
[4] N. B. Brandt, D. B. Gitzu, A. M. Josher, B. P. Kotrubenko, and A. A. Nikolaeva, Sov. "Pribory i Technika Experimenta" **n.3**, 256 (1976)
[5] M. Tinkham, J. Low Temp. Phys. **35**, 147 (1979)
[6] R. Tidecks, *Current Induced Nonequilibrium Phenomena in Quasi-One-Dimensional Superconductors* (Springer, New York, 1990).
[7] A. M. Kadin, L. N. Smith, and W. J. Skocpol, J Low Temp Phys. **38**, 497 (1980).
[8] L. Kramer and R. Rangel, J Low Temp. Phys **57**, 391 (1984)
[9] W. J. Skocpol, M. R. Beasley, and M. Tinkham, J Appl. Phys. **45**, 4054 (1974).
[10] X. Yang and R. Tidecks, Phys. Rev Lett. **66**, 2822 (1991).

Remanent magnetization of layered and isotropic superconductors (abstract)

Yu. V. Bugoslavsky, A. A. Minakov, and S. I. Vasyurin
General Physics Institute 117942, Vavilov st. 38, Moscow, Russia

There are contradicting data on the anisotropy of remanent magnetization of high-temperature superconductors.[1-3] To clarify the mechanism of this anisotropy we performed a comparative study of thermoremanent (TRM) and isothermal remanent (IRM) magnetizations. We report on the results obtained on layered single crystals of LaCrSuO and RBaCuO (R=Y,Gd) families as well as on isotropic soft alloy Bi:Pb:Sn and nontextured ceramic YBaCuO samples. The experiments were done by means of a vibrating-sample magnetometer. The external magnetic field up to 8 kOe was applied to magnetize the samples at arbitrary directions. It was found that all the studied plate-like samples show the effect of "easy remanent magnetization axis:" the vectors of IRM and TRM tend to point along the normal of the plate at any magnetizing or cooling angle. In the case of TRM this effect can be well described considering the influence of the sample shape. This fact was proved by measurements on samples with substantially different aspect ratios. Thus, we argue that the anisotropy of TRM is not related to anisotropic flux trapping. The anisotropy of IRM is a more complex phenomenon, as it involves inhomogeneous flux distribution in the sample. Nevertheless, it was found that the dependence of IRM direction on the magnetizing angle is also governed mainly by the sample shape. The corrections to the effective demagnetization factors were calculated, which arise due to the flux distribution. The analysis of the absolute value of IRM on the magnetizing angle allows one to distinguish between the influence of the critical current anisotropy and the sample shape.

[1] U. Jaron *et al.*, Phys. Rev. B **44**, 531 (1991).
[2] S. Kolesnik *et al.*, Cryogenics **32**, 979 (1992).
[3] T. Habisreuther *et al.*, Proceedings of the European Conference on Applied Superconductivity, Gottingen, 1993.

 0021-8979/94/76(10)/7142/1/$6.00 © 1994 American Institute of Physics

Two types of additional maxima in magnetization curves of layered superconductors (abstract)

Yu. V. Bugoslavsky and A. A. Minakov
General Physics Institute, 117942 Vavilov St. 38, Moscow, Russia

We report on magnetic measurements of LaSrCuO and YBaCuO single crystals in order to clear up their anomalous behavior and to attribute it to the crystals' anisotropic properties. Magnetization curves were obtained by means of a vibrating sample magnetometer at temperatures from 4.2 to 90 K. The magnetic field up to 8 kOe was applied at various angles with respect to the crystal c axis. Our main findings are that there are two physically different types of additional maxima, as ruled out from the evolution of magnetization curves with varying the tilt angle of the external field. One type of the maxima is attributed to anisotropic flux penetration into a sample and flux-line-lattice rotation with increasing the field. We provide an experimental justification of this explanation. The second type of maxima is related to an anomalous increase of the critical current in magnetic field which is often referred to as the "fishtail" phenomenon. It was found that the existence of the fishtail is closely related to the anisotropy of flux pinning. On this basis a qualitative model was developed to describe this phenomenon. The model takes into account vortex interaction with stretched pinning sites and the vortex bending due to stray fields in the sample. The formation of staircase flux lines is also assumed, as specific for layered superconductors. The qualitative explanation of the fishtail is as follows. At low fields the flux lines are strongly curved. When increasing the field, they straighten and fit the linear pinning sites better, which gives rise to more effective flux line fixing. The proposed model allows to describe the angular and temperature dependencies of the additional maximum position.

"Effective radius" of the 4*f* electrons in $REBa_2Cu_3O_7$, RE=Dy, Ho, Er (abstract)

Yu. A. Koksharov and P. K. Silaev
Department of Physics, Moscow State University, Moscow 119899, Russia

It is well known that in most high-temperature superconductors rare earth (RE) ions and superconducting copper-oxygen planes coexist as rather isolated subsystems. It would be expected that the "magnetic" $4f$ electrons are to be strongly localized as it takes place in many oxides.[1] On the other hand, significant crystal-field (CF) splitting of RE ground states is evidence that the "effective radius" of the $4f$ electron wave functions (WF) could be large.[2–4] This matter could be responsible for the disappearance of the superconductivity in Pr_{123} since the "effective radius" of the $4f$ electron WF increases from Yb to Ce. There is the adequate complete information about CF splitting in $HoBa_2Cu_3O_7$ (Ho_{123}) from inelastic neutron scattering experiments. The energies of low-lying levels are known also for Dy_{123}[3,4] and Er_{123}.[3] To compute CF splitting in RE_{123} compounds the hydrogen-like one-electron radial WF $R(r)=(rN)\exp(-alpha\ r)$ are used. Only five parameters are taken into account to accord the calculated and experimental data: alpha, N, and effective charges of nearest oxygen, copper, and barium ions. The minimal discrepancy for Ho_{123} is small enough for such simple approximation. The minimum is observed with enough magnitude of alpha than the one in the case of free Ho_{3+} ion. The same is true for Dy_{123} and Er_{123}. This fact points out the strong localization of the $4f$ one-electron radial wave function and probably on the small covalent mixture of $4f$ ("magnetic") and $3d$-$2p$ ("superconducting") orbitals.

[1] G T Trummell *et al*, Phys Rev **92**, 1387 (1953).
[2] A. Furrer *et al*, Phys. Rev B **38**, 4616 (1988).
[3] B D Dunlap *et al.*, J Magn Magn. Mater. **68**, L139 (1987)
[4] A Furrer *et al.*, J Magn Magn Mater. **76–77**, 594 (1988)

 0021-8979/94/76(10)/7143/1/$6 00 © 1994 American Institute of Physics

Helicoidal, magnetic vortex in a current-carrying superconductor in a longitudinal magnetic field: New exact solution (abstract)

Yuri A. Genenko
Donetsk Phystech, 340114 Donetsk, Ukraine

A resistive state in a type-II superconductor (SC) is conditioned by the Abrikosov magnetic vortex motion in them. In absence of external magnetic field the entry of vortex rings of a transport current self field determines the resistivity oneset.[1] Being applied along the current-carrying SC cylinder the magnetic field does not affect the entry of self-field vortex loops, because of force-free geometry.[2] In a latter case other vortex configurations, more likewise a field line pattern, seem to face less edge barrier against vortex entry and determine the resistivity onset. In this work an exact solution for helicoidal magnetic vortex is found in a London approximation, similar to magnetic helicoidal configurations known in magnetism. The Gibbs free energy of the current-carrying SC cylinder in a parallel magnetic field is constructed and the edge barrier problem of irreversible entry of helicoid into the SC sample is solved. An optimal parameter of helicoid is chosen by minimization of critical SC parameters (current or field) for vortex entry. The phase diagram of resistive state in coordinates current field is evaluated. An essential difference of magnetic behavior between thin (of radius $R<1$, London penetration depth) and thick ($R\gg1$) samples is shown. The latter exhibit the field-dependent critical current J_{cr} due to the helicoid entry in almost all of the field region $H<H_c$, the thermodynamic critical field, while for $R<1$ J_{cr}, almost field-independent, is determined by the vortex ring entry.

[1] Yu. A. Genenko, Physica C **215**, 343 (1993); Phys. Rev B (in press).
[2] A. M. Campbell and J. E. Evetts, *Critical Currents in Superconductors* (Taylor & Francis, London, 1972).

 0021-8979/94/76(10)/7144/1/$6.00 © 1994 American Institute of Physics

Ga substitution effect on magnetic and magnetostrictive properties of $TbFe_2$ compounds

Y. J. Tang, Y. B. Feng, and H. L. Luo
Institute of Physics, Academia Sinica, Beijing 100080, People's Republic of China

S. M. Pan
General Research Institute for Non-Ferrous Metals, CNNC, Beijing 100088, People's Republic of China

In the present paper magnetic and magnetostrictive properties of $Tb(Fe_{1-x}Ga_x)_2$ ($x=0-0.2$) compounds were investigated. It was found that the iron moment of the compounds does not seem to vary much for $x\leqslant 0.12$. The Curie temperatures of the compounds decrease continuously by substituting Ga for Fe, which was attributed to the decrease of the R-T coupling strength due to Ga substitution. The intersublattice coupling constant J_{RFe} was evaluated by molecular field model. The decrease of J_{RFe} with increasing Ga content was found and related to the decrease of the number of the Tb-Fe interaction pairs when replacing Fe with Ga. By using an x-ray diffractometer the samples were step scanned with Cu radiation at a higher Bragg angle 2θ ranging from 71° to 74° to study the cubic (440) reflection. The splitting of (440) reflection for $X\leqslant 1.2$ was clearly seen and the easy direction magnetostriction λ_{111} of the compounds was calculated. It was found that λ_{111} decreases with increasing Ga content. This was attributed to the decrease of magnetic properties of the compounds. The polycrystal magnetostriction λ_s of the compounds has also been studied.

I. INTRODUCTION

Substitution of Fe with other transition metals, such as Mn, Co, Ni, Al, etc., in RFe_2 cubic Laves compounds are of considerable interest because in some cases such substitution can improve the magnetostriction of the compounds.[1–4] According to Clark *et al.*[5] the magnetostriction of such compounds are highly anisotropic, exhibiting different magnetostrictive characters depending on their easy magnetization direction, i.e., $\lambda_{111}\gg\lambda_{100}$. The huge λ_{111}'s are allowed because two inequivalent tetrahedral rare earth sites exist in the C15 structure while the potentially huge values of λ_{100} are shorted out because of the high tetrahedral symmetry at the rare earth site, which means that only transition metal contributes to λ_{100}. It was found[2] that the magnetostriction of $Tb_{0.3}Dy_{0.7}(Fe_{1-x}T_x)_2$ decreases when replacing Fe with Ni or Co. Teter *et al.*[3] also found that the low Tb concentration samples with Mn substitution do show a tendency to have a lower $\Delta H/\lambda$ ratio than the pure iron ones in a twinned single crystal of Mn substituted Terfenol-D. Recent studies[1,6] have found that substituting Fe with Mn in $Tb_xDy_{1-x}Fe_2$ compounds could shift the magnetocrystalline anisotropy compensation composition to higher Tb content and was effective to improve their magnetostriction because of the Mn influence on the magnetocrystalline anisotropy; and Mn substitution in $DyFe_2$ increases the magnetostriction at room temperature, especially in low fields, which is suggested to be caused by λ_{100} increase. It was also found[7] that the magnetostriction shows a significant increase with substituting a small amount of Mn in $Y_{0.1}Tb_{0.9}(Fe_{1-x}Mn_x)_2$ compounds. These results suggested that transition metals could play a relative important role in improving the magnetostriction of RFe_2 compounds through R-T interaction, especially at low fields.

Although the theory of anisotropy and magnetostriction is well developed for the rare-earth sublattice in RFe_2 Laves compounds, a detailed understanding of the effect of the transition metals on magnetostriction proved to be elusive. A better knowledge of such an effect both from experimental and theoretical points of view may lead to some discoveries of new giant magnetostrictive materials at relatively low field.

In the present study magnetic and magnetostrictive properties of $Tb(Fe_{1-x}Ga_x)_2$ ($x=0-0.2$) compounds were measured in order to reveal the substitution effect.

II. EXPERIMENT

The $Tb(Fe_{1-x}Ga_x)_2$ ($x=0-0.2$) compounds were arc melted in a magnetocontrolled arc furnace under an atmosphere of very pure argon, and annealed at 900 °C for a week under a purified-argon atmosphere. X-ray analysis showed that all samples were single phase of cubic Laves structure (C15). Curie temperature was obtained by extrapolating the σ^2-T curve to $\sigma^2=0$. Saturation magnetization (σ_s) was measured in the extraction magnetometer with field up to 60 kOe at 1.5 K. Polycrystal magnetostriction λ_s was measured by using the strain gauge method in applied field up to 20 kOe at room temperature and was obtained by using parallel strain $\lambda_\parallel$ and perpendicular strain $\lambda_\perp$, to applied magnetic field as follows:

$$\lambda_s=\tfrac{2}{3}(\lambda_\parallel-\lambda_\perp). \tag{1}$$

 0021-8979/94/76(10)/7145/3/$6.00 © 1994 American Institute of Physics

TABLE I. Lattice constant a, Curie temperature T_c, and intersublattice coupling constant J_{RFe} for $Tb(Fe_{1-x}Ga_x)_2$ compounds. The values $Z_{RFe}=12$, $Z_{FeR}=6$, $S_{Fe}=0.78$, $g_R=3/2$, and $J=6$ are used in the calculation.

X	a (Å)	T_c (K)	$-J_{RFe}$ (10^{-22} J)
0	7.346	694	2.1
0.03	7.360	662	1.6
0.06	7.370	614	0.9
0.09	7.383	593	0.6
0.12	7.391	545	0.3

By using an x-ray diffractometer, the samples in powder form were step scanned with Cu radiation at a higher Bragg angle 2θ ranging from 71° to 74° in order to study the cubic (440) reflection. The absolute error of the measurement for the lattice constant is less than 0.002 Å. The easy direction magnetostriction λ_{111} of the compounds was calculated by:[8]

$$\lambda_{111}=\Delta\alpha, \tag{2}$$

where $\Delta\alpha$ is the deviation of the angle between neighboring edges of the distorted cube from $\pi/2$.

III. RESULTS AND DISCUSSION

The lattice constants of $Tb(Fe_{1-x}Ga_x)_2$ ($x=0-0.12$) compounds were measured by x-ray diffraction and listed in Table I. It could be found that they increase with increasing Ga content, obeying Vegard's law. Studying the magnetic behavior of $TbFe_2$ compounds both as a single crystal and polycrystal from previous research,[5] we found that even at 120 kOe it was impossible to saturate the polycrystal samples at 4.2 K. In the present study, the polycrystal moment is reduced by about 10% below the single-crystal value. Assuming the same reduction of the moment for $Tb(Fe_{1-x}Ga_x)_2$ compounds, we obtained from the saturation data an iron magnetic contribution $(1.56\pm0.03)\mu_B$ for the entire concentration range.

Although the iron moment does not seem to vary much in the studied composition range, the Curie temperatures T_c of $Tb(Fe_{1-x}Ga_x)_2$ compounds decrease continuously by substituting Ga for Fe. This is evidence that the greatest contribution to T_c values is given by the interactions involving the iron atoms. T_c reduction can be attributed to the decrease of the R-T coupling strength due to Ga substitution. On the basis of molecular field theory the R-T intersublattice-coupling constant J_{RFe} can be obtained by:[9]

$$(J_{RFe}/k)^2=\frac{9(T_C-T_C^Y)T_C}{4Z_{RFe}Z_{FeR}S_{Fe}(S_{Fe}+1)(g_R-1)^2J(J+1)}, \tag{3}$$

where T_c and T_c^Y represent the Curie temperatures of the compounds in which R is magnetic ($J\neq0$) or R is nonmagnetic ($J=0$), respectively; k is Boltzmann constant. Some parameters used in the calculation are listed in Table I. Here YFe_2 was used as the $J=0$ compound in the calculation. The magnetic-coupling strength constants derived from Eq. (3) are listed in Table I. For $TbFe_2$, J_{RFe} is 2.1×10^{-22} J, which agrees well with $153k$ (yields a value of 2.3×10^{-22} J) estimated from Mössbauer spectra for RFe_2 compounds[10] and somewhat smaller than 19.1 K for J_{RFe}/k (yields a value of 2.6×10^{-22} J) derived from high field measurements,[9] and 2.93×10^{-22} J evaluated by *ab initio* calculations.[11] The decrease of J_{RFe} with increasing Ga content is apparently seen from Table I. This can be related to the decrease of the number of the Tb-Fe interaction pairs when replacing Fe with Ga.

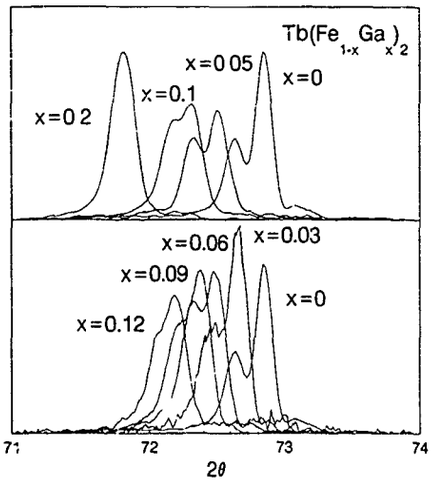

FIG. 1. X-ray spectra for $Tb(Fe_{1-x}Ga_x)_2$ compounds

$TbFe_2$, whose easy direction is parallel to [111], presents a rhombohedral distortion at room temperature. We suppose that no easy direction change occurs for the entire concentration range for $Tb(Fe_{1-x}Ga_x)_2$ ($x=0-0.2$) compounds. In this study λ_{111} was determined from the splitting of the high Bragg angle (440) reflection. The splitting of the (440) reflection due to the distortion is of the same order of magnitude as the one due to the doublet $K\alpha_1$, $K\alpha_2$; actually a triplet is observed. So the reflection created by $K\alpha_2$ is deducted from the whole reflection using a standard method. Figure 1 shows the x-ray spectra after deduction for the compounds. For $TbFe_2$, the calculated distortion is 0.0024, which corresponds to a rhombohedral angle $\alpha_R=89.86°$. This result shows a good agreement with single crystal data[5] and

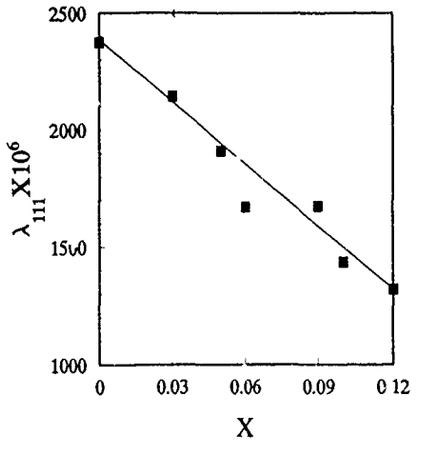

FIG. 2. Ga concentration dependence of λ_{111} for $Tb(Fe_{1-x}Ga_x)_2$ compounds

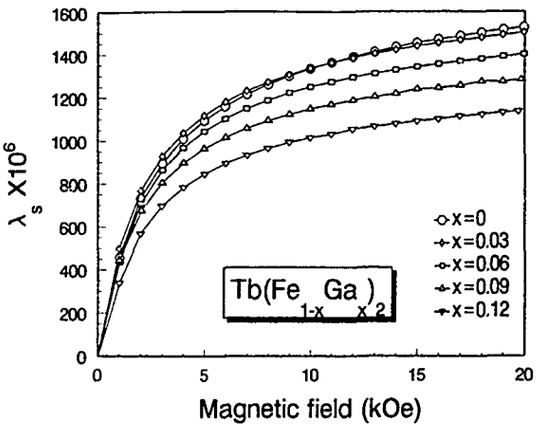

FIG. 3. Magnetic field dependence of polycrystal magnetostriction for $Tb(Fe_{1-x}Ga_x)_2$ compounds.

previous x-ray studies for $TbFe_2$.[12] The splitting of the (440) reflection is clearly seen from Fig. 1. It decreases with increasing Ga content. When $X=0.2$ the splitting disappears, which means that the distortion becomes too small to be measured at room temperature. It could also be found from Fig. 2 that λ_{111} decreases linearly with increasing Ga content, which can be attributed to the decrease of magnetic properties of the compounds. It is well known that the large magnetostriction in RFe_2 compounds is due to the interactions of the anisotropic cloud of the $4f$ electrons with the crystal field and transition metals. According to the single-ion model, the magnetostriction varies with temperature as $\sigma_R^3(T)$. Assuming that the R sublattice moments decrease with decreasing Curie temperature, the rapid decrease in T_c with increasing Ga content results in a strong decrease of $\sigma_R(T)$ at room temperature, which in return leads to a marked reduction in magnetostriction. Figure 3 shows the polycrystal magnetostriction λ_s versus applied magnetic field at room temperature for the compounds. It can be seen that the magnetostriction of the compounds are not saturated even at 20 kOe. We note that the magnetostriction at 20 kOe drops with increasing Ga content. This situation is not the same as that for $Y_{0.1}Tb_{0.9}(Fe_{1-x}Mn_x)_2$ compounds in which the magnetostriction shows a significant increase with a small amount of Mn compounds.[7] This suggests that substitution Ga cannot improve the saturated magnetostriction for $TbFe_2$ compound.

IV. CONCLUSION

In conclusion we would like to point out that:

(1) while the iron moment does not seem to vary much in the studied composition range for $Tb(Fe_{1-x}Ga_x)_2$ ($x=0-0.12$) compounds, the Curie temperatures T_c decrease continuously by substituting Ga for Fe, which was attributed to the decrease of the R-T coupling strength due to Ga substitution. The decrease of J_{RFe} with increasing Ga content, which was obtained by molecular field model, can be related to the decrease of the number of the Tb-Fe interaction pairs when replacing Fe with Ga.

(2) The splitting of (440) reflection for $x \leq 1.2$ was clearly seen and the easy direction magnetostriction λ_{111} of the compounds was calculated. It was found that λ_{111} decreases with increasing Ga content, which was attributed to the decrease of magnetic properties of the compounds. By using the strain gauge method, we found that substitutional Ga cannot improve the polycrystal magnetostriction for the $TbFe_2$ compound.

[1] T. Funayama, T. Kobayashi, I Sakai, and M. Sahashi, Appl. Phys. Lett. **61**, 114 (1992).
[2] A E. Clark, J. P. Teter, and O. D. McMasters, IEEE Trans. Magn. **MAG-23**, 3526 (1987).
[3] J. P. Teter, A E. Clark, M. Wun-Fogle, and O D McMasters, IEEE Trans. Magn. **MAG-26**, 1748 (1990).
[4] A. E. Clark, J. P. Teter, and M. Wun-Fogle, J. Appl. Phys. **69**, 5771 (1991).
[5] A. E. Clark, *Ferromagnetic Materials*, edited by E. P. Wohlfarth (North-Holland, Amsterdam, 1980), Vol. 1, p. 531.
[6] M. Sahashi, T. Kobayashi, and T. Funayama, Proceedings of the Tenth International Workshop on Rare-earth Magnets and Their Applications, Kyoto, Japan, May 16–19, 1989, p. 347.
[7] H. Y. Yang, H. Q. Guo, B. G. Shen, L. Y. Yang, J. Yuan, and J. G. Zhao, Phys. Status Solidi A **129**, K107 (1992).
[8] R. Z. Levitin and A S. Markosyan, J. Magn. Magn. Mater. **84**, 247 (1990).
[9] J. P. Liu, F. R. de Boer, and K. H. J. Bushow, J. Magn. Magn. Mater **98**, 291 (1991).
[10] B. Bleaney, G. J. Bowden, J M. Cadogan, R. K. Day, and J. B. Dunlop, J. Phys. F: Metal Phys. **12**, 795 (1982)
[11] M. Liebs, K. Hummler, and M Fahnle, J. Magn. Magn. Mater. **124**, 239 (1993).
[12] B. Barbara, J. P. Giraud, J. Laforest, R. Lemaire, E. Siaud, and J. Schweizer, Physica **86-88B**, 155 (1977).

Comparison of the dynamic magnetomechanical properties of $Tb_{0.27}Dy_{0.73}Fe_2$ and $Tb_{0.30}Dy_{0.70}Fe_2$

D. Kendall[a] and A. R. Piercy
Department of Mathematical Sciences, University of Brighton, Brighton BN2 4GJ, United Kingdom

Comparison is made between the magnetomechanical properties of $Tb_{0.27}Dy_{0.73}Fe_2$ (27 Tb) and $Tb_{0.30}Dy_{0.70}Fe_2$ (30 Tb), two commercially available compositions of the giant magnetostrictive alloy Terfenol-D. The quasi-static magnetostriction (as a function of bias field) and the dynamic strain coefficient (as a function of bias field and frequency) are shown for the two compositions at room temperature, using stress bias values of 0 and 9 MPa. The energy loss per cycle as a function of frequency is also given. The data for the static magnetostriction versus bias field shows 30 Tb to exhibit a significantly greater increase in initial slope and saturation strain when stress bias is applied compared to that seen for 27 Tb, which possesses superior magnetostriction at zero stress bias. A similar trend is observed in the data for the dynamic strain coefficient with 30 Tb again performing better under stress bias. The widening of the static strain hysteresis loop observed for stressed 30 Tb is seen to manifest itself in the low frequency energy loss per cycle; however 27 Tb is observed to possess the higher eddy current loss at 1 kHz. Data for the ratio d/χ, a quantity which is dependent only on magnetization processes and material constants, are shown which suggests that the application of a stress bias affects the magnetization processes, but differently for the two compositions.

INTRODUCTION

The magnetomechanical properties of Terfenol-D of nominal composition $Tb_{0.27}Dy_{0.73}Fe_2$ have been extensively investigated for use in actuator and transducer devices (see the review by Jiles[1]). It has also been widely reported that the composition $Tb_{0.30}Dy_{0.70}Fe_2$, under stress bias, has a high saturation magnetostriction and a high differential (quasi-static) strain coefficient (the burst effect[2]) making the material suitable for use in actuators, but little has been reported on the dynamic properties and frequency response of this composition. In this article, a comparison is made of the static and dynamic magnetomechanical properties of commercial samples of $Tb_{0.27}Dy_{0.73}Fe_2$ and $Tb_{0.30}Dy_{0.70}Fe_2$, both with and without stress bias.

EXPERIMENT

The magnetomechanical properties of the Terfenol-D samples were determined at room temperature in an electromagnet using a strain gauge to measure the static and dynamic magnetostriction and search coils to monitor the drive field and dynamic magnetization in the material. A drive field of 2 kA m^{-1} rms (5.6 kA m^{-1} peak-to-peak) was employed. The energy loss per cycle per unit volume (W) was calculated from the measured values of the peak drive field, the magnitude of the dynamic relative permeability (μ_{r33}) and the phase of μ_{r33} with respect to the drive field (the loss angle, δ_B).

Stress bias was applied to a sample in the electromagnet using a rig comprising perspex head and tail pieces held together by three bolts. The compressive stress was supplied by a spring on each bolt and the rig was calibrated using a load cell in order subsequently to allow the force to be determined through the number of turns on the bolts. The amount of perspex between the ends of the sample and the pole pieces was kept to a minimum to reduce demagnetizing effects.

Both samples were manufactured by ETREMA of Edge Technologies, Ames, Iowa, and were 6 mm in diameter and cut to a length of 64 mm to fit the stress rig. In this article the sample of composition $Tb_{0.27}Dy_{0.73}Fe_2$ is referred to as 27 Tb and the sample of composition $Tb_{0.30}Dy_{0.70}Fe_2$ as 30 Tb.

RESULTS AND DISCUSSION

The quasi-static magnetostriction as a function of bias field is shown in Fig. 1 for the two Terfenol-D compositions under 0 and 9 MPa stress bias. It is clear from these plots that applying a stress to 30 Tb transforms the material from one that is inferior to 27 Tb with respect to initial slope and high-field magnetostriction to one that is superior. The high

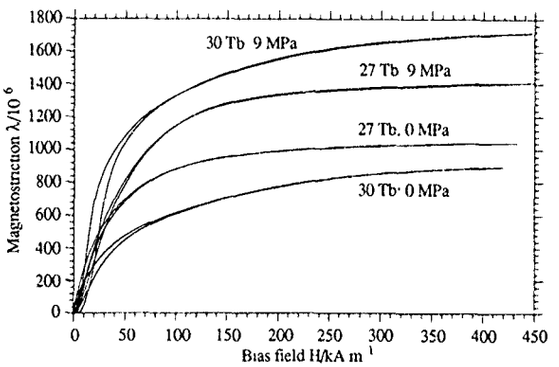

FIG 1 Static magnetostriction as a function of bias field for $Tb_{0.27}Dy_{0.73}Fe_2$ and $Tb_{0.30}Dy_{0.70}Fe_2$ under 0 and 9 MPa stress bias at room temperature.

[a]Present address. DRA, Holton Heath, Poole, Dorset BH16 6JU, United Kingdom.

 0021-8979/94/76(10)/7148/3/$6.00 © 1994 American Institute of Physics

TABLE I. Summary of the magnetomechanical properties of $Tb_{0.27}Dy_{0.73}Fe_2$ and $Tb_{0.30}Dy_{0.70}Fe_2$ at 0 (plain) and 9 MPa (italic) stress bias.

Composition	$d_{33max\ 70\ Hz}$ / nm A^{-1}		H_{d33max} / kA m^{-1}		λ_{sat} / 10^{-6}		W_{hyst} / J m^{-3} $cycle^{-1}$		$W_{eddy\ 1\ kHz}$ / J m^{-3} $cycle^{-1}$	
$Tb_{0.27}Dy_{0.73}Fe_2$	15.3	*10.4*	12.5	*30.0*	1100	*1490*	3.8	*4.0*	7.9	*17.9*
$Tb_{0.30}Dy_{0.70}Fe_2$	10.5	*16.2*	4.5	*22.0*	990	*1840*	3.8	*9.0*	3.8	*12.9*

initial slope for the 30 Tb composition under stress bias has been termed the burst effect[2] and is thought to be due to jumping[3] of the magnetization in a domain from the easy direction perpendicular to the axis of the rod to that closest to this direction. The maximum theoretical saturation strain for a ⟨112⟩ oriented rod of Terfenol-D is approximately 1250×10^{-6} unstressed and 2080×10^{-6} stressed (assuming $\lambda_{111}=1640\times10^{-6}$ and $\lambda_{111}/\lambda_{100}=16$). Values for the saturation strain λ_{sat} obtained by extrapolation against $1/H$, are shown in Table I and it is clear that neither composition has the theoretical value under zero stress. This may be partly attributed to axial misalignment of the Terfenol-D grains although, while the 27 Tb sample is 12% lower than the theoretical value, the 30 Tb composition is almost 21% lower. This behavior is not reflected when stress bias is applied since, although the theoretical maximum has not been reached (a higher stress bias is required[4]), the saturation strain for 30 Tb is 350×10^{-6} greater than that for 27 Tb. If the initial state of magnetization for 30 Tb under zero stress is not equivalent to the ideal demagnetized state, then this composition may possess positive magnetostriction when compared to the ideal state and hence the measured saturation strain will be less than that predicted from theory. Conversely, if the initial state of magnetization for 27 Tb is closer to the ideal state, the saturation strain will more nearly approach the theoretical value. The 30 Tb composition possesses a higher room temperature anisotropy than 27 Tb and hence the initial states of demagnetization or remanence are likely to be different. When a stress is applied, easy directions perpendicular to the rod are occupied, resulting in a negative magnetostriction compared with the ideal demagnetized state and more available strain on the application of a field.

The observed trend in the initial slope of the plots of magnetostriction versus bias field in Fig. 1 is reflected in the data for the dynamic strain coefficient (d_{33}) as a function of bias field shown in Fig. 2, with 30 Tb performing better under stress bias than 27 Tb. If the dynamic magnetization processes are the same as those under quasistatic conditions, then the burst effect mechanism could be responsible for the differences observed dynamically. The magnitude of the dynamic strain coefficient is not as high as the incrementally determined value (which can be as large as 90 nm A^{-1} for 30 Tb[5]), although we have found that d_{33} increases markedly with the magnitude of the drive field. This field dependence arises because at low drive fields the slope of the minor loop is less than the slope of the static strain curve, but as the drive field is increased, the magnetostriction is forced to execute a loop of greater slope due to the limited width of the hysteresis of the static curve.

Figure 3 shows d_{33} as a function of frequency for the two compositions under stress bias values of 0 and 9 MPa. The observed flat response, which has been reported[6,7] previously for unstressed 27 Tb, is expected because the critical frequency, at which eddy current effects are significant, is greater than 1 kHz. (The similarity between the magnitude of d_{33} under 0 and 9 MPa stress bias is coincidental through the choice of bias field. See d_{33} at 30 kA m^{-1} in Fig. 2.) The graph of Fig. 4 shows the energy loss per cycle (W) as a function of frequency. The observed widening of the static strain hysteresis loop for 30 Tb at 9 MPa is seen to manifest itself in the low frequency energy loss per cycle (W_{hyst}), which has similar values for 27 Tb unstressed and stressed and for 30 Tb unstressed, but which is more than 50% larger for 30 Tb stressed. The data in Table I show that both compositions exhibit higher eddy current loss ($W_{eddy}=W-W_{hyst}$)

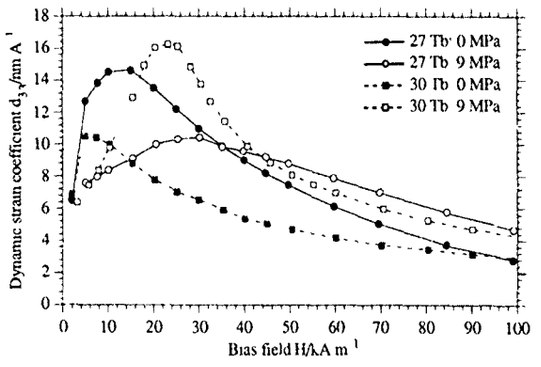

FIG 2 Dynamic strain coefficient as a function of bias field for $Tb_{0.27}Dy_{0.73}Fe_2$ and $Tb_{0.30}Dy_{0.70}Fe_2$ under 0 and 9 MPa stress bias at room temperature using a 70 Hz, 2 kA m^{-1} rms drive field

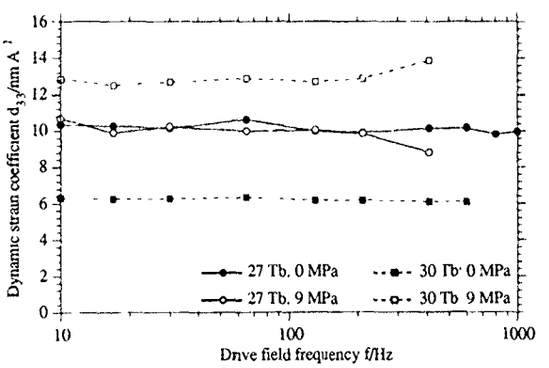

FIG. 3 Dynamic strain coefficient as a function of frequency for $Tb_{0.27}Dy_{0.73}Fe_2$ and $Tb_{0.30}Dy_{0.70}Fe_2$ under 0 and 9 MPa stress bias at a bias field of 30 kA m^{-1} using a 2 kA m^{-1} rms drive field

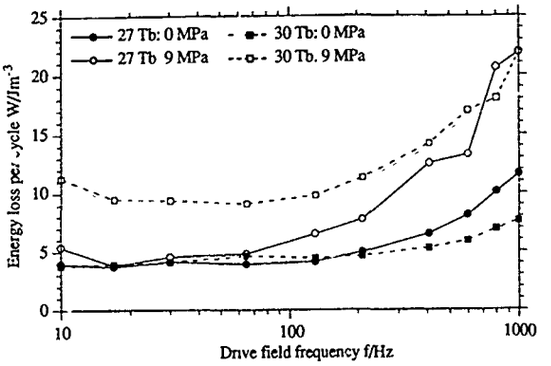

FIG. 4. Energy loss per cycle as a function of frequency for $Tb_{0.27}Dy_{0.73}Fe_2$ and $Tb_{0.30}Dy_{0.70}Fe_2$ under 0 and 9 MPa stress bias at a bias field of 30 kA m^{-1} using a 2 kA m^{-1} rms drive field.

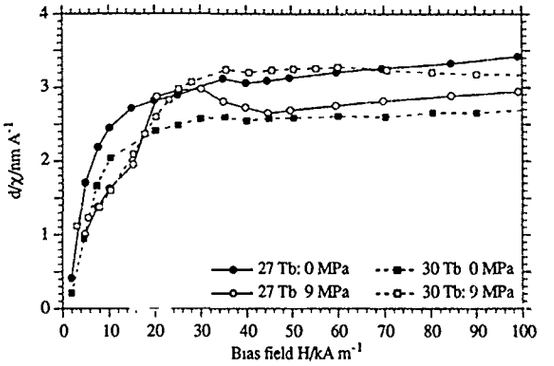

FIG. 5. The ratio d/χ as a function of bias field for $Tb_{0.27}Dy_{0.73}Fe_2$ and $Tb_{0.30}Dy_{0.70}Fe_2$ under 0 and 9 MPa stress bias at room temperature using a 70 Hz, 2 kA m^{-1} rms drive field.

at 1 kHz when stressed, with 27 Tb being the higher. In consequence, the total loss for 27 Tb with stress bias exceeds that for 30 Tb at frequencies above 1 kHz. Part of the increase in apparent eddy current loss can be attributed, from a classical eddy current consideration, to the increase in μ_{r33} at the bias field value used. However, not all of the increase can be accounted for in this way, suggesting that either the eddy current losses behave nonclassically under stress or that other loss mechanisms become significant.

The ratio of the dynamic strain coefficient to the dynamic magnetic susceptibility, d/χ, is a quantity which is dependent only on magnetization processes and material constants and therefore can give information on the magnetization processes taking place.[6,8] This ratio as a function of bias field is shown in Fig. 5 for the two compositions under 0 and 9 MPa stress bias. The two plots for 27 Tb are seen to exhibit similar trends, with the application of stress causing a decrease in the magnitude of d/χ. The plots for 30 Tb also show a similar trend, although in this case the application of stress increases d/χ. These observations suggest that stress bias changes the magnetization processes, but in different ways depending on the composition. Finally we note that at low bias fields, the magnitude of d/χ for 30 Tb is smaller, which suggests an increased number of 180° walls and gives support to the suggestion that different demagnetized states occur for the two compositions.

CONCLUSION

Some of the important magnetomechanical properties are summarized in Table I for the two compositions of Terfenol-D. It is proposed that the performance of transducer devices that are driven at a few kHz would be enhanced by the use of $Tb_{0.30}Dy_{0.70}Fe_2$ when compared to $Tb_{0.27}Dy_{0.73}Fe_2$, not only in terms of the magnetostriction attainable, but also from the point of view of eddy current losses.

ACKNOWLEDGMENT

This work has been carried out with the support (D. Kendall) of the DRA (Maritime Division), Portland, UK.

[1] D. C. Jiles, J. Phys. D: Appl. Phys. **27**, 1 (1994).
[2] R. D. Greenough, A. J. Wilkinson, A. Jenner, A. Parvinmehr, and M. Schulze, IMechE **C391/072**, 109 (1989).
[3] A. E. Clark, J. P. Teter, and O. D. McMasters, J. Appl. Phys. **63**, 3910 (1988).
[4] D. C. Jiles, J. E Ostenson, C. V. Owen, and T. T. Chang, J. Appl. Phys. **64**, 5417 (1988).
[5] A. G. Jenner, R. D. Greenough, A. J. Wilkinson, and A. Parvinmehr, IEEE Trans. Magn. **MAG-26**, 2589 (1990)
[6] D. Kendall and A. R Piercy, J. Appl. Phys. **73**, 6174 (1993).
[7] D. Kendall and A. R. Piercy, *Magnetoelastic Effects and Applications*, edited by L Lanotte (Elsevier, The Netherlands, 1993), p. 111.
[8] D. Kendall and A. R. Piercy, IEEE Trans. Magn. **MAG-26**, 1837 (1990).

Anisotropy in twinned terfenol-D crystals

D. G. Lord and D. Harvey
Joule Physics Laboratory and Science Research Institute, University of Salford, Salford M5 4WT, United Kingdom

The highly magnetostrictive cubic compound Terfenol-D ($Tb_{0.3}Dy_{0.7}Fe_2$) solidifies via a {211} dendritic growth front when grown by a free-standing zone technique. The resulting material is usually composed of dendritic plates often containing crystallographic twins, the predominant plate and twin plane being the $(1\bar{1}1)$ orthogonal to the $(\bar{2}\bar{1}1)$ growth plane. Results of room temperature magnetic torque analysis from (011) disk specimens, having differing twin densities, are presented which yield both the magnetic anisotropy constants, $K_1=-1.6\times10^5$ J/m^3 and $K_2=-0.16\times10^5$ J/m^3, and the relative parent/twin volume. Magnetic susceptibility data both parallel and transverse to the applied field are presented which, in conjunction with the anisotropy results, emphasize the importance of twin density on magnetoelastic response for typical application geometries.

I. INTRODUCTION

The cubic Laves phase ternary compound $Tb_{0.3}Dy_{0.7}Fe_2$ (Terfenol-D) is of significant interest technologically for actuator and transducer applications as it possesses a large magnetostriction to anisotropy ratio near room temperature. Commercially available material, grown by a free-standing zone technique, solidifies via a {211} dendritic growth front producing samples composed of dendritic plates which often contain crystallographic twin boundaries, the predominant plate and twin boundary plane being the {111} orthogonal to the growth front plane.[1,2] Such material exhibits significant magnetoelastic strain, of the order of 1500 ppm in moderate applied fields around 100 kA/m, the development of which, with increasing field, is characterized by discontinuous changes in strain at particular fields.[3]

The magnetic anisotropy, determined by the material composition, is such that anisotropy compensation is achieved at about 280 K;[4] above this temperature, the easy directions for the magnetization are along the ⟨111⟩ axes. It is the anisotropy, influenced by the defect nature of the material, which in the main determines the form of the strain evolution whether this is by domain wall motion or magnetization rotation. The presence of (111) twin boundaries leads to a complication in that not all the easy axes are continuous across either the twin or the dendrite boundaries. In order to gain a better understanding of the interaction of the magnetization and the strain, this article reports room temperature measurements of the anisotropy in such twinned Terfenol-D samples which, along with susceptibility and transverse susceptibility observations, demonstrate the importance of the parent/twin concentration on sample response.

II. EXPERIMENT

Samples used in this investigation were prepared in the form of 8-mm-diam rods by Edge Technologies Inc. by a free-standing zone technique using a zone rate of 38 cm/h. Disk specimens for torque curve analysis, 3 mm in diameter and 1 mm thick, were produced by spark erosion with disk faces parallel to the (011) plane orthogonal to the $(\bar{2}\bar{1}1)$ growth plane. Bar specimens used in measurements of the magnetic susceptibility, 50 mm in length and 5 mm by 5 mm in square cross section, were similarly produced with the long direction parallel to the growth axis and the faces mutually orthogonal and parallel to the (011) and $(1\bar{1}1)$ planes. All planar surfaces, aligned by x-ray back-reflection, were diamond polished to a 1/4 μm finish.

Torque curves were obtained from anti-clockwise rotation of a 650 kA/m magnetic field in the plane of the (100) disks using a Penoyer-type torque magnetometer[5] in which the specimen torque was balanced by an opposing torque produced by a known current passing through a coil, attached to the specimen suspension, which was located in a field from a fixed permanent magnet. All data reported here were taken at a room temperature of 293 K. Differential magnetic susceptibility data were obtained by subjecting the bar specimens to a dc and superimposed ac magnetic field directed along the long bar axis. The ac field of 5 kA/m and frequency 82 Hz was constant, while the dc field was ramped at a rate of 2 kA/m/s. Two pairs of mutually orthogonal pick-up coils were placed around the specimen to detect the transverse magnetization changes in both the $[1\bar{1}1]$ and [011] directions and one coil, with an associated air-flux compensation coil, was placed to detect susceptibility parallel to the applied fields and the $[\bar{2}\bar{1}1]$ direction. Signals in-phase with the ac magnetic field were detected by a lock-in amplifier. All measurements reported were obtained at zero applied stress and at room temperature.

III. RESULTS AND DISCUSSION

The spatial dependence of the magnetocrystalline anisotropy energy, $E(K)$, can be expressed phenomenologically for a cubic crystal as

$$E(K)=K_0+K_1(\alpha_1^2\alpha_2^2+\alpha_2^2\alpha_3^2+\alpha_3^2\alpha_1^2)+K_2(\alpha_1^2\alpha_2^2\alpha_3^2) \quad (1)$$

where K_n are the anisotropy constants and α_i are the direction cosines of the magnetization relative to the cubic axes of the crystal. The presence of both parent(p) and twin(t) oriented material in the specimens is accounted for by assuming a relative fractional parent-to-twin volume, c, such that $c=0.5$ for equal p and t volume content. The magnetic anisotropy energy and magnetization in both parent and twin are of necessity the same: only their relative crystallographic orientations differ. In Fig. 1 we show the anisotropy energy profiles for both twin and parent material superimposed on

 0021-8979/94/76(10)/7151/3/$6.00 © 1994 American Institute of Physics

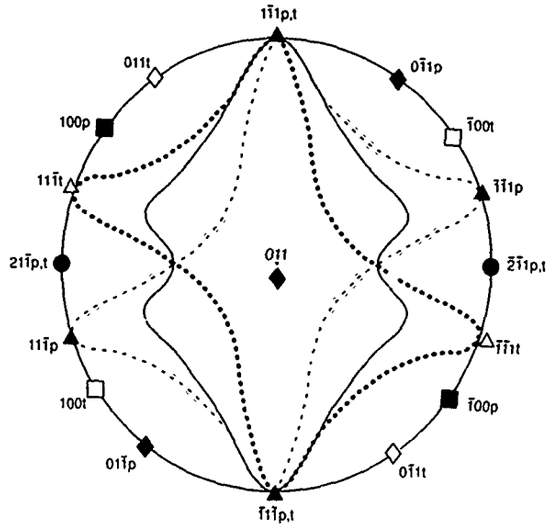

FIG. 1. Polar plot of anisotropy energy superimposed on the stereographic projection of the (011) plane showing parent (p) and twin (t) directions for a (111) twinning plane (dotted and dashed lines represent parent and twin, respectively, and full line represents the energy of the combination of equal parent and twin volumes).

the stereographic projection of the (011) plane of the disk specimen. The profiles are constructed from Eq. (1) using equal negative values of K_1 and K_2 and a K_0 value of half the radius of the projection. The easy ⟨111⟩ directions are clearly indicated by the larger radial values of the profile. Indicated on the figure are the parent and twin directions relative to the predominant (111) twinning plane.[1,2,6] It can be seen from Fig. 1 that the parent and twin are related by a rotation of 70.54° about the surface normal of the (011) plane. The solid energy profile in this figure represents the effective anisotropy energy of the combination of the assumed equal p and t volumes constructed by expressing the energy of the twin in terms of its direction cosines relative to the parent cubic axes. It is this profile that will produce the

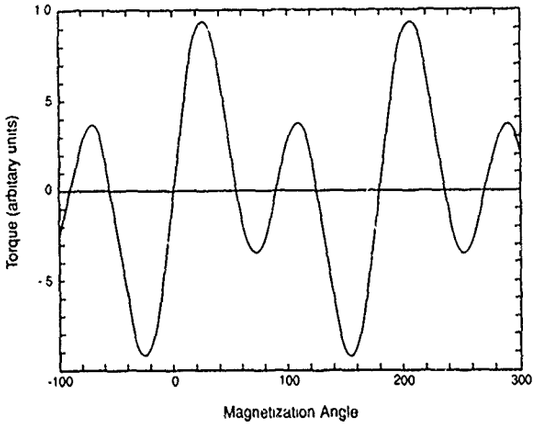

FIG. 2. Expected torque curve from magnetization rotation in the (011) for ⟨111⟩ easy axis cubic crystal. Zero angle is for magnetization along the [100] direction

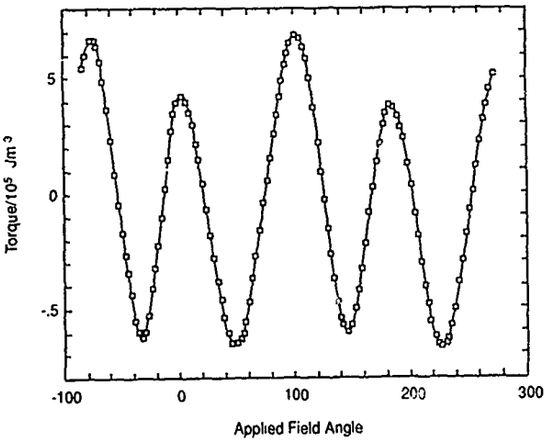

FIG. 3. Experimental torque curve from Terfenol-D (011) disk Zero angle is for field (650 kA/m) along parent [100] direction

resulting torque curve where the torque, corrected for misalignment of the field and the magnetization, is $-dE(K)/d\theta$, θ being the field angle with respect to the parent [100] direction.

The torque expected from an untwinned disk is shown in Fig. 2 and can be compared to an experimental curve from a (011) twinned sample shown in Fig. 3. Torque curves have been obtained from a number of samples, of differing twin density, and analyzed by a curve fitting procedure to yield both the relative twin density c and the anisotropy constants. The values found are $K_1 = -(1.60 +/- 0.08) \times 10^5$ J m^{-3} and $K_2 = -(0.16 +/- 0.01) \times 10^5$ J m^{-3} which compare favorably with previous data for K_1 though not with the previous scattered data for K_2. The values of c have been correlated with estimates of twin density from polarized optical micrographs of the disk surfaces, two examples of which are

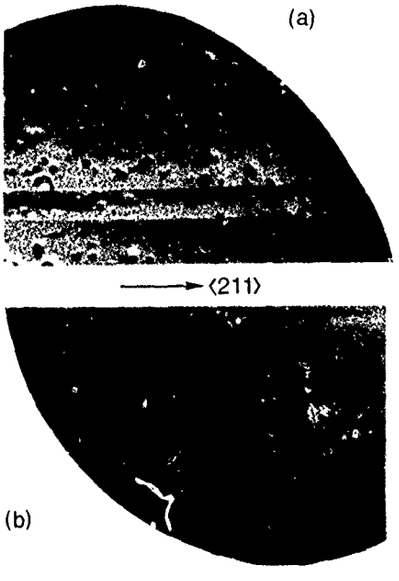

FIG. 4 Polarized optical micrographs from (011) Terfenol-D disks showing differences in twin (darker areas) density between disk (a) and disk (b).

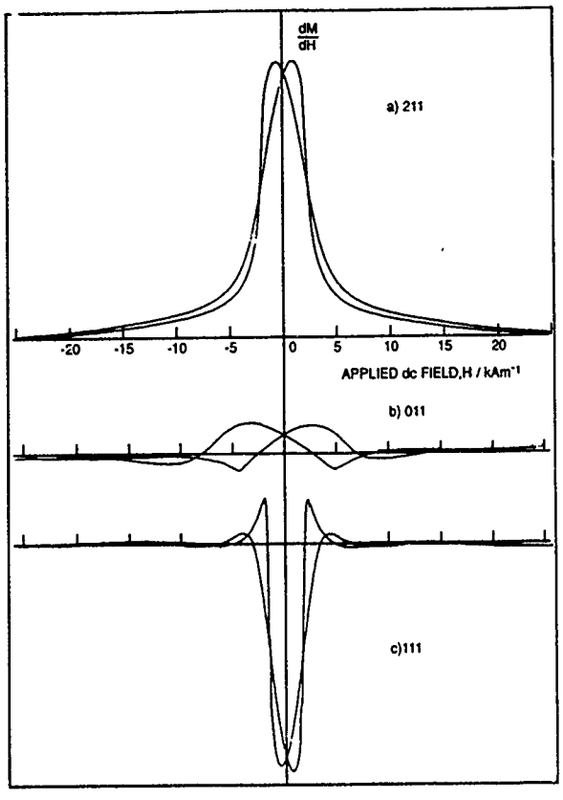

FIG. 5. Differential magnetic susceptibility data measured parallel to (a) [211] growth direction, (b) [011], and (c) [111] where applied dc and ac fields are parallel to [211]. Sensitivity for (b) and (c) is approximately ten times greater than for (a).

shown in Fig. 4, where the twins correspond to the lower reflectance areas and the straightness of the twin boundaries are clearly observed. Excellent agreement has been found for values of c between 0.3 as in Fig. 4(a) and 0.5 (the more typical material) as in Fig. 4(b).

Differential susceptibility and transverse susceptibility data in the mutually orthogonal $[\bar{2}\bar{1}1]$, [011], and $[1\bar{1}1]$ direction from a bar specimen with an optically estimated parent/twin density of $c=0.45$ is shown in Fig. 5. For a specimen with $c=0.50$, it may be expected that the high symmetry of the anisotropy energy about the $[\bar{2}\bar{1}1]$ bar axis, as seen in Fig. 1, would yield zero transverse magnetization as there would be equal populations distributed symmetrically with respect to the bar axis, even accounting for the anisotropic effect of the magnetostriction.[7] The small transverse susceptibility signals from the [011] and $[1\bar{1}1]$ are therefore due to the asymmetry in the anisotropy energy introduced by the inequality in parent and twin volumes. Indeed, the variations show excellent agreement both in field dependence and magnitude to the magnetostriction data obtained in these directions[3] and indicate that the magnetization distribution, as a function of applied field, is far from straightforward.

IV. CONCLUSIONS

The magnetic anisotropy constants in twinned Terfenol-D materials have been obtained from room temperature torque curve analysis from (011) plane disk specimens of varying twin content. Consideration of the anisotropy energy as a function of twin content clearly demonstrates the potential symmetry of currently available float-zone material for the case of equal parent/twin volumes. Where any inequality exists, the anisotropy, and hence magnetoelastic strain, will be asymmetrically disposed to the growth direction. The only crystal direction in which behavior is symmetrical in twinned or untwinned material is the ⟨111⟩ normal to the predominant twin plane. To manufacture device material using such a geometry would yield large strains with exceptional strain coefficients as seen from the ⟨111⟩ data in Fig. 5.

[1] A. E. Clark, J. P. Teter, and O. D. McMasters, J. Appl. Phys. **63**, 3910 (1988).
[2] M. Al-Jiboory, D. G. Lord, Y. J. Bi, J. S. Abell, A. M. H. Hwang, and J. P. Teter, J. Appl. Phys. **73**, 6168 (1993).
[3] J. P. Teter, M. Wun-Fogle, A. E. Clark, and K. Mahoney, J. Appl. Phys. **67**, 5004 (1990).
[4] M. Al-Jiboory and D. G. Lord, IEEE Trans. Mag. **26**, 2583 (1990).
[5] R. F. Penoyer, Rev. Sci. Instrum. **30**, 711 (1959).
[6] Y. J. Bi, J. S. Abell, and A. M. H. Hwang, J. Magn. Magn. Mater. **99**, 159 (1991).
[7] J. P. Teter, A. E. Clark, and O. D. McMasters, J. Appl. Phys. **61**, 3887 (1987).

Published without author corrections

Device oriented magnetoelastic properties of $Tb_xDy_{1-x}Fe_{1.95}$ ($x=0.27$, 0.3) at elevated temperatures

K. Prajapati, R. D. Greenough, and A. G. Jenner
Department of Applied Physics, University of Hull, Hull HU6 7RX, United Kingdom

In order to assess the potential of the highly magnetostrictive compound Terfenol-D (composition $Tb_xDy_{1-x}Fe_{1.95}$, where $x=0.3$ or 0.27) for device applications in the temperature range 20–300 °C, measurement of magnetostrictive strain (λ), differential strain coefficient (d_{33}), and magnetomechanical coupling coefficient (k_{33}) have been made against applied dc field ($\leq$120 kA/m), uniaxial pressure ($\leq$20 MPa), and temperature. Comparing the two compositions at elevated temperatures has shown that large grain oriented material of the composition $Tb_{0.3}Dy_{0.7}Fe_{1.95}$ has higher strains and d coefficients at elevated temperatures than small grain oriented material of composition $Tb_{0.27}Dy_{0.73}Fe_{1.95}$, but for optimum coupling efficiency $Tb_{0.27}Dy_{0.73}Fe_{1.95}$ is preferable.

I. INTRODUCTION

The pseudobinary rare earth-iron compound Terfenol-D[1] ($Tb_xDy_{1-x}Fe_{1.95}$, where x is typically 0.27 or 0.3) generates large magnetostrictive strains (~1500 ppm) which can be used in a variety of applications. For a particular composition, the magnetomechanical properties depend on three principal factors: the applied field, temperature, and especially in grain oriented material, the applied stress.[2] Although some measurements have been made at elevated temperatures,[3] previous work has concentrated mainly on the room temperature properties. However, operation at higher temperatures is desirable for some applications and the present work was conducted to provide a more comprehensive assessment of magnetomechanical performance to temperatures up to 300 °C.

The two main constraints on the range of temperature over which Terfenol-D can be used are (i) the magnetocrystalline anisotropy, because at low temperatures the competing anisotropies of the Tb and Dy ions causes the easy axis of magnetization to switch from the $\langle 111\rangle$ to the $\langle 100\rangle$ axes,[4] and (ii) the exchange energy which decreases as the temperature approaches the Curie temperature, T_c, and causes the magnetostriction to decrease monotonically in accordance to single ion theory.[5] Within these constraints lies a useful range of temperature and the following results indicate how the performance of Terfenol-D can be optimized in this range.

The two compositions chosen for comparative purposes are $x=0.30$ (grain oriented, large grains), which is particularly susceptible to the application of applied uniaxial prestress along the $[11\bar{2}]$ grain growth axis,[6] and $x=0.27$ (grain oriented, small grains), chosen to minimize magnetocrystalline anisotropy at room temperature.[1] The grain structure in both compositions is typical of commercially available material.

II. EXPERIMENTAL TECHNIQUES

Commercial grade samples, prepared by a free float zone process, were in the form of rods 50 to 100 mm long and 6 mm diameter, with the $[11\bar{2}]$ growth direction along the rod axis. Magnetostrictive strain, λ, measured with strain gauges, were measured in dc fields $\leq$120 kA/m and with uniaxial stresses $\leq$20 MPa applied along the $[11\bar{2}]$ axis. The magnetostrictive strain coefficient $d_{33}(=d\lambda/dH)$ were obtained by differentiating the static λ-H curves. Coupling coefficients (k_{33}) were obtained from the magnetomechanical resonance. The measurements were undertaken in a noninductively wound furnace to obtain temperatures $\leq$300 °C (±1 °C) with samples contained in an argon atmosphere. Approximately 5% variation in measurements from sample to sample was expected and found.

III. RESULTS AND DISCUSSION

Data have been collected for λ, d_{33}, and k_{33} as functions of applied field, stress, and temperature. For each magnetostriction isothermal in Figs. 1 and 2, the uniaxial pressure and applied field have been chosen to yield the maximum d coefficient. At room temperature for $x=0.3$, after a sharp increase in strain at low fields (known as the "burst effect"[4]), at 120 kA/m the strain is almost doubled. The isofield contours decrease slowly with temperature at low

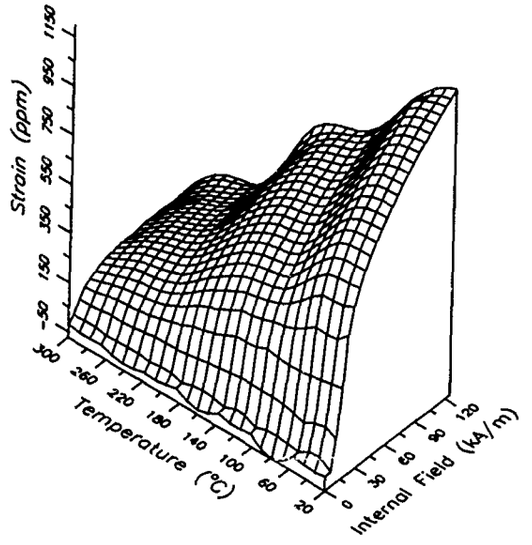

FIG. 1. Strain profile at optimum pressure bias conditions for maximum d_{33} as a function of temperature and internal magnetic field for $x=0.30$ composition.

 0021-8979/94/76(10)/7154/3/$6.00 © 1994 American Institute of Physics

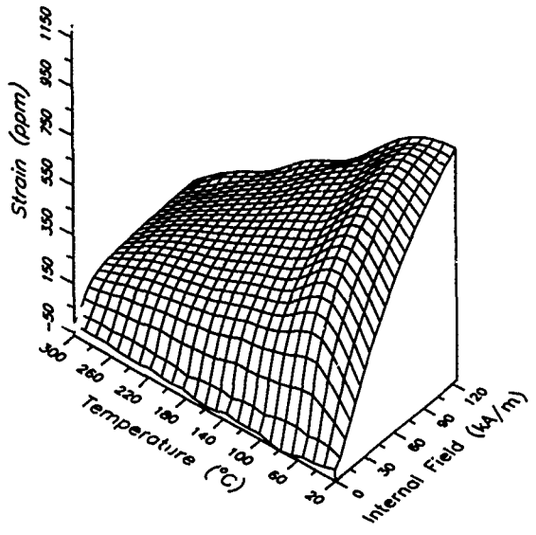

FIG. 2. Strain profile at optimum pressure bias conditions for maximum d_{33} as a function of temperature and internal magnetic field for $x=0.27$ composition.

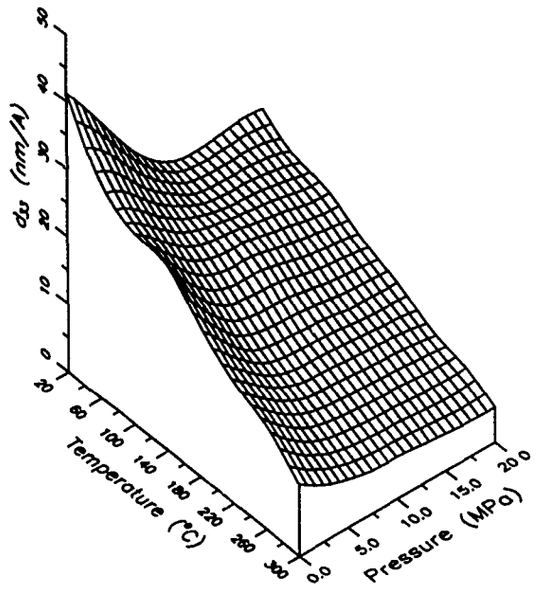

FIG. 4. Variation in optimum d_{33} with pressure and temperature for $x=0.27$.

fields (<30 kA/m) but the decrease in the 120 kA/m contour in this sample is clearly not monotonic. Although magnetic saturation has not been achieved, it is expected that these strains should decrease with temperature approximately as m^3 [where m is the reduced magnetization (M_T/M_0)].[5] The maximum at ~140 °C interrupts this pattern and is evident in fields as low as 30 kA/m. For practical applications this effect at 140 °C is an added bonus because unexpectedly larger strains can be generated. For the sample with $x=0.27$ the decrease in isofield strains with temperature are almost monotonic for any field strength. The different behaviors of the $x=0.3$ and 0.27 samples is explained by the competing anisotropies of the Tb and Dy ions. For $x=0.3$ the anisotropy minimum is at $T=-10$ °C with maximum strains at 25 °C; and for $x=0.27$, the minimum in anisotropy occurs at approximately $T=20$ °C, with the maximum strain at ~60 °C (comparable with findings by Clark *et al.*[3]).

Along each isothermal contour for d_{33} (Figs. 3 and 4) fields have been applied to give the largest d coefficient for each applied pressure. For $x=0.3$ in the range $20 \leq T \leq 200$ °C, an enhanced d coefficient is present at low pressures due to the combined effects of applied stress and grain orientation.[4] The level of stress becomes less critical for $T>200$ °C, where the small magnetocrystalline anisotropy[5] renders the applied stress less effective in regu-

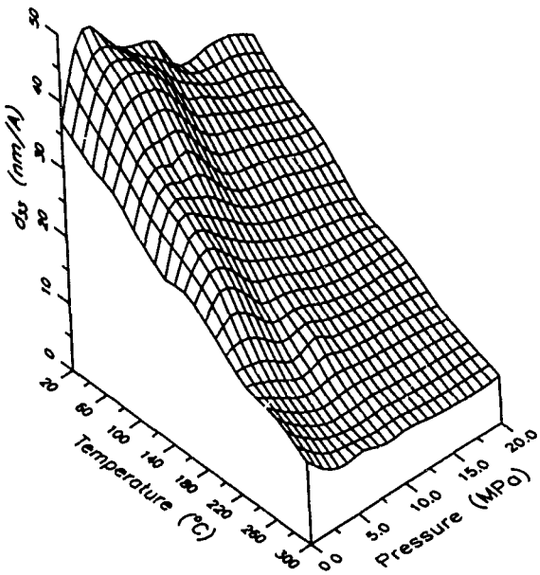

FIG. 3. Variation in optimum d_{33} with pressure and temperature for $x=0.30$

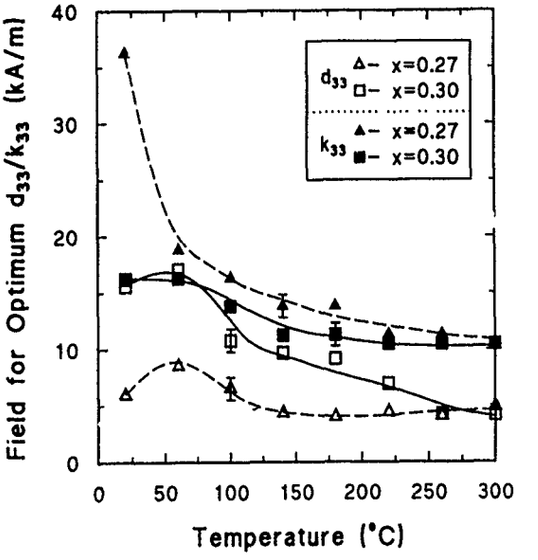

FIG. 5. dc bias fields required to obtain maximum d_{33} and k_{33} as a function of temperature for $x=0.27$ and 0.30.

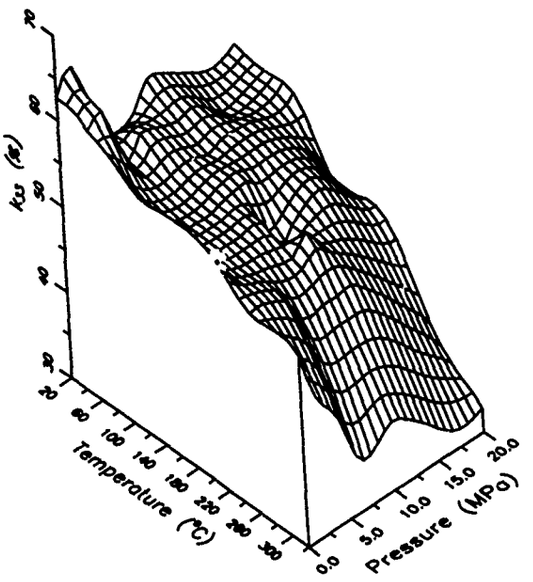

FIG. 6. Surface plot showing the variation in optimum k_{33} with pressure and temperature for $x=0.30$.

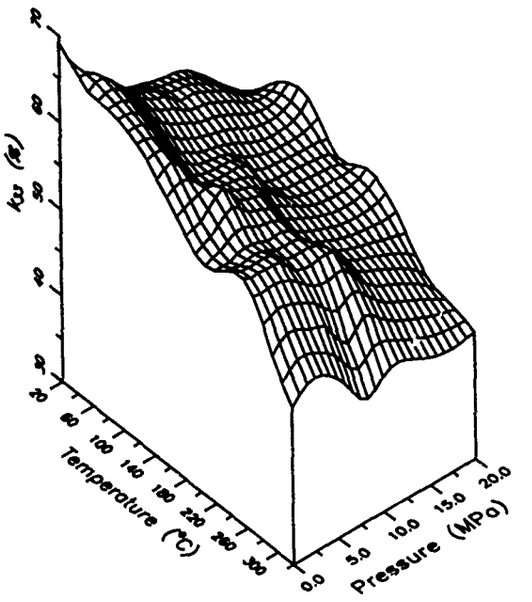

FIG. 7. Surface plot showing the variation in optimum k_{33} with pressure and temperature for $x=0.27$.

lating the magnetization processes. This is the case for $x=0.27$ at most temperatures until an imbalance between the Tb and Dy anisotropies emerges at low temperatures ($T\leqslant 40$ °C). Due to the magnetocrystalline anisotropy, undulations occur in the d_{33} surface for $x=0.30$, whereas this surface for $x=0.27$ is comparatively smooth. The oscillation on the room temperature isothermal for $x=0.30$ have been observed in other samples with the same composition and are reported elsewhere.[7] From the application point of view there is a clear advantage in employing Terfenol-D with $x=0.30$ for $T\leqslant 100$ °C. Provided pressure loading is kept in the range 2–10 MPa. Larger fields are required compared with $x=0.27$ (Fig. 5) and some control will be needed to maintain them in the range 10–17 kA/m.

The surfaces representing optimum magnetomechanical coupling as a function of temperature and pressure are very irregular for both compositions (Figs. 6 and 7). This is not surprising because k_{33} depends on d coefficient, permeability, and elastic compliance.[2] At elevated temperatures ($T\sim 300$ °C), for $x=0.30$, k_{33} is very strongly dependent on pressure. It decreases from ~0.5 to ~0.35 between zero and 7 MPa, representing a reduction in transducer efficiency from 25% to 12%. For $x=0.27$ the lowest observed value for k_{33}, regardless of pressure or temperature is ~0.45. It is concluded that pressure dependent effects on k_{33} in large grain oriented material are a disadvantage and small grain oriented material ($x=0.27$) is preferable.

IV. CONCLUSIONS

For practical applications the present results show that large grain oriented material with the composition $Tb_{0.3}Dy_{0.7}Fe_{1.95}$ produces better strain and d coefficients at elevated temperatures provided the applied field is controlled. For optimum coupling efficiency at elevated temperatures, the small grain oriented material with composition $Tb_{0.27}Dy_{0.73}Fe_{1.95}$ is preferable.

ACKNOWLEDGMENTS

The authors wish to thank EPSRC and Geo Measurement Systems, for the financial support given to K. Prajapati and staff in the Department of Applied Physics who assisted with this work.

[1] A. E. Clark, R. Abbundi, and W. R. Gillmore, IEEE Trans. Mag. **14**, 542 (1978).
[2] R. D. Greenough, A. G. I. Jenner, M. P. Schulze, and A. J. Wilkinson, J. Magn. Magn. Mat. **101**, 75 (1991).
[3] A. E. Clark and D. N. Crowder, IEEE Trans. Mag. **21**, 1945 (1985).
[4] A. E. Clark, J. Teter, and O. D. McMasters, J. Appl. Phys. **63**, 3910 (1988).
[5] E. Callen and H Callen, Phys. Rev. **129**, 578 (1963).
[6] J. D. Verhoeven, E. D. Gibson, O. D. McMasters, and H H. Baker, Met. Trans. A **18A**, 223 (1987).
[7] N. Galloway, R. D. Greenough, A. G. Jenner, and M. P. Schulze (these proceedings).

Influence of hydrogen on the magnetic properties of Terfenol-D

L. Ruiz de Angulo, J. S. Abell, and I. R. Harris
School of Metallurgy and Materials, University of Birmingham, Birmingham, United Kingdom

The reactions with hydrogen of the C15-type Laves phase $Tb_{0.27}Dy_{0.7}Fe_2$ have been studied by differential thermal analysis and the influence of this hydrogenation upon the magnetic properties was observed with a Curie–Faraday balance and a vibrating sample magnetometer. It has been found that a slightly rare earth rich composition allows the hydrogenation to take place at room temperature. Two endothermic peaks observed on heating under 1.2 bar of hydrogen are attributed to hydrogen desorption, due possibly to the form of the pressure isotherms. At a pressure of 1.2 bar, the amorphization and disproportionation peaks are combined as a single peak, but a higher pressures these two phenomena separate into two peaks. After the first absorption/desorption cycle, the hydrogenation occurs at temperatures as low as −75 °C, and is highly exothermic and very rapid in nature. The magnetic susceptibility of the compound suffers a dramatic drop when it is hydrided, and the magnetization at 1100 kA m^{-1} falls from 77.5 J T^{-1} kg^{-1} to 9.2 J T^{-1} kg^{-1}. When heated in hydrogen, a peak in susceptibility was observed at about the same temperatures as those of the amorphization/disproportionation reactions. The Curie point of the amorphous hydrided material was found to be around 68 °C, with a magnetization at room temperature and 1100 kA m^{-1} of 46 J T^{-1} kg^{-1}. The fully disproportionated material had a magnetization of 82 J T^{-} kg^{-1} at 1100 kA m^{-1}, which was related to the proportion of α-Fe formed during the disproportionation reaction.

I. INTRODUCTION

The RTM_2 (R=rare earth, TM=transition metal) type Laves phase compounds have been studied in the last few years for their interesting magnetic properties and hydrogen-absorption capacity, see, for example, Refs. 1–2. Upon hydrogenation, these compounds exhibit substantial changes in their magnetic properties. In addition, the pseudobinary Terfenol-D ($Tb_{0.27}Dy_{0.73}Fe_2$) has outstanding magnetorestrictive properties combining a low crystalline anisotropy with a huge magnetorestriction at room temperature.[3] In the light of these studies, it is therefore interesting to investigate the hydrogenation behavior of this compound.

II. EXPERIMENT

The material used in the present work was $Tb_{0.27}Dy_{0.73}Fe_{1.93}$ ($RFe_{1.93}$). Lumps (a single coarse particle of ≈200 mg) were introduced to a specially constructed differential thermal analyzer (DTA) with a hydrogen atmosphere (HDTA), and were subjected to different pressures with a heating rate of 3 °C per min. The material obtained was used for measurements on a vibrating sampler magnetometer (VSM), and for x-ray diffractometry using Co K_α and Cu K_α radiation. Curie–Faraday balance measurements were performed by hydrogenating freshly cut lumps of around 30 mg, *in situ*. In this case, a hydrogen pressure of 1 bar was employed.

A. Hydrogen absorption

HDTA was performed in order to investigate the influence of the rare earth grain boundary phase on the hydrogenation process. It was found that, when the material was single phase and in lump form, the hydrogenation process took place at about 280 °C, and at about 120 °C when in the form of crushed powder. However, the compound $RFe_{1.93}$ (3.5 at. % of free rare earth) reacts very rapidly at temperatures close to room temperature, even as a lump. Figure 1 shows the HDTA trace of lumps of $RFe_{1.93}$ heated in a hydrogen atmosphere at 1.2, 3, and 5 bar initial pressure.

Three exothermic peaks and two endothermic peaks were seen in the trace, corresponding to the run at 1.2 bar of H_2. At higher pressures four, exothermic peaks, but only one endothermic peak, were observed. X-ray diffraction examination of the material was carried out after each peak of the 1.2 bar run. After the first exothermic peak, the material had an expanded cubic structure, indicating hydrogen absorption in the crystalline state. The x-ray diffraction (XRD) patterns of the samples hydrogenated after each endothermic peak showed different rhombohedral structures. On hydrogenation at 400 °C, very broad x-ray peaks corresponding to RH_2 and α-Fe could be seen. At temperatures above 500 °C, much sharper peaks, corresponding to RH_2 and α-Fe were observed. When heated under 5 bar to 300 °C, no x-ray peaks, but a broad maximum, can be observed, thus indicating

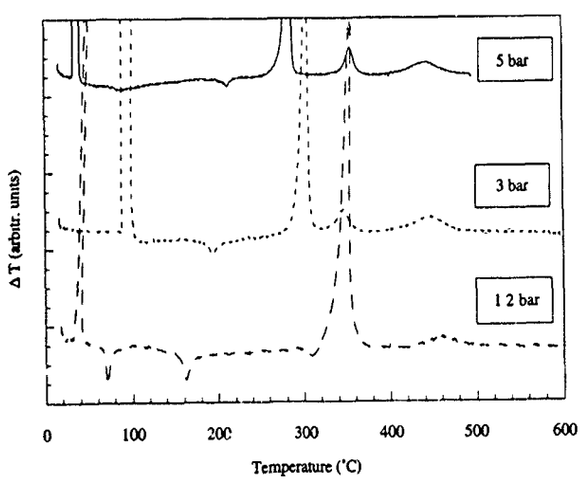

FIG. 1. HDTA traces of $Tb_{0.27}Dy_{0.73}Fe_{1.93}$($RFe_{1.93}$) at different pressures.

 0021-8979/94/76(10)/7157/3/$6.00 © 1994 American Institute of Physics

amorphous material. Finally, the diffraction pattern of the sample heated under 5 bar to 400 °C is very similar to the one heated to the same temperature at 1.2 bar. The endothermic peaks move to higher temperatures with increasing pressure, and this could indicate that they are related to the form of the pressure isotherms rather than to any change in the structure or state. This data are consistent with the work of others researchers.[2,4]

These results indicate that, below 280 °C in this range of pressures, Terfenol-D absorbs hydrogen while maintaining a crystalline structure. The second exothermic peak observed at 1.2 bar can be ascribed to the combination of the hydrogen induced amorphization and the disproportionation reaction. These two reactions separate at higher pressures due to a lowering of the amorphization temperature. This lowering of the amorphization temperature with pressure has already been reported in other Laves phases such as $TbFe_2$ (Ref. 5) and $GdFe_2$ [6]

It was observed that, when cycles of absorption/desorption were performed, the initial hydrogenation reaction would take place immediately at room temperature. To investigate if this could be done at lower temperatures, a lump of $RFe_{1.93}$ was hydrided, and then desorbed by heating under vacuum to 350 °C and then cooled. At room temperature, 5 bar of argon was introduced, and the sample chamber was cooled with liquid nitrogen. When the temperature was −125 °C, the argon was replaced by 1.2 bar of H_2. At around −75 °C, a sharp and strong exothermic peak (ΔT=52 °C) was observed. From this point and apart from the hydrogen absorption peak at 40 °C, the trace was the same as that for 1.2 bar H_2 shown in Fig. 1. One possible contribution to the low hydrogenation temperature is the very clean surface obtained in this material after hydrogen decrepitation. This behavior also indicates very rapid hydrogen diffusion in this system.

B. VSM measurements

Figure 2 shows the magnetization obtained for $RFe_{1.93}$ material heated in hydrogen at 1.2 bar to different temperatures. It can be seen that the cubic hydride is still unsaturated at 1100 kA/m, giving a magnetization of 9.2 J T^{-1} kg^{-1}. The rhombohedral hydrides (70 °C and 160 °C) exhibit a behavior close to paramagnetism. These observations agree with work by Annapoorni *et al.*[2]

The sample heated to 400 °C is easier to magnetize, and a magnetization at 1100 kA/m of 50 J T^{-1} kg^{-1} was obtained. From the experiments on the HDTA, this value should correspond to a mixture of amorphous plus very finely disproportionated material. To measure the real value of the amorphous material, one sample was heated under 5 bar of hydrogen up to 300 °C and then quenched. The XRD studies confirmed the amorphous state of the material. The amorphous material was found to be easy to magnetize, and a magnetization at 1100 kA/m of 46 J T^{-1} kg^{-1} was obtained. The sample heated to 500 °C at 1.2 bar had a magnetization of 82 J T^{-1} kg^{-1} at 1100 kA/m. This value is close to the theoretical value of 86 J T^{-1} kg^{-1} expected for a fully disproportionated material consisting of α-Fe and RH_2.

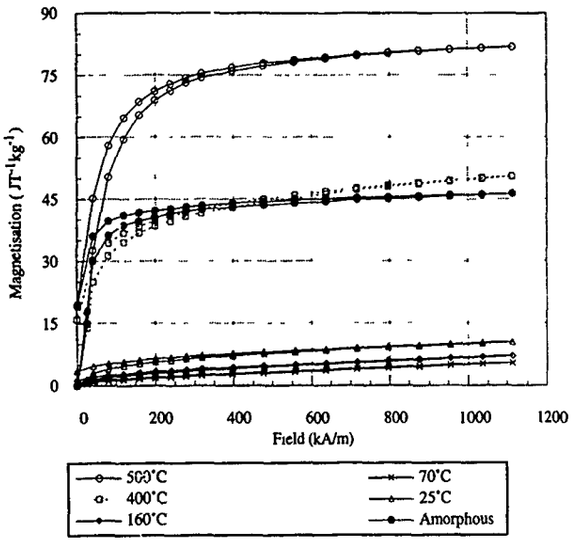

FIG. 2. Magnetization of $RFe_{1.93}$ samples heated in 1.2 bar H_2 to different temperatures and in 5 bar H_2 to 300 °C (amorphous).

C. Curie–Faraday balance experiments

The results of the Curie–Faraday balance experiment are shown in Fig. 3. Upon hydrogenation, there is a sudden drop in magnetic susceptibility, which is consistent with the VSM measurements. Between 350 and 520 °C, the susceptibility increases as the hydrogenated material starts to disproportionate, with the formation of α-Fe. On cooling, the susceptibility increases steadily, as would be expected from the presence of free iron.

After the initial drop at 57 °C, the susceptibility decreases slowly with the temperature up to around 180 °C, after which the temperature exhibits an increase. Another interesting feature is the peak between 260 and 350 °C, which is approximately the temperature range where the HDTA displays the combined amorphization/disproportionation peak. The increase in magnetic suscepti-

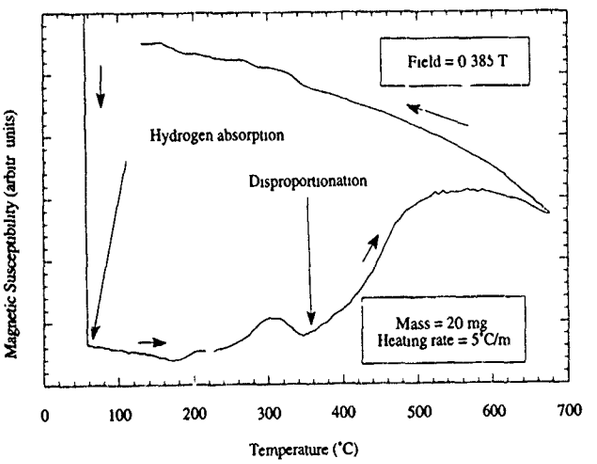

FIG. 3. Curie–Faraday balance trace of $RFe_{1.93}$ heated under 1 bar of hydrogen.

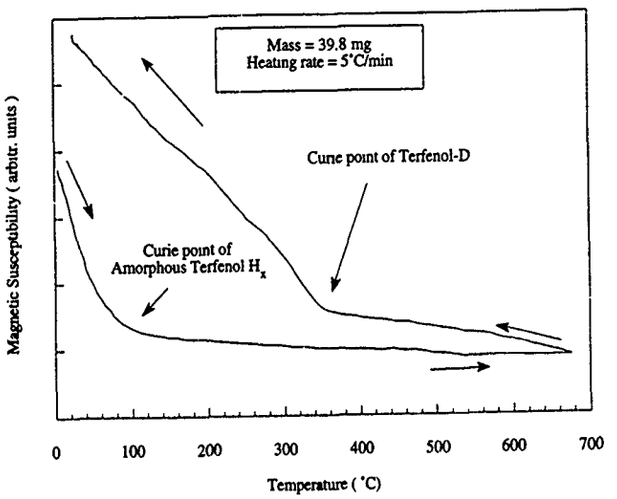

FIG. 4. Curie–Faraday balance trace of hydrogen induced amorphized $RFe_{1.93}$ heated under vacuum.

bility from 180 to 300 °C could be related to the loss of hydrogen prior to amorphization, as suggested by Manwaring *et al.*[7] What is not understood at this stage is the reason for the decrease in susceptibility from 300 to 350 °C.

Finally, 39.8 mg of $RFe_{1.93}$ were hydrogenated in the Curie–Faraday balance, heated to 380 °C, and then cooled. After this treatment, the resulting material should be mainly amorphous. After evacuating the chamber, the sample was heated under vacuum. The resultant trace is shown in Fig. 4. On heating, it can be seen that the Curie point for the amorphous Terfenol-D hydride, under these conditions, is around 68 °C (in this work the Curie point was defined as the intersection of the tangents of the two different parts of the curve). On cooling, another Curie point can be observed at around 370 °C. These results show that, when heated under vacuum, the hydrogen amorphized Terfenol reverts to its original crystalline structure.

D. Conclusions

The pseudobinary Laves phase, Terfenol-D, exhibits interesting and complex reactions with hydrogen. The initial hydrogenation can take place at a very low temperature under low hydrogen pressure. As is the case with other RTM_2 compounds, it is possible to induce amorphization with the introduction of hydrogen in the structure. The transformation of the rhombohedral hydride structure to the amorphous state is accompanied by a recovery of magnetization at room temperature. This amorphous material has a Curie point close to 70 °C.

ACKNOWLEDGMENTS

Thanks are due to the School of Metallurgy and Materials for the provision of student grant support for L. Ruiz de Angulo. Thanks are also due to Rare Earth Products for the provision of material.

[1] K. Aoki, X-G. Li, and T. Masumoto, Acta Metall. Mat. **40**, 1717 (1992).
[2] S. Annapoorni, Markandeyulu, and K. V. S. Rama Rao, J. Appl. Phys. **65**, 4955 (1989).
[3] A. E. Clark *Ferromagnetic Materials*, edited by E. P. Wohlfarth (North-Holland, New York, 1980) Vol. 1.
[4] D. G. R. Jones, P. J. McGuiness, J. S. Abell, and I. R. Harris, J. Less-Common Met. **158**, 153 (1990).
[5] K. Aoki, X-G. Li, and T. Masumoto, Mater. Sci. Forum **88–89**, 439 (1992).
[6] K. Aoki, X-G. Li, and T. Masumoto, Acta Metall. Mat. **40**, 221 (1992).
[7] C. A. F. Manwaring, D. G. R. Jones, L. Ruiz de Angulo, and I. R. Harris, Z. Phys. Chem. **179**, 133 (1993).

Control of Terfenol-D under load

A. G. Jenner, R. D. Greenough, and D. Allwood
Department of Applied Physics, University of Hull, Hull HU6 7RX, United Kingdom

A. J. Wilkinson
Department of Electronic Engineering, University of Hull, Hull HU6 7RX, United Kingdom

A vibration control case study is described which demonstrates the application of magnetostrictive (Terfenol-D) actuators. The magnetomechanical properties of the material suggests that when incorporated in devices for applications a nonlinear response will result. This case study compares the performance of two kinds of control strategy (both discrete), a conventional proportional and integral (PI) algorithm and a variable structure algorithm (DVSC) in both servo and cancellation/regulation roles. Both strategies were implemented on an INMOS[7] transputer based microcontroller with a sampling period of 300 μs. The results presented show that the control behavior of the DVSC strategy offers significant advantages over the PI strategy when controlling actuators with nonlinear characteristics, i.e., the rejection of a 5 Hz disturbance with a gain of −36 dB compared to a gain of −15 dB when using the PI strategy.

I. INTRODUCTION

The exceptional magnetomechanical properties of the rare earth compounds generically known as Terfenol-D, have been shown to offer a great potential for a variety of transducer and actuator applications.[1,2] This potential is now being realized with the development of linear and rotary actuators but such devices usually require advanced instrumentation to implement servo controlled loops, for example, linear micropositioning or active vibration control.[3]

Actuator/transducer performance is sensitive to operating conditions and requires device designs to take into account the specification and working conditions that are unique to each application. This sensitivity is due to the nonlinear response of Terfenol-D.[4] To achieve control over operating performance, strategies are employed that cater to both the nonlinear magnetomechanical material properties and the responses from the associated mechanical components. At best, the overall system response can be considered linear with a gain that varies with the operating point.[3]

Here, servo actuators that achieve predescribed displacement wave forms (i.e., triangle, sine or step) are described. These form the basis of an active vibration control (AVC) system in which two types of control algorithms (both discrete) are incorporated, a conventional proportional and integral (PI) type and a variable structure control (DVSC) type. A vibration control case study is presented to compare these two types of control algorithms.

II. EXPERIMENTAL TECHNIQUES

In order to demonstrate the potential of Terfenol-D in servo actuators and in active vibration control (AVC), Terfenol-D based actuators were constructed and two of these incorporated in a system arranged in the form of one table carried by another (Fig. 1). These actuators have built-in adjustable prestress to place the material on the optimum gain magnetostriction curve, permanent magnets to bias the material in the middle of the approximately linear region of the strain (λ)-field (H) curve, a drive coil to implement actuation signal, and a complete magnetic circuit to reduce flux loss.[3]

The actuators in the system can be used as individual units to implement servo tests or together with the lower actuator causing a disturbance of the level two table for antivibration (AV) tests. The aim of the AV control is to minimize the impact of any disturbance on the level one table using only the measurement of the position via linear variable displacement transducers (LVDTs), type GTX2500 (RDP, Ltd., Wolverhampton, UK) of the two tables to create a drive signal for the top actuator. Two control algorithm types, a conventional proportional and integral (PI) type, and a variable structure control (DVSC) type, both discrete, were implemented on a INMOS[5] transputer based microcontroller with a sampling period of 300 μs.[4]

III. RESULTS AND DISCUSSION

The overall response of the level one table/antivibration actuator system must be linear and of appropriate speed and character in order to cancel the vibration of the level two table. This must be achieved in spite of the nonlinear behavior of the Terfenol-D material. The presence of sensor two

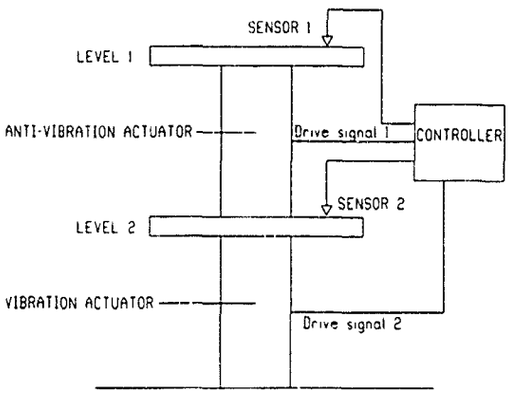

FIG. 1. Schematic of vibration experiment consisting of a vibration table in the form of one table carried by another.

 0021-8979/94/76(10)/7160/3/$6.00 © 1994 American Institute of Physics

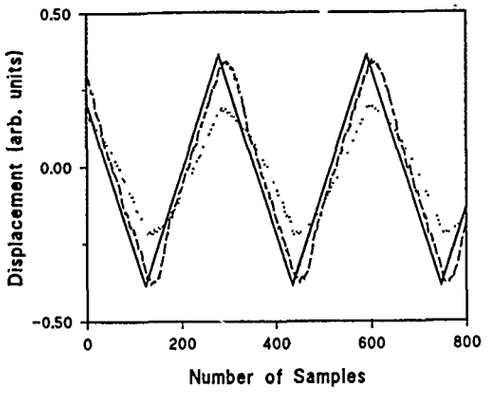

FIG. 2. Displacement of level one table position under DVSC (---) and PI (···) control in response to a triangular demand signal (—).

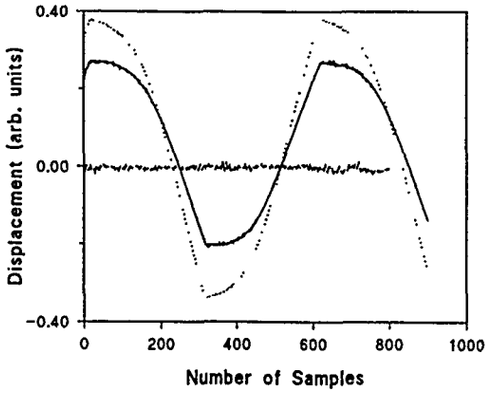

FIG. 4. Table displacements in response to a 5 Hz vibration actuation drive signal. Level one table displacement (—), level two (···), and "canceled" level one displacement under DVSC control as reference (~-~-~).

offers the possibility of using feed-forward control strategies to reduce the effects of the disturbance on the level one table.

To test the actuators and the control algorithms servo experiments were implemented with the use of predetermined demand displacement wave forms. The response of level one actuator to both triangular and step demand (frequency 10 Hz) signals supplied to the DVSC and PI controllers is shown in Figs. 2 and 3. No drive is supplied to the vibration actuator (level 2) in these experiments. It can be seen that the DVSC algorithm shows a superior signal following property particularly when using a step demand, it has the ability to suppress the excitation of unwanted mechanical resonances whilst responding to the demand in a desired way.

Variable structure control (VSC) is a modern nonlinear switching control technique[6] which can be described, for a second order process, as a means of constraining the dynamic behavior to that of a desired first order process response using switched feedback control, i.e., switching between positive and negative feedback. In the implementation of this control approach, the feedback gains which are switched are typically much larger than those used in PI control. Thus, there is an equivalent increase in control system immunity to process gain and behavior variations such as those caused by Terfenol-D. Here, the approach used to control the level one actuator was to use a computer based form of VSC with a discrete form of the switching line.[7] In a practical device such as the level one actuator, additional compensation dynamics must be used to ensure good performance, such as the incorporation of integral action to prevent steady state errors which may cause the DVSC to act inappropriately. If in certain situations the dynamics of the device are suspected to be higher than second order, then lead compensation in the form of discrete zeros must be incorporated into the feedback signal path. This prevents higher order resonances from being excited by the DVSC control.

The response of the level one and level two table to a 5 Hz drive signal applied to the vibration actuator when the DVSC controller is used to drive the antivibration actuator is shown in Fig. 4. The difference between using either PI or DVSC control to drive the antivibration actuator in cancellation is highlighted in Fig. 5, using the same input drive levels shown in Fig. 4, with the resulting amplitude reduction for each type (from spectrum analysis at 5 Hz) as −15 and −36 dB for the PI and DVSC algorithms, respectively.

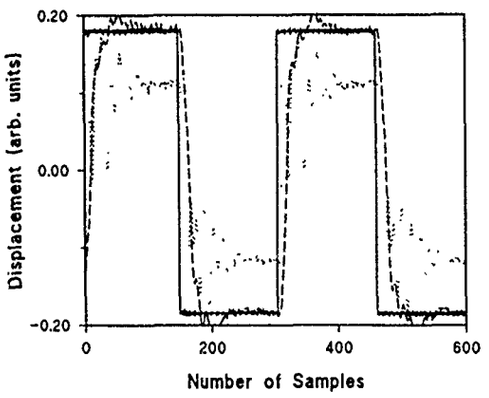

FIG. 3 Displacement of level one table position under DVSC (---) and PI (···) control in response to a step demand signal (—).

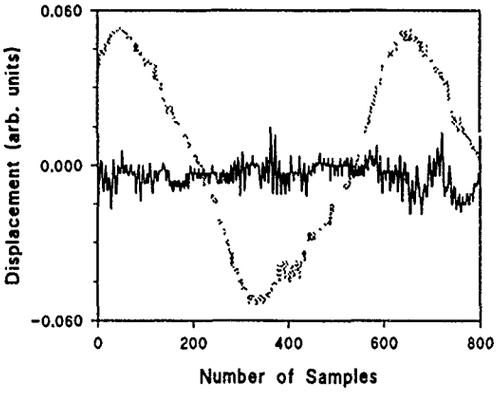

FIG. 5. Relative "canceled" level one table displacements under DVSC (—) and PI (·) control showing reduced effects of a 5 Hz vibration actuator drive signal using the same drive levels as shown in Fig. 4.

IV. CONCLUSION

Antivibration control has been illustrated with Terfenol-D based actuators incorporated in a device consisting of one table carried by another. Two implementations of computer based control have been demonstrated, a PI algorithm and a novel DVSC approach. Both algorithms were implemented using an INMOS[7] transputer based microcontroller. The DVSC algorithm demonstrated superior antivibration and demand signal following properties, with a resulting −36 dB in amplitude cancellation for a 5 Hz vibration signal. The DVSC approach showed particular superior behavior in its response to a step demand. It appeared to be able to suppress the excitation of unwanted mechanical resonances while at the same time responding to the step demand in a desired way.

ACKNOWLEDGMENTS

The authors wish to thank the staff in the Departments of Applied Physics and Electronic Engineering who assisted with this work and its presentation.

[1] R. D. Greenough, A. G. Jenner, M. P. Schulze, and A. J. Wilkinson, J. Magn. Magn. Mater. **101**, 75 (1991).

[2] F. Claeyssen, N. Lhermet, and R. Le Letty, Actuator 94, Proceedings of the 4th Int. Conf. on New Actuators, Bremen, Germany, June 1994, p. 203.

[3] R. D. Greenough, A. G. Jenner, and A. J. Wilkinson, *Machine Actuators & Control*, IMechE. Seminar Series Vol. 67 (IMechE, London, 1993).

[4] R. D. Greenough, M. P. Schulze, A. G. Jenner, and A. J. Wilkinson, IEEE Trans Magn. **27**, 5346 (1991).

[5] INMOS is a member of the SGS-Thomson group of companies.

[6] V. I. Utkin, Automat. Remote Contr. **44**, 1105 (1983).

[7] R. D. Greenough, A. G. Jenner, A. J. Wilkinson, and A. Parvinmehr, U.S.A Patent No. 893-10286-3 (Appl. 1989).

Pressure dependencies of magnetostrictive strain and *d* coefficient in Terfenol-D after thermal or magnetic annealing

N. Galloway,[a] R. D. Greenough, A. G. I. Jenner, and M. P. Schulze
Department of Applied Physics, University of Hull, Hull HU6 7RX, United Kingdom

The pressure dependence of the magnetostrictive strain coefficient, d_{33}, and maximum strains in applied fields of 120 kA m^{-1} have been measured in samples of Terfenol-D before and after thermal or magnetic annealing. Application of an annealing field, H_a, parallel to the ⟨111⟩ axes which are normal to grains oriented along the [11$\bar{2}$] axis, leads to an increase in d_{33} of as much as 81%, with applied uniaxial prestresses as low as 3 MPa. The variation of optimum d_{33} values as a function of stress applied along the [11$\bar{2}$] axis shows anomalous oscillations after magnetic annealing. The thermal and magnetic effects of the annealing procedures are discussed and a mechanism to explain magnetic annealing is proposed.

INTRODUCTION

Investigations have been made previously into the effects of thermal[1] and magnetic[2,3] annealing on the magnetostrictive properties of Terfenol-D. Of these, the most comprehensive study was made by Verhoeven on grain oriented samples with the annealing fields applied parallel to the ⟨111⟩ axes which are perpendicular to the [11$\bar{2}$] grain growth direction. After heat treatment followed by magnetic annealing, one particular sample ($Tb_{0.318}Dy_{0.682}Fe_{1.963}$) subsequently produced an increase in the maximum anisotropic magnetostrictive strain, λ_{max}, measured in an applied field of 3 kOe and, more striking, an unusually large magnetostrictive strain coefficient, d_{33} $(=d\lambda/dH)$ in the absence of any applied uniaxial stress. The application of a prestress is usually considered essential to generate such a response in samples which have not been subjected to magnetic anneal.[4] As part of the same investigation, other samples still required ~1.7 MPa to obtain enhanced levels of λ_{max} and d_{33}, even after magnetic annealing.

The response to a magnetic field anneal depends on the conditions of the samples prior to the anneal. Grain orientation is clearly essential and while the rare earth (RE)-iron ratio regulates the magnetoelastic coupling, the Tb:Dy ratio controls the magnetocrystalline anisotropy. The consequences of these two compositional factors are not unrelated; the application of a uniaxial prestress induces additional anisotropy via the magnetoelastic coupling which, by virtue of the sign of the magnetostriction, causes magnetic moments to rotate away from the stress axis. The purpose of the present work is to investigate the effects of thermal annealing which can induce compositional changes and magnetic annealing which induces magnetic anisotropy. Of particular interest are the resultant magnetostrictive properties gauged by the pressure dependencies of λ_{max} and d_{33}. While providing some insight into the magnetization processes which generate the magnetostriction, the results are of potential value for practical applications.

EXPERIMENTAL TECHNIQUES

A furnace capable of reaching ~1000 °C was situated between the 8 in. diameter poles of an electromagnet to generate annealing fields, H_a, ~1000 kA m^{-1}. The sample enclosure was evacuated and repeatedly flushed with argon, before filling to a pressure of ~1/2 atm. Samples were wrapped in tantalum foil to minimize oxidation. Cooling rates of ~25 °C/min were used.

Commercial grade samples of material were prepared by a free float zone process, ~140 mm long and ~6 mm diameter, grain orientated with the [11$\bar{2}$] axes parallel to the rod axis. Polishing and etching were used to reveal grain structure at each end for the purposes of orientation. Gross misorientation of grains along the lengths of the samples were detectable with a nondestructive scanning technique.[5] The nominal compositions of each sample provided by the manufacturers are given in Table I, together with their individual heat treatments and magnetic annealing conditions. Sample "C" was cut into four equal lengths C1,...,C4. Prior to treatment, these four sections did not display any significant differences in magnetostrictive behavior.

Room temperature magnetostrictive strains in DC fields (≤120 kA m^{-1}) were measured using strain gauges with fields, applied uniaxial stresses, and strain measurement directions along the [11$\bar{2}$] direction of the oriented grains. Data were differentiated numerically to obtain values for the *d* coefficients.

TABLE I. Sample compositions with annealing conditions and annealing procedures.

Sample	Composition	Measurement stages
A	$Tb_{0.3}Dy_{0.7}Fe_{1.95}$	(i) As received (ii) Thermal anneal 950 °C 7 h Magnetic anneal $H_a \parallel [11\bar{1}]$ (iii) Thermal anneal 950 °C 7 h Thermal anneal $H_a \parallel [110]$
B	$Tb_{0.32}Dy_{0.68}Fe_{1.95}$	As for sample A
C		
C1		(i) Magnetic anneal 950 °C 8 h $H_a \parallel [11\bar{1}]$
C2	$Tb_{0.32}Dy_{0.68}Fe_{1.95}$	(ii) Thermal anneal 950 °C 8 h
C3		(iii) As received
C4		(iv) As for sample C1

[a]DRA, Holton Heath, Poole, Dorset, UK.

 0021-8979/94/76(10)/7163/3/$6.00 © 1994 American Institute of Physics

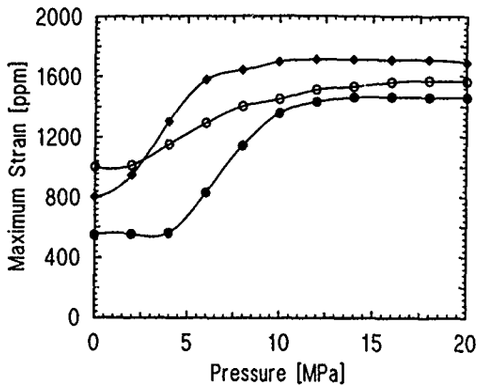

FIG. 1. Sample A: pressure dependence of the maximum strains at 120 kA m^{-1} for material composition $Tb_{0.3}Dy_{0.7}Fe_{1.95}$ as received (●), magnetically annealed with H_a applied parallel to the [110] axis (○) and [11$\bar{1}$] axis (♦).

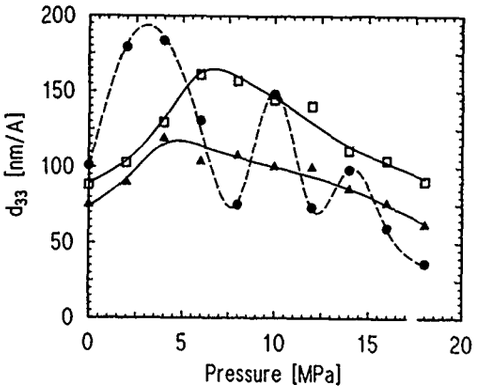

FIG. 3. Sample B: pressure dependence of the d coefficient for as received (□), magnetically annealed with H_a applied parallel to the [110] axis (▲) and [11$\bar{1}$] axis (●).

RESULTS

For *sample A*, the maximum strains at 120 kA m^{-1} and maximum d coefficients as functions of pressure in "as received" material are compared with results after the sample was magnetically annealed twice, once with H_a applied approximately parallel to the [111] direction and then along the [110] direction (Figs. 1 and 2). Both annealing directions improve λ_{max} slightly at low pressures but the response of d_{33} to magnetic annealing is more pronounced than λ_{max}. An exceptionally large d_{33}~260 nm A^{-1} is observed with a prestress of 10 MPa when annealed with H_a along the [111] axis. *Sample B*, having the same history of treatment as sample A, exhibits the same kind of response, viz., a small increase in λ_{max} at low pressures after magnetic anneal, regardless of the direction of H_a. The change in d-coefficient response is far greater, with d_{33}~190 nm A^{-1} at ~3 MPa (Fig. 3) but in this sample an oscillatory variation of d_{33} with pressure is very strong after applying H_a along the [111] axis. Similar oscillations can be seen in the results from sample A, but much weaker.

Sample C1 and *C2* received identical heat treatments except the annealing field was not applied to C2. The purpose of this procedure was to identify how much of the subsequent magnetostrictive response was due to the application of H_a rather than thermally induced compositional changes. The effects of the magnetic anneal over and above the thermal effects are clear. Heat treatment alone (Fig. 4) moves the peak in the d_{33} to a lower pressure (~8 MPa) but the magnitude is not increased; magnetic annealing doubles the maximum d coefficient and reduces the required prestress from 14 to 3 MPa. *Sample C4* shows an almost identical change in behavior to sample C1 (Fig. 5).

DISCUSSION

It is observed that magnetic annealing has a more marked effect on the pressure dependent behavior of d_{33} than on λ_{max}. A reduction in uniaxial prestresses to achieve maximum d_{33} indicates that magnetic annealing introduces extra anisotropy which assists in the preferential distribution of moments along the [111] axis prior to the application of a magnetizing field.[6] Magnetization then proceeds by the ma-

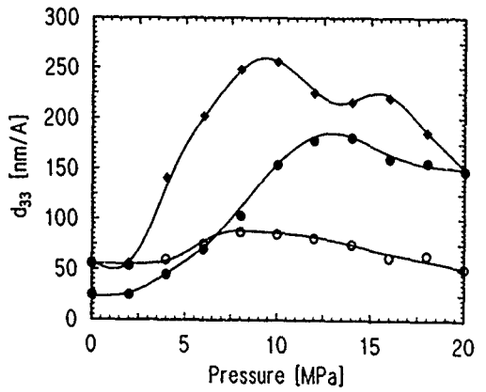

FIG. 2. Sample A: pressure dependence of the d coefficient for as received (●), magnetically annealed with H_a applied parallel to the [110] axis (○) and [11$\bar{1}$] axis (♦).

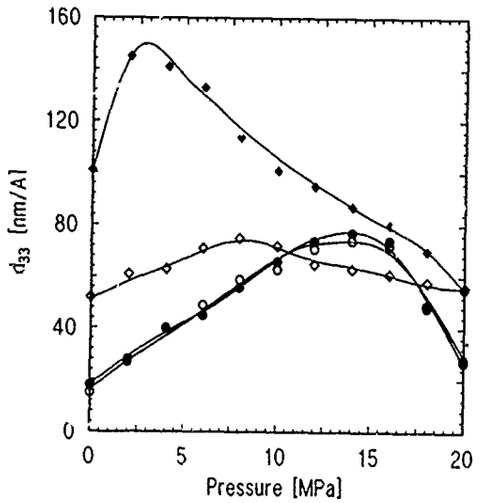

FIG. 4. d_{33} vs pressure for the composition $Tb_{0.32}Dy_{0.68}Fe_{1.95}$ thermally annealed sample C2 (◇) or magnetically annealed sample C1 (♦), compared with the "as received" performances for C1 (●) and C2 (○).

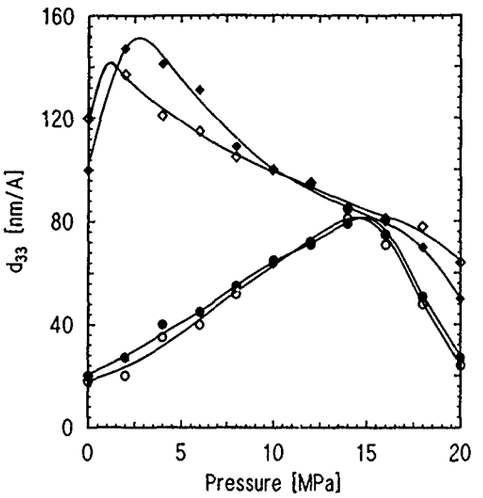

FIG. 5 d_{33} vs pressure for the composition $Tb_{0.32}Dy_{0.68}Fe_{1.95}$ magnetically annealed samples C1 (♦) and C4 (◇) compared with performances prior to annealing, C1 (●) and C4 (○).

jority of moments rotating away from the [111] direction towards the [11$\bar{2}$] axis and the corresponding magnetostrictive response, as gauged by the magnitude of d_{33}, is maximized. The maximum strain λ_{max} depends on the final state of magnetization rather than the processes through which it is achieved. Hence the magnitude of λ_{max}, as expected, is virtually independent of anisotropy induced by magnetic annealing (Table II).

In addition to the initial distribution of moments amongst the ⟨111⟩ axes, the subsequent magnetization processes which determine the magnitude of d_{33} are also influenced by the shapes of the anisotropy surfaces.[7] The combined effects of three anisotropies, mangetocrystalline and induced anisotropies from the application of stress or magnetic annealing, will regulate the surface shape. When uniaxial pressure is applied the balance of the three energy components is perturbed and the surface modified. It is considered that the oscillations in d_{33} as a function of pressure in samples A and B after magnetic annealing originate not only from the initial distribution of moments but from pressure induced periodic undulations in the energy surfaces.

The effects of magnetic annealing could be of value for practical purposes (for example, to reduce the level of prestress required to gain maximum d coefficient) provided the response of any sample to post production processing can be predicted. In the present work, no correlation is evident between the pre- and post-annealed d coefficients. However, the magnitude of the prestress required to achieve an optimum d coefficient is lower for material containing a higher Tb:Dy ratio (Table II).

In the absence of an annealing field, changes occur at elevated temperatures causing, for instance, a reduction of the bias pressure for optimum d coefficient in sample C2. Compositional changes such as the diffusion of RE ions from the grain boundaries maximize interatomic magnetoelastic coupling,[2] which enhances the pressure sensitivity. Only if the magnetoelastic coupling is strong enough will a sample of material be susceptible to magnetic annealing. Then, in cooling from T_c to room temperature, the annealing field retains the moments along a particular ⟨111⟩ direction and the maximum macroscopic contraction will develop along the aligned [11$\bar{2}$] grain axes as the spontaneous magnetostriction develops. This lowers the free energy and after annealing is completed the contraction will then be retained, as observed in practice, until sufficient energy is supplied to redistribute the moments among all the ⟨111⟩ axes. In other words, magnetic annealing could be magnetostrictively driven.

TABLE II. Increases in the d coefficient (d_{33}) and maximum strains at 120 kA m^{-1} (λ_{max}) observed in each sample and maximum d coefficients measured with optimum applied stress (σ) and field (H)

Sample	d_{33} (%)	λ_{max} (%)	max. d_{33} (rm A^{-1})	Opt. σ (MPa)	Opt. H (kA m^{-1})
A	44	17	260	9.5	12
B	18	~0	190	3.0	15
C1	81	~0	145	3 0	19
C4	73	~0	135	1.5	11

CONCLUSIONS

The d coefficient is particularly responsive to magnetic annealing as seen in both its magnitude and the optimum pressure bias. The thermal element of a magnetic anneal process is important in controlling the composition, which maximizes the magnetoelastic coupling. A spontaneous magnetostrictive deformation that accompanies magnetic annealing could be the origin of the extra anisotropy which subsequently causes moments to align preferentially along the field anneal direction.

ACKNOWLEDGMENTS

The authors are grateful to the SERC, DRA, and staff at the University of Hull for their support, in particular K.P.

[1] J. D. Verhoeven, J. E. Ostenson, E. D. Gibson, and O. D. McMasters, J. Appl Phys. **66**, 772 (1989).
[2] N. Galloway, M. P Schulze, R. D. Greenough, and D. C. Jiles, Appl. Phys. Lett. **63**, 842 (1993).
[3] N. Galloway, R. D. Greenough, M. P. Schulze, and A. G. I. Jenner, J. Magn. Magn. Mater. **119**, 117 (1993).
[4] A. E. Clark, J. P. Teter, and O. D McMasters, J. Appl. Phys. **63**, 3910 (1988).
[5] M P. Schulze, Thesis, University of Hull, 1991.
[6] J. B. Thoelke and D. C. Jiles, J. Magn. Magn. Mater. **104–107**, 1453 (1992).
[7] D. C. Jiles and J B. Thoelke, IEEE Trans. Magn **27**, 5352 (1991).

Effect of bias magnetic field on the magnetostrictive vibration of amorphous ribbons

Naoshi Asuke
Toppan Printing Co., Ltd., Sugito Saitama 345, Japan

Tatsuru Namikawa and Yohtaro Yamazaki
Tokyo Institute of Technology, Nagatsuta, Midori-ku, Yokohama 227, Japan

Electromagnetic waves generated from the magnetostrictive vibrations of amorphous ribbons under nonuniform bias fields were investigated. The sample ribbon 80 mm in length was placed on a plastic support board where both edges of the ribbon were free. In a uniform bias field generated by a Helmholtz coil, four resonance peaks of 27, 54, 81, and 107 kHz were detected. The nonuniform magnetic fields were generated by single-pole magnetic heads. Two single-pole magnetic heads with 3 mm spacing between the ribbon were moved along the ribbon. When the heads were located at 10 and 70 mm from an edge of the ribbon, the frequency of the detected response was 54 kHz, i.e., the detected response was the second resonance peak. The other resonance peaks (81, 107, and 129 kHz) could also be separated by adjusting the positions of the heads. Therefore, the electromagnetic response of the magnetostrictive vibrations of amorphous ribbons could be controlled by applying appropriate nonuniform bias magnetic fields. From the results, it is suggested that a magnetostrictive amorphous ribbon not only sends one bit data but also sends multiple bit data with the aid of bias magnetic fields.

INTRODUCTION

Some amorphous magnetic ribbons have large magnetostrictive coefficients and they have been applied to many devices.[1] When an ac magnetic field is applied to a magnetostrictive ribbon with a uniform dc magnetic field, a mechanical vibration is induced. Through the analysis of mechanical resonance, the magnetomechanical coupling factor k of the material is determined.[2–8] The vibrations have many resonance points which depend on the sample's shape and induce electromagnetic waves which can be detected by an antenna. It is expected that, through amorphous ribbons, we can send multiple bit data by separating the resonance mode.

In this study, we observe the resonance peaks of amorphous ribbons for uniform and nonuniform bias magnetic fields, to investigate the separation of the vibration modes.

EXPERIMENT

The schematic of the experimental setup is presented in Fig. 1. An exciting coil of 34 mm in diameter and 200 turns was placed 35 mm apart from the detecting coil. The signal from the sample was detected by a figure-eight coil, so as to eliminate the exciting signal. The measurement was made in the frequency range from 10 to 200 kHz. The exciting current was from 44 to 2 mA. The exciting coil generated ac magnetic fields of about 3.0 to 0.2 Oe rms, at the center of the coil.

The figure-eight coil consists of two rectangles with a size of 80×25 mm^2 and 10 turns. The signal from the figure-eight coil was measured by a network/spectrum analyzer. The wave form and phase of the exciting voltage were monitored by an oscilloscope.

A Metglas™ 2826MB ($Fe_{40}Ni_{38}Mo_4B_{18}$) (Refs. 6 and 9) amorphous ribbon with size of 80×12 mm^2 and thickness of 0.03 mm was used, as a sample. The sample ribbon was as cast and placed on a plastic support board. The sample ribbon was not fixed and both edges were free. The position of the ribbon was adjusted so that an edge of the ribbon was located near the center of the figure-eight coil. In order to apply a uniform bias field to the sample ribbon, a Helmholtz coil was added.

Figure 2 shows the schematic diagram for generating nonuniform field patterns by using single-pole magnetic heads. The single-pole heads were made of soft steel plates $50\times15\times0.3$ mm^3, and a copper wire of 0.2 mm was wound 200 turns. The space between the single-pole heads and amorphous ribbon was 3 mm. The magnetic field from the single-pole head was 6 Oe at the surface of the amorphous ribbon.

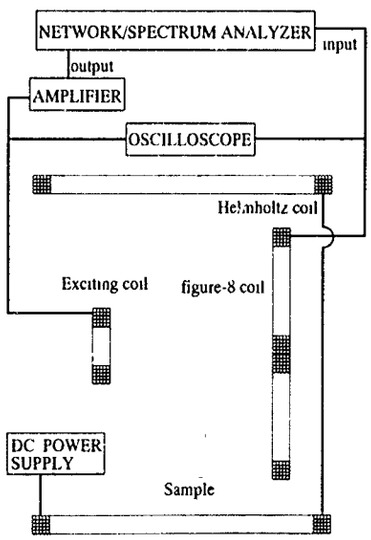

FIG. 1. Schematic diagram of experimental apparatus.

 0021-8979/94/76(10)/7166/3/$6.00 © 1994 American Institute of Physics

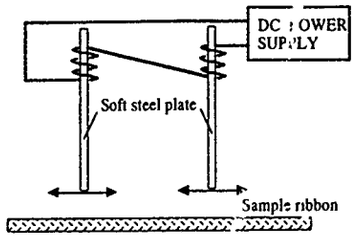

FIG. 2. Schematic diagram for generating nonuniform field patterns by using single-pole magnetic heads.

RESULTS AND DISCUSSION

Figure 3 shows the power spectrum measured with a uniform magnetic field of 4 Oe. The frequencies of the peak points were 27, 54, 81, and 107 kHz, and correspond to the first, second, third, and fourth harmonics, respectively. The peak observed at 116 kHz was expected to be a resonance of the transverse mode. We use the relationship between the resonance frequency and the length of the media as

$$f_n = nv/(2l), \tag{1}$$

where f_n is the nth resonance frequency, l is the length of the media, and v is the velocity of sound. We calculate the resonance frequencies from the first to the fourth as 27, 54, 81, and 107 kHz by using Eq. (1) and $v = 4320$ m/s.

In other amorphous ribbons, Metglas 2605SC ($Fe_{81}B_{13.5}Si_{3.5}C_2$),[10] 2605S-2 ($Fe_{78}Si_9B_{13}$),[10] and 2605CO ($Fe_{67}Co_{18}B_{14}Si_1$),[11] the power spectra did not generate sharp peaks provided the sample ribbons were as cast.

Figure 4 shows the power spectrum with a uniform magnetic field of 4 Oe, where the two positions of 20 and 60 mm from an edge of the ribbon were fixed to the support board by using a pair of thin plastic plates (0.2 mm thick). Only one peak of 54 kHz was detected in this case. Considering Eq. (1) and the result of Fig. 4, this peak is expected to be the second harmonic resonance, and the fixing positions correspond to the nodes for the vibration. Therefore, other harmonic modes were suppressed.

Figure 5 shows the separation of the resonance peaks using nonuniform magnetic fields. The power spectrum without peaks, shown as A in the figure was obtained when no

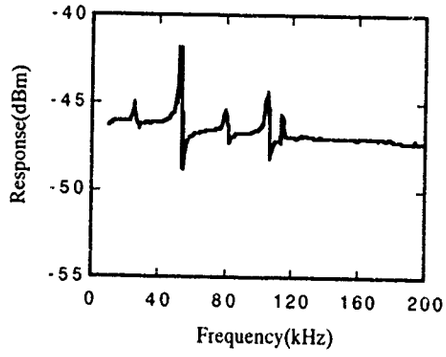

FIG 3 Power spectrum of magnetostrictive vibrations with a uniform magnetic field.

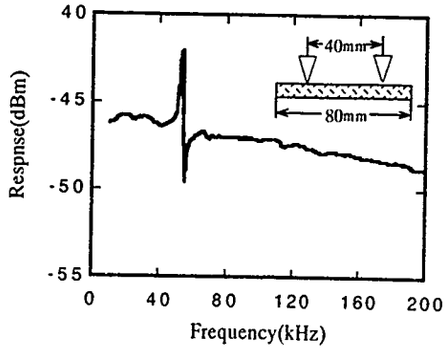

FIG. 4. Power spectrum with a uniform magnetic field for a confined amorphous ribbon. Two positions of the ribbon were fixed to the support board by using a pair of thin plastic plates.

uniform field nor nonuniform field were applied. The following results were obtained with nonuniform magnetic fields. Curves B–E were obtained by using a pair of single-pole magnetic heads. The spaces between the heads are shown in the figure. The distances from the edges of the ribbon to the heads are equal for both ends. The frequencies of the highest peaks for the head distances and polarities were 54, 81, 107, and 129 kHz for 60, 30, 40, and 54 mm, respectively. Curves B and D were obtained with magnetic heads having different polarities. The peaks in curves B, C, and D correspond to the

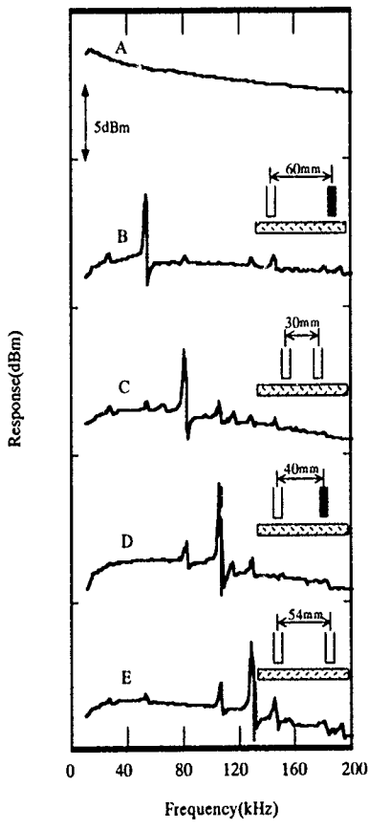

FIG. 5. Separation of resonance peaks, A: without magnetic field, B–E: nonuniform magnetic fields are applied with magnetic heads. Magnetic polarities of the heads are indicated by black and white.

second, third, and fourth resonance peaks in Fig. 3. The peak in curve E is not observed in Fig. 3, however, we estimate the fifth harmonic frequency as 135 kHz using Eq. (1). Therefore the peak can be assigned to the fifth resonance. It is noted that the intensities of the highest peaks are almost equal, compared with Fig. 3.

The power spectra that we obtain by the measurements relate to the magnetomechanical coupling factor k of the material. It is expected that more than six resonance peaks may be detected when the magnetomechanical coupling factor of sample ribbons is increased.

CONCLUSIONS

The relationship between the resonances in the magnetostrictive vibration of amorphous ribbons and bias magnetic field patterns was investigated. The first, second, third, and fourth harmonic peaks were detected in an amorphous ribbon 80 mm in length and 12 mm in width, with a uniform bias field. Specific resonance peaks were detected with nonuniform magnetic bias patterns which were generated with a pair of single-pole magnetic heads. Therefore, the response of the harmonics frequencies could be controlled by applying appropriate nonuniform bias magnetic fields. From the result, it is suggested that a magnetostrictive amorphous ribbon not only sends one bit data but also sends multiple bit data with the aid of bias magnetic fields.

ACKNOWLEDGMENT

We wish to thank Dr. G. Sugiura for discussions on this study.

[1] K. Mori, IEEE Trans. Magn. **MAG-20**, 942 (1984).
[2] M. A. Mitchell, J. R. Cullen, R. Abbundi, A. Clark, and H. Savage, J. Appl. Phys. **50**, 1627 (1979).
[3] M. Broha and J. van der Borst, J. Appl. Phys. **50**, 7594 (1979).
[4] C. Modzelewski, H. T. Savage, L. T. Kabacoff, and A. E. Clark IEEE Trans. Magn. **MAG-17**, 2837 (1981).
[5] L. T. Kabacoff, J. Appl. Phys. **53**, 8098 (1982).
[6] P. M. Anderson III, J. Appl. Phys. **53**, 8101 (1982).
[7] L. T. Kabacoff and M. Wun-Fogle, J. Appl. Phys. **57**, 3499 (1985).
[8] M. Wun-Fogle, H. T. Savage, L. T. Kabacoff, K. B. Hathaway, J. M. Merchant, and B. Beihoff, J. Appl. Phys. **64**, 5405 (1988).
[9] Metglas™ is an Allied Corporation registered trademark.
[10] M. L. Spano, K. B. Hathaway, and H. T. Savage, J. Appl. Phys. **53**, 2667 (1982).
[11] A. Hernando, C. Aroca, and V. Madurga, J. Appl. Phys. **53**, 2297 (1982).

AUTHOR INDEX

Abad, H.–(10) 6294
Abarra, E. N.–(10) 6292
Abdouche, R.–(10) 7084
Abele, M. G.–(10) 6247, 6853
Abell, J. S.–(10) 7157
Acher, O.–(10) 6570
Adams, C. P.–(10) 6229
Adenwalla, S.–(10) 6443
Aeppli, G.–(10) 6788
Aharoni, Amikam–(10) 6977
Ahlers, D.–(10) 6453
Aksay, I. A.–(10) 6778
Albuquerque, E. L.–(10) 6552
Al-Kanani, H. J.–(10) 6359
Allen, P.–(10) 7074
Allia, P.–(10) 6817
Allwood, D.–(10) 7160
Al-Omari, I. A.–(10) 6159
Altounian, Z.–(10) 6038, 6796, 7084
Alves, E.–(10) 6906
Amado, M. M.–(10) 6851
Ames, Edwin A.–(10) 6197
Andrä, W.–(10) 6510
Ankner, J. F.–(10) 6284, 7092
Antonov, A. S.–(10) 6365
Antropov, V. P.–(10) 6705
Aoki, Y.–(10) 6919
Arai, K. I.–(10) 6994
Arnaudas, J. I.–(10) 6180
Aronson, M. C.–(10) 7049
Arrott, A. S.–(10) 7031
Artman, J. O.–(10) 6307
Arutyunov, K. Yu.–(10) 7139
Arzhnikov, A. K.–(10) 7032
Ashraf, M. M.–(10) 6831
Asti, G.–(10) 6268
Asuke, Naoshi–(10) 7166
Attenkofer, K.–(10) 6453
Awschalom, D. D.–(10) 6656

Bader, S. D.–(10) 6419, 6425
Badía, F.–(10) 6481
Balbás, L. C.–(10) 6989
Baldokhin, Yu. V.–(10) 6496
Baldomir, D.–(10) 6564, 7034
Baltensperger, W.–(10) 6980
Bao, Xiaohua–(10) 6626
Barbara, B –(10) 6676
Barbeta, V. B.–(10) 7121
Barnard, J. A.–(10) 6478, 6522
Bärner, K.–(10) 6925
Barradas, N. P.–(10) 6104, 6537
Bass, J.–(10) 6610
Batlle, X.–(10) 6481
Batlogg, B.–(10) 6789
Bauer, G.–(10) 6290, 6291
Beach, R. S.–(10) 6117, 6209
Beatrice, C.–(10) 6817
Beauvillain, P.–(10) 6078
Bedell, Kevin S.–(10) 6130
Beliën, P.–(10) 6604
Belov, S. I.–(10) 6353
Bender, H.–(10) 6281
Ben-Dor, L.–(10) 7121
Bennett, L. H.–(10) 6044, 6519, 6950
Berg, L.–(10) 6986
Berkowitz, A. E.–(10) 6117, 6209, 6292, 6331
Bernardi, Johannes–(10) 6241
Berry, S. D.–(10) 6284
Bespyatykh, Yurij–(10) 6895, 6895
Beyers, R.–(10) 6618
Bhatia, S. N.–(10) 6944
Bhatnagar, A. K.–(10) 6107, 6110
Bian, X.–(10) 6796, 7084
Binek, C.–(10) 6528
Bishop, D. J.–(10) 6788, 6789
Blanco, J. A.–(10) 6118
Bland, J. A. C.–(10) 6093, 6440
Blendell, J. E.–(10) 6950
Blinkin, V. A.–(10) 6892
Bloemen, P. J. H.–(10) 7081
Boardman, Alan–(10) 6895
Bödeker, P.–(10) 6096
Boekema, Carel–(10) 6703
Bolzoni, F.–(10) 6268
Booth, J. G.–(10) 6359
Borchers, J. A.–(10) 6284, 7092
Borghs, G.–(10) 6281
Bounouh, A.–(10) 6078
Braga, M. E.–(10) 6851
Brand, R. A.–(10) 6293, 6528, 6912
Braun, Hans-Benjamin–(10) 6177, 6310
Brewer, E. G.–(10) 6232
Bröhl, K. Z.–(10) 6096
Broholm, C.–(10) 6788
Broussard, P. R.–(10) 6437
Brown, L. M.–(10) 6440
Brown, S. D.–(10) 6386
Brück, E.–(10) 6913
Bruno, P.–(10) 6972
Bruton, W. D.–(10) 6110
Bruynseraede, C.–(10) 6281
Bruynseraede, Y.–(10) 6604
Bucher, E.–(10) 6133, 6788, 6789
Buckley, M. E.–(10) 6093
Budnick, J. I.–(10) 6576
Bugoslavsky, Yu. V.–(10) 7142, 7143
Burkel, E.–(10) 6295
Busbridge, S. C –(10) 7006
Buschow, K. H. J.–(10) 6035, 6731, 6837, 6843, 6851
Bushida, K.–(10) 6198
Butler, W. H.–(10) 6805, 6808
Buyers, W. J. L.–(10) 7075

Cabassi, R.–(10) 6268
Cable, J. W.–(10) 6359
Cabral, C., Jr.–(10) 6601
Cacuffo, R –(10) 7034
Cadieu, F. J.–(10) 6059, 6068, 6760
Cadogan, J. M.–(10) 6038, 6138, 6150
Cai, Jian-Wang–(10) 7043
Camp, F. E.–(10) 6265
Canfield, P. C.–(10) 6121, 7049
Cao, Lei–(10) 6711, 6714, 6746
Cao, Y.–(10) 7127
Carbone, C.–(10) 6966
Carbucicchio, Massimo–(10) 6626
Carl, A.–(10) 6116
Carra, P.–(10) 6474
Castro, J.–(10) 7034
Cavalleri, A.–(10) 6332
Cebollada, A.–(10) 6618
Celotta, R. J.–(10) 6992
Cerdonio, M.–(10) 6332
Cerva, H.–(10) 6238
Chamberlin, R. V.–(10) 6401
Chandra, G.–(10) 6501
Chang, Ching-Ray–(10) 6493, 6588
Chang, Kuo En–(10) 6262
Chang, W. D.–(10) 6582
Chantrell, R. W.–(10) 6368, 6407, 6811
Chapman, J. N.–(10) 6440, 6613
Chappert, C.–(10) 6078
Che, Hao–(10) 6347
Chen, C. T.–(10) 6477
Chen, C.-T.–(10) 6525
Chen, C. Y.–(10) 6516
Chen, E. Youjun–(10) 6616
Chen, F.–(10) 6941, 7127
Chen, Hong–(10) 6720, 6749, 6849
Chen, J.–(10) 6291
Chen, J. P.–(10) 6316
Chen, L. H.–(10) 6814
Chen, Qixu–(10) 6579
Chen, S. K.–(10) 7071
Chen, X.–(10) 6038
Chen, Y. Y.–(10) 6516
Cheng, Ben-Pai–(10) 6725
Cheng, S. F.–(10) 6525, 7009, 7027
Cheng, Zhao-Hua–(10) 6711, 6714, 6734
Cheng, Zhao-hua–(10) 6746
Cherny, A. S.–(10) 7117
Chevalier, B.–(10) 6344
Chien, C. L.–(10) 6081
Chin, T. S.–(10) 6582, 6834, 7071
Ching, K. M.–(10) 6582
Ching, W. Y.–(10) 6047, 7046
Chiou, Gwo-Ji–(10) 6862
Chou, Stephen Y.–(10) 6673, 6679
Chouairi, A.–(10) 6989
Chrisey, D. B.–(10) 6823
Christodoulou, Chris N.–(10) 6041
Chu, C W –(10) 6941, 7127
Chu, T. Y.–(10) 6834
Chubing, Peng–(10) 6769, 7102
Chui, S. T.–(10) 6449
Ciria, M.–(10) 6180
Clark, A. E.–(10) 7009
Clausen, K. N.–(10) 6788
Clegg, S. J.–(10) 6371
Clemens, Bruce M.–(10) 6617
Cobb, J. L.–(10) 6110
Cochrane, R. W.–(10) 6796, 7075
Coehoorn, R.–(10) 7081
Coey, J. M. D.–(10) 6632, 7068
Collocott, S. J.–(10) 6138
Cooper, B. R.–(10) 6226
Cooper, Bernard R –(10) 6130
Corno, J.–(10) 6078
Correia, J. G –(10) 6906
Costa, J. L –(10) 7030
Costa-Kramer, J. L.–(10) 6204
Cottam, M. G.–(10) 6549, 6883
Cowen, J. A.–(10) 6567
Cowley, R. A.–(10) 6274
Crespo, P.–(10) 6322
Cubitt, R –(10) 6784
Cuccoli, Alessandro–(10) 6362
Cullen, J. R.–(10) 7027

Daboo, C.–(10) 6440
Dahlberg, E. Dan–(10) 6196, 6396, 6616
Danilova, N. P.–(10) 7139
Daosheng, Dai–(10) 6769, 7102
Das, B. N.–(10) 6823
da Silva, M. F.–(10) 6104, 6537, 6906
Davies, H. A.–(10) 6244
Davis, R. L.–(10) 6138
Dawson, F. P.–(10) 6871, 6874
Day, R K.–(10) 6153
De Boeck, J.–(10) 6281
de Boer, F. R.–(10) 6214, 6217, 6740, 6743, 6837, 6913, 7040
de Boer, R.–(10) 6843
de Francisco, C.–(10) 7133
de Groot F. M. F.–(10) 6453
de Jonge, W. J. M.–(10) 6607, 7081
de Julián, C.–(10) 6573, 6840
Dekoster, J.–(10) 6428
de la Fuente, C.–(10) 6180
Delamare, Jérôme–(10) 6865
Dellalov, V. S.–(10) 6560
del Moral, A.–(10) 6180
Demangeat, C.–(10) 6989
Demokritov, S –(10) 7091
DeSimone, Antonio–(10) 7018
Detlefs, C.–(10) 6453
Devine, M. K.–(10) 7015
Dhard, C. P.–(10) 6944
DiBari, R. C.–(10) 6284
Diep, H. T.–(10) 6350, 7093
Dikshtein, I. E.–(10) 6880
Dikshtein, Igor–(10) 6895, 6895
Dimitrov, D. V.–(10) 6799
Ding, J.–(10) 7074
DiVincenzo, D. P–(10) 6195
Diviš, M.–(10) 6214
Dobbertin, D.–(10) 6618
Dobysheva, L. V.–(10) 7032
Dogan, F.–(10) 6778
Doi, M.–(10) 6642
Dong, Shengzhi–(10) 6053
Dorantes-Dávila, J.–(10) 6328
Dresselhaus, M. S.–(10) 6291
Dreyssé, H.–(10) 6328, 6989
Du, Y. W.–(10) 6490
Duh, J G.–(10) 6582
Dunlap, R. A –(10) 6113, 6338, 6499, 6501, 6737
Dunlop, J. B.–(10) 6138, 6150, 6153
Dupas, C.–(10) 6558
Dupuis, V.–(10) 6676
Dye, J. L.–(10) 6567

Eberhardt, W.–(10) 6966
Ebert, H.–(10) 6453
Eckert, D.–(10) 6268, 6717
Edwards, Brandon–(10) 6271

El-Hilo, M.–(10) 6368, 6407, 6802, 6811
Engel, Brad N.–(10) 6075, 6959
Engle, E.–(10) 6396
Engle, Emily–(10) 6196
Erwin, R. W.–(10) 6284, 6778
Eschrig, H.–(10) 6214
Escorial, A. Garcia–(10) 6322
Espeso, J. I.–(10) 6118
Étourneau, J.–(10) 6344
Evetts, J. E.–(10) 6513

Fadley, C S.–(10) 6452, 6477
Falco, Charles M.–(10) 6075, 6959
Falenschek, J.–(10) 6986
Falicov, L. M.–(10) 6595
Farrow, R F. C.–(10) 6617, 6618
Faschinger, W.–(10) 6290
Fassbender, J.–(10) 6100
Fayeulle, S.–(10) 6676
Fazleev, N. G.–(10) 6347, 6896
Felcher, G. P.–(10) 6443
Feng, Y B.–(10) 6591, 6594, 6903, 7145
Feng, Yuan-Bing–(10) 7043
Fenimore, P. W.–(10) 6192
Fernandez-Baca, J. A.–(10) 6359
Fernando, A S –(10) 6159
Ferré, J.–(10) 6983
Feutrill, E.–(10) 7074
Fidler, J.–(10) 7053
Fidler, Josef–(10) 6241
Fiévet, F.–(10) 6570
Fiévet-Vincent, F.–(10) 6570
Filipkowski, M. E.–(10) 6437, 7090, 7092
Fiorani, D.–(10) 7034
Fischer, P.–(10) 6453
Fischer, Paul B.–(10) 6673
Fischer, R.–(10) 7053
Fisk, Z.–(10) 6121, 7049, 7052
Fitzsimmons, M. R.–(10) 6295
Foldeaki, M –(10) 6737
Folks, L.–(10) 6391, 7074
Fondado, A.–(10) 6564
Forgan, E. M.–(10) 6784
Fraerman, Andrey A –(10) 6671
Frait, Z.–(10) 6897
Freitag, M.–(10) 6425
Freitas, P. P.–(10) 6104, 6537
Fritzsch, L –(10) 6510
Fruchart, D.–(10) 6035
Fry, J L –(10) 6347, 6896
Fuerst, C D –(10) 6056, 6144, 6232, 6301
Fujiki, N. M.–(10) 6338
Fujimori, H.–(10) 6790
Fujiwara, H.–(10) 6522
Fukamichi, K.–(10) 6682
Fukunaga, H.–(10) 6846
Fulmek, Paul L.–(10) 6561
Funayama, T.–(10) 7024
Furdyna, J. K.–(10) 6290, 6291

Galloway, N –(10) 7163
Galtier, M –(10) 6558, 6983
Gama, S.–(10) 6585
Gammel, P. L –(10) 6789
Gangopadhyay, S.–(10) 6319, 6522
Gao, L –(10) 6941
Gao, Y H.–(10) 6740
García-Jastida, A. J –(10) 6564
García-Otero, J.–(10) 6564
Garg, Anupam–(10) 6168
Garifullin, I. A.–(10) 6096, 6889
Gay, J. M.–(10) 6676
Ge, Sen-Ling–(10) 6725
Ge, X.–(10) 6490
Ge, Y. P –(10) 6843
Gebel, B.–(10) 6717
Gehring, P. M.–(10) 6180
Geldart, D. J. W.–(10) 6338
Genenko, Yuri A.–(10) 7144
Gerlach, B.–(10) 7000
Gervais, B.–(10) 6661
Gester, M.–(10) 6440
Ghidini, M.–(10) 6661
Gibbs, M. R. J.–(10) 6534
Gider, S.–(10) 6656
Giebultowicz, T. M.–(10) 6290, 6291
Gignoux, D.–(10) 6118
Giri, Anit K.–(10) 6573
Girt, Er.–(10) 6038
Givord, D.–(10) 6661
Gnezdilov, V. P.–(10) 6883
Gómez Sal, J. C.–(10) 6118
Gong, Hua-Yang–(10) 6711, 6714, 6734
Gong, Hua-yang–(10) 6746
Gong, W.–(10) 6156
Gong, X. G.–(10) 7037
González, A.–(10) 6564
González, J. M.–(10) 6573, 6840
Goremychkin, E. A.–(10) 6124
Goryunov, Yu. V –(10) 6096, 6889
Goto, T.–(10) 6682
Graf, T.–(10) 7052
Grandjean, F.–(10) 6731
Greaves, S J.–(10) 6802
Greene, R. L –(10) 6953
Greenough, R. D.–(10) 6371, 7154, 7160, 7163
Grigereit, T. E.–(10) 6772
Grigorenko, A. N.–(10) 6335
Grigor'ev, L. A.–(10) 7099
Grishin, A.–(10) 6947
Grishin, A M.–(10) 6560, 6965
Grolier, V –(10) 6983
Grünberg, P.–(10) 6604, 7091, 7092
Grundy, P. J.–(10) 6090, 7003
Gu, E –(10) 6440
Gudat, W.–(10) 6966
Guillot, M.–(10) 6035
Guntherodt, G.–(10) 6100
Guo, G.–(10) 6490
Guo, Hong–(10) 6374
Guo, Hui-qun–(10) 6746, 6763
Guo, X.–(10) 6465
Guozhong, Li–(10) 7102
Gurney, B. A.–(10) 6805
Gurney, Bruce A.–(10) 6616
Gusev, Sergey A.–(10) 6671
Gutfleisch, O.–(10) 6256, 6825
Gutierrez, C. J.–(10) 7090, 7092

Habib, J. M.–(10) 6950
Hadjipanayis, G. C.–(10) 6156, 6316, 6319, 6543, 6799, 7065
Haiying, Chen–(10) 7102
Han, D. H.–(10) 6591, 6900
Handstein, A –(10) 6717
Hanisch, K.–(10) 6528
Harada, Yasoo–(10) 6667
Harbison, J P –(10) 6278
Hargraves, P.–(10) 6338
Harmon, B. N.–(10) 6474, 6705
Harp, G. R.–(10) 6462, 6471
Harper, J. M.–(10) 6601
Harris, I. R –(10) 6050, 6256, 6825, 6831, 7157
Harris, V G.–(10) 6322
Hart, R.–(10) 6519
Harvey, D.–(10) 7151
Haupt, L –(10) 6925
Hauser, Hans–(10) 6561
Havela, L.–(10) 6214, 6217, 6913, 7040
Hay, J. N.–(10) 6831
He, P.–(10) 6084
He, Y·L.–(10) 6446
Hegde, H.–(10) 6059, 6068, 6760
Hellman, F –(10) 6292
Helman, J. S.–(10) 6980
Helmolt, R. v.–(10) 6824
Hempel, K. A –(10) 6062
Henderson Lewis, L.–(10) 6235
Henmi, H.–(10) 6919
Her, Trao–(10) 6703
Herbst, J. F.–(10) 6056, 6144, 6301
Hernández, Laura–(10) 7093
Hernando, A.–(10) 6322
Heyderman, L. J.–(10) 6613
Hillebrands, B.–(10) 6100
Hines, W. A.–(10) 6576
Ho, G. H.–(10) 6477, 6525
Hoffmann, H.–(10) 6507
Holden, T. M.–(10) 6229
Holody. P.–(10) 6610
Homma, M.–(10) 6828
Honda, T.–(10) 6994
Hono, K.–(10) 6790
Hood, Randolph Q.–(10) 6595
Horwitz, J.–(10) 6823
Hossain, S.–(10) 6522
Howard, B.–(10) 6788
Hsieh, W. T.–(10) 7124
Hu, B. C.–(10) 6516
Hu, Bo-Ping–(10) 6383
Hu, Ji-Fan–(10) 6383
Hu, W. Y.–(10) 6751
Hu, Xiao–(10) 7108
Hu, Z.–(10) 6147, 6162, 6731
Hua, S. Z.–(10) 6519
Huang, Der-Ray–(10) 6862
Huang, F.–(10) 6434
Huang, H. L –(10) 6892
Huang, J. C. A.–(10) 6516
Huang, M. Q.–(10) 6648
Huang, Ming-Zhu–(10) 6047, 7046
Hucht, A.–(10) 6341
Humphrey, F. B.–(10) 6204
Hundley, M F.–(10) 7052
Huse, D. A –(10) 6789

Ido, Hideaki–(10) 6165
Idzerda, Y. U.–(10) 6437, 6452, 6477, 6525
Iñiguez, J.–(10) 7133
Inoue, Yoshiharu–(10) 6653
Ioffe, A. F.–(10) 7099
Isaacs, E. D.–(10) 6133
Isnard, O.–(10) 6035
Izco, C –(10) 6564

Jack, K. H.–(10) 6620
Jakubovics, J. P.–(10) 6099, 6513
James, R. D.–(10) 7012
Jardim, R. F –(10) 6585, 7121
Jarratt, J. D –(10) 6478
Jaswal, S. S.–(10) 6159
Jedryka, E –(10) 6428
Jehan, D.–(10) 6274
Jenner, A. G –(10) 7154, 7160
Jenner, A G. I.–(10) 7163
Jensen, J. H.–(10) 6853
Jeong. S. Y.–(10) 6084
Jerems, F –(10) 6371
Jerome, R.–(10) 7087
Jeyadevan, B –(10) 6325
Ji, J. T.–(10) 6490
Jiang, Xiuguang–(10) 6953
Jiang, Z S.–(10) 6490
Jiles, D. C –(10) 7015
Jin, S.–(10) 6814, 6929
Johnson, M. T–(10) 7081
Johnson, M. T.–(10) 6100
Johnson, S.–(10) 7049
Jones, D. G. R –(10) 6825
Jones, T.–(10) 7034
Jonker, B. T.–(10) 6294
Jou, C J.–(10) 7136
Joven, E –(10) 6180
Judy, Jack–(10) 6579
Julian, S. R –(10) 6137
Jung, Hyung Jin–(10) 6877
Jungblut, R.–(10) 6100
Jungermann, J.–(10) 6293

Kaczmarek, W. A.–(10) 6065
Kaduwela, A. P –(10) 6477
Kalceff, W.–(10) 6153
Kalogirou, O –(10) 6722
Kamzin, A. S.–(10) 7099
Kang, I. K –(10) 7021
Kasuya, Tadao–(10) 6934
Katori, H. Aruga–(10) 6682
Kawasaki, Masahito–(10) 6708
Kawazoe, Yoshiyuki–(10) 7108
Keimer, B.–(10) 6778
Keirstead, Rick–(10) 6579
Kemner, K. M.–(10) 6322
Kendall, D –(10) 7006, 7148
Kent, A. D.–(10) 6656
Keramidas, V. G.–(10) 6287
Kergadallan, Y.–(10) 7040
Kergoat, R.–(10) 7087
Kes, P. H.–(10) 6784
Keune, W.–(10) 6293, 6528, 6912
Khaliullin, G. G –(10) 6096, 6889
Khasanov, B. M.–(10) 6353
Khats'ko, E N.–(10) 7117
Khizroev, S.–(10) 6953
Kief, M T –(10) 6522
Kim, A. S.–(10) 6265
Kim, Chul Sung–(10) 6877
Kim, J. D.–(10) 6513
Kim, S R.–(10) 7021
Kim, Y H –(10) 6099
Kim, Young-Suk–(10) 6087
Kinderlehrer, D.–(10) 7012
Klabunde, K J –(10) 6316, 6319
Klasges, R.–(10) 6966
Kleemann, W.–(10) 6528
Kleiman, R. N –(10) 6788, 6789
Klik, Ivo–(10) 6493, 6588
Knobel, M.–(10) 6817
Knülle, M –(10) 6453
Kobayashi, T –(10) 7024
Kobayashi, Y.–(10) 6919
Kocharian, A. N –(10) 6127, 6186
Koksharov, Yu. A –(10) 7143
Kolb, E –(10) 6558
Kolotyrkin, P Ya.–(10) 6496
Komada, Norikazu–(10) 6041
Komuro, Matahiro–(10) 6637
Kong, Lin-Shu–(10) 6711, 6714
Kong, Lin-shu–(10) 6746
Konig, H.–(10) 6474
Konrad, A.–(10) 6871, 6874
Koon, N. C.–(10) 6823
Korotkova, Natalia A –(10) 6671
Kortan, A R.–(10) 6110
Kouvel, J. S –(10) 6965
Krause, R. F –(10) 7065
Krauss, Peter R.–(10) 6673
Krebs, J J –(10) 6294, 6452, 7090, 7092
Kronmuller, H.–(10) 7053
Kryshtal, R G.–(10) 6880
Ku, H. C –(10) 6582, 7124

Kübler, J.–(10) 6694
Kubo, H.–(10) 6504
Kuhrt, C.–(10) 6238, 7068
Kume, Minoru–(10) 6667, 6793
Kunkel, H. P–(10) 6356
Kuroki, Kazuhiko–(10) 6667, 6793
Kwon, H. W.–(10) 6050
Kyriakidis, J.–(10) 6113

Labarta, A.–(10) 6481
Labbé, H. J.–(10) 6883
Lacerda, A.–(10) 6121, 7052
Lado, I.–(10) 6564
Lafford, Tamzin A.–(10) 6534
Lagarikov, A. N.–(10) 6365
Lai, W. Y.–(10) 6484
Lai, Wu-Yan–(10) 6383
Lai, Wuyan–(10) 6487
Langer, J.–(10) 6510
Langouche, G.–(10) 6428
Larson, Allen C.–(10) 6217, 7049
Lashmore, D. S.–(10) 6519
Lavielle D.–(10) 6825
Lawson, A. C.–(10) 7049
Lawther, D. W.–(10) 6501
Leal, J. L.–(10) 6537
LeClair, P.–(10) 6546
Lee, C. H.–(10) 6516
Lee, J.-G.–(10) 7031
Lee, K. C.–(10) 7124, 7136
Lee, S.-F–(10) 6610
Lee, S. L.–(10) 6784
Lee, S. R.–(10) 7021
Lee, Seung Wha–(10) 6877
Lee, Young Jong–(10) 6877
Lee, Young-Sook–(10) 6820
Lefakis, Harry–(10) 6616
Leonowicz, M.–(10) 6244
Leupold, H. A.–(10) 6253, 6856, 6859
Levin, K.–(10) 6935
Levy, Peter M.–(10) 6619
Li, Dongqi–(10) 6419, 6425
Li, Hong-Shuo–(10) 6138
Li, Shuxiang–(10) 6487
Li, W. Z.–(10) 6740
Li, W-Z.–(10) 6743
Li, W-H.–(10) 7124, 7136
Liang, Bing–(10) 6746, 6763
Liang, N. T.–(10) 6516
Liao, S. Y–(10) 6516
Liechtenstein, A I –(10) 6705
Lim, S. H.–(10) 7021
Lin, C H –(10) 6834
Lin, Chin–(10) 6766
Lin, D. L –(10) 6347
Lin, H.-J.–(10) 6477, 6525
Lin, X.–(10) 6543
Lind, D. M.–(10) 6284
Liou, S. H.–(10) 6304
Liou, Y.–(10) 6516
Liu, Cong-Xiao–(10) 6766
Liu, Den-ke–(10) 6749
Liu, Gui-Chuan–(10) 6383
Liu, K.–(10) 6081
Liu, S –(10) 6757
Liu, Y–(10) 6304
Liu, Zun-Xiao–(10) 6725, 6728, 6766
Loberg, B.–(10) 6947
Lochner, E –(10) 6284
Lockwood, D. J –(10) 6883
Loison, D –(10) 6350
Loloee, R –(10) 6610
Long, Gary J –(10) 6731
Lonzarich, G G –(10) 6137
López-Quintela, A –(10) 7034
López Quintela, M A –(10) 6564
Lord, D. G.–(10) 7003, 7151
Lord, J S –(10) 6504
Loss, Daniel–(10) 6177
Lottis, D. K.–(10) 6396
Lu, C. L.–(10) 6516
Luo, H. L.–(10) 6484, 6591, 6900, 6903, 7145
Luo, He-Lie–(10) 7043
Lyberatos, A.–(10) 6407
Lynn, J. W.–(10) 6772, 6778, 7124, 7136

Ma, Ru-Zhang–(10) 6720
Ma, Ru-zhang–(10) 6749, 6849
MacLaren, J. M.–(10) 6069, 6805, 6808
Maeda, Atsushi–(10) 6667, 6793
Mahía, J.–(10) 7034
Majetich, S. A.–(10) 6307
Majkrzak, C. F.–(10) 7092
Maletta, H.–(10) 6217
Malhotra, S. S.–(10) 6304
Mandrus, D.–(10) 7052
Mankey, G. J.–(10) 6434
Mao, Ming–(10) 6038
Mao, Weihua–(10) 6053
Maple, M. B.–(10) 6137, 7121
Maraner, A.–(10) 6332
Marasinghe, G. K.–(10) 6731
Margarian, A.–(10) 6138, 6150, 6153
Marinero, E.–(10) 6287
Markert, J. T.–(10) 6110
Marks, R.–(10) 6617
Marks, R. F.–(10) 6618
Marques, J. G.–(10) 6906
Martinez, N –(10) 6825
Mason, T. E.–(10) 6789
Mathieu, Ch.–(10) 6100
Matson, M.–(10) 6396
Matsui, M.–(10) 6642
Mattheis, R.–(10) 6510
Mayergoyz, I. D.–(10) 6956, 7130
McCormack, M.–(10) 6929
McGuire, T. R.–(10) 6601
McHenry, M E –(10) 6307
McKay, Susan R.–(10) 6197, 7117
McKinley, J D.–(10) 7114
McLane, G. F.–(10) 6253
McMichael, R. D.–(10) 6301, 6519
McMorrow, D. F.–(10) 6274
McMullan, G. J.–(10) 6137
Medved, A V.–(10) 6880
Mégy, R.–(10) 6078
Meigs, G.–(10) 6477, 6525
Meisner, G P.–(10) 6259
Melamud, M.–(10) 6044
Mélinon, P –(10) 6676
Melo, A. A.–(10) 6537, 6906
Melo, L V –(10) 6537
Mendik, M. –(10) 6897
Meng, R L –(10) 6941
Meng, X –(10) 6796, 7084
Mergia, K –(10) 6380
Meservey, R –(10) 6546
Messoloras, S.–(10) 6380
Metzger, Robert M.–(10) 6626
Middleton, D P.–(10) 6731
Miller, B H.–(10) 6616
Miller, J –(10) 6531
Miltat, J.–(10) 7087
Minakov, A. A.–(10) 7142, 7143
Mira, J.–(10) 6564, 7034
Miraglia, S.–(10) 6035
Mishra, R K –(10) 6301
Mishra, S –(10) 6731
Mishra, S K –(10) 6700
Mitamura, H.–(10) 6682
Miteva, S –(10) 7118
Mitsuoka, Katsuya–(10) 6637
Mohri, K –(10) 6198
Molnár, S. von–(10) 6656
Moodera, J. S.–(10) 6101, 6546
Mook, H. A –(10) 6784
Mootoo, D. M.–(10) 6101
Morawe, Ch –(10) 6096
Morón, C.–(10) 6840
Mortensen, K.–(10) 6784, 6788, 6789
Moschel, A.–(10) 6560
Moshchalkov, V. V –(10) 6604
Movshovich, R.–(10) 6121
Mühge, Th.–(10) 6096
Muir, W. B.–(10) 6796, 7084
Mukai, Toshio–(10) 6653
Müller, K.-H.–(10) 6268, 6717
Mulloy, M.–(10) 6558, 6983
Muñoz, J. M.–(10) 7133
Murata, K.–(10) 6682
Murphy, A. S.–(10) 7065
Murthy, A. S.–(10) 6543, 6799

Na, J. G.–(10) 6484, 6900
Nakamura, H.–(10) 6828
Nakamura, Yoshihisa–(10) 6540
Nakatsuka, K.–(10) 6325
Nakotte, H.–(10) 6214, 6217, 6913, 7040
Namikawa, Tatsuru–(10) 7166
Nashi, H.–(10) 6642
Nashima, Osamu–(10) 6165
Nastasi, M. A.–(10) 6295
Naugle, D. G –(10) 6107, 6110
Navarathna, A.–(10) 6068, 6760
Nedkov, I.–(10) 7118
Ni, Qiang–(10) 6720, 6749, 6849
Niarchos, D –(10) 6380, 6722
Nicholson, D M. C.–(10) 6805, 6808
Nicolaides, G.–(10) 6380
Nielsen, Morten–(10) 6374
Nigam, A. K.–(10) 6501, 6944
Nikitin, P. I.–(10) 6335
Nikitov, Sergey–(10) 6895, 6895
Nikolaeva, A. A.–(10) 7139
Nikolayev, E. I.–(10) 6560
Ninham, B. W.–(10) 6065
Nishikawa, Madoka–(10) 6667
Niska, J.–(10) 6947
Noda, M.–(10) 6198
Nogués, J.–(10) 7030
Noh, T. H.–(10) 7021
Nolting, W.–(19) 6691
Nowak, U.–(10) 6341
Nozières, J. P.–(10) 6661
Nunez, V.–(10) 6290, 6291
Nurgaliev, T –(10) 7118
Nyenhuis, J. A.–(10) 6909

O'Brien, W. L.–(10) 6462, 6468, 6471
O'Connor, Charles J.–(10) 6820
Oda, Kiwamu–(10) 6165
O'Donnell, K –(10) 7068
Oglesby, C. S –(10) 6133, 6789
O'Grady, K –(10) 6368, 6407, 6802, 6811
Ogura, Takashi–(10) 6667
Oh, Young Jei–(10) 6877
Oikawa, Satoru–(10) 6793
Okada, M –(10) 6828
Onda, N.–(10) 6897
Osborn, R –(10) 6124
Oseroff, S. B.–(10) 6564, 7034
O'Shea, M. J.–(10) 6174
Osofsky, M. S –(10) 6437
Otani, Y.–(10) 6661
Ould-Mahfoud, S –(10) 6078
Ounadjela, K.–(10) 7078
Paillard, V–(10) 6676
Pan, C Y–(10) 6751
Pan, Qi–(10) 6725, 6728
Pan, S. M.–(10) 6903, 7145
Pan, Shu-Ming–(10) 6720
Pan, Shu-ming–(10) 6749, 6849
Panchanathan, V.–(10) 6259
Panina, L. V.–(10) 6198, 6365
Panwar, Sunil–(10) 6220, 6223
Papaefthymiou, V.–(10) 6319
Paramonov, V. P.–(10) 6365
Park, Jae Yun–(10) 6877
Park, M. C.–(10) 6278
Park, S. J.–(10) 6965
Park, Seung Iel–(10) 6877
Park, Y. S.–(10) 6278
Park, Yongsup–(10) 6443
Parker, M. R.–(10) 6522
Parkin, S. S. P.–(10) 6462, 6471, 6613, 6617, 6618
Pashkevich, Yu. G.–(10) 6892
Pastor, G. M.–(10) 6328
Paul, D. I.–(10) 6271
Paul, D M –(10) 6784
Pearson, D. P. A.–(10) 6531
Pearson, J.–(10) 6425
Pedersen, J. S –(10) 6788
Pelloth, J.–(10) 6912
Peng, J. L –(10) 6953
Peré, D.–(10) 6825
Perera P.–(10) 6174
Perettie, Donald J.–(10) 6579
Perez, A.–(10) 6676
Perez, J P.–(10) 6676
Peterman, D. W.–(10) 6886
Petford-Long, Amanda K.–(10) 6099, 6513
Petrov, Yu. I.–(10) 6496
Pfandzelter, R.–(10) 6431
Pfeffer, R. L –(10) 6287
Pfleiderer, C –(10) 6137
Pick, Š.–(10) 6328
Pierce, D T –(10) 6992
Piercy, A. R.–(10) 7006, 7148
Pini, M G.–(10) 6555
Pinkerton, F. E.–(10) 6056, 6144
Pinto, R. P.–(10) 6851
Pitcher, P G –(10) 6531
Plaskett, T. S.- (10) 6104, 6601
Ploessl, R.–(10) 6440
Politi, P.–(10) 6555
Pollard, R. J.–(10) 6090
Popova, M. N.–(10) 7105
Portwine, W.–(10) 6284
Potenziani, E., II–(10) 6856, 6859
Potter, C. D.–(10) 6604
Prajapati, K –(10) 7154
Pratt, W. P, Jr –(10) 6610
Pringle, O. A.–(10) 6731
Prinz, G. A.–(10) 6452, 6477, 6525, 7090, 7092
Prodi, G. A.–(10) 6332
Prokeš, K.–(10) 6214, 6217, 6913, 7040
Psycharis, V.–(10) 6722
Purdy, J. H.–(10) 6371
Purwanto, A –(10) 6214, 6217, 7040
Pynn, R.–(10) 6295

Qi, X.–(10) 6356
Qingqing, Fang–(10) 6769
Qiu, Z Q.–(10) 6419, 6425
Quandt, E.–(10) 7000

Rabedeau, T. A –(10) 6617, 6618
Rader, O.–(10) 6966
Rahman, M. A.–(10) 6868

Ramesh, R.–(10) 6287, 6929
Ramirez, A. P.–(10) 6133
Rani, R.–(10) 6068, 6760
Rao, D.–(10) 6117
Rao, K. V.–(10) 6204, 6965, 7030
Rathnayaka, K. D. D.–(10) 6107
Rau, C.–(10) 6431
Ravel, F.–(10) 6570
Rebizant, J.–(10) 6214, 7040
Reich, G. R.–(10) 6127
Rejcek, J. M.–(10) 6896
Renard, D.–(10) 6558
Renard, J. P.–(10) 6078, 6558
Rennert, Peter–(10) 6459
Rensing, Noa M.–(10) 6617
Restorff, J. B.–(10) 7009
Rettori, A.–(10) 6555
Richter, M.–(10) 6214
Ricketts, J.–(10) 6784
Riedi, P. C.–(10) 6504
Rinaldi, D.–(10) 7034
Ritcey, S. P.–(10) 6499
Rivas, J.–(10) 6564, 7034
Robinson, R. A.–(10) 6214, 6217, 7040
Rodríguez Fernández, J.–(10) 6118
Roesler, G. M., Jr.–(10) 6437
Rojdestvenski, I. V.–(10) 6549
Röll, A –(10) 6295
Rosov, N.–(10) 6772
Rothberg, G. M.–(10) 6278
Rots, M.–(10) 6428, 6537
Rozenstein, Dmitry B.–(10) 6671
Rubinstein, M.–(10) 6823
Ruiyi, Fang–(10) 6769
Ruiz de Angulo, L.–(10) 7157
Ryan, D. H.–(10) 6038, 6138, 6150, 6189, 6374, 6377

Sachtler, W. M. H.–(10) 6576
Saettas, L.–(10) 6722
Sahashi, M.–(10) 7024
Sakakibara, T.–(10) 6682
Sakuma, Akimasa–(10) 6637
Salamanca-Riba, L.–(10) 6519
Salgueiro da Silva, M.–(10) 6344
Samarasekara, P.–(10) 6068, 6760
Samwer, K.–(10) 6824, 6925
Sánchez, R. D.–(10) 6564
Sanchez-Castro, Carlos–(10) 6130
Sandratskii, L. M.–(10) 6694
Sang, H.–(10) 6490
Sarrao, J. L.–(10) 7052
Sarychev, A. K.–(10) 6365
Sasaki, I.–(10) 7024
Sastry, P. V. P. S. S –(10) 6944
Sato, H.–(10) 6919
Satpathy, S.–(10) 6700
Saxena, Siddharth S.–(10) 6820
Scalettar, R. T –(10) 6452
Schad, R.–(10) 6604
Schäfer, M.–(10) 6604, 7092
Schäfer, R.–(10) 6604
Schelp, L. F.–(10) 6081
Schloemann, E.–(10) 6059
Schmidt, J. E.–(10) 6081
Schmidt, S.–(10) 6510
Schnitzke, K.–(10) 6238
Scholz, B.–(10) 6293
Schrefl, T –(10) 7053
Schreiber, F.–(10) 6096
Schreyer, A.–(10) 7092
Schroeder, P. A.–(10) 6610
Schuller, Ivan K.–(10) 7091
Schultz, L.–(10) 6238
Schulze, M. P.–(10) 7163
Schumann, F. O.–(10) 6093
Schütz, G –(10) 6453
Schwarzacher, W.–(10) 6519
Sechovsky, V.–(10) 6919
Sechovský, V.–(10) 6214, 6217, 6913, 7040
Seed, R. G.–(10) 6962
Seemann, K.–(10) 7000
Sellmyer, D. J.–(10) 6084, 6159, 6304
Seret, A.–(10) 6214
Seshu, B.–(10) 6107
Seyoum, H M.–(10) 6950
Shafranovsky, E. A –(10) 6496
Shah, S. I.–(10) 6543
Shaheen, S. A.–(10) 6754
Shan, Z. S.–(10) 6084
Sharrock, M. P.–(10) 6413
Shaw, K. A.–(10) 6284
Shearwood, C.–(10) 6534
Shen, Bao-Gen–(10) 6711, 6714, 6734
Shen, Bao-gen–(10) 6746, 6763, 6849
Shen, J. X.–(10) 6084, 6304
Sheng, Q. G.–(10) 6226
Sheng, Zhang–(10) 6769
Shieh, J. H.–(10) 7124
Shih, W. Y.–(10) 6778
Shim, In Bo–(10) 6877
Shin, D. H.–(10) 6507
Shin, Sung-Chul–(10) 6087
Shin, T.–(10) 6278
Shinjo, T.–(10) 6919
Shkar, V. F.–(10) 6560
Shoji, H.–(10) 6642
Shukh, A. M.–(10) 6507
Shyr, S. T.–(10) 7136
Si, Qimiao–(10) 6935
Sikafus, K. E.–(10) 6295
Silaev, P. K.–(10) 7143
Simion, B. M.–(10) 6287
Simpson, A.–(10) 6274
Singh, David J.–(10) 6688
Singh, Ishwar–(10) 6220, 6223
Singh, R. R. P.–(10) 6452
Sitter, H.–(10) 6290
Skomski, R.–(10) 7059
Slavin, A. N.–(10) 6335, 6549
Smith, G. S.–(10) 6295
Smith, P. A. I.–(10) 7074
Snowman, Daniel P.–(10) 7117
Soares, J. C.–(10) 6104, 6537, 6906
Sobolev, V. L.–(10) 6892
Sogomonian, A. S.–(10) 6186
Somekh, R.–(10) 6513
Song, Lin–(10) 6383
Sorensen, C. M.–(10) 6316, 6319
Sousa, J. B.–(10) 6344, 6851
Speriosu, V. S.–(10) 6805
Speriosu, Virgil S.–(10) 6616
Spirlet, J. C.–(10) 6214, 7040
Springholz, G.–(10) 6291
Srinivas, V.–(10) 6501
Stadelmaier, H. H.–(10) 6265
Stähler, S.–(10) 6453
Steierl, G.–(10) 6431
Steinitz, M. O.–(10) 6229
Stewart, R. J.–(10) 6380
Stoyonov, P –(10) 6284
Street, R.–(10) 6386, 6391, 7074
Ström-Olsen, J. O.–(10) 6796, 7084
Stroscio, Joseph A –(10) 6992
Stüchelli, N.–(10) 6788
Suefuji, R.–(10) 6828
Sugawara, T.–(10) 6790
Sugimoto, S.–(10) 6828
Sugita, Yutaka–(10) 6637
Sugiyama, Kiyohiro–(10) 6165
Sun, Yun-Xi–(10) 6725, 6766
Sutton, M.–(10) 6038, 6796, 7075, 7084
Suzuki, P. A.–(10) 6585
Suzuki, Shinya–(10) 6708
Suzuki, Shunji–(10) 6708
Suzuki, Takashi–(10) 6934
Svoboda, P.–(10) 6214, 6217
Swaddling, P.–(10) 6274
Swainson, I. P.–(10) 7075
Swann, C.–(10) 6543
Swartzendruber, L. J.–(10) 6950
Swartzenruber, L. J.–(10) 6519
Swinnen, B.–(10) 6428

Tagawa, Ikuya–(10) 6540
Tagirov, L. R.–(10) 6096
Takahashi, H.–(10) 6642
Takahashi, Hiromasa–(10) 6637
Takahashi, Migaku–(10) 6642
Takahashi, Takehiro–(10) 6165
Takanashi, K.–(10) 6790
Takano, K.–(10) 6292
Takebayashi, Shigeto–(10) 6653
Tanaka, C.–(10) 6307
Tanaka, M.–(10) 6278
Tang, Jinke–(10) 6820
Tang, N.–(10) 6740, 6743, 6837
Tang, Y. J.–(10) 6903, 7145
Tappert, J.–(10) 6293
Taslakov, M.–(10) 7118
Tattam, C.–(10) 6831
Tautz, F. S.–(10) 6137
Tayurskii, D. A.–(10) 6353
Tedstone, S. F.–(10) 6831
Teitelman, M.–(10) 6443
ter Haar, Leonard W.–(10) 7111
Teter, J. P.–(10) 7009, 7027
Thevuthasan, S.–(10) 6452, 6477
Thomas, G.–(10) 6287
Thomas, L.–(10) 6676
Thompson, J. D.–(10) 6121, 7049, 7052
Thomson, T.–(10) 6504
Tiberto, P.–(10) 6817
Tiefel, T. H.–(10) 6814, 6929
Tilak, A. S.–(10) 6856, 6859
Timasheva, E. V.–(10) 6365
Tindall, D A.–(10) 6229
Tobin, J. G.–(10) 6465
Tognetti, Valerio–(10) 6362
Tohji, K.–(10) 6325
Tomita, H.–(10) 6846
Tondra, Mark–(10) 6616
Toney, M. F –(10) 6618
Tong, S. Y.–(10) 6465
Tonner, B. P.–(10) 6462, 6468, 6471
Torres, L.–(10) 7133
Toshimura, T.–(10) 6846
Tracy, K.–(10) 6760
Trallori, L.–(10) 6555
Tsai, K. L.–(10) 6567
Tsay, H. L –(10) 7136
Tsifrinovich, V. I –(10) 6898
Tsoukatos, A.–(10) 6799
Tsymbal, E –(10) 7091
Tuaillon, J.–(10) 6676
Tuan, N. C.–(10) 7040
Tun, Z –(10) 7075
Turchinskaya, M. J.–(10) 6950

Uhl, M.–(10) 6694
Um, Young Rang–(10) 6877
Unguris, J.–(10) 6992
Usadel, K. D.–(10) 6560

Vaia, Ruggero–(10) 6362
Valet, T.–(10) 7087
van Alphen, E. A. M.–(10) 6607
van den Berg, H. A M –(10) 6559
Van Esch, A.–(10) 6281
van Heijden, P. A. A –(10) 6607
Van Hook, H. J.–(10) 6059
Van Hove, M. A.–(10) 6477
Van Roy, W.–(10) 6281
Vasyurin, S. I.–(10) 7142
Vavra, W.–(10) 6525
Vázquez-Vázquez, C –(10) 7034
Vega, A.–(10) 6691, 6989
Veillet, P.–(10) 6078
Vélu, E.–(10) 6558
Veneva, A.–(10) 7118
Verbanck, G.–(10) 6604
Verdier, M.–(10) 6256
Verrucchi, Paola–(10) 6362
Vescovo, E –(10) 6966
Viau, G.–(10) 6570
Victora, R. H.–(10) 6069
Villain, J.–(10) 6555
Vinai, F.–(10) 6817
Vitale, G.–(10) 6332
Vitebskii, I. M.–(10) 6892
Vittoria, C.–(10) 6962
Von Dreele, R. B.–(10) 7049
von Helmolt, R.–(10) 6925
von Känel, H.–(10) 6897
Vorst, M. T. H. van de–(10) 7081
Vyas, Gayatri–(10) 7111

Wada, M.–(10) 6846
Waddill, G. D.–(10) 6465
Wakiyama, T.–(10) 6642
Walker, M. J.–(10) 650
Wallace, W. E.–(10) 6648
Wan, H –(10) 6331
Wang, Fang-Wei–(10) 6711, 6714, 6734
Wang, Fang-wei–(10) 6746, 6763
Wang, G.-C.–(10) 6446
Wang, J. L.–(10) 6740
Wang, J.-L –(10) 6743
Wang, J. P –(10) 6591
Wang, J. Y.–(10) 6843
Wang, Kai-Ying–(10) 6383
Wang, Shyh-Jier–(10) 6862
Wang, Xindong–(10) 6474
Wang, Yi-Zhong–(10) 6383
Wang, Z.–(10) 6356, 6737
Wang, Zhenxi–(10) 6487
Wang, Zhigang–(10) 6540
Ward, R. C. C.–(10) 6274
Warren, Garry W.–(10) 6262
Watson, M –(10) 6802
Watson, M. L.–(10) 6481
Watson, R. E –(10) 6044
Weber, H.–(10) 6947
Wecker, J –(10) 6238, 6824, 6925
Wei, Mark S.–(10) 6673, 6679
Weissman, M. B.–(10) 6192
Welch, D. O.–(10) 6235
Weller, D –(10) 6078, 6116
Wells, M. R.–(10) 6274
Wendhausen, P A. P.–(10) 6268, 6717
Westphal, C.–(10) 6477
White, R. M.–(10) 6396
Wiarda, D.–(10) 6189, 6377
Widom, A.–(10) 6962
Wiedmann, Michael H.–(10) 6075
Wigen, P. E.–(10) 6886, 7078
Wilhoit, Dennis R.–(10) 6616
Wilkinson, A. J.–(10) 7160
Wilks, Carlos W.–(10) 6959
Williams, A. J.–(10) 6831
Williams, Gwyn–(10) 6356
Williams, P I.–(10) 7003
Willis, R. F.–(10) 6434
Wilson, M. J.–(10) 6090
Winand, J. M.–(10) 6214
Wirth, S –(10) 6268

Witcraft, B.–(10) 6986
Withanawasam, L –(10) 7065
Wojciechowski, S.–(10) 6244
Wolf, J. A.–(10) 6452, 7092
Wolters, H.–(10) 6537
Woodward, R. C.–(10) 7074
Woollam, J. A.–(10) 6084
Wu, K. T.–(10) 6516
Wu, S. Z.–(10) 6434
Wu, T. C.–(10) 6814
Wun-Fogle, M.–(10) 7009
Wylie, M. T.–(10) 6784

Xiao, H.–(10) 6477
Xiao, John Q.–(10) 6081
Xiong, Q.–(10) 7127
Xu, Jun-Hao–(10) 6965
Xu, Xie–(10) 6754
Xu, Zu-Xiong–(10) 6720
Xu, Zu-xiong–(10) 6749, 6849
Xuan, Ping–(10) 6053
Xue, De-Yan–(10) 6720
Xue, De-yan –(10) 6749, 6849
Xue, Y. Y.–(10) 6941, 7127

Yakhmi, J V.–(10) 6944
Yamada, Takashi–(10) 6667
Yamaguchi, M.–(10) 6994
Yamamoto, H.–(10) 6919
Yamashita, F.–(10) 6846
Yamazaki, Yohtaro–(10) 7166
Yampolskii, S. V.–(10) 6560
Yang, F. M.–(10) 6740
Yang, F.-M.–(10) 6156
Yang, Fuming–(10) 6743
Yang, H. D.–(10) 7136
Yang, J.–(10) 6522
Yang, Ji-Lian–(10) 6720
Yang, Ji-lian–(10) 6749
Yang, Jun–(10) 6053
Yang, Jyh-Shinn–(10) 6493, 6588
Yang, Q.–(10) 6610
Yang, W. T.–(10) 6516
Yang, Y.–(10) 6319
Yang, Ye–(10) 6487
Yang, Ying-Chang–(10) 6725, 6728
Yang, Yingchang–(10) 6053
Yang, Z. J.–(10) 6499
Yao, J. M.–(10) 6834, 7071
Yao, Y. D.–(10) 6516
Yao, Yeong-Der–(10) 6862
Yaron, U.–(10) 6788, 6789
Ye, M.–(10) 6886
Yee, O. P.–(10) 6909
Yeh, T.–(10) 6986
Yelon, W B –(10) 6147, 6162, 6731
Yelsukov, E. P.–(10) 7032
Yethiraj, M.–(10) 6784
Yewondwossen, M.–(10) 6113, 6501
Yewondwossen, M. H.–(10) 6499
Yonnet, Jean-Paul–(10) 6865
Young, S. J.–(10) 6871, 6874
Yu, C. T.–(10) 6484
Yu, Chengtao–(10) 6487
Yue, J.–(10) 6986

Zabel, H.–(10) 6096, 7092
Zawadzki, J.–(10) 6717
Zazo, M.–(10) 7133
Zeng, D. C.–(10) 6837
Zeng, Y. W.–(10) 6743
Zeng, Zhi–(10) 7043
Zha, Yuyao–(10) 6935
Zhan, Wen-Shan–(10) 6711, 6734
Zhan, Wen-shan–(10) 6746, 6763
Zhang, Bai-Sheng–(10) 6720
Zhang, Bai-sheng–(10) 6749
Zhang, Bo–(10) 6763
Zhang, F.–(10) 6452
Zhang, G. W.–(10) 7037
Zhang, J. Z.–(10) 6751
Zhang, Jun-Xian–(10) 6734
Zhang, Jun-xian–(10) 6763
Zhang, S. Y.–(10) 6490
Zhang, Shufeng–(10) 6619, 6993
Zhang, X.-G.–(10) 6805, 6808
Zhang, Xiao-Dong–(10) 6725
Zhang, Y. B.–(10) 6084
Zhang, Y. D.–(10) 6576
Zhang, Z.–(10) 6576, 6700, 7078
Zhao, J. G.–(10) 6484, 6900, 7037
Zhao, Jian-Gao–(10) 6714, 6734
Zhao, Jian-gao–(10) 6763
Zhao, R. W.–(10) 6740
Zhao, T.–(10) 6837
Zhao, X. G.–(10) 6484
Zhao, Z. G.–(10) 6837, 6843
Zheng, Q. Q.–(10) 6751, 7037
Zheng, Qing-Qi–(10) 7043
Zhong, Xue-Fu–(10) 6047
Zhou, L.–(10) 7078
Zhou, P. Y.–(10) 6335
Zhou, Ping–(10) 6868
Zhou, Yuqing–(10) 6487
Zhu, J. J.–(10) 6743
Zhu, Y.–(10) 6235
Zimmermann, G –(10) 6062
Zinn, W.–(10) 7091
Zschack, P.–(10) 6133
Zuberek, R.–(10) 6534
Zuckermann, Martin–(10) 6374
Zuo, F.–(10) 6953

From AIP Press
in cooperation with the American Vacuum Society

AVS Classics Series in Vacuum Science and Technology

Series editor, H. Fredrick Dylla, CEBAF, Newport News, VA, and College of William and Mary, Williamsburg, VA

Vacuum Technology and Space Simulation
D.J. Santeler, D.H. Holkeboer, D.W. Jones, and F. Pagano

While specific projects have changed in the 30 years since this book was first published, the need for large, complex vacuum facilities has not. And despite new developments in pumping, measurement, and outgassing, this book will remain, for many years to come, the standard of practical vacuum operation.

1993, 350 pages, illustrated, ISBN 1-56396-123-7, paper
$35.00 **Members $28.00**

Field Emission and Field Ionization
Robert Gomer

This authoritative work was based on four lectures presented at Harvard University in 1958. When it was written, field emission was one of the few techniques available for surface studies, and the attainment of ultra-high vacuum was a little-known art. Though more sophisticated treatments have been developed, Gomer's pioneering work remains extremely relevant.

1993, 200 pages, illustrated, ISBN 1-56396-124-5, paper
$35.00 **Members $28.00**

Handbook of Electron Tube and Vacuum Techniques
Fred Rosebury

This handbook was originally prepared so that workers would have a single source for learning the procedures and materials needed to construct tubes and other evacuated devices. Even now, as space and high-vacuum research yield new information daily, much of the subject matter in this seminal work—such as properties of materials—are as cogent as they were in 1964 when the book was first published.

1993, 600 pages, illustrated, ISBN 1-56396-121-0, paper
$35.00 **Members $28.00**

The Physical Basis of Ultrahigh Vacuum
P.A. Redhead, J.P. Hobson, and E.V. Kornelsen

Written 25 years ago, this book explains both the design and use of UHV systems and components, as well as the underlying physical principles on which the performance of the equipment depends. The close association of these underlying physical principles with the practical problems inherent in UHV equipment makes this a fundamental resource, still sought after by today's researchers.

1993, 500 pages, illustrated, ISBN 1-56396-122-9, paper
$35.00 **Members $28.00**

Ionized Gases
A. von Engel

Though based on the author's lectures for undergraduates at Oxford, this classic 1955 work is also a valuable resource today for practitioners in atomic physics, astrophysics, spectroscopy, and, most especially, semiconductors. Researchers and graduate students will find that von Engel's ideas hold up remarkably well.

1994, 344 pages, ISBN 1-56396-272-1, illustrated, paper
$35.00 **Members $28.00**

Vacuum Sealing Techniques
Alexander Roth

This volume presents numerous techniques developed in the early '60s for the construction of vacuum seals, providing critical insights into the design and construction of the vacuum system's constituent parts and the proper assembly of the system. Extensively researched, this work covers a variety of sealing techniques and design concepts that are relevant to this day.

1994, 860 pages, ISBN 1-56396-259-4, illustrated, paper
$35.00 **Members $28.00**

Basic Data of Plasma Physics: The Fundamental Data on Electrical Discharges in Gases
Sanborn C. Brown

This 1966 reference work is a compilation of some of the most important plasma physics articles published during the late 1950s and the early 1960s. It offers a wealth of useful information on elastic-collision and charge-transfer cross sections, mobility and diffusion, electron attachment and detachment, and recombination. Numerous fundamental principles make this a much- consulted handbook on the physical phenomena, measurements, and properties of plasma physics.

1994, 344 pages, ISBN 1-56396-273-X, illustrated, paper
$35.00 **Members $28.00**

To order, call toll-free: 1-800-488-BOOK

Or mail check, money order, or purchase order to:

American Institute of Physics
c\o AIDC • P.O. Box 20
Williston, VT 05495

Shipping & Handling: $2.75 first book ($7.50 foreign)
$.75 each additional book.

Credit card orders will not be billed until the book is shipped.
Members of AIP Member Societies are entitled to a 20% discount.

Books of the American Institute of Physics
500 Sunnyside Boulevard
Woodbury, NY 11797

Entertaining, Informative, Innovative...

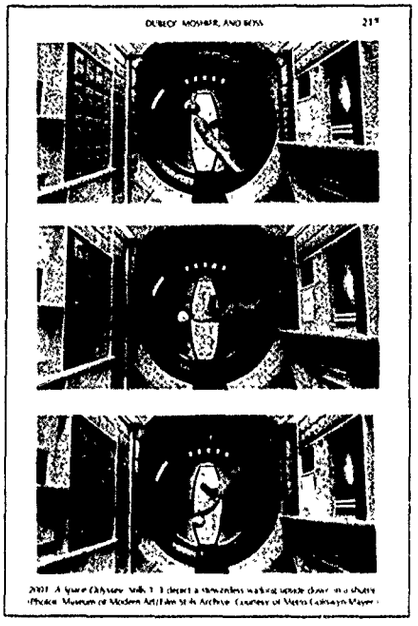

4 New Books from AIP Press.

Fantastic Voyages

Learning Science Through Science Fiction Films

Leroy W. Dubeck, Suzanne E. Moshier, and Judith E. Boss

By revealing the facts behind the fiction of some of the finest sci-fi films, ***Fantastic Voyages*** offers a novel approach to teaching science—using science fiction to illustrate fundamental concepts of physics, astronomy, and biology.

Each film scene depicts a scientific principle, or its violation, reinforcing concepts that are taught in more traditional ways. The chapter Electricity and Magnetism discusses the use of computers in *Blade Runner*. Under astronomy, *2001* is examined as it relates to ancient astronauts. In the chapter Evolution, *Planet of the Apes* is studied in detail.

Helpful end-of-chapter exercises, together with more than 20 movie stills, further aid readers to grasp the technical material. Nonscience majors, science fiction enthusiasts, and film buffs will find this work both enjoyable and instructive.

1993, 400 pages, ISBN 1-56396-195-4, paper, illustrated
$40.00 **Members $32.00**

The Physics of Golf

Theodore P. Jorgensen

In ***The Physics of Golf***, you'll learn how to apply the principles of dynamics and energy to perfect your golf stroke, to choose the right clubs, and to make the handicap system work optimally. Using stroboscopic photographs and an ingenious mathematical calculation, the author shows you how small changes in your swing can increase the distance the ball travels.

This engaging book provides many more tips concerning the critical components of a good swing, helping you to play better and to get more enjoyment out of your round.

1993, 156 pages, ISBN 0-88318-955-0, paper, illustrated
$35.00 **Members $28.00**

Time Machines

Time Travel in Physics, Metaphysics, and Science Fiction

Paul J. Nahin

Time Machines takes you on an exhilarating journey through the intriguing theories of scientists and the far-flung imaginations of writers. Explore the ideas of time travel from the first account in English literature — Samuel Madden's 1733 *Memoirs of the Twentieth Century* — to the latest theories of physicists such as Kip Thorne and Igor Novikov.

This accessible work covers a variety of topics including the history of time travel in fiction; the fundamental scientific concepts of time, spacetime, and the fourth dimension; time-travel paradoxes; the speculations of Einstein, Richard Feynman, Kurt Gödel, and others; and much more.

1993, 512 pages,ISBN 0-88318-935-6, cloth, illustrated
$45.00 **Members $36.00**

"Most of the Good Stuff"

Memories of Richard Feynman

Laurie M. Brown and John S. Rigden

Prominent physicists such as John Wheeler, Freeman Dyson, Hans Bethe, Julian Schwinger, Murray Gell-Mann, David Pines, and others offer intimate reminiscences of their colleague and perceptive explanations of Feynman's trail-blazing work. These essays uncover the precocious undergraduate, the young scholar at Cornell, the theoretician in his prime at Caltech, and the mature teacher and mentor.

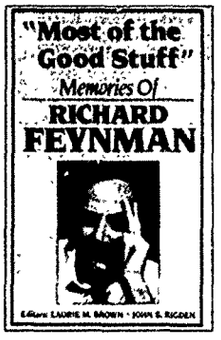

Highlighting both the charm and the brilliance of Feynman, ***"Most of the Good Stuff"*** is an engrossing collection for enthusiasts—scientists and nonscientists alike—awed and entertained by one of the century's greatest minds.

1993, 181 pages, illustrated
ISBN 0-88318-870-8, cloth
$35.00 **Members $28.00**

To order, call toll-free: 1-800-488-BOOK
Or mail check, money order, or purchase order to:
American Institute of Physics • c/o AIDC
P.O. Box 20 • Williston, VT 05495

Shipping & Handling: $2 75 first book, $.75 each additional book.
Credit card orders will not be billed until the book is shipped.

AIP PRESS
Books of the American Institute of Physics
500 Sunnyside Boulevard
Woodbury, NY 11797

A TOUR OF THE SUBATOMIC ZOO

A Guide to Particle Physics

Cindy Schwarz, *Vassar College*

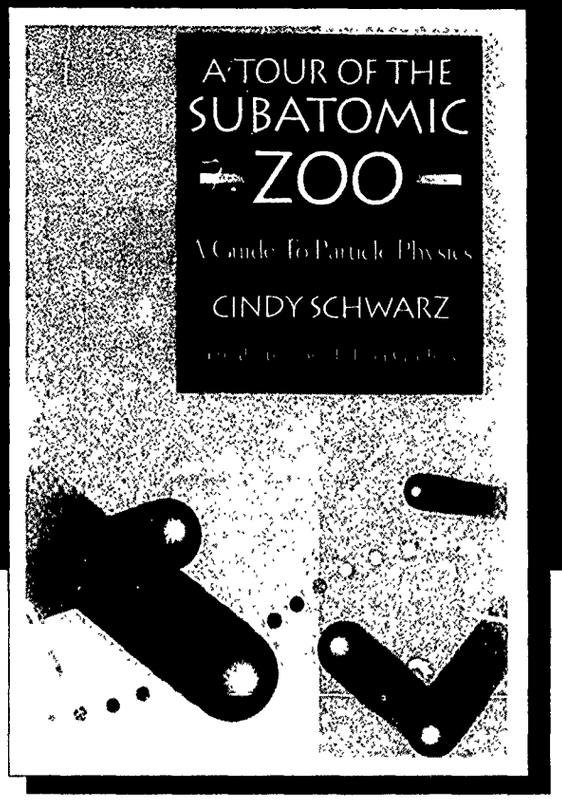

"A great little book, and if every physics textbook were like this, physics classrooms would be crowded."

—Scitech Book News

With hardly a mathematical formula, Ms. Schwarz clearly explains the substance of elementary particle physics. The book guides readers through the subatomic "zoo," populated by some of the most dramatic discoveries of modern science—notably, quarks, leptons, and the basic forces that govern their interactions.

Most important, this tour is conducted in terms that are easily understood—even by those who have no prior particle physics background. Each chapter in this book begins with an overview of concepts and ends with a summary and self-tests to help readers gauge their understanding.

If you're involved in teaching science to the non-scientist, think about using this book. It's been used successfully to introduce future lawyers, politicians, and parents to the ideas, terminology, and techniques of high energy physics and it's given them a unique historical perspective on the field.

1992, 128 pages, illustrated
ISBN 0-88318-954-2, paper
$25.00 ***Members $20.00**

*Members of AIP Member Societies are entitled to a 20% discount.

ORDER FORM

❑ **Yes!** Please send me ___ copy(ies) of ***A Tour of the Subatomic Zoo*** by Cindy Schwarz (ISBN 0-88318-954-2) at **$25 00 per copy ($20.00 for Members.)**

Shipping: $2.75 first book ($7.50 foreign), $.75 each additional book.

METHOD OF PAYMENT

❑ Check enclosed (payable in U S dollars to the **American Institute of Physics** and drawn on a bank in the United States)

❑ Charge my credit card ❑ AMEX ❑ VISA ❑ MasterCard

Cardholder name (please print)_____

Acct No _____ Exp Date _____

Signature _____

(Credit card orders not valid without signature)

Name _____

Organization_____

Address_____

City/State/Zip_____

☎ FOR FAST SERVICE, CALL TOLL-FREE:

1-800-488-BOOK (2665)

In Vermont: (802) 862-0095

Or mail to:

American Institute of Physics • c/o AIDC
P.O. Box 20 • Williston, VT 05495

AIP PRESS

American Institute of Physics
500 Sunnyside Boulevard
Woodbury, NY 11797-2999

9472

AIP

AMERICAN INSTITUTE OF PHYSICS
500 Sunnyside Blvd., Woodbury, New York 11797-2999 · (516) 576-2268

Under U.S. copyright law, the transfer of copyright from the author(s) should be explicitly stated to enable the publisher to disseminate the work to the fullest extent. The following transfer must be signed and returned to the Editor's office before the manuscript can be accepted for publication. Please note that if the manuscript has been prepared as a Work Made For Hire, the transfer should be signed by both employer and employee. Address requests for further information or exceptions to the Office of Rights and Permissions, American Institute of Physics (AIP), 500 Sunnyside Blvd., Woodbury, New York 11797-2999 · (516) 576-2268.

TRANSFER OF COPYRIGHT AGREEMENT

Copyright to the unpublished and original article, including copyright to the abstract forming part thereof, entitled

_____

submitted by the following author(s) (names of all authors)_____

_____

is hereby transferred to American Institute of Physics (AIP) for the full term thereof throughout the world, BUT SUBJECT to the following rights reserved to the author(s) and to acceptance of the article for publication in

_____
Name of Journal

AIP shall have the right to publish the article in any medium or form, or by any means, now known or later developed.

AIP shall have the right to register copyright in the article and the accompanying abstract in its name as claimant, whether separately or as part of the journal issue or other medium in which such work is included.

The author(s) reserve the following rights:

(1) All proprietary rights other than copyright, such as patent rights.
(2) The right, after publication by AIP, to grant or refuse permission to third parties to republish all or part of the article or translations thereof. In the case of whole articles, such third parties must obtain AIP's written permission as well. However, such permission will not be refused by AIP except at the direction of the author. AIP may grant rights with respect to journal issues as a whole.
(3) The right, after publication by AIP, to use all or part of the article and abstract in compilations or other publications of the author's own works, and to make copies of all or part of such material for the author's use for lecture or classroom purposes.
(4) If the article has been prepared by an employee within the scope of his or her employment, the employer reserves the right to make copies of the work for its own internal use. If the article was prepared under a U.S. Government contract, the government shall have the rights under the copyright to the extent required by the contract.

The author(s) agree that all copies of the article or abstract made under any of the above reserved rights shall include a copyright notice in the AIP's name. The author(s) represent and warrant that the article is original with them, that it does not infringe any copyright or other rights in any other work, or violate any other rights, and that the author(s) own the copyright in it or are authorized to transfer it. If each author's signature does not appear below, the signing author(s) represent that they sign this agreement as authorized agents for and on behalf of all the authors, and that this agreement and authorization is made on behalf of all the authors.

_____
Signature Date

_____
Name (print)

If the manuscript has been prepared as a Work Made For Hire, the transfer should be signed by the employee (above) and by the employer (below):

_____
Name of Employer (print)

_____
Signature Name (print) Title Date

A work prepared by a U.S. Government officer or employee as part of his or her official duties is not eligible for U.S. copyright, however, foreign copyright laws may differ. Thus, **this form should be signed even by U.S. Government** officers or employees. Signing of this form will not affect U.S. copyright law provisions in the case of works of the U.S. Government. If all the authors are in this category, check the box here and return the signed form. ☐

AMERICAN INSTITUTE OF PHYSICS

500 Sunnyside Boulevard, Woodbury, NY 11797-2999

The American Institute of Physics is a not-for-profit membership corporation chartered in New York State in 1931 for the purpose of promoting the advancement and diffusion of the knowledge of physics and its application to human welfare. Leading societies in the fields of physics, astronomy, and related sciences are its members.

The Institute publishes its own scientific journals as well as those of its member societies; publishes both technical and general interest books; provides abstracting and indexing services; provides on-line database and e-mail services; disseminates reliable information on physics to the public; collects and analyzes statistics on the profession and on physics education; encourages and assists in the documentation and study of the history and philosophy of physics; cooperates with other organizations on educational projects at all levels; and collects and analyzes information on Federal programs and budgets.

Member Societies

The American Physical Society
Judy Franz, Executive Officer
One Physics Ellipse
College Park, MD 20740-3844

Optical Society of America
David W. Hennage, Executive Director
2010 Massachusetts Avenue, N.W.
Washington, DC 20036

Acoustical Society of America
Charles Schmid, Executive Director
500 Sunnyside Blvd., Woodbury, NY 11797-2999

The Society of Rheology
Andrew M. Kraynik, Secretary
Department 1512
Sandia National Labs
Albuquerque, NM 87185

American Association of Physics Teachers
Bernard V. Khoury, Executive Officer
One Physics Ellipse
College Park, MD 20740-3845

American Crystallographic Association
William L. Duax, Executive Officer
P.O. Box 96, Endicott Station
Buffalo, NY 14205-0096

American Astronomical Society
Peter B. Boyce, Executive Officer
1630 Connecticut Avenue, N.W.
Washington, DC 20009

American Association of Physicists in Medicine
Sal Trofi, Executive Director
One Physics Ellipse
College Park, MD 20740-3846

American Vacuum Society
William D. Westwood, Secretary
Bell-Northern Research, Ltd.
P.O. Box 3511, Station C
Ottawa, Ontario K1Y 4H7, Canada

American Geophysical Union
A. F. Spilhaus, Jr., Executive Director
1630 Connecticut Avenue, N.W.
Washington, DC 20009

Affiliated Societies

American Institute of Aeronautics and Astronautics, American Meteorological Society, American Nuclear Society, ASM International, Astronomical Society of the Pacific, Division of Physical Chemistry of ACS, Engineering Information, Inc., The Geological Society of America, Instrument Society of America, International Association of Mathematical Physicists, International Centre for Diffraction Data, Materials Research Society, Microscopy Society of America, Nuclear and Plasma Sciences Society of IEEE, Physics/Astronomy Section of the Council on Undergraduate Research, Physics Section of AAAS, Society for Applied Spectroscopy, SPIE—The International Society for Optical Engineering

Corporate Associates: Approximately 175 leading corporations, by their membership, participate in and contribute to the support of AIP

Publications

Physical Review A · Bernd Crasemann, *Editor,* Physics Dept., University of Oregon, Eugene, OR 97403
Physical Review B · P.D. Adams, *Editor,* The American Physical Society, 1 Research Rd., Box 1000, Ridge, NY 11961
Physical Review C · Sam Austin, *Editor,* Cyclotron Labs., Michigan State University, E. Lansing, MI 48824
Physical Review D · Lowell S. Brown and D.L. Nordstrom, *Editors,* APS, 1 Research Rd., Box 1000, Ridge, NY 11961
Physical Review E · Irwin Oppenheim, *Editor,* Dept. of Chemistry, Massachusetts Institute of Technology, Cambridge, MA 02139
Physical Review Abstracts · Reid Terwilliger, *Editor,* APS, One Physics Ellipse, College Park, MD 20740-3844
Physical Review Letters · J. Sandweiss, G. Basbas, S.G. Brown, and G.L. Wells, *Editors,* APS
APS News · Brian Schwartz, *Editor,* APS, One Physics Ellipse, College Park, MD 20740-3844
Bulletin of The American Physical Society · Brian Schwatz, *Editor,* APS, One Physics Ellipse, College Park, MD 20740-3844
Reviews of Modern Physics · David Pines, *Editor,* Loomis Lab. of Physics, 1110 W. Green St., Urbana, IL 61801
The Journal of the Acoustical Society of America · Daniel W. Martin, *Editor-in-Chief,* 7349 Clough Pike, Cincinnati, OH 45244
American Journal of Physics · Robert H. Romer, *Editor,* 222 Merrill Science Bldg., Box 2262, Amherst College, Amherst, MA 01002
The Astronomical Journal · Paul W. Hodge, *Editor,* Astronomy Dept. FM-20, University of Washington, Seattle, WA 98195
Publications of the Astronomical Society of the Pacific · Howard E. Bond, *Editor,* Space Telescope Science Institute, Baltimore, MD 21218
Bulletin of the American Astronomical Society · Peter B. Boyce, *Editor,* AAS
The Astrophysical Journal · Helmut A. Abt, *Managing Editor,* Kitt Peak National Observatory, Box 26732, Tucson, AZ 85726
The Journal of Chemical Physics · J.C. Light, *Editor,* James Franck Institute, The University of Chicago, Chicago, IL 60637
Journal of Mathematical Physics · Roger G. Newton, *Editor,* Indiana Univ., The Poplars, Rm. 324, Bloomington, IN 47405
Physics of Fluids · A. Acrivos, *Editor,* The Levich Institute, Steinman 202, CCNY, Convent Ave. at 140 St., New York, NY 10031
Physics of Plasmas · Ronald C. Davidson, *Editor,* Plasma Phys. Lab., Princeton Univ., P.O. Box 451, Princeton, NJ 08543
Journal of Applied Physics · Steven J. Rothman, *Editor,* Argonne Natl. Lab., Box 8296, Argonne, IL 60439-8296
Applied Physics Letters · Hartmut Wiedersich, *Editor,* Argonne Natl. Lab., Box 8296, Argonne, IL 60439-8296
Review of Scientific Instruments · Thomas H. Braid, *Editor,* Argonne Natl. Lab., Box 8293, Argonne, IL 60439-8293
Journal of Physical and Chemical Reference Data · Jean W. Gallagher, *Editor,* NIST, MS221/A3223, Gaithersburg, MD 20899
Physics Today · Gloria B. Lubkin, *Editor,* AIP, One Physics Ellipse, College Park, MD 20740-3843
Computers in Physics · Lewis Holmes, *Editor,* One Physics Ellipse, College Park, MD 20740-3843
Chaos · David K. Campbell, *Editor,* Dept. of Physics, University of Illinois-UC, Urbana, IL 61801
Journal of Vacuum Science and Technology A · Gerald Lucovsky, *Editor,* Dept. of Physics, N. Carolina State Univ., Raleigh, NC 27650
Journal of Vacuum Science and Technology B · Gary E. McGuire, *Editor,* MCNC, Research Triangle Park, NC 27709
Surface Science Spectra · C. E. Bryson, *Editor,* Surface/Interface, Inc., Mountain View CA 94041, Gary McGuire, *Editor,* MCNC, NC 27709
Medical Physics · J. S. Laughlin, *Editor,* Memorial Sloan-Kettering Cancer Center, 1275 York Ave., New York, NY 10021
Noise Control Engineering Journal · Alan H. Marsh, *Editor-in-Chief,* DyTec Engineering, Inc., 5092 Tasman Dr., Huntington Beach, CA 92649
Powder Diffraction · Deane K. Smith, *Editor-in-Chief,* Dept. of Geosci. and Mineralogy, Penn State Univ., University Park, PA 16802
AAPT Announcer · Bernard V. Khoury, *Editor,* AAPT, One Physics Ellipse, College Park, MD 20740-3845
The Physics Teacher · Clifford E. Swartz, *Editor,* Phys. Dept., State University of New York, Stony Brook, NY 11794
Journal of Rheology · Arthur B. Metzner, *Editor,* Dept. of Chemical Engineering, University of Delaware, Newark, DE 19716
Journal of the Optical Society of America A · Bahaa E. A. Saleh, *Editor,* 2010 Massachusetts Ave., N.W., Washington, DC 20036
Journal of the Optical Society of America B · Paul F. Liao, *Editor,* 2010 Massachusetts Ave., N.W., Washington, DC 20036
Applied Optics · William T. Rhodes, *Editor-in-Chief,* Dept. of Electr. & Computer Eng., Univ. of Colorado, Boulder, CO 80309-0425
Optics Letters · Peter W. E. Smith, *Editor,* Bellcore, 331 Newman Springs Rd., Red Bank, NJ 07701
Optics and Photonics News · Andrea Pendleton, *Editor,* 2010 Massachusetts Ave., N.W., Washington, DC 20036
Journal of Lightwave Technology · Donald B. Keck, *Editor,* Corning Glass Works, Sullivan Park FR29, Corning, NY 14830
The Journal of Undergraduate Research in Physics · R. E. Adelberger, *Editor,* Physics Dept., Guilford College, Greensboro, NC 27410

AIP Conference Proceedings

Acoustical Physics
Astronomy Reports
Astronomy Letters
Crystallography Reports
JETP
JETP Letters
Low Temperature Physics
Optics and Spectroscopy
Physics-Doklady
Physics of Atomic Nuclei
Physics of the Solid State
Plasma Physics Reports
Physics of Particles and Nuclei
Semiconductors
Journal of Optical Technology
Technical Physics
Technical Physics Letters

Current Physics Index (CPI), quarterly and annual subject index with abstracts to all the above journals
General Physics Advance Abstracts (GPAA), semimonthly advance abstracts of AIP-published physics literature
Searchable Physics Information Notices (SPIN), monthly computer-readable tape of abstracts
Current Physics Microform (CPM), monthly microfilm edition of all the above journals
Current Physics Reprints (CPR), on-demand copies of any article in any of the above journals
Physics Briefs (PB), semimonthly comprehensive index with abstracts to the world literature of physics
PINET, an online physics information network

Governing Board 1994–1995

Roland W. Schmitt, *Chair**
Reuben E. Alley
Benjamin Bederson
Roger A. Bell
Marc H. Brodsky (*ex officio*)*
Robert L. Beyer*
Patricia E. Cladis
Charles Counselman, III
G. Brent Dalrymple*
Robert L. Dixon
William L. Duax
Judy R. Franz
Roderick M. Grant (*ex officio*)*
Joseph E. Greene
David Hennage
David W. Hoffman*
Karen L. Johnston
Frank J. Kerr
Bernard V. Khoury*
Cari Kisslinger
Patricia K. Kuhl
Donald N. Langenberg
Tingye Li
Harry Lustig*
Christopher H. Marshall
Gregory B. McKenna
Duncan T. Moore
Norman F. Ness
C. Robert O'Dell
C. Kumar N. Patel
Burton Richter
Barrett H. Ripin
J. William Rogers, Jr.
Charles E. Schmid*
Benjamin Snavely
A. F. Spilhaus, Jr.
Hugo Steinfink
Richard Stern
Howard G. Voss*
Martin Walt
* executive committee

AIP Officers

Marc H. Brodsky, *Executive Director and CEO*
Roderick M. Grant, *Secretary*
Arthur T. Bent, *Treasurer and CFO*
Theresa C. Braun, *Director of Human Resources*
Darlene Carlin-Walters, *Vice President, Publishing*
John S. Rigden, *Director of Physics Programs*

Publishing Services

James J. Donohue, *Director Publishing Services*
Edward P. Greeley, *Director Advertising and Exhibits*
Douglas LaFrenier, *Director of Marketing*
Peggy Judd, *Director of Information Technology*
Maria Taylor, *Publisher AIP Press*
Carol Fleming, *Manager Publishing II Branch*
Doreene A. Berger, *Manager Journal Production I Division*
Maya Flikop, *Manager Translation Program Division*
John T. Scott, *Manager Editorial Operations Division*
Brian Schmitt, *Division Manager Circulation and Fulfillment Division*
Cheryl Taub, *Manager Composition I Division*
Denise Weiss, *Manager Books and Special Projects*
Janice Wilmot, *Manager Production II Division*

APPLIED PHYSICS LETTERS: Current Table of Contents

Applied Physics Letters, a companion publication to the *Journal of Applied Physics*, is published weekly by the American Institute of Physics. Its letters are timely, short reports devoted to important new findings in applied physics. The contents list below is from a recent issue.

APPLIED PHYSICS LETTERS

Vol 65, No 17, 24 October 1994

CODEN APPLAB ISSN 0003-6951

OPTICS

2121 **Single-beam time-resolved Z-scan measurements of slow absorbers** — L C Oliveira S C Zilio

2124 **Bright red light-emitting organic electroluminescent devices having a europium complex as an emitter** — Junji Kido Hiromichi Hayase Kenichi Hongawa Katsutoshi Nagai Katsuro Okuyama

2127 **Selective ablation of a hydrogenated amorphous silicon thin layer by the second-harmonic radiation of a transversely excited atmospheric CO_2 laser** — Tetsumi Sumiyoshi Yutaka Hiromiya Akira Shiratori Minoru Obara Katsunori Ishii

2130 **Novel tunable semiconductor lasers using continuously chirped distributed feedback gratings with ultrahigh spatial precision** — H Hillmer H -L Zhu A Grabmaier S Hansmann H Burkhard K Magari

FLUIDS, PLASMAS, AND ELECTRICAL DISCHARGES

2133 **Repetitively pulsed relativistic klystron amplifier** — Jerrold S Levine Bruce D Harteneck

CONDENSED MATTER (STRUCTURE, MECHANICAL AND THERMAL PROPERTIES)

2136 **Metallic glass formation in highly undercooled $Zr_{41.2}Ti_{13.8}Cu_{12.5}Ni_{10.0}Be_{22.5}$ during containerless electrostatic levitation processing** — Y J Kim R Busch W L Johnson A J Rulison W K Rhim

2139 **Direct growing of lightly doped epitaxial silicon without misfit dislocation on heavily boron-doped silicon layer** — Ho-Jun Lee Chang-Soo Kim Chul Hi Han Chioong Ki Kim

2142 **Fabricating nanoscale structures on Au surface with scanning tunneling microscope** — K Besocke S Hashimoto

2145 **Two kinds of nitrogen atoms in nitrogen-substituted, highly crystalline graphite prepared by chemical vapor deposition** — T Matsui M Yudasaka R Kikuchi Y Ohki S Yoshimura

2148 **Enhanced confinement of electrons at room temperature using a superlattice reflector** — D Campi C Rigo C Caccia tore H -C Neitzert

2151 **Three-dimensional electrostatic potential, and potential-energy barrier, near a tip-base junction** — Li-Hong Pan Thomas E Sullivan Vallorie J Pendler Paul H Cutler Nicholas M Miskovsky

2154 **Fabrication of a periodically domain-inverted structure in $LiNbO_3$ thin film by a domain-transfer technique** — Hiroshi Momii Kazumi Kawamoto Kenchi Ito

2156 **New synthetic route to the formation of fullerene superconductors** — J H Hwang C Y Mou H S Sheu Y Wang M K Wu

SEMICONDUCTORS

2159 **$Ga_xIn_{1-x}As/AlAs$ resonant tunneling diodes grown by atmospheric pressure metalorganic chemical vapor deposition** — B P Keller J C Yen S P DenBaars U K Mishra

2162 **Crystalline phases of II-VI compound semiconductors grown by pulsed laser deposition** — W P Shen H S Kwok

2165 **Low resistance ohmic contacts on nitrogen ion bombarded InP** — F Ren S J Pearton J R Lothian S N G Chu W K Chu R G Wilson C R Abernathy S S Pei

2168 **Low temperature mobility limiting defects in CdTe/CdMnTe multi-quantum-well structures** — M Godlewski C I Harris J P Bergman B Monemar A Waag

2171 **Preparation of crystallographically aligned layers of silicon carbide by pulsed laser deposition of carbon onto Si wafers** — L Rimai R Ager W H Weber J Hangas B D Poindexter

2174 **Hydrogenation of multiple-quantum-well optical-modulator structures** — T K Woodward, J E Cunningham, W Y Jan A Kastalsky

2177 **Electrical properties of thermal oxide grown using dry oxidation on *p*-type 6H-silicon carbide** — Dev Alok, P K. McLarty, B J Baliga

2179 **Negative differential conductance frequency resonances in *X* valley superlattice minibands** — A Sibille, J F Palmier H Wang R Planel

2182 **Nanocrystal size modifications in porous silicon by preanodization ion implantation** — L. Pavesi, G Giebel, F Ziglio, G Mariotto F Priolo, S U Campisano, C Spinella

2185 **Growth and characterization of thallium- and gold-doped $PbSe_{0.78}Te_{0.22}$ layers lattice matched with BaF_2 substrates** — Patrick J McCann Srinath K Aanegola, John E Furneaux

2188 **Nondestructive mapping of carrier concentration and dislocation density in n^+-type GaAs** — D C Look, D C Walters, M G Mier, J R Sizelove

2191 **Spectroscopy of hydrogen-related complexes in GaP:Zn** — M D McCluskey, E E Haller, J Walker, N M Johnson

2193 **Optical monitoring of the growth of heavily doped GaAs by chemical beam epitaxy and of the *in situ* etching of GaAs using CBr_4** — T B Joyce T J Bullough, T Farrell

2196 **Design of high-performance quantum well electron transfer modulators via self-consistent modeling** — Jin Wang J E Zucker, J P Leburton, T Y Chang, N J Sauer

2199 **Observation of sulfur-terminated GaAs(001)-(2×6) reconstruction by scanning tunneling microscopy** — Shiro Tsukamoto, Nobuyuki Koguchi

2202 **Measurement of nonuniform distribution of strain in InGaAs/GaAs quantum wires** — Yu-Pei Chen, Jason D Reed, William J Schaff, Lester F Eastman

2205 **Carbon doping of AlAs using CCl_4 and CBr_4 during growth by metalorganic molecular-beam epitaxy** — C R Abernathy, J D MacKenzie W S Hobson, P W Wisk

2208 **Electrically active subthreshold damage in Si ion implanted with Si, Ge, and Sn** — P Kringhøj, J S Williams, C Jagadish

2211 **Determination of the GaN/AlN band offset via the (-/0) acceptor level of iron** — J Baur, K Maier, M Kunzer, U Kaufmann, J Schneider

2214 **Conduction-band engineering in piezoelectric [111] multiple quantum well *p-i-n* photodiodes** — J L Sanchez-Rojas A. Sacedon F Calle E Calleja E Muñoz

2217 **Selective epitaxial growth of GaInP by low-pressure metal-organic chemical-vapor deposition using ethyldimethylindium as in source** — Shih-Hsiung Chan Simon Ming Sze Chun-Yen Chang, W. I Lee

2220 **Magnetron sputter epitaxy of Si_mCe_n/Si(001) strained-layer superlattices** — P Sutter, C Schwarz E Müller V Zelezny S Goncalves Conto, H von Kanel

2223 **Bandwidth enhanced metal-semiconductor-metal photodetectors based on backgated *ip* structures** — E Greger, K Reingruber P Riel G H Döhler, J Rosenzweig, M Ludwig

2226 **Infrared absorption of holes in a parabolic quantum well** — M Sundaram, S J Allen, Jr M R Geller, P F Hopkins, K. L Campman A C Gossard

2229 **Oxidation of silicon nitride prepared by plasma-enhanced chemical vapor deposition at low temperature** — Wen-Shiang Liao Chi-Huei Lin, Si-Chen Lee

SUPERCONDUCTORS

2232 **Insulating boundary layer and magnetic scattering in $YBa_2Cu_3O_{7-\delta}$/Ag interfaces over a contact resistivity range of 10^{-6}–10^{-3} Ω cm²** — S C Sanders S E Russek, C C Clickner, J W Ekin

2235 **CUMULATIVE AUTHOR INDEX**

Subscription information may be obtained by writing Marketing Services at the American Institute of Physics.